

INMATEH -

**AGRICULTURAL
ENGINEERING**

MAY - AUGUST

No liability is assumed by the editorial staff for the content of scientific papers and opinions published in this volume. They represent the author's point of view

Managing Editorial Board - INMA Bucharest

Editor in Chief

Lucian-Ionel CIOCA, Professor, PhD.Eng., "Lucian Blaga" University of Sibiu

Executive Editor

Lucreția POPA
PhD.Eng, SR I

Assistant Editor

Nicolae-Valentin VLADUȚ
PhD.Eng, SR I
Mihai-Gabriel MATAȚHE
PhD.Eng, SR I

Logistic support, database

Virgil MURARU
PhD.Eng, SR I

Scientific Secretary

Cârdei Petre, math.

Official translator

RADU Daniela-Cristina, English

Editorial Board

- *QUENDLER Elisabeth – Austria, Vienna, Univ. of Natural Resources & Applied Life Sciences;*
- *Ir. HUYGHEBAERT Bruno – Belgia, Walloon Agricultural Research Center CRA-W;*
- *Van IMPE F.M. Jan – Belgia, KU Leuven University*
- *FABBRO Dal Inacio Maria - Brazil, Campinas State University;*
- *ATANASOV Atanas – Bulgaria, "Angel Kanchev" University of Rousse*
- *MOLINOS-SENANTE María – Chile, Pontificia Universidad Católica - Vicedecana, Escuela de Ingeniería UC*
- *BILANDZIJA Nikola – Croatia, Zagreb University, Faculty of Agriculture;*
- *KOSUTIC Silvio – Croatia, Zagreb University, Faculty of Agriculture;*
- *KOVACEV Igor - Croatia, Zagreb University, Faculty of Agriculture;*
- *GONZÁLEZ Omar – Republic of Cuba, Central University "Marta Abreu" de las Villas;*
- *KATHIJOTES Nicholas – Cyprus, University of Nicosia;*
- *HERAK David - Czech Republic, Czech University of Agriculture Prague;*
- *BORCHARD Nils – Finland, Natural Resources Institute Finland (Luke);*
- *SAUER Johannes – Germany, Technical University Munich;*
- *FENYVESI László – Hungary, Hungarian Institute of Agricultural Engineering Godollo;*
- *PEEYUSH Soni - India, Indian Institute of Technology, Kharagpur;*
- *MOHAMMADREZA Alizadeh – Iran, Department of Agricultural Engineering, Rice Research Institute of Iran (RRII);*
- *De WRACHIEN Daniele - Italy, State University of Milan;*
- *BIOCCA Marcello - Italy, Agricultural Research Council, Agricultural Engineering Research Unit;*
- *COLANTONI Andrea – Italy, University Viterbo;*
- *SARAUSSKIS Egidijus – Lithuania, Vytautas Magnus University, Faculty of Agricultural Engineering;*
- *KRIAUCIUNIENE Zita - Lithuania, Vytautas Magnus University;*
- *DUKE Mike – New Zealand, University of Waikato, Faculty of Science and Engineering;*
- *EWEMOJE Temitayo Abayomy – Nigeria, University of Ibadan, Faculty of Technology, Department of Agricultural and Environmental Engineering;*
- *SKIERUCHA Wojciech – Poland, Institute of Agro-physics Polish Academy of Sciences, Lublin;*
- *EKIELSKI Adam - Poland, Warsaw University of Life Sciences;*
- *KOT Sebastian - Poland, Czestochowa University of Technology*
- *SAVIN Lazar– Serbia, University of Novi Sad, Faculty of Agriculture, Department of Agricultural Engineering;*
- *SIMIKIC Mirko– Serbia, University of Novi Sad, Faculty of Agriculture, Department of Agricultural Engineering;*
- *MARTINOV Milan - Serbia, Faculty of Agriculture, Department of Agricultural Engineering,*
- *TURAN Jan – Slovakia, Technical University Kosice, Dept Elect & Multimedia Commun, Kosice;*
- *MADYIRA M. Daniel - South Africa, University of Johannesburg, Mechanical Engineering Science Department*
- *COZ FERNANDEZ Alberto – Spain, University of Cantabria, School of Nautical Studies, Department of Chemistry and Process & Resource Engineering;*
- *ERTEKIN Can - Turkey, Akdeniz University Antalia;*
- *KABAŞ Önder –Turkey, Antalia, Agricultural Scientific Research Institute of Batı Akdeniz;*
- *SELVI Kemal Çağatay - Turkey, Samsun, University of Ondokuz Mayıs, Faculty of Agriculture, Department of Machines for Agriculture;*
- *ÖTLEŞ Semih - Turkey, Ege University, Engineering Faculty, Food Engineering Department;*
- *MARUSCHAK Pavlo - Ukraine, Ternopil Ivan Pul'uj National Technical University, Department of Technical Mechanics and Agricultural Engineering;*
- *BULGAKOV Volodymyr – Ukraine, National University of Life and Environmental Sciences of Ukraine;*
- *PARASCHIV Gigel - Romania, Politehnica University of Bucharest;*
- *VOICU Gheorghe - Romania, Politehnica University of Bucharest;*
- *BIRIŞ Sorin - Romania, Politehnica University of Bucharest;*
- *MAICAN Edmond - Romania, Politehnica University of Bucharest;*
- *FILIP Nicolae - Romania, Technical University Cluj Napoca;*
- *COZAR Onuc-Romania, „Babes-Bolyai” University of Cluj-Napoca Romania, Faculty of Physics;*
- *VLASE Sorin - Romania, “Transilvania” University of Braşov;*
- *ȚENU Ioan - Romania, USAMV Iași;*
- *HERIŞANU Nicolae - Romania, Politehnica University of Timisoara;*
- *MARSAVINA Liviu - Romania, Politehnica University of Timisoara*
- *MARINCA Vasile - Romania, Politehnica University of Timisoara*
- *GERGEN Iosif - Romania, USAMVB Timișoara;*
- *BORDEAN Despina-Maria - Romania, USAMVB Timișoara;*
- *BUNGESCU Sorin - Romania, USAMVB Timișoara;*
- *RODINO Steliana – Romania, ICEADR, Bucharest;*
- *VOICEA Iulian - Romania, INMA Bucharest;*
- *DEAK Gyorgy - Romania, INCDPM Bucharest;;*
- *BELC Nastasia - Romania, IBA Bucharest;*
- *BUȚU Alina - Romania, INCDSB Bucharest;*
- *PAUN Mihaela - Romania, INCDSB, Bucharest*

INMATEH - Agricultural Engineering journal is indexed in the next international databases:
ELSEVIER /SciVerse SCOPUS, CLARIVATE - WEB of SCIENCE- Emerging Sources Citation Index (ESCI),
ULRICHS Web: Global Serials Directory, CABI, SCIPRO, Index COPERNICUS International, EBSCO Publishing,
Elektronische Zeitschriftenbibliothek

INMATEH - Agricultural Engineering

vol. 73, no.2 / 2024

e-ISSN: 2068 – 2239; p: ISSN: 2068 – 4215

<https://inmateh.eu/>

E-mail: inmatehjournal@gmail.com

Edited by: **INMA Bucharest**

Copyright: INMA Bucharest / Romania

National Institute for Research-Development of Machines and Installations
Designed for Agriculture and Food Industry - INMA Bucharest
6, Ion Ionescu de la Brad Blvd., sector 1, Bucharest, ROMANIA

CONTENT

| | | Page(s) |
|----|--|---------|
| 1. | <p>STUDY THE THERMAL PERFORMANCE OF DRYING TOMATOES PROCESS USING A SOLAR ENERGY SYSTEM / دراسة التأثير الحراري لعملية تجفيف الطماطم باستخدام نظام الطاقة الشمسية Ahmed M. EL-SHEIKHA¹⁾, Mohamed R. DARWESH^{2,3)}, Rashad HEGAZY⁴⁾, Mahmoud OKASHA⁵⁾, Nada H. MOHAMED¹⁾ ¹⁾Agricultural Engineering Dept., Faculty of Agriculture, Damietta University, Egypt ²⁾Agricultural Engineering Dept., Faculty of Agriculture, Tanta University, Egypt ³⁾ Faculty of Technology of Industry and Energy, Samannoud Technological University, Egypt ⁴⁾Agricultural Engineering Department, Faculty of Agriculture, Kafrelsheikh University, Kafrelsheikh 33516, Egypt ⁵⁾Agricultural Engineering Research Institute (AEnRI), Agricultural Research Center (ARC), Giza 12611/ Egypt</p> | 13 |
| 2. | <p>VIBRATION PARAMETER CALIBRATION AND TEST OF TIGER NUT BASED ON DISCRETE ELEMENT METHOD / 基于离散元法的油莎豆振动参数标定与试验 Shikuan MA¹⁾, Xiaoning HE^{*1)}, Hao ZHU³⁾, Zhixin LIU¹⁾, Dongwei WANG¹⁾, Shuqi SHANG¹⁾, Guanghui LI²⁾ ¹⁾ College of Electrical and Mechanical Engineering, Qingdao Agricultural University, Qingdao/ China ²⁾ Shandong Saline Modern Agriculture Co., Ltd, Dongying/ China ³⁾ Nanjing Agricultural University, Nanjing/ China</p> | 30 |
| 3. | <p>DESIGN AND RESEARCH ON FEEDING COMPONENTS OF WHEAT FLOUR PARTICLE SIZE DETECTION DEVICE / 小麦制粉粒度检测装置供料部件设计与研究 Mingxu WANG^{1,2)}, Haojun ZHAO¹⁾, Saiqiang LI¹⁾, Jiangfeng OUYANG¹⁾, Junyong WU³⁾, Hengda ZHANG⁴⁾ School of Mechanical & Electrical Engineering, Henan University of Technology, Zhengzhou, China Henan Key Laboratory of Grain and Oil Storage Facility & Safety, Henan Univ. of Technology, Zhengzhou, China Hebei Pingle Flour Machinery Group Co., Ltd., Zhengding, China Buler (Wuxi) Commercial Co., Ltd., Wuxi, Jiangsu, China</p> | 40 |
| 4. | <p>DESIGN AND EXPERIMENT OF ANNULAR AIR-BLOWING ASSISTED SEED GUIDING DEVICE FOR CORN NO-TILL SEEDER / 玉米免耕播种机环形气吹辅助导种装置设计与试验 Haojie ZHOU¹⁾, Chunling ZHANG^{*1,2)}, Tao LIU¹⁾, Yazi WANG¹⁾, Jun FANG¹⁾, Antai HU¹⁾ ¹⁾ College of Engineering, Anhui Agricultural University, Hefei, Anhui, 230036, China²⁾ Engineering Laboratory of Intelligent Agricultural Machinery Equipment, Anhui, Hefei, 230036, China</p> | 50 |
| 5. | <p>OPTIMISED DESIGN AND SIMULATION ANALYSIS OF LONGITUDINAL FLOW CORN CONE THRESHING DEVICE / 纵轴流玉米锥形脱粒装置优化设计与仿真分析 Jinliang GONG^{1,2)}, Zengjia LUO³⁾, Yanfei ZHANG³⁾ ¹⁾ Collaborative Innovation Center for Shandong's Main crop Production Equipment and Mechanization, Qingdao, Shandong, China; ²⁾ School of Mechanical Engineering, Shandong University of Technology, Zibo, Shandong, China ³⁾ School of Agricultural Engineering and Food Science, Shandong University of Technology, Zibo, Shandong, China</p> | 63 |
| 6. | <p>CENTRIFUGAL SPRAYING SYSTEM DESIGN AND DROPLET DISTRIBUTION CHARACTERIZATION FOR MAIZE PLANT PROTECTION UAV / 玉米植保无人机离心喷施系统设计与雾滴分布特性试验 Jiaxun HE¹⁾, Keke SUN¹⁾, Taojie WANG¹⁾, Zhihua SONG¹⁾, Lichao LIU^{1,2)} ¹⁾ College of Engineering, Anhui Agricultural University, Hefei, Anhui, China ²⁾ Engineering Laboratory of Intelligent Agricultural Machinery Equipment, Anhui, Hefei, China</p> | 73 |
| 7. | <p>YOUNG APPLE FRUITS DETECTION METHOD BASED ON IMPROVED YOLOV5 / 基于改进 YOLOv5 的苹果幼果检测方法 Yonghui DU¹⁾, Ang GAO¹⁾, Yuepeng SONG^{1,2,3)}, Jing GUO^{1,2,3)}, Wei MA⁴⁾, Longlong REN^{1,2,3)} ¹⁾ Shandong Agricultural University, College of Mechanical and Electrical Engineering / China; ²⁾ Shandong Provincial Key Laboratory of Horticultural Machinery and Equipment / China; ³⁾ Shandong Provincial Engineering Laboratory of Agricultural Equipment Intelligence / China ⁴⁾ Institute of Urban Agriculture, Chinese Academy of Agricultural Sciences / China</p> | 84 |
| 8. | <p>HYDROPONIC VERTICAL SYSTEMS: ENHANCING CLIMATE RESILIENCE, WATER EFFICIENCY, AND URBAN AGRICULTURE / SISTEME VERTICALE HIDROPONICE: INTENSIFICAREA REZISTENȚEI LA CLIMĂ, EFICIENȚEI APEI ȘI AGRICULTURII URBANE Iuliana GĂGEANU¹⁾, Ana-Maria TĂBĂRAȘU^{*1)}, Cătălin PERSU¹⁾, Gabriel GHEORGHE¹⁾, Mihaela NIȚU^{*1)}, Dan CUBESCU¹⁾, Alexandru IONESCU¹⁾, Dragoș ANGHELACHE¹⁾ National Institute of Research – Development for Machines and Installations Designed to Agriculture and Food Industry, Romania</p> | 94 |
| 9. | <p>MATLAB-BASED DESIGN AND ANALYSIS OF SMALL RICE TRANS-PLANTER IN HILLY AREAS / 基于 MATLAB 的丘陵地区小型水稻插秧机的设计与分析 Hao WANG¹⁾, Xiaobo ZHOU^{*1)}, Xiayu WU¹⁾, Yuling DAN¹⁾, Hongchun CHU¹⁾, Jin CHEN¹⁾ ¹⁾ Sichuan Academy of Agricultural Machinery Science / China</p> | 110 |

| | | Page(s) |
|-----|--|---------|
| 10. | OPTIMIZATION AND EXPERIMENT OF CUTTING PARAMETERS OF ALFALFA DISC-TYPE MOWER / 圆盘式苜蓿切割器参数优化与试验 Yong YOU [*] , Pengzhan HU, Lu ZHU, Haiyi WANG, Yunting HUI, Decheng WANG China Agricultural University, College of Engineering, Beijing / China | 119 |
| 11. | DETECTION METHOD OF CORN LEAF DISEASES BASED ON CA-YOLOv8 / 基于 CA-YOLOv8 的玉米叶病检测方法 Miao XU ¹⁾ , Xuan ZHANG ^{*2)} , Na MA ¹⁾ , Yanwen LI ¹⁾ ¹⁾ College of Information Science and Engineering, Shanxi Agricultural University, Taigu / China; ²⁾ College of Agricultural Engineering, Shanxi Agricultural University, Taigu / China | 129 |
| 12. | SOIL STRESS ANALYSIS AT DIFFERENT DEPTHS AFTER AGRICULTURAL VEHICLE OPERATION / 农业车辆作业后不同深度的土壤应力分析 Jun GUO ¹⁾ ; Enhui SUN ^{*1)} ; Yue YANG ¹⁾ ; Jun LU ¹⁾ ¹⁾ School of Automotive Engineering, Yancheng Institute of Technology, Yancheng, China | 139 |
| 13. | RESEARCH ON THE DOA-BP-BASED TEMPERATURE AND HUMIDITY PREDICTION MODEL FOR COMMERCIAL CULTIVATION OF AGARICUS BISPORUS / 基于 DOA-BP 的双孢菇工厂化生产温湿度预测模型研究 Tianhua LI ¹⁾ , Yinhang DONG ¹⁾ , Guoying SHI ¹⁾ , Guanshan ZHANG ¹⁾ , Chao CHEN ²⁾ , JianchangSU ⁴⁾ ¹⁾ Shandong Agricultural University, College of Mechanical and Electrical Engineering/ China; ²⁾ Shandong Century Smart Agricultural Technology Co., LTD; ³⁾ Shandong Qihe Biotech Co., LTD | 149 |
| 14. | PHYSICO-CHEMICAL, CULTURE VIABILITY, AND SENSORY FEATURES OF KEFIR ICE CREAM AS AFFECTED BY VARIOUS <i>Saccharomyces cerevisiae</i> ATCC 36858 CONCENTRATIONS / FISIKO-KIMIA, VIABILITAS KULTUR, DAN FITUR SENSORIK ES KRIM KEFIR YANG DIPENGARUHI OLEH BERBAGAI KONSENTRASI <i>Saccharomyces cerevisiae</i> ATCC 36858 Muhammad Fajrul Arief ¹⁾ , Lilik Eka Radiati ¹⁾ , Ria Dewi Andriani ¹⁾ , Dedi Fardiaz ²⁾ , Laprianika Reta Hapita Sari ³⁾ ¹⁾ Faculty of Animal Science, Universitas Brawijaya, Malang / Indonesia ²⁾ Faculty of Dentistry, Universitas Muhammadiyah, Sidoarjo / Indonesia ³⁾ Faculty of Medicine, Universitas Airlangga, Surabaya / Indonesia | 162 |
| 15. | DESIGN AND TESTING OF A VARIABLE FERTILIZATION SYSTEM BASED ON SOIL NUTRIENT DETECTION / 基于土壤养分检测的变量施肥系统的设计与试验 Jie LIU ¹⁾ , Fanxia KONG ¹⁾ , Lili Yi ¹⁾ , Yubin LAN ^{1,2)} , Xin HAN ¹⁾ , Minhui ZHANG ¹⁾ , Lei LIU ¹⁾ , Pengcheng LV ¹⁾ , Zhao JIE ³⁾ ¹⁾ College of Agricultural Engineering and Food Science, Shandong University of Technology, Zibo/China; ²⁾ National Sub-Centre for International Collaboration Research Centre for Agricultural Aviation Intelligent Equipment, Zibo/China; ³⁾ UNDOF Procurement Service Station No. 4, Shenyang/China | 176 |
| 16. | DESIGN AND EXPERIMENTAL OPTIMIZATION OF V-SHAPED HAMMER FOR HAMMER MILL / 锤片式粉碎机 V 型锤片设计及试验优化 Haijun Zhang ^{1,2)} , Yi Qian ²⁾ , Haiqing Tian ²⁾ ¹⁾ Huzhou Vocational and Technical College, Intelligent Manufacturing and Elevator College, Huzhou / China; ²⁾ Inner Mongolia Agricultural University, College of Mechanical and Electrical Engineering, Hohhot / China | 191 |
| 17. | TRACTOR DESIGN ANALYSIS AND RESEARCH BASED ON KANO - AHP MODEL AND JACK / 基于 KANO—AHP 模型与 JACK 的拖拉机设计分析与研究 Yuanqi LIU, Bin QI [*] , Tengyun MA, Yuchao REN, Jiyuan SUN, Bohan ZHANG College of Agricultural Engineering and Food Science, Shandong University of Technology / China | 201 |
| 18. | RESEARCH ON SLAM AND PATH PLANNING METHOD FOR INSPECTION ROBOT IN ORCHARD ENVIRONMENT / 果园环境中巡检机器人的 SLAM 和路径规划方法研究 Pengcheng LV, Minhui ZHANG, Jie LIU, Lei LIU, Lili YI [*] Shandong University of Technology, Collage of Agricultural Engineering and Food Science, ZiBo, China | 213 |
| 19. | MULTI-TARGET DETECTION METHOD FOR MAIZE PESTS BASED ON IMPROVED YOLOv8 / 基于改进 YOLOv8 的玉米害虫多目标检测方法 Qiuyan LIANG ¹⁾ , Zihan ZHAO ¹⁾ , Jingye SUN ¹⁾ , Tianyue JIANG ²⁾ , Ningning GUO ¹⁾ , Haiyang YU ¹⁾ , Yiyuan GE ¹⁾ ¹⁾ School of Mechanical Engineering, Jiamusi University, Jiamusi, Heilongjiang / China; ²⁾ College of Information and Electronic Technology, Jiamusi University, Jiamusi, Heilongjiang / China | 227 |
| 20. | MECHANICAL PROPERTIES OF CERASUS HUMILIS AT DIFFERENT TEMPERATURES FOR POSTHARVEST DAMAGE ANALYSIS / 欧李采收后在不同温度下的力学特性研究分析 Bin TONG, Junlin HE [*] , Jingpu ZHOU, Tao WANG, Huhu YANG College of Agricultural Engineering, Shanxi Agricultural University, Taigu / China104 | 239 |
| 21. | LOCAL PATH PLANNING METHOD BASED ON SMOOTH TIME ELASTIC BAND ALGORITHM FOR ORCHARD ROBOTIC LAWN MOWER / 基于 S-TEB 算法的果园割草机器人局部路径规划研究 Minhui ZHANG, Pengcheng LV, Jie LIU, Lei LIU, Huibin ZHU, Lili YI [*] Shandong University of Technology, Collage of Agricultural Engineering and Food Science / China | 249 |

| | | Page(s) |
|-----|--|---------|
| 22. | <p>DESIGN AND TEST OF SUPPLEMENTAL FEEDING PUSHER DEVICE FOR CATTLE STABLE / 牛场补饲推料装置设计与试验</p> <p>Yumeng XIAO ¹⁾, Taowei JIAO¹⁾, Wenjie ZHAO ¹⁾, Hengxu ZHU¹⁾, Hongming ZHANG²⁾, Pengpeng SUN²⁾, Wei LI^{*1)}</p> <p>¹⁾ Northwest A&F University, College of Mechanical and Electronic Engineering/ China; ²⁾ Northwest A&F University, College of Information Engineering/China</p> | 263 |
| 23. | <p>DYNAMIC-ENERGY ANALYSIS OF A ROTARY TILLER WITH A VERTICAL ROTATION AXIS ԴՐՂԱԶԻԳ ՊՏՏԱՆ ԱՌԱՆՑՔՈՎ ՀՈՂԱՄՇԱԿ ՖՐԵԶԻ ԴԻՆԱՄԻԿԱԿԱՆ-ԷՆԵՐԳԵՏԻԿԱԿԱՆ ՀԵՏԱԶՈՏՈՒԹՅՈՒՆ</p> <p>Arshaluys TARVERDYAN¹⁾, Artur ALTUNYAN¹⁾, Gevorg HARUTYUNYAN²⁾, Albert GRIGORYAN¹⁾</p> <p>¹⁾Scientific Research Institute for Agricultural Mechanization and Automation, Armenian National Agrarian University, Yerevan, Armenia ²⁾Aspirant at Agricultural Engineering Faculty</p> | 275 |
| 24. | <p>DESIGN AND TESTING OF A VARIABLE SPRAY SYSTEM BASED ON PTO PROTOCOLS / 基于 PTO 协议的变量喷雾系统设计与试验</p> <p>Lei LIU¹⁾, Fanxia KONG^{*1)}, Lili YI¹⁾, Yubin LAN^{1,2)}, Xin HAN¹⁾, Jie ZHAO³⁾, Jie LIU¹⁾, Pengcheng LV¹⁾, Minhui ZHANG¹⁾</p> <p>¹⁾ College of Agricultural Engineering and Food Science, Shandong University of Technology, Zibo/China ²⁾ National Sub-Centre for International Collaboration Research Centre for Agricultural Aviation Intelligent Equipment, Zibo/China ³⁾ UNDOF Procurement Service Station No.4, Shenyang/China</p> | 285 |
| 25. | <p>DESIGN AND EXPERIMENT OF SPIRAL-RIBBON BLADE COMBINATION MECHANISM OF STRAW AND MANURE INCLINED MIXING CONVEYOR / 秸秆粪便斜式混配输送机螺旋-螺带组合机构设计与试验</p> <p>Tiejun WANG, Peng YIN, Li DU, Rui ZHOU, Yuanjuan GONG, Hongguang CUI[*]</p> <p>Shenyang Agricultural University, College of Engineering, Shenyang/ China</p> | 299 |
| 26. | <p>DESIGN AND EXPERIMENTAL VERIFICATION OF SELF-PRIMING HOT AIR TEMPERATURE CHANGING DEVICE FOR GRAIN DRYER / 粮食干燥机自吸式热风变温装置设计与试验验证</p> <p>Zhao-Xin LIU^{1,2)}, Gang CHE^{1,2)}, Lin WAN^{1,2)}, Hong-Chao WANG¹⁾, Zheng-Fa CHEN¹⁾, Hao-Chen WANG¹⁾</p> <p>¹⁾College of Engineering, Heilongjiang Bayi Agricultural University, Daqing / P.R.China ²⁾Key Laboratory of Intelligent Agricultural Machinery Equipment in Heilongjiang Province, Daqing / P. R. China</p> | 310 |
| 27. | <p>VIBRATION TESTING AND ANALYSIS OF THE PICKUP HEADER OF STRAW FORAGE HARVESTER UNDER MULTI-SOURCE EXCITATION / 秸秆饲料收获机捡拾割台在多源激励下的振动试验与分析</p> <p>Qiaofei MU^{1,2)}, Haiqing TIAN^{*1,2)}, Ziqing XIAO^{1,2)}, Chunxiang ZHUO^{1,2)}, Xiaoyu XUE^{1,2)}, Leifeng TANG^{1,2)}</p> <p>¹⁾ Inner Mongolia Agricultural University, College of Mechanical and Electrical Engineering, Hohhot/China; ²⁾ Inner Mongolia Engineering Research Centre of Intelligent Equipment for the Entire Process of Forage and Feed Production, Hohhot, China</p> | 324 |
| 28. | <p>DESIGN AND EXPERIMENT OF A MULTI-CHANNEL REAL-TIME WEIGHING DEVICE / 多路实时称量装置设计与试验</p> <p>Lingyu LIU, Xiangcai ZHANG³⁾, Xianliang WANG, Zhongcai WEI, Xiupei CHENG, Yujie ZHANG, Xinkai JIAO</p> <p>School of Agricultural Engineering and Food Science, Shandong University of Technology, Zibo, China</p> | 338 |
| 29. | <p>DESIGN AND TESTING OF A SOWING DRONE BASED ON RICE PRECISION STRIP SEEDING 水稻精量化条直播播种无人机的设计与试验</p> <p>Liangchen HOU¹⁾, Xin HAN¹⁾, Yubin LAN¹⁾, Jingbo BAI²⁾, Zhikang DING¹⁾, Xuejian ZHANG³⁾, Maochang SONG¹⁾, Kailu WANG¹⁾</p> <p>¹⁾School of Agricultural and Food Science, Shandong University of Technology, Zibo, China; ²⁾Shandong Siyuan Agricultural development Co., LTD, Zibo, China; ³⁾Institute of Agricultural Economics and Information Technology, Ningxia Academy of Agricultural and Forestry Sciences, Ningxia, China</p> | 351 |
| 30. | <p>OPTIMIZATION DESIGN AND EXPERIMENT OF AUTOMATIC LEVELING SYSTEM FOR ORCHARD OPERATING PLATFORM IN HILLY AND MOUNTAINOUS AREAS / 丘陵山区果园作业平台自动调平系统的优化设计与试验</p> <p>Huijie SHANG¹⁾, XinCheng LI^{*1)}, Chengfu ZHANG²⁾, Cuiyun XU²⁾, Yaxiu HOU¹⁾, Mingtao JIA¹⁾</p> <p>¹⁾ College of Mechanical and Electrical Engineering, Qingdao Agricultural University, Shandong / China ²⁾ Gaomi Yifeng Machinery Co., Ltd. / China</p> | 364 |

| | | Page(s) |
|-----|--|---------|
| 31. | <p>INVESTIGATION OF THE REACTION OF SOIL TO MOVEMENT BY PLATES AT VARIOUS INCLINED ANGLES BASED ON 2D-DEM / 基于二维离散元法对倾角条件影响土壤-板接触系统相互作用的研究 Liangyu YUAN, Jun GE [*], Chengmao CAO, Kuan QIN, Yan SUN, Liangfei FANG School of Engineering, Anhui Agricultural University, Hefei, Anhui / China</p> | 375 |
| 32. | <p>DESIGN DEVELOPMENT AND RESULTS OF EXPERIMENTAL RESEARCH ON GRAIN DAMAGE BY A NEW SCREW CONVEYOR / РОЗРОБКА КОНСТРУКЦІЇ ТА РЕЗУЛЬТАТИ ЕКСПЕРИМЕНТАЛЬНОГО ДОСЛІДЖЕННЯ ПОШКОДЖЕННЯ ЗЕРНА НОВИМ ГВИНТОВИМ КОНВЕЄРОМ Volodymyr BULGA KOV¹⁾, Adolfs RUCINS^{*2)}, Ivan HOLOVACH¹⁾, Oleksandra TROKHANI AK¹⁾, Dmytro POLISHCHUK³⁾ ¹⁾ National University of Life and Environmental Sciences of Ukraine, 15, Heroyiv Oborony Str., Kyiv / Ukraine ²⁾ Latvia University of Life Sciences and Technologies, Ulbroka Research Centre, Stopinu Municipality/ Latvia ³⁾ Taras Shevchenko National University of Kyiv, 64/13, Volodymyrska Str.</p> | 383 |
| 33. | <p>SIMULATION PARAMETER CALIBRATION AND TEST OF PAK CHOI SEEDS BASED ON DISCRETE ELEMENT METHOD / 基于离散元的小白菜种子仿真参数标定与试验 Guoqiang DUN^{*1)}, Chaoxia ZHANG²⁾, Xinin Ji²⁾, Qingjun MENG²⁾, Quanbao SHENG²⁾, Lei WANG²⁾ ¹⁾ Harbin Cambridge University, Intelligent Agricultural Machinery Equipment Engineering Laboratory, China; ²⁾ Northeast Forestry University, College of Mechanical and Electrical Engineering, Harbin / China</p> | 391 |
| 34. | <p>DEVELOPMENT OF MATHEMATICAL MODEL FOR ESTIMATING THE RICE MILLING DEGREE BASED ON FLUORESCENCE IMAGE / PENGEMBANGAN MODEL MATEMATIKA UNTUK MENDUGA DERAJAT SOSOH BERAS BERDASARKAN CITRA FLUORESENSI Zakky MOCHAMAD ¹⁾, Ahmad USMAN ²⁾, Subrata I DEWA MADE ²⁾, Suhil MARDISON ³⁾ ¹⁾ Agricultural and Biosystem Engineering Study Program, Faculty of Agricultural Engineering and Technology, IPB University, Indonesia; ²⁾ Department of Mechanical and Biosystem Engineering, Faculty of Agricultural Engineering and Technology, IPB University, Indonesia; ³⁾ Indonesian Agricultural Engineering Polytechnic, Tangerang, Indonesia</p> | 406 |
| 35. | <p>HEAT TRANSMISSION THROUGH WALLS OF COMPOSITE MATERIAL WITH CLAY MATRIX/ TRANSMITEREA CALDURII PRIN PERETI DE MATERIAL COMPOZIT CU MATRICE DE LUT Elena SURDU¹⁾, Dana-Claudia FARCAȘ-FLAMAROPOL¹⁾, Radu I. IATAN¹⁾, Petru CÂRDEI²⁾, Nicoleta SPOREA¹⁾, Gheorghita TOMESCU¹⁾, Ion DURBACĂ¹⁾ ¹⁾ U.N.S.T "POLITEHNICA" of Bucharest, Bucharest / Romania ²⁾ INMA Bucharest, Bd. Ion Ionescu de la Brad, No.6, Romania, 013813</p> | 416 |
| 36. | <p>MECHANICAL AND THERMAL PROPERTIES OF COMPOSITE MATERIALS OBTAINED WITH SLUDGE MATRIX AND AGRICULTURAL WASTE INSERTS / PROPRIETĂȚI MECANICE ȘI TERMICE ALE MATERIALELOR COMPOZITE OBȚINUTE CU MATRICE DE NĂMOL ȘI INSERȚII DIN DEȘEURI AGRICOLE Dana-Claudia FARCAȘ-FLAMAROPOL¹⁾, Elena SURDU¹⁾, Radu I. IATAN¹⁾, Petru CÂRDEI²⁾, Georgiana ENĂCHESCU¹⁾, Iuliana PRODEA¹⁾, Ion DURBACĂ¹⁾ ¹⁾ U.N.S.T "POLITEHNICA" of Bucharest, no. 313, Splaiul Independentei, sector 6, Bucharest, 060042, Romania ²⁾ INMA Bucharest, 6 Bd. Ion Ionescu de la Brad, Romania, 013813</p> | 427 |
| 37. | <p>SIMULATION AND OPTIMIZATION OF THE SPOON-WHEEL TYPE MAIZE PRECISION SEED-METERING DEVICE BASED ON VIBRATION / 勺轮式玉米精量排种器在振动条件下的仿真与优化 Qing Wang[#], Dandan Han^{**}, Lin Chen, Yuxia Huang, Wei Li, Chao Tang College of Mechanical & Electrical Engineering, Sichuan Agricultural University, Ya'an/China</p> | 435 |
| 38. | <p>EVALUATION OF THE CORRELATION BETWEEN THE COLOR OF DIFFERENT WHEAT VARIETIES AND WEATHER CONDITIONS USING RGN UAV-BASED IMAGES / ОЦЕНКА НА ЗАВИСИМОСТТА МЕЖДУ ЦВЕТА ПРИ РАЗЛИЧНИ СОРТОВЕ ПШЕНИЦА И МЕТЕОРОЛОГИЧНИТЕ УСЛОВИЯ ИЗПОЛЗВАЙКИ RGN ИЗОБРАЖЕНИЯ БАЗИРАНИ НА UAV Asparuh I. ATANASOV ¹⁾; Atanas Z. ATANASOV ^{*2)} ¹⁾ Technical University of Varna, / Bulgaria; ORCID 0000-0001-9898-8472 ²⁾ University of Ruse "Angel Kanchev", 7017 Ruse, / Bulgaria</p> | 453 |
| 39. | <p>NON-DESTRUCTIVE PREDICTION OF OIL AND FREE FATTY ACID OF OIL PALM FRUITLETS USING NEAR-INFRARED SPECTROSCOPY AND HYBRID CALIBRATION METHOD / PREDIKSI KANDUNGAN MINYAK DAN ASAM LEMAK BEBAS BUAH SAWIT SECARA NON-DESTRUKTIF MENGGUNAKAN NEAR-INFRARED SPECTROSCOPY DAN METODE KALIBRASI HYBRID I WAYAN Budiastara^{*1,2)}, SUTRISNO Marjan¹⁾, NISSA Adiarifia¹⁾, INNA Novianty³⁾, YUNISA Tri Suci¹⁾ ¹⁾ IPB University, Department of Mechanical and Biosystem Engineering / Indonesia; ²⁾ IPB University, Centre for Research on Engineering Application in Tropical Agriculture / Indonesia; ³⁾ IPB University, Study Program of Computer Engineering / Indonesia</p> | 463 |

| | | Page(s) |
|-----|---|---------|
| 40. | <p>DESIGN AND EXPERIMENT OF PROGRESSIVE SEED-CLEANING MECHANISM FOR AIR-PRESSURE MAIZE PRECISION SEED-METERING DEVICE / 气压式玉米精量排种器递进性清种装置设计与试验</p> <p>Wen-sheng SUN¹⁾, Shu-juan YI¹⁾, Hai-long QI²⁾, Yi-fei LI^{1,3)}, Zhi-bo DAI¹⁾, Yu-peng ZHANG¹⁾, Song WANG¹⁾</p> <p>¹⁾College of Engineering, Heilongjiang Bayi Agricultural University, Daqing / P.R.China ²⁾Heilongjiang Beidahuang Modern Agricultural Service Group Zhongrong Agricultural Machinery Co., Ltd, Harbin / P.R.China ³⁾College of Engineering, Northeast Agricultural University, Harbin/P.R.China</p> | 473 |
| 41. | <p>RESEARCH ON CURVED PATH-TRACKING CONTROLLER OF RICE TRANSPLANTER BASED ON H-INFINITY STATE FEEDBACK CONTROL / 基于H无穷状态反馈控制的插秧机曲线路径跟踪控制器研究</p> <p>Yueqi MA^{1,2)}, Ruijuan CHI^{1,2)}, Yantao ZHAO^{1,2)}, Chao BAN^{1,2)}, Tong SU^{1,2)}, Zhengrong LI^{1,2)}</p> <p>¹⁾ College of Engineering, China Agricultural University, Beijing, China ²⁾ Vehicle Intelligent Control Laboratory, China Agricultural University, Beijing, China</p> | 487 |
| 42. | <p>DETECTION OF BLACK HEART DISEASE IN SEED POTATO BASED ON TRANSMISSION SPECTROSCOPY TECHNIQUE / 基于透射光谱技术的马铃薯种薯黑心病检测研究</p> <p>Xianhe WANG¹⁾, Min HAO^{1,*)}, Xingtai CAO¹⁾, Yutao ZHANG¹⁾</p> <p>¹⁾College of Electromechanical Engineering, Inner Mongolia Agricultural University, Hohhot, Inner Mongolia Autonomous Region, China</p> | 501 |
| 43. | <p>CLIMATE QUALITY EVALUATION AND FINE ZONING OF GUANGXI SPECIALIZED FORAGE RICE "ZHONGZAO 39" / 广西专用饲料稻“中早39”气候品质评价与精细化区划</p> <p>Mengxiang TAN¹⁾, Yan HE^{1,*)}, Xuanke WU²⁾, Yucong LI¹⁾, Wei HUANG²⁾, Ying XIE¹⁾</p> <p>¹⁾ Guangxi Zhuang Autonomous Region Institute of Meteorological Science, Nanning, China ²⁾ Liuzhou Meteorological Bureau, Liuzhou, China</p> | 513 |
| 44. | <p>DESIGN AND EXPERIMENTAL STUDY ON FERTILIZATION PERFORMANCE OF CRANK ROCKER DEEP APPLICATION MECHANISM / 曲柄摇杆式深施机构的设计与施肥性能试验研究</p> <p>Jinlong FENG^{1,*)}, Dongxue CHEN²⁾, Qichao LI¹⁾, Hua LI¹⁾</p> <p>¹⁾ College of Mechanical and Electrical Engineering, Lingnan Normal University; Zhanjiang 524048, China ²⁾ Teacher education college, Lingnan Normal University; Zhanjiang, China</p> | 524 |
| 45. | <p>DESIGN AND SIMULATION ANALYSIS OF THE TUBER HARVEST SCREENING MACHINE / 块茎收获物清选机的设计与模拟分析</p> <p>Wenliang LIU¹⁾, Changyou WEI¹⁾, Feng LIU^{1,*)}, Caiyu JIANG¹⁾, Fei PENG¹⁾, Jiaqi WANG¹⁾</p> <p>¹⁾Jilin Agricultural Machinery Research Institute, Changchun, China</p> | 534 |
| 46. | <p>EXPERIMENTAL STUDY OF LYCIUM BARBARUM BRUISING DURING VIBRATION HARVESTING / 枸杞振采收集中果实碰撞损伤分析与试验</p> <p>Qingyu CHEN¹⁾, Rui KANG²⁾, Naishuo WEI¹⁾, Yunlei FAN¹⁾, Zeyu WANG¹⁾, Jianguo ZHOU¹⁾, Lingxin BU³⁾, Yu CHEN¹⁾, Jun CHEN^{*)}</p> <p>¹⁾ College of Mechanical and Electronic Engineering, Northwest A&F University, Yangling, China; ²⁾ German-Sino School of Business & Technology, FOM University of Applied Sciences, Essen, Germany; ³⁾ College of Mechatronic Engineering, North Minzu University, Yinchuan, Ningxia, China</p> | 546 |
| 47. | <p>MULTI-OUTPUT REGRESSION PREDICTION OF PNEUMATIC SUBMERGING RESISTANCE AND DISTURBANCE AREA BASED ON NEURAL NETWORK / 基于神经网络的气动深松阻力及扰动面积多输出回归预测</p> <p>Xia Li^{1,2)}, Xuhui Wang^{1,2)}, Jinyou Xu^{*)}, Xinglong Li^{1,2)}, Zhangjun Jiang^{1,2)}, Birong You^{1,2)}</p> <p>¹⁾ Tianjin Key Laboratory for Advanced Mechatronic System Design and Intelligent Control, School of Mechanical Engineering, Tianjin University of Technology, Tianjin / China; ²⁾ National Demonstration Center for Experimental Mechanical and Electrical Engineering Education, Tianjin University of Technology, Tianjin / China</p> | 559 |
| 48. | <p>DYNAMIC DRYING CHARACTERISTICS OF ALFALFA UNDER SOLAR ENERGY-HEAT PUMP COMBINED DRYING CONDITIONS / 太阳能-热泵联合干燥条件下紫花苜蓿动态干燥特性</p> <p>WenBin GUO^{*)}, Shuo CHENG^{1,2)}, ZhiKang CUI^{1,2)}, DongLi HE³⁾, XuHui ZHANG^{1,2)}, TianYu SHI^{1,2)}, ShanZhu QIAN^{1,2)}, JianQiang DU^{1,2)}</p> <p>¹⁾ College of Mechanical and Electrical Engineering, Inner Mongolia Agricultural University, Hohhot, China; ²⁾ Inner Mongolia Engineering Research Centre of Intelligent equipment for the entire process of forage and feed production, Hohhot, China; ³⁾ Research Institute of Inner Mongolia First Machinery Group Co. Ltd, China</p> | 569 |
| 49. | <p>EFFICIENCY ANALYSIS AND EVALUATION OF VARIABLE FERTILIZER SPREADING BASED ON REALTIME SPECTRAL INFORMATION ON WHEAT / 基于实时光谱信息的小麦变量施肥效率分析与评价</p> <p>Man CHEN¹⁾, Zhichang CHANG¹⁾, Chengqian JIN^{1,*)}, Yinyan SHI^{2,*)}</p> <p>¹⁾ Nanjing Institute of Agricultural Mechanization, Ministry of Agriculture and Rural Affairs, Nanjing, / China; ²⁾ College of Engineering, Nanjing Agricultural University, Nanjing, Jiangsu / China</p> | 581 |

| | | Page(s) |
|-----|---|---------|
| 50. | <p>WHEAT GRAINS AUTOMATIC COUNTING BASED ON LIGHTWEIGHT YOLOv8 / 基于轻量化的 YOLOv8 小麦籽粒自动计数研究</p> <p>Na MA¹⁾, Zhongtao Li, Qingzhong KONG College of Information Science and Engineering, Shanxi Agricultural University, Taigu/China</p> | 592 |
| 51. | <p>RESEARCH ON THE STEERING CHARACTERISTICS OF ELECTRO-HYDRAULIC COUPLED STEERING SYSTEM OF SELF-DRIVING TRACTOR / 自动驾驶拖拉机电液耦合转向特性研究</p> <p>Guangfei XU¹⁾, Qun SUN¹⁾, Meizhou CHEN²⁾, Jian WU¹⁾, Jiwei FENG³⁾, Peisong DIAO²⁾, Chenqiang YIN⁴⁾ ¹⁾ College of Mechanical and Automotive Engineering, Liaocheng University, Liaocheng, China; ²⁾ College of Agricultural Engineering and Food Science, Shandong University of Technology, Zibo, China; ³⁾ School of Mechanical Engineering, Southeast University, Nanjing, China. ⁴⁾ School of Machinery and Automation, Weifang University, Weifang, China</p> | 603 |
| 52. | <p>RESEARCH ON PARAMETER MATCHING METHOD OF PURE ELECTRIC HORTICULTURAL MACHINERY DRIVELINE BASED ON WORKING CONDITION CHARACTERISTICS / 考虑作业工况特性的纯电动园艺作业机械动力传动系统参数匹配方法研究</p> <p>Dongyang WANG^{1,2)}, Zhanyu LI¹⁾, Jiangtao JI²⁾, Weixiang LIU²⁾, Zuohua DONG³⁾, Hongmei ZHU¹⁾, Lijun BAO⁴⁾ ¹⁾ College of Automotive and Transportation Engineering, Shenzhen Polytechnic University, Shenzhen/China; ²⁾ College of Agricultural Equipment Engineering, Henan University of Science and Technology, Luoyang/China; ³⁾ Changzhou Dongfeng Agricultural Machinery Group Co., Ltd., Changzhou/China ⁴⁾ Beijing Research Institute of Commercial Machinery, All China Federation of Supply and Marketing Cooperatives, Beijing/China</p> | 613 |
| 53. | <p>A PRIMARY INVESTIGATION OF SEPARATING ALFALFA STEMS AND LEAVES BY CHOPPING AND BLOWING METHOD / 苜蓿切断-气吹茎叶分离方法初步研究</p> <p>Bojun CAO¹⁾, Tianlin ZUO¹⁾, Bei WU^{1,2)}, Tianci HUANG¹⁾, Huaiyuan QIAN¹⁾ ¹⁾ Hunan Agricultural University, College of Mechanical and Electrical Engineering, Changsha/China; ²⁾ Hunan Key Laboratory of Intelligent Agricultural Machinery and Equipment, Changsha/China</p> | 624 |
| 54. | <p>RESEARCH ON SIMULTANEOUS LOCALIZATION AND MAPPING METHOD FOR ORCHARDS BASED ON SCAN CONTEXT AND NDT-ICP FUSION SCHEME / 基于扫描上下文和 NDT-ICP 融合方案的果园同步定位与绘图方法研究</p> <p>Zhen QIN¹⁾, Hongxia WANG¹⁾, Pengcheng LV²⁾ * ¹⁾ School of Information and Control Engineering of Qingdao University of Technology, Qingdao, China ²⁾ Shandong University of Technology, College of Agricultural Engineering and Food Science, Zibo, China</p> | 636 |
| 55. | <p>AGRICULTURAL PLANT PROTECTION UNMANNED AERIAL VEHICLE SPRAY PATH PLANNING BASED ON ANT COLONY ALGORITHM / 基于蚁群算法的农业植保无人机作物喷洒路径规划</p> <p>Mingda HE¹⁾, Xinyan YANG²⁾ ¹⁾ Chengdu Sport University, Chengdu, Sichuan, 610000, China; ²⁾ Chengdu Normal University, Chengdu, 611130, China</p> | 647 |
| 56. | <p>APPLYING MACHINE LEARNING FOR ENVIRONMENTAL FACTOR PREDICTION ON DESIGNING IOT APPLIED HYDROPONIC SYSTEM / ỨNG DỤNG PHƯƠNG PHÁP HỌC MÁY ĐỂ DỰ ĐOÁN CÁC YẾU TỐ MÔI TRƯỜNG TRONG THIẾT KẾ HỆ THỐNG THỦY CANH IOT</p> <p>Van-Tinh NGUYEN*, Tan-Hoang NGUYEN, Ngoc-Kien NGUYEN School of Mechanical Engineering, Hanoi University of Science and Technology, Hanoi, Vietnam</p> | 658 |
| 57. | <p>DESIGN AND OPTIMIZATION OF A VACUUM SYSTEM FOR A LARGE STORAGE TANK CLEANING ROBOT / 大型贮罐清理机器人吸尘系统的设计与研究</p> <p>Yong TIAN¹⁾, Zhengtao WANG²⁾, Jian SONG¹⁾, Fuxiang XIE¹⁾, Hongwei WANG¹⁾ ¹⁾ School of Machinery and Automation, Weifang University, Shandong/ China; ²⁾ WindSun Science & Technology Co., Ltd., Shandong / China</p> | 668 |
| 58. | <p>EXPERIMENTAL RESEARCH ON THE EXTRACTION OF POLYPHENOLS FROM NETTLE, LAVENDER AND SAGE USING THE PERCOLATION METHOD / CERCETĂRI EXPERIMENTALE PENTRU EXTRAȚIA POLIFENOLILOR DIN URZICĂ, LAVANDĂ ȘI SALVIE PRIN METODA PERCOLĂRII</p> <p>Ana-Maria TĂBĂRAȘU^{1,2)}, Iuliana GĂGEANU¹⁾, Nicolae-Valentin VLĂDUȚ¹⁾, Mihai-Gabriel MATAACHE¹⁾, Dragoș-Nicolae ANGHELACHE¹⁾ ¹⁾INMA Bucharest / Romania; ²⁾POLITEHNICA University / Romania</p> | 678 |
| 59. | <p>RESEARCH ON AGRICULTURAL LOGISTICS DISTRIBUTION PATH PLANNING CONSIDERING UAV ENDURANCE MILEAGE LIMIT / 考虑无人机续航里程限制的农业物流配送路径规划研究</p> <p>Yebiao XU * School of Economics and Management, Wuhan Railway Vocational College of Technology, Wuhan / China</p> | 688 |

| | | Page(s) |
|-----|---|---------|
| 60. | <p>DESIGN AND EXPERIMENT OF DOUBLE-ROW WHEEL SELF-PROPELLED CHINESE CABBAGE HARVESTER / 双行轮式自走型大白菜收获机设计与试验</p> <p>Wenyu TONG¹⁾, Yanwei YUAN¹⁾, Shenghe BAI^{1,2)}, Kang NIU¹⁾, Chengxu LV¹⁾, Liming ZHOU¹⁾</p> <p>¹⁾ Chinese Academy of Agricultural Mechanization Sciences Group Co., Ltd, National Key Laboratory of Agricultural Equipment Technology, Beijing 100083, China; ²⁾ China Agricultural University, Beijing 100083, China.</p> | 702 |
| 61. | <p>SEED DISCHARGE PERFORMANCE TEST OF AIR SUCTION SEED DISCHARGER FOR SMALL VEGETABLE SEEDS / 面向小粒蔬菜种子的气吸排种器排种性能试验</p> <p>YanJun LI^{1,2)}, Yichao NING^{*2)}, Fuxiang XIE^{*1)}, Yang Bai¹⁾</p> <p>¹⁾School of Machinery and Automation, Weifang University, Weifang/China; ²⁾ State Key Laboratory of Agricultural Equipment Technology, Beijing/China</p> | 721 |
| 62. | <p>A REVIEW OF INTELLIGENT HEADER TECHNOLOGY FOR GRAIN COMBINE HARVESTER/ 谷物联合收获机智能化割台技术研究综述</p> <p>Jin WANG^{1,2)}, Fuqiang GOU^{1,2)}, Zhenjie QIAN¹⁾, Youliang NI¹⁾, Chengqian JIN^{*1,3)}</p> <p>¹⁾Nanjing Institute of Agricultural Mechanization, Ministry of Agriculture and Rural Affairs, Jiangsu / China ²⁾ Graduate School of Chinese Academy of Agricultural Sciences, Beijing / China ³⁾ School of Agricultural Engineering and Food Science, Shandong University of Technology, Shandong / China</p> | 731 |
| 63. | <p>A REVIEW OF APPLICATION OF WATER JET TECHNOLOGY IN AGRICULTURE / 水射流技术在农业领域的应用研究现状</p> <p>Lixue ZHU¹⁾, Wenxuan LUO¹⁾, Hongnan HU^{*1)}, Shiang ZHANG¹⁾, Yifan SHI¹⁾, Shinian HUANG</p> <p>¹⁾College of Mechanical and Electrical Engineering, Zhongkai Univ.of Agriculture and Engineering, Guangzhou, China</p> | 745 |
| 64. | <p>DESIGN AND TESTING OF PEANUT SIEVING PROTOTYPE MACHINE / 花生清选筛台架的设计与试验</p> <p>Dongjie LI¹⁾, Jialin HOU^{*1)}, Dongwei WANG^{2,3)}, Zengcun CHANG¹⁾</p> <p>¹⁾ Shandong Agricultural University, College of Mechanical and Electrical Engineering/ China ²⁾ Yellow River Delta Intelligent Agricultural Equipment Industry Academy, Shandong / China; ³⁾ Qingdao Agricultural University, College of Mechanical and Electrical Engineering / China</p> | 760 |
| 65. | <p>ENGINEERING PROPERTIES OF COMMON BEAN (PHASEOLUS VULGARIS L.) IN PERSPECTIVE OF PHYSICAL AND FRICTIONAL PARAMETERS FOR THRESHING MACHINE DESIGN / የቦሎ (Phaseolus vulgaris L.) የምህንድስና ባህሪያት ለመውቁያ ማሽን ዲዛይን በአካላዊ እና ፍራክሽናል መለኪያዎች አገናኛ</p> <p>Biniam ZEWDIE¹⁾, Adesoji M. OLANIYAN²⁾, Amana WAKO¹⁾, Dereje ALEMU³⁾, Tamrat LEMA³⁾</p> <p>¹⁾ School of Mechanical, Chemical, & Materials Engineering, Departments of Agricultural Machinery Engineering, Adama Science and Technology University, P.O. Box 1888, Adama, Ethiopia. ²⁾ Department of Agricultural and Bioresources Engineering, Faculty of Engineering, Federal University Oye-Ekiti, Ikole-Ekiti Campus, Post Code 370001, Ikole-Ekiti, Nigeria. ³⁾ Ethiopian Institute of Agricultural Research; Agricultural Engineering Research, Melkassa Agricultural Research Center, P.O.Box 436, Adama, Ethiopia</p> | 771 |
| 66. | <p>ANALYSIS ON PATH OPTIMIZATION OF AGRICULTURAL WAREHOUSE LOGISTICS HANDLING ROBOT BASED ON POTENTIAL FIELD ANT COLONY ALGORITHM / 基于势场蚁群算法的农业仓库物流搬运机器人路径优化研究</p> <p>Yunyun WANG¹⁾, Mingzhe XIE^{*2)}</p> <p>¹⁾ School of Management, Wuhan University of Technology, Wuhan, Hubei/ China ²⁾ School of Economics and Management, Ningbo University of Technology, Ningbo, Zhejiang/ China</p> | 784 |
| 67. | <p>DETECTION OF PESTICIDE RESIDUES IN WHITE TEA FRESH LEAVES BASED ON HYPERSPECTRAL AND ARTIFICIAL INTELLIGENCE MODELS / 基于高光谱和人工智能模型的白茶鲜叶农药残留检测</p> <p>Weiqiang PI¹⁾, Rongyang WANG^{*1)}, Jingrui CHENG¹⁾, Qinliang SUN¹⁾, Guanyu LIU¹⁾, Yong WANG¹⁾</p> <p>¹⁾ Huzhou Vocational and Technical College, College of Intelligent Manufacturing and Elevator, Huzhou / China</p> | 796 |
| 68. | <p>DESIGN AND EXPERIMENT OF AUTOMATIC FILM AND TAPE CUTTING SYSTEM FOR COTTON PRECISION FILM-LAYING HOLE SEEDER / 棉花精量铺膜穴播机自动断膜带系统设计与试验</p> <p>Shenghe BAI^{1,2)}, Yanwei YUAN^{1,2)}, Liang WEI²⁾, Gaoyong XING^{1,2)}, Liming ZHOU²⁾, Kang NIU²⁾, Bo ZHAO²⁾, Shuhui LI³⁾, Yuqi WANG²⁾, Wenyu TONG²⁾, Shuaiyang ZHANG²⁾, Lijing LIU^{1,2)}, Xuejun ZHANG⁴⁾, Yongliang YU⁵⁾</p> <p>¹⁾ China Agricultural University, Beijing, China; ²⁾ Chinese Academy of Agricultural Mechanization Sciences Group Co., Ltd, National Key Laboratory of Agricultural Equipment Technology, Beijing, China ³⁾ Gongzhuling City eight Wu town agricultural machinery technology extension service section, Ji Lin, China ⁴⁾ College of Mechanical and Electrical Engineering, Xinjiang Agricultural University, Urumqi, China ⁵⁾ Xinjiang Tiancheng Agricultural Machinery Manufacturing Co., Ltd., Tiemenguan, China</p> | 807 |

| | | Page(s) |
|-----|--|---------|
| 69. | <p>CALIBRATION AND TESTING OF SALINE SOIL PARAMETERS BASED ON EDEM DISCRETE ELEMENT METHODOLOGY / 基于 EDEM 离散元方法的盐碱土壤参数标定与测试 Xiaoning HE¹⁾, Shikuan MA¹⁾, Zhixin LIU¹⁾, Dongwei WANG¹⁾, Shuqi SHANG^{*1)}, Guanghui LI²⁾, Hongxiu LI²⁾ ¹⁾ College of Electrical and Mechanical Engineering, Qingdao Agricultural University, Qingdao/ China ²⁾ Shandong Saline Modern Agriculture Co., Ltd, Dongying / China</p> | 822 |
| 70. | <p>EXPERIMENTAL STUDY ON THE CLEANING PERFORMANCE OF BIONIC SCREEN BASED ON EARTHWORM MOTION CHARACTERISTICS / 基于蚯蚓运动特征的仿生筛清选性能试验研究 Yongtao YU, Yanjun LI, Fuxiang XIE*, Jian SONG College of Machinery and Automation, Weifang University, Weifang, China</p> | 834 |
| 71. | <p>CALIBRATION AND EXPERIMENTATION OF DISCRETE META-SIMULATION PARAMETERS OF ASTRAGALUS MEMBRANACEUS / 黄芪离散元仿真参数的标定与试验 Xiangyu GAO^{1,2)}, Xuejie MA¹⁾, Xiangdong LIN^{*1)}, Qianqian SUN^{*1)}, Zhanfeng HOU^{*1,3)}, Xiaoming ZHANG^{*4)} ¹⁾ College of Mechanical and Electrical Engineering, Inner Mongolia Agricultural University, Inner Mongolia, Hohhot / China; ²⁾ Inner Mongolia First Machinery Group Corporation, Baotou / China; ³⁾ Inner Mongolia Engineering Research Center of Intelligent equipment for the entire process of forage and feed production, Inner Mongolia, Hohhot / China ⁴⁾ Hohhot Agriculture and Animal Husbandry Technology Promotion Center, Hohhot, Inner Mongolia / China</p> | 845 |
| 72. | <p>OPTIMIZATION OF JOINT SAND BARRIER SPACING AND CHARACTERIZATION OF WIND AND SAND FLOW STUDY BASED ON CFD NUMERICAL SIMULATION / 基于 CFD 数值模拟的联合沙障间距优化与风沙流特征研究 Ming YAN¹⁾, Afang JIN^{*1)}, Wenxiu GAO¹⁾ ¹⁾ College of Mechanical Engineering, Xinjiang University, Urumqi 830046 / China</p> | 855 |
| 73. | <p>RESEARCH REGARDING AGRICULTURAL BIONIC BLADE DEVELOPMENT BASED ON THE MECHANISM OF THE CUTTING-SAWING MOTION OF THE CAMPONOTUS MANDIBLE / 基于弓背蚁上颚切-锯运动机理的农业仿生刀开发研究 Zhu ZHAO^{1,2)}, Dongli SHUI¹⁾, Fengbo LIU¹⁾, Bintong ZHAO³⁾, Zhongnan WANG^{*1)} ¹⁾ Liaoning Agricultural Technical College, Yingkou / China; ²⁾ Tacheng Vocational and Technical College, Tacheng / China; ³⁾ College of Engineering, Shenyang Agricultural University, Shenyang / China</p> | 870 |

STUDY THE THERMAL PERFORMANCE OF DRYING TOMATOES PROCESS USING A SOLAR ENERGY SYSTEM

دراسة التأثير الحراري لعملية تجفيف الطماطم باستخدام نظام الطاقة الشمسية

Ahmed M. EL-SHEIKHA¹⁾, Mohamed R. DARWESH^{2,3)}, Rashad HEGAZY⁴⁾,
Mahmoud OKASHA⁵⁾, Nada H. MOHAMED¹⁾

¹⁾Agricultural Engineering Dept., Faculty of Agriculture, Damietta University, Egypt

²⁾Agricultural Engineering Dept., Faculty of Agriculture, Tanta University, Egypt

³⁾Food Industry Technology Dept., Faculty of Technology of Industry and Energy, Samannoud Technological University, Egypt

⁴⁾Agricultural Engineering Department, Faculty of Agriculture, Kafrelsheikh University, Kafrelsheikh 33516, Egypt

⁵⁾Agricultural Engineering Research Institute (AENRI), Agricultural Research Center (ARC), Giza 12611/ Egypt

Tel: +20-1003133841; E-mail: mahmoudokasha1988@yahoo.com

Corresponding author: Mahmoud Okasha

DOI: <https://doi.org/10.35633/inmateh-73-01>

Keywords: Dryer; Solar energy; Tomato; Greenhouse

ABSTRACT

This study developed a hybrid solar greenhouse dryer (lean-to) incorporated with a solar collector and photovoltaic (PV) system for smallholder processors of tomatoes and evaluated the thermal performance of forced convection mixed-mode solar dryer with two pretreatments of fresh tomatoes (halves and slices) with salt and sugar. Tomatoes dipped in a 40% sucrose solution for 72 hours before drying exhibited a greater initial drying rate than those treated with salt. The hourly average incident solar radiation without a reflector was 673.8 (± 14.2) W/m² outside and 754.6 (± 284.5) W/m² inside the lean-to solar dehydrator during operation. The incident solar radiation in the collector ranged from 390.3 to 1156.0 W/m², indicating higher levels at the tilt angle. The hourly average air temperatures outside and inside the solar dehydrator and solar collector during the experiment, respectively, were 30.7 (± 2.3), 52.7 (± 10.1), and 30.7 (± 2.3), 79.7 (± 26.9) °C for the salt treatment and 31.0 (± 2.0), 55.1 (± 15.3), and 31.0 (± 2.0), 84.8 (± 28.0) °C for the sugar treatment. Thus, the solar dehydrator and the solar collector raised the dehydrating air temperatures over the outside for the salt and sugar treatment by an average of 22.0, 49.0, 24.1, and 53.8 °C, respectively. The average hourly air-relative humidity inside the solar dehydrator was 33.5%, while outside was 47.2%. The pretreated tomatoes had an initial moisture content of 93.1% (w.b). The solar dehydrator's thermal efficiency was 72.21%, and its drying efficiency was 56.48%. Consequently, solar energy contributed 84.28 and 71.18% of the generated heating power. The solar dehydrator lost 15.72 and 28.82% of its remaining solar energy due to exhausted air. The solar dehydrator had a daily average energy of 59.375 kWh, and the heating power was 47.473 kWh during the experimental period (29 h).

المخلص

تهدف هذه الدراسة الى تطوير مجفف هجين يعمل بالطاقة الشمسية للبيوت الزجاجية مُدمج مع مجمع شمسي ونظام خلايا ضوئية لصغار مُصنعي الطماطم. كما تناولت الدراسة تقييم الأداء الحراري للمجفف الشمسي ذو الحمل الحراري الممزوج مع نوعين من المعالجة المسبقة للطماطم (أصناف وشرائح) باستخدام الملح والسكر. أظهرت الطماطم التي غُطست في محلول سكر بنسبة 40% لمدة 72 ساعة قبل التجفيف معدل تجفيف أولي أكبر من تلك التي تم معامتها بالملح. كان متوسط الإشعاع الشمسي الساقط في الساعة بدون العاكس 673.8 (± 14.2) واط/مترمربع في الخارج و754.6 (± 284.5) واط/مترمربع داخل مجفف التجفيف الشمسي أثناء التشغيل. تراوح الإشعاع الشمسي الساقط على المجمع الشمسي بين 390.3 و1156.0 واط/مترمربع، مما يدل على مستويات أعلى عند زاوية الميل. كانت متوسطات درجات حرارة الهواء خارج المجفف الشمسي وداخله ومجمع الطاقة الشمسية خلال التجربة على التوالي 30.7 (± 2.3)، 52.7 (± 10.1)، و30.7 (± 2.3)، 79.7 (± 26.9) درجة مئوية للمعالجة بالملح و31.0 (± 2.0)، 55.1 (± 15.3)، و31.0 (± 2.0)، 84.8 (± 28.0) درجة مئوية للمعالجة بالسكر. وبالتالي، رفع المجفف الشمسي والمجمع الشمسي درجة حرارة الهواء المجفف عن الخارج لكلا من المعاملة بالملح والسكر بمعدل 22.0، 49.0، 24.1، و53.8 درجة مئوية، وعلى التوالي. كان متوسط الرطوبة النسبية للهواء داخل المجفف الشمسي 33.5%، بينما كانت بالخارج 47.2%. وبلغت نسبة الرطوبة الأولية للطماطم المعالجة مسبقاً 93.1% (على أساس الوزن الرطب). وبلغت الكفاءة الحرارية للمجفف الشمسي 72.21%، وكانت كفاءة التجفيف 56.48%. وبالتالي، ساهمت الطاقة الشمسية بنسبة 84.28 و71.18% من طاقة التسخين المتولدة. وقد فقد المجفف الشمسي 15.72 و28.82% من طاقته الشمسية المتبقية بسبب الهواء الخارج. وبلغ متوسط الطاقة اليومية للمجفف الشمسي 59.375 كيلووات ساعة، بينما كانت قدرة التسخين 47.473 كيلووات ساعة خلال الفترة التجريبية (29 ساعة).

INTRODUCTION

Tomato (*Lycopersicon esculentum* Mill.) is a commonly cultivated vegetable worldwide, boasting a productivity of approximately 182,301,395 tons from an area of 4,848,384 ha. China, the USA, Turkey, India, and Egypt are leading global tomato producers.

Egypt produced 6,275,443 tons of tomatoes in 2022 (FAO, 2022). After harvest, the drying process is implemented by many local processors as an effective means to extend the shelf life of tomato crops (Li, 2021). Solar energy is a well-established and renewable source, especially for low-temperature heating. Solar drying is the most optimal solution to overcome artificial mechanical and natural sun drying drawbacks. Moreover, adopting solar energy for crop drying offers both environmental benefits and economic viability in developing countries. Providing energy for agricultural applications is contingent upon advancing solar energy systems with optimal thermal performance, exceptional reliability, and competitive economic features. This advancement must attain a stage where optimal thermal performance and reliability can be attained for a wide range of solar energy applications. For solar energy to be economically viable, solar energy systems must exhibit high annual utilization, extended lifespan, and meticulous design tailored to the specific application and location, thus enabling a realistic evaluation of solar energy as a feasible alternative energy source. Consequently, solar energy is a viable heat source for drying various crops. Because of the uncertain rise in fossil fuel prices and the potential depletion, it has received significant attention in recent years (Abdellatif et al., 2015; Ramos et al., 2015). Fruits and vegetables, including potato slices, red peppers, cherry tomatoes, banana slices, and tomatoes, have been subjected to solar drying techniques. There have been few studies conducted on the solar drying of cherry tomatoes. Several studies were conducted to investigate the thermal and mass transfer balance in hybrid solar dryers and the effectiveness of solar greenhouse dryers (Azam et al., 2020). Patil and Gawande (2016) reviewed various techniques employed in greenhouse dryers and solar tunnels, focusing on forced and natural convection methods. Using tunnels and greenhouses for solar drying proves to be highly suitable for rural areas. Using these dryers leads to substantial fuel savings and enhances the product's quality regarding color, taste, and aroma. The enhancement of dried agricultural products' quality is of utmost importance, and this can be accomplished by implementing pretreatment methods that ensure product preservation and enhance their visual appeal. Osmosis is a convenient and effective method for pretreating fruit before drying. Immersing products in the solution reduces costs by removing water. Osmosis pretreatment might enhance the drying rate of cashew apples by impacting both their quality and drying kinetics compared to fruits that have not undergone pretreatment (Shahi et al., 2016). The dryer and collector had average energy efficiencies of 50.5%, and 34.98%, respectively. Tiwari and Tiwari (2016) studied the exergoeconomic of PV-thermal mixed-mode greenhouse solar dryer. Lakshmi et al. (2019) investigated stevia leaf drying in a mixed-mode forced convection solar dryer. The dryer's overall efficiency was approximately 33.5%. The dryer's payback duration is approximately 0.65 years. A hybrid solar drying system, including a greenhouse dryer, a flat plate solar collector (FPSC), and a PV system, was investigated in some literature using forced thermal convection drying mode.

Thus, this study involves developing a solar greenhouse dryer for post-harvest tomato drying and evaluating the thermal performance of hybrid forced convection mixed-mode greenhouse dryers, integrating tomato load, solar air collectors, and PV system operation.

MATERIALS AND METHODS

The trials were performed at the Faculty of Agriculture, University of Damietta (31°39'07.05" E, longitude; 31°25'38.24" N, latitude) from August 20th, 2022, to August 26th, 2022.

Description of the solar dehydrator (lean-to)

It comprises space heating for pre-heating the drying air, a drying chamber, and a reflector for increasing the solar radiation intensity. The structural frame comprises 12.7 mm diameter hot-dipped galvanized pipes with anti-corrosion qualities. The structural frame consists of beams, posts, and rafters that can be assembled on the spot by joining parts, bolts, and nuts with no welding points to secure optimal anti-corrosion performance. It was 2.0 m long, 1.0 m wide, 0.96 m high vertical back wall (reflector), 40 cm high vertical front wall, 1.15 m rafter length. The rafter tilt angle is 17.97° for August. The net dehydration surface area is 2.0 m², and the net air volume is 1.36 m³. The drying tray is a 2.0 m long and 1.0 m wide galvanized wire mesh with a 2.0 m² surface area. Below the drying tray lies an air chamber comprising two layers of a 2.0 mm thick firm galvanized sheet. These layers are separated by a 2.5 cm space and filled with loosely packed rock-wool insulation to lessen heat energy gain or loss. It was 2.0 m long, 1.0 m wide, 40 cm deep, 2.0 m² surface area, and 0.8 m³ space volume. To circulate the dehydrated air through the solar dehydrator, an electric forced air fan with a power of 38 W, a speed of 2000 rpm, and operating at a current of 220 V is positioned at the center of the eastern side (lateral section) of an air chamber. This fan is connected to an air duct with a diameter of 12 cm. On the opposite side, the solar dehydrator's gable incorporates a circular opening with a 12 cm diameter (inlet for drying air) at its center.

This configuration ensures that air enters the upper section's solar dehydrators and descends through the drying tomatoes before being expelled from the dehydrator. The solar dehydrator is located 10 cm above the floor level using four metallic legs over a cubic concrete block (20×20 cm), as shown in Fig. 1.

The dehydration chamber's upper surface was covered by a perforated galvanized steel sheet, and the other sides were covered with solid galvanized steel sheets. The solar dehydrator is equipped with a transparent polycarbonate sheet that is 2.0 mm thick, providing UV protection and allowing for high radiation transmission to optimize the dehydrator's solar radiation. A 2.0 mm thick sheet of nickel chrome was applied to the vertical back wall as a solar reflector. The solar dehydrator was in an East-West orientation.

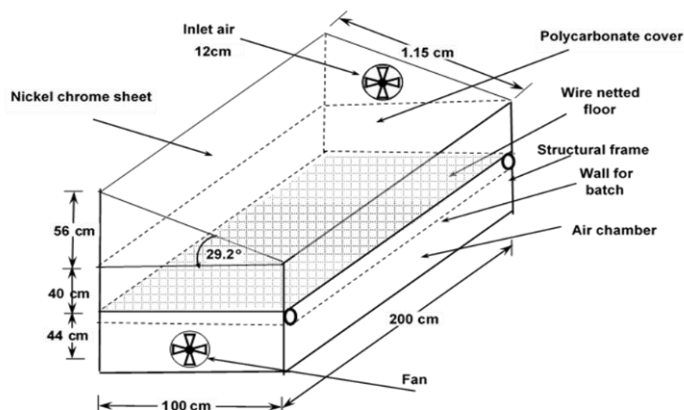


Fig. 1 – Simplified scheme and picture of solar dehydrator (lean-to architectural form)

Flat plate air solar collector

It comprises space heating for pre-heating the air, a wooden box, and an absorber plate for increasing the intensity of solar radiation. It was inclined with 30° and supplied the lean-to solar dryer with auxiliary heat. The structural frame was made from wood with a 2.0 m^2 surface area (2.0 m long, 1.0 m wide), 0.15 m depth, and 0.3 m^3 space volume. It had 2.5 cm rock-wool insulation to lessen heat gain or loss. It has a black-painted aluminum corrugated sheet of 0.002 m thick, and the thermal conductivity coefficient was $204 \text{ W/m}\cdot^\circ\text{C}$, which was utilized to absorb thermal solar radiation and used it to heat the air, which moves up toward the solar dryer. A 0.10 m fiberglass insulation layer was installed to insulate the absorber plate from the backside to minimize heat energy gain or loss. The upper surface of the solar collector was protected by a polycarbonate sheet measuring 0.002 m , maintaining a gap of approximately 0.10 m between the absorber sheet and polycarbonate to facilitate airflow. The upward movement of hot air from the collector toward the lean-to solar dryer occurs through an insulated tube measuring 0.15 m in diameter, as depicted in Fig. 2.

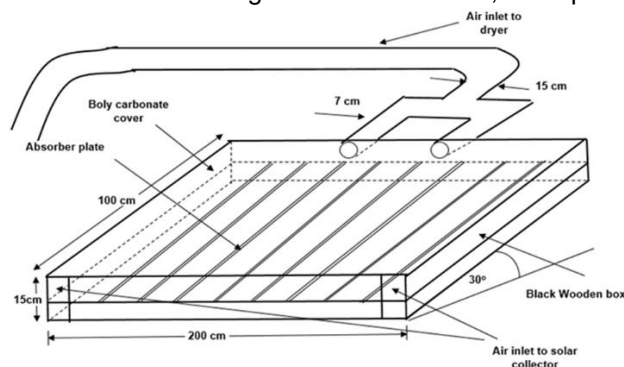


Fig. 2 – Simplified scheme of flat plate air solar collector (architectural form)

Solar photovoltaic cell (PV) panels

The PV system included a 385 W ASEM PV panel, a charge controller with $12 \text{ V}/24 \text{ V}$ capabilities and load current up to 20 A , and a 12 V battery with a rated current of 17 A h . Inverter (Yumatsu JAPAN 220V $50\text{Hz}/60\text{Hz}$ Power capacity: 2000VA). This was used to convert the current to DC, which comes from the PV panel and is integrated into the battery. The PV panel's inclination was set to 30° in a southerly direction. The PV system was used to power a DC fan, which helped optimize the drying process, as revealed in Fig. 3.



Fig. 3 – Tomatoes spread under natural sun drying

Experimental parameters of PV-solar collector incorporated with greenhouse dryer

An evaluation was performed to measure the performance of the greenhouse dryer when used outdoors, specifically for drying tomatoes. The initial trials were performed at varying airflow rates of 2.10, 3.12, and 4.18 m³/min, utilizing the DC speed controller to regulate the DC fan's flow rate. The optimal airflow rate of 3.12 m³/min was elected for drying tomatoes. Fresh tomatoes were purchased from the local market in 2022. Before the drying process, the selected fresh tomatoes were subjected to a cleaning and pre-conditioning procedure, which involved the removal of foreign impurities and immaturity. As a result, a homogeneous size of tomatoes unaffected by bacteria and fungi was chosen for the experimental investigation. These tomatoes were carefully graded by hand, with a preference for smaller sizes (0.020-0.035 m diameter). After washing, the tomatoes were divided into two groups of equal weight (7.0 kg each). Fresh tomatoes were halved and sliced, then osmotically treated with sugar. They were compared to halved and sliced tomatoes, treated with salt, and dried in the greenhouse dryer. The fruits treated osmotically with sugar are cut into halves and slices and dipped in a 40% sucrose solution for 72 h (10.5-liter water/ 2.8 kg sugar/ 7kg of tomatoes). The samples were stored at 5°C before beginning the experiments and then allowed to reach room temperature.

Measurements

The ambient weather and various parameters of the greenhouse dryer (GD) were measured using instruments, including a meteorological weather station (Vantage Pro 2, DeVise, USA). This allowed for accurately evaluating the macroclimatic conditions surrounding the developed drying system. These measurements comprise various weather factors, including solar radiation intensity on a horizontal plane, dry-bulb air temperature, air relative humidity, and wind speed. The weather station is beside the solar dehydrator (about five meters away). The collected data were stored in a computer file for data acquisition. The speed of dehydrated air was measured thrice daily at the drying air inlet and outlet locations throughout the experimental duration. This was conducted using a vane LCD Digital Anemometer (Montreal, Canada). Solar radiation intensity was measured using disk-solarimeters (TENMARS TM-207, Taiwan). They were placed horizontally with the dryer and were inclined toward the PV module and the solar collector. Temperature and relative humidity were measured by a weather anemometer sensor (Pasport, 1000 series, USA). Measurements of the relative humidity in the ambient air and inside the dryer were conducted using the Amprobe THWD-5. The dryer's airflow rate and wind speed were measured using an airflow meter/Hotwire anemometer. The moisture content of tomatoes was determined using an electric oven dryer set at a temperature of 70 ± 1°C (ASAE 1991). The initial, final, and instantaneous moisture contents were calculated based on dry basis according to Mumba (1996), as follows in Eqs. 1–3:

$$M_0 = \frac{W_0 - W_d}{W_d} \quad (1)$$

$$M_f = \frac{W_{wet} - W_d}{W_d} \quad (2)$$

$$M_t = \left[\frac{(M_0 + 1)W_0}{W_t} - 1 \right] = \frac{(W_t - W_d)}{W_d} \quad (3)$$

where:

M_0 denotes the initial moisture content [%], W_0 represents the initial weight of sample [kg], W_d represents the weight of dry matter [kg], M_f implies the final moisture content [%], M_t implies the instantaneous moisture content [%], and W_t represents the weight of sample at time (t) [kg].

Thermal energy balance analysis

An energy analysis of tomato drying with a PV solar collector integrated with a lean-to solar dryer is presented in this study. The steady-state energy equations are used to optimize tomato drying conditions (Hepbasli, 2008).

The net energy balance between the inlet and outlet can be represented by Eq. 4:

$$\sum E_{in} = \sum E_{out} \quad (4)$$

where E_{in} denotes the net energy input, [W], E_{out} represents the net energy outlet, [W].

Solar collector's thermal balance

The solar collector's thermal balance was determined as follows in Eqs. 5–7:

$$E_{in,coll} = E_{out,coll} \quad (5)$$

$$E_{in,coll} = (E_{out,coll} + E_{heat\ transferred} + E_{infiltration}) \quad (6)$$

$$E_{u,coll} = E_{in,coll} - (E_{heat\ transferred} + E_{infiltration}) \quad (7)$$

The energy input and heat gain of the solar collector are computed by Duffie and Beckman (2013); Usub et al. (2008), as follows in Eqs. 8–10:

$$E_{in,coll} = E_{solar,coll} = A_{coll} \int_0^t I_{coll} \quad (8)$$

$$E_{u,coll} = m_a \times C_{p,a} (T_{a,in} - T_{a,out}) \quad (9)$$

$$m_a = \rho_a \times V_a = \rho_a \times u_a \times A_{coll} \quad (10)$$

where m_a denotes the air mass flow rate, [kg/s]; A_{coll} represents the collector area [m²], u_a implies air speed, [m/s]; and ρ_a stands for the air density, [kg/m³].

Hence, collector efficiency (η_{coll}) is calculated as follows in Eqs. 11–13:

$$\eta_{coll} = \frac{E_{u,coll}}{E_{in,coll}} \quad (11)$$

$$E_{loss} = E_{heat\ transfer} + E_{infiltration} \quad (12)$$

$$E_{heat\ transfer} = E_{wall} + E_{ground} + E_{loss,tube} \quad (13)$$

Heat losses from solar collector surfaces can be determined according to Sahin and Sumnu (2005), as follows in Eqs. 14 and 15:

$$E_{heat\ transfer(surfaces)} = U_{coll,surf} \times A_{coll,surf} \times dT \quad (14)$$

$$U_{coll,surf} = \frac{1}{\left(\frac{1}{h_{conv,abs-g}} + \frac{x_1}{h_{rad,abs-g}} + \frac{1}{h_{rad,g-amb}} + \frac{x_1}{h_{conv,g-amb}} \right)} \quad (15)$$

Where:

$U_{coll,surf}$ denotes the overall heat transfer coefficient for the solar collector surfaces [W/m².K],

$A_{coll,surf}$ denotes the solar collector's area [m²], and dT refers to the temperature difference [K].

Heat losses from collector walls and ground to air

The convective and conductive resistances of the overall heat transfer coefficient were determined as follows in Eq. 16:

$$U_{coll,wg} = \frac{1}{\left(\frac{1}{h_i} + \frac{x_1}{k_1} + \frac{x_2}{k_2} + \frac{x_3}{k_3} + \frac{1}{h_o} \right)} \quad (16)$$

where h_i and h_o represent the heat transfer coefficients for internal and external surfaces [W/m².K], respectively, x_i is the layer's thickness [m], k_i is the layer's thermal conductivity [W/m.K].

The solar collector's walls and ground heat losses can be determined using Eq. 17:

$$E_{heat\ transfer(wall,ground)} = U_{coll,wg} \times A_{coll,wg} \times dT \quad (17)$$

where $U_{coll,wg}$ refers to the overall heat transfer coefficient [W/m².K], $A_{coll,wg}$ stands for the solar collector's area of walls and ground [m²], and dT denotes the temperature difference [K].

Heat transfer by convection from the collector

The convective heat transfer coefficient caused by wind is calculated based on *Duffie and Beckmen (2013)*, as follows in Eq. 18:

$$h_{g-amb, coll} = 2.8 + (3.0 \times W_s) \quad (18)$$

The convective heat transfer coefficient for air over the absorber surface can be calculated by determining the Reynolds Number (Re) and Nusselt number (Nu) *Bergman et al. (2011)*, as follows in Eqs. 19–21:

$$Re = \frac{u_{a, coll} \times \rho_a \times D_{h, coll}}{\nu_a} \quad (19)$$

$$Nu = \frac{h_{conv, abs-a} \times D_h}{k_a} = 0.0158 Re^{0.8} \quad (20)$$

$$h_{conv, abs-a} = \frac{k_a \times Nu}{D_{h, coll}} \left(\frac{W}{m^2 \times ^\circ C} \right) \quad (21)$$

where $D_{h, coll}$ stands for the air passes hydraulic width (m), and is determined according to *Cengel et al. (2003)*, as follows in Eq. 22:

$$D_{h, coll} = \frac{4(D \times H)}{2(D + H)} \quad (22)$$

where D_{coll} and H_{coll} represent the actual width and height of the air passes [1 m and 0.08 m, respectively], D_h is the air pass width [m], ν is the air viscosity [m^2/s], T_{abs} is the absorber temperature [$65^\circ C = 338K$], and T_{amb} is the surrounding temperature [$31^\circ C = 304K$]. Thus, $h_{conv, abs-a} = 1.746 \text{ W/m}^2.K$; and heat loss below the absorber is obtained as shown in Eq. 23:

$$E_{conv, (abs-a)} = A_{abs} \times h_{conv, abs-a} \times (T_{abs} - T_{amb}) \quad (23)$$

where A_{abs} represents the contact area between the absorber and the air within the collector [m^2].

Collector's radiation heat transfer ($E_{rad, coll}$)

The radiation heat transfer coefficients can be determined by employing Eqs. 24 and 25 given by *Duffie and Beckmen (2013)* for the interactions between the sky and the collector glass cover and between the absorber and collector glass cover.

$$h_{rad, g-s} = \varepsilon_g \times \sigma \times (T_g^2 + T_s^2) \times (T_g + T_s) \quad (24)$$

$$h_{rad, abs-g} = \frac{\sigma \times (T_{abs}^2 + T_g^2) \times (T_{abs} + T_g)}{\frac{1}{\varepsilon_{abs}} + \frac{1}{\varepsilon_g} - 1} \quad (25)$$

where ε_{abs} represent the emissivity of the absorber surface [assumed 0.98], ε_g represents the emissivity of the glass surface [assumed 0.92], and σ represents the Stefan-Boltzmann constant [$5.67 \times 10^8 \text{ W/m}^2.K^4$]. The sky temperature (T_s) is calculated according to *Duffie and Beckmen (2013)*, as in Eq. 26.

$$T_s = 0.0552 \times (T_{amb})^{1.5} \quad (26)$$

where T_s and T_{amb} are expressed in Kelvin. The losses caused by radiation and convection from the insulation layer surrounding the sides and bottom of the solar collector were determined using Eq. 17.

Tube heat losses between the collector and greenhouse dryer

The connection tube, which links the collector and greenhouse dryer, was constructed using tin and insulated with fiberglass. Therefore, the total heat transfer coefficient for the tube (U_{tube}) is determined in Eq.27:

$$U_{tube} = \frac{1}{\left(\frac{1}{r_i h_i} + \frac{x_1}{k_1} + \frac{x_2}{k_2} + \frac{1}{r_o h_o} \right)} \quad (27)$$

where r_i and r_o represent the inner and outer layer radius, [m], in order. The heat losses from the connection tube ($E_{loss, tube}$) are expressed as follows in Eq. 28:

$$E_{loss, tube} = 2\pi L \times \frac{(T_i - T_o)}{\left(\frac{1}{r_i h_i} + \frac{\ln\left(\frac{r_2}{r_1}\right)}{k} + \frac{1}{r_o h_o} \right)} \quad (28)$$

where $h_o = h_d$ stands for the conductive heat-transfer coefficient across the insulation, [$\text{W}/\text{m}^2\cdot^\circ\text{C}$] and is determined as follows in Eq. 29:

$$h_d = \frac{K_{gf}}{d_i} \quad (29)$$

where K_{gf} stands for thermal conductivity for fiberglass 0.043 [$\text{W}/\text{m}\cdot^\circ\text{C}$], and d_i denotes the average insulation thickness [0.05 m].

Greenhouse dryer's thermal balance

In order to estimate the thermal performance of the tomato dryer, the GD underwent experiments in which the heat balance and theoretical analysis were applied according to Dewanto *et al.* (2002); Lewicki (1998), as follows in Eq. 30:

$$E_{in,dryer} = (E_{net,coll} + E_{sol,dryer}) \quad (30)$$

$$E_{out,dryer} = (E_{evap} + E_{loss})$$

$$E_{net,dryer} = E_{sol,dryer} + E_{net,coll} - (E_{evap} + E_{loss})$$

Heat gain to the greenhouse dryer

Solar energy in the greenhouse dryer can be determined by considering the solar radiation and surface area, as follows in Eq. 31:

$$E_{sol,dryer} = I_{dryer} \times A_{dryer} \quad (31)$$

where I_{dryer} represents the horizontal insolation on the GD, [W/m^2], and A_{dryer} denotes the area of the GD, [m^2]. The collector transfers heat to the GD, resulting in a useful heat gain as expressed in Eq. 32:

$$E_{net,coll} = E_{u,coll} \times E_{loss,tube} \quad (32)$$

Heat evaporated from the greenhouse dryer

The overall thermal energy required for evaporation (E_{evap}) comprises two components: sensible heat (E_{sens}), which raises the temperature of tomatoes to the desired level, and latent heat energy (E_{latent}), which vaporizes water from tomatoes, as follows in Eq. 33:

$$E_{evap} = E_{sens} \times E_{latent} \quad (33)$$

The estimation of the sensible heat required to increase the temperature of tomato (E_{sens}) can be determined as follows in Eq. 34:

$$E_{sens} = m_t \times C_{p,t} \times \Delta T_t = \rho_t \times V_t \times C_{p,t} \times \Delta T_t \quad (34)$$

where m_t represents fresh tomatoes rate, [kg/s], $C_{p,t}$ stands for tomato's specific heat, [$4.08 \text{ kJ}/\text{kg}\cdot^\circ\text{C}$], ρ_t denotes tomato's density [$672.78 \text{ kg}/\text{m}^3$], $T_{t,in}$ refers to the tomato's inlet temperature to the dryer, [$^\circ\text{C}$], and $T_{t,out}$ denotes the tomato's outlet temperature from the dryer, [$^\circ\text{C}$].

The latent heat required for vaporizing water from tomatoes can be determined as follows in Eq. 35:

$$E_{latent} = mw \times \lambda_w \quad (35)$$

where mw represents the water removal rate from tomatoes, [kg/s], and λ_w denotes the latent heat of water vaporization, [$2300 \text{ kJ}/\text{kg}$].

Hence, the dryer efficiency (η_{dryer}) is determined as follows in Eq. 36:

$$\eta_{dryer} = \frac{E_{evap}}{E_{in,dryer}} \quad (36)$$

Heat losses from the greenhouse dryer via convection and radiation

By convection

The convection heat loss coefficient from the greenhouse dryer ($h_{conv,a,dryer}$) was determined using Eqs.19–22.

By radiation

The radiation heat transfer coefficient between the greenhouse covers and the sky and between the cover and the tomatoes was determined using Eqs. 24 and 25.

Thermal radiation losses can be attributed to the surfaces of the dryer cover and the dried product. The losses of radiant heat were minimal because of the low temperatures of the surface. The heat losses by radiation from the cover surface ($E_{rad,f}$) were calculated as follows in Eq. 37:

$$E_{rad,f} = A_f \times \varepsilon_f \times F_{c-d} \times \delta = [(T_{f,out})^4 - (T_{a,out})^4] \tag{37}$$

where ε_f refers to the surface emissivity [assumed 0.93 for the cover], and F_{c-d} denotes the dryer wall's cover surface (Bergman et al., 2011).

Fan's heat losses in the greenhouse dryer

In the forced convection greenhouse dryer system, the heat losses through the transparent cover are significantly lower than the direct heat loss through the exhaust vent (Mohsenin, 2020).

Thermal balance for PV panel

$$E_{net,pv} = E_{gain} - E_{loss} \tag{38}$$

$$E_{loss} = E_{operating} - E_{infiltration} \tag{39}$$

The photovoltaic efficiency (η_{PV}) and the solar system's overall efficiency ($\eta_{overall}$) were calculated according to Eltawil et al. (2018), as follows in Eqs. 40 and 41:

$$\eta_{PV} = \frac{E_{out,PV}}{E_{in,PV}} = \frac{V_{max,PV} \times I_{max,PV}}{Ins_{PV} \times A_{PV}} \times 100 \tag{40}$$

$$\eta_{overall} = \frac{E_{out,dryer}}{E_{in,coll} + E_{in,dryer} + E_{in,fan}} \times 100 \tag{41}$$

where: η_{PV} represents photovoltaic efficiency [%], $V_{max,PV}$ refers to the maximum PV voltage for power [V], $I_{max,PV}$ refers to the maximum PV current for power [A], Ins_{PV} denotes the insolation in the same plane of PV module [W/m^2], A_{PV} denotes the area of solar module [m^2], $\eta_{overall}$ implies the solar system's overall efficiency [%], $E_{out,dryer}$ implies the dryer output, $E_{in,coll}$ denotes the insolation input on the collector, $E_{in,dryer}$ represents the incident solar energy on the dryer, and $E_{in,fan}$ refers to the DC fan energy consumption.

RESULTS AND DISCUSSION

Intensity of incident solar radiation

The dehydration of tomatoes was performed utilizing the developed drying system that was incorporated with the flat plate air solar collector (FPASC) and operated using a solar PV system. The dehydration process of tomatoes included 72 hours of bright sunshine, with 25 hours for salt pretreatment and 29 hours for sugar pretreatment in the lean-to solar dehydrator. These measurements were recorded and utilized in the dehydration process. The experiment involved measuring and monitoring the intensity of solar radiation on horizontal ($I_{ho} = I_{dryer}$) and inclined ($I_{inclined} = I_{collector} = I_{PV}$) surfaces. The results are summarized and presented in Table 1.

Table 1

Hourly average incident solar radiation measured and recorded outside (R_o), inside the solar dehydrator (R_i) and inclined solar collector, PV panels during the experiment, and the maximum and minimum values

| Date | | $R_o, W/m^2$ | Lean-to | | | Solar collector = PV panels |
|------------|------|--------------|--------------------------|---------------------------|----------------------|-----------------------------|
| | | | R_i Reflected, W/m^2 | R_i Horizontal, W/m^2 | R_i Total, W/m^2 | R_i Inclined, W/m^2 |
| 20/08/2022 | Max. | 633.0 | 87.7 | 519.6 | 607.3 | 1120 |
| | Min. | 266.8 | 36.8 | 190.3 | 227.1 | 540.0 |
| | Mean | 455.6 | 58.0 | 355.2 | 413.2 | 897.8 |
| | SD | ±183.3 | ±26.5 | ±164.7 | ±190.2 | ±220.3 |
| 21/08/2022 | Max. | 928.3 | 213.2 | 882.4 | 1091.9 | 1131.0 |
| | Min. | 275.5 | 69.0 | 285.4 | 285.3 | 399.0 |
| | Mean | 596.0 | 155.4 | 528.6 | 684.0 | 878.6 |
| | SD | ±210.2 | ±56.1 | ±220.4 | ±257.2 | ±239.3 |
| 22/08/2022 | Max. | 932.5 | 242.0 | 885.5 | 1127.5 | 1186.0 |
| | Min. | 301.2 | 59.5 | 238.3 | 297.8 | 430.0 |
| | Mean | 702.3 | 178.5 | 625.2 | 803.7 | 839.1 |
| | SD | ±227.1 | ±64.7 | ±232.8 | ±295.1 | ±254.6 |
| Average | Max. | 831.3 | 180.9 | 762.5 | 942.2 | 1145.7 |
| | Min. | 281.2 | 55.1 | 238.0 | 270.0 | 456.3 |
| | Mean | 584.6 | 130.6 | 503.0 | 633.6 | 871.8 |
| | SD | ±196.8 | ±49.1 | ±206.0 | ±247.5 | ±238.1 |

| Date | | Ro, W/m ² | Lean-to | | | Solar collector = PV panels |
|------------|------|----------------------|--------------------------------|---------------------------------|----------------------------|-------------------------------|
| | | | Ri Reflected, W/m ² | Ri Horizontal, W/m ² | Ri Total, W/m ² | Ri Inclined, W/m ² |
| 23/08/2022 | Max. | 943.4 | 266.5 | 887.6 | 1154.1 | 1214.0 |
| | Min. | 441.3 | 59.4 | 248.3 | 307.7 | 353.0 |
| | Mean | 737.3 | 187.8 | 622.8 | 822.8 | 840.2 |
| | SD | ±170.4 | ±74.8 | ±217.7 | ±289.1 | ±275.7 |
| 24/08/2022 | Max. | 964.8 | 277.2 | 915.8 | 1193.0 | 1135.0 |
| | Min. | 309.0 | 66.5 | 256.7 | 323.2 | 320.0 |
| | Mean | 696.7 | 199.9 | 622.9 | 810.6 | 807.1 |
| | SD | ±209.1 | ±68.0 | ±214.8 | ±276.9 | ±290.8 |
| 25/08/2022 | Max. | 1033.3 | 182.0 | 1045.1 | 1227.1 | 1092 |
| | Min. | 329.3 | 91.0 | 225.0 | 316.0 | 341.0 |
| | Mean | 701.9 | 140.8 | 680.2 | 821.0 | 862.2 |
| | SD | ±244.2 | ±34.4 | ±282.0 | ±316.4 | ±236.7 |
| 26/08/2022 | Max. | 953.9 | 178.0 | 1011.6 | 1189.6 | 1224.0 |
| | Min. | 86.9 | 84.3 | 157.0 | 241.3 | 420.0 |
| | Mean | 707.9 | 134.6 | 642.2 | 776.8 | 864.6 |
| | SD | ±298.8 | ±25.5 | ±307.7 | ±333.3 | ±260.6 |
| Average | Max. | 973.9 | 225.9 | 965.0 | 1191.0 | 1166.3 |
| | Min. | 291.6 | 75.3 | 221.8 | 297.1 | 358.5 |
| | Mean | 711.0 | 165.8 | 642.0 | 807.8 | 843.5 |
| | SD | ±54.5 | ±59.1 | ±255.6 | ±304.0 | ±266.0 |

The incident total solar radiation inside the lean-to solar dehydrator comprised transmitted and reflected solar radiation for salt and sugar pretreatment ranged between 270.0, 942.2 W/m² and 297.1, 1191.0 W/m². The average hourly incident solar radiation outside and inside that dehydrator for salt and sugar pretreatment, without reflector was 584.6 (±196.8), 633.6 (±247.5) W/m² and 711.0 (±54.5), 807.8 (±304.0) W/m², respectively, which realized the polycarbonate cover had an average transmittance of 87.35% (±9.6) per hour. The solar radiation inside the lean-to solar dehydrator changed hourly because of the polycarbonate cover's transmittance, which is influenced by the solar incident angle. The incident total solar radiation inside the solar collector for salt and sugar pretreatment, respectively, ranged between 456.3, 1145.7 W/m² and 358.5, 1166.3 W/m², and the tilt angle recorded higher insolation than on the horizontal level. The variation in average insolation and wind speed is depicted in Fig. 4.

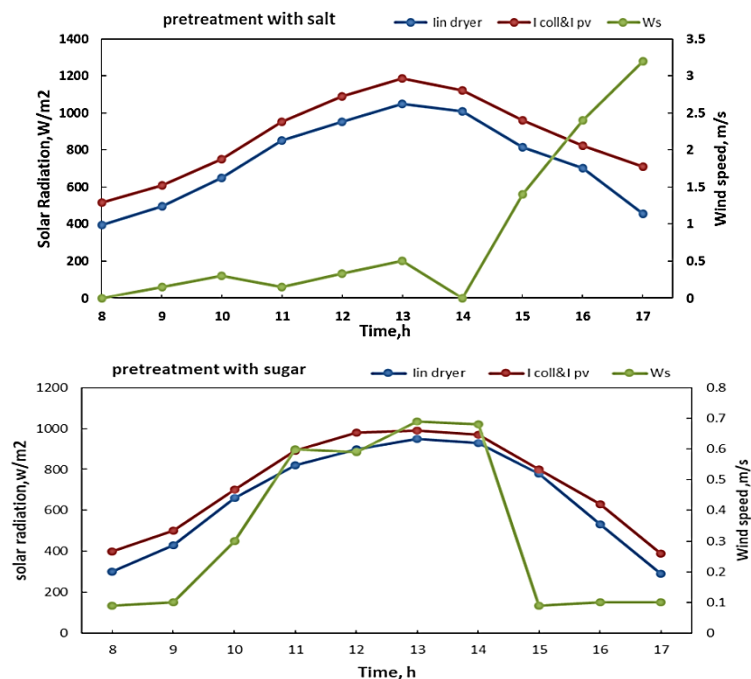


Fig. 4 – The drying system's average insolation and wind speed variation

The influence of the polycarbonate cover on the solar dehydrator was examined by plotting the incident solar radiation inside and outside the dehydrator, as shown in Figs. 5 and 6. The regression equations provided the best-fit correlations between incident solar radiation inside and outside for the solar dehydrator and solar collector, as follows in Eqs. 42, and 43:

$$R_i(\text{lean} - t_o) = 1.2080 (R_o) \tag{42}$$

$$R_i(\text{solar collector}) = 1.3348 (R_o) \tag{43}$$

The regression analysis revealed correlation coefficients of 0.9865 and 0.9462 between incident solar radiation inside and outside the solar dehydrator and solar collector, respectively ($P > 0.001$). The regression equation showed that each equation's slope almost equals the effective transmittance of the solar dehydrator cover (polycarbonate sheet). Regression analysis also showed that 10.47% and 9.49% of the outside incident solar radiation were reflected into the surrounding space of the solar dehydrator and solar collector, respectively.

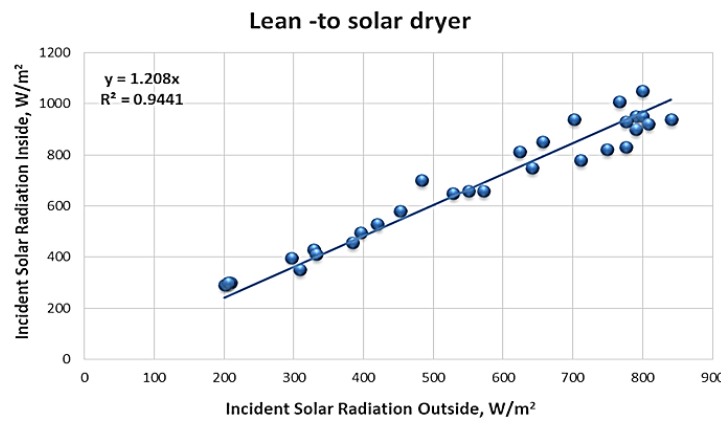


Fig. 5 – Incident solar radiation inside and outside the lean-to solar dehydrator

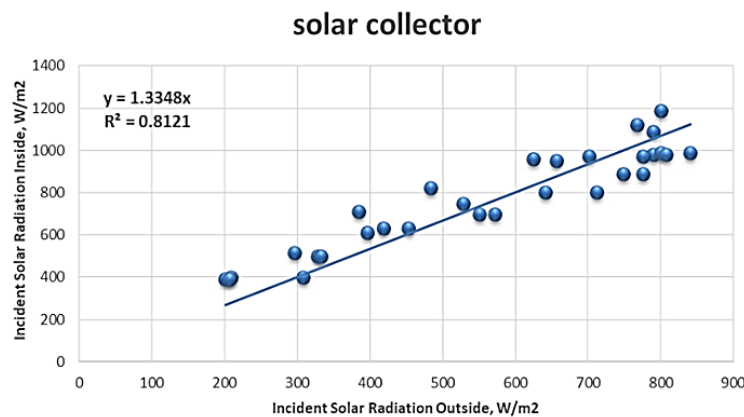


Fig. 6 – Incident solar radiation on and outside the solar collector

The relation between reflected solar radiation and incident solar radiation inside the solar dehydrator was investigated. The data regarding reflected solar radiation during the experiment were utilized to establish the correlation with incident solar radiation within the lean-to solar dehydrator (Fig. 7). The regression analysis showed a linear correlation between these two parameters, resulting in the best fit. The regression analysis also unveiled a high-significance relationship ($r = 0.7584$; $P > 0.001$). The equation used for regression analysis to find the optimal fit under certain experimental conditions is as follows in Eq. 44:

$$R_r = 0.1604(R_i) \tag{44}$$

Regression analysis also showed that the total reflected radiation from the vertical back wall almost represented 16.04% of the total incident solar radiation inside the lean-to solar dehydrator. Therefore, the reflector increased the total incident solar radiation inside the solar dehydrator over the outside incident solar radiation. Due to the lower values of solar altitude angles and higher values of solar azimuth angles and solar incident angles in the early morning and late afternoon, there was scattering in the data measured at those times.

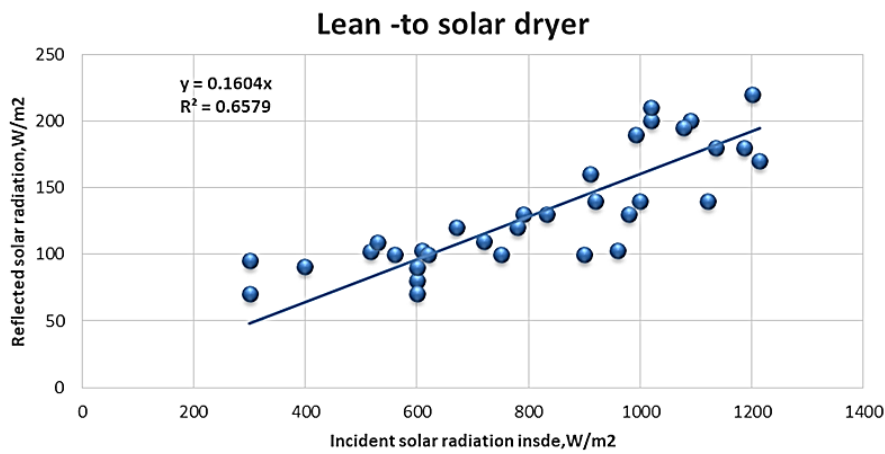


Fig. 7 – Reflected solar radiation against incident solar radiation inside the lean-to solar dehydrator during the experiment

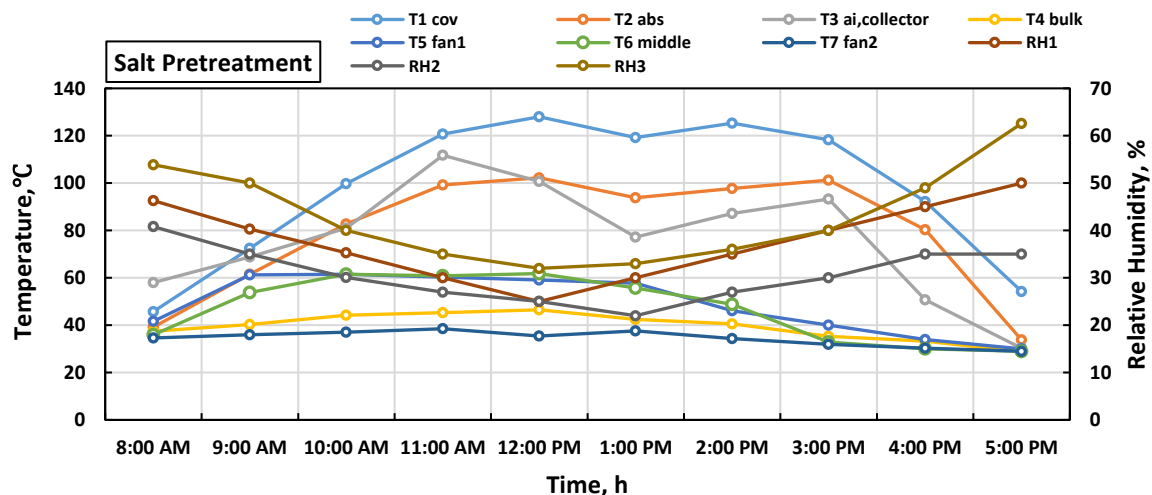
Dehydrating-air-temperature

Average hourly air temperatures outside and inside the solar dehydrator and solar collector during the experiment, respectively, were 30.7 (±2.3), 52.7 (±10.1), and 30.7 (±2.3), 79.7 (±26.9) for the salt treatment and 31.0 (±2.0), 55.1 (±15.3), and 31.0 (±2.0), 84.8 (±28.0) for the sugar treatment. Thus, the solar dehydrator and the solar collector increased the dehydrating air temperatures over the outside for the salt and sugar treatment by an average of 22.0, 49.0°C, and 24.1, 53.8°C, respectively. Consequently, the increasing percentages in dehydrating-air temperatures for the solar dehydrator system were 77.90%, 145.80%, 80.80%, and 180.30%, respectively.

Dehydrating-air-relative-humidity

During the dehydration process of tomatoes, the average hourly relative humidity inside the collector (RH1) and inside the solar dehydrator (RH2) was 33.5% (±7.7) and 29.1% (±7.4), respectively. The relative humidity of the outside air in salt pretreatment was 45.7% (±7.6). Regarding the sugar treatment, the average hourly relative humidity inside the solar collector (RH1) and the solar dehydrator (RH2) was measured to be 35.9% (±5.9) and 32.2% (±5.5), respectively.

Meanwhile, the relative humidity of the outside air was found to be 47.2% (±6.9). As a result, the solar collector reduced the relative humidity of the dehydrating air by 27.5% and 28.0% for the salt and sugar pretreatments, respectively, compared to the outside air relative humidity. Furthermore, the solar dehydrator effectively lowered the air-relative humidity for salt and sugar pretreatments by 4.3% and 5.7%, respectively. Fig. 8 illustrates the drying system's average temperatures and relative humidity variations. The recorded drying temperatures inside the dryer exceeded the surrounding temperature (T_{out} side). Simultaneously, the relative humidity level inside the GD (RH_{in}) was less than the outside (RH_{out})



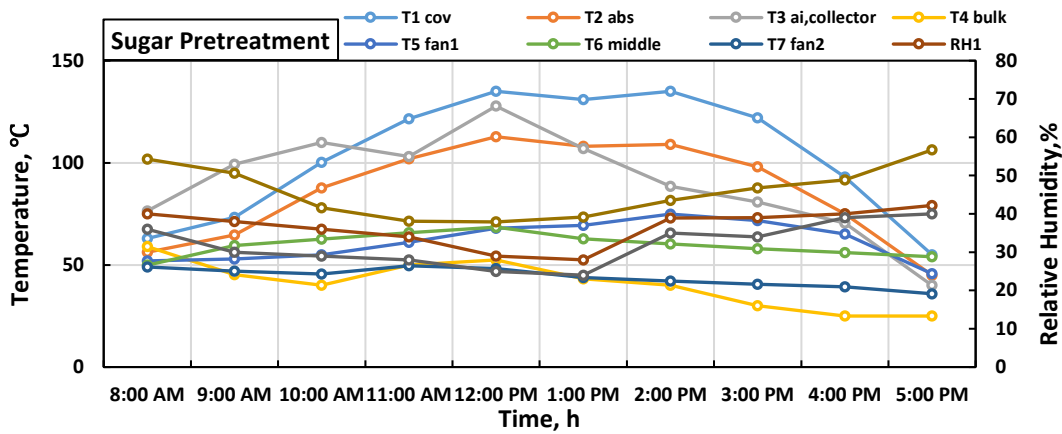


Fig. 8 – Variation of temperature and air relative humidity for salt and sugar pretreatments

Moisture content

Fig. 9 presents the moisture content variations of tomatoes at different times of the day for two treatments applied in the drying process. Increasing the duration of the drying process resulted in a decrease in the tomato's moisture content. The data concluded that the drying process of various tomato treatments follows a consistent drying rate and then transitions to a declining one. The tomatoes' moisture contents (w.b.), which dried inside the dryer for two treatments (salt and sugar) were 93.1% (10.20%) and 95.1% (11.30%), respectively. Moisture absorption during tomato pretreatment affects initial moisture content. For salt treatment, the dried tomatoes achieved equilibrium moisture content in the dryer after 20 and 25 hours for slices and halves, respectively. For sugar treatment, equilibrium moisture content was achieved by the dried tomatoes in the dryer after 23 and 29 hours for slices and halves, respectively.

To assess the impact of solar energy on heating power, the recorded data from the solar dehydrator's heating process were graphed against internal solar energy for both pretreatments, as shown in Figs. 10 and 11. The regression analysis results showed a remarkably significant linear relationship ($r = 0.9213$ and $r = 0.9253$, in order; $P > 0.001$). The regression equations with the best fit were as shown in Eqs. 45 and 46:

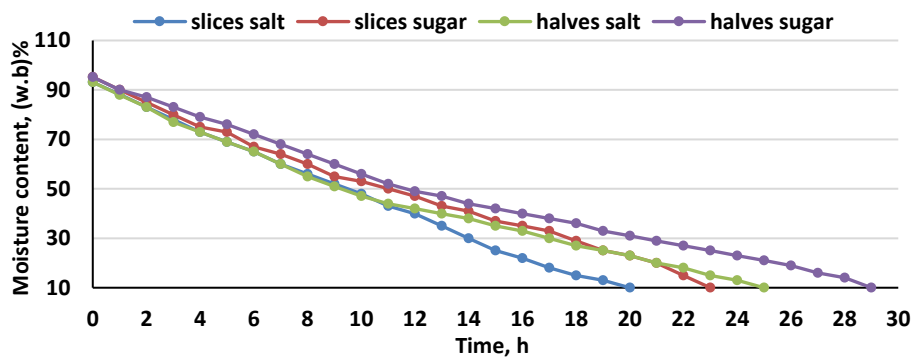


Fig. 9 – Variation of tomatoes moisture contents for salt and sugar treatments inside the lean-to solar dryer

$$H_p (salt) = 0.8428 (q) \tag{45}$$

$$H_p (sugar) = 0.7118 (q) \tag{46}$$

Regression analysis shows that 84.28% and 71.18% of solar energy were used for heating power in the tomato dehydrator system. The solar dehydrator lost the remaining solar energy (15.72% and 28.82%, respectively) through various modes of heat transfer (radiation, convection, conduction, and exhausted air) to the surroundings.

Useful heat gain and heat losses

During the experiment, the dryer's average heat gain ranged from 1350 to 1850 Wh per day. The quantity of heat that proved useful displayed variations over the experimental duration owing to the changes in weather. The reduction in the ambient air temperature (T_{amb}) led to a decrease in the useful heat gain because of the diminished temperature difference between the hot air inside the dryer and the air flowing from the collector to the dryer.

In the lean-to solar dryer, the average daily heat gain for evaporating moisture from tomatoes decreased from 60% to 5% at the beginning and end of the dehydration process. The remaining heat was lost through convection, conduction, and radiation. It is essential to acknowledge that the increase in temperature difference between the solar dryer's interior and the surrounding air increases heat losses.

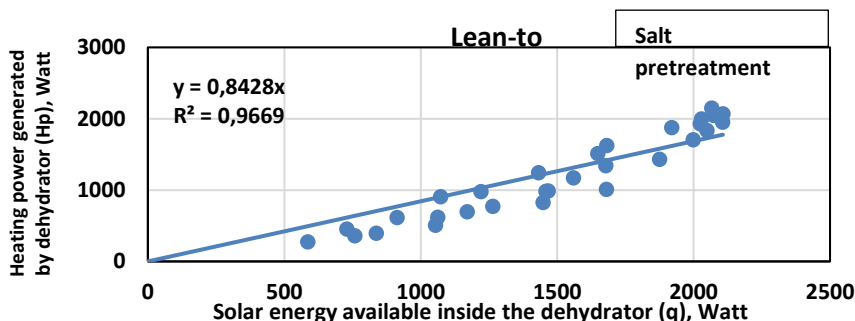


Fig. 10 – Heating energy generated by the lean-to solar dehydrator against solar energy inside the dehydrator for salt pretreatment

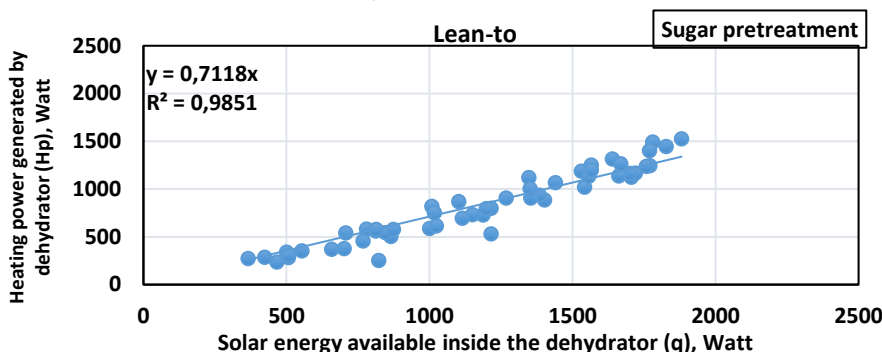


Fig. 11 – Heating energy generated by the lean-to solar dehydrator against solar energy inside the dehydrator for the sugar pretreatment

Assessing the relationship between solar energy and heating power is necessary to evaluate the solar dehydrator's thermal performance and overall efficiency. The solar dehydrator was found to provide an average diurnal solar energy of 54.939 kWh, while generating a heating power of 39.670 kWh for salt pretreatment during the 25-hour dehydrating process. Thus, the solar dehydrator attained an overall thermal efficiency of 76.2%. As a result, the exhausted dehydrating air lost about 23.8% of the heating power. The average daily total solar energy within the lean-to solar dehydrator and the generated heating power during the experimental period (29 hours) amounted to 59.375 kWh and 47.473 kWh, respectively. Consequently, the total thermal efficiency of the lean-to solar dehydrator reached 79.95%. As a result, the dehydrator experienced a loss of approximately 20.05% in heating power when the dehydrating air was discharged. The solar dryer exhibited minimal heat infiltration through the door and connections; hence, it was disregarded. During cloudy hours, the remaining usable energy produced by the PV module can be stored in the battery, along with the energy required for operating the DC fan. The solar energy inside the lean-to solar dehydrator (E_{in}), solar energy outside (E_{out}), the overall thermal efficiency (η_{th}), and the energy losses during each hour throughout the dehydrating process are summarized and presented in Table 2.

Overall thermal efficiency

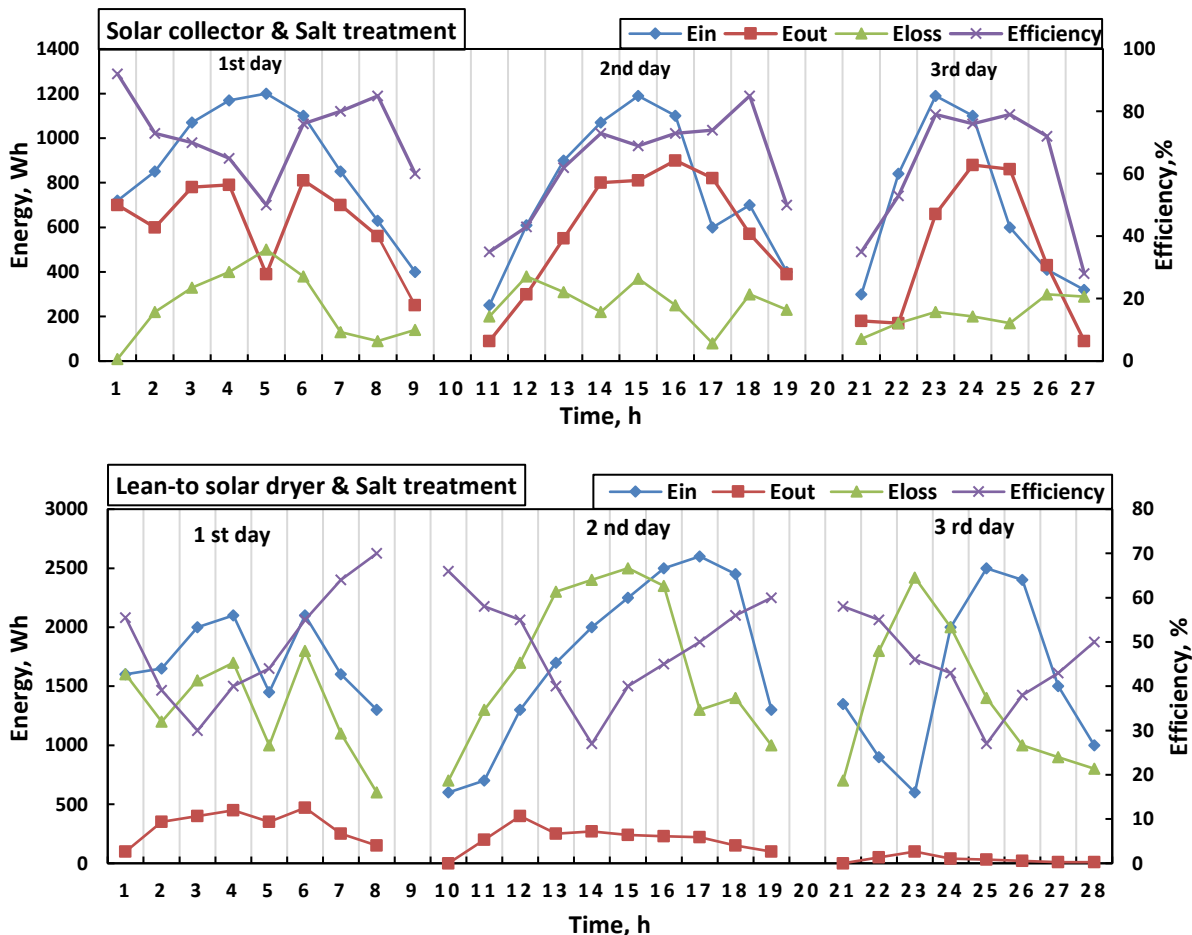
The drying system was assessed, including energy analysis, energy efficiency, and time-dependent changes in energy loss. The drying system component's input, output, energy losses, and efficiency are illustrated in Figs. 12 and 13. The average overall efficiency for the salt and sugar pretreatment was 53.5% and 48.1%, respectively. The salt pretreatment was the best because of its short drying time of 25 hours. The presence of clouds, which caused solar radiation to scatter, decreased the efficiency of various components and input energy within the drying system. An increased disparity between output and input energy resulted in reduced efficiency. The collector's mean efficiency was 65.1% and 57.5% for the salt and sugar pretreatment, respectively. In contrast, the solar dryer's optimal mean efficiency has a comparable pattern to solar collectors. This result is associated explicitly with the drying time, whereby the salt experiment on slices exhibited the shortest period. The collector's efficiency was noted to be at its peak on the first day and displayed a continuous decline throughout the second, third, and fourth days. This can be because the drying rate initially started at a high value and gradually decreased over time until the end of the experiment.

Nonetheless, the sugar trial yielded the highest mean efficiency for the PV system. It could be because of the solar radiation incident on the PV panel throughout the experiment. Figs. 12 and 13 rely on the thermal analysis of the solar system, considering solar radiation and weather conditions during the experiment. These figures' energy inputs in (E_{in}) depend on the solar radiation during the experiment. The energy output (E_{out}) is the energy that exits each part of the drying system after use. The E_{loss} represents the disparity between E_{in} and E_{out} for the solar collector; the energy input (E_{in}) denotes the energy acquired from solar radiation, which progressively increases from morning until 1:00 p.m. and decreases until the day's ending. The energy output (E_{out}) refers to the energy expelled through the outlet after accounting for energy losses (E_{loss}) from the bottom, sides, and cover.

Table 2

The solar energy inside the lean-to solar dehydrator (E_{in}), solar energy outside (E_{out}), the overall thermal efficiency (η_{th}), and the energy losses during each hour throughout the dehydrating process

| Solar collector | Salt pretreatment | | | | Sugar pretreatment | | | |
|-----------------|-------------------|----------------|-----------------|---------------|--------------------|----------------|-----------------|---------------|
| | E_{in} , Wh | E_{out} , Wh | E_{loss} , Wh | Efficiency, % | E_{in} , Wh | E_{out} , Wh | E_{loss} , Wh | Efficiency, % |
| | 887.8 | 620.0 | 244.4 | 72.3 | 806.0 | 530.0 | 246.0 | 63.9 |
| | 757.8 | 581.1 | 260.0 | 62.7 | 644.0 | 256.0 | 283.0 | 56.0 |
| | 680.0 | 467.0 | 207.0 | 60.3 | 333.8 | 390.0 | 147.0 | 60.9 |
| | - | - | - | - | 348.0 | 405.0 | 161.0 | 49.3 |
| Solar dryer | 1725.0 | 315.0 | 1318.8 | 49.7 | 1725.0 | 144.0 | 1290.0 | 56.1 |
| | 1740.0 | 206.0 | 1695.0 | 49.7 | 1155.0 | 71.0 | 1015.0 | 53.7 |
| | 1531.0 | 32.4 | 1377.5 | 45.0 | 655.0 | 40.0 | 550.0 | 52.5 |
| | - | - | - | - | 817.9 | 49.0 | 573.0 | 51.5 |
| PV panels | 503.0 | 38.9 | 414.4 | 12.0 | 437.0 | 392.0 | 46.0 | 11.7 |
| | 444.0 | 51.0 | 378.0 | 12.5 | 395.0 | 372.0 | 47.1 | 13.5 |
| | 358.8 | 40.4 | 322.5 | 14.9 | 199.0 | 181.5 | 53.5 | 13.4 |
| | - | - | - | - | 221.0 | 215.0 | 55.7 | 17.9 |



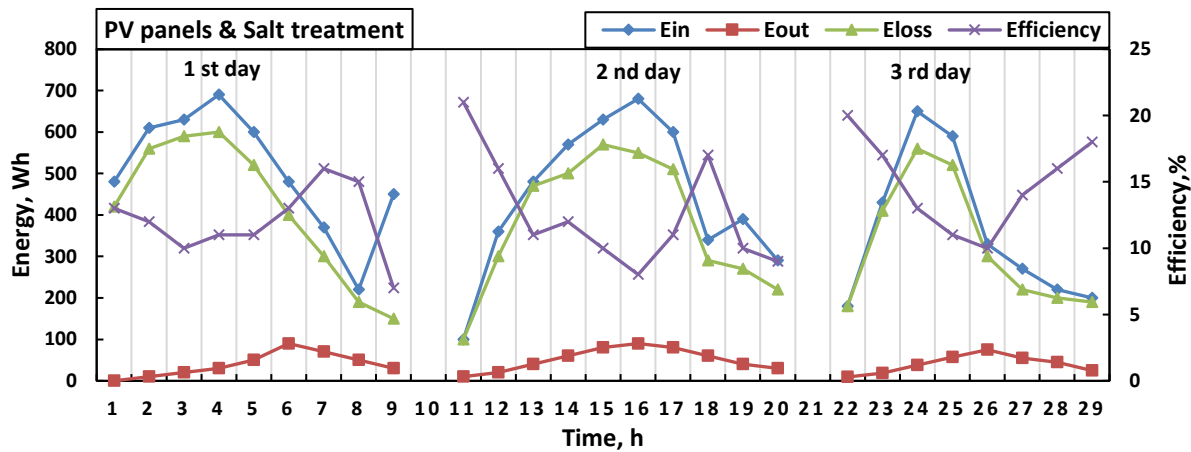
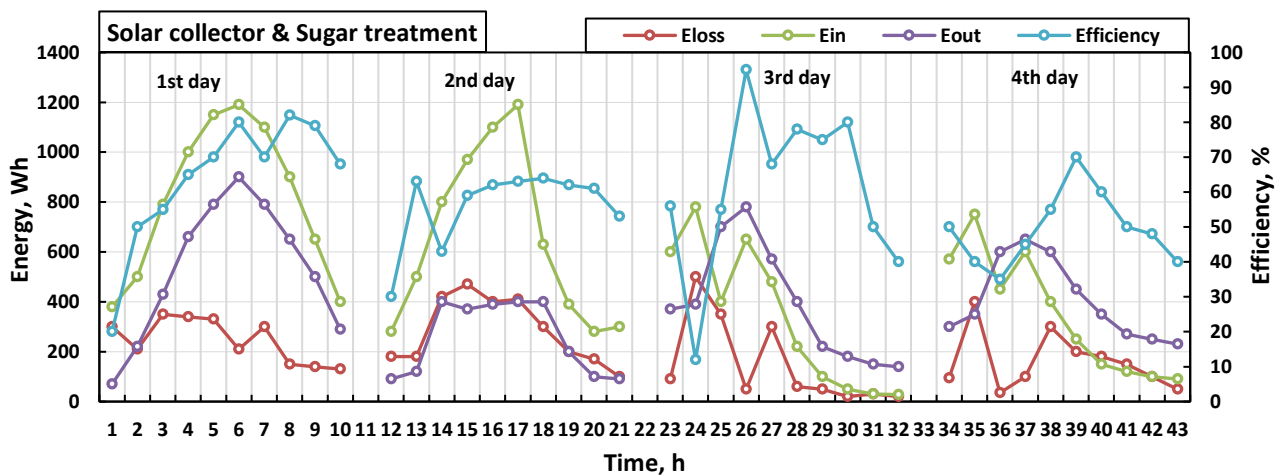


Fig. 12 – The calculated energy input (E_{in}), energy output (E_{out}), energy loss (E_{loss}), and efficiency for collector, dryer, and PV for salt treatment of slices and halves tomatoes

The E_{out} started with a small value, progressively escalating in response to the strength of solar radiation until reaching a maximum, followed by a gradual decline by day's end. The solar collector's efficiency has an inverse relationship with energy loss. The dryer's performance may vary based on weather conditions, as shown in Figs. 12 and 13. The E_{out} implies the energy released upon the evaporation of moisture from the tomatoes; beginning at a high level, it progressively decreases in correspondence with the moisture content until the solar drying process ends. The value was significantly higher on the initial day because of the high reduction in the tomato's moisture content. Afterward, a decrease was observed on the second day because of the tomato moisture content reduction, eventually reaching its lowest point on the third day when the moisture content became exceedingly low. PV panels had a behavior similar to solar collectors, but their efficiency trend differed regarding energy input and loss. Furthermore, it was varied based on the weather conditions. The useful energy is exploited to dry the tomatoes in the drying system by quickly lessening the tomato's moisture content to a safe level. Hence, the usefulness of solar energy diminished over time. The results demonstrated a progressive rise in E_{loss} with passaging drying time throughout each day until mid-day, after which it declined. Air temperature and moisture content are critical factors that significantly influence E_{loss} . Additionally, it was noted that E_{loss} initially exhibited a high value in these trials. The results revealed that energy efficiency exhibited higher on the first day than the last, which can be attributed to increased losses during the drying process. Additionally, the temperature variation led to an elevation in the E_{loss} resulting from radiation and convection heat exchange between the internal cover and other dryer elements. The significant temperature variation observed between the indoor and outdoor air of the dryer suggests that the chosen dryer design exhibited a high-efficiency level.



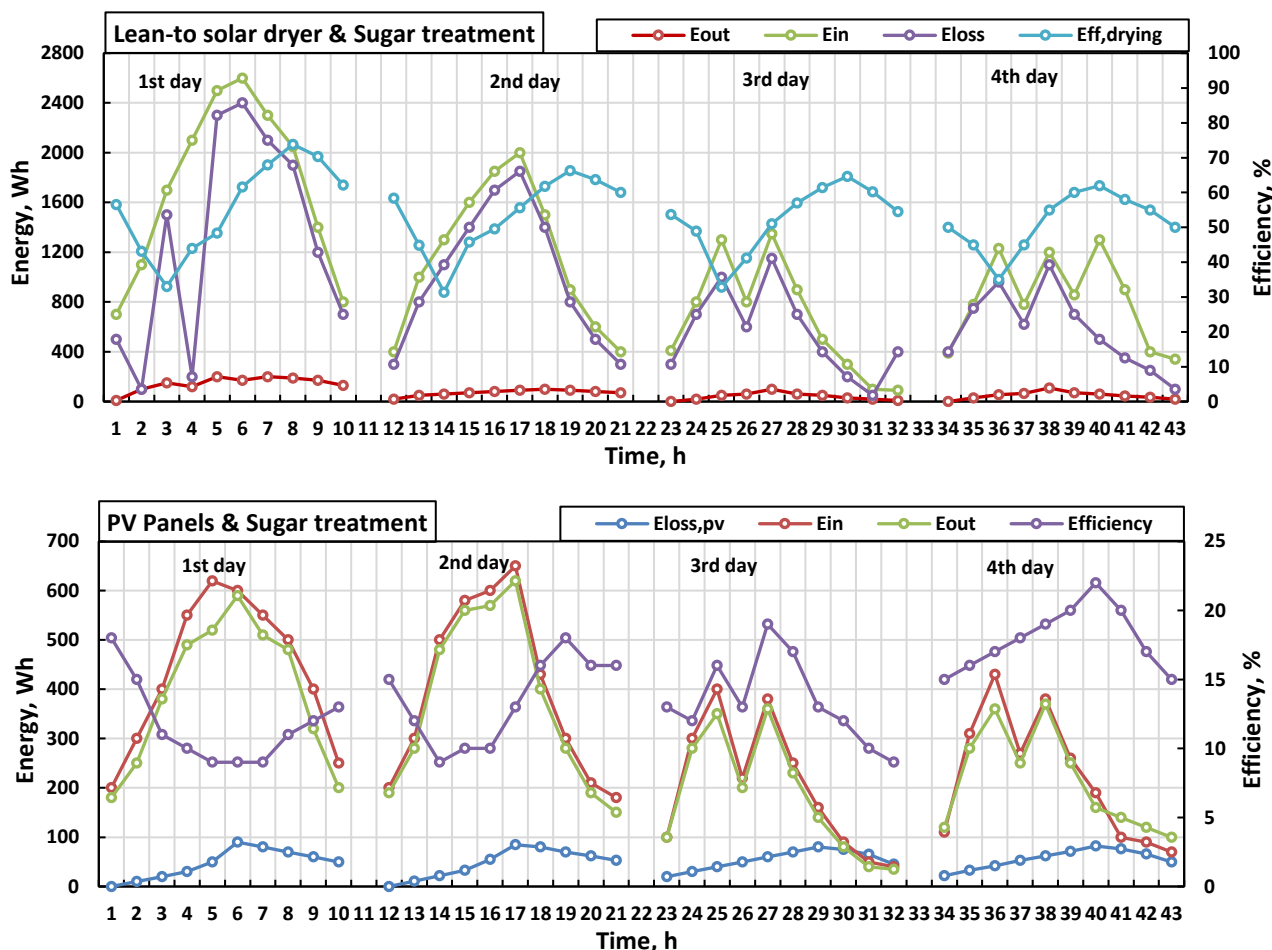


Fig. 13 – The calculated energy input (E_{in}), energy output (E_{out}), energy loss (E_{loss}), and efficiency for collector, dryer, and PV for sugar treatment of slices and halves tomatoes

CONCLUSIONS

The solar dryer (lean-to) was developed to optimize the absorption of solar radiation for efficient heat gain. The solar drying system's thermal efficiency was examined by investigating its mixed-mode forced convection. The moisture content was removed using solar-heated air with temperatures ranging from 40 to 60°C, air-relative humidity between 19 and 40%, and incident solar radiation ranging from 400 to 1200 W/m². As a result, the solar dehydrator utilized a suction blower to expel water vapor, enabling the transfer of sensible and latent heat during the evaporation process of water. Different pretreatments before drying were examined to detect the optimal treatment. Further, energy for various components of the lean-to-solar dryer was analyzed. The results showed that the dried tomatoes attained the state of equilibrium moisture content within the drying equipment for slices and halves (salt) after 20 and 25 hours, respectively. In contrast, sugar treatment was 23 and 29 h, respectively. The initial drying rate of tomato slices was higher than the halves. The tomato slices that underwent salt pretreatment and were dried in the dryer exhibited the shortest drying time compared with those that underwent sugar pretreatment. Tomato halves were dipped in sucrose solution (40%) and then dried in the dryer for 72 h, which had the longest drying period. Increasing the energy difference between input and output reduces efficiency. The highest level of mean efficiency for the PV system was observed on the fourth day during the sugar pretreatment phase (slices and halves of tomatoes). The average overall efficiencies for the salt and sugar pretreatments were 53.5% and 48.1%, respectively. The salt pretreatment was the optimal choice, resulting in the shortest drying time of 25 hours. The mean efficiency for the collector was 65.1 and 57.5% for the salt, and sugar pretreatment, respectively.

REFERENCES

[1] Abdellatif, S.M., El-Hadidi, Y.M., & Mohammed, E.M. (2015). Thermal performance analysis for solar collector air heater assisted solar modified-Quonset dryer. *Journal of Soil Sciences and Agricultural Engineering, Mansoura University* 6(10), 1217–1236. <https://dx.doi.org/10.21608/jssae.2015.43796>

- [2] ASAE (1991). *Standards*. American society of agricultural engineers, st. Joseph. Michigan.
- [3] Azam, M.M., Eltawil, M.A., & Amer, B.M. (2020). Thermal analysis of PV system and solar collector integrated with greenhouse dryer for drying tomatoes. *Energy*, 212, 118764. <https://doi.org/10.1016/j.energy.2020.118764>
- [4] Bergman, T.L., Lavine, A.S., Incropera, F.P., & DeWitt, D.P. (2011). *Introduction to heat transfer*. John Wiley & Sons.
- [5] Cengel, A. (2003). *Heat transfer: A practical approach*. New York: McGraw-Hill.
- [6] Dewanto, V., Wu, X., Adom, K.K., & Liu, R.H. (2002). Thermal processing enhances the nutritional value of tomatoes by increasing total antioxidant activity. *Journal of agricultural and food chemistry*, 50(10), 3010–3014. <https://doi.org/10.1021/jf0115589>
- [7] Duffie, J. A., & Beckman, W.A. (2013). *Solar engineering of thermal processes*. New York, N.Y.: John Wiley and Sons. <http://doi.org/10.1002/9781118671603>
- [8] Eltawil, M.A., Azam, M.M., & Alghannam, A.O. (2018). Energy analysis of hybrid solar tunnel dryer with PV system and solar collector for drying mint (*Mentha Viridis*). *Journal of Cleaner Production* 181, 352–364. <https://doi.org/10.1016/j.jclepro.2018.01.229>
- [9] Faostat (2018). <http://www.fao.org/faostat/ar/#data/QC>.
- [10] FAO (2022). *Food and Agriculture Organization of the United Nations*. FAOSTAT Available at <https://www.fao.org/faostat/en/#data/QCL>, accessed on 04/03/2024.
- [11] Hepbasli, A. (2008). A key review on exergetic analysis and assessment of renewable energy resources for a sustainable future. *Renew Sustain Energy Rev.*, 12(3), 593–661. <https://doi.org/10.1016/j.rser.2006.10.001>
- [12] Lakshmi, D.V.N., Muthukumar, P., Layek, A., & Nayak, P.K. (2019). Performance analyses of mixed mode forced convection solar dryer for drying of stevia leaves. *Solar Energy*, 188, 507–518. <https://doi.org/10.1016/j.solener.2019.06.009>
- [13] Lewicki, P.P. (1998). Some remarks on rehydration of dried foods. *Journal of Food Engineering*, 36(1), 81–87. [https://doi.org/10.1016/S0260-8774\(98\)00022-3](https://doi.org/10.1016/S0260-8774(98)00022-3)
- [14] Li, M. (2021). Research on color correction method of greenhouse tomato plant image based on high dynamic range imaging. *NMATEH - Agricultural Engineering*, 64(2), 393-402. <https://doi.org/10.35633/inmateh-64-39>
- [15] Mohsenin, N.N., (2020). *Physical properties of plant and animal materials: v. 1: physical characteristics and mechanical properties*. Routledge.
- [16] Mumba, J. (1996). Design and development of a solar grain dryer incorporating photovoltaic powered air circulation. *Energy Convers Manag.* 37(5), 615-621. [https://doi.org/10.1016/0196-8904\(95\)00205-7](https://doi.org/10.1016/0196-8904(95)00205-7)
- [17] Patil, R., & Gawande, R. (2016). A review on solar tunnel greenhouse drying system. *Renewable and sustainable energy reviews*, 56, 196–214. <https://doi.org/10.1016/j.rser.2015.11.057>
- [18] Ramos, I.N., Brandao, T.R.S., & Silva, C.L.M. (2015). Simulation of solar drying of grapes using an integrated heat and mass transfer model. *Renewable Energy*, 81, 896–902. <https://doi.org/10.1016/j.renene.2015.04.011>
- [19] Sahin, S., & Sumnu, S.G. (2005). *Physical properties of foods*. USA: Springer. <https://hdl.handle.net/11511/70305>
- [20] Shahi, M.M.N., Sabetghadam, M., & Athari, M. (2016). The Effect of Osmotic and Ultrasound Pretreatment on Some Physicochemical Features of Avocado. *International Journal of Pharmaceutical Research & Allied Sciences*, 5(4), 121–131.
- [21] Tiwari, S., & Tiwari, G.N. (2016). Exergoeconomic analysis of photovoltaic-thermal (PVT) mixed mode greenhouse solar dryer. *Energy*, 114, 155–164. <https://doi.org/10.1016/j.energy.2016.07.132>
- [22] Usub, T., Lertsatitthanakorn, C., Poomsa-ad, N., Wiset, L., Yang, L., & Siriamornpun, S. (2008). Experimental performance of a solar tunnel dryer for drying silkworm pupae. *Biosystems Engineering*, 101(2), 209–216. <https://doi.org/10.1016/j.biosystemseng.2008.06.011>

VIBRATION PARAMETER CALIBRATION AND TEST OF TIGER NUT BASED ON DISCRETE ELEMENT METHOD

基于离散元法的油莎豆振动参数标定与试验

Shikuan MA¹⁾, Xiaoning HE^{*1)}, Hao ZHU³⁾, Zhixin LIU¹⁾, Dongwei WANG¹⁾, Shuqi SHANG¹⁾, Guanghui LI²⁾

¹⁾ College of Electrical and Mechanical Engineering, Qingdao Agricultural University, Qingdao/ China

²⁾ Shandong Saline Modern Agriculture Co., Ltd, Dongying/ China

³⁾ Nanjing Agricultural University, Nanjing/ China

Corresponding author: Xiaoning HE

Tel: +8618306391208; E-mail: 944286200@qq.com

DOI: <https://doi.org/10.35633/inmateh-73-02>

Keywords: parameter calibration, Tiger nut, discrete element, the electromagnetic vibration feeder

ABSTRACT

In this study, the parameters of tiger nut were calibrated based on discrete element method, and significant influencing factors and optimal levels were selected by Plackett-Burman test, steepest climb test and center compound test, and verified by electromagnetic vibration hopper bench test. The results show that the relative error between the simulated resting angle and the actual resting angle is only 0.381%. The fitting degree of the model is 96.32% and 94.57% respectively, which can provide theoretical basis for the study of the parameters and discrete element simulation of tiger nut.

摘要

本研究基于离散元法对油莎豆参数进行标定, 采用 Plackett-Burman 试验、最陡爬坡试验和中心复合试验筛选出显著影响因素及最优水平, 进行电磁振动料斗台架试验进行验证。结果表明: 仿真休止角与实际休止角相对误差仅为 0.381%; 电磁振动料斗输送时间的预测模型拟合度为 96.32%, 质量流率拟合度为 94.57%, 可为油莎豆参数特性研究以及离散元仿真工作提供理论依据。

INTRODUCTION

Tiger nut is known as “underground walnut”. It has high oil yield and its yield ranks first among oil crops (Rebezov *et al.*, 2023; Udefa *et al.*, 2020; Sobhy *et al.*, 2015). It is a new economic crop with high comprehensive utilization value (Wang *et al.*, 2022; Guo *et al.*, 2021; Umukoro *et al.*, 2020; Pascual *et al.*, 2000). Automatic feeding is an important part of Tiger nut seed selection and processing, and conveying stability is an important evaluation index of feeding quality. At present, electromagnetic vibration hoppers are mostly used in China to transport peanuts, corn and other materials in an orderly manner. However, problems such as backward slip and in-situ beating during the transportation of Tiger nut are prominent, which seriously affect the efficiency of Tiger nut seed selection. At the same time, there are few studies on the basic theory of Tiger nut, and it is impossible to determine the motion law of Tiger nut under high frequency vibration, and the transportation accuracy is not high in actual operation (Xing *et al.*, 2017; Singh *et al.*, 2020; Mišljen *et al.*, 2016). Therefore, it is of great significance to study the basic physical parameters of Tiger nut for realizing the accurate and stable feeding of Tiger nut and promoting the development of Tiger nut industrial chain.

In the process of automatic feeding, the trajectory of Tiger nut is complex and changeable under the action of high frequency vibration of electromagnetic vibration hopper. EDEM software is often used for discrete element simulation to explore the movement law of agricultural granular materials and the best operating parameters of the machine. At present, most of the researches on the calibration of material parameters only verify the accuracy of the calibration parameters through the angle of repose test, which is different from the actual working conditions of the material, resulting in the simulation conclusion cannot guide the actual production well (Hao *et al.*, 2019; Wang *et al.*, 2020; Wu *et al.*, 2020; Shi *et al.*, 2022). The research objects are mostly peanut seeds, potatoes, wheat grains and other materials. There are few studies on the calibration of the parameter characteristics of the simulation model of Tiger nut tubers.

¹⁾ Xiaoning HE, Prof. Ph.D. Eng.; Shikuan MA, M.S. Stud. Eng.; Zhixin LIU, M.S. Stud. Eng.; Dongwei WANG, Prof. Ph.D. Eng.; Shuqi SHANG, Prof. Ph.D. Eng.

²⁾ Guanghui LI, M.S. Stud. Eng. ;

³⁾ Hao ZHU, M.S. Stud. Eng.

In this paper, the intrinsic parameters and contact parameters of Tiger nut tubers were determined by physical experiments. The simulation model was established in EDEM software to simulate the accumulation state of Tiger nut. Taking the angle of repose of Tiger nut as the response value, the Plackett-Burman test was used to screen out the significant influencing factors, and the central composite test of response surface method was used to obtain the optimal level. Through the bench test of electromagnetic vibration hopper, the motion state of Tiger nut was reflected and verified by conveying time and mass flow rate. This paper can provide a theoretical reference for the application of discrete element method to the study of small seed parameter characteristics and the study of motion state under high frequency vibration.

MATERIALS AND METHODS

Determination of intrinsic parameters of Tiger nut tubers

A total of 1000 grains were randomly selected from the Tiger nut samples and placed in a combined sieve for manual screening and separation. 100 grains were randomly selected, and the three-axis size was measured using a vernier caliper. The results are shown in Table 1.

Table 1

Triaxial dimension of the Tiger nut tubers

| Triaxial Dimension | Small Tuber | Medium Tuber | Large Tuber |
|--------------------|-------------|--------------|-------------|
| Length L/mm | 12.05±0.77 | 13.34±0.93 | 14.78±1.06 |
| Width W/mm | 10.31±0.64 | 13.14±0.85 | 14.45±1.02 |
| Height H/mm | 9.83±0.59 | 13.36±0.87 | 12.93±0.81 |

The average moisture content of Tiger nut was 48.90% according to the wet basis representation method.

The cylindrical sample compression test of randomly selected Tiger nut was carried out by microcomputer controlled electronic universal testing machine, and the average Poisson's ratio of Tiger nut was 0.478.

Determination of elastic modulus and shear modulus

The Tiger nut was randomly selected and the original height was measured. Then it was fixed on the test machine platform and pressurized along the height direction of Tiger nut at a loading speed of 0.1 mm/s (Hao *et al.*, 2021). The software post-processing module was used to read the real-time data of load and deformation, and 100 tests were repeated. The shear modulus of Tiger nut tubers ranged from 105 MPa~127 MPa, with an average of 116.82 MPa.

$$E = \frac{\sigma}{\varepsilon} = \frac{F/A}{\lim_{T \rightarrow 0} \left(\frac{\Delta T}{T} \right)} \quad (1)$$

where:

E is the elastic modulus of Tiger nut, [MPa]; σ is the maximum compressive stress, [MPa]; ε is strain; F is the axial load, [N]; A is the contact area, [mm²]; ΔT is the high deformation of Tiger nut, [mm]; G is the shear modulus of Tiger nut, [MPa];

Determination of friction coefficient between Tiger nut tuber and steel plate

In this experiment, the static friction coefficient between Tiger nut tubers and steel plates was measured by a self-made friction coefficient measuring device. The test device is shown in Fig.1.

Four Tiger nut tubers (Wu *et al.*, 2020) were bonded using glue and placed flat on a horizontal steel plate. The sliding friction angle was determined by measuring the inclination angle at which the tuber started sliding downwards on the slope. The static friction coefficient between the Tiger nut tuber and the steel plate was calculated based on 50 repeated tests, ranging from 0.15 to 0.35, averaging 0.26. The rolling friction coefficient was also measured using the same method, resulting in a range of 0.017 to 0.035, with an average value of 0.027.

Determination of friction coefficient between Tiger nut tubers

The Tiger nut tubers were closely arranged according to the shape. The bottom of some large-sized Tiger nut tubers was removed and adhered to the plane test plate, as shown in Fig. 2 (Wu *et al.*, 2020). The above tests were repeated as a whole as a material to be tested, and the static friction coefficient between the tubers of Tiger nut ranged from 0.26~0.44, with an average value of 0.34. The rolling friction coefficient between Tiger nut tubers ranged from 0.027~0.045, with an average of 0.035.



Fig. 1 – Static friction coefficient measurement



Fig. 2 – Measurement of friction coefficient between tubers



Collision restitution coefficient test

The high-speed camera was used to collect and process the image of tuber falling motion, and the recovery coefficient of Tiger nut was determined (Liu et al., 2018). The materials to be tested are steel plate and Tiger nut tuber plate. The test height is 200 mm, and the vertical height between the chute of electromagnetic vibration hopper and the material box is set.

The material to be inspected is attached to the slope instrument, and the slope angle is 30°. The Tiger nut tubers were fixed on a tripod, and the vertical height from the material to be inspected was 200 mm. After the free fall of the tuber, the complete motion process is collected by a high-speed camera, and the trajectory image is generated as shown in Fig. 3.

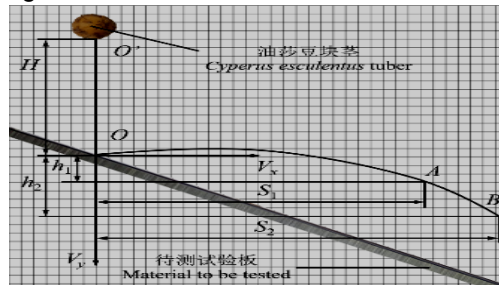


Fig. 3 – Principle of crash recovery coefficient determination test

O' is the original position; O is the origin; H is the OO' distance, [mm]; A and B are the observation points; h₁ and h₂ are the height displacements, [mm]; S₁ and S₂ are the horizontal displacements, [mm]; V_x and V_y are the horizontal and vertical fractional velocities, [m·s⁻¹];

The calculation formula of the recovery coefficient of Tiger nut is as follows:

$$e = \frac{|V_n|}{|V_n^0|} = \left| \frac{\sqrt{V_x^2} \cos[60^\circ + \arctan C \tan(V_y/V_x)]}{V_0 \cos 30^\circ} \right| \tag{2}$$

where:

e is the collision recovery coefficient of Tiger nut tuber-tested material; v₁ is the instantaneous separation velocity in the normal direction of the collision point between the Tiger nut tuber and the material to be tested, [m/s]; v₀ is the instantaneous contact velocity of the collision between the Tiger nut tuber and the material to be tested, [m/s]; H₁ is the maximum height of collision rebound between Tiger nut tubers and materials to be tested, [mm]; H₀ is the falling height of Tiger nut tuber, [mm];

Repeated 50 tests, the range of collision recovery coefficient between Tiger nut tubers was 0.28~0.45, and the average value was 0.36. The collision recovery coefficient of Tiger nut tuber-steel plate ranged from 0.60~0.76, with an average of 0.70.

Angle of repose determination test

The actual accumulation test of Tiger nut was carried out by using the device shown in Fig. 4 (Jia et al., 2021).



Fig. 4 – Physical Repose angle test of Tiger nut tubers

According to the pre-test, the lifting speed of the cylinder was set to be 0.1 m/s, and the tuber fell under the action of gravity. After the oil sands pile was stabilized, the lifting was stopped, and then the positive and negative sides of the oil sands pile were photographed horizontally with the steel plate platform (Han et al., 2019; Pan et al., 2020).

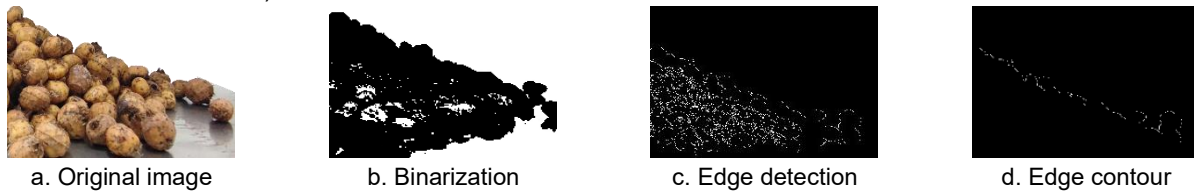


Fig. 5 – Edge contour extraction and fitting process of stacking angle

Image processing was performed using MATLAB to remove the internal interference contour of the Tiger nut, and only the outer contour was retained, as shown in Fig. 5. The software Origin was imported to linearly fit the outer contour of the Tiger nut, as shown in Fig. 6 (Pue et al., 2019; Tekeste et al., 2018; Coetzee et al., 2016). The angle of repose of the actual stacking test of Tiger nut tubers was 30.70 ° by repeating the test for 100 times and taking the average value.

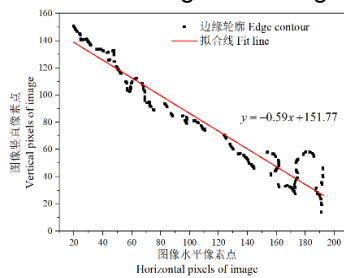


Fig. 6 – Boundary fitting of one-side stacking angle

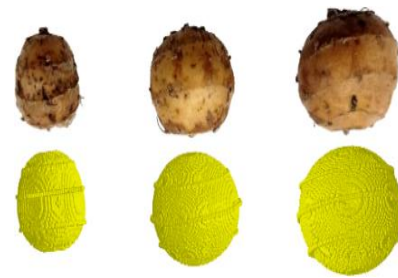


Fig. 7 – Discrete element model of Tiger nut tubers

Tiger nut tuber model and Tiger nut tuber contact mechanic model

The three-dimensional dimensions and shape characteristics of tuber were determined by using a three-dimensional laser scanner. By scanning to reconstruct its morphological features, the software automatically fills in three discrete element models of the model, as shown in Fig. 7. The Hertz-Mindlin (no slip) contact model was selected for simulation. The Hertz-Mindlin (no slip) contact model was selected for simulation.

Plackett-Burman Design experiment

Between the references and the experiments in this paper, the range of each parameter is determined as shown in Table 2, and the experimental design table and results are shown in Table 3. The significance analysis of Plackett-Burman test parameters is shown in Table 4. Regression model equation represented by the coding factor is:

$$\eta = 29.91 - 0.17A + 0.17B + 0.29C + 0.49D + 1.40E + 2.28F - 0.14G - 0.43H + 0.50J \tag{3}$$

Table 2

Factors and levels table of Plackett-Burman Design

| Symbol | Parameter | Level | |
|--------|---|-------|-------|
| | | -1 | +1 |
| A | Tiger nut Poisson 's ratio | 0.464 | 0.486 |
| B | Density of Tiger nut /(kg·m ⁻³) | 2700 | 3000 |
| C | Shear modulus of Tiger nut /MPa | 105 | 127 |
| D | Recovery coefficient between tubers of Tiger nut | 0.28 | 0.45 |
| E | Static friction coefficient between Tiger nut tubers | 0.26 | 0.44 |
| F | Rolling friction coefficient between Tiger nut tubers | 0.027 | 0.045 |
| G | Tiger nut-steel plate recovery coefficient | 0.60 | 0.76 |
| H | Tiger nut-steel plate static friction coefficient | 0.15 | 0.35 |
| J | Tiger nut-steel plate rolling friction coefficient | 0.017 | 0.035 |
| K | virtual parameter | — | — |

Table 3

Design and results of Plackett-Burman test scheme

| No. | A | B | C | D | E | F | G | H | I | J | K | Repose angle $\eta/(\circ)$ |
|-----|----|----|----|----|----|----|----|----|----|----|----|-----------------------------|
| 1 | -1 | 1 | 1 | -1 | 1 | 1 | 1 | -1 | -1 | -1 | 1 | 34.039 |
| 2 | 1 | 1 | 1 | -1 | -1 | -1 | 1 | -1 | 1 | 1 | -1 | 26.418 |
| 3 | -1 | -1 | -1 | -1 | -1 | -1 | -1 | -1 | -1 | -1 | -1 | 26.424 |
| 4 | 0 | 0 | 0 | 0 | 0 | 0 | 0 | 0 | 0 | 0 | 0 | 29.741 |
| 5 | 1 | -1 | 1 | 1 | 1 | -1 | -1 | -1 | 1 | -1 | 1 | 31.06 |
| 6 | -1 | 1 | 1 | 1 | -1 | -1 | -1 | 1 | -1 | 1 | 1 | 25.776 |
| 7 | -1 | 1 | -1 | 1 | 1 | -1 | 1 | 1 | 1 | -1 | -1 | 30.372 |
| 8 | 1 | -1 | -1 | -1 | 1 | -1 | 1 | 1 | -1 | 1 | 1 | 26.065 |
| 9 | 1 | 1 | -1 | 1 | 1 | 1 | -1 | -1 | -1 | 1 | -1 | 33.441 |
| 10 | -1 | -1 | 1 | -1 | 1 | 1 | -1 | 1 | 1 | 1 | -1 | 33.189 |
| 11 | 0 | 0 | 0 | 0 | 0 | 0 | 0 | 0 | 0 | 0 | 0 | 29.46 |
| 12 | 0 | 0 | 0 | 0 | 0 | 0 | 0 | 0 | 0 | 0 | 0 | 29.84 |
| 13 | 1 | 1 | -1 | -1 | -1 | 1 | -1 | 1 | 1 | -1 | 1 | 30.729 |
| 14 | -1 | -1 | -1 | 1 | -1 | 1 | 1 | -1 | 1 | 1 | 1 | 30.978 |
| 15 | 1 | -1 | 1 | 1 | -1 | 1 | 1 | 1 | -1 | -1 | -1 | 31.06 |

The overall model $P < 0.01$, indicating a significant difference, the determination coefficient $R_2 = 0.9973$, indicating that the regression model is suitable for 99.73% of the test data. After ignoring the non-significant factors, comparing the F values, the order of the influence of each factor on the test angle of repose is $F > E > J > D > H > C$.

Design of steepest ascent experiment

In summary, the static friction coefficient (E) and rolling friction coefficient (F) between Tiger nut tubers were selected as the test factors, and the value range was further determined by the steepest climbing test. By increasing E and F from low level to high level with equal step length, the relative error δ between the angle of repose of simulation test η and the angle of repose of actual test θ can be calculated according to formula (4). The test scheme and results are shown in table 5.

The significant influencing factors of the simulated angle of repose are selected as the test factors, and the range of values is reduced by the steepest climbing test. The relative error δ between the simulated angle of repose η and the actual angle of repose θ is:

$$\delta = \frac{|\eta - \theta|}{\theta} \times 100\% \quad (4)$$

Table 4

Plackett - Burman design regression model analysis of variance of characteristic parameters

| Source | Standardization effect | Sum of squares | Contribution rate/% | F value | p value |
|--------|------------------------|----------------|---------------------|---------|------------|
| Model | — | 95.62 | — | 102.56 | 0.0014** |
| A | -0.33 | 0.34 | 0.33 | 3.74 | 0.1487 |
| B | 0.33 | 0.33 | 0.33 | 3.71 | 0.1495 |
| C | 0.59 | 1.04 | 1.03 | 11.60 | 0.0423* |
| D | 0.97 | 2.83 | 2.79 | 31.52 | 0.0112* |
| E | 2.80 | 23.47 | 23.19 | 261.79 | < 0.001*** |
| F | 4.55 | 62.20 | 61.46 | 693.93 | < 0.001*** |
| G | -0.28 | 0.24 | 0.23 | 2.65 | 0.2023 |
| H | -0.86 | 2.23 | 2.20 | 24.84 | 0.0155* |
| J | 0.99 | 2.94 | 2.91 | 32.81 | 0.0106* |

The static friction coefficient (E) between Tiger nut tubers was determined to be 0.305 at low level and 0.395 at high level. The rolling friction coefficient (F) between Tiger nut tubers was 0.0315 at low level and 0.0405 at high level, which was optimized by Central Composite test.

Table 5

Design and results of path of steepest ascent method

| NO. | E | F | Repose angle $\eta/^\circ$ | Relative error $\delta/\%$ |
|-----|-------|--------|----------------------------|----------------------------|
| 1 | 0.26 | 0.027 | 28.912 | 5.825 |
| 2 | 0.305 | 0.0315 | 29.911 | 2.571 |
| 3 | 0.35 | 0.036 | 31.282 | 1.896 |
| 4 | 0.395 | 0.0405 | 32.039 | 4.362 |
| 5 | 0.44 | 0.045 | 32.984 | 7.439 |

Central Composite test

In order to obtain the optimal parameter combination and explore the significance of the influence of the static friction coefficient (E) and the rolling friction coefficient (F) between the tubers of Tiger nut on the simulated angle of repose, the Central Composite test was carried out by Design-Expert V10.0.1. In the data pre-processing interface, five central points were set up, and a total of 13 groups of angle repose tests were carried out. The test results are shown in table 6.

The regression equation of static friction coefficient (E) and rolling friction coefficient (F) between Tiger nut tubers can be obtained by regression fitting of the test results:

$$\eta = 30.38 + 1.11E + 0.46F - 0.27EF - 0.43E^2 - 0.37F^2 \tag{5}$$

Table 6

Scheme and results of Central Composite Design

| NO. | E | F | Repose angle $\eta/^\circ$ | Relative error $\delta/\%$ |
|-----|----------|----------|----------------------------|----------------------------|
| 1 | -1 | -1 | 27.725 | -9.6905 |
| 2 | 0 | -1.41421 | 29.164 | -5.0033 |
| 3 | 1.41421 | 0 | 31.683 | 3.2020 |
| 4 | 0 | 0 | 30.561 | 0.4528 |
| 5 | 0 | 1.41421 | 30.746 | 0.1498 |
| 6 | 0 | 0 | 30.132 | 1.8501 |
| 7 | 0 | 0 | 31.035 | 1.0912 |
| 8 | 0 | 0 | 30.235 | 1.5147 |
| 9 | 1 | 1 | 30.256 | 1.4463 |
| 10 | -1 | 1 | 28.963 | 5.6580 |
| 11 | -1.41421 | 0 | 27.984 | 8.8469 |
| 12 | 0 | 0 | 29.954 | 2.4300 |
| 13 | 1 | -1 | 30.091 | 1.9837 |

Table 7

Analysis of variance of Central Composite Design regression model

| Source | Sum of squares | Degree of freedom | Mean square | F value | p value |
|----------------|----------------|-------------------|-------------|---------|------------|
| Model | 13.84 | 5 | 2.77 | 10.04 | 0.0043** |
| E | 9.88 | 1 | 9.88 | 35.84 | < 0.001*** |
| F | 1.66 | 1 | 1.66 | 6.01 | 0.0440* |
| EF | 0.29 | 1 | 0.29 | 1.04 | 0.3408 |
| E ² | 1.31 | 1 | 1.31 | 4.75 | 0.0657 |
| F ² | 0.97 | 1 | 0.97 | 3.51 | 0.1030 |
| Residual error | 1.93 | 7 | 0.28 | — | — |
| Misfit term | 1.20 | 3 | 0.40 | 2.21 | 0.2292 |
| Pure error | 0.73 | 4 | 0.18 | — | — |

Through the analysis of variance of the Central Composite Design regression model, the coefficient of variation C.V. is 1.76%. The smaller the coefficient of variation C.V. is, the more reliable the test data is, and the test results are highly reliable. Ignoring the non-significant factors, comparing the F values, the order of the influence of each factor on the angle of repose of the test is E>F.

Fig. 8 shows the influence of the interaction between the static friction coefficient and the rolling friction coefficient on the simulated angle of repose. When the F level is less than 0.25, the η value increases slowly, but with the increase of E, it increases rapidly and then gradually slows down. When the F level is greater than 0.25, the η value does not change significantly, but increases slowly with the increase of E.



Fig. 8 – Effect of Repose angle of Tiger nut tuber

Angle of repose verification test

In the Design-Expert optimization interface, the actual angle of repose of Tiger nut was optimized. The simulation test was carried out under the parameter conditions of the optimized solution to find the most similar parameter conditions to the actual angle of repose, that is, the static friction coefficient between Tiger nut tubers was 0.35 and the rolling friction coefficient was 0.036. Under the optimal parameter conditions, the simulation test is repeated for 10 times to take the average value, and the simulated angle of repose is 30.583°, and the error with the actual angle of repose is only 0.381%. The Tiger nut stacking test is shown in Fig. 9. The trend of the unilateral contour curve of the Tiger nut heap is similar, and the results show that the calibrated Tiger nut parameters are in line with reality.



Fig. 9 – Comparison between physical and simulation experiment of Repose angle of Tiger nut tuber

Electromagnetic vibration hopper verification test

When the electromagnetic vibrating hopper works, the hopper performs a composite movement under the action of the electromagnetic vibrator, as shown in Fig. 10. So that the heaps of Tiger nut tubers are dispersed, and then the spiral track rises slowly, thereby achieving orderly transportation (SINGH *et al.*, 2020; Nguyen *et al.*, 2018). In the bench test, a total of 1000 small, medium and large Tiger nut tubers with a ratio of 12: 9: 5 were selected according to the proportion of collected samples. The diameter of the hopper was 300 mm and the height was 120 mm. When Tiger nut tubers began to slide evenly from the spiral track, the quality of Tiger nut tubers was recorded every minute, and the mass flow rate was calculated. The test was repeated 20 times under the same voltage condition, and the average value was taken.



Fig. 10 – Electromagnetic vibration hopper test

Simulated test

In the simulation experiment, the STL files of Tiger nut tubers and hopper models were imported into EDEM. The number ratio of small, medium and large Tiger nut tubers was 12: 9: 5, the diameter of the hopper was 300 mm, and the height was 120 mm, which was consistent with the actual test.

The compound motion of the hopper is simulated by adding ‘Sinusoidal Translation Kinematic’ and ‘Sinusoidal Rotation Kinematic’ sinusoidal motion functions in the vertical and horizontal circumferential directions. The amplitude is nonlinearly proportional to the voltage. The effective voltage range is selected to be 190–250 V by pre-test. In the simulation, the operating voltage of the electromagnetic vibrator is changed by adjusting and Z_0 .

Table 8

| Relationship between working voltage and amplitude | | |
|--|-----------------------------|---------------------------------------|
| Voltage U/V | Vertical amplitude Z_0/mm | Angular amplitude $\theta_0/(^\circ)$ |
| 190 | 0.334 | 0.534 |
| 200 | 0.349 | 0.571 |
| 210 | 0.360 | 0.603 |
| 220 | 0.365 | 0.629 |
| 230 | 0.377 | 0.665 |
| 240 | 0.391 | 0.692 |
| 250 | 0.402 | 0.727 |

RESULTS

Analysis of test results

The three motion states of the heaps of Tiger nut tubers in the electromagnetic vibration hopper are shown in Fig. 11. After the simulation test, in order to facilitate observation, the three kinds of Tiger nut tubers were dyed black, the green and blue respectively in the post-processing interface, and the “Grid Bin Group” module was added to the spiral track chute to read the quality of the fallen Tiger nut tubers over time and calculate the mass flow rate. At the same time, the total time T required for each test to complete the transportation is recorded.

In addition, the top view and front view of the movement trajectory of Tiger nut tubers during sorting transportation are shown in Fig. 12. Taking the simulation test of voltage $U=220$ V (vertical amplitude $Z_0=0.365$, angular amplitude $\theta_0=0.629$) as an example, under the action of vibration, the heaps of Tiger nut tubers first gradually spread from the bottom of the hopper to the surroundings, and then transported upwards along the spiral track, and finally fell from the chute to complete the transportation.

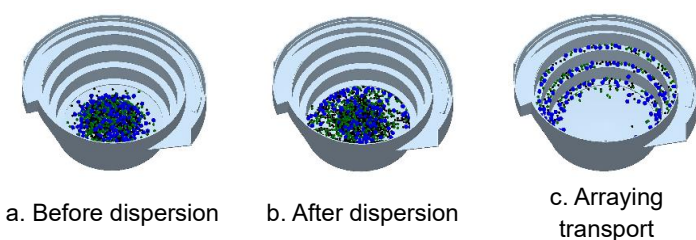


Fig. 11 – Three movement states of Tiger nut tubers

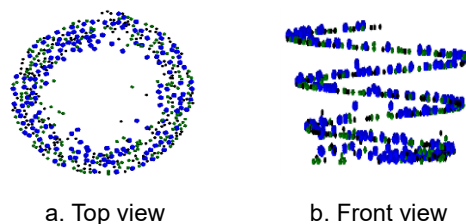


Fig. 12 – Sorting conveying motion trajectory

In the actual test and simulation test, the transmission time curve under different operating voltages is shown in Fig. 13, the change trend of the two curves is basically the same, and the fitting degree of the prediction model is 96.32%. In the simulation experiment, when the working voltage U is lower than 220 V, the movement rate of Tiger nut tubers increases obviously with the increase of working voltage U , when the working voltage U is higher than 220 V, some Tiger nut tubers appear in situ beating on the spiral track or even fall back to the bottom of the hopper. This phenomenon is consistent with the actual test, indicating that the Tiger nut tuber model is reliable and realistic.

As shown in Fig. 14, the change trend of the two curves is basically the same, and the fitting degree of the prediction model is 94.57%. When the operating voltage is in the range of 190–230 V, the mass flow rate increases obviously, and when the operating voltage is in the range of 230–250 V, the mass flow rate tends to be stable.

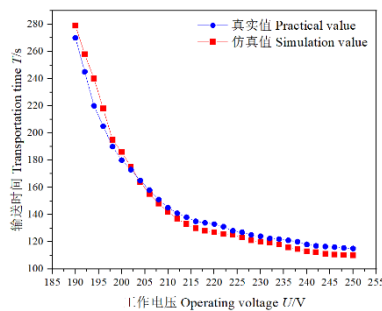


Fig. 13 – Measured results of total transportation time

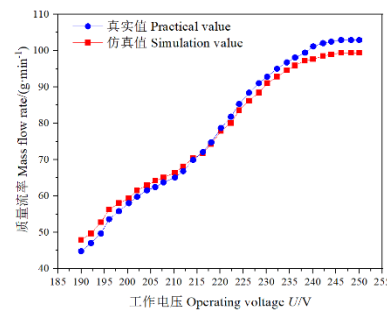


Fig. 14 – Measured results of mass flow rate

By comparing conveying time and mass flow rate at different voltages, it is found that as voltage increases, the actual measured conveying time initially exceeds the simulated value, then becomes smaller and tends to stabilize. The actual measured mass flow rate, on the other hand, starts lower than the simulated value, then increases and tends to stabilize. This inverse relationship between conveying time and mass flow rate results in a curve that accurately represents the actual situation. Overall, the simulation results align well with the actual test results, providing a reliable reflection of real-world operation.

CONCLUSIONS

(1) The results showed that the static friction coefficient and rolling friction coefficient between Tiger nut tubers had a very significant positive effect on the angle of repose of the simulation test. Other contact parameters have no significant effect on the simulated angle of repose.

(2) The central composite test yielded a reliable quadratic regression model using static friction coefficient and rolling friction coefficient as variables, which were identified as significant influencing factors. To optimize the angle of repose for Tiger nut tubers, numerical optimization was employed. The optimal combination of static friction coefficient and rolling friction coefficient was determined to be 0.35 and 0.036, respectively. The simulated angle of repose for Tiger nut tubers was 30.583° , with a negligible error of only 0.381% compared to the actual test results.

(3) The electromagnetic vibration hopper verification test results demonstrated a close resemblance between the motion state of the actual test and the simulation test of Tiger nut tubers across various working voltages. The prediction model for transportation time exhibited a high fitting degree of 96.32%, while the fitting degree for mass flow rate was 94.57%. These calibration results for the intrinsic parameters and contact parameters of Tiger nut are reliable and accurately reflect the actual test outcomes. They serve as a valuable reference for studying Tiger nut parameters, as well as providing a theoretical basis for discrete element simulation of Tiger nut and optimization of electromagnetic vibration hopper parameters.

ACKNOWLEDGEMENT

The author was supported by the New Variety Breeding and Industrialization Demonstration Project of High Yield and High Quality Tiger nut. (Project No. 211100110100).

REFERENCES

- [1] Coetzee C.J. (2016). Calibration of the discrete element method and the effect of particle shape. *Powder Technology*, 297: 50–70. South Africa.
- [2] Guo Tingting, Wan Chuyun, Huang Fenghong, et al. (2021). Research Progress on main nutritional components and physiological functions of Tiger nut (油莎豆主要营养成分及生理功能研究进展). *Chinese Journal of oil crops*, 43: 1174–1180. China.
- [3] Han S.W., Lee C.S., Paz Z.M.A. et al. (2019). Calibration Factor for ASCE 41-17 Modeling Parameters for Stocky Rectangular RC Columns. *Applied Sciences, Multidisciplinary Digital Publishing Institute*, 9(23): 5193. Republic of Korea.
- [4] Hao Jianjun, Long Sifang, Li Hao, et al. (2019). Construction of discrete element model and calibration of simulation parameters for machine harvesting yam (机收麻山药离散元模型构建及其仿真参数标定). *Journal of agricultural engineering*, 35(20): 34–42. China.

- [5] Jia Honglei, Deng Jiayu, Deng Yanling, et al. (2021). Contact parameter analysis and calibration in discrete element simulation of rice straw. *International Journal of Agricultural and Biological Engineering*, 14(3): 72–81. China.
- [6] Mišljen P., Matijević M., Despotović Z. (2016). Modeling and Control of Bulk Material Flow on the Electromagnetic Vibratory Feeder. *Automatika*, 57(4): 936–947. Republic of Serbia.
- [7] Nguyen V.X., Golikov N.S. (2018). Analysis of material particle motion and optimizing parameters of vibration of two-mass GZS vibratory feeder. *Journal of Physics: Conference Series*, 1015: 052020. Vietnam.
- [8] Pan Yanxin, Yuan Chengfu, Jing Siyuan, et al. (2020). Simulation and optimization of irrigation schedule for summer maize based on SWAP model in saline region. *International Journal of Agricultural and Biological Engineering*, 13(3): 117–122. China.
- [9] Pascual B., Maroto J.V., López-Galarza S., et al. (2000). Chufa (Tiger nut L. var. sativus Boeck.): an unconventional crop. Studies related to applications and cultivation. *Economic botany*, 439–448. Spain.
- [10] Pue J.D., Emidio G.D., Flores R.D.V., et al. (2019). Calibration of DEM material parameters to simulate stress-strain behaviour of unsaturated soils during uniaxial compression. *Soil and Tillage Research*, 194: 104303. Belgium.
- [11] Rebezov M., Usman Khan M., Bouyahya A. et al. (2023). Nutritional and technical aspect of tiger nut and its micro-constituents: An overview. *Food Reviews International*, 39(6): 3262-3282. Russian.
- [12] Shi Linrong, Zhao Wuyun, Yang Xiaoping. (2022). Effects of typical corn kernel shapes on the forming of repose angle by DEM simulation. *International Journal of Agricultural and Biological Engineering*, 15(2): 248–255. China.
- [13] Singh C., Chandravanshi M.L. (2020). Performance and noise analysis of vibratory feeder using dynamic rubber spring model. Proceedings of the Institution of Mechanical Engineers, Part C: *Journal of Mechanical Engineering Science*, 234(2): 530–543. Indian.
- [14] Sobhy H.M., Ahmad S.S., Azoz H.A., et al. (2015). Hepatoprotective effect of fennel and tiger nut on biochemical parameters and DNA damage in rats. *Egyptian Journal of Chemistry and Environmental Health*, 1(1): 18-37. Australia.
- [15] Tekeste M.Z., Mousaviraad M., Rosentrater K.A. (2018). Discrete Element Model Calibration Using Multi-Responses and Simulation of Corn Flow in a Commercial Grain Auger. *Transactions of the ASABE*, 61(5): 1743–1755. USA.
- [16] Udefa A.L., Amama E.A., Archibong E.A., et al. (2020). Antioxidant, anti-inflammatory and anti-apoptotic effects of hydro-ethanolic extract of Tiger nut L. (tiger nut) on lead acetate-induced testicular dysfunction in Wistar rats. *Biomedicine & pharmacotherapy*, 129: 110491. Italy.
- [17] Umukoro S., Okoh L., Igweze S.C., et al. (2020). Protective effect of Tiger nut (tiger nut) extract against scopolamine-induced memory loss and oxidative stress in mouse brain. *Drug Metabolism and Personalized Therapy*, 35(3): 20200112. Nigeria.
- [18] Wang Liming, Fan Shengyuan, Cheng Hongsheng, et al. (2020). Calibration of pig manure contact parameters based on EDEM (基于 EDEM 的猪粪接触参数标定). *Journal of agricultural engineering*, 36(15): 95–102. China.
- [19] Wang Zhicheng, Li Shuangshou, Liang Xiong, et al. (2022). Development status and Prospect of Tiger nut industry in China (中国油莎豆产业发展现状与前景展望). *Technology and industry*, 22(01): 62–67. China.
- [20] Wu Mengchen, Cong Jinling, Yan Qin, et al. (2020). Calibration and experiment of discrete element simulation parameters of peanut seed particles (花生种子颗粒离散元仿真参数标定与试验). *Journal of agricultural engineering*, 36(23): 30–38. China.
- [21] Xing Jiejie, Xu Liming, Liu Xudong, et al. (2017). Simulation and experiment of corn seed dispersion, sorting and transportation in electromagnetic vibration hopper (电磁振动料斗内玉米种子分散与排序输送仿真及试验). *Journal of agricultural engineering*, 33(13): 32–39. China.

DESIGN AND RESEARCH ON FEEDING COMPONENTS OF WHEAT FLOUR PARTICLE SIZE DETECTION DEVICE

小麦制粉粒度检测装置供料部件设计与研究

Mingxu WANG^{1,2)}, Haojun ZHAO¹⁾, Saiqiang LI¹⁾, Jiangfeng OUYANG¹⁾, Junyong WU³⁾, Hengda ZHANG⁴⁾

School of Mechanical & Electrical Engineering, Henan University of Technology, Zhengzhou 450001, China
Henan Key Laboratory of Grain and Oil Storage Facility & Safety, Henan University of Technology, Zhengzhou 450001, China
Hebei Pingle Flour Machinery Group Co., Ltd., Zhengding 050800, China
Buler (Wuxi) Commercial Co., Ltd., Wuxi, Jiangsu 214142, China
Tel: 18623717728.; E-mail: wmx20032002@163.com
DOI: <https://doi.org/10.35633/inmateh-73-03>

Keywords: Wheat milling; particle size detection; shaftless screw; Box-Behnken model

ABSTRACT

To address the issues of poor timeliness and delayed feedback in traditional wheat milling processes for manual particle size detection, a wheat milling online particle size detection device has been designed. This paper focuses on the design optimization of the key feeding component in the device, which affects the accuracy of particle size detection. The feeding component adopts shaftless screw blades. Through theoretical analysis, the main parameter ranges affecting the throughput capacity of the shaftless screw conveyor are determined. A Box-Behnken experiment is designed to obtain the optimal parameter combination for each factor: outer diameter of screw blades 23.8 mm, inner diameter of screw blades 6.4 mm, pitch 11.2 mm, and blade rotation speed 288.9 r/min. Simulation and test stand experiments are conducted using the above parameter combination. The simulation results show that the average throughput capacity of the feeding component is 2.85 kg/h, while the average throughput capacity of the test stand experiment is 2.84 kg/h, with a coefficient of variation of uniformity of 1.33%. These results indicate that the above parameter combination meets the design requirements for the feeding component in the device.

摘要

针对传统小麦制粉工艺人工粒度检测时效性差、反馈迟滞等问题，设计了小麦制粉在线粒度检测装置，本文针对装置中的影响装置检测准确率的关键供料部件进行设计优化。供料部件采用无轴螺旋叶片，通过理论分析确定影响无轴螺旋输送能力的主要参数取值范围，设计 Box-Behnken 试验得到各因素的最优参数组合为：螺旋叶片外径 23.8mm，螺旋叶片内径 6.4mm，螺距 11.2mm，叶片转速 288.9r/min。采用上述参数组合进行仿真与台架试验，仿真结果为供料部件平均输送能力为 2.85kg/h，台架试验的平均输送能力为 2.84kg/h，均匀性变异系数为 1.33%，结果表明上述参数组合能够满足装置中供料部件的设计要求。

INTRODUCTION

In wheat milling, the particle size curve of the ground material serves as a direct indicator of the milling machine's technical efficiency (Zhao et al, 2009). Traditional flour mills typically rely on manual sieving to determine the particle size distribution of the ground material (Wen et al, 2013), leading to issues like poor timeliness, delayed feedback, and an inability to detect subtle fluctuations in processing quality. To address these challenges, the development of an online particle size detection equipment for the wheat milling industry is imperative. While online particle size detection technology has been extensively researched in industries like mining and coal mining (Wang et al, 2018; Li et al, 2021; Wang et al, 2021; Bidas et al, 2021), its application in wheat milling is still in its nascent stages. This paper proposes a novel approach based on the dynamic image method (Yang., 2018), introducing an online particle size detection device for wheat processing during the milling process. This device not only resolves the limitations of traditional manual offline detection methods but also facilitates seamless integration with milling machines, enabling automated and real-time adjustment of grinding parameters.

In terms of material feeding in the equipment, the application of shaftless screw blade mechanisms is ideal for the wheat milling industry, which demands strict cost and energy consumption control along with long equipment lifespans. Shaftless screw blades possess the desired characteristics (Cheng et al, 2016; Ananth et al, 2023) and have been widely utilized in various industries in recent years. For instance, Ma designed a simulated lunar soil active filling device based on shaftless screw blade design principles (Ma et al, 2019).

Wang applied shaftless screw blades to biomass screw continuous pyrolysis equipment feeders, addressing issues such as high mass, energy consumption, and susceptibility to mechanical interference associated with shafted screw feeders (Wang *et al*, 2017). Jiang optimized the structural parameters of sterilizers' shaftless screw heating conveyors using a particle swarm algorithm and verified the optimized parameters using COMSOL software (Jiang *et al*, 2020). Orefice conducted an analysis of the effect of screw shaft size on material conveying efficiency using discrete element analysis, finding that smaller screw shafts led to higher productivity and efficiency (Orefice *et al*, 2017). Bangura designed a spiral groove wheel manure spreading device, and experimental verification revealed improvements in both manure discharge quantity and uniformity (Bangura *et al*, 2020).

This paper is based on the principle of shaftless screw conveying to design the key shaftless screw feeding component in the wheat milling particle size detection device. The structural parameters of the screw in the feeding component are crucial, as their stability directly affects the accuracy of particle size identification in the final device operation. Therefore, based on the throughput demand of the device process, the various parameters of the shaftless screw blades are designed. Utilizing the discrete element method, a quadratic regression orthogonal Box-Behnken combined experiment is conducted to determine the optimal combination of parameters for the screw conveying blades. Subsequently, experimental verification is performed on the test stand. This study aims to provide a reference for the design of wheat milling sub-material particle size detection devices and the optimization of shaftless screw design.

MATERIAL AND METHODS

The Overall Structure of The Device

The structural working principle of the wheat processing particle size detection device is illustrated in Figure 1. The device primarily consists of feeding components, a vibrating feeder, a collection box, a capturing unit, and a cleaning unit. Its operation relies on a PLC control system, with parameters controlled via a touchscreen interface. The working process of the device is as follows: sample material is fed into the particle size detection device from beneath the grinding roller via a Sampling component, where it vertically descends through the material inlet; the feeding device transports the sample material to the vibrating feeder; the material descends from the end of the vibrating feeder in a "single-layer material waterfall" form; the capturing unit captures images of the descending particles using backlighting; and the images are then analysed for particle size information using proprietary algorithms upon transmission to a computer. In practical applications, one PLC control system can manage multiple particle size detection devices.

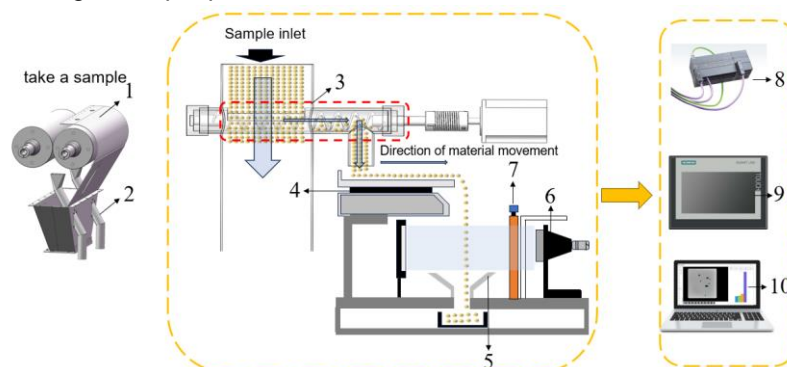


Fig. 1 - Device Structure and Working Principle

1- Grinding roller; 2-Sampling component; 3-Feeding component; 4-Vibrating feeder; 5-Collection box; 6-Capturing unit; 7-Cleaning unit; 8-PLC; 9-Touchscreens; 10-Recognition software

Feeding Component Working Principle

The material flows into the inlet pipe and falls into the entrance of the feeding component. The shaftless screw blade, driven by a stepper motor, continuously rotates in the specified direction. The material falls into the feeding trough of the vibrating feeder at the rear end of the feeding device.

Design of Shaftless Screw Blade Structure and Parameters

In order to ensure the conveying state and uniformity of materials when they are conveyed to the vibrating feeder, and to avoid blockages in the conveying device, it is crucial to maintain a stable conveying state of the materials. The conveying state of the materials ultimately affects the accuracy of particle size identification. When materials are in motion within the shaftless screw conveying device, the shape and size parameters of the shaftless screw directly influence the trajectory of the materials (Motaln *et al*, 2017).

Therefore, detailed design of the shaftless screw is required to determine key parameters such as the outer diameter, inner diameter, and pitch of the shaftless screw blades.

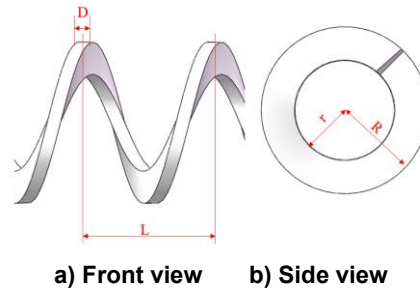


Fig. 2 - Schematic Diagram of Shaftless Screw Blade Structure

D - Thickness of screw blade; *L* - Pitch; *R* - Outer diameter of screw blade; *r* - Inner diameter of screw blade

The outer diameter *D*, inner diameter *d*, pitch *L*, and operating speed *n* of the shaftless screw conveyor should satisfy equations (1) to (4) respectively (Xiang et al, 2010; Erhie et al, 2021).

Screw outer diameter:

$$D \geq K \left[\frac{Q}{\varphi \rho C} \right]^{\frac{2}{5}} \quad (1)$$

In the equation, *D* represents the outer diameter of the screw blade in meters (m); *K* is the material characteristic coefficient, taken as 0.049; φ is the fill coefficient, taken as 0.3; ρ is the material unit bulk density, 407.9 kg/m³; *C* is the inclination coefficient, taken as 1 when horizontal; *Q* is the screw conveying capacity, in this device, *Q* has been verified by the previous test, and its conveying capacity is 2.88 kg/h when it meets the process requirements of the device.

Screw inner diameter:

$$d = (0.2 \sim 0.35) D \quad (2)$$

Pitch:

$$L = (0.5 \sim 2.2) D \quad (3)$$

Operating speed:

$$n \leq \frac{A}{\sqrt{D}} \quad (4)$$

In the equation, *n* represents the operating speed in revolutions per minute (r/min), *A* is the comprehensive material coefficient, taken as 50. The selection of *K*, φ , ρ , *C*, and *A* can be referenced from relevant literature (Zhang et al, 2010; Bates, 2008).

According to equation (1), the outer diameter of the shaftless screw blade only needs to be greater than 11 mm to meet the design requirements. The width of the material inlet of the vibrating feeder is 45 mm. To prevent material from blocking and overflowing on the chute, the maximum outer diameter of the shaftless screw blade is set to 30 mm. To avoid material flow obstruction inside the shaftless screw blade, based on the material's flow characteristics, the minimum flow space for the material should be at least 3 times the size of the material particles (Zhu et al, 2023).

Thus:
$$D \geq 3m \quad (5)$$

In the equation, *m* represents the average diameter of the material, in millimetres (mm).

The average diameter of the large particles of the ground material from the type I mill used in the experiment is 6.6 mm. Therefore, the minimum outer diameter of the selected screw blade is 19.8 mm.

Substituting the range of screw blade outer diameters, 19.8 to 30 mm, into equation (4), the operating speed should be 288.68 to 355.34 r/min. To ensure the strength and flexibility of the screw blade, a thickness of 2 mm (*e*) is selected for the screw blade. Based on practical usage, for equations (2) and (3), *d* is taken as 0.3*D* and *L* is taken as 0.5*D*, which means the inner diameter of the screw blade ranges from 5.94 to 9 mm, and the pitch ranges from 9.9 to 15 mm. According to Ji, the gap between the screw outer diameter and the barrel wall has a significant impact on the conveying efficiency and operating power (Ji, 2021). When designing screw conveyors, the gap should be smaller than the size of the particles to reduce power consumption and material damage. Considering this, a gap of 2 mm between the screw outer diameter and the barrel wall is selected.

Simulation Experiment

To explore the optimal operating conditions of the shaftless screw blades, simulation experiments are conducted on the screw pitch, outer diameter of the screw blades, inner diameter of the screw blades, and blade rotation speed. The aim is to determine the optimal combination of parameters for the screw blades.

Simulation Model

This design focuses on the sub-material of the Type I skin mill. The "Polyhedral" particle model, newly added in EDEM 2022, is adopted. Figure 3(a) shows the plan view and front view of the particles under the Type I skin mill, presenting an overall "rectangular prism" shape. After measuring the length, width, and height of 100 sub-material particles, their average dimensions are determined to be 6.3 mm, 3.7 mm, and 1.2 mm, respectively. Ultimately, the simulated particle model adopts the particles shown in Figure 3(b), with their dimensions set to the measured average values. Referring to the contact parameter determination method in the GEEM library and literature (Li et al, 2019; Chen et al, 2023; Hoshishima et al, 2021), the contact parameters between the sub-material particles and stainless steel are measured, as shown in Table 1. The calibration method of discrete element parameters for sub-material particles and experimental details will be reported separately.

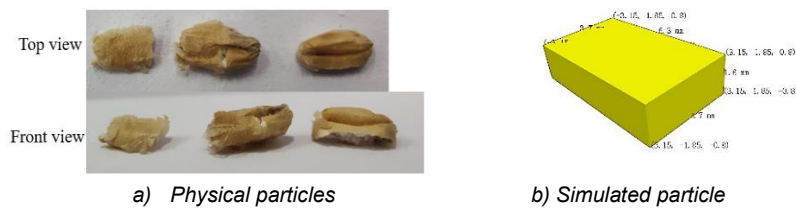


Fig. 3 - Ground down actual and simulated particles

Table 1

| EDEM simulation model parameter | | |
|---------------------------------|--------------------------------|---------------------|
| Item | Argument | Numerical value |
| Ground stock | Poisson's ratio | 0.33 |
| | Shear modulus /[Pa] | 2.088×10^8 |
| | density /[kg/m ³] | 1270 |
| Stainless steel | Poisson's ratio | 0.274 |
| | Shear modulus /[Pa] | 7×10^{10} |
| | density /[kg/m ³] | 7800 |
| Ground stock - Ground stock | Collision recovery coefficient | 0.241 |
| | Static friction factor | 0.619 |
| | Rolling friction factor | 0.055 |
| Ground stock - Stainless steel | Collision recovery coefficient | 0.176 |
| | Static friction factor | 1.364 |
| | Rolling friction factor | 0.399 |

The simplified simulation model of the sampling component built in SolidWorks is imported into EDEM, as shown in Figure 4. To ensure the accuracy of the experiment, material particles are generated with a normal distribution. The particle factory is set above the inlet, and a flow detection sensor is added at the end of the shaftless screw sampler for convenient processing of the experimental results. The sensor captures the conveying capacity for 8 seconds and calculates the average value. Simulation parameters are set according to the experimental plan, with a total simulation duration of 15 seconds.

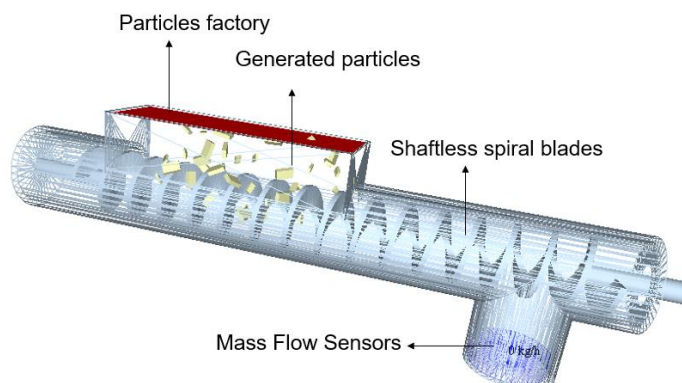


Fig. 4 - Simulation Model of Shaftless Screw

Experimental Factors and Experimental Indicators

As deduced from the parameter design in the previous section, the conveying capacity of the shaftless screw blade is related to the outer diameter, inner diameter, pitch, and rotational speed of the screw blade. To find the optimal parameters for the shaftless screw blade, Design Expert 13 is used to analyse these four influencing factors through experimental trials. The ranges of the outer diameter, inner diameter, pitch, and rotational speed of the screw blade are set to 19.8-30 mm, 5.94-9 mm, 9.9-15 mm, and 288.68-355.34 r/min respectively.

RESULTS

Box-Behnken Combination Experiment

Based on the designed ranges of four influencing factors mentioned earlier, Design Expert 13 was employed to conduct a Box-Behnken experiment with four factors at three levels. The independent variables included the outer diameter of the helical blade, the inner diameter of the helical blade, the pitch, and the rotational speed of the helical blade. The response value was the conveying capacity at the end of the shaftless spiral feeder. The aim was to seek the optimal operating parameters for the shaftless helical blade. The experiment consisted of 29 simulation runs, with 5 sets of trials established at the central level. The experimental factors and their codes are shown in Table 2, and the experimental results are presented in Table 3.

Table 2

| Experimental Factors and Codes | | | | |
|--------------------------------|---|---|-----------------------------|---|
| Code | Factor | | | |
| | Spiral blade outer diameter A / [mm] | Spiral blade inner diameter B / [mm] | Pitch of spiral C / [mm] | Rotational speed of spiral blades D / [r·min ⁻¹] |
| 1 | 30 | 9 | 15 | 355.34 |
| 0 | 24.9 | 7.47 | 12.45 | 322.01 |
| -1 | 19.8 | 5.94 | 9.9 | 288.68 |

Table 3

| Experimental Results and Design | | | | | |
|---------------------------------|-------------------------------|-------------------------------|-------------------|-------------------------------------|-----------------------------|
| Serial number | Spiral blade outer diameter A | Spiral blade inner diameter B | Pitch of spiral C | Rotational speed of spiral blades D | conveying capacity Y/[kg/h] |
| 1 | 24.9 | 7.47 | 12.45 | 322.01 | 9.527 |
| 2 | 30 | 7.47 | 15 | 322.01 | 11.761 |
| 3 | 30 | 7.47 | 12.45 | 288.68 | 10.527 |
| 4 | 24.9 | 7.47 | 15 | 288.68 | 7.217 |
| 5 | 24.9 | 5.94 | 12.45 | 355.34 | 6.731 |
| 6 | 24.9 | 9 | 12.45 | 355.34 | 4.663 |
| 7 | 24.9 | 5.94 | 15 | 322.01 | 8.639 |
| 8 | 30 | 7.47 | 12.45 | 355.34 | 12.638 |
| 9 | 24.9 | 7.47 | 12.45 | 322.01 | 8.006 |
| 10 | 19.8 | 7.47 | 12.45 | 288.68 | 3.58 |
| 11 | 24.9 | 7.47 | 12.45 | 322.01 | 9.987 |
| 12 | 24.9 | 5.94 | 9.9 | 322.01 | 4.378 |
| 13 | 24.9 | 7.47 | 12.45 | 322.01 | 8.033 |
| 14 | 19.8 | 7.47 | 9.9 | 322.01 | 2.226 |
| 15 | 19.8 | 7.47 | 12.45 | 355.34 | 7.233 |
| 16 | 24.9 | 7.47 | 15 | 355.34 | 10.967 |
| 17 | 24.9 | 7.47 | 12.45 | 322.01 | 7.842 |
| 18 | 24.9 | 9 | 15 | 322.01 | 11.53 |
| 19 | 24.9 | 7.47 | 9.9 | 355.34 | 10.059 |
| 20 | 30 | 7.47 | 9.9 | 322.01 | 6.213 |
| 21 | 19.8 | 7.47 | 15 | 322.01 | 9.589 |
| 22 | 24.9 | 7.47 | 9.9 | 288.68 | 2.131 |
| 23 | 24.9 | 5.94 | 12.45 | 288.68 | 3.628 |
| 24 | 24.9 | 9 | 12.45 | 288.68 | 2.484 |
| 25 | 19.8 | 9 | 12.45 | 322.01 | 6.377 |
| 26 | 24.9 | 9 | 9.9 | 322.01 | 3.435 |
| 27 | 19.8 | 5.94 | 12.45 | 322.01 | 10.777 |
| 28 | 30 | 9 | 12.45 | 322.01 | 9.661 |
| 29 | 30 | 5.94 | 12.45 | 322.01 | 10.231 |

Using Design Expert 13 to analyse the experimental results, the analysis of variance is shown in Table 4. Additionally, the response surface regression equation for the conveying capacity, given by equation (6), is obtained.

Table 4

| Analysis of Variance | | | | | |
|----------------------|----------------|----|-------------|--------|--------|
| Source | Sun of Squares | df | Mean Square | F | P |
| Model | 214.77 | 14 | 15.34 | 3.40 | 0.0144 |
| A | 37.63 | 1 | 37.63 | 8.34 | 0.0119 |
| B | 3.24 | 1 | 3.24 | 0.7180 | 0.4110 |
| C | 81.44 | 1 | 81.44 | 18.06 | 0.0008 |
| D | 43.03 | 1 | 43.03 | 9.54 | 0.0080 |
| AB | 3.67 | 1 | 3.67 | 0.8130 | 0.3825 |
| AC | 0.8236 | 1 | 0.8236 | 0.1826 | 0.6757 |
| AD | 0.5944 | 1 | 0.5944 | 0.1318 | 0.7220 |
| BC | 3.67 | 1 | 3.67 | 0.8147 | 0.3820 |
| BD | 0.2134 | 1 | 0.2134 | 0.0473 | 0.8309 |
| CD | 4.36 | 1 | 4.36 | 0.9675 | 0.3420 |
| A² | 5.26 | 1 | 5.26 | 1.17 | 0.2984 |
| B² | 12.43 | 1 | 12.43 | 2.76 | 0.1191 |
| C² | 3.02 | 1 | 3.02 | 0.6705 | 0.4266 |
| D² | 13.99 | 1 | 13.99 | 3.10 | 0.1000 |
| Residual | 63.15 | 14 | 4.51 | | |
| Lack of Fit | 59.15 | 10 | 5.91 | 5.91 | 0.0507 |
| Pure Error | 4.00 | 4 | 1.00 | | |
| Cor Total | 277.92 | 28 | | | |

$$Y=8.68+1.77A-0.5195B+2.61C+1.89D+0.9575AB-0.4537AC-0.3855AD+0.9585BC-0.2310BD -1.04CD+0.9007A^2-1.38B^2-0.6828C^2-1.47D^2 \tag{5}$$

In the equation, A, B, C and D are coded values.

Response Surface Analysis

Using Design Expert, response surface plots are obtained to illustrate the effects of various interaction factors on the conveying capacity, as shown in Figure 5. In the plot, factors other than the interaction factors are kept at their midpoint values.

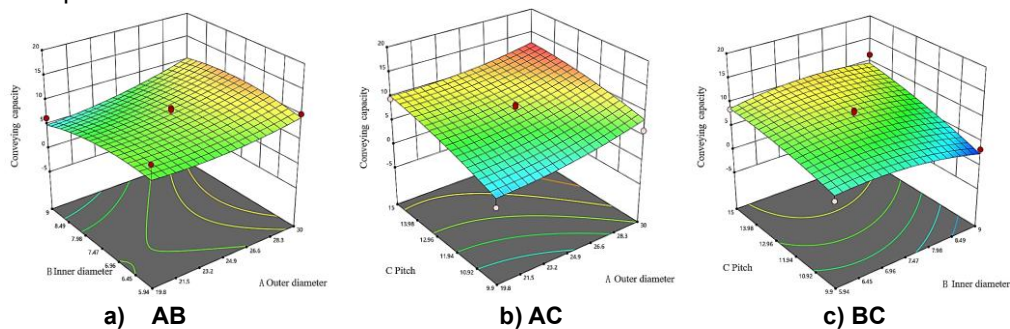


Fig. 5 - The effects of the AB, AC, and BC interactions on the conveying capacity

As shown in Figure 5(a), the conveying capacity of the screw device increases steadily with the increase in blade outer diameter. Analysing the reason, with the increase in blade outer diameter, the filling volume of the material inside the screw device increases, thereby improving the conveying capacity of the screw mechanism. When the blade outer diameter is small, the conveying capacity of the screw mechanism decreases with the increase in blade inner diameter, and the rate of decrease becomes faster after reaching a certain value. Analysing the reason, with the increase in blade inner diameter, the gap inside the mechanism increases, resulting in increased fluidity of the material inside the screw device, thereby reducing the conveying capacity. When the blade outer diameter is large, the conveying capacity increases with the increase in blade inner diameter, but after reaching the peak, it slowly decreases. Analysing the reason, when the outer diameter is large, with the increase in inner diameter, the filling volume of the material inside the screw increases. However, after exceeding a certain degree, the increase in fluidity of the material has a more significant impact on the conveying capacity.

As shown in Figure 5(b), the curvature of the contour lines for the AC interaction is lower compared to those for the AB and BC interactions, indicating that the interaction between AC is not as significant as the other two groups. The conveying capacity of the screw device increases steadily with the increase in blade outer diameter. The conveying capacity of the screw device increases with the increase in pitch. Analysing the reason, with the increase in pitch, the gaps for material filling gradually increase, and more material fills the spaces between the screws, thereby increasing the conveying capacity of the material. This is similar to the findings in Figure 5(a).

As shown in Figure 5(c), the conveying capacity of the screw device gradually decreases with the increase in inner diameter and increases with the increase in pitch. This is similar to the findings in Figure 5(a).

Targeting the optimization of the objective function, using the Optimization function in Design Expert 13 with a target conveying capacity of 2.88 kg/h, the optimal combination parameters obtained are as follows: A (blade outer diameter) = 23.8 mm, B (blade inner diameter) = 6.4 mm, C (pitch) = 11.2 mm, D (blade speed) = 288.9 r/min. Conducting experiments based on the optimal combination parameters yields a conveying capacity of 2.85 kg/h, with an error of 1.04% compared to the predicted value. The experimental and predicted values are consistent, providing a reference for the design of the screw conveyor.

OPTIMIZED PARAMETER BENCH TRIAL

Experimental Material and Equipment

Using laboratory-made Type I skin mill sub-material that complies with production standards as the experimental material, as shown in Figure 6; applying a prototype of the self-made wheat milling sub-material particle size detection device for the throughput capacity test on the test stand, the experimental setup of the device feeding component test stand is depicted in Figure 7, with some structures made transparent for ease of experimental observation.

Experimental Design and Methodology

The experimental setup involves uniformly pouring the test material above the inlet. To accurately measure the feeding component's throughput over a unit of time and assess the overall operational stability of the device, the vibration feeder within the device is also activated and its conveying parameters are set. The material will then fall into the receiving bin at the end of the vibration feeder. To ensure precision in the experiment, timing starts the moment the material reaches the receiving bin. The experiment consists of 5 sets, with each set lasting 5 minutes.

The evaluation criterion used in this experiment is the coefficient of variation (CV) of throughput uniformity. A smaller coefficient of variation indicates less fluctuation in the feeding component's throughput, signifying more uniform feeding. The CV is calculated for each set of 5 statistical time periods, with each period lasting 15 seconds. During each time period, material is manually collected using a material receiving device. The calculation for the coefficient of variation is as follows:

$$\bar{m} = \frac{\sum_{i=1}^x m_i}{x} \quad i=1,2,\dots,5 \quad (6)$$

$$s = \sqrt{\frac{\sum_{i=1}^x (m_i - \bar{m})^2}{x-1}} \quad i=1,2,\dots,5 \quad (7)$$

$$\delta = \frac{s}{\bar{m}} \times 100\% \quad (8)$$

In the equation,

\bar{m} represents the average throughput within five-time intervals, g;

m_i represents the throughput within the i -th time interval, g;

x represents the quantity within the statistical time interval, where n equals 5;

s represents the standard deviation of throughput within each statistical time interval of a set of experiments, g;

δ represents the coefficient of variation of throughput uniformity, expressed as a percentage, %.



Fig. 6 - Laboratory-made material

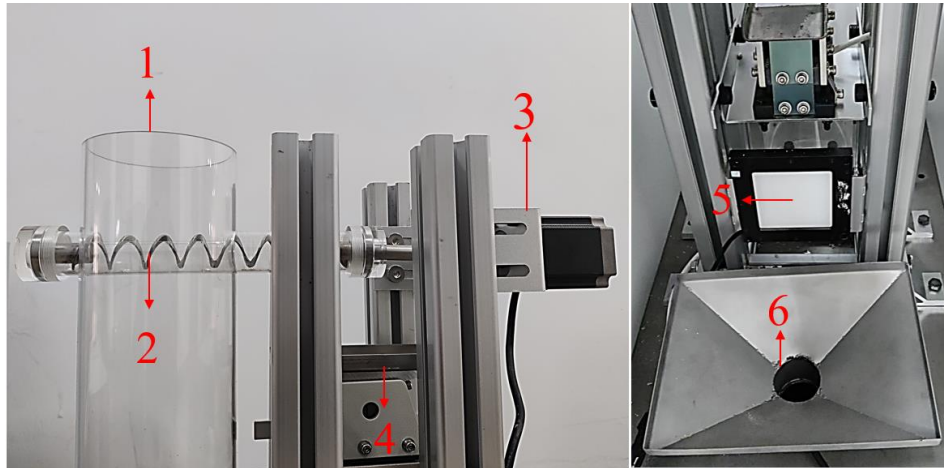


Fig. 7 - Bench Trial

1- Inlet; 2- Sampling Screw; 3- Drive Motor; 4- Vibrating Feeder and its Chute; 5- Backlight; 6- Receiving Hopper

Experimental Results and Analysis

The experimental results of the test stand are shown in Table 5.

Table 5

| Number of times | Bench trial data | |
|----------------------|-----------------------------|--|
| | Conveying capacity / [kg/h] | Coefficient of variation of uniformity / % |
| 1 | 2.71 | 1.34 |
| 2 | 2.83 | 1.28 |
| 3 | 2.81 | 1.42 |
| 4 | 2.91 | 1.29 |
| 5 | 2.79 | 1.33 |
| Average value | 2.81 | 1.33 |

According to Table 5, the average throughput capacity of the sampling device is 2.84 kg/h, the coefficient of variation of uniformity for the five experiments is 1.33%, indicating good stability in the operation of the device. The discrepancy may be attributed to measurement errors or insufficient material dispersion during manual operation, which affected its throughput performance. However, it still meets the requirements for device usage.

The results from both the Box-Behnken combination experiment and the parameter optimization bench test indicate that the designed parameters, with a helical blade outer diameter of 23.8 mm, inner diameter of 6.4 mm, pitch of 11.2 mm, and blade speed of 288.9 r/min, can be effectively implemented in the design of this apparatus. They satisfactorily meet the design requirements for the feeding components of the device. Additionally, this chapter conducts an analysis of the response surface experiment results, providing some guidance for the design optimization of the shaftless helix. Furthermore, the similarity between the research outcomes of this study and those documented in relevant literature (Ma et al, 2019; Zhu et al, 2023; Wulantuya et al, 2020) validates the correctness of the research content and results presented in this paper.

CONCLUSIONS

This study focuses on the shaftless screw blades of the spiral feeding component in the wheat processing particle size online detection device, with the throughput capacity of the screw conveyor as the target. A Box-Behnken experiment with four factors and three levels is conducted using Design Expert 13. A quadratic regression equation is established, with a throughput capacity target of 2.88 kg/h.

The optimal parameter combination is determined to be: outer diameter of screw blades 23.8 mm, inner diameter of screw blades 6.4 mm, pitch 11.2 mm, and blade rotation speed 288.9 r/min. Simulation experiments based on the optimal parameter combination yield a throughput capacity of 2.85 kg/h for the screw blades, with a prediction error of 1.04%, validating the reliability of the multi-objective optimization model. Further experiments on the test stand using the optimal parameter combination show an average throughput capacity of 2.84 kg/h for the test stand prototype, with an average coefficient of variation of throughput uniformity in the test stand experiments of 1.33%, confirming the reliability of the device operation. Additionally, the assembly of the wheat processing particle size online detection device is completed, and the device operates smoothly with stable operation of the feeding components and no occurrence of material blockages.

ACKNOWLEDGEMENT

This research was supported by Training plan of young backbone teachers in colleges and universities in Henan Province (2020GGJS088), Opening subject of Henan key laboratory of grain and oil storage construction and safety (2021KF-B02), Science and Technology Research Project of Henan (No.232103810084) and Science and Technology Key Research Program of Henan Provincial Department of Education (24A460004)

REFERENCES

- [1] Ananth V.L., Arun K.K., Shrivathsan S., et al. (2023). Design of shaftless spiral conveyor for transportation of bulk materials[C]//*AIP Conference Proceedings*. AIP Publishing, 2869(1).
- [2] Bates L. (2008). Screw conveyors[J]. *Bulk solids handling: equipment selection and operation*: 197-220.
- [3] Bangura K., Gong H., Deng R.L., et al. (2020). Simulation analysis of fertilizer discharge process using the Discrete Element Method (DEM) [J]. *PLoS One*, 15(7): e0235872.
- [4] Bidas M, Galecki G. (2021). The concept of a screw conveyor for the vertical transport of bulk materials [J]. *Mining Machines*.
- [5] Cheng Luyang, Zhao Chunhui, Wang Ke. (2016). Shaftless Screw Conveyor (无轴螺旋输送机) [J]. *Hoisting and Transporting Machinery*, (08):16-18.
- [6] Chen Yong, Gao Xiaoxun, Jin Xin, et al. (2023). Parameter calibration and experiment of discrete element Simulation for the seeds of Yousa bean (油莎豆排种离散元仿真参数标定与试验)[J]. *Transactions of the Chinese Society for Agricultural Machinery*, 54(12):58-69.
- [7] Erhie E.O., Hillsden D., Sidhu A.S., et al. (2021). *Shaftless Screw Conveyor Design* [J].
- [8] Hoshishima C., Ohsaki S., Nakamura H., et al. (2021). Parameter calibration of discrete element method modelling for cohesive and non-spherical particles of powder [J]. *Powder Technology*, 386: 199-208.
- [9] Jiang Xiang, Cai Jianrong, Sun Li, et al. (2020). Structure Optimization Design of shaftless Spiral Heating Conveyor for Sterilization Machine (杀菌机的无轴螺旋加热输送机结构优化设计) [J]. *Packaging and Food Machinery*, 38(01):42-46.
- [10] Ji Yu. (2021). Numerical Simulation of particle flow characteristics in screw conveyor based on CFD-DEM (基于 CFD-DEM 螺旋输送机内颗粒流动特性数值模拟研究) [D]. *Northeast Petroleum University*.
- [11] Li Fengli, Tao Yanhui, Chen Jianghui. (2019). Discrete element parameter calibration of sunflower seeds based on accumulation test (基于堆积试验的食葵种子离散元参数标定)[J]. *Journal of Agricultural Mechanization Research*, 46(09):209-215.
- [12] Li Wenbo, Hao Bing, Zhao Hu, et al. (2021). Research and application of ore particle size image online analysis system (矿石粒度图像在线分析系统的研究与应用) [J]. *Mining Machinery*, 49(04):47-50.
- [13] Ma Chao, Liu Fei, Zeng Ting, et al. (2019). Development of an active filling device for simulative lunar soil with shaftless spiral (无轴螺旋式模拟月壤主动填充装置研制) [J]. *Journal of Deep Space Exploration*, 6(01):57-62.

- [14] Motaln M., Lerher T. (2024). Innovative Approaches to Wear Reduction in Horizontal Powder Screw Conveyors: A Design of Experiments-Guided Numerical Study[J]. *Applied Sciences*, 14(7): 3064.
- [15] Orefice L., Khinast J.G. (2017). DEM study of granular transport in partially filled horizontal screw conveyors[J]. *Powder Technol*, 305: 347-356.
- [16] Wang Mingfeng, Xu Qiang, Jiang Enchen et al. (2017). Design and pilot test of feeders for axial spiral continuous pyrolysis of biomass (生物质无轴螺旋连续热解装置送料器设计及中试) [J]. *Transactions of the Chinese Society of Agricultural Engineering*, 33(04):83-88.
- [17] Wang R., Zhang W., Shao L. (2018). Research of ore particle size detection based on image processing [C] // *Proceedings of 2017 Chinese Intelligent Systems Conference: Volume II*. Springer Singapore, 505-514.
- [18] Wang Z., Li D., Zheng X., et al. (2021). A novel coal dust characteristic extraction to enable particle size analysis [J]. *IEEE Transactions on Instrumentation and Measurement*, 70: 1-12.
- [19] Wen Suorang, Yang Lei. (2013). Application of on-line particle size detection in flour production (浅谈在线粒度检测在面粉生产过程中的应用) [J]. *Grain Processing*, 38(04):17-19.
- [20] Xiang Dongzhi, Xu Yuwei. (2010). Design parameter selection of spiral conveyer (螺旋输送机设计参数的选择和确定)[J]. *Cement Technology*, (1): 29 – 33.
- [21] Yang Lin (2018). Research on Dynamic Image Particle Size and Shape measurement System (动态图像颗粒粒度粒形测量系统研究) [D]. *Shandong University of Technology*.
- [22] Zhang Chen, Guo Weicheng, Zhang Kai et al. (2010). Determination and Optimization of Design Parameters of Vertical Screw Conveyor (垂直螺旋输送机设计参数确定与优化)[J]. *Machinery Design & Manufacture*, (10):56-58.
- [23] Zhao Xuejing (2009). Study on equivalent grain size and equivalent grain size curve in wheat milling (小麦制粉中当量粒度与当量粒度曲线研究) [J]. *Food Processing*, 34(02):16-18+58.
- [24] Zhu H., Wu X., Bai L., et al. (2023). Design and experiment of a soybean shaftless spiral seed discharge and seed delivery device[J]. *Scientific Reports*, 13(1): 20751.
- [25] Wulantuya, Wang H., Wang C., et al. (2020). Theoretical Analysis and experimental study on the process of conveying agricultural fiber materials by screw conveyors[J]. *Engenharia Agrícola*, 40(5): 589-594.

DESIGN AND EXPERIMENT OF ANNULAR AIR-BLOWING ASSISTED SEED GUIDING DEVICE FOR CORN NO-TILL SEEDER

玉米免耕播种机环形气吹辅助导种装置设计与试验

Haojie ZHOU¹⁾, Chunling ZHANG^{*1 2)}, Tao LIU¹⁾, Yazi WANG¹⁾, Jun FANG¹⁾, Antai HU¹⁾

¹⁾ College of Engineering, Anhui Agricultural University, Hefei, Anhui, 230036, China

²⁾ Engineering Laboratory of Intelligent Agricultural Machinery Equipment, Anhui, Hefei, 230036, China

Tel: +86-18715160995; E-mail: zhangcl@ahau.edu.cn

DOI: <https://doi.org/10.35633/inmateh-73-04>

Keywords: air-blowing, auxiliary seed guide, seed guide tube, experiment, seed guide device

ABSTRACT

In the process of seed introduction, there is a problem of seed falling disorderly due to the collision between the seed and tube wall, which seriously affects the uniformity of seed spacing in the field. To solve this problem, this paper designed a kind of annular air-blowing auxiliary seed guide device. After a series of simulation experiments, theoretical research, and high-speed camera bench experiments, the optimal parameter selected combination of the critical structure of the seed guide device. The experimental results showed that when the annular air-blowing assisted seed guide tube was used, the positive air pressure was 2 KPa, the airway angle was 150°, the airway outlet width was 12 mm, and the distribution pore diameter was 4 mm. When the forward speed was 6 km/h (the rotation speed of the seed metering disc was 25.30 rpm), the seed sowing effect was the best in the seed guide device; the qualified rate was 88.36%, and the coefficient of variation was 12%. This study provides a reference for improving seed spacing uniformity and can be used to optimize seed guide tubes.

摘要

导种过程中存在着因种子与管壁碰撞引起的种子无序下落的问题，此问题严重影响了种子在田间的粒距均匀性。针对此问题，本文设计了一种环形气吹辅助导种装置，经过一系列的仿真实验，理论研究，高速摄像台架实验，选取导种装置关键结构的最优参数组合。实验结果表明采用环形气吹辅助导种管，正风压为 2 KPa，气道角度 150°、气道出口宽度 12 mm，分配气孔直径 4 mm，在前进速度为 6km/h(排种盘转速 25.30rpm)时种子在导种装置内，种播效果最好到达最好，合格率达到 88.36%，变异系数 12%。导种效果好，该研究为提高播种粒距均匀性提供了借鉴，能够用于导种管的优化。

INTRODUCTION

Sowing operation is an essential primary link in agricultural production, and the precision seeding device is an integral part of realizing agricultural modernization (Dayoub *et al.*, 2021; Lei *et al.*, 2021). Accurate sowing position and grain spacing distribution are the key to proper sowing of corn. The value of precise positioning and seeding lies not only in saving seeds and reducing costs but also in improving the quality of seeding, making seedlings orderly, improving the utilization rate of light energy and soil power, and providing highly consistent operating objects for the midterm management and harvesting, to effectively improve the yield per unit area (Liu *et al.*, 2017; Huang, 2015; Liu, 2013). Therefore, improving the uniformity of corn seed sowing has significant effects on the later growth and yield of corn. Scholars at home and abroad have conducted a series of studies on seed guide technology and device. For corn, a large grain crop, in the process of seed introduction, the seed guide device is required to restrict the movement of seeds, control the movement of seeds in three-dimensional space, and prevent the collision between seeds and seed guide tube, to meet the requirements of precision seeding.

After leaving the seed metering device, due to the inertia of the rotary table of the seed metering device, the seeds cannot fall along a straight line only by gravity. The collision between the seeds and the seed guiding device will be caused by the vibration and displacement of the machine. The results of Wang Qing's field experiment showed that as the forward speed increased, the vibration of the seeder became more intense, and the peak vibration acceleration became larger (Wang *et al.*, 2024). Resulting in the longer migration time of the seeds in the seed guiding device.

Haojie Zhou, U.G. Stud.; Chunling Zhang, Lecturer; Tao Liu, M.S. Stud.; Yazi Wang, M.S. Stud.; Jun Fang, M.S. Stud.; Antai Hu M.S. Stud.

Wang Jinwu used high-speed photography and took the finger clip corn precision seeder as the research carrier. The test results showed that when the working speed was 15 rpm~45 rpm, and the tilt angle was 0 °, the lateral displacement of the seed front and side tracks increased with the increase of the working speed; When the working speed was more significant than 35 rpm, the seed trajectory and the position distribution of the falling point are gradually dispersed, and the coefficient of variation of plant spacing becomes larger; When the working speed is 30 rpm and the tilt angle is -12°~12°, the trajectory seed throwing angle decreases with the increase of the tilt angle (Wang *et al.*, 2017). Sweden Vaderstad company is a high-speed planter that uses pneumatic projection technology to control the planting trajectory to achieve accurate planting. This falling method can reduce the collision between seed and seed metering tube and improve the precision of the seed dropping (Chen *et al.*, 2022). Zhang Yunhe designed a pressure-holding precision seed-metering device for corn, which uses a guide plate to control the movement trajectory of corn seeds. The experimental results show that the device can effectively improve the accuracy of seed dropping (Zhang *et al.*, 2023). Zhao Shuhong designed a corn seed guiding device that limits the seed pod's movement trajectory by combining the wrist seeder with the V-slot (Zhao *et al.*, 2018). Li Yuhuan designed a straight-line seed-pushing device for air-suction corn metering device. The device is equipped with a straight-line seed-feeding device during the seed-feeding process. When the machine is working, the seeds arriving at the seed-pushing area will be pushed by the airflow, move downward straight away from the seed metering disc, and then quickly reach the seed bed along the seed guide tube (Li *et al.*, 2020).

Kocher took the new and old seed guide tubes produced by John Deere company of the United States as the test object using its precision seeder to conduct a comparative test on the seeding performance. The results showed that the new seed guide tube's seeding performance was better, mainly caused by the smooth inner wall of the new seed guide tube and the rough inner wall of the old seed guide tube (Kovher M.F. *et al.*, 2011). Yazgi studied the effect of different seed guide tube shapes on seed metering performance under various operating speeds and theoretical seed spacing test conditions. Regarding the seed metering qualification rate, the performance of a plastic bellows-type seed guide tube is much worse than that of a smooth metal surface (Yazgi A., 2016). Yatskul studied that the diameter of the pneumatic seed guide tube commonly used by foreign agricultural machinery enterprises (Horse, Kuhn, and John Deere) is mostly 20~30 mm, which can achieve a better sowing effect (Yatskul A. *et al.*, 2018). Endrerud used the combination of the seed guide tube and ditcher to conduct a numerical simulation to study how the kinetic energy of seed sliding from the seed guide tube is affected by the ditcher's diameter, inclination angle, and bending radius. The test shows that when the seed guide tube is tilted to 45°, the diameter does not affect on the energy loss. When the seed guide tube is divided into a smooth horizontal, inclined plane and smoothly transits to the shape of an arc curve, this time, the collision energy is minimized (Endrerud H.C., 1999).

Therefore, in order to improve the uniformity of corn planting spacing, a kind of annular air-blowing assisted seed guide device was designed in this paper. Through theoretical analysis and fluid numerical simulation, the key structural parameters were determined. The rationality and accuracy of the design were verified by bench test, and the optimal combination of operation parameters was obtained. This study can provide a theoretical basis and technical support for the innovative design of a corn precision seeding device.

MATERIALS AND METHODS

The following is a schematic diagram of seeds bouncing inside the seed guide tube. A new type of seed guide tube will be designed to avoid such bounce.

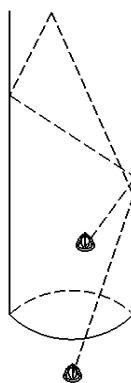


Fig. 1 - Schematic diagram of seed bouncing inside the seed guide tube

Whole structure design

The square cross-section seed guide tube was used as the research carrier, and the annular air-blowing auxiliary seed guide device was installed in the linear seed guide section. The annular air-blowing additional seed guide device mainly comprises an upper annular airway, inclined guide airway, fan airflow interface, distribution hole, and other components. The overall structure is shown in Fig. 2.

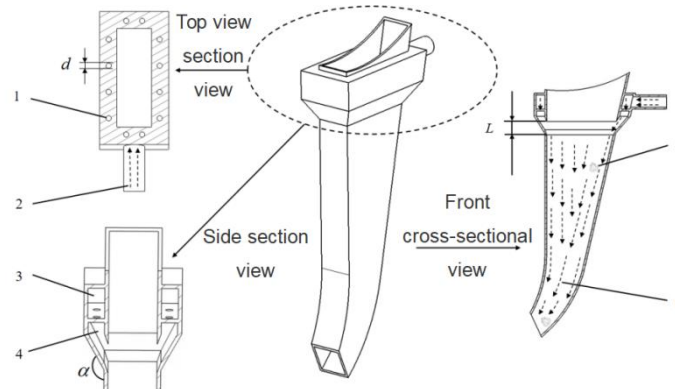


Fig. 2 - Overall and partial structure diagram of annular air-blowing auxiliary seed guide device

1 - distribution hole; 2 - air flow interface of fan; 3 - upper annular airway; 4 - inclined guide airway; 5 - corn grain; 6 - air flow direction
 Note: α is the angle between the inclined guide airway and the tube wall of the seed guide tube, d is the diameter of the distribution pore, L is the width of the distribution airway

During the seeding operation, the annular air-blowing auxiliary seed guide device is installed on the precision seed metering device, and the airflow interface of the fan is connected to the supporting fan. After the fan sets a specific air pressure, the seed guide device continuously provides a high-speed stable air flow. After entering the upper annular airway, the airflow will fill the upper airway and then enter the lower inclined plane to guide the airway through the distribution hole. At this time, a uniform airflow will be formed in the seed guide device continuously downward along the inclined plane. The seeds distributed by the seed metering device migrate to the airflow area of the annular air-blowing auxiliary seed guiding device and scurry downward along the seed guiding tube curve under high-speed airflow. This device shortens the running time of seeds in the tube and reduces the number of collisions.

Design of key components

Inclined airway

When the seeds enter the air flow area of the seed guide device, they will be subjected to forces in different directions, and the force diagram is shown in Fig 3:

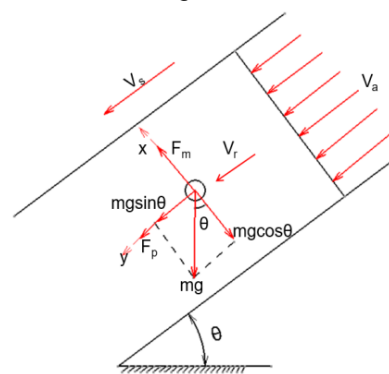


Fig. 3 - Schematic diagram of seed force in the seed guide device

Note: mg – Gravity; F_m - Magnus effect force; θ - air flow angle; v_r - relative velocity of seed and air flow; v_a - air velocity; v_s -seed velocity

According to the theory of gas-solid two-phase flow, the force acting on the corn seed in the air passage with an air flow angle of θ is:

$$F_p = \mu \rho S v_r^2 \tag{1}$$

where:

$$v_r = v_a + v_s \tag{2}$$

$$v_a = \frac{Q}{S_T} \quad (3)$$

where μ - resistance coefficient of corn seed, taking 0.22;
 ρ - air density at normal temperature(20°C), taking 1.205 kg/m³;
 S - relative contact area between seed and air flow, m²;
 v_r - relative velocity of seed and air flow, m/s;
 v_a - air velocity, m/s;
 v_s - seed velocity, m/s;
 Q - air flow, m³/s;
 S_T — cross-sectional area of seed guide device, m²;

Force analysis of seed in seed guide device:

$$F_x = F_m - mg\cos\theta \quad (4)$$

$$F_y = F_p + mg\sin\theta \quad (5)$$

where: F_x – the force of seed in the vertical direction of seed guide device, N;
 F_m — Magnus effect force, N; m — corn seed mass, kg;
 g — acceleration of gravity, m/s²;
 F_y — the force of seed along the curve of seed guide tube, N.

Without contacting the tube wall of the seed guide tube, the force on the vertical movement direction of the seed is constrained by the pressure difference force and Magnus effect force generated by the airflow; under the joint action of airflow resistance and gravity component $mg\sin\theta$ along the direction of seed guide curve, the differential equation of seed motion is obtained from cameral principle:

$$\frac{dv_{sx}}{dt} = \frac{F_m}{m} - g\cos\theta \quad (6)$$

$$\frac{dv_{sy}}{dt} = \frac{\mu\rho S}{m} \left(\frac{Q}{S_T} + v_s\right)^2 + g\sin\theta \quad (7)$$

According to the above formula, when the seed does not collide with the tube wall, its motion acceleration in the tube is affected by the airflow velocity, seed velocity, and air flow angle θ influence. When the corn seed leaves the seed metering device, the seed speed is affected by the angular speed of the rotation of the seed metering plate, which can be regarded as a constant quantity. Since the air velocity is mainly related to the wind speed provided by the fan, it can be kept constant by artificially changing the wind speed. In order to avoid the collision and bounce between the seed and the soil due to the excessive partial velocity in the horizontal direction when the seed leaves the seed guide device, the air flow angle in the tube should be controlled. And it is relevant with an inclined guide airway α . Too large airflow angle will lead to the failure of the design of the pores of the upper distribution channel behind, and too small air flow angle will lead to the loss of the air flow of the annular channel to go down, resulting in eddy currents that disturb the falling of seeds. The angle of the inclined airway in the range of 140°~160° is selected as the later influencing factor.

Airway outlet width L and distribution pore diameter d

In order to ensure the good seeding function of corn seeds under high-speed airflow, the width of the airway outlet should be less than the shortest side length of the nozzle of the seed guide tube. At the same time, if the width of the airway guided by the high-speed airflow is too narrow, the air pressure entering the seed guide tube will be lost, and the aerodynamic resistance will increase (Sokolov E. and Zingel, 1977). Therefore, the outlet width of the intake port is 10~20 mm as the later influencing factor. Both too-large and too-small distribution pores will make the air flow in the airway unevenly distributed into the seed guide tube. According to the size of the design structure and relevant research (Wang et al., 2020), the diameter of the distribution pore is between 3~6 mm as the subsequent influencing factor.

Fan air flow interface and air flow size

The air flow interface of the fan is connected with the pressure-resistant starting hose, and the fan provides a continuous flow of air. The fan model is YASHIBA small drag pump fan, with a working speed of ≤ 3500 rpm and a working pressure between -7 kPa and 7 kPa. The diameter of the large rotating small connector is 16 mm, and the diameter of the air flow interface of the fan should be equal to its outer diameter, taking 16 mm.

Experimental methods

Simulation

The single-factor simulation test was carried out on the critical structural parameters affecting the seed guide effect, the ideal parameter combination was selected for the orthogonal experiment, and the optimal combination of the annular air-blowing auxiliary seed guide device was selected. The test factors and their levels are shown in Table 1:

Table 1

| Single factor influencing factor level | | | |
|--|---------------------------------------|----------------------------|-----------------------------------|
| Level | Inclined airway angle $\alpha/^\circ$ | Airway outlet width L / mm | Distribution pore diameter d / mm |
| 1 | 140 | 10 | 3 |
| 2 | 145 | 12 | 4 |
| 3 | 150 | 14 | 5 |
| 4 | 155 | 16 | 6 |
| 5 | 160 | 18 | |
| 6 | | 20 | |

The critical link of the annular air-blowing auxiliary seed guide device is the selection of wind pressure. High or low wind pressure will affect the movement of seeds in the seed guide tube. 2 kPa, 3 kPa, and 4 kPa were used for fluent software simulation experiments, and the ideal wind pressure was selected.

By counting the absolute value of the velocity difference at the midpoint of the length and width of the section ($v = |v_4 - v_2| + |v_3 - v_1|$), it can be seen whether the seed movement is stable during the process of the seed guide tube. The schematic diagram is shown in Fig 4:

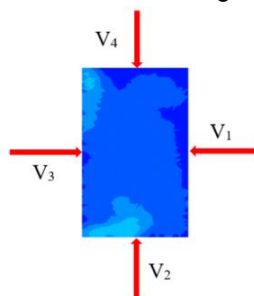


Fig. 4 - Schematic diagram of velocity at the midpoint of section length and width

V_1 - V_4 - the velocities in the four directions of the selected cross-section: right, down, left, up.

Bench test

In order to study the seed guiding effect of the auxiliary seed guiding device of the annular device, the JSP-12 seed metering device performance test bench was used in this experiment. The bench test was carried out in the intelligent agricultural machinery equipment laboratory of Anhui Agricultural University; the i-speed 3 high-speed cameras were used to record the movement of seeds in the seed guiding tube. The data processing software of the seed metering device test bed was used to record the corn seed spacing. It mainly counts the plant spacing of corn seeds to obtain the qualified rate and variation coefficient of sowing.



Fig. 5 - JSP seeder performance test bench

1 - drive motor; 2 - high-speed camera; 3 - scoop wheel seed metering device; 4 - annular air blowing auxiliary seed guiding device; 5 - positive pressure air pipe; 6 - test bed control cabinet

RESULTS

Results and analysis of simulation

Three different wind pressures were simulated and analyzed, and the experimental results are shown in Fig 6:

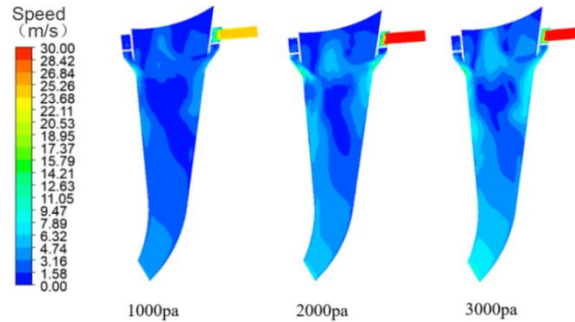


Fig. 6 - Front velocity nephogram under different wind pressures

It can be seen that when the wind pressure is equal to 1 kPa, the airflow inside the pipe is small due to the existence of the distribution airway, which cannot play the role of making the seeds fall rapidly and stably; When the wind pressure is equal to 3 kPa, the turbulence inside the pipe is considerable, which cannot provide stable acceleration for the seeds; At 2 kPa, the air flow in the tube is evenly distributed, which is suitable for the steady falling of sources. 2 kPa air pressure is selected as the inlet air pressure of the seed guide device.

Inclined airway angle

In order to ensure the consistency of test factors, set the airway width as 16 mm and the diameter of the distribution pore as 4 mm, and carry out single-factor numerical simulation for different inclined airway angles. The simulation cloud diagram is shown in Fig. 7 and Fig. 8:

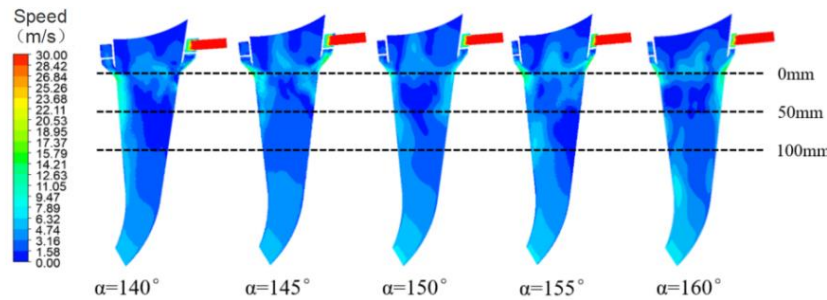


Fig. 7 - Frontal velocity nephogram

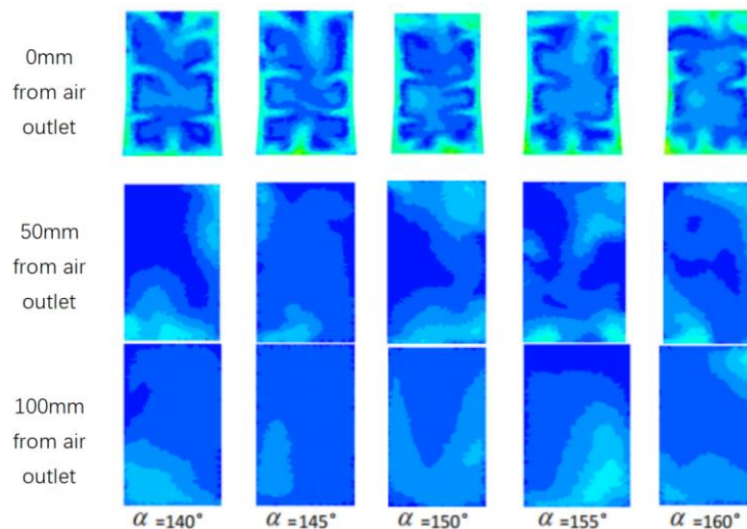


Fig. 8 - Local velocity nephogram of seed guide device

The simulation results are imported into the Origin for drawing, and the influence of different airway angles on the velocity difference in the opposite position is shown in Fig. 9:

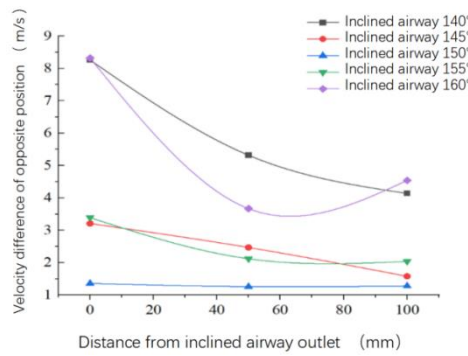


Fig. 9 - Influence of different airway angles on velocity difference in the opposite position

It can be concluded that when the inclined airway angle is between 145° and 155°, the absolute value of the velocity difference at the opposite position of the midpoint of the section is significantly less than 140° and 160°. In order to make the later design of the seed guide tube more in line with the requirements of the experimental design, 145°, 150° and 155° are selected as the factor levels of the later orthogonal test.

Airway width

In order to ensure the accuracy of the single factor simulation, reduce the test error, and ensure the unity of other variables, set the inclined airway angle = 150° and the distribution pore diameter *d* is 4 mm. Then the single factor experiment was carried out on the airway, and the numerical simulation was carried out on different airway widths.

The results are shown in Fig.10 and Fig.11.

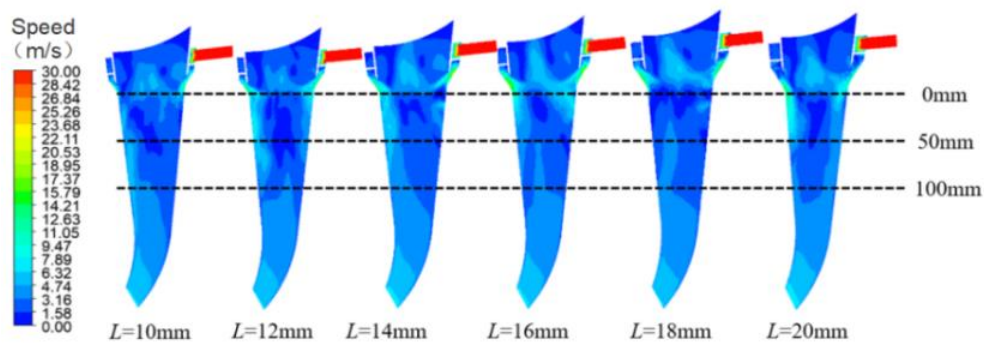


Fig. 10 - Frontal velocity nephogram

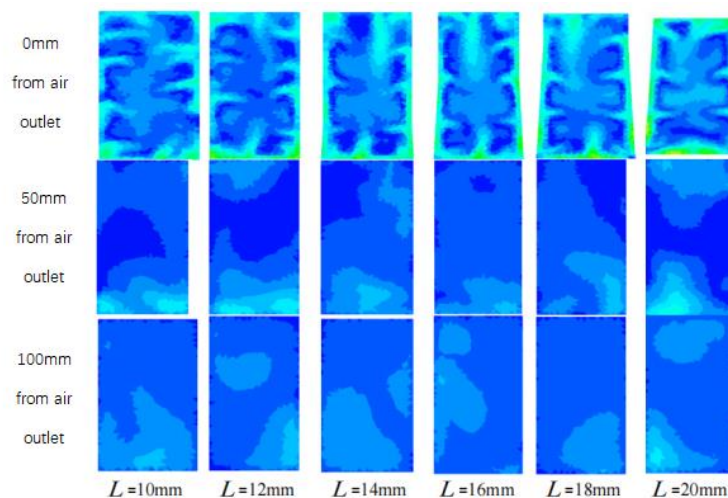


Fig. 11 - Local velocity nephogram of seed guide device

The results were imported into the Origin for drawing, and the influence of different airway widths on the velocity difference in the opposite position was obtained, as shown in Fig.12:

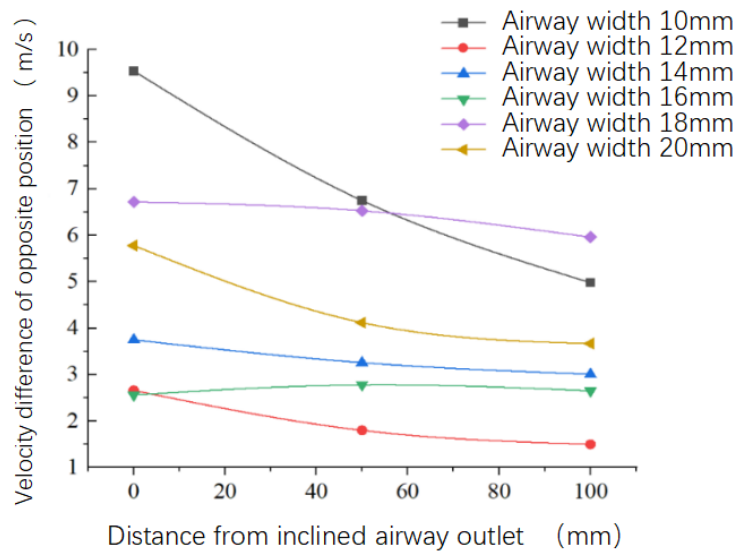


Fig. 12 - Influence of different airway widths on velocity difference in the opposite position

It can be seen from the figure that when the airway width is 12 mm~16 mm, the absolute value of the velocity difference in the opposite position of the experimental index is maintained at a low level relative to the other three factors and are all lower than 4 m/s. In the following orthogonal exploratory analysis, 12 mm, 14 mm and 16 mm were used as the influencing factors.

Distribution pore diameter

In order to ensure the reliability of single factor simulation, the inclined airway angle is set uniformly $\alpha=150^\circ$, the airway width $d=16$ mm. The single-factor experiment was carried out on the distribution pores diameter, and the numerical simulation of different pore diameters was carried out. The simulation cloud diagram is shown in Fig.13 and Fig.14:

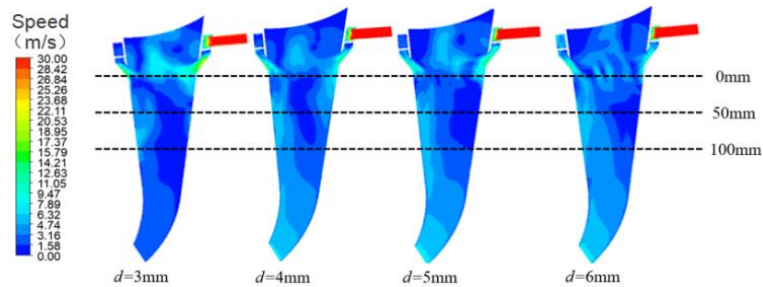


Fig. 13 - Frontal velocity nephogram

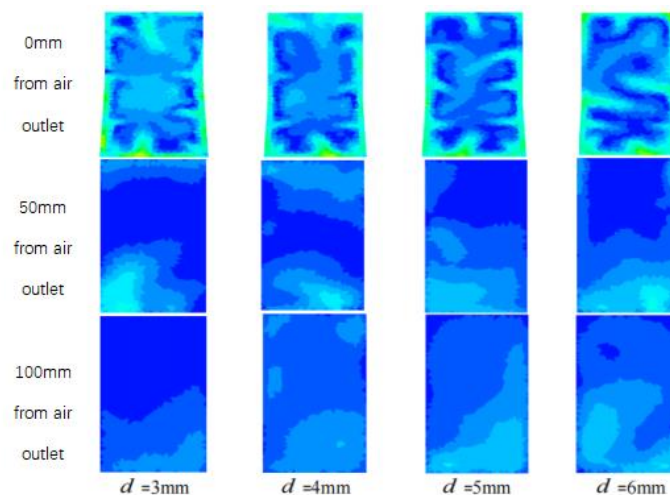


Fig. 14 - Local velocity nephogram of seed guide device

Import the results into the Origin for drawing, and get the influence of different distribution pore diameters on the velocity difference in the opposite position, as shown in Fig. 15:

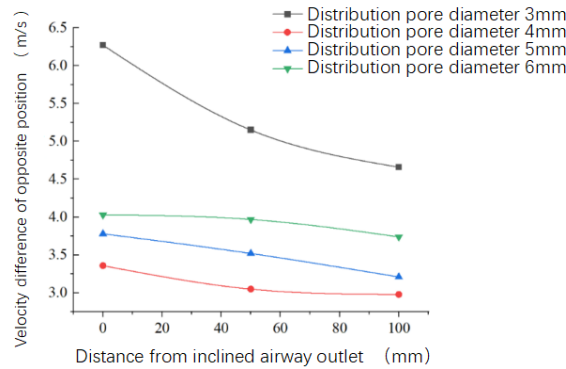


Fig. 15 - Influence of different distribution pore diameter on velocity difference in the opposite position

Therefore, when the distribution pore diameter $d \geq 4$ mm, the velocity difference in the opposite position in the device section is slight. In order to ensure the accuracy of the orthogonal test, 4 mm, 5 mm, and 6 mm are selected as the influencing factors of the interaction.

Results and analysis of the orthogonal experiment

In order to obtain the interaction effect of three factors on the airflow inside the tube and the optimal parameter combination, the Box-Behnken experimental design principle (Wang et al., 2021; Araujo et al., 2017) was adopted. The coding table of the designed experimental factors is shown in Table 2:

Table 2

| Code | Factor | | |
|------|---------------------------------------|--------------------------|---------------------------------|
| | Inclined airway angle $\alpha/^\circ$ | Airway outlet width L/mm | Distribution pore diameter d/mm |
| 1 | 145 | 12 | 4 |
| 0 | 150 | 14 | 5 |
| -1 | 155 | 16 | 6 |

In this experiment, the three-factor three-level quadratic orthogonal rotation combination scheme was used to carry out the multi-factor investigation. The sum of the absolute values of the velocity difference was calculated to judge the airflow stability. The significance of the main factors was analyzed α , the airway outlet width L, distribution pore diameter D, and the absolute value of velocity difference (take the average value) is set respectively as x_1 , x_2 , x_3 and y. The orthogonal test scheme and results are shown in Table 3:

Table 3

| Serial Number | Factor | | | y /m·s ⁻¹ |
|---------------|----------------|-------------------|-------------------|----------------------|
| | $x_1 / ^\circ$ | x_2 / mm | x_3 / mm | |
| 1 | 1 | 1 | 0 | 1.86 |
| 2 | 0 | 0 | 0 | 2.78 |
| 3 | 0 | 0 | 0 | 3.44 |
| 4 | 1 | 0 | -1 | 4.89 |
| 5 | 0 | 1 | -1 | 2.6 |
| 6 | 1 | 0 | 1 | 4.02 |
| 7 | -1 | 0 | 1 | 2.79 |
| 8 | 0 | 0 | 0 | 4.21 |
| 9 | -1 | 1 | 0 | 1.31 |
| 10 | 1 | -1 | 0 | 3.54 |
| 11 | 0 | 0 | 0 | 1.68 |
| 12 | 0 | -1 | 1 | 3.65 |
| 13 | -1 | -1 | 0 | 2.61 |
| 14 | 0 | 1 | 1 | 2.64 |
| 15 | -1 | 0 | -1 | 2.67 |
| 16 | 0 | 0 | 0 | 2.62 |
| 17 | 0 | -1 | -1 | 2.5 |

On the basis of the test, the Design-Expert software was used to carry out multiple regression fitting analysis on the test results, and the regression equation of the sum y of the velocity difference at the opposite position of the midpoint of the section was obtained as:

$$y = 2.61 + 0.65x_1 + 0.99x_2 + 0.11x_3 + 0.13x_1x_2 - 0.065x_2x_3 + 0.75x_1^2 - 0.11x_2^2 + 0.05x_3^2 \quad (8)$$

Variance analysis of the Box-Behnken test model was carried out on the experimental results. The results are shown in Table 4. The absolute value y of the velocity difference of the opposite position of the section's midpoint is significant, and the regression equation mismatch is not significant ($P > 0.05$). From the P value of variance analysis, it can be concluded that the inclined airway angle and the airway outlet width have a significant impact on the model, and the distribution pore diameter had a general effect on the model.

Table 4

Variance analysis of the Box-Behnken quadratic regression model

| Variance source | Velocity difference y at the opposite position of the midpoint of the section | | | |
|--------------------|---|-------------------|--------|---------|
| | Sum of squares | Degree of freedom | F | P |
| Model | 13.76 | 9 | 137.1 | <0.0001 |
| x_1 | 3.39 | 1 | 304.29 | <0.0001 |
| x_2 | 7.78 | 1 | 697.85 | <0.0001 |
| x_3 | 0.092 | 1 | 8.29 | 0.0237 |
| x_1x_2 | 0.070 | 1 | 6.30 | 0.0404 |
| x_1x_3 | 0.000 | 1 | 0.000 | 1.0000 |
| x_2x_3 | 0.017 | 1 | 1.52 | 0.2580 |
| x_1^2 | 2.35 | 1 | 210.85 | <0.0001 |
| x_2^2 | 0.054 | 1 | 4.80 | 0.0646 |
| x_3^2 | 0.010 | 1 | 0.93 | 0.3659 |
| Residual | 0.078 | 7 | | |
| Lack of fit | 0.061 | 3 | 4.91 | 0.0793 |
| Pure error | 0.017 | 4 | | |
| Sum | 13.84 | 16 | | |

In order to study the interaction between multiple factors, two factors are selected as variables, and the other variable is fixed at zero level to obtain the response surface curve in Fig. 16.

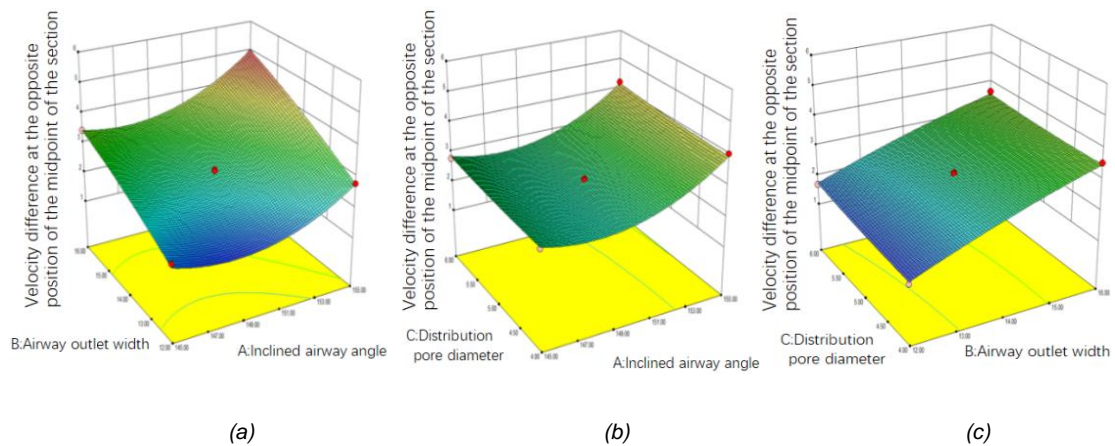


Fig. 16 - Influence of various factors on the velocity difference of the opposite position of the midpoint of the section

As shown in Fig. 16 (a), the inclined airway angle and the airway's outlet width significantly impact the cross-section airflow velocity difference. When the distribution pore diameter is fixed, the velocity difference increases with the increase of the inclined airway angle and the outlet width of the airway; Fig.16 (b) shows that when the outlet width of the airway is fixed, the distribution pore diameter and the inclined airway angle have interactive effects on the velocity difference. With the decrease of the angle and diameter, the sum of the velocity difference becomes smaller; Fig.16 (c) shows that the interaction between the distribution pore diameter and the airway outlet width is not apparent.

From the single-factor experiment results, it can be concluded that the inclined airway angle of 150° is the better single factor air blowing structure, and the outlet width of 12 mm is the better air-blowing structure; In the orthogonal experiment, the simulation effect of No. 9 is the best, and the velocity difference on the opposite position of the midpoint of the section is the smallest, so the selected factors are the inclined airway angle of 150°, the airway outlet width of 12 mm, and the distribution pore diameter of 4 mm.

Results and analysis of bench test

Repeat each group of tests three times, calculate the qualified rate and coefficient of variation of the obtained results, take the average value record, import the results into Origin, and draw a dotted line diagram for comparison. The results are shown in Fig.17:

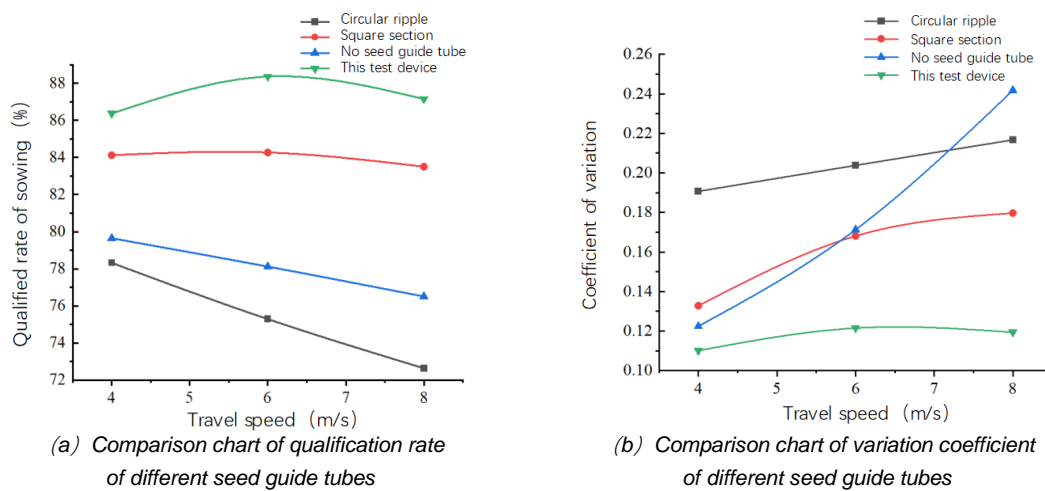


Fig. 17 - Comparison results of seed guide performance

Compared with the seed guide device without a seed guide tube and two kinds of spoon wheel seed metering device, the seed guide performance of the annular air-blowing auxiliary seed guide device designed in this paper has been greatly improved. Compared with the square cross-section seed guide tube, the qualified rate of sowing increased by about 3%, and the coefficient of variation decreased by more than 4%; compared with the mode without seed guide tube, the pass rate can be increased by up to 10% under the condition of high-speed seeding, the coefficient of variation is reduced by about 10%, and the seeding accuracy is significantly improved. The seed metering effect is shown in Fig.18.



Fig. 18 - Seed metering effect

The bench test was carried out. The experimental results showed that the seed metering effect of the seed guide device with air blowing was statistically analyzed. Compared with the seed guide tube without air blowing, the qualified seeding rate increased by 3.2%, with a slight increase, and the coefficient of variation decreased by 7.3%, significantly reducing the coefficient of variation.

CONCLUSIONS

In order to solve the problem of uneven seed spacing caused by the collision between corn seeds and the tube wall of the seed guide tube when sowing, a kind of auxiliary seed guide device with an annular device was designed.

Single-factor simulation analysis and orthogonal experiment were carried out with wind pressure, inclined airway angle, airway outlet width, and distribution pore diameter as experimental indexes. The test results showed that when the wind pressure was 2 kPa, the inclined airway angle was 150°, the outlet width of the airway was 12 mm, and the distribution pore diameter was 4 mm, it was suitable to be used as the key component parameters of the seed guide device.

When the forward speed was 6 km/h (the rotation speed of the seed metering plate was 25.30 rpm), the air pressure was 2 kPa, the inclined airway angle was 150°, the outlet width of the airway was 12 mm, and the diameter of the distribution pore was 4 mm, the qualified rate of sowing reached 88.36%, and the coefficient of variation was 12%, which had high sowing uniformity. The effect is better than that of a round cross-section seed guide tube, square cross-section seed guide tube, and no seed guide tube.

ACKNOWLEDGEMENT

This work was supported by Anhui colleges and universities project under Grand NO.2022AH050897.

REFERENCES

- [1] Araujo, M., Santos, M., de Oliveira, M., Matos, R., Matos, M. (2017). Box–Behnken design applied to optimize the ultrasound-assisted extraction of petroleum biomarkers in river sediment samples using green analytical chemistry. *Analytical Methods*, 9(40), 1039. <https://doi.org/10.1039/C7AY01470H>.
- [2] Chen, K., Yuan, Y., Zhao, B., Zhou, L., Zhou, L., Niu, K., Dong, X., Jin, X., Zheng, Y. (2022). Design of dynamic compensation system for corn seeding position based on fuzzy PID control and analysis of bench test (玉米播种位置动态补偿系统设计与台架试验分析). *INMATEH - Agricultural Engineering*, 67(2), 394-405. <https://doi.org/10.35633/inmateh-67-40>.
- [3] Dayoub, E., Lamichhane, J., Céline S., Philippe D., Pierre M. (2021). Early-Stage Phenotyping of Root Traits Provides Insights into the Drought Tolerance Level of Soybean Cultivars. *Agronomy*, 11(1), 188. <https://doi.org/10.3390/agronomy11010188>.
- [4] Endrerud, H. (1999). Influence of tube configuration on seed delivery to a coulter. *Journal of Agricultural Engineering Research*, 74(2), 177-184. <https://doi.org/10.1006/jaer.1999.0449>.
- [5] Huang, J. (2015). Effect of Precision Sowing and Traditional Sowing on the Growth and Income of Corn (精量播种与传统播种对玉米生长发育及收益的影响). *Journal of Anhui Agricultural Sciences*, 0(5), 29-31. <https://doi.org/10.13989/j.cnki.0517-6611.2015.05.010>.
- [6] Kovher, M., Coleman, J., Smith, J., Kachman, S. (2011). Corn seed spacing uniformity as affected by seed tube condition. *Applied Engineering in Agriculture*, 27(2), 177-183.
- [7] Lei, X., Hu, H., Yang, W., Liu, L., Liao, Q., Ren, W. (2021). Seeding performance of air assisted centralized seed-metering device for rapeseed (油菜小麦兼用气送式直播机集排器参数优化与试验). *International Journal of Agricultural and Biological Engineering*, 14(5), 79-87. <https://doi.org/10.25165/j.ijabe.20211405.5349>.
- [8] Li, Y., Yang, L., Zhang, D., Cui, T., Zhang, K., Xie, C., Yang, R. (2020). Analysis and test of linear seeding process of maize high-speed precision metering device with air suction (气吸式玉米高速精量排种器直线投种过程分析与试验). *Transactions of the Chinese Society for Agricultural Engineering*, 36(9), 26-35. <https://doi.org/10.11975/j.issn.1002-6819.2020.09.003>.
- [9] Liu, Y., Xu, Y., Wang, Y., Yang, H., Gao, P., Wang, J. (2017). Effect of Precision Sowing on Growth and Economic Benefit of Maize (精量穴播对玉米生长发育及经济效益的影响). *Heilongjiang Agricultural Science*, (04), 12-15. <https://doi.org/10.11942/j.issn10022767.2017.04.0012>.
- [10] Liu, X. (2013). Research on Mechanized Maize Precision Sowing (玉米精量播种机械化技术研究). *Agricultural Science & Technology and Equipment*, 223(1), 66-67. <https://doi.org/10.3969/j.issn.1674-1161.2013.01.027>.
- [11] Sokolov, E.R., Zingel, H. (1977). *Ejector*, Beijing: Science Press.
- [12] Wang, J., Tang, H., Wang, J., Shen, H., Feng, X., Huang, H. (2017). Analysis and Experiment of Guiding and Dropping Migratory Mechanism on Pickup Finger Precision Seed Metering Device for Corn (指夹式

- 玉米精量排种器导种投送运移机理分析与试验). *Transactions of the Chinese Society for Agricultural Machinery*, 48(1), 29-37+46. <https://doi.org/10.6041/j.issn.1000-1298.2017.01.005>.
- [13] Wang, C., Li, H., He, J., Wang, Q., Lu, C., Wang, J. (2020). Design and Experiment of Pneumatic Wheat Precision Seed Casting Device in Rice-wheat Rotation Areas (稻麦轮作区气动式小麦精准投种装置设计与试验). *Transactions of the Chinese Society for Agricultural Machinery*, 51(5), 43-53. <https://doi.org/10.6041/j.issn.1000-1298.2020.05.005>.
- [14] Wang, W., Cai, D., Xie, J., Zhang, C., Liu, L., Chen, L. (2021). Parameter Calibration of Discrete Element Model for Dense Forming of Corn Straw Powder (玉米秸秆粉料致密成型离散元模型参数标定). *Transactions of the Chinese Society for Agricultural Machinery*, 52(7), 127-134. <https://doi.org/10.6041/j.issn.1000-1298.2021.03.013>.
- [15] Wang, Q., Han, D., Xu, Y., Huang, Y., Tang, C., Li, W. (2024). Experimental study on the seeding performance of the spoon-wheel maize seed-metering device under vibration conditions (勺轮式排种器在振动条件下的排种性能试验研究). *INMATEH - Agricultural Engineering*, 72(1), 324-338. <https://doi.org/10.35633/inmateh-72-30>.
- [16] Yazgi, A. (2016). Effect of seed tubes on corn planter performance. *Applied Engineering in Agriculture*, 32(6), 783-790. <https://doi.org/10.13031/aea.11274>.
- [17] Yatskul, A, Lemiere, J. (2018). Establishing the conveying parameters required for the air-seeders. *Biosystems Engineering*, 166, 1-12. <https://doi.org/10.1016/j.biosystemseng.2017.11.001>.
- [18] Zhao, S., Chen, J., Wang, J., Chen, J., Yang, C., Yang, Y. (2018). Design and Experiment on V-groove Dialing Round Type Guiding-seed Device (精量播种机V型凹槽拨轮式导种部件设计与试验), *Transactions of the Chinese Society of Agricultural Machinery*, 49(6). 146-158. <https://doi.org/10.6041/j.issn.1000-1298.2018.06.017>.
- [19] Zhang, Y., Cheng, J., Zhang, X., Shi, Z., Wang, M., Wu, H., Fu, H. (2023). Design and experiment of pressure-holding precision seed-metering device for maize (压持式玉米精量排种器的设计与试验). *INMATEH – Agricultural Engineering*, 69(1), 159-169. <https://doi.org/10.35633/inmateh-69-14>.

OPTIMISED DESIGN AND SIMULATION ANALYSIS OF LONGITUDINAL FLOW CORN CONE THRESHING DEVICE

纵轴流玉米锥形脱粒装置优化设计与仿真分析

Jinliang GONG^{1,2*}, Zengjia LUO³⁾, Yanfei ZHANG^{3*)}

¹⁾ Collaborative Innovation Center for Shandong's Main crop Production Equipment and Mechanization, Qingdao, Shandong, 266109, China

²⁾ School of Mechanical Engineering, Shandong University of Technology, Zibo, Shandong, 255000, China

³⁾ School of Agricultural Engineering and Food Science, Shandong University of Technology, Zibo, Shandong, 255000, China
Tel: +86 18265338441; E-mail: gjlwing@sdut.edu.cn; 1392076@sina.com

DOI: <https://doi.org/10.35633/inmateh-73-05>

Keywords: corn harvester; conical threshing drum; threshing concave plate; simulation test

ABSTRACT

Aiming at the high crushing rate and impurity rate of corn kernel machine harvesting in the Huanghuaihai region, a longitudinal flow conical variable pitch threshing device is designed, which adopts the combined threshing element of "plate teeth + ribs" and the combined threshing concave plate of "leftward round tube type + vertical round tube type". The cob model was established, and the force analysis of the cob threshing process was carried out, and the type of threshing drum and the installation angle of the threshing concave plate round tube were determined as the main influencing factors, and the collision force on the corn cob was taken as the test index. Using EDEM discrete element simulation software, simulation tests were carried out on different types of threshing drums and threshing concave plates with different installation angles of round tubes with corn cobs, and the better threshing method was finally determined: a conical threshing drum at a drum speed of 450 r/min, and a combination of left-facing round-tube-type + vertical round-tube-type threshing concave plates with an installation angle of 10° (front-sparse and back-dense type) were used. Compared with the vertical circular tube type threshing concave plate, the corn cob contact force decreased from 313.5 N to 247.3 N, which was optimal for threshing in the range allowed by the corn kernel destructive force.

摘要

针对黄淮海地区玉米籽粒机收时破碎率和含杂率高等问题,设计了一种纵轴流锥形变螺距脱粒装置,采用“板齿+纹杆”的组合式脱粒元件以及“左向圆管型+垂直圆管型”的组合式脱粒凹板。建立了果穗模型并对果穗脱粒过程进行受力分析,确定了以脱粒滚筒类型和脱粒凹板圆管安装角度为主要影响因素,以玉米果穗受到的碰撞力为试验指标,利用EDEM离散元仿真软件,分别对不同类型的脱粒滚筒和不同圆管安装角度的脱粒凹板与玉米果穗进行仿真试验,最终确定了较优的脱粒方式:在滚筒转速为450r/min下,采用锥形脱粒滚筒,安装角度为10°的左向圆管型+垂直圆管型组合式脱粒凹板(前疏后密型)。与垂直圆管型脱粒凹板相比,玉米果穗接触力由313.5N下降到247.3N,在玉米籽粒破坏力允许的范围脱粒效果最优。

INTRODUCTION

With the continuous improvement of the level of mechanized corn harvesting, corn harvester types and functions are becoming more and more abundant. The Huanghuaihai region is one of China's five major corn planting areas (Wang et al., 2018), with the corn sowing area accounting for more than 30% of the national corn area, but cob machine harvesting accounts for 95.2% while seed machine harvesting accounts for only 4.8%. Cob harvesting mainly involves picking and peeling, while kernel harvesting can be completed in one go, including picking, peeling, threshing, cleaning, and collection of work (Cattaneo et al., 2021). With time-saving, increased harvesting efficiency, and lower harvesting costs, corn kernel harvesting is more in line with the direction of the overall process of mechanization development (Cui et al., 2019). The issue of high kernel breakage and impurity content occurs during higher moisture content corn harvesting, which has become a key issue to be addressed in corn kernel harvesting in the Huanghuaihai region.

One of the key components of a corn kernel harvester is the threshing device, and differences in threshing device performance have a significant impact on kernel breakage (Steponavičius et al., 2018). Most experts and scholars at home and abroad research from the crushing mechanism of corn kernels and mechanical structure optimization. For example, Vlădut et al., (2022), rounding of the angular portion of the gridded concave plate ensures threshing quality.

Khawaja et al., (2022), explored the mechanism of corn kernel breakage by studying the forces on corn inside the threshing device through DEM software. Aneliak et al. (2023), determined the threshing efficiency by studying the material movement of alfalfa in a threshing unit. Hou et al. (2023), improved the threshing form and threshing elements, and the threshing efficiency was greatly improved. Deng et al., (2023), designed a high moisture content corn threshing device, determined the optimal operating parameters, the effect was more satisfactory. Cujbescu et al., (2021), achieved low-loss threshing by investigating the effect of threshing device length on threshing quality. Geng et al., (2020), analyzed the collision contact between the flexible spike tooth and the cob, and designed the flexible spike tooth with a reduction in the rigidity of the impact. EDEM is commonly used in discrete element simulation tests, and the standardization of corn cob model affects the accuracy of simulation results. Due to the different morphology of the cob and the lack of adhesion on the surface, the corn cob model was established by SolidWorks 3D modeling software and imported into EDEM software, and the model was filled by the sphere combination method, and the number of filled balls was 24 (Yan et al., 2020; Wang et al., 2023). The leftward round tube type threshing concave plate can reduce the collision force on the corn cob. In the past, the installation angle of the round tube of the threshing concave plate was less studied, and the agricultural machinery design manual mentioned that the installation angle of the round steel tube should not be too large, and excessive installation angle of the round steel tube may lead to blockage of corn cobs in the threshing drum. (Editor-in-chief of China Academy of Agricultural Machinery, 2007).

Therefore, in order to solve the problems of kernel breakage rate and high impurity rate in the process of corn kernel harvesting in the Huanghuaihai region, this paper designs a conical threshing device, which adopts the combined threshing element of "plate teeth + ribs" and the combined threshing concave plate of "leftward round tube type + straight round tube type". It verifies the mechanical properties of the threshing device through simulation tests, so as to provide reference for the research of longitudinal flow corn conical threshing devices.

MATERIALS AND METHODS

Structure

The overall structure of corn conical variable pitch threshing device is shown in Fig. 1, which mainly consists of a feeding hopper, screw blade, threshing drum, plate teeth, D-type ribs, cover plate, threshing concave plate, separating concave plate, and debris deflector plate. The support frame fixes the upper cover plate and the segmented combined threshing concave plate together to form the threshing chamber. Inside the device, there are plate-tooth threshing elements fixed on the circumferential surface of the first half of the threshing drum; in order to offset the movement of the core axial side during threshing as well as the drum's imbalance, the latter half of the drum adopts D-type grain rods arranged alternately in the left and right grain directions. The threshed corn kernels shaft are discharged at the tail end through the debris deflector.

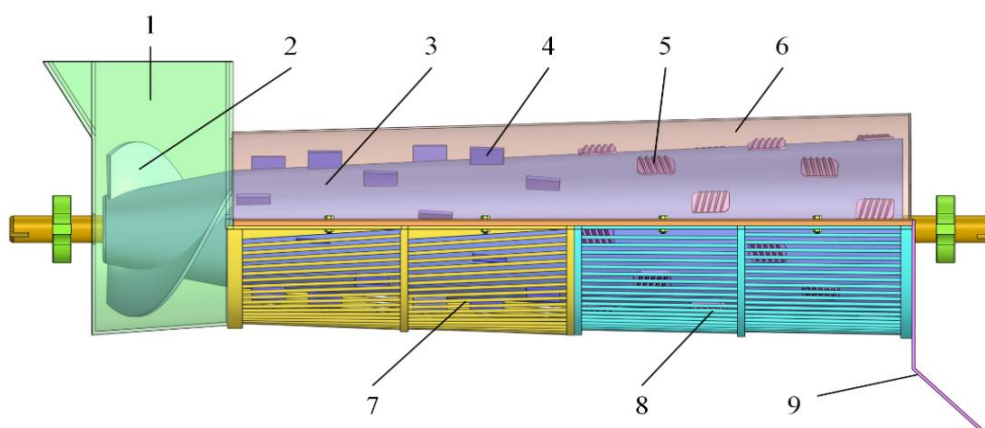


Fig. 1 - Structural diagram of variable pitch corn threshing device

1.feed hopper; 2.spiral blade; 3.threshing drum; 4.plate teeth; 5.D-type ribs; 6.cover plate; 7.threshing concave plate; 8.separation concave plate; 9. discharge deflector plate

Working Principle

The conical variable pitch threshing unit mainly consists of four stages such as feeding, threshing, separating and discharging as shown in Fig. 2.

During operation, the power system drives the input shaft of the conical drum, which in turn makes the threshing drum rotate at high speed; when the corn cob reaches the spiral blade through the feeding hopper, the cob enters the threshing chamber through the thrust effect of the spiral blade to complete the cob feeding process. The spiral arrangement of plate teeth with axial thrust effect, the cob along the axial movement, by the impact of the plate teeth, collision and threshing concave plate extrusion, in the plate teeth and threshing concave plate under the joint action of the part of the cob on the grain is gradually removed. In the second half of the drum, as the diameter of the cob becomes smaller, the circular tube gap of the concave plate decreases, the cob is rubbed under the action of the ripple bar, the cob that has not been threshed continues to be threshed, the corn kernels are separated from the cob through the circular tube gap of the concave plate. After the completion of the threshing, the corn kernel shaft is discharged through the end of the discharging port, and the whole process of threshing is completed.

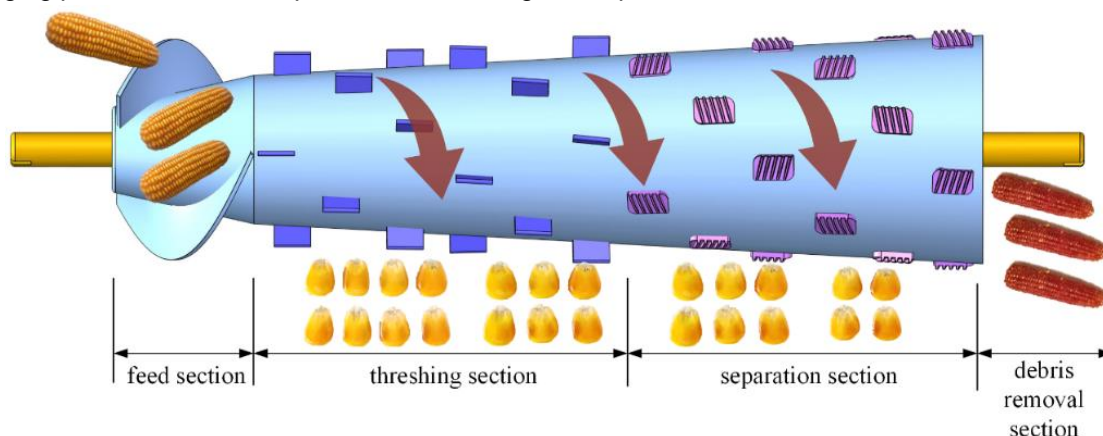


Fig. 2 - Hematic working diagram of the conical variable pitch threshing device

Determination of key parameters

Determination of the parameters of the conical threshing drum

The length of the drum has a significant impact on the threshing quality. The longer the drum, the greater the quality of the whole machine and the working load, and the corn kernels and corn cobs are seriously broken. The threshing drum length is calculated as:

$$L \geq q / q_0 \quad (1)$$

In the formula, L - roller length, m; q - threshing device feeding volume, kg/s; q_0 - unit length of the drum can withstand the feeding volume, in the corn harvester to take the value of 3~4 kg/(s·m).

To feed 6 kg/s into the (1) formula can be obtained, the longitudinal axial flow conical threshing drum length L value range of 1.5 to 2 m. In order to ensure the quality of threshing under the premise of consideration of the machine power consumption and the weight of the relationship between the length of the drum in this paper will take the value of 1.6 m.

When corn cobs enter the drum, the impact force on the plate teeth is relatively large. Therefore, the threshing drum adopts a conical design with a "small diameter at the front and large diameter at the rear". As the diameter decreases towards the front end, the linear velocity of the plate teeth also decreases. This means that the impact force on the cobs during the feeding process is reduced, which helps to minimize grain breakage. (Wang et al., 2021).

The formula for calculating the linear velocity is as follows:

$$D = d_a + 2h_t \quad (2)$$

$$v = \frac{\pi D n}{60} \quad (3)$$

where D -- the diameter of the root circle of the drum teeth, mm; d_a -the diameter of the drum at point a , mm; h_t - the height of the threshing element, the plate teeth are taken as 50 mm, and the ribs are taken as 30 mm.

According to the new edition of agricultural mechanics, the recommended conical roller diameter for the big end is generally 450~550 mm, and the diameter for the small end is 350~450 mm (Geng, 2011), the small end of the diameter of this paper takes 360 mm, roller cone angle of 6°, the big end of the diameter is 528 mm.

Determination of threshing element spacing

The speed of movement of corn cobs in the drum affects the rate of threshing. When the cobs are just fed into the threshing room, cobs between the individual density is larger, the seeds are arranged more densely, and threshing is more difficult (Li et al., 2017). At this point, it is necessary to reduce the speed of axial movement of the cob within the drum as a means of increasing the number of contacts of the threshing element with the corn cob. The combined threshing element adopts the arrangement of equiangular conical spirals with gradually increasing pitch, effectively extending the threshing time and the number of threshing actions. With the shedding of corn kernels, the density of the material gradually decreases, and the pitch increases to aid material flow. That is, the use of small load, multi-circulation threshing method, effectively reducing the kernel breakage.

The parametric equations of the equiangular conic helix are as follows:

$$\begin{cases} x = ce^{m_a t} \sin \zeta \cos t \\ y = ce^{m_a t} \sin \zeta \sin t \\ z = ce^{m_a t} \cos \zeta \end{cases} \quad (4)$$

In the formula, c - the distance of the start of the helix from the top of the cone; ζ - the half cone angle of the threshing drum, 3° ; t - the angle parameter (taking the value $2k\pi$, $k \geq 0$); m_a are constant values.

The radius of the helix is given by Eq.(4):

$$\rho = \sqrt{x^2 + y^2} = ce^{m_a t} \sin \zeta \quad (5)$$

The helix pitch is:

$$\rho = ce^{4\pi m_a} \quad (6)$$

Then the kth pitch is:

$$L_k = Z_k - Z_{k-1} = c \left[e^{2m_a k\pi} - e^{2m_a (k-1)\pi} \right] \cos \zeta \quad (7)$$

From equation (4), $R_{\min} = c \sin \zeta = 180$ mm, the calculation gives $c = 3439.32$.

The average length of corn cob in Huanghuaihai region is about 210 mm (Chen et al., 2020), and the initial threshing spacing of the selected threshing plate teeth is 2/3 of the cob length, so $L_1=140$ mm, so it can be obtained from equation (7):

$$L_1 = Z_1 - Z_0 = c \left(e^{2\pi m_1} - 1 \right) \cos \zeta = 140 \text{ mm}$$

The calculation gives: $m_1 = 0.006359$.

The maximum radius of the drum is known to be $R_5=264$ mm, which can be obtained by substituting into equation (4): $x = 180e^{m_4 8\pi} \cos 8\pi = 264$, calculated as $m_4 = 0.019196$.

The whole section of this design is divided into 4 pitches, and m_1 and m_4 are linearly interpolated and calculated to obtain $m_2 = 0.010638$ and $m_3 = 0.014917$. Substituting $m_1 \sim m_4$ into equation (7) gives the pitch: $L_1=140$ mm, $L_2=253$ mm, $L_3=406$ mm, $L_4=632$ mm.

Parameterization of segmented combined concave plates

In threshing, the separation of seeds is accomplished by the joint action of the drum and the concave plate, and most of the conventional concave plate adopt the grid-type concave plate, which is easy for the seeds to collide with the top of the cross partition plate, resulting in serious seed crushing. For this reason, the concave plate designed in this paper adopts a round tube-type structure, when compared with the angular grid-type concave plate, the round tube-type concave plate with a rounded surface is favorable to reduce the impact on the cob and reduce the seed damage.

As shown in Fig. 3(a) and (b), segmented combination threshing concave plates are arranged in a leftward circular tube type and a vertical circular tube type. The diameter of round pipe is 16 mm Q235 structural steel with superior material performance. The welding direction of the round steel pipe in the leftward round pipe type concave plate deviates from the axis of the concave plate by a certain angle; the welding direction of the round steel pipe in the vertical round pipe type concave plate is perpendicular to the bracket of the concave plate.

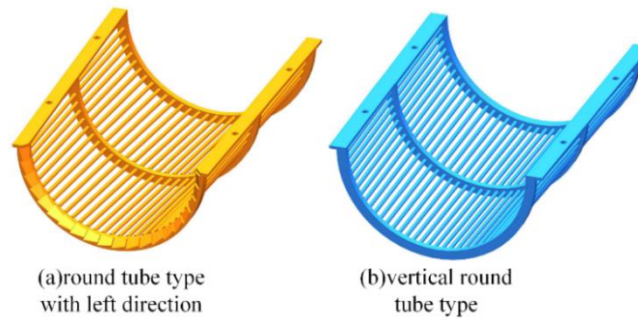


Fig. 3 - Structure of the concave plate for two mounting orientations

In this paper, in order to verify the effect of the concave plate of two installation directions on the collision strength of the cob, the force analysis is carried out between the round tube and the cob of two installation directions, as shown in Figs. 4 and 5.

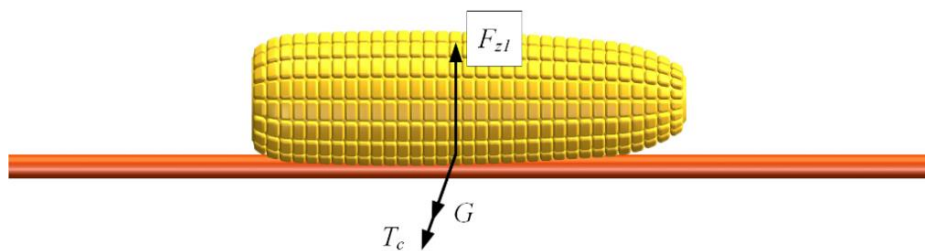


Fig. 4 - Front view of the force on the fruit cob and the vertical circular tube type concave plate

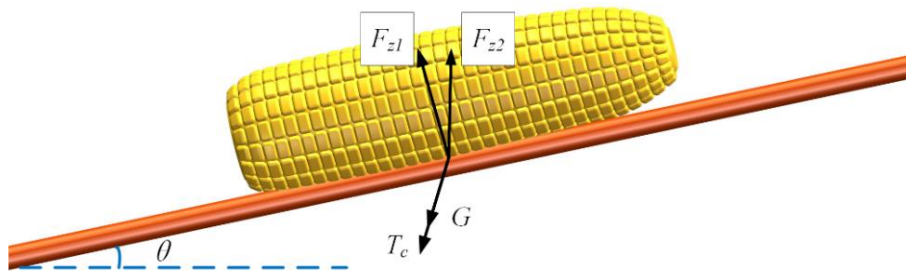


Fig. 5 - Front view of the cob and the leftward circular tube type concave plate under force

As can be seen from Figs. 4 and 5, during the contact between the cob and the circular steel tube, the cob force calculation formula can be expressed as respectively:

$$F_{z1} = (G + T_c) \cos \frac{\beta}{2} \tag{8}$$

$$F_{z2} = (G + T_c) \cos \frac{\beta}{2} \cos \theta \tag{9}$$

In the formula, F_{z1} is the collision reaction force of the cob by the vertical type round steel tube, N; F_{z2} - the collision reaction force of the cob by the leftward type round steel tube, N; T_c - the collision force of the cob on the round steel tube, N; β - the cone angle of the threshing drum, 6° ; θ - the angle of the round steel tube deviating from the axis to the left.

From equations (8) and (9):

$$F_{z1} - F_{z2} = (G + T_c) \cos \frac{\beta}{2} (1 - \cos \theta) > 0 \tag{10}$$

From equation (10), $F_{z1} > F_{z2}$. Under the condition of a certain threshing drum speed, the collision force experienced by the cob is constant. At this point, the collision reaction force experienced by the cob in the vertical round steel tube is greater than that in the left round steel tube.

This confirms that the left circular tube type threshing concave plate effectively reduces the collision force experienced by the cob. Therefore, the use of a left-oriented threshing concave plate in the first half of the threshing drum is conducive to reducing seed breakage.

In the second half of the threshing drum, where the density and diameter of the cob are smaller, a vertical circular tube-type concave plate with a smaller gap is used in conjunction with the ripple-type threshing element. It relies on the rubbing force for flexible threshing, thereby facilitating the separation of seeds and grains.

RESULTS

EDEM-based simulation test and analysis

Modeling of corn cob collisions

The material parameters and material contact parameters of the corn cob and threshing unit are shown in Tables 1 and 2.

Table 1

| Model material parameters | | |
|---|--------------------|----------------------|
| Parameter name | Corn cob | Threshing device |
| Poisson's ratio | 0.4 | 0.3 |
| Shear modulus [Pa] | 1.30×10^8 | 3.5×10^{10} |
| Densities [$\text{kg} \cdot \text{m}^{-3}$] | 1197 | 7850 |

Table 2

| Model contact parameters | | |
|--------------------------|---------------------------|--------------------------|
| Parameter name | Between the ears of fruit | Ears of fruit with steel |
| Crash recovery factor | 0.182 | 0.659 |
| Static friction factor | 0.44 | 0.326 |
| Kinetic friction factor | 0.008 | 0.02 |

Threshing drum simulation test and analysis

Threshing drum simulation test method

Simulation tests allow for simulating the threshing process of the cob in the threshing chamber. Using the type of threshing drum as an influencing factor, the study was carried out on cylindrical and conical drums with plate teeth and ripple bar matching threshing elements, and the concave plate types were all of the vertical round tube type. In the EDEM software, the pellet plant was set up at the feeding port with a pellet mass of about 0.25 kg each and a generation rate of 24 per second, so the feed rate was about 6 kg/s. The mechanical simulation test of corn cob was carried out under the conditions of roller speed of 400 r/min and simulation time of 10s.

Analysis of threshing drum simulation test results

The force cloud maps of corn cob under different types of threshing drums were output by EDEM post-processing module, as shown in Fig. 6(a) and (b).

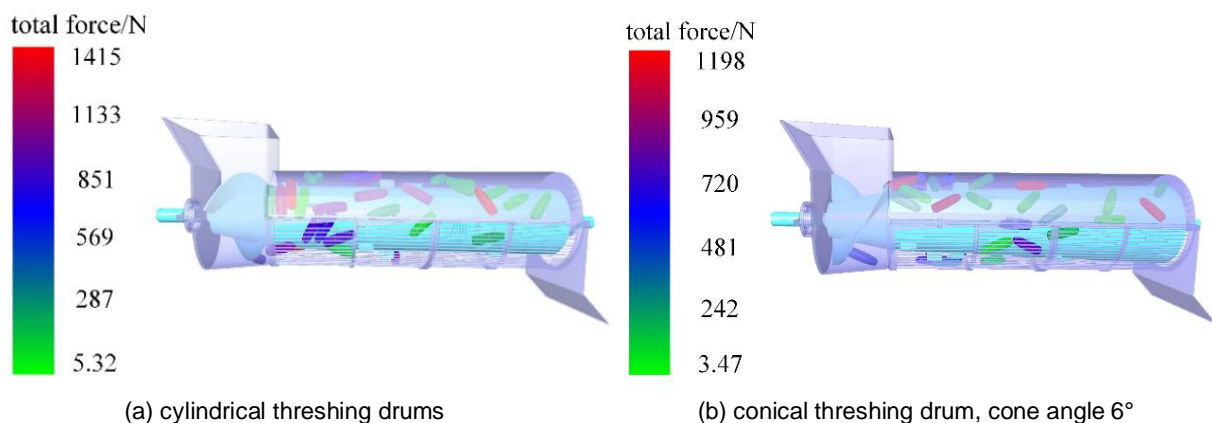


Fig. 6 - Cloud diagram of cob force process under different threshing drums

As seen in the cloud view of the force process on the corn cob in Fig. 6, close to half of the corn cobs were blue or red inside the cylindrical threshing device. However, the number of dark-colored cobs was lower in the conical threshing unit compared to the former, indicating that the conical threshing unit reduces the impacts from the threshing elements under the same constraints and employs a "small load, many cycles" threshing method.

Through the EDEM software post-processing module of the total force exerted on the corn cob, the data were summarized, and the average contact force between the threshing element and the cob was obtained through calculation and imported into the data visualization software Origin for data plotting, as shown in Fig.7.

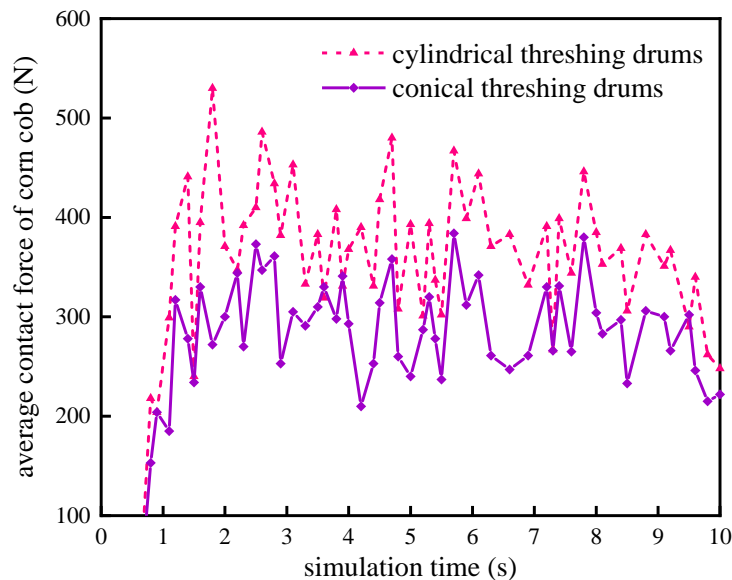


Fig. 7 - Line graph of force on corn cob at different threshing drums

As can be seen in Fig. 7, from 0 to 0.7 s, the cob produced by the pellet plant enters the threshing chamber through the spiral blades. From 0.7 to 6.5 s, the cob contacts the plate tooth threshing element. During this stage, each sudden change in cob force means a collision between the cob and the cob, and the cob and the threshing element, but the cob is subjected to the contact force of the cylindrical threshing drum as a whole more than that subjected to the cone-shaped threshing drum's Contact force. From Fig. 7 conical threshing drum line graph can be seen, the cob in the conical threshing drum in the first half of the intensive degree of force mutation compared to the second half of the more intensive, indicating that the use of variable pitch structure arrangement of the threshing element helps to increase the number of times and prolong the time of threshing; in the second half of Fig. 7, along with the shedding of grains, the radius of the cob decreases, cob force mutation number of times to reduce the number of cob collision, so cob collision number is reduced. Thus, the rationality of using a ripple type threshing element in the latter half of the threshing drum and a larger pitch structure was confirmed, and all subsequent studies used conical variable pitch threshing drums.

Simulation test and analysis of threshing concave plate

Threshing concave plate simulation test method

In this subsection, by using EDEM simulation software, the circular steel pipe installation angle is selected as the influencing factor, and the circular steel pipe installation angles of the leftward circular pipe-type concave plate are 8°, 10°, and 12°, respectively, and these are compared with the vertical circular pipe-type concave plate. Conical threshing drums were used for all threshing units, and drum speeds of 250, 350, 450, and 550 r/min were selected.

Analysis of threshing concave plate simulation test results

The force cloud diagrams of corn cobs under different threshing concave plates were output by EDEM post-processing module, as shown in Fig. 8(a) to (d).

Within the threshing device under the leftward circular tube-type threshing concave plate, as can be seen from the cloud diagram of the force process of the corn cob in Fig. 8(b), the corn cob has a darker portion of the corn cob than in Fig. 8(a) and Fig. 8(c); and for the threshing device with a vertically circular tube-type threshing concave plate in Fig. 8(d), the corn cob has a darker portion of the corn cob than in the first three.

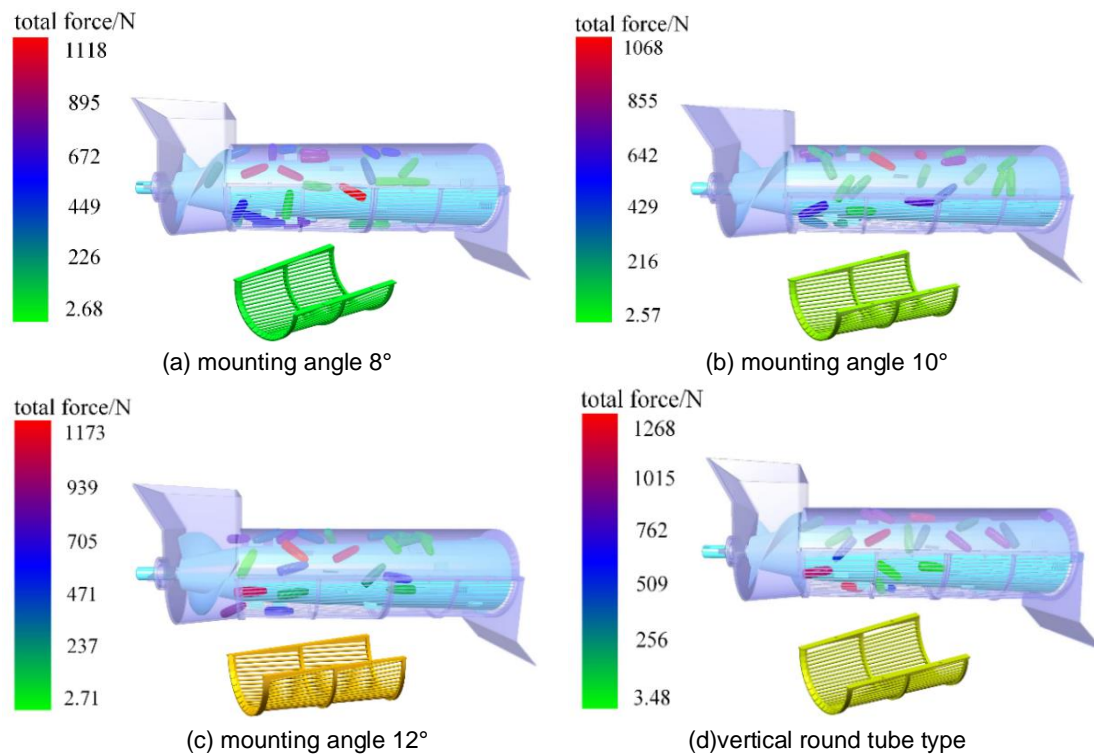


Fig. 8 - Cloud diagram of the force process of the cob under the threshing concave plate with different installation angles of the round tube

The average contact force applied to the corn cob was calculated by the post-processing module and the results are shown in Table 3.

Table 3

Simulation results of threshing concave plate with different round tube installation angles [unit: N]

| Drum speed [r/min] | Threshing concave plate round tube installation angle | | | |
|--------------------|---|--------------------|--------------------|--------------------------|
| | mounting angle 8° | mounting angle 10° | mounting angle 12° | vertical round tube type |
| 250 | 131.6 | 128.3 | 153.1 | 186.5 |
| 350 | 163.7 | 169.2 | 207.8 | 235.4 |
| 450 | 256.8 | 247.3 | 276.2 | 313.5 |
| 550 | 365.4 | 358.6 | 382.4 | 423.7 |

The data were plotted in Table 3 by Origin plotting software to obtain the change curve of corn cob contact force under different drum speeds and round tube installation angles, as shown in Fig. 9.

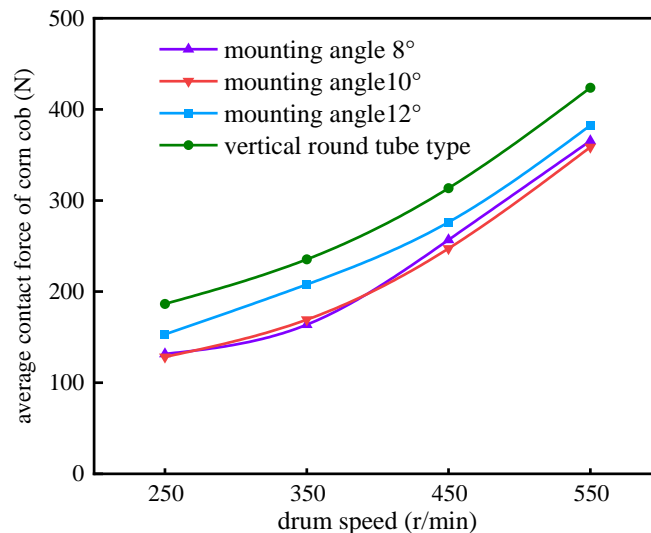


Fig. 9 - Variation of contact force of corn cob at different round tube mounting angles

As can be seen from Fig. 9, with the gradual increase in drum speed, the average contact force on the corn cob is also increasing to varying degrees; at the same speed, the contact force on the cob is smaller in the former compared to the three installation angles of the leftward circular tube-type threshing concave plate and the vertical circular tube-type threshing concave plate, confirming that the leftward circular tube-type threshing concave plate can reduce the contact force on the corn cob.

When the threshing drum is at a lower rotational speed, the contact force of the vertical round tube-type threshing concave plate on the corn cob is greater than that of the leftward round tube-type threshing concave plate; the contact force on the corn cob under the round steel tube mounted at an angle of 8° and 10° threshing concave plate is approximately the same. When the threshing drum is at a higher speed, the contact force on the corn cob under the threshing concave plate at an angle of 8° for the installation of the round steel tube is greater than that on the corn cob under the threshing concave plate at an angle of 10° for the installation of the round steel tube; the corn cob under the threshing concave plate at an angle of 12° for the installation of the round steel tube and the vertical round tube is subjected to a larger contact force, and the kernels are easy to be broken. From the perspective of reducing the collision force, seed crushing rate, comprehensive analysis of the data in Table 3 and Figure 9 curve, select the round steel pipe installation angle of 10 ° threshing concave plate, and the simulation test results are more satisfactory.

CONCLUSIONS

A conical threshing unit was designed using SolidWorks software with combined threshing elements and the threshing elements were arranged according to variable pitch. A combined threshing concave plate was used and the main structure and parameters were determined.

Using EDEM software, simulation tests were carried out on the type of drum and the installation angle of the concave plate circular steel pipe, and the conical drum was better than the cylindrical drum; the installation angle of the concave plate circular steel pipe was optimal at 10°, which was conducive to reducing the collision force of the seeds.

ACKNOWLEDGEMENT

This work was funded by the Key Research and Development Program of Shandong Province (Major Innovative Project in Science and Technology) (2020CXGC010804), Shandong Provincial Natural Science Foundation (ZR2021MC026), the Collaborative Innovation Center for Shandong's Main crop Production Equipment and Mechanization.

REFERENCES

- [1] Cattaneo A., Sanchez M V., Torero M., et al. (2021). Reducing food loss and waste: Five challenges for policy and research [J]. *Food Policy*, Vol. 98, pp.101974.
- [2] Chen R.J., Zhang J., Liu X.Z., et al. (2020). Research on breeding technology of new maize varieties in Huanghuaihai [J] (黄淮海玉米新品种育种技术研究). *China Seed Industry*, Vol. (02), pp. 22-24.
- [3] Cui T., Fan C.L., Zhang D.X., et al. (2019). Analysis of research progress of mechanized corn harvesting technology [J] (玉米机械化收获技术研究进展分析). *Journal of Agricultural Machinery*, Vol. 50(12), pp.1-13.
- [4] Cujbescu D., Gageanu I., Iosif A. (2021). Mathematical modeling of ear grain separation process depending on the length of the axial flow threshing apparatus. *INMATEH - Agricultural Engineering*, Vol. 65(3), pp. 101-110.
- [5] Deng Y.J., Zhang G.H., Zhang A.Q., et al. (2023). Experimental analysis of threshing maize seeds with high moisture content. *INMATEH - Agricultural Engineering*, Vol. 69(1), pp. 131-144.
- [6] Geng D.Y., Tan D.L., Yu X.R., et al. (2020). Design and test of threshing element of corn flexible threshing drum [J] (玉米柔性脱粒滚筒脱粒元件设计与试验). *Journal of Jilin University (Engineering Edition)*, Vol. 50(05), pp.1923-1933.
- [7] Geng D.Y. (2011). *New Agricultural Mechanics [M]* (新编农业机械学). Beijing: National Defense Industry Press.
- [8] Hou Y.X., Shang S.Q., Li X., et al. (2023). Discrete element method (EDEM) simulation and parameter optimization: Design and testing of a low-loss and high-efficiency corn threshing device. *INMATEH - Agricultural Engineering*, Vol. 71(3), pp. 194-204.
- [9] Khawaja A.N., Khan Z.M. (2022). DEM study on threshing performance of "compression-oscillation" thresher [J]. *Computational Particle Mechanics*, Vol. 9(6), pp. 1233-1248.

- [10] Li X.P., Ma L., Geng L.X., et al. (2017). Performance test and parameter optimization of corn seed bionic thresher [J] (玉米种子仿生脱粒机性能试验与参数优化). *Journal of Agricultural Engineering*, Vol. 33(05), pp. 62-69.
- [11] Aneliak M., Kuzmych A., Stepanenko S., Lysaniuk V. (2023). Study of the process of threshing leguminous grass seeds with a drum-type threshing device. *INMATEH - Agricultural Engineering*, Vol. 71(3), pp. 83-92. <https://doi.org/10.35633/inmateh-71-06>
- [12] Steponavičius D., Pužauskas E., Špokas L., Jotautienė E., Kemzūraitė A., Petkevičius S. (2018). Concave design for high-moisture corn ear threshing [J]. *Mechanics*, Vol. 24(1), pp.80-91.
- [13] Vladut N.V., Biris S.Ş., Cardei P. et al. (2022). Contributions to the Mathematical Modeling of the Threshing and Separation Process in An Axial Flow Combine [J]. *Agriculture*, Vol. 12(10), pp. 1520.
- [14] Wang Y.G., Zhang G.H., Zhang H., et al. (2018). Analysis of the current situation of summer corn harvesting in the Huanghuaihai region [J] (黄淮海地区夏玉米收获现状分析). *Chinese Journal of Agricultural Mechanical Chemistry*, Vol. 39(11), pp. 112-115.
- [15] Wang Z.D., Cui T., Zhang D.X., et al. (2021). Design and test of low-loss variable-diameter threshing drum for corn harvester [J] (玉米收获机低损变径脱粒滚筒设计与试验). *Journal of Agricultural Machinery*, Vol. 52(08), pp. 98-105.
- [16] Wang H.B., Fan Z.P., Urantuya, et al. (2023). Parameter calibration of a discrete element model for the simulation of spiral conveying of kneaded corn stover [J] (揉碎玉米秸秆螺旋输送仿真离散元模型参数标定). *China Agricultural Science and Technology Bulletin*, Vol. 25(03), pp.96-106.
- [17] Yan B.X., Wu G.W., Fu W.Q., et al. (2020). Research on the influence factors of high seed placement position of corn precision sowing based on EDEM [J] (基于 EDEM 的玉米精播高位投种着床位置影响因素研究). *Journal of Agricultural Machinery*, Vol. 51(S2), pp. 47-54.
- [18] ***China Agricultural Machinery Research Institute, ed. (2007). *Agricultural machinery designs manual* [M] (农业机械设计手册 下). Beijing: China Agricultural Science and Technology Press.

CENTRIFUGAL SPRAYING SYSTEM DESIGN AND DROPLET DISTRIBUTION CHARACTERIZATION FOR MAIZE PLANT PROTECTION UAV

玉米植保无人机离心喷施系统设计与雾滴分布特性试验

Jiaxon HE¹⁾, Keke SUN¹⁾, Taojie WANG¹⁾, Zhihua SONG¹⁾, Lichao LIU^{1,2)}

¹⁾ College of Engineering, Anhui Agricultural University, Hefei, Anhui, 230036, China

²⁾ Engineering Laboratory of Intelligent Agricultural Machinery Equipment, Anhui, Hefei, 230036, China

Tel: +86 15705603452; E-mail: llchao@ahau.edu.cn

Corresponding author: Lichao Liu

DOI: <https://doi.org/10.35633/inmateh-73-06>

Keywords: aviation spraying operation, centrifugal nozzle parameters, spraying system, droplet distribution characterization

ABSTRACT

Aiming at the problem that the ground plant protection machine is difficult to enter for plant protection in the middle and late stages of maize field, this paper designs a UAV centrifugal spraying system for maize plant protection based on centrifugal nozzle and plant protection UAV. A single nozzle parameter test was carried out, and the results showed that the droplet size is related to the liquid supply flow rate and the nozzle speed. According to the optimal biological particle size theory, the nozzle parameters with the liquid supply flow rate of 1000 mL/min and the rotation speed of 14000 r/min are selected to test the droplet distribution characteristics under actual operation conditions, and the droplet size, droplet density, coverage and other important indicators of aviation spraying operations are analyzed. The experimental results show that the flight speed of the UAV significantly affects the droplet distribution in the bottom layer of maize. The droplet coverage and droplet deposition of each sampling layer decrease with the increase of flight speed. When the flight speed is 1.5 m/s, the coefficient of variation of the centrifugal spraying system is the smallest, and the droplet deposition effect is the most uniform. This study can provide a reference for the parameter optimization and correct use of centrifugal plant protection UAV in the middle and late plant protection operations of high-stalk crops such as maize.

摘要

针对玉米中后期田间郁闭，地面植保机难以下田进行植保的问题，本文基于离心喷头和植保无人机设计了一款用于玉米植保的无人机离心喷施系统。开展了单喷头参数试验，结果表明：雾滴粒径与供液流量、喷头转速均相关，且结合最佳生物粒径理论，选择供液流量为1000 mL/min，转速为14000 r/min的喷头参数进行实际作业情况下的雾滴分布特性试验，分析雾滴粒径、雾滴密度、覆盖率等航空喷施作业的重要指标。试验结果表明：无人机的飞行速度显著影响玉米底层的雾滴分布，各采样层的雾滴覆盖率和雾滴沉积量的变化趋势均随着飞行速度的增大而减小，在飞行速度为1.5m/s时离心喷施系统的变异系数最小，雾滴沉积效果最均匀。该研究为离心喷头植保无人机在玉米等高秆作物中后期植保作业的参数优化和正确使用提供参考依据。

INTRODUCTION

Maize is one of the three major food crops in China, widely planted and with high yield, not only an important food resource, but also an important raw material in industry and animal husbandry, with high market and social value. The Huang-Huai-Hai region is the main planting area of summer maize in China, since 2015, the Ministry of Agriculture and Rural Development has organized the zero-growth action of chemical fertilizer and pesticide use, and after several years of implementation, the utilization rate of pesticides in China has significantly improved. However, in the middle and late stage of maize growth, the plants are high and the closed rows are formed by field depression. The efficiency of traditional artificial application is low, while the existing spray rod sprayer is difficult to enter, and the injury rate is high (Liu et al., 2022), and most of the sprayer use pressure nozzle, easy to block. Vigorously promoting green control and precision scientific medication, the use of plant protection drones for maize mid- and late-stage pest control is currently a more reasonable solution (Xie et al., 2022; Yang et al., 2020).

China's plant protection UAVs use atomization nozzle is mainly divided into pressure nozzle and centrifugal nozzle, pressure nozzle in the requirement of small droplet size is easy to block, centrifugal nozzle particle size change can be controlled by the rotational speed in real time (Chen *et al.*, 2018). Compared to pressure nozzles, centrifugal nozzles have better atomization, pesticide cost savings, and long life span in spraying facilities (Dong *et al.*, 2018). Yu *et al.*, (2023), developed a rotary nozzle for UAV spraying, and explored the influence of three factors on the droplet size of the centrifugal nozzle from the flow rate, rotation speed and mesh number, which provided a certain technical basis for the research and optimization of the spray parameters of the centrifugal nozzle. Chen *et al.*, (2023), used CFD simulation to study the downwash airflow and droplet distribution of the six-rotor UAV, and combined RBFNN and GA to optimize the parameters of the spraying system. Jane *et al.*, (2021), conducted experiments in vineyards, and three different types of drones and two different types of nozzles were evaluated. It was concluded that the vortex airflow and the arrangement position of the nozzle were the two main reasons affecting the difference in spray performance. Gavali *et al.*, (2023), used PIV technology to study the droplet deposition characteristics of centrifugal sprayers, and concluded that at a constant rotational speed, the friction force between the ejected liquids decreases, and changing the liquid mass will cause the droplet diameter to increase. Chen *et al.*, (2017), studied the effect of wind field on the penetration and uniformity of droplet deposition in the effective spraying area through the actual spraying operation test. Fritz *et al.*, (2009), investigated the effect of different flight speeds of plant protection aircraft on the particle size of fog droplets using wind tunnel testing methods. Biglia *et al.*, (2022), carried out experiments on fog droplet deposition in vineyards with different flight speeds of drones and spray nozzles, and the results showed that: the flight speed of the drones had a significant effect on the amount of fog droplet deposition in different canopies of grapes. All the above studies provide reference for the optimization of nozzle operation parameters, but the spraying problem of high stalk dense planting crops has not been solved.

This paper designs a centrifugal spraying system applicable to plant protection drones, controls the rotational speed of the centrifugal nozzle through the wireless control module, and then changes the size of the droplet size, carries out a test on the droplet deposition and distribution characteristics of plant protection drones in the middle and late stages of maize, and investigates the parameter indexes such as the droplet size, density, coverage, and deposition rate of the maize field with different sample points, in order to provide references for the effective application of plant protection drones in maize in the middle and late stages of plant protection.

MATERIAL AND METHODS

DESIGN OF CENTRIFUGAL SPRAYING SYSTEMS FOR UAV

The structure of the maize plant protection drone is shown in Fig. 1, in which the drone platform adopts the DJI T20 plant protection drone, and the centrifugal spraying system consists of the centrifugal nozzle and wireless control system which are modularized and designed to form an independent system installed on the plant protection drone.

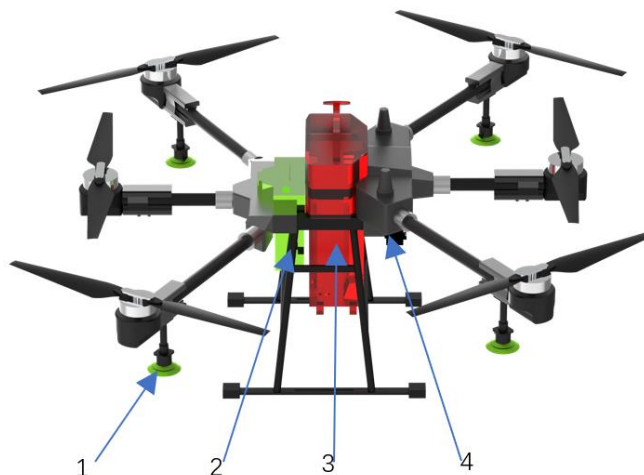


Fig. 1 - Schematic diagram of centrifugal plant protection drone structure

1. centrifugal nozzle; 2. plant protection drone; 3. medicine cabinet; 4. control box

The main structure includes centrifugal nozzle, liquid pipeline, microcontroller and remote control. When working, the remote control of the UAV controls the flow of the nozzle, and the start-stop and speed of the centrifugal nozzle are realized by the independently developed remote control system, which sends commands to the control box of the centrifugal spraying system through the hand-held remote control to realize the one-key start and speed regulation of the nozzle. The speed control process is realized by the microcontroller in the control box through PWM (pulse width modulation) technology, adjusting the duty cycle of PWM to control the rotational speed of the centrifugal spray nozzle to change the droplet size. The total weight of the centrifugal spraying system is small, which has less influence on the drug carrying capacity of the plant protection UAV, the weight of the centrifugal spraying system is 1 kg.

Nozzle structure

The plant protection UAV uses centrifugal nozzle, the main structure of the designed centrifugal nozzle is shown in Fig. 2a including the drive motor, atomizing disk, electronic speed controller and waterproof shell. The drive motor of the centrifugal nozzle adopts a brushless DC motor with 12 V power supply. The output shaft of the drive motor is connected to the end of the atomizing disk, and the atomizing disk is disc-shaped and divided into two parts, as shown in Fig. 2b and 2c. Controlled by the single-chip microcomputer, the brushless motors rotate to drive the atomizing disk. The liquid is sent to the atomization disk through the inlet. Under the action of centrifugal force, the liquid is shunted along the water tank on the atomization disc, and then atomized into small droplets through the fine line atomization groove. Finally, the small droplets are spiraled out through the atomizing groove on the outer edge of the tooth tip.

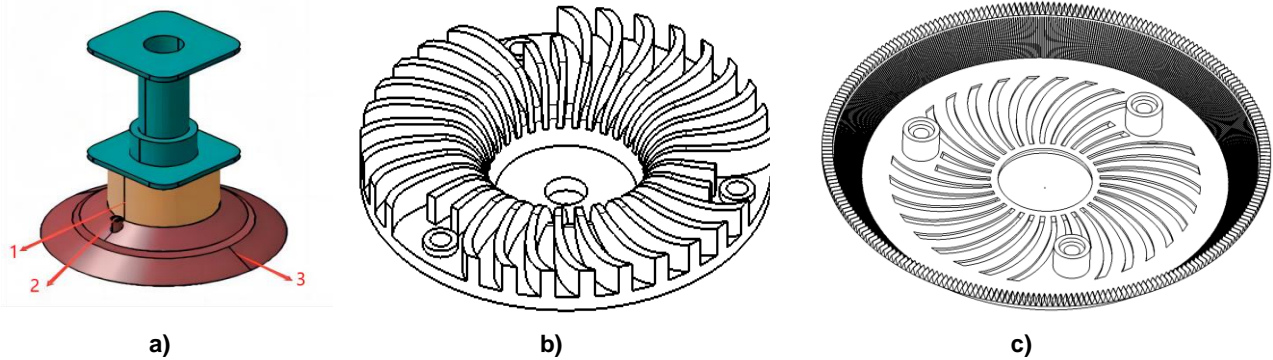


Fig. 2 - Structure of nozzle and atomization disk
 1. brushless motor; 2. Inlet; 3. fogging tray

Wireless control system for centrifugal nozzles

The wireless control system is designed to achieve the purpose of changing the droplet size by changing the rotational speed of the centrifugal nozzle, and the control system includes three modules: power supply module, nozzle control module, and remote control module.

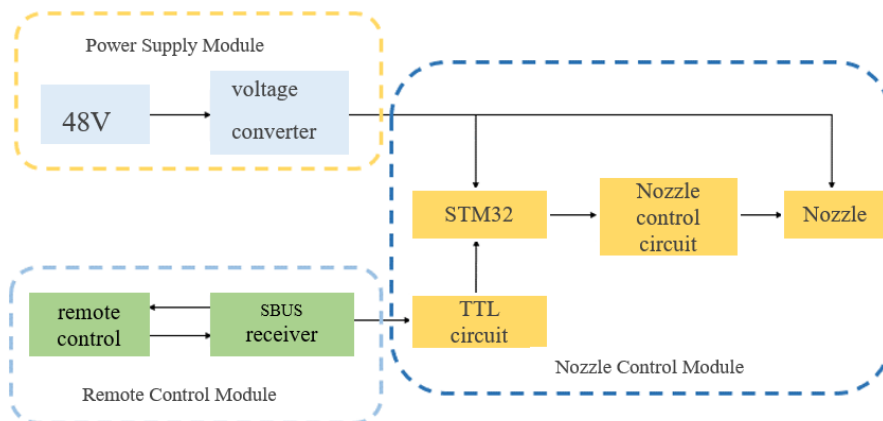


Fig. 3 - Control system composition

Power modules

As shown in Fig. 4, the whole control system is powered by the 51.8 V battery of the UAV, which is converted to 12 V and 3.3 V through the voltage conversion module. As shown in Fig. 5, the voltage is converted to 3.3 V by LDO voltage regulator PW8600 and linear circuit to provide power for the MCU main control chip and the remote control receiver, and converted to 12 V by DC-DC power supply chip PW2906 and buck circuit to provide power for the brushless ESC.

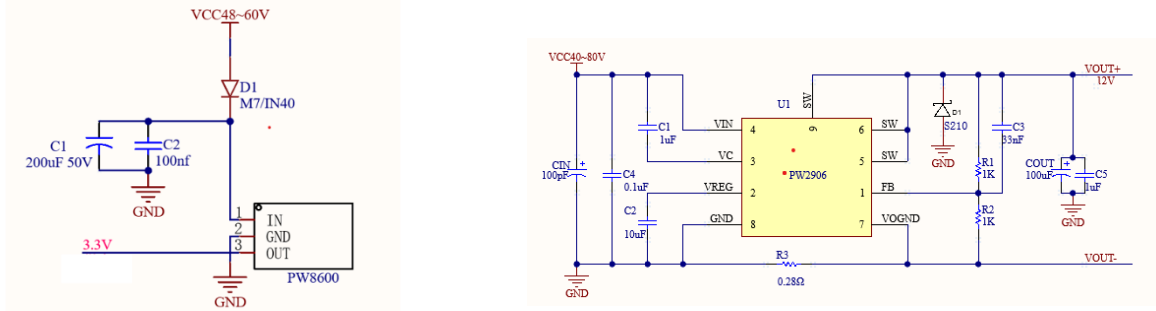


Fig. 4 - Circuit diagram of the power supply module of the control system

Remote control module

The remote control module is mainly a remote control, SBUS receiver. Through the handheld remote control commands are sent to the spraying system of the wireless receiver module in the control box. The remote control and receiver are selected from WFLY's ET08 and RD201W models, respectively. The remote control transmits key values to the receiver through a 2.4GHz wireless signal. The receiver communicates with the microcontroller through the SBUS serial port, and the microcontroller receives and parses the SBUS signal through the serial interrupt function in the program, converting the key value into a PWM wave value and transmitting it to the brushless electric controller to control the start stop, speed, etc. of the centrifugal nozzle.

Printhead control module

The start-stop and speed change of centrifugal nozzle is realized by the remote control system developed independently, and the microcontroller in the control box realizes the start-stop and speed change of centrifugal nozzle through PWM technology, and adjusts the duty cycle of PWM to control the rotational speed of centrifugal nozzle to change the size of droplet particle size. stm32 microcontroller accepts and analyzes the SBUS signal from the remote control module through the serial interrupt function of the program and converts the key value into PWM wave value, and amplifies the output signal through field effect tube to control the start-stop and rotational speed of centrifugal nozzle. The key value will be converted to PWM wave value, and through the field effect tube will be the output signal amplification, so as to control the centrifugal nozzle start-stop, speed and so on. Single nozzle control circuit diagram shown in Fig. 5.

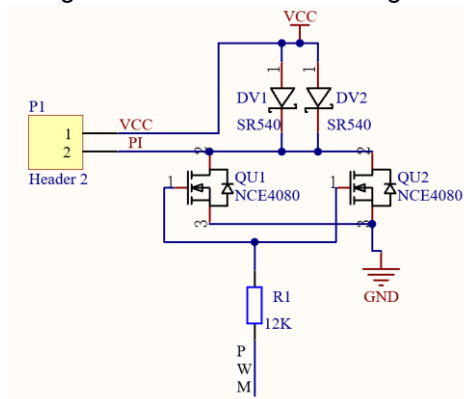


Fig. 5 - PWM control circuit

SINGLE NOZZLE PARAMETER TEST

Centrifugal nozzle speed and PWM signal duty cycle calibration

The atomization effect of the centrifugal nozzle is closely related to the rotational speed of the nozzle, the rotational speed of the centrifugal nozzle is controlled by adjusting the PWM duty cycle; in order to more accurately control the rotational speed of the nozzle, it is necessary to establish a deterministic function relationship between the PWM duty cycle and the motor speed. For this purpose, a laser speed meter is used to measure the centrifugal nozzle speed under different PWM, and the results are shown in Fig. 6.

As can be seen in Fig. 6, when the voltage is 12 V and the PWM frequency is 500 Hz, the centrifugal nozzle speed and the PWM duty cycle are approximately linear, and the centrifugal nozzle speed can be better controlled by adjusting the PWM duty cycle using the PWM signal generator.

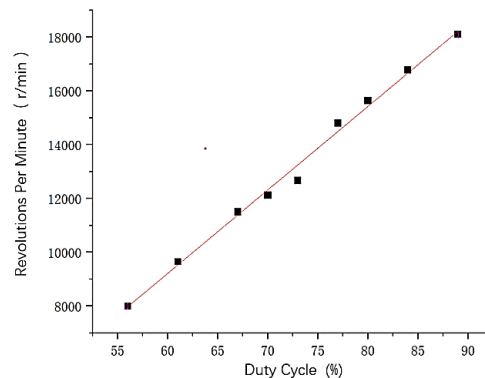


Fig. 6 - Relationship between nozzle speed and PWM duty cycle

Centrifugal nozzle speed and droplet size calibration

In order to clarify the numerical relationship between atomizing disk flow and motor speed and droplet particle size, and to find the centrifugal spray nozzle operating parameters with the bio-optimal particle size to satisfy plant diseases, the relevant tests were carried out in a suitable environment.

Test platform

A set of centrifugal nozzle parameter testing platform is designed, which mainly consists of centrifugal nozzle, brushless water pump, medicine tank, microcontroller, support frame and YE180-A laser particle size meter. The centrifugal nozzle is controlled by a wireless control system designed to change the speed of the centrifugal nozzle. The centrifugal nozzle, brushless water pump, and medicine tank are connected through transparent rubber hoses. The microcontroller controls the brushless water pump to change the flow rate of the nozzle, and the support frame can adjust the height of the nozzle according to testing needs. In the actual plant protection operations, the flight height of the UAV is usually higher than the crop canopy 1~3 m (Qiu et al., 2013), the test set the centrifugal nozzle from the laser particle size meter test beam 1.5 m, the transmitting end and the receiving end of the laser line is placed directly below the centrifugal nozzle, the laser particle size meter is connected to the computer, the computer running the laser particle size analyzer dedicated NKT analysis software can be derived from the Dv10, Dv50, Dv90 particle size distribution map and cumulative distribution map and other data. According to the purpose of this paper, Dv50 data is mainly used as the average particle size of droplet group to study the relationship between nozzle speed, flow rate and droplet particle size.

Taking into account the outdoor wind speed, light and other environmental factors may have an impact on the test results, this test will be completed indoors as shown in Fig. 7.



Fig. 7 - Test system for centrifugal nozzle parameters

1 - Centrifugal nozzle; 2 - Support frame; 3 - Guide rails; 4 - Laser particle size analyzer analysis software; 5 - Laser particle sizer

Test results analysis

As shown in Fig. 8, the droplet size is related to the supply flow rate and nozzle speed, and the higher the flow rate and the lower the speed, the larger the droplet size. At the same flow rate, the higher the rotational speed, the smaller the droplet size. Fig. 8b shows the nozzle test D_{v50} data, in the nozzle speed from 8000 r/min to 12000 r/min process, the droplet size changes in a larger magnitude, the speed reaches 12000 r/min after the size change curve tends to flatten.

When the nozzle rotational speed is the same, the effect of the liquid supply flow rate on the droplet particle size is not consistent, the flow rate being in the interval of 500 mL/min to 650 mL/min, 800 mL/min to 1000 mL/min, the degree of change in the droplet particle size at different centrifugal rotational speeds is relatively small compared to the degree of change in the droplet particle size outside the flow rate interval. Centrifugal atomizing nozzles have small droplet size distribution and narrow droplet spectrum width, which have obvious advantages over pressure atomizing nozzles. Combined with Fig. 8a and 8c, it can be seen that in the parametric test of a single nozzle, by adjusting the liquid supply flow rate and nozzle rotation speed, a number of droplets can have a particle size of less than 35 μm . For example, if the liquid supply flow rate is 650 ml and the nozzle rotation speed is 14,000 r/min, the D_{v10} data is 43.263 μm , the D_{v90} data is 118.753 μm , and the D_{v50} data is 74.357 μm , according to the fog droplet spectral width representation equation:

$$\frac{D_{V90}-D_{V10}}{D_{V50}} \quad (1)$$

The width of the droplet spectrum can be obtained as 1.02 less than 2.0, which is in line with the quality technical index of spraying operation.

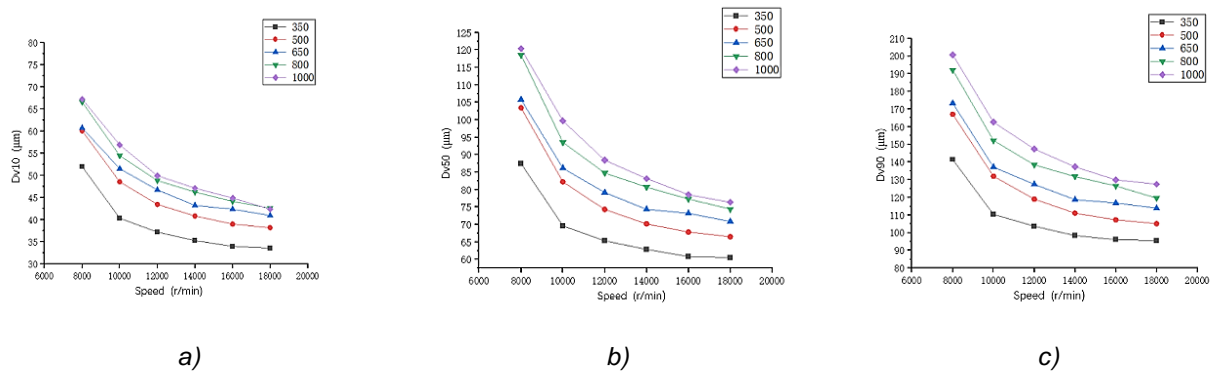


Fig. 8 - Flow rate, rotational speed and particle size of droplets

There is a relationship between droplet size and pesticide efficacy of bio-optimal particle size, pesticide spraying technology theory research that the control of flying pests is suitable for the use of small insecticide droplets of 10 to 50 μm , the control of foliar crawling pest larvae is suitable for the use of insecticide droplets of 30 to 150 μm , the spraying of fungicide control of plant diseases is suitable for the use of droplets of 30 to 150 μm , and herbicide spraying is suitable for the use of coarse droplets of 100 to 300 μm (Chen *et al.*, 2021; Uk *et al.*, 1997; Yuan *et al.*, 2015; Zhang *et al.*, 2022). Considering the factors of droplet evaporation, drift, penetration, and droplet adhesion on leaves, the centrifugal nozzle parameters in this paper were selected to supply liquid at a flow rate of 1,000 mL/min, and the nozzle rotational speed was 14,000 r/min.

DROPLET DISTRIBUTION CHARACTERIZATION TEST AND RESULT ANALYSIS

Experimental site and conditions

The experiment was conducted on September 10, 2022 at the test site of Anhui Agricultural University, Anhui Province, China. The maize planted in the trial site was a late-maturing fresh maize variety, which was in the filling stage at that time, with an average plant height of about 200 cm, planting row spacing of 60 cm, and an average plant spacing of 25 cm. The day of the trial was a sunny day, with an average air temperature of 21°C, an easterly wind, a wind speed of 0.6-1.2 m/s, and a relative humidity of 48%. In order to reduce the effect of morning and evening field fog, the experiment was selected in the afternoon.

Experimental material

Fog droplet sampling uses water-sensitive test paper with a specification of 35 mm \times 110 mm, with a yellow background color that changes to blue when exposed to water, which can be used to detect the distribution status of fog droplets in the field.

Experimental design

In the experimental field, a 30m×20m experimental area was selected for sampling point arrangement, three collection strips with 5 m interval were set up, six maize plants with 1 m interval were selected for each collection strip, and three layers of vertical sampling points were set up for each maize plant at a distance of 0.3 m from the ground (bottom), 1 m (middle), and 1.7 m (canopy), and water-sensitive test papers were arranged on the maize leaves at each sampling point to form a three-dimensional sampling point. Each sampling point was arranged with water-sensitive test paper on maize leaves to form a three-dimensional sampling point. The schematic layout of the field test paper is shown in Fig. 9. The UAV flight path was operated according to the arrow direction, and the sampling belt was located in the middle of the spray pattern extending to both sides. According to the results of the matching test calculations of the parameters of plant protection UAV flight height, operation width and application amount in the previous experiments and the related articles on the impact of plant protection UAV parameters on maize plant protection (Wang *et al.*, 2023; Qin *et al.*, 2014), the flight height of the UAV was set to 4 m, and water was used instead of pesticide for the test. During the test, the UAV used the conventional reciprocating flight application mode to carry out spraying operations on maize, and the interval between each route was 3 m. A schematic diagram of the test paper arrangement for the field test is shown in Fig. 9. The test plot was open and unobstructed, and the maize growth was more consistent.

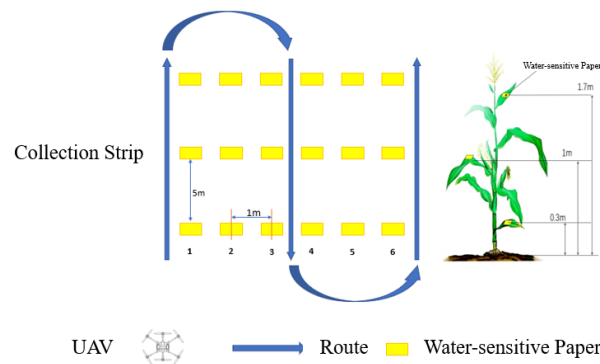


Fig. 9 - Schematic layout of water-sensitive test strips

Three common speed sorties (Wang *et al.*, 2021), 1.5 m/s, 3 m/s and 4.5 m/s treatments, were set up for testing the droplet deposition distribution characteristics of UAV sprayed droplets at different sampling locations in maize plants under different flight speeds, and the specific experimental parameters are shown in Table 1.

Table 1

Test design for droplet distribution characteristics

| Sortie | Speed (m/s) | Height (m) | Flux (L·min) | Nozzle Speed (r/min) |
|--------|-------------|------------|--------------|----------------------|
| 1 | 1.5m/s | 4m | 4 | 14000 |
| 2 | 3m/s | 4m | 4 | 14000 |
| 3 | 4.5m/s | 4m | 4 | 14000 |

Data collection and processing

After the completion of each set of tests the water sensitive papers were collected one by one in a sealed bag by serial number and brought back to the laboratory for processing. A scanner was used to scan the collected water-sensitive paper into a grayscale image with a resolution of 600 dpi and saved in jpg format. The scanned images were imported into the image processing software Deposit Scan and analyzed to obtain the deposition characteristics, including droplet density, coverage, deposition volume and other parameters.

In order to characterize the uniformity of droplet deposition among the collection points in the test, it can be evaluated by the coefficient of variation (CV) of the density of droplet coverage (or deposition) at different collection points within the effective spraying area of the UAV, and the smaller the value is, the better the droplet uniformity is. The coefficient of variation (CV) is calculated as:

$$CV = \frac{SD}{\bar{X}} \times 100\% \quad (2)$$

$$SD = \sqrt{\frac{\sum_{i=1}^n (X_i - \bar{X})^2}{N - 1}} \quad (3)$$

where:

SD is the standard deviation of the same group of test collection samples; X_i is the droplet density (or deposition) of each collection point; \bar{X} is the average value of droplet density (or deposition) of each group of test collection points; N is the number of test collection points of each group.

RESULTS AND ANALYSES

Particle size distribution of droplets at different flight speeds

Figure 10 shows the comparison of the droplet volume median diameter (VMD) at different sampling locations for each test sortie, from which it can be seen that at the same sampling level, the value of VMD decreases with the increase of the flight speed from 1.5 m/s to 4.5 m/s; the flight speed significantly affects the droplet size at the same sampling level. For example, in the bottom layer of maize plants, the corresponding droplet volume median diameters at flight speeds of 1.5, 3, and 4.5 m/s were 98.87, 75.67, and 72.73 μm , respectively.

The droplet volume median diameters at 3 m/s decreased by 35.94% compared with that at 1.5 m/s. The basic trend of VMD in different sampling layers at the same speed was maximum in the canopy layer, followed by the middle layer and minimum in the bottom layer. However, when the UAV flight speed was 1.5 m/s, it can be seen from the figure that the VMD of the bottom layer was 98.87 μm larger than that of the middle layer, 92.64 μm , which was opposite to the results of 3 m/s and 4 m/s.

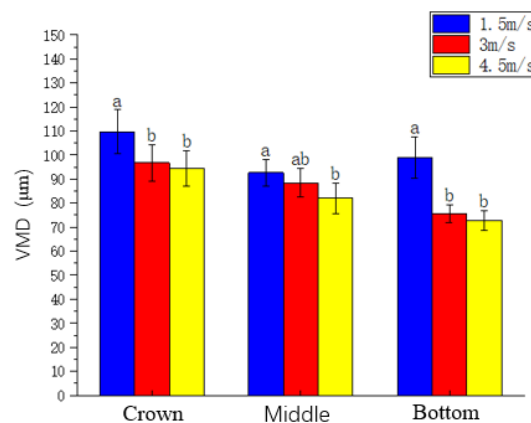


Fig. 10 - Particle size distribution of droplets at different flight speeds

(Data in the table are mean \pm standard error. Different lowercase letters in the same column indicate that the different treatments were tested by Turkey's method at the $P < 0.05$ level)

Characterization of droplet deposition at each sampling point at different flight speeds

There is a close relationship between droplet coverage density and droplet size, application rate and flight speed. Under the same droplet size and application rate, it can be seen in Fig.11 that among the three flight speeds of the experimental treatments, the droplet coverage density of each sampling point under the same speed has the same trend with the sampling position, and the droplet coverage density of the bottom layer is the largest at 1.5 m/s, the droplet coverage density of the canopy layer is the largest at 3 m/s and 4.5 m/s, and the maximum droplet coverage density of the three speeds occurs in different positions.

The maximum droplet coverage density at the slower speed of 1.5 m/s was 432.09 droplets/cm² at the bottom of sampling point 1, and the minimum was 41.43 droplets/cm² at the bottom of sampling point 6 at the speed of 4.5 m/s. This experiment used the same multi-route reciprocal spraying as the actual operation, and it can be seen that the droplet deposition pattern is highly consistent among the collection points in the spraying area of the UAV under the same treatment.

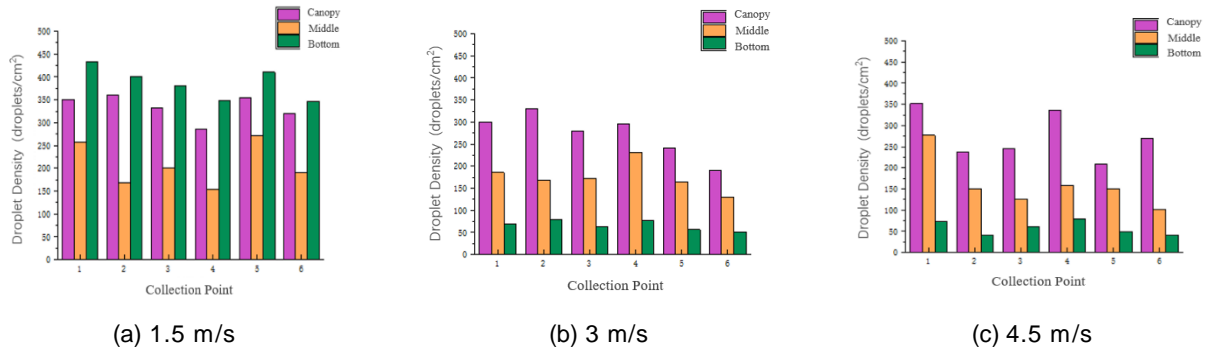


Fig. 11 - Distribution of droplet deposition characteristics at each sampling point for different flight speeds

Analysis of droplet density, coverage and droplet deposition

Table 2

| Parameters of droplet deposition characteristics for each sampling layer | | | | | | | |
|--|--------|---|---|----------------------------------|--|------------------------|--------------------------------------|
| Sampling Point | Sortie | Droplet Density (droplets/cm ²) | Coefficient of Variation of Droplet Density | Deposition (µm/cm ²) | Coefficient of Variation of Deposition | Coverage (%) | Coefficient of Variation of Coverage |
| Canopy | 1 | 334.16±28.14 ^a | 8.42 | 0.313±0.02 ^a | 5.55 | 23.63±1.9 ^a | 7.86 |
| | 2 | 273.05±50.02 ^a | 18.32 | 0.297±0.07 ^a | 24.27 | 14.44±4.7 ^b | 32.39 |
| | 3 | 274.48±57.52 ^a | 20.96 | 0.287±0.09 ^a | 31.33 | 13.15±6.3 ^b | 48.19 |
| Middle | 1 | 206.44±47.27 ^a | 22.90 | 0.171±0.05 ^a | 29.80 | 8.19±2.6 ^a | 31.91 |
| | 2 | 174.94±32.97 ^a | 18.85 | 0.138±0.05 ^a | 35.34 | 7.53±2.3 ^a | 30.23 |
| | 3 | 160.19±60.91 ^a | 38.02 | 0.118±0.07 ^a | 58.67 | 4.95±2.9 ^a | 58.44 |
| Bottom | 1 | 386.29±34.72 ^a | 8.99 | 0.365±0.04 ^a | 11.07 | 28.21±3.9 ^a | 13.72 |
| | 2 | 65.52±11.45 ^b | 17.48 | 0.040±0.01 ^b | 27.25 | 3.09±1.1 ^b | 34.09 |
| | 3 | 57.47±16.14 ^b | 28.10 | 0.034±0.01 ^b | 33.05 | 1.63±0.6 ^b | 38.10 |

(Data in the table are mean ± standard error. Different lowercase letters in the same column indicate that the different treatments were tested by Turkey's method at the P<0.05 level)

Table 2 shows the droplet deposition parameters of each sampling level, and it is not difficult to find that the flight speed significantly affects the droplet coverage, droplet density and deposition amount of the same sampling level, and the trends of droplet coverage and droplet deposition amount of each sampling level (canopy, middle and bottom) decrease with the increase of the flight speed, and only the droplet density of the canopy level of sorties 2 and 3 (with the flight speed of 3 m/s and 4.5 m/s) do not conform to this law, but the values of the two were very close to each other. In the canopy sampling position, the average droplet density of sortie 1 (flight speed of 1.5 m/s) reached 334.16/cm², and the extreme difference between the sorties was 61.11/cm², but the difference was not significant (P=0.064). Similarly, the droplet densities in the middle layer were 160.19~206.44 droplets/cm², which was not significant, but the droplet densities in the bottom layer were significant, and the droplet density in the bottom layer of flight 1 exceeded the droplet density in the canopy layer to reach 386.29 droplets/cm², and the minimum droplet density in the bottom layer of flight 3 was 57.47 droplets/cm², which was much smaller than the droplet density in the canopy layer. The reason for this is that, when the flight speed is small, the downwash airflow reaches the ground and spreads upward to a certain height, which leads to the obvious difference in the bottom layer data. The pattern of change of droplet deposition and droplet density of each sortie is generally consistent, the maximum deposition is in the bottom layer of sortie 1, and the minimum value is in the bottom layer of sortie 3, which is 0.365 µm/cm² and 0.034 µm/cm², respectively.

A comprehensive analysis of the data in Table 4 reveals that under the operational treatments in this study, the difference in the fog droplet deposition effect at flight speeds of 3 m/s and 4.5 m/s is not significant, but the difference between these two sorties and the fog droplet deposition effect at a flight speed of 1.5 m/s is more significant. In this study, the coefficient of variation CV value was used to measure the uniformity of fog droplet deposition among the collection points within the UAV spraying area in the experiment.

Table 4 shows that the coefficients of variation for droplet deposition, droplet coverage and droplet density at 1.5 m/s are smaller than those of the other two groups, which indicates that under the operating conditions of this paper, the droplet deposition effect of the centrifugal spraying system of the maize plant protection drone is most uniform at a flight speed of 1.5 m/s. The coefficients of variation for droplet density at the maize crown, middle and lower layers at both the flight speeds of 1.5 and 3 m/s are less than 50%, which is in line with the provisions of MH/T 1002.1-2016 "Quality Technical Indicators of Agricultural Aerial Operations Part 1: Spraying Operations" on the uniformity of droplet distribution in constant spraying operations, and the coefficient of variation of droplet density in the middle layer at a flight speed of 4.5 m/s was 58.44% slightly higher than the operational standard. Considering the requirements of actual operation on the efficiency of the UAV and the utilization rate of pesticides, a flight speed of 3 m/s can be considered for operation in actual operation.

CONCLUSIONS

In this paper, a set of maize plant protection UAV centrifugal spraying system was designed based on DJI T20 UAV platform, and the performance test of single nozzle and the field test of the droplet distribution characteristics of the whole system under different flight speeds were carried out. According to the analysis of the experimental results in this study, the coefficient of variation of fog droplet density in the crown, middle and lower layers of maize at 1.5 m/s and 3 m/s flight speeds is less than 50%, which is in line with the provisions of the quality technical indexes of agricultural aerial operations. When the flight speed is 4.5 m/s, the coefficient of variation of droplet density in its middle layer is 58.44% which is slightly higher than the operation standard, and the coefficients of variation of the crown and the bottom layer are also in accordance with the regulations. A flight speed of 3 m/s can be considered for the actual operation.

ACKNOWLEDGEMENT

This work was supported by Anhui Provincial Science and Technology Special Project, No.2022296906020008.

REFERENCES

- [1] Biglia, A., Grella, M., Bloise, N., et al. (2022). UAV-spray application in vineyards: Flight modes and spray system adjustment effects on canopy deposit, coverage, and off-target losses. *The Science of the total environment*, Vol. 845, 157292.
- [2] Chen, C., Li, S., Wu, X., et al. (2021). Analysis of droplet size uniformity and selection of spray parameters based on the biological optimum particle size theory. *Environmental research*, Vol. 204 (Pt B), 112076.
- [3] Chen, J., Liu, W., Yuan, Y. (2018). Current status and development trend of the use of drone atomising nozzle (无人机雾化喷头的使用现状与发展趋势). *China Plant Protection Guide*, Vol. 38, Issue 03, 66-70.
- [4] Chen, Q., Zhang, J., Zhang, C., et al. (2023). CFD analysis and RBFNN-based optimization of spraying system for a six-rotor unmanned aerial vehicle (UAV) sprayer. *Crop Protection*, Vol.174, Issue 106433, 0261-2194.
- [5] Chen, S., Lan, Y., Bradley, K. F., et al. (2017). Effect of wind field below the rotor of a multi-rotor UAV on aerial spraying droplet deposition (多旋翼无人机旋翼下方风场对航空喷施雾滴沉积的影响). *Journal of Agricultural Machinery*, Vol. 48, Issue 08, 105-113.
- [6] Dong, K., Chen, H., Zheng, Y., et al. (2018). Design and test of centrifugal nozzle for plant protection drone (植保无人机离心喷头的设计与试验). *Journal of China University of Metrology*, Vol. 29, Issue 03, 265-268.
- [7] Fritz, B. K., Hoffmann, W. C., Bagley, W. E. (2009). Effects of spray mixtures on droplet size under aerial application conditions and implications on drift. *Applied Engineering in Agriculture*, Vol. 26, Issue 1, 21-29.
- [8] Liu, L., Sun, K., Zhang, Q., et al. (2022). Maize plant protection UAV hot dance spraying system design and droplet distribution characteristics test (玉米植保无人机热雾喷施系统设计与雾滴分布特性试验). *Journal of Agricultural Machinery*, Vol. 53, Issue 12, 80-88.
- [9] Pankaj, G., Shashidhar, K. (2023). Experimental analysis of spray droplet deposition behaviour for centrifugal assisted spinning disc sprayer. *Materials Today: Proceedings*. Vol. 92, Issue 1, 258-263.
- [10] Qin, W., Xue, X., Zhou, L., et al. (2014). Effects of unmanned helicopter spraying parameters on the distribution of droplet deposition in maize canopy (无人直升机喷雾参数对玉米冠层雾滴沉积分布的影响). *Journal of Agricultural Engineering*, Vol. 30, Issue 05, 50-56.

- [11] Qiu, B., Wang, L., Cai, D., et al. (2013). Effects of flight height and speed of unmanned helicopter on spray deposition distribution (无人直升机飞行高度与速度对喷雾沉积分布的影响). *Journal of Agricultural Engineering*, Vol. 29, Issue 24, 25-32.
- [12] Ru, Y., Fang, S., Xue, J., et al. (2023). Experimental study of the influence factors of the droplet size of rotary nozzles during manned helicopter spraying operations. *Crop Protection*, Vol. 177, 106550.
- [13] Uk, S. (1977). Tracing insecticide spray droplets by sizes on natural surfaces. The state of the art and its value. *Pesticide Science*, Vol. 8, Issue 5, 501-509.
- [14] Wang, C., Herbst, A., Zeng, A., et al. (2021). Assessment of spray deposition, drift and mass balance from unmanned aerial vehicle sprayer using an artificial vineyard. *Science of The Total Environment*, Vol. 777, Issue 146181, 0048-9697.
- [15] Wang, L., Xu, M., Hou, Q., et al. (2021). Numerical verification on influence of multi-feature parameters to the downwash airflow field and operation effect of a six-rotor agricultural UAV in flight. *Computers and Electronics in Agriculture*, Vol. 190, 106425.
- [16] Wang, Z., Hussain, M., Yin, J., et al. (2023). Analysis of droplet deposition and maize (*Zea Mays L.*) growth control: application of ethephon by small unmanned aerial vehicle and electric knapsack sprayer. *Field Crops Research*. Vol. 292, 108822
- [17] Xie, D., Chen, L., Liu, L., et al (2022). Actuators and sensors for application in agricultural robots: A review. *Machines*, Vol. 10, Issue 10, 913.
- [18] Yang, Y., Zhang, B., Zha, J. et al. (2020). Real-time extraction of navigation lines between rows of maize (玉米行间导航线实时提取). *Journal of Agricultural Engineering*, Vol. 36, Issue 12, 162-171.
- [19] Yuan, H., Wang, G. (2015). Relationship between droplet size and coverage density and pesticide control effect (雾滴大小和覆盖密度与农药防治效果的关系). *Plant Protection*, Vol. 41 Issue 06, 9-16.
- [20] Zhang, H., Lan, Y., Wen, S., et al. (2022). Modelling the adhesion of fog droplets on rice plants under the action of UAV rotor wind field (无人机旋翼风场作用下雾滴在水稻植株上的黏附量模型构建). *Journal of Agricultural Engineering*, Vol. 38, Issue 18, 40-50.

YOUNG APPLE FRUITS DETECTION METHOD BASED ON IMPROVED YOLOv5

/ 基于改进 YOLOv5 的苹果幼果检测方法

Yonghui DU¹⁾, Ang GAO¹⁾, Yuepeng SONG^{1,2,3*)}, Jing GUO^{1,2,3)}, Wei MA⁴⁾, Longlong REN^{1,2,3,*)}¹⁾ Shandong Agricultural University, College of Mechanical and Electrical Engineering/ China;²⁾ Shandong Provincial Key Laboratory of Horticultural Machinery and Equipment/ China;³⁾ Shandong Provincial Engineering Laboratory of Agricultural Equipment Intelligence/ China;⁴⁾ Institute of Urban Agriculture, Chinese Academy of Agricultural Sciences/ China

E-mail: renlonglong@sdau.edu.cn

DOI: <https://doi.org/10.35633/inmateh-73-07>**Keywords:** YOLOv5; Young apple fruit; Prediction layer; CA attention mechanism; GIOU loss function**ABSTRACT**

The intelligent detection of young apple fruits based on deep learning faced various challenges such as varying scale sizes and colors similar to the background, which increased the risk of misdetection or missed detection. To effectively address these issues, a method for young apple fruit detection based on improved YOLOv5 was proposed in this paper. Firstly, a young apple fruits dataset was established. Subsequently, a prediction layer was added to the detection head of the model, and four layers of CA attention mechanism were integrated into the detection neck (Neck). Additionally, the GIOU function was introduced as the model's loss function to enhance its overall detection performance. The accuracy on the validation dataset reached 94.6%, with an average precision of 82.2%. Compared with YOLOv3, YOLOv4, and the original YOLOv5 detection methods, the accuracy increased by 0.4%, 1.3%, and 4.6% respectively, while the average precision increased by 0.9%, 1.6%, and 1.2% respectively. The experiments demonstrated that the algorithm effectively recognized young apple fruits in complex scenes while meeting real-time detection requirements, providing support for intelligent apple orchard management.

摘要

基于深度学习的苹果幼果智能化检测面临诸多挑战如尺度大小不一、颜色与背景相近等，会导致误检或漏检的风险增加。为了有效解决这些问题，本文提出一种基于改进 YOLOv5 的苹果幼果检测方法，首先建立苹果幼果数据集，再者在检测模型的检测头中添加预测层，在检测脖颈 (Neck) 中添加四层 CA 注意力机制，并引入 GIOU 函数作为模型的损失函数，以提高模型的整体检测性能。在验证数据集上的准确率达到 94.6%，平均精度为 82.2%；与 YOLOv3、YOLOv4 和原始的 YOLOv5 检测方法相比，准确率分别提升 0.4%、1.3%、4.6%，平均精度分别提升 0.9%、1.6%、1.2%。试验证明，该算法能在满足实时检测要求的前提下，能够有效地识别复杂场景中的苹果幼果，为智能化苹果园管理提供支持。

INTRODUCTION

China, as the world's largest producer and consumer of apples, played a crucial role in rural revitalization and increasing farmers' income (Jiang et al., 2023). However, one of the constraints currently faced was the rising labor cost year by year, especially in the apple industry, which has become an important factor restricting its development. In apple production, the management of fruits and vegetables served as a crucial link. At present, it mainly depended on manual labor to complete, but there were problems of high labor intensity and low production efficiency. Therefore, there was an urgent need to improve the intelligent level of apple fruits and vegetables management to cope with the challenges of the current industrial development.

Achieving reliable detection and recognition of young apple fruits is crucial for the intelligence of fruit and vegetable management. In recent years, with the continuous advancement of deep learning technology, object detection techniques have been widely applied in the agricultural sector (Kamilaris et al., 2018). In the field of young apple fruit detection, various improved models have emerged successively. Tian et al. optimized the YOLOv3-based model with DenseNet, significantly improving detection speed to just 0.304 seconds per frame (Tian et al., 2019). To address the challenge of nighttime fruit detection, Sun et al. optimized the Retina-PVTv2 model by introducing a gradient-coordination mechanism, leading to a significant improvement in nighttime fruit detection accuracy (Sun et al., 2022).

Yonghui DU, M.Sc. Stud. Eng.; Ang Gao, M.Sc. Stud. Eng.; Yuepeng Song, Prof. Ph.D. Eng.; Jing GUO Prof. Ph.D. Eng.; Wei MA Prof. Ph.D. Eng.; Longlong Ren Lecturer Ph.D. Eng;

Li et al. focused on addressing the issue of small-sample datasets and proposed an integrated U-Net segmentation model, which significantly improved the accuracy and generalization ability of image segmentation, achieving accurate detection of nighttime young apple fruits (Li et al., 2021).

Sun et al. successfully applied the BFP-Net, an FPN layer-optimized model, to the task of detecting young apple fruits, effectively improving detection accuracy and efficiency (Sun et al., 2022). Wang et al. proposed an R-FCN young apple fruits detection network capable of detecting small targets with similar background colors (Wang et al., 2019). Song et al. achieved young apple fruits recognition by adding non-local modules and squeeze-and-excitation modules to the YOLOv4 model, achieving an average precision of 96.9% (Song et al., 2021). Jiang et al. added non-local attention mechanisms and convolutional block attention mechanisms to the YOLOv4 model, enabling efficient recognition under conditions such as high glare, shadows, blurriness, and severe occlusion (Jiang et al., 2022). Wang et al. improved the YOLOv5s model, achieving an accuracy of 95.8% in young fruits detection while reducing model load (Wang et al., 2021). Additionally, the detection of other fruits such as kiwi, green peach, and citrus bears some similarity to young fruits detection.

The above scholars had detected and achieved good detection results for young apple fruits. However, as far as the detection of young apple fruits was concerned, the problems of smaller target and similar colors to the background were still the focus of research. Therefore, in this paper, a young apple fruits detection method based on improved YOLOv5 was designed to better recognize and distinguish the young fruits from the background and improve the overall detection performance.

MATERIALS AND METHODS

YOLOv5 algorithm

The YOLOv5 algorithm was mainly composed of four parts: the Input, the Backbone, the Neck and the Head (Park et al., 2023). The Mosaic data enhancement technology (Bochkovskiy et al., 2020) was used on the input side, which was able to randomize the size, cropping and alignment of the data set to achieve more flexible and diverse data processing. The backbone network was the core of YOLOv5s network, which was mainly used to extract image features for target detection (Arifando et al., 2023). The neck network was located between the backbone network and the head network, and its function was to extract the features extracted from the backbone network in a deeper way to improve the robustness of the model. The head network was the output part of the target detection model and was responsible for target detection using the previously extracted features. It consists of multiple convolutional and detection layers, where the detection layer mainly implements the process of target detection.

Due to differences in network depth and width, YOLOv5 has undergone several evolutions, resulting in various versions, including YOLOv5s, YOLOv5m, YOLOv5l, and YOLOv5x. Considering the design requirements of this study and to ensure accuracy, the research was based on the YOLOv5s as the foundational model, with improvements made using the YOLOv5-6.0 version. Figure 1 illustrates the network structure diagram of YOLOv5s.

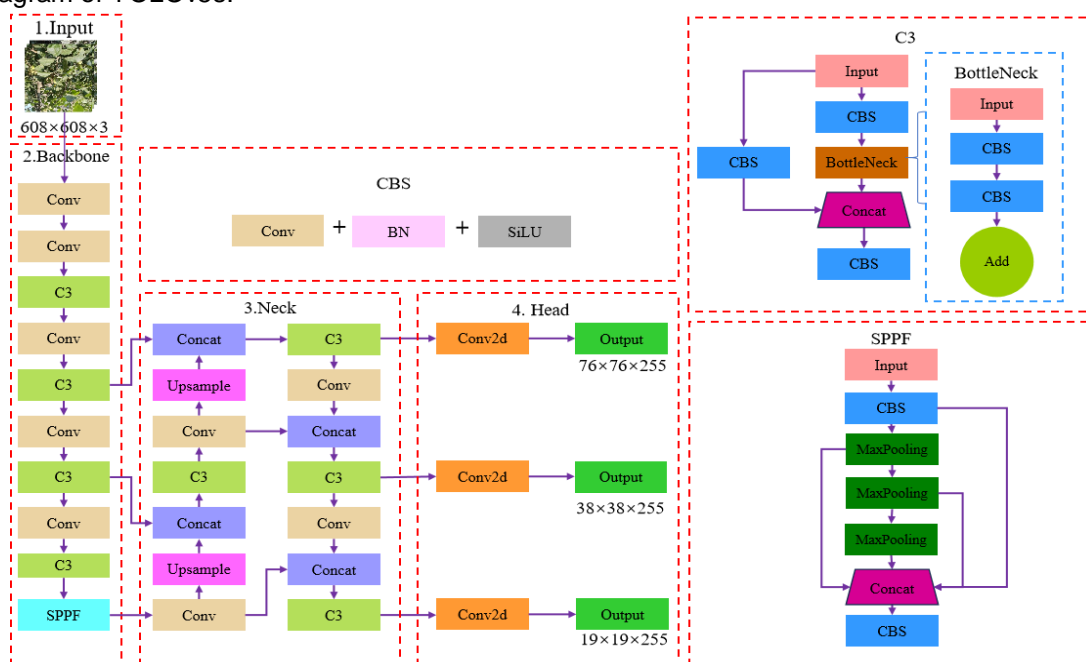


Fig. 1 - Network structure of YOLOv5s

Improved YOLOv5 algorithm

In this paper, the YOLOv5 model was improved on top of it. Firstly, a prediction layer was added to the detection head of the detection model. Secondly, four layers of CA attention mechanism were incorporated into the detection neck (Neck), and the GIOU function was introduced as the model's loss function to enhance the overall detection performance. The network structure of the improved model in this study is illustrated in Figure 2.

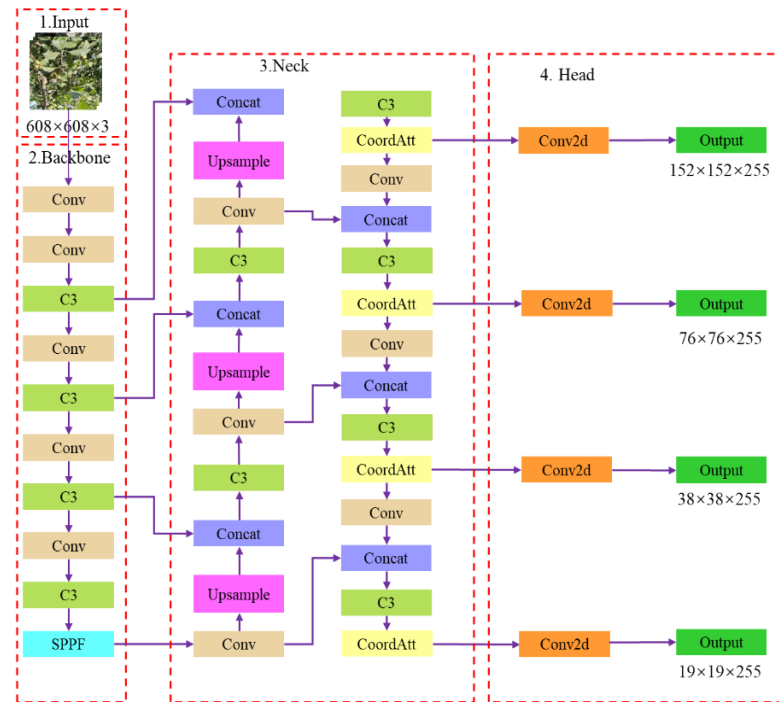


Fig. 2 - Improved network structure

Multi-scale detection head

As could be seen in Figure 1, in the original YOLOv5 model, YOLOv5 detected the target by three different sizes of prediction layers. If the input size was 608 × 608, the three prediction layer sizes of 19 × 19, 38 × 38, and 76 × 76 were obtained at the time of detection (Carrasco et al., 2021). As the depth of the input passed to the detection layer gradually increases, the possibility of information loss in the process of passing the features extracted from the shallow layer to the deeper layer gradually increases, placing higher demands on the feature extraction capability of the network structure (Changgao et al., 2021). This suggests that the features extracted in the deeper structure through multiple dimensionality reduction operations may not be able to adequately express the information of the image, and thus the design of appropriate multi-scale prediction layers becomes crucial.

The research object of this paper was young apple fruits. Since the size of the near apple fruits was larger relative to the size of the far ones during the shooting, it was often easy to miss the detection problem for the small-scale apple fruits. To solve this problem, this paper used multi-scale detection head to add a shallow prediction layer in the Head network. It was specifically used to detect small-scale young apple fruits. The improved Head network was shown in Figure 3.

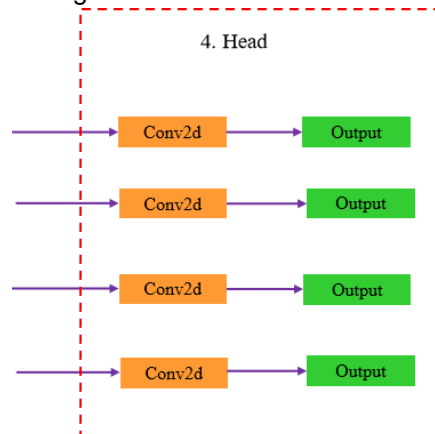


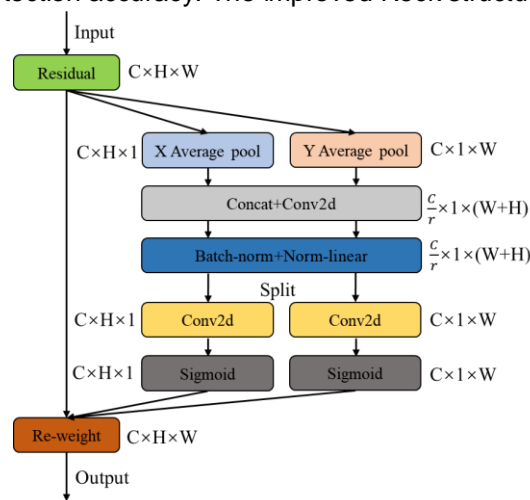
Fig. 3 - Improved Head network

Introduction of CA attention mechanisms

The attention mechanism was a widely used technique in current deep learning, endowing models with the ability to finely select information when processing images. Similar to the attention mechanism in human vision, this technique enables models to focus on key information within vast amounts of data, thereby disregarding unnecessary information (Aijun et al., 2022).

At the early stage of the growth of young apple fruits, they might have features that were similar to or not distinct enough from the background, which added difficulties to the detection. The introduction of CA (Coordinate attention) attention mechanism (Hou et al., 2021) could enhance the features related to young apple fruits and automatically select the most representative feature channels, thus improving the accuracy of recognition. CA attention mechanism improved the robustness of recognition by assigning different weights to each channel, which enabled the model to adaptively handle these changes (Pham et al., 2023). Compared with other complex attention mechanisms, CA attention mechanism had lower computational complexity, which made it more efficient in dealing with real-time or large-scale young apple fruits recognition tasks, and reduced the consumption of computational resources and time. The specific implementation process is shown in Fig.4.

In this study, CA attention mechanism modules were introduced after each C3 module in the Neck network to enhance the model's detection accuracy. The improved Neck structure is depicted in Figure 5.



Note: Input is the input; C is the number of image channels; H is the image height; W is the image width; r is the downsampling reduction ratio; X Average pool is the horizontal average pooling; Y Average pool is the vertical average pooling; Non-linear is the nonlinear activation function; Sigmoid is the activation function; Re-weight is the weight acquisition; Output is the output.

Fig. 4 - Schematic diagram of CA attention mechanism module

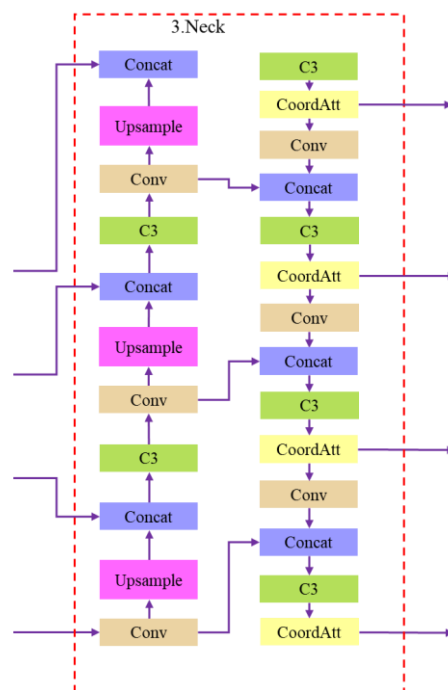


Fig. 5 - Diagram of the improved Neck structure

Optimizing the loss function

In the original YOLOv5 model, the CIOU loss function (Zheng *et al.*, 2023) was adopted as the regression loss function of the model. It effectively improved the localization accuracy of the bounding box by integrating the intersection and concurrency ratio (IOU) between the predicted box and the real box, the center point distance, with the aspect ratio (Aswal *et al.*, 2023, Zhang *et al.* 2022). However, in the specific task of young apple fruits recognition, there might be significant variations in the shape and size of young fruits, which makes the CIOU loss function show some limitations in terms of stability. In contrast, the GIOU loss function (Rezatofghi *et al.*, 2019) had higher stability when dealing with targets with large variations in shape and size, which helped to improve the performance of the model in the task of young apple fruits recognition. Meanwhile, the GIOU loss function was able to consider the spatial relationship between the bounding boxes more comprehensively, which helped the model to locate the position of the young apple fruits more accurately. Therefore, in order to improve the stability of the model, the GIOU loss function was used instead of the CIOU loss function in this paper.

The GIOU loss function makes the predicted bounding box closer to the real bounding box by introducing the area of the smallest outer rectangle as a penalty term (Rani, 2021). This design makes the GIOU loss function perform stably in solving the problem of the degree of bounding box overlap, regardless of whether the two overlap or not. The GIOU loss function model is shown in Figure 6.

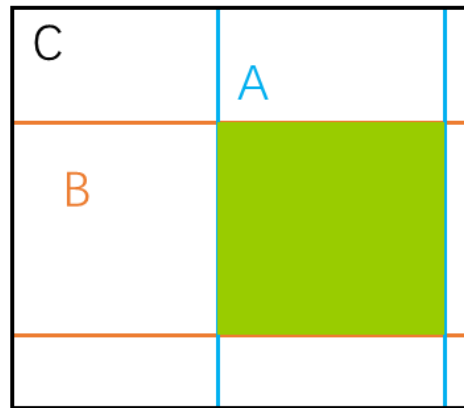


Fig. 6 - GIOU loss function model

$$GIOU = IOU - \frac{|C - |A \cup B||}{|C|} \quad (1)$$

$$IOU = \frac{|A \cap B|}{|A \cup B|} \quad (2)$$

where: A is the area of the prediction frame; B is the area of the real frame; C is the area of the smallest rectangle containing the prediction frame A and the real frame B .

RESULTS

Data set preprocessing and evaluation indicators

The image data used in this study were sourced from the apple experimental field at Shandong Agricultural University, located at approximately 117.12296° E longitude and 36.200713° N latitude. The data were collected in early May 2023 to ensure their timeliness. All images in the datasets were uniformly formatted as .jpg files with dimensions of 608x608 pixels for ease of subsequent processing. The dataset was annotated using labeling software to ensure data quality. In total, there were 7536 images in the dataset, which were divided into training, validation, and testing sets in an 8:1:1 ratio for model training and performance evaluation purposes.

To validate the effectiveness of the algorithm proposed in this paper, performance evaluation of the algorithm was conducted using metrics such as Precision (P), Recall (R), Average Precision (AP), and Mean Average Precision (mAP) (Jubayer *et al.*, 2021, Ye *et al.*, 2023). The following are the formulas used to calculate these parameters:

$$P = \frac{TP}{TP + FP} \quad (3)$$

$$R = \frac{TP}{TP + FN} \quad (4)$$

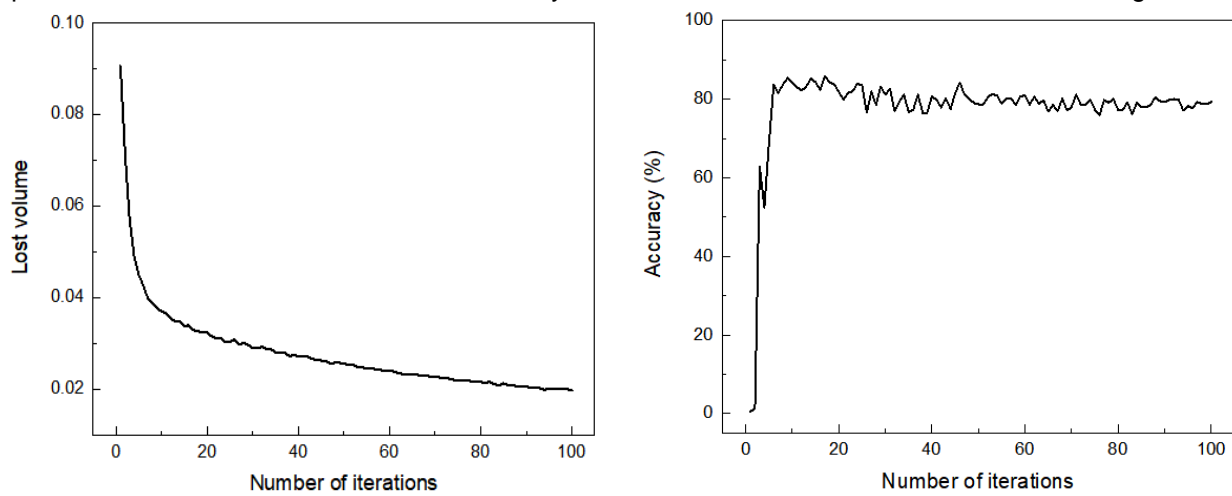
$$AP = \int_0^1 P(R) dR \quad (5)$$

$$mAP = \frac{1}{K} \sum_{i=1}^K AP(i) \tag{6}$$

where: P denotes accuracy, %; R denotes recall, %; AP denotes average precision, %; mAP denotes mean average precision, %; TP denotes the number of correctly detected young apple fruits, pcs; FP denotes the number of wrongly detected young apple fruits, pcs; FN denotes the number of missed young apple fruits, pcs; TN denotes the number of detected backgrounds, pcs; K is the number of categories of young apple fruits in the dataset, pcs.

Training of young apple fruits model

By adding a prediction layer, CA attention mechanism, and optimizing the GIOU loss function to the YOLOv5s model, the accuracy of the model in identifying young apple fruits was improved. To validate the proposed detection method, loss curve and accuracy curve of the improved model were plotted. Figure 7(a) depicted the loss curve during model training. After multiple iterations of training, the loss curve exhibited a noticeable decreasing trend, stabilizing around 0.025 with increasing iterations and gradually leveling off. Figure 7(b) illustrated the accuracy curve during model training. At the beginning of training, the recognition accuracy was relatively low. However, with an increase in the number of iterations, the accuracy gradually improved and stabilized around 80%. This clearly demonstrated the effectiveness of model training.



a) Model Training Loss Lost Plot; (b) Model training precision graph

Fig. 7 - Model training Loss, accuracy plot

Improvement program for young apple fruits

In the same experimental environment, eight tests of the improvement scheme were conducted to evaluate the impact of each improvement module in the YOLOv5 model improved in this paper on the performance of young apple fruit detection. The experimental results were shown in Table 1, where "√" indicates the use of the corresponding module.

Table 1

Test results

| Test number | Predictive layer | CA | GIOU | Accuracy (%) | Mean average precision (%) |
|-------------|------------------|----|------|--------------|----------------------------|
| (1) | | | | 90.0 | 81.0 |
| (2) | √ | | | 90.2 | 82.6 |
| (3) | | √ | | 89.9 | 82.2 |
| (4) | | | √ | 92.2 | 80.9 |
| (5) | √ | √ | | 93.2 | 82.4 |
| (6) | √ | | √ | 92.1 | 81.4 |
| (7) | | √ | √ | 93.8 | 82.5 |
| (8) | √ | √ | √ | 94.6 | 82.2 |

Trial (1) was the trial of the original model, which served as the baseline for the following seven sets of trial comparisons. Trial (2) was the trial with only the prediction layer added, which improved accuracy by 0.2% and mean average precision by 1.6%. Trial (3) was the trial with only the CA attention mechanism added, which showed a 0.1% decrease in accuracy but a 1.2% improvement in mean average precision.

Trial (4) was the trial with only the GIOU loss function introduced, and the accuracy was improved by 2.2%, but the mean average precision decreased by 0.1%. Trial (5) was a trial that added both the prediction layer and the CA attention mechanism, with the accuracy improved by 3.2% and the mean average precision improved by 1.4%. Trial (6) was a trial with the addition of both the prediction layer and the introduction of the GIOU loss function, with the accuracy improved by 2.1% and the mean average precision improved by 0.4%. Trial (7) was the trial of adding CA attention mechanism and introducing GIOU loss function at the same time, the accuracy was improved by 3.8%, and the mean average precision was improved by 1.5%. Trial (8) was the trial of the improved method in this paper, the accuracy was improved by 4.6%, and the mean average precision was improved by 1.2%. After the ablation test, it was found that all the improvement points and their synergies with each other positively affected the model and enhanced the detection of young apple fruits. This fully proved the effectiveness and correctness of the improvement method proposed in this paper, making it advantageous in the detection task.

Comparison tests of young apple fruits based on improved YOLOv5

Classical detection methods including YOLOv3, YOLOv4, and YOLOv5 were selected for young apple fruits detection and compared with the detection method proposed in this paper to validate its superiority in detecting young apple fruits. The detection results are presented in Table 2.

Table 2

Comparative test results

| Detection Models | Accuracy (%) | Mean average precision (%) |
|---------------------------|--------------|----------------------------|
| YOLOv3 | 94.2 | 81.3 |
| YOLOv4 | 92.9 | 80.6 |
| YOLOv5 | 90.0 | 81.0 |
| Methodology of this paper | 94.6 | 82.2 |

Based on the comparison results in Table 2, it could be seen that the proposed detection method in this paper improved the accuracy by 0.4% and the mean averaged accuracy by 0.9% over the YOLOv3 model. Compared with the YOLOv4 model, the accuracy was improved by 1.3% and the mean average precision was improved by 1.6%. Compared with the original YOLOv5 model, the accuracy was improved by 4.6% and the mean average precision was improved by 1.2%. In each parameter index, the model in this paper outperforms the accuracy and mean average accuracy of the YOLOv3, YOLOv4 and YOLOv5 models.

Validation analysis of apple young fruits visualization based on improved YOLOv5

Using the same set of test images, YOLOv3, YOLOv4, YOLOv5, and the model proposed in this paper were tested and visually analyzed, as shown in Figure 8.





Fig. 8 - Comparison of the detection effect of different methods on young apple fruits

In terms of the actual detection effect, the method in this paper showed better detection effect in the detection of young apple fruits at different distances and with leaves as the background. In contrast, YOLOv3, YOLOv4 and YOLOv5 had some degree of missed detection and false detection. The method in this paper could more accurately detect all the young apple fruits and showed higher detection accuracy. In conclusion, the method in this paper could significantly improve the effectiveness of feature extraction, effectively reduce the loss of detail information, and it improved the detection accuracy of young apple fruits.

CONCLUSIONS

To address current challenges in young apple fruits detection, such as significant variations in target sizes and diverse detection environments, in this paper, on the basis of YOLOv5 model, the prediction layer and CA attention mechanism were introduced on, and the GIOU loss function was used. It was proved through experiments that compared with the traditional YOLOv5 algorithm, the improved method proposed in this paper increased the prediction accuracy by 3.6% and the mean average accuracy by 1.2%. The method could better realize the detection of young apple fruits in natural scenes.

Although the current method has achieved certain results in young apple fruits detection, there are still some limitations, such as the single variety and lack of wide applicability. To overcome these limitations, future work will focus on further improvements, including collecting data from more varieties, optimizing network models, and addressing detection challenges in complex environments.

ACKNOWLEDGEMENT

We are very grateful to all the authors for their support and contribution with the manuscript. This work is partly supported by: Innovation Team Fund for the Fruit Industry of Shandong's Modern Agricultural Technology System (SDAIT-06-12), the State Key Laboratory of Mechanical System and Vibration (Grant No. MSV202002), and the Modern Agriculture Coarse Grain Industry Technology System Project of Shandong Province (SDAIT-15-05).

REFERENCES

- [1] Aijun, G., Gao, A.N.G., Chunming, Y., Zhilong, Z., Zhang, J. I., & Jinglong, Z. (2022). Dropping ear detection method for corn harvester based on improved Mask-RCNN. *INMATEH-Agricultural Engineering*, 66(1), pp.31-40. Shandong/China. <https://doi.org/10.35633/inmateh-66-03>
- [2] Arifando, R., Eto, S., & Wada, C. (2023). Improved YOLOv5-based lightweight object detection algorithm for people with visual impairment to detect buses. *Applied Sciences*, 13(9), 5802, Kyushu/Japan.
- [3] Aswal, D., Shukla, P., & Nandi, G. C. (2021). Designing effective power law-based loss function for faster and better bounding box regression. *Machine Vision and Applications*, 32(4), 87, India.
- [4] Bochkovskiy, A., Wang, C. Y., & Liao, H. Y. M. (2020). Yolov4: Optimal speed and accuracy of object detection. *arxiv preprint arxiv:2004.10934*, Russia.
- [5] Carrasco, D. P., Rashwan, H. A., García, M. Á., & Puig, D. (2021). T-YOLO: Tiny vehicle detection based on YOLO and multi-scale convolutional neural networks. *IEEE Access*, 11, 22430-22440, Spain.
- [6] Changgao, Xia., Wanlei, Ni, Kun Jiang, & Xiaofan, Li (2022). A real-time detection model for identification of citrus during different growth stages in orchards. *INMATEH-Agricultural Engineering*, 68(3), pp.373-382. Jiangsu/China. <https://doi.org/10.35633/inmateh-68-37>
- [7] Fan, X.Y., Fan, F. Kao, J.F. Yu, C.K. Hua, Jiang, Y., & Qian, C.H., (2023). Research on visual detection technology for liquid crystal panel electrode defect by improved YOLOv7 (基于改进 YOLOv7 的液晶面板电极缺陷视觉检测技术研究). *Journal of Electronic Measurement and Instrumentation* (09), 225-233. doi:10.13382/j.jemi.B2306576, Jiangsu/China.
- [8] Hou, Q., Zhou, D., & Feng, J., (2021). Coordinate attention for efficient mobile network design. *In Proceedings of the IEEE/CVF conference on computer vision and pattern recognition*. pp. 13713-13722, Singaporean.
- [9] Jiang, G.Q., Yang, Z.Y., Huo, Z.Q., Luo, J.W., & Zhao, C.J., (2023). Apple detection method before thinning fruit based on improved YOLOv5 model (基于改进 YOLOv5 网络的疏果前苹果检测方法). *Jiangsu Agricultural Science* (14), 205-215. doi:10.15889/j.issn.1002-1302.2023, 14.028, Hebei/China.
- [10] Jiang, M., Song, L., Wang, Y., Li, Z., & Song, H., (2022). Fusion of the YOLOv4 network model and visual attention mechanism to detect low-quality young apples in a complex environment. *Precision Agriculture*, 1-19, Shaanxi/China.
- [11] Jubayer, F., Soeb, J. A., Mojumder, A. N., Paul, M. K., Barua, P., Kayshar, S., ... & Islam, A. (2021). Detection of mold on the food surface using YOLOv5. *Current Research in Food Science*, 4, 724-728, Bangladesh.
- [12] Kamilaris, A., & Prenafeta-Boldú, F.X., (2018). Deep learning in agriculture: A survey. *Computers and electronics in agriculture*, 147, 70-90, Spain.
- [13] Li, Q., Jia, W., Sun, M., Hou, S., & Zheng, Y., (2021). A novel green apple segmentation algorithm based on ensemble U-Net under complex orchard environment. *Computers and Electronics in Agriculture*, 180, 105900, Shandong/China.
- [14] Pham, T. N., Nguyen, V. H., & Huh, J. H. (2023). Integration of improved YOLOv5 for face mask detector and auto-labeling to generate dataset for fighting against COVID-19. *The Journal of Supercomputing*, 79(8), 8966-8992, Korea.
- [15] Park, J., Bae, J., Im, J., Kim, B., & Jeong, J. (2023). LED-Display Defect Detection based on YOLOv5 and Transformer. *IEEE Access*, Korea.
- [16] Rani, E. (2021). LittleYOLO-SPP: A delicate real-time vehicle detection algorithm. *Optik*, 225, 165818, India.
- [17] Rezatofghi, H., Tsoi, N., Gwak, J., Sadeghian, A., Reid, I., & Savarese, S. (2019). Generalized intersection over union: A metric and a loss for bounding box regression. *In Proceedings of the IEEE/CVF conference on computer vision and pattern recognition* (pp. 658-666), Australia.

- [18] Song, H. B., Jiang, M. Mei, Wang, Y. F., & Song, L., (2021). Efficient detection method for young apples based on the fusion of convolutional neural network and visual attention mechanism (融合卷积神经网络与视觉注意机制的苹果幼果高效检测方法). *Journal of Agricultural Engineering* (09), 297-303, Shaanxi/China.
- [19] Sun, M., Xu, L., Chen, X., Ji, Z., Zheng, Y., & Jia, W., (2022). Bfp net: balanced feature pyramid network for small apple detection in complex orchard environment. *Plant Phenomics*, Shandong/China.
- [20] Sun, M., Xu, L., Luo, R., Lu, Y., & Jia, W., (2022). GH Former-Net: Towards more accurate small green apple/begonia fruit detection in the nighttime. *Journal of King Saud University-Computer and Information Sciences*, 34(7), 4421-4432, Shandong/China.
- [21] Tian, Y., Yang, G., Wang, Z., Wang, H., Li, E., & Liang, Z., (2019). Apple detection during different growth stages in orchards using the improved YOLO-V3 model. *Computers and electronics in agriculture*, 157, 417-426, Beijing/China.
- [22] Wang, D., & He, D., (2021). Channel pruned YOLO V5s-based deep learning approach for rapid and accurate apple fruitlet detection before fruit thinning. *Biosystems Engineering*, 210, 271-281, Shaanxi/China.
- [23] Wang, D., & He, D., (2019). Recognition of apple targets before fruits thinning by robot based on R-FCN deep convolution neural network (基于 R-FCN 深度卷积神经网络的机器人疏果前苹果目标的识别). *Journal of Agricultural Engineering* (03), 156-163, Shaanxi/China.
- [24] Wanzhi Zhang, Yuelin Han, Chen Huang, & Zhiwei Chen. (2022). Recognition method for seed potato buds based on improved YOLOv3-tiny. *INMATEH-Agricultural Engineering*, 67(2), Shandong/China.
- [25] Ye Xia, Xiaohui Lei, Herbst, A., & Xiaolan LYU. (2023). Research on pear inflorescence recognition based on fusion attention mechanism with Yolov5. *INMATEH-Agricultural Engineering*, 69(1), pp.11-20. Nanjing/China. <https://doi.org/10.35633/inmateh-69-01>
- [26] Zhang X. H., Yan J. X., Ma B., Ju J. S., Shen Q. F., & Wu Y. J., (2022). Research on abnormal detection method of side guard based on improved YOLOv5s (基于改进 YOLOv5s 的护帮板异常检测方法研究). *Journal of Engineering Design* (06), 665-675, Shaanxi/China.
- [27] Zheng, Z., Wang, P., Liu, W., Li, J., Ye, R., & Ren, D. (2020, April). Distance-IoU loss: Faster and better learning for bounding box regression. *In Proceedings of the AAAI conference on artificial intelligence* Vol. 34, No. 07, pp. 12993-13000, Tianjin/China.

HYDROPONIC VERTICAL SYSTEMS: ENHANCING CLIMATE RESILIENCE, WATER EFFICIENCY, AND URBAN AGRICULTURE

SISTEME VERTICALE HIDROPONICE: INTENSIFICAREA REZISTENȚEI LA CLIMĂ, EFICIENȚEI APEI ȘI AGRICULTURII URBANE

Iuliana GĂGEANU¹⁾, Ana-Maria TĂBĂRAȘU^{*1)}, Cătălin PERSU¹⁾, Gabriel GHEORGHE¹⁾, Mihaela NIȚU^{*1)},
Dan CUJBESCU¹⁾, Alexandru IONESCU¹⁾, Dragoș ANGHELACHE¹⁾

National Institute of Research – Development for Machines and Installations Designed to Agriculture
and Food Industry, Romania

Tel: 0730417449; E-mail: anamariatabarasu22@yahoo.com; Tel: 0746689449; E-mail: rosumihaelan@yahoo.com

DOI: <https://doi.org/10.35633/inmateh-73-08>

Keywords: Vertical farming; Hydroponic systems; Artificial light; Mathematical modelling.

ABSTRACT

This paper explores hydroponic vertical systems as a sustainable solution to modern agricultural challenges, particularly those posed by climate change. Hydroponics, a method of growing plants without soil using nutrient-rich water solutions, offers significant advantages over traditional farming. Vertical systems maximize space efficiency by growing plants in stacked layers, making them ideal for urban environments with limited space. These systems provide a controlled environment that mitigates the impacts of extreme weather, ensuring consistent crop production. The paper reviews various hydroponic techniques, including deep water culture, nutrient film technique, flood and drain, and drip irrigation. It highlights the efficiency of water use in hydroponics, crucial for areas facing water scarcity. Advanced technologies, such as sensors, automated nutrient delivery, and LED lighting, are employed to optimise growing conditions, enhance resource use efficiency, and improve crop yields. LED lights, in particular, offer energy efficiency, customizable spectra, and low heat output. Mathematical models are used to maximize plant development and resource efficiency, providing a framework for understanding plant-environment interactions. Despite high initial setup costs and the need for technical expertise, hydroponic systems present long-term economic and environmental benefits. This paper underscores hydroponic vertical systems' potential to revolutionize urban agriculture, ensuring food security and sustainability amidst climate change challenges.

REZUMAT

Această lucrare explorează sistemele verticale hidroponice ca o soluție durabilă la provocările agricole moderne, în special cele generate de schimbările climatice. Hidroponia, o metodă de cultivare a plantelor fără sol folosind soluție de apă bogată în nutrienți, oferă avantaje semnificative față de agricultura tradițională. Sistemele verticale maximizează eficiența spațiului prin creșterea plantelor stratificat, făcându-le ideale pentru mediile urbane cu spațiu limitat. Aceste sisteme oferă un mediu controlat care atenuează impactul vremii extreme, asigurând o producție constantă a culturilor. Lucrarea trece în revistă diferite tehnici hidroponice, inclusiv cultura în apă adâncă, tehnica filmului nutritiv, inundarea și scurgerea și irigarea prin picurare. Subliniază eficiența utilizării apei în hidroponie, crucială pentru zonele care se confruntă cu deficitul de apă. Tehnologiile avansate, cum ar fi senzorii, livrarea automată a nutrienților și iluminatul cu LED-uri, sunt folosite pentru a optimiza condițiile de creștere, a îmbunătăți eficiența utilizării resurselor și a îmbunătăți randamentul culturilor. LED-urile, în special, oferă eficiență energetică, spectre personalizabile și putere termică scăzută. Modelele matematice sunt folosite pentru a maximiza dezvoltarea plantelor și eficiența resurselor, oferind un cadru pentru înțelegerea interacțiunilor plante-mediu. În ciuda costurilor inițiale mari de instalare și a necesității de expertiză tehnică, sistemele hidroponice prezintă beneficii economice și de mediu pe termen lung. Această lucrare subliniază potențialul sistemelor verticale hidroponice de a revoluționa agricultura urbană, asigurând securitatea alimentară și sustenabilitatea în mijlocul provocărilor legate de schimbările climatice.

INTRODUCTION

One of the most important worldwide issues of the twenty-first century is climate change, which has a significant influence on many industries, including agriculture. Due to agriculture's natural sensitivity to weather, there are serious threats to global food security as a result of weather patterns becoming more unpredictable. Climate change has a wide range of consequences on agriculture, including changes in agricultural production, livestock health, and the occurrence of diseases and pests. For the purpose of creating

plans to lessen negative effects and guarantee sustainable agricultural practices, it is essential to comprehend these implications (*El-Ghobashy et al., 2023; FAO, 2016; FAO, 2023a; Stein, 2021*).

One of the most direct effects of climate change on agriculture is the alteration in crop yields. Changes in temperature, precipitation patterns, and the increased frequency of extreme weather events such as droughts, floods, and heatwaves can severely affect crop productivity. Higher temperatures can accelerate crop maturation but also reduce the period of grain filling, leading to lower yields. For example, staple crops like wheat, maize, and rice are highly sensitive to temperature changes, with even slight increases potentially resulting in significant yield reductions (*Lobell et al., 2011*). Additionally, altered precipitation patterns can lead to water stress in some regions, while others may experience excessive rainfall, both of which can negatively impact crop growth (*FAO, 2023b*).

The distribution and prevalence of agricultural pests and diseases are influenced by climate change, potentially leading to increased crop and livestock losses. Warmer temperatures and higher humidity levels can create favourable conditions for pests and pathogens, resulting in more frequent and severe outbreaks (*Patterson et al., 2015*). For instance, the range of the European corn borer, a major pest for maize, is expected to expand northwards with rising temperatures, affecting areas previously unexposed to this pest. Similarly, changes in climate can alter the life cycles and population dynamics of many insect vectors, increasing the spread of plant and animal diseases.

The impacts of climate change on agriculture extend beyond biological effects, encompassing significant socio-economic dimensions. Reduced agricultural productivity can lead to higher food prices, increased food insecurity, and livelihood challenges for farmers, particularly in developing countries where agriculture is a primary source of income (*FAO, 2023b*). Smallholder farmers are especially vulnerable due to their limited capacity to adapt to changing conditions and invest in resilient agricultural practices.

Addressing the challenges posed by climate change to agriculture requires comprehensive adaptation and mitigation strategies. These include developing climate-resilient crop varieties, improving water management practices, adopting sustainable soil management techniques, and enhancing pest and disease control measures. Additionally, integrating advanced technologies such as precision agriculture or vertical farming, which uses data-driven approaches to optimise farming practices, can help mitigate the adverse effects of climate change (*Benke & Tomkis, 2017; Mir et al., 2022*).

Hydroponics, the method of growing plants without soil by using nutrient-rich water solutions, offers a promising solution to combat the adverse effects of climate change on crop production. As climate change alters weather patterns, increases the frequency of extreme weather events, and affects water availability, hydroponics provides a controlled environment for agriculture, mitigating many of these challenges (*Chang et al., 2018; Maucieri et al., 2017; Niu & Masabni, 2018*).

Vertical hydroponic systems represent a significant innovation in agricultural technology, aimed at maximizing space efficiency and resource use in plant cultivation. Unlike traditional horizontal farming, these systems grow plants in vertically stacked layers, which is particularly advantageous in urban environments with limited space (*Avgoustaki & Xydis, 2020; Despomier, 2013; FAO, 2022*).

The paper presents a review of the characteristics of hydroponic vertical systems, their advantages and disadvantages, as well a series of technical solution employed for implementing and operating these systems and turning them in means of combating climate changes effects on agriculture and supplying fresh food to the growing population, especially that clustered in urban areas.

MATERIALS AND METHODS

Hydroponic systems are typically housed in greenhouses or indoor environments where conditions such as temperature, humidity, and light can be tightly controlled. This control protects crops from extreme weather events like droughts, floods, and storms, which are becoming more frequent due to climate change (*Asha et al., 2023; Tusi & Shimazu, 2021*).

Hydroponics allows for continuous crop production throughout the year, regardless of external weather conditions. This stability is crucial as climate change leads to unpredictable growing seasons and affects traditional agricultural timelines (*Graves, 1983; Sharma et al., 2018*).

Hydroponic systems use water more efficiently than traditional soil-based agriculture. Water is recirculated in a closed-loop system, significantly reducing the amount needed for crop growth. This efficiency is particularly important as climate change exacerbates water scarcity in many regions (*Debnath & Mohiudin, 2020; Zhang et al., 2022*).

In traditional farming, a significant amount of water is lost to evaporation and runoff. Hydroponics minimizes these losses, ensuring that more water is available for plant uptake, which is critical in areas facing water shortages (Carotti et al., 2023; Goldammer, 2019).

In hydroponic systems, nutrients are delivered directly to plant roots in a soluble form, ensuring optimal uptake. This direct delivery can lead to faster growth rates and higher yields compared to traditional farming, which can be hindered by poor soil quality and nutrient availability affected by climate conditions. The controlled environment of hydroponic systems reduces the incidence of soil-borne diseases and pests. This reduction minimizes crop losses and the need for chemical pesticides, which can be harmful to the environment (Gruda, 2020; Hosseinzadeh et al., 2017; Son et al., 2020).

Hydroponics can be implemented in urban areas, utilizing spaces like rooftops, abandoned buildings, and vertical farms. This adaptability helps alleviate the pressure on rural agricultural land, which may be increasingly affected by climate change (Dumitrescu et al., 2022; GVR, 2021).

By decoupling crop production from arable land, hydroponics mitigates the impact of land degradation caused by climate change. This method ensures food production can continue even as fertile land becomes scarce.

Hydroponic farms can integrate renewable energy sources such as solar or wind power to run their systems, reducing reliance on fossil fuels and minimizing their carbon footprint. This integration is aligned with climate change mitigation strategies. These systems also allow precise control over the amount and type of fertilizers used, reducing the risk of over-fertilization and nutrient runoff, which can contribute to environmental pollution and greenhouse gas emissions (Aiswarya & Vidhya, 2023; Cristea et al. 2024).

They often use advanced technologies such as sensors, automated nutrient delivery, and data analytics to monitor and optimise growing conditions. These technologies enhance resource use efficiency and crop management, making agriculture more resilient to climate variability. Hydroponics can support the growth of a wide variety of crops, including those that might struggle in changing soil and climate conditions. This diversity can help stabilize food supply chains impacted by climate change (Asher & Edwards, 1983; Charumathi et al., 2017; Cho et al., 2017; Hati & Singh, 2021).

Hydroponic systems rely on a variety of technologies to optimise plant growth, improve efficiency and ensure sustainability (Nguyen et al., 2016).

Irrigation and nutrient delivery systems

Depending on the manner of irrigating and delivering nutrient to the crops, hydroponics is divided in various types, as follows:

1. Deep water culture

Deep Water Culture (Figure 1) or direct water culture is a type of hydroponic farming method in which the roots of the plants are continually suspended in nutrient-rich, oxygenated water solution (Sambo et al., 2019).

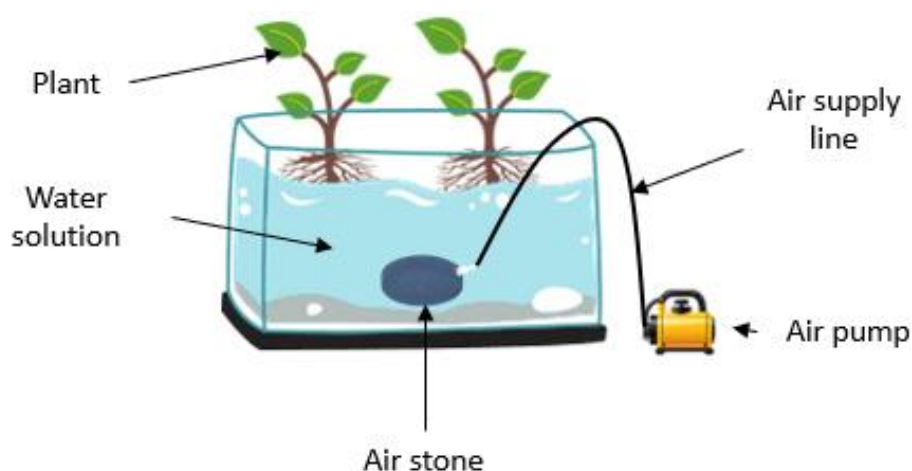


Fig. 1 – Deep water culture plant growing
(adapted from Syed et al., 2021)

Deep water culture works in the following manner:

- A reservoir is filled with water – nutrient solution, plants are placed in net pots as such or filled with an inert substrate (clay pebbles, hydro cocos) and immersed in the water – nutrient mixture;

- An air pump and air stone are used to oxygenate the water mixture, ensuring that plant roots receive adequate oxygen. This prevents roots from rotting and promotes healthy plant growth;
- The water nutrient solution is constantly monitored and adjusted as to maintain the correct pH and nutrient levels;
- The plants are continuously submerged in the nutrient solution thus allowing them to take up water and nutrients in an efficient manner.

2. Nutrient Film Technique (NFT)

Nutrient Film Technique – NFT (Figure 2) is a popular hydroponic method that involves a continuous flow of nutrient-rich water over the roots of plants. This technique is widely used due to its efficiency, simplicity, and effectiveness in providing nutrients to plants (Guzman-Valvidia et al., 2019).

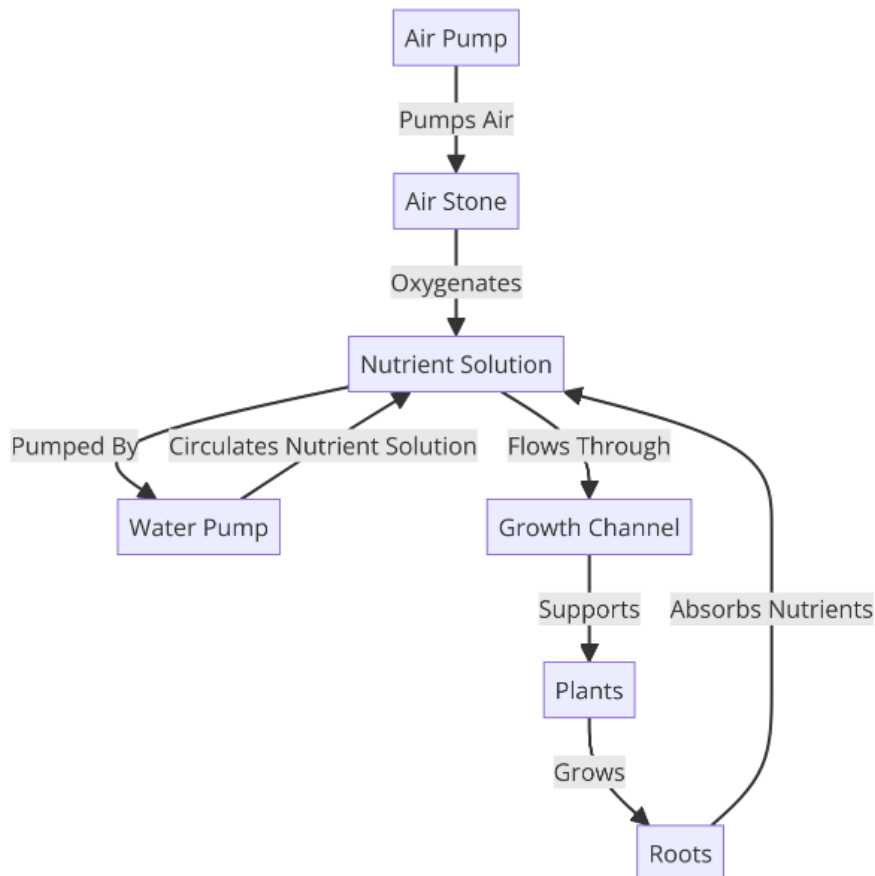


Fig. 2 – Nutrient film technique plant growing diagram

Nutrient film technique works in the following manner:

- Plants are placed in an inclined channel type growth tray made of inert materials;
- A pump continuously delivers the nutrient-rich water solution from the reservoir to the growth channels;
- The solution flows down the slope inside the growth channel, forming a thin film of nutrient-rich water that is absorbed by the roots of plants;
- The roots of plants are constantly exposed to air as well to the nutrient solution, thus receiving the required oxygen for a healthy development;
- After flowing through the growth channels, the excess nutrient solution (that is not absorbed by the plants) drains back into the reservoir and is recirculated.

3. Flood and drain

Flood and Drain (Figure 3) is a system that involves the periodic flooding and draining of the nutrient solutions. Basically, there are two phases of its operation. The **flood** is when the water and nutrients flow the growing areas, flowing over the plants' roots, followed by the second phase – **draining** (Putra & Yuliado, 2015; Clyde-Smith & Campos, 2023).

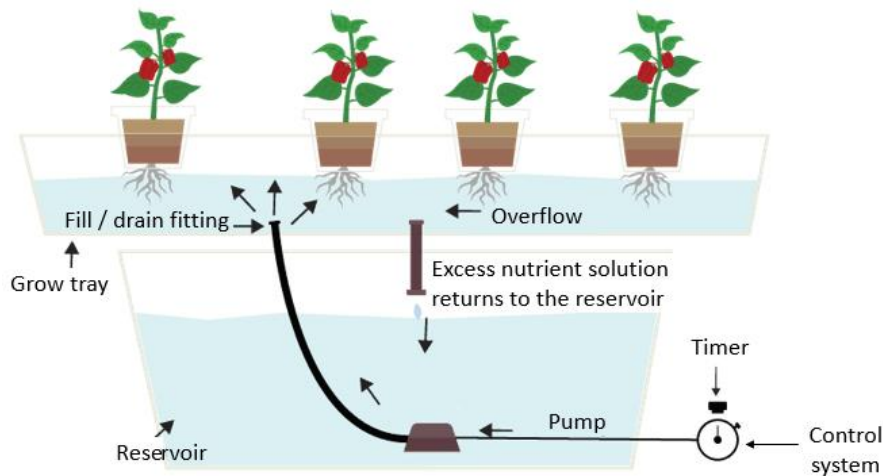


Fig. 3 – Flood and drain technique plant growing

(<https://www.trees.com/gardening-and-landscaping/ebb-and-flow-hydroponics>)

Flood and drain system works in the following manner:

- Plants are placed in wire pots / mineral substrate in a growth tray with one or multiple openings at the bottom part, situated above a water tank;
- The water tank is filled with water – nutrient solution and through the means of a pump is distributed to the grow tray at intervals regulated by a timer;
- After a preset time of flooding the growth tray, the opening (s) of the growth tray allows the excess water to drain in the reservoir below, thus leaving the plants with the ability to intake oxygen through the roots;
- After a preset time, the flooding process resumes, followed again by draining of the growth trays in the determined cycle.

4. Drip irrigation

Drip irrigation (Figure 4) is a type of micro-irrigation system that has the potential to save water and nutrients by allowing water to drip slowly to the roots of plants, either from above the substrate surface or buried below the surface (Perez et al., 2024).

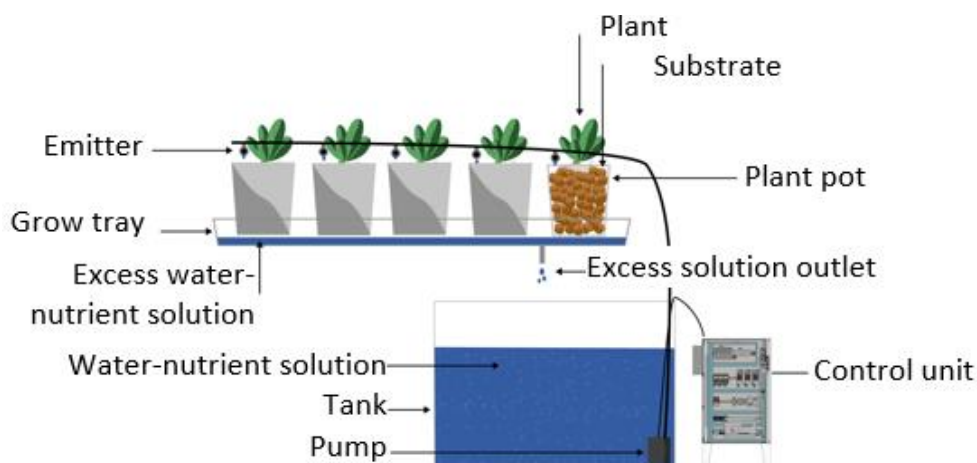


Fig. 4 – Flood and drain technique plant growing

(adapted from <https://hydroplanner.com/blog/hydroponics-drip-system-EN>)

Drip irrigation hydroponic systems work in the following manner:

- Plants are placed in individual containers or in a larger growth tray, supported by a growing medium (substrate) such as clay pebbles, coco coir, perlite, or rock wool.
- A tank is filled with the nutrient-rich water solution.
- A water pump is used to transport the nutrient solution from the reservoir to the plants.

- A network of hoses and drip emitters deliver the nutrient solution directly to the base of each plant.
- An automation system is used to control the pump, ensuring the nutrient solution is delivered at regular intervals.
- The excess water-nutrient solution is collected back in the reservoir.

Lighting systems

Lighting systems for hydroponics are a critical component of indoor gardening and plant cultivation, enabling growers to simulate natural sunlight and provide the necessary light spectrum for photosynthesis. In hydroponics, where plants are grown without soil, optimizing light conditions is essential to promote healthy growth, flowering, and fruiting. These artificial lighting systems replicate the sun's intensity and spectrum, allowing plants to grow indoors all year-round, regardless of outdoor weather conditions. Different types of growth lights (Figure 5), such as fluorescent, high-intensity discharge (HID), and light-emitting diode (LED) lights, are used to meet the specific needs of various plant species and growth stages. Fluorescent lights are often favoured for seedlings and leafy greens due to their lower intensity and cooler operation, while HID lights, including metal halide (MH) and high-pressure sodium (HPS), offer higher intensity suitable for larger, flowering plants (Arcel *et al.*, 2021; Avgoustaki & Xydis, 2021; Bures *et al.*, 2018; Jager, 2024; Smith, 1982).

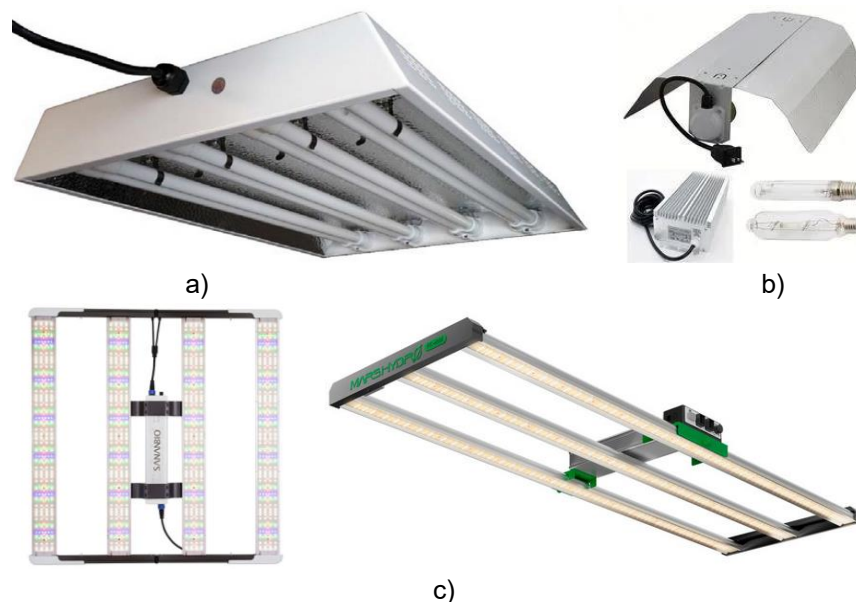


Fig. 5 – Growth lights used for hydroponic systems

a) – fluorescent lights (<https://www.hydrocentre.com>), b) – HID lights (<https://www.nosoilsolutions.com/>), c) – LED lights (<https://www.sananbiofarm.com/>; <https://marshydro.eu/>)

LED lights have become increasingly popular in recent years due to their energy efficiency, long lifespan, and customizable light spectrum, which can be tailored to the precise needs of the plants. Properly managing the duration, intensity, and spectrum of light ensures that hydroponic plants receive optimal conditions to maximize growth and yields, making lighting systems a pivotal factor in the success of hydroponic gardening (Jin *et al.*, 2023; Matysiak *et al.*, 2021; Najera *et al.*, 2022; Sellaro *et al.*, 2010).

The **advantages** of using LED lights in hydroponic systems are listed as follows (Lobiuc *et al.*, 2017; Pennisi *et al.*, 2019; Phum *et al.*, 2024; Tharun & Padmasine, 2023):

- **Energy efficiency** - LED lights are highly energy-efficient compared to traditional lighting systems such as fluorescent and high-intensity discharge (HID) lights. They consume less electricity while providing the same or even higher levels of light output, resulting in lower energy bills and reduced environmental impact.
- **Long lifespan** - LED lights have a significantly longer lifespan than other types of grow lights. They can last up to 50,000 hours or more, which means fewer replacements and lower maintenance costs over time.
- **Customizable light spectrum** - LED lights can be engineered to emit specific wavelengths of light that are most beneficial for plant growth. This allows growers to tailor the light spectrum to the needs

of their plants at different growth stages, optimizing photosynthesis and improving overall plant health and yields.

- **Low heat output** - LED lights produce much less heat compared to HID and fluorescent lights. This reduces the risk of heat stress and burn damage to plants, allowing the lights to be placed closer to the plants. Additionally, lower heat output minimizes the need for additional cooling systems, saving on energy costs.
- **Compact and flexible design** - LED grow lights are available in a variety of shapes and sizes, making them adaptable to different growing spaces. Their compact and flexible design makes it easier to install them in tight or uniquely shaped areas, maximizing the use of available space.
- **Improved growth and yields** - Due to their ability to provide a tailored light spectrum, LED lights can enhance plant growth, improve flowering and fruiting, and increase yields. The precise control over light wavelengths ensures that plants receive the optimal light conditions for each stage of growth.
- **Durability and safety** - LED lights are more durable and robust compared to other lighting options. They are less prone to breakage and can withstand environmental fluctuations better. Additionally, they do not contain harmful substances like mercury, making them safer for both the grower and the environment.
- **Instant On/Off** - LED lights reach full brightness instantly, unlike some HID lights that require a warm-up period. This instant on/off capability is beneficial for controlling light cycles precisely, which is important for maintaining consistent growth conditions.
- **Lower light degradation** - LEDs maintain their light output over a longer period, experiencing less degradation compared to other types of grow lights. This means that the intensity and quality of light remain more consistent, contributing to stable and reliable plant growth.
- **Long-term cost-effectiveness** - Although the initial investment for LED lights may be higher than for other types of grow lights, their energy efficiency, long lifespan, and lower maintenance costs make them a more cost-effective option in the long term.

The **disadvantages** of using LED lights in hydroponic systems are considered as follows (*Naz et al., 2021; Phum et al., 2024; Tharun & Padmasine, 2023*):

- **Initial Cost** - LED lights generally have a higher upfront cost compared to other types of grow lights like fluorescent and HID lights. This initial investment can be a significant barrier for small-scale growers or those new to hydroponics.
- **Light Intensity** - Although LED technology has improved, some LED grow lights may not provide the same level of light intensity as high-intensity discharge (HID) lights. This can be a disadvantage for plants that require very high light levels, such as some fruiting and flowering plants.
- **Spectrum Limitations** - Not all LED lights offer a full-spectrum light that mimics natural sunlight. Some cheaper models may provide a narrow spectrum that isn't suitable for all stages of plant growth. Ensuring that the LED lights cover the necessary wavelengths for photosynthesis and development is crucial, which can be challenging with lower-quality products.
- **Heat Distribution** - While LED lights produce less heat than HID lights, the heat they do generate is often concentrated in a smaller area. Without proper heat sinks or cooling systems, this can potentially cause localized heating issues, affecting plant health if the lights are placed too close.
- **Complexity in Selection** - The market for LED grow lights is vast, with many different models and specifications. Choosing the right LED light can be complex and confusing, especially for beginners. The need to understand specifications such as light spectrum, intensity, and coverage area can be overwhelming.
- **Lifespan Variability** - Although LEDs have a long lifespan, their actual longevity can vary significantly based on the quality of the components and manufacturing. Poor-quality LEDs may degrade faster, leading to reduced light output over time.
- **Electrical Requirements** - High-power LED systems can require specific electrical setups, such as additional wiring or circuit adjustments, to handle their power needs safely and efficiently. This can add to the installation complexity and cost.
- **Limited Penetration** - LED lights often have less light penetration compared to HID lights. This means that the light may not reach the lower parts of larger plants effectively, potentially impacting the growth of lower leaves and branches.

- **Potential for Over-Saturation** - LED lights can sometimes provide too much light in specific wavelengths, leading to issues like light bleaching or nutrient imbalances. Plants may develop symptoms of overexposure if the light intensity and spectrum are not carefully managed.
- **Dependence on Technology** - LED systems rely on electronic components and sophisticated technology, which can sometimes lead to issues with reliability and the need for technical support. Problems with drivers, diodes, or other electronic parts can necessitate repairs or replacements, which can be costly and time-consuming.

RESULTS

Developing and using mathematical models in hydroponic systems has become essential for maximising plant development, resource efficiency, and environmental control. To attain optimal efficiency and yield, hydroponic farming needs careful management over a number of parameters. A foundation for comprehending and forecasting the intricate relationships between plant physiology and environmental variables is provided by mathematical models. These models include kinetic models that depict rates of nutrient intake as well as dynamic and eco-physiological models that mimic the time-dependent behaviour of plant growth and interactions with the environment.

Dynamic models can be used to determine the optimal root zone temperature (RZT) for different growth stages, ensuring that plants receive the right amount of nutrients and water throughout their lifecycle. Eco-physiological models help in understanding how plants respond to changes in nutrient availability, temperature, and other environmental factors, which is essential for optimizing nutrient formulations and irrigation schedules. The use of Artificial Neural Networks (ANNs) and machine learning techniques has further enhanced the modelling of hydroponic systems by enabling the prediction of plant growth and yield based on historical data and current environmental conditions. These models are particularly effective in handling non-linear relationships and can adapt to new data, making them suitable for the dynamic environments of hydroponic farming.

Below are presented a series of mathematical models that contribute to the various approaches of estimating and controlling plant growth using hydroponic systems.

1. Dynamic response of plant growth (*Aji et al., 2020*)

$$WR(t) = \frac{\Delta W}{\Delta t}, [\%] \quad (1)$$

This model determines the response of plant growth ($WR(t)$) measuring the sensitivity of changes in plant weight (ΔW , [g]) in relation to the change in time (Δt , [d]).

The Dynamic Response of Plant Growth model, represented by Equation (1), quantifies the sensitivity of plant growth in response to changes in environmental conditions over time. This model is pivotal for predicting how plants will respond to varying nutrient levels and environmental factors, enabling precise adjustments to optimise growth rates. By measuring the change in plant weight over time, this model helps in identifying the most effective growth conditions and allows for dynamic adjustments to maintain optimal growth.

2. Ion concentration in the culture crop solution model (*Carmassi et al., 2004*)

$$U = V \times C_{n-1} + V_R \times C_R - V \times C_n, [\text{mmol}] \quad (2)$$

This model derives from the balance equation for nutrient by the plants (U) over the period between n and $n-1$ [days]. V is the volume of the system [l], C is the total ionic concentration of the nutrient solution [mM] and V_R [l] and C_R [mM] represent the volume and ionic concentration of the nutrient solution added to the system in a given interval.

The model depicted in Equation (2) focuses on the nutrient balance within the hydroponic solution. This model ensures that plants receive the appropriate levels of nutrients by monitoring and adjusting the ionic concentration of the solution. The accurate management of nutrient levels is crucial for preventing deficiencies and toxicities, which can significantly impact plant health and yield. This model helps in maintaining a stable nutrient environment, which is essential for the continuous and healthy growth of plants in hydroponic systems.

3. Mathematical model for monitoring carbon dioxide concentration (*Laktionov et al., 2018*)

$$\varphi_{CO_2}^{sour} - \varphi_{CO_2}^{vent} - \varphi_{CO_2}^{phot} = 0, [\text{ppm}] \quad (3)$$

where $\varphi_{CO_2}^{sour}$ is the amount of carbon dioxide the enters the system; $\varphi_{CO_2}^{vent}$ is the amount of carbon dioxide lost from the system through ventilation and $\varphi_{CO_2}^{phot}$ is the amount of carbon dioxide consumed by the plants through photosynthesis.

This model is based on the distribution of carbon dioxide occurring in two simultaneous processes: the movement on CO_2 in an opposite direction compared to the concentration gradient and the movement caused by air currents. Carbon dioxide is a critical component of photosynthesis, and its optimal concentration can significantly influence plant growth. This model accounts for the carbon dioxide entering the system, losses due to ventilation, and consumption by plants. By ensuring a balanced carbon dioxide level, this model supports the enhancement of photosynthetic efficiency and overall plant productivity.

4. Computational fluid dynamics techniques model (*Rezvani et al., 2021*)

$$\frac{\partial(\rho\phi)}{\partial t} + \nabla \times (\partial\bar{u}\phi) = \nabla \times (\Gamma\nabla\phi) + S_\phi \quad (4)$$

where ρ is the density (kg m^{-3}), t is time, ∇ is divergence operator, and ϕ represents the concentration of the dimensionless transported quantity (momentum, mass, anergy), \bar{u} (m s^{-1}) is the component of the velocity vector, Γ represents the diffusion coefficient (m^2s^{-1}) and S_ϕ is the source term indicating the changes in the amount of manner in the transfer.

This model is essential for understanding the distribution and flow of the nutrient solution, which directly affects nutrient availability to plant roots. By modelling the movement and concentration of the solution, this approach helps in designing efficient delivery systems that ensure uniform nutrient distribution and prevent issues such as stagnation or uneven nutrient uptake.

5. Water uptake model (WUS) (*Lopez Mora et al., 2024*)

$$ET_o = [0.408\Delta(R_n - G) + 37u_2\gamma(e_s - e_a) \times (T + 273)^{-1}][\Delta + \gamma(1 + u_2C_d)]^{-1}, [\text{mmh}^{-1}] \quad (5)$$

where: Δ [$\text{KPa} \times \text{C}^{-1}$] represents the slope of the relationship between the saturation vapor pressure and temperature; R_n and G [$\text{MJm}^{-2}\text{h}^{-1}$] represent the net variation at crop surface, respectively substrate heat flux at substrate surface; γ [KPaC^{-1}] represents the psychrometric constant; u_2 [ms^{-1}] is the average hourly wind speed; $e_s - e_a$ [KPa] is the air's vapour pressure deficit; T [$^{\circ}\text{C}$] is the hourly temperature of the air; C_d [sm^{-1}] represents the day and night factor (0.24 for day hours and 0.96 for night hours).

This model is used to calculate crop Evapotranspiration (ET_o) in hourly periods [mmh^{-1}] and incorporates various environmental factors such as temperature, wind speed, and vapor pressure deficit to calculate the hourly water uptake by plants. By optimizing water use, this model supports sustainable practices in hydroponic farming, which is particularly important in regions facing water scarcity.

These mathematical models collectively contribute to the precision and efficiency of hydroponic systems. By enabling detailed monitoring and control of various factors affecting plant growth, they support the development of more resilient and productive agricultural practices. The integration of these models with advanced technologies such as sensors and automation further enhance their applicability, making hydroponic systems a viable solution for sustainable agriculture in the face of climate change.

The implementation of hydroponic systems in agriculture presents a myriad of advantages and challenges. As the agricultural industry seeks sustainable and efficient methods to address the growing concerns of climate change and food security, hydroponic systems offer a promising solution (*Lubna et al., 2022; Magwaza et al., 2020; Sarkar & Majumer, 2015*).

Table 1 outlines the numerous benefits of hydroponic systems, such as controlled environment agriculture, efficient water use, and enhanced crop yields. Conversely, Table 2 highlights the potential drawbacks associated with these systems, including high initial setup costs and the need for technical expertise. Together, these tables offer a balanced view of the hydroponic approach, supported by recent literature, and aid in evaluating its viability for future agricultural practices.

Table 1

Advantages of hydroponic systems

| Advantage | References |
|---|--|
| Controlled Environment Agriculture | <i>Al-Kodmany, 2018; Kozai, 2018; Kumar & Singh, 2024</i> |
| Efficient Water Use | <i>Park & Williams, (2024); Savvas, 2003; Kozai, 2018; Verdoliva et al., 2021; Zimmermann & Fisher, 2020; Clyde-Smith & Campos, 2023</i> |
| Enhanced Crop Growth and Yield | <i>Butt, 2010; Etesami et al., 2023; Kozai, 2018;</i> |
| Adaptability to Urban and Unconventional Spaces | <i>Al-Kodmany, 2018; Despommier, 2010; Richa et al., 2020</i> |
| Energy and Resource Efficiency | <i>Graamans et al., 2018; Kozai, 2018; van Straten et al., 2011</i> |
| Innovative Crop Management | <i>van Straten et al., 2011</i> |
| Reduced Need for Chemical Pesticides | <i>Jones, 2014; Resh, 2012; Velazquez-Gonzalez et al., 2022</i> |
| Consistent and Predictable Crop Production | <i>Butturini & Marcelis, 2019; Kozai, 2018</i> |
| Reduced Land Use | <i>Al-Kodmany, 2018; Despommier, 2010; Van Delden et al., 2021</i> |
| Potential for Higher Nutritional Quality | <i>Barbosa et al., 2015; Pantanella et al., 2012</i> |

Table 2

Disadvantages of hydroponic systems

| Disadvantage | References |
|---------------------------------------|--|
| High Initial Setup Costs | <i>Kozai, 2018; Resh, 2012; van Tuiji et al., 2018</i> |
| Technical Expertise Required | <i>Delaide et al., 2016; Jones, 2014; Resh, 2012</i> |
| Dependency on Electricity | <i>Graamans et al., 2018; Kozai, 2018; Promratrak L., 2017</i> |
| Potential for Waterborne Diseases | <i>Jones, 2014; Savvas, 2003; van Tuiji et al., 2018</i> |
| High Energy Consumption | <i>Graamans et al., 2018; Promratrak L., 2017; van Straten et al., 2011; Velazquez-Gonzalez et al., 2022; Xydis et al., 2017</i> |
| Limited Crop Variety | <i>Barbosa et al., 2015; Butt, 2010; Promratrak L., 2017</i> |
| Continuous Monitoring Needed | <i>Jones, 2014; Resh, 2012; van Tuiji et al., 2018</i> |
| System Failures Can Be Catastrophic | <i>Butt, 2010; Delaide et al., 2016; Jones, 2014</i> |
| Limited Organic Certification | <i>Butturini & Marcelis, 2019; Delaide et al., 2016; Resh, 2012;</i> |
| Nutrient Solution Management | <i>Jones, 2014; Promratrak L., 2017; Savvas, 2003; Van Delden et al., 2021</i> |
| Limited Scalability for Certain Crops | <i>Butt, 2010; Promratrak L., 2017</i> |
| High Initial Learning Curve | <i>Delaide et al., 2016; Jones, 2014; Resh, 2012</i> |
| Need for High-Quality Water | <i>Savvas, 2003; van Tuiji et al., 2018</i> |
| High Operational Costs | <i>Graamans et al., 2018; Kozai, 2018</i> |

In summary, hydroponic systems present a transformative approach to modern agriculture, offering substantial benefits such as efficient water use, enhanced crop yields, adaptability to urban environments, and reduced need for chemical pesticides, as highlighted in Table 1. However, these advantages come with notable challenges, as detailed in Table 2, including high initial setup costs, the requirement for technical expertise, and dependency on electricity. By weighing these pros and cons, stakeholders can make informed decisions about implementing hydroponic systems. This balanced perspective underscores the potential of hydroponics to contribute to sustainable and resilient agricultural practices, particularly in the face of global challenges like climate change and urbanization.

CONCLUSIONS

By analysing hydroponic vertical systems, the following conclusions can be drawn:

- the implementation of hydroponic vertical systems offers a significant solution to the challenges posed by climate change on traditional agriculture. These systems provide a controlled environment that shields crops from extreme weather events, ensuring stable crop production irrespective of external climatic conditions;
- hydroponic systems utilize water more efficiently compared to conventional soil-based agriculture. by recirculating water in a closed-loop system, these systems significantly reduce water usage, making them particularly beneficial in regions facing water scarcity. This efficient water use is crucial as climate change exacerbates water shortages globally;

- the direct delivery of nutrients to plant roots in hydroponic systems ensures optimal nutrient uptake, leading to faster growth rates and higher yields. The controlled environment minimizes the occurrence of soil-borne diseases and pests, reducing the need for chemical pesticides and promoting healthier crop production;
- vertical hydroponic systems maximize space utilization by growing plants in vertically stacked layers. This innovation is especially advantageous in urban environments where space is limited, contributing to urban agriculture and reducing pressure on rural agricultural lands;
- these systems can integrate renewable energy sources such as solar or wind power, reducing reliance on fossil fuels and minimizing their carbon footprint. This integration aligns with global climate change mitigation strategies and promotes sustainable agricultural practices;
- hydroponic systems employ advanced technologies such as sensors, automated nutrient delivery, and data analytics to monitor and optimise growing conditions. These technologies enhance resource use efficiency, making agriculture more resilient to climate variability and improving overall productivity;
- the development and use of mathematical models in hydroponic systems are essential for maximizing plant development and resource efficiency. These models help in understanding and predicting the complex interactions between plant physiology and environmental variables, leading to better management practices and higher yields;
- the use of LED lights in hydroponic systems offers several advantages, including energy efficiency, customizable light spectra, and low heat output. LED lights can be tailored to meet the specific needs of different plant species and growth stages, ensuring optimal growth conditions and improving crop yields;
- despite the high initial setup costs, hydroponic systems are cost-effective in the long term due to their efficiency and reduced operational costs. The precise control over growing conditions results in consistent and predictable crop production, contributing to food security;
- by minimizing water and nutrient runoff, hydroponic systems reduce environmental pollution. Additionally, the reduced need for chemical pesticides and fertilizers lessens the impact on surrounding ecosystems, promoting more sustainable agricultural practices;
- the adoption of hydroponic systems faces several challenges, including the need for technical expertise, continuous monitoring, and high initial setup costs. Addressing these challenges requires investment in education and training, as well as support from governmental and non-governmental organizations to promote the adoption of hydroponic farming;
- hydroponic vertical systems hold great potential for the future of agriculture, particularly in urban areas. As technology advances and becomes more accessible, these systems are likely to play a critical role in ensuring food security and sustainability in the face of climate change.

ACKNOWLEDGEMENT

This work was supported by the Romanian Ministry of Research Innovation and Digitalization, through the project “Intelligent plant growth systems under controlled environmental conditions” – PN 23 04 01 04–Ctr. 9N/01.01.2023.

REFERENCES

- [1] Aishwarya, J.M., Vidhya, R. (2023). Study on the Efficiency of a Hydroponic Treatment for Removing Organic Loading from Wastewater and Its Application as a Nutrient for the “*Amaranthus campestris*” Plant for Sustainability. *Sustainability*, 15, 7814, <https://doi.org/10.3390/su15107814>
- [2] Al-Kodmany, K. (2018). The Vertical Farm: A Review of Developments and Implications for the Vertical City. *Buildings*, 8(2), 24, <https://doi.org/10.3390/buildings8020024>
- [3] Aji, G.K., Hatou, K., Morimoto, T. (2020). Modeling the Dynamic Response of Plant Growth to Root Zone Temperature in Hydroponic Chili Pepper Plant Using Neural Networks. *Agriculture*, 10, 234. <https://doi.org/10.3390/agriculture10060234>
- [4] Arcel, M. M., Lin, X., Huang, J., Wu, J., Zheng, S. (2021). The application of LED illumination and intelligent control in plant factory, a new direction for modern agriculture: A Review. *Journal of Physics: Conference Series*. 1732, 012178. doi:10.1088/1742-6596/1732/1/012178.
- [5] Asha S. V., Agarwal S., Dubey H., Jain L C., (2023). A study on hydroponic farming. *IJFMR*, Vol. 5, Issue 2, 23022286, E-ISSN: 2582-2160
- [6] Asher, C. J., and Edwards, D. G. (1983). “Modern solution culture techniques” in *Inorganic plant nutrition*. eds. A. Pirson and M. H. Zimmermann (Berlin, Heidelberg: Springer), 94–119.

- [7] Avgoustaki, D.D., Xydis, G., (2020). Indoor Vertical Farming in the Urban Nexus Context: Business Growth and Resource Savings. *Sustainability*, 12, 1965
- [8] Avgoustaki, D.D., Xydis, G., (2021). Energy cost reduction by shifting electricity demand in indoor vertical farms with artificial lighting. *Biosystems Engineering*, Volume 211, 219-229, <https://doi.org/10.1016/j.biosystemseng.2021.09.006>
- [9] Barbosa, G. L., Gadelha, F. D. A., Kublik, N., Proctor, A., Reichelm, L., Weissinger, E., Wohlleb, G. M., & Halden, R. U. (2015). Comparison of Land, Water, and Energy Requirements of Lettuce Grown Using Hydroponic vs. Conventional Agricultural Methods. *International Journal of Environmental Research and Public Health*, 12(6), 6879-6891
- [10] Benke, K., and Tomkins, B. (2017). Future food-production systems: vertical farming and controlled-environment agriculture. *Sustain. Sci. Pract. Policy* 13, 13–26. doi: 10.1080/15487733.2017.1394054
- [11] Bures, S., Urrestarazu Gavilán, M., Kotiranta, S. (2018). Artificial lighting in agriculture [online]. *Horticulture Library*, available at <https://www.valoya.com/artificial-lighting-in-agriculture/> (accessed on 23.05. 2024)
- [12] Butt, S. J. (2010). Hydroponic Green Farming Initiative: Report and Case Study. *United Nations Development Programme*
- [13] Butturini, M., & Marcelis, L. F. M. (2019). Vertical Farming in Controlled Environment Agriculture: Influence of Environmental Factors on Yield and Resource Use Efficiency of Leafy Greens. *Acta Horticulturae*, 1266, 333-342
- [14] Carmassi, G., Maggini, R., Incrocci, L. (2004). Modelling Ion Concentration in the Culture Solution of Closed-Loop Hydroponics. *Acta Hort.* 654, ISHS.
- [15] Carotti, L., Pistilo, A., Zauli, I., Meneghello, D., Martin, M., Pennisi, G., Gianquinto, G., Orsini, F. (2023). Improving water use efficiency in vertical farming: Effects of growing systems, far-red radiation and planting density on lettuce cultivation. *Agricultural Water Management*. Volume 285, 1, 108365, <https://doi.org/10.1016/j.agwat.2023.108365>
- [16] Chang, C.L., Hong, G.F., Fu, W.L., (2018). Design and implementation of a knowledge-based nutrient solution irrigation system for hydroponic applications. *Trans. Asabe*, 61, 369–379
- [17] Charumathi, S., Kaviya, R. M., Kumariyarsi, J., Manisha, R., and Dhivya, P. (2017). Optimization and control of hydroponics agriculture using IOT. *Asian J. Appl. Sci. Technol.* 1, 96–98
- [18] Cho, W. J., Kim, H.-J., Jung, D. H., Kang, C. I., Choi, G.-L., and Son, J.-E. (2017). An embedded system for automated hydroponic nutrient solution management. *Trans. ASABE* 60, 1083–1096. doi: 10.13031/trans.12163
- [19] Clyde-Smith, D., Campos, L.C., (2023). Engineering Hydroponic Systems for Sustainable Wastewater Treatment and Plant Growth. *Appl. Sci.*, 13, 8032. <https://doi.org/10.3390/app13148032>
- [20] Cristea, M., Vladut, N.V., Ungureanu, N. (2024) Using solar energy as non-conventional alternative energy in small and medium-sized farms, *INMATEH-Agricultural Engineering*, Volume 72, No. 1, pp. 631-643, <https://doi.org/10.35633/inmateh-72-56>
- [21] Debnath S., Mohiudin G. (2020). Irrigation and Fertigation in Protected Cultivation, In: Protected Cultivation and Smart Agriculture, New Delhi Publishers, pp. 40-54. ISBN: 978-81-948993-2-7, doi: 10.30954/NDP-PCSA.2020.5
- [22] Delaide, B., Goddek, S., Gott, J., Soyeurt, H., & Lambert, S. (2016). Lettuce (*Lactuca sativa* L. var. Sucrine) Growth Performance in Complemented Aquaponic Solution Outperforms Hydroponics. *Water*, 8(10), 467
- [23] Despomier D. (2010). The vertical farm – Feeding the world in the 21st century. Thomas Dunne Books. ISBN: 978-0-312-61139-2
- [24] Despomier D., (2013). Farming up the city: The rise of urban vertical farms. *Trends Biotechnol.* 31, 388–389
- [25] Dumitrescu, L., Veringa, D., Matche, M.G., Vladutoiu, L.C. (2022). Preliminary results of the analysis of the main microclimate factors in an urban farm module, *INMATEH-Agricultural Engineering*, Volume 67, No. 2, pp. 278-284, <https://doi.org/10.35633/inmateh-67-28>
- [26] El Ghobashy, H., Shaban, Y., Okasha, M., El-Reheem S.A., Abdelgawad, M., Ibrahim, R., Ibrahim, H., Abdelmohsen, K., Awad, M., Cottb., Elmeadawy M., Fathy, W., El-Sayed, K. (2023). Development and evaluation of a dual-purpose machine for chopping and crushing forage crops, *Heliyon*, Vol. 9, Issue 4, <https://doi.org/10.1016/j.heliyon.2023.e15460>

- [27] Etesami, H., Jeong, B.R., Glick, B.R. (2023). Biocontrol of plant diseases by *Bacillus* Spp. *Physiological and Molecular Plant Pathology*, Volume 126, 102048, <https://doi.org/10.1016/j.pmpp.2023.102048>
- [28] FAO. (2016). The state of food and agriculture. Climate change, agriculture and food security. ISBN 978-92-5-109374-0, Download <http://www.fao.org/3/a-i6030e.pdf> (accessed on 14.05.2024)
- [29] FAO. (2023a). Land Use. In: FAOSTAT. Rome. <https://www.fao.org/faostat/en/#data/RL> Download: <https://doi.org/10.4060/cc8166en-fig59> (accessed on 14.05.2024)
- [30] FAO. (2023b). World Food and Agriculture – Statistical Yearbook 2023. Rome. <https://doi.org/10.4060/cc8166en>
- [31] FAO, Rikolto and RUAFA, (2022). Urban and peri-urban agriculture sourcebook – From production to food systems. Rome, FAO and Rikolto. <https://doi.org/10.4060/cb9722en>
- [32] Goldammer T. (2019). Greenhouse Management - A Guide to Operations and Technology, Apex Publishers, ISBN (13): 978-0-9675212-4-4
- [33] Graamans, L., van den Dobbelaer, A., Meinen, E., & Stanghellini, C. (2018). Plant Factories, Crop Transpiration and Energy Balance. *Agricultural Systems*, 153, 138-147
- [34] Graves, W. R. (1983). Hydroponic Plant Culture as a Method for Studying Plant Mineral Nutrition. *HortScience*, 18(5), 595-598
- [35] Gruda, N.S. (2020). Advances in horticultural soilless culture. Burleigh Dodds Science Publishing. 442 pages, e-ISBN:9781003048206, <https://doi.org/10.1201/9781003048206>
- [36] GVR. (2021). Hydroponics Market Size, Share & Trends Analysis Report By Type, By Crop Type (Tomatoes, Lettuce, Peppers, Cucumbers, Herbs, and Others), By Crop Area, By Region, And Segment Forecasts, 2024 – 2030. Available online: <https://www.grandviewresearch.com/industry-analysis/hydroponics-market/methodology> (accessed on 10 May 2024)
- [37] Guzmán-Valdivia, C.H., Talavera-Otero, J., Désiga-Orenday, O. (2019). Turbulent Kinetic Energy Distribution of Nutrient Solution Flow in NFT Hydroponic Systems Using Computational Fluid Dynamics. *AgriEngineering*, 1, 283-290. <https://doi.org/10.3390/agriengineering1020021>
- [38] Hati, A.J., Singh, R.R., (2021). Smart Indoor Farms: Leveraging Technological Advancements to Power a Sustainable Agricultural Revolution. *AgriEngineering*, 3, 47
- [39] Hosseinzadeh, S., Verheust, Y., Bonarrigo, G., and Van Hulle, S. (2017). Closed hydroponic systems: operational parameters, root exudates occurrence and related water treatment. *Rev. Environ. Sci. Biotechnol.* 16, 59–79. doi: 10.1007/s11157-016-9418-6
- [40] Jager S., (2024). Vertical farming (plant factory with artificial lighting) and its produce: consumer insights, *Current Opinion in Food Science*. Volume 56, 101145
- [41] Jin, W., Formiga Lopez, D., Heuvelink, E., Marcelis L.F.M. (2023). Light use efficiency of lettuce cultivation in vertical farms compared with greenhouse and field. *Food Energy Secur.* 12: e391. <https://doi.org/10.1002/fes3.391>
- [42] Jones, J. B. (2014). Hydroponics: A Practical Guide for the Soilless Grower. CRC Press.
- [43] Kozai, T. (2018). "Smart Plant Factory: The Next Generation Indoor Vertical Farms." Springer. E-ISBN 978-981-13-1065-2. <https://doi.org/10.1007/978-981-13-1065-2>
- [44] Kumar, P., Singh, J. (2024). Hydroponic: An Eco-friendly Future. In: Kumar, N. (eds) Hydroponics and Environmental Bioremediation. Springer Water. Springer, Cham. https://doi.org/10.1007/978-3-031-53258-0_9
- [45] Laktionov, I., Vovna, O., Cherevko, O., Kozlovskaya, T. (2018). Mathematical model for monitoring carbon dioxide concentration in industrial greenhouses. *Agronomy Research* 16(1), 134-146, <https://doi.org/10.15159/AR.17.074>
- [46] Lobell, D. B., Schlenker, W., & Costa-Roberts, J. (2011). Climate Trends and Global Crop Production Since 1980. *Science*, 333(6042), 616-620
- [47] Lobiuc A., Vasilache V., Pintilie O., Stoleru T., Burducea M., Oroian M., Zamfirache M. M. (2017). Blue and red LED illumination improves growth and bioactive compounds contents in acyanic and cyanic *Ocimum basilicum* L. microgreens, *Molecules*, 22, 14
- [48] Lubna, F.A., Lewus, D.C., Shelford, T.J., Both, A.-J. (2022). What You May Not Realize about Vertical Farming. *Horticulturae*, 8, 322. <https://doi.org/10.3390/horticulturae8040322>
- [49] López Mora, M.F., Quintero Castellanos, M.F., González Murillo, C.A., Borgovan, C., Salas Sanjuan, M.d.C., Guzmán, M. (2024). Predictive Model to Evaluate Water and Nutrient Uptake in Vertically Grown

- Lettuce under Mediterranean Greenhouse Conditions. *Horticulturae*, 10, 117. <https://doi.org/10.3390/horticulturae10020117>
- [50] Magwaza, S.T., Magwaza, L.S., Odindo, A.O., Mditshwa, A., (2020). Hydroponic technology as decentralised system for domestic wastewater treatment and vegetable production in urban agriculture: A review. *Sci. Total Environ.*, 698, 134154
- [51] Matysiak, B., Kaniszewski, S., Dyśko, J., Kowalczyk, W., Kowalski, A., Grzegorzewska, M. (2021). The Impact of LED Light Spectrum on the Growth, Morphological Traits, and Nutritional Status of 'Elizium' Romaine Lettuce Grown in an Indoor Controlled Environment. *Agriculture*, 11, 1133. <https://doi.org/10.3390/agriculture11111133>
- [52] Maucieri, C., Nicoletto, C., Junge, R., Schmutz, Z., Sambo, P., and Borin, M. (2017). Hydroponic systems and water management in aquaponics: a review. *Ital. J. Agron.* 11, 1–31. doi: 10.4081/ija.2017.1012
- [53] Mir M. S., Naikoo N. B., Kanth R. H., Bahar F.A., Anwar Bhat M., Nazir A., Sheraz Mahdi S., Amin Z., Singh L., Raja W., Saad AA, T. Bhat A, Palmo T., Ahngar T. A., (2022). Vertical farming: The future of agriculture: A review, *The Pharma Innovation Journal*, SP-11(2): 1175-1195
- [54] Nájera, C., Gallegos-Cedillo, V.M., Ros, M., Pascual, J.A. (2022). LED Lighting in Vertical Farming Systems Enhances Bioactive Compounds and Productivity of Vegetables Crops. *Biol. Life Sci. Forum*, 16, 24. <https://doi.org/10.3390/IECHo2022-12514>
- [55] Naz S., Haq A.H.M., Rahman M., Khatun M., (2021). An Initiative for Developing Low Cost Hydroponic System. *Haya Saudi J Life Sci.*, ISSN 2415-623X, doi: 10.36348/sjls.2021.v06i01.003
- [56] Niu, G., Masabni, J. (2018). Plant Production in Controlled Environments. *Horticulturae*, 4, 28. <https://doi.org/10.3390/horticulturae4040028>
- [57] Nguyen N.T., McInturf S., Mendoza-Cozatl D.G., (2016). Hydroponics: A Versatile System to Study Nutrient Allocation and Plant Responses to Nutrient Availability and Exposure to Toxic Elements. *J Vis Exp.*, (113): 54317. doi: 10.3791/54317
- [58] Pantanella, E., Cardarelli, M., Colla, G., Rea, E., & Marcucci, A. (2012). Aquaponics vs. Hydroponics: Production and Quality of Lettuce Crop. *Acta Horticulturae*, 947, 217-223
- [59] Park Y., Williams K.A., (2024). Organic hydroponics: A review. *Scientia Horticulturae. Volume 324*, 112604
- [60] Patterson, D. T., Westbrook, J. K., Joyce, R. J. V., Lingren, P. D., & Rogasik, J. (2015). Weeds, Insects, and Diseases. *Climatic Change*, 43(4), 711-727
- [61] Pennisi, G., Orsini, F., Blasioli, S. et al. (2019). Resource use efficiency of indoor lettuce (*Lactuca sativa* L.) cultivation as affected by red:blue ratio provided by LED lighting. *Sci Rep* 9, 14127. <https://doi.org/10.1038/s41598-019-50783-z>
- [62] Perez, S.L., Ferro, R.B., Corrêa, B. Casarin R., Correa K., Blanco K.C., Bagnato V.S., (2024). Enhanced vegetable production in hydroponic systems using decontamination of closed circulating fluid. *Sci Rep* 14, 602. <https://doi.org/10.1038/s41598-023-50974-9>
- [63] Phum, Teo E., Chan, K. Y., Mokhtar, S.M., Lee C.L. (2024) Effect of LED Wavelength and Power on the Hydroponic Indoor Vegetable Farming. *Universal Journal of Agricultural Research Vol. 12(1)*, pp. 41 – 50, doi: 10.13189/ujar.2024.120105
- [64] Promratrak L. (2017). The effect of using LED lighting in the growth of crops hydroponics. *International Journal of Smart Grid and Clean Energy*, vol. 6, no. 2, pp. 133-140, doi: 10.12720/sgce.6.2.133-140
- [65] Putra, P. A., and Yuliando, H. (2015). Soilless culture system to support water use efficiency and product quality: a review. *Agric. Agric. Sci. Procedia* 3, 283–288. doi: 10.1016/j.aaspro.2015.01.054
- [66] Resh, H. M. (2012). *Hydroponic Food Production: A Definitive Guidebook for the Advanced Home Gardener and the Commercial Hydroponic Grower*. CRC Press
- [67] Rezvani, M., Shamshiri, R.R., Hamed, I.A., Abyane, H.Z., Godarzi, M., Momeni, D. (2021). Greenhouse Crop Simulation Models and Microclimate Control Systems, A Review, in *Next-Generation Greenhouses for Food Security*, Intechopen, ISBN 978-1-83968-076-2, DOI: 10.5772/intechopen.92515
- [68] Richa A., Touil S., Fizir M., Martinez V. (2020). Recent advances and perspectives in the treatment of hydroponic wastewater: a review. *Reviews in Environmental Science and Bio/Technology*, Volume 19, 945–966
- [69] Sarkar, A., Majumder, M. (2015). Opportunities and Challenges in Sustainability of Vertical Farming: A Review. *Journal of Advanced Agricultural Technologies*, 2(3), 81-86

- [70] Sambo P., Nicoletto C., Giro A., Pii Y., Valentinuzzi F., Mimmo T., Lugli P., Orzes G., Mazzetto F., Astolfi S., Terzano R., Cesco S. (2019). Hydroponic Solutions for Soilless Production Systems: Issues and Opportunities in a Smart Agriculture Perspective. *Frontiers in Plant Science*, Vol. 10. ISSN: 1664-462X, doi:10.3389/fpls.2019.00923
- [71] Savvas, D. (2003). Hydroponics: A Modern Technology Supporting the Application of Integrated Crop Management in Greenhouse. Food and Agriculture Organization
- [72] Sellaro, R., Crepy, M., Trupkin, S.A., Karayekov, E., Buchovsky, A.S., Rossi, C. Casal, J.J. (2010). Cryptochrome as a Sensor of the Blue/Green Ratio of Natural Radiation in Arabidopsis. *Plant Physiology*, Vol. 154, pp. 401–409
- [73] Sharma, N., Acharya, S., Kumar, K., Singh, N., Chaurasia, O. P., (2018). Hydroponics as an advanced technique for vegetable production: An overview. *J. Soil Water Conserv.* 17, 364
- [74] Smith H. (1982). Light quality, photoperception, and plant strategy. *Annual Review of Plant Physiology* 33, 1882-8
- [75] Son J. E., Kim H.J., Ahn T.I., (2020). Plant Factory (Second Edition) An Indoor Vertical Farming System for Efficient Quality Food Production. Chapter 20 – Hydroponic Systems, ISBN 978-0-12-816691-8, <https://doi.org/10.1016/B978-0-12-816691-8.00020-0>
- [76] Stein E.W. (2021). The Transformative Environmental Effects Large-Scale Indoor Farming May Have On Air, Water, and Soil. *Air Soil Water Res.*, 14, 1178622121995819
- [77] Syed, A.A., Z.A. Khan, S.H. Chattha, I.A. Shaikh, M.N.H.A. Ali, Z.R. Bughio, S.H. Dahri and G.B. Buriro. (2021). Comparative assessment of hydroponic and geponic cultivation systems for sustainable Spinach cultivation. *Pakistan Journal of Agricultural Research*, 34(4): 678-688
- [78] Tharun, R., Padmasine, K.G. (2023). A Review of Grow-light Farming, Hydroponics, Automated Irrigation System, Smart Farming and Spectrum LED. *International Journal of Research Publication and Reviews*, Vol 4, no 3, pp 4706-4711. <https://doi.org/10.55248/gengpi.2023.4.3.34385>
- [79] Tusi, A., Shimazu, T. (2021). Real-time comparison of several transpiration methods for estimating greenhouse ventilation rate via water vapour balance method. *INMATEH-Agricultural Engineering*, Volume 78, No. 3, pp. 81-90, <https://doi.org/10.35633/inmateh-63-09>
- [80] Van Delden, S.H., SharathKumar, M., Butturini, M., Graamans, L.J.A., Heuvelink, E., Kacira, M., Kaiser, E., Klamer, R.S., Klerkx, L., Kootstra, G., et al., (2021). Current status and future challenges in implementing and upscaling vertical farming systems. *Nat. Food*, 2, 944–956
- [81] van Straten, G., van Ooteghem, R., van Henten, E. J., & De Gelder, A. (2011). Optimal Control of Greenhouse Cultivation. CRC Press, ISBN 9781420059618
- [82] Van Tuiji E., Hospers G.-J., vn den Berg L. (2018). Opportunities and Challenges of Urban Agriculture for Sustainable City Development. *European Spatial Research Policy*, Vol. 25 No. 2, <https://doi.org/10.18778/1231-1952.25.2.01>
- [83] Velazquez-Gonzalez, R.S., Garcia-Garcia, A.L., Ventura-Zapata, E., Barceinas-Sanchez, J.D.O., Sosa-Savedra, J.C., (2022). A Review on Hydroponics and the Technologies Associated for Medium- and Small-Scale Operations. *Agriculture*, 12, 646. <https://doi.org/10.3390/agriculture12050646>
- [84] Verdoliva S.G., Gwyn-Jones D., Detheridge A., Robson P., (2021). Controlled comparisons between soil and hydroponic systems reveal increased water use efficiency and higher lycopene and β -carotene contents in hydroponically grown tomatoes. *Sci Hort.* 15, 279: 109896. doi: 10.1016/j.scienta.2021.109896
- [85] Xydis G. A., Liaros S., Botsis K., (2017). Energy demand analysis via small scale hydroponic systems in suburban areas – An integrated energy-food nexus solution. *Science of the Total Environment*, Volume 593-594, pp. 610-617
- [86] Zhang, X., Cao, D., Wang, M., Cui, G., Shi, Y., Cui, Y. (2022). Nutrient deficiency diagnosis in whole hydroponic lettuce based on random forest, *INMATEH-Agricultural Engineering*, Volume 78, No. 3, pp. 81-90, <https://doi.org/10.35633/inmateh-68-08>
- [87] Zimmermann M., Fisher M., (2020). Impact assessment of water and nutrient reuse in hydroponic systems using Bayesian Belief Networks. *Journal of Water Reuse and Desalination*, 10 (4): 431–442, <https://doi.org/10.2166/wrd.2020.026>
- [88] <https://www.trees.com/gardening-and-landscaping/ebb-and-flow-hydroponics> (accessed on 03.06.2024)
- [89] <https://hydroplanner.com/blog/hydroponics-drip-system-EN> (accessed on 03.06.2024)

- [90] <https://www.hydrocentre.com.au/4-x-55w-star-light-t5-fluro-system-with-lamps-110w> (accessed on 04.06.2024)
- [91] <https://www.nosoilsolutions.com/different-types-grow-lights/> (accessed on 04.06.2024)
- [92] <https://www.sananbiofarm.com/> (accessed on 04.06.2024)
- [93] <https://marshydro.eu/products/new-fc4000-evo-led-grow-light/> (accessed on 05.06.2024)

MATLAB-BASED DESIGN AND ANALYSIS OF SMALL RICE TRANS-PLANTER IN HILLY AREAS

基于 MATLAB 的丘陵地区小型水稻插秧机的设计与分析

Hao WANG¹⁾, Xiaobo ZHOU^{*1)}, Xiayu WU¹⁾, Yuling DAN¹⁾, Hongchun CHU¹⁾, Jin CHEN¹⁾

¹⁾ Sichuan Academy of Agricultural Machinery Science / China;

Tel: +86-18828286534; E-mail: zhouxb79@163.com

DOI: <https://doi.org/10.35633/inmateh-73-09>

Keywords: Hilly Area, Rice Transplanter, Structural Design, Kinematic Analysis, Finite Element Analysis.

ABSTRACT

A small-scale paddy rice transplanter for hilly and mountainous areas faces issues such as few suitable machines, poor transplanting results, and low adaptability and efficiency of large transplanters in small fields. To address these problems, a four-row small-scale paddy rice transplanter was designed, driven by an engine with chain transmission. The machine structure mainly consists of a frame, engine, paddy field wheels, seedling tray, transplanting mechanism, reversing gearbox, and electromagnetic clutch, with a total weight of only 50 kg, facilitating transportation and operation. MATLAB was used for kinematic simulation and analysis of the transplanting mechanism, plotting displacement diagrams of the seedling needles and motion characteristic curves of the transplanting mechanism. ANSYS software was employed for finite element analysis of key components to ensure they meet operational requirements. Experimental studies were conducted with transplanting speed as the experimental factor, using floating rate and missing insertion rate as test indicators. Results showed that under specified transplanting conditions, the floating rate stabilized at around 2.9% and the missing insertion rate at approximately 4.8%. These findings indicate that the designed small-scale transplanter can effectively meet the requirements for rice transplanting operations in hilly areas.

摘要

针对丘陵山区小地块的深泥脚田水稻种植机具少，插秧效果不佳，大型插秧机在小田块中适应性差、效率低等问题，设计了一款四行小型水稻插秧机，采用发动机驱动整机，链式传动。整机结构主要由机架、发动机、水田轮、秧盘和插秧机构、换向减速器和电磁离合器等组成，整机质量只有 50kg，方便转运与作业。利用 MATLAB 对插秧机构进行仿真分析，并编程绘制出秧针的位移图和插秧机构的运动特性曲线；利用 ANSYS 软件对关键部件进行有限元分析，确保所设计的零部件能满足使用要求；以漂秧率和漏插率为试验指标，插秧机前进速度为试验因素，进行试验研究，得到插秧机在规定范围内插秧作业时，漂秧率基本稳定在 2.9% 左右，漏插率基本在 4.8% 左右。结果表明，所设计的小型插秧机能够基本满足丘陵地区的水稻插秧作业。

INTRODUCTION

As one of the essential food crops for human beings, rice has a relatively long history of cultivation and consumption, and more than half of the world's population consumes rice. China is the country with the most extended history of rice cultivation in the world, planting rice as early as six or seven thousand years ago, and is currently the world's first rice-producing country (Cai et al., 2017; Lou et al., 2020; Hafijur et al., 2022). In recent years, with the development of agricultural mechanization, rice transplanter has gradually replaced the traditional manual planting method (Chen et al., 2022; Li et al., 2022; Yang et al., 2024). Compared with artificial planting, mechanized rice trans-planting can better control plant spacing and transplanting depth, which is conducive to the growth and management of seedlings in the later stage, and ensures both transplanting efficiency and quality (Fu et al., 2023; Hu et al., 2024; Kumar et al., 2023).

Hilly areas have complex terrain, fragmented fields, significant height differences, inconvenient road access, centralized large-scale production organization difficulties, agricultural machinery and agronomic technology mismatches, and the existing rice trans-planting equipment can't meet the high-speed development of large-area mechanized rice production in hilly areas. Therefore, there is a need for more customized small rice transplanting machines that adapt to the characteristics of hilly terrace fields.

Hao Wang, Assistant Engineer; Xiaobo Zhou, Senior Agronomist; Xiayu Wu, Engineer;

Yuling Dan, Assistant Engineer; Hongchun Chu, Senior Agronomist; Jin Chen, Senior Engineer;

In 2022, Li et al. designed a small impeller energy-taking rice transplanter in a labor-saving operation, carried out a detailed optimization design for the transplanting mechanism of the box mechanism, and analyzed and evaluated the key components by using finite element simulation (Li et al., 2022). In 2022, Mao G. et al. carried out a comparative field experiment between a light and simple rice transplanter and a small-scale direct seeding rice transplanter in hilly mountainous areas, and concluded that light and simple rice transplanter and small-scale rice direct seeding machine can't meet the high-speed development of large-scale mechanized rice production in hilly terrace fields using the structure of the machine, the production efficiency, and the rice yield of three aspects. Comparison and analysis of light type rice transplanter is more suitable for rice cultivation in hilly mountainous areas (Mao et al., 2022).

In this paper, given the dilemma of rice transplanter in hilly areas facing no "excellent machine" available, a 2ZQS-4 four-row small rice transplanter is designed to provide reference and reference for the design of rice transplanter in hilly areas.

MATERIAL AND METHODS

STRUCTURAL DESIGN

The overall structure and working principle

The overall structure of the 2ZQS-4 rice transplanter is shown in Fig.1A. It mainly consists of frame 1, engine 2, paddy wheel 3, transmission system 4, seedling tray 5 and rice transplanter mechanism 6. When working in the field, the rice transplanter power is provided by engine 2, the engine output power is transmitted to the paddy wheel 3 through the commutation reducer, and the axle transmits the power synchronously to the rear rice seedling plate 5 and the transplanting mechanism 6 through the commutation reducer to ensure that the rice transplanter realizes the synchronization of the power during the operation. The rice-planting mechanism adopts a crank-rocker type mechanism, and the input and output end of the paddy wheel axle are respectively equipped with electromagnetic clutches, which control the rice-planting and travelling operations of the rice-planting machine through the clutches.

Because the operation process of rice transplanter is more complicated, the rice transplanting operation needs the forward speed, the left and right moving speed of the seedling box and the rotary movement of the rice transplanting mechanism to cooperate with each other in order to accurately and correctly take down the seedlings and insert them into the paddy field, so all the parts of the whole machine's power are supplied by the gasoline engine, and the operation of the rice transplanter is controlled by the ratio between the reducer and the transmission chain (Xu et al., 2022; Zhu et al., 2023). Moreover, the seedling needles are fastened to the seedling needle holder by bolts so that the depth of rice transplanting can be adjusted, and the corresponding tilt angle of the seedling needle holder can be adjusted to ensure that the needles can pick up the rice seedlings smoothly. The three-dimensional model diagram of the rice transplanter is shown in Fig. 1B.

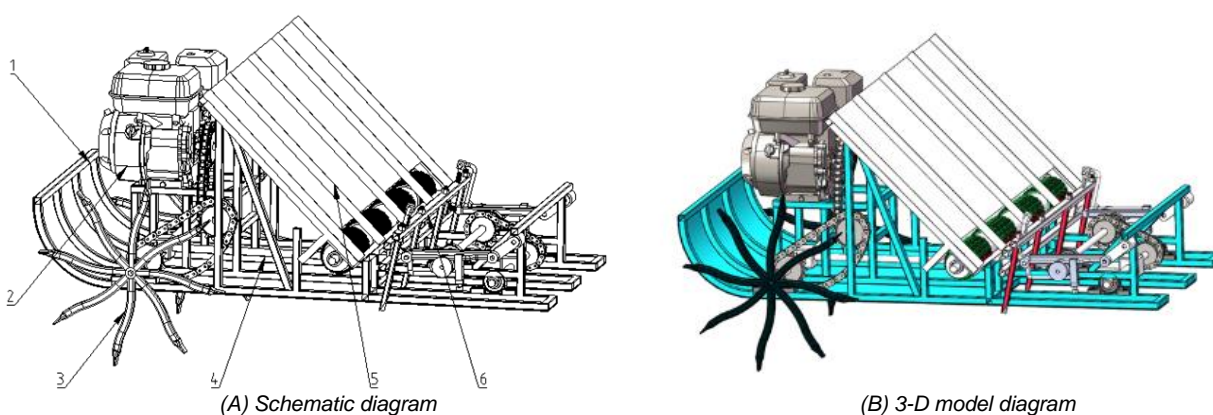


Fig. 1 – The overall structure of 2ZQS-4 rice transplanter

1-frame; 2-engine; 3-paddy wheel; 4-transmission system; 5-rice paddy; 6-rice transplanter mechanism.

The transmission system design

The transmission system of the 2ZQS-4 rice transplanter as a whole is shown in Fig. 2, which mainly consists of an engine, reversing reducer, transmission sprocket, transmission shaft, electromagnetic clutch, etc.

The power of the whole machine is provided by engine 8, and the power of the rice transplanter is matched with each other in terms of the forward movement of the rice transplanter, the movement of the seedling box, and the operation of the rice transplanting mechanism, so as to ensure that the rice transplanter can pick up the rice seedlings smoothly in its operation, and that the transplanting distance of the rice seedlings is 150 mm.

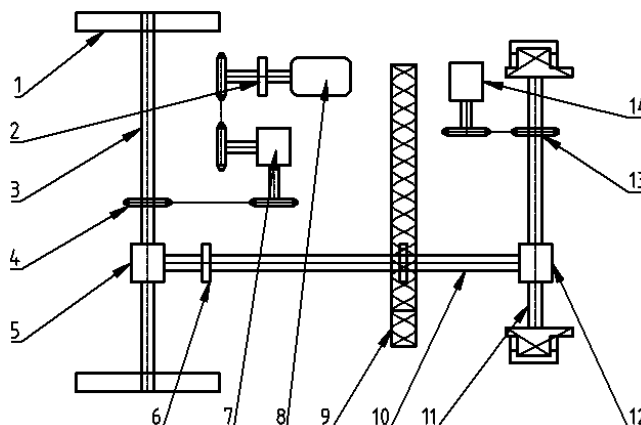


Fig. 2 – ZZQS-4 rice transplanter transmission system schematic diagram

1-Paddy wheel; 2-Electromagnetic clutch; 3-Wheel shaft; 4-Sprocket; 5-Reversing reducer; 6-Electromagnetic clutch; 7-Reversing reducer; 8-Engine; 9-Seedling box; 10-Main drive shaft; 11-Transplanting mechanism drive shaft; 12-Reversing reducer; 13-Sprocket; 14-Transplanting mechanism.

In order to make the rice transplanter work smoothly in the deep mud foot field, the design of its wheel diameter is 800 mm, then the rice transplanter wheel rotates for one week, and the forward displacement of the machine S calculation formula is shown in the equation (1).

$$S = \pi D \tag{1}$$

It was calculated that $S=2513.27$ mm.

There is a slight loss in transmission efficiency because the wheel slips in the paddy field, and the power is transmitted to the crank of the rice-planting mechanism through the reducer and chain (Cai et al., 2012; Kumar et al., 2021). So, the wheel rotates for one week, and the number of rice transplanting times M is calculated as shown in equation (2).

$$M = \frac{S\eta}{N} \tag{2}$$

where: M - Number of rice planting, (times);

H -Total efficiency, ($\eta=80\%$);

N - plant spacing, ($N=150$ mm);

Calculated $M = 13$. That is, the wheel rotates for one week, the rice transplanter inserts seedlings 13 times, and the forward speed of the rice transplanter is set at 0.5 m/s, then the crank rotation speed of the rice transplanter mechanism can be obtained as 3.25 r/s.

Main technical parameters

The main technical parameters of the rice transplanter are shown in Table 1.

Table 1

| Main technical parameters of ZZQS-4 rice transplanter | |
|---|-----------------|
| Parameter Name | Parameter Value |
| Model | ZZQS-4 |
| Rated engine power/(kW) | 3.3 |
| Rated engine speed/(r/min) | 3600 |
| Overall dimensions (L×W×H)/(mm) | 1500×1200×1200 |
| Operating speed/(m/s) | 0.25~0.75 |
| Number of rice-planting rows/(row) | 4 |
| Diameter of paddy wheel/(mm) | 800 |
| Row spacing/(mm) | 300 |
| Plant spacing/(mm) | 150 |
| Transplanting box length/(mm) | 600 |
| Transplanting mechanism type | Crank Rocker |

KINEMATICS SIMULATION ANALYSIS OF RICE TRANSPLANTER MECHANISM

The mathematical model

The principle of the rice-planting mechanism is shown in Fig. 3, the crank AD rotates around the rotary center A, the rocker BC is hinged on the frame AB, the connecting rod CD is hinged on BC and AD respectively, the seedling needle EF is fixed on the connecting rod CD. The CDEF forms a fixed quadrilateral structure, and the tip of the seedling needle is the F point. When working, the crank rotates around point A uniformly, driving the seedling needle to realize the seedling picking and inserting operation.

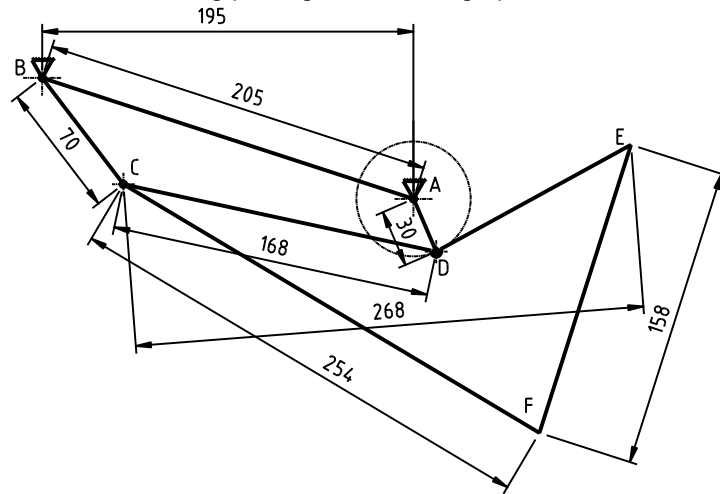


Fig. 3 – Schematic diagram of rice-planting mechanism

The closed-loop vector diagram of the rice planting mechanism is shown in Fig. 4, and the right-handed right-angle coordinate system is established with the crank rotation center as the coordinate origin.

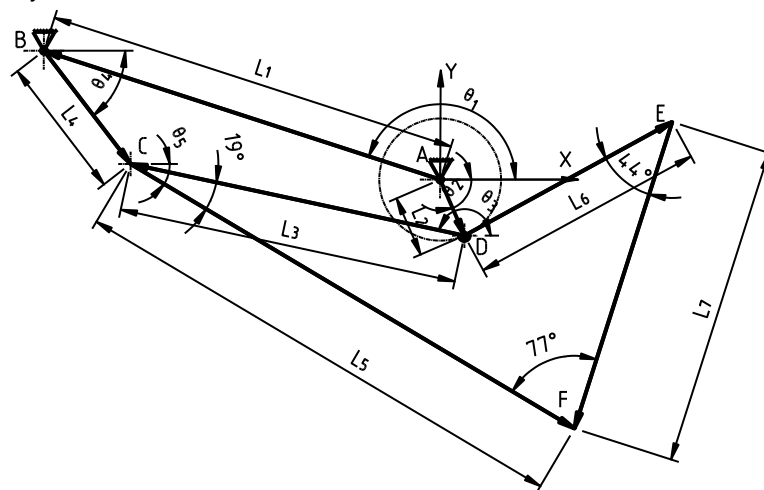


Fig. 4 – Closed-loop vector diagram of rice-planting mechanism

Establish the vector equation of the mechanism, as shown in equation (3).

$$\vec{l}_1 + \vec{l}_4 = \vec{l}_2 + \vec{l}_3 \tag{3}$$

Decomposing the above vector equation into x and y coordinate axes gives the displacement equation, as shown in equation (4).

$$\begin{cases} l_1 \cos \theta_1 + l_4 \cos \theta_4 = l_2 \cos \theta_2 + l_3 \cos \theta_3 \\ l_1 \sin \theta_1 + l_4 \sin \theta_4 = l_2 \sin \theta_2 + l_3 \sin \theta_3 \end{cases} \tag{4}$$

Derivation of the above displacement equation concerning time yields the velocity equation, the matrix form of which is given in equation (5).

$$\begin{bmatrix} -l_3 \sin \theta_3 & l_4 \sin \theta_4 \\ l_3 \cos \theta_3 & -l_4 \cos \theta_4 \end{bmatrix} \begin{bmatrix} \omega_3 \\ \omega_4 \end{bmatrix} = \begin{bmatrix} l_2 \sin \theta_2 \omega_2 \\ -l_2 \cos \theta_2 \omega_2 \end{bmatrix} \tag{5}$$

Derivation of the velocity equation concerning time yields the acceleration equation, the matrix form of which is given in equation (6).

$$\begin{bmatrix} -l_3 \sin \theta_3 & l_4 \sin \theta_4 \\ l_3 \cos \theta_3 & -l_4 \cos \theta_4 \end{bmatrix} \begin{bmatrix} \alpha_3 \\ \alpha_4 \end{bmatrix} = \begin{bmatrix} l_2 \sin \theta_2 \alpha_2 + l_2 \cos \theta_2 \omega_2^2 + l_3 \cos \theta_3 \omega_3^2 - l_4 \cos \theta_4 \omega_4^2 \\ -l_2 \cos \theta_2 \alpha_2 + l_2 \sin \theta_2 \omega_2^2 + l_3 \sin \theta_3 \omega_3^2 - l_4 \sin \theta_4 \omega_4^2 \end{bmatrix} \quad (6)$$

The displacement equation for point F of the seedling tip is shown in equation (7).

$$\begin{cases} X_F = l_1 \cos \theta_1 + l_4 \cos \theta_4 + l_5 \cos \theta_5 \\ Y_F = l_1 \sin \theta_1 + l_4 \sin \theta_4 + l_5 \sin \theta_5 \end{cases} \quad (7)$$

Derivation of the displacement equation gives its velocity equation, as shown in equation (8).

$$\begin{cases} X' = -l_4 \sin \theta_4 \omega_4 - l_5 \sin \theta_5 \omega_5 \\ Y' = l_4 \cos \theta_4 \omega_4 + l_5 \cos \theta_5 \omega_5 \end{cases} \quad (8)$$

Derivation of the velocity equation gives its acceleration equation, as shown in equation (9).

$$\begin{cases} X'' = -l_4 \cos \theta_4 \omega_4^2 - l_4 \sin \theta_4 \alpha_4 + l_5 \cos \theta_5 \omega_5^2 - l_5 \sin \theta_5 \alpha_5 \\ Y'' = -l_4 \sin \theta_4 \omega_4^2 + l_4 \cos \theta_4 \alpha_4 - l_5 \sin \theta_5 \omega_5^2 + l_5 \cos \theta_5 \alpha_5 \end{cases} \quad (9)$$

From the above schematic and vector diagram:

$$\theta_5 = -(180^\circ - (\theta_3 - 19^\circ)) \quad (10)$$

Simulation Model

The Simulink kinematic simulation model is established based on the above mathematical modelling program, as shown in Fig. 5. The simulation initial condition table is shown in Table 2 (Kumar et al., 2022; Li, 2024).

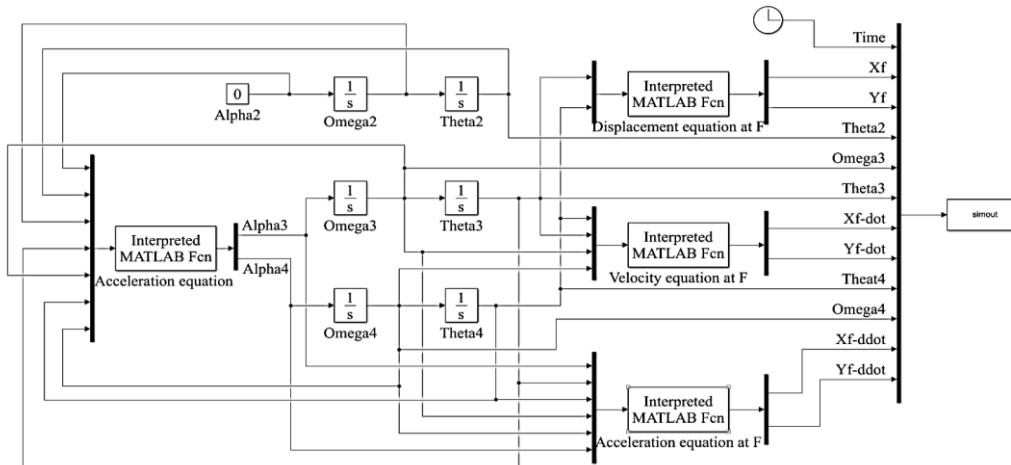


Fig. 5 – Simulink simulation model diagram

Table 2

| Simulation initial condition table | |
|------------------------------------|-----------------|
| Parameter Name | Parameter Value |
| l_1 / (mm) | 205 |
| l_2 / (mm) | 30 |
| l_3 / (mm) | 168 |
| l_4 / (mm) | 70 |
| l_5 / (mm) | 254 |
| θ_1 / (rad) | 2.8274 |
| θ_2 / (rad) | -1.1694 |
| θ_3 / (rad) | 2.9322 |
| θ_4 / (rad) | -0.9076 |
| ω_2 / (rad/s) | -20.42 |
| ω_3 / (rad/s) | 1.4682 |
| ω_4 / (rad/s) | -11.1526 |
| Machine forward speed / (m/s) | 0.5 |
| Simulation time / (s) | 1 |

RESULTS

Simulation results and analysis

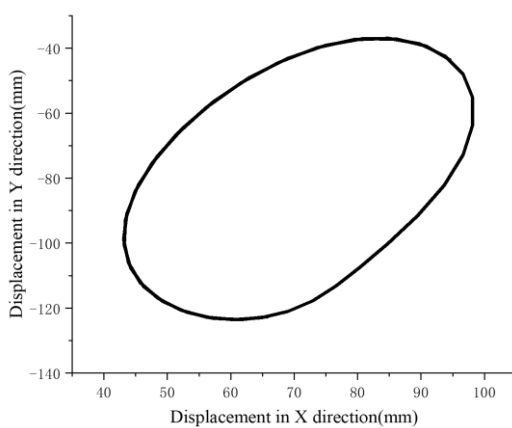
Through simulation, the displacement of the tip of the seedling needle at point F is shown in Fig. 6A. The seedling needle does regular periodic movement, and basically becomes parallel with the seedling tray when picking up seedlings at the front end so as to avoid injuring seedlings to the maximum extent. To effectively insert seedlings into the ground and lower the rate of drifting and floating seedlings, the seedling needle must be essentially in a vertical position after being picked up (Ma, 2023).

From the simulation results, the horizontal and vertical velocity change rule of the rice-planting mechanism is shown in Fig. 6B and Fig. 6C. The velocity change range of the horizontal direction is $-0.44\text{m/s}\sim 0.60\text{m/s}$, and the velocity change range of the vertical direction is $-0.94\text{m/s}\sim 0.87\text{m/s}$. The rice-planting mechanism's motion is a stable periodic simple harmonic motion.

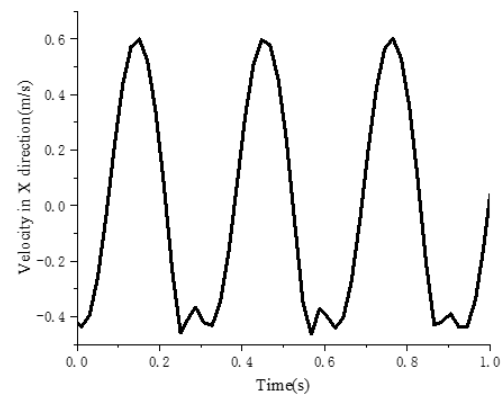
From the simulation results, the acceleration change rule of the horizontal and vertical direction of the rice-planting mechanism is shown in Fig. 6D and Fig. 6E. The acceleration change range of the horizontal direction is $-6.17\text{m/s}^2\sim 18.70\text{m/s}^2$, and the acceleration change range of the vertical direction is $-20.64\text{m/s}^2\sim 13.98\text{m/s}^2$. The rice-planting mechanism's motion is a stable periodic simple harmonic motion.

From the simulation results, the angular velocity change rule of the transplanting mechanism is shown in Fig. 6F. The angular velocity change range is $-5.55\text{rad/s}\sim 3.61\text{rad/s}$. The angular velocity of the transplanting mechanism is a stable cyclic change. There will be no considerable vibration in the process of the movement, and it can stably carry out the transplanting operation, prolonging the service life of the whole rice transplanter.

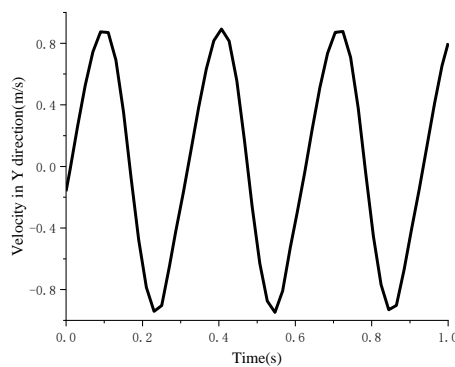
Through the kinematics simulation of the rice-planting mechanism and simulation of its complex motion process, its motion characteristics can be more intuitively analyzed, thus providing a reference for the subsequent dynamics analysis, finite element simulation, test and optimization design.



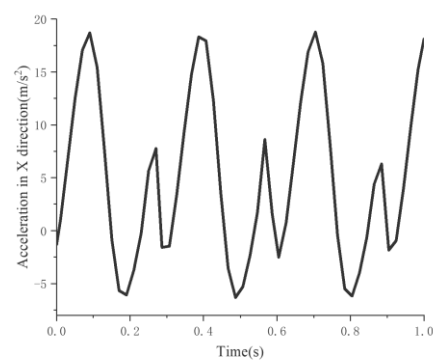
(A)



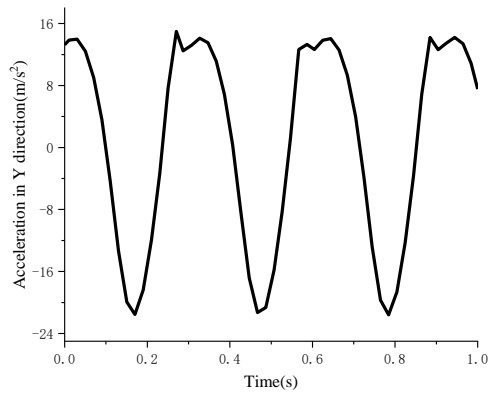
(B)



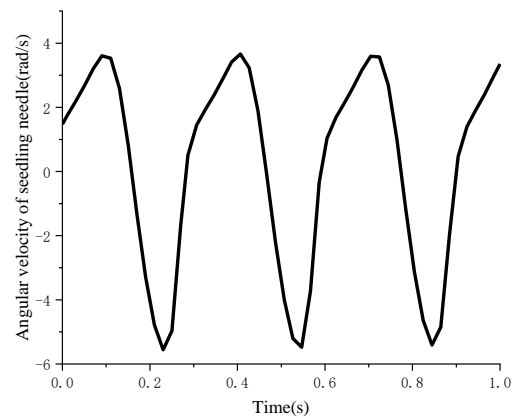
(C)



(D)



(E)



(F)

Fig. 6 – Kinematic simulation analysis results

A-Displacement diagram of F point of the tip of seedling needle; B-Variation of horizontal velocity of rice interpolation mechanism; C-Variation of vertical velocity of rice interpolation mechanism; D-Accelerating change of horizontal velocity of rice transplanting mechanism; E-Accelerating change of vertical direction of rice transplanting mechanism; F-Angular velocity change rule diagram of rice-planting mechanism.

FINITE ELEMENT SIMULATION ANALYSIS

Through the above kinematic analysis and observation of actual operating conditions, in the rice transplanter machine, in terms of strength and stiffness, what is the most prone to fracture is the crank of the rice transplanter mechanism, so using ANSYS to analyze the finite element of the crank, study its stress, strain and deformation will lay a foundation for the development of the rice transplanter machine at a later stage (Wen et al., 2019; Zhang et al., 2021).

Simulation model

After three-dimensional modeling by using SolidWorks software, it is imported into Workbench, and the selected material of the crank is Hardened 45 Steel (Zhang et al., 2021). After importing it into the software, meshing is carried out with tetrahedral cells as the primary type, boundary conditions and constraints are set, and the maximum force obtained through dynamics analysis is applied to it.

Simulation results and analysis

After finite element analysis, the total displacement analysis of the crank can be obtained as shown in Fig. 7A, from which it can be seen that the displacement change at any point out of the crank is minimal, and the displacement change at the maximum is only 0.295 mm.

The stress analysis cloud diagram of the crank is shown in Fig. 7B, and the strain analysis cloud diagram is shown in Fig. 7C; the maximum stress suffered by the crank is 363.43 MPa, and the maximum strain is 0.002, the yield strength of 45 steel is 355 MPa, and the tensile strength is 6000 MPa, so it can be seen that the crank designed meets the needs of use completely.

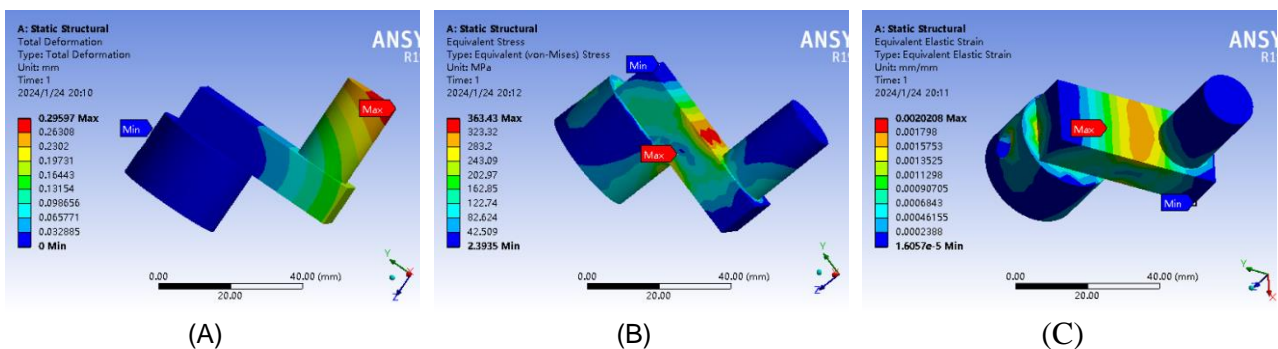


Fig. 7 – The result of finite element simulation

A-Crank total displacement analysis cloud diagram; B-Crank stress analysis cloud; C-Crank Strain Analysis.

EXPERIMENTAL RESEARCH

Blanket seedlings cultivated in 3-inch trays were used for transplanting tests in winter paddy fields, and the drift rate and leakage rate in the selected range were measured by varying different forward speeds of the rice transplanter and selecting a length of 5 meters at the same speed (Luo *et al.*, 2020). Each set of tests was repeated three times, and the results were averaged. The drift and leakage rates' formulas are shown in equation (11). The test results are shown in Table 3.

$$P = \frac{Z_P}{Z} \times 100\% \quad (11)$$

$$L = \frac{Z_L}{Z} \times 100\%$$

where:

- P - Drift seedling rate, (%);
- L - Leakage rate, (%);
- Z_P - Total number of drifted rice plants, (plants);
- Z_L - Total number of missed insertions, (plants);
- Z - Total number of transplanted seedlings, (plants).

Table 3

| Table of test results | | |
|----------------------------------|-------------------------|------------------|
| Transplanter forward speed (m/s) | Drift seedling rate (%) | Leakage rate (%) |
| 0.3 | 2.95 | 4.67 |
| 0.4 | 2.93 | 4.78 |
| 0.5 | 2.91 | 4.83 |
| 0.6 | 2.96 | 4.88 |
| 0.7 | 3.12 | 5.51 |

From the above test results, it can be seen that the rice transplanter will increase the drift rate and leakage rate as the forward speed increases. The main reason is that, with the increase in forward speed, the frequency of transplanting will also increase, which leads to the seedling needle entering the next action before the seedlings are stabilized, and the seedling box can't move in time to send the seedlings to the designated position. However, the overall test results show that the rice transplanter can meet the corresponding national standards.

CONCLUSIONS

In this paper, for the problem of lack of rice transplanter in deep mud foot fields in hilly and mountainous areas, a ZZQS-4 four-row small rice transplanter is designed, with a row spacing of 300 mm and plant spacing of 150 mm, and the transplanting mechanism adopts a crank-linkage structure, which makes the whole machine compact and lightweight. It is very suitable for transplanting rice seedlings in small plots of land in hilly and mountainous areas.

The kinematic simulation of the rice-planting mechanism shows that when the rice-planting machine operates within the predetermined speed range, the movement is stable, and there is no violent vibration, which meets the requirement of stability. The rice-planting operation can be carried out safely and effectively in the field. The finite element analysis of the key components shows that the whole machine structure is reasonably designed, and the materials selected can meet the strength and stiffness of use.

The field test results of the rice transplanter show that when the rice transplanter operates within the designed forward speed, the rate of drifting rice seedlings is basically maintained at about 2.9%, and the rate of leakage is stabilized at about 4.8%, which can meet the relevant standards.

In summary, the four rows of small rice transplanter can meet the requirements of rice transplanter operation in small plots in hilly mountainous areas, and the whole machine is reasonable in design and stable in structure, which can provide a certain reference value for the design and development of rice transplanter in hilly areas.

REFERENCES

- [1] Cai, J., (2017). Cracking the hilly mountainous area rice machine insertion technology promotion problems (破解丘陵山区水稻机插技术推广难题). *Agricultural Machinery Science and Technology Promotion*, Vol. 2, pp. 31-33, Beijing/China.

- [2] Cai, H., (2012). *Research on the insertion mechanism of high-speed rice transplanter* (高速水稻插秧机分插机构研究). (Degree Dissertation). Jilin University, Jilin/China.
- [3] Chen, J., Bo, K., W, J., (2022). Adaptability test of rice transplanter equipped with Bei-Dou satellite navigation system for driving operation (水稻插秧机搭载北斗卫星导航系统驾驶作业适配性试验). *Agricultural Machinery Science and Technology Promotion*, Vol. 4, pp. 44-45, Beijing/China.
- [4] Fu, Q., Wang, Y., Ma, Z., (2023). YOLOv5-AC: A Method of Uncrewed Rice Transplanter Working Quality Detection. *Agronomy*, Vol. 13, Issue 9, Switzerland.
- [5] Hafijur R, Mizanur M R, Saiful M K A I, (2022). Mechanical Rice Transplanting in Bangladesh: Current Situation, Technical Challenges, and Future Approach. *Journal of Biosystems Engineering*, Vol. 47, pp.417-427, Korea.
- [6] Hu, X., Zhang, X., Li, Y., (2024). Application of mathematical modeling in rice transplanter operation optimization (数学建模在水稻插秧机作业优化中的应用). *Agricultural Mechanization Research*, Vol. 46, pp. 186-189, Heilongjiang/China.
- [7] Kumar A.M., Uttam K., Gourav S., (2021). Development and performance evaluation of a manually operated paddy transplanter for root-washed seedlings. *Journal of Agricultural Engineering*, Vol. 58, pp. 323-342, India.
- [8] Kumar N.S., Kumar M.N., Singh S.T., (2023). Influence of transplanting techniques and age of wash root type seedlings on planting attributes of paddy rice. *Cogent Food & Agriculture*, Vol. 9, Issue 1, United Kingdom.
- [9] Kumar S.L., Kumar M.N., Mohd J., (2022). Optimization and evaluation of machine–field parameters of remotely controlled two-wheel paddy transplanter. *Journal of Field Robotics*, Vol. 39, pp. 984-998, United Kingdom.
- [10] Li H., (2022). Intelligent rice transplanter unmanned key technology research (智能化水稻插秧机无人驾驶关键技术研究). (Degree Dissertation). *Shandong Agricultural University*, Shandong/China.
- [11] Li N., (2024). Optimization of rice transplanter control system based on mathematical partial differential algorithm (基于数学偏微分算法的水稻插秧机控制系统优化). *Agricultural Mechanization Research*, Vol. 46, pp. 234-238, Heilongjiang/China.
- [12] Luo C., Li H., Wang M., (2020). Design and experimental study of small rice transplanter (小型水稻插秧机设计与试验研究). *Agricultural Mechanization Research*, Vol. 42, pp. 76-80, Heilongjiang/China.
- [13] Ma Z., (2023). Comparative analysis of simultaneous side-deep fertilization of mechanically transplanted rice and conventional fertilization of mechanically transplanted rice (机插秧同步侧深施肥与机插秧常规施肥对比试验分析). *Southern Agricultural Machinery*, Vol. 54, pp. 53-55+67, Jiangxi/China.
- [14] Mao, G., Wu X., Lin, S., (2022). Field trials of light and simple rice transplanter and small direct seeding machine for planting different varieties of rice in ethnic minority mountainous areas (轻简型水稻插秧机和小型直播机在少数民族山区种植不同品种水稻的田间试验). *Southern Agricultural Machinery*, Vol.53, pp.5-8, Jiangxi/China.
- [15] Wen C., Wang H., Wang M., (2019). Optimized design and simulation analysis of rice transplanter splitting mechanism (水稻插秧机分插机构优化设计与仿真分析). *Journal of Hubei University of Technology*, Vol. 34, pp.36-39, Hubei/China.
- [16] Xu, X., Zhou, M., Chen, X., (2022). Processing Method of Gearbox with Non-Circular Gear Train and Its Application in Rice Potted Seedling Transplanting Mechanism. *Agriculture*, Vol.10, pp.1676-1676, Switzerland.
- [17] Yang S., Song Y., Xue, J., (2024). Research on multi-sensor combination localization of rice transplanter based on vision supplement (基于视觉补充的水稻插秧机多传感器组合定位研究). *Journal of Huazhong Agricultural University*, Vol. 1, pp. 1-13, Hubei/China.
- [18] Zhang, N., Cheng, L., Liu, J., (2021). Finite element optimization analysis of a new type of rice transplanter frame (一种新型插秧机机架的有限元优化分析). *Electromechanical Engineering Technology*, Vol.50, pp.32-34, Guangdong/China.
- [19] Zhu, D., Gao, K., Xue, K., (2023). Vibration analysis and parameter optimization of seedling pushing device of transplanting mechanism with planetary elliptic gears. *Journal of the Chinese Institute of Engineers*, Vol. 46, pp. 154-162, United Kingdom.

OPTIMIZATION AND EXPERIMENT OF CUTTING PARAMETERS OF ALFALFA DISC-TYPE MOWER

圆盘式苜蓿切割器参数优化与试验

Yong YOU*, Pengzhan HU, Lu ZHU, Haiyi WANG, Yunting HUI, Decheng WANG

China Agricultural University, College of Engineering, Beijing / China

Tel: +86 10 010-62737977; +86 10 010-62737208; E-mail: youyong@cau.edu.cn;

Corresponding author: Yong You;

DOI: <https://doi.org/10.35633/inmateh-73-10>

Keywords: forage, alfalfa harvesting, disc-type cutter, mower, low-loss cutting

ABSTRACT

Optimization and experimental research on the cutting parameters of the cutter were carried out to solve the high re-cutting rate and loss rate under high-speed harvesting of alfalfa disc-type cutter. Kinematics theory was used to analyze the movement trajectory and cutting area of the cutter in the cutting process, and theoretical calculations to carry out an analysis of the factors affecting the re-cutting area of the cutter. A working parameters adjustable cutting test bench was designed and produced, and cutting experiments of alfalfa were conducted using this test bench combined with response surface methodology. The optimized factors combination was solved by quadratic fitting function, and the value of cutterhead diameter, blade twist angle, and cutting inclination angle was 407.04 mm, 4.21°, and 4.51°, respectively. The verification test showed that the average re-cutting rate and loss rate were 1.48% and 3.13%, less than national standard requirements for alfalfa harvesting quality (re-cutting rate <1.5%; loss rate <4%), low-loss cutting of alfalfa was achieved, and the harvesting quality of the disc-type cutter was improved.

摘要

针对圆盘式苜蓿切割器高速收获下重割率及损失率高的问题,开展了切割器切割参数优化与试验研究。运用运动学理论分析了割刀切割过程中的运动轨迹及切割区域,通过理论计算进行了切割器重割面积影响因素分析。设计并搭建了一款作业参数可调切割试验台架,结合响应曲面试验方法,利用切割试验台架开展苜蓿田间收割试验。利用二次拟合方程求得最优参数组合为刀盘直径 407.04 mm、割刀扭转角 4.21°、切割倾角为 4.51°。验证试验结果表明,最优参数组合下平均损失率为 3.13%、平均重割率为 1.48%,小于苜蓿收获质量的国家标准要求(损失率 <4%;重割率 <1.5%),实现了苜蓿的低损失切割,提升了圆盘式切割器高速收获下的作业质量。

INTRODUCTION

With the introduction of policies such as national planting structure adjustment, "grain to fodder" and returning farmland to grass, the planting area of forage grass in China has further increased (Chen et al., 2015; Jiang et al., 2016; Li et al., 2020; Zhu et al., 2022; Wang et al., 2017; Guo et al., 2019). Forage industry development cannot be separated from the support of machinery and equipment, disc mowers with high efficiency, and no vibration characteristics, in modern mower products have a wide range of applications (Fu et al., 2018; Zhao et al., 2014; Hou et al., 2020; Xie et al., 2020; Vasiliev N. et al., 2021; Otroshko S. et al., 2021). Disc-type forage cutter still has the problem of high re-cutting rate and loss rate under high-speed harvesting at this stage, which limits the development of the forage industry.

Aiming at efficient and low-loss crop harvesting, there have been many related researches, domestically and abroad. Song et al. (2020) prepared a self-sharpening cutter with a metal-ceramic gradient to achieve low-damage cutting of alfalfa by maintaining the cutting performance of the cutter during harvesting. Du et al (2022) designed a bionic blade for a single-row tea harvester based on the curved structure of cricket incisors according to the bionic principle, which reduces the tea-cutting resistance and power consumption. Hao et al, (2018), found that different shapes of cutting blades had a significant effect on the energy consumption of the equipment and field performance during the harvesting of manzanita. Shi et al, (2017), optimized the parameters such as cutting speed, cutting inclination angle, and a working speed of an orderly harvester for artemisia by orthogonal tests to improve the cutting performance of the harvester. Fu (2014) and Wu (2017) determined the optimum region for the blade twist angle and the cutting inclination angle based on the complex

vector theory. Johnson Phillip C. et al (2012) designed a pendulum cutting mechanism for the cutting of mango grass stalks, and the study showed that the energy required for cutting is directly proportional to the cutting speed, and there exists the optimum cutting bevel angle so that the cutting consumes the least amount of energy. Zhang et al (2019) studied the optimum blade slant cutting angle for rice stalks under-supported and unsupported cutting to provide a reference for the height adjustment of the rice harvester cutting table. Hou et al, (2020), analyzed the effect of different blade angles and slant cutting angles of disc cutter knives on the cutting quality of castor beans to obtain optimum operating parameters through experimentation. Chandra Gupta, (1992), designed a rotary single-disc sugarcane cutter test bench, and the optimal operating parameters of the single-disc sugarcane cutter were obtained through computerized acquisition of the mechanical power and cutting torque of the cutter. In summary, relevant scholars mainly aim at reducing the crop-cutting power consumption and improving the operational performance of cutting machine tools at present, and have conducted research around the design of crop stalk cutting tools and optimization of cutting parameters by methods such as computer simulation and analysis or cutting test platform, and have achieved certain results. However, the disc-type forage cutter is prone to produce multiple cutting areas under high-speed harvesting, repeated cutting of forage and stubble, leading to the phenomenon of uneven stubble height, which affects the yield of perennial forage such as alfalfa and the quality of the next round of growth. Therefore, it is of great significance to carry out the theoretical analysis of the cutting system of the disc-type cutter and the influence factors of re-cutting, and to research on the matching relationship of the cutting parameters to improve the harvesting quality of the mower during high-speed harvesting.

This paper carries out theoretical research on disc-cutting systems according to the kinematics principle, and explores the relationship between the re-cutting area and cutting parameters. A parameter adjustable cutting test bench is constructed, and key cutting parameters are optimized by response surface test to reduce the cutting loss rate and re-cutting rate, the harvesting quality of the cutter at high-speed harvesting is improved.

MATERIALS AND METHODS

Theoretical analysis of cutting systems

● Cutting kinematics analysis

The disc-type cutter adopts the unsupported cutting method to cut the alfalfa, suitable cutting speed is the first condition for successful completion of the cutting action. In addition, the mower cutting system often adopts two special structures twisting cutter and tilting disc. Tilting the cutterhead at an angle to the ground can reduce the stubble height and improves the cutting quality of the alfalfa; at the same time, make the cutting mode from cross-cutting to oblique cutting, reduce the cutting resistance and power consumption (Li, 2014; Dong, 2020). Blade twisted at a certain angle can make the back of the knife produce an upward thrust to the stalks after the stalks were cut off, reducing the re-cutting phenomenon and cutting losses.

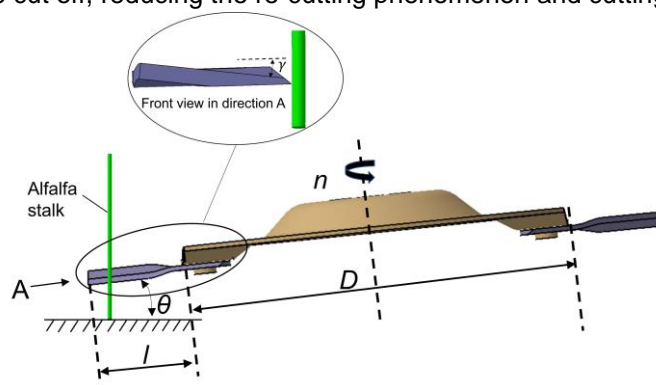


Fig. 1 - Working principle diagram

Note: n is the rotation speed of the cutterhead; D is the cutterhead diameter; l is the blade length that extends out of the cutterhead; γ is the blade twist angle; θ is the cutting inclination angle

To determine the movement trajectory of the blade and the cutting area, the kinematical cutting process of the disc mower is analyzed. The cutterhead mainly consists of the left and right cutter discs, as shown in Fig. 2 and Fig. 3. A, B and C, D are points in the same position of blades 1, 2, and 3, 4, respectively. The center O of the disc circle is the basis for the establishment of a coordinate system, the equation of motion of the points A, B, C, and D is:

$$\begin{cases} x_{oA} = 2r + l_1 + (\Delta l + r) \cos \phi \\ y_{oA} = (\Delta l + r) \sin \phi + v_m t \end{cases} \quad (1)$$

$$\begin{cases} x_{oB} = 2r + l_1 + (l + r) \cos \phi \\ y_{oB} = (l + r) \sin \phi + v_m t \end{cases} \quad (2)$$

$$\begin{cases} x_{oC} = (\Delta l + r) \sin \phi \\ y_{oC} = (\Delta l + r) \cos \phi - v_m t \end{cases} \quad (3)$$

$$\begin{cases} x_{oD} = (l + r) \sin \phi \\ y_{oD} = (l + r) \cos \phi - v_m t \end{cases} \quad (4)$$

Where: r is the cutterhead diameter, (mm);

l is the blade length extending out of the slide palm, (mm);

l_0 is the length of the blades, (mm);

l_1 is the cutterhead spacing, (mm);

Δl is the difference between the ' l ' and ' l_0 ', (mm);

v_m is the speed of the tractor, (m/s);

Φ is the blade rotated angle relative to initial position, ($^\circ$);

According to the trajectory equations, the movement trajectories of the points on the blade and the composed cutting area are plotted in Fig. 2. Curves 1A and 2A represent the movement trajectories of point A on blades 1 and 2, respectively, and curve 3A represents the movement trajectory of point A on blade 1 after the cutterhead is rotated by an angle of 2π ; The rest of the points on the cutterhead have a same motion trajectory rule to A.

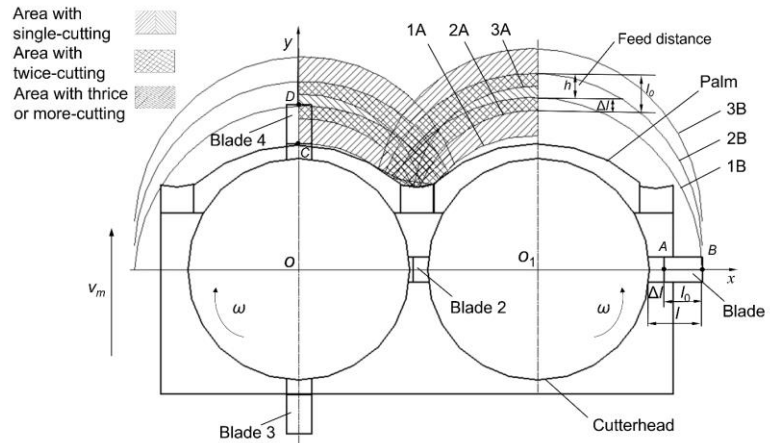


Fig. 2 - Cutting area diagram of disc cutter

h is the feed distance of the cutter, mm; O is the coordinate origin (the center of the left cutterhead circle); O_1 is the circle center of the right cutterhead.

During the cutting process, the trajectory equation of blade 2 lags π phases behind blade 1, and the trajectory equation of blade 3 lags π phases behind blade 4. According to the above motion equations, the absolute motion trajectory equations of each point on the blade are further introduced.

$$y_{2A} = (\Delta l + r) \sin \left[\arccos \left(\frac{x - 2r - l_1}{\Delta l + r} \right) \right] + \frac{v_m}{\omega} \left[\arccos \left(\frac{x - 2r - l_1}{\Delta l + r} \right) + \pi \right] \quad (5)$$

$$y_{1B} = (l + r) \cos \left[\arcsin \left(\frac{x}{l + r} \right) \right] + \frac{v_m}{\omega} \arcsin \left(\frac{x}{l + r} \right) \quad (6)$$

$$y_{2C} = (\Delta l + r) \cos \left[\arcsin \left(\frac{x}{\Delta l + r} \right) \right] + \frac{v_m}{\omega} \left[\arcsin \left(\frac{x}{\Delta l + r} \right) + \pi \right] \quad (7)$$

$$y_{1D} = (l + r) \cos \left[\arcsin \left(\frac{x}{l + r} \right) \right] + \frac{v_m}{\omega} \arcsin \left(\frac{x}{l + r} \right) \quad (8)$$

where: ω is the angular velocity of the blade, (rad/s);

● **Theoretical analysis of factors influencing re-cutting area**

The cutting trajectory of the cutter blade is related to the forward speed v_m of the tractor, the angular velocity ω of the cutterhead, the length l of the cutterhead, and the radius r of the cutterhead. As shown in Fig. 3, in determining the theoretical length of the cutter blade extending out of the cutterhead, there is a reduction of the re-cutting area and the top of the cutterhead does not produce a missed cut. Therefore, to reduce the re-cutting area and avoid missed cuts at the top of neighboring blades, it is necessary to ensure that the feed distance h is equal to the length of the blade l_0 , which is determined by the forward speed v_m of the tractor and the angular velocity ω of the cutterhead together.

$$y_B = v_m \frac{\pi}{2\omega} + R \quad (9)$$

$$y_A = v_m \frac{\frac{\pi}{2} + \alpha}{\omega} + r_1 \quad (10)$$

where: y_B is the tractor moves forward distance after the blade turning at $\pi/2$ angle, (mm);
 y_A is the tractor moves forward distance after the blade turning at $(\pi/2+\alpha)$ angle, (mm);
 R is the distance from the blade top to the cutterhead center, (mm);
 r_1 is the distance from the blade root to the cutterhead center, (mm);
 α is the angle between adjacent blades, take π ;
Let $y_B=y_A$, i.e.

$$\frac{v_m \pi}{2\omega} + R = v_m \frac{\frac{\pi}{2} + \alpha}{\omega} + r_1 \quad (11)$$

$$R - r_1 = l_0 = \frac{v_m \alpha}{\omega} \quad (12)$$

The relationship between the radius r and the re-cutting area was analyzed to obtain the velocity equations of the points on the cutter, take the first derivatives of the motion equations of the points at the root and the top of the blade. To achieve alfalfa cutting successfully, the linear velocity of the blade root must be faster than the minimum velocity of unsupported cutting of alfalfa v_{min} . Taking point C as an example, its velocity equation is shown in Equation (13), and according to the velocity synthesis theorem, the absolute velocity of point C is shown in Equation (14).

$$\begin{cases} v_{xc} = (\Delta l + r)\omega \cos \phi \\ v_{yc} = -(\Delta l + r)\omega \sin \phi - v_m \end{cases} \quad (13)$$

$$v_c = \sqrt{v_{xc}^2 + v_{yc}^2} = \sqrt{(\Delta l + r)^2 \omega^2 - 2v_m(\Delta l + r)\omega \sin \phi + v_m^2} \quad (14)$$

The angle ϕ is $\pi/2$ when point C is rotated to the horizontal position, point C has the minimum absolute velocity at this time. For a determined blade length l_0 and cutterhead angular velocity ω , i.e.:

$$r \geq \frac{v_m + v_{min}}{\omega} \quad (15)$$

At the determined forward speed of the tractor, the angular velocity of the cutterhead, and the blade length, the trajectory equation of the cutterhead was integrated, and the cutting area as a function of the cutterhead radius was obtained, as shown in Fig. 3. Due to the complexity of solving the intersection of the blade trajectory, it is difficult to directly solve all the re-cutting area. To represent the relationship between the cutterhead radius and the re-cutting area intuitively, take two identical intervals between the cutterhead center and the edge of the cutterhead, the area between the two curves under different cutterhead radius r was calculated.

$$S_1 = \int_{-20}^0 (y_{1D} - y_{2C}) dx \quad (16)$$

$$S_2 = \int_{-r}^{-r+20} (y_{1D} - y_{2C}) dx \quad (17)$$

$$S_i = \frac{S_1}{S_2}, \quad \left(r \geq \frac{v_m + v_{min}}{\omega} - \Delta l \right) \quad (18)$$

where: S_1 is the area between y_{1D} and y_{2C} on the interval $[-20, 0]$ mm, (mm²);

S_2 is the area between y_{1D} and y_{2C} on the interval $[-r, -r+20]$ mm, (mm²).

$$Y_{2C} = \int y_{2C} dx = \frac{(\Delta l + r)^2 \arcsin\left(\frac{x}{\Delta l + r}\right)}{2} + xr \arcsin\left(\frac{x}{\Delta l + r}\right) + \frac{x\sqrt{(\Delta l + r)^2 - x^2}}{2} + \frac{v_m(\Delta l + r)}{\omega} \sqrt{1 - \left(\frac{x}{\Delta l + r}\right)^2} + \frac{\pi v_m x}{\omega} \quad (19)$$

$$Y_{1D} = \int y_{1D} dx = \frac{(l + r)^2 \arcsin\left(\frac{x}{l + r}\right)}{2} + xr \arcsin\left(\frac{x}{l + r}\right) + \frac{x\sqrt{(l + r)^2 - x^2}}{2} + \frac{v_m(l + r)}{\omega} \sqrt{1 - \left(\frac{x}{l + r}\right)^2} \quad (20)$$

The relationship between cutterhead radius and re-cutting area under different tractor speeds and cutterhead angular velocity is shown in Fig. 4. The re-cutting area is positively correlated with the cutter feed distance, and small feed distance can reduce the re-cutting area of the cutterhead, but the slower tractor speed, and faster cutterhead angular velocity will increase the power consumption; in the determined feed distance, the re-cutting area is positively correlated with the cutterhead radius, and the reduction of the radius can reduce the re-cutting area of both two sides of the cutterhead, and the cutting effect will be improved.

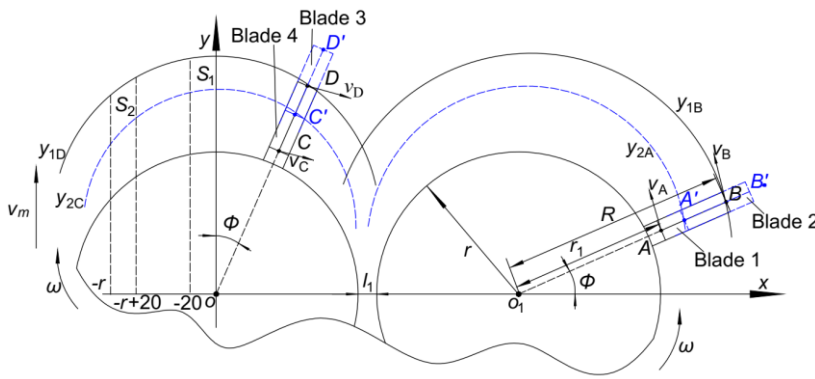


Fig. 3 - Motion parameters diagram of blade

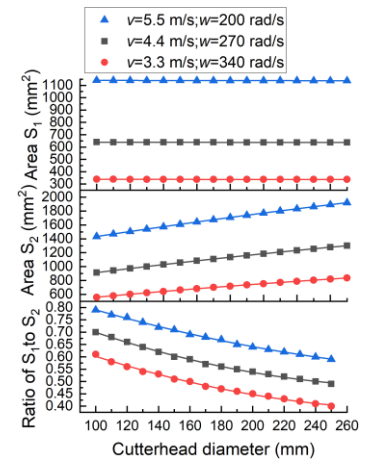


Fig. 4 - Relationship between cutter radius and re-cutting area

Response surface Box-Behnken experiment

● **Experiment equipment and materials**

A cutting test bench was built to explore the influence on the cutting effect of the cutting parameters. The test bench mainly consists of a suspension frame, transmission system, lifting components, and cutterhead assembly, as shown in Fig. 5.

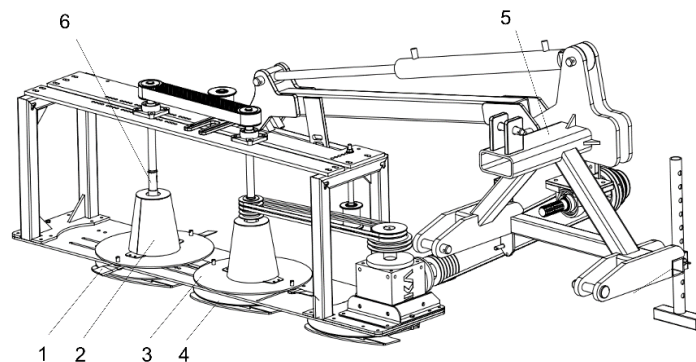


Fig. 5 - Structure diagram of cutting test bench

1 - blade; 2 - drum; 3 - cutterhead; 4 - slide palm; 5 - suspension frame; 6 - cutterhead mounting shaft

A response surface experiment was carried out by using the cutting test bench to optimize the cutting parameters of the disc cutter. The experiment was conducted in October 2022 at the alfalfa planting test field of the National Forage Industry Technology System of Qingdao Agricultural University, (Jiaozhou, Qingdao, Shandong Province, China). The surface of the field was levelled, and the alfalfa cultivar was ‘Zhongmu No. 3’. The alfalfa was in the late bud stage and early flowering stage during the experiment, with good growth and no collapse phenomenon. The height of alfalfa plants was measured to be about 400–600 mm.

● **Experimental factors and levels**

Three experiment factors were selected: cutterhead diameter X_1 , blade twist angle X_2 , and cutting inclination angle X_3 . The cutterhead rotation speed of 2640 r/min and tractor speed of 4.4 m/s were determined through the pre-test before carrying out the Box-Behnken test, three factor levels are the cutterhead diameter of 350-480 mm, the blade twist angle of 0-8 °, the cutting inclination angle of 0-8 °, respectively. The factor level codes are shown in Table 1.

Table 1

| Coding of factor levels | | | |
|-------------------------|-----------------------------------|--------------------------------|--|
| Level | Cutterhead diameter X_1 (mm) | Blade twist angle X_2 (°) | Cutting inclination angle X_3 (°) |
| -1 | 350 | 0 | 0 |
| 0 | 415 | 4 | 4 |
| 1 | 480 | 8 | 8 |

● Experimental indicators

The test indicators were selected as loss rate Y_1 and re-cutting rate Y_2 , each test indicator was calculated as follows:

(1) loss rate

The total loss rate for harvesting is calculated according to Equation (21):

$$S = S_z + S_l \quad (21)$$

where: S is the total harvest loss rate;

S_z is overcutting loss rate (the ratio of the stubble mass overcutting to stubble mass required left);

S_l is missed cutting loss rate (the ratio of the stubble mass missed cutting to stubble mass required left);

(2) re-cutting rate

The re-cutting rate is the ratio of the mass of headless nodes per unit area to the mass of alfalfa to be harvested, it is calculated according to Equation (22):

$$S_e = \frac{g_w}{g_z} \quad (22)$$

where: S_e is the re-cutting rate;

g_w is the actual mass of headless grass nodes harvested per unit area, g/m^2 ;

g_z is the total mass of harvested alfalfa per unit area, g/m^2 ;

Measurements of operational indicators at the test site are shown in Fig. 6:



Fig. 6 - Situation of experimental field
a) cutting parameter adjustment; b) working process

RESULTS

Experimental results

Based on the Box-Behnken quadratic regression orthogonal test design scheme, including 17 test points, including 12 analytical factors and 5 zero estimation errors, the test scheme and test results are shown in Table 2.

Table 2

| Quadratic regression orthogonal response surface test results | | | | | | |
|---|-------|-------|-------|--------------------|--------------------------|--|
| Experimental number | X_1 | X_2 | X_3 | Loss rate $Y_1/\%$ | Re-cutting rate $Y_2/\%$ | |
| 1 | 350 | 4 | 8 | 3.63 | 1.32 | |
| 2 | 350 | 0 | 4 | 3.89 | 1.51 | |
| 3 | 350 | 8 | 4 | 3.84 | 1.26 | |
| 4 | 350 | 4 | 0 | 3.76 | 1.46 | |
| 5 | 415 | 4 | 4 | 3.08 | 1.41 | |
| 6 | 415 | 4 | 4 | 3.05 | 1.4 | |
| 7 | 415 | 0 | 8 | 3.79 | 1.49 | |
| 8 | 415 | 4 | 4 | 3.09 | 1.43 | |
| 9 | 415 | 8 | 0 | 3.85 | 1.54 | |
| 10 | 415 | 8 | 8 | 3.72 | 1.34 | |
| 11 | 415 | 0 | 0 | 3.93 | 1.71 | |
| 12 | 415 | 4 | 4 | 3.09 | 1.45 | |
| 13 | 415 | 4 | 4 | 3.1 | 1.42 | |
| 14 | 480 | 4 | 0 | 3.94 | 1.7 | |
| 15 | 480 | 8 | 4 | 4 | 1.47 | |
| 16 | 480 | 4 | 8 | 3.8 | 1.49 | |
| 17 | 480 | 0 | 4 | 4.26 | 1.57 | |

● **Regression model**

According to the sample data in Table 2, the analysis of variance of the quadratic regression equation of the loss rate Y_1 and re-cutting rate Y_2 on three factors was established through Design-Expert 13 software, and the results are shown in Table 3.

Table 3

| Analysis of variance of experimental results | | | | | | | | |
|--|-----------|----|---------|----------|-----------------|----|---------|-----------|
| Source | Loss rate | | | | Re-cutting rate | | | |
| | Squares | DF | F value | P value | Squares | DF | F value | P value |
| Models | 2.45 | 9 | 218.55 | <0.001** | 0.2 | 9 | 36.71 | <0.0001** |
| X_1 | 0.0968 | 1 | 77.62 | <0.001** | 0.06 | 1 | 86.92 | <0.0001** |
| X_2 | 0.0264 | 1 | 21.21 | 0.002** | 0.0561 | 1 | 84.38 | <0.0001** |
| X_3 | 0.0364 | 1 | 29.23 | 0.001** | 0.0741 | 1 | 111.45 | <0.0001** |
| X_1X_2 | 0.011 | 1 | 8.84 | 0.0207* | 0.0056 | 1 | 8.46 | 0.0227* |
| X_1X_3 | 0 | 1 | 0.02 | 0.8914 | 0.0012 | 1 | 1.84 | 0.2168 |
| X_2X_3 | 0 | 1 | 0.02 | 0.8914 | 0.0001 | 1 | 0.1504 | 0.7097 |
| X_1^2 | 0.8068 | 1 | 646.95 | <0.001** | 0.0001 | 1 | 0.0142 | 0.9083 |
| X_2^2 | 0.961 | 1 | 770.59 | <0.001** | 0.0035 | 1 | 5.32 | 0.0544 |
| X_3^2 | 0.2907 | 1 | 233.08 | <0.001** | 0.02 | 1 | 30.14 | 0.0009** |
| Lack of Fit | 0.0072 | 3 | 6.53 | 0.0507 | 0.0032 | 3 | 2.86 | 0.1681 |
| Pure Error | 0.0015 | 4 | | | 0.0015 | 4 | | |
| Cor Total | 2.46 | 16 | | | 0.2244 | 16 | | |

Note: $P < 0.01$ (extremely significant, **), $P < 0.05$ (significant, *)

The P-values of the response surface models for loss rate Y_1 and re-cutting rate Y_2 are less than 0.001 from the analysis in Table 3, indicating that the regression models are highly significant and statistically significant; the P-values of the lack of fit terms are all greater than 0.05, indicating that the regression equations are well fitted: their coefficients of determination, R^2 , are 0.9965 and 0.9793, respectively, indicating that more than 95% of the response values can be explained by these 2 models. Therefore, the model can be used to optimize the cutting parameters.

The magnitude of the P-value of each parameter reflects its role in influencing the regression equation. The model insignificant regression terms were removed and the loss rate Y_1 and re-cutting rate Y_2 models were optimized as follow:

$$Y_1 = 3.08 + 0.11X_1 - 0.058X_2 - 0.068X_3 - 0.053X_1X_2 + 0.438X_1^2 + 0.478X_2^2 + 0.263X_3^2 \tag{23}$$

$$Y_2 = 1.44 + 0.085X_1 - 0.084X_2 - 0.096X_3 - 0.038X_1X_2 + 0.070X_3^2 \tag{24}$$

Based on the results of the regression equation analysis, the response surface was plotted using Design Expert software.

● **Analysis of the influence of interaction factors on cutting effect**

From the response graph of the influence of each factor on the loss rate Y_1 , it can be learned that the change rule of the response surface is consistent with the results of the ANOVA of the regression equation and the model, and the overall trend of the influence of the cutterhead diameter X_1 , the blade twist angle X_2 and the cutting inclination angle X_3 are moderate, the loss rate Y_1 is small. The main reason is that the cutterhead diameter affects the linear velocity; if the linear velocity is too small or too large, it will cause cutting loss; similarly, the cutter blade twist angle X_2 and cutting inclination angle X_3 determine the movement state of alfalfa after being cut and the cutting inclination angle, the three should be moderate to ensure the lower loss rate of harvesting.

From the factors on the re-cutting rate Y_2 response graph can be learned, the change rule of the response surface and the regression equation analysis of variance results and the model is consistent, the overall impact of the trend for the smaller the cutterhead diameter, the larger the cutterhead twist angle, and the larger the cutting inclination angle X_3 , the smaller the re-cutting rate Y_2 . The main reasons are: when the cutterhead diameter is bigger, the cutterhead linear velocity is bigger, and the linear velocity is too big to cause

excessive cutting and leaf loss; the bigger the blade twist angle is, the better the effect of the cutting inclination angle is on the lifting of the stalks, and avoiding the stalks from being cut repeatedly by the cutterhead; and the bigger cutting inclination angle is benefit for the alfalfa's feeding and flow.

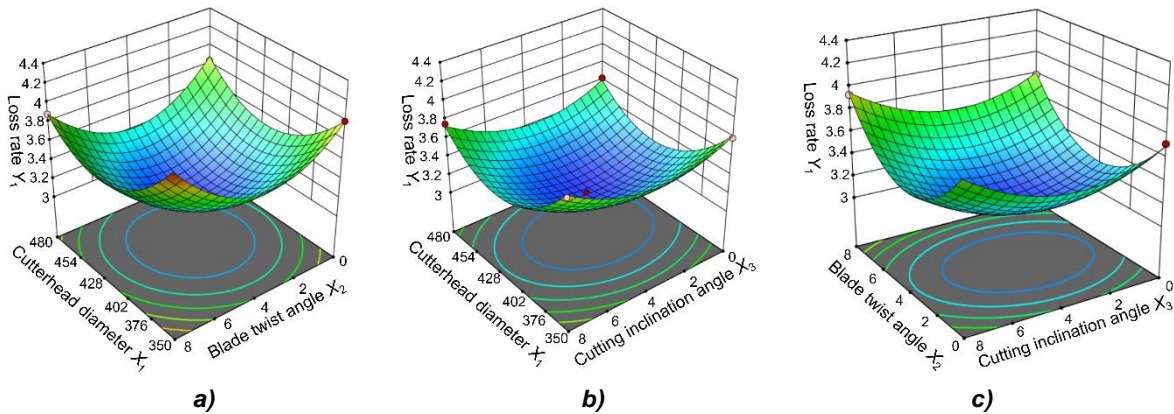


Fig. 7 - Response surface for double factors and loss rate
 a) X_1 and X_2 interaction; b) X_1 and X_3 interaction; c) X_2 and X_3 interaction

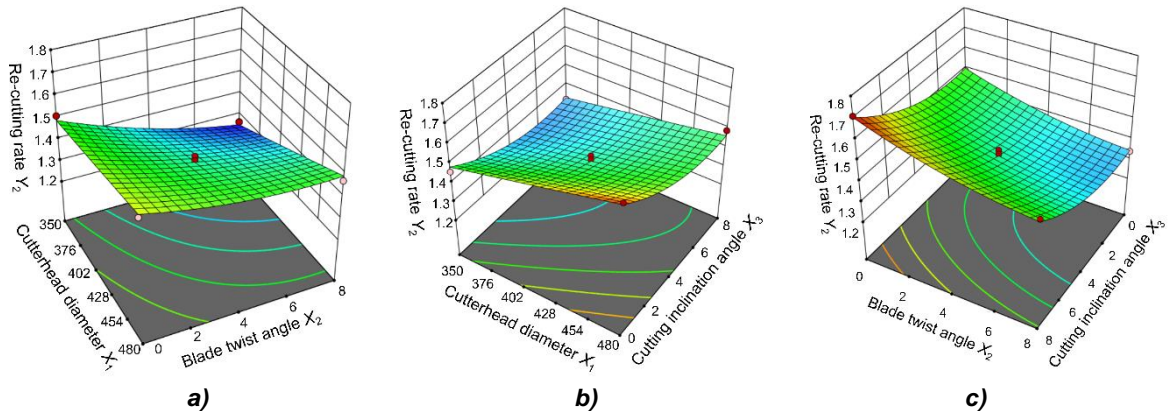


Fig. 8 - Response surface for double factors and re-cutting rate
 a) X_1 and X_2 interaction; b) X_1 and X_3 interaction; c) X_2 and X_3 interaction

● **Parameter optimization and verification experiments**

To reduce the loss rate and re-cutting rate, the alfalfa harvesting standards (minimum loss rate and re-cutting rate $\leq 1.5\%$) were taken as the parameter optimization conditions, and the optimal parameter combinations were solved by using the Design-Expert software; the solution methods were as follows:

Objective function:
$$\begin{cases} f = \min Y_1 \\ f = Y_2 \leq 1.5\% \end{cases} \quad (25)$$

Boundary constraint function:
$$\begin{cases} 350 \leq X_1 \leq 480 \\ 0 \leq X_2 \leq 8 \\ 0 \leq X_3 \leq 8 \end{cases} \quad (26)$$

Design-Expert software was used to solve the optimization of each parameter. The optimal parameter combinations were obtained as cutterhead diameter (X_1) 407.04 mm, blade twist angle (X_2) 4.21°, and cutting inclination angle (X_3) 4.51°, which resulted in a loss rate of 3.07% and a re-cutting rate of 1.40%.

Verification test

To verify the optimal parameter combinations solved by the software, the verification test was carried out, and the test was repeated three times. Considering the rationality of mechanical structure and the convenience of measurement, the cutterhead diameter was set to 407 mm, the blade twist angle was set to 4°, and the cutting inclination angle was 4.5°. The results of the validation test are shown in Fig. 9, the alfalfa stubble is cut flush, the stubble height is following the standard, and the phenomenon of re-cutting and missed cutting is less.



Fig. 9 - Verification test effect
 a) mowed alfalfa b) alfalfa stubble

The results of the verification test are shown in Table 4. They show that under the optimal parameter combination, the average value of the loss rate is 3.13% (with a difference of 0.06% from the software solution value), less than national standard requirements for alfalfa harvesting re-cutting rate (1.5%), the standard deviation is 7.72%, and the coefficient of variation is 2.47%; the average value of the re-cutting rate is 1.48% (with a difference of 0.08% from the software solution value), less than national standard requirements for alfalfa harvesting loss rate (4%), the standard deviation is 15%, and the coefficient of variation is 10.14%; the harvesting effect is ideal, and optimization effect is obvious.

Table 4

| Results of verification test | | | | | |
|------------------------------|------|------|------|------|-------|
| Experimental indicators | 1 | 2 | 3 | S.D. | C.V. |
| Loss rate $Y_1(\%)$ | 3.21 | 3.10 | 3.08 | 7.72 | 2.47 |
| Re-cutting rate $Y_2(\%)$ | 1.40 | 1.46 | 1.59 | 15 | 10.14 |

CONCLUSIONS

(1) The theoretical study of the disc-type cutting system was carried out, the cutting area of the cutter was analyzed and mapped by kinematics theory, and the effects of feed distance and cutterhead radius on the re-cutting area of the cutter under high-speed harvesting were studied.

(2) A set of parametrically adjustable cutting test bench was built, and alfalfa field high-speed harvesting tests were conducted using the test bench. The test results showed that the order of significance of the factors affecting the loss rate was cutterhead diameter, cutting inclination angle, and blade twist angle, the effect of each factor on the re-cutting rate was highly significant.

(3) The optimal parameter combination of the disc cutter under high-speed harvesting was 407.04 mm for the cutterhead diameter, 4.21° for the blade twist angle, and 4.51° for the cutting inclination angle; the verification test showed that the average value of the loss rate under the optimal parameter combination was 3.13% and the average value of the re-cutting rate was 1.48%, which achieved the low-loss cutting effect under high-speed harvesting of the disc-type cutter.

ACKNOWLEDGEMENT

This work was supported by “Shandong Province Science and Technology-based Small and Medium-sized Enterprises Innovation Capacity Enhancement Project (2022TSGC2508) and China Forage and Grass Research System (CARS-34-21)”

REFERENCES

- [1] Chen, L., Yu, Z., Mao, P., Sun, H., (2015), Development situation of forage grass industry and current status of forage quality safety in China(中国饲草产业发展概况及饲草料质量安全现状). *Feed Industry*, vol. 36, no. 5, pp: 56-60, Jilin/China.
- [2] Chandra, P.G., Moses, F.O., (1992), Design of the Revolving Knife-type Sugarcane Base cutter. *Transactions of the ASABE*, vol. 35, no. 6, pp:1747-1752, United States.
- [3] Du, Z., Li, D., Ji, J., Zhang, L., Li, X., Wang, H., (2022), Bionic Optimization Design and Experiment of Reciprocating Cutting System on Single-Row Tea Harvester. *Agronomy (Basel)*, vol. 12, no. 6, pp: 1309, Switzerland

- [4] Dong, R., (2020), *Simulation and Experimental Study on Cutting Process of Silage Corn Harvesting Header* (青贮玉米收获割台切割过程仿真及试验研究), MSc Thesis, Jilin University, Jilin/China.
- [5] Fu, Z., (2014), *Study on Cutting System for Two Discs Mower Conditioner* (双圆盘式刈割压扁机切割系统研究), PhD Thesis, China Agricultural University, Beijing/China.
- [6] Fu, Z., Wang, D., Li, W., Huang, Y., (2018), Design and Experiment of Two-disc Rotary Mower of Alfalfa (双圆盘式苜蓿旋转切割器设计与试验). *Transactions of the Chinese Society for Agricultural Machinery*, vol. 49, pp: 214-220, Beijing/China.
- [7] Guo, T., Xue, B., Bai, J., Sun, Q., (2019), Discussion of the present situation of China's forage grass industry development: An example using alfalfa and oats (刍议中国牧草产业发展现状—以苜蓿、燕麦为例). *Pratacultural Science*, vol. 36, no. 5 pp: 1466-1474, Gansu/China.
- [8] Gan, H., Mathanker, S., Momin, A., Kuhns, B., Stoffel, N., Hansen, A., Grift, T., (2018), Effects of three cutting blade designs on energy consumption during mowing-conditioning of *Miscanthus Giganteus*. *Biomass and Bioenergy*, vol. 109, pp: 166-171, United Kingdom.
- [9] Hou, J., Bai, J., Yao, E., Zhu, H., (2020), Design and Parameter Optimization of Disc Type Cutting Device for Castor Stem. *IEEE Access*, vol. 8, pp: 191152-191162, United States.
- [10] Jiang, Y., Zhang, J., Nan, Z., Wang, L., (2016), Competitiveness analysis of alfalfa international trade in China (中国苜蓿国际贸易竞争力分析). *Pratacultural Science*, vol. 33, no. 2, pp: 322-329, Gansu/China.
- [11] Johnson, P.C., Clementson, C.L., Mathanker, S.K., Grift, T., Hansen, A., (2012), Cutting energy characteristics of *Miscanthus x giganteus* stems with varying oblique angle and cutting speed. *Biosystems Engineering*, vol. 112, no. 1, pp: 42-48, United States.
- [12] Li, X., Yin, X., Zhou, X., Li, P., (2020), Countermeasures and Suggestions for High Quality Development of Forage Industry in China (我国饲草产业高质量发展的对策和建议). *ACTA AGRESTIA SINICA*, vol. 28, no. 4, pp: 889-894, Beijing/China.
- [13] Li, Z., (2014), Design and Experiments of the Rape Disc-cutter (圆盘式油菜切割器的设计与试验). MSc Thesis, Hunan Agricultural University, Hunan/China.
- [14] Otroshko S.A., Shevtsov A.V., Sharikov N.D., (2021), An innovative technical solution to the issue of conditioning forage grasses. *IOP conference series Earth and environmental science*, vol. 901, no. 1, ISSN: 1755-1307, pp: 012049, United Kingdom. DOI: 10.1088/1755-1315/901/1/012049
- [15] Song, Y., Wang, Z., Wu, K., Li, F., Song, Z., Yang, X., (2020), Fabrication of Self-sharpening Blades with Metaloceramics Materials and Low-damaged Cutting Mechanism of Alfalfa (金属陶瓷自磨刃割刀对苜蓿低损伤切割机理分析). *Transactions of the Chinese Society for Agricultural Machinery*, vol. 51, no. 10, pp: 421-426, 309 Beijing/China.
- [16] Shi, Y., Chen, M., Wang, X., Zhang, Y., Odhiambo, M., (2017), Dynamic Simulation and Experiments on *Artemisia selengensis* Orderly Harvester Cutter (芦蒿有序收获机切割器动力学仿真与试验). *Transactions of the Chinese Society for Agricultural Machinery*, vol. 48, no. 2, pp: 110-116, Beijing/China.
- [17] Vasiliev N., Kudryavtsev A., Golubev A., Vyacheslav, V., (2021), Research Results of the Modified Working Tool of the Combined Rotary Mower. *Agricultural Engineering (Moscow)*, no. 3, pp: 10-18, Moscow/Russia.
- [18] Wu, B., (2017), *Optimization and Experimental Study on Mechanical System of Alfalfa Mower Conditioner* (苜蓿刈割压扁收获机械系统的优化和试验研究). PhD Thesis, China Agricultural University, Beijing/China.
- [19] Wang, D., He, C., Wu, H., You, Y., (2017), Review of Alfalfa Full-mechanized Production Technology (苜蓿生产全程机械化技术研究现状与发展分析). *Transactions of the Chinese Society for Agricultural Machinery*, vol. 48, no. 8, pp: 1-25, Beijing/China.
- [20] Xie, S., Zhao, H., Yang, S., Xie, Q. Yang, M., (2020), Design, Analysis and Test of Small Rotary Lawn Mower of Single-Disc Type. *INMATEH Agricultural Engineering*, vol. 62, no. 3, pp: 89-98, Cuernavaca/Mexico.
- [21] Zhao, M., Zhang, N., Yang, T., Shi, Y., (2014), Design and Experiment of Virtual Prototype of Double Disc Mower Cutter (双圆盘割草机切割器虚拟样机设计与试验). *Transactions of the Chinese Society for Agricultural Machinery*, vol. 45, no. 8, pp: 101-105, Beijing/China.
- [22] Zhu, H., Jin, J., (2022), An Empirical Analysis on the Development of Alfalfa Forage Industry from the Perspective of Grain Security. *Animal Husbandry and Feed Science*, vol. 43, no. 4, pp: 73-79, United States.
- [23] Zhang, C., Chen, L., Xia, J., Zhang, J., (2019) Effects of blade sliding cutting angle and stem level on cutting energy of rice stems. *International Journal of Agricultural and Biological Engineering*, vol. 6, no. 12, pp: 75-81, United States.

DETECTION METHOD OF CORN LEAF DISEASES BASED ON CA-YOLOv8

/ 基于 CA-YOLOv8 的玉米叶病检测方法

Miao XU¹⁾, Xuan ZHANG^{*2)}, Na MA¹⁾, Yanwen LI¹⁾¹⁾ College of Information Science and Engineering, Shanxi Agricultural University, Taigu/ China;²⁾ College of Agricultural Engineering, Shanxi Agricultural University, Taigu/ China;Tel: +86 18434764827; E-mail: zhangxuan727@126.comDOI: <https://doi.org/10.35633/inmateh-73-11>**Keywords:** corn leaf, disease detection, YOLOv8, attention mechanism, Coordinate Attention(CA)**ABSTRACT**

In order to achieve efficient and accurate detection of common corn leaf diseases such as leaf blight, gray spot disease, and rust, a corn leaf disease detection method based on CA-YOLOv8 was proposed. In this method, the Coordinate Attention(CA) attention mechanism was added after the feature map output from the Neck part to enhance the feature extraction capability of the model. The experimental results showed that the precision, recall and mean average precision(mAP) of the CA-YOLOv8 model on the test set were 94.08%, 90.53% and 97.38%, respectively. Compared with the YOLOv8, YOLOv8+SE and YOLOv8+CBAM models, the mAP was improved by 2.15, 0.86 and 2.35 percentage points, respectively. Compared with Faster R-CNN, YOLOv5s, YOLOv7, and YOLOv8 models, the mAP has increased by 63.53, 29.24, 3.21, and 2.15 percentage points, respectively. The study showed that the CA-YOLOv8 model can provide a technical reference for the development of a portable intelligent corn leaf disease detection system.

摘要

为了实现以叶枯病、灰斑病、锈病等玉米常见叶病的高效准确检测，提出了一种 CA-YOLOv8 的玉米叶病检测方法。该方法在 Neck 部分输出的特征图之后加入 CA 注意力机制，以便提升模型的特征提取能力。试验结果表明，CA-YOLOv8 模型在测试集上的精确率、召回率和平均精度均值分别为 94.08%、90.53% 和 97.38%。对比 YOLOv8、YOLOv8+SE 和 YOLOv8+CBAM 模型，平均精度均值 mAP 分别提升了 2.15、0.86、2.35 个百分点。与 Faster R-CNN、YOLOv5、YOLOv7 和 YOLOv8 模型相比，mAP 分别提升了 63.53、29.24、3.21 和 2.15 个百分点。研究表明，CA-YOLOv8 模型能够为便携式智能玉米叶病检测系统开发提供技术参考。

INTRODUCTION

Corn is a globally important crop for food, feed and industrial raw materials, and the stabilization of corn production plays an important role in food security, farmers' incomes and the national economy (Song et al., 2023; Cui et al., 2023). However, corn diseases seriously affect corn production (Zhang et al., 2021). There are many types of corn diseases worldwide that are difficult to identify, among which corn gray spot, corn leaf blight and corn rust are the most common (Zibani et al., 2022). The traditional methods for detecting corn leaf disease mainly rely on manual observation and identification, which are not only inefficient but also limited by manual experience and skills (Song et al., 2023). Therefore, efficient and accurate detection of corn leaf disease is crucial for yield improvement.

In recent years, with the generation of large-scale labelled data and the rapid improvement of computer processing capabilities, deep learning technology has achieved rapid development in the field of plant disease detection (Yang et al., 2023; Zhang et al., 2024). Due to its high extraction of high-dimensional features from targets, the effect of plant disease detection in complex situations has been significantly improved. At present, plant disease detection algorithms based on deep learning mainly include multi-stage object detection algorithms represented by Faster R-CNN (Ren et al., 2017) and single-stage object detection algorithms represented by YOLO series (Shao et al., 2022).

Sun et al. proposed a multi-scale feature fusion instance detection method based on convolutional neural network for maize leaf blight detection with a mAP of 91.83%, which is about 20% higher than the original SSD algorithm (Sun et al., 2020). Zhang et al. optimized convolutional neural network using Multi-Activation Function (MAF) module to detect maize leaf disease, and used transfer learning and warm-up methods to accelerate training, improving the accuracy of traditional artificial intelligence methods (Zhang et al., 2021).

Chen et al. proposed a lightweight corn disease recognition model, DFCANet (Dual Fusion Blocks with Coordinate Attention Networks), with an average recognition accuracy of 98.47% (Chen et al., 2022). Bi et al. proposed the CD-Mobilenetv3 model to identify corn leaf disease, replacing the SE module of original model with the EAC module, and introducing dilated convolution into the model. The accuracy on open-source datasets reached as high as 98.23% (Bi et al., 2023). Dai et al. (2023) proposed a multi-task deep-learning-based system for enhanced precision detection and diagnosis of corn leaf diseases (MTDL-EPDCLD) to enhance the detection and diagnosis of corn leaf disease, and developed a mobile application utilizing the Q_t framework. Song et al., (2023), proposed a high-accuracy detection method based on Attention Generative Adversarial Network (Attention-GAN) and few-shot learning. GAN are used to expand data and generate more training samples. An attention mechanism was introduced to enable the model to focus more on important parts of the image, thereby improving model performance.

The above research indicates that deep learning has achieved certain results in the detection of corn leaf disease. However, most methods with high detection accuracy have problems such as multiple parameters, high computational power, and slow detection speed. Methods with low computational complexity and fast detection speed have lower detection accuracy, and the network's generalization and adaptability to complex environments are insufficient. YOLOv8 is the latest version of the YOLO (You Only Look Once) series of object detection algorithms released by Ultralytics. Compared to previous versions, YOLOv8 has faster inference speed, higher accuracy, and is easier to train and adjust (Hussain et al., 2023). Therefore, this study takes YOLOv8 as the basic model and improves it to realize efficient and accurate detection of corn leaf disease, which can not only ensure the stability of corn production, but also provide technical support for the development of portable intelligent corn leaf disease detection system.

MATERIALS AND METHODS

Dataset construction

The corn leaf disease images used in this study were from the publicly available dataset PlantDoc (<https://github.com/pratikkayal/PlantDoc-Dataset>) (Singh et al., 2020), which includes corn gray leaf spot, corn leaf blight, and corn rust. After screening, 70 corn gray spot images, 116 corn leaf blight images, and 114 corn rust images were obtained. Fig. 1 shows sample images of different leaf diseases in the dataset.

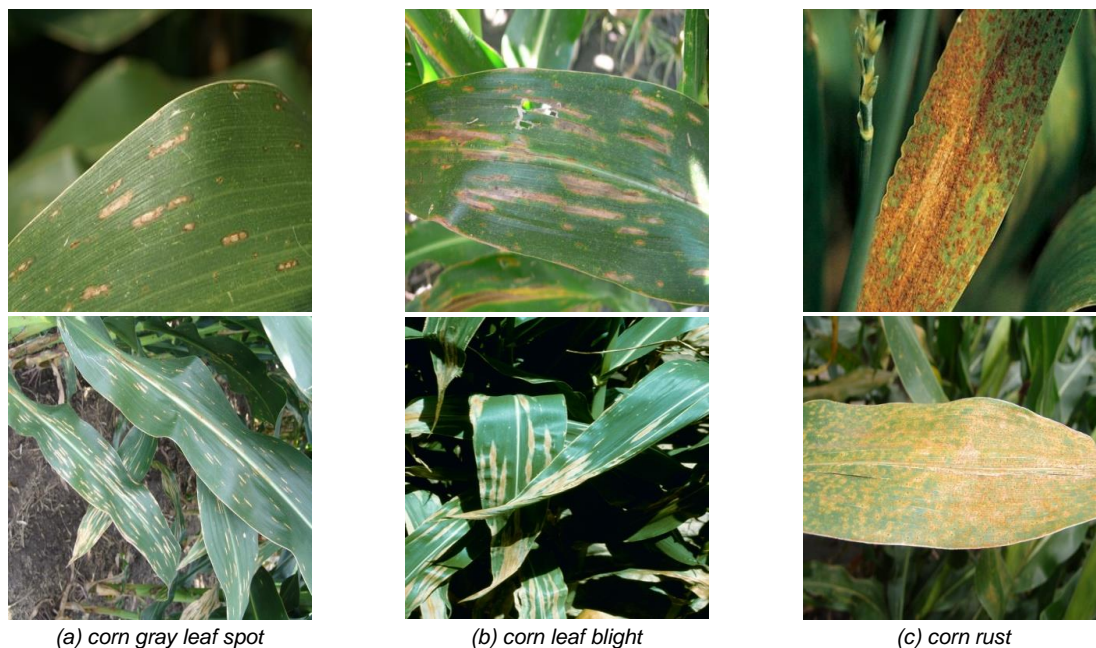


Fig. 1 - Sample images of corn leaf disease

Due to the insufficient sample size of the dataset, the model cannot converge during the training process. In order to improve the effectiveness of the network training model and enhance its generalization ability, and prevent overfitting caused by insufficient training samples, image enhancement methods were used to expand the dataset, resulting in 1470 images of corn diseases including 500 images of corn gray spot, 486 images of corn leaf blight, and 484 images of corn rust. The training set, validation set and test set were divided according to the ratio of 8:1:1, and the annotation number of different leaf diseases in the divided dataset is shown in Table 1.

Table 1

Annotation number of different corn diseases

| Disease | Training set | Validation set | Test set | Total |
|---------------------|--------------|----------------|------------|-------------|
| corn gray leaf spot | 529 | 56 | 72 | 657 |
| corn leaf blight | 813 | 71 | 96 | 980 |
| corn rust | 453 | 56 | 50 | 559 |
| Total | 1795 | 183 | 218 | 2196 |

CA-YOLOv8 model

YOLOv8 belongs to the single-stage object detection algorithm, which only needs to extract features once to achieve object detection. Compared with previous networks, YOLOv8 improves the detection speed and accuracy while reducing the number of network parameters. For corn leaf disease images in different backgrounds, a lightweight version of YOLOv8n was selected as the base network for improvement. In this paper, CA (Coordinate attention) mechanism is added after the feature map output of the Neck part to improve the ability of the model to extract features and improve the detection accuracy of the model. The network structure name is defined as CA-YOLOv8. The CA-YOLOv8 network structure is shown in Fig. 2.

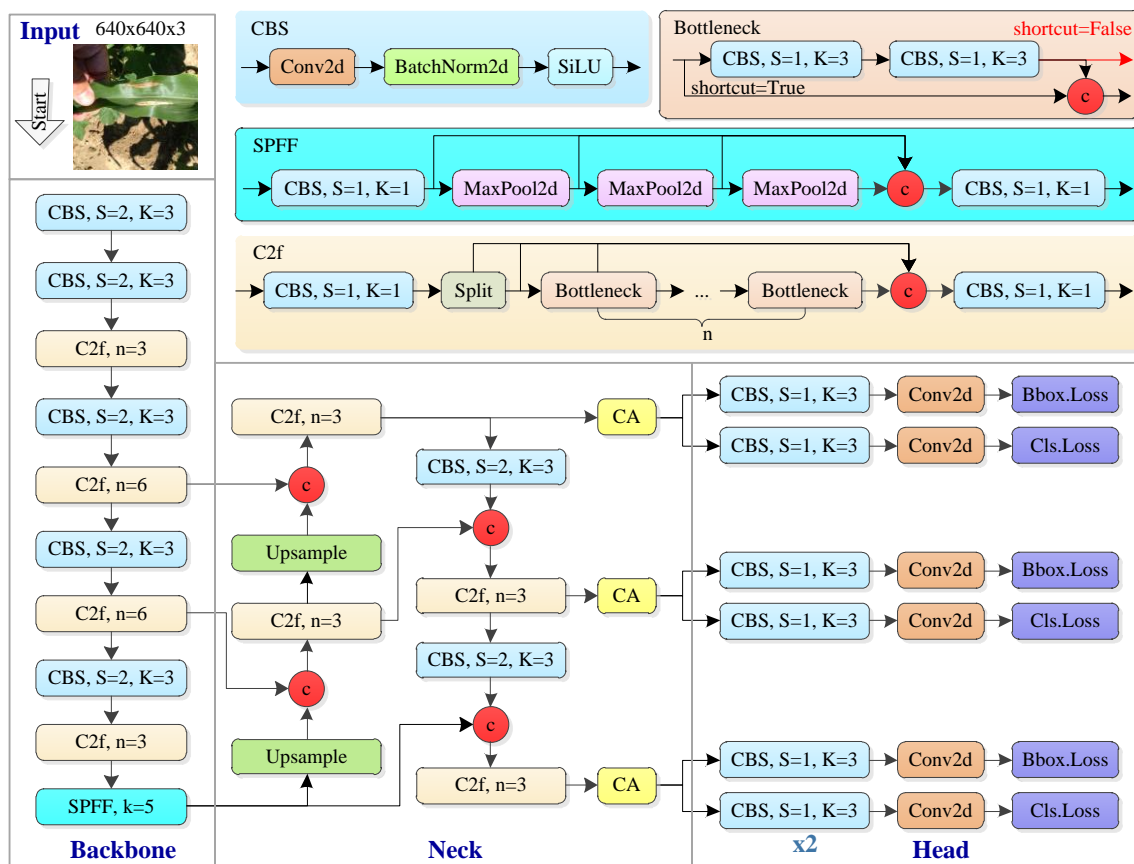


Fig. 2 - CA-YOLOv8 network structure

YOLOv8 model

The YOLOv8 network model uses the Backbone for feature extraction, the Neck for feature fusion, and the Head for detection and recognition. YOLOv8 integrates many excellent technologies in real-time object detection, and its main features are as follows:

(1) The input end uses an adaptive scaling method to adjust the image size to 640*640, while using mosaic data augmentation to improve model robustness.

(2) The backbone consists of CBS module, C2f module, and SPFF module using the CSP concept. The CBS module is a combination of convolution, normalization, and SiLU activation function, which can improve model stability, accelerate convergence speed, and prevent gradient disappearance.

Compared to the C3 module, C2f adds skip connections and additional Split operations, allowing the model to obtain richer gradient flow information. SPFF adaptively fuses feature information of various scales through pooling and convolution operations, which can enhance the feature extraction ability of the model.

- (3) The neck uses the idea of PAN-FPN to remove the convolution in the upsampling stage of PAN-FPN in YOLOV5, and replaces the C3 module with the C2f module.
- (4) The head uses a Decoupled-Head structure to separate the classification and detection heads, capturing information on targets of different scales and improving the accuracy of object detection.

CA attention mechanism

Attention mechanism can help neural networks focus on information that is more critical to the current task, reduce attention to other information, and thus improve the performance and accuracy of the model. Squeeze and Excitation Networks (SENet) learn adaptive channel weights to make the model focus more on useful channel information (Hu et al., 2020), but only consider attention in the channel dimension and cannot capture attention in the spatial dimension. The Convolutional Block Attention Module (CBAM) extracts positional attention information through large-scale kernel convolution, but convolution can only extract local relationships and lacks the ability to extract remote relationships (Woo et al., 2018). Moreover, paying attention to images from both spatial and channel perspectives requires more computational resources and higher complexity. Coordinate Attention (CA) can encode horizontal and vertical position information into channel attention (Hou et al., 2021), enabling mobile networks to focus on a wide range of position information without excessive computational complexity. Fig. 3 shows a comparison diagram of different attention modules.

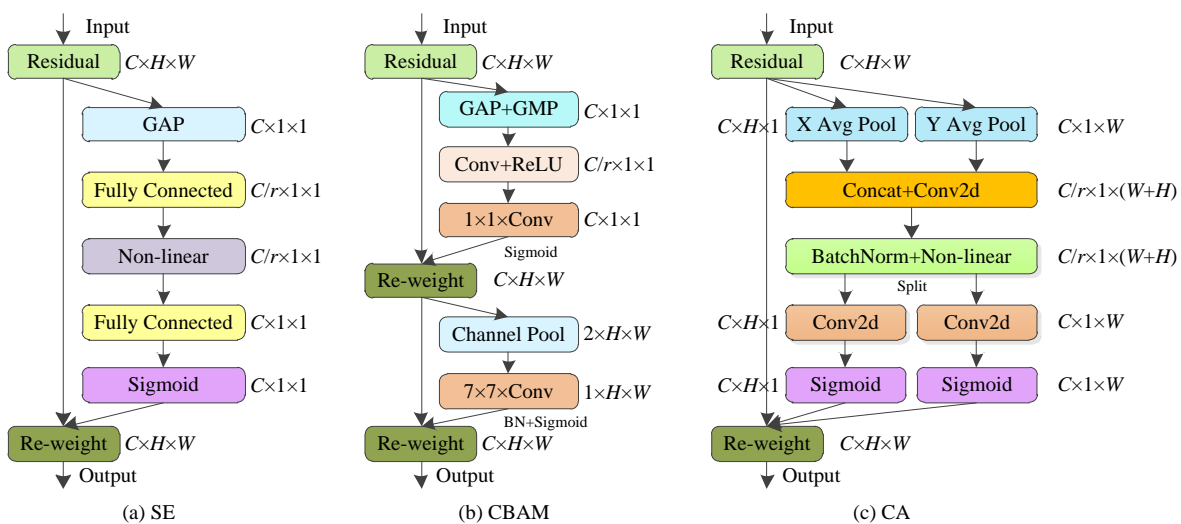


Fig. 3 - Comparison of different attention modules

C, H, W – the number of channels, height, and width of the feature map; GAP – Global Avg Pool; GMP – Global Max Pool; X Avg Pool – one-dimensional horizontal global pooling; Y Avg Pool – one-dimensional vertical global pooling.

The input of the CA attention mechanism is usually a feature map $[C, H, W]$, which is usually the output of a certain layer in a convolutional neural network (CNN). CA consists of two steps: coordinate information embedding and coordinate attention generation.

In the coordinate information embedding step, CA will perform global average pooling on the input feature map in the width and height directions, respectively, to obtain the feature maps $[C, H, 1]$ in the width direction and $[C, 1, W]$ in the height direction. This method captures remote spatial interactions with precise position information, avoids compressing all spatial information into the channel, and can help the network locate targets more accurately.

In the coordinate attention generation step, the above two feature mappings are firstly merged to obtain a new feature layer $[C, 1, W+H]$, and the merged feature layer is feature transformed using the 1×1 convolution, BN normalization and nonlinear activation function operation to obtain a richer representation. Subsequently, the width and height direction features were separated from the above feature layers, and the two separate feature layers were transposed to restore the dimensions of width and height, resulting in two feature layers $[C, H, 1]$ and $[C, 1, W]$. Afterwards, 1×1 convolution and sigmoid function are applied to the separated feature layers for feature transformation to make their dimensions consistent with the input, respectively. Finally, the original input feature map is multiplied by the attention scores in the width and height directions to obtain the output of the CA attention mechanism.

Experimental Platform and Network Parameter Settings

The experiment used a GPU model of NVIDIA GeForce RTX 3090, running memory of 35GB, programming language of Python 3.6, deep learning framework of PyTorch 1.12, and GPU acceleration library of CUDA 11.4. To shorten the training time of the network, the freezing training method is adopted. When freezing the backbone network for training, the initial learning rate is set to 0.01 and the batch processing volume is set to 2. After unfreezing, the learning rate of network training is set to 0.0001, the batch size is set to 2, and the number of iterations is 100.

Model evaluation indicators

In order to verify the detection performance of the algorithm proposed in this study, Precision (P), Recall (R), Average Precision (AP), and Mean Precision (mAP) were used as evaluation indicators, and the model performance was evaluated by comparing the detection image differences between the model in this paper and other models.

RESULTS

Experiment of CA-YOLOv8 model

In order to verify the performance of the CA-YOLOv8 model, 147 corn leaf disease images in the test set were tested and evaluated, and Table 2 shows the detection results of CA-YOLOv8 algorithm on different corn leaf diseases. Table 2 shows that the average accuracy of the CA-YOLOv8 algorithm can reach 97.38%, with an accuracy rate of 94.08% and a recall rate of 90.53%.

Table 2

Detection results with different corn leaf diseases of CA-YOLOv8 model

| Disease | P | R | AP |
|---------------------|-------|-------|-------|
| | [%] | [%] | [%] |
| Corn gray leaf spot | 95.77 | 93.06 | 99.37 |
| Corn leaf blight | 90.82 | 88.54 | 97.84 |
| Corn rust | 95.65 | 90.00 | 94.93 |
| Average | 94.08 | 90.53 | 97.38 |

Part of the detection examples are shown in Fig. 4. It can be seen that CA-YOLOv8 algorithm proposed in this paper can accurately detect different corn leaf diseases, and the recognition results are also good for the complex background in Fig. 4 (d) ~ (f). Due to the high risk of misjudgement or loss in complex backgrounds, the CA-YOLOv8 model can focus on a wide range of positional information to achieve accurate detection of different leaf diseases. In summary, the CA-YOLOv8 model proposed in this paper can accurately detect different corn leaf diseases, and has good detection performance for small targets, multiple targets, complex backgrounds, etc.

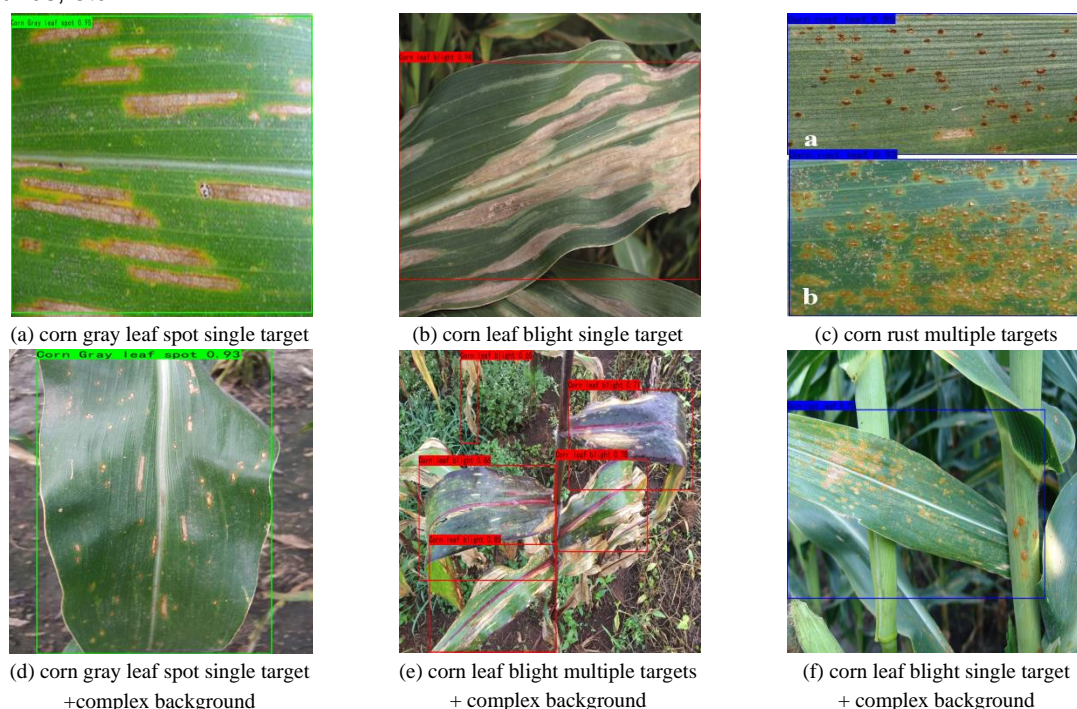


Fig. 4 - Detection results of CA-YOLOv8 model

Comparison of CA-YOLOv8 model and YOLOv8 model with different attention mechanisms

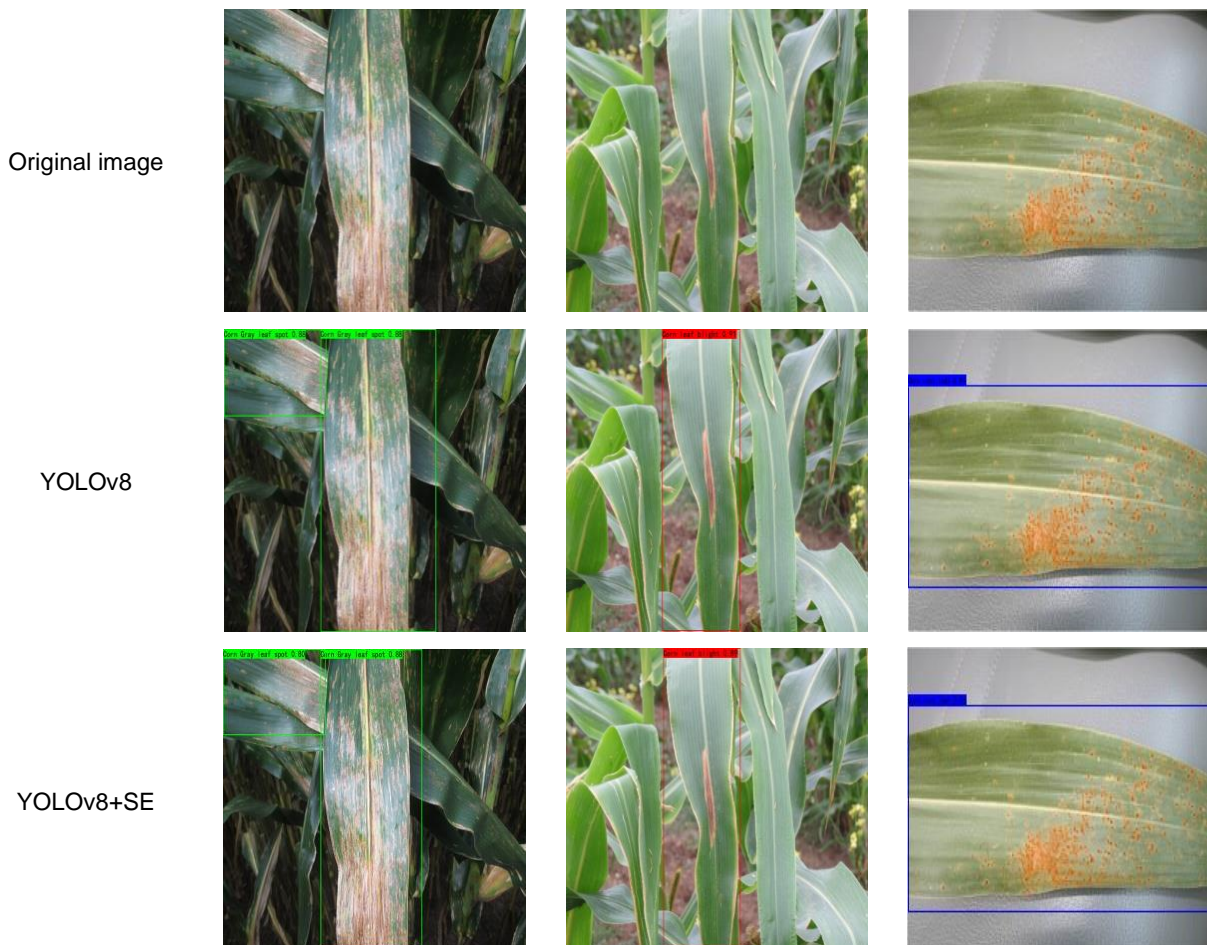
To verify the effectiveness of the attention mechanism used in this paper, the improved YOLOv8 model with CA (abbreviated as CA-YOLOv8) was compared with the original YOLOv8 model (abbreviated as YOLOv8), the YOLOv8 model with SE (abbreviated as YOLOv8+SE), and the YOLOv8 model with CBAM (abbreviated as YOLOv8+CBAM) in disease detection experiments on the test set. As shown in Table 3, the CA-YOLOv8 model has the highest AP for three different corn leaf diseases. Compared with the YOLOv8, YOLOv8+SE, and YOLOv8+CBAM models, its mAP has increased by 2.15, 0.86, and 2.35 percentage points, respectively. The CA-YOLOv8 model improved detection accuracy with almost no increase in model memory usage.

Table 3

Comparison of YOLOv8 model with different attention mechanisms

| Model | AP | | | mAP | Size of the Weight Files |
|-------------|---------------------|------------------|-----------|-------|--------------------------|
| | corn gray leaf spot | corn leaf blight | corn rust | | |
| | [%] | [%] | [%] | [%] | [MB] |
| YOLOv8 | 98.85 | 95.52 | 91.31 | 95.23 | 42.7 |
| YOLOv8+SE | 97.64 | 96.49 | 95.42 | 96.52 | 42.8 |
| YOLOv8+CBAM | 96.82 | 95.15 | 93.12 | 95.03 | 43.0 |
| CA-YOLOv8 | 99.37 | 97.84 | 94.93 | 97.38 | 42.9 |

Fig. 5 (a) shows the detection results of multiple corn gray spot disease leaves under complex background, Fig. 5 (b) shows the detection results of single corn leaf blight disease leaf under complex background, and Fig. 5 (c) shows the detection results of single corn rust disease leaf. It can be seen that the YOLOv8, YOLOv8+SE, YOLOv8+CBAM, and CA-YOLOv8 models can correctly detect corn leaf disease in different backgrounds, while the CA-YOLOv8 model has higher detection accuracy.



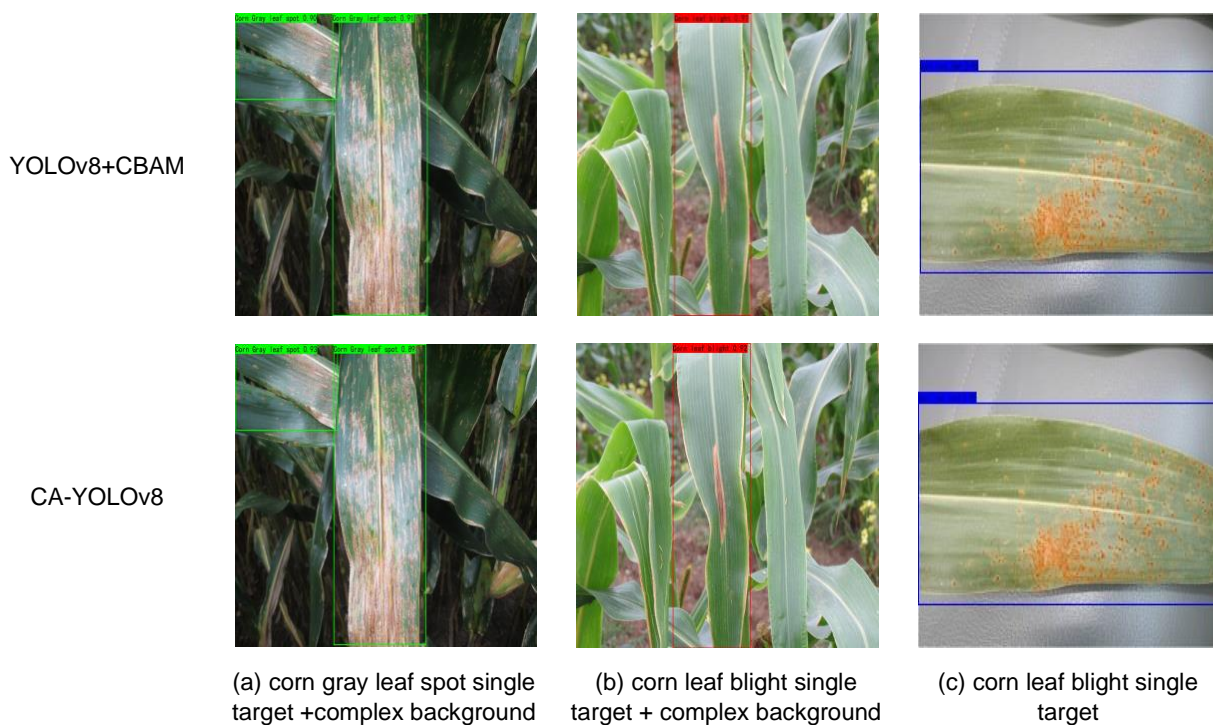


Fig. 5 - Detection results of YOLOv8 model with different attention mechanisms

Comparison with other models

In order to explore the detection effects of different models on three types of corn leaf diseases, the performance of different models on the test set were compared, as shown in Table 4. The results showed that the CA-YOLOv8 model had the highest average accuracy in detecting three types of corn leaf diseases compared with other models. Compared with the Faster R-CNN, YOLOv5s, YOLOv7 and original YOLOv8 models, the mAP of CA-YOLOv8 model improved by 63.53, 29.24, 3.21 and 2.15 percentage points respectively. The memory usage of the CA-YOLOv8 model is only 0.1 MB higher than that of the original YOLOv8 model.

Table 4

| Model | AP | | | mAP | Size of the Weight Files |
|--------------|---------------------|------------------|-----------|-------|--------------------------|
| | corn gray leaf spot | corn leaf blight | corn rust | | |
| | [%] | [%] | [%] | [%] | [MB] |
| Faster R-CNN | 37.41 | 28.68 | 35.67 | 33.85 | 521.6 |
| YOLOv5s | 68.70 | 57.20 | 78.52 | 68.14 | 27.0 |
| YOLOv7 | 93.63 | 93.86 | 95.03 | 94.17 | 142.3 |
| YOLOv8 | 98.85 | 95.52 | 91.31 | 95.23 | 42.7 |
| CA-YOLOv8 | 99.37 | 97.84 | 94.93 | 97.38 | 42.9 |

To better evaluate the performance of detection models, the results of different models were visualized, as shown in Fig. 6. Fig. 6 (a) shows the detection results of single corn gray spot disease leaf under complex background. It can be seen that the Faster R-CNN model failed to detect gray spot disease leaf, while the YOLOv5s, YOLOv7, YOLOv8, and CA-YOLOv8 models were able to correctly detect gray spot disease leaf. The CA-YOLOv8 model has the highest confidence level. Fig. 6 (b) shows the detection results of multiple corn leaf blight diseases. It can be seen that the Faster R-CNN model has false positives and omissions, the YOLOv5s model has false positives, the YOLOv8 model has false positives, and both the YOLOv7 and CA-YOLOv8 models can correctly detect multiple corn leaf blight diseases. However, the confidence of the CA-YOLOv8 model is better than that of YOLOv7. Fig. 6 (c) shows the detection results of single corn rust leaf under simple background. It can be seen that the Faster R-CNN model failed to detect corn rust leaves, while the YOLOv5s, YOLOv7, YOLOv8, and CA-YOLOv8 models were able to correctly detect corn rust leaves. The CA-YOLOv8 model has the highest confidence level. In summary, the CA-YOLOv8 model can accurately detect three types of corn leaf diseases under different backgrounds, and has the highest confidence compared to other models.

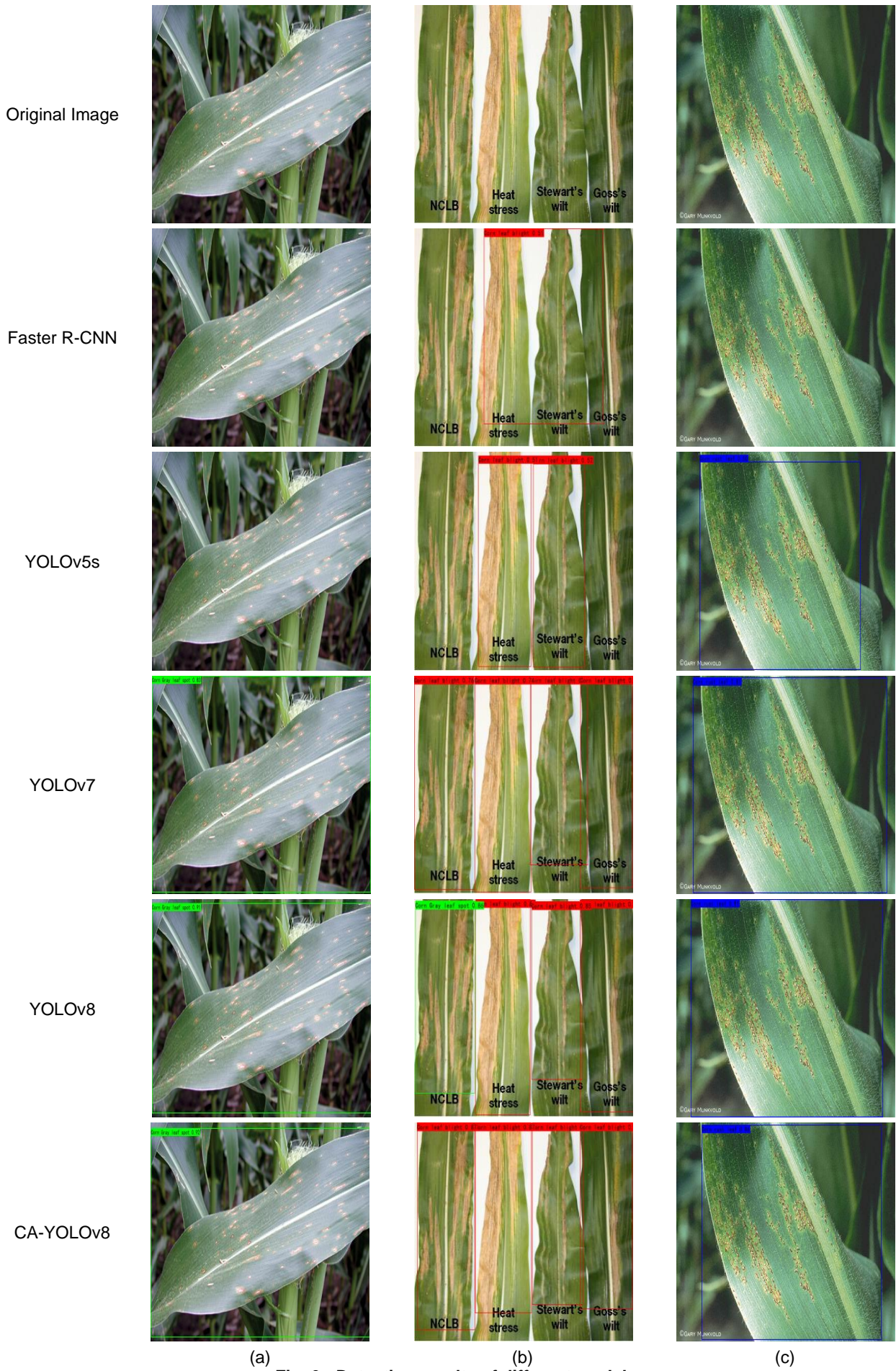


Fig. 6 - Detection results of different models

CONCLUSIONS

(1) A CA-YOLOv8 corn leaf disease detection model was proposed for the detection of corn gray spot, corn leaf blight, and corn rust. The CA attention mechanism was added to the feature map output from the Neck part of the network, which helps the model to better locate and identify the target, improve the detection accuracy of the model, and hardly increase the memory occupation of the model.

(2) In order to verify the performance of the CA-YOLOv8 model, four groups of experiments were set up for comparative analysis. The four groups of experiments were YOLOv8, YOLOv8+SE, and YOLOv8+CBAM, and the CA-YOLOv8 model proposed in this paper. The experimental results showed that the mAP of the CA-YOLOv8 model was the highest.

(3) Under the same experimental conditions, compared with Faster R-CNN, YOLOv5s, YOLOv7, and YOLOv8 models, the CA-YOLOv8 model achieved better results on the corn leaf disease dataset, with mAP improvements of 63.53, 29.24, 3.21, and 2.15 percentage points, respectively.

The experiment fully proves that the CA-YOLOv8 model not only improves the evaluation indicators, but also achieves good visual effects. This study can provide technical reference for the development of a portable intelligent corn leaf disease detection system.

ACKNOWLEDGEMENT

This research, titled "Detection of corn leaf diseases based on CA-YOLOv8", was funded by the Basic Research Program of Shanxi Province (Research on wheat grain appearance quality detection based on computer vision).

REFERENCES

- [1] Bi, C., Xu, S., Hu, N., Zhang, S., Zhu, Z., & Yu, H. (2023). Identification method of corn leaf disease based on improved Mobilenetv3 model. *Agronomy*, 13(2), 300. <https://doi.org/10.3390/agronomy13020300>
- [2] Chen, Y., Chen, X., Lin, J., Pan, R., Cao, T., Cai, J., Yu, D., Cernava, T., & Zhang, X. (2022). DFCANet: A Novel Lightweight Convolutional Neural Network Model for Corn Disease Identification. *Agriculture*, 12(12), 2047. <https://doi.org/10.3390/agriculture12122047>
- [3] Cui, S., Su, Y.L., Duan, K., & Liu, Y. (2023). Maize leaf disease classification using CBAM and lightweight Autoencoder network. *Journal of ambient intelligence and humanized computing*. 14:7297–7307. <https://doi.org/10.1007/s12652-022-04438-z>
- [4] Dai, D., Xia, P., Zhu, Z., & Che, H. (2023). MTDL-EPDCLD: A Multi-Task Deep-Learning-Based System for Enhanced Precision Detection and Diagnosis of Corn Leaf Diseases. *Plants*, 12(13), 2433. <https://doi.org/10.3390/plants12132433>
- [5] Hussain, M. (2023). YOLO-v1 to YOLO-v8, the Rise of YOLO and Its Complementary Nature toward Digital Manufacturing and Industrial Defect Detection. *Machines*, 11(7), 677. <https://doi.org/10.3390/machines11070677>
- [6] Hu, J., Shen, L., Albanie, S., Sun, G., & Wu, E. (2020). Squeeze-and-Excitation Networks. *IEEE Transactions on Pattern Analysis and Machine Intelligence*, 42(8), 2011-2023. [10.1109/TPAMI.2019.2913372](https://doi.org/10.1109/TPAMI.2019.2913372)
- [7] Hou, Q., Zhou D., & Feng J. (2021). Coordinate attention for efficient mobile network design. *IEEE Computer Society, Proceedings of the 2021 IEEE Conference on Computer Vision and Pattern Recognition*, Washington: 13713-13722. [10.48550/arXiv.2103.02907](https://doi.org/10.48550/arXiv.2103.02907)
- [8] Ren, S., He, K., Girshick, R., & Sun, J. (2017). Faster R-CNN: towards real-time object detection with region proposal networks. *IEEE Transactions on Pattern Analysis & Machine Intelligence*, 39(6), 1137-1149. [10.1109/TPAMI.2016.2577031](https://doi.org/10.1109/TPAMI.2016.2577031)
- [9] Shao, M., Zhang, J., Feng, Q., Chai, X., Zhang, N., Zhang, W. (2022). Research progress of deep learning in detection and recognition of plant leaf diseases (深度学习在植物叶部病害检测与识别的研究进展). *Smart Agriculture*, 4(1), 29-46. (in Chinese) [10.12133/j.smartag.SA202202005](https://doi.org/10.12133/j.smartag.SA202202005)
- [10] Singh, D., Jain, N., Jain, P., Kayal, P., Kumawat, S., & Batra, N. (2020). PlantDoc: A dataset for visual plant disease detection. *CoDS COMAD 2020: 7th ACM IKDD CoDS and 25th COMAD ACM*, 249–253. [10.1145/3371158.3371196](https://doi.org/10.1145/3371158.3371196)
- [11] Song, Y., Zhang, H., Li, J., Ye, R., Zhou, X., Dong, B., & Li, L. (2023). High-Accuracy Maize Disease Detection Based on Attention-GAN and Few-Shot Learning. *Plants*, 12(17), 3105. <https://doi.org/10.3390/plants12173105>

- [12] Sun, J., Yang, Y., He, X., & Wu, X. (2020). Northern maize leaf blight detection under complex field environment based on deep learning. *IEEE Access*, 8, 33679-33688. [10.1109/ACCESS.2020.2973658](https://doi.org/10.1109/ACCESS.2020.2973658)
- [13] Woo, S., Park, J., Lee, JY., Kweon, I.S. (2018). CBAM: Convolutional Block Attention Module. In: Ferrari, V., Hebert, M., Sminchisescu, C., Weiss, Y. (eds) *Computer Vision – ECCV 2018. ECCV 2018. Lecture Notes in Computer Science*, 11211, 3-19. https://doi.org/10.1007/978-3-030-01234-2_1
- [14] Yang, J., Zuo, H., Huang, Q., Sun, Q., LI, S., & Li, Li. (2023). Lightweight Method for Crop Leaf Disease Detection Model Based on YOLO v5s (基于 YOLO v5s 的作物叶片病害检测模型轻量化方法). *Transactions of the Chinese Society for Agricultural Machinery*, (in Chinese) <https://link.cnki.net/urlid/11.1964.S.20230914.1537.031>
- [15] Zhang, L., Ba, Y., & Zeng, Q. (2024). Grape Disease Detection Algorithm Based on StyleGAN2-ADA and Improved YOLO v7 (基于 StyleGAN2-ADA 和改进 YOLO v7 的葡萄病害检测方法). *Transactions of the Chinese Society for Agricultural Machinery*, 55(01): 241-252. (in Chinese) <https://link.cnki.net/urlid/11.1964.s.20231115.0946.006>
- [16] Zhang, Y., Wa, S., Liu, Y., Zhou, X., Sun, P., & Ma, Q. (2021). High-Accuracy Detection of Maize Leaf Diseases CNN Based on Multi-Pathway Activation Function Module. *Remote Sensing*, 13(21), 4218. <https://doi.org/10.3390/rs13214218>
- [17] Zibani, A., Ali, S., & Benslimane, H. (2022). Corn diseases in Algeria: first report of three *Bipolaris* and two *Exserohilum* species causing leaf spot and leaf blight diseases. *Cereal Research Communications*, 50(3), 449-461. [10.1007/s42976-021-00192-8](https://doi.org/10.1007/s42976-021-00192-8)

SOIL STRESS ANALYSIS AT DIFFERENT DEPTHS AFTER AGRICULTURAL VEHICLE OPERATION

农业车辆作业后不同深度的土壤应力分析

Jun GUO¹⁾; Enhui SUN^{*1)}; Yue YANG¹⁾; Jun LU¹⁾

¹⁾ School of Automotive Engineering, Yancheng Institute of Technology, Yancheng, 224051, China

E-mail: sun_enhui13@163.com

DOI: <https://doi.org/10.35633/inmateh-73-12>

Keywords: Stress-strain, Soil compaction, Porosity ratio, Consolidation coefficient, Orthogonal test

ABSTRACT

In modern agriculture, with the development and widespread use of agricultural mechanization, mechanical compaction of soils has become a growing problem, resulting in soil degradation in the field. Based on the Boussinesq solution, the soil stress formula for the circular load area is derived, and MATLAB is used to simulate the stress-strain relationship of the soil at different depths. The results show that under the same load conditions, as the soil depth increases, the soil stress gradually decreases, with the most significant stress change occurring at 0.2 m depth. Soil compression experiments conducted using a consolidation instrument revealed that the soil void ratio dropped rapidly under loading of 50-200 kPa, and the decline slowed after 400 kPa. When the soil void ratio decreases to 0.2-0.4, the soil stress changes tend to stabilize. Comparison between the theoretical formula and the compression experimental data indicates that the soil stress gradually decreases as the thickness of the soil layer increases and the pressure load increases, verifying the linear relationship predicted by the theoretical formula.

摘要

在现代农业中，随着农业机械化的发展和广泛使用，土壤的机械压实已成为一个日益严重的问题，导致田间土壤退化。基于 Boussinesq 解推导了圆形荷载面积的土壤应力公式，利用 MATLAB 模拟土壤不同深度的应力-应变，结果表明：相同载荷条件下，土壤深度增加，土壤应力逐渐减小，在 0.2m 处应力变化最大。通过固结仪进行土壤压缩实验，结果表明：土壤孔隙比在 50-200kPa 的加载下迅速下降，在 400kPa 后下降速度减缓。当土壤孔隙比降低到 0.2-0.4，土壤的应力变化趋于稳定。通过理论公式与压缩实验数据对比结果表明：土壤应力随土层厚度增加以及压力载荷增加逐渐减小，验证理论公式的线性关系。

INTRODUCTION

Agriculture plays an important role in a country's political and economic independence (Daneshvar *et al.*, 2023). With the development of agriculture, field machinery operations have become common, and people's dependence on agricultural machinery has increased. When machinery operates in the field, the traction and load of tillage machinery gradually increase, leading to greater compaction. The stress on the soil profile may exceed the soil's internal strength, resulting in changes to its physical, chemical, and biological properties, increased soil density and mechanical resistance, and reduced macropores (Zhang *et al.*, 2005). This, in turn, affects crop growth in the field, as the stress from mechanical operations exceeds soil stability, leading to soil degradation.

Current research on soil stress-strain in China primarily focuses on the physical properties of soil after compaction, including factors such as soil moisture content, bulk density, porosity, and firmness that affect the internal stress-strain of soil. Based on soil stress research, soil compression tests were conducted at different depths to explore changes in soil stress-strain, providing both theoretical and experimental foundations for mitigating soil mechanical compaction.

Although agricultural machinery has been further developed, the damage to topsoil and subsoil remains significant. Soil compaction in farmland primarily results from the stress transfer within the soil under external loads, which causes soil particles to aggregate due to regular tillage compaction. This, in turn, alters the physical and chemical properties of the soil (Naveed *et al.*, 2016).

¹ Jun Guo, Ph.D. Eng.; Enhui Sun, Master; Yue Yang, Master; Jun Lu, Ph.D. Eng.

Large agricultural machinery operations and livestock trampling generate stress transfer and shear stress in the soil, increasing the mass per unit volume and reducing soil porosity (Carman *et al.*, 2002). Previous studies have shown that soil compaction from agricultural vehicles can be mitigated by reducing tire inflation pressure and increasing vehicle speed. Currently, many solutions focus on tire design, primarily by reducing the load or increasing the contact area.

Arvidsson *et al.*, (2005), proved that tire inflation pressure significantly influences soil stress and displacement at a depth of 0.3 m. By further investigating the impact of wheel load on subsoil stress and validating the commonly used stress propagation model, they found that soil stress measured at a depth of 10 cm is highest under the greatest wheel load, indicating that both inflation pressure and wheel load affect vertical soil stress near the surface. Lamandé *et al.*, (2007) studied the stress and deformation induced by loading the soil with undisturbed samples. By comparing the measured vertical stress with that calculated by the Söhne model, they found that doubling the contact area reduces stress-strain in the topsoil, with contact stress determining stress in the topsoil, while subsoil stress depends mainly on the load. Keller *et al.*, (2005), developed a model in Visual Basic that predicts vertical stress distribution under a rubber track mounted on an agricultural vehicle, providing a realistic estimate of the vertical stress at the contact point of the rubber track with the soil, thereby improving the prediction of soil stress and compaction risk for rubber-tracked agricultural vehicles. Keller *et al.*, (2016), used the Arvidsson probe to measure vertical stress and found, through finite element simulation, that soil properties had little effect on vertical stress. Lamandé *et al.*, (2018), analyzed the compaction effect of the same vehicle on the soil using both wheeled and crawler traveling devices and measured the distribution of vertical stress at the contact surface between the rubber crawler and the soil along the length of the crawler. Through the SoilCare project, Piccoli *et al.*, (2022), studied the use of soil improvement planting systems to alleviate topsoil and internal soil compaction. Ahmed Salih Mohammed *et al.*, (2023) used statistical modeling methods to comprehensively analyze temperature, ground granulated blast furnace slag (GGBFS) and other research parameters and evaluate their impact on the compressive strength of concrete. The experiments showed that multiple factors affect the compressive strength of soil. Through comparative experiments, Pieniżek, (2023), concluded that in the traditional farming system (CONV), suitable and efficient grain varieties should be selected to allow them to grow under lower fertilization conditions, so as to increase grain yield and reduce soil degradation. Song *et al.*, (2023), mixed sedimentary soil with cultivated land, compost and biochar by volume ratio to make the soil have higher water holding capacity and reduce soil loss.

Tong, (2017), determined soil strain in the contact area based on wheel movement, calculated stress for each contacting soil unit using the stress-strain relationship of vehicle-driving soil, integrated stress along the tread direction, and dynamically computed rigid ring-soil forces. Ding, (2020), discovered that increasing vehicle speed can reduce vertical stress in the soil, suggesting that vehicles should operate at higher speeds whenever possible to minimize soil compaction risk. Li *et al.*, (2010), through actual soil tests, demonstrated that controlling soil stress within the Spc (elastic zone) effectively reduces soil compression deformation, indicating that if soil pre-consolidation pressure is lower than tire ground contact pressure, agricultural machinery operations will exacerbate soil compaction and soil structure damage. Wang *et al.*, (2011), proposed using the impact principle to detect soil compaction and established a relationship model between the impact rod and soil resistance to reflect soil compaction levels. Song *et al.*, (2015), investigated the linear relationship between resistivity and soil moisture content and compaction based on the original resistivity model of soil compaction. He *et al.*, (2017), established a linear correlation between moisture content, density, pre-consolidation pressure in the soil environment, and soil stress transfer under external force through uniaxial compression tests, aiming to predict soil compaction degree. Wang *et al.*, (2018), explored the influence of soil stress on soil unit density and compaction during the transfer process of different nodes by studying tire pressure, axle load, and mechanical compaction times of agricultural machinery. They also identified the influence of soil profile stress and the number of agricultural machinery compactions using the discrete element method. Xu, (2020), designed a multi-directional wireless earth pressure sensor and developed a soil stress dynamic detection system for the sensor to study changes in earth pressure during soil compaction.

Considerable research has been conducted on soil compaction, resulting in a series of solutions, but most have focused on seeking remedies within agricultural machinery itself, with little emphasis on mitigating mechanical compaction from the soil itself. Currently, research on compacted soil predominantly centers on its physical and chemical properties, yielding gradual effects on alleviating soil compaction.

Assessment of soil compaction degree relies on physical quantities associated with soil compaction. Unlike the deep soil examined in soil mechanics, the soil in contact with the wheel, studied in vehicle ground mechanics, is primarily surface soil (Zhuang, 2002). The process of soil compaction is typically divided into three steps (O'SullivanMF et al., 1999): stress application to the soil surface during tire-soil interaction, stress transmission within the soil, and soil stress-induced changes in soil structure. This article focuses on the "stress transfer within the soil" process, investigating soil stress at various depths during soil compaction and identifying effective methods to alleviate soil mechanical compaction.

Building upon previous research on soil compressive stress transfer, this study addresses the limitations of existing stress transfer investigations by theoretically deducing stress transfer at various depths in the soil. Theoretical analysis of soil stress is conducted using compression test methods, with an experimental plan tailored to existing soil conditions. Soil compression tests are carried out to validate the feasibility of the soil stress theory, utilizing data obtained from the tests to examine relationships between various parameters.

MATERIALS AND METHODS

The specific research objectives are as follows:

(1) Theoretical derivation

Theoretical formulas are analyzed to establish a formula suitable for this research, and MATLAB is employed to simulate the linear relationship of the theoretical formula.

(2) Design and analysis of soil compression test

A test plan is designed in accordance with the existing soil compression test method, meeting the requirements of this study. The WG single-lever consolidation instrument (medium and low pressure) and the NSIF geotechnical test control data acquisition and processing system are utilized for the test.

Theoretical analysis

In previous stress studies, simulation and modeling methods were the primary approaches for calculating soil stress transfer. Existing analysis models all assumed that the soil is a homogeneous, elastic, and isotropic medium (Van den Akker, 2004). Treating the soil as an elastic-plastic material (Smith et al., 2000), Boussinesq deduced the stress solution at any point of the soil when the semi-infinite soil elastic body was subjected to a concentrated load in 1855 (Fig. 1).

$$\sigma_z = \frac{3Pz^3}{2\pi R^5} = \frac{3P}{2\pi R} \cos^3 \theta \tag{1}$$

where P represents the concentrated load acting on the soil surface, R denotes the distance from point M to the center point, and θ is the angle between the R line and the vertical axis Z .

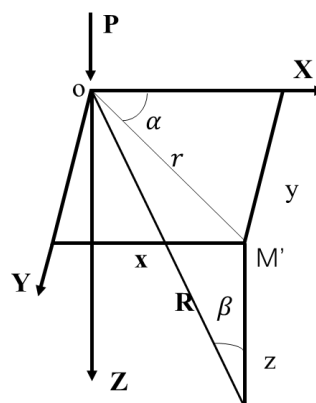


Fig. 1 - Stresses caused by concentrated loads in the vertical direction

Considering the vertical normal stress analysis in this study:

$$\sigma_z = \frac{3Pz^3}{2\pi(x^2 + y^2 + z^2)^{\frac{5}{2}}} = \frac{3P}{2\pi z^2} \times \frac{1}{\left[1 + \left(\frac{r}{z}\right)^2\right]^{\frac{5}{2}}} = \alpha \frac{P}{z^2} \tag{2}$$

In the formula: $R^2 = r^2 + z^2$, $r^2 = x^2 + y^2$;

$$\alpha = \frac{3}{2\pi} \times \frac{1}{\left[1 + \left(\frac{r}{z}\right)^2\right]^{\frac{5}{2}}}$$

is the stress coefficient, it is a function of r and z .

The instrument used for the soil compression experiment in this study employs a circular loading surface, so the stress under the corner point of the circular area under the action of a uniform load (Fig. 2) is:

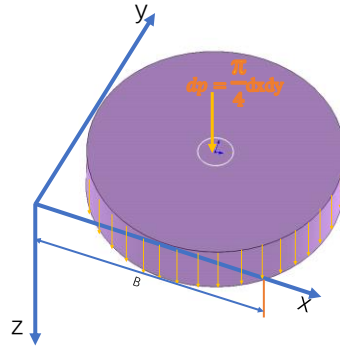


Fig. 2 - Stress under uniform circular load corner

The microelement $dxdy$ is taken in the load surface, and the distributed load on the microelement is replaced by the concentrated force $dp = dxdy$, then, from the Bucinnaiske solution, it can be deduced that the point M at the depth z under the corner point O is subjected to the concentrated force.

The vertical stress can be obtained from the formula:

$$d\sigma_z = \frac{3z^3 p \frac{\pi}{4}}{2\pi(x^2 + y^2 + z^2)^{\frac{5}{2}}} dxdy = \frac{3z^3 p}{8(x^2 + y^2 + z^2)^{\frac{5}{2}}} dxdy \tag{3}$$

$$\sigma_z = \frac{3pz^3}{8} \int_0^l \int_0^b \frac{1}{(x^2 + y^2 + z^2)^{\frac{5}{2}}} dxdy = \frac{p}{8} \left[\frac{mn(m^2 + 2n^2 + 1)}{(m^2 + n^2)(1 + n^2)\sqrt{m^2 + n^2 + 1}} + \arctan \frac{m}{n\sqrt{m^2 + n^2 + 1}} \right] \tag{4}$$

In the formula: $m = \frac{l}{b}$, $n = \frac{z}{b}$, l and b are the lengths of the load acting on the farmland soil surface, respectively (Gao, 2018).

Simplify the above formula $\sigma_z = \alpha_c p$

$$\alpha_c = \frac{1}{8} \left[\frac{mn(m^2 + 2n^2 + 1)}{(m^2 + n^2)(1 + n^2)\sqrt{m^2 + n^2 + 1}} + \arctan \frac{m}{n\sqrt{m^2 + n^2 + 1}} \right]$$

is the stress coefficient.

The concentration factor is influenced by both the loading environment and the soil environment. Currently, soil moisture content significantly affects the concentration coefficient, with the coefficient increasing as soil moisture content rises, according to research by *Chen et al.*, (2012). However, when moisture content is high, soil deformation after compression is substantial (*Defossez P. et al.*, 2003).

Simulation of stress in the subsoil

Using the soil sample taken in this experiment as an example, the soil stress σ_z is generated by successively loading P . P ranges from 0 to 800 kPa for the test. When P ranges from 0 to 800 kPa, the distance Z between the loading point and the stress prediction point directly below is 0.02 m, 0.04 m, 0.06 m.

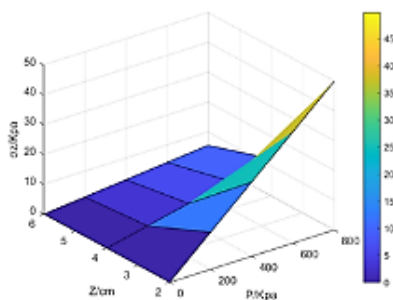


Fig. 3- σ_z Relationship between soil P stress and surface stress

From Fig. 3, it can be observed that using MATLAB software to analyze the theoretical formula above, there exists a relatively stable linear relationship between σ_z and P . Under the same pressure load condition, as the soil depth increases, the soil stress gradually decreases, with the most significant change occurring at 0.02 m. Under the same soil depth, soil pressure gradually increases, and the internal stress of the soil changes slowly. Due to the shallow sampling depth, the change in stress-strain is small when the loading force is low, hence the relationship between σ_z and P shown in Fig.3. When soil moisture content and wet density change, the linear relationship also remains stable.

Experimental Tests and Methods

The soil at the test site is wetland soil. Retrieved soil samples underwent rapid uniaxial compression experiments. Simultaneously, the WG-type single-lever consolidation instrument (medium and low pressure) and NSIF geotechnical tests produced by Nanjing Soil Instrument Factory Co., Ltd. were employed to control the test site. The data acquisition and processing system detected changes in the soil due to compaction, measured soil deformation and pressure, and evaluated the relationship between porosity ratio and loading pressure, as well as the consolidation coefficient and loading pressure after soil compression.

The experimental device is depicted in Fig.4, consisting mainly of the WG-type single-lever consolidation instrument (medium and low pressure), the NSIF geotechnical test control data acquisition and processing system, three dial indicators, a data collector, weights at all levels, and the test soil samples and tools.



Fig. 4 - WG type single lever consolidation instrument

The soil used in the experiment was sourced from Yancheng Institute of Technology, taken from the original soil within the 0-10 cm cultivated layer of the experimental land. Soil samples were retrieved using a ring knife with a diameter of 79.8 mm and a height of 20 mm to prepare samples located 0.02 m, 0.04 m, and 0.06 m away from the sampling ground. Each parameter's soil samples were tested multiple times, and the data were recorded (five sets of test data were analyzed for this test). A thin layer of Vaseline (Tager *et al.*, 2013) was applied to the inner wall of the soil cutting ring knife used in the experiment, with the cutting edge facing downwards, and placed onto the soil sample. A soil cutter was used to cut the soil sample into soil columns slightly larger than the diameter of the ring cutter. Then, the ring knife was pressed vertically downward, and cutting proceeded while applying pressure until the soil sample protruded from the ring knife. The remaining soil at both ends was cut off and smoothed, and the outer wall of the ring knife was wiped clean. Throughout the cutting process, careful observation of the soil sample's condition was maintained. Any remaining undisturbed soil samples after cutting were wrapped in wax paper and placed in sealed bags for supplementary testing.

(1) Connect the test device, as shown in Fig.4, and place the container holding the soil sample in the pressure frame according to the test regulations, with the height of the soil sample set at 2 cm.

(2) Before commencing the test, adjust the lever to the horizontal position. To ensure optimal contact between the test soil sample and the upper and lower parts of the instrument, apply a precompression pressure of 1 kPa first according to geotechnical operating procedures. Then, adjust the dial indicator so that the pointer reads zero. Subsequently, load according to the test procedure (removing the preload weight before loading). When the soil sample sinks under pressure, causing the lever to tilt, rotate the handwheel counterclockwise to restore the lever to the horizontal position. Throughout the loading process, collect a set of data every hour until the end of pressurization.

(3) The maximum applied load for this test is 800 N. A 50 cm² soil sample container is used for the compression test. During the 50 cm² pressurization process, pressure is applied to the test soil sample through a pressure transfer plate with a diameter of 8 cm. The soil consolidation instrument is loaded step by step according to pressure levels of 50, 100, 200, 400, and 800 kPa.

(4) During the pressurization process of the test soil samples, apply the loading force to the soil samples every two loading intervals of 1 hour. After all loading levels have been applied, the test is completed once the instrument is deemed stable. Throughout the process, the NSIF geotechnical test control data acquisition system will record the vertical settlement of the pressure transfer plate and monitor the relationship between the void ratio of the ring cutter and the loading pressure, soil consolidation coefficient, and loading pressure. The ratio of pre-compressive stress to principal stress provides soil stability assessment, with values between 0.1 and 0.5 indicating weak soil conditions.

(5) Monitor soil compression by conducting compression tests on prepared soil samples using a soil consolidation instrument. Simultaneously, the NSIF geotechnical test control data acquisition and processing system will monitor and record the vertical settlement of the pressure transfer plate due to successive loading, followed by monitoring the void ratio and loading pressure of the ring cutter, and the relationship between soil consolidation coefficient and loading pressure.

(6) Analyze the changes in compressive modulus parameters, void ratio-load curve (e-p), and consolidation coefficient-load curve (cv-p) of the test soil samples based on results obtained by the NSIF geotechnical test control data acquisition and processing system.

RESULTS

Soil Compression Test Results

In Table 1 to Table 6, the vertical settlement obtained by applying the initial load is zero. Since the soil is inelastic and difficult to calculate, it is typically assumed and calculated as semi-elastic soil in actual calculations. Thus, the soil is considered a semi-infinite medium that satisfies uniform, continuous, and isotropic properties. During the experiment, the influence of the container's side wall prevents lateral deformation of the soil, which differs somewhat from the deformation of unconfined soil. However, the soil deformation observed in the test still provides valuable guidance for calculating the actual soil stress-strain distribution.

Table 1

Soil compression deformation test under lateral limit conditions 1

| Pressure plate area/cm ² | Apply load / kPa | Vertical sedimentation / cm | Porosity ratio | Modulus / MPa | Compression factor / MPa ⁻¹ |
|-------------------------------------|------------------|-----------------------------|----------------|---------------|--|
| 40.24 | 0 | | 0.964 | 0 | |
| 40.24 | 50 | 3.437 | 0.627 | 0.291 | 6.752 |
| 40.24 | 100 | 4.392 | 0.533 | 1.047 | 1.876 |
| 40.24 | 200 | 5.272 | 0.447 | 2.271 | 0.865 |
| 40.24 | 400 | 6.061 | 0.369 | 5.072 | 0.387 |
| 40.24 | 800 | 6.835 | 0.293 | 10.335 | 0.190 |

Table 2

Soil compression deformation test under lateral limit conditions 2

| Pressure plate area/cm ² | Apply load / kPa | Vertical sedimentation/cm | Porosity ratio | Modulus / MPa | Compression factor / MPa ⁻¹ |
|-------------------------------------|------------------|---------------------------|----------------|---------------|--|
| 40.24 | 0 | | 0.964 | 0 | |
| 40.24 | 50 | 4.190 | 0.553 | 0.239 | 8.230 |
| 40.24 | 100 | 4.923 | 0.481 | 1.364 | 1.440 |
| 40.24 | 200 | 5.646 | 0.410 | 2.764 | 0.711 |
| 40.24 | 400 | 6.326 | 0.343 | 5.884 | 0.334 |
| 40.24 | 800 | 6.954 | 0.281 | 12.739 | 0.154 |

Table 3

Soil compression deformation test under lateral limit conditions 3

| Pressure plate area / cm ² | Apply load / kPa | Vertical sedimentation / cm | Porosity ratio | Modulus / MPa | Compression factor / MPa ⁻¹ |
|---------------------------------------|------------------|-----------------------------|----------------|---------------|--|
| 40.24 | 0 | | 0.964 | 0 | |
| 40.24 | 50 | 4.615 | 0.555 | 0.240 | 8.181 |
| 40.24 | 100 | 5.086 | 0.465 | 1.086 | 1.809 |
| 40.24 | 200 | 5.868 | 0.388 | 2.557 | 0.768 |
| 40.24 | 400 | 6.571 | 0.319 | 5.692 | 0.345 |
| 40.24 | 800 | 7.241 | 0.253 | 11.942 | 0.165 |

Table 4

Soil compression deformation test under lateral limit conditions 4

| Pressure plate area / cm ² | Apply load / kPa | Vertical sedimentation / cm | Porosity ratio | Modulus / MPa | Compression factor / MPa ⁻¹ |
|---------------------------------------|------------------|-----------------------------|----------------|---------------|--|
| 40.24 | 0 | | 0.964 | 0 | |
| 40.24 | 50 | 3.447 | 0.626 | 0.290 | 6.771 |
| 40.24 | 100 | 4.692 | 0.504 | 0.803 | 2.446 |
| 40.24 | 200 | 5.749 | 0.400 | 1.892 | 1.038 |
| 40.24 | 400 | 6.613 | 0.315 | 4.626 | 0.425 |
| 40.24 | 800 | 7.425 | 0.235 | 9.856 | 0.199 |

Table 5

Soil compression deformation test under lateral limit conditions 5

| Pressure plate area / cm ² | Apply load / kPa | Vertical sedimentation / cm | Porosity ratio | Modulus / MPa | Compression factor / MPa ⁻¹ |
|---------------------------------------|------------------|-----------------------------|----------------|---------------|--|
| 40.24 | 0 | | 0.964 | 0 | |
| 40.24 | 50 | 2.388 | 0.730 | 0.419 | 4.690 |
| 40.24 | 100 | 3.508 | 0.620 | 0.892 | 2.201 |
| 40.24 | 200 | 4.352 | 0.537 | 2.369 | 0.829 |
| 40.24 | 400 | 5.044 | 0.469 | 5.783 | 0.340 |
| 40.24 | 800 | 5.710 | 0.404 | 12.021 | 0.163 |

Table 6

Soil compression deformation test under lateral limit conditions 6

| Pressure plate area / cm ² | Apply load / kPa | Vertical sedimentation / cm | Porosity ratio | Modulus / MPa | Compression factor / MPa ⁻¹ |
|---------------------------------------|------------------|-----------------------------|----------------|---------------|--|
| 40.24 | 0 | | 0.964 | 0 | |
| 40.24 | 50 | 4.042 | 0.567 | 0.247 | 7.940 |
| 40.24 | 100 | 5.378 | 0.567 | 0.247 | 7.940 |
| 40.24 | 200 | 6.481 | 0.436 | 0.748 | 2.626 |
| 40.24 | 400 | 7.387 | 0.328 | 1.814 | 1.083 |
| 40.24 | 800 | 8.147 | 0.239 | 4.413 | 0.445 |

Through the step-by-step loading compression experiment of the test soil, the compressive curve of the void ratio of the test soil and the external load under confinement conditions, and the variation of the compressive modulus of the test soil sample due to loading and compression were obtained. It can be observed from the following charts (Fig. 5) that as the external load increases, the soil undergoes rapid compression initially. The soil decreases rapidly during the loading process of 50-200 kPa, while the compressive modulus increases slowly during this process. Due to the gradual loading of the soil, the soil consolidation coefficient gradually decreases, indicating a slowing down of the degree of soil consolidation. The soil porosity ratio decreases slowly after loading at 400 kPa, and the compressive modulus increases rapidly after loading at 200 kPa. A larger soil void ratio corresponds to a smaller allowable bearing capacity of the soil. When the soil void ratio is reduced to 0.2-0.4, the stress-strain of the test soil tends to stabilize, further verifying the linear relationship shown by the theoretical derivation formula. The data error of the consolidation instrument range during the test can be ignored for multiple tests.

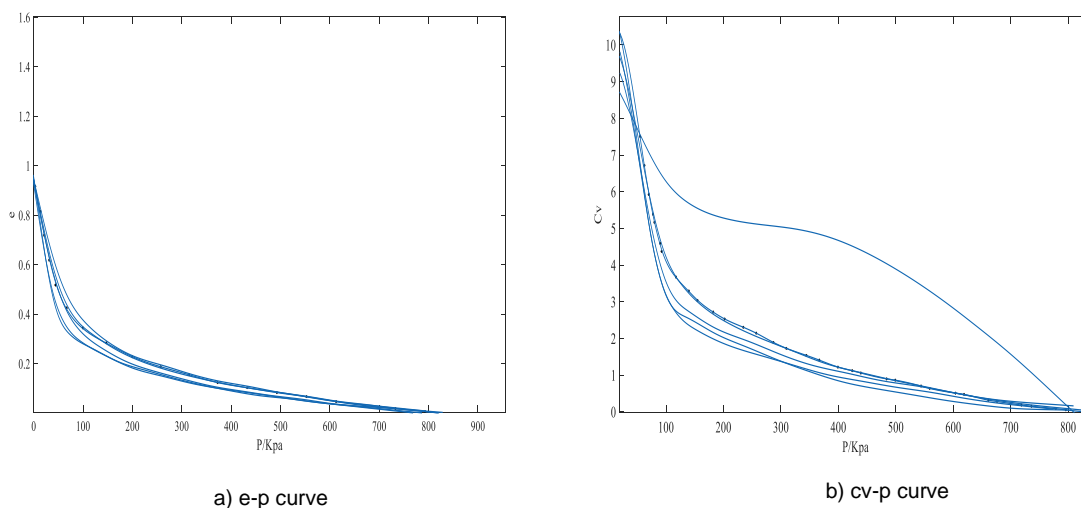


Fig. 5 - Soil compression test results

CONCLUSIONS

Based on the Boussinesq solution, the soil stress formula for the circular load area was derived, providing a theoretical basis for analyzing the stress distribution of soil under mechanical loads. Soil compression experiments were conducted, revealing that the soil void ratio decreased rapidly within a certain pressure range (50 - 200 kPa), and the decline trend slowed down after 400 kPa. Moreover, when the soil void ratio decreased to 0.2 - 0.4, the soil stress change tended to stabilize, providing experimental evidence for the compression characteristics of the soil. It helps to further understand the mechanical response and change laws of the soil under agricultural mechanization operations, providing theoretical support for reducing soil compaction, protecting soil structure and quality, and optimizing the use of agricultural machinery.

ACKNOWLEDGEMENT

This work was supported by Founding for school-level research projects of Yancheng Institute of Technology (grant 154203635), from the Yancheng Institute of Technology, of Yancheng, Jiangsu Province, China. We would like to thank Editage for providing English language editing. We are also grateful to the editor and anonymous reviewers for providing helpful suggestions to improve the quality of the present paper.

REFERENCES

- [1] Carman, K., (2002), Compaction characteristics of towed wheels on clay loam in a soil bin. *Soil and Tillage Research*, 65(1), 37-43. [https://doi.org/10.1016/S0167-1987\(01\)00281-1](https://doi.org/10.1016/S0167-1987(01)00281-1)
- [2] Chen, Z., Wang, D., Li, L., Shan R., (2012), Tensile and shear characteristics test of corn stover peel. (玉米秸秆皮拉伸和剪切特性试验), *Journal of Agricultural Engineering*, 28(21), 59-65. <https://doi:10.3969/j.issn.1002-6819.2012.21.009>
- [3] Daneshvar, A., Radfar, R., Ghasemi, P., Bayanati, M., Pourghader Chobar, A., (2023), Design of an Optimal Robust Possibilistic Model in the Distribution Chain Network of Agricultural Products with High Perishability under Uncertainty. *Sustainability*, 15, 11669. <https://doi.org/10.3390/su151511669>
- [4] Défossez, P., Richard, G., Boizard, H., et al., (2003), Modeling change in soil compaction due to agricultural traffic as function of soil water content. *Geoderma*, 116(1-2), 89-105. [https://doi.org/10.1016/S0016-7061\(03\)00096-X](https://doi.org/10.1016/S0016-7061(03)00096-X)
- [5] Ding, Z., (2020), Study on soil shear and compaction process of track/wheeled combined harvester on paddy field. (履带/轮式联合收获机对稻田土壤剪切及压实作用过程研究), Jiangsu University. <https://doi:10.27170/d.cnki.gjsuu.2020.000973>
- [6] Gao, X.Y., (2018), *Soil Mechanics*. (土力学), Peking University Press, Beijing, 81-85.
- [7] He, T., Cong, W., Adam B E, Ding, Q., Yang, Y., Huo, L., (2017), Study on soil stress transfer coefficient based on com-paction analysis model. (基于压实分析模型的土壤应力传递系数研究), *Transactions of the CSAM*, 48(06), 59-65. <https://doi: 10.6041/j.issn.1000-1298.2017.06.007>
- [8] Lamandé, M., Greve, M.H., Schjønning, P., (2018), Risk assessment of soil compaction in Europe—Rubber tracks or wheels on machinery. *Catena*, 167(41), 353-362. <https://doi.org/10.1016/j.catena.2018.05.015>
- [9] LI, C., Ding, Q., Chen, Q., (2010), Determination and analysis of advanced consolidation pressure in paddy soil. (水稻土的先期固结压力测定与分析), *Transactions of the Chinese Society of Agricultural Engineering*, 26(08), 141-144. <https://doi: 10.3969/j.issn.1002-6819.2010.08.024>
- [10] Lamandé, M., Schjønning, P., Tøgersen, F.A., (2007), Mechanical behaviour of an undisturbed soil subjected to loadings: Effects of load and contact area. *Soil and Tillage Research*, 91-106. <https://doi.org/10.1016/j.still.2007.09.002>
- [11] Mohammed, A.K., Hassan, A.M.T., Mohammed, A.S., (2023), Predicting the Compressive Strength of Green Concrete at Various Temperature Ranges Using Different Soft Computing Techniques. *Sustainability*, 15, 11907. <https://doi.org/10.3390/su151511907>
- [12] Naveed, M., Schjønning, P., Keller, T., et al., (2016), Quantifying vertical stress transmission and compaction-induced soil structure using sensor mat and X-ray computed tomography. *Soil and Tillage Research*, 158. <https://doi.org/10.1016/j.still.2015.12.006>
- [13] O'Sullivan, M.F., Henshall, J.K., Dickson, J.W., (1999), A simplified method for estimating soil compaction. *Soil and Tillage Research*, 49(4), 325-335. [https://doi.org/10.1016/S0167-1987\(98\)00187-1](https://doi.org/10.1016/S0167-1987(98)00187-1)
- [14] Piccoli, I., Seehusen, T., Bussell, J., Vizitu, O., Calciu, I., Berti, A., Börjesson, G., Kirchmann, H., Kätterer, T., Sartori, F., et al., (2022), Opportunities for Mitigating Soil Compaction in Europe—Case Studies from the SoilCare Project Using Soil-Improving Cropping Systems. *Land*, 11(2). <https://doi.org/10.3390/land11020223>
- [15] Pieniżek, J.M., (2023), The Influence of Cropping Systems on Photosynthesis, Yield, and Grain Quality of Selected Winter Triticale Cultivars. *Sustainability*, 15, 11075. <https://doi.org/10.3390/su151411075>
- [16] Smith, R., Ellies, A., Horn, R., (2000), Modified Boussinesq's equations for nonuniform tire loading. *Journal of Terramechanics*, 37(4), 207-222. [https://doi.org/10.1016/S0022-4898\(00\)00007-0](https://doi.org/10.1016/S0022-4898(00)00007-0)
- [17] Song, J., LI, S.C., Liu, B., Xu, X., Wang, C., Nie, L., (2015), Quantitative evaluation method of compaction degree of unsaturated soil based on resistivity characteristics, (基于电阻率特性的非饱和土

- 压实度定量评价方法). *Journal of Chang'an University (Natural Science Edition)*, 35(06), 33-41. [https://doi: JournalArticle/5b3c22e1c095d70f00a9c1aa](https://doi.org/10.1016/j.still.2013.12.001)
- [18] Song, Y., Kim, S.; Koo, H., Kim, H., Kim, K., Lee, J., Jang, S., Lee, K.C., (2023), Assessing the Suitability of Sediment Soil to Be Reused by Different Soil Treatments for Forest Agriculture. *Sustainability*, 15, 11477. <https://doi.org/10.3390/su151511477>
- [19] Tagar, A.A., Ji, C., Ding, Q., et al., (2014), Soil failure patterns and draft as influenced by consistency limits: an evaluation of the remolded soil cutting test. *Soil and Tillage Research*, 137, 58-66. <https://doi.org/10.1016/j.still.2013.12.001>
- [20] Keller, T., Arvidsson, J., (2016), A model for prediction of vertical stress distribution near the soil surface below rubber-tracked undercarriage systems fitted on agricultural vehicles. *Soil and Tillage Research*, 116-124. <https://doi.org/10.1016/j.still.2015.07.014>
- [21] Keller, T., (2005), A Model for the Prediction of the Contact Area and the Distribution of Vertical Stress below Agricultural Tyres from Readily Available Tyre Parameters. *Biosystems Engineering*, 85-96. <https://doi.org/10.1016/j.biosystemseng.2005.05.012>
- [22] Keller, T., Ruiz, S., Stettler, M., Berli, M., (2016), Determining Soil Stress beneath a Tire: Measurements and Simulations. *Soil Science Society of America Journal*, 80: 541-553. <https://doi.org/10.2136/sssaj2015.07.0252>
- [23] Tong, K., (2017), Study on dynamic contact force model of tire-soft road surface. (轮胎-松软路面动态接触力模型研究). Jilin University. [https://doi:CNKI:CDMD:2.1017.156238](https://doi.org/10.1016/j.still.2004.03.021)
- [24] Van den Akker, Jan J.H., (2004), SOCOMO: a soil compaction model to calculate soil stresses and the subsoil carrying capacity. *Soil and Tillage Research*, 79(1), 113-127. <https://doi.org/10.1016/j.still.2004.03.021>
- [25] Wang, J.F., Chen, X.X., (2011), Application of impact principle in soil compaction measurement technology. (冲击原理在土壤压实测量技术中的应用). *Agricultural Equipment and Vehicle Engineering*, (02), 49-51. [https://doi:10.3969/j.issn.1673-3142.2011.02.016](https://doi.org/10.3969/j.issn.1673-3142.2011.02.016)
- [26] Wang, X.L., (2018), Research on soil compaction evaluation and combined shoveling and ripping technology of agricultural machinery. (农机作业土壤压实评价及组合铲松土技术研究). China Agricultural University.
- [27] Xu, J.X., (2020), Research on multi-directional wireless soil pressure sensor and monitoring system in farmland. (农田多向无线土压力传感器及监测系统的研究). Northeast Agricultural University. [https://doi: 10.27010/d.cnki.gdbnu.2020.000953](https://doi.org/10.27010/d.cnki.gdbnu.2020.000953)
- [28] Zhang, X.Y., Sui Y.Y., (2005), Research progress of mechanical soil compaction in farmland. (农田土壤机械压实研究进展). *Transactions of the CSAM*, 36(6), 122-125. [https://doi:10.3969/j.issn.1000-1298.2005.06.033](https://doi.org/10.3969/j.issn.1000-1298.2005.06.033)
- [29] Zhuang, J.D., (2002), *Calculation of automobile ground mechanics*. (计算汽车地面力学). Beijing: China Machine Press, Beijing.

RESEARCH ON THE DOA-BP-BASED TEMPERATURE AND HUMIDITY PREDICTION MODEL FOR COMMERCIAL CULTIVATION OF AGARICUS BISPORUS

基于 DOA-BP 的双孢菇工厂化生产温湿度预测模型研究

Tianhua LI¹⁾, Yinhang DONG¹⁾, Guoying SHI^{1*)}, Guanshan ZHANG¹⁾, Chao CHEN²⁾, Jianchang SU³⁾

¹⁾ Shandong Agricultural University, College of Mechanical and Electrical Engineering/ China;

²⁾ Shandong Century Smart Agricultural Technology Co., LTD

³⁾ Shandong Qihe Biotech Co., LTD

E-mail: sgy509@sdau.edu.cn

DOI: <https://doi.org/10.35633/inmateh-73-13>

Keywords: Mushroom house environment, Temperature and humidity prediction, BP neural network, DOA optimization algorithm, Algorithm fusion.

ABSTRACT

Accurate prediction of environmental changes in *Agaricus bisporus* cultivation is essential for better managing climatic conditions within mushroom houses, ultimately enhancing the yield and quality of *Agaricus bisporus*. However, traditional control systems for *Agaricus bisporus* production environments can only monitor the current conditions and lack the ability to predict environmental changes, leading to issues such as delayed feedback on environmental data and the effectiveness of control measures. In response to these challenges, this study establishes a temperature and humidity prediction model based on the DOA-BP algorithm. Experimental results demonstrate that the DOA optimization algorithm exhibits strong global search capabilities. By rapidly searching for optimal weights and biases, it overcomes the drawback of the BP neural network getting stuck in local minima, accelerates network convergence, and improves the performance of the BP neural network. The MAE values for temperature and humidity prediction inside the mushroom house are 0.021 and 0.013, respectively. The RMSE values are 0.044 and 0.038, respectively, and the R2 values are 0.976 and 0.968, respectively. Through validation, the DOA-BP temperature and humidity prediction model proposed in this study accurately predicts the temperature and humidity inside mushroom houses. This model can enhance environmental control for cultivation, optimize resource utilization, and reduce production costs effectively.

摘要

精准预测双孢菇生产环境变化有助于更好的管理菇房内的气候条件，提高双孢菇产量与质量。但传统的双孢菇生产环境控制系统只能对当前环境状况进行监测，无法对环境变化做出预判，导致环境数据的反馈和调控措施的生效都存在滞后性等问题。针对以上问题，本文建立了基于 DOA-BP 的温湿度预测模型，实验结果表明，DOA 优化算法具有较强全局搜索能力，通过快速搜索最优权值和偏置，克服了 BP 神经网络陷入局部极小值的缺点，加快网络收敛速度，提高了 BP 神经网络的性能。该预测模型对菇房内温湿度预测的 MAE 值分别为 0.021、0.013，RMSE 值分别为 0.044、0.038，R2 值为 0.976、0.968。通过验证，本研究提出的 DOA-BP 温湿度预测模型能够精准预测菇房温湿度，可以更好的控制栽培环境，还可以合理安排资源利用，降低生产成本。

INTRODUCTION

To achieve precision, standardization, and year-round production of *Agaricus bisporus*, the rapid development of environmentally controlled closed-system factory production is evident (Mao et al., 2018). Temperature and humidity, as crucial environmental factors in the growth process of *Agaricus bisporus*, play a significant role throughout the entire cultivation cycle, directly influencing the quality and yield of *Agaricus bisporus*. Closed mushroom house environmental control systems can analyse and make regulatory decisions on monitored environmental factors. However, they lack the capability to predict future environmental changes, resulting in a certain lag in the feedback of abrupt environmental data and the effectiveness of control measures (Zhao et al., 2020).

Tianhua Li, Professor; Yinhang Dong, Postgraduates; Guoying Shi, Senior experimentalist; Guanshan Zhang, Doctoral students; Chao Chen, Undergraduate; Jianchang Su, Researcher.

Therefore, establishing a high-precision prediction model with temperature and humidity as output variables is crucial. This model aims to anticipate the changing trends of temperature and humidity within the mushroom house over a future period, allowing timely adjustments to maintain optimal conditions for stable *Agaricus bisporus* production.

Greenhouse microclimate prediction models can be categorized into mechanistic models and data models (Chen *et al.*, 2017). Mechanistic models simulate and predict greenhouse environmental conditions based on fluid dynamics and heat and mass transfer mechanisms (Zhou *et al.*, 2014). However, due to the dynamic interdependence of various environmental factors within the greenhouse, these models require extensive physical parameters and environmental data, leading to challenges such as complex modelling and poor adaptability (Saberian *et al.*, 2019).

Data models, also known as black boxes, employ data fitting algorithms to ensure the predicted values align with actual values (Wang *et al.*, 2009). Previous studies, such as that by Zong *et al.*, (2022), utilized multiple linear regression, support vector machine regression, and random forest regression to construct nighttime hourly temperature prediction models under three different weather conditions in the greenhouse. Zou Weidong *et al.*, (2015), improved the extreme learning machine for predicting temperature and humidity in a sunlight greenhouse.

Mao Xiao Juan *et al.*, (2023), proposed a grey wolf optimization algorithm-based long short-term memory network model for greenhouse temperature prediction. However, these models were limited by a finite number of samples, and some were only studied under specific seasons or meteorological conditions, restricting their generalization capabilities.

Tian *et al.*, (2020), proposed a combination method of MA-ARIMA-GASVR based on mining historical temperature data time-series information to establish a temperature prediction model. However, this model is relatively complex, demanding substantial computational resources and time, limiting its practical application.

Zu *et al.*, (2023), introduced a sparrow search algorithm (SSA)-optimized long short-term memory network (LSTM) greenhouse environment prediction model. Yet, the limited local search capabilities of this optimization algorithm may lead to local optimal solutions, impacting the model's overall search capabilities and optimization effectiveness.

Zhang *et al.*, (2021), established an Elman neural network prediction model based on collected environmental historical data. However, this model may encounter challenges such as gradient vanishing or exploding when predicting long time series, making it difficult to stabilize training networks and affecting predictive performance.

The aforementioned studies share common issues, including limited coverage of sample data, biased model selection, complexity, and susceptibility to locally optimal solutions (Johnstone *et al.*, 2021). In this paper, a DOA-BP-based industrial production environment prediction model for *Agaricus bisporus* was proposed. With the advantages of the DOA optimization algorithm, such as strong global search ability, parallelism and simplicity, the weight and bias of the BP network were accelerated to optimize, and environmental data of different regions of mushroom houses were collected through multiple groups of sensors. The 3sigma criterion and linear interpolation method were used to process the original data, and the input matrix of the processed environmental data was constructed according to the time series and input into the DOA-BP model for training, to achieve the accurate prediction of the production environment of the *Agaricus bisporus*.

This study compares the total energy consumption and environmental data between Mushroom House 28, which uses temperature and humidity data predicted by the DOA-BP model for climate control, and Mushroom House 29, which uses real-time sensor data for climate control. The results show that Mushroom House 28's temperature control equipment consumed 10.8% less total energy, and its humidification equipment consumed 15.4% less total energy compared to Mushroom House 29. Overall, Mushroom House 28's total energy consumption was 12.6% lower than that of Mushroom House 29. Additionally, the temperature and humidity in Mushroom House 28 remained stable and within optimal ranges, while Mushroom House 29 also maintained optimal temperature and humidity ranges, but with greater fluctuations.

The remaining sections of this article are organized as follows. In the second section, the DOA and BP algorithms are individually elaborated, and the fusion process of the two algorithms is summarized. The third section discusses the source and processing methods of the required data. In the fourth section, validation of the fusion algorithm is conducted, and its practical application in the field is demonstrated. The conclusion of this article is presented in the fifth section.

MATERIALS AND METHODS

DOA-BP ENVIRONMENTAL PREDICTION MODEL

DOA optimization algorithm

The Dingo Optimization Algorithm (DOA), proposed by Hernán Peraza-Vázquez and colleagues in 2021, is a novel bio-inspired algorithm (Hernán et al., 2021). This algorithm draws inspiration from the hunting strategies of wild dingoes in Australia, including group attacks, grouping strategies, scavenging behaviour, and the incorporation of survival tactics (Cai et al., 2023). These additions enhance the overall efficiency and performance of the method, endowing it with strong optimization capabilities and rapid convergence speed.

The fundamental mathematical model of the algorithm is as follows.

1. Population Initialization

$$\vec{x}_i(t) = lb_i(t) + rand(ub_i(t) - lb_i(t)) \quad (1)$$

where $\vec{x}_i(t)$ represents the position of the current optimizing individual, whose value varies between the lower search boundary lb_i and the upper search boundary ub_i of the Australian wild dog individual; t is the iteration number, $rand$ is a randomly generated number uniformly distributed between $[0,1]$.

2. Hunting strategy

1) Group Attack: Australian dingoes engage in coordinated group attacks when hunting large prey. They work together to locate the prey's position and surround it for a group attack. As illustrated in Figure 1, this behaviour can be described by (2).

$$\vec{x}_i(t+1) = \beta_1 \sum_{k=1}^{na} \frac{[\vec{\varphi}_k(t) - \vec{x}_i(t)]}{na} - \vec{x}_*(t) \quad (2)$$

When $random < P$ and $random < Q$ are satisfied. Where $random$ is a uniformly generated random number in the range $[0,1]$, and P and Q are the probability values for the dingo population to execute their respective strategies. In this context, $\vec{x}_i(t+1)$ represents the new position of an individual, na is a randomly generated integer inversely proportional to $[2, sizepop/2]$, where $sizepop$ is the total population size. Additionally, $\vec{\varphi}_k(t)$ denotes the set of individuals that will attack, with $\varphi \in X$, where X is a randomly generated dingo population. $\vec{x}_i(t)$ is the current optimizing individual, $\vec{x}_*(t)$ is the best individual found in the previous iteration, and β_1 is a uniformly generated random number in the range $[-2,2]$, serving as a scaling factor for the magnitude of individual movement trajectories.

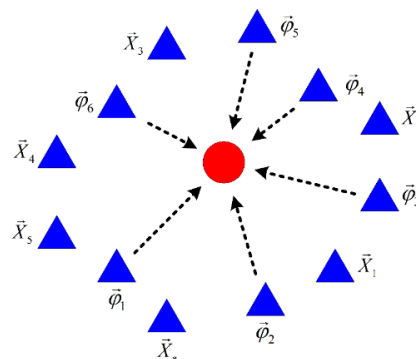


Fig. 1 - Group Attack Strategy

2) Persecution Strategy: Australian dingoes, when hunting small animals such as rabbits, employ a strategy where individual dingoes continuously pursue and approach the prey until it is captured individually. This behaviour can be described by (3).

$$\vec{x}_i(t+1) = \vec{x}_*(t) + \beta_1 * e^{\beta_2} * (\vec{x}_{r_1}(t) - \vec{x}_i(t)) \quad (3)$$

When $random < P$ is satisfied the following actions are executed. $\vec{x}_i(t+1)$ represents the new position of the individual, where $\vec{x}_i(t)$ is the current optimizing individual, and $\vec{x}_*(t)$ is the best individual found in the previous iteration. β_1 is the same as in (2), and β_2 is a uniformly generated random number in the range $[-1,1]$. r_1 is a random number generated from the range $[1, sizepop]$, and $\vec{x}_{r_1}(t)$ is the position of the randomly selected individual at index r_1 , where $i \neq r_1$.

3) Scavenging: Australian dingoes exhibit scavenging behaviour when randomly wandering in their habitat and come across carrion as a food source. This behaviour can be described by (4).

$$\vec{x}_i(t+1) = \frac{1}{2} \left[e^{\beta_2} * \vec{x}_{r_1}(t) - (-1)^\sigma * \vec{x}_i(t) \right] \tag{4}$$

When $random > P$ is satisfied, the following actions are executed. $\vec{x}_i(t+1)$ represents the new position of the individual, where $\vec{x}_i(t)$ is the current optimizing individual. $\vec{x}_{r_1}(t)$ is the position of the randomly selected individual at index r_1 , where $i \neq r_1$. β_2 is the same as in (3), and σ is a uniformly generated random number in the range $[0, 1]$.

4) Survival Strategy: Due to reasons such as illegal hunting, Australian dingoes are facing the risk of extinction. The survival rate of Australian dingoes is described by (5). (6) is applicable when the survival rate is less than or equal to 0.3.

$$survival(i) = \frac{fitness_{max} - fitness(i)}{fitness_{max} - fitness_{min}} \tag{5}$$

$$\vec{x}_i(t) = \vec{x}_*(t) + \frac{1}{2} \left[\vec{x}_{r_1}(t) - (-1)^\sigma * \vec{x}_{r_2}(t) \right] \tag{6}$$

Where $fitness_{max}$ and $fitness_{min}$ are the fitness values of the best and worst individuals in the current generation, and $fitness(i)$ is the current fitness value of the i th individual. The training data error absolute value is used as the individual fitness value, where $\vec{x}_i(t)$ represents the dingo individual with a lower survival rate that will be updated. r_1 and r_2 are random numbers generated within the range $[1, sizepop]$, and $r_1 \neq r_2$. $\vec{x}_*(t)$ is the best individual found in the previous iteration.

Bp neural network

BP neural network is a concept proposed by *Rumelhart et al.* and other scientists in 1986. Each layer of neurons is fully connected with the adjacent layer of neurons, and there is no connection between neurons in the same layer and no feedback connection between neurons in each layer. It is a feedforward neural network system with hierarchical structure trained according to the error reverse propagation algorithm (*Xu et al., 2017*). Its training algorithm is simple, can handle various types of data, and has good adaptability to nonlinear problems (*Huang et al., 2020*).

This paper adopts a three-layer BP neural network, consisting of the input layer, hidden layer, and output layer. The number of nodes in the input and output layers is set to 6 and 2, respectively. The number of nodes in the hidden layer is determined based on the empirical formula (*Ding et al., 2023*) (7).

$$j = \sqrt{m+n} + a \tag{7}$$

In the formula, n represents the number of nodes in the input layer, m is the number of nodes in the output layer, j is the number of nodes in the hidden layer, based on experience, choosing a between 1 and 10 often helps to find a balance between computational efficiency and model accuracy. According to (7), the preferred range for j is 4 to 13.

Figure 2 shows the topology of BP neural network, where h is the output of the hidden layer, Y is the output of the output layer, W_{ij} is the weight between the j^{th} neuron of the hidden layer and the i neuron of the input layer, b_j is the bias of the j^{th} neuron of the hidden layer, and W_{ij} is the weight between the j^{th} neuron of the hidden layer and the l neuron of the output layer. b_1 and b_2 are the bias of neurons in the output layer.

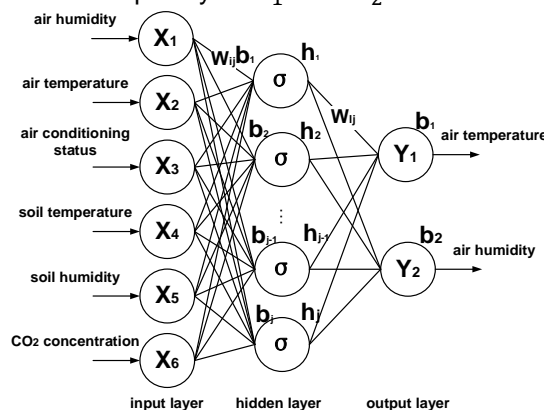


Fig. 2 - Structure of BPNN network

DOA-BP network fusion model

In the BPNN model, weights and biases play a crucial role in the model's fitting capability. In traditional BPNN models, weights and biases are typically set randomly based on empirical experience, which may lead the model to get stuck in local minima during network training, making it challenging to achieve optimal performance. Therefore, the DOA optimization algorithm is employed, known for its robust global search capabilities. Through hunting and survival strategies, optimal parameters are obtained for assigning and training the weights and biases of the BP neural network. This approach helps overcome the drawback of susceptibility to local minima, accelerates network convergence, and enhances the performance of the neural network. The algorithmic process is illustrated in Figure 3, and the specific steps are outlined below.

(1) DOA Initialization: Initialize individual positions by randomly generating a certain number of dingo individuals within the boundary conditions of the search space. Set their positions as random combinations of weights and biases.

(2) Fitness Evaluation: Input historical environmental data and perform forward propagation through the BP neural network to generate predicted values. Calculate the prediction error of each individual corresponding to the BP neural network, and evaluate the fitness of each individual using the loss function.

(3) Selection and Replication: Select individuals with better performance based on their fitness values. Retain these individuals for generating the next generation, and replicate the selected individuals to maintain the population size.

(4) Update Individual Positions: Update individual positions through group attacks, grouping strategies, and scavenging behaviour, ensuring that the updated positions do not exceed the allowable range of weights and biases.

(5) Convert the updated individual positions into combinations of weights and biases, and apply them to the BPNN model. Evaluate the positions through the fitness function to identify the individual with the optimal fitness.

(6) Update the Best Individual: Select the dingo individual with the best fitness value in the population as the current best individual. Record and update the global optimum solution.

(7) Check whether the set error or maximum iteration conditions are met. If satisfied, set the global optimal weights and biases as the parameters for the BPNN. If not satisfied, return to step (2).

(8) Model Prediction: Input new environmental data into the optimized BP neural network. Generate prediction results through forward propagation. Output the predicted temperature and humidity values.

(9) Model Evaluation and Validation: Evaluate the predictive performance of the model using a test dataset and calculate error metrics.

Through these steps, the weights and biases of the BP neural network will be set to search and optimize in the solution space of the DOA. By iteratively updating individual positions, the algorithm eventually finds the individual with the minimum fitness value, and its corresponding weights and biases are considered as the optimal parameters for the BPNN model.

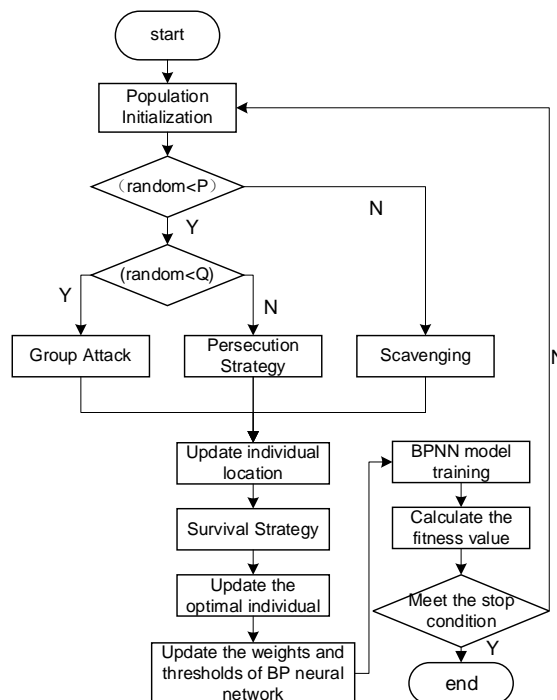


Fig. 3 - DOA-BPNN Flowchart

Model evaluation metrics

To provide a visual representation of the predictive performance and accuracy of the model, the mean absolute error (*MAE*), root mean square error (*RMSE*), and coefficient of determination (*R*²) are selected as performance evaluation metrics for the model (*Liang et al., 2023*). Here, *N* represents the number of test samples, *y_i* is the actual value, *ŷ_i* is the predicted value, and *ȳ_i* is the mean value.

$$MAE = \frac{1}{N} \sum_{i=1}^N |y_i - \hat{y}_i| \tag{8}$$

$$RMSE = \sqrt{\frac{1}{N} \sum_{i=1}^N (y_i - \hat{y}_i)^2} \tag{9}$$

$$R^2 = \frac{\sum_{i=1}^N (y_i - \bar{y}_i)^2}{\sum_{i=1}^N (y_i - \bar{y}_i)^2} \tag{10}$$

DATA SOURCE AND PROCESSING

Overview of the experimental area

The experimental site is located at the Shandong Century Smart Agriculture Technology Co., Ltd. *Agaricus bisporus* Cultivation Base in Jining City, Shandong Province, China, specifically in Mushroom House No. 28 (35.224°N, 116.929°E). The mushroom house measures 18 m in length, 6.5 m in width, and 4.6 m in height. It is constructed using 100 mm thick polyurethane insulation boards, with a ground surface of 180 mm thick cement hardening. Each mushroom house has an area of approximately 117 m² and is equipped with two sets of aluminium alloy planting racks. These racks are 15 m long, and 1.4 m wide in planting face, with a layer height of 600 mm, totalling 6 layers.

The mushroom house is equipped with an intelligent temperature control system, humidification system, and ventilation system. When the temperature changes, the temperature control system activates the air conditioning through an S-shaped temperature control pipeline. In case of an increase in carbon dioxide concentration, the ventilation system extracts air from the mushroom house through the return air vent and introduces fresh air through the fresh air vent. When humidity decreases, the humidification system is activated, and the solenoid valve is opened for spray humidification.

Internet of Things data acquisition system

Build a greenhouse environment IoT data acquisition system, real-time and accurate. Obtaining environmental information is the premise and guarantee of realizing greenhouse environmental prediction. The IoT data-acquisition system mainly consists of a CPU (*Teik et al., 2021*), perception module and the transmission module is composed of the sensing module to complete the air temperature and relative humidity. Measurement of degree, carbon dioxide concentration and soil temperature and humidity, complete the collection of air conditioner on/off status. The relevant parameters of the sensor are shown in Table 1. The overall system architecture is shown in Figure 4.

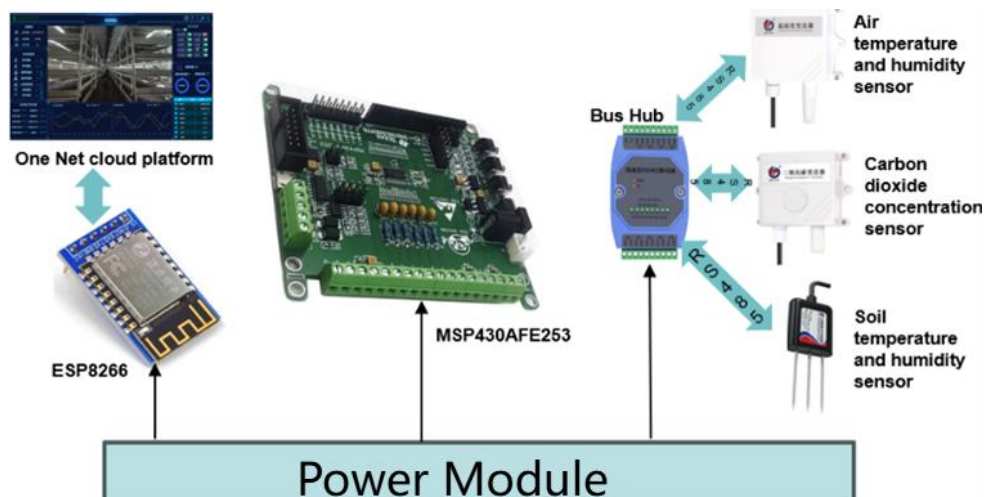


Fig. 4 - Lot system architecture diagram

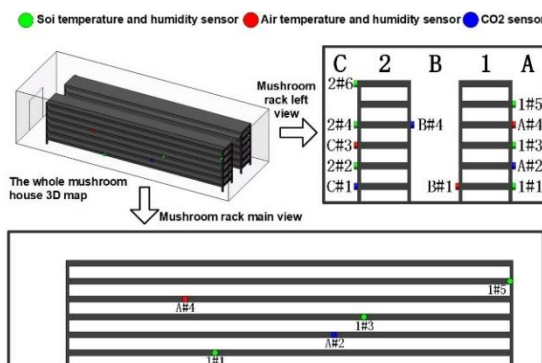


Fig. 5 - Three-dimensional map of sensor layout position

To ensure the accuracy of collecting environmental data in the mushroom house, the following sensor layout scheme is employed: Two sets of planting racks (15 m, 6 layers each), sensors are placed at 5 m intervals on 1st layer of Planting Rack #1 (1#1), 3rd layer of Planting Rack #1 (1#3), 5th layer of Planting Rack #1 (1#5), 2nd layer of Planting Rack #2 (2#2), 4th layer of Planting Rack #2 (2#4), and 6th layer of Planting Rack #2 (2#6). Air temperature and humidity sensors are placed on the west side of A#4 (1st layer, 4th layer of Planting Rack #1), east side of B#1 (1st layer of Planting Rack #1), and east side of C#3 (3rd layer of Planting Rack #2). CO2 sensors are placed on the west side of A#2 (2nd layer of Planting Rack #1), east side of B#4 (4th layer of Planting Rack #2), and east side of C#1 (1st layer of Planting Rack #2).

This optimized sensor layout maximizes the sensing range, reduces blind spots and overlapping areas, avoids resource waste and redundancy, and enhances detection accuracy and reliability.

The schematic diagram of the sensor deployment positions is shown in Figure 5, where the top left corner represents the overall three-dimensional view of the mushroom house, the top right corner is the main view of the mushroom rack, and the bottom shows the side view of Planting Rack #1. During the experiment, two sets of planting racks inside the mushroom house were used for the cultivation of *Agaricus bisporus* using the covered soil cultivation method, and the mushrooms were in the fruiting body growth stage (mushrooming stage and mushrooming period). The experimental site is illustrated in Figure 6.



Fig. 6 - Interior environment of mushroom house

a) East aisle; b) Centre aisle; c) West aisle

Table 1

| Sensor parameters | | | |
|--------------------------------------|--------------|--|--|
| Sensor type | Model | Range | Precision |
| Air temperature and humidity sensor | RS-WS-N1-2-* | Temperature: -40°C~+80°C Humidity:0%RH~100%RH | Temperature: ±0.4°C Humidity: ±2%RH |
| CO2 sensor | RS-CO2*-*-2 | 0-5000ppm | ±30ppm+3%F.S |
| Soil temperature and humidity sensor | RS-WS-*-TR-1 | Temperature: -40°C~+80°C Humidity:0%RH~100%RH | Temperature: ±0.5°C Humidity: ±3%RH |

Data collection and preprocessing

Data collection

Through the intelligent data collection system, automatically collect six types of data: air temperature, air humidity, soil temperature and humidity, CO₂ concentration, and air conditioner on/off status (0/1), was conducted from May 3, 2023, to June 7, 2023. This period corresponds to the fruiting body growth stage of *Agaricus bisporus* (fruiting stage and mushrooming period). The sampling interval was 10 minutes, resulting in 5040 data points for a single environmental parameter and a total of 30,240 data points.

The environmental data from May 3, 2023, to June 1, 2023, were used as the training set, while the data from June 2, 2023, to June 7, 2023, were used as the validation set for model verification. Some raw data, as illustrated in Figure 7 (taking the temperature data from May 3, 2023, to May 18, 2023, as an example), indicate the presence of missing data and instances of abrupt temperature changes to zero.

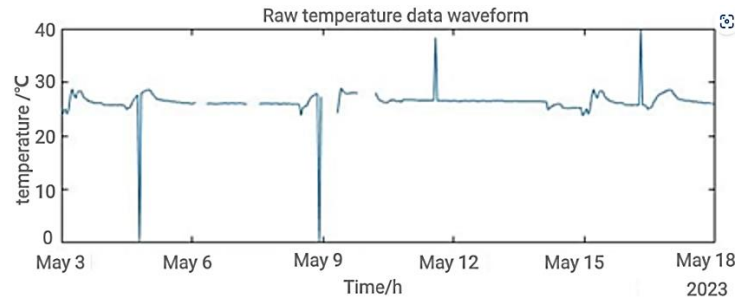


Fig. 7 - Partial raw data

Data preprocessing

Exposing sensors to prolonged high-humidity environments in the mushroom house can affect their accuracy. Additionally, issues such as network transmission quality and control equipment malfunctions may lead to anomalies and data gaps, impacting the accuracy of the prediction model. In this study, the 3-sigma criterion is employed to eliminate outliers from the collected raw data, and linear interpolation is used to impute missing data. As shown in Figure 8 (taking the temperature data from May 3, 2023, to May 18, 2023, as an example), the upper part displays temperature data after removing outliers, while the lower part shows temperature data after interpolation.

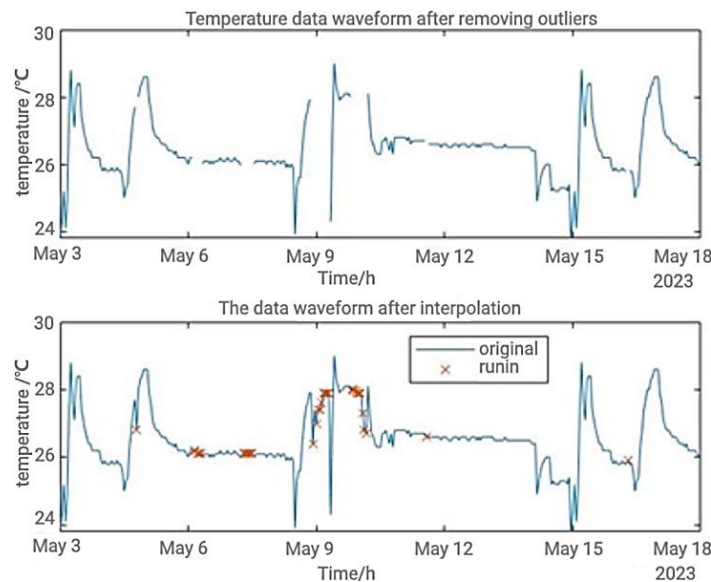


Fig. 8 - Data preprocessing

Data normalization

Normalization of data eliminates differences in range and dimensionality among various environmental parameters within the mushroom house, enhancing the stability, accuracy, and efficiency of the model. This ensures consistent weights for features, thereby better adapting to the modelling process (Liang *et al.*, 2023).

$$X_i = \frac{x_i - x_{i\min}}{x_{i\max} - x_i} \quad (11)$$

Here, X_i represents the normalized value, and x_i is the environmental data within the sample dataset X . $x_{i\min}$ and $x_{i\max}$ represent the minimum and maximum values of the data belonging to the sample before normalization.

TEST

Test platform

The platform configuration used for training is as follows: operating system Windows 10 Professional 64-bit, processor 12th Gen Intel Core i9-12900KF, graphics card NVIDIA GeForce RTX 3090, and memory 128GB. The programming software used is Matlab R2023a.

Model parameter settings

The parameter settings are as follows: In the DOA optimization model, a larger population size can expand the search space and improve global search capabilities, but it increases computational complexity. Set the total number of dingoes to 200. The probability of hunting or scavenging strategy, P, is set to 0.5, and the probability of group attack or persecution, Q, is set to 0.7. The search boundaries define the range of individual searches for new solutions. A larger search boundary can expand the search space, aiding global search but may slow down the search speed. The upper and lower search boundaries of the population individuals, lb_i and ub_i , are set to -10 and 10, respectively.

The selected three-layer BP neural network model has an input layer with 6 nodes and an output layer with 2 nodes. Through program execution, under the same sample set and number of training iterations, the root mean square error (RMSE) for different numbers of hidden layer nodes is calculated, as shown in Figure 9. When the number of hidden layer nodes is 14, the RMSE is minimized.

Therefore, the BP neural network model is configured with 14 hidden layer nodes, and the activation function for each neuron is the sigmoid function: $\sigma(x) = 1/(1 + e^{-x})$. The loss function used is the mean square error $E = \frac{1}{2} \sum_{l=1}^k (d_l - y_l)^2$, with a learning rate ϵ set to 0.01. The training target for the minimum error is set to 0.0001, and the time step, determining the utilization of historical information and model prediction performance, is set to 15. The maximum number of iterations is set to 1000. The parameter settings for the DOA-BP prediction model are summarized in Table 2.

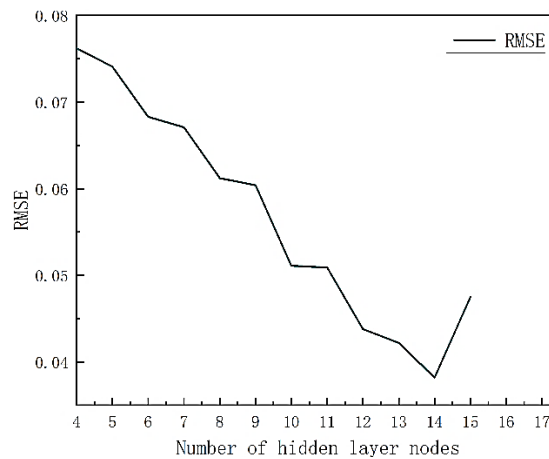


Fig. 9 - Root mean square error corresponding to node number of different hidden layers

Table 2

| Model parameter Settings | |
|------------------------------|------------------|
| Name of parameter | Parameter values |
| Population quantity | 200 |
| Probability of P | 0.5 |
| Probability of Q | 0.7 |
| Learning rate | 0.01 |
| Network layer number | 3 |
| Input layer node | 5 |
| Hidden layer node | 13 |
| Output layer node | 2 |
| Time step | 15 |
| Search boundary | -10~10 |
| Target minimum error | 0.001 |
| Maximum number of iterations | 1000 |

RESULT AND ANALYSIS

Data preprocessing impact analysis

Table 3 presents a comparative analysis of the DOA-BP prediction model's temperature forecasting performance before and after data preprocessing. From the table, it can be observed that, after data preprocessing, the DOA-BP model's Mean Absolute Error (MAE) and Root Mean Square Error (RMSE) for temperature prediction decreased by 0.005 and 0.057, respectively, compared to before preprocessing. The coefficient of determination (R^2) increased by 0.075. Similarly, for humidity prediction, the MAE and RMSE decreased by 0.009 and 0.0047, respectively, and R^2 increased by 0.057. This indicates that data missing and anomalies have a negative impact on the prediction model, demonstrating the effectiveness of using the 3-sigma criterion and linear interpolation for data preprocessing.

Table 3

Comparative analysis of DOA-BP prediction model's effect on temperature prediction before and after data preprocessing

| Temperature | MAE | RMSE | R^2 |
|-------------------|-------|-------|-------|
| Before repair | 0.026 | 0.101 | 0.901 |
| After restoration | 0.021 | 0.044 | 0.976 |
| Humidity | MAE | RMSE | R^2 |
| Before repair | 0.022 | 0.085 | 0.911 |
| After restoration | 0.013 | 0.038 | 0.968 |

Prediction results and comparative analysis

The obtained DOA-BP prediction model was used to forecast the temperature and humidity inside the mushroom cultivation facility for the next 5 days. The results are depicted in Figure 10.

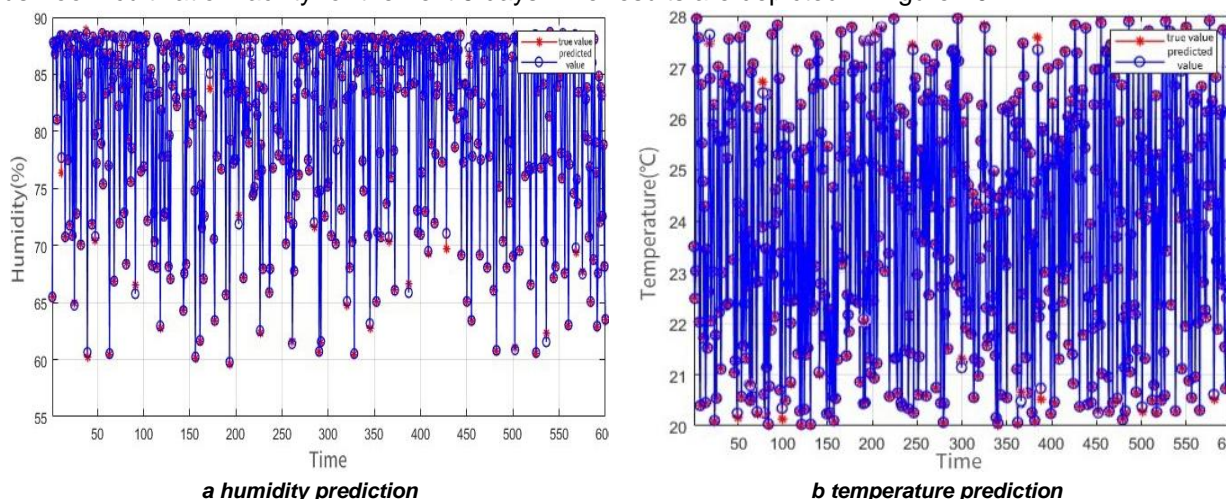


Fig. 10 - Prediction results of temperature and humidity in mushroom house based on DOA-BP

The DOA-BP model achieved R^2 , MAE, and RMSE values of 0.976, 0.021, and 0.044 for temperature prediction, respectively. For humidity prediction, the model achieved R^2 , MAE, and RMSE values of 0.968, 0.013, and 0.038, respectively.

To validate the scientific and superior performance of the proposed DOA-BP neural network prediction model, this study conducted a comparative analysis of predictive performance with BP neural network, genetic algorithm optimized BP neural network (GA-BP), and particle swarm optimization optimized BP neural network (PSO-BP) under the same input parameters and computational environment. As seen in Table 4, For humidity prediction, the R^2 of DOA-BP model increased by 8.3%, 5.9%, and 5.4% compared to BP model, GA-BP model, and PSO-BP model, respectively. Moreover, the MAE and RMSE decreased by 12.5%, 54.2% compared to BP model, 30%, 48.2% compared to GA-BP model, and 8.7%, 46.9% compared to PSO-BP model. As seen in Table 5, for temperature prediction in the mushroom cultivation facility, the R^2 of DOA-BP model increased by 6%, 4.6%, and 4.4% compared to BP model, GA-BP model, and PSO-BP model, respectively. Additionally, the MAE and RMSE decreased by 35%, 56.3% compared to BP model, 40.9%, 51.9% compared to GA-BP model, and 38.1%, 51.3% compared to PSO-BP model.

The number of iterations in which the best performance of each model for temperature and humidity prediction appears respectively were 132 and 174 for DOA-BP, 352 and 326 for BP, 205 and 241 for GA-BP, and 197 and 225 for PSO-BP. In conclusion, the DOA-BP model demonstrated superior predictive performance, accurately forecasting temperature and humidity in the mushroom cultivation facility, while also improving model efficiency.

Table 4

Comparison of humidity evaluation indexes predicted by models

| Model(humidity) | MAE | RMSE | R ² | Iterations |
|-----------------|-------|-------|----------------|------------|
| BP | 0.020 | 0.087 | 0.913 | 352 |
| GA-BP | 0.023 | 0.079 | 0.925 | 205 |
| PSO-BP | 0.021 | 0.078 | 0.927 | 197 |
| DOA-BP | 0.013 | 0.038 | 0.968 | 132 |

Table 5

Comparison of temperature evaluation indexes predicted by models

| Model(temperature) | MAE | RMSE | R ² | Iterations |
|--------------------|-------|-------|----------------|------------|
| BP | 0.024 | 0.096 | 0.912 | 316 |
| GA-BP | 0.030 | 0.085 | 0.922 | 241 |
| PSO-BP | 0.023 | 0.083 | 0.926 | 225 |
| DOA-BP | 0.021 | 0.044 | 0.976 | 174 |

Experimental validation

Mushroom house No. 28 and Mushroom house No. 29 of the mushroom culture base of Shandong Century Smart Agricultural Technology Co., LTD., Jining City, Shandong Province, were selected. The two mushroom houses were in the fruiting stage, and the suitable temperature range was 20-24°C and the suitable humidity range was 80-85%. The automatic environmental control system of mushroom room No. 28 uses the temperature and humidity data predicted by the DOA-BP model to adjust temperature and humidification, while the automatic environmental control system of mushroom room No. 29 directly adjusts temperature and humidification according to the real-time sensor data. The observation time is from July 1, 2023 to July 4, 2023, and the environmental data is collected every 10 minutes. Record the total power consumed by the device. The total electric energy consumption and environmental data of the equipment in Room No. 28 and Room No. 29 were compared and analysed. As shown in the table 5, the total electric energy consumed by the temperature regulating equipment in Room 28 is reduced by 10.8% compared with room 29, the total electric energy consumed by the humidifying equipment is reduced by 15.4% compared with room 29, and the total electric energy is reduced by 12.6% compared with room 29.

Figure 11 shows the temperature data and humidity data of mushroom room No. 28 and No. 29 within 5 days. The overall temperature and humidity of mushroom room No. 28 changed steadily, and always kept within the appropriate temperature and humidity range; Room No. 29 kept the overall temperature and humidity within the appropriate range. But the temperature and humidity change range was large.

Based on the above analysis, the DOA-BP temperature and humidity prediction model proposed in this study can accurately predict the temperature and humidity of mushroom houses, which can better control the cultivation environment, rationally arrange the utilization of resources, and reduce the production cost.

Table 6

Power consumption of equipment

| Room | thermostat consumes electricity (KW*h) | humidifier consumes electrical energy (KW*h) | Total electric energy (KW*h) |
|-----------------------|--|--|------------------------------|
| Mushroom house No. 28 | 371 | 231 | 602 |
| Mushroom house No. 29 | 416 | 273 | 689 |

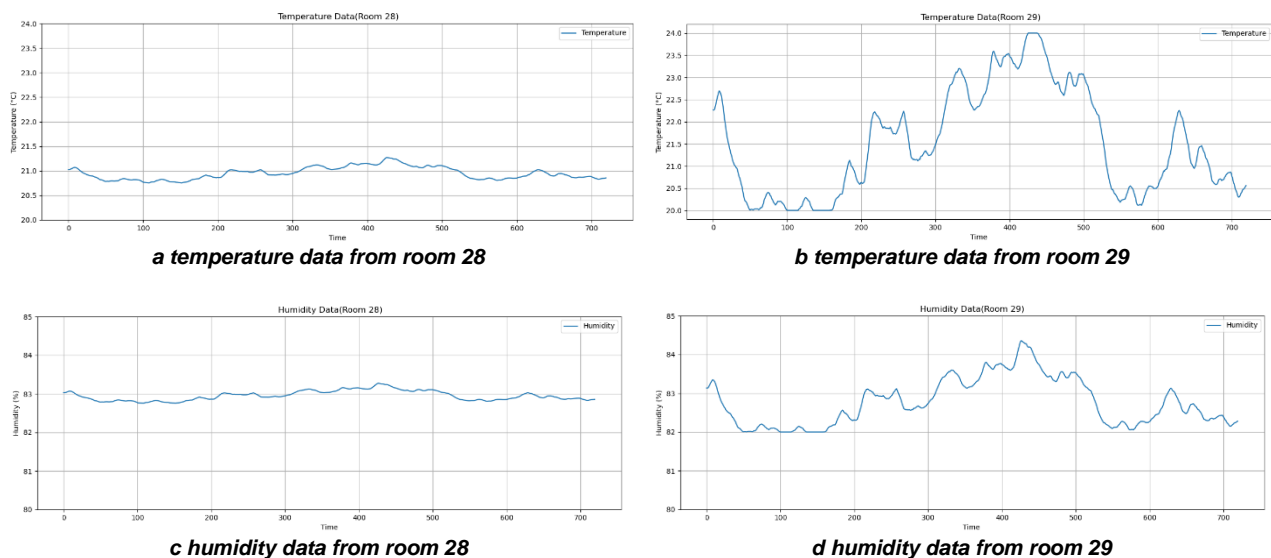


Fig. 11 - The change of the overall temperature and humidity of the mushroom house

CONCLUSIONS

(1) The temperature and humidity prediction model for the industrialized production of *Agaricus bisporus* based on the DOA-BP proposed in this study utilizes the strong global search capability of the DOA optimization algorithm to perform rapid search and optimization of the weights and thresholds of the BP neural network. This approach addresses issues such as low model prediction accuracy resulting from manually setting weights and biases through random empirical methods. It helps overcome the drawbacks of easily falling into local minima, accelerates network convergence, and improves the overall performance of the neural network.

(2) The greenhouse environment Internet of Things data acquisition system is used to obtain environmental information in real-time and accurately. At the same time, the abnormal environmental data collected is eliminated based on the 3sigma criterion, and the missing data is interpolated by the linear interpolation method. The input matrix of the processed environmental data is constructed according to the time series and input into the DOA-BP model for training. The accuracy of temperature and humidity prediction is significantly improved by the model, which provides a guarantee for realizing the accurate prediction of the greenhouse environment.

(3) Experimental results indicate that the model achieves determination coefficients (R^2) of 0.976 and 0.968 for temperature and humidity predictions, respectively. The performance surpasses that of BP neural networks, genetic algorithm-optimized BP neural networks, and particle swarm optimization-optimized BP neural networks. While enhancing prediction accuracy, the model also considers operational efficiency, thus improving the overall predictive performance. It exhibits notable superiority in predicting the temperature and humidity of the *Agaricus bisporus* production environment.

(4) Through validation, the DOA-BP temperature and humidity prediction model proposed in this study accurately forecasts the conditions in mushroom houses. It enables better control of cultivation environments and facilitates efficient resource allocation, thereby reducing production costs.

ACKNOWLEDGEMENT

This work was supported by the Major Science and Technology Innovation Project of Shandong Province: Research and Development and Industrialization of key technologies for intelligent Factory Production of edible fungi (2022CXGC010609); Shandong Vegetable Industry Technology System Project (SDAIT-05-11)

REFERENCES

- [1] Chen L., Du S., Li J., He Y., Liang M. (2017). Online identification method of parameters for greenhouse temperature prediction self-adapting mechanism model (温室环境温度预测自适应机理模型参数在线识别方法). *Transactions of the Chinese Society for Agricultural Engineering*, Vol. 33, pp. 315-321.
- [2] Cai X., Zhu J., Liu M., Liu J., Meng Z., Yu Y. (2023). Peak shaving strategy of electric vehicles based on an improved dingo optimization algorithm (基于改进野狗优化算法的电动汽车调峰策略). *Energy Storage Science and Technology*, Vol. 12, pp. 1913-1919.

- [3] Ding G., Shi X., Hu J. (2023). Prediction model of the aeration oxygen supply for aerobic composting using CGA-BP neural network (基于 CGA-BP 神经网络的好氧堆肥曝气供氧量预测模型). *Transactions of the Chinese Society for Agricultural Engineering*, Vol. 39, pp. 211-217.
- [4] Johnstone C., Sulungu ED. (2021). Application of neural network in prediction of temperature: a review. *Neural computing and applications*, Vol. 33, pp. 11487-11498.
- [5] Huang Y., Xiang Y., Zhao R., Cheng Z. (2020). Air quality prediction using Improved PSO-BP neural network. *IEEE Access*, vol. 8, pp. 346-353.
- [6] Hernán P., Adrian F., Gustavo E., Ana B., Jonás V., Fernando R. (2021). A bio-inspired method for engineering design optimization inspired by dingoes hunting strategies. *Mathematical Problems in Engineering*, Vol. 138, pp. 1-19.
- [7] Liang W., Xue W., Ma J., Cheng L., Xu H. (2023). Soft measurement of main steam flow in municipal solid waste incinerator based on WOA-Elman neural network (基于 WOA-Elman 神经网络的城市固废焚烧炉主蒸汽流量软测量). *Control Engineering*, Vol. 31, pp. 1-7.
- [8] Mao H., Jin C., Chen Y. (2018). Research progress and prospect on control methods of greenhouse environment (温室环境控制方法研究进展分析与展望). *Transactions of the Chinese Society for Agricultural Machinery*, Vol. 49, pp. 1-13.
- [9] Mao X., Bao T., Xun G., Li D., Wang B., Ren N. (2023). Prediction of temperature in the greenhouse of vegetable growing based on GWO-LSTM (基于 GWO-LSTM 的设施蔬菜温室温度预测). *Journal of Chinese Agricultural Mechanization*, vol. 44, pp. 116-123.
- [10] Rumelhart D., Hinton G., Williams J. (1986). Learning representations by back-propagating errors. *Nature*, Vol. 323, pp. 533-536.
- [11] Saberian A., Sajadiye S. (2019). The effect of dynamic solar heat load on the greenhouse microclimate using CFD simulation. *Renewable Energy*, Vol. 138, pp. 722-737.
- [12] Tian D., Wei X., Wang Y., Zhao A., Mu W., Feng J. (2020). Prediction of temperature in edible fungi greenhouse based on MA-ARIMA-GASVR (基于 MA-ARIMA-GASVR 的食用菌温室温度预测). *Transactions of the Chinese Society for Agricultural Engineering*, Vol. 36, pp. 190-197.
- [13] Teik TS., Krishnen G., Khulidin KA., Tahir M., Hashim M., Khairudin S. (2021) Automated controlled environment mushroom house. *Advances in Agricultural and Food Research Journal*, Vol. 2.
- [14] Wang D., Wang M., Qiao X. (2009). Support vector machines regression and modeling of greenhouse environment. *Computers and Electronics in Agriculture*, Vol. 66, pp. 46-52.
- [15] Xu B., Dan H., Li L. (2017). Temperature prediction model of asphalt pavement in cold regions based on an improved BP neural network. *Applied Thermal Engineering*, Vol. 120, pp. 568-580.
- [16] Zhou W., Li Y., Wang X. (2014). Model predictive control of air temperature in greenhouse based on CFD unsteady model (基于 CFD 非稳态模型的温室温度预测控制). *Transactions of the Chinese Society for Agricultural Machinery*, Vol. 45, pp. 335-340.
- [17] Zou W., Zhang B., Yao F., He C. (2015). Verification and forecasting of temperature and humidity in solar greenhouse based on improved extreme learning machine algorithm (基于改进型极限学习机的日光温室温湿度预测与验证). *Transactions of the Chinese Society for Agricultural Engineering*, 31, 194-200.
- [18] Zhao Q., Song Z., Li Q., Zheng W., Liu Y., Zhang Z. (2020). Multi-point prediction of temperature and humidity of mushroom based on CNN-GRU (基于 CNN-GRU 的菇房多点温湿度预测方法研究). *Transactions of the Chinese Society for Agricultural Machinery*, Vol. 51, pp. 294-303.
- [19] Zhang J., Shan H., Jing X., Li C., Zhang C., Liu H. (2021). Prediction method of greenhouse environmental factors based on Elman neural network (基于 Elman 神经网络的温室环境因子预测方法). *Journal of Chinese Agricultural Mechanization*, vol. 42, pp. 203-208.
- [20] Zong C., Wang J., Song W., Gen R., Liu P., Xu D. (2022). Construction and validation of hourly air temperature prediction model in solar greenhouse at night (基于天气预报的日光温室夜间逐时气温预测模型构建). *Transactions of the Chinese Society for Agricultural Engineering*, Vol. 38, pp. 218-225.
- [21] Zu L., Liu P., Zhao Y., Li T., Li H. (2023). Solar greenhouse environment prediction model based on SSA-LSTM (基于 SSA-LSTM 的日光温室环境预测模型研究). *Transactions of the Chinese Society for Agricultural Machinery*, Vol. 54, pp. 351-358.

PHYSICO-CHEMICAL, CULTURE VIABILITY, AND SENSORY FEATURES OF KEFIR ICE CREAM AS AFFECTED BY VARIOUS *Saccharomyces cerevisiae* ATCC 36858 CONCENTRATIONS

/

FISIKO-KIMIA, VIABILITAS KULTUR, DAN FITUR SENSORIK ES KRIM KEFIR YANG DIPENGARUHI OLEH BERBAGAI KONSENTRASI *Saccharomyces cerevisiae* ATCC 36858

Muhammad Fajrul Arief¹⁾, Lilik Eka Radiati¹⁾, Ria Dewi Andriani¹⁾, Dedi Fardiaz²⁾, Laprianika Reta Hapita Sari³⁾

¹⁾ Faculty of Animal Science, Universitas Brawijaya, Malang / Indonesia

²⁾ Faculty of Dentistry, Universitas Muhammadiyah, Sidoarjo / Indonesia

³⁾ Faculty of Medicine, Universitas Airlangga, Surabaya / Indonesia

Tel: +6281336236208; E-mail: lilik.eka@ub.ac.id

DOI: <https://doi.org/10.35633/inmateh-73-14>

Keywords: acidity, ethanol, FESEM, melting rate, nutritional content, overrun, viscosity

ABSTRACT

The purpose of this research was to determine the character of kefir ice cream enrichment with *Saccharomyces cerevisiae* ATCC 36858 in various concentration. The study was conducted using a complete randomized design with 4 treatments (T0=0%; T1=0.33%; T2=0.66%; T3=1% *S. cerevisiae* ATCC 36858 (w/v)) and 4 repetitions. The results of the study were processed using ANOVA and DMRT. The treatment increases acidity, ethanol, viscosity and decreases the pH value, overrun, and melting rate of the product ($p < 0.05$). The micro nutrients (C, O, K, Ca, P, Cl, S, Na, Mg, Si) and macro nutrients (protein and fat) has changed ($p > 0.05$). The lactic acid bacteria and yeast content has decrease of 10^5 CFU/g during 28 days of storage. T2 has a good overall acceptance value with flavor and texture favored by panelists.

ABSTRAK

Tujuan penelitian ini adalah untuk mengetahui karakter es krim kefir yang diperkaya dengan *Saccharomyces cerevisiae* ATCC 36858 dalam berbagai konsentrasi. Penelitian dilakukan menggunakan rancangan acak lengkap dengan 4 perlakuan (T0=0%; T1=0,33%; T2=0,66%; T3=1% *S. cerevisiae* ATCC 36858 (w / v)) dan 4 pengulangan. Hasil penelitian diolah menggunakan ANOVA dan DMRT. Perlakuan mampu meningkatkan keasaman, etanol, viskositas dan menurunkan nilai pH, overrun, dan laju leleh produk ($p < 0,05$). Kandungan mikro nutrient (C, O, K, Ca, P, Cl, S, Na, Mg, Si) dan makro nutrient (protein dan lemak) mengalami perubahan ($p > 0,05$). Kandungan bakteri asam laktat dan ragi mengalami penurunan sebesar 10^5 CFU/g selama 28 hari penyimpanan. T2 adalah produk yang memiliki nilai penerimaan keseluruhan terbaik. Sebagai kesimpulan, T2 mampu menghasilkan produk dengan rasa dan tekstur yang disukai oleh panelis.

INTRODUCTION

Recently, efforts have been made to decrease the use of chemical drugs and increase lifestyle changes and natural therapies, such as by drinking kefir. Kefir that contains high probiotic is considered to be a new approach to effective treatment of various metabolic disorders. World Health Organization (WHO) defines probiotics as living microorganisms with beneficial health effects on the human body when consumed in sufficient quantities. Lactic acid bacteria (LAB) and *Saccharomyces* sp are part of the kefir grain ecosystem. Furthermore, they are able to survive over long storage periods in frozen systems such as kefir ice cream matrix that includes nutritive constituents such as milk proteins and fat.

Ice cream is a complex multiphase system that consists of dispersed air cells, coalescence fat globules, crystal ice, and aqueous phase with dissolved mineral and suspended proteins (*Indonesian National Standardization Agency, 1995*). Ice cream has good potential to be used as probiotic vehicle because of its composition as well as its acceptable flavor and texture (*Agustin et al., 2021*). Recently, new ice cream formulations have been developed with various probiotics, one of them is kefir ice cream. Incorporating kefir grain into the ice cream mix (ICM) is expected to help reduce the sugar and fat contents of the probiotic ice cream. ICM made from fermented milk has a simpler sugar and fat content that significantly affects the sensory quality of probiotic ice cream (*Jardines et al., 2020*). However, there were still many shortcomings in the product including flavor, texture, melting, color, and nutritional content.

Senaka et al (2013) reported that kefir grain produces ethanol during its fermentation process, thus affecting the sensory quality of the final product. Akalin et al (2018) argued that enrichment on ice cream with probiotic has significantly increased the acidity of product. In addition, Khademi et al (2022) also reported that probiotic inside the formulation significantly affects the physicochemical and sensory properties especially fatty acid profile of sourness. On the contrary, utilization of *Saccharomyces boulardii* in combination with *Lactobacillus rhamnosus* GG in probiotic ice cream formulations gives insignificant affect to its sensory quality (Goktas et al., 2022). This was due to the role of *Saccharomyces* sp.

In general, *S. cerevisiae* serves to produce functional food due to their antimicrobial activity against pathogen (Suhendar, 2023; Zhang et al., 2024) and as an antioxidant agent (Adi, 2022; Bamba et al., 2024). Radiati et al (2022) reported that the addition of *S. cerevisiae* ATCC 36858 by 1% (w/v) into goat's milk kefir formulations resulted in antimicrobial activity of 25, 28, and 22 mm zone inhibition against *Escherichia coli*, *Streptococcus typhi*, and *Klebsiella pneumoniae* respectively, β -galactosidase of 120.33 U/g protein, and antioxidant activities of 72% DPPH inhibition. They argued that β -galactosidase from *S. cerevisiae* convert milk fat into short-chain fatty acids that are useful material for the host to improve probiotic ice cream texture acceptance. Based on this description, the use of *S. cerevisiae* ATCC 36858 was thought to produce kefir ice cream. The purpose of this research was to determine the character of kefir ice cream enrichment with *S. cerevisiae* ATCC 36858 in various concentration. The novelty of this study is *S. cerevisiae* population reconstruction to produce kefir ice cream that has good overall acceptance.

MATERIALS AND METHODS

MATERIAL

S. cerevisiae ATCC 36858 (10^7 CFU/g) (0; 0.33; 0.66; 1 % w/v) and kefir grains (*Lactobacillus plantarum*, *L. cremoris*, *Streptococcus cremoris*, and *Saccharomyces* sp.) were obtained from the Animal Product Technology Laboratory, Animal Science Faculty of Universitas Brawijaya. Commercial goat's milk was obtained from local farmers, Malang, Indonesia. Glucose as sweetener and mono-acyl glycerol (MAG) as emulsifier were obtained from Subur Kimia Jaya, Indonesia. Egg yolk as stabilizer and salt (NaCl) as flavor agent were obtained from traditional market, Malang, Indonesia.

GOAT'S MILK KEFIR PREPARATION

Goat milk kefir was made based on the method of Radiati et al (2022) with slight modification by adding 0; 0.33; 0.66; and 1% (w/v) *S. cerevisiae* ATCC 36858 and 4% (w/v) kefir grain into goat's milk. The mixture was put into a non-plastic glass jar with a volume of 1000 ml. The fermentation process was carried out for 48 hours at room temperature. After that, the mixture was filtered using a fine sieve to separate grains from the liquid. The liquid was stored in a 4°C refrigerator for temporary storage or directly used to produce kefir ice cream.

KEFIR ICE CREAM PRODUCTION

Kefir ice cream was produced using a protocol from Zoumpopoulou et al (2021) with slight modification by putting kefir goat's milk, MAG, glucose, salt, and egg yolk into a bowl to make ICM. The dosage of ingredients was listed in Table 1. The ICM was homogenized, then put into ice cream machine (GEA ICE – 1530) for 45 minutes. The thickened ICM was taken using a spatula and stored into an airtight plastic container to be stored in a freezer (-20°C) for 4 hours before being used for research. Stirring was done every 4 hours to keep kefir ice cream's viscosity in good condition.

Table 1

| Formulation of kefir ice cream enrichment with <i>S. cerevisiae</i> ATCC 36858 in various concentration | | | | | |
|---|------|--------------|-----|-----|-----|
| Ingredients | | T0 (control) | T1 | T2 | T3 |
| Goat's milk | [mL] | 750 | 750 | 750 | 750 |
| MAG | [g] | 3 | 3 | 3 | 3 |
| Glucose | [mL] | 120 | 120 | 120 | 120 |
| Egg yolk | [mL] | 300 | 300 | 300 | 300 |
| Kefir grains | [g] | 30 | 30 | 30 | 30 |
| Salt | [g] | 2 | 2 | 2 | 2 |
| <i>S. cerevisiae</i> ATCC 36858 | [g] | 0 | 2.5 | 5 | 7.5 |

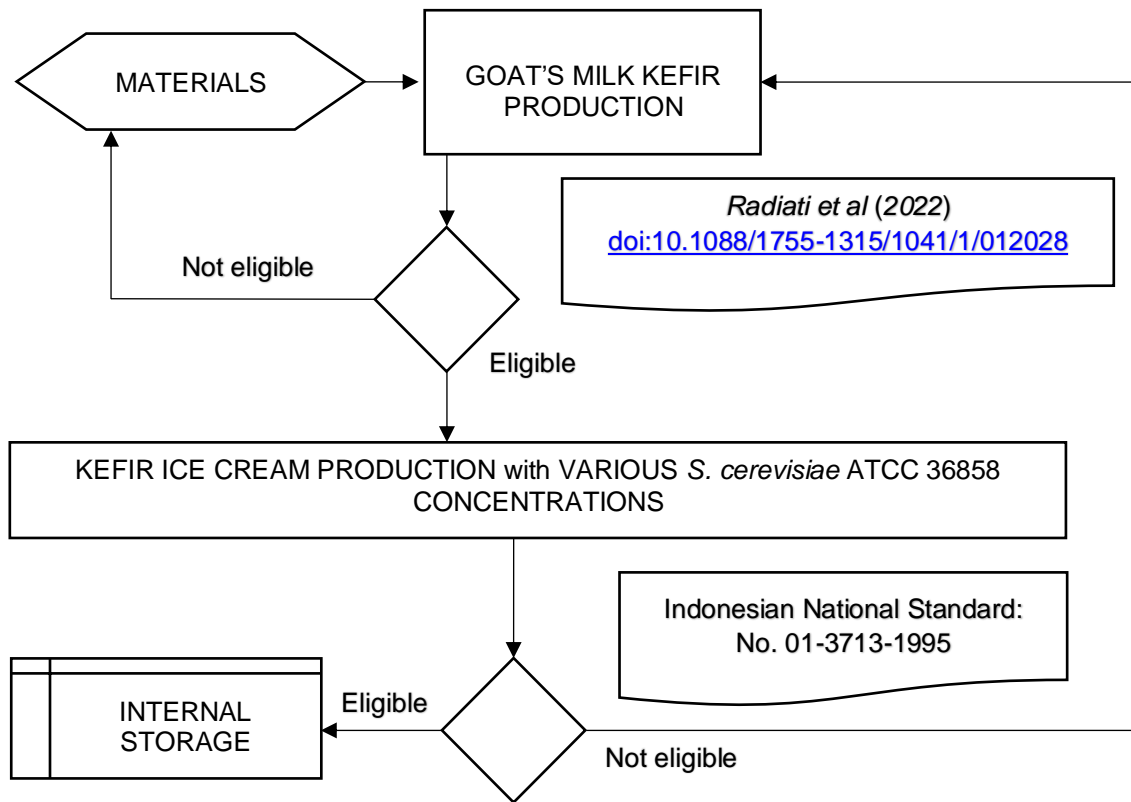


Fig. 1 – Producing of kefir ice cream

VIABILITY of CULTURE

Enumeration was carried out based on protocol by *Arief et al (2024)* with slight modification. The viability of culture (LAB and yeast) inside kefir ice cream products were determined throughout storage time. LAB and yeast were incubated in Man Rogosa Sharpe (MRS) broth (t=24 hours; T=37°C) and yeast extract, peptone, dextrose (YPD) broth (t=48 hours; T=37°C), respectively. 0.9% NaCl solution serial dilution of kefir ice cream was created and homogenized for 2 min. Serial dilutions were prepared and 100 μL from each dilution was spread to MRS and YPD agar plates for LAB and yeast, respectively. The viability of LAB and yeast were calculated using Equation 1.

$$Viability\ of\ culture = \frac{a}{((1 \times b) + (0,1 \times c) \times d)} \tag{1}$$

Where:

- a* = Calculated colony
- b* = Sum of Petri dish on the first dilution
- c* = Sum of petridish on the next dillution
- d* = First dilution

PHYSICO-CHEMICAL FEATURES DETERMINATION

Kefir ice cream was melted at room temperature and characterized for pH by potentiometric method (Digimed DM20), titratable acidity by titration method and expressed as a lactic acid percentage, viscosity by viscometer (NDJ-8S) at 30 rpm for 30 seconds, total protein by Kjeldhal method, fat by Gerber method, and ethanol content by titration method based on Indonesian National Standard 01-2891-1992 (*Indonesian National Standardization Agency 1992*).

MELTING FEATURES DETERMINATION

Melting testing was carried out based on protocol by *Muse and Hartel (2004)* with slight modifications. A sample of kefir ice cream blocks (6cm×6cm×3cm) with mass ±100 gr. The initial temperature of ice cream was -17°C. Then they were placed on a wire screen. The sample was placed in a controlled temperature chamber at 25°C. The dripped volume was recorded after 30 minutes, 60 minutes, and 90 minutes and calculated as percentage drainage using Equation 2.

$$\frac{a}{b} \times 100\% \tag{2}$$

where: *a* = Mass of melted ice cream; *b* = Mass of frozen ice cream

OVERRUN FEATURES DETERMINATION

Overrun calculations were carried out based on *Kozłowicz et al. (2019)* with slight modifications. The mass of ICM was weighed as and recorded as "a". The mass of kefir ice cream was weighed and recorded as "b". Mass weighing was carried out according to the theory of the equation that 1 gram is equivalent to 1 cm³. Overrun was calculated using Equation 3.

$$\frac{b - a}{a} \times 100\% \quad (3)$$

where:

a = Mass of ICM; b = Volume of kefir ice cream

COLOR FEATURES DETERMINATION

Color determination was carried out based on protocol by *Kozłowicz et al. (2019)* with slight modification. The color values of probiotic ice cream in terms of L*, a*, and b* values were determined using a CR-400 ChromaMeter (Konica Minolta, Japan) instrument.

MORPHOLOGY AND MINERAL CONTENT FEATURES DETERMINATION

Kefir ice cream was melted at room temperature and were characterized for morphology based on *Florczuk et al. (2022)* using field emission scanning electron microscopy (FESEM) – Energy Dispersive Spectroscopy (EDS) from the FESEM Thermo Scientific Quattro with EDS detector was used to capture the surface morphology of kefir ice cream. The same engine was used to calculate the weight percentages of components.

SENSORY FEATURES

Sensory evaluation was carried out based on protocol by *Hanafi et al. (2022)* with slight modification. In this analysis, 30 panelists (15 men dan 15 woman) present their personal responses written using a hedonic scale on 1 to 5 (1: very bad, 2: dislike, 3: not too bad, 4: good and 5: very good) during the education period held to provide knowledge about probiotic ice cream in two hours meeting. Ethical clearance regarding the use of panelists based on protocol by Guidelines for the Code of Ethics for Research and Community Service Universitas Brawijaya.

EXPERIMENTAL DESIGN AND DATA ANALYZES

The experimental design used in this study was a Completely Randomized Design (CRD) with four treatments 0%; 0.33%; 0.66%; 1% (w/v) *S. cerevisiae* ATCC 36858 addition and four repetitions respectively. Kefir ice cream's formulation can be seen in Table 1. Statistical analysis was performed for all measurement data using Microsoft Excel with One Way Analysis of Variance (ANOVA). The differences between treatments were tested further using Duncan's Multiple Range Test (DMRT) analysis with a significance level of 0.05.

BEST TREATMENT DETERMINATION

The analysis for determining the best formulation was carried out by the method of De Garmo (*Alfadila et al. 2020*). Determining the best treatment begins with grouping all observation parameters and scoring. Then calculate the weight value (WV) to determine the treatment value, the best value, and the worst value. Then calculated the effectiveness value (EV) with the Equation 4.

$$\frac{(a-b)}{(c-b)} \quad (4)$$

where:

a = Treatment value; b = Worst value; c = Best value

After that, the calculation of the product value for each observation parameter was carried out using the Equation 5.

$$a \times b \quad (5)$$

where:

a = Effectiveness value; b = Weight value

RESULTS

Culture Viability of Kefir Ice Cream

The initial count of LAB viability was 2.35×10^7 CFU/g for control and all treatments. The results showed that the control and all treatments decreased the viability of LAB by 1×10^4 and 5×10^5 CFU/g on day 1st to day 7th; 4×10^5 and 1×10^6 CFU/g on day 14th; 1×10^6 and 4×10^5 CFU/g on day 21st to day 28th respectively. While the initial count of yeast viability for control and all treatments was 9.11×10^4 ; 9.13×10^4 ; 9.15×10^4 ; 9.20×10^4 CFU/g respectively. The results showed that control and all treatments decreased the viability of yeast by 1×10^4 and 2×10^3 CFU/g on day 1st; 2×10^3 CFU/g on day 7th; 1×10^4 CFU/g on day 14th; 2×10^4 CFU/g on day 21st to day 28th for control and all treatment respectively.

Kefir grains used in this study contained *L. plantarum*, *L. cremoris*, *S. cremoris*, and *Saccharomyces* sp as much as 4% (w/v). Meanwhile, the treatment used in this study was the addition of *S. cerevisiae* ATCC 36858 strains as much as 0.33, 0.66, and 1% (w/v). The probiotic community was thought to have a positive impact on human health. Akalin et al (2018) argue that *Lactobacillus* sp is classified as LAB which can help maintain human digestive health. Bamba et al (2024) argue that *Saccharomyces* sp is a yeast that can establish mutualism symbiosis with LAB. Arief et al (2024) reported that the viability of LAB and yeast during ice cream production showed a good viability rate. Unfortunately, there were several factors that can reduce this number when entering the storage stage. Probiotic products should contain viable count of microorganisms at numbers ranging from 10^6 to 10^9 CFU/g during their shelf-life (Bullock & Gruen, 2023).

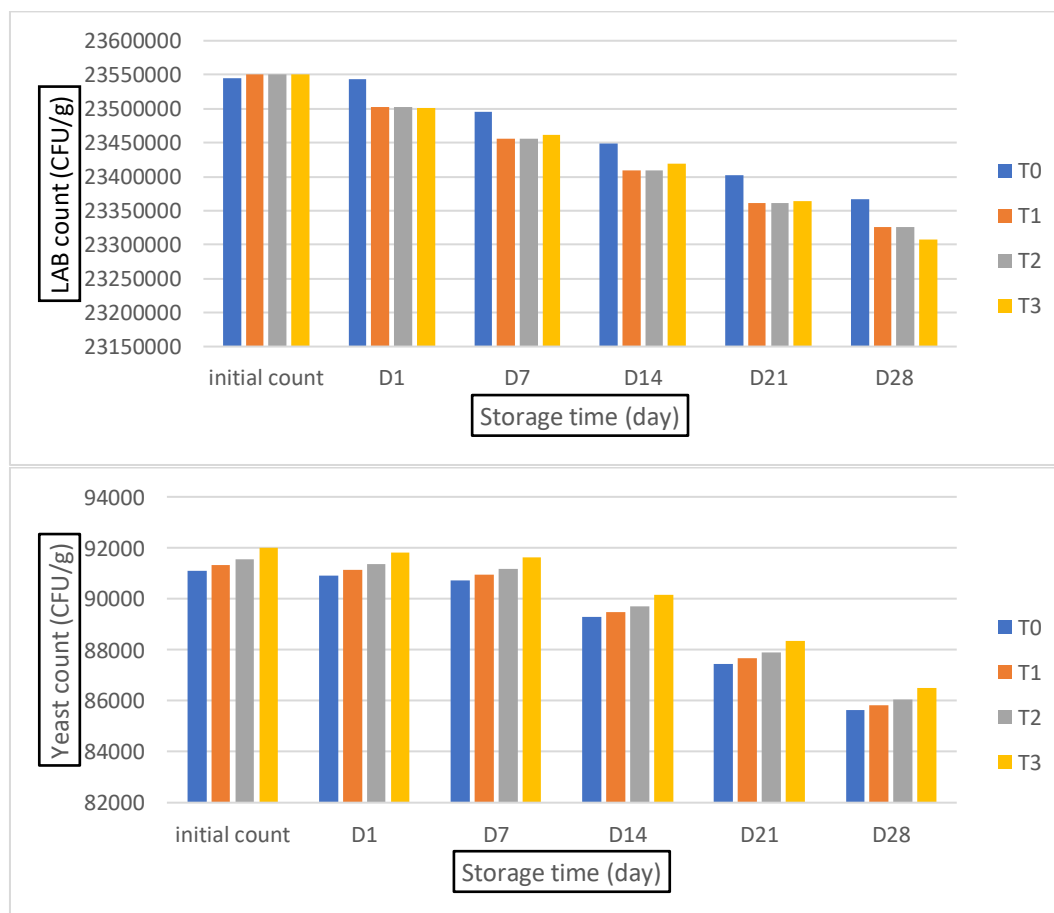


Fig. 2 - Viability of culture (LAB and yeast) in kefir ice cream product during 28 days storage period

Fig. 2 shows the viability of LAB and yeast in kefir ice cream product. For the record, the calculation of viable count of *S. cerevisiae* ATCC 36858 was put together with *Saccharomyces* sp. During the ice cream production, LAB and yeast were inoculated at level of 2.354529×10^7 and 9.1100×10^4 CFU/g respectively. The initial count results showed that the decrease in viability of LAB was higher than that of yeast (Fig. 2). Many LAB suffer a rapid loss of their viability if stored at temperatures below -17°C (Goktas et al., 2022). This could be due to the yeasts which are more adaptable to low temperature than bacteria.

As expected, the probiotic numbers in ice cream products were in a decrement trend during the storage time but importantly none of the ice cream products harbored probiotics below 8.5634×10^4 CFU/g. This level was within the suitable level to be classified as probiotic products based on Codex Alimentarius. The number of LAB and yeast is at least $10^6 - 10^9$ and 10^4 CFU/g, respectively (Codex, 2018).

The decrement of viable culture number was probably because of the freezing stage which caused some damage to cells and finally they died (Corradini et al., 2014). Cruz et al (2022) argued that decrement of viable LAB and yeast in the product may be related to competition. The decrease of viable counts during storage time could be caused by the low temperature (-20°C) storage condition. Following the D-28th of storage period, viable counts of LAB and yeast were at 2.3308100×10^7 and 8.5634×10^4 CFU/g levels, respectively. This result can be critical for the numbers because the LAB has decreased drastically as much as 1×10^6 CFU/g in D-14th storage, while yeast experienced a drastic decrease as much as 2×10^4 CFU/g on D-21st storage. These findings suggest that the product storage should not be more than 28 days.

Physico-chemical Features of Kefir Ice Cream

There was a significant increase in acidity, ethanol and viscosity, but this was not the case with protein inside kefir ice cream (Table 2). The difference that causes an increase in acidity and ethanol appears significantly in T0 with T1. There was also a significant decrease in pH (D-1), pH (D-28), overrun, melting in 30 minutes, 60 minutes, and 90 minutes, but this did not occur in fat inside kefir ice cream (Table 2). The difference that causes a decrease in pH D-1st and D-28th appears significantly in T2 with T1 and T1 with control. While against overrun there was a significant difference in T1 with control. Unfortunately, there was no significant difference between treatments despite a decrease in melting in 30; 60; and 90 minutes.

Table 2

| Effect of various <i>S. cerevisiae</i> ATCC 36858 concentrations on physico-chemical features of kefir ice cream | | | | | |
|--|--------|---------------------------|--|---------------------------|---------------------------|
| Attributes | | Control (T0) | Concentration of <i>S. cerevisiae</i> ATCC 36858 | | |
| | | | T1 | T2 | T3 |
| pH (D-1 st) | [pH] | 6.71 ± 0.03 ^c | 6.34 ± 0.03 ^b | 6.29 ± 0.03 ^a | 6.25 ± 0.02 ^a |
| pH (D-28 th) | [pH] | 6.68 ± 0.02 ^c | 6.27 ± 0.02 ^b | 6.23 ± 0.03 ^a | 6.21 ± 0.01 ^a |
| Acidity | [%] | 0.18 ± 0.00 ^a | 0.34 ± 0.08 ^b | 0.37 ± 0.02 ^b | 0.38 ± 0.00 ^b |
| Fat | [%] | 3.20 ± 0.01 | 3.15 ± 0.13 | 3.13 ± 0.13 | 3.11 ± 0.12 |
| Protein | [%] | 3.35 ± 0.21 | 3.65 ± 0.36 | 3.68 ± 0.36 | 3.69 ± 0.34 |
| Ethanol | [%] | 0.50 ± 0.03 ^a | 0.69 ± 0.06 ^b | 0.76 ± 0.07 ^b | 0.88 ± 0.08 ^b |
| Overrun | [%] | 31.13 ± 0.22 ^b | 27.05 ± 0.82 ^a | 27.00 ± 0.82 ^a | 26.99 ± 0.85 ^a |
| Melting in 30 min | [%] | 27 ± 0.05 ^a | 25 ± 0.06 ^a | 19 ± 0.06 ^a | 14 ± 0.06 ^a |
| Melting in 60 min | [%] | 39 ± 0.05 ^a | 34 ± 0.06 ^a | 27 ± 0.06 ^a | 25 ± 0.06 ^a |
| Melting in 90 min | [%] | 87 ± 0.05 ^a | 81 ± 0.06 ^a | 77 ± 0.06 ^a | 69 ± 0.06 ^a |
| Viscosity | [m.Pa] | 65.15 ± 6.12 ^a | 70.08 ± 6.19 ^a | 81.93 ± 6.26 ^b | 83.29 ± 6.33 ^b |

Means in the same row with different superscript differ significantly (p<0.05)

Kozłowicz et al (2019) argued that LAB and yeast as kefir grains are enclosed in a polysaccharide known as kefiran and protein matrix. McGhee et al (2015) argued that the microbial fermentation of kefir product produces organic compounds such as lactic acid and ethanol. Under favorable conditions, the fermentation process begins and leads to the increased number of their viability and produces various metabolites at the end of the process. Therefore, in making this kefir ice cream, nutritional conditioning was well maintained to meet the life needs of LAB and yeast by adding *S. cerevisiae* ATCC 36858 to the formula. Radiati et al (2022) reported that *S. cerevisiae* ATCC 36858 in grain kefir complex improved bioactive compound of goat's milk kefir and simultaneously gave some improvement by producing antimicrobial activity, antioxidant, and β - galactosidase enzyme. Besides that, this enzyme converts milk fat into short-chain fatty acids that are useful material for the host.

Bamba et al (2023) reported that *S. cerevisiae* produced glycerol and ethanol around 1.1 and 5.4 g/L at 48 h of cultures respectively. In addition, Khademi et al (2022) reported that *S. cerevisiae* could lower the pH value continuously during culture and reached a value of 4.4 pH. Furthermore, Gut et al (2022) reported that from 5.5 to 6.5 pH led to the increased survival of LAB and yeast during storage. The ice cream matrix could become a good vehicle for LAB and yeast culture which contained milk protein and fat.

High fat content can provide support considerably higher viability of probiotic strains during production and storage (Zoumpopoulou et al 2021).

The fat content of kefir ice cream product changed between 3.20% and 3.11%. In the particular case, this implies overcoming intrinsic hurdles such as the beating step, where air is incorporated known as overrun and storage under freezing temperatures. *Dutra et al (2015)* stated similarly that in general, addition of LAB and yeast resulted in lower overrun levels in comparison with control.

The overrun defines the structure of the final product, since the presence of air gives the kefir ice cream an agreeable creamy texture. *Jardines et al (2020)* reported that commercially, the overrun of all the probiotic ice cream was low, which were indicated to be between 50% and 80%. An increase in *S. cerevisiae* ATCC 36858 used decreased the overrun of kefir ice cream. A higher overrun led to a slower melting because air cells acted as an isolator medium (*Deosarkar et al., 2016*). Melting rate feature affects the formation of hardness texture of the final product. The increased proportion of *S. cerevisiae* ATCC 36858 is able to improve viscosity while decreasing the melting of kefir ice cream.

The melting was also associated with the overrun. These current findings show that increasing the amount of *S. cerevisiae* ATCC 36858 reduces overrun, causing kefir ice cream to melt more slowly. *Akbari et al (2019)* reported that low air cell incorporation might function as an insulator inside the kefir ice cream structure. Whereas, *Arief et al (2023)* reported that the addition of partially mixed fat derived from egg yolk was able to form a fat bond which could stabilize the air bubble and foam in the ice cream structure, which subsequently reduced the melting around 80 – 90 % when the block of kefir ice cream was allowed to melt at room temperature for 2 hours.

Viscosity feature is the resistance of fluids to changes in movement relative to each other (*Fitri et al., 2020*). The viscosity value will appear when the molecules in the fluid friction against each other. The increase in the viscosity of kefir ice cream containing *S. cerevisiae* ATCC 36858 was probably due to the high-water retention of insoluble materials based on their low soluble content. *Alfadila et al (2020)* argued that the increment indicated the significant effect of LAB on texture of the ice cream in viscosity. *Popescu et al (2021)* argued that enhanced viscosity can be achieved with the interaction of milk protein or by the interaction between soluble and insoluble compound.

Color Feature of Kefir Ice Cream

The results showed that the addition of *S. cerevisiae* ATCC 36858 with various concentrations was able to produce a brighter product than the control (Table 3). This was because *S. cerevisiae* ATCC 36858 produces products that tend to be greenish and yellowish significantly. Based on the DMRT test, it was known that the color tendency of T1 and T2 products was bright yellowish and bright greenish respectively. The duration of product storage for 28 days was able to significantly reduce product brightness (Table 3). DMRT tests show that the difference between treatments that cause a decrease in brightness tends to be greenish occurs insignificantly, while the yellowish color turns bluish. DMRT tests show that there was a significant difference in each treatment of yellow to bluish color change.

Table 3

| Effect of various <i>S. cerevisiae</i> ATCC 36858 concentrations on color features of kefir ice cream day 1 st and day 28 th | | | | | | |
|--|-------------------------|-------------------------|-------------------------|-------------------------|-------------------------|-------------------------|
| Sample | D-1 st | | | D-28 th | | |
| | L* | a* | b* | L* | a* | b* |
| Control (T0) | 84.47±0.32 ^a | -5.95±0.03 ^a | 11.45±0.05 ^a | 83.14±0.43 ^a | -6.02±0.03 ^a | 11.31±0.05 ^c |
| T1 | 86.84±0.33 ^b | -5.91±0.03 ^b | 12.36±0.06 ^b | 84.87±0.65 ^a | -5.74±0.02 ^a | 10.78±0.05 ^b |
| T2 | 87.62±0.33 ^c | -5.84±0.03 ^c | 12.21±0.06 ^b | 84.31±0.43 ^a | -5.67±0.02 ^a | 10.65±0.05 ^b |
| T3 | 88.41±0.34 ^c | -5.77±0.02 ^c | 12.06±0.06 ^b | 83.30±0.43 ^a | -5.60±0.02 ^a | 10.52±0.05 ^a |

Means in the same row with different superscript differ significantly (p<0.05). L* values show the light intensity between 0 – 100, a* values show the redness (+) to green (-) and b* values show yellowness (+) to blueness (-) color.

Color feature of kefir ice cream is one of the most critical quality indicators accepted by panelist. L* (brightness) of kefir ice cream changed between 84.47 and 88.41 observed for all treatment. The addition of 1% *S. cerevisiae* ATCC 36858 resulted in significantly higher L* compared to control. After 28 days of storage time, differences in L* value of kefir ice cream were found to be significant. *Sarwar et al (2021)* reported that with the exception of yellowness, all kefir ice cream products prepared with fat replacers had significantly better appearance acceptance than control. In terms of a* (redness) dan b*(yellowness) of kefir ice cream, a* values changed in the range of – 5.95 to – 5.77 whereas b* values product altered in the range of 11.45 to 12.06. An improvement in a* values of all kefir ice cream products containing *S. cerevisiae* ATCC 36858 was observed after 28 days of storage time whereas a decrement was observed for a* and b* values.

Structure and mineral of Kefir Ice Cream

FESEM results showed that the particles were formed from agglomerations of various sizes (Fig. 3). The particles seemed to be trying to form large spheres. At 100X magnification, these tiny particles were not clearly visible. Fig 3 shows that the addition of *S. cerevisiae* ATCC 36858 to the formula affects the agglomeration process. The particles in the treatment showed increased agglomeration activity compared to the control. The agglomerations formed were observed using 100X magnification to obtain overall results and continued using 500X and 1,000X magnifications. The results of the enlargement showed that the appearance of voids gradually began to fade as the concentration of *S. cerevisiae* ATCC 36858 increased.

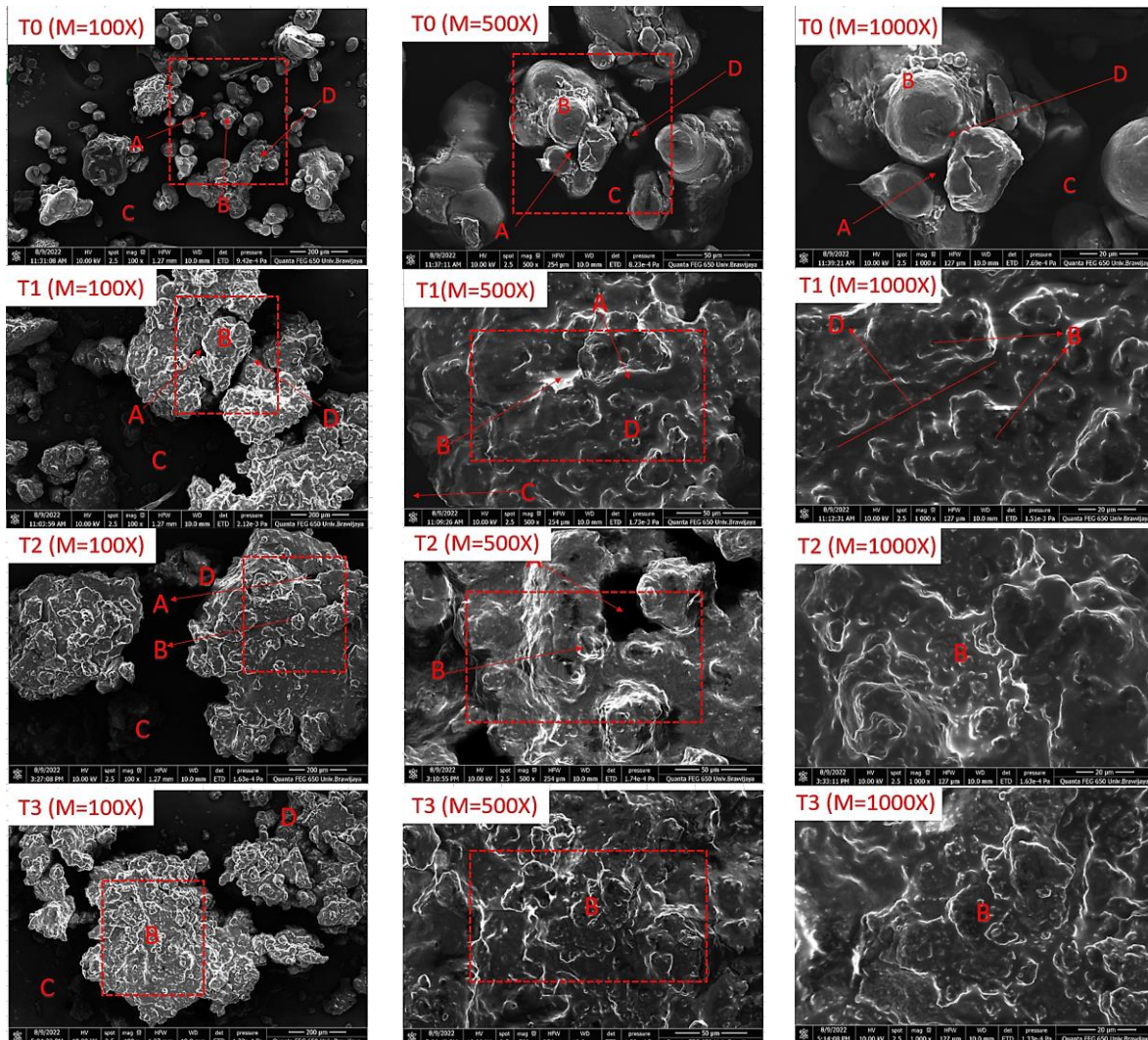


Fig. 3 - The FESEM result of enrichment kefir ice cream with *S. cerevisiae* ATCC 36858

Appearance of kefir ice cream enrichment with *S. cerevisiae* ATCC 36858 in various concentration based on FESEM-EDS overview. A – Voids that thwart the formation of agglomerations, B – Fat droplets attempt to attract particles around them to unite, C – Water as a solvent has the potential to dissolve the particles formed to become a homogeneous solution, D – Fat droplets attempt to form agglomerations with the help of casein micelles. Agglomeration was formed if no voids were found in them. An increase in the concentration of *S. cerevisiae* ATCC 36858 of at least 0.33% was able to minimize the appearance of voids. This was evidenced by the disappearance of voids in T1 and T2 which were observed using 1,000X magnification. This was further strengthened by the absence of voids in the T3 formula that was observed using 500X magnification.

FESEM + EDS results showed that the addition of *S. cerevisiae* ATCC 36858 also affected the mineral content of kefir ice cream (Fig. 4). The mineral levels contained in kefir ice cream were C (56.92 – 65.43%), O (30.37 – 41.02%), K (0.70 – 1.04%), Cl (0.43 – 0.73%), Ca (0.28 – 0.96%), P (0.26 – 0.82%), Na (0.25 – 0.36%), S (0.00 – 0.26%), Mg (0.00 – 0.22%), and Si (0.00 – 0.13%). These micronutrients come from the ingredients used to produce kefir ice cream such as, goat's milk (Ca, Mg, P, and K), glucose (C and O), egg yolk (P, Ca, and Mg), and salt (Na and Cl). Based on result, it was known that kefir ice cream has an average of C (61.85 ± 3.86), O (34.90 ± 5.15), K (0.88 ± 0.24), Ca (0.62 ± 0.38), P (0.55 ± 0.33), Cl (0.59 ± 0.26), S (0.15 ± 0.13), Na (0.27 ± 0.05), Mg (0.09 ± 0.11), and Si (0.05 ± 0.06).

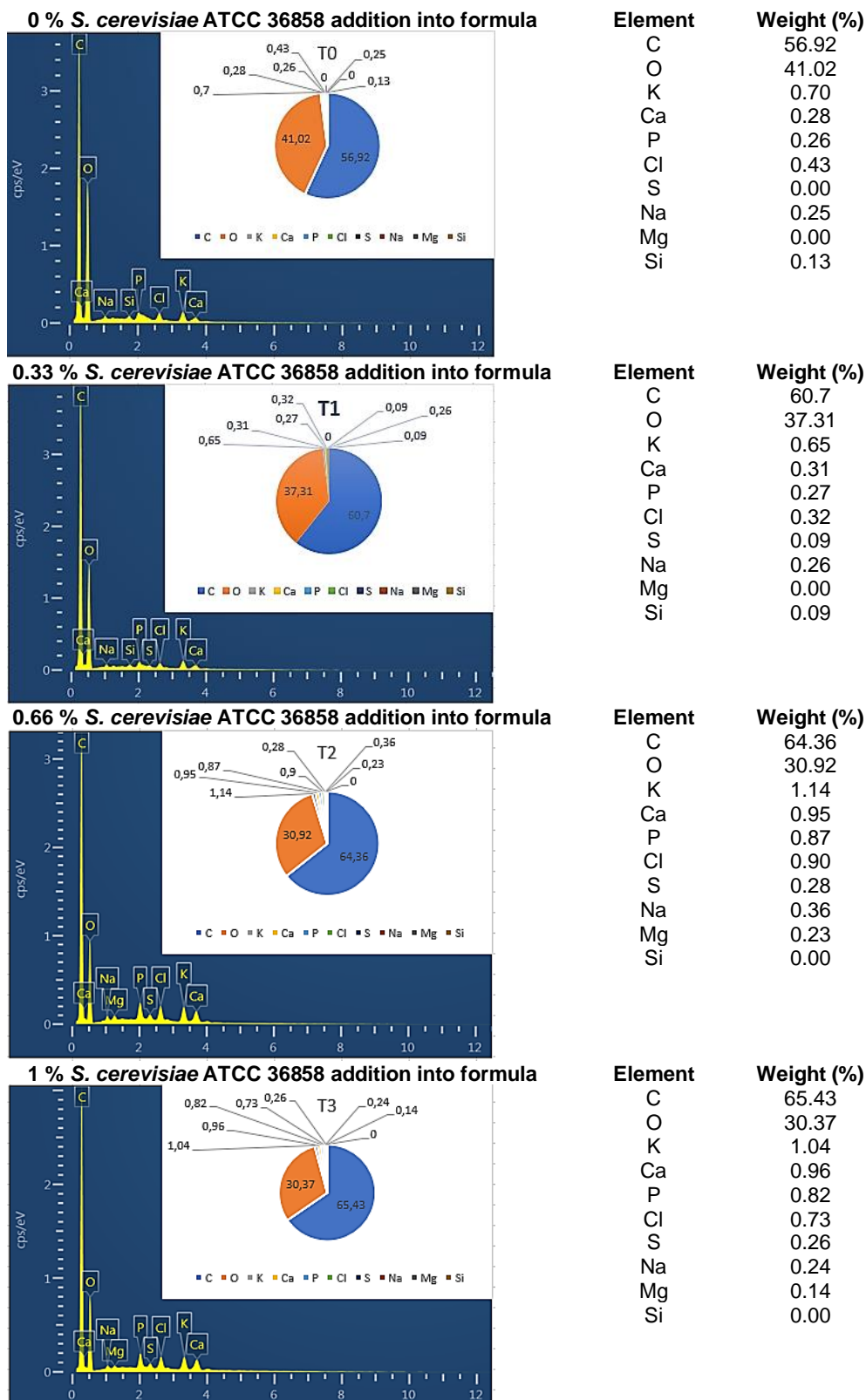


Fig. 4 - Mineral contents of kefir ice cream enrichment with *S. cerevisiae* ATCC 36858 in various concentration for each treatment assessment result by FESEM-EDS

The difference in micronutrient content of each treatment was thought to be caused by LAB and yeast activities. Ali *et al* (2022) report that *S. cerevisiae* is known to be an obligate aerobe so they require oxygen for cellular respiration. Georgiev *et al* (2024) report that glucose is a monosaccharide that easily fermented by *S. cerevisiae* as a food source to produce phytase enzymes and cause increased phosphorus levels during the milk fermentation process. Casertano *et al.* (2022) argued that micronutrient such as mineral and vitamin should not result in disagreeable flavors negatively affecting the panelists acceptance.

Salari *et al.* (2021) argued that macro minerals such as Ca, Mg, Na, and K are essential for controlling blood pressure, while micro minerals such as Si are able to help repair cell damage. Unfortunately, although kefir ice cream was made from goat's milk, no Zn content was found in them. Fernandes *et al.* (2022) argued that Zn is a mineral derived from milk-based foods that functions as an antioxidant and strengthens the body's immune system. Even so, Umam *et al.* (2021) reported that goat's milk kefir supplemented with *S. cerevisiae* ATCC 36858 has good antioxidants and peptide bonds to support the consumer's immune system. However, excess minerals are also not good for the body. Warren and Hartel (2018) argued that excess consumption of Na causes poisoning, even in acute circumstances can cause hypertension. Karim and Aider (2022) also argued that excess K causes side effects such as stomach ache and heart attack. Therefore, consumption of kefir ice cream needs to be maintained even in order to obtain optimal health effects.

Sensory Features of Kefir Ice Cream

Hedonic tests show that the addition of *S. cerevisiae* ATCC 36858 with various concentrations can significantly affect flavor, melting, texture, color, and overall acceptance (Table 4). Unfortunately, the results of the DMRT test showed that there was no significant difference between the treatment of all sensory features. However, each product has its own acceptance value for each treatment (Fig. 5). The most favorable products by the panelists were T2 (flavor) and T3 (melting, texture, and color). Whereas the least favorable ones were T3 (flavor) and T0 (melting, texture, and color). While the favorite product category was T2 because it has the highest overall acceptance value.



Fig. 5 - The hedonic assessment result of enrichment kefir ice cream with *S. cerevisiae* ATCC 36858.

As a general rule, the addition of *S. cerevisiae* ATCC 36858 into a kefir ice cream implies the need to assure the viability of LAB and yeast without altering its sensory features. Some physico-chemical features affect sensory features. Zhang *et al.* (2024) reported that the differences in the overrun step of kefir ice cream were related to the acidifying capacity of the LAB and yeast cultures, which affects the origin protein. Khademi *et al.* (2022) argued that the sensory feature of textural appearance corresponded to whether a sample cut smoothly or crumbled when cut into with a spoon. Gut *et al.* (2022) reported that graininess was related to whether the surface had the typical appearance of a full fat product or icy appearance of fat-free ice cream.

Table 4

| Effect of various <i>S. cerevisiae</i> ATCC 36858 concentrations on sensory features of kefir ice cream | | | | |
|---|--|------------------------|------------------------|------------------------|
| Attributes | Concentration of <i>S. cerevisiae</i> ATCC 36858 | | | |
| | Control (T0) | T1 | T2 | T3 |
| Flavor | 3.67±0.95 ^a | 3.53±1.13 ^a | 4.00±0.74 ^a | 2.90±0.71 ^a |
| Melting | 2.76±0.93 ^a | 3.80±0.61 ^a | 3.86±0.77 ^a | 3.90±0.80 ^a |
| Texture | 3.50±0.93 ^a | 3.63±0.76 ^a | 3.93±0.78 ^a | 4.00±0.74 ^a |
| Color | 3.40±0.77 ^a | 3.53±0.50 ^a | 3.63±0.66 ^a | 3.73±0.82 ^a |
| Overall | 3.23±0.81 ^a | 3.76±0.62 ^a | 3.90±0.80 ^a | 3.80±0.80 ^a |

Means in the same row with different superscript differ significantly (p<0.05)

The appearance term air holes described whether or not discrete air pockets were observed as the panelists scraped the surface of the kefir ice cream with a spoon. The appearance term stickiness referred to product cohesion. Fig. 3 shows that the particles were formed from agglomerations of various sizes, due to the addition of *S. cerevisiae* ATCC 36858. The particles in the treatment showed the increased agglomeration activity compared to the control. Void spaces within the casein matrix were spherical, showing that they were formed by fat droplets interrupting the aggregation of casein micelles (Yuzhen *et al.*, 2023). In general, there was only fat droplet per void space. The casein micelles thus were surrounded by each fat droplet separating it from the others. An increase in the concentration of *S. cerevisiae* of at least 0.33% was able to minimize the appearance of voids (Fig.3). These evidenced by the disappearance of voids in T1 and T2 observed using 1,000X magnification. This was further strengthened by the absence of voids in the T3 formula which observed using 500X magnification.

Table 5

| Attributes | Treatment | | | | Best Value | Worst Value | Differ |
|------------|-----------|------|------|------|------------|-------------|--------|
| | T0 | T1 | T2 | T3 | | | |
| Flavor | 5.00 | 6.00 | 6.16 | 6.00 | 6.16 | 5.00 | 1.16 |
| Melting | 5.16 | 6.00 | 6.36 | 6.26 | 6.26 | 5.16 | 1.10 |
| Texture | 5.23 | 6.00 | 6.36 | 6.40 | 6.40 | 5.23 | 1.16 |
| Color | 5.03 | 5.23 | 5.33 | 5.43 | 5.43 | 5.03 | 0.40 |
| Overall | 5.63 | 6.10 | 6.40 | 6.20 | 6.40 | 5.63 | 0.77 |

| Attributes | WV | Treatment | | | | | | | |
|------------|------|-----------|------|------|------|------|------|------|------|
| | | T0 | | T1 | | T2 | | T3 | |
| | | EV | PV | EV | PV | EV | PV | EV | PV |
| Flavor | 0.26 | 0.00 | 0.00 | 0.85 | 0.22 | 1.00 | 0.26 | 0.85 | 0.22 |
| Melting | 0.13 | 0.00 | 0.00 | 0.81 | 0.10 | 1.03 | 0.13 | 1.00 | 0.13 |
| Texture | 0.20 | 0.00 | 0.00 | 0.68 | 0.13 | 0.97 | 0.19 | 1.00 | 0.20 |
| Color | 0.06 | 0.00 | 0.00 | 0.50 | 0.03 | 0.75 | 0.05 | 1.00 | 0.06 |
| Overall | 0.33 | 0.00 | 0.00 | 0.60 | 0.20 | 1.00 | 0.33 | 0.73 | 0.24 |
| Total | 1.00 | 0.00 | 0.00 | 3.44 | 0.68 | 4.75 | 0.96 | 4.58 | 0.85 |

Note:

| | | |
|----|---|---|
| WV | = | Weight value |
| EV | = | Effectivity value |
| PV | = | Product value, Best treatment was determined by the highest score of PV |

The results showed that kefir ice cream produced with LAB and yeast cultures only (control), present a less intense aroma and kefir flavor than the product prepared with *S. cerevisiae* ATCC 36858 cultures (Table 5). The addition of *S. cerevisiae* ATCC 36858 does not modify the sensory features of the control intensely. Unfortunately, T3 was thought to have an off flavor due to too much addition of *S. cerevisiae* ATCC 36858, resulting in lactic acid and acidity extremely. The authors suggested that the use of *S. cerevisiae* ATCC 36858 was only 0.66% because there was no significant difference between T2 and T3, mainly with respect to the product acidity and sensory features. Overall, T2 had the best value compared to other treatments. T2 has sufficient pH, acidity, and ethanol compared to other treatments so that it has the right flavor. T2 has enough overrun and viscosity to slow down the melting rate to produce textures that were quite desirable. In the present study, the best treatment of kefir ice cream was determined by de Garmo method. The score of the T0, T1, T2, and T3 product value was 0.00; 0.68; 0.96; and 0.85 respectively. This result shows that the optimum concentration of *S. cerevisiae* ATCC for use was 5 g per 750 ml (T2) as the best treatment.

CONCLUSIONS

The addition of *S. cerevisiae* ATCC 36858 with a concentration of 0.66% was the best treatment to obtain the highest overall acceptance value. The addition of more than 0.66% makes kefir ice cream a very acidic product and the flavor was not liked by panelists. An addition of less than 0.66% was still less to get the sensation of flavor and texture from kefir ice cream products. In addition, LAB and yeast in kefir ice cream can survive for 28 days at – 20°C.

ACKNOWLEDGEMENT

This study was supported by funds and the scheme of Research Grand Universitas Brawijaya by the List of Budget Implementation Fills number SP DIPA-023.17.2.677512/2021 for the grant on this study.

REFERENCES

- Adi, P. (2022). The Beneficial and Detrimental Role of Fungi for Humans. <https://masalahrom.my.id/biologi/peran-menguntungkan-dan-merugikan-jamur-bagi-manusia/> [Accessed on 01.01.2022]
- Agustin, C., Nurliyani, N., & Jamhari, J. (2021). Ice Cream Characteristic with Cured Egg Yolk Powder as Whipping Cream Replacer. *Journal of Animal Science and Technology*, 16(1), 11–20. <https://doi.org/10.21776/ub.jitek.2021.016.01.2>
- Akalın, A. S., Kesenkas, H., Dinkci, N., Unal, G., Ozer, E., & Kınık, O. (2018). Enrichment of Probiotic Ice Cream with different dietary fibers: Structural characteristics and culture viability. *Journal of Dairy Science*, 101(1), 37–46. <https://doi.org/10.3168/jds.2017-13468>
- Akbari, M., Eskandari, M. H., & Davoudi, Z. (2019). Application and Functions of Fat Replacers in Low-Fat Ice Cream: A Review. In *Trends in Food Science and Technology* (Vol. 86, pp. 34–40). Elsevier Ltd. <https://doi.org/10.1016/j.tifs.2019.02.036>
- Ali, S. A., Syed, M. G. S., Uroosa, E., Muneera, N. B., & Muhammad, S. (2022). A Novel Approach to Improve the Nutritional Value of Black Gram (*Vigna mungo* L.) by the Combined Effect of Pre-Gelatinization and Fermentation by *Lactobacillus* sp. E14 and *Saccharomyces cerevisiae* MK-157: Impact on Morphological, Thermal, and Chemical Structural Properties. *LWT – Food and Technology*, 114216. <https://doi.org/10.1016/j.lwt.2022.114216>
- Alfadila, R., Baskara, R., Anandito, K., & Siswanti, D. (2020). Effects of Sweeteners on Physical, Chemical, And Sensory Quality of Soymilk Ice Cream with Orange Juice (Citrus Sinensis) Addition. *Journal of Agricultural Product Technology*: Vol. XIII (Issue 1)
- Arief, M. F., Ria, D. A., Rosyidi, D., & Radiati, L. E. (2023). Effect of Goat Kefir Utilization on Physicochemical Quality and Sensory Attributes of Ice Cream Probiotic. *Advances in Biological Sciences Research*: pp. 247 – 257. https://doi.org/10.2991/978-94-6463-116-6_32
- Arief, M. F., Rosyidi, D., & Radiati, L. E. (2024). Characteristics of Functional Ice Cream Produced with Goat's Milk Kefir in Combination with Mono-acylglycerol. *Livest. Anim. Res.* 22(1): 68-76. <https://doi.org/10.20961/lar.v22i1.78614>
- Bamba, T., Yoshimi, H., Kyohei, U., Chieko, S., Tomohiro, H., Kazumi, K., Masako, O., Akihiko, K., & Tomohisa, H. (2024). Comprehensive Metabolic Profiling of *Geotrichum candidum* and Comparison with *Saccharomyces cerevisiae*. *Journal of Bioscience and Bioengineering*: Vol. 137 (1): 9 – 15. <https://doi.org/10.1016/j.jbiosc.2023.10.004>
- Bengoa, A. A., Iraporda, C., Garrote, G.L., & Abraham, A.G. (2019). Kefir Micro-organisms: Their Role in Grain Assembly and Health Properties of Fermented Milk. *Journal of Applied Microbiology* (Vol. 126, Issue 3, pp. 686–700). Blackwell Publishing Ltd. <https://doi.org/10.1111/jam.14107>
- Bullock, Y. & Gruen, I. (2023). Effect of Strained Yogurt on the Physico-chemical, Texture, and Sensory Properties of Low-fat Frozen Desserts. *Food Chemistry Advances*, 2, 100161. <https://doi.org/10.1016/j.focha.2022.100161>
- Casertano, M., Vincenzo, F., & Danilo, E. (2022). Psychobiotics, Gut Microbiota and Fermented Foods Can Help Preserving Mental Health. *Food Research International*, 110892. <https://doi.org/10.1016/j.foodres.2021.110892>
- Corradini, S. A. S., Madrona, G. S., Visentainer, J. V., Bonafe, E. G., Carvalho, C. B., Roche, P. M., & Prado, I. N. (2014). Sensorial and fatty acid profile of ice cream manufactured with milk of crossbred cows fed palm oil and coconut fat. *Journal of Dairy Science*, 97(11), 6745–6753. <https://doi.org/10.3168/jds.2014-8290>

- Codex Alimentarius. (2018). International Food Standards for Fermented Milks. World Health Organization.
- Cruz, C., Fonte, C. P., Simone, A. D., Oppong, F. K., Jeatt, W., & Rodgers, T. L. (2022). Effect of homogenisation on fat droplets and viscosity of aged ice cream mixes. *Chemical Engineering Science*, 260. <https://doi.org/10.1016/j.ces.2022.117857>
- Deosarkar, S. S., Kalyankar, S. D., Pawshe, R. D., Khedkar, C. D. (2016). Ice Cream: Composition and Health Effects. *Encyclopedia of Food and Health*. <https://doi.org/10.1016/B978-0-12-384947-2.00385-8>
- Dutra, R. M., Gennari, A., Volpato, G., Volken, & Souza, C. F. (2015). Lactose Hydrolysis in Milk and Dairy Whey using Microbial β -Galactosidases. *Enzyme Research*. <https://doi.org/10.1155/2015/806240>
- Fernandes, M. L. P., Souza, A. C., Junior, P. S. P. C., Verissimo, L. A. A., Pylro, V. S., Dias, D. R., & Schwan, R. F. (2022). Sugary Kefir Grains as the Inoculum for Developing a Low Sodium Isotonic Beverage. *Food Research International*, 111257. <https://doi.org/10.1016/j.foodres.2022.111257>
- Fitri, A. S., & Yolla, A. N. F. (2020). Analysis of Chemical Compounds on Carbohydrates. *SAINTEKS*, Vol. 17 (1): 45 – 52
- Florczuk, A., Aneta, D., & Marek, A. (2022). An Evaluation of the Effect of Curdlan and Scleroglucan on the Functional Properties of Low-Fat Processed Cheese Spreads. *LWT*, 163, 113564. <https://doi.org/10.1016/j.lwt.2022.113564>
- Georgiev, D., Milena, K., Ana, C.O., & Yordan, M. (2024). Investigation of the Potential of Yeast Strains for Phytase Biosynthesis in a Two-Step Screening Procedure. *Journal of Microbiological Methods*, 106890. <https://doi.org/10.1016/j.mimet.2024.106890>
- Goktas, H., Dikmen, H., Bekiroglu, H., Cebi, N., Dertli, E., & Sagdic, O. (2022). Characteristics of Functional Ice Cream Produced with Probiotic *Saccharomyces boulardii* in Combination with *Lactobacillus rhamnosus* GG. *LWT*, 153, 112489. <https://doi.org/10.1016/j.lwt.2021.112489>
- Gut, A. M., Vasiljevic, T., Yeager, T., & Donkor, O. N. (2022). Anti-salmonella Properties of Kefir Yeast Isolates: An in Vitro Screening for Potential Infection Control. *Saudi Journal of Biological Sciences*, 29(1), 550–563. <https://doi.org/10.1016/j.sjbs.2021.09.025>
- Hanafi, F. N. A., Kamaruding, N. A., & Shaharuddin, S. (2022). Influence of Coconut Residue Dietary Fiber on Physicochemical, Probiotic (*Lactobacillus Plantarum* ATCC 8014) Survivability and Sensory Attributes of Probiotic Ice Cream. *LWT*, 154. <https://doi.org/10.1016/j.lwt.2021.112725>
- Indonesian National Standardization Agency. (1992). Ice Cream Testing Standards. Indonesian National Standard: Testing of Livestock Products. SNI 01-2891-1992. Indonesia.
- Indonesian National Standardization Agency. (1995). Indonesian National Standard: Ice Cream. SNI 01-3713-1995. Indonesia.
- Jardines, A. P., Arjona-Román, J. L., Severiano-Pérez, P., Totosaus-Sánchez, A., Fiszman, S., & Escalona-Buendía, H. B. (2020). Agave Fructans as Fat and Sugar Replacers in Ice Cream: Sensory, Thermal and Texture Properties. *Food Hydrocolloids*, 108. <https://doi.org/10.1016/j.foodhyd.2020.106032>
- Karim, A., & Aider, M. (2022). Comprehensive Utilisation of Electro-Activated Whey-Based Media in Cell Growth, Metabolite Production and Aroma Compounds Synthesis Using a Starter Culture Originated from Kefir Grains. *International Dairy Science Journal*. <https://doi.org/10.1016/j.idairyj.2021.105276>
- Khademi, F., Naghizadeh, R. S., Younesi, M., Motamedzadegan, A., Rabiei, K., Shojaei, M., Rokni, H., & Falsafi, M. (2022). Effect of Probiotic Bacteria on Physicochemical, Microbiological, Textural, Sensory Properties and Fatty Acid Profile of Sour Cream. *Food and Chemical Toxicology*, 166. <https://doi.org/10.1016/j.fct.2022.113244>
- Kozłowicz, K., Góral, M., Góral, D., Pankiewicz, U., & Bronowicka-Mielniczuk, U. (2019). Effect of Ice Cream Storage on the Physicochemical Properties and Survival of Probiotic Bacteria Supplemented with Zinc Ions. *LWT*, 116, 108562. <https://doi.org/10.1016/j.lwt.2019.108562>
- McGhee, C. E., Gupta, B. P., & Park, Y. W. (2015). Evaluation of Total Fatty Acid Profiles of Two Types of Low-Fat Goat Milk Ice Creams. *Journal of Animal Sciences*. <https://doi.org/10.4236/ojas.2015.51003>
- Muse, M. R., & Hartel, R. W. (2004). Ice Cream Structural Elements that Affect Melting Rate and Hardness. *Journal of Dairy Science*, 87(1), 1–10. [https://doi.org/10.3168/jds.S0022-0302\(04\)73135-5](https://doi.org/10.3168/jds.S0022-0302(04)73135-5)
- Popescu, L., Bulgaru, V., & Siminiuc, R. (2021). Effect of Temperature, pH and Amount of Enzyme Used in the Lactose Hydrolysis of Milk. *Food and Nutrition Sciences*. <https://doi.org/10.4236/fns.2021.1212091>
- Radiati, L. E., Hati, D. L., Fardiaz, D., & Sari, L. R. H. (2022). Effect of *Saccharomyces cerevisiae* Probiotic Properties of Goat's Milk Kefir. *IOP Earth and Environmental Science*, 1041, 012028. <https://doi.org/10.1088/1755-1315/1041/1/012028>

- Salari, A., Sara, G., Alireza, G., Lida, J., Mohammad, H., & Asma, A. (2021). Effect of Kefir Beverage Consumption on Glycemic Control: A Systematic Review and Meta-Analysis of Randomized Controlled Clinical Trials. *Complementary Therapies in Clinical Practice*. <https://doi.org/10.1016/j.ctcp.2021.101443>
- Sarwar, A., Aziz, T., Al-Dalali, S., Zhang, J., Din, J., Chen, C., Cao, Y., Fatima, H., & Yang, Z. (2021). Characterization of Synbiotic Ice Cream Made with Probiotic Yeast *Saccharomyces boulardii* CNCM I-745 in Combination with Inulin. *LWT*, 141, 110910. <https://doi.org/10.1016/j.lwt.2021.110910>
- Senaka, R. C., Evans, C. A., Adams, M. C., & Baines, S. K. (2013). Production of Probiotic Ice Cream from Goat's Milk and Effect of Packaging Materials on Product Quality. *Small Ruminant Research*, 112(1–3), 174–180. <https://doi.org/10.1016/j.smallrumres.2012.12.020>
- Suhendar, A. (2023). Beneficial of *Saccharomyces Sp* in Food Production. <https://homecare24.id/jamur-saccharomyces-sp-bermanfaat-dalam-pembuatan/> [Accessed on 04.10.2023].
- Umam, A. K., Lilik, E. R., Kevin, H. P. S., & Siti, N. K. (2021). Study of Antioxidant Activity, Peptides, and Chemical Quality of Goat Milk on the Different Post-Acidification Periods During Cold Storage. *Advances in Biological Sciences Research*, 18: 178 – 182. <https://doi.org/10.2991/absr.k.220207.037>
- Warren, M. M., & Hartel, R. W. (2018). Effects of Emulsifier, Overrun, and Dasher Speed on Ice Cream Microstructure and Melting Properties. *Food Science*. <https://doi.org/10.1111/1750-3841.13983>
- Yuzhen, J., Zhengbiao, G., Li, C., Caiming, L., Zhaofeng, L., & Yan, H. (2023). Physicochemical Characterization of Debranched Waxy Rice Starches and Their Effect on the Quality of Low-Fat Ice Cream Mixtures. *Bioscience*, 103485. <https://doi.org/10.1016/j.fbio.2023.103485>
- Zhang, B., Cuiying, Z., Jin, L., Penghui, Z., Yibin, L., Changqing, D., & Guoliang, Y. (2024). The Effect of Different Starter Cultures of *Lactobacillus paracasei* M104 and *Pediococcus pentosaceus* M103 on the Physicochemical and Microbial Qualities of Fermented Goat Milk. *Journal of Animal Science and Technology*, 14(2), 70–77. <https://doi.org/10.21776/ub.jitek.2019.014.02.1>
- Zoumpopoulou, G., Myro, L., Rania, A., Athanasia, A., Voula, A., Konstantinos, P., Ekaterini, M., & Effie, T. (2021). Kaimaki Ice Cream as a Vehicle for *Limosilactobacillus fermentum* ACA-DC 179 to Exert Potential Probiotic Effects: Overview of Strain Stability and Final Product Quality. *International Dairy Journal*. <https://doi.org/10.1016/j.idairyj.2021.105177>

DESIGN AND TESTING OF A VARIABLE FERTILIZATION SYSTEM BASED ON SOIL NUTRIENT DETECTION

基于土壤养分检测的变量施肥系统的设计与试验

Jie LIU¹⁾, Fanxia KONG^{*1)}, Zhao JIE²⁾, Lili Yi¹⁾, Yubin LAN^{1,3)}, Xin HAN¹⁾, Minhui ZHANG¹⁾, Lei LIU¹⁾, Pengcheng LV¹⁾

¹⁾College of Agricultural Engineering and Food Science, Shandong University of Technology, Zibo/China

²⁾The Forth procurement service station, Troop 32680, Shenyang/China

³⁾National Sub-Centre for International Collaboration Research Centre for Agricultural Aviation Intelligent Equipment, Zibo/China

Tel: +86-18653372858; E-mail: kfx0309@163.com

Corresponding author: Fanxia Kong

DOI: <https://doi.org/10.35633/inmateh-73-15>

Keywords: Agricultural machinery; Precision variable fertilization; Soil; Nutrient detection; Automatic control

ABSTRACT

In order to solve the problems of low correlation between variable fertilizer application system and soil nutrient content detection and insufficient real-time performance, a variable fertilizer application system based on real-time soil nutrient content detection was developed. This paper describes the structure, working principle and design of key components of the soil information acquisition and fertilizer application system. It includes the simulation and analysis of fertilizer application using the discrete element method and the selection of curved blade fertilizer application discs. The system uses STM32F429IGT6 microcontroller and ROS higher-level computer for decision making. The device detects soil nutrients in real time, adjusts the fertilizer motor speed accordingly, and runs autonomously along the planned path. The decision coefficient R^2 between the fertilizer application rate and the speed of the fertilizer application wheel is not less than 0.97, and the relative error between the actual fertilizer application rate and the theoretical fertilizer application rate is up to 5.91%, with the maximum value of the coefficient of variation (CV) of 10.18%. The indoor bench test shows that the relative error between the actual fertilizer application rate and the target fertilizer application rate within a single operating grid is up to 6.2%, with the maximum value of CV being 6.64%. The field test in the orchard showed that the maximum relative error between the actual fertilizer application and the target fertilizer application in a single operation grid was 6.3%, and the maximum value of CV was 12.34%, and the fertilizer application was completed in the operation grid, which demonstrated that the device was able to realize real-time and accurate variable fertilizer application according to the soil nutrient information.

摘要

针对变量施肥系统与土壤养分含量检测之间的关联性程度低，实时性不足的问题，开发了一种基于土壤养分实时检测的变量施肥系统。本文介绍了土壤信息采集与施肥系统的结构、工作原理和关键部件的设计。其中包括利用离散元法对撒肥进行仿真和分析，以及对弯曲形叶片撒肥盘的选择。系统采用 STM32F429IGT6 微控制器和 ROS 上位机进行决策。装置能实时检测土壤养分，相应地调整施肥电机转速，并沿着规划的路径自主运行。排肥量与排肥轮转速之间决定系数 R^2 不小于 0.97，实际排肥量与理论排肥量相对误差最大为 5.91%，变异系数最大值为 10.18%，室内台架试验表明，单个作业栅格内的实际施肥量与目标施肥量的相对误差最大值为 6.2%，变异系数最大值为 6.64%。果园田间试验表明，单个作业栅格内的实际施肥量与目标施肥量的相对误差最大值为 6.3%，变异系数最大值为 12.34%，且施肥均在作业栅格中完成，试验表明，该装置能够根据土壤养分信息实现实时精准变量施肥。

INTRODUCTION

Fertilizer is an indispensable key factor in agricultural production, many orchards in China still use the traditional manual fertilization, which leads to inaccurate fertilizer application, leakage and the practice of inadequate and excessive fertilization is pervasive, resulting in environmental contamination and pollution. (Liu et al., 2019). So, how to achieve automation of precise variable fertilizer application is the current urgent need to solve the problem (Xu et al., 2023). Researchers at home and abroad have done a lot of research on the structural design of the fertiliser discharge device, the linkage between soil nutrient information and variable fertiliser application, and the integration of the control system (Pawase et al., 2024).

Bo Wang et al. addressed the problems of over-application of fertiliser and poor uniformity of fertiliser discharge in maize fertiliser planter (Wang et al., 2022). A set of precision sensing and control system for maize fertiliser planter was studied. In the study of variable rate fertiliser application based on working prescription charts, the 'SOILECTION' fertiliser system produced by Open Ag-chem Instrumentation Co., Ltd. in the United States, can be used for dry or liquid fertiliser application. It adjusts the application rates of nitrogen, phosphate and potash according to the fertiliser prescription chart (Poncet et al., 2018). Bai Qiwei and other research for the orchard fruit tree fertiliser problem, developed a set of accurate variable automatic target fertiliser application device and its control system. The volume of the slot of the fertilizer discharge wheel can be automatically adjusted according to the target fertilization amount of fruit trees and the size of the canopy diameter, which can meet the requirements of precise and variable automatic fertilization of different sizes of fruit trees with different fertilizer requirements. (Bai et al., 2021).

Domestic and foreign variable fertilizer application equipment and control technology mainly relies on external information collection and offline analysis, fertilizer application often adopts the uniform fertilizer application method, and manual operation reduces the efficiency (Zhang J., Liu G. et al., 2019; Przywara et al., 2015; Fan et al., 2024). In view of the above problems, this paper explores a series of accurate variable fertilizer application equipment and control system based on soil nutrient detection. Soil-integrated sensors are used to detect the nutrient information in the soil grid, and the relationship between the target fertilizer requirement of plant growth in the grid and the variables such as the speed of the fertilizer wheel, the width of fertilizer application, the speed of the fertilizer wagon, and the actual fertilizer content in the soil, and the control rules of the wheel speed, and add the path planning and navigation technology is implemented in the fertilizer application apparatus, enabling it to traverse, sample, and apply fertilizer along a designated route. This facilitates a more precise correlation between variable fertilizer application and soil nutrients, while also enhancing the intelligence of the fertilizer application device.

MATERIALS AND METHODS

Structure of the whole machine

The whole machine structure consists of a medium-size crawler robot chassis equipped with soil information collecting device, fertilizer discharging device and control system. The soil information collection device consists of drilling mechanism, coupling, soil collection sensor, electric actuator, fixed frame, etc.; the fertilizer discharge device consists of fertilizer discharge box, fertilizer discharge wheel, fertilizer discharge pipe, fertilizer spreading wheel, fertilizer spreading belt, fixed frame, etc.; the control system consists of STM32F429IGT6 microcontroller, decision making host computer based on the development of ROS (Robot Operating System) system, VCU of the crawler chassis, motor driver, Hall sensor, GNSS (Global Navigation Satellite System), etc.. The structure of the whole device is shown in Figure 1.

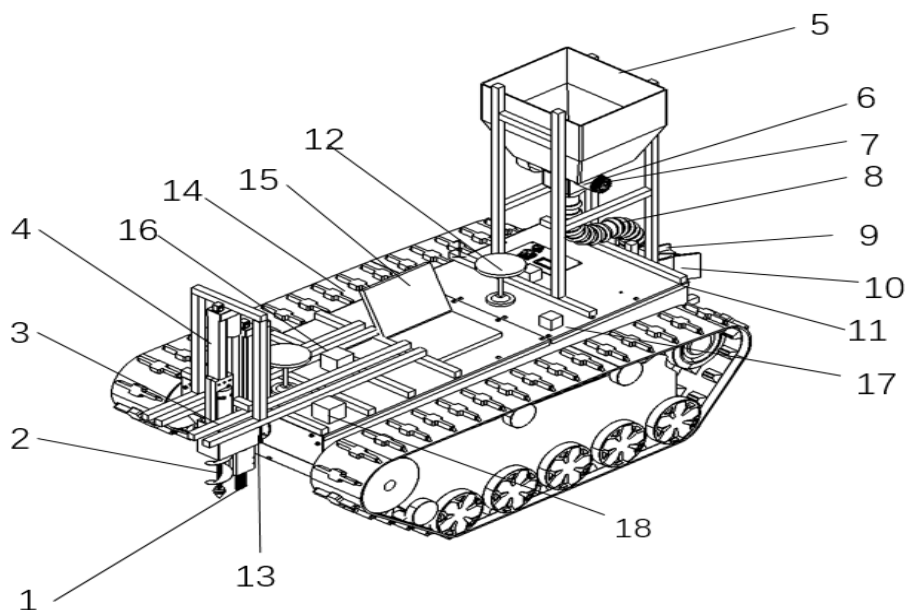


Fig. 1 - Structure of variable fertilization device based on soil nutrient detection

1. Soil integrated sensor; 2. Driller; 3. Coupler; 4. Linear actuator; 5. Compost Bin; 6. Fertilizer motor; 7. Hall encoder; 8. Fertilizer pipe;
9. Spinner fertilizer spreader; 10. Protecting band driller; 11. Fertilizer moto; 12. Dual Antenna GNSS-RTK; 13. Mounting;
14. Caterpillar traveling chassis; 15. ROS upper computer; 16. 24V DC power supply; 17. 12V DC power supply; 18. Control box

Working Principle

Before the operation of the machine, the GNSS carried by the chassis is first used to locate the sampling points in the operation area and control the whole machine to move according to the pre-planned path. During the operation of the machine, the RTK_GNSS receiver will acquire the latitude and longitude information of the current position of the whole machine in real time, and upload the data to the ROS host computer mounted on the vehicle through the RS232 serial port. The vehicle speed of the fertilizer application operation of the device is controlled within the range of 0-2 meters per second, starting from the head of the vineyard rows and moving forward, while the speed of the fertilizer application vehicle is monitored by the Hall sensor in real time. The schematic diagram of the control system of this device is shown in Figure 2.

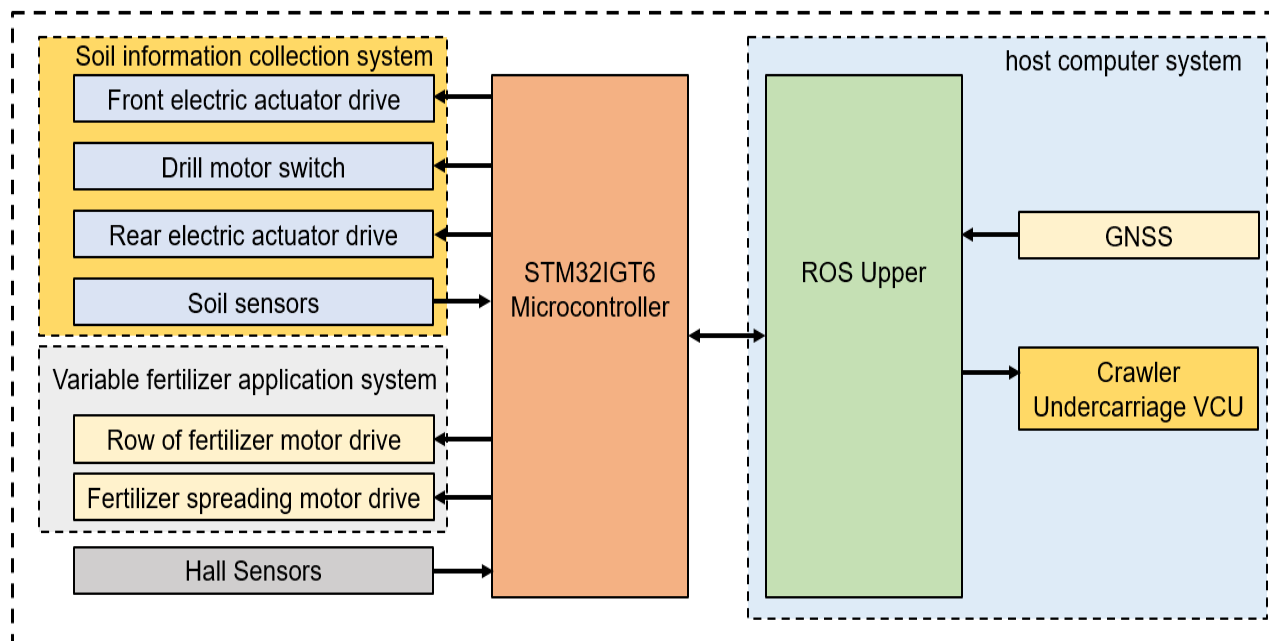


Fig. 2 - Schematic diagram of control system of variable fertilization device based on soil nutrient detection

When the instrument arrives at the specified sampling point, the travel speed is reduced to 0 m/s. At this time, the host computer sends acquisition instructions to the microcontroller, instructing the soil sampler to begin acquiring soil information. The size of the sampling grid is set according to the actual soil structure (taking into account the differences in row spacing of different crops, e.g. row spacing is 3.5-5 m for apples, 1.5-2.5 m for peaches and 1-2 m for vines) (Walton J.C. et al., 2009).

The soil nutrient detection structure consists of two electric actuators: the front electric actuator fixes the 42GP-775 24V planetary gear motor (torque 28 kg.cm), which is connected to the auger to form a soil loosening device; the rear electric actuator is connected to the soil synthesis sensor through the sensor fixing piece to form a collecting device. The structure of the soil sampling device is shown in Figure 3(a). During soil sampling, the loosening device first loosens the soil, and then the collecting device starts working to collect soil information. The microcontroller uploads the soil data read by the sensor to the host computer control system through serial communication, and the control system sends control instructions to the microcontroller according to the fertilizer requirement of fruit trees, fertilizer truck speed, fertilizer spreading width and soil nutrient information collected, so as to automatically adjust the rotational speed of the fertilizer discharge motor (20-60 rpm).

Fertilizer device consists of fertilizer discharging mechanism and fertilizer spreading mechanism, in which fertilizer discharging mechanism adopts external grooved wheel structure, fertilizer discharging mechanism consists of fertilizer box and 12V DC motor with deceleration device, which is connected to fan blade spindle by coupling, with fertilizer brush set in fertilizer outlet slot, and fertilizer discharge pipe connected to outlet of slot. The fertilizer spreading device consists of a 12V DC motor and a fertilizer spreading disc connected to the motor rotation axis by a flange. The construction principle of fertilizer spreader is shown in Figure 3(b,c). By changing the rotational speed of the fertilizer discharge motor, the amount of fertilizer discharged will change, and the fertilizer will be transported to the fertilizer spreading disc for spreading through the fertilizer discharge pipe.

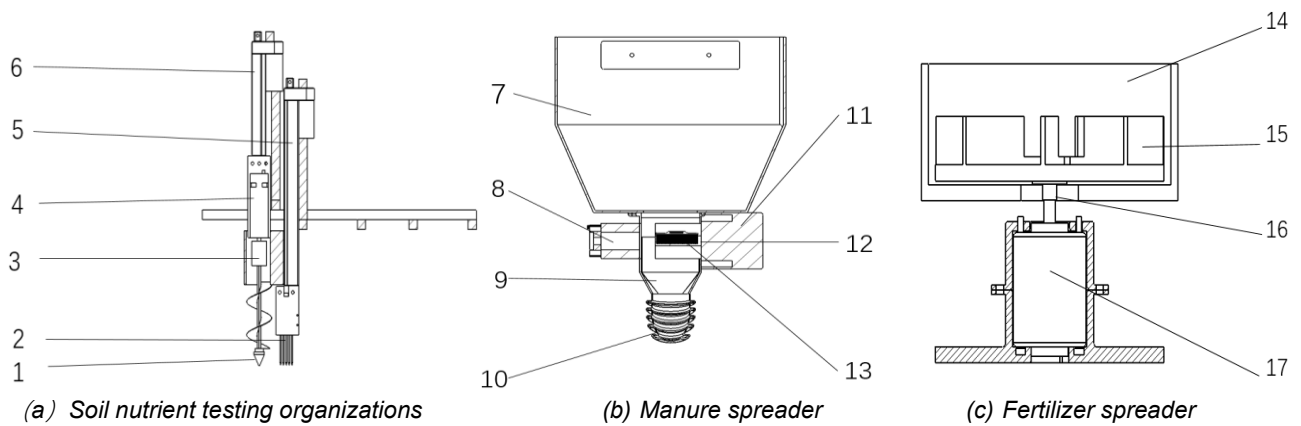


Fig. 3 Schematic diagram of soil information collection mechanism and fertilizer application mechanism

- 1. Drill; 2. Soil acquisition sensor; 3. Coupling; 4. Planetary gear reduction motor; 5. Rear electric push rod; 6. Front electric push rod;
- 7. Fat box; 8. Outer wheel; 9. Manure box; 10. Fertilizer can; 11. Fertilizer discharge motor; 12. Fertilizer fan leaf; 13. Fertilizer brush;
- 14. protected zone; 15. Manure spreader; 16. Ring flange; 17. Fertilizer motor

Calibration of the effect of fertilizer discharge device and fertilizer spreader

The volume of fertilizer discharged per revolution of the external chute wheel type fertilizer discharger is the total mass of fertilizer particles in the forced and driven layers, and the theoretical volume of fertilizer discharged per revolution can be calculated according to formula (1) (.

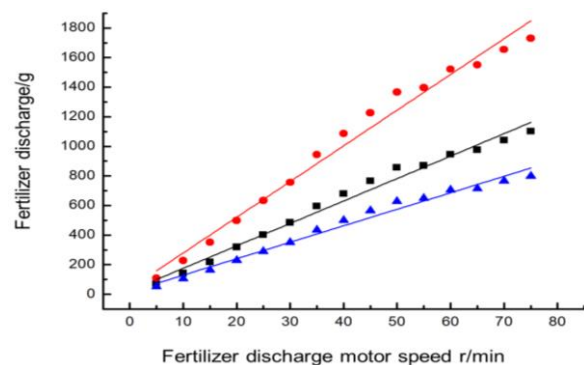
$$q = q_1 + q_2 = \pi dls\gamma\left(\frac{\alpha(n)f}{t} + c(n)\right) \tag{1}$$

q for the fertilizer discharge per turn of the fertilizer discharge, g/r; q_1 is the amount of fertilizer discharged from the forced layer per revolution of the fertilizer discharger, g; q_2 for each revolution of the fertilizer discharger is driven out of the fertilizer, g; d for the diameter of the grooved wheel, cm; l for the working length of the grooved wheel, cm; s for the grooved wheel grooves of the end area, cm²; γ is the density of fertilizer, g/cm³; $\alpha(n)$ is the filling coefficient of fertilizer to the groove of the grooved wheel; t is the pitch between the groove teeth of the grooved wheel, cm; f is the cross-sectional area of the groove of the grooved wheel, cm²; $c(n)$ is the characteristic coefficient of the driving layer (calculated thickness), cm. The test was conducted with the three different granular fertilizers with the bulk density of 750 kg/m³ urea, 850 kg/m³ calcium superphosphate and 880 kg/m³ potassium nitrate as test materials, and the density of the granular fertilizers was calculated by the method of (1). Fertilizers as test materials, by (1) formula were calculated to obtain the theoretical per-rotation discharge of granular fertilizers urea for 16.56 g, calcium superphosphate for 26.46 g, potassium nitrate for 12.17 g.

The fertilizer discharger discharges the fertilizer at 5, 10, 15, 20, 25, 30, 35, 40, 45, 50, 55, 60, 65, 70, 75 r/min discharging speed for 1 minute, the fertilizer collection box collects the discharged fertilizer, and the electronic scale weighs the mass of the discharged fertilizer. Each fertilizer was subjected to the above experimental procedure 10 times at different rotational speeds and the average of the 10 discharges was calculated. The test platform was set up indoors as shown in Fig. 4(a), and the relationship between the rotational speed of the discharge wheel and the actual amount of fertilizer discharged by the three kinds of granular fertilizer is shown in Figure 4(b).



(a) Indoor test platform



(b) Fertilizer Displacement versus RPM

Fig. 4 - Fertilizer discharge calibration test

In Fig. 4(b), with the increase of the rotational speed of the fertilizer discharge wheel, the amount of fertilizer discharged increases, and the fertilizer discharge amount and the rotational speed of the fertilizer discharge wheel are subjected to one-way linear regression analysis, resulting in a one-way linear regression model between the two as (2).

$$q = kn_r + b \tag{2}$$

Where n_r is the rotational speed of the fertiliser wheel, r/min; q is the volume of fertiliser discharged by the fertiliser discharger, g; k, b are the coefficients and constants of the univariate linear regression model, respectively, and the values of k, b are different under the conditions of different fertilisers, and the results of the significance test of each regression model are shown in Table 1.

Table 1

| Regression results and significance test | | | | |
|---|--------|--------|----------------|---------|
| Fertilizer type | k | b | R ² | P-value |
| urea (NH ₂) ₂ CO | 0.9685 | 15.481 | 0.98 | 0.0071 |
| calcium superphosphate (Ca(OH) ₂) | 0.9729 | 16.841 | 0.98 | 0.0045 |
| potassium nitrate | 0.9556 | 17.668 | 0.97 | 0.0069 |

As can be seen from Table 1, the values of the coefficients of determination R² of the univariate linear regression models established for different granular fertilizers in terms of rotational speed and fertilizer discharge were not less than 0.97, and the P values were all less than 0.01, and the univariate linear regression equations between the fertilizer discharge volume of the three granular fertilizers and the rotational speed of the fertilizer discharge wheels were all particularly significant and with high degree of fit, which had practical significance. In Figure 4(b), the same type of fertilizer from the speed 5-75 r/min, the amount of fertilizer discharged is a gradient of rising. If the rotational speed of the fertilizer discharge wheel is less than 20 rpm, the fertilizer discharge mechanism of the outer groove wheel will shake severely and the amount of fertilizer discharged will be low. When the rotating speed of the fertilizer discharge wheel is higher than 60 r/min, the rotating speed of the outer groove wheel is too fast, and the fertilizer cannot be filled into the fertilizer cavity by gravity in time, and the amount of fertilizer discharged is also seriously low, based on the above situation. The rotational speed of the fertilizer discharge wheel and the amount of fertilizer discharged cannot satisfy the linear relationship, so the rotational speed of the fertilizer discharge wheel is limited to the range of 20-60 rpm to meet the needs of different fertilizer discharge amounts in the operation grid area. The rotational speed of the fertilizer wheel is limited to 20-60 rpm to meet the needs of different fertilizer discharges in the working grid area. The calibration results of three kinds of fertilizer under each speed are shown in Table 2-4. From Table 2-4, it can be seen that in the range of 20-60 rpm, the relative error between the actual fertilizer discharge and the theoretical fertilizer discharge is within 6%, and the accuracy of fertilizer discharge meets the requirements, which can be further used for precise variable fertilization.

Table 2

| Fertiliser Discharger Rotation Speed and Fertiliser Discharge of Urea Granular Fertiliser | | | | |
|---|----------------|-----------------------|--------------------|------------------------------|
| Motor speed (r/min) | Mean value / g | Theoretical value / g | Relative Error / g | Coefficient of variation / % |
| 20 | 318.98 | 331.2 | 3.69 | 6.49 |
| 30 | 484.43 | 496.8 | 2.49 | 8.69 |
| 40 | 679.22 | 662.4 | 2.54 | 7.46 |
| 50 | 855.99 | 828 | 3.38 | 6.67 |
| 60 | 946.30 | 993.6 | 4.76 | 7.01 |

Table 3

| Rotational speed of fertiliser discharger and fertiliser discharge of calcium superphosphate granular fertiliser | | | | |
|--|----------------|-----------------------|--------------------|------------------------------|
| Motor speed (r/min) | Mean value / g | Theoretical value / g | Relative Error / g | Coefficient of variation / % |
| 20 | 499.19 | 559.7 | 5.67 | 8.21 |
| 30 | 756.09 | 793.8 | 4.75 | 13.78 |
| 40 | 1085.81 | 1058.4 | 2.59 | 10.68 |
| 50 | 1365.60 | 1323 | 3.22 | 9.89 |
| 60 | 1521.87 | 1587.6 | 4.14 | 8.65 |

Table 4

| Rotational speed of fertiliser discharger and discharge rate of potassium nitrate granular fertiliser | | | | |
|---|----------------|-----------------------|--------------------|------------------------------|
| Motor speed (r/min) | Mean value / g | Theoretical value / g | Relative Error / g | Coefficient of variation / % |
| 20 | 229.02 | 243.4 | 5.91 | 9.33 |
| 30 | 349.80 | 365.1 | 4.19 | 10.18 |
| 40 | 499.16 | 486.8 | 2.54 | 9.57 |
| 50 | 627.67 | 608.5 | 3.15 | 9.16 |
| 60 | 704.50 | 730.2 | 3.52 | 7.36 |

Calibration of the spreading effect of fertiliser discs

In this paper, a reasonable balanced fertilisation was carried out according to the law of fertiliser demand of grapes, taking into account the spreading width of fertilisers, and three kinds of spreading disc rotation speeds were selected for verification. Firstly, by analysing the movement and force of the fertiliser particles in the spreading disc and in the air, ignoring the bouncing between the fertilisers and the spreading disc and the interaction force between the fertilisers, it was found that the speed of the granular fertilisers when they left the discs was mainly related to the rotational speed of the discs, v , and the calibre R of the discs (Gou Y., Li H. et al., 2022). The speed of granular fertiliser when leaving the disc is mainly related to the rotational speed v of the disc and the diameter R of the disc, while the spreading width is mainly related to the spreading height H under the condition of a certain rotational speed (Liu C. et al., 2017). The force analysis of the granular fertiliser movement is shown in Figure 5.

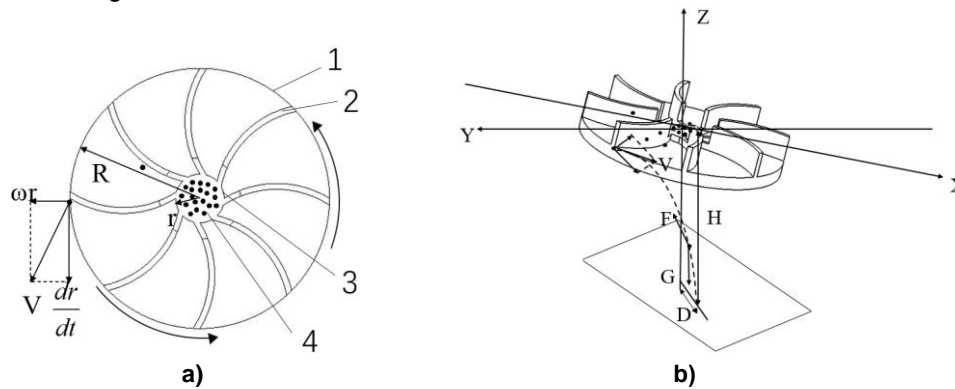


Fig. 5 - Motion analysis of granular fertilizer

1. Fertilizer spreading disc; 2. Blade; 3. Fertilizer falling area; 4. Granular fertilizer; 5. r is the radius of the fertilizer falling area;
6. R fertilizer disc radius; 7. v is the speed of the granular fertilizer when it leaves the disc at the moment of t ; 8. is the angular speed of the fertilizer spreading disc rotation; 9. G is the gravitational force of the movement in air; 10. F is the resistance during the movement in the air; 11. X is the width of the fertilizer spreading width; 12. H is the height of the fertilizer spreading; 13. D the width of fertilizer spreading.

Fertilizer spreading disc is a key component of the fertilizer spreading device, its operational performance is excellent or not directly affects the accuracy and stability of fertilizer spreading, therefore, EDEM was used to build the simulation model of the fertilizer spreading disc, analyse the impact of changes in the parameters of the spreading disc on the accuracy and stability of fertilizer spreading, and select the optimal spreading structure. Fertilizer contact area of the spreading device model is PLA material and 3D printed, using SolidWorks in accordance with the ratio of 1:1 to build and import the model into the EDEM software, combined with the literature to determine the model parameters as shown in Table 5 (Dun et al., 2016; Xin et al., 2023; Liu et al., 2021).

Table 5

| Pre-treatment parameters setting | | |
|----------------------------------|-----------------------------|-------------------|
| Items | Parameters | Numerical value |
| Granular Fertilizer | Poisson's ratio | 0.25 |
| | modulus of rigidity / Pa | 1.1×10^8 |
| | Densities / kg/m^3 | 750 |
| PLA Consumables | Poisson's ratio | 0.42 |
| | modulus of rigidity / Pa | 2.6×10^9 |
| Pellet-Pellet | Densities / kg/m^3 | 1260 |
| | Crash factor | 0.3 |

As shown in Figure 8(b), the y-axis direction is the fertilizer spreading direction, the origin O is the centre of the fertilizer spreading width, the right side of the fertilizer spreading disc takes the value of the positive direction of the x-axis as positive, and the negative direction of the x-axis takes the value of the negative direction, and the collecting area is divided into a single-column fertilizer collecting matrix with a width of 100 mm, and the quality of fertilizer particles of the six fertilizer collecting boxes in the single-column collecting matrix represents the concentration of the particles of the fertilizers scattered along the spreading width after the fertilizer spreader passes through the collecting matrix (Liu et al., 2022). The quality of the fertilizer particles in each single column collection matrix is shown in Figure 9. By comparing the fertilizer spreading results of three different blade structures with the same parameters, it can be seen that the three-blade fertilizer spreading discs are more concentrated when they are close to the y-axis, and the quality of granular fertilizer of the three kinds of blades is obviously asymmetric about the y-axis, and the spreading area of linear and wedge blades is to the right of the whole with respect to that of curved blades, while the curved blades are close to the centre of fertilizer spreading. The spreading area of the linear blade and wedge-shaped blade is to the right of that of the curved blade, while the granular fertilizer quality of the curved blade is more concentrated near the centre of fertilizer spreading, and the overall change is smoother.

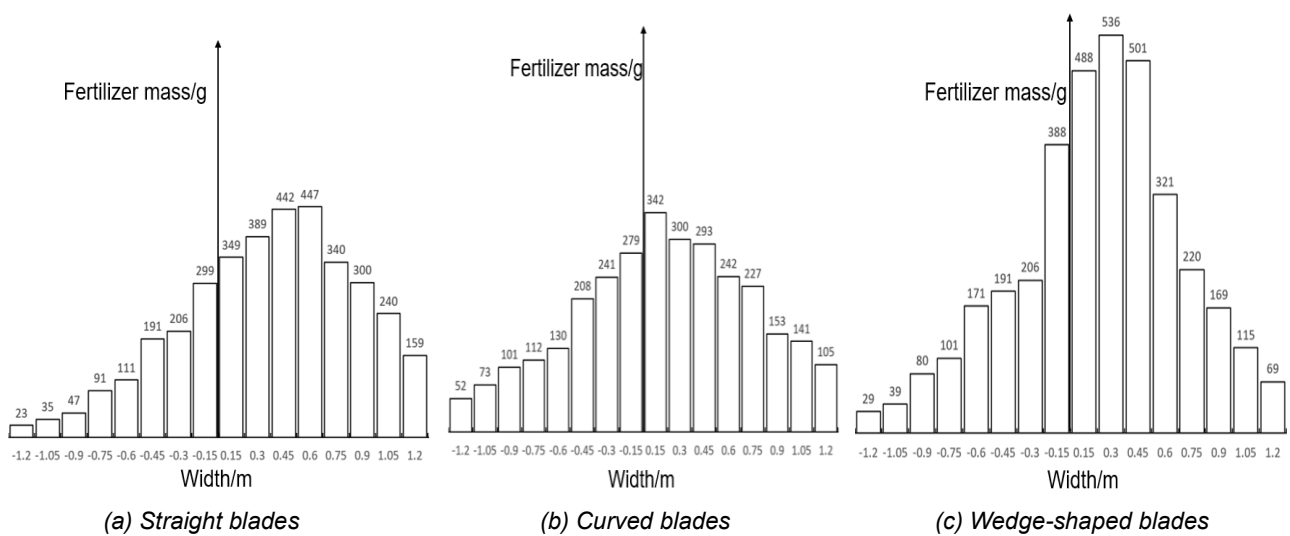


Fig. 9 - Histogram of fertilizer spreading distribution

Fertiliser application control model and control system design

In this study, the relationship between the nutrient content estimation points x_i and the sampling points x_a in the sampling grid area was calculated using the radial basis function method and combined with statistical laws. From equation (3), the nutrient content values $Z(x_i)$ were calculated for the four estimation points of (4) (Rastgou M. et al., 2022).

$$Z(x_i) = \sum_{j=1}^5 w_j e^{-\frac{1}{2\sigma^2}(\|x_i - x_a\|)^2} \tag{3}$$

where $\|x_i - x_a\|$ is the Euclidean distance between the estimated point x_i and the point to be measured x_a , σ is the standard deviation of the Gaussian function. w_i is the weight of the known point x_a .

$$Z(x_1), Z(x_2), Z(x_3), Z(x_4) \tag{4}$$

The soil nutrient content values of the four estimation points and one sampling point within the sampling grid described above, totalling five points, were each assigned a different weight δ_i in equation (5) to derive the mean soil nutrient distribution value S_v in the operational grid (Daou L. et al., 2021).

$$S_v = \frac{\sum_{i=1}^5 Z(x_i)\delta_i}{\sum_{i=1}^5 \delta_i} \tag{5}$$

When fertiliser is applied according to a given target fertiliser application rate for fruit trees, common methods for determining the target fertiliser application rate include the geotechnical zoning (level) allocation method, the target yield allocation method and the soil effective nutrient correction coefficient method. Combined with the actual situation, this paper adopts the soil effective nutrient correction coefficient method, and equation (6) is used to calculate the target fertiliser application rate in the sampling grid.

$$y_i = \frac{N_a T - 0.15 S_v \mu_N}{\omega_f \eta_{Nf}} \quad (6)$$

where 0.15 is the soil quick-acting nutrient coefficient, y_i is the amount of fertiliser applied, g; N_a is the nutrient uptake per unit of crop yield, g; T is the target yield, g; S_v is the soil test value, mg/kg μ_N is the soil effective nutrient correction coefficients for N, P and K of 0.65, 0.5 and 0.80 respectively, and ω_f is the nutrient content in the fertiliser, % and η_{Nf} is the fertiliser utilisation rate, %.

The fertiliser is applied according to the target fertiliser quantity required for the growth of the fruit trees in the collection grid, and the relationship between the target fertiliser quantity y_i , g; the fertiliser application wheel speed n_τ , m/s; the fertiliser vehicle speed v , m/s; the fertiliser application width β , m; and the fertiliser application rate q , g; in a single collection grid is as follows Formula (7).

$$y_i = \frac{10000 q n_\tau}{v \beta} \quad (7)$$

Substituting equation (2) into equation (7) and simplifying yields:

$$10000 k n_\tau^2 + b n_\tau - y_i v \beta = 0 \quad (8)$$

In the orchard fertilization test, the chassis moves forward according to the set speed, and when the positioning system detects that the fertilization device arrives at the sampling grid, the host computer sends the acquisition command to the STM32F429IGT6 microcontroller, thus controlling the acquisition device to perform soil sampling and according to the acquisition of various soil parameters, so as to realize the automatic and accurate variable fertilization of fruit trees.

Solving for n_τ in equation (8) gives.

$$n_{\tau 1} = \frac{-b + \sqrt{b^2 + 40000 k y_i v \beta}}{20000 k} \quad (9)$$

$$n_{\tau 2} = \frac{-b - \sqrt{b^2 + 40000 k y_i v \beta}}{20000 k} \quad (10)$$

Analysis of (9) (10) formula can be seen, if y_i , v , β any one of the three values of 0, the device does not need to apply fertilizer, fertilizer wheel rotation speed is 0, $n_{\tau 1}$ in accordance with the actual situation, $n_{\tau 2}$ is not 0, the device discharges fertilizer, not in accordance with the actual situation; so to sum up, the formula (9) will be used as a fertilizer discharge system to obtain the control rules, imported into the device control system on the fertilizer wheel rotation speed for automatic control.

After the system is turned on and reset, the vehicle travels from the ground at a constant speed according to the set vehicle travel path, the positioning system detects that the implement arrives at the first working grid when the implement stops, the STM32F429IGT6 controls the soil information collecting device to collect soil parameters, the soil integrated sensor uploads the collected information to the ROS host computer decision system through the serial port, and the decision system quickly derives the rotational speed of the fertilizer discharger according to equation (9), generates an adjustable duty cycle pulse waveform PWM wave, and sends the instruction to the STM32F429IGT6 through the serial port, the decision system quickly derives the rotational speed of the fertilizer discharging device, generates an adjustable duty cycle pulse waveform PWM wave, and sends the instruction to STM32F429IGT6 through the serial port, and the microcontroller controls the rotation of the fertilizer discharging motor, which drives the fertilizer discharging wheels to apply the fertilizer, and before the device performs the operation, the rotational speed of the universal spreading device spreads the fertilizer according to the actual required fertilizer spreading width set in the decision system. During the fertilizer application period, the traveling machine moves forward at a speed of 1 m/s until it reaches the next working area, and during the soil information sampling period, the fertilizer spreading motor stops rotating and no fertilizer is applied. The hardware wiring diagram is shown in Figure 10.

Test condition

In order to verify whether the range of fertilizer application rate of the experimental device and the control system meets the requirements of fruit trees for different granular fertilizers in different growth periods, as well as the match between the width of fertilizer application and the width of fruit trees between rows, indoor experiments and field tests for soil information acquisition and variable fertilization, respectively, were conducted using grapevines as an example.

Grapes in China are mainly grown on the plains in areas with fertile soil and good irrigation conditions. Cultivation methods in vineyards mainly include hedgerow and trellis cultivation. The row spacing of grapes varies according to the cultivar and environment, usually ranging from 0.6 m to 1.5 m and 2.5 m to 3.5 m. Fertilization is usually a combination of organic and chemical fertilizers. Depending on the stage of growth of the fruit trees, grapes need to be fertilized several times during the year. Fertilizers are applied according to the nutrient content of the soil and the nutritional needs of the fruit trees. Indoor simulated variable fertilization trials are usually conducted in vineyards with row spacing of 1.5 m × 1.5 m, while variable fertilization trials based on soil nutrient content detection are conducted in mature vineyards with row spacing of approximately 1.5 m × 2 m.

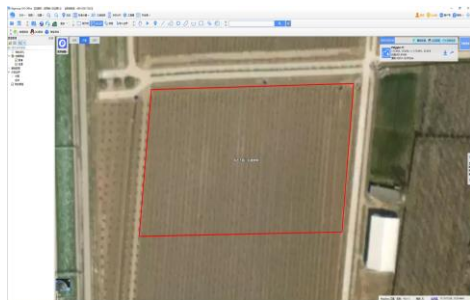
Indoor simulated variable fertilization trials

This system uses an STM32F429IGT6 type microcontroller to control the fertilizer application motor and fertilizer spreading motor. The simulated collected nutrient content of the raster soil was input to the ROS higher-level computer decision system, and the ROS higher-level computer quickly calculated the required rotational speed of the fertilizer discharge wheel according to equation (9) and sent commands to the STM32F429IGT6, which then controlled the rotational speeds of the fertilizer discharge motor and the fertilizer spreading motor. The indoor simulated variable fertilizer application test is shown in Figure 5(a) and Figure 9(a).

In the experiment, the planting distance was set at 1.5m×1.5m row spacing, and the selected test soil grid was 1.5m×0.5m. 6,800 plants could be planted per hectare, and the selected nitrogen content of urea was 46.6%, the phosphorus content of calcium superphosphate was 45.59%, and the potassium content of potassium nitrate was 38.6%. 100 kg of calcium superphosphate and 50 kg of potassium nitrate were applied per 667 square meters. The fertilizer requirement of each vine is different at each stage of the growing period, and the nitrogen requirement of a single fruit tree throughout the year is 200-600 g, phosphorus is 150-300 g and potassium is 200-400 g. Setting the target fertilizer application in the fertilizer grid is 50, 100, 150, 200, 300 g granular urea, 100, 200, 300 g granular calcium superphosphate and 400, 500 g granular potassium nitrate. 80, 120, 180, 250, 300 g of granular potassium nitrate were applied, and the fertilization test was carried out sequentially. According to the size of the fertilizer grid and the target speed of fertilizer application, the maximum driving speed of the simulated fertilizer truck was controlled to be from 1 m/s to 1.5 m/s. For the same target fertilizer application, the operation was repeated three times, and the mass of fertilizer after application was weighed by an electronic scale to obtain the actual amount of fertilizer applied, and the average value of the three trials and the coefficient of variation of the amount of fertilizer applied were calculated.

Field trials

The soil sampling device and fertilizer application device were mounted on an unmanned sports chassis, and the experiment was conducted at the foot of 1,000 mu vineyard in Hantai County, Zibo City, Shandong Province (N37.07420°, E117.91777°). The ambient temperature at that time was 19°C to 27°C and the relative humidity was 13%, and the exact location is shown in Figure 12.



(a) Vineyard Map



(b) Vineyard field scenes

Fig. 12 - Test site

The test procedure is shown in Figure 13.

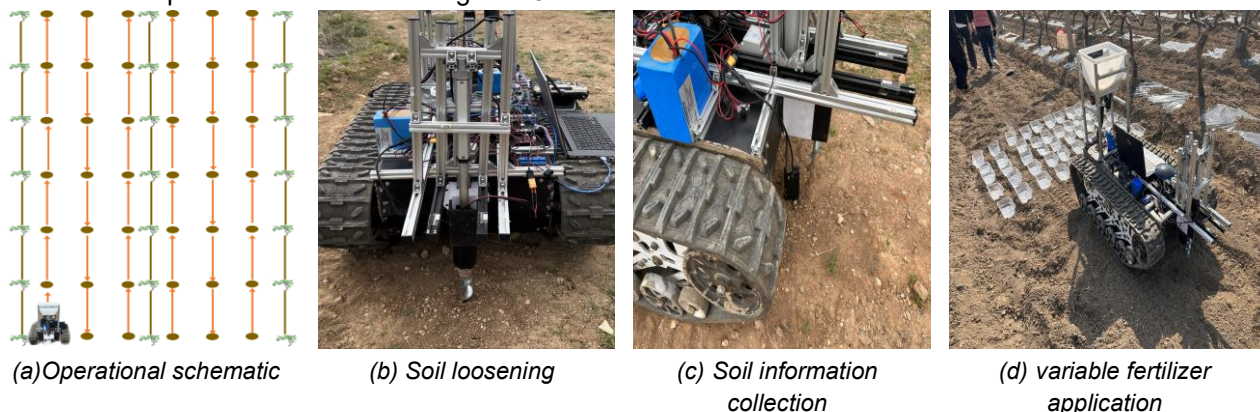


Fig. 13 - Field trial of variable rate fertilization based on soil nutrient testing

According to the actual nutrient content of the soil in the fertilization area and the target fertilizer requirement for grape growth, the developed soil information collection and fertilization device and control system were used to fertilize a 50m×1.5m orchard area. Granular fertilizer urea 30, 60, 90 g, calcium superphosphate 130, 160, 200 g, potassium nitrate 40, 70, 100 g were applied, and nine fertilizer spreading grids of 1.5m×0.5m each were selected for the sampling and fertilization test. In the test process, according to the actual collection of soil nutrient content and fruit tree growth fertilizer requirement, the fertilizer application vehicle speed is set to 1 m/s, and the soil sampling device automatically collects soil data for on-demand fertilization. For the same target fertilizer application amount, 3 trials were conducted, the collection box was placed in the fertilizer spreading area, and the mass of fertilizer in the collection box was weighed to determine the actual amount of fertilizer discharged and to evaluate the uniformity of fertilizer spreading width. Finally, the average of the 3 trials and the coefficient of variation of the fertilizer application rate were calculated.

RESULTS AND ANALYSIS

The results of the indoor simulated variable fertilization test are shown in Table 6; the results of the orchard variable fertilization test are shown in Table 7.

Table 6

Results of indoor simulated variable fertilization experiment

| Type of fertiliser | Vehicle speed (m/s) | Element Type | Soil nutrient content (mg/kg) | Target fertiliser application rate/(g) | Average fertiliser application/(g) | Relative error/(%) | Coefficient of variation/(%) |
|---|---------------------|--------------|-------------------------------|--|------------------------------------|--------------------|------------------------------|
| urea (NH ₂) ₂ CO | 1m/s | N | 15 | 50 | 53.1 | 6.20 | 5.21 |
| | | | 16 | 100 | 102.7 | 2.70 | 6.34 |
| | | | 17 | 150 | 145.6 | 2.93 | 5.98 |
| | | | 18 | 200 | 194.9 | 2.55 | 2.21 |
| | | | 20 | 300 | 290.2 | 3.27 | 3.41 |
| calcium superphosphate (Ca(OH) ₂) | 1.5m/s | P | 16 | 100 | 103.1 | 3.10 | 4.23 |
| | | | 18 | 200 | 193.4 | 3.30 | 5.45 |
| | | | 20 | 300 | 296.5 | 1.17 | 6.64 |
| | | | 22 | 400 | 390.7 | 2.33 | 2.27 |
| potassium nitrate | 1m/s | K | 24 | 500 | 489.8 | 2.04 | 5.65 |
| | | | 54 | 80 | 78.3 | 2.13 | 3.36 |
| | | | 56 | 120 | 124.4 | 3.67 | 2.39 |
| | | | 59 | 180 | 188.1 | 4.50 | 1.83 |
| | | | 51 | 250 | 259.0 | 3.60 | 5.82 |
| | | | 50 | 300 | 311.3 | 3.77 | 5.52 |

The indoor simulation experiments in Table 6 show that the maximum relative error between the actual amount of urea fertiliser applied to the grapes in the grid and the target amount of fertiliser is 6.2%, the maximum relative error in the amount of calcium superphosphate applied is 3.3%, the maximum relative error in the amount of potassium nitrate applied is 4.5%, and the maximum value of the coefficient of variation of the amount of fertiliser applied is 10.52%.

The width of the spread from the edge of the fertiliser grid is the maximum distance of -0.17 m, and the locations of the fertiliser drops are all within the area of the fertiliser grid. The locations were all within the range of the fertiliser grid.

Table 7

Table 7 Precision variable fertilization in orchard field

| Type of fertiliser | Vehicle speed m/s | Element type | Soil nutrient content mg/kg | Target fertiliser application rate/g | Average fertiliser application/g | Relative error/% | Coefficient of variation/% |
|---|-------------------|--------------|-----------------------------|--------------------------------------|----------------------------------|------------------|----------------------------|
| urea (NH ₂) ₂ CO | 1m/s | N | 9 | 30 | 31.8 | 6 | 10.83 |
| | | | 10 | 60 | 63.8 | 6.3 | 11.26 |
| | | | 11 | 90 | 87.2 | 3.1 | 9.32 |
| calcium superphosphate (Ca(OH) ₂) | 1m/s | P | 13 | 130 | 133.9 | 3 | 7.41 |
| | | | 14 | 160 | 154.7 | 3.3 | 12.34 |
| | | | 16 | 200 | 209.3 | 4.6 | 10.43 |
| potassium nitrate | 1m/s | K | 50 | 40 | 38.6 | 3.5 | 7.33 |
| | | | 52 | 70 | 74.3 | 6.5 | 8.2 |
| | | | 54 | 100 | 105.0 | 5 | 9.61 |

The coefficient of variation within a single fertilizer grid in the vineyard test was generally higher than that in the indoor simulation experiment, mainly due to the fact that the rotational speed of the fertilizer wheels was not stable enough when the fertilizer applicator was operating in the orchard, especially in the rough conditions along the roadside. However, based on the target fertilizer application rate of the vines in the grid, the actual soil nutrient content, the fertilizer application width, and the vehicle speed of the fertilizer application device, the system could automatically adjust the rotational speed of the fertilizer discharge wheel, which resulted in the relative error of the fertilizer application rate of a single vine being less than 6.5%, with a maximum coefficient of variation of 12.34%. Through the real-time detection of the actual soil nutrient content in the fertilizer grid based on the built-in soil nutrient sensor, it ensures that the fertilizer drop locations are all within the fertilizer grid. Therefore, the fertilizer application device combines the collection device and the control system to realize the precise variable fertilization of different fruit trees in the grid for different granular fertilizer needs.

In addition, the orchard validation experiments of this device and control system were conducted in vineyards with the same ridge spacing and the same selected grape variety. However, the ridge spacing of different grape varieties varies greatly, so when sampling and fertilizing a large area in vineyards with different planting densities, it is necessary to improve the structure of the soil nutrient detection device again to improve the detection efficiency and accuracy. In addition, the device was mainly tested for three kinds of granular fertilizers, namely urea, calcium superphosphate and potassium nitrate, and further experimental studies are needed to investigate the application effects of powder and liquid fertilizers.

CONCLUSIONS

(1) Using unmanned technology, the relationship between the target fertiliser application rate and the rotational speed of the fertiliser spreading wheel, the speed of the fertiliser spreading vehicle, the width of the fertiliser spreading width and the actual nutrient content of the soil, as well as the control rules of the rotational speed of the fertiliser spreading wheel were established according to the actual content of soil nutrients in the fertiliser spreading grid and the target fertiliser application rate of different fruit tree varieties.

(2) Through the comparative analyses of simulation test, indoor test and orchard test on three kinds of fertiliser spreading blades, the results showed that the curved blades were more uniform in spreading effect.

(3) The results of the indoor simulation test showed that when applying urea granular fertiliser, the maximum error of fertiliser application in a single grid was 6.2%, the maximum error of calcium superphosphate fertiliser application amount was 3.30% and the maximum error of potassium nitrate fertiliser application amount was 4.5%.

(4) The field test in the orchard showed that the integrated soil nutrient sensor could accurately detect the nutrient content in different farm grids and could meet the requirement of precise variable fertiliser application for fruit tree growth in the farm grids. The maximum relative error of fertiliser application within a single spacing was 6.5% and the maximum coefficient of variation was 12.43%.

ACKNOWLEDGEMENT

The work was supported by Top Talents Program for One Case One Discussion from Shandong Province (Lu Zheng Ban Zi [2018] No. 27), and Technology small courtyard project supported by Ministry of Education, Ministry of Agriculture and Rural Affairs, and China Association for Science and Technology (Department of Teaching and Research Letter [2022] No.7), and Key R&D Program Funding Project in Zibo City (2019ZBXC053).

REFERENCES

- [1] Bai Qiwei, Zhang Xin, Luo Hongpin, Li Guanglin (2021). Automatic target precise variable fertilization control system for facility orchard (设施果园自动对靶精准变量施肥控制系统), *Transactions of the Journal of Agricultural Engineering*, vol.37(12), pp.28-35, Chongqing/China.
- [2] Bo Wang, Yafei Wang, Hui Wang, Hanping Mao, Liming Zhou (2022). Research on accurate perception and control system of fertilization amount for corn fertilization planter. *Frontiers in Plant Science*, vol.13, pp.1074945, Zhenjiang/China
- [3] Cai Rui (2023). Design and test of variable fertilizer application device for corn (玉米变量施肥装置的设计与试验). *Transactions of the Northwest Agriculture and Forestry University*, pp.001776, Xianyang/China.
- [4] Daou Laurent, Garnier Éric, Shipley Bill (2021). Quantifying the relationship linking the community - weighted means of plant traits and soil fertility. *Ecology*, vol.102(9), e03454, Quebec/Canada.
- [5] Dun Guoqiang, Chen Haitao, Feng Yining, Yang Jilong, Li Ang, Zha Shaohui, (2016). Optimization and test of key component parameters of fertilizer blending device based on EDEM software (基于 EDEM 软件的肥料调配装置关键部件参数优化与试验). *Transactions of the Journal of Agricultural Engineering*, vol.32 (07), pp.36-42, Haerbin/China.
- [6] Chengsai Fan, Ruiyin He, Yinyan Shi, Linan He (2024). Structure and operation mode of centrifugal side-throwing organic fertilizer spreader for greenhouses. *Powder Technology*, pg.119457, Nanjing/China.
- [7] Gou Yujiang, Li Huiying, Wang Daming, He Huibo (2022). Design and simulation optimization of small variable fertilizer spreader based on EDEM (基于 EDEM 的小型变量撒肥机设计与仿真优化). *Transactions of the Agricultural Mechanization Research*, vol.44 (11), pp.65-71+76, Chongqing/China.
- [8] Jiqin Zhang, Gang Liu, Chengming Luo, Hao Hu, Jiayun Huang, (2019). MOEA/D-DE based bivariate control sequence optimization of a variable-rate fertilizer applicator. *Computers and electronics in agriculture*, vol.167, pp.105063, Beijing/China.
- [9] Liu Xiaodong, Hu Rui, Wang Denghui, Lu Bang, Wang Wanchao, Ding Youchun (2021). Optimization and test of fertilizer discharger based on granular fertilizer motion model (基于颗粒肥料运动模型的排肥器优化与试验). *Transactions of the Journal of Agricultural Machinery*, vol.52 (12), pp.85-95, Wuhan/China.
- [10] Liu Cailing, Li Yanni, Song Jiannong, Ma Tuo, Wang Mengmeng, Wang Xujian (2017). Performance analysis and test of centrifugal dump disk fertilizer spreader based on EDEM (基于 EDEM 的离心甩盘撒肥器性能分析与试验), *Transactions of the Journal of Agricultural Engineering*, vol.33 (14), pp.32-39, Beijing/China.
- [11] Liu Mochun, Zhao Qingji, Han Shouqiang, Song Zhanyhua, Li Fade, Yan Yinfa (2022). Design and test of self-propelled directional fertilizer spreader for mulberry plantation (桑园自走式变比配肥定向撒肥机设计与试验). *Transactions of the Journal of Agricultural Machinery*, vol.53 (S2), pp.120-130+140, Taian/China.
- [12] Liu Ji'ai, Shu Aiping, Liu Guangrong, Li Zuzhang, Liu Zengbing, Gao Zheng (2019). Progress of research on fertilizer application affecting soil traits and microbiome (施肥影响土壤性状和微生物组的研究进展), *Transactions of the Biotechnology Bulletin*, vol.35 (09), pp.21-28, Nanchang/China.
- [13] Poncet A, Fulton J., McDonald T., Knappenberger T. (2018). Effect of heterogeneous field conditions on corn seeding depth accuracy and uniformity. *Applied Engineering in Agriculture*. vol.34.5, pp.819-830, Michigan/USA.
- [14] Pranav Pramod Pawase, Sachin Madhukar Nalawade, Avdhoot Ashok Walunj, (2024). Comprehensive study of on-the-go sensing and variable rate application of liquid nitrogenous fertilizer. *Computers and Electronics in Agriculture*, vol.216, pp. 108482, Rahuri / India.

- [15] Przywara Artur (2015). The impact of structural and operational parameters of the centrifugal disc spreader on the spatial distribution of fertilizer. *Agriculture and Agricultural Science Procedia*, vol.7, pp.215-222, Głęboka/Poland.
- [16] Rastgou M., Bayat H., Mansoorizadeh M., Gregory A. S. (2022). Estimating soil water retention curve by extreme learning machine, radial basis function, m5 tree and modified group method of data handling approaches. *Water Resources Research*, vol.58(4), e2021WR031059, Hamedan/Iran.
- [17] Walton J., Roberts R., Dayton L. (2009). Grid soil sampling adoption and abandonment in cotton production [J]. *Precision Agriculture*, vol.11, 135-147, TN/USA.
- [18] Xin Mingjin, Jiang Zhiwen, Chen Tianyou (2023). Design and test of inflow-type centrifugal fertilizer lifter for paddy fields (导流式水田离心扬肥器设计与试验), *Transactions of the Journal of Agricultural Engineering*, vol.39 (15), pp.67-75, Shenyang/China.
- [19] Xu Yang, Du Sen, Zhong Yonghong (2023). Fifteen Years of Progress and Prospects of the Soil Testing and Fertilizer Application Project (测土配方施肥项目十五年进展与展望), *Transactions of the Soil and Fertilizer China*, vol.03, pp.236-244, Beijing/China.
- [20] Yang Liwei, Chen Longsheng, Zhang Junyi (2019). Experiment on uniformity of fertilizer spreading by centrifugal disc spreader (离心圆盘式撒肥机撒肥均匀性试验). *Transactions of the Journal of Agricultural Machinery*, vol,50 (S1), pp.108-114, Beijing/China.

DESIGN AND EXPERIMENTAL OPTIMIZATION OF V-SHAPED HAMMER FOR HAMMER MILL

锤片式粉碎机 V 型锤片设计及试验优化

Haijun ZHANG^{1,2)}, Yi QIAN²⁾, Haiqing TIAN²⁾

¹⁾ Huzhou Vocational and Technical College, Intelligent Manufacturing and Elevator College, Huzhou / China;

²⁾ Inner Mongolia Agricultural University, College of Mechanical and Electrical Engineering, Hohhot / China

Tel: +086-0572-2363665; E-mail: zhanghj320@163.com

DOI: <https://doi.org/10.35633/inmateh-73-16>

Keywords: Hammer mill, Feed, Grinding, V-shaped hammer, Parameter optimization, Orthogonal tests, ANSYS analysis

ABSTRACT

Low productivity and high electricity consumption are considered problems of the hammer mill, which is widely used in current feed production. In this paper, a folded V-shaped hammer was designed to improve the performance of the hammer mill. To determine the optimal design parameters of the new hammer, the single-factor test and orthogonal tests were carried out with the inclination angle of hammer, the angle of hammer head, and the distance of hammer head as the influencing factors, and the productivity and output per kWh as evaluation indexes. The order of the influence on the productivity and output per kWh were the inclination angle of hammer > the angle of hammer head > the distance of hammer head. The parameters were optimized based on the orthogonal tests with the following results: the angle of hammer head was 160°, inclination angle of hammer was 110°, and the inclination distance of hammer head was 24 mm. The static analysis and modal analysis were carried out on the optimized hammer by using ANSYS software. The results showed that the new hammer satisfies the strength and stiffness requirements during working, does not resonate, and has good dynamic characteristics. The new hammer can effectively improve the performance of the hammer mill, and the research results can provide theoretical basis for the optimization design of the hammer mill.

摘要

针对目前生产中普遍使用的锤片式粉碎机存在生产率低、能耗高的问题。本文以 CPS-420 型锤片式粉碎机为研究样机，对锤片式粉碎机物料粉碎过程和物料力学特性进行分析，设计了折线式 V 型锤片，提高粉碎机性能。为确定锤片最佳设计参数，以锤片倾角、锤头角度和倾角距离为因素，以生产率和度电产量为评价指标，开展了单因素试验和正交试验，结果表明：影响生产率和度电产量的因素主次顺序均为锤头角度 > 锤片倾角 > 倾角距离。基于正交试验进行参数优化，优化结果为：锤头角度为 160°、锤片倾角为 110° 和倾角距离为 24 mm。对优化后的锤片进行静力学分析和模态分析，结果表明：锤片满足工作时的强度和刚度要求，不会发生共振，有较好的动态特性。新型锤片能有效提高锤片式粉碎机的性能，研究结果可为锤片式饲料粉碎机的优化设计提供理论依据。

INTRODUCTION

Feed grinding can increase the surface area of feed and improve its palatability and digestibility for livestock. Therefore, a large amount of feed needs to be ground every year (Mugabi et al., 2017; Wang et al., 2020; Barnwal et al., 2015). The hammer mill is a widely used grinding equipment in feed processing, and it has the advantages of low price, simple structure and easy operation (Chen et al., 2017; Qian, 2021). However, there are still some problems, such as low productivity and high electricity consumption with the hammer mill (Li et al., 2019; Cao et al., 2016; Wang et al., 2020).

The material is ground by the hammer in the grinding chamber. The hammer is key part that affect the productivity and electricity consumption of the hammer mill (Li et al., 2019; Qian, 2021). In recent years, researches on the hammer of the hammer mill in China and abroad have mainly focused on the arrangement, manufacturing process and numbers of the hammer, etc.

Xu Wei *et al.*, (2021), took the minimum deformation of the traditional hammer as the optimization objective and used the response surface method and genetic algorithm to optimize the structure parameters of the hammer. Bochat *et al.*, (2015), designed a new hammer and performed comparative experiments. The results showed that the new hammer was more efficient than the traditional hammer. Su Congyi *et al.*, (2016), designed a new hammer and performed comparative experiments. The results showed that the new hammer reduced the centrifugal inertia force of the material and the density of the material ring, the efficiency of the hammer mill was improved by 25% to 28%. Ma Qian *et al.*, (2016), studied the influence of the hammer inclination angle on the grinding performance by using computational fluid dynamics methods. Simulation results showed that the hammer with an inclination angle could improve the flow field characteristics of the grinding chamber and the efficiency of the hammer mill. CPS-420 hammer mill was taken as the experimental prototype, Li Xiuqing, (2021), designed an edged hammer and an angled hammer, discrete element simulation and grinding performance tests were carried out. The results showed that both the edged hammer and the angled hammer could improve the grinding performance. The angled hammer could change the flight trajectory of materials, reduce movement speed of materials, and the angled hammer was beneficial to sieve. The hammer mill with an inclined hammer was beneficial for reducing electricity consumption. The edged hammer could break more material bonding keys, improve the production efficiency of the hammer mill.

In this work, a hammer mill CPS-420 produced by machinery factory of Inner Mongolia Agricultural University in China was taken as the prototype. Considering the existing problems with the hammer mill, the grinding process of materials in the grinding chamber was analysed, a folded V-shaped hammer was designed to improve the performance of the hammer mill, and the key structural parameters of the new hammer affecting the performance of the hammer mill were determined. The orthogonal tests were used to optimize the structural parameters of the hammer, and the optimal combined parameters were determined. The research results can provide a reference for the optimal design of the hammer mill.

MATERIALS AND METHODS

• Overall structure and working principle

The hammer mill used in this study is mainly composed of an outlet, a frame, a motor, a feeding hopper, a sieve, and a hammer. The structure diagram of the hammer mill is shown in Figure 1. When the hammer mill is working, the feed materials enter the grinding chamber through the feeding hopper. It is first ground by the hammer and then further ground by the impact between the feed and sieve. When the feed particle size is smaller than the sieve hole diameter, the feed is discharged from the outlet.

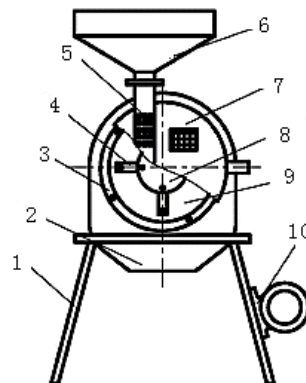


Fig. 1 - Structure diagram of the hammer mill

1-Frame; 2-Outlet; 3-Sieve frame and sieve; 4-Hammer; 5-Air inlet of feeding mouth; 6-Feeding hopper; 7-Cover plate of grinding chamber; 8-Hammer frame; 9-Grinding chamber; 10-Motor

Table 1

| Specification of hammer mill | |
|------------------------------|----------------|
| Specification | Value |
| Size (LengthxWidthxHeight) | 650x380x930 mm |
| Motor power | 3 kW |
| Rotational speed of rotor | 4 400 r/min |
| Number of hammers | 24 |
| Sieve width | 170 mm |
| sieve hole diameter | 3 mm |
| Productivity | 900~950 kg/h |

● **Principle analysis of material grinding**

When the hammer mill is working, the materials in the grinding chamber are mainly ground by the combined action of the hammer, the sieve, and material particles. The schematic diagram of movement of material particles in the grinding chamber is shown in Figure 2. The linear speed of the hammer is v . Assuming that the impact between the hammer and the material is a frontal impact, the speed of the material after the impact is v_1 , which is the same as v . Energy transfer is completed at the moment of impact, the kinetic energy of the high-speed rotating hammer is transferred to the material particles. After impact, the material particles move in the direction of v_1 and impact with the sieve in the grinding chamber. The kinetic energy of the material particles decreases, and the lost energy during the impact process is used to destroy the cohesive force of the material particles themselves, causing the material to quickly grind.

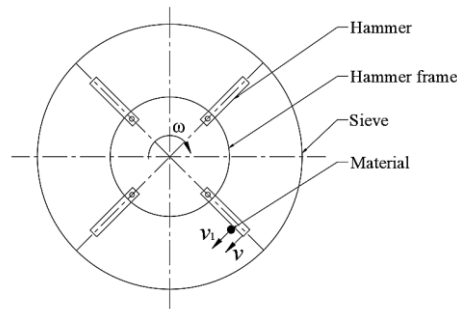


Fig. 2 - Schematic diagram of movement of material particles

● **Design of V-shaped hammer for the hammer mill**

According to Figure 2, the material particles enter the grinding chamber from the feeding hopper and mainly impact with the side surface of the hammer end. Without considering the influence of factors such as air flow resistance and friction on the hammer, the following equation can be obtained from the impulse momentum theorem (Qian, 2021).

$$P\Delta t = m_1(v - v_2) \tag{1}$$

where: P is the impact force between the hammer and the material, N; m_1 is the mass of hammer, kg; Δt is the impact time between hammer and material, s; v is the speed of the hammer before impact, m/s; v_2 is the speed of the hammer after impact, m/s.

According to Eq. (1), if the speed of hammer and the speed of material are constant, the impact of the hammer on the material is increased with the increases of m_1 , accelerating the grinding efficiency of large particle materials into small particles, thereby improving the grinding performance of the hammer mill.

In addition, it found that the impact angle of particles thrown onto the sieve after being impacted by the hammer affects the sieving effect of the material. The impact of the hammer on the material particles in the grinding chamber is shown in Figure 3.

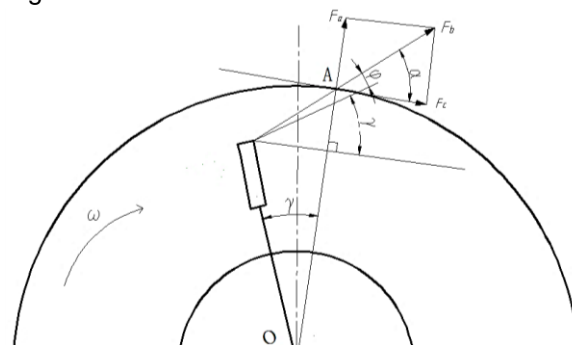


Fig. 3 - Schematic diagram of material particles impacting screen plate

It can be seen from Figure 3 that after the traditional hammer impacts with material particles, its ejection angle is φ , point A is the impact point between the material and the sieve, α is the impact angle, γ is the angle between the centre line of the hammer and the radial centre line of point A on the sieve, F_b is the combined force of the material particles under the impact of the hammer, F_a and F_c are the positive and side impact force, they are the two components of F_b . The following equations can be obtained (Du, 2015):

$$\alpha = \varphi + \gamma \tag{2}$$

$$F_a = F_b \sin \alpha \tag{3}$$

An analysis of Eq. (2) and Eq. (3) show that the larger the impact angle, the greater the positive impact force, which is more conducive to the grinding and sieving effect of the material. The optimized hammer should increase the impact angle of the material on the sieve, so that the ground material can be quickly sieved out and achieve efficient grinding of the material.

During the working process of the hammer mill, the material is mainly ground by the impact between the end of the hammer and the material. Based on the above theory and referring to the picking mechanism of the straw baler (Qian, 2021), a new design scheme of a folded hammer structure was proposed. The end of the hammer was designed as a V-shaped structure with a fold line, which can improve the quality of the hammer appropriately. On the other hand, it increases the impact probability between the hammer and the material, thereby improving the grinding efficiency of the hammer mill. The schematic diagram and physical picture of the new hammer structure are shown in Figure 4.



Fig. 4 - Parameters of V-shaped hammer

Note: In Fig.4a: a- Inclination angle of hammer; b-Angle of hammer head; c-Inclination distance of hammer head

• Design of hammer thickness

The overall thickness of the hammer has a significant impact on the grinding performance of the hammer mill. If the hammer is too thin, it will cause its wear resistance to deteriorate and require frequent replacement, which not only increases the labour intensity of maintenance workers but also increases the cost of material grinding. The hammer is too thick, although it increases the probability of the material being hit, the load on the rotor of the hammer mill will increase, resulting in huge electricity consumption.

Therefore, based on the structural parameters of the grinding chamber of the CPS-420 hammer mill, the thickness of the hammer was designed by the following equation:

$$Z = K_2 B / \delta \quad (4)$$

where: Z is the thickness of hammer; K_2 is the density coefficient of hammer configuration. Generally, K_2 is taken as 0.2~0.42; B is the width of grinding chamber, $B=170$ mm; δ is the total count of hammer, $\delta=24$.

Based on the analysis of the density of the prototype hammer in this study, it was found that K_2 is 0.42. According to Eq. (4), the thickness of the new hammer was calculated to be 2.98 mm, for processing convenience, Z was taken as 3 mm.

In addition, the effective impact area between the traditional rectangular hammer of the hammer mill and the material is determined by the following equation:

$$S_1 = B_1 \times P_1 \quad (5)$$

where: S_1 is the effective impact area of the traditional hammer, mm^2 ; B_1 is the thickness of the traditional hammer, mm; P_1 is the length of the traditional hammer, mm.

Bringing B_1 and P_1 into Eq. (5), it can be obtained $S_1 = 2.5 \times 101 = 252.5(\text{mm}^2)$.

The optimized hammer end is a double-sided structure, and the effective impact area of the hammer is:

$$S_2 = B_2 \times (P_2 + P_3) \quad (6)$$

where: S_2 is the effective impact area of the optimized hammer, mm^2 ; B_2 is the thickness of the optimized hammer, mm; P_2 and P_3 are the lengths of the optimized hammer and its head, respectively, mm.

Bringing B_2 , P_2 and P_3 into Eq. (6), it can be obtained $S_2 = 3 \times (105 + 11) = 348(\text{mm}^2)$

According to the analysis of Eq. (5) and Eq. (6), it can be seen that the effective impact area of the optimized hammer is about 1.4 times greater than that of the traditional hammer, thereby increasing the probability of impact between the material and the hammer.

• Design of hammer length

The length of the hammer affects the gap between the hammer and sieve. When the hammer mill is working, there is a material circulation layer between the end of the hammer and the sieve that rotates with the hammer. When the distance between the end of the hammer and the sieve is too large, the small particle materials have been ground near the end of the hammer are not easy to be sieved out. If the distance is too small, the velocity of the circulation layer increases, the particle size of the material is low, and it increases the electricity consumption.

It was found that the distance between the end of the hammer and the sieve is generally between 7 mm to 10 mm (Qian *et al.*, 2020). In this paper, the distance is 9 mm.

The length of the hammer is determined by the following equation:

$$r_1 = R_1 - \Delta R - L_i \quad (7)$$

where: r_1 is the distance from the centre of the pin shaft installation hole to the end of the hammer, mm; R_1 is the radius of the sieve, $R_1=195$ mm; ΔR is the distance between the end of the hammer and the sieve, $\Delta R = 9$ mm; L_i is the distance from the centre of the rotor to the centre of the pin shaft installation hole, $L_i=92$ mm.

Bringing R_1 , ΔR and L_i into Eq. (7), it can be obtained $r_1 = 94$ mm.

● Parameter design of hammer experiment

The design of the new hammer structure of the hammer mill should not only satisfy the hammer installation size, but also consider the distance between the end of the hammer and the sieve. The angle of hammer head of the new hammer directly affects the grinding characteristics of the hammer. Considering the motion characteristics of the ground material in the grinding chamber and the structural parameters of the hammer mill, the ranges of hammer head were set to 90° to 150° ; considering the wear angle and position of the end of the hammer, the inclination distances of hammer head were set to 15 mm to 30 mm. In addition, the circulation area between the end of the hammer and the sieve in the grinding chamber has a significant impact on the sieving and grinding of the material. The airflow characteristics in the circulation area are closely related to the inclination angle of hammer. According to Qian *et al.*, (2021), it was found that when the inclination angle of hammer changes from 140° to 165° , the material can achieve better sieving performance. Therefore, the inclination angles of hammer were set to 140° to 165° .

● Experimental design

In order to study the influence of the structural parameters of the new hammer on the grinding performance of the hammer mill, and determine the optimal hammer structure parameters. The experiment of grinding performance was carried out based on the inclination angle of hammer, the angle of hammer head, and the inclination distance of hammer head.

● Experimental materials and equipment

Corn grain was selected as the test material. The average moisture content of corn grain was 13.2%. The variety of corn used was JINSHAN-126, with a moisture content of 13.20% and bulk density of 723 kg/m^3 . The test equipment included a TCS-150 type electronic scale (accuracy of 0.01 kg), a BT223S type electronic balance (accuracy of 0.001 g), an electric energy meter, a stopwatch and a drying box, etc.

● Evaluation indexes

In order to objectively and accurately evaluate the grinding performance of the hammer mill, according to the Chinese national standard (GB/T 6971-2007) (China National Standardization Committee, 2007), the productivity and electricity consumption per ton were taken as the performance evaluation indexes.

The calculation equations are given by Eq. (8) and Eq. (9) (China National Standardization Committee, 2007).

$$E = m/t_c \quad (8)$$

$$Y = Z/Q \quad (9)$$

where:

E is the productivity, t/h; m is the material mass, t; t_c is the material grinding time, h.

Y is the output per kWh, t/kWh; Q is the electricity consumption, kWh; Z is the output, t.

● Test procedures

The new hammers with different structural parameters were installed on the hammer mill to carry out the grinding performance tests. The test procedures were as follows:

(1) The hammer mill ran no-load firstly, and after the no-load power stabilizes, the spindle speed was measured to verify whether the speed meets the requirements of the hammer mill.

(2) The hammer mill ran with load, and it ran smoothly for 1 to 2 minutes, after confirming that there are no abnormal phenomena, the grinding performance test was carried out according to the test scheme.

(3) In order to increase the accuracy of experimental data, each group of tests was repeated three times. The average values were taken as the test results.

RESULTS

- **Single-factor test results and analysis**

- Results and analysis of the inclination angle of hammer*

The values 140°, 145°, 150°, 155°, 160°, and 165° were selected as the inclination angle of hammer, productivity and output per kW·h tests were carried out. The test results are shown in Table 2.

Table 2

| Inclination angle of hammer | Productivity | Output per kWh |
|-----------------------------|--------------|----------------|
| [°] | [t/h] | [t/kWh] |
| 140 | 0.89 | 5.12 |
| 145 | 0.94 | 4.93 |
| 150 | 1.02 | 4.80 |
| 155 | 1.07 | 4.72 |
| 160 | 0.98 | 4.82 |
| 165 | 0.92 | 5.13 |

It can be seen from Table 2 that with the inclination angle of hammer increases, the productivity first increases and then decreases, and the output per kWh first decreases and then increases. When the inclination angles of hammer were 155°, the productivity was highest and the output per kWh per ton of material was lowest; from the trend of changes in productivity and output per kWh, it can be seen that the better inclination angle ranges of the hammer were 150° to 160°.

- Results and analysis of the angle of hammer head*

90°, 100°, 110°, 120°, 130°, and 140° were selected as the angle of hammer head, productivity and output per kW·h tests were carried out. The test results are shown in Table 3.

Table 3

| Angle of hammer head | Productivity | Output per kWh |
|----------------------|--------------|----------------|
| [°] | [t/h] | [t/kWh] |
| 90 | 0.96 | 5.03 |
| 100 | 0.99 | 4.87 |
| 110 | 1.04 | 4.82 |
| 120 | 1.02 | 4.90 |
| 130 | 0.93 | 5.12 |
| 140 | 0.89 | 5.08 |

It can be seen from Table 3 that with the angle of hammer head increases, the productivity first increases and then decreases, the output per kWh shows a waveform trend. When the angle of hammer head was 110°, the productivity was highest and the output per kWh was lowest. From the trend of changes in productivity and output per kWh, it can be seen that the better angles of hammer head were 100° to 120°.

- Results and analysis of the inclination distance of hammer head*

The values 15 mm, 18 mm, 21 mm, 24 mm, 27 mm and 30 mm were selected as the inclination distance of hammer head, productivity and output per kWh per ton of material tests were carried out.

The test results are shown in Table 4.

Table 4

| Inclination distance of hammer head | Productivity | Output per kWh |
|-------------------------------------|--------------|----------------|
| [mm] | [t/h] | [t/kWh] |
| 15 | 0.97 | 5.01 |
| 18 | 0.90 | 4.92 |
| 21 | 0.95 | 4.83 |
| 24 | 1.03 | 4.84 |
| 27 | 1.01 | 4.81 |
| 30 | 0.98 | 4.92 |

It can be seen from Table 4 that with the inclination distance of hammer head increases, the productivity first decreases and then increases, and then decreases again.

The output per kWh first increases and then decreases. When the inclination distance of hammer head was 24 mm, the productivity was the highest; when the inclination distance of hammer head was 27 mm, the output per kWh was the lowest; from the trend of changes in productivity and output per kWh, it can be seen that the better inclination distances of hammer head were 24 mm to 30 mm.

- **Orthogonal tests results and analysis**

In order to obtain the optimal working parameters combination of the hammer, three-factor, and three level orthogonal tests were carried out. According to the single-factor test results, the level of each factor was determined as shown in Table 5.

Table 5

| Level of factor | Inclination angle of hammer | Angle of hammer head | Inclination distance of hammer head |
|-----------------|-----------------------------|----------------------|-------------------------------------|
| | A | B | C |
| | [°] | [°] | [mm] |
| 1 | 150 | 100 | 24 |
| 2 | 155 | 110 | 27 |
| 3 | 160 | 120 | 30 |

The results of the orthogonal tests are shown in Table 6. It can be seen from Table 6 that the range of factor B in productivity test and output per kWh test was 0.1 and 0.2 respectively, both of which were the maximum values, indicating that the factor B had the greatest impact on productivity and output per kWh. The range of factor A was 0.06 and 0.08 respectively, both of which were greater than factor C, indicating that the factor A had a secondary impact on the productivity and output per kWh; The range of factor C was 0.05 and 0.06 respectively, both of which were the smallest, indicating that the factor C had the smallest impact on productivity and output per kWh. Using the range analysis method, the rankings of the three factors according to the importance to the productivity and output per kWh were obtained, successively, they were factor B > factor A > factor C. The combined optimal parameters of productivity were as follows: B₂A₁C₁. The combined optimal parameters of output per kWh were as follows: B₂A₃C₁.

The B₂ level of factor B was selected twice, so B₂ was the optimal level for factor B. The C₁ level of factor C was selected twice, so C₁ was the optimal level for factor C. The A₃ level and A₁ level of factor A were selected once each, therefore, the optimal level of factor A was between A₃ and A₁. It can be seen from Table 6 that the E_{k1} plus Y_{k1} was less than E_{k3} plus Y_{k3}, so the A₃ was the optimal level for factor A. The final combined optimal parameters were as follows: B₂A₃C₁.

Table 6

| Factor test number | Inclination angle of hammer | Angle of hammer head | Inclination distance of hammer head | Empty column D | Productivity E | Output per kW·h Y |
|--|-----------------------------|----------------------|-------------------------------------|----------------|--|-------------------|
| | A | B | C | | | |
| | [°] | [°] | [mm] | \ | [t/h] | [t/kWh] |
| 1 | 1 | 1 | 1 | 1 | 0.97 | 4.84 |
| 2 | 1 | 2 | 2 | 2 | 1.03 | 4.87 |
| 3 | 1 | 3 | 3 | 3 | 0.98 | 4.86 |
| 4 | 2 | 1 | 2 | 3 | 0.92 | 4.97 |
| 5 | 2 | 2 | 3 | 1 | 0.96 | 5.04 |
| 6 | 2 | 3 | 1 | 2 | 0.93 | 4.81 |
| 7 | 3 | 1 | 3 | 2 | 0.87 | 4.78 |
| 8 | 3 | 2 | 1 | 3 | 1.08 | 5.20 |
| 9 | 3 | 3 | 2 | 1 | 0.94 | 4.85 |
| E _{k1} | 0.99 | 0.92 | 0.99 | 0.96 | | |
| E _{k2} | 0.93 | 1.02 | 0.96 | 0.94 | | |
| E _{k3} | 0.96 | 0.95 | 0.94 | 0.99 | | |
| E _{Range R} | 0.06 | 0.1 | 0.05 | 0.03 | | |
| E Importance ranking affected by the three factors | | | | | B>A>C | |
| E Optimal parameter | | | | | B ₂ A ₁ C ₁ | |
| Y _{k1} | 4.86 | 4.86 | 4.95 | 4.91 | | |
| Y _{k2} | 4.9 | 5.04 | 4.90 | 4.82 | | |
| Y _{k3} | 4.94 | 4.84 | 4.89 | 5.01 | | |
| Y _{Range R} | 0.08 | 0.2 | 0.06 | 1.78 | | |
| Y Importance ranking affected by the three factors | | | | | B>A>C | |
| Y Optimal parameter | | | | | B ₂ A ₃ C ₁ | |

Note: E_{k1}, E_{k2}, and E_{k3} represented the average value of the sum of the three evaluation indicators of productivity for the same parameter at the same level, t/h; Y_{k1}, Y_{k2}, and Y_{k3} represented the average value of the sum of the three evaluation indicators of output per kW·h for the same parameter at the same level, t/kWh.

- **Static results and analysis of the hammer**

The hammer is the key component of the hammer mill. Static analysis of the optimized hammer will be carried out, which can identify dangerous cross-sectional areas in the design, and improve the shortcomings in the design. In this work, static analysis on the optimized hammer was carried out by ANSYS software. The mesh is shown in Figure 5.

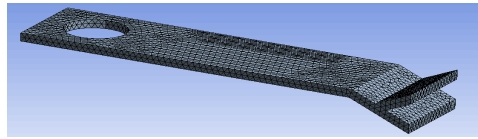


Fig. 5 - Hammer mesh

Due to the high-speed rotation of the hammer in the grinding chamber, compared to the unloaded situation, the load on the hammer under loading is relatively large, so only the loading situation was analysed and calculated.

According to the momentum theorem, the impact force between the material and the hammer is as follows:

$$P\Delta t_1 = m_1\Delta v \quad (10)$$

where: Δt_1 is the contact time between the material and the hammer, s; Δv is the variable of velocity of hammer after contact with the material, m/s; m_1 is the mass of hammer, kg; P is the impact force between the material and the hammer, N .

Bringing Δt_1 , m_1 and Δv into Eq.(10), it can be obtained $P = \frac{0.00493 \times (85.2 - 45.6)}{0.001} = 195.2(N)$.

The impact force, the rated speed, the constraints, etc. of the material and hammer were added to the hammer, and the static calculation and solution on the hammer were carried out. The equivalent stress cloud map and deformation cloud map of the hammer are shown in Figure 6.

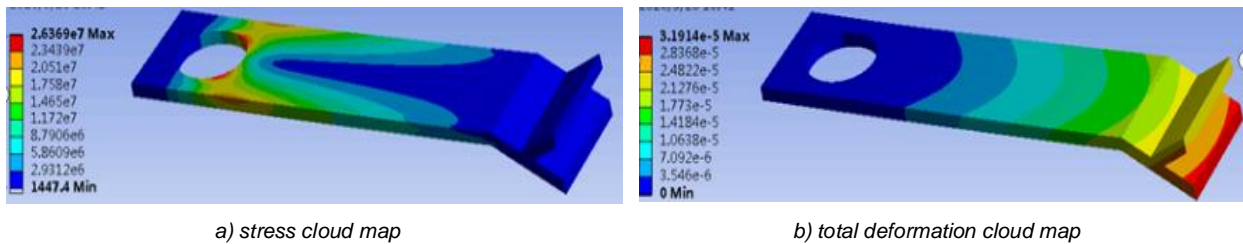


Fig. 6 - Static analysis simulation cloud chart of new hammer

It can be seen from Figure 6a that the stress of the hammer was mainly concentrated at the circular hole that matched with the pin shaft, the stress variation range was 0.0145 MPa to 26.37 MPa. The stress of the hammer was mainly between 0.01445 MPa to 14.7 MPa. The material of the hammer was 45# steel, its yield strength was 355 MPa, which was much greater than the maximum stress of the hammer. From the stress analysis, the hammer satisfies the strength and stiffness requirements during working.

It can be seen from Figure 6b that the maximum deformation in the X direction was 7.41 μm . The maximum deformation in the Y direction was 4.35 μm . The maximum deformation in the Z direction was 7.42 μm . The total deformation was 31.9 μm . Therefore, the deformation of the hammer was very small, and there will be no structural damage during working.

- **Modal results and analysis of the hammer**

Objects with different structures have different natural frequencies. When the external excitation frequency is consistent with the natural frequency, the object will resonate. Therefore, modal analysis of key components is crucial. Modal results of the new hammer are shown in Figure 7. According to the working principle of the hammer, the maximum excitation frequency of the hammer during working is the excitation frequency generated by the rotor rotating at the rated speed. The maximum speed of the rotor was 4400 r/min, so the maximum excitation frequency of the hammer was 73.33 Hz. The first-order to sixth order natural frequencies of the hammer were 7.556 Hz, 8.377 Hz, 9.563 Hz, 10.450 Hz, 11.880 Hz and 11.109 Hz, respectively, the maximum excitation frequency of the hammer was much greater than the natural frequency. Therefore, resonance was effectively avoided and the dynamic characteristics are good.

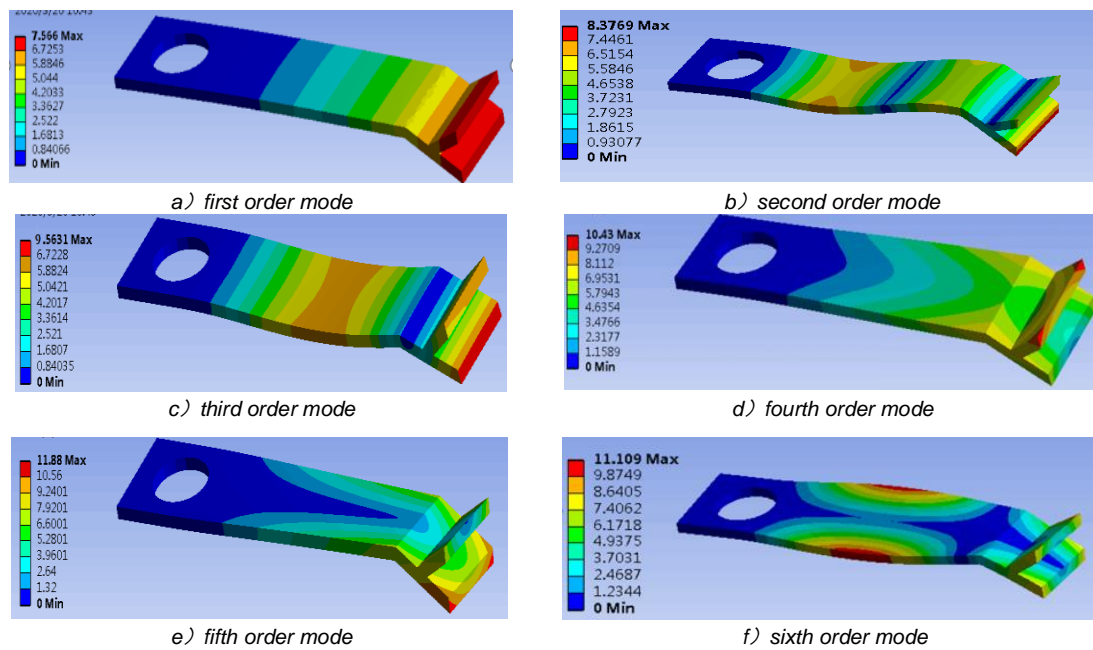


Fig. 7 - Modal results and analysis of the new hammer

The previous studies mainly focused on the structure of the hammer mill and the shape of the grinding chamber, with the goal of improving the efficiency and reducing energy consumption of the hammer mill, a series of studies were carried out. Hammer is a key component for crushing materials, some scholars have studied the material and wear resistance of hammer, but have not studied the structure and shape of hammer. Therefore, this article focuses on optimizing the design of hammer, a folded V-shaped hammer was designed. The hammer mill installed the V-shaped hammer, which not only improved production efficiency but also reduced energy consumption. The research results can provide theoretical basis for the optimization design of the hammer mill.

CONCLUSIONS

1. Taking the hammer of CPS-420 hammer mill as the studied object, the grinding process of materials in the grinding chamber was analysed. It was found that changing the shape of the hammer reasonably could increase the probability of material being hit. Combined with the dynamic characteristics of material grinding, a design scheme of a folded V-shaped hammer was proposed, the folded V-shaped hammer effectively increased the contact area with the material, thereby it effectively improved the grinding performance of the hammer mill.

2. Taking the inclination angle of hammer, the angle of hammer head, and the inclination distance of hammer head as the influencing factors, and the productivity and output per kWh as evaluation indexes, the grinding performance of the hammer mill was experimentally studied through single factor test and orthogonal tests. The results of the single factor test showed that the optimal parameter range for the inclination angle of hammer was 150° to 160° , the optimal parameter range for the angle of hammer head was 100° to 120° , and the optimal parameter range for the inclination distance of hammer head was 24 mm to 30 mm. The orthogonal tests results showed that the rankings of the three factors according to the importance to the productivity and output per kWh were obtained, successively, they were the angle of hammer head, the inclination angle of hammer and the inclination distance of hammer head. The final combined optimal parameters of the hammer are as follows: 160° the angle of hammer head, 110° the inclination angle of hammer and 24 mm the inclination distance of hammer head.

3. The static analysis and modal analysis were carried out on the optimized hammer by using ANSYS software. The static analysis results showed that the stress variation range of the new hammer was 0.0145 MPa to 26.37 MPa. The stress of the hammer was mainly concentrated at the circular hole that matched with the pin shaft. The total deformation was $31.9 \mu\text{m}$, the hammer satisfies the strength and stiffness requirements during working. The modal analysis results showed that the first-order to sixth order natural frequencies of the hammer were 7.556 Hz, 8.377 Hz, 9.563 Hz, 10.450 Hz, 11.880 Hz and 11.109 Hz, respectively, the maximum excitation frequency of the hammer was 73.33 Hz, which was much greater than the natural frequency, resonance was effectively avoided and the dynamic characteristics were good.

ACKNOWLEDGEMENT

This research was funded by the National Natural Science Foundation of China (51765055)

REFERENCES

- [1] Barnwal, P., Singh, K. K., Sharma, A. et al. (2015). Influence of pin and hammer mill on grinding characteristics, thermal and antioxidant properties of coriander powder. *Journal of Food Science and Technology*, 52(12), 7783-7794. <https://doi.org/10.1007/s13197-015-1975-0>
- [2] Bochat, A., Wesolowski, L., Zastempowski, M. (2015). A comparative study of new and traditional designs of a hammer mill. *Transactions of the ASABE*, 58(3), 585-596. <https://doi.org/10.13031/trans.58.10691>
- [3] Cao Liying, Zhang Yuepeng, Zhang Yubao et al. (2016). Influence of screen parameters optimization on screening efficiency of feed hammer mill. *Transactions of the Chinese Society of Agricultural Engineering*, 32(22), 284-288. <https://doi.org/10.11975/j.issn.1002-6819.2016.22.039>
- [4] Chen Junyu, Liu Bao, Li Pengfei. (2017). Study on motion state of mill hammer based on clearance joint. *Modern Machinery*, (4), 55-59. <https://doi.org/CNKI:CDMD:2.1018.960617>
- [5] Wang Di, He Changbin, Tian Haiqing, et al. (2020). Parameter optimization and experimental research on the hammer mill. *INMATEH Agricultural Engineering*, 62 (03): 341-350. <https://doi.org/10.35633/inmateh-62-36>
- [6] Wang Di, He Changbin, Wang Haiqing, et al. (2020). Design and experimental optimization of air oil triangle level for hammer mill. *INMATEH Agricultural Engineering*, 61 (02): 315-322. <https://doi.org/10.35633/inmateh-61-34>
- [7] Du Jianan, (2015). *Design and experimental research on wing shaped screen of hammer grinder*, MSc dissertation, Inner Mongolia Agricultural University, Hohhot/China
- [8] Li Xiuqing, (2021). *Simulation of corn grinding process of hammer mill and experimental study of hammer performance based on discrete element method*, MSc dissertation, Inner Mongolia Agricultural University, Hohhot/China
- [9] Li Zhen, Wei Anning, Cao Liying et al. (2019). Experimental research and optimal design of new feed hammer grinder's smashing performance. *Feed Industry*, 40(5), 6-10. <https://doi.org/10.13302/j.cnki.fi.2019.05.002>
- [10] Liu Weigang, (2019). *Analysis of straw grinding characteristics and optimization of grinding equipment*, MSc dissertation, Guizhou University, Guizhou/China
- [11] Ma Qian, Liu Fei, Zhao Manquan, (2016). Analysis of grinding Mechanism and Optimization of Hammer Structure of a grinder. *Journal of Agricultural Engineering*, 32 (Supplement 2): 7-15. <https://doi.org/10.11975/j.issn.1002-6819.2016.z2.002>
- [12] Mugabi, R., Eskridge, K. M., Weller, C. L. (2017). Comparison of experimental designs used to study variables during hammer milling of corn bran. *Transactions of the ASABE*, 60(2), 537-544. <https://doi.org/10.13031/trans.11656>
- [13] Qian Yi, Wang Di, Zhang Jue, et al. (2020). Numerical simulation and experimental research on the airflow field of the irregular screen of a grinder. *Journal of China Agricultural University*, 25 (03): 79-87. <https://doi.org/10.11841/j.issn.1007-4333.2020.03.10>
- [14] Qian Yi, (2021). *Optimization design and experimental research on the rotor structure of hammer grinder*, MSc dissertation, Inner Mongolia Agricultural University, Hohhot/China
- [15] Su Congyi, Wang Yongchang, Yu Xinguo et al. (2016). Cutting edge hammer blade is a new way to improve the efficiency of grinder. *Feed Industry*, 2016, 37 (01): 12-18. <https://doi.org/10.13302/j.cnki.fi.2016.01.003>
- [16] Xu Wei, Cao Chunping, Sun Yu. (2021). Optimization design of hammer structure parameters of hammer mill. *Journal of Agricultural Mechanization Research*, 43(1), 27-33. <https://doi.org/10.13427/j.cnki.njyi.2021.01.006>
- [17] ***China Agricultural Machinery Standardization Technical Committee, (2007), *Technical specification of quality evaluation for grinders, NY/T1554-2007*, Standards Press of China, Beijing/China.
- [18] ***China Agricultural Machinery Standardization Technical Committee, (2007), *Test method for feed mill, GB/T6971-2007*, Standards Press of China, Beijing/China.

TRACTOR DESIGN ANALYSIS AND RESEARCH BASED ON KANO - AHP MODEL AND JACK

基于 KANO—AHP 模型与 JACK 的拖拉机设计分析与研究

Yuanqi LIU, Bin QI ^{*}), Tengyun MA, Yuchao REN, Jiyuan SUN, Bohan ZHANG

College of Agricultural Engineering and Food Science, Shandong University of Technology / China;

Tel: +86-15966964198; E-mail: sduid@163.com

DOI: <https://doi.org/10.35633/inmateh-73-17>

Keywords: Kano model, Analytic hierarchy process, Agricultural machinery modeling design, Jack ergonomic simulation

ABSTRACT

In order to make the tractor better meet the needs of users under the premise of satisfying the use of functions, the Kano - AHP model is used to design the appearance of the tractor. Firstly, the emotional needs of users are collected, and the tractor modeling is designed according to the requirements combined with the Kano model. The design scheme is displayed through Rhino in the form of three-dimensional modeling. According to the design requirement index was summarized by Kano model, the tractor modeling hierarchical structure model was established by using analytic hierarchy process, the weights of each index were obtained, and the best design scheme was selected according to the weights. Finally, the selected best scheme was imported into Jack ergonomics simulation software for stress analysis and comfort analysis of the lower back, and the analysis results were used to check whether the scheme met the man-machine physiological standards.

摘要

为了使拖拉机在满足使用功能的前提下更好的满足用户需求，现使用 Kano—AHP 模型对拖拉机进行外观的造型设计。首先收集用户的情感需求，结合 Kano 模型并根据需求设计拖拉机造型，通过 Rhino 将设计方案通过三维建模的形式展现出来；结合 Kano 模型总结出的设计需求指标，使用层次分析法建立拖拉机造型层次结构模型，得出各指标权重，依据权重选出最佳设计方案。最后将选出的最佳方案导入 Jack 人机工程仿真软件进行下背部受力分析和舒适度分析，通过分析结果检验该方案是否符合人机生理标准。

INTRODUCTION

With the development of The Times, the innovation of agricultural machinery is also urgent, more agricultural personnel put forward higher requirements for tractors, not only to meet the needs of functional use, the appearance should also be more in line with the user's aesthetic, which puts forward higher requirements for designers. According to the research literature, such as Wu, (2019), in order to enhance the market competitiveness of tractor enterprises and improve economic benefits, the tractor's practical value and aesthetic needs are combined, so that the user is the center. Li et al. (2023) combined the analytic hierarchy process and fuzzy comprehensive evaluation method to evaluate the three tractor modeling schemes and screened out the best scheme. In the application of the analytic hierarchy process, the tractor modeling features are disassembled into different levels and elements, which are used to calculate the weight value of each design element. Hridoy et al., (2020), combined Analytic Hierarchy Process (AHP), Kano and Quality Function Deployment (QFD) to design the tractor seat. Based on the existing problems of the seat, the requirements were determined, and then the weights were calculated to guide the design. Zhou et al., (2023), combined the analytic hierarchy process with the analysis network process, obtained the humanistic design elements of the intelligent pension products, and put forward a new design model so that the humanistic design factors can be reasonably applied in the design. Zhang et al., (2023), used the man-machine simulation and analysis software Jack to improve the tractor cab, the overall comfort of the tractor cab was improved. Shi et al., (2023), combined the analysis of controllability, visibility, and working posture comfort in Jack, summarized the design defects of the driver's cab of an electric monorail crane, and put forward optimization strategies. Wang et al., (2018), carried out an ergonomic analysis of agricultural machinery cabs through Jack, including driving comfort point, back stress critical value, seat, control device, etc., to improve the comfort and safety of agricultural machinery cabs.

The above literature has achieved good results in identifying innovation needs and providing innovative methods, reducing the limitations of a single method, but in many cases, it still cannot solve practical problems. For example, the combination of Kano and AHP cannot verify whether the designed product meets the man-machine requirements; only Jack is used for man-machine inspection of existing products, but Kano and AHP cannot obtain and analyze user requirements.

To sum up, in this paper, a variety of methods will be used to combine the way of tractor modeling design. The first part is the combination of Kano model and analytic hierarchy process. In this part, the needs of target users, namely design elements, are obtained, arranged, and compared, and the needs with high priority are met first. According to the design elements, the hierarchical structure model is constructed to select the best solution. Finally, the selected scheme is imported into Jack for simulation analysis to verify whether it is reasonable in terms of ergonomics, so as to provide method support for the innovation of tractor modeling design.

Jack is a very classic man-machine simulation analysis software (*Li et al., 2013*), but the research on how to apply it in tractor modeling and combine it with Kano and AHP to complete the design is still blank. The combination of Jack and the first two methods enables the man-machine aspect of tractor design to be further tested, thus improving the design efficiency and accuracy, which is also the main innovation point of this paper.

MATERIALS AND METHODS

Kano model is the overall data prioritization of user needs by obtaining user satisfaction with product shape and function. By using the Kano model, the product development team can comprehensively classify the user needs, and formulate corresponding product strategies according to the importance of each demand attribute, so as to improve user satisfaction and market competitiveness. This is shown in Figure 1. The X-axis coordinate is the degree of fulfillment of the user's needs and the Y-coordinate is the user satisfaction. Kano model proposes five demand attributes: Attractive attribute(A); One-dimensional attribute(O); Indifference attribute(I); Must-be attribute(M); Reverse attribute(R) (*Kano et al., 1984*).

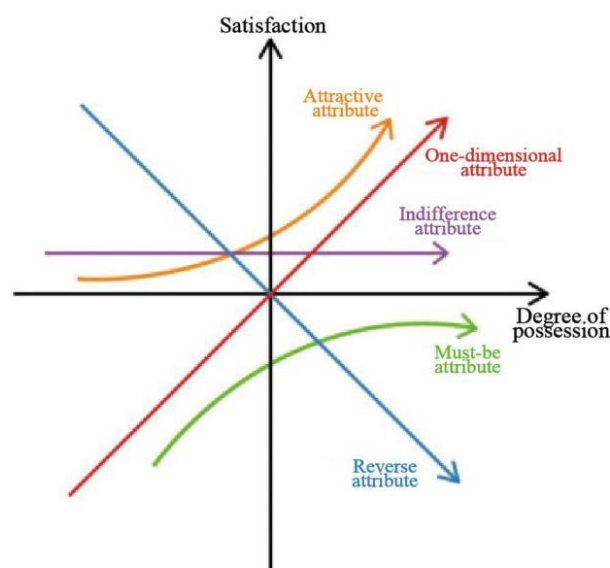


Fig. 1 - Kano model

The interpretation of each demand is as follows: Attractive demand (charm attribute): a function/service that exceeds the user's expectation, with a high degree of perfection of the function/service, the user's satisfaction will increase significantly, but without the function/service, the user's satisfaction will not decrease significantly; One-dimensional demand (One-dimensional attribute): a certain function/service will improve the satisfaction, without which the satisfaction will decrease; Indifference demand (Indifference attribute): the presence or absence of a function/service does not affect satisfaction; Must-be demand (Must-be attribute): the presence of a function/service does not increase satisfaction, but the absence of it decreases satisfaction; Reverse demand (reverse attribute): the absence of a feature/service leads to higher satisfaction (*Akao et al., 1994*).

Table 1 shows the mapping between the questionnaire options and each requirement.

Table 1

| Functional Requirements | | Demand attributes | | | | |
|-------------------------|----------------|-------------------|-------------|----------------|------------|------|
| | | Reverse problem | | | | |
| | | Dislike | Put up with | Doesn't matter | Rightly so | Like |
| Positive questions | Dislike | Q | R | R | R | R |
| | Put up with | M | I | I | I | R |
| | Doesn't matter | M | I | I | I | R |
| | Rightly so | M | I | I | I | R |
| | Like | O | A | A | A | Q |

By investigating the user intention, the demand type of the tractor design is obtained.

According to the Kano model, the questionnaire is designed and investigated. Each index attribute in the questionnaire contains forward questions and reverse questions so that the average satisfaction score of users on the functional index can be calculated. By classifying the subsequently obtained data, users' demand types for product functions can be obtained (Cohen et al., 1996).

Better-Worse coefficient analysis is a demand satisfaction analysis method based on the Kano model that is used to determine the importance and priority of product features. This method determines which functions are of the greatest concern and priority to users through the comparison of different features.

The Better coefficient, the satisfaction coefficient, is:

$$Better = (A + O) / (A + O + M + I) \tag{1}$$

The Worse coefficient, i.e. the dissatisfaction coefficient, is:

$$Worse = -(O + M) / (A + O + M + I) \tag{2}$$

The absolute value of the Better-Worse coefficient is generally between 0 and 1, which represents the user's satisfaction with the existence of the function. According to the value of the coefficient, a four-quadrant distribution diagram of the demand attributes can be obtained.

The value of the Better coefficient is the vertical coordinate, the absolute value of the Worse coefficient is the horizontal coordinate, the average of the value of the Better coefficient and the absolute value of the Worse coefficient is the quadrantal dividing line, and the four-quadrant diagram of the better-worse coefficient is drawn. The first quadrant is the expected attribute; the function of this quadrant should be satisfied first. The second quadrant is the charm attribute; the function of this quadrant should be satisfied first. The third quadrant is the indifference attribute; the function of this quadrant is not usually provided. The fourth quadrant is the necessary attribute; the function of this quadrant must be satisfied (Song et al., 2023).

The Analytic Hierarchy Process (AHP) (Saaty et al., 1989) is a multi-criteria decision analysis method designed to help decision makers deal with the complex relationship between multiple criteria and multiple alternatives. The core idea of this method is to hierarchize the decision problem, decompose the complex problem into several relatively simple sub-problems, and get the final decision result by comparing and judging each sub-problem.

According to the analysis of questionnaire data obtained by Kano model and the analytic hierarchy process, the hierarchical structure model of tractor modeling factor evaluation can be obtained.

According to the design elements, the 9-level scale method can be used to construct the judgment matrix (Guo et al., 2023). The judgment matrix is a pairwise comparison between the indicators of the same layer, that is, the criterion layer and the sub-criterion layer are compared respectively, and the value is assigned according to the relative scale of 1-9, and the importance of the design elements is expressed according to the value. The scale table of the judgment matrix is shown in Table 2.

Table 2

Scale table of judgment matrix

| Relative importance Degree assignment (i/j) | Implication | Scale specification |
|---|-------------------------|--|
| 1 | Equally important | Indicator i is as important as indicator j |
| 3 | Slightly important | Indicator i is slightly more important than indicator j |
| 5 | Obvious importance | Indicator i is obviously more important than indicator j |
| 7 | Strongly important | Indicator i is more important than indicator j |
| 9 | Extremely important | Indicator i is extremely important compared to indicator j |
| 2, 4, 6, 8 | Use when you compromise | The degree of importance is determined according to the adjacent scale |

According to the constructed judgment matrix, the weight of each element can be obtained by using the arithmetic average method.

1. Each column of the judgment matrix is normalized, that is:

$$\bar{x}_{ij} = \frac{x_{ij}}{\sum_{i=1}^n x_{ij}} \quad (i=1,2,3,\dots,n) \tag{3}$$

2. Sum the processed matrices by row, that is:

$$\check{\omega}_i = \sum_{j=1}^n \bar{x}_{ij} \quad (i = 1,2,3,\dots,n) \tag{4}$$

3. The weight vector can be obtained by processing the result of the sum:

$$\omega_i = \check{\omega}_i / n \tag{5}$$

After the relative weight of each design element is obtained, it is necessary to carry out a consistency test. First, it is necessary to obtain the maximum feature root of the judgment matrix according to the weight, and then obtain the consistency test value CI. Then, the test coefficient of the judgment matrix can be obtained according to the standard value of RI in Table 3.

1. Find the maximum eigenroot of the judgment matrix (where the weight is multiplied by the matrix, n represents the order of the matrix, and represents the weight of each row in the matrix):

$$\lambda_{max} = \sum_{i=1}^n \frac{(AW)_i}{nw_i} \tag{6}$$

2. Find the consistency test value of each indicator:

$$CI = \frac{\lambda_{max} - n}{n - 1} \tag{7}$$

3. Calculate the test coefficient of the judgment matrix:

$$CR = \frac{CI}{RI} \tag{8}$$

Table 3

RI standard values

| Rank | 1 | 2 | 3 | 4 | 5 | 6 | 7 | 8 | 9 |
|----------|---|---|------|------|------|------|------|------|------|
| RI value | 0 | 0 | 0.52 | 0.89 | 1.12 | 1.26 | 1.36 | 1.41 | 1.46 |

Through the weight of analytic hierarchy process, the index that has a greater weight in the tractor modeling design can be obtained, but the evaluation and scoring of experts are more subjective, and it is impossible to know whether the best scheme meets the man-machine standard. Therefore, Jack (*Badler et al., 1992*) was used to analyze the stress and comfort of the lower back while holding the steering wheel.

RESULTS

According to the results of the questionnaire to obtain the user intention, two types of tractor design requirements are obtained, namely functional requirements and comfort requirements. Each requirement contains its specific indicators, i.e., six items each of functional requirements and comfort requirements, as shown in Table 4.

Table 4

| Demand index of tractor modeling design | | | |
|---|--------|---|--|
| Type of demand | Number | Demand items | Instructions |
| Functional Requirements n | n1 | Water heater | Provision of hot drinking water |
| | n2 | Cab ceiling | Shelter from rain and sun |
| | n3 | Sound insulation and noise reduction device | Effectively prevent transmission noise |
| | n4 | Air conditioner | Optional cooling or heating |
| | n5 | Windshield wiper | Clean the windshield |
| | n6 | Floodlight | Work area lighting |
| Comfort Requirements m | m1 | Instrument panel | Display driving information |
| | m2 | Driver's seat | Stress on the lower back |
| | m3 | Hand control device | Gear hanging comfort |
| | m4 | Control panel layout | Operation control panel comfort |
| | m5 | Steering wheel | Comfort on the steering wheel |
| | m6 | Foot control device | Pedal comfort |

Use questionnaires to collect data, so as to obtain the initial needs of users. A total of 150 questionnaires were issued and 135 valid questionnaires were collected.

According to formulas (1) and (2), attribute statistics are carried out on the questionnaire data, and the results are shown in Table 5, and the demand attribute quadrant diagram is shown in Figure 2.

Table 5

| Statistics of tractor design requirements | | | | | | | | | |
|---|----------------------|----|----|----|----|---|--------------------|-------------------|-----------------------------|
| No. | Number of selections | | | | | | Better coefficient | Worse coefficient | Better-Worse classification |
| | A | O | M | I | R | Q | | | |
| n1 | 72 | 35 | 20 | 8 | 0 | 0 | 0.793 | -0.407 | A |
| n2 | 65 | 38 | 21 | 7 | 4 | 0 | 0.786 | -0.450 | A |
| n3 | 16 | 11 | 50 | 56 | 2 | 0 | 0.203 | -0.459 | I |
| n4 | 16 | 23 | 25 | 65 | 4 | 2 | 0.302 | -0.372 | I |
| n5 | 10 | 18 | 90 | 13 | 3 | 1 | 0.214 | -0.824 | M |
| n6 | 25 | 66 | 36 | 5 | 3 | 0 | 0.689 | -0.772 | O |
| m1 | 34 | 70 | 7 | 13 | 11 | 0 | 0.839 | -0.621 | O |
| m2 | 6 | 46 | 54 | 25 | 4 | 0 | 0.397 | -0.763 | M |
| m3 | 26 | 31 | 25 | 45 | 7 | 1 | 0.449 | -0.441 | I |
| m4 | 14 | 19 | 22 | 67 | 13 | 0 | 0.270 | -0.336 | I |
| m5 | 21 | 72 | 15 | 9 | 17 | 1 | 0.795 | -0.744 | O |
| m6 | 8 | 6 | 17 | 26 | 75 | 3 | 0.246 | -0.404 | I |

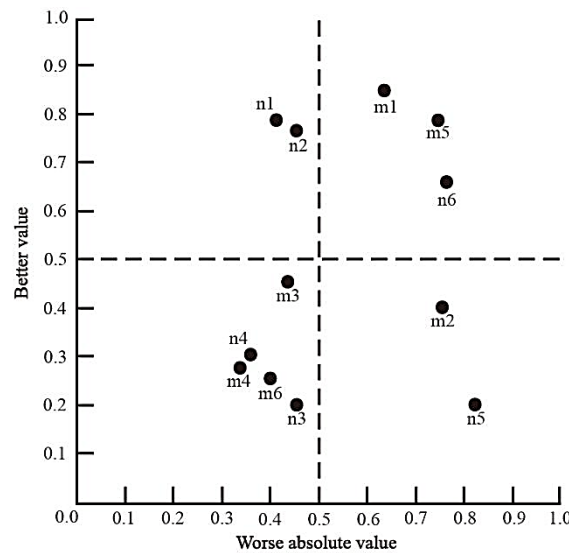


Fig. 2 - Quadrantal distribution of demand attributes

The results show that the following 7 requirements need to be met in the tractor design: the attractive demands are water heater n1 and cab ceiling n2; the One-dimensional demand is lighting function n6, instrument panel m1 and steering wheel m5; the Must-be demands are the wiper n5 and the driver's seat m2.

In the design of tractor modeling, the basic needs of users must be met, in addition to the need to try to meet the expectations of the needs and the excitement of the needs. According to this, the preliminary design of the tractor modeling is carried out, and the scheme is modeled with Rhino 7 (McNeel et al., 2023). The design of the modeling scheme is shown in Figure 3.

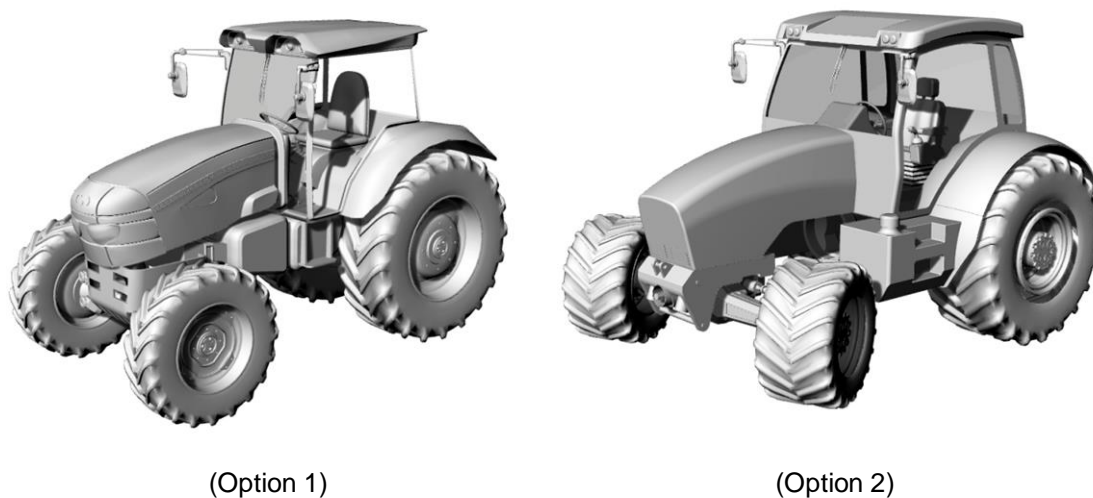


Fig. 3 - Tractor modeling scheme

The obtained hierarchical structure model of tractor modeling factor evaluation is shown in Table 6.

Table 6

| Hierarchical structure model of tractor modeling factor | | |
|---|------------------------|---|
| Target layer | Criterion layer | Subcriterion layer |
| Tractor modeling | Feature N ₁ | Water heater N ₁₁ Cab ceiling N ₁₂ Floodlight N ₁₃ Windshield wiper N ₁₄ |
| | Comfort N ₂ | Instrument panel N ₂₁ Steering wheel N ₂₂ Driver's seat N ₂₃ |

Questionnaires were sent to 5 experts to evaluate and score each element according to the 9-level scale rule. According to the scoring results given by experts, a judgment matrix is constructed, in which:

The judgment matrix of the tractor modeling factor is:

| | | | |
|----------------------|----------|----------------------|----------------------|
| | M | N₁ | N₂ |
| N₁ | | 1 | 2 |
| N₂ | | 1/2 | 1 |

The judgment matrix among indicators in the functional criterion layer is:

| | | | | | |
|-----------------------|----------------------|-----------------------|-----------------------|-----------------------|-----------------------|
| | N₁ | N₁₁ | N₁₂ | N₁₃ | N₁₄ |
| N₁₁ | | 1 | 1/7 | 1/3 | 1/2 |
| N₁₂ | | 7 | 1 | 3 | 4 |
| N₁₃ | | 3 | 1/3 | 1 | 2 |
| N₁₄ | | 2 | 1/4 | 1/2 | 1 |

The judgment matrix among indexes of the comfort criterion layer is as follows:

| | | | | |
|-----------------------|----------------------|-----------------------|-----------------------|-----------------------|
| | N₂ | N₂₁ | N₂₂ | N₂₃ |
| N₂₁ | | 1 | 1/5 | 1/7 |
| N₂₂ | | 5 | 1 | 1/2 |
| N₂₃ | | 7 | 2 | 1 |

Based on formula (3) - Formula (8), the weights of each evaluation index of tractor modeling design can be obtained, as shown in Table 7.

Table 7

| Index weights of tractor modeling design evaluation system | | | | | | |
|--|------------------------|----------------------------------|----------------------------|----------------------|-----------------|-------------|
| Criterion layer | Criterion layer weight | Subcriterion layer | Subcriterion layer weights | Comprehensive weight | λ_{max} | CR |
| Feature N ₁ | 0.667 | Water heater N ₁₁ | 0.074 | 0.049 | 4.021 | 0.008 < 0.1 |
| | | Cab ceiling N ₁₂ | 0.568 | 0.379 | | |
| | | Floodlight N ₁₃ | 0.225 | 0.150 | | |
| | | Windshield wiper N ₁₄ | 0.134 | 0.089 | | |
| Comfort N ₂ | 0.333 | Instrument panel N ₂₁ | 0.076 | 0.025 | 3.016 | 0.015 < 0.1 |
| | | Steering wheel N ₂₂ | 0.334 | 0.111 | | |
| | | Driver's seat N ₂₃ | 0.591 | 0.197 | | |

If CR values in the table are all less than 0.1, the judgment matrix passes the consistency test, and the data are valid data.

In order to obtain the best scheme, it is necessary to compare the two schemes, construct a judgment matrix, and combine formula (3) - formula (5) to obtain the specific index weights of each scheme layer, as shown in Table 8.

Table 8

| Weights of specific indicators at the solution layer | | | | | | | |
|--|-----------------|-----------------|-----------------|-----------------|-----------------|-----------------|-----------------|
| Index | N ₁₁ | N ₁₂ | N ₁₃ | N ₁₄ | N ₂₁ | N ₂₂ | N ₂₃ |
| Option 1 | 0.333 | 0.250 | 0.667 | 0.333 | 0.667 | 0.167 | 0.143 |
| Option 2 | 0.667 | 0.750 | 0.333 | 0.667 | 0.333 | 0.833 | 0.857 |

By the weight of each specific index, the total weight of the two schemes can be calculated: the weight of each index in the scheme is multiplied by the corresponding comprehensive weight, and then the result is added (Su et al., 2018). The total weight of scheme 1 is 0.304; the total weight of scheme 2 is 0.696. According to the weight results, scheme 2 is the best scheme. Since the judgment matrices of the scheme layer are consistent matrices, no consistency test is needed and the data is valid.

The combination of the above two methods has been able to obtain a specific tractor design scheme, but from the actual effect, it may not be able to pass the man-machine inspection; if not verified, it is easy for users to use the tractor faster driving fatigue phenomenon.

According to the above methods and results, the conclusion was drawn that the steering wheel and driving seat have a large weight in the tractor modeling design, indicating that these two indicators are more important, so in order to exclude contingency, Jack should be used to carry out man-machine simulation analysis of the scheme to increase its objectivity.

The Rhino model of the best scheme was converted into .wrl format and imported into Jack(9.0), and the Chinese adult male virtual character model in the 50th percentile was constructed according to GB/T 10000-1988 (Zhu *et al.*, 2022), and its posture was changed to driving state, as shown in Figure 4 and Figure 5 respectively. Figure 4 shows the specific data of the virtual human model, and Figure 5 shows the posture display of the virtual human driving state.

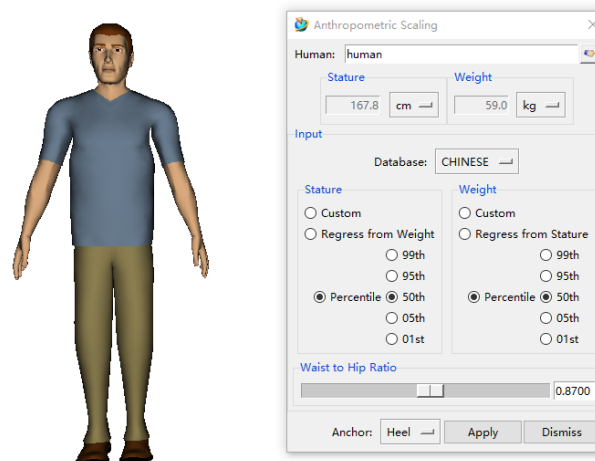


Fig. 4 - Human data model



Fig. 5 - The virtual person driving state

The comfort level of the seat is the most easily addressed, which is directly related to the stress on the lower back when holding the steering wheel. Only when the stress is within the appropriate range can the driver operate the tractor stably and comfortably. Therefore, the stress analysis on the lower back is one of the important analysis items in Jack's simulation analysis (Liu *et al.*, 2013).

When analyzing the stress on the lower back, the stress on the fourth and fifth lumbar vertebrae of the lower lumbar vertebrae of the driver was mainly analyzed, through which it could be checked whether the stress situation of the driver met the NIOSH standard (Sun *et al.*, 2022). The specific simulation analysis interface is shown in Figure 6.

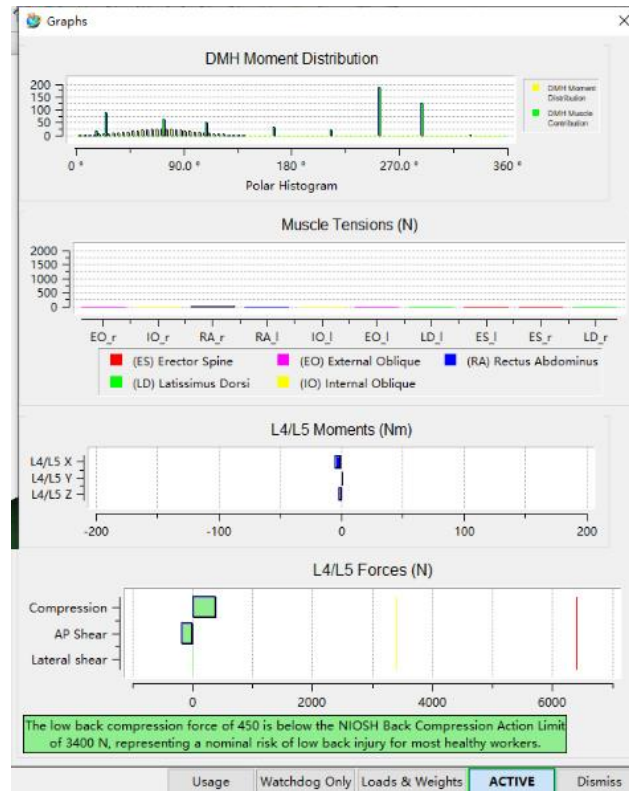


Fig. 6 - Stress analysis diagram of lower back

As can be seen from Figure 6, when the virtual driver is driving, the force on the fourth and fifth lumbar vertebrae of the lower back is 450N, while the pressure limit stipulated in the NIOSH standard is 3400N, so the driver is in a safe state.

The Comfort Assessment in Jack was used to analyze the driver's comfort (Liu et al., 2022). The comfort value range given by Porter's data source is -60 to 60, within which the driver's operating comfort is considered acceptable. The green bar chart indicates the difference between the actual measured value and the standard value; if the yellow bar chart appears, it indicates that the joint is beyond the comfort range of the human body and causes physical discomfort.

Figure 7 is the analysis diagram of joint comfort, from which it can be seen that the driver's joints are all within the range of human comfort in the driving state.

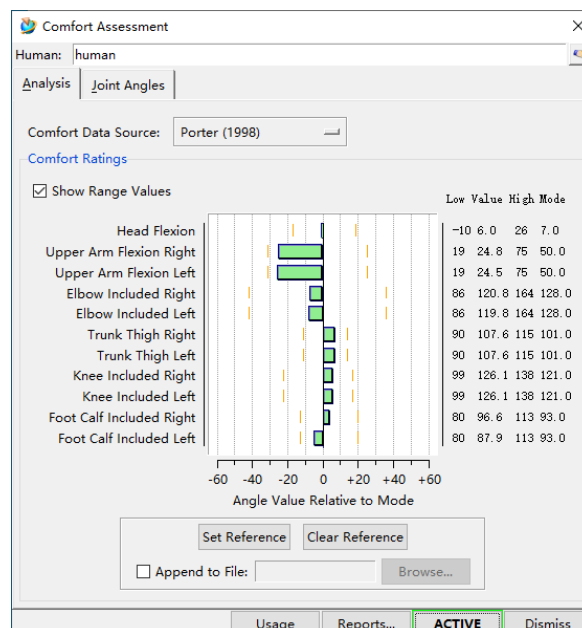


Fig. 7 - Analysis of Joint Comfort

Secondly, the Krist data source tool is used to score the joint comfort, ranging from 0 to 80. The smaller the number, the greater the comfort. The specific analysis interface is shown in Figure 8. It can be seen from the figure that the driver's comfort under this posture meets the man-machine standard.

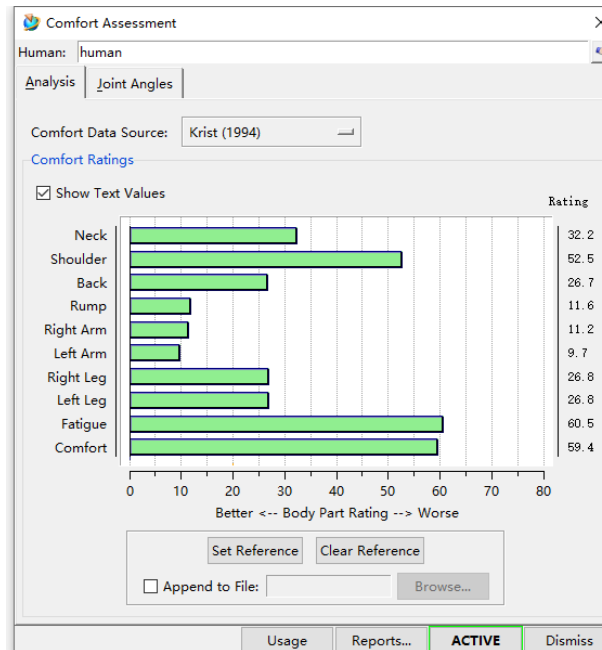


Fig. 8 - Comfort score

In order to increase the rationality of the design method in this paper, the model of scheme 1 is also imported into Jack for analysis, and the comfort score obtained is shown in Figure 9. Compared with Figure 8, it can be concluded that the comfort score of scheme 1 is generally higher than that of scheme 2.

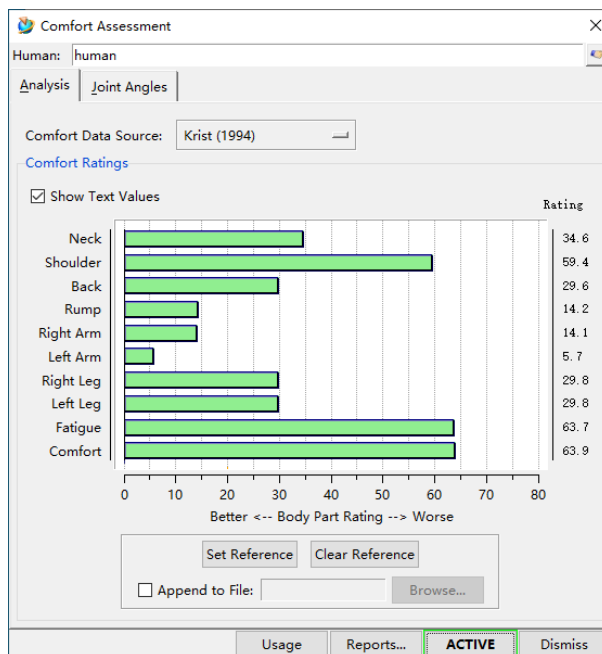


Fig. 9 - Scheme 1 Comfort rating

Through the use of Jack, it can be concluded that the tractor model designed in this paper is in line with the man-machine standard. With respect to appearance design in the field of industrial design, subjective and objective evaluation design methods are usually adopted. The application of Kano and AHP is the most common among subjective methods, while Jack is the most common among objective methods. Combining the three methods, on the one hand, the most commonly used methods in design are adopted, and the results are reasonable.

On the other hand, the combination of subjectivity and objectivity makes the result more convincing. In comparison, most other design methods have been eliminated and not used because of their greater subjective contingency. Therefore, the use of this combination method increases the efficiency of design from the side and shortens the design cycle.

CONCLUSIONS

For product modeling, especially for agricultural machinery design, in order to improve user satisfaction, it is more and more important to meet the functional and psychological needs of users. In this paper, Kano model is used to analyze user requirements and guide the design of tractor appearance. AHP is used to calculate the weight of each design element and select the best design scheme. Jack was used for simulation analysis of the best scheme to check whether it conforms to the man-machine physiological standard.

The results show that: Kano model and analytic hierarchy process can accurately express and screen out user needs, so as to guide the tractor appearance design and select the best scheme; For the inspection of the best scheme, Jack can provide better man-machine data support. By comparing the comfort scores of the two schemes, it is concluded that the scores of scheme 2 are generally 2-3 points lower those that of scheme 1, and the score of "shoulder" is 6.9 points lower. At the same time, the stress of the lumbar spine in the scheme is 450 N, which is far lower than the specified pressure limit of 3400 N. This shows that combining the three methods to design the appearance of the tractor is effective, and provides experience for the future product design.

Because of the difference in driving posture, the score of "left arm" in Plan 2 is 4 points higher than that in plan 1 in the comfort score, which is also a design accident and should be avoided as much as possible. Although the combination of various design methods has been adopted to meet the needs of users as far as possible, the demand analysis of this design is still incomplete due to the influence of other practical factors, such as the age of users and the color and material of the products, and other design-influencing factors have not been deeply considered, which is also an aspect that needs attention and the future design.

ACKNOWLEDGEMENT

This work was supported by the Shandong Province Science and Technology minor enterprises Innovation Ability Project (Project number: 2023TSGC1014).

REFERENCES

- [1] Akao, Y. (1994). Development history of quality function deployment [J]. *The Customer Driven Approach to Quality Planning and Deployment*, 339: 90.
- [2] Badler, N.I., Phillips, C.B., Webber, B.L. (1992). *Simulating Humans: Computer Graphics, Animation, and Control* [C]. Oxford Univ Press.
- [3] Cohen, L., John, J. (1996). Quality function deployment: How to make QFD work for you [C]. *Journal of Product Innovation Management*, 13(2):183-184.
- [4] Guo, L.; Yi, J.; Wang, H. (2023). Research on situation assessment of industrial control network based on analytic Hierarchy process. *J. Xi'an Univ. Technol*, 1–8.
- [5] Hridoy, R.M.; Parvez, M.S.; Mohsin, N. (2020). Joining Methods of Analytic Hierarchy Process (AHP), Kano Model and Quality Function Deployment (QFD) to Improve the Tractor's Seat Design for Tractor Drivers in Bangladesh[J]. *American Journal of Industrial and Business Management*, 10(05): 1073.
- [6] Kano, N. (1984). Attractive quality and must-be quality[J]. *Journal of the Japanese society for quality control*, 31(4): 147-156.
- [7] Li, J.; Han, Y.; Hu, C. (2023). Evaluation of tractor modeling design based on analytic hierarchy process and fuzzy comprehensive evaluation[J]. *Industrial Design*, (06):148-150.
- [8] Li, Y.; Chen, D.K.; Yu, S.H.; Li, Z. (2013). Research of Design Evaluation Method Based on the Jack Human Model[J]. *Applied Mechanics and Materials*, 365–366:117–20.
- [9] Liu, S.; Wang, X.; Chen, D.; Wang, S.; et al. (2013). Cockpit simulation and ergonomic analysis based on JACK[J]. *Computer and modernization*, (08):106-110.
- [10] Liu, G.; Tang, D.; Gao, X. (2022). Ergonomic design of cervical rehabilitation trainer based on Jack simulation[J]. *Mechanical Design*, 39(06):155-160.

- [11] McNeel North America. (2023). Rhino 3D. Retrieved from <https://www.rhino3d.com/>(2023,10,11).
- [12] Shi, Y.; Xu, G.; Xing, Y. et al. (2023). Ergonomics analysis of driver cab of electric monorail crane based on JACK simulation[J]. *Chinese Journal of Construction Machinery*, 21(02):139-144.
- [13] Song, Y.; Zhang, N.; Liu, Y.; Wu, T. et al. (2023). Research on satisfaction of Qipao customization service based on Kano model[J]. *Silk*, 60(09):62-72.
- [14] Saaty, T.L. Paul Fatti. (1989). Decision making for leaders: The analytical hierarchy process for decisions in a complex world[C]. *European Journal of Operational Research*, 42(1):107-109.
- [15] Su, K.; Liao, Y. (2018). Improved design of electric tractor cab ergonomics based on Jack[J]. *Mechanical Design*, 35(8):106-110.
- [16] Sun, R.; Wei, J.; Chen, Y. (2022). Simulation and evaluation of upper limb occupational injury of maintenance personnel based on JACK[J]. *China safety production science and technology*, 18(08):222-227.
- [17] Wu, Z. (2019). Research on tractor design based on product system design method[J]. *Industrial Design*, (07):159-160.
- [18] Wang, J.; Zhang, J. (2018). Ergonomic analysis and simulation of agricultural machinery cab based on Jack[J]. *Agricultural Mechanization Research*, 40(06):246-251+256.
- [19] Zhou, Z.; Wang, L.; Ye, R.; Yue, H. (2023). A humanistic-care factors application hierarchical design-model for intelligent elderly products [J]. *Heliyon*, 9(03):e13734.
- [20] Zhang, F.; Liu, G.; Zhang, L. et al. (2023). Ergonomic simulation analysis and design improvement of backhoe excavator cab based on Jack [J]. *Mechanical Design*, 40(06):145-152.
- [21] Zhu, Z.; Wu, Y.; Han, J. (2022). A prediction method of coal burst based on analytic hierarchy process and fuzzy comprehensive evaluation [J]. *Frontiers in Earth Science*, 9: 834958.

RESEARCH ON SLAM AND PATH PLANNING METHOD FOR INSPECTION ROBOT IN ORCHARD ENVIRONMENT

果园环境中巡检机器人的 SLAM 和路径规划方法研究

Pengcheng LV, Minhui ZHANG, Jie LIU, Lei LIU, Lili YI*

Shandong University of Technology, Collage of Agricultural Engineering and Food Science, Zibo, China

Corresponding author: Lili YI; Tel: +86 18553308656; E-mail: yili0001@sdut.edu.cn

DOI: <https://doi.org/10.35633/inmateh-73-18>

Keywords: Orchard robots; Autonomous navigation; SLAM; Path planning

ABSTRACT

Orchard robots play a crucial role in agricultural production. Autonomous navigation serves as the foundation for orchard robots and eco-unmanned farms. Accurate sensing and localization are prerequisites for achieving autonomous navigation. However, current vision-based navigation solutions are sensitive to environmental factors, such as light, weather, and background, which can affect positioning accuracy. Therefore, they are unsuitable for outdoor navigation applications. LIDAR provides accurate distance measurements and is suitable for a wide range of environments. Its immunity to interference is not affected by light, colour, weather, or other factors, making it suitable for low objects and complex orchard scenes. Therefore, LiDAR navigation is more suitable for orchard environments. In complex orchard environments, tree branches and foliage can cause Global Positioning System (GNSS) accuracy to degrade, resulting in signal loss. Therefore, the major challenge that needs to be addressed is generating navigation paths and locating the position of orchard robots. In this paper, an improved method for Simultaneous Localization and Mapping (SLAM) and A-star algorithm is proposed. The SLAM and path planning method designed in this study effectively solves the problems of insufficient smoothness and large curvature fluctuation of the path planned in the complex orchard environment, and improves the detection efficiency of the robot. The experimental results indicate that the method can consistently and accurately fulfil the robot's detection needs in intricate orchard environments.

摘要

果园机器人在农业生产中发挥着至关重要的作用。自主导航是果园机器人和生态无人农场的基础。准确的感知和定位是实现自主导航的先决条件。然而，目前基于视觉的导航解决方案对光线、天气和背景等环境因素非常敏感，会影响定位精度。因此，它们不适合户外导航应用。激光雷达可提供精确的距离测量，适用于各种环境。它的抗干扰能力不受光线、颜色、天气或其他因素的影响，因此适用于低矮物体和复杂的果园场景。因此，激光雷达导航更适合果园环境。在复杂的果园环境中，树枝和树叶会导致全球定位系统（GNSS）精度降低，造成信号丢失。因此，需要解决的主要挑战是生成导航路径和定位果园机器人的位置。在本文中，我们提出了一种改进的同步定位与地图构建（SLAM）方法和 A-star 算法。本研究设计的 SLAM 和路径规划方法有效解决了复杂果园环境下规划路径的平滑度不够和曲率波动较大的问题，提高了机器人的巡检效率。实验结果表明，该方法能稳定、准确地满足机器人在复杂果园环境中的巡检需求。

INTRODUCTION

As China vigorously develops smart agriculture, the use of agricultural robots can effectively solve the challenges of rural labour shortage and labour intensity. China has issued a series of policy documents to support smart agriculture, such as the "14th Five-Year Plan" Robotics Industry Development Plan and the "14th Five-Year Plan" National Agricultural and Rural Informatization Development Plan, in which it is clearly stated that it is necessary to develop precision agriculture and support and encourage the Agricultural robot research and development and application, in order to accelerate the process of agricultural modernization. With the increasing diversity and complexity of the application scenarios of orchard robots, the autonomous navigation performance of the robot has put forward higher requirements. Robot navigation technology mainly includes Simultaneous localization and mapping technology (SLAM) and path planning technology. SLAM is the process by which a moving robot determines its own position and creates a map through sensors carried in the surrounding environment.

Path planning technology creates the optimal navigation path for the robot to reach the target location according to different task objectives and requirements, according to the robot's operating width, minimum turning radius, operating strips and other parameters, and with the goal of minimizing operating energy consumption, the robot automatically plans a full-coverage operating path without repetitive omissions within the operating area, which is the basic requirement for autonomous robot operation (Wang *et al.*, 2022).

The orchard inspection robot belongs to the modern intelligent mobile robot. Its main function is to familiarize with the orchard environment, find a suitable path to reach the target point, and complete the whole task. Robot autonomous navigation is the basis for realizing robot intelligence, and it is also the key to realize robot autonomous walking to reach the destination and complete specific tasks. In the process of autonomous navigation, the robot must ensure its own safety and not cause damage to the surrounding environment.

Simultaneous localization and mapping, as one of the key technologies in the field of mobile robotics, has made great progress through the development of recent years (Davison *et al.*, 2007). The SLAM system is divided into vision SLAM and LIDAR SLAM according to the different sensors (Pire *et al.*, 2017). Due to the camera's sensitivity to light, vision SLAM technology is difficult to land in the actual production of orchards, and the application scene is limited (Zhou *et al.*, 2021). On the other hand, laser SLAM uses LiDAR (laser radar) as the main sensor, which is characterized by high robustness and high accuracy, and is more friendly to long lifecycle SLAM systems and suitable for operation in complex outdoor scenes such as orchards (Xue *et al.*, 2023). In recent years, many laser SLAM algorithms have been proposed. Zhang *et al.* proposed the classic and representative LOAM (LiDAR Odometry and Mapping) in 2014, which opens up the precedent of feature extraction for 3D point clouds and is useful for subsequent algorithms (Zhang *et al.*, 2014). The algorithm extracts edge and plane points in the point cloud according to the curvature size, and the algorithm extracts edge points and plane points in the point cloud according to the curvature size, and participates in frame-to-frame matching (Scan-to-Scan) and frame-to-map matching (Scan-to-Map), which improves the efficiency of point cloud alignment, but due to the lack of loopback detection and back-end optimisation, the cumulative error is larger in large-scale scenes. In 2018, LeGo-LOAM (Lightweight and Ground-Optimized LiDAR Odometry and Mapping) algorithm was proposed by Shan *et al.* (Shan *et al.*, 2018). This algorithm optimises the front-end odometry, introduces the concept of keyframes, and adds loopback detection to LOAM, which greatly reduces the computation amount. LIO-SAM is the sequel of LeGO-SLAM authors, which implements tightly coupled laser inertial odometry on the basis of graph optimization framework, and adopts factor graph optimization to realize the fusion of introducing GPS factor and loopback detection factor, and this algorithm is compared with LOAM and LIOM algorithms horizontally, and the end-to-end error under the park dataset is 0.04 m, which is better than the 121.74 m of LOAM algorithm and the 34.6 m of LIOM, and it has better global consistency, although this algorithm is more consistent than LOAM algorithm, and it has more accuracy (Shan *et al.*, 2020).

The purpose of path planning is to plan an optimal collision-free path from the start point to the end point in a map environment. Dijkstra *et al.* proposed the shortest path planning algorithm which uses breadth-first search to search for paths (Dijkstra *et al.*, 1959). Seet *et al.* proposed the A-star algorithm, which reduces the search nodes and improves the efficiency of path search by using a heuristic evaluation function (Seet *et al.*, 2004). Fox *et al.* proposed the DWA, which dynamically samples velocities in the robot's sampling space based on the robot's kinematic model and the current motion parameters and selects the optimal trajectory (Fox *et al.*, 1997). To address the problem of insufficient DWA evaluation functions, Chang *et al.* proposed an improved DWA algorithm based on Q-learning, which modifies and extends the evaluation functions by adding two more evaluation functions in order to improve the navigation performance and to achieve higher navigation efficiency and success rate in complex and unknown environments (Chang *et al.*, 2021). Rösmann *et al.* proposed a time-elastic segmentation algorithm based on multi-objective optimization, which ensures that the robot outputs smooth trajectories while satisfying kinematic constraints (Rösmann *et al.*, 2015).

In this paper, an inspection robot navigation system designed for complex scenes in orchards, as shown in Figure 1, is introduced. A SLAM system based on multiline LiDAR is designed to meet the robot's inspection needs in outdoor scenes such as orchards. Firstly, the LiDAR scanned images of the vineyard environment are collected, and the original point cloud of the vineyard is subjected to data processing, and then features such as edges and corners are extracted from the scanned images, and the point cloud is matched using the NDT-ICP algorithm. Finally, these features are used to construct a 3D point cloud map of the environment. The 3D point cloud map is converted to a 2D raster map, and the improved A-star algorithm is used for global path planning to improve the navigation efficiency and help the robot quickly plan the optimal path. Finally, the robot is realized to complete the high-precision navigation inspection task in the complex scene of the orchard.

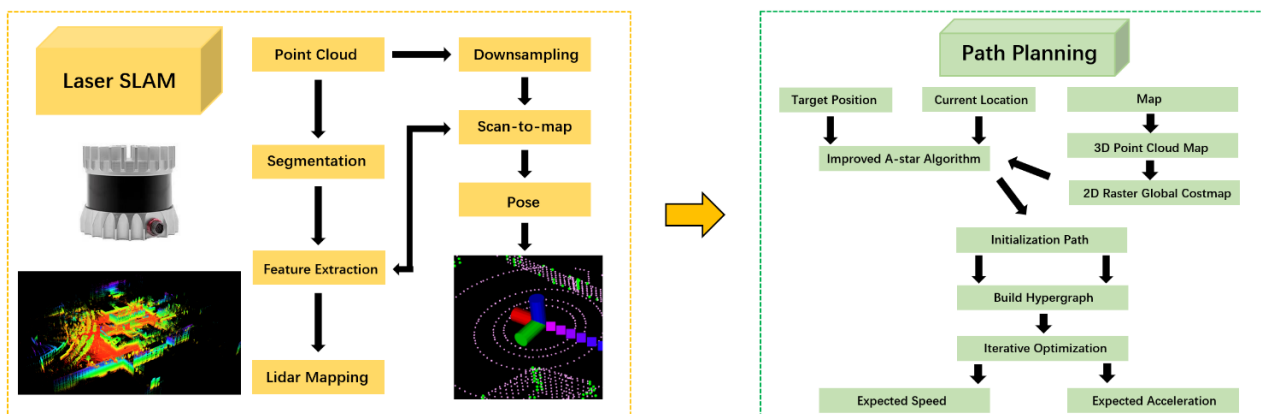


Fig. 1 – System framework

MATERIALS AND METHODS

Radar point cloud information acquisition

In order to study the SLAM and path planning methods for inspection robots in orchard environments, a 132-meter × 144-meter rectangular plot in a vineyard in Huantai County, Zibo City, Shandong Province (N37.07420°, E117.91777°) was selected for data acquisition. Figure 2 depicts the actual vineyard. The grapes in the orchard are planted using the ridge planting method, which involves the planting of grapes in single rows on each ridge, with a distance of three meters between the rows.



Fig. 2 – The Grapevine

The map query function of Bigemap GIS Office software was used to locate the test site, as shown in Figure 3.



Fig. 3 – The test site

An orchard robot was designed for the purpose of data collection and field experiments. This robot fixes the Ouster 64-line lidar to the centre of the crawler chassis by means of a radar bracket with an aluminium profile, and the centre of the LIDAR is located at a distance of 1 m from the ground, which ensures that the LIDAR is not obstructed and ensures that the accuracy of the SLAM construction is guaranteed. In addition, the two GNSS antennas are screwed to the strong magnetic suction cups and fixed in the forward direction and backward direction of the crawler chassis at a distance of 1 m to ensure that there is no obstruction above the antennas to ensure that good positioning signals are received.

Concurrently, it is imperative to guarantee that the corresponding centers of the two GNSS antennas align with the central axis of the crawler chassis. This configuration enables the GNSS-RTK to obtain the position data of the orchard robot in real time, and the accuracy reaches centimetre level. Finally, the AI processor is installed, which is connected to the robot's underlying control driver board via serial cable, to the GNSS-RTK positioning receiver via USB cable, and to the LiDAR adapter box via Ethernet cable. The tracked chassis of the orchard robot is powered by a buck module that steps down the 48 V to 24 V for the LIDAR and 48 V to 5 V for the AI processor.



Fig. 4 – Tracked mobile platform for orchard robots

- 1. External Monitor; 2. Artificial Intelligence (AI) Processors;
- 3. Crawler-Type Mobile Chassis; 4. Dual-Antenna GNSS-RTK; 5. 64-Line 3D LiDAR.

Figure 5 shows the hardware connection diagram of the orchard robot.

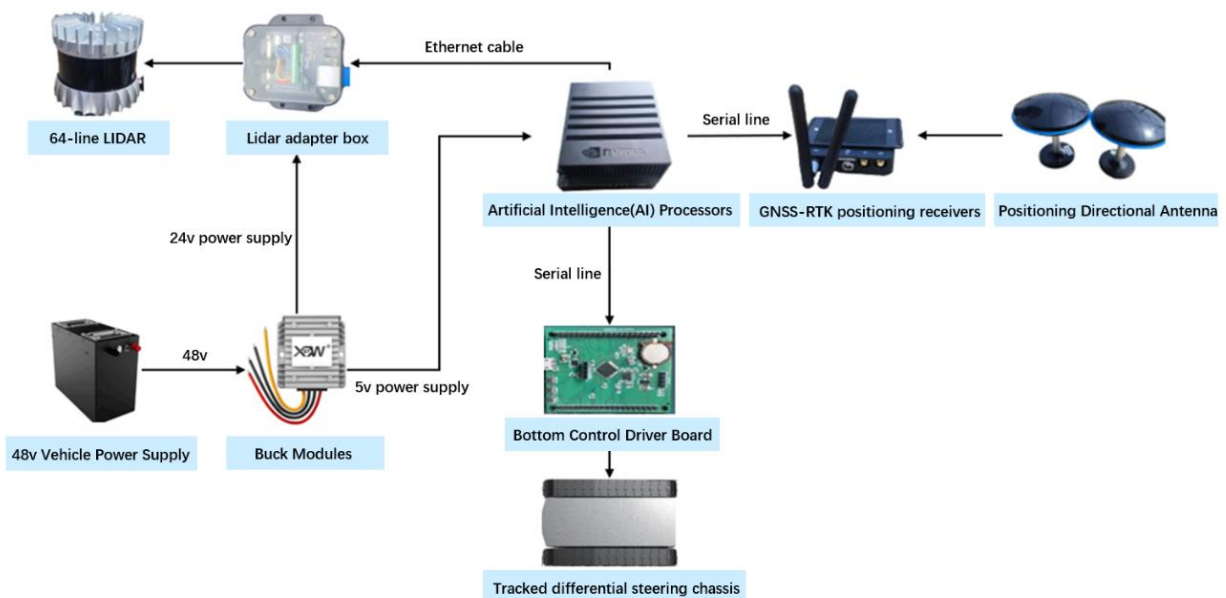


Fig. 5 – Hardware Connection Diagram of Orchard Work Robot

Multi-Line LiDAR-Based SLAM Algorithm Design and verification

In outdoor orchard environments, the position of the sun changes all the time from sunrise to sunset, and the intensity of the sunlight varies over time, which can cause vision sensors to misidentify objects or locate them inaccurately. However, laser sensors do not require an external light source because they emit their own laser beams, which are not affected by lighting problems. Therefore, a lightweight, ground-optimized laser ranging and mapping method, the structure of which is schematically shown in Fig. 6, was adopted.

The LeGo-LOAM algorithm consists of four main parts, which are point cloud segmentation, feature extraction, radar odometry, and map construction. The loopback detection used in the LeGo-LOAM algorithm is relatively simple, and the loopback matching process uses the Iterative Closest Point (ICP) and Euclidean distance combination, which is established for low drift cases, and when running in scenes with large distance ranges, it accumulates large errors and produces large scale drifts. To address this problem, new spatial constraints are added to the loopback detection process, a constraint relationship is established between the current frame point cloud data and the first three frames of point cloud data, and the bit position of the current frame is recursively solved from the first three frames of point cloud data to reduce the accumulation of error, and finally the current point cloud is mapped to the global map based on graph optimization to complete the establishment of a high-precision map.

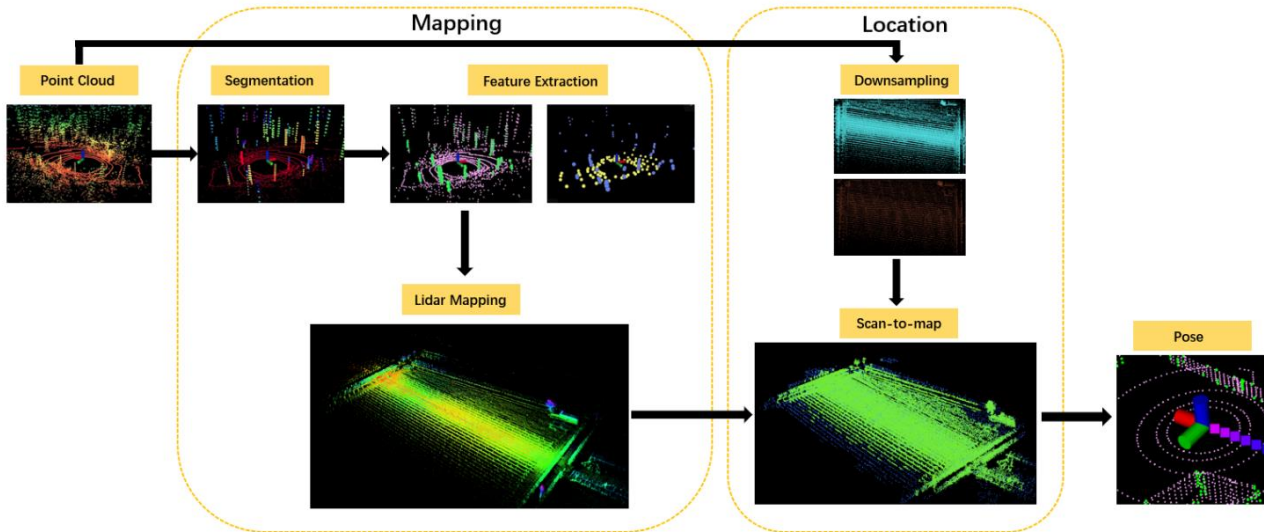


Fig. 6 – Multi-line LiDAR-based SLAM system structure diagram

The algorithm improvement process is as follows:

1) The scanned point cloud data is clustered and ground segmented to segment out the non-ground points, while the point cloud data is filtered. In the process of feature matching, the distance image level is evenly divided into equal sub-images, and the plane smoothness of the points in each row of each sub-image is calculated, and the plane smoothness is used as an index to extract the feature information of the current frame, and the feature points are divided into edge points and planar points according to the plane smoothness as an index, and the formula for calculating the plane smoothness is shown in equation (1):

$$c = \frac{1}{|S| \cdot \|r_i\|} \left\| \sum_{j \in S, j \neq i} r_j - r_i \right\| \quad (1)$$

where S is the set of 5 points before and after point i in the same direction; r_i is the Euclidean distance from point i to LIDAR in the distance image; r_j is the Euclidean distance from point j to LIDAR in the distance image.

2) The extracted feature points are traversed to distinguish the edge points from the plane points, and the constraint relations from the edge points to the straight line and the plane points to the plane are constructed respectively. The distance from an edge point to a straight line is shown in equation (2):

$$D_\varepsilon = \frac{\left| \left(\bar{X}_{(k+1,i)}^L - \bar{X}_{(k,j)}^L \right) \times \left(\bar{X}_{(k+1,i)}^L - \bar{X}_{(k,l)}^L \right) \right|}{\left| \bar{X}_{(k,j)}^L - \bar{X}_{(k,l)}^L \right|} \quad (2)$$

where D_ε is the shortest distance from the edge point to the straight line; $\bar{X}_{(k,i)}^L$ is the coordinate of point i in the k th complete scan in the radar coordinate system; $\bar{X}_{(k,j)}^L$ is the coordinate of point j in the k th complete scan in the radar coordinate system; $\bar{X}_{(k+1,i)}^L$ is the coordinate of point i in the $k+1$ st complete scan in the radar coordinate system; and $\bar{X}_{(k+1,j)}^L$ is the coordinate of point j in the $k+1$ st complete scan in the radar coordinate system.

The distance from the plane point to the plane is shown in equation (3):

$$D_H = \frac{\left| \left(\bar{X}_{(k+1,i)}^L - \bar{X}_{(k,j)}^L \right) \cdot \left(\bar{X}_{(k,j)}^L - \bar{X}_{(k,n)}^L \right) \times \left(\bar{X}_{(k,l)}^L - \bar{X}_{(k,m)}^L \right) \right|}{\left| \left(\bar{X}_{(k,j)}^L - \bar{X}_{(k,\eta)}^L \right) \times \left(\bar{X}_{(k,j)}^L - \bar{X}_{(k,m)}^L \right) \right|} \quad (3)$$

Where D_H is the shortest distance from the plane point to the plane; $\bar{X}_{(k,m)}^L$ is the coordinate of point m in the k th complete scan under the radar coordinate system; $\bar{X}_{(k+1,m)}^L$ is the coordinate of point m in the $k+1$ th complete scan under the radar coordinate system.

3) Calculate the distance between the current frame point cloud data and the previous three frames point cloud data by the point to line and point to plane distance formula, when there are two frames of point cloud data with close distance, match the edge points or plane points in them, for the edge points, match them by the segmented segmentation point labels; for the plane points, match them by the segmented plane point labels. Comparing the difference between the description vectors of the two frames of point cloud data, the similarity of the two frames of data is calculated, and the similarity calculation process is shown below:

$$\cos(\theta) = \frac{\sum_{i=1}^n (x_i \times y_i)}{\sqrt{\sum_{i=1}^n (x_i)^2} \times \sqrt{\sum_{i=1}^n (y_i)^2}} \quad (4)$$

where $\cos(\theta)$ is the cosine of the two vectors; n is the dimension of the vector.

The range of cosine value is $[-1, 1]$, when $\cos(\theta)$ is closer to 1, it represents that the direction of the two vectors is closer, the higher the similarity of the two vectors; when $\cos(\theta)$ is closer to -1, it represents that the direction of the two vectors tends to the opposite direction, the lower the similarity of the two vectors.

4) When the similarity between two frames of data that are close to each other is high, the feature similarity matching is recognized to be completed, and the current frame of point cloud data is used to project the bit position through a frame of point cloud data at the previous moment. The error function is minimized by calculating the rotation matrix and translation matrix between the two point clouds. Assuming that the two point clouds are $X = \{x_1, x_2, \dots, x_{np}\}$, $P = \{p_1, p_2, \dots, p_{nx}\}$, and the error function is shown in equation (5):

$$E(R, t) = \frac{1}{n} \sum_{i=1}^n \|x_i - Rp_i - t\|^2 \quad (5)$$

where R is the rotation matrix; t is the translation matrix.

The rotation matrix R and the translation matrix t satisfy the following relationship:

$$x_i = Rp_i + t \quad (6)$$

Calculate the centre of mass of the two sets of point clouds as shown in equations (7) and (8):

$$u_x = \frac{1}{n} \sum_{i=1}^n X_i \quad (7)$$

$$u_p = \frac{1}{n} \sum_{i=1}^n P_i \quad (8)$$

The two sets of point clouds are moved towards the origin to remove the centre of mass, and the coordinates of the two point clouds after the removal of the centre of mass are shown in Eqs. (9) and (10):

$$X = \{X_i - u_x\} \quad (9)$$

$$P = \{P_i - u_p\} \quad (10)$$

Set the matrix W :

$$W = \sum_{i=1}^n x_i p_i^T \quad (11)$$

Obtained by SVD decomposition:

$$W = U \Sigma V^T \quad (12)$$

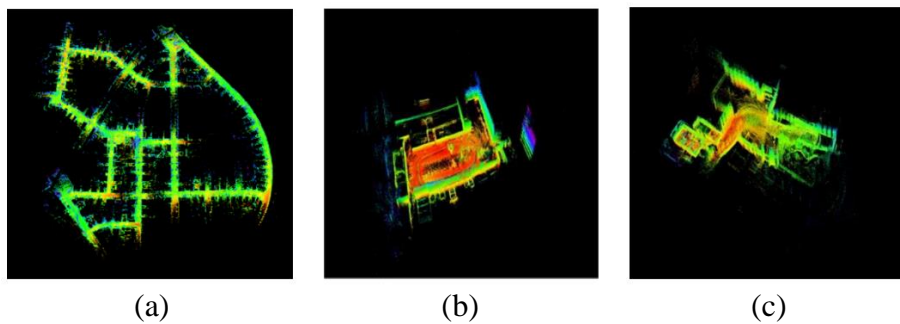
The rotation matrix R and the translation matrix t can be obtained:

$$R = UV^T \quad (13)$$

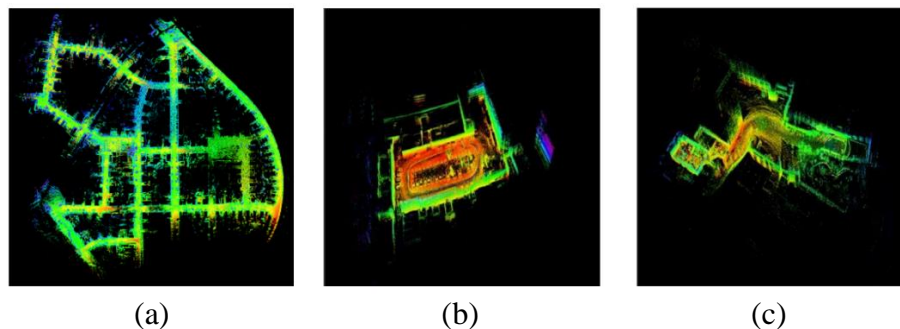
$$t = u_x - Ru_p \quad (14)$$

After aligning the two point cloud frames by the obtained rotation and translation matrices, each feature set is bound to the LiDAR's position to generate a local feature point cloud map, and the local point cloud data is fused to the global map, and the final global map is obtained through optimization.

In this paper, the feasibility, reliability and accuracy of the improved LeGo-LOAM algorithm are verified by the KITTI dataset, and the verification experiments are designed as follows: the same dataset is run using the LeGo-LOAM algorithm and the improved LeGo-LOAM algorithm, and the LeGo-LOAM algorithm and the improved LeGo-LOAM algorithm are compared with the improved LeGo-LOAM algorithm in terms of the graph building effect, the running time, and the CPU occupancy rate. LeGo-LOAM algorithm and the improved LeGo-LOAM algorithm are compared in three aspects: building effect, running time and CPU utilization. In order to ensure the accuracy of the test, this paper conducts several tests and takes the average value. The map constructed by LeGo-LOAM algorithm is shown in Figure 7, and the map constructed by the improved LeGo-LOAM algorithm is shown in Figure 8. The comparison results of the two algorithms are shown in Table 1.



(a) (b) (c)
Fig. 7 – Maps constructed by the LeGo-LOAM algorithm



(a) (b) (c)
Fig. 8 – Maps constructed by the improved LeGo-LOAM algorithm

As can be seen from the comparison of Fig. 7 and Fig. 8, the maps constructed by the improved LeGo-LOAM algorithm are clearer compared to the maps constructed by the LeGo-LOAM algorithm, which reduces the error generated by the accumulation, and handles the edge contours better (Wei *et al.*, 2023).

As can be seen from Table 1, the two algorithms have roughly the same building time, and the CPU occupancy rate of the improved LeGo-LOAM algorithm is slightly higher than that of the LeGo-LOAM algorithm, but the difference is very small. Comparing the two algorithms in terms of building time, building effect and CPU occupancy, the improved LeGo-LOAM algorithm is better than LeGo-LOAM algorithm.

Table 1

| Algorithm comparison test results | | | |
|-----------------------------------|-----------|------------|-------------------|
| Data set | Algorithm | Time (min) | CPU Occupancy (%) |
| First data set | LeGo-LOAM | 1.50 | 24 |
| | Ours | 1.50 | 29 |
| Second data set | LeGo-LOAM | 1.25 | 23 |
| | Ours | 1.24 | 25 |
| Third data set | LeGo-LOAM | 2.43 | 31 |
| | Ours | 2.44 | 36 |

Inspection Robot Path Planning System

The global path planning takes the 2D raster cost map converted from the 3D point cloud map as input, and takes the shape of the robot, the dynamics model and the motion performance into consideration when planning the path, and adopts the multi-constraint Bessel curve fusion to improve the A-star path planning algorithm to plan the optimal path from the robot's current position to the desired target position, and in this process, it is necessary to continuously adjust the robot's position in the process of motion, so that new paths can be generated by each iteration, and through the continuous iteration, the optimal path of the global path in the process of navigation of the robot in the orchard is obtained, as shown in Fig. 9.

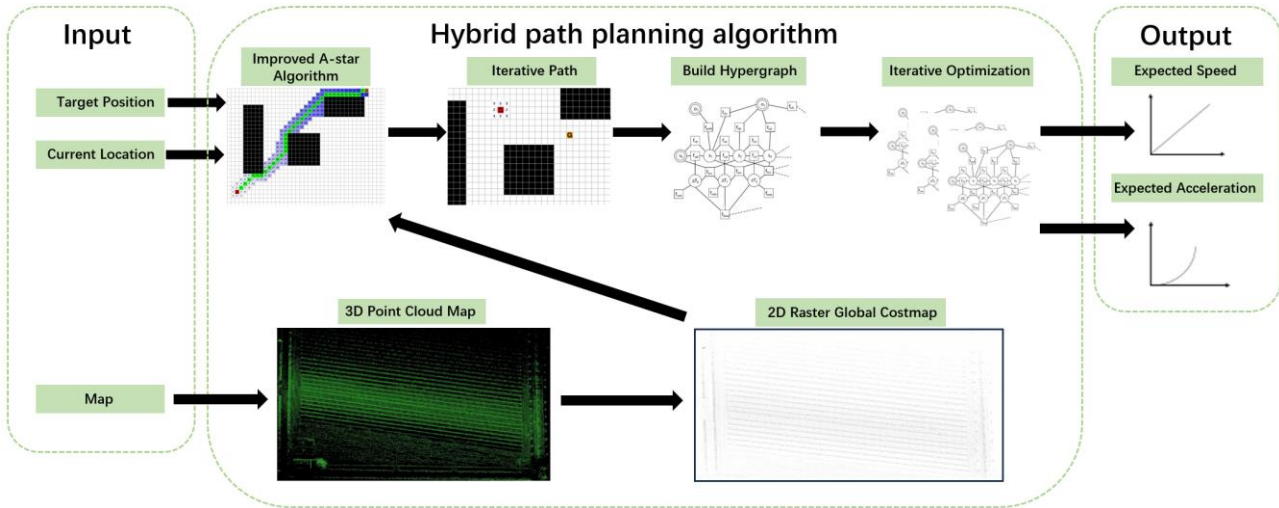


Fig. 9 – Flowchart of the route planning system

The advantage of A-star algorithm as a common heuristic search algorithm is that it can find the optimal solution quickly and also ensure the correctness of the optimal solution when pathfinding and path planning work.

The cost function $f(n)$ of the A-star algorithm is denoted as:

$$f(n) = g(n) + h(n) \tag{15}$$

Here, a simplified version of the vineyard simulation map is drawn using MATLAB to test the improved A-star full-coverage path planning algorithm. The map size is 30*30 raster units as shown in Fig.10.

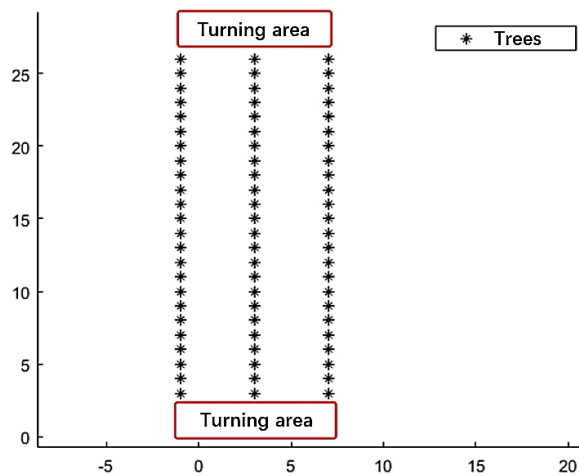


Fig. 10 – Simulated Orchard Environment Map

The traditional A-star algorithm global path planning work is shown in Fig.11, and the A-star full-coverage path planning algorithm for global path planning work is shown in Fig.12.

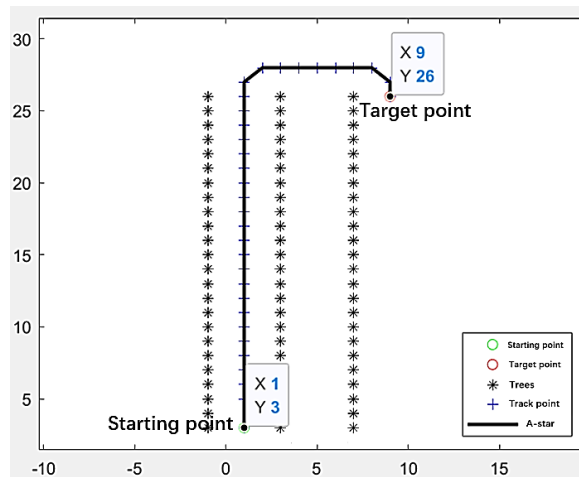


Fig. 11– Simulation of Traditional A-star Algorithm Planning

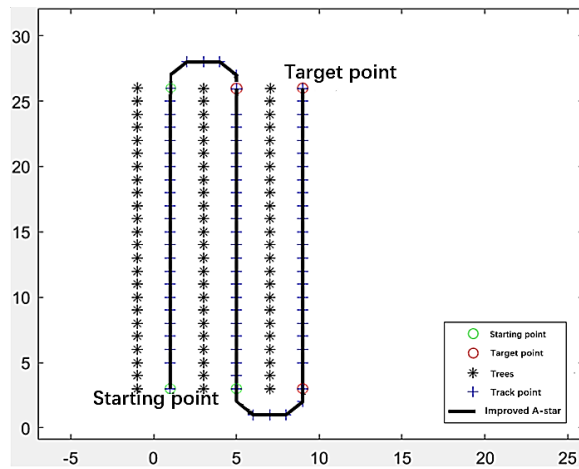


Fig. 12 – Simulation of Improved A-star Full Coverage Path Planning Algorithm

Relative to Fig. 11, it can be seen from Fig. 12 that the improved A-star full-coverage path planning algorithm can plan a collision-free, full-coverage shortest path.

However, the improved path trajectory in Fig. 12 has more turns and folds, which can cause the robot to change direction during travel and thus lose control, and the efficiency is greatly reduced, so Bessel curves will be used to plan the paths for the improved A-star algorithm under kinematic constraints to make them closer to the theoretical travel paths.

The shape of the Bezier curve is determined by the control points. Different Bezier curves can be created by adjusting the position and number of control points.

When $n=1$, the first order Bessel curve is a straight line with the expression.

$$P^1(t) = (1-t)P_0 + tP_1 = \sum_{i=0}^1 C_1^i (1-t)^{1-i} t^i P_i \quad (16)$$

When $n=2$, the second-order Bessel curve is parabolic and at most the first-order derivative is not constant, with the expression.

$$P^2(t) = (1-t)^2 P_0 + 2t(1-t)P_1 + t^2 P_2 = \sum_{i=0}^2 C_2^i (1-t)^{2-i} t^i P_i \quad (17)$$

The formula for the third-order Bessel curve when $n=3$, with at most the second-order derivatives not being constant, is expressed as.

$$P^3(t) = (1-t)^3 P_0 + 3t(1-t)^2 P_1 + 3t^2(1-t)P_2 + t^3 P_3 = \sum_{i=0}^3 C_3^i (1-t)^{3-i} t^i P_i \quad (18)$$

When $n \geq 3$, the curve is a higher order Bessel curve. The first to third order Bessel curve images are shown in Fig. 13.

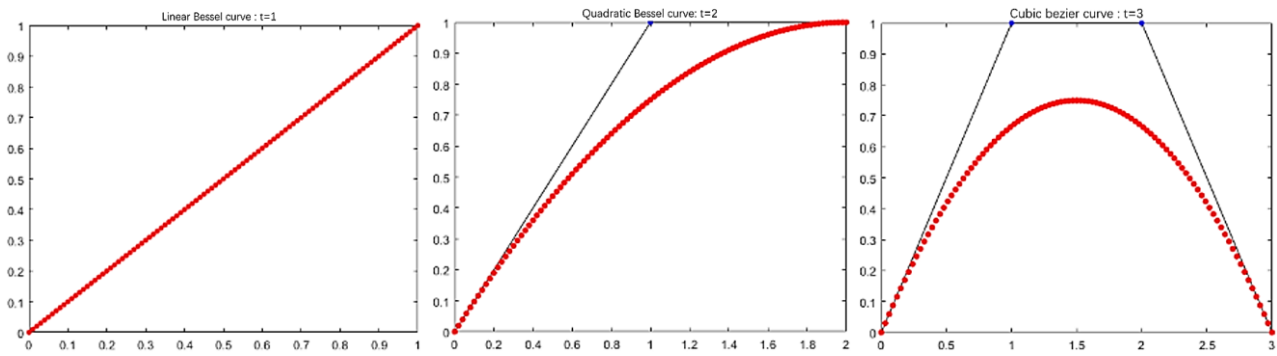


Fig. 13 – First- to third-order Bessel plots

When the trajectory is smoothed, it should be ensured that the robot kinematic constraints are satisfied to ensure that the cost is minimized when the robot trajectory is tracked. The curvature continuity constraint is of paramount importance in ensuring smooth turning during robot travel. In order to avoid unstable phenomena such as violent turns during trajectory tracking by the robot, it is essential that the curvature changes of adjacent path segments on the path are continuous. This is achieved by ensuring that the third-order Bessel curve, which is the basis of the curvature continuity constraint, has continuous second-order derivatives.

The flowchart of the improved A-star algorithm based on constraint Bessel curves is shown in Fig. 14.

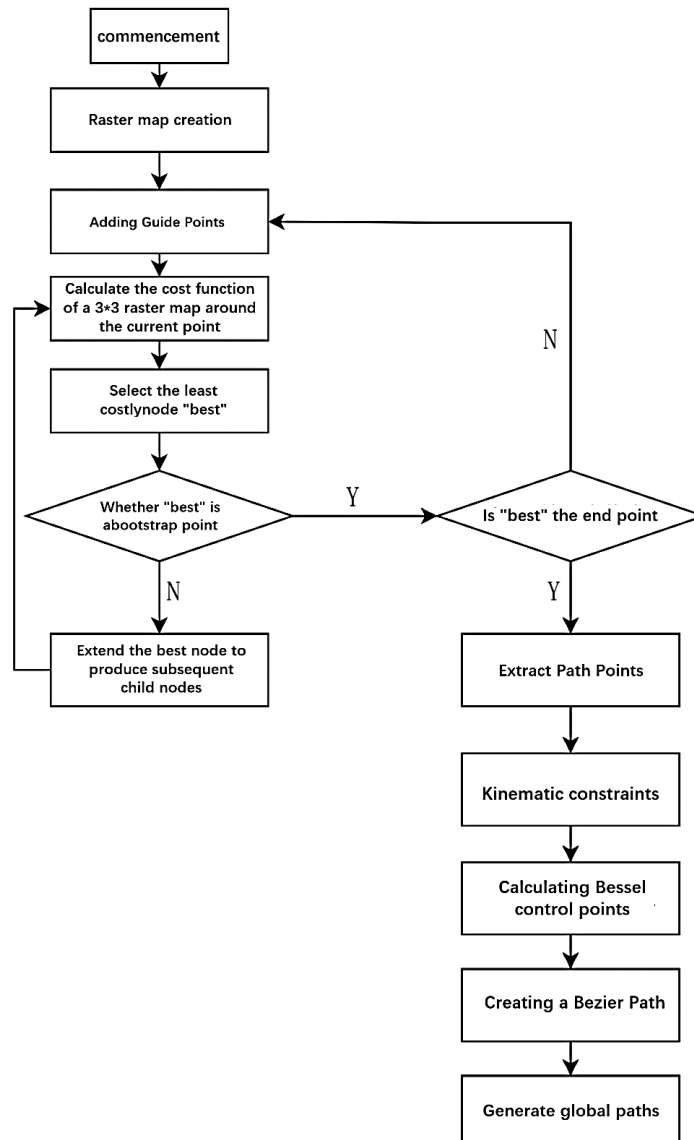


Fig. 14 – Flowchart of Improved A-star Algorithm Based on Constraint Bessel Curve

Through Figure 15, it can be found that the A-star algorithm with added Bessel curve optimization is smoother in the ground head turnaround region, which is more suitable for the orchard scene operation, while the global path optimized by the unconstrained Bessel curve has an abrupt change of curvature in the connection between the straight line and the turnaround path, which is not smooth.

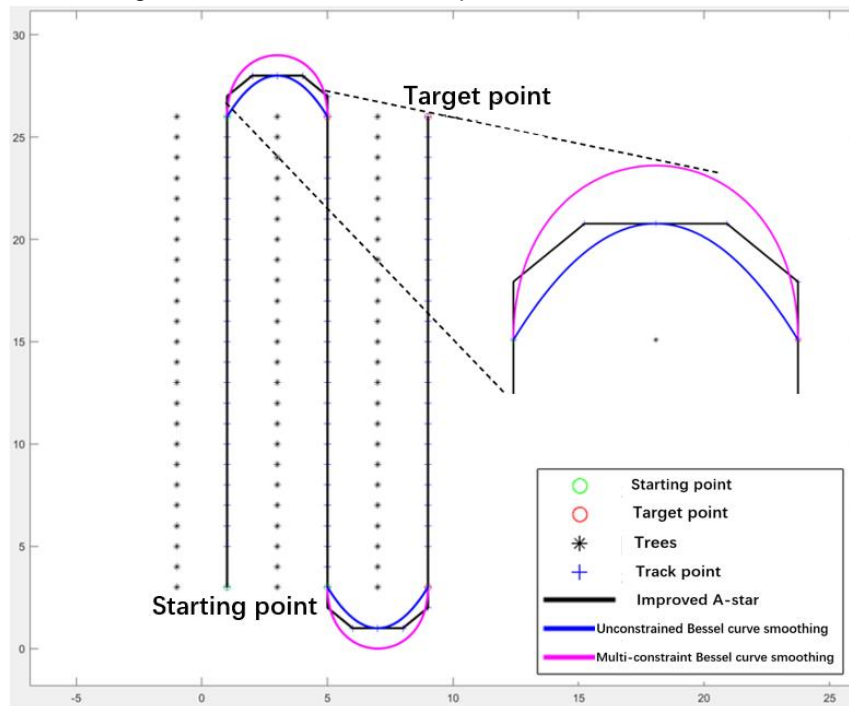


Fig. 15 – A-star Algorithm before and after Bessel Curve Optimization

RESULTS

Details of SLAM algorithm testing based on multi-line LiDAR

Before the orchard robot works, it establishes a three-dimensional point cloud map for the orchard and transforms it into a two-dimensional raster map that can be used for navigation, and generates an optimized global path according to the two-dimensional raster map in the Robot Operating System (ROS) to start the unmanned inspection operation at the starting point. In the process of robot driving, the artificial intelligence processor receives the data from the localization receiver through the serial communication, and analyses and transforms it into the localization point information under the absolute coordinate system, and receives the localization point information through the control module, and after calculation, it sends the linear velocity and angular velocity information to the bottom control driver board of the tracked vehicle, so as to let the vehicle carry out the inspection operation along the globally planned path.

First, the inspection operation area is selected, because the path in the vineyard is mainly divided into two parts, one is the straight line path in the inspection area, and the other is the turnaround path in the ground turnaround area, so two rows of vineyard are selected as the test area, as shown in Figure 16.

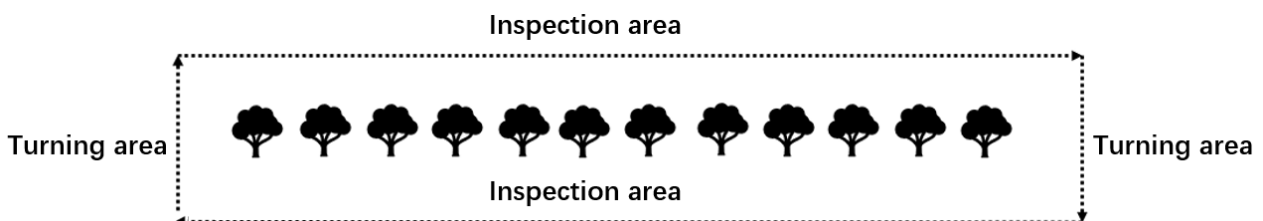


Fig. 16 – Schematic diagram of the inspection operation area

Second, as shown in Figure 16, the orchard inspection robot is controlled to loop back at 1.0 m/s according to the rectangular frame, record the 3D point cloud data at 10 Hz, and run the improved SLAM algorithm in order to construct a high-precision 3D point cloud map of the vineyard, as shown in Figure 17.

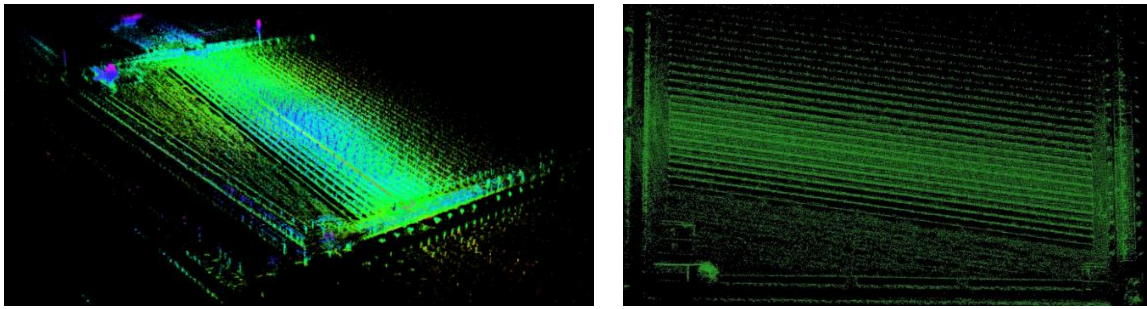


Fig. 17 – High-precision 3D point cloud map of the vineyard

Finally, the map conversion function package is launched to generate and update the 2D raster map from the high precision map in real time. The generated 2D raster map is shown in Figure 18.



Fig. 18 – Vineyard 2D Grid Map

The 3D point cloud map constructed by the improved SLAM algorithm is clearer and denser than the map constructed by the LeGo-LOAM algorithm, the data is more complete, the processing of the edge contour is better, and the converted 2D raster map can satisfy the robot's navigational accuracy requirements in the orchard environment.

Inspection Robot Path Planning System Test Details

When launching the Global Path Planning feature package, you need to import a 2D raster map of the test area. The map information is obtained by subscribing to the map information through the ROS theme. Then specify the starting and target points of the orchard robot and add guidance points. The global path is generated by the comb-type full-coverage algorithm and the improved A-star path planning algorithm with multi-constraint Bessel curves, and the global path is displayed using MATLAB, as shown in Fig. 19.

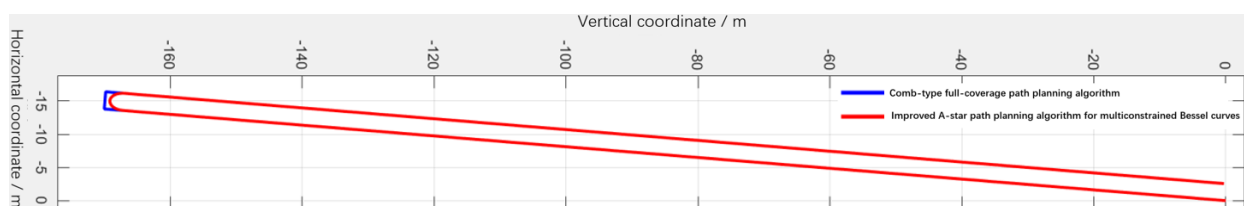


Fig. 19 – Improved A-star path planning algorithm for multi constrained Bessel curves

From Fig. 19, it can be seen that the A-star algorithm with the addition of Bessel curve optimization is smoother in the ground-head turning region, which is more suitable for the operation of the orchard scene. Next, the navigation parameters are set, the sampling time is set to 0.1s, the traveling speed is set to 1m/s, the basic forward-looking distance is set to $L_{d0}=1\text{m}$, the gain coefficient of pure tracking algorithm speed control is set to $K_v=1$, and the integration adjustment coefficient is set to $K_i=0.5$, and the initial lateral bias and heading error are not set, and the startup command is inputted into the ROS terminal to control the orchard robot to start trajectory tracking and to record the Robot position information.

Save the driving trajectory point data in txt format and import the txt format file into MATLAB to display the trajectory as shown in Fig. 20.

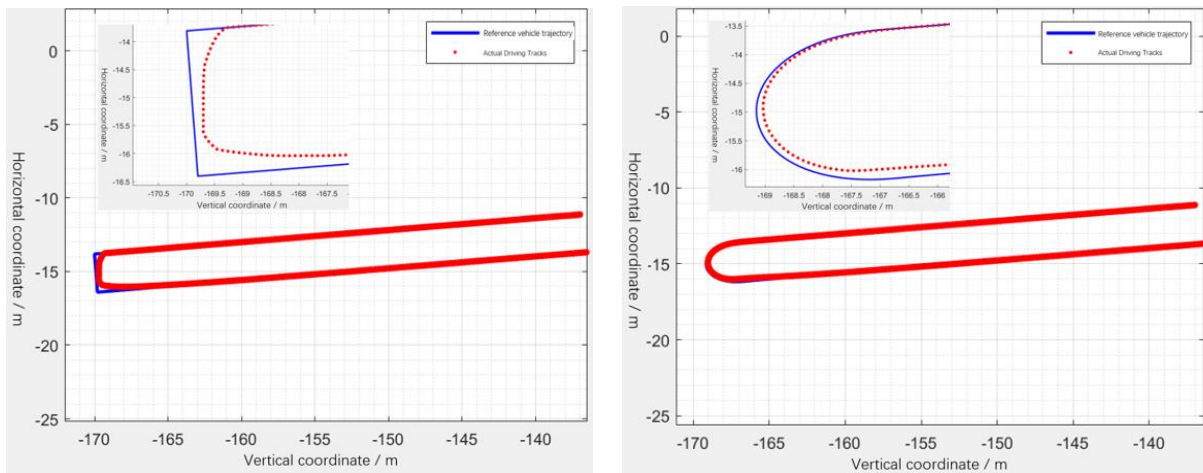


Fig. 20 – Comparison chart of tracking effect

The lateral deviations of the sampled points are saved in txt format, and then the txt format file is imported into MATLAB to display the trajectory tracking errors of the two planning algorithms, as shown in Fig. 21 and Table 2.

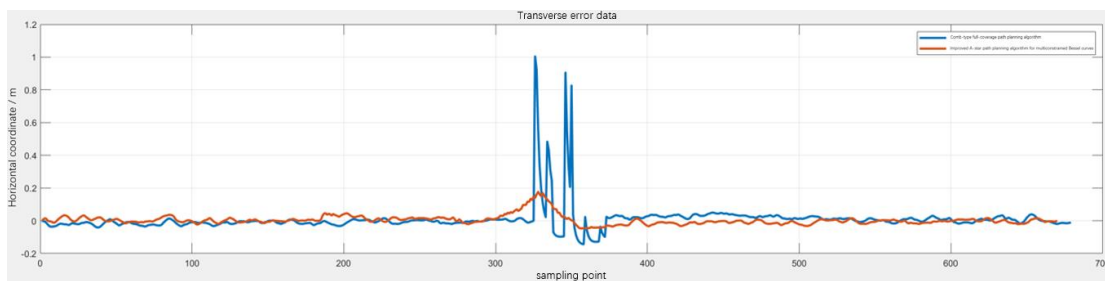


Fig. 21 – Comparison of lateral tracking deviation between two algorithms for path planning

Table 2

Lateral deviation of two planning paths under a pure tracking algorithm

| Route planning methodology | Different test paths | Average lateral deviation/m | Maximum lateral deviation/m |
|--|----------------------|-----------------------------|-----------------------------|
| Comb-type full coverage | linear path | 0.0162 m | 0.0505 m |
| | U-turn path | 0.2580 m | 1 m |
| | Overall path | 0.0300 m | 1 m |
| Improved A-star for multiconstrained Bessel curves | linear path | 0.0157 m | 0.0457 m |
| | U-turn path | 0.1081 m | 0.1768 m |
| | Overall path | 0.0176 m | 0.1768 m |

Experimental analysis shows that the path generated by the improved A-star algorithm based on constrained Bessel curves meets the requirements of full-coverage trajectory smoothing, and experiments show that the average lateral deviation of the straight line path during trajectory tracking is 0.0157 m, while the average lateral deviation of the trajectory tracking turn path is 0.1081 m, and the robot travels smoothly and the steering amplitude fluctuates less to meet the requirements of the robot autonomous unmanned operation.

CONCLUSIONS

This paper presents a novel autonomous detection and navigation system for orchard robots that integrates SLAM (Simultaneous Localization and Mapping) and path planning algorithms. Field tests in vineyards have validated the efficacy of the algorithms proposed in this paper. The research outcomes are of paramount importance in reducing labour costs and fostering the advancement of precision agriculture.

ACKNOWLEDGEMENT

The project supported by the R&D of low-speed unmanned autonomous navigation controller Project under Grant (No.2022TSGC1175).

REFERENCES

- [1] Chang L., Shan L., Jiang C., Dai Y., et al. (2021) Reinforcement based mobile robot path planning with improved dynamic window approach in unknown environment. *Auton. Robot.* 45, 51–76.
- [2] Davison A., Reid I., Molton N., Stasse O., et al. (2007). MonoSLAM: Real-time single camera SLAM. *IEEE Trans. Pattern Anal. Mach.Intell.* 29, 1052–1067.
- [3] Dijkstra, E. W., et al. (1959) A note on two problems in connexion with graphs. *Numerische Mathematik.* 1, 269–271.
- [4] Fox, D., Burgard, W., & Thrun, S., et al. (1997) The dynamic window approach to collision avoidance. *IEEE Robotics & Automation Magazine.* 4(1), 23-33.
- [5] Pire T., Fischer T., Castro G., De Cristóforis P., Civera J., Berlles J., et al. (2017) S-PTAM: Stereo parallel tracking and mapping. *Robot.Auton. Syst.* 93, 27–42.
- [6] Rösmann C., Hoffmann F., Bertram T., et al. (2015) Timed-elastic-bands for time-optimal point-to-point nonlinear model predictive control. In *Proceedings of the 2015 European Control Conference (ECC)*, Linz, Austria, 15–17 July. 3352–3357.
- [7] Shan T., Englot B., et al. (2018) LeGO-LOAM: Lightweight and ground-optimized lidar odometry and mapping on variable terrain. *IEEE/RSJ International Conference on Intelligent Robots and Systems (IROS)*. 4758-4765.
- [8] Shan T., Englot B., Meyers D., et al. (2020) LIO-SAM: Tightly-coupled lidar inertial odometry via smoothing and mapping. *IEEE/RSJ international conference on intelligent robots and systems (IROS)*. 5135-5142.
- [9] Seet B., Liu G., Lee B., Foh C., Wong K., Lee K., et al. (2004) A-STAR: A mobile ad hoc routing strategy for metropolis vehicular communications. In *Proceedings of the Networking 2004: Networking Technologies, Services, and Protocols; Performance of Computer and Communication Networks; Mobile and Wireless Communications Third International IFIP-TC6 Networking Conference*, Athens, Greece, 9–14 May; Springer: Berlin/Heidelberg, Germany. 989–999.
- [10] Wang N., Han Y., Wang Y., et al. (2022) Research progress on full-coverage operational planning for agricultural robots (农业机器人全覆盖作业规划研究进展). *Transactions of the Chinese Society for Agricultural Machinery*, Vol. 53, Issue S1: 1-19.
- [11] Wei Y., et al. (2023) *Research on orchard robot navigation system based on fusion of LiDAR and millimeter wave radar (基于激光雷达和毫米波雷达融合的果园机器人导航系统研究)*. Shandong Agricultural University.
- [12] Xue G, Li R, Zhang Z., et al. (2023) Research Status and Development Trend of SLAM Algorithm Based on 3D LiDAR (基于 3D 激光雷达的 SLAM 算法研究现状与发展趋势). *Information and Control*, vol. 52, Issue (01): 18-36.
- [13] Zhou Z., Cao J., Di S., et al. (2021) Overview of 3D LiDAR SLAM algorithms (3D 激光雷达 SLAM 算法综述). *Chinese Journal of Scientific Instrument*, vol. 42, Issue (09): 13-27.
- [14] Zhang J., Singh S., et al. (2014) LOAM: Lidar odometry and mapping in real-time. *Robotics: Science and Systems Conference.* 2(9): 1-9.

MULTI-TARGET DETECTION METHOD FOR MAIZE PESTS BASED ON IMPROVED YOLOv8

基于改进 YOLOv8 的玉米害虫多目标检测方法

Qiuyan LIANG¹, Zihan ZHAO¹, Jingye SUN¹, Tianyue JIANG², Ningning GUO¹, Haiyang YU¹, Yiyuan GE^{*1}

¹ School of Mechanical Engineering, Jiamusi University, Jiamusi, Heilongjiang / China;

² College of Information and Electronic Technology, Jiamusi University, Jiamusi, Heilongjiang / China

Tel: 13089679130; E-mail: geyiyuan@qq.com

Corresponding author: Yiyuan Ge

DOI: <https://doi.org/10.35633/inmateh-73-19>

Keywords: object detection; maize pests; yolov8; DAttention; SCConv

ABSTRACT

When maize is afflicted by pests and diseases, it can lead to a drastic reduction in yield, causing significant economic losses to farmers. Therefore, accurate and efficient detection of maize pest species is crucial for targeted pest control during the management process. To achieve precise detection of maize pest species, this paper proposes a deep learning detection algorithm for maize pests based on an improved YOLOv8n model: Firstly, a maize pest dataset was constructed, comprising 2,756 images of maize pests, according to the types of pests and diseases. Secondly, a deformable attention mechanism (DAttention) was introduced into the backbone network to enhance the model's capability to extract features from images of maize pests. Thirdly, spatial and channel recombination convolution (SCConv) was incorporated into the feature fusion network to reduce the miss rate of small-scale pests. Lastly, the improved model was trained and tested using the newly constructed maize pest dataset. Experimental results demonstrate that the improved model achieved a detection average precision (mAP) of 94.8% at a speed of 171 frames per second (FPS), balancing accuracy and efficiency. The improved model can be deployed in low-computing-power mobile devices to achieve real-time detection, and in the future, more types of maize pests can be detected by adding multi-category datasets and training with new models with more computational power, which is important for the healthy development of maize agriculture.

摘要

玉米发生病虫害时会导致产量骤减使农民遭受重大经济损失。因此，准确、高效的玉米害虫种类检测在病虫害防治过程中可进行针对性防治。为了获得准确玉米害虫种类检测，本文提出了一种基于改进 YOLOv8n 的玉米害虫深度学习检测算法：首先，根据玉米病虫害种类，构建了玉米害虫数据集，共计 2756 张玉米害虫图像；其次，在主干网络中引入具有可变形注意力机制 (DAttention) 来提高算法模型对玉米害虫图像的特征提取能力；然后，针对不同尺度玉米害虫，在特征融合网络中引入空间和通道重组卷积 (SCConv)，降低小目标害虫的漏检率；最后，基于自建玉米害虫数据集对改进后的模型进行训练和测试。实验结果表明，改进后的模型在 171 帧每秒 (FPS) 的速度下实现了 94.8% 的检测平均精度 (mAP)，平衡了准确性和效率，可将改进的模型部署在低算力移动设备中实现实时检测，未来可通过添加多类别数据集和使用计算能力更强的新模型进行训练，实现更多种类的玉米害虫检测，对玉米农业健康发展具有重要意义。

INTRODUCTION

Maize is one of the most important cereal crops in the world, yet its yield is severely threatened by pests and diseases. These afflictions can lead to reduced yield, quality degradation, and even total crop failure. Consequently, early detection and targeted control of these pests and diseases are crucial for ensuring the quantity and quality of maize production. Early warning and forecasting are foundational to the effective control of maize pests and play a significant role in the agricultural management and decision-making processes related to maize production. Currently, the detection of maize pests primarily relies on manual inspection by agricultural technicians, which is time-consuming and labor-intensive (Tian et al., 2020; Qi et al., 2021).

¹ Qiuyan Liang, Assoc. Prof., Ph.D.; Zihan Zhao, master degree; Jingye Sun, master degree; Tianyue Jiang, master degree; Ningning Guo, master degree; Haiyang Yu, master degree; Yiyuan Ge, Prof., Ph.D.

Additionally, the acquisition of pest information in some remote areas is delayed. Therefore, exploring a rapid, efficient, cost-effective, and accurate real-time detection method to identify maize pests, which helps reduce the use of chemical pesticides, lower production costs, and protect the ecological environment, holds significant practical value (Xinlu *et al.*, 2023; Xu *et al.*, 2023).

Convolutional Neural Networks (CNNs) possess richer feature extraction capabilities compared to traditional image detection algorithms, improving both accuracy and speed of detection. Representative CNN models include AlexNet (Yuan and Zhang, 2016), VGGNet (Jun *et al.*, 2018), GoogLeNet (Al-Qizwini *et al.*, 2017), ResNet (Targ *et al.*, 2016), DenseNet (Zhu and Newsam, 2017), Faster RCNN (Ren *et al.*, 2017), and the YOLO series (Redmon *et al.*, 2016; Redmon and Farhadi, 2017, 2018; Bochkovskiy *et al.*, 2020; Ge *et al.*, 2021; Wang *et al.*, 2023). With the advancement of artificial intelligence technology, deep learning methods have been extensively applied to crop pest detection (Maican *et al.*, 2023; Xintao *et al.*, 2023; Zongwang *et al.*, 2023; Zhang *et al.*, 2023; Ronghua *et al.*). For instance, literature (Hao *et al.*, 2020) utilized an improved SSD network for detecting rice pests, enhancing normalization and activation functions, which improved the identification rate and detection speed of rice pests, achieving an mAP of 79.3%.

Zhang *et al.*, (2022), proposed an improved model based on YOLOv4, utilizing contextual information and a multi-scale mixed attention mechanism to enhance the biological features of pests and integrate feature information, thereby improving pest detection accuracy, with the improved model achieving an accuracy of 80.16%. Xiaoyu *et al.*, (2023), introduced an improved YOLOv5 model designed to identify and locate small target pests by adding additional feature extraction layers at the cost of some detection speed, achieving a detection accuracy of 92%. Hui *et al.*, (2023), presented a pest identification method based on an improved YOLOv7, incorporating Transformer and CBAM modules and making enhancements to the loss function to boost pest detection performance, with an mAP of 91.6%. Zhu *et al.*, (2023), proposed a new object detection model, Poly-YOLOv8, which features a loss calculation algorithm insensitive to order and introduces a loss ratio factor based on the perimeter of polygons, outperforming other models in accurately and effectively detecting areas infected by maize leaf pests.

The aforementioned deep learning methods are capable of effectively learning target features from training data and can detect maize pests with certain levels of accuracy and efficiency. Among these, the YOLOv8 algorithm exhibits high detection precision. However, there are still some issues concerning the detection of maize pests that remain unresolved.

In recent years, research has rarely focused on the identification of maize pests; even when it has, it has only identified and detected a limited number of pest categories. Consequently, the lack of a comprehensive maize pest dataset hinders precise identification. Additionally, due to uncertain factors such as lighting and occlusion, the accuracy of existing methods in complex backgrounds is not high. Therefore, in this paper, a large-scale maize pest dataset was first constructed, which includes 2,756 images of five types of maize pests. Subsequently, the Deformable Attention mechanism (DAttention) (Zhu *et al.*, 2020) was incorporated based on the YOLOv8n framework to capture richer feature information of maize pests and enhance the model's feature extraction capability.

Using Spatial and Channel Recombination Convolution (SCConv) (Li *et al.*, 2023), feature fusion was performed for different scales of pest categories, reducing the miss rate of small target pests. Finally, the proposed method, embedded into the YOLOv8n algorithm, achieved accurate detection of multiple categories of maize pests. The improved YOLOv8n network model can be deployed on mobile embedded platforms, such as patrol robots, and holds promising prospects for applications in mobile target detection based on video streams.

MATERIALS AND METHODS

YOLOV8 ALGORITHM PRINCIPLES

The YOLOv8 algorithm is divided into five versions based on model size: v8n, v8s, v8m, v8l, and v8x. As the model size increases, its accuracy improves, while the detection speed gradually decreases. This allows for the selection of network models of varying depths and widths depending on the requirements of tasks such as object detection, image classification, instance segmentation, and keypoint detection. Given the hardware limitations of the deployment devices for maize pest detection, this paper utilizes the YOLOv8n model, which is compact yet highly precise. The network structure of YOLOv8n, as shown in Figure 1, comprises three main components: the Backbone, the Neck, and the Detection Head.

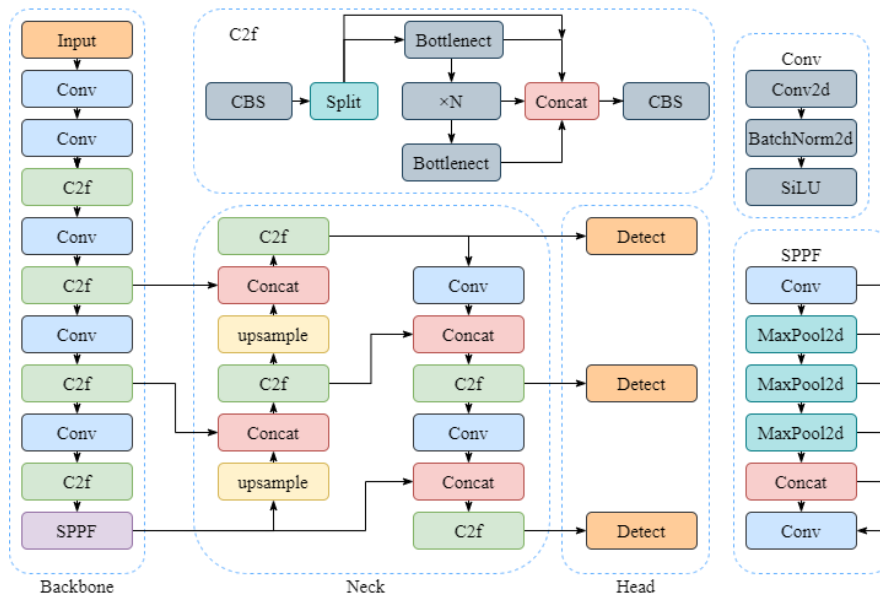


Fig. 1 - YOLOv8n network structure diagram

Backbone

The Backbone component primarily focuses on feature extraction from maize pest targets, utilizing the CSPDarknet-53 framework, which is composed of CBS, C2F, SPPF, and other modules. Specifically, the C2F module draws on the design philosophy of ELAN from YOLOv7 (Wang *et al.*, 2023) and the C3 module from YOLOv5, replacing all the original C3 modules with C2F (CSPLayer_2Conv) modules for residual learning. Additionally, more branches are added within this module. Inspired by CSP and ELAN, it employs numerous skip connections and additional Split operations, integrating gradient variations from beginning to end into the feature map. The Conv convolution modules and C2F modules are serially stacked four times, with each stack referred to as a stage. Ultimately, the SPPF (Spatial Pyramid Pooling Fusion) module, used in architectures like YOLOv5, is employed to fix the vector size of different scale feature maps.

Neck

The Neck component primarily handles the feature fusion of extracted maize pest characteristics, employing the Feature Pyramid Network (FPN) (Lin *et al.*, 2017) and Path Aggregation Network (PAN) (Liu *et al.*, 2018) from YOLOv5 to achieve both bottom-up and top-down feature pyramids. Similar to the Backbone, the C2F module replaces the C3 module in the Neck. YOLOv8n eliminates the 1x1 convolution used in YOLOv5 and YOLOv6 before upsampling, directly performing upsampling operations on features output at different stages of the Backbone.

Head

The Head component primarily converts feature maps of maize pests into prediction results, accurately predicting the location, category, and bounding box information of maize pests. It is an improvement on the YOLOv5 model, replacing the Anchor-Based coupled head with an Anchor-Free decoupled head. The Decoupled-Head structure is used, with the classification branch and the regression branch that employs Distribution Focal Loss (DFL), thus separating the classification and detection heads. The Head has three scales - large, medium, and small - of feature map detection heads, enabling the detection of maize pests of varying sizes.

To further enhance the detection speed and accuracy of the algorithm, improvements were made to the YOLOv8n model. Based on YOLOv8n, DAttention was introduced to enhance the model's feature fusion capabilities. Additionally, SCConv was employed to improve feature fusion capabilities and increase the detection precision for small targets, thereby enhancing the detection performance for maize pests.

Optimization of Feature Extraction Network Based on DAttention

In the YOLOv8n model, DAttention is inserted prior to the SPPF network in the backbone to optimize the process. This helps the model to better extract features of maize pests at different scales, thereby allowing the model to better focus on the crucial parts of the maize and pests, improving the accuracy and robustness of detection.

DAttention is an attention mechanism used in neural networks. In traditional attention mechanisms, weights are calculated based on a fixed-location attention model. However, in deformable attention, the shape and size of the attention model can be dynamically adjusted to better adapt to the characteristics of different tasks and input data, enhancing the feature extraction capability of the backbone network. The model of the deformable attention mechanism is shown in Figure 2.

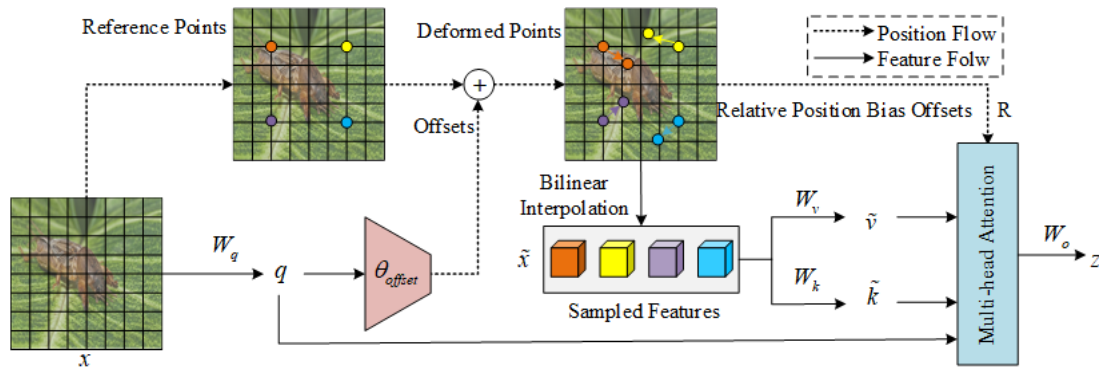


Fig. 2 - Deformable attention module

- (1) Given a feature map of maize pests, $x \in R^{H \times W \times C}$, generate a uniform grid of points over $p \in R^{H_G \times W_G \times 2}$ as a reference.
- (2) Linearly project the feature map onto query token $q = xW_q$, then input it into a lightweight network, θ_{offset} , to generate offsets $\Delta\theta_{offset(q)}$.
- (3) Sample at the positions of the deformed points, which serve as key and value, and together with the query, pass them into the multi-head attention mechanism.
- (4) Concatenate the features from each head and project them through W_o to obtain the final output.

When processing images of maize pests, DAttention focuses only on a small key area of the image, maintaining good performance while significantly reducing computational load. In the selection of sampling points, DAttention does not process the entire maize pest image rigidly; rather, it uses a dynamic selection mechanism that allows the model to focus more on the regions that are most relevant to the current task. Additionally, DAttention can adapt to different sizes of maize pests, making it effective in the identification tasks involving various types of maize pests.

Optimization of Feature Fusion Network Based on SCConv

SCConv combines spatial and channel information by performing concatenation operations across channel and spatial dimensions, enabling the network to better utilize the correlations between features in both spatial and channel aspects. In maize pest detection, SCConv helps the model better integrate multi-level features, thus enhancing the model's adaptability to different scales and complex backgrounds, and reducing the model's miss rate.

The SCConv model, as shown in Figure 3, consists of two units: the Spatial Reconstruction Unit (SRU) and the Channel Reconstruction Unit (CRU), arranged sequentially. The input features first pass through the SRU, resulting in spatially refined features, and then through the CRU, which refines the features at the channel level to produce the output. The SCConv module effectively utilizes the spatial and channel redundancy among features and can be seamlessly integrated into any CNN architecture to reduce redundancy among intermediate feature mappings and enhance the CNN's feature representation capabilities.

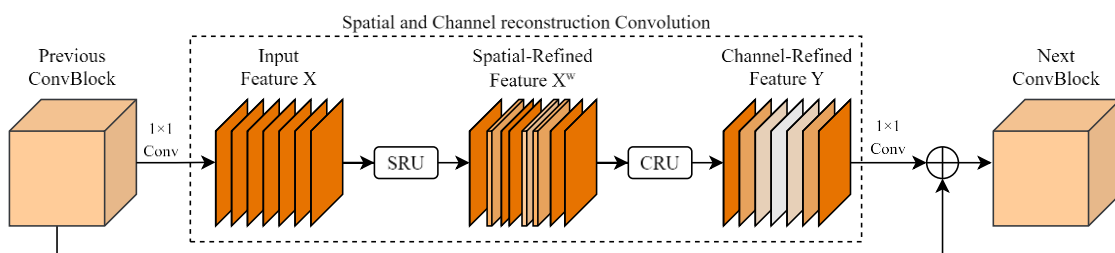


Fig. 3 - Spatial and Channel reconstruction convolution

(1) SRU - Spatial Reconstruction Unit

To utilize the spatial redundancy of features, a Spatial Reconstruction Unit (SRU) is introduced, as depicted in Figure 4, utilizing separation and reconstruction operations.

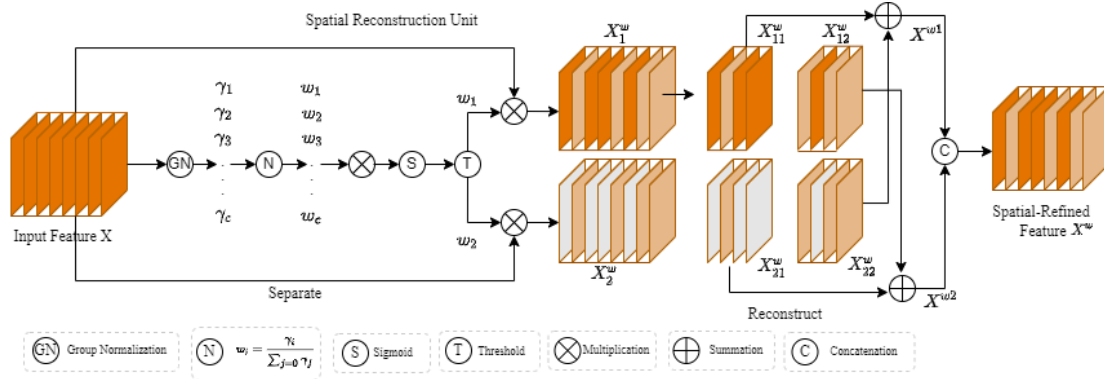


Fig. 4 - The architecture of Spatial Reconstruction Unit

The purpose of the separation operation is to distinguish feature maps with high spatial information content from those with less information. The scaling factor in Group Normalization (GN) is used to assess the information content in different feature maps, as shown in equations (1) to (3):

$$X_{out} = GN(X) = \gamma \frac{X - \mu}{\sqrt{\sigma^2 + \epsilon}} \tag{1}$$

$$W_\gamma = \{w_i\} = \frac{\gamma_i}{\sum_{j=1}^c \gamma_j}, i, j = 1, 2, \dots, C \tag{2}$$

$$W = Gate(Sigmoid(W_\gamma(GN(X)))) \tag{3}$$

where:

μ and σ are the mean and standard deviation of X , γ and β are trainable variables, and ϵ is a very small positive constant added for division stability. A larger γ represents greater variability between pixels, indicating richer spatial information.

The reconstruction operation adds features rich in information to those with less information, generating more informative features, thereby saving space. Using a cross-reconstruction operation, the weighted different information features are fully integrated to strengthen the information flow between them. Then, the cross-reconstructed features X^{w_1} and X^{w_2} are concatenated to produce a finely mapped spatial feature X^w , as indicated in equation (4):

$$\begin{cases} X_1^w = W_1 \otimes X, \\ X_2^w = W_2 \otimes X, \\ X_{11}^w \oplus X_{22}^w = X^{w_1}, \\ X_{21}^w \oplus X_{12}^w = X^{w_2}, \\ X^{w_1} \cup X^{w_2} = X^w. \end{cases} \tag{4}$$

where:

\otimes represents element-wise multiplication, \oplus is the summation of elements, and \cup is the union operation.

Applying SRU to the intermediate input feature X not only separates information-rich features from those with less information but also reconstructs them, enhancing representative features and suppressing redundant features in the spatial dimension.

(2) CRU - Channel Reconstruction Unit

The Channel Reconstruction Unit (CRU) utilizes a splitting transformation and fusion strategy to reduce redundancy in the channel dimension as well as computational costs and storage. The CRU structure is illustrated in Figure 5.

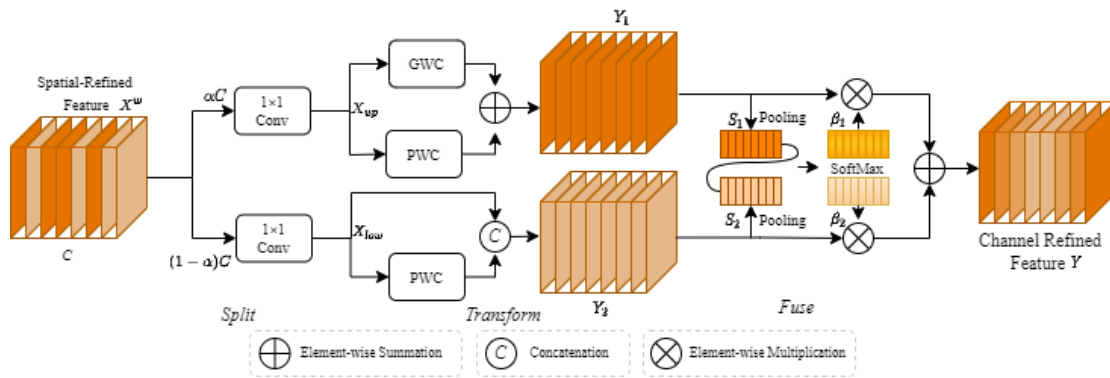


Fig. 5 - The architecture of Channel Reconstruction Unit

The splitting operation divides the input refined spatial features X^w into two parts, one with a channel count of αC and the other with a channel count of $(1-\alpha)C$, and then compresses the channel count of both groups of features using a 1×1 convolution, resulting in X_{up} and X_{low} .

The transformation operation takes the input X_{up} as the input for "rich feature extraction," undergoing GWC and PWC separately, and then the outputs are added to get the output Y_1 . The input X_{low} acts as a supplement for "rich feature extraction," undergoing PWC, and the result is combined with the original input to form Y_2 .

The fusion operation uses a simplified SKNet method to adaptively merge Y_1 and Y_2 . First, global average pooling is used to combine global spatial information and channel statistics, obtaining pooled S_1 and S_2 . Then, Softmax is applied to S_1 and S_2 to obtain feature weight vectors β_1 and β_2 , and finally, these feature weight vectors are used to produce the output $Y = \beta_1 Y_1 + \beta_2 Y_2$, Y as the refined channel features.

SCConv is a plug-and-play architectural unit that can be directly used to replace standard convolutions in convolutional neural networks. Incorporating SCConv into models can improve performance by reducing redundant features of maize pests and significantly lower the complexity and computational cost of the YOLOv8n model for maize pest detection, yielding better results in detecting small target maize pests.

Design of Maize Pest Detection Model Based on Improved YOLOv8n

Building on the structure of the YOLOv8n network, DAttention is added to the C2F module before the SPPF in the backbone network, and SCConv is added to the feature fusion network in the Head, following the C2F module. The improved YOLOv8n algorithm is illustrated in Figure 6.

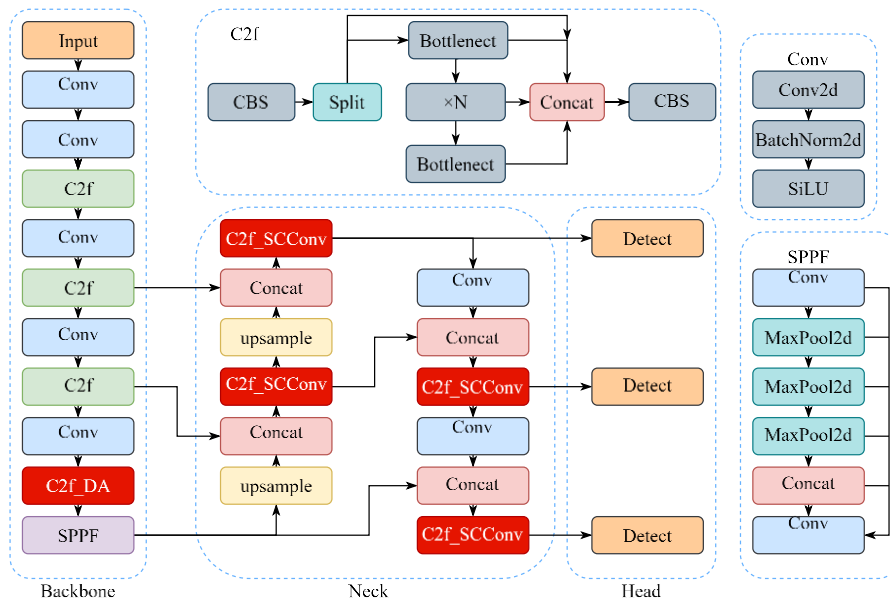


Fig. 6 - Improved YOLOv8n network structure

The introduction of the DAttention module enhances the feature extraction capability for maize pests. Initially, the YOLOv8n model extracts feature maps from the original maize pest images. Subsequently, the DAttention module is added to the C2F to enhance the extraction of features at smaller scales. This integration combines feature channels and spatial dimensions to form an attention mechanism. The focused range information from this attention mechanism is then multiplied with the input feature maps, allowing for adaptive feature refinement and thereby strengthening the feature extraction capability for maize pests.

The inclusion of SCConv enables simultaneous processing of both spatial (shape, structure) and channel (color, depth) information of images, making SCConv more precise and efficient in analyzing maize pest images. Embedded into the feature fusion network, SCConv increases detection precision for small targets, thereby enhancing the overall detection performance of the model.

Construction of the Experimental Dataset

The experimental dataset consists of 2,756 images of maize pests, including five types: aphids, mole crickets, wireworms, red spiders, and corn borers. The images of these five pest categories are shown in Figure 7. The dataset is divided into training, testing, and validation sets with a ratio of 7:1:2.



Fig. 7 - Images of corn pests
a) mole cricket; b) wireworm; c) corn borer; d) red spider; e) aphids

Configuration of the Experimental Environment

The experimental environment for this study is a Windows 10 system, with an Intel i7-11800H CPU, 16GB of RAM, and an RTX4060 (8GB) GPU. All models are implemented using PyTorch. Initially, frozen training is employed, where certain convolutional layer weights are kept unchanged to retain the features learned during the pre-training phase. This approach better adapts the model to the new dataset and helps prevent overfitting. Since the initial parameters of the original model are already optimal, the model is trained with the default initial network parameters to ensure stable training. The parameters are as follows: a confidence level of 0.5, 100 training epochs, a learning rate of 1×10^{-3} for the first 50 epochs with a batch size of 16, and a learning rate of 1×10^{-4} for the last 50 epochs with a batch size of 8. During the frozen training phase, fine-tuning is performed with a smaller batch size to avoid overfitting, which requires less GPU memory. In the unfrozen phase, normal training with larger GPU memory usage is performed, hence the batch size is set to 8 for the latter 50 epochs. The input image size for the model is 640×640 . The basic configuration of the local computer is shown in Table 1.

Table 1

| Basic configuration of the local computer | |
|---|-----------------------------|
| Computer Configuration | Specific parameters/version |
| operating system | Windows 10 |
| CPU | Intel i7-11800HQ |
| RAM | 12GB |
| GPU | NVIDIA RTX-4060(8G) |
| Python | 3.9 |
| PyTorch | 1.9.0 |
| CUDA | 11.3 |

Model Performance Evaluation Metrics

To validate the detection performance of images, the following model evaluation metrics are provided:

(1) **Precision (P)**: Precision measures the accuracy of the model and is defined as the proportion of true positive predictions out of all positive predictions made by the model.

The formula is as follows:

$$P = \frac{TP}{TP + FP} \tag{5}$$

(2) **Recall (R)**: Recall measures the comprehensiveness of the model and is defined as the proportion of true positives that were correctly identified by the model out of all actual positives. The formula is as follows:

$$R = \frac{TP}{TP + FN} \tag{6}$$

(3) **Average Precision (AP)**: Average Precision assesses the detection performance of the model by calculating the precision for each sample. The formula is provided below:

$$AP = \int_0^1 P(R) dR \tag{7}$$

(4) **Mean Average Precision (mAP)**: Mean Average Precision is a comprehensive evaluation metric that considers the precision of the model across different categories and is the average of the AP values across all categories. The formula is as follows:

$$mAP = \frac{1}{C} \sum_{i=1}^C AP_i \tag{8}$$

where:

AP_i represents the AP for an individual category, and C represents the total number of categories.

RESULTS

Analysis of the Experimental Process

The dataset images were input into the improved YOLOv8n model for training, with results shown in Figure 8. The loss curve displays the training errors over the dataset during training. For bounding box, category, and confidence losses, a sharp decline was observed in the first 10 iterations, indicating high learning efficiency. Subsequently, the loss curve gradually stabilized. Conversely, for accuracy and recall, the model initially showed good learning efficiency with rapid increases in values, achieving good average precision and recall rates within dozens of iterations, and then stabilizing in later iterations.

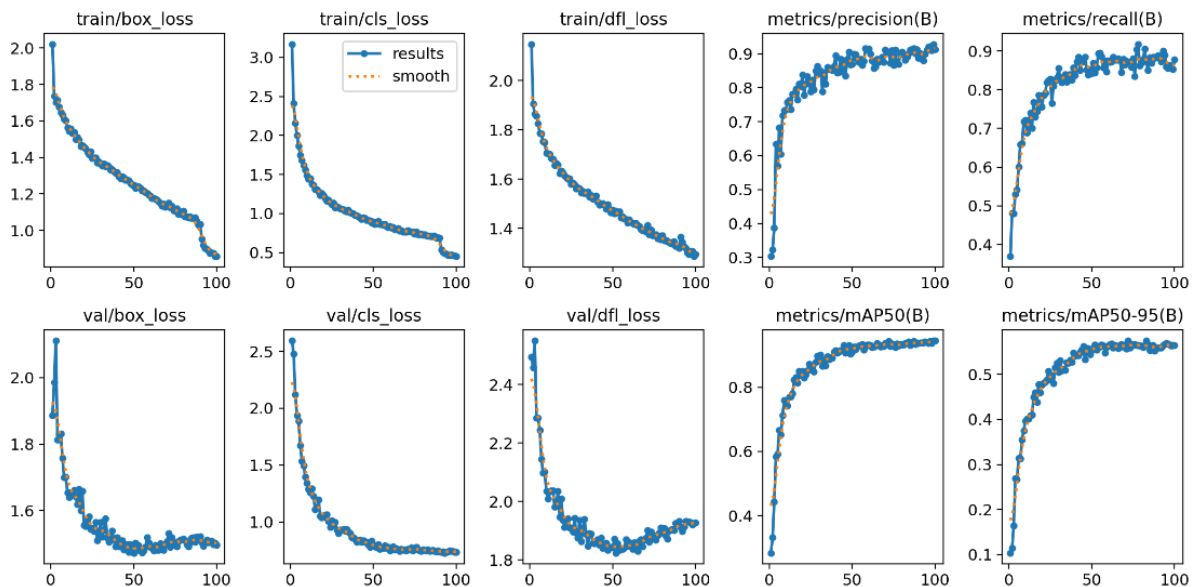


Fig. 8 - Loss function training results

Analysis of Experimental Results

To validate the performance of the improved YOLOv8n model in detecting five types of maize pests, 276 images were randomly selected for testing and evaluation with the improved algorithm. The experimental results are shown in Figure 9.

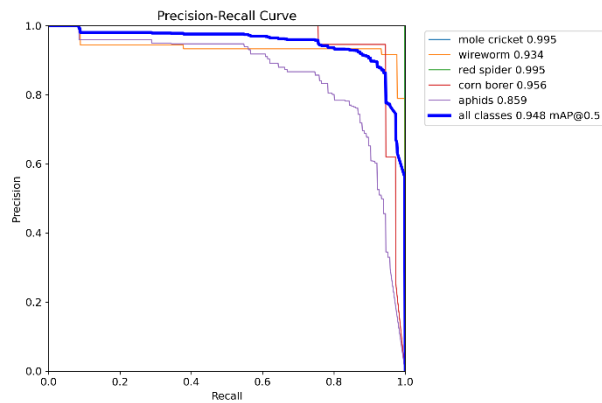


Fig. 9 - The mAP value of improve YOLOv8n

After incorporating the DAttention and SCCnov modules, the YOLOv8n algorithm achieved an mAP of 94.8%. Among these, the AP values for mole cricket and red spider were the highest at 99.5%, while the lowest AP value for aphids was 85.9%. The AP values for other maize pests ranged from high to low with corn borer at 95.6%, and wireworm at 93.4%. Overall, the improved YOLOv8n algorithm demonstrated good detection performance for maize pests. The significant difference in AP values between aphids and other pests is mainly due to their smaller size and higher color overlap with the maize background, resulting in relatively poorer detection performance. However, there was a 2.9% improvement compared to the original YOLOv8n algorithm.

To further demonstrate the detection effectiveness of the improved YOLOv8n algorithm on maize pests, a visual analysis was conducted on the five types of maize pests. The detection results are displayed in Figure 10, with detection boxes for mole cricket, aphids, red spider, corn borer, and wireworm colored in red, yellow, orange, peach, and pink, respectively. Predicted categories and confidence levels are displayed at the top left corner of each box.



Fig. 10 - Various pest detection results chart

As shown in Figure 10, despite complex backgrounds, small sizes of various maize pests, and some occlusions, the improved YOLOv8n algorithm accurately identified all five categories of maize pests. The highest confidence level was for the red spider at 90%, and the lowest was for the mole cricket at 75%. The detection boxes were also well-fitted, accurately locating and identifying each category of maize pests. Thus, the improved YOLOv8n algorithm provides accurate localization and identification of maize pests, demonstrating good detection performance on small and occluded targets across different categories.

MODEL COMPARATIVE ANALYSIS

To explore the performance enhancements brought by incorporating the DAttention attention mechanism and SCCnov module into the YOLOv8n model and to validate the effectiveness of each component, a comparative ablation study was conducted. The study analyzed the experimental data on precision, recall, mAP, and FPS during the training processes of YOLOv5, YOLOv8n, YOLOv8n with DAttention, YOLOv8n with SCCconv, and YOLOv8n with both DAttention and SCCconv. A comparison of the evaluation metrics for different models is shown in Table 2.

Table 2

| Comparison table of evaluation index parameters of different models | | | | | | |
|---|------------|--------|-------------|----------|-------|-----|
| Model | DAttention | SCConv | Precision/% | Recall/% | mAP/% | FPS |
| YOLOv5 | | | 94.5 | 78.3 | 86.4 | 128 |
| YOLOv8n | | | 89.3 | 98 | 92.7 | 181 |
| YOLOv8n | √ | | 87.2 | 98 | 93.8 | 185 |
| YOLOv8n | | √ | 89.6 | 97 | 93.2 | 169 |
| YOLOv8n | √ | √ | 93.2 | 93.5 | 94.8 | 171 |

As can be seen from Table 2, although the YOLOv5 model performs well in terms of precision, it has relatively lower recall, mAP, and FPS. YOLOv8n maintains high precision and recall, and also improves mAP and FPS, indicating that the YOLOv8n model has been optimized for accuracy and detection speed, making it more effective for detecting maize pest targets.

Introducing DAttention into YOLOv8n resulted in a slight decrease in precision from 89.3% to 87.2%, but an increase in mAP from 92.7% to 93.8%. This suggests that DAttention helps the YOLOv8n model better balance precision and recall overall, thus enhancing the mAP value. The addition of DAttention also reduces the computational load, leading to an increase in FPS.

Adding SCConv to YOLOv8n increased the precision to 89.6%, with a slight decrease in recall to 97%, and an improvement in mAP to 93.2%, but a decrease in FPS to 169. This shows that while SCConv improves precision, it has a minimal impact on recall but does reduce processing speed.

When both DAttention and SCConv are introduced into YOLOv8n, precision increased from 89.3% to 93.2%, and mAP reached the highest value of 94.8%. Meanwhile, FPS reached 171. The improved YOLOv8n algorithm sacrificed some detection speed, but achieved superior performance in detection accuracy.



(a) YOLOv8n;

(b) YOLOv8n-DAttention;

(c) YOLOv8n-SCConv;

(d) YOLOv8n-DAttentionSCConv

Fig. 11 - Different Model Detection Results

To validate the improvements of different models on the YOLOv8n algorithm, the detection effects of maize pests were analyzed subjectively through visual inspection. The detection results of the different models are shown in Figure 11.

From Figure 11, it is evident that different YOLOv8n models can accurately identify maize pests, with detection accuracies exceeding 70%. Among these, the original YOLOv8n model had the lowest recognition accuracy, while the YOLOv8n model with both DAttention and SCConv achieved the highest detection accuracy, with the bounding boxes more closely fitting the targets. However, the original YOLOv8n model experienced false detections when identifying corn borers, with one target being identified with two prediction boxes. The improved YOLOv8n model, with better integration of features from different scales of maize pests, more accurately recognized maize pests and enhanced detection performance.

Small datasets can limit the model from acquiring sufficient regularities and features, and changing the initial conditions or the presence of random disturbances can lead to model instability. Large datasets provide more information and training samples, which helps to learn sample features and improve model generalization, and also reduces the phenomenon of overfitting of the model to the dataset.

CONCLUSIONS

In response to the challenges posed by maize being susceptible to pest and disease damage, low yield, complex detection backgrounds, and the difficulty in identifying small-sized maize pests, this paper presents a multi-target detection method for maize pests based on the improved YOLOv8n. Initially, the DAttention module was introduced into the backbone network of YOLOv8n to enhance the model's feature extraction capabilities. Subsequently, the SCConv convolution was incorporated into the Head module to improve the model's feature fusion capabilities and to obtain richer feature information about maize pests. Ultimately, the proposed method was embedded into the YOLOv8n algorithm, achieving accurate detection of multiple categories of maize pests. Experimental results demonstrate that the improved YOLOv8n algorithm reached an mAP of 94.8%, an increase of 2.1% over the original YOLOv8n, although the FPS decreased from 181 to 171. The improved algorithm for multi-target detection of corn pests improves the accuracy, but the detection speed relatively decreases. Overall, the algorithm can meet the requirements of multi-target detection of corn pests.

In future research, the multi-class pest dataset can be increased, a larger dataset can be established for training, and the trained model can be applied to the identification and detection of various field pests. As the preliminary data labeling consumes a lot of time, online fast labeling can be established to reduce the preliminary preparation time. In terms of modeling, the model is made more lightweight by reducing the computational complexity and memory occupation of the model, and the lightweight complex model can be deployed on mobile detection equipment to achieve real-time on-site detection, which is convenient for agricultural technicians to use to prevent pests in time.

ACKNOWLEDGEMENT

This research, titled "Multi-Target Detection Method for Maize Pests Based on Improved YOLOv8n", was funded by Basic Scientific Research Expenses Project of Universities in Heilongjiang (2023-KYYWF-0571); Heilongjiang Province Excellent Young Teachers Basic Research Support Program (YQJH2023218); Key Laboratory Open Topics of Field Agricultural Equipment Engineering Technology in Heilongjiang(TJNY202302); Science and Technology Plan Innovation Incentive Program of Jiamusi (NY2023JL0006); Heilongjiang Province Department of Education Science and Technology Innovation Team Construction Plan Project (2021-KYYWF-0639).

REFERENCES

- [1] Al-Qizwini, M., Barjasteh, I., Al-Qassab, H., and Radha, H. (2017). Deep learning algorithm for autonomous driving using Google net. In *2017 IEEE Intelligent Vehicles Symposium (IV)*. IEEE.
- [2] Bochkovskiy, A., Wang, C.-Y., and Liao, H.-Y. M. (2020). Yolov4: Optimal speed and accuracy of object detection. *arXiv preprint arXiv:2004.10934*.
- [3] Ge, Z., Liu, S., Wang, F., Li, Z., and Sun, J. (2021). Yolox: Exceeding yolo series in 2021. *arXiv preprint arXiv:2107.08430*.
- [4] Hao, S., Ling, W., and Luquan, S. (2020). An improved SSD network model for rice pest identification. *Journal of Zhengzhou University (Science Edition)*, 52:49–54.
- [5] Hui, Z., Biao, H., and Hongjun, W. (2023). Research on pest identification algorithms in complex agricultural environments based on improved yolov7. *Journal of Agricultural Machinery*, 54:246–254.
- [6] Jun, H., Shuai, L., Jinming, S., Yue, L., Jingwei, W., and Peng, J. (2018). Facial expression recognition based on VGGNet convolutional neural network. In *2018 Chinese Automation Congress (CAC)*. IEEE.

- [7] Li, J., Wen, Y., and He, L. (2023). SCConv: Spatial and channel reconstruction convolution for feature redundancy. In *2023 IEEE/CVF Conference on Computer Vision and Pattern Recognition (CVPR)*. IEEE.
- [8] Lin, T.-Y., Dollár, P., Girshick, R., He, K., Hariharan, B., and Belongie, S. (2017). Feature pyramid networks for object detection. In *2017 IEEE Conference on Computer Vision and Pattern Recognition (CVPR)*. IEEE.
- [9] Liu, S., Qi, L., Qin, H., Shi, J., and Jia, J. (2018). Path aggregation network for instance segmentation. In *2018 IEEE/CVF Conference on Computer Vision and Pattern Recognition*. IEEE.
- [10] Maican, E., Iosif, A., and Maican, S. (2023). Precision corn pest detection: Two-step transfer learning for beetles (coleoptera) with MobileNet-SSD. *Agriculture*, 13(12):2287.
- [11] Qi, C., Liudi, Y., and Qiuling, W. (2021). Monitoring and analysis of lepidopteran pests during the flowering and grain-filling stages of summer maize in luohu city. *Shandong Agricultural Sciences*, 53:105–110.
- [12] Redmon, J., Divvala, S., Girshick, R., and Farhadi, A. (2016). You only look once: Unified, real-time object detection. In *2016 IEEE Conference on Computer Vision and Pattern Recognition (CVPR)*. IEEE.
- [13] Redmon, J. and Farhadi, A. (2017). Yolo9000: Better, faster, stronger. In *2017 IEEE Conference on Computer Vision and Pattern Recognition (CVPR)*. IEEE.
- [14] Redmon, J. and Farhadi, A. (2018). Yolov3: An incremental improvement. *arXiv preprint arXiv:1804.02767*.
- [15] Ren, S., He, K., Girshick, R., and Sun, J. (2017). Faster R-CNN: Towards real-time object detection with region proposal networks. *IEEE Transactions on Pattern Analysis and Machine Intelligence*, 39(6):1137–1149.
- [16] Ronghua, Z., Xue, B., and Jiangchuan, F. (2024). Pest target detection algorithm in complex scenes: YOLOv8-extend. *Smart Agriculture (Bilingual)*, pages 1–14.
- [17] Targ, S., Almeida, D., and Lyman, K. (2016). Resnet in Resnet: Generalizing residual architectures. *arXiv preprint arXiv:1603.08029*.
- [18] Tian, H., Wang, T., Liu, Y., Qiao, X., and Li, Y. (2020). Computer vision technology in agricultural automation—a review. *Information Processing in Agriculture*, 7(1):1–19.
- [19] Wang, C.-Y., Bochkovskiy, A., and Liao, H.-Y. M. (2023). YOLOv7: Trainable bag-of-freebies sets new state-of-the-art for real-time object detectors. In *2023 IEEE/CVF Conference on Computer Vision and Pattern Recognition (CVPR)*. IEEE.
- [20] Xiaoyu, T., Qiuchi, X., and Xiaoning, H. (2023). Agricultural pest detection based on improved YOLOv5. *Journal of South China Normal University (Natural Science Edition)*, 55:42–49.
- [21] Xinlu, J., Tian'en, C., and Cong, W. (2023). A review of deep learning algorithms for agricultural pest detection. *Computer Engineering and Applications*, 59:30–44.
- [22] Xintao, D., Shen, W., and Qing, Z. (2023). Research on detection methods for major pests of summer maize based on improved YOLOv4. *Shandong Agricultural Sciences*, 55:167–173.
- [23] Xu, W., Li, W., Wang, L., and Pompelli, M. F. (2023). Enhancing corn pest and disease recognition through deep learning: A comprehensive analysis. *Agronomy*, 13(9):2242.
- [24] Yuan, Z.-W. and Zhang, J. (2016). Feature extraction and image retrieval based on AlexNet. In Falco, C. M. and Jiang, X., editors, *Eighth International Conference on Digital Image Processing (ICDIP 2016)*. SPIE.
- [25] Zhang, C., Hu, Z., Xu, L., and Zhao, Y. (2023). A YOLOv7 incorporating the Adan optimizer based corn pests identification method. *Frontiers in Plant Science*, 14.
- [26] Zhang, W., Sun, Y., Huang, H., Pei, H., Sheng, J., and Yang, P. (2022). Pest region detection in complex backgrounds via contextual information and multi-scale mixed attention mechanism. *Agriculture*, 12(8):1104.
- [27] Zhu, R., Hao, F., and Ma, D. (2023). Research on polygon pest-infected leaf region detection based on YOLOv8. *Agriculture*, 13(12):2253.
- [28] Zhu, X., Su, W., Lu, L., Li, B., Wang, X., and Dai, J. (2020). Deformable DETR: Deformable transformers for end-to-end object detection. *arXiv preprint arXiv:2010.04159*.
- [29] Zhu, Y. and Newsam, S. (2017). DenseNet for dense flow. In *2017 IEEE International Conference on Image Processing (ICIP)*. IEEE.
- [30] Zongwang, L., Shuaixin, Q., and Fuyan, S. (2023). Lightweight grain storage pest detection method based on improved YOLOv5s. *Journal of the Chinese Cereals and Oils Association*, 38:221–228.

MECHANICAL PROPERTIES OF CERASUS HUMILIS AT DIFFERENT TEMPERATURES FOR POSTHARVEST DAMAGE ANALYSIS

欧李采后在不同温度下的力学特性研究分析

Bin TONG, Junlin HE^{*}), Jingpu ZHOU, Tao WANG, Huhu YANG
 College of Agricultural Engineering, Shanxi Agricultural University, Taigu / China;
 Tel: +86-0354-6288400; E-mail: hejunlin26@126.com
 Corresponding author: Junlin He
 DOI: <https://doi.org/10.35633/inmateh-73-20>

Keywords: mechanical damage, postharvest treatment, *Cerasus humilis*, temperature, mechanical properties

ABSTRACT

In this study, the mechanical properties of three varieties of *cerasus humilis* at different temperatures were systematically investigated by whole fruit puncture test, exocarp uniaxial tensile test and mesocarp uniaxial compression test. It was found that puncture test could not only reflect the shear mechanics of the exocarp in vivo at the tissue level, but also characterize the resistance level of fruit to puncture damage at the macro level. The environmental temperature had significant negative and positive effects on puncture failure stress and puncture failure deformation of *cerasus humilis* ($p < 0.05$). The stress and elastic modulus of exocarp tension and mesocarp compression were significantly affected by ambient temperature ($p < 0.05$). This study combined with temperature change to study the mechanical properties of *cerasus humilis* provides a necessary theoretical basis for the prediction of fruit damage and the development of postharvest treatment equipment.

摘要

本文采用全果穿刺试验、外果皮单轴拉伸试验和中果皮单轴压缩试验，系统研究了3个欧李品种在不同温度下的力学特性研究。穿刺试验结果反映了环境温度对欧李穿刺破坏应力和穿刺破坏变形分别有显著的负向和正向影响($p < 0.05$)。研究发现，穿刺试验不仅能在组织水平上反映果皮在体内的剪切力学，而且能在宏观水平上表征果实对穿刺损伤的抵抗水平。而外果皮拉伸试验和中果皮压缩试验结果反映了环境温度对欧李外果皮拉伸和中果皮压缩的破坏应力和弹性模量有显著的负向影响($p < 0.05$)。本研究以温度为自变量研究欧李的力学特性，为预测欧李的损伤和后续分拣储存运输等处理设备的改进提供重要的理论基础。

INTRODUCTION

Cerasus humilis, in the world distribution is mainly concentrated in the north of China's thirteen provinces, municipalities and autonomous region (Liu *et al.*, 2005). Its pulp contains 17 amino acids needed by the human body and a large number of vitamin C, vitamin B2, vitamin E and potassium, phosphorus, zinc, selenium and other minerals, and it is one of the fruits with the highest calcium content (Li.,2015). In addition to its nutrient rich characteristics, the root system of *cerasus humilis* is well-developed and can grow under adverse conditions such as drought and low temperature. It plays an important role in preventing soil erosion and protecting the soil and sand (Liang *et al.*, 2008; Liu *et al.*, 2013). At present, the bottleneck that restricts the development of the *cerasus humilis* industry in China is mainly the backwardness of harvesting methods and grading, packaging and transportation machines, resulting in mechanical damage to the fruit. Therefore, basic research on mechanical damage of *cerasus humilis* has become very urgent (Zhang *et al.*, 2018).

For the research on the mechanical properties of fruits, there were relevant studies on apples as early as 2008. The researchers used methods of stretching the exocarp and compressing the mesocarp to study the mechanical properties of fruits such as apples, tomatoes and cherries (Li *et al.*, 2012; Alamar *et al.*, 2008; An *et al.*, 2020). In the meantime, a large number of systematic studies on the tissue mechanics of other fruits have shown that environmental temperature can affect the mechanical properties of various fruits (De *et al.*, 2015; Desmat *et al.*, 2002). For example, in the study of tomatoes, cherries and bayberries, it was found that temperature had a significant negative effect on the failure stress, elastic modulus and failure energy of the mesocarp (Han *et al.*, 2022; Lana *et al.*, 2005; Yang *et al.*, 2007).

Bin Tong, As.M.S.Stud.; Junlin He, Prof.Ph.D.Eng.; Jinpu Zhou, As.M.S.Stud.; Tao Wang, As.M.S.Stud.; Huhu Yang, As.M.S.Stud

Nevertheless, the study of the sensitivity of the mechanical properties of *Cerasus humilis* to ambient temperature is still very rare in the world. Only a few studies have investigated the basic physical and mechanical properties of *Cerasus humilis* (Bin *et.al*, 2020; Shaohua *et.al*, 2021). For example, in Shilei's paper, only the compressive failure mechanical properties and elastic modulus of whole fruit were investigated (Shilei *et.al*, 2023). For the exocarp and mesocarp and the influence of temperature on the mechanical properties of differences, more in-depth research was not done.

However, the harvest period of *Cerasus humilis* is usually from early August to October, and the process from orchard picking to market sales of *Cerasus humilis* requires many processing operations, such as orchard picking, sorting and packaging, transportation and storage, which can expose these *Cerasus humilis* fruits to different environmental temperatures. Therefore, the study of *Cerasus humilis* mechanical properties combined with temperature change is necessary, which can provide a vital theoretical basis for fruit damage prediction and the development of postharvest treatment equipment.

MATERIALS AND METHODS

Materials

The materials for this experiment were selected from the fruits of three varieties of *Cerasus humilis*: Nongda No.5, Nongda No.6, and Nongda No.7. The ripening period of the *Cerasus humilis* is divided into two stages: the orange-red stage and the bright red stage, and in order to ensure the quality of the *Cerasus humilis* during transportation and storage, the usual choice was to pick it during the orange-red period. That's why it was chosen to pick *Cerasus humilis* fruits during the orange-red period and then they were inspected to make sure that the fruits were intact and not damaged by hand-picking or damaged by pests or diseases. The experiment required the harvesting of approximately 300 similarly sized *Cerasus humilis* fruits to be used for the study. Subsequently, after cleaning and drying the surface of the picked *Cerasus humilis* samples, they were transported back to the laboratory and stored in the laboratory freezer, with a storage temperature set at 5°C.

Determination of puncture mechanical properties

Test setup

All possible ambient temperatures to which *Cerasus humilis* may be exposed from the time of picking to the time of sale are usually between 5~35°C. Therefore, three temperatures, 5°C, 20°C and 35°C, were chosen as independent variables for this experimental design. A constant temperature and humidity chamber (Zhongwei Instrument Co., Ltd., Guangdong, China) was chosen for storing the *Cerasus humilis* fruits in order to achieve the three ambient temperatures set for the experiment. The storage time for each group of *Cerasus humilis* specimens was 30 minutes and all tests were carried out at 60% relative humidity to ensure that the conditions required for the tests were achieved (Alique *et.al*, 2005). In this experimental study, 30 samples of each of the three varieties of *Cerasus humilis* were used, for a total of 90 *Cerasus humilis* samples, and each of these *Cerasus humilis* samples was randomly assigned into three groups of 10 *Cerasus humilis* fruits each. And these samples were used to complete the puncture test.

Puncture test

The instrument used for the puncture test was a texture analyzer (Chaotech Instruments Co., Ltd., Xiamen, China). The procedure of the puncture test was as follows: firstly, one fruit was randomly removed from a sample group of *Cerasus humilis* in a constant temperature and humidity chamber, for example, one from the group with the temperature set to 5°C was taken. Considering the influence of external environmental temperature, only one *Cerasus humilis* fruit was selected for each experiment, and the experimental time was controlled to be about 1 minute. Next, the displacement of each experiment was set to 15% deformation, and the puncture position was selected at the bottom of the fruit (Fig.1.a). The testing mode of this puncture test was compression, with a pretest speed of 2 mm/s, a mid-test speed of 0.5 mm/s, and a post-test speed of 10 mm/s. The load trigger force was 0.05 N, and the probe was P2. During the test, the penetration force and displacement data have been recorded in real time by the texture analyzer. Finally, formulas (1) and (2) were used to calculate the puncture failure force and puncture failure energy of *Cerasus humilis* fruits:

$$\sigma_p = \frac{F_{p\max}}{A} \quad (1)$$

$$E_{prec} = \int_0^{D_{p\max}} F dD \quad (2)$$

In the formulas: σ_p - puncture failure stress, MPa; F_{pmax} - peak puncture force, N; A - bottom area of puncture probe, mm²; E_{prec} - puncture failure energy, mJ; D_{pmax} - puncture failure deformation, mm; F - real-time puncture force, N; D - real-time probe displacement, mm.

Determination of tissue mechanical properties

Test setup

As with the puncture test, for the study of the tissue mechanical properties of *Cerasus humilis*, three temperatures were also set, 5°C, 20°C and 35°C, as independent variables. Humidity was set at 60%. The time for storage of each set of samples was similarly set at 30 minutes. Again, in order to minimize the influence of external factors, only one sample was taken in a single experiment and the experiment time was kept to no more than 1 minute as far as possible. The experiment entailed each *Cerasus humilis* fruit being made into a standard exocarp or mesocarp sample. In order to investigate the effects of different varieties and ambient temperatures on the tissue mechanical properties of *Cerasus humilis*, all samples were divided into 2 tissue types × 3 varieties × 3 temperatures for a total of 18 groups. Each group was allocated 10 fruit samples to be used for replicated tests. A total of 180 *Cerasus humilis* fruits were used in this experiment (Han et al, 2022).

Tensile test of exocarp

For the tensile test, nine sets of fruit samples (3 varieties×3 temperatures) were selected as materials for the tensile test. The steps for a single experiment were: firstly, one fruit sample was randomly selected from the constant temperature and humidity chamber at some set temperature for each experiment. Next, the one was made into an exocarp sample with a length of 50 mm and a width of 7 mm. Preparation of exocarp samples began with a circular cut along the center transverse section of the fruit using a circular cut fruit knife to obtain a circular cut slightly larger than the standard sample size. A blade was then used to cut a standard exocarp sample of 7 mm in width and 50 mm in length from the annular section along the direction of the equatorial cross-section. Finally, the mesocarp residue was removed from the exocarp sample and the standard sample preparation was completed. The prepared samples were immediately subjected to exocarp tensile test using an electronic universal material testing machine (INSTRON, Boston, the USA) until fracture (Fig.1.b). The testing mode of this experiment was tension, and the testing speed was set to 1 mm/s. The electronic universal testing machine has recorded the test data of tensile force and displacement in real time. Finally, using the following formulas to calculate the mechanical parameters such as the elastic modulus of the exocarp (Li et al, 2012). Each set of experiment requires 10 repetitions.

$$\sigma_e = \frac{F_{e\max}}{wd} \quad (3)$$

$$\varepsilon_e = \frac{\Delta L}{L} \quad (4)$$

$$E_e = \frac{\sigma_e}{\varepsilon_e} \quad (5)$$

$$E_{rece} = \int_0^{\Delta L} F_e d\Delta L \quad (6)$$

In the formulas: σ_e - tensile failure stress of exocarp, MPa; $F_{e\max}$ - peak tensile force of exocarp, N; w - cross-sectional width of exocarp, mm; d - cross-sectional thickness of exocarp, mm; ε_e - tensile failure strain of exocarp; ΔL - The difference in length of the exocarp before and after the tensile test, mm; L - initial length of exocarp, mm; E_e - Tensile modulus of elasticity of exocarp, MPa; E_{rece} - Elongation loss efficiency of exocarp, mJ; F_e - actual tensile strength of the exocarp, N.

Compression test of mesocarp

The compression test of the mesocarp of *Cerasus humilis* fruit could be generally referred to the steps of the tensile test of the exocarp. Preparation of mesocarp samples was also done by using the blade to cut out standard samples of 10 mm length by 7 mm width by 5 mm height. It is important to note that samples should be ensured that the exocarp has been completely removed before the compression test is carried out. One *Cerasus humilis* fruit was removed from the constant temperature and humidity chamber and prepared as a standard mesocarp sample.

Immediately thereafter, a downward compression test was performed along the vertical axis of the device using the P36R probe of the texture analyzer (Fig.1.c). Set the pre-test speed to 2 mm/s, the speed during the test to 1 mm/s, and the post-test speed to 10 mm/s. And set the load triggering force to 0.05 N and the deformation to 70%. The compression force and displacement test data have been recorded in real time by the texture analyzer, and then mechanical parameters such as the elastic modulus of the mesocarp were calculated using formulas similar to (3) to (6).

Statistical analysis

Statistical analysis was conducted using SAS9.4 software (SAS Software Research Institute, USA), using multiple analysis of variance (MANOVA) and Pearson correlation analysis. The minimum significant difference method was used for multiple comparisons, and the significance level was set to 0.05.

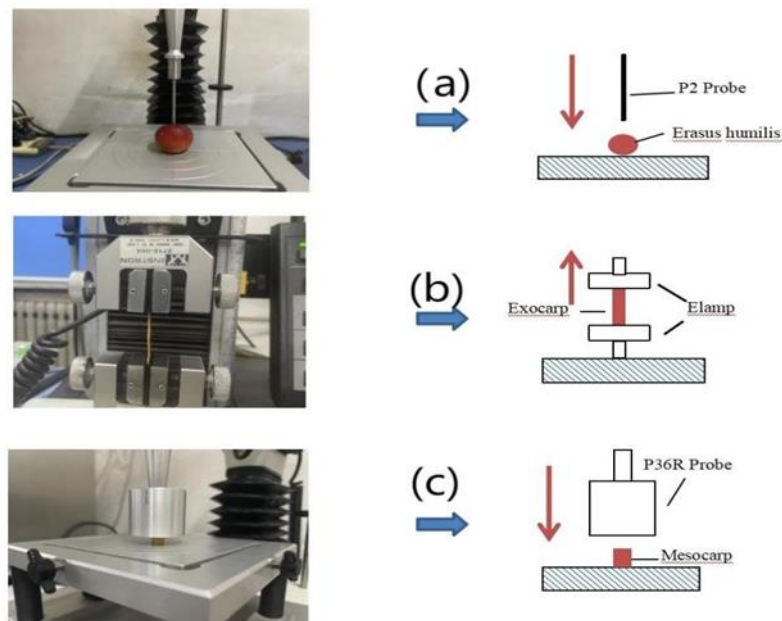


Fig. 1 - (a) Puncture test of *Cerasus humilis*; (b) Tensile test of exocarp; (c) Compression test of mesocarp

RESULTS

Mechanical properties of *cerasus humilis*

Puncture force displacement curve of *Cerasus humilis*

Figure 2.a shows the puncture force displacement curve of the *cerasus humilis* sample during the puncture test. From the beginning, the curve rose nearly linearly until it reached the peak point A, which indicated the beginning of rupture of the exocarp of *cerasus humilis*. In contrast, this phase of linear relationship between puncture force and displacement reflected the role of the exocarp and mesocarp in jointly resisting the externally applied puncture load. The shaded part in the figure represented the puncture failure energy. The abscissa of the peak point was the puncture failure deformation (displacement of the probe at the time of puncture failure), which was the maximum shear deformation allowed for the entire puncture process of the exocarp of *cerasus humilis* in order not to rupture. The ordinate of the peak point was the peak puncture force, which was the maximum shear force that the exocarp of *cerasus humilis* experienced before it ruptured.

And at this stage AB in the figure, the curve dropped sharply, which indicated that the exocarp has failed and only the mesocarp was left to resist for the external puncture load. At the same time, it is easy to see that the resistance of the mesocarp was much less than the combined resistance of the exocarp and mesocarp. Therefore, the exocarp played a crucial role in resisting puncture damage and protecting the *cerasus humilis* fruit (Costa *et.al*, 2016). The puncture force curve of the BC segment gradually flattened in the later stage, demonstrating the resistance of the mesocarp to external puncture loads in the absence of the exocarp.

The effect of temperature

Based on the puncture tests conducted on three different varieties of Nongda No. 5, Nongda No. 6 and Nongda No. 7 at 5°C, 20°C and 35°C, respectively, the relevant experimental data obtained are shown in Figure 2. b, c, d. In order to be able to accurately and consistently depict the discrete distribution of the experiment data, independent of outliers, the figure is presented as a box plot.

For the data obtained, SAS software was used for processing and data was analyzed using MANOVA and Pearson correlation analysis.

The results showed that the puncture failure stress of *Cerasus humilis* was significantly affected ($p < 0.05$) by changes in temperature. The puncture failure stress at 5°C was 1.70, 1.58 and 1.52 times higher than that at 35°C for Nongda No.5, Nongda No.6 and Nongda No.7, respectively. The ability of the exocarp of *Cerasus humilis* to resist external puncture forces could be assessed using puncture failure stress values. The exocarp of *Cerasus humilis* consists of a cuticle and several layers of dermal cells. The cuticle is a composite biopolymer composed mainly of amorphous polyesters, trace waxes and hydrolyzed polysaccharides (Fich *et al.*, 2016). At low temperatures, the polyester that formed keratin maintains limited rotational and vibrational degrees of freedom, as well as limited translational motion, while at high temperatures, it becomes more porous, allowing translational motion between the long hydrocarbon chains of the keratin network (Matas *et al.*, 2004). The decrease in exocarp puncture failure stress with increasing temperature may be attributed to this phenomenon.

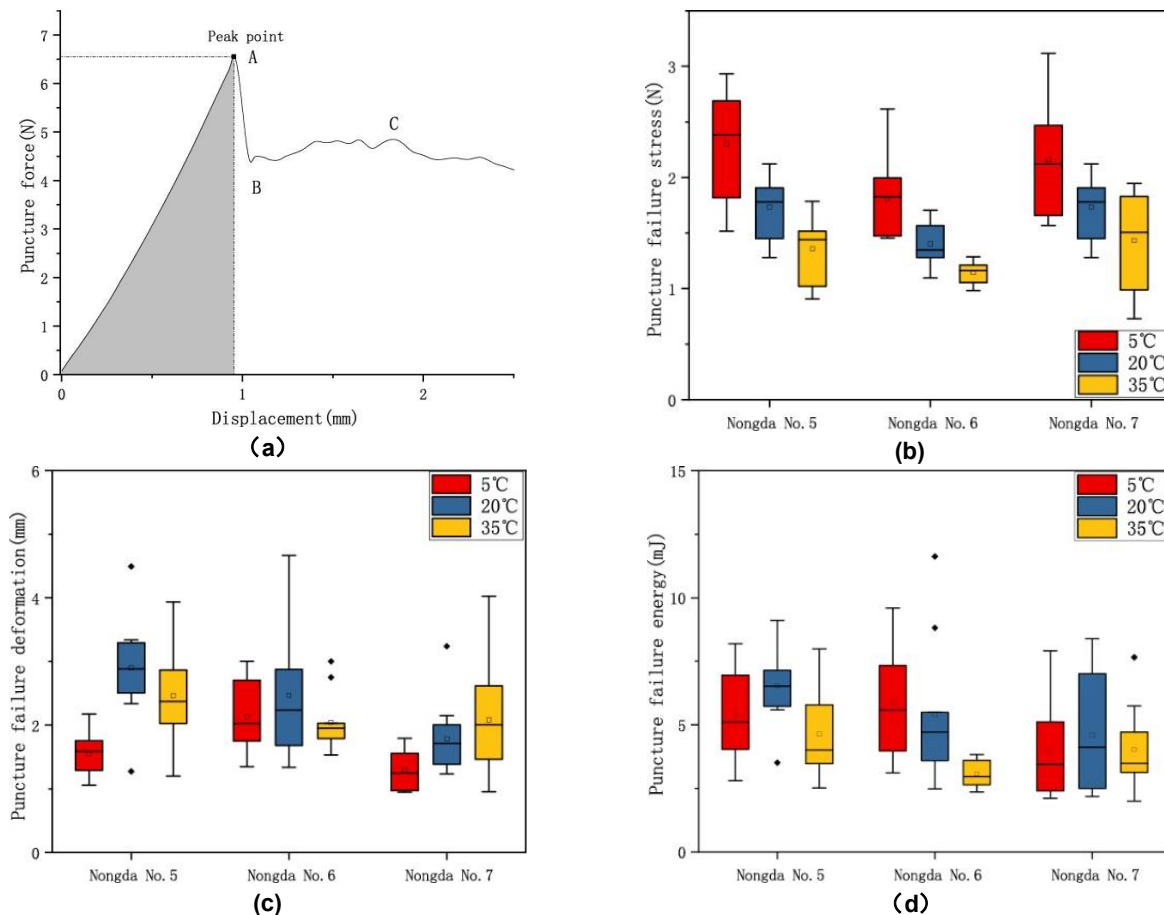


Fig. 2 - (a) Puncture force-deformation curve; (b)~(d) Result of fruit puncture tests at different ambient temperatures - puncture failure stress, puncture failure deformation and puncture failure energy

The change in temperature also had a significant effect ($p < 0.05$) on the puncture failure deformation of Nongda No.5 and Nongda No.7. The effect on them was that their puncture failure strain decreases with the increase of temperature. However, the puncture failure deformation of Nongda No.6 at 5~35°C seems to be inconsistent with this rule. The probe displacement of Nongda No.5, Nongda No.6 and Nongda No. 7 when puncture failure occurred at 35°C was 1.59, 0.97 and 1.62 times that at 5°C. The pericarp of *Cerasus humilis* consists of two layers: the exocarp is on the outside, and the mesocarp is between the exocarp and the core. In the process of puncture, the probe first applied puncture force to the exocarp, and the exocarp was supported by the lower mesocarp. Therefore, the displacement of the probe when the puncture failed indicates the comprehensive resistance of the exocarp and mesocarp to the external puncture force. The higher displacement of the probe during puncture failure indicated that the exocarp was malleable while the mesocarp was soft. The mesocarp of *Cerasus humilis* is composed of many cells, and its cell wall is mainly composed of cellulose. Its polysaccharide matrix is formed by pectin binding to proteins through Ca^{2+} bridges (Posé *et al.*, 2019).

As the temperature increased, the viscosity of pectin and cellulose decreased, and the adhesion between cells weakened, resulting in a paste like appearance of the mesocarp under external mechanical puncture (Karatas *et al.*, 2016). According to the experimental results, in general, the mechanical properties of the mesocarp and exocarp were affected by temperature to some extent. So, it can be stated that the temperature affected the puncture failure deformation of *Cerasus humilis*.

In addition, the temperature did not significantly affect ($p > 0.05$) the puncture failure energy of Nongda No.5 and Nongda No.7. Nevertheless, it had a significant effect on the puncture failure energy of Nongda No.6 ($p < 0.05$). Figure 2.a shows that when the puncture failure energy reached its peak, the shadow area surrounding the curve was the puncture failure energy. According to formulas (1-4), it can also be seen that the peak puncture force and its corresponding real-time probe displacement determine the puncture failure energy during the puncture process. Therefore, the puncture failure energy in the process of *Cerasus humilis* puncture would be affected by the puncture force and puncture failure deformation. This result seems to explain that the puncture failure energy of Nongda No.5 and Nongda No.7 was not affected by the temperature, but the temperature had a negative impact on the puncture failure energy of Nongda No.6. In summary, the puncture test could reflect the ability of *Cerasus humilis* to resist puncture damage. Therefore, data such as puncture failure stress could be obtained through puncture tests, and was used as an indicator to evaluate the ability of this *Cerasus humilis* to resist puncture damage.

Tissue mechanical properties of *Cerasus humilis* Organizational loading force displacement curve

According to Figure 3, when the tensile test began, the exocarp began to deform under the action of the universal testing machine. The curve of the tensile force from the beginning to the peak of the tensile force was approximately linear. After reaching the peak point, the tensile force began to decline sharply, indicating that the exocarp had completely broken. And what happened was that the tension decreased very quickly to zero after the break. The peak tensile value and the maximum tensile deformation value were the vertical and horizontal coordinates of this point respectively, and the shadow area surrounded by the curve before the peak tensile value represented the tensile failure energy. During the compression process of the mesocarp, its phenomenon was similar to the tensile test of exocarp. The curve also raised linearly, and the compressive force gradually decreased after reaching the peak point. But a little differently, the force did not decrease to zero. Subsequently, the curve showed an upward trend. This phenomenon indicated that at the peak point, the mesocarp tissue was partially damaged and several cracks were produced. The external load continued to be applied, leading to crack propagation. The reason why the compression force did not decrease to 0 was that there were still residual tissues that can withstand external forces after local damage to the mesocarp. As the compression deformation gradually expanded, the contact area of the sample under compression was increasing, which led to an upward trend in the subsequent compression force curve. The peak compressive force and maximum compressive deformation values are the vertical and horizontal coordinates of the first peak point, respectively, while the compressive failure energy is the shadow area enclosed by the curve before the first peak point.

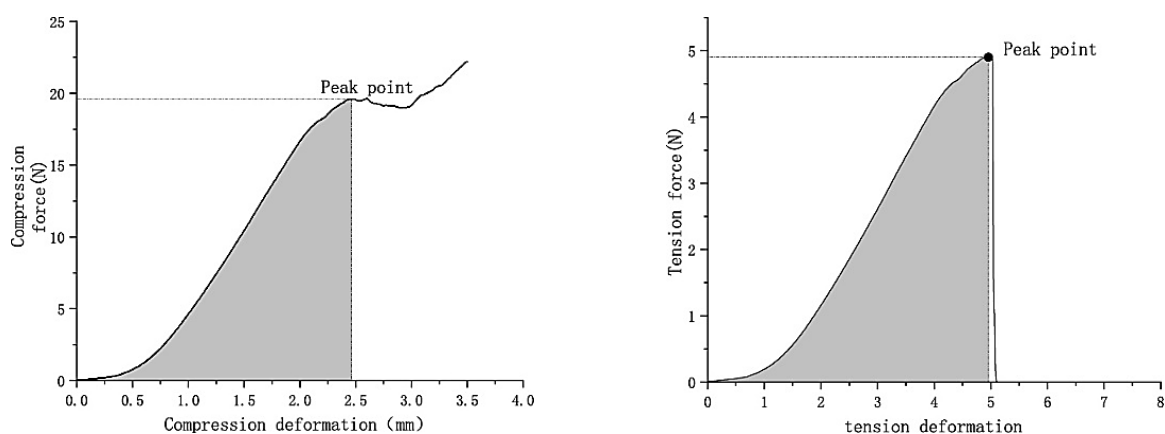


Fig. 3 - Compression force - compression deformation and tension force - tension deformation

Mechanical properties of exocarp during stretching process

The mechanical properties of the exocarp of three varieties of *Cerasus humilis* fruits subjected to tensile tests under three different temperature conditions are shown in Figure 4. The tensile failure stress of the exocarp of *Cerasus humilis* was significantly affected by temperature ($p < 0.05$) and decreased with increasing temperature. The tensile failure stress of the exocarp of Nongda No.5, Nongda No.6 and Nongda No.7 at 5°C was 1.21, 1.57 and 1.52 times higher than that at 35°C, respectively. In addition, temperature had a significant positive effect ($p < 0.05$) on the tensile failure strain of the exocarp of Nongda No.5 and Nongda No.7, with the tensile failure strains of the exocarp of Nongda No.5 and Nongda No.7 at 35°C being 1.71 and 1.42 times higher than that at 5°C. The failure strain is related to the ductility of the exocarp, so the test results seem to indicate that temperature can raise this property.

Like the tensile failure stress, the tensile elastic modulus of the exocarp of *Cerasus humilis* was also significantly ($p < 0.05$) affected by temperature, decreasing as temperature increased. The tensile modulus of elasticity of the exocarp of Nongda No.5, Nongda No.6 and Nongda No.7 varied from 14.48 ~ 6.41 MPa, 9.30 ~ 4.93 MPa, and 15.00 ~ 7.07 MPa, respectively, within the range of temperature change from 5°C to 35°C. The tensile modulus of elasticity of the exocarp of Nongda No.5, Nongda No.6 and Nongda No.7 at 5°C was 2.26, 1.89 and 2.12 times higher than that at 35°C, respectively. Moreover, the effect of temperature on the tensile failure energy of the exocarp of the three *Cerasus humilis* species can be seen in Figure 4. However, the tensile damage energy of the exocarp of Nongda No.5, Nongda No.6 and Nongda No.7 was not significantly affected by temperature ($p > 0.05$).

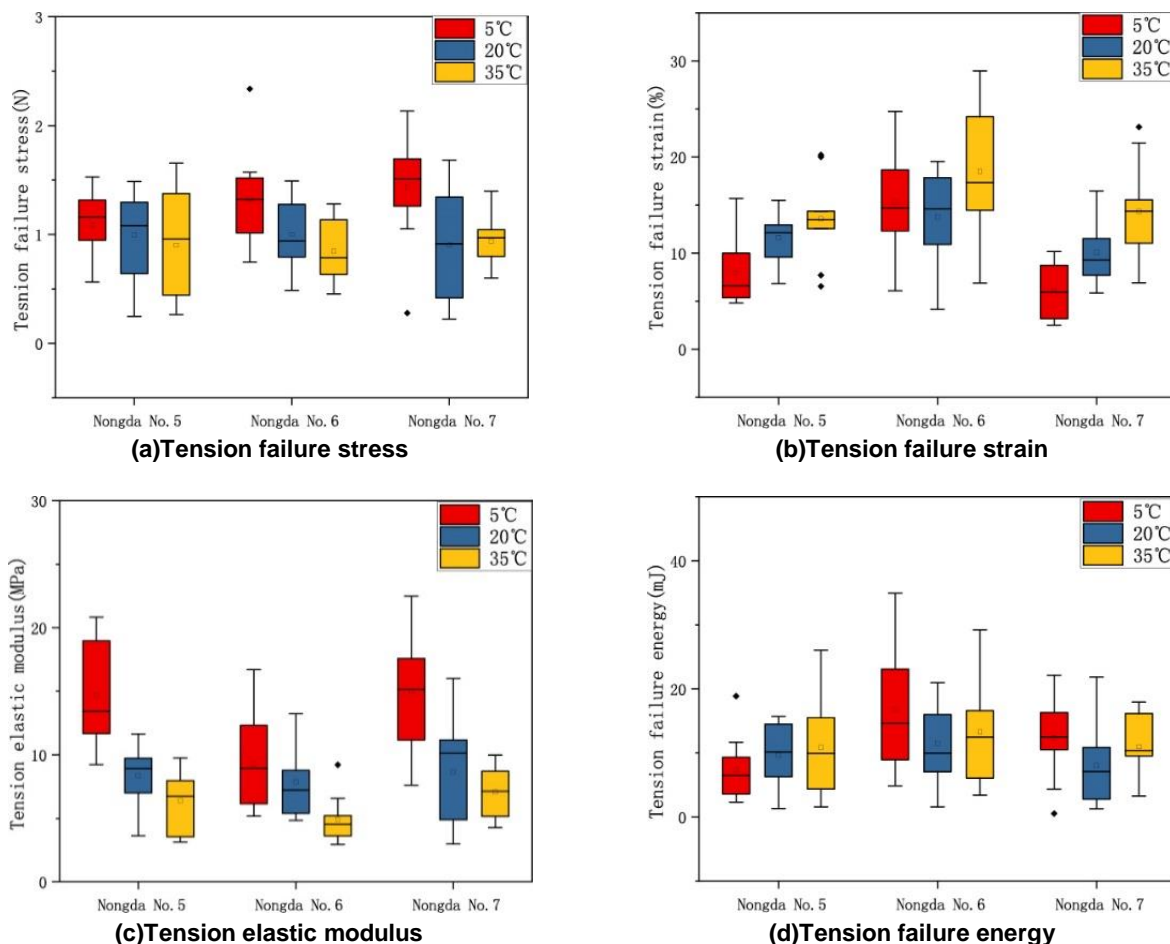


Fig. 4 - Mechanical properties of *Cerasus humilis* exocarp during tension test

It is easy to see that the tensile mechanical properties of the exocarp of different varieties of *Cerasus humilis* were different at different temperatures. During stretching, the rupture of the exocarp specimen at the macroscopic level was actually the rupture of the cuticle of the exocarp specimen, while at the microscopic level it was the separation of the dermal cell layers of the exocarp specimen from each other.

Since the microstructural morphology of the cuticle network and the viscosity of the pectin in the cell wall could be affected by temperature (Brüggenwirth *et al.*, 2016), which in turn affected the state of movement of the exocarp during stretching. The higher the temperature, the less viscous the pectin in the cell wall of the exocarp, and the easier it was for neighboring cells to segregate. This was characterized on a macroscopic level by a reduction in tensile force. So, it can be affirmed that temperature was significantly affecting the tensile mechanical properties of the exocarp of *Cerasus humilis*.

Mechanical properties of mesocarp during compression

The tissue mechanical properties of mesocarp of three varieties of *Cerasus humilis* fruits when subjected to compression tests at three different ambient temperature conditions are shown in Figure 5. As in the case of exocarp stretching, temperature also significantly affected ($p < 0.05$) the compressive failure stress of the mesocarp of *Cerasus humilis*. The compressive failure stress of mesocarp decreased with increasing temperature. The compression failure stress of the mesocarp of Nongda No.5, Nongda No.6 and Nongda No.7 *Cerasus humilis* at 5°C was 3.47, 2.27 and 1.52 times higher than that at 35°C, respectively.

There was a significant negative correlation ($p < 0.05$) between the compression failure strain of mesocarp of Nongda No.7 and the ambient temperature, whereas the ambient temperature did not significantly affect the compression failure strain of mesocarp of Nongda No.5 and Nongda No.6 *Cerasus humilis* ($p > 0.05$). With reference to the mesocarp compression test of tomato, the maturity of the tomato fruit and the type of force applied affect the magnitude of the compressive strain. Therefore, the reason for this test result may be the different shape of mesocarp cells of these three *Cerasus humilis* after ripening, as well as the difference in microstructure causing the type of force applied to their mesocarp when compressed.

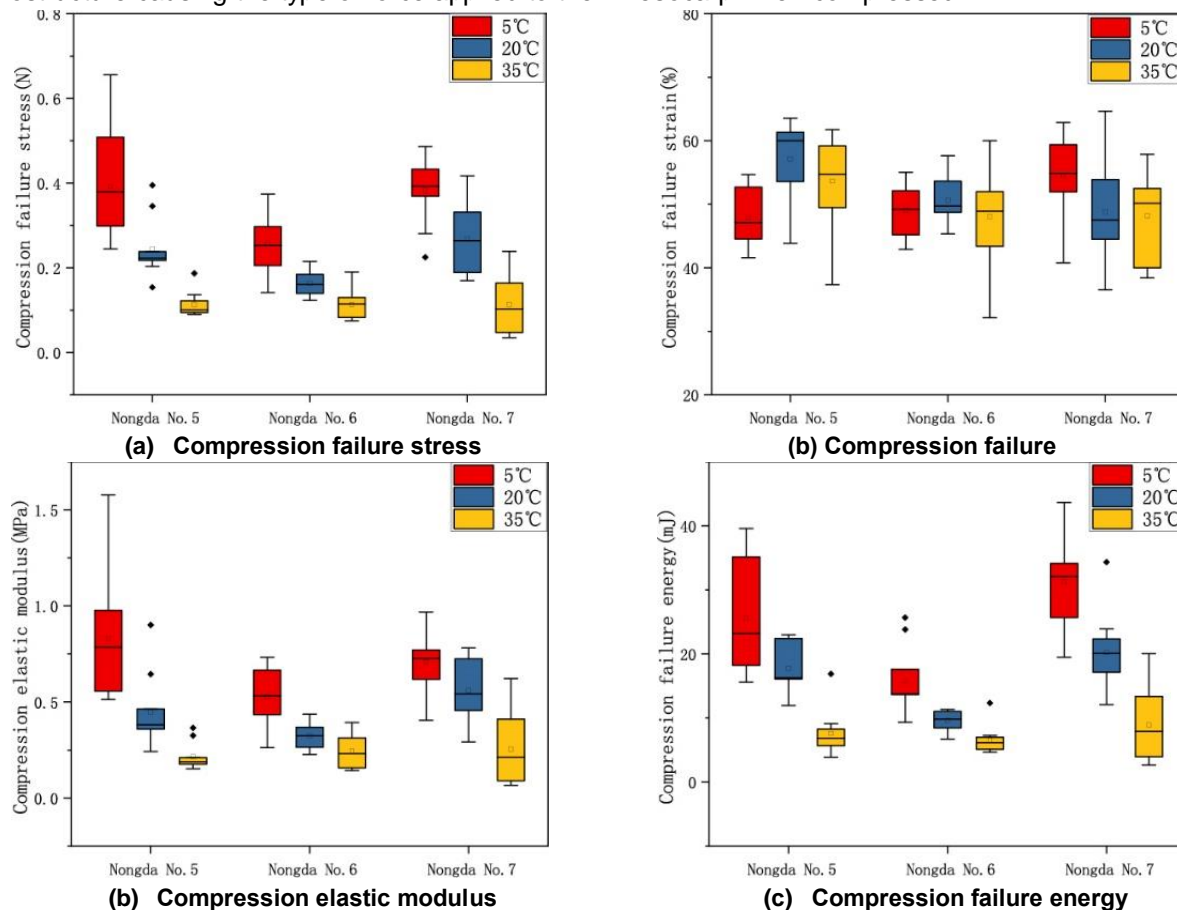


Fig. 5 - Mechanical properties of *Cerasus humilis* mesocarp during compression test strain

There was a significant negative correlation ($p < 0.05$) between mesocarp compressive elastic modulus and failure energy and temperature in *Cerasus humilis* compared to failure strain. In the interval of temperature conditions from 5°C to 35°C, the compression elastic modulus of mesocarp of Nongda No.5, Nongda No.6 and Nongda No.7 varied in the range of 0.83 ~ 0.22 MPa, 0.52 ~ 0.24 MPa, and 0.71 ~ 0.26 MPa, respectively; and the compression failure energy of mesocarp of Nongda No.5, Nongda No.6 and Nongda No.7 varied in

the range of 25.69 ~ 7.60 mJ, 15.79 ~ 6.60 mJ and 31.25 ~ 8.92 mJ, respectively. The compressive elastic modulus of mesocarp of Nongda No.5, Nongda No.6 and Nongda No.7 at 5°C was 3.77, 2.17 and 2.73 times higher than that at 35°C, respectively. The compression failure energy of mesocarp of Nongda No.5, Nongda No.6 and Nongda No.7 at 5°C was 3.38, 2.39 and 3.50 times higher than that at 35°C, respectively.

During compression, mesocarp specimens of *Cerasus humilis* first experienced elastic-plastic deformation, followed by microcrack development and expansion. Pectinase activity, viscosity of pectin and cellulose, and water content in mesocarp cells were altered by temperature (Chahal *et al.*, 2020), which in turn affected mesocarp firmness. This changed the moment of onset, the initial state (e.g., type, direction, number), and the rate of expansion of the cracks in the mesocarp specimen. Therefore, the effect of temperature on the mechanical properties of the mesocarp of *Cerasus humilis* should not be neglected.

CONCLUSIONS

In this study, the puncture mechanical properties and tissue mechanical properties of *Cerasus humilis* fruits at different temperatures were investigated by puncture, tensile and compression tests. Firstly, based on the results of the *Cerasus humilis* fruit puncture test, the methodology used and the data obtained not only reflect the shear mechanical properties of the *Cerasus humilis* exocarp at the tissue level, but at the same time characterize the degree of resistance of *Cerasus humilis* fruits to puncture damage at the macroscopic level. Temperature had a significant negative effect on *Cerasus humilis* puncture failure stress and a significant positive effect on *Cerasus humilis* puncture failure deformation ($p < 0.05$).

Additionally, based on the tensile and compression test, temperature had a significant effect ($p < 0.05$) on the tensile failure stress of *Cerasus humilis* exocarp and the compressive damage stress of mesocarp, as well as on the modulus of elasticity of both of them. As the temperature increased from 5°C to 35°C, the modulus of elasticity of the exocarp of Nongda No.5, Nongda No.6, and Nongda No.7 varied from 14.48 to 6.41 MPa, 9.30 to 4.93 MPa, and 15.00 to 7.07 MPa, respectively; and the modulus of elasticity of the mesocarp of Nongda No.5, Nongda No.7, and Nongda No.5 varied from 0.83 to 0.22 MPa, 0.52 to 0.24 MPa, and 0.71 to 0.26 MPa, respectively. At the same time, it is not difficult to see that as the temperature increases, the tissue damage stress and elastic modulus of *Cerasus humilis* were gradually decreasing. Therefore, in combination with the results of the puncture test, it could be concluded that low temperatures had a positive effect on reducing mechanical damage in *Cerasus humilis*.

Furthermore, due to the textural differences between different parts of the *Cerasus humilis* caused by the distribution of lithocyte, the modulus of elasticity, destructive stress, and destructive strain of the exocarp of the *Cerasus humilis* and the mesocarp of the *Cerasus humilis* differed significantly, with the value of the modulus of elasticity of the exocarp of the *Cerasus humilis* being higher than that of the mesocarp of the *Cerasus humilis*. So, the exocarp was more protective against mechanical damage to the fruit.

Eventually, this study provided systematic mechanical property parameters of *Cerasus humilis* and its tissues, which provided systematic basic parameters for numerical simulation methods to predict mechanical damage of *Cerasus humilis*.

ACKNOWLEDGEMENT

This research was supported by Supported by Fundamental Research Program of Shanxi Province (Grant Agreement No202203021221174)

REFERENCES

- [1] Alique R., Zamorano, J., Martinez, M., Alonso, J. (2005). Effect of heat and cold treatments on respiratory metabolism and shelf-life of sweet cherry, type picota cv "Ambrunes". *Postharvest Biology and Technology*, Madrid/Spain, vol.35, issue 2, pp.153-165;
- [2] Alamar M., Vanstreels E., Oey, M., Molto E., Nicolai B. (2008). Micromechanical behaviour of apple tissue in tensile and compression tests: Storage conditions and cultivar effect. *Journal of Food Engineering*, Cranfield / England, vol.86, issue 3, pp.324-333;
- [3] An X., Li Z., Zude-Sasse M., Tchuénbou-Magaia F., Yang Y. (2020). Characterization of textural failure mechanics of strawberry fruit. *Journal of Food Engineering*, Xianyang/China, vol.282, article number:110016;
- [4] Brüggewirth M., Knoche M. (2016). Factors affecting mechanical properties of the skin of sweet cherry fruit. *Journal of the American Society for Horticultural Science. American Society for Horticultural Science*, Jork / Germany, vol.141, issue 1, pp.45-53;

- [5] Costa F. (2016). Mechanical investigation to assess the peel contribution in apple fruit. *Postharvest Biology and Technology*, Trento/Italy, vol.111, pp.41–47;
- [6] Chahal A., Ciolkosz D., Puri V., Liu J., Jacobson M. (2020). Factors affecting wood-bark adhesion for debarking of shrub willow. *Biosystems Engineering*, PA / USA, vol.196, pp.202–209;
- [7] De Oliveira, G., Correa, P., Botelho, F., De Oliveira, A. (2015). Mechanical properties of tomatoes subjected to an induced compression during storage. *Journal of Texture Studies*, MG/Brazil, vol.46, issue 4, pp.293-301;
- [8] Desmet M., Lammertyn, J., Verlinden, B., Nicolai, B. (2002). Mechanical properties of tomatoes as related to puncture injury susceptibility. *Journal of Texture Studies*, Leuven/Belgium, vol.33, issue 3, pp.415-429;
- [9] Fich E., Segerson, N., Rose, J. (2016). The Plant Polyester Cutin: Biosynthesis, Structure, and Biological Roles. *Annual Review of Plant Biology*, NY/USA, vol.67, issue 1, pp. 207-233;
- [10] Han X., An X., Fadji T., Li Z., Khojastehpour M. (2022). Textural thermos-mechanical properties of sweet cherry for post-harvest damage analysis. *Journal of Texture Studies*, Xianyang/China, vol.53, issue 4, pp.453-464;
- [11] Karatas M., Arslan N. (2016). Flow behaviours of cellulose and carboxymethyl cellulose from grapefruit peel. *Food Hydrocolloids*, Elazig/Turkey, vol.58, pp.235-245;
- [12] Liu L., Liu G. (2005). The effect of different carbon sources on *Cerasus humilis* tissue culture seedlings (不同碳源对钙果组培苗的影响), *Northern Horticulture*, Beijing/China, issue 5, pp.68;
- [13] Li X. (2015). Determination and analysis of nutritional content in *Cerasus humilis*. (欧李的营养成分测定与分析), *Journal of Agriculture*, Shanxi/China, vol.5, issue 8, pp.97-100;
- [14] Liu C.Kuang M. (2013). Manufacture of *Cerasus humilis* compound health beverage (枸杞钙果复合运动饮料的研制). *Northern Horticulture*, Jilin/China, issue 17, pp.129-131;
- [15] Liang W., Cui D., Zhang G. (2008). Study on brewing technology of Chinese dwarf cherry fermented wine. (钙果发酵酒酿造工艺的研究). *China Brewing*, Liangning/China, issue 22, pp.72-74;
- [16] Li Z., Li P., Yang H., Liu J., Xu Y. (2012). Mechanical properties of tomato exocarp, mesocarp and locular gel tissues. *Journal of Food Engineering*, Xianyang/China, vol.111, issue 1, pp.82-91;
- [17] Lana M., Tijskens L., Kooten O. (2005). Effects of storage temperature and fruit ripening on firmness of fresh cut tomatoes. *Postharvest Biology and Technology*, Brasilia/ Brazil, vol.35, issue 1, pp.87-95;
- [18] Liu Z., Li Z., Yue T., Diels E., Yang Y. (2020). Differences in the cell morphology and microfracture behaviour of tomato fruit (*Solanum Lycopersicon L.*) tissues during ripening. *Postharvest Biology and Technology*, Xianyang/China, vol.164, article number:111182;
- [19] Matas A., Cobb E., Bartsch J., Paolillo D., Niklas K. (2004). Biomechanics and anatomy of *Lycopersicon esculentum* fruit peels and enzyme-treated samples. *American Journal of Botany*, Malaga/Spain, vol.91, issue 3, pp.352-360;
- [20] Posé S., Paniagua C., Matas A. J., Gunning A. P., Morris V. J., Quesada M. A., Mercado J. A. (2019). A nano structural view of the cell wall disassembly process during fruit ripening and postharvest storage by atomic force microscopy. *Trends in Food Science and Technology*, Malaga / Spain, vol.87, pp.47-58;
- [21] Yang Z., Zheng Y., Cao S., Tang S., Ma S., Li N. (2007). Effects of storage temperature on textural properties of Chinese bayberry fruit. *Journal of Texture Studies*, Xianyang/China, vol.38, issue 1, pp.166-177;
- [22] Zhang W., Du X., He J. (2018). Simulation analysis and experiment of combing pluck of *Cerasus humilis*(钙果梳刷采摘仿真分析与试验). *Agricultural Engineering*, Shanxi/China, vol.8, issue 5, pp.89-94;
- [23] Bin W., Junlin H., Shujuan Z., Lili L. (2020). Nondestructive testing of soluble solids content in *Cerasus humilis* using visible / near-infrared spectroscopy coupled with wavelength selection algorithm. *INMATEH Agricultural Engineering*, Shanxi/China, Vol.61, issue. 2, pp. 251-262.
- [24] Shaohua L., Junlin H., Nan W. (2021). Design and experimental study of the comb-type harvesting test bench for *Cerasus humilis*. *INMATEH Agricultural Engineering*, Shanxi/China, Vol.63, issue. 1, pp. 261-270. <https://doi.org/10.35633/inmateh-63-26>
- [25] Shilei K., Yanshun X., Bin T., Jingpu Z., Junlin H. (2023). Study on the characteristics of *Cerasus humilis* free falling impact. *INMATEH Agricultural Engineering*, Shanxi/China, Vol.71, issue.3, pp. 725-733. <https://doi.org/10.35633/inmateh-71-63>

LOCAL PATH PLANNING METHOD BASED ON SMOOTH TIME ELASTIC BAND ALGORITHM FOR ORCHARD ROBOTIC LAWN MOWER

基于 S-TEB 算法的果园割草机器人局部路径规划研究

Minhui ZHANG¹, Pengcheng LV¹, Jie LIU¹, Lei LIU¹, Huibin ZHU¹, Lili YI ^{*1}

¹ Shandong University of Technology, Collage of Agricultural Engineering and Food Science / China

Tel: +86 18553308656; E-mail: yili0001@sdut.edu.cn

DOI: <https://doi.org/10.35633/inmateh-73-2-1>

Keywords: Local path planning, S-TEB, Orchard Robotic Lawn Mower

ABSTRACT

This paper proposes a local path planning algorithm method named S-TEB (Smooth Time Elastic Band), aimed at fulfilling the requirement of full coverage for ORLMs (Orchard Robotic Lawn Mowers) during mowing operations. Firstly, by analyzing the tracking control mode of ORLMs in operational scenarios, control points are selected reasonably. Subsequently, utilizing B-spline curves, the path is optimized to generate the optimal trajectory and speed for ORLMs that satisfy multiple objectives and constraints. Finally, multiple simulations and field experiments were conducted in actual operational environments, with a speed of 0.6 m/s. Experimental results show that in scenarios involving obstacle avoidance, the minimum distance between the automatic lawnmower and the outer contour of obstacles is 4 cm. Compared to the traditional TEB planning algorithm, there is a 4.23% increase in mowing coverage area. These findings provide theoretical and technical support for local path planning in the operational scenarios of ORLMs.

摘要

本文提出了一种名为 S-TEB 的局部路径规划方法，以满足果园割草机器人在割草作业中的全覆盖需求。首先，通过分析果园割草机器人在作业场景下的追踪控制模式，合理选取控制点。然后，利用 b 样条曲线对路径进行优化，生成满足多目标、多约束条件的自动割草机最优轨迹和速度。最后，在实际作业环境中进行了多次仿真和实车试验，速度为 0.6 m/s。试验结果显示，在绕行障碍物场景中，果园割草机器人与障碍物外轮廓的最小距离为 4cm。相比传统 TEB 规划算法，割草面积覆盖率提升了 4.23%，为果园割草机器人作业过程中的局部路径规划提供了理论和技术支持。

INTRODUCTION

As a consequence of the long-term decline in the number of people of working age, countries around the world are exploring the use of unmanned agricultural machinery driving technologies (Zhao *et al.*, 2023; Zhong *et al.*, 2020). Grass cutting is an inevitable aspect of agricultural operations. Conducting local path planning and autonomous obstacle avoidance for ORLMs (Orchard Robotic Lawn Mowers) has significant theoretical and practical implications. The use of ORLMs in agricultural production is becoming increasingly prevalent (Huang *et al.*, 2023). Among the essential technologies ensuring the safe operation of ORLMs is real-time obstacle detection and local path planning after encountering obstacles (Wen *et al.*, 2022). This research aims to explore and implement the S-TEB (Smooth Time Elastic Band) algorithm for local path planning in ORLMs, contributing to the advancement of autonomous agricultural machinery technology.

The local path planning algorithms can be divided into graph-based local path planning, sample-based local path planning, curve interpolation fitting-based local path planning, and reinforcement learning-based local path planning (Weixin *et al.*, 2021). Yang *et al.*, (2024), introduced a risk assessment-based local path planning algorithm, which extracted and reconstructed active lane-changing scenarios and longitudinal collision prevention scenarios from high-dimensional datasets for validation and evaluation. The proposed algorithm reduced risks and improved driving efficiency, especially during speed and trajectory changes.

In the ORLMs field, Shi *et al.* (2023) proposed a local path planning method based on Bezier curves improving the problem of discontinuous curvature in planned paths.

¹ Minhui Zhang, M.S. Stud. Eng; Pengcheng Lv, M.S. Stud. Eng; Jie Liu, M.S. Stud. Eng; Lei Liu, M.S. Stud. Eng; Huibin Zhu, M.S. Stud. Eng; Lili Yi, Prof. Ph.D.

Liu et al. (2019), presented an obstacle avoidance path planning algorithm that utilized fifth-degree polynomial functions on the basis of improved shortest path method, addressing the issue of discontinuous curvature in the shortest path method. Zhang et al., (2019), based on the basis of original work (Qiu et al., 2020), introduced dynamic identification zones and improved the selection range of control points for Bezier curves, this results in a smoother curvature of the plan. Guo et al., (2022), proposed a local path planning algorithm based on B-spline curves and an improved rapidly exploring random tree algorithm, enhancing the efficiency and smoothness of the algorithm.

Existing agricultural machinery path planning algorithms are mostly designed for field operations, whereas the requirements for ORLMs operations are distinct, necessitating a certain level of coverage in path planning to maximize weed cutting efficiency (Yang et al., 2015). In the operational scenarios of ORLMs, various types of obstacles exist, including temporarily parked agricultural machinery, taller fruit trees or other traffic participants. The characteristics of ORLMs dictate that they cannot perform complex trajectory movements, thus requiring higher smoothness in trajectory planning (Wu et al., 2022).

In the aspect of environmental perception and localization, environment perception and localization are crucial steps for ORLMs to achieve autonomous movement and task execution. Traditional ORLMs often rely on buried metal wires to demarcate lawn boundaries, which can lead to higher installation costs and inflexibility in adapting to changes in mowing areas (Chen et al., 2023; Qin et al., 2023). This approach is inadequate for dynamic orchard environments. Yang et al., (2022), addressed this limitation by equipping ORLMs with an omnidirectional camera and an Inertial Measurement Unit (IMU). They utilized the camera to capture surrounding landmarks, thereby obtaining more precise position and orientation information. The fusion of data from multiple sensors enhances the robot's understanding of the environment and its localization accuracy. In this field, Huo et al., (2024), proposed a method that combines data from LiDAR and visual sensors for precise orchard robot localization. Furthermore, Kang et al., (2020), introduced a visual perception method based on deep learning, enabling orchard robots to achieve real-time environmental perception and modeling.

In terms of path planning and coverage rate, path planning and coverage rate are central to the execution of mowing tasks by orchard robots. Effective path planning algorithms ensure efficient obstacle avoidance and path optimization, thereby enhancing coverage rates. In related studies, Wang et al., (2023), proposed a path planning method based on the propagation wavefront algorithm, achieving favorable results in orchard environments. Zhang et al., (2022), investigated the feasibility of using deep learning techniques for path planning, implementing efficient orchard robot path planning through model predictive control. Additionally, Li et al., (2022), introduced a path planning strategy combining potential field methods and genetic algorithms, enabling orchard robots to autonomously navigate obstacles and optimize paths. However, it is noted that during obstacle avoidance, the smoothness of the path is poor, making it difficult for the lawnmower to follow its trajectory accurately during actual operations.

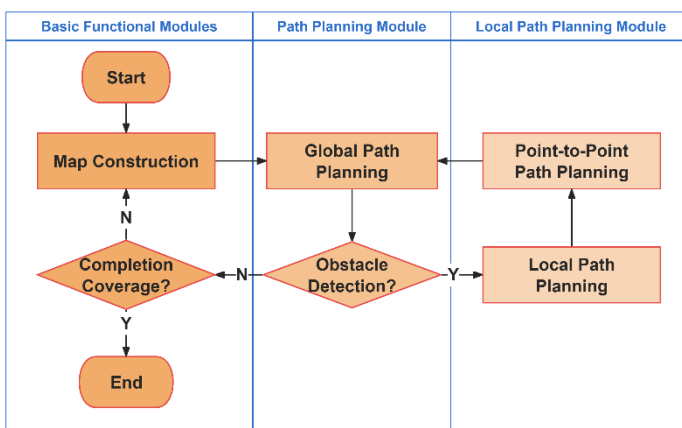


Fig. 1 - The Path planning flow chart for ORLMs

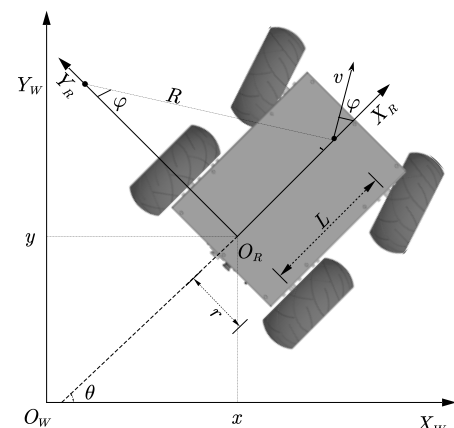


Fig. 2 - The motion model for ORLMs

This paper addresses the characteristics of ORLMs and their operational scenarios, studying the problem of local path planning for ORLMs in various driving environments. Based on the traditional TEB algorithm, the S-TEB algorithm is proposed to adapt to the practical operational requirements of lawnmowers. By selecting control points judiciously and introducing B-spline curves, the proposed algorithm aims to achieve smoother paths while covering a larger area. The objective is to provide technical references for the automation, intelligence, safety, and efficiency of ORLMs navigation.

MATERIALS AND METHODS

In the domain of ORLMs, path planning is a key task because it determines both the action strategy and the safety of ORLMs in complex environments. The proposed S-TEB local path planning algorithm in this paper aims to address the action of ORLMs when encountering obstacles. The primary workflow of the algorithm, as shown in Fig. 1, consists of two crucial steps: first, the TEB algorithm is used to generate a global path based on map information. The TEB algorithm, known for its efficient trajectory generation and optimization capabilities, is widely used in autonomous navigation (Xia *et al.*, 2022; Zhou *et al.*, 2020). Then, when ORLMs encounter obstacles, the S-TEB algorithm is used for replanning. Compared to conventional methods, the S-TEB algorithm shows a significant improvement in obstacle avoidance performance, enabling more adaptive path adjustments to avoid obstacles. By integrating these two steps, our algorithm ensures safe navigation of ORLMs amidst obstacles while striving to achieve maximum area coverage, thereby increasing the efficiency and reliability of path planning.

ORLMs motion mode

In the context of local path planning for ORLMs, the Ackermann motion model plays a central role. This is because ORLMs need to consider their spatial motion characteristics during local path planning to ensure safe and efficient traversal of obstacles and reaching of target points. The Ackermann motion model provides an optimal framework for ORLMs systems to predict and plan their motion trajectories.

To ensure collision-free ORLMs with road edges and obstacles, the ORLMs is abstracted as a rectangular model. The coupled dynamics of the vehicle suspension are not considered. The mass of the ORLMs body is uniformly distributed, and the center of mass is located on the longitudinal geometric line of symmetry of the robot. However, it may not be on the transverse geometric line of symmetry. In addition, the tire sideslip problem has been neglected.

The motion model for ORLMs is shown in Fig. 2. In order to accurately simulate the Ackermann steering mode of the ORLMs, two basic coordinate systems have been introduced: the Cartesian coordinate system W ($X_w-O_w-Y_w$), and the frenet coordinate system R ($X_R-O_R-Y_R$). The coordinates of the ORLMs are $S = (x, y, \theta)$, where (x, y) is the position of the smart car in the world coordinate system, θ is the angle between the longitudinal axis of the ORLMs and the world coordinate system. The steering angle of the front wheels of the ORLMs is denoted as φ , with a maximum steering angle constraint given by $\varphi \leq \varphi_{max}$. The wheelbase between the front and rear wheels is denoted by L , and the angular velocity of the rear wheels is denoted by ω . The turning radius of the ORLM is denoted by r .

The relationship between the turning radius r , the wheelbase L , and the steering angle φ of the front wheels should satisfy the following equation (Li *et al.*, 2023):

$$r = \frac{L}{\tan[\varphi(t)]} \quad (1)$$

The relationship between the steering angle of the front wheels and the angular velocity is given by Equation (2).

$$\omega(t) = \frac{v(t)}{r(t)}, \varphi(t) = \arctan\left[\frac{\omega(t)L}{v(t)}\right] \quad (2)$$

In the equation, $\varphi(t)$ represents the real-time steering angle of the ORLMs. The kinematic state equation of the ORLMs is shown in Equation (3).

$$\dot{S}(t) = \begin{bmatrix} \dot{x}(t) \\ \dot{y}(t) \\ \dot{\theta}(t) \end{bmatrix} = \begin{bmatrix} \cos[\theta(t)] \\ \sin[\theta(t)] \\ \tan\left[\frac{\varphi(t)}{L}\right] \end{bmatrix} v(t) \quad (3)$$

In the equation, $\dot{S}(t)$ represents the derivative of the pose state of the ORLMs, $[\dot{x}(t), \dot{y}(t), \dot{\theta}(t)]^T$ represents the position state of the ORLMs.

Vehicle control method

Stanley is a trajectory tracking algorithm based on geometry. Its main idea is to use the center of the front wheel as the reference point, without the need for a preview distance, to directly calculate the lateral error and heading error from the center of the front wheel to the target trajectory.

Assume that the current lateral error $e=0$, so the vehicle only needs to turn through the angle θ_e , and the vehicle can always drive along the target trajectory. In this case, let $\delta(t) = \theta_e(t)$. In order to eliminate the lateral error, construct a triangle, it can be obtained:

$$\tan \delta_e = \frac{e}{d\omega} \tag{4}$$

$d = \frac{v}{k}$ into the above formula, the following is obtained:

$$\delta_e = \tan^{-1} \left(\frac{ke}{v} \right), \delta(t) \in [\delta_{min}, \delta_{max}] \tag{5}$$

$$\delta(t) = \theta_e(t) + \tan^{-1} \left(\frac{ke}{v} \right), \delta(t) \in [\delta_{min}, \delta_{max}] \tag{6}$$

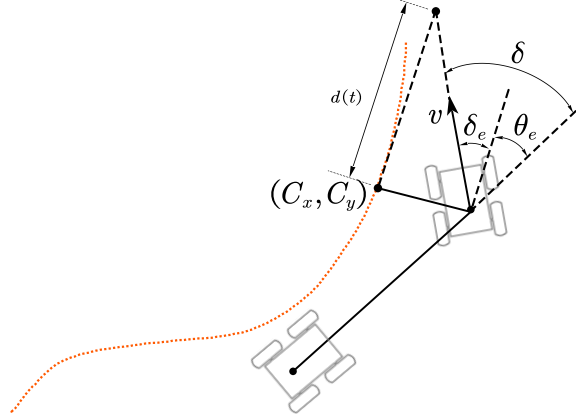


Fig. 3 - Schematic diagram of Stanley trajectory tracking control algorithm

ORLMs generally operates at low speed. In order to solve the noise problem, a positive constant k_s is added. The final corner is:

$$\delta(t) = \theta_e(t) + \tan^{-1} \left(\frac{ke}{k_s + v} \right) \tag{7}$$

Principle of TEB algorithm

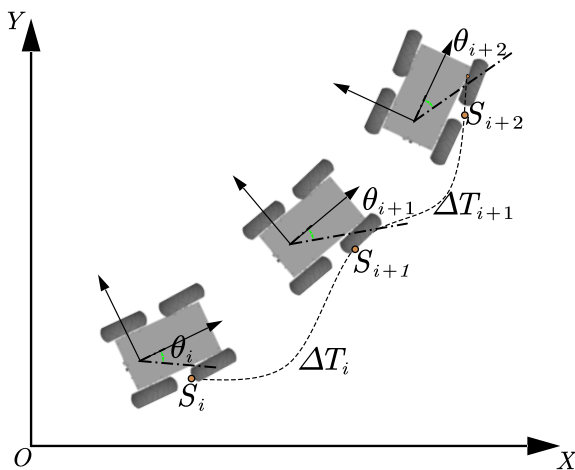


Fig. 4 - The relationship between bit position and time interval with TEB algorithm

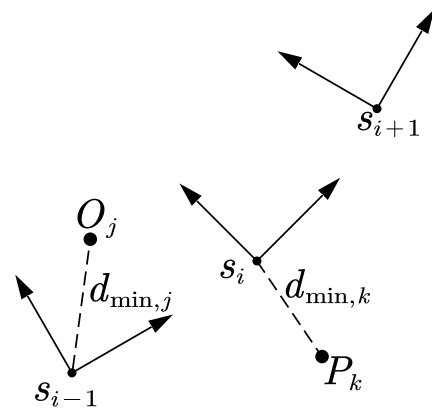


Fig. 5 - Abstract graph of pose and time interval relationship in TEB algorithm

The global path of the TEB algorithm consists of poses relative to discretized pose points $S_i(x_i, y_i, \theta_i)^T$. In this context, (x_i, y_i) represents the position of discrete path points, and θ_i denotes the angle between the direction of motion of the ORLMs and the X-axis of the world map, as shown in Fig. 4. At this point, the pose sequence can be represented as:

$$Q = \{S_i\}_{i=0, \dots, n} \tag{8}$$

The time interval ΔT_i denotes the time required for the ORLMs to move from the current position point S_i to the next position point S_{i+1} in the sequence Q . The time interval ΔT_i is the time required for the ORLMs to move from the current position point S_i to the next position point S_{i+1} in the sequence Q (Dai et al., 2022). Therefore, the trajectory formed by the TEB algorithm consists of two sets of time interval sequences and

position point sequences. Therefore, the trajectory formed by the TEB algorithm consists of two sets of time interval sequences and position point sequences. The time interval sequence can be expressed as:

$$\tau = \{\Delta T_i\}_{i=0,1,\dots,n-1} \tag{9}$$

The optimization sequence consisting of the position and time of the intelligent cart in the TEB algorithm can be expressed as follows:

$$B = (Q, \tau) = \{s_1, \Delta T_1, s_2, \Delta T_2, \dots, s_{n-1}, \Delta T_{n-1}, s_n\} \tag{10}$$

The central concept behind the TEB algorithm is to determine the optimal sequence of vehicle poses within specified time intervals. This optimization problem is formulated as a nonlinear least-squares cost function, aiming to aggregate the weighted sum of B^* values.

In the objective function B constituted by the optimization sequence, the relationship between each position point and time is affected by the TEB constraints. Usually, the TEB constraints contain four types of constraints: incomplete kinematics constraints, acceleration and velocity constraints, obstacle point and global path point constraints, and shortest time constraints (Wu et al., 2021).

In most cases, ORLMs needs to follow the global path points to navigate around obstacles and complete local path planning (Jiang et al., 2022). The global path planning algorithm treats ORLMs as a point mass, and the planned global path is an ideal trajectory. However, in real-world scenarios, due to constraints such as its own dynamics, ORLMs cannot completely follow the global path (Huang et al., 2023). Therefore, it is necessary to further consider the information of global path points and obstacles, establish reasonable constraints, and plan paths that conform to reality.

The distance between the local path point and the global path point is expressed as $d_{min,k}$, and the distance between the local path point and the obstacle is expressed as $d_{min,j}$, its simplified diagram is shown in Fig. 5, point O_j represents an obstacle, and point P_k represents the path point of the global path. The obstacle avoidance penalty function of TEB is as follows:

$$f_{obstacle} = e_{\tau}(-d_{min,j}, -r_{O_{min}}, k, S, n) \tag{11}$$

In order to ensure that the ORLMs do not collide with road edges and obstacles, the ORLMs are abstracted as a rectangular model and a kinematic model. In the formula, $r_{O_{min}}$ represents the lower limit of the minimum distance set between the smart car and the obstacle. Similarly, the number of penalty terms following the global path can be expressed as:

$$f_{path} = e_{\tau}(d_{min,j}, r_{P_{max}}, k, S, n) \tag{12}$$

$r_{P_{max}}$ is the upper limit of the allowed deviation from the global path points. The penalty function takes effect when the distance of the smart trolley from the obstacle is less than the set lower limit distance, or the distance from the path point is greater than the set upper limit distance. If it is within the allowed range, the penalty function outputs 0.

Optimize TEB algorithm

Incomplete Kinematic Constraints are constraints that contain generalized coordinate derivatives of the system and are not integrable. The turning radius of the ORLMs is limited by its own turning radius, which belongs to incomplete kinematic constraints. Fig. 6 shows the relationship between bit position and time interval with TEB algorithm when turning.

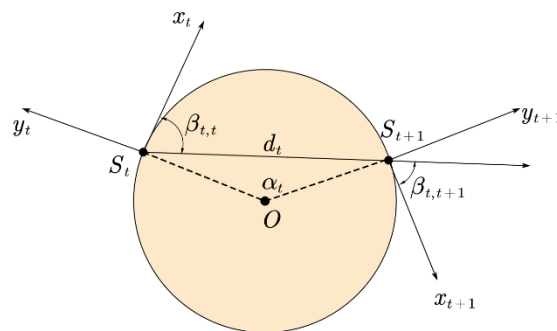


Fig. 6 - Schematic diagram of ORLMS turning motion

The displacement of the non-complete kinematic constraint of the AMR between two neighboring attitude points is a path composed of a segment of arcs. In Fig. 6, the displacements of the ORLMs from point S_i to point S_{i+1} are on arcs with constant curvature, thus they satisfy the following equations.

$$\beta_{t,t} = \beta_{t,t+1} \quad (13)$$

$$d_{t,t+1} = \begin{pmatrix} x_{t+1} - x_t \\ y_{t+1} - y_t \\ 0 \end{pmatrix} \quad (14)$$

$$\begin{bmatrix} \cos \beta_{t,t} \\ \sin \beta_{t,t} \\ 0 \end{bmatrix} d_{t,t+1} = d_{t,t+1} \begin{bmatrix} \cos \beta_{t,t+1} \\ \sin \beta_{t,t+1} \\ 0 \end{bmatrix} \quad (15)$$

Where: $\beta_{t,t}$ and $\beta_{t,t+1}$ are the angles between the traveling direction of the ORLMS and the X-axis of the world coordinates, so the cost equation of the incomplete kinematic constraints is shown as follows.

$$f(x_t, x_{t+1}) = \left\| \left[\begin{pmatrix} \cos \beta_{t,t} \\ \sin \beta_{t,t} \\ 0 \end{pmatrix} + \begin{pmatrix} \cos \beta_{t,t+1} \\ \sin \beta_{t,t+1} \\ 0 \end{pmatrix} \right] d_{t,t+1} \right\|^2 \quad (16)$$

When the ORLMS with Ackermann structure turns, the turning radius must not be smaller than its minimum turning radius, therefore, its constraint is shown as follows.

$$r(x_{t+1}, x_t) = \left| \frac{v_t}{\omega_t} \right| \geq \left| \frac{d_t}{2 \sin \frac{\alpha_t}{2}} \right| = r_{\min} \quad (17)$$

The smart trolley needs to satisfy the incomplete kinematics constraints, and also needs to satisfy that the turning radius of the smart trolley is not less than its minimum turning radius, $r_t \geq r_{\min}$.

● Velocity and acceleration constraints

The constraints of velocity and acceleration are composed of the Euclidean distance between two neighboring attitude points S_i and S_{t+1} and the time ΔT_i needed for the motion between the two points, and the constraints are formed by obtaining the rotational and translational velocities of the intelligent trolley, whose solution formulas are shown as follows.

$$v \approx \frac{1}{\Delta T_i} \left\| \begin{pmatrix} x_{t+1} - x_t \\ y_{t+1} - y_t \end{pmatrix} \right\| \quad (18)$$

$$\omega_t \approx \frac{\beta_{t+1} - \beta_t}{\Delta T_i} \quad (19)$$

Similarly, the average linear acceleration and average angular acceleration can be obtained from the linear and angular velocities of two consecutive postures, shown as follows.

$$a_t = \frac{2(v_{t+1} - v_t)}{\Delta T_i + \Delta T_{i+1}} \quad (20)$$

$$a_\omega = \frac{2(\omega_{t+1} - \omega_t)}{\Delta T_i + \Delta T_{i+1}} \quad (21)$$

● Minimum time constraint

The TEB algorithm combines the time information between the neighboring position points of the ORLMS, different from the traditional local path planning algorithm which takes the shortest distance as the optimization criterion, the TEB algorithm takes the shortest time as the optimization criterion.

The objective function takes the square of the sum of the time intervals between all the position points as the optimal index, and its expression is shown as follows.

$$f_{\text{short_time}} = \left(\sum_{i=0}^n \Delta T_i \right)^2, i \in N \quad (22)$$

Constraints on Obstacle Points and Global Paths

Usually, the ORLMS needs to follow the global path points to avoid obstacles and complete the local path planning. The global path planning algorithm treats the ORLMS as a mass point, and the planned global path is an ideal path. However, in reality, the ORLMS cannot follow the global path completely due to its own dynamics and other constraints. Therefore, it is necessary to further consider the global path points and obstacle information to construct reasonable constraints and plan a realistic path.

● The trajectory planning constraints

For a curve composed of discrete points with equal lateral spacing, the magnitude of the first derivative of the trajectory points is positively correlated with the length of the curve. That is, the smaller the first derivative of the trajectory points, the smoother the curve. Hence, the cost function C_{smooth} for smoothness can be derived as:

$$C_{smooth} = W_{length} \sum_{i=1}^n (l'(s_i))^2 \tag{23}$$

where W_{length} is the distance weight, and $l'(s_i)$ is the lateral displacement of the agricultural machinery at the longitudinal distance s_i .

● **Severity of danger**

The severity of danger is assessed based on the distance of ORLMs from obstacles when circumventing static obstacles. Let d denote the straight-line distance between the ORLMs and the obstacle.

The cost function for the severity of danger is denoted as C_{danger} .

$$C_{danger} = \begin{cases} 0, & d > d_2 \\ \frac{W_{danger}}{d}, & d_1 \leq d < d_2 \\ +\infty, & d \leq d_1 \end{cases} \tag{24}$$

In the formula, W_{danger} represents the weight of the severity of danger, d_1 is the risk distance in meters (m), and d_2 is the safety distance in meters (m). Beyond the safety distance, it is assumed that there is no collision risk between the agricultural robot and the obstacle, and the cost is 0. Within the risk distance, it is assumed that there is a collision risk between the agricultural robot and the obstacle, and the cost is considered infinite. Between the risk distance and the safety distance, the severity of danger is inversely proportional to d .

● **Selecting Control Points**

In the actual operation process, the task target point of the lawn mower is abstracted as shown in the Fig. 7. As is commonly understood, curvature denotes the degree of curvature exhibited by a curve. Altering the radius of a circle, smaller radii yield larger curvatures, resulting in more pronounced curvature of the curve. Conversely, larger radii lead to smaller curvatures, resulting in a smoother curve. Illustrated in the diagram are three curves denoted as $l_1, l_2,$ and $l_3,$ respectively. These curves are positioned on circles centered at points $O_1, O_2,$ and $O_3,$ with radii denoted as $R_1, R_2,$ and $R_3,$ respectively. If curvature is denoted by K :

$$K = \frac{1}{r} \tag{25}$$

For a general curve, the degree of curvature varies at different positions. This variation in curvature can be described using curvature. Curvature denotes the degree of curvature of a curve at a certain point and can be obtained by computing the second derivative of the curve.

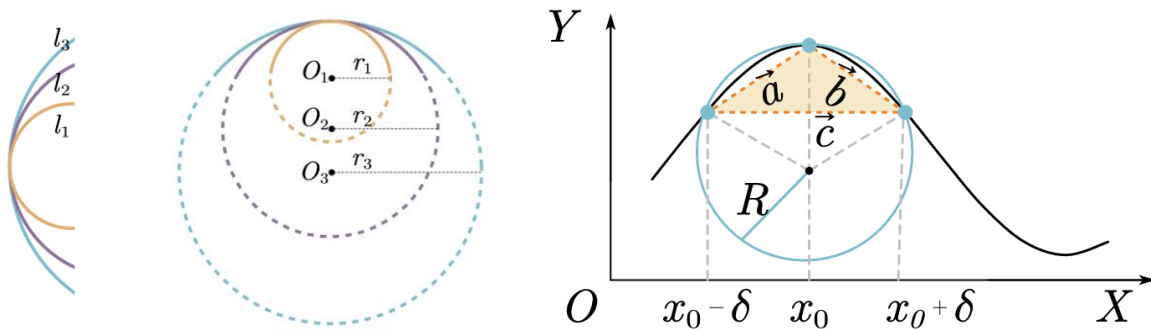


Fig. 7 - Curvature models

In the curve, some positions exhibit significant curvature while others are relatively flat. To compute the curvature of point x_0 on the curve, a point to the left is selected and another to the right of $x_0, x_0 - \delta$ and $x_0 + \delta$ respectively. These three points collectively determine a circle, the radius of which is named R , as δ tends towards zero, this circle becomes the osculating circle of the curve at point x_0 . By calculating the radius of the osculating circle, the curvature of the curve at point x_0 can be determined.

According to the circumscribed circle formula:

$$R = \frac{abc}{4S} \tag{26}$$

S is the area of the circumcircle determined by three points $a, b,$ and c representing the lengths of the three sides. The directed area of the parallelogram formed by vectors a and b can be represented by the determinant $det(\vec{a}, \vec{b})$.

$$R = \frac{abc}{4S} = \frac{|\vec{a}| \times |\vec{b}| \times |\vec{c}|}{4 \times \det(\vec{a}, \vec{b})} \tag{27}$$

Dividing both sides by δ^3 it is obtained:

$$R = \frac{\sqrt{[f(x_0 + \delta) - f(x_0 - \delta)]^2 + 4\delta^2} \cdot \sqrt{[f(x_0 + \delta) - f(x_0)]^2 + \delta^2} \cdot \sqrt{[f(x_0) - f(x_0 - \delta)]^2 + \delta^2}}{2|\delta f(x_0 + \delta) + \delta f(x_0 - \delta) - 2\delta f(x_0)|} \tag{28}$$

When δ approaches 0, the radius of the osculating circle is r , thus r is the limit of R , resulting in:

$$r = \lim_{\delta \rightarrow 0} R = \frac{(1 + (f'(x_0))^2)^{\frac{3}{2}}}{|f''(x_0)|} \tag{29}$$

As the result:

$$K = \frac{1}{r} = \frac{|f''(x_0)|}{(1 + (f'(x_0))^2)^{\frac{3}{2}}} = \frac{2|(x_1 - x_2)(y_2 - y_3) - (x_2 - x_3)(y_1 - y_2)|}{\sqrt{(x_1 - x_2)^2 + (y_1 - y_2)^2}^3} \tag{30}$$

Through detailed calculations and analysis, a significant conclusion is reached: when the parameter k undergoes substantial changes, employing a strategy of multiple control points can effectively ensure the safety of autonomous robotic systems (ORLMs) during operation. When k changes from 0 to non-zero, it evaluates to true. When the change in k exceeds 0.26, the evaluation result is true. This can be expressed with the following formula:

$$\begin{cases} \text{true,} & \text{if}(k_{\text{previous}} = 0) \text{ or if}(k = 0) \\ \text{true,} & \text{if}(|k_{\text{previous}} - k|) > 0.26 \\ \text{false,} & \text{otherwise} \end{cases} \tag{31}$$

Where k_{previous} represents the previous value of k .

Implementing this strategy enables the ORLMs system to adapt more flexibly to various environments and situations. Moreover, when faced with complex road conditions, it can navigate and plan paths more robustly. Therefore, selecting multiple control points is an effective approach to enhance the safety and stability of ORLMs systems, which holds crucial significance for the advancement of autonomous robotics technology.

● **B-spline curve smoothing strategy**

For the initial path obtained from the TEB algorithm, a cubic uniform B-spline curve smoothing strategy is introduced to optimize the path smoothing. The formula for a B-spline curve can be expressed as:

$$P(u) = \sum_{i=0}^n N_{i,p}(u) \cdot P_i \tag{32}$$

Where $P(u)$ is a point on the curve, u is the parameter, n is the number of control points minus 1, P is the degree of the B-spline minus 1, $N_{i,p}(u)$ is the B-spline basis function, and P_i is a control point.

When $k=3$, the mathematical expression for the cubic uniform B-spline curve is:

$$P(u) = \sum_{i=0}^n N_{i,3}(u) \cdot P_i \tag{33}$$

After introducing the smoothing strategy, line segments around the turning points in the path are replaced by curves, resulting in smoother local paths being generated.

● **Smoothness evaluation function**

This paper designs a smoothness function Q_k to calculate the overall smoothness of the path during algorithm. This function is represented as:

$$Q_k = \sum_{i=2}^{k-1} abs\left(\arccos\frac{D_1^2 + D_2^2 - D_3^2}{2D_1D_2}\right) \cdot \frac{180}{\pi} \tag{34}$$

In the equation, D_1 , D_2 , and D_3 represent the distances between any three adjacent path nodes. The expression is given by:

$$\begin{cases} D_1 = \sqrt{(x_{i+1} - x_i)^2 + (y_{i+1} - y_i)^2} \\ D_2 = \sqrt{(x_{i+2} - x_{i+1})^2 + (y_{i+2} - y_{i+1})^2} \\ D_3 = \sqrt{(x_{i+2} - x_i)^2 + (y_{i+2} - y_i)^2} \end{cases} \quad (35)$$

In equation, a larger value of Q_k indicates that there are more acute angles between adjacent path nodes, meaning the path is more tortuous; conversely, a smaller value represents a smoother path.

Overall, in optimizing the navigation process of ORLMs, the main improvement directions include selecting control points reasonably, adding danger constraints, and increasing velocity constraints. By selecting control points reasonably, the smoothness and coverage area of path planning can be improved. Additionally, the danger penalty function makes ORLMs more cautious when encountering obstacles or complex road conditions, thereby enhancing its navigational safety. Furthermore, increasing velocity constraints helps balance the speed and safety of ORLMs, ensuring stability during the navigation process. These improvement measures collectively influence the path planning and navigation process of ORLMs, aiming to enhance its adaptability, safety, and stability in various environments and conditions.

RESULTS

● Simulation

In order to verify the effectiveness of the improved S-TEB local planning algorithm, the algorithm was integrated into the ROS robot operating system for simulation experiments, and then actual experimental tests were conducted on the Ackerman differential robot^[6]. The purpose is to verify the improved S-TEB algorithm. There are 3 aspects of performance: first, the effectiveness of planning safe motion trajectories at obstacles; second, the effectiveness of smoothing the planned path; third, the effectiveness of accurately reaching the target point.

In the simulation environment shown in Fig. 8, the left side is the location of the simulation environment and its obstacles, and the right side is the environment map constructed using SLAM. In the map, the innermost circle is the obstacle, the first circle is the expansion distance of the obstacle, and the second circle is the safe distance.

To validate the effectiveness of the S-TEB local path planning algorithm, simulation experiments were conducted in the ROS system. The operating system utilized is Ubuntu 18.04, through the gazebo and RVIZ platform in ROS-melodic system co-simulation, in the gazebo platform to build the simulation environment and set up the physical simulation map, in the RVIZ platform to display the obstacles and the intelligent car model, the ORLMs trajectory through the ROS control.

First, establish a map of the plowed path. The global path consists of smooth curves formed by connecting trajectory points.

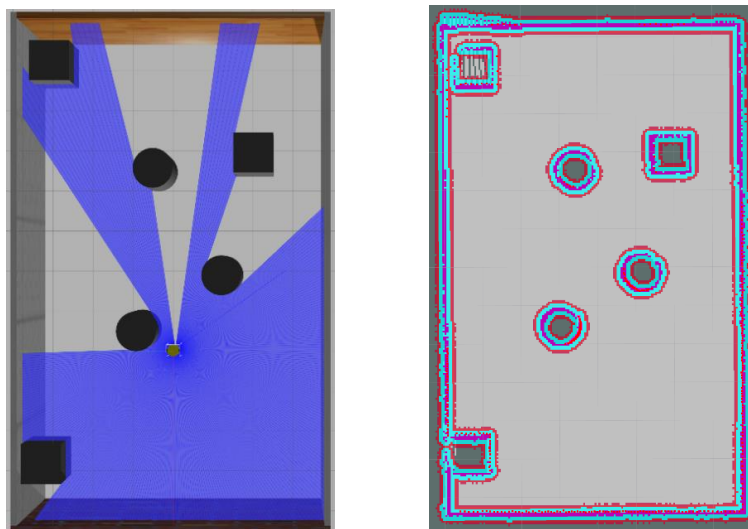


Fig. 8 - Simulation environment and map constructed by slam

Subsequently, employing the aforementioned formula, the process of selecting control points ensues. These meticulously chosen control points are then integrated into the B-spline curve for optimization, resulting in the refinement of the local path. This iterative procedure seamlessly harmonizes mathematical precision with real-world application, culminating in a locally optimized trajectory tailored to the intricacies of the environment.

Through the fusion of algorithmic finesse and practical utility, the refined path intricately weaves through obstacles, ensuring optimal traversal efficiency and enhancing the navigational capabilities of the autonomous system. This meticulous optimization not only fosters smoother trajectory planning but also bolsters the system's adaptability and resilience amidst dynamic operational scenarios.

The comparison between paths circumventing square and circular obstacles, as depicted in Fig. 9 and Fig. 10, reveals a notable distinction. The green line illustrates the path planned using the conventional TEB algorithm, while the red line signifies the path charted using the enhanced S-TEB algorithm. It is discernible from these illustrations that the path generated by the improved S-TEB algorithm exhibits enhanced smoothness and encompasses a larger coverage area compared to its traditional counterpart.

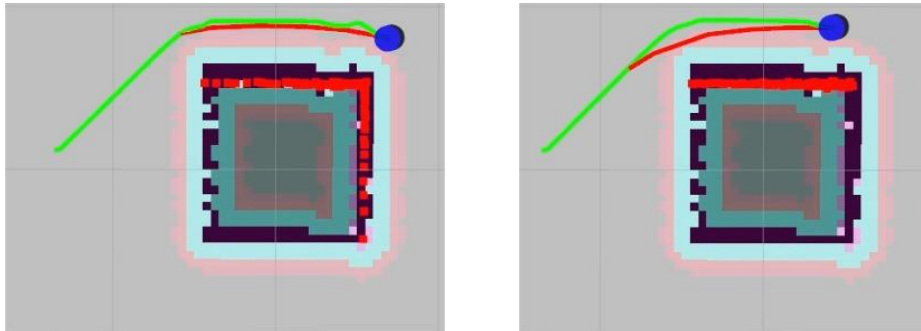


Fig. 9 Comparison chart of path planning under square obstacle scenario

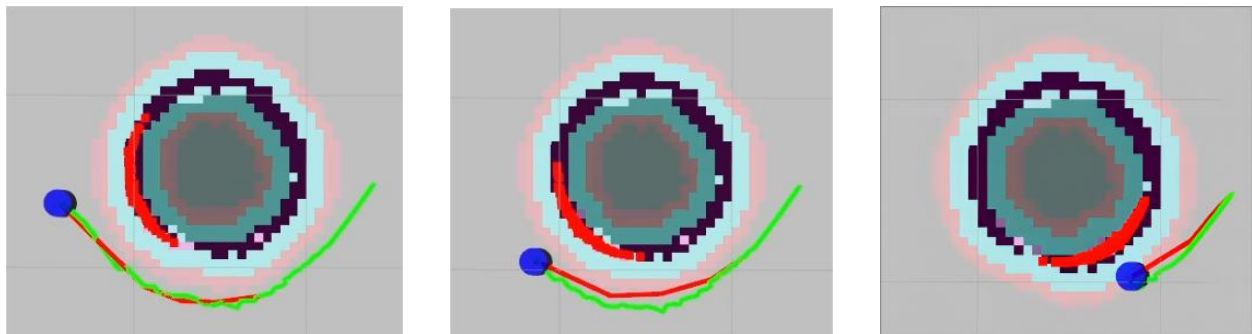


Fig. 10 Comparison chart of path planning under circular obstacle scenario

Experiment



Fig. 11 – Local Path Planning Experiment to ORLMs

Standardized grape vineyards ensure a high degree of consistency in row spacing, plant spacing and pruning methods, which provides an ideal basis for orchard robots to work in and plan paths. Furthermore, the data collection and analysis of the standardized grape vineyard is more convenient. Consequently, the standardized grape vineyard is selected as the experimental environment for the orchard robot.

Through continuous testing and optimizing in this environment, the mature technology solution can be gradually extended to other types of orchards or agricultural fields, thereby promoting the intelligent upgrading of the entire agricultural production process. The experimental test scenario mirrors the real-world operational conditions encountered by ORLMs and is set within a standardized grape vineyard environment. This scenario comprises two cylindrical obstacles and one cuboid obstacle strategically placed to simulate dynamic obstacles commonly encountered in agricultural settings. By replicating these realistic conditions, the performance of the robots in effectively navigating around obstacles can be thoroughly evaluated. This carefully designed experimental setup ensures that the outcomes accurately reflect the capabilities and effectiveness of the robotic systems in real-world agricultural applications.

In this series of scientific research experiments, a variety of sensors and intelligent control modules were integrated into the ORLMs. The RTK positioning system provides centimeter-level ultra-high-precision positioning, while the 64-line 3D LIDAR offers detailed obstacle information through its omni-directional field of view and high-precision detection capability. It is noteworthy that the ROS operating system was implemented on the Nvidia Jetson Orin NX hardware platform, which was paired with the VCU vehicle control unit to serve as the ORLMs's intelligent brain.



Fig. 12 – Local Path Planning Experiment to ORLMs in the spring

The SLAM was adopted to construct a point cloud map and employ RTK (Real-Time Kinematic) devices for online localization. As shown in Fig. 13, a 3D point cloud map of the current scene is opened in Reconstruct Visualization Interface. This map is employed to delineate the effective identification area, which is instrumental in the process of identifying potential obstacles. Subsequently, the 2D Pose Estimate tool is employed. In order to approximate the location and orientation of the current vehicle on the map, it is necessary to remotely move the vehicle by a distance of between one and two meters. Concurrently, it is essential to monitor the alterations in the vehicle's coordinate system within the designated visualization area to ascertain the precision of the initialized vehicle position. The 2D Nav Goal tool is employed to select a target point on the map, and the TEB (Timed Elastic Band) global path planner will generate a global path from the starting point to the target point.

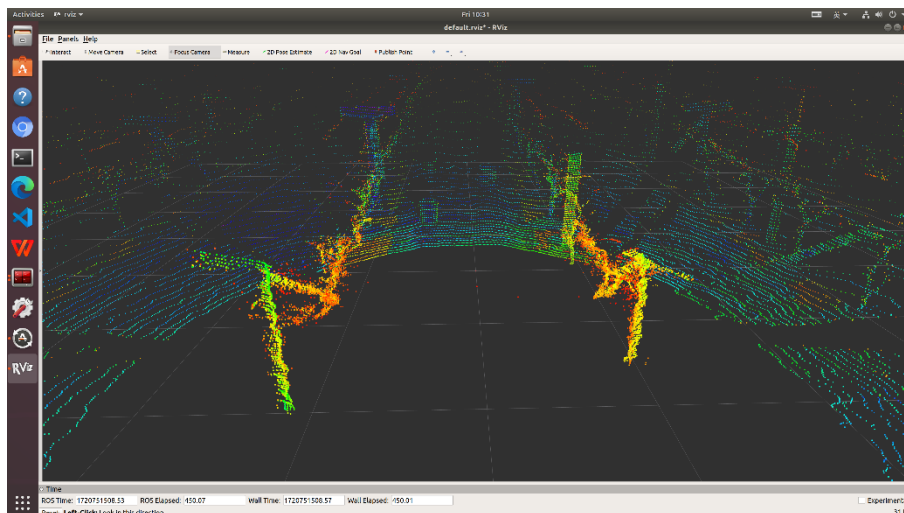


Fig. 13 – The Point Cloud Plots from the experiment

The ORLMs operated at a speed of approximately 0.6 m/s, traversing from a fixed starting point to a fixed endpoint. Within the program, both the traditional TEB and S-TEB algorithms were separately employed to replace the local path planning module, each followed by ten experimental obstacle avoidance tests. The obstacle conditions were based on the model depicted in Fig. 12, with a standardized grape vineyard environment featuring row spacing of 1.5 meters and a minimum distance of 4 cm from obstacles. Experimental parameter data were collected using ROS tools such as rqt and rosbag, and analyzed based on the evaluation metrics that were developed. The results, depicted in Fig. 14, show that the coverage area increased by 4.23%. To facilitate observation of data changes, the numerical values of the x-axis and y-axis coordinates underwent non-uniform scaling.

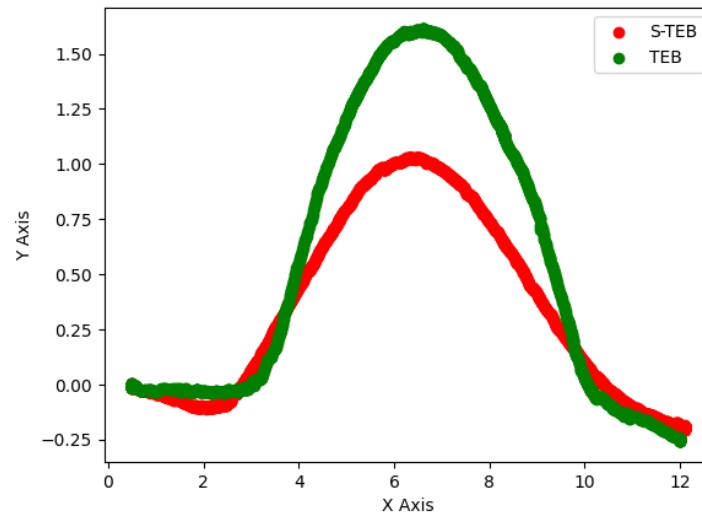


Fig. 14 Comparison diagram of experimental paths

From the Fig. 14, it can be observed that neither of the two path planning methods resulted in collisions with obstacles. Compared to the traditional TEB algorithm, the motion planner of the proposed TEB-CA algorithm maintains a smaller distance relative to obstacles and covers a larger area of weed growth. Additionally, there is minimal fluctuation in speed and angle, ensuring stable control and reducing the probability of rollover during turning and obstacle avoidance. The planned travel path meets the dynamic constraint requirements of the mobile robot, with various state quantities changing accordingly.

1. Obstacle Avoidance from Start to Goal:

The experimental results demonstrate the efficacy of the S-TEB algorithm in enabling the ORLMs to navigate from the starting point to the target point while effectively avoiding obstacles in the environment. Through real-world testing scenarios, the ORLMs successfully circumvented various obstacles encountered along the path, showcasing its robust obstacle avoidance capability.

2. Enhanced Smoothness in Local Path Planning:

Incorporating the S-TEB algorithm into the ORLM's local path planning process yielded notable improvements in trajectory smoothness. By adjusting parameters such as velocity and acceleration profiles, the ORLMs was able to generate smoother paths, minimizing abrupt changes in direction and velocity. This enhanced smoothness not only contributes to the overall navigation efficiency but also ensures a more stable and predictable trajectory for the ORLMs.

3. Mowing Coverage Area Increases:

Analysis of the experimental data reveals that the implementation of the improved S-TEB algorithm has resulted in a notable enhancement in mowing coverage area, with a significant increase of 4.23%.

CONCLUSIONS

This paper optimizes the ORLMs local path planning algorithm by incorporating the B-spline curve time elastic band local path planning algorithm, and proposes the S-TEB algorithm for improved local path planning based on this optimization.

In this paper, the SLAM method was adopted to construct a point cloud map and utilized RTK (Real-Time Kinematic) devices for online localization. In a standardized vineyard environment, two cylindrical obstacles and one cuboid obstacle were set up to evaluate the performance of robots in avoiding dynamic obstacles.

The experimental results demonstrate that the paths planned using the improved S-TEB algorithm exhibit smoother trajectories and cover a larger area compared to those generated by the traditional TEB algorithm, showcasing enhanced navigation capabilities. This research provides valuable insights and guidance for autonomous navigation of agricultural robots in complex environments.

While this study successfully explores the effectiveness of the improved S-TEB algorithm in the local path planning of ORLMs and demonstrates a significant improvement with a 4.23% increase in coverage area, there are still areas that require further investigation. Specifically, this research did not analyze dynamic obstacles, which could be a crucial factor in actual orchard environments. Therefore, future research could consider expanding the scope of experiments to include in-depth analysis and testing of dynamic obstacles to comprehensively assess the performance of ORLMs in real orchard operations. Additionally, further optimization of algorithm parameters and path planning strategies could enhance the navigation efficiency and stability of ORLMs. Overall, while this study provides valuable insights for the development of orchard robot technology, there are still many directions to explore and improve upon to achieve higher levels of autonomy and operational efficiency.

ACKNOWLEDGEMENT

The work was supported by the R&D of low-speed unmanned autonomous navigation controller Project under Grant (No.2022TSGC1175).

REFERENCES

- [1] Chen Ruiyun, Tian Wenbin, Bao Haibo, Li Duan, Xie Xinhao, Zheng Yongjun, Tan Yu., (2023). Three-dimensional environment perception technology for agricultural wheeled robots: A review (农业轮式机器人三维环境感知技术研究进展). *Smart Agriculture*, 5(4), 16-32. <https://doi.org/10.12133/j.smartag.SA202308006>
- [2] Dai Wanyu, Zhang Lijuan, Wu Jiafeng, Ma Xianghua, (2022). Research on Local Path Planning Algorithm Based on Improved TEB Algorithm (改进 TEB 算法的局部路径规划算法研究). *Computer Engineering and Applications*, 58(8), 283-288. <https://doi.org/10.3778/j.issn.1002-8331.2108-0290>
- [3] Guo Chengyang, Liu Meichen, Gao Zeng, Zhou Jianguo, Chen Jun, (2020). Research on agricultural machinery obstacle avoidance method based on improved artificial potential field method. *Journal of Chinese Agricultural Mechanization*, 41(3), 152-157. <https://doi.org/10.13733/j.jcam.issn.2095-5553>
- [4] Jiang H., Pi J., Li A., Yin C. (2022). Dynamic Local Path Planning for Intelligent Vehicles Based on Sampling Area Point Discrete and Quadratic Programming. *IEEE Access*, vol. 10, pp.70279-70294, 2022, <https://doi.org/10.1109/ACCESS.2022.3183154>
- [5] Hang P., Yan, Y., Fu, X., Chen, H., Liu, Y., (2023, April). Research on local path planning of intelligent vehicle based on improved dynamic window approach. In *Third International Conference on Artificial Intelligence and Computer Engineering (ICAICE 2022)* (Vol. 12610, pp. 1326-1334). SPIE. <https://doi.org/10.1117/12.2671069>
- [6] Huang X., Yi J., Shen T., (2023). Research on automatic lawn mower system based on differential GPS and IMU fusion. In *2023 3rd Asia-Pacific Conference on Communications Technology and Computer Science (ACCTCS)*, 26-432, IEEE. <https://doi.org/10.1109/ACCTCS58815.2023.00056>
- [7] Huo, F., Zhu, S., Dong, H., Ren, W., (2024). A new approach to smooth path planning of Ackerman mobile robot based on improved ACO algorithm and B-spline curve. *Robotics and Autonomous Systems*, 175, 104655. <https://doi.org/10.1016/j.robot.2024.104655>
- [8] Kang H., Zhou H., Chen C., (2020). Visual perception and modeling for autonomous apple harvesting. *IEEE Access*, 8, 62151-62163. <https://doi.org/10.1109/ACCESS.2020.2984556>
- [9] Li Y., Li J., Zhou W., Yao Q., Nie J., Qi X., (2022). Robot Path Planning Navigation for dense planting red jujube orchards based on the joint improved A* and DWA algorithms under laser SLAM. *Agriculture*, 12(9), 1445. <https://doi.org/10.3390/agriculture12091445>
- [10] Li J., Zhang Z., (2023, August). AUV Local Path Planning Based on Fusion of Improved DWA and RRT Algorithms. In *2023 IEEE International Conference on Mechatronics and Automation (ICMA)* (pp. 935-941). IEEE. <https://doi.org/10.1109/ICMA57826.2023.10216263>
- [11] Liu Z., Lü Z., Zheng W., Zhang W., Cheng X., (2019). Design of obstacle avoidance controller for agricultural tractor based on ROS. *International Journal of Agricultural and Biological Engineering*, 12(6), 58-65. <https://doi.org/10.25165/j.ijabe.20191206.4907>

- [12] Qin J., Sun R., Zhou K., Xu Y., Lin B., Yang, L., ... & Wu, C., (2023). Lidar-Based 3D Obstacle Detection Using Focal Voxel R-CNN for Farmland Environment. *Agronomy*, 13(3), 650. <https://doi.org/10.3390/agronomy13030650>
- [13] Qiu Z., Zhao N., Zhou L., Wang M., Yang L., Fang H., ... & Liu Y., (2020). Vision-based moving obstacle detection and tracking in paddy field using improved yolov3 and deep SORT. *Sensors*, 20(15), 4082. <https://doi.org/10.3390/s20154082>
- [14] Shi Yangjie, Cheng Xinhui, Xi Xiaobo, (2023). Research progress on the path tracking control methods for agricultural machinery navigation (农业机械导航路径跟踪控制方法研究进展). *Transactions of the Chinese Society of Agricultural Engineering (Transactions of the CSAE)*, 39(15), 1-14. <https://doi.org/10.11975/j.issn.10026819.202304004>
- [15] Wang, Z., Li, P., Li, Q., Wang, Z., Li, Z., (2023). Motion Planning Method for Car-Like Autonomous Mobile Robots in Dynamic Obstacle Environments. *IEEE Access*, 11, 137387-137400. <https://doi.org/10.1109/ACCESS.2023.3339539>
- [16] Weixin, Z., Wang, D., Chen, Z., (2021). Autonomous operation path planning method for unmanned agricultural machinery (无人驾驶农机自主作业路径规划方法). *Transactions of the Chinese Society of Agricultural Engineering*, 37(16), 1-7. <https://doi.org/10.11975/j.issn.1002-6819.2021.16.001>
- [17] WEN Yu, HUANG Jiang-shuai, JIANG Tao, SU Xiao-jie, (2022). Safe and smooth improved time elastic band trajectory planning algorithm (安全平滑的改进时间弹性带轨迹规划算法). *Control and Decision*, 37(08), 2008-2016. <https://doi.org/10.13195/j.kzyjc.2021.0068>.
- [18] Wu, J., Ma, X., Peng, T., Wang, H., (2021). An improved timed elastic band (TEB) algorithm of autonomous ground vehicle (AGV) in complex environment. *Sensors*, 21(24), 8312. <https://doi.org/10.3390/s21248312>
- [19] Wu, M.H., Yu, J.C., Lin, Y.C., (2022, August). Study of Autonomous Robotic Lawn Mower Using Multi-Sensor Fusion Based Simultaneous Localization and Mapping. In 2022 International Conference on Advanced Robotics and Intelligent Systems (ARIS), Taipei, Taiwan, 2022, pp. 1-4, <https://doi.org/10.1109/ARIS56205.2022.9910445>
- [20] XIA Changgao, DING Weibing, HAN Jangyi, (2022). Research on path planning algorithm combining B-splines with improved APF (融合 B 样条与改进 APF 的路径规划算法研究). *Journal of Chongqing University of Technology (Natural Science)*, 36(6), 48-54. [https://doi.org/10.3969/j.issn.1674-8425\(z\)](https://doi.org/10.3969/j.issn.1674-8425(z))
- [21] Yang, J., Chung, S. J., Hutchinson, S., Johnson, D., Kise, M., (2015, May). Omnidirectional-vision-based estimation for containment detection of a robotic mower. In 2015 IEEE International Conference on Robotics and Automation (ICRA) (pp. 6344-6351). IEEE. <https://doi.org/10.1109/ICRA.2015.7140090>
- [22] Yang Lili, Tang Xiaoyu, Wu Sixian, (2024). Local path planning for autonomous agricultural machinery on farm road (机耕道自动驾驶农机局部路径规划). *Transactions of the Chinese Society of Agricultural Engineering (Transactions of the CSAE)*, 40(1), 27-36. (in Chinese with English abstract). <https://doi.org/10.11975/j.issn.1002-6819.202307231>
- [23] Yang, L., Xu, Y., Liang, Y., Qin, J., Li, Y., Wang, X., Wu, C., (2022). Extraction of straight field roads between farmlands based on agricultural vehicle-mounted LiDAR. *International Journal of Agricultural and Biological Engineering*, 15(5), 155-162. <https://doi.org/10.25165/j.ijabe.20221505.6933>
- [24] Zhang Qiang, Chen Bingkui, Liu Xiaoyong, (2019). Ant colony optimization with improved potential field heuristic for robot path planning. *Transactions of the Chinese Society for Agricultural Machinery*, 50(5), 23-32. <https://doi.org/10.6041/j.issn.1000-1298.2019.05.003>
- [25] Zhang, X., Zhu, T., Du, L., Hu, Y., Liu, H., (2022). Local path planning of autonomous vehicle based on an improved heuristic bi-rrt algorithm in dynamic obstacle avoidance environment. *Sensors*, 22(20), 7968. <https://doi.org/10.3390/s22207968>
- [26] Zhao Chunjiang, FAN Beibei, LI Jin, FENG Qingchun, (2023). Agricultural robots: Technology progress, challenges and trends (农业机器人技术进展、挑战与趋势). *Smart Agriculture*, 5(4), 1-15. <https://doi.org/10.12133/j.smartag.SA202312030>
- [27] Zhong, X., Tian, J., Hu, H., Peng, X., (2020). Hybrid path planning based on safe A* algorithm and adaptive window approach for mobile robot in large-scale dynamic environment. *Journal of Intelligent & Robotic Systems*, 99(1), 65-77. <https://doi.org/10.1007/s10846-019-01112-z>
- [28] Zhou, X., Wang, Z., Ye, H., Xu, C., Gao, F., (2020). Ego-planner: An ESDF-free gradient-based local planner for quadrotors. *IEEE Robotics and Automation Letters*, 6(2), 478-485. <https://doi.org/10.1109/LRA.2020.3047728>

DESIGN AND TEST OF SUPPLEMENTAL FEEDING PUSHER DEVICE FOR CATTLE STABLE

牛场补饲推料装置设计与试验

Yumeng XIAO¹⁾, Taowei JIAO¹⁾, Wenjie ZHAO¹⁾, Hengxu ZHU¹⁾, Hongming ZHANG²⁾, Pengpeng SUN²⁾, Wei LI^{*1)}

¹⁾ Northwest A&F University, College of Mechanical and Electronic Engineering/ China;

²⁾ Northwest A&F University, College of Information Engineering/China

Tel: +86-139-0925-8177; E-mail: liweizibo@nwsuaf.edu.cn

DOI: <https://doi.org/10.35633/inmateh-73-22>

Keywords: livestock machinery; design; beef cattle; assisted feeding; auger; push feeder

ABSTRACT

This paper proposed a supplemental feeding pusher based on beef cattle's auxiliary feeding needs to solve the traditional feeding mode of manual work, labor intensity, and inconsistent manual work standards. Firstly, the conveyed feed particles movement process was established as a motion model and the basis of the design parameters of the screw conveyor was explained. ANSYS static analysis module was used to ensure that the structural parameters of the discharging device were reasonable, ANSYS vibration modal analysis module was used to verify the frame strength and stability. According to the theoretical design of the trial prototype, the control system with STM32F103RE microcontroller as the core was carried out. Finally, the orthogonal test was conducted with the screw shaft speed, sweeping roller brush height, and traveling speed as test factors; different parameters were set to verify the effect of supplemental feeding and pushing, and parameter optimization of the test results was carried out using Design-Expert software. The optional combination of working parameters was determined to be the feeding screw shaft speed 188 r/min, the sweeping roller brush speed 160 r/min, and the work speed 0.26 m/s. The test demonstrated that the residual feed width was 0.73 m, and the transverse coefficient of variation was 14.9%, which could satisfy the needs of auxiliary feeding for beef cattle. This study reduced feed waste and met the cattle feeding needs to the greatest extent, and it could provide a reference for auxiliary feeding machinery.

摘要

为解决传统饲喂方式以人工作业为主、劳动强度大、作业标准不统一且效率低的问题，本文基于肉牛辅助饲喂需求设计了一种的补饲推料机。首先，对输送的饲料颗粒运动过程建立运动模型并说明螺旋输送装置设计参数依据，利用 ANSYS 静力学分析模块确保下料装置结构参数合理，并利用 ANSYS 振动模态分析模块验证机架强度和稳定性；根据理论设计试制样机，对以 STM32F103RE 单片机为核心的补料清扫控制系统进行了设计。最后，以螺旋轴转速、清扫滚刷高度、行驶速度为试验因素进行正交试验，设置不同参数验证补饲推料效果，使用 Design-Expert 软件对试验结果进行参数优化，结果表明，当送料螺旋轴转速为 188 r/min，清扫滚刷转速为 160 r/min，行进速度为 0.26 m/s 时，余料幅宽为 0.73 m，横向变异系数为 14.9%，能够满足肉牛辅助饲喂的需求该研究减少了饲料的堆积浪费，最大程度上满足动物的采食需求，可为辅助饲喂机械的设计优化提供参考。

INTRODUCTION

With the development of science and technology empowering the beef cattle breeding industry, feeding methods are constantly changing from traditional feeding methods to TMR methods at this stage (Zhong et al., 2020), but most beef cattle farms currently have a low degree of automation (Bae et al., 2023). During the feeding process of beef cattle, it often happens that straw and other remaining roughage accumulated in the trough or the grass is arched away from the feeding area due to the preference for concentrate feed (Greter et al., 2015), resulting in a decline in cattle intake and feed waste (Da Borso et al., 2017).

The traditional solution is to sweep scattered feed manually or drive the feed truck to push the remnant feed, which is inefficient, and the operation effect cannot be effectively guaranteed. If scattered feed is not pushed back promptly, it may lead to a buildup of fermentation, affecting the stable environment and cattle health (Nabokov et al., 2020; Liu et al., 2016). Cattle's feeding and living environment directly affect their growth conditions (Tangorra and Calcante, 2018; Moya et al., 2011). In the long run, it not only causes the waste of feed but also affects the cattle quality (Cummins et al., 2009) and reduces the economic value (Álvarez-Rodríguez et al., 2020), so the research on assisted feeding robots has been generated (Pavkin et al., 2023).

Auxiliary feeding equipment like supplemental feeding equipment and pushing machinery is an essential part of intelligent farming (Alameer et al., 2020; Pavkin et al., 2021), which can improve the efficiency of feed utilization as well as the eating quality of beef cattle (Mosquera et al., 2021; Bisaglia, 2012). Many researchers have recently focused on automated feeding robots (Bisaglia, 2023; Yang et al., 2022). Uzedhe et al. presented an on-farm automated feeding robotic system that consisted of automatic navigation, which could provide 26.6 kg of feed automatically at 1.233 km/h, but it was incapable of tipping and pushing loose material and was not suitable for automatic feeding of beef cattle (Uzedhe et al., 2023). The cow intelligent pushing robot developed by Zhang et al. used a straight-faced pushing plate to push the material and acquired images through a webcam; however, the recognition rate of this method for the QR code was easily affected by environmental factors (Zhang et al., 2023). Chen et al. used the 9ITL-650 feeding robot as a platform and constructed an ultra-wideband autonomous navigation system, but the device had a single function, and it could not satisfy the replenishment feeding as well as sweeping and other operations (Chen et al., 2024). Bakirov et al. developed a robotic control system for cattle shed feeding and carried out an operational procedure that allowed for automated feeding of typical cattle yards. However, it lacked pushing and sweeping functions to meet complete automation requirements (Bakirov et al., 2020).

In summary, due to the problem of frequent replenishment and pushing of materials in beef cattle farms, there is a lack of an integrated cattle farm auxiliary feeding machine that can simultaneously realize automatic replenishment, moving materials, and cleaning. Considering the problems of existing feeding machinery, a structure and working method of a supplemental feeding pusher are proposed. Automatically achieving timely replenishment, pushing, and cleaning can solve the problem of low grass utilization as it is removed from the feeding area by the cattle.

MATERIALS AND METHODS

Machine structure and working principle

Structure of supplemental feeding pusher

The supplemental feeding pusher consists of the traveling chassis, discharging device, sweeping device, power supply, navigation module and central control module. As shown in Fig. 1, the device can push back the feed along the feed routing trajectory to facilitate beef cattle feeding. At the same time, it carries a silo that can add following the remaining feed in the process of the feeding of the beef cattle. For the operating environment of beef farms, the traveling chassis is steered by the front axle and driven by the rear axle, and the system adopts the UWB (ultra-wide band) positioning mode and integrates the IMU (micro-inertial measurement unit) data information for navigation. Considering loose-feeding as the mainstream of livestock breeding, the application scenario of the designed supplemental feeding pusher is loose-feeding mode, with an open range of cattle activities and fixed feeding points.

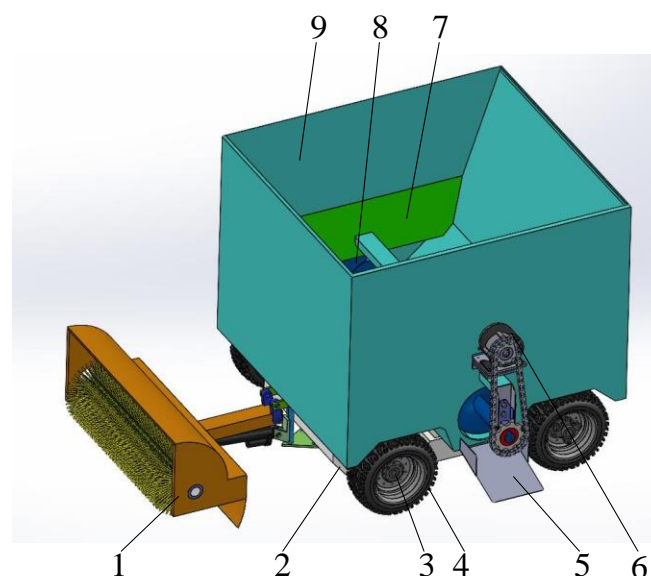


Fig. 1 - Structure of the supplemental feed pusher

1. Cleaning device; 2. Frame; 3. Wheel encoder; 4. Rolling wheel; 5. Feeding plate;
6. Motor; 7. Leak-proof baffle; 8. Feeding screw; 9. Silo

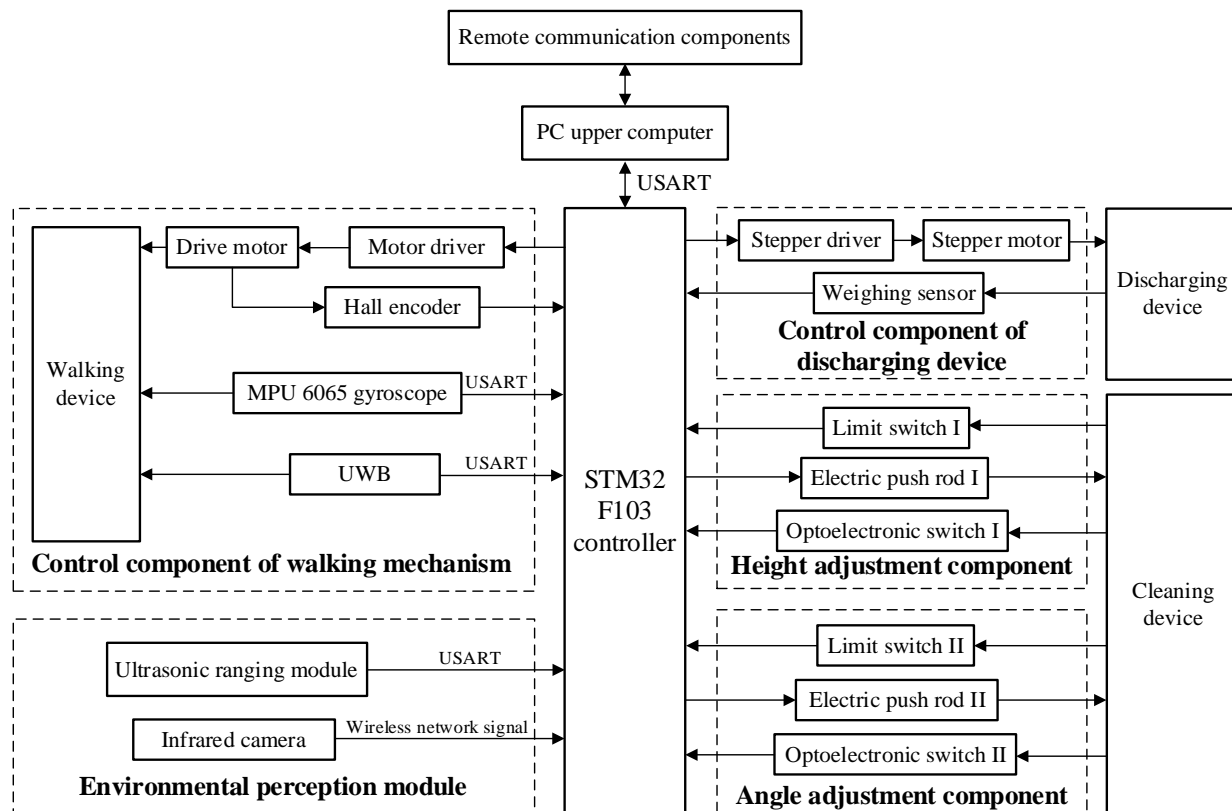


Fig. 2 - Overall control system diagram for the supplemental feeding pusher

The microcontroller integrates microprocessor, memory and other parts to form a miniature computing system, with reliability and fast operation advantages. Given the beef cattle feeding requirements, the composition of the hardware part of the supplemental feeding pusher control system is determined. The STM32F103 microcontroller is the total controller of the whole system, which is connected to the ultrasonic range sensor, load cell and other modules. The overall control system diagram for the supplemental feeding pusher is shown in Fig. 2.

Working principle and technical parameters

According to the requirements of the beef cattle breeding feeding link, firstly, the TMR (total mixed ration) spreading wagon completes the feed sprinkling in the stable. After 1.5 h of centralized feeding by the spreading wagon, the supplemental feeding pusher carries out the pushing and supplemental feeding operation. The working method of the designed supplemental feeding pusher system is as follows: after turning on the power supply unit, it makes a fixed stop at the starting point A position, and then through the system distance measuring sensor, the distance to the cattle neck yoke railings is measured.

After entering the area to be operated, stop at the starting point A position, measure the distance to the border cattle neck yoke fence through the system distance measuring sensor, adjust the distance between the left and right of the AB section, and get ready to enter the working state. After entering the feeding area through the B point, monitor the distance to the border cattle neck yoke fence in real time in the process of the straight operation of the BC section, and control the distance from the border to a certain extent.

During the operation of the feeding area, set up a suitable working mode in advance, and the supplementary feeding pusher will carry out the supplementary feeding and cleaning operation; after completing the operation of one side of the feeding area, it will drive to the cattle house D. After finishing the work in the feeding area on one side, it will drive to the D section of the stable, turn at the DE section at the end of the stable, and complete the pushing and feeding operation on the other side. The main technical parameters of the supplemental feed pusher are shown in Table 1.

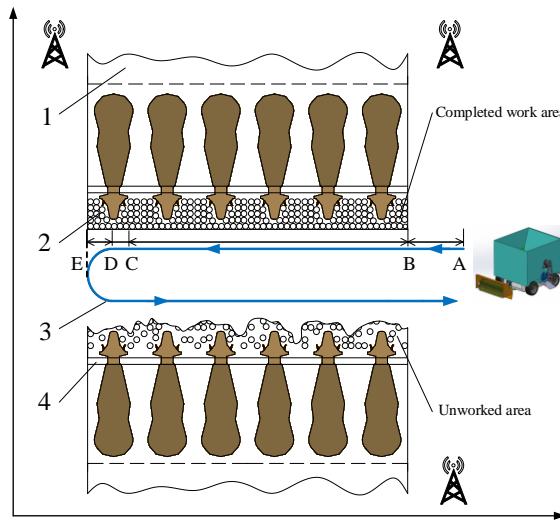


Fig. 3 - Schematic diagram of the operation of the supplemental feeding pusher
 1. Beef cattle activity area; 2. Feeding area; 3. Operating track; 4. Neck yoke

Table 1

| Main technical indexes of feeding pusher | |
|--|----------------|
| Parameters | Values |
| Overall dimensions (lengthx widthx height) /mmx mmx mm | 1350×1200×1450 |
| Quantity of material in storage /m ³ | 3.2 |
| Silo Flow Pattern | Integral flow |
| Operating speed /(m/s) | ≤0.4 |
| Weight /kg | 165 |

Design and analysis of supplemental feeding pusher components

Design and simulation verification of discharging device

In order to realize the supplemental forage function of the supplemental feed pusher, it is required that the feed stored in the silo can be uniformly and steadily fed to the feeding area. The feeding device mainly consists of a silo, conveying screw, anti-leakage baffle, motor, weighing device and other parts, as shown in Figure 4. The screw conveyor has the advantages of simple structure and reliable work, and it is easy to control frequency in the actual production. By selecting different motor speeds, it is easier to control the amount of feed accurately. To avoid the problem of "hygroscopic agglomeration" caused by the accumulation of feed in the silo for too long a period, a side length of 1200 mm square funnel-type silo is used. When working, the motor drive conveyor screw rotates through the chain, through the guide plate to avoid uneven feeding and clogging phenomenon, and then fall into the conveyor screw blade. The feed plate has a tilt angle to ensure that the feed is thrown to the scope of the feeding area. When discharging is stopped, the motor stops, and the remaining forage in the silo can be a leakage barrier to block to avoid wastage.

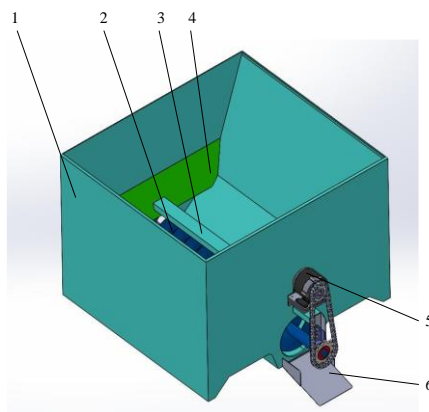


Fig. 4 - Structure of the discharging device

1. Bin; 2. Feeding screw; 3. Guide plate; 4. Leak-proof baffle; 5. Motor; 6. Feeding plate

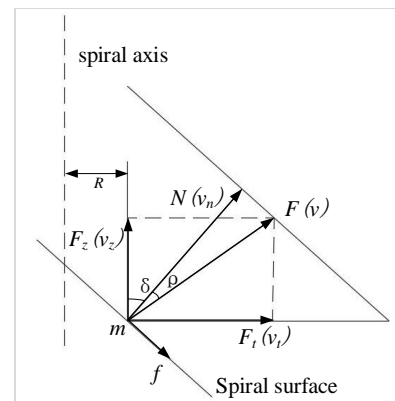


Fig. 5 - Mechanical and kinematic decomposition of the conveying medium

Theoretical analysis of the process of material transfer in the discharging device is made, and the following assumptions are put forward: it is assumed that the material filling coefficient in the spiral discharging device was the same, without considering the compression of the material in the spiral. Take the material at the distance R from the axis as the object of study, and the force and motion decomposition of the mass point m is shown in Figure 5. It can be seen that v_n is the velocity of the point m along the direction normal to the helical surface, and due to the existence of friction between the material and the helical blades, v is the actual speed of the point m . The helical lift angle of the feeding screw is expressed according to the equation (1).

$$\tan\delta = \frac{S}{\pi D_m} \quad (1)$$

where:

δ is the helical lift angle at which the mass point m is located at that position, [°];

D_m is the diameter at which the mass point m is located at that position, [m];

S is the pitch of the spiral, [m].

In the force decomposition of Fig. 5, the axial force and circumferential force are expressed according to equation (2):

$$\begin{cases} F_t = F \sin(\rho + \delta) \\ F_z = F \cos(\rho + \delta) \end{cases} \quad (2)$$

where:

F is the combined force exerted on the mass m , [N];

F_z is the axial component forces exerted on the mass, [N];

F_t are the circumferential component forces exerted on the mass, [N];

δ is the helical lift angle at which the mass point m is located at that position, [°];

ρ is the equivalent friction angle, approximating the v and v_n deviation amount, [°].

From equations (1) and (2), it can be seen that with the increase of δ , F_z decreases while F_t increases, and the main movement of the conveyed material gradually becomes rotary around the axis. According to the structure of the screw conveying device and the relevant parameters, take out the diameter of the mouth of the material is 275 mm, the diameter of the helical blade is 200 mm, and S is 135 mm.

The simplified 3D model was imported into ANSYS to verify the stability of the discharging device. The simplified 3D model was imported into ANSYS to analyze the force situation and simulate the deformation and stress situation of the feeding screw. The analysis results are shown in Fig. 6.

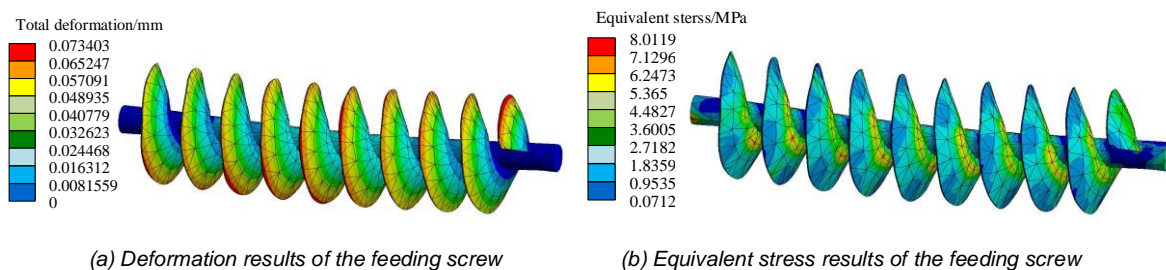


Fig. 6 - Analysis results of the feeding screw

According to the results in Fig. 6(a), the screw was deformed under the action of self-weight, torsional moment and material transfer. The main deformation area was the spiral blade and intermediate shaft position. The maximum deformation is 0.073403 mm, which occurred at the maximum radius of the spiral blade at both ends. The deformation of the edge of the spiral blade was more significant than that at the root position. In Fig. 6(b), the stress of the feeding screw was concentrated in the contact position of the screw blade and the screw shaft. The stress was gradually dispersed and reduced with the increase of the screw radius, and the maximum stress was far less than the yield strength of Q235 235MPa. After analyzing and verifying, the discharging device structure can meet the strength requirements.

Structural design of the cleaning device

The cleaning device can quickly complete the directional sweeping operation of scattered feed, mainly including sweeping brush, brush groove, roller motor and electric actuator. The structure is shown in Fig. 7.

Brush strips are arranged on the periphery of the motor, and the feed left from the gap between the brush clusters in the front row can be cleaned by the brush clusters in the back row, which can prevent the incomplete cleaning phenomenon. In addition, the cleaning brush tufts are installed in the brush groove so they can be replaced after long-term use, reducing maintenance costs. This structural form can realize the collection and discharge of materials and complete both circumferential tangential sweeping and axial pushing during operation.

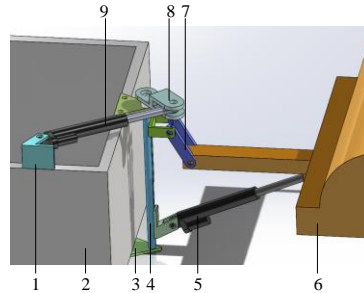


Fig. 7 - Sketch of the structure of the cleaning device

1. Mounting bracket; 2. Frame; 3. Fixed plate; 4. Centre shaft; 5. Electric actuator 1; 6. Brush roller; 7. Connecting plate; 8. Rotating bracket; 9. Electric actuator 2

To improve the feed pushing rate, the height position and working angle of the sweeping device can be controlled by the electric actuator 1 and the electric actuator 2 to complete the sweeping operation of the feed in different directions so that the lower edge of the sweeping brush is in close contact with the ground. When the cleaning device is not working, the vertical direction is raised by 0~70 mm, the lower edges of the cleaning brush and dust cover are not in contact with the ground, and the cleaning device is restored to the initial position.

Vehicle structure design and simulation verification

The frame is integral to the connection between the various working parts. During operation, it is subjected to dynamic loads and vibration from other working parts. When the frequency of the external vibration source and the inherent frequency of the frame are close to, or even coincide with, it is easy to produce damage to the parts. Therefore, modal analysis is used to determine the vibration characteristics of the frame to avoid resonance phenomena and to ensure the reliability of the feeding pusher.

The vibration differential equation of the system during the working process of the supplemental feeding and pushing device, with no external changing load on the frame and ignoring the damping effect, is shown in equation (3):

$$[M]\{x''\} + [K]\{x\} = \{0\} \tag{3}$$

where: $[M]$ is the mass matrix of the frame;

$[K]$ is the stiffness matrix of the frame;

$\{x''\}$ is the acceleration vector matrix;

$\{x\}$ is the displacement vector matrix;

The modal analysis of the frame was carried out using ANSYS Workbench. Generally, the low-order vibration mode plays a relatively important role in the working device, so the transverse axis of the first six orders of the mode of the intrinsic frequency and vibration mode were considered. The modal analysis result is shown in Table 2, and the modal vibration pattern is shown in Figure 8.

Table 2

| Rack modal analysis results | | | |
|-----------------------------|--------------------------|-------------------------------|--------------------------------------|
| Modal order | Intrinsic frequency (Hz) | Relative deformation peak(mm) | Description of the vibration pattern |
| 1 | 15.398 | 2.288 | Bend around the X axis |
| 2 | 31.215 | 3.082 | Bend around the Z axis |
| 3 | 37.198 | 3.196 | Bend around the Z axis |
| 4 | 53.055 | 2.865 | Bend around the Y axis |
| 5 | 60.657 | 3.182 | Bend around the X axis |
| 6 | 66.606 | 3.425 | Bend around the Y axis |

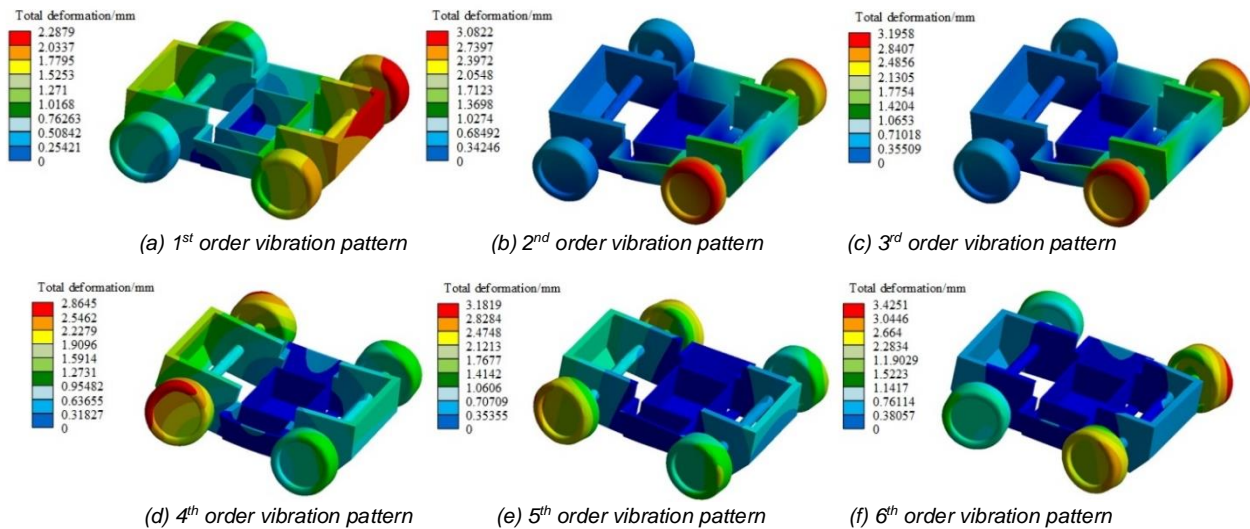


Fig. 8 - The first six orders of the modal vibration pattern of the frame

As seen from Fig. 8, the areas where larger amplitude and deformation occurred were the front and rear ends of the frame, and the deformation inside the frame was minor. The frame carried the weight of the discharging device, and it was affected by the vibration of the discharging device and the sweeping device when they were working, which concentrated the force and vibration in the position of the two ends of the rack, resulting in poor stability. The maximum speed of the drum motor was 5.67 r/s, and the vibration frequency generated by the external stimulation was less than the minimum frame inherent frequency, so the frame would not resonate with other parts during the working process. The structural design is reasonable and meets the stability requirements.

RESULTS

Feeding pusher performance experiment

Experimental conditions

The selected test site was in Yangling District, Shaanxi Province (34°28'N, 108°07'E). The test instruments and materials included a 48 V battery, I/O module terminals, Mini3sPlus UWB module, MPU9250 gyroscope, E3F-DS304C photoelectric switch, HC-SR04 ultrasonic sensor, E6B2-CWZ6 encoder, tape measure, and vernier caliper.

Discharge test

Orthogonal experimental design

According to the theoretical analysis of each working part in the previous period, it was determined that the main factors affecting the working effect of the supplemental feeding pusher were the screw shaft rotation speed, the roller brush rotation speed and the traveling speed as the test factors. Ten 5 m×3 m measurement areas were taken in the test stable. The distance of scattered feed from the cattle neck yoke in each region was measured before the test as the initial offset μ_0 . The residual feed width and uniformity were taken as the test indexes, in which the residual feed width could be measured directly, and the transverse coefficient of variation illustrated the uniformity, and the calculation is shown in equation (4).

$$\begin{cases} CV = \frac{\sigma}{\mu} \\ \sigma = \sqrt{\frac{1}{n-1} \sum_{i=1}^n (\mu_i - \mu_0)^2} \end{cases} \quad (4)$$

where:

- CV is the transverse coefficient of variation, [%];
- σ is the standard deviation;
- n is the number of sampling areas;
- μ_i is the average distance of the residual feed in the i sampling area after the operation, [m];
- μ is the average of μ_i , [m].

Experimental program and results

In order to avoid material accumulation on the inner wall of the silo, the proposed screw shaft speed range was 150 r/min~220 r/min; with reference to the working parameters of similar machinery, the preliminary selection of the sweeping roller brush speed range was 120 ~200 r/min; the proposed range of traveling speeds of the supplemental feeding pusher was 0.1~0.4 m/s. The orthogonal test was used to study the influence of each factor on the machine, and the code levels of factors are shown in Table 3.

Table 3

| Test Code and levels of factors | | | |
|---------------------------------|--|--|--------------------------------|
| Code | Test factors | | |
| | Feeding screw shaft speed, x_1 / (r/min) | Sweeping roller brush speed, x_2 / (r/min) | Traveling speed, x_3 / (m/s) |
| +1.682 | 220 | 200 | 0.4 |
| +1 | 205.8 | 183.8 | 0.34 |
| 0 | 185 | 160 | 0.25 |
| -1 | 164.2 | 136.2 | 0.16 |
| -1.682 | 150 | 120 | 0.1 |

The test was conducted according to the test factors in Table 3, the test and measurement process shown in Fig. 9, and the test results in Table 4.



Fig. 9 - Supplemental feeding pusher discharging test

(a) Test Scene

(b) Measurement process

Table 4

| Experimental results | | | | | |
|----------------------|---------------|---------------|-------------|-------|--------|
| No | Test factors | | | Y (m) | CV (%) |
| | x_1 (r/min) | x_2 (r/min) | x_3 (m/s) | | |
| 1 | 164.2 | 136.2 | 0.16 | 1.08 | 19.2 |
| 2 | 205.8 | 136.2 | 0.16 | 0.87 | 17.6 |
| 3 | 164.2 | 183.8 | 0.16 | 1.12 | 16.2 |
| 4 | 205.8 | 183.8 | 0.16 | 0.95 | 15.8 |
| 5 | 164.2 | 136.2 | 0.34 | 0.96 | 17.5 |
| 6 | 205.8 | 136.2 | 0.34 | 0.98 | 15.9 |
| 7 | 164.2 | 183.8 | 0.34 | 1.02 | 15.3 |
| 8 | 205.8 | 183.8 | 0.34 | 1.08 | 14.7 |
| 9 | 150 | 160 | 0.25 | 1.05 | 17.0 |
| 10 | 220 | 160 | 0.25 | 1.07 | 14.1 |
| 11 | 185 | 120 | 0.25 | 0.80 | 19.1 |
| 12 | 185 | 200 | 0.25 | 0.91 | 14.0 |
| 13 | 185 | 160 | 0.1 | 1.04 | 18.6 |
| 14 | 185 | 160 | 0.4 | 0.90 | 14.9 |
| 15 | 185 | 160 | 0.25 | 0.62 | 14.5 |
| 16 | 185 | 160 | 0.25 | 0.73 | 13.7 |
| 17 | 185 | 160 | 0.25 | 0.66 | 14.9 |
| 18 | 185 | 160 | 0.25 | 0.71 | 13.8 |
| 19 | 185 | 160 | 0.25 | 0.79 | 15.1 |
| 20 | 185 | 160 | 0.25 | 0.87 | 15.0 |
| 21 | 185 | 160 | 0.25 | 0.76 | 14.5 |
| 22 | 185 | 160 | 0.25 | 0.89 | 15.2 |
| 23 | 185 | 160 | 0.25 | 0.71 | 14.8 |

Analysis of test results

Multiple regression was fitted to the results using Design-Expert 13.0 software to obtain the regression equations for the residual material distance from the neck yoke width *Y* and the transverse coefficient of variation *CV*, respectively. It could test the effect of each test factor on the significance of the model.

(1) Residual feed width from the cattle yoke *Y*

According to the results of the ANOVA, the model $F=7.37$ indicated that the model was significant. For the grading accuracy of the test indicators, the order of influence of the test factors and the interactions between the factors was $x_1^2, x_3^2, x_2^2, x_1x_3, x_2, x_1, x_3, x_1x_2, x_2x_3$, where x_1^2, x_3^2 had a highly significant influence; x_2^2 had a significant influence; x_1x_3 had a slightly significant; $x_2, x_1, x_3, x_1x_2, x_2x_3$ had no significant impact.

The non-significant factors were removed and re-analyzed by ANOVA to obtain the regression equation of each experimental factor on the residual feed distance from the neck yoke width *Y* according to equation (5) and the results are presented in table 5:

$$Y = 0.7482 + 0.0575x_1x_3 + 0.1168x_1^2 + 0.0443x_2^2 + 0.0850x_3^2 \tag{5}$$

Table 5

Results of ANOVA for residual feed distance from cattle neck yoke width

| Source | Sum of squares | Degree of freedom | Mean square | <i>F</i> | <i>P</i> |
|-------------|----------------|-------------------|-------------|----------|-------------|
| Modal | 0.4107 | 9 | 0.0456 | 7.37 | 0.0008*** |
| x_1 | 0.0052 | 1 | 0.0052 | 0.8392 | 0.3763 |
| x_2 | 0.0158 | 1 | 0.0158 | 2.56 | 0.1338 |
| x_3 | 0.0034 | 1 | 0.0034 | 0.5491 | 0.4719 |
| x_1x_2 | 0.0008 | 1 | 0.0008 | 0.1292 | 0.7250 |
| x_1x_3 | 0.0265 | 1 | 0.0265 | 4.27 | 0.0592* |
| x_2x_3 | 0.0002 | 1 | 0.0002 | 0.0323 | 0.8601 |
| x_1^2 | 0.2168 | 1 | 0.2168 | 35.23 | < 0.0001*** |
| x_2^2 | 0.0321 | 1 | 0.0321 | 5.05 | 0.0427** |
| x_3^2 | 0.1148 | 1 | 0.1148 | 18.55 | 0.0009*** |
| Residual | 0.0805 | 13 | 0.0062 | | |
| Lack of fit | 0.0162 | 5 | 0.0032 | 0.4029 | 0.8342 |
| Error | 0.0643 | 8 | 0.0080 | | |
| Total | 0.4912 | 22 | | | |

Note: *** denotes highly significant, ** denotes significant, * denotes slightly significant, same as Table 6

(2) Transverse coefficient of variation

According to the ANOVA results, the model $F=19.59$ indicated that the model was significant. For the transverse coefficient variation, the order of magnitude of the effects of the test factors and the interactions between the factors on it were $x_1, x_3, x_3^2, x_2^2, x_2, x_1^2, x_1x_2, x_2x_3, x_1x_3$, where $x_1, x_2, x_3, x_2^2, x_3^2$ had a highly significant influence; x_1x_2, x_1x_3, x_2x_3 had no significant influence. The non-significant factors were removed and re-analyzed by ANOVA to obtain the regression equation of each experimental factor on the transverse coefficient variation according to equation (6) and the results are presented in table 6:

$$CV = 14.61 - 0.6647x_1 - 1.23x_2 - 0.8510x_3 + 0.3610x_1^2 + 0.7146x_2^2 + 0.7853x_3^2 \tag{6}$$

Table 6

Results of ANOVA for transverse coefficient variation

| Source | Sum of squares | Degree of freedom | Mean square | <i>F</i> | <i>P</i> |
|----------|----------------|-------------------|-------------|----------|-------------------------|
| Modal | 170.84/168.38 | 9 | 6.35 | 19.59 | < 0.0001***/< 0.0001*** |
| x_1 | 57.13 | 1 | 6.03 | 18.62 | 0.0008*** |
| x_2 | 6.03 | 1 | 20.61 | 63.62 | < 0.0001*** |
| x_3 | 9.89 | 1 | 9.89 | 30.53 | < 0.0001*** |
| x_1x_2 | 0.6050 | 1 | 0.6050 | 1.87 | 0.1949 |

| Source | Sum of squares | Degree of freedom | Mean square | F | P |
|-------------|----------------|-------------------|-------------|--------|-----------|
| X_1X_3 | 0.0050 | 1 | 0.0050 | 0.0154 | 0.9030 |
| X_2X_3 | 0.2450 | 1 | 0.2450 | 0.7562 | 0.4003 |
| X_1^2 | 2.07 | 1 | 2.07 | 6.39 | 0.0252** |
| X_2^2 | 8.11 | 1 | 8.11 | 25.04 | 0.0002*** |
| X_3^2 | 9.80 | 1 | 9.80 | 30.24 | 0.0001*** |
| Residual | 1.84 | 5 | 1.24 | | |
| Lack of fit | 2.37 | 8 | 0.2961 | 1.24 | 0.3722 |
| Error | 4.21 | 13 | 0.3240 | | |
| Total | 61.35 | 22 | | | |

Response surface analysis

The experimental results were analyzed by Design-Expert 13.0 software to derive the response surfaces of the significant interactions of feeding screw shaft speed x_1 , sweeping roller brush speed x_2 and travel speed x_3 on the residual feed width Y and transverse coefficient of variation CV as shown in Figure 10.

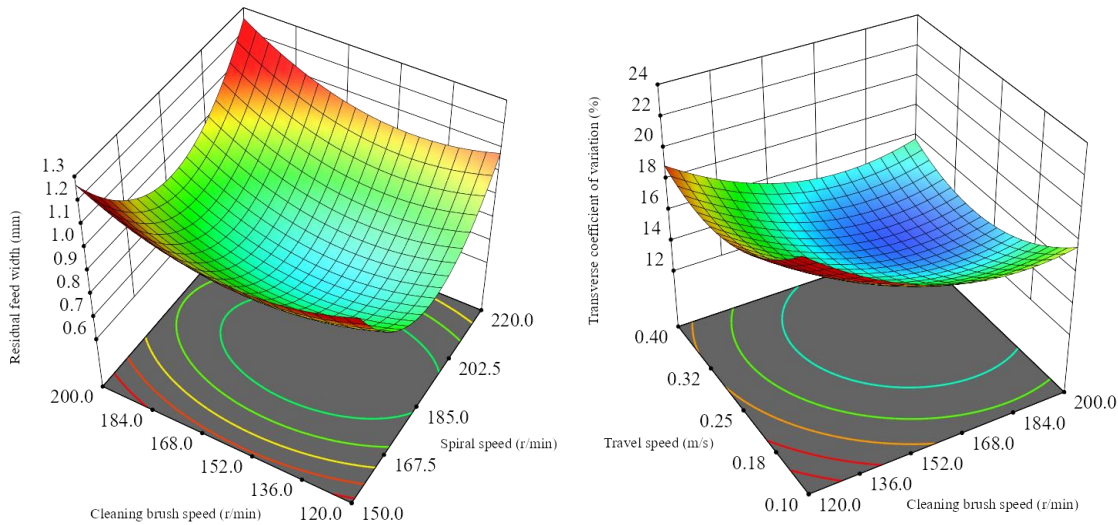


Fig. 10 - Response surface for the interaction between residual feed width and transverse coefficient of variation
 (a) $x_3=0.4$ m/s
 (b) $x_1=185$ r/min

When the traveling speed = 0.4 m/s, the response surface of the interaction between the screw shaft rotation speed and the sweeping brush rotation speed is shown in Fig. 10(a). When the sweeping brush rotation speed was certain, the residual material width showed a decreasing and increasing trend with the increase of the screw shaft rotation speed. The screw rotation speed of the feeding screw influenced the discharged amount and the movement of the material when it was thrown out. The horizontal initial velocity of feed particles was easy to pile up in the non-feeding zone when the screw shaft rotation speed was too low, but when the rotational speed was too high, the discharged amount increased, so the preferred rotational speed of the screw shaft was in the range of 185.0-202.5 r/min. When the rotational speed of the screw shaft was certain, the residual material width showed a decreasing and then increasing tendency with the increasing rotational speed of the sweeping brush. The preferred rotational speed range of the sweeping brush was in the range of 136.0-168.0 r/min.

When the rotational speed of the spiral axis = 185 r/min, the response surface of the interaction between the sweeping brush speed and traveling speed is shown in Fig. 10(b). When the traveling speed was certain, the CV showed a decreasing trend as the speed of the sweeping brush increased and was gradually flattened out because the sweeping brush affected the total amount of pushed feed per unit of time, increasing the efficiency of sweeping. But when the sweeping brush speed exceeded a specific range, the vibration of the whole machine caused by the sweeping device increased, so the optimal range of the sweeping brush speed was 152.0~184.0 r/min; when the speed of the sweeping brush was certain, the CV showed a decreasing and then increasing trend with the increase of the traveling speed, and the better traveling speed was 0.25~0.32 m/s.

Parameter optimization

To obtain the best operational performance parameters of the supplemental feed pusher, the regression model was optimized based on the obtained test results and regression equations with the constraints.

The system of objective and constraint equations is shown in equation (7):

$$\begin{cases} \min Y(x_1, x_2, x_3) \\ \min CV(x_1, x_2, x_3) \\ 150r/min \leq x_1 \leq 220r/min \\ 120r/min \leq x_2 \leq 200r/min \\ 0.1m/s \leq x_3 \leq 0.4m/s \end{cases} \quad (7)$$

The optimal solution was 187.6 r/min for the feeding screw shaft, 160.8 r/min for the sweeping roller brush, and 0.26 m/s for the traveling speed. The residual feed from the cattle neck yoke after the operation of the supplemental feeding push device was 0.71 m in width, with a transverse coefficient of variation of 14.3%.

Experimental validation

Considering the optimized working parameters and operational feasibility, the feeding screw shaft speed was set at 188 r/min, the sweeping roller brush speed at 160 r/min, and the travel speed at 0.26 m/s for the test. The other test conditions were the same as above, and the test results are shown in Table 7.

Table 7

| Effectiveness of feeding pusher operation at optimum parameters | | | | | |
|---|---------------|---------------|-------------|-------|--------|
| No. | Test factors | | | Y (m) | CV (%) |
| | x_1 (r/min) | x_2 (r/min) | x_3 (m/s) | | |
| 1 | 188 | 160 | 0.26 | 0.70 | 15.9 |
| 2 | 188 | 160 | 0.26 | 0.79 | 16.3 |
| 3 | 188 | 160 | 0.26 | 0.75 | 13.8 |
| 4 | 188 | 160 | 0.26 | 0.67 | 15.4 |
| 5 | 188 | 160 | 0.26 | 0.77 | 14.6 |
| 6 | 188 | 160 | 0.26 | 0.72 | 13.5 |
| Average value | 188 | 160 | 0.26 | 0.73 | 14.9 |

After six tests, the average width of the residual feed was 0.73 m, and the average value of the calculated transverse coefficient of variation was 14.9%, which was able to satisfy the auxiliary feeding needs of beef cattle breeding (width of scattered feed less than 0.75 m).

CONCLUSIONS

(1) Through theoretical analysis, device design and cattle farm tests, a supplemental feeding pusher was developed, which is more adaptable to cattle farms of different breeding scales and more suitable for intensive cattle farms.

(2) The three-factor, five-level orthogonal test established the regression model using test factors and evaluation indexes. The optimal combination of the working parameters was determined to be the screw shaft speed of 188 r/min, the sweeping roller brush speed of 160 r/min, and the traveling speed of 0.26 m/s, providing the basis for the selection of the machine working parameters of the supplemental feeding pusher.

(3) The test showed that the prototype machine had stable performance. The measured residual feed width was 0.73 m, the lateral coefficient of variation was 14.9%, and the test index met the needs of beef cattle auxiliary feeding. It can reduce the problem of high labor-intensity manual operation and effectively improve supplemental feeding and cleaning efficiency.

ACKNOWLEDGEMENT

This study was supported by the Shaanxi Livestock and Poultry Breeding Double-chain Fusion Key Project (2022GD-TSLD-46) and in part by SCO Institute of Modern Agricultural Development Program, Northwest A&F University.

REFERENCES

- [1] Alameer, A., Kyriazakis, I., Dalton, H. A., Miller, A.L. & Bacardit, J. (2020). Automatic recognition of feeding and foraging behavior in pigs using deep learning. *Biosystems Engineering*, 197, 91-104.
- [2] Álvarez-Rodríguez, J., Casasús, I., Blanco-Penedo, I., & Sanz, A. (2020). Effect of Feeding Level and Breed on the Daily Activity Budget of Lactating Beef Cows Fed Total Mixed Ration. *Agriculture*, 10(6), 195.
- [3] Bae, J., Park, S., Jeon, K., & Choi, J.Y. (2023). Autonomous System of TMR (Total Mixed Ration) Feed Feeding Robot for Smart Cattle Farm. *International Journal of Precision Engineering and Manufacturing*, 24, 423-433.

- [4] Bakirov, S.M., Logachev, O.V., & Shlyupikov, S.V. (2020). Justification of parameters of automatic control system of robot feed distribution in cattle barn. *IOP Conference Series Earth and Environmental Science*, 422, 12057.
- [5] Bisaglia, C., Belle Z., Berg, G.V. & Pompe, J.C. (2012). Automatic vs. conventional feeding systems in robotic milking dairy farms: a survey in The Netherlands. <https://www.researchgate.net/publication/267555832>.
- [6] Bisaglia, C., Lazzari, A., Giovinazzo, S., & Brambilla, M. (2023). Automatic Feeding Systems for Cattle in Italy: State of the Art and Perspectives. *AIIA 2022: Biosystems Engineering Towards the Green Deal*, 373-381.
- [7] Chen Z.J., Wang H.F., Zhou M.C., Zhu J., Chen J.H., & Li B. (2024) Design and Experiment of an Autonomous Navigation System for a Cattle Barn Feed-Pushing Robot Based on UWB Positioning. *Agriculture*, 14(5), 694.
- [8] Cummins, B., Kiely, P.O., Keane, M.G. & Kenny, D.A. (2009). Feed Intake Pattern, Behaviour, Rumen Characteristics and Blood Metabolites of Finishing Beef Steers Offered Total Mixed Rations Constituted at Feeding or Ensiling. *Irish Journal of Agricultural and Food Research*, 48, 57-73.
- [9] Da Borso, F., Chiumenti, A., Sigura, M., & Pezzuolo, A. (2017). Influence of automatic feeding systems on design and management of dairy farms. *Journal of Agricultural Engineering*, 48-52.
- [10] Greter, A.M., Miller-Cushon N.E.K., McBride, B.W., Widowski, T.M., Duffield, T.F. & DeVries T.J. (2015) Short communication: Limit feeding affects behavior patterns and feeding motivation of dairy heifers. *Journal of Dairy Science*, 98, 1248-1254.
- [11] Liu Y.F., Sun F.F., Wan F.C., Zhao H.B., Liu X.M., You W., Cheng H.J., Liu G. F., Tan X. W. & Song, E. L. (2016). Effects of Three Feeding Systems on Production Performance, Rumen Fermentation and Rumen Digesta Particle Structure of Beef Cattle. *Animal Bioscience*, 29, 659-665.
- [12] Mosquera, I. L. Q., Fierro, J. E. R., Zacarias, J. R. O., Montero, J. B., Quijano, S. A. C. & Huamanchahua, D. (2021). Design of an Automated System for Cattle-Feed Dispensing in Cattle-Cows. *2021 IEEE 12th Annual Ubiquitous Computing, Electronics & Mobile Communication Conference*, 671 - 675.
- [13] Moya, D., Mazzenga, A., Holtshausen, L., Cozzi, G., González, L. A., Calsamiglia, S., Gibb, D. G., McAllister, T. A., Beauchemin, K. A. & Schwartzkopf-Genswein, K. (2011). Feeding behavior and ruminal acidosis in beef cattle offered a total mixed ration or dietary components separately. *Journal of Animal Science*, 89(2), 520–530.
- [14] Pavkin, D.Y., Nikitin, E.A., Shilin, D.V., Belyakov, M.V., Golyshkov, I.A., Mikhailichenko, S. & Chepurina, E. (2023). Development Results of a Cross-Platform Positioning System for a Robotics Feed System at a Dairy Cattle Complex. *Agriculture*, 13(7), 1442.
- [15] Pavkin, D.Y., Shilin, D.V., Nikitin, E.A. & Kiryushin, I.A. (2021). Designing and Simulating the Control Process of a Feed Pusher Robot Used on a Dairy Farm. *Applied Science*, 11(22), 10665.
- [16] Nabokov, V. I., Novopashin, L. A., Denyozhko, L.V., Sadov, A. A., Ziablitskaia, N.V., Volkova, S.A., & Speshilova I.V. (2020). Applications of feed pusher robots on cattle farmings and its economic efficiency. *International Transaction Journal of Engineering Management & Applied Sciences & Technologies*, 2020,11(14): 14-20.
- [17] Tangorra, F. M. & Calcante, A. (2018). Energy consumption and technical-economic analysis of an automatic feeding system for dairy farms: Results from a field test. *Journal of Agricultural Engineering*, 49, 228-232.
- [18] Uzedhe, G.O., Akinloye, E.B.O. & Febaide, I.C. (2023). Development of an Animal Farm Robotic Feeding System. *Tropical Journal of Science and Technology*, 4(1), 14-22.
- [19] Yang L., Xiong B.H., Wang H., Chen R.P., & Zhao Y.G. (2022). Research Progress and Outlook of Livestock Feeding Robot (家畜饲喂机器人研究进展与发展展望). *Smart Agriculture*, 4(02):86-98.
- [20] Zhang Q., Ren H. L., & Hu J.H. (2023). Design and Experiment of Intelligent Feed-pushing Robot Based on Information Fusion (基于信息融合的智能推料机器人设计与试验), *Transactions of the Chinese Society for Agricultural Machinery*, 54(6):78-84.
- [21] Zhong R.Z., Zhao C.H., Feng P., Wang Y.T., Zhao X.L., Luo D.W., Cheng L., Liu D. & Fang Y. (2020) Effects of feeding ground versus pelleted total mixed ration on digestion, rumen function and milk production performance of dairy cows. *International Journal of Dairy Technology*, 73, 22-30.

DYNAMIC-ENERGY ANALYSIS OF A ROTARY TILLER WITH A VERTICAL ROTATION AXIS

ՈՒՐԱՍԶԻԳ ԴՏՏԱՆ ԱՌԱՆՑՔՈՎ ՀՈՂԱՄՇԱԿ ՖՐԵԶԻ ԴԻՆԱՄԻԿԱԿԱՆ- ԷՆԵՐԳԵՏԻԿԱԿԱՆ ՀԵՏԱԶՈՏՈՒԹՅՈՒՆ

Arshaluys TARVERDYAN¹⁾, Artur ALTUNYAN^{1*)}, Gevorg HARUTYUNYAN²⁾, Albert GRIGORYAN¹⁾

¹⁾Scientific Research Institute for Agricultural Mechanization and Automation, Armenian National Agrarian University, Yerevan, Armenia

²⁾Aspirant at Agricultural Engineering Faculty

Tel: +37455327325; E-mail: arturaltunyan@gmail.com

Corresponding author: Artur Altunyan

DOI: <https://doi.org/10.35633/inmateh-73-23>

Keywords: rotary tiller, planetary drive, resistance moment, energetic characteristics, traction resistance

ABSTRACT

The article considers the issue of dynamic and energy analysis of the rotary tiller with planetary transmission gear and vertical rotation axis designed for orchards and vineyards. In the result of investigations, analytical expressions have been derived, which enable to determine the resistance force factors of the cultivated medium affecting the rotary tiller and to set up their changing patterns during a single rotation of the rotor in conditions of forward movement of the aggregate/working unit. It has been confirmed that in case of binary symmetric blades located at 120 degree, the resistance forces transmitted from the tiller satellites to the rotor shaft mutually balance each other, as a result of which the traction resistance force of the unit receives the possible minimum value. As regard to the resistance moments transmitted from the tiller satellites to the rotor shaft and to their main moments, it should be noted that they change significantly during a single rotation of the rotor. Particularly, the extreme values of the main moment for each tiller satellite are obtained at the finite points of the rotor's diameter perpendicular to the forward movement of the tillage machine. Based on the driving and resistance force factors of the machine, as well as the differential equation of the motion, the term has been identified by means of the energy research of the rotary tiller, in case of which the angular acceleration of the rotor's shaft will be equal to zero and the machine will operate without oscillations and vibrations.

ԱՍՓՈՓԱԳԻՐ

Հոդվածում դիտարկվում է պլանետարային հաղորդակով, ուղղահիգ պտտման առանցքով պտղատու և խաղողի այգիների հողամշակ ֆրեզի դինամիկական և էներգետիկ վերլուծության խնդիրը: Հետազոտությունների արդյունքում ստացվել են անալիտիկ արտահայտություններ, որոնք հնարավորություն են տալիս որոշելու հողամշակ ֆրեզի վրա ազդող մշակվող միջավայրի դինամիկական ուժային գործոններն ու սահմանելու դրանց փոփոխման օրինաչափությունները ռոտորի մեկ պտույտի ընթացքում, ագրեզատի համընթաց շարժման պայմաններում: Հաստատվել է, որ 120 աստիճանի տակ տեղակայված երկուսական սիմետրիկ դանակների դեպքում սատելիտ ֆրեզներից ռոտորի լիսեռին փոխանցվող դինամիկական ուժերը փոխադարձ հավասարակշռում են իրար, ինչի հետևանքով ագրեզատի քարշային դինամիկական ուժը ստանում է հնարավոր նվազագույն արժեքը: Ինչ վերաբերվում է ֆրեզ-սատելիտներից ռոտորի լիսեռին փոխանցվող դինամիկական մոմենտներին և դրանց գլխավոր մոմենտին, ապա դրանք ռոտորի մեկ պտույտի ընթացքում փոփոխվում են զգալի չափով: Մասնավորապես գլխավոր մոմենտն իր էքստրեմալ արժեքները, յուրաքանչյուր ֆրեզ-սատելիտի համար, ստացվում են ֆրեզ-մեքենայի համընթաց շարժմանն ուղղահայաց ռոտորի տրամագծի ծայրակետերում: Առաջարկվող պլանետարային հաղորդակով հողամշակ ֆրեզի էներգետիկական հետազոտության միջոցով, հիմք ընդունելով մեքենայի շարժող և դինամիկական ուժային գործոնները, ինչպես նաև շարժման դիֆերենցիալ հավասարումը, սահմանվել է պայմանը, որի դեպքում ռոտորի լիսեռի անկյունային արագացումը հավասար կլինի 0-ի, մեքենան կաշխատի առանց ցնցումների և վիբրացիայի:

INTRODUCTION

The inter-row cultivation of gardens, as well as inter-trunk and near-trunk cultivation of trees in accordance with the agrotechnical requirements is an essential prerequisite for the yield capacity increase and quality improvement of the product in orchards. Furthermore, the latter are ensured by the accurate and timely implementation of the mentioned agrotechnical activities (*Manaenkov, 2017; Kupryashkin & Gusev, 2020, Khort et al., 2020; Bordoni et al., 2019*).

The operational practice of rotary tillers in the inter-trunk and inter-row spaces has enabled to develop their main agrotechnical requirements (*Panov & Tokushev, 2005; Koval, 2010; Tarverdyan et al., 2024*) and at the same time to state that the machines with active working parts are more effective. These are mainly rotary tillers with horizontal or vertical rotation axis equipped with mechanical or hydraulic transmission gears (*Parkhomenko, 2012; Kupryashkin & Gusev, 2020; Tarverdyan et al., 2024; Panov, 1963; Byshov, 2017; Tarverdyan & Sargsyan, 2015, Hegazy et al., 2014; Abo-Habaga et al., 2018*).

Their structural peculiarities enable to maximally adapt the machine to the cultivation of inter-trunk spaces observing the implementation rules of agrotechnical requirements. The distinctive advantages of machines of this series are introduced in many research works (*Kupryashkin & Gusev, 2020; Byshov, 2017; Tarverdyan & Sargsyan, 2015; Mosatovskiy, 1980; Ahmadi, 2017; Raparelli et al., 2021*).

However, the operational practice of the tillers with vertical axis and the analysis of literature data signify that they are not free from defects either (*Panov & Tokushev, 2005; Panov, 1963; Tarverdyan & Sargsyan, 2015*).

Particularly, in this case the thrown out mass of cultivated soil is rather large, and at the same time it is mentioned that the way of elimination of this shortcoming is the correct selection of the shape and geometrical parameters of the tiller's blades (*Mosatovskiy, 1980*).

Considering also the circumstance that the operational reliability of the existing machines is low, especially in the soil types of the Republic of Armenia, which stand out for high content of rocks and gravel, an attempt was made to develop rotary tillers with vertical rotation axis possibly free from the above stated shortcomings and suitable for the cultivation of inter-tree, inter-trunk and inter-vine spaces in orchards and vineyards.

The attempts to solve the mentioned problem through optimization of the shape and profile of the existing tiller's blades with vertical rotation axis failed to bring out the expected results, though partial improvement in some indicators has taken place (*Kupryashkin & Gusev, 2020; Koval, 2010; Byshov, 2017; Chatkin, 2007; Wusong et al., 2024; Li S.T. et al., 2016*). Based on the afore stated, the goal and objectives of the presented research work has been developed.

The key objective of the current work was to develop a rotary tiller with vertical rotation axis, which could enable to cultivate the inter-row and inter-trunk spaces in orchards with minimum energy consumption, meanwhile ensuring minimum horizontal movement of the soil mass throughout the cultivation process.

It is apparent that the only way to solve the problem is to make fundamental changes in the tiller's structure.

MATERIALS AND METHODS

Based on the results of our previous investigations (*Tarverdyan et al., 2024; Tarverdyan & Hayrapetyan, 2019*), an attempt was made to develop a transmission gear of a tiller with vertical axis, which will be able to provide high rotation numbers of working tillers (200–250 rpm) in case of relatively lower rotation numbers of the rotor (50–80 rpm). It is a planetary mechanism of external gear with immobile/fixed annular/sun wheel (Fig. 1).

It consists of an annular fixed wheel (3), mounted to the support (2) attached to the tiller's frame (1), satellites (4) rolled thereto, the rotation axis of which is installed in the grooves of rotor housing/casing (5) with bearings. The tillers discs (6) are rigidly attached to the free ends of the rotation axes of the satellites (4), on which the tiller's blades (7) are mounted in a symmetrical pattern.

The rotor (5) of the tilling machine receives the rotational movement via belt or chain transmission (8). The rotational motion is transmitted from the power take-off shaft of the tractor or hydraulic motor to the rotor (5) of the rotary tiller which in this case acts as a driver of planetary mechanism; due to the rotor's rotation the satellites (4) roll over the ring belt of the fixed annular wheel (3) with the multiplied angular velocity of the gear ratio of the mechanism. In terms of qualitative evaluation, the selected mechanism enables to solve the raised problem: to get the large angular, and hence, blades' linear speeds/velocities of the rotary tillers (working parts) with small diameter in case of relatively small rotation numbers of the rotor.

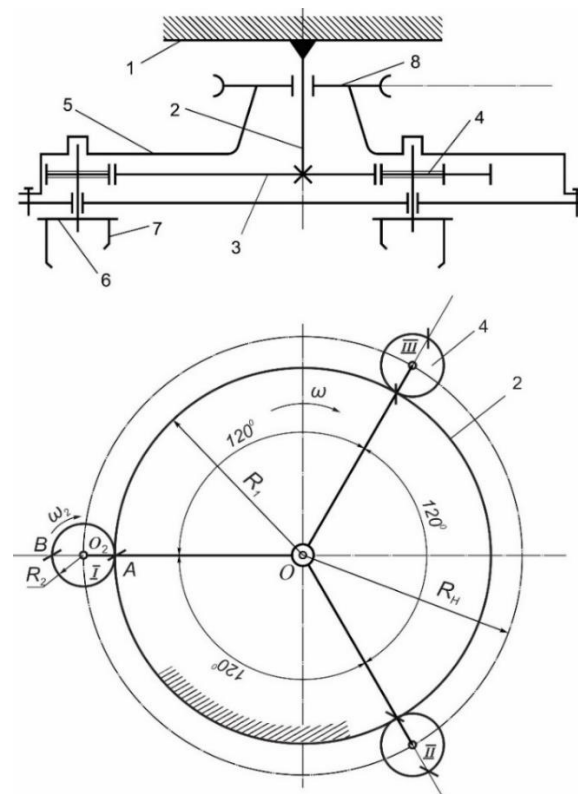


Fig. 1 – Schematic diagram of a rotary tiller with a planetary drive for the cultivation of near-trunk and inter-trunk areas of orchards

The kinematic analysis of the proposed mechanism was conducted in the first article of the series related to the discussed problem (Tarverdyan et al, 2024), and the expressions of the trajectory Equation (1), velocities Equation (2) and accelerations Equation (3) for the arbitrary point of the tiller’s blades of the machine were derived:

$$\begin{cases} x = V \cdot t \pm (R_1 + R_2) \cdot \sin\omega t - R_2 \sin(i + 1)\omega t \\ y = (R_1 + R_2) \cdot \cos\omega t - R_2 \cos(i + 1)\omega t \end{cases} \quad (1)$$

$$\begin{cases} V_x = V \pm \omega[(R_1 + R_2) \cdot \cos\omega t - R_2(i + 1) \cdot \cos(i + 1)\omega t] \\ V_y = -\omega[(R_1 + R_2) \cdot \sin\omega t - R_2(i + 1) \cdot \sin(i + 1)\omega t] \end{cases} \quad (2)$$

$$\begin{cases} a_x = \mp \omega^2[(R_1 + R_2) \cdot \sin\omega t - R_2(i + 1)^2 \cdot \sin(i + 1)\omega t] \\ a_y = -\omega^2[(R_1 + R_2) \cdot \cos\omega t - R_2(i + 1)^2 \cdot \cos(i + 1)\omega t] \end{cases} \quad (3)$$

where: V_x, V_y are the speed components of any fixed point for the tiller’s blade [m/s], a_x, a_y - acceleration components of any fixed point for the tiller’s blade [m/s²], V - velocity of forward movement of the aggregate [m/s], t - time of movement [s], R_1 - radius of relatively fixed sun gear, [m], R_2 - planet gear radius, [m], $i = \frac{R_1}{R_2}$ – transmission ratio, ω - angular speed of the planetary mechanism driver [min⁻¹].

Based on the results of kinematic studies of the mechanism, a force analysis of the mechanism was performed, analytical expressions were obtained, which enable to determine the resistance force factors affecting the blades of the tilling machine depending on the kinematic and geometric parameters of the machine (Tarverdyan et al, 2024).

In particular for the option of the rotary tiller with planetary transmission gear equipped with three satellites at 120°, based on the principles of mechanics (Zinoviev, 1975; Loytsyansky & Lurie, 2006), the scheme of resistance force factors (Fig.2) affecting the rings of the tilling machine and their determination expressions (Tarverdyan et al, 2024) have been developed.

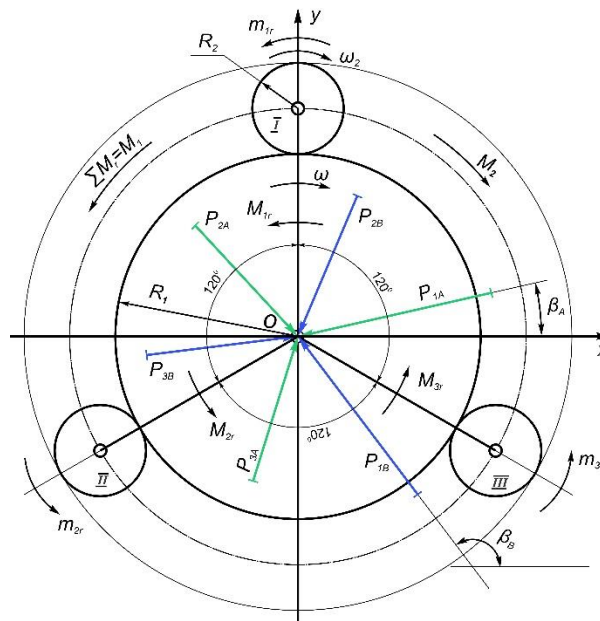


Fig. 2 – Scheme of resistance force factors affecting the rotary tiller with planetary mechanism

Since the resistance moments (m_r^k and M_r^k) applied to the satellites and drivers act in one plane, hence, the total resistance or the main resistance moment applied to the drive shaft will be determined in the following way (Tarverdyan et al., 2024, eq. 17):

$$M_1 = m_r^I + M_r^I + m_r^{II} + M_r^{II} + m_r^{III} + M_r^{III}, \quad (4)$$

where m_r is the the moment of resistance forces towards the planet gear axis [N.m], M_r – moment of resistance forces towards the planetary mechanism drive axis [N.m].

Having the value of the resistance moment (M_1) applied to the driving rotor’s shaft of the rotary tiller, it will be possible to determine the torque/moment (M_2) applied to the drive shaft and the power of the engine.

The resistance moment ($m_r^{(k)}$) applied to one satellite (k) and the resistance moment ($M_r^{(k)}$) applied to the rotor’s shaft therefrom are determined through the following expressions (Tarverdyan et al., 2024).

$$m_r^{(k)} = -P_A \cdot R_2 \cos[(i + 1)\varphi + \beta_A] - P_B \cdot R_2 \cos[(i + 1)\varphi + \beta_B]. \quad (5)$$

$$M_r^{(k)} = P_A \cdot R_2 (i + 1) \cos(\varphi + \beta_A) - P_B \cdot R_2 (i + 1) \cos(\varphi + \beta_B). \quad (6)$$

For the A and B blades of conditional I, II and III satellites $tg\beta_A$ and $tg\beta_B$ are determined with the following expressions (in the formulae the sign of numerator refers to A blade, and denominator - to B blade):

I satellite

$$\left. \begin{aligned} \text{A blade: } tg\beta_A &= -\frac{\omega[R_H \sin\varphi - R_2(i + 1)\sin(i + 1)\varphi]}{V \pm \omega[R_H \cos\varphi - R_2(i + 1)\cos(i + 1)\varphi]} \\ \text{B blade: } tg\beta_B &= -\frac{\omega[R_H \sin\varphi + R_2(i + 1)\sin(i + 1)\varphi]}{V \pm \omega[R_H \cos\varphi + R_2(i + 1)\cos(i + 1)\varphi]} \end{aligned} \right\} \quad (7)$$

II satellite

$$\left. \begin{aligned} \text{A blade: } tg\beta_A &= \frac{-\omega R_2 (i + 1) \{ \cos(60 - \varphi) + \cos[(i + 1)\varphi - 60] \}}{V \pm \omega R_2 (i + 1) \{ \sin(60 - \varphi) - \sin[(i + 1)\varphi - 60] \}} \\ \text{B blade: } tg\beta_B &= -\frac{-\omega R_2 (i + 1) \{ \cos(60 - \varphi) - \cos[(i + 1)\varphi - 60] \}}{V \pm \omega R_2 (i + 1) \{ \sin(60 - \varphi) + \sin[(i + 1)\varphi - 60] \}} \end{aligned} \right\} \quad (8)$$

III satellite

$$\left. \begin{aligned} \text{A blade: } tg\beta_A &= -\frac{\omega R_2 (i + 1) \{ \cos(\varphi + 30) - \cos[150 - \varphi(i + 1)] \}}{V \mp \omega R_2 (i + 1) \{ \sin(\varphi + 30) + \sin[150 - \varphi(i + 1)] \}} \\ \text{B blade: } tg\beta_B &= -\frac{\omega R_2 (i + 1) \{ \cos(\varphi + 30) + \cos[150 - \varphi(i + 1)] \}}{V \mp \omega R_2 (i + 1) \{ \sin(\varphi + 30) - \sin[150 - \varphi(i + 1)] \}} \end{aligned} \right\} \quad (9)$$

As regard to the forces applied to the drive shaft – $P_{A_0}^I; P_{B_0}^I; P_{A_0}^{II}; P_{B_0}^{II}; P_{A_0}^{III}; P_{B_0}^{III}$, they form a planar convergent force system, the vector sum of which comes forth as the main vector R applied to the drive shaft.

In case of small differences in the resistance forces applied to the tiller blades, which is confirmed via empiric data, the forces applied to the drive rotor are balanced (R=0), which practically leads to the abrupt reduction in the traction resistance of the unit.

Thus, the energy indicators of the machine are mainly and primarily related to the resistance moment loads. Taking into account the hypothesis about the equality of resistance forces applied to the tillers' blades, the resistance moment applied to the rotor's shaft of the rotary tiller can be practically determined in the following way:

$$M_1 = \sum_{k=1}^{III} (M_r^k + m_r^k) \text{ or inserting the values of } m_r^{(k)} \text{ and } M_r^{(k)} \text{ from Equations (5) and (6), it will be obtained:}$$

$$M_1 = PR_2 \cdot \sum_{k=1}^{III} \{ (i + 1) \cos(\varphi + \beta_A^{(k)}) - (i + 1) \cos(\varphi + \beta_B^{(k)}) - \cos[(i + 1)\varphi + \beta_A^{(k)}] - \cos[(i + 1)\varphi + \beta_B^{(k)}] \} \quad (10)$$

It is necessary to take into account that when determining the total resistance moment (M_1) through Equation (10) expression it is required to calculate the values of β_A^k and β_B^k in the expressions for each satellite and place it in Equations (7), (8) and (9) expressions, respectively.

RESULTS AND ANALYSIS

To present the changing patterns of resistance moments applied to the satellite-tiller and drive rotor shaft more vividly, let's build the graphs of their changes during a single rotation of the rotor per the expressions of Equations (5), (6) and (10) in case of the following numerical values: $V=1 \text{ m/s}$, $\omega=5 \text{ s}^{-1}$, $\omega_2=25 \text{ s}^{-1}$, $i=4$, $R_1=0.2 \text{ m}$, $R_2=0.05 \text{ m}$.

Considering the introduced data of (Konstantinov, 2019; Kupryashkin & Gusev, 2020; Tarverdyan & Sargsyan, 2015; Akimov, 2017; Ahmadi, 2017) in the conducted research works, it is conditionally assumed that $P=150 \text{ N}$. The graphs designed with the mentioned data are presented in Figure 3.

It is noteworthy that the resistance forces applied to the satellite blades during the tiller operation change their signs, anyhow, the directions of the resistance moments raised from those forces stay unchanged; this is the reason why the total resistance moments are introduced in absolute values (Zinoviev, 1975).

It follows from Fig. 3 that the variation patterns of resistance moments applied to the three satellites located at 120° are absolutely identical upon 120° –phase deviation.

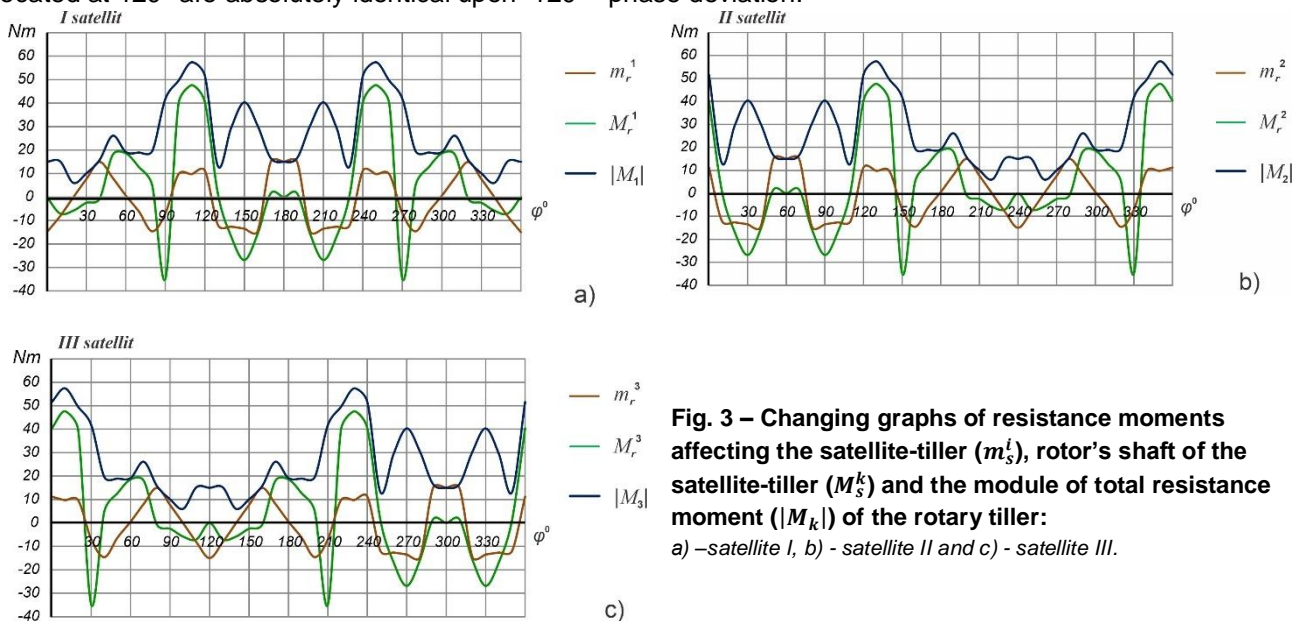


Fig. 3 – Changing graphs of resistance moments affecting the satellite-tiller (m_s^i), rotor's shaft of the satellite-tiller (M_s^k) and the module of total resistance moment ($|M_k|$) of the rotary tiller:
 a) –satellite I, b) - satellite II and c) - satellite III.

In Figure 4 the changing graph of total resistance moment ($\sum M$) applied to the drive-rotor's shaft of the tilling machine is depicted. It follows from the graph that from the standpoint of energy and uniform work of the tiller the extreme values of total resistance moment, being at the top interest point, are formed in the finite diameter points perpendicular towards the forward movement of the aggregate.

After the determination of resistance moment applied to the shaft of the drive rotor, it is crucial to identify the optimal geometrical and kinematic parameters of the transmission gear rings, in case of which the uniformity of the mentioned moment during the working cycle will be maximum or the changing amplitude will be minimum.

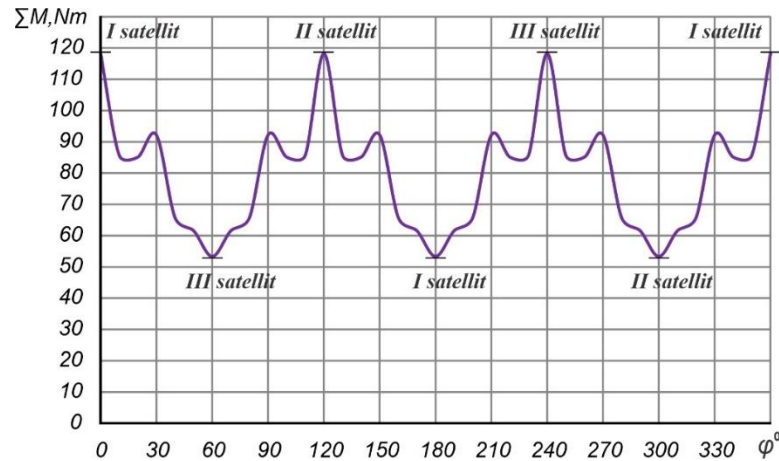


Fig. 4 – Changing graph of total resistance moment affecting the rotor’s shaft of the rotary tiller with three satellite tillers located at 120°

It is obvious that in order to ensure the intended stable work mode of the machine, it is necessary to apply force couple with M_2 moment, which should be equal to the total resistance moment of the soil environment $\sum M_r$, in large or marginal case (for practicality, let’s denote $\sum M_r$ as M_1 in further expressions). To solve the proposed problem, it is necessary to perform energy analysis of the rotary tiller with planetary transmission gear. The analysis was conducted according to the scheme presented in Figure 5. The expression of kinetic energy of the mechanism looks as follows according to well-known theories of classical mechanics (Zinoviev, 1975; Loytsyansky & Lurie, 2006):

$$W = (W_1 + 3W_2 + W_V), \tag{11}$$

where $W_1 = \frac{J_1\omega^2}{2}$ is the kinetic energy of the drive rotor (1, Fig. 5),

$W_2 = \frac{J_2\omega_2^2}{2} + \frac{m_2V_{O2}^2}{2}$ is the kinetic energy of satellite (the satellite performs complex motion: rotational and forward), $W_V = \frac{m_1V^2}{2}$ is the kinetic energy of the forward movement of the rotor (general mass).

The kinetic energy of the rotary tiller along the driving ring of the mechanism, i.e., drive-rotor’s shaft will be:

$$W_r = \frac{J_r\omega^2}{2} \tag{12}$$

where J_r - is the resulting moment of inertia.

Considering that $\omega_2 = (i + 1) \omega$, V_{O_2} will be $V_{O_2} = R_2(i + 1)\omega$, for the forward movement of the unit, based on the conservation term of kinematic parameters, in case of three satellites installed at 120°, the following expression has been obtained (Tarverdyan et al., 2024): $V \leq 6\omega(i + 1)R_2$.

Placing the values of the above-mentioned quantities in Equation (11) and equating the right parts of Equations (11) and (12), it is obtained:

$$\frac{J_p\omega^2}{2} = \frac{J_1\omega^2}{2} + \frac{3J_2(i + 1)^2\omega^2}{2} + \frac{3m_2R_2^2(i + 1)^2\omega^2}{2} + \frac{36m_1R_2^2(i + 1)^2\omega^2}{2},$$

wherefrom:

$$J_p = J_1 + 3(i + 1)^2(J_2 + m_2R_2^2 + 12m_1R_2^2), \tag{13}$$

where J_1 is the moment of rotor’s inertia: $J_1 = \frac{P_1R_D^2}{2g}$ ($m_1 = \frac{P_1}{g}$ is the rotor’s mass, P_1 is the total rotor’s weight, R_D is the radius of rotor-drive case), J_2 is the satellite’s inertia moment: $J_2 = \frac{P_2R_2^2}{2g}$ ($m_2 = \frac{P_2}{g}$ is the satellite mass).

Taking into account the above stated expressions and denotations, the kinematic energy of the mechanism will be determined through the following expression:

$$W = \frac{\omega^2}{4g} [P_1 R_D^2 + 6(i + 1)^2 \cdot (P_2 R_2^2 + 6P_1 R_2^2)]. \tag{14}$$

To get the equation of the motion of the mechanism, the Lagrange's equation is used for the generalized coordinate φ (Zinoviev, 1975; Loytsyansky & Lurie, 2006).

$$\frac{d}{dt} \frac{\partial W}{\partial \dot{\varphi}} - \frac{\partial W}{\partial \varphi} = P_\varphi. \tag{15}$$

In the discussed problem, the position of any ring of the mechanism is determined through the generalized φ coordinate, and in the result of force analysis the resistance moment M_1 was already determined, hence the driving force factor M_2 .

Obviously in Equation (15) expression, it can be accepted that the moment M is risen by the active forces as a generalized force factor (P_φ). Since the active forces come forth as both driving and resistant ones, the resulted moment can be presented as the difference in the force factors of driving and resistance moments (Zinoviev, 1975).

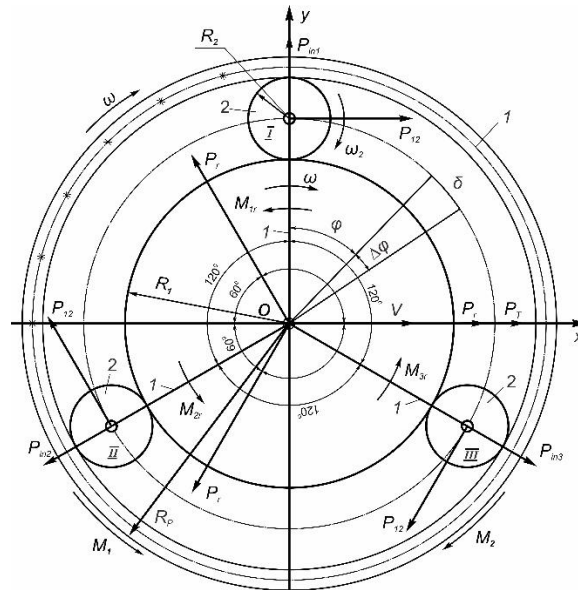


Fig. 5 – Scheme for the dynamic study of the planetary driving mechanism of a rotary tiller.

Besides, the traction resistance force P_T (Figure 5) of the aggregate and satellites' inertial forces P_{in} should be considered as important force factors. Inertial forces of the satellites (centrifugal forces), $P_{in1} = P_{in2} = P_{in3} = m_2 \omega^2 \cdot (R_1 + R_2)$, which are equal in modulus, are directed towards each other at 120° and practically balance each other relative to the axis of the driver.

To receive the analytical expression of the generalized force (P_φ), it is given the generalized coordinate (φ) an elementary increment ($\delta\varphi$) and the elementary work (δA) performed on that elementary displacement is determined.

The work of the traction resistance force performed on the elementary displacement is determined in the following way:

$$\delta A_{(P_T)} = P_T \cdot (R_1 + R_2) \delta\varphi \cdot \cos\varphi. \tag{16}$$

Since the traction resistance force is directed towards x axis, and $(R_1 + R_2) \delta\varphi \cdot \cos\varphi$ is the projection of the elementary displacement on the same axis.

As regard to the satellites' inertial forces, they mutually balance each other relative to the driver's axis and besides, their work performed on the elementary displacement $(R_1 + R_2) \delta\varphi$ is equal to zero, since those forces are perpendicular towards elementary displacement.

Not only the inertial but also the resistance forces (P_r) applied to the rotor shaft are mutually balanced. This circumstance is paramount importance in terms of uniform operation of the rotary tiller and abrupt decline in the traction resistance of the unit. This is one of the most important findings of the planetary transmission gear.

The elementary work performed by the active force factors will be determined through the following expression in the discussed case:

$$\delta A = [M_2 - M_1 - P_T \cdot (R_1 + R_2) \cdot \cos\varphi] \cdot \delta\varphi \quad (17)$$

Since according to definition $\delta A = P_\varphi \cdot \delta\varphi$, hence:

$$P_\varphi = M_2 - M_1 - P_T(R_1 + R_2) \cdot \cos\varphi. \quad (18)$$

The partial derivative of the kinetic energy expression Equation (14) per the generalized ($\dot{\varphi}$) speed will be:

$$\frac{\partial W}{\partial \dot{\varphi}} = \frac{1}{2g} [P_1 R_D^2 + 6(i+1)^2 \cdot (P_2 R_2^2 + 6P_1 R_2^2)] \cdot \dot{\varphi}. \quad (19)$$

When deriving the obtained expression Equation (19) per time, it will be obtained:

$$\frac{d}{dt} \cdot \frac{\partial W}{\partial \dot{\varphi}} = \frac{1}{2g} [P_1 R_D^2 + 6(i+1)^2 \cdot (P_2 R_2^2 + 6P_1 R_2^2)] \cdot \ddot{\varphi}. \quad (20)$$

By placing the right parts of Equations (18) and (20) expressions in the Lagrange expression Equation (15) and considering that $\frac{\partial W}{\partial \varphi} = 0$ (the kinematic energy of the mechanism according to Equation (14) expression is not dependent on the generalized coordinate) the differential equation for the movement of the proposed mechanism will be obtained:

$$\frac{1}{2g} [P_1 R_D^2 + 6(i+1)^2 \cdot (P_2 R_2^2 + 6P_1 R_2^2)] \cdot \ddot{\varphi} = M_2 - M_1 - P_T(R_1 + R_2) \cdot \cos\varphi,$$

wherefrom the angular acceleration of the drive rotor will be:

$$\ddot{\varphi} = \frac{2g[M_2 - M_1 - P_T(R_1 + R_2) \cdot \cos\varphi]}{P_1 R_D^2 + 6(i+1)^2 \cdot (P_2 R_2^2 + 6P_1 R_2^2)} \quad (21)$$

For the uniform work of the rotor's drive, and hence, for that of rotary tiller, it is required that its angular acceleration- $\ddot{\varphi} = 0$, i.e., the driving moment (M_2) applied to the rotor, should balance the resistance forces, that is:

$$M_2 = M_1 - P_T(R_1 + R_2) \cdot \cos\varphi. \quad (22)$$

To use the received expression Equation (22) in practice, it is necessary to consider not only the theoretical research results Equation (10) for the definition of M_1 changing patterns, but also first of all the real changing patterns and quantities resulted from the scientific experimental research. In this regard, it is worthwhile mentioning once more, that in case of rotary tiller the real resistance force factors of the medium is possible to determine only empirically then comparing them with the theoretically obtained results. Only in this way is it possible to apply this expression Equation (22) and determine the minimum value of the driving power in case of which the work would be implemented uniformly without any undesired shocks and vibrations.

CONCLUSIONS

1. In the result of the dynamic analysis of the rotary tiller with planetary transmission gear, analytical expressions have been derived, which make it possible to determine the resistance force factors of the medium theoretically, which affect the shaft of satellite tillers and rotor drive and particularly the total resistance moment and its changing pattern throughout a single rotation of the rotor.

2. As a result of dynamic and energy analysis, the term has been set up, in case of which the ratio of total resistance and driving moment/torque should compensate the lack of angular acceleration ($\ddot{\varphi} = 0$) of the rotor's shaft.

Only then it is possible to identify the minimum value of driving moment or the power, in case of which the working mode of the rotary tiller will be uniform without any fluctuations and vibrations.

3. The transmission gear mechanism of the rotary tiller with three satellites located at 120° enables not only to ensure uniform work of the machine, but also most importantly, in this condition, the main vector of the cutting resistance forces in the soil environment equals to zero on the rotor's shaft, as a result of which the traction resistance force of the working unit possibly gets its minimum value.

ACKNOWLEDGEMENTS

The work was supported by the Science Committee of MESCS RA, in the frames of the research project № 21APP-2D015

REFERENCES

- [1] Abo-Habaga M., Imara Z., Okasha M. (2018). Development of a Combine Hoeing Machine for Flat and Ridged Soil, *Journal of Soil Sciences and Agricultural Engineering*, 9(12), pp.817-820. <https://doi.org/10.21608/jssae.2018.36548>
- [2] Akimov A.P., Koketantinov Yu.V., Turovskiy B.V. (2017). Mathematical model of interaction of milling knives with soil (Математическая модель взаимодействия фрезерного ножа с почвой). *Bulletin of the Kazan State Agrarian University*, №4(46), pp.67-71. https://doi.org/10.12737/article_5a5f06808b59a5.62332052
- [3] Bordonni M., Vercesi A., Maerker M., Ganimede C., Reguzzi M.C., Capelli E., Wei X., Mazzoni E., Simoni S., Gagnarli E., Meisina C., (2019), Effects of vineyard soil management on the characteristics of soils and roots in the lower Oltrepò Apennines (Lombardy, Italy), *Science of The Total Environment*, Vol. 693, <https://doi.org/10.1016/j.scitotenv.2019.07.196>
- [4] Vyshov N.V., (2017), Modern technical facilities for working in gardens (Современные технические средства для работы в садах). *Scientific journal of Kuban SAU (Научный журнал Куб ГАУ)*, №134, <https://doi.org/10.21515/1990-4665-134-082>
- [5] Chatkin M.N., (2007) *Kinematics and dynamics of the working parts of the rotary tillers with screw elements (Кинематика и динамика ротационных почвообрабатывающих рабочих органов с винтовыми элементами)*. Publishing house of Mordovia State University, Saransk, 316 p.
- [6] Hegazy R.A., Abdelmotaleb, Z.M. Imara, Okasha M.H. (2014), Development and Evaluation of Small-Scale Power Weeder, *Journal of Agricultural Engineering (MJAE)*, Vol. 31, Issue 3, pp. 703-728, <https://doi.org/10.21608/MJAE.2014.98430>
- [7] Iman Ahmadi, (2017), A torque calculator for rotary tiller using the laws of classical mechanics, *Soil and Tillage Research*, Volume 165, Pages 137-143, <https://doi.org/10.1016/j.still.2016.08.009>
- [8] Khort D., Filippov R., Smirnov I., Kutuyev A. and Semichev S., (2020), Automated section for milling soil in near-trunk zones of orchard, *E3S Web of Conferences* 161,01068. <https://doi.org/10.1051/e3sconf/202016101068>
- [9] Konstantinov Yu. V., (2019) Calculation method of resistance and resistance moment to the soil cutting with a straight disk blade of the cutter (Методика расчета сопротивления и момента сопротивления резанию почвы прямым пластинчатым ножом фрезы). *Tractors and Agricultural Machinery*, vol. 86 №5, p. 31-39. <https://doi.org/10.31992/0321-4443-2019-5-31-39>
- [10] Koval Zh.L.. (2010) *Development of a rotary tiller with energy-saving cutting working parts (Разработка почвообрабатывающей машины с энергосберегающими фрезерными рабочими органами)*. Thesis for the Candidate of Mechanical Sciences, Moscow.
- [11] Kupryashkin V.F., Gusev A.Yu., (2020) Justification of the parameters and operating modes of a self-propelled rotary tiller with combined rotation of active working parts (Обоснование параметров и режимов работы самоходной почвообрабатывающей фрезы с комбинированным вращением активных рабочих органов). *Scientific Review. International scientific and practical journal*. Saransk, - pp. 42-48. №2,
- [12] Li S.T., Yang L., Niu P., et al (2016). Design and study on the edge curve of blade of a handheld tiller's rotary blade, *INMATEH-Agricultural Engineering*, 51(3): 5-12, Bucharest, Romania.
- [13] Loytsyansky L.G., Lurie A.I., (2006), *Course of theoretical mechanics (Курс теоретической механики)*, volume 2., Moscow
- [14] Manaenkov K.A., (2017), Improving soil cultivation in near- trunk strips of intensive gardens (Совершенствование обработки почвы в приствольных полосах интенсивных садов). *Technologies of food and processing industry.(Технологии пищевой и перерабатывающей промышленности)*, №3 (17) pp. 28-34
- [15] Mosatovskiy V.B., (1980), *Study of the process of near-trunk spaces cultivation in intensive gardens with vertical tillers and justification of the types and parameters of their working parts (Исследование процесса обработки приствольных полос в интенсивных садах вертикальными фрезами и обоснование типов и параметров их рабочих органов)*. Thesis for the candidate of technical sciences, Chisinau.
- [16] Panov I.M., (1963), *Rotary tillage machines and tools (Ротационные почвообрабатывающие машины и орудия)*. Moscow.

- [17] Panov I.M., Tokushev Zh.E., (2005) *Theory, design and calculation of rotary tilling machines (Теория, конструкция и расчет ротоционных почвообрабатывающих машин)*. Publ. House of Kokshetau University, Kokshetau, 314 p.
- [18] Parkhomenko G.G., (2012), *Tillage in rows of orchards and vineyards. Processes, devices. (Обработка почвы в рядах садов и виноградников. Процессы, устройства)*. LAP LAMBERT Academic Publishing, ISBN 978-3-659-30811-6, p.148, Saarbrücken, Germany
- [19] Raparelli T., Ivanov A., Pepe G. and Eula G. (2021), "Analysis of the energy consumption of a rotary harrow", *Journal of Agricultural Engineering*, 52(2). <https://doi.org/10.4081/jae.2021.1132>
- [20] Tarverdyan A., Sargsyan S. (2015) The Dynamics of Tiller with Vertical Axis for The Cultivation of Inter-Trunk Spaces in Orchards / *Bulletin of National Agrarian University of Armenia*, Armenian National Agrarian University, Yerevan №4, pp 75-84.
- [21] Tarverdyan A.P., Altunyan A.V., Grigoryan A.S. (2024) Force analysis of a rotary tiller with a vertical rotation axis, *INMATEH-Agricultural Engineering* №72(1), p. 454-465, <https://doi.org/10.35633/inmateh-72-40>
- [22] Tarverdyan A.P., Hayrapetyan H.H., (2019), Kinematic and dynamic Study of the rotary crusher transmission gear in the potato digger. *Agriscience and Technology*, Armenian National Agrarian University, Yerevan, №4(68),
- [23] Wusong XIAO, Po NIU, Pan WANG, Yingjie XIE, Fei XIA, (2024) Simulation analysis and optimization of soil cutting of rotary blade by ANSYS/LS-DYNA, *INMATEH-Agricultural Engineering*, 72(1): 22-32, Bucharest, Romania <https://doi.org/10.35633/inmateh-72-02>
- [24] Zinoviev, V.A., (1975) *Course on the theory of mechanisms and machines (Курс теории механизмов и машин)*, Moscow, "Science".

DESIGN AND TESTING OF A VARIABLE SPRAY SYSTEM BASED ON PTO PROTOCOLS

基于 PTO 协议的变量喷雾系统设计与试验

Lei LIU¹⁾, Fanxia KONG^{*1)}, Lili YI¹⁾, Yubin LAN^{1,2)}, Xin HAN¹⁾, Jie ZHAO³⁾, Jie LIU¹⁾, Pengcheng LV¹⁾, Minhui ZHANG¹⁾

¹⁾ College of Agricultural Engineering and Food Science, Shandong University of Technology, Zibo/China

²⁾ National Sub-Centre for International Collaboration Research Centre for Agricultural Aviation Intelligent Equipment, Zibo/China

³⁾ UNDOF Procurement Service Station No.4, Shenyang/China

Tel: +8618653372858; E-mail: kfx0309@163.com

Corresponding author: Fanxia Kong

DOI: <https://doi.org/10.35633/inmateh-73-24>

Keywords: PTO Protocol; PWM; Electromagnetic Spray nozzle; Variable spraying

ABSTRACT

The aim of this research is to address the issues of low precision in variable spraying within the existing farmland application system, whereby nozzles cannot be controlled independently and low pesticide utilisation is observed. A variable spraying system based on PTO protocol has been designed. The system comprises an STM32 microcontroller as the control core, including the host computer, multi-channel controller, electronic switch, and electromagnetic spray nozzle. The master control unit receives the spray amount set by the user and calculates the duty cycle of the corresponding nozzle, which is then sent to the multiplex controller in real time through CAN communication. The multiplex controller adjusts the on-off frequency and duty cycle of each electromagnetic nozzle in real time according to the duty cycle of the corresponding nozzle it receives, thus enabling the nozzles to be controlled independently. This study offers theoretical and technical support for the independent control of spray nozzles and the optimisation of pesticide utilisation for variable spray systems based on PTO protocols.

摘要

针对现有农田施药系统变量喷雾精准化程度低、喷头不能独立控制及农药利用率低等问题，该研究设计了一种基于 PTO 协议的变量喷雾系统。系统以 STM32 单片机为控制核心，包括上位机、多路控制器、电子开关、电磁喷头等。主控接收用户设置的喷药量并计算对应喷头的占空比，通过 CAN 通讯实时发送到多路控制器；多路控制器根据接收的对应喷头的占空比，实时调节各个电磁喷头的通断频率与占空比，从而实现喷头的独立控制。该研究为基于 PTO 协议的变量喷雾系统提供了实现喷头独立控制和提高农药利用率的理论和技术支持。

INTRODUCTION

The control of crop pests, diseases, and weeds is one of the most important aspects of agricultural production. At present, the use of pesticides is still an important means of controlling pests, diseases, and weeds, and for achieving stable and high yields (He et al., 2020; Qi et al., 2022; Feng et al., 2021; Qiu et al., 2015). With the advancement of intelligent agricultural production and mechanization, crop protection machine operations have gradually replaced traditional manual spraying operations, improving the efficiency and safety of spraying. However, traditional crop protection operations do not take into account the uneven distribution of pests, diseases, and weeds in the operation area and typically use the same amount of pesticide across the entire area. This practice can lead to pesticide overuse, ecological degradation, and other problems. Variable spraying technology can adjust the dosage in real time according to the target information, thus reducing the amount of liquid used (Chu et al., 2021; He et al., 2019; He et al., 2022).

Experts from both within and outside the field have conducted comprehensive research on variable spraying technology from a variety of perspectives. Wang et al., (2022), conducted research using fuzzy control technology to investigate the influence of vehicle speed on spraying volume per unit area. This led to the development of a speed-following adaptive variable spray system. Li et al., (2016), designed a pulse-width modulated spraying system operating at frequencies exceeding 20 Hz, with the objective of studying the effects of PWM frequency and duty cycle on spraying characteristics. This research provides a theoretical basis for the application of high-frequency solenoid valves in PWM variable application systems and parameter selection.

Ramon *et al.*, (2021), employed PWM technology to regulate the solenoid valve and, consequently, the flow rate of the nozzle, with the objective of reducing the quantity of pesticides utilised, thus minimising environmental pollution and cutting down agricultural costs. Butt *et al.*, (2019), conducted an investigation on the impact of various nozzle types and duty cycles on the pressure at the nozzle orifice. The findings indicated that solenoid valve pulses result in pressure loss at the nozzle. Li *et al.*, (2022), investigated the impact of PWM duty cycle and frequency on spray drift characteristics. Their findings indicated that the duty cycle has a greater influence on spray drift than the frequency. They demonstrated that PWM duty cycles set in the range of 20% to 70% can effectively reduce the potential for drift in PWM spray.

A solenoid valve is a quick-acting suction mechanism that is operated by electromagnetism. The electromagnetic force is generated when the solenoid coil is energized. This force overcomes the spring force, causing the spool to move away from the valve and the valve to open. Conversely, when the solenoid coil is de-energised, the spring force pushes the spool towards the valve, closing the valve. The variable flow rate is achieved by rapidly controlling the valve in and out (Liu *et al.*, 2022; Fan *et al.*, 2021).

The aim of the study was to address the issues of low precision and low effective utilisation of pesticides in the current variable spraying system. To achieve this end, a variable spraying system based on PTO protocol was designed. The control system primarily consists of a host computer, an STM32 microcontroller, a multi-channel controller, electronic switches, and electromagnetic spray nozzles. The generation of multi-channel PWM signals, which independently control the frequency and duty cycle of each spray nozzle, enables precise control of the spray operation. This is done to assess the performance of the electromagnetic nozzle and to achieve independent control of the nozzle, thereby enhancing the precision of variable spraying.

MATERIALS AND METHODS

Variable spray control system design

Design Requirements for Variable Spray Control System

Aiming at the issues of low precision in variable spraying in the current agricultural application system, the inability to control the nozzle independently, and low pesticide efficiency, this paper designs a variable spraying system based on PTO protocol. The variable spray system developed based on the PTO protocol is installed on the spray bar of a self-propelled high clearance sprayer. Since the spraying width of the self-propelled high clearance sprayer is wide, the amount of pesticide applied within the spraying area is different and needs to be adjusted according to the speed, crop, pest and disease, etc., so each nozzle is independently controlled to achieve real-time and accurate adjustment of the amount of pesticide applied (Wang *et al.*, 2023). To meet the sprayer's basic spray parameters and the need for independent nozzle control, the control system must output multiple PWM signals to independently control the frequency and duty cycle of each nozzle. In order to ensure the accuracy and performance of independent control of the nozzle, an electromagnetic nozzle is proposed, as detailed in Table 1 of the technical specifications.

Table 1

| Electromagnetic nozzle main technical indicators | |
|---|------------------------|
| Parametric | Numerical value |
| Pressure range / MPa | 0.15~0.8 |
| Flow range / (L•min ⁻¹) | 0~6.0 |
| Rated voltage / V | 12 |
| Duty Cycle Range / % | 0~100 |
| Open time / ms | 15 |
| Close time / ms | 10 |
| Frequency ranges / Hz | 0~25 |

Variable Spray Control System Components

The variable rate spray system based on the PTO protocol mainly consists of a host computer, a main controller, a multiplex controller, an electronic switch, an electromagnetic spray nozzle, etc., as shown in Fig. 1. The host computer is used to input the spray rate and send it to the master controller. RTK_GNSS implements RTK differential positioning via UM482, which collects the position and speed information of the equipment in real time and transmits it to the main controller through the serial port. The main controller uses the STM32F103c8t6 chip as its core, calculates the required frequency and duty cycle information according to the received spray rate and operating speed information, integrates it into a complete data according to the custom PTO protocol format and transmits it to the multiplexer controller via CAN bus. The multiplexing controller utilizes the STM32F407vet6 chip as the core, and according to the received PTO protocol data, performs CRC check, extracting frequency and duty cycle information, and then outputs this data to the electronic switches, controlling multiple electronic switches to turn on and off. The electromagnetic nozzle is connected to the electronic switch, when the electronic switch is open, the nozzle opens, and the liquid is sprayed, when the electronic switch is closed, the nozzle closes, and the liquid stops spraying. The amount of spray can be adjusted by modifying the duty cycle and frequency of the PWM signal via the PTO protocol.

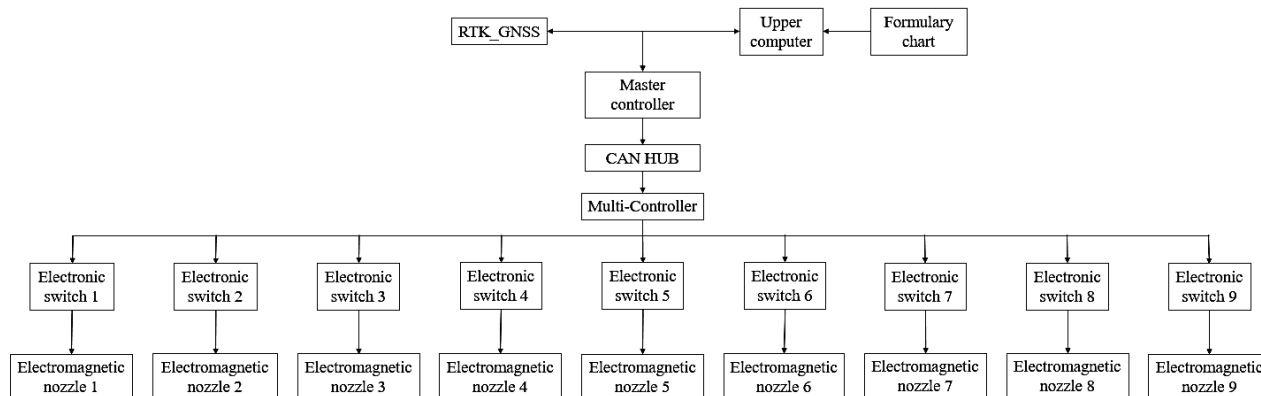


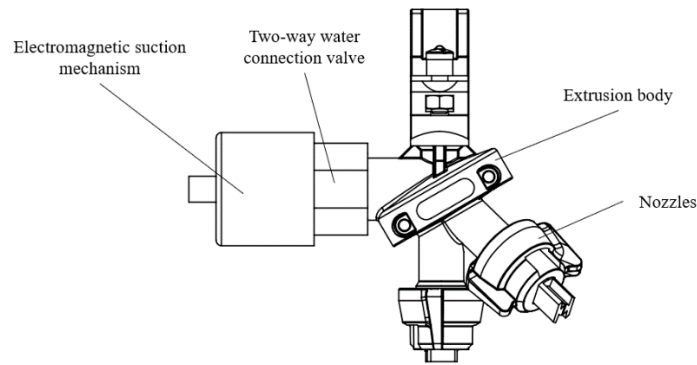
Fig. 1 – PTO protocol variable spray system components

Hardware Design

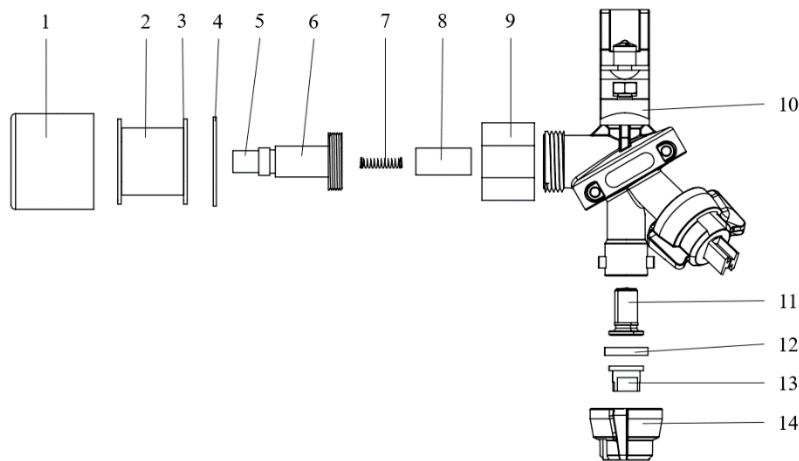
Electromagnetic nozzles

As shown in Fig.2, the electromagnetic nozzle mainly consists of an electromagnetic suction mechanism, a two-way water connection valve, a spray body, nozzles and other components. Among them, the solenoid suction mechanism adopts a 2W025-08 solenoid valve, which mainly includes a solenoid coil housing, solenoid coil, winding skeleton, fixed iron core, return spring, valve spool, and so on. The ring is installed inside the solenoid coil case to secure the solenoid coil and winding skeleton; the fixed iron core is fixedly connected to the sleeve by a snap, and both of them are placed inside the solenoid coil; the valve spool is positioned in the inner cavity of the sleeve, which can slide freely; the valve spool and the fixed iron core are equipped with reset springs between them; the other end of the sleeve is connected to the threaded two-way water connection valve. The two-way water connection valve features a central hole in the centre for the two-way water connection valve outlet, surrounded by 12 holes for the two-way water connection valve inlet, the two-way water connection valve on both sides of the thread connecting the electromagnetic suction mechanism and the spray body. Spray body model ARAG 4012747, the spray body has three ports, inlet, return port, outlet, return port including the inner cavity and is set in a ring on the outside of the inner cavity of the outer cavity, the inner cavity is connected to the outlet of the two-way water connection valve, the outer cavity is connected to the inlet of the two-way water connection valve, the spray body also includes the nozzle converter part, rotating can be used to select the use of three nozzles, respectively, with SF11006, SF11008, CFA11006 fan nozzle, spray angle being 110°.

The working principle is that when the electromagnetic suction mechanism of the coil is energised, its internal magnetic field magnetises the fixed iron core and the valve core, the valve core is attracted away from the bidirectional water connection valve outlet by the magnetic force, and the liquid is sprayed from the nozzle outlet; when the electromagnetic coil is de-energised, the magnetic field disappears, and the valve core moves away from the iron core under the action of the return spring, blocking the central through hole of the bidirectional water connection valve, and the liquid is blocked. By adjusting the PWM duty cycle, i.e. the on/off time within a single cycle of the nozzle, the spray flow rate can be adjusted and the on/off frequency of the nozzle can be controlled by adjusting the on/off frequency of the solenoid valve.



a. Electromagnetic nozzle assembly diagram

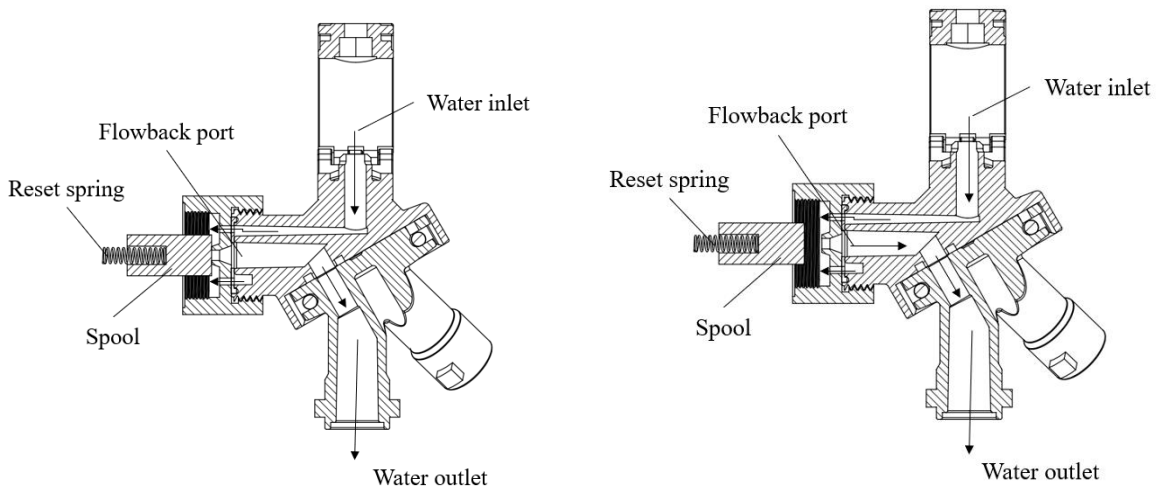


b. Electromagnetic nozzle main parts

Fig. 2 – Electromagnetic nozzle structure

- 1 - Solenoid shell; 2 - Solenoid coil; 3 - Winding skeleton; 4 - Fixed iron core; 5 - Sleeve; 6 - Reset spring;
- 7 - Valve spool; 8 - Gasket; 9 - Two-way through the water connection valve; 10 - Spray body; 11 - Screen;
- 12 - Gasket; 13 - Nozzle; 14 - Nozzle cap

For the automatic opening and closing of the sprayer body, a return port is designed to include an inner chamber and an outer chamber arranged in an annular shape on the outside of the inner chamber. The water inlet and outlet are connected to the outer and inner return port cavity. Since the direct use of the spool directly blocking the return port sealing is poor, the two-way water connection valve is designed to enhance the sealing. The two-way water connection valve features a central hole and 12 holes evenly distributed around the hole for the two-way water connection valve outlet and water inlet, respectively. The water inlet is connected to the outer cavity of the return port, and the water outlet is connected to the inner cavity of the return port.



a. Closed state internal structure

b. On-state internal structure

Fig. 3 – Internal structure of two-way water connection valve and spray body section

Figure 3 displays the two-way water connection valve and the internal structure of the sprayer body. Closed state, the valve spool blocks the outlet, preventing the liquid from the water inlet, flow to the two-way water connection valve is blocked; conductive state, the valve spool moves away from the two-way water connection valve outlet, allowing the liquid to flow from the two-way water connection valve outlet out of the water, into the spray body outlet.

Calculate the radius of the outlet of the bi-directional through-connection valve according to the maximum flow rate required by the technical specifications.

$$Q = K_L A \Delta p^m \tag{1}$$

Q is the flow rate through the outlet of the bi-directional water connection valve, [l/min];

K_L – throttle factor;

A – throttle port flow area, [m²];

Δp – differential pressure before and after throttle orifice, [N/m²];

m – throttle port shape factor

In the formula throttle coefficient according to experience usually take 0.7, throttle port shape coefficient, elongated holes $m = 1$, thin-walled holes $m = 0.5$. After calculating, this paper bidirectional flow through the water connection valve outlet cross-section radius of 2 mm.

Microcontroller Selection

The control system STM32 microcontroller selected STM32F103c8t6 chip from STMicroelectronics, a total of 48 pins, the maximum clock frequency of 72MHz; the main control of the multi-controller selected STM32F407vet6 chip from STMicroelectronics, a total of 100 pins, the maximum clock frequency of 168MHz. This controller can communicate with CAN bus interface, I2C, 485, SPI, and USART. It can also output PWM signals and operates within a temperature range of -40°C ~ 85°C. The microcontroller has the advantages of high working stability and reliability, efficient code efficiency, many peripheral interfaces, and low power consumption, which can adapt to withstand the harsh environment of agricultural environments and fulfil the requirements of variable rate spray control.

Multiple controllers

The multiplex controller serves as the core of the PTO protocol variable spray system. It receives the PTO protocol sent by the STM32 microcontroller for CRC check and extract the frequency and duty cycle information of the relevant PWM channel, and then outputs the PWM frequency and duty cycle through the electronic switch to control the on-off frequency and duty cycle of the electromagnetic nozzle, so that the medicine is sprayed according to the set spray volume. The multiplex controller uses STM32F407vet6 chip as the central processor, TJA1050 as the CAN communication chip, PMOS tube as the electronic switch, in addition to the clock circuit, reset circuit, and so on. The schematic block diagram of the multiplexer is shown in Fig. 4, and the physical diagram is shown in Fig. 5.

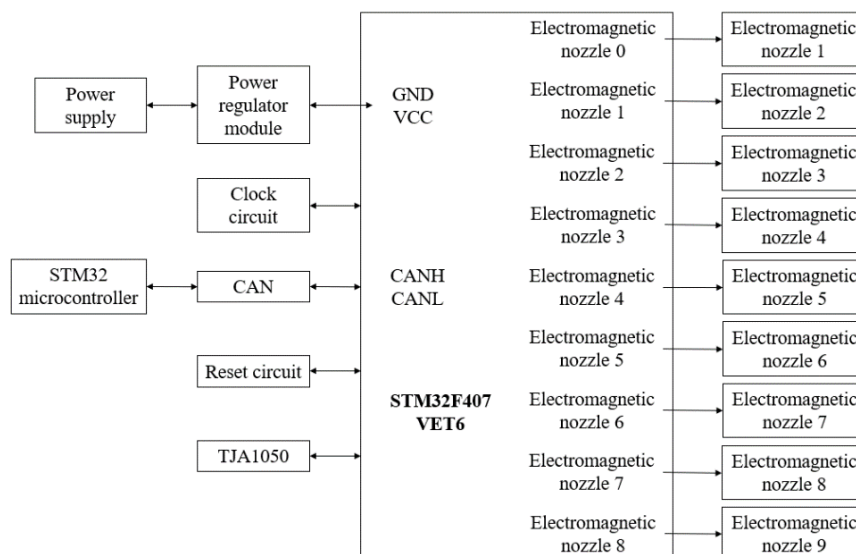


Fig. 4 – Multi-Controller block diagram

The power supply is connected to the microcontroller through the power regulator module to ensure stable power supply during operation. The STM32 microcontroller is linked to the multiplexer via the CAN bus module to transmit the integrated PTO protocol to the multiplexer. During the spraying operation, according to the PTO protocol data is received in real time, it extracts the corresponding frequency and duty cycle information of the channel and controls the on/off time of each electronic switch by adjusting the frequency and duty cycle of the PWM signal, thus controlling the on/off time of each electromagnetic nozzle and realising the control of the spray flow of each nozzle.



Fig. 5 – Multi-Controller Physical Diagram

The multiplex controller contains nine electronic switches, with each switch controlling a group of nozzles. The circuit diagram for the electronic switch circuit diagram is shown in Fig. 6. Each electronic switch consists of one PMOS tube, one transistor, four resistors, and one LED. Through the RC port input level signal controls the electronic switch to turn on and off. When the RC port input high level signal, the electronic switch is closed, the LED light is open, the electromagnetic nozzle suction, the nozzle spray liquid; RC port output low level signal, the electronic switch is disconnected, the LED light is closed, the electromagnetic nozzle is closed, the nozzle stops spraying liquid.

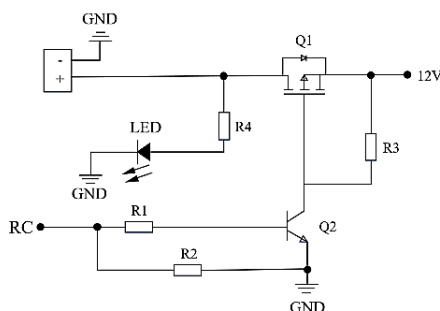


Fig. 6 – Electronic switch circuit diagram

Software system design

Programme design

The variable-rate spraying control program was developed based on the MDK5 development environment, in accordance with the basic operational requirements of variable-rate spraying and specifications such as the flow control algorithm. The workflow of the variable-rate spraying system was designed in accordance with the PTO protocol. Upon initialisation of the system, the STM32F103 MCU first receives the spray rate input from the host computer, converts the spray rate into a PWM duty cycle, and incorporates the frequency and duty cycle information into the PTO protocol, as shown in Fig. 7. The data then transmitted to the STM32F407 microcontroller through the CAN bus. The STM32F407 microcontroller performs CRC checksum data parsing on the received PTO protocol and extracts the relevant frequency and duty cycle information. Subsequently, the microcontroller receives the frequency and duty cycle information, which it uses to regulate the on/off switch of each electronic switch. Each electronic switch is responsible for regulating the on/off operation of an electromagnetic nozzle. The spraying of liquid occurs when the electromagnetic nozzle is open, and the liquid ceases to be sprayed when the electromagnetic nozzle is closed. By adjusting the on/off time of the electromagnetic nozzle in relation to the unit of time, the spray rate can be modified in order to achieve variable spraying.

The development of the PTO protocol variable spray control program is described in this paper, which also outlines the process of downloading the program to STM32F103 and STM32F407 microcontrollers using the ST-LINK V2 downloader for debugging and experimental verification. The workflow is depicted in Fig. 8.



Fig. 7 – PTO protocol data format

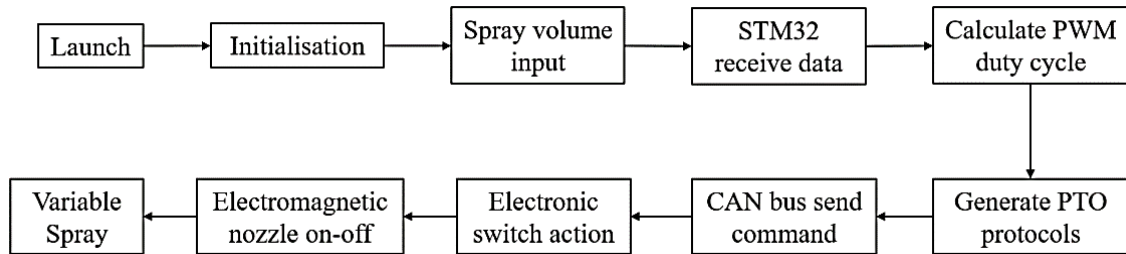


Fig. 8 – PWM signal output process

Flow regulation algorithm

In this study, a multiplex controller is utilized to receive and process the PTO protocol data and generate a multiplex adjustable PWM signal to regulate the variable spray nozzle, thereby achieving variable spray. Fig. 9 illustrates the PWM digital signal, the PWM duty cycle for a single pulse cycle, and the pulse period ratio (Yin et al., 2022). The pulse signal duty cycle calculation formula is as follows:

$$\alpha = \frac{t_0}{T} \times 100\% \tag{2}$$

α is the duty cycle of the pulse signal, [%];

t_0 — the on-time (high level output time), [s];

T — the pulse period, [s]

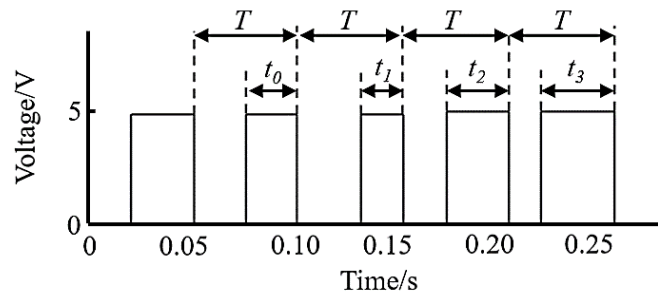


Fig. 9 – PWM digital signal

It can be observed that as the PWM duty cycle increases, the high-level output time also increases, as does the electromagnetic nozzle length and the number of nozzle sprays per unit time. Conversely, a shorter high-level output time leads to a shorter electromagnetic nozzle and a reduction in the number of nozzle sprays per unit time. Consequently, the actual flow rate of the nozzle, the duty cycle of the pulse signal, and the maximum flow rate of the nozzle are related as follows:

$$Q_0 = a \cdot \alpha + b \tag{3}$$

Q_0 is the actual flow rate of the nozzle, [l/min];

a, b - the constant

During the operational process, the machine's travel speed is subject to change. This results in a corresponding change in operating speed, which in turn affects the uniformity of drug application per unit area. In order to maintain a consistent spray effect, it is essential dynamically adjust the spray flow in real time in response to changes in speed.

The optimal demand flow rate of the outlet line is designated as $q(t)$ at the present moment t . The demand flow rate is calculated from the real-time vehicle speed obtained from the speed sensor. The following relationship exists between machine forward speed, application rate, spray width, and spray flow rate:

$$q(t) = m \frac{Qv'(t)W}{60000} \quad (4)$$

$q(t)$ is the demand flow at time t , [l/min];

Q — the amount applied per unit area, [l/min];

$v'(t)$ — the speed at which the machine is travelling at time t , [km/h];

W — the nozzle spacing, [cm];

m — the number of nozzles

Operational performance test

In order to evaluate the operational performance of the designed variable spray control system based on the PTO protocol for electromagnetic spray nozzles, a variable spray test bench was constructed and the developed control system then installed on the spray test bench. The effectiveness of the control system and the performance characteristics of the electromagnetic spray nozzle were assessed at the Precision Agriculture Laboratory of Shandong University of Technology in May 2024.

Test set-up

The test equipment includes a microcomputer-controlled nozzle, a comprehensive performance precision test bench, a high-speed camera, a filling light, a data acquisition system, a computer, an electromagnetic nozzle, a multi-channel controller, and other components, as shown in Fig.10. The physical diagram of the electromagnetic nozzle is depicted in Fig. 11. The nozzles connected to the nozzle were SF11006, SF11008, CFA11006 fan nozzle, spray angle of 110° , pressure range of 0.15 ~ 0.8 MPa. The test was performed on the CFA11006 fan nozzle.

The precision test bench consists of a hydraulic spraying system, a mist collection tank, a pressure monitoring system, and other components. During operation, the computer sends the PWM duty cycle and frequency to the main control through the serial port, which is then transmitted to the multi-channel controller via the CAN bus. setup enables the nozzle flow to be controlled through the opening and closing time of the control spool. The operator enters the required frequency and duty cycle in accordance with the test requirements. The duty cycle is the primary parameter of PWM precision spray technology, as it directly determines the size of the spray flow. If the on-time of the nozzle in a single cycle differs significantly from the set on-time, it will result in a reduction in spray precision. In order to verify the control accuracy of the designed PWM electronically controlled precision spray control system, the actual duty cycle of the nozzle spray was tested. This involved measuring the spray time of the electromagnetic spray nozzle in a single cycle under different pressures. This was done by a high-speed camera in order to verify the designed electromagnetic spray nozzle's working performance. The high-speed camera employed was the Photron FASTCAM Mini AX, which boasts excellent light sensitivity, high-quality imaging capabilities, and versatility, allowing for real-time display on both analogue and digital monitors.

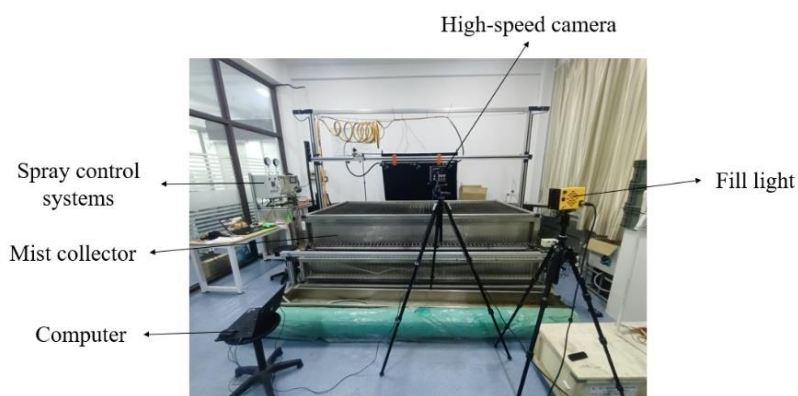


Fig. 10 – Test bench



Fig. 11 – Electromagnetic nozzle physical picture

Test methods

In order to verify the linear relationship between the spool conduction duty cycle and the set duty cycle, the designed solenoid nozzle was installed on the test bench, and the solenoid nozzle on-off test was carried out in the pressure range of 0.2 to 0.8 MPa. The pulse width modulation (PWM) signal frequency was set to 10 Hz, and the pressure values were set to 0.2, 0.3, 0.4, 0.5, 0.6, 0.7, and 0.8 MPa, respectively. A high-speed camera is employed to capture images, and the number of images containing spray droplets in a single cycle is multiplied by the frame length of the high-speed camera to obtain the on-time of the electromagnetic nozzle in a single cycle. During the test, the pulse-width modulation (PWM) duty cycle is incremented from 0 to 100% by 1% each time. The spraying time is then measured for 5-6 cycles under each duty cycle. The average value of the middle 3 sets of on/off time data is taken to find the spraying time and the corresponding spool on/off duty cycle in a single cycle. This is then compared with the set duty cycle. The high-speed camera is capable of capturing images at a rate of 4000 frames per second, with each pixel measuring 1024×1024. The interface for shooting is illustrated in Fig. 12. A single pulse-width modulation cycle under a high-speed camera captures the electromagnetic nozzle spray process, as illustrated in Fig. 13.

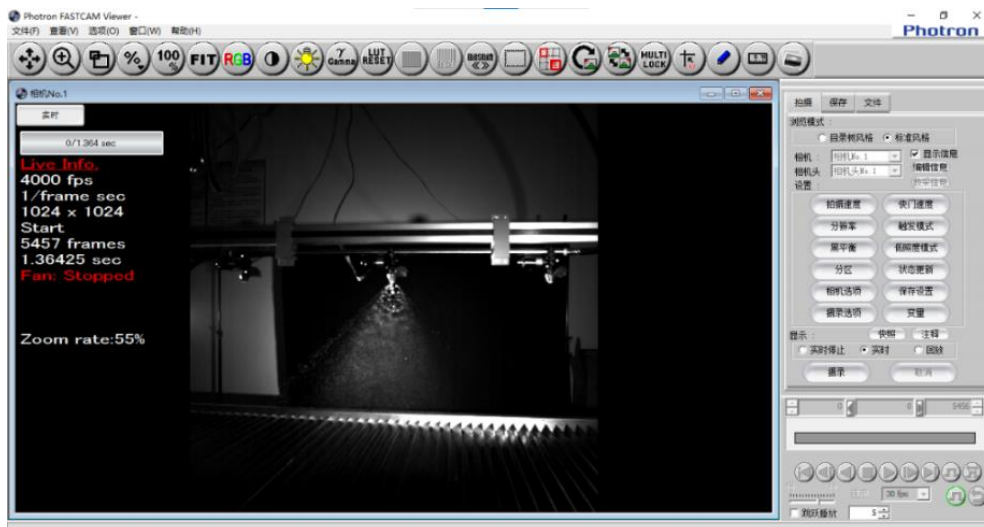


Fig. 12 – High-speed camera shooting interface

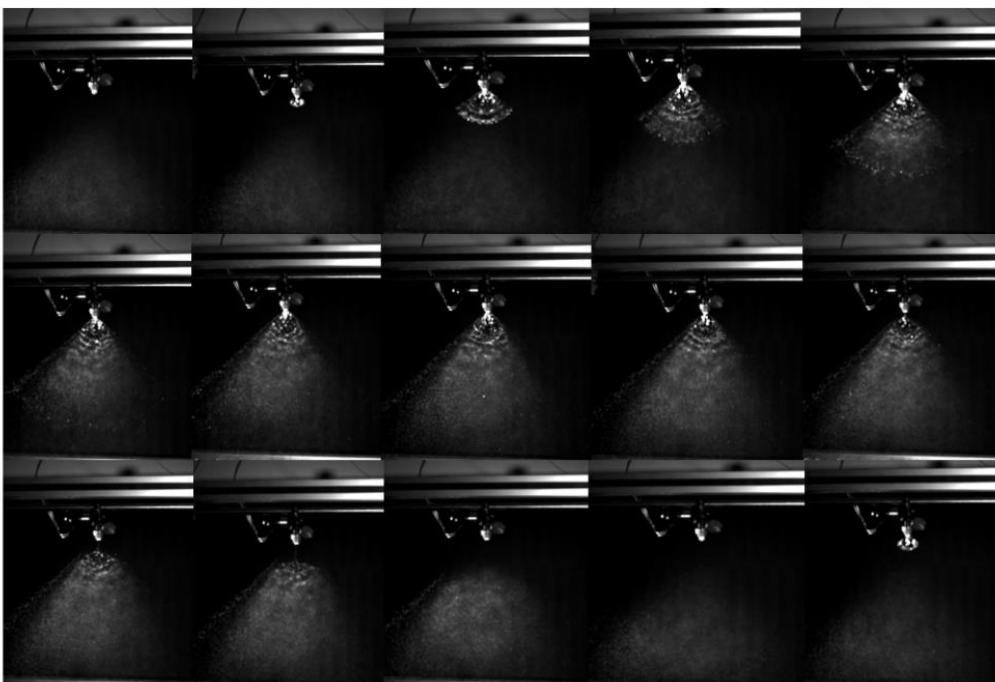


Fig. 13 - Spraying process with a single PWM cycle of the electromagnetic nozzle

RESULTS

The range of duty cycles at which the electromagnetic nozzle can operate at different pressures is presented in Table 2. At a pressure of 0.2 to 0.3 MPa, the minimum duty cycle at which the electromagnetic nozzle can be activated is 8%. At a pressure of 0.4 MPa, the minimum duty cycle is 9%. At a pressure of 0.5 to 0.6 MPa, the minimum duty cycle is 10%. Finally, at a pressure of 0.7 to 0.8 MPa, the minimum duty cycle is 11%. In the range of 0.2 to 0.8 MPa, the maximum duty cycle that can be closed by the electromagnetic nozzle is 94%. This phenomenon can be attributed to the two-way water connection with the spool side, which is subject to liquid pressure. The spool is reset in order to overcome the pressure of liquid reset, and the pressure is relatively low. This makes it easier to completely close the nozzle. However, as the pressure increases, the spool is reset with greater difficulty, and it becomes more challenging to completely close the nozzle.

Table 2

| System pressure (MPa) | 0.2 | 0.3 | 0.4 | 0.5 | 0.6 | 0.7 | 0.8 |
|-----------------------|------|------|------|-------|-------|-------|-------|
| Duty Cycle Range (%) | 8~94 | 8~94 | 9~94 | 10~94 | 10~94 | 11~94 | 11~94 |

The selected duty cycle range for the electromagnetic nozzle work performance test was 11% to 94%. The actual duty cycle error of the electromagnetic nozzle under different pressures is shown in Table 3. At a duty cycle of [11%, 94%], the maximum value of the maximum relative error of the actual duty cycle on-time is 137%, the maximum value of the average relative error is 17%, the maximum value of the maximum absolute error is 19.7 ms, and the maximum value of the root mean square error is 9.8 ms. At a duty cycle of [15%, 94%], the maximum value of the maximum relative error of the actual duty cycle on-time is 75.2%, the maximum value of the average relative error is 16.4%, the maximum value of the maximum absolute error is 19.7 ms, and the maximum value of the root-mean-square error is 9.5 ms. At a duty cycle of [20%, 94%], the maximum value of the maximum relative error of the actual duty cycle on-time is 38.2%, the maximum value of the average relative error is 12.1%, the maximum value of the maximum absolute error is 19.7 ms, and the maximum value of the root-mean-square error is 9.1 ms. When the duty cycle is [20%, 94%], the relative errors of the actual duty cycle on-time under different pressures are all low, indicating that the spray system has poor control effect on the electromagnetic nozzle in the range of duty cycle [11%, 20%], and has good control stability and reliability in the range of duty cycle [20%, 94%], which is able to meet the basic requirements of variable spraying.

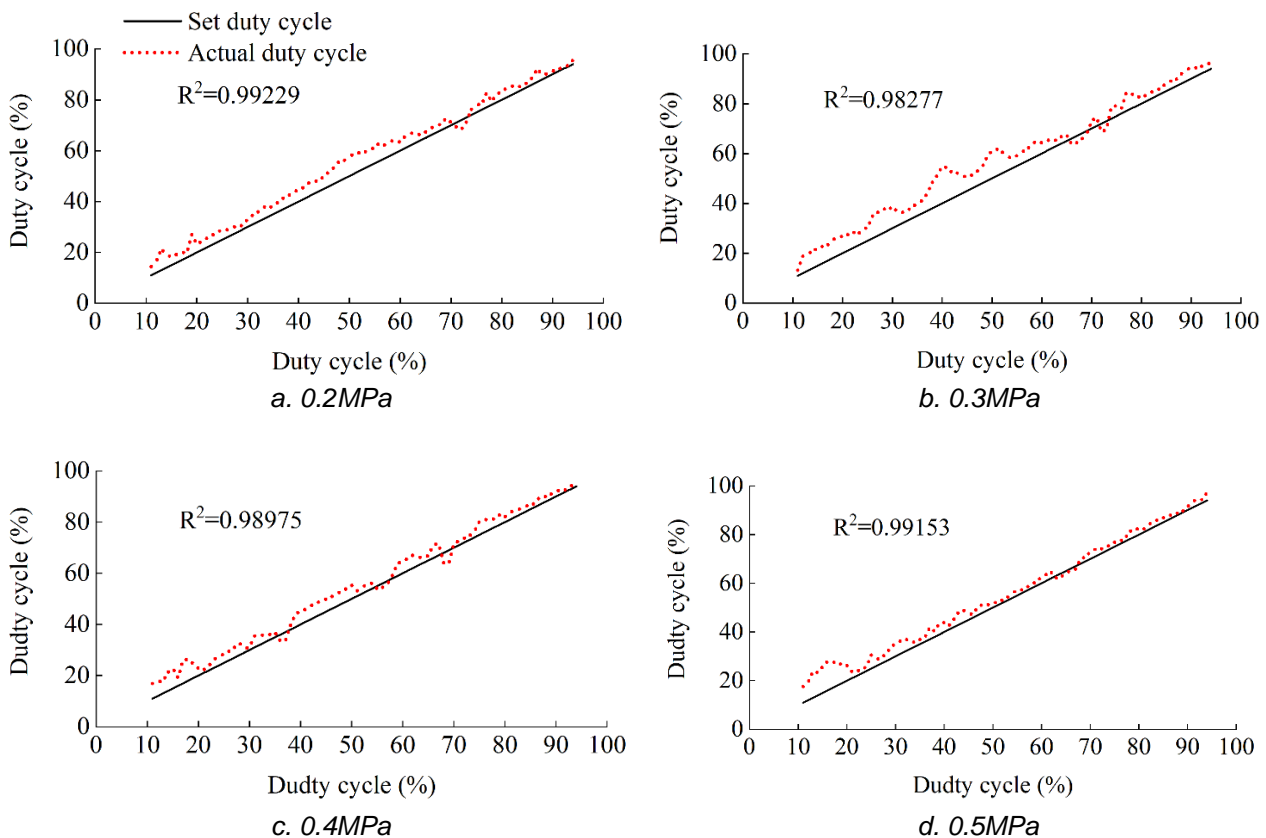
Table 3

| Spray pressure / MPa | Duty cycle range | Maximum relative error / % | Average relative error / % | Maximum absolute error / ms | RMSE / ms |
|----------------------|------------------|----------------------------|----------------------------|-----------------------------|-----------|
| 0.2 | [11%, 94%] | 64.6 | 6.42 | 8.4 | 3.7 |
| | [15%, 94%] | 42.8 | 4.31 | 8.1 | 3.3 |
| | [20%, 94%] | 16.4 | 3.27 | 8.1 | 2.9 |
| 0.3 | [11%, 94%] | 57.2 | 12.7 | 14.9 | 8.2 |
| | [15%, 94%] | 51.4 | 11.4 | 14.9 | 7.9 |
| | [20%, 94%] | 36.8 | 10.5 | 14.9 | 7.4 |
| 0.4 | [11%, 94%] | 54.2 | 8.6 | 9.2 | 4.7 |
| | [15%, 94%] | 54.1 | 4.3 | 9.2 | 4.7 |
| | [20%, 94%] | 14.3 | 2.1 | 5.3 | 2.2 |
| 0.5 | [11%, 94%] | 60.3 | 10.8 | 12.8 | 7.1 |
| | [15%, 94%] | 44.7 | 6.7 | 12.8 | 6.5 |
| | [20%, 94%] | 31.8 | 3.9 | 11.4 | 4.2 |
| 0.6 | [11%, 94%] | 80.7 | 8.2 | 17.4 | 6.5 |
| | [15%, 94%] | 75.2 | 4.2 | 17.4 | 6.2 |
| | [20%, 94%] | 38.2 | 4.1 | 17.4 | 5.8 |

| Spray pressure / MPa | Duty cycle range | Maximum relative error / % | Average relative error / % | Maximum absolute error / ms | RMSE / ms |
|----------------------|------------------|----------------------------|----------------------------|-----------------------------|-----------|
| 0.7 | [11%, 94%] | 45.4 | 14.8 | 15.1 | 8.4 |
| | [15%, 94%] | 36.8 | 14.3 | 12.9 | 8.2 |
| | [20%, 94%] | 32.6 | 9.6 | 11.4 | 7.1 |
| 0.8 | [11%, 94%] | 137 | 17.0 | 19.7 | 9.8 |
| | [15%, 94%] | 68.3 | 16.4 | 19.7 | 9.5 |
| | [20%, 94%] | 26.9 | 12.1 | 19.7 | 9.1 |

A comparison of the PWM set duty cycle the actual duty cycle at different pressures is presented in Fig.14. This can be observed by combining Table 3 and Fig.14a, Fig.14c, Fig.14d, and Fig.14e. At system pressures of 0.2, 0.4, 0.5, and 0.6 MPa, the average relative error between the actual duty cycle and the set duty cycle in the range of [11%, 94%] is 6.42%, 8.6%, 10.8%, and 8.2%, respectively. These values are considered unsuitable for practical applications due to their significant magnitude. The relative errors between the actual duty cycle and the set duty cycle in the range of [20%, 96%] are less than 4.1%, and the linearity is high, with the linear regression coefficients of determination exceeding 0.98. When combined with Table 3 and Fig.14b, Fig.14f, and Fig.14g, it can be observed that the actual duty cycle is greater than the set duty cycle in the range of [11%, 94%] at the system pressures of 0.3, 0.7, and 0.8 MPa, with average relative errors of 12.7%, 14.8%, and 17%, respectively. However, the data exhibits a high degree of linearity, with the coefficient of determination of the linear regression exceeding 0.98.

After repeated tests, the analysis shows that during the spool closure process, the liquid creates a certain resistance to the spool, and the pressure in the spray body and the spring work together to produce a resetting force on the spool. When the system pressure is 0.3 MPa, the low pressure in the spray body results in a small resetting force. After the electromagnetic force disappears, the resetting force cannot overcome the resistance of the liquid in time to close the spool. Similarly, when the system pressure is 0.7 MPa and 0.8 MPa, the liquid resistance is too great, preventing the spool from closing in time. However, when the system pressure is 0.2 MPa, due to the liquid resistance to the spool being insufficient, the spring reset force can close the spool in time. Conversely, when the system pressure is 0.4, 0.5, and 0.6 MPa, the reset force is sufficient, and the liquid resistance to the spool is minimal, allowing the spool to close in a timely manner.



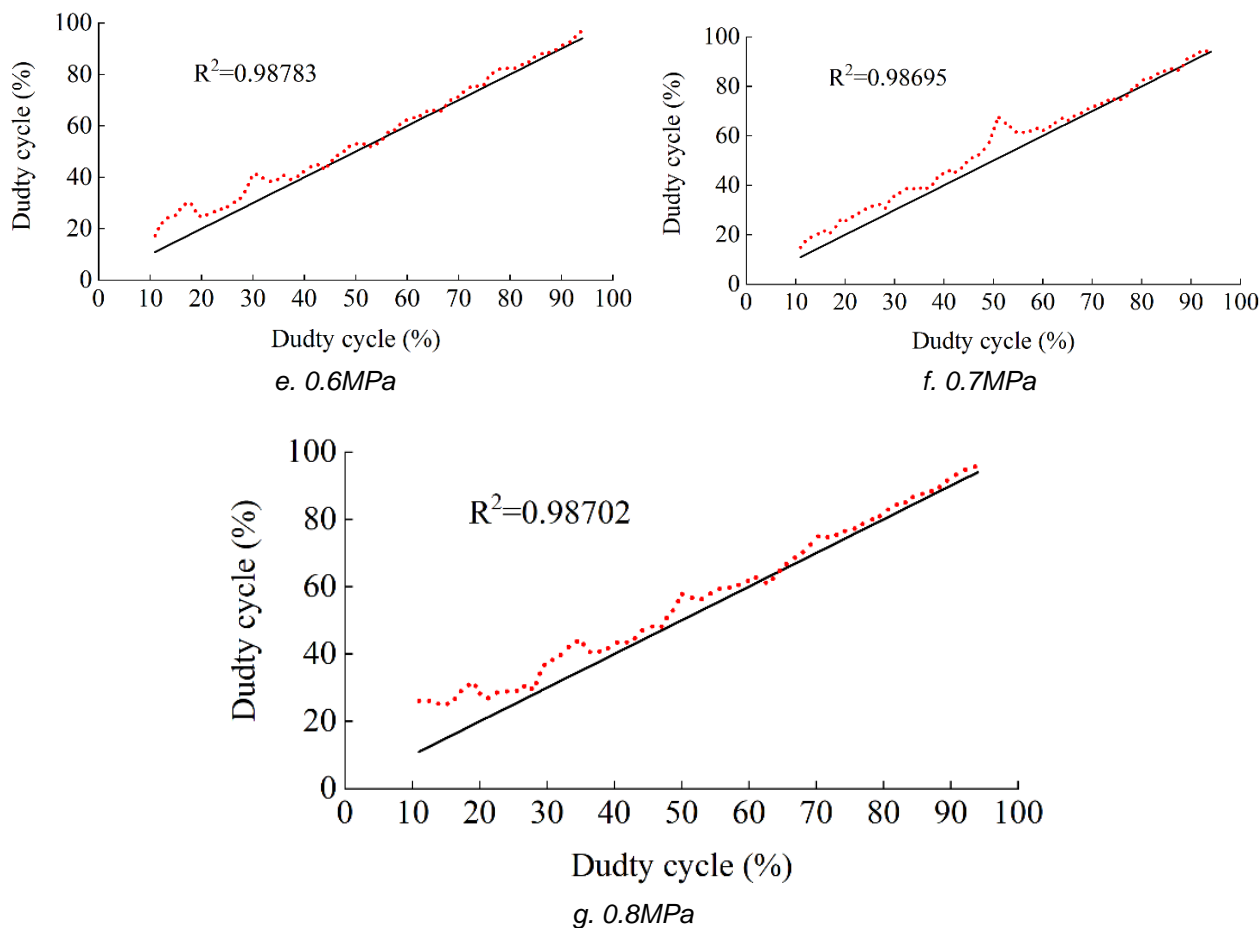


Fig. 14 – Set duty cycle and actual duty cycle at different pressures of electromagnetic nozzle

CONCLUSIONS

The aim of this study was to address the limitations of the existing farmland application system, which is characterised by low precision in variable spraying. The design and analysis of a variable spraying system based on the PTO protocol were conducted, and the results were verified through experimental testing. This system is capable of independently controlling the spray amount of each spray nozzle according to the application demand, offering a potential solution to the aforementioned issues.

In the designed variable spray system, the upper computer inputs the spray amount and sends it to the main controller. RTK_GNSS, using the um482, achieves RTK differential positioning, collecting the real-time position and speed information of the equipment and sending it to the main controller via the serial port. The main controller, with the STM32 at its core, calculates the required frequency and duty cycle based on the received spray amount and speed information, and sends this data via the CAN bus to the multiplex controller. The multiplex controller extracts the corresponding frequency and duty cycle information and outputs it to the electronic switches, controlling the on-off states of multiple switches. This controls the PWM duty cycle and frequency of each electromagnetic nozzle, achieving independent regulation of each nozzle's flow.

The test results for the electromagnetic nozzle at a PWM frequency of 10 Hz are as follows: at a pressure of 0.2 to 0.3 MPa, the minimum duty cycle for the electromagnetic nozzle is 8%; at a pressure of 0.4 MPa, the minimum duty cycle is 9%; at a pressure of 0.5 to 0.6 MPa, the minimum duty cycle is 10%; Finally, at a pressure of 0.7 to 0.8 MPa, the minimum duty cycle is 11%.

In a pressure range of 0.2 to 0.8 MPa, the maximum duty cycle that can be achieved by the electromagnetic nozzle is 94%. When the PWM signal frequency is 10 Hz, the system pressure at 0.2, 0.3, 0.4, 0.5, 0.6, 0.7, and 0.8 MPa is as follows: when the duty cycle is between 11% and 94%, the average relative error between the actual duty cycle and the set duty cycle is 6.42%, 12.7%, 8.6%, 10.8%, 8.2%, 14.8%, and 17.0%, respectively. When the duty cycle is between 20% and 94%, the average relative error between the actual duty cycle and the set duty cycle is 3.27%, 10.5%, 2.1%, 3.9%, 4.1%, 9.6%, and 12.1%, respectively.

The results demonstrate that the spray system exhibits inadequate control of the electromagnetic nozzle in the duty cycle range of 11% to 20%. Conversely, it exhibits optimal control stability and reliability in the duty cycle range of 20% to 94%. This performance is sufficient to meet the fundamental requirements of variable spraying.

ACKNOWLEDGEMENT

This work was supported by (Lu Zheng Ban Zi [2018] No. 27), the Technology Small Courtyard project by the Ministry of Education, Ministry of Agriculture and Rural Affairs, and the China Association for Science and Technology (Department of Teaching and Research Letter [2022] No. 7), as well as the Key R&D Program Funding Project in Zibo City (2019ZBXC053).

REFERENCES

- [1] Butts T.R., Luck J.D., Fritz B.K. et al. (2019). Evaluation of spray pattern uniformity using three unique analyses as impacted by nozzle, pressure, and pulse-width modulation duty cycle. *Pest management science*, Vol.75, Issue S7: 1875-1886.
- [2] Chu Wei-Wen (2021). Analysis of short boards and enhancement countermeasures for the development of plant protection mechanisation in China (我国植保机械化发展短板与提升对策分析). *Journal of Chinese Agricultural Mechanization*, Vol, 42, Issue S1: 46-51.
- [3] Fan Yu, Yang Jianguo, He Yuhai (2021). Study on dynamic characteristics of high-speed solenoid valve with double reset springs (双复位弹簧高速电磁阀动态特性研究). *Chinese Internal Combustion Engine Engineering*, Vol, 42, Issue S4: 101-108.
- [4] Feng Yaoning, Pei Liang, Chen Xiao et al. (2021). A review of key technologies for variable application (变量施药关键技术综述). *Journal of Chinese Agricultural Mechanization*, Vol, 42, Issue S12: 65-71.
- [5] He Xiongkui. (2019). Research progress of plant protection machinery and application technology in China (中国植保机械与施药技术研究进展). *Chinese Journal of Pesticide Science*, Vol, 21, Issue Z1: 921-930.
- [6] He Xiongkui. (2020). Research status and development proposal of precision application technology and equipment in Chin (中国精准施药技术和装备研究现状及发展建议). *Smart Agriculture*, Vol. 2, Issue S1: 133-146.
- [7] He Xiongkui. (2022). Progress of efficient plant protection machinery and precision application technology (高效植保机械与精准施药技术进展). *Journal of Plant Protection*, Vol, 49, Issue S1: 389-397.
- [8] Li Longlong, He Xiongkui, Song Jianli, et al. (2016). Spray characteristics of pulse width modulated variable nozzle based on high frequency solenoid valve (基于高频电磁阀的脉宽调制变量喷头喷雾特性). *Transactions of the Chinese Society of Agricultural Engineering*, Vol, 32, Issue S1: 97-103.
- [9] Liu Yong, Wang Yunsheng, Hu Wenwen, et al. (2022). Research and development of an agricultural solenoid valve control system integrating near and far (远近一体的农用电磁阀控制系统研发). *Acta Agriculturae Shanghai*, Vol, 38, Issue S1: 101-107.
- [10] Longlong Li, Liping Chen, Ruirui Zhang, et al. (2022). Spray drift characteristics of pulse-width modulation sprays in wind tunnel. *International Journal of Agricultural and Biological Engineering*, Vol.15, Issue S4: 7-15.
- [11] Qi Yachong, Yang Huimin, Chen Yifei, et al. (2022). Current status and prospect of variable spray target detection technology (变量喷雾靶标探测技术研究现状与展望). *Journal of Chinese Agricultural Mechanization*, Vol, 43, Issue S6: 83-89.
- [12] Qiu Baijing, Yan Run, Ma Jing, et al. (2015). Analysis of the research progress of variable spray technology (变量喷雾技术研究进展分析). *Transactions of the Chinese Society for Agricultural Machinery*, Vol, 46, Issue S3: 59-72.
- [13] Ramón Salcedo, Zhu H., Ozkan E., et al. (2021). Reducing ground and airborne drift losses in young apple orchards with PWM-controlled spray systems. *Computers and Electronics in Agriculture*, Vol, 189, Issue S6: 0168-1699.
- [14] Wang Runtao, Liu Yao, Wang Shuwen, et al. (2022). Design and test of speed-following variable spraying system based on fuzzy control (基于模糊控制的车速跟随变量喷雾系统设计与试验). *Transactions of the Chinese Society for Agricultural Machinery*, Vol, 53, Issue S6: 110-117.

- [15] Wang Yalin, Yin Xiang, Yang Shuang, et al. (2023). Design and test of electronically controlled precision spray control system based on PWM (基于 PWM 的电控精量喷雾控制系统设计与试验). *Journal of Chinese Agricultural Mechanization*, Vol, 44, Issue S5: 81-88.
- [16] Yin Xiang, Wang Yalin, Du Juan, et al. (2022). Design and test of electronically controlled precision nozzle body based on PWM (基于 PWM 的电控精量喷嘴体设计与试验). *Transactions of the Chinese Society of Agricultural Engineering*, Vol, 38, Issue S1: 18-26.

DESIGN AND EXPERIMENT OF SPIRAL-RIBBON BLADE COMBINATION MECHANISM OF STRAW AND MANURE INCLINED MIXING CONVEYOR

秸秆粪便斜式混配输送机螺旋-螺带组合机构设计与试验

Tiejun WANG, Peng YIN, Li DU, Rui ZHOU, Yuanjuan GONG, Hongguang CUI^{1*}

Shenyang Agricultural University, College of Engineering, Shenyang / China;

Tel: +8613804060603; E-mail: chg7763@syau.edu.cn

DOI: <https://doi.org/10.35633/inmateh-73-25>

Keywords: agricultural machinery; straw; manure; inclined mixing conveyor; spiral blade; ribbon blade

ABSTRACT

In order to solve the problem of poor mixing effect of inclined spiral conveyor, this paper designed an inclined spiral and ribbon blade combination conveying device. The mechanics and kinematics analysis of the movement process of the material unit in each mechanism was carried out, on which key devices and components were designed based. Effects of the speed of main shaft (X_1), the full coefficient (X_2) and the angle of inclination (X_3) on the mixing uniformity (Y_1) and the residual rate of material (Y_2) were explored. Three-dimensional quadratic regression orthogonal rotation central combination experiment method combined with response surface method was used to conduct experiments and explore the interaction effects of influence factors on indicators. A regression model of influence factors and evaluation indicators was established through the analysis of variance. The significant factors affecting Y_1 were ordered of X_3 , X_2 , X_1 , and the significant factors affecting Y_2 were ordered of X_2 , X_1 , and X_3 . In the interaction of factors, X_1X_2 had a significant impact on Y_1 and Y_2 ; X_1X_3 had an extremely significant impact on Y_1 ; X_2X_3 had an extremely significant effect on Y_1 and a significant impact on Y_2 . The optimal structure and working parameters combination were determined to be 50 rpm for the speed of main shaft, 60% for the full coefficient, and 19° for the angle of inclination, while the verification experiments demonstrated that the mixing uniformity and residual rate of material corresponding to the verification test were 90.37% and 5.31%, respectively. The inclined device with combined spiral and ribbon blade developed in this study meets the design requirements for the misprocess of the fertilizer utilization of agricultural organic wastes.

摘要

为解决倾斜螺旋叶片输送机输送秸秆与畜禽粪便混合效果不佳的问题,设计了一种适用于作物秸秆与畜禽粪便混合用于肥料生产的螺旋叶片与螺带叶片组成的斜式混合输送装置,并对其进行设计和性能试验。结合物料单元体在关键机构中的动力学与运动学分析,确定机构主要结构及工作参数。采用三元二次回归正交旋转中心组合试验方法,以主轴转速、充满系数和倾斜角度为试验因素,以混合均匀度和物料残留率为评价指标,实施试验并对其结果进行分析,建立影响因素与评价指标回归模型。结果表明:影响混合均匀度的主次因素是倾斜角度、充满系数、主轴转速,影响物料残留率的主次因素是充满系数、主轴转速、倾斜角度;确定最优参数组合为:主轴转速 50 r/min、充满系数 60%、倾斜角度 19°,在此条件下混合均匀度和物料残留率分别达到 90.37%、5.31%,试验验证结果表明,所设计机构满足技术要求。

INTRODUCTION

Crop straw and livestock manure are important fertilizer source materials for organic fertilizers (Dong et al., 2019; Chen et al., 2020). Their mixing and transportation links are important factors affecting the quality and efficiency of fertilizer production (Li et al., 2012). The integrated treatment of mixing and transportation can ensure the production quality and improve the production efficiency of fertilizer production at the same time (Ştefan et al., 2019&2021). The research and development of small-scale mixed transportation collaborative operation devices can provide technical support for improving the utilization rate of agricultural waste in local fertilizer (Zhang et al., 2020).

Researchers at domestic and abroad explored the mixing and conveying mechanism of agricultural waste. Such as straw and cow manure from the perspective of material flow characteristics and mechanical working parameters through experimental optimization and simulation (Chupshev et al., 2019; Savinyh et al., 2020; Sakai et al., 2015). The solid mixing test to the twin spiral ribbon mixer can be used to simulate the mixing uniformity and the torque of the mixing shaft with DEM of packing height and blade speed (Simons et al., 2016).

EDEM software was used to simulate and analyse the flow characteristics of corn stalk powder under the current working conditions of the spiral feeder. LIGGGHTS (LAMMPS improved for general granular and granular heat transfer simulations) software was used to solve the discrete element model to study the effects of rotational speed, filling rate, particle number ratio and loading mode on the mixing quality of dispersed particles in the horizontal blade mixer. It is found that the particle number ratio has the greatest effect on the mixing performance, and diffusion mixing has more advantages than convection mixing (Mohammadreza et al., 2020).

The installation experiment stand of horizontal screw conveying device was built, and a spiral-pneumatic coupling conveying device was designed, which provided a feasible device structure for the study of screw conveying and kneading corn stalk (Wulantuya et al., 2016 & 2019). The scholars quantitatively analysed the motion characteristics of straw particles by means of the discrete element method, high-speed tracer particle photography and comparison of test images, which provided a better analysis method for obtaining appropriate discrete element parameters and motion rules of material characteristics (Ştefan et al., 2018; Feng et al., 2017; Zhou et al., 2015). The scholars researched on ration mixers with different mixing components through high-speed photography technology, that provided an effective way to analyse the mixing process and type distribution of materials, the relationship between work and structural parameters and special mixing phenomena (Wang et al., 2017; Li et al., 2017; Wang et al., 2020; Yu et al., 2015).

Aiming at the problems such as unsatisfactory mixing effect, not applicable for material mixing, and no function of conveying material in horizontal spiral ribbon mixing, this paper designs a spiral-ribbon inclined mixing conveyor device for crop straw and manure production. Based on the dynamic and kinematic analysis and test of the material unit in each mechanism of the device, the influence of the key structure, working parameters and their interaction on the production capacity and working effect of the device is analysed and verified. The optimal structure and working parameters are proposed to realize the integrated treatment of the mixed transportation of crop straw, manure and sewage in the process of fertilizer production.

MATERIALS AND METHODS

Machine structure and working principle

The structure of the straw manure inclined mixing conveyor is shown in Fig.1, which is mainly composed of spiral blade, spiral ribbon blade, mechanical housing, support, spindle, frame, motor. The spindle can adjust the horizontal angle between the spindle and the ground under the action of the electric push rod support. From bottom to top, spiral blade with equal pitch, spiral ribbon blade with equal pitch, and spiral blade with variable pitch are arranged along the spindle in order to realize the mixing and transportation of straw manure under inclined conditions according to the principle of convection and shear mixing.

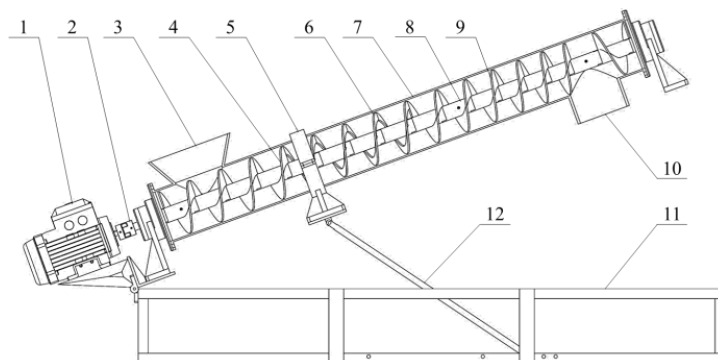


Fig. 1 - Machine structure diagram

1- Speed regulating motor; 2- Coupling; 3- Feeding port; 4- Equal pitch spiral mechanism; 5- Support; 6- Equal pitch spiral ribbon mechanism; 7- Mechanical housing; 8- Spindle; 9- Variable pitch spiral mechanism; 10- Discharge port; 11- Frame; 12- Angle adjustment bracket

When the machine works, the crushed straw, livestock and poultry manure enter through the feeding port 3 and are transported to the discharge port 10 in the spiral direction. Materials are pre-mixed in the vertical direction of each spiral section of the equal pitch spiral mechanism 4, and secondary mixing is carried out in the horizontal and vertical directions of the hollow structure of the spiral ribbon blade of the equal pitch spiral mechanism 6 in each spiral section. That is, the unmixed materials have different movements due to the difference in forces in every direction, resulting in the coexistence of multiple mixing forms such as convection and shear. Therefore, the variable pitch spiral mechanism 9 is recompressed along the decreasing pitch direction and finally discharged downward through the discharge port 10, at the upper end of the device.

Analysis and design of key components

The spiral-ribbon combined mechanism is the key component of the inclined mixing conveyor, which directly affects the performance of the mixing conveyor. The horizontal angle of the spindle is the main parameter reflecting the mixing force of the spiral ribbon mechanism on the straw manure material, and the spiral lift angle is the main parameter reflecting the spiral mechanism on the straw manure material conveying force. Refer to the main parameter relation of spiral conveying mechanism:

$$Q = 47 D^2 \Psi S n \gamma C \tag{1}$$

where: Q is the productivity, kg/h; D is the outer diameter of the helix, m; Ψ is the full coefficient; S is the pitch, m; n is the speed of main shaft, r/min; γ is the bulk weight of the material, kg/m³; C is the inclination correction factor, the corresponding value is taken according to the inclination angle.

In this paper, the relevant parameters are determined based on the operation conditions and requirements such as the fertilizer source material ratio, the geometric length range of straw silk, and the unit power productivity of the previous straw kneading process determined by the research group's previous research results (Wang et al., 2021a & 2021b). The design machine productivity $Q=800$ kg/h, material bulk weight $\gamma=200$ kg/m³, equal pitch spiral (spiral ribbon) mechanism $D=2R_1=2R_2=0.30$ m, the width of spiral ribbon mechanism $d=0.1D=0.03$ m, the spiral pitch of equal pitch spiral (spiral ribbon) mechanism $S_1=S_2=0.10$ m. The mechanism designed in this paper operates in the inclined state. When the full coefficient takes down the limit value 0.4 and the inclination angle takes up the upper limit value, that is, $C_{min}=0.4$, $n_{max}=59.10$ rad/min.

While determining the design parameters, it is necessary to further determine the main factors affecting the working performance of the spiral-ribbon combined device through the force and movement analysis of the material (Ştefan et al., 2017). Straw and manure materials are regarded as material unit with a mass of m in the analysis, and it is assumed that the friction factors between all parts at any position in the device are f , and the friction angles between materials and components are φ . The quality of materials in the space of the equal pitch spiral and spiral ribbon mechanism in the device is the same. According to the helical lift angle and other conditions, the effect of the force in the spiral blade plane is transformed into the projected amount of the force in the vertical and horizontal xOy planes formed along the main axis.

Equal pitch spiral mechanism

The simplified force analysis of the material unit in the equal pitch spiral mechanism is shown in Fig. 2.

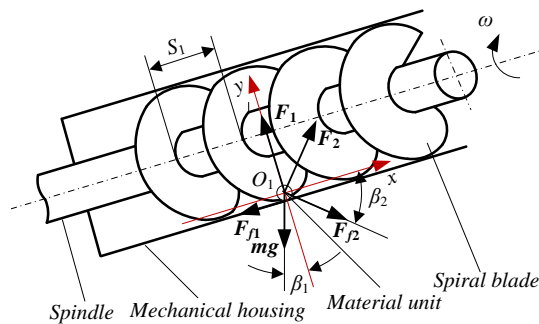


Fig. 2 - Force analysis diagram of material unit in oblique spiral mechanism with equal pitch

Note: F_1 is the supporting force of the mechanical housing on the material unit, N; F_2 is the positive pressure of the spiral blade with equal pitch on the material unit in xO_1y plane, N; F_{f1} is the friction force between the mechanical housing and the material unit, N; F_{f2} is the friction force between the equal pitch spiral blade and the material unit in the xO_1y plane, N; ω is the angular speed of the spindle rotation, rad/s; β_1 is the horizontal inclination angle of the main shaft, °; β_2 is the lift angle of the equal pitch spiral blade, °.

The three-dimensional space motion equation of the material unit is established from Fig. 2. The contact position between the material element and the surface of the spiral blade and the surface of the casing is determined by the radius R of the spiral blade and the displacement angle β_0 (Hewko et al., 2015). In the hypothetical case, the coordinates of the material unit are determined by Eq. (2):

$$\begin{cases} x_A = (R_1 - K) \cos \beta_0 + K \cos^2 \beta_0 \\ y_A = R_1 \sin \beta_0 \\ z_A = \frac{S_1(\omega t_1 - \beta_0)}{2\pi} \end{cases} \tag{2}$$

where:

x_A is the x coordinate of the material unit in the process of the equal pitch spiral mechanism movement, m; y_A is the y coordinate of the material unit during the motion of the constant pitch spiral mechanism, m; z_A is the z coordinate of the material unit during the motion of the constant pitch spiral mechanism, m; R_1 is the spiral radius of the equal pitch spiral mechanism, m; β_0 is the displacement angle of the material unit during the motion of the equal pitch spiral mechanism, rad; t_1 is the movement time of the material unit, s; K is the material coefficient; S_1 is the pitch, mm.

It can be seen from Eq. (2) that when the spiral radius R and pitch S are fixed, the displacement and acceleration of the material during movement are related to the speed of main shaft n and the inclination angle β_1 . The appropriate range should be determined to meet the design requirements.

Spiral ribbon mechanism with equal pitch

The simplified force and motion analysis of the material unit in the spiral ribbon mechanism are shown in Fig. 3. As can be seen from Fig. 3a, the conditions to ensure the movement of materials along the spiral direction are:

$$\begin{cases} \sum F_{x2} = F_4 \sin \beta_3 + F_{f4} \cos \beta_3 - F_{f3} - F_{f5} - mg \sin \beta_1 \geq 0 \\ \sum F_{y2} = F_3 + F_4 \cos \beta_3 - F_{f4} \sin \beta_3 - F_5 - mg \cos \beta_1 \geq 0 \end{cases} \quad (3)$$

where: F_{x2} is the resultant force of the material unit in the x direction during the movement of the constant pitch spiral ribbon mechanism, N; F_{y2} is the resultant force of the material unit in y direction during the movement of the constant pitch ribbon mechanism, N.

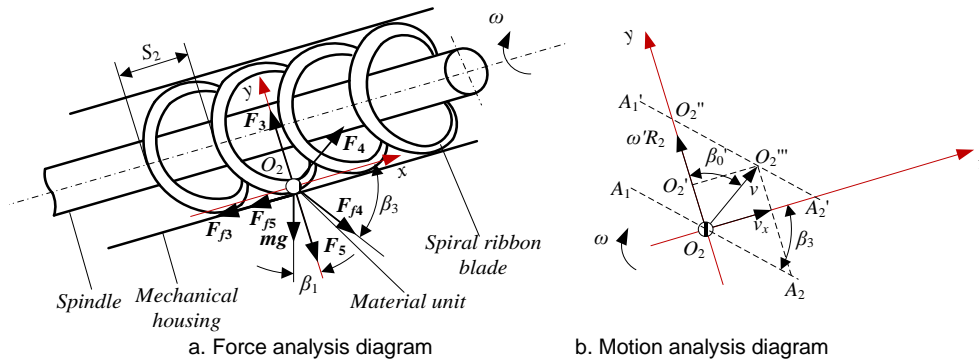


Fig. 3 - Force and motion analysis diagram of material unit in oblique spiral ribbon mechanism with equal pitch

Note: F_3 is the supporting force of the mechanical housing on the material unit in oblique spiral ribbon mechanism with equal pitch, N; F_4 is the positive pressure of the spiral ribbon blade on the material unit in xO_2y plane, N; F_5 is the pressure of the upper material on the material unit during the movement of the equal pitch spiral ribbon mechanism, N; F_{f3} is the friction force between the mechanical housing and the material unit in oblique spiral ribbon mechanism with equal pitch, N; F_{f4} is the friction force between the spiral ribbon blade and the material unit in the xO_2y plane, N; F_{f5} is the friction force between the materials in oblique spiral ribbon mechanism with equal pitch, N; β_3 is the lift angle of the equal pitch spiral ribbon blade, °.

According to Coulomb's formula:

$$\tan \beta_1 \leq \frac{F_4(\sin \beta_3 + \tan \varphi \cos \beta_3) - (F_3 + F_5) \tan \varphi}{F_4(\cos \beta_3 - \tan \varphi \sin \beta_3) + F_3 - F_5} \quad (4)$$

The motion analysis of the material unit in the constant pitch spiral ribbon mechanism is shown in Fig. 3b. After t_2 time of movement, the material unit moves in a circle with the angular speed ω' less than the rotation of the main shaft, resulting in displacement $l_{O_2O_2}$. Relative movement with the spiral ribbon blade at the same time results in displacement $l_{O_2O_2''}$.

$$v^2 = v_x^2 + v_y^2 = v_x^2 + (\omega R_2 - \tan \beta_3 v_x)^2 \quad (5)$$

$$\tan \beta_0' = \frac{l_{O_2'O_2}}{l_{O_2O_2}} = \frac{l_{O_2'O_2}}{l_{O_2O_2} - \tan \beta_3 l_{O_2'O_2}} = \frac{v_x}{\omega R_2 - \tan \beta_3 v_x} \quad (6)$$

where: v is the speed of the material unit in the constant pitch spiral ribbon mechanism, m/s; v_x is the axial component velocity of the material unit during the movement of the constant pitch ribbon mechanism, m/s; v_y is the radial component velocity of the material unit during the movement of the constant pitch ribbon mechanism, m/s; R_2 is the spiral radius of the constant pitch ribbon mechanism, m; β_0' is the displacement angle of the material unit during the movement of the constant pitch spiral ribbon mechanism, rad.

According to the theorem of kinetic energy, the force between matter and material F_5 , can be expressed as:

$$F_5 = m \frac{v^2}{R_2} \tag{7}$$

The instantaneous inter body force of the material unit can be obtained by connecting the vertical Eqs. 3-7:

$$F_5 = \frac{m\omega^2 R_2}{1 + \tan \beta_0 \tan \beta_3} \left(\frac{1}{1 + \tan \beta_0 \tan \beta_3} + \tan^2 \beta_0' \right) \tag{8}$$

When the force between the material unit overcomes its own gravity ($F_5 \geq mg$), and achieves the best mixing effect along the negative direction of the x axis ($\beta_0' = -90^\circ$), then the speed of main shaft $n_{\min} = 25 \text{ rad/min}$.

Spiral mechanism with unequal pitch

The simplified force analysis of the material unit in the variable pitch spiral mechanism is shown in Fig. 4. During the movement of the variable pitch spiral mechanism, the material unit is subjected to the following forces: Its own gravity mg , the thrust F_6 and friction force F_{f6} of the rear material, the positive pressure F_7 and friction force F_{f7} of the spiral blade behind the forward direction, the positive pressure F_8 and friction force F_{f8} of the spiral blade in the forward direction, the resistance F_{f8} and friction force F_{f9} of the front material, the pressure F_{10} and friction force F_{f10} of the mechanical housing.

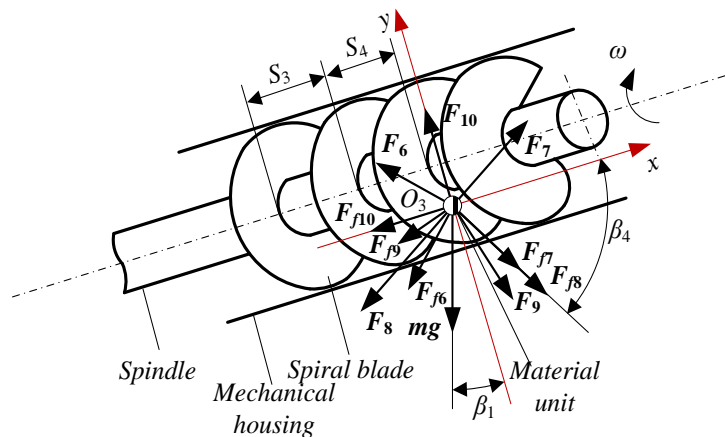


Fig. 4 - Force analysis diagram of material unit in oblique spiral mechanism with unequal pitch

The variable pitch spiral mechanism belongs to the quantitative variable pitch spiral structure, in which the movement law of each monomer material in the bin is not the same, and there are irregular changes due to the change of spiral moment. To ignore the difference between monomer material and the interaction force between materials, the calculation formula of the quantitative variable pitch spiral structure flowmeter is adopted (Xu et al., 2021):

$$Q = \frac{E \cdot 60 \gamma \psi n L}{10^9} = \frac{47 D^2 \gamma \psi n \sum_{i=3}^t S_i^2}{t S_3 + (t-1) S_4 + (t-2) S_5 + \dots + S_t} \tag{9}$$

where:

E is the blanking volume per turn per unit length, m^3 ; L is the length of the spiral body, mm ; t is the serial number of the spiral segment.

The length of the variable pitch spiral mechanism is designed $L = 400 \text{ mm}$, and five spiral segments are designed, which are S_3 to S_7 . According to Eq. (9), when the actual blade diameter, filling rate, density and rotational speed are fixed, the influence of the variable pitch of the feed section on the flow rate is mainly considered. Concerning Xu et al. (2021), the design values of the spiral pitch in the variable pitch mechanism are $S_3 = 0.10 \text{ m}$, $S_4 = 0.09 \text{ m}$, $S_5 = 0.08 \text{ m}$, $S_6 = 0.07 \text{ m}$ and $S_7 = 0.06 \text{ m}$, respectively.

To sum up, to further clarify the influence of the speed of main shaft, full coefficient and inclination angle on the mixing effect and conveying capacity of the machine, this paper carries out experimental analysis and optimization.

Experiment design

Experiment condition

The experiment was carried out at the Northeast Horticultural Engineering Scientific Observation Station of the Ministry of Agriculture and Rural Affairs. The experimental straw was harvested and air-dried corn straw (*variety: Wanying 178*) from Beishan Scientific Research Base of Shenyang Agricultural University. The manure for the experiment was taken from fresh manure of surrounding farmers. The experiment fertilizer source material ratio (corn straw dry matter mass to fertilizer mass ratio) was 23%. The geometric length of straw silk was 10 to 50 mm (*Wang et al., 2017a*). The average moisture content of straw and cow manure was 15.36% and 65.12%, respectively.

Experiment equipment included electronic analysis balance (*Germany Sartoris QUINTIX224-1CN*), digital display electric constant temperature drying oven (*Shanghai Sunshine Experimental Instrument Co., LTD. 101-0A*), DC regulated power supply (*Yuride UTP1306S*), variable-speed motor (*Pfield 10RK60RGN-CF*), incline meter (homemade), electronic scale.

Experiment factors and indexes

Three-dimensional quadratic regression orthogonal rotation central combination experiment method, combined with response surface method, was used to conduct experiments and explore the interaction effects of influence factors on indicators. Effects of the speed of main shaft (X_1), the full coefficient (X_2) and the angle of inclination (X_3) on the mixing uniformity (Y_1) and the residual rate of material (Y_2) were explored.

According to the relevant research on the mixing characteristics of materials and the comparative analysis of the theory and test of the detection method of mixing uniformity (*Wulatuya et al., 2016; Wang et al., 2013*), the physical method was adopted in this experiment, the soybean (the variety was Dongdou NO.1) was used as the tracer to detect the mixing uniformity. According to the total mass of the feeding material in each experiment level, the corresponding quality of soybeans were put in equal proportion (from the thousand grain weight of soybeans to the corresponding quality of the feeding material), so that the quality of soybeans in the unit mass of the feeding material was equal, which was regarded as the quantity of soybeans contained in the unit mass of the feeding material was equal. During the experiment, the samples were taken 10 times at the outlet at the same time interval, about 250 g each time. The parameter value of the tracer quantity under the experiment level was calculated with the corresponding value n_i of the tracer quantity measured at each time, and the mixing uniformity Y_1 (%) was calculated according to Eq. (10). The material quality was weighed before and after each level experiment, and the material residue rate Y_2 (%) was calculated according to Eq. (11).

The experiment process and samples were shown in Fig. 5. According to the analysis of the aforementioned documents and the mixing process, the value range of each factor and the experiment factor levels were shown in Table 1.

$$Y_1 = (1 - S/\bar{n}) \times 100\% \quad (10)$$

$$Y_2 = (T_1 - T_2)/T_1 \times 100\% \quad (11)$$

where:

S is the standard deviation of the number of tracers; \bar{n} is the average value of the number of tracers; T_1 is the mass of the feed-in material, kg; T_2 is the mass of discharged material, kg.



Fig. 5 - Experimental apparatus (left) and collected sample (right)

Table 1

Factors and levels of combination experiment

| Levels | Factors | | |
|------------|------------------------|------------------|-------------------|
| | Speed of main shaft | Full coefficient | Inclination angle |
| | [r·min ⁻¹] | [%] | [°] |
| | X_1 | X_2 | X_3 |
| 1.682 | 60.00 | 80.00 | 35.00 |
| 1 | 52.90 (53.00) | 71.89 (72.00) | 29.93 (30.00) |
| 0 | 42.50 | 60.00 | 22.50 |
| -1 | 32.10 (32.00) | 48.11 (48.00) | 15.07 (15.00) |
| -1.682 | 25.00 | 40.00 | 10.00 |
| Δj | 10.40 (10.50) | 11.89 (12.00) | 7.43 (7.50) |

Note: The parameters in parentheses were the parameters taken in the experiment. Adjusted the calculation results according to the feasibility of actual operation, and taken the values in parentheses.

RESULTS

A total of 23 groups of experiment were considered, and each group was repeated three times. The results were taken as the average value. The experiment scheme design and result analysis were shown in Table 2, where X_1 , X_2 , and X_3 are factor coded values specified in Table 1. Using Design-Expert software, multiple regression analysis was carried out by mixing uniformity Y_1 and material residue rate Y_2 as response indexes, and speed of main shaft, full coefficient, and inclination angle as influencing factors to obtain the regression model.

Table 2

Experimental plan and results

| No. | Speed of main shaft | Full coefficient | Inclination angle | Y_1 | Y_2 |
|-----|------------------------|------------------|-------------------|-------|-------|
| | [r·min ⁻¹] | [%] | [°] | [%] | [%] |
| 1 | 1 | 1 | 1 | 81.12 | 6.84 |
| 2 | 1 | 1 | -1 | 93.73 | 6.90 |
| 3 | 1 | -1 | 1 | 80.14 | 3.32 |
| 4 | 1 | -1 | -1 | 84.41 | 4.87 |
| 5 | -1 | 1 | 1 | 80.88 | 8.18 |
| 6 | -1 | 1 | -1 | 87.41 | 7.89 |
| 7 | -1 | -1 | 1 | 80.58 | 6.15 |
| 8 | -1 | -1 | -1 | 82.24 | 6.88 |
| 9 | 1.682 | 0 | 0 | 84.29 | 5.41 |
| 10 | -1.682 | 0 | 0 | 80.13 | 7.85 |
| 11 | 0 | 1.682 | 0 | 85.49 | 7.95 |
| 12 | 0 | -1.682 | 0 | 80.68 | 3.80 |
| 13 | 0 | 0 | 1.682 | 80.46 | 5.81 |
| 14 | 0 | 0 | -1.682 | 90.89 | 7.88 |
| 15 | 0 | 0 | 0 | 88.22 | 5.56 |
| 16 | 0 | 0 | 0 | 87.72 | 5.73 |
| 17 | 0 | 0 | 0 | 87.17 | 4.85 |
| 18 | 0 | 0 | 0 | 88.79 | 5.04 |
| 19 | 0 | 0 | 0 | 88.26 | 5.19 |
| 20 | 0 | 0 | 0 | 87.24 | 4.80 |
| 21 | 0 | 0 | 0 | 87.40 | 5.31 |
| 22 | 0 | 0 | 0 | 86.67 | 5.39 |
| 23 | 0 | 0 | 0 | 88.77 | 5.44 |

Experiment results variance analysis

It can be seen from Table 3, the effects of the speed of main shaft (X_1), full coefficient (X_2), and inclination angle (X_3) on mixing uniformity and material residue rate were very significant ($P < 0.01$). The secondary terms of speed of main shaft and inclination angle had great significant effects on mixing uniformity and material residue rate ($P < 0.01$). The quadratic terms of the full coefficient had a great significant influence on the mixing uniformity ($P < 0.01$) and have a significant influence on the material residue rate ($P < 0.05$).

Table 3

Data significance experiment and analysis of variance

| Source of variation | The mixing uniformity Y_1 | | | | The residual rate of material Y_2 | | | |
|---------------------|-----------------------------|----|---------|-----------|-------------------------------------|----|---------|-----------|
| | SS | DF | F value | P value | SS | DF | F value | P value |
| Model | 328.72 | 9 | 62.42 | <0.0001** | 39.35 | 9 | 37.95 | <0.0001** |
| x_1 | 17.07 | 1 | 29.18 | 0.0001* | 9.3 | 1 | 80.74 | <0.0001** |
| x_2 | 41.72 | 1 | 71.29 | <0.0001** | 17.79 | 1 | 154.41 | <0.0001** |
| x_3 | 132.97 | 1 | 227.24 | <0.0001** | 2.23 | 1 | 19.38 | 0.0007** |
| x_1x_2 | 2.9 | 1 | 4.96 | 0.0442* | 0.7859 | 1 | 6.82 | 0.0215* |
| x_1x_3 | 9.44 | 1 | 16.13 | 0.0015** | 0.1685 | 1 | 1.46 | 0.2481 |
| x_2x_3 | 21.79 | 1 | 37.24 | <0.0001** | 0.7839 | 1 | 6.8 | 0.0217* |
| x_1x_1 | 56.97 | 1 | 97.36 | <0.0001** | 3.31 | 1 | 28.76 | 0.0001** |
| x_2x_2 | 39.9 | 1 | 68.18 | <0.0001** | 0.5668 | 1 | 4.92 | 0.0450* |
| x_3x_3 | 7.11 | 1 | 12.14 | 0.0040** | 4.5 | 1 | 39.04 | <0.0001** |
| Lack of Fit | 3.15 | 5 | 1.13 | 0.417 | 0.7023 | 5 | 1.41 | 0.3156 |

Among the interaction factors, the interaction of the speed of main shaft and full coefficient (X_1X_2) had significant effects on mixing uniformity and material residue rate ($P<0.05$). The interaction of the speed of main shaft and inclination angle (X_1X_3) had a great significant effect on the mixing uniformity ($P<0.01$). The interaction between the full coefficient and the inclination angle (X_2X_3) had a great significant effect on the mixing uniformity ($P<0.01$) and a significant effect on the material residue rate ($P<0.05$). The coefficient of determination is $R_1^2=0.98$, $R_2^2=0.96$. The significant level F_R of the regression equation, the F_{L_f} value and P value of the mismatch experiment were greater than 0.05, indicating that the relationship between the regression equation were statistically significant. At the significant level of $P=0.05$, non-significant items were eliminated and the regression model of each factor and index Y was simplified as follows:

$$\hat{Y}_1 = 87.80 + 1.12X_1 + 1.75X_2 - 3.12X_3 + 0.60X_1X_2 - 1.09X_1X_3 - 1.65X_2X_3 - 1.89X_1^2 - 1.58X_2^2 - 0.67X_3^2 \quad (12)$$

$$\hat{Y}_2 = 5.26 - 0.83X_1 + 1.14X_2 - 0.40X_3 + 0.31X_1X_2 + 0.31X_2X_3 + 0.47X_1^2 + 0.19X_2^2 + 0.53X_3^2 \quad (13)$$

Analysis of influencing factors

The calculation results of the response surface of each experiment factor and its interaction on the experiment index were shown in Fig. 6. It can be seen from the figure that the primary and secondary order of the influence of each experiment factor on the mixing uniformity was inclination angle>full coefficient>speed of main shaft; and the primary and secondary order of the influence of each experiment factor on the material residual rate was full coefficient>speed of main shaft>inclination angle.

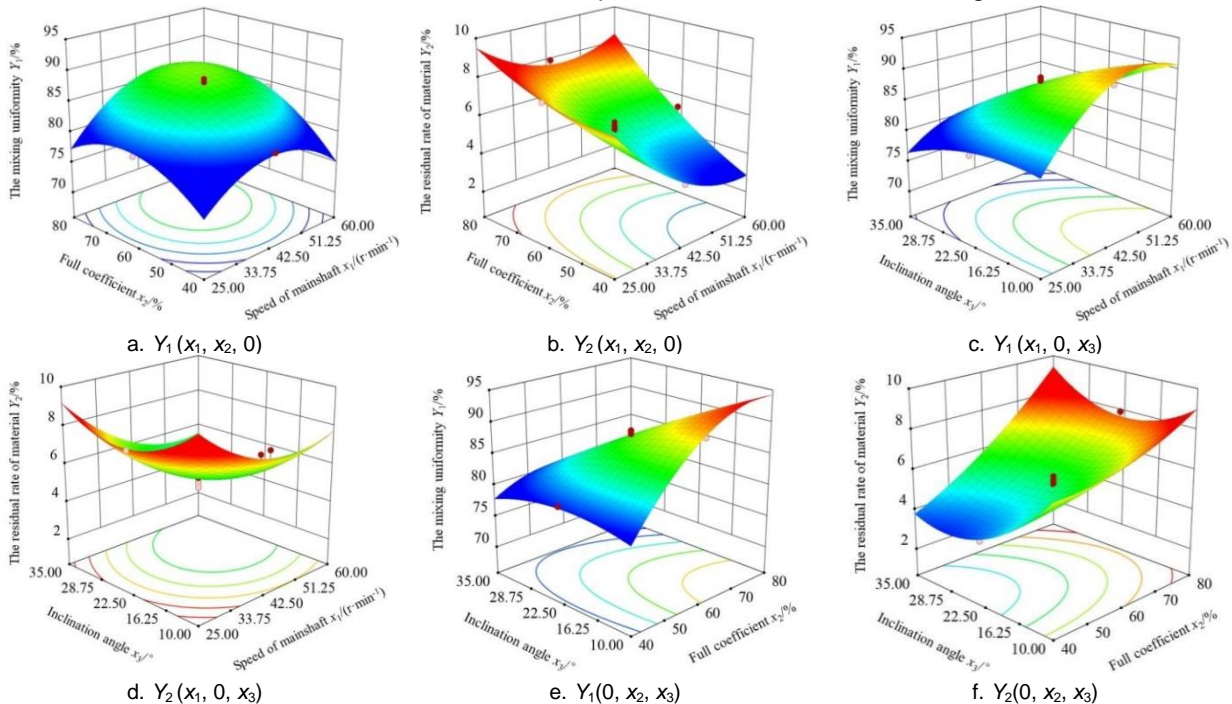


Fig. 6 - Response surface analysis of the factors' interaction effect on the index

Fig. 6a and 6b showed the response surface diagram of the influence of the speed of main shaft and full coefficient interaction (X_1X_2) on Y_1 and Y_2 when the inclination angle (X_3) was zero level value (22.50°). The analysis showed that when X_1 and X_2 gradually increase within the experiment range, Y_1 first increases and then decreases, and Y_2 gradually increases. When x_2 was constant and x_1 increases gradually within the experiment range, Y_1 also increases first and then decreases, and Y_2 gradually decreases. At the same time, x_2 determines the total amount of the materials in the device per unit of time. When x_2 value was low, there was less material, the active diffusion movement ability between materials was weak, the shear effect of mixing parts on materials was reduced, the mixing effect was unsatisfactory, and the materials were less attached to the shell and the mixing mechanism. When the x_2 value was high, there were more materials, and the diffusion effect between materials was limited by the movement space. Meanwhile, under the same speed (under the power input) the driving force of the stirring parts was more dispersed, which affected the convective mixing process and reduces the mixing effect, and more materials were attached to the housing and stirring parts. When x_2 was constant, increasing x_1 appropriately to transport power input could improve the mixing effect, but when x_1 was too large, the input power was larger, driving the material movement speed up, and the material residue was less, but different bulk weight materials were easy to form different mixing material areas in the housing, resulting in uncoordinated convection and diffusion movement conditions in the horizontal and vertical directions of the material, thus reducing the mixing effect.

Fig. 6c and 6d showed the response surface diagram of the influence of the interaction between the speed of main shaft and inclination angle (X_1X_3) on Y_1 and Y_2 when the full coefficient (X_2) was zero horizontal value (60%). According to the analysis, when X_1 was constant and in the lower level of the experiment range, when X_3 gradually increased in the experiment range, Y_1 first increases and then decreases, and Y_2 first decreases and then increases with the increase of X_3 . When X_1 was constant and in the higher level of the experiment range, X_3 gradually increases in the experiment range, Y_1 and Y_2 gradually decrease. When X_3 and X_1 gradually increase within the experiment range, Y_1 first increases and then slightly decreases, and Y_2 gradually decreases. This was because when X_2 was certain, that is, the total amount of materials in the device in unit time was the same; the same X_3 meant the same material was subject to the same external force in unit time. Increasing X_1 increased the disorderly motion speed of the material, thereby improving the mixing effect, and reducing the time of material attachment to the housing and accumulation on the mixing parts, thus increasing the discharge and reducing the material residual rate.

Fig. 6e and 6f were the response surface diagrams of the influence of the full coefficient and inclination angle interaction (X_2X_3) on Y_1 and Y_2 when the speed of main shaft (X_1) was zero horizontal value (42.5 r/min). It could be seen from the analysis that if X_2 was a fixed value, when X_3 gradually increased in the lower level of the experiment range, Y_1 had insignificant change, and Y_2 first decreases and then slightly increases. If X_2 was a fixed value, when X_3 gradually increased in the higher level of the experiment range, Y_1 gradually decreases and Y_2 gradually increases. When X_3 and X_2 gradually increased within the experiment range, Y_1 gradually increases and Y_2 gradually increases. This was because when X_1 was certain (the input power is certain) the same X_2 was the same material in the unit time force effect is equal, X_2 and X_3 increased to improve the gravity effect of the material, further increasing the mixing movement time of the material in the housing, improve the mixing effect. But at the same time, increased the time of the material attached to the housing and mixing parts. The adhesion strength was improved and the discharge quantity is reduced.

Parameter optimization and verification test

Set the target parameter the mixing uniformity and the material residual rate to maximize, and the factors parameter to the range of experiment to obtain the optimal working parameter combination of the spiral-ribbon inclined combined mixing device: the speed of main shaft was 48.73 r/min, the full coefficient was 58.45%, and the inclination angle was 19.10° , the overall operation effect being the best. The predicted mixing uniformity will be 88.97% and the material residue rate will be 5.11%.

In order to further verify the reliability and applicability of the mathematical model, the optimization results were tested and verified under the same experiment conditions, while the actual test results and the model prediction values were analysed for error. Considering the operability of the test, the optimization results were adjusted as follows: the spindle speed was 50 r/min, the fullness coefficient was 60%, and the inclination angle was 19° , and three repeated tests were carried out to obtain the best working parameter combination. The average values of the test values of uniformity and material residue

rate were 90.37% and 5.31%, respectively, which were close to the predicted values of the model. The relative error between the actual and predicted values didn't exceed 0.5%, indicating the established model and analysis results were valid.

CONCLUSIONS

In this paper, mixing uniformity and material residue rate are used as the performance indexes of the diagonal mixing conveyor of straw and manure. Combine with the theoretical analysis of the stress theory to materials in different structures and the test results of prototypes under theoretical assumptions, the following conclusions are drawn:

1) The inclined mixing conveyor completes the feeding, mixing, and conveying of straw silk and cow manure in succession through the spiral-ribbon combined mechanism, which can realize the mixed conveying of straw manure.

2) The result shows that the order of influence of each factor on mixing uniformity is as follows: inclination angle, full coefficient, and speed of main shaft. The order of influence of interaction of factors on mixing uniformity is as follows: speed of main shaft and full coefficient, speed of main shaft and inclination angle, full coefficient and inclination angle. The order of influence of each factor on material residual rate is as follows: full coefficient, speed of main shaft, and inclination angle. The order of influence of interaction of factors on material residual rate is as follows: the speed of main shaft and the full coefficient, full coefficient and inclination angle.

3) According to the response surface method, the optimal parameter combination is as follows: speed of main shaft 50 r/min, full coefficient 60%, inclination angle 19°, corresponding to the mean value of mixing uniformity and material residue rate are 90.37% and 5.31% respectively.

ACKNOWLEDGEMENT

The study was supported by the Liaoning Province Natural Science Foundation of Innovation Capacity Promotion Joint Fund (2022-NLTS-19-05). The authors thank relevant scholars for their assistance in the literature.

REFERENCES

- [1] Chen Shan, Han Hui, Zhang Xin, et al. (2020), Analysis on the agricultural ecological cycle model of planting and farming combination (种养结合的农业生态循环模式探析), *Territory & Natural Resources Study*, vol.185, no.2, pp.63-65, Harbin/China.
- [2] Chupshev A., Teryushkov V., Konovalov V., et al. (2019), Functional model of energy consumption for mixing with a vertical paddle mixer [C]. *XII International Scientific Conference on Agricultural Machinery Industry, IOP Conference Series: Earth and Environmental Science*, vol.403, 012102.
- [3] Dong Hongmin, Zuo Lingling, Wei Sha, et al. (2019), Establish manure nutrient management plan to promote green development of integrated crop-livestock production system, *Bulletin of Chinese Academy of Sciences*, vol.34, no.2, pp.180-189, Beijing/China.
- [4] Feng Junxiao, Lin Jia, Li Shizhong, et al. (2017), Calibration of discrete element parameters of particle in rotary solid state fermenters (秸秆固态发酵回转筒内颗粒混合状态离散元参数标定), *Transactions of the CSAM*, vol.46, no.3, pp.208-213, Beijing/China.
- [5] Hewko B.M., Popovich P.V., Diachun A.Y., et al. (2015), The study of bulk material kinematics in a screw conveyor-mixer, *INMATEH - Agricultural Engineering*, vol.47, no.3, pp.155-162, Bucharest / Romania.
- [6] Li Liqiao, Wang Defu, Li Chao, et al. (2017), Design and experimental optimization of combined-type ration mixer of drum and blade (转筒与桨叶组合式日粮混合机设计与试验优化), *Transactions of the CSAM*, vol.48, no.10, pp.67-75, Beijing/China.
- [7] Li Ruxin, Geng Aijun, Zhao He, et al. (2012), Rheologic behavior of chopped corn stalks during rotary compression (碎玉米秸秆卷压过程的流变行为试验), *Transactions of the CSAE*, vol.28, no.18, pp.30-35, Beijing/China.
- [8] Mohammadreza E., Amirsalar Y., Behrooz J., et al. (2020), Assessment of bi-disperse solid particles mixing in a horizontal paddle mixer through experiments and DEM, *Powder Technology*, vol.381, pp.129-140, Lausanne/Switzerland.
- [9] Sakai M., Shigeto Y., Basinskas G., et al. (2015), Discrete element simulation for the evaluation of solid mixing in an industrial blender, *Chemical Engineering Journal*, vol.279, pp.821-839, Lausanne/Switzerland.

- [10] Savinyh P., Aleshkin A., Turbanov N., et al. (2020), Investigation of impact of technological and structural parameters upon energy indicators of work of mixer, *19th International Scientific Conference Engineering for Rural Development, Engineering for Rural Development*, vol.19, pp.1338-1348.
- [11] Simons T.A.H., Bensmann S., Zigan S., et al. (2016), Characterization of granular mixing in a helical ribbon blade blender, *Powder Technology*, vol.293, pp.15-25, Lausanne / Switzerland.
- [12] Ștefan V., Cârdei P., Vlăduț N.V., et al. (2018), Mathematical model for particle motion applied on a manure spreading apparatus used in environmentally friendly technology, *Environmental Engineering and Management Journal*, January, vol.17, no.1, pp. 217-227, Iasi / Romania.
- [13] Ștefan V., David L., Popa L., et al. (2017), Use of theoretical mathematical relations for calculating the application and mass flow rate of a rear delivery vertical axis manure spreader, *16th International scientific conference engineering for rural development proceedings*, vol.16, May 24-26, pp.1284-1291
- [14] Ștefan V., Sfârșu R. & Popa L. (2019), Experimental results on the solid organic fertilizer machine MG 5. *E3S Web of Conferences* 112, 03007.
- [15] Ștefan V., Zaica A., Adrian Iosif. (2021), Research on the uniformity degree of solid organic fertilizers distribution, *INMATEH-Agricultural Engineering*, vol.65, no.3, pp.495-504, Bucharest/Romania. <https://doi.org/10.35633/inmateh-65-51>
- [16] Wang Defu, Dang Chunxue, Huang Huinan, et al. (2020), Mechanism Analysis and parameter optimization of paddle-type ration mixer (桨叶式日粮混合机机理分析与参数优化), *Transactions of the CSAM*, vol.51, no.6, pp.122-131, Beijing/China.
- [17] Wang Defu, Li Chao, Li Liqiao, et al. (2017), Mechanism analysis and parameter optimization of blade-type feed mixer (叶板式饲料混合机混合机理分析与参数优化), *Transactions of the CSAM*, vol.48, no.12, pp.98-104, Beijing/China.
- [18] Wang Ruifang, Li Zhanyong, Dou Rubiao, et al. (2013), Simulation on random motion and mixing characteristic for soybean in rotary drum (水平转筒内大豆颗粒随机运动与混合特性模拟), *Transactions of the CSAM*, vol.44, no.6, pp.93-99, Beijing/China.
- [19] Wang Ruili, Yu Jin, Wang Tiejun, et al. (2021c), Experimental study on molding technology for a mixture of corn straw and cow manure, *BioResources*, vol.16, no.1, pp.1740-1756, USA.
- [20] Wang Tiejun, Wang Ruili, Sun Junde, et al. (2021a), Parameter optimization of the small-scale compost technology with localization maize stover and livestock manure (秸秆-粪便属地化微贮制肥工艺参数优化), *Transactions of the CSAE*, vol.37, no.2, pp.251-257, Beijing/China.
- [21] Wang Tiejun, Wang Tieliang, Cui Hongguang, et al. (2021b), Design and experiment of adjustable feeding straw bale-breaking and rubbing filament machine (喂入调节式秸秆破包揉丝机设计与试验), *Transactions of the CSAM*, vol.52, no.6, pp.148-158, Beijing/China.
- [22] Wulantuya, Qing Lin, Wang Chunguang. (2019), Design of screw-pneumatic coupling conveying device for crushed corn straw (揉碎玉米秸秆螺旋—气力耦合输送装置设计), *Transactions of the CSAE*, vol.35, no.6, pp.29-38, Beijing/China.
- [23] Wulantuya, Wang Chunguang, Qi Shaohua, et al. (2016), Analysis and test of theoretical model of screw conveyor for rubbing and breaking corn straw (揉碎玉米秸秆螺旋输送理论模型分析与试验), *Transactions of the CSAE*, vol.32, no.22, pp.18-26, Beijing/China.
- [24] Xu Xuemeng, Li Feixiang, Li Yongxiang, et al. (2019), Design and experiment of quantitative variable pitch screw (定量变距螺旋结构设计及试验), *Transactions of the CSAM*, vol.50, no.12, pp.89-97, Beijing/China.
- [25] Yu Keqiang, Li Liqiao, He Xun, et al. (2015), Experimental design and principle analysis on paddle-wheel total mixed ration mixer (转轮式全混合日粮混合机试验设计与机理分析), *Transactions of the CSAM*, vol.46, no.7, pp.109-117, Beijing/China.
- [26] Zhang Huipeng. (2020), Big country and small farmers: structural contradiction and governance difficulty - Take the management of agricultural ecological environment as an example, *Journal of China Agricultural University Social Sciences*, vol.37, no.1, pp.15-24, Beijing/China.
- [27] Zhou Jingzhi, Zhou Xingzhi, Feng Junxiao, et al. (2015), Rotary cycle of crushed straw material bed and complete mixing time of layers in rotary cylinder (回转筒内秸秆碎料回转周期和料层完全混合时间研究), *Transactions of the CSAM*, vol.46, no.8, pp.178-185, 238, Beijing/China.

DESIGN AND EXPERIMENTAL VERIFICATION OF SELF-PRIMING HOT AIR TEMPERATURE CHANGING DEVICE FOR GRAIN DRYER

粮食干燥机自吸式热风变温装置设计与试验验证

Zhao-Xin Liu^{1,2)}, Gang Che^{*1,2)}, Lin Wan^{*1,2)}, Hong-chao Wang¹⁾, Zheng-Fa Chen¹⁾, Hao-Chen Wang¹⁾

¹⁾College of Engineering, Heilongjiang Bayi Agricultural University, Daqing / P.R.China

²⁾Key Laboratory of Intelligent Agricultural Machinery Equipment in Heilongjiang Province, Daqing / P.R.China

Tel: +86-459-13836961617; E-mail: chegang180@126.com

Corresponding author: Gang Che

DOI: <https://doi.org/10.35633/inmateh-73-26>

Keywords: self-priming, variable temperature device, mutual mixing, Fluent, combination test

ABSTRACT

During the grain drying process, in order to adjust the temperature, it is necessary to match the proportion of hot and cold air. This is the problem that the two components in the mixed gas cannot fully mix with each other in a short period of time, resulting in the problem that it takes a long time for the gas flow temperature to reach a stable value. Based on the process and technical requirements of the dryer, a self-priming hot air temperature changing device suitable for the dryer was designed. The two gas components used to improve the variable temperature ratio of the dryer are fully mixed with each other in a short time and a short distance, thereby reducing the loss caused by the food not reaching safe moisture. Based on Bernoulli's principle and the basic theory of airflow mixing in fluid dynamics, a mathematical model of airflow mixing in the constriction section of the main pipeline was established. Fluent was used to numerically simulate the distribution of uniform mixing distance and temperature field in the necking section. The results show that the mixing uniformity in the necking section reaches 75%-80%, which effectively improves the mixing efficiency. A self-priming hot air temperature change device test bench developed independently was used, and the quadratic orthogonal rotation combined test method was used for parameter optimization. Design-Expert.V8.0.6.1 was used for analysis and testing, and the regression equation and response surface were obtained to analyze the effects. Interaction between factors to determine the best combination of optimization parameters: when the number of air inlet pipes is 3.16, the incision axial angle is 27.6°, the temperature difference is 43.5°C, and the pipe diameter is 23.8 mm, the post-mixing temperature is 50.93°C, and the mixing distance is uniform is 39.33 mm. The test results are consistent with the optimization results. The self-priming hot air temperature changing device of the dryer has certain practical application value.

摘要

在谷物干燥过程中,为调节温度,需要根据冷热空气的比例配比。为混合气体中的两种组分在短时间内无法充分相互混合,导致气流温度达到稳定值需要较长时间的问题。基于干燥机的工艺与技术要求,设计了一种适用于干燥机自吸式热风变温装置。用于提高干燥机变温配比的两种气体组分短时间、短距离的充分相互混合,进而减少粮食未达到安全水分造成损失。基于流体动力学中伯努利原理和气流混和的基本理论,建立了在主管道缩颈段的气流混配的数学模型。运用 Fluent 对缩颈段内混合均匀距离和温度场的分布情况进行了数值模拟。结果表明:在缩颈段混合均匀度达到 75~80%,有效的提高了混合效率。采用自主研发的自吸式热风变温装置试验台,应用二次正交旋转组合试验方法进行参数优化,运用 Design-Expert.V8.0.6.1 进行分析检验,得到回归方程和响应曲面,分析各影响因素之间的交互作用,以确定优化参数最佳组合:当进气管数量为 3.16、切口轴向角 27.6°、温差 43.5°C、导管直径 23.8mm 时混后温度为 50.93°C,混合均匀距离为 39.33mm,试验结果与优化结果相符合,干燥机自吸式热风变温装置具有一定的实际应用价值。

INTRODUCTION

According to the National Bureau of Statistics' announcement on grain output data in 2022, the country's total grain output was 686.53 million tons (1,373.1 billion kilograms), an increase of 3.68 million tons (7.4 billion kilograms) compared with 2021, an increase of 0.5%. Among them, grain output is 633.24 million tons (1,266.5 billion catties), an increase of 490,000 tons (1 billion catties) compared with 2021. However, every year due to climate reasons, the drying time is not enough to reach safe moisture, resulting in losses of up to 5% of the total output. Therefore, it is crucial to reduce the temperature uniformity time of the mixed airflow and accurately control it (*Chen et al., 2020*).

Rice drying usually uses two drying methods: traditional natural drying and mechanical drying. The traditional natural drying method is easily affected by various factors such as climate and site. In recent years, the sales of drying devices have increased year by year, so research on the precise adjustment of rice drying devices is very necessary. In terms of drying technology research *Jiang and Liu (2009)* tested two drying processes, low constant temperature drying and variable temperature drying, on a batch circulation rice dryer; domestic scholar (*Liu et al., 2023*) studied the technology and performance of the rice variable temperature homogeneous drying device; it was conducted experimental research on the variable temperature and quality-preserving drying technology and control process of rice (*Li, 2019*); in terms of mixed flow investigation, research by *Ahri Ozkan (Fahri et al., 2006)* and others has verified that the Venturi effect can significantly increase the solubility of oxygen in water. *Song Kangkang* used the CFD method to analyze the solid-liquid two-phase flow field of the SH20 mixed-discharge integrated device, and improved the design of the device (*Song et al., 2023*). Therefore, a stable temperature changing device is an important prerequisite for ensuring drying quality (*Hang et al., 2014*). The temperature-changing mechanical system of the dryer is mostly separated from the cold air inlet and the hot air inlet. Cold and hot air fan blowers are used to work at the same time to control temperature changes. There is room for improvement in both its energy consumption and real-time temperature changing level.

MATERIALS AND METHODS

Self-priming hot air temperature changing device and its working principle

The self-priming hot air temperature changing device includes an air volume hot air inlet connected to a heating fan blower, and a mixer outlet connected to a drying device. The main pipeline consists of an inlet section, a constriction section and a diffusion section, as shown in Fig. 2. The fan blower is shown in Fig. 1. The fan blower is a hot air supply device. The tail of the air inlet pipe is placed in the constriction section. The hot air in the main pipe passes through the constriction section and creates a pressure difference with the atmospheric pressure, causing the air to enter from the air inlet pipe and mix with the air in the main pipe for cooling. When the temperature required for drying needs to be changed, the sliding plate of the variable temperature adjustment device is driven by the drive motor and forms staggered openings with the fixed plate to control the amount of air entering and thereby control the temperature.

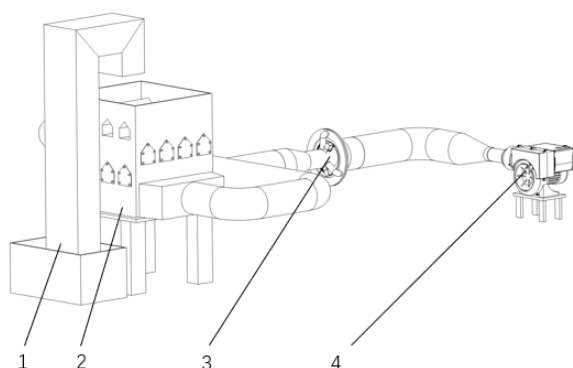


Fig. 1 - Variable temperature drying test bench

1. Elevator; 2. Dryer; 3. Temperature changing device;
4. Heating fan blower;

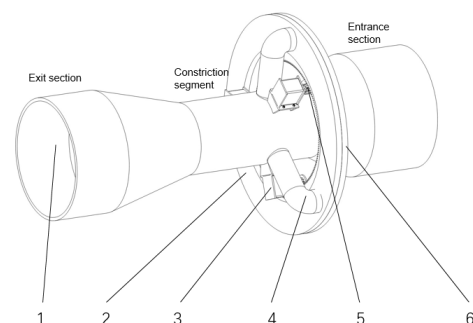


Fig. 2 - Self-priming hot air temperature changing device

1. Main pipe; 2. Fixed plate; 3. Drive motor; 4. Inlet pipe;
5. Drive gear; 6. Sliding plate

Design calculation of air inlet size

During the design and research of hot and cold air flow mixing devices, the principle of hot and cold air ratio is that hot and cold air are mixed according to a certain ratio, and a new equilibrium state is reached after mixed flow and heat transfer within a certain distance. The temperature changing device in this article adopts negative pressure self-priming air inlet. The air flow mixing angle is analyzed as intersecting air flow mixing. During the mixing process, the cold air enters the main pipe through the air inlet pipe. When the cold air passes through the tail of the air inlet pipe, it is cold air due to its guiding role. When the spiral enters through an oblique cut, entrainment is formed inside the airflow, the expansion angle increases, and the mixing becomes more complete, thereby forming a uniform airflow, that is, uniform mixing can be achieved within a short distance. The area of the near-air opening and closing section of the cold air is shown in Fig. 2:

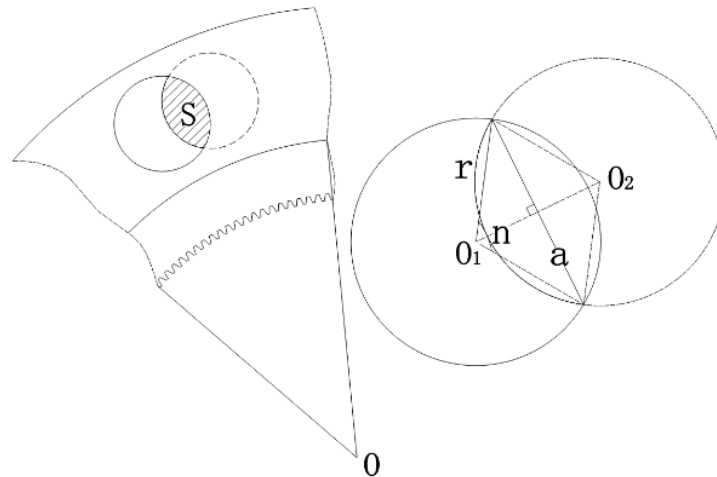


Fig. 3 - Close air opening and closing section

$$a = 2rsinn \tag{1}$$

$$S \approx r^2(0.017n - sinn\sqrt{1 - \sin^2 n}) \tag{2}$$

where:

r is the radius of the intake pipe, [mm]; n is the sector angle, [°]; a is the chord length, [mm]; Bernoulli's equation for spiral flow is:

$$\frac{\gamma}{\gamma-1} \frac{p}{\rho} + \frac{1}{2} V^2 = C(n) \tag{3}$$

where:

γ is the helix angle, [°]; p is pressure, [Pa]; ρ is density, [kg/m³]; V is the flow rate, [m/s]; $C(n)$ is a constant;

The amount of cold air proportioned through the intake pipe per unit time and the cross-sectional air volume of the hot air in the constriction section of the main pipe are equal to the mixed cross-sectional air volume. According to the above equations 1, 2, and 3, the expression is:

$$V_3\pi R^2 + V_2S = V_m\pi R^2 \tag{4}$$

where:

R is the radius of the necked section pipe, [mm]; V_3 is the flow velocity of the necked section pipeline, [m/s]; V_2 is the flow rate of cold air into the pipe, [m/s]; S is the cold air inlet area, [m²]; V_m is the wind speed after mixing, [m/s];

In order to meet the requirements of drying air volume adjustment and to obtain the minimum hot air temperature, it is assumed that the temperature fluctuation is ±1°C, the hot air temperature is 40~70°C, and the ambient temperature is 20. Determining the wind speed of the main duct by changing the wind speed and then the pressure of the necked section has no effect on its indicators. Determine the structural parameters according to the changes in the temperature of the main duct. The combined equations 1, 2, and 3 yield that the opening area of the main duct is approximately no more than 0.0023 m², combined with the size of the main pipeline necking section, determine the circular section radius to be 16 mm, the number is 3 and they are evenly distributed in the main pipeline necking section.

Intake pipe design

The intake pipe is installed in the necked section of the main pipe. A circular hole is set 135 mm from the beginning of the necked section. The tail of the intake pipe is placed in the circular hole and has a beveled arc opening and a horseshoe shape. The tail of the intake pipe has both a radial angle α and an axial angle β of the incision with the intake pipe itself, as shown in Fig. 4. The tail of the inlet pipe in the necked section of the main pipe is arranged in a spiral inside the pipe, so that when the cold air passes through the tail of the inlet pipe, the cold air enters through a spiral bevel due to its guiding function, and the air flow is entrained inside, and the expansion angle increases. At the same time, the hot gas in the main pipe also has a certain spiral guide, and its mixing is more uniform, thereby forming a uniform mixed gas. And the tail of the intake pipe faces the direction of the main pipe airflow, which prevents backflow.

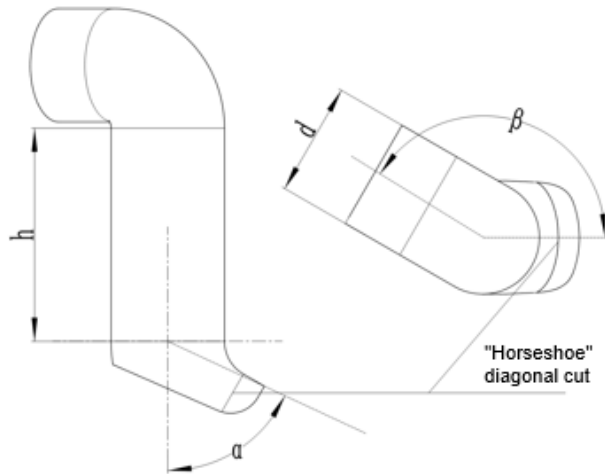


Fig. 4 - Intake pipe structure diagram

Design and optimization of adjusting plate

The air volume adjustment device consists of a fixed plate and a sliding plate. The fixed plate and the sliding plate are respectively provided with circular holes in the center. An internal ring gear is arranged on the inner circumference of the sliding plate. The fixed plate and the sliding plate are evenly provided with holes along their circumferences. The fixed plate is fixedly connected with the head of the air intake pipe. When the temperature required for drying needs to be changed, the sliding plate of the air volume adjustment device is driven by the motor and forms staggered openings with the fixed plate to control the amount of air entering and thereby control the temperature.

Since the fixed plate and the sliding plate are installed closely, an annular slideway is provided on the inner circumference of the opposite fixed plate, and an annular slide rail is provided on the inner end surface of the sliding plate. The annular slideway and the annular slide rail fit together. The installation enables the sliding disc to rotate on the surface of the fixed disc.

Since the design of friction on the slide rail is relatively complex, formula 5 for calculating the radial toroidal friction moment is:

$$M = \int_{R_2}^{R_1} dM = \frac{2}{3} \mu mg (R_1^3 - R_2^3) \tag{5}$$

$$S \approx 3\pi r^2 \tag{6}$$

$$R_1 - R_2 > 2r \tag{7}$$

where: R_1 is the radius of the outer circular surface, [mm]; R_2 is the radius of the inner circular surface, [mm]; μ is the friction coefficient of the sliding disk material; m is the mass of the sliding disk, [kg]; g is the gravity acceleration, [m/s²]; S is the cold air inlet Area, [m²]; r is the radius of the intake pipe, [mm];

Through formulas 5, 6, and 7, the equation is calculated: in order to ensure that the material of the adjustment plate is unique, (polyamide) material was selected for 3D printing in the test, which is stable and reliable while minimizing the distance between the inner and outer slideways as much as possible. The optimal structure obtained is that the radius of the inner slideway R_1 is approximately 247.5 mm, and the radius of the outer slideway R_2 is approximately 332.5 mm.

NUMERICAL SIMULATION ANALYSIS

Build mathematical models

The solver in Fluent software is used to perform simulation calculations. The continuity equation in the Cartesian coordinate system is Formula 8:

$$\frac{\partial}{\partial x_i}(\rho u_i) = 0 \quad (8)$$

The momentum equation is equation 9:

$$\frac{\partial}{\partial x_i}(\rho u_i u_j) = \frac{\partial}{\partial x_i} \left[\mu_e \left(\frac{\partial u_i}{\partial x_j} + \frac{\partial u_j}{\partial x_i} \right) \right] + \rho g_j - \frac{\partial}{\partial x_j} \left(p + \frac{2}{3} \mu_e \frac{\partial u_i}{\partial x_i} \right) \quad (9)$$

The energy equation is equation 10:

$$\frac{\partial}{\partial x_i}(\rho u_i i) = \frac{\partial}{\partial x_i} \left[\mu \left(\frac{1}{Pr} + \frac{\mu_i}{Pr_t} \right) \frac{\partial i}{\partial x_i} \right] \quad (10)$$

where:

ρ is density, [kg/m³]; u is velocity, [m/s]; p is pressure, [Pa]; μ_e is effective viscosity; $\mu_e = \mu + \mu_t$; μ is molecular viscosity; μ_t is turbulent viscosity; i is specific enthalpy; Pr is molecular Prandtl Number; $Pr = \mu C_p / \lambda$; C_p is specific constant pressure heat capacity; λ is thermal conductivity; turbulent Prandtl number $Pr_t = \mu_t C_p / \lambda_t$; λ_t is eddy flow thermal conductivity; in the calculation process Pr_t is usually set to 0.85;

Since the fluid domain model is relatively simple, the simple-C solver is selected for solution. Commonly used turbulence models in Fluent include Standard, RNG, Realizable, etc. Considering the existence of rotating uniform shear flow, Realizable's k -epsilon model is selected to simulate airflow mixing. Turbulent viscosity is calculated as equation 11:

$$\mu_t = \rho C_\mu \frac{k^2}{\varepsilon} \quad (11)$$

The Realizable k -epsilon turbulent kinetic energy transport equation is equation 12:

$$\frac{\partial \rho}{\partial t}(\rho k) + \frac{\partial}{\partial x_i}(\rho k u_i) = \frac{\partial}{\partial x_j} \left[\left(\mu + \frac{\mu}{\sigma_k} \right) \frac{\partial k}{\partial x_j} \right] + G_k + G_b - \rho \varepsilon - Y_m + S_k \quad (12)$$

The Realizable k -epsilon turbulent dissipation rate transport equation is equation 13:

$$\frac{\partial}{\partial t}(\rho \varepsilon) + \frac{\partial}{\partial x_j}(\rho \varepsilon u_j) = \frac{\partial}{\partial x_j} \left[\left(\mu + \frac{\mu}{\sigma_\varepsilon} \right) \frac{\partial \varepsilon}{\partial x_j} \right] + \rho C_{1\varepsilon} S \varepsilon - \rho C_{2\varepsilon} \frac{\varepsilon^2}{k + \sqrt{\nu \varepsilon}} - C_{1\varepsilon} \frac{\varepsilon}{k} C_{3\varepsilon} G_b + S_\varepsilon \quad (13)$$

where:

G_k is the generation of turbulent kinetic energy caused by the average velocity gradient; G_b is the generation of turbulent kinetic energy caused by buoyancy; Y_m is the effect of the pulsating expansion of compressible turbulent flow on the total dissipation rate; $C_{1\varepsilon}$, $C_{2\varepsilon}$, $C_{3\varepsilon}$ are empirical constants; the default values are $C_{1\varepsilon}=1.44$, $C_{2\varepsilon}=1.92$, $C_{3\varepsilon}=0.09$; σ_k , σ_ε are the Prandtl coefficients corresponding to turbulent kinetic energy and turbulent kinetic energy dissipation rate respectively; β is thermal expansion Coefficient; M_t is the turbulent Mach number; a is the speed of sound, [m/s];

Setting of boundary conditions

Taking the self-priming hot air temperature changing device as the prototype, a simplified three-dimensional model of the fluid domain was established and imported into ANSYS, and the fluid domain was divided into volume meshes (Papkov et al., 2023). The hot air flow passes through the inlet section, constriction section, and diffusion section in sequence. When passing through the constriction section, the pressure difference between the constriction section and the atmospheric pressure causes the air to enter from the air inlet pipe and mix with the main pipe air to achieve cooling. The mixed gas enters the dryer inlet duct through the inlet section.

In order to make the simulation close to reality, this paper uses the steady-state flow field for simulation. The two-phase flow medium is air, and SWF is selected as the wall function.

The fluid domain model has an arc wall, so a curvature correction coefficient is added to improve the authenticity of the model. During the simulation process, the inlet section port is set to the velocity inlet gas flow rate of 5m/s and the temperature is set to 60°C. The inlet pipe port of the constriction section is set to the pressure inlet. Its initial gauge pressure is set to 0 MPa and the temperature is set to 20°C. The diffusion section port is set to the pressure outlet gauge, the pressure is set to 0MPa, and the temperature is set to 20°C.

Numerical simulation analysis of necking section

When the mixed gas passes through the constriction section, the two components, which have low pressure and fast flow rate, do not mix with each other. Therefore, the length of the constriction section is 135 mm at the beginning of the constriction section and its length is 60 mm for temperature monitoring (Gao et al., 2018; Han et al., 2023; Kavga et al., 2023; Liu et al., 2023). 13 temperature monitoring points are evenly selected in each section. Point 5 is shown in Fig. 5 for instantaneous monitoring, and the temperature of each cross-section monitoring point is shown in Fig. 6.

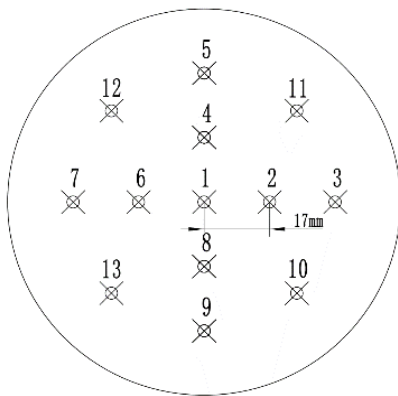


Fig. 5 - Section monitoring selected points

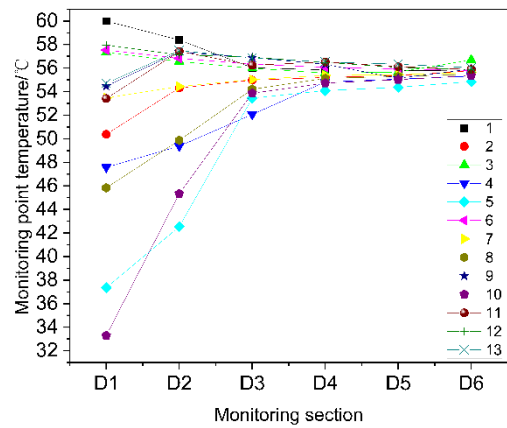


Fig. 6 - Temperature point and line diagram of cross-section monitoring points

The length of the necking section is 60 mm at 135 mm from the beginning, and monitoring is performed every 10 mm. The relationship between the monitoring sections (a, b, c, d, e, f) and temperature is shown in Fig. 7. The results show that: From a to b, the gas is still in stratified flow. From b to f, the temperature tends to be between 42°C and 58°C and gradually becomes stable. The temperature changes at each monitoring point in the b to c section are relatively large according to Gao and Jiang (2018). The temperature changes at each monitoring point in section e ~ f are relatively small; the temperature changes around monitoring points 4 and 5, and between 13, 9 and 10 are particularly obvious. The cloud images of each section are shown in Fig. 7.

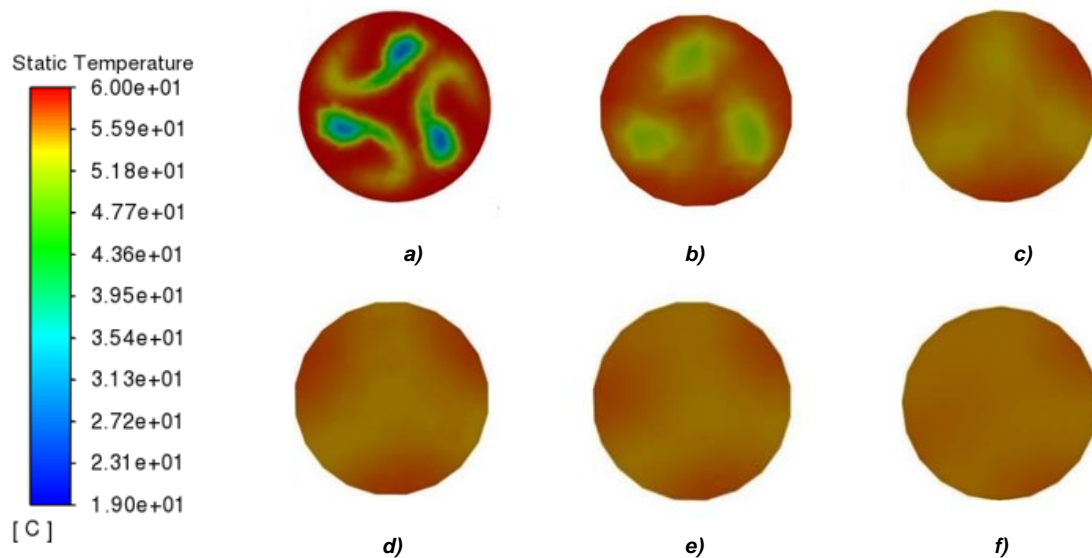


Fig. 7- Cross-section temperature distribution cloud chart

Experimental analysis of the impact of various factors on experimental indicators

When the number of intake pipes is determined to be 3, the diameter of the intake pipe is 32 mm, the flow velocity of the main pipe is 5 m/s, the temperature difference between hot and cold air is 40°C and other parameters are certain, the number of axial angles of the incisions at the end of the intake pipe is set to 15°, 30°, and 45°, thereby obtaining a graph of the temperature after mixing of hot and cold air, the uniform distance of mixing, and the axial angle of the incision at the end of the intake pipe, as shown in Fig. 8.

It can be seen from the fig. that the axial angle of the incision has a significant impact on the uniform mixing distance, but the influence on the temperature is not significant. When the axial angle of the incision is set to 15°, the distance for uniform air flow mixing is 45 ~ 50 mm. When the axial angle is set to 30°, the distance required for the airflow to be evenly mixed is 40 ~ 42 mm. When the axial angle of the incision is set to 45°, the distance required for the airflow to be evenly mixed is 57 ~ 62 mm. When the axial angle of the incision is 30°, the mixing distance is relatively short. When the axial angle of the incision is smaller, the torsional force on the airflow is smaller, and the bevel angle of the cold air entering the hot air is smaller, and the mixing distance is longer. When the axial angle of the incision is larger, the torsional force on the airflow is greater, and the oblique angle at which the cold air enters the hot air is larger, causing the cold air to enter the surface layer of the hot air in the main pipe, which is not conducive to the heat conduction of the gas, making the mixing distance longer.

Under the condition that the number of air inlet pipes is 3, the pipe diameter is 32 mm, the axial angle of the incision is 30°, the flow rate of the main pipe is 5 m/s and other parameters are certain, the temperature difference between the hot and cold air is set to 20°C, 40°C, and 60°C respectively, thus obtaining the curve of the temperature after mixing of hot and cold air and the mixing uniform distance and temperature difference, as shown in Fig. 9. It can be seen from the fig. that the temperature difference has a significant impact on the mixing temperature. When the temperature difference is set to 20°C, the temperature at which the airflow is evenly mixed is 58 ~ 58.5°C. When the temperature difference is set at 40°C, the temperature at which the airflow is evenly mixed is 56 ~ 57°C. When the temperature difference is set to 60°C, the temperature at which the airflow is evenly mixed is 53 ~ 55°C. Therefore, as the temperature difference expands, the temperature after mixing is lower, and the lower the temperature can be adjusted. The larger the range, the more accurate real-time temperature variable mixing can be achieved.

When it is determined that the diameter of the air inlet pipe is 32 mm, the axial angle of the incision is 30°, the flow rate of the main pipe is 5 m/s, the number of air inlet pipes is 1, 3, 5, and other parameters as in the test are certain, thus obtaining the curve diagram of the temperature after mixing of hot and cold air, the uniform distance of mixing and the number of air intake pipes, as shown in Fig. 10.

It can be seen from the fig. that the number of air inlet pipes has a significant impact on the mixing temperature and uniform mixing distance. When the number of air inlet pipes is set to 1, the temperature at which the air flow is evenly mixed is 57 ~ 58°C. When the number of air inlet pipes is set to 5, the temperature at which the air flow is evenly mixed is 58 ~ 59°C. Therefore, when the number of pipes is 1, the temperature of the mixed air flow is the lowest, the adjustable range is the largest to meet greater temperature changing needs. When the number of air inlet pipes is set to 1, the distance for uniform air flow mixing is 125 ~ 150 mm. When the number of air inlet pipes is set to 3, the distance for uniform air flow mixing is 40 ~ 42 mm. When the number of air inlet pipes is set to 5, the temperature for uniform air flow mixing is 35 ~ 37 mm, so as the number of tubes increases, the distance for uniform airflow mixing becomes shorter.

After determining that the number of air inlet pipes is 3, the axial angle of the incision is 30°, the flow rate of the main pipe is 5 m/s, and other parameters are certain, the diameter of the air inlet pipes is set to 22 mm, 32 mm, and 42 mm respectively, so as to obtain a mixture of hot and cold air. The curves of the temperature after mixing, the mixing uniform distance and the diameter of the air inlet pipe are shown in Fig. 11.

It can be seen from the fig. that the diameter of the air inlet pipe has a significant impact on the mixing temperature. When the pipe diameter is 22 mm, the temperature at which the airflow is evenly mixed is 57 ~ 57.5°C. When the pipe diameter is 32 mm, the temperature at which the airflow is evenly mixed is 56 ~ 57°C. When the pipe diameter is 42 mm, the temperature at which the air flow is evenly mixed is 55.5 ~ 56°C. Therefore, as the pipe diameter expands, the temperature after mixing is lower, and the lower the temperature can be adjusted. The larger it is, the more accurate real-time temperature-changing mixing can be achieved.

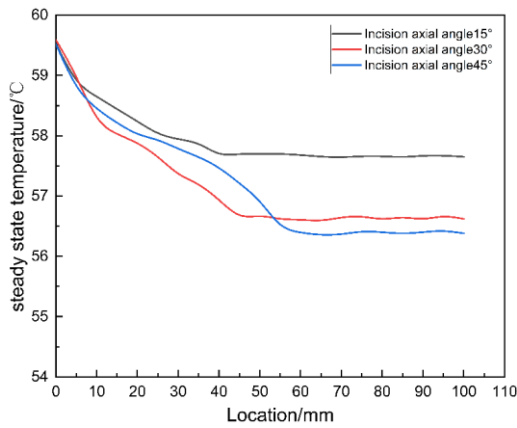


Fig. 8 - Effect of axial angle of incision on performance indicators

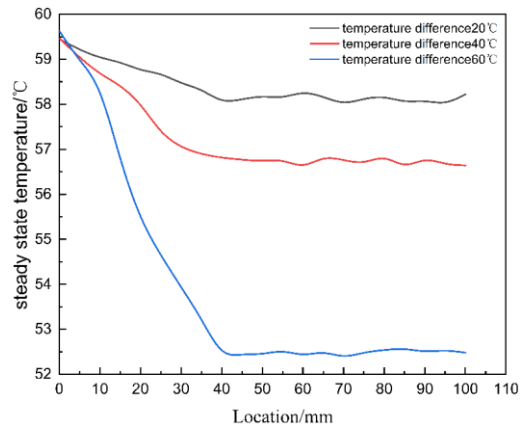


Fig. 9 - Effect of temperature difference angle on performance indicators

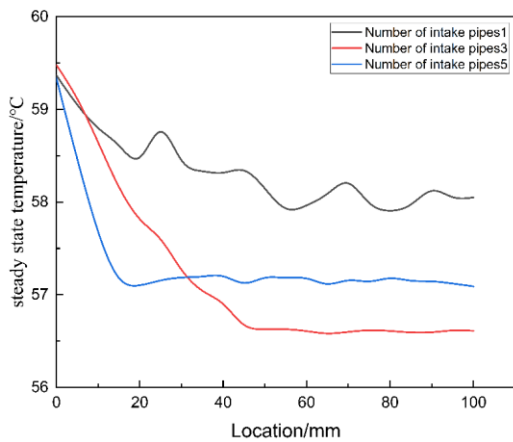


Fig. 10 - The impact of the number of intake pipes on performance indicators

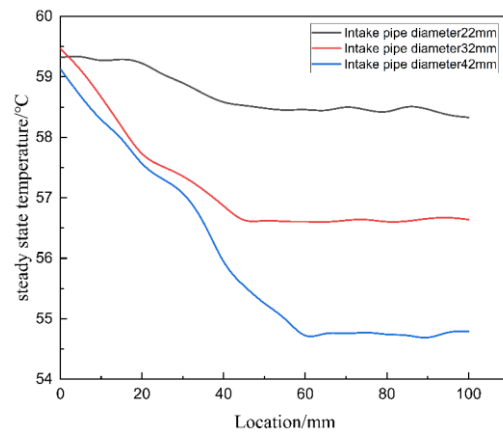


Fig. 11 - Effect of intake pipe diameter on performance indicators

RESULTS

Experimental design and response analysis

Taking the number of air inlet pipes X_1 , the axial angle of the incision X_2 , the temperature difference X_3 and the diameter of the air inlet pipe X_4 of the variable temperature device as test factors, the uniform mixing distance Y_1 and the mixing temperature Y_2 as optimization indicators, a quadratic orthogonal rotation of four factors and five levels was used. Through the combined design test, the optimized structure of each working component on the mixing device was determined, and the test factor range and level coding table were compiled, as shown in Table 1.

Table 1

| Factor Level Coding | | | | |
|---------------------|---------------------------------------|-----------------------------------|--------------------------------------|------------------------------------|
| Coding | Number of intake pipes X_1 [PCS] | Incision axial angle X_2 [°] | Temperature difference X_3 [°C] | Intake pipe diameter X_4 [mm] |
| +2 | 5 | 60 | 50 | 42 |
| +1 | 4 | 45 | 40 | 37 |
| 0 | 3 | 30 | 30 | 32 |
| -1 | 2 | 15 | 20 | 27 |
| -2 | 1 | 0 | 10 | 22 |
| | 1 | 15 | 10 | 5 |

Table 2

| Coding | Experimental factors | | | | Test indicators | |
|--------|------------------------|----------------------------|------------------------|----------------------------|-------------------------------|--------------------------|
| | Number of intake pipes | Incision axial angle X_2 | Temperature difference | Intake pipe diameter X_4 | Mixing uniform distance Y_1 | Mixing temperature Y_2 |
| | X_1 [PCS] | [°] | X_3 [°C] | [mm] | [mm] | [°C] |
| 1 | -1 | -1 | -1 | -1 | 54.72 | 58.25 |
| 2 | 1 | -1 | -1 | -1 | 47.23 | 56.44 |
| 3 | -1 | 1 | -1 | -1 | 57.46 | 55.58 |
| 4 | 1 | 1 | -1 | -1 | 57.71 | 56.09 |
| 5 | -1 | -1 | 1 | -1 | 48.71 | 58.82 |
| 6 | 1 | -1 | 1 | -1 | 34.32 | 53.37 |
| 7 | -1 | 1 | 1 | -1 | 58.78 | 56.48 |
| 8 | 1 | 1 | 1 | -1 | 46.31 | 53.73 |
| 9 | -1 | -1 | -1 | 1 | 46.27 | 58.41 |
| 10 | 1 | -1 | -1 | 1 | 41.22 | 57.62 |
| 11 | -1 | 1 | -1 | 1 | 47.04 | 57.2 |
| 12 | 1 | 1 | -1 | 1 | 44.02 | 57.96 |
| 13 | -1 | -1 | 1 | 1 | 48.77 | 56.31 |
| 14 | 1 | -1 | 1 | 1 | 36.87 | 52.59 |
| 15 | -1 | 1 | 1 | 1 | 47.85 | 56.28 |
| 16 | 1 | 1 | 1 | 1 | 39.99 | 55.2 |
| 17 | -2 | 0 | 0 | 0 | 57.34 | 56.38 |
| 18 | 2 | 0 | 0 | 0 | 41.89 | 53.44 |
| 19 | 0 | -2 | 0 | 0 | 38.18 | 57.78 |
| 20 | 0 | 2 | 0 | 0 | 55.26 | 55.3 |
| 21 | 0 | 0 | -2 | 0 | 50.06 | 58.87 |
| 22 | 0 | 0 | 2 | 0 | 43.03 | 56.7 |
| 23 | 0 | 0 | 0 | -2 | 51.33 | 56.54 |
| 24 | 0 | 0 | 0 | 2 | 37.41 | 58.76 |
| 25 | 0 | 0 | 0 | 0 | 55.71 | 50.28 |
| 26 | 0 | 0 | 0 | 0 | 52.97 | 51.45 |
| 27 | 0 | 0 | 0 | 0 | 52.97 | 51.45 |
| 28 | 0 | 0 | 0 | 0 | 53.25 | 51.36 |
| 29 | 0 | 0 | 0 | 0 | 51.61 | 52.04 |
| 30 | 0 | 0 | 0 | 0 | 52.51 | 52.09 |

As shown in Table 2, the model of mixed uniform distance $P < 0.01$ indicates that the model is statistically significant, and the test result of the lack of fit item is $P = 0.2635 > 0.05$, which is an insignificant item, indicating that the fit of the regression equation is good and has practical significance. The uniform mixing temperature model $P < 0.01$ indicates that the model is statistically significant, and the test result of the lack of fit item is $P = 0.5052 > 0.05$, which is an insignificant item, indicating that the regression equation has good fitting properties and has practical significance. After eliminating non-influencing factors, the regression equations of uniform mixing distance and uniform mixing temperature are obtained, which are divided into equations 14 and 15:

$$Y_1 = 53.16 - 3.98X_1 + 3.16X_2 - 2.01X_3 - 3.37X_4 + 0.99X_1X_2 - 1.99X_1X_3 + 0.42X_1X_4 + 0.50X_2X_3 - 1.88X_2X_4 + 1.50X_3X_4 - 0.80X_1^2 - 1.53X_2^2 - 1.57X_3^2 - 2.11X_4^2 \quad (14)$$

$$Y_2 = 51.45 - 0.84X_1 - 0.34X_2 - 0.80X_3 + 0.30X_4 + 0.58X_1X_2 - 0.73X_1X_3 + 0.39X_1X_4 + 0.28X_2X_3 + 0.42X_2X_4 - 0.43X_3X_4 - 0.79X_1^2 + 1.20X_2^2 + 1.51X_3^2 + 1.48X_4^2 \quad (15)$$

The response surface of the interaction between the number of inlet pipes and the axial angle of the incisions on the uniform mixing distance can be seen from Fig. 12a. When the number of inlet pipes remains unchanged, as the axial angle of the incisions increases, the uniform mixing distance first increases and then there is a decreasing trend; when the axial angle of the incision remains unchanged, the number of air inlet pipes increases, the uniform mixing distance shows a decreasing trend, the overall trend changes are more obvious and the range of change is smaller, and the overall trend becomes stable.

The response surface of the interaction between the number of air inlet pipes and the temperature difference on the uniform mixing distance can be seen from Fig. 12b: when the number of air inlet pipes remains unchanged, as the temperature difference increases, the uniform mixing distance first increases and then decreases; When the temperature difference remains unchanged, as the number of air inlet pipes increases, the uniform mixing distance first increases and then decreases. The overall trend changes relatively smoothly and has a small range of change.

The response surface of the interaction between the axial angle of the incision and the diameter of the inlet pipe on the uniform mixing distance can be seen from Fig. 12c: when the axial angle of the incision remains unchanged, as the diameter of the inlet pipe increases, the uniform distance of mixing decreases. Small trend: when the diameter of the inlet pipe remains unchanged, as the axial angle of the incision increases, the uniform mixing distance first increases and then decreases. The overall trend changes are more obvious and the range of changes is larger.

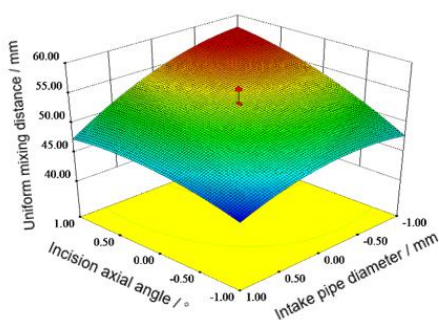
The response surface of the interaction between the temperature difference and the diameter of the air inlet pipe on the uniform mixing distance can be seen from Fig. 12d: when the diameter of the air inlet pipe remains unchanged, as the temperature difference increases, the uniform mixing distance shows a decreasing trend; when the temperature difference is constant, with the increase of the diameter of the inlet pipe, the mixing uniform distance increases first and then decreases, and the overall trend changes more obviously and the change range is larger.

The response surface of the interaction between the number of air inlet pipes and the axial angle of the incision on the mixing temperature can be seen from Fig. 12e: It can be seen from the fig. that when the number of air inlet pipes remains unchanged, as the axial angle of the incision increases, the mixing temperature increases first, the trend decreases and then increases; when the axial angle of the incision remains unchanged, the number of intake pipes increases, and the mixing temperature first decreases and then increases. The overall trend changes are more obvious and the range of changes is smaller, and the overall trend is stable.

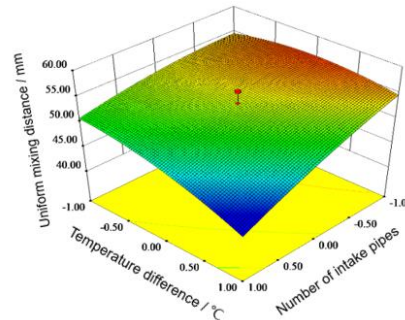
The response surface of the interaction between the number of air inlet pipes and the temperature difference on the mixing temperature can be seen from Fig. 12f: when the number of air inlet pipes remains unchanged, as the temperature difference increases, the mixing temperature first decreases and then increases. When the temperature difference remains unchanged, as the number of air inlet pipes increases, the mixing temperature first decreases and then increases. The overall trend changes relatively smoothly and has a small range of change.

The response surface of the interaction between the axial angle of the incision and the diameter of the tube on the mixing temperature can be seen from Fig. 12g: when the axial angle of the incision remains unchanged, as the diameter of the inlet tube increases, the mixing temperature first decreases, then increases; when the diameter of the inlet pipe remains unchanged, as the axial angle of the incision increases, the mixing temperature shows a trend of increasing first. The overall trend changes are more obvious and the range of changes is larger.

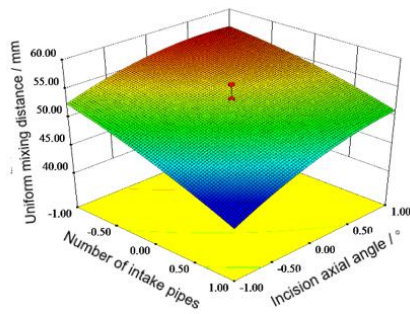
The response surface of the interaction between temperature difference and pipe diameter on the mixing temperature can be seen from Fig. 12h: when the diameter of the inlet pipe remains unchanged, as the temperature difference increases, the mixing temperature shows a decreasing trend; when the temperature difference is constant, with the increase of the diameter of the inlet pipe, the mixing temperature increases first and then decreases, and the overall trend changes more obviously and the change range is larger.



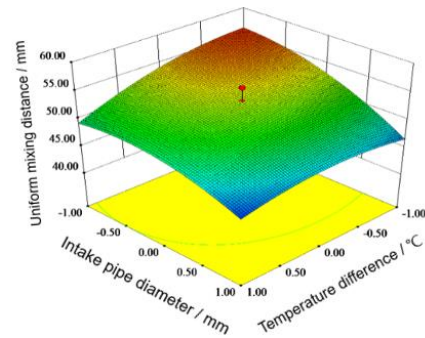
a) Effects of the axial angle of the incision and the diameter of the inlet pipe on the uniform mixing distance



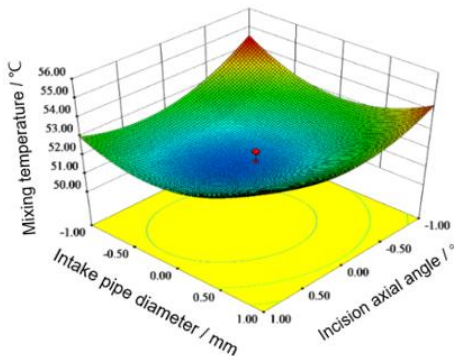
b) Effect of temperature difference and number of air inlet pipes on uniform mixing distance



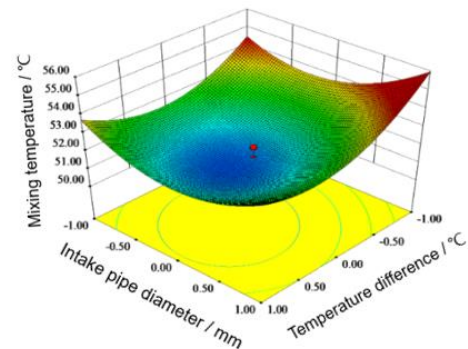
c) Effect of the number of air inlet pipes and the axial angle of the incision on the uniform mixing distance



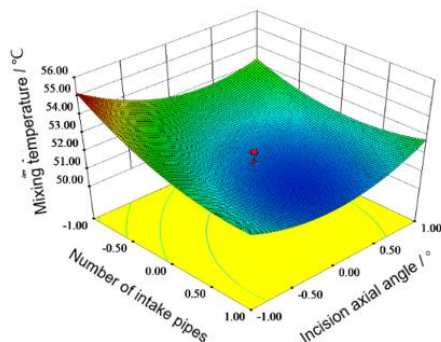
d) Effects of intake pipe diameter and temperature difference on uniform mixing distance



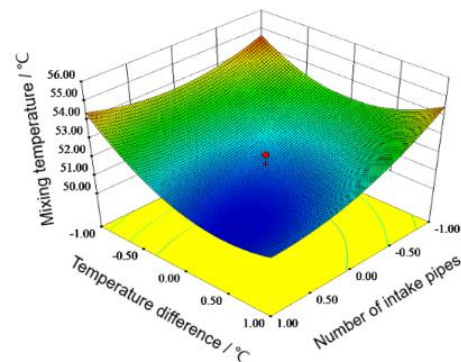
e) Inlet pipe diameter and cut axial angle on mixing temperature



f) Intake pipe diameter and temperature difference on mixing temperature



g) Effect of the number of intake pipes and the axial angle of the incision on the mixing temperature



h) Effect of the number of intake pipes and temperature difference on the mixing temperature

Fig. 12 - The impact of interactive factors on test indicators

Test equipment and methods

The equipment required for the test bench includes (Keshun Measurement and Control) temperature and humidity transmitter, (Jianda Nishina) wind speed sensor, tape measure and other test devices. The test location was conducted in the Intelligent Drying Laboratory of Heilongjiang Bayi Agricultural University. The temperature variable device was connected to the fan blower and drying device as shown in Fig.13. Before the test, three (Keshun Measurement and Control) temperature and humidity transmitters are evenly installed at the fan blower pipe outlet. When the temperature is stable, the average temperature of the three points is taken. Set up 3 (Jianda Nishina) wind speed sensors evenly. When the wind speed is stable, take the average of 3 wind speeds. The average temperature of the experimental environment is about 10°C. Monitoring is performed every 10 mm after the air inlet duct, a total of 10 times, with a total length of 100 mm. Select 5 points evenly in each section, repeat 5 times, and process the data collected each time.



Fig. 13 - Variable temperature drying test bench

Test data optimization and verification

Using Design-Expert 8.0.6 software to optimize, select three sets of optimization data and take the average value to obtain the post-mixing temperature of 50.93 when the number of air intake pipes is 3.16, the axial angle of the incision is 27.6°, the temperature difference is 43.5°C, and the diameter of the intake pipe is 23.8 mm, the mixing uniform distance is 39.33 mm. During the experimental verification process, the number of air inlet pipes was selected to be 3, the axial angle of the incision was 27°, the temperature difference was 45°C, the diameter of the air inlet pipe was 24 mm, and monitoring was performed every 15 mm after the air inlet pipe. Repeat the test 5 times to take the average, the result is that the temperature after mixing is 51.24°C, and the uniform mixing distance is 38.94 mm. A system of objective equations and constraint equations:

$$\left\{ \begin{array}{l} \min Y_1 \\ \min Y_2 \\ 1 \leq X_1 \leq 5 \\ 0^\circ \leq X_2 \leq 60^\circ \\ 10^\circ\text{C} \leq X_3 \leq 50^\circ\text{C} \\ 22\text{mm} \leq X_4 \leq 42\text{mm} \\ 0 \leq Y_1(X_1, X_2, X_3, X_4) \leq 1 \\ 0 \leq Y_2(X_1, X_2, X_3, X_4) \leq 1 \end{array} \right. \quad (16)$$

Relative error:

$$\delta = \frac{\Delta}{L} \times 100\% \quad (17)$$

where:

Δ absolute error; L truth value.

Table 3

| Optimization and test results | | |
|-------------------------------|----------------------------|---------------------------------|
| Project | Mixing temperature [°C] | Uniform mixing distance [mm] |
| Optimization Results | 50.93 | 39.33 |
| Actual results | 51.24 | 38.94 |
| Relative error [%] | 6.04 | 9.76 |

It can be seen from Table 3 that there is not much difference between the optimized value and the experimental value, and all indicators are at a relatively good level.

CONCLUSIONS

Using the principle of theoretical mechanics friction torque to analyze the friction of the slide rail in the air volume adjustment device, the results show that while ensuring that the material is unique, stable and reliable, the distance between the inner and outer slides should be minimized as much as possible to obtain the optimal. The structure has an inner slide radius R_1 of approximately 247.5 mm, and an outer slide radius R_2 of approximately 332.5 mm. Using Bernoulli's principle of fluid dynamics and the basic theory of airflow mixing to combine mathematical equations, the results show that the pipe opening area is approximately no more than 0.0023 m². Combined with the size of the main pipe necking section, the circular cross-section radius is determined to be 16 mm.

Fluent was used to numerically simulate the distribution of uniform mixing distance and temperature field in the necking section. Taking the uniform mixing distance and uniform mixing temperature as test indicators, the number of intake pipes, the axial angle of the incision, the temperature difference and the diameter of the intake pipe were initially selected as the test indicators. A single-factor simulation performance test analysis was conducted based on Fluent software. The results showed that: the mixing was uniform in the necking section. The degree reaches 75 ~ 80%, and the above factors have a relatively obvious impact on the test indicators.

A test bench was built to conduct a four-factor and five-level quadratic regression orthogonal rotation combined test on the number of intake pipes, incision axial angle, temperature difference and intake pipe diameter. Design-Expert.V8.0.6.1 software was used to optimize the analysis and test indicators. The uniform mixing distance and mixing temperature both meet the requirements of the technical specifications for drying machinery quality evaluation indicators, and the uniform mixing distance is 39.33 mm and the mixing temperature is 50.93°C. The actual data is that the uniform mixing distance is 38.94 mm and the mixing temperature is 51.24°C. The relative errors are respectively are 9.76% and 6.04%, the error between the optimized value and the experimental value is small, and all indicators are at a relatively good level.

ACKNOWLEDGEMENT

This project is supported by the Natural Science Foundation of Heilongjiang Province (LH2022E098).

REFERENCES

- [1] Chen, Y.J. (2020). Analysis of my country's food security situation (我国粮食安全形势分析). *Comprehensive agricultural development in China*. Vol.11, pp. 11-14. Beijing/China.
- [2] Fahri, O., Mualla, O. Ahmet, B. (2006). Experimental investigations of air and liquid injection by venturi tubes. *Water and Environment Journal*. Vol.20(3), pp. 114-122. United States.
- [3] Gao, L.J., Jiang X.X. (2018). Analysis of flow field in water chamber of a certain condenser (某凝汽器水室流场分析). *Mechanical Engineers*. Vol.04, pp. 105-107. Heilongjing/China.
- [4] Han, M.L., Zhou.D.K., Chen, X. (2023). Aerodynamic calculation of aircraft external flow field based on FLUENT (基于 FLUENT 的飞行器外流场气动计算). *China high-tech*. Vol. (14). pp. 111-112. Beijing/China.
- [5] Hang, Y. (2014). Application of grain drying mechanization technology (谷物干燥机械化技术的应用). *Agricultural technology and equipment*. Vol.01, pp. 42-43. Liaoning/China.
- [6] Jiang, F., Hang R. (2022). Analysis of fluid flow characteristics in reducing pipes based on FLUENT (基于 FLUENT 的异径管管内流体流动特性分析). *Welded pipe*. Vol.45(11), pp. 27-30+38. Shanxi/China.
- [7] Jiang, S.J., Liu.Q.J. (2009). Research on variable temperature drying technology of rice (稻谷变温干燥工艺研究). *Grain and feed industry*. Vol.02, pp.10-12. Wuhan/China.
- [8] Kavga, A., Thomopoulos, V., Pischinas, E., Tsiapanitis, D., Nikolakop P. (2023). Design and simulation of a greenhouse in a computational environment (ANSYS/FLUENT) and an automatic control system in a LABVIEW environment. *Simulation Modelling Practice and Theory*. pp. 129. Netherlands.
- [9] Li, H. (2019). Design and implementation of improved Venturi fertilizer mixer (改进型文丘里混肥器的设计与实现). *Hebei Agricultural University*. Hebei/China.
- [10] Li, H.I. (2019). Experimental research on temperature-variable and quality-preserving drying technology and control process of rice (水稻变温保质干燥工艺及控制过程的试验研究). *Heilongjiang Bayi Agricultural University*. Heilongjing/China.

- [11] Liu, C.S., Chen, S.Y., Xiao, S.W., Ma, L.X., Zhang Y., Chen, S. (2023). Technology research and performance verification of rice variable temperature homogeneous drying device (稻谷变温均质干燥装置工艺研究与性能验证). *Journal of Agricultural Machinery*. pp. 366-372. Beijing/China.
- [12] Liu, X.H., Xiang Z.L., Tan P., Chen W., Feng J.Y. (2023). Analysis and optimization of internal flow field of heat dissipation system expansion structure based on Fluent (基于 Fluent 的散热系统扩流结构内部流场分析及优化). *Journal of Jilin University (Engineering Edition)*. Vol.1-14. pp.10-11. Jilin/China.
- [13] Ozkan, F., Ozturk, M., Baylar, A. (2006). Experimental investigations of air and liquid injection by venturi tubes. *Water and Environment Journal*. Vol.20(3). pp. 114-122. England.
- [14] Song, K.K., Li, M.Q., Hang, T.C., Song, D.S. (2023). Analysis of solid-liquid mixing performance of integrated mixing and discharge device based on CFD (基于 CFD 的混排一体化装置固液混合性能分析). *Petroleum machinery*. Vol.51(01), pp. 101-139. Hubei/China.
- [15] Papkov, V., Shadymov, N., Pashchenko, D. (2023). CFD-modeling of fluid flow in Ansys Fluent using Python-based code for automation of repeating calculations. *International Journal of Modern Physics C*. Vol.34(9). Singapore.

VIBRATION TESTING AND ANALYSIS OF THE PICKUP HEADER OF STRAW FORAGE HARVESTER UNDER MULTI-SOURCE EXCITATION

秸秆饲料收获机捡拾割台在多源激励下的振动试验与分析

Qiaofei MU^{1,2)}, Haiqing TIAN^{*1,2)}, Ziqing XIAO^{1,2)}, Chunxiang ZHUO^{1,2)}, Xiaoyu XUE^{1,2)}, Leifeng TANG^{1,2)}

¹⁾ Inner Mongolia Agricultural University, College of Mechanical and Electrical Engineering, Hohhot/China;

²⁾ Inner Mongolia Engineering Research Centre of Intelligent Equipment for the Entire Process of Forage and Feed Production, Hohhot 010018, China;

Tel: 15947019846; E-mail: 2022202050021@emails.imau.cn; hqtian@126.com

DOI: <https://doi.org/10.35633/inmateh-73-27>

Keywords: Agricultural machinery; Pick-up header; Multi-source excitation; operational transfer path analysis

ABSTRACT

The complex vibration field in agricultural equipment during field operations not only predisposes key mechanical components to fatigue failure, but also leads to crop losses. This study introduces the Operating Transfer Path Analysis (OTPA) method to identify the vibration sources in the pickup header of a straw forage harvester. Finite element modal analysis, vibration testing, and operating transfer path analysis were conducted on the header frame. The findings indicate that excitation sources, including the hammer claw device, transmission, and dust box on the pickup header, are prone to resonant coupling with the header frame. The analysis reveals that the right transmission output shaft contributes 18.3% to the vertical vibrations on the right side panel of the frame. Meanwhile, the left transmission output shaft accounts for 29.4% of the horizontal vibrations on the left side panel. Additionally, the transmission input end is responsible for 54.8% of the horizontal vibrations on the front beam, while the dust box end contributes 45% to the forward vibrations on the rear beam. By identifying the primary transmission paths, the most effective strategies for the vibration reduction and optimization design of the pickup header can be developed. Furthermore, this study offers a theoretical foundation and experimental references for the vibration reduction optimization of other agricultural machinery.

摘要

农业装备在田间收获作业时复杂的振动场不仅易导致机械关键部件疲劳破坏，还会造成农作物收获损失。本研究引入工况传递路径分析方法（OTPA）作为识别秸秆饲料收获机捡拾割台振动原因的手段。对割台机架进行有限元模态分析、振动试验分析和工况传递路径分析。结果表明：捡拾割台上锤爪装置、变速箱以及除尘箱体等激励源易与割台机架发生共振耦合。其中，变速箱右输出端对机架右侧板垂直方向上振动贡献占比 18.3%；变速箱左输出端对机架左侧板水平方向上振动贡献占比 29.4%；变速箱输入端对机架前梁水平方向上振动贡献占比 54.8%；除尘箱体轴承端对机架后梁前进方向上振动贡献占比 45%。通过确定主要的传递路径，可为捡拾割台的减振优化设计制定最有效的改进方案。同时，本研究可为其他农业装备的减振优化提供理论依据和试验参考。

INTRODUCTION

Crop straw, as an important agricultural by-product, has received much attention in recent years globally, especially in China (Lu et al., 2014; McKendry et al., 2002). Yellow storage feed harvesting equipment integrates operations such as cutting, picking up, dust removal, and baling of crop straw into a seamless process that converts the straw into filamentous material for livestock use, significantly enhancing straw resource utilization efficiency (Awad et al., 2022; El Ghobashy et al., 2023).

During operation, the yellow silage harvesting equipment experiences significant vibration due to the road surface excitation and the concurrent functioning of multiple components. According to relevant data, 80% of mechanical structure damage is attributed to fatigue, while 75% is related to vibration (Yao, and Y et al., 2020; An et al., 2020; Lai, S, and P et al., 2018). To address the vibration issues in agricultural harvesting equipment and mitigate vibration intensity, numerous scholars have undertaken related research.

Scholars have integrated modal analysis with experimental validation to optimize structures by shifting their natural frequencies away from the range of external excitation forces. For example, Jiang and colleagues enhanced the frame structure of a rapeseed cutting and drying machine using finite element analysis. By tuning the frame's natural frequency to circumvent resonance, they performed a finite element static analysis on the optimized structure (Jiang et al., 2017). Scholars have integrated theoretical calculations, experimental computations, and simulation analysis to mitigate the risk of resonance in agricultural equipment. Through structural optimization, they successfully isolated external excitation frequencies, thereby achieving significant vibration reduction and overall optimization (Chen et al., 2020). In summary, most scholars primarily employ methods such as vibration testing and simulation analysis to optimize and improve the damaged parts of harvesting equipment, with the main research focusing on the establishment of vibration models (Nakata, Yuji, and Takao et al., 2010), vibration and comfort analysis of cab seats (Ahmadian, Seyed, and Barat et al., 2014), and vibration of cutter knives and cutting tables (Chuan-Udom et al., 2017; Chen, Han, Lu et al., 2012).

In fact, agricultural harvesting equipment is subject to dynamic loads from various sources of excitation during operation. The vibrations from different sources can create complex vibrational couplings, leading to intense vibrations throughout the machinery (Harikrishnan, and Varun et al., 2017). Therefore, in order to more precisely reduce vibration and noise in agricultural harvesting equipment, it is necessary to obtain the vibration characteristics of each excitation source in the harvesting equipment, as well as the vibration transmission paths and their contributions.

Operating Transfer Path Analysis (OTPA) serves as an essential tool for analysing the transmission of structural vibrations and noise. It is routinely employed to assess the vibrational contributions of various transfer paths, aiming to pinpoint the primary paths responsible for vibration (Chen et al., 2023). Researchers have utilized the OTPA method in the automotive industry, with De Klerk et al. employing it to investigate tire vibration noise and assess the influence of structural and acoustic pathways on noise at specific points (De, Alexander et al., 2010). Moreover, the OTPA method has been employed in the agricultural machinery sector. Notably, Qi Quan and his team applied the OTPA method to pinpoint structural noise sources within an excavator cabin. Through comparison of synthetic and actual measured signals, they confirmed the method's effectiveness (Qi et al., 2017). The Operational Transfer Path Analysis (OTPA) method has evolved over an extended period and found applications across various fields. However, the application of the OTPA method in agricultural straw harvesting equipment remains relatively uncommon, particularly in the domain of straw feed harvesting equipment research.

The study aims to conduct parametric modeling of the pickup header on the straw feed harvester. Modal analysis will be employed to determine the modal parameters of the frame. Additionally, field vibration tests on the pickup header have been conducted, analysing the header and its various working components under diverse operating conditions. Ultimately, the study utilizes the Operational Transfer Path Analysis (OTPA) method to analyse vibration test data under various working conditions. This analysis assesses the contributions of different transmission paths originating from the primary excitation sources under specified conditions. It identifies the primary excitation source and its transmission path affecting the pickup header frame, pinpointing the underlying cause of the frame's vibration and deformation. The anticipated results of this study are expected to offer a theoretical foundation and novel insights into developing strategies for vibration reduction and noise control in straw feed harvester pickup headers, as well as aiding the structural design and development of new models. Furthermore, these findings are crucial for fostering the rapid expansion of agricultural equipment and accelerating the development of agricultural mechanization globally.

MATERIAL AND METHODS

Finite element modeling of the pickup header

This paper examines the pickup header of a straw forage harvester. The pickup header frame model was constructed using SolidWorks (2018) 3D software. To accommodate finite element calculations and enhance finite element analysis efficiency, the model was suitably simplified.

The simplification scheme is as follows:

1. Ignore supports that have minimal impact on the structural stiffness and strength;
2. Disregard the effects of welding and bolted connections on the material properties of components;
3. Ignore small holes, chamfers, and other structures smaller than the mesh size that have a significant effect on finite element calculations but not a major impact on model quality.

The simplified frame of the pickup header is shown in Figure 1.

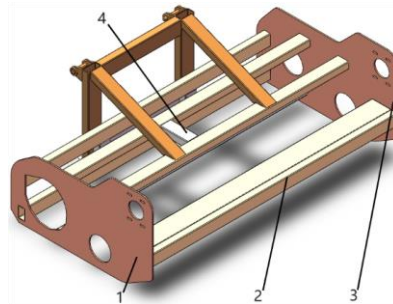


Fig. 1 - Simplified frame for pickup header

1. Right side panel of the frame; 2. Frame front beam; 3. Left side panel of the frame; 4. Frame rear beam.

Save the simplified 3D model of the frame in STP format and import it into ANSYS(19.0). The model's material properties are defined as Q235 steel, featuring an elastic modulus of 210 GPa, a Poisson's ratio of 0.3, and a density of 7850 kg/m³. Subsequently, the model was meshed with an element size of 5 mm. Upon completion of the meshing process, it yielded a total of 668,922 nodes and 315,187 elements.

The header vibration test

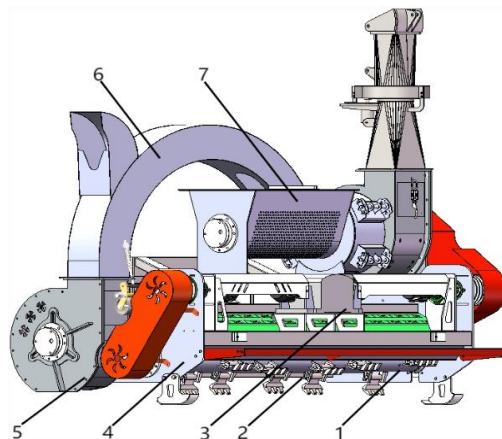


Fig. 2 - Straw forage harvester pick up header

1. Hammer Claw Device; 2. Conveying device; 3. Transmission; 4. Right side panel of the frame; 5. Conveyor box; 6. Ejection device; 7. Dust box.

This study focuses on the straw forage harvester pickup header (shown in Figure 2), analysing the vibration contribution of primary excitation sources (such as the hammer claw, conveying auger, dust removal systems, and transmission) at various engine speeds, transmitted through their respective paths to the pickup header frame during harvester downtime. To eliminate interference from external excitations during the analysis of the main excitation sources, the experiment was performed in a controlled stationary vibration test environment on a paved surface for the straw feed harvester. The experiment took place at the Hongchang Machinery Factory, located in Hohhot, Inner Mongolia Autonomous Region, China. The experimental conditions are designed based on engine speed, which ranges from 1000 r/min to 2000 r/min, increasing by 200 r/min for each condition. This results in a total of six different conditions, with each condition being tested for a duration of 60 seconds. The experimental condition corresponding to an engine speed of 1600 r/min is designated as the target response condition. The remaining conditions are used to establish a condition transfer path analysis model.

Prior to the experiment, the DH5902N data acquisition instrument from Donghua Testing Company was selected, with a sampling frequency set to 2.56 kHz. Subsequently, triaxial accelerometers were positioned near the excitation sources. The positive X direction of the accelerometers was aligned with the forward direction of the pickup cutter bed, the positive Y direction was set vertically upward from the ground, and the Z direction represented the transverse motion of the pickup cutter bed, with its positive direction defined by the right-hand rule.

The distribution of measurement points on the pickup header is detailed in Table 1.

Figure 3 shows the installation diagram of these measurement points on the straw forage harvester's pickup header, and Figure 4 provides the schematic diagram of the vibration test setup for the straw forage harvester.

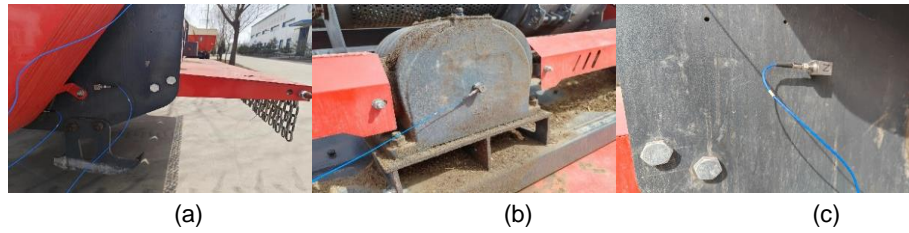


Fig. 3 - Header frame part measurement point
 (a) Right side panel of the frame; (b) Transmission; (c) Left side panel of the frame.



Fig. 4 - Field test of straw feed harvester

Table 1

Pickup header frame measuring point layout table

| Response Points | Positions | Measurement point | Positions |
|-----------------|-------------------------------|-------------------|---------------------------------|
| 1 | Right side panel of the frame | 2 | Hammer-claw drive shaft |
| | | 3 | Transmission right output shaft |
| | | 4 | Conveyor box end |
| 5 | Left side panel of the frame | 6 | Transmission left output shaft |
| | | 7 | Conveyor drive shafts |
| | | 8 | Dust box drive shaft |
| 10 | Frame front beam | 9 | Transmission input end |
| 12 | Frame rear beam | 11 | Dust box end |

Establishment and validation of the OTPA model for the pickup header

Operational Transfer Path Analysis (OTPA) method

The OTPA method is an enhancement of the traditional Transfer Path Analysis (TPA) method. Its model utilizes an 'input-transfer path-output' representation to analyse vibrations in mechanical systems (Xia et al., 2021; Liao et al., 2021). The theoretical formula for OTPA is:

$$P(\omega) = \sum_{j=1}^m T_j(\omega)P_j(\omega) + \sum_{i=1}^m TT_i(\omega)Q_i(\omega) \tag{1}$$

where: P represents the vibration at the target point; ω represents the excitation frequency of the signal; TT_i ($i = 1, 2, \dots, n$) denotes the transfer function of the vibration signal from the i th position to the target point; Q_i represents the vibration response signal at the i th position, characterized by the root mean square value of acceleration measured at the point; P_j represents the acoustic pressure response signal at the j th position.

In practical applications, the vibration signals from different excitation sources are integrated into the input signal matrix X , and the response data of the target point are integrated into the output matrix Y . The transfer function matrix T is used to reflect the relationship between the input signals and the output responses. Where $Y = X \cdot T$. It follows that:

$$T = (X^T X)^{-1} X^T Y = G_{XX}^{-1} G_{XY} \tag{2}$$

where: G_{XX} represents the auto power spectrum of the input signal; G_{XY} represents the cross power spectrum between the input signal and the output signal.

In the field of engineering, signals are often affected by noise and crosstalk. Therefore, to avoid interference between input signals, the technique of truncated Singular Value Decomposition (SVD) is introduced into the computational process. The new mathematical expression for the vibration system then becomes:

$$X_{real} T = Y_{Ture} + \varepsilon = Y \tag{3}$$

where: X_{real} represents the input matrix of excitation data obtained from actual measurements; ε represents the small error amount caused by coupling and crosstalk among the measured input signals; Y_{Ture} represents the true output of the system under ideal conditions; Y represents the output values of the system obtained from measurements.

Assuming the number of system inputs is n and the number of operating conditions is s , the signal matrix is subjected to Singular Value Decomposition (SVD), as shown in equation (9):

$$X_{real} = U \Sigma V^T \tag{4}$$

where: U is an $s \times s$ unitary matrix; V is an $n \times n$ unitary matrix; Σ in an $s \times n (s \geq n)$ diagonal matrix.

This can be represented by equation (10):

$$\Sigma = \text{diag}(\sigma_1, \sigma_1, \dots, \sigma_n) \tag{5}$$

where: $\sigma_1 \geq \sigma_2 \geq \dots \geq \sigma_n \geq 0$. Connecting equations (2-8) to (2-10), the transfer function matrix T can be expressed as:

$$T = \sum_{i=1}^n \left(\frac{u_i^T (Y_{Ture} + \varepsilon)}{\sigma_i} \right) v_i \tag{6}$$

where: u_i and v_i are the i th column vectors of the unitary matrices U and V , respectively.

The contribution of the i th input to the j th output through the transfer path is:

$$Y_{i,j}^{contri} = X_i Y_{i,j} \tag{7}$$

The formula for calculating the contribution rate of singular values is:

$$CR = \frac{\sigma_i}{\sum_{i=1}^n \sigma_i} \times 100\% \tag{8}$$

In matrix decomposition, truncation of smaller singular values is commonly employed to ensure the stability of the inversion operation. The truncated singular value matrix is denoted as $\bar{\Sigma}$ and the formula for calculating the transfer matrix is:

$$\bar{T} = \bar{X} + Y = V \bar{\Sigma}^{-1} U^T Y = \sum_{i=1}^{n-l} \frac{u_i^T Y}{\sigma_i} v_i \tag{9}$$

Establishment of the OTPA model

The modal analysis and vibration testing of the pickup header indicate that the primary deformation areas of the pickup header frame are the side panels and the front and rear over-bridge sections. Consequently, measurement points 1, 5, 10, and 12 were positioned on the left and right sides, as well as the front and rear bridge beams of the pickup cutter bed frame, serving as model response points. The remaining measurement points were positioned on the operational components of the cutter bed frame, serving as model excitation points. Under the target condition of 1600 r/min, a 4x8 OTPA model was developed, as illustrated in Figure 5.

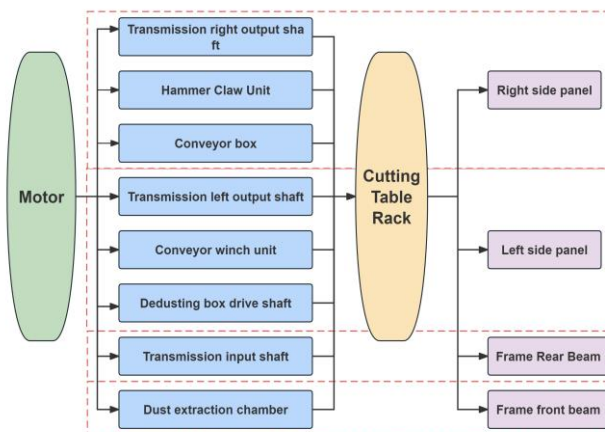


Fig. 5 - Pick up header OTPA vibration transmission path diagram

Validation of the OTPA model

The established OTPA model requires validation for source leakage detection. Typically, the coherent function is utilized to verify if the model output is induced by the model input and to identify any significant missing transfer paths.

According to the Multiple-Input Single-Output (MISO) system, the relationship between inputs and outputs can be expressed as follows:

$$S_{yy} = S_{vv} + S_{ee} \tag{10}$$

where: S_{yy} represents the auto power spectrum of the output signal; S_{vv} represents the portion of the output signal power spectrum caused by the input signal; S_{ee} represents the portion of the output signal power spectrum caused by non-input signals (noise, unreferenced excitations, system errors, etc.).

Therefore, the cross-correlation function of the system can be expressed as:

$$\zeta_{y,x}^2 = 1 - \frac{S_{ee}}{S_{yy}} \tag{11}$$

In practical engineering, it is desirable for the coherence function value to be as high as possible, and it typically needs to satisfy a coherence function value $\zeta_{y,x}^2 \geq 0.6$ (Zheng, and Qian et al., 2016).

According to Equation (11), the vibration data under the target operating condition is processed to validate the established OTPA model, yielding the coherent function of the system under this condition. The results are shown in Figure 6:

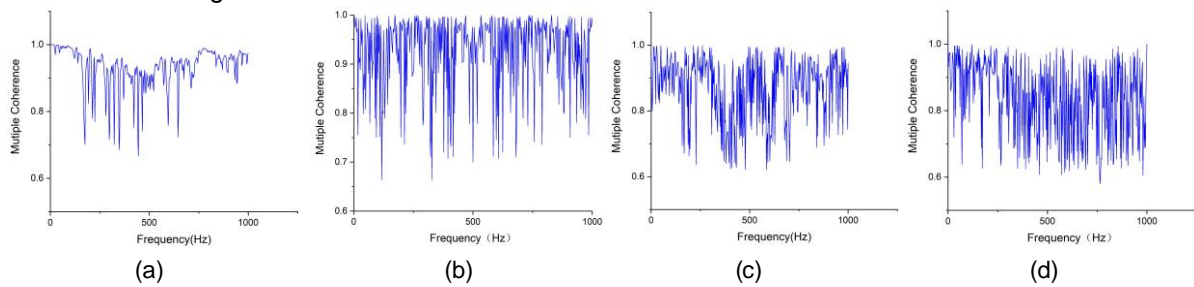


Fig. 6 - Re-coherence function of header vibration model

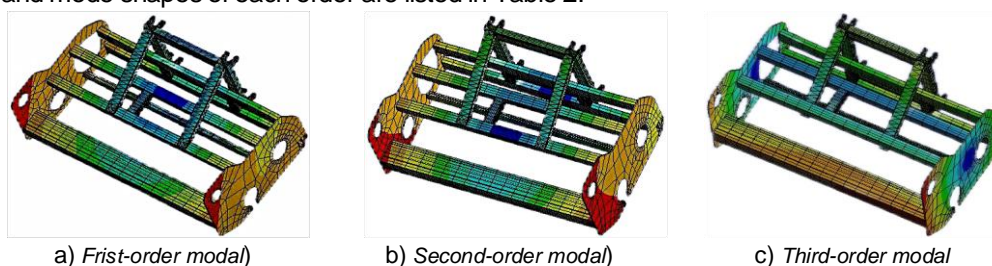
- (a). Model re-coherence function for vibration on the right side of the frame;
- (b). Model re-coherence function for vibration on the left side of the frame;
- (c). Model re-coherence function for frame front beam vibration;
- (d). Model re-coherence function for frame rear beam vibration.

As illustrated in the figure, the coherence function values between the input and output signals under the target operating conditions are generally above 0.6, thereby meeting the engineering requirement of 0.6. This indicates that the primary excitation sources of the model output signals originate from the vibrations observed at the measurement points, with no significant excitation sources or transfer paths omitted. Thus, the vibration data from the specified excitation and response points can be utilized to develop a model for analysing the transfer paths under these operating conditions.

RESULTS AND DISCUSSION

Modal analysis

Taking into account the actual working conditions of the pickup cutter bed, a modal analysis was performed on the pickup cutter bed in a free state. The model imposed no constraints on the translational and rotational degrees of freedom in the X, Y, and Z directions. The first six non-zero modal frequencies and corresponding mode shapes were calculated and analysed. Utilizing ANSYS Workbench(19.0), the first six natural frequencies and mode shape contour plots of the pickup header frame were obtained. The simulation results are shown in Figure 7, and the frequencies and mode shapes of each order are listed in Table 2.



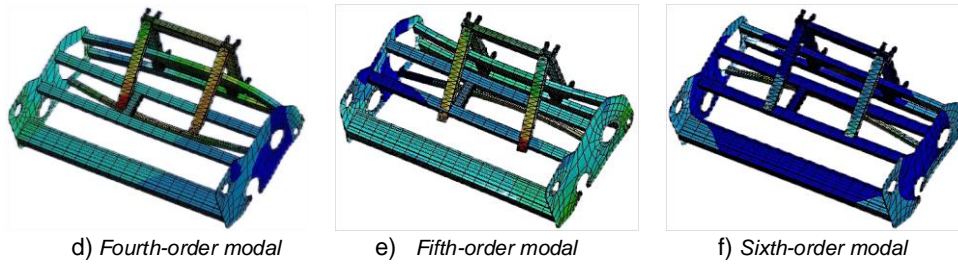


Fig. 7 - The front sixth-order modal shapes of the pickup header frame

Table 2

Modal results of finite element analysis

| Modal order | Frequency/Hz | Modal shape characteristics |
|-------------|--------------|---|
| 1 | 8.3284 | Bending of left and right side panels along the z-axis |
| 2 | 9.7012 | Torsion of the front beam along the z-axis |
| 3 | 15.549 | Torsion of the rear beam along the z-axis |
| 4 | 29.959 | Torsion + bending of rear beam along z-axis |
| 5 | 32.741 | Torsion + bending of right beam and right side panel along z-axis |
| 6 | 35.624 | Torsion + bending of the frame along the z-axis |

The detailed results of each mode from the finite element modal analysis are presented in Table 2. The first six modes include both bending and torsional modes. The first six natural frequencies of the pickup header frame range from 0 to 40 Hz. The fourth, fifth, and sixth natural frequencies are relatively concentrated between 30 and 35 Hz. The corresponding vibration modes involve the torsion and bending of the left and right side panels as well as the front and rear cross beams. When external excitations fall within the 30 to 35 Hz range, resonance may occur in the frame, resulting in overall torsion and bending deformation of the structure.

Time-domain analysis of experimental results

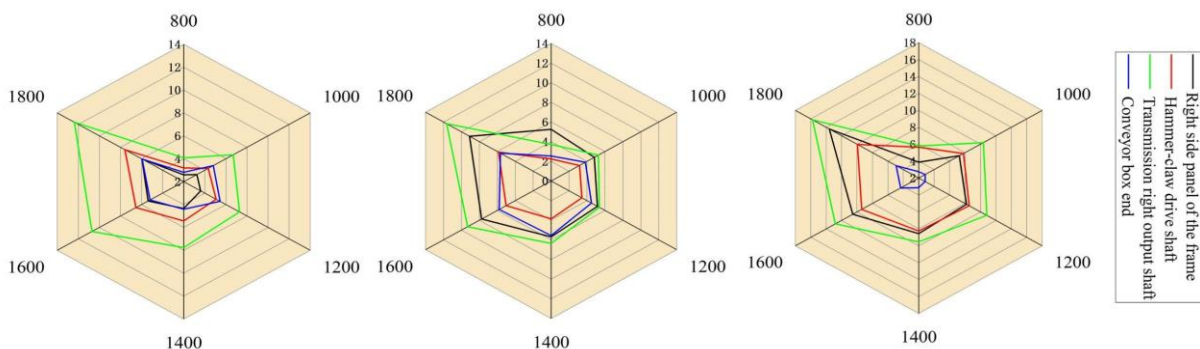
The intensity of cutter bar vibration is a key indicator for assessing the operational condition of agricultural machinery. Using the root mean square (RMS) value of vibration acceleration to measure vibration intensity effectively reflects the amplitude and energy intensity of the structure.

The calculation is shown in Equation (12):

$$RMS = \sqrt{\frac{1}{N} \sum_{k=1}^n x_k^2} = \sqrt{\frac{x_1^2 + x_2^2 + x_3^2 + \dots + x_k^2}{N}} \tag{12}$$

In the equation: x_k represents the vibration signal; N is the number of trials.

The vibration acceleration signals collected from the belt are processed to extract the root mean square values of the acceleration from the time-domain signals recorded at the measurement points. The specific values for the 12 measurement points on the harvester frame are shown in Figure 8.



(a) Rack right side X-direction (b) Rack right side Y-direction (c) Rack right side Z-direction

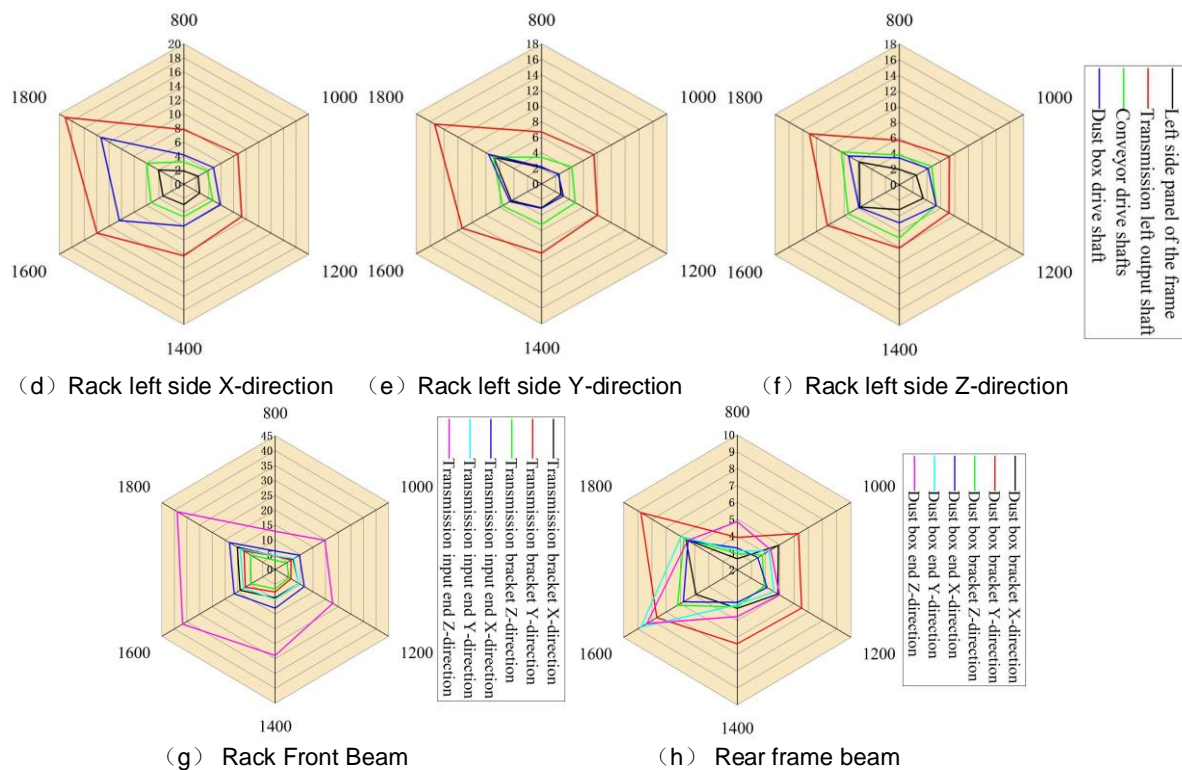


Fig. 8 - Root mean square value of vibration acceleration of measuring points under different working conditions of frame

(a ~ c) Root-mean-square value of vibration acceleration at the right side of the frame. (d ~ f) Root-mean-square of vibration acceleration at the left measurement point of the rack. (g) Root-mean-square value of vibration acceleration at measurement points on the front beam of the frame. (h) Root-mean-square value of vibration acceleration at the rear beam measurement point of the frame.

Analysis of acceleration signals at multiple vibration measurement points under varying operating conditions indicates a consistent upward trend in vibration magnitude in the X, Y, and Z directions as engine speed increases. At the target operating speed of 1600 r/min, the RMS value of vibration acceleration for the entire header frame shows a significant increase. This suggests that under these conditions, the excitation frequency from a specific source closely aligns with the header frame's natural frequency, resulting in a resonance effect.

Analysis of the vibration responses of the right side plate of the header frame to various excitation sources under different operating conditions indicates that the vibration amplitude at the right output shaft end of the transmission (measurement point 3) is consistently higher in all three axes compared to other measurement points. The difference in vibration amplitudes is most pronounced at the target operating speed of 1600 r/min, suggesting that the vibrations on the right side of the header frame are predominantly due to excitation from the rotational motion of the transmission's right output shaft. Further analysis reveals that the vibration excitation in the Z-axis at the drive shaft end of the hammer claw device (measurement point 2) is particularly pronounced. This finding suggests that during the operation of the pickup header, the excitation from the hammer claw device primarily influences the transverse vibration of the header frame's right side plate. The analysis results indicate that the primary sources of vibration affecting the right side of the header frame, ranked by impact, are the transmission right output shaft (measurement point 3), the hammer claw device (measurement point 2), and the conveyor housing (measurement point 4).

Comparison of the vibration responses from various excitation sources on the left side of the harvester frame under different operating conditions reveals that the vibration amplitudes at the left output shaft end of the transmission (measurement point 6) in the X, Y, and Z directions exceed those at other measurement points. This trend is further accentuated at the target operating speed of 1600 r/min. This finding suggests that the predominant factor influencing vibration on the left side of the harvester frame is the vibrational excitation from the rotational movement of the transmission's left output shaft end. Under each operating condition, the vibrational excitation at the drive shaft end of the dust removal device (measurement point 8) in the X-direction is notably prominent. This suggests that the dust removal device has a significant impact on the vibration of the harvester frame's left side plate in the longitudinal direction during operation. This is likely due to the fact that the excitation generated by the operation of the dust removal device primarily propagates along the X-axis.

A comprehensive analysis reveals that the main excitation sources influencing the vibration of the left side plate of the harvester frame, ranked from strongest to weakest, are the left output shaft of the transmission (measurement point 6), the dust removal device (measurement point 8), and the conveying auger device (measurement point 7).

Analysis of the vibration responses of the header frame front beam under various operating conditions shows that the vibration amplitude at the transmission input end in the horizontal direction exceeds those in other directions. This suggests that the primary influence on the vibration of the header frame front beam is the horizontal vibration excitation originating from the transmission input end. At the target operating speed of 1600 r/min, significant changes in the vibration amplitudes are observed for both the header frame front beam and the transmission input end. This observation suggests that resonance coupling between the transmission input end and the front beam may occur under this test condition.

Analysis of the vibration responses of the header frame rear beam under various operating conditions clearly shows that the vibration amplitudes at the dust box end are significant in both the horizontal and vertical directions. At the target operating speed of 1600 r/min, there is a considerable sudden increase in vibration amplitude. At the same operating speed of 1600 r/min, the vibration amplitude of the header frame rear beam significantly increases in both horizontal and vertical directions. This observation suggests that at this operating speed, the excitation from the dust collector box may resonate with a particular natural frequency of the frame's rear beam.

In summary, the pickup header undergoes varying degrees of vibrational deformation on both the left and right sides of the frame, as well as at the front and rear beams, due to multiple excitation sources. At the target operating speed of 1600 r/min, the impact on the frame is particularly significant, aligning with the results of the modal analysis of the cutting table frame.

Frequency domain analysis of experimental results

The time-domain signals from vibration tests at various measurement points on the pickup header were analysed using Fast Fourier Transform (FFT). A total of 2048 analysis points were selected, with a rectangular window applied, and amplitude correction was performed on the window. This process produced the frequency spectrum characteristics for each measurement point. The frequency amplitude table is shown in Table 3:

Table 3

The vibration frequency and amplitude of the main excitation source in the target condition

| Measurement point | Peak number | X-direction | | Y-direction | | Z-direction | |
|-------------------|-------------|----------------|------------------------|----------------|------------------------|----------------|------------------------|
| | | Frequency / Hz | Amplitude / $m*s^{-2}$ | Frequency / Hz | Amplitude / $m*s^{-2}$ | Frequency / Hz | Amplitude / $m*s^{-2}$ |
| 2 | 1 | 408.7 | 1.492 | 33.75 | 4.9 | 175 | 1.724 |
| | 2 | 33.75 | 1.367 | 476.8 | 2.476 | 183.75 | 1.526 |
| | 3 | 443.1 | 1.239 | 408.7 | 2.417 | 170.625 | 1.435 |
| 3 | 1 | 613.1 | 2.541 | 33.75 | 2.437 | 183.7 | 3.042 |
| | 2 | 31.75 | 2.39 | 443.1 | 1.388 | 170.6 | 1.771 |
| | 3 | 647.5 | 2.159 | 609.3 | 1.264 | 158.7 | 1.29 |
| 4 | 1 | 183.7 | 1.55 | 34.3 | 2.437 | 183.7 | 3.042 |
| | 2 | 338.7 | 1.122 | 443.1 | 1.388 | 170.6 | 1.771 |
| | 3 | 341.8 | 1.004 | 91.8 | 1.264 | 158.7 | 1.29 |
| 6 | 1 | 44.3 | 4.427 | 960 | 2.085 | 449.3 | 5.16 |
| | 2 | 960 | 2.49 | 933.1 | 1.936 | 35.85 | 2.486 |
| | 3 | 946.8 | 1.906 | 42.5 | 1.726 | 483.7 | 2.064 |
| 7 | 1 | 771.8 | 1.891 | 449.3 | 2.198 | 414.3 | 2.319 |
| | 2 | 763.8 | 1.125 | 791.2 | 1.128 | 771.8 | 1.891 |
| | 3 | 733.1 | 0.959 | 763.7 | 1.081 | 483.7 | 1.746 |
| 8 | 1 | 449.3 | 4.817 | 485.6 | 1.527 | 449.7 | 1.342 |
| | 2 | 480.6 | 3.129 | 481.2 | 1.326 | 480.6 | 0.903 |
| | 3 | 476.8 | 2.669 | 491.2 | 1.065 | 617.5 | 0.855 |
| 9 | 1 | 451.2 | 9.153 | 901.8 | 3.205 | 798.1 | 11.778 |
| | 2 | 69.375 | 3.749 | 901.7 | 2.984 | 34.75 | 10.145 |
| | 3 | 277.5 | 2.537 | 416.25 | 2.979 | 867.5 | 9.881 |
| 12 | 1 | 849.3 | 1.699 | 849.3 | 5.47 | 755 | 4.061 |
| | 2 | 69.3 | 1.154 | 416.2 | 3.09 | 759.3 | 1.894 |
| | 3 | 35 | 1.054 | 63.125 | 1.067 | 647.5 | 1.43 |

The vibration frequency at the transmission output shaft is primarily determined by the rotational speed of the power output shaft. The vibration frequency of the hammer claw device is primarily determined by the frequency at the drive pulley. The vibration frequency of the conveyor box is primarily determined by the frequency at the conveyor shaft bearing cover. As shown in Table 3, the vibration amplitude of the hammer claw device is the largest, reaching up to $4.9 \text{ m}^*\text{s}^{-2}$ in the Y-direction (vertical direction). This is because the hammer-claw drive shaft is the first component to come into contact with the straw, leading to significant variations in vibration amplitude. The frequently occurring vibration frequencies at Measurement Points 2, 3, and 4 in the X and Y directions—33.75 Hz, 31.75 Hz, 34.3 Hz, and 91.8 Hz—are closely aligned with the fundamental and harmonic frequency range of the header frame's natural frequency, which is between 29 and 35 Hz. This proximity makes it prone to resonance coupling phenomena.

The vibration frequencies of the conveying device and the dust box are primarily dominated by the fundamental and higher frequencies of the drive pulley. As can be seen from Table 3, the vibration amplitude at the transmission's left output shaft is higher than that of the conveying device and dust box, with the greatest amplitude occurring in the Z-direction (horizontal direction), reaching up to $5.16 \text{ m}^*\text{s}^{-2}$. Additionally, the frequencies occurring in all three directions at the transmission's left output shaft—44.3 Hz, 42.5 Hz, and 35.85 Hz—are close to the sixth-order natural frequency of the frame, making it susceptible to frame resonance coupling phenomena.

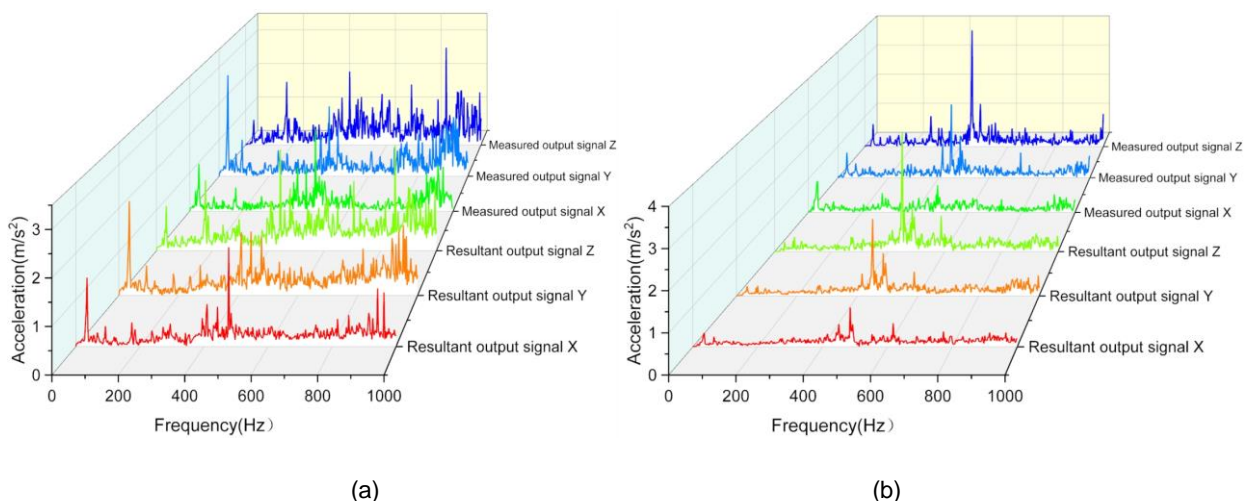
The vibration frequency at the transmission input end is caused by the engine speed, with a notably significant vibration amplitude in the Z-direction (horizontal direction). The maximum amplitude reaches $11.778 \text{ m}^*\text{s}^{-2}$. This is due to the triangular configuration of the transmission's input and output shafts. Among these, the frequency of 69.4 Hz in the X-direction falls within the double frequency range of the sixth-order natural frequency of the frame, and the frequency of 34.75 Hz in the Z-direction is close to the fifth-order natural frequency of the frame. These conditions are likely to cause resonance coupling between the transmission and the front beam of the header frame.

Measurement Point 11, located at the dust box end, exhibits a vibration amplitude in the Y-direction (vertical direction) that is higher than in other directions, with the maximum vibration amplitude reaching $5.47 \text{ m}^*\text{s}^{-2}$. Among these, the frequencies of 69.3 Hz, 63.1 Hz, and 35 Hz occurring in the X- and Y-directions fall within the fundamental and double frequency range of the sixth-order natural frequency of the frame. Therefore, these frequencies are likely to cause resonance coupling in the frame.

Comparing the excitation frequencies with the modal parameters of the header frame reveals that Measurement Points 2, 3, 6, 9, and 12 all have frequencies within the fundamental and harmonic frequency range of the header frame's natural frequencies, which is between 30 and 35 Hz. Therefore, when the straw forage harvester is operating normally, excitation sources such as the hammer claw device, transmission, conveyor box, and dust box can induce resonance in the header frame. Consequently, it is necessary to analyse the vibration transmission paths and contribution levels from each excitation source to the response points on the header frame.

Analysis of transmission path results under operating conditions

According to the principles of the Operational Transfer Path Analysis (OTPA) method, establishing a model requires constructing an input signal matrix and a corresponding target response point matrix. The experimental data under the target conditions were processed and analysed according to Equation (9). The synthesized vibration data from the model response points were then compared with the actual measured data, with the results shown in Fig. 9.



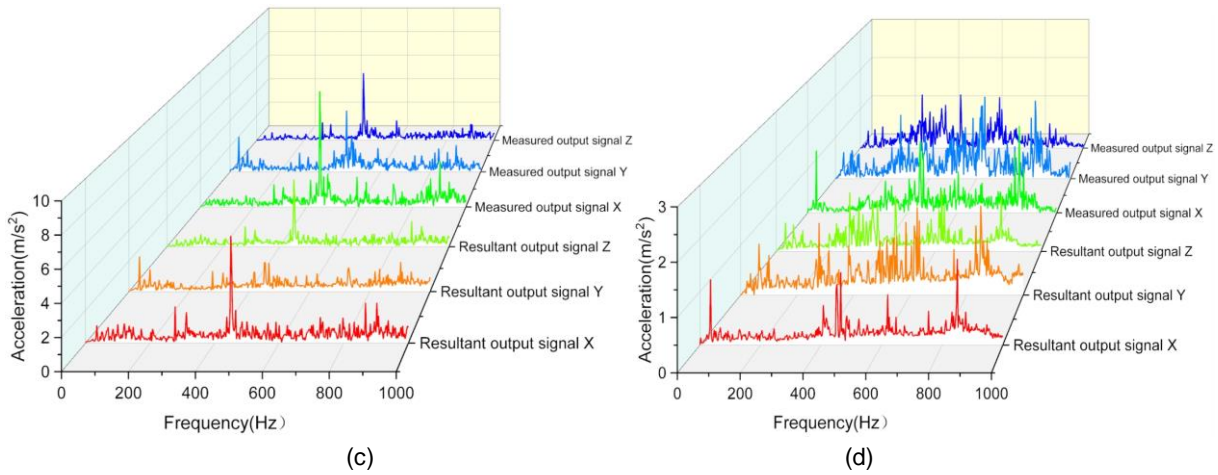


Fig. 9 - Comparison between the synthetic signal and the measured signal

(a) Rack right hand side working condition transfer path analysis model; (b) Rack left hand side working condition transfer path analysis model; (c) Frame front beam working condition transfer path analysis model; (d) Frame rear beam working condition transfer path analysis model.

As demonstrated in Figure 9, the output signal synthesized by the OTPA model closely matches the measured signal. The model displays consistent magnitude and variation trends within the analysis frequency band, effectively capturing the vibration transmission from various excitation sources on the straw forage harvester's pickup header to the designated response points on the header frame.

Building on this foundation, the validated model for operational condition transfer path analysis can be employed to determine the vibration contributions of each measurement point to the response points on the header frame at the characteristic frequencies under specified operational conditions, as outlined in Equation (7). By analysing the contribution of each transfer path to the structural vibrations at characteristic frequencies under test conditions, the influence on the four response points of the pickup header is determined, as illustrated in Figure 10.

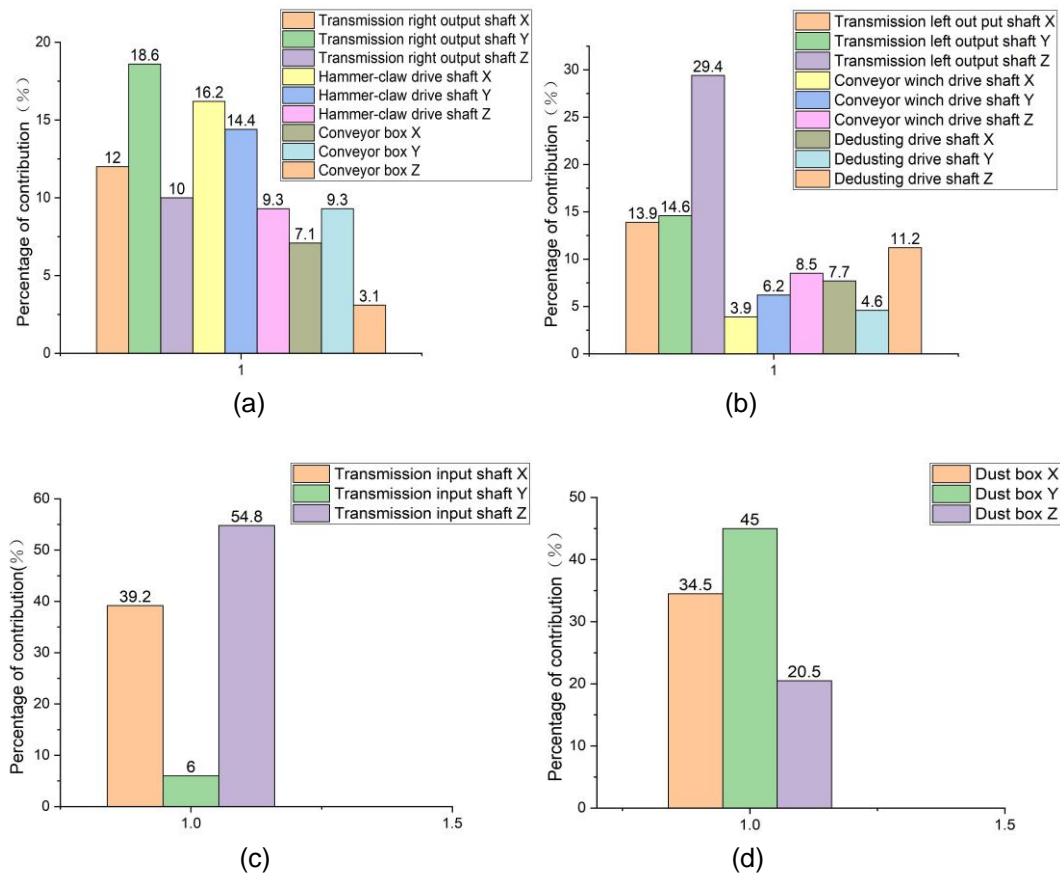


Fig. 10 - Characteristic frequency points of each path contribution diagram

(a) Excitation vibration contribution from the right side of the frame; (b) Excitation vibration contribution from the left side of the frame; (c) Excitation vibration contribution from the front beam of the frame; (d) Excitation vibration contribution from the rear beam of the frame.

Analysis of the vibration contribution diagram for the right side of the frame indicates that the transmission output end and the hammer-claw drive shaft are the primary contributors to the vibration on the right side of the header, accounting for 40% and 39% respectively. The primary contributors to vibration on the right side of the frame are: the transmission output end, accounting for 18.58% of the vertical vibrations; and the hammer-claw drive shaft, which contributes 16.24% to forward vibrations and 14.35% to vertical vibrations. Observations indicate that the largest contributions to the forward and vertical directions of the right side panel of the pickup header frame come from various transfer paths, whereas the lateral contributions are the smallest. Therefore, in optimizing vibration reduction for the pickup header, priority should focus on the forward and vertical directions of the frame's right-side panel.

Analysis of the vibration contribution diagram for the left side of the frame shows that the transmission output end accounts for a significant 57.89% of the vibrations, markedly more than the other two measurement points. The transmission output end is the most significant contributor to the horizontal vibrations of the frame's left side, accounting for 29.41%. This observation reveals that excitation sources contribute predominantly to the lateral vibrations of the left side panel of the pickup header, with the smallest contribution in the forward direction. Therefore, in optimizing vibration reduction for the pickup header, particular emphasis should be placed on mitigating the impact of the gearbox output shaft end on the lateral vibrations of the left side panel.

Analysis of the vibration contribution diagram for the frame's front beam indicates that the transmission input end primarily contributes to vibrations in the forward and horizontal directions of the header, accounting for 39.2% and 54.8% respectively. The primary vibration contributions from the transmission input end are in the Z, X, and Y directions, respectively. This indicates that the excitation sources predominantly affect the front beam of the pickup header in the forward and horizontal directions. Consequently, in optimizing vibration reduction for the front beam of the pickup header, particular emphasis should be placed on mitigating the transmission's impact on the forward and horizontal directions.

The analysis of the vibration contribution diagram for the frame's rear beam reveals that the dust box end primarily contributes to vibrations in the forward and vertical directions of the header, accounting for 45% and 34.5% respectively. At the dust box end, the vibration contributions are ordered as follows: Y-axis, X-axis, and Z-axis. This analysis shows that the excitation source contributes most significantly to the vertical vibrations of the pickup header's rear beam, and least to the horizontal vibrations. During the vibration damping optimization for the rear beam of the pickup header, emphasis should be placed on mitigating the impact of excitation from the dust box in the vertical direction.

In summary, during operation, the pickup header of the straw forage harvester is primarily influenced by excitations from the power input shaft, the left and right output shafts of the transmission, the hammer-claw drive shaft, and the dust box. These influences are specifically manifested in the forward and vertical vibrations of the header frame's right side plate, the horizontal vibrations of the left side plate, and the forward and horizontal vibrations of the front beam, as well as the vertical vibrations of the rear beam.

CONCLUSIONS

This study focuses on the pickup header of a straw forage harvester. By integrating modal analysis, vibration testing, and operational transfer path analysis, the vibration characteristics of the pickup header frame and its excitation sources were identified. Additionally, the primary transfer paths and their contribution levels to the vibration of the pickup header were identified. The key findings are as follows:

- (1) The vibration characteristics of the pickup header frame are as follows: the primary response areas to excitation sources are located on the left and right sides, as well as the front and rear beams of the frame. Additionally, the excitation frequencies of sources like the hammer claw device, transmission output shaft, transmission input shaft, and dust box closely match the natural frequencies of the pickup header, potentially causing resonance coupling.
- (2) The study examined the feasibility of using the Operational Transfer Path Analysis (OTPA) method, based on Singular Value Decomposition (SVD), to analyse the transmission paths of vibrations from excitation sources to the frame of the straw forage harvester's pickup header. An OTPA model was developed to map excitation points to response points. The model's accuracy was validated by comparing the agreement between simulated synthetic signals and measured signals within the study frequency range. This provides a theoretical basis for the structural optimization of the pickup header.
- (3) The main transmission path contributions are as follows: For the right side panel of the frame, the primary contributors are the transmission's right output shaft (vertical direction) and the hammer-claw drive shaft (forward and horizontal directions). For the left side panel of the frame, the primary contributor is the transmission's left output shaft (horizontal direction). For the front beam of the frame, the primary

contributor is the transmission's input shaft (forward and horizontal directions). For the rear beam of the frame, the primary contributor is the dust box end (forward and vertical directions).

In summary, this study has identified the fundamental causes of vibration deformation in the pickup header of the straw forage harvester. This provides crucial insights for optimizing vibration reduction and structural design in new models of the pickup header, offering valuable references for the development of other agricultural equipment as well. Moreover, it provides a theoretical basis and new perspectives for optimizing vibration reduction and structural design, with potential applications in multi-source excitation load studies and vibration improvements for other electromechanical products.

ACKNOWLEDGEMENTS

We acknowledge that this work was supported by the National Natural Science Foundation of China (52365035), the Inner Mongolia Autonomous Region Science and Technology Programme (2022YFDZ0024), the National Natural Science Foundation of China (32071893), the Innovation and Entrepreneurship Training Programme for College Students of Inner Mongolia Agricultural University (202310129084) and the Priority Agricultural Engineering Projects (YLXKZX-NND-NYGCZD001).

REFERENCES

- [1] Awad, Mahmoud, et al. (2022) A combined machine for collecting and chop rice straw. *Heliyon*. 8.8. <https://doi.org/10.1016/j.heliyon.2022.e10412>
- [2] An, Xue, et al. (2020). Characterization of textural failure mechanics of strawberry fruit. *Journal of Food Engineering*. 282: 110016. <https://doi.org/10.1016/j.jfoodeng.2020.110016>
- [3] Ahmadian, Hossein, Seyed Reza Hassan-Beygi, and Barat Ghobadian. (2014). Investigating a power tiller handle and seat vibration on transportation mode. *Agricultural Engineering International: CIGR Journal* 16.4: 194-206.
- [4] Chen, Shuren, et al. (2020). Modal vibration response of rice combine harvester frame under multi-source excitation. *Biosystems engineering*. 194: 177-195. <https://doi.org/10.1016/j.biosystemseng.2020.04.002>
- [5] Chuan-Udom, Somchai. (2017). Development of a cutter bar driver for reduction of vibration for a rice combine harvester. *Asia-Pacific Journal of Science and Technology* 15.7. 572-580.
- [6] Chen Shuren, Han Hongyang, and Lu Qiang. (2012). Modal Analysis of Header for Type 4LZ 2. 0 Combine Harvester (4LZ-2.0 型联合收获机割台模态分析). *Transactions of the Chinese Society for Agricultural Machinery*, 43(S1): 90-94. <https://doi.org/10.6041/j.issn.1000-1298.2012.S0.018>
- [7] Chen Jun-fei, et al. (2023). Transfer path analysis of product packaging system under random vibration (随机振动下产品包装系统传递路径分析). *Journal of Vibration Engineering*, 36(02): 507-516. DOI:10.16385/j.cnki.issn.1004-4523.2023.02.022. <https://doi.org/10.16385/j.cnki.issn.1004-4523.2023.02.022>
- [8] De Klerk, Dennis, and Alexander Ossipov. (2010). Operational transfer path analysis: Theory, guidelines and tire noise application. *Mechanical systems and signal processing*. 24.7:1950-1962. <https://doi.org/10.1016/j.ymssp.2010.05.009>
- [9] El Ghobashy, Hossam, et al. (2023). Development and evaluation of a dual-purpose machine for chop and crushing forage crops. *Heliyon*. 9.4. <https://doi.org/10.1016/j.heliyon.2023.e15460>
- [10] Guo, Rong, et al. (2015). A novel visual transfer path analysis method with coupled vibration source based on inverse substructuring technique. <https://doi.org/10.11908/j.issn.0253-374x.2015.04.015>
- [11] Harikrishnan, P. M., and Varun P. Gopi. (2017). Vehicle vibration signal processing for road surface monitoring. *IEEE Sensors Journal*. 17.16: 5192-5197. <https://doi.org/10.1109/JSEN.2017.2719865>
- [12] Jiang, Yajun, et al. "Vibration analysis and improvement for frame of 4SY-2.9 typed rape windrower." *Transactions of the Chinese Society of Agricultural Engineering* 33.9 (2017): 53-60. <https://doi.org/10.11975/j.issn.1002-6819.2017.09.007>
- [13] Lu, Wang, et al. (2014). Classification and comparison of physical and chemical properties of corn stalk from three regions in China. *International Journal of Agricultural and Biological Engineering*. 7.6: 98-106. <https://doi.org/10.3965/j.ijabe.20140706.012>
- [14] Liao Xuhui, et al. (2021). Improved operational transfer path analysis (改进的工况传递路径分析). *Journal of Vibration and Shock*, 40(12):196-202+218. <https://doi.org/10.13465/j.cnki.jvs.2021.12.024>

- [15] Lai, Z. N., S. Yang, and P. Wu. (2018). Speed-throttling combined optimization for high reliability in parallel centrifugal pump system. *Journal of drainage and irrigation machinery engineering*. 36.12: 1205-1210.
- [16] McKendry, Peter. (2002) Energy production from biomass (part 2): conversion technologies. *Bioresource technology* 83.1: 47-54. [https://doi.org/10.1016/S0960-8524\(01\)00119-5](https://doi.org/10.1016/S0960-8524(01)00119-5)
- [17] Nakata, Toshimichi, Yuji Sogabe and Takao Araki. (2010) Vibration property of a rubber crawler system when traveling over bumps. *Engineering in Agriculture, Environment and Food*. 3.2: 47-53. <https://doi.org/10.11165/eaef.3.47>
- [18] QI Quan, et al. (2017). Structure-borne Noise Source Identification of an Excavator's Cab based on Operational Transfer Path Analysis (基于 OTPA 方法的挖掘机驾驶室结构噪声源识别). *Noise and Vibration Control*, 37(02): 80-84. <https://doi.org/10.3969/j.issn.1006-1355.2017.02.017>
- [19] Xia, Erli, et al. (2021) A modified dynamic stiffness calculation method of rubber isolator considering frequency, amplitude and preload dependency and its application in transfer path analysis of vehicle bodies. *Applied acoustics*. 175: 107780. <https://doi.org/10.1016/j.apacoust.2020.107780>
- [20] Yao, T. T., and Y. Zheng. (2020) Finite element analysis of stress, deformation and modal of head cover in axial-flow hydro-turbine. *Journal of Drainage and Irrigation Machinery Engineering* 38.1: 39-44. <https://doi.org/10.3969/j.issn.1674-8530.18.0140>
- [21] Zheng Qi-ming, Qian Jing. (2016). Improvement of the Operational Transfer Path Model of a Label Sewing Machine Using Multiple Coherence Analysis (利用改进重相干分析改进订标机工况传递路径模型). *Noise and Vibration Control*, 36(03):169-173. <https://doi.org/10.3969/j.issn.1006-1335.2016.03.035>

DESIGN AND EXPERIMENT OF A MULTI-CHANNEL REAL-TIME WEIGHING DEVICE

多路实时称量装置设计与试验

Lingyu LIU, Xiangcai ZHANG^{*}, Xianliang WANG, Zhongcai WEI, Xiupei CHENG, Yujie ZHANG, Xinkai JIAO¹

School of Agricultural Engineering and Food Science, Shandong University of Technology, Zibo (255000), China

Tel: +86-15169235925; E-mail: zxcai0216@163.com

Corresponding author: Xiangcai Zhang

DOI: <https://doi.org/10.35633/inmateh-73-28>**Keywords:** seeding rate detection, SPI, pressure sensors, LabVIEW upper computer, DEM**ABSTRACT**

During the sowing operation, the consistency and stability of the row dispenses of a seeder are important indicators for evaluating sowing performance. A multi-channel real-time weighing device was designed to study and analyze the consistency of row dispenses in seeder under identical conditions, as well as the stability of dispenses from a seed dispenser. This device utilized two Arduino boards as controllers for data acquisition, processing, and transmission. Based on the Serial Peripheral Interface (SPI), data exchange between multiple Arduinos was achieved in a master-slave configuration, allowing for data acquisition from 14 pressure sensors in a one-master, one-slave setup. Pressure data was collected using pressure sensors, HX711 converter chips, and Arduino. LabVIEW was utilized as the upper computer to read data from the Arduino host serial port and provide real-time display and storage. This paper presents the structural and working principles of the device. Experimental tests on the weighing unit were conducted using a test bench to evaluate measurement errors. The absolute error mean ranged from 0.143 g to 0.262 g. Additionally, the impact of the seed impact force on the error was simulated using EDEM. The device was used to evaluate a six-row wheat seeder under the experimental conditions of the groove wheel having a length of 2.5 cm and a groove wheel speed of 25 r/min. The maximum coefficient of variation for seeding stability (Y_1) was 2.38%, the minimum was 0.83%, and the mean was 1.21%. The coefficient of variation for consistency of seeding in rows (Y_2) was 1.86%.

摘要

在进行播种作业时，播种机的各行排量一致性和排量稳定性是评价播种性能的重要指标。为了研究和分析在相同条件下，同一播种机的各行排量一致性，以及单一排种器的排量稳定性，设计了一种多路实时称量装置。该装置以两块 Arduino UNO 作为控制器，用于装置数据的采集、处理和传输；基于 SPI 通信原理，实现多 Arduino 的主从机数据交换，一主一从时，可实现 14 个压力传感器的数据采集；通过应变式压力传感器、HX711 A/D 转换芯片和 Arduino 实现压力数据采集；应用 LabVIEW 上位机用于读取 Arduino 主机串口的数据，并进行实时显示和存储。本文介绍了该装置的结构构成以及工作原理，通过台架试验，检验了称重单体的测量误差，并对误差做出了分析，绝对误差均值在 0.143g 至 0.262g 之间，并通过 EDEM 离散元仿真模拟了种子冲击力大小对误差的影响。运用该装置检验了 6 行单箱小麦播种机在外槽轮开度 2.5cm、槽轮转速 25r/min 的试验条件下，排量稳定性变异系数最大值为 2.38%，最小值为 0.83%，均值为 1.21%，各行排量一致性变异系数为 1.86%。

INTRODUCTION

With the development of precision agriculture, seeding detection technology is gradually becoming one of the research hotspots to achieve intelligent seeding, providing essential technical support to enhance seeding quality (Ding et al., 2021; He et al., 2021; Ramasamy, 2021). Improving seeding uniformity to ensure crop seedlings are uniform and strong can provide favorable conditions for crop growth, laying a foundation for increasing yields in the early stages (Wang et al., 2024).

Since the 1980s, research on seeding detection technology has been carried out both domestically and internationally (Li et al., 2022). In the early stages, mechanical alarms were used, such as on the NODET air-suction seeder developed in France (Zhao et al., 2003), where an actively fitted spring plate would strike a raised shield to trigger an alarm using metal components but could only determine the working status of the seeder.

¹ Lingyu Liu, M.Sc. Stud. Eng.; Xiangcai Zhang, Ph.D. Eng.; Xianliang Wang, Ph.D. Eng.; Zhongcai Wei, Ph.D. Eng.; Xiupei Cheng, Ph.D. Eng.; Yujie Zhang, M.Sc. Stud. Eng.; Xinkai Jiao, M.Sc. Stud. Eng.

Based on the sensing principles of different detection devices for seeds, the existing detection methods mainly include mechanical-electrical, machine vision, photoelectric sensing, capacitive sensing (Taghinezhad *et al.*, 2013), and piezoelectric sensing (Sebastián Rossi *et al.*, 2023). Drake *et al.* (1991) combined high-speed photography with image processing technology to measure and analyze the motion of seeds falling from the seed outlet. Zhang *et al.* (2013) used red high-brightness light-emitting diodes in conjunction with a photoresistor as the sensing component for seeds, coupled with a microcontroller, to design a photoelectric seed and fertilizer detection system. Wu *et al.* (2014) used pressure sensors to monitor the real-time changes in the mass of the seed box and provide feedback to adjust the seeder's speed to control the seeding quantity. This enables the detection of key information such as blockages, seeding quantity, seeding frequency, misplanting, overplanting, and seed motion status (Karimi *et al.*, 2017; Zhang *et al.*, 2022; Zhou *et al.*, 2022). However, there is a lack of a detection device specifically for detecting the consistency of seeding quantities in each row of seeders, and existing seeding detection devices developed domestically and internationally suffer from issues such as single application, limited detection channels that are difficult to install and dismantle, poor environmental adaptability, high costs, and a lack of mature technical systems and marketable products (Li & Yang, 2018; Wang *et al.*, 2021; Zhang *et al.*, 2021; Zagainov Nikolay *et al.*, 2023).

To address this, research was conducted on aspects such as the structure of the weighing unit, operational principles, error analysis, and upper and lower machine program design. The weighing device was designed and characterized by its multi-channel, real-time display and synchronous operation. This device provides technical and data support for assessing the consistency and stability of the row dispenses of a seeder and also serves as a foundational reference for the design of other agricultural machinery in areas such as broadcast sowing, row sowing, and irrigation.

MATERIALS AND METHODS

General structure and working principle

The overall schematic diagram of the multi-channel real-time weighing device is illustrated in Fig. 1, which is comprised mainly of the LabVIEW upper computer, Arduino master, Arduino slave, weighing unit, and Serial Peripheral Interface (SPI) communication system. The LabVIEW upper computer, Arduino master, and Arduino slave adopt a three-tier distributed structure.

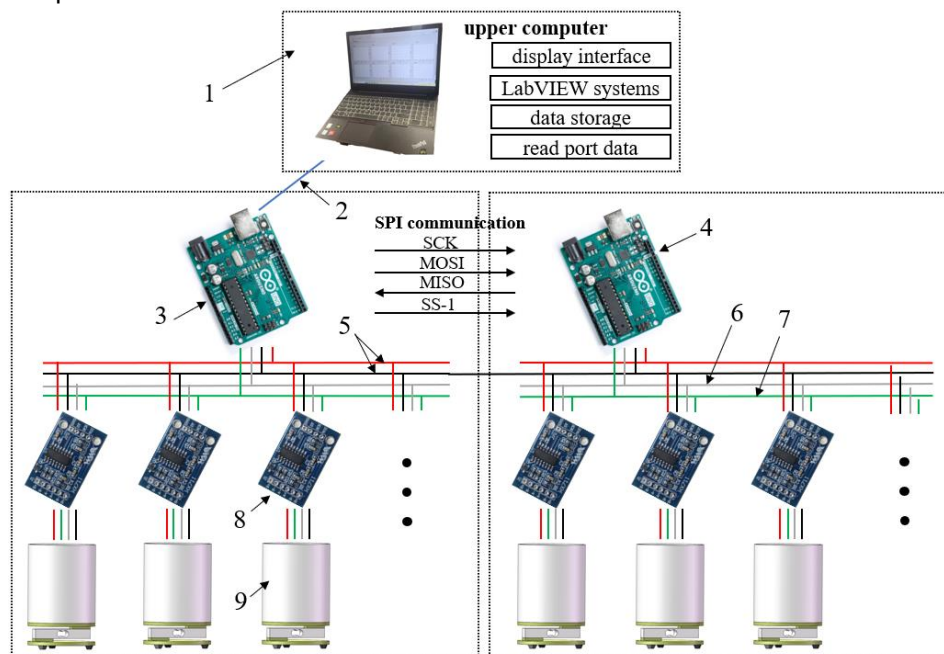


Fig. 1 - The overall schematic diagram of the device

1 – LabVIEW upper computer; 2 – Type-B to Type-A; 3 – Arduino master; 4 – Arduino slave; 5 – 5v power supply; 6 – SCK cord; 7 – DT cord; 8 – HX711 converter chip; 9 – weighing unit

The multi-channel real-time weighing device was designed with a master unit and a slave unit, comprising 8 weighing units (theoretically expandable up to 14), capable of simultaneously conducting real-time monitoring of 8 targets. Each weighing unit was primarily composed of a pressure sensor and a weighing cylinder, which function to acquire the weight of the target and output its mass.

The Arduino master unit is responsible for collecting real-time data from its own weighing units, selecting the communication slave unit, collecting real-time data from the slave unit weighing units, integrating all the data, and printing it via the serial port. The Arduino slave unit was tasked with collecting real-time data from its own weighing units and transmitting the data to the master unit upon selection. SPI communication was employed for the Arduino master unit to select the Arduino slave unit and perform data exchange. The LabVIEW control system runs on a computer equipped with LabVIEW 2018 software. Through LabVIEW software programming, it reads, separates, displays, and stores data from the Arduino master unit via the serial port. During operation, each weighing unit was placed beneath the weighing target, and the target continuously enters each weighing unit, enabling multi-channel real-time weighing.

Weighing unit structure

The schematic diagram of the weighing unit structure is shown in Fig. 2. The weighing unit is one of the main functional components of the multi-channel real-time weighing device, designed to acquire the weighing target and output the target's mass. It primarily consists of a weighing cylinder, upper fixed plate, strain gauge pressure sensor, spacer, HX711 converter chip, lower fixed plate, and foot pad. During operation, the unit remained in a static state.

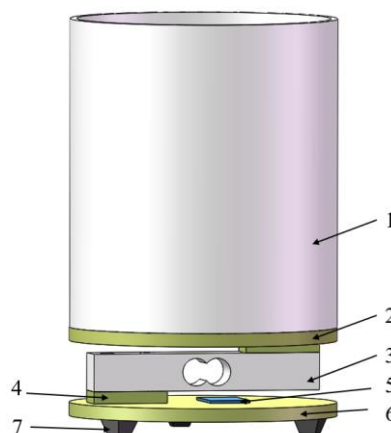


Fig. 2 - The schematic diagram of the weighing unit structure

1 – weighing cylinder; 2 – upper fixed plate; 3 – strain gauge pressure sensor; 4 – spacer; 5 – HX711 converter chip; 6 – lower fixed plate; 7 – foot pad

In Fig. 2, both the upper fixed plate and lower fixed plate are made of acrylic plates. Three rubber foot pads are fixed to the lower surface of the lower fixed plate to provide support and stability to the entire working component. The HX711 converter chip is secured to the upper surface of the lower fixed plate by two rivets, positioned closely to the pressure sensor without affecting signal transmission. According to the working principle of the strain gauge pressure sensor, the lower left and upper right ends of the pressure sensor are respectively fixed to the lower fixed plate and upper fixed plate through acrylic spacers and bolts. The weighing cylinder is fixed to the upper surface of the upper fixed plate with two bolts, serving to support the seeds discharged by a single seed dispenser.

Principles of data acquisition

The data acquisition of this device primarily consists of a strain gauge pressure sensor, an HX711 converter chip, and an Arduino board. A 5 kg range pressure sensor was selected to meet the test requirements of GB/T 9478-2005 for grain strip planter testing methods. The pressure sensor is used to sense external pressure changes and generate corresponding voltage signals for output to the HX711 converter chip. The strain gauge pressure sensor is an elongated prism-shaped elastic element with a hollow center that undergoes slight elastic deformation when force is applied. There is a strain gauge on each of its upper and lower surfaces, with two pressure resistors within each strain gauge. When the elastic element deforms due to force, the upper strain gauge experiences tension while the lower strain gauge undergoes compression, and causing a change in resistance in the resistive wire leading to an imbalance in the original bridge configuration. The four pressure resistors form a full bridge circuit, enhancing measurement accuracy (Ghanbari & Rezazad, 2022; Gu et al., 2024). The operational principle is depicted in Fig. 3. In the process of connecting the four lead wires of the pressure sensor to the HX711 converter chip, the black wire connects to E-, the white wire connects to S-A, the red wire connects to E+, and the green wire connects to S+A.

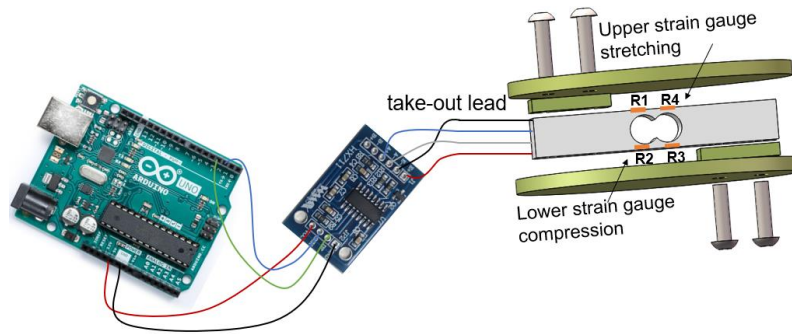


Fig. 3 - Strain gauge pressure sensor working principle diagram

The HX711 is a 24-bit A/D converter chip specifically designed for high-precision weighing sensors. In comparison to similar chips, the HX711 integrates features such as a stable power supply and an on-chip clock oscillator, eliminating the need for external peripheral circuits required by other chips of the same type. It is characterized by high integration, fast response speed, and strong anti-interference capability, which not only saves costs but also enhances the performance and reliability of the entire system. The main function of the HX711 is to amplify the voltage signal generated by the pressure sensor and convert the voltage signal into a digital signal. In this device, the A channel of the HX711 with a 128-gain is utilized, and the analog differential input of HX711 Channel A can be directly connected to the differential output of the pressure sensor. To fully utilize the input dynamic range of the A/D converter, it is necessary to amplify the relatively small voltage signal generated by the bridge sensor, and then the on-chip A/D converter will convert the voltage signal into a digital signal for output.

This device utilizes two Arduino boards to read the digital signals output by multiple HX711 converter chips and performs calculations with the intermediate value *GapValue* to determine the mass of the heavy object. The system frequency was set at 9600 for both boards, with one serving as the master to read data from the sensors to which it is connected. The master simultaneously selects the slave, receives data from the sensors connected to the slave, and prints the data on the master's serial port. The second board functions as the slave, reading data from its own connected sensors. When selected by the master board to establish communication, it transmits the collected data to the master board.

The *GapValue* is an intermediary variable used in the calculation of the mass of the heavy object. By adjusting its value, the pressure sensor can be calibrated.

The formula for calculating the mass of the heavy object is Eq. 1.

$$M = \frac{D}{GapValue} \tag{1}$$

where: *M* is the mass of the heavy object. *D* is Sensor reading. *GapValue* is intermediary variable.

$$GapValue = \frac{X \cdot 0.86 \cdot 2^{24}}{4.3} \tag{2}$$

where: *X* is magnifying power.

Due to the varying slope characteristics of different pressure sensors, the *GapValue* calculated by the formula represents the theoretical value, and actual calibration of each pressure sensor is required. In order to improve computational speed and reduce storage space resource usage, many programs scale the received AD sample values during data processing, resulting in the loss of lower-order data bits. As a result, the measurement accuracy of the program is around 1 g. By not scaling the data, reducing the *GapValue* value by a factor of 100, and dividing the output data by 100, the output mass results can retain two decimal places.

Due to the limited volume of the weighing cylinder during operation, in order to improve the accuracy of the data for this experiment, calibration was performed using a 1 kg standard weight. The calibration procedure involves burning the program onto the Arduino board with no weight on the pressure sensor, opening the serial monitor, and observing an initial reading of 0 g. The 1000 g standard weight was then placed on the pressure sensor, and the displayed value on the serial monitor is observed. If the value was higher than expected, the *GapValue* was increased and the Arduino program is re-burned. If the value is lower, the *GapValue* was decreased. This process was repeated multiple times until the value is accurate, indicating successful calibration. The *GapValue* values for each sensor are provided in Table 1.

Table 1

The *GapValue* values for each sensor

| Number | 1 | 2 | 3 | 4 | 5 | 6 | 7 | 8 |
|--------|------|------|------|------|------|------|------|------|
| Value | 4.30 | 4.29 | 4.21 | 4.25 | 4.30 | 4.28 | 4.15 | 4.16 |

Principles of SPI

In order to collect data from multiple sensors and achieve modularity in the system, the Serial Peripheral Interface (SPI) was adopted. SPI is a high-speed, full-duplex, synchronous communication bus. SPI operates in a master-slave configuration, allowing one master device to communicate with multiple slave devices. The master device selects different slave devices for communication using separate SS/CS signal lines and performs bidirectional data exchange under the control of the SCK (serial clock) signal (Yang & Ding, 2012).

The system consists of one master and one slave board, with a bus utilizing four data lines for data transfer. These lines are connected through pins 10, 11, 12, and 13 of the Arduino UNO, serving as the control signal line SS-1 (slave select), the data signal line MOSI (master out slave in), the data signal line MISO (master in slave out), and the control signal line SCK for communication. To ensure the stability of the communication process, the GND(Ground) pins of the master and slave devices are connected. To guarantee the stability of data transmission in SPI communication, the communication clock starts with a 2x clock division, and eventually, the communication clock for the multi-channel real-time weighing device was set to SPI_CLOCK_DIV16 to define it as one-sixteenth of the system clock frequency.

During communication, the master initiates SPI by setting the SS-1 pin of the slave device to a low logic level, selecting the desired slave for communication. The selected slave board detects the initiation, establishes communication, and data is synchronously exchanged between the master and slave boards during the communication process. When the master detects the transmission of the "p" character from the slave device, it concludes one communication session by setting the SS-1 pin of the slave device to a high logic level, deselecting the slave. The slave device then disregards the host, and when not selected, the MOSI signal line remains in a high impedance state, awaiting the next communication session with the host.

Principles of LabVIEW

LabVIEW is a graphical development environment language that provides the necessary development environment for various applications such as data acquisition, instrument control, measurement analysis, and data display (Gong & Zhang, 2020). Upon the initialization of LabVIEW software, this device configured the serial port using VISA, initialized the selected serial port at a communication frequency of 9600, and set the VISA resource name as "Arduino master serial port.". Serial port data was read, and a regular expression is used to search for the presence of the character "p" in the input string, which is then split into sub-strings. After splitting, the sub-strings are converted into numerical values, placed in an array, and displayed on the front panel. By indexing the array, the variation of individual sensor data curves is displayed in real-time on the front panel of the software. Simultaneously, utilizing file writing functionality to store the data from each sensor in a local folder on the computer, for subsequent data processing and analysis. The LabVIEW front panel interface is shown in Fig. 4, and the overall workflow of the LabVIEW system is depicted in Fig. 5.

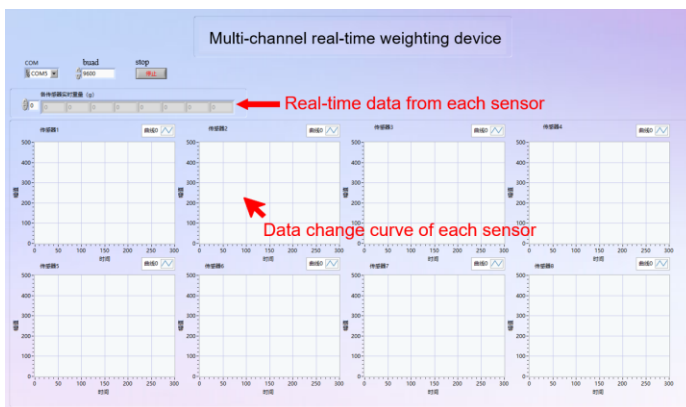


Fig. 4 - The LabVIEW front panel interface

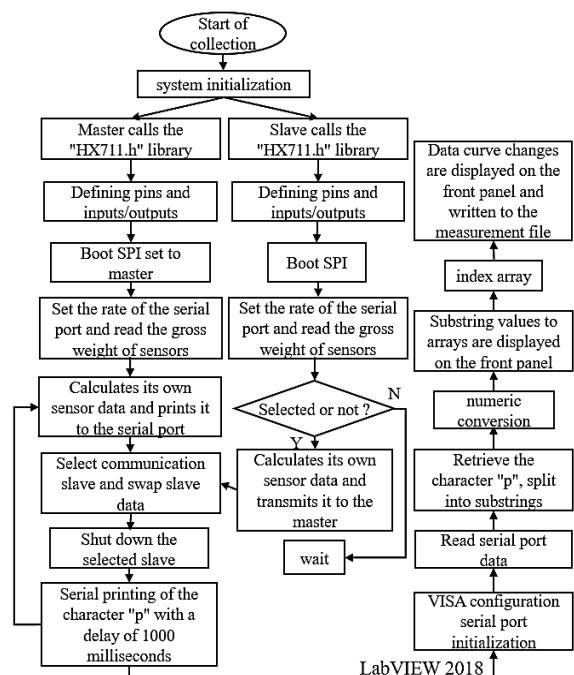


Fig. 5 - Overall workflow of the LabVIEW system

Principles of circuit

The hardware circuit connections of the device primarily consist of a pressure sensor, HX711 conversion chip, and Arduino board forming the signal processing circuit, as well as the SPI communication circuit for communication between the Arduino master and slave. The schematic diagram of the device circuit is shown in Fig. 6.

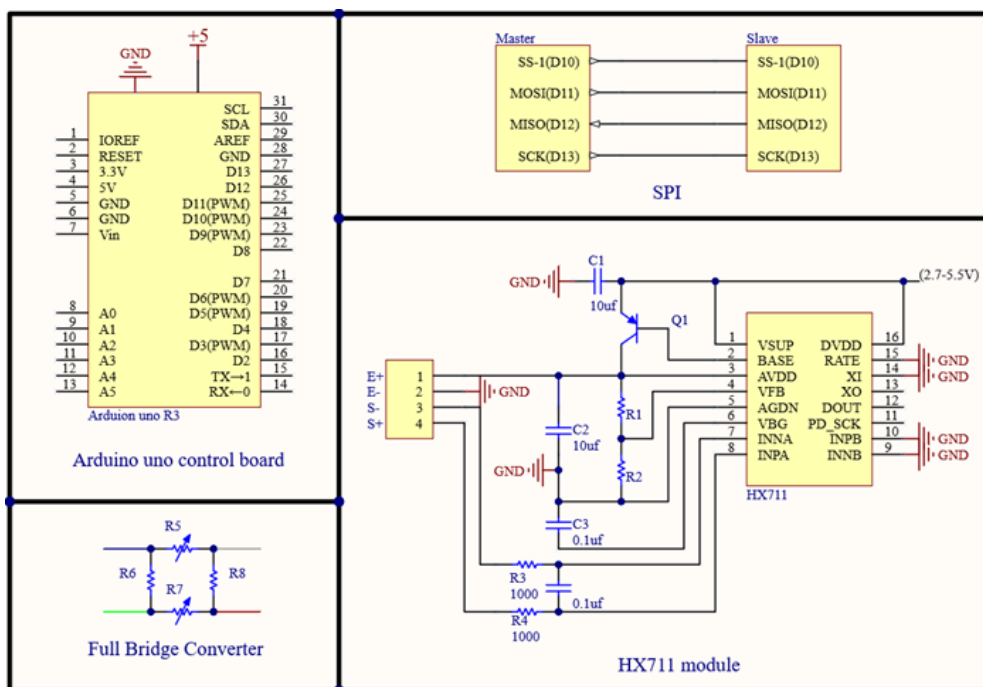


Fig. 6 - The schematic diagram of the device circuit

The Arduino master and slave can each connect up to seven strain gauge pressure sensors. In this design, four strain gauge pressure sensors are connected to both the master and slave Arduino boards. When connecting the HX711 conversion chip to the Arduino board, it is necessary to define the pins on the Arduino board. The VCC of the HX711 was connected to the 5V power output of the Arduino board, and the GND was connected to the GND pin R3 of the Arduino board. The 2, 4, 6, and 8 pins of the Arduino master and slave were defined as output ports and connected to the SCK output pulses of each HX711. The 3, 5, 7, and 9 pins of the Arduino master and slave were defined as input ports and connected to the DT for data reading from each HX711. The 10, 11, 12, and 13 pins of the Arduino master and slave were defined and connected for SPI communication. The Arduino master was connected to the LabVIEW upper computer via a Type-B to Type-A cable.

Bench test error measurements method

In order to analyze the error between the measured values and the true values of the pressure sensor during operation, a bench test experiment was designed, as shown in Fig. 7. The row seeder of a wheat seed dispenser with external groove wheel was fixed on the bench, with a seed box mounted above the seeder. A weighing unit was placed 20 cm below the seeder outlet, driven by a stepper motor to rotate the seed dispenser with a groove wheel. The groove wheel has a length of 2.5 cm and the groove wheel speed of 25 r min^{-1} . The seed box was filled with wheat seeds, and the stepper motor was activated to start seeding. The seeds fell into the weighing cylinder underneath the working part in sequence. After rotating the stepper motor for two full rotations, it was stopped. The maximum value measured by the weighing unit at the end of seeding was taken as the measured value. The mass of the discharged seeds was measured using a high-precision balance with a precision of one thousandth as the true value. Absolute error and relative error analyses were conducted based on the measured values from the weighing unit and the true values from the high-precision balance. Each test was repeated three times to take the average value. The seeds in the weighing cylinder were then emptied, and the stepper motor was set to rotate for 4 full rotations before stopping, and the above test was repeated. The experiment was conducted by incrementing 2 rotations each time until the stepper motor completed 20 rotations, totaling 10 sets of experiments.

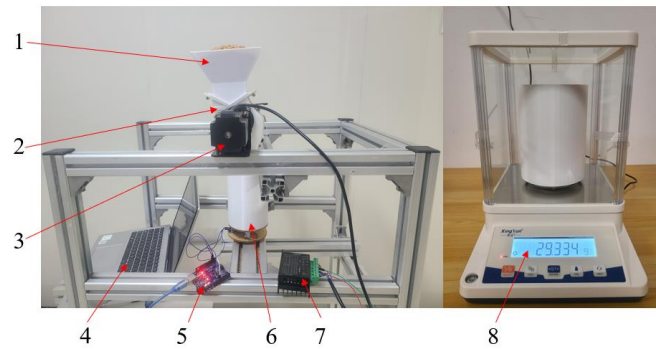


Fig. 7 - The bench test experiment

1 – seed box; 2 – seed dispenser with external groove wheel; 3 – stepper motor; 4 – computer; 5 – Arduino board; 6 – weighing unit; 7 – motor controller; 8 – high-precision balance; 9 – weighing unit

Impact error simulation method

When wheat seed is discharged from the seed dispenser, it acquires an initial velocity (v_a) and collides with the bottom of the weighing cylinder after falling a height (h), generating an impact force (P) at the moment of collision. The schematic diagram of the seed collision motion is shown in Fig. 8. Due to the random direction of the wheat seeds during descent and their irregular shapes, the direction of the impact force when they collide with the bottom of the weighing cylinder is also not fixed. The impact force direction is always perpendicular to the contact surface between the wheat seed and the bottom of the weighing cylinder. If the seed is considered a particle, the motion equation when it falls to a height (h) can be expressed as:

$$h = v_a \cdot t + \frac{1}{2} g t^2 \tag{3}$$

where: v_a is initial velocity of wheat seeds (m/s); g is the gravitational acceleration

The time t for the seed to fall is:

$$t = \frac{-v_a + \sqrt{v_a^2 + 2gh}}{g} \tag{4}$$

where: h is seed drop height (m).

During the impact process considered as a point particle, there exists a gravitational force (G) and a normal pressure (P) acting on the particle. According to the principle of kinetic energy:

$$\frac{1}{2} m v_a^2 + G(t+t_1) = P \cdot t_1 \tag{5}$$

where: t_1 is normal pressure action time (s).

Bringing the time t into Eq. (5) yields:

$$P = \frac{m v_a^2}{2 t_1} + mg \left(\frac{-v_a + \sqrt{v_a^2 + 2gh}}{t_1 g} + 1 \right) \tag{6}$$

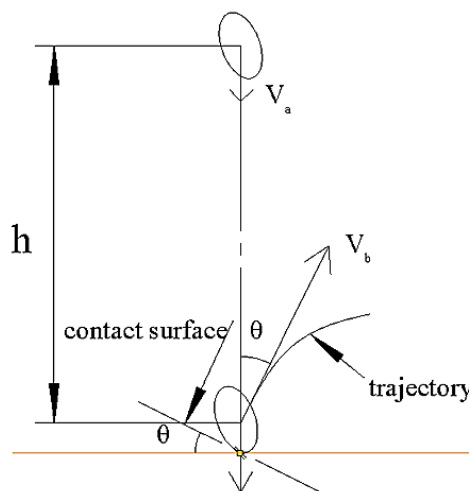


Fig. 8 - The schematic diagram of the seed collision motion

From Eq. (6), it can be observed that, with other conditions remaining constant, the impact force increases as the duration (t_i) of positive pressure decreases or as the height (h) of seed descent increases. In order to measure and analyze the impact of the impact force (P) on the pressure sensor reading during collision, EDEM discrete element simulation experiments were conducted. To simplify the calculation process, based on the measurement of the physical properties of Jima 22 seeds and references from literature, wheat seeds were equivalently modeled as ellipsoidal particles using five spherical particles. The model had a major axis length of 6.49 mm and minor axis length of 3.3 mm. The particle model is shown in Fig. 9, and the key parameters (Yu *et al.*, 2018; Yu *et al.*, 2020) for seed-DEM simulation are presented in Table 2.

Table 2

Basic parameters of seed and discrete element models

| Parameters | Value |
|---|--------------------|
| seed triaxial size (mm×mm×mm) | 6.49×3.36×3.05 |
| seed Poisson's ratio | 0.434 |
| seed shear modulus (Pa) | 5.24×10^7 |
| seed density (kg/m ³) | 1223 |
| ABS Plastic Poisson's ratio | 0.6 |
| ABS Plastic shear modulus (Pa) | 8.96×10^8 |
| ABS Plastic density (kg/m ²) | 1060 |
| seed-to-seed collision coefficient | 0.407 |
| coefficient of static friction between seeds | 0.523 |
| coefficient of kinetic friction between seeds | 0.082 |
| seed - ABS collision coefficient | 0.507 |
| seed - ABS static friction coefficient | 0.563 |
| seed - ABS coefficient of kinetic friction | 0.051 |

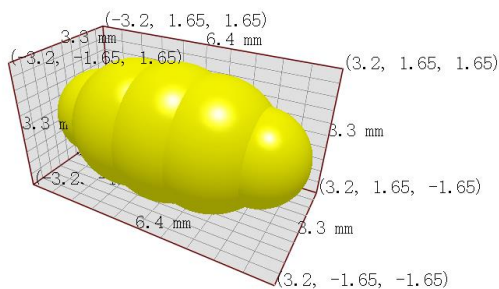


Fig. 9 - Particle model

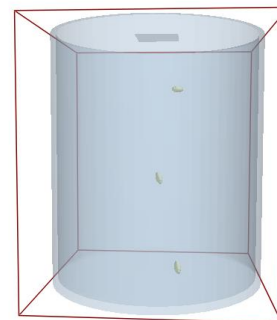


Fig. 10 - Simulation

Using SolidWorks 2016 modeling software, a three-dimensional model of the weighing cylinder component was created and then imported into the EDEM environment in .igs format for analysis. The simulation employed the default Hertz-Mindlin non-sliding contact model to analyze the impact force of wheat seed. A grain factory was established 115 mm directly above the weighing cylinder, and at the start of the simulation, seed particles were created with a velocity of 1.5 m/s along the negative Y-axis. To capture more data points and accurately reflect the collision process, the simulation was paused near the collision, and the time step was set to 10% of the Rayleigh Time Step. Data was stored at intervals of 1×10^{-5} s before continuing the simulation. During playback of the animation, it was observed that the positions of the seed before and after collision were continuous. The simulation experiment, as shown in Fig. 10, was repeated 20 times. The mass of a single wheat seed simulated particle was 0.0435 g.

Indoor experiment method

In order to assess the operational stability of the entire system and LabVIEW software, the coordination between the LabVIEW upper computer and the control system, the reliability of the pressure sensor operation, and the real-time performance and reliability of SPI communication, the multi-channel real-time weighing device was employed. Using a six-row wheat seeder as the experimental subject, indoor tests were conducted under the same experimental conditions to evaluate the consistency and stability of the sowing quantities for each row of the seeder. The experimental setup is depicted in Fig. 11.

On September 25, 2023, the experiments were conducted at the Agricultural Machinery and Equipment Testing Laboratory of Shandong University of Technology. The experimental equipment consisted mainly of a 6-row wheat seeder, with the groove wheel having a length of 2.5 cm and a groove wheel speed of 25 r/min, seeds in the seed box exceeding half of the box volume; a multi-channel real-time weighing device; an electromagnetic force electronic balance with an accuracy of 1×10^{-3} g; a stepper motor with a motor speed of 25 r/min; the wheat variety used for sowing was *Jimai 22*; weighing buckets; and brushes, among others.

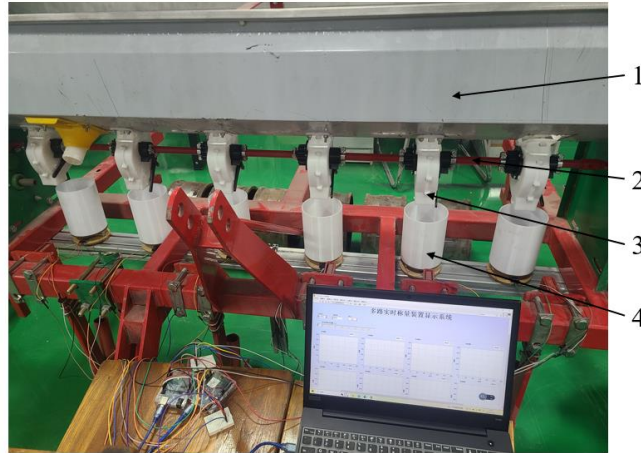


Fig. 11 - Indoor experiment

1 – seed box; 2 – propshaft; 3 – seed dispenser; 4 – weighing unit

The experiment was a static test, in which six weighing units were randomly selected from the multi-channel real-time weighing device to determine the consistency and stability of the sowing quantities for each row of the six-row wheat seeder. Prior to the start of the experiment, the stepper motor was connected to the seeding machine transmission shaft via a coupling to drive the seed dispenser for rotation. The weighing units of the multi-channel real-time weighing device were placed under each seed dispenser according to the settings from the simulation analysis. The distance between the bottom of the seeding openings and the bottom of the weighing cylinders was approximately 11 cm, designed for assessing the sowing quality of each seed dispenser. After emptying the seed box, the seeds were poured into the seed box and waited for the sowing to begin.

At the beginning of the experiment, the multi-channel real-time weighing device was started and allowed 3 seconds to stabilize before initiating the stepper motor to drive the seeder for sowing. The stepper motor ran at a speed of 25 r/min for 30 seconds, during which the multi-channel real-time weighing device displayed and recorded the experimental data. This procedure was repeated 5 times. To analyze the sowing quantity stability of each seed dispenser, the coefficient of variation for seeding stability Y_1 was used as an evaluation indicator. The sowing quality of each seed dispenser was then input into Eq. (7) for calculation.

$$\begin{cases} m_s = \frac{\sum_{i=1}^n m_{si}}{n} \\ Y_1 = \frac{\sqrt{\frac{1}{n-1} \sum_{i=1}^n (m_{si} - m_s)^2}}{m_s} \cdot 100 \end{cases} \quad (7)$$

where:

m_s is average seed quality from 5 experiments (g); m_{si} is scheduled seed quality at time i (g); n is measurement times, $n=5$. Y_1 is the coefficient of variation for seeding stability (%).

To analyze the consistency of sowing quantities for each row of the seeder, the coefficient of variation for consistency of seeding in rows Y_2 was used as the evaluation indicator based on the sowing quality of each seed dispenser. The average sowing quantity from the 5 experiments for each seed dispenser was calculated and considered as the sowing quantity for that seed dispenser. Utilizing Eq. (8), the sowing quantity was subjected to inter-row sowing quantity consistency variation analysis.

$$Y_2 = \frac{\sqrt{\frac{1}{n-1} \sum_{i=1}^n (m_{si} - m_s)^2}}{m_s} \cdot 100 \quad (8)$$

where:

m_s is average seed quality from six seed dispensers (g). m_{si} is seed quality from the i th dispenser (g). n is the number of dispensers, $n=6$. Y_2 is the coefficient of variation for consistency of seeding in rows (%).

RESULTS

Results of bench test

In order to clearly observe the changes in the absolute error, a curve depicting the changes in the absolute error was plotted, as shown in Fig. 12. The bench test experimental results are presented in Table 3.

Table 3

The bench test experimental results

| Number | Absolute error 1(g) | Absolute error 2(g) | Absolute error 3(g) | Mean absolute error (g) | Mean relative error (‰) |
|--------|---------------------|---------------------|---------------------|-------------------------|-------------------------|
| 1 | 0.129 | 0.211 | 0.196 | 0.179±0.044 | 6.08 |
| 2 | 0.216 | 0.133 | 0.114 | 0.154±0.054 | 2.67 |
| 3 | 0.322 | 0.137 | 0.037 | 0.165±0.145 | 1.85 |
| 4 | 0.305 | 0.087 | 0.291 | 0.228±0.122 | 1.97 |
| 5 | 0.195 | 0.141 | 0.109 | 0.148±0.043 | 1.02 |
| 6 | 0.300 | 0.244 | 0.242 | 0.262±0.033 | 1.48 |
| 7 | 0.194 | 0.136 | 0.261 | 0.197±0.063 | 0.97 |
| 8 | 0.103 | 0.300 | 0.192 | 0.198±0.099 | 0.86 |
| 9 | 0.075 | 0.038 | 0.315 | 0.143±0.150 | 0.54 |
| 10 | 0.147 | 0.205 | 0.121 | 0.158±0.043 | 0.49 |

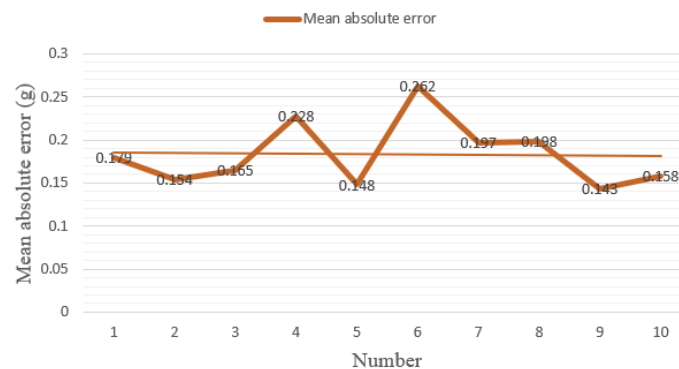


Fig. 12 - The curve of the changes in the absolute error

In the 10 sets of experimental data, the mean absolute error of the individual weighing units was randomly distributed between 0.143 g and 0.262 g, with a mean of 0.184 g. Two main factors contribute to this absolute error: the inherent error of the strain gauge pressure sensor and the impact component's force along the vertical direction during the seed's descent. The maximum and minimum mean relative errors of the weighing units are 6.08‰ and 5.4‰, respectively. As wheat seeds continue to be discharged, the mass of the wheat seeds increases, leading to a gradual reduction in the impact of absolute errors on the measurement results and an overall decreasing trend in relative errors.

Results of simulation

Analysis of collision data showed that the magnitude of the force generated in the negative Y-axis direction during collision was random, ranging from 1.508 N to 3.121 N, with a mean value of 2.220 N. The influence on the pressure sensor ranged from 0.110 g to 0.275 g, with a mean impact of 0.183 g.

The sampling frequency of the pressure sensor is 10 Hz, while the frequency at which Arduino reads sensor data is 2 Hz. When the moment of seed impact synchronizes with the data acquisition time of the pressure sensor, the impact force affects the real pressure data. As the seeds fell and accumulated, impact force simulation analyses were conducted with 500 and 1000 static seeds in the weighing cylinder, observing the changes in seed velocity to examine the process of impact force transmission, as shown in Fig. 13. In Fig. 13a, with no seed accumulation, the impact force acts directly on the bottom of the weighing cylinder. In Fig. 13b, with 500 seeds accumulated, the impact force is transmitted among the seeds, as indicated by the color of the arrows; when the impact force acts at the bottom of the cylinder, its magnitude decreases. In Fig. 13c, with 1000 seeds accumulated, the variation of impact force with time steps was observed. During the transmission of impact force, due to reasons such as inter-seed gaps and friction, the force cannot be transmitted to the bottom of the weighing cylinder.

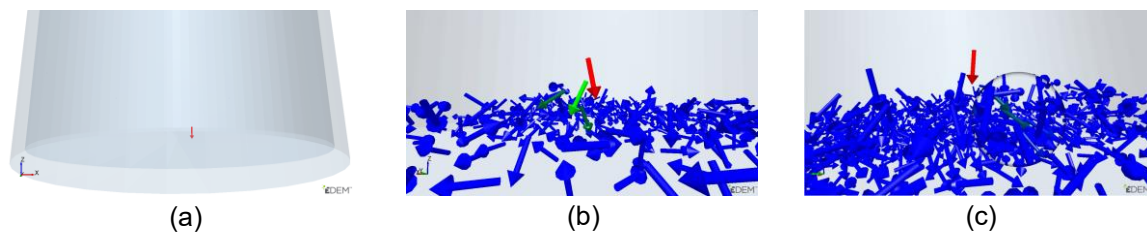


Fig. 13 – Process of impact force transmission

(a) With no seed accumulation; (b) With 500 seeds accumulated; (c) With 1000 seeds accumulated

Results of Indoor experiment

The experimental data results are shown in Table 4. The table includes the sowing quality data from 5 experiments for 6 seed dispensers, the calculated results of the coefficient of variation for seeding stability Y_1 , and the calculated results of the coefficient of variation for consistency of seeding in rows Y_2 . The calculation method for Y_1 involves taking the average of the five measurements of a single seed dispenser, computing the standard deviation of the sowing quantity for that seed dispenser, and then calculating the sowing quantity stability coefficient for the individual seed dispenser. Among the 6 seed dispensers, the maximum sowing quantity stability coefficient is 2.38%, the minimum is 0.83%, and the mean is 1.21%. The calculation method for Y_2 involves calculating the average sowing quantity from the 5 experiments for each seed dispenser, considering it as the sowing quantity for that seed dispenser, and then computing the standard deviation of the average sowing quantity for the 6 seed dispensers to determine the coefficient of variation for consistency of seeding in rows. The coefficient of variation for consistency of seeding in rows is 1.86%.

Table 4

The experimental data results

| Number | Seed dispenser 1 quality(g) | Seed dispenser 2 quality(g) | Seed dispenser 3 quality(g) | Seed dispenser 4 quality(g) | Seed dispenser 5 quality(g) | Seed dispenser 6 quality(g) | Y_2 (%) |
|------------------|-----------------------------|-----------------------------|-----------------------------|-----------------------------|-----------------------------|-----------------------------|-----------|
| 1 | 192.85 | 193.58 | 193.30 | 198.96 | 196.66 | 201.02 | - |
| 2 | 191.08 | 190.23 | 196.34 | 196.85 | 198.37 | 201.87 | - |
| 3 | 193.42 | 192.11 | 205.07 | 194.20 | 201.17 | 202.72 | - |
| 4 | 191.91 | 192.89 | 194.94 | 197.59 | 199.32 | 199.50 | - |
| 5 | 188.70 | 189.81 | 194.96 | 195.47 | 199.56 | 196.05 | - |
| mean quality (g) | 191.59 | 191.72 | 196.92 | 196.61 | 199.07 | 200.23 | 1.86 |
| Y_1 (%) | 0.96 | 0.86 | 2.38 | 0.94 | 0.83 | 1.31 | - |

As the transmission shaft of the seeder is driven by the stepper motor to rotate at a constant speed, there was no slippage of the ground wheels or shaking of the seeder. The seeders rotate synchronously at a constant speed, leading to a small value of the coefficient of variation for seeding stability. Additionally, due to the consistent groove wheel length of each seed dispenser and the uniform distribution of wheat seeds in the seed box, coupled with the small individual mass of wheat seeds, the calculation value of the coefficient of variation for consistency of seeding in rows was also relatively small.

CONCLUSIONS

(1) A multi-channel real-time weighing device has been designed that collects real-time data from various pressure sensors through Arduino controllers and displays and stores it in the LabVIEW upper computer. This device can be applied to monitor the operational quality of agricultural machinery such as row seeding, broadcast sowing, and irrigation equipment.

(2) By utilizing SPI communication, the data exchange between the master and slave Arduino boards has been achieved. In a one-master, one-slave configuration, it is possible to simultaneously collect data from 14 pressure sensors. Each slave device is an independent Arduino controller, enabling modularity that is beneficial for future expansion and improvement of functionalities. Based on the working principle of strain pressure sensors, the design of the weighing unit is reasonable, resulting in stable operation of the entire system with low production costs. This makes it easier to promote the device.

(3) The results of the bench test and indoor test demonstrate the reliability of the device, with the mean absolute error of the weighing unit ranging from 0.143 g to 0.262 g. According to simulation results, the impact of a single wheat seed on the weighing unit falls between 0.11 g and 0.275 g, with a mean impact value of 0.183 g. Under the preset test conditions, the coefficient of variation for seeding stability ranges from a maximum of 2.38% to a minimum of 0.83%, with a mean of 1.21%, while the coefficient of variation for consistency of seeding in rows was 1.86%.

ACKNOWLEDGEMENT

This research was supported by the National Natural Science Foundation of China (Grant No. 32101631 & No. 51805300), the Youth Innovation Team Project of Shandong Colleges and Universities, Science and Technology Program of Guizhou Province (QKHZDZX[2024]004) and China National Tobacco Corporation Guizhou Provincial Company Technology Project (2024520000240066).

REFERENCES

- [1] Drake, T.G. (1991) Granular flow: physical experiments and their implications for microstructural theories. *Journal of Fluid Mechanics*, Vol. 225, 121-152. <https://doi.org/10.1017/S0022112091001994>
- [2] Ding Youchun, Wang Kaiyang, Liu, Xiaodong. et al. (2021) Research progress of seeding detection technology for medium and small size seeds (中小粒径种子播种检测技术研究进展). *Transactions of the Chinese Society of Agricultural Engineering*, Vol.37:8, 30-41. <https://doi.org/10.11975/j.issn.1002-6819.2021.08.004>
- [3] Gong Yang, Zhang Pan. (2020) Multi-channel wireless A/D acquisition system based on NRF24L01 and LABVIEW. *MATEC Web of Conferences*. Vol. 309, 01001. <http://doi.org/10.1051/mateconf/202030901001>
- [4] Ghanbari M., Rezazadeh G. (2022) Investigating Static and Dynamic Behavior of the Strain Gauge Type Pressure Sensor in Exposure to Thermal Stresses. *Arabian Journal for Science and Engineering*, Vol.47, 8931-8944. <http://doi.org/10.1007/S13369-021-06443-4>
- [5] Gu Tingwei, Yuan Shengjun, Gu Lin. et al. (2024) Research on dynamic calibration and compensation method of strain-gauge type force sensor. *Sensor Review*, Vol.44, No.1, 68-80. <http://doi.org/10.1108/sr-08-2023-0330>
- [6] He Xiantao, Zhang Dongxing, Yang Li. et al. (2021) Design and experiment of a GPS-based turn compensation system for improving the seeding uniformity of maize planter. *Computers and Electronics in Agriculture*, Vol.187, p.106250. <https://doi.org/10.1016/j.compag.2021.106250>
- [7] Karimi Hadi, Navid Hosseni, Besharati Bahram. et al. (2017) A practical approach to comparative design of non-contact sensing techniques for seed flow rate detection. *Computers and Electronics in Agriculture*. Vol.142, 164-172. <https://doi.org/10.1016/j.compag.2017.08.027>
- [8] Li Daoliang, Yang Hao. (2018) State-of-the-art Review for Internet of Things in Agriculture (农业物联网技术研究进展与发展趋势分析). *Transactions of the Chinese Society for Agricultural Machinery*, Vol.49, 1-20. <https://doi.org/10.6041/j.issn.1000-1298.2018.01.001>
- [9] Li Runtao, Wang Xianliang, Yao Yanchun. et al. (2022) Research on intelligent detection technology of seed planter (播种机智能检测技术研究). *Journal of Chinese Agricultural Mechanization*, Vol.43, 93-101. <https://doi.org/10.13733/j.jcam.issn.2095-5553.2022.05.014>
- [10] Navid H., Ebrahimian S., Gassezadeh H. R. et al. (2011) Laboratory evaluation of seed metering device using image processing method. *Australian Journal of Agricultural Engineering*, Vol.2, 1-4. <https://api.semanticscholar.org/CorpusID:61725810>
- [11] Ramasamy, S. (2021) Sustainable Development in Agriculture Through Information and Communication Technology (ICT) for Smarter India. *International Journal of Social Ecology and Sustainable Development*, Vol.12:3, ISSN:1947-8402. <https://doi.org/10.4018/IJSESD.2021070106>
- [12] Rossi Sebastián, Scola Ignacio Rubio, Bourges Gastón et al. (2023) Improving the seed detection accuracy of piezoelectric impact sensors for precision seeders. Part I: A comparative study of signal processing algorithms. *Computers and Electronics in Agriculture*, Vol.215, p.104449. <https://doi.org/10.1016/j.compag.2023.108449>
- [13] Taghinezhad J., Alimardani R., Jafari A. (2013) Design a capacitive sensor for rapid monitoring of seed rate of sugarcane planter. *Agricultural Engineering International: The CIGR e-journal*, Vol.15, 23-29. <https://cigrjournal.org/index.php/Ejournal/article/view/2576/1791>

- [14] Wu Mingliang, Yang Yang, Guan Chunyun. et al. (2014) Design and test of a control system for rapeseed metering device based on pressure sensor for seed quantity control (基于压力传感器的油菜排种量控制系统的设计与试验). *Journal of Hunan Agricultural University (Natural Sciences)*, Vol.40:5, 536-540. <https://doi.org/10.13331/j.cnki.jhau.2014.05.015>
- [15] Wang Tongzhao, Quan Qiquan, Tang Dewei. et al. (2021) Effect of hyperthermal cryogenic environments on the performance of piezoelectric transducer. *Applied Thermal Engineering*, Vol.193, p.116725. <https://doi.org/10.1016/j.applthermaleng.2021.116725>
- [16] Wang Weiwei, Song Lanzhou, Shi Wenbing. et al. (2024) Design and Experiment of Air-suction Double-row Staggered Precision Seed Metering Device for Maize Dense Planting (气吸双行错置式玉米密植精量排种器设计与试验). *Transactions of the Chinese Society for Agricultural Machinery*, Vol.55:3, 53-63. <https://doi.org/10.6041/j.issn.1000-1298.2024.03.005>
- [17] Yang, B., Ding, X. W. (2012) Design of SPI bus communication in the multi-channel data acquisition systems. *Advanced Materials Research*, Vol.532, 187-191. <http://doi.org/10.4028/www.scientific.net/AMR.532-533.187>
- [18] Yu Jiayang, Lu Caiyun, Wei Ruxue. et al. (2018) Simulation test on the performance of wheat precision seed discharger based on discrete element method (基于离散元法的小麦精量排种器性能模拟试验). *Jiangsu Agricultural Sciences*, Vol.46:8, 225-228. <http://doi.org/10.15889/j.issn.1002-1302.2018.08.057>
- [19] Yu Qingxu, Liu Yan, Chen Xiaobing. et al. (2020) Calibration and Experiment of Simulation Parameters for Panax notoginseng Seeds Based on DEM (基于离散元的三七种子仿真参数标定与试验). *Transactions of the Chinese Society for Agricultural Machinery*, Vol.51:2, 123-132. <http://doi.org/10.6041/j.issn.1000-1298.2020.02.014>
- [20] Zagainov Nikolay, Kostyuchenkov Nikolay, Huang Yu Xiang. et al. (2023) Line laser based sensor for real-time seed counting and seed miss detection for precision planter. *Optics and Laser Technology*, Vol.167, p.109742. <http://dx.doi.org/10.1016/J.OPTLASTEC.2023.109742>
- [21] Zhao Baitong, Zhang Xiaohui, Kong Qingyong. et al. (2003) Current status and development trend of monitoring systems for precision seeders at home and abroad (). *Shandong Agricultural Machinery*, Vol.12, 14-16.
- [22] Zhang Jicheng, Chen Haitao, Ouyang Binlin. et al. (2013) Monitoring system for precision seeders based on a photosensitive sensor (基于光敏传感器的精密播种机监测装置). *Journal of Tsinghua University (Science and Technology)*, Vol.53:2, 265-268. <https://doi.org/10.16511/j.cnki.qhdxxb.2013.02.018>
- [23] Zhang Yang, Zhu Bin, Xie Bo. et al. (2013) Visual image and radio signal fusion identification based on convolutional neural networks. *Journal of Optics*, Vol.50, 237-244. <http://dx.doi.org/10.1007/s12596-020-00672-w>
- [24] Zhang Xiwen, Hou Zhanfeng, Xuan Chuangzhong. (2022) Design and experiment of recognition system for coated red clover seeds based on machine vision (基于机器视觉的包衣红三叶种子识别系统的设计与试验). *INMATEH Agricultural Engineering*, Vol.66, no.1, 62-72. <https://doi.org/10.35633/inmateh-66-06>
- [25] Zhou L.M., Niu K., Chen K.K. et al. (2022) Design and test of real-time monitoring system for non-contact fertilization flow (非接触施肥流量实时监测系统的设计与试验). *INMATEH Agricultural Engineering*, Vol.66, no.1, 351-360. <https://doi.org/10.35633/inmateh-66-35>

DESIGN AND TESTING OF A SOWING DRONE BASED ON RICE PRECISION STRIP SEEDING

水稻精量化条直播播种无人机的设计与试验

Liangchen HOU¹⁾, Xin HAN^{*1)}, Yubin LAN^{*1)}, Jingbo BAI²⁾, Zhikang DING¹⁾,
Xuejian ZHANG³⁾, Maochang SONG¹⁾, Kailu WANG¹⁾

¹⁾School of Agricultural and Food Science, Shandong University of Technology, Zibo (255000), China;

²⁾Shandong Siyuan Agricultural development Co., LTD, Zibo (25000), China;

³⁾Institute of Agricultural Economics and Information Technology, Ningxia Academy of Agricultural and Forestry Sciences, Ningxia (750002), China

Tel: +86-15953359191; +86-13922707507; E-mail: hanxin_1979@163.com ylan@sdut.edu.cn

DOI: <https://doi.org/10.35633/inmateh-73-29>

Keywords: UAV, direct sowing in strips, external grooved wheel seeder, simulation analysis, control system

ABSTRACT

In order to solve the problem that the wind field disturbs the trajectory of falling seeds and causes the seeds to be unable to be arranged in equidistant rows when the UAV is spreading rice, a shot seeding device that can sow five rows of pelleted rice seeds at the same time was designed. The unit is centered on an external grooved wheel seed metering device and a seed acceleration unit for row seeding and hole sowing. The airflow simulation of the rotor wind field of the UAV was carried out by simulation software to explore the changes in the wind field of the UAV during operation. The position where the wind field disturbance is minimized is chosen for the seed guide tube arrangement. The position with the least wind field disturbance is chosen to arrange the seed guide tube and combine it with a seed acceleration device to reduce the influence of the UAV wind field airflow on the direction of seed movement. The operational effectiveness of the seeding device with and without wind was verified by an indoor test and an outdoor flight seeding test, respectively. Simulation results show that: when the mouth of the seed guide pipe is 0.9 m away from the paddle, the wind field has the smallest influence on the sowing results. The results of the bench test show that: when the rotational speed is 30-45 r/min, the coefficient of variation of the discharge rate of each row (CVR) and total seed discharge rate stability (CVT) are less than 1.98% and 0.84%, and the seed breakage rate is less than 0.95%, which all conform to the UAV fly sowing industry standards. The outdoor mud box test shows that: when the baffle angle changes by 26%, 58%, and 71%, each slot wheel hole can store 5-10, 3-5 and 1-3 seeds respectively, and the UAV operates at a speed of 2 m/s-3 m/s, the pass rate of hybrid rice is greater than 86%, which meets the agronomic requirements of rice sowing operation.

摘要

为解决无人机在水稻撒播时, 普遍存在风场扰动种子下落的轨迹和种子无法成穴排布的问题, 设计了一种可同时播种六行颗粒状水稻种子的射种装置。该装置由一个外槽轮式排种装置和种子加速装置为核心, 实现了精准行播和穴播的功能。通过仿真软件对无人机进行了旋翼风场的气流仿真模拟, 探究风场的变化特性。确定风场扰动最小的位置去布置导种管。加速装置和无人机的气流分析都是为了减少无人机风力对种子运动方向的影响。在室内试验和室外飞行播种试验中, 分别验证在无风场和有风场下播种装置的作业效果。仿真结果表明: 导种管道口距离桨叶为 0.9m 时, 风场对播种结果影响最小; 台架试验结果表明: 转速处于 30-45r/min 时, 每行排种率的变异系数小于 1.98%、总排量稳定性的变异系数小于 0.84%、种子破损率小于 0.95%等都符合无人机飞播行业标准; 室外泥盒试验表明: 挡板角度变化 26%、58%、71%时, 每个槽轮孔可以分别储存 5-10 粒、3-5 粒、1-3 粒种子, 且无人机以 2m/s-3m/s 速度下作业, 杂交稻合格率均大于 86%, 满足水稻直播作业的农艺要求。

INTRODUCTION

As one of the three major food crops in the world, rice is closely related to people's lives. Ensuring rice yield is of great significance to meet the food demand of China and the world. Rice mechanized planting operation is the most critical and weakest link in the three major production processes of rice cultivation, planting, and harvesting. Moreover, rice planting is the most important factor hindering the production of mechanized rice at present. Therefore, it is very necessary to improve the efficiency of rice mechanized planting and the level of automatic operation (Luo et al., 2019).

In recent years, agricultural aviation technology has been developing rapidly at home and abroad because of its advantages of not being restricted by the operating environment, higher operating efficiency, less impact on crop growth, and low operating costs at the same time. Agricultural aviation assumes an important role in the development of modern precision aerial agriculture. In this study, the autonomous design of UAV can achieve route planning, land-like flight, autonomous obstacle circling, automatic return, flexible take-off, and landing through the data fusion of multiple sensors. It also proves that the efficiency, cost, and stability of land-based equipment are not as good as UAVs. Super-hybrid rice is a type of hybrid rice with greater tillering capacity and higher yields. When sowing by direct seeding technology, only 1~3 grains/hole are generally needed, of which 2 grains/hole are preferred, with a plant spacing of about 10 cm and a row spacing of about 30 cm. but often land equipment operates at a slower speed. Therefore, there is an urgent need to study the precision sowing technology of hybrid rice using drones as a carrier (Zhou *et al.*, 2014). In this paper, hybrid rice is taken as the research object, and the research and design are carried out for precise and quantitative row sowing and hole sowing (Luo *et al.*, 2019).

At present, drone seeding is categorized as row seeding and spread seeding, but regular distribution of cavities cannot be achieved. The field of seeding using drones has developed rapidly in recent years. In response, the land-based equipment has the disadvantages of easily getting stuck in the soil and low operating efficiency. Seeding by drones has become a new type of rice cultivation (Wan *et al.*, 2021). Among them, Gao Xuemei *et al.* developed a rice and fertilizer spreading device. The device mainly used centrifugal force to spill rice seeds along the outlet of the spreading device. However, the influence of the wind field of the UAV and the parameter matching problem of the spreading disc resulted in poor spreading uniformity (Gao *et al.*, 2022).

Huang Xiaomao *et al.* designed a row sowing device for both rice and oilseed rape. The device adopted a split seed dispenser and folded seed guide tube program, which could reduce the wind field impact and achieved the position of the falling seeds arranged in strips. However, the speed of rice seed drop plus was limited, resulting in the seeds not being able to penetrate 1-2 cm below the soil, making it difficult to meet agronomic requirements. Rice seeds floated on the soil surface and were easily eaten by birds and rats. The seeds also floated away due to the external wind (Huang *et al.*, 2020; Huang *et al.*, 2022); Li Wencheng *et al.* designed an oilseed rape drone fly sowing device, which could realize oilseed rape in rows and rows. However, the seed guide tube he designed was too long, which was a big hidden danger to the safety of the flight (Li *et al.*, 2020; Zhang *et al.*, 2020); Song Cancan *et al.* designed a method to achieve spreading through high-speed airflow, which in turn achieved uniform fertilizer spreading. However, the uniformity of that program was general (Song *et al.*, 2018; Song *et al.*, 2020).

He Weizhuo *et al.* designed a seed acceleration device with friction wheel force, which accelerated the rice seed significantly and did not hurt the seed. This solution could achieve row sowing but not hole sowing, improve the uniformity of the position of seed fall and reduce the effect of airflow from the drone on the trajectory of the seed. In this study, the seed sowing method was improved by increasing friction based on others (He *et al.*, 2022). At the same time, an external grooved wheel seed metering device was designed to achieve an equalized distance between two adjacent seed-filled holes. The wind field airflow was simulated under the UAV by simulation software to simulate the change of wind field under the rotor surface, so that the optimal location of the seed discharge point could be determined and the effect of UAV wind on the seed trajectory could be reduced (Shen *et al.*, 2018; Zhang *et al.*, 2019).

In this paper, an external grooved wheel seed metering device is designed, where the volume of the grooves and the rotational speed of the grooved wheel can be precisely controlled and adjusted to accurately group the seeds and adjust the seed flow rate and the falling frequency (Zeng *et al.*, 2021). The acceleration of the seed by the friction wheel reduces the effect of the wind field on the seed trajectory and allows the seed to penetrate deeper into the soil. Compared with other drone seeding methods, this solution can make the seed drop location evenly distributed and reduce the impact of the wind field on the seed trajectory. It provides a reference for the subsequent UAV rice direct seeding technology.

MATERIALS AND METHODS

Flying seeding drone machine structure and principle

The whole machine is divided into three main parts: drone platform, seed discharge device, and seeding device, as shown in Fig. (1). Among them, the grooved wheel seed discharger and seed acceleration device are fixedly connected to the frame of the UAV through fixing parts.



Fig. 1 - Three-dimensional roadmap



Fig. 2 - Physical drawing of rice flying seeding drone

This experiment uses an independently designed X8 co-axial counter-propeller UAV as a power platform to ensure hovering and flight attitude during operation. The seeding device is divided into three processes: seed filling, seed carrying, and seed shooting. The seed-filling process is the free fall of rice seeds from the seed box to the inlet of the grooved wheel under the effect of gravity. The seed is transported to the accelerating device during the rotation of the grooved wheel. The trough wheel is rotated by a 42-step motor, and the rotational speed is controlled by a handheld remote control that establishes communication with the motor drive module and the signal transmitter. Different rotational speeds control the flow of seed output from the trough wheel per unit of time. The chute wheels uniformly control the seed drop, and then the seed dispenser carries the seed from each chute wheel opening to the acceleration device. The acceleration device consists of two motors that control the opposite rotation of two friction wheels. The acceleration unit consists of two motors that control the opposite rotation of two friction wheels. The friction wheels provide the seeds with a friction force, and then the seeds enter the acceleration device and are instantly squeezed by the two friction wheels to use the friction force to accelerate them, and then after passing through the pipeline, they pass through the wind field under the rotor blades of the UAV and are shot into the soil at a distance of 1-2 cm, to complete the fly sowing operation.

Table 1

| Rice seeding drone-specific parameters | |
|---|---|
| Parametric | Numerical value |
| Overall dimensions (LxWxH)/(mm) | 1100 × 1100 × 950 (Arm deployment) 600 × 600 × 950 (Arm Removal) |
| Seeding method | Strip sowing, hole sowing |
| Number of lines of work | 6 |
| Sowing rate (dry weight of rice seed)/ (kg/min) | 1-3 |
| The rotational speed of groove wheel / (r/min) | 30-45 |
| Working width / (m) | 1-2.1 |
| Operating altitude / (m) | 1-2 |
| Operational flight speed / (m/s) | 1.5-2.5 |
| Seedbox capacity / (kg) | 18 |
| Maximum Endurance / (min) | 16 |
| Overall quality / (kg) | 35.06 |

Sowing device layout

Rice UAV flying and seeding control system

The whole control system is divided into the UAV flight control system, sowing control system, and monitoring system, as shown in Figure 3 below. The mission platform consists of two parts: the trough wheel and the acceleration device. The trough wheel is printed by a 3D printer using PLA material to print out the mold and installed for use. The grooved wheel controls the rotational speed and thus the flow of rice seeds through a type 42 stepper motor and a motor driver. The groove baffle of the groove wheel can be rotated along the axis at an appropriate angle to effectively control the size of the groove hole and the quantity of rice seeds.

The acceleration device uses a friction wheel driven by a motor to accelerate the rice seed and then complete the sowing operation. The friction wheel is made of rubber, which is elastic and does not harm the rice seeds. The maximum speed of the motor is up to 9000 r/min, which ensures a high seed ejection speed. The motor is controlled by an electronic speed controller (ESC). External stm32f1 microcontroller controls ESC and thus controls the friction wheel speed and stepping motor speed. One of the monitoring systems, consisting of a piezoresistive weight sensor. Sensor set two order alarm prompts, in the seed box balance of 5 kg and 2 kg when the remote control alarm occurs. The motors are set up to monitor the identification and alarm when one of the accelerators jams. In which the whole flight control system is linked to the seeding main controller for signal interaction and information transfer.

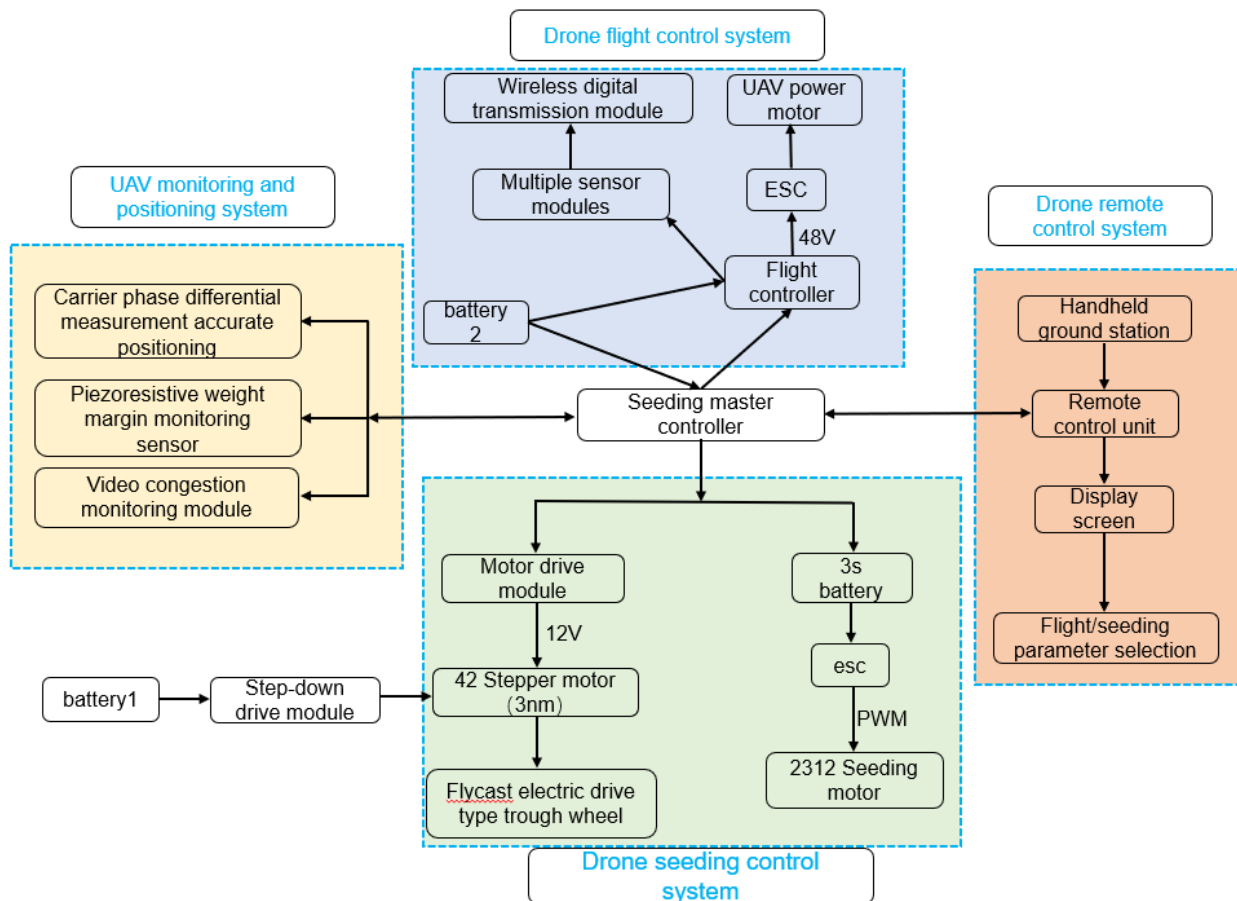


Fig. 3 - Block diagram of UAV rice seeding control system structure

The rice seeding UAV consists of the flight control system, ground control system, propulsion system, power system, and seeding control system as follows (4). The fuselage is made of carbon-brazed dimensional material, and the flight-sowing UAV control system adopts DJI-A3, including a control master module, power module, GPS module, LED module, Lightbridge2, and image transmission module (Bian et al., 2024). The motors are DJI E5000 series, with a pull force of 7kg. Since the single-axis dual propellers have a 10%-30% power loss, the minimum single-axis pull force is 9.8kg. The arm carries sockets, which can be plugged and unplugged to reduce the storage volume. The flight control system is the brain of the UAV, mainly responsible for the autonomous flight of the UAV. The ground control system works in conjunction with the flight control system to control the flight of the UAV, and you can choose automatic flight settings or manual operation. The propulsion system is responsible for powering the UAV to climb, hover, fly, and land. The power system consists of a battery and a power distribution unit (PDU), which powers the propulsion system, the rice seeding system, and the flight control system. The rice seeding system consists of a seed supply system and a seed discharge system. The grooved wheel can precisely control the flow and frequency of the falling rice seeds, and the friction wheel is responsible for shooting the seeds under the soil in batches at intervals to achieve hole sowing.

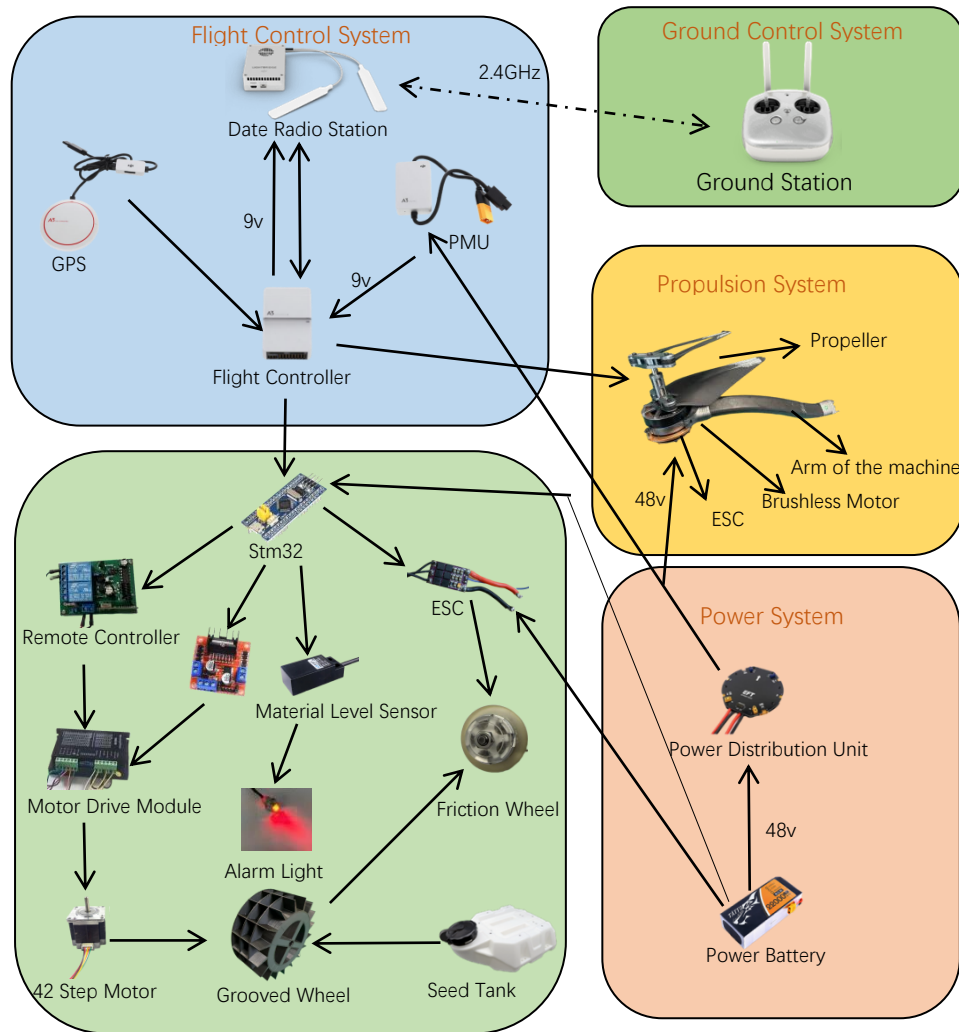


Fig. 4 - Components of the UAV and the workflow of each system

Design and parameterization of key seeding devices for rice drones **Seeder design**

Rice seeds need to be treated before sowing. Firstly, the outer layer of the rice seed is wrapped with a layer of hard powder, which is rich in fertilizers and nutrients that promote the growth and development of the rice seed. The seeds are then hardened and treated to approximate the shape of a sphere. The hardness and volume can be customized in the device. This technique is called 'seed dressing'. In this paper, the rice seed is set as a sphere with a diameter of 5 mm.

The design of the friction wheel extrusion direct injection device is shown in Figure (5) below: the frequency of rice seed drop controlled by the grooved wheel of the previous link is 2 or 4 seeds in a group. The falling seeds then pass through the seed distributor into the gap between the two friction wheels. When the seed passes through the friction wheel A and friction wheel B, the two friction wheels rotate at a high speed in the opposite direction, giving the seed two friction forces in the same direction respectively, and quickly shoot the rice seed into the soil, the rice seed will have a short residence time in the guide and during the drop. In this paper, the motor is fixed inside the friction wheel, and the friction wheel is rotated by the motor. The accelerating motor is an external rotor brushless motor, and the model of the motor is DJI-2312A. In order to ensure that the seeds are in full contact with the friction wheels, the gap between the two friction wheels is set to 3.5 mm. The catheter is mounted at the bottom of the guide rail. Due to the error in the production process of the coated seeds, the diameters are slightly different. Setting a tension spring underneath the two motor holders allows the friction wheels to adapt to seeds of different diameters and reduces the seed breakage rate.

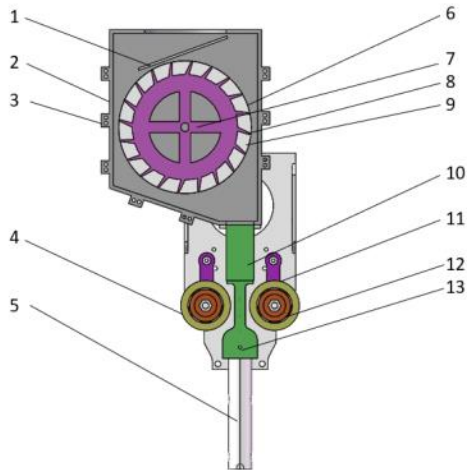


Fig. 5 - Overall structure of the sowing device

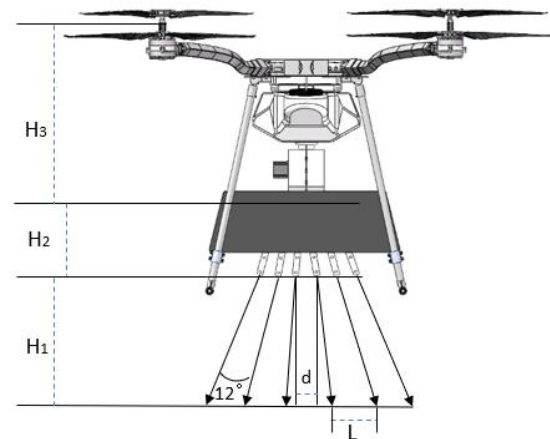


Fig. 6 - Key Component Arrangement

1. Seed stopper; 2. Grooved wheel housing; 3. Screw fixing parts; 4. Rubber wheel; 5. Seed guide tube; 6. Adjusting stopper; 7. Rotating shaft; 8. Grooved wheel hole; 9. Grooved wheel; 10. Seed tube; 11. Flexible motor holder; 12. Brushless motor; 13. Guide rail
 H_1 refers to the direct distance between the pipe and the ground; H_2 refers to the distance for seed acceleration; H_3 is the distance between the rotor surface and the seed inlet, d refers to the distance between two neighboring pipes, and L refers to the row spacing

In this paper, coated rice seeds were used as the research object for sowing. Before the experiment, special equipment was used to wrap a layer of powder and solution containing nutrients such as fertilizer on the outer layer of the seeds. When the seeds were dried the outer layer of material hardened and the shape of the seeds was made into a ball shape. Compared to other drone seeding, such as centrifugal spreading (Gao *et al.*, 2022) and seeding by gravity (Huang *et al.*, 2020), it is not possible to give the seeds increased acceleration. In this paper, the device applies a strong friction force to the seed so that the seed has the initial speed to better cross the wind field and enter the soil. This can effectively realize the orderly arrangement of seeds on the ground and improve the uniformity of sowing. At the same time, the control to adjust the opening and closing angle between two neighboring seed dispensers can control the size of the row spacing, and the layout of the conduit and acceleration device is shown in Fig. 6.

At the same time, the hard texture of the coated seeds, rich in fertilizer and other nutrients will slowly dissolve in the water to promote seed germination, so that the layout reduces the risk of rice seeds floating on the surface of the soil being eaten by birds, rats, or even washed away by the rain, resulting in a lack of seedlings. At the same time, it also enables the seeds to be not affected by the ambient wind or the rotor winds of the drone resulting in an uneven density of the landing site, thus causing poor permeability in the later stages and thus triggering the risk of diseases and insect pests.

Grooved wheel design

In this paper, an external grooved wheel seed metering device is designed as shown in Fig. 7, where the number of seeds inside the groove is controlled by controlling the angle of baffle. Where the power of the groove wheel is provided by a stepper motor (3 Nm 42 stepper motor). The power is provided by the UAV battery (model 22000aAh, 6s, 25.2v). The power supply is connected to the buck module and a remote control system is established with the motor driver, signal receiver, and remote control. The remote control system of the grooved wheel is shown in Fig. 8 below, and the grooved wheel is equipped with six circles of grooved holes on the outside, with 20 grooved holes in each circle. The baffle plate is used to regulate the volume of the holes, the larger the opening of the baffle plate, the smaller the volume of the holes in the wheel and the smaller the inflow of rice seed. The groove wheel uses a 2.4 GHz remote control (AT9S PRO) with 12 buttons to control the start, stop and speed of the groove wheel. The microcontroller controls the speed of the seed metering motor, and its signal transmission is based on the 1, 2, 8, 9, and 10 buttons, so that the number of rice seeds falling into each groove is basically the same, reducing the missed seeding rate and repetition rate.

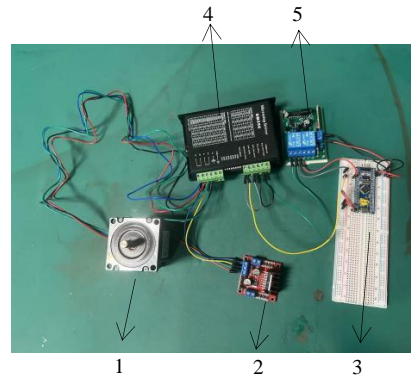
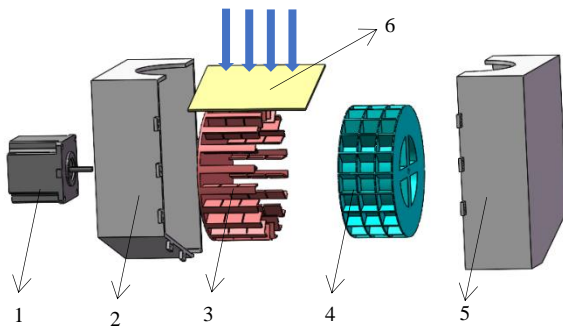


Fig. 7 - Seed Discharger Structure Diagram **Fig. 8 - Motor control system wiring diagram**
 1 - 42 Stepping motor; 2 - Left grooved wheel housing; 3 - Seed stopper angle opening and closing plate; 4 - Grooved wheel;
 5 - Right grooved wheel housing; 6 - Seed stopper; 1 - 42 Stepper motor; 2 - L298 motor drive module;
 3 - Stm32 microcontroller; 4 - Motor driver; 5 - Receiver

The diameter of the grooved wheel, the structure and the number of holes have a greater impact on the performance of fly-sowing operations. When the sowing volume and operating speed are certain, the number of grooved wheel holes is inversely proportional to the rotational speed of the grooved wheel. If the diameter of the grooved wheel is too small, the grooved wheel rotational speed is high, which will lead to an increase in the rate of seed breakage; if the diameter of the grooved wheel is too large, the volume of the seed discharge device is large, which is not suitable for unmanned aerial sowing operations. Comprehensive consideration, the external dimensions of the grooved wheel are designed to be 95 mm in diameter and 101 mm in length. The grooved wheel has a number of slotted wheel holes on the outside to group the seeds.

In order to facilitate the smooth discharge of seeds from the groove, the wall of the groove side is designed to be an inclined quadrilateral with an inclination angle of 40° . Compared with a square, this structure not only makes it easier for seeds to escape from the groove, but also reduces the risk of the groove wheel getting stuck. The inclination of the groove wall is conducive to rapid seed filling and seeding. During operation, in order to ensure the seeding volume during fast flight operation, each groove is designed to be filled with 1-10 seeds, and the number of seeds can be freely adjusted.

The adjustment process is as follows: (1) baffle opening 0%, slot wheel hole in the maximum capacity of rice seed volume state, a single hole of about 10-15 grains, at this time the speed is higher, the seeding volume is larger, the flight speed is relatively fast suitable for strip seeding; (2) baffle opening 26%, slotted wheel hole can hold 5-10 rice seeds; (3) baffle opening 58%, slotted wheel hole can hold 3-5 rice seeds; (4) baffle opening 71%, and slotted wheel hole can hold 1-3 rice seeds.

Simulation environment construction

The airflow disturbance in the wind field of motion under the rotor of the UAV is large and has an effect on the trajectory of the falling seeds. There may also be a region with less airflow disturbance under the rotor. In this paper, the wind field is simulated to find the location of the optimal seed guide. This is done to reduce the airflow disturbance on the seed trajectory. The environment for the simulation is built and the simplified model for the flow field calculation is shown in Fig. 9.

The flow field computational domain is modelled as a cuboid, which represents the operational environment in which the UAV is located. The rotating region where the propeller is located represents the dynamic domain grid. The face ABCD of the rectangular body is set as the velocity inlet, the face EFGH is the pressure outlet, and the other faces are set as walls. The position of the airframe is 2.5 m from the bottom of the rectangular body and 1.0 m from the top, and the rotational speed of the propeller is set to 2000 r/min in the dynamic domain to simulate the three-dimensional CFD (Computational fluid dynamic) model of the downwash airflow of the UAV at the flight speeds of 1.9 m/s, 2.2 m/s, and 2.85 m/s, and the hovering state, respectively. The velocity maps of different planning surfaces are also analyzed to explore the distribution law of the airflow.

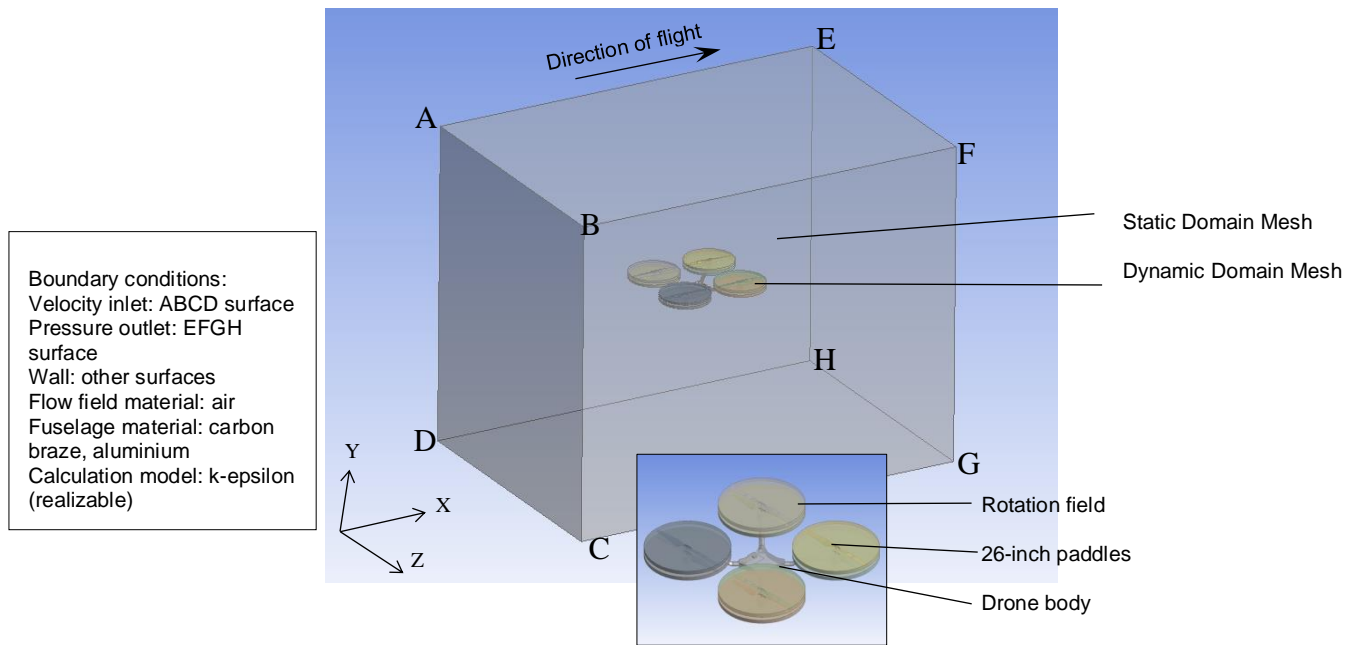


Fig. 9 - Simulation environment construction

Method

Field seeding effect test

1. Seeding system bench test

Through the bench test, verify whether the various row seeding performance of the system meets the agronomic requirements of rice sowing.

1.1 Determination of test indexes

Referring to the test method stipulated in "NY/T3881-2021 Technical Specification for Quality Evaluation of Remote-Controlled Flying Seeder", the test indicators are the coefficient of variation of the discharge rate of each row (CVR) and total seed discharge rate stability (CVT) and breakage rate *P*, and the calculation formulas are as follows, respectively:

$$C_{vT} = \frac{\sqrt{\frac{1}{i-1} \sum (x_i - \bar{x})^2}}{\bar{x}} \times 100\% \tag{1}$$

$$C_{vR} = \frac{\sqrt{\frac{1}{j-1} \sum (y_j - \bar{y})^2}}{\bar{y}} \times 100\% \tag{2}$$

$$P = \frac{m_i}{m_1} \tag{3}$$

x is the mean total discharge per unit of time, g/min; *x_i* is the total discharge per unit of time for the *i*-trial, g/min; *y* is the mean row discharge, g/min; *y_j* is the discharge for the *j*th row, g/min; CVR is the coefficient of variation of the discharge rate for each row, and CVT is the coefficient of variation of total seed discharge rate stability.

1.2 Test program and materials

The test scheme was to fix the UAV and the row seeding operation task platform on a 150mmx80mmx9mm table made of aluminum profiles as shown in Figure 10. In this paper, the pill box was used instead of the seed box to complete the test subsequent customized large-scale specifically for this shape of rice seed box. In this paper, the pill granulation of rice seeds was considered as a test object, and the sample bags were fixed at the mouth of the seed guide tube, to receive the rows in the amount of seed discharged per unit of time. Setting the groove wheel speed at 45 r/min (using the seventh channel of the remote control) corresponded to the degree of openness of 0%, 26%; setting the groove wheel speed at 30 r/min corresponded to a degree of openness of 58%, 71%. The weight of seeds discharged from each row was collected and recorded within 1 minute using a counting bag, from which the quality of broken seeds was screened to calculate the breakage rate. In the experiment, to facilitate the calculation of seed weight, the mass of the seed-coated fertilizer was not removed and the coated seeds were weighed directly.

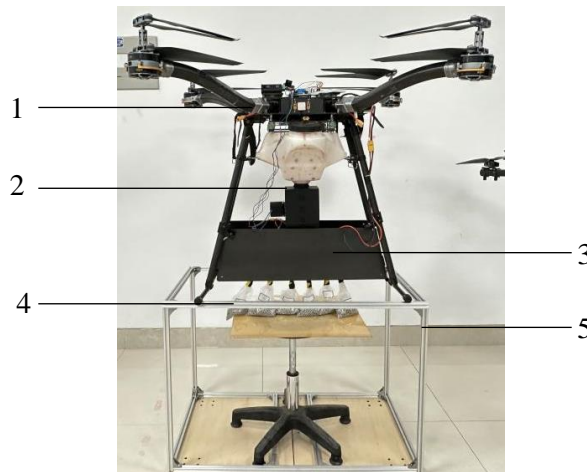


Fig. 10 - Bench test of seed discharge performance
 1 - drone flying platform; 2 - grooved wheels; 3 - seeding device; 4 - counting bag; 5 - table stand

2. Sample machine field test trials

2.1 Test program and materials

The prescribed UAV flight height setting was based on the pre-simulation results derived from the seed guide tube mouth at a distance of 0.9 m from the rotor surface for the test; the flight altitude was set at 1.2 m, the flight speed at 1.5-2.5 m/s. The test site was in the Shandong University of Science and Technology, on the lawn behind the library, this place is wide open and unobstructed. On the day of the test the environmental winds were south-easterly winds, 1-3.5 m/s, the air humidity was 25%. Six rows of mud boxes (containing water, simulating a rice field) were arranged as shown in Figure 11, with a width of about 2.3 m, and the target sowing effect was 1.8 m, covering the maximum sowing width. The UAV flew over the mud box several times and recorded the probability of the number of seeds and the corresponding number of seeds at 250 positions continuously according to the national rice sowing enforcement standards. The pass rate, miss seeding rate and re-seeding rate were tested at different angles of the baffle. Records were repeated three times and averaged.

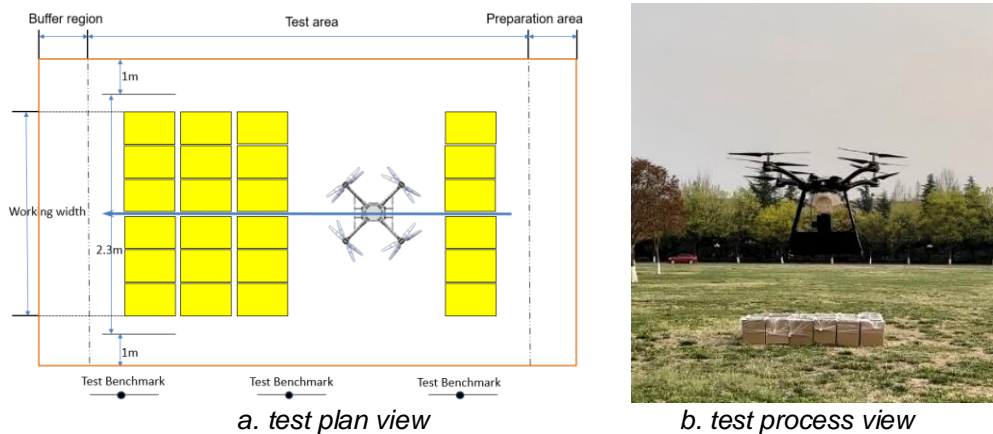


Fig. 11 - UAV seeding performance test

2.2 Test indicators

There were four indicators of the test: pass rate, reseedling rate, leakage rate, breakage rate.

$$M_j = \frac{n_{mj}}{N} \times 100\% \tag{4}$$

$$Q_j = \frac{n_{Qj}}{N} \times 100\% \tag{5}$$

$$R_j = \frac{n_{Rj}}{N} \times 100\% \tag{6}$$

$$p = \frac{m}{M_n} \times 100\% \tag{7}$$

RESULTS

Determination of seed guide port position parameters

After several simulations, the velocity clouds of the UAV wind field at different speeds at different angles were derived as follows in Figure 12.

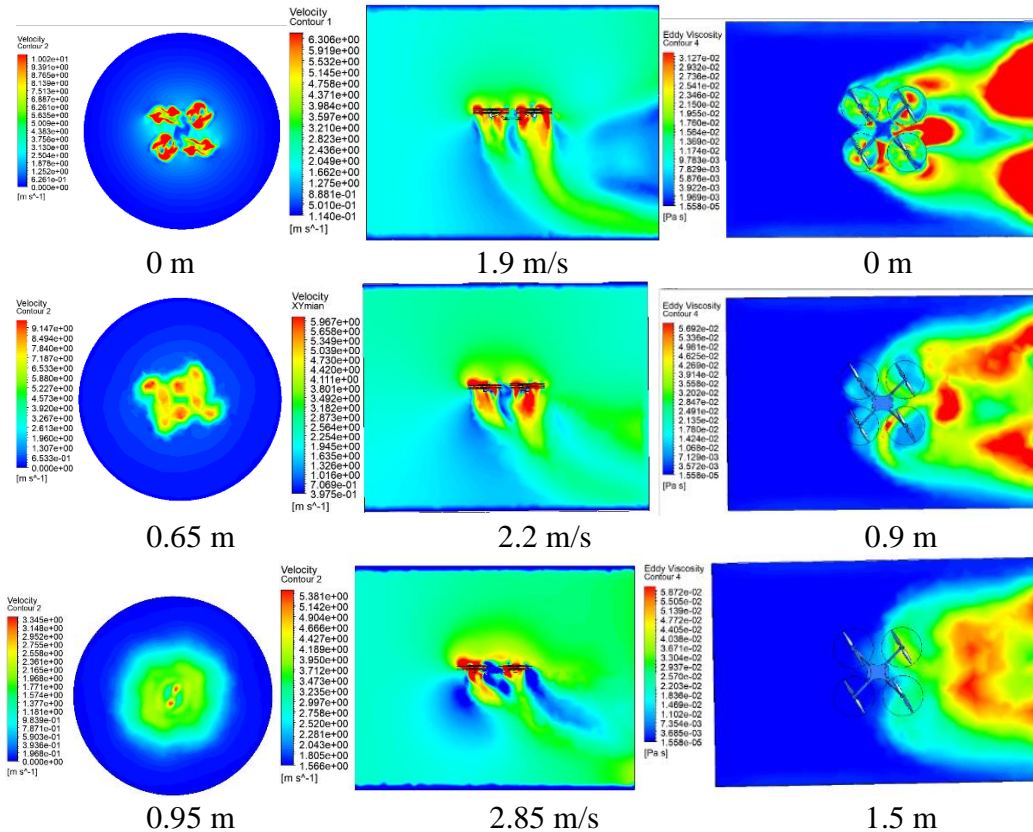


Fig. 12 - Velocity clouds at different angles of the flow field in which the UAV was located

The surface where the paddle was located was set as the horizontal plane. The velocity cloud of the XZ surface was observed at 0 m, -0.65 m, and -0.95 m from the horizontal plane respectively through the simulation post-processing software CFD-Post. From the first column of the three graphs in Fig. 12, it can be seen that the airflow was relatively concentrated at 0 m, and the airflow velocity was relatively high, and the airflow was distributed in four regions; at -0.65 m, the airflow in the corresponding regions of the four rotors gradually started to contract in one region but did not form a region completely, and its airflow velocity started to decrease; at -0.95 m, the airflow basically formed a region, and the airflow velocity was obviously reduced. At -0.95 m, the airflow basically formed a region, and its airflow speed decreased significantly.

From the second column of graphs, it can be seen that when flying at three different speeds, at 1.9 m/s, the airflow was shifted at -1.2 m; at 2.2 m/s the airflow was deflected at -1.0 m; at 2.85 m/s, the airflow was deflected at -0.85m. The velocity cloud maps from different heights during flight showed the distribution of the UAV in the XZ plane. The rotor flow field velocity distribution was symmetrically distributed with the centerline of the UAV fuselage, and along the -Y direction, the airflow was gradually weakened and shifted backward. When the UAV was flying at a speed of 2.85 m/s, the rotor airflow velocity around the fuselage was stronger at y=0 m; between y=0 m and y=-0.9 m, the airflow velocity was stronger, and mainly downward mixing was distributed; between y=-0.90 m and y=-1.5 m, the airflow velocity distribution showed a tendency to move backward and downward (with respect to the flight direction);

Taking flight safety as the premise, the fuselage should not fly close to the ground, and comparing the airflow fields at three different heights, it was found that the airflow velocity gradually decreased with the decrease of height when hovering, and the airflow velocity distribution showed a backward trend when flying forward, and the airflow velocity was the smallest directly under y=-0.9 m. Therefore, the seed guide orifice is arranged at a distance of 0.9 m below the paddle blade, which was conducive to reducing the influence of the rotor airflow velocity on seed drift after seed dropping.

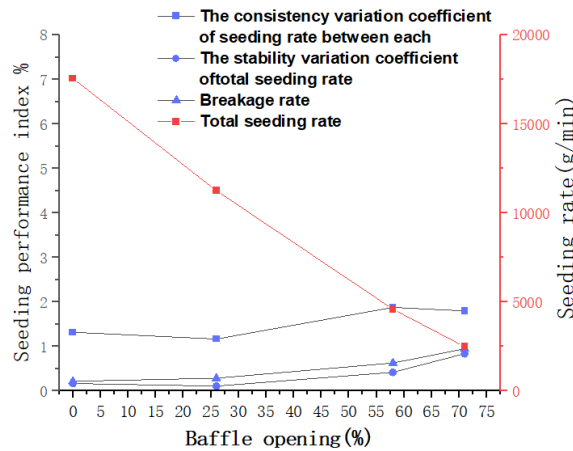
Bench test data and result analysis

According to the ‘NY/T3881-2021 Technical Specification for Quality Evaluation of Remote-Controlled Flying Seeders’, CVR is less than or equal to 5 percent, CVT is less than or equal to 2.6 percent, and the rate of breakage is less than or equal to 2 percent. According to the regulations, the data from multiple trials of CVR can be used to represent the working level as the average of the data. As can be seen from the following table and figure, CVT, CVR, and breakage rate are low, and their maximum values are 0.84%, 1.88%, and 0.95% respectively, which all satisfy the indexes, and the seeding rate of each seed guide tube mouth has small ups and downs and is stable. When the rotational speed is 45 r/min, the seed guide tube seeding rate is the maximum of 2995 g/min, and as the volume of the groove increases the displacement of seeds is gradually increasing. Through the analysis of the device seed discharger design is in line with the requirements of practical applications.

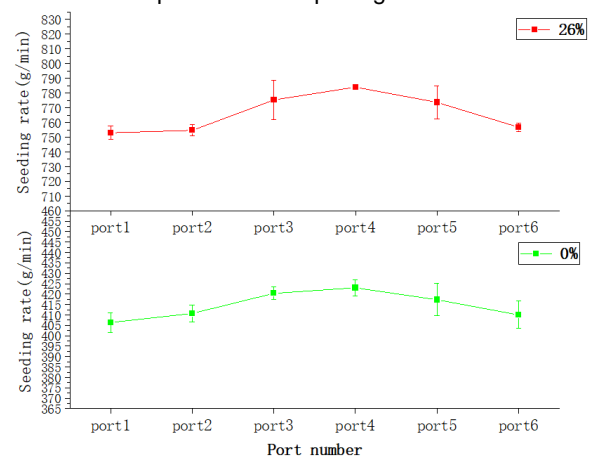
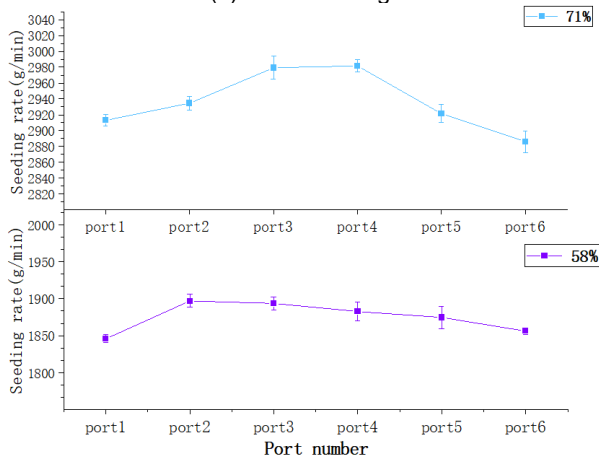
Table 1

Bench test results of the fly-by-wire device

| Flap opening | Row-by-row seeding / g | | | | | | Total displacement /g·min ⁻¹ | CVR / % | CVT / % | Average value / % | Breakage rate / % |
|--------------|------------------------|------|------|------|------|------|---|---------|---------|-------------------|-------------------|
| | 1 | 2 | 3 | 4 | 5 | 6 | | | | | |
| 0% | 2920 | 2941 | 2967 | 2986 | 2912 | 2901 | 17552 | 1.13 | 0.17 | 1.32 | 0.22 |
| | 2906 | 2938 | 2995 | 2973 | 2934 | 2882 | 17531 | 1.41 | | | |
| | 2913 | 2925 | 2976 | 2986 | 2918 | 2875 | 17593 | 1.42 | | | |
| 26% | 1848 | 1887 | 1892 | 1889 | 1890 | 1856 | 11262 | 1.04 | 0.11 | 1.17 | 0.29 |
| | 1850 | 1903 | 1903 | 1868 | 1860 | 1852 | 11236 | 1.29 | | | |
| | 1841 | 1901 | 1886 | 1891 | 1874 | 1861 | 11254 | 1.16 | | | |
| 58% | 754 | 753 | 778 | 785 | 761 | 756 | 4587 | 1.78 | 0.42 | 1.88 | 0.63 |
| | 757 | 752 | 787 | 782 | 782 | 760 | 4620 | 1.98 | | | |
| | 748 | 759 | 761 | 785 | 778 | 754 | 4585 | 1.87 | | | |
| 71% | 401 | 413 | 417 | 419 | 411 | 403 | 2464 | 1.78 | 0.84 | 1.80 | 0.95 |
| | 408 | 406 | 421 | 427 | 415 | 416 | 2493 | 1.89 | | | |
| | 410 | 413 | 423 | 423 | 426 | 410 | 2505 | 1.74 | | | |



(a) Total seeding rate and coefficient of variation with respect to baffle opening



(b) and (c) Comparison of seeding rates of each port

Fig. 13 - Seeding performance

The aircraft was fixed on the pedestal and the mud box was moved below to test the planting effect of the device as shown below:

Table 2

| Effectiveness at different effective lengths | | | | | |
|--|---------------------|---------------------|----------------|--------------------|-----------------|
| Flap opening | Number of particles | Satisfactory rate/% | Leakage rate/% | Rebroadcast rate/% | Breakage rate/% |
| 71% | 1-3 | 89.56 | 2.23 | 8.21 | 0.81 |
| 58% | 3-5 | 90.64 | 2.11 | 6.25 | 0.55 |
| 26% | 5-10 | 93.77 | 2.13 | 4.10 | 0.43 |

Site test data and data analysis

Through the change of the grooved wheel baffle to control the volume of different individual holes of the grooved wheel, the test analysis was carried out, and it was verified that the fly sowing device based on the UAV platform could achieve effective sowing for points with different numbers of seeds as shown in Figure 14 below. Due to the characteristics of the use, the rice seeds unlike fertilizers, pesticides, etc. cannot be used in excess. In order to ensure the overall pass rate, the volume of grooved wheel grooves was designed with redundancy. The purpose was to reduce the leakage of sowing, so it could be appropriate for more seeds. The trial was conducted at a minimized flight speed to satisfy a moderate or redundant amount of seed at each position. The aim was to reduce the probability of missed sowing and to guarantee that the yield of rice would not be reduced at a later stage. According to the experimental test under three different effective lengths of the grooved wheel, when the rotational speed of the grooved wheel was 45 r/min and the baffle opening was 26%, the qualification rate was 88.94%; when the rotational speed of the grooved wheel was 30 r/min, at the time of the baffle opening of 58%, the qualification rate was 86.89%, and at the time of the baffle opening of 71%, the qualification rate was 86.18%, and its sowing effect was very close to the ground effect of mechanical operation. However, when the position of the seed guide was higher, after 2 m and 2.5 m tests, the pass rate was 83.4% and 76.8%, the effect was not as good as for the height of 1.2 m. The reason may be that the trajectory of the seeds was affected by the wind force of the drone. The results weren't as good as the indoor tests because of the effects of the drone's wind.



Fig. 14 - Schematic diagram of sowing effect

Table 3

| Effectiveness at different effective lengths | | | | | |
|--|---------------------|---------------------|----------------|------------------|-----------------|
| Flap opening | Number of particles | satisfactory rate/% | leakage rate/% | reseeding rate/% | breakage rate/% |
| 71% | 1-3 | 86.18 | 3.16 | 10.66 | 0.73 |
| 58% | 3-5 | 86.89 | 2.84 | 10.27 | 0.45 |
| 26% | 5-10 | 88.94 | 2.47 | 8.59 | 0.31 |

CONCLUSIONS

(1) In order to solve the problem that the wind field disturbs the trajectory of falling seeds and causes the seeds to be unable to be arranged in equidistant rows when the UAV is spreading rice, a shot seeding device that can sow five rows of pelleted rice seeds at the same time was designed. The unit was centered on an external grooved wheel seed metering device and a seed acceleration unit for row seeding and hole sowing. The general control system and the process of seeding unit design are described.

(2) In order to reduce the influence of the airflow in the wind field of the UAV on the trajectory of the seeds, the characteristics of the airflow changes below the paddles during the operation of the UAV were analyzed. The variation of the cross-section velocity cloud map at different heights under a hovering state was analyzed and the result that the wind speed was smaller at 0.95 m was obtained. The change of velocity cloud map in XY plane under the flight speed of 1.9 m/s, 2.2 m/s and 2.85 m/s was analyzed and it was concluded that the wind field was shifted at 0.85 m when the drone is working at 2m/s.

Taking into account, that the minimum area of airflow disturbance was 0.9 m from the rotor surface, it was determined that the optimal position of the seed guide was 0.9 m from the rotor surface, in order to guarantee the accuracy of the seed drop point.

(3) The results of the indoor tests showed that the greater the angle of the baffle, the smaller the number of seeds in each position on the ground. When the baffle angle was 26%, 58%, and 71% respectively, the CVR was $\leq 1.88\%$, the CVT was $\leq 0.84\%$, and the breakage rate was $\leq 0.95\%$. The test results met the standards, indicating that the device met the operational requirements.

(4) The results of the outdoor mud box test showed that hole sowing and strip sowing could be realized when the sowing volume varied. The feasibility of this seeding method was verified. Compared with the traditional sowing operation, this device can ensure that the seed falling position is orderly, and can efficiently complete the hole sowing operation. The qualification rates of 1-3 seeds, 3-5 seeds, and 5-10 seeds were 86.18%, 86.89%, and 88.94%, respectively, and the test results were in line with the operational requirements.

ACKNOWLEDGEMENTS

This research was funded by the Ningxia Key Research and Development Plan Project (2023BCF01051); the National Key R&D Program of China, Large Load Plant Protection Intelligent UAV Creation and Application (2023YFD2000200). We would also like to thank the anonymous reviewers for their important suggestions and comments to improve our article.

REFERENCES

- [1] Bian Z.H., Lan Y.B., et al. (2024). Effect of nozzle angle of plant protection unmanned aerial vehicle on droplet deposition distribution. *INMATEH - Agricultural Engineering*, Vol.72(1), pp. 214–223.
- [2] Gao X.M., You Z.Y., Wu H.C., (2022). Design and testing of a green manure seed-spreading device based on a UAV platform [J]. *Transactions of the Chinese Society for Agricultural Machinery*, 53(11): 76-85.
- [3] He W.Z., Liu W., Jiang R., et al. (2022). Control system design and experiments of UAV shot seeding device for rice [J]. *Transactions of the CSAE*, 38(18): 51-61.
- [4] Huang X.M., Xu H.W., Zhang S., et al. (2020). Design and experiment of a rape aerial seeding in lines device[J]. *Transactions of the CSAE*, 36(5): 78-87.
- [5] Huang X.M., Zhang S., Zhu Y.Z., et al. (2022). Seeding process analysis and test of the air conveying rapeseed aerial seeding device [J]. *Transactions of the CSAE*, 38(17): 31-41.
- [6] Luo X.W., Xie F.P., Qu Y.G. et al. (2004). Comparative test of different planting methods for rice production [J]. *Transactions of the CSAE*, 20(1): 136 - 139.
- [7] Luo X.W., Wang Z.M., Zeng S., et al. (2019). Recent advances in mechanized direct seeding technology for rice[J]. *Journal of South China Agricultural University*, 40(5): 1-13.
- [8] Shen A., Zhou S.D., Wang M., et al. (2018). Simulation analysis of flow field of multi-rotor UAV[J]. *Flight Mechanics*, 36(4): 29-33.
- [9] Song C.C., Zhou Z.Y., Zang Y., et al. (2020). Variable-rate control system for UAV-based granular fertilizer spreader[J]. *Computers and Electronics in Agriculture*, 180: 105832.
- [10] Song C.C., Zhou Z.Y., Jiang R., et al. (2018). Design and parameter optimization of pneumatic rice sowing device for unmanned aerial vehicle[J]. *Transactions of CSAE*, 34(6): 80 – 88.
- [11] Wan J.J., Qi L.J., Zhang H., et al. (2021) Research status and development trend of UAV broadcast sowing technology in China[C]//2021 ASABE Annual International Virtual Meeting. Michigan, USA: *American Society of Agricultural and Biological Engineers*, 1-12.
- [12] Zeng S., Tan Y.P., Wang Y., et al. (2020). Structural design and parameter determination for fluted-roller fertilizer applicator. *International Journal of Agricultural and Biological Engineering*, 13(2): 101-110.
- [13] Zhang H., Qi L.J., Wu Y.L., et al. (2019). Distribution characteristics of rotor downwash airflow field under spraying on orchard using unmanned aerial vehicle[J]. *Transactions of the CSAE*, 35(18): 44-54.
- [14] Zhang, Q.S., Zhang, K., Liao Q.X., et al. (2020). Design and experiment of rapeseed aerial seeding device used for UAV. *Transactions of the CSAE*, 36, 138-147.
- [15] Zhou Z.Y., Yuan W., Chen S.D., (2014). Current status and future directions of rice plant protection machinery in China[J]. *Guangdong Agricultural Sciences*, 41(15): 178-183.

OPTIMIZATION DESIGN AND EXPERIMENT OF AUTOMATIC LEVELING SYSTEM FOR ORCHARD OPERATING PLATFORM IN HILLY AND MOUNTAINOUS AREAS

丘陵山区果园作业平台自动调平系统的优化设计与试验

Huijie SHANG¹⁾, XinCheng LI^{*1)}, Chengfu ZHANG²⁾, Cuiyun XU²⁾, Yaxiu HOU¹⁾, Mingtao JIA¹⁾

¹⁾ College of Mechanical and Electrical Engineering, Qingdao Agricultural University, Shandong / China

²⁾ Gaomi Yifeng Machinery Co., Ltd. / China

Tel: +86-0532-58957391; E-mail: xincheng_li@163.com

Corresponding author: XinCheng Li

DOI: <https://doi.org/10.35633/inmateh-73-30>

Keywords: Horizontal and vertical automatic leveling, ADAMS simulation, optimized design, Text

ABSTRACT

A multifunctional leveling platform for orchard in hilly and mountainous areas is developed. The platform design optimizes the double circuit hydraulic system and the horizontal and vertical bidirectional leveling structure to realize synchronous adjustment. Based on the attitude sensor, an intelligent detection and control system is developed to realize the automatic leveling and platform stabilization. The test results show that the platform can reach the maximum climbing capacity of 30° and the limit leveling angle of 15°, which can meet the requirements of orchard operation in large slope and complex terrain, and provide theoretical basis for the future design of orchard operation platform in hilly and mountainous areas.

摘要

本文研发一种适用于丘陵山区果园的多功能调平作业平台。该平台设计优化了双回路液压系统及横、纵双向调平结构可实现同步调节，并基于姿态传感器，开发了智能检测控制系统实现作业平台自动调平与机身稳定。试验结果表明，该平台最大爬坡能力达到 30°、极限调平角度达到 15°，能满足大坡度复杂地形果园作业的要求，可为今后丘陵山区果园作业平台的设计提供理论依据。

INTRODUCTION

With the continuous expansion of orchard planting area, fruit tree planting has become an important branch of agriculture (*China Smart Agriculture Development Research Report, 2021*). China's orchards are mainly distributed in hilly and mountainous areas, the terrain in these areas is undulating, not suitable for large-scale mechanical operations, and traditional operation methods such as manual ladder climbing, tree climbing, etc. have great potential safety hazards, and the operation efficiency is low (*Li et al., 2021*).

The research of foreign orchard machinery started earlier, and the Windegger Picking Platform series produced by N.P. Seymour company in Italy can be turned on all wheels, and the workbench can be lifted in two stages, and the angle can be adjusted, which has a wide range of applicability. The Piattaforma orchard platform produced by Macfrut in Italy has a two-stage scissor lifting mechanism, which can realize cross-slope leveling and longitudinal slope leveling at the same time, with a lifting height of 3.85 m, and has the functions of multiple people working at the same time to complete picking and transportation (*Lu et al., 2023*). The Bielevatore picking platform jointly designed and produced by D'Amico and the Faculty of Engineering of the University of Bari in Italy is connected to the tractor through a three-point suspension mechanism, and has two telescopic booms, the working platform on each telescopic arm can be controlled independently, and the operating platform is equipped with an air source to complete the pruning operation with pruning tools such as saws and scissors (*Meng et al., 2012*). However, the environmental and topographic characteristics of foreign countries are not fully applicable to the mechanical operation of orchards in China, and the structural function needs to be further optimized (*Ding et al., 2022*).

Liu Dawei developed a small orchard lifting platform for citrus orchards in the hilly and mountainous areas of southern China, and leveled by the telescopic hydraulic cylinder through the "secondary leveling" method, but the leveling method was manual leveling, which had low leveling accuracy and low operation efficiency (*Liu et al., 2022*).

Qiu Wei developed a folding arm lifting leveling platform based on the characteristics of hilly and mountainous areas of orchards and orchard operations in southern China, and verified the tipping stability in hilly and mountainous areas through theoretical calculation, simulation analysis, and prototype test analysis, which has certain reference significance in the operation and the design of related machinery (Qiu et al., 2018).

In recent years, domestic research on orchard platforms has made rapid progress, but most of them are still in the stage of theoretical design or prototype trial production, and most of them are miniaturized machinery with small load, which has certain limitations in the scope of application (Fan et al., 2017). The stability of existing products of agricultural machinery manufacturers is not good enough when operating on slopes, and it is not suitable for use in hilly and mountainous orchards (Duan et al., 2018; Chaoran et al., 2019).

MATERIALS AND METHODS

Overall platform structure and parameters

The overall structure of the operating platform is shown in Figure 1.

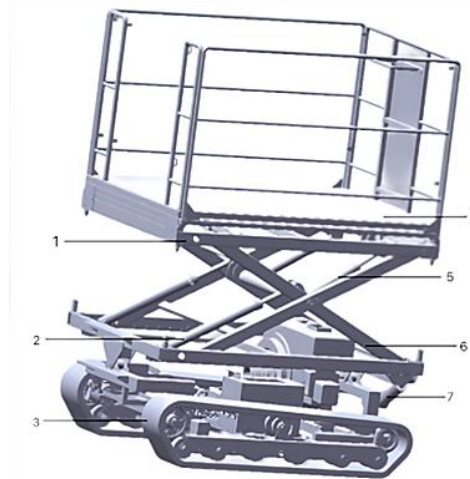


Fig. 1 - 3D model of the overall structure of the operation platform

a) Upper frame; 2 - Lifting mechanism; 3 - Track; 4 - Bearing platform; 5 - Longitudinal adjustment mechanism; 6 - Fork cutting mechanism; 7 - Transverse levelling mechanism

The leveling structure of orchard platform includes longitudinal leveling structure and transverse leveling structure. The platform has four degrees of freedom: lift, pitch, roll and expansion. The leveling structure of the orchard platform is a key component designed to ensure stable operation of the platform on uneven terrain (Fan et al., 2017).

Table 1

Main parameters of operation platform

| Item | Technical parameter |
|---|---------------------|
| Overall dimensions (length × width × height) (cm) | 185×130×198 |
| Maximum size of table (length × width) (cm) | 175×210 |
| Load rating (kg) | 300 |
| Lifting height range (cm) | 0-100 |
| Maximum horizontal leveling angle (°) | ±15 |
| Maximum longitudinal leveling angle (°) | ±15 |
| Maximum gradeability (°) | 30 |
| Track grounding length (cm) | 130 |

Longitudinal leveling structure design

Considering the topography characteristics of gentle hilly orchards and combined with Chinese Adult Body Size Standards, it can be seen that the lifting height of the workbench up to 2.2 m can fully meet the requirements of orchard operations (Fan et al., 2019). Therefore, a single-stage scissor-fork lifting mechanism was selected and improved into a folding arm scissor-fork lifting mechanism with more independent and flexible movement on this basis.

Considering the rationality of structure, installation position of hydraulic cylinder and leveling angle, the structural parameters determined are shown in Table 2.

Table 2

| Basic parameters of longitudinal leveling structure | | |
|---|------|---------------|
| Parameter | Unit | Numeric value |
| L_{O_1N} | mm | 410 |
| L_{O_1M} | mm | 160 |
| L_{O_1D} | mm | 560 |
| β | ° | 88 |

The thrust F_2 of the horizontal hydraulic cylinder is related to the pitch Angle and lifting height of the workbench. In the design process, the values of L_{O_1M} and β should be increased and the values of L_{O_1D} and L_{O_1N} should be reduced as far as possible.

In Figure 2, obtaining equilibrium equation in the XOY coordinates:

$$\begin{cases} x_{OD_1} = L_{OQ_1} \cos \alpha + L_{O_1D_1} \cos (\alpha + \varphi) \\ y_{OD_1} = L_{OQ_1} \sin \alpha + L_{O_1D_1} \sin (\alpha + \varphi) \end{cases} \quad (4)$$

Since $\tan \theta = \frac{y_{OD_1} - h}{x_{OD_1}}$, we get:

$$\begin{aligned} \theta &= \arctan \frac{(L_{OQ_1} - L_{EH}) \sin \alpha + L_{O_1D_1} \sin (\alpha + \varphi)}{L_{OQ_1} \cos \alpha + L_{O_1D_1} \cos (\alpha + \varphi)} \\ \varphi &= \arccos \frac{L_{QM}^2 + L_{ON}^2 - (LMN - y)^2}{2L_{O_1M} \cdot L_{O_1N}} \end{aligned} \quad (5)$$

where: y is the displacement of the piston rod of the longitudinally leveled hydraulic cylinder, and LMN is the length of the pitching hydraulic cylinder MN .

It can be seen from the formula that the leveling angle of the knuckle arm scissor longitudinal leveling structure is related to the displacement of the piston rod and the installation position of the hydraulic cylinders for lifting and longitudinal leveling (Li et al., 2022). According to the determined dimension parameters of the longitudinal leveling structure, the longitudinal leveling hydraulic cylinder stroke of 1500 mm can meet the requirements of the installation position and the leveling Angle, and the longitudinal leveling Angle of the workbench is increased to 15°. The specific dimensions are shown in Table 2.

Horizontal leveling structure design

The horizontal leveling structure is responsible for adjusting the left and right tilt Angle of the orchard platform. The schematic diagram of the designed structure is shown in Figure 3.

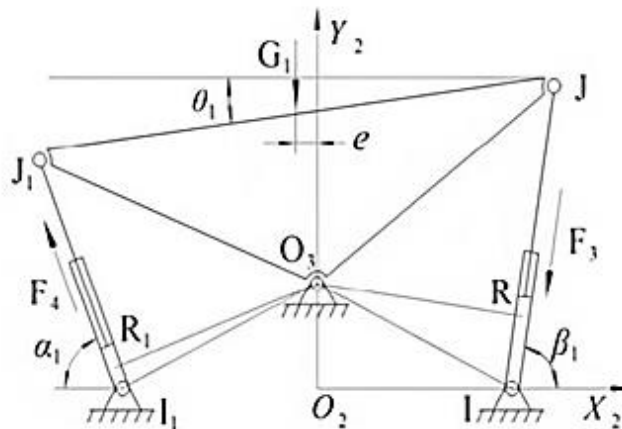


Fig. 3 - Horizontal leveling structure diagram

The hydraulic cylinder I_1J_1 the opposite movement of the IJ , the frame rotates around the O_3 point, and the worktable tilts at a certain angle θ_1 to achieve the purpose of roll leveling.

$$\begin{cases} \angle IO_3R = \beta_1 - \angle IO_3O_2 \\ L_{O_3R} = L_{IO_3} \cos \angle IO_3R \\ \angle I_1O_3R_1 = \alpha_1 - \angle I_1O_3O_2 \\ L_{O_3R_1} = L_{I_1O_3} \cos \angle I_1O_3R_1 \\ F_3 \cdot L_{O_3R} + F_4 \cdot L_{O_3R_1} = G_1 e \end{cases} \quad (6)$$

where: F_3 and F_4 are the thrust of the roll hydraulic cylinder.

According to the selected cylinder, $1.45F_3 = F_4$ is obtained, therefore:

$$F_4 = G_1 \frac{0.6e}{L_{IO_3} \cos(\beta_1 - \angle IO_3O_2) + L_{I_1O_3} \cos(\alpha_1 - \angle I_1O_3O_2)} \quad (7)$$

It can be seen from the formula that: the increase of the hydraulic cylinder will lead to the increase of the hydraulic cylinder thrust. In the design of the workbench components, the center of gravity is reduced to reduce the required thrust of the hydraulic cylinder, and the roll stability of the platform can also be increased.

Increasing L_{IO_3} and $L_{I_1O_3}$ will reduce the thrust required by the hydraulic cylinder, but too much L_{IO_3} and $L_{I_1O_3}$ will lead to insufficient stroke of the hydraulic cylinder, which cannot meet the leveling requirements of the design. It is necessary to select an appropriate value for the structural parameters, which can not only reduce the thrust required by the hydraulic cylinder, but also make the structure more reasonable and meet the design requirements.

The specific dimensions are shown in Table 3.

$$\begin{cases} X_{JJ_1} = L_{I_1J_1} \cos \alpha_1 + L_{I_1I} + L_{LJ} \cos \beta_1 \\ Y_{J_1} = L_{LJ} \cos \beta_1 - L_{I_1J_1} \cos \alpha_1 \end{cases} \quad (8)$$

Horizontal adjustable table angle:

$$\begin{cases} X_{JJ_1} = L_{I_1J_1} \cos \alpha_1 + L_{I_1I} + L_{LJ} \cos \beta_1 \\ Y_{J_1} = L_{LJ} \cos \beta_1 - L_{I_1J_1} \cos \alpha_1 \end{cases} \quad (9)$$

$$\theta_1 = \arctan \frac{L_{LJ} \sin \beta_1 - L_{I_1J_1} \sin \alpha_1}{L_{I_1J_1} \cos \alpha_1 + L_{I_1I} + L_{LJ} \cos \beta_1} \quad (10)$$

The installation position, installation size and stroke of hydraulic cylinder are directly related to the transverse adjustable angle. The installation position and installation size are affected by the frame structure. Considering the design requirements of the horizontal leveling angle, the hydraulic cylinder with the stroke amount is selected, and the appropriate size is selected for other structures according to the design requirements and structural characteristics. The specific size is shown in Table 3.

Table 3

| Basic parameters of horizontal leveling structure | | |
|---|------|-----------------|
| Argument | Unit | Numerical value |
| α_1 | ° | 28 ~ 70.5 |
| L_{IO_3} | mm | 264 |
| L_{IJ} | mm | 320 ~ 390 |
| L_{I_1I} | mm | 373 |

ANSYS finite element analysis of leveling structures

According to the actual force and constraints of the frame, the frame is constrained and loaded 3000 N, as shown in Figure 4. Because the horizontal leveling hydraulic rod is not the main force component, only the finite element analysis of the shear fork lifting structure and the longitudinal leveling hydraulic rod is needed.

The designed platform material uses Q235, and its mechanical properties parameters are shown in Table 4.

Table 4

| Q235 material mechanical performance parameters | | | | | |
|---|-----------------------------|------------------------------|----------------------|------------------------|-----------------|
| Type of material | Modulus of elasticity (GPa) | Density (kg/m ³) | Yield strength (MPa) | Tensile strength (MPa) | Poisson's ratio |
| Q235 | 210 | 7800 | 235 | 400 | 0.28 |

The distribution of stress and deformation, the maximum stress and deformation position can be obtained by simulation, and whether the structure meets the strength requirements can be obtained by referring to the parameter table.

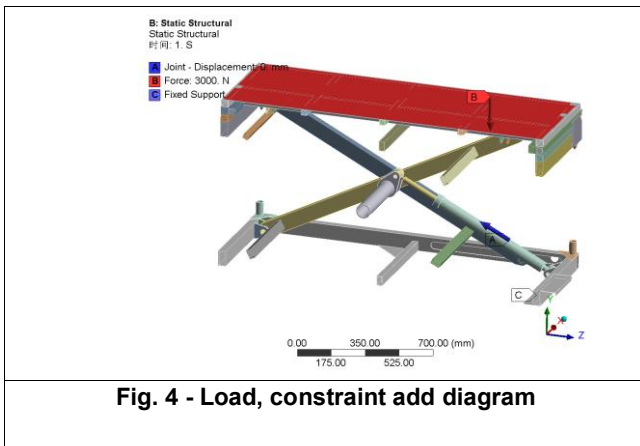


Fig. 4 - Load, constraint add diagram

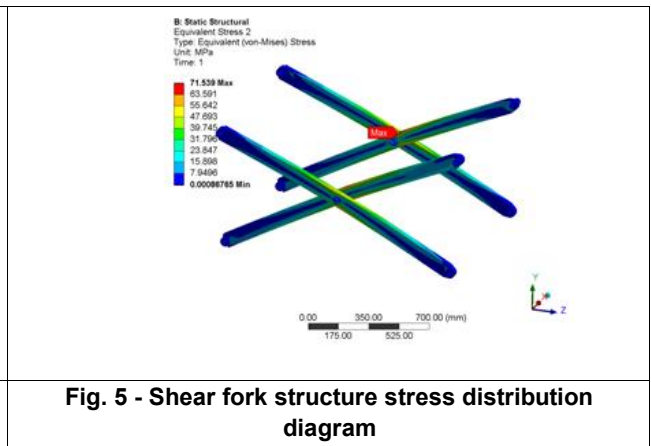


Fig. 5 - Shear fork structure stress distribution diagram

According to the stress distribution of the diagonal support and support rod of the scissor structure. The maximum stress on the system is calculated to be 71.539 MPa, as shown in Figures 5 and 6, observed in Part B. The load acting on the cylinder causes a lower stress on the lower scissor section A.

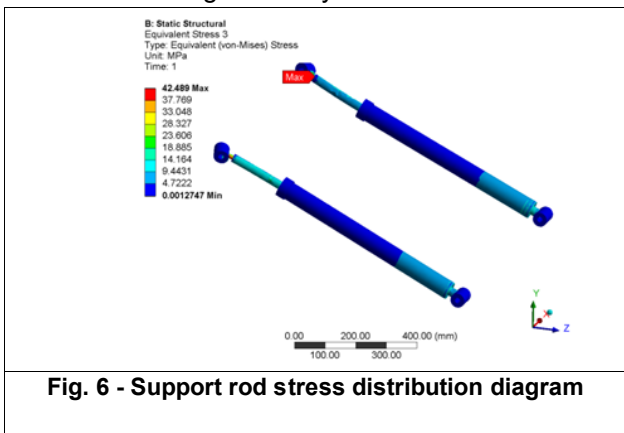


Fig. 6 - Support rod stress distribution diagram

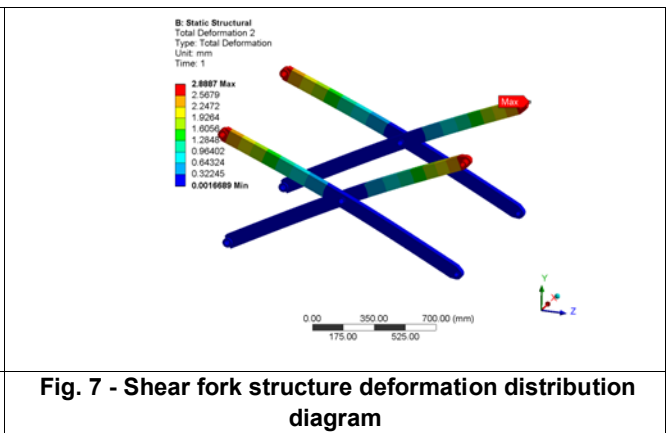


Fig. 7 - Shear fork structure deformation distribution diagram

Figure 7 shows the deformation of the upper table and the upper splicing head under load. The calculated deformation is 0.1173 mm under no-load condition. When the maximum load is applied to the platform, the deformation is 0.694 mm, which is a six-fold increase in deformation. The analysis results show that when the scissors profile is made of Q235 material, the lowest safety factor observed at the joint of the scissors is 4.3, and the safety factor of the pin made of Q235 material is 6.5, both of which are greater than 3. Therefore, the safety factor is within the acceptable range of the system to be designed.

Design of double circuit hydraulic system

The basic configuration circuit is shown in Figure 8. The relief valve, check valve, hydraulic lock and other basic hydraulic circuits are configured. With the introduction of the automatic leveling system, the configuration of the hydraulic circuit has been partially changed.

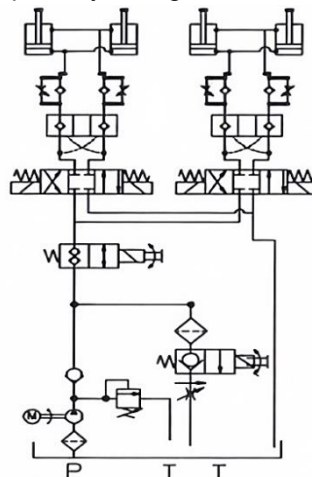


Fig. 8 - Hydraulic system basic schematic diagram

Mechanical analysis of tipping factors

The orchard platform on the slope is divided into three kinds of posture: longitudinal, oblique and transverse. In order to determine the factors affecting the tipping angle, the slope mechanics of the platform was analyzed. Figure 9 shows the stress diagram of the orchard operating platform under longitudinal and transverse attitude.

Where: G_1 - total platform weight; G_2 - total load weight; H - linear distance between platform center of mass and load center of mass; h - height of platform center of mass; L_1, L_2 - respectively, the distance from the center of the front and rear support wheels to the center of the platform along the slope; L_Z - track grounding length; F - driving force; α - slope angle; f_p - the frictional resistance of the slope against the platform; b - track width; L - two track distance; O_1, O_2, O_3, O_4, O_5 - they are respectively the rear support wheel, front support wheel, left track edge, left track, right track and slope contact points.

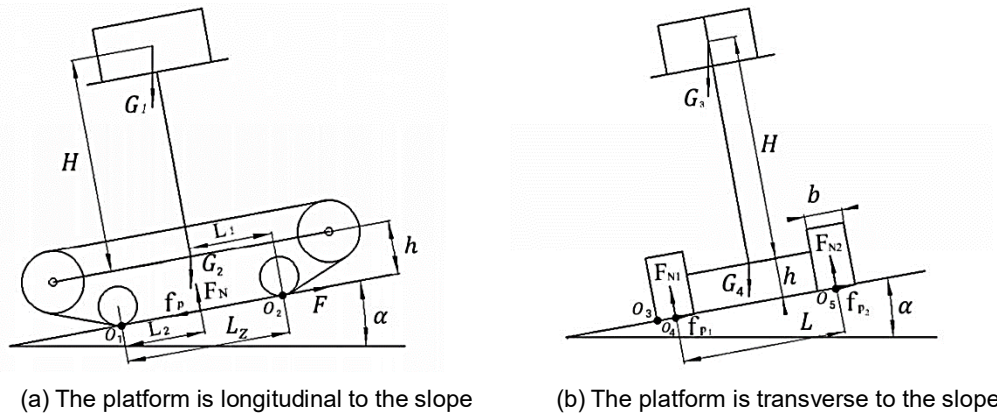


Fig. 9 - Force diagram under two slope attitudes

When the platform is longitudinal on the slope, the force analysis shows that with the increase of slope Angle, the platform will tip over along the O_1 point, and the torque equilibrium equation $\sum M_{O_1} = 0$ can be obtained:

$$G_1 \cos \alpha (L_1 - L_2) - G_1 \sin \alpha (H + h) + G_2 \cos \alpha (L_1 - L_2) - G_2 \sin \alpha h - F_N L_2 = 0 \tag{11}$$

When the slope Angle α gradually increases, the supporting force F_N of the slope towards the track gradually moves to O_2 point. When F_N fully acts on the support wheel of the track, that is, $L_2 = 0$, the critical tipping state occurs. Therefore, the condition that the platform does not roll over vertically is $L_2 \geq 0$. Therefore:

$$\alpha \leq \arctan \frac{(G_1 + G_2)(L_Z - L_1)}{G_1(H + h) + G_2 h} \tag{12}$$

As can be seen from the above formula, the platform tipping Angle is related to the total weight of the machine, the height of the load center of mass and the load position.

When the platform is transversally on the slope, with the increase of the slope Angle, the platform turns transversally along the O_1 point, and the moment equilibrium equation $\sum M_{O_3} = 0$ can be obtained:

$$G_2 \cos \alpha \left(\frac{L+b}{2}\right) - G_2 \sin \alpha b + G_1 \cos \alpha \left(\frac{L+b}{2}\right) - G_3 \sin \alpha (H + h) - P_{N1} \frac{b}{2} - F_{N2} \left(\frac{b}{2} + L\right) = 0 \tag{13}$$

When the platform is in a critical tipping state, both F_{N1} and F_{N2} are 0, so the conditions for not tipping are $F_{N1} \geq 0$ and $F_{N2} \geq 0$. Therefore:

$$\alpha \leq \arctan \frac{(G_1 + G_2) \left(\frac{L+b}{2}\right)}{G_1(H + h) + G_2 h} \tag{14}$$

It is concluded that the lateral slope of the platform is related to the total weight of the load, the height of the centroid of the load and the position of the load. When the table is inclined to the slope, the tipping slope is between the longitudinal tipping slope and the transverse tipping slope under the condition that the load, load height and load position are unchanged.

Dynamic simulation optimization analysis

According to the above force analysis, it can be seen that the tipping slope of the orchard platform should be tested by comprehensively considering the different posture of the platform on different slopes (the Angle between the track and the ground in the direction of the platform is divided into three cases: 0°, 45° and 90°) load size, load height and load position. Therefore, the tilting test bench is set up in ADAMS, as shown in Figure 10.

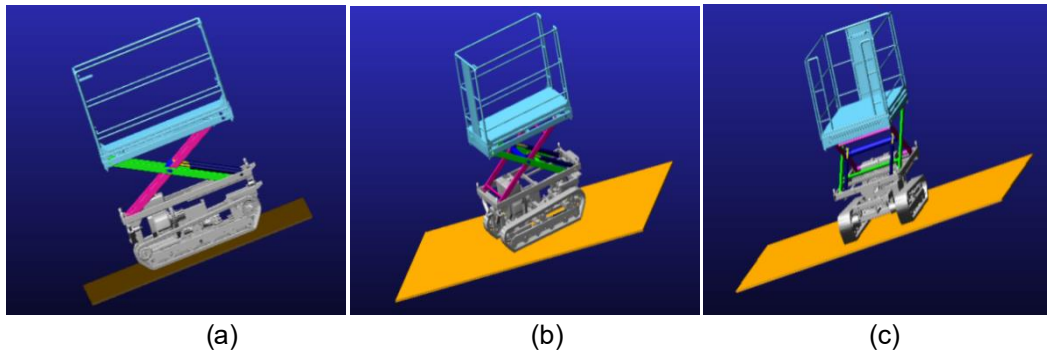


Fig. 10 - Simulation process diagram of orchard platform
(a) 0°; (b) 45°; (c) 90°

The test bench (*Chinese research criteria, 2011*) rotates at a certain angular speed and performs simulation under different loads of 1200, 1420, 1640, 1860, 2080 and 2300 mm at different stroke elevations and 0, 50, 100, 150, 200, 250 and 300 kg at three different poses. When the supporting force of the track is 0, the inclination Angle of the test stand is recorded as the tipping slope. As the test bench is turned over, the longitudinal or transverse structure begins to level until the limit position is reached, as shown in Figure 11.

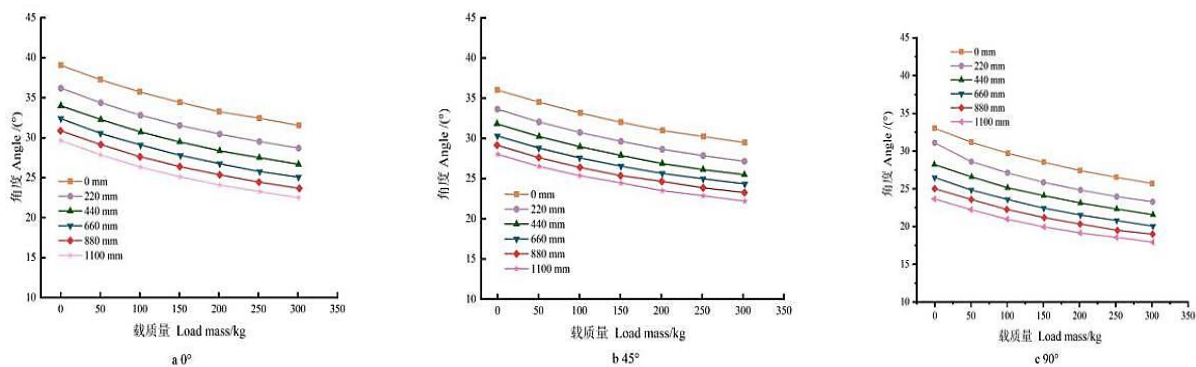


Fig. 11 - Simulation results of orchard platform tipping
(a) 0°; (b) 45°; (c) 90°

It can be seen from the simulation results that, when the lifting height and load are constant, the ultimate tipping slope of the platform in the vertical, oblique and transverse posture gradually decreases. In addition, under the three attitudes, the lifting height and load increase, and the extreme limit tipping slope of the platform will decrease. Shear-fork structure levelling raises the work platform, allowing the center of gravity of the platform to move along the slope, which is beneficial for improving the vertical anti-overturning ability of the platform. Because both oblique and lateral attitude leveling require the involvement of the roll leveling mechanism, which improves the anti-roll ability of the platform.

Overall, the maximum ultimate tipping slope was reduced by 1.3%, and the minimum ultimate tipping slope was increased by 15.1%, which significantly improved the safety of the platform.

Dynamic walking simulation analysis

In order to verify that the platform can be levelled according to the levelling design requirements when it passes the uneven road surface (*Liu et al., 2009*), different obstacle roads can be set up in ADAMS to simulate and analyze the dynamic levelling performance of the workbench. After analyzing the basic characteristics of orchard pavement, it can be simplified into two kinds of obstacle pavement: single wave and continuous wave.

The slow running speed of agricultural machinery during operation is generally lower than 2 km/h, and the minimum speed can reach 0.2 km/h. Due to the large amount of orchard work and the slow running speed of the platform, the simulation speed is set to 0.72 km/h and the STEP function is used to control the platform.

Track chassis inclination and table inclination are measured. Track chassis inclination reflects the influence of road surface changes on the platform, and table inclination reflects the degree of leveling to offset the influence of road surface. By comparing the two, it is possible to obtain the leveling performance of the platform when passing different obstacles. Fig.12 shows the simulation results.

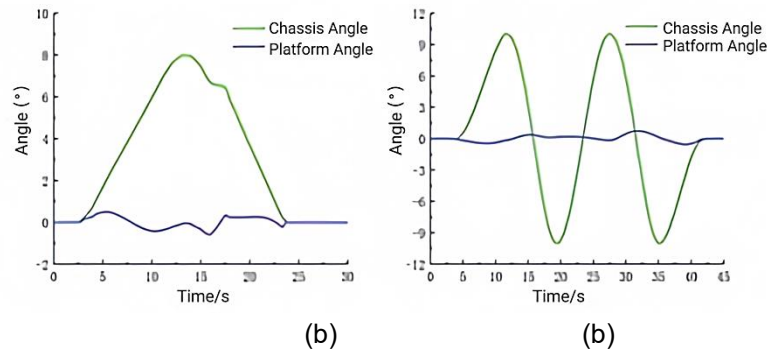


Fig. 12 - Simulation results of dynamic leveling
a) Single waveform; (b) Continuous waveform

It can be seen from the figure that under a single waveform obstacle, the chassis Angle changes with the change of the obstacle, the maximum roll is 8° , and the workbench Angle fluctuates to a certain extent, but it is always maintained within the range of 0.75° . Since the two sides of the track are rigidly connected together, when passing a single waveform obstacle, there will be a corner hanging, and there will be fluctuations at 16s.

However, when encountering fluctuations, the angle of the platform is still maintained near 0° , showing better leveling performance. Under continuous waveform fault, the Angle of the chassis fluctuates with the change of the waveform, the change range is $\pm 10^\circ$, the Angle of the platform is floating in the range of 0.73° , and the longitudinal leveling performance is good. It can be seen that the terrain change has a great impact on the orchard platform, but the leveling can effectively reduce this impact, so that the workbench is stable and maintained near 0° , which can meet the requirements of orchard operation in hilly and mountainous areas.

RESULTS

Platform field test

The prototype of orchard multifunctional automatic leveling operation platform is shown in Figure 13.



Fig. 13 - Working platform prototype

Build a leveling test site, design different gradients, and test the dynamic leveling performance of the operating platform during the ramp driving. The operating platform is uphill at a speed of 1km/h, and the Angle value of the platform is recorded in real time by the inclination sensor. Each slope Angle was tested four times respectively, and the recorded data were shown in Table 5.

Table 5

| Dynamic leveling performance test | | | | | |
|-----------------------------------|------------------------|-------------------|------------------|--------------------|--------------------|
| Slope Angle / (°) | | Platform no-load | | Platform full load | |
| Longitudinal Angle / (°) | Transverse Angle / (°) | Leveling time / s | Leveling error/s | Leveling time / s | Leveling error / s |
| | 0 | 0 | 0 | 0 | 0 |
| 0 | 5 | 1.04 | 0.64 | 1.16 | 0.58 |
| | 10 | 1.18 | 0.78 | 1.25 | 0.95 |
| | 15 | 1.30 | 0.82 | 1.33 | 1.05 |
| | 0 | 1.36 | 0.47 | 1.28 | 0.62 |
| 7 | 5 | 2.02 | 0.60 | 2.20 | 0.97 |
| | 10 | 2.20 | 0.63 | 2.35 | 1.06 |
| | 15 | 2.42 | 0.80 | 2.58 | 1.12 |
| | 0 | 1.63 | 0.62 | 1.79 | 0.73 |
| 14 | 5 | 2.49 | 0.74 | 2.70 | 1.09 |
| | 10 | 2.60 | 0.80 | 2.78 | 1.20 |
| | 15 | 2.77 | 0.85 | 2.99 | 1.30 |
| | 0 | 1.20 | 0.64 | 3.00 | 0.85 |
| 21 | 5 | 2.83 | 0.79 | 3.35 | 1.20 |
| | 10 | 3.05 | 0.86 | 3.44 | 1.28 |
| | 15 | 3.33 | 0.89 | 3.60 | 1.34 |
| | 0 | 2.57 | 0.62 | 3.12 | 0.93 |
| 30 | 5 | 3.45 | 0.80 | 3.94 | 1.32 |
| | 10 | 3.78 | 0.82 | 4.30 | 1.40 |
| | 15 | 3.90 | 0.93 | 4.33 | 1.43 |

The test results of leveling performance are shown in Table 5. When the platform is fully loaded, the average value of the platform leveling error is within $0^{\circ}\sim 1.5^{\circ}$, and the dynamic leveling time has a certain relationship with the ramp and load mass. When the transverse Angle is within 15° and the longitudinal Angle is within 30° , the leveling time is less than 4.5 s. It can realize the horizontal state of the operating platform during the ramp driving and maintain the stability of goods transportation.

CONCLUSIONS

(1) In this paper, the scheme of horizontal and vertical leveling of orchard operation platform is designed. The longitudinal leveling structure is improved on the basis of the shear fork lifting structure, which will not add too much structure. The simulation analysis is carried out, and according to the simulation results, the structure is further optimized to improve its safety strength.

(2) The static analysis of the platform was carried out, and the dynamic simulation optimization was carried out in ADAMS. The tilting test platform was established, and the leveling accuracy and walking stability of the platform under different attitude, slope and load were analyzed and verified.

(3) The dynamic leveling performance of the platform prototype is tested to check the horizontal state and transportation stability of the platform on the ramp.

ACKNOWLEDGEMENT

The research was funded by Shandong Province agricultural major application technology innovation project (Grant SD2019NJ001).

REFERENCES

- [1] Ahmadi I. (2011). Dynamics of tractor lateral overturn on slopes under the influence of position disturbances (model development), *Journal of Terramechanics*, Volume 48, Issue 5, Pages 339-346.
- [2] Chaoran S., Hiroshi N., Hiroshi S., Juro M., Katsuaki O. (2019). Physics engine application to overturning dynamics analysis on banks and uniform slopes for an agricultural tractor with a rollover protective structure[J]. *Biosystems Engineering*, 185:150-160.
- [3] Ding Shaowen, Sun Zhenzhong, Li Qinglan. (2022). Improving the level of agricultural mechanization and promoting the sustainable development of agriculture (提高农业机械化水平, 促进农业可持续发展) [J]. *Contemporary Agricultural Machinery*, (10): 39+41.

- [4] Duan Z.H., Qiu W., Ding W.M., Liu Y.D., Huang L. (2018). Tilting stability analysis and experiment of the 3-DOF lifting platform for hilly orchards [J]. *International Journal of Agricultural and Biological Engineering*, 11(6): 73–80.
- [5] D'Esnon A.G., Rabatel G., Pellenc R., Journeau A., Aldon M.J. (1987). Magali: A self-propelled robot to pick apples. *American Society of Agricultural Engineers (USA)*.
- [6] Eryilmaz B., Wilson B.H. (2005). Unified modeling and analysis of a proportional valve[J]. *Journal of the Franklin Institute*, 343 (1): 48–68.
- [7] Fan G.J., Li Z., Feng T.T., Zhang H., Qin F., Sun X.H. (2019). Kinematics Modeling and Analysis of Leveling Mechanism of Orchard Work Platform Based on Screw Theory [J]. *Journal of Physics: Conference Series*, 1237(5).
- [8] Fan Guiju, Wang Yongzhen, Zhang Xiaohui, Zhao Jinying, Song Yuepeng. (2017). Design and experiment of automatic Leveling Control System for orchard lifting Platform [J]. *Transactions of the Chinese Society of Agricultural Engineering* (果园升降平台自动调平控制系统设计与试验), MSc Thesis, 33(11): 38-46.
- [9] Franceschetti B., Rondelli V., Ciuffoli A. (2019). *Comparing the influence of Roll-Over Protective Structure type on tractor lateral stability* (J). *Saf Sci*, 115: 42-50.
- [10] Gao Q.M., Gao F., Tian L., Li L.J., Ding N.G., Xu G.Y., Jiang D.W. (2014). Design and development of a variable ground clearance, variable wheel track self-leveling hillside vehicle power chassis (V2-HVPC)[J]. *Journal of Terramechanics*, 56:77–90.
- [11] General Administration of Quality Supervision, Inspection and Quarantine of the People's Republic of China, Standardization Administration of China GB/T14172-2009 (2011). *Bench test method for Vehicle static Rollover stability* [S]. Beijing: Standards Press of China,
- [12] Institute of Policy and Economics, China Academy of Information and Communications Technology, Chinese People's Research Center for Smart Agriculture and Digital Countryside Development. (2021). *China Smart Agriculture Development Research Report: New generation of information technology to help rural revitalization* [R/OL]. China mail tunnels.
- [13] Li W.H., Kang F., (2020). Design and Analysis of Steering and Lifting Mechanisms for Forestry Vehicle Chassis[J]. *Mathematical Problems in Engineering*, 1–16.
- [14] Li Zhao, Fan Guiju, Liang Zhao, Niu Chengqiang. (2020). Work space analysis and experiment of orchard working platform based on D-H method [J]. *Transactions of the Chinese Society of Agricultural Engineering*, 36(16): 25-34.
- [15] Liu Dawei, Xie Fangping, Li Xu, Wang Xiaolong. (2015). Design and experiment of small orchard lifting operation platform [J]. *Transactions of the Chinese Society of Agricultural Engineering* (小型果园升降作业平台的设计与试验), 31(03):113-121.
- [16] Liu Xining, Zhu Haitao, Ba Heti. (2009). Development of Lupergod LG-1 multifunctional orchard machine [J]. *Xinjiang Agricultural Mechanization*, (1):42-44.
- [17] Leonard K.E., Woody V.O. (2000) Automatic leveling system: US6106402 [P]
- [18] Meng Xiangjin, Shen Congju, Tang Zhihui, Jia Shouxing, Zheng Xuan, Zhou Yan, Liu Wei. (2012). Current situation and development of orchard working machinery (果园作业机械的现状与发展), *Journal of agricultural machinery*, (25):114-117. DOI: 10.16167 / j.carol carroll nki. 1000-9868.2012.25.011.
- [19] Ren Raine. (2022). Promote the steady improvement of agricultural mechanization application level [J]. *China Fruit Science*, (05):129-130.
- [20] Schutte A.D., Udawadia F.E. (2010). New approach to the modeling of complex multi-body dynamical systems [J]. *Journal of Applied Mechanics*, 78(2):856-875.
- [21] Thamsuwan O., Galvin K., Tchong-French M., Aulck L., Boyle L. N., Ching R. P., McQuade K. J., Johnson P. W. (2020). Comparisons of physical exposure between workers harvesting apples on mobile orchard platforms and ladders, part 2: Repetitive upper arm motions[J]. *Applied Ergonomics*, 89:103192.
- [22] Xiang Li. Analysis on changes of fruit production in China in 2021. (2023). (2021 年我国水果生产变动简析), *China Fruit Industry Information*, 40(02):28-43. (in Chinese)

INVESTIGATION OF THE REACTION OF SOIL TO MOVEMENT BY PLATES AT VARIOUS INCLINED ANGLES BASED ON 2D-DEM

基于二维离散元法对倾角条件影响土壤-板接触系统相互作用的研究

Liangyu YUAN, Jun GE ^{*}), Chengmao CAO, Kuan QIN, Yan SUN, Liangfei FANG ¹

School of Engineering, Anhui Agricultural University, Hefei, Anhui / China

Tel:(+86) 150 7791 2067; E-mail: gejunahau@ahau.edu.cn

Corresponding author: Ge Jun

DOI: <https://doi.org/10.35633/inmateh-73-31>

Keywords: soil-plate interaction system, 2D-DEM, varied inclination angle, Terramechanics

ABSTRACT

In order to investigate the soil reactions influenced by the single plate with the inclination angles from 0° to 75°, an in-house code of 2D DEM has been developed in this study. An iron flat plate penetrated soil by a constant velocity of 1 mm/s in the study. In the penetration test, the maximum vertical force was 753.8 N which was generated by the 0° plate. In addition, it was found that the less the inclination angle, the greater the vertical force. Furthermore, a greater force in the horizontal direction has been generated at 45° of the inclination angle. This research can provide a theoretical reference for optimizing tools that contact soil, for example, patterns/lugs on wheels, earthmoving blades (such as rotary cultivators, bulldozers, weeding machines etc.) and grouser of tracks.

摘要

本研究旨在利用二维离散元仿真方法对单板倾角从 0°变化到 75°时土壤反力变化进行研究。在仿真试验过程中, 钢材料平板以 1mm/s 的恒定速度向土壤中贯入。试验结果显示, 贯入试验土壤最大反力为 0°板产生的 753.8N, 与此同时, 还发现垂直反力与板的倾角呈现反比关系, 而水平反力峰值出现在倾角 45°左右。这项研究为优化触土工具提供了理论参考, 如胎花、推土刀片 (旋耕机、推土机、除草机等) 和履刺等。

INTRODUCTION

When machines operate under water flow or other weak soil conditions, the running gear needs to produce greater traction, by using lugged wheels, for example (Holthusen *et al.*, 2018; Md-Tahir *et al.*, 2019; Rasool *et al.*, 2018). Meanwhile, those soil conditions, such as the tiller machine in paddy fields, demand machines with a smaller earth contact pressure (Tian *et al.*, 2021; Jiang *et al.*, 2021). Since it is a fundamental problem in the field of terramechanics, research on the influence of lugs or plates on soil reaction forces has always attracted the attention of researchers (Wong, 2010; Zhu *et al.*, 2023; Ravula *et al.*, 2021).

Initially, as described by Gill & Vanden Berg (1968) in their book, *Soil Dynamics in Tillage and Traction*, in reaction analysis, the soil was regarded as an isotropic and homogeneous material. The main experimental method for examining the different soil conditions is the soil bin test, and researchers have achieved excellent results when using this method (Wong, 2001; Wei *et al.*, 2022; Stefanow & Dudziński, 2021).

In the Asian region, the water fields have a wide range of soil conditions because of water contents and region differences. Number of studies have been carried out on the interaction between machinery/tools and paddy soil, such as the running gear of rice transplanter/tiller and soil interaction system (Jia *et al.*, 2016; Nassiraei *et al.*, 2020). Wang *et al.* (1993, 1995) conducted two sets of the wider-spaced lugs of the lugged wheel on the cutting resistance of the metal surface in the wheel-soil interaction system. However, they used the fixed lug-wheel, and, therefore, there was no mention of the effect of changes in the inclination angle. Hermawan *et al.* (1996, 1997 & 1998) implemented a series of experiments to investigate the effect of angle changes on single movable lugs, movable lug wheels, and fixed lug wheels under wet loam soil conditions.

¹ Yuan Liangyu, Stud. Eng.; Ge Jun, Lecturer PhD. Eng.; Cao Chengmao, Prof. PhD. Eng.; Qin Kuan, Assoc. Prof. PhD. Eng.; Sun Yan, Assoc. Prof. M.S. Eng.; Fang Liangfei, Lecturer PhD. Eng.

However, given the disregard of the effect of lug spacing in those studies, *Watyotha et al. (2001)* investigated the effect of circumferential angle, lug spacing, and wheel slip on forces produced by a cage wheel in a laboratory soil bin, which was filled with a high-moisture-content Bangkok clay soil. They found that changes in the circumferential angle may significantly affect the lateral force, whereas the smallest change or the largest average lug force is generated by the 20° lug spacing. Besides the conventional methods, in consideration of the efficiency and repeatability of the soil test, computer-aided methods have gradually been widely adopted (*Wong, 2001; Zhang et al., 2020*).

Initially, the FEM was used to investigate the tool/tire-soil interaction system. *Abo-Elnor et al., (2004)*, investigated the soil-blade interaction with sandy soil using 3D FEM. The cutting forces were found to be significantly affected by factors such as blade-cutting width, lateral boundary width, and soil swelling. Until present, the FEM is still used to do concerning research on the items as the soil-blade interaction (*Arefi et al., 2022*). The discrete/distinct element method (DEM) was proposed by *Cundall et al. (1979)*. From then on, it has been used to investigate the tool/tire-soil interaction system, especially the soil under the condition of a low moisture content (*Ucgull & Saunders, 2020*). Furthermore, some situations that are practically difficult to achieve in reality, such as the continuous movement of soil particles under tires/tools, can be easily investigated by DEM (*Nakanishi et al., 2020; Ravula et al., 2021; Jiang et al., 2017*). Researchers also utilized the DEM to study the plate/blade-soil interaction system. For example, *Tsuji et al., (2012)*, conducted research on the soil-pushing behavior of a bulldozer blade using a 3D DEM simulation. The result indicated that the size of the cohesive bond force significantly affected the behavior of the particles. However, there are few researchers focused on the effects of the plate inclination angle on soil action and force, though some researchers have conducted soil experiments on the impact of the plate/blade inclination angle. *Yang et al., (2014)*, carried out an experiment that focused on the change of the plate under different inclination angles and movement directions. Base on the aforementioned and previous research (*Ge et al., 2019*), the purpose is to investigate the effects of the plate inclination angle, from 0° to 75°, on soil reaction forces using the two-dimensional (2D) DEM approach in this study.

A non-cohesive soil DEM model and a 5 × 77 × 100 mm plate have been used for this study. The simulation consisted of two parts: calibrate and determine the parameters and moduli for soil particles; and the plate penetrating the soil at a certain depth with different inclined plates.

MATERIALS AND METHODS

First, a soil model should be established, as it is the foundation of the DEM simulation. An in-house 2D DEM code has been developed with a plate-soil system. As a 2D DEM was used in this study, the particles were treated as circular rigid bodies. The study aimed to understand the effect of the plate inclination angle, and the soil model was treated as a linear contact model. To calibrate the soil model, a penetration experiment needed to be performed first.

Soil-soil band

Contact detection is a prerequisite for the calculation of interaction forces between elements (*Zang & Zhao, 2013*). As mentioned in *INTRODUCTION*, non-cohesive soil was used in this study. These soil particles were piled up layer by layer and were aggregated to form a compound test soil (*Horabik & Molenda, 2016*).

For DEM simulation, the macro-scale forces are determined by the microscopic relationship between particles. In this study, every soil particle was regarded as a rigid solid, and the algorithm could be illustrated by an elastoplastic system consisting of spring and damping, as shown in Fig. 1.

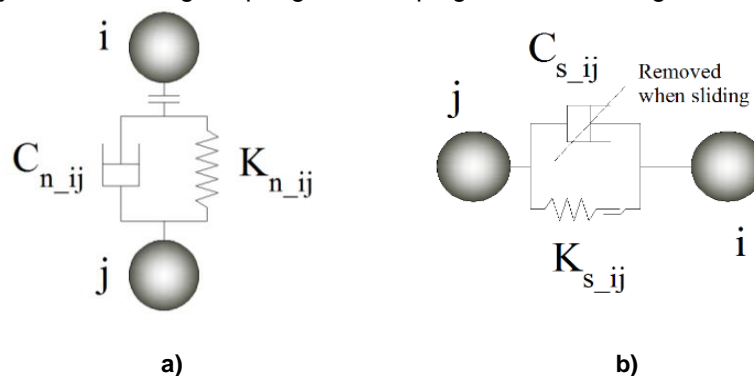


Fig. 1 – Contact model for particles in 2D-DEM
(a) – in normal direction, (b) – in tangential direction

On the basis of the model shown in Fig. 1, it can be seen that the force between particles i and j was divided into two directions: the normal direction and the tangential direction. If the force on particle i in the normal direction is represented by F_{n_i} and the force of the same particle in the tangential direction is represented by F_{s_i} , F_{n_i} and F_{s_i} can be calculated by Equations (1) and (2), as follows:

$$F_{n_i} = K_{n_{ij}}\mu_{n_{ij}} + C_{n_{ij}}v_{n_{ij}} \tag{1}$$

where:

$C_{n_{ij}}$ and $K_{n_{ij}}$ are the coefficients of damping and elasticity in the normal direction, respectively. The parameter $\mu_{n_{ij}}$ is the relative displacement of particles i to j in the normal direction, which is illustrated in Fig. 2, and the parameter $v_{n_{ij}}$ is the relative velocity of particles in the normal direction.

$$F_{s_i} = \begin{cases} K_{s_{ij}}(\Delta x_{pre} + \Delta x) + C_{s_{ij}}v_{s_{ij}} & (f_s < \mu f_n) \\ \mu f_n + C_{s_{ij}}v_{s_{ij}} & (f_s \geq \mu f_n) \end{cases} \tag{2}$$

where:

$C_{s_{ij}}$ and $K_{s_{ij}}$ are the coefficients of damping and elasticity in the tangential direction, respectively. Δx_{pre} is the displacement from the previous step, and Δx is the displacement from the previous step to the present step, which is illustrated in Fig. 2. The parameter of $v_{s_{ij}}$ is the relative velocity from the previous step to the present step. Equation (2) contains a judgment between f_s and μf_n . μ is the frictional modulus between particles i and j , and the normal force f_n is calculated by Equation (3). f_s is the initial time force, which can be expressed by Equation (4), as follows:

$$f_n = K_{n_{ij}}\mu_{n_{ij}} \tag{3}$$

$$f_s = f_s^0 + K_{s_{ij}}\Delta x \tag{4}$$

where: f_s^0 is the force at the previous step.

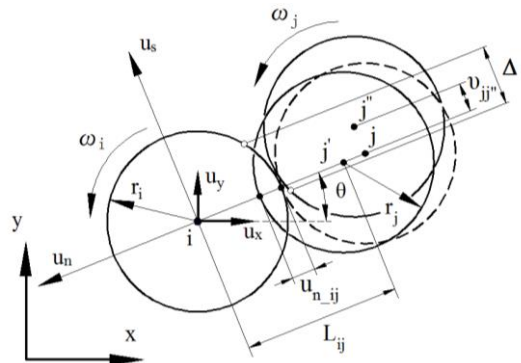


Fig. 2 – The position (displacement) changes in the normal and tangential directions

In Fig. 2, it can be seen that a global coordinate system x - y and a relative coordinate system u_s - u_n have been established to calculate the banding force and moment between particles i and j . In addition, particles i and j have an angular velocity of ω_i and ω_j , respectively. On the basis of these, there should be a rolling resistance moment M_{ij} between the two particles. Specifically, in this study, the parameter M_{ij} was obtained by Equation (5), as follows:

$$M_{ij} = -\alpha b f_n \tag{5}$$

where: f_n is the same parameter as that shown in Equation (3), and α is a constant coefficient of the resistance moment. Parameter b is half the contact length at the overlap between the two particles. If there is an arbitrary element k , the motions of this element should be governed by Newton's second law for the 2D DEM algorithm, as expressed in Equation (6):

$$\begin{cases} m_k \dot{v}_k = F_k \\ I_k \dot{\omega}_k = M_k \end{cases} \tag{6}$$

where:

m_k and I_k are the mass and the inertia moment of element k , respectively. v_k and ω_k are the velocity and the angular velocity of element k , respectively. Parameter F_k represents the resultant force on element k ; meanwhile, the resultant moment on element k is represented by M_k .

Soil-plate interaction

The plate had a rectangular shape, which consisted of circular shapes, as shown in Fig. 3.

Soil particles are checked to see whether they were in contact with the plate or not. If contact is detected, the interaction relationship and mechanical algorithm are the same as those introduced in last section. If a total number of nn particles were in contact with the plate, the force acting on the plate could be calculated and expressed as follows:

$$\begin{cases} F_x = \sum_0^{nn} F_i^x & (x - axis) \\ F_y = \sum_0^{nn} F_i^y & (y - axis) \end{cases} \quad (7)$$

In Equation (7):

F_x and F_y are the respective force components on the plate in the direction of the x-axis and the y-axis.

F_i^x and F_i^y represent the component force on a single element when in contact with the plate.

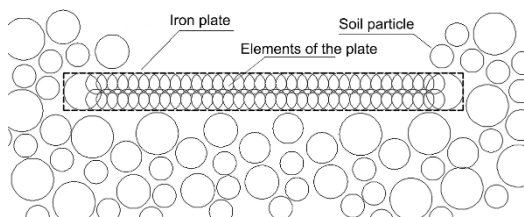


Fig. 3 – Description of the iron plate in the 2D-DEM

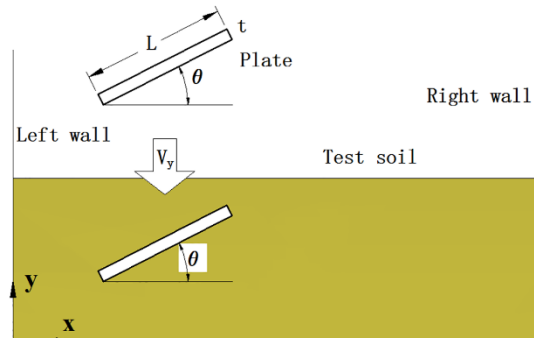


Fig. 4 – Movement of the plate in the soil bin

Experiment and parameter determination

Generally, there are two methods for calibrating the parameters of the DEM soil model: the first method is to repeat the tests on numerous occasions, and after every test, compare the results and check whether they are close to the results of either the in situ measurements or the laboratory experiments; the second method directly determines the input parameters to be equal to the soil test results (Coetzee, 2019). In this study, the first method was utilized.

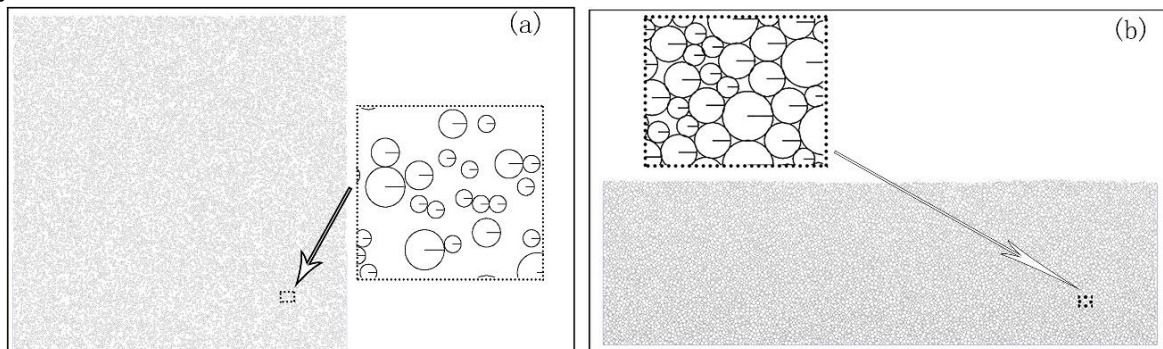


Fig. 5 – Soil particles have been packed in the soil bin:

a) - The soil particles are randomly distributed initially; b) - The particles were settled after a free-falling process

Table 1

| Soil parameters in DEM test 4 | | |
|-------------------------------|----------------|-------------------|
| Items | Value | Unit |
| Particle number | 14,973 | |
| Particle density | 2,600 | kg/m ³ |
| Diameters of particles | 1.5; 2.5; 3.5 | mm |
| Frictional modulus | 0.48 | |
| Elastic modulus Kn, Ks | 50,000, 12,500 | N/m |

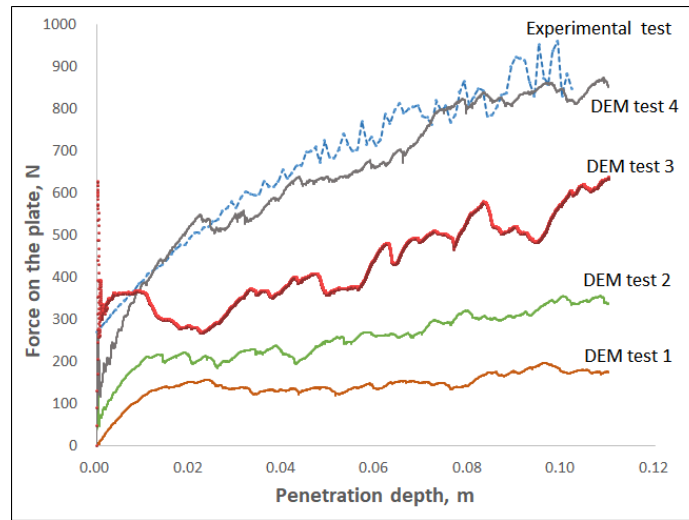


Fig. 6 – A series of DEM trial tests compared with the laboratory experiment

Before conducting the simulation test, a laboratory experiment of penetration testing was performed. The plate, with dimensions of 5 × 77 × 100 mm (thickness × width × length), was set horizontally above the soil surface in the soil bin. The results of the experiment are shown in Fig. 6. In the simulation, according to the established particle–particle bonding rules, a total of 14,973 soil elements were deposited in a soil bin that was 1 m in length, 1 m in height, and 0.3 m in width, as shown in Fig. 5. As a plate with an inclination angle of 0° was used for calibration, the plate was set just above the position of the highest soil particles. After a series of simulation tests, the reaction force results were plotted on a graph, as shown in Fig. 6.

Based on Fig. 6, DEM test 4 matches the laboratory results. The maximum value of the reaction force was 964.87 N in the laboratory experimental test, and it was 873.0 N in DEM test 4. Moreover, the increasing slopes were also similar to each other, DEM test 4 was still considered to be close enough to the laboratory results. Therefore, the soil model with the equivalent parameters of DEM test 4, as shown in Table 1, were used for the planned DEM tests.

RESULTS

A plate with dimensions of 77 × 100 × 5 mm was determined for the DEM tests. After the soil model was calibrated, the plates with 0°, 15°, 30°, 45°, 60° and 75° inclination angles were used for the experiments. The results of the DEM experiments are shown in Fig. 7.

Fig. 7 shows the stress distribution of soil disturbed by plates at different inclination angles during soil penetration at a depth of 100 mm. This demonstrates that the soil reacted to the plate penetration, and when the inclination angle was changed, the soil reacted differently. When the inclination angle changed from 0° to 75°, the forces exerted on the plate were recorded, and the relationship between the forces and the penetration depth is shown in Fig. 8a and Fig. 8b.

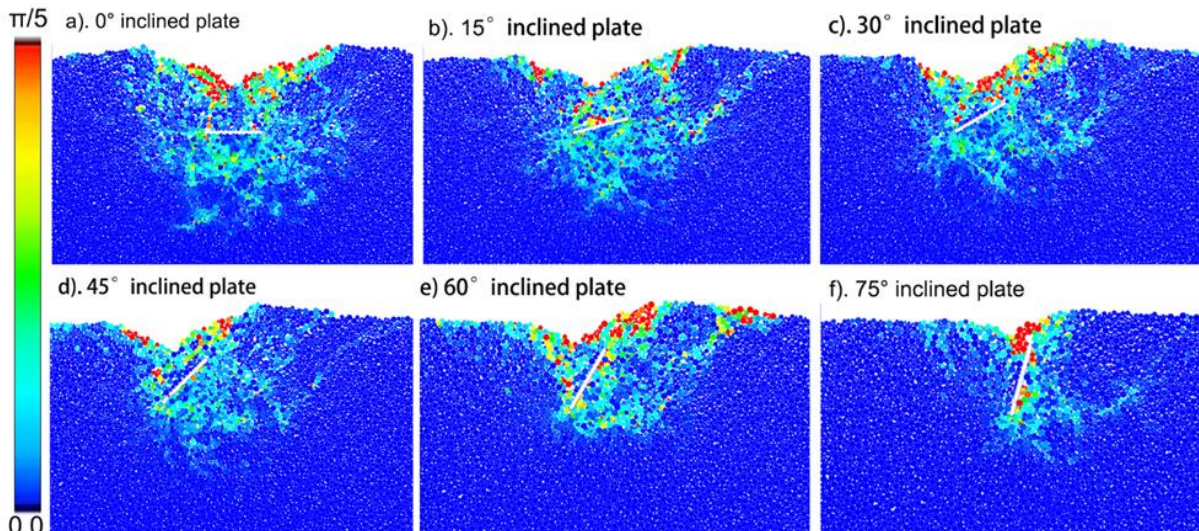


Fig. 7 – Plates with various inclination angles penetrated into the soil at a depth of 100 mm

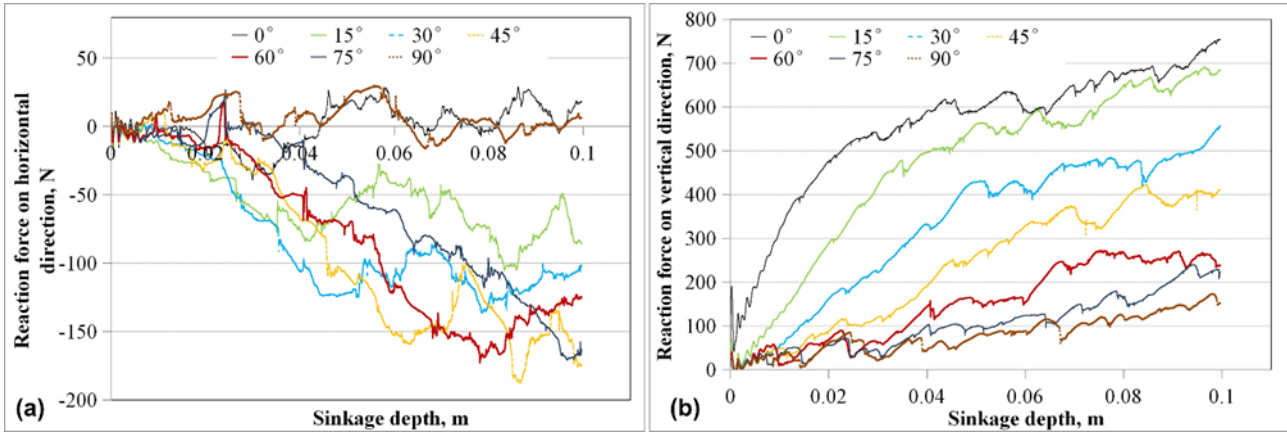


Fig. 8 – Relationship between the forces exerted on the plates and the penetration depth:
 (a) - in the horizontal direction, (b) - in the vertical direction

In Fig. 4, it can be seen that the x-axis was in the horizontal direction and the y-axis was in the vertical direction. As shown in Fig. 8a, the horizontal force components of the plates with inclination angles of 0° and 90° have a similar trend with an increasing penetration depth, and their values are close to 0 N. The remaining plates, with inclination angles at 15°, 30°, 45°, 60°, and 75°, are similar to those with angles of 0° and 90° when the penetration depth was < 25 mm. However, if the depth was >25 mm, the horizontal force components at inclination angles of 15° and 30° decreased with an increase in penetration depth, until a depth of approximately 50 mm, and then, they almost kept at 70 and 110 N, respectively, until the plate ceased. In contrast, the plates with inclination angles of 45°, 60°, and 75° decreased almost proportionally to an increase in the penetration depth above 25 mm. The minimum value of the force, -187.6 N, could be achieved using a 45° inclination plate at a depth of 86.6 mm.

Unlike Fig. 8a, Fig. 8b shows that the vertical force components of different inclination plates separated from each other. In addition, the greater the inclination angle, the lower the force value. Except for the 0° plate, under a certain slope rate, the force component of all the plates increased with an increase in penetration depth. In the case of the 0° plate, the force component increased rapidly at a depth of under 25 mm and then increased only gradually with a subsequent increase in depth. The maximum value of the force component was 753.8 N at a depth of 100 mm.

During the penetration process, the relationship between the soil reaction force and the inclination angle has been plotted on a graph, as shown in Fig. 9.

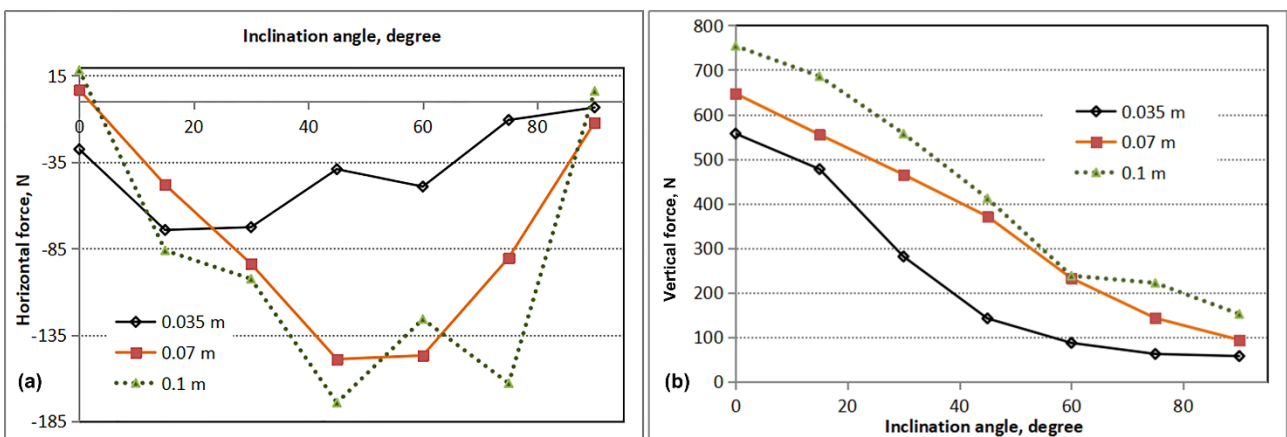


Fig. 9 – The relationship of forces and inclination angle
 (a) - in the horizontal direction, (b) - in the vertical direction

It can be seen from Fig. 9 that depths of 35, 70, and 100 mm were studied. The figure shows that a change in the inclination angle has a limited effect on the horizontal force component at a depth of 35 mm.

However, if the depths are at 70 or 100 mm, the relationship between the force and the change in depth is similar to a parabolic curve, and the minimum value of the force occurs, in both cases, at an inclination angle of 45°. However, according to Fig. 9b, the vertical force components have a close relationship with changes in the inclination angle. At all depth levels, the perpendicular plate produced the lowest soil reaction force. It can also be seen that a plate with an inclination angle that is perpendicular to the soil surface produces a lower resistance force, as shown in Figs 8 and 9.

CONCLUSIONS

In this study, a non-cohesive DEM soil model was used, calibrated by laboratory penetration experiments. Using this soil model and a plate with dimensions of 5 × 77 × 100 mm, the effects of changes to the inclination angle on the forces generated during a penetration test were investigated. Based on the results of the DEM simulation and the discussion introduced in section 3, the following concluding remarks can be made:

- (1) The 2D DEM method is sufficient to meet the research needs for investigating the soil reaction forces, which are affected by changing inclination angles. The whole process has been successfully carried out in this study.
- (2) During the penetration process, the maximum value of the vertical force component was 753.8 N, which was generated by a 0° inclination angle plate at a depth of 100 mm, at which point the penetration test was stopped. It was found that the greater the inclination angle, the greater the vertical force.
- (3) For the movement of a bulldozer blade, the vertical angle should be maintained to minimize resistance. If the lugs on the tire/track are considered, the inclination angle should be closer to 45° to generate a greater traction force.

ACKNOWLEDGEMENT

This research was supported by the project of the Natural Science Foundation of Anhui Province (2308085ME160).

REFERENCES

- [1] Abo-Elnor, M., Hamilton, R., Boyle, J. T. (2004). Simulation of soil–blade interaction for sandy soil using advanced 3D finite element analysis, *Soil and Tillage Research*, Vol. 75, Iss. 1, pp. 61-73. Egypt;
- [2] Arefi, M., Karparvarfard, S. H., Azimi-Nejadian, H., Naderi-Boldaji, M. (2022). Draught force prediction from soil relative density and relative water content for a non-winged chisel blade using finite element modelling, *Journal of Terramechanics*, Vol. 100, pp. 73-80. Iran;
- [3] Coetzee, C. J. (2019). Particle upscaling: Calibration and validation of the discrete element method, *Powder Technology*, Vol. 344, pp. 487-503. South Africa;
- [4] Cundall, P. A., Strack, O. D. L. (1979). A discrete numerical model for granular assemblies, *Geotechnique*, Vol. 29, Iss. 1, pp. 47-65. UK;
- [5] Ge, J., Zhang, D. S., Wang, X. L., Cao, C. M., Fang, L. F., Duan, Y. M. (2019). Tractive performances of single grouser shoe affected by different soils with varied moisture contents, *Advances in Mechanical Engineering*, Vol. 11, Iss. 5, no.1687814019849133. Hefei/China;
- [6] Gill, W. R., Berg, G. E. V. (1968). Soil dynamics in tillage and traction, Agricultural Research Service, U.S. Department of Agriculture. *America Agriculture Handbook No. 316*. United States;
- [7] Hermawan, W., Oida, A., Yamazaki, M. (1996). Measurement of soil reaction forces on a single movable lug, *Journal of Terramechanics*, Vol. 33, Iss. 2, pp. 91-101. Japan;
- [8] Hermawan, W., Oida, A., Yamazaki, M. (1997). The characteristics of soil reaction forces on a single movable lug, *Journal of Terramechanics*, Vol. 34, Iss. 1, pp. 23-35. Japan;
- [9] Hermawan, W., Yamazaki, M., Oida, A. (1998). Experimental analysis of soil reaction on a lug of a movable lug wheel, *Journal of Terramechanics*, Vol. 35, Iss. 2, pp. 119-135. Indonesia;
- [10] Holthusen, D., Brandt, A. A., Reichert, J. M., Horn, R., Fleige, H., Zink, A. (2018). Soil functions and in situ stress distribution in subtropical soils as affected by land use, vehicle type, tire inflation pressure and plant residue removal, *Soil and Tillage Research*, Vol. 184, pp. 78-92. Brazil;
- [11] Horabik, J., Molenda, M. (2016). Parameters and contact models for DEM simulations of agricultural granular materials: A review, *Biosystems Engineering*, Vol. 147, pp. 206-225. Poland;

- [12] Jia, H., Guo, M., Yu, H., Li, Y., Feng, X., Zhao, J., Qi, J. (2016). An adaptable tillage depth monitoring system for tillage machine, *Biosystems Engineering*, Vol. 151, pp. 187-199. Jilin/China;
- [13] Jiang, M., He, J., Wang, J., Zhou, Y., Zhu, F. (2017). Discrete element analysis of the mechanical properties of deep-sea methane hydrate-bearing soils considering interparticle bond thickness, *Comptes Rendus Mécanique*, Vol. 345, pp. 868-889. Shanghai/China;
- [14] Jiang, Q. J., He, Z. L., Wang, Y. W., Wang, J. (2021). Optimizing the working performance of a boat-type tractor using central composite rotatable design and response surface method, *Computers and Electronics in Agriculture*, Vol. 181, 105944. Hangzhou/China;
- [15] Md-Tahir, H., Zhang, J., Xia, J., Zhang, C., Zhou, H., Zhu, Y. (2019). Rigid lugged wheel for conventional agricultural wheeled tractors - Optimising traction performance and wheel–soil interaction in field operations, *Biosystems Engineering*, Vol. 188, pp.14-23. Wuhan/China;
- [16] Nakanishi, R., Nakashima, H., Miyasaka, J., Ohdoi, K. (2020). Tractive performance analysis of a lugged wheel by open-source 3D DEM software, *Journal of Terramechanics*, Vol. 92, pp. 51-65. Japan;
- [17] Nassiraei, A. A. F., Skonieczny, K. (2020). Grousers improve drawbar pull by reducing resistance and generating thrust at the front of a wheel, *Journal of Terramechanics*, Vol. 91, pp. 73-84. Canada;
- [18] Rasool, S., Raheman, H. (2018). Improving the tractive performance of walking tractors using rubber tracks, *Biosystems Engineering*, Vol. 167, pp. 51-62. India;
- [19] Ravula, P., Acar, G., Balachandran, B. (2021). Discrete element method-based studies on dynamic interactions of a lugged wheel with granular media, *Journal of Terramechanics*, Vol. 94, pp. 49-62. United States;
- [20] Stefanow, D., Dudziński, P. A. (2021). Soil shear strength determination methods – State of the art, *Soil and Tillage Research*, Vol. 208, 104881. Poland;
- [21] Tsuji, T., Nakagawa, Y., Matsumoto, N., Kadono, Y., Takayama, T., Tanaka, T. (2012). 3-D DEM simulation of cohesive soil-pushing behavior by bulldozer blade, *Journal of Terramechanics*, Vol. 49, Iss. 1, pp. 37-47. Japan;
- [22] Ucgul, M., Saunders, C. (2020). Simulation of tillage forces and furrow profile during soil-mouldboard plough interaction using discrete element modelling, *Biosystems Engineering*, Vol. 190, pp. 58-70. Australia;
- [23] Wang, X. L., Yamazaki, M., Tanaka, T. (1993). Dynamic behaviour of an open lugged wheel under paddy soil conditions, *Journal of Terramechanics*, Vol. 30, Iss. 3, pp. 191-203. Japan;
- [24] Wang, X. L., Yamazaki, M., Tanaka, T. (1995). Characteristics of soil reactions of an open lugged wheel under paddy soil conditions, *Journal of Terramechanics*, Vol. 32, Iss. 3, pp. 115-125. Japan;
- [25] Watyotha, C., Gee-Clough, D., Salokhe, V. M. (2001). Effect of circumferential angle, lug spacing and slip on lug wheel forces, *Journal of Terramechanics*, Vol. 38, Iss. 1, pp. 1-14. Thailand;
- [26] Wei, H. Q., Ai, Q., Zhao, W. Q., Zhang, Y. T. (2022). Modelling and experimental validation of an EV torque distribution strategy towards active safety and energy efficiency, *Energy*, Vol. 239, Part A, 121953. Beijing/China;
- [27] Wong, J. Y. (2001). Theory of ground vehicles. 3rd ed. New York: *John Wiley & Sons*. Canada;
- [28] Wong, J. Y. (2010). Terramechanics and off road vehicle engineering: Terrain behavior, off-road vehicle performance and design. 2nd ed. UK: *Elsevier*. Canada;
- [29] Yang, Y., Sun, Y., Ma, S., Yamamoto, R. (2014). Characteristics of normal and tangential forces acting on a single lug during translational motion in sandy soil, *Journal of Terramechanics*, Vol. 55, pp. 47-59. Japan;
- [30] Zang, M., Zhao, C. (2013). Numerical Simulation of Rigid Wheel Running Behavior on Sand Terrain on sand terrain, Singapore, *APCOM & ISCM*. Guangzhou/China;
- [31] Zhang, R., Pang, H., Dong, W. C., Li, T., Liu, F., Zhang, H., Hu, Z. Y., Li, J. Q. (2020). Three-dimensional Discrete Element Method simulation system of the interaction between irregular structure wheel and lunar soil simulant, *Advances in Engineering Software*, Vol. 148, 102873. Shanghai/China;
- [32] Zhu, J., Shen, Y., Hao, P., Liu, J., Li, Y., Wang, K., Zou, M. (2023). Modeling of flexible metal wheel for pressurized lunar rover and traction performance prediction. *Journal of Field Robotics*, Vol. 40, Issue 8, pp. 2030-2041. Tianjin/China

DESIGN DEVELOPMENT AND RESULTS OF EXPERIMENTAL RESEARCH ON GRAIN DAMAGE BY A NEW SCREW CONVEYOR

РОЗРОБКА КОНСТРУКЦІЇ ТА РЕЗУЛЬТАТИ ЕКСПЕРИМЕНТАЛЬНОГО ДОСЛІДЖЕННЯ ПОШКОДЖЕННЯ ЗЕРНА НОВИМ ГВИНТОВИМ КОНВЕЄРОМ

Volodymyr BULGAKOV¹⁾, Adolfs RUCINS^{*2)}, Ivan HOLOVACH¹⁾,
Oleksandra TROKHANIYAK¹⁾, Dmytro POLISHCHUK³⁾

¹⁾ National University of Life and Environmental Sciences of Ukraine, 15, Heroyiv Oborony Str., Kyiv, UA 03041 / Ukraine

²⁾ Latvia University of Life Sciences and Technologies, Ulbroka Research Centre, 1, Instituta Str., Ulbroka, Ropazu Region, Stopinu Municipality, LV 2130 / Latvia

³⁾ Taras Shevchenko National University of Kyiv, 64/13, Volodymyrska Str.,

*Corresponding author's e-mail: adolfs.rucins@lbtu.lv

DOI: <https://doi.org/10.35633/inmateh-73-32>

Keywords: transportation, grain material, screw conveyor, bladed working body.

ABSTRACT

The article presents an experimental stand for laboratory research of a screw conveyor with a bladed working body. Based on the results of experimental studies, the corresponding response surface regression equations were constructed to establish the influence of controllable factors upon the degree of damage to the grain materials. It was established that the main factor affecting the increase in the amount of the grain damage was factor $x_3(n)$, the rotation frequency of the bladed working body. The increase in factors $x_1(D)$ and $x_2(\psi)$ led to a decrease in the amount of the grain damage. Based on the results of comparative experimental studies to determine the degree of damage to the grain material during its transportation by the screw and blade working bodies, it was established that the bladed working body provided a reduction in the degree of damage to the grain material with a simpler manufacturing technology.

АНОТАЦІЯ

В статті представлена експериментальна установка для дослідження шнекового транспортера із лопатевим робочим органом. За результатами експериментальних досліджень побудовані відповідні рівняння регресії, поверхні відгуку для встановлення впливу на ступінь пошкодження зернових матеріалів керованих факторів. Встановлено що основним фактором, який впливає на збільшення величини травмування зерна є фактор $x_3(n)$, частота обертання лопатевого робочого органу. Збільшення величин факторів $x_1(D)$ та $x_2(\psi)$ призводить до зменшення величини травмування зерна. На основі результатів порівняльних експериментальних досліджень з визначення ступеня травмування зернового матеріалу при його транспортуванні гвинтовим та лопатевим робочими органами встановлено, що лопатевий робочий орган забезпечує зменшення ступеня пошкодження зернового матеріалу при простішій технології виготовлення.

INTRODUCTION

Screw conveyors are widely used in the transportation of grain, seed materials, and granular mineral fertilizers, which experience significant damage during their transportation. The main causes of damage to the agricultural materials are the entry of their particles into the gap between the rotating working body and the stationary inner surface of the guide pipe, resulting in damage to the materials. It has been established that the existing designs of the working parts of screw conveyors do not fully satisfy the functional requirements for damage to the grain materials.

Thus, the designs of screw conveyors with the working bodies of a round cross-section are made of high-carbon steels that are subjected to heat treatment (Hewko et al., 2015; Sokil et al., 2018; Aulin et al., 2019; Lyashuk et al., 2019; Hevko et al., 2019). However, such spirals can only be produced in an uncalibrated state, with subsequent calibration per step, with a length of 3...6 m. Therefore, their thermal treatment is too complicated. They also have low productivity since the circular cross-section of the spiral does not provide a concentrated guiding force in the axial direction when transporting the material.

Strip spirals are characterized by significantly higher efficiency, but they have low durability, since the low-carbon steels used in their manufacture are quickly destroyed when the spirals operate at small radii of curvature, due to the occurrence of banner stresses during rotation (Hevko et al., 2015; Hevko et al., 2016; Bulgakov et al., 2022).

Also, the selection of constructive and kinematic parameters of the working bodies of conveyors, depending on the rheological properties of grain materials, cannot completely solve this problem (Pascuzzi *et.al.*, 2024; Bulgakov *et.al.*, 2022).

Therefore, the task of developing new constructions of working bodies of conveyors, which will have a simple manufacturing technology and ensure the implementation of the process of transportation of grain materials with less damage to the grain material, is urgent.

An urgent task in development is new constructions of the working bodies of conveyors that will have a simple manufacturing technology and ensure implementation of the process of transportation of the grain materials with less damage to the grain material. The purpose of research is to reduce damage to the grain materials during their transportation by a screw conveyor, by creating an improved screw construction with bladed working parts, and experimental justification of its parameters.

MATERIALS AND METHODS

To solve this problem, an experimental stand has been developed to study a screw conveyor with a bladed working body, the diagram of which is shown in Fig. 1. It consists of frame 10 on which a screw conveyor is placed, containing a guide pipe 7 in which a bladed working body 6 is located. On the loading side of the material hopper 5 is installed, and in the unloading area there is a window with an adjustable damper 9 and a brake on the auger shaft 8. The working element is driven from the electric motor 3 through a safety clutch 4.

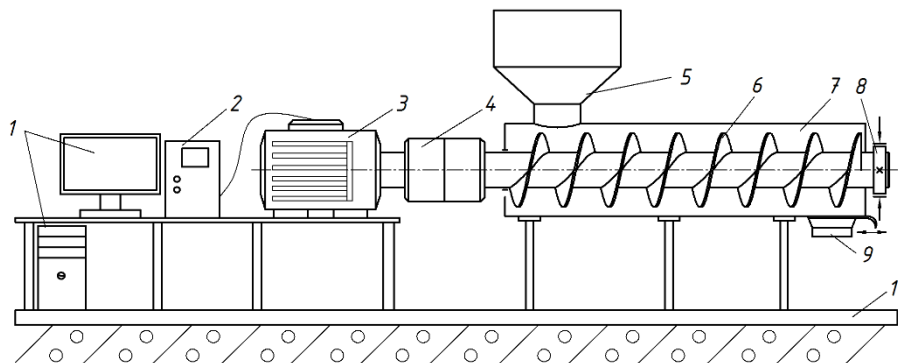


Fig. 1 - Diagram of an experimental stand for the investigation of the screw conveyor with a bladed working body

To start the engine and adjust its rotation speed, frequency converter 2 (Altivar 71) with Power Suite v.2.5.0 software is used. The Altivar 71 system is connected to the network and computer 1.

When the required rotation speed is set, using a computer through the Altivar 71 system, a command is transmitted to the electric motor, and through a safety clutch it begins to rotate the shaft of the blade working body with the set parameters. First, the grain material is loaded into the hopper and, at a certain rotation speed of the working body and according to specified parameters, the material is transported to the unloading zone into a measuring vessel.

A general view of the stand for studying the screw conveyor and the bladed working body is shown in Fig. 2.



Fig. 2 - General view of the stand for the investigation of the screw conveyor (a) and a screw working body, consisting of individual blades (b)

It is advisable to manufacture the blades for the working body of the conveyor by twisting a sheet material and then welding them to a cylindrical shaft. It has been established that it is advisable to use flat blades with a mirror reflection relative to the vertical in the range from 0° to 90° (full range 180°), since it is not rational to produce blade sectors with an angular pitch of up to 20° , both from the point of view of their manufacture (large quantity) and from point of view of their composition (Hevko, et al., 2019).

To determine the degree of damage to the grain material during its transportation by the developed bladed working body of the auger conveyor into a measuring vessel, taking into account the dimensional and geometric parameters of the grain, which contained about 100 grains, three grain samples were first taken before moving. Next, the number of the damaged grains was checked and the percentage of the damaged grain material was determined before its transportation. Grains with knocked out germs were not taken into account, and only crushed grains were consider. Based on the difference in the number of damaged grains before and after transportation, the degree of damage to the grain material was determined depending on the changing structural and kinematic parameters of the blade working body of the screw conveyor.

To obtain a comparative indicator of the damaged material, the mass of the damaged grain in the sample mass was recalculated using the formula:

$$T = \frac{m_1 - m_2}{m_n} \cdot 100, \% \quad (1)$$

where m_1 – mass of the damaged grain after its moving by the conveyor, kg; m_2 – mass of the damaged grain after moving by the conveyor, kg; mass of the damaged grain for transportation, kg; m_n – mass of the sample, kg.

The damaged grains were those that had the following damage: crushed germs, damaged germs, damaged grain shell, damaged endosperm, damaged endosperm shell, broken grain, mechanically compressed grain. This damage for various crops, the transportation of which was experimentally studied, is shown in Fig. 3.



Fig. 3 - General view of grains with damage:

a – peas; b – maize; c – wheat

In addition, there are presented grains, selected from the total mass with standard volumes (up to 1 decimeter per cube) after their transportation. As it is evident from the photos, presented in Fig. 3. damage occurs during transportation of all the types of grains. The most damage occurs to the maize grains. In all cases, the greatest damage is damage (chips) of the outer surfaces, as well as continuous transverse cracks, splitting of seeds into two approximately equal parts, etc.

When conducting a multifactorial experiment in order to determine the degree of damage to the grain material by the bladed working body, the variable factors were: the pipe diameter D , the filling factor ψ of the conveyor and the rotational speed n of the bladed working body.

Since during the experiments the variable independent factors are heterogeneous and have different units of measurement, and the numbers expressing the value of these factors are of different orders, they were brought to a unified calculation system by moving from actual values to coded ones, presented in Table 1.

The investigation of the material damage made it possible to determine its dependence on many factors characterizing the process, namely: the internal diameter of the pipe D , (m); the filling factor ψ ; the rotation speed n (rpm) of the blade working body.

Investigations on damage to the grain material with a bladed working body were carried out during transportation of such materials with the corresponding volumetric mass: peas – $700 \text{ kg}\cdot\text{m}^{-3}$; wheat – $760 \text{ kg}\cdot\text{m}^{-3}$; maize – $800 \text{ kg}\cdot\text{m}^{-3}$ with moisture content $W = 12\text{...}15\%$, which made it possible to construct analytical regression equations.

Table 1

Results of the factor coding and levels of their variation in the research of damage to grain material

| Factors | Designation | | Interv. of variation | Levels of variation, natur. / codified | | |
|---|-------------|--------|----------------------|--|--------|--------|
| | Code | Natur. | | | | |
| The inner diameter of the pipe D , m | X_1 | x_1 | 0.02 | 0.06/-1 | 0.08/0 | 0.1/+1 |
| The filling factor of the conveyor, ψ | X_2 | x_2 | 0.2 | 0.3/-1 | 0.5/0 | 0.7/+1 |
| Rotation speed n of the blade working body, rpm | X_3 | x_3 | 200 | 200/-1 | 400/0 | 600/+1 |

The processing of the data, obtained from the experimental array, was carried out on a PC, using well-known methods and methods of statistical processing, using the well-known methods of the correlation and regression analysis to ultimately obtain empirical regression equations (Adler, et al., 1976; Dushinskyi, 1998). To obtain a regression model for the optimization parameter, an appropriate multifactorial experimental design was selected, which was implemented in the following sequence.

The response function (optimization parameter), i.e., determined in an experimental way, are presented as mathematical models of a full quadratic polynomial (Adler et al., 1976; Dushinskyi 1998):

$$T = b_0 + b_1x_1 + b_2x_2 + b_3x_3 + b_{12}x_1x_2 + b_{13}x_1x_3 + b_{23}x_2x_3 + b_{11}x_1^2 + b_{22}x_2^2 + b_{33}x_3^2, \quad (2)$$

where $b_0, b_1, b_2, b_3, b_{12}, b_{13}, b_{23}, b_{11}, b_{22}, b_{33}$ – coefficients of the corresponding values x_i ; x_1, x_2, x_3 – relevant factors to be coded.

The values of the coefficients of the regression equations, presented in Table. 2.

Table 2

Value of coefficients of regression equations

| Coeffic. | b_0 | b_1 | b_2 | b_3 | b_{12} | b_{13} | b_{23} | b_{11} | b_{22} | b_{33} |
|----------|-------|--------|--------|-------|----------|----------|----------|----------|----------|----------|
| peas | 0.360 | -0.028 | -0.024 | 0.092 | 0 | -0.002 | 0 | -0.004 | 0.0060 | -0.0040 |
| maize | 0.318 | -0.022 | -0.026 | 0.085 | 0 | -0.0022 | 0 | -0.0036 | 0.0054 | -0.0036 |
| wheat | 0.270 | -0.025 | -0.026 | 0.075 | 0 | -0.002 | 0 | -0.0032 | 0.0048 | -0.0032 |

General form of the regression equation for the magnitude of the grain damage during transportation by a screw conveyor with a bladed working element depending on the pipe diameter D , the conveyor filling coefficient ψ and the rotation speed n of the bladed working element, i.e. $T_{(x_1, x_2, x_3)} = f(D, \psi, n)$ according to the results of full factorial experiments, 3^3 in coded quantities is equal to:

– for transportaion of peas:

$$T_{(x_1, x_2, x_3)} = 0.36 - 0.028x_1 - 0.024x_2 + 0.092x_3 + 0x_1x_2 - 0.002x_1x_3 + 0x_2x_3 - 0.004x_1^2 + 0.006x_2^2 - 0.004x_3^2; \quad (3)$$

– for transportaion of maize:

$$T_{(x_1, x_2, x_3)} = 0.318 - 0.022x_1 - 0.026x_2 + 0.085x_3 + 0x_1x_2 - 0.0022x_1x_3 + 0x_2x_3 - 0.0036x_1^2 + 0.0054x_2^2 - 0.0036x_3^2; \quad (4)$$

– for transportaion of wheat:

$$T_{(x_1, x_2, x_3)} = 0.27 - 0.025x_1 - 0.026x_2 + 0.075x_3 + 0x_1x_2 - 0.002x_1x_3 + 0x_2x_3 - 0.0032x_1^2 + 0.0048x_2^2 - 0.0032x_3^2. \quad (5)$$

The assessment of the statistical significance of the coefficients of the regression equation and the verification of the adequacy (correspondence) of the obtained theoretical distribution of random variables of the regression equations to the real experimental process were made according to method (Lyashuk et al., 2019). The statistical significance of the coefficient assessment of the regression equation and the verification of the adequacy (correspondence) of the obtained theoretical distribution of random variables of the regression equations to the real experimental process were carried out according to the method (Lyashuk et al., 2019). In natural quantities (coordinates), the regression equation (3 – 5), after transforming and simplifying the expressions, is accepted in its final form:

– for transportation of peas:

$$T_{(D, \psi, n)} = 0.252 + 0.511D - 0.275\psi + 0.0011n - 0.0014Dn - 10D^2 + 0.15\psi^2 - 0.00000033n^2; \quad (6)$$

– for transportation of maize:

$$T_{(D,\psi,n)} = 0.228 + 0.475D - 0.25\psi + 0.00101n - 0.001023Dn - 9D^2 + 0.135\psi^2 - 0.000000297n^2; \quad (7)$$

– for transportation of wheat:

$$T_{(D,\psi,n)} = 0.203 + 0.389D - 0.22\psi + 0.000903n - 0.00099Dn - 8D^2 + 0.12\psi^2 - 0.000000264n^2. \quad (8)$$

The obtained regression equations (6 – 8) may be used to determine the degree of the grain damage T during transportation by a screw conveyor with a bladed working body, depending on the diameter of the pipe D , the filling factor ψ of the conveyor and the rotation speed of the bladed working body when transporting peas, maize, wheat to the following limits of change in the input factors: $0.06 \leq D \leq 0.1$ (m); $0.3 \leq \psi \leq 0.7$; $100 \leq n \leq 500$ (rpm).

RESULTS

Using the developed STATISTICA application program for the PC, a graphical reproduction of intermediate general regression models in the form of quadratic responses and their two dimensional sections of the grain damage value T as a function of two variable factors $x_{i(1,2)}$ with a constant level of the corresponding third factor $x_{i(3)} = \text{const}$ (Fig. 4 – Fig. 6) was built.

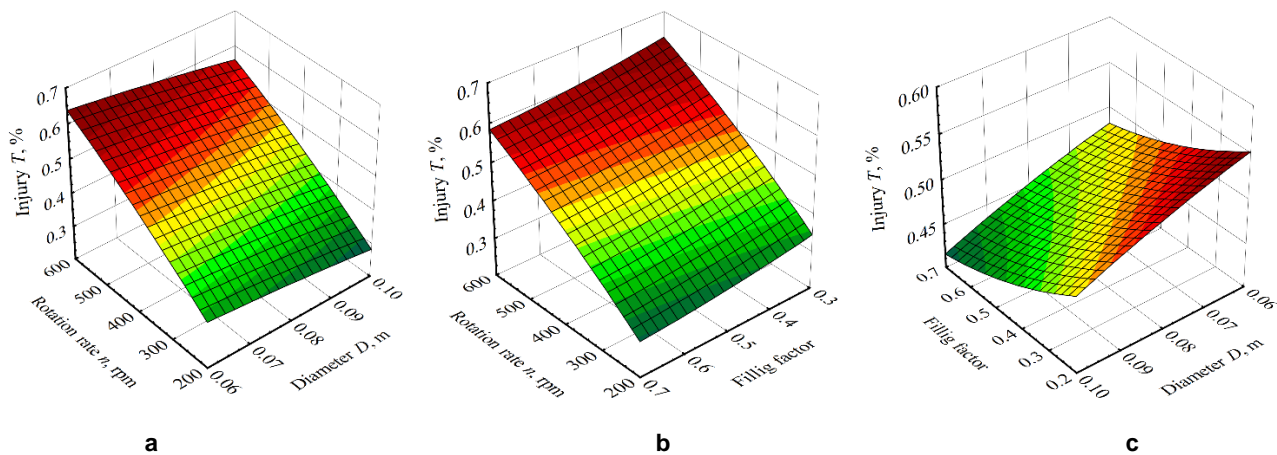


Fig. 4 - Response surface of the magnitude of damage to the pea grains depending on:
 a) $T = f(D; n)$; b) $T = f(n; \psi)$; c) $T = f(\psi; n)$

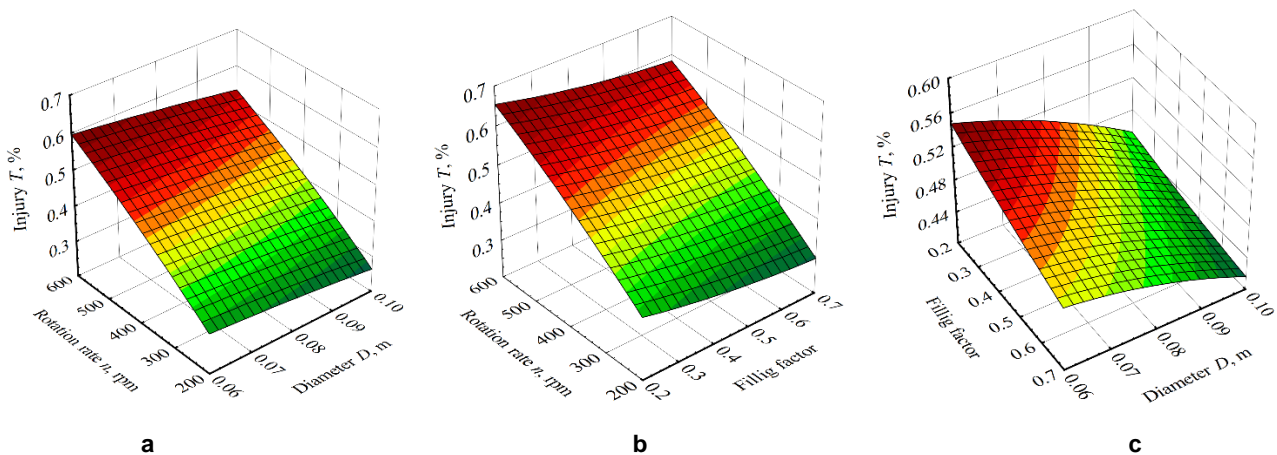


Fig. 5 - Response surface of the magnitude of the maize grain damage depending on:
 a) $T = f(D; n)$; b) $T = f(n; \psi)$; c) $T = f(\psi; n)$

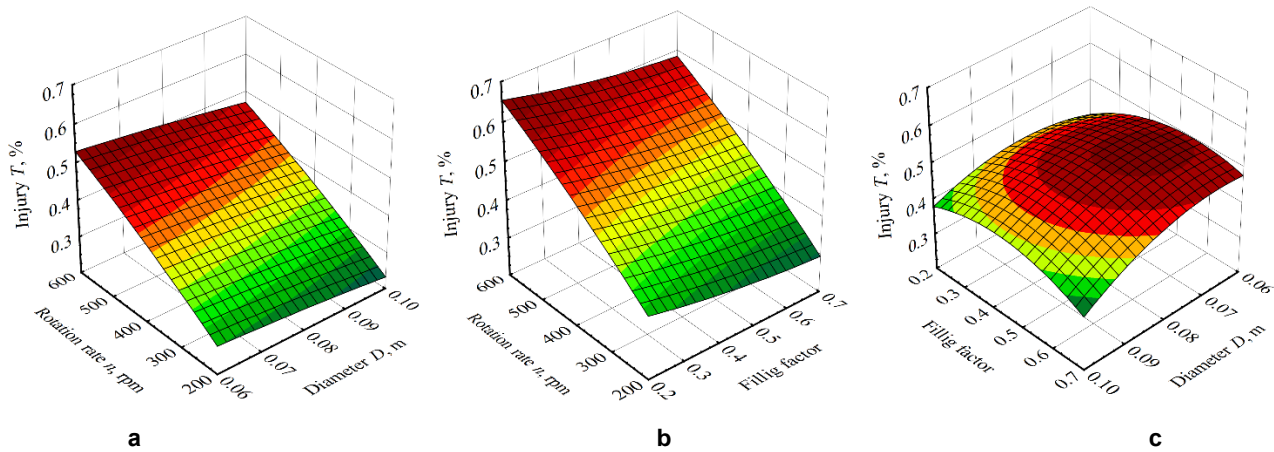


Fig. 6 - Response surface of the magnitude of the wheat grain damage depending on:

a) $T = f(D; n)$; b) $T = f(n; \psi)$; c) $T = f(\psi; n)$

Analysis of the above regression equations shows that the main factor influencing the increase in the amount of the grain damage is factor $x_3(n)$, the rotation speed of the blade working body. An increase in factors $x_1(D)$ and $x_2(\psi)$ leads to a decrease in the amount of the grain damage. Therefore the rational value of the frequency is the rotation speed of the blade working body within the range of $100 \leq n \leq 500$ (rpm).

When the diameter D of the guiding pipe changes within 0.06...0.1 m, the damage to the grain material, namely peas, maize and wheat, decreases by 12...13.5%; when the rotation speed of the blade working body changes within 200...600 rpm, the damage to the grain increases by 48...50%, and in the range of changes in the conveyor filling coefficient ψ from 0.3 m to 0.7 m, the damage is reduced by 10%.

The results of comparative experimental investigations to determine the degree of damage to the grain material during its transportation by a screw working body (a solid line), as well as by a bladed working body (a dashed line) on the rotation speed n at various values of the conveyor filling coefficient ψ and on the diameter D of the guiding pipe also at different values of the conveyor filling coefficient ψ are respectively presented in Fig. 7 and Fig. 8.

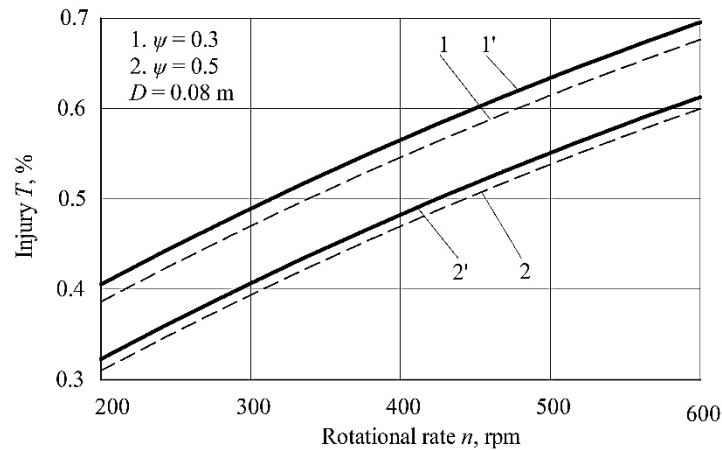


Fig. 7 - Dependences of damage to the grain material T , %, caused by the screw working body (a solid line)

Analysis of the graphical dependencies, depicted in Figs. 6 and 7. showed that the use of a bladed working body, in comparison with the screw one, ensures a reduction in the degree of damage to the grain material.

So, for the rotation speed of the blade working body, which is in the range of 200...600 rpm, the degree of damage to the grain material decreases by 1.07...1.1 times.

When the diameter of the guiding pipe D changes within 0.06...0.1 m, the degree of damage to the grain material, when using a bladed working body, decreases by 1.04...1.07 times.

Therefore it is advisable to use instead of helical spirals flat blades inclined to the axis of rotation, which are attached to the cylindrical shaft of the base. It is advisable to produce such blades by cutting and trimming the sheet material, followed by welding them to the cylindrical shaft.

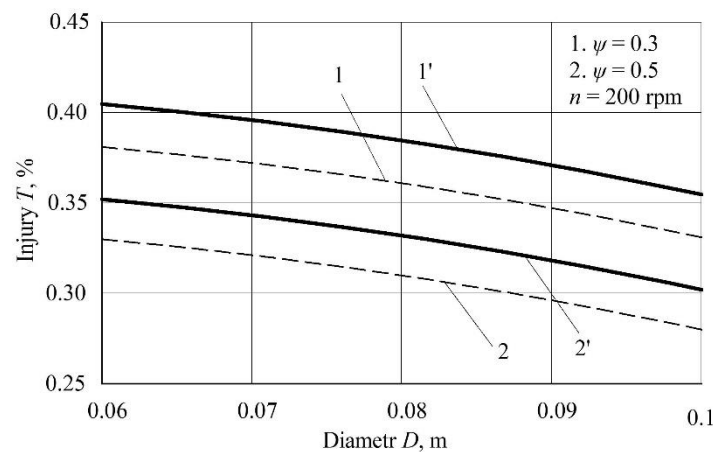


Fig. 8 - Dependences of damage to the grain material T , %, caused by the screw working element (a solid line) and a bladed one (a dashed line) on the diameter of the guide pipe D at different conveyor filling coefficients ψ

Consequently, the proposed design of the bladed working body provides stable standard dimensions of the working body section at low cost and simpler manufacturing technology, and also carries out the process of transporting the grain materials with less damage.

CONCLUSIONS

Based on the analysis of literary sources and patent search, an experimental stand was developed and manufactured to study a screw conveyor with a bladed working body, which will improve the functional and operational characteristics of screw conveyors. The proposed design of the blade working body ensures stable standard dimensions of the working body section at low cost and simpler manufacturing technology, and also carries out the process of transporting the grain materials with less damage.

Based on the results of experimental studies, the corresponding response surface regression equations were constructed to establish the influence of controllable factors on the degree of damage to the grain materials. It has been found out that the main factor influencing the increase in the amount of the grain damage is factor $x_3(n)$, rotation speed n of the blade working body. An increase in factors $x_1(D)$ and $x_2(\psi)$ leads to a decrease in the amount of the grain injury. Therefore, a rational value of frequency n is the rotation speed of the blade working body within the range of $100 \leq n \leq 500$ (rpm).

Analysis of the results of the comparative experimental investigations to determine the degree of damage to the grain material during its transportation by a screw working body and a bladed working body at different values of the conveyor filling factor from the rotation speed n and the diameter of the guiding pipe D showed that a bladed screw conveyor provides a reduction in the degree of damage to the grain material.

The proposed design of the blade working body ensures stable standard dimensions of the working body section at low cost and simpler manufacturing technology, and also carries out the process of transporting the grain materials with less damage.

REFERENCES

- [1] Adler, Yu. P., Markova, E. V., Granovsky, Yu. V. (1976). Planning the experiment in search of optimal conditions. *Nauka*, 279 p.
- [2] Aulin, V. V., Pankov, A. O., Zamota, T. M., Lyashuk, O. L., Hrynkiv, A. V., Tykhyi, A. A., Kuzyk, A. V. (2019). Development of mechatronic module for the seeding control system. *INMATEH - Agricultural Engineering*, 59(3), 181-188. <https://doi.org/10.35633/INMATEH-59-20>
- [3] Bulgakov, V., Trokhaniak, O., Adamchuk, V., Chernovol, M., Korenko, M., Dukulis, I., & Ivanovs, S. (2022). A study of dynamic loads of a flexible sectional screw conveyor. *Acta Technologica Agriculturae*, 25(3), 131-136. doi:10.2478/ata-2022-0020
- [4] Bulgakov, V., Trokhaniak, O., Klendii, M., Ivanovs, S., & Dukulis, I. (2022). Research on the Impact of the Operating Modes and Main Design Parameters on the Efficiency of the Machine for Preparing and Packing Slaked Lime. *INMATEH - Agricultural Engineering*, 67(2), 323-330. <https://doi.org/10.35633/inmateh-67-33>
- [5] Dushynskiy V. V. (1998). Fundamentals of scientific research. Theory and practice with software. Kyiv, National Technical University of Ukraine "Ihor Sikorsky Kyiv Polytechnic Institute". 408 p.

- [6] Hevko R. B., Zalutskyi S. Z., Tkachenko I. G., Klendiy O. M. (2015). Development and investigation of reciprocating screw with flexible helical surface. *INMATEH: Agricultural engineering*, 46(2), 133-138.
- [7] Hevko R. B., Rozum R. I., Klendiy O. M. (2016). Development of design and investigation of operation processes of loading pipes of screw conveyors. *INMATEH: Agricultural engineering*, 50(3), 89-96.
- [8] Hevko, R. B., Zalutskyi, S. Z., Hladyo, Y. B., Tkachenko, I. G., Lyashuk, O. L., Pavlova, O. M., Pohrishchuk, B. V., Trokhaniak, O. M., Dobizha, N. V. (2019). Determination of interaction parameters and grain material flow motion on screw conveyor elastic section surface. *INMATEH - Agricultural Engineering*, 57(1), 123-134.
- [9] Hewko, B. M., Popovich, P. V., Diachun, A. Y., Lyashuk, O. L., Liubachivskyi, R. O. (2015). The study of bulk material kinematics in a screw conveyor-mixer. *INMATEH - Agricultural Engineering*, 47(3), 155-162.
- [10] Lyashuk, O., Vovk, Y., Sokil, B., Klendii, V., Ivasechko, R., Dovbush, T. (2019). Mathematical model of a dynamic process of transporting a bulk material by means of a tube scraping. *Agricultural Engineering International: CIGR Journal*, 21(1), 74-81.
- [11] Pascuzzi, S., Łyp-Wrońska, K., Gdowska, K., Paciolla, F. (2024). Sustainability Evaluation of Hybrid Agriculture-Tractor Powertrains. *Sustainability*, 16(3), 1184
- [12] Sokil, B., Lyashuk, O., Sokil, M., Popovich, P., Vovk, Y., Perenchuk, O. (2018). Dynamic effect of cushion part of wheeled vehicles on their steerability International. *Journal of Automotive and Mechanical Engineering*, 15 (1), 4880-4892.

SIMULATION PARAMETER CALIBRATION AND TEST OF PAK CHOI SEEDS BASED ON DISCRETE ELEMENT METHOD

基于离散元的小白菜种子仿真参数标定与试验

Guoqiang DUN^{*1)}, Chaoxia ZHANG²⁾, Xinin JI²⁾, Qingjun MENG²⁾, Quanbao SHENG²⁾, Lei WANG²⁾

¹⁾ Harbin Cambridge University, Intelligent Agricultural Machinery Equipment Engineering Laboratory, Harbin / China;

²⁾ Northeast Forestry University, College of Mechanical and Electrical Engineering, Harbin / China;

Tel: +86 13836027042; E-mail: dunguoqiangpaper@163.com

DOI: <https://doi.org/10.35633/inmateh-73-33>

Keywords: Pak Choi seeds; discrete element simulation; angle of repose, seed-metering device

ABSTRACT

Physical property parameter measurements and simulation model parameter calibrations of Pak Choi seeds were conducted to address the lack of accurate parameters for discrete elemental seed discharging simulation tests in the seed-metering device. Firstly, physical tests were utilized to determine the basic physical parameters and contact parameters of Pak Choi seeds. The results of these physical tests served as the basis for determining the range of simulation parameters. The Plackett-Burman test was employed to screen out factors that significantly affected the simulated angle of repose from the test parameters, including static friction coefficient between Pak Choi seeds-Pak Choi seeds and rolling friction coefficient between Pak Choi seeds-Pak Choi seeds. The optimal interval of these two factors was determined using the Steepest Climb Test. Subsequently, the regression equation between the significance parameters and the angle of repose was obtained through the Central Composite Designs test, and the best parameter combinations were obtained with the measured stacking angle of 24.3° as the optimisation target value: Pak Choi seeds-Pak Choi seeds static friction coefficient of 0.486, Pak Choi seeds-Pak Choi seeds rolling friction coefficient of 0.104. Finally, simulation and bench comparison tests were carried out for stacking angle and Pak Choi seed discharger performance evaluation. The relative error of the angle of repose was found to be 0.288%, while average relative errors for qualified sowing rate, replanting rate, and missed sowing rate were all less than 5%. These results demonstrate that calibrated Pak Choi seed simulation parameters are reliable and can serve as a reference for design optimization of Pak Choi seed dischargers in academic research writing standards.

摘要

针对小白菜种子在排种器中进行离散元排种仿真模拟试验缺乏准确参数, 对小白菜种子进行物性参数测量及仿真模型参数标定。首先, 采用物理试验测定小白菜种子的基本物性参数及接触参数, 以物理试验结果为基础, 确定仿真参数范围, 利用 Plackett-Burman 试验从各组试验参数中筛选出对堆积角影响显著的因素: 小白菜种子-小白菜种子静摩擦系数、小白菜种子-小白菜种子滚动摩擦系数, 并进一步通过最陡爬坡试验确定两因素最优区间。再通过二次通用旋转组合试验得到显著性参数与堆积角之间得回归方程, 并以实测堆积角 24.3° 为优化目标值获得最佳参数组合: 小白菜种子-小白菜种子间静摩擦系数 0.486、小白菜种子-小白菜种子间滚动摩擦系数 0.104。最后, 开展了堆积角对比试验及小白菜排种器的仿真与台架对比试验, 得到堆积角的相对误差为 0.288%, 排种器的合格率、重播率、漏播率的平均相对误差小于 5%。由此表明, 标定的小白菜种子仿真参数具有可靠性, 可为小白菜排种器的设计优化提供参考。

INTRODUCTION

Pak Choi, an annual or biennial plant of the genus Brassica, it is widely loved for its rich nutritional elements and certain medicinal values. In recent years, the planting area of Pak Choi has been increasing year by year in China, the traditional artificial seeding method and the existing seeding equipment have been unable to meet the production needs of Pak Choi, to promote the high efficiency of mechanized Pak Choi seeding device is imminent. The seed-metering device is the core component of seeding machinery (Wang et al., 2023; Song et al., 2023), and the interaction forces between seed populations and between seeds and the discharger are very complex during the working process. To study the mechanical precision seed discharger suitable for sowing Pak Choi seeds, the EDEM software based on the discrete element theory can be used to simulate the seeding process in the seed-metering device and analyze the movement law of Pak Choi seeds in the seed discharger, to provide a reference for the design and optimization of the seed-metering device

(Zeng *et al.*, 2021). Due to the irregular shape of Pak Choi seeds, the direct simulation with the calibrated spherical particle parameters in EDEM software may result in a large error with the physical test results, therefore, discrete element simulation parameters need to be calibrated for Pak Choi seeds.

In recent years, many scholars at home and abroad have studied the calibration of simulation parameters based on discrete elements for agricultural materials such as maize seeds, *Cucurbita ficifolia* seeds, *Adzuki Bean Seeds*, *Agropyron seeds*, *Panax notoginseng Seed* and *white radish seed*. Chen *et al.*, (2018) used a multi-sphere model (MS) approach to establish a single seed model of maize seeds based on the physical properties of seeds of different shapes, such as horse-tooth and spherical-cone, and verified the feasibility and validity of the particle ensemble of maize seeds and the individual seed particle modelling approach. Ding *et al.*, (2023) used response surface method (RSM) and machine learning were utilized for optimization inversion of the parameters, calibration of parameters for discrete element simulation of *Cucurbita ficifolia* seeds was completed. Liu *et al.*, (2022), samples were used to determine the DEM parameters of *Adzuki Bean Seeds* using a combination of physical tests and virtual calibration. Hou *et al.*, (2020), used a combination of physical and simulation tests to calibrate and align the discrete elemental simulation parameters of *Agropyron seeds*. Yu *et al.*, (2020), used reverse engineering technology to establish a discrete elemental model of *Panax quinquefolium* seeds in EDEM software based on the bonded particle model and calibrated the optimal contact parameters between *Panax quinquefolium* seeds and ABS plastics by combining bench tests and simulation tests. Yan *et al.* (2022), created a discrete elemental model of radius white radish seeds using multiball bonding, and analyzed the optimal ball particle filling radius of white radish seeds by combining the relative error rate of stacking angle with the simulation time. In summary, the discrete element method is widely used in the simulation parameter calibration of agricultural material particles, but there are fewer discrete element simulation parameter calibrations for spherical small-size seeds such as Pak Choi seeds.

In this study, based on the discrete element simulation calibration method for agricultural material particles at home and abroad, the basic physical property parameters and contact parameters of Pak Choi seeds were measured by physical tests, using the simulated angle of repose of Pak Choi seeds as the test index and the physical property parameters as the test factors, the most significant test factors were screened out by the Plackett-Burman test, and the steepest climb test was conducted to select the optimal value region for the screened out significant test factors, then the optimal parameter combination is determined by the secondary generalized rotary combination test, and the determined discrete element simulation calibration parameters are subjected to simulation test to verify the discrepancy with the physical test, to provide a reference for the design and simulation study of the mechanical precision seed-metering device for Pak Choi.

MATERIALS AND METHODS

Determination of material properties of Pak Choi seeds

Measurement of triaxial dimensions and mass

The test selected Jinyu Shenghui four-season Pak Choi seeds widely planted in the northeast region as the object to measure experimental research, to reduce seed error and improve the accuracy of the measurement, from 50 g of Pak Choi seeds randomly selected 100 Pak Choi seeds for measurement, a way to ensure that the measurement of the size and quality of the seed has randomness. The length (L), width (W), and height (H) of each seed were measured and recorded in three directions using the Airex three-button electronic digital vernier calipers (accuracy of 0.01 mm), as shown in Figure 1. UTP-313 electronic balance scale (accuracy of 0.001 g) was used to repeat the measurement of 100 seeds 10 times record the data each time and take the average value.



Fig. 1 - Triaxial dimensional measurement of Pak Choi seed

The data were statistically organized to give a mean value of 1.74 mm with a standard deviation of 0.12 mm for the length of Pak Choi seeds, 1.63 mm with a standard deviation of 0.10 for the width, 1.53 mm with a standard deviation of 0.11 for the height, and a mean value of about 0.0025 g for the seed mass. The length, width, and height size distribution statistics of Pak Choi seeds are shown in Figure 2, all of which are normally distributed, and the overall shape of the seeds is similar to that of a sphere. Based on the seed length, width, and height, the equivalent diameter, sphericity, and volume of the Pak Choi seeds are calculated by applying Equations (1), (2), and (3).

$$D_e = \sqrt[3]{LWH} \tag{1}$$

$$S_p = \frac{D_e}{L} \times 100\% \tag{2}$$

$$V = \frac{4}{3} \pi lwh \tag{3}$$

where: L, W, H is the length, width, height of Pak Choi seeds, mm; D_e is the equivalent diameter of Pak Choi seeds, mm; S_p is the sphericity of Pak Choi seeds, %; V is the volume of Pak Choi seeds, mm³; l, w, h is the semiaxis of the length, width, and height of Pak Choi seeds, mm.

The equivalent diameter of Pak Choi seeds was calculated to be about 1.63 mm, the sphericity was about 93.7%, and the mean value of the volume was about 2.262 m4m³.

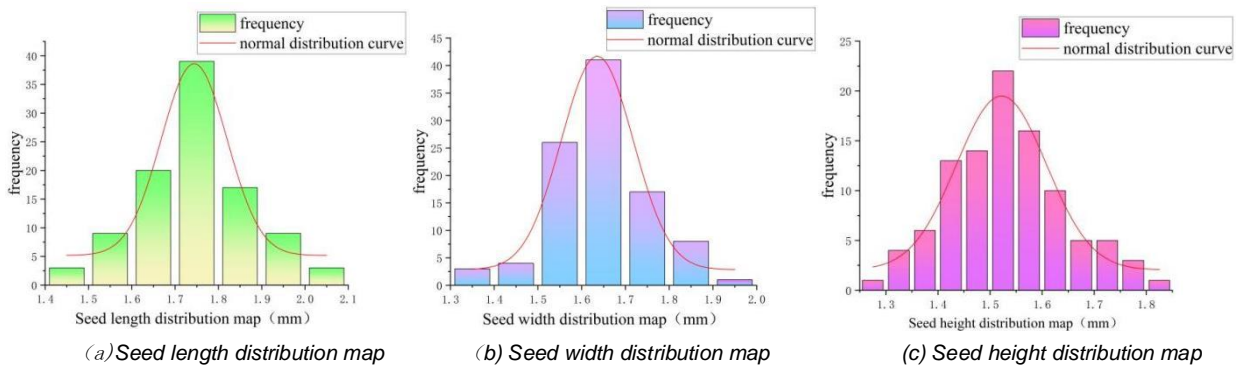


Fig. 2 - Seed triaxial size and volume distribution diagram

Density and moisture content measurement

To measure the density of Pak Choi seeds by the immersion method (Du et al., 2023), 10g of Pak Choi seeds were randomly weighed using a UTP-313 electronic balance scale with an accuracy of 0.001 g, 40 ml of pure water was injected into a measuring cylinder with a range of 100 ml, and 10 g of weighed seeds were placed into the measuring cylinder, and the volume of the horizontal plane of the cylinder at this point in time was recorded as V_2 . Substituting into Equation (4), the density of the Pak Choi seeds was calculated. Repeat the test 5 times and take the average. Repeat the test 5 times, take the average value of 1.082 g/cm³ for the density of Pak Choi seeds.

$$p = \frac{m}{V_2 - V_1} \tag{4}$$

where: p is the density of Pak Choi seeds, g/cm³; m is the addition of the mass of Pak Choi seeds, g; V_1 is the volume of pure water injected into the cylinder, cm³; V_2 is the volume of the cylinder after the addition of seeds, cm³.

The drying method was used to measure the water content of Pak Choi seeds, 10 g of Pak Choi seeds were randomly weighed using an electronic balance scale with an accuracy of 0.001 g, placed in a drying oven with the temperature set to 105°C, and dried continuously for 8 hours, and the seeds were cooled in the drying oven and taken out to be weighed again and recorded, substituting the mass of the seeds before drying m_a and the mass of the seeds after drying m_b into the Equation (5) the water content of the seeds was calculated to be 7.82%.

$$M_c = \frac{m_a - m_b}{m_a} \times 100\% \tag{5}$$

where: m_c is the moisture content of Pak Choi seeds, %; m_a is the mass of Pak Choi seeds before drying, g; m_b is the mass of Pak Choi seeds after drying, g.



Fig. 3 - Moisture content testing device

Poisson's ratio

Poisson's ratio is an elastic constant reflecting the lateral deformation of the material. Due to the small Pak Choi seeds and thin seed coat, the pressure deformation test was used to measure the Poisson's ratio of Pak Choi seeds. 10 Pak Choi seeds were randomly selected, the electronic digital vernier calipers was used for each seed length, thickness was measured and data were recorded. The universal pressure testing machine was used to measure the entire seed along the thickness of the seed to apply pressure, when the surface of the seed ruptured, applying pressure was immediately stopped. The deformation of the seed thickness direction was recorded, the electronic digital vernier calipers was used to measure the deformation of the seed length direction, the Poisson's ratio of Pak Choi seeds was calculated according to the Equation (6). The test was repeated 10 times to take the average value of 0.342 for the Pak Choi seeds Poisson's ratio.

$$u = \frac{g'}{g} = \frac{y_1 - y_2}{b_1 - b_2} \quad (6)$$

where: u is the Poisson's ratio of Pak Choi seeds; g' is the deformation in the length direction of Pak Choi seeds; g is the deformation in the thickness direction of Pak Choi seeds; y_1 is the length of Pak Choi seeds before being pressed, mm; y_2 is the length of Pak Choi seeds after being pressed, mm; b_1 is the thickness of Pak Choi seeds before being pressed, mm; b_2 is the thickness of Pak Choi seeds after being pressed, mm.

Determination of modulus of elasticity and shear modulus

The compression method was used to measure the modulus of elasticity and shear modulus of the seeds, using electronic digital display vernier calipers to randomly measure the thickness of 10 Pak Choi seeds, placing the seeds with the measured thickness horizontally on the pressure tester, applying pressure in the direction of the thickness of the Pak Choi seeds and recording the compression pressure-displacement data of the seeds during compression, and deriving the modulus of elasticity of the Pak Choi seeds according to Equation (7). The modulus of elasticity of Brassica juncea seeds was obtained as 4.56×10^7 Pa by repeating the test 10 times and taking the average value.

$$E = \frac{z}{g} \quad (7)$$

where: E is the modulus of elasticity of Pak Choi seeds, Pa; z is the maximum compressive stress, Pa; g is the linear strain of Pak Choi seeds.

The shear modulus of Pak Choi seeds was calculated according to Equation (8), and the shear modulus of Pak Choi seeds was obtained to be 1.66×10^7 Pa.

$$C = \frac{E}{2(1+u)} \quad (8)$$

where: C is the shear modulus of Pak Choi seeds, pa; u is the Poisson's ratio of Pak Choi seeds.

Measurement of Static friction coefficient

Measurement of the static friction coefficient between Pak Choi seeds and PLA material was carried out by the inclined plane sliding method (Xu *et al.*, 2023), and the test device used was a homemade static friction angle measuring device made from PLA material, which had a length, width, and height of 150mm×80mm×20mm. In determine the coefficient of static friction between the Pak Choi seeds and the PLA material, because the Pak Choi seeds are bulk materials with small size and easy to tumble. In order to prevent Pak Choi seeds from tumbling, the inclined plane test was carried out by 4 Pak Choi seeds were glued together to form a Pak Choi seeds group, with reference to the relevant literature (Wang *et al.*, 2022; Zhou *et al.*, 2018), as shown in Figure 4a. Turning the rocking handle, so that the PLA plate end of the placed seeds is slowly and uniformly elevated, When the seed slides downward on the inclined PLA plate, immediately stop the rotation of the rotor shaft, the inclined PLA plate will be fixed and the use of electronic protractor to measure the angle α between the inclined plane and the horizontal plane, and then use the Equation (9) to calculate the coefficient of static friction between the Pak Choi seeds and the PLA plate.

$$u_g = \tan \alpha \quad (9)$$

where: u_g is the coefficient of static friction indicated; α is the angle of sliding friction.

The static friction coefficient of between Pak Choi seeds was also determined by the inclined plane method, in order to more accurately measure the coefficient of static friction between Pak Choi seeds, the test seeds were made into seed boards with adhesive and pasted on the test plane of measuring device, so that the cabbage seeds could be arranged as closely as possible, as shown in Figure 4b. Place the Pak Choi seeds group on the Seed board, slowly turn the Rocking handle until the Pak Choi seeds group appears to slide on the seed board, stop rotating and record the inclined plane angle at this time. The experiments were repeated for 10 times in each group, and the average value was obtained. The average value of static friction coefficient between Pak Choi seeds and PLA material was 0.46, and the average value of static friction coefficient between Pak Choi seeds was 0.52.

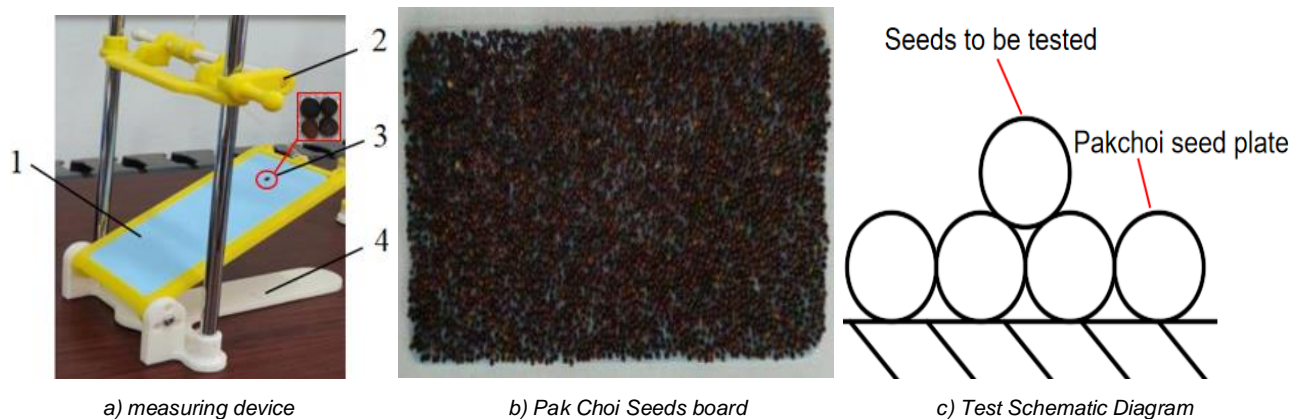


Fig. 4 - Test for determination of static friction coefficient between seeds

1. PLA plate; 2. Rocking handle; 3. Pak Choi seeds group; 4. Rack

Measurement of rolling friction coefficient

The rolling friction coefficient between Pak Choi seeds and PLA material as well as between Pak Choi seeds was determined using the inclined rolling method. The test setup for determining the rolling friction coefficient between seeds and PLA material consisted of two plates made of PLA material, with one of the plates inclined at 30°. The Pak Choi seed is placed at a fixed height $b = 0.075$ m, $\theta = 30^\circ$ inclined plate, the Pak Choi seed is released with an initial speed of 0, the seed rolls along the inclined plate to the PLA horizontal panel and comes to rest. The rolling distance T of the Pak Choi seed on the PLA horizontal panel is measured and recorded, the schematic diagram is shown in Figure 5, the rolling friction coefficient between Pak Choi seeds and PLA material can be obtained by applying equation (10). Determination of the rolling friction coefficient between Pak Choi seeds and Pak Choi seeds test method is the same as above, the test device will be replaced by two PLA boards for two pieces of Pak Choi seeds plate.

The average coefficient of rolling friction between Pak Choi seeds and PLA material as well as the Pak Choi seeds was 0.163 and 0.098, respectively, after 10 times repeated tests.

$$mg \cdot \sin\theta \times b = u_s mg(\cos\theta \times b + T) \quad (10)$$

where: u_s is the rolling friction coefficient; m is the mass of Pak Choi seeds, kg; g is the gravitational acceleration of the seeds, m; α is the inclination angle of the inclined plane, m/s²; b is the rolling length of the inclined plane, m; T is the rolling length of the horizontal plane, m.

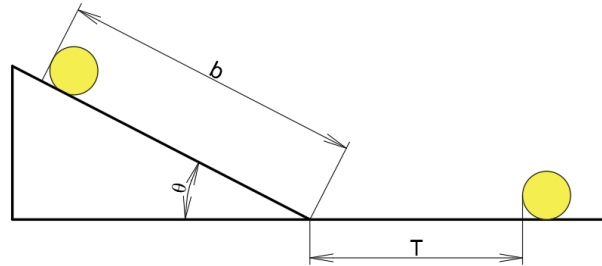


Fig. 5 - Schematic diagram of inclined plane rolling friction test measurement

Determination of Collision Recovery Coefficient

The collision recovery coefficient is the ratio of the normal relative separation velocity to the normal relative approach velocity at the contact point of the two objects before and after the collision (Xie et al., 2022), which is an important parameter for EDEM software simulation and has a relatively large impact on the qualification rate of the seed-metering device. The collision bounce test was used to determine the collision recovery coefficients between Pak Choi seeds and PLA materials and between Pak Choi seeds, the test setup has a computer, scale, coordinate grid paper, PLA board, high-speed camera, the PLA board was placed horizontally on the desktop, and the coordinate grid paper was pasted on the wall using tape to make a backdrop, as shown in Figure 6.



Fig. 6 - Collision restitution coefficient measurement test

1. Computer; 2. Scale; 3. Grid paper; 4. PLA material; 5. High-speed photography camera.

In the Pcc3.7 software, the number of frames is set to 2500 frames, and a seed is released from the height of $H_r=250\text{mm}$ to fall freely, and the high-speed camera is controlled to record the whole motion process of the seed falling on the PLA plate and rebounding, and the principle is shown in Figure 7. The maximum rebound height h_r of the collision of the Pak Choi seeds on the PLA plate reflected in the coordinate grid paper was intercepted and the data were recorded. Applying Equation (11), the coefficient of recovery of collision between Chinese Pak Choi seeds and PLA material was calculated.

To determine the coefficient of recovery of collision between Pak Choi seeds, the PLA material plate was replaced with a Pak Choi seed plate placed horizontally on the tabletop, and the test method was the same as above. The test was repeated 10 times to obtain the average rebound height of Pak Choi seeds on PLA material at $h=56\text{ mm}$ and on Pak Choi seed plates at $h=22\text{ mm}$, the collision recovery coefficient between the Pak Choi seeds and PLA material as well as the Pak Choi seeds 0.473, 0.297.

$$e = \frac{v_t}{v_0} = \sqrt{\frac{h_r}{H_r}} \tag{11}$$

where:

e is the collision recovery coefficient; v_t is the normal relative approach velocity before the collision, m/s; v_0 is the normal relative separation velocity after the collision, m/s; h_r is the maximum height of the seed rebound, mm; H_r is the initial height of the seed drop, m.

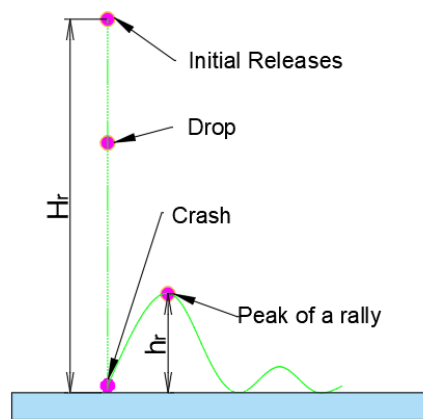


Fig. 7 - Schematic diagram of the collision recovery coefficient determination test

Material angle of repose Test

The material angle of repose reflects the friction characteristics and scattering performance between seeds and seeds, which is related to the physical properties of the contact materials and seeds, and its calibration can effectively reflect the reasonableness and reliability of the seed friction characteristics parameters. This test uses the funnel method to measure the material pile (*Liu et al., 2020; Gong et al., 2021*), and the test device uses a homemade angle of repose tester. Use the baffle plate to block the lower drop port, pour 15g of Pak Choi seeds into the upper funnel at a uniform speed, open the baffle plate quickly, the seeds fall freely and form a seed pile on the bottom disk, and wait until the seed pile is completely stationary, use an electronic protractor to measure the angle between the right half of the taper and the base plate, as shown in Figure 8. At the same time, in order to reduce the error that exists in the human measurement of the angle of repose, an image processing method was used to analyze the test photos, the frontal image of the seed pile was captured with a high-definition camera, and the image of the right side of the seed pile was grayscale processing, binarization processing, the extraction of the image boundary pixel points and the boundary pixel points were fitted by MATLAB, and the angle of the fitted straight line with the horizontal plane is the physical angle of repose of the Pak Choi seeds, as shown in Figure 9. The test was repeated 10 times to take its average value, and the angle of repose was obtained as 24.3°.

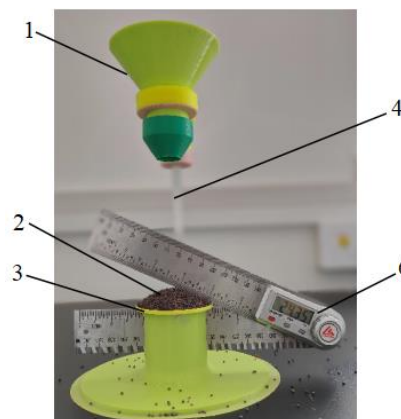


Fig. 8 - Angle of repose determination test

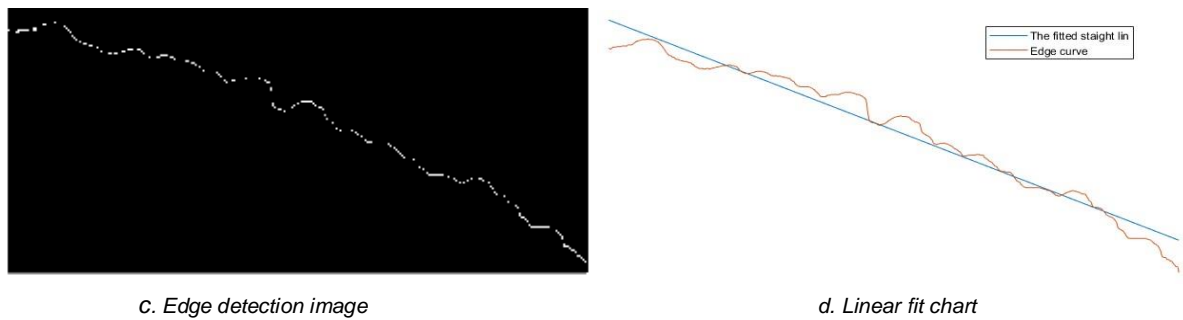
1. Funnel; 2. Pak Choi seeds; 3. Brackets; 3. Base support; 5. Digital Angle Measuring Ruler



a. The right half image of the seeds pile



b. Binary image



c. Edge detection image

d. Linear fit chart

Fig. 8 - Image processing of Pak Choi seeds pile

Discrete element modelling and simulation parameter calibration

Pak Choi seeds simulation modeling

To make the simulation model of seeds closer to the size and shape of the actual seeds, the basic physical properties data of Pak Choi seeds were obtained through the preliminary physical test measurements, using SolidWorks 3D modeling software, according to the shape of the seeds as well as the average of the three-axis dimensions of the modeling, the 3D model of the seeds was saved as an stl file format, and the seed model was imported into the EDEM software, the discrete element simulation model of Pak Choi seed was established by using the method of spherical particle polymerization filling model, shown in Figure 10.



Fig. 10 - Pak Choi seeds granules and their discrete element models

Material angle of repose simulation test

The angle of repose simulation test was carried out using EDEM software, as shown in Figure 11, and the contact parameters between seed populations and between seeds and PLA materials were set up in EDEM software by combining the pre-measured data on the physical properties of Pak Choi seeds. Since the surface of Pak Choi seeds is smooth and has no adhesion, the Hertz-Mindlin no-contact model was chosen for the simulation contact model. At the same time, the same geometric model of the measuring device as the bench test measuring device was imported into the EDEM software, and the material was set to PLA material. A virtual plane was established above the funnel to generate a total amount of 30g seed model, and the generation time was set to 1 second. To ensure the continuity of the simulation test, the time step was set to 3.44244×10^{-6} s, the total simulation time was 6s, and the virtual simulation test was the same as the bench test.

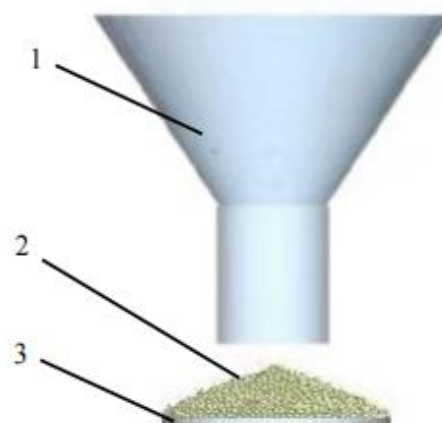


Fig. 11 - Angle of repose simulation test

1. Funnel; 2. Pak Choi seeds; 3. Chassis.

RESULTS

Plackett-Burman Test

Design-Expert 10.0 software was applied to carry out the Plackett-Burman experimental design to screen out the experimental factors that had significant effects on the seed angle of repose of Pak Choi using the seed angle of repose of Pak Choi as the experimental index (Bai *et al.*, 2022).

A-H is taken to indicate the actual test factors, respectively, and +1 indicates a high level and -1 indicates a low level in each test factor. Based on the measured values of the previous physical tests, the range of values of each test factor was determined as shown in Table 1.

The experimental design scheme is shown in Table 2, and a total of 12 groups of tests were designed, and the angle of repose of each group of tests was simulated by EDEM software.

Table 1

Plackett-Burman test parameter table

| Serial number | Experimental factors | Low level (-1) | High Level (+1) |
|---------------|--|-------------------|-------------------|
| A | Poisson's ratio of Pak Choi seeds | 0.24 | 0.53 |
| B | Shear modulus of Pak Choi seeds / Pa | 1.2×10^7 | 3.8×10^7 |
| C | Pak Choi seeds - Pak Choi seeds collision recovery coefficient | 0.24 | 0.56 |
| D | Pak Choi seeds - Pak Choi seeds rolling friction coefficient | 0.083 | 1.24 |
| E | Pak Choi seeds - Pak Choi seeds static friction coefficient | 0.36 | 0.71 |
| F | Pak Choi seeds - PLA plastic collision recovery coefficient | 0.45 | 0.88 |
| G | Pak Choi seeds - PLA plastic rolling friction coefficient | 1.43 | 1.92 |
| H | Pak Choi seeds - PLA plastic static friction coefficient | 0.28 | 0.53 |

Table 2

Plackett-Burman test protocol and results

| Serial number | A | B | C | D | E | F | G | H | Angle of repose / ° |
|---------------|----|----|----|----|----|----|----|----|---------------------|
| 1 | 1 | 1 | -1 | 1 | 1 | 1 | -1 | -1 | 26.65 |
| 2 | -1 | 1 | 1 | -1 | 1 | 1 | 1 | -1 | 25.97 |
| 3 | 1 | -1 | 1 | 1 | -1 | 1 | 1 | 1 | 28.12 |
| 4 | -1 | 1 | -1 | 1 | 1 | -1 | 1 | 1 | 27.76 |
| 5 | -1 | -1 | 1 | -1 | 1 | 1 | -1 | 1 | 22.46 |
| 6 | -1 | -1 | -1 | 1 | -1 | 1 | 1 | -1 | 27.22 |
| 7 | 1 | -1 | -1 | -1 | 1 | -1 | 1 | 1 | 22.52 |
| 8 | 1 | 1 | -1 | -1 | -1 | 1 | -1 | 1 | 14.48 |
| 9 | 1 | 1 | 1 | -1 | -1 | -1 | 1 | -1 | 18.97 |
| 10 | -1 | 1 | 1 | 1 | -1 | -1 | -1 | 1 | 24.86 |
| 11 | 1 | -1 | 1 | 1 | 1 | -1 | -1 | -1 | 31.92 |
| 12 | -1 | -1 | -1 | -1 | -1 | -1 | -1 | -1 | 17.56 |

The analysis of variance (ANOVA) of the test results was performed by Design-Expert software to obtain the significance results of each test parameter on the angle of repose of the test indexes, as shown in Table 3. In the ANOVA table, the p-value is used to assess the extent to which each test factor affects the test metrics, i.e., to measure whether the effects of different test factors on the results are statistically significant.

As can be seen from Table 3, the P-value of the rolling friction coefficient (D) and the static friction coefficient (E) of Pak Choi seeds - Pak Choi seeds is less than 0.01, indicating that the effect on the angle of seed stacking is highly significant, and the P-value of the collision recovery coefficient (C) of Pak Choi seeds - Pak Choi seeds is less than 0.05 on the angle of repose is significant, while the other test factors are greater than 0.5, and the effect on the angle of repose is not significant.

Table 3

Significance analysis of test parameters

| Source | Sum of squares | Degree of freedom | Mean square | F number | P value |
|--------|----------------|-------------------|-------------|----------|----------|
| Model | 273.82 | 8 | 34.23 | 25.81 | 0.0110* |
| A | 0.84 | 1 | 0.84 | 0.63 | 0.4849 |
| B | 10.29 | 1 | 10.29 | 7.76 | 0.0687 |
| C | 21.63 | 1 | 21.63 | 16.31 | 0.0273* |
| D | 165.54 | 1 | 165.54 | 124.84 | 0.0015** |
| E | 56.64 | 1 | 56.64 | 42.71 | 0.0073** |
| F | 0.14 | 1 | 0.14 | 0.11 | 0.7642 |
| G | 13.29 | 1 | 13.29 | 10.02 | 0.0506 |
| H | 5.45 | 1 | 5.45 | 4.11 | 0.1356 |

Note: ** indicates highly significant effect ($p < 0.01$), * indicates significant effect ($0.01 < p < 0.05$).

Steepest Climb Test

The steepest climb test was conducted based on the highly significant parameters of rolling friction coefficient between Pak Choi seeds-Pak Choi seeds (D) and static friction coefficient between Pak Choi seeds-Pak Choi seeds (E) screened by the Plackett-Burman test as a quick way to determine the optimal region of each significant factor relative to the test index. The relative error between the actual angle of repose and the simulated angle of repose was used as the test index, and D and E were used as the test factors. In the EDEM software angle of repose simulation experiments, the rolling friction coefficient between Pak Choi seeds-Pak Choi seeds was selected as 0.083-0.124, the static friction coefficient between Pak Choi seeds-Pak Choi seeds was selected as 0.36-0.72, and all other non-significant factors were used as the average values of physical tests. The results of the steepest climb test design are shown in Table 4. The results show that the relative error of the 3 sets of simulation tests is minimized, which shows that the optimal interval is near the 3 sets of tests. Therefore, the Pak Choi seeds-Pak Choi seeds static friction coefficients of 0.43-0.57 and the Pak Choi seeds-Pak Choi seeds rolling friction coefficients of 0.091-0.107 were selected as the range of test factor levels for the subsequent Central Composite Designs test.

Table 4

The steepest climbing test design scheme and results

| Serial number | Pak Choi seeds - Pak Choi seeds static friction coefficient | Pak Choi seeds - Pak Choi seeds rolling friction coefficient | Angle of repose / (°) | Relative error / % |
|---------------|---|--|-----------------------|--------------------|
| 1 | 0.36 | 0.083 | 19.75 | 18.72 |
| 2 | 0.43 | 0.091 | 22.37 | 8.65 |
| 3 | 0.50 | 0.099 | 23.46 | 3.45 |
| 4 | 0.57 | 0.107 | 25.63 | 5.47 |
| 5 | 0.63 | 0.115 | 29.95 | 23.25 |
| 6 | 0.72 | 0.124 | 32.83 | 32.7 |

Central Composite Designs test

Test Methods

After obtaining the optimal range of intervals for the significant factors through the steepest climb test, the optimal parameter combinations for the static friction coefficient and rolling friction coefficients between Pak Choi seeds-Pak Choi seeds in the simulation test were obtained for the further development of Pak Choi seeds. Using the simulated angle of repose as the test index, the two-factor, five-level Central Composite Designs test was conducted using Design-Expert software and EDEM software, and the simulation factor coding table is shown in Table 5.

Table 5

Factor level coding table

| Level | Pak Choi seeds - Pak Choi seeds static friction coefficient | Pak Choi seeds - Pak Choi seeds rolling friction coefficient |
|--------|---|--|
| 1.414 | 0.57 | 0.107 |
| 1 | 0.55 | 0.105 |
| 0 | 0.5 | 0.099 |
| -1 | 0.45 | 0.093 |
| -1.414 | 0.43 | 0.091 |

The experimental design scheme and simulation results are shown in Table 6.

Table 6

| Serial number | Pak Choi seeds - Pak Choi seeds static friction coefficient / A | Pak Choi seeds - Pak Choi seeds static friction coefficient / B | Angle of repose β / ° |
|---------------|---|---|-----------------------------|
| 1 | -1 | -1 | 21.43 |
| 2 | 1 | -1 | 24.03 |
| 3 | -1 | 1 | 24.53 |
| 4 | 1 | 1 | 27.63 |
| 5 | -1.414 | 0 | 22.28 |
| 6 | 1.414 | 0 | 26.64 |
| 7 | 0 | -1.414 | 21.46 |
| 8 | 0 | 1.414 | 25.75 |
| 9 | 0 | 0 | 23.63 |
| 10 | 0 | 0 | 23.11 |
| 11 | 0 | 0 | 22.93 |
| 12 | 0 | 0 | 24.07 |
| 13 | 0 | 0 | 21.26 |

Angle of repose analysis of variance

Multiple regression was fitted to the experimental data (Table 6) using the software Design-Expert software 10.0, and the results of the analysis of variance of the regression model were obtained, as shown in Table 7. The results show that the p-value of the model is less than 0.01, indicating that the regression model is extremely significant. The P-values of A (static friction coefficient between Pak Choi seeds-Pak Choi seeds) and B (rolling friction coefficient between Pak Choi seeds-Pak Choi seeds) were both less than 0.01, indicating that the effect on angle of repose was extremely significant. The P-value of A^2 (quadratic term of coefficient of static friction between Pak Choi seeds-Pak Choi seeds) was less than 0.05, indicating a significant effect on angle of repose, while the P-values of the other factors were greater than 0.05, indicating a non-significant effect on angle of repose. The out-of-fit term $P=0.954 > 0.05$, which is not significant, indicates that the model is well-fitted and there are no other significant factors affecting the test index.

The regression equation between the contact parameters and the angle of repose (β) is obtained by eliminating the factors that do not have a significant effect on the angle of repose as:

$$\beta = +23.28 + 1.48A + 1.6B + 0.77A^2 \quad (12)$$

Table 7

Heap angle analysis of variance results

| Source | Sum of squares | Degree of freedom | Mean square | F number | P value |
|-------------|----------------|-------------------|-------------|----------|----------|
| Model | 43.34 | 5 | 8.67 | 12.28 | 0.0024** |
| A | 17.60 | 1 | 17.60 | 24.93 | 0.0016** |
| B | 20.37 | 1 | 20.37 | 28.86 | 0.0010** |
| AB | 0.063 | 1 | 0.063 | 0.089 | 0.7747 |
| A^2 | 4.71 | 1 | 4.71 | 6.68 | 0.0363* |
| B^2 | 1.09 | 1 | 1.09 | 1.54 | 0.2542 |
| Residual | 4.94 | 7 | 0.71 | | |
| Lack of fit | 0.35 | 3 | 0.12 | 0.10 | 0.9540 |
| Pure error | 4.59 | 4 | 1.15 | | |
| Sum | 48.28 | 12 | | | |

Note: ** indicates highly significant effect ($p < 0.01$), * indicates significant effect ($0.01 < p < 0.05$).

Response surface analysis

The Design-Expert software was applied to generate the response surface plots of the coefficient of static friction of Pak Choi Seeds-Pak Choi Seeds versus the rolling friction coefficient of Pak Choi Seeds-Pak Choi Seeds, as shown in Figure 12.

The angle of repose increases with the increase in the rolling friction coefficient between the Pak Choi Seeds-Pak Choi Seeds due to the increase in the Pak Choi Seeds-Pak Choi Seeds rolling friction coefficient and the corresponding increase in the shear stress and consequent increase in the angle of repose.

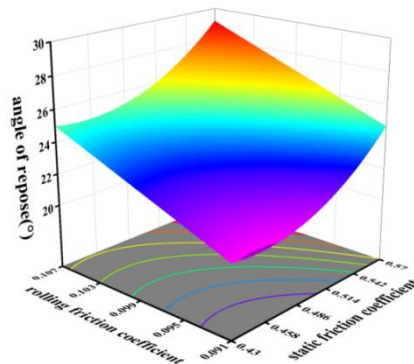


Fig. 12 - Pak Choi seed packing angular response surface

Optimization of parameters

Using the optimization module of Design-Expert software, the regression model was optimally solved with the measured angle of repose as the target value to minimize the error between the angle of repose simulation test results and the physical test angle of repose results, and the objective and constraint Equations are shown below:

$$\begin{cases} \beta(A, B) = 24.3 \\ S.t \begin{cases} 0.41 \leq A \leq 0.57 \\ 0.091 \leq B \leq 0.107 \end{cases} \end{cases} \quad (13)$$

The resulting optimization results in a Pak Choi seeds - Pak Choi seeds static friction coefficient of 0.486, Pak Choi seeds - Pak Choi seeds rolling friction coefficient of 0.104.

Verification test

Angle of repose verification test

To verify the reliability and authenticity of Pak Choi seeds after simulation calibration, the results of the angle of repose simulation test were compared with those of the physical test angle of repose. For the angle of repose simulation test, the above-determined static friction coefficient of 0.522 and rolling friction coefficient of 0.101 between Pak Choi species were used as simulation parameters, and the average values of the physical tests were used for other non-significant parameters. The relative error between the simulation test result of 24.23° and the physical test angle of repose of 24.30° was obtained to be 0.288%, and the results proved the validity of the calibrated simulation parameters.

Seed-metering device verification test

To further verify the reliability of the discrete meta-model and simulation parameters of Pak Choi seeds, the homemade horizontal disk type cabbage precision seeder was used to carry out the simulation test of seeding performance and bench test in the intelligent agricultural machinery and equipment engineering laboratory of Harbin Cambridge College, and to calculate the relative errors of its simulation value and the measured value of the qualification rate, the reseeding rate, and the leakage rate with the formula:

$$\begin{aligned} g &= \frac{n_1}{n} \times 100\% \\ j &= \frac{n_2}{n} \times 100\% \\ k &= \frac{n_3}{n} \times 100\% \end{aligned} \quad (14)$$

where: n is the number of theoretical rows of particles, grains; n_1 is the number of seeds single qualified, grains; n_2 is the number of seeds reseeded, grains; n_3 is the number of seeds missed, grains.

Seed-metering device simulation test

The horizontal disk-type Pak Choi precision seed discharger used in this study has a total of 12 type holes evenly distributed on the discharging disk, and a brush is installed at the exit of the seed box for seed cleaning. SolidWorks software was used to model the seed displacer in three dimensions, and it was saved in stl format and imported into EDEM software, the material of the wall of the seed displacer was set as PLA material, and the material of the brushes was set as nylon plastic. Referring to the above calibration results and related literature, the material and contact parameters of the seed displacer wall, seed cleaning brush, and Pak Choi seeds were set as shown in Table 8 (Dun et al., 2020; Li et al., 2024). Hertz-Mindlin (no slip) contact model was used between the seeds and the seed discharger, between the brushes and between the seeds, and the rotational speed of the seed discharging disk was set to 30 r/min, and a total of 800 Pak Choi seed models were generated in the seed box, and the simulation time was set to 18 s, as shown in Figure. 13. Continuously measure the number of seed filling in 200 type holes in the simulation test, 1 seed filling in the type holes for seed filling qualified n_1 , 2 or more for reseeding n_2 , less than 1 for leakage n_3 , using the Equation (14) to calculate the rate of qualified, reseeding rate, leakage rate of the seed in the type holes, repeat the three tests to take the average value.

Table 8

Material parameters required for seeding simulation

| Project | Attribute | Numeric value |
|---------------------------------|--|--------------------|
| Pak Choi seeds | Poisson's ratio | 0.375 |
| | Shear modulus / Pa | 1.66×10^7 |
| | Density / ($\text{kg} \cdot \text{m}^3$) | 1082 |
| PLA plastic | Poisson's ratio | 0.3 |
| | Shear modulus / Pa | 1.04×10^7 |
| | Density / ($\text{kg} \cdot \text{m}^3$) | 1290 |
| Nylon plastic | Poisson's ratio | 0.4 |
| | Shear modulus / Pa | 1.1×10^8 |
| | Density / ($\text{kg} \cdot \text{m}^3$) | 1150 |
| Pak Choi seeds - Pak Choi seeds | collision recovery coefficient | 0.292 |
| | Coefficient of static friction | 0.52 |
| | Coefficient of rolling friction | 0.098 |
| Pak Choi seeds - PLA plastic | collision recovery coefficient | 0.473 |
| | Coefficient of static friction | 0.46 |
| | Coefficient of rolling friction | 0.163 |
| Pak Choi seeds - nylon plastic | collision recovery coefficient | 0.45 |
| | Coefficient of static friction | 0.50 |
| | Coefficient of rolling friction | 0.01 |

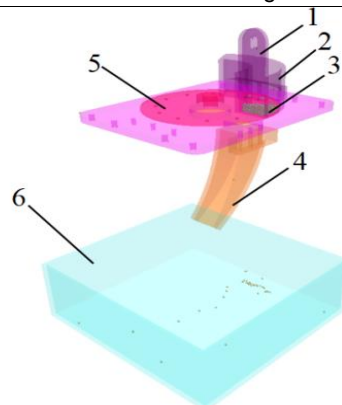


Fig. 13 - Sowing device simulation experiment

1. Brush; 2. Seed box; 3. Pak Choi seeds; 4. Seed tubes; 5. Seed tray; 6. Seed collection bin.

Seed-metering device bench test: The same batch of Jinyu Shenghui four-season Pak Choi seeds as the above test was selected for the bench test, and the seed-metering device was made with 3D rapid prototyping technology, and the material was PLA plastic. The test setup consisted of a seed-metering device, seed-metering device mounting bracket, motor with the motor controller, homemade sand spreader with sand

spreader controller, and conveyor belt as shown in Figure 14. To better achieve the experimental effect, according to the actual small Pak Choi breeding agronomic requirements, the plant spacing is 10 cm as a standard, the seed grain spacing is greater than 1.5 times the theoretical grain spacing for the leakage of seed, the seed grain spacing is less than or equal to 0.5 times the theoretical grain spacing for the re-sowing. At the beginning of the test, the white sand was poured into the sand spreader, the sand spreader was started and the operating speed of the conveyor belt was set to 0.5 m/s. After the sand was discharged uniformly and continuously, the motor speed was set to 25 r/min seed rowing was started, and the test was conducted to measure the plant spacing of 200 seeds, and the statistical data were brought into Equation (14) to calculate the qualification rate of the seeds, the reseeding rate, and the omission rate, and the trial was repeated for three times. The average value was taken.

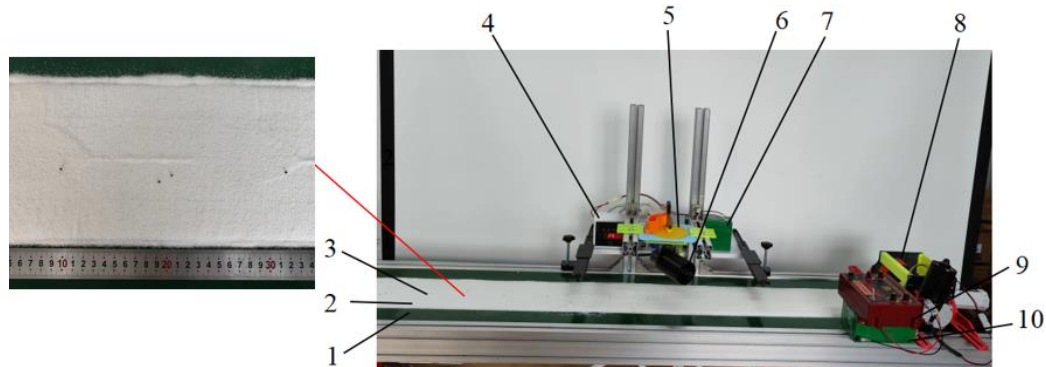


Fig. 14 - Sowing device test rig experiment

1. Conveyor belt; 2. Sand; 3. Pak Choi seeds; 4. Seeding Controller; 5. Seed-metering device; 6. Electrical machinery; 7. Battery; 8. Sand laying machine; 9. Sand spreading machine controller; 10. Sand paver battery.

Test results and analyses

The results of simulation and bench test are obtained as follows: the average values of qualified rate are 85.33% and 84.67%, respectively, with a relative error of 0.78%; the average values of replay rate are 8.17% and 8.5%, respectively, with a relative error of 3.88%; and the average values of missed seeding rate are 6.5% and 6.83%, respectively, with a relative error of 4.83%. The results of the simulation test and the bench test were less than 5%. The results show that the seed discrete element model and simulation parameter calibration are reliable, and the simulation and test qualification rate, reseeding rate and leakage rate meet the agronomic requirements of Pak Choi sowing.

CONCLUSIONS

(1) The basic physical parameters of Pak Choi seeds were determined through physical tests mainly including triaxial dimensions, mass, density, water content, Poisson's ratio, modulus of elasticity, shear modulus, and the equivalent diameters, sphericities, and volumes of the seeds were calculated by applying formulas, and the static friction coefficients, rolling friction coefficients, collision recovery coefficients, and angle of repose of the seeds were measured through the mechanical property test device constructed by the company independently.

(2) The physical property parameters determined in the physical tests were used as the basis for the selection of parameters for the simulation tests, the Plackett-Burman test was carried out to select the parameters that highly significantly affected the angle of repose: Pak Choi seeds - Pak Choi seeds static friction coefficient and Pak Choi seeds - Pak Choi seeds rolling friction coefficient. The optimal range interval of the highly significance parameter was further determined by the steepest climb test.

(3) Using the simulated angle of repose as the test index, the Design-Expert software and EDEM software were used to carry out the Central Composite Designs test, and the regression equation between the highly significance parameter and the angle of repose was obtained. The regression equation was optimally solved using the measured angle of repose (24.3°) as the target value. It was obtained the optimal simulation parameters: Pak Choi seed - Pak Choi seed static friction coefficient of 0.486, Pak Choi seed - Pak Choi seed rolling friction coefficient of 0.104.

(4) Pak Choi seeds angle of repose simulation and bench test error rate of 0.288%, seed dispenser simulation test and bench test qualified sowing rate of 85.33%, 84.67%, respectively, replanting rate of 8.17%, 8.5%, missed sowing rate of 6.5%, 6.83%, respectively, verified that the relative error rate between the two is not more than 5%, there is no significant difference, so the simulation of the calibration parameters with a certain degree of reliability and authenticity, can be used as a reference for the operation simulation of Pak Choi seed dispenser. The simulation parameters have certain reliability and authenticity, which can provide a certain reference for the relevant operation simulation of Pak Choi seed discharger.

REFERENCES

- [1] Bai, J., Xie, B., Yan, J., Zheng, Y., Liu, N., Zhang, Q. (2023). Moisture content characterization method of wet particles of brown rice based on discrete element simulation, *Powder Technology*, vol.428, 118775. <https://doi.org/10.1016/j.powtec.2023.118775>
- [2] Chen, Z., Yu, J., Xue, D., Wang, Y., Zhang, Q., Ren, L. (2018). An approach to and validation of maize-seed-assembly modelling based on the discrete element method. *Powder Technology*, 167-183.
- [3] Ding, X., Wang, B., He, Z., Shi, Y., Li, K., Cui, Y., ... & Yang Q. (2023). Fast and precise DEM parameter calibration for *Cucurbita ficifolia* seeds. *Biosystems Engineering*, 258-276.
- [4] Du, X., Liu, C. (2022). Prediction of DEM parameters of coated fertilizer particles based on GA-BP neural network. *Engenharia Agrícola*.
- [5] Dun, G., Fan, X., Yang, Y., Li, H., Wang, C., Chen, H., ... & Du, JI. (2020). Improved design and experiment of a plug-in soybean seed metering device based on discrete element (基于离散元的插装式大豆排种器改进设计及试验). *Journal of Huazhong Agricultural University*, 39(03), 135-144.
- [6] Gong, X., Bai, X., Huang, H., Zhang, F., Gong, Y., Wei, D. (2021). DEM parameters calibration of mixed biomass sawdust model with multi-response indicators. *INMATEH - Agricultural Engineering*, 65(3), 183-192. <https://doi.org/10.35633/inmateh-65-19>
- [7] Hou, Z., Dai, L., Chen, Z., Qiu, Y., Zhang, X. (2020). Measurement and calibration of physical property parameters for Agropyron seeds in a discrete element simulation (冰草种子物性参数测定与离散元仿真参数标定). *Transactions of the Chinese Society of Agricultural Engineering*, 36(24):46-54
- [8] Li, W., Xu, H., Li, X., Li, H., Xu, R. (2023). Design and Experiment of Horizontal Disc Soybean Single-grain Precision Seed Metering Device (水平圆盘式大豆单粒精密排种器的设计与试验). *Journal of Agricultural Mechanization Research*, 46(06): 109-115.
- [9] Liu, F., Li, D., Zhang, T., Lin, Z., Zhao, M. (2020). Analysis and calibration of quinoa grain parameters used in a discrete element method based on the repose angle of the particle heap. *INMATEH Agricultural Engineering*, 61(2), 77-86. <https://doi.org/10.35633/inmateh-61-09>
- [10] Liu, Y., Mi, G., Zhang, S., Li, P., Huang Y. (2022). Determination of Discrete Element Modelling Parameters of Adzuki Bean Seeds. *Agriculture*, 12(5), 626-626.
- [11] Song, W., Wan, Y., Zhou, B., Kuang, F., Xiong, W., Liao J., ... & Zhang, S. (2020). Design and experiment of combined cavity-type precision hole-drop seed-metering device for rice. *INMATEH Agricultural Engineering*, 71(2), 25-43. <https://doi.org/10.35633/inmateh-71-02>
- [12] Wang, S., Lu, M., Liu, X., Ji, J., Chen, P. (2022). Calibration and analysis of discrete element simulation parameters of Chinese cabbage seeds. *PloS one*, 17(6), e0270415-e0270415.
- [13] Wang, Y., Kang, X., Wang, G., Ji, W. (2023). Numerical Analysis of Friction-Filling Performance of Friction-Type Vertical Disc Precision Seed-Metering Device Based on EDEM. *Agriculture*, 13(12).
- [14] Xie, B., Bai, J., Yan, J., Zhao, S., Liu, N., Zhang Q (2023). Calibration of white rice simulation parameters based on discrete element method. *INMATEH Agricultural Engineering*, 71(3), 215-224. <https://doi.org/10.35633/inmateh-71-18>
- [15] Xu, T., Fu, H., Liu, M., Feng, W., Zhang, R., Wang, Y., Wang, J. (2023). Ellipsoidal seed modeling and simulation parameter selection based on the discrete element method. *Materials Today Communications*, vol.37, 106923. <https://doi.org/10.1016/j.mtcomm.2023.106923>
- [16] Yan, J., Wei, S., Hu D., Liu, Q., Zhang, F. (2022). Calibration of discrete element contact parameters for white radish seed particle (白萝卜种子颗粒模型离散元接触参数标定与试验). *Journal of the Chinese Agricultural Mechanization*, 24(05).
- [17] Yu, Q., Liu, Y., Chen X., Sun, K., Lai, Q. (2019). Calibration and Experiment of Simulation Parameters for *Panax notoginseng* Seeds Based on DEM (基于离散元的三七种子仿真参数标定与试验). *Journal of the Chinese Agricultural Mechanization*, 51(02), 123-132
- [18] Zeng, Z., Man, X., Cao, X., li, Z., Wang, X. (2021). Critical Review of Applications of Discrete Element Method in Agricultural Engineering (离散元法在农业工程研究中的应用现状和展望). *Transactions of the Chinese Society for Agricultural Machinery*, 52(04), 1-20.
- [19] Zhou, H., Hu, Z., Chen, J., Lv, X., Xie, N. (2018). Calibration of DEM models for irregular particles based on experimental design method and bulk experiments. *Powder Technology*, vol.332, 210-223.

DEVELOPMENT OF MATHEMATICAL MODEL FOR ESTIMATING THE RICE MILLING DEGREE BASED ON FLUORESCENCE IMAGE

PENGEMBANGAN MODEL MATEMATIKA UNTUK MENDUGA DERAJAT SOSOH BERAS BERDASARKAN CITRA FLUORESENSI

Zakky MOCHAMAD^{1*)}, Ahmad USMAN²⁾, Subrata I DEWA MADE²⁾, Suhil MARDISON³⁾

¹⁾Agricultural Engineering Science Study Program, Faculty of Agricultural Engineering and Technology, IPB University, Indonesia;

²⁾Department of Mechanical and Biosystem Engineering, Faculty of Agricultural Engineering and Technology, IPB University, Indonesia;

³⁾ Indonesian Agricultural Engineering Polytechnic, Tangerang, Indonesia

Tel: +62816414894; E-mail: zakky_1979mochamad@apps.ipb.ac.id

DOI: <https://doi.org/10.35633/inmateh-73-34>

Keywords: quality, rice, milling degree, development model

ABSTRACT

This research aims to develop a mathematical model for estimating the milling degree of milled rice based on fluorescent imaging. The materials used were the Ciherang, IR64 and Mekongga varieties which are widely grown and consumed by Indonesian people. The experiment was conducted by varying the polishing time starting from 0 seconds to 34 seconds with 1 second intervals. Six grains of polished rice were taken to record their images using a camera with 365 nm UV fluorescent ring light. The data collected in this research were milling degree obtained by gravimetric method, milling degree obtained using a milling meter and color values of fluorescent images of milled rice by image processing. The results showed that prediction of milling degree using the RGB color model has the coefficient of determination between 0.8001 – 0.8652, which is considered as potential to be used as a model for estimating the degree of milled rice based on fluorescence images. The RGB color model shows that the image red signal has the highest coefficient of determination compared to green and blue signals. For all of the three varieties in this study, the Ciherang variety has a predictive model equation for the image red signal $y = 3.9027x - 429.61$, the IR64 variety has a predictive model equation for the image red signal $y = 3.7344x - 415.01$, and the Mekongga variety has a predictive model equation for the image red signal $y = 3.5627x - 388.86$.

ABSTRAK

Penelitian ini bertujuan untuk mengembangkan model matematika untuk menduga derajat sosoh beras giling berdasarkan pencitraan fluoresen. Bahan yang digunakan adalah varietas Ciherang, IR64 dan Mekongga yang banyak ditanam dan dikonsumsi oleh masyarakat Indonesia. Percobaan dilakukan dengan memvariasikan waktu pemolesan mulai dari 0 detik hingga 34 detik dengan interval 1 detik. Enam butir beras yang telah disosoh diambil untuk direkam gambarnya dengan menggunakan kamera dengan lampu cincin fluoresen UV 365 nm. Data yang dikumpulkan dalam penelitian ini adalah derajat sosoh yang diperoleh dengan metode gravimetri, derajat sosoh yang diperoleh dengan menggunakan alat ukur milling meter dan nilai warna citra fluoresen beras giling dengan pengolahan citra. Hasil penelitian menunjukkan bahwa prediksi derajat sosoh menggunakan model warna RGB memiliki nilai koefisien determinasi antara 0.8001 - 0.8652, sehingga model ini berpotensi untuk digunakan sebagai model penduga derajat sosoh beras giling berdasarkan citra fluoresensi. Model warna RGB menunjukkan bahwa sinyal warna merah pada citra memiliki nilai koefisien determinasi yang paling tinggi dibandingkan dengan sinyal warna hijau dan biru. Untuk ketiga varietas dalam penelitian ini, varietas Ciherang memiliki persamaan model prediksi untuk sinyal merah citra $y = 3.9027x - 429.61$, varietas IR64 memiliki persamaan model prediksi untuk sinyal merah citra $y = 3.7344x - 415.01$, dan varietas Mekongga memiliki persamaan model prediksi untuk sinyal merah citra $y = 3.5627x - 388.86$.

INTRODUCTION

Rice is a strategic food consumed by most of the world's population. Rice is a grain whose outer husk has been removed by shucking. Rice consumption per capita in 2023 experienced a slight increase compared to 2022, from 256.2 grams/cap/day (93.5 kg/cap/year) to 257.0 grams/cap/day (93.8 kg/cap/year) (*National Food Agency, 2024*). Rice sold in the market is generally milled rice. The degree of milling is the detachment of the aleurone and sub-aleurone layers in rice grains (*Patria et al., 2021*). The degree of milling greatly affects the physical characteristics and nutritional content of rice (*Hasnelly et al., 2020*). Milling will increase the shelf life of rice (*Febriandi et al., 2017*).

Rice quality is a result of combination of grain physical and chemical characteristics. The physical characteristics of rice are degree of milling, whiteness, translucency, grain length, foreign matter, head rice, and chalkiness, while the chemical characteristics are amylose content, gelatinase temperature, and gel consistency (Bhattacharya, 2011). Indonesia has rice quality requirements defined in Indonesian National Standards (SNI) 6128:2020, published by the National Standardization Agency (NSA), in which there are six parameters for general quality requirements and eight parameters for special requirements for the quality of milled rice. One of the general requirement parameters to determine the quality of milled rice is the degree of milling (National Standardization Agency, 2020).

The rice quality estimation in the market is conducted by looking at the color of rice, smelling the aroma of rice and feeling the texture of rice. This method has weaknesses, namely perceptions that are not the same between one person and another and the fatigue factor of the person. Meanwhile, the determination of the degree of milling based on SNI is qualitatively based on the coloring method (*methylene blue*). In addition to expensive equipment, the use of certain chemicals can also increase evaluation costs. Other unfavorable aspects are the long time required and the waste generated from the process. Based on this, the current determination of general quality requirements for rice in Indonesia still needs improvement and enhancement of its measurement methods. The method that will be developed to identify the general quality requirements of rice is the use of optical-based technology.

The development of non-destructive technology based on optical characteristics has now been widely applied in various fields, including agriculture. Near Infrared (NIR) is one of the non-destructive technologies that can determine the quality of a product with the ability to analyze up to a depth of 5 mm from a product, this technology is different from image processing which only sees the outer appearance. NIR technology involves chemical activities that occur to a depth of 5 mm when the product is subjected to photon energy emitted from the energy source. *Mardison, (2010)*, used NIR technology to determine the chemical content of *Jatropha* non-destructively, and *Angkat, (2012)*, used NIR technology to determine the nitrogen content in soil non-destructively.

Image processing technology as one optical-based data set has been used to determine the quality of agricultural products visually and the application of this technology has reached the stage of real-time process on agricultural machineries. The uses of camera as sensor and image processing to analyze the image is known as machine vision as done by *Ahmad et al., (2010)*, in developing an orange sorting machine with real-time image processing capability.

Image processing is the process of observing and analyzing an object without having direct contact with the object being observed. The process and analysis involve visual perception with input data obtained in the form of images of the objects being observed. Image processing techniques include image sharpening, highlighting certain features of an image, image correction of out-of-focus or blurry images (*Ahmad, 2005*). Normal color image shows an object just like our eyes see the object directly, contains a set of data as a representative of the object but the data can be extracted and processed by computer to facilitate quantitative analysis. The available data in the normal color image represent what can be seen by eyes only because normal camera works at the same range of wavelength with human eyes. However, more data can be obtained from image if the object is excited with light that covers wider wavelength such as ultraviolet (UV) in combination with visible wavelength to produce fluorescence image. Fluorescence is light emitted by an atom or molecule after absorbing high-energy light. The principle that occurs is that the electrons in the molecule are first excited by absorbing light from a beam, then the electrons move from the ground electronic state to one of various vibrational states in the excited electronic state. After that the molecule will quickly lose the remaining vibrational energy through collisions and fall back to one of the various vibrational levels in the ground electronic state while emitting light in the form of fluorescence (*Lakowicz, 2006*).

Fluorescent imaging systems consist of camera with several additional components such as excitation light source, light transmitting and collecting optical components, and emission filters. Light sources that are often used are LEDs, halogen lamps, and diode lasers. A digital camera has sensors which are divided into two types, namely CCD sensors and CMOS sensors. Fluorescence imaging is closely related to the excitation wavelength because it involves the process of fluorescence. Fluorescence occurs when light is induced into the test material or sample. This material consists of atoms or molecules that have certain energy levels. When light hits a substance, the photon energy is used to excite the atoms or molecules to a higher energy level (*Albani, 2007*).

Research on rice using fluorescence imaging through UV light excitation has been carried out for example to determine the freshness of the rice with the results of the fluorescent intensity being strongly correlated with the freshness of the milled rice at 0.819 (*Hachiya et al., 2009*). Other research was to determine the origin of rice using hyperspectral fluorescence image analysis with the results showing that hyperspectral fluorescence imaging technology can be used to discriminate the rice with different origin with high levels of 98.89% (*Kim et al., 2020*). The fluorescence imaging can be used also to measure the degree of graininess of rice based on UV spectrum characteristics and the results showing that the most influential measurement parameters in estimating the degree of graininess are the duration of deposition, the shape of the sample, and the concentration of the n-hexane solvent for Ciherang variety (*Mardison, 2019*). Detecting the distribution of rice bran residue on the surface of rice was also conducted using fluorescence imaging with the SLC prediction error result being 2.44% (*Chen and Kuo, 2014*), and determination of multiple rice quality parameters simultaneously using image analysis method with the result of the regression coefficient (R) were 0.9916, 0.9691, 0.9938, 0.9929, 0.9649, and 0.9377 for length, width, length-to-width ratio, head rice, percentage of chalky rice, and lime content (*Fang et al., 2014*).

Based on the mentioned problem, it is necessary to design an alternative method to analyze the quality of milled rice which is cheap, fast and does not damage the rice and is environmentally friendly. One technology that has the potential to be applied is fluorescent imaging. This research aims to develop a model for predicting the degree of milled rice based on fluorescent images.

MATERIALS AND METHODS

Samples Collection

The samples used were three varieties of rice (Ciherang, IR64 and Mekongga varieties). A total of 315 samples of rice weighing 100 grams per sample were prepared. The three varieties were selected in this research because they are widely grown and consumed by Indonesian people.

Equipment

The equipment for processing whole grain into rice, namely the Zaccaria brand PAZ-1 DTA rice mill, is used to remove husk and produce whole rice kernel and directly polish the rice kernel until white rice was obtained. The TRG05B type SATAKE brand rice grader is used to separate head, broken and rice groats. Rice milling meter type New MM1D made by SATAKE, Japan is used to measure polishing parameters which are expressed in whiteness (%), transparency (%) and milling degree values and analytical scales. Equipment for image processing, namely a 48 MP 4K Monocular Microscope Camera which is connected to a Digital Video Microscope Electronic Monitor, a UV ring fluorescent lamp with a wavelength of 365 nm, and an image recording chamber with lighting controller.

Procedure

The research stages include sample preparation, image recording, image processing and analysis of the data, development of rice milling degree model, and the stages can be seen in Figure 1. The procedures for the research are explained as follow.

1) Sample collecting

Samples in the form of whole paddy grains were taken from a local paddy breeder under the supervision of Indonesian Center for Rice Standard Evaluation in Sukamandi, West Java. The varieties used in this stage are the Ciherang, IR64 and Mekongga. The three varieties were collected, 15 kg each that meets quality standards as commercial paddy rice, in order to obtain sample uniformity (pure variety).

2) Sample weighing

Samples in the form of whole grain were weighed, 100 g for each sample. The number of samples used were 105 samples for each variety, making the total number of samples being 315 for three varieties. Each sample then was packaged in plastic packaging and labeled for each treatment.

3) Husk removing

The husk was removed from the whole grain and then the kernel was weighed to obtained the yield and then the rice kernels were put again into the same plastic packaging.

4) Whole kernel selection

The husked rice produced in the previous step consists of whole rice, head rice, broken grains and rice groats. Sorting was carried out to select only whole kernels for further processing and then put again the whole rice kernels into the same plastic packaging.

5) Polishing process

The samples that contain only the whole rice kernels were polished with 35 levels of polishing degree based on process duration with the same machine and the same parameter setting. The duration applied were 0, 1, 2, 3, 4, 5, 6, 7, 8, 9, 10, 11, 12, 13, 14, 15, 16, 17, 18, 19, 20, 21, 22, 23, 24, 25, 26, 27, 28, 29, 30, 31, 32, 33, and 34 seconds as treatments. After finishing the polishing process, each sample was weighed again and was put again into the same plastic packaging.

6) Polished kernel selection

Polishing process caused breakage to some kernels making the sample not being uniform. For better data, only whole kernels and kernels with small broken parts (head kernel) were selected for further analysis.

7) Measurement of milling degree

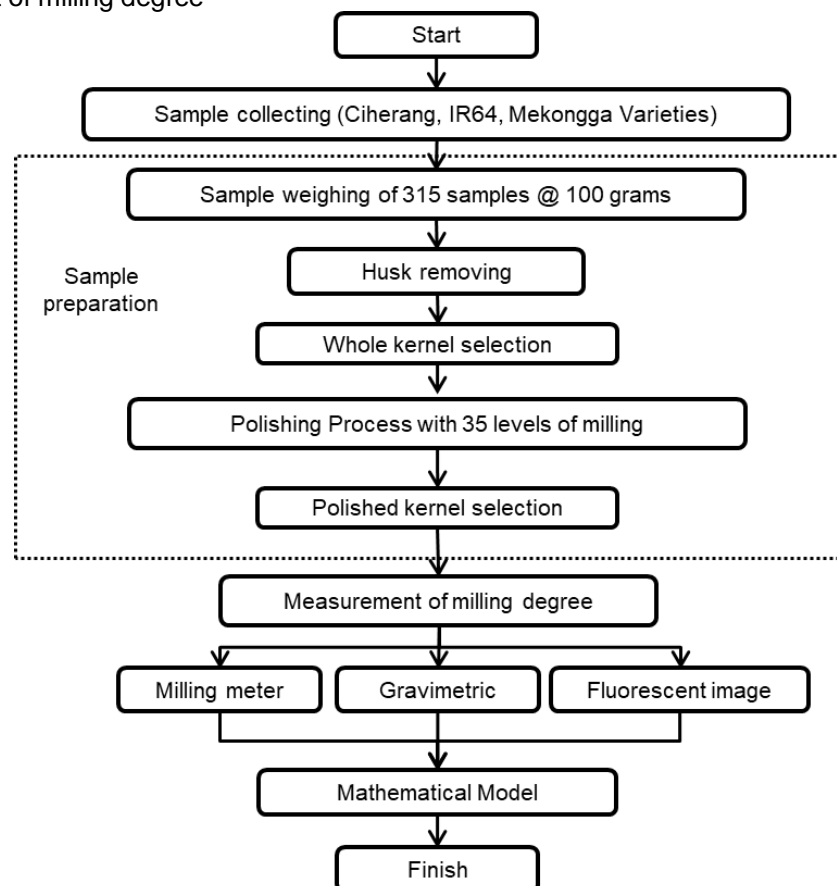


Fig. 1 - The development of a mathematical model for rice milling degree estimation using fluorescent images

Measuring the degree of milling of the polished rice kernels is done by knowing loss of sample weight after polishing with the initial condition is that the rice kernel before polishing which is known as gravimetric method (Patria et al., 2021). The DM in this research was calculated using Equation 1 where DM is milling degree, W_p is weight of milled rice (g) and W is weight of whole rice kernel (g).

$$DM = \frac{1 - W_p}{W} \times 100\% \quad (1)$$

Milling degree measurements was also carried out using a rice milling meter that directly gives the results obtained: whiteness (%), transparency (%) and milling degree values (no unit). As for estimation of the milling degree based on fluorescence image by image processing and analysis, the equipment used was arranged as shown in Figure 2. The stages were carried out starting from sample preparation, image capturing and saving the image in the JPG format in the computer connected to the camera, and finally image processing and analysis to obtain the desired features using ImageJ image analysis software. The equipment used to capture image of arranged rice kernels, 6 rice kernels of that were placed on a tray which was covered with a black cloth. In the image capture process, a resolution of 1920 x 1080 pixels was applied and the distance between the camera and the object was 15 cm. Lighting was provided by an 8W UV fluorescent ring lamp, which was placed at the end of the camera lens.

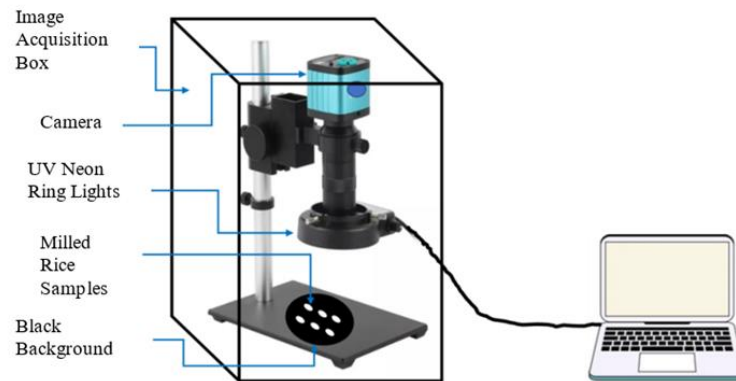


Fig. 2 - The development of a mathematical model for rice milling degree estimation using fluorescent images

Color analysis of digital images is carried out using two color models, namely red-green-blue (RGB) color model and hue-saturation-intensity (HSI) color model. According to *Ahmad, (2005)* color processing using RGB colors is easy and simple, because the color information in the computer is packaged in the same model. The RGB color model is an additive basic color model, that is, colors are formed by combining light energy from the three basic colors in various ratios. The HSI color model with hue (H), saturation (S) and intensity (I) color components, can be converted from the RGB color space. The HSI color model is the color model that best suits human's visual interpretation. Hue value expresses color position by angle where red is 0 or 360 degrees, green is 120 degrees and blue is 240 degrees. Any angle value between 0 and 360 stated a unique color according to the wavelength. Saturation value expresses strength of color where 0 is very weak and 1 is strongest color (saturated color). Intensity expresses the brightness of color where 0 means no light so any color will be black and maximum brightness will turn any color to white. The relationship between RGB and HSI color components are expressed by Equation 2 – 4.

$$H = \arccos\left(\frac{2R-G-B}{2\sqrt{(R-G)^2+(R-G)(G-B)}}\right) \quad (2)$$

$$S = 1 - \frac{3 \cdot \min(R,G,B)}{R+G+B} \quad (3)$$

$$I = \frac{R+G+B}{3} \quad (4)$$

If $B > G$ then the hue value is $360-H$. Color conversion from RGB to HSI can use the original RGB values.

Analysis

The RGB and HSI color components as the results of the fluorescence image processing were analyzed using linear regression. The linear regression equation can be calculated using Equation 5 where Y is degree of milling obtained using gravimetric method and milling meter, a is slope of the regression line, X is equal values of color components in RGB and HSI color models, and b is a constant.

$$Y = aX + b \quad (5)$$

According to (*Usman dan Akbar, 2008*) the R^2 value has no units (dimensions), the closer it is to 1, the stronger the relationship between variables. When $0.20 < R^2 \leq 0.40$ means the correlation is low, when $0.40 < R^2 \leq 0.60$ the correlation is somewhat low, when $0.60 < R^2 \leq 0.80$ the correlation is quite high, and when $0.80 < R^2 \leq 0.99$ the correlation is high, and 1 means the correlation is very high.

RESULTS AND DISCUSSION

Gravimetric and Milling Meter Correlation

According to *Khatun et al., (2019)*, rice grains are composed of 5.9 – 6.4% bran including aleurone, 5.6 – 9.9% sub-aleurone, 82.5 – 83.8% endosperm, and 1.3 – 1.5 germ as shown in Figure 3.

Based on a literature study, a milling degree of 100% is assumed to be 11.5% by gravimetric method. In this study, the results of measuring milling degrees using the gravimetric method with milling degrees using a milling meter are as shown in Table 1.

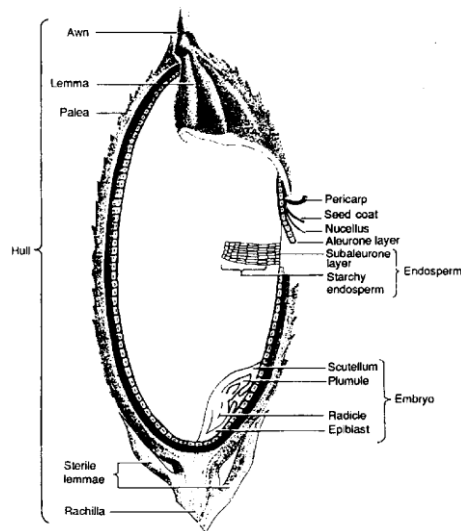


Fig 3 - Rice grain structure (Khatun et al., 2019)

Table 1
Degree of Milling Gravimetric and Milling Meter

| No | Variety | Gravimetric (%) | | Milling Meter | |
|----|----------|-----------------|-----------|---------------|-------------|
| | | Range | Average | Range | Average |
| 1 | Ciherang | 0 – 12.88 | 8.05±3.65 | 0 – 119.00 | 75.64±36.20 |
| 2 | IR64 | 0 – 14.35 | 8.18±3.75 | 0 – 121.56 | 72.13±40.03 |
| 3 | Mekongga | 0 – 11.20 | 7.22±3.09 | 0 – 124.00 | 78.25±37.25 |

Rice milling meter type New MM1D made by SATAKE, Japan, has a degree of milling value from 0 - 199, and in the table, the degree of milling using the milling meter is above 100, so it is necessary to convert the milling meter value into a percentage of the degree of milling on a scale of 0 - 100%.

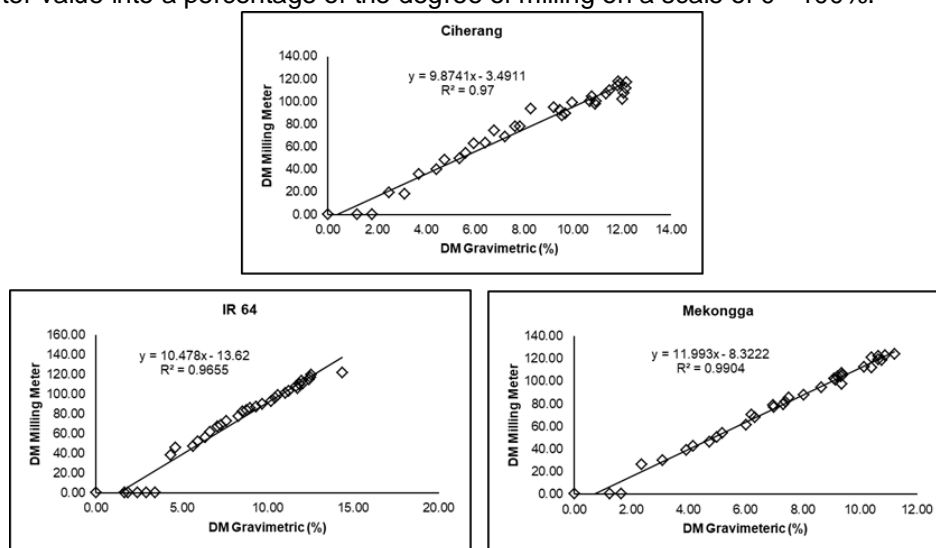


Fig. 4 - Relationship of milling degree analyzed by Gravimetric method and measured by milling meter

Figure 4 shows the relationship between the degree of milling analyzed by Gravimetric method and measured by milling meter. The R² value of the Ciherang variety is 0.97, the R² of the IR64 variety is 0.9655, and the R² of the Mekongga variety is 0.9904. The three varieties show high relationships between the degree of milling obtained using the two different methods. Based on this, the degree of milling using a milling meter can be used as the degree of milling of milled rice to build the mathematical model.

Correlation of Gravimetric, Milling Meter and Fluorescent Image

The number of samples used to estimate milling degree are 315, with 30 g/sample of 105 samples for each variety. For all of 105 samples of each variety, 35 different milling time treatments were applied with three repetitions. The color values generated in this study were obtained from six randomly selected rice grains in each sample to produce the images. The image recording results can be seen in Figure 5.

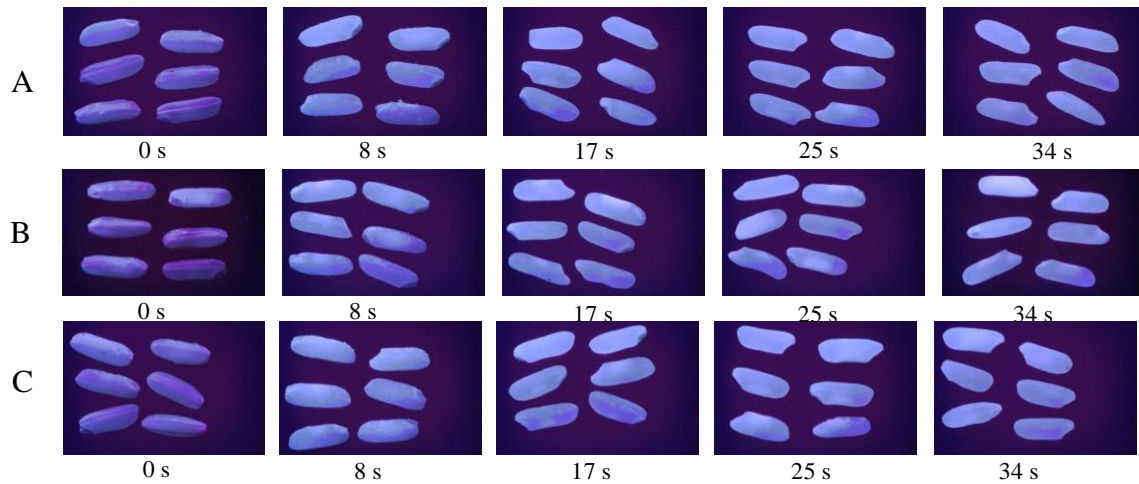


Fig. 5 - Image recording results of (A) Ciherang, (B) IR64, and (C) Mekongga varieties

The image obtained in the image recording is then analyzed with the ImageJ application. After receiving the RGB value, the value of six rice grains is averaged to become the value of 1 sample. The calculation results of each sample are then made into a graph using Microsoft Excel software.

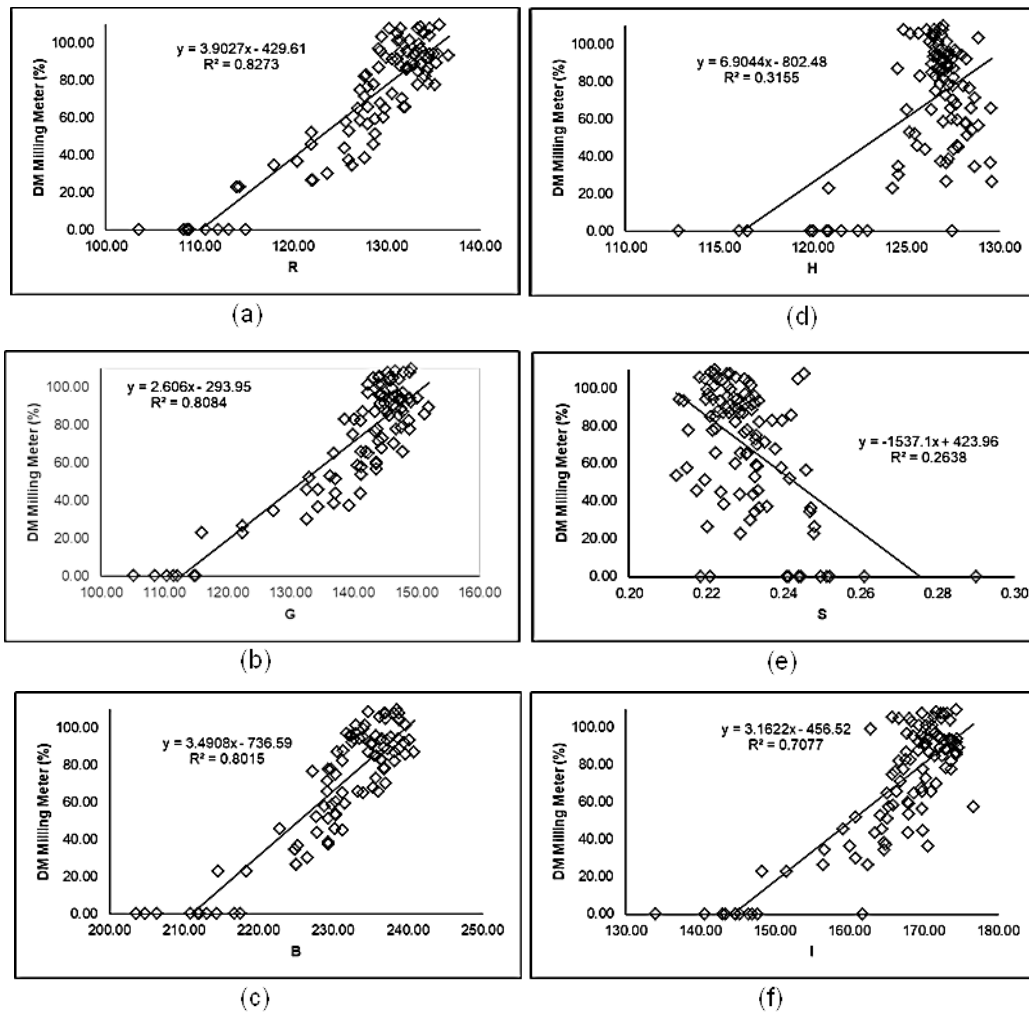


Fig. 6 - Correlation between the degree of milling measured by milling meter and estimated using fluorescence image on Ciherang variety using (a) red signal, (b) green signal, (c) blue signal, (d) hue color component, (e) saturation color component, and (f) intensity color component

In Figure 6, the correlation between the degree of milling using a milling meter and the color values of R, G, B of Ciherang varieties represented by R^2 are 0.8273, 0.8084, 0.8015, respectively, which is categorized as a high correlation and show that RGB color values have positive correlation with the length of milling time. The RGB color model in fluorescence images has the potential to be used to estimate the degree of milling rice of Ciherang variety. The relationship between the degree of milling using a milling meter with the HSI color model of Ciherang variety are 0.3155, 0.2638, 0.7077. For the three R^2 respectively and for the HSI color method, the correlation between the degree of milling and the color values of HSI is categorized as low to high. The strongest correlation of the Ciherang variety is between the degree of milling with image red signal and the estimation model equation is $y = 3.9027x - 429.61$.

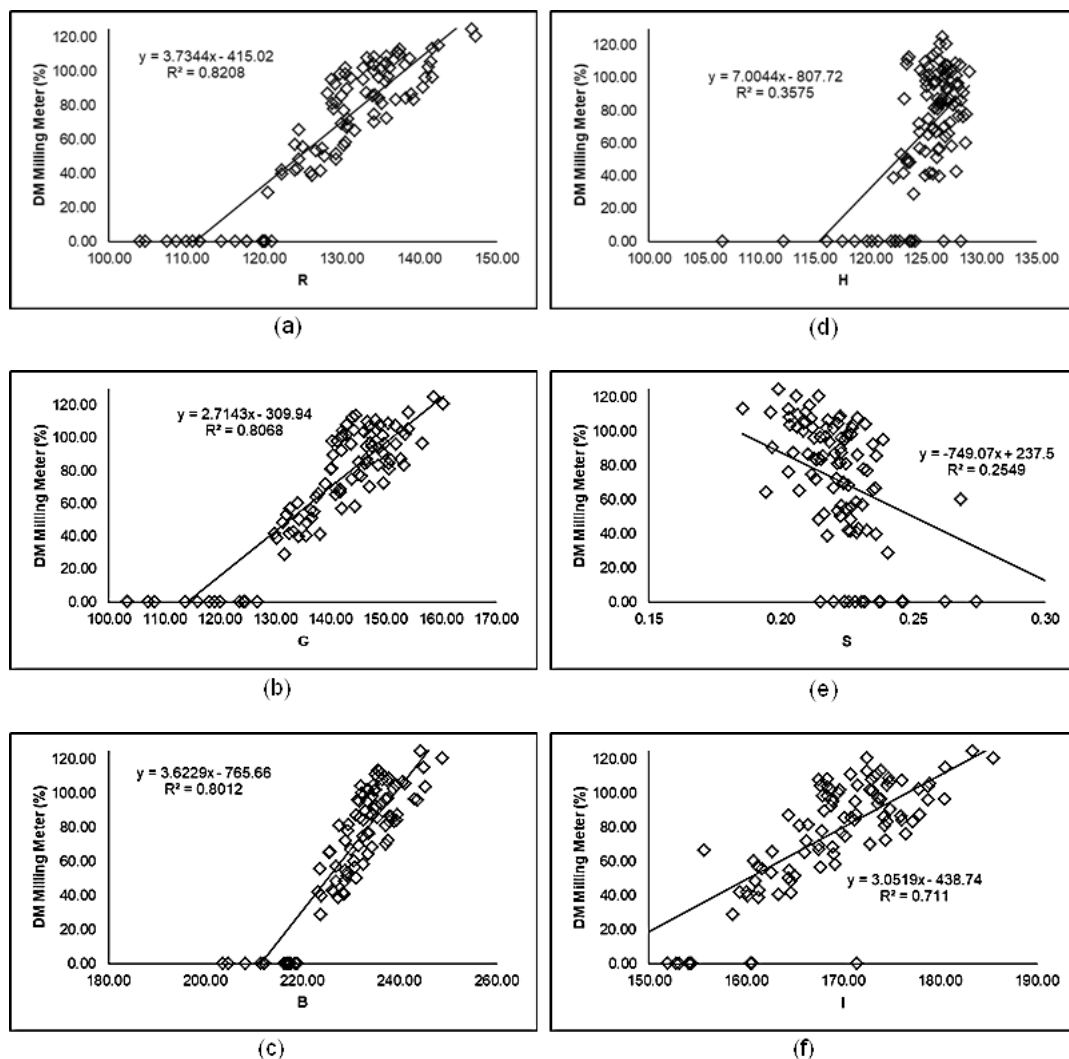


Fig. 7 - Correlation between the degree of milling measured by milling meter and estimated using fluorescence image on IR64 variety using (a) red signal, (b) green signal, (c) blue signal, (d) hue color component, (e) saturation color component, and (f) intensity color component

In Figure 7, the correlation between the degree of milling using a milling meter and the color values of R, G, B of IR64 varieties represented by R^2 are 0.8208, 0.8068, 0.8012, respectively, which is categorized as a high correlation and show that RGB color values have positive correlation with the length of milling time. The RGB color model in fluorescence images has the potential to be used to estimate the degree of milling rice for IR64 variety. The correlation between the degree of milling using a milling meter with the HSI color model of IR64 variety are 0.3575, 0.2549, 0.711, respectively. For the HSI color model categorized as low correlation to high correlation. The strongest relationship for IR64 varieties is between the degree of milling with image red signal and the estimation model equation $y = 3.7344x - 415.01$.

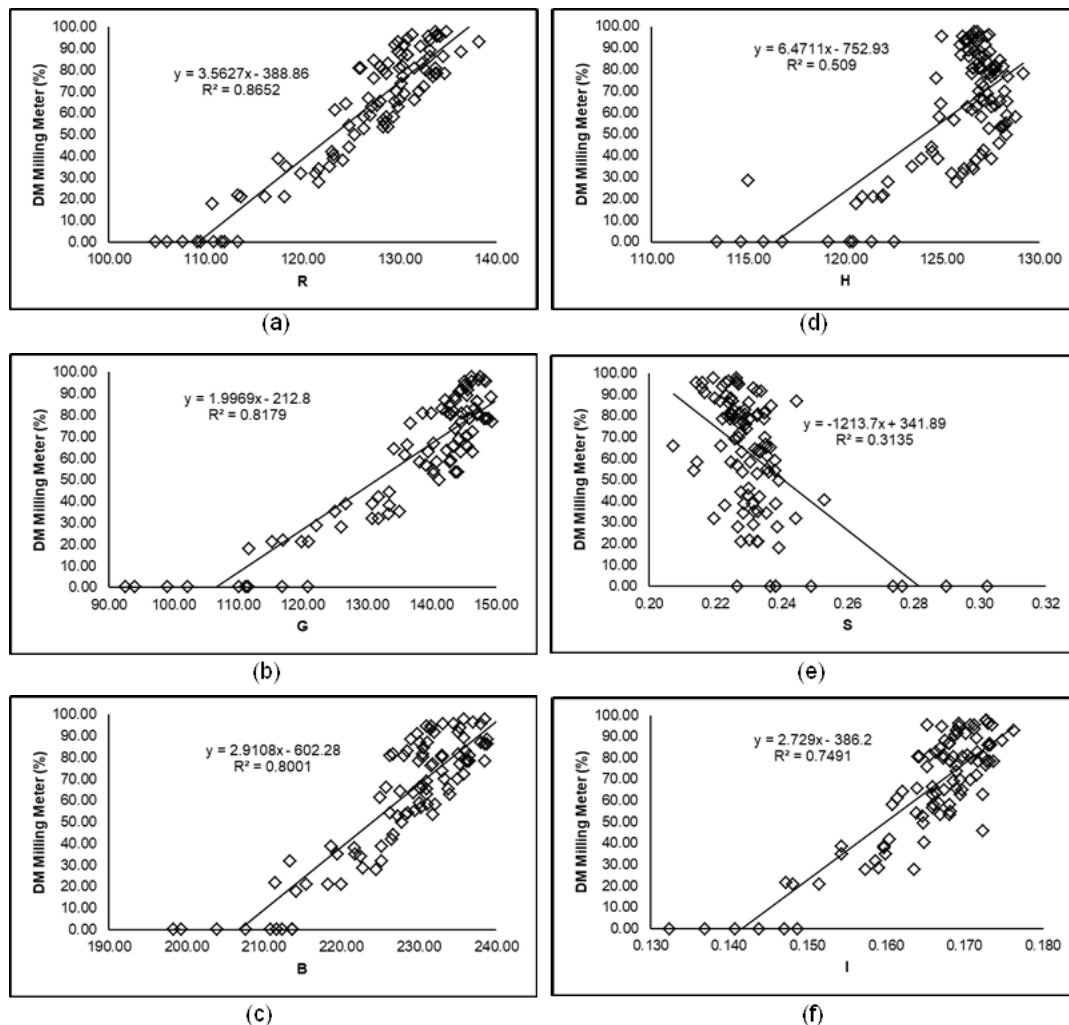


Fig. 8 - Correlation between the degree of milling measured by milling meter and estimated using fluorescence image on Mekongga variety using (a) red signal, (b) green signal, (c) blue signal, (d) hue color component, (e) saturation color component, and (f) intensity color component

In Figure 8, the correlation between the degree of milling using a milling meter and the color values of R, G, B of IR64 varieties represented by R^2 are 0.8652, 0.8179, 0.8001 respectively, which is categorized as a high correlation and show that RGB color values have positive correlation with the length of milling time. The RGB color model in fluorescence images has the potential to be used to estimate the degree of milling rice for Mekongga variety. The correlation between the degree of milling using a milling meter with the HSI color model of Mekongga variety are 0.509, 0.3135, 0.7491, respectively. For the HSI color model categorized as low correlation to high correlation. The strongest relationship of the Mekongga variety is the correlation between the degree of milling with image red signal and the estimation model equation $y = 3.5627x - 388.86$.

For the three varieties, the RGB color model has the potential to be used as a parameter for estimating the milling degree of milled rice, while the HSI color model cannot be used for estimating the milling degree. In the image analysis, the image red signal has the largest R^2 among the green and blue signals in the three varieties. According to (Ahmad, 2005), the RGB color model is an additive principal color model where colors are formed by combining the light energy of the three primary colors in various comparisons.

CONCLUSIONS

The mathematical model for estimating the milling degree of milled rice based on fluorescence images having the potential to be developed is the RGB color values with a coefficient of determination between 0.8001 - 0.8652, categorized as high for Ciherang, IR64 and Mekongga varieties.

The RGB color values shows that the image red signal has the highest coefficient of determination compared to green and blue signals. For all of the three varieties in this study, the Ciherang variety has a predictive model equation for the image red signal $y = 3.9027x - 429.61$, the IR64 variety has a predictive model equation for the image red signal $y = 3.7344x - 415.01$, and the Mekongga variety has a predictive model equation for the image red signal $y = 3.5627x - 388.86$.

REFERENCES

- [1] Ahmad, U. (2005). *Digital Image Processing and Programming Techniques (Pengolahan Citra Digital dan Teknik Pemrogramannya)*. Graha Ilmu. Yogyakarta (ID). ISBN: 979-756-072-6.
- [2] Ahmad, U., Mardison, S., Rudy, T., and Ana, N. (2010). Development of automatic grading machine prototype for citrus using image processing. *Australian Journal of Agricultural Engineering* 1 165-169.
- [3] Albani, J. R. (2007). *Principles and Applications of Fluorescence Spectroscopy*. Blackwell Publishing company.
- [4] Angkat, A. R. (2012). *Development of a Soil Nitrogen Content Data Acquisition System Based on Infrared Sensors as a Guideline for Determining Fertilizer Dosage (Pengembangan Sistem Akuisisi Data Kadar Nitrogen Tanah Berbasis Sensor Infra Merah sebagai Pedoman Penentuan Dosis Pemupukan)*. [Doctoral dissertation, IPB University]. Bogor (ID).
- [5] *** National Food Agency. (2024). *National Food Consumption Situation in 2023 (Situasi Konsumsi Pangan Nasional Tahun 2023)*. Jakarta (ID).
- [6] *** National Standardization Agency. (2020). *SNI No. 6128:2020 Rice*. National Standardization Agency. Jakarta (ID).
- [7] Bhattacharya, K. R. (2011). *Rice quality*. Springer. Singapore.
- [8] Chen, W.T., Kuo, Y.F. (2014). Detecting Bran Residue Distribution on Rice Surface Using Fluorescence Imaging. *ASABE and CSBE/SCGAB Annual International Meeting*. Montreal, Quebec Canada.
- [9] Febriandi, E., Rizal, S., Sri, W. (2017). Studi Sifat Fisikokimia dan Fungsional Padi Lokal (Mayang Pandan) pada berbagai Tingkat Derajat Sosoh. *Jurnal Penelitian Pascapanen Pertanian*, vol.14, 79 - 87.
- [10] Fang, C., Hu, X., Sun, C., Duan, B., Xie, L., and Zhou, P. (2014). Simultaneous Determination of Multi Rice Quality Parameters Using Image Analysis Method. *Food Analytical Methods*, vol.8, 70-78.
- [11] Hachiya, M., Asanome, N., Goto, T., Noda, T. (2009). Fluorescence Imaging with UV-Excitation for Evaluating Freshness of Rice. *Japan Agricultural Research Quarterly*, vol.43, 193-198.
- [12] Hasnelly, H., Evi, F., Shelvi, P. A., and Hervelly, H. (2020). Effect of Degree of Milling on Physical Quality and Nutritional Value of Some Rice Types (Pengaruh Derajat Penyosohan terhadap Mutu Fisik dan Nilai Gizi Beberapa Jenis Beras). *agriTECH*, vol.40.
- [13] Khatun, A., Waters, D. L. E., and Liu, L. (2019). A Review of Rice Starch Digestibility: Effect of Composition and Heat-Moisture Processing. *Starch – Stärke*, vol.71.
- [14] Kim, M.J., Lim, J., Kwon, S. W., Kim, G., Kim, M. S., Cho, B.-K., Baek, I., Lee, S. H., Seo, Y., and Mo, C. (2020). Geographical Origin Discrimination of White Rice Based on Image Pixel Size Using Hyperspectral Fluorescence Imaging Analysis. *Applied Sciences*, vol.10.
- [15] Lakowicz, J. R. (2006). *Principles of Fluorescence Spectroscopy*. Third Edition/Ed. Springer. Singapore.
- [16] Mardison, S. (2010). *Nondestructive Determination of Chemical Composition of Jatropha Seeds by NIR Method and Artificial Neural Networks (Penentuan Komposisi Kimia Biji Jarak Pagar Secara Nondestruktif dengan Metode NIR dan Jaringan Saraf Tiruan)*. [Thesis, IPB University]. Bogor (ID).
- [17] Mardison, S. (2019). *Development of a Rice Milling Degree Measurement Method Based on Ultra-Violet Spectrum Absorbance Characteristics (Pengembangan Metode Pengukuran Derajat Sosoh Beras Berdasarkan Karakteristik Absorbansi Spektrum Ultra-Violet)*. [Doctoral dissertation, IPB University]. Bogor (ID).
- [18] Patria, D. G., Sukamto, Sumarji. (2021). *Rice Science and Technology (Ilmu dan Teknologi Beras)*. Literasi Nusantara. Malang, Jawa Timur (ID).
- Usman, H., Akbar, P. (2008). *Introduction to Statistics (Pengantar Statistika)*. PT Bumi Aksara. Jakarta (ID).

HEAT TRANSMISSION THROUGH WALLS OF COMPOSITE MATERIAL WITH CLAY MATRIX

/

TRANSMITEREA CALDURII PRIN PERETI DE MATERIAL COMPOZIT CU MATRICE DE LUT

Elena SURDU¹⁾, Dana-Claudia FARCAȘ-FLAMAROPOL¹⁾, Radu I. IATAN¹⁾,
Petru CÂRDEI²⁾, Nicoleta SPOREA¹⁾, Gheorghîța TOMESCU¹⁾, Ion DURBACĂ¹⁾

¹⁾U.N.S.T "POLITEHNICA" of Bucharest, no. 313, Splaiul Independentei, sector 6, Bucharest, 060042, Romania

²⁾ INMA Bucharest, Bd. Ion Ionescu de la Brad, No.6, Romania, 013813

Tel: 0722298477; E-mail: cladidff@gmail.com

Tel: 0726142837; E-mail: petru_cardei@yahoo.com

DOI: <https://doi.org/10.35633/inmateh-73-35>

Keywords: *insulating materials, composites, clay, agricultural waste, properties, thermal conductivity, heat transfer*

ABSTRACT

The article presents results obtained for the thermal characterization of composite materials with clay matrix and inserts from agricultural waste (MCMLIDA). The experiments carried out led to the estimation of the coefficient of thermal conductivity of the bricks made from the MCMLIDA composite material. MCMLIDA composite materials have physical properties dependent on the parameters of the manufacturing process, one of the most important being the concentration of the insert. MCMLIDA materials were tested for eleven insert concentrations and four types of inserts (maize cobs, walnut husks, wheat straw, wool). Only the materials with the first two types of inserts had the necessary cohesion for the experiments over the entire range of concentrations (0-50%). It was found that the values of the conductivity coefficient of those materials were between 0.4 and 0.8 W/(mK), values that placed them in the area of good insulating materials from a thermal point of view. It was also observed that thermal conductivity increased (along with a decrease in insulating capacity) as the amount of insertion in the matrix was increased.

REZUMAT

Articolul prezintă rezultate obținute pentru caracterizarea termică a materialelor compozite cu matrice de lut și inserții din deșeuri agricole (MCMLIDA). Experimentele efectuate au condus la estimarea coeficientului de conductivitate termică a cărămizilor fabricate din materialul compozit MCMLIDA. Materialele compozite MCMLIDA au proprietăți fizice dependente de parametri procesului de fabricare, unul dintre cei mai importanți fiind concentrația inserției. Au fost testate materialele MCMLIDA pentru unsprezece concentrații ale inserției și patru tipuri de inserție (tocătură de coceni de porumb, tocătură de coji de nuca, tocătură de paie de grâu, lână). Numai materialele cu primele două tipuri de inserții au avut coeziunea necesară experimentelor pe tot intervalul de concentrații (0-50%). A fost constatat că valorile coeficientului de conductivitate al acestor materiale sunt cuprinse între 0.4 și 0.8 W/(mK), valori care le situează în zona materialelor bune izolatoare din punct de vedere termic. De asemenea, se constată creșterea conductivității termice (odată cu scăderea capacității izolatoare) pe măsură ce este sporită cantitatea de inserție în matrice.

INTRODUCTION

According to some research, (Popa et al., 1986; Vlădeș, 1974), heat transfer is the field of thermodynamics that deals with heat energy exchanges between bodies. Heat transfer occurs under the influence of a temperature difference. The second law of thermodynamics in Clausius's formulation states that this transfer takes place by itself only from the higher temperature to the lower temperature. Also, according to the mentioned research, the three heat transmission mechanisms are: conduction, convection and radiation. Thermal conduction is one of the ways of transmitting heat between two media at a certain temperature difference, in which, unlike convection and radiation, energy transfer occurs through collisions between neighboring elementary particles, close to close, throughout the mass of the environment.

Although, as shown in other paper, (Gavrila, 2000), in most cases encountered in practice, heat transmission is carried out simultaneously through two or all three of the mentioned mechanisms, but in the present paper, the heat loss will be analyzed only through conductivity.

For the composite materials used in the field of construction and not only, the phenomenon of heat transmission is very important.

Sometimes thermal insulation is followed, other times conductivity through the walls built from composite materials common in civil constructions. The physical properties, and especially the thermal ones, have been studied for composite materials with clay matrices, clay, silts, etc. (*Lertwattanaruket et al., 2011; Florescu et al., 2019; Quagliarini et al., 2015; Abanto et al., 2017; Calatan et al., 2020*).

Calatan et al., (2020), even studied the optimal proportions of clay and sand in the mortar, in order to obtain a maximum resistance to bending for bricks, but also a satisfactory thermal insulation. Paper and cellulose residues were used to make adobe bricks (*Muñoz et al., 2020*). Compression resistance was increased by up to 190%, thermal conductivity was reduced by up to 30%, water resistance was increased so that the standards were respected, and toxicity values decreased by up to 20%. A mathematical model with finite elements for a wall built with adobe bricks was presented by *Tarque et al., (2010)*, but the model was only mechanical and not thermomechanical. It is, however, a starting point for the construction of elementary thermomechanical models. Measuring thermal conductivity is not an easy problem to solve, as *Mosquera et al., (2014)*, showed. They estimated the effective thermal conductivity of an adobe using a theoretical and a theoretical-empirical method. It showed that only in five cases out of eighteen, the results of the two paths were close enough. *Zhengrong et al., (2024)*, argued that the durability of 3D printed buildings had attracted increasing attention in research. As a basis for evaluating energy efficiency and sustainability, it is crucial to consider the thermal performance of 3D printed walls during the structural design phase. 3D printed walls exhibit anisotropic thermo-physical properties and complex heat transfer processes. For such a model, information about dimensions, directions and properties is essential. The mathematical model is one of a thermal network suitable for objects with changing directions of thermal conductivities. Numerical simulation of the anisotropic 3D printed wall with complex geometry shows that the reinforced structures and cavities cause alternating surface temperature distributions with an average temperature difference of about 0.75°C. Due to the barrier effect of the inclined printed structure, the triangular cavities show higher temperatures than the square cavities. The proposed model is significant for characterizing the relationship between structure and thermal performance and can be used to optimize the thermal design of 3D printed walls. It is shown that the thermal insulator performance of the structure can be significantly improved by using less material and reducing the mass/weight. *Araújo et al., (2022)*, manufactured lightweight 3D printed cement composites by replacing traditional fine aggregates with slightly expanded clay aggregates to improve thermal insulation. The 100% replacement led to a decrease in thermal conductivity from 1.19 W/mK, to 0.68 W/mK. A theoretical model combined with an operational solution using the MATLAB program, for heat transmission of heat through any wall, was given by *Mižáková et al., (2021)*.

In this article, experimental results are given regarding the conductivity coefficient for composite materials with clay matrix and inserts of shredded corn husks, respectively shredded walnut husks. Also, theoretical and empirical solutions are proposed for the heat flow through the adobe wall and for the amount of heat transmitted through an adobe wall of a given area. A numerical solution with finite elements is given using the facilities of the MATLAB program, for the temperature distribution on the section perpendicular to the side faces of the wall.

MATERIALS AND METHODS

In order to estimate the heat transfer (thermal energy) through the walls built from composite materials with clay matrix and agricultural waste, the theory of heat transfer is used together with the results of experiments measuring the conductivity coefficient. Using the results of this method with two main components, formulas for particular cases, partially extrapolable, are obtained.

The theory of heat transfer through the wall of composite material is taken from some works (*Popa et al., 1986; Vladea, 1974; Gavrița, 2000; Gavrița, 2003*). The simplest possible model is approached to be able to observe the consequences of the introduction of inserts from agricultural waste in relation to the material from pure clay or other construction materials.

The experimental results from which the values of the thermal conductivity coefficient resulted were made within the applied research of the authors regarding the uses of the above-mentioned composite materials.

Bricks of composite material with dimensions 40x40x30 mm, made of composite material with clay matrix and inserts from agricultural waste (shredded corn cobs, walnut shell and wheat straw, respectively wool waste), figure. 1a, were mounted in the slot (fig. 1b) of a box with plasterboard walls, as can be seen in Figure 1c.

Inside the box, a source was inserted that provided a good approximation of the internal temperature of 100°C. Knowing the thermal conductivity coefficient of the plasterboard and taking into account the temperatures measured on the external surfaces of the box (on the plasterboard surface and on the external surface covered with composite material bricks), the coefficient of thermal conductivity of the composite material with which the box slot was covered was deduced, in points on its longitudinal axis.

Calculation relations from sources were used (https://www.scrigroup.com/casa-masina/constructii/TRANSFERUL-DE-CALDURA-IN-CONST22834.php#google_vignette; <https://www.baduc.ro/fise/2601001019.pdf>; <https://construiestesingur.wordpress.com/2010/12/15/ce-este-conductivitatea-termica-%CE%BB/>; https://ro.wikipedia.org/wiki/Conductivitate_termic%C4%83).

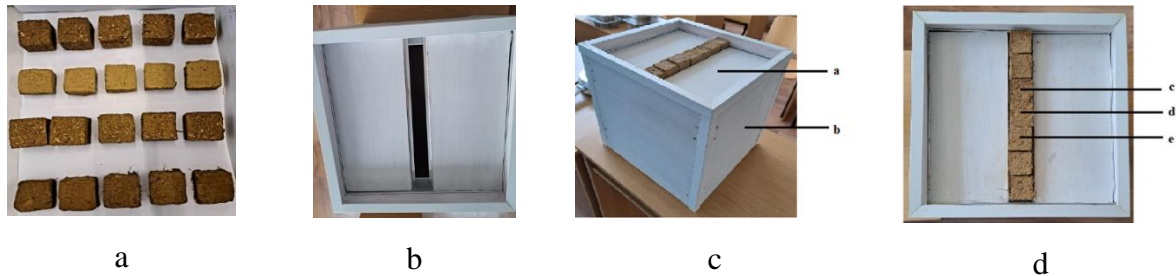


Fig. 1 - The components of the experimental system

a - bricks made of composite material; b - box with a slot made for moving the bricks; c - bricks mounted in the slot of the box with the heat source, ready for measurement; d - measurement points on the brick wall.

The composite materials with an insert of chopped walnut shells showed satisfactory cohesion in the range of insert concentrations 0-50%. The material with an insert of straw shredding showed cohesion only up to an insert concentration of 15%, and the material with an insert from wool waste only up to a value of 10% of the insert concentration.

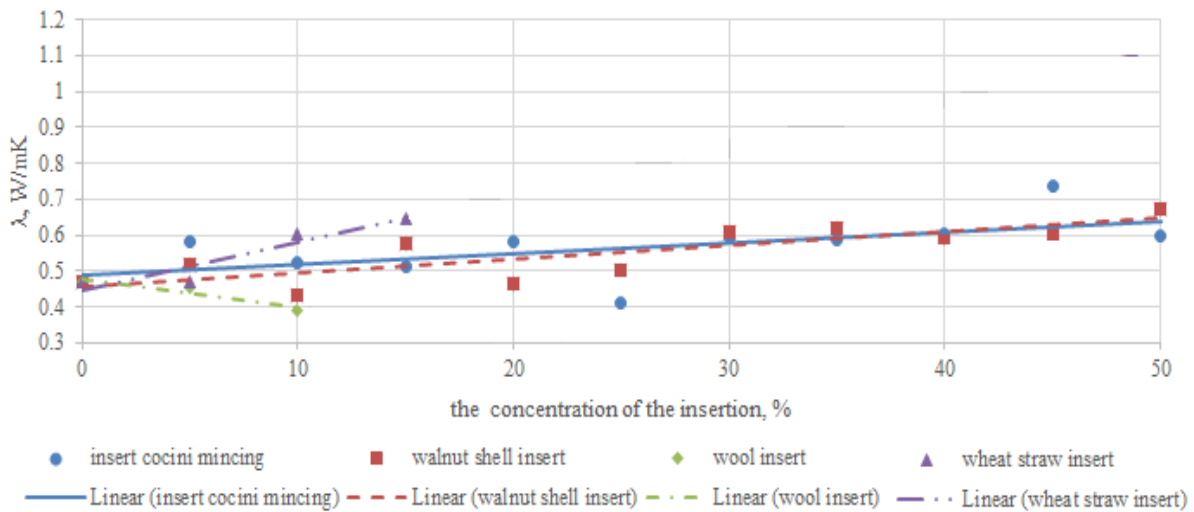


Fig. 2 - The variation of the thermal conductivity coefficient for the four types of composite materials, depending on the concentration of the insert

After a minimum statistical processing, the thermal conductivity coefficient values were obtained, specified in the graphic representation in Figure 2. Knowing the constant temperature inside the box, $T_{ic} = 100^{\circ}\text{C}$, generated by an electrical resistance, for calculating the heat flow through the walls, q (it was assumed that the thermal energy was transmitted outside the box only perpendicular to the walls), the relations (https://www.scrigroup.com/casa-masina/constructii/TRANSFERUL-DE-CALDURA-IN-CONST22834.php#google_vignette; <https://www.baduc.ro/fise/2601001019.pdf>; <https://construiestesingur.wordpress.com/2010/12/15/ce-este-conductivitatea-termica-%CE%BB/>; https://ro.wikipedia.org/wiki/Conductivitate_termic%C4%83) are valid:

$$q = \lambda_R \frac{T_{ic}-T_a}{g_{ps}} = \lambda_R \frac{T_{ic}-T_b}{g_{pl}} = \lambda_c \frac{T_{ic}-T_c}{g_c} = \lambda_d \frac{T_{ic}-T_d}{g_c} = \lambda_e \frac{T_{ic}-T_e}{g_c}, [W/m^2] \quad (1)$$

where: q - heat flow through the walls, W/m^2 ;

λ_R - thermal conductivity of the box, $W/(mK)$;

$\lambda_{c,d,e}$ – thermal conductivity in points c, d, e , W/(mK);
 T_{ic} – the temperature inside the box, °C;
 T_a – the temperature measured at point a , °C;
 T_b – the temperature measured at point b , °C;
 T_c – the temperature measured at point c , °C;
 T_d – the temperature measured at point d , °C;
 T_e – the temperature measured at point e , °C;
 g_{pl} – side wall thickness (gypsum), mm;
 g_{ps} – upper wall thickness (gypsum), mm;
 g_c – composite material thickness (brick), mm.

From equalities (1), relations (2) result:

$$\lambda_c = \lambda_R \frac{g_c T_{ic} - T_a}{g_{pl} T_{ic} - T_c}, \quad \lambda_d = \lambda_R \frac{g_c T_{ic} - T_a}{g_{pl} T_{ic} - T_d}, \quad \lambda_e = \lambda_R \frac{g_c T_{ic} - T_a}{g_{pl} T_{ic} - T_e} \quad [W/(mK)] \quad (2)$$

The average thermal conductivity coefficient, λ_c , was obtained by averaging the conductivity coefficients determined in points c, d and e , according to equality (3):

$$\lambda_c = \frac{\lambda_c + \lambda_d + \lambda_e}{3} \quad [W/(mK)] \quad (3)$$

Figure 2 shows the most important information: the thermal conductivity coefficient values for each of the 4 materials and the trend line. Thus, it is shown that for 3 of the 4 materials, the conductivity coefficient increased with the insertion concentration. Therefore, for sufficiently studied materials, the thermal insulation decreased with the increase of the insertion concentration.

The thermal conductivity coefficients were calculated according to the formulas (1-3) that can also be found in the paper of Dobritoiu, (2024). These formulas use the thickness of the walls of the box in which the heat source is located and the coefficient of thermal conductivity of the gypsum wall, as well as the temperatures measured at three points on the surface of the composite bricks. The last measured data can be found in the same source (Dobritoiu, 2024).

The technology of obtaining the bricks, their behavior over time (dimensional and appearance changes), the mechanical tests (bending stress and compression stress) as well as the statistical processing of the results were described by some authors. Following the research carried out, the results obtained on composite materials with clay matrix and agricultural waste insertion (nut shells, cobs, wheat straw, wool) will be compared with other biodegradable and sustainable composite materials, such as those with mud matrix and sawdust/seed husk insert (Surdu, 2023; Farcas-Flamaropol, 2023).

In order to summarize the above, the technological flow diagram - thermal conductivity determination figure 3 was drawn up, for the composite materials with clay matrix and agricultural waste insert.

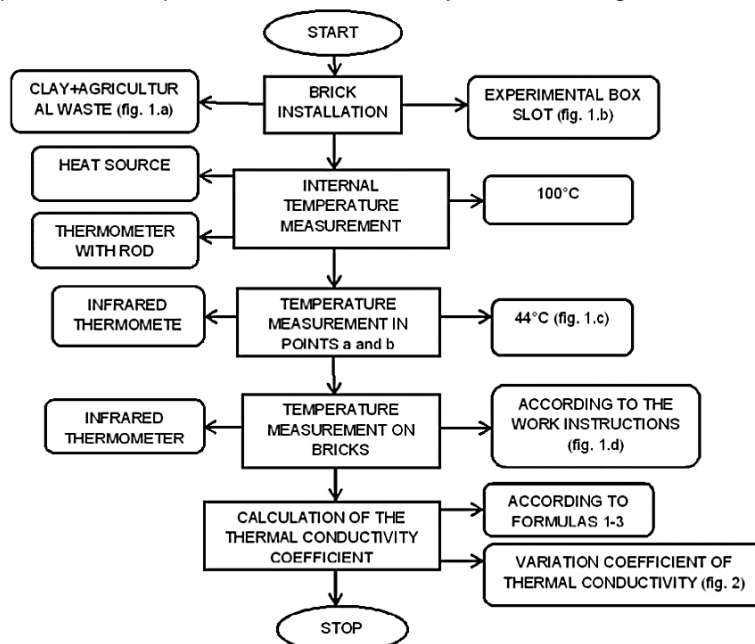


Fig. 3 - Diagram in technological flow - determination of thermal conductivity

RESULTS AND DISCUSSION

1. Heat loss through plain walls

The first approximation of heat loss through a MCMLIDA brick wall was made according to *Gavrila, (2003)*, assuming that the homogeneous plane wall had an infinitely long length, in relation to the thickness δ . It was assumed that the heat transfer was unidirectional along the Ox , axis, perpendicular to the wall surface. The conductive thermal transfer equation, in steady state, became a differential equation with simple partial derivatives (*Gavrila, 2003*):

$$\nabla^2 T = \frac{\partial^2 T}{\partial x^2} + \frac{\partial^2 T}{\partial y^2} + \frac{\partial^2 T}{\partial z^2} = 0 \quad (4)$$

For the three-dimensional case, x, y, z were the coordinates of the generic point in the wall space. For the 1- dimensional case, equation (4) became an ordinary, elementary differential equation:

$$\frac{d^2 T}{dx^2} = 0 \quad (5)$$

with the conditions at the limits of the interval (the limits of the wall along the axis Ox):

$$\text{for } x = 0, T = T_1, \text{ for } x = \delta, T = T_2 \quad (6)$$

Schematization of the geometry of the model is given in figure 4.

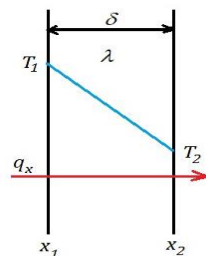


Fig. 4 - The geometry of the ideal wall for the elementary mathematical model of heat transmission through conduction, after the work (*Gavrila, 2003*)

The general solution of the differential equation (2) was:

$$T = k_1 x + k_2 \quad (7)$$

The integration constants k_1 and k_2 were found using the boundary conditions (6):

$$k_1 = \frac{T_1 - T_2}{\delta}, \quad k_2 = T_1 \quad (8)$$

Finally, the temperature distribution on the wall thickness had the expression:

$$T(x) = \frac{T_2 - T_1}{\delta} x + T_1 \quad (9)$$

Using Fourier's law, the equation of the unit heat flow was obtained, in W/m^2 :

$$q = \frac{\lambda}{\delta} (T_1 - T_2) \quad (10)$$

and the total thermal flow, Q_S (in W), would have the expression:

$$Q_S = \frac{\lambda}{\delta} A (T_1 - T_2) \quad (11)$$

where λ is the coefficient of thermal conductivity, and A is the finite area of the wall through which heat is transferred. The unit thermal flow is the amount of heat transferred in the unit of time through the unit of surface:

$$q = \frac{dQ_S}{dA} = \frac{d}{dA} \left(\frac{dQ}{dt} \right) = \frac{d^2 Q}{dA dt} \quad (12)$$

in which:

$$Q_S = \lim_{t \rightarrow 0} \left| \frac{\Delta Q}{\Delta t} \right| = \frac{dQ}{dt} \quad (13)$$

Q_S is the heat flow, and Q is the amount of heat (energy, J).

2. The influence of the insert concentration in the composite material on the unit heat flow and on the total heat flow

The thermal conductivity coefficient does not appear in the temperature distribution on the wall thickness (6), but the unitary thermal flow and the total thermal flow (10, 11) contain thermal conductivity as a factor and, therefore, these parameters depend on the thermal conductivity coefficient. In the experiments measuring the coefficient of thermal conductivity, it was found to change with the change of the concentration of insertion in the material.

For the composite material with clay matrix and corn cobs insert, the linear regression of the thermal conductivity coefficient in relation to the insert concentration was found as:

$$\lambda(c) = 0.003c + 0.487374 \quad (14)$$

For the composite material with a clay matrix and an insert made of chopped walnut shells, the linear regression of the coefficient of thermal conductivity, in relation to the insert concentration, was found in the form:

$$\lambda(c) = 0.0037997c + 0.456344 \quad (15)$$

Formulas (14) and (15) show that the value of the thermal conductivity coefficient is a function dependent on the concentration of the insert material in the composite. From formula (13), taking into account formulas (14) and (15), the formulas of the unitary heat flux on the walls of composite material with clay matrix and insert of corn husks (16) and for the composite material with matrix of clay and insert made of chopped walnut shells (17):

$$q(T_1, T_2, \delta, c) = \frac{\lambda(c)}{\delta} (T_1 - T_2) = \frac{0.003c + 0.487374}{\delta} (T_1 - T_2) \quad (16)$$

$$q(T_1, T_2, \delta, c) = \frac{\lambda(c)}{\delta} (T_1 - T_2) = \frac{0.0037997c + 0.456344}{\delta} (T_1 - T_2) \quad (17)$$

In the technique, two important concepts are used to determine the properties of walls, influenced by their geometry and physical structure (<https://www.isover.ro/parametrii-importanti-coeficientii-u-si-r>). The thermal insulation performance of a wall is represented by the thermal transfer coefficient U , expressed in $W/(m^2K)$, or by the thermal resistance R , expressed in $(m^2K)/W$.

The formulas of these synthetic characteristics of the insulation capacity of the walls are given in the report:

$$U = \frac{\lambda}{\delta}, \quad R = \frac{\delta}{\lambda} \quad (18)$$

It can be seen, from relation (18), that the value of the thermal transfer coefficient U , and the thermal resistance R , depend directly, respectively inversely proportionally, on the thermal conductivity coefficient. Considering the empirically deduced formulas (14) and (15), it is found that these insulation characteristics of the studied composite materials can be tentatively programmed in the production process by choosing an insert and a suitable insert concentration.

3. A numerical solution of the heat transfer

For cases closer to reality (three-dimensional or two-dimensional simplifications, walls with complex shapes, with multiple joints, with a layered structure, etc.), the solution of equation (1) becomes more complicated. The solution exists, in general, for correctly set boundary conditions, but the solutions themselves can no longer be described by elementary, but by approximations (series of functions). There are often cases where equation (1) is solved by finite difference schemes or the finite element method.

Figure 5 shows a solution obtained by using the finite element method, using the MATLAB solution program for equations with partial derivatives. The solution of the MATLAB program works for planar domains (2D). The border portion of the box that contains the heat source was represented by a rectangle with a length of 280 mm (7 bricks with sides of 40 mm each) and a width equal to the height of one brick. A value of 30 mm was accepted as the approximate value of the height of the bricks (they are not formed at exactly the same value). On the inside of the box, the temperature is hypothetically constant (100°C), and on the outside, also constant, at 21°C (ambient temperature). A constant average temperature of 60°C was entered on the ends of the row of bricks, the program not accepting the variable temperature with the coordinate on the width of the wall (40 mm). In these conditions, at the border, the temperature distribution on the thickness of the wall (30 mm) showed as in figure 5. To calculate the thermal flow and the amount of heat lost, the solution from figure 5 (the matrix of values corresponding to the considered finite elements) was taken and it was multiplied by the ratio between the coefficient of thermal conductivity and the thickness of the bricks (the height of the rectangle in figure 5), then by the area the considered wall.

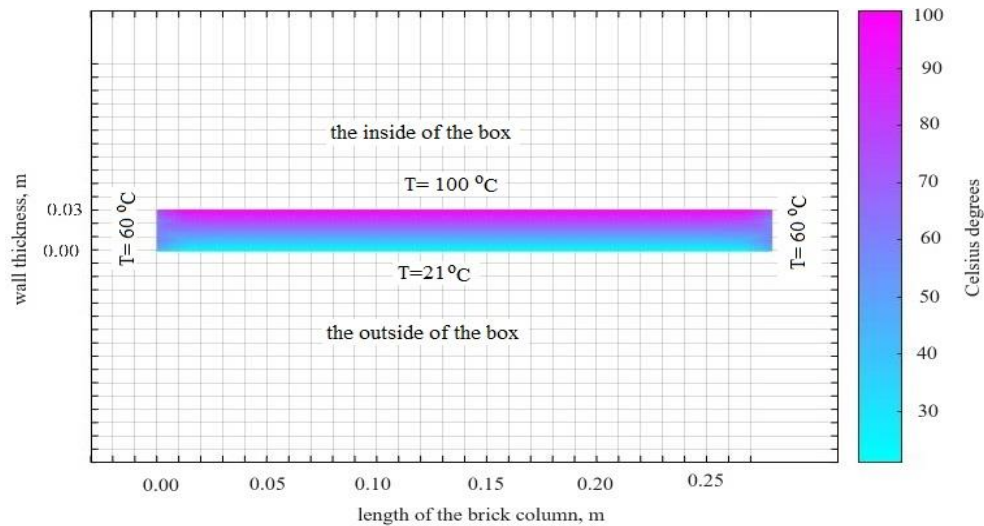


Fig. 5 - Temperature variation inside the wall (assembly) of seven bricks used to determine the coefficient of thermal conductivity (fig. 1c)

Mathematical models with finite elements for walls from MCMLIDA were also presented by *Florescu et al., (2019)*. In the same work, the behavior of some stratified walls made of the same type of materials was also studied. This type of models can also be made in the case of composite materials with clay matrices and inserts of chopped corn cobs or walnut shells, experimentally researched and presented in the present article. Also, some authors use mathematical models to verify the empirical results and extend the results (*Abanto et al., 2020*).

Following the research, the following results were obtained:

- the value of the thermal transfer coefficient is directly proportional to the thermal conductivity;
- following the research carried out, a composite material with a suitable concentration of insertion can be chosen in order to obtain the value of the optimal heat transfer coefficient;
- figure 5 shows the temperature variation inside the wall in order to determine the thermal conductivity coefficient.

For the theoretical verification of the measurement method, figure 6 will show the temperature variation along the normal to the plane wall. This variation is simple, linear, and does not depend on the coefficient of thermal conductivity. Increasing the wall thickness linearly decreases (for this solution) the temperature at any point inside the wall.

Figure 7 shows graphically the dependence of the unitary flow of heat through a brick of composite material with a clay matrix with a thickness of 30 mm, in the version with an insert of shredded corn cobs and in the version with an insert of shredded walnut shells. It can be seen that for both composites, the increase in the concentration of the insert makes the brick material a better conductor of heat, therefore a weaker insulator.

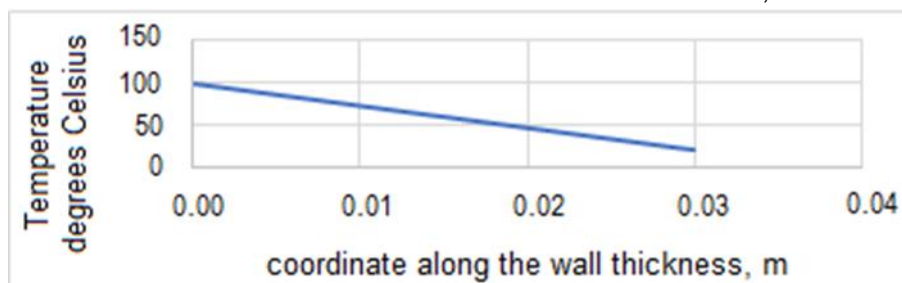


Fig. 6 - Theoretical variation of temperature on the thickness of the brick wall from MCMLIDA

A confirmation of the values of the coefficient of thermal conductivity is also noted in the relevant literature. *Lertwattanakul et al.* found thermal conductivity coefficient values between 0.1 and 1.7 W/mK, for bricks with clay matrix and various insertion materials (*Lertwattanakul et al., 2011, fig.1, page 55*).

As can be seen from figure 2, the thermal conductivity coefficient λ , values found in the present experiments varied between 0.4 and 0.8 W/(mK).

Florescu et al, (2019), used for the mathematical models of the walls made of adobe bricks, values of the coefficient of thermal conductivity between 0.17 and 0.47 W/mK. Abanto et al., (2017), determined, for construction materials of the same type as those studied in the present research, values between 0.25 and 0.334 W/(mK) of the coefficient of thermal conductivity. For composite materials (mortar, clay and sand) Calatan et al., (2020), determined optimal recipes that maximize bending resistance and reach thermal conductivity coefficient values between 0.17 and 0.38 W/mK.

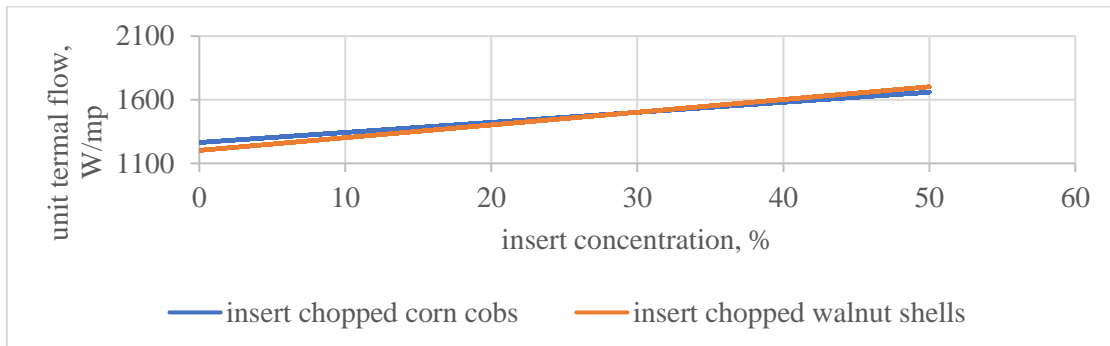


Fig. 7 - The variation of the unit heat flow through a MCMLIDA brick, with a thickness of 30 mm, in the version with an insert of chopped corn cobs and in the version with an insert made of chopped walnut shells

Figure 7 shows graphically the variation of the unitary heat flow depending on two variables: the concentration of the insert and the thickness of the bricks. The functions of two variables (13) and (14) were used for representation. Functions (13) and (14) have a theoretical-empirical character, because the general structure was deduced through the theory of heat transfer. The law of the dependence of the coefficient of thermal conductivity on the concentration of the insert, which appeared in the numerator of the fraction, was determined empirically with the help of statistical processing of the experimental data. It can be seen that the variation of the unit heat flux with the insertion concentration was linear, for both materials. The dependence of the unit thermal flow on the wall thickness was hyperbolic, so that the reduction of heat losses could be done preferentially, by changing the thickness of the brick and/or by choosing the appropriate concentration of the insert. Formulas (13) and (14) also show that the unit heat flow depended linearly on the temperature difference on the two faces (inside and outside) of the composite brick.

The variation of the unitary heat flow through adobe walls made of clay matrix with an insert of corn cobs shreds, depending on the concentration of the insert and the thickness of the wall, is represented graphically in figure 8. It can be seen that the variation with the thickness of the wall is much more intense than the dependence of the insertion concentration, non-linear, hyperbolic. The variation of the unitary heat flow with the concentration of the insert shows that with the increase of the concentration of the insert, the thermal conductivity of the wall increases, so the thermal insulation capacity decreases.

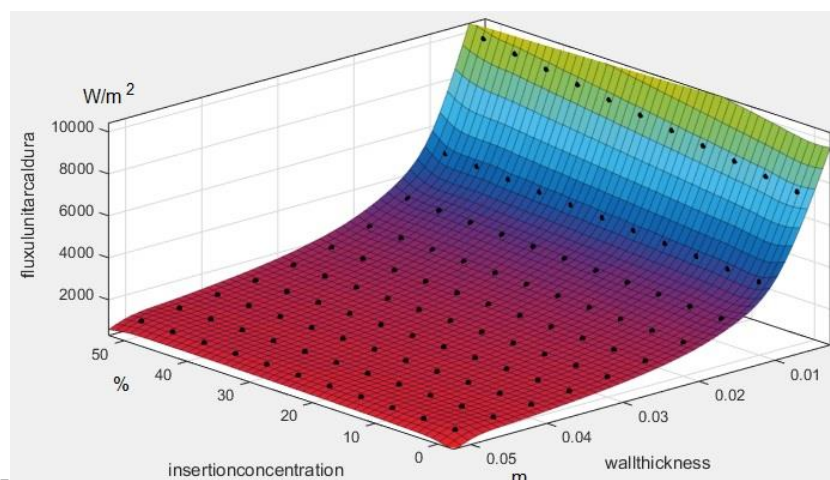


Fig. 8 - The variation of the unit heat flux with the insertion concentration and with the wall thickness

A last piece of information obtained later on the coefficient of thermal conductivity of composite materials with a clay matrix and an insert of shredded corn cobs, respectively chopped walnut shells, showed a strong dependence of the coefficient of thermal conductivity on the density of the final product and a significant one of product moisture (Table 1).

Also, there was a significant dependence on the compression force in the brick manufacturing process. This information is useful for future research regarding the structure of a formula of the thermal conductivity of the parameters of the manufacturing process, of the raw material and of the final product.

Table 1

Correlation values between the conductivity coefficient and the main parameters of the manufacturing process and of the finished material

| Material | Pressing force, N | Initial humidity, % | Initial density, g/cm ³ | Initial humidity, % | Initial density, g/cm ³ | Humidity after 2 weeks, % | Density after 2 weeks, g/cm ³ |
|--------------------------------|-------------------|---------------------|------------------------------------|---------------------|------------------------------------|---------------------------|--|
| Clay matrix with corn cobs | 0.590 | 0.486 | -0.340 | 0.522 | -0.432 | -0.398 | -0.804 |
| Clay matrix with walnut shells | 0.747 | 0.660 | -0.775 | 0.839 | -0.743 | 0.718 | -0.800 |

The dependence of the coefficient of thermal conductivity on the density of the raw material, of the product at the exit from manufacturing and after two weeks of storage, was, without exception, an inverse one. This is a serious indication of a formula for the coefficient of thermal conductivity in relation to the density of the material. This observation also confirms the fact that the density of the studied composites decreased with the increase of the insertion concentration, and the coefficient of thermal conductivity increased.

CONCLUSIONS

The usefulness of composite materials in construction is well known, especially if it is adobe. Their properties as thermal and sound insulators recommend them. Neither are the resistance to compression nor bending negligible, so there are many constructions made of these materials or that use them for infill walls, false walls or infill material.

Present research has found methods to obtain composite materials based on clay matrices and various insertion materials including agricultural waste, whose final properties can be programmed by choosing the characteristic parameters of the raw material and the technological process.

For now, the only control parameter of the properties of the obtained composite materials is the concentration of the insert material in the matrix. However, there are other important parameters in the process of obtaining composite materials, which have been insufficiently studied.

Some important conclusions relative to the thermal properties that are all related to the coefficient of thermal conductivity are stated below.

C1) The values of the coefficient of thermal conductivity obtained for the composite materials with clay matrix and chipping insert from corn cobs or walnut shells (0.4-0.8 W/(mK)) place them among the good thermal insulating materials;

C2) Within the limits of the insert concentrations in which the materials work (composite materials have cohesion and adhesion between matrix and insert 0-50% for the materials specified in conclusion C1), the coefficient of thermal conductivity increases with the volume of the insert concentration. Materials become weaker insulators (better heat conductors), as the concentration of insertion increases. In relation to this behavior, it should be specified that the bending and compressive strengths also decrease with the increase of the insertion concentration;

C3) The research continues and recent results show that the value of the coefficient of thermal conductivity depends inversely on the density of the material. With one exception, the coefficient of thermal conductivity is significantly related to the humidity of the material in all three specified technological stages. Also, there is a significant relationship between the coefficient of thermal conductivity and the pressing force in the brick mold.

C4) Conclusions C1-C3 also generate future research directions:

- the rigorous selection of the process parameters, of the raw material, control and regulation of the brick formation process and optimal storage parameters to obtain final products with improved qualities;
- re-evaluating the linear and non-linear regressions found in the preliminary experiments, in order to obtain possible optimal work regimes, including the qualities of the final product, but also energy and material consumption;
- the consideration of some alternative recipes for composite materials, with other agricultural or other waste, important suggestions being present in the literature;
- the research of complex solutions including complex, pre-stratified walls, in order to obtain adequate and optimal mechanical and thermal (in the future and acoustic) properties.

REFERENCES

- [1] Dobritoiu I. E., (2024), Experimental research on obtaining composite materials and evaluating the corresponding thermal characteristics (Cercetari experimentale privind obtinerea materialelor composite si evaluarea caracteristicilor termice corespunzatoare), *Scientific Report Number 5*, National University of Science and Technology Politehnica Bucharest, Doctoral School of Mechanical Engineering and Mechatronics;
- [2] Flamaropol-Farcaș C.D., Surdu E., Iatan I.R., Cârdei P., Mare R., (2023). Preliminary research regarding the creation of a category of composite material based on a mud matrix and agricultural waste as filler materials (Cercetări preliminare privind realizarea unui material compozit, bazat pe matrice de nămol și deșeuri agricole, ca materiale de umplutură), *INMATEH–Agricultural Engineering*, vol.71(3), pp.205-214. Bucharest, Romania. <https://doi.org/10.35633/inmateh-71-17>
- [3] Florescu E.R., Bica S.M., (2019), Thermal properties of an adobe brick wall: adapting traditional techniques to contemporary living standards, *Proceedings of SOCIOINT 2019- 6th International Conference on Education, Social Sciences and Humanities*, Istanbul, Turkey;
- [4] Gabriela Calatan, Andreea Hegyi, Carmen Dico, Henriette Szilagyi, (2020), Opportunities Regarding the Use of Adobe-bricks within Contemporary Architecture, *Procedia Manufacturing*, Volume 46, pp.150-157, <https://doi.org/10.1016/j.promfg.2020.03.023>;
- [5] Gavrilă L., (2000), *Transfer phenomena (Fenomene de transfer)*, vol I, II, Bacău/Romania, ALMA MATER Publishing House, ISBN 973-99487-7-4, ISBN 973-99487-6-6;
- [6] Gavrilă L., (2003), *Transfer phenomena (Fenomene de transfer) Volume II*, <https://cadredidactice.ub.ro/gavrilalucian/files/2011/05/fdtou-curs-081.pdf>;
- [7] Ginés A. Abanto, Mustapha Karkri, Gilles Lefebvre, Manfred Horn, Jose L. Solis, Mónica M. Gómez, (2017), Thermal properties of adobe employed in Peruvian rural areas: Experimental results and numerical simulation of a traditional bio-composite material, *Case Studies in Construction Materials*, Volume 6, pp.177-191, <https://doi.org/10.1016/j.cscm.2017.02.001>;
- [8] Lertwattanaruk P., Chorksiwanna J., (2011), The Physical and Thermal Properties of Adobe Brick Containing Bagasse for Earth Construction, *International Journal of Building Urban Interior and Landscape Technology*, Volume 1;
- [9] Mižáková J., Hrehová S., Hošovský A., (2021), Simulation model of Heat Transfer through the Wall, *International Journal of Applied Mathematics and Informatics*, Volume 15; e-ISSN: 2074-1278;
- [10] Mosquera, P., Cañas, I., Cid-Falceto, J., Marcos, F. (2014), Determination of the Thermal Conductivity in Adobe with Several Models, *ASME Journal of Heat Transfer and Mass Transfer March*, Volume 136(3): 031303. <https://doi.org/10.1115/1.4025560>;
- [11] Muñoz P., Letelier V., Muñoz L., Bustamante M.A., (2020), Adobe bricks reinforced with paper & pulp wastes improving thermal and mechanical properties, *Construction and Building Materials*, Volume 254 (4), 119314, <https://doi.org/10.1016/j.conbuildmat.2020.119314>;
- [12] Popa B. et al. (1986), *Thermotechnical engineer's manual, (Manualul inginerului termotehnician (MIT))*, Volume 1, Technical Publishing House, Bucharest, Romania;
- [13] Quagliarini E., D'Orazio M., Lenci S., (2015), 16 - The properties and durability of adobe earth-based masonry blocks, *Eco-Efficient Masonry Bricks and Blocks*, Woodhead Publishing, pp.361-378, ISBN 9781782423058, <https://doi.org/10.1016/B978-1-78242-305-8.00016-4>;
- [14] Rísia A. Araújo, Antônio E. Martinelli, Kleber C. Cabral, André F.O.A. Dantas, Iago F.D. Silva, Allynson A.C. Xavier, Ana L. Santos, (2022), Thermal performance of cement-leca composites for 3D printing,

- Construction and Building Materials*, Volume 349, 128771, ISSN 0950-0618, <https://doi.org/10.1016/j.conbuildmat.2022.128771>;
- [15] Surdu E., Farcaș-Flamaropol C.D., Cârdei P., Durbacă I., Sporea N., Research on The Recovery of Some Agricultural Waste for Manufacturing of Composite Materials with Clay Matrices, *The 18th International Conference of Constructive Design and Technological Optimization in Machine Building Field OPROTEH 2023* (ISSN 2457 – 3388).
- [16] Torque N., Camata G., Espacone E., Varum H., Blondet M., (2010), Numerical modelling of in-plane behaviour of adobe walls, *SÍSMICA 2010 – 8º Congresso de sismologia e engenhariasísmica*, University of Aveiro, Portugal;
- [17] Vlădeanu I., (1974), *Treatise on technical thermodynamics and heat transmission, (Tratat de termodinamica tehnica si transmiterea caldurii)*, Didactic and Pedagogical Publishing House, Bucharest, Romania;
- [18] Zhengrong Li, Wenjing Xing, Jingting Sun, Xiwen Feng, Heyu Wang, (2024), Thermal network model for anisotropic heat transfer in 3D printed complex geometry structures, *Building and Environment*, Volume 254, 111381, ISSN 0360-1323, <https://doi.org/10.1016/j.buildenv.2024.111381>;
- [19] https://www.scrigroup.com/casa-masina/constructii/TRANSFERUL-DE-CALDURA-IN-CONST22834.php#google_vignette(accessed on 22.03.2024);
- [20] <https://www.baduc.ro/fise/2601001019.pdf>(accessed on 22.03.2024);
- [21] <https://construiestesingur.wordpress.com/2010/12/15/ce-este-conductivitatea-termica-%CE%BB/> (accessed on 22.03.2024);
- [22] https://ro.wikipedia.org/wiki/Conductivitate_termic%C4%83 (accessed on 22.03.2024);
- [23] <https://www.isover.ro/parametrii-importanti-coeficientii-u-si-r> (accessed on 22.03.2024).

MECHANICAL AND THERMAL PROPERTIES OF COMPOSITE MATERIALS OBTAINED WITH SLUDGE MATRIX AND AGRICULTURAL WASTE INSERTS

PROPRIETĂȚI MECANICE ȘI TERMICE ALE MATERIALELOR COMPOZITE OBȚINUTE CU MATRICE DE NĂMOL ȘI INSERȚII DIN DEȘEURI AGRICOLE

Dana-Claudia FARCAȘ-FLAMAROPOL¹⁾, Elena SURDU^{1*)}, Radu I. IATAN¹⁾,
Petru CÂRDEI^{2*)}, Georgiana ENĂCHESCU¹⁾, Iuliana PRODEA¹⁾, Ion DURBACĂ¹⁾

¹⁾U.N.S.T "POLITEHNICA" of Bucharest, no. 313, Splaiul Independentei, sector 6, Bucharest, 060042, Romania

²⁾ INMA Bucharest, 6 Bd. Ion Ionescu de la Brad, Romania, 013813

Tel: 0723213708; E-mail: elena.surdu@yahoo.com

Tel: 0726142837; E-mail: petru_cardei@yahoo.com

DOI: <https://doi.org/10.35633/inmateh-73-36>

Keywords: composite, sludge, agricultural waste, mechanical testing, thermal conductivity, civil engineering applications

ABSTRACT

The article describes the achievement and values of the mechanical and thermal characteristics of composite materials with sludge matrix and the insertion of agricultural waste, focusing on the compressive strength and thermal conductivity coefficient. These two characteristics are essential for civil engineering applications. The compressive strength and thermal conductivity coefficient depend significantly on the insertion concentration in the composite material: the compression strength decreases, and the thermal conductivity coefficient increases as the insertion concentration increases.

For mud matrix composites and seed husk insert, the compressive strength varies between 0.375 MPa and 2.292 MPa. In the case of sawdust insert, the compressive strength varies between 0.149 MPa and 2.292 MPa. These values indicate that composite materials are at the lower limit of strength of building materials, but have good insulating properties due to the low coefficient of thermal conductivity. These features recommend using them for supporting walls in light, floor-free buildings, and for partitions with good thermal insulation properties.

REZUMAT

Articolul descrie obținerea și valorile caracteristicilor mecanice și termice ale materialelor compozite cu matrice de nămol și inserție de deșeuri agricole, punând accent pe rezistența la comprimare și coeficientul de conductivitate termică. Aceste două caracteristici sunt esențiale pentru aplicațiile în construcții civile. Rezistența la comprimare și coeficientul de conductivitate termică depind semnificativ de concentrația de inserție în materialul compozit: rezistența la comprimare scade, iar coeficientul de conductivitate termică crește pe măsură ce crește concentrația de inserție.

Pentru compozitele cu matrice de nămol și inserție de coji de semințe, rezistența la comprimare variază între 0,375 MPa și 2,292 MPa. În cazul inserției de rumeguș, rezistența la comprimare variază între 0,149 MPa și 2,292 MPa. Aceste valori indică faptul că materialele compozite se situează la limita inferioară de rezistență a materialelor de construcții, dar au bune proprietăți izolatoare datorită coeficientului scăzut de conductivitate termică. Aceste caracteristici recomandă utilizarea lor pentru pereți de susținere în clădiri ușoare, fără etaje, și pentru pereți despărțitori cu bune proprietăți de izolare termică.

INTRODUCTION

Sustainable sludge recovery is a solution for the increased management of sludge stocks resulting from the wastewater treatment of urban, industrial systems and dredging works of lakes, canals, and rivers. According to FAO's AQUASTAT database (Global Information System of the EU Water and Agriculture Organisation) of 2020, 56% from global freshwater abstraction are released into the environment as waste water (in the form of industrial effluents and agricultural drainage waters), while the remaining 44% are consumed in agriculture, the report said, for irrigation of land (<https://data.apps.fao.org/aquastat/?lang=en>). Increased discharges of industrial waste water, improperly cleaned, clean wastewater and wastewater infiltrations from agricultural activities (from soils directly into groundwater) have led to water quality degradation around the world. Even today, in many developed countries, most wastewater is discharged directly into the environment without proper treatment.

Another important issue is the management of sewage sludge, where most of the pollutants present in wastewater are concentrated. A typical sludge treatment scheme provides for the preliminary reduction of the water content of the original sludge, biological/chemical stabilization, with or without electricity production, and a later phase of chemical conditioning and mechanical dehydration, designed to further reduce the water content of the sludge. Clearly, the intention is to minimize the volume of sludge to be removed outside the sewage treatment plant.

As for the methods of managing excess sludge, the most used are waste storage, incineration, evacuation to seas and oceans, re-use in agriculture (directly or after composting) and reuse for the production of cement, bricks and asphalt. According to (https://www.researchgate.net/figure/Sludge-management-2016-Eurostat-Data-Explorer-2020_fig2_353333820) in 2020, about 40% of the total sludge produced in the European Union is used in agriculture. Another method of removing sludge, which has also been most used for many years, is storage. Recently, due to the impact of leachate production and equivalent CO₂ emissions, legislation has become stricter, and the method of sludge storage began to be less used in many European countries. On the other hand, in recent years, sludge incineration has been increasingly used in European countries, due to significant improvements in this process, such as the high technological level, reducing costs and reducing emissions.

The recovery method proposed consists of drying by vibratory sieving and use to obtain materials useful in construction (*Dumitrescu-Tivig D-C, 2024*). The materials are varied, including mud matrix composite materials of different concentrations, obtained from seed husk or sawdust shredders. A number of sludge characteristics are detailed in the material in the paper (*Batali and Carastoian, 2015*). Characterizations of the physical properties of such materials also appear in papers (*Parra-Saldivar and Batty, 2006; Silveira et al., 2012; Parisi et al., 2014; Correa et al., 2006; Zhou et al., 2022; Kumar et al., 2024*), as well as in many other works, many authors operating on composite materials with sludge matrices, clay, etc.

The article begins with the description of experiments conducted to determine the mechanical properties and thermal conductivity coefficient of bricks made from sludge and agricultural materials. It continues with the results obtained and concludes with comments and conclusions drawn from data processing and comparing them with other types of materials used in construction.

MATERIALS AND METHODS

To evaluate the mechanical and thermal properties of mud matrix composite materials and agricultural waste inserts, compression experiments were conducted, as well as experiments for determining the coefficient of thermal conductivity.

Experiments for determining the compressive strength

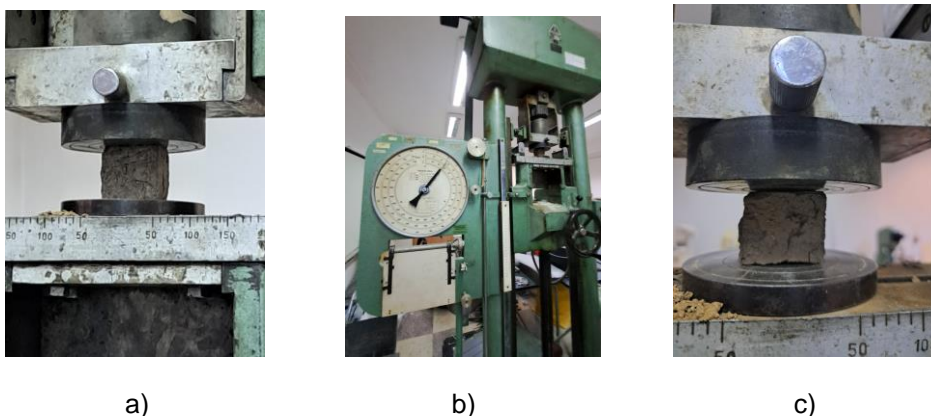


Fig. 1 - Devices for mechanical testing

a - laying and alignment of the parts on the press support of the mechanical test machine ZDM 50,000 N from the mechanical test laboratory of the Faculty of Construction Bucharest; b - applied force; c - brick after compression.

The mechanical properties of bricks or briquettes built from mud matrix composite material and seed husk or sawdust insert are multiple. In the experiments whose results are described in this article, only the strength of the bricks at crushing (compression) was measured.

Two mechanical characteristics of the bricks produced have already been measured: the density of the bricks made of composite material and the mass of the final product (*Farcas-Flamaropol et al., 2023; Ghiga, 2021*). The first mechanical characteristics as mentioned importance are: mass, density and resistance to compression. Important are then the elastic characteristics: the modulus of elasticity, Poisson's coefficient, tensile strength and compressive strength (*Ghiga, 2021*).

The compression test was performed using the ZDM 50,000 N test machine for measuring the resistance to compression, bending and traction. For each material concentration, three samples were used to calculate the average compressive strength. The evidence was put on a media stand. The compressive force (figure 1-b) has been read.

Then, the following features were calculated: the area of the compression section:

$$A = b \cdot h \quad (1)$$

where: A - area of the compression section, mm²;
 b, h - dimensions of the brick, mm.

and compressive strength:

$$R_{compr} = \frac{F}{A} \quad (2)$$

where: R_{compr} - compressive strength, N/mm² (MPa);
 F - compression force, N.

The strength of the bricks at compression was determined as an average value, corresponding to the three samples tested. Experimental data was stored in tables and then used for synthetic graphical representations.

Experiments for determining the coefficient of thermal conductivity

For the determination of thermal transfer of mud bricks with seed husk insert or sawdust, a box of fire-resistant material (plasterboard) was used, having on the upper wall a slit in which the bricks are tightly inserted. Inside the box there is a heat source that heats the box on the inside to 100 °C. The ambient temperature and the measuring distance will be the same. The outside temperature on the bricks is measured with a digital infrared thermometer. For each material concentration, three temperatures will be measured, on three bricks as shown in figure 2. The thickness of the brick must be measured and the average density of the three bricks calculated. The data is stored in tables and subsequently used for statistical processing.



Fig. 2 - Measuring the external temperature on bricks

a - laying of bricks b - temperature measuring devices.

Calculations of thermal conductivity coefficients are made according to the formulas (3.1)-(3.3) in the source written by *Dobritoiu, (2024)*. These formulas use the thicknesses of the walls of the box in which the heat source is found and the coefficient of thermal conductivity of the wall made of plasterboard, as well as temperatures measured at three points on the surface of the composite bricks. The ratio between the temperature generated by the heat source inside the box and the temperature measured on the outer surface of the bricks together with the thickness of the brick, allows determining the thermal conductivity coefficient of the brick.

The experimental data comprised numerical sequences, with the first sequence representing the concentration of the insertion material and the second sequence representing either the compressive mechanical strength or the thermal conductivity.

The statistical tool used to investigate the relationships between mechanical strength and insertion concentration, as well as thermal conductivity and insertion concentration, was both nonlinear and linear regression analysis. Observing the graphical distribution of the experimental data, a second-degree polynomial interpolation function was found suitable for the dependence of mechanical strength on insertion concentration. For the dependence of thermal conductivity on insertion concentration, the graphical representation indicated the use of linear regression (first-degree polynomial).

The accuracy of the proposed statistical models was estimated using the coefficient of determination R^2 . The accuracy of the regression formulas increases as R^2 approaches the value of 1. It was observed that the interpolation formulas for the dependence of mechanical strength on insertion concentration are more accurate than the regression formulas for the thermal conductivity coefficient.

Regarding the errors generated in the experiments, these were tested only to detect any potential outliers, but no such anomalies were found. On the other hand, there were experimental data points, so it was preferred not to eliminate any of them.

RESULTS

In this paragraph, the results of the statistical processing of experimental data obtained by measurement and preprocessing shall be presented. It highlights the variations in mechanical and thermal characteristics of composite materials with clay matrix and seed insert, respectively sawdust, depending on the concentration of the insert in the material. The trendlines for assessing the overall variation of thermal and mechanical characteristics according to the concentration of the insert are also presented.

The behaviour of mechanical compressive strength according to the concentration of the insert in the material

The variation in compressive strength according to the insertion concentration of the bricks in the mud matrix composite material and seed shell insert is plotted in Figure 3.

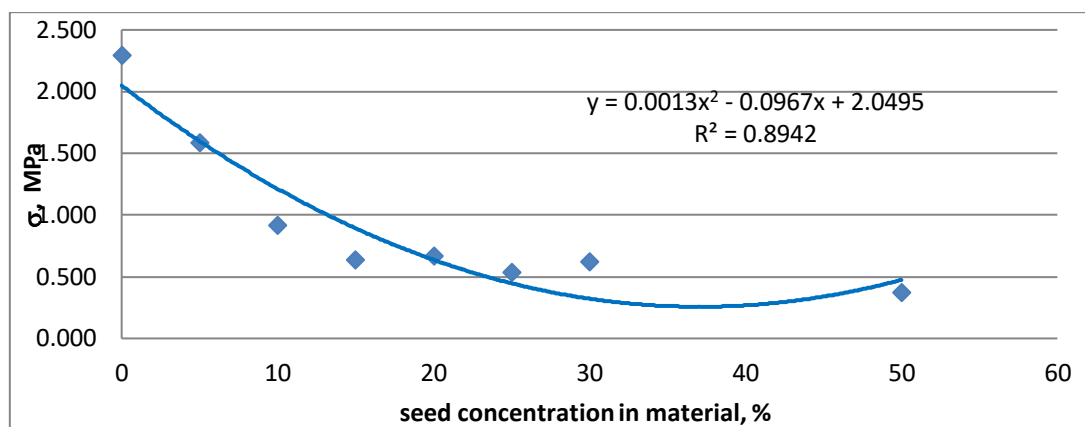


Fig. 3 - Variation of the crushing limit resistance of the sludge matrix composite material and seed husk insert, with the concentration of seed husks

The resistance of the bricks to compression, obtained from the composite material with sludge matrix and seed shell insert, decreases with increasing the concentration of seed shells. The decrease in quantity does not have a linear influence. The trend line, expressed by the regression line equation, indicates that the compressive strength decreases as the seed husk content in the composite material increases. Compression resistance values for sludge matrix and seed husk insert composite variants range from 0.375 MPa to 2.292MPa.

The variation in compressive strength, depending on the insertion concentration of the bricks in the mud matrix composite material and sawdust insert, is plotted in Figure 4. In this case, the compressive strength of the bricks decreases with the increase in the concentration of sawdust. The decrease does not have a linear relationship. Compression resistance values for mud matrix composite variants and sawdust insert range from 0.149 MPa to 2.292 MPa.

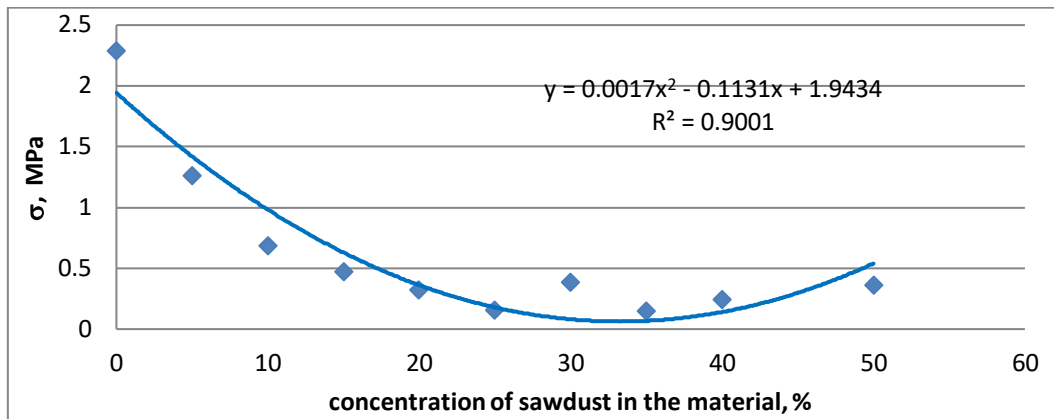


Fig. 4 - Variation of the crushing limit resistance of the matrix composite material sludge and sawdust insert, with sawdust concentration

Variation of thermal conductivity coefficient to sludge matrix composite materials

The variation in thermal conductivity of the sludge matrix composite and seed husk insert according to the concentration of the seed husks can be observed in Figure 5. According to the trend line, thermal conductivity increases with the insertion concentration, but relatively slowly. The minimum thermal conductivity is 0.4089 W/mK, while the maximum is 0.59989 W/mK.

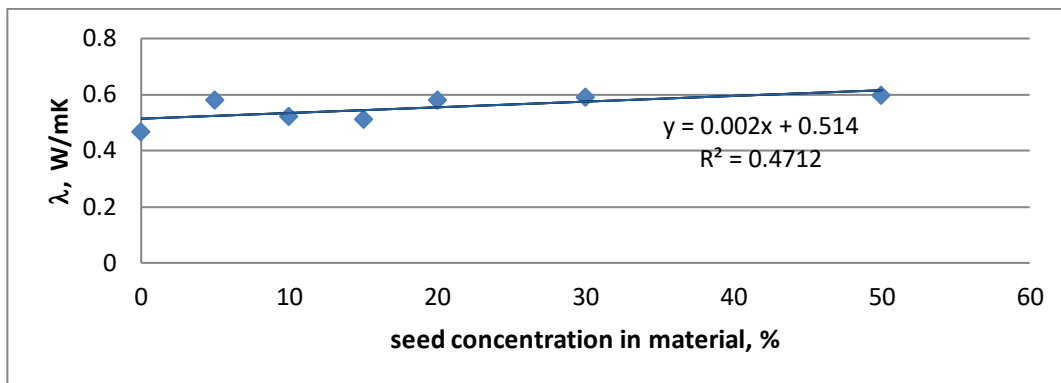


Fig. 5 - Variation of thermal conductivity of the composite material (sludge matrix with seed husk insert) with the concentration of seed husk insert

The variation in thermal conductivity of the sludge matrix composite and sawdust insert according to the concentration of sawdust can be observed in Figure 6. According to the trend line, the thermal conductivity increases with the insertion concentration. The minimum thermal conductivity is 0.430946 W/mK, while the maximum is 0.674512 W/mK.

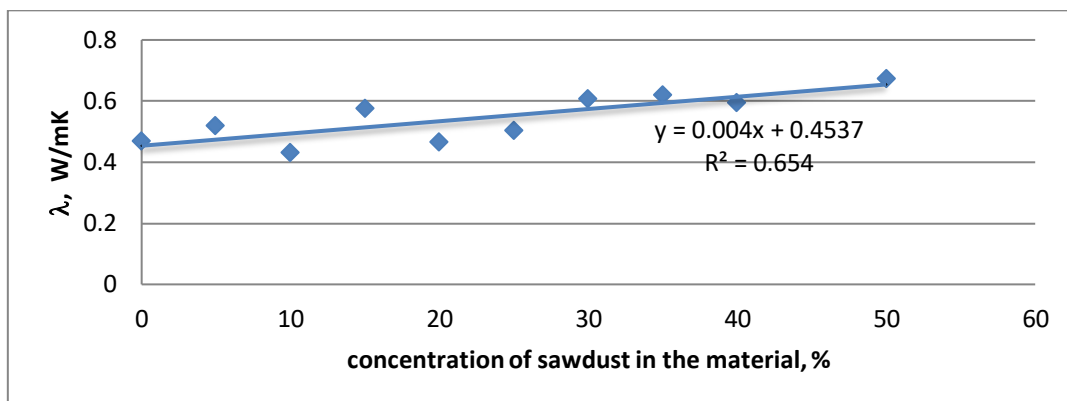


Fig. 6 - Variation of thermal conductivity of composite material (sludge matrix with sawdust insert) with the concentration of sawdust insert

For comparison, according to the paper (<https://www.imaterial.ro/exterioroare/caramizi-perfromante-termic.html>), the thermal conductivity of hollow bricks Heluz Family is 0.066/0.089 W/mK (with/without polystyrene insert), and they have an acoustic insulation index of 37 dB. Ordinary ceramic bricks have a thermal conductivity ranging from 0.15 to 0.202 W/mK and an acoustic insulation index ranging from 51 to 55 dB. Also, according to the source (https://www.heluz.com/files/57255_00-Technicky-list-EN.pdf), the thermal conductivity of the ground Heluz P15 25 brick is 0.26 W/mK, and the Heluz P15 30 bricks of the same family, have a thermal conductivity of 0.165 W/mK, according to the paper (https://www.heluz.com/files/vyrobky/prohlaseni-o-vlastnostech/311897-20305.00+_en-v4.pdf). Measured values for the thermal conductivity of the sludge matrix composite material and seed husk insert, as well as those with sawdust insert, fit well in the given intervals in literature for the thermal conductivity of materials of this type, as evidenced by the works (Parra-Saldivar & Batty, 2006; Revuelta-Acosta et al., 2010; Jové-Sandoval et al., 2023).

The mechanical and thermal properties of composite materials with sludge matrix and agricultural waste insert are a potential resource in construction, having multiple applications such as small load-bearing wall, wall filler, thermal insulation and acoustic insulation. For this purpose, important properties of these materials, such as compressive strength and thermal conductivity, were tested.

Mechanical properties

Compression resistance is one of the most important characteristics for assessing the load bearing of materials used in construction.

For comparison, table 1 provides values of compressive strength of materials commonly used in construction, according to the paper (<https://www.rombadconstruct.ro/rezistenta-la-compresiune.html>). For example, Heluz P15 30 bricks have an average compression strength of 15 MPa and a normalized value of 17.2 MPa (Danciu et al., 2017). These values are used to highlight the performance and potential of compressive strength of composite materials, in comparison with traditional materials used in construction.

Table 1

Compression resistance for a few reference materials in construction

| Material | Compression resistance, MPa |
|-----------------------|-----------------------------|
| Poros limestone | 2.7 |
| Lightweight concrete | 8.1 |
| Clay brick | 9.8 |
| Common heavy concrete | 31.9 |
| Limestone | 76.0 |
| Silico-calc brick | 11.0 |
| Pinewood | 44.1 |
| Granite | 181.4 |

The mud matrix composite bricks and seed husk insert are positioned at the lower limit of the materials used in the construction field.

In literature, there is little work studying the mechanical properties of composite bricks based on mud matrices or clay with vegetable and/or dung inserts. One of the remarkable works confirms the results obtained in the experiments carried out. The authors of this paper provide for the compressive strength of bricks of this type, coming from various areas of the planet, values ranging from 0.29 to 3.04 MPa, respectively, range within which the performance of the proposed composite material variants for research also fit (Silveira et al., 2012). The correct framing of the measured compressive strength of the sludge matrix composite materials and seed shell insert is also confirmed by (Oliveira et al., 2021), which includes a wide range of such materials, some of which are of recent conception.

Thermal properties

For thermal properties, taking into account the available experimental data and the fact that the elaborated composite materials are intended for applications in the field of civil engineering and related fields, thermal conductivity was chosen. This is an appropriate measure for characterizing the ability of a material to be a good heat insulator or conduct heat.

According to the trend line, the thermal conductivity of the sludge matrix composite material and seed shell insert increases with the insertion concentration, in a relatively slow way. The minimum value of thermal conductivity is 0.4089 W/mK, while the maximum value is 0.59989 W/mK. For the material with sawdust insert, the thermal conductivity increases with the insertion concentration. The minimum value of thermal conductivity is 0.430946 W/mK, while the maximum value is 0.674512 W/mK.

Compared to the usual building materials, the composite with sludge matrix and seed shell insert, as well as the one with sawdust insert, have a thermal conductivity value comparable to that of plasterboard or dry, according to the work (<https://www.rombadconstruct.ro/tabel-cu-conductivitate-termica-a-materialelor-de-constructii.html>). It also falls within the range of thermal conductivity of other materials such as Agloporite concrete, asbestos, cast gypsum, gravel (stuffing), limestone, hollow core stones made of light concrete, solid stones made of light concrete according to DIN 18152, solid stones made of natural tuff or expanded clay, expanded clay concrete on quartz sand with pore-laying, concrete, brick for furnace, etc. (<https://builder.techinfus.com/ro/uteplenie/teploprovodnost-uteplitelej.html>). The thermal conductivity range covered by the sludge matrix composite material and seed shell insert is less common in most building materials (<https://www.rombadconstruct.ro/tabel-cu-conductivitate-termica-a-materialelor-de-constructii.html>; <https://builder.techinfus.com/ro/uteplenie/teploprovodnost-uteplitelej.html>).

CONCLUSIONS

Composite materials with sludge matrix and agricultural waste inserts are an alternative solution to early III millennium building materials. However, from the point of view of their structure and source, they are older than most of the materials used today in construction, small-sized ones with clay or mud walls are used for thousands of years. In this context, a new impetus in the research activity was the subject of knowledge as accurately as possible of the properties of these materials and the variation of these properties according to various parameters of the composition of materials or the technological training process. These materials have important applications both in the construction of small-sized houses, possibly with strength structures reinforced with wooden or concrete beams, and in the realization of the filler walls, separation and isolation. The possibility of dressing them in a hygienic way makes them usable as walls without load-bearing (insulators, separators, etc.) in modern and sanitary safe and fire-resistant buildings.

Mechanical bending strength, but especially when compressing, recommends bricks as strength materials for small houses, cottages, etc. Thermal conductivity recommends composite materials for the insulating wall (thermal, acoustic). Low density leads to the realization of light walls and the possibility of obtaining low loads for a strength structure made of wood, concrete or metal. Obviously, in the future, a health approach study for these materials must also be carried out, in order to eliminate possible sources of infection for residents of buildings built with such materials.

The basic properties of these composite materials are strongly influenced by the concentration of the insert, giving the manufacturer the opportunity to supply composites with programmable properties. However, among the parameters that characterize the raw material and the technological process, there are some important ones that have not been taken into account in the research whose results have been described, such as insert grain and material pressing speed in forming matrix. These issues remain to be resolved in the future, especially if the applications suggested in the exposed research will prove viable.

The important conclusions in this article are as follows:

C1) The thermal conductivity for the composite material with seed husk insert increases with the insertion concentration, relatively slowly. The minimum value of thermal conductivity is 0.4089 W/mK, and the maximum is 0.59989 W/mK.

C2) The thermal conductivity of the composite material with sludge matrix and sawdust insert increases with the insertion concentration. The minimum value of thermal conductivity is 0.430946 W/mK, and the maximum is 0.674512 W/mK.

C3) The compressive strength of the bricks in the sludge matrix composite material and seed shell insert decreases as the concentration of seed shells in the composite material increases. The values of the compression resistance vary between 0.375 MPa and 2.292 MPa, placing the bricks of this composite at the lower limit of the usual building materials.

C4) For composite materials with sludge matrix and sawdust insert, the compressive strength of the bricks decreases with increasing sawdust concentration. The decrease is not linear, and the values of the compressive strength for these composite variants vary between 0.149 MPa and 2.292 MPa.

REFERENCES

- [1] Batali, L., & Carastoian, A. (2015). Geotechnical characterization of sludge from treatment plants for their disposal (Caracterizarea, din punct de vedere geotehnic, a nămolurilor de la stațiile de epurare, în vederea depozitării lor), *Revista Construcțiilor*, (117), 56-59.
- [2] Correa, A., Teixeira, V. H., Lopes, S. P., & de Oliveira, M. S. (2006). Evaluation of physical and mechanical properties of adobe bricks. *Ciência e Agrotecnologia*, 30(3), 503-515.
- [3] Danciu, A. M., Crișan, O-A., Orban, M., & Lakatos, E. S. (2017). Utilization of sludge from wastewater treatment plants from a circular economy perspective (Valorificarea nămolurilor provenite de la stațiile de tratare a apelor uzate din perspectiva economiei circulare), *The 17th International Multidisciplinary Conference "Professor Dorin Pavel-Founder of Romanian Hydropower"*, Sebeș.
- [4] Dobritoiu, I. E. (2024). *Experimental research on obtaining composite materials and evaluating their thermal characteristics*. Scientific Report Number 5, National University of Science and Technology Politehnica Bucharest, Doctoral School of Mechanical Engineering and Mechatronics.
- [5] Dumitrescu-Tivig, D-C. (2024). *Experimental research on sludge dehydration for practical use (Cercetari experimentale privind obtinerea materialelor compozite si evaluarea caracteristicilor termice corespunzatoare)*, Scientific Report Number 5, National University of Science and Technology Politehnica Bucharest, Doctoral School of Mechanical Engineering and Mechatronics.
- [6] Farcas-Flamaropol, D-C., Surdu, E., Iatan, I. R., Cardei, P., & Mare, R. (2023). Preliminary research regarding the creation of a category of composite material based on a mud matrix and agricultural waste as filler materials, *INMATEH-Agricultural Engineering*, 71(3), pp.205-214.
- [7] Ghiga, D. (2021). Summary of Doctoral Thesis, *Modern techniques for strengthening masonry structures (Tehnici moderne de consolidare a structurilor din zidarie)*, Gheorghe Asachi Technical University of Iași.
- [8] Jové-Sandoval, F., García-Baños, E. M., & Barbero-Barrera, M. M. (2023). Characterisation and thermal improvement of adobe walls from earth-straw lightweight panels. *MRS Advances*.
- [9] Kumar, R., Singh, V., & Bansal, A. (2024). Experimental research on the physical and mechanical properties of rice straw-rice straw ash composite materials. *International Journal of Interactive Design and Manufacturing*, 18, 721–731. <https://doi.org/10.1007/s12008-024-01741-1>.
- [10] Oliveira, C., Silveira, D., Varum, H., Parisi, F., Miccoli, L., Solís, M., Rodríguez-Mariscal, J. D., & Tarque, N. (2021). Mechanical Characterization of Adobe Masonry. In *Structural Characterization and Seismic Retrofitting of Adobe Constructions: Experimental and Numerical Developments*. Springer.
- [11] Parisi, F., Asprone, D., Fenu, L., & Prota, A. (2014). Experimental characterization of Italian adobe bricks reinforced with straw fibres. *9th International Masonry Conference*, Guimarães, Portugal.
- [12] Parra-Saldivar, M. S., & Batty, W. (2006). Thermal behaviour of adobe constructions. *Building and Environment*, 41.
- [13] Revuelta-Acosta, J. D., Garcia-Diaz, A., Soto-Zarazua, G. M., & Rico-Garcia, E. (2010). Adobe as a Sustainable Material: A Thermal Performance. *Journal of Applied Sciences*, 10(19), 2211-2216.
- [14] Silveira, D., Varum, H., Costa, A., Martins, T., Pereira, H., & Almeida, J. (2012). Mechanical properties of adobebricks in ancient constructions. *Construction and Building Materials*.
- [15] Zhou, T., Wang, X., Ma, B., Zhang, Z., & Tan, W. (2022). Seismic performance of new adobe bricks masonry: Design and experiment. *Advances in Structural Engineering*, 25(2), 277-289. <https://doi.org/10.1177/13694332211046349>
- [16] <https://data.apps.fao.org/aquastat/?lang=en>
- [17] https://www.heluz.com/files/20255_10-Technicky-list-EN.pdf
- [18] https://www.heluz.com/files/vyrobky/prohlaseni-o-vlastnostech/311897-20305.00+_en-v4.pdf
- [19] <https://www.imaterial.ro/exteroare/caramizi-perfromante-termic.html>
- [20] <https://www.researchgate.net/figure/Sludge-management-2016-Eurostat-Data-Explorer-2020>
- [21] <https://www.rombadconstruct.ro/rezistentia-la-compresiune.html>
- [22] <https://www.rombadconstruct.ro/tabel-cu-conductivitate-termica-a-materialelor-de-construcii.html>
- [23] <https://builder.techinfus.com/ro/uteplenie/teploprovodnost-uteplitelej.html>

SIMULATION AND OPTIMIZATION OF THE SPOON-WHEEL TYPE MAIZE PRECISION SEED-METERING DEVICE BASED ON VIBRATION

勺轮式玉米精量排种器在振动条件下的仿真与优化

Qing WANG[#], Dandan HAN^{**}, Lin CHEN, Yuxia HUANG, Wei LI, Chao TANG¹

College of Mechanical & Electrical Engineering, Sichuan Agricultural University, Ya'an/China

Tel: 08352883018; E-mail: handd1988@126.com

Corresponding author: Dandan Han

DOI: <https://doi.org/10.35633/inmateh-73-37>

Keywords: maize; spoon-wheel type; seed-metering device; vibration; optimization; discrete element method

ABSTRACT

The DEM (discrete element method) simulation and optimization of the shapes and quantity of spoons of spoon-wheel disc in the spoon-wheel seed-metering device under vibrational conditions are investigated in this paper. EDEM (Engineering-DEM) software was adopted to establish DEM models of 'Zhongyu No.3' coated maize seeds and the spoon-wheel seed-metering device first, and four additional spoons of various shapes (labeled as K1~K5, respectively) were designed. The test results indicated that the acceleration of seeds in the Y-direction in spoons (K2~5) was all less fluctuating than those in the original spoon (K1), and the multiple rate was the largest in spoon (K5). The ultimate optimal working speed of the spoon-wheel maize precision planter in southwest China was identified as 3 km/h, with 22 spoons and the ideal spoon shape being K3. The bench validation test was executed under vibrational conditions based on the optimal spoon structure and operation settings. The qualified rate exceeded 94.5% at an operating speed of 3~4 km/h, while the multiple rate was less than 4%, the leakage rate was lower than 1.5%, and the variation coefficient was smaller than 25.5%. The variety adaptability test was launched when the working speed was 3 km/h. The qualified rates of various maize varieties were all more than 96.5%; the multiple and leakage rates were both less than 2%, which satisfied the technical requirements of maize precision sowing in southwest China. The qualified rates of various maize varieties were all more than 96.5%, and the multiple and leakage rates were both less than 2%, which satisfied the technical requirements of maize precision sowing in southwest China.

摘要

本文研究了振动条件下勺轮式排种器中排种盘勺轮的形状和数量的 DEM(离散元法)仿真和优化。首先采用 EDEM (工程-离散元法)软件建立了"仲玉 3 号"包衣玉米种子和勺轮式排种器的 DEM 模型, 并设计了 4 个不同形状的附加勺子(分别标记为 K1~K5)。试验结果表明, 勺子(K2~5)内种子在 Y 方向的加速度波动均小于原勺子(K1), 且勺子(K5)内种子加速度的重播指数最高。最终确定西南地区勺轮玉米精量播种机的最佳工作速度为 3 km/h, 勺子数量为 22 个, 理想勺子形状为 K3。根据最佳勺子结构和操作设置, 在振动条件下进行了台架验证试验。在工作速度为 3~4 km/h 时, 合格指数超过 94.5%, 重播指数小于 4%, 漏播指数小于 1.5%, 变异系数小于 25.5%。在工作速度为 3 km/h 时进行了品种适应性试验, 各玉米品种合格指数均在 96.5% 以上, 重播指数和漏播指数均小于 2%, 满足了西南地区玉米精量播种的技术要求。

INTRODUCTION

The operating environment of the planter in the field has an immediate impact on seeding efficacy (Yang et al., 2015; Liao et al., 2020). Since of the sticky soil and uneven terrain in southwest China, the planter will generate vibrations in the field due to the undulation of the ground, and the seed-metering device will also be vibrated up and down at the same time, which will lead to a decrease in sowing quality, as evidenced by an increase in leakage rate and poor plant distribution uniformity (Jiang et al., 2011; Boydas et al., 2007). Consequently, the influential issue of vibration on the seeding performance of planters has gradually attracted widespread attention from scholars at home and abroad (Joseph et al., 2004; Moore., 1991; Zhao et al., 2010).

¹ Qing Wang, M.S. Stud. Agr.; Dandan Han, Lecturer. Ph.D. Eng.; Lin Chen, Prof. Ph.D. Eng.; Yuxia Huang, M.S. Stud. Agr.; Chao Tang, M.S. Stud. Agr.; Wei Li M.S. Stud. Eng.

(#These authors contributed equally to this work and should be considered co-first authors.)

A less uniform spacing of seeds discharged from the seed-metering device into the seed furrow can be triggered by field vibrations of the planter, as dictated by Yang et al. (Yang et al., 2016; Yang et al., 2016). It has been investigated that planter vibration could enormously interfere with the seeding process of the seed-metering device, thus diminishing the uniformity of plant distribution and impairing the planter's functionality (Emrah., 2021). Wang et al. conducted field vibration tests on the 2BMZ-2 no-till precision maize planter, and the effects of vibration loads on the performance of the seed-metering device and maize seed falling trajectory were analyzed, establishing the groundwork for improving the seeding performance of the finger clip seed-metering device (Wang et al., 2015). The mathematical models of the vibration systems of the spade punch maize precision planter and the 2BM-5 air-suction no-till planter were constructed to explore the planter's vibration properties in the field (Zhang et al., 2014; Zhang et al., 2009; Liu et al., 2016). To investigate the effects of various vibration frequency intervals and amplitudes on seeding performance, the vibration test results of the 2BFQ-6 precision combine seeder in the field were conducted as guidance by Liao et al, providing a reference basis for research on increasing beneficial vibration intervals in practice (Liao et al., 2022; Zheng et al., 2023). Once the effects of vibration on the seeding performance of the seed-metering device have been identified, the ultimate objective is to enhance performance by eliminating the vibration impact. Wu et al. elevated the target seeding rate of a rapeseed centralized seed-metering device at different vibration frequencies by adjusting the longitudinal distance (Wu et al., 2022). The study by Min Y.B. et al. aimed to investigate the optimum vibration condition of the seed hopper on the vacuum suction nozzle seeder for improving seeding performance (Min Y.B. et al., 2008). Turgut et al. study that the planting units operate at different amplitudes and frequencies depending on the soil conditions of the field and the amplitude and frequency of the vibration vary according to the planter characteristics such as the planter weight, tire type, and tire pressure, as well as the surface smoothness of the field, the ratio of stone and clod (Turgut N. et al., 1992). The laboratory tests and field trials confirmed the expediency of using the engineering sample of the planting machine equipped with the vibration-pneumatic planting device, according to research by Aksenov et al. (Aksenov A.G. et al., 2018). Vishnyakov A.A. et al studied the main factors influencing the quality of seeding by vibration device are determined and according to research results, a graph of their influence on estimates of seeding was constructed (Vishnyakov A.A. et al., 2015).

Seed-metering device is the centerpiece of the planter (Huang et al., 2022; Bai et al., 2022; Su et al., 2022). Depending on how it operates, the seed-metering device can be classified as mechanical or pneumatic (Han et al., 2018; Shi et al., 2019; Gao et al., 2023). The spoon-wheel seed-metering device is a kind of mechanical that primarily relies on gravity to achieve seed-cleaning and seed-voting, which has the advantages of being less susceptible to damage, better sowing quality, and the ability to adapt to seeds with significant shape variations, among other things (Guo et al., 2019; Zhang et al., 2023), and it is the most widely used in production practice in southwest China. To identify the mechanism by which vibrations cause the seed-metering device to miss-sowing, the forces on the seeds during the seed-filling and seed-cleaning processes of the spoon-wheel seed-metering device are examined in this work. The major components of the seed-metering device are simulated and optimized to discover the ideal structure, which is subsequently verified in bench tests to reduce miss-sowing and increase spacing uniformity under vibration.

MATERIALS AND METHODS

Design of the spoon-wheel seed-metering device

Structure and working principle of the seed-metering device

The seed-metering device is the core component of the planter, and its structural parameters directly determine the sowing quality. The spoon-wheel seed-metering device, which is more typically adopted on planters in southwest China, consists of a rear shell, seed-guiding wheel, spacer plate, spoon-wheel disc, front shell, and other parts. The concrete structure of the seed-metering device is depicted in Fig. 1(a).

The seed-metering device is mainly fixed to and supported by the rear shell. The seeds are ladled up by the spoon on the spoon-wheel disc and delivered to the seed-guiding wheel. The initial position of the seed delivery from the spoon to the seed-guiding wheel is dictated by the opening location of the spacer plate, which separates the spoon-wheel disc from the seed-guiding wheel. The seed-guiding wheel receives the seed from the spoon-wheel disc and neatly releases it from the seed-metering device. The movement of seeds in the seed-metering device will be easily observed via the transparent front shell.

Everything that happens with the spoon-wheel seed-metering device can be divided into seed-filling, seed-cleaning, seed-delivery, seed-protection, and seed-voting, as illustrated in Fig. 1(b).

The seeds are fed into the seed-filling zone via the seeds-inlet, the spoon-wheel disc, and the seed-guiding wheel together rotate in tandem with the seeding shaft. The seeds are loaded into the spoon hole under the combined action of gravity and the stirring of the spoon-wheel disc and then arrive at the opening position of the spacer plate via the seed-cleaning zone with the rotation of the spoon-wheel disc. After entering the seed-delivery zone, the single seed will disengage from the seed-metering device in the seed-voting zone under the joint action of gravity and centrifugal force and fall into the corresponding groove of the seed-guiding wheel from the opening position of the spacer plate, completing the entire seeding process.

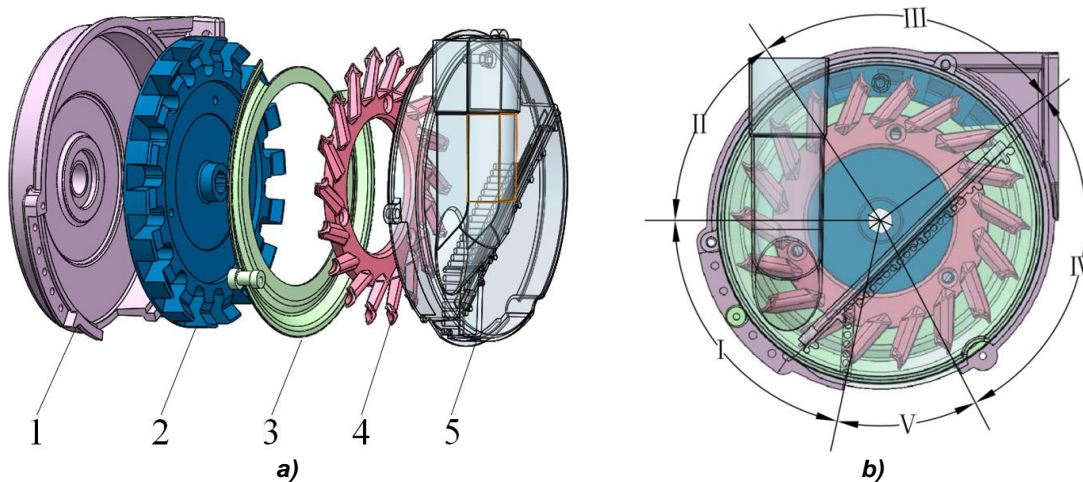


Fig. 1 - Schematic diagram of the spoon-wheel seed-metering device

a) Spoon-wheel seed-metering device; b) Diagram of the working process

1. Rear shell; 2. Seed-guiding wheel; 3. Spacer plate; 4. Spoon-wheel disc; 5. Front shell;

I. Seed-filling zone; II. Seed-cleaning zone; III. Seed-delivery zone; IV. Seed-protecting zone; V. Seed-voting zone

Force analysis of the seed-filling process

A good seed-filling effect is required for the seeding performance of the spoon-wheel seed-metering device (Pareek et al., 2021). The seed-metering device is driven by the ground wheel when the planter is running in the field. The seeds in the seed-filling zone are disturbed by the stirring action of the spoon-wheel disc, and the seeds near the spoon will follow the disc in a circular motion, thus fulfilling the seed-filling process. Planters may be subject to vibration during field operations due to the sticky soil and uneven terrain in southwest China. The seed-metering device will also be vibrated up and down with the planter. The forces on the seed during the seed-filling process are displayed in Fig. 2. The vibrating force on the seed-metering device is simplified to a vertical force in this paper.

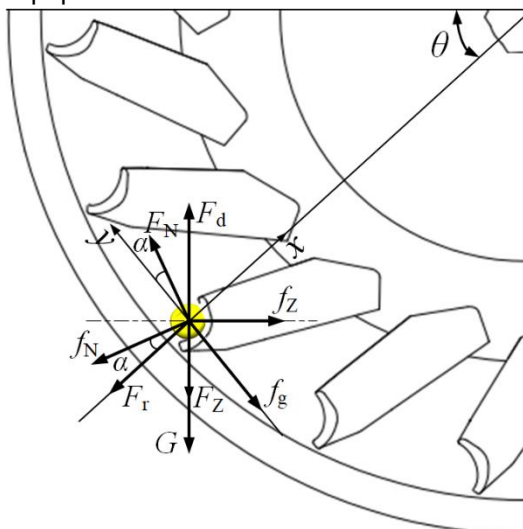


Fig. 2 - Force analysis diagram of the seed-filling process

The following equations can be derived from the analytical depiction of the forces on the seeds during the seed-filling process shown in Fig. 2.

$$F_r = mr\omega^2 \tag{1}$$

$$G = mg \tag{2}$$

$$f_N = F_N \tan \beta_1 \tag{3}$$

$$f_z = F_z \tan \beta_2 \tag{4}$$

$$f_g = F_g \tan \beta_3 \tag{5}$$

Where:

F_r is the centrifugal force generated by the seed's rotation with the spoon-wheel disc in N, G is gravity of seed in N, f_N is the frictional force between the inner spoon wall and the seed in N, f_z is the inter-population frictional force in N, f_g is the frictional force between the spacer plate and the seed in N, m is the seed mass in kg, r is the distance between the seed centroid and the center of the spoon-wheel disc in m, ω is the angular velocity of the seed in rad/s, g is the gravitational acceleration in m/s², F_N is the supporting force exerted on the seed by the inner spoon wall in N, F_z is the extrusion force produced by the seed population in N, β_1 is the friction angle between the seed and the spoon in (°), β_2 is the friction angle between the seed and the spacer plate in (°), β_3 is the friction angle between the seeds in (°).

The seed will be securely placed in the spoon after the seed-filling process is done. The resultant force of the forces acting on the seed in the x-axis direction is 0. The supporting force (F_N) exerted on the seed by the inner spoon wall is collated as follows:

$$F_N = \frac{F_z \sin \theta + G \cos \theta + f_N \cos \theta + F_r - f_z \cos \theta - F_d \sin \theta}{\sin \alpha} \tag{6}$$

where: F_d is the vertical vibrating force exerted on the seed by the seed-metering device vibrating in the field with the planter in N, α is the inclination angle of the spoon (°); and θ is the angle between the spoon and the center of the spoon-wheel disc (°).

As can be observed from Eq. (6), the supporting force (F_N) applied to the seed by the inner spoon wall diminishes as the vertical vibrating force (F_d) exerted on the seed by the vibration of the seed-metering device increases. Thus, the supporting force on the seed by the inner spoon wall is needed to be greater than 0 ($F_N > 0$) for the seed inside the spoon to remain in place. Otherwise, the supporting force (F_N) exerted on the seed by the inner spoon wall will be zero when the vertical vibrating force (F_d) surpasses a particular value, resulting in seed-filling failure and missed sowing.

Force analysis of the seed-cleaning process

When there are multiple seeds in the spoon, the seeds located on the outside of the spoon will gradually detach from the spoon and fall back into the seed-filling zone again under the combined force of gravity and other external forces, leaving only one seed in the spoon, which is referred to as the “seed-cleaning process” of the spoon-wheel seed-metering device. In this case, the single seed inside the spoon is exposed to gravity (G), the supporting force (F_N) exerted on the seed by the inner spoon wall, the frictional force (f_N) between the inner spoon wall and the seed, the centrifugal force (F_r) generated by the rotation of the seed with the spoon-wheel disc, the frictional force (f_g) between the spacer plate and the seed, and the vertical vibrating force (F_d) caused by the vibration of the seed-metering device. The forces acting on the seed during the seed-cleaning process are illustrated in Fig. 3.

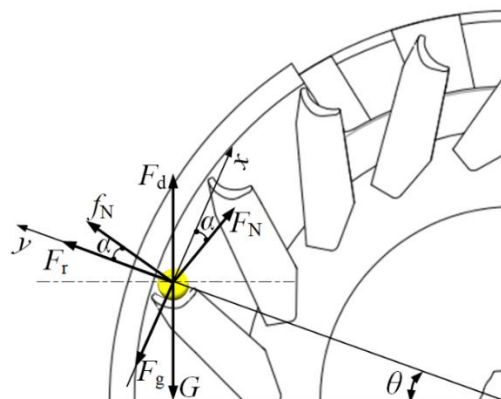


Fig. 3 - Force analysis diagram of the seed-cleaning process

The resultant force of the projected forces on the seed in the x-axis is:

$$F_x = f_N \sin \alpha + F_N \cos \alpha + F_d \cos \theta - G \cos \theta - f_g \tag{7}$$

Smooth seed cleaning can only be achieved during the seed-cleaning process if the resultant force of the projected forces in the x-axis on the seed is greater than zero. In this instance, the supporting force (F_N) on the seed by the inner spoon wall satisfies the following relationship:

$$F_N > \frac{G \cos \theta + f_g - f_N \sin \alpha - F_d \cos \theta}{\cos \alpha} \tag{8}$$

When the seed-metering device vibrates vigorously in the field with the planter, an increase in the vertical vibrating force (F_d) exerted on the seed by the vibration of the seed-metering device will result in a reduction in the supporting force (F_N) provided by the inner spoon wall. The seed-cleaning function of the seed-metering device is unaffected unless the vibrating force (F_d) is within a specific range. Consequently, if the seed-metering device vibrates excessively when the planter is in the field, it will lead to excessive seed-cleaning, which will trigger all of the seeds in the spoon to be shaken back into the seed-filling zone, resulting in an airlift of the seed spoon and unsuccessful sowing.

Planters will inevitably vibrate when operating in the field due to the sticky soil and uneven terrain in southwest China. Hence, it is required to optimize the structure of the existing spoon-wheel seed-metering device to make it more adaptable to the working circumstances in southwest China.

Optimized design of the spoon-wheel seed-metering device

Structural optimization of the spoon

The spoon-wheel disc is the core component of the spoon-wheel seed-metering device, and the spoon of the spoon-wheel disc is the primary working portion for taking and carrying seeds. The seed-filling, seed-cleaning, and seed-delivery effects of the seed-metering device are influenced by the spoon's shape (Jia et al., 2018). According to the above-mentioned forces on the seed during the seed-filling and seed-cleaning process, as well as the spoon design requirements, this paper is devoted to optimizing the spoon structure to lower the leakage rate caused by vibrations during the seed-metering device's function in the field.

The spoon employed in the existing spoon-wheel seed-metering device is based on a tetrahedral construction with a cylinder at an angle in particular through, eliminating the part where they are intersected, and the spoon hole is made on the curved surface formed on the tetrahedron (Jia et al., 2018). The specific structure of the spoon is illustrated in Fig. 4. The central axis of the cylinder is denoted by Y_1 , R_1 is the radius of the cylinder, and α_1 is the angle between the cylinder and the tetrahedron. To guarantee that the spoon can successfully scoop up more than one seed at a time, the spoon hole is required to be larger than the maximum length of the maize seed. Accordingly, the radius of the spoon hole and the size of the maize seed has the following relationship:

$$2R > L \tag{9}$$

R_{min} is the minimum radius of the cylinder in mm and L is the maximum length of the maize seed in mm.

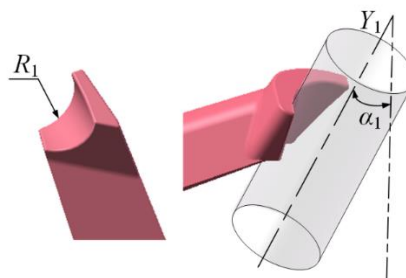


Fig. 4 - Schematic diagram of the shape of the original spoon hole

It can be observed that the vibration will mostly result in a reduction of the supporting force (F_N) on the seed by the inner spoon wall from the analysis of the forces on the seed during the seed-filling and seed-cleaning processes. To ameliorate the substantial leaping of the seeds triggered by vibrations that detach them from the spoon, the original spoon hole was twice incised with a cylinder of radius R_2 . In this instance, the angle formed by the axes of cylinder 2 (Y_2) and cylinder 1 (Y_1) is β . The optimal structure of the spoon nest can be acquired by eliminating the intersection between cylinder 2 and the original spoon nest. The structural layout of the sliced spoon nest is depicted in Fig. 5.

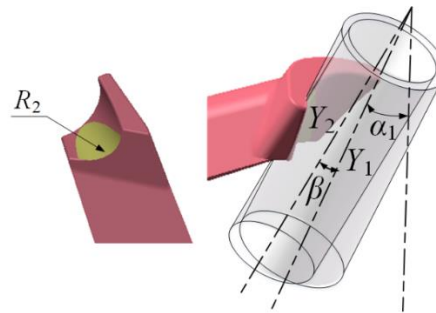


Fig. 5 - Schematic diagram of the improved spoon hole

Structural optimized design of the spoon

The maize variety that is commonly grown in southwest China is 'Zhongyu No. 3'. The measurement of the triaxial dimensions of maize seeds has been completed in the preliminary stage, and the results are listed in Table 1. The optimized spoon nest is based on the original structure for secondary cutting and shaping. The criterion " $R_2 < R_1$ " needs to be fulfilled to avoid interfering with the current seed-filling function of the spoon nest and disrupting the general shape of the original spoon nest. $2R_2$ should be longer than the average length of the maize seeds to comply with the design requirements of the spoon nest. As indicated in Table 1, the average length of maize seeds was 10.92 mm, and R_2 was determined to be 5.5 mm in this paper.

Table 1

| Triaxial sizes of 'Zhongyu No. 3' maize seeds | | | |
|---|-------------|------------|-------------|
| Seeds | Length [mm] | Width [mm] | Height [mm] |
| Flat | 10.92 | 8.31 | 4.96 |
| Spherical | 8.90 | 8.43 | 7.15 |

Analyzing the forces acting on the seed throughout the seed-filling and seed-cleaning processes reveals that the inclination angle (β) between the cylinder and the tetrahedron is essential for guaranteeing the seeds to fill the spoon hole smoothly. The seed travels from the spoon into the groove of the seed-guiding wheel mainly relying on gravity when the seed-metering device is in use. The spoon was 3D modeled with SolidWorks (version 2022) at different angles (β). In particular, when β is greater than 10° , it will conflict with the contoured shape of the original spoon. Additionally, without altering the profile of the original spoon, the bigger the β , the larger the overall shape of the spoon will be, which will result in multiple seeds filling the spoon at one time, thus affecting the single rate of seeding. The original spoon was thereby designated K1, and K2, K3, K4, and K5 are the spoons that were designed for an β 1° , 3° , 5° , and 7° , respectively. The structures of various spoons are depicted in Fig. 6.

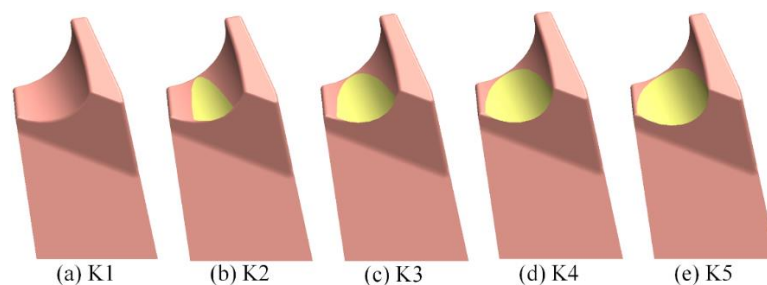


Fig. 6 - Different structures of spoon holes

Simulation and optimization DEM particle modelling

Maize seeds can be classified as "flat" and "spherical" according to the morphological characteristics of 'Zhongyu No. 3'. Statistically, there are around 74% flat maize seeds and roughly 26% spherical seeds. The coated maize seeds were virtually modeled in SolidWorks using their length, width, and height measurements from Table 1, and the 3D models were then imported into the EDEM software (version 2018) in '.step' format. The Multi-sphere method was executed to establish the DEM models of maize seeds, as shown in Fig. 7.

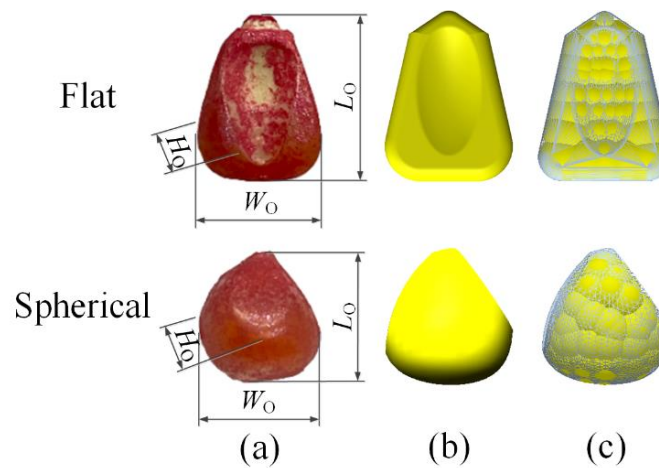


Fig. 7 - Models of maize seed
 (a) Physical figure; (b) 3D model; (c) EDEM model

DEM modelling of the seed-metering device

The spoon-wheel type seed-metering device is essentially composed of the rear shell, seed-guiding wheel, spacer plate, spoon-wheel disc, and transparent front shell. To conserve simulation time, elements unrelated to seed movement, such as bearings and bolts, were omitted without compromising simulation results. The simplified 3D model of the seed-metering device built with SolidWorks was loaded into the EDEM's pre-processing module in '.step' format. Aluminum alloy was adopted as the basic material for the spoon wheel discs. The DEM characteristics of the 'Zhongyu No. 3' coated maize seeds have been measured and calibrated in advance (Han *et al.*, 2023). The contact parameters between the maize seeds and the seed-metering device are listed in Table 2.

Table 2

| Simulation input parameters of maize and seed-metering device | | |
|---|-------|----------------------|
| Parameters | Maize | Seed-metering device |
| Poisson's ratio | 0.398 | 0.250 |
| Shear modulus [MPa] | 177 | 27000 |
| Density [g/cm ³] | 1.094 | 2.700 |
| Restitution coefficient [with maize] | 0.380 | 0.675 |
| Static friction coefficient [with maize] | 0.237 | 0.444 |
| Rolling friction coefficient [with maize] | 0.029 | 0.103 |

A virtual particle factory is followed by building above the inlet of seeds once the simulation parameters have been set. The movability of the spoon-wheel disc and seed-guiding wheel were arranged to be linear rotation, and the rotating speed of each group during the simulation was equal to the working speed of the planter. For all of the components were subjected to vertical vibration to simulate how the seed-metering device would operate under vibrational conditions, and the specific vibration parameters are indicated in Table 3.

A total of about 1500 particles were generated by the virtual factory based on the number of seeds in the chamber during the actual operation of the seed-metering device. Wherein 26% were spherical seeds and 74% were flat seeds.

The rotating time of the spoon-wheel disc and the seed-guiding wheel, as well as the vertical movement time of the seed-metering device, were started from 0.5 s when the particle generation in the chamber was complete and in a stable state. To extract motion information of particles in EDEM as precisely as feasible, the EDEM time step was set to 1×10^{-5} s, and data was recorded every 0.01 s.

The simulated working process of the spoon-wheel seed-metering device is illustrated in Fig. 8.

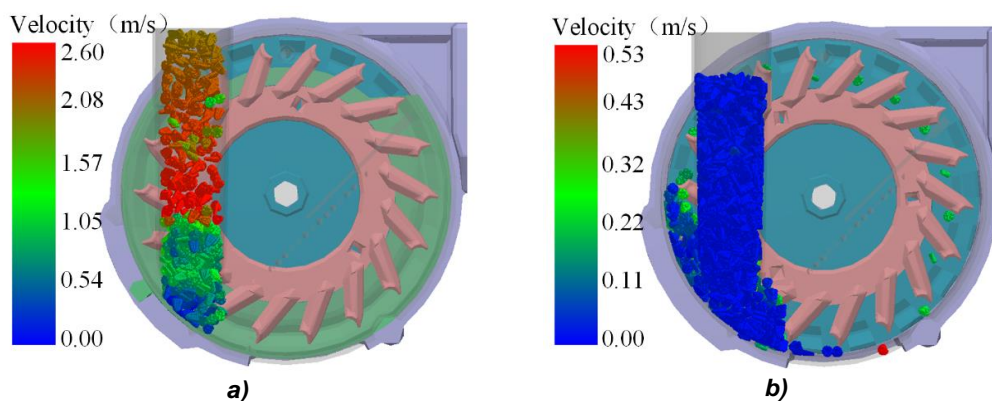


Fig. 8 - The working simulation process of the seed-metering device
 a) Particle generating process; b) Seed arranging process

The different seeding phases of the spoon-wheel seed-metering device during the working process are depicted in Fig. 9.

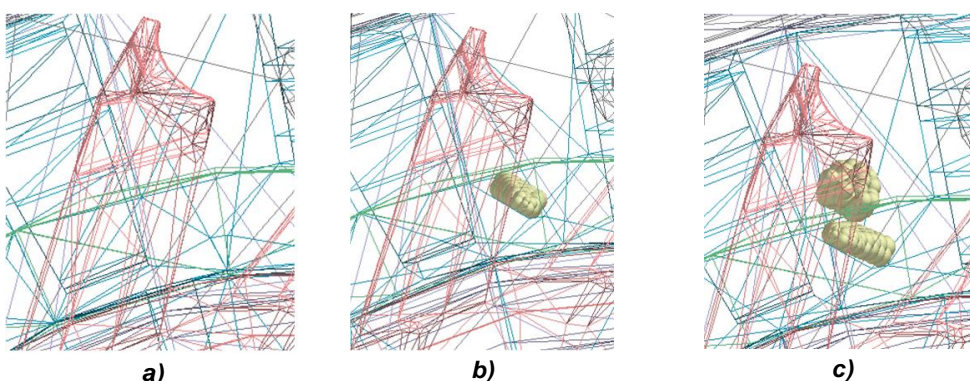


Fig. 9 - The seeding statuses of the seed-metering device
 a) Leakage sowing state; b) Qualified sowing state; c) Multiple sowing state

Simulation of the spoon-wheel disc

Experimental design

The spoon quantity and the disc’s diameter are the essential structural parameters of the spoon-wheel seed-metering device. The seed-metering device’s overall constructional dimensions are determined by the diameter of the spoon-wheel disc, while its speed is dictated by the spoon quantity used. In this regard, the working speed of the planter and the linear velocity at the spoon of the spoon-wheel disc are correlated as displayed in (Ding et al., 2018):

$$\frac{v_1}{v_2} = \frac{Zk}{2\pi R} \tag{10}$$

Where v_1 is the working speed of the planter in m/s; v_2 is the linear speed at the spoon of the spoon-wheel disc in m/s; R is the radius of the spoon-wheel disc in mm; Z is the number of the spoons; k is the theoretical plant spacing in mm.

At the same planter working speed and equivalent theoretical plant spacing, an increase in the number of spoons could reduce the rotation velocity of the spoon-wheel disc and thus improve the seeding performance. To investigate the influence of spoon-wheel discs with various numbers of spoons on the seeding performance under vibrational conditions, the optimization of the number of spoons was focused on in this section. The angle between two spoons on the spoon-wheel disc is φ_1 , with the spoon quantity (Z) and angle (φ_1) having the following relationship:

$$\varphi_1 = \frac{360^\circ}{Z} \tag{11}$$

The spoon mounted on the spoon-wheel disc is required to match the groove of the seed-guiding wheel, and the two components are synchronized with the seeding shaft. Consequently, the spoon-wheel disc and seed-guiding wheel need to be designed in compliance with the following condition: $\varphi_1 = \varphi_2$. The structure of the spoon-wheel disc and seed-guiding wheel are schematically diagrammed in Fig. 10.

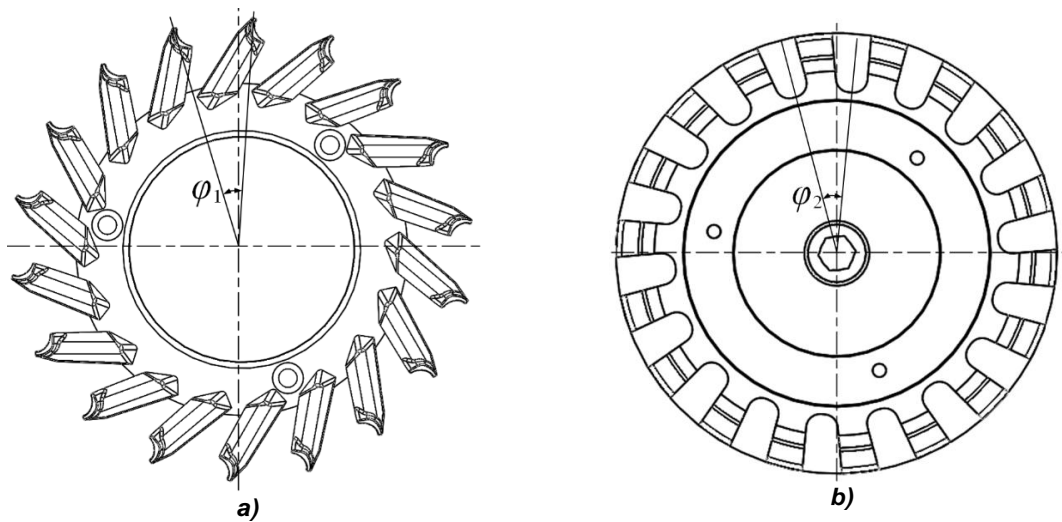


Fig. 10 - Schematic diagrams of the structure of spoon-wheel disc and seed-guiding wheel
 a) Spacing angle of the dipper wheel; b) spacing angle of the guide wheel

As noticed from Eq. (11), the angle between two spoons (φ_1) will decrease as the number of spoons (Z) extends while the diameter of the spoon-wheel disc remains constant. Currently, the most common quantity of spoons used in spoon-wheel devices is 18. Without altering the diameter of the spoon-wheel disc, up to 24 spoons can be manufactured. The number of spoons for comparative tests was selected at 18, 20, 22, and 24. Furthermore, it should be noted that the spoons of K2~4 are relatively neatly ordered as a result of the previously compared simulations of spoon-wheel discs with various spoon shapes. Therefore, the original spoon shape K1 and K2~4 were chosen for the comparative trials. A comparative test was carried out with the planter working at a speed of 3 to 6 km/h since the planter is less efficient while operating at a forward speed of 2 km/h in the field.

To obtain the optimal working parameters combination of the seed-metering device, the three factors-four levels orthogonal test was conducted in this part with the working speed, number of spoons, and structures of spoon holes as test factors, and the qualified rate, multiple rate, leakage rate, and variation coefficient of seeding as evaluation indicators. The orthogonal table $L^{16}(4^5)$ was selected, and the test factors and levels are listed in Table 3. The theoretical plant spacing was fixed at 20 cm in each trial group according to the agronomic requirements of maize cultivation in southwest China.

Table 3

| Factors and levels of the orthogonal test | | | |
|---|------------------------|--------------------|----------------------------|
| Levels | Factors | | |
| | A Working speed [km/h] | B Number of spoons | C Structure of spoon holes |
| 1 | 3 | 18 | K1 |
| 2 | 4 | 20 | K2 |
| 3 | 5 | 22 | K3 |
| 4 | 6 | 24 | K4 |

To simulate the field operation of the planter as well as for the measurement and statistics of each evaluation indicator, a 20 m-long seed bed was created under the seed-metering device to imitate the linear motion of the planter pulled by the tractor. The material properties of the seedbed and the variables governing the interaction between the seed and the seedbed were referred to in the earlier study findings (Lei et al., 2020; Wang et al., 2023). The specific parameter settings are shown in Table 4.

Table 4

| Simulation parameters setting of rubber and maize | | | | | | |
|---|-----------------|---------------------|------------------------------|--------------------------------------|--|---|
| Parameters | Poisson's ratio | Shear modulus [MPa] | Density [g/cm ³] | Restitution coefficient [with maize] | Static friction coefficient [with maize] | Rolling friction coefficient [with maize] |
| Rubber | 0.47 | 2900 | 1.350 | 0.0001 | 10 | 10 |

Note: To avoid seeds bouncing, the mechanical parameters of contact between maize and rubber are not true values.

The material properties of the seedbed and the variables governing the interaction between the seed and the seedbed were referred to in the earlier study findings (Lei *et al.*, 2020; Wang *et al.*, 2023). The specific parameter settings are shown in Table 4.

RESULTS

Simulation test results and analysis of the spoon hole

The analysis of the forces on the seed throughout the seed-filling and seed-cleaning processes revealed that the primary cause of the leaking of seeds was the seeds detached from the spoon holes. The original spoon hole (K1) was pre-simulated under vibrational conditions to better investigate the cause of the seeds falling back to the seed-filling zone in the event of vibration. The front shell is displayed as "Filled" in EDEM so that the phenomenon of leakage inside the seed-metering device can be observed. The opacity of the front shell is set to 0.1, while the spoon-wheel disc is set to 1. Following the observation of several seed-dropping procedures, it emerged that the seeds were most likely to detach from the spoon hole in the Y-direction during the seed-cleaning stage under vibrational conditions.

The phenomenon of leaking of the spoon-wheel seed-metering device under vibrational and the dropping direction of the seed is illustrated in Fig.11.

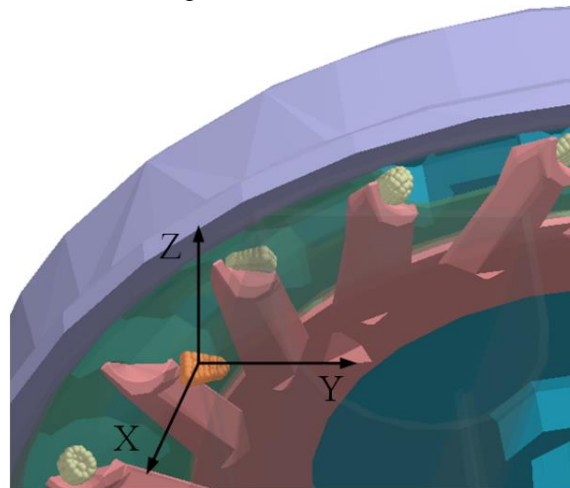


Fig. 11 - The dropping direction of maize seed

To optimize the seeding performance of the seed-metering device under vibrational conditions, comparative vibration tests were conducted for the spoon-wheel type planter at different working speeds. The vibration testing trials and analysis of the spoon-wheel planter in the field were performed in the foregoing period. DEM simulation tests were conducted on the aforementioned spoon-wheel discs with varied spoon holes under vibrational conditions for the spoon-wheel seed-metering device. In contrast, to analyze the stability of seeds moving in the Y-direction inside the spoon, three seeds with successful seed delivery were chosen at random after each group of simulations was completed.

The velocities of the selected seeds in the Y-direction inside the spoon during the seed-cleaning stage were exported, and the averaged values of their velocities were fitted by a MATLAB program to obtain the acceleration curves of the seeds concerning time.

The maximum difference between the acceleration of the seed and the spoon itself in the Y-direction for various spoon hole structures was calculated and gained by using the acceleration curve of the spoon itself as a baseline. Due to the considerable variation of the initial acceleration when the seed enters the spoon and the acceleration just before it is going to be released from the spoon and delivered to the seed-guiding wheel, the accelerations at these two limiting positions cannot be compared.

Comparisons of the Y-directional acceleration of seeds from the five kinds of spoon holes are illustrated in Figs. 12~16, respectively.

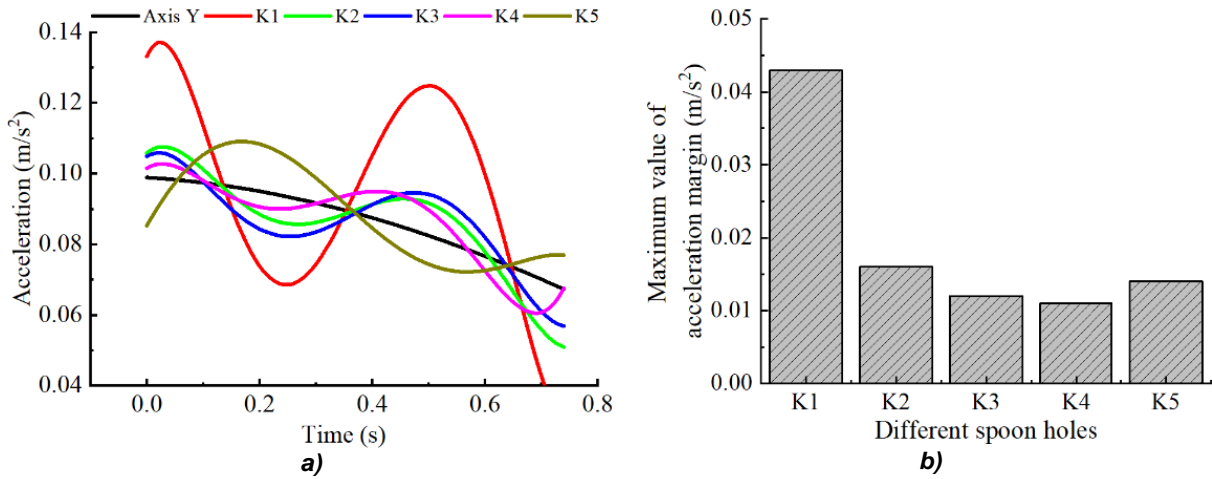


Fig. 12 - Comparative diagram of seed acceleration in the y-direction at a working speed of 2 km/h
 a) Acceleration change curve; b) Maximum difference of acceleration

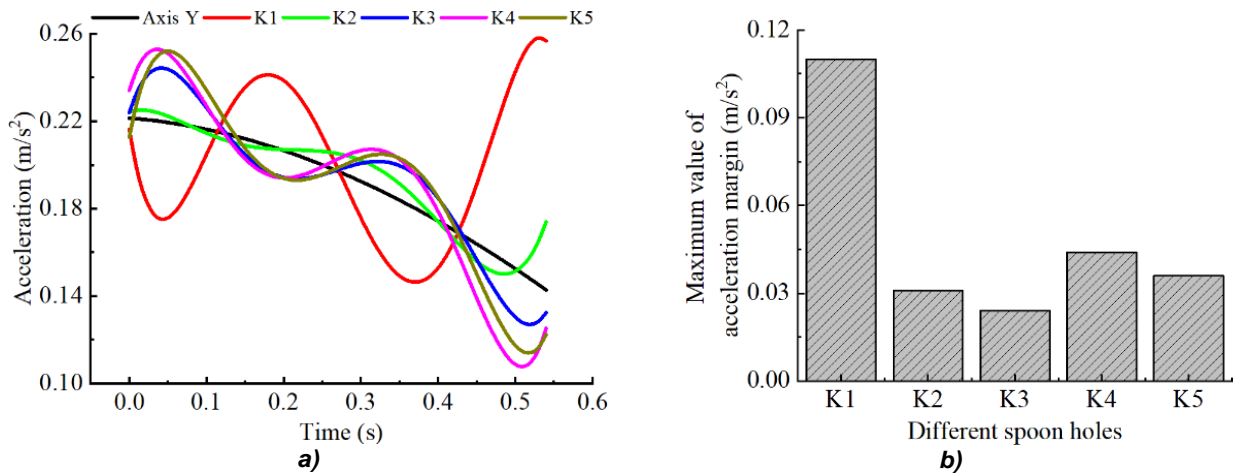


Fig. 13 - Comparative diagram of seed acceleration in the y-direction at a working speed of 3 km/h
 a) Acceleration change curve; b) Maximum difference of acceleration

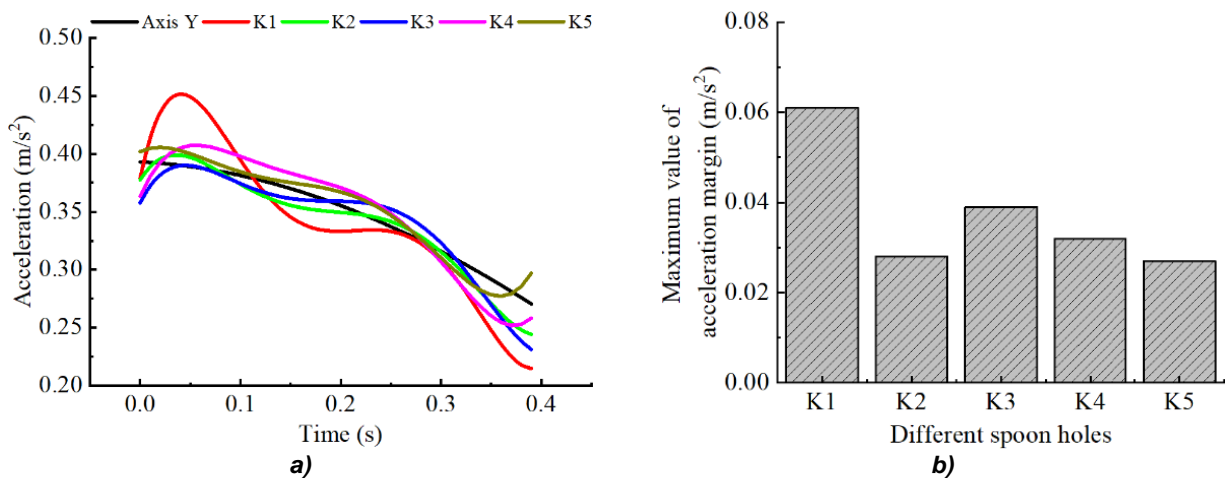


Fig. 14 - Comparative diagram of seed acceleration in the y-direction at a working speed of 4 km/h
 a) Acceleration change curve; b) Maximum difference of acceleration

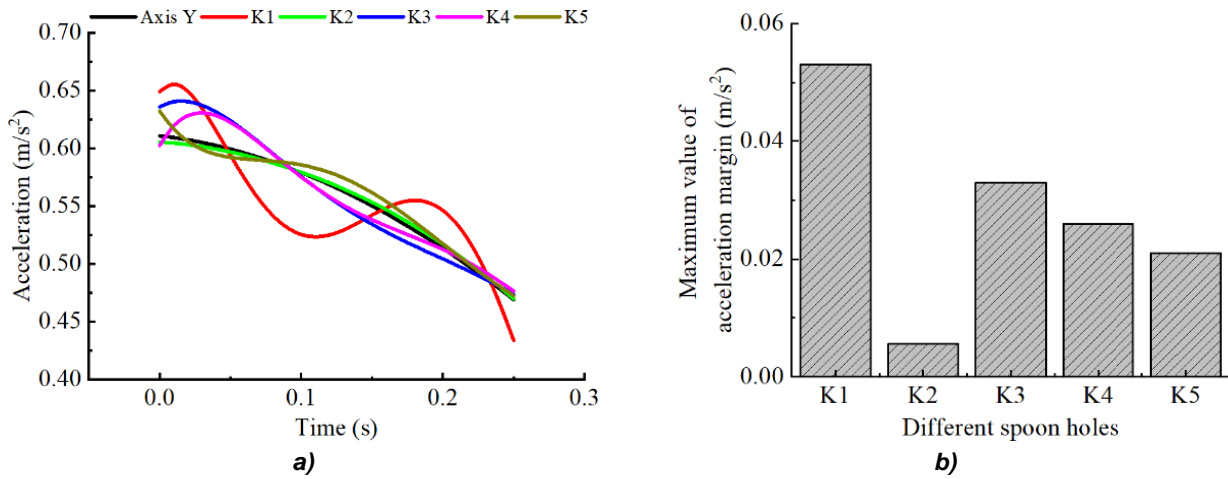


Fig. 15 - Comparative diagram of seed acceleration in the y-direction at a working speed of 5 km/h
 a) Acceleration change curve; b) Maximum difference of acceleration

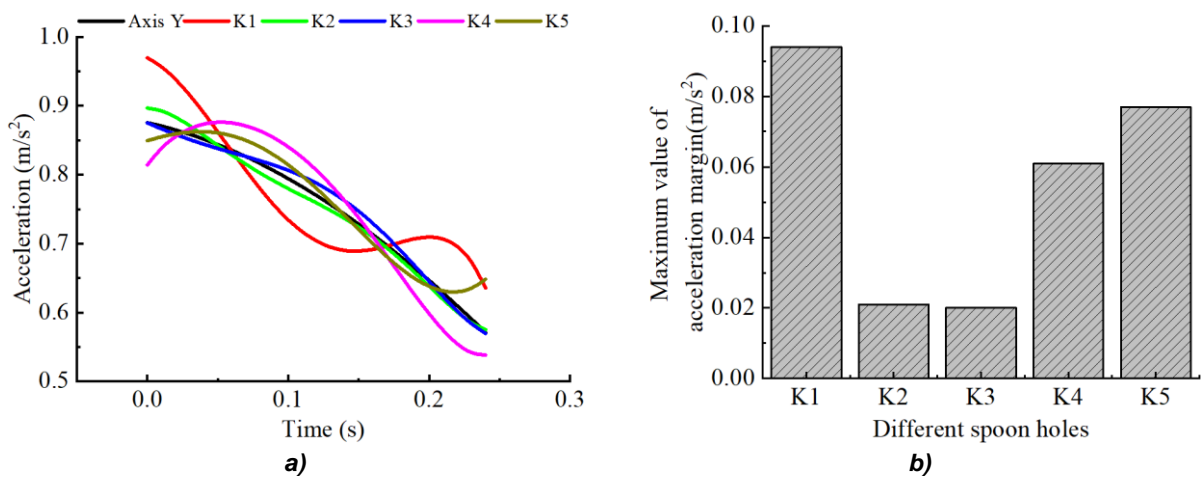


Fig. 16 - Comparative diagram of seed acceleration in the y-direction at a working speed of 6 km/h
 a) Acceleration change curve; b) Maximum difference of acceleration

It was revealed that the acceleration in the Y-direction of seeds in spoons K2-5 was less fluctuating than those in spoon K1 when the working speed was 2-6 km/h by analyzing the variation in an acceleration of maize seeds at a variety of working speeds and within diverse spoon structures, which indicates that the seeds would be more stable in these four spoons of K2-5. The anomalous states of the seeds being fed from the spoon-wheel disc into the seed-guiding wheel in the DEM simulation are reseeding (2 or more seeds in the seed-guiding wheel) and missing (0 seeds in the seed-guiding wheel). In addition to comparing the stability of seeds moving in the Y-direction, it is required to evaluate the aberrant states of seeds entering the seed-guiding wheel from the spoon-wheel disc within the five species of spoons. The results are shown in Fig. 17.

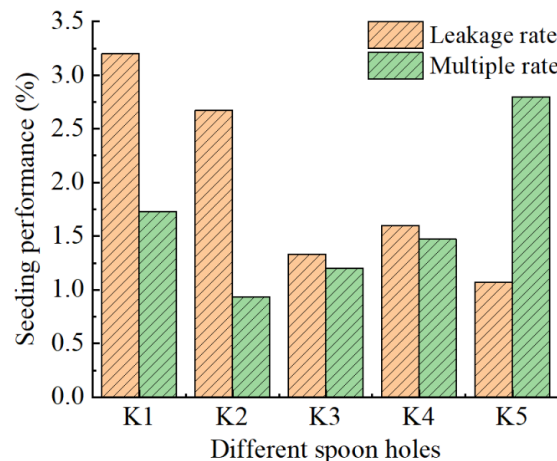


Fig. 17 - Comparison of the seeding performance of various spoon-wheel discs

According to Fig. 16, the leakage rate of all four species of spoons (K2~5) is lower than the rate of the original spoon (K1), while the multiple rate of spoon (K5) is the highest. Therefore, the seeding performance of spoons (K2~4) is relatively more stable.

Simulation of the spoon-wheel disc experimental results and analysis

Each set of DEM simulation tests was repeated thrice, and the distance between seeds was measured using the post-processing tool “ruler” in EDEM, as indicated in Fig. 18.

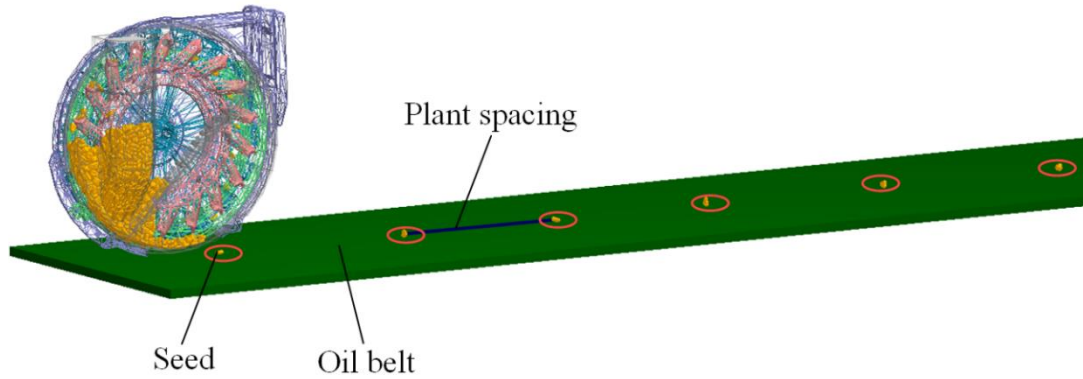


Fig. 18 - Simulation result of the seed-metering device on the oil belt

The design scheme and results of the orthogonal test are listed in Table 5.

Table 5

| Simulation results of the orthogonal test | | | | | | | |
|---|---|---|---|--------------------|-------------------|------------------|---------------------------|
| No. | A | B | C | Qualified rate [%] | Multiple rate [%] | Leakage rate [%] | Variation coefficient [%] |
| 1 | 1 | 1 | 1 | 96.15 | 1.13 | 2.72 | 20.73 |
| 2 | 1 | 2 | 2 | 97.25 | 0.05 | 2.70 | 20.55 |
| 3 | 1 | 3 | 3 | 97.45 | 1.14 | 1.41 | 17.10 |
| 4 | 1 | 4 | 4 | 97.01 | 1.30 | 1.69 | 22.74 |
| 5 | 2 | 1 | 2 | 94.59 | 2.13 | 3.28 | 27.82 |
| 6 | 2 | 2 | 1 | 93.36 | 3.97 | 2.67 | 27.64 |
| 7 | 2 | 3 | 4 | 95.93 | 2.91 | 1.16 | 25.71 |
| 8 | 2 | 4 | 3 | 93.47 | 4.73 | 1.80 | 25.13 |
| 9 | 3 | 1 | 3 | 90.93 | 4.80 | 4.27 | 27.50 |
| 10 | 3 | 2 | 4 | 91.97 | 4.32 | 3.71 | 29.62 |
| 11 | 3 | 3 | 1 | 95.83 | 1.09 | 3.08 | 24.73 |
| 12 | 3 | 4 | 2 | 91.94 | 3.38 | 4.68 | 31.52 |
| 13 | 4 | 1 | 4 | 88.41 | 3.76 | 7.83 | 31.80 |
| 14 | 4 | 2 | 3 | 88.78 | 4.85 | 6.37 | 29.02 |
| 15 | 4 | 3 | 2 | 90.92 | 1.67 | 7.41 | 27.32 |
| 16 | 4 | 4 | 1 | 90.72 | 2.72 | 6.56 | 29.68 |

Analysis of variance (ANOVA) was executed to examine the findings of the orthogonal test, and the results are presented in Table 6.

Table 6

| Variance analysis of orthogonal test results | | | | | | | |
|--|--------------------|----------------|----|-------------|---------|---------|--------------|
| Dependent variable | Source of variance | Sum of squares | Df | Mean square | F-value | P-value | Significance |
| Qualified rate | A | 111.031 | 3 | 37.010 | 42.118 | 0.000 | ** |
| | B | 15.059 | 3 | 5.020 | 5.712 | 0.034 | * |
| | C | 4.034 | 3 | 1.345 | 1.530 | 0.300 | - |

| Dependent variable | Source of variance | Sum of squares | Df | Mean square | F-value | P-value | Significance |
|-----------------------|--------------------|----------------|----|-------------|---------|---------|--------------|
| Multiple rate | Error | 5.272 | 6 | 0.879 | | | |
| | A | 18.170 | 3 | 6.057 | 14.948 | 0.003 | ** |
| | B | 6.075 | 3 | 2.025 | 4.998 | 0.045 | * |
| | C | 10.169 | 3 | 3.390 | 8.365 | 0.015 | * |
| Leakage rate | Error | 2.431 | 6 | 0.405 | | | |
| | A | 63.157 | 3 | 21.052 | 135.507 | 0.000 | ** |
| | B | 3.300 | 3 | 1.100 | 7.080 | 0.021 | * |
| | C | 2.668 | 3 | 0.889 | 5.724 | 0.034 | * |
| Variation coefficient | Error | 0.932 | 6 | 0.155 | | | |
| | A | 201.468 | 3 | 67.156 | 56.552 | 0.000 | ** |
| | B | 32.593 | 3 | 10.864 | 9.149 | 0.012 | * |
| | C | 18.027 | 3 | 6.009 | 5.060 | 0.044 | * |
| | Error | 5.145 | 6 | 0.858 | | | |

*Note: * means significant influence in 95% confidence interval, ** means significant influence in 99% confidence interval, - means no significant influence.

As observed in Table 6 of the ANOVA of the orthogonal test results, the effects of planter working speed (A) and spoon count (B) were both extremely significant and generally significant for all evaluation indicators, respectively. The spoon shape (C) had a typically considerable impact on the multiple rate, leakage rate, and variation coefficient, while it did not affect the qualified rate. It was discovered that the working speed of the planter extremely affects the seeding performance and that adding the number of spoons can improve seeding properties to some amount. While optimizing the shape of spoons will not enhance the qualified rate or the variation coefficient of plant spacing, it may somewhat ameliorate the multiple rate and leakage rate.

The orthogonal test results were evaluated for extreme differences, and the results are indicated in Table 7.

Table 7

Results of the extreme difference analysis

| Evaluation indicators | Factors | Levels | | | | Extreme Difference | Optimal level | Optimal combination |
|-----------------------|---------|----------------|----------------|----------------|----------------|--------------------|---------------|--|
| | | k ₁ | k ₂ | k ₃ | k ₄ | | | |
| Qualified rate | A | 96.97 | 94.34 | 92.67 | 89.71 | 7.29 | 1 | |
| | B | 92.52 | 92.84 | 95.03 | 93.29 | 2.19 | 3 | A ₁ B ₃ C ₃ |
| | C | 94.02 | 93.68 | 92.66 | 93.33 | 1.36 | 3 | |
| Multiple rate | A | 0.91 | 3.44 | 3.40 | 3.25 | 2.53 | 1 | |
| | B | 2.96 | 3.30 | 1.70 | 3.03 | 1.60 | 3 | A ₁ C ₂ B ₃ |
| | C | 2.23 | 1.81 | 3.88 | 3.07 | 2.07 | 2 | |
| Leakage rate | A | 2.13 | 2.23 | 3.94 | 7.04 | 4.91 | 1 | |
| | B | 4.53 | 3.86 | 3.27 | 3.68 | 1.26 | 3 | A ₁ B ₃ C ₃ |
| | C | 3.76 | 4.52 | 3.46 | 3.60 | 1.06 | 3 | |
| Variation coefficient | A | 20.28 | 26.58 | 28.34 | 29.46 | 8.06 | 1 | |
| | B | 26.96 | 26.71 | 23.72 | 27.27 | 3.25 | 3 | A ₁ B ₃ C ₃ |
| | C | 25.70 | 26.80 | 24.69 | 27.47 | 2.78 | 3 | |

As revealed in Table 8 of the analysis of extreme differences in orthogonal test results, the primary and secondary factors affecting the qualified rate were A>B>C, and the optimal parameters combination was A₁B₃C₃. The major and secondary factors regarding the multiple rate were A>C>B, and the optimum set of combined factors was A₁C₂B₃. The principal and subsidiary factors that affected the leakage rate were A>B>C, and the ideal portfolio was A₁B₃C₃.

The priority factors influencing the coefficient of variation were $A > B > C$, and the optimized set was $A_1 B_3 C_3$. The results of the extreme difference analysis further indicated that the optimal levels of the planter working speed (A) and the number of spoons (B) were identical for each evaluation index, which were A_1 and B_3 , respectively. The preferred level of spoon shape (C) for the multiple rate was C_2 , while the intended level for the other three evaluation indicators was C_3 . Taking into account the fact that a slightly higher multiple rate throughout the sowing process would not detract from the overall working effectiveness of the planter. The integrated analysis ultimately concluded that the best working speed of the spoon-wheel maize precision planter is 3 km/h, the ideal number of spoons is 22, and the equivalent spoon shape is K3 under the conditions of sticky soil in southwest China.

Bench validation tests

Validation test of the spoon-wheel disc

The orthogonal test optimization results of DEM simulation ultimately led to the conclusion that 22 spoons and the shape of K3 contribute to the ideal structure of the spoon-wheel disc. A 3D model of the seed-guiding wheel with an identical number of grooves (22) was sketched, and the aluminum alloy material was adopted for 3D printing. Comparative bench tests of seeding performance at different working speeds were carried out for the optimized disc (S1), the original spoon-wheel disc (18 spoons, S2), and the commercially available spoon-wheel disc with 24 spoons (S3). The results are summarized in Table 8.

Table 8

| | Qualified rate [%] | | | Multiple rate [%] | | | Leakage rate [%] | | | Variation coefficient [%] | | |
|---|--------------------|-------|-------|-------------------|------|------|------------------|-------|------|---------------------------|-------|-------|
| | S1 | S2 | S3 | S1 | S2 | S3 | S1 | S2 | S3 | S1 | S2 | S3 |
| 3 | 97.45 | 94.33 | 94.67 | 1.14 | 1.34 | 1.67 | 1.41 | 4.33 | 3.66 | 20.28 | 25.63 | 25.17 |
| 4 | 94.70 | 92.00 | 93.33 | 3.82 | 4.03 | 3.67 | 1.48 | 3.97 | 3.00 | 25.42 | 27.02 | 28.05 |
| 5 | 93.38 | 90.26 | 91.00 | 2.95 | 3.85 | 4.27 | 3.67 | 5.89 | 4.73 | 26.11 | 31.43 | 30.94 |
| 6 | 90.05 | 87.33 | 89.74 | 3.26 | 2.00 | 4.12 | 6.69 | 10.67 | 6.14 | 28.17 | 32.09 | 31.18 |

As seen from Table 8, the qualified rate of the optimized spoon-wheel disc under vibrational conditions with different forward speeds can reach over 90%, which is higher than that of the original spoon-wheel disc (18 spoons) and the spoon-wheel disc (24 spoons) already available on the market. The multiple rates are all lower than 5%, the leakage rates are all smaller than 7%, and the variation coefficients are all less than 30%. The seeding performance is improved compared with that before optimization, and satisfies the design specifications.

Variety adaptability test

With a working speed of 3 km/h and a theoretical plant spacing of 20 cm, several species of seeds, including 'Zhengdan 958', 'Ziyu 46', 'Chuandan 99', 'Denghai 618', and 'Zhengda 999', were selected to investigate the variety adaptability of the optimized spoon-wheel disc. The averaged values were retrieved by replicating each group of tests thrice, and the results are indicated in Table 9.

Table 9

| Maize varieties | Qualified rate [%] | Multiple rate [%] | Leakage rate [%] | Variation coefficient [%] |
|-----------------|--------------------|-------------------|------------------|---------------------------|
| Zhengdan 958 | 96.97 | 1.63 | 1.40 | 21.50 |
| Ziyu 46 | 96.65 | 1.73 | 1.62 | 22.17 |
| Chuandan 99 | 97.30 | 1.53 | 1.17 | 21.53 |
| Denghai 618 | 97.07 | 1.26 | 1.67 | 21.42 |
| Zhengda 999 | 97.19 | 1.28 | 1.53 | 20.14 |

The results revealed that the optimized spoon-wheel disc had higher adaptation to maize seeds, with the qualified rate of all five maize varieties being greater than 96.5%, the multiple rate and leakage rate being both less than 2%.

CONCLUSIONS

Based on the actual demand for precision sowing of maize under vibrational conditions in the hilly areas of Southwest China, the key structure and working parameters affecting the precision sowing of the spoon-wheel seed-metering device under vibrational conditions was analyzed. The critical parameters related to the sowing performance of the planter was optimized and examined. The main conclusions are as follows:

(1) According to the analysis of forces on the seeds during the seed-filling and seed-cleaning processes under vibrational conditions, it was ascertained that the vertical vibrating force exerted on the seed by the vibration of the seed-metering device will induce a reduction in the supporting force on the seed by the inner spoon wall, which will increase the leakage rate of the seed-metering device under vibrational conditions. To address this issue, the simulated optimization and tests of the structures and number of spoons are carried out in this paper.

(2) To the characteristics of the forced seeds in the spoon under vibrational conditions, the spoon-wheel discs with varied spoon structures were designed, and DEM simulation compared tests was conducted with the acceleration variation of seeds in the Y-direction in the spoon as the evaluation index to analyze the stability of different spoon shapes on seeds during the seed-cleaning process. The superior spoon shape was ultimately defined as K2~4.

(3) The optimal spoon structure was further evaluated by conducting a three-factor and four-level orthogonal test with the working speed, the number and structure of the spoon as the test factors, and the qualified rate, multiple rate, leakage rate, and variation coefficient of plant spacing as the evaluation indexes, and the ultimate best spoon shape of the spoon-wheel disc was K3, and the number of spoons was 22.

(4) The optimized spoon-wheel disc to different maize varieties has a sowing qualified rate greater than 96.5%, multiple and leakage rates both less than 2%, which complies with national standard requirements, and has a good variety of adaptability, as indicated by the results of the variety adaptability test.

ACKNOWLEDGEMENT

This work was supported by the Natural Science Foundation of Sichuan Province (2022NSFSC0138), the Technological Innovation R&D Projects of Chengdu Science and Technology Bureau (2022YF0501141SN), and the Listing Project of Rural Revitalization Research Institute of Sichuan Tianfu District (XZY1-11).

REFERENCES

1. Aksenov A. G., Izmaylov A. lu., Dorokhov. A.S., Sibirev A.V. (2018). Onion bulbs orientation during aligned planting of seed-onion using vibration-pneumatic planting device. *INMATEH - Agricultural Engineering*. Vol.55, No.2, pp.63-77. Moscow /Russian.
2. Bai, W., Li, Y., Yu, H., Zhao, D., Li, X., Zhao, X. (2022). Design and simulation optimization of positive and negative pressure seed-metering device (正负压式精量排种器设计与仿真优化). *Journal of Hebei Agricultural University*, Vol.45, No.4, pp115-122. Baoding/China.
3. Boydas, M. G., Turgut, N. (2007). Effect of vibration, roller design, and seed rates on the seed flow evenness of a studded feed roller. *Applied Engineering in Agriculture*, Vol.23, No.4, pp. 413-418. Erzurum/Turkey.
4. Ding, L., Yang, L., Liu, S., Yan, B., He, X., Zhang, D. (2018). Design of air suction high speed precision maize seed metering device with assistant seed filling plate (辅助充种种盘玉米气吸式高速精量排种器设计). *Transactions of the Chinese Society of Agricultural Engineering*, Vol.34, No.22, pp.1-11. Beijing/China.
5. Emrah, K. (2021) Field-scale evaluation of parameters affecting planter vibration in single seed planting. *Measurement*, Vol.184. Igdır/Turkey.
6. Gao, X., Xie, G., Li, J., Shi G., Lai, Q., Huang, Y. (2023). Design and validation of a centrifugal variable-diameter pneumatic high-speed precision seed-metering device for maize. *Biosystems Engineering*, Vol.227, pp.161-181. Yangling/China.
7. Guo, X., Zhang, H., Wu, J., Chen, T. (2019) Simulation research on spoon type seed metering device of sunflower seed based on EDEM (基于 EDEM 的勺轮式葵花排种器离散元仿真研究). *Journal of Chinese Agricultural Mechanization*, Vol.40, No.2, pp.19-24. Kunming/China.

8. Han, D, Xu, Y., Huang, Y., He, B., Dai, J., Lv, X., Zhang, L. (2023). DEM parameters calibration and verification for coated maize particles. *Computational Particle Mechanics*, Vol.10, No.6, pp.1931-1941. Yaan/China.
9. Han, D., Zhang, D., Jing, H., Yang, L., Cui, T., Ding, Y., Wang, Z., Wang, Y., Zhang, T. (2018). DEM-CFD coupling simulation and optimization of an inside-filling air blowing maize precision seed-metering device. *Computers and Electronics in Agriculture*, Vol.150, pp.426-438. Beijing/China.
10. Huang, Y., Li, P., Dong, J., Chen, X., Zhang, S., Liu, Y. (2022). Design and experiment of side-mounted guided high speed precision seed metering device for soybean (大豆高速播种机侧置导引式精量排种器设计与试验). *Transactions of the Chinese Society for Agricultural Machinery*, Vol.53, No.10, pp.44-53. Yangling/China.
11. Jia, S., Wei, L., Chen, C., Qiao, H., Li, H. (2018). Structure design of spoon wheel planter and analysis of seeds force (勺轮式排种器结构设计与种子受力分析). *Journal of Jilin Institute of Chemical Technology*, Vol.35, No.9, pp.41-45. Jilin/China.
12. Jia, S., Wei, L., Zhang, Z., Hao, S., Liu, Y., Sun, Z. (2018). Design and simulation of spoon wheel type seed metering device based on discrete element theory (基于离散元理论的勺轮式排种器设计与仿真). *Research and Exploration in Laboratory*, Vol.37, No.12, pp.124-128. Jilin/China.
13. Jiang, X., Zheng, J., Chi, Z. (2011). Study of mechanized seeding machinery selection for single corn planting in hilly area's rape stubble (丘陵山地油菜茬玉米净作机械化播种机械选型研究). *Southwest China Journal of Agricultural Sciences*, Vol.24, No.4, pp.1261-1264. Chengdu/China.
14. Joseph, G. L., Mike, R. (2004). Corn response to within row plant spacing variation. *Agronomy Journal*, Vol.96, No.5, pp.1464-1468. Wisconsin/America.
15. Lei, X., Yang, W., Yang, L., Liu, L., Liao, Q., Ren, W. (2020). Design and experiment of seed hill-seeding centralized metering device for rapeseed (油菜精量穴播集中排种装置设计与试验). *Transactions of the Chinese Society for Agricultural Machinery*, Vol.51, No.2, pp.54-64. Yaan/China.
16. Liao, Y., Li, C., Liao, Q., Wang, L. (2020). Research progress of seed guiding technology and device of planter (播种机导种技术与装置研究进展分析). *Transactions of the Chinese Society for Agricultural Machinery*, Vol.51, No.12, pp.1-14. Wuhan/China.
17. Liao, Y., Qi, T., Liao, Q., Zeng, R., Li, C., Gao, L. (2022). Vibration characteristics of pneumatic combined precision rapeseed seeder and its effect on seeding performance (气力式油菜精量联合直播机振动特性及对排种性能影响). *Journal of Jilin University (Engineering and Technology Edition)*, Vol.52, No.5, pp.1184-1196. Wuhan/China.
18. Liu, Y., Liu, F, Zhao, M., Dong, S., Zhang, X. (2016). Analysis of vibration test and vibration theory of air-suction no-tillage planter (气吸式免耕播种机的振动测试与振动理论分析). *Journal of China Agricultural University*, Vol.21, No.10, pp.109-116. Huhehaote/China.
19. Min Y. B., Kim S. T., Kwon H. D., Moon S. W., Kang D. H. (2008). Effect of the seed hopper vibration on the seeding performance of the vacuum suction nozzle seeder. *Journal of Biosystems Engineering*, Vol.33, No.3, pp. 179-185. Gyeongsang/Korea.
20. Moore, S. H. (1991) Uniformity of plant spacing effect on soybean population parameters. *Crop Science*, Vol.31, No.4, pp.1049-1051. State of Louisiana/America.
21. Pareek, C., Tewari, V., Machavaram, R., Nare, B. (2021). Optimizing the seed-cell filling performance of an inclined plate seed metering device using integrated ANN-PSO approach. *Artificial Intelligence in Agriculture*, Vol.5, pp.1-12. Kharagpur/India.
22. Shi, L., Sun, B., Zhao, W., Yang, X., Xin, S., Wang, J. (2019). Optimization and test of performance parameters of elastic air suction type corn roller seed-metering device (弹性气吸嘴式玉米滚轮排种器排种性能参数优化与试验). *Transactions of the Chinese Society for Agricultural Machinery*, Vol.50, No.10, pp.88-95+207. Lanzhou/China.
23. Su, W., Chen, Z., Lai, Q., Jia, G., Lv, Q., Tian, B. (2022) Design and test of wheel-spoon type precision seed-metering device for Chinese herbal medicine pinellia ternate (轮勺式半夏精密排种器设计与试验). *Transactions of the Chinese Society for Agricultural Machinery*, Vol.53, No.9, pp.60-71. Kunming/China.
24. Turgut N., Ulger P., Ozsert I. (1992). The effect of vibration upon the longitudinal seed distribution for some delivery mechanisms, in: *Agricultural Mechanization 14th National Congress*, pp.112-124. Samsun/Turkey.

25. Vishnyakov A. A., Vishnyakov A. S., Klak A. I. (2015). Seeding of rapeseed by the use of vibration sowing device of a seeder. *Tractors and Agricultural Machinery*, Vol.82, No.10, pp.36-39. Krasnoyarsk/Russia.
26. Wang, B., Liao, Q., Wang, L., Shu, C., Cao, M., Du, W. (2023). Design and test of air-assisted seed-guiding device of precision hill-seeding centralized seed-metering device for sesame. *Agriculture* Vol.13, No.2, pp.393. Wuhan/China.
27. Wang, Q., Zhu, L., Li M., Huang, D., Jia, H., Zhuang, J. (2019). Vibration characteristics of corn no-tillage finger-type precision planter and its effect on seeding performance (指夹式玉米免耕精密播种机振动特性及对排种性能的影响). *Transactions of the Chinese Society of Agricultural Engineering*, Vol.35, No.9, pp.9-18. Changchun/China.
28. Wu, W., Chang, C., Li, T., Hu, H., Zhou, Z., Yang, W., Guo, J., Zhu, P., Li, J., Hu, J., Cheng, H., Tao, Y., Zhou, W., Deng, F., Chen, Y., Ren, W., Lei, X. (2022). Seed-filling characteristics of a centralized seed-metering device for rapeseed caused by vibration. *Agriculture*, Vol.12, NO.07, pp.965. Yaan/China.
29. Yang, L., Yan, B., Cui, T., Yu, Y., He, X., Liu, Q., Liang, Z., Yin, X., Zhang, D. (2016). Global overview of research progress and development of precision maize planters. *International Journal of Agricultural and Biological Engineering*, Vol.9, No.1, pp.9-26. Beijing/China.
30. Yang, L., Yan, B., Zhang, D., Zhang, T., Wang, Y., Cui, T. (2016). Research Progress on Precision Planting Technology of Maize (玉米精密播种技术研究进展). *Transactions of the Chinese Society for Agricultural Machinery*, Vol.47, No.11, pp.38-48. Beijing/China.
31. Yang, L., Zhang, R., Gao, N., Cui, T., Liu, Q., Zhang, D. (2015). Performance of no-till corn precision planter equipped with row cleaners. *International Journal of Agriculture and Biological Engineering*, Vol.8, No.5, pp.15-25. Beijing/China.
32. Zhang, R., Liu, H., Wei, G., Zhou, J., Shi, S., Li, H., He, T. (2023). Design and test of key components of scoop type precision sorghum seed metering device (勺式高粱精量排种器关键部件设计与试验). *Journal of Agricultural Mechanization Research*, Vol.45, No.12, pp.215-219. Jinan/China.
33. Zhang, X., Li, C., Li, J., Zou, M. (2014). Mathematic vibration model of spade punch planter of maize. Trans (铲式玉米精密播种机振动特性模型建立与试验). *Transactions of the Chinese Society for Agricultural Machinery*, Vol.45, No.2, pp.88-93. Changchun/China.
34. Zhang, X., Li, C., Tang, Q., Yang, Y., Ma, Y. (2009). Vibration properties of spade punch planter of maize (铲式玉米精密播种机振动特性试验). *Journal of Shenyang Agricultural University*, Vol.40, No.6, pp.732-735. Shenyang/China.
35. Zhao, Z., Li, Y., Chen, J., Xu, L. (2010). Numerical analysis and laboratory testing of seed spacing uniformity performance for vacuum-cylinder precision seeder. *Biosystems Engineering*, Vol.106, No.4, pp.344-351. Zhenjiang/China.
36. Zheng, J., Liao, Y., Qi, T., Liao, Q., Gao, L., Liu, J. (2023). Effect of vibration on performance of pneumatic rapeseed precision metering device (振动对气力式油菜精量排种器性能影响). *Journal of Huazhong Agricultural University*, Vol.42, No.2, pp.233-242. Wuhan/China.

EVALUATION OF THE CORRELATION BETWEEN THE COLOR OF DIFFERENT WHEAT VARIETIES AND WEATHER CONDITIONS USING RGN UAV-BASED IMAGES

ОЦЕНКА НА ЗАВИСИМОСТТА МЕЖДУ ЦВЕТА ПРИ РАЗЛИЧНИ СОРТОВЕ ПШЕНИЦА И МЕТЕОРОЛОГИЧНИТЕ УСЛОВИЯ ИЗПОЛЗВАЙКИ RGN ИЗОБРАЖЕНИЯ БАЗИРАНИ НА UAV

Asparuh I. ATANASOV ¹⁾; Atanas Z. ATANASOV ^{*2)}

¹⁾ Technical University of Varna, / Bulgaria; ORCID 0000-0001-9898-8472

²⁾ University of Ruse "Angel Kanchev", 7017 Ruse, / Bulgaria

Tel: +359 885 497 406; E-mail: aatanasov@uni-ruse.bg

DOI: <https://doi.org/10.35633/inmateh-73-38>

Keywords: precision agriculture, remote sensing, UAV, vegetation indices, NDVI

ABSTRACT

The present work investigates the dependences between weather conditions and the specific characteristics of nine wheat varieties and the reflection of light spectra. The obtained images captured with an unmanned aerial vehicle UAV model DJI Mavic 2 Pro and RGN camera reflect the state of vegetation of wheat varieties depending on environmental factors and the specific morphological features of each variety. The differences are analyzed and presented by variety, highlighting the relationship between the factors through reflected light and the condition of the investigated winter wheat varieties. The study provides valuable information for future research on the influence of meteorological conditions on the accuracy of the results obtained with UAV imaging.

РЕЗЮМЕ

Настоящата работа изследва зависимостите между метеорологичните условия и специфичните особености на девет сорта пшеница и отражението на спектри от светлината. Получените изображения заснети с безпилотен летателен апарат UAV модел DJI Mavic 2 Pro и RGN камера отразяват състоянието на вегетацията на сортовете пшеница зависимост от факторите на околната среда и специфичните морфологични особености на всеки сорт. Анализирани са разликите и е представено по сортове връзката между факторите посредством отразената светлина и състоянието на изследваните сортове зима пшеница. Проучването дава ценна информация при бъдещи изследвания за влиянието на метеорологичните условия върху точността на получените резултати при заснемането с UAV.

INTRODUCTION

Reflective vegetation indices are keys in precision agriculture. The peculiarities of obtaining them significantly influence the correct reading of the received information and subsequent planning of agrotechnical activities. Proving dependencies between different factors is carried out using the methods of mathematical statistics for processing data from various practical and experimental studies. In precision agriculture, the study of the dependences between different dimensions of the environment and parameters of agricultural crops is the key. The process involves monitoring the entire life cycle of crops over an extended period of time. During this period, many of the factors have random values that are difficult to predict.

A basic approach in analysing data is the regression model, which characterizes the dependencies between the obtained data. In the article of Jiang *et al.*, (2020), a platform for remote sensing of unmanned aerial vehicles (UAV) is investigated, which creates a map of the monitored area of the normalized differential vegetation index (NDVI). An assessment of the influence of the parameters of the UAV operation modes on the correctness of the generated data is made. Khabba *et al.*, (2020), proposes a method to determine the pattern when registering the reflected light. He analyses the data obtained during the vegetation of winter wheat grown in semi-arid conditions and the influence of irrigation.

The influence of the process in the processing of chickpeas by means of PFE was made by Angelova *et al.* (2022). The study examines the relationship between 4 factors and 4 parameters and analyses the dependencies.

Through regression analysis (Sellam et al., 2016) establishes a relationship between a set of variables as area under cultivation, annual rainfall and food price index and their effects on rice yield. The study, through regression analysis, assesses environmental factors and their impact on crop yield. By means of multi-factorial analysis, it is determined which factors are important for decision-making. A 10-year sample period from 1990-2000 was examined for environmental factors. Linear regression was applied to establish a relationship between the independent variables and crop yield as the dependent variable. Ganeva-Kiryakova, (2020), uses a methodology to determine the condition of winter rape before and after wintering and to estimate the duration of flowering. The study was aimed to determine the states of culture and was conducted in the Python programming language. The factors: good, average and poor for each parameter, (duration of flowering) are determined by experts. The 10 variables used correspond to Sentinel-2 channels with 10 m and 20 m spatial resolution; all input data that were determined to be abnormal at the 5% significance level were excluded in post-treatments using a regression model for the process under consideration.

A study of the applicability and effectiveness of the methodology was done in Atanasov et al., (2022). It confirms the validity of the obtained vegetation indices from the considered methodology compared with satellite data. Some authors (Feng H. et al., 2022) investigate the performance of RGB imagery and hyperspectral data for monitoring crop growth based on multi-time estimation of the comprehensive growth index. Other authors (Dong T. et al., 2019) explore the potential of vegetation indices for crop leaf area index estimation, with a focus on comparing red-edge reflectance based and the visible reflectance based.

The aim of the study is to determine how meteorological factors and the specificity of wheat varieties affect the accuracy of the data obtained for the recorded sunlight reflected by the crop in the visible and near infrared area.

MATERIALS AND METHODS

1. Study area

The experiment was conducted in the experimental field of the Dobrudja Agricultural Institute in the city of General Toshevo, Bulgaria during the economic year 2021-2022 on a field with coordinates: (43.657536 N, 28.021847 E) in the Dobrudja region, Bulgaria. The geography of the area is a plateau with an average altitude of about 230 m, (Fig. 1.). The climate is temperate, but the winter is harsh because of the incessantly blowing winds. The soils of the area are chernozem.



Fig. 1 - Location of the experimental plot

The seeding plan of the experimental trial field with designated cultivars is shown in Fig. 2. Each variety is sown in beds 1.25 m wide and 20 m long with two repetitions. Each variety is tested with two replicates to ensure the accuracy of the result. Roman numerals indicate the varieties as follows: I – Shibil; II - GT 7-190; III – Enola; IV – Chudomira; V – Fedora; VI – Annapurna; VII - Indje; VIII – Andronia; IX – Avenue.

| A | | B | | C | |
|---|----------|---|-----------|---|----------|
| 1 | Shibil | 1 | Chudomira | 1 | Inje |
| 2 | Shibil | 2 | Chudomira | 2 | Indje |
| 3 | GT 7-190 | 3 | Fedora | 3 | Andronia |
| 4 | GT 7-190 | 4 | Fedora | 4 | Andronia |
| 5 | Enola | 5 | Annapurna | 5 | Avenue |
| 6 | Enola | 6 | Annapurna | 6 | Avenue |

Fig. 2 - Planting plan of the individual varieties of the experiment

2. UAV Images acquisition

In the experiment was used MAPIR Survey3W Camera RGN (Company Peau Productions sub-brand of MAPIR) photosensor type: Sony Exmor R IMX117- 12 MP; photo 4000x3000, lens 41° HFOV, 47mm; external GPS/GHSS ublox UBX-G7020-KT. The camera is mounted on the DJI Mavic 2 Pro UAV shown in Fig. 3. The sensor matrix is a Bayer type. Each photocell converts the light falling on it in the spectrum it detects into an electric charge. The three colours correspond to reflections with different lengths of electromagnetic waves. Each of these colours have a different energy, a different frequency of propagation, which is the main reason they have a different reflection and a different amount of scattering in the atmosphere.



Fig. 2 - DJI Mavic 2 Pro with MAPIR Survey3W camera mounted

3. Data collection and processing

The input factors and their magnitudes on which the reflection from the leaf mass of the different varieties of winter wheat depends are analysed to obtain the dependencies by varieties. The factors considered are those on which the spectral reflectance of light is assumed to strongly depend and would directly change the result of remote spectral sensing. Disturbances (inaccuracies) in obtaining information about agricultural crops strongly depend on a group of factors depending on meteorological nature: E - illumination (lx), CCT - correlated colour temperature (K), Cloudiness (%).

There is a second group of factors related to morphological features of the investigated crops (in the specific case, winter wheat): the wax coating, plant flowers, and physiological signs such as the leaf area, which is determined by the parameter Flag leaf width (mm). The specified groups of factors directly determine the reflectance in the different spectral bands and influence the obtained vegetation indices. The measurement of light characteristics was performed with an HPCS-320 spectrometer, which uses an optical CCD sensor (Hangzhou Hopoo Light&Color Technology Co.Ltd). All measurements were taken during the flight missions.

The most common vegetation index is NDVI, which compares the difference in the reflected red spectrum of light (660 nm) and infrared (850 nm). The camera used for the MAPIR Survey3W-RGN experiment recorded the reflectance in the red – 660 nm, green – 550 nm, and infrared – 850 nm, and this channel was obtained after repositioning the blue. It is 20 nm wide as opposed to the other two which are 10 nm each. The speed of the UAV is much less than that of the diaphragm. By default, in flight with 10 ms⁻¹ shutter speed is set to 1/500 s. These are factors that can be controlled, but they do not affect the results.

The considered factors form a large amount of information regarding the dependencies in obtaining vegetation indices, but in the present study only the most significant ones will be considered. With the set goals of the study, E - lighting (lx), CCT - correlated colour temperature (K), the wax coating were selected, and the investigated parameters were the colour values registered by the camera used.

Table 1 presents the natural data for the factors: lighting, colour temperature and wax deposit (scored: 1 absent, 5 medium, 9 strong) according to the dates in which the studies were made, as well as the digital data for the reflectance of red, green and infrared. Digital colour values were obtained after processing the RGN images with the Pix4D software product [Pix4D, 2024, <https://www.pix4d.com/>]. Due to the equal size of the investigated areas, the colour values are presented as an absolute value of the channel in the image.

Due to the equal size of the investigated areas, the colour values are presented as an absolute value of the channel in the image. On each of the observation dates marked as an experiment, it is a recording of the studied field with 300 separate photos, which are processed until they are compiled into one image with the program product Pix4D and a digital model of the surface is obtained. Then the area of each individual experiment (variety) was marked to determine the differences in reflectance and obtain vegetation indices such as NDVI, SAVI and others. For the presented study period, 3,600 photographs were obtained. Each of them contains information about an area of the experiment.

Table 1

Obtained data for the factors (Xi) and parameters (Yi) of the regression model for 2022

1. Wheat variety - Shibil

| No of trial | 1 | 2 | 3 | 4 | 5 | 6 | 7 | 8 | 9 | 10 | 11 | 12 |
|-----------------|---------------------------|--------------------------|---------------------------|------------------------|-------------------------|-------------------------|-------------------------|-------------------------|-------------------------|--------------------------|--------------------------|-------------------------|
| Date | 26 th of March | 5 th of April | 26 th of April | 3 rd of May | 10 th of May | 17 th of May | 25 th of May | 31 th of May | 7 th of June | 21 th of June | 28 th of June | 5 th of July |
| E - (kix), X1 | 90.39 | 84.82 | 28.59 | 52.96 | 84.83 | 97.30 | 103.61 | 125.96 | 172.73 | 109.11 | 126.82 | 106.71 |
| CCT (K), X2 | 5978 | 6087 | 6802 | 6409 | 6251 | 6089 | 6154 | 6012 | 5903 | 6004 | 6024 | 6036 |
| Wax coating, X3 | 1 | 1 | 1 | 1 | 1 | 1 | 1 | 1 | 1 | 1 | 1 | 1 |
| Red (R) Y1 | 2792.50 | 2932.27 | 1491.33 | 2802.84 | 3161.78 | 4127.28 | 4499.87 | 3860.67 | 3554.31 | 4316.57 | 2051.94 | 4573.80 |
| Green (G) Y2 | 2477.20 | 2465.29 | 1070.29 | 1823.88 | 2306.19 | 3349.07 | 3703.05 | 3098.58 | 2834.01 | 3987.12 | 1678.66 | 4020.48 |
| Nir (NIR) Y3 | 2744.46 | 3698.63 | 2329.50 | 4020.00 | 3649.35 | 4617.35 | 5410.29 | 3924.37 | 4635.60 | 4088.97 | 1574.95 | 3478.66 |

2 Wheat variety - GT 7-190

| | | | | | | | | | | | | |
|-----------------|---------|---------|---------|---------|---------|---------|---------|---------|---------|---------|---------|---------|
| Wax coating, X3 | 3 | 3 | 3 | 3 | 3 | 3 | 3 | 3 | 5 | 5 | 5 | 5 |
| Red (R) Y1 | 2761.01 | 3039.93 | 1763.92 | 3088.77 | 3689.34 | 4378.4 | 4403 | 4443.3 | 3504.84 | 4145.73 | 2281.74 | 4615.98 |
| Green (G) Y2 | 2483.8 | 4132.06 | 1171.52 | 1946.83 | 2620.75 | 3659.46 | 3547.35 | 3492.43 | 2848.83 | 3885.8 | 1826.06 | 4071.97 |
| Nir (NIR) Y3 | 2896.51 | 3961.36 | 3209.7 | 4421.41 | 4952.83 | 5277.89 | 5551.22 | 5649.97 | 4554.46 | 3605.02 | 1710.74 | 3478.33 |

3 Wheat variety -Enola

| | | | | | | | | | | | | |
|-----------------|---------|---------|---------|---------|---------|---------|---------|---------|---------|---------|---------|---------|
| Wax coating, X3 | 1 | 1 | 1 | 1 | 1 | 1 | 1 | 1 | 1 | 3 | 3 | 3 |
| Red (R) Y1 | 1515.96 | 3102.09 | 1449.31 | 2678.34 | 3670.8 | 4374.25 | 4144.62 | 4234.97 | 3278.34 | 3755.66 | 2306.25 | 4138 |
| Green (G) Y2 | 1189.66 | 2695.73 | 1085.7 | 1781.94 | 2645.66 | 3636.42 | 3520.79 | 3253.8 | 2621.14 | 3281.55 | 1866.03 | 3706.34 |
| Nir (NIR) Y3 | 2867.34 | 3965.25 | 2211.6 | 3728.54 | 4728.26 | 5232.11 | 4582.52 | 4789.5 | 4214.2 | 3402.53 | 1757.04 | 3012.23 |

4 Wheat variety - Chudomira

| | | | | | | | | | | | | |
|-----------------|---------|---------|---------|---------|---------|---------|---------|---------|---------|---------|---------|---------|
| Wax coating, X3 | 1 | 1 | 1 | 1 | 1 | 1 | 1 | 1 | 1 | 7 | 7 | 7 |
| Red (R) Y1 | 2607.34 | 3154.05 | 1380.9 | 2863.9 | 3325.65 | 4248 | 4303.42 | 2760.41 | 2590.56 | 4121.9 | 1533.53 | 4916.74 |
| Green (G) Y2 | 2297.16 | 2568.26 | 1021.37 | 1925.34 | 2426.88 | 3378.61 | 3447.15 | 2084.37 | 2052.66 | 3851.35 | 1385.34 | 4388.36 |
| Nir (NIR) Y3 | 3082.32 | 4082.15 | 2382.12 | 3890.49 | 3925.73 | 4957.77 | 5117.74 | 3903.15 | 3171.67 | 3759.33 | 1237.25 | 3757.12 |

5 Wheat variety - Fedora

| | | | | | | | | | | | | |
|-----------------|---------|---------|---------|---------|---------|---------|---------|---------|---------|---------|---------|---------|
| Wax coating, X3 | 1 | 1 | 1 | 1 | 1 | 1 | 1 | 1 | 1 | 1 | 1 | 1 |
| Red (R) Y1 | 2942.46 | 3185.56 | 1576.42 | 2712.21 | 3739.24 | 4578.08 | 4450.51 | 3305.78 | 3239 | 4115.59 | 2020.17 | 4875.29 |
| Green (G) Y2 | 2685.99 | 2786.88 | 1176.5 | 1840.68 | 2799.08 | 3766.5 | 3565.96 | 2478.95 | 2597.79 | 3662.98 | 1696.25 | 4361.33 |
| Nir (NIR) Y3 | 3255.19 | 4171.4 | 2700.81 | 3716.65 | 4961.87 | 5719.2 | 5598.86 | 4502.57 | 4334.1 | 4172.9 | 1628.92 | 3702.58 |

6 Wheat variety - Anapurna

| | | | | | | | | | | | | |
|-----------------|---------|---------|---------|---------|---------|---------|---------|---------|---------|---------|---------|---------|
| Wax coating, X3 | 1 | 1 | 1 | 1 | 1 | 1 | 1 | 1 | 1 | 5 | 5 | 5 |
| Red (R) Y1 | 3054.22 | 3419.77 | 1574.75 | 2445.95 | 3193.59 | 4234.93 | 4270.4 | 3295.17 | 2456.08 | 3620.09 | 2366.41 | 3783.52 |
| Green (G) Y2 | 2891.94 | 3232.62 | 1169.46 | 1736 | 2326.88 | 3458.78 | 3569.54 | 2557.42 | 1925.47 | 3305.18 | 1915.44 | 3366.82 |
| Nir (NIR) Y3 | 3202.97 | 4216.59 | 2625.54 | 3756.46 | 3726.4 | 5028.16 | 4959.43 | 4372 | 2948.09 | 3650.47 | 1720.79 | 2637.01 |

7 Wheat variety - Indje

| | | | | | | | | | | | | |
|-----------------|---------|---------|---------|---------|---------|---------|---------|---------|---------|---------|---------|---------|
| Wax coating, X3 | 1 | 1 | 1 | 1 | 1 | 1 | 1 | 1 | 1 | 3 | 3 | 3 |
| Red (R) Y1 | 2462.99 | 2988.33 | 1536.22 | 2606.83 | 2776.2 | 4300.49 | 4076.33 | 2178.02 | 2300.37 | 3952.12 | 1552.48 | 4742.07 |
| Green (G) Y2 | 2241.82 | 2451.72 | 1054.71 | 1714.4 | 2076.13 | 3357.41 | 3086.98 | 1629.74 | 1769.63 | 3469.46 | 1289 | 4181.02 |
| Nir (NIR) Y3 | 2951.68 | 3963.24 | 2779 | 3563.4 | 2923.42 | 5204.84 | 4843.25 | 2971.87 | 2837.72 | 3353.73 | 1197.11 | 3610.3 |

8 Wheat variety - Andronia

| | | | | | | | | | | | | |
|-----------------|---------|---------|---------|---------|---------|---------|---------|---------|---------|---------|---------|---------|
| Wax coating, X3 | 1 | 1 | 1 | 1 | 1 | 1 | 1 | 1 | 1 | 7 | 7 | 7 |
| Red (R) Y1 | 2842.37 | 2896.55 | 1562.37 | 2914.43 | 3392.21 | 4524.32 | 4333.98 | 3581.02 | 3198.75 | 4196.9 | 1566.21 | 4480.42 |
| Green (G) Y2 | 2556.9 | 2478.46 | 1042.71 | 1792.37 | 2268.08 | 3841.41 | 3571.87 | 2674.91 | 2515.28 | 3800.43 | 1328.19 | 3998.89 |
| Nir (NIR) Y3 | 2919.83 | 3810.36 | 2891.69 | 4141.21 | 4516.21 | 5651.67 | 5189.25 | 4635.68 | 4341.62 | 3969 | 1210.34 | 3260.39 |

9 Wheat variety - Avenu

| | | | | | | | | | | | | |
|------------------------|---------|---------|---------|---------|---------|---------|---------|---------|---------|---------|---------|---------|
| Wax coating, X3 | 1 | 1 | 1 | 1 | 1 | 1 | 1 | 1 | 1 | 9 | 9 | 9 |
| Red (R) Y1 | 2751.58 | 3069.53 | 1451.99 | 2589.26 | 3363.95 | 4313.13 | 3498.1 | 3748.19 | 2611.72 | 3996.54 | 1986.68 | 4014.65 |
| Green (G) Y2 | 2458.5 | 2666.62 | 1037.82 | 1613.94 | 2403.67 | 3628.55 | 2608.83 | 3113.77 | 2122.4 | 3712.48 | 1614.84 | 3520.77 |
| Nir (NIR) Y3 | 2876.07 | 3850.61 | 2493.57 | 3657.12 | 4202.2 | 5067.37 | 3825.47 | 4218.64 | 3269.77 | 3791.92 | 1553.01 | 2849.27 |

The two factors X_1 and X_2 are the same for the entire experiment, therefore they will not be presented with numerical values in the following tables. Each of the varieties will be considered separately as a regression model.

The optimal values of the parameters $Y_j, j = 1,2,3$ and the description of the echo surfaces for a larger area of the factor space require a regression model more complex than the linear one. This corresponds to a full factorial experiment – PFE of type 2^m and its derivatives. In this case, describing the optimum can be done with a polynomial of the second degree, (Mitkov A., 2011). The polynomial chosen for the experiment is of the form:

$$\hat{Y}_j = b_0 + \sum_{i=1}^m b_i \hat{x}_i + \sum_{\substack{i,k=1 \\ i < k}}^m b_{i,k} \hat{x}_i \hat{x}_k + \sum_{i=1}^m b_{ii} \hat{x}_i^2 \tag{1}$$

where: \hat{Y}_j is estimation of parameter Y_j ; b_0 is a coefficient equal to 1; b_i coefficients of the regression equation; i is the index of factors 1 to 3; \hat{x}_i coded values of the factors from Table 3; m – number of factors.

Finding the values for the quantities in the particular case is in a second-order polynomial. In it, the factors vary on three levels or more. Table 2 shows the variation and coding of the five-level factors.

Table 2

Levels of variation and factor coding of the regression model

| Levels | E - (κlx), X1 | | CCT (K), X2 | | Wax coating, X3 | |
|-------------------------|----------------|--------------|----------------|--------------|-----------------|--------------|
| | Nature. values | Code. values | Nature. values | Code. values | Nature. values | Code. values |
| Low $X_{0i+\alpha_i}$ | 28.59 | +1.682 | 5903 | +1.682 | 1 | +1.682 |
| X_{0i+J} | 65.63 | +1 | 6231.125 | +1 | 3 | +1 |
| Average X_{0j} | 98.65 | 0 | 6145.75 | 0 | 5 | 0 |
| X_{0i-J} | 135.69 | -1 | 6473.875 | -1 | 7 | -1 |
| Above $X_{0i-\alpha_i}$ | 172.73 | -1.682 | 6802 | -1.682 | 9 | -1.682 |
| A step J | 37.04 | - | 325.125 | - | 2 | - |

The area of the optimum is first described by a first-order plan, then the centre of the PFE or a fractional replica of it is chosen as the centre of the new plan. More appropriately selected key points are added to the plan. A rotatable central-composition plan is obtained - RCKP, (Mitkov A., 2011; Andonova-Vakarelska T., 2017). Added points lie on the coordinate axes at a distance α from the center of the plan.

Table 3

Rotatable central-composite plan in three factors

| | | | | | | | | | | | | |
|------------|---------|---------|---------|---------|---------|---------|---------|---------|---------|---------|---------|---------|
| X1 | 0.000 | 0.000 | 1.682 | 1.000 | 0.000 | 0.000 | 0.000 | -1.000 | -1.682 | 0.000 | -1.000 | 0.000 |
| X2 | 1.682 | 1.682 | -1.682 | -1.000 | 0.000 | 1.682 | 0.000 | 1.682 | 1.682 | 1.682 | 1.682 | 1.682 |
| X3 | 1.000 | 1.000 | 1.000 | 1.000 | 1.000 | 1.000 | 1.000 | 1.000 | 1.000 | 1.000 | 1.000 | 1.000 |
| X12 | 0.000 | 0.000 | -2.829 | -1.000 | 0.000 | 0.000 | 0.000 | -1.682 | -2.829 | 0.000 | -1.682 | 0.000 |
| X13 | 0.000 | 0.000 | 1.682 | 1.000 | 0.000 | 0.000 | 0.000 | -1.000 | -1.682 | 0.000 | -1.000 | 0.000 |
| X23 | 1.682 | 1.682 | -1.682 | -1.000 | 0.000 | 1.682 | 0.000 | 1.682 | 1.682 | 1.682 | 1.682 | 1.682 |
| X11 | 0.000 | 0.000 | 3.364 | 2.000 | 0.000 | 0.000 | 0.000 | -2.000 | -3.364 | 0.000 | -2.000 | 0.000 |
| X22 | 3.364 | 3.364 | -3.364 | -2.000 | 0.000 | 3.364 | 0.000 | 3.364 | 3.364 | 3.364 | 3.364 | 3.364 |
| X33 | 2.000 | 2.000 | 2.000 | 2.000 | 2.000 | 2.000 | 2.000 | 2.000 | 2.000 | 2.000 | 2.000 | 2.000 |
| Y1 | 2792.50 | 2932.27 | 1491.33 | 2802.84 | 3161.78 | 4127.28 | 4499.87 | 3860.67 | 3554.31 | 4316.57 | 2051.94 | 4573.80 |
| Y2 | 2477.20 | 2465.29 | 1070.29 | 1823.88 | 2306.19 | 3349.07 | 3703.05 | 3098.58 | 2834.01 | 3987.12 | 1678.66 | 4020.48 |
| Y3 | 2744.46 | 3698.63 | 2329.50 | 4020.00 | 3649.35 | 4617.35 | 5410.29 | 3924.37 | 4635.60 | 4088.97 | 1574.95 | 3478.66 |

This is how the star points are obtained, α is a star arm. The value of $\alpha=1.682$ proposed by Mitkov T., (2011), against the number of factors $m=3$ according to the formula $\alpha = 2^{\frac{m}{4}}$. A symmetric plane is obtained, which is orthogonal to the central composition, as shown in Table 3.

The points of the rotatable plane are arranged so that when the coordinate axes are rotated, the dispersion distribution does not change. As a result of a proper choice of the number of replicates for observations in the centre of the plan, an almost uniform distribution of variance can be achieved throughout the area. This area does not depend on the distance to the centre of the plan. Such planning is called uniform-planning.

Statistical analysis was performed with the statistical processing software IBM SPSS Statistics (*www.ibm.com, 2024*) and quadratic model coefficients were determined.

RESULTS

The results of statistical processing are given in Table 4. The obtained values for the dependences between Y1 and the input parameters are presented in table 4. In table 5 the dependence between the input parameters and Y2 is presented and table 6 with the parameter Y3, which for variety 1 remains unity throughout the period.

Table 4

Results of regression analysis of factors against Y1 in variety 1
Model Summary

| Model | R | R Square | Adjusted R Square | Std. Error of the Estimate |
|-------|--------------------|----------|-------------------|----------------------------|
| 1 | 0.675 ^a | 0.456 | 0.252 | 849.64183 |

a. Predictors: (Constant), X22, X12, X11

ANOVA^a

| Model | | Sum of Squares | df | Mean Square | F | Sig. |
|-------|------------|----------------|----|-------------|-------|--------------------|
| 1 | Regression | 4845333.897 | 3 | 1615111.299 | 2.237 | 0.161 ^b |
| | Residual | 5775129.965 | 8 | 721891.246 | | |
| | Total | 10620463.862 | 11 | | | |

a. Dependent Variable: Y1

b. Predictors: (Constant), X22, X12, X11

Table 5

Results of regression analysis of factors against Y2 in variety 1
Model Summary

| Model | R | R Square | Adjusted R Square | Std. Error of the Estimate |
|-------|--------------------|----------|-------------------|----------------------------|
| 1 | 0.708 ^a | 0.501 | 0.313 | 778.73592 |

a. Predictors: (Constant), X22, X12, X11

ANOVA^a

| Model | | Sum of Squares | df | Mean Square | F | Sig. |
|-------|------------|----------------|----|-------------|-------|--------------------|
| 1 | Regression | 4865354.853 | 3 | 1621784.951 | 2.674 | 0.118 ^b |
| | Residual | 4851437.028 | 8 | 606429.628 | | |
| | Total | 9716791.880 | 11 | | | |

a. Dependent Variable: Y2

b. Predictors: (Constant), X22, X12, X11

Table 6

Results of regression analysis of factors against Y3 in variety 1
Model Summary

| Model | R | R Square | Adjusted R Square | Std. Error of the Estimate |
|-------|--------------------|----------|-------------------|----------------------------|
| 1 | 0.519 ^a | 0.270 | -0.004 | 1059.61460 |

a. Predictors: (Constant), X22, X12, X11

ANOVA^a

| Model | | Sum of Squares | df | Mean Square | F | Sig. |
|-------|------------|----------------|----|-------------|-------|--------------------|
| 1 | Regression | 3318141.040 | 3 | 1106047.013 | 0.985 | 0.447 ^b |
| | Residual | 8982264.862 | 8 | 1122783.108 | | |
| | Total | 12300405.902 | 11 | | | |

a. Dependent Variable: Y3

b. Predictors: (Constant), X22, X12, X11

The obtained high Fisher's criterion $F = 0.985$ for a significance level of 0.05 confirms that the null hypothesis is rejected and the criterion is significant. The coefficient of determination R^2 for factors Y_1 and Y_2 is about 0.5, from which it follows that 50% of the change in parameters $Y_j, j = 1,2,3$ are included in the model. For factor Y_3 , the coefficient is 0.27, which is expected for the specific case. In cultivar Shibil, the wax coating remained low throughout the study period.

Evaluation of the significance of the factors compared to the obtained coefficients according to Student's criterion, for a significance level $\alpha = 0,05$, that is: $Y = 1, \alpha = 0.95$, with the number of degrees of freedom $k = n - 1 = 11$. Compared with the calculated coefficients B, it is seen which are the significant factors. Table 7 presents the significant coefficients with their values.

Table 7

| Significance of coefficients | | | |
|------------------------------|------------|----------|--------|
| Model | | B | t |
| Dependent Variable: Y1 | (Constant) | 3829.247 | 6.893 |
| | X12 | 542.373 | 0.629 |
| | X11 | -281.983 | -0.507 |
| | X22 | -42.422 | -0.107 |
| Dependent Variable: Y2 | (Constant) | 2929.690 | 5.754 |
| | X12 | 435.264 | 1.676 |
| | X11 | -138.482 | -0.559 |
| | X22 | 80.879 | 0.443 |
| Dependent Variable: Y3 | (Constant) | 4624.698 | 6.675 |
| | X12 | 562.744 | 1.593 |
| | X11 | -475.646 | -1.411 |
| | X22 | -307.951 | -1.239 |

Fig. 4 shows the maximum values of the factors compared to each other for Shibil variety. The wax coating factor for the variety throughout the period is constant. A maximum of the values is seen where the factors X_1 and X_2 are involved.

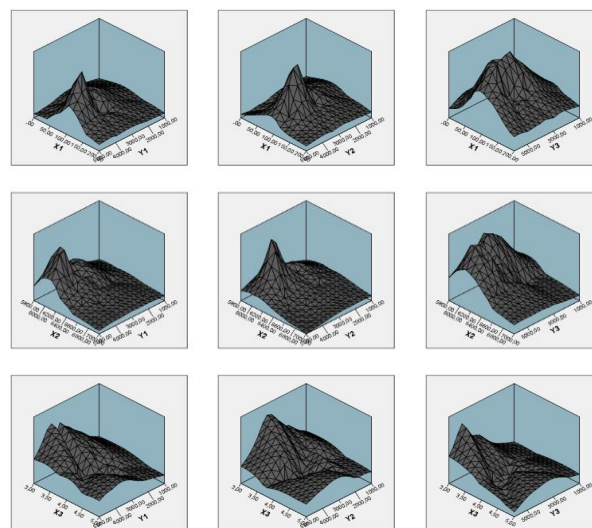
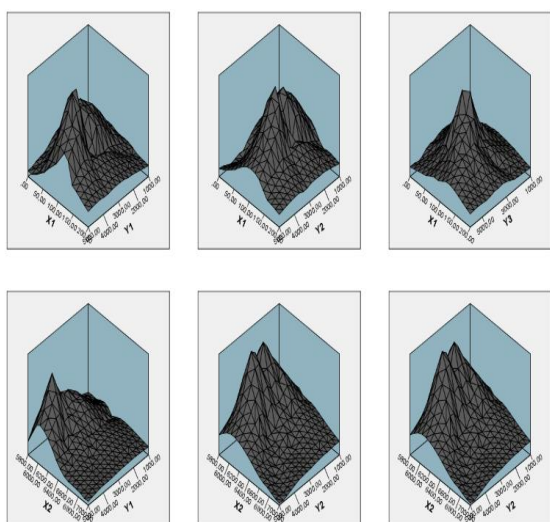


Fig. 4 - Dependencies of the factors in Shibil variety; Fig. 5 - Dependencies of the factors in variety GT 7-190

The results obtained for variety GT 7-190 are presented in Fig. 5. In addition to the strong dependence on X_2 colour temperature and the obtained values, the strong dependence on the wax coating X_3 is also visible. For the Enola variety, the results have similar trends to the GT 7-190 variety.

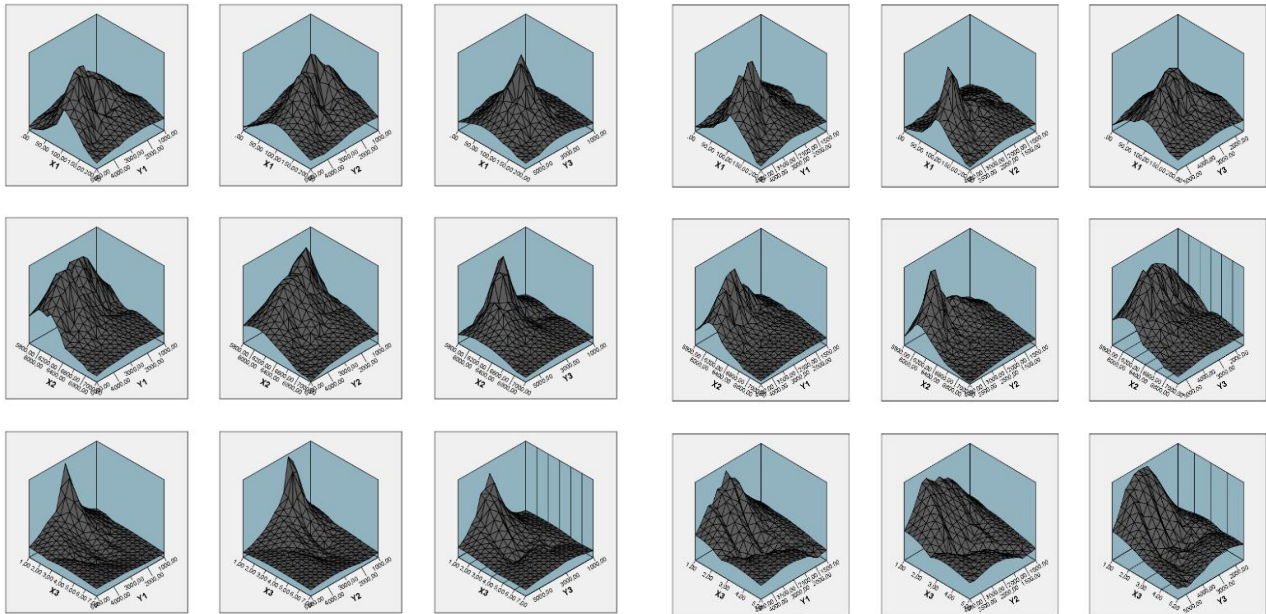


Fig. 6 - Dependencies of the factors in the Chudomira variety

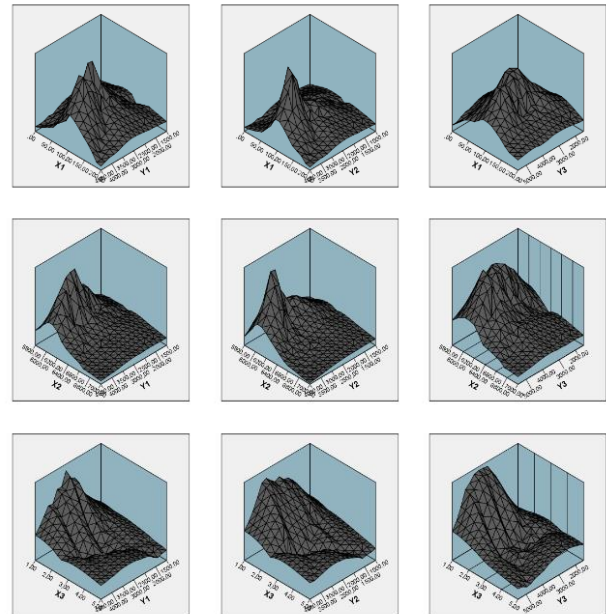


Fig. 7 - Dependencies of factors in variety Annapurna

In the case of the Chudomira variety (Fig. 7), the general tendency of the dependencies is similar to the previous varieties, but there are sharper dependencies. A very strong dependence to the reflection in the infrared range (Y3) is observed and a strong influence of the wax coating (X3), which in the variety increases significantly as the maturity stage approaches.

The Fedora variety, like Shibil, retains a constant value of the wax coating (X3), which is almost absent. This is the prerequisite for the two varieties to have similar trends. In the visible spectrum of the reflection, the Fedora variety in the conducted experiment has a lighter colour than Shibil. But the reflection in the infrared spectrum (Y3) is similar.

Factor dependencies for Annapurna cultivar are shown in Fig. 7. In this variety, it is characteristic that the X3 factor (wax coating) is absent at the beginning of development and then increases to average values. This can also be seen from the graph where there is a strong dependence. In the Inje variety, there is a close relationship, although the X3 wax coating is low, but the trend of change is similar to that of Annapurna.

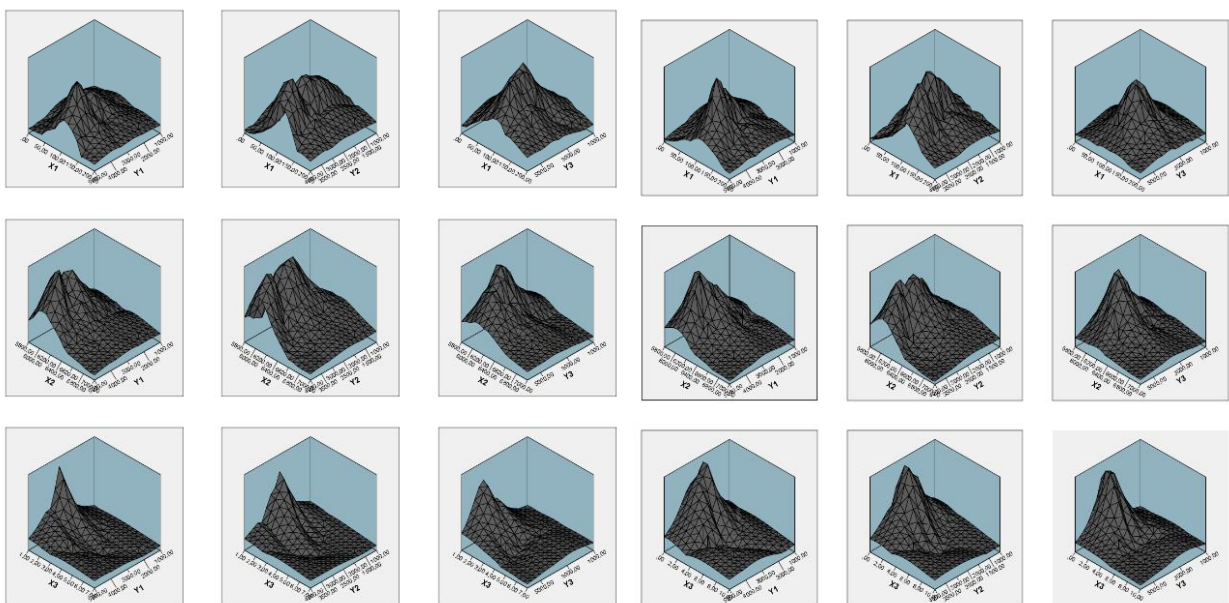


Fig. 8 - Dependencies of the factors in Andronia variety

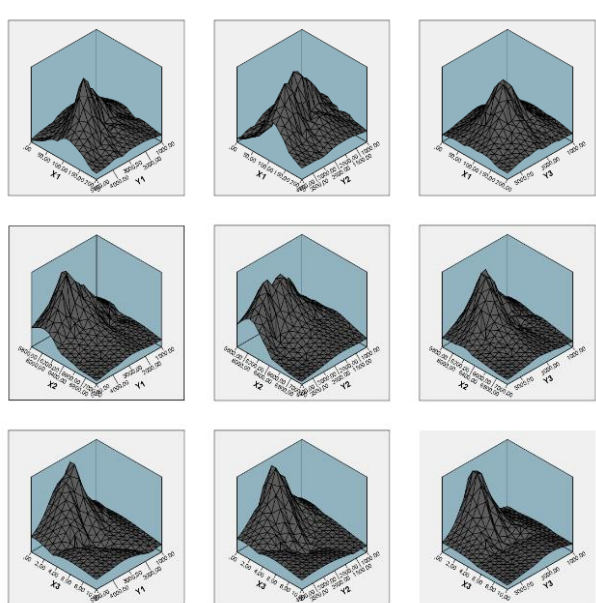


Fig. 9 - Dependencies of the factors in the Avenue variety

The varieties Andronia (Fig. 8) and Avenue (Fig. 9) do not have a wax coating in the initial stage of their development. In the grain formation stage, it increases to a medium value in the first and a high value in the second. In the visible spectrum, Andronia is dark green and Avenue is green in colour. These features are visible on the graphs reflecting the dependences of the factors between the two varieties.

The overall analysis of the dependencies shows a very strong dependence of the factor X3 (wax coating), which actually changes the amount of reflected light in all spectra. This greatly changes the reflective vegetation indices in remote spectral analysis. Factors X1 and X2 influence to a lesser extent. The influence of the X3 factor on the resulting NDVI reflectance index is shown in Table 8.

Table 8

Results of linear regression analysis for the dependence of X3 on NDVI

| <i>Regression Statistics</i> | |
|------------------------------|-------------|
| Multiple R | 0.844504113 |
| R Square | 0.713187197 |
| Adjusted R Square | -1.2 |
| Standard Error | 2.032265819 |
| Observations | 1 |

| ANOVA | | | | |
|-------------------|-----------|-----------|-----------|-----------|
| | <i>df</i> | <i>SS</i> | <i>MS</i> | <i>F</i> |
| Regression | 12 | 102.69896 | 8.558246 | 24.865947 |
| Residual | 10 | 41.301044 | 4.130104 | |
| Total | 22 | 144 | | |

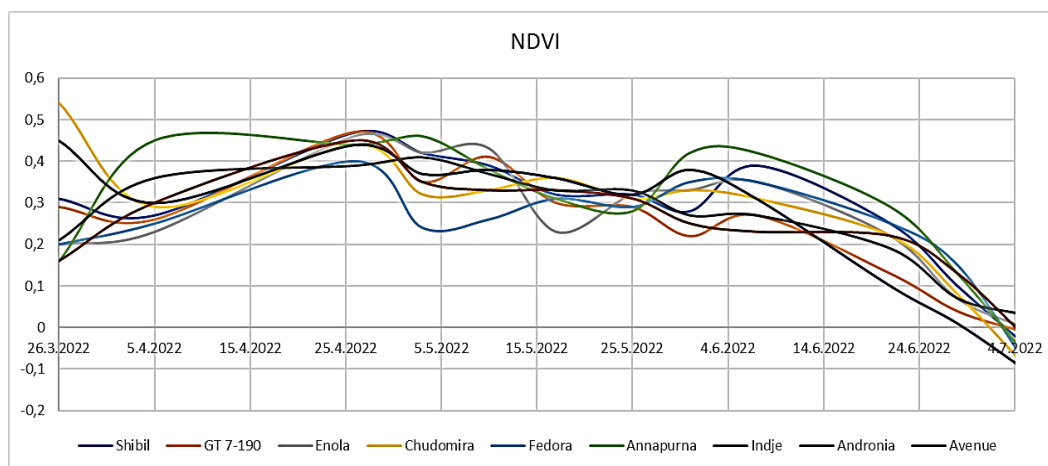


Fig. 10 - Obtained tendencies for changes in NDVI by varieties for the observed period

Fig. 10 summarizes the trends of changes in the reflective vegetation index NDVI by varieties for the considered period. The result was obtained by the program product Pix4D after processing the photographic material and marking the area with the corresponding variety. A calibration image for solar radiation intensity is introduced into the program. Which largely reduces factors X1 and X2 but is strongly influenced by X3. The wax coating directly changes the degree of reflection.

CONCLUSIONS

An active-passive experiment was conducted to investigate the correctness of obtaining reflective vegetation indices. A regression model was obtained that provides information on the influence of the three factors: E - lighting (lx), CCT - correlated colour temperature (K) and Wax coating (quantitative assessment) on the parameters of the model, which represent the digital values of the three colours: Y1 - red, Y2 - green and Y3 - near infrared.

The strong dependence of the parameters on the obtained reflective vegetation indices has been proven. The most significant influence is the factor wax coating, which changes the texture of the leaf mass, which changes the reflection in all spectra. It was found that as its value increases, the NDVI index does not reach large numerical values.

This gives us reason to reach the conclusion that: in agricultural crops (varieties) which during their growing season accumulate a wax coating, it is normal to lower the value of the reflective vegetation indices without it being related to crop stress. Differentiation of the dependencies between the factors and the development of trends in the change of the vegetation indices in the different varieties is the key for the correct interpretation of the data and the planning of the subsequent agrotechnical measures. The survey provides indispensable information for the breeding activity and aims to create a database of NDVI variation. It is planned to continue the research, with the main goal being the recognition of wheat varieties using photogrammetry data.

ACKNOWLEDGEMENT

This study is financed by the European Union-NextGenerationEU, through the National Recovery and Resilience Plan of the Republic of Bulgaria, project № BG-RRP-2.013-0001-C01.

REFERENCES

- [1] Andonova-Vakarelska, T. (2017). Approbation of the methodology for experimental research and processing of results in automated production, XXVI ISTC "ADP-2017", *Collection of reports*, pp. 417-422, (in Bulgarian).
- [2] Angelova, T., Goranova, Z., Petrova, T., Ruskova, M., Penov, N., Simitchiev, A., Zhonisova, M. (2022). Influence of some process parameters on the water solubility index of chickpea extrudates, *Journal of Mountain Agriculture on the Balkans (JMAB)*, Vol 25, Issue 4, pp. 335-348, (in Bulgarian).
- [3] Atanasov, A., Bankova, A., Zhecheva, G. (2023^a). Observation of the vegetation processes of agricultural crops using small unmanned aerial vehicles in Dobrudja region. *Bulgarian Journal of Agricultural Science*, 29 (No 1), pp.176–181. <https://agrojournal.org/29/01-21.html>
- [4] Atanasov, A., Bankova, A., Zhecheva, G. (2023^b). Result Processing Methodology for the Vegetation Processes Remote Sensing by a Small Unmanned Aerial Vehicle, *Bulgarian Journal of Agricultural Science*, 29 (No 3), pp. 564–569. <https://agrojournal.org/29/03-22.html>
- [5] Atanasov, A., Mihova, G., Mihaylov, R. (2022). Applicability and efficiency of remote sensing of agricultural areas. *Bulgarian Journal of Agricultural Science*, 28 (5), pp. 933–943, ISSN 1310-0351. <http://www.agrojournal.org/28/05-21.pdf>
- [6] Dong, T., Liu, J., Shang, J., Qian, B., Ma, B., Kovacs, J.M., Walters, D., Jiao, X., Geng, X., Shi, Y. (2019). Assessment of red-edge vegetation indices for crop leaf area index estimation. *Remote Sens. Environ.*, 222, pp. 133–143. <https://doi.org/10.1016/j.rse.2018.12.032>
- [7] Feng, H., Tao, H., Li, Z., Yang, G., Zhao, C. (2022). Comparison of UAV RGB Imagery and Hyperspectral Remote-Sensing Data for Monitoring Winter Wheat Growth. *Remote Sens.*, 14, p.3811. <https://doi.org/10.3390/rs14153811>
- [8] Ganeva-Kiryakova, DG. (2020). *Assessment of the condition of winter rapeseed crops in northeastern Bulgaria by satellite and terrestrial data*, [Doctoral dissertation, Field of higher education: 4. "Natural science"], (in Bulgarian).
- [9] Jiang, R., Wang, P., Xu, Y., Zhou, Z., Luo, X., Lan, Y., Zhao, G., Sanchez-Azofeifa, A., & Laakso, K. (2020). Assessing the Operation Parameters of a Low-altitude UAV for the Collection of NDVI Values Over a Paddy Rice Field. *Remote Sensing*, 12(11), p.1850. <https://doi.org/10.3390/rs12111850>
- [10] Khabba, S., Er-Raki, S., Toumi, J., Ezzahar, J., Ait Hssaine, B., Le Page, M., & Chehbouni, A. (2020). A Simple Light-Use-Efficiency Model to Estimate Wheat Yield in the Semi-Arid Areas. *Agronomy*, 10(10), p.1524.
- [11] Kunze, L., Amaral, T., Mauro Pereira Moraes, L., José Monteiro Oliveira, J., Gomes Bispo Junior, A., Parros Machado de Sousa, E. and Cordeiro, R. (2018). Classification Analysis of NDVI Time Series in Metric Spaces for Sugarcane Identification. *In Proceedings of the 20th International Conference on Enterprise Information Systems (ICEIS 2018)*, pp. 162-169. DOI: [10.5220/0006709401620169](https://doi.org/10.5220/0006709401620169)
- [12] Mitkov, A., (2011), Theory of Experiment, *Danube Press*, Ruse, (in Bulgarian);
- [13] Sellam, V., Poovammal, E. (2016). Prediction of Crop Yield using Regression Analysis, *Indian Journal of Science and Technology*, Vol 9(38), DOI: [10.17485/ijst/2016/v9i38/91714](https://doi.org/10.17485/ijst/2016/v9i38/91714)
- [14] Stefanov, N. (2012). Application of the factorial experiment for determining the efficiency of a water turbine, *Scientific papers of the University of Ruse*, Volume 51, Series, pp. 138-142, (in Bulgarian);

NON-DESTRUCTIVE PREDICTION OF OIL AND FREE FATTY ACID OF OIL PALM FRUITLETS USING NEAR-INFRARED SPECTROSCOPY AND HYBRID CALIBRATION METHOD

PREDIKSI KANDUNGAN MINYAK DAN ASAM LEMAK BEBAS BUAH SAWIT SECARA NON-DESTRUKTIF MENGGUNAKAN NEAR-INFRARED SPECTROSCOPY DAN METODE KALIBRASI HYBRID

I Wayan BUDIASTRA^{*1,2}, Sutrisno MARJAN¹, Nissa ADIARIFIA¹, Inna NOVIANTY³, Yunisa Tri SUCI¹

¹IPB University, Department of Mechanical and Biosystem Engineering / Indonesia;

²IPB University, Centre for Research on Engineering Application in Tropical Agriculture / Indonesia;

³IPB University, Study Program of Computer Engineering / Indonesia;

Tel: +622518623026; E-mail: wbudiastra@apps.ipb.ac.id

DOI: <https://doi.org/10.35633/inmateh-73-39>

Keywords: free fatty acid, hybrid calibration, NIR, oil content, oil palm fruitlets

ABSTRACT

The study used near-infrared reflectance spectroscopy and hybrid calibration methods to predict oil and free fatty acid content of oil palm fruitlets non-destructively. The reflectance and chemical content of oil palm fruitlets were measured and the calibration between near infrared spectra and chemical content was performed using hybrid calibration methods. The developed hybrid calibration model was validated to predict oil and free fatty acid of other oil palm fruitlets. The best models to predict oil and free fatty acid of oil palm fruitlets respectively were the hybrid model of Partial Least Square-Artificial Neural Network with 25 factor components ($R^2 = 0.96$; $SEP = 2.21\%$, $RPD = 4.79$) and 19 factor components ($R^2 = 0.96$; $SEP = 0.25\%$, $RPD = 4.24$) using Savitzky-Golay first derivative spectra pre-treatment.

ABSTRAK

Penelitian ini menggunakan spektroskopi inframerah dekat dan metode kalibrasi hibrid untuk memprediksi kandungan minyak dan asam lemak bebas buah sawit secara nondestruktif. Reflektan dan kandungan kimia buah sawit diukur dan kalibrasi antara spektra inframerah dekat dan kandungan kimia dilakukan menggunakan metode kalibrasi hibrid. Model kalibrasi hibrid yang dibangun divalidasi untuk memprediksi kandungan minyak dan asam lemak bebas buah sawit lainnya. Model terbaik untuk memprediksi masing masing kandungan minyak dan asam lemak bebas buah sawit adalah model hibrid Partial Least Square-Artificial Neural Network dengan input 25 factor component ($R^2 = 0,96$; $SEP = 2,21\%$, $RPD = 4,79$) dan 19 factor component ($R^2 = 0,96$, $SEP = 0,25\%$, $RPD = 4,24$) menggunakan pretreatment spektra turunan pertama Savitzky-Golay.

INTRODUCTION

Palm oil is one of the most important commodities in the world for vegetable oil production (Murphy et al., 2021). Oil and free fatty acid (FFA) content are the important criteria for quality of oil palm fruitlets (OPF) or crude palm oil (CPO). According to quality standard for CPO in Indonesian Standard of SNI 01-2901-2006, the maximum allowable FFA content in CPO is 5% (BSN, 2006). When the FFA content exceeds this limit, it can cause rancidity and damage to the oil, reducing its shelf life (Akbar et al., 2022).

Presently, determination of oil and free fatty acid content of OPF is carried out destructively in the chemical laboratory that require a long time and complicated procedures. Several non-destructive technologies for assessing the oil and free fatty acid of OPF have been explored, including those based on electrical properties (Sinambela et al., 2020; Mellyana et al., 2024), image analysis (Makky, 2016), and near-infrared spectroscopy (NIRS) (Makky and Soni, 2014; Iqbal, 2015; Novianty et al., 2020, Novianty et al., 2022). The advantages of implementing NIR technology in agriculture include rapid response times, competitive costs, and being non-destructive (Blanco and Villarroya, 2002). Makky and Soni, (2014), predicted the FFA content of OPF using artificial neural network (ANN) calibration methods with a VIS-NIR series spectrometer.

¹ I Wayan BUDIASTRA, Assoc.Prof. Dr.Agr.Eng; Sutrisno MARJAN, Prof.Dr.Agr.Eng; Nissa ADIARIFIA, MS Agr.Eng; Inna NOVIANTY, Dr.Agric. Eng; Yunisa Tri SUCI, PhD.Stud.Agr. Eng

Iqbal *et al.*, (2018), developed a predictive model for the FFA content of OPF using absorbance in the wavelengths of 700-2500 nm from NIRFlex N-500 spectrometer and Partial Least Square Regression (PLSR) calibration, but the result was not satisfied. The better results of NIR method in predicting oil content of OPF were obtained using absorbance in the wavelengths of 1000-1500 nm from NIRFlex N-500 spectrometer and using Partial Least Square (PLS) calibration (Novianty *et al.*, 2020) and empirical mode decomposition calibration method (Novianty *et al.*, 2022).

Recently, a hybrid method combining Partial Least Square-Artificial Neural Network (PLS-ANN) is studied as an alternative prediction model in many fields, including near infrared spectroscopy. Idrus and Kim, (2019), successfully applied PLS-ANN in predicting blood haemoglobin using near-infrared spectrum. PLS-ANN showed a better quality compared to PLS in terms of coefficient of determination and mean square error value. A similar result is also shown by Yu *et al.*, (2018), in the prediction of consumer liking scores of ready-to-drink green tea beverages and Song *et al.*, (2014), for inversion of inland water chlorophyll-a using PLS-ANN. Therefore, this research aims to assess hybrid calibration method and NIR spectroscopy to predict oil and FFA content in OPF non-destructively.

MATERIALS AND METHODS

Sample Preparation and NIR Measurement

About 396 samples of OPF (*Elaeis guineensis* Jacq. Var. tenera) were harvested from Cikabayan Farm, IPB University. The samples consisted of 10 groups of maturity age (number months from full bloom) namely 3 months, 4 months, 4 months 1 week, 4 months 2 weeks, 4 months 3 weeks, 5 months, 5 months 1 week, 5 months 2 weeks, 5 months 3 weeks, and 6 months. The identification of sample age was established by considering the point at which OPF undergo a significant change in oil content, which typically occurs within 4 to 6 months. (Novianty *et al.*, 2020, Akbar *et al.*, 2022). NIR spectrum data acquisition was carried out using the NIRFlex N-500 spectrometer (BUCHI Labortechnik AG, Switzerland) equipped with fibre optic solid by shooting the gun of the fibre optic solid to the sample in the wavelength range of 1000-1500 nm with a 0.4 nm interval, a scan speed of 3 scans/s and the ambient temperature around 22 – 25 °C. Before NIR measurement, the spectrometer was calibrated by using a standard reference material with known characteristics. The selection of 1000-1500 nm wavelength was based on the previous research results (Novianty *et al.*, 2120, Novianty *et al.*, 2022) that showed more accurate prediction in determining chemical content of OPF. The light energy reflected by the OPF samples was captured by the detector as reflectance data or spectrum data, which was then recorded by the instrument.

Chemical Content Measurement

Oil content of OPF samples was determined using Soxhlet extraction method (AOAC, 2000) as described in Novianty *et al.*, (2020). The determination of free fatty acid content in the OPF is using titration method according to AOAC 940.28 procedures (AOAC, 2003; Irfan *et al.*, 2023).

NIR Spectra Pre-treatments

Reflectance spectra was transformed to absorbance and some NIR spectra pre-treatments were carried out in order to reduce noise, baseline shift, and enhance peak or variation of spectra namely the first derivative Savitzky-Golay pre-treatment (SG1), normalization (N01), and standard normal variate (SNV). The spectra pre-treatments improved the accuracy of prediction by NIR spectroscopy (Budiastra *et al.*, 2020).

The Development of Calibration Model

A hybrid calibration method that combined multivariate analysis and artificial neural network (PLS-ANN, PCA-ANN) and a single multivariate calibration of PCR and PLSR were applied to develop calibration between spectra data and chemical content of OPF. PCR is suitable for large datasets (NIR spectra) (Perera *et al.*, 2021) and produces principal components (PC) as representations of new uncorrelated variables resulting from the transformation (Costantini *et al.*, 2024). Meanwhile, PLS extracts predictors for the analysis of dependent and independent variables (Liu *et al.*, 2022) and generates factor components (FC) as representations of new data related to the original data (NIR spectra). ANN is a tool for modelling non-linear statistical data where complex relationships between various inputs (NIR spectra) and outputs (chemical data) are modelled for pattern recognition (Hamdani *et al.*, 2023).

PCR and PLSR calibration were carried out to obtain some numbers of PC and FC and then correlated with chemical data using software the Unscrambler X. Meanwhile, hybrid models are a combination of multivariate analysis of PCA or PLS and Artificial Neural Network model. In hybrid model (PCA-ANN and PLS-ANN), some numbers of PC extracted from PCA and FC from PLS were input to ANN model (Figure 1).

Hidden layer that was used in this study consisted of 1 (one) layer with 2 neuron per layer. The output layer represented the oil or FFA content that was predicted by the hybrid model. Hybrid model utilized a feed-forward neural network trained by a back propagation algorithm (multi-layer perceptron) using software Rapid Miner.

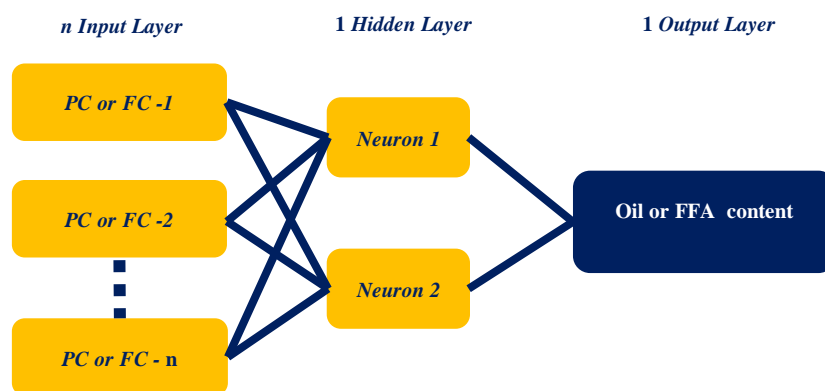


Fig. 1 - Hybrid calibration model (PCA-ANN, PLS-ANN)

Model Evaluation

The statistical parameters used to evaluate calibration and prediction models include the coefficient of determination (R^2), standard error of calibration (SEC), standard error of prediction (SEP), coefficient of variation (CV), residual predictive deviation (RPD), and consistency. A good model's validity can be assessed based on the following statistical parameters, such as R^2 value ≈ 1 , $SEP \approx SEC \approx 0$, $RPD \geq 2$, consistency values within the range of 80-110%, and $CV < 10\%$ (Munawar et al., 2019; Palou et al., 2023).

RESULTS

NIR spectra of oil palm fruitlets

Fig. 2(A) illustrates the original absorbance spectra obtained from NIRS measurements on oil palm fruitlets. There are some variations in absorbance spectra of ten maturities of OPF, indicating variation in its chemical content. The spectra peak at wavelengths of 1200 and 1450 nm indicates the water absorption. The water content of OPF is high so it is identified visually from spectra. The oil and FFA content absorption peaks (have C-O and O-H bonds) could not be identified, but it was estimated in the wavelength ranges of 1200-1300 nm and 1408-1470 nm (Iqbal, 2015; Lengkey et al., 2013; Sudarno et al., 2017). So, it is necessary to find out the methods to identify the absorption peak of oil and FAA in the NIR region.

One of the most powerful of spectra pre-treatment that could show more absorption peaks than original spectra is the first derivative Savitzky-Golay pre-treatment (SG1). The results of the spectrum refinement process with the first derivative Savitzky-Golay pre-treatment (SG1) can be seen in Fig. 2(B). The oil palm fruitlets spectra after correction with SG1 form a more slender pattern with clearer peaks and valleys compared to the original spectra, especially for FFA content. This is because the first derivative functions as a separator for chemical components that experience overlapping (Bou-Orm et al., 2020).

The result of another spectra pre-treatment, namely normalization (N01), can be observed in Fig. 2(C). Normalization pre-treatment forms a pattern that is similar to the original spectra but with a narrower range between spectra values. Normalization pre-treatment serves to reduce the range of reflectance values into the range of 0-1, thereby minimizing the effect of sample particle size differences (Lengkey et al., 2013). However, normalization could not exhibit especially oil and FFA absorption peaks, similar to original spectra.

Meanwhile, Fig. 2(D) represents the result of standard normal variate (SNV) pre-treatment. It can be observed from Fig. 2(D), SNV pre-treatment reduces the interference of noise waves, resulting in a smoother and denser spectrum (Nurhasanah et al., 2019). Similar to normalization spectra pre-treatment, the SNV also could not show the absorption peaks of oil and FFA.

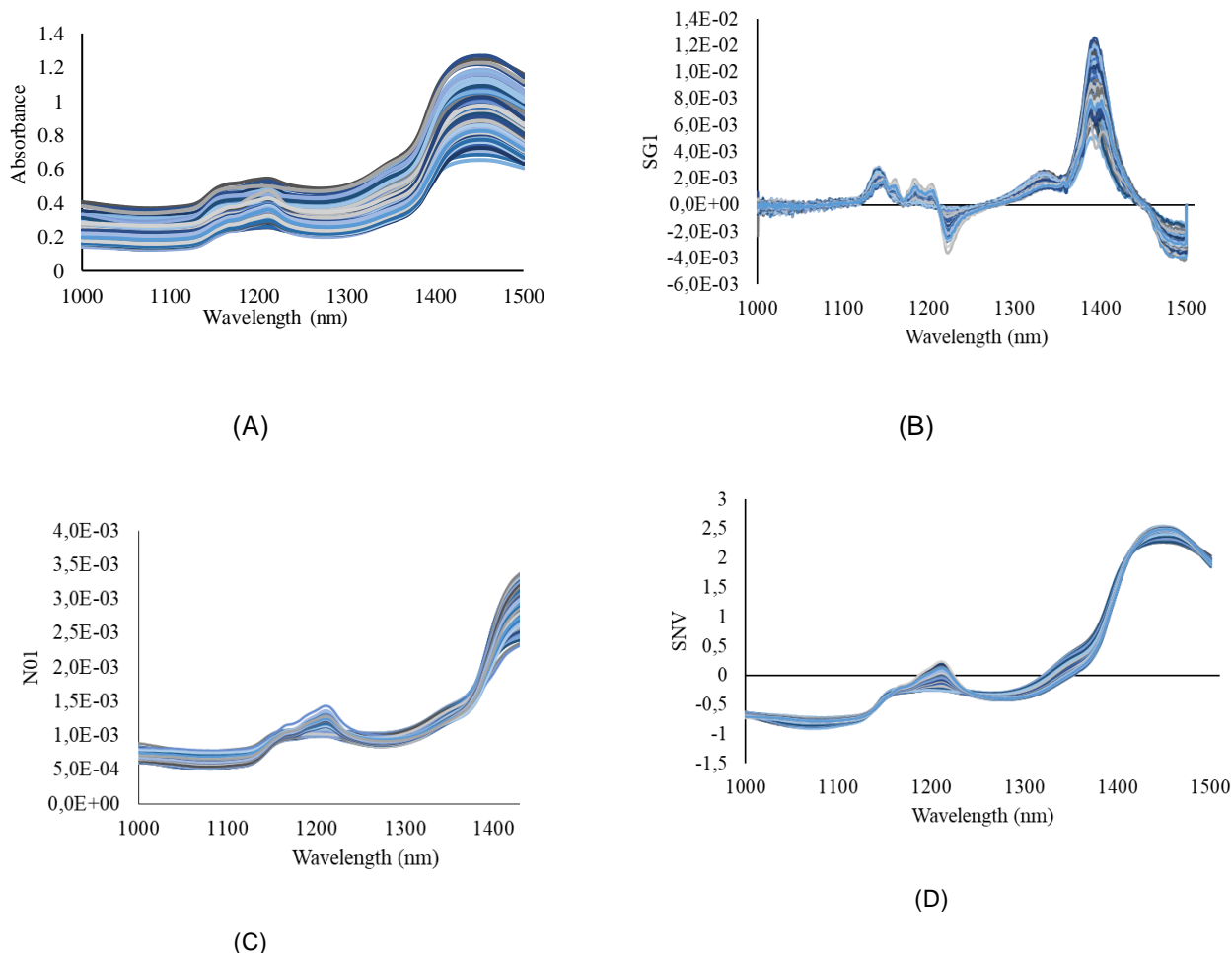


Fig. 2 - NIR Spectra of OPF : (A) -Original ; (B) -SG1 ; (C) - N01 ; (D) -SNV

Oil and Free Fatty Acid (FFA) Content in Oil palm fruitlets

The oil content and FFA of samples of 10 maturity age are shown in Table 1. The oil content of OPF ranges from 0.64% to 45.65%. As FFA content ranged from 1.08% to 5.51%. The oil and FFA content of OPF increased from unripe OPF (3 months age) to ripe OPF (6 months age). The oil content of OPF is significantly higher than FFA content. The variation of oil and FFA content of the samples is good enough to develop a good calibration, indicated by their standard deviation.

Table 1

The oil and FFA content of oil palm fruitlets

| Chemical content | Calibration/Training [n=277] | | | | Validation/Testing [n=119] | | | |
|------------------|------------------------------|--------------------|---------|---------|----------------------------|--------------------|---------|---------|
| | Mean | Standard Deviation | Minimum | Maximum | Mean | Standard Deviation | Minimum | Maximum |
| Oil [%] | 21.79 | 9.60 | 0.64 | 45.65 | 21.64 | 10.58 | 0.67 | 45.56 |
| FFA [%] | 3.28 | 1.11 | 1.08 | 5.51 | 3.41 | 1.07 | 1.09 | 5.25 |

Calibration and Prediction Results for Oil Content

Table 2 shows the results of calibration and validation using four kinds of calibration methods at different spectra pre-treatments. PLSR calibration results are better than PCR ones. These results are as predicted since PLSR include the chemical content in the transformation of the spectra into the factor components which is used in calibration with chemical content of OPF. Meanwhile, PCR used spectra data only in transformation of the spectra to the principle components without involving chemical content of OPF.

Table 2

| Pre-Treatment | Method | Input | Calibration [n=277] | | Validation [n=119] | | | Consistency [%] |
|---------------|---------|-------|---------------------|--------|--------------------|--------|------|-----------------|
| | | | R ² | SEC[%] | SEP [%] | CV [%] | RPD | |
| Original | PCR | 22 PC | 0.82 | 4.10 | 4.52 | 20.89 | 2.34 | 90.79 |
| | | 23 PC | 0.83 | 3.99 | 4.24 | 19.61 | 2.49 | 93.93 |
| | | 24 PC | 0.82 | 4.06 | 4.25 | 19.63 | 2.49 | 95.61 |
| | PLSR | 12 FC | 0.84 | 3.83 | 3.82 | 20.41 | 2.77 | 86.67 |
| | | 14 FC | 0.88 | 3.27 | 3.80 | 17.57 | 2.78 | 85.95 |
| | | 15 FC | 0.90 | 3.01 | 3.82 | 17.66 | 2.77 | 78.74 |
| | PCA-ANN | 22 PC | 0.88 | 3.30 | 4.23 | 19.55 | 2.50 | 78.03 |
| | | 23 PC | 0.90 | 3.05 | 3.75 | 17.32 | 2.82 | 81.22 |
| | | 24 PC | 0.91 | 2.89 | 3.91 | 18.07 | 2.71 | 73.87 |
| | PLS-ANN | 20 FC | 0.94 | 2.38 | 2.66 | 12.28 | 3.98 | 89.60 |
| | | 21 FC | 0.94 | 2.32 | 2.66 | 12.18 | 3.98 | 88.05 |
| | | 22 FC | 0.94 | 2.36 | 2.59 | 11.99 | 4.08 | 91.14 |
| SG1 | PCR | 23 PC | 0.82 | 4.11 | 4.66 | 21.54 | 2.27 | 88.25 |
| | | 24 PC | 0.82 | 4.08 | 4.62 | 21.36 | 2.29 | 88.30 |
| | | 25 PC | 0.82 | 4.07 | 4.62 | 21.36 | 2.29 | 88.10 |
| | PLSR | 7 FC | 0.87 | 3.52 | 4.21 | 19.45 | 2.51 | 83.72 |
| | | 8 FC | 0.89 | 3.24 | 4.01 | 18.51 | 2.64 | 80.97 |
| | | 9 FC | 0.90 | 3.00 | 3.85 | 17.79 | 2.75 | 78.02 |
| | PCA-ANN | 15 PC | 0.87 | 3.43 | 4.05 | 18.70 | 2.61 | 84.68 |
| | | 16 PC | 0.88 | 3.32 | 4.01 | 18.53 | 2.64 | 82.87 |
| | | 17 PC | 0.87 | 3.49 | 4.37 | 20.18 | 2.42 | 79.92 |
| | PLS-ANN | 16 FC | 0.94 | 2.28 | 2.54 | 11.73 | 4.17 | 89.80 |
| | | 24 FC | 0.96 | 1.88 | 2.22 | 10.24 | 4.77 | 84.92 |
| | | 25 FC | 0.96 | 1.86 | 2.21 | 10.21 | 4.79 | 84.33 |
| N01 | PCR | 19 PC | 0.82 | 4.06 | 4.41 | 20.37 | 2.40 | 92.01 |
| | | 20 PC | 0.83 | 3.99 | 4.37 | 20.17 | 2.42 | 91.49 |
| | | 25 PC | 0.83 | 3.92 | 4.36 | 20.13 | 2.43 | 89.98 |
| | PLSR | 12 FC | 0.87 | 3.47 | 4.17 | 19.29 | 2.53 | 83.08 |
| | | 13 FC | 0.88 | 3.47 | 3.93 | 18.18 | 2.69 | 83.98 |
| | | 14 FC | 0.90 | 3.08 | 3.90 | 18.02 | 2.71 | 78.90 |
| | PCA-ANN | 19 PC | 0.89 | 3.24 | 4.44 | 20.52 | 2.38 | 72.95 |
| | | 20 PC | 0.86 | 3.55 | 4.27 | 19.71 | 2.48 | 83.15 |
| | | 21 PC | 0.89 | 3.20 | 4.28 | 19.78 | 2.47 | 74.71 |
| | PLS-ANN | 22 FC | 0.94 | 2.35 | 2.66 | 12.27 | 3.98 | 88.50 |
| | | 23 FC | 0.95 | 2.35 | 2.35 | 10.87 | 4.50 | 92.19 |
| | | 25 FC | 0.95 | 2.09 | 2.42 | 11.20 | 4.37 | 86.21 |
| SNV | PCR | 23 PC | 0.82 | 4.12 | 4.43 | 20.45 | 2.39 | 93.07 |
| | | 24 PC | 0.82 | 4.06 | 4.43 | 20.45 | 2.39 | 91.84 |
| | | 25 PC | 0.82 | 4.04 | 4.39 | 20.27 | 2.41 | 92.19 |
| | PLSR | 11 FC | 0.85 | 3.76 | 4.55 | 21.04 | 2.32 | 82.47 |
| | | 14 FC | 0.89 | 3.18 | 3.96 | 18.31 | 2.67 | 80.23 |
| | | 15 FC | 0.90 | 3.09 | 4.01 | 18.52 | 2.64 | 77.08 |
| | PCA-ANN | 20 PC | 0.88 | 3.29 | 4.27 | 19.72 | 2.48 | 77.03 |
| | | 23 PC | 0.89 | 3.22 | 4.13 | 19.06 | 2.56 | 78.04 |
| | | 24 PC | 0.90 | 3.04 | 4.23 | 19.56 | 2.50 | 71.76 |
| | PLS-ANN | 24 FC | 0.94 | 2.37 | 2.53 | 11.68 | 4.19 | 93.80 |
| | | 25 FC | 0.95 | 2.10 | 2.55 | 11.80 | 4.14 | 82.35 |
| | | 26 FC | 0.95 | 2.14 | 2.49 | 11.51 | 4.25 | 85.99 |

Notes: Blue Block = Best model for hybrid calibration method with and without pre-treatments ; Yellow Block = The Best Model

This result agrees with *Budiastra et al., 2020* that compared PLS and PCR calibration method in predicting trigonelline and chlorogenic acid of intact coffee bean and *Kumiasari et al., 2018* in predicting soluble solid of persimmon. Similarly, PLS-ANN calibration method is much better than PCA-ANN in any pre-treatments. This result confirms that PLS calibration method is always better than PCR. PLS-ANN calibration method is better than PLSR and PCA-ANN calibration method is better than PCR. It means that hybrid model gives the best performance in predicting oil content of OPF. This result agrees with the results of previous research which examined hybrid methods (PLS-ANN) in predicting blood haemoglobin (*Idrus and Kim, 2019*) and inversion of inland water chlorophyll-a (*Song et al., 2014*). The hybrid model is better than single PLSR or PCR since it could compensate the non-linear relationships between NIR spectra and chemical content of OPF.

Commonly, spectra pre-treatment improves calibration and validation performance compared to the original spectra (without pre-treatment). However, in this study, this only happened with the PLS-ANN method. Spectra pre-treatments combined with the PLS-ANN method provided higher calibration and validation performance compared to the original spectra as indicated by lower errors (SEC, SEP), and higher RPD values (Table 2). This also shown that the PLS-ANN method requires a larger number of components (FC) to develop better calibration and validation results.

The best model to predict oil content of OPF is PLS-ANN with 25 Factor Component (FC) input using SG1 pre-treatment ($R^2 = 0.96$; SEC= 1.86%, SEP= 2.21%, CV= 10.21%, RPD = 4.79). This result agrees with *Lengkey et al., (2013)*, that also found that the best pre-treatment for oil prediction of oil content of *Jatropha Curcas L* was using first derivative Savitzky-Golay. The first derivative of Savitzky-Golay pre-treatment was effective in improving accuracy (*Bou-Orm et al., 2020*) because the percentage of moisture content in OPF in this study was high enough in unripe OPF. This result is slightly better than *Novianty et al., (2022)*, that used EMD-ANN calibration method. The result is much better than *Novianty et al., 2020* that used similar instrument and PLS calibration in predicting oil content of OPF. But the result is not better than *Makky and Soni, (2014)*, ($R^2=0.98$) and *Sudarno et al., (2017)*, ($R^2=0.95$) that used different NIR instruments and wavelength region. However, the PLS-ANN is a promising hybrid method to improve accuracy of NIR spectroscopy in determining oil content of OPF.

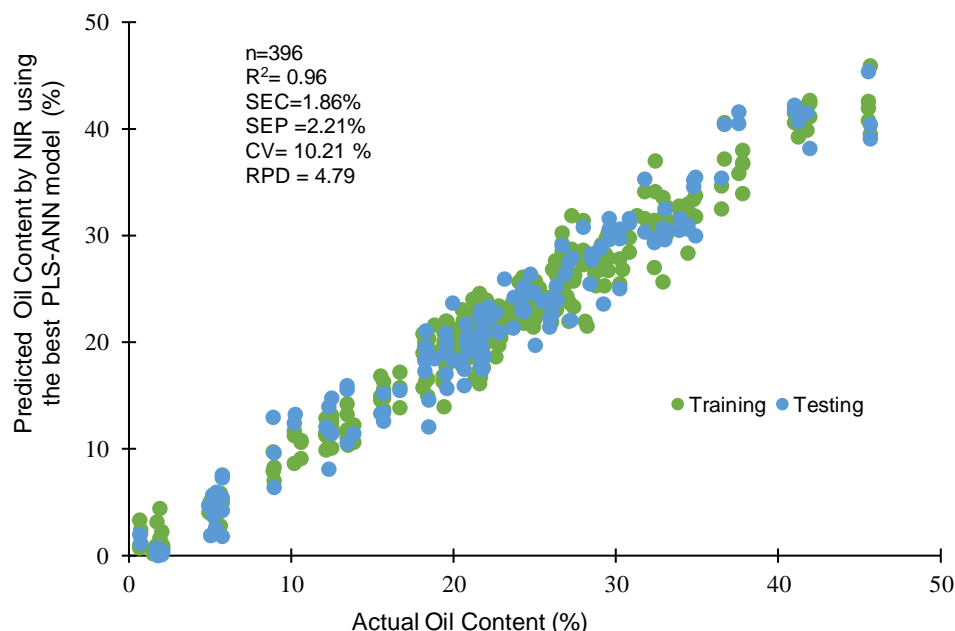


Fig. 3 - Plot of predicted oil content by NIR using the best PLS-ANN model vs actual oil content

Fig. 3 shows the plot of predicted oil content by NIR using the best PLS-ANN model and the chemically tested one of oil content. The high coefficient of determination (R^2) value of 0.96, a low SEC value of 1.86%, a low SEP value of 2.21%, a low CV value of 10.21%, and high RPD value of 4.79 indicate that this model is excellent for predicting oil content in OPF non-destructively.

Calibration and Prediction Results for FFA Content

The calibration results of the model using the original absorbance spectra could not produce satisfactory models for predicting FFA content, except for PLS (17 FC) and hybrid model (Table 3).

Table 3

The calibration and validation results for predicting FFA content in oil palm fruitlets

| Pre-Treatment | Method | Input | Calibration [n = 277] | | Validation [n = 119] | | | Consistency [%] |
|---------------|---------|-------|----------------------------|---------|---------------------------|--------|-------|--------------------|
| | | | R ² | SEC [%] | SEP [%] | CV [%] | RPD | |
| Original | PCR | 10PC | 0.54 | 0.75 | 0.74 | 21.74 | 1.45 | 101.82 |
| | | 13PC | 0.60 | 0.71 | 0.67 | 19.53 | 1.62 | 106.18 |
| | | 20PC | 0.77 | 0.53 | 0.61 | 17.79 | 1.77 | 87.92 |
| | PLSR | 10FC | 0.77 | 0.54 | 0.61 | 17.82 | 1.77 | 88.60 |
| | | 12FC | 0.83 | 0.46 | 0.61 | 16.97 | 1.77 | 80.19 |
| | | 15FC | 0.90 | 0.36 | 0.51 | 14.90 | 2.12 | 70.47 |
| | PCA-ANN | 10PC | 0.56 | 0.78 | 0.78 | 22.93 | 1.38 | 99.35 |
| | | 13PC | 0.62 | 0.70 | 0.71 | 20.98 | 1.50 | 97.94 |
| | | 17PC | 0.83 | 0.46 | 0.53 | 15.58 | 2.03 | 86.98 |
| | PLS-ANN | 10FC | 0.77 | 0.54 | 0.53 | 15.52 | 2.03 | 102.09 |
| 13FC | | 0.85 | 0.43 | 0.53 | 14.03 | 2.03 | 89.32 | |
| 15FC | | 0.88 | 0.38 | 0.43 | 12.69 | 2.49 | 88.63 | |
| SG1 | PCR | 10PC | 0.75 | 0.56 | 0.59 | 17.23 | 1.83 | 95.20 |
| | | 13PC | 0.78 | 0.52 | 0.54 | 16.00 | 1.97 | 95.36 |
| | | 25PC | 0.81 | 0.48 | 0.52 | 15.29 | 2.06 | 93.07 |
| | PLSR | 6FC | 0.83 | 0.46 | 0.54 | 15.81 | 2.00 | 84.99 |
| | | 16FC | 0.97 | 0.19 | 0.62 | 18.22 | 1.73 | 30.56 |
| | | 19FC | 0.98 | 0.15 | 0.64 | 18.90 | 1.67 | 23.56 |
| | PCA-ANN | 10PC | 0.58 | 0.73 | 0.80 | 23.51 | 1.34 | 91.52 |
| | | 13PC | 0.73 | 0.59 | 0.62 | 18.26 | 1.73 | 95.00 |
| | | 24PC | 0.87 | 0.40 | 0.48 | 14.00 | 2.25 | 83.45 |
| | PLS-ANN | 12FC | 0.93 | 0.31 | 0.32 | 9.52 | 3.32 | 94.44 |
| 16FC | | 0.95 | 0.26 | 0.28 | 8.29 | 3.81 | 90.58 | |
| 19FC | | 0.96 | 0.23 | 0.25 | 7.45 | 4.24 | 90.36 | |
| N01 | PCR | 10PC | 0.53 | 0.77 | 0.75 | 21.96 | 1.44 | 102.55 |
| | | 13PC | 0.68 | 0.63 | 0.66 | 19.24 | 1.64 | 96.47 |
| | | 25PC | 0.80 | 0.49 | 0.52 | 15.33 | 2.06 | 94.36 |
| | PLSR | 13FC | 0.87 | 0.41 | 0.51 | 14.91 | 2.12 | 80.69 |
| | | 25FC | 0.97 | 0.51 | 0.65 | 19.14 | 1.65 | 31.01 |
| | | 29FC | 0.98 | 0.16 | 0.68 | 20.08 | 1.57 | 23.68 |
| | PCA-ANN | 10PC | 0.45 | 0.83 | 0.84 | 24.61 | 1.28 | 98.55 |
| | | 13PC | 0.71 | 0.63 | 0.64 | 18.76 | 1.68 | 99.06 |
| | | 15PC | 0.81 | 0.48 | 0.57 | 16.87 | 1.87 | 84.34 |
| | PLS-ANN | 22FC | 0.93 | 0.29 | 0.34 | 9.94 | 3.17 | 84.56 |
| 25FC | | 0.95 | 0.34 | 0.30 | 8.67 | 3.64 | 88.05 | |
| 29FC | | 0.96 | 0.22 | 0.27 | 7.93 | 3.98 | 82.25 | |
| SNV | PCR | 10PC | 0.57 | 0.73 | 0.77 | 22.58 | 1.40 | 94.76 |
| | | 13PC | 0.67 | 0.65 | 0.69 | 20.18 | 1.56 | 93.98 |
| | | 25PC | 0.81 | 0.49 | 0.53 | 15.63 | 2.02 | 92.00 |
| | PLSR | 13FC | 0.86 | 0.41 | 0.51 | 14.94 | 2.11 | 80.77 |
| | | 24FC | 0.96 | 0.22 | 0.61 | 18.05 | 1.75 | 35.36 |
| | | 26FC | 0.97 | 0.19 | 0.63 | 18.40 | 1.72 | 30.55 |
| | PCA-ANN | 10PC | 0.44 | 0.83 | 0.89 | 26.05 | 1.21 | 93.97 |
| | | 13PC | 0.68 | 0.66 | 0.70 | 20.45 | 1.54 | 95.39 |
| | | 17PC | 0.84 | 0.44 | 0.54 | 15.79 | 2.00 | 82.39 |
| | PLS-ANN | 23FC | 0.94 | 0.28 | 0.32 | 9.44 | 3.34 | 87.67 |
| 24FC | | 0.93 | 0.29 | 0.32 | 9.54 | 3.31 | 90.30 | |
| 26FC | | 0.94 | 0.27 | 0.30 | 8.89 | 3.55 | 87.57 | |

Notes: Blue Block = Best model for hybrid calibration method with and without pre-treatments; Yellow Block = The Best Model

Similar to oil content, the PLSR is more accurate than PCR. The PLS-ANN is more accurate than PCA-ANN in any pre-treatment spectra. Spectra pre-treatments also increase calibration and prediction performance in FFA content. It is caused by the ability of spectra pre-treatment to reduce noise, overlapping absorption peaks (SG1) and enhance spectra differences (N01 or SNV) in relatively small amount of FFA content of oil palm fruitlets.

Table 3 also shows that the first derivative Savitzky-Golay (SG1) pre-treatment is the best pre-treatment for all calibration models. This result agrees with *Lengkey et al., 2013* that also found that the best pre-treatment for prediction of FFA content of *Jatropha Curcas L* was using first derivative Savitzky-Golay.

The PCR needs more numbers of PC in order to make a good calibration and prediction in any spectra pre-treatment. Conversely, The PLS needs less numbers of FC to develop a good calibration and prediction.

The best model for predicting FFA content is the PLS-ANN model with a pre-treatment first derivative Savitzky-Golay (SG1) of 19 FC (Table 3). This result agrees with *Lengkey et al., (2013)*, that also found that the first derivative of Savitzky-Golay pre-treatment was the best pre-treatment for predicting FFA content of *Jatropha Curcas* using PLS. The result is better than *Iqbal et al., (2018)*, ($R^2=0.24$ and $RPD=1.27$) that used the similar instrument, which might be due to the ability of PLS-ANN to compensate a non-linearities relationship between NIR spectra and FFA content of OPF. The accuracy is lower than *Makky and Soni (2014)* due to the different instrument and wavelength region used (400-1000 nm).

Fig.4 illustrates the plot of predicted FFA content by NIR using the best model (PLS-ANN using 19 FC with SG1) and the chemically tested one of FFA content. The high coefficient of determination (R^2) value of 0.96, a low SEC value of 0.23%, a low SEP value of 0.25%, a low CV value of 7.45%, and high RPD value of 4.24 indicate that this model is excellent in predicting FFA content of OPF.

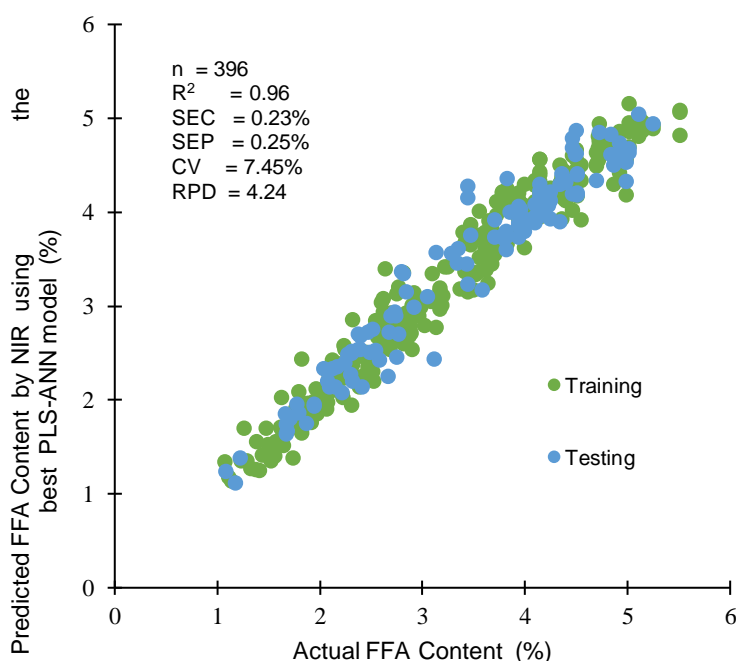


Fig. 3 - Plot of predicted FFA content by NIR using the best PLS-ANN model vs actual FFA content

CONCLUSIONS

The hybrid method of PLS-ANN increased accuracy of NIR spectroscopy in predicting oil and FFA content of OPF non-destructively. The best model to predict oil content of OPF was PLS-ANN with 25 Factor Component (FC) input and using Savitzky-Golay first derivative pre-treatment ($R^2 = 0.96$; SEC=1.86%, SEP=2.21%, CV=10.21%, RPD = 4.79). For FFA content, the best model was also PLS-ANN with 19 FC input using Savitzky-Golay first derivative pre-treatment ($R^2 = 0.96$; SEC=0.23%, SEP=0.25%, CV=7.45%, RPD = 4.24). The PLS-ANN model developed can be used as a rapid and non-destructive method for determining oil and FFA content in oil palm fruitlets.

ACKNOWLEDGEMENTS

We would like to thank the Directorate of Research, Technology and Community Services, Ministry of Education, Culture, Research and Technology, for cooperation and support through the research grant in Fiscal Year 2023 (contract number: 18901/IT3.D10/PT.01.02/M/T/2023).

REFERENCES

- [1] Akbar, A.R., Legowo M.A.C., and Rustiani K. (2022). Determination of Harvesting Time Based on the Variation of Fruitlet Abortion Days in Smallholder Oil Palm Plantations: A Case Study in Tanah Laut Regency, South Kalimantan. *Agritech*, vol. 24, no. 2, pp.167-173, Indonesia;
- [2] AOAC. 2000. *Official Method of Analysis of The Association of Official Analytical of Chemist*. 17th edition. Gaithersburg, MD, USA: The Association of Official Analytical Chemist, Inc;
- [3] [AOAC. 2003. *AOAC 940.28 procedures Fatty Acids (Free) in Crude and Refined Oils. Titration Method*. The Association of Official Analytical Chemist, Inc;
- [4] Blanco, M., I. Villarroya. (2002). NIR spectroscopy: a rapid-response analytical tool. *TrAC*, vol. 21, no. 4, pp.240-250;
- [5] [BSN] National Standardization Agency. 2006. *SNI 01-2901-2006*. Jakarta: BSN;
- [6] Budiastira I. W., Sutrisno, S. Widyoutomo, and P.C. Ayu. (2020). Determination of trigonelline and chlorogenic acid (CGA) concentration in intact coffee beans by NIR spectroscopy. *Agricultural Engineering International: CIGR Journal*, vol. 22, no. 1, pp.163-168;
- [7] Bou-Orm, N., AlRomaithi, A. A., Elrmeithi, M., Ali, F. M., Nazzal, Y., Howari, F. M., & Al Aydarroos, F. (2020). Advantages of first-derivative reflectance spectroscopy in the VNIR-SWIR for the quantification of olivine and hematite. *Planetary and Space Science*, 188;
- [8] Costantini, E., Lang, K. M., Sijtsma, K., & Reeskens, T. (2024). Solving the many-variables problem in MICE with principal component regression. *Behavior Research Methods*, vol.56, no.3, pp.1715–1737;
- [9] Hamdani, A., N. A. Ganai, and J. Bashir. (2023). Artificial neural networks for data mining in animal sciences. *Bulletin of the National Research Centre*, vol. 47, no.68, pp.1-8;
- [10] Idrus, M.N.E and S.C. Kim. (2019). Artificial neural network and partial least square in predicting blood hemoglobin using near-infrared spectrum. *Indonesian Journal of Electrical Engineering and Computer Science*, vol.16, no. 2, pp. 701-708;
- [11] Iqbal, Z. (2015). *Prediction of Oil Palm Fresh Fruit Bunch (FFB) Chemical Content Using NIR Spectroscopy*. M.S. thesis. Agricultural and Biosystem Engineering Department. IPB University, Indonesia.
- [12] Iqbal, Z., S. Herodian, S. Widodo. (2018). Non-Destructive Evaluation Of Free Fatty Acid (FFA) Of Oil Palm Fresh Fruit Bunch (FFB) Using NIR Spectroscopy. *Jurnal Teknik Pertanian Lampung*, vol. 7, no.2, pp. 80-87, Indonesia;
- [13] Irfan, I., Aji, I. F., & Yunita, D. (2023). Application of Near Infrared Spectroscopy (NIRS) in the Measurement of Oil Loss and Its Accuracy Compared To Soxhlet Method. *Jurnal Agroindustri*, vol. 13, no. 2, pp. 107–120, Indonesia;
- [14] Kurniasari I, Y.A. Purwanto, I.W Budiastira, Ridwani S. (2017). Prediction of Tannin and NonSoluble Solid Content of Persimmon (*Diospyros kaki L.*) Using NIR Spectroscopy. *Jurnal Teknik Pertanian*, vol. 5, no. 3, pp. 245-252;
- [15] Lengkey, L.C.E., Sari, D.P., Budiastira, I.W., Seminar, K.B., Purwoko, B.S. (2013). Prediction of chemical contents of *Jatropha curcas L.* Seeds IP-3P by near infrared reflectance method. *Acta Horticulturae*, 1011, pp.335–342;
- [16] Liu, C., X. Zhang, T. T. Nguyen, J. Liu, T. Wu, E. Lee, and X. M. Tu. (2022). Partial least squares regression and principal component analysis: similarity and differences between two popular variable reduction approaches. *Gen Psychiatr*, 35, pp.1-5;
- [17] Makky, M, and P. Soni. (2014). In situ quality assessment of intact oil palm fresh fruit bunches using rapid portable non-contact and non-destructive approach. *Journal of Food Engineering*, 120, pp.248-259;
- [18] Makky, M. (2016). A Portable Low-cost Non-destructive Ripeness Inspection for Oil Palm FFB. *Agriculture and Agricultural Science Procedia*, 9, pp. 230-240;
- [19] Mellyana V., I W. Budiastira, Irmansyah, Y.A. Purwanto. (2024). Electrical Properties for Non-destructive Determination of Free Fatty Acid and Moisture Content in Oil Palm Fruit. *International Journal on Advanced Science Engineering Information Technology*, vol.14, no.2, pp. 641-649.
- [20] Munawar, A. A., Kusumiyati, Hafidh, Hayati, R., & Wahyuni, D. (2019). The application of near infrared technology as a rapid and non-destructive method to determine vitamin C content of intact mango fruit. *INMATEH - Agricultural Engineering*, vol. 58, no. 2, pp.1–12;

- [21] Murphy, D. J., Goggin, K., & Paterson, R. R. M. (2021). Oil palm in the 2020s and beyond: challenges and solutions. *CABI Agriculture and Bioscience*, vol. 2, no.1, pp. 1–22;
- [22] Novianty, I. K. B. Seminar, Irzaman, I. W. Budiastira. (2020). Improving the accuracy of near-infrared (NIR) spectroscopy method to predict the oil content of oil palm fresh fruits. *IOP Conf. Series: Earth and Environmental Science*, 460, pp.1-8;
- [23] Novianty, I., R. G. Baskoro, M. I. Nurulhaq, and M.A. Nanda. (2022). Empirical mode decomposition of near-infrared spectroscopy signals for predicting oil content in palm fruits. *Information Processing in Agriculture*, vol. 10, no. 3, pp.289-300;
- [24] Nurhasanah, Siregar K, Zulfahrizal. (2019). Prediction of Rice Moisture Content Using NIRS with PLS Method and Pre-Treatment Standard Normal Variate, Derivative I, Savitzky Golay Smoothing. *Jurnal Ilmu Mahasiswa Pertanian*, vol. 4, no. 1, pp. 628-637, Indonesia;
- [25] Palou A., P. Jimenez, J. Casals, I. Masalo. (2023). Evaluation of the Near Infrared Spectroscopy (NIRS) to predict chemical composition in *Ulva ohnoi*. *Journal of Applied Phycology* 35, pp. 2007-2015;
- [26] Perera, K. D. C., G. K. Weragoda, R. Haputhanthri, S. K. Rodrigo. (2021). Study of concentration dependent curcumin interaction with serum biomolecules using ATR-FTIR spectroscopy combined with Principal Component Analysis (PCA) and Partial Least Square Regression (PLS-R). *Vibrational Spectroscopy*, 116, pp. 1-9;
- [27] Sinambela, R., T. Mandang, I. D. M. Subrata, W. Hermawan. (2020). Application of an inductive sensor system for identifying ripeness and forecasting harvest time of oil palm. *Scientia Horticulturae*, 265, pp. 1-6;
- [28] Song, K, Li L., Li S., Tedesco, L., Duan H., Li Z., Shi K., Du J., Zhao Y., Shao T. (2014). Using Partial Least Squares-Artificial Neural Network for Inversion of Inland Water Chlorophyll-a. *IEEE Transactions on Geoscience and Remote Sensing* vol. 52, no. 2, pp.1502-1517;
- [29] Sudarno, Divo, D.S., Tauvik, R., Baiq, L. W., Fabrice, D., Yong, Y.Y., and Jean, P.C. (2017). Rapid determination of oil content in dried-ground oil palm mesocarp and kernel using near infrared spectroscopy. *JNIRS*, vol. 25, no. 5, pp. 338–347;
- [30] Yu Peigen, Mei Yin Low, Weibiao Zhou. (2018). Development of a partial least squares-artificial neural network (PLS-ANN) hybrid model for the prediction of consumer liking scores of ready-to-drink green tea beverages. *Food Research International* 103, pp. 68-75.

DESIGN AND EXPERIMENT OF PROGRESSIVE SEED-CLEANING MECHANISM FOR AIR-PRESSURE MAIZE PRECISION SEED-METERING DEVICE

气压式玉米精量排种器递进性清种装置设计与试验

Wen-sheng SUN¹⁾, Shu-juan YI^{*1)}, Hai-long QI²⁾, Yi-fei LI^{1,3)}, Zhi-bo DAI¹⁾, Yu-peng ZHANG¹⁾, Song WANG¹⁾

¹⁾College of Engineering, Heilongjiang Bayi Agricultural University, Daqing/P.R.China

²⁾Heilongjiang Beidahuang Modern Agricultural Service Group Zhongrong Agricultural Machinery Co., Ltd, Harbin / P.R.China

³⁾College of Engineering, Northeast Agricultural University, Harbin/P.R.China

Tel: +86-459-13836961877; E-mile: yishujuan_2005@126.com;

Corresponding author: Shu-juan Yi

DOI: <https://doi.org/10.35633/inmateh-73-40>

Keywords: maize, seed-metering device, seed-cleaning mechanism, design, experiment

ABSTRACT

In order to improve the sowing performance of air-pressure maize dense planting high-speed precision seed-metering device and reduce the occurrence of multiple and missed seeds phenomenon, a seed-cleaning mechanism with progressive seed scraper was designed. The structure and working principle of the seed-metering device and seed-cleaning mechanism are described, the mechanical model before and after the excess seed enters the seed cleaning area is established, and the design parameters of the key components of the seed-cleaning mechanism are determined through the method of theoretical analysis. The experiments of single-factor and multi-factor are conducted with seed clearing angle, operating speed, positive pressure value of blower as influencing factors, and with qualified index, miss index, multiple index as the experimental indexes. The results show that the optimal seed-clearing performance parameter combination of the seed-cleaning mechanism is seed-clearing angle of 0.024°, operating speed of 10 km/h, positive pressure value of 6.0 kPa, verification test of the parameter combination of the qualified index of 98.11%, multiple index of 1.44%, miss index of 0.45%. In the comparative experiment, the qualified index of the device with seed-cleaning mechanism increased by about 2.3% compared to the device without seed-cleaning mechanism, and the multiple index decreased by about 2.2%. The seed-cleaning mechanism is reasonably designed to meet the seed clearing operation requirements of air-pressure maize dense planting high-speed precision seed-metering device.

摘要

为提高气压式玉米密植高速精量排种器的播种作业性能,减少漏播、重播现象的发生,设计了一种带有递进性刮种刀的清种装置。阐述了排种器、清种装置的结构与工作原理,建立了多余种子进入清种区前后的力学模型,得到了风机正压值与作业速度是影响清种装置清种性能的主要因素,通过理论分析的方法确定了清种装置关键部件的设计参数。以清种角度、作业速度、风机正压值为影响因素,以粒距合格指数、重播指数、漏播指数为试验指标进行了单因素试验,确定了合理的因素变化范围进行了多因素试验,得到了清种装置的最佳清种性能参数组合并对其进行了试验验证以及对比试验。结果表明,清种装置最优清种性能参数组合为清种角度 0.024°、作业速度 10km/h、风机正压值 6.0kPa,验证试验该参数组合的合格指数为 98.11%、重播指数 1.44%、漏播指数 0.45%,对比试验中带有清种装置的排种器较无清种装置的排种器合格指数提高了 2.3%左右,重播指数降低了 2.2%左右,清种装置设计合理可满足气压式高速密植精量排种器对清种装置的清种作业要求。

INTRODUCTION

Maize is one of the most widely grown crops in the world, with multiple attributes such as feed, food, medicine and economy (Huma et al., 2019). Considering the whole production chain of maize, the quality of sowing directly affects the yield and quality of maize (Testa et al., 2016).

¹Wen-sheng Sun, Ph.D.; Shu-juan Yi, Prof. Ph.D.; Hai-long Qi, bachelor degree; Yi-fei Li, Ph.D.; Zhi-bo Dai, master degree; Yu-peng Zhang, master degree; Song Wang, Ph.D.

Precision planting technology is an important means of improving the quality of maize sowing (Nardon *et al.*, 2022), which is based on the agronomic requirements of maize planting seeds according to a certain plant spacing, row spacing, sowing depth into the seed bed, which can ensure a reasonable growth space for the plant. Corn precision seed-metering device is the core working part to realize the precision planting technology (Zhang *et al.*, 2023; Van *et al.*, 2020), air-pressure seed-metering device, as a kind of pneumatic precision seed-metering device, has the advantages of good adaptability to seeds, does not hurt the seeds, and is suitable for high-speed sowing, etc., but the internal structure is more complicated. As an important part of seed-metering device, seed-cleaning mechanism is a key component to avoid the phenomenon of multiple seeds, and its reasonable design has an important impact on the operational performance of seed-metering device (Younis *et al.*, 2020; Ramesh *et al.*, 2015; Li *et al.*, 2021).

In the whole working process of seed-metering device, seed cleaning is an important link to reduce the index of the multiple and miss, and current scholars have carried out in-depth research on the seed cleaning process of seed-metering device (Li *et al.*, 2023; Liquan *et al.*, 2021; Zhang *et al.*, 2023). Qi Bing designed a circumferential seed-cleaning device for the problem of serious reseeding in the low-speed operation of set-row maize precision seed-metering device (Qi *et al.*, 2015). Aiming at the problems of high reseeding index of air-suction maize seed-metering device and the difficulty of ensuring the rationality of the design of seed clearing mechanism, Ding Li optimized the design of seed clearing mechanism of seed-metering device, which is well adapted to different varieties of maize seeds (Ding *et al.*, 2019). In addition to maize, Hu designed a double-sided seed clearing mechanism consisting of seed clearing scraper and disturbing air nozzle for the problem that the seed clearing performance of internal cotton air-suction seed-metering device is poor (Hu *et al.*, 2022). He designed a positive pressure airflow seed clearing device for improving the qualified index of coated hybrid rice pneumatic seed-metering device (He *et al.*, 2022). However, current scholars have less research on the seed clearing device of air-pressure maize dense planting high-speed precision seed-metering device.

Aiming at the problem that the high multiple index of air-pressure maize dense planting high-speed precision seed-metering device leads to the decline of its performance, this study designs a seed-cleaning mechanism with a progressive seed scraper, which can be adjusted by a single-degree-of-freedom rod-slider mechanism to adapt to the seed clearing requirements for different sizes and shapes of maize seeds, and provides design references for the research of seed clearing device of pneumatic high-speed dense planting precision seed-metering device.

MATERIALS AND METHODS

MATERIAL

Structure and working principle of seed-metering device

The schematic diagram of the air-pressure seed-metering device is shown in Fig. 1 (a) and (b), which mainly consists of seeding plates, seed-cleaning mechanism, shell, seed blocking net, seed blocking plate, connecting plate, motor, pressure relief wheel, and its connecting frame. When seed-metering device is in operation, the blower delivers airflow to the device chamber, forming a positive pressure chamber. The internal chamber of seeding plates is connected to the outside world, creating a pressure difference between the inside and outside of the shape hole, ensuring stable pressure attachment of maize seeds to the shape hole. The two chambers on the left and right are symmetrically arranged as independent seeding units, and the two seeding plates are fixed and installed at a certain angle to achieve differential time interlaced seeding two rows of one device.

The entire working process of the device can be divided into four stages: filling, cleaning, carrying, and feeding. The working principle is shown in Fig. 1 (c). Maize seeds are divided into two symmetrical seeding chambers through the guide plate on the shell through the air inlet, and are disturbed by the air flow and the grooves of the seeding plates in the waiting seed filling area. The motor drives the seeding plates to rotate, and maize seeds are continuously pressed onto the shape holes by the airflow to rotate at a uniform speed. When the seeds are transferred to the seed cleaning area, the seed-cleaning mechanism removes excess seeds from the shape hole, keeping only single seed. When the single seed is transported to the unloading point, the pressure relief wheel will block the inner side of the hole at the unloading point, and the pressure difference received by the seed will disappear. With the assistance of gravity and air flow, it will be thrown away from the device through the seed discharge pipe, and one seeding operation cycle will be completed.

Structure and working principle of seed-cleaning mechanism

There are significant differences in the shape and size of maize seeds, and when they are pressed onto the surface of shape hole by the airflow, they may not fully cover the surface of the hole. When airflow passes through the uncovered area of the hole, it will carry other seeds and press them onto the surface of the hole again, causing multiple seeds in one hole, seriously affecting the seeding performance of the device (Xu et al., 2023). The seed-cleaning mechanism with progressive seed scraper is mainly composed of an adjustment mechanism and executing mechanism, as shown in Fig. 1 (d). The adjustment mechanism is a single degree of freedom rod slider mechanism consisting of three rotating pairs and one moving pair; the executing mechanism mainly consists of base, arc-shaped frame, scraper blade, and scraper blade fixing frame. One end is fixed on the positioning hole of the shell, and the other end slides on the sliding groove of the shell to adjust the cleaning angle of the scraper blade to meet the cleaning requirements of seeds of different sizes and shapes. The seed-cleaning mechanism is symmetrically arranged on both sides of seeding plates. When shape hole carrying multiple seeds passes through the cleaning area, three Suona shaped scraper blades are used to perform a progressive seed cleaning operation on the excess seeds, gradually reducing the proportion of excess seeds occupying the hole area and ensuring only a single seed that is pressed into the hole.

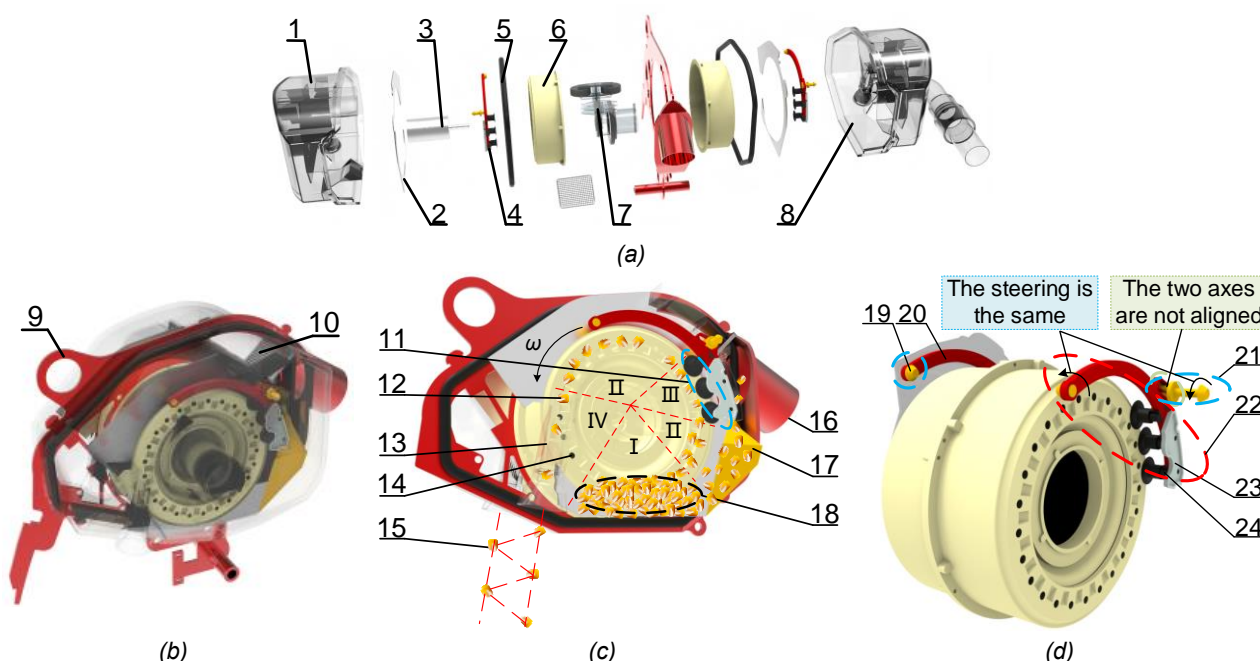


Fig. 1 - Structure and working principles diagram of seed-metering device and seed-cleaning mechanism

1. shell 1; 2. seed blocking plate; 3. motor; 4. seed-cleaning mechanism; 5. seals; 6. seeding plate; 7. pressure relief wheel and its connecting frame; 8. shell 2; 9. connecting plate; 10. seed blocking net; 11. progressive seed scraper; 12. unloading point; 13. seed discharge pipe; 14. shape hole; 15. maize; 16. air inlet; 17. guide plate; 18. waiting seed filling area; 19. positioning hole; 20. arc-shaped frame; 21. adjustment mechanism; 22. executing mechanism; 23. base; 24. scraper blade fixing frame; I. seed filling area; II. seed cleaning area; III. seed carrying area; IV. seed feeding area.

METHODS

Before excess seed enters the clearing area

In this study, the diameter d_1 of shape hole was 5.5 mm. Based on the three-axis size, thousand grain weight of the tested maize (Table 1), and previous experimental observations, the probability of three seeds appearing in a hole was relatively low.

Table 1

| Information of test seed | | | | | |
|---|--------------|-------------------------|-------------|------------|----------------|
| Seed pictures | Variety name | Thousand grain weight/g | Length / mm | Width / mm | Thickness / mm |
|  | Demeya No.1 | 304.3 | 11.12±0.70 | 10.14±0.62 | 5.56±0.69 |

The analysis of the situation where two seeds are attached to the same type of hole can be divided into four situations: the inner and outer seeds are placed horizontally (Fig. 3a); the outer seeds are placed horizontally and the inner seeds are placed laterally (Fig.3b); the inner and outer seeds are placed laterally (Fig.3c); the outer seeds are placed laterally and the inner seeds are placed horizontally (Fig.3d). Considering the rationality of the internal structure layout of the device, seed-cleaning mechanism is located on the outside of seeding plates for single-sided cleaning, and the scraper applies force to the seed (excess seed) on the outside of the hole for cleaning operation. Define k_i as the ratio of the area S_i (approximated as a circle) of the excess seed covering shape hole to entire area S of the hole:

$$k_i = \frac{S_i}{S} = \frac{4S_i}{\pi d_2^2} \tag{1}$$



Fig. 2 - Different states of compression attachment of two seeds on shape hole

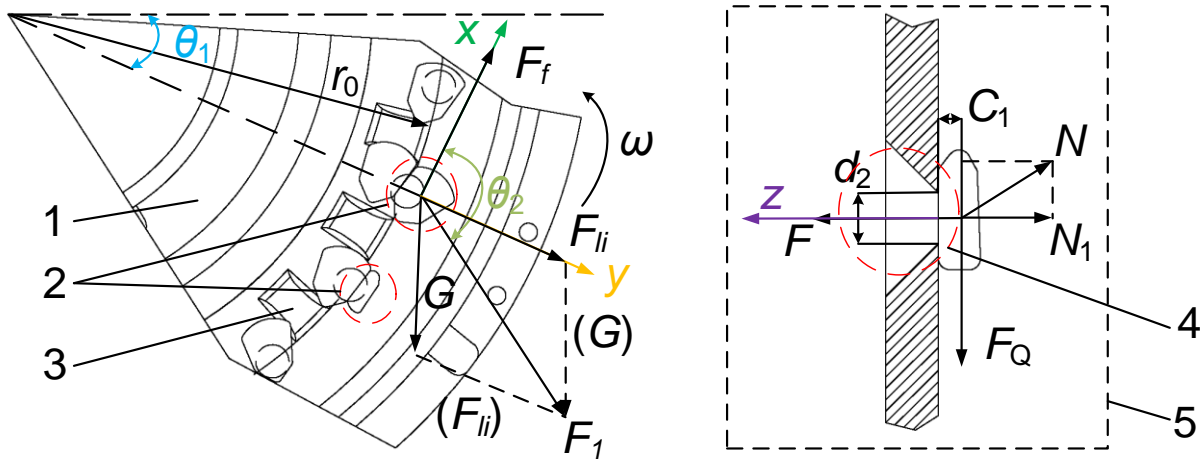


Fig. 3 - Schematic diagram of the forces on the excess seeds before enters the clearing area

1. seeding plate; 2. excess seeds; 3. groove; 4. shape hole; 5. forces of excess seed z-axis direction.

Perform force analysis on the excess seed before entering the seed cleaning area, as shown in Fig. 3. Establish xyz three-dimensional coordinate system with the seed center of gravity as the coordinate origin. The x-axis direction is the tangential direction of seeding plate, the y-axis direction is the radial direction of the plate, and the z-axis is the axis of shape hole. Excess seed will be subjected to centrifugal force F_{li} , air resistance F_z (negligible), airflow pressure force F , gravity G , as well as frictional force F_f and support force N_1 caused by the force N from shape hole before entering the seed cleaning area. F_Q is the combined force on the seed in the xy plane, and a mechanical equation is established based on the D'Alembert's principle:

$$\begin{cases} F \frac{\sqrt{k_i} d_2}{2} = C_1 F_Q \\ F = \Delta P S_i \\ F_1 = \sqrt{G^2 + F_{li}^2 + 2F_{li}G \sin \theta_1} \\ F_Q = \sqrt{F_f^2 + F_1^2 + 2F_f F_1 \cos \theta_2} \end{cases} \tag{2}$$

where:

θ_1 is the angle between the radial and horizontal directions where the seed is located, ($^\circ$); θ_2 is the angle between F_f and F_1 , ($^\circ$); C_1 is the distance from the seed centroid to the hole of seeding plate, (m); ΔP is the pressure difference inside and outside the mold hole, (Pa).

Equations 1~2 can be organized as follows:

$$\sqrt{k_i^3} = \frac{8K_1K_2C_1}{\Delta P\pi d^3} \sqrt{F_{li}^2 + G^2 + F_f^2 + 2GF_{li}\sin\theta_1 + 2F_f\sqrt{F_{li}^2 + G^2} + 2GF_{li}\sin\theta_1\cos\theta_2} \quad (3)$$

which:

$$\begin{cases} F_{li} = m\omega^2r \\ G = mg \end{cases} \quad (4)$$

where: m is seed quality, (kg); ω is the angular velocity of seeding plate, (rad/s); r is the distance from the seed centroid to the center of seeding plate, (m).

From equation (3), it can be seen that, under the condition that the structure of the device is determined, the ratio k_i is positively correlated with the distance C_1 and the angular velocity ω and negatively correlated with the pressure difference ΔP . When the outer seed is in a lateral position, the distance C_1 from the seed centroid to the hole is larger, making it easier to clear the seed. Angular velocity ω of the plate and the pressure difference ΔP has a significant impact on the seed cleaning process, and will be used as influencing factor to explore its impact on the seed cleaning performance of seed-cleaning mechanism in the following text.

After excess seed enters the clearing area

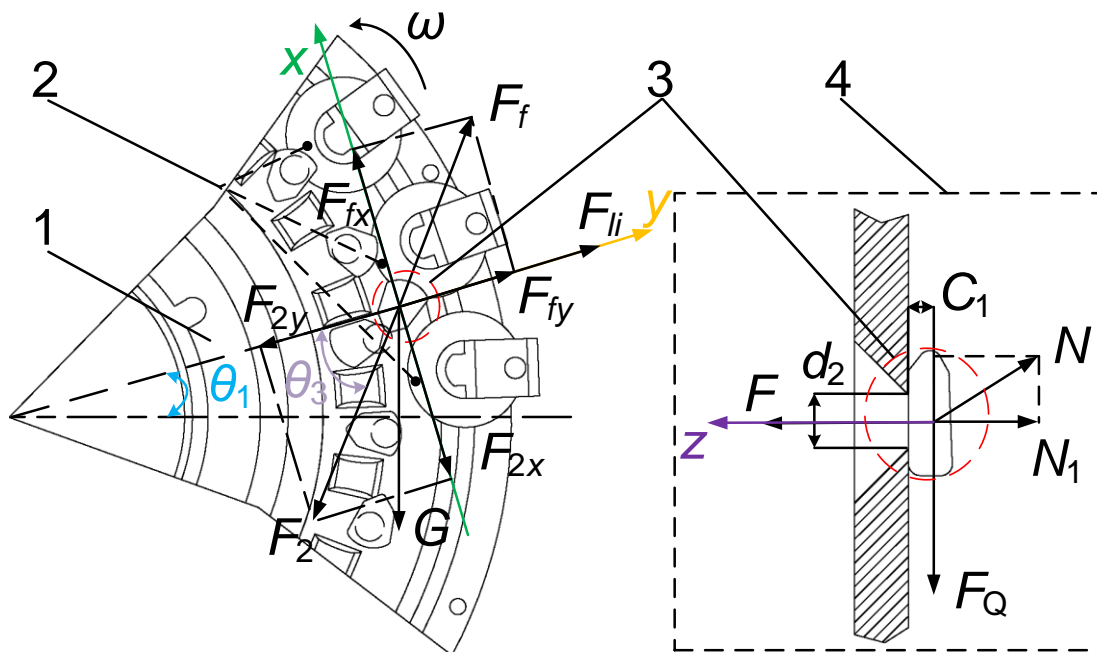


Fig. 4 - Schematic diagram of the forces on the excess seeds after entering the clearing area
 1. seeding plate; 2. seed scraper; 3. excess seed; 4. forces of excess seed z-axis direction.

After the excess seed enter the seed cleaning area (Fig. 4), it will be subjected to centrifugal force F_{li} , air flow pressure force F , gravity G , as well as forces N from shape hole and F_2 from scraper. The force N exerted by the hole on the seed can be decomposed into frictional force F_f and supporting force N_1 . The force F_2 exerted by the seed scraper on the seeds can be decomposed into F_{2x} and F_{2y} on the x-axis and y-axis, respectively.

Establish the mechanical equilibrium equation:

$$\begin{cases} \sum F_x = 0 \Rightarrow F_{fx} = G \cos\theta_1 + F_2 \sin\theta_3 \\ \sum F_y = 0 \Rightarrow F_{fy} = G \sin\theta_1 + F_2 \cos\theta_3 - F_{li} \\ \sum F_z = 0 \Rightarrow F = N_1 \end{cases} \quad (5)$$

which:

$$\begin{cases} F_f = \mu N_1 \\ F_f = \sqrt{F_{fx}^2 + F_{fy}^2} \end{cases} \quad (6)$$

where:

θ_3 is the angle between the radial position of the seed and F_2 , ($^\circ$); F_{fx} is the component of F_f in the x -axis direction, (N); F_{fy} is the component of F_f in the y -axis direction, (N); μ is the friction coefficient between the seed and seeding plate.

Equations 1 and Equations 5~6 can be organized as follows:

$$k_i = \frac{4}{\mu \Delta P \pi d^3} \sqrt{(G \cos \theta_1 + F_1 \sin \theta_2)^2 + (G \sin \theta_1 + F_1 \cos \theta_2 - F_{li})^2} \quad (7)$$

From equation (7), when the structural dimensions and working conditions of the device are determined, the required ratio k_i is positively correlated with the force F_1 of the scraper on the seeds. As the scraper increases its force F_1 on the seeds, the k_i will decrease until excess seeds are removed and the cleaning is completed, and so that the design of the seed-cleaning mechanism should meet the principle of gradually reducing the proportion k_i of the excess seed to the hole area.

Parametric design of key components

As a key component of seed-cleaning mechanism, the rationality of the structure and parameter design of the scraper directly affects the effectiveness of the seed cleaning operation of the device. The main structural parameters of the seed scraper include the disk diameter of the scraper blade, the number of scraper blades, the distance between the center of each scraper blade and the center of seeding plate at the starting cleaning position, respectively, the center angle between adjacent scraper blades, and the adjustable seed-clearing angle range.

To cushion the collision between the seeds and the seed scraper, and avoid damaging the seeds, the shape of the scraper blade is designed to be similar to the Suona shape, and the material is nitrile rubber. Due to the fact that seed cleaning is not effective when the number of seed scrapers is low. When the number is large, the seed scrapers that first come into contact with the seeds have already removed excess seeds from the hole, making the seed scrapers that come into contact with the seeds ineffective in clearing the seeds afterwards. Therefore, it is advisable to design three seed scrapers. In the preliminary experiment, it was observed that when the disk diameter of the scraper blade was large, there was a phenomenon of "over-clearing", which caused the single seed on the hole to be removed and missed seeding occurred. When the diameter was small, the clearing effect was not obvious and led to multiple seeding. Considering the limitations of the structure size of the device chamber, the disk diameter d_2 was designed to be 22 mm, and the diameter of blade body was taken as half of the base diameter to be 11 mm. The blade length was 9 mm. An arc with inclination angle from 0° to 90° was designed between the body and the disk. The scraper blade is equipped with a through-hole with a diameter of 5.5 mm, which is installed on the fixing frame by matching with countersunk screws, as shown in Fig. 5 (a).

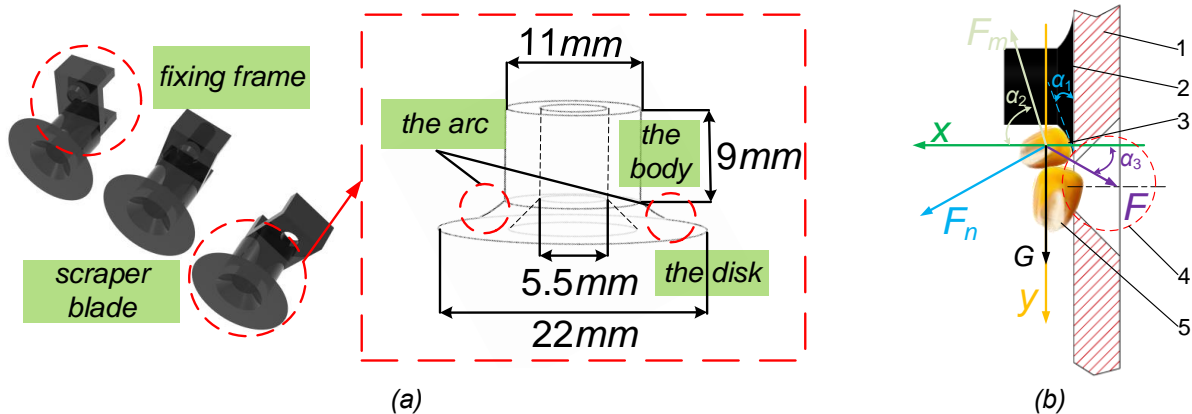


Fig. 5 - Schematic diagram of the structure of the scraper blade and the forces on the excess seed
 1. seeding plate; 2. seed scraper; 3. seed B; 4. shape hole; 5. seed A.

Perform force analysis on the excess seeds on the arc as shown in the Fig. 5 (b), and establish the dynamic equation as follows:

$$\begin{cases} ma_x = F_n \cos \alpha_1 + F_m \cos \alpha_2 - F \cos \alpha_3 \\ ma_y = F_n \sin \alpha_1 - F_m \sin \alpha_2 + F \sin \alpha_3 + G \end{cases} \quad (8)$$

where: a_x is the acceleration of excess seeds in the positive x -axis direction, ($m \cdot s^{-2}$); a_y is the acceleration of excess seeds in the positive y -axis direction, ($m \cdot s^{-2}$); α_1 is the angle between F_n and the positive x -axis, ($^\circ$); α_2 is the angle between F_m and the positive x -axis, ($^\circ$); α_3 is the angle between F and the negative x -axis, ($^\circ$);

F_n is the force exerted by the scraper on excess seeds, (N); F_m is the force exerted by seed A on seed B, (N).

The conditions for excess seed to fall are:

$$\begin{cases} a_x > 0 \\ a_y > 0 \end{cases} \quad (9)$$

When the working speed of the device is constant with the pressure inside the chamber, excess seeds enter the seed cleaning area, and with the rotation of seeding plate, the arc angle α_1 where the excess seeds are located will gradually increase, causing the force F_n to gradually increase, increasing the probability of excess seeds falling off.

To reduce the proportion of excess seeds occupying the hole area k_i , the distance between the center of each scraper blade and the center of seeding plate gradually decreases. At the same time, to prevent the cleaned seeds from colliding with the pressed seeds during the process of falling back into the waiting seed filling area, the starting cleaning position of the scraper blade I is designed on the x-axis. Referring to the Agricultural Machinery Design Manual (*Agricultural Machinery Design Manual: The First Volume.*, 2007), the adjustment range Δd of the scraper blade I is -2~8 mm (overlapping with the center of the hole is 0, negative inward, positive outward). Establish a Cartesian coordinate system with the center of the seeding plate as the coordinate origin, the horizontal direction as the x-axis, and the vertical direction as the y-axis, as shown in Fig. 6.

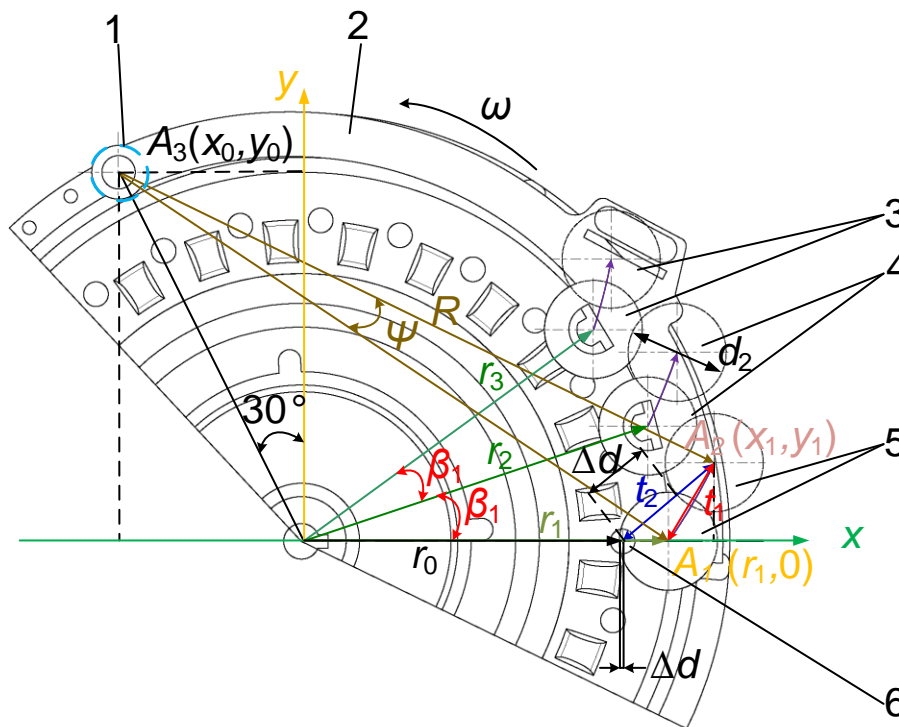


Fig. 6 - Schematic analysis of the key parameters of the seed scraper

1. positioning hole; 2. arc-shaped frame; 3. scraper blade III; 4. scraper blade II; 5. scraper blade I; 6. hole I.

When the hole I rotates to the x-axis, the distance between the disk of the scraper blade I and the center of the hole is -2 mm, and the distance r_0 between the center of the hole and the center of seeding plate is 72 mm.

The equation for the starting position of the seed scraper for seed cleaning is established as follows:

$$\begin{cases} r_1 = r_0 + \frac{d_2}{2} - 2 \\ r_2 = r_1 - \Delta r \\ r_3 = r_2 - \Delta r \end{cases} \quad (10)$$

where:

r_1 is the distance between the center of scraper blade I and the center of seeding plate, (m); r_2 is the distance between the center of scraper blade II and the center of seeding plate, (m); r_3 is the distance between the center of scraper blade III and the center of seeding plate, (m); Δr is the decreasing distance from the scraper blade to the center of seeding plate, value 1 mm.

After calculation, the distances from the center of the scraper blades I, II, and III to the center of seeding plate are 81 mm, 80 mm, and 79 mm, respectively. To prevent interference between the scraper blades, the center angle β_1 of adjacent scraper blades should meet the following requirements:

$$\frac{\pi}{180^\circ} \times \beta_1 \left(\frac{d_2}{2} + r_0 + \Delta d \right) > d_2 \tag{11}$$

After calculation, the center angle β_1 not less than 15.56° . After meeting the condition of no interference between the scraper blades, the smaller the center angle, the closer the connection between the scraper and the longer the continuous clearing time. Considering the convenience of processing, Center angle β_1 takes a value of 16° .

The seed scraper can adjust and rotate around the positioning hole based on the rod slider mechanism within a certain angle range, and the location of the positioning hole should minimize the distance from the center of seeding plate without affecting the normal operation of the plate, so as to reduce the chamber volume and reduce the fan loss. Considering the convenience of processing, the coordinates $A_3 (x_0, y_0)$ of the positioning hole are determined to be $(-45, 45\sqrt{3})$. Points A_1 and A_2 are the center of the disk where the adjustable angle of scraper blade I starts and ends, respectively. The scraper blade I rotates around the positioning hole with R as the radius and the adjustable angle is ψ .

The position relation equation of the seed scraper is established as:

$$\begin{cases} \cos \psi = \frac{2R^2 - t_1^2}{2R} \\ t_1 = \sqrt{(x_1 - r_1)^2 + y_1^2} \\ x_1 - r_0 = \sqrt{t_2^2 - y_1^2} \\ t_2 = \frac{d_2}{2} + \Delta d \\ R^2 = (x_1 - x_0)^2 + (y_1 - y_0)^2 \end{cases} \tag{12}$$

where: t_1 is the distance between point A_1 and point A_2 , (m); $A_2 (x_1, y_2)$ are coordinates of the endpoint where scraper blade I can be adjusted.

According to triangular geometry:

$$R^2 = (r_1 - x_0)^2 + y_0^2 \tag{13}$$

By combining equations 12~13, it can be determined that the adjustable seed-clearing angle range ψ of the seed scraper is $0\sim5^\circ$.

RESULTS AND DISCUSSIONS

Experimental condition

In order to investigate the optimal seed clearing performance of seed-cleaning mechanism of the device, the bench performance test was carried out in the high-speed precision seeding laboratory of Heilongjiang Bayi Agricultural University. The test conditions and seeding effect are shown in Fig. 7.

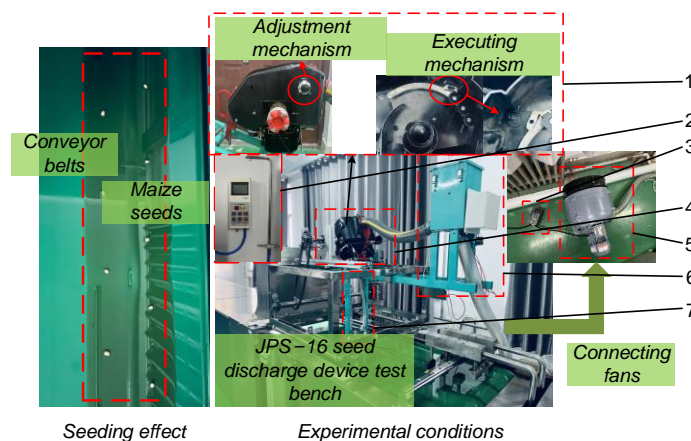


Fig. 7 - Experimental conditions and effects

1. seed-cleaning mechanism; 2. DP2000 intelligent pressure and wind velocity air volume meter; 3. frequency converter;
4. air-pressure precision seed-metering device; 5. HTB-multi-stage blower; 6. seed-supply device; 7. seed guide tube.

The main test equipment includes air-pressure precision seed-metering device, seed-cleaning mechanism, HTB-multi-stage blower, JPS-16 seed discharge device test bench, seed guide tube, seed-supply device, frequency converter and DP2000 intelligent pressure and wind velocity air volume meter. The maize seed variety used in the experiment is "Demeya No. 1", and the material parameters were shown in Table 1.

Experimental factors and Indexes

In order to explore the effect of seed clearing operation of seed-cleaning mechanism, the seed-clearing angle ψ , the operating speed V , and the positive pressure of blower P were taken as the influencing factors, and the qualified index W_1 , multiple index W_2 , and miss index W_3 were taken as the test indexes. The average value of each horizontal test was repeated three times as the test results. The formula of qualified index W_1 , multiple index W_2 and miss index W_3 is as follows:

$$\begin{cases} W_1 = \frac{n_1}{N} \times 100\% \\ W_2 = \frac{n_2}{N} \times 100\% \\ W_3 = \frac{n_3}{N} \times 100\% \end{cases} \quad (14)$$

where: n_1 is the number of passes; n_2 is the number of duplicates; n_3 is the number of leaks; N is the total number of zones.

Set the theoretical plant spacing as L_r , the actual distance between neighboring seeds discharged by the device as L_s , $L_s < 0.5L_r$ for duplicates, $L_s > 1.5L_r$ for leaks, and $0.5L_r < L_s < 1.5L_r$ for passes.

Experiments of single-factor

Considering the actual working conditions, the seed clearing angle ψ is $0 \sim 5^\circ$, the operating speed V is $10 \sim 16$ km/h, and the positive pressure P is $3.5 \sim 6.0$ kPa as the factor range.

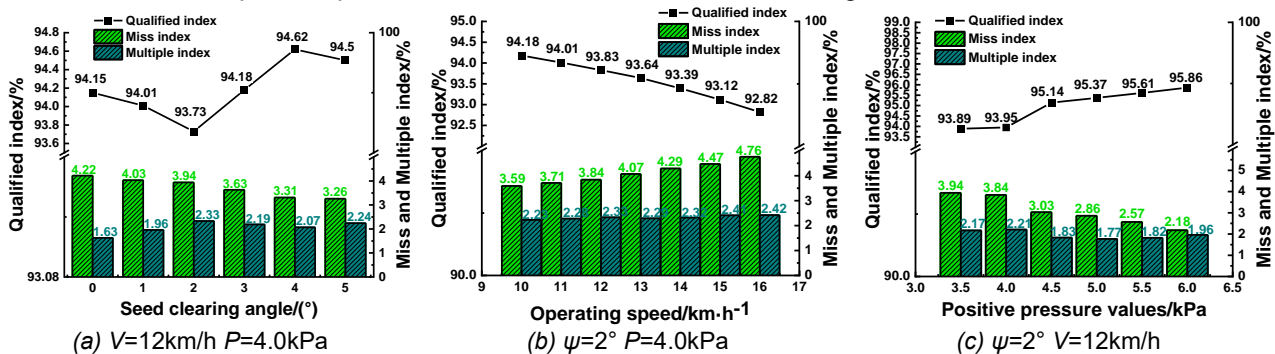


Fig. 8 - Influence of single-factor on test index

(1) Effect of seed clearing angle on the test index

Set the operating speed of 12 km/h, the positive pressure value is 4.0 kPa, and select the seed clearing angle of $0 \sim 5^\circ$ every 1° as a level value for the single-factor test, and get the effect of the seed clearing angle on the experimental index as shown in Fig. 8 (a). As can be seen from the figure, with the increase of the seed clearing angle, miss index is a decreasing trend. The lowest miss index is 3.26% when the seed clearing angle is 5° . With the increase of the seed clearing angle, multiple index first increased and then stabilized. The lowest multiple index is 1.63% when the seed clearing angle is 0° . Qualified index is greater than 93%.

(2) Effect of operating speed on the test index

The seed clearing angle was set to 2° , the positive pressure value was set to 4.0 kPa, and the operating speed of $10 \sim 16$ km/h was selected as a horizontal value for every 1 km/h to set the test bench. The influence of operating speed on the experimental index was shown in Fig. 8 (b). As can be seen from the figure, with the increase of operating speed, miss index generally shows an upward trend, and the highest miss index is 4.76% when the operating speed is 16 km/h. Multiple index fluctuates around 2.3%, and the lowest multiple index is 2.23% when the operating speed is 10 km/h. Qualified index gradually decreases, reaching a minimum of 92.82% at the operating speed of 16 km/h. It can be seen from the results that qualified index gradually decreases when the operating speed of the seed feeder is $10 \sim 16$ km/h, while multiple index tends to be stable after the gradual increase. It is said that seed-cleaning mechanism reduces the degree to which multiple index is affected by the operating speed, while an increase in operating speed will relatively reduce the filling time of the seeder, leading to an increase in the miss index.

(3) Effect of the positive pressure on the test index

Set seed clearing angle to 2 ° and the operating speed to 12 km/h. Select the positive pressure value from 3.5 to 6.0 kPa every 0.5 kPa as one horizontal value for the experiment. The impact of the positive pressure value on the experimental index is shown in Fig. 8 (c). As shown in the figure, with the increase of positive pressure, the overall miss index shows a decreasing trend. At a positive pressure of 6.0 kPa, miss index reaches its lowest point of 2.18%; multiple index first increases and then fluctuates within the range of 1.77% to 1.96%. When the positive pressure value is 4.0 kPa, multiple index reaches the highest of 2.21%; qualified index gradually increases, reaching a maximum of 95.86% when the positive pressure value is 6.0kPa. From the results, it can be seen that when the positive pressure value is between 3.5 and 4.0 kPa, the increase in pressure of blower increases the possibility of multiple seeds in a hole. However, at 4.5 and 6.0 kPa, multiple index is all less than 2%, indicating that seed-cleaning mechanism reduces the degree to which multiple index is affected by the positive pressure value.

Experiments of multi-factor

Based on the results of the single-factor test, the range of seed clearing angle was determined to be 0~4°, the range of operating speed to be 10~12 km/h, and the range of positive pressure values to be 4.0~6.0 kPa, and a three-factor, five-level Central Composite experimental design was conducted. The coding of the test factors is shown in Table 2, where x1, x2, and x3 are the coded values of the seed clearing angle, operating speed, and positive pressure value, respectively.

Table 2

| Experimental factor code table | | | | |
|--------------------------------|----------|-------------------------|----------|--|
| Coded values | Factor | | | |
| | x1 / (°) | x2 / km·h ⁻¹ | x3 / kPa | |
| -1.682 | 0 | 10 | 4.0 | |
| -1 | 1 | 10.4 | 4.4 | |
| 0 | 2 | 11 | 5.0 | |
| 1 | 3 | 11.6 | 5.6 | |
| 1.682 | 4 | 12 | 6.0 | |

The experimental program and results are shown in Table 3.

Table 3

| Experimental design and results | | | | | | |
|---------------------------------|--------|--------|--------|-------------------|-------------------|-------------------|
| Number | x1 | x2 | x3 | W ₁ /% | W ₂ /% | W ₃ /% |
| 1 | -1 | -1 | -1 | 94.39 | 2.47 | 3.14 |
| 2 | 1 | -1 | -1 | 94.41 | 2.86 | 2.73 |
| 3 | -1 | 1 | -1 | 93.94 | 2.28 | 3.78 |
| 4 | 1 | 1 | -1 | 93.84 | 2.65 | 3.51 |
| 5 | -1 | -1 | 1 | 96.94 | 1.19 | 1.87 |
| 6 | 1 | -1 | 1 | 96.43 | 2.01 | 1.56 |
| 7 | -1 | 1 | 1 | 96.63 | 1.14 | 2.23 |
| 8 | 1 | 1 | 1 | 96.23 | 1.91 | 1.86 |
| 9 | -1.682 | 0 | 0 | 94.82 | 1.31 | 3.87 |
| 10 | 1.682 | 0 | 0 | 95.77 | 2.09 | 2.14 |
| 11 | 0 | -1.682 | 0 | 96.35 | 2.01 | 1.64 |
| 12 | 0 | 1.682 | 0 | 95.47 | 1.82 | 2.71 |
| 13 | 0 | 0 | -1.682 | 93.67 | 2.42 | 3.91 |
| 14 | 0 | 0 | 1.682 | 97.48 | 1.66 | 0.86 |
| 15 | 0 | 0 | 0 | 95.38 | 1.05 | 3.57 |
| 16 | 0 | 0 | 0 | 95.96 | 2.03 | 2.01 |
| 17 | 0 | 0 | 0 | 94.83 | 1.76 | 3.41 |
| 18 | 0 | 0 | 0 | 95.12 | 1.99 | 2.89 |
| 19 | 0 | 0 | 0 | 95.09 | 1.37 | 3.54 |
| 20 | 0 | 0 | 0 | 94.96 | 1.76 | 3.28 |
| 21 | 0 | 0 | 0 | 95.61 | 1.61 | 2.78 |
| 22 | 0 | 0 | 0 | 95.02 | 1.37 | 3.61 |
| 23 | 0 | 0 | 0 | 95.22 | 1.04 | 3.74 |

The data in the Table 3 was processed using Design Expert 12 software to obtain the quadratic equation analysis of variance for the qualified index W₁, multiple index W₂, and miss index W₃, as shown in Table 4.

In the table, the *P*-value of the regression models for the qualified index, multiple index, and miss index are all less than 0.01, indicating that the regression model is extremely significant. The *P*-value of the lack of fit are all greater than 0.05, indicating that the regression model has good fitting. In the analysis of variance of the qualified index, operating speed *x*₂, and the positive pressure value *x*₃ show significant effects. In the analysis of variance of the multiple index, seed clearing angle *x*₁, the positive pressure value *x*₃, and the quadratic term *x*₃² are all significant; In the analysis of variance of the miss index, seed clearing angle *x*₁, operating speed *x*₂, the positive pressure value *x*₃, the quadratic terms *x*₂², and *x*₃² are all significant. The other factors are not significant.

Excluding insignificant factors, the regression equations for qualified index *W*₁, multiple index *W*₂, and miss index *W*₃ are obtained:

$$\begin{cases} W_1 = 151.37 - 11.63x_2 + 1.98x_3 + 0.51x_2^2 \\ W_2 = 18.88 + 0.23x_1 - 6.4x_3 + 0.57x_3^2 \\ W_3 = -130.71 - 0.26x_1 + 21.73x_2 + 6.23x_3 - 0.97x_2^2 - 0.76x_3^2 \end{cases} \quad (15)$$

Table 4

| The quadratic equation analysis of variance | | | | | | |
|---|-----------------|-----------------|----------------|-----------------|----------------|-----------------|
| Source | Qualified index | | Multiple index | | Miss index | |
| | Sum of squares | <i>p</i> -value | Sum of squares | <i>p</i> -value | Sum of squares | <i>p</i> -value |
| Model | 20.29 | < 0.0001** | 4.36 | 0.0083** | 14.01 | 0.0012** |
| <i>x</i> ₁ | 0.027 | 0.667 | 0.98 | 0.01* | 1.33 | 0.0325* |
| <i>x</i> ₂ | 0.66 | 0.0483* | 0.0554 | 0.49 | 1.10 | 0.0487* |
| <i>x</i> ₃ | 18.88 | < 0.0001** | 2.05 | 0.0009** | 8.49 | < 0.0001** |
| <i>x</i> ₁ <i>x</i> ₂ | 0.00 | 0.99 | 0.0006 | 0.94 | 0.0008 | 0.95 |
| <i>x</i> ₁ <i>x</i> ₃ | 0.086 | 0.45 | 0.086 | 0.39 | 1.8e-15 | 1.00 |
| <i>x</i> ₂ <i>x</i> ₃ | 0.033 | 0.64 | 0.0078 | 0.79 | 0.0722 | 0.59 |
| <i>x</i> ₁ ² | 0.021 | 0.70 | 0.11 | 0.33 | 0.0372 | 0.70 |
| <i>x</i> ₂ ² | 0.52 | 0.0755 | 0.41 | 0.076 | 1.86 | 0.01* |
| <i>x</i> ₃ ² | 0.062 | 0.52 | 0.67 | 0.0287* | 1.14 | 0.046* |
| Residual | 1.82 | | 1.44 | | 3.03 | |
| Lack of Fit | 0.81 | 0.36 | 0.34 | 0.77 | 0.5790 | 0.85 |
| Pure Error | 1.01 | | 1.09 | | 2.45 | |
| Cor Total | 22.11 | | 5.79 | | 17.04 | |

Note: * indicates a significant impact; ** indicates a highly significant impact.

To explore the impact trend of interaction terms on multiple and miss indices, a contour map is drawn as shown in Fig. 9. Fig. 9a, 9b, 9c, 9d, 9e, and 9f respectively showing the effects of the other two factors on multiple and miss index, explored at seed clearing angle of 2°, operating speed of 11 km/h, and positive pressure value of 5 kPa.

In Fig.9a, when operating speed is constant, multiple index gradually increases with the increase of seed clearing angle. However, when seed clearing angle is constant, multiple index does not change significantly with operating speed, indicating that the influence of operating speed on seed clearing angle is not significant, which is consistent with the results of the analysis of variance. In Fig. 9b, when seed clearing angle is between 0~3.6° and positive pressure value is between 4.5~6.0 kPa, multiple index is lower.

In Fig. 9c, when operating speed is constant, multiple index gradually decreases with the increase of the positive pressure value. However, when the positive pressure value is constant, multiple index does not change much with operating speed.

For miss index, in Fig.9d, when operating speed is less than 10.8 km/h, miss index decreases as seed clearing angle increases. However, when operating speed is greater than 10.8 km/h, miss index is relatively high, indicating that seed-cleaning mechanism has a better cleaning effect under sub-high-speed operation.

In Fig.9e, when seed clearing angle is constant, miss index decreases with the increase of the positive pressure value. When the positive pressure value is below 5 kPa, seed-cleaning mechanism's effect is not obvious. The reason is that low chamber pressure is not conducive to seed filling, and the seeds attached to shape hole are unstable during the seeding process. When the positive pressure value is higher than 5 kPa, the lowest value of miss index is 1%, indicating that the cleaning effect of seed-cleaning mechanism is better when the positive pressure value of the blower is higher.

In Fig. 9f, when operating speed is constant, miss index gradually decreases with the increase of the positive pressure value. However, when the positive pressure value is constant, miss index increases with the increase of operating speed, indicating that operating speed and positive pressure value have a significant impact on miss index, which is consistent with the results of the variance analysis.

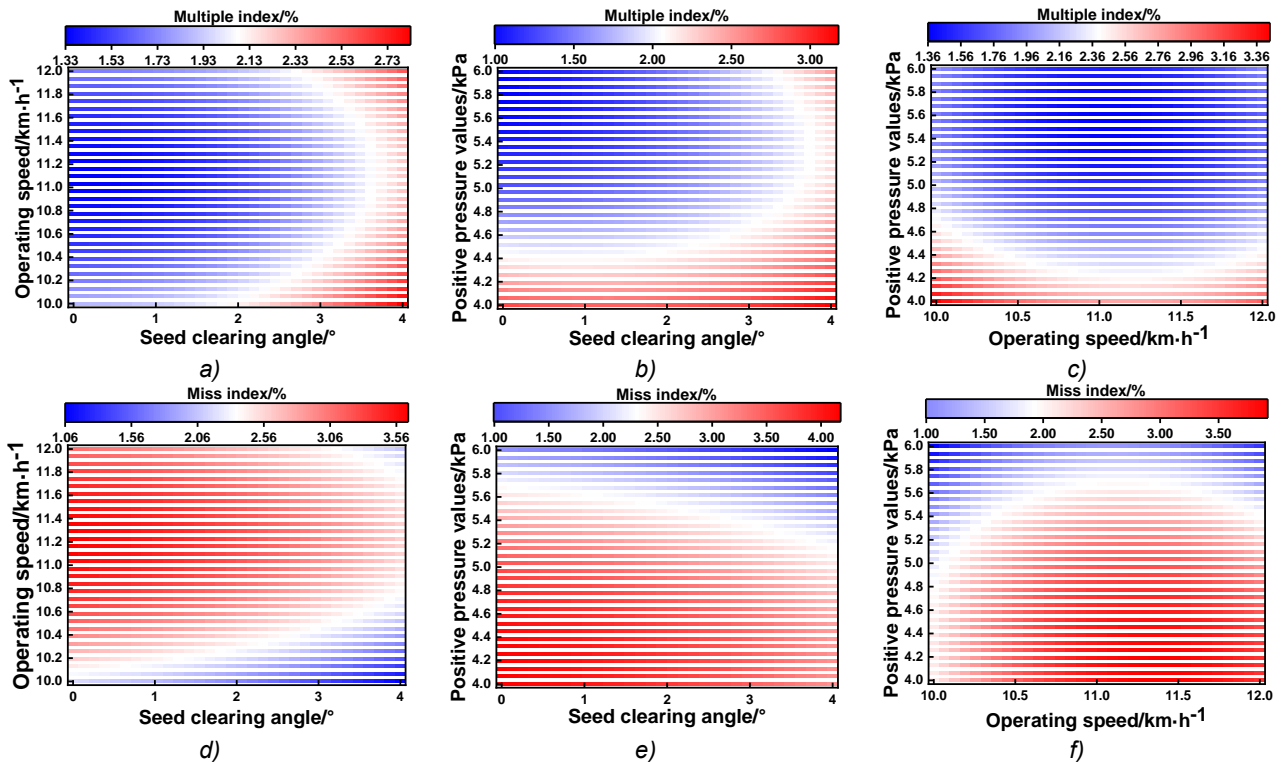


Fig. 9 - Effect of interactivity on test index

In order to obtain the optimal seed cleaning performance of seed-cleaning mechanism and improve the operation performance of the device, the highest qualified index and the lowest miss and multiple index were found within the range of factors, and the optimization equation was established:

$$\begin{cases} \max W_1 \\ \min W_2 \\ \min W_3 \\ 0^\circ \geq x_1 \geq 4^\circ \\ 10\text{km/h} \geq x_2 \geq 12\text{km/h} \\ 4.0\text{kPa} \geq x_3 \geq 6.0\text{kPa} \\ 1 \geq W_1(x_1, x_2, x_3) \geq 0 \\ 1 \geq W_2(x_1, x_2, x_3) \geq 0 \\ 1 \geq W_3(x_1, x_2, x_3) \geq 0 \end{cases} \quad (16)$$

The optimal seed cleaning performance parameter combination of the device was obtained as follows: seed clearing angle 0.024°, operating speed 10 km/h, and positive pressure value 6.0 kPa. Under this parameter combination, qualified index is 98.218%, multiple index is 1.426%, and miss index is 0.356%. In order to verify the optimization results of parameters, verification tests were carried out on JPS-16 seed discharge device test bench. Combined with the actual test conditions, test parameters were set according to seed clearing angle of 0°, operating speed of 10 km/h, and the positive pressure value of 6.0 kPa. The qualified index is 98.11%, multiple index is 1.44%, and miss index is 0.45%. The deviation between the actual result and the parameter optimization is less than 0.2%. The optimized parameter combination can make the seed clearing device achieve better seed clearing performance.

Comparative experiment

In order to investigate the improvement of seed-cleaning mechanism of the device designed under the optimal combination of seed cleaning parameters, the device installed (Fig. 10a) and the device not installed (Fig. 10b) were used for comparison test.

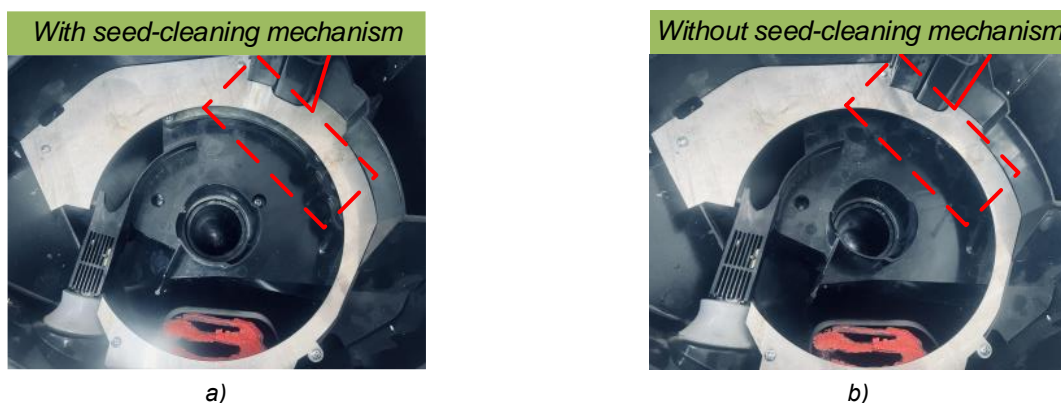


Fig. 10 - Comparison with and without seed-cleaning mechanism

The test conditions of the device without installation were set according to the operating speed of 10 km/h and the positive pressure value of 6.0 kPa. The test was repeated for five groups and the data obtained were shown in Table 5. In the table, the qualified index of the device with seed-cleaning mechanism increased by about 2.3% compared with the device without seed-cleaning mechanism, multiple index decreased by about 2.2%, and miss index changed little and were all less than 1%. The results showed that the seed filling effect was better and the phenomenon of missing sowing was less under the optimal combination of seed cleaning parameters. The miss index of the device with seed-cleaning mechanism was lower than that of the device without installation. The phenomenon of "over-clearing" did not occur in the device.

Table 5

| Comparative test results | | | | | |
|--------------------------|---------------------------------------|--------------------|-------------------|---------------|----------------------------------|
| Test number | Seed-cleaning device installed or not | Qualified index /% | Multiple index /% | Miss index /% | Difference in qualified index /% |
| 1 | Installed | 97.96 | 1.56 | 0.48 | 2.27 |
| | No | 95.69 | 3.78 | 0.53 | |
| 2 | Installed | 98.05 | 1.48 | 0.47 | 2.24 |
| | No | 95.81 | 3.68 | 0.51 | |
| 3 | Installed | 98.12 | 1.47 | 0.41 | 2.28 |
| | No | 95.84 | 3.72 | 0.44 | |
| 4 | Installed | 98.12 | 1.42 | 0.46 | 2.36 |
| | No | 95.76 | 3.77 | 0.47 | |
| 5 | Installed | 98.06 | 1.49 | 0.45 | 2.28 |
| | No | 95.78 | 3.69 | 0.53 | |

In conclusion, seed-cleaning mechanism with progressive seed scraper is reasonable in design, which reduces multiple index of the device, avoids the occurrence of "over-clearing" phenomenon, and improves the operation performance of the device.

CONCLUSIONS

In this study, the main factors affecting the seed clearing performance of the seed-cleaning mechanism were determined to be the pressure of blower and the operating speed. Based on single-factor results, the range of seed-cleaning angle is determined to be 0~4°, the range of operating speed is 10~12 km/h, and the range of positive pressure of blower is 4.0~6.0 kPa. The optimal combination of cleaning performance parameters for seed-metering device was obtained, which included a cleaning angle of 0.024°, an operating speed of 10 km/h, and a positive pressure value of 6.0 kPa. Under this parameter combination, the qualified index is 98.218%, the multiple index was 1.426%, and the miss index was 0.356%. According to the actual test conditions, the test parameters were set in accordance with the cleaning angle of 0°, the operating speed of 10 km/h, and the positive pressure value of 6.0 kPa. The qualified index under the verification test is 98.11%, the multiple index is 1.44%, and the miss index is 0.45%. In the comparative experiment, the qualified index of seed-metering device with seed-cleaning mechanism increased by about 2.3% compared to without seed-cleaning mechanism, the multiple index decreased by about 2.2%, and the miss index was all less than 1%. This indicates that the reasonable design of the seed-cleaning mechanism can meet the cleaning operation requirements of the seed-metering device.

ACKNOWLEDGEMENT

The study was funded by the Heilongjiang Province Key Research and Development Program Major Projects, China (2022ZX05B02) and Ltd. 2023 Pilot Project on Integration of Agricultural Machinery R&D, Manufacturing, and Promotion and Application.

REFERENCES

- [1] Ding, L., Yang, L., Zhang, D. X., & Cui, T. (2019). Parametric Design and Test of Seed Cleaning Mechanism of Air-suction Maize Seed-metering Device. *Transactions of the Chinese Society of Agricultural Machinery*, Vol. 50, Issue 9, pp. 47-56.
- [2] Huma, B., Hussain, M., Ning, C., & Yuesuo, Y. (2019). Human benefits from maize. *Sch. J. Appl. Sci. Res*, Vol. 2, Issue 2, pp. 4-7.
- [3] Hu, M. J., Xia, J. F., Zhou, M. K., Liu, Z. Y., & Xie, D. Y. (2022). Design and Experiment of Seed-Cleaning Mechanism for Inside-Filling Pneumatic Cotton Precision Seed-Metering Device. *Agriculture*, Vol. 12, Issue 8, pp. 1217.
- [4] He, S. Y., Zang, Y., Huang, Z. S., Tao, W. Y., Xing, H., Qin, W., Jiang, Y. C., & Wang, Z. M. (2022). Design of and experiment on a cleaning mechanism of the pneumatic single seed metering device for coated hybrid rice. *Agriculture*, Vol. 12, Issue 8, pp. 1239.
- [5] Li, C., Cui, T., Zhang, D. X., Yang, L., He, X. T., Li, Z. M., Jing, M. S., Dong, J. Q., & Xing, S. L. (2023). Design and experiment of a centrifugal filling and cleaning high-speed precision seed metering device for maize. *Journal of Cleaner Production*, Vol. 426, pp. 139083.
- [6] Liquan, T., Yongsen, X., Zhao, D., & Zhan, S. (2021). Design and performance test of direct seed metering device for rice hill. *INMATEH-Agricultural Engineering*, Vol. 64, Issue 2, pp. 257-268.
- [7] Li, Y. H., Yang, L., Zhang, D. X., Cui, T., He, X. T., & Hu, H. (2021). Design and test of double-side cleaning mechanism for air-suction maize seed-metering device. *Transactions of the Chinese Society of Agricultural Machinery*, Vol. 52, Issue 7, pp. 29-39.
- [8] Nardon, G. F., & Botta, G. F. (2022). Prospective study of the technology for evaluating and measuring in-row seed spacing for precision planting: A review. *Spanish Journal of Agricultural Research*, Vol. 20, Issue 4, pp. e02R01-e02R01.
- [9] Qi, B., Zhang, D. X., Liu, Q. W., Yang, L., Shi, S., & Cui, T. (2015). Design and experiment of cleaning performance in a centralized pneumatic metering device for maize. *Transactions of the Chinese Society of Agricultural Engineering*, Vol. 31, Issue 1, pp. 20-27.
- [10] Ramesh, B., Reddy, B. S., Veerangoud, M., Anantachar, M., Sharanagouda, H., & Shanwad, H. K. (2015). Properties of cotton seed in relation to design of a pneumatic seed metering device. *Indian Journal of Dryland Agricultural Research and Development*, Vol. 30, Issue 1, pp. 69-76.
- [11] Testa, G., Reyneri, A., & Blandino, M. (2016). Maize grain yield enhancement through high plant density cultivation with different inter-row and intra-row spacings. *European Journal of Agronomy*, Vol. 72, pp. 28-37.
- [12] Van Loon, J., Krupnik, T. J., López-Gómez, J. A., Timsina, J., & Govaerts, B. (2020). A standard methodology for evaluation of mechanical maize seed meters for smallholder farmers comparing devices from Latin America, Sub-Saharan Africa, and Asia. *Agronomy*, Vol. 10, Issue 8, pp. 1091.
- [13] Xu, J., Sun, S. L., He, Z. K., Wang, X. M., Zeng, Z. H., Li, J., & Wu, W. B. (2023). Design and optimisation of seed-metering plate of air-suction vegetable seed-metering device based on DEM-CFD. *Biosystems Engineering*, Vol. 230, pp. 277-300.
- [14] Younis, S. M., Sheded, R. S. M., Ali, T. H., & Ibrahim, M. M. (2020). Development of a drum seeding metering unit for sowing vegetable plug tray seedlings. *Plant Archives*, Vol. 20, Issue 1, pp. 3119-3130.
- [15] Zhang, X. R., Yang, Y. M., Wang, Q. J., Li, H. W., Zhang, Z. F., & Liu, J. X. (2023). Design and experiment of pneumatic seed clearing mechanism for pin-hole tube wheat plot precision sowing device. *International Journal of Agricultural and Biological Engineering*, Vol. 16, Issue 4, pp. 85-95.
- [16] Zhang, Y. H., Cheng, J. P., Zhang, X. J., Shi, Z. L., Wang, M. J., Wu, H. F., & Fu, H. (2023). Design and experiment of pressure-holding precision seed-metering device for maize. *INMATEH-Agricultural Engineering*, Vol. 69, Issue 1, pp. 159-169.
- [17] *** *Agricultural Machinery Design Manual: The First Volume* (农业机械设计手册:上册) (2007). Beijing: China Agricultural Science and Technology Press. (in Chinese).

RESEARCH ON CURVED PATH-TRACKING CONTROLLER OF RICE TRANSPLANTER BASED ON H-INFINITY STATE FEEDBACK CONTROL

基于 H 无穷状态反馈控制的插秧机曲线路径跟踪控制器研究

Yueqi MA^{1, 2)}, Ruijuan CHI^{*1, 2)}, Yantao ZHAO^{1, 2)}, Chao BAN^{1, 2)}, Tong SU^{1, 2)}, Zhengrong LI^{1, 2)}

¹⁾ College of Engineering, China Agricultural University, Beijing 100083, China

²⁾ Vehicle Intelligent Control Laboratory, China Agricultural University, Beijing 100083, China

*Corresponding authors. Email: chiruijuan@cau.edu.cn

DOI: <https://doi.org/10.35633/inmateh-73-41>

Keywords: Unmanned transplanter; Path-tracking; H-infinity control; Linear matrix inequality

ABSTRACT

The accuracy of curved path-tracking for headland turning of transplanters is crucial to maintaining the row spacing precision required for rice planting. To address this issue, a method based on H-infinity state feedback control is proposed. In this method, the requirement of robustness is transformed into linear matrix inequalities (LMIs) to optimize the gain coefficients of the control law. The simulation test show that this method outperforms the Linear Quadratic Regulator (LQR) when facing uncertain parameters (longitudinal speed and cornering stiffness) and path curvature disturbance. In addition, the field test results show that when the transplanter tracks a 1/4 circular arc path with a radius of 2 meters, the mean value of the absolute lateral error and the absolute heading angle error using this controller are 0.029 m and 3.69°, respectively. The maximum absolute lateral error is 0.072 m, and 64% of the absolute lateral error are less than 0.04 m, meeting practical requirements. Compared with the LQR controller with feed forward control, the mean value of the absolute lateral error is reduced by 36%. This method meets the accuracy and robustness requirements for unmanned rice transplanter turning at the headland.

摘要

水稻插秧机地头转向时的曲线路径跟踪效果影响着水稻插秧机每行作业前期水稻插植的行距精度。为了提高无人插秧机曲线路径跟踪的鲁棒性，保证水田复杂环境下插秧机地头转向的精度，提出了一种基于 H 无穷状态反馈控制的插秧机曲线路径跟踪控制器设计方法。该方法将控制器对于不确定参数（纵向速度、轮胎侧偏刚度）和扰动项（路径曲率扰动）的鲁棒性需求转化为线性矩阵不等式（Linear Matrix Inequality, LMI）的形式，并以此作为约束求解最优控制律增益系数，实现控制器对于不确定参数和扰动项的鲁棒性。仿真试验结果表明，该方法在系统存在不确定参数和扰动项时，相较于线性二次调节器（Linear Quadratic Regulator, LQR）具有更好的路径跟踪效果。田间试验结果表明，插秧机在跟踪半径为 2m 的 1/4 圆弧路径时，该控制器控制下的曲线路径跟踪的横向偏差绝对值均值和航向角偏差绝对值均值分别为 0.029m、3.69°，横向偏差绝对值的最大值为 0.072m，绝对值小于 0.04m 的横向偏差占 64%，满足实际需求。相较于前馈 LQR 控制器，横向偏差绝对值均值降低 36%。该方法满足插秧机地头转向时曲线路径跟踪的精度与鲁棒性需求。

INTRODUCTION

Path-tracking control technology is the key to improving the accuracy and efficiency of unmanned agricultural machinery operations. Unmanned rice transplanters are a typical representative of unmanned agricultural machinery, and improving the accuracy of rice planting through path-tracking control is an inevitable requirement for precision agriculture. Currently, the straight-line path-tracking accuracy of unmanned rice transplanters has basically met the requirements, while the curved path-tracking accuracy still needs to be improved. The accuracy of curved path-tracking during the headland turning of the rice transplanter affects the row spacing precision of rice planting in the early stage of each row operation (Li et al., 2023; Gang et al., 2022). Therefore, the research on curved path-tracking control of rice transplanters is of great significance for improving the operational precision of unmanned rice transplanters.

The main algorithms applied in agricultural machinery path-tracking control include PID algorithm (Gökçe et al., 2021), fuzzy control (Dekhterman et al., 2024), pure pursuit algorithm (Li et al., 2018), LQR algorithm (Hossain et al., 2022), MPC algorithm (Simonelli et al., 2023), and sliding mode control (SMC) (Ji et al., 2023).

All authors' names and titles: Yueqi MA, Ph.D. candidate; Ruijuan CHI, Associate Professor; Yantao ZHAO, Master's candidate; Chao BAN, Ph.D. candidate; Tong SU, Master's candidate; Zhengrong LI, Master's candidate.

In terms of straight-line path-tracking control, *Tang et al (2018)* improved the adaptability of straight-line path-tracking of rice transplanters to vehicle speed under pure tracking algorithm control. *He et al (2022)* and *Chi et al (2022)* applied the MPC algorithm to the straight-line path-tracking of rice transplanters and achieved optimal results. To date, the accuracy of straight-line path-tracking control for agricultural machinery and even rice transplanters has met the requirements. However, because the curvature of the expected path is not considered in the design of the straight-line path-tracking controller, the adaptability of the above methods to curved path-tracking is poor. They are not suitable for being directly applied to curved path-tracking.

Li et al (2018) improved the accuracy of rice transplanter curved path-tracking by adjusting the look-ahead distance of the pure pursuit algorithm based on vehicle speed and path curvature. They also introduced a coefficient to multiply the desired front wheel angle when the lateral error exceeds a certain threshold, enabling the controller to simultaneously control lateral error and heading angle error. However, this approach does not guarantee the optimal response of the pure pursuit controller to lateral error. Based on the pure pursuit algorithm, *Yang et al (2022)* proposed a path-tracking algorithm based on the optimal target point for agricultural machinery. The curve tracking error was reduced by more than 20% compared to the pure pursuit algorithm. Although the above methods have improved the adaptability of the path-tracking controller to path curvature, the controller design is all based on the vehicle kinematic model. This kind of model does not consider the path curvature factors and has weak adaptability to curved path-tracking (*Gong, et al., 2014*). There are also designed curved path-tracking controllers for vehicles based on vehicle kinematic tracking error models that include expected path curvature factors. For example, based on the vehicle kinematic tracking error model, *Oh and SEO (2023)* proposed an adaptive control and sliding mode control based curved path-tracking algorithm, which further enhances the adaptability of autonomous vehicles to uncertain parameters based on pure sliding mode control. *Kim et al (2023)* calculated the tracking error based on image information and compared the path-tracking control accuracy of LQR and traditional sliding mode control based on the vehicle kinematic tracking error model. The experimental results showed that LQR was better than traditional sliding mode control. *Taghia et al (2017)* used a sliding mode controller with disturbance observer to control the path-tracking of tractors based on the vehicle kinematic tracking error model. However, the vehicle kinematic tracking error model ignores the lateral speed. When the rice transplanter performs large curvature headland turning in paddy fields, the lateral speed is relatively high. Therefore, the above method is also difficult to adapt to the curved path-tracking of the rice transplanter headland turning.

The establishment of the tracking error model based on the two-degree-of-freedom vehicle dynamics simultaneously considers path curvature and lateral speed. Therefore, this paper adopts the tracking error model based on the two-degree-of-freedom (Two-DOF) vehicle dynamics to design the curved path-tracking controller for the transplanter. There are three main types of interference in the system after the linearization of the tracking error model based on Two-DOF vehicle dynamics: the path curvature disturbance caused by the curved path, the longitudinal speed uncertainty and the cornering stiffness uncertainty caused by the complex dynamic paddy field environment. Combined with robust control (*Su, 2010*), the design of the path-tracking controller can improve the robustness of the controller and reduce the influence of the above factors on the control accuracy.

Currently, methods for enhancing the robustness of path-tracking controllers for agricultural machinery often involve supplementing traditional algorithms such as PID and pure pursuit with fuzzy control (*Tang et al., 2018*), neural networks (*Shojaei and Taghavifar, 2022*), optimization algorithms such as PSO (*Gökçe et al., 2021*), as well as manually designed coefficient determination strategies (*Li et al., 2018*). These methods typically require iterative adjustments, consuming considerable time, and may not easily converge to the optimal solution. The H-infinity state feedback controller is a robust feedback controller (*Su, 2010*). In the design, the robustness requirements of the system for uncertain parameters and disturbances can be transformed into the form of linear matrix inequalities (LMIs), which can be used as a constraint to efficiently solve the gain coefficient of optimal control law and achieve the robustness of the controller. In recent years, the application of H-infinity state feedback control in non-agricultural vehicles has been increasing, but its development in agricultural machinery has been relatively limited. *Rath and Subudhi (2022)* proposed a robust MPC control algorithm based on the H-infinity index, which improves the robustness of unmanned underwater vehicles to environmental disturbances while ensuring that their path-tracking control meets control constraints. *Legrand et al (2022)* designed a path-tracking controller for off-road vehicles based on H2/H-infinity control. It improved the robustness of the off-road vehicle path-tracking controller to uncertain parameters such as road slope, cornering stiffness, and road adhesion coefficient.

Gagliardy et al (2022) designed a path-tracking controller for autonomous vehicles during automatic following based on H-infinity state feedback control, which improved the robustness of autonomous vehicles to path curvature disturbance, front vehicle acceleration disturbance, and longitudinal speed uncertainty in a simulation environment. In agricultural machinery, Fukumoto et al (2022) applied H-infinity state feedback control to the arm length control mechanism in automatic spinach harvesters. In the path-tracking control of rice transplanters, the H-infinity state feedback control has not yet been applied and practiced. To this end, a curved path-tracking controller is designed for rice transplanters based on H-infinity state feedback control.

To improve the accuracy of curved path-tracking for transplanter headland turning, taking the tracking error model based on Two-DOF vehicle dynamics as the model, based on the H-infinity state feedback control, a curved path-tracking controller is designed. Finally, the control accuracy of the proposed controller is verified by using the YANMAR VP6E rice transplanter.

MATERIALS AND METHODS

Experimental materials

The experimental platform is the modified YANMAR VP6E rice transplanter shown in Fig. 1, and the basic parameters are shown in Table 1. The accelerator pedal and brake pedal of the transplanter are modified to be controlled by an electric push rod, and the speed of transplanter is controlled by a STM32 controller adjusting the electric push rod. The steering of the transplanter is controlled by a controller driving a DC motor-driven gear mechanism, thereby regulating the rotation of the steering wheel. The front wheel angle sensor measures the front wheel angle in real time, thereby achieving closed-loop control of the front wheel angle of the transplanter. The navigation equipment is the CHC CGI-610 centimeter-level integrated navigation system, configured to send data at a frequency of 10Hz according to the GPCHC data transmission protocol. During path-tracking, the STM32 controller first receives the pose of the transplanter sent by the integrated navigation, and then calculates the state error based on the actual rice transplanter pose and the expected path point input in advance. Finally, based on the state error matrix and the control law input in advance, the expected front wheel angle is calculated to achieve path-tracking of the rice transplanter.

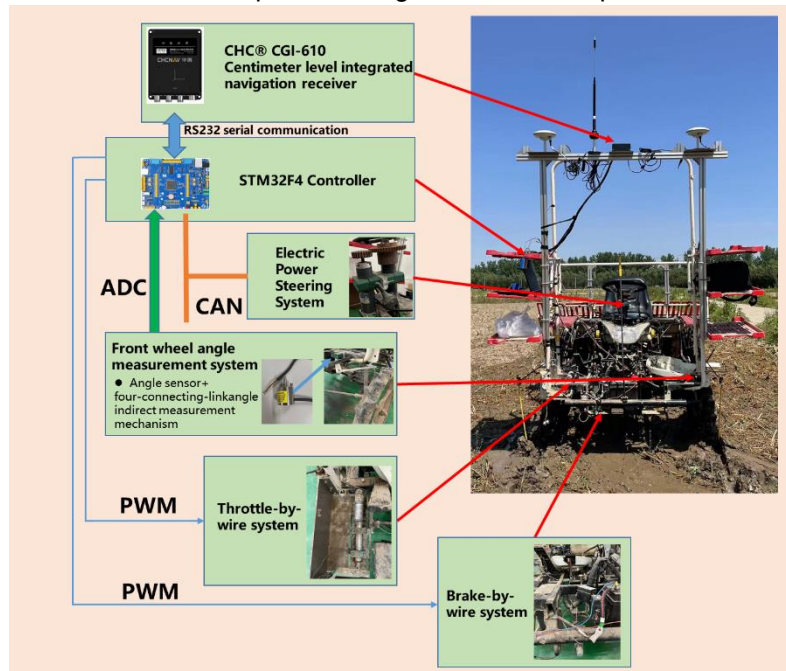


Fig. 1 - Modified YANMAR VP6E rice transplanter

Table 1

| Basic vehicle parameters | |
|--|--------|
| Parameters | Values |
| Vehicle mass m , (kg) | 496 |
| Distance from the center of mass to the front axle a , (m) | 0.65 |
| Distance from the center of mass to the rear axle b , (m) | 0.4 |
| Moment of inertia around the z-axis I_z , (kg/m ²) | 124 |
| The maximum front wheel absolute angle $\delta_m / (^\circ)$ | 57 |

Tracking error model

A tracking error model based on Two-DOF vehicle dynamics is used to design the curved path-tracking controller of the rice transplanter. The tracking error model is shown in Fig. 2. According to two-DOF vehicle dynamic model, the tire slip angle formula, and the relationship between the front wheel angle and the front wheel sideslip angle, the state space equation of the tracking error model can be derived and simplified, as shown in Eq. (1) (Hossain et al., 2022).

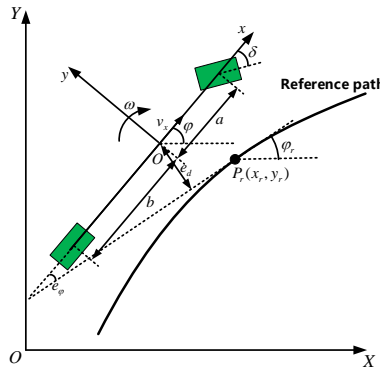


Fig. 2 - Tracking error model

$$\begin{cases} \dot{X} = AX + BU + CW \\ Y = DX \end{cases} \quad (1)$$

where:

$$A = \begin{bmatrix} 0 & 1 & 0 & 0 \\ 0 & -\frac{2C_{af} + 2C_{ar}}{mv_x} & \frac{2C_{af} + 2C_{ar}}{m} & -\frac{2aC_{af} - 2bC_{ar}}{mv_x} \\ 0 & 0 & 0 & 1 \\ 0 & -\frac{2aC_{af} - 2bC_{ar}}{I_z v_x} & \frac{2aC_{af} - 2bC_{ar}}{I_z} & -\frac{2a^2C_{af} + 2b^2C_{ar}}{I_z v_x} \end{bmatrix} \quad B = \begin{bmatrix} 0 \\ \frac{2C_{af}}{m} \\ 0 \\ \frac{2aC_{af}}{I_z} \end{bmatrix} \quad C = \begin{bmatrix} 0 \\ -\frac{2aC_{af} - 2bC_{ar}}{mv_x} - v_x \\ 0 \\ -\frac{2a^2C_{af} + 2b^2C_{ar}}{mv_x} \end{bmatrix}$$

$$X = \begin{bmatrix} e_d \\ \dot{e}_d \\ e_\phi \\ \dot{e}_\phi \end{bmatrix} \quad U = \delta \quad W = \dot{\phi}_r$$

where:

m is the mass of rice transplanter; v_x is the longitudinal speed; I_z is the moment of inertia around the z -axis; a is the longitudinal distance between the center of mass and the front axle; b is the longitudinal distance between the center of mass and the rear axle; ϕ is the heading angle of rice transplanter; ϕ_r is the heading angle of reference path; δ is the front wheel steering angle; C_{af} is the cornering stiffness of front wheel; C_{ar} is the cornering stiffness of rear wheel; e_d is the lateral error between the center of mass and the nearest reference path point ahead; e_ϕ is the heading angle error between the center of mass and the nearest reference path point ahead, and D is the output matrix.

Controller design based on H-infinity state feedback control

When controlling the curved path-tracking, the controller designed based on the tracking error model of two-DOF vehicle dynamics is mainly affected by three factors: path curvature disturbance $W = \dot{\phi}_r = \frac{v_x}{r}$, longitudinal speed uncertainty, and cornering stiffness uncertainty. The H-infinity state feedback controller is a robust feedback controller that can effectively enhance the robustness of the control system to path curvature disturbance and uncertain parameters.

Design principles of the controller

For the open-loop system described in Eq. (1) in the form of
$$\begin{cases} \dot{X} = AX + BU + CW \\ Y = DX \end{cases} \quad (Su, 2010),$$
 H-infinity

state feedback control achieves asymptotic stability of the system by designing an optimal control law $U = KX$, making the disturbance term W having as little gain as possible on the output Y , that is, the infinity norm $\|T_{WY}(s)\|_{\infty}$ of the closed-loop transfer function $T_{WY}(s) = D[sI - (A + BK)]^{-1}C$ from W to Y is as small as possible, thus achieving system's robustness to disturbances. At the same time, if the problem of solving the optimal control law gain coefficient K mentioned above is transformed into a convex optimization problem containing LMIs, it can greatly simplify the solving process and improve the solving efficiency. When the parameters in matrices A , B and C are uncertain, the LMIs problem with uncertain parameters can be transformed into solving the LMIs problem corresponding to the upper and lower bounds of the uncertain parameters only based on the properties of convex function and amplification technique. In this way, it is ensured that the sensitivity of system to disturbances is reduced while the robustness of system to uncertain parameters is improved.

Lemma

To transform the solving of the gain coefficient of the control law into a convex optimization problem with LMIs, and to address issues related to parameter uncertainty and disturbances, the following lemma needs to be used (Su, 2010):

Lemma 1 (Su, 2010):

For a given constant $\gamma > 0$ and the system state equation
$$\begin{cases} \dot{X} = AX + CW \\ Y = DX \end{cases}$$
, the following two conditions

are equivalent:

(1) The system is asymptotically stable with EE (Energy to Energy) gain $\Gamma_{ee} < \gamma$;

(2) There is a symmetric matrix $P > 0$, such that
$$\begin{bmatrix} A^T P + PA & PC & D \\ C^T P & -\gamma I & 0 \\ D^T & 0 & -\gamma I \end{bmatrix} < 0$$

where X is the state quantity; W is the disturbance, and Y is the output.

Lemma 2 (Boyd et al., 1994): When $f(x)$ is a convex function defined on a compact convex set Ω , $f(x) < 0, x \in \Omega \Leftrightarrow f(x) < 0, x \in \Omega_E$, where Ω_E represents the pole of the convex set.

Lemma 3 (Amplification technique) (Boyd et al., 1994): For symmetric matrix Y , real matrices Γ and ψ with appropriate dimensions, if there is a matrix Λ satisfying $\Lambda^T \Lambda \leq I$, then the inequality $Y + \Gamma \Lambda \psi + \psi^T \Lambda^T \Gamma^T < 0$ holds if and only if there is a constant $\epsilon > 0$, such that $Y + \epsilon \Gamma \Gamma^T + \epsilon^{-1} \psi^T \psi < 0$.

Lemma 4 (Schur complement lemma) (Boyd et al., 1994): $S_{22} < 0, \begin{bmatrix} S_{11} & S_{12} \\ S_{21} & S_{22} \end{bmatrix} < 0 \Leftrightarrow S_{11} - S_{12} S_{22}^{-1} S_{21} < 0$.

Solving the gain coefficient of control law

For model (1), according to Lemma 1, the problem of reducing the output gain caused by path curvature disturbance can be transformed into a convex optimization problem with LMIs shown as Eq. (2). After solving Eq. (2) to obtain the matrix F and matrix G , the gain coefficient $K = FG^{-1}$ of the controller control law making system resistant to path curvature disturbance can be obtained first.

$$\begin{aligned} & \text{miny} \\ & \text{s.t.} \begin{bmatrix} (AG + BF) + (AG + BF)^T & C & GD \\ C^T & -\gamma I & 0 \\ (GD)^T & 0 & -\gamma I \end{bmatrix} < 0 \\ & P > 0 \end{aligned} \tag{2}$$

Proof: Multiply the left and right ends of the first LMI in Eq. (2) by symmetric matrix $\text{diag}(P, E, E)$, it is obtained that:

$$\begin{bmatrix} P(AG + BF)P + P(AG + BF)^T P & PC & PGD \\ C^T P & -\gamma I & 0 \\ (GD)^T P & 0 & -\gamma I \end{bmatrix} < 0 \tag{3}$$

Let $K = FG^{-1}$, $G = P^{-1}$, substituting into Eq.(3), it can be obtained that

$$\begin{bmatrix} P(A + BK) + (A + BK)^T P & PC & D \\ C^T P & -\gamma I & 0 \\ D^T & 0 & -\gamma I \end{bmatrix} < 0 \tag{4}$$

Eq. (4) is the form that satisfies Lemma 1, thus proved.

At this point, the problem solved by Eq. (2) is only to reduce the interference of path curvature disturbance on the tracking performance of the controller.

The controller also needs to consider robustness to uncertain parameters. Based on Eq. (2), the robustness of the controller to longitudinal speed is introduced. The longitudinal speed of the vehicle exists in matrices A , B and C , and the linear matrix in Eq. (2) can be regarded as a function of v_x . It is known that the set of v_x is a convex set, and the left linear matrix of the first LMI in Eq. (2) is a convex function. Therefore, substituting the poles of the convex set of v_x into Eq. (2), Eq. (5) can be obtained as follow:

$$\begin{aligned} & \min \gamma \\ \text{s.t.} & \begin{bmatrix} \text{sys}(A_i G + B_i F) & C_i & GD \\ C_i^T & -I & 0 \\ (GD)^T & 0 & -\gamma I \end{bmatrix} < 0 \quad i = 1, 2, \dots, n \\ & G > 0 \end{aligned} \tag{5}$$

where, n is the number of poles on the convex set of v_x ; A , B and C are the matrices corresponding to v_x at the i th pole of the convex set of v_x .

Combined with Lemma 2, it can be inferred that the gain coefficient $K = FG^{-1}$ of control law obtained by solving Eq. (5) can make the controller robust to path curvature disturbance and longitudinal speed.

To introduce the uncertainty term of cornering stiffness into the tracking error model based on Two-DOF vehicle dynamics, uncertainty terms ΔA and ΔB are introduced into Eq. (1). Thus, Eq. (1) is transformed into the form of the parameter perturbation model (Su 2010), as shown in Eq. (6).

$$\begin{cases} \dot{X} = (A + \Delta A)X + (B + \Delta B)U + (C + \Delta C)W \\ Y = DX \end{cases} \tag{6}$$

$$\text{Where, } \Delta A = \begin{bmatrix} 0 & 1 & 0 & 0 \\ 0 & -\frac{2\tilde{C}_{af} + 2\tilde{C}_{ar}}{mv_x} & \frac{2\tilde{C}_{af} + 2\tilde{C}_{ar}}{m} & -\frac{2a\tilde{C}_{af} - 2b\tilde{C}_{ar}}{mv_x} \\ 0 & 0 & 0 & 1 \\ 0 & -\frac{2a\tilde{C}_{af} - 2b\tilde{C}_{ar}}{I_z v_x} & \frac{2a\tilde{C}_{af} - 2b\tilde{C}_{ar}}{I_z} & -\frac{2a^2\tilde{C}_{af} + 2b^2\tilde{C}_{ar}}{I_z v_x} \end{bmatrix} \Delta B = \begin{bmatrix} 0 \\ \frac{2\tilde{C}_{af}}{m} \\ 0 \\ \frac{2a\tilde{C}_{af}}{I_z} \end{bmatrix}$$

$$\Delta C = \begin{bmatrix} 0 \\ -\frac{2a\bar{C}_{af} - 2b\bar{C}_{ar}}{mv_x} - v_x \\ 0 \\ -\frac{2a^2\bar{C}_{af} + 2b^2\bar{C}_{ar}}{mv_x} \end{bmatrix} \quad \tilde{C}_{af} = \lambda \bar{C}_{af} \quad \tilde{C}_{ar} = \lambda \bar{C}_{ar} \quad \bar{C}_{af} = \frac{C_{af \max} - C_{af \min}}{2} \quad \bar{C}_{ar} = \frac{C_{ar \max} - C_{ar \min}}{2} \quad |\lambda| \leq 1$$

Then, according to the method of handling parameter perturbation models (Su 2010), ΔA and ΔB can be represented in the following form:

$$[\Delta A \quad \Delta B \quad \Delta C] = H\Lambda[E_1 \quad E_2 \quad E_3] \tag{7}$$

where $\Lambda = \text{diag}(\lambda, \lambda, \lambda)$

$$H = \begin{bmatrix} 0 & 1 & 0 & 0 \\ 0 & 0 & 0 & 1 \end{bmatrix}^T E_1 = \begin{bmatrix} 0 & -\frac{2\bar{C}_{af} + 2\bar{C}_{ar}}{mv_x} & \frac{2\bar{C}_{af} + 2\bar{C}_{ar}}{m} & -\frac{2a\bar{C}_{af} - 2b\bar{C}_{ar}}{mv_x} \\ 0 & -\frac{2a\bar{C}_{af} - 2b\bar{C}_{ar}}{I_z v_x} & \frac{2a\bar{C}_{af} - 2b\bar{C}_{ar}}{I_z} & -\frac{2a^2\bar{C}_{af} + 2b^2\bar{C}_{ar}}{I_z v_x} \end{bmatrix} E_2 = \begin{bmatrix} \frac{2\bar{C}_{af}}{m} \\ \frac{2a\bar{C}_{af}}{I_z} \end{bmatrix}$$

$$E_3 = \begin{bmatrix} -\frac{2a\bar{C}_{af} - 2b\bar{C}_{ar}}{mv_x} v_x \\ -\frac{2a^2\bar{C}_{af} + 2b^2\bar{C}_{ar}}{mv_x} \end{bmatrix}$$

Finally, combined with Eqs. (5), (6) and (7) and the amplification technique (Su, 2010), the problem of solving the gain coefficient of the control law for the curved path-tracking controller of a rice transplanter based on H-infinity state feedback control, which is robust to uncertain parameters (longitudinal speed and cornering stiffness) and path curvature disturbance, can be transformed into a convex optimization problem with LMIs as follows:

$$\begin{aligned} & \min \gamma \\ \text{s.t.} & \begin{bmatrix} \text{sys}(A_i G + B_i F) & GC_i & G & (E_{1i} R + E_2 F)^T & GH \\ * & -\gamma I & 0 & E_{3i}^T & 0 \\ * & * & -\gamma I & 0 & 0 \\ * & * & * & -\varepsilon_i I & 0 \\ * & * & * & * & -\varepsilon_i^{-1} I \end{bmatrix} < 0 \quad i = 1, 2, \dots, n \quad (8) \\ & P > 0 \\ & P = P^T \end{aligned}$$

where:

$\text{sys}(\bullet) = \bullet + \bullet^T$; n is the number of poles on the convex set of v_x ; A_i, B_i, C_i, E_{1i} and E_{3i} are the matrices corresponding to v_x at the i -th pole of the convex set of v_x ; $*$ is the symmetric element in the symmetric matrix.

Proof: first, there is:

$$\begin{aligned} & \text{sys}(A_i P + \Delta A_i P + B_i K P + \Delta B K P) \\ & = \text{sys}(A_i P + H \Lambda E_{1i} P + B_i K P + H \Lambda E_2 K P) \\ & = \text{sys}(A_i P + B_i K P) + \text{sys}(H \Lambda (E_{1i} + E_2 K) P) \end{aligned} \quad (9)$$

Combined Lemma 3 with Lemma 4, it is obtained that

$$\begin{aligned} & \begin{bmatrix} \text{sys}(PA_i + P\Delta A_i + PB_i K + P\Delta B K) & P(C_i + \Delta C_i) & D \\ (C_i + \Delta C_i)^T P & -\gamma I & 0 \\ D^T & 0 & -\gamma I \end{bmatrix} \\ & = \begin{bmatrix} \text{sys}(PA_i + PB_i K) & PC_i & D \\ C_i^T P & -\gamma I & 0 \\ D^T & 0 & -\gamma I \end{bmatrix} + \text{sys} \left\{ \begin{bmatrix} PH \\ 0 \\ 0 \end{bmatrix} \Lambda [E_{1i} + E_2 K \quad E_{3i} \quad 0] \right\} \\ & < \begin{bmatrix} \text{sys}(PA_i + PB_i K) & PC_i & D \\ C_i^T P & -\gamma I & 0 \\ D^T & 0 & -\gamma I \end{bmatrix} + \varepsilon_i \begin{bmatrix} PH \\ 0 \\ 0 \end{bmatrix} \begin{bmatrix} PH \\ 0 \\ 0 \end{bmatrix}^T + \varepsilon_i^{-1} [E_{1i} + E_2 K \quad E_{3i} \quad 0]^T [E_{1i} + E_2 K \quad E_{3i} \quad 0] \quad (10) \\ & = \begin{bmatrix} \text{sys}(PA_i + PB_i K) & PC_i & D & (E_{1i} + E_2 K)^T & PH \\ * & -\gamma I & 0 & E_{3i}^T & 0 \\ * & * & -\gamma I & 0 & 0 \\ * & * & * & -\varepsilon_i I & 0 \\ * & * & * & * & -\varepsilon_i^{-1} I \end{bmatrix} \end{aligned}$$

Multiplying $diag (P^{-1}, I, I, I, I)$ on both sides of the above equation, it is obtained that:

$$\begin{bmatrix} \text{sys} (A_i P^{-1} + B_i K P^{-1}) & C_i & P^{-1} D & (E_{1i} P^{-1} + E_{2i} K P^{-1})^T & P^{-1} H \\ * & -\gamma I & 0 & E_{3i}^T & 0 \\ * & * & -\gamma I & 0 & 0 \\ * & * & * & -\varepsilon_i I & 0 \\ * & * & * & * & -\varepsilon_i^{-1} I \end{bmatrix} \quad (11)$$

Let $F = K P^{-1}$ and $G = P^{-1}$, the above formula can be transformed as follows:

$$\begin{bmatrix} \text{sys} (A_i G + B_i F) & C_i & G D & (E_{1i} G + E_{2i} F)^T & G H \\ * & -\gamma I & 0 & E_{3i}^T & 0 \\ * & * & -\gamma I & 0 & 0 \\ * & * & * & -\varepsilon_i I & 0 \\ * & * & * & * & -\varepsilon_i^{-1} I \end{bmatrix} \quad (12)$$

Thus, Eq. (8) is proved.

Finally, using the LMI toolkit in Matlab to solve the convex optimization problem shown in Eq. (8), the matrix F and G can be obtained. Then the gain coefficient of the control law for the curved path-tracking controller of a rice transplanter based on H-infinity state feedback control, which is robust to uncertain parameters (longitudinal speed and cornering stiffness) and path curvature disturbance, can be obtained. The control law is $U = KX = FG^{-1}X$.

RESULTS AND ANALYSIS

Reference path and initial pose of the rice transplanter

According to the relationship between working spacing and turning radius, the headland turning mode of the rice transplanter should be T -turn, which is composed of 1/4 arc and straight-line (Trendafilov and Tihanov, 2022). Combined with the actual situation of the rice transplanter headland turning, a 1/4 arc with a radius of 2 m is selected as the reference path to evaluate the curved path-tracking effect of the path-tracking controller.

At the beginning of the experiment, the initial heading angle of the transplanter is adjusted to 90° and the initial front wheel angle to 0° in the geodetic coordinate system. The controller first obtains the starting position (x_0, y_0) of the transplanter, and then use $(x_0 + 0.02 \text{ m}, y_0 + 0.06 \text{ m})$ as the starting point of the reference path to make a 1/4 arc with a radius of 2 m clockwise. This serves as the reference path for the transplanter curved path-tracking, then discretizes the reference path into 40 reference path points at an interval of $\Delta x = 0.05 \text{ m}$.

Determination of system model parameters and controller parameters

To calculate the control law gain coefficient of the controller, it is necessary to determine all parameters in Eq. (8). To obtain the range of longitudinal speed variation, the PID algorithm is used to control the longitudinal speed of the rice transplanter to maintain around 0.7 m/s, then let the transplanter turn along a 1/4 arc with a radius of 2 m, and obtain the speed measured by the integrated navigation. The variation curve of the longitudinal speed is shown in Fig. 3. From Fig. 3, it can be seen that the longitudinal speed of the rice transplanter is basically maintained between 0.5 m/s and 0.8 m/s. Therefore, the nominal longitudinal speed v_x during the path-tracking process is selected as 0.7 m/s, and the upper bound $v_{x_{\max}}$ and lower bound $v_{x_{\min}}$ of the longitudinal speed are 0.5 m/s and 0.8 m/s, respectively.

To obtain the nominal value and range of cornering stiffness, based on the identification results of the cornering stiffness of the transplanter in reference (Li et al., 2020) and combined with magic formulas, the cornering stiffness of the transplanter tire used in the experiment is estimated. The upper and lower limits of the cornering stiffness of the front and rear tires are obtained as 625 N/rad, 250 N/rad, 776 N/rad and 258N/rad, respectively. The nominal cornering stiffness C_{af} of the front tire was 400 N/rad, and the nominal cornering stiffness C_{ar} of the rear tire was 517 N/rad.

As the output of the H-infinity state feedback controller increases, the conservatism of the controller will improve, leading to a decrease in control accuracy. Thus, the designed H-infinity state feedback controller only controls the lateral error and heading angle error, and does not control their rate of change. The output matrix $D = diag (1, 0, 1, 0)$ is selected.

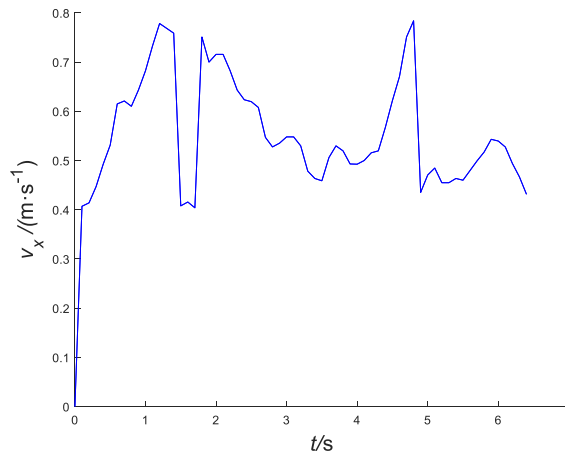


Fig. 1 - Longitudinal speed variation curve

To acquire the LQR controller (which has relatively good tracking performance) to be compared with the H-infinity state feedback controller, and to verify the improvement effect of the H-infinity state feedback controller on the curved path-tracking accuracy of the transplanter, leveraging the method described in reference (Xu *et al.*, 2022) for calculating the gain coefficients of the LQR controller control law, based on experience, the parameter of the control input weight of the LQR controller is selected to be 0.1, based on the parameters in Table 1 and the nominal longitudinal speed and nominal cornering stiffness, the weight parameters of the state error weight matrix Q in the calculation of the LQR controller control law gain coefficient are exhaustively tested from 1 to 100 with 4 intervals through CarSim-Simulink co-simulation, the state error weight matrix $Q = \text{diag}(49, 1, 25, 1)$ that minimizes the mean absolute lateral error is obtained.

Simulation experiments and discussions

To verify the impact of path curvature disturbance and parameter uncertainty on the tracking accuracy of the controller path, and to verify the effectiveness of the H-infinity state feedback controller, the LQR controller, feedforward LQR controller, and H-infinity state feedback controller in tracking the path described in section 3.2 are compared through CarSim-Simulink co-simulation.

The control laws of the H-infinity state feedback controller and the LQR controller are as follows:

$$U = KX \quad (13)$$

The control law of the feedforward LQR controller (obtained according to the method in reference (Xu and Liu, 2022) is as follows:

$$U = KX + \dot{\varphi}_r [a + b - bK_3 + \frac{mv_x^2}{a+b} (-\frac{b}{2C_{af}} - \frac{a}{2C_{ar}} K_3 + \frac{a}{2C_{ar}})] \quad (14)$$

where, K_3 is the third element in the matrix K .

The simulation time step is set to 1ms, and the parameters of the transplanter are set as shown in Table 1. The initial state is the same as described in Section 3.2. To make the simulation effect closer to the actual application effect in paddy fields, the function of longitudinal speed variation with time is approximately fitted based on the actual longitudinal speed of the rice transplanter when turning in the paddy field obtained in Section 3.3, as shown in Eq. (15).

$$v_x = 0.6 + 0.2 \sin\left(\frac{\pi}{2}t - \frac{\pi}{4}\right) \text{ (m/s)} \quad (15)$$

During the simulation experiment, the above function is input into the simulation model to change the longitudinal speed of the transplanter in real time, so that the influence of the complex environment of paddy fields on the longitudinal speed of the transplanter is simulated. The corresponding relationship between cornering stiffness and load in Carsim is estimated and designed based on the nominal cornering stiffness obtained in section 3.3 and the magic formula. In the simulation process, taking the rice transplanter controlled by the LQR controller as an example, the cornering stiffness change curve is output, as shown in Fig. 4 (d).

During the experiment (so as the field test), the tracking error is calculated by the method described in reference (Xu *et al.*, 2022). Finally, the simulation results of path-tracking are shown in Fig. 4, and the simulation data statistics are shown in Table 2.

The simulation results are analyzed according to Fig. 4 and Table 2. In terms of lateral error, the H-infinity state feedback controller considering path curvature disturbance and parameter uncertainty, has the best tracking performance, followed by the feedforward LQR controller, and the LQR controller is the worst. From the perspective of heading angle error, the performance of the H-infinity state feedback controller is relatively poor compared to the other two controllers. The overall tracking performance of the three controllers based on the proximity between the actual path and the reference path of the rice transplanter is evaluated, the H-infinity state feedback controller has the best tracking performance, followed by the feedforward LQR controller, and the LQR controller is the worst.

Figs. 3 and 4 (d) can represent the changes in uncertain parameters during the simulation process. The longitudinal speed is generally between 0.5 m/s and 0.8 m/s; the cornering stiffness of the front tire is generally between 200 N/rad and 600 N/rad, and the cornering stiffness of the rear tire is generally between 300 N/rad and 800 N/rad. The path curvature disturbance in this experiment is approximately $W = \dot{\phi}_r = \frac{v_x}{r} = \frac{0.7}{2} = 0.35 \text{ (s}^{-1}\text{)}$. The above experimental results show that when there are uncertain parameters and path curvature disturbance, the LQR controller has relatively poor path-tracking performance due to not considering the above two issues. After incorporating feedforward control, improvements are made to address the issue of path curvature disturbance, resulting in improved path-tracking performance. For the H-infinity state feedback controller, due to its consideration of robustness to path curvature disturbance and uncertain parameters, it achieves the best path-tracking performance.

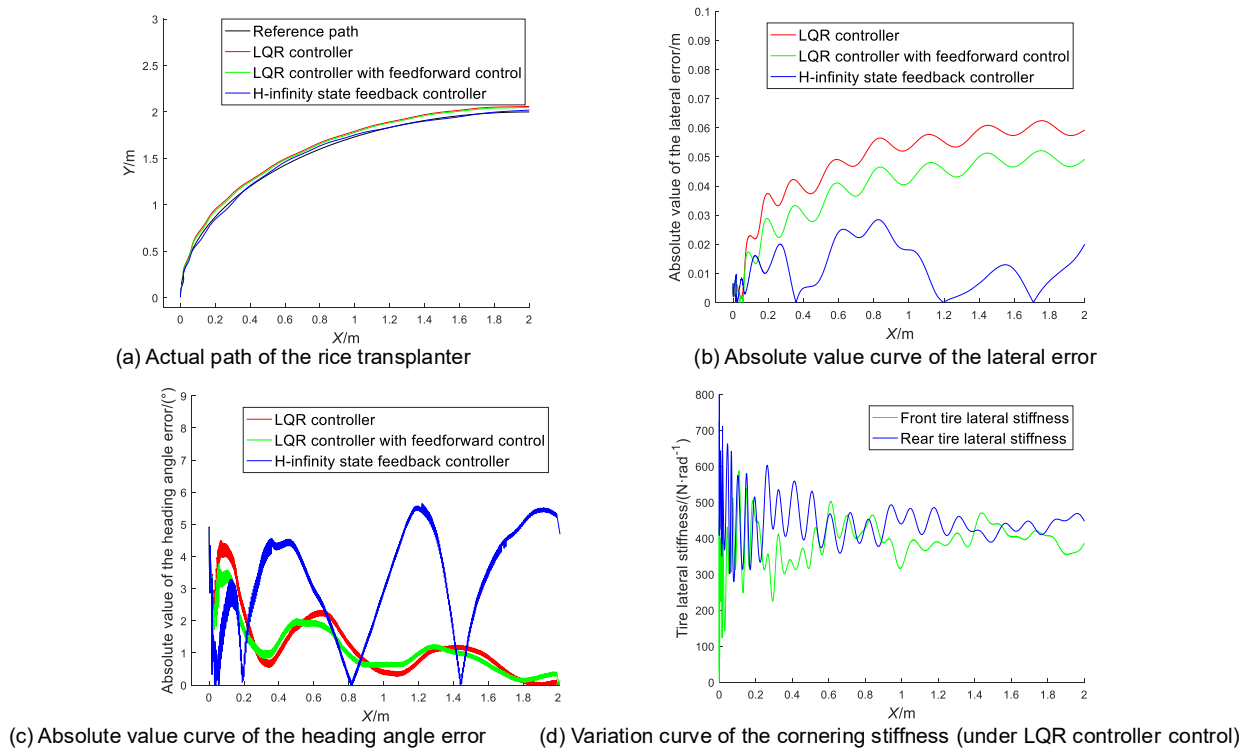


Fig. 4 - Simulation test results

Table 2

Data statistics of the simulation results

| Controllers | Lateral error | | | Heading angle error | | |
|--------------------------------------|-------------------------|----------------------------|---------------------------------------|---------------------------|------------------------------|-----------------------------------|
| | Mean absolute value / m | Maximum absolute value / m | Absolute value less than 0.04 m / (%) | Mean absolute value / (°) | Maximum absolute value / (°) | Absolute value less than 5° / (%) |
| LQR controller | 0.036 | 0.062 | 48 | 1.98 | 4.94 | 100 |
| Feedforward LQR controller | 0.029 | 0.052 | 60 | 1.81 | 4.94 | 100 |
| H-infinity State Feedback Controller | 0.011 | 0.028 | 100 | 2.97 | 5.65 | 95 |

Field experiments and discussions

To verify the actual effectiveness of the controller, the feedforward LQR controller and H-infinity state feedback controller will be used for actual vehicle control. During the path-tracking process of the rice transplanter, the PID algorithm is used to maintain the longitudinal speed v_x around 0.7 m/s. The experimental scenario is shown in Fig. 5.

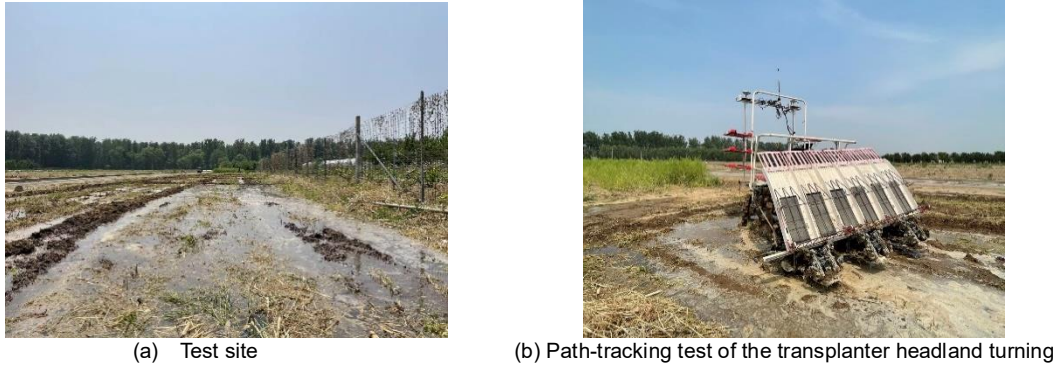


Fig. 5 - Experimental scenario of curved path-tracking for the rice transplanter on the field

After the experiment, the actual path and absolute lateral error variation curves of the rice transplanter under the feedforward LQR controller and the H-infinity state feedback controller, as well as the absolute heading angle error variation curve, can be obtained as shown in Fig. 6. The specific statistical data is shown in Table 3.

As shown in Fig. 6, the actual path of the rice transplanter under the control of the H-infinity state feedback controller is closer to the expected path than the actual path under the feedforward LQR controller. The lateral error of the H-infinity state feedback controller is generally smaller than that of the feedforward LQR controller, but the heading angle error is larger than that of the feedforward LQR controller.

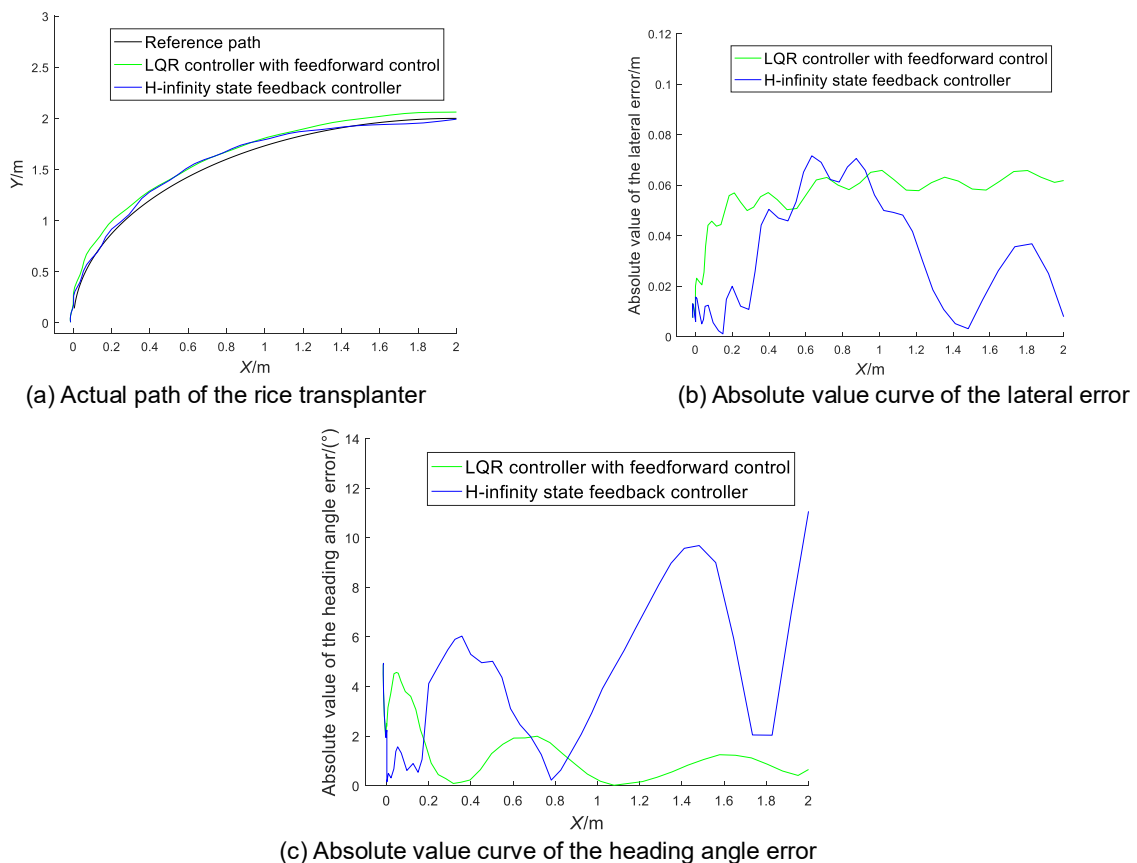


Fig. 6 - Field test results

Table 3

Comparison of the tracking error

| Controllers | Lateral error | | | | Heading angle error | | | |
|--------------------------------------|-------------------------|----------------------------|----------------------------|--------------------------------------|---------------------------|------------------------------|------------------------------|-----------------------------------|
| | Mean absolute value / m | Maximum absolute value / m | Minimum absolute value / m | Absolute value less than 0.04m / (%) | Mean absolute value / (°) | Maximum absolute value / (°) | Minimum absolute value / (°) | Absolute value less than 5° / (%) |
| Feedforward LQR controller | 0.045 | 0.066 | 0.008 | 29 | 1.93 | 4.93 | 0.09 | 100 |
| H-infinity State Feedback Controller | 0.029 | 0.072 | 0.003 | 64 | 3.69 | 10.98 | 0.16 | 72 |

According to Table 3, the absolute lateral error under the H-infinity state feedback controller is reduced by 36% compared to the feedforward LQR controller, and the percentage of absolute lateral error less than 0.04 m is increased by 121%. However, for the absolute heading angle error, the mean value under the feedforward LQR controller is reduced by 48% compared to that under the H-infinity state feedback controller, and the percentage of error less than 5° under the feedforward LQR controller is increased by 39% compared to the H-infinity state feedback controller.

In summary, the control accuracy of the H-infinity state feedback controller for curved path-tracking of unmanned rice transplanters meets practical requirements and can be applied to headland turning control of unmanned rice transplanters. The actual path of the rice transplanter under its control is closer to the expected path compared to the LQR controller with feedforward control. The lateral error is reduced and the heading angle error is improved. Overall, the H-infinity state feedback controller has better path-tracking performance and stronger robustness.

CONCLUSIONS

(1) To improve the accuracy of curved path-tracking when unmanned rice transplanters turns at the headland, a design method for a curved path-tracking controller of a rice transplanter based on H-infinity state feedback control is proposed. This method transforms the robustness requirements of the controller to uncertain parameters (longitudinal speed, cornering stiffness) and disturbance (path curvature disturbance) into the form of LMIs, and uses it as a constraint to solve the gain coefficient of optimal control law, achieving the robustness of the controller to uncertain parameters and disturbance.

(2) The simulation test results show that when the rice transplanter tracks the path of a 1/4 arc with a radius of 2 m, and the longitudinal speed and cornering stiffness fluctuate, the path-tracking performance of LQR controller is relatively poor due to not considering path curvature disturbance and parameter uncertainty. After incorporating feedforward control, improvements are made to address the issue of path curvature disturbance, resulting in improved path-tracking performance. For the H-infinity state feedback controller, due to its consideration of robustness to path curvature disturbance and uncertain parameters, it can achieve better path-tracking performance than the LQR controller and the feedforward LQR controller.

(3) The field test results show that when the rice transplanter tracks the path of a 1/4 arc with a radius of 2 m, the mean absolute values of lateral error and heading angle error under the H-infinity state feedback controller are 0.029 m and 3.69°, respectively. The maximum absolute lateral error is 0.072 m, and the absolute lateral errors less than 0.04 m account for 64%. Compared with the feedforward LQR controller, the mean absolute lateral error is reduced by 36%. It has been verified that the proposed path-tracking algorithm meets the accuracy and robustness requirements of path-tracking when the transplanter turns at the headland.

ACKNOWLEDGEMENTS

The work was supported by the National Natural Science Foundation of China (52172396).

REFERENCES

- [1] Boyd, S., Ghaoui, L.E., Feron, E., Balakrishnan, V. (1994). Linear Matrix In-equalities in Systems and Control Theory. SIAM Studies in Applied Mathematics. <https://epubs.siam.org/doi/book/10.1137/1.9781611970777>

- [2] Chi, R.J., Xiong, Z.X., Jiang, L.T., Ma, Y.Q. and Huang, X.L., Zhu, X.L. (2022). Path-tracking control algorithm of transplanter based on model prediction (基于模型预测的插秧机路径跟踪控制算法). *Transactions of the Chinese Society for Agricultural Machinery*, Vol. 53(11), pp. 22-30, 99. (in Chinese)
- [3] Dekhterman, S. R., Cichon, M. T., Norris, W. R., Nottage, D., Soylemezoglu, A. (2024). Hierarchical rule-base reduction fuzzy control for constant velocity path-tracking of a differential steer vehicle. *Journal of Field Robotics*. Vol. 41, pp. 718-734. <https://doi.org/10.1002/rob.22287>
- [4] Fukumoto, T., Chida, Y., Tanemura, M. (2022). Improved tracking performance by H^∞ control for an automatic spinach harvester. *IFAC-Papers OnLine*, Vol. 55(25), pp. 265-270. <https://doi.org/10.1016/j.ifacol.2022.09.357>
- [5] Gagliardi, G., Casavola, A., Toscano, S. (2022). Linear Parameter Varying Control Strategies for Combined Longitudinal and Lateral Dynamics of Autonomous Vehicles. *2022 European Control Conference (ECC), (London, United Kingdom)*. Vol. 2022, pp.181-186. <https://doi.org/10.23919/ECC55457.2022.9838177>
- [6] Gang, M., Kim, H.-J., Jeon, C.-W., Yun, C. (2022). Design and Testing of Headland Turning Algorithms Based on Transition Distance Prediction for Autonomous Rice Transplanter. *Journal of the ASABE*, Vol. 65(6), pp. 1277-1291. Doi: 10.13031/ja.14952
- [7] Gökçe, B., Koca, Y. B., Aslan, Y., Gökçe, C. O. (2021). Particle swarm optimization-based optimal PID control of an agricultural mobile robot. *Comptes rendus de l'Académie bulgare des Sciences*. Vol. 74(4), pp. 568-575. DOI: 10.7546/CRABS.2021.04.12
- [8] Gong, J.W., Jiang, Y., Xu, W. (2014). Model Predictive Control for Self-driving Vehicles. Beijing: Beijing institute of technology Press. (in Chinese)
- [9] He, J., Hu, L., Wang, P., Liu, Y.X., Man, Z.X., Tu, T.P., Yang, L.N., Li, Y.Y., Yi, Y.L., Li, W.C., Luo, X.W. (2022). Path-tracking control method and performance test based on agricultural machinery pose correction. *Computers and Electronics in Agriculture*, Vol. 200, pp. 107185. <https://doi.org/10.1016/j.compag.2022.107185>
- [10] Hossain, T., Habibullah, H., Isiam, R. (2022). Steering and Speed Control System Design for Autonomous Vehicles by Developing an Optimal Hybrid Controller to Track Reference Trajectory. *Machines*, Vol. 10, pp. 420. <https://doi.org/10.3390/machines10060420>
- [11] Ji, X., Ding, S.H., Wei, X.H., Cui, B.B. (2023). Path-tracking of unmanned agricultural tractors based on a novel adaptive second-order sliding mode control. *Journal of the Franklin Institute*, Vol. 360(8), pp. 5881-5831. <https://doi.org/10.1016/j.jfranklin.2023.03.053>
- [12] Kim, S., Jang, M., La, H., Oh, K. (2023). Development of a Particle Filter-Based Path-tracking Algorithm of Autonomous Trucks with a Single Steering and Driving Module Using a Monocular Camera. *Sensors*, Vol. 23, pp. 3650. <https://doi.org/10.3390/s23073650>
- [13] Legrand, R., Claveau, F., Chevrel, P., Rancinangue, B., Dollet, A. (2022). H_2/H^∞ robust lateral control of an off-road two-steering-axle vehicle on slippery sloping soils. *IFAC-Papers OnLine*, Vol. 55(25), pp. 187-192. <https://doi.org/10.1016/j.ifacol.2022.09.345>
- [14] Li, G., Wang, Y., Guo, L.F., Tong, J.H., He, Y. (2018). Improved pure pursuit algorithm for rice transplanter path-tracking (插秧机导航路径跟踪改进纯追踪算法). *Transactions of the Chinese Society for Agricultural Machinery*, Vol. 49(05), pp. 21-26. (in Chinese)
- [15] Li, Y.B., Li, H., Guo, X.N. (2020). Online parameter identification of rice transplanter model based on IPSO-EKF algorithm. *INMATEH - Agricultural Engineering*, Vol. 61(2), pp. 25-34. <https://doi.org/10.35633/inmateh-61-03>
- [16] Li, Y.M., Wu, T., Xiao, Y.F., Gong, L., Liu, C.L. (2023). Path planning in continuous adjacent farmlands and robust path-tracking control of a rice-seeding robot in paddy field. *Computers and Electronics in Agriculture*, Vol. 210, 107900. <https://doi.org/10.1016/j.compag.2023.107900>
- [17] Oh, K., Seo, J. (2023). Development of a Sliding-Mode-Control-Based Path-Tracking Algorithm with Model-Free Adaptive Feedback Action for Autonomous Vehicles. *Sensors*, Vol. 23, pp. 405. <https://doi.org/10.3390/s23010405>

- [18] Rath, B.N., Subudhi, B. (2022). A robust model predictive path following controller for an Autonomous Underwater Vehicle. *Ocean Engineering*, Vol. 244, pp. 110265. <https://doi.org/10.1016/j.oceaneng.2021.110265>
- [19] Shojaei, K., Taghavifar, H. (2022). Input-output feedback linearization control of a tractor with n-trailers mechanism considering the path curvature. Proceedings of the Institution of Mechanical Engineers. *Part C: Journal of Mechanical Engineering Science*, Vol. 236(17), pp. 9700-9715. <https://doi.org/10.1177/09544062221088236>
- [20] Simonelli, R., Höffmann, M., Patel, S., Büskens, C. (2023). Optimal Path-tracking: Benchmarking an NMPC for a Wide-Span Autonomous Agricultural Machine. *2023 European Control Conference (ECC), (Bucharest, Romania)*. Vol. 2023, pp.1-7. <https://doi.org/10.23919/ECC57647.2023.10178268>
- [21] Su, H. Y. (2010). Basic Theory of Robust control. Beijing: Science Press. (in Chinese)
- [22] Taghia, J., Wang, X., Lam, S., Katupitiya, V. (2017). A sliding mode controller with a nonlinear disturbance observer for a farm vehicle operating in the presence of wheel slip. *Robot*, Vol. 41(1), pp. 71-88. <https://doi.org/10.1007/s10514-015-9530-4>
- [23] Tang, X.T., Tao, J.F., Li, Z.T., Li, Y.M., Liu, C.L. (2018). Fuzzy control optimization method for stability of path-tracking system of automatic transplanter (自动驾驶插秧机路径跟踪系统稳定性模糊控制优化方法). *Transactions of the Chinese Society for Agricultural Machinery*, Vol. 49(01), pp. 29-34. (in Chinese)
- [24] Trendafilov, K., Tihanov, G. (2022). Comparative Analysis of the Headland Width when Making T-turns by a Mounted Machine-Tractor Unit on an Irregularly-Shaped Field. *INMATEH-Agricultural Engineering*, Vol. 67(2), pp. 221-232. <https://doi.org/10.35633/inmateh-67-22>
- [25] Xu, M.Z., Liu, Q.H. (2022). Design and simulation of intelligent vehicle trajectory tracking control algorithm based on LQR and PID (基于 LQR 和 PID 的智能车轨迹跟踪控制算法设计与仿真). *Journal of Taiyuan University of Technology*, Vol. 53(5), pp. 877-885. (in Chinese)
- [26] Yang, Y., Li, Y.K., Wen, X., Zhang, G., Ma, Q.L., Cheng, S.K., Qi, J., Xu, L.Y., Chen, L.Q. (2022). An optimal goal point determination algorithm for automatic navigation of agricultural machinery: Improving the tracking accuracy of the Pure Pursuit algorithm. *Computers and Electronics in Agriculture*, Vol. 194, pp. 106760. <https://doi.org/10.1016/j.compag.2022.106760>

DETECTION OF BLACK HEART DISEASE IN SEED POTATO BASED ON TRANSMISSION SPECTROSCOPY TECHNIQUE

基于透射光谱技术的马铃薯种薯黑心病检测研究

Xianhe WANG¹⁾, Min HAO^{1,*)}, Xingtai CAO¹⁾, Yutao ZHANG¹⁾

¹⁾College of Electromechanical Engineering, Inner Mongolia Agricultural University, Hohhot, Inner Mongolia Autonomous Region 010018, China

*Corresponding authors, Email: hhhthaomin@163.com

DOI: <https://doi.org/10.35633/inmateh-73-42>

Keywords: Neural networks, Transmission spectroscopy, Black heart, Seed Potatoes

ABSTRACT

Black heart disease is one of the screening indicators of seed potatoes, which has a serious impact on the quality and yield of potato, and at present there are fewer non-destructive testing methods for internal defects of seed potatoes. This paper aims to utilize non-destructive testing technology to quickly identify qualified and black hearted seed potatoes, and then to protect yield and food security. In this paper, transmission spectroscopy system was utilized to collect the spectral data of 104 qualified seed potatoes and 104 black hearted seed potatoes in 450~940 nm band. Subsequently, four algorithms, namely Savitzky-Golay (SG), Standard Normal Variate (SNV), Multiplicative Scatter Correction (MSC) and First-order Derivative (FD), were utilized to pre-process the seed potatoes spectral data to improve the data noise ratio. Feature wavelength extraction was made using Competitive Adaptive Reweighted Sampling (CARS) and Successive Projections Algorithm (SPA) to enhance the sample data characteristics and improve the model interpretability. The construction of classification models for qualified and black hearted seed potatoes relied on two deep learning techniques, Convolutional Neural Networks (CNN) and Recurrent Neural Network (RNN), which were trained and tested for the feature bands respectively. The experimental results showed that SG-CARS-CNN was the optimal combination of classification algorithms, and the classification accuracies of both the training set and the test set reached 100%, which improved the accuracy of the test set by 3.85% compared with that of the traditional machine learning algorithms, and provided an accurate method for the rapid screening of qualified seed potatoes.

摘要

黑心病是马铃薯种薯筛选指标之一，对马铃薯的品质和产量有严重的影响，而目前针对马铃薯种薯内部缺陷无损检测方法较少，本文旨在利用无损的检测技术快速识别合格与黑心马铃薯种薯，进而保障马铃薯产量和粮食安全。本文利用透射光谱系统采集 104 个合格种薯和 104 个黑心种薯 450~940nm 波段光谱数据，随后利用 SG 卷积平滑 (SG)、标准正态变换法 (SNV)、多元散射校正法 (MSC) 和一阶导数 (FD) 4 种算法对马铃薯种薯光谱数据预处理，以提高数据信噪比；利用竞争性自适应重加权采样法(CARS)和连续投影算法(SPA)进行特征波长提取，以强化样本数据特征和提高模型可解释性；合格与黑心马铃薯种薯分类模型的构建依赖于卷积神经网络(CNN)和循环神经网络(RNN) 2 种深度学习技术，分别对特征波段进行训练与测试。试验结果表明，SG-CARS-CNN 为最优分类算法组合，训练集和测试集分类准确度均达到 100%，相比于传统机器学习算法测试集准确率提高了 3.85%，为快速筛选合格马铃薯种薯提供准确方法。

INTRODUCTION

Potato is the fourth largest food crop in China, with high nutritional and economic value, strong adaptability, large yield, wide range of uses (Wang et al., 2018), and the quality of seed potatoes directly affects the level of potato production in China. No. 1 of the 2024 central document states that the production of food and important agricultural products should be grasped to ensure national food security and food security of the country with the experience of the "Ten Million Project" (Jiang et al., 2024). Therefore, in order to accelerate the modernization of agriculture and fight a good battle for the seed industry (Ning et al., 2021), efficient screening of excellent seed potatoes is one of the important guarantees for food security in China.

Xianhe Wang, Student; Min Hao, Associate professor; Xingtai Cao, Student; Yutao Zhang, Student.

Black heart disease is one of the important screening indicators of seed potatoes, and its use in seeding can lead to the spread of the disease, reduce yield and affect food safety and other hazards. Seed potatoes are usually screened by machine and by hand. According to China's seed potatoes quality standard (GB/T 29377-2012), the permissible rate of black heart disease is 0.1% (GB/T 29377-2012, 2012). Manual screening is overly dependent on manual judgment, low detection and sorting precision (Tiwari *et al.*, 2020), and unable to screen out black heart disease seed potatoes, while machine screening is mainly for potatoes weight and shape screening, and there is a certain limitation on the screening of black heart disease seed potatoes. In the field of agriculture, spectral detection technology is usually used in plant disease detection and internal quality detection of agricultural products, with the advantages of being non-destructive and accurate. Since black heart disease of seed potatoes belongs to the internal defects of agricultural products, it is feasible to use spectral detection technology to screen out seed potatoes containing black heart disease.

At present, most of the potato quality detection uses traditional machine learning algorithms to extract features and construct quality detection models. Zhou *et al.* (2012) used diffuse reflectance spectra by the second-order derivative and normalized combination of the model built on the test set of samples identified the correct rate of 92.31%. Gao *et al.* (2013) used partial least squares discriminant model (PLS-DA) to establish a discriminant model for potato black heart disease, and verified the feasibility of the method. Han *et al.* (2021) used principal component analysis combined with partial least squares discriminant model (PCA-PLS-DA) to establish a discriminant model of potato black heart disease, and its accuracy was 96.73%. Foreign studies on potato black heart disease are fewer and still remain in the detection of potato nutrients. Abukmeil *et al.* (2022) estimated the nutrients in potato plants by detecting the reflectance of potato leaves, thus replacing the destructive method of chemical experiments.

However, traditional machine learning algorithms have low detection accuracy and weak generalization ability, resulting in decreased performance in practical production. In recent years, deep learning algorithms have been developed, which are fast, accurate and efficient, and can effectively extract features to improve production efficiency and automation. Khorramifar *et al.* (2022) predicted potato soluble solids pH using artificial neural network (ANN) with an accuracy of 92%. Gupta *et al.* (2023) used convolutional neural network (CNN) for potato leaf disease classification with 90% accuracy.

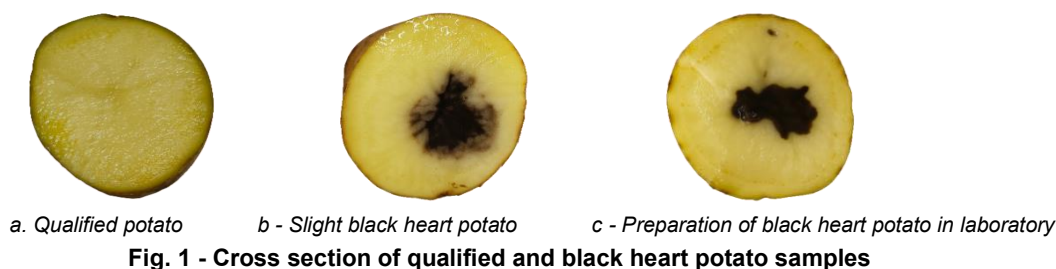
In summary, domestic and foreign research on potato defect detection mainly stays in the research of potato skin, dry matter, nutrient elements, ring rot and so on. Our country has a very low permission rate for black heart disease seed potatoes, and there is less research on the detection of black heart disease defects in potato, and the detection accuracy is lower. Therefore, for the current problem of low screening accuracy of seed potatoes containing black heart disease, this paper proposes a study on black heart disease detection in seed potatoes based on transmission spectroscopy technology, using visible-near infrared spectrometer to collect transmission spectroscopy data of seed potatoes, and establishing a dichotomous classification model of seed potatoes with black heart disease by comparing and analyzing multiple algorithmic combination models to meet the requirements of screening black heart disease in seed potatoes in China.

MATERIALS AND METHODS

Sample collection and preparation

Ulanchoabu is the potato capital, located in the central part of the Inner Mongolia Autonomous Region. The study varieties used were field-harvested Ulanchoabu purple-flowered white seed potatoes, which are characterized by thin skin, large tubers, good shape, and few pests and diseases. Since seed potatoes containing black heart disease could not be directly observed, this paper used the field sample harvesting method and laboratory sample preparation method for sample collection, with 104 qualified seed potatoes and 104 black hearted seed potatoes, totaling 208. The cross section of qualified and black heart potato samples are shown in Fig. 1a, 1b and 1c. Black heart potatoes are completely different from certified potatoes. Blackheart potatoes are rotten, soft and smelly on the inside.

Potato black heart disease is caused by high temperature and hypoxic conditions. The laboratory sample preparation method is: field-harvested seed potatoes were vacuum-sealed and transferred to a thermostat and stored at 40° C for 27 h. During this period, the temperature was adjusted to 3° C at 6-h intervals to minimize the respiration rate and stored for 1 h. The temperature was adjusted to 3° C at 6-h intervals to minimize the respiration rate.



Transmission Spectroscopy Data Acquisition System

Transmission spectroscopy data acquisition system mainly includes: DELL laptop, Ocean View spectroscopy acquisition software, Ocean Optics USB4000 micro-spectrometer, optical fiber, collimator mirror, twelve 60 W halogen lamps. Ocean Optics USB4000 spectrometer has spectral band range of 450 nm ~ 940 nm and a total of 3151 bands; halogen lamp is added in the bulb halogen gas at high temperatures to achieve luminescence, with high luminous efficacy, long life, it will not affect the quality of the samples, the transmittance system of twelve 60 W halogen lamps is placed in the experimental samples of the upper-left 45° and the upper-right 45°. The structure of transmission spectrum data acquisition system is shown in Fig. 2, the light passes through the sample, and is transmitted to the spectrometer through the collimating mirror and optical fiber, and then the optical signal is converted into an electrical signal.

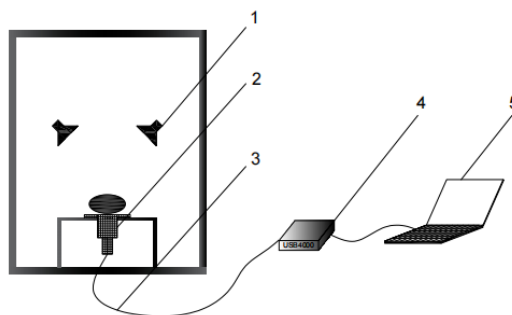


Fig. 2 - Structure of transmission spectrum data acquisition system
1 - Halogen lamp; 2 - Collimator; 3 - Fiber optic; 4 - USB4000 Spectrometer; 5 - Laptop

In order to ensure the stability of the test and its accuracy, the spectrometer needs to be switched on and warmed up for 30 min before the test, and after the spectrometer and the light source are stabilized, the reference correction is carried out, respectively, by using the blackboard and the collection of standard cellophane (yellow) to cover the collimating mirror, to obtain the dark-field light intensity and the reference light intensity, with the aim of eliminating the systematic error and maintaining the consistency of the measurement results.

$$T = \frac{T_s - T_d}{T_r - T_d} \quad (1)$$

In the formula, T is the transmissivity, T_s is the original light intensity, T_r is the reference light intensity, T_d is the dark field light intensity.

Data preprocessing

During the experimental process, the transmission spectroscopy data acquisition system will generate electronic noise, ambient temperature fluctuations and other interferences, and the differences in the size and shape of the experimental samples will affect the consistency of the spectral data. Therefore, in order to reduce the influence of environmental noise, improve the signal-to-noise ratio of spectral data, and optimize the model performance (Li et al., 2024; Liu et al., 2024), it is necessary to preprocess the transmission spectral data of the black heart seed potatoes before building the model. In this paper, the preprocessing method uses the most commonly used SG convolutional smoothing, standard normal transform method, multiple scattering correction (MSC) and first-order derivatives (FD) four algorithms, and the optimal preprocessing algorithms are derived from the comparative analysis of traditional machine learning models using support vector machine (SVM).

Characteristic Wavelength Extraction Competitive Adaptive Reweighted Sampling (CARS)

The Competitive Adaptive Reweighted Sampling (CARS) method aims to select the most competitive band combinations (Zhao *et al.*, 2023). Monte Carlo sampling is used to select some samples for modeling, and the remaining samples are used as a prediction set to build a partial least squares (PLS) model to obtain the regression coefficients for the first wavelength:

$$|K_i| (i = 1, 2, \dots, p) \quad (2)$$

The combinations of wavelengths with higher weights are filtered as a new subset using the exponential decay function:

$$r_i = ae^{-bj} (j = 1, 2, \dots, N) \quad (3)$$

In the formula, j denotes the j^{th} Monte Carlo sampling; N denotes the total number of Monte Carlo sampling; a and b are constants.

After several calculations, the evaluation of weights is used for variable selection:

$$\omega_i = |K_i| / \sum_{i=1}^p |K_i| (i = 1, 2, \dots, p) \quad (4)$$

Finally, the subset with the smallest root mean square error of validation (RMSECV) is chosen as the characteristic wavelength of black heart disease in seed potatoes by selecting cross validation.

Successive Projection Algorithm (SPA)

Successive projection algorithm (SPA) is a forward iterative method of feature variable screening, by projecting one wavelength onto another wavelength to compare the size of the projection vector, the wavelength with larger projection is used as the feature wavelength; with each iteration, SPA selects the wavelength with the least covariance with the screened feature wavelength as the new feature wavelength, which minimizes the covariance feature; the cycle repeats itself and the wavelengths obtained subset contains most of the data variability and is used as the final feature wavelength. Therefore, SPA is less sensitive to noise and outliers, and feature wavelength extraction can effectively reflect the essential characteristics of the data (Arshaghi *et al.*, 2021). Transmission spectroscopy data acquisition system is susceptible to noise interference, so it is chosen to utilize SPA for feature wavelength extraction of the data pre-processed by SG.

Neural network model

Convolutional neural network (CNN)

Convolutional neural network (CNN) is one of the typical deep learning algorithms, the core of which is to use convolutional and pooling layers to extract data features and classify them through fully connected layer (Al-Adhaileh *et al.*, 2023; Huang *et al.*, 2022). The model has two convolutional layers with 16 and 32 convolutional kernels, respectively. Since the ReLU function has an input value equal to itself in the positive interval and an output of 0 in the negative interval, it makes the network nonlinear; since the ReLU function always has a gradient of 1 on the positive semiaxis, which does not decrease with the number of layers, it is a better solution compared to other activation functions such as Sigmoid or Tanh activation functions that can better mitigate the gradient vanishing problem. Therefore, utilizing the ReLU function as the activation function of the model is more helpful for model training.

$$ReLU = \max(0, x) \quad (5)$$

In the formula, x denotes the feature input in the network.

The two pooling layers reduce the data dimensionality and prevent overfitting, with kernel sizes set to 1 and 2, step sizes of 2 for both. After combining with the ReLU activation function, the nonlinear expression ability of the network can be increased to improve the model generalization ability. The fully connected layer unfolds the feature wavelengths of different samples into one-dimensional vectors for integration, and uses the Softmax function to map the feature representations learned from the convolutional and pooling layers to the samples (Rogers *et al.*, 2023), and ultimately realizes the role of a classifier that transforms from the feature wavelengths to the qualified and the black heart seed potatoes. The structure simplification diagram of CNN classification model is shown in Fig.3.

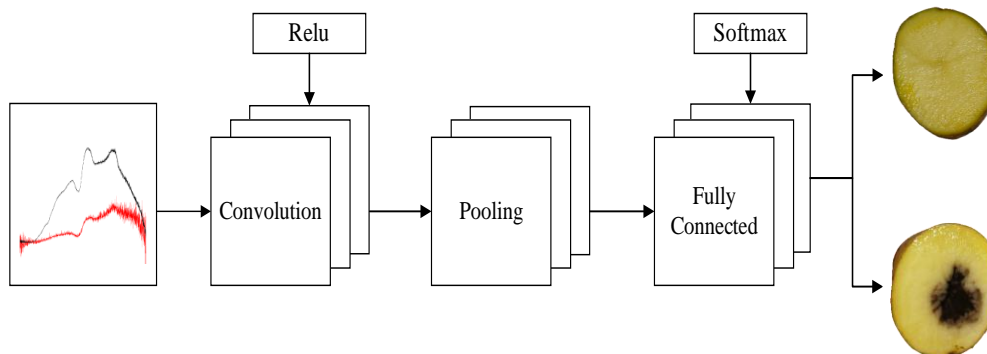


Fig. 3 - Structure simplification diagram of CNN classification model

Recurrent neural network (RNN)

Recurrent neural network (RNN) consists of input layer, hidden layer and output layer, with weight sharing property and memory function. The core of RNN is the hidden layer, which optimizes the model and improves the classification ability through the way of neuron cyclic connection. The weight sharing property is manifested in the fact that the recurrent network uses the same parameters to process the data at each moment, which makes the model reduce the parameters during learning, and reduces the risk of overfitting. The recurrent network has a certain memory ability by processing sequential data, which is mainly manifested in the fact that the network takes into account the influence of inputs from other moments every time it processes data or outputs, and transmits and saves the key information through the memory units in the network, which gives the network a "memory" function. The network is endowed with the function of "memory". The weight sharing and memory function can effectively reduce the complexity of the model and give the dependence of each neuron in the network, which can more powerfully explain the relationship between the feature wavelength and the classification results in the classification of qualified and black heart disease seed potatoes. The structure of the RNN classification model is shown in Fig. 4.

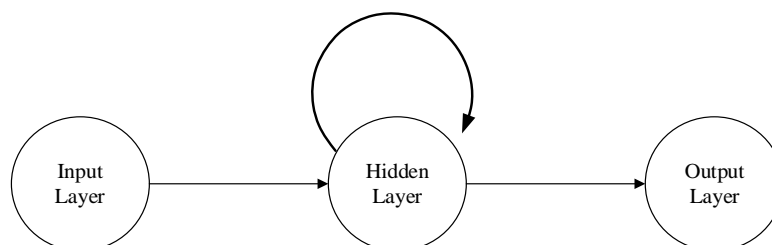


Fig. 4 - Structure simplification diagram of RNN classification model

RESULTS AND ANALYSIS

Data preprocessing

In order to avoid oversaturation, the integration time of the spectrometer was set to 100 ms, and the acquisition band was 450 ~ 940 nm, 104 transmission spectra of qualified seed potatoes and 104 transmission spectra of black-centered seed potatoes were collected, totaling 208 samples of data. The average curve of wavelength-transmission of qualified and black-cored potatoes are shown in Fig. 5.

Due to the cell death of the pith tissue in the center of black heart seed potatoes tubers, the central part of the tubers became black and partly cracked and hollow, which was manifested as the loss of water and hardening, and as shown in Fig. 1b and Fig. 1c, the transmittance of black-centered potatoes was obviously lower than that of normal potatoes, and the two presented the maximum difference at 717 nm, and at 652 nm, and the maximum difference at 652 nm, and at 652 nm. The maximum difference between the two was at 717 nm, and the absorption peaks were obvious near 652 nm, 717 nm and 814 nm.

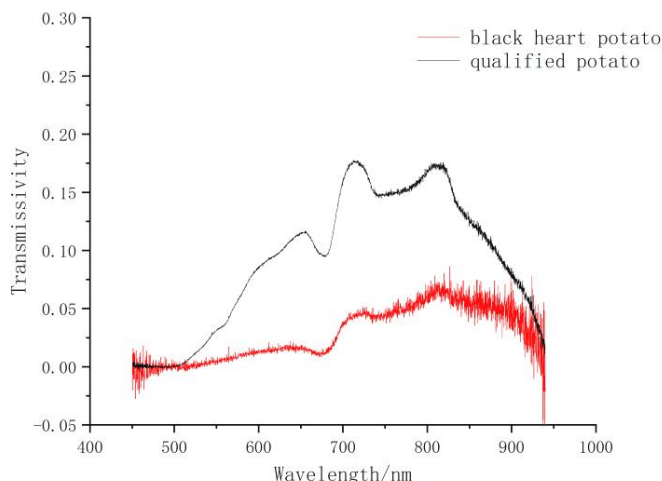


Fig. 5 - Wavelength-transmissivity curve of qualified potato and black heart potato

Table 1 shows the support vector machine discriminant model (SVM) using different preprocessing methods.

Table 1

Classification models of different preprocessing methods based on SVM

| Algorithmic | Training set | | Test set | |
|-------------|------------------|-----------------|------------------|-----------------|
| | Number of Errors | Correctness / % | Number of Errors | Correctness / % |
| Raw | 10 | 93.59 | 4 | 92.31 |
| SG | 4 | 97.44 | 2 | 96.15 |
| SNV | 9 | 94.23 | 3 | 94.23 |
| MSC | 6 | 96.15 | 4 | 92.31 |
| FD | 11 | 92.95 | 5 | 90.38 |

The classification models of different preprocessing methods based on SVM are shown in Table 1, by comparing and analyzing the number of misclassification and correct rate of different preprocessing methods, the number of misclassification in the correction set of first-order derivative (FD) method is 11, with a correct rate of 92.95%, and the number of misclassification in the prediction set is 5, with a correct rate of 90.38%; the number of misclassification in the correction set of Savitzky-Golay is 4, with a correct rate of 97.44%, and the number of misclassification in the prediction set is 2, with a correct rate of 96.15%; among the four preprocessing methods first order derivative (FD) has the lowest classification accuracy and S-G convolutional smoothing has the highest classification accuracy.

In summary, the Savitzky-Golay will be used to preprocess the transmission spectral data of seed potatoes. However, this preprocessing method does not meet the black heart disease allowable rate of seed potatoes quality standard (GB18133-2000) formulated in China, and the spectral band dimension is large, which is weak for model interpretation, so the spectral data preprocessed by Savitzky-Golay will be downgraded to extract the most relevant features.

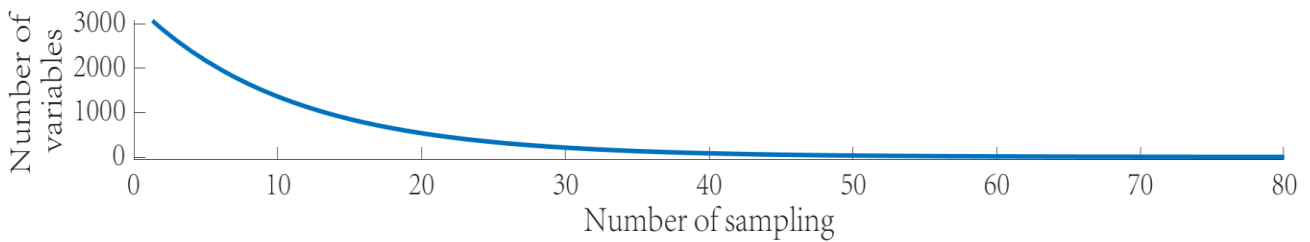
Characteristic Wavelength Extraction

The transmission spectral data acquisition system is used to obtain 3151 feature information; however, the number of these features is huge and contains irrelevant noise, not all features are beneficial to model building, irrelevant features will lead to a reduction in the accuracy of the model, and the huge feature latitude cannot meet the real-time, accuracy, and interpretability of the model detection (Lakshmanan et al., 2023). So, in order to meet the requirements of fast and accurate modeling, improve the model interpretation ability, reduce the consumption of computational calculations, and enhance the model performance. In this paper, Competitive Adaptive Reweighted Sampling (CARS) and Successive Projection Algorithm (SPA) were utilized for feature wavelength extraction, and were combined with Convolutional Neural Network (CNN) and Recurrent Neural Network (RNN) to build a binary classification model.

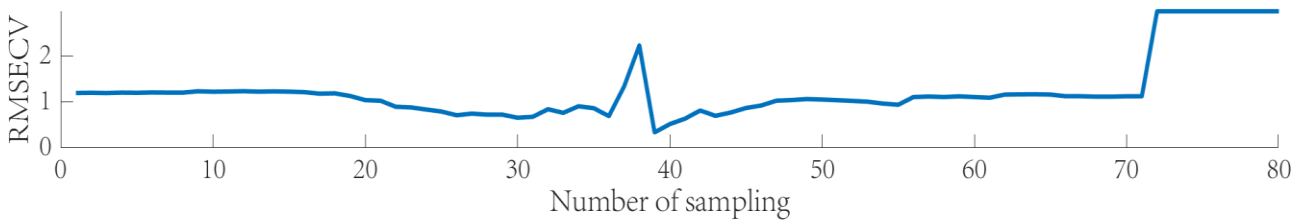
Competitive Adaptive Reweighted Sampling (CARS)

In this paper, the CARS algorithm was utilized to downscale the spectral data pre-processed by SG respectively, using 80 times Monte Carlo sampling and 5-fold cross-validation, and its running results are shown in Fig. 6.

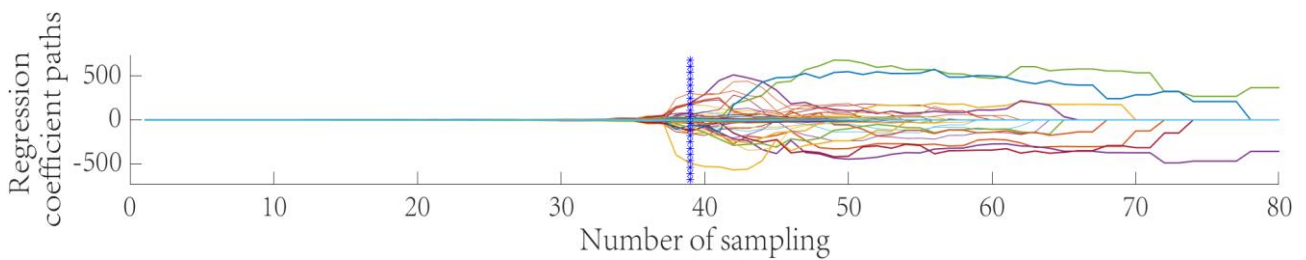
From Fig. 6b, it can be seen that the cross-validation RMS error gradually decreases in the first 30 samples, indicating that the feature variables with less relevance to the black hearted seed potatoes are eliminated; the fluctuation of the RMS error of the cross-validation is larger in the 30th to 39th samples, in which the 38th sampling eliminates some important parameters; then the minimum cross-validation RMS error is obtained in the 39th sampling, which achieves the optimal extraction of feature wavelengths, and 83 feature wavelengths are obtained at this time, accounting for 2.63% of the whole band.



a - Number of variables



b - Root mean square error of cross-validation



c - Regression coefficient paths

Fig. 6 - Variables selected by SG-CARS method

Successive Projection Algorithm (SPA)

The minimum value of the number of wavelengths is set to 1, and the maximum value is set to 50, and the spectral data after S-G preprocessing are downgraded, and as the number of selected feature wavelengths increases the root mean square error decreases, and finally 30 feature wavelengths are extracted, accounting for 0.95% of the full wavelength range, and at this time, the root mean square error is 0.168. The SPA selects this point because the feature wavelengths already contain the feature information of the original spectral data and has interpretability. The variables selected by SG-SPA method is shown in Fig. 7.

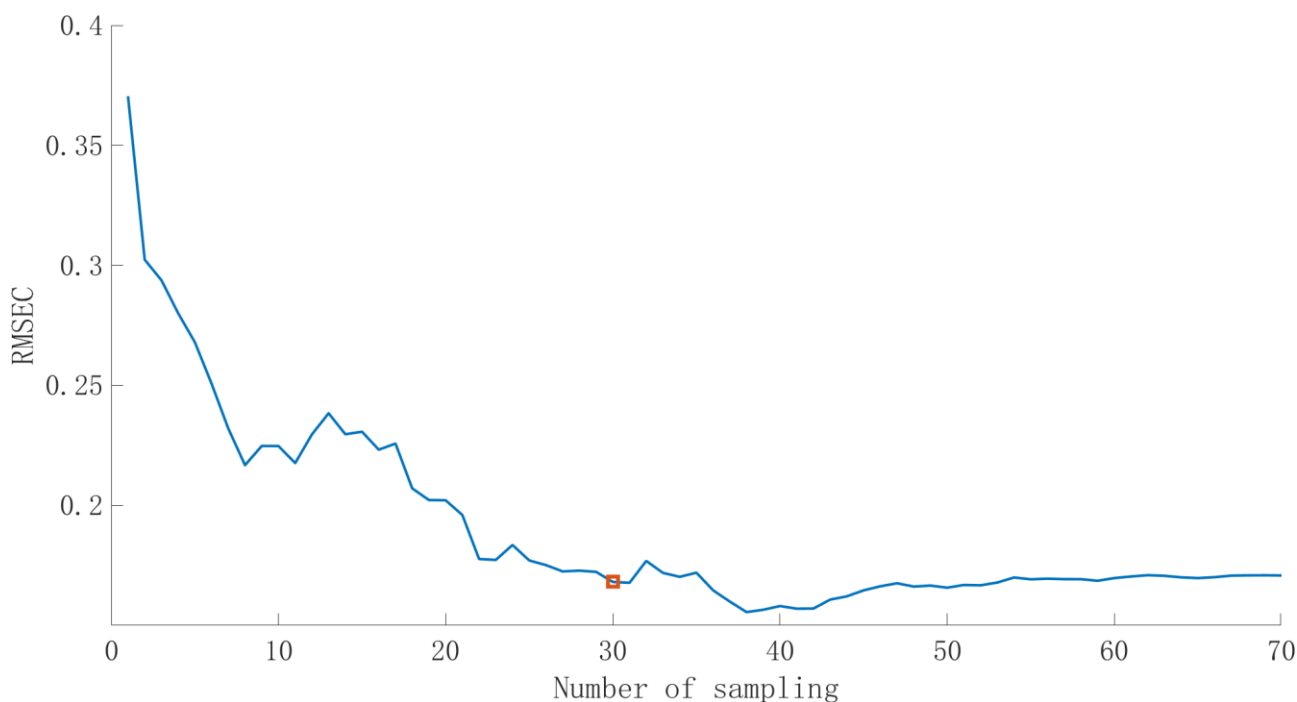


Fig. 7 - Variables selected by SG-SPA method

Modeling the classification of black heart and qualified potatoes

Data set segmentation

The KS algorithm (Kennard-Stone, KS) is used to divide the dataset, the core of which is to iteratively select the features that are least similar to those in the current training set, so that the samples in the training set are dispersed as much as possible as a way to cover the sample space more comprehensively and strengthen the interpretability of the model structure. The feature distribution of seed potatoes spectral data is complex, and the use of the KS algorithm can effectively capture the overall structure of seed potatoes spectral data and improve the stability and classification ability of the model. Using the KS algorithm to divide the data set according to the ratio of 3:1, 152 and 56 sample data were obtained for the training set and test set, respectively, and qualified seed potatoes were set as class 1 samples, and black hearted seed potatoes were set as class 2 samples.

CNN classification modeling

The model sets the initial learning rate of the CNN model to 0.01, the regularization parameter to 0.01, and the number of iterations to 100, and the SG preprocessed data are used to extract features and build the CNN classification model using CARS and SPA, respectively.

Table2

Combined classification model of different algorithms based on CNN

| Algorithmic combination | Training set accuracy/% | Test set accuracy/% |
|-------------------------|-------------------------|---------------------|
| RAW-CARS-CNN | 90.38 | 82.69 |
| RAW-SPA-CNN | 83.97 | 88.46 |
| SG-CARS-CNN | 100 | 100 |
| SG-SPA-CNN | 98.72 | 100 |

The combined classification model of different algorithms based on CNN are shown in Table 2, the classification accuracy of the CNN model built after extracting the feature wavelengths of the unprepared data is lower than that of the CNN model after SG preprocessing, and the combination of SG-CARS-CNN algorithms has the highest classification accuracy, with the classification accuracy of 100% in both the training set and the test set. The SG-CARS-CNN training set and test set confusion matrix are shown in Fig. 8 and Fig. 9.

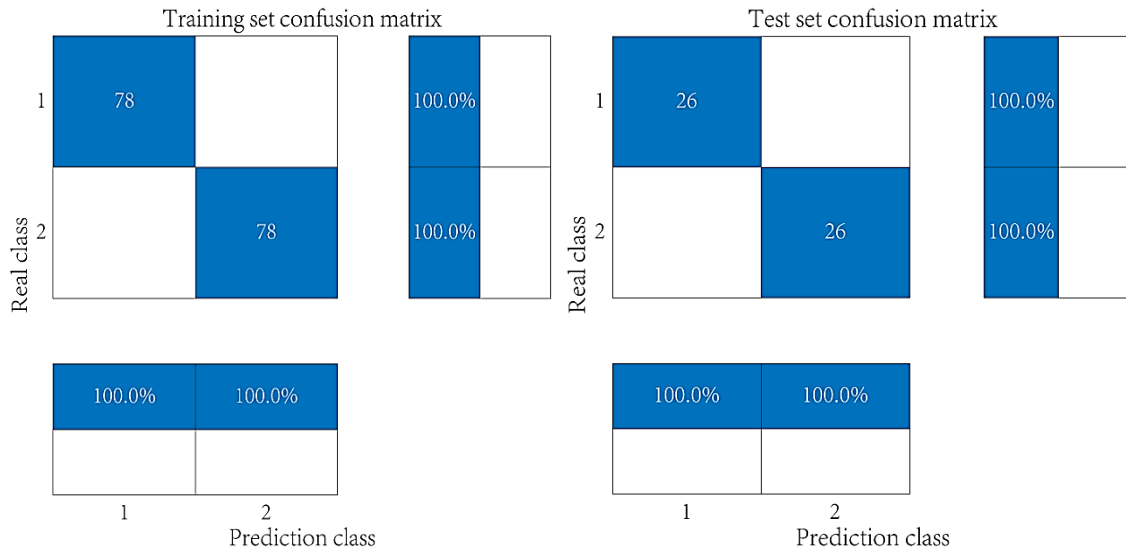


Fig. 8 - SG-CARS-CNN training set and test set confusion matrix

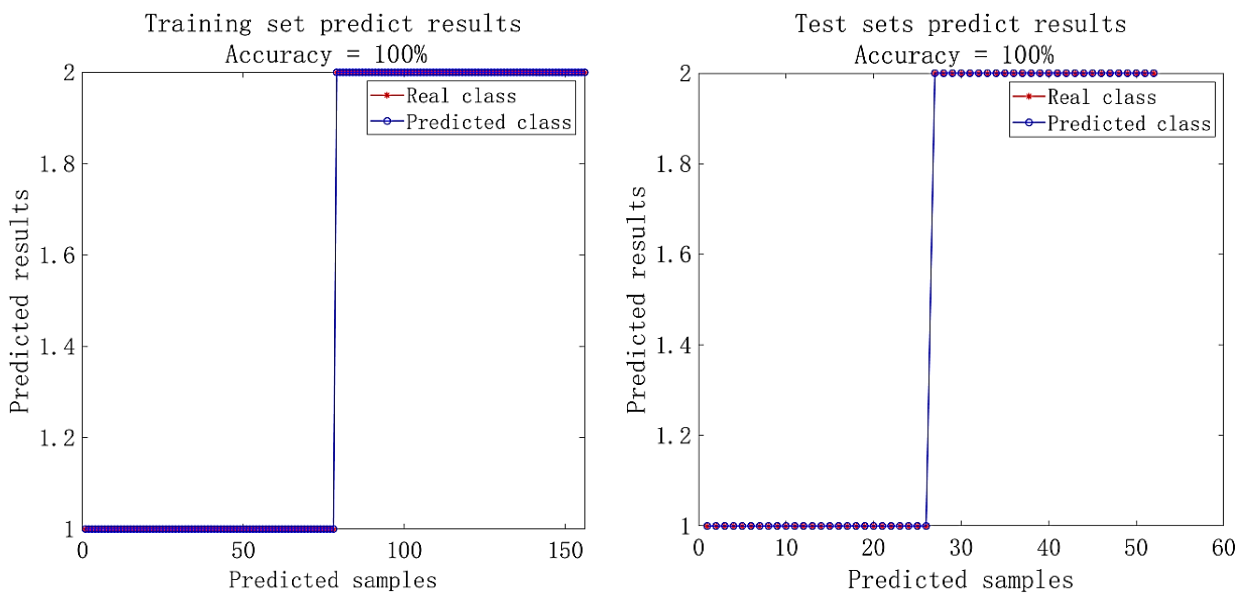


Fig. 9 - SG-CARS-CNN training set and test set accuracy

RNN classification modeling

The dataset division and model parameter settings are the same as CNN, and the RNN binary classification model is constructed using the SG preprocessed data after the feature wavelengths are extracted by CARS and SPA, respectively.

The SG-CARS-RNN training set and test set accuracy are shown in Fig. 10, the accuracy of the training set is 98.08%, in which all of the class 1 samples are successfully recognized, and three of the class 2 samples are misclassified as class 1 samples; the accuracy of the test set is 98.08%, in which all of the class 1 samples are accurately recognized, and one of the class 2 samples is misclassified as class 1 sample.

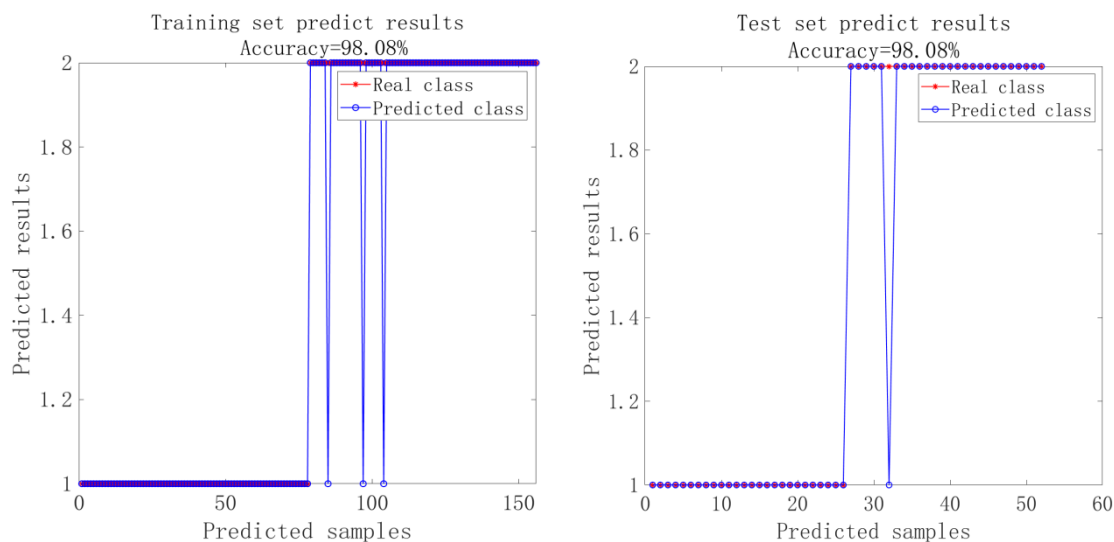


Fig. 10 - SG-CARS-RNN training set and test set accuracy

Table 3 shows the comparison of different combined classification models based on CNN and RNN, in the RNN model, the SG-CARS-RNN algorithm combination training set and test set have the highest classification accuracy, both of which are 98.08%; while in the CNN model, the SG-CARS-CNN algorithm combination training set and test set have the highest classification accuracy, both of which are 100%, which has an advantage of 1.92% over the RNN model.

Table3

Comparison of different combined classification models based on CNN and RNN

| Model | Algorithmic combination | Training set accuracy/% | Test set accuracy/% |
|-------|-------------------------|-------------------------|---------------------|
| CNN | SG-CARS-CNN | 100 | 100 |
| | SG-SPA-CNN | 98.72 | 100 |
| RNN | SG-CARS-RNN | 98.08 | 98.08 |
| | SG-SPA-RNN | 92.31 | 92.31 |

CONCLUSIONS

In this paper, the detection of black heart disease in seed potatoes was realized based on the fusion of transmission spectroscopy and neural network.

(1) Utilizing different preprocessing methods has an impact on the accuracy of the established classification model of qualified and black hearted seed potatoes, among the four preprocessing methods utilizing Savitzky-Golay preprocessing could achieve the highest classification accuracy, and the classification accuracy of the SG-SVM test set was 96.15%.

(2) Using CARS to extract the characteristic wavelengths of the seed potatoes spectral data pre-processed by Savitzky-Golay, 83 characteristic wavelengths were extracted from the original 3151 wavelengths, which accounted for 2.63% of the whole band; and using SPA to extract the characteristic wavelengths of the seed potato spectral data pre-processed by Savitzky-Golay, which finally extracted 30, which accounted for 0.95% of the whole band.

(3) After SG preprocessing, CNN and RNN classification models were built using CARS and SPA, respectively. Among the CNN models, the combined SG-CARS-CNN algorithm had the highest classification accuracy, reaching 100% in both the training and test sets; among the RNN models, the combined SG-CARS-RNN algorithm had the highest classification accuracy, with 98.08% in both its training and test sets. Although SPA extracted more concise feature wavelengths, none of the classification algorithms built using SPA had less accuracy than CARS, which is more suitable for feature wavelength extraction from seed potatoes spectral data.

The combined SG-CARS-CNN algorithm was finally used as a black heart disease detection model for seed potato, and its classification accuracy reached 100% in both the training and test sets. Therefore, this study can accurately classify qualified and black hearted seed potatoes and reach the black heart disease allowable rate of seed potato quality standard (GB18133-2000) formulated in China.

ACKNOWLEDGEMENTS

The work was supported by the National Natural Science Foundation of China (No. 62366041).

REFERENCES

1. Abukmeil, R., Al-Mallahi, A. (2022). In-field scanning of the spectrum potato plant leaves for a less destructive technique to estimate nutrients. *CSBE/SCGAB 2022 Annual Conference*, Charlottetown, Prince-Edward-Island.
2. Al-Adhaileh, M. H., Verma, A., Aldhyani, T. H., Koundal, D. (2023). Potato blight detection using fine-tuned CNN architecture. *Mathematics*, Vol. 11(6), pp. 1516. <https://doi.org/10.3390/math11061516>
3. Arshaghi, A., Ashourin, M., Ghabeli, L. (2021). Detection and Classification of Potato Diseases Potato Using a New Convolution Neural Network Architecture. *Traitement du Signal*, Vol. 38(6), pp.1783-1791. <https://doi.org/10.18280/ts.380622>
4. Gao, H.L., Li, X.Y., Xu, M.M., Huang, T., Tao, H.L., & Li, X.J. (2013). Transmission hyperspectral detection method for weight and black heart of potato (马铃薯黑心病和单薯质量的透射高光谱检测方法). *Transactions of the Chinese Society of Agricultural Engineering*, Vol.29(15), pp.279-285. (In Chinese). <https://doi.org/10.3969/j.issn.1002-6819.2013.15.034>
5. GB/T 29377-2012 (2012). *Code of practice for virus free seed potatoes grading and inspection (马铃薯脱毒种薯级别与检验规程)*. (In Chinese).
6. Gupta, H.K., & Shah, H.R. (2023). Deep Learning-Based Approach to Identify the Potato Leaf Disease and Help in Mitigation Using IOT. *SN Computer Science*, Vol.4(4), pp.333. <https://doi.org/10.1007/s42979-023-01758-5>
7. Han, Y.F., Lv, C.X., Yuan, Y.W., Yang, B.N., Zhao, Q.L., Cao, Y.F., & Yin, X.Q. (2021). PLS-Discriminant Analysis on Potato Blackheart Disease Based on VIS-NIR Transmission Spectroscopy (PLS-DA 优化模型的马铃薯黑心病可见近红外透射光谱检测). *Spectroscopy and Spectral Analysis*, Vol. 41(04), pp.1213-1219. (In Chinese). [https://doi.org/10.3964/j.issn.1000-0593\(2021\)04-1213-07](https://doi.org/10.3964/j.issn.1000-0593(2021)04-1213-07)
8. Huang, W., Zhao, Z., Sun, L., & Ju, M. (2022). Dual-branch attention-assisted CNN for hyperspectral image classification. *Remote Sensing*, Vol.14(23), pp.6158. <https://doi.org/10.3390/rs14236158>
9. Jiang, C.Y. (2024). China's No. 1 central document for 2024 (2024 年中央一号文件的突出亮点). *Rural Finance Research*, Vol. 2024(02), pp.3-13. <https://doi.org/10.16127/j.cnki.issn1003-1812.20240209.001>
10. Khorrarifar, A., Sharabiani, V. R., Karami, H., Kisalaei, A., Lozano, J., Rusinek, R., & Gancarz, M. (2022). Investigating Changes in pH and Soluble Solids Content of Potato during the Storage by Electronic Nose and Vis/NIR Spectroscopy. *Foods*, Vol. 11 (24), pp.4077-4077. <https://doi.org/10.3390/foods11244077>
11. Lakshmanan, M. K., Boelt, B., & Gislum, R. (2023). A chemometric method for the viability analysis of spinach seeds by near infrared spectroscopy with variable selection using successive projections algorithm. *Journal of Near Infrared Spectroscopy*, Vol.31(1), pp.24-32. <https://doi.org/10.1177/09670335221138955>
12. Li, X.T., Zhang, F., Feng, J. (2024). Convolutional Neural Network Combined with Improved Spectral Processing Method for Potato Disease Detection (卷积神经网络结合改进光谱处理方法用于马铃薯病害检测). *Spectroscopy and Spectral Analysis*, Vol. 44(01), pp. 215-224. (In Chinese). [https://doi.org/10.3964/j.issn.1000-0593\(2024\)01-0215-10](https://doi.org/10.3964/j.issn.1000-0593(2024)01-0215-10)
13. Liu, W.Z., Zhou, X.J., Ping, F.J., Su, Y., Ju, Y.L., Fang, Y.L., Yang, J.H. (2024). Detection of Key Indicators of Ripening Quality in Table Grapes Based on Visible-near-infrared Spectroscopy (基于可见-近红外光谱的鲜食葡萄成熟品质关键指标检测). *Transactions of the Chinese Society for Agricultural Machinery*, Vol. 55(02), pp. 372-383. (In Chinese). <https://doi.org/10.6041/j.issn.1000-1298.2024.02.037>
14. Rogers, M., Blanc-Talon, J., Urschler, M., & Delmas, P. (2023). Wavelength and texture feature selection for hyperspectral imaging: a systematic literature review. *Journal of Food Measurement and Characterization*, Vol. 17(6), pp. 6039-6064. <https://doi.org/10.1007/s11694-023-02044-x>
15. Tiwari, D., Ashish, M., Gangwar, N., Sharma, A., Patel, S., Bhardwaj, S. (2020). Potato leaf diseases detection using deep learning. *2020 4th International Conference on Intelligent Computing and Control Systems (ICICCS)*, Vol. 2020, pp. 461-466. <https://doi.org/10.1109/ICICCS48265.2020.9121067>
16. Vallese, Federico Danilo; Garcia Paoloni, Maria Soledad; Springer, Valeria; Fernandes, David Douglas de Sousa; Diniz, Paulo Henrique Gonçalves Dias; Pistonesi, Marcelo Fabián. (2024). Exploiting the successive projections algorithm to improve the quantification of chemical constituents and

- discrimination of botanical origin of Argentinean bee-pollen [J]. *Journal of Food Composition and Analysis*, <https://doi.org/10.1016/j.jfca.2023.105925>.
17. Wang, F., Li, Y.Y., Peng, Y.K., Yang, B.N., Li, L., Yin, X.Q. (2018). Hand-held Device for Non-destructive Detection of Potato Quality Parameters (便携式马铃薯多品质参数局部透射光谱无损检测装置). *Transactions of the Chinese Society for Agricultural Machinery*, Vol. 49(07), pp. 348-354. (In Chinese). <https://doi.org/10.6041/j.issn.1000-1298.2018.07.042>
 18. Zhou, Z., Li, X.Y., Gao, H.L., Tao, H.L., & Li, P. (2012). Comparison of diffuse reflection and transmission mode of visible/near infrared spectroscopy for detecting black heart of potato (漫反射和透射光谱检测马铃薯黑心病的比较). *Transactions of the Chinese Society of Agricultural Engineering*, Vol. 28(11), pp. 237-242. (In Chinese)

CLIMATE QUALITY EVALUATION AND FINE ZONING OF GUANGXI SPECIALIZED FORAGE RICE "ZHONGZAO 39"

广西专用饲料稻“中早 39”气候品质评价与精细化区划

Mengxiang TAN¹⁾, Yan HE^{1,*}, Xuanke WU²⁾, Yucong LI¹⁾, Wei HUANG²⁾, Ying XIE¹⁾

¹⁾ Guangxi Zhuang Autonomous Region Institute of Meteorological Science, Nanning, 530022, China

²⁾ Liuzhou Meteorological Bureau, Liuzhou, 545000, China

*Corresponding author's Email: t-mactmx@163.com

DOI: <https://doi.org/10.35633/inmateh-73-43>

Keywords: Rice; Specialized Forage Rice; Climate Quality; Zoning

ABSTRACT

Using the staged sowing experiment data and rice quality data of the specialized forage rice "Zhongzao 39" (hereinafter referred to as "Z-39") conducted in Nanning, Guangxi, combined with climate and geographic information data, the meteorological factors that play a key role in the formation of rice quality for the specialized forage rice "Z-39" are screened and determined. Based on the actual planting of specialized forage rice in Guangxi and the critical disaster causing indicators of "Z-39" specialized forage rice, the climate quality zoning index of "Z-39" is determined. GIS fine grid spatial simulation analysis method is used for refined spatial simulation analysis on key meteorological factors. The zoning indicator method and path analysis method are fully used for refined level zoning of the climate quality of Guangxi specialized forage rice "Z-39". It includes three levels: optimal, high-quality, and suboptimal. Ultimately, a refined zoning map for the climate quality of "Z-39" is developed, and the results are in line with the actual situation of forage rice cultivation in Guangxi. The aim is to provide a scientific basis for the rational planning and sustainable development of the specialized forage rice "Z-39" in Guangxi.

摘要

利用在广西南宁开展的专用饲料稻“中早 39”分期播种试验数据以及稻米品质数据，结合气候资料和地理信息数据，筛选确定对专用饲料稻“中早 39”稻米品质形成起关键作用的气象因子，结合广西专用饲料稻实际种植情况以及专用饲料稻“中早 39”致灾临界指标等，确定“中早 39”气候品质区划等级指标，并利用 GIS 细网格空间模拟分析方法对关键气象因子进行精细化空间模拟分析，综合利用区划指标及通径分析法，对广西专用饲料稻“中早 39”气候品质进行最优、优质和次优三个等级的精细化等级区划，研制出广西专用饲料稻“中早 39”稻米气候品质精细化区划图，分区结果符合广西饲料稻种植实际情况，以期为专用饲料稻“中早 39”在广西种植提供合理规划布局和可持续发展提供科学依据。

INTRODUCTION

Rice is the main grain crop in China. With the improvement of living standards, the pursuit of rice quality is also increasing. The quality of rice is a comprehensive trait, and its quality is not only influenced by its own genetic characteristics, but also meteorological conditions (Sreenivasulu *et al.*, 2022; Zahra *et al.*, 2022). During the growth and development period of rice, there are sensitive periods for multiple meteorological factors, during which changes in meteorological conditions can have varying degrees of impact on the quality of rice (Mousa *et al.*, 2024). Specialized forage rice is a type of rice specially made into forage for animals (Jang *et al.*, 2024). According to the different parts of use, forage rice can be divided into two categories: one is rice used to forage single stomach animals such as pigs and chickens, with the breeding goal centered on yield and nutrient content.

Another type is whole plant forage for herbivorous livestock, which is different from general rice breeding in that it targets the biological yield and nutrient content of the whole plant.

¹ Mengxiang Tan (Engineer), Yan He (Senior Engineer), Xuanke Wu (Senior Engineer), Yucong Li (Assistant Engineer), Wei Huang (Engineer), Ying Xie (Engineer)

With the continuous diversification of food types, the per capita consumption of rice is gradually decreasing, creating objective conditions and market demand for the development of forage rice. It is an inevitable trend for the future development of rice to appropriately reduce planting area for people's consumption according to demand, and then diversify the development of rice, and expand more on rice foraging. "Zhongzao 39" (hereinafter referred to as "Z-39") is a high-yielding, multi resistant, and medium maturing early indica rice variety. It is widely planted as early rice in double cropping rice regions such as Guangxi, Jiangxi, Hunan, and Anhui. The variety has a wide range of adaptability, high yield, excellent rice quality, and good resistance (Han, 2012). In recent years, "Z-39" has also been widely planted in Guangxi.

There are many reports on the relationship between rice quality and meteorological conditions around the world. Japan, South Korea, the United States and other countries have cultivated specialized forage rice varieties suitable for their own national conditions through advanced agricultural technology (Jang et al., 2022; Ma et al., 2024). However, due to various reasons, research on specialized forage rice in China has stagnated and fallen behind, and there is still no complete system of specialized forage rice varieties. Moreover, most studies are limited to the impact and related analysis of meteorological factors on the quality of edible rice or other agricultural products (Cheng et al., 2022; Wakatsuki et al., 2024; Dong et al., 2024; Zhao et al., 2023a; Chen et al., 2024), and there is still a gap in the study of the relationship between the quality of specialized forage rice and meteorological factors, as well as the formulation of meteorological indicators for rice quality. Therefore, based on the entire growth period of rice, taking the specialized forage rice "Z-39" as the test variety, the key meteorological factors that affect the quality of forage rice are analyzed to determine the climate quality evaluation technical indicators of "Z-39", and establish a climate quality evaluation model. Based on the climate indicators of rice quality, the rice planting areas in Guangxi are divided, aiming to provide a scientific basis for high-quality rice breeding and cultivation.

MATERIAL AND METHODS

Test location and materials

Guangxi is located in the low-latitude region of southern China, with a warm climate, abundant heat, abundant rainfall, rainy and hot seasons, abundant sunshine, and favorable climate resources for the development of rice. Guangxi has a long history of planting rice and is one of the main double cropping rice areas in China. Over the years, the planting area and yield of rice have ranked first among grain crops.

The experiment was conducted from March to August 2019 at the Agricultural College Farm of Guangxi University (N22° 48', E108° 22'). The tested variety is the early indica forage rice "Z-39", with a total growth period of 114 days and a thousand grain weight of 28 g. This variety has excellent rice quality, good resistance, and all rice quality indicators have reached the 5th grade of the Ministry of Quality for Edible Rice Varieties (Wu et al., 2015).

Data source

The daily meteorological data was from 89 meteorological stations in Guangxi Zhuang Autonomous Region from 1960 to 2020, including average temperature, maximum temperature, minimum temperature, solar radiation, and rainfall. The data was sourced from the Guangxi Zhuang Autonomous Region Meteorological Information Center. The geographic information data also came from the Meteorological Information Center of Guangxi Zhuang Autonomous Region, mainly including 1:250000 Guangxi administrative boundaries and administrative points. The Guangxi Digital Elevation Model (DEM) data was sourced from geospatial data clouds, mainly including longitude, latitude, altitude, slope, and aspect, with a resolution of 100 × 100 m.

Experimental design

The staged sowing experiment was divided into 7 sowing periods, with an interval of 15 days between each sowing period. A random block arrangement design was used, with a small area of 12.5 m² (length 5.2 m x width 2.4 m), repeated three times. No walkway was left between the small communities, and a 60 cm wide walkway was left between the repetitions. The conventional method of seedling cultivation involved manual transplanting around the 4-leaf stage, with a row spacing of 30 cm x 13 cm and 3 seedlings per hole. 5 rows were transplanted in each plot, with 40 holes in each row and 600 seedlings in each split plot, moderate fertilization level. Other field management were carried out according to local high-yield practices.

Measurement projects and research methods

(1) Determination of growth period and rice quality

The main growth periods of the three test points were recorded, including sowing period, emergence period, transplanting period, full heading period, maturity period and full growth period. Heading period refers to the date when 50% of the plants in the region head out, and maturity period refers to the physiological maturity date when 95% of the rice in the region turns yellow. 3 kg rice samples were randomly selected from each rice plot for determination and analysis of rice quality indexes. The quality indicators of rice mainly include brown rice percentage (%), milled rice percentage (%), full milled rice percentage (%), chalky grain percentage, chalkiness degree, amylose content (%), alkali digestibility value, gel consistency, protein content (%), and hydrolyzed amino acids (Zhao *et al.*, 2022). They are measured according to the method of GB/T 15683-2008 High Quality Rice.

(2) A Fine Grid Spatial Simulation Analysis Method based on GIS Technology

Using GIS technology and climate resource fine grid spatial simulation analysis method, based on the climate quality zoning indicators of the specialized forage rice "Zhongzao39", a spatial analysis model for the climate quality of Guangxi specialized forage rice "Zhongzao39" is established by comprehensively considering the effects of five factors: longitude, latitude, altitude, slope, and aspect. The inverse distance weight interpolation method is used to simulate and analyze the influencing factors in the indicators using a 100×100 m fine grid. Residual correction analysis is carried out to analyze the spatial refinement distribution of climate quality of Guangxi forage rice "Zhongzao39". The expression for the relationship between climate quality zoning indicators and geographical elements is as follows:

$$Y = f(\phi, \lambda, h, s, a) + \varepsilon \quad (1)$$

where:

Y represents the climatic quality zoning indicators of the specialized forage rice "Z-39"; ϕ , λ , h , s , and a respectively represent geographic elements such as latitude, longitude, altitude, slope, and aspect; ε is the residual term, called the comprehensive geographic residual.

(3) Path analysis method

There are two common methods for establishing indicator weights: subjective weighting and objective weighting (Włodarczyk *et al.*, 2023). Subjective weighting methods can be divided into expert scoring, expert ranking, Analytic Hierarchy Process (AHP), Rank Sum Ratio (RSR), and more. Objective weighting methods include factor analysis, component analysis, and more (Zhao *et al.*, 2023b). The method of path analysis is used to allocate the weights of meteorological factors in climate quality indicators. Path analysis is a method of connecting the correlation coefficient with the direct and indirect effects of two variables based on a linear regression equation. The path analysis theory shows that the simple correlation coefficient (r_{ny}) between any independent variable X_n and the dependent variable Y is the sum of the direct path coefficients (P_{ny}) of X_n and Y and the indirect path coefficients (P_{nj}) of all X_n and Y , that is, the total effect of X_n on Y . In the case where multiple independent variables interact to affect a dependent variable, each independent variable has a different degree of influence on the dependent variable. There are also cases where one independent variable affects the dependent variable through other independent variables. In path analysis, the calculation of path coefficient is difficult, but after linear regression calculation through software, the standard coefficient of the equation is the calculated path coefficient.

The simple correlation coefficient is the sum of the indirect path coefficient and the direct path coefficient, which is the result obtained during correlation analysis.

Related formulas are as follows:

The direct path coefficient P_{ny} of X_n and Y = standard coefficient

The indirect path coefficient of X_n and Y = correlation coefficient (r_{ny}) x direct path coefficient (P_{ny})

The decision coefficient $R^2(n) = 2 \times P_{ny} \times r_{ny} - (P_{ny})^2$

P_{ny} is the direct path coefficient between the independent variable n and the dependent variable Y ; R_{nj} is the correlation coefficient between the independent variable n and the independent variable j ; R_{ny} is the correlation coefficient between the independent variable n and the corresponding variable Y .

RESULTS AND ANALYSIS

Screening and determination of major meteorological influencing factors

Forage rice has different requirements or breeding objectives based on its utilization location and purpose. For the rice used for forage, high rice yield ($> 8250 \text{ kg/hm}^2$), high crude protein content ($\geq 12\%$), and high roughening rate ($\geq 80\%$) are required (Zhang *et al.*, 2008). In this study, protein content and brown rice rate are used to represent the quality of forage rice.

Based on the field stage sowing experiment data, rice quality data, and meteorological data, the correlation between the quality indicators (protein content and brown rice rate) of forage rice "Z-39" and meteorological factors during each growth period is analyzed (as shown in Tables 1 and 2).

Table 1 shows that the protein content of forage rice "Z-39" is significantly correlated with the average temperature throughout the full growth period and the lowest temperature from sowing to transplanting. It is significantly correlated with the highest temperature, average temperature, daily solar radiation, and rainfall from transplanting to full heading period. It is significantly correlated with the highest temperature, lowest temperature, average temperature, daily solar radiation, and rainfall from sowing to full heading period. There is no significant correlation with the meteorological factors studied from full heading to maturity period and from transplanting to maturity period.

Table 1

Correlation between Protein Content of Specialized Forage Rice "Z-39" and Meteorological Factors at Different Growth Stages

| Growth stage | Highest temperature | Lowest temperature | Average temperature | Diurnal variation of temperature | Daily average solar radiation | Humidity | Rainfall |
|---------------------------------------|---------------------|--------------------|---------------------|----------------------------------|-------------------------------|----------|----------|
| Full growth period | 0.456 | 0.474 | 0.483* | 0.100 | 0.477 | -0.266 | -0.349 |
| Sowing and transplanting period | 0.418 | 0.557* | 0.467 | 0.400 | 0.362 | 0.299 | 0.005 |
| Transplanting and full heading period | 0.782** | 0.477 | 0.596** | 0.444 | 0.569* | -0.467 | -0.619** |
| Full heading and maturity period | 0.334 | -0.221 | -0.363 | -0.277 | -0.228 | -0.27 | -0.022 |
| Sowing and full heading period | 0.514* | 0.702** | 0.519* | 0.094 | 0.571* | -0.233 | -0.523* |
| Transplanting and Maturity period | 0.434 | 0.439 | 0.440 | 0.190 | 0.414 | -0.291 | -0.406 |

Note: * indicates significant correlation at the 0.05 level (bilateral); ** indicates significant correlation at the 0.01 level (bilateral).

Table 2

Correlation between brown rice rate of specialized forage rice "Z-39" and meteorological factors at different growth periods

| Growth period | The highest temperature | The lowest temperature | Average temperature | Diurnal variation of temperature | Daily average solar radiation | Humidity | Rainfall |
|---|-------------------------|------------------------|---------------------|----------------------------------|-------------------------------|----------|----------|
| Full growth period | -0.177 | -0.412 | -0.357 | 0.382 | -0.319 | -0.044 | 0.276 |
| Sowing and transplanting period | -0.253 | -0.226 | -0.256 | -0.261 | -0.394 | -0.172 | -0.169 |
| Transplantation and full heading period | -0.098 | -0.363 | -0.261 | -0.292 | 0.022 | -0.422 | 0.055 |
| Full heading and maturity period | -0.696* | -0.811** | -0.711** | -0.786** | -0.695** | 0.406 | 0.434 |
| Sowing and full heading period | -0.418 | -0.270 | -0.246 | 0.809** | -0.416 | -0.467 | -0.051 |
| Transplantation and maturity period | -0.308 | -0.567* | -0.423 | 0.351 | -0.364 | 0.075 | 0.419 |

Note: * indicates significant correlation at the 0.05 level (bilateral); ** indicates significant correlation at the 0.01 level (bilateral).

Table 2 shows that the brown rice rate of forage rice "Z-39" is not significantly correlated with the meteorological factors during the full growth period, from sowing to transplanting period, and from transplanting to full heading period. It is significantly negatively correlated with the highest temperature, the lowest

temperature, average temperature, daily temperature range, daily solar radiation, and the lowest temperature range from transplanting to maturity period. It is highly positively correlated with the diurnal variation of temperature from sowing to full heading period.

Xie et al. (2010), Xu, et al. (2021) and Yao et al. (2021) believed that high temperatures during the heading and filling period of rice could reduce the brown rice rate, milled rice rate, and protein content, leading to a decrease in rice yield and quality. Yang et al. (2023) found that low temperatures during the booting, heading, and filling periods can reduce the full head rice rate and taste score of rice. Based on the above correlation analysis, eight main meteorological factors are selected and determined for the evaluation of climate quality in "Z-39": the highest temperature from transplanting to full heading period, the lowest temperature from sowing to full heading period, the rainfall from transplanting to full heading period, the average temperature from transplanting to full heading period, the maximum temperature from full heading to maturity period, the minimum temperature from full heading to maturity period, and the average temperature from full heading to maturity period, and diurnal variation of temperature from sowing to full heading period.

Construction of a single climate quality index model for rice quality

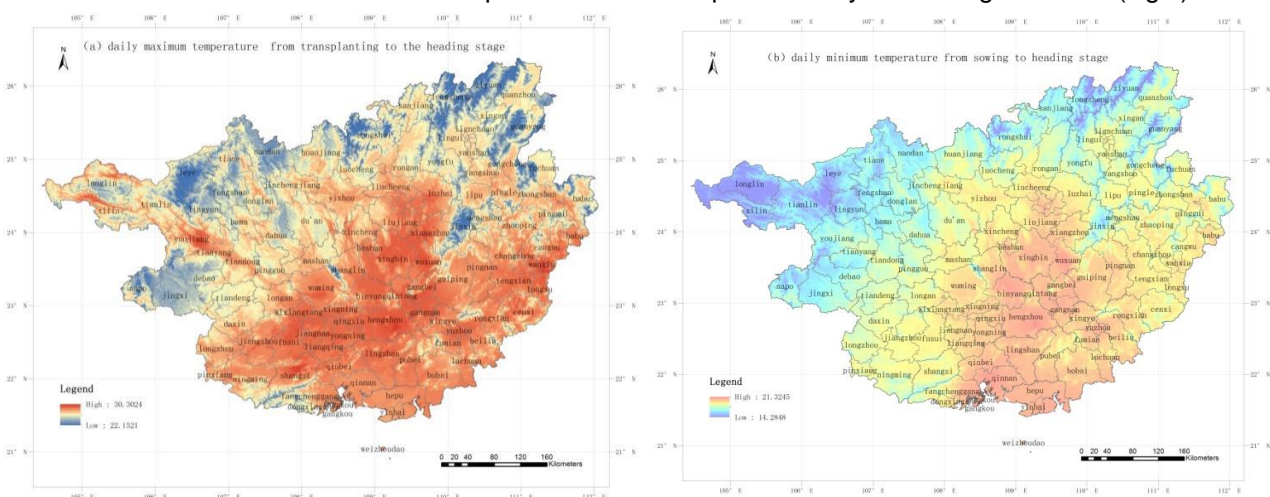
Stepwise linear regression, quadratic model, cubic model, and exponential distribution are used to fit and analyze the meteorological factors closely related to protein content and brown rice rate. Comparing the fitting effects of each model, the model with high fitting degree is selected to establish a single climate indicator model for the quality of forage rice "Zhongzao39". The model results are shown in Table 3.

Table 3

Climate model for single index quality of specialized forage rice "Z-39"

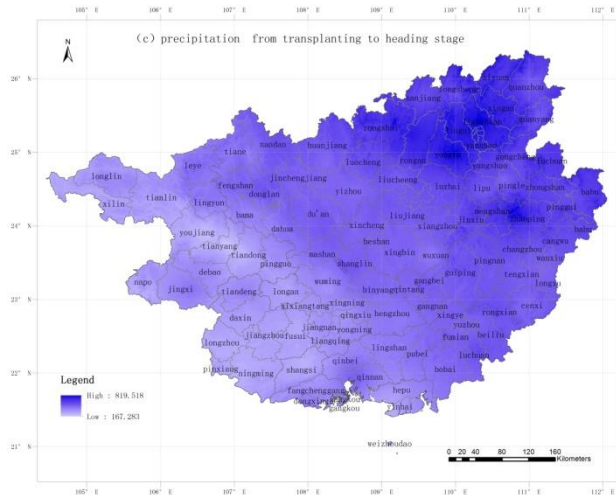
| Quality index | Meteorological factors | Regression equations |
|-----------------|---|---|
| Protein | The highest temperature from transplantation to full heading period | $Y = 0.029X_{2-T_m}^2 - 1.734X_{2-T_m} + 32.786$ |
| Protein | The lowest temperature from sowing to full heading period | $Y = 0.115X_{4-T_i} + 4.457$ |
| Protein | Rainfall from transplantation to full heading period | $Y = -0.003X_{2-R} + 7.896$ |
| Protein | Average temperature from transplantation to full heading period | $Y = 0.138X_{2-\bar{T}} + 3.287$ |
| Brown rice rate | The highest temperature from full heading to maturity period | $Y = 0.051X_{3-T_m}^2 - 3.767X_{3-T_m} + 32.786$ |
| Brown rice rate | The lowest temperature from full heading to maturity period | $Y = -0.136X_{3-T_i}^2 + 6.325X_{3-T_i} + 5.987$ |
| Brown rice rate | Average temperature from full heading to maturity period | $Y = -0.056X_{3-\bar{T}}^2 + 2.684X_{3-\bar{T}} + 47.944$ |
| Brown rice rate | Diurnal variation of temperature from sowing to full heading period | $Y = 73.05 + 0.712T$ |

A spatial simulation analysis model is established for the 8 key meteorological factors and the 5 factors of longitude, latitude, altitude, slope and slope direction respectively. The residual correction of the model analysis structure is carried out to obtain the 100x100 m refined spatial distribution map of the 8 key meteorological factors (Fig.1).

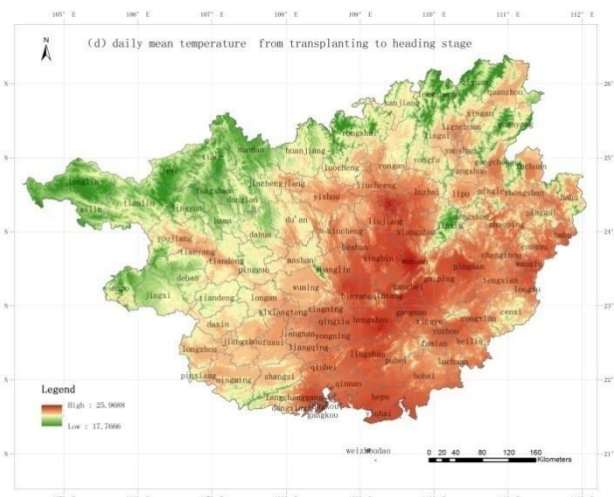


(a) The highest transplanting to full heading period

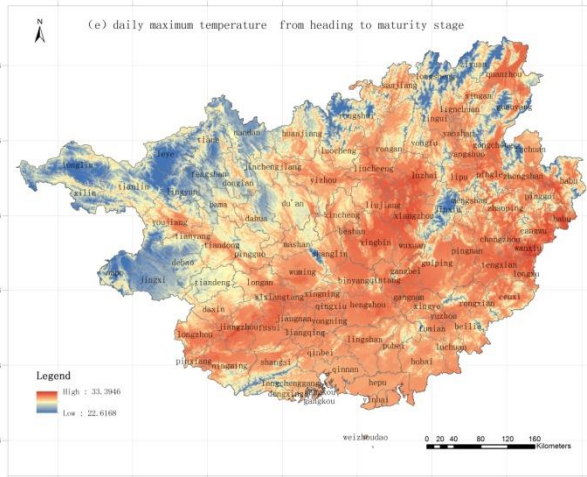
(b) The lowest temperature from sowing to full heading period



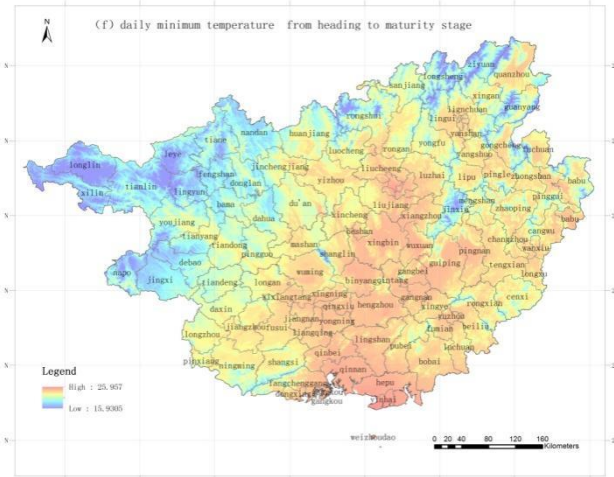
(c) Rainfall from transplanting to full heading period



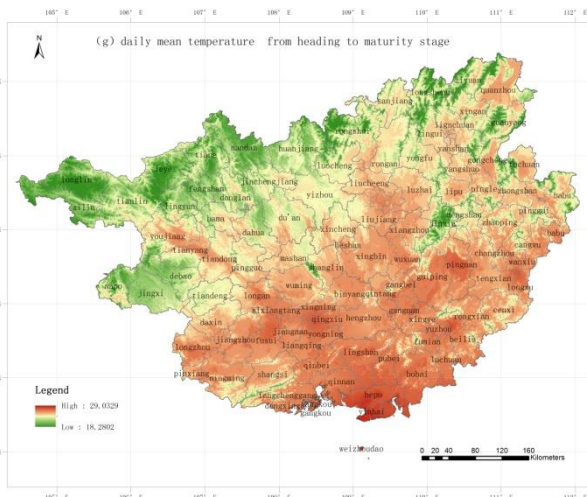
(d) Average temperature from transplanting to full heading period



(e) The highest temperature from full heading stage to maturity period



(f) The lowest temperature from full heading stage to maturity period



(g) Average temperature from full heading stage to maturity period



(h) Diurnal variation of temperature from sowing to full heading period

Fig. 1 - Refined distribution map of Guangxi specialized forage rice "Z-39"

Establishing evaluation indicators for climate quality grading of rice

According to the requirements for the quality indicators of forage rice "Z-39", and taking into account the expert scoring method, combined with the climate background of rice cultivation in Guangxi, the critical disaster indicators for each growth stage of rice in Guangxi, and the analysis of suitable meteorological conditions for each growth period of "Z-39", the evaluation and grading indicators for the climate quality zoning of "Z-39" in Guangxi are determined (Table 4).

Table 4

Climate quality zoning index for specialized forage rice "Z-39"

| Key meteorological factors | The highest quality area | High quality area | Secondary Quality Zone |
|--|--------------------------|-------------------|------------------------|
| The highest temperature from transplantation to full heading period (°C) | 29-32 | 27.5-29 | <27.5 >32 |
| The lowest temperature from sowing to full heading period (°C) | >20.5 | 17.5-20.5 | <17.5 |
| Rainfall from transplantation to full heading period (mm) | 400-500 | 500-630 | >630 <400 |
| Average from transplantation to full heading period (°C) | 25-30 | 22.5-25 | <22.5 >30 |
| The highest temperature from full heading to maturity period (°C) | <31 | 31-32.5 | >32.5 |
| The lowest temperature from full heading to maturity period (°C) | 22-24 | 20.5-22 24-26 | <20.5 >26 |
| Average from full heading to maturity period (°C) | 23-26 | 21-23 26-27.5 | <21 >27.5 |
| Diurnal variation of temperature from sowing to full heading period (°C) | >9.8 | -9.8 | <7 |

Determining the weight of climate quality zoning indicators

The simple correlation coefficient, direct path coefficient, and indirect path coefficient between the quality of the special forage rice "Z-39" and key meteorological factors are integrated and calculated (Table 5). The weights of each factor based on a correlation coefficient weight of 40% and a direct path coefficient weight of 60% are calculated. According to calculations, the weights of the highest temperature from transplanting to full heading period (X1), lowest temperature from sowing to full heading period (X2), rainfall from transplanting to full heading period (X3), average temperature from transplanting to full heading period (X4), the highest temperature from full heading to maturity period (X5), the lowest temperature from full heading to maturity period (X6), average temperature from full heading to maturity period (X7), and diurnal variation of temperature from sowing to full heading period (X8) in the climate quality zoning of forage rice "Zhongzao39" are 18.3%, 13.8%, 6.4%, 23.9%, 9.5%, 7.5%, 14.6%, and 6%, respectively.

Table 5

Path analysis between the quality of specialized forage rice "Z-39" and meteorological factors

| Key meteorological factors | Simple correlation coefficient | Direct path coefficient | Indirect path coefficient |
|----------------------------|--------------------------------|-------------------------|---------------------------|
| X1 | 0.78 | 2.57 | -1.79 |
| X2 | 0.7 | 1.78 | -1.08 |
| X3 | -0.62 | -0.42 | -0.2 |
| X4 | 0.6 | -3.94 | 4.54 |
| X5 | -0.7 | 0.92 | -1.62 |
| X6 | -0.81 | 0.36 | -1.17 |
| X7 | -0.71 | -1.93 | 1.22 |
| X8 | 0.81 | 0.07 | 0.74 |

Climate zoning of rice quality of Guangxi forage rice "Z-39"

Based on the climate quality zoning indicators and the spatial distribution of key meteorological factors of the special forage rice "Z-39", the spatial stacking function of GIS is used to stack the key meteorological factors with different weights corresponding to the zoning indicators at the same level. This result in a thematic map of the refined climate quality zoning of Guangxi specialized forage rice "Z-39" based on the stacking of key meteorological factors (Figure 2). As shown in Figure 2, the climate quality optimal zone, high-quality zone, and sub-optimal zone specialized forage rice "Z-39" account for 19.0%, 26.6%, and 54.4%, respectively.

The optimal areas are mainly distributed in most parts of central Guangxi, southeastern Guangxi, and northwestern Guangxi, including Huanjiang, Liuzhou, Liujiang, Luzhai, Shanglin, Binyang, Laibin, Xiangzhou, Wuxuan, Guigang, Fangchenggang, Xingye, Lingshan, Shangsi, Hepu, Pingnan, Cenxi, Cangwu and other counties (cities), as well as parts of Baise, Hechi, Hezhou, and Wuzhou. The thermal conditions in this area are suitable, and the matching of light, temperature, and water is optimal. Currently, the area for planting forage rice is the largest, especially in the Guizhong Basin area. If the planting time and structure are arranged reasonably, the specialized forage rice planted can achieve higher yield and better quality.

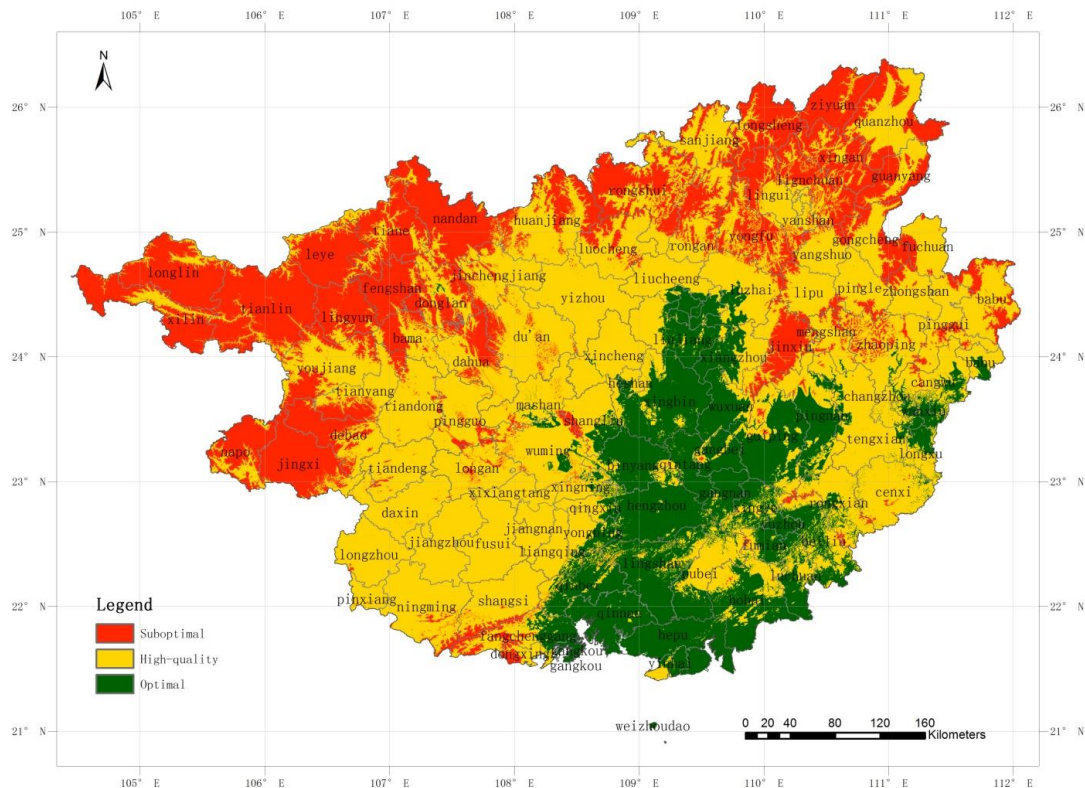


Fig. 2 - Fine climate quality zoning map of Guangxi specialized forage rice "Z-39"

The high-quality areas are mainly distributed in the southwest and northeast of Guangxi, as well as in some parts of cities such as Baise, Hechi, and Yulin. These areas need to cooperate with good field management measures, strengthen the prevention and control of diseases, pests, and meteorological disasters to harvest high-quality specialized forage rice.

The areas with sub-optimal climate quality are mainly distributed in northern Guangxi, western Guangxi, and southern Guangxi, including most counties (cities) such as Xilin, Longlin, Lingyun, Leye, Fengshan, Tian'e, Nandan, Longsheng, Resources, and Napo, as well as some counties (cities) such as Tianlin, Bama, Donglan, Rongshui, Guanyang, Jinxiu, Gongcheng, and Fangchenggang. Cold damage is more frequent in spring in the northern part of the area, while high temperature and heat damage is more likely to occur in the Baise area in the west. There are fewer areas for planting specialized forage rice in the south, which is generally not suitable for the cultivation of specialized forage rice and the improvement of rice quality.

DISCUSSIONS

(1) The key meteorological factors affecting the quality of special forage rice "Z-39". Temperature and light have a crucial impact on rice quality among various meteorological factors (*Lu et al., 2024*). Among them, temperature during the filling period, sunshine hours, and amylose content, brown rice rate, milled rice rate, full milled rice rate, and alkaline digestion value are negatively correlated (*Huang et al., 2021; Feng et al., 2024*). *Lv et al. (2021)* found that low temperature stress during the heading period can seriously affect the photosynthetic rate of rice, thereby reducing the polished rice rate and head milled rice rate. *Suung (2020)* and *Ahmed et al. (2015)* found that the content of amylose in rice usually decreases with increasing temperature.

This study uses staged sowing experimental data conducted in Nanning, Hengyang, and Nanchang, combined with local meteorological observation data for statistical analysis, the correlation between the rice quality elements (protein content, brown rice rate) of the specialized forage rice "Z-39" and meteorological factors in the full growth period of rice is analyzed. On this basis, eight meteorological factors that had significant correlation with rice quality factors and played a key role in rice quality of Z-39 were selected. The quality of rice is not only controlled by the genetic genes of the variety, but also by environmental factors, cultivation measures, and fertilization conditions (Kashiwagi, 2021; Mahmood et al., 2024). The study only analyzes and studies the climate factors that affect the specialized forage rice "Z-39". In actual production, various factors such as soil conditions, different cultivation methods, pest and disease effects, and planting management levels can also affect the quality of rice. Therefore, the next research needs to further systematically identify the demand of rice for climate resources under different influencing factors.

(2) Climate quality zoning and grading indicators for specialized forage rice "Z-39". Climate impact assessment of agricultural products is the study of the relationship between their quality and climate. Based on a climate quality assessment model and comprehensive evaluation, the climate quality level of agricultural products is determined (Jin et al., 2015). Yang et al. (2022) used Hubei's characteristic fragrant rice yellow felt as an example to construct a climate evaluation model for the quality of yellow felt and conduct quantitative evaluation. Based on the modeling results of the quality and key meteorological factors of "Z-39" rice, combined with the climatic characteristics of special forage rice cultivation, suitable meteorological conditions for each growth stage, especially the key growth stage, as well as restrictive meteorological conditions and disaster critical indicators, the climate grade index of rice quality planted in Guangxi for "Z-39" is determined, providing a reference for optimizing the layout of special forage rice cultivation in Guangxi.

(3) The climate quality classification of specialized forage rice "Z-39" in Guangxi. The promotion of agricultural products based on climate quality level zoning plays an important guiding role (Yan et al., 2024). The evaluation and zoning of climate quality levels, such as Dong Tibetan red rice in Hunan, green dates in Guangdong, and Wogan in Guangxi, have achieved certain benefits in crop promotion and meteorological services (Chen et al., 2021; Tan et al., 2021). Based on the climate quality zoning index of "Z-39", GIS spatial fine grid zoning method is used for fine grid spatial simulation analysis of key meteorological factors affecting rice quality. Then a refined climate quality zoning map for specialized forage rice "Z-39" is developed. The zoning results are divided into three zones: the best climate quality zone, the best climate quality zone, and the second best climate quality zone. The zoning results are more detailed and accurate, and also more in line with the actual distribution, providing a scientific basis for further optimizing the breeding layout.

CONCLUSIONS

This study focused on the specialized forage rice variety "Z-39" widely planted in Guangxi, and rice protein content and brown rice rate were selected as its quality evaluation indicators. The meteorological factors that played a key role in the quality elements of the specialized forage rice "Z-39" were: the highest temperature from transplanting to full heading period, the lowest temperature from sowing to full heading period, the rainfall from transplanting to full heading period, the average temperature from transplanting to full heading period, the highest temperature from full heading to maturity period, the lowest temperature from full heading to maturity period, the average temperature from full heading to maturity period, and diurnal variation of temperature from sowing to full heading period. The climate quality zoning indicators for the specialized forage rice "Z-39" were developed and the climate quality of specialized forage rice "Z-39" was classified. The optimal, high-quality, and sub-optimal climate quality areas accounted for 19.0%, 26.6%, and 54.4%, respectively. The optimal climate quality areas were mainly located in the central, southeastern, and northwestern regions of Guangxi.

ACKNOWLEDGEMENTS

China Meteorological Administration Joint Research Project on Meteorological Capacity Enhancement (22NLTSY013), National Agricultural Science and Technology Achievement Transformation Project (2014GB2E100281), Guangxi Science and Technology Key R&D Program Project (Guike AB17195037).

REFERENCES

1. Ahmed, N., Tetlow, I. J., Nawaz, S., Iqbal, A., Mubin, M., Nawaz ul Rehman, M. S., Butt, A., Lightfoot, D. A., Maekawa, M. (2015). Effect of high temperature on grain filling period, yield, amylose content and activity of starch biosynthesis enzymes in endosperm of basmati rice. *Journal of the Science of Food and Agriculture*, Vol. 95, pp. 2237-2243. England.
2. Chen, B., Tong, R., Gao, X., Chen, Y. (2024). A novel dynamic decision-making method: Addressing the complexity of attribute weight and time weight. *Journal of Computational Science*, Vol. 77, pp. 102228. Netherlands.
3. Chen, H., Lin, J., Yang, K., Wang, P., Yang, F., Chen, H., Chen, T., Li, L., Li, L., Chen, F. (2021). Construction and Application of Climate Quality Evaluation Model for Indian Jujube (青枣气候品质等级评价模型构建及应用). *Journal of Applied Meteorological Science*, Vol. 32, pp. 443-455. Beijing/China.
4. Cheng, F., Liu, Z., Zhang, S. (2022). The Evaluation of Climatic-Ecology Condition for the Rice Quality Formation and Its Distribution Laws in China (稻米品质形成的气候生态条件评价及我国地域分布规律), *Acta Ecologica Sinica*, Vol. 22(5), pp. 636-642. Beijing/China.
5. Dong, Z., Chen, M., Srivastava, K. A., Mahmood, U. H., Ishfaq, M., Shi, X., Zhang, Y.Q., Moussa, M. G., Li, X., Hu, C., Zhang F. (2024). Climate changes altered the citrus fruit quality: A 9-year case study in China. *Science of the Total Environment*, Vol. 923, pp. 171406. Netherlands.
6. Feng, X., Xu, J., Shen, Z., Wang, D., Xu, C., Chen, S., Zhang, X., Xiao, Y. (2024). Effect of Sowing Date on Grain Yield and Quality of Indica-Japonica Hybrid Yongyou 1540 and its Climate-Related Mechanism (播期对籼粳杂交稻甬优 1540 产量、品质的影响及其与气候因子的相关性). *China Rice*, Vol. 30(1), pp. 108-114+117. Zhejiang/China.
7. Han, J., (2012). Planting performance and high-yield cultivation techniques of early indica variety ZhongZao 39 in Yuyao (早籼品种中早 39 在余姚的种植表现及高产栽培技术). *China Rice*, Vol. 18(1), pp. 63-64. Zhejiang/China.
8. Huang, M., Cao, J.L., Liu, Y., Zhang, M.Y., Hu, L.Q., Xiao, Z.W., Chen, J.N., Cao, F.B. (2021). Low-temperature stress during the flowering period alters the source-sink relationship and grain quality in field-grown late-season rice. *Journal of Agronomy and Crop Science*, Vol. 207(5), pp. 833-839. Germany.
9. Jang, Y., Sharavdorj, K., Ahn, Y., Cho, J. (2024). Effects of Planting Density and Nitrogen Fertilization on the Growth of Forage Rice in Reclaimed and General Paddy Fields. *Plants*, Vol. 13(1), pp. 13. Switzerland.
10. Jang, Y., Sharavdorj, K., Nadalin, P., Lee, S., Cho, J. (2022). Growth and Forage Value of Two Forage Rice Cultivars According to Harvest Time in Reclaimed Land of South Korea. *Agronomy*, Vol. 12(12), pp. 3118. Switzerland.
11. Jin, Z., Wang, Z., Yao, Y., Li, R.Z., Wang, Y.F., Lu, J.W., Ye, J.G., Xu, P. (2015). Evaluation of Climate Quality Grade of Tea in Zhejiang Province (浙江省茶叶气候品质等级评价). *Chinese Journal of Ecology*, Vol. 34(5), pp. 1456-1463. Liaoning/China.
12. Kashiwagi, T. (2021). Effect of rice grain protein QTL, TGP 12, on grain composition, yield components, and eating quality with different nitrogen applications. *Field Crops Research*, Vol. 263, pp. 108051. Netherlands.
13. Lu, B., Xu, C., Li, Z., Tang, X., Yang, F., Xu, D., Zhu, G., Zhang, J., Jiang, Y., Li, W., Liu, Z., Ding, Y., Li, G. (2024). Influence of the temperature during grain filling stage and nitrogen application rate on yield and quality of indica hybrid rice. *Field Crops Research*, Vol. 309, pp. 109333. Netherlands.
14. Lv, Y., Zhou, K., Tang, S., Gao, D., Zhang, S., Huang, W., He, P., Zhou, B. (2021). Effects of Chilling Stress at Heading Stage on Yield Traits and Grain Quality of Rice (抽穗期低温胁迫对水稻产量性状及稻米品质的影响). *Hunan Agricultural Sciences*, Vol. 12, pp. 23-25+29. Hunan/China.
15. Ma, K., Zhao, X., Lu, B., Wang, Y., Yue, Z., Zhang, L., Diao, X., Yuan, X.Y. (2024). Effect of Ecological Factors on Nutritional Quality of Foxtail Millet (*Setaria italica*L.). *Agronomy*, Vol. 14(2), 387. Switzerland.
16. Mahmood, N., Liu, Y., Zheng, X., Munir, Z., Pandiselvam, R., Zhang, Y., Saleemi, M. A., Yves, H., Sufyan, M., Lei, D. (2024). Influences of emerging drying technologies on rice quality. *Food Research International*, Vol. 184, pp. 114264. USA.

17. Mousa, A. M., Ali, A. M. G., Omar, A. E., Alharbi, K., Abd El-Moneim, D., Mansour, E., & Elmorsy, R. S. (2024). Physiological, Agronomic, and Grain Quality Responses of Diverse Rice Genotypes to Various Irrigation Regimes under Aerobic Cultivation Conditions. *Life*, Vol. 114(3), pp. 370. Switzerland.
18. Seung, D. (2020). Amylose in starch: Towards an understanding of biosynthesis, structure and function. *New Phytologist*, Vol. 228(5), pp. 1490-1504. England.
19. Sreenivasulu, N., Zhang, C., Tiozon, R. N., & Liu, Q. (2022). Post-genomics revolution in the design of premium quality in a high-yielding background to meet consumer demands in the 21st century. *Plant Communications*, Vol. 3(3), pp. 100271. USA.
20. Tan, Z., Luo, Z., Wang, J. (2021). Climatic Suitability Planting Regionalization of Orah's Fruit Quality Grade in Guangxi (广西'沃柑'果实品质等级气候适宜性种植区划研究). *Chinese Agricultural Science Bulletin*. Vol. 37(5), pp. 65-74. Beijing/China.
21. Wakatsuki, H., Takimoto, T., Ishigooka, Y., Nishimori, M., Sakata, M., Saida, N., Akagi, K., Makowski, D., Hasegawa, T. (2024). A dataset for analyzing the climate change response of grain quality of 48 Japanese rice cultivars with contrasting levels of heat tolerance. *Data in brief*, Vol. 54, pp.110352. USA.
22. Włodarczyk, Z., Ziernicka-Wojtaszek, A., Kędzior, R., Mazur, J. (2023). Flowering Phenology of Shrub Roses as a Sensitive Indicator of Meteorological Variability in Central Europe. *Journal of Horticultural Research*, Vol. 31(2), pp. 175-190. Poland.
23. Wu, M. F., Wu, H.Y., Zhang, W., Sun, L.F. (2015). Characteristics and cultivation points of early rice Zhongzao 39 (in Chinese). *Journal of Zhejiang Agricultural Sciences* (早稻中早 39 的特征特性及栽培要点), Vol. 56(5), pp. 648-649. Zhejiang/China.
24. Xie, X., Li, B., Li, Y., Li, H., Zhao X., Yang, S., Wang, Z. (2010). Effects of High Temperature Stress on Yield Components and Grain Quality during Heading Stage (抽穗期高温胁迫对水稻产量构成要素和品质的影响). *Chinese Journal of Agrometeorology*, Vol. 31(3), pp. 411-415. Beijing/China.
25. Xu, Y., Chu, C., Yao, S. (2021). The impact of high-temperature stress on rice: challenges and solutions. *The Crop Journal*, Vol. 9(5), pp. 963-976. China
26. Yan, X., Muneer, A.M., Qin, M., Ou, J., Chen, X., He, Z., Liu, Y., Cheng, Z., Su, D., Liu, R., Wu, L. (2024). Establishing quality evaluation standards for pomelo fruit: The role of harvesting time and appearance characteristic. *Postharvest Biology and Technology*, Vol. 212, pp. 112863. Netherlands.
27. Yang, M., Liu, Z., Xiao, W., Han, Y. (2022). Construction and quantitative evaluation of climate evaluation model of fragrant rice quality in Xiaogan city (孝感市香米品质气候评价模型构建与定量评价). *Hubei Agricultural Sciences*, Vol. 61(3), pp. 21-25+31. Hubei/China.
28. Yang, Y., Han, L., Li, M. (2023). Zoning of Climatic Quality Grades for Dong Tibetan Red Rice in Hunan Province (湖南侗藏红米气候品质等级区划). *Chinese Journal of Agrometeorology*, Vol. 44(12), pp.1147-1154.
29. Yao, D.P., Wu, J., Luo, Q.H., Shen, H., Zhuang, W., Xiao, G., Li, J., Li, Y., Deng, Q., Lei, D., Bai, B. (2021). Comprehensive evaluation of high temperature tolerance of six varieties during grain-filling period based on key starch physicochemical indexes. *LWT*. Vol. 148, pp. 111804. England.
30. Zahra, N., Hafeez, M. B., Nawaz, A., Farooq, M. (2022). Rice production systems and grain quality. *Journal of Cereal Science*, Vol. 105, pp. 103463. England.
31. Zhang, J., Liu, X, Cao, Z. (2008). Current status and perspectives of research and utilization of forage rice. *Acta Prataculturae Sinica*, Vol. 05, pp. 151-155.
32. Zhao, D., Zhang, C., Li, Q., Liu, Q. (2022). Genetic control of grain appearance quality in rice. *Biotechnology Advances*, Vol. 60, pp. 108014. England.
33. Zhao, W., Ban, Y., Su, Z., Li, S., Liu, X., Guo, Q., Ma, P. (2023a). Colonization ability of bacillus subtilisNCD-2 in different crops and its effect on rhizosphere microorganisms. *Microorganisms*, Vol. 11(3), pp. 776. Switzerland.
34. Zhao, Y., Lv, X., Shen, X., Wang, G., Li, Z., Yu, P., & Luo, Z. (2023b). Determination of Weights for the Integrated Energy System Assessment Index with Electrical Energy Substitution in the Dual Carbon Context. *Energies*, Vol. 16(4), pp. 2039. Switzerland.

DESIGN AND EXPERIMENTAL STUDY ON FERTILIZATION PERFORMANCE OF CRANK ROCKER DEEP APPLICATION MECHANISM

曲柄摇杆式深施机构的设计与施肥性能试验研究

Jinlong FENG^{1*}, Dongxue CHEN², Qichao LI¹, Hua LI¹

¹) College of Mechanical and Electrical Engineering, Lingnan Normal University; Zhanjiang 524048, China

²) Teacher education college, Lingnan Normal University; Zhanjiang 524048, China

*Corresponding author's E-mail: 37002165@qq.com

DOI: <https://doi.org/10.35633/inmateh-73-44>

Keywords: crank rocker arm; deep implementation institutions; spray hole diameter; experimental research; pump pressure; fertilizer

ABSTRACT

In response to the poor fertilization performance of the deep application mechanism of the deep application liquid fertilizer applicator under multiple parameters, the fertilization variation of the crank rocker deep application mechanism under multiple working parameters is explored. To obtain the fertilization variation of the crank rocker deep application mechanism, a fertilization performance test bench for the crank rocker deep application mechanism is developed. On this test bench, the crank speed, liquid pump pressure, and spray hole diameter are used as experimental factors, and fertilizer application rate is used as experimental indicators. A composite design scheme of rotation center is adopted to establish a relationship model and response surface diagram between experimental influencing factors and influencing indicators. Design Expert 8.0.10 software is used to analyze and optimize the experimental data. The optimal results are a crank speed of 145.80 r/min, a liquid pump pressure of 0.25 MPa, a spray hole diameter of 3.02 mm, a fertilizer application rate of 28.6 mL, and a fertilizer loss rate of 1.95%. At this time, the fertilization performance of the mechanism is optimal. This parameter combination is applied for testing and verification to verify its rationality. The results can ensure that the crank rocker deep application mechanism has good working performance when working under multiple parameters, providing theoretical reference for designing deep application liquid fertilizer machines with simple structure and optimal fertilization performance.

摘要

针对深施型液态施肥机的深施机构多参数下施肥性能差等问题，探索了多工作参数下的曲柄摇杆式深施机构施肥变化规律，为了得到曲柄摇杆式深施机构的施肥变化规律，研制了曲柄摇杆式深施机构的施肥性能试验台。在该试验台上以曲柄转速、液泵压力和喷孔直径为试验因素，施肥量为试验指标，采用旋转中心复合设计方案，建立试验影响因素和影响指标的关系模型及响应曲面图，并运用 Design-Expert 8.0.10 软件对试验数据进行分析和优化，最优结果：曲柄转速为 145.80 r/min、液泵压力为 0.25 MPa、喷孔直径 3.02 mm、施肥量为 28.6 mL 和施肥损失率为 1.9%，此时机构施肥性能最优，应用此参数组合进行测试验证，验证了其合理性。该研究结果可保证曲柄摇杆式深施机构在多参数下工作时，机具具有良好的工作性能，为设计结构简单且具有较好施肥性能的深施型液态施肥机提供理论参考。

INTRODUCTION

With the promotion and popularization of liquid fertilizers, deep application liquid fertilizing machines with high fertilizer efficiency have been widely recognized and applied. The deep application mechanism is an important working component of the deep application liquid fertilizer applicator, which is the executing component of deep application of liquid fertilizer into the soil. Its fertilization directly affects the quality and efficiency of fertilization (da Silva and Magalhães, 2019; Sharma and Khar, 2022; Ramarao et al., 2024). A well performing deep application mechanism can reduce the impact of soil on the deep application mechanism, thereby ensuring the trajectory posture of the fertilizer spraying needle entering the soil and improving the fertilization performance of the mechanism.

Jinlong Feng, Lecturer, Ph.D.; Dongxue Chen, assistant engineer, Ph.D.; Qichao Li, Associate professor, Ph.D.; Hua Li, professor, Ph.D.

At present, the deep application mechanism of the deep application liquid fertilizer applicator mainly proposes three forms of deep application mechanisms: elliptical gear planetary system, fully elliptical gear planetary system, and non-circular gear planetary system (Wafiqah *et al.*, 2024; Gilvan *et al.*, 2023; Wang *et al.*, 2022). Kinematic and simulation analysis, structural optimization, and corresponding bench tests have been conducted on the three mechanisms. After optimization, although the inertia force of the three mechanisms has decreased and the number of punctures per unit time has increased, the machining accuracy requirements are high, especially for the relative position between the planetary carrier and the gear shaft. This has resulted in an increase in the machining cost of the deep application mechanism, and the fertilizer loss rate is still high (Wang *et al.* 2022; Chen *et al.* 2023; Zhou *et al.* 2023). Therefore, on the premise of further reducing the fertilizer loss rate, a crank rocker deep application mechanism is proposed. It uses the insertion mechanism of the transplanting machine as the research and development basis of the crank rocker deep application mechanism. Utilizing the trajectory characteristics of the crank rocker mechanism, the verticality of the deep application mechanism into the soil is further improved, thereby reducing fertilizer loss and processing costs. Indoor bench tests were conducted on the deep application mechanism device, using response surface design method to fit the functional relationship between factors and response values, and analyzing the regression equation to seek the optimal process parameters, providing a reference for the design and optimization of deep application liquid fertilizer equipment.

MATERIAL AND RESEARCH METHODS

The overall structure of the crank rocker depth application mechanism

The deep application mechanism is an important executing component of the deep application liquid fertilizer applicator. Based on the operating characteristics of the deep application liquid fertilizer applicator, the deep application mechanism is designed in the form of a crank rocker, consisting of a front swing arm spindle seat 2, a crank 4, a fertilizer spray needle 5, and other parts. The structure is shown in Fig. 1.

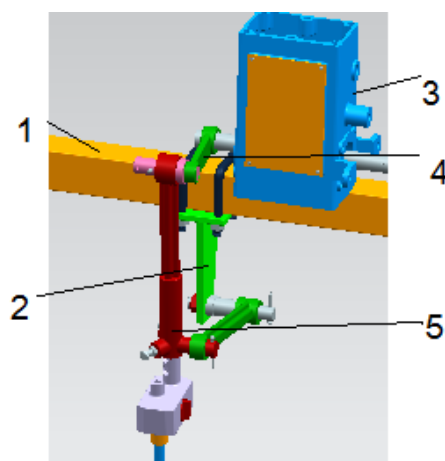


Fig. 1 - Schematic diagram of deep application mechanism

1. Main beam, 2. Front swing arm spindle seat, 3. Spray automatic control valve, 4. Left crank arm, 5. Fertilization spray needle assembly

The rotation of the shaft of the spray control valve 3 drives the rotation of the crank 2, which in turn drives the movement of the fertilizer spraying needle. The trajectory of the fertilizer spraying needle meets the requirements of deep fertilization. The movement of the fertilizer spraying needle causes the front swing arm spindle seat 2 to swing slightly, and the fertilizer spraying needle deeply applies liquid fertilizer to the soil, thereby achieving the deep application of liquid fertilizer. The power of the crank rocker deep application mechanism is transmitted to the crank through the transmission system. Through the rotational motion of the crank, the reciprocating motion of the rocker is driven to achieve the up and down movement of the spray needle, completing piercing and fertilizing. According to agricultural requirements, the depth of liquid fertilizer application is around 100-130 mm. Therefore, the deep application mechanism is designed to ensure that the spraying point of the needle is within the spraying zone of 70-120 mm below the surface. Due to the ease of penetration of the fertilizer spraying needle into the soil, a 30 mm needle tip is welded below the spraying area, which not only facilitates penetration into the soil but also reduces the risk of clay formation when the needle moves upward. Each nozzle has two liquid outlet holes, reducing the number of spray needles and improving work efficiency.

Test equipment

To study the fertilization performance of the crank rocker deep application mechanism under the combinations of certain performance parameters, a liquid fertilizer deep application test bench is designed. The test bench is shown in Fig. 2.

The liquid fertilization test device mainly consists of components such as 1: the motor that drives the pump, 2: the piston pump, 3: the fertilizer spraying needle, 4: the crank, 5: the self-control spraying system, 6: the fertilizer tank, 7: the motor that drives the small sprocket, and 8: the frequency converter. The deep construction mechanism is the main working component. The working process is as follows: after the three-phase asynchronous motor that drives the pump starts, the liquid pump begins to work. At this time, the flow path of liquid fertilizer is from the liquid fertilizer tank through the outlet pipe to the liquid pump. After being pressurized by the liquid pump, it becomes a high-pressure liquid and passes through the pipeline system to the automatic spraying system. After passing through the automatic spraying system, the liquid fertilizer is finally applied to the soil through the crank rocker hole digging fertilization mechanism.

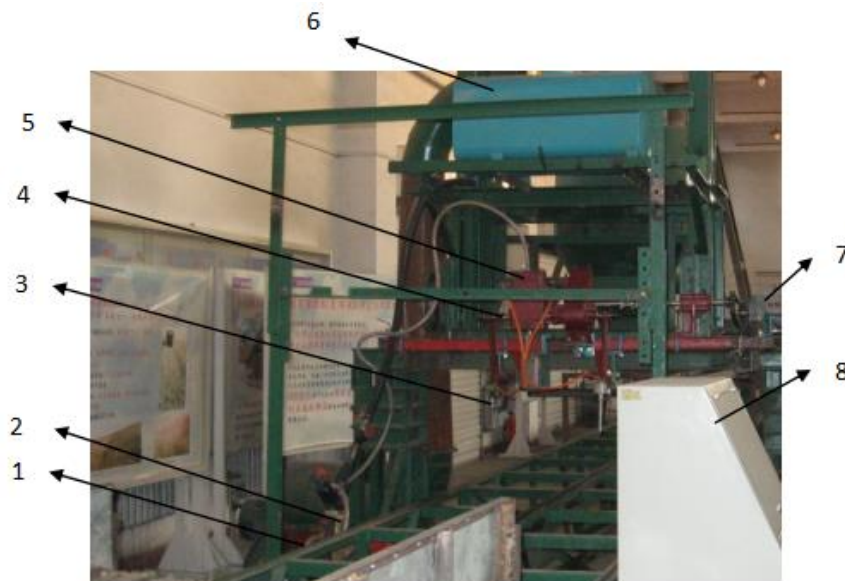


Fig. 2 - Test bench of the crank rocker deep application mechanism

1. Motor that drives the pump, 2. Piston pump, 3. Fertilizer spraying needle, 4. Crank, 5. Self-controlled spray system, 6. Fertilizer box, 7. Motor that drives the sprocket, 8. Frequency converter

Test design

The fertilization amount and fertilization loss rate are indicators for evaluating the fertilization performance of deep application mechanisms. The main working parameters that affect fertilization include liquid pump pressure, spray hole diameter, and crank speed. The above three factors are determined as experimental factors of fertilization. Single-factor and three-factor five level quadratic rotation orthogonal experimental designs are adopted, and the experimental coding table is shown in Table 1. Design expert 8. 0. 10 is used to process experimental data and analyze the impact of various factors on the fertilizer application rate and fertilizer loss rate of deep application mechanisms (Wang *et al.*, 2023; Zhang *et al.*, 2021; Yang *et al.*, 2023).

Table 1

| Test level coding table | | | |
|-------------------------|---------------------|--------------------------|---------------------|
| Coding value | Pump pressure / MPa | Spray hole diameter / mm | Crank speed / r/min |
| Upper star arm (1.68) | 0.23 | 4.6 | 167 |
| Higher level (1) | 0.3 | 4 | 150 |
| Zero level (0) | 0.4 | 3 | 125 |
| Lower level (-1) | 0.5 | 2 | 100 |
| Lower level (-1.68) | 0.57 | 1.3 | 83 |

RESULTS AND ANALYSIS

Single-factor experiment

When the crank speed is 125 r/min and the nozzle diameter is 3 mm, the effect of liquid pump pressure on fertilizer application rate is studied. The five levels of experimental factors are 0.2 MPa, 0.3 MPa, 0.4 MPa, 0.5 MPa and 0.6 MPa, respectively.

Five repeated experiments at each level are conducted, totaling 25 experiments. Design expert 8. 0. 10 is used to analyze the experimental data, and the relationship curve between liquid pump pressure and fertilizer application rate is shown in Fig. 3.

As shown in Fig. 3, when the crankshaft speed and nozzle diameter are constant and the liquid pump pressure varies in the range of 0.2 - 0.6 MPa, the applied fertilizer increases as the pressure increases. The reason is that the crankshaft speed and the key component cam speed of the distributor are the same during the fertilization. Therefore, when using the deep injection mechanism for fertilization, the opening and closing duration of the distribution valve remains unchanged, and the fertilizer gradually increases as the liquid pump pressure increases.

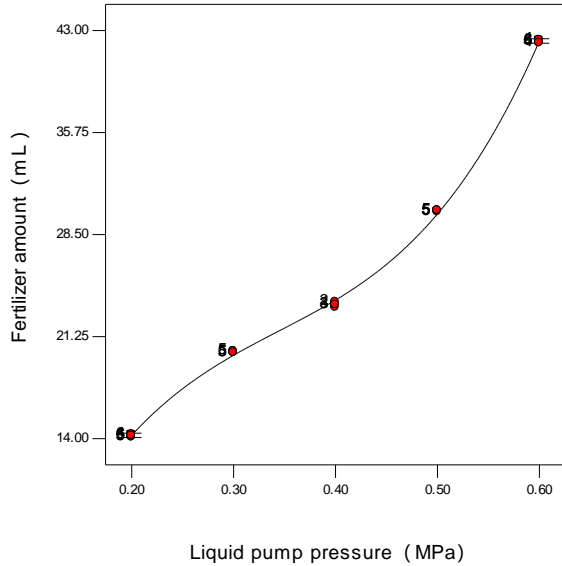


Fig. 3 - The effect of liquid pump pressure on fertilizer application rate

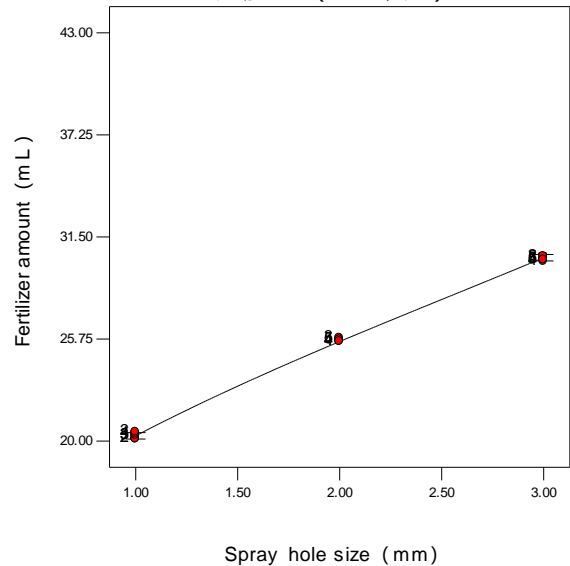


Fig. 4 - The influence of spray hole diameter on fertilizer application rate

When the crank speed is 125 r/min and the liquid pump pressure is 0.4 MPa, the influence of spray hole diameter on fertilizer application rate is studied. The five levels of experimental factors are 1 mm, 2 mm, 3 mm, 4 mm and 5 mm, respectively. 5 repeated experiments at each level are conducted, totaling 25 experiments. Design expert 8. 0. 10 is used to analyze the experimental data, and the relationship curve between the diameter of the spray hole and the fertilizer application rate is shown in Fig. 4.

As shown in Fig. 4, when the crank speed and liquid pump pressure are constant and the spray hole diameter varies in the range of 1-5 mm, the applied fertilizer increases with the increase of diameter. The reason is that the pressure of the liquid pump and the opening and closing duration of the distribution valve remain unchanged, and the fertilizer gradually increases with the increase of the spray hole diameter.

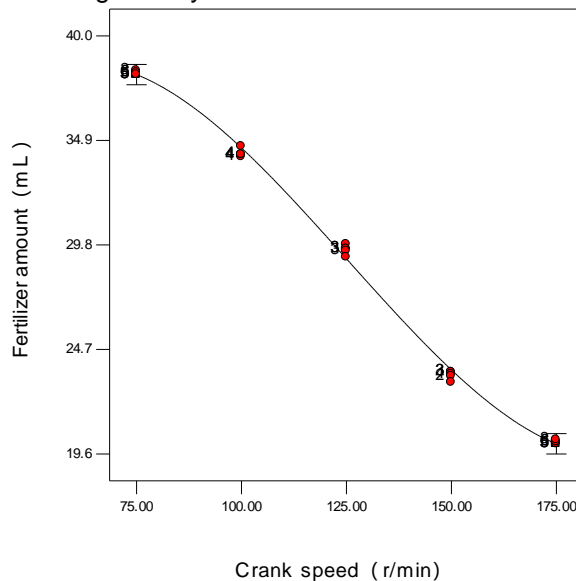


Fig. 5 - The influence of crank speed on fertilizer application rate

When the spray hole diameter is 3 mm and the liquid pump pressure is 0.4 MPa, the effect of crank speed on fertilizer application rate is studied. The five levels of experimental factors are 100 r/min, 125 r/min, 150 r/min, 175 r/min, and 200 r/min, respectively. 5 repeated experiments at each level are conducted, totaling 25 experiments. Design expert 8. 0. 10 is used to analyze the experimental data, and the relationship curve between crank speed and fertilizer application rate is shown in Fig. 5.

From Fig. 5, it can be seen that when the spray hole diameter and the liquid pump pressure are constant and the crankshaft speed varies in the range of 75-175 r/min, the applied fertilizer decreases with the increase of the speed. The reason is that the pressure of the liquid pump and the diameter of the spray hole remain unchanged. As the crankshaft speed increases, the opening and closing duration of the distribution valve will gradually decrease, and the fertilizer will also gradually decrease.

Multi-factor experiment

On the basis of a single factor, an orthogonal rotation experiment is conducted, and the experimental scheme and results are shown in Table. 2. Design expert 8. 0. 10 is used to analyzed the experimental data in Table. 2, and the response surfaces of the effects of liquid pump pressure and spray hole diameter, liquid pump pressure and crank speed, and spray hole diameter and crank speed on fertilizer application rate are shown in Figs. 6, 7, and 8, respectively. The response surfaces of the effects of liquid pump pressure and spray hole diameter, liquid pump pressure and crank speed, and spray hole diameter and crank speed on fertilizer loss rate are shown in Figs. 9, 10, and 11, respectively. The multi-factor variance analysis is shown in Tables. 3 and 4 (Rubeis et al., 2024; Sommermann and Cartmell, 2024; Riess, 2023).

When the significance level is $F_{0.05}$, as shown in Table 3, the effects of x_1, x_2, x_3, x_1^2 and x_2^2 on fertilizer are significant, and are the effective items of the model. After removing insignificant terms, the fitted regression equation is as follows:

$$y_1 = 59.735 - 140.546x_1 - 4.849x_2 - 0.3742x_3 + 311.06x_1^2 + 4.098x_2^2 \tag{1}$$

When the significance level is $F_{0.05}$, as shown in Table 4, the effects of x_1, x_2, x_3, x_1^2 and x_2^2 on fertilizer are significant, and are the effective items of the model. After removing insignificant terms, the fitted regression equation is as follows:

$$y_2 = 28.37 + 10.92x_1 + 1.67x_2 - 0.72x_3 - 0.50x_1x_3 + 50.15x_1^2 + 0.0051x_3^2 \tag{2}$$

Table 2

Secondary rotation orthogonal experiment scheme and results

| No. | Experimental factors | | | Performance indexes | |
|-----|------------------------------|-----------------------------------|--|--|-----------------------------------|
| | Pump pressure x_1 / MPa | Spray hole diameter x_2 / mm | Crank speed x_3 / r.min ⁻¹ | Fertilizer y_1 / mL ⁻¹ | Fertilizer loss rate y_2 / % |
| 1 | -1 | -1 | -1 | 22.2 | 1.2 |
| 2 | 1 | -1 | -1 | 42.9 | 2.9 |
| 3 | -1 | 1 | -1 | 31.4 | 1.2 |
| 4 | 1 | 1 | -1 | 56.4 | 4.5 |
| 5 | -1 | -1 | 1 | 16.2 | 4.3 |
| 6 | 1 | -1 | 1 | 36.9 | 3.2 |
| 7 | -1 | 1 | 1 | 25.3 | 1.8 |
| 8 | 1 | 1 | 1 | 50.3 | 4.2 |
| 9 | -1.68 | 0 | 0 | 20.6 | 2.7 |
| 10 | 1.68 | 0 | 0 | 54.2 | 5.4 |
| 11 | 0 | -1.68 | 0 | 21.5 | 1.1 |
| 12 | 0 | 1.68 | 0 | 41.5 | 4.1 |
| 13 | 0 | 0 | -1.68 | 36.8 | 1.1 |
| 14 | 0 | 0 | 1.68 | 20.8 | 5.2 |
| 15 | 0 | 0 | 0 | 30.5 | 2.3 |
| 16 | 0 | 0 | 0 | 29.5 | 2.7 |
| 17 | 0 | 0 | 0 | 30.5 | 2.2 |
| 18 | 0 | 0 | 0 | 29.5 | 2.3 |
| 19 | 0 | 0 | 0 | 29.5 | 2.9 |
| 20 | 0 | 0 | 0 | 30.0 | 2.8 |
| 21 | 0 | 0 | 0 | 29.5 | 2.4 |
| 22 | 0 | 0 | 0 | 30.5 | 2.5 |
| 23 | 0 | 0 | 0 | 31.0 | 2.6 |

Table 3

Variance analysis of the influence of various factors on fertilizer application rate

| Sources | Square sum | Degree of freedom | F-value | Significance (P>F) |
|----------|------------|-------------------|---------|--------------------|
| Model | 2427.33 | 9 | 88.87 | <0.0001 |
| x_1 | 455.09 | 1 | 149.96 | <0.0001 |
| x_2 | 1601.90 | 1 | 527.84 | <0.0001 |
| x_3 | 191.27 | 1 | 63.03 | <0.0001 |
| x_1x_2 | 9.24 | 1 | 3.05 | 0.1045 |
| x_1x_3 | 0.01 | 1 | 0.000 | 0.0946 |
| x_2x_3 | 0.03 | 1 | 0.003 | 10.9682 |
| x_1^2 | 153.79 | 1 | 50.68 | <0.0001 |
| x_2^2 | 16.70 | 1 | 5.50 | 0.0355 |
| x_3^2 | 0.079 | 1 | 0.026 | 0.8743 |
| Errors | 39.45 | 13 | | |
| Sum | 2466.78 | 22 | | |

Table 4

Analysis of variance on the impact of various factors on fertilizer loss rate

| Sources | Square sum | Degree of freedom | F-value | Significance (P>F) |
|----------|------------|-------------------|---------|--------------------|
| Model | 56.72 | 9 | 19.96 | < 0.0001 |
| x_1 | 16.67 | 1 | 52.78 | < 0.0001 |
| x_2 | 9.50 | 1 | 30.09 | 0.0001 |
| x_3 | 19.16 | 1 | 60.69 | < 0.0001 |
| x_1x_2 | 0.61 | 1 | 1.92 | 0.1896 |
| x_1x_3 | 0.85 | 1 | 6.33 | 0.0258 |
| x_2x_3 | 0.85 | 1 | 2.68 | 0.1258 |
| x_1^2 | 4.01 | 1 | 12.65 | 0.0035 |
| x_2^2 | 0.019 | 1 | 0.063 | 0.9378 |
| x_3^2 | 4.0 | 1 | 12.65 | 0.0035 |
| Errors | 4.10 | 13 | | |
| Sum | 60.82 | 22 | | |

As shown in Fig. 6, when the spray diameter is constant and the liquid pump pressure varies in the range of 0.1-0.6 MPa, the applied fertilizer gradually increases with the increase of liquid pump pressure. When the pressure of the liquid pump is constant and the diameter of the spray hole varies in the range of 1-5 mm, the applied fertilizer gradually increases with the increase of the spray hole diameter. The response surface changes faster in the direction of the spray hole diameter than the liquid pump pressure. According to Table. 3, the F value of the effect of liquid pump pressure on fertilizer application y_1 is 149.96, and that of spray hole diameter on fertilizer application y_1 is 527.84. Therefore, the influence of spray hole diameter on fertilizer application is greater than that of liquid pump pressure.

From Fig. 7, it can be seen that when the liquid pump pressure is constant and the crank speed varies in the range of 100-150 r/min, the applied fertilizer gradually decreases with the increase of crank speed. When the crankshaft speed is constant and the liquid pump pressure varies in the range of 0.1-0.6 MPa, the fertilizer application rate gradually increases with the increase of pressure. The response surface changes faster in the direction of pump pressure than the crankshaft speed.

According to Table 3, the F value of the effect of crank speed on fertilizer application y_1 is 63.03, and that of liquid pump pressure on fertilizer application y_1 is 149.96. Therefore, the influence of liquid pump pressure on fertilizer application is greater than that of crank speed.

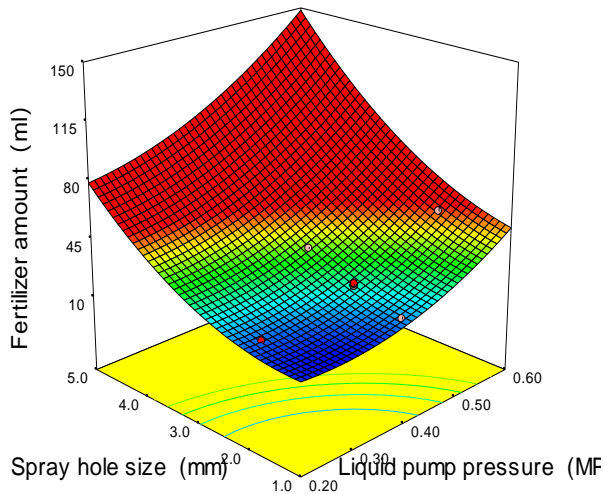


Fig. 6 - Response surface diagram of the influence of spray hole diameter and liquid pump pressure on fertilizer application rate

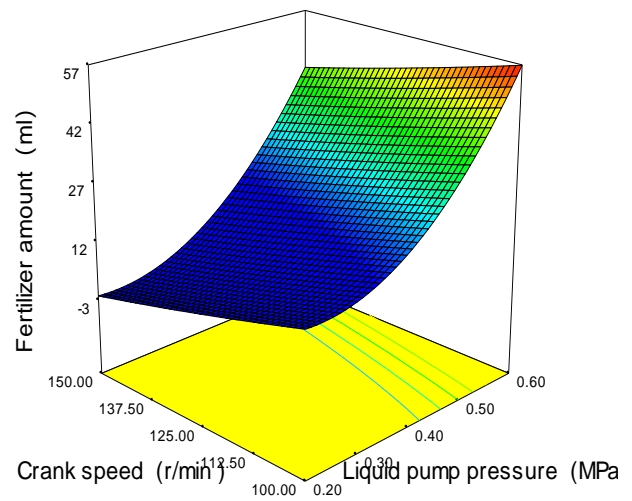


Fig. 7 - Response surface diagram of the influence of crank speed and liquid pump pressure on fertilizer application rate

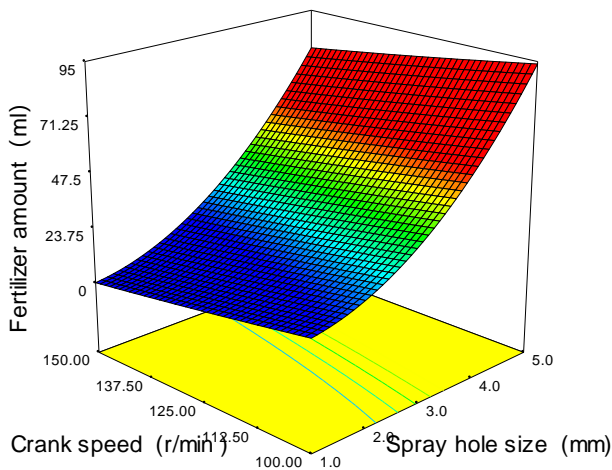


Fig. 8 - Response surface diagram of the influence of crank speed and spray diameter on fertilizer application rate

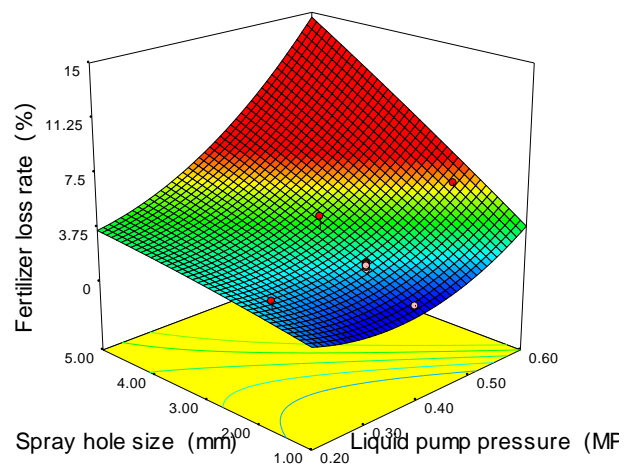


Fig. 9 - Response surface graph of the influence of spray hole diameter and liquid pump pressure on fertilizer loss rate

As shown in Fig. 8, when the spray hole diameter is constant and the planetary carrier speed varies in the range of 100-150 r/min, the applied fertilizer gradually decreases with the increase of the planetary carrier speed. When the crankshaft speed is constant and the spray hole diameter varies in the range of 1-5 mm, the applied fertilizer gradually increases with the increase of spray hole diameter. The response surface changes faster in the direction of the spray hole diameter than the crank speed. According to Table 3, the F -value of the effect of crank speed on the fertilizer application y_2 is 63.03, and that of spray diameter is 527.84. Therefore, the influence of spray hole diameter on fertilizer application is greater than that of crank speed.

According to Fig. 9, when the nozzle diameter is constant and the liquid pump pressure varies within the range of 0.1 - 0.6 MPa, the fertilizer loss rate gradually increases with the increase of liquid pump pressure. When the liquid pump pressure is constant and the spray hole diameter varies in the range of 1-5 mm, the fertilizer loss rate gradually increases with the increase of spray hole diameter. The response surface changes faster in the direction of liquid pump pressure than the spray hole diameter. According to Table 4, the F value effect of liquid pump pressure on fertilizer loss rate y_2 is 52.78, and that of spray hole diameter on fertilizer loss rate y_2 is 30.09. Therefore, the influence of liquid pump pressure on fertilizer loss rate is greater than that of spray hole diameter.

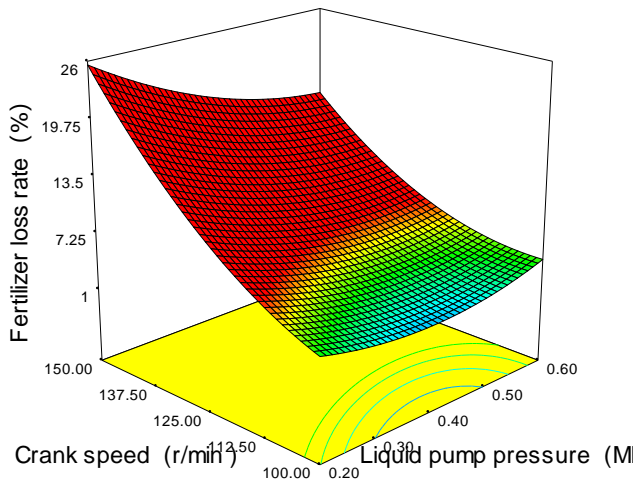


Fig. 10 - Response surface diagram of the influence of crank speed and liquid pump pressure on fertilizer loss rate

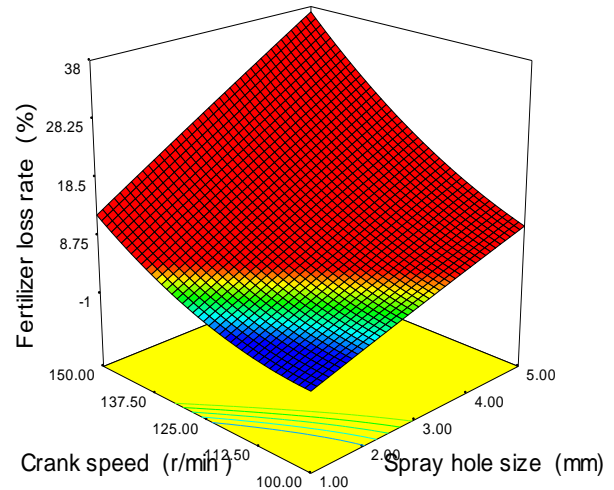


Fig. 11 - Response surface graph of the influence of crank speed and spray hole diameter on fertilizer loss rate

As shown in Fig. 10, when the liquid pump pressure is constant and the crank speed varies in the range of 100-150 r/min, the fertilizer loss rate gradually increases with the increase of crank speed. When the crankshaft speed is constant and the liquid pump pressure varies in the range of 0.1 - 0.6 MPa, the fertilizer loss rate gradually increases with the increase of pressure. The response surface changes rapidly in the direction of crank speed and slowly in the direction of liquid pump pressure. According to Table 4, the F value of the effect of crank speed on fertilizer loss rate y_2 is 60.69, and that of liquid pump pressure on fertilizer loss rate y_2 is 52.78. Therefore, the influence of crank speed on fertilizer loss rate is greater than that of liquid pump pressure.

As shown in Fig. 11, when the spray hole diameter is constant and the crank speed varies in the range of 100-150 r/min, the fertilizer loss rate gradually increases with the increase of crank speed. When the crankshaft speed is constant and the spray hole diameter varies in the range of 1-5 mm, the fertilizer loss rate gradually increases with the increase of spray hole diameter. The response surface changes rapidly in the direction of crank speed and slowly in the direction of spray hole diameter. As shown in Table. 4, the F -value of the effect of crank speed on fertilizer loss rate y_2 is 60.69, and that of nozzle diameter on fertilizer loss rate y_2 is 30.09. Therefore, the influence of crank speed on fertilizer loss rate is greater than that of spray hole diameter.

Experimental optimization and validation

To obtain the optimal parameter combination of liquid pump pressure, spray hole diameter, and crank speed, with fertilizer application rate and fertilizer loss rate as performance indicators and agronomic requirements as boundary conditions, the regression equations of fertilizer application rate and fertilizer loss rate are analyzed, and a nonlinear programming mathematical model is obtained as follows:

$$\begin{cases} y_1 \in (20,30) \\ y_2 \in (0,3) \\ s.t. 0.1 \leq x_1 \leq 0.6 \\ 1 \leq x_2 \leq 5 \\ 100 \leq x_3 \leq 150 \end{cases} \tag{3}$$

where the objective function used in parameter optimization is as follows (1) and (2):

$$\begin{cases} y_1 = 59.735 - 140.54x_1 - 4.849x_2 - 0.3742x_3 + 311.060x_1^2 + 4.0980x_2^2 \\ y_2 = 28.37 + 10.92x_1 + 1.67x_2 - 0.7x_3 - 0.5x_1x_3 + 50.15x_1^2 + 0.005x_3^2 \end{cases} \tag{4}$$

Application Software Design Expert 8 .0.10 pairs of (3) and (4) are optimized for parameter solving, the optimal parameter combination of hydraulic pump pressure, spray hole diameter and crank speed, that is, the crank speed is 145.80 r/min; the hydraulic pump pressure is 0.25 MPa; the nozzle diameter is 3.02 mm; the output fertilizer amount is 28.6 mL, and the fertilizer loss rate is 1.95%, which meet the requirements of fertilization performance.

Five sets of validation tests were conducted with the optimal crank speed of 145.80 r/min, liquid pump pressure of 0.25 MPa, and spray hole diameter of 3.02 mm. The validation results are shown in Table 5. The verification results are consistent with the optimization results of Design expert 8. 0. 10. The error mainly refers to the error caused by equipment accuracy and human operation during the experimental process. The validation test results are close to the predicted results under the optimal combination, with good consistency, indicating that the optimization model is feasible, the research results are available and provide reference for the design of fertilization equipment.

Table 5

| Verification test results | | | | |
|---|---|----------------------------------|---------------------------------|------------------------------------|
| Factors | | | Performance indexes | |
| Pump pressure $x_1 / \text{r} \cdot \text{min}^{-1}$ | Spray hole diameter x_2 / MPa | Crank speed x_3 / mm | Fertilizer y_1 / mL | Fertilizer loss rate $y_2 / \%$ |
| 0.25 | 3.02 | 145.8 | 28.6 | 1.95 |
| | | | 28.5 | 2.01 |
| | | | 28.5 | 2.33 |
| | | | 28.4 | 2.12 |
| | | | 28.4 | 2.10 |

CONCLUSIONS

(1) A crank rocker fertilization performance test bench was established, and a single factor experiment was designed. The results showed that as the crank speed increased, the fertilization amount gradually decreased; as the spray hole diameter increased, the fertilization gradually increased; as the liquid pump pressure increased, the fertilization amount gradually increased.

(2) A quadratic orthogonal rotation combination design experiment was adopted to establish a mathematical model for the performance indicators and experimental factors of fertilizer application rate, and the influence of interaction relationship on dynamic characteristics was analyzed.

(3) Design Expert 8 0.10 software was used to analyze and optimize the experimental results. When the crank speed was 145.80 r/min, the liquid pump pressure was 0.25 MPa, and the nozzle diameter was 3.02 mm, the fertilization of the crank rocker deep application mechanism was optimal. That is, the crank speed was 145.80 r/min; the liquid pump pressure was 0.25 MPa; the nozzle diameter was 3.02 mm; the output fertilization amount was 28.6 mL, and the fertilization loss rate was 1.95%.

ACKNOWLEDGMENTS

The work was supported by the Postdoctoral Science Foundation of Heilongjiang Province of China (Grant No. LBH-Z18254), Guangdong basic and applied basic research fund project (2021A1515011790), Special project for doctoral talents of Lingnan Normal University (ZL2021019).

REFERENCES

- [1] Chen, J.N., Zhang, X.W., Liu, L.M., Ma, X.X., Yao, K., Cheng, D. (2023). Design and experiment of a non-circular gear corn bowl seedling transplanting mechanism with clamped stem (夹茎式非圆齿轮玉米钵苗移栽机构设计与试验). *Journal of Agricultural Engineering*, 39(18), 30-40. (In Chinese) <https://dx.doi.org/10.11975/j.issn.1002-6819.202306011>
- [2] da Silva, M.J., Magalhães, P.S.G. (2019). Modeling and design of an injection dosing system for site-specific management using liquid fertilizer. *Precision Agriculture*, 20, 649-662. <https://doi.org/10.1007/s11119-018-9602-5>
- [3] Gilvan, M. B., José, F. S., Rovian, B., Alfran, T. M., Marcelo, S. d. F. (2023). Pollutant emissions from a tractor towing a seeder-fertilizer in an area with controlled machinery traffic. *Ciência Rural*, 53(6), 1-6. <http://doi.org/10.1590/0103-8478cr20230173>
- [4] Ramarao, S., Azman, E. A., Tajidin, N. Ismail, R., Yahya, B. (2024). Characterization of Liquid Organic Fertilizer (LOF) Derived from Unmarketable Vegetables and Fruits. *Pertanika Journal of Tropical Agricultural Science*, Vol. 47(2), 559-573. DOI:10.47836/pjtas.47.2.15
- [5] Riess, I. (2023). Analysis of Experimental Results of Defect Concentrations in the Surface Layer of Acceptor Doped Ceria. *Russian Journal of Electrochemistry*, 59(3), 169-172. <http://dx.doi.org/10.1134/S1023193523030114>

- [6] Rubeis, T. d., Ciccozzi, A., Paoletti, D., Ambrosini, D. (2024). Experimental analysis of insulating materials using Guarded Hot Box - Preliminary results. *Journal of Physics: Conference Series*, 2685, 012033. Doi:10.1088/1742-6596/2685/1/012033
- [7] Sharma, A., Khar, S. (2022). Current developments in vegetable transplanters in developing countries: a comprehensive review. *International Journal of Vegetable Science*, 28(5), 417-440. <https://doi.org/10.1080/19315260.2022.2046672>
- [8] Sommermann P., Cartmell. M.P., (2024). Dynamics of an omnidirectional pendulum energy harvester: A comparative analysis between numerical and experimental results. *International Journal of Non-Linear Mechanics*, 159, March 2024, 104588. <https://doi.org/10.1016/j.ijnonlinmec.2023.104588>
- [9] Wafiqah, A., Retnaningtyas, E., Wahyuni, D.S.C., Andini. A., Anjarsari, Y., Khotimah, R. A. N., Abdulaziz, U., Ansari, A. S., Rochman, N. T. (2024). Jamu waste as liquid organic fertilizer (LOF) and its quality analysis. *Materials Today: Proceedings*, March 2024, 1-6. <https://doi.org/10.1016/j.matpr.2024.03.057>
- [10] Wang, J.F., Liu, Y.F., Weng, W.X., Wang, J.W., Fu, Z.D., Wang, Z.T. (2022). Design and experiment of sliding groove rotary deep fertilization device for paddy field side (滑槽回转式水田侧深施肥装置设计与试验). *Journal of Agricultural Machinery*, 53(10), 76-85. (In Chinese) <http://dx.doi.org/10.6041/j.issn.1000-1298.2022.10.008>
- [11] Wang, J.F., Fu, Z.D., Weng, W.X., Wang, Z.T., Wang, J.W., Yang, D.Z. (2023). Design and Experiment of Double row Fertilizer Discharger for Deep Fertilization on the Side of Conical Plate Pushing Plate in Paddy Fields(圆锥盘推板式水田侧深施肥双行排肥器设计与试验). *Journal of Agricultural Machinery*, 54(02), 53-62. (In Chinese) <http://dx.doi.org/10.6041/j.issn.1000-1298.2023.02.005>
- [12] Wang, J.W., Liu, Z.M., Sun, X.B., Tang, H., Wang, Q., Zhou, W.Q. (2022). Design and Experiment of Fertilizing Device for Deep Application of Liquid Fertilizer with Target Fertilizing System (深施型液肥对靶点施装置设计与试验). *Journal of Agricultural Machinery*, 53(11), 152-162. (In Chinese) <http://dx.doi.org/10.6041/j.issn.1000-1298.2022.11.015>
- [13] Wang, J.W., Yan, D.W., Wang, Q., Tang, H., Wang, J.F., Zhou, W.Q. (2021). Design and Experiment of Jet Type Inter Plant Weeding Device in Paddy Fields (射流式水田株间除草装置设计与试验). *Journal of Agricultural Machinery*, 52(11), 78-85+94. (In Chinese) <http://dx.doi.org/10.6041/j.issn.1000-1298.2021.11.008>
- [14] Yang, X.L., Chen, B., Xing, H., Zhen, W.B., Qi, L. (2023). Design and Experiment of Sliding Knife Trenching Pneumatic Injection Liquid Fertilizer Atomization Side Deep Fertilization Device (滑刀开沟-气力引射式液肥雾化侧深施肥装置设计与试验). *Journal of Agricultural Engineering*, 39(16), 13-25. (In Chinese) <http://dx.doi.org/10.11975/j.issn.1002-6819.202212124>
- [15] Zhang, L.Y., He, Y.C., Yang, H.J., Tang, Z.H., Zheng, X., Meng, X.J. (2021). Analysis of the Relationship between the Development Status of Liquid Fertilization Machinery and Modern Agriculture (液体施肥机械发展现状与现代农业关系分析). *Journal of Chinese Agricultural Mechanization*, 42(04), 34-40. (In Chinese) <https://doi.org/10.13733/j.jcam.issn.2095-5553.2021.04.06>
- [16] Zhou, H.L., Liu, J.G., Yu, G.H., Qi, P., Wang, L., Zheng, J. (2023). Research on the seedling picking mechanism of vegetable transplanter with helical gear non-circular gear planetary gear system (蔬菜移栽机斜齿轮-非圆齿轮行星轮系取苗机构研究). *Journal of Agricultural Machinery*, 54(08), 77-86. (In Chinese) <http://dx.doi.org/10.6041/j.issn.1000-1298.2023.08.007>

DESIGN AND SIMULATION ANALYSIS OF THE TUBER HARVEST SCREENING MACHINE

块茎收获物清选机的设计与模拟分析

Wenliang LIU¹⁾, Changyou WEI¹⁾, Feng LIU^{1,*)}, Caiyu JIANG¹⁾, Fei PENG¹⁾, Jiaqi WANG¹⁾

¹⁾Jilin Agricultural Machinery Research Institute, Changchun, 130022, China

*Corresponding author's Email: 531845652@qq.com

DOI: <https://doi.org/10.35633/inmateh-73-45>

Keywords: Tuber harvest, Simulation, Experimental study, Vibration screening, Air separation, Flexible cleaning

ABSTRACT

In this paper, a screening machine was designed to remove the impurities in the tuber harvest, which integrates the functions of vibration screening, air separation, and flexible polishing. Discrete element simulation analysis was carried out to investigate the movement of tuber harvest and soil in the machine and the effect of polishing and removing impurities, the rationality of the structure, and the size were verified. Orthogonal tests were designed and carried out, with the rate of impurity, loss, and crushing as indicators and crank speed, impeller speed, and polishing roller speed as factors. The optimum working parameters were obtained: crank speed 280.12 r/min, impeller speed 1056.27 r/min, polishing roller speed 405.02 r/min, the impurity content was 0.29%, the loss rate was 1.01%, and the breakage rate was 0.11%. Through experimental verification, the actual value and theoretical value are basically the same, which verifies the rationality.

摘要

本文以清除块茎收获物中掺杂的杂质为目标,设计了一种集振动筛分、风选除杂、柔性清理功能于一体的清选机;并对清选作业过程进行离散元仿真分析,探究了块茎收获物和土壤在装置内的运动情况和清选除杂作业效果,验证了装置结构和尺寸设计的合理性;设计并开展正交试验,以含杂率、损失率、破碎率为指标,曲柄转速、叶轮转速、清理辊转速为因素,通过建立二次多项式回归方程和响应面模型,预测样机的最优工作参数组合:曲柄转速 280.12 r/min、叶轮转速 1056.27 r/min、抛光辊转速 405.02 r/min,此时含杂率 0.29%、损失率 1.01%、破碎率 0.11%。对预测结果优化后进行试验验证,得到预测值和优化值相近,验证了优化参数的合理性。

INTRODUCTION

Tubers are located beneath the earth's surface, making them susceptible to soil and other impurities during harvest. Additionally, newly harvested tubers have a higher water content and are prone to mildew deterioration (Zhou *et al.*, 2023). Therefore, it is essential to promptly clean the tubers after harvest in preparation for drying, dehydration, or further processing (Zhu *et al.*, 2022).

A soil-wash cleaning system for small-sized root crops, developed by Zhang *et al.* (2022) from Henan Agricultural University, breaks and separates larger soil clods by the collision and friction between tubers, and then separates the fine impurities on the tuber surface by the friction between the tuber and the sand. This design uses sand as a detergent, which requires inputting sand first and then filtering out the sand, increasing the machine's complexity, large size, and high energy consumption. Chen *et al.* (2015) and others used a flexible roller beating mechanism and a flexible rolling removing impurities mechanism and used spring teeth and flexible hammers to hit the material to complete the removing impurities operation, thereby realizing the root and soil separation of deep-rooted and stem-type medicinal materials. Due to the machine's poor operating stability, it is not suitable for operations with a large amount of feeding materials and has a high damage rate. Therefore, the existing root and soil separation technology and equipment for rhizomes cannot meet the requirements of beans and soil separation. It is necessary to conduct in-depth research on the mechanism of bean and soil separation and innovate in the structural design of the separation device. In this paper, a tuber harvest screening machine was designed to clean and remove impurities in the fluidization process, and the performance test of related operation parameters was carried out for the reference of relevant researchers.

Wenliang Liu, Associate Researcher; Changyou Wei, Research Intern; Feng Liu, Senior Engineer; Caiyu Jiang, Associate Researcher; Fei Peng, Engineer; Jiaqi Wang, Engineer.

Impurities in the harvested tubers: one is soil and grass stems mixed in the tuber harvest, and the other is soil and roots attached to the tuber skin. According to the types and characteristics of impurities in the harvest, the design scheme of the whole machine is determined. Firstly, the soil doped in the harvest is cleaned by the screening device; secondly, the grass stems are cleaned by the air separation unit; finally, the soil and roots attached to the tuber surface are cleaned by the polishing device. As shown in the design scheme in Fig. 1, the tuber harvest screening machine is mainly composed of three parts: vibrating screen motion, negative pressure air separation unit, and drum cleaning device, and each part is powered by an independent motor. The research content is very meaningful for the development of the tuber harvest screening machine technology.

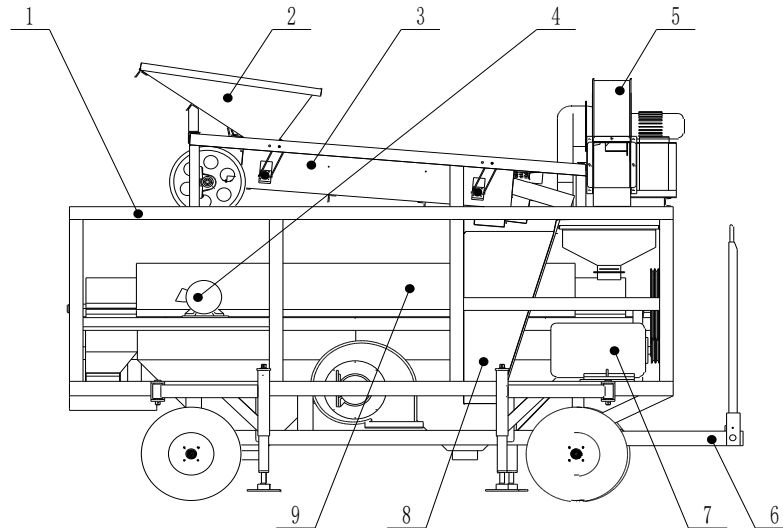


Fig. 1 - Overall structure of the tuber harvest screening machine

1 - Frame; 2 - Feeding hopper; 3 - Screening device; 4 - Screening device dynamo; 5 - Air separation unit; 6 - Hitch frame; 7 - Polishing device dynamo; 8 - Impurity removal slide; 9 - Polishing device

MATERIALS AND METHODS

Design screening device

As shown in Fig. 2, the structure of the screening device is mainly composed of pulley I, crank, connecting rod, suspension rod, and vibrating screen. The crank is firmly connected with the connecting rod, and the connecting rod is rotated with the vibrating screen. The vibrating screen is hinged with the frame by four suspension rods of equal length, and the whole vibrating screen is inclined to a certain angle with the horizontal direction. When working, the dynamo of the screening device drives pulley I. Due to the driving connecting rod driving the vibrating screen, it makes a reciprocating swing. The amplitude can be changed by adjusting the length of the connecting rod, the vibration frequency can be changed by adjusting the crank speed, and the screen angle can be changed by adjusting the length of the suspension rods. The working principle of the screening device is to separate impurities from the tubers using a sieve based on the difference in the three-axis size of the harvested material (Tao et al., 2023).

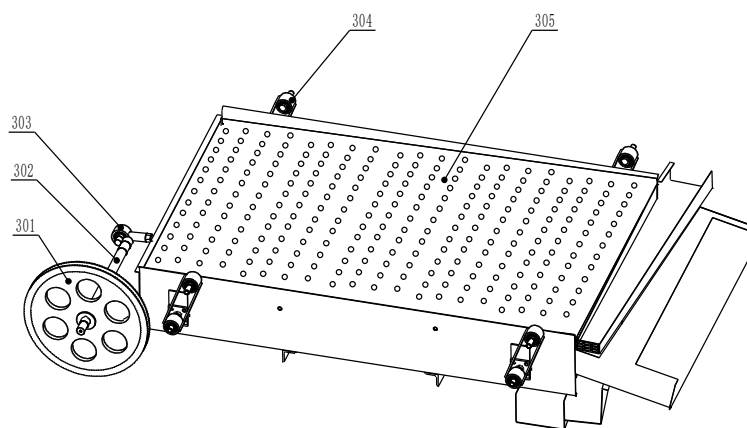


Fig. 2 - Screening device

301 - Pulley I; 302 - Crank; 303 - Connecting rod; 304 - Suspension rod; 305 - Vibrating screen

(1) Dimensional design of connecting rod and suspension rod

According to the requirements of the Agricultural Machinery Design Manual, the length of the connecting rod should be more than 5 times that of the crank, and the angle between the connecting rod and the suspension rod should be as close as possible to 90 degrees. Therefore, the length of the suspension rod should also be much larger than the length of the crank (*Chinese Academy of Agricultural Mechanization Sciences, 2007*). The length of the screening device crank is generally 23 - 30 mm, so the length of the connecting rod is designed to be 175 mm, and the length of the suspension rod is designed to be 155 mm, which is the design requirement of agricultural machinery.

(2) Design vibration direction angle and screen surface inclination angle

Directly, the vibration direction angle ε and the screen surface inclination angle α affect the motion speed of the material and the dispersion on the screen surface. Relevant studies have shown that $\varepsilon + \alpha$ is usually $5^\circ - 15^\circ$, the larger the $\varepsilon + \alpha$, the larger the amplitude of the screening device and the stronger the separation capacity (*Du et al., 2022; Qiu et al., 2022*). Combined with the screen surface load and separation effect, the design takes $\varepsilon + \alpha = 11^\circ$, $\alpha = 5^\circ$, $\varepsilon = 6^\circ$.

(3) Measuring friction angle

Using the inclined plane method, after many tests, the average result is obtained as the friction angle φ : friction angle $\varphi = 28^\circ$.

(4) Analyzing vibration status and calculating crank speed

To get a better screening effect, the tubers should try to keep in contact with the screen surface at all times and not be thrown up when on the screen. At the same time, the forward sliding distance of tubers on the screen surface should be greater than the reverse sliding distance to achieve the feeding function (*Tong et al., 2020; Ishtiaque et al., 2022; An et al., 2022*). According to this operation requirement, it is necessary to analyze the vibration state of the tuber on the screen. As shown in Fig. 3, it is assumed that the vibrating screen moves in the direction of OM in a positive direction, while the crank rotates in a clockwise direction.

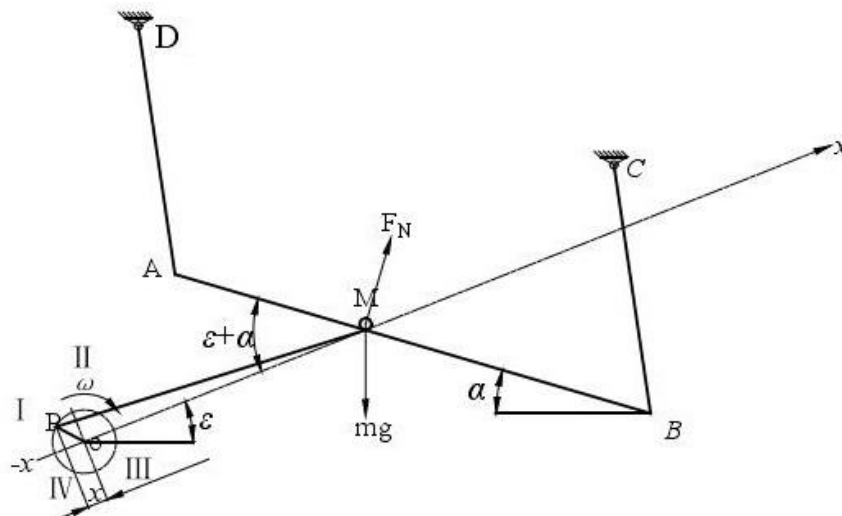


Fig. 3 - Sketch of vibrating screen motion

The vibrating screen motion can be expressed as follows:

$$\text{Displacement: } x = -r \cos \omega t \tag{1}$$

$$\text{Linear velocity: } v = x' = \frac{dx}{dt} = \omega r \sin \omega t \tag{2}$$

$$\text{Acceleration: } a = x'' = \frac{d^2x}{dt^2} = -\omega^2 r \cos \omega t \tag{3}$$

where: x - displacement, m; r - crank length, m; ω - angular velocity, rad/s; v - linear velocity, m/s; a - acceleration, m/s^2 ; t - time, s.

As shown in Fig. 3, according to formula (3), the acceleration is positive and the direction is to the right, when the crank OP is located in the I and IV quadrants. The tuber moves with the shaker and the acceleration is consistent with the shaker acceleration. The inertia force I of the tuber on the screen is to the left, and the formula is $I = -ma = -m\omega^2 r \cos \omega t$. where: I - inertial force, N; m - mass, kg; a - acceleration, m/s^2 . At this time, the forces acting on the tuber are inertia force I , gravity mg , support reaction force F_N , friction force f ,

where: in friction force $f = \mu F_N = F_N \tan \varphi$.

So, the screen surface support reaction:

$$F_N = mg \cos \alpha - l \sin (\varepsilon + \alpha)$$

Set a_s as the acceleration of tuber sliding upward along vibrating screen, then:

$$ma_s = -l \cos (\varepsilon + \alpha) - mg \sin \alpha - f \quad (4)$$

Substituting I. f into the above formula is:

$$ma_s = m\omega^2 r \cos \omega t \cos (\varepsilon + \alpha) - mg \sin \alpha - [mg \cos \alpha + m\omega^2 r \cos \omega t \sin (\varepsilon + \alpha)] \frac{\sin \varphi}{\cos \varphi} \quad (5)$$

m is divided by both sides of the equation and then multiplied by $\cos \varphi$, so the following can be obtained:

$$\begin{aligned} \cos \varphi a_s &= \omega^2 r \cos \omega t [\cos (\varepsilon + \alpha) \cos \varphi - \sin (\varepsilon + \alpha) \sin \varphi] - g (\sin \alpha \cos \varphi + \cos \alpha \sin \varphi) \\ &= \omega^2 r \cos \omega t \cos (\varepsilon + \alpha + \varphi) - g \sin (\alpha + \varphi) \end{aligned} \quad (6)$$

$\varepsilon + \alpha = 11^\circ$ and $\varphi = 28^\circ$ are known, then $\cos (\varepsilon + \alpha + \varphi) > 0$.

Divide $\cos (\varepsilon + \alpha + \varphi)$ by both sides of Formula (6):

$$\frac{\cos \varphi}{\cos (\varepsilon + \alpha + \varphi)} a_s = \omega^2 r \cos \omega t - g \frac{\sin (\alpha + \varphi)}{\cos (\varepsilon + \alpha + \varphi)} \quad (7)$$

From $\varphi = 28^\circ$, it can be inferred that $\cos \varphi > 0$, and since $\cos (\varepsilon + \alpha + \varphi) > 0$, $\frac{\cos \varphi}{\cos (\varepsilon + \alpha + \varphi)} > 0$, according to Formula (7), when $a_s > 0$, the tuber slides upwards along the vibrating screen. At this point:

$$\omega^2 r \cos \omega t > g \frac{\sin (\alpha + \varphi)}{\cos (\varepsilon + \alpha + \varphi)} \quad (8)$$

Similarly, the condition for the tuber to slide downwards along the screen surface is:

$$-\omega^2 r \cos \omega t > g \frac{\sin (\alpha - \varphi)}{\cos (\varepsilon + \alpha - \varphi)} \quad (9)$$

The tubers are thrown on the screen under the following conditions:

$$-\omega^2 r \cos \omega t \geq g \frac{\cos \alpha}{\sin (\varepsilon + \alpha)} \quad (10)$$

$k_s = g \frac{\sin (\alpha + \varphi)}{\cos (\varepsilon + \alpha + \varphi)}$, is called the up slip index. $k_x = g \frac{\sin (\alpha - \varphi)}{\cos (\varepsilon + \alpha - \varphi)}$, is called the down slide index (Fu, 2019).

$k_p = g \frac{\cos \alpha}{\sin (\varepsilon + \alpha)}$, is called the throwing index. Given $\varepsilon = 6^\circ$, $\alpha = 5^\circ$, $\varphi = 28^\circ$, the calculation can be: $k_s = 6.87$; $k_x = 4$; $k_p = 51.16$.

According to Formulas (8) and (10), when $\cos \omega t = 1$, $-\cos \omega t = 1$, the crank critical angular velocity formula can be obtained:

$$\omega_s = \sqrt{\frac{k_s}{r}} \quad (11)$$

$$\omega_p = \sqrt{\frac{k_p}{r}} \quad (12)$$

And since $n = \frac{30\omega}{\pi}$, Formulas (11) and (12) can be transformed into:

$$n_s = \frac{30}{\pi} \sqrt{\frac{k_s}{r}} \quad (13)$$

$$n_p = \frac{30}{\pi} \sqrt{\frac{k_p}{r}} \quad (14)$$

where n_s represents the crank speed when sliding up, r/min; n_p represents the crank speed when thrown up, r/min; r represents the length of the crank, m; k_s represents the up slide index; k_p represents the upthrow index.

In order that the forward sliding distance of the tuber on the screen surface should be larger than the reverse sliding distance, the crank speed n should be: $n_s < n < n_p$.

Substituting the minimum crank length $r_{\min} = 23$ mm, $k_s = 6.87$, $k_p = 51.16$ into Formula (13) and (14), it can be obtained $n_s = 165.12$ r/min, $n_p = 450.6$ r/min, and the obtained crank speed range of screening device 165.12 r/min - 450.6 r/min.

Design Air separation unit

As shown in Fig. 4, the air separation unit consists of a support, a driving motor, and a fan casting. The grass roots separated and mixed in the tubers are discharged from the machine and wind power is generated by fan rotation, which is the working principle of the Air separation unit (Zhou et al., 2022; Zhao et al., 2023). The Air separation unit is installed above the end of the vibrating screen, the suction outlet is toward the screen surface, and the outlet is toward the outside of the body. The driving motor is a centrifugal fan with a power of 2.2 kW and a rated speed of 2900 r/min.

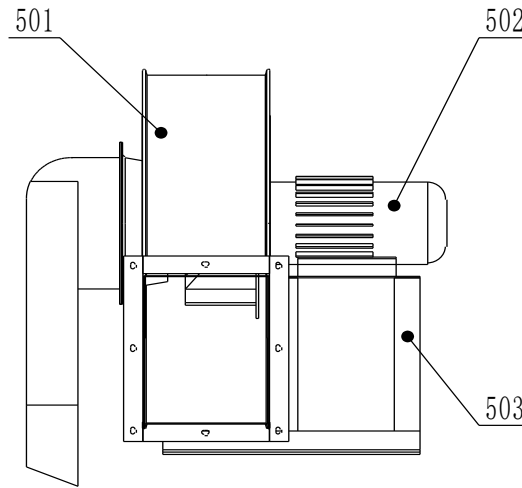


Fig. 4 - Air separation unit
 501 - Fan casting; 502 - Air separation unit dynamo; 503 - Support

Design polishing device

The structure of the polishing device is shown in Fig. 5, which is mainly composed of a polishing room, a feed hopper, a pulley II, a settling box, an impurity removal fan, and an outlet hopper. The polishing room is of horizontal structure. The polishing roller, as shown in Fig. 6, consists of a polishing shaft and a nylon brush mounted on it (Wang et al., 2018; Zhang et al., 2023). At work, the tubers enter the cleaning room from the hopper, and as the polishing roller rotates along the spiral to the discharge port, the tubers rub against each other in the fluidized movement process. At the same time, the nylon brush frictions the surface of the tubers. Under the action of multiple forces, the tubers are separated from the surface attachments such as soil and roots, and discharged through the hopper, and the soil impurities are discharged through the lower shell through the settling box. The impurities of the root are blown out of the machine under the action of the impurity fan.

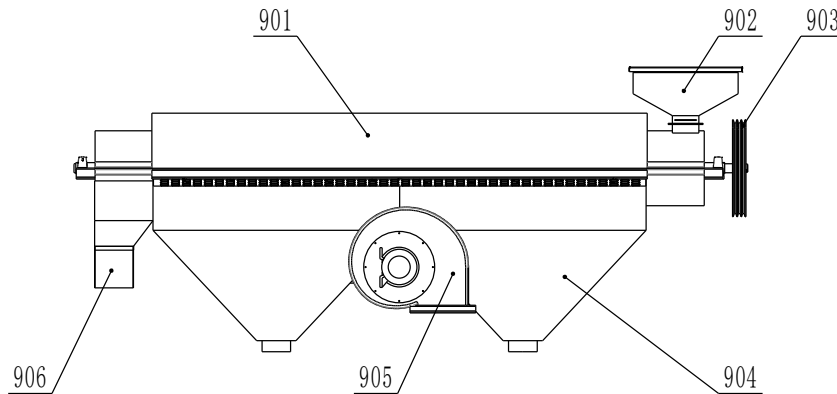


Fig. 5 - Polishing device
 901- Polishing room; 902 - Feed hopper; 903 - Pulley II; 904 - Settling box; 905 - Impurity removal fan; 906 - Outlet hopper



90031 - Nylon brush; 90032 - Polishing shaft
Fig. 6 - Polishing roller

Calculate the polishing roller diameter

According to the Agricultural Machinery Design Manual, the calculation formula for the design parameters of the polishing roller (including the brush installed on the roller shaft) is:

$$A_q = \frac{60\pi n e D^2}{Q} \tag{15}$$

$$l = e D \tag{16}$$

where: A_q - movement area per unit output of the polishing roller, $70 \text{ m}^2/\text{kg}$; n - polishing roller speed, 400 r/min ; e - polishing roller length and diameter ratio, 8 ; polishing roller diameter, m ; and Q - polishing machine output per hour, 1000 kg/h .

According to Formula (15), the diameter of the cleaning roller $D = 0.34 \text{ m} = 340 \text{ mm}$ can be obtained, and according to Formula (16), the length of the cleaning roller $l = 2720 \text{ mm}$.

Calculate the polishing roller speed

The speed of the polishing roller determines the movement speed and collision force of the crop. The calculation formula for the speed of the cleaning roller is:

$$n = \frac{60v}{\pi D} \tag{17}$$

where n - cleaning roller speed, r/min ; v - cleaning roller linear speed, m/s ; and D - diameter of the cleaning roller, m .

Generally, the linear speed of the cleaning roller is $6 \text{ m/s} - 10 \text{ m/s}$ (Yang et al., 2023; Ji et al., 2021). According to Formula (17), the speed of the cleaning roller is $337 \text{ r/min} - 562 \text{ r/min}$.

Discrete element simulation analysis

It is difficult to observe the operation process because the entire device is a closed structure. Discrete element simulation analysis is carried out by EDEM software to observe the movement and the operating effect of tubers and soil and fibrous roots in the device, and verify the rationality of the parameter and structural design.

(1) Establishing models for crops, soil, and fibrous roots

In this paper, the length of the tuber modeling is 7 mm ; the width is $13 - 14 \text{ mm}$, the height is $12 - 13 \text{ mm}$ and the soil diameter is 3 mm . The length of the root is 5 mm . The bonding bond between the tuber, soil and fibrous roots can withstand the force and deformation caused by collision, friction, extrusion, kneading, etc. When it reaches a certain degree, the bonding fails and the soil or fibrous root particles are separated from the parent (Jiang et al., 2023; Yu, 2022). As shown in Fig. 7, the model is established through particle combination, including the tuber, soil, and bonding models.

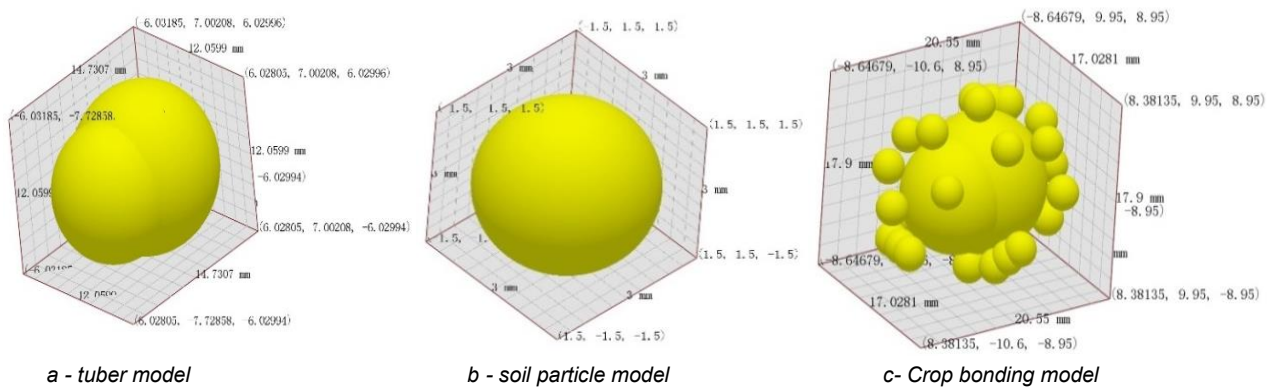


Fig. 7 - Model building

(2) Simulation process

During the simulation, the particle factory is set up and the particles are generated dynamically inside the hopper. The particles entering the polishing chamber through the hopper are polished for simulation and discharged from the rear discharge port after the whole polishing process (Zhang et al., 2022; Sadek et al., 2021; Sarkar et al., 2021).

The particle generation speed is set as 1500 grains/s and the line speed into the hopper is set as 0.7 m/s . The acceleration of gravity is 9.8 m/s^2 . Set the fixed time step to the time step of 16.04% , the step size to $2E - 5 \text{ s}$, and the mesh size to 2.5 R . The simulation situation is shown in Fig. 8.

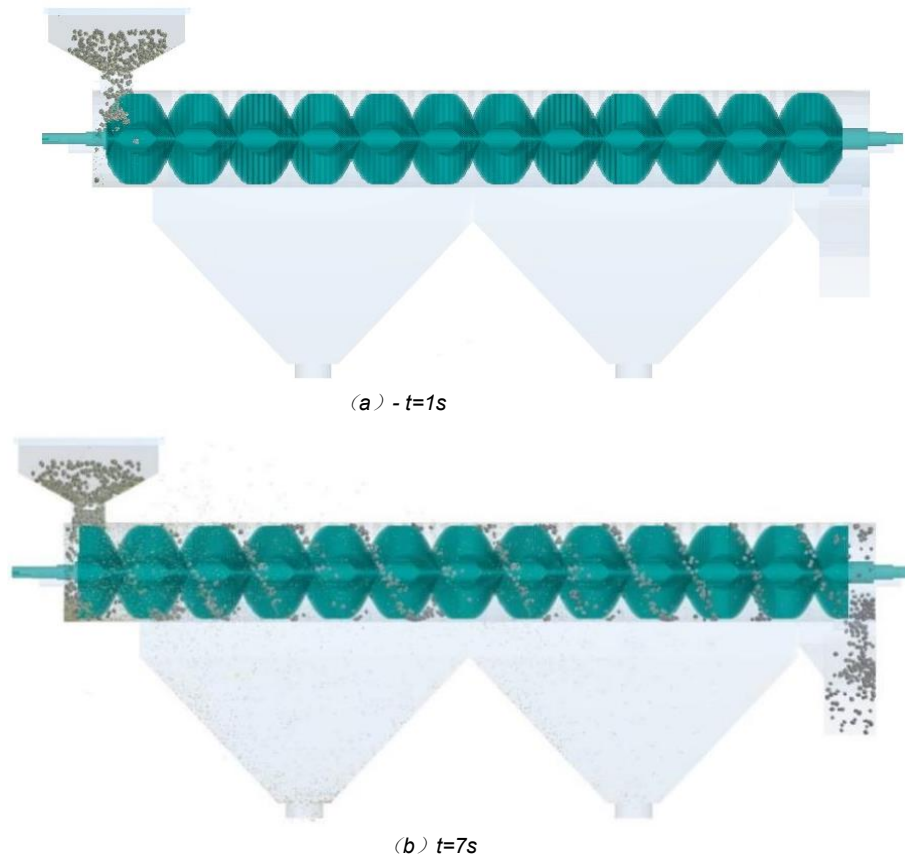


Fig. 8 - Simulation situation

(3) Analyze simulation results

From the simulation process, it can be clearly seen that the effect of the crop polishing operation throws off more impurities in the beginning stage. At the end of the polishing chamber, there were basically no impurities falling, indicating that the length of the polishing roller is reasonable. And because there were more crops gathered under the polishing room near the settling box, the polishing effect was best here. However, in the actual operation process, the entire polishing room would be filled with crops, and this effect would be achieved everywhere in the polishing room.

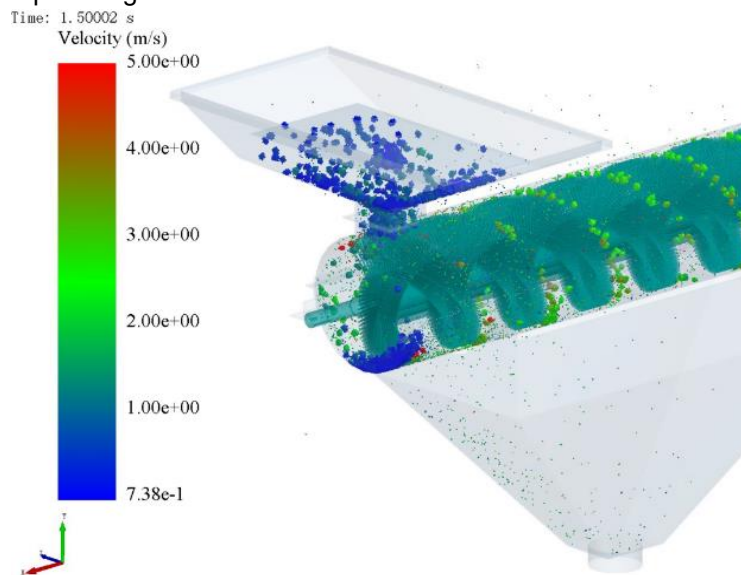


Fig. 9 - Article velocity vector diagram of simulation process

The particles' velocity field distribution in the simulation process is shown in Fig. 9. It can be seen that the crops enter the polishing room through the hopper and contact the polishing roller at the front of the polishing room. Due to the impact of the rotating polishing roller, the speed is relatively fast.

The particles close to the nylon brush are thrown up by the nylon brush rotation, and a certain acceleration is obtained, and the speed is also relatively fast. The particles between the spiral nylon brush are forced to withstand the thrust action, rotate axially, and move toward the discharge port at a uniform speed.

RESULTS

Design factor level

The impurity rate, loss rate, and crushing rate selected during the experiment were used as evaluation indicators, and the feeding amount remained constant at 1000 kg/h.

(1) The impurity rate is calculated as follows:

$$\eta_1 = \frac{n_1}{n_2} \tag{18}$$

Where η_1 represents the impurity content, %; n_1 represents the mass of impurities in the material after operation, kg; and n_2 represents the mass of mixture after operation, kg. (Ishiaque et al., 2022)

(2) The loss rate is calculated as follows:

$$\eta_2 = \frac{n_3}{n_3+n_4} \tag{19}$$

Where η_2 represents the loss rate, %; n_3 represents the loss of tubers, kg; and n_4 represents the mass of tuber harvested through the device, kg.

(3) The crushing rate is as follows:

$$\eta_3 = \frac{n_5}{n_6} \tag{20}$$

Where η_3 represents the crushing rate, %; n_5 represents the mass of broken tubers, kg; and n_6 represents the mass of harvested tubers, kg. (An et al., 2022; Fu, 2019; Zhou et al., 2022)

Test design

In advance, the single-factor test was carried out to develop the rule that the three test indexes, including the impurity rate, loss rate, and crushing rate, were affected by five factors (the screen inclination angle of the screening device, the crank speed of the screening device, the impeller speed of the air separation unit, the polishing roller speed of the polishing device, and the clearance of the polishing chamber of the polishing device). It is concluded that the factors and levels that have a great influence on the cleaning, screening and impurity removal effects of tuber harvest were as follows: crank speed: 254 r/min - 314 r/min, impeller speed: 900 r/min - 1700 r/min, and polishing roller speed: 378 r/min - 452 r/min. According to the above test results, the factors and levels of the orthogonal test were selected: crank speed: 254, 284, 314 r/min, impeller speed: 900, 1100, 1300 r/min, and polishing roller speed: 380, 410, 440 r/min. The test was designed using Design-Expert software, and 17 groups of tests were estimated. The test data results are shown in Table 1.

Table1

Orthogonal test table and results

| Number | Crank speed r/min | Impeller speed r/min | Polishing roller speed r/min | Impurity rate % | Loss rate % | Crushing rate % |
|--------|-------------------|----------------------|------------------------------|-----------------|-------------|-----------------|
| 1 | 284 | 1300 | 380 | 0.44 | 1.52 | 0.24 |
| 2 | 314 | 1100 | 440 | 0.52 | 1.76 | 0.19 |
| 3 | 254 | 900 | 410 | 0.42 | 1.42 | 0.17 |
| 4 | 284 | 1100 | 410 | 0.32 | 1.03 | 0.13 |
| 5 | 254 | 1100 | 440 | 0.47 | 1.53 | 0.16 |
| 6 | 284 | 1100 | 410 | 0.29 | 0.96 | 0.12 |
| 7 | 284 | 900 | 380 | 0.39 | 1.33 | 0.17 |
| 8 | 314 | 1300 | 410 | 0.52 | 1.78 | 0.25 |
| 9 | 284 | 1100 | 410 | 0.29 | 1.05 | 0.12 |
| 10 | 254 | 1100 | 380 | 0.44 | 1.42 | 0.14 |
| 11 | 284 | 1100 | 410 | 0.31 | 1.04 | 0.12 |
| 12 | 254 | 1300 | 410 | 0.47 | 1.59 | 0.24 |
| 13 | 314 | 900 | 410 | 0.46 | 1.61 | 0.19 |
| 14 | 284 | 1300 | 440 | 0.54 | 1.66 | 0.26 |
| 15 | 314 | 1100 | 380 | 0.43 | 1.63 | 0.17 |
| 16 | 284 | 1100 | 410 | 0.3 | 1.09 | 0.11 |
| 17 | 284 | 900 | 440 | 0.43 | 1.43 | 0.18 |

The regression equations containing the impurity rate, loss rate, and crushing rate are obtained by fitting the data.

$$Y_1 = 0.30 + 0.016A + 0.034B + 0.033C + 0.015AC + 0.015BC + 0.090A^2 + 0.075B^2 + 0.073C^2 \tag{21}$$

$$Y_2 = 1.03 + 0.10A + 0.095B + 0.060C + 0.010BC + 0.33A^2 + 0.23B^2 + 0.22C^2 \tag{22}$$

$$Y_3 = 0.12 + 0.011A + 0.035B + 0.023A^2 + 0.070B^2 + 0.023C^2 \tag{23}$$

where: Y_1 - impurity rate; Y_2 - loss rate; Y_3 - crushing rate; A - crank speed; B - impeller speed; C - polishing roller speed.

Interpretation of results

Analyze the significance of impurity rate

Table2

Analysis of variance of impurity rate

| Source of variation | Quadratic sum | Degree of freedom | Mean square error | F-value | P-value | Significance |
|---------------------|---------------|-------------------|-------------------|---------|---------|-----------------|
| Model | 0.11 | 9 | 0.012 | 63.86 | <0.0001 | Significant |
| A | 2.113E-003 | 1 | 2.113E-003 | 10.91 | 0.0131 | |
| B | 9.113E-003 | 1 | 9.113E-003 | 47.08 | 0.0002 | |
| C | 8.450E-003 | 1 | 8.450E-003 | 43.65 | 0.0003 | |
| AB | 2.500E-005 | 1 | 2.500E-005 | 0.13 | 0.7299 | |
| AC | 9.00E-004 | 1 | 9.00E-004 | 4.65 | 0.0680 | |
| BC | 9.00E-004 | 1 | 9.00E-004 | 4.65 | 0.0680 | |
| A ² | 0.034 | 1 | 0.034 | 177.17 | <0.0001 | |
| B ² | 0.024 | 1 | 0.024 | 123.17 | <0.0001 | |
| C ² | 0.022 | 1 | 0.022 | 115.12 | <0.0001 | |
| Residuals | 1.355E-003 | 7 | 1.936E-004 | | | |
| Undrafted item | 6.750E-004 | 3 | 2.250E-004 | 1.32 | 0.3837 | Not significant |
| Pure error | 6.800E-004 | 4 | 1.700E-004 | | | |
| Sum total | 0.11 | 16 | | | | |

According to the data in Table 2, P-value 0.0001 < 0.01, F-value = 63.86, the model effect was significant, and the P - value of the missing item was 0.3837 > 0.05, indicating that there was no missing factor and the model was stable. R² = 0.988, regression items A², B² and C² were extremely significant under P < 0.001, regression items A, B and C were significant under P < 0.05, and the remaining items P > 0.1 were not significant. The factors that affected the impurity content were A > B > C, that is, crank speed > impeller speed > polishing roller speed.

Analyze the significance of loss rate

Table3

Analysis of variance of loss rate

| Source of variation | Quadratic sum | Degree of freedom | Mean square error | F-value | P-value | significance |
|---------------------|---------------|-------------------|-------------------|---------|---------|-----------------|
| Model | 1.18 | 9 | 0.13 | 90.32 | <0.0001 | significant |
| A | 0.084 | 1 | 0.084 | 57.85 | 0.0001 | |
| B | 0.072 | 1 | 0.072 | 49.70 | 0.0002 | |
| C | 0.029 | 1 | 0.029 | 19.82 | 0.003 | |
| AB | 0.000 | 1 | 0.000 | 0.000 | 1.0000 | |
| AC | 1.000E-004 | 1 | 1.000E-004 | 0.069 | 0.8006 | |
| BC | 4.000E-004 | 1 | 4.000E-004 | 0.28 | 0.6160 | |
| A ² | 0.47 | 1 | 0.47 | 321.37 | <0.0001 | |
| B ² | 0.23 | 1 | 0.23 | 157.33 | <0.0001 | |
| C ² | 0.20 | 1 | 0.20 | 137.73 | <0.0001 | |
| Residuals | 0.010 | 7 | 1.453E-003 | | | |
| Undrafted item | 1.250E-003 | 3 | 4.167E-004 | 0.19 | 0.9002 | not significant |
| Pure error | 8.920E-003 | 4 | 2.230E-003 | | | |
| Sum total | 1.19 | 16 | | | | |

From the data in Table 3, P < 0.0001, F = 90.32, the model was significant, and P = 0.9002 > 0.05 of the missing item indicates that was no missing factor and the model was stable. R² = 0.9915. When P < 0.001, regression items A², B² and C² were extremely significant; when P < 0.05, regression items A, B and C were significant, while the other items were not. The factors affecting the loss rate are as follows: A > B > C; namely, crank speed > impeller speed > polishing roller speed.

Analyze the significance of crushing rate

Table 4

| Source of variation | Quadratic sum | Degree of freedom | Mean square error | F-value | P-value | Significance |
|---------------------|---------------|-------------------|-------------------|---------|---------|-----------------|
| Model | 0.038 | 9 | 4.249E-003 | 79.31 | <0.0001 | Significant |
| A | 1.012E-003 | 1 | 1.012E-003 | 18.90 | 0.0034 | |
| B | 9.800E-003 | 1 | 9.800E-003 | 182.93 | <0.0001 | |
| C | 6.125E-004 | 1 | 6.125E-004 | 11.43 | 0.0117 | |
| AB | 2.500E-005 | 1 | 2.500E-005 | 0.47 | 0.5165 | |
| AC | 0.000 | 1 | 0.000 | 0.000 | 1.0000 | |
| BC | 2.500E-005 | 1 | 2.500E-005 | 0.47 | 0.5165 | |
| A ² | 2.132E-003 | 1 | 2.132E-003 | 39.73 | 0.0002 | |
| B ² | 0.021 | | 0.021 | 385.12 | <0.0001 | |
| C ² | 2.132E-003 | 1 | 2.132E-003 | 39.79 | 0.0004 | |
| Residuals | 3.750E-004 | 7 | 5.357E-005 | | | |
| Undrafted item | 1.750E-004 | 3 | 5.833E-005 | 1.17 | 0.4262 | not significant |
| Pure error | 2.000E-004 | 4 | 5.000E-005 | | | |
| Sum total | 0.039 | 16 | | | | |

Table 4 shows that the regression model with $P < 0.0001$ was extremely significant. The missing item ($P = 0.4262 > 0.05$) was not significant, indicating there was a good fit. By analyzing the P-values of the primary and secondary and interaction terms of each factor, it can be seen that the P-values of B and B² were < 0.0001 , and the influence was extremely significant; the P-values of A, C, A² and C² were < 0.05 , and the influence was significant. According to the F-value in the table, the main order of factors was $B > A > C$, that is, impeller speed $>$ crank speed $>$ polishing roller speed.

Parameter optimization and experimental verification

The three selected factors were optimized by Design-Expert 8.0.6 software to predict the test indexes and obtain the optimal parameter combination of optimization results. In the optimization process, the three test indexes including impurity rate, loss rate and crushing rate were set to the minimum, and the optimization process and results are shown in Table 5.

Table 5

| Name | Goal | Lower Limit | Upper Limit | Lower Weight | Upper Weight | Importance | | |
|--------------------------------|------------------------------|--------------------|------------------------|---------------|--------------|---------------|--------------|----------|
| A:Vibrating screen crank speed | Within the range | 254 | 314 | 1 | 1 | 3 | | |
| B: Fan impeller speed | Within the range | 900 | 1300 | 1 | 1 | 3 | | |
| C: Polishing roller speed | Within the range | 380 | 440 | 1 | 1 | 3 | | |
| Impurity rate | Minimal | 0.29 | 0.54 | 1 | 1 | 5 | | |
| loss rate | Minimal | 0.96 | 1.78 | 1 | 1 | 4 | | |
| Crushing rate | Minimal | 0.11 | 0.26 | 1 | 1 | 3 | | |
| Solutions | | | | | | | | |
| Number | Vibrating screen crank speed | Fan impeller speed | Polishing roller speed | Impurity rate | Loss rate | Crushing rate | Desirability | |
| 1 | 280.12 | 1056.27 | 405.02 | 0.295172 | 1.0132 | 0.113804 | 0.963 | Selected |

The predicted results are: the crank speed was 280.12 r/min, the impeller speed was 1,056.27 r/min, and the cleaning roller speed was 405.02 r/min. The impurity rate, loss rate and crushing rate were 0.29%, 1.01%, and 0.11%, respectively.

According to the actual operating conditions and operational feasibility, the predicted results were verified. The test parameters were set as integers; the crank speed was 284 r/min, the impeller speed was 1100 r/min, and the polishing roller speed was 410 r/min. The test was repeated three times. As shown in Table 6, the average value of impurity rate, loss rate and crushing rate was basically the same as the predicted value, meeting the design requirements of the machine tools.

Table 6

| Validation test results | | | |
|-------------------------|-----------------|-------------|-----------------|
| Number of trials | Impurity rate % | Loss rate % | Crushing rate % |
| 1 | 0.29 | 1.03 | 0.15 |
| 2 | 0.30 | 1.05 | 0.13 |
| 3 | 0.31 | 1.07 | 0.12 |
| Mean | 0.30 | 1.05 | 0.13 |

CONCLUSIONS

(1) In this paper, a kind of tuber harvest polishing machine is designed, and the screening device, air separation unit and polishing device are designed in detail and their parameters are calculated. The centrifugal volute suction fan with a power of 2.2 kW is selected for the air separation unit. The polishing device is designed as a combination structure of a double helix nylon brush and cylinder screen.

(2) The particle model of soil and fibrous roots attached to the surface of tuber harvest was established by EDEM software. The movement of tuber harvest, soil, and roots in the plant and the effect of polishing and removing impurities were analyzed by discrete element simulation, which finally verified the rationality of the structure and size design of the plant.

(3) To verify the rationality of the optimized parameters, the quadratic polynomial regression equation and response surface were employed to establish the model by determining the influence law of the interaction between different factors on the evaluation index. Among them, the impurity rate, loss rate, and crushing rate were used as evaluation indexes, and the crank speed, impeller speed, and polishing roller speed were used as factors. According to the best working parameters predicted by the software, and combined with the actual working needs of the machine, the software prediction results were optimized and verified.

The research content of this paper has certain reference significance for the design and simulation analysis of the tuber harvest screening machine. The design tested some factors that affected the operation effect due to the limitations of the test cycle and parts processing conditions. In the future, studies can be conducted on the influence of other factors, such as the inclination angle of the roller, the brush wire material, etc.

ACKNOWLEDGEMENTS

Science and technology development plan of Jilin Province "Study on Key Equipment of Whole Mechanized Operation Mode of Farmland Ginseng" (20230202037NC).

REFERENCES

- [1] An, Z., Wang, R., Liu, P., & Fan, J. (2022). Design Study of a New Type of Flat Body Cleaning Device. *Journal of Electronics and Information Science*, Vol. 7(1), pp. 99-102. <http://dx.doi.org/10.23977/jeis.2022.070117>
- [2] Chen, X.S., Ma, X., Chen, G.R., Qi, L., Wu, T., Zeng, L.C. (2015). Research on root-soil separation device for deep-rooted Chinese medicinal materials. *Mechanical Design*, Vol. 32 (07), pp.65-70. DOI: 10.13841/j.cnki.jxsj.2015.07.014
- [3] Chinese Academy of Agricultural Mechanization Sciences (2007). *Agricultural Machinery Design Manual* (农业机械设计手册). China Agricultural Science and Technology Press, Beijing, China. (In Chinese)
- [4] Du, J., Heng, Y., Zheng, K., Luo, C., Zhu, Y., Zhang, J., & Xia, J. (2022). Investigation of the burial and mixing performance of a rotary tiller using discrete element method. *Soil and Tillage Research*, Vol. 220, pp. 105349. <https://doi.org/10.1016/j.still.2022.105349>
- [5] Fu Y. (2019). *Study on screening device for wet peanut pods* (鲜花生荚果筛选装置试验研究). Shenyang Agricultural University. (In Chinese). DOI: 10.27327/d.cnki.gshnu.2019.000323
- [6] Ishtiaque, A., Singh, S., Lobell, D., Fishman, R., & Jain, M. (2022). Prior crop season management constrains farmer adaptation to warming temperatures: evidence from the Indo-Gangetic Plains. *Science of the Total Environment*, Vol. 807, pp. 151671. <https://doi.org/10.1016/j.scitotenv.2021.151671>
- [7] Ji, J., Sang, Y., He, Z., Jin, X., & Wang, S. (2021). Designing an intelligent monitoring system for corn seeding by machine vision and Genetic Algorithm-optimized Back Propagation algorithm under precision positioning. *PLoS one*, Vol. 16(7), pp. e0254544. <https://doi.org/10.1371/journal.pone.0254544>
- [8] Jiang, Q., Liu, Y., Zhou, X., Yang, Y., Zhang, J., Jiang, B., Mao, D., Yang, Y., & Fu, Y. (2023). Intelligent Control Knowledge-Based System for Cleaning Device of Rice–Wheat Combine Harvester. *International*

- Journal of Pattern Recognition and Artificial Intelligence*, Vol. 37(07), pp. 2359015. <https://doi.org/10.1142/S0218001423590152>
- [9] Qiu, W., Ma, X., Cao, H., Huang, T., She, X., Huang, M., Wang, Z., & Liu, J. (2022). Improving wheat yield by optimizing seeding and fertilizer rates based on precipitation in the summer fallow season in drylands of the Loess Plateau. *Agricultural Water Management*, Vol. 264, pp. 107489. <https://doi.org/10.1016/j.agwat.2022.107489>
- [10] Sadek, M. A., Chen, Y., & Zeng, Z. (2021). Draft force prediction for a high-speed disc implement using discrete element modelling. *Biosystems engineering*, Vol. 202, pp. 133-141. <https://doi.org/10.1016/j.biosystemseng.2020.12.009>
- [11] Sarkar, P., Upadhyay, G., & Raheman, H. (2021). Active-passive and passive-passive configurations of combined tillage implements for improved tillage and tractive performance: A review. *Spanish journal of agricultural research*, Vol. 19(4), pp. e02R01-e02R01. <https://doi.org/10.5424/sjar/2021194-18387>
- [12] Tao, J., Leng, J., Lei, X., Wan, C., Li, D., Wu, Y., Yang, Q., Wang, P., Feng, B., & Gao, J. (2023). Effects of selenium (Se) uptake on plant growth and yield in common buckwheat (*Fagopyrum esculentum Moench*). *Field Crops Research*, Vol. 302, pp. 109070. <https://doi.org/10.1016/j.fcr.2023.109070>
- [13] Tong, J., Jiang, X. H., Wang, Y. M., Ma, Y. H., Li, J. W., & Sun, J. Y. (2020). Tillage force and disturbance characteristics of different geometric-shaped subsoilers via DEM. *Advances in Manufacturing*, Vol. 8, pp. 392-404. <https://doi.org/10.1007/s40436-020-00318-x>
- [14] Wang, Q., Wu, W., & Zhu, H. (2018). Design and test of screw cleaning mechanism for corn (玉米螺旋式清选装置的设计与试验). *Transactions of the CSAE*, Vol. 34(20), pp. 12-19. (In Chinese). DOI:10.11975/j.issn.1002-6819.2018.20.002
- [15] Yang, W., Ma, X., Ma, R., & Yang, C. (2015). Design and Experiment of Drum Type Brush Removing Soil Device (滚筒式毛刷清扫土装置的设计与试验). *Journal of Agricultural Mechanization Research*, Vol. 37(12), pp. 197-200. (In Chinese). DOI:10.3969/j.issn.1003-188X.2015.12.043
- [16] Yu, C. (2022). *Analysis and Simulation Test of Rice Grain Movement Trajectory in Rice Flexible Polishing Machine* (大米柔性抛光机内米粒运动轨迹分析与仿真试验). Wuhan Polytechnic University. (In Chinese). DOI: 10.27776/d.cnki.gwhgy.2022.000370
- [17] Zhang, X., Liu, X., Fan, C., Pei, Y., Wang, D., Zhou, P., Chen, X., Zhao, R., Zhou, X., Song, Q., Hou, Y., Zhang, Y., Liu, R., Lin, G. (2022). A "soil-washing" dry cleaning system for small-particle root crops (一种"以土洗土"的小粒径根茎作物干洗系统). Henan Province: [P] CN202110484627.9, 2022-11-22. (In Chinese)
- [18] Zhang, C., Geng, D., Xu, H., Li, X., Ming, J., Li, D., & Wang, Q. (2023). Experimental Study on the Influence of Working Parameters of Centrifugal Fan on Airflow Field in Cleaning Room. *Agriculture*, Vol. 13(7), pp. 1368. <https://doi.org/10.3390/agriculture13071368>
- [19] Zhang, S., Fu, J., Zhang, R., Zhang, Y., & Yuan, H. (2022). Experimental study on the mechanical properties of friction, collision and compression of tiger nut tubers. *Agriculture*, Vol. 12(1), pp. 65. <https://doi.org/10.3390/agriculture12010065>
- [20] Zhao, G., Wu, P., Liu, F., Li, S., Zhang, J., Dang, Y., Wang, L., Wang, S., Cheng, W., Cai, T., & Fan, T. (2023). Plow layer management during the fallow season can enhance the wheat productivity and resource utilization in a semi-arid region. *Soil and Tillage Research*, Vol. 228, pp. 105633. <https://doi.org/10.1016/j.still.2022.105633>
- [21] Zhou, J., Sun, W., & Liang, Z. (2023). Research on discrete element flexible model of Jerusalem artichoke roots and tubers during harvest period (收获期菊芋根-块茎离散元柔性模型研究). *Transactions of the CSAM*, Vol. 54(10), pp. 124-132. (In Chinese). DOI: 10.6041/j.issn.1000-1298.2023.10.011
- [22] Zhou, X., WANG, Z., TIAN, L., Su, Z., & Ding, Z. (2022). Numerical Simulation and Experiment of Cleaning Performance of Combine Harvester under the Action of Conical Fan. *Engineering in Agriculture, Environment and Food*, Vol. 15(2), pp. 61-71. https://doi.org/10.37221/eaef.15.2_61
- [23] Zhu, C., Chen, B., Li, J., Liu, Y., Yang, L., Wang, W., & Zhang, H. (2022). Design and Testing of the Peanut Pod Cleaning Device. *Processes*, Vol. 11(1), pp. 106. <https://doi.org/10.3390/pr11010106>

EXPERIMENTAL STUDY OF LYCIUM BARBARUM BRUISING DURING VIBRATION HARVESTING

枸杞振采收过程中果实碰撞损伤分析与试验

Qingyu CHEN¹⁾, Rui KANG²⁾, Naishuo WEI¹⁾, Yunlei FAN¹⁾, Zeyu WANG¹⁾, Jianguo ZHOU¹⁾,
Lingxin BU³⁾, Yu CHEN¹⁾, Jun CHEN^{*1)}

¹⁾ College of Mechanical and Electronic Engineering, Northwest A&F University, Yangling 712100, China;

²⁾ German-Sino School of Business & Technology, FOM University of Applied Sciences, Essen 45141, Germany;

³⁾ College of Mechatronic Engineering, North Minzu University, Yinchuan, Ningxia 750021, China

Tel: +86 135721917773; E-mail: chenjun_jdxy@nwsuaf.edu.cn

DOI: <https://doi.org/10.35633/inmateh-73-46>

Keywords: *L. barbarum*; vibration harvesting; high-speed photography; drop test; explicit dynamics; response surface method

ABSTRACT

Lycium barbarum L. (*L. barbarum*) is an economic crop with high added value and profit. Vibration harvesting is a suitable mechanized harvesting method for *L. barbarum*. It bruises easily during harvesting due to the softness and vulnerability of fresh ripe fruit, resulting in economic losses. This study analyzed the fruit drop and collision during vibration harvesting. High-speed photography was used to obtain the impact speed and angle of the falling fruit, and a kinematic analysis of the collision with the collection surface was conducted. The majority of the fruit had an impact speed of 3-6 m/s and an impact angle of 30-90° with the collection surface. A drop test was conducted to assess fruit bruising, and the impact speed was converted to the drop height. An orthogonal rotation experiment was conducted, and mathematical model was established between the drop height, impact angle, and impact material, and the fruit bruise rate, maximum impact force, recovery coefficient, and impact time. The effects of the factors on the fruit bruise rate, maximum impact force, recovery coefficient, and impact time were analyzed. The test results show that a vibration harvesting device for *L. barbarum* should be designed to reduce the height between the fruit and the collection surface and utilize a tilted collection surface and high cushioning materials to reduce the fruit bruising. This study provides guidance for subsequent research on the bruising of *L. barbarum* during vibration harvesting and harvester design.

摘要

枸杞作为一种经济作物，具有较高的附加值和利润。振动采收是枸杞机械化采收的适宜方法，由于枸杞鲜果柔嫩易损，采收过程中容易损伤造成经济损失。本研究针对枸杞振动采收中的果实跌落收集过程进行研究，通过高速摄影技术获取果实振采脱落速度与角度，对果实脱落后碰撞过程进行运动学分析，研究发现绝大多数枸杞果实与收集面的撞击速度在 3~6m/s，撞击角度为 30~90°。采用跌落试验的方法进行损伤研究，将撞击速度转变为跌落高度。通过三因素三水平二次正交旋转组合试验，建立了跌落高度、碰撞角度、碰撞材料与果实损伤率、最大冲击力、恢复系数和碰撞时间之间的数学模型，分析各因素对果实损伤率、最大冲击力、恢复系数和碰撞时间的影响。分析实验结果发现，较低的跌落高度与碰撞角度，以及添加更具缓冲能力的碰撞材料能够有效减少果实损伤，为后续枸杞损伤研究与采收机的设计提供参考。

INTRODUCTION

Lycium barbarum L. (*L. barbarum*) is a deciduous shrub belonging to the *Lycium* genus in the Solanaceae family. The fruit contains many nutritional components, such as polysaccharides, fatty acids, carotenoids, and phenolic compounds, that nourish the liver and kidneys, improve vision, enhance immunity, and delay aging (Xiao et al., 2022; Ma et al., 2022).

Qingyu Chen, Ph.D. Stud. Eng.; Rui Kang, M.S. Eng.; Naishuo Wei, Ph.D. Stud. Eng.; Yunlei Fan, Ph.D. Stud. Eng.; Zeyu Wang, M.S. Stud. Eng.; Jianguo Zhou, Ph.D. Stud. Eng.; Lingxin Bu, Ph.D. Eng.; Yu Chen, Ph.D. Eng.; Jun Chen, Prof. Ph.D. Eng.

As a valuable tonic in traditional Chinese medicine, *L. barbarum* is processed in various ways, including drying, making tea, pulping, and brewing (Ma et al., 2018; Bora et al., 2019). China is the largest producer of *L. barbarum*. It is mainly planted in Ningxia, Qinghai, and Xinjiang due to favorable soil, climate, and temperature (Shen et al., 2016; Skenderidis et al., 2019).

As an economic crop, *L. barbarum* has high added value and profit. As the planting area and production have increased, mechanized harvesting will become common in recent years (Zhao et al., 2021; Chen et al., 2021; Chen et al., 2022a). Field trials have demonstrated that vibration harvesting can substantially improve harvest efficiency, with a ripe fruit picking rate of over 90%, making it a suitable mechanized harvesting method (Chen et al., 2019; Zhang et al., 2018; He et al., 2017; Bu et al., 2020; Hu et al., 2020). In vibration harvesting, the fruit is subjected to a force greater than its binding force, causing it to fall off and land on the collection device. Due to the softness and vulnerability of fresh fruit, the impact can cause bruising or skin rupture, resulting in bruised fruit, accelerated spoilage, and blackening of the bruised area after drying, affecting its market value and economic benefits (Zhao et al., 2019). Therefore, it is necessary to develop a method to reduce fruit bruising during vibration harvesting.

Research methods for assessing fruit bruising include drop, pendulum, compression, and electronic fruit. Measurement methods include the use of impact force sensors, high-speed photography, and photosensitive lamination (Öztekin & Gungor, 2020; Opara & Pathare, 2014; Stroppek & Golacki, 2020). Hussein et al. (2020) used drop tests to analyze the impact of fruit collision on the level of fruit bruising. Wang et al. (2020) utilized a pendulum test to assess the impact of lychee fruit and established a method to predict the bruising degree based on the impact energy. Chen et al. (2018) studied the bruise characteristics of thick-skinned citrus fruit under different load conditions and the ability of different materials to reduce fruit bruising. Xu et al. (2015) used a micro-impact recorder to quantify the mechanical impact of blueberries in a packaging line. However, the electronic fruit is not suitable for *L. barbarum* fruits due to their small size, low weight, and unique shape. The compression test is typically used to analyze the static pressure of mechanical hands acting on fruits. This test is not suitable for assessing bruising occurring during collisions. The pendulum test is commonly used to analyze the bruise area and volume of fruits. However, this process is cumbersome when many tests are conducted. Therefore, it is more appropriate to use drop test to study the bruise rate of *L. barbarum* fruit during vibration harvesting (Zulkifli et al., 2020; Celik et al., 2017).

Linden et al. (2006) found that tomato fruit absorbs kinetic energy when struck, and when the energy exceeds the tissue failure threshold, mechanical bruising will occur, leading to skin cracking in severe cases. Bao et al. (2017) indicated that different drop heights result in different energy intensities absorbed by the blueberry fruit, with higher heights resulting in a higher impact energy and increased fruit bruising. For the apple and peach, the addition of cushioning materials can absorb part of the impact energy. Different materials have different densities, elasticities, and abilities to reduce fruit bruising (Jarimopas et al., 2007; Ahmadi et al., 2010). In addition, Zhou et al. (2016) discovered that the collision angle can affect fruit bruising of sweet cherry.

This study analyzed the impact process between falling *L. barbarum* and the collection device during vibration harvesting, and evaluated the relationship between fruit damage indicators and collection parameters through drop test. This provides a new analysis method and experimental reference for subsequent vibration harvesting damage experiments during the collection process.

MATERIALS AND METHODS

Response analysis of fruit drop

The working principle of the *L. barbarum* vibration harvester is to convert the uniform rotation of the motor into the reciprocating motion of the vibrating rod using a transmission. The vibrating rod causes the branches to swing. When the applied force exceeds the binding force of the fruit and the fruit stem, the fruit falls off. As shown in Figure 1, a high-speed camera (I-Speed LT, Olympus Co., Ltd., Japan; 1280 × 1024 resolution; 10,000 frames per second (fps) maximum) was used to record the fruit drop at 1,000 fps as the vibration harvester was operating. The vibration harvester is handheld and portable, mainly consists of a handle, a shell, a motor, a crank-swinging lever, a clamping rod and a vibrating rod. The experiment and operating parameters (swing angle of 49.58°, swing radius of 72.53 mm, and swing frequency of 11.21 Hz) of the vibration harvester have been described in the paper (Chen et al., 2022b). I-Speed software was used to track the dropping fruit and obtain the initial velocity and angle of the fruits. A total of 109 groups of data were collected.

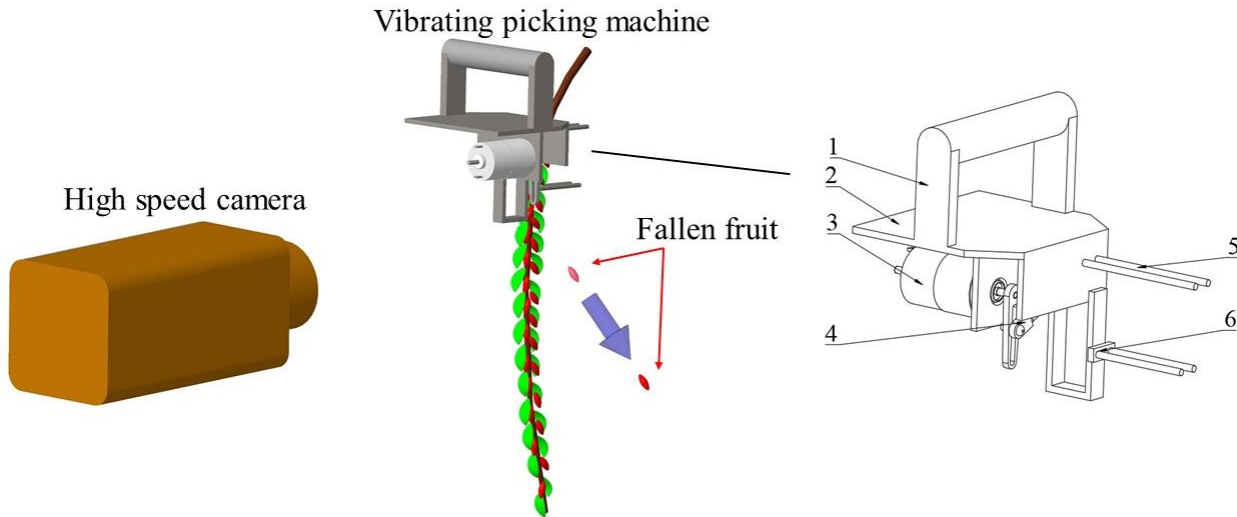


Fig. 1 - Schematic diagram of fruit drop

(1) hand shank, (2) shell, (3) DC motor, (4) a crank-swinging lever, (5) clamping rod, (6) vibrating rod.

Analysis of collision after fruit detachment

After the fruit falls off, it drops at a certain speed and angle with a parabolic motion due to gravity until it collides with the collection surface. The reason for bruising after detachment is the collision between the fruit and the plane. This article focuses on the collision between the fruit and the plane.

In vibration harvesting, the fallen fruit has a certain initial velocity, the initial direction of motion can be oblique upward or oblique downward. The schematic diagram of the motion analysis is shown in Figure 2. The air resistance is ignored.

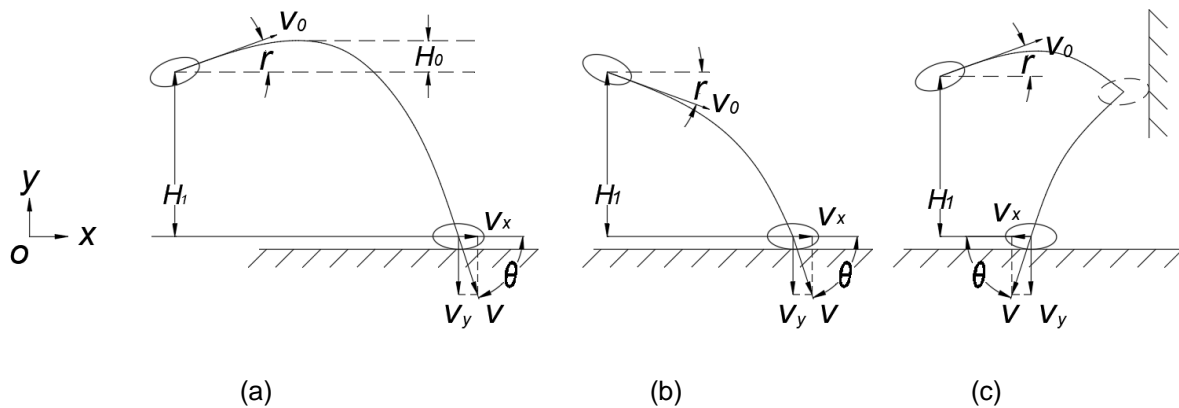


Fig. 2 - Schematic diagram of fruit movement after detachment

If the motion is oblique upward (Figure 2a), the fruit moves upward and decelerates. After it reaches the highest point, it moves downward, accelerates, and collides with the collection surface.

The maximum height in the vertical direction is defined as follows:

$$H_0 = \frac{V_0^2 \sin^2 r}{2g} \tag{1}$$

where:

H_0 is the height the fruit moves upward, m; V_0 is the instantaneous velocity of the fruit after detachment, m/s; r is the angle between the fruit's direction of motion and the horizontal plane, °; g is the acceleration of gravity, which is 9.8 m/s².

After the fruit has reached the maximum height, it falls to the collection surface with a vertical velocity of:

$$V_y = \sqrt{2g(H_0 + H_1)} = V_0 \sin r + \sqrt{2gH_1} \quad (2)$$

where: V_y is the vertical velocity of the fruit when it impacts the collection surface, m/s; H_i is the height of the fruit from the collection surface, m.

If the detachment direction is oblique downward (Figure 2b), the fruit drops with uniform acceleration until it collides with the collection surface. The maximum vertical velocity is:

$$V_y = V_0 \sin r + \sqrt{2gH_1} \quad (3)$$

Therefore, the maximum vertical velocity at which the fruit collides with the collection surface is not affected by the detachment direction.

The fruit moves at a constant speed in the horizontal direction, and if it collides with the wall of the collection device or the harvesting equipment, the post-separation velocity of the fruit is related to the coefficient of restitution (the ratio of the separation velocity after collision to the approach velocity before collision):

$$V_x = e^n V_0 \cos r \quad (4)$$

where: V_x is the horizontal velocity of the fruit as it falls to the collection surface, m/s; e is the coefficient of restitution after the fruit has collided with the wall; n is the number of collisions. e depends on the collision material, and it has a value of 0.2-0.8.

The final collision velocity of the fruit as it hits the collection surface is:

$$V = \sqrt{V_y^2 + V_x^2} = \sqrt{(V_0 \sin r + \sqrt{2gH_1})^2 + (e^n V_0 \cos r)^2} \quad (5)$$

where: V is the final collision velocity of the fruit as it hits to the collection surface, m/s.

The maximum collision velocity of the fruit as it hits the collection surface is:

$$V_{\max} = \sqrt{V_{y\max}^2 + V_{x\max}^2} = \sqrt{(V_0 \sin r + \sqrt{2gH_1})^2 + (V_0 \cos r)^2} \quad (6)$$

where:

V_{\max} is the vertical maximum collision velocity of the fruit as it hits to the collection surface, m/s; $V_{y\max}$ is the vertical maximum collision velocity of the fruit as it hits to the collection surface, m/s; $V_{x\max}$ is the horizontal maximum collision velocity of the fruit as it hits to the collection surface, m/s.

The impact angle of the fruit as it hits the collection surface is:

$$\theta = \arctan \frac{V_y}{V_x} \quad (7)$$

where: θ is the impact angle of the fruit as it hits the collection surface, °.

Kinematic analysis of the collision after detachment shows that the maximum velocity and angle of collision between the fruit and the collection surface depend on the initial velocity and angle of fruit detachment and the height of the fruit from the collection surface. According to formulas 6 and 7, combined with the initial velocity and angle of the fruit obtained, the velocity and angle of the fruit hitting the collection surface can be obtained, providing data support for bruise experiment.

Bruise experiment

A drop test is a common method for assessing fruit bruising. Since it is difficult to achieve a stable initial velocity and angle for *L. barbarum* fruits in experiments, the movement of the fruit from the oblique throwing of the bodies was converted into the free fall movement, the collision velocity and angle are converted into the drop height of the fruits (by formula 8) and the angle of the collision plane (by adjusting the angle of the plate change the collision angle), respectively.

According to the free-fall formula, the following can be derived:

$$H = \frac{v^2}{2g} \quad (8)$$

where: H is the drop height of the fruit, m; v is the collision velocity of the fruit, m/s.

The fruit used in the experiment was obtained from the Ningxia Zhengqihong *L. barbarum* Industry Development Co., Ltd., Gangou Village, Sanying Town, Yuanzhou District, Guyuan City, Ningxia Hui Autonomous Region (36°17'32.9"N, 106°6'41.5"E). The variety used was Ningqi 7.

The shrubs were artificially pruned into standardized hedge cultivation mode, with the shrubs' age of 3-4 years. The experiment was conducted on July 10, 2023. *L. barbarum* shrubs with good growth conditions, no pests or diseases, and no damage were selected. The branches were cut down in the field and collected to ensure the freshness of the fruits. Ripe fruits were picked and used immediately in the experiment.

As shown in Figure 3, the experimental device consisted of a fruit guide tube, an impact sensor (model: DYZ-100, range: 0-20N, accuracy: 0.3%, Bengbu Dayang Sensor System Engineering Co., Ltd.), a portable force measurement instrument (model: DY920, accuracy: 0.05%, rate: 3200 times/second, Bengbu Dayang Sensor System Engineering Co., Ltd.), and a high-speed camera. The guide tube was installed vertically; it was replaceable, and the position could be adjusted to ensure that the fruits fell from the same height onto the same area of the collection device. The impact sensor was cushioned with 5-mm thick material, and the position and angle were adjustable. In addition, a sponge was placed around the collision material to prevent secondary bruising.

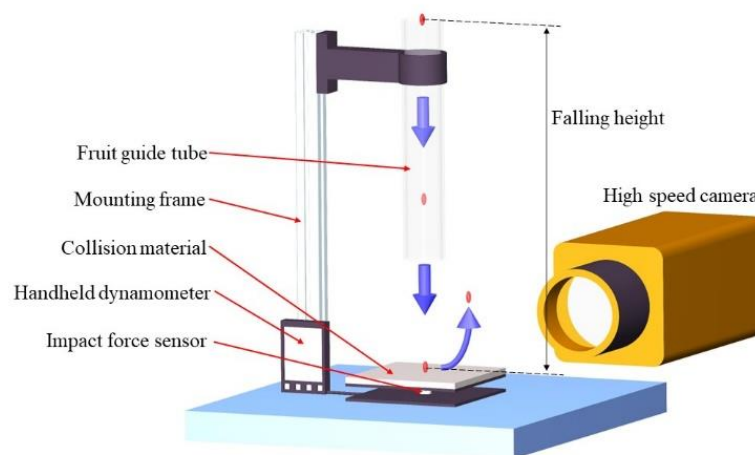


Fig. 3 - Schematic diagram of the fruit drop test

Fruit bruise assessment

The degree of fruit bruising is directly related to the energy absorbed by the fruit during the impact. The potential energy of the fruit during the impact is converted into kinetic energy, and elastic-plastic deformation of the fruit occurs, resulting in bruising (Bai et al., 2017). After the fruit collides with the collision plane, the color of the bruised area does not change significantly, and the bruised area is soft and flat. After the fruit dries, the surface becomes black, resulting in economic losses. Since the most *L. barbarum* are made into dried fruits and sold afterwards, all samples were dried after the drop test according to the Agricultural Industry Standard (NY/T2966-2016) of China, which specifies standards for harvesting, cleaning, dewaxing, draining, loading, drying, cooling, unloading, and removing impurities. The fresh fruits were immersed for 10 s in a solution of food-grade sodium bicarbonate (baking soda) with a concentration of 2% to remove wax. The fruit was dried using a small household fruit dryer (model: MR6255, Morphy Richards UK Ltd.). After drying, fruit with a color that did not meet the standard requirements (some areas are black, clearly different from other fruits) were manually selected and were considered bruised fruit. The fruits before and after drying are shown in Figure 4.

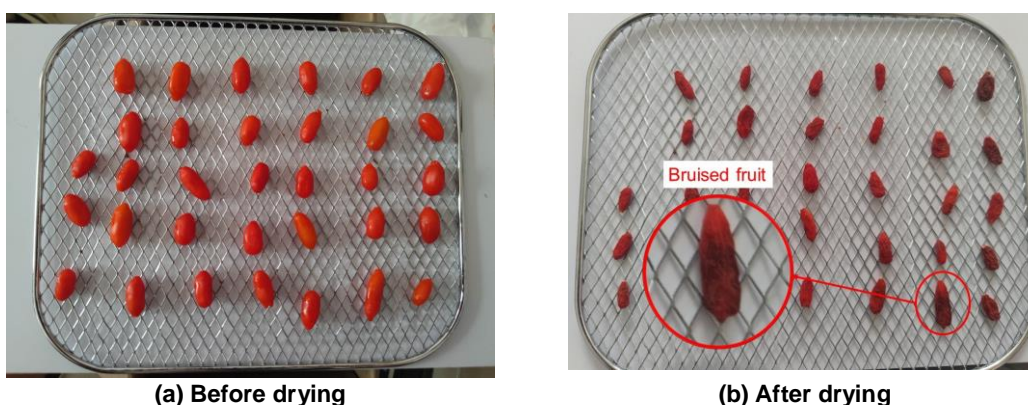


Fig. 4 - Drying detection of fruit bruise

The main purpose of this experiment was to investigate the level of bruising occurring after vibration harvesting of ripe fruits. The experimental indicators included the fruit bruise rate I_s , maximum impact force I_f (peak force during impact process, measured by force measurement instrument), restitution coefficient I_R (the ratio of velocity after rebound to velocity before impact, measured by high-speed camera), and collision time I_T (the time of contact between the fruit and the collection surface, measured by high-speed camera). The calculation formula for the fruit bruise rate is as follows:

$$I_s = \frac{N_s}{N} \times 100\% \tag{9}$$

where: N is the total number of dried fruits, and N_s is the number of bruised dried fruits.

RESULTS AND ANALYSIS

Analysis of fruit drop

Figure 5 shows a scatterplot between the initial velocity and angle of the fruit after vibration harvesting. The collision speed of the fruit as it hit the collection surface was related to the height of the fruit. Based on the growing parameters and the harvesting conditions of ripe fruits, the drop height was set at 0.5 m. Calculated by combining formulas 6 and 7, the scatterplot between the collision speed and angle of the fruit hit the collection surface is shown in Figure 6. Most of the fruit had an impact velocity of 3-6 m/s and an impact angle of 30-90°. Based on the analysis results and formula 8, 60-180 cm and 30-90 ° were used as experimental parameters for response surface analysis.

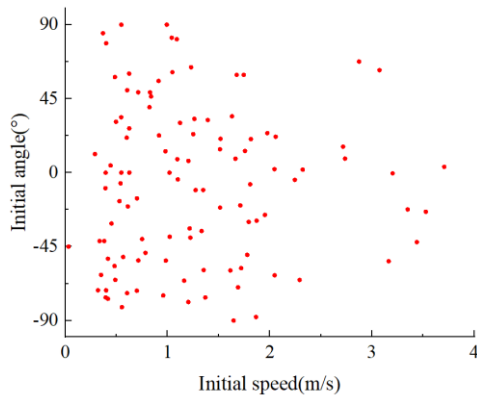


Fig. 5 - Scatterplot between the initial velocity speed and angle of the fruit

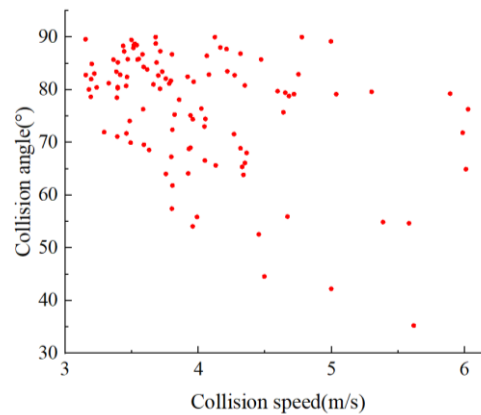


Fig. 6 - Scatterplot between the collision speed and angle of the fruit

Experimental protocol and results

A response surface analysis was conducted to evaluate the effects of different variables. A quadratic orthogonal rotation experiment was used. The factor coding is listed in Table 1, and the experimental protocol and results are presented in Table 2. Seventeen groups of experiments were conducted. The average value of the test data was used as the result of this group. The design of the experimental protocol and the analysis of the results were performed using the Design Expert 12 software.

Table 1

Codes of factors

| Code | Drop height / [cm] | Collision angle / [°] | Collision material |
|------|--------------------|-----------------------|--------------------|
| -1 | 60 | 30 | 1 |
| 0 | 120 | 60 | 2 |
| 1 | 180 | 90 | 3 |

Table 2

Experiment schemes and results

| | Dropping height A | Impact angle B | Impact material C | Fruit bruise rate I_s / % | Maximum impact force I_f / N | Recovery coefficient I_R | Impact time I_T / ms |
|---|----------------------|-------------------|----------------------|--------------------------------|-----------------------------------|-------------------------------|---------------------------|
| 1 | -1 | -1 | 0 | 16.67 | 0.61 | 0.71 | 5 |

| | Dropping height A | Impact angle B | Impact material C | Fruit bruise rate I_s / % | Maximum impact force I_F / N | Recovery coefficient I_R | Impact time I_T / ms |
|----|----------------------|-------------------|----------------------|--------------------------------|-----------------------------------|-------------------------------|---------------------------|
| 2 | 1 | -1 | 0 | 35.56 | 1.55 | 0.34 | 6 |
| 3 | -1 | 1 | 0 | 32.43 | 0.87 | 0.34 | 7 |
| 4 | 1 | 1 | 0 | 78.94 | 2.65 | 0.24 | 7 |
| 5 | -1 | 0 | -1 | 6.67 | 0.95 | 0.55 | 3 |
| 6 | 1 | 0 | -1 | 36.36 | 1.86 | 0.39 | 2 |
| 7 | -1 | 0 | 1 | 51.85 | 1.01 | 0.40 | 3 |
| 8 | 1 | 0 | 1 | 77.27 | 2.03 | 0.26 | 4 |
| 9 | 0 | -1 | -1 | 10.34 | 0.89 | 0.62 | 3 |
| 10 | 0 | 1 | -1 | 36.36 | 1.77 | 0.41 | 3 |
| 11 | 0 | -1 | 1 | 42.86 | 1.47 | 0.48 | 2 |
| 12 | 0 | 1 | 1 | 62.50 | 2.17 | 0.36 | 6 |
| 13 | 0 | 0 | 0 | 54.05 | 1.58 | 0.37 | 6 |
| 14 | 0 | 0 | 0 | 31.82 | 1.79 | 0.46 | 5 |
| 15 | 0 | 0 | 0 | 52.63 | 1.42 | 0.37 | 3 |
| 16 | 0 | 0 | 0 | 70.97 | 1.63 | 0.54 | 4 |
| 17 | 0 | 0 | 0 | 41.38 | 1.52 | 0.34 | 4 |

Experimental results

Regression equations were established to fit the experimental results. The fruit bruise rate I_s , maximum impact force I_F , and recovery coefficient I_R were the dependent variables, and dropping height A , impact angle B and impact material C were the independent variables.

The polynomial regression equations are as follows:

$$I_s = 44.20 + 13.46A + 14.70B + 18.09C + 3.70AB - 1.07AC - 1.60B \quad (10)$$

$$I_F = 1.52 + 0.58A + 0.37B + 0.15C + 0.21AB + 0.03AC - 0.05BC \quad (11)$$

$$I_R = 0.42 - 0.09A - 0.11B - 0.06C + 0.08AB + 0.01AC + 0.03BC \quad (12)$$

Analysis of variance was performed; the results are listed in Table 3. The results indicate that the p-values of the fruit bruise rate, maximum impact force, and recovery coefficient are less than 0.05, indicating that the models are statistically significant. Factors A , B , and C had significant effects on the fruit bruise rate, maximum impact force, and recovery coefficient ($p < 0.05$), and factor AB had a significant effect on the maximum impact force and recovery coefficient. The other factors had non-significant effects. The p-values of the lack-of-fit term were greater than 0.05, indicating no lack-of-fit factors in the regression equations.

The response surfaces of the parameters are shown in Figures 7-9. Equation (10) and the results in Table 3 indicate that the collision material had the greatest influence on the fruit bruise rate, followed by the drop height and the collision angle. Equation (11) and the results in Table 3 show that the drop height had the greatest influence on the maximum impact force, followed by the collision angle and the collision material. Equation (12) and the results in Table 3 demonstrate that the collision angle had the greatest influence on the recovery coefficient, followed by the drop height and the collision material.

As shown in Figures 7a, 8a, and 9a, as the drop height increased, the fruit bruise rate and maximum impact force increased, whereas the recovery coefficient decreased. As the drop height increased, the impact velocity of the fruit increased, resulting in higher kinetic energy and a greater impact force. The fruit underwent elastic deformation and plastic deformation due to the impact, increasing the energy required for the fruit to undergo plastic deformation, causing a bruised area, resulting in an increase in fruit bruise rate (*Fu et al., 2017*). Subsequently, a decrease in the energy of the fruit's rebound, resulting in a decrease in the recovery coefficient occurred.

As shown in Figures 7b, 8b, and 9b, as the collision material changed from 1 to 3, the fruit bruise rate and maximum impact force increased, whereas the recovery coefficient decreased. The reason is that the kinetic energy of the fruit is converted into elastic deformation energy of the fruit and the collision material during the collision due to the elasticity of the collision material. If the collision material has low elasticity, the impact force is higher, and less elastic potential energy is retained, resulting in greater plastic deformation energy of the fruit (Xia *et al.*, 2020; Guan *et al.*, 2023). Thus, the fruit bruise rate increased, and the recovery coefficient decreased.

As shown in Figures 7c, 8c, and 9c, as the collision angle increased, the fruit bruise rate and the maximum impact force increased, whereas the recovery coefficient decreased. Most studies on the collision angle have focused on its effect on the degree of fruit bruising (Zhou *et al.*, 2019; Bao *et al.*, 2017).

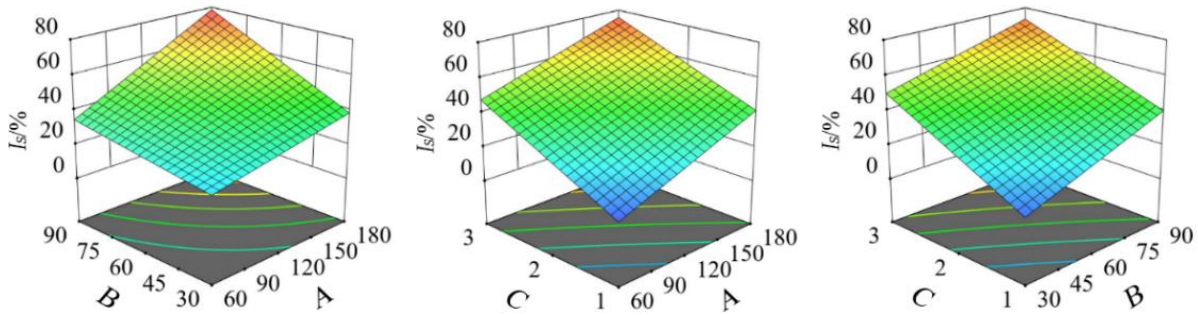


Fig. 7 - Response surface of influence of various factors on the fruit bruise rate

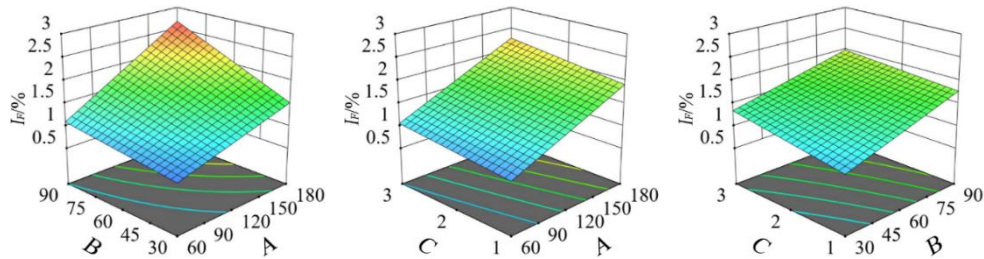


Fig. 8 - Response surface of influence of various factors on the maximum impact force

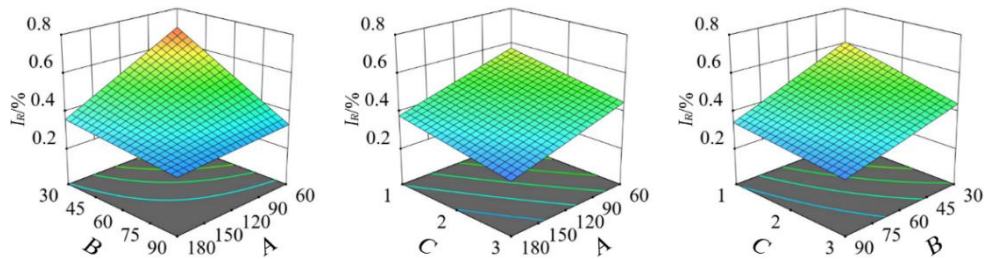


Fig. 9 - Response surface of influence of various factors on the restitution coefficient

Table 3

| Variance analysis | | | | | | |
|-------------------|---------------------|----------------|--------------------|-------------|--------|--------|
| | Sources of Variance | Sum of Squares | Degrees of Freedom | Mean Square | F | p |
| Fruit bruise rate | model | 6012.73 | 6 | 1002.12 | 7.32 | 0.0033 |
| | A | 1815.33 | 1 | 1815.33 | 13.27 | 0.0045 |
| | B | 1372.88 | 1 | 1372.88 | 10.03 | 0.01 |
| | C | 2619.07 | 1 | 2619.07 | 19.14 | 0.0014 |
| | AB | 190.72 | 1 | 190.72 | 1.39 | 0.2651 |
| | AC | 4.56 | 1 | 4.56 | 0.0333 | 0.8588 |
| | BC | 10.18 | 1 | 10.18 | 0.0744 | 0.7906 |
| | lack of fit | 500.64 | 6 | 83.44 | 0.3846 | 0.8579 |

| | Sources of Variance | Sum of Squares | Degrees of Freedom | Mean Square | F | p |
|----------------------|---------------------|----------------|--------------------|-------------|--------|---------|
| | pure error | 867.73 | 4 | 216.93 | | |
| | total sum | 7381.11 | 16 | | | |
| Maximum impact force | model | 4.15 | 6 | 0.6923 | 21.77 | <0.0001 |
| | A | 2.7 | 1 | 2.7 | 84.99 | <0.0001 |
| | B | 1.08 | 1 | 1.08 | 33.98 | 0.0002 |
| | C | 0.183 | 1 | 0.183 | 5.75 | 0.0374 |
| | AB | 0.1764 | 1 | 0.1764 | 5.55 | 0.0403 |
| | AC | 0.003 | 1 | 0.003 | 0.0951 | 0.7641 |
| | BC | 0.0081 | 1 | 0.0081 | 0.2547 | 0.6247 |
| | lack of fit | 0.2425 | 6 | 0.0404 | 2.14 | 0.2406 |
| | pure error | 0.0755 | 4 | 0.0189 | | |
| | total sum | 4.47 | 16 | | | |
| Recovery coefficient | model | 0.2097 | 6 | 0.0349 | 7.84 | 0.0025 |
| | A | 0.0685 | 1 | 0.0685 | 15.35 | 0.0029 |
| | B | 0.0903 | 1 | 0.0903 | 20.25 | 0.0011 |
| | C | 0.0253 | 1 | 0.0253 | 5.68 | 0.0384 |
| | AB | 0.0225 | 1 | 0.0225 | 5.05 | 0.0485 |
| | AC | 0.0001 | 1 | 0.0001 | 0.0224 | 0.8839 |
| | BC | 0.003 | 1 | 0.003 | 0.6783 | 0.4294 |
| | lack of fit | 0.0173 | 6 | 0.0029 | 0.4215 | 0.835 |
| | pure error | 0.0273 | 4 | 0.0068 | | |
| | total sum | 0.2543 | 16 | | | |

Collision time

Due to the limited frame rate of high-speed cameras, the accuracy of the contact time obtained from experiments is at the millisecond level, resulting in lack of detailed data. The experimental results and the Design-Expert 12 software were used to perform quadratic regression fitting.

The polynomial regression equation with the collision time t_T as the response function is:

$$t_T = 4.4 + 0.125A + 0.875B + 0.5C - 0.25AB + 0.5AC + 1BC + 0.675A^2 + 1.18B^2 - 2.08C^2 \quad (13)$$

The result of the analysis of variance is listed in Table 4. p-values of the collision time regression model were less than 0.05, indicating that the model was statistically significant. Factors B , B^2 , and C^2 had a significant effect on the fruit bruise rate ($p < 0.05$), whereas the other factors were not significant. The p-value of the lack-of-fit term was greater than 0.05, indicating no lack-of-fit factors in the regression equation.

As shown in Figure 10, as the collision angle increased, the collision time first decreased and then increased. When the angle is small, the fruit slides after contacting the collision plane.

Ripe fruit is relatively slender and will roll when subjected to a force. A smaller collision angle caused the fruit to collide with the collision plane a second time, making it difficult to distinguish the collision occurrences and increasing the collision time. When the collision angle was greater than or equal to 60° , the fruit only collided once before rebounding and leaving the collision plane.

When the collision angle was 60° , the fruit was sliding after it collided with the collision plane, leaving the contact surface and decreasing the contact time.

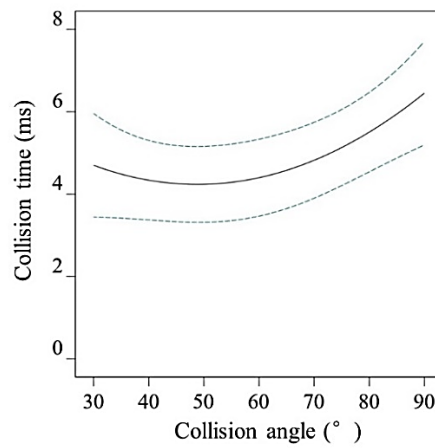


Fig. 10 - Influence of collision angle on collision time

Table 4

Variance analysis of the impact time

| Sources of Variance | Sum of Squares | Degrees of Freedom | Mean Square | F | p |
|---------------------|----------------|--------------------|-------------|--------|--------|
| Model | 38.08 | 9 | 4.23 | 5.43 | 0.0181 |
| A | 0.125 | 1 | 0.125 | 0.1606 | 0.7006 |
| B | 6.13 | 1 | 6.13 | 7.87 | 0.0263 |
| C | 2 | 1 | 2 | 2.57 | 0.153 |
| AB | 0.25 | 1 | 0.25 | 0.3211 | 0.5886 |
| AC | 1 | 1 | 1 | 1.28 | 0.2944 |
| BC | 4 | 1 | 4 | 5.14 | 0.0578 |
| A ² | 1.92 | 1 | 1.92 | 2.46 | 0.1605 |
| B ² | 5.81 | 1 | 5.81 | 7.47 | 0.0292 |
| C ² | 18.13 | 1 | 18.13 | 23.28 | 0.0019 |
| lack of fit | 0.25 | 3 | 0.0833 | 0.0641 | 0.9761 |
| pure error | 5.2 | 4 | 1.3 | | |
| total sum | 43.53 | 16 | | | |

Correlation analysis

The recovery coefficient is typically used to evaluate the degree of fruit bruising. The correlation between the fruit bruise rate, maximum impact force, recovery coefficient, and collision time was analyzed using Pearson correlation analysis by SPSS Statistics 27 software. Due to the insufficient sample size of less than 30, the normality of the data was assessed. The test results showed that all four datasets were normally distributed.

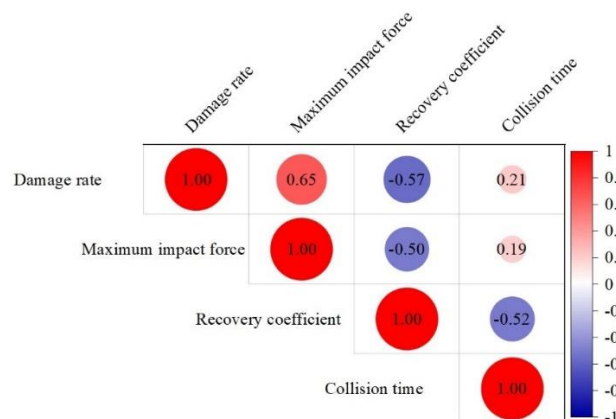


Fig. 11 - Correlation coefficient between various indicators

As shown in Figure 11, Pearson correlation analysis showed that the fruit bruise rate was significantly negatively correlated with the recovery coefficient ($p=0.003$) and significantly positively correlated with the maximum impact force ($p<0.001$). The recovery coefficient was significantly negatively correlated with the maximum impact force ($p=0.003$). However, the collision time was not significantly correlated with the fruit bruise rate, the maximum impact force, or the recovery coefficient ($p>0.05$). A significant correlation existed between the fruit bruise rate, the maximum impact force, and the recovery coefficient, indicating that the maximum impact force and recovery coefficient can be used to replace the fruit bruise rate to evaluate the bruise severity of *L. barbarum* fruits.

Based on the above, in order to reduce fruit bruise during vibration harvesting, the design of vibration harvester should consider reducing the height between the fruit and the collection surface, reducing the speed at which the fruit is dropped, making the fruit collide with the collection surface at a smaller angle, and using softer collection material.

CONCLUSIONS

This study analyzed the collision bruise during the falling and collection process of *L. barbarum* fruits after vibration harvesting. The following experimental results and conclusions were obtained:

(1) High-speed photography was used to obtain the initial velocity and angle of fruits after vibration harvesting. A kinematic analysis of the fruit's collision with the collection surface was performed. The impact speed of most fruits was 3-6 m/s, and the impact angle was 30-90°.

(2) A drop test was adopted based on fruit impact speed and angle, and an orthogonal rotation experiment was conducted to establish a mathematical model between the drop height, collision angle, collision material, and the fruit bruise rate, maximum impact force, recovery coefficient, and collision time. The collection parameters had significant effects on the fruit bruise rate, maximum impact force, and recovery coefficient, whereas the collision angle had a significant effect on the collision time.

(3) The correlation between the fruit bruise rate, maximum impact force, recovery coefficient, and collision time was analyzed. The experimental results indicated a significant correlation between the fruit bruise rate, maximum impact force, and recovery coefficient. The maximum impact force and recovery coefficient can be used to replace the fruit bruise rate to evaluate the degree of bruising of *L. barbarum* fruits.

(4) This study indicated that reducing the height between the fruit and the collection surface and using a tilted collection surface and materials with high cushioning capabilities substantially reduced fruit bruising during vibration harvesting. The results provide a basis for the research and design of vibration harvesting machines to reduce fruit bruising.

ACKNOWLEDGEMENT

This study was supported by the National Natural Science Foundation of China (32272001) and Key Research and Development Program of Ningxia Hui Autonomous Region (2022BBF01002).

REFERENCES

- [1] Ahmadi, E., Ghassemzadeh, H. R., Sadeghi, M., Mohammad, M., & Zarif, N. S. (2010). The effect of impact and fruit properties on the bruising of peach. *Journal of Food Engineering*, 97(1), 110-117. <https://doi.org/10.1016/j.jfoodeng.2009.09.024>
- [2] Bao, Y., Yang, C., Zhao, Y., Zhao, Y., Liu, X., & Guo, Y. (2017). Collision injury assessment of mechanical harvesting blueberry fruit based on collision deformation energy. *Transactions of the Chinese Society of Agricultural Engineering*, 33(16), 283-292. <http://dx.doi.org/10.11975/j.issn.1002-6819.2017.16.037>
- [3] Bora, P., Ragaei, S., & Abdel-Aal, E-S. M. (2019). Effect of incorporation of goji berry by-product on biochemical, physical and sensory properties of selected bakery products. *LWT*, 112, 108225. <https://doi.org/10.1016/j.lwt.2019.05.123>
- [4] Bu, L., Hu, G., Chen, C., Sugirbay, A., & Chen, J. (2020). Experimental and simulation analysis of optimum picking patterns for robotic apple harvesting. *Scientia Horticulturae*, 261, 108937. <https://doi.org/10.1016/j.scienta.2019.108937>
- [5] Celik, H. K. (2017). Determination of bruise susceptibility of pears (Ankara variety) to impact load by means of FEM-based explicit dynamics simulation. *Postharvest Biology and Technology*, 128, 83-97. <http://dx.doi.org/10.1016/j.postharvbio.2017.01.015>

- [6] Chen, H., Yin, Y., Pan, H., Bao, X., Li, S., Xu, Q., & Xu, X. (2018). Loss factor analysis of mechanical damage and cushioning protection measure for Citrus reticulate Blanco. *Transactions of the Chinese Society of Agricultural Engineering*, 34(1), <https://doi.org/258-266.10.11975/j.issn.1002-6819.2018.01.035>
- [7] Chen, J., Zhao, J., Chen, Y., Bu, L., Hu, G., & Zhang, N. (2019). Design and Experiment on Vibrating and Comb Brushing Harvester for *Lycium barbarum*. *Transactions of the Chinese Society for Agricultural Machinery*, 50(01), 152-161+95. <https://doi.org/10.6041/j.issn.1000-1298.2019.01.016>
- [8] Chen, Q., Zhang, S., Hu, G., Zhou, J., Zhao, J., Chen, Y., Chen, J., Gao, S., Chen, Y., & Shi, T. (2022a). Parameter Optimization of the Harvest Method in the Standardized Hedge Cultivation Mode of *Lycium barbarum* Using Response Surface Methodology. *Horticulturae*, 8(4), 308. <https://doi.org/10.3390/horticulturae8040308>
- [9] Chen, Q., Zhang, S., Wei, N., Li, P., Hu, G., & Chen, J. (2022b). Parameter Optimization of the Swing Harvesting of *Lycium barbarum* L. Based on Response Surface Methodology; *Proceedings of the 2022 Chinese Automation Congress, CAC 2022, November 25, 2022 - November 27, 2022, Xiamen, China*, <https://doi.org/10.1109/CAC57257.2022.10055703>
- [10] Chen, Y., Zhao, J., Hu, G., & Chen, J. (2021). Design and Testing of a Pneumatic Oscillating Chinese L. *barbarum* Harvester. *Horticulturae*, 7(8), 214. <https://doi.org/10.3390/horticulturae7080214>
- [11] Fu, H., He, L., Ma, S., Manoj, K., Chen, D., Zhang, Q., Wang, S. (2017). 'Jazz' Apple Impact Bruise Responses to Different Cushioning Materials. *Transactions of the ASABE*, 60(2), 327-36. <https://doi.org/10.13031/trans.11946>
- [12] Guan, X., Li, T., Zhou, F. (2023). Determination of bruise susceptibility of fresh corn to impact load by means of finite element method simulation. *Postharvest Biology and Technology*, 198, 112227. <https://doi.org/10.1016/j.postharvbio.2022.112227>
- [13] He, M., Kan, Z., Li, C., Wang, L., Yang, L., & Wang, Z. (2017). Mechanism analysis and experiment on vibration harvesting of L. *barbarum*. *Transactions of the Chinese Society of Agricultural Engineering*, 33(11), 47-53. <https://doi.org/10.11975/j.issn.1002-6819.2017.11.006>
- [14] Hu, G., Bu, L., & Chen, J. (2020). Simulation to determination of significant parameters on apple stress for combing harvesting in trellis trained trees. *Scientia Horticulturae*, 274, 109654. <https://doi.org/10.1016/j.scienta.2020.109654>
- [15] Hussein, Z., Fawole, O. A., & Opara, U. L. (2019). Bruise damage susceptibility of pomegranates (*Punica granatum*, L.) and impact on fruit physiological response during short term storage. *Scientia Horticulturae*, 246, 664-674. <https://doi.org/10.1016/j.scienta.2018.11.026>
- [16] Hussein, Z., Fawole, O. A., & Opara, U. L. (2020). Harvest and Postharvest Factors Affecting Bruise Damage of Fresh Fruits. *Horticultural Plant Journal*, 6(1), 1-13. <https://doi.org/10.1016/j.hpj.2019.07.006>
- [17] Jarimopas, B., Singh, S. P., Sayasoonthorn, S., & Jagjit, S. (2007). Comparison of package cushioning materials to protect post-harvest impact damage to apples. *Packaging Technology and Science*, 20(5), 315-24. <https://doi.org/10.1002/pts.760>
- [18] Linden, V. V., Ketelare, D. B., Desmet, M., & Baerdemaeker, D. J. (2006). Determination of bruise susceptibility of tomato fruit by means of an instrumented pendulum. *Postharvest Biology and Technology*, 40(1), 7-14. <http://dx.doi.org/10.1016/j.postharvbio.2005.12.008>
- [19] Ma, A., Carradori, S., Casadei, M. A., Paolicelli, P., Petralito, S., Ragno, R., & Cesa, S. (2018). *Lycium barbarum* polysaccharides: Extraction, purification, structural characterisation and evidence about hypoglycaemic and hypolipidaemic effects. A review. *Food Chemistry*, 254, 377-389. <https://doi.org/10.1016/j.foodchem.2018.01.176>
- [20] Ma, R., Zhang, X., Thakur, K., Zhang, J., & Wei, Z. (2022). Research progress of *Lycium barbarum* L. as functional food: phytochemical composition and health benefits. *Current Opinion in Food Science*, 47, 100871. <https://doi.org/10.1016/j.cofs.2022.100871>
- [21] Opara, U., & Pathare, P. (2014). Bruise damage measurement and analysis of fresh horticultural produce—A review. *Postharvest Biology and Technology*, 91, 9-24. <http://dx.doi.org/10.1016/j.postharvbio.2013.12.009>
- [22] Öztekin, Y., & Gungor, B. (2020). Determining impact bruising thresholds of peaches using electronic fruit. *Scientia Horticulturae*, 262, 109046. <https://doi.org/10.1016/j.scienta.2019.109046>
- [23] Shen, T., Zhou, X., Shi, J., Li, Z., Huang, X., Xu, Y., & Chen, W. (2016). Determination Geographical Origin and Flavonoids Content of L. *barbarum* Using Near-Infrared Spectroscopy and Chemometrics. *Food analytical methods*, 9, 68-79. <https://doi.org/10.1007/s12161-015-0175-x>

- [24] Skenderidis, P., Lampakis, D., Giavasis, I., Leontopoulos, S., Petrotos, K., Hadjichristodoulou, C., & Tsakalof, A. (2019). Chemical Properties, Fatty-Acid Composition, and Antioxidant Activity of *L. barbarum* (*Lycium barbarum* L. and *Lycium chinense* Mill.) Fruits. *Antioxidants*, 8(3), 60. <https://doi.org/10.3390/antiox8030060>
- [25] Stroppek, Z., & Golacki, K. (2020). Bruise susceptibility and energy dissipation analysis in pears under impact loading conditions. *Postharvest Biology and Technology*, 163, 111120. <https://doi.org/10.1016/j.postharvbio.2020.111120>
- [26] Wang, W., Zhang, S., Fu, H., Lu, H., & Yang, Z. (2020). Evaluation of litchi impact damage degree and damage susceptibility. *Computers and Electronics in Agriculture*, 173, 105409. <https://doi.org/10.1016/j.compag.2020.105409>
- [27] Xia, M., Zhao, X., Wei, X., Guan, W., Wei, X., Xu, C., Mao, L. (2020). Impact of packaging materials on bruise damage in kiwifruit during free drop test. *Acta Physiologiae Plantarum*, 42(7), 119. <https://doi.org/10.1007/s11738-020-03081-5>
- [28] Xiao, Z., Deng, Q., Zhou, W., & Zhang, Y. (2022). Immune activities of polysaccharides isolated from *Lycium barbarum* L. What do we know so far?. *Pharmacology & Therapeutics*, 229, 107921. <https://doi.org/10.1016/j.pharmthera.2021.107921>
- [29] Xu, R., Takeda, F., Krewer, G., & Li, C. (2015). Measure of mechanical impacts in commercial blueberry packing lines and potential damage to blueberry fruit. *Postharvest Biology and Technology*, 110, 103-113. <http://dx.doi.org/10.1016/j.postharvbio.2015.07.013>
- [30] Zhang, W., Zhang, M., Zhang, J., & Li, W. (2018). Design and experiment of vibrating *L. barbarum* harvester. *Transactions of the Chinese Society for Agricultural Machinery*, 49(7), 97-102. <https://doi.org/10.6041/j.issn.1000-1298.2018.07.012>
- [31] Zhao, J., Ma, T., Inagaki, T., Chen, Q., Gao, Z., Sun, L., Cai, H., Chen, C., Li, C., Zhang, S., Tsuchikawa, S., & Chen, J. (2021). Finite Element Method Simulations and Experiments of Detachments of *Lycium barbarum* L. *Forests*, 12(6), 699. <https://doi.org/10.3390/f12060699>
- [32] Zhao, J., Sugirbay, A., Chen, Y., Zhang, S., Liu, F., Bu, L., Chen, Y., Wang, Z., & Chen, J. (2019). FEM explicit dynamics simulation and NIR hyperspectral reflectance imaging for determination of impact bruises of *Lycium barbarum* L. *Postharvest Biology and Technology*, 155, 102-110. <https://doi.org/10.1016/j.postharvbio.2019.05.024>
- [33] Zhou, J., He, L., Karkee, M., & Zhang, Q. (2016). Effect of catching surface and tilt angle on bruise damage of sweet cherry due to mechanical impact. *Computers and Electronics in Agriculture*, 121, 282-289. <https://doi.org/10.1016/j.compag.2016.01.004>
- [34] Zulkifli, N., Hashim, N., Harith, H. H., & Shukery, M. F. M. (2020). Finite element modelling for fruit stress analysis - A review. *Trends in Food Science & Technology*, 97, 29-37. <https://doi.org/10.1016/j.tifs.2019.12.029>

MULTI-OUTPUT REGRESSION PREDICTION OF PNEUMATIC SUBMERGING RESISTANCE AND DISTURBANCE AREA BASED ON NEURAL NETWORK

基于神经网络的气动深松阻力及扰动面积多输出回归预测

Xia LI^{1,2)}, Xuhui WANG^{1,2)}, Jinyou XU^{*1,2)}, Xinglong LI^{1,2)}, Zhangjun JIANG^{1,2)}, Birong YOU^{1,2)}

¹⁾ Tianjin Key Laboratory for Advanced Mechatronic System Design and Intelligent Control, School of Mechanical Engineering, Tianjin University of Technology, Tianjin / China;

²⁾ National Demonstration Center for Experimental Mechanical and Electrical Engineering Education, Tianjin University of Technology, Tianjin / China

Tel: +15200158817; E-mail: yj20220152@stud.tjut.edu.cn

DOI: <https://doi.org/10.35633/inmateh-73-47>

Keywords: pneumatic subsoiling, neural network, multiple output regression prediction, traction resistance, disturbed area

ABSTRACT

The current field of pneumatic subsoiling prediction focuses on a single task and neglects the possible interrelationships between different outputs. In order to improve prediction accuracy and reduce the number of algorithmic model establishments, this study conducted field experiments on soil in autumn and winter. Neural network algorithms RBF (radial basis neural network), BP (backward propagation neural network), DNN (deep learning network), and CNN (convolutional neural network) were used to make multi-output regression predictions for changing the traction resistance and disturbance area affected by different levels of subsoiling velocity, depth, and pressure value in the process of pneumatic subsoiling. The evaluation indexes RMSE, MAE, and R^2 were compared with the single output regression model, and the accuracy of the four models with the highest accuracy was compared with that of its own single output model to prove the correlation between traction resistance and disturbance area. The results showed that the R^2 of the four model test sets of RBF, BP, DNN, and CNN were 0.9999, 0.9966, 0.9986, and 0.9762, respectively. The R^2 values of the disturbance area are 0.9997, 0.9924, 0.9968, and 0.9715, respectively. RBF has the highest R^2 and the lowest RMSE and MAE, indicating that the RBF model has the best prediction effect. Compared with the single output regression model of the RBF model, the prediction accuracy of both outputs is higher, so it can be used to predict the subsoiling drag resistance and disturbance area.

摘要

针对目前气动深松预测领域多聚焦于单一任务，忽略了不同输出之间可能存在的相互关系。为了提高预测的精确性，并且减少算法模型建立次数，本研究对秋冬两个季节下的土壤进行田间试验，利用神经网络算法 RBF（径向基神经网络）、BP（逆向传播神经网络）、DNN（深度学习网络）、CNN（卷积神经网络）对气动深松过程中改变受不同水平的深松速度、深度、气压值影响的牵引阻力及扰动面积值进行多输出回归预测，利用评价指标 RMSE、MAE、 R^2 与单输出回归模型进行对比评估，将四个模型中精度最高的与本身的单输出模型的精度进行对比，证明牵引阻力及扰动面积之间的相关性。结果表明：RBF、BP、DNN、CNN 四个模型测试集牵引阻力的 R^2 分别为 0.9999、0.9966、0.9986、0.9762。扰动面积的 R^2 分别为 0.9997、0.9924、0.9968、0.9715。RBF 的 R^2 最高，RMSE、MAE 最低，可见 RBF 模型预测效果效果最好，且相较于 RBF 模型的单输出回归模型两个输出的预测精度都较高，因此可用于深松牵引阻力及扰动面积的预测。

INTRODUCTION

Soil is the basis of sustainable agricultural development (Lou et al., 2021). Compaction is one of the factors causing soil degradation (Iman et al., 2017), which makes the soil more vulnerable to erosion by wind and water, causing economic and ecological damage to society (Thomas et al., 2019). It is urgent to improve compaction and break the bottom of the plow (Su et al., 2021).

Xia Li, Ph.D. Eng.; Xuhui Wang, MS.Stud.Eng.; Jinyou Xu, Associate Prof, Ph.D. Eng.; Xinglong Li, MS.Stud.Eng.; Zhangjun Jiang, MS.Stud.Eng.; Birong You, MS.Stud.Eng.

A subsoiler is a mechanical device that acts on soil (Odey *et al.*, 2018), which can crush soil, increase soil moisture content, and promote plant root growth (Aday *et al.*, 2019). Plowing in compacted soil requires high traction (Askari *et al.*, 2017). Many ways of reducing drag have been studied at home and abroad, such as vibration and pneumatic drag reduction. Different drag reduction methods have their own characteristics.

Vibration subsoiling relies on vibration to reduce drag. Shi *et al.* explored the disturbance effect of vibration subsoiling on soil by using the discrete element method combined with field test verification (Shi *et al.*, 2021). By using the TST5910 dynamic signal test and analysis system, Dong *et al.* tested and analyzed the vibration response characteristics of the frame of the 1ST-460 vibration subsoiler (Dong *et al.*, 2022).

Compared with vibration subsoiling, pneumatic subsoiling uses high-pressure gas to break through the soil aggregates at the bottom of the plough, thus reducing the resistance and strengthening the soil disturbance. Zuo *et al.* used pneumatic subsoiling to conduct air jet tests on cultivated soil, analyzed the characteristics of pneumatic subsoiling, and verified the feasibility of pneumatic subsoiling (Zuo *et al.*, 2016; Zuo *et al.*, 2017). Zhang designed a hot-air subsoiling machine and explored the subsoiling characteristics of the hot-air subsoiling machine combined with the soil tank test (Zhang *et al.*, 2022). Feng *et al.* conducted a simulation test of pneumatic subsoiling based on the pressure splitting method and explored the effect of pneumatic subsoiling operation under the combination test of different pressure values and subsoiling depth (Feng *et al.*, 2019). Li *et al.* established an aerodynamic model of pneumatic subsoiling and explored the effects of three factors, namely different plowing depth, air pressure, and speed, on traction resistance (Li *et al.*, 2022). Su *et al.* investigated the vibration characteristics of the pneumatic subsoiler and optimized the structure of the subsoiler. The optimized subsoiler avoids resonance phenomena and prolongs service life (Su *et al.*, 2022). Zuo *et al.* explored the variation rule of soil porosity in pneumatic deep panasonic and analyzed the porosity increase rate as an index. The results show that the atmospheric pressure and horizontal distance have a significant effect on the porosity increase rate (Zuo *et al.*, 2017).

The application of machine learning to agriculture can help researchers save a lot of time and experience. In order to reduce the maintenance cost of machine damage caused by abnormal operation, Gao *et al.* (2022) realized the control of tillage under the condition of non-uniform soil height in the field. Improved random forest was used to conduct regression prediction of tillage depth, and a prediction model of tillage depth was established.

Li *et al.* (2023) used RF, SVR, XGBoost and BP models to make regression prediction of traction resistance in the process of pneumatic subsoiling by taking five factors as input: ploughing depth, velocity, air pressure, soil bulk density and water content. The results showed that the prediction accuracy of RF model was the highest (Li *et al.*, 2023). When the output of the regression prediction is multiple dimensions, the number of models required will be reduced, and the prediction accuracy of the model can also be improved if there is a correlation between the multiple output factors. In order to optimize the pneumatic subsoiler, it is very important to explore the relationship between the pneumatic subsoiler and soil parameters. It is of great significance to apply multi-output neural network model to pneumatic subsoiling.

In this study, four neural network models, RBF, BP, DNN, and CNN, were used to simultaneously predict the traction resistance and soil disturbance area in different seasons at the same location on the basis of pneumatic subsoiling. Then, the model with the highest prediction accuracy was found among the four models. When comparing the single prediction of the traction resistance and disturbance area of the model, the accuracy of the model was improved.

MATERIALS AND METHODS

Test site and materials

The test site is located in the experimental field (39°19'n, 116°17'e) outside Langfang Ward Technology Co., LTD., 40 meters northwest of the intersection of 602 Xiang Road and Huimin East Road, Liuquan Town, Gu'an County, Langfang City, Hebei Province. The soil type of the experimental field was loam (clay 12.1%; silica 39.8%; sand 48.1%). The tractor is a John Deere 6B-954 tractor. The test shovel is a chisel-type shovel with air holes at the tip of the crank shovel. The model is JBT9788-1999. There is also an S-type digital tension meter, a laptop, a plugboard, and an air pump. The air pump is connected with the subsoiling shovel through the gas pipe to realize pneumatic subsoiling.

The details are shown in Figure 1 below.

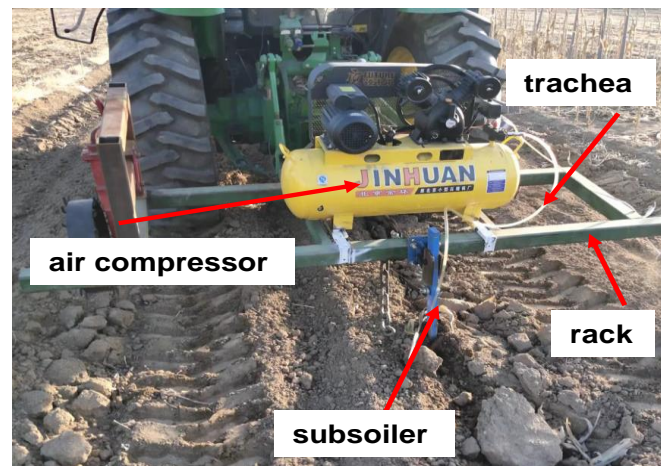


Fig.1 - Pneumatic subsoiling equipment

The experimental data include traction resistance and disturbance area, in which the traction resistance is obtained by the tension sensor. The tension sensor is connected by a chain to one end of the subsoiling shovel and the other end to the frame, which is powered by a battery. In the process of subsoiling, the subsoiling shovel pulls the iron chain to generate traction resistance, and the tension sensor receives the value and transmits it to the computer, as shown in Figure 2(a). The disturbance surface is obtained by the plugboard method, as shown in Figure 2(b) below. The insert board is composed of a wood strip with a length and width of 10 mm and a height of 500 mm, respectively. After the loose soil has been deeply loosened to reveal the disturbed surface, place the insert board on it. Then place A2 paper behind the insert board and trace the shape of the disturbed surface along the top of the strip.



(a)



(b)

Fig. 2 - Traction resistance and disturbance area data acquisition

The data were divided into two groups, one in the autumn and one in the winter. In order to measure the moisture content and bulk density of soil in different seasons, 100 cm³ soil samples were randomly sampled at 12 points in the field by the ring knife method. Taking the dry mass of the soil as the soil volume, the soil sample was placed in a drying oven with a temperature of 105° for 24 hours, and the soil bulk density was obtained after being weighed again. The soil water content was measured at 12 points, and the soil depth range of water content collection was 20-30 cm. The specific operation method is to weigh the collected soil once, then put it in the oven to dry until the water completely evaporates, and then weigh the dried soil. The proportion of the reduced value of the soil weight in the dried soil weight is the moisture content. The collected autumn and winter soil parameters are shown in the following table:

Table 1

| Soil parameters in autumn and winter | | |
|--------------------------------------|----------------------|----------------------------------|
| Season | Moisture content (%) | Unit weight (kg/m ³) |
| Autumn | 20.9 | 1580 |
| Winter | 18.3 | 1940 |

In the field experiment, there were 5 levels of working pressure (0, 0.2, 0.4, 0.6, 0.8 MPa), 3 levels of subsoiling speed (1, 2, 3), and 4 levels of subsoiling depth (20, 25, 30, 35 cm). Traction resistance and disturbance surface data were respectively measured in the experiments of the two seasons, with 60 sets of data for each season and a total of 120 sets of data. In Figures 3-4, the four tillage depths were taken as horizontal coordinates to compare the changes in traction resistance and disturbance area under different pressures and tillage speeds. It can be seen from the figure that the traction resistance in winter is significantly higher than that in autumn, and the disturbance area is smaller than that in autumn.

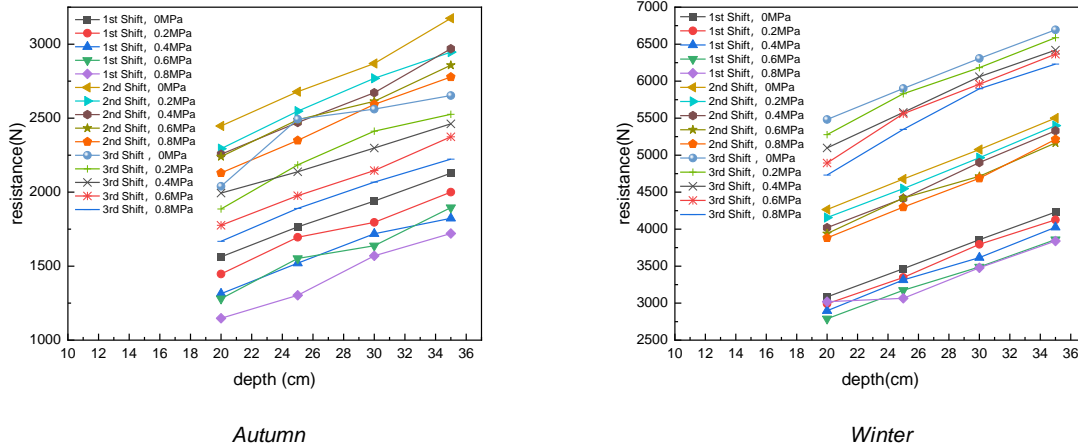


Fig. 3 - Traction resistance data at different velocities, depths, and working pressures

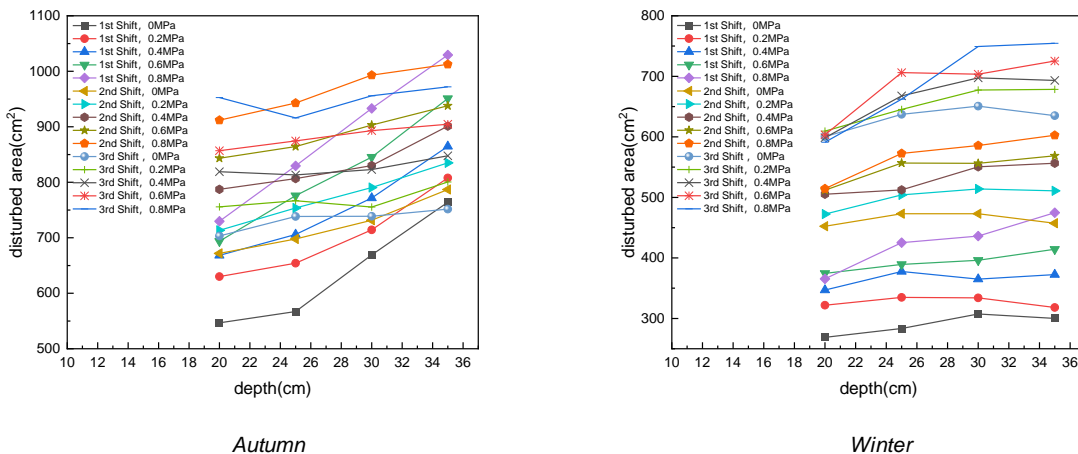


Fig. 4 - Disturbance area data at different velocities, depths, and working pressures

Neural network multiple output regression prediction model

RBF neural network: It is a radial basis neural network with an uncomplicated structure and three layers, namely the input layer, hidden layer, and output layer. Because of its simple structure, fast learning speed, and ability to approximate arbitrary nonlinear functions (Kou, 2022), it is often widely used in the fields of time series analysis, pattern recognition, graph processing, etc. The mathematical expression of the model refers to the formula in Melagraki's paper as follows (Melagraki. et al., 2006):

$$y_j = \sum_{i=1}^n \omega_{ij} e^{-\frac{\|x_p - c_i\|^2}{2\sigma^2}} \quad (j = 1, 2, \dots, p) \tag{1}$$

Where: y_j is the j th output of the network;

ω_{ij} - the link weight from the hidden layer to the output layer;

n - the number of hidden layer nodes;

X_p - the p th input sample;

c_i - the center of the network hidden layer node;

σ - the variance of the Gaussian function.

A BP neural network is a kind of neural network based on error-reverse propagation that contains only one hidden layer and can approximate any nonlinear system with arbitrary accuracy (Wang, 2014). The number of nodes in the hidden layer is calculated by referring to the following formula 2 in Qian's paper (Qian, et al., 2021). During the training process, the BP model constantly updates itself to fit the characteristics of new data. Therefore, the model has very high adaptability (Tang, 2018).

$$a \leq 4\sqrt{i(y+3)+1} \tag{2}$$

where: a is the number of neurons in the hidden layer;

i - the number of neurons in the input layer;

y - the number of neurons in the output layer;

When the number of hidden layer neurons in the BP neural network used in this study is calculated to be 10, the prediction effect is the best.

DNN is a deep learning network with one input layer, multiple hidden layers, and one output layer, and the hidden layers are fully connected. There are four processes in training DNN models: forward propagation, reverse propagation, weight gradient calculation, and updating. The core of the forward propagation process is to calculate the next hidden layer from the previous hidden layer, and the specific equation is as follows: The focus of backpropagation is to use the gradient of loss function to calculate the gradient of weight and bias and use the chain rule to backpropagate the gradient layer by layer. The output formula 3 of the DNN model is shown as follows in Song's paper (Song et al., 2019):

$$y = f\left(\sum_{i=1}^n \omega_i x_i + \theta\right) \tag{3}$$

where: ω_i is the weight coefficient;

n - the number of neurons in the input layer;

X_i - the neural network input;

θ - the bias;

f is the activation function;

CNN Neural Network: The CNN network has been widely used in image recognition, object detection, and other fields, has achieved good results, and is also used to perform data regression prediction tasks. The structure of the neural network includes a convolutional layer, a pooling layer, and a fully connected layer.

RESULTS

Multiple output prediction results

In this experiment, five factors that can affect the effect of pneumatic subsoiling, namely subsoiling speed, depth, pressure value, moisture content, and soil bulk density, were selected as input indexes for model training, and the predicted results were traction resistance and disturbance area. The 60 groups of data from the autumn experiment and the 60 groups of data from the winter experiment were combined to build a data set, and the 120 groups of data were randomly arranged, with the first 60 groups of data used in the model training process and the last 10 groups of data used in the test process. When building the model, it is necessary to normalize the data, then train the model with the training set, verify the model with the test set after the training is completed, and then reverse normalize the predicted data and calculate the error to evaluate the model performance.

In this study, MATLAB 2023a software was used for modeling. Open the software to create four windows, and enter the code for each neural network. Figures 5-12 show the specific prediction results:

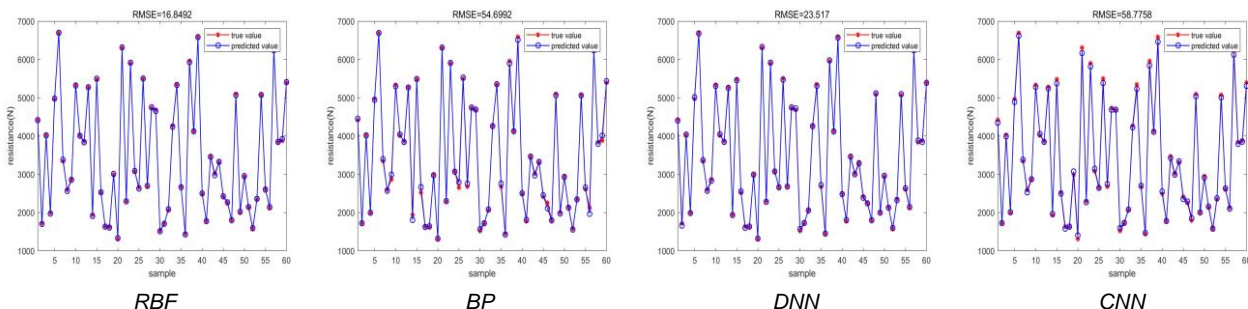


Fig. 5 - The fitting plot of four models when predicting traction resistance in the training set

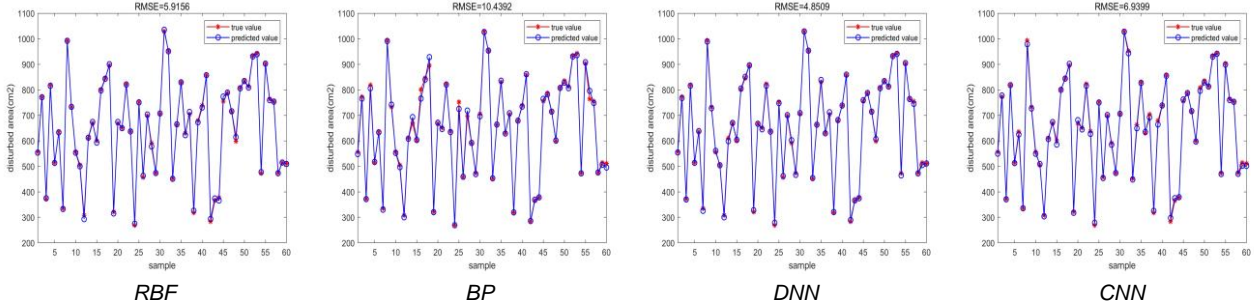


Fig. 6 - The fitting plot of four models when predicting the disturbance area in the training set

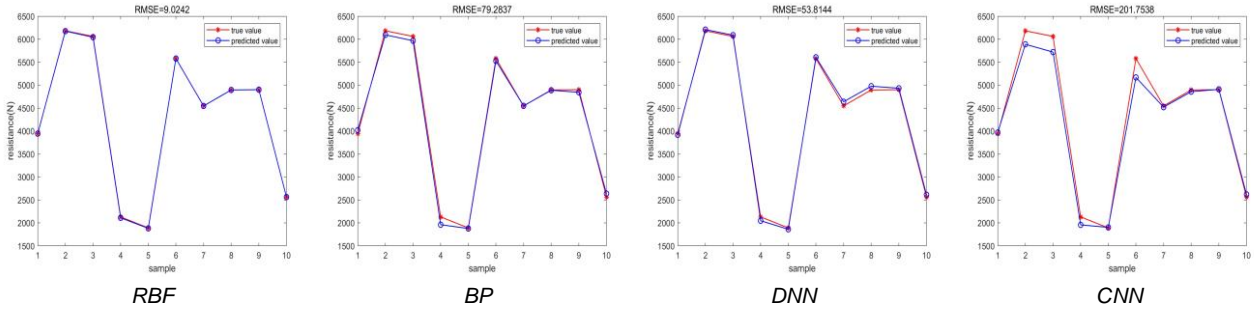


Fig. 7 - The fitting plot of the four models when predicting traction resistance in the test set

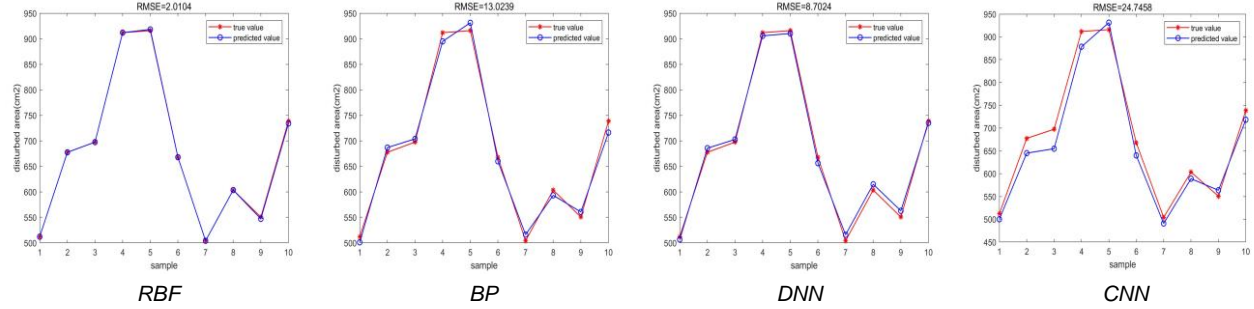


Fig. 8 - The fitting plot of the four models when predicting the disturbance area in the test set

The graph below is a regression graph of the four neural networks, representing the degree of fit of the respective models. The higher the degree of fitting, the smaller the error between the true value and the predicted value, and the better the prediction effect of the network.

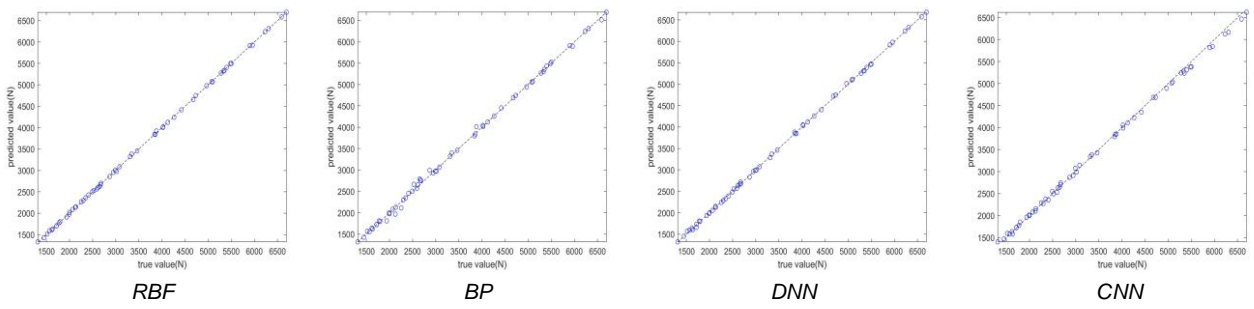


Fig. 9 - The regression plot of four models predicting traction resistance in the training set

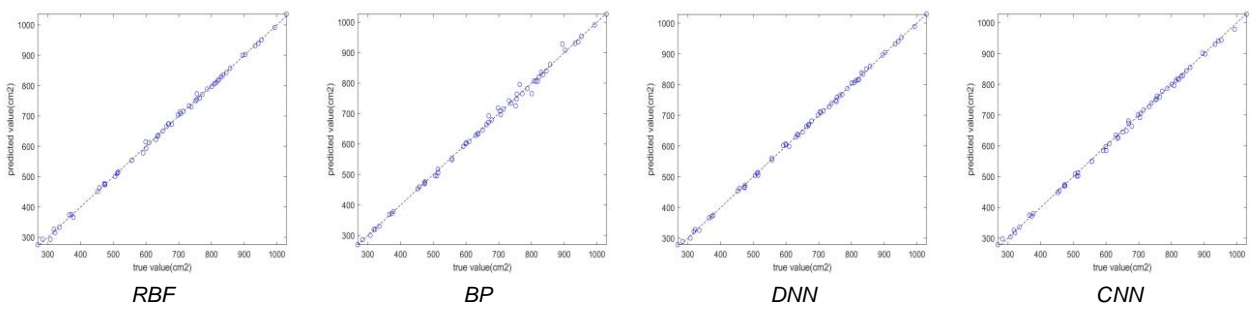


Fig. 10 - The regression plot of four models predicting the disturbance area in the training set

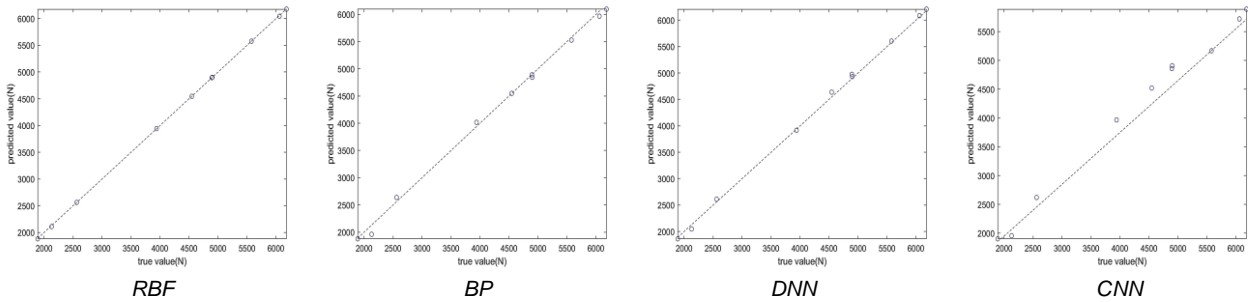


Fig. 11 - The regression plot of four models predicting traction resistance in the test set

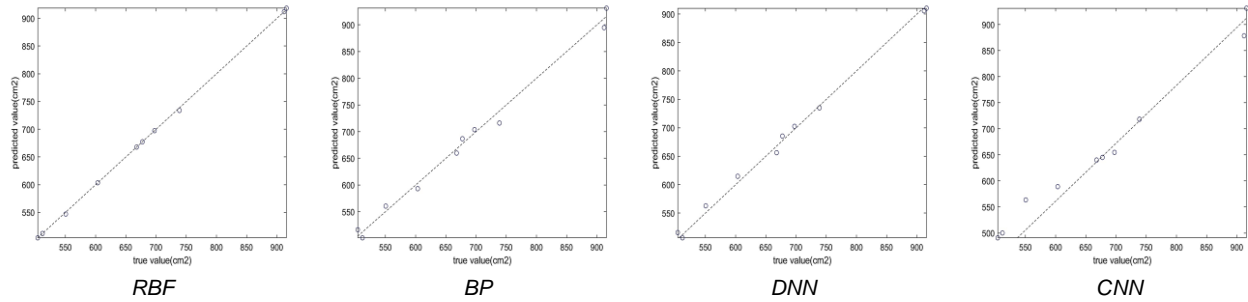


Fig. 12 - The regression plot of four models predicting the disturbance area in the test set

After the regression prediction calculation of the model, the measured results of the performance evaluation coefficients of the four models are shown in the table below and the radar chart. Through comparative analysis, it can be seen that among the four models in the prediction results, the prediction accuracy of the CNN model is the lowest, and the R^2 value of the prediction data of traction resistance and disturbance area of the RBF model in the test set is the largest. Therefore, the prediction accuracy of the RBF model is the highest, and the fitting effect is the best.

Table 2

Prediction accuracy of drag resistance for four models

| Model | Training | | | Testing | | |
|-------|----------|--------|--------|---------|---------|---------|
| | R^2 | RMSE | MAE | R^2 | RMSE | MAE |
| RBF | 0.9998 | 16.849 | 13.792 | 0.9999 | 9.024 | 5.739 |
| BP | 0.998 | 54.699 | 34.994 | 0.9966 | 79.284 | 63.089 |
| DNN | 0.9997 | 23.517 | 19.63 | 0.9986 | 53.814 | 47.1 |
| CNN | 0.9983 | 58.776 | 47.322 | 0.9762 | 201.754 | 138.624 |

Table 3

Prediction accuracy of the disturbance area of four models

| Model | Training | | | Testing | | |
|-------|----------|--------|-------|---------|--------|--------|
| | R^2 | RMSE | MAE | R^2 | RMSE | MAE |
| RBF | 0.9987 | 5.916 | 4.362 | 0.9997 | 2.01 | 1.067 |
| BP | 0.998 | 10.439 | 6.551 | 0.9924 | 13.024 | 12.184 |
| DNN | 0.9993 | 4.851 | 3.742 | 0.9968 | 8.702 | 8.118 |
| CNN | 0.9986 | 6.94 | 5.486 | 0.9715 | 24.746 | 22.501 |

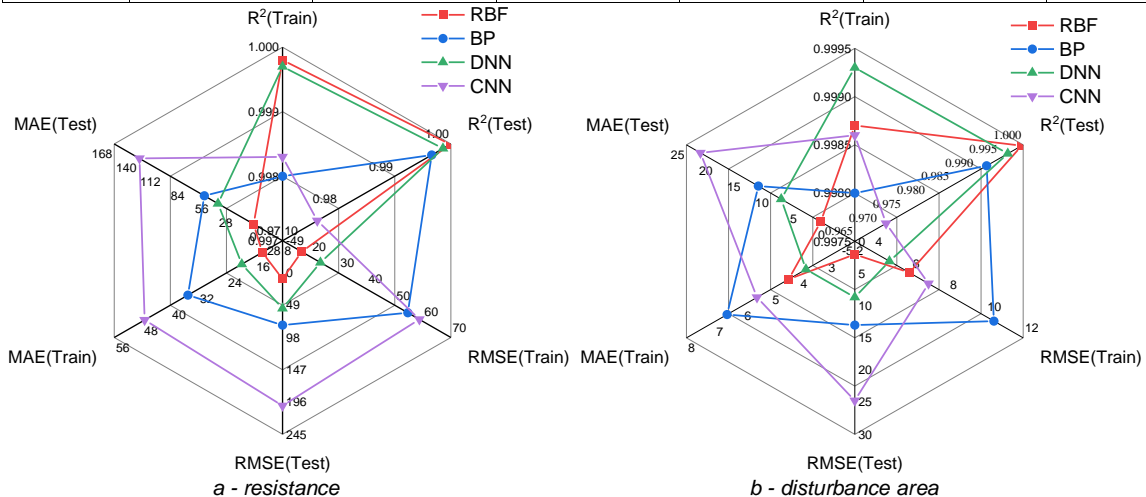


Fig. 13 – Comparison of the evaluation indicators of the four models

Single output prediction results

Based on the above RBF neural network, the prediction effect is the best, and whether the accuracy of RBF neural network multi-output regression prediction is improved compared with its single output regression prediction is studied. The RBF neural network was used to predict the traction resistance and disturbance area, respectively, and the data were obtained after training, as shown in Tables 4 and 5 below. The evaluation indexes of the RBF single-output model in the test set were compared with those of the RBF multi-output model, as shown in the figure below, where R and DA are shorthand for resistance and disturbance area, respectively.

Table 4

Prediction accuracy of traction resistance of the RBF neural network

| Model | Training | | | Testing | | |
|-------|----------------|-------|--------|----------------|-------|-------|
| | R ² | RMSE | MAE | R ² | RMSE | MAE |
| RBF | 0.9998 | 16.73 | 13.711 | 0.9999 | 9.246 | 6.025 |

Table 5

Prediction accuracy of the disturbance area of the RBF neural network

| Model | Training | | | Testing | | |
|-------|----------------|-------|-------|----------------|------|-------|
| | R ² | RMSE | MAE | R ² | RMSE | MAE |
| RBF | 0.9987 | 5.908 | 4.355 | 0.9997 | 2.01 | 1.107 |

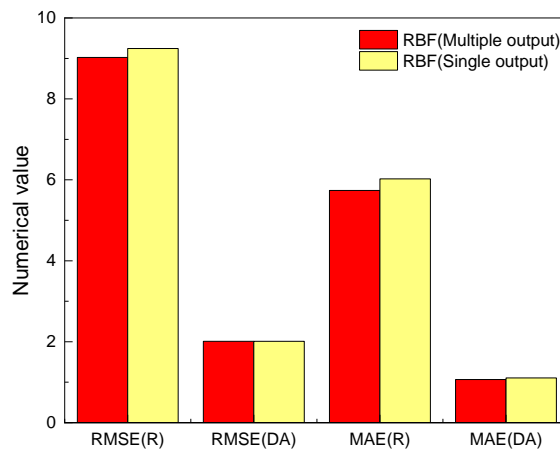


Fig. 14 - Comparison of evaluation indexes of the multi-output RBF model and the single-output RBF model

Referring to the Pearson algorithm used in Li's paper (Li et al., 2023) to conduct correlation analysis on velocity, depth, pressure, bulk density, water content, and resistance, this study added disturbance area on this basis to explore the correlation between resistance and disturbance area. As can be seen from the figure below, there is a strong correlation between volume weight and resistance. There is a strong correlation between water content and disturbance area.

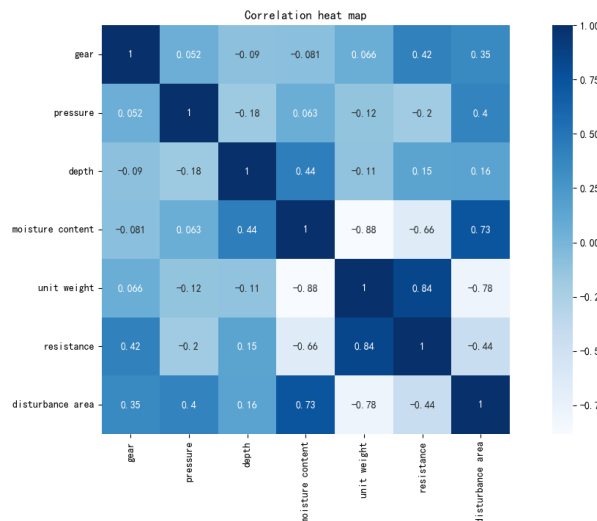


Fig. 15 - Correlation diagram

CONCLUSIONS

In this study, four neural network models (RBF, BP, DNN, and CNN) were used to make regression predictions of traction resistance and disturbance area of pneumatic subsoiling machines under the same test site in autumn and winter with inputs of subsoiling depth, velocity, pressure value, bulk density, and water content, and R^2 , RMSE, and MAE as evaluation indexes. The prediction results show that the RBF model has the highest prediction accuracy, and the R^2 , RMSE, and MAE of the traction resistance in the test set are 0.9999, 9.024, and 5.739, respectively, and the disturbance area is 0.9997, 2.01, and 1.067. Compared with the single output model of RBF, the MAE of the double output model of RBF is slightly lower in terms of drag resistance and disturbance area. The results show that the RBF multi-output model has a better prediction effect. Pearson correlation analysis also proves that there is a negative correlation between drag resistance and disturbance area in the process of pneumatic subsoiling. This correlation can be used to improve the accuracy of regression prediction and provide technical support for intelligent research on pneumatic subsoiling.

ACKNOWLEDGEMENT

This research was funded by the National Natural Science Foundation of China (grant nos.32171902, 32060417).

REFERENCES

- [1] Aday, S.H., & Ramadhan, M.N. (2019). Comparison between the draft force requirements and the disturbed area of a single tine, parallel double tines and partially swerved double tines subsoilers. *Soil & Tillage Research*, 191, 238-244. <https://doi.org/10.1016/j.still.2019.02.011>
- [2] Askari M., Shahgholi G., & Abbaspour-Gilandeh Y. (2017). The effect of tine, wing, operating depth and speed on the draft requirement of subsoil tillage tines. *Research in Agricultural Engineering*, 63(4), 160-167. <http://dx.doi.org/10.17221/4/2016-RAE>
- [3] Dong, X.Q., Zheng, H.N., Chen, S., Li, Y.L., Song, J.N., & Wang, J.C. (2022). Test and analysis of vibration characteristics of vibration subsoiler. *INMATEH-Agricultural Engineering*, 68(3), 906-917. <https://doi.org/10.35633/inmateh-68-90>
- [4] Feng, Z.Z., Li, X., Wang, W.X., Yan, Y.M., & Chen, F.X. (2019). Simulation test of pneumatic subsoiling based on pressure splitting method (基于气压劈裂法的气动深松模拟试验). *Agricultural mechanization research*, 41(11),178-184. <https://link.cnki.net/doi/10.13427/j.cnki.njyi.2019.11.031>
- [5] Gao, A.F. (2022). *Research on tillage depth prediction model based on improved random forest (基于改进随机森林的耕深预测模型研究)*(Master's Degree Thesis, Changchun University of Technology).
- [6] Iman, A. (2017). Effect of soil, machine, and working state parameters on the required draft force of a subsoiler using a theoretical draft-calculating model. *Soil Research*, 55(4), 389-400. <https://doi.org/10.1071/SR16193>
- [7] Kou, L.Y. (2022). *Climate data prediction based on improved RBF neural network (基于改进 RBF 神经网络的气候数据预测研究)*(Msc Thesis. Southwest University of Science and Technology).
- [8] Li, X., Jiang, Z.J., Wang, S.C., Li, X.L., Liu, Y., & Wang, X.H. (2023). A study of a model for predicting pneumatic subsoiling resistance based on machine learning techniques. *Agronomy*,13,1079. <https://doi.org/10.3390/agronomy13041079>
- [9] Li, X., Wang, S.C., Meng, H.W, Qu, Q.J., & Jia, Y.W. (2022), Research on drag reduction mechanism of pneumatic subsoiler and establishment of resistance mathematical model. *Canadian Journal of Soil Science*, 102(2), 531-548. <http://dx.doi.org/10.1139/cjss-2021-0101>
- [10] Lou, S.Y., He, J., Li, H.W., Wang, Q.J., Lu, C.Y., Liu, W.Z., Liu, P., Zhang, Z.G., & Li, H. (2021). Current knowledge and future directions for improving subsoiling quality and reducing energy consumption in conservation fields. *Agriculture*, 11, 575. <https://doi.org/10.3390/agriculture11070575>
- [11] Melagraki, G., Afantitis, A., Makridima, K., Sarimveis, H., & Lgglessi-Markopoulou, O. (2006). Prediction of toxicity using a novel RBF neural network training methodology. *Journal of Molecular Modeling*, 12, 297-305. <https://doi.org/10.1007/s00894-005-0032-8>
- [12] Odey, S.O., & Manuwa, S.I. (2018). Subsoiler development trend in the alleviation of soil compaction for sustainable agricultural production. *International Journal of Engineering Inventions*, 7(8), 29-38. <https://www.researchgate.net/publication/329972623>

- [13] Qian, J.G., Xu, W., Mu, L.L., & Wu, A.H. (2021). Calibration of soil parameters based on intelligent algorithm using efficient sampling method. *Underground Space*, 6(3), 329-341. <https://doi.org/10.1016/j.undsp.2020.04.002>
- [14] Shi, Z.M., Chen, T.H., Li, S.T., Yang, L., & Yang, M.J. (2021). Impact of vibration on tillage performance of subsoilers using the discrete element method (DEM). *INMATEH-Agricultural Engineering*, 64(2), 89-98. <https://doi.org/10.35633/inmateh-64-08>
- [15] Song, W.J., Choi, S.G., & Lee, E.S. (2019). Prediction and comparison of electrochemical machining on shape memory alloy(SMA) using deep neural network(DNN). *Journal of Electrochemical Science and Technology*, 10(3), 276-283. <https://doi.org/10.33961/jecst.2019.03174>
- [16] Su, H.J., Cui, H.M., Li, F.Y., Chaolun Yideer., Zhu, Y.X., & Ma, Z.P. (2022). Vibration characteristics analysis and structure optimization of air-pressure subsoiler. *Noise & Vibration Worldwide*, 53(1-2), 12-23. <https://doi.org/10.1177/09574565211052695>
- [17] Su, H.J., Cui, H.M., Li, F.Y., & Fan, T. (2021). Optimization design of an air-pressure subsoiler type. *INMATEH-Agricultural Engineering*, 63(1), 145-154. <https://doi.org/10.35633/inmateh-63-15>
- [18] Tang, Z.X. (2018). *Research and implementation of air quality prediction based on BP neural network (基于 BP 神经网络的空气质量预测研究与实现)*(Master's Degree Thesis, Xidian University).
- [19] Thomas, K., Maria, S., Tino, C., Rainer, H., & Dani, O. (2019). Historical increase in agricultural machinery weights enhanced soil stress levels and adversely affected soil functioning. *Soil & Tillage Research*, 194, 104293. <https://doi.org/10.1016/j.still.2019.104293>
- [20] Wang, Z.Q. (2014). *Establishment of NOx emission prediction model of GA-BP diesel engine and its application on real ship (GA-BP 柴油机 NOx 排放预测模型的建立及实船应用研究)*(Master's Degree Thesis, Dalian Maritime University).
- [21] Zhang, M.X. (2022). *Design and test of hot air deep soil opening tank test bed(热风式深松土槽试验台的设计与试验)*. (Master's Degree Thesis, Anhui Agricultural University).
- [22] Zuo, S.J. (2016), *Experimental study on the characteristics and techniques of pneumatic subsoiling (气压深松特性及技术的试验研究)*(Ph.D. Thesis, Northeast Agricultural University).
- [23] Zuo, S.J., Kong, D.G., Chen, H.X., Han, Y., Zhang, Y., & Liu, C.S. (2017), Design of pneumatic subsoiling machine based on pressure splitting principle(基于气压劈裂原理的气压深松机设计). *Chinese Journal of Agricultural Mechanization*, 38(4), 5-10.
- [24] Zuo, S.J., Kong, D.G., Liu, C.S., Li, Z.H., Zhang, C, Chen, S., & Wu, Y.F. (2017). Test and analysis of soil porosity with pneumatic subsoiling(气压深松土壤孔隙度测试与分析). *Transactions of the Chinese Society of Agricultural Engineering (Transactions of the CSAE)*, 33(1), 162-166.

DYNAMIC DRYING CHARACTERISTICS OF ALFALFA UNDER SOLAR ENERGY-HEAT PUMP COMBINED DRYING CONDITIONS

太阳能-热泵联合干燥条件下紫花苜蓿动态干燥特性

WenBin GUO ^{*1,2)}; Shuo CHENG ^{1,2)}; ZhiKang CUI ^{1,2)}; DongLi HE ³⁾; XuHui ZHANG ^{1,2)};
TianYu SHI ^{1,2)}; ShanZhu QIAN ^{1,2)}; JianQiang DU ^{1,2)}

¹⁾ College of Mechanical and Electrical Engineering, Inner Mongolia Agricultural University, Hohhot 010018, China;

²⁾ Inner Mongolia Engineering Research Centre of Intelligent equipment for the entire process of forage and feed production, Hohhot 010018, China;

³⁾ Research Institute of Inner Mongolia First Machinery Group Co. Ltd, China

Tel: 13848109315; E-mail: CS985761@163.com; wenbingwb2000@sina.com

DOI: <https://doi.org/10.35633/inmateh-73-48>

Keywords: solar-heat pump drying system, alfalfa, drying characteristics, mathematical model, moisture diffusivity, activation energy

ABSTRACT

To promote the application of solar energy-heat pump combined drying technology in forage processing and enhance the drying efficiency of alfalfa, an experimental study was conducted. The research utilized a solar energy-heat pump drying system and a mesh belt dynamic drying device to investigate the drying characteristics of alfalfa. Drying characteristic curves were obtained, and the drying model and parameters were determined through model comparison. The study also analysed the impact of factors such as hot air velocity, temperature, alfalfa stacking thickness, turning angle of the spinner rack, and conveyor belt speed on the drying characteristic curves and parameters of alfalfa. A predictive model for alfalfa moisture content was developed, and the effective moisture diffusivity and activation energy were calculated. The findings revealed that alfalfa does not exhibit a constant speed drying stage, and its drying primarily occurs during the deceleration drying stage. The Logarithmic model was found to accurately describe the moisture change pattern during the dynamic drying process of alfalfa, with a model fitting coefficient R^2 exceeding 0.994, with an effective moisture diffusivity ranging from $2.776 \times 10^{-10} \text{ m}^2/\text{s}$ to $4.7324 \times 10^{-9} \text{ m}^2/\text{s}$, and an activation energy of 37.02 kJ/mol. The study suggests that increasing the hot air velocity and temperature, reducing the conveyor belt speed, and adjusting the alfalfa stacking thickness can further enhance the drying rate and reduce the drying time.

摘要

为推动太阳能-热泵联合干燥技术在饲草加工领域的应用,改善苜蓿干燥效率和效果,借助太阳能-热泵干燥系统及其网带式动态干燥装置对苜蓿进行了干燥特性试验研究,获取了干燥特性曲线,并通过模型对比确定了干燥模型及参数。分析了热风风速、温度、苜蓿堆积厚度、转架偏转角度、输送带移动速度等因素对苜蓿干燥特性曲线与参数的影响,得到了苜蓿水分比预测模型,同时计算得到有效水分扩散率和活化能。结果表明苜蓿无恒速干燥阶段,其干燥主要发生在降速干燥阶段,Logarithmic模型可以精准描述苜蓿动态干燥过程中的水分变化规律,模型拟合决定系数 R^2 大于 0.994。有效水分扩散率介于 $2.776 \times 10^{-10} \text{ m}^2/\text{s} \sim 4.7324 \times 10^{-9} \text{ m}^2/\text{s}$ 、活化能为 37.02 KJ/mol,可通过增加热风风速、温度、降低输送带移动速度、苜蓿堆积厚度,进一步增大干燥速率,缩短干燥时间。

INTRODUCTION

Alfalfa, a perennial leguminous forage grass, is prized for its adaptability, high nutritional value, and abundant yield. With a protein content surpassing that of corn and rich in essential amino acids and trace elements, it is extensively cultivated in China's Inner Mongolia region, boasting a national planting area of 6.355 million mu and an annual yield of 4.224 million tons in 2021. Due to its substantial yield and harvest timing during the rainy season, rapid moisture reduction after harvest is crucial to prepare alfalfa for feed processing and minimize the impact of weather conditions on the drying process (Liu Z. H., 2022).

Drying is a critical step in preserving and storing alfalfa, directly influencing its quality. High-temperature dehydration can lead to the loss of aromatic amino acids and protein aging, resulting in reduced digestibility and palatability when used as feed. After experimenting with various drying methods, solar energy hot air drying has emerged as a suitable, energy-efficient, and cost-effective approach for alfalfa processing (Sun Q. Y. et al., 2022).

However, the fluctuating temperatures of sunlight exposure, influenced by natural conditions such as day-night alternation and varying weather, pose challenges in meeting the demands for continuous drying of large quantities of alfalfa during the harvesting period. Therefore, a solar energy-heat pump combined drying method is adopted in this study. This method demonstrates high efficiency, low energy consumption, and strong continuity, and has been widely applied in the agricultural material processing field (Wang Q. *et al.*, 2012; Anfal A.H., 2022). Analysing the drying characteristics of alfalfa under these conditions and determining relevant drying processes can offer valuable insights for improving the efficiency of alfalfa drying processing. Singh and his team have designed a dynamic drying device, which can increase the hot air temperature and drying efficiency (Singh P., 2010). In a study by Li Y.Y., the moisture changes of alfalfa during the drying process using hot air drying technology were investigated. Experiments were conducted on alfalfa density, the distance between the heating plate and the material, and heating temperature to explore the moisture change patterns under different influencing factors (Li Y.Y., 2020).

This study focuses on fresh alfalfa and conducts dynamic drying experiments under solar energy-heat pump combined drying conditions. It involves plotting drying characteristic curves, establishing drying models, analysing the effects of hot air temperature, air velocity, material pile thickness, turning angle of the spinner rack, and conveyor belt speed on the drying characteristics of alfalfa, and optimizing dynamic drying processes. The results obtained will promote the application of solar energy-heat pump combined drying technology in forage processing, thereby enhancing the drying processing capacity of alfalfa.

MATERIALS AND METHODS

Materials

The experimental materials used in the study were fresh purple alfalfa grown in the grasslands in Horinger County (figure 1), Hohhot City, Inner Mongolia Autonomous Region, with an initial moisture content of approximately $76\% \pm 2\%$. The alfalfa had 3 times mowing, and the second batch was used for the experiments, leaving a stubble height of 5~6 cm (Luo S H *et al.*, 2024), and the stubble was neatly cut to facilitate regrowth.



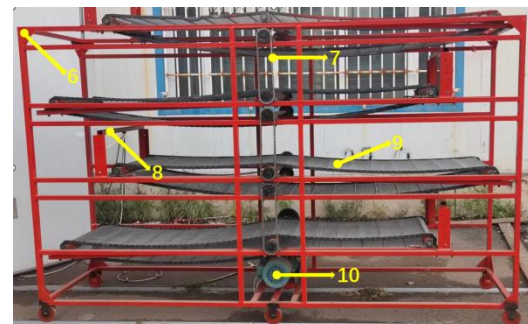
Fig. 1 - Fresh alfalfa

Instruments and equipment

The experimental setup utilized was the TGS-2 solar energy-heat pump combined drying system (figure 2a), comprising solar collectors, a drying chamber, a control system, a dehumidification system, and a dynamic drying device (figure 2b). During operation, air heated by the solar collectors is directed into the drying chamber from the bottom by fans, facilitating the drying of alfalfa on the dynamic mesh belt drying bed. To optimize drying efficiency, adjacent layers of the mesh belt move in opposite directions during drying. This allows the material to transition from one layer to the next, ensuring thorough contact with the hot air and achieving dynamic drying. When sunlight intensity decreases and the temperature inside the drying chamber drops below the set drying temperature, the control system will switch from solar drying to solar energy-heat pump combined drying mode, with the heat pump supplementing the drying heat to maintain a constant drying temperature.



(a)



(b)

Fig. 2 - (a) Solar-heat pump combined drying system; (b) Dynamic drying device

1. Solar collector; 2. Dehumidification system; 3. Drying room; 4. Mesh belt drying bed; 5. Control system; 6. Drying frame; 7. Drive chain; 8. Swivel frame; 9. Drying bed; 10. Electric motor

Drying Process

To investigate the impact of temperature, air velocity, material pile thickness, turning angle of the spinner rack, and conveyor belt speed on drying characteristics, and minimize loss of alfalfa leaves and nutrients, specific parameters were selected. Hot air temperatures of 45, 50, 55, 60, and 65°C were chosen, along with hot air velocities of 1.5, 3.0, 4.5, 6.0, and 7.5 m/s. Material pile thicknesses of 4, 7, 10, 13, and 16 cm were considered, as well as turning angles of 0°, 5°, 10°, 15°, and 20°, and conveyor belt speeds of 0.01, 0.02, 0.04, 0.08, and 0.16 m/s. Prior to the experiment, the levels of each experimental factor were adjusted according to the experimental design, and the equipment was preheated for half an hour before commencing the experiment.

Test metrics

The dry-base moisture content

The definition of moisture content on a dry basis is the ratio of the mass of water in a material to the mass of dry matter in the material. The calculation formula is as follows:

$$M_t = \frac{m_t - m_d}{m_d} \quad (1)$$

where: M_t is the dry-base moisture content, (g/g); m_t is the quality of alfalfa at a certain moment (g), m_d is the weight of alfalfa dry matter (g).

Drying rate

The drying rate can reflect the drying characteristics, describing the weight of water removed from the material per unit of time. The formula for calculation is as follows:

$$D_R = \frac{M_{t1} - M_{t2}}{t_1 - t_2} \quad (2)$$

where:

M_{t1} and M_{t2} are the moisture of samples (g/g) at time t_1 and t_2 (minutes), respectively.

Moisture ratio

The moisture ratio represents the proportion of the moisture content at a certain point in the drying process to the initial moisture content. The smaller the ratio of the moisture content, the more water loss, thereby reflecting the speed of drying. The formula for calculating the moisture content is as follows:

$$MR = \frac{M_t}{M_0} \quad (3)$$

where: M_t , M_0 are moisture content (g/g) at any time, initial moisture content (g/g).

Mathematical modelling and Statistical Analysis

Drying of alfalfa is a complex non-steady-state heat and mass transfer process, thus mathematical models can be used to describe the trend of moisture change in alfalfa during drying (Simal S, 1997). Negligible deformation and shrinkage of alfalfa during drying are ignored, and the proposed mathematical models were employed to analyse the drying process. The details are shown in Table 1.

Table 1

| Name | Equation |
|----------------------------|--|
| Page | $MR = \exp(kt^n)$ |
| Logarithmic | $MR = a \exp(-kt) + c$ |
| Two-term model | $MR = a \exp(-k_0 t) + b \exp(-k_1 t)$ |
| Approximation of diffusion | $MR = a \exp(-kt) + (1-a) \exp(-kat)$ |

The data obtained from the experiments are subjected to nonlinear regression analysis. The evaluation criteria for the goodness of fit of the models include the coefficient of determination R^2 , chi-square χ^2 , and root mean square error $RMSE$ (Chang Jiang D. et al., 2017). The model with the highest R^2 value and the lowest χ^2 and $RMSE$ values is considered the best model to describe the drying characteristics. Drying characteristic curves are plotted for mathematical model data analysis. The above indicators are used to evaluate the mathematical models, and calculated as follows.

$$R^2 = \frac{\sum_{i=1}^N \left(MR_{pre,i} - \overline{MR_{exp}} \right)^2}{\sum_{i=1}^N \left(MR_{exp,i} - \overline{MR_{exp}} \right)^2} \quad (4)$$

$$\chi^2 = \frac{\sum_{i=1}^N \left(MR_{exp,i} - MR_{pre,i} \right)^2}{N - P} \quad (5)$$

$$RMSE = \sqrt{\frac{\sum_{i=1}^N \left(MR_{pre,i} - MR_{exp,i} \right)^2}{N}} \quad (6)$$

where: $MR_{exp,i}$ is the experimental dimensionless moisture ratio, $MR_{pre,i}$ is the predicted dimensionless moisture ratio, N is the number of observations, and P is the number of constants in the mathematical model.

Effective Moisture Diffusivity

The effective moisture diffusivity can reflect the moisture migration mechanism during the material drying process, describing the evaporation of moisture within a certain period under specific conditions. It is of great significance for analysing internal moisture diffusion and process optimization. As alfalfa drying primarily occurs during the deceleration drying stage, the effective moisture diffusivity can be calculated using a simplified form of Fick's second law. Assuming negligible volume shrinkage of the drying material and a constant diffusion coefficient and temperature, the effective diffusivity can be expressed as:

$$MR = \frac{8}{\pi^2} \exp\left(-\frac{\pi^2 D_{eff} t}{4L^2}\right) \quad (7)$$

The equation (7) can be expressed in logarithmic form as follows:

$$\ln(MR) = \ln\left(\frac{8}{\pi^2}\right) - \frac{\pi^2 D_{eff}}{4L^2} t \quad (8)$$

By plotting $\ln(MR)$ against drying time as coordinates and obtaining the slope of the line, the effective moisture diffusivity can be then determined.

$$S = \frac{\ln(MR) - \ln\left(\frac{8}{\pi^2}\right)}{t} = \frac{\pi^2 D_{eff}}{4L^2} \quad (9)$$

where: D_{eff} is the effective moisture diffusivity (m^2/s), L is half of the alfalfa thickness (m), S is the slope, and t is the drying time (minutes).

Activation energy

The drying activation energy represents the energy required to remove the moisture from 1 mole of material, and its value directly reflects the difficulty of the drying process. A higher value indicates a more difficult drying process (Onwude D.I. et al., 2016). Therefore, this study aims to measure the difficulty of alfalfa drying under dynamic conditions by calculating the activation energy. The activation energy is calculated using the Arrhenius equation to establish the relationship between the effective diffusivity and the activation energy, as follows:

$$D_{eff} = D_0 \exp\left[-\frac{E_a}{R(T + 273.15)}\right] \quad (10)$$

where: D_0 is the pre-exponential factor (m^2/s), E_a is the activation energy (kJ/mol), R is the ideal gas constant ($8.314 kJ/mol$), T is the absolute temperature ($^{\circ}C$).

The equation (10) can be expressed in logarithmic form as follows:

$$\ln D_{eff} = \ln D_0 - \frac{E_a}{R} \frac{1}{T + 273.15} \quad (11)$$

By plotting a line with $\ln(D_{eff})$ and $1/(T+273.15)$ as coordinates, the slope of the line can be determined, and thus the activation energy can be calculated.

RESULTS

Analysis of drying characteristics under different wind speeds

When the temperature was 55 °C, the alfalfa was stacked to a thickness of 7 cm, the turning angle of the spinner rack was 0°, and the conveyor belt moved at a speed of 0.01 m/s, the drying characteristic curves under different wind speeds were obtained, as shown in Figure 3. As the drying time increased, the drying rate showed a trend of initial increase followed by a decrease (figure 3a), without a constant speed drying stage. This is similar to the curves obtained for alfalfa drying under static conditions (*Shi Q et al., 2013*). During the initial stage of drying, the alfalfa experienced a preheating phase (*Cowen A.A. et al., 2008*), characterized by a rapid increase in temperature (figure 3b) and subsequent decrease in the dry-base moisture content (figure 3c), leading to a linear rise in the drying rate. When the solar energy-heat pump system provided heat exclusively for evaporating moisture, the alfalfa temperature stopped rising and entered a constant temperature phase (figure 3b), causing the drying rate to decrease to a lower level. By the drying time reached 170 minutes, the wet basis moisture content fell below 18% (the dry-base moisture content below 22%), reaching a safe moisture content level.

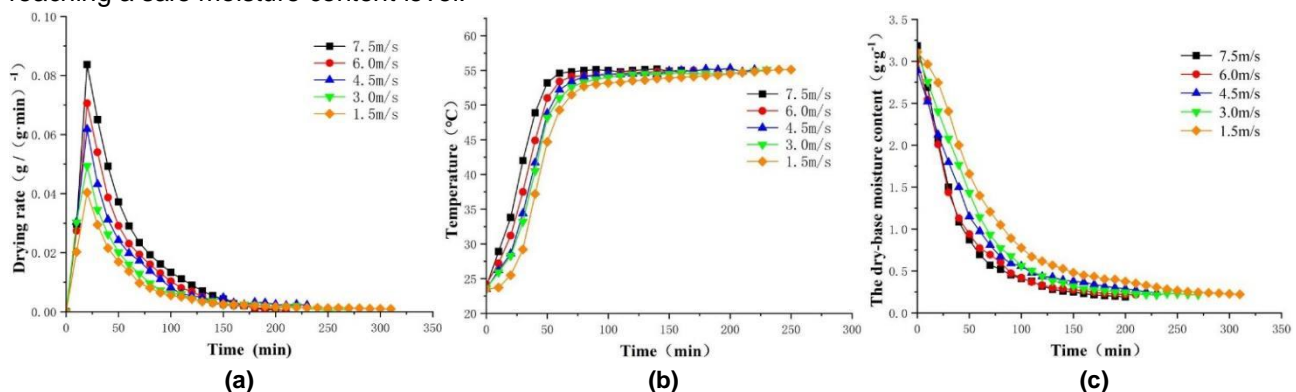


Fig. 3 - (a)Effect of wind speed on drying rate; (b)Effect of wind speed on alfalfa warming; (c)Effect of wind speed on the water content of alfalfa

The impact of varying wind speeds on the drying rate, moisture content, and temperature of alfalfa was interconnected. Higher wind speeds resulted in a faster drying rate during the preheating phase (figure 3b), an earlier transition to the constant temperature phase (figure 3b), and a shorter time to reach the target moisture content (figure 3c). This acceleration was attributed to the increased wind speed expediting the removal of moisture from the drying chamber, thereby requiring less time to achieve equilibrium and resulting in a more rapid increase in alfalfa temperature. Specifically, at wind speeds of 1.5, 3.0, 4.5, 6.0, and 7.5 m/s, the times required for alfalfa to reach the target moisture content were 310, 270, 230, 210, and 200 minutes, respectively. Higher wind speeds accelerated the evaporation rate of moisture, leading to reduced drying time (*YunHong Liu et al., 2016*). Compared to static drying (*Qian W. et al., 2018*), the moisture content decreases more rapidly and the time required for drying is shorter during mesh belt dynamic drying.

Characterization of drying at different temperatures

Drying characteristic curves for alfalfa at various temperatures were obtained under specific conditions, including a wind speed of 7.5m/s, an alfalfa stacking thickness of 10 cm, a spinner rack turning angle of 0°, and a conveyor belt speed of 0.01 m/s, as depicted in Figure 4. Over time, the drying rate curve displayed an initial increase followed by a decrease (figure 4a). Obviously, there were both acceleration and deceleration drying stages, with no constant speed drying stages. Moreover, the primary drying process occurred during the deceleration stage. The drying temperature significantly impacted the drying rate and heating effect of the alfalfa. Higher temperatures led to greater heat absorption by the alfalfa as well as a faster temperature increase (figure 4b). The higher the maximum drying rate (figure 4a), the faster the dry-base moisture content decreased (figure 4c). This was because in the initial stage of drying, the alfalfa surface contained a higher amount of free water, which rapidly evaporated with rising temperature, leading to an increase in the drying rate. As drying progressed, the internal moisture of the alfalfa, including bound water, began to migrate outward and evaporate. However, due to the influence of the internal tissue structure, the rate of moisture diffusion decreased, leading the alfalfa into the deceleration drying stage. At this point, the temperature tended to stabilize, and the drying rate continued to decline until the alfalfa reached the desired moisture content.

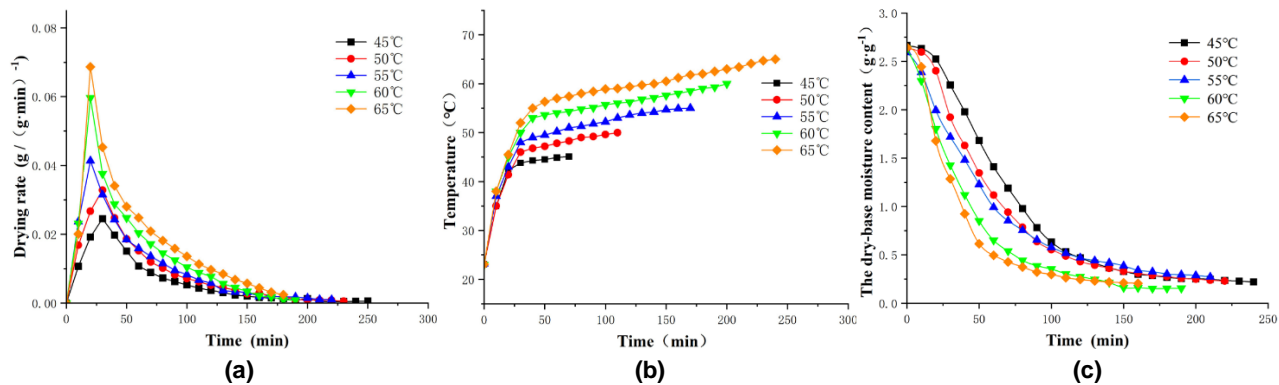


Fig. 4 - (a) Effect of temperature on drying rate; (b) Effect of temperature on alfalfa warming; (c) Effect of temperature on the water content of alfalfa

The trend of the drying characteristic curves of alfalfa remained consistent at different inlet air temperatures. It was evident that higher temperatures resulted in a faster drying rate (figure 4a) and a more pronounced decrease in the dry-base moisture content of the alfalfa (figure 4c). The alfalfa temperature increased more rapidly (figure 4b), the value tended to be larger when the temperature reached equilibrium, leading to a shorter time to reach the target moisture content. This aligns with results obtained under static drying conditions, as higher temperatures accelerated the diffusion of moisture within the alfalfa, increased the heat flow between the alfalfa and the hot air, enhanced the rate of heat transfer, and ultimately led to a rapid increase in alfalfa temperature (figure 4b), accelerating the outward transfer of moisture (Xiao H.W. *et al.*, 2010).

Characterization of drying under different stack thicknesses

When the temperature was 45°C, the wind speed was 7.5 m/s, the conveyor turning angle was 0°, and the conveyor belt speed was 0.01 m/s, dynamic drying characteristic curves for alfalfa at various stacking thicknesses were obtained, as depicted in Figure 5. Under dynamic drying conditions, stacking thickness significantly affected the dry-base moisture content of the alfalfa (figure 5c). Smaller stacking thickness led to a more pronounced decrease in moisture content and a faster temperature increase (figure 5b). This was due to the easy access of hot air into the spaces between alfalfa particles during dynamic drying, promoting efficient heat exchange and timely moisture removal, thus accelerating internal moisture migration and diffusion within the alfalfa. Moreover, higher stacking thickness (13 cm and 16 cm) increased alfalfa density per unit area, impacting the entry of hot air into interstitial spaces between the alfalfa particles for heat exchange.

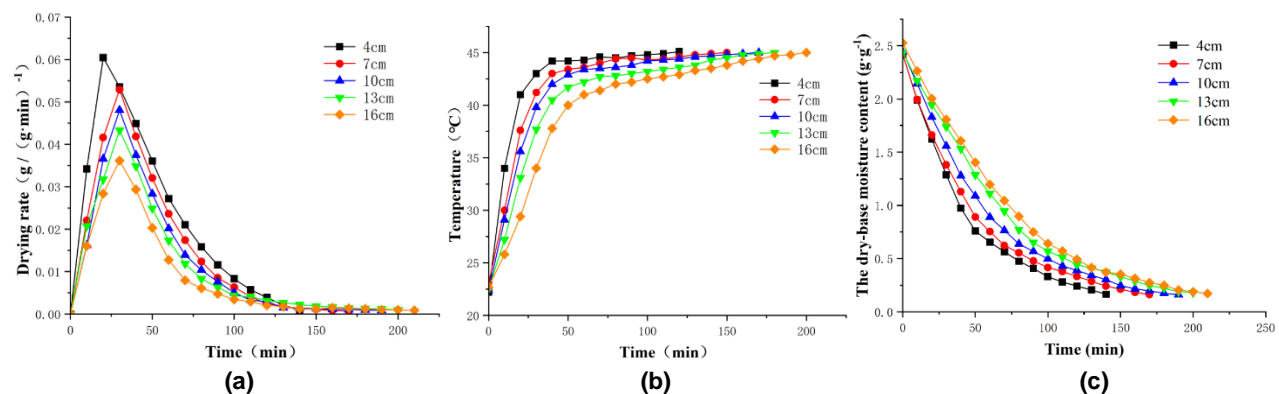


Fig. 5 - (a) Effect of stack thickness on drying rate; (b) Effect of stack thickness on the warming of alfalfa; (c) Effect of stack thickness on water content

Additionally, stacking thickness had a differential impact on alfalfa's drying rate (figure 5a). A smaller stacking thickness resulted in a higher maximum drying rate and shorter drying time. This reaffirms that even under dynamic drying conditions, thin-layer alfalfa drying offers the advantage of a faster drying rate, a similar conclusion to that obtained under static drying conditions (Hu Y.Q. *et al.*, 2022). As stacking thickness decreased, the alfalfa's absorption rate of thermal energy increased under continuous hot air action, leading to an accelerated drying rate. Conversely, as stacking thickness increased, the alfalfa's drying rate gradually declined. This was because as stacking thickness gradually reached the maximum inside the drying chamber, the removal of moisture content per unit time had already peaked (Kamruzzaman M *et al.*, 2010).

Analysis of drying characteristics under different deflection angles of rotary frame

Under the conditions of a temperature of 60°C, an alfalfa stacking thickness of 7 cm, a wind speed of 7.5 m/s, and a conveyor belt speed of 0.01 m/s, drying characteristic curves for alfalfa at different turning angles of the conveyor were obtained, as shown in Figure 6.

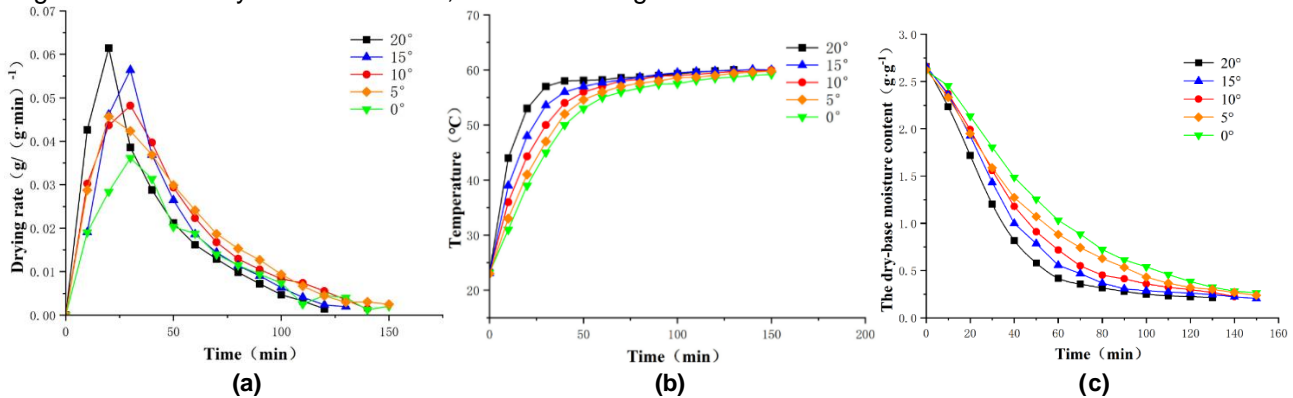


Fig. 6 - (a) Effect of deflection angle on drying rate; (b) Effect of deflection angle on alfalfa warming; (c) Effect of deflection angle on water content

In the initial stage of alfalfa drying, different turning angles had a significant impact on the drying rate, temperature increase, and moisture content change of the alfalfa. Furthermore, a larger turning angle of the spinner rack resulted in a greater tilt angle between the direction of alfalfa placement on the conveyor and the flow direction of the hot air. This led to a more pronounced drying effect of the hot air on the surface moisture of the alfalfa, causing rapid loss of free water from the alfalfa surface and a higher drying rate in the initial drying stage (figure 6a). As a result, the alfalfa temperature rose rapidly (figure 6b), and the dry-base moisture content decreased quickly (figure 6c). After entering the deceleration drying stage, the differences in drying characteristic parameters caused by different turning angles gradually diminished, and the drying rate, temperature, and dry basis moisture content of the alfalfa essentially reached consistency at the same drying time. It is therefore concluded that the different turning angles of the conveyor do not affect the time it takes for the alfalfa to dry to a safe moisture content.

Analysis of drying characteristics under different conveyor belt moving speeds

Compared to static drying, the movement of the conveyor belt can optimize airflow positioning during the drying process, thereby improving drying efficiency. However, a faster conveyor belt speed is not necessarily better. When the temperature was 65°C, the stacking thickness was 10 cm, the wind speed was 7.5 m/s, and the turning angle of the spinner rack was 0°, drying characteristic curves for alfalfa at different conveyor belt speeds were obtained (Figure 7).

It's evident that varying conveyor belt speeds resulted in significant differences in drying rate, temperature, and moisture content patterns over time. A slower conveyor belt speed led to a faster increase in the drying rate during the acceleration drying stage, with a higher maximum value. In the deceleration drying stage, the time required for alfalfa to reach a safe moisture content was shorter. This suggests that a slower conveyor belt speed allowed for more thorough contact between the hot air medium and the alfalfa, enhancing heat and mass transfer effects and thus improving drying efficiency and quality. For instance, at a conveyor belt speed of 0.16 m/s, the drying time required for alfalfa to reach a safe moisture content was 128 minutes (figure 7c), whereas at a speed of 0.01 m/s, the drying time was only 80 minutes (figure 7c), reducing the drying time by 37.5%. It's worth noting that at a conveyor belt speed of 0.16 m/s, the belt was prone to vibration, leading to the shedding of alfalfa leaves during the experiment.

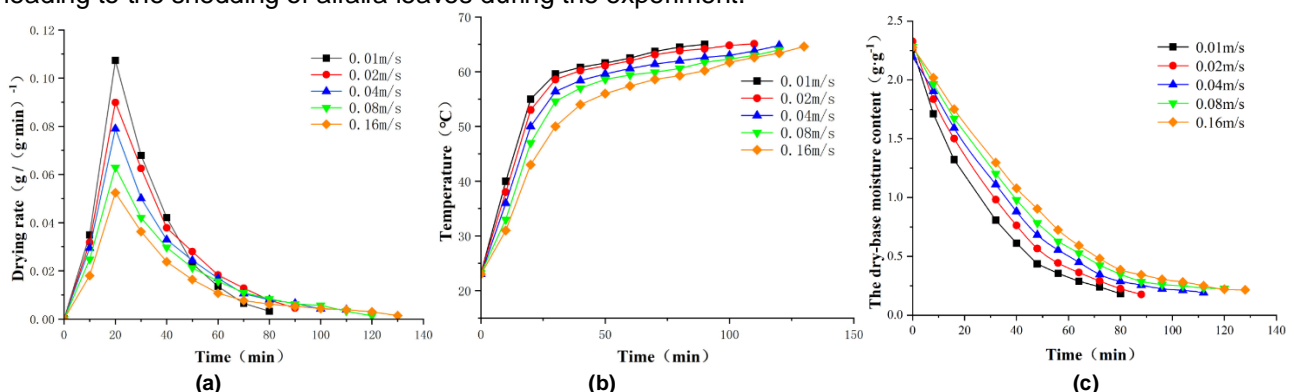


Fig. 7 - (a) Effect of conveyor speed on drying rate; (b) Effect of conveyor speed on alfalfa warming; (c) Effect of conveyor speed on moisture content

Model fitting of drying curves

To further analyse the drying characteristics of alfalfa under dynamic drying conditions and predict the moisture change during the drying process, four drying models were non-linearly fitted. The R^2 , χ^2 , $RMSE$ values of the four drying mathematical models obtained are shown in Table 2. It can be observed that the R^2 values of the fitted curves for all four models are greater than 0.97, and the χ^2 and $RMSE$ values are less than 0.003 and 0.034, respectively. Among them, the Logarithmic model has the best fitting effect, with an R^2 value exceeding 0.994, and the lowest χ^2 and $RMSE$ values among the four models. Therefore, the Logarithmic model can effectively describe the moisture change pattern of alfalfa during dynamic drying, well predict the moisture content of alfalfa at a certain moment, and analyse its moisture migration trend.

Table 2

Model parameters and Statistical analysis result of drying kinetic models

| Models | R^2 | χ^2 | $RMSE$ |
|----------------------------|---------|----------|---------|
| Page | 0.98368 | 0.00159 | 0.02738 |
| Logarithmic | 0.99454 | 0.00140 | 0.01479 |
| Two-term model | 0.98109 | 0.00297 | 0.03160 |
| Approximation of diffusion | 0.97988 | 0.00186 | 0.03334 |

Table 3

Logarithmic Model fitting results

| Drying condition | Parameters | | |
|------------------|------------|---------|----------|
| | a | k | c |
| 7.5 m/s | 0.9987 | 0.02874 | 0.06091 |
| 6.0 m/s | 0.9422 | 0.02656 | 0.07113 |
| 4.5 m/s | 1.0138 | 0.01736 | 0.03301 |
| 3.0 m/s | 0.9572 | 0.02085 | 0.07783 |
| 1.5 m/s | 0.9807 | 0.01767 | 0.06281 |
| 45 °C | 0.9767 | 0.01684 | 0.08089 |
| 50 °C | 1.0772 | 0.01481 | 0.01169 |
| 55 °C | 1.0109 | 0.01879 | 0.04810 |
| 60 °C | 0.9658 | 0.02217 | 0.06770 |
| 65 °C | 1.0051 | 0.03098 | 0.05742 |
| 4 cm | 0.9460 | 0.03384 | 0.07109 |
| 7 cm | 0.9870 | 0.01901 | 0.05898 |
| 10 cm | 0.9293 | 0.01918 | 0.10794 |
| 13 cm | 0.9701 | 0.01721 | 0.11071 |
| 16 cm | 0.9961 | 0.01302 | 0.08722 |
| 0° | 1.0098 | 0.01883 | 0.05204 |
| 5° | 0.9799 | 0.02215 | 0.06010 |
| 10° | 1.0275 | 0.02858 | 0.04556 |
| 15° | 1.1063 | 0.02299 | -0.00872 |
| 20° | 1.014 | 0.03175 | 0.04079 |
| 0.01m/s | 1.0755 | 0.01843 | -0.04009 |
| 0.02m/s | 1.0574 | 0.01990 | -0.01417 |
| 0.04m/s | 1.0574 | 0.02269 | -0.02646 |
| 0.08m/s | 1.2723 | 0.01836 | -0.22371 |
| 0.16m/s | 1.0738 | 0.03294 | -0.01281 |

The Logarithmic model fitting results obtained are shown in Table 3. To analyse the relationship between the model parameters (a , k , c) and the experimental factors, including drying air velocity, drying temperature, stacking thickness of alfalfa, turning angle of the spinner rack, and conveyor belt speed, the regression equations of Logarithmic model parameters are obtained using multivariate statistical analysis:

$$a = 0.708 + 0.004T + 0.005V + 0.005M + 0.002N + 0.678V_m \tag{12}$$

$$k = 0.022 + 0.000063T + 0.001042V - 0.001378M + 0.000205N + 0.061296V_m \tag{13}$$

$$c = 0.326 - 0.004431T - 0.004333V - 0.000091M + 0.000553N - 0.634629V_m \tag{14}$$

where: T is the drying temperature in °C, V is the drying air velocity in m/s, M is the stacking thickness in cm, N is the turning angle of the spinner rack in °, and V_m is the moving speed of the conveyor belt in m/s.

From the above expression, it can be seen that the drying air velocity, drying temperature, stacking thickness of alfalfa, turning angle of the spinner rack, and conveyor belt speed all have an impact on the model parameters a , k , and c . By substituting the expressions 12-14 into the Logarithmic equation, the predicted model for the moisture content of alfalfa can be obtained, as shown in expression 15.

The prediction of alfalfa moisture content during dynamic drying can be carried out based on the experimental conditions.

$$MR = (0.708 + 0.004T + 0.005V + 0.005M + 0.002N + 0.678V_m) \exp[-(0.022 + 0.000063T + 0.001042V - 0.001378M + 0.000205N + 0.061296V_m) \cdot t] + (0.326 - 0.004431T - 0.004333V - 0.000091M + 0.000553N - 0.634629V_m) \tag{15}$$

Validation of Logarithmic model

To verify the accuracy of the model, experimental conditions were set as follows: hot air velocity of 7.5 m/s, hot air temperature of 55°C, stacking thickness of 7 cm, turning angle of the spinner rack at 0°, and conveyor belt speed at 0.01 m/s. A comparison of the experimental values and the model-predicted values was conducted, and the results are shown in Figure 8. The fitting accuracy between the experimental and predicted values is high ($R^2 > 0.998$), confirming that the Logarithmic model can effectively describe the moisture change pattern of alfalfa during the drying process.

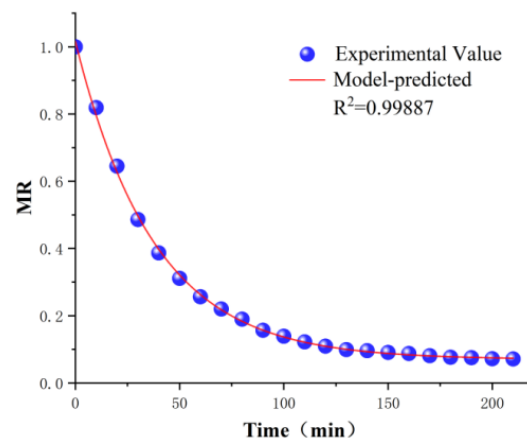


Fig. 8 - Validation of Logarithmic model

Moisture Diffusivity

From the drying rate curves under different conditions, it can be observed that alfalfa drying under solar energy-heat pump drying mainly occurred during the deceleration drying stage. During this stage, resistance controlled the mass transfer process, and moisture transfer during the drying process was influenced by diffusion. The effective moisture diffusivity during dynamic drying was calculated, as shown in Table 4.

Table 4

| Effective diffusivity for alfalfa under different drying | | | | | | |
|--|-----------------------|-------------------------|---------------|----------------|---|--|
| Temperature [°C] | Air velocity [m/s] | Stack thickness [cm] | Angles [°] | Speed [m/s] | D_{eff} [m ² ·s ⁻¹] | |
| 45 | 7.5 | 10 | 0 | 0.01 | 1.9323×10 ⁻⁹ | |
| 50 | 7.5 | 10 | 0 | 0.01 | 2.1499×10 ⁻⁹ | |
| 55 | 7.5 | 10 | 0 | 0.01 | 2.2533×10 ⁻⁹ | |
| 60 | 7.5 | 10 | 0 | 0.01 | 2.4180×10 ⁻⁹ | |
| 65 | 7.5 | 10 | 0 | 0.01 | 3.1067×10 ⁻⁹ | |
| 55 | 1.5 | 7 | 0 | 0.01 | 1.0049×10 ⁻⁹ | |
| 55 | 3.0 | 7 | 0 | 0.01 | 1.2849×10 ⁻⁹ | |
| 55 | 4.5 | 7 | 0 | 0.01 | 1.5604×10 ⁻⁹ | |
| 55 | 6.0 | 7 | 0 | 0.01 | 1.6155×10 ⁻⁹ | |
| 55 | 7.5 | 7 | 0 | 0.01 | 1.7466×10 ⁻⁹ | |
| 45 | 7.5 | 4 | 0 | 0.01 | 4.7324×10 ⁻⁹ | |
| 45 | 7.5 | 7 | 0 | 0.01 | 4.4360×10 ⁻⁹ | |
| 45 | 7.5 | 10 | 0 | 0.01 | 2.8720×10 ⁻⁹ | |
| 45 | 7.5 | 13 | 0 | 0.01 | 1.0524×10 ⁻⁹ | |
| 45 | 7.5 | 16 | 0 | 0.01 | 2.7760×10 ⁻¹⁰ | |
| 60 | 7.5 | 7 | 0 | 0.01 | 1.0391×10 ⁻⁹ | |
| 60 | 7.5 | 7 | 5 | 0.01 | 1.2978×10 ⁻⁹ | |
| 60 | 7.5 | 7 | 10 | 0.01 | 1.3683×10 ⁻⁹ | |

| Temperature [°C] | Air velocity [m/s] | Stack thickness [cm] | Angles [°] | Speed [m/s] | D_{eff} [m ² ·s ⁻¹] |
|---------------------|-----------------------|-------------------------|---------------|----------------|---|
| 60 | 7.5 | 7 | 15 | 0.01 | 1.3976×10 ⁻⁹ |
| 60 | 7.5 | 7 | 20 | 0.01 | 1.4464×10 ⁻⁹ |
| 65 | 7.5 | 10 | 0 | 0.01 | 2.3254×10 ⁻⁹ |
| 65 | 7.5 | 10 | 0 | 0.02 | 2.3021×10 ⁻⁹ |
| 65 | 7.5 | 10 | 0 | 0.04 | 2.2808×10 ⁻⁹ |
| 65 | 7.5 | 10 | 0 | 0.08 | 2.2744×10 ⁻⁹ |
| 65 | 7.5 | 10 | 0 | 0.16 | 2.1847×10 ⁻⁹ |

The effective moisture diffusivity of alfalfa ranged from 2.776×10^{-10} to 4.7324×10^{-9} m²/s. This result is similar to the range of effective moisture diffusivity reported by Madamba (*Madamba P.S. et al., 1996*), which is $10^{-12} \sim 10^{-8}$ m²/s for drying materials. The results in Table 4 demonstrate that the effective moisture diffusivity increases with higher air velocity, as it accelerates the heat exchange between the moisture in alfalfa and the air, leading to an increase in effective moisture diffusivity. The effective moisture diffusivity increased with temperature. This was because the heightened temperature within the drying chamber increased the energy of water molecules, resulting in a faster transition frequency and accelerated moisture transfer to the material surface. This further enhanced the efficiency of heat and mass transfer, ultimately leading to an increase in effective moisture diffusivity. Moreover, an increase in stacking thickness lengthened the distance for bound water evaporation within the alfalfa, leading to greater resistance to moisture migration and a decrease in effective moisture diffusivity.

An increase in the turning angle of the spinner rack also led to an increase in effective moisture diffusivity. This was because with a larger turning angle, the alfalfa experienced greater impact from the hot air, making it easier for the hot air to pass through the alfalfa layer and carry away moisture, thereby accelerating the migration of moisture in the alfalfa. Additionally, a decrease in conveyor belt speed increased effective moisture diffusivity. This was because a slower speed allowed the hot air to more easily penetrate the internal gaps of the alfalfa layer, causing rapid evaporation of surface moisture. When the surface moisture concentration was lower than the internal moisture concentration, a concentration gradient was formed, thereby reducing the resistance to moisture diffusion and increasing effective moisture diffusivity. In summary, variations in the levels of the various experimental factors impacted the effective moisture diffusivity during alfalfa drying. Therefore, in practical processing, reasonable process parameters can be selected based on production needs and the above results to improve the efficiency and effectiveness of alfalfa drying.

Activation energy

The slope of the $\ln(D_{eff})$ versus $1/(T+273.15)$ curve obtained from Figure 9 allows for the calculation of the activation energy E_a of alfalfa.

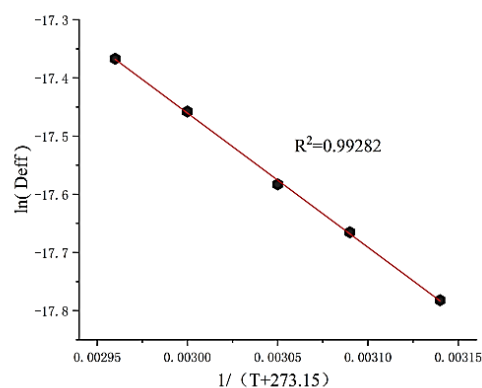


Fig. 9 - The relationship between change of $\ln(D_{eff})$ and $1/(T+273.15)$

The calculated activation energy is 37.02 kJ/mol when the air velocity is 7.5 m/s, the stacking thickness is 10 cm, the turning angle of the spinner rack is 0°, and the conveyor belt speed is 0.01 m/s. This indicates that at least 37.02 kJ of energy is required to remove 1 mole of water during the dynamic drying process. This value is lower than the activation energy of 38.34 kJ/mol obtained for lemongrass by Thi Van Linh Ngu-yen (*Nguyen T et al., 2019*).

Additionally, based on the research results of Azeez (Azeez L et al., 2017), the activation energy of agricultural materials generally falls within the range of 12.7~110 kJ/mol. Therefore, it can be concluded that under the conditions of solar-heat pump combined drying, the difficulty level of dynamically drying alfalfa is moderate, similar to that of drying other agricultural materials.

The activation energy of alfalfa falls within the normal range, indicating the feasibility of the drying method adopted for alfalfa in this study. In practical processing, adjustments can be made to the process parameters such as stacking thickness and particle size of alfalfa to further reduce the activation energy and enhance the effective moisture diffusivity.

CONCLUSIONS

In this study, a dynamic drying test platform is constructed under the conditions of solar-heat pump combined drying. The dynamic drying characteristics of alfalfa are studied by considering factors such as hot air velocity, temperature, alfalfa stacking thickness, turning angle of the spinner rack, and conveyor belt speed. The drying characteristic curves obtained show that the drying rate of alfalfa exhibits an increasing and then decreasing trend, without a constant speed drying stage. The drying process mainly occurs in the deceleration drying stage. During this stage, the moisture content of alfalfa continuously decreases, and the decreasing rate shows a pattern of initially fast and then slow decline. The temperature also corresponds to a pattern of rapid increase followed by a tendency to stabilize.

The analysis of the influence of various experimental factors on the drying characteristic curves reveals the following trends: Higher air velocity accelerates the temperature increase and drying rate of alfalfa, reducing the time to reach the safe moisture content level. Moreover, elevated drying temperatures enhance heat absorption by the alfalfa, leading to faster temperature rise and higher drying rates, resulting in a swifter decrease in moisture content. Furthermore, a smaller stacking thickness prompts a quicker temperature increase, faster drying rates, and a more rapid decrease in moisture content during dynamic drying. Additionally, a greater turning angle of the spinner rack initiates a faster initial decrease in moisture content, accelerated temperature rise, and quicker drying rates for alfalfa. However, the impact of the turning angle diminishes during the deceleration drying stage, exerting minimal influence on the total time for alfalfa to reach the safe moisture content level. A slower conveyor belt speed leads to a quicker increase in drying rate and a shorter time to reach the safe moisture content level.

Comparison and regression analysis of drying models show that the Logarithmic model is the optimal model for describing the moisture change during dynamic drying of alfalfa, with a fitting determination coefficient R^2 being greater than 0.994, and χ^2 and $RMSE$ being both less than 0.003 and 0.034, respectively. Multivariate statistical regression analysis of the model parameters a, k, and c reveals that each experimental factor has an impact on the model parameters. A predictive model for moisture content during dynamic drying of alfalfa is developed and validated. Additionally, calculations indicate that the effective moisture diffusivity of alfalfa ranges from $2.776 \times 10^{-10} \text{m}^2/\text{s}$ to $4.7324 \times 10^{-9} \text{m}^2/\text{s}$, with an activation energy of 37.02 kJ. These results suggest that under solar energy-heat pump combined drying conditions, the difficulty of dynamic drying of alfalfa is moderate. Furthermore, process parameters can be adjusted according to production requirements to further improve drying efficiency and effect.

ACKNOWLEDGEMENT

This study was supported by the National Natural Science Foundation of China (Funding No.32360852). Inner Mongolia Science and Technology Project (Funding No.2022YFDZ0032 and 2022YFDZ0022). Inner Mongolia Natural Science Foundation (Funding No.2023LHMS03004).

REFERENCES

- [1] Al-Hamdani A., Jayasuriya H., Pathare P. B., Al-Attabi Z., (2022), Drying Characteristics and Quality Analysis of Medicinal Herbs Dried by an Indirect Solar Dryer. *Food Science*, vol.11, no. 24, Oman.
- [2] Azeez, L., Adebisi, S. A., Oyedeji, A. O., (2017). Bioactive compounds' contents, drying kinetics and mathematical modelling of tomato slices influenced by drying temperatures and time. *Journal of the Saudi Society of Agricultural Sciences*, Nigeria.
- [3] Cowen, A. A., Abu-Ghannam N., Frias J., (2008). Modeling dehydration and rehydration of cooked soybeans subjected to combined microwave-hot-air drying[J]. *Innovative Food Science & Emerging Technologies*, vol. 9, no. 1, pp. 129-137, Ireland.

- [4] Ding, C. J., Yang, M. S., (2017), Drying Characteristics and Mathematical Models of Chinese Wolfberry in DC High Voltage Electric Field (直流高压电场中枸杞的干燥特性与数学模型研究). *Transactions of the Chinese Society for Agricultural Machinery*, vol. 48, no. 6, pp. 302-311, Huhhot/China.
- [5] Hu, Y. Q., Fan, Y., Yang, L. W., (2022). Study on thin layer drying characteristics and color and quality of alfalfa (苜蓿薄层干燥特性及颜色和品质). *Pratacultural Science*, vol. 39, no. 9, pp. 1861-1868, Shanghai/China.
- [6] Kamruzzaman, M., Islam, M. N. (2010). Kinetics of Dehydration of Aroids and Developed Dehydrated Aroids Products. *Journal of Chemical Engineering*, vol. 24, no. 19, Bangladesh.
- [7] Liu, Y. H., Li, X. F., Miao, S., (2016). Drying Characteristics of Apple Slices during Contact Ultrasound Reinforced Heat Pump Drying(南瓜片超声-远红外辐射干燥特性及微观结构). *Transactions of the Chinese Society for Agricultural Machinery*, vol. 47, no. 2, pp. 228-236, Henan/Cina.
- [8] Li, Y.Y., Che, G., Wan, L., (2020), Experimental research on the process of radon hot air drying based on visual recognition(基于视觉识别的苜蓿远红外热风干燥工艺试验研究). *Journal of Chinese Agricultural Mechanization*, vol. 41, no. 1, pp. 83-88, Heilongjiang/China.
- [9] Luo, S. H., Liu, F. Y., Yan, W. D., Wang, W. H., (2019), *Scale-up low-loss alfalfa hay production modification method. Patent*, NO.CN201910722727. 3, China.
- [10] Liu, Y. H., Li, X. F., Miao, S., (2016). Drying Characteristics of Apple Slices during Contact Ultrasound Reinforced Heat Pump Drying(南瓜片超声-远红外辐射干燥特性及微观结构). *Transactions of the Chinese Society for Agricultural Machinery*, vol. 47, no. 2, pp. 228-236, Henan/Cina.
- [11] Madamba, P. S., Driscoll, R. H., Buckle, K. A., (1996). The thin-layer drying characteristics of garlic slices. *Journal of Food Engineering*, vol. 29, no. 1, pp. 75-97, Philippines.
- [12] Nguyen, T., Nguyen, M., Nguyen, D., (2019). Model for Thin Layer Drying of Lemongrass (*Cymbopogon citratus*) by Hot Air. *Processes*, vol. 7, no. 1, Ho Chi Minh City /Vietnam.
- [13] Onwude, D. I., Hashim, N., Janius, R. B., (2016). Modeling the thin-layer drying of fruits and vegetables: A review. *Comprehensive reviews in food science and food safety*, vol. 15, no. 3, pp. 599-618, Malaysia.
- [14] Qian, W., Yang, S.K., Liu, G.L., (2018). Optimization of Drying Process Parameters of Solar Herbage Dry Equipment (太阳能牧草干燥成套设备干燥工艺参数优化). *Transactions of the Chinese Society for Agricultural Machinery*, vol. 49, no. 8, pp. 110-118, Huhhot/China.
- [15] Singh, P.L., (2011). Silk cocoon drying in forced convection type solar dryer [J]. *Applied Energy*, vol. 88, no. 5, pp. 1720-1726, India.
- [16] Simal, S., Deya, E., Frau, M., (1997), Simple Modelling of Air Drying Curves of Fresh and Osmotically Pre-dehydrated Apple Cubes. *Journal of Food Engineering*, vol. 33, pp. 139-150, Spain.
- [17] Shi, Q. L., Zheng, Y. Q., Zhao, Y., (2013), Mathematical modeling on thin-layer heat pump drying of vacon (*Smallanthus sonchifolius*) slices. *Energy Conversion & Management*, vol. 71, pp. 208-216, Shandong/China.
- [18] Sun, Q. Y., Yu, Q. N., Jia, Z. C., (2022), Research Progress of Forage Drying Technology and Equipment (牧草干燥技术与装备研究进展), *Acta Agrestia Sinica*, vol. 30, no. 1, pp. 1-11, Shandong/China.
- [19] Wang, Q. X., Wang, D. C., Du, J. Q., (2012), Design and Experiment of Heat Pump Assisted Solar Energy Heat-storage Drying Equipment for Herbage Seed (牧草种子热泵辅助型太阳能储热干燥设备与试验). *Transactions of the Chinese Society for Agricultural Machinery*, vol. 43, pp. 222-226.
- [20] Xiao, H. W., Gao, Z. J., Lin, H., (2010). Air impingement drying characteristics and quality of carrot cubes. *Journal of Food Process Engineering*, vol. 33, no. 5, pp. 899-918, Beijing/China.

EFFICIENCY ANALYSIS AND EVALUATION OF VARIABLE FERTILIZER SPREADING BASED ON REALTIME SPECTRAL INFORMATION ON WHEAT

基于实时光谱信息的小麦变量施肥效率分析与评价

Man CHEN¹⁾, Zhichang CHANG¹⁾, Chengqian JIN^{1*)}, Yinyan SHI^{2*)}

¹⁾ Nanjing Institute of Agricultural Mechanization, Ministry of Agriculture and Rural Affairs, Nanjing, Jiangsu / China;

²⁾ College of Engineering, Nanjing Agricultural University, Nanjing, Jiangsu / China;

Tel: +8602584346113; E-mail: jinchengqian@126.com; shiyinyan@njau.edu.cn

DOI: <https://doi.org/10.35633/inmateh-73-49>

Keywords: Wheat; Variable fertilization; Spectral information; Economic benefits

ABSTRACT

Studying the effect of variable fertilization during the elongation stage on winter wheat production in the rice-wheat rotation area is critical for evaluating the application effect and economic benefits of variable fertilization technology. The variable fertilization experiment of wheat was carried out in Jiangsu province by using the self-developed fertilizer applicator. Three fertilization methods were used to conduct a comparative analysis of the fertilization amount, population structure, and yield of winter wheat during the elongation stage. On this basis, the economic feasibility of variable fertilization during the elongation stage was evaluated. The experimental results showed that the control accuracy of variable-rate fertilization with fertilization equipment was greater than 95%. After variable fertilization, the coefficient of variation of Normalized Difference Vegetation Index (NDVI) values in the winter wheat crop canopy spectral data remained between 0.076 and 0.125, and the Christensen uniformity coefficient remained between 0.901 and 0.940. Compared with the traditional empirical balance method for quantitative fertilization of plots, the real-time variable fertilization plot used 13.6 kg/ha less fertilizer during the elongation stage. The findings validate that implementing variable fertilization can help reduce nitrogen fertilizer input, improve nitrogen fertilizer utilization efficiency, reduce environmental pollution, and enhance the sustainability of agricultural production.

摘要

本研究以小麦品种杨麦 25 为研究对象, 对自行研制的基于冬小麦生长实时信息的变量施肥机进行了研究。在江苏金坛小麦种植基地进行了不同施肥模式的田间试验。比较分析了 3 种施肥方式冬小麦的拔节期施肥量、群体结构和产量。在此基础上, 对拔节期变量施肥经济性进行了评价。试验结果表明, 施肥装备变量施肥的控制精度均大于 95%。变量施肥后冬小麦冠层光谱数据 NDVI 值变异系数保持在 0.076 ~ 0.125 之间, 克里斯琴森均匀系数保持在 0.901 ~ 0.940 之间。相比于传统经验平衡法定量施肥地块, 实时变量施肥地块在拔节期少投入了 13.6 kg/ha 的肥料, 但是产量却提升了 436.3 kg/ha, 收益增加了 1213.6 元/ha。本研究可为在长江中下游稻麦轮作区推广变量施肥技术的试点应用提供理论参考。

INTRODUCTION

As one of the main grain crops in China, wheat ranks second only to rice in terms of planting area and total yield. As the main grain-producing area in southern China, Jiangsu mainly adopts the special planting and production method of rice-wheat rotation. The potential of grain yield is maximized through this method, and the comprehensive productivity of grain crops is also improved (Huang *et al.*, 2020).

Increasing nitrogen fertilizer application within a certain range can increase the yield and improve the quality of winter wheat. Fertilization during the elongation stage is not only beneficial for delaying the aging of winter wheat plants and improving grain yield but also for forming a reasonable population and balancing winter wheat yield. However, unreasonably increasing the application of chemical fertilizers has also caused serious problems in China, such as excessive application, an unreasonable application structure, and a low utilization rate of chemical fertilizers (Huang *et al.*, 2020).

Man Chen, Associate Prof. Ph.D. Eng.; Zhichang Chang, Stud. Eng.; Chengqian Jin, Prof. Ph.D. Eng.; Yinyan Shi, Associate Prof. Ph.D. Eng..

In China, the nitrogen fertilizer utilization rate is only 30–50% (Wu *et al.*, 2019). Excessive and unreasonable use of chemical fertilizers causes the waste of chemical fertilizers, reduces their utilization efficiency, and causes huge economic losses, as well as serious environmental pollution (e.g., water pollution and soil compaction) and even reduces the yield and quality of food (Sun *et al.*, 2019). Therefore, the rational and scientific application of fertilizers is crucial for the sustainable production of winter wheat.

Variable rate fertilization technology relies on modern advanced scientific and technological advancements. With a comprehensive understanding of field soil, crops, and environmental information, professionals can use the technology to perform fertilization operations in small areas according to quantity and demand. This approach meets the nutritional requirements of crops and also aids in achieving the goal of scientific and rational fertilization, improving fertilizer utilization efficiency, and balancing the environment and economic development (He *et al.*, 2023; Ma *et al.*, 2023). Research on this technology has produced significant social, economic, and environmental benefits. To achieve online detection of phosphorus fertilizer, Maleki *et al.* used visible light near-infrared sensors and designed variable-rate fertilization machinery for the precise application of a base fertilizer to winter wheat. The actual application of phosphorus fertilizer by the machinery was 28.75 kg/ha, which was 1.25 kg/ha less than the traditional application (Maleki *et al.*, 2008).

Xinwei *et al.* developed a wheat fertilization expert decision-making system and a remote precision control system on the basis of using the active remote sensing spectrometer Green Seeker to diagnose wheat nitrogen nutrition. The response time and precision of the fertilization decision-making system reached an average of 3.6 s and 3.62%, respectively, meeting the accuracy requirements of remote variable control fertilization (Li *et al.*, 2019). Furthermore, Jinbin *et al.* designed a variable-rate fertilizer applicator control system for a more efficient field-spray variable-rate fertilization operation and conducted an analysis and a test. The average error of the system's fertilizer flow fluctuated around 6% (Bai *et al.*, 2022). Similarly, to achieve positioning fertilization based on the root position of corn seedlings, Shuo *et al.* designed a motor-driven positioning fertilization control system. He proposed a threshold control algorithm, and the average response time of the system was 0–8 s (Zhao *et al.*, 2019). Similarly, to design a real-time variable-rate fertilizer applicator in the field, Man *et al.* used near-Earth spectroscopy detection technology, achieving variable-rate fertilization operations based on wheat growth. The precision of the fertilizer applicator's fertilizer control exceeded 90%, which can meet the requirements of precise fertilization (Chen *et al.*, 2015). The development of the abovementioned variable fertilization equipment provides technical support for the variable fertilization operation during the *elongation stage* of winter wheat.

Currently, two main forms of fertilization operations exist based on crop growth. One form aims to obtain the spectral data of crops within the plot through remote sensing technology, to analyze crop growth offline, and to generate prescription maps. Based on geographical location information and prescription maps, variable fertilization machines implement variable fertilization operations. The second is to rely on ground sensors, which measure the crop growth in the working area in real time according to the spectral sensor at the front end of the fertilization machine to calculate the target fertilization amount, thus guiding the variable fertilization control system to achieve variable fertilization operations. Regardless of the form used, a fertilization model based on crop spectral information is a prerequisite for achieving precise variable fertilization. Models based on the normalized difference vegetation index (NDVI) (Yu *et al.*, 2023), leaf area index (Zhang *et al.*, 2010), and nitrogen fertilizer optimization algorithm (Chen *et al.*, 2018) have been widely used in the variable fertilization of winter wheat. These models are all based on analyzing the differences in crop canopy spectral data in the work area, deducing the nutrients required for wheat production, and establishing precise variable decision-making models to achieve on-demand fertilizer supply within the plot.

This study focused on the Yangmai 25 wheat variety and used a self-developed variable fertilization machine based on the real-time growth of winter wheat for variable fertilization during the *elongation stage*. More specifically, this rice variety grows in the rice-wheat rotation area in the middle and lower reaches of the Yangtze River. Field experiments were conducted on increasing nitrogen fertilizer application during the winter wheat *elongation stage* in different areas with blank fertilization, traditional experience balanced fertilization, and real-time variable fertilization. These three fertilization methods were used to conduct a comparative analysis of the fertilization amount, population structure, and yield of winter wheat during the *elongation stage*. On this basis, the economic feasibility of variable-rate fertilization during the elongation stage was evaluated, providing a theoretical basis and reference for the promotion and application of precision agriculture variable-rate fertilization technology in rice-wheat rotation areas in Jiangsu. Meanwhile, this study will provide useful experience for green and sustainable production of winter wheat.

MATERIALS AND METHODS

Variable-rate fertilization system

In this study, to perform variable fertilization of winter wheat, the project team used a self-developed dual-channel-strip fertilization machine, with a width of 2 m and a spacing of 210 mm between fertilization rows. The fertilization equipment uses Green Seeker optical sensors as the monitoring mechanism for analyzing wheat nutrient requirements, the external groove wheel fertilizer applicator as the fertilizer discharge mechanism of the variable-rate fertilizer applicator, the electric motor as the driving power mechanism of the fertilizer discharge device, and the on-board computer, coordinator, and STM32 microcontroller to form the variable-rate fertilizer control execution mechanism, implementing online variable-rate fertilizer control of the variable-rate fertilizer applicator (Chen *et al.*, 2016). Fig. 1 shows the system's working principle.

In the process of variable fertilization, to obtain the normalized vegetation index of the wheat crop canopy, a spectral monitoring system first scans the wheat crop canopy, and the obtained data are transmitted to the vehicle control terminal. Next, the variable fertilization decision system is activated by the vehicle control terminal, the intelligent variable fertilization control program is executed to generate real-time target fertilization amount, and the target fertilization amount is transmitted to the STM32 controller. At the same time, the fertilization operation speed is monitored by the STM32 controller based on the GPS/BDS speed measurement system, the speed of the fertilizer applicator is monitored by the speed sensor, and the opening of the fertilizer applicator is monitored by the displacement sensor, thereby forming a closed-loop feedback control. Finally, the variable fertilization decision-making system guides the controller to adjust the real-time operation status of the motor based on the built-in algorithm, indirectly adjusting the opening and speed of the fertilizer feeder, thereby achieving online adjustment of the fertilization amount and achieving the goal of precise variable fertilization.

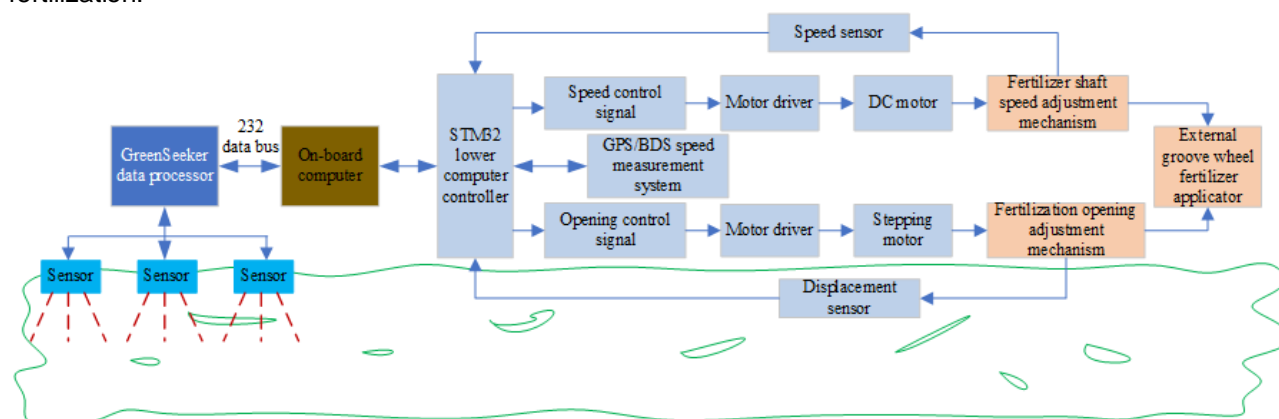


Fig. 1 – Real time measurement system for harvesting area.

Test conditions

The field experiment was conducted from November 2019 to June 2020 at the Shahu Agricultural Machinery Professional Cooperative Experimental Base in Zhulin Town, Jintan District, Changzhou City, Jiangsu (31° 73' N and 119° 47' E), using fertilizer in the winter wheat elongation stage. The test area is located in the Taihu Lake Basin of China. The terrain is mainly plain, with little topographic relief, and the altitude is between 10 and 60 m. The experimental area belongs to a subtropical monsoon climate with distinct four seasons, mild and humid climate, with an average annual temperature of around 15°C and abundant precipitation, with an annual precipitation of approximately 1,000 mm and an average annual sunshine of 2,000 h.

The experimental area has formed a two-crop cultivation system, with rice and wheat rotation as the main crop, and has achieved full mechanized production. The previous crop in this study was rice, and the current wheat variety was Yangmai 25. Wheat is mainly sown through mechanized drilling with a row spacing of 17–20 cm. The traditional experience balance method applies 600 kg/ha of compound fertilizer (total nutrient $\geq 45\%$; N:P₂O₆:K₂O = 25:12:8) to the base fertilizer, and during the elongation stage, 225 kg/ha of urea (total nitrogen $\geq 46.4\%$) is applied. Nitrogenous fertilizers are no longer applied during other stages.

Test settings

Based on the existing planting layout of the Shahu Agricultural Machinery Professional Cooperative Experimental Base, this study randomly selected nine experimental fields: three blank control plots (marked CK-01, CK-02, and CK-03); three quantitative fertilization plots using traditional empirical balance method

(marked FB-01, FB-02, and FB-03); and three real-time variable fertilization plots (marked FV-01, FV-02, and FV-03). Each experimental field adopts a unified management mode. On November 7, 2019, machine drilling was performed on each plot, and bottom fertilizer was applied. On March 11, 2020, top dressing during the jointing period was applied. On June 7, 2020, wheat was harvested using a harvester.

In all experimental areas, the base fertilizer was added with 600 kg/ha of compound fertilizer per the conventional empirical balanced fertilization method, as shown in Fig. 2(a). Fertilization during the green period was performed in different ways. Among them, the blank control area was not fertilized. The traditional experience balance method for quantitative fertilization of plots uses traditional precision fertilization machines for quantitative fertilization (225 kg/ha). A variable fertilization machine developed by the project team was used in the real-time variable fertilization plot to perform variable fertilization operations based on the real-time growth of winter wheat, as shown in Fig. 2(b). The speed of the fertilization operation should be controlled at around 1.2 m/s.

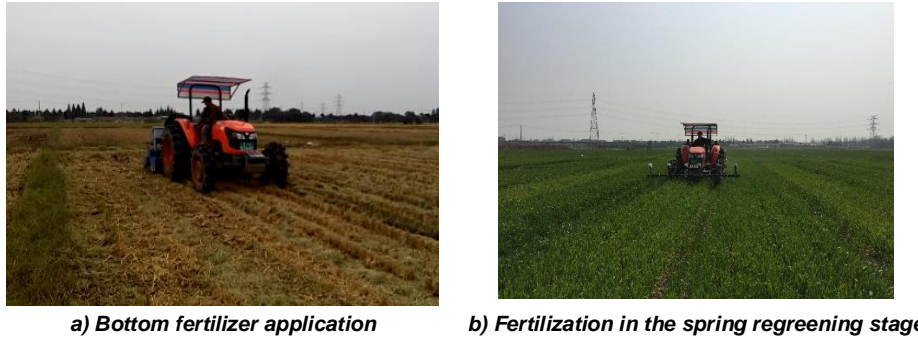


Fig. 2 – Fertilization of winter wheat

Test method

Based on the actual situation of winter wheat production in the Shahu Agricultural Machinery Professional Cooperative Experimental Base, a real-time target fertilization calculation model based on the NDVI value of winter wheat crop canopy was established (Yang *et al.*, 2015). The target fertilization calculation was as follows:

$$\Delta I_i = \frac{1.02}{1 + e^{-11.62(D_{above0}/D_{grow} - 0.25)}} \times I_{max} - I_i \quad (1)$$

$$\Delta M_i = \begin{cases} 10.213 + 2787.3\Delta I_i - 21171\Delta I_i^2 + 56776\Delta I_i^3 & \Delta I_i > 0.70 \\ 7.0405 + 1701.4\Delta I_i - 11435\Delta I_i^2 + 31065\Delta I_i^3 & 0.65 \leq \Delta I_i \leq 0.70 \text{ [kg/ha]} \\ 0.4502 + 1314.9\Delta I_i - 11148\Delta I_i^2 + 39654\Delta I_i^3 & \Delta I_i < 0.65 \end{cases} \quad (2)$$

$$M_{vi} = \Delta M_i + M_0 \text{ [kg/ha]} \quad (3)$$

$$M_v = \sum_{i=1}^n \frac{v \cdot L_{sf} \cdot T}{1000} M_{vi} \text{ [kg]} \quad (4)$$

where:

ΔI_i is the difference between the actual NDVI value of the wheat crop canopy at the i -th sampling time and the theoretical optimal value; D_{above0} refers to the number of days when the daily average temperature remains stable above 0°C from wheat sowing to spectral measurement; and D_{grow} is the total growth cycle of winter wheat. I_{max} is the maximum NDVI value of the winter wheat crop canopy in the experimental area; I_i is the NDVI value of the winter wheat crop canopy at the i -th sampling point. Furthermore, ΔM_i is the fertilizer deficiency of the experimental plot at the i -th sampling time, [kg/ha]; M_{vi} is the target fertilization amount within the i -th sampling time, [kg/ha]; M_0 is the traditional empirical balance method quantitative fertilization amount, [kg/ha]. Additionally, M_v is the target fertilization amount within the experimental plot, [kg]; v is the real-time speed of the top-dressing operation, [m/s]. L_{sf} is the effective width of fertilization, [m]. T is the sampling period of the fertilization system, [s], and n is the number of winter wheat crop canopy NDVI values collected in the experimental area.

ΔM_i is a positive value, indicating that wheat lacks fertilizer in the early stage and needs to be supplemented with nitrogen fertilizer, based on the traditional empirical balance method for quantitative fertilization. Excessive fertilization in the early stage of wheat is indicated by a negative value of ΔM_i , meaning that it is necessary to apply less nitrogen fertilizer, based on the traditional empirical balance method for quantitative fertilization.

According to the historical data of the experimental area, I_{\max} in this study was 0.732, M_0 was 225 kg/ha, L_{sf} was 2.0 m, T was 1.0 s, $D_{\text{above}0}$ was 116, D_{grow} was 225, and M_{vi} had a maximum value of 220 kg/ha and a minimum value of 0.

The actual fertilization amount for the real-time variable fertilization plot using the variable fertilization machine developed by the project team was calculated as follows:

$$M_c = M_{cb} - M_{ca} \quad [\text{kg}] \quad (5)$$

where:

M_c is the actual fertilization amount of the real-time variable fertilization plot, [kg]; M_{cb} is the mass of fertilizer loaded into the fertilization box before fertilization, [kg]; and M_{ca} is the remaining fertilizer mass in the fertilization box after fertilization, [kg].

The control accuracy of variable-rate fertilization was calculated as follows:

$$P_M = \left(1 - \frac{|M_c - M_{vi}|}{M_c}\right) \times 100\% \quad [\%] \quad (6)$$

where: P_M is the control accuracy of the real-time variable fertilization system, [%].

Spectral information of the winter wheat crop canopy was collected after 15 days of fertilization. Based on the distribution of NDVI values in the winter wheat crop canopy, the changes in winter wheat population structure after fertilization were analyzed along with the effectiveness of fertilization. To analyze the NDVI data of the winter wheat crop canopy, this study used the coefficient of variation and the Christiansen uniformity coefficient, as follows:

$$C_{ul} = 1 - \frac{\sum_{i=1}^n |I_i - \bar{I}|}{\sum_{i=1}^n I_i} \quad (7)$$

$$C_{vI} = \frac{\sqrt{\sum_{i=1}^n (I_i - \bar{I})^2 / n}}{\bar{I}} \quad (8)$$

$$\bar{I} = \frac{\sum_{i=1}^n I_i}{n} \quad (9)$$

where: C_{ul} is the Christiansen uniformity coefficient of NDVI in the winter wheat crop canopy; C_{vI} is the coefficient of variation of NDVI in the winter wheat crop canopy; I_i is the NDVI value of the winter wheat crop canopy at the i -th sampling point; \bar{I} is the mean NDVI value of the winter wheat crop canopy in the experimental area; and n is the number of winter wheat crop canopy NDVI values collected in the experimental area.

After the season's wheat matures, the five-point sampling method was used to manually collect and thresh the wheat, weigh it, and measure its yield. Through the coefficient of variation and the Christiansen uniformity coefficient, the uniformity of winter wheat yield within the plot was analyzed:

$$C_{uY} = 1 - \frac{\sum_{i=1}^n |Y_i - \bar{Y}|}{\sum_{i=1}^n Y_i} \quad (10)$$

$$C_{vY} = \frac{\sqrt{\sum_{i=1}^n (Y_i - \bar{Y})^2 / n}}{\bar{Y}} \quad (11)$$

$$\bar{Y} = \frac{\sum_{i=1}^n Y_i}{n} \quad (12)$$

where: C_{uY} is the Christiansen uniformity coefficient of yield within the winter wheat plot; C_{vY} is the coefficient of variation of yield within winter wheat plots; Y_i is the winter wheat yield at the i -th sampling point, [kg]; \bar{Y} is the average winter wheat yield in the experimental area, [kg]; and n is the number of sampling points for winter wheat yield in the experimental area, with a value of 5.

Afterward, a wheat combine harvester was used to harvest the wheat, and a weighbridge was used to finely measure the wheat yield in each experimental area.

Based on the area of each experimental plot, the yield was converted into hectare yield, as follows:

$$Y_c = \frac{Y_s}{S} \times 10000 \quad [\text{kg/ha}] \quad (13)$$

where:

Y_s is the actual yield of the experimental area, [kg]; Y_c is the converted yield per hectare of the experimental area, [kg/ha]; and S is the area of the real-time variable fertilization plot, [m²].

This study calculated the economic benefits of wheat top dressing in the experimental area on a hectare basis. The specific calculations were as follows:

$$P_r = P_{cw} \times Y_c - P_{cf} \times Y_{cf} \quad \text{[[yuan/ha]} \tag{14}$$

$$Y_{cf} = \frac{M_c}{S} \times 10000 \quad \text{[kg/ha]} \tag{15}$$

where: P_r is the profit per hectare of the experimental area, [yuan/ha]; Y_{cf} is the amount of fertilizer input per hectare in the experimental area, [kg/ha]; P_{cw} is the purchase price of current season wheat, [yuan/kg]; and P_{cm} is the price of urea for the current season, [yuan/kg]. In this study, the value of P_{cw} was 2.73 yuan/kg, and the value of P_{cf} was 1.645 yuan/kg.

Data analysis

The results were processed by Microsoft Office Excel (version 2021, Microsoft Corp., USA) and Matlab (version 2021a, MathWorks Corp., USA). Single factor analysis of variance (ANOVA) was carried out with IBM SPSS Statistics (version 24, IBM Corp., USA). The significance test was carried out by the Tukey test. The significance level was $p < 0.05$.

RESULTS

Analysis of variable-rate fertilization effect

In the early stage for fertilization operations, the variable fertilization machine developed by the project team was used in the variable fertilization experimental area, and Table 1 shows the fertilization amount results. The fertilization machine could calculate the target fertilization amount for each plot in real time based on the different growth of winter wheat, which was 57.14 kg, 55.43 kg, and 62.19 kg. According to the fertilizer requirements of different plots, 58.47 kg, 54.57 kg, and 63.83 kg of fertilizer were applied to the fertilization equipment. The control accuracy of variable-rate fertilization with fertilization equipment was greater than 95% in three fertilization experimental areas, with the optimal control accuracy reaching 98.42% and the lowest control accuracy reaching 97.43%. This indicates that the fertilization equipment has good variable system control performance and can ensure good system control accuracy.

Table 1

| Statistical data on fertilization amount in variable fertilization areas | | | | | |
|--|---------------|---------------|------------|------------|-----------|
| Plot | M_{cb} (kg) | M_{ca} (kg) | M_c (kg) | M_v (kg) | P_M (%) |
| FV-01 | 200 | 141.53 | 58.47 | 57.14 | 97.73 |
| FV-02 | 200 | 145.53 | 54.57 | 55.43 | 98.42 |
| FV-03 | 200 | 136.17 | 63.83 | 62.19 | 97.43 |

Analysis of wheat population growth structure

Figure 3 and Table 2 show the NDVI values of wheat crop canopy spectral data in each experimental area before and after the application of fertilizer in the winter wheat elongation stage.

Table 2

| Statistical data of wheat crop canopy spectral data in the experimental area | | | | | | | | | | |
|--|---------------------------------|-------|-------|----------|----------|--------------------------------|-------|-------|----------|----------|
| Plot | I_{df} (during fertilization) | | | | | I_{af} (after fertilization) | | | | |
| | Max. | Min. | Mean | C_{vi} | C_{ul} | Max. | Min. | Mean | C_{vi} | C_{ul} |
| CK-01 | 0.856 | 0.109 | 0.522 | 0.302 | 0.750 | 0.876 | 0.179 | 0.615 | 0.177 | 0.863 |
| CK-02 | 0.805 | 0.171 | 0.516 | 0.238 | 0.793 | 0.818 | 0.237 | 0.610 | 0.132 | 0.893 |
| CK-03 | 0.829 | 0.218 | 0.541 | 0.330 | 0.708 | 0.847 | 0.294 | 0.615 | 0.192 | 0.835 |
| FB-01 | 0.815 | 0.206 | 0.495 | 0.215 | 0.824 | 0.827 | 0.366 | 0.601 | 0.111 | 0.911 |
| FB-02 | 0.822 | 0.143 | 0.519 | 0.210 | 0.825 | 0.833 | 0.346 | 0.616 | 0.111 | 0.908 |
| FB-03 | 0.866 | 0.214 | 0.489 | 0.247 | 0.801 | 0.884 | 0.377 | 0.603 | 0.131 | 0.896 |

| Plot | I_{af} (during fertilization) | | | | | I_{af} (after fertilization) | | | | |
|-------|---------------------------------|-------|-------|----------|----------|--------------------------------|-------|-------|----------|----------|
| | Max. | Min. | Mean | C_{vi} | C_{ul} | Max. | Min. | Mean | C_{vi} | C_{ul} |
| FV-01 | 0.782 | 0.175 | 0.577 | 0.166 | 0.871 | 0.797 | 0.475 | 0.659 | 0.076 | 0.940 |
| FV-02 | 0.844 | 0.132 | 0.534 | 0.236 | 0.813 | 0.857 | 0.46 | 0.642 | 0.095 | 0.927 |
| FV-03 | 0.850 | 0.101 | 0.442 | 0.364 | 0.695 | 0.891 | 0.433 | 0.605 | 0.125 | 0.901 |

As shown in Fig. 4, the growth of winter wheat in each experimental area was uneven, and there were certain spatial differences in growth. The statistical data in Table 2 show that the maximum NDVI value of winter wheat crop canopy spectral data in the experimental area was 0.866 and that the minimum value was 0.101. This indicates that there are areas with good growth and areas with poor growth in the experimental area. The spatial differences in winter wheat growth are not considered in the traditional empirical balance method for quantitative fertilization, making it difficult to achieve on-demand fertilization. Based on the spectral data of winter wheat crop canopy, variable fertilization can be quantitatively applied according to the different growth conditions of winter wheat, which can further improve the utilization efficiency of fertilizers. Moreover, owing to the adoption of a unified production management method in the early stage, there was not much difference in wheat growth among different experimental intervals. The maximum and minimum NDVI values of winter wheat crop canopy spectral data in each experimental area were 0.577 and 0.442, respectively. The maximum and minimum coefficients of variation were 0.364 and 0.166, respectively. The maximum value of the Christensen uniformity coefficient was 0.871, and the minimum value was 0.695. Therefore, the data from each experimental area are universal and can objectively reflect the production situation of winter wheat in the region.

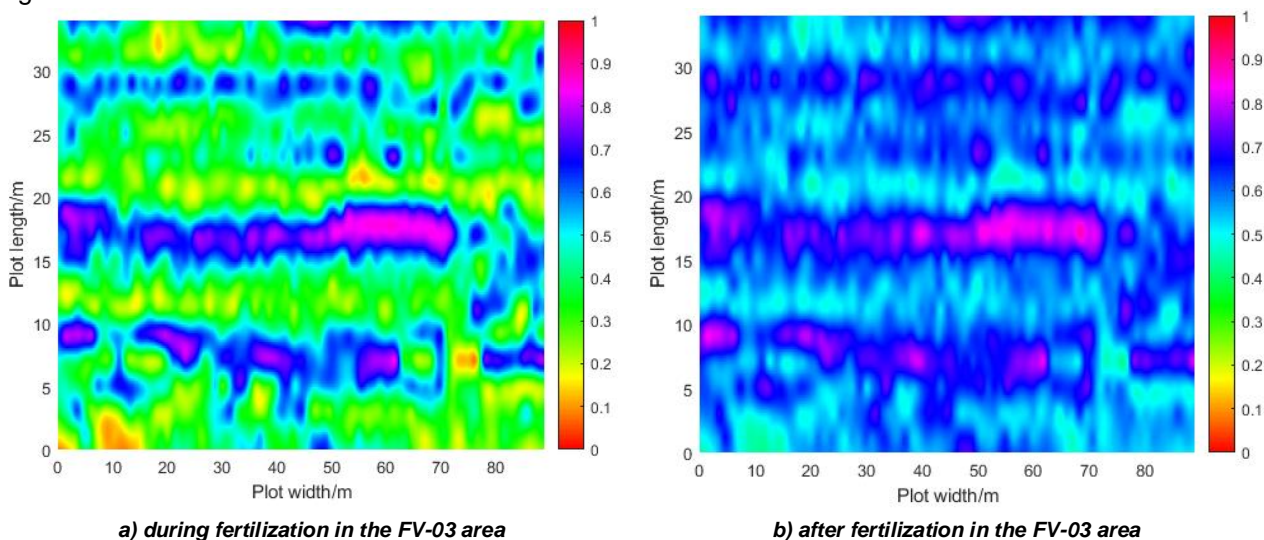


Fig. 3 – Visualization of wheat crop canopy spectral data before and after fertilization

As shown in Fig. 4 and Table 2, the spatial differences in winter wheat growth after the application of jointing fertilizer varied in each experimental area. No chemical fertilizer was applied during the jointing period in the blank control area, and the spatial differences of winter wheat in the planting area were not significantly improved. Among them, the NDVI coefficient of variation of winter wheat crop canopy spectral data in the CK-03 area decreased by 0.138, and the Christensen uniformity coefficient increased by 0.127, showing the best performance among all blank control areas. After the quantitative fertilization of 225 kg/ha urea during the elongation stage using the traditional experience balance method in the fertilization area, the spatial differences of winter wheat in the planting area were improved to a certain extent. Among them, the NDVI coefficient of variation of winter wheat crop canopy spectral data in the FB-03 area decreased by 0.116, and the Christensen uniformity coefficient increased by 0.095, showing the best performance among all traditional empirical balance method quantitative fertilization areas. In the real-time variable fertilization area, the spatial differences of winter wheat in the planting area were significantly improved after variable fertilization based on spectral data of the winter wheat crop canopy during the jointing period.

Among them, the NDVI coefficient of variation of winter wheat crop canopy spectral data in the FV-03 area decreased by 0.239, and the Christensen uniformity coefficient increased by 0.206, showing the best performance among all variable fertilization areas. These results indicate that variable fertilization can be applied according to the spatial differences in winter wheat growth, which effectively improves the population diversity of winter wheat in the planting area. Long-term excessive or insufficient fertilization can seriously damage the soil structure, exacerbate soil nutrient imbalance, and affect the overall growth and later yield of crops. In contrast, based on the actual growth of crops, reasonable variable fertilization and required inputs are beneficial for improving soil structure, balancing soil nutrients, and increasing crop growth and yield.

Field test result analysis

To further analyze the effect of different fertilization methods during the elongation stage on the production efficiency of winter wheat, a five-point sampling method was used to analyze the spatial differences in wheat yield among different plots in the experimental area.

Fig. 4(a) and (d) shows the yield data of each sampling point in the blank control plot. The maximum value of the yield at the sampling point was 0.685 kg, and the minimum value was 0.454 kg. The coefficient of variation between sampling points in each plot was 0.132, 0.126, and 0.134, and the Christensen uniformity coefficient was 0.894, 0.892, and 0.891.

Fig. 4(b) and (d) shows the yield data of each sampling point in the traditional empirical balance method for the quantitative fertilization of plots. The maximum value of yield at the sampling points was 0.710 kg, and the minimum value was 0.524 kg. The coefficient of variation between sampling points in each plot was 0.107, 0.109, and 0.099, and the Christensen uniformity coefficient was 0.905, 0.913, and 0.908.

Fig. 4(c) and (d) shows the yield data of each sampling point in the real-time variable fertilization plot. The maximum value of the yield at the sampling point was 0.722 kg, and the minimum value was 0.585 kg. The coefficient of variation between sampling points in each plot was 0.067, 0.058, and 0.058, and the Christensen uniformity coefficient was 0.938, 0.949, and 0.947.

The results showed that there was a significant spatial difference in yield among the blank control plots, followed by the traditional empirical balance method for quantitative fertilization plots, while the spatial difference in winter wheat yield among the real-time variable fertilization plots was relatively balanced. Thus, variable-rate fertilization improves the population structure of winter wheat growth, provides a good foundation for crop photosynthesis, and serves as a good framework platform for the ultimate high yield of winter wheat.

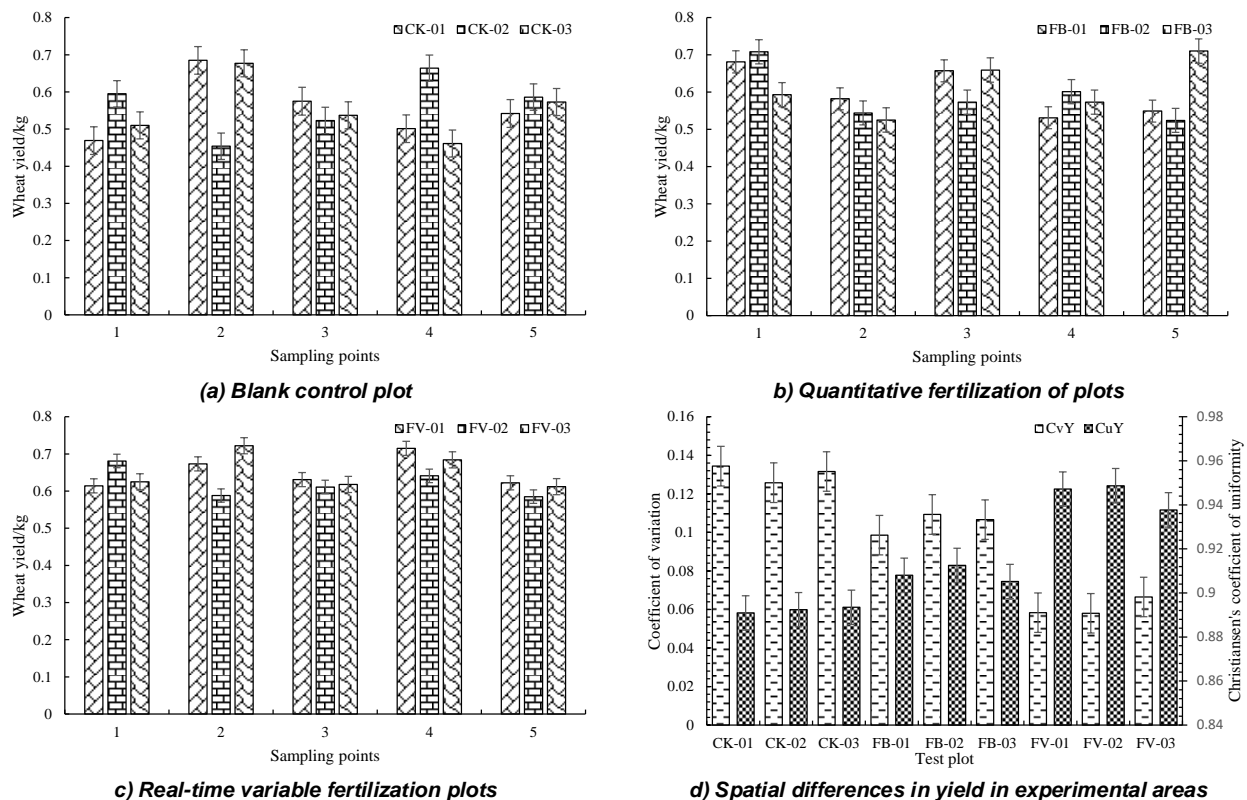


Fig. 4 – Sampling statistics of winter wheat yield in experimental plots

Analysis of economic benefits of fertilization during the elongation stage

In addition to the difference in fertilizer application during the elongation stage, a unified management model was adopted for winter wheat in each experimental area in this study. Therefore, it was assumed that the production management investment in each experimental area was consistent, so this paper only discusses the economic benefits of winter wheat caused by different fertilizer applications during the jointing period. Owing to the different areas of each experimental area, the measurement units were unified and the economic benefits of winter wheat on a per-hectare basis were evaluated, as shown in Table 3. The average winter wheat yield in the blank fertilized plot was 5,679.2 kg/ha, the fertilization amount during the elongation stage was 0, and the average profit was 15,504.1 yuan/ha. The average yield of winter wheat in the plot fertilized with the traditional empirical balance method was 6,060.5 kg/ha, the fertilization amount during the elongation stage was 225 kg/ha, and the average profit was 16,174.9 yuan/ha. The average winter wheat yield of the real-time variable fertilization plot was 6,496.8 kg/ha, the fertilization amount during the elongation stage was 211.4 kg/ha, and the average profit was 17,388.5 yuan/ha. From this, it can be seen that applying fertilizer during the elongation stage can effectively promote the winter wheat yield increase, increase yield by more than 381.3 kg/ha, and increase income by more than 670.8 yuan/ha. Compared with the traditional empirical balance method for the quantitative fertilization of plots, the real-time variable fertilization plot used 13.6 kg/ha less fertilizer during the elongation stage, but the yield increased by 436.3 kg/ha and the income increased by 1,213.6 yuan/ha. This indicates that implementing variable fertilization technology can effectively improve the economic benefits of winter wheat cultivation.

Table 3

Statistics for the intelligent measurement results in different job scenarios

| Plot | Length (m) | Width (m) | Ys (kg) | Yc (kg/ha) | Ycf (kg/ha) | Pr (yuan/ha) |
|-------|------------|-----------|---------|------------|-------------|--------------|
| CK-01 | 67 | 32 | 1253.0 | 5844.3 | 0 | 15,954.9 |
| CK-02 | 67 | 30 | 1114.0 | 5542.2 | 0 | 15,130.2 |
| CK-03 | 67 | 28 | 1060.1 | 5651.0 | 0 | 15,427.1 |
| FB-01 | 92 | 32 | 1758.7 | 5973.8 | 225.0 | 15,938.2 |
| FB-02 | 92 | 30 | 1704.1 | 6174.3 | 225.0 | 16,485.7 |
| FB-03 | 92 | 30 | 1665.2 | 6033.3 | 225.0 | 16,100.8 |
| FV-01 | 89 | 30 | 1753.5 | 6567.3 | 219.0 | 17,568.5 |
| FV-02 | 89 | 30 | 1675.4 | 6274.8 | 204.4 | 16,794.0 |
| FV-03 | 89 | 34 | 2011.8 | 6648.3 | 210.9 | 17,802.9 |

CONCLUSIONS

A winter wheat jointing-stage fertilization experiment was conducted in Jintan, Jiangsu, China, to explore the effectiveness and economic benefits of variable fertilization technology in the rice-wheat rotation area in the middle and lower reaches of the Yangtze River.

(1) The control accuracy of variable fertilization equipment was greater than 95% and that it had good variable system control performance.

(2) There were certain spatial differences in the growth of winter wheat, and the population structure could be effectively improved through variable fertilization. After variable fertilization, the coefficient of variation of NDVI values in winter wheat crop canopy spectral data remained between 0.076 and 0.125, and the Christensen uniformity coefficient remained between 0.901 and 0.940. The coefficient of variation of winter wheat yield within the plot remained between 0.058 and 0.067, while the Christensen uniformity coefficient remained between 0.938 and 0.949.

(3) Compared with the traditional empirical balance method for quantitative fertilization of plots, the real-time variable fertilization plot used 13.6 kg/ha less fertilizer during the elongation stage, but the yield increased by 436.3 kg/ha and the income increased by 1,213.6 yuan/ha.

ACKNOWLEDGEMENT

We greatly appreciate the careful and precise reviews by the anonymous reviewers and editors. This research was financially supported by the Science and Technology Innovation Engineering Project of the Chinese Academy of Agricultural Sciences (Office of the Chinese Academy of Agricultural Sciences (2014) No. 216).

REFERENCES

- [1] Bai, J.B., Tian, M. & Li, J.Q. (2022). Analysis and precision test of variable fertilization control system (变量施肥控制系统分析与精度试验). *Journal of Agricultural Mechanization Research*, Vol.9, pp.22-28. DOI: 10.13427/j.cnki.njyi.2022.09.040
- [2] Chen, M. Shi, Y.Y., Wang, X.C., Sun, G.X. & Li, Y.B. (2015). Design and experiment of variable rate fertilizer applicator based on crop canopy spectral reflectance (基于光谱探测的小麦精准追肥机设计与试验). *Transactions of the Chinese Society of Agricultural Machinery*, Vol.46, pp.26-32. DOI: 10.6041/j.issn.1000-1298.2015.05.005
- [3] Chen, M. Shi, Y.Y., Wang, X.C., Sun, G.X. & Li, Y.B. (2016). Design and experiment of optimization control system for variable fertilization in winter wheat field based on fuzzy PID (基于模糊PID的冬小麦变量追肥优化控制系统设计与试验). *Transactions of the Chinese Society of Agricultural Machinery*, Vol.47, pp.71-76. DOI: 10.6041/j.issn.1000-1298.2016.02.010
- [4] Chen, M., Yang, Z.J., Wang, X.C., Shi, Y.Y. & Zhang, Y. (2018). Response characteristics and efficiency of variable rate fertilization based on spectral reflectance. *Int J Agric & Biol Eng*, Vol.11, pp.152-158. DOI: 10.25165/j.ijabe.20181106.4086
- [5] He, Y.C., Yang, Y., Yi, X.k. & Wang, W.P. (2023). Simulation and experiment of influencing factors of fertilization accuracy based on variable rate fertilization system (基于变量施肥系统的施肥准确性影响因素仿真与试验). *Journal of Chinese Agricultural Mechanization*, Vol.44, pp.51-57, 86. DOI: 10.13733/j.jcam.issn.2095-5553.2023.10.008
- [6] Huang, Q.N., Dang, H.Y., Huang, T.M., Hou, S.B. & Wang C.H. (2020). Problems in fertilization and fertilizer reduction in wheat production of China (我国小麦施肥问题与化肥减施). *Scientia Agricultura Sinica*, Vol.53, pp.4813-4815. DOI: 10.3864/j.issn.0578-1752.2020.23.008
- [7] Huang, X.M., Xu, X.P., He, P., Wang, X.B., Yang, L.F., Qiu, S.J., Zhao, S.C. & Zhou, W. (2020). Yield response to NPK fertilization and the main impacts in production of winter wheat in Yangtze River catchments of China (长江流域冬小麦氮磷钾肥增产效应及其影响因素). *Journal of Plant Nutrition and Fertilizers*, Vol.26, pp.1059-1068. DOI: 10.11674/zwf.20103
- [8] Li, X.W., Tian, M. & Xiao, X. (2019). Design of wheat fertilization decision-making and control system based on quick diagnosis (基于小麦养分快速诊断的施肥决策与控制系统设计). *Journal of Northeast Agricultural Sciences*, Vol.44, pp.23-27. DOI: 10.16423/j.cnki.1003-8701.2019.02.005
- [9] Ma, Xu., Zhao, X., Liu, S.S., Wang, Y.W., Wang, X.C. & Li, Z.H. (2023). Design and experiment of solid particle fertilizer variable rate fertilization device for high-speed rice transplanter (水稻高速插秧机固体颗粒肥料变量施肥装置设计与试验). *Transactions of the Chinese Society of Agricultural Machinery*, Vol.54, pp.99-110. DOI: 10.6041/j.issn.1000-1298.2023.09.010
- [10] Maleki, M.R., Mouazen, A.M., Ketelaere, B.D., Ramon, H. & Baerdemaeker, J.D. (2008). On-the-go variable-rate phosphorus fertilisation based on a visible and near-infrared soil sensor. *Biosystems Engineering*, Vol.99, pp.35-46. DOI: 10.1016/j.biosystemseng.2007.09.007
- [11] Sun, C.J., He, Q.M., Teng, W.J. & Wu, M.Q. (2019). Research on present situation of precision fertilization and seed sowing device for wheat (小麦精准施肥播种装置现状研究). *Journal of Chinese Agricultural Mechanization*, Vol.40, pp.30-34. DOI: 10.13733/jcam.issn.2095-5553.2019.07.06
- [12] Wu, L.Q., Wu, L., Cui, Z.L., Chen, X.P. & Zhang F.S. (2019). Optimal regional nitrogen, phosphorus, potassium rates recommendations and special fertilizer formulae study for wheat in China (中国小麦区域氮磷钾肥推荐用量及肥料配方研究). *Journal of China Agricultural University*, Vol.24, pp.30-40. DOI: 10.11841/i.issn.1007-4333.2019.11.04
- [13] Yang, B.H., Chen, J.L., Chen, L.H., Cao, W.X., Yao, X. & Zhu, Y. (2015). Estimation model of wheat canopy nitrogen content based on sensitive bands (基于敏感波段的小麦冠层氮含量估测模型). *Transactions of the Chinese Society of Agricultural Engineering (Transactions of the CSAE)*, Vol.31, pp.176-182. DOI: 10.11975/j.issn.1002-6819.2015.22.024

- [14] Yu, H.F., Xu, H.L., Ding, Y.Q, Yang, Z.N., Dou, X.L., Li, Q. & Guan, X.T. (2023). Wheat canopy vegetation index measurement method based on narrow band spectral image analysis (基于窄带光谱图像分析的小麦冠层植被指数测量方法研究). *Journal of Nanjing Agricultural University*, Vol.46, pp.189-199. DOI: 10.7685/jnau.202112021
- [15] Zhang, J.J., Liu, H.B., Xi, L. & Ma, X.M. (2010). Construction and application of wheat variable fertilization system based on model (基于生长模型的小麦变量施肥决策系统构建与应用). *Journal of Henan Agricultural University*, Vol.44, pp.591-595. DOI: 10.1645/j.cnki.1000-2340.2010.05.012
- [16] Zhao, S., Zong, Z. & Liu, G. (2019). Design and test on position fertilization control system based on motor drive (基于电机驱动的定位施肥控制系统设计与试验). *Transactions of the Chinese Society of Agricultural Machinery*, Vol.50, pp.91-114. DOI: 10.6041/j.issn.1000-1298.2019.S0.015

WHEAT GRAINS AUTOMATIC COUNTING BASED ON LIGHTWEIGHT YOLOv8

基于轻量化的 YOLOv8 小麦籽粒自动计数研究

Na MA^{*}, Zhongtao LI, Qingzhong KONG

College of Information Science and Engineering, Shanxi Agricultural University, Taigu/China

Tel: +86-13834188480; E-mail: manasxau@163.com

DOI: <https://doi.org/10.35633/inmateh-73-50>**Keywords:** wheat grains, counting, object detection, YOLOv8**ABSTRACT**

In order to accurately and quickly achieve wheat grain detection and counting, and to efficiently evaluate wheat quality and yield, a lightweight YOLOv8 algorithm is proposed to automatically count wheat grains in different scenarios. Firstly, wheat grain images are collected under three scenarios: no adhesion, slight adhesion, and severe adhesion, to create a dataset. Then, the neck network of YOLOv8 is modified to a bidirectional weighted fusion BiFPN to establish the wheat grain detection model. Finally, the results of wheat grain counting are statistically analyzed. Experimental results show that after lightweight improvement of YOLOv8 with BiFPN, the mAP (mean Average Precision) value of wheat grain detection is 94.7%, with a reduction of 12.3% in GFLOPs. The improved YOLOv8 model now requires only 9.34 ms for inference and occupies just 4.0 MB of memory. Compared with other models, the proposed model in this paper performs the best in terms detection accuracy and speed comprehensively, better meeting the real-time counting requirements of wheat grains.

摘要

为了准确、快速实现小麦籽粒目标检测和计数，更为高效的对小麦品质和产量进行评估，提出一种轻量化的 YOLOv8 算法实现不同场景下小麦籽粒自动计数。首先采集无粘连、轻微粘连、重度粘连 3 种场景下的小麦籽粒图像创建数据集。然后将 YOLOv8 的 neck 网络改成双向加权融合的 BiFPN，建立小麦籽粒检测模型。最后，对小麦籽粒计数结果进行统计。试验结果表明，YOLOv8 进行 BiFPN 的轻量化改进后，小麦籽粒检测 mAP 值为 94.7%，GFLOPs 减少了 12.3%。改进后的 YOLOv8 模型推理时间仅需 9.34ms，内存占用仅为 4.0MB。将改进后的 YOLOv8 模型与其他模型相比，本文提出的模型在检测精度和速度综合方面性能最优，更能满足小麦籽粒实时计数要求。

INTRODUCTION

Wheat grains are one of the primary cereal crops for humans, possessing abundant nutritional value (Sun *et al.*, 2021; Liu *et al.*, 2022). Rich in starch, proteins, fats, vitamins, and minerals, wheat grains serve as essential sources of energy and nutrients for the human body. Additionally, they are crucial for wheat breeding programs. These programs typically involve cultivating and researching wheat in small experimental fields to estimate yield. Once the actual yield meets the expected targets, the cultivation is scaled up for widespread planting. Yield estimation has always been a critical indicator in wheat breeding, and obtaining accurate counts of wheat grains through statistics is a vital factor for yield prediction (Zhang *et al.*, 2023). Therefore, rapid detection and counting of wheat grains can efficiently evaluate wheat quality and yield. Moreover, it enables the adoption of more rational and scientific planting methods during wheat promotion to achieve increased production.

The traditional method for counting wheat seeds involves manually counting the wheat grains, requiring counters to be constantly attentive and patient (Wang *et al.*, 2023). The counting process is extremely tedious, time-consuming, and labor-intensive, making it prone to subjective errors and leading to inconsistent results among different individuals. Additionally, the reproducibility is poor, and it is difficult to directly identify high-quality seeds with the naked eye. Therefore, there is a need for an objective, reproducible, fast, and economically reliable method of measurement.

In recent years, deep learning has been widely applied in different fields with promising results, and the integration of traditional agriculture with deep learning has become a trend (Saleem *et al.*, 2021; Attri *et al.*, 2023). Su *et al.* (2023) proposed an improved YOLOv5 model for detecting brown spot regions in adzuki beans. The improved YOLOv5 model achieved detection accuracy, recall rate, and mAP of 94.7%, 88.2%, and 92.5%, respectively.

Wang *et al.* (2024) proposed a method called YOLO-EfficientNet for identifying the growth status of hydroponic lettuce. It achieved excellent scores of 95.78 for Val-acc, 94.68 for Test-acc, 96.02 for Recall, 96.32 for Precision, and 96.18 for F1-score. Gai *et al.* (2023) proposed an improved YOLOv4 deep learning algorithm for detecting cherry fruits. It is proposed to increase the network based on the YOLO-V4 backbone network CSPDarknet53 network, combined with DenseNet. The density between layers, the a priori box in the YOLO-V4 model, is changed to a circular marker box that fits the shape of the cherry fruit. The results show that the mAP value obtained by using the improved YOLO-V4 model network in this paper is 0.15 higher than that of YOLOv4. To address weed detection and identification amidst complex field backgrounds, Peng *et al.* (2023) integrated the CBAM attention mechanism into YOLOv7. The enhanced algorithm achieved an average precision (mAP) of 91.15%, surpassing the original YOLOv7 algorithm by 2.06%. Researchers have conducted extensive studies on seed counting using deep learning methods. Zhao *et al.* (2023) proposed a P2PNet-Soy method for automatic counting of soybean seeds. The superiority of the proposed P2PNet-Soy in soybean seed counting and localization over the original P2PNet was confirmed by a reduction in the value of the mean absolute error, from 105.55 to 12.94. Xiang *et al.* (2023) proposed a method called YOLO POD for counting soybean pods. Building upon YOLO X, they added a block for predicting pod quantity, modified the loss function, and introduced the Convolutional Block Attention Module (CBAM). The results show that the R2 between the predicted and actual pod counts by YOLO POD reached 0.967, which is an improvement of 0.049 over YOLO X. A lightweight real-time wheat seed detection model, YOLOv8-HD, based on YOLOv8, was previously proposed. YOLOv8-HD achieves an average precision (mAP) of 99.3%, which is 16.8% higher than YOLOv8. The memory footprint of the YOLOv8-HD model is 6.35 MB (Ma *et al.*, 2024).

From the above research, it can be seen that there is an urgent need for a method that can perform fast and accurate real-time counting of seed. Therefore, this study proposes a wheat grain real-time detection model named YOLOv8-BIFPN, focusing on counting accuracy and speed. Firstly, images of wheat grains in different scenarios were collected as the dataset. Then, building upon the YOLOv8 base model (Yang *et al.*, 2023; Hussain *et al.*, 2023), BiFPN with bidirectional weighted fusion was introduced to accelerate the model's execution speed and achieve wheat grain object detection (Yu *et al.*, 2024; He *et al.*, 2023). Furthermore, the improved YOLOv8-BiFPN was compared with current mainstream object detection algorithms. The results showed that the proposed algorithm has significant advantages in both wheat grain detection accuracy and speed, meeting the practical demand for wheat grain counting and laying a foundation for the development of precision agriculture technology.

MATERIALS AND METHODS

Data Acquisition and Pre-processing

The wheat grains used in the experiment are of the variety Longmai 6197. These grains are compact, resistant to lodging, and have stable high yield characteristics, making them a new variety of drought-resistant and high-yielding wheat. Three scenarios were set up for the experiment: wheat with slight adhesion, wheat without adhesion, and wheat with severe adhesion. A total of 300 images were collected, with 100 images for each scenario. Some of the data are shown in Figure 1, where the wheat grains are placed on a black cushion to enhance the contrast of the images. The photographic equipment used in the experiment was the Huawei P40 Pro Plus smartphone. A certain amount of wheat grains were mixed with wheat husks and straw, and then lightly shaken to randomly scatter them on the experimental platform, ensuring the random distribution of wheat grains, husks, and straw.

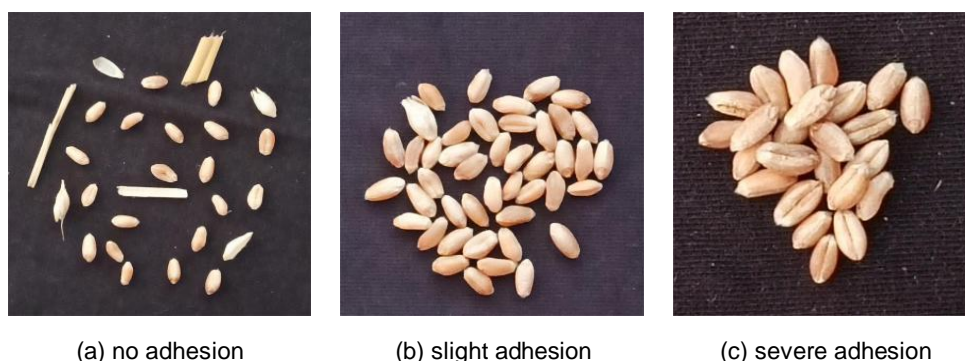


Fig.1 - Partial Data Collection

Using the Labellmg software for annotation, wheat grains are labeled as "w", husks are labeled as "k" and stalks are labeled as "g". After annotating the data, it is randomly divided into training, validation, and test sets in a ratio of 7:2:1. Finally, there are 210 images in the training set, 60 images in the test set, and 30 images in the validation set.

YOLOv8 Model

YOLOv8 is an advanced SOTA model developed by Ultralytics. Building upon the success of previous YOLO versions, it introduces new features and improvements, further enhancing its performance and flexibility. Based on the principles of speed, accuracy, and ease of use, YOLOv8 is an excellent choice for tasks such as object detection, image segmentation, and image classification (Terven et al., 2023). YOLOv8 is capable of performing detection, classification, and segmentation tasks. The main improvement in YOLOv8 is the C2f module, depicted in Figure 2. It is a further refinement of ELAN, primarily replacing the convolutions in ELAN's computational modules with Bottleneck modules. ELAN serves as the main module for the Backbone. ELAN consists of three parts: Cross Stage Partial; Computational module; 1x1 convolutions, as shown in Figure 3.

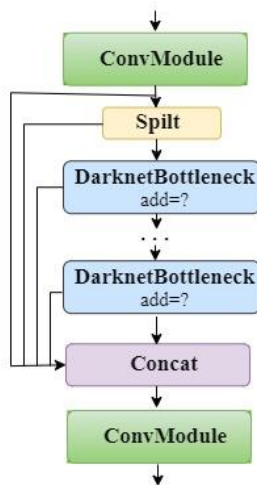


Fig. 2 - C2f model

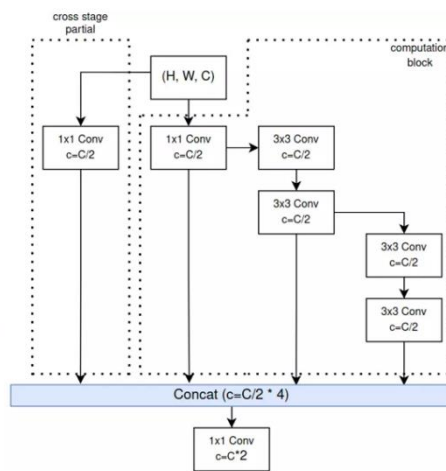


Fig. 3 - ELAN model

BiFPN Model

BiFPN (Bi-directional Feature Pyramid Networks) is an enhanced version of the FPN network structure. FPN relies on a backbone and incorporates bottom-up, top-down, feature fusion, lateral connections, and feature integration, primarily for object detection tasks. This structure is weighted and bidirectional, involving both top-down and bottom-up structures. By constructing bidirectional channels, it achieves cross-scale connections, directly fusing features from the feature extraction network with relatively large features from the bottom-up path. It preserves shallower semantic information without losing too much deep semantic information.

BiFPN features bidirectional connections, adaptive feature adjustment, modular design, efficiency, and performance improvement (Chen et al., 2021). It allows information to propagate bidirectionally between different resolution levels, better integrating low-level and high-level features, thereby enhancing object detection accuracy. The specific structure of BiFPN is illustrated in Figure 4.

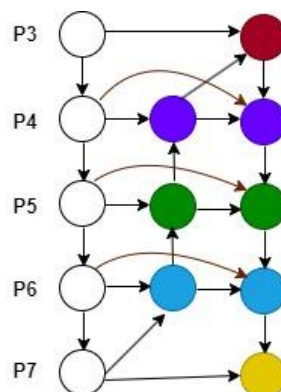


Fig. 4 - BiFPN model

Improved YOLOv8

The counting of wheat grains is easily disrupted by wheat stalks and husks, especially since husks closely resemble wheat grains. Additionally, accurately detecting clumped wheat grains presents a significant challenge. In order to enhance the detection performance of wheat grains, especially under conditions of adhesion and impurities, the YOLOv8 neck network was replaced with BiFPN. The introduction of BiFPN allows information to propagate across different resolutions, aiding the model in better understanding the features of targets in various scenarios. The improved structure diagram is shown in Figure 5.

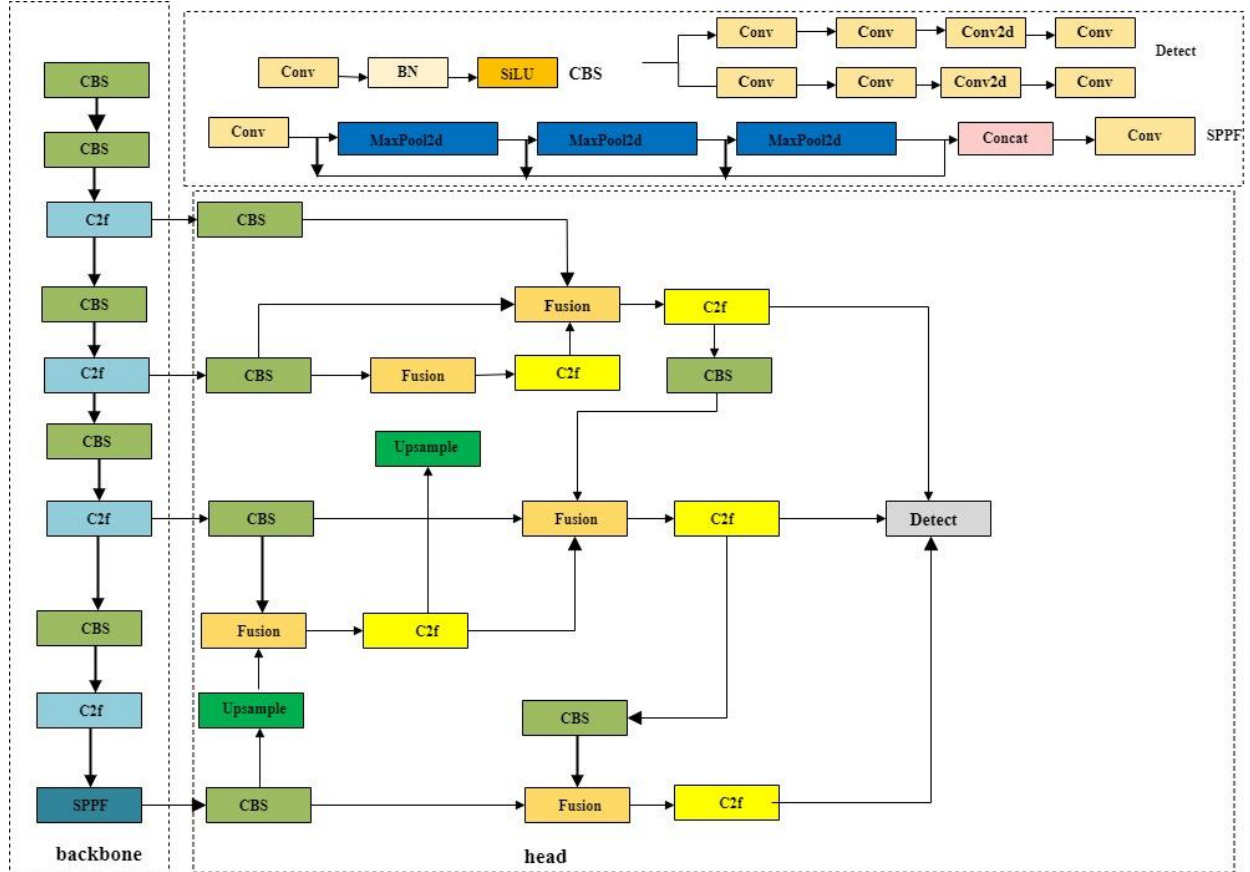


Fig. 5 - Improved YOLOv8 Architecture Diagram

Classic detection models YOLOv3, YOLOv5, YOLOv6, YOLOv8 were used to detect wheat seed data. The model with the highest detection accuracy and fastest detection speed was selected from the experimental results, and further improved using BiFPN to select the optimal wheat grain counting model.

Model Evaluation Metrics

Wheat grain object detection needs to balance accuracy and speed. Therefore, this experiment employs precision (P), recall (R), and mean average precision (mAP). The confusion matrix is a metric used to evaluate model results, which is part of model assessment. It calculates metrics such as precision and recall. TP : True Positive, predicting positive class as positive; FP : False Positive, predicting negative class as positive; FN : False Negative, predicting positive class as negative; TN : True Negative, predicting negative class as negative.

Precision calculation formula is:

$$P = \frac{TP}{FP+TP} \tag{1}$$

Recall calculation formula is:

$$R = \frac{TP}{TP+FN} \tag{2}$$

mAP calculation formula is:

$$AP = \frac{TN+TP}{TP+TN+FP} \tag{3}$$

$$mAP = \frac{\sum_{i=1}^C AP_i}{C} \tag{4}$$

FLOPs stands for floating point operations, which can be used to measure the complexity of algorithms/models. GFLOPs represents one billion floating point operations. In the field of deep learning, especially during the training and inference processes of models, GFLOPs are often used to describe the computational requirements of models and the computing capabilities of hardware.

Grad-CAM heat maps are a visualization method used in object detection to understand the decision-making process of deep neural networks in image classification tasks (Wang *et al.*, 2023). Through these heat maps, it can be observed which regions of the input image are crucial for the network model's decision-making during classification. The computation of the heat map involves calculating the gradient weights of the target class with respect to the feature maps of the network's final layer, multiplying these weights with the feature maps to obtain the heat map. This process visualizes the network model's attention to different regions. When observing the heat map, the importance of corresponding regions can be judged based on the intensity of colors. Brighter colors indicate that the features in that region significantly contribute to the detection results, while darker colors suggest less significant contributions.

RESULTS

The operating system used for the experiment was Windows 11. The GPU model was NVIDIA GeForce RTX 2060. The CPU model was Intel(R) Core(TM) i7-10875H CPU @ 2.30GHz. The system memory was 16GB and the solid-state drive had 512GB. The GPU acceleration libraries used were CUDA 11.6 and cuDNN 8.7. The Python version used was Python 3.8, and the deep learning framework PyTorch 1.13.1. The image size for deep learning training was 640x640 pixels, with 12 images per batch, and 100 epochs of training. In the experiment, a pre-trained model was used for transfer learning. Applying pre-training as the basis for transfer learning in a new task can significantly improve model performance, reduce training time, and consume fewer computational resources.

Comparison of Detection Performance of Different Models

Using YOLO series algorithms to detect wheat grains, the results are shown in Table 1. From Table 1, it can be seen that the detection accuracy of YOLOv3 (Lawal *et al.*, 2021) and YOLOv6 (Li *et al.*, 2022) is not high and the speed is slow. Although YOLOv8 has high detection accuracy, its detection GFLOPs are not as good as YOLOv5 (Jocher *et al.*, 2022). Therefore, in order to balance detection speed and accuracy, improvements were made to YOLOv8 and YOLOv5.

Table 1

| Results of different YOLO algorithms detection | | | | | |
|--|-------------|------|------|-----------------------|--------|
| Scene | Category | P/% | R/% | mAP _{0.5} /% | GFLOPs |
| YOLOv3 | Mean | 89 | 87.2 | 93.5 | 282.2 |
| | Wheat seeds | 98.5 | 97.9 | 99.4 | |
| | Straw | 79.4 | 80 | 86.5 | |
| | Husk | 89 | 83.7 | 94.5 | |
| YOLOv5 | Mean | 90.6 | 70.3 | 86.4 | 7.1 |
| | Wheat seeds | 99 | 95.6 | 99.2 | |
| | Straw | 78.7 | 50 | 68 | |
| | Husk | 94.1 | 65.1 | 92 | |
| YOLOv6 | Mean | 87.2 | 76.6 | 84.8 | 11.8 |
| | Wheat seeds | 96.9 | 97.2 | 99.2 | |
| | Straw | 71.1 | 65 | 69.5 | |
| | Husk | 93.6 | 67.6 | 85.8 | |
| YOLOv8 | Mean | 97.6 | 96.8 | 95 | 8.1 |
| | Wheat seeds | 99.9 | 97.4 | 99.3 | |
| | Straw | 79.5 | 80.2 | 86.9 | |
| | Husk | 95.9 | 93 | 98.8 | |

Improved Algorithm Performance

After improving YOLOv8 and YOLOv5 with BiFPN, the results are shown in Table 2. YOLOv5-BiFPN achieved an AP of 99.3% for wheat grain detection, an AP of 76.7% for husk detection, an AP of 97% for straw detection, and an mAP of 91.4%. YOLOv8-BiFPN achieved an AP of 99.5% for wheat grain detection, an AP of 87.3% for husk detection, an AP of 97.4 for straw detection, and an mAP of 94.7%. The GFLOPs of YOLOv5-BiFPN were 6.4, and those of YOLOv8-BiFPN were 8.1, the same as YOLOv5. From the above experimental results, it can be seen that the mAP of YOLOv8-BiFPN in multiple scenarios is 94.7%, which is respectively 8.3% higher than YOLOv5, and the AP of wheat grain, straw, and husk is respectively 0.3%, 19.3%, and 5.4% higher than YOLOv5, and 0.2%, 10.6%, and 0.4% higher than YOLOv5-BiFPN. Although the GFLOPs of YOLOv5-BiFPN decreased, its detection accuracy did not surpass that of YOLOv8.

Table 2

Improved algorithm detection results

| Scene | Category | P/% | R/% | mAP _{0.5} /% | mAP _{0.5:0.95} /% | GFLOPs |
|--------------|-------------|------|------|-----------------------|----------------------------|--------|
| YOLOv5-BiFPN | Mean | 87.7 | 85.5 | 91.4 | 67.9 | 6.4 |
| | Wheat seeds | 98 | 96.6 | 99.3 | 81.7 | |
| | Straw | 67.7 | 73.4 | 76.7 | 52.9 | |
| | Husk | 97.4 | 86.4 | 97 | 69 | |
| YOLOv8-BiFPN | Mean | 95.6 | 91.2 | 94.7 | 75.1 | 7.1 |
| | Wheat seeds | 99 | 98.7 | 99.5 | 83.9 | |
| | Straw | 93.7 | 75 | 87.3 | 63.4 | |
| | Husk | 94.2 | 1 | 97.4 | 78 | |

To further compare the performance of the improved algorithms, this study plotted the loss functions of YOLOv3, YOLOv5, YOLOv6, YOLOv5-BiFPN, and YOLOv8-BiFPN, as shown in Figure 6. From Figure 6, it can be observed that the box_loss, cls_loss, and dfl_loss curves of YOLOv3, YOLOv5, YOLOv6, YOLOv5-BiFPN, and YOLOv8-BiFPN all continuously decrease during 100 epochs of training until they stabilize. Compared to other YOLO series algorithms, YOLOv8-BiFPN exhibits faster convergence speed on the training set, effectively extracting wheat grain features and accelerating the model convergence rate.

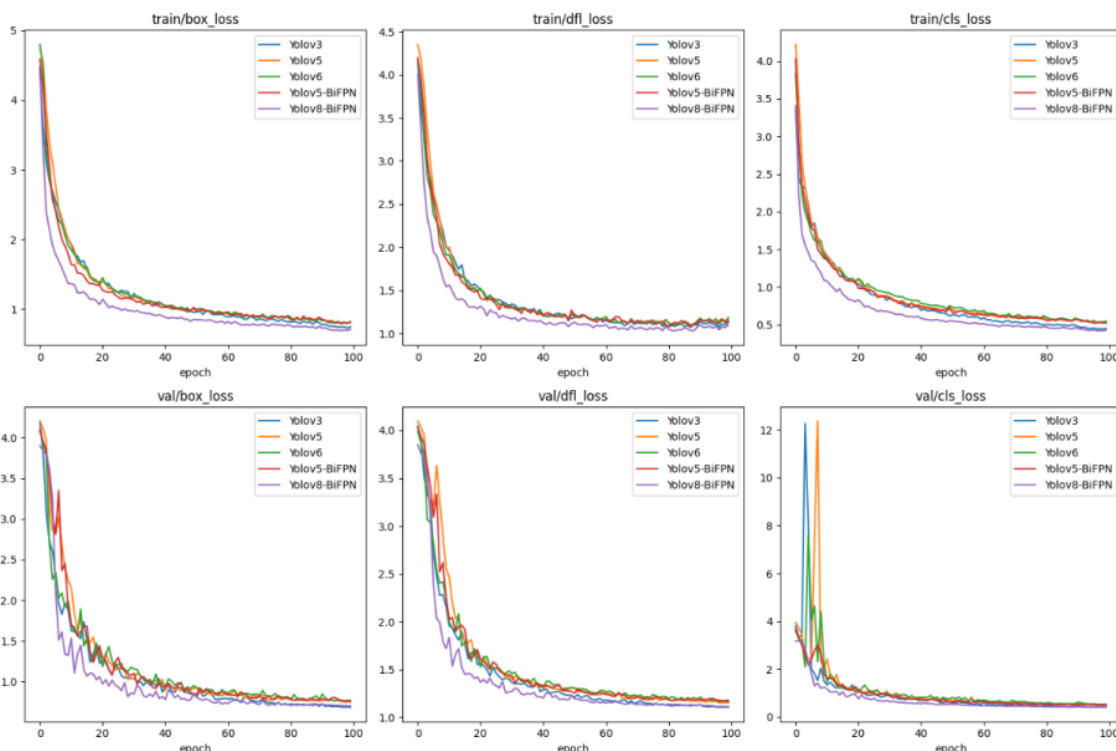


Fig. 6 - Comparison of loss functions for different models

This study compared the precision, recall, mAP_{0.5}, and mAP_{0.5:0.95} of YOLOv3, YOLOv5, YOLOv6, YOLOv5-BiFPN, and YOLOv8-BiFPN models, as shown in Figure 7. It can be observed from Figure 7 that YOLOv8-BiFPN outperforms other algorithms in all aspects.

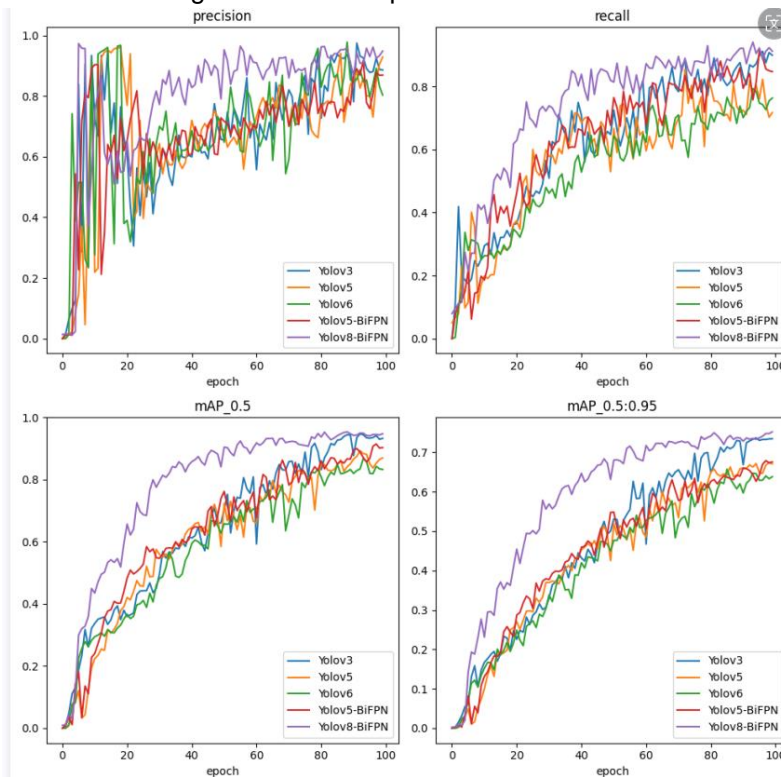


Fig. 7 - Performance curves of different algorithms

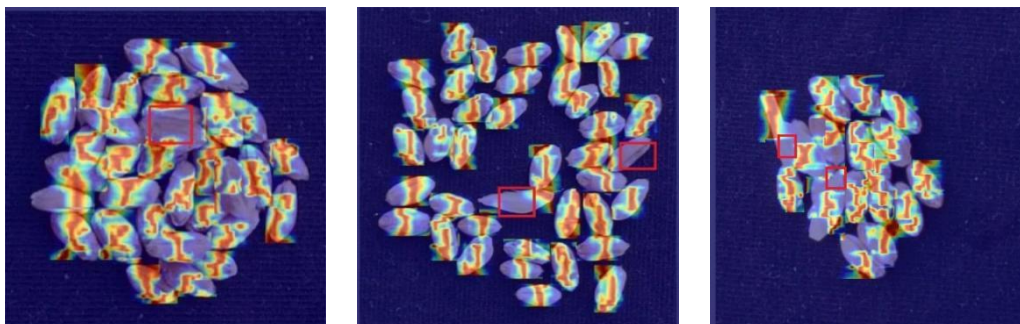
Table 3 compares the speed of the YOLOv8-BiFPN and YOLOv5-BiFPN models using parameters such as FPS, Latency, and size. FPS indicates the number of photos that can be processed per second, serving as a measure of detection speed. Latency represents the inference time, while size denotes the model's memory footprint. From Table 3, it can be observed that although YOLOv8-BiFPN has slightly larger memory requirements, both the inference speed and detection speed of YOLOv8-BiFPN are superior to those of YOLOv5-BiFPN.

Table 3

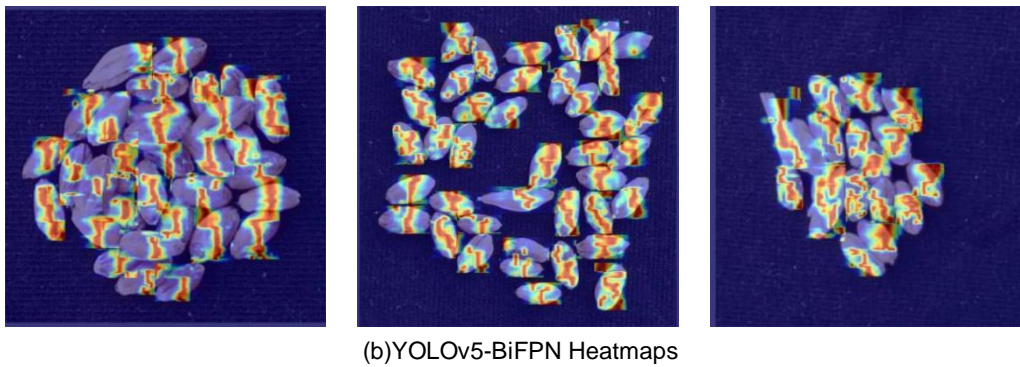
Comparison of Lightweighting Between YOLOv8-BiFPN and YOLOv5-BiFPN Models

| Model | Latency | FPS | size |
|--------------|---------|-------|------|
| YOLOv8-BiFPN | 9.34ms | 107.1 | 4.0M |
| YOLOv5-BiFPN | 12.61ms | 79.3 | 3.5M |

To better compare the feature extraction capabilities of the models, heatmaps of wheat grain detection using YOLOv8-BiFPN and YOLOv5-BiFPN were plotted as shown in Figure 8. The portion circled in red boxes in the figure indicates areas where the feature extraction of YOLOv5-BiFPN is less prominent. This demonstrates that the feature extraction capability of YOLOv8-BiFPN is superior to that of YOLOv5-BiFPN.



(a)YOLOv8-BiFPN Heatmaps



(b)YOLOv5-BiFPN Heatmaps

Fig. 8 - Comparison of Heatmaps

Counting Wheat Grains

Using the YOLOv8-BiFPN model for counting in different scenarios yields the results depicted in Figure 9. From the figure, it's evident that the YOLOv8-BiFPN model can effectively detect wheat grains, stalks, and husks in various scenes, accurately determining their quantities.



(a)no adhesion

(b)slight adhesion

(c)severe adhesion

Fig. 9 - Counting results in different scenarios

The wheat grain target detection and counting results were obtained using YOLOv8-BiFPN and YOLOv5-BiFPN models under scenarios of no adhesion, slight adhesion, and severe adhesion, with a total of 60 images, 20 for each scenario. The counting results are presented in Tables 4 and 5. Calculation errors include errors in wheat grain counting, wheat husk counting, and wheat straw counting. Detection errors encompass misidentification, missed detection, and duplicate detection. Due to the prevalence of detection errors, such as mistaking wheat husks for wheat grains or wheat husks for wheat straws, detailed classification of detection errors was not provided here.

Due to situations where counting errors and detection errors occur simultaneously, the total correct count for various scenarios does not equal 20. From the Tables 4 and 5, it can be observed that YOLOv8-BiFPN exhibits high detection and counting accuracy. In scenarios without adhesion, the counting and detection accuracy of YOLOv8-BiFPN is 70%, with a counting error rate of 25% and a detection error rate of 15%. In scenarios with slight adhesion, the counting and detection accuracy is 75%, with a counting error rate of 15% and a detection error rate of 15%. In scenarios with severe adhesion, the counting and detection accuracy is 55%, with a counting error rate of 25% and a detection error rate of 40%.

YOLOv5-BiFPN, on the other hand, achieves a counting and detection accuracy of 35% in scenarios without adhesion, with a counting error rate of 30% and a detection error rate of 45%. In scenarios with slight adhesion, the counting and detection accuracy is 40%, with a counting error rate of 25% and a detection error rate of 60%. In scenarios with severe adhesion, the counting and detection accuracy is 10%, with a counting error rate of 60% and a detection error rate of 55%.

Table 4

YOLOv8-BiFPN counting results

| Scene | counting and detection correct | counting errors | Detection errors |
|-----------------|--------------------------------|-----------------|------------------|
| no adhesion | 14 | 5 | 3 |
| slight adhesion | 15 | 3 | 3 |
| severe adhesion | 11 | 5 | 8 |

Table 5

YOLOv5-BiFPN counting results

| Scene | counting and detection correct | counting errors | Detection errors |
|-----------------|--------------------------------|-----------------|------------------|
| no adhesion | 7 | 6 | 9 |
| slight adhesion | 8 | 5 | 12 |
| severe adhesion | 2 | 12 | 11 |

YOLOv5-BiFPN and YOLOv8-BiFPN partial counting results are shown in Figure 10. In the first image of Figure 10(a), YOLOv5-BiFPN redundantly detects wheat stems and misses wheat husks, while in the first image of Figure 10(b), YOLOv8-BiFPN falsely detects wheat husks as wheat grains and misses wheat stems. In the second image of Figure 10(a), YOLOv5-BiFPN redundantly detects wheat stems, whereas in the second image of Figure 10(b), YOLOv8-BiFPN detects and counts correctly. In the third image of Figure 10(a), YOLOv5 incorrectly detects wheat husks as wheat grains, misses wheat stems, and duplicates counts of wheat grains. However, in the third image of Figure 10(b), YOLOv8-BiFPN detects and counts accurately.



Fig. 10 - Partial detection and counting result images

Based on the analysis above, it can be seen that the improved algorithms perform poorly in counting and detecting wheat grains in severely adhesive scenarios compared to other situations. This indicates that wheat grains are difficult to identify in severe adhesion conditions. Meanwhile, comparing experimental data reveals that both models show improved detection and counting accuracy in mildly adhesive situations. When comparing the counting errors and detection errors of YOLOv5-BiFPN, it is evident that the detection error rate is higher than the counting error rate.

Analysis of the experimental result graphs shows that YOLOv5-BiFPN exhibits a higher detection error rate for wheat husks and stems. The graphs frequently show misidentifications of wheat husks as stems and issues with repeated detection of stems.

In conclusion, the detection and counting accuracy of YOLOv8-BiFPN are higher than those of YOLOv5-BiFPN. Therefore, selecting YOLOv8-BiFPN for wheat grain detection and counting is a scientifically reasonable approach.

CONCLUSIONS

This study successfully developed a lightweight wheat grain detection model based on the improved YOLOv8, named YOLOv8-BiFPN, aiming to improve the accuracy and speed of wheat grain counting.

(1) This study created three scenarios of wheat grain datasets: non-adherent, slightly adherent, and severely adherent.

(2) BiFPN was introduced into the neck network of YOLOv8 in this study to achieve lightweighting of the YOLOv8 model. The improved model achieved a wheat grain detection mAP of 94.7%, with a 12.3% reduction in GFLOPs. The inference time of the improved YOLOv8 model was only 9.34 ms, with a memory footprint of only 4.0 MB, meeting the real-time counting requirements for wheat grains.

(3) The improved model YOLOv8-BiFPN was compared with YOLOv3, YOLOv5, YOLOv8, and YOLOv5-BiFPN in this study, showing that YOLOv8-BiFPN was superior in both detection accuracy and speed.

(4) Using the improved YOLOv8-BiFPN for wheat grain counting in different scenarios, the counting and detection accuracy were 70% in the non-adherent scenario, 75% in the slightly adherent scenario, and 55% in the severely adherent scenario. The algorithm's performance in severely adherent scenarios was lower compared to other scenarios, indicating difficulties in wheat grain identification under severe adherence conditions.

The shortcomings in this experiment lie in the decreased detection accuracy of the improved YOLOv8-BiFPN compared to YOLOv8. Therefore, further research can be conducted to improve YOLOv8 in order to find a wheat grain detection algorithm that enhances accuracy while maintaining faster detection speed. Additionally, the current algorithm exhibits relatively lower detection and counting accuracy in severely cluttered scenes. Optimization of the model can be continued to enhance the accuracy of wheat grain detection in severely cluttered scenarios.

ACKNOWLEDGEMENT

This research, titled "Wheat grains automatic counting based on lightweight YOLOv8", was funded by the Basic Research Program of Shanxi Province (202303021212115).

REFERENCES

- [1] Attri I, Awasthi L K, Sharma T P, et al. (2023). A review of deep learning techniques used in agriculture [J]. *Ecological Informatics*, 102217.
- [2] Chen J, Mai H S, Luo L, et al. (2021). Effective feature fusion network in BiFPN for small object detection[C]// *IEEE international conference on image processing (ICIP)*. IEEE, 699-703.
- [3] Gai R, Chen N, Yuan H. (2023). A detection algorithm for cherry fruits based on the improved YOLO-v4 model [J]. *Neural Computing and Applications*, 35(19): 13895-13906.
- [4] He L, Wei H, Wang Q. (2023). A New Target Detection Method of Ferrography Wear Particle Images Based on ECAM-YOLOv5-BiFPN Network [J]. *Sensors*, 23(14): 6477.
- [5] Hussain M. (2023). YOLO-v1 to YOLO-v8, the rise of YOLO and its complementary nature toward digital manufacturing and industrial defect detection [J]. *Machines*, 11(7): 677.
- [6] Jocher G, Chaurasia A., Stoken A., et al. (2022). Ultralytics/YOLOv5: v6. 2-YOLOv5 Classification models, Apple M1, Reproducibility, ClearML and Deci.ai integrations [J]. *Zenodo*, 12-16.
- [7] Lawal M.O. (2021). Tomato detection based on modified YOLOv3 framework [J]. *Scientific Reports*, 11(1): 1-11.
- [8] Li C., Li L., Jiang H., et al. (2022). YOLOv6: A single-stage object detection framework for industrial applications [J]. *arxiv preprint arxiv:2209*.
- [9] Liu X. (2022). *Research on Automatic Counting of wheat seed based on Image Processing*. Bachelor's Thesis, Anhui Agriculture University, Hefei, China (In Chinese with English abstract).

- [10] Ma N., Su Y., Yang L., et al. (2024). Wheat Seed Detection and Counting Method Based on Improved YOLOv8 Model [J]. *Sensors*, 24(5): 1654.
- [11] Peng M., Zhang W., Li F., et al. (2023). Weed detection with Improved Yolov 7[J]. *EAI Endorsed Transactions on Internet of Things*, 9(3): 1-2.
- [12] Saleem M.H., Potgieter J., Arif K.M. (2021). Automation in agriculture by machine and deep learning techniques: A review of recent developments [J]. *Precision Agriculture*, 22(6): 2053-2091.
- [13] Su P., Li H., Wang X., et al. (2023). Improvement of the YOLOv5 Model in the Optimization of the Brown Spot Disease Recognition Algorithm of Kidney Bean [J]. *Plants*, 12(21): 3765.
- [14] Sun J., Zhang L., Zhou, X., et al. (2021). Detection of rice seed vigor level by using deep feature of hyperspectral images. *Transactions of the CSAE*, 37(14): 171-178. (in Chinese with English abstract)
- [15] Terven J., Córdova-Esparza D.M, Romero-González J.A. (2023). A comprehensive review of YOLO architectures in computer vision: From YOLOv1 to YOLOv8 and YOLO-nas [J]. *Machine Learning and Knowledge Extraction*, 5(4): 1680-1716.
- [16] Wang L., Zhang Q., Feng T. et al. (2023). Research on wheat grain counting method based on YOLOv7-ST model [J]. *Transactions of the Chinese Society for Agricultural Machinery*, 54(10): 188-197.
- [17] Wang S., Zhang Y. (2023). Grad-CAM: understanding AI models [J]. *Comput. Mater. Contin*, 76: 1321-1324.
- [18] Wang Y., Wu M., Shen Y. (2024). Identifying the Growth Status of Hydroponic Lettuce Based on YOLO-EfficientNet [J]. *Plants*, 13(3): 372.
- [19] Xiang S., Wang S., Xu M. et al. (2023). YOLO POD: a fast and accurate multi-task model for dense Soybean Pod counting [J]. *Plant methods*, 19(1): 8.
- [20] Yang G., Wang J., Nie Z., et al. (2023). A lightweight YOLOv8 tomato detection algorithm combining feature enhancement and attention [J]. *Agronomy*, 13(7): 1824.
- [21] Yu C., Shin Y. (2024). SAR ship detection based on improved YOLOv5 and BiFPN [J]. *ICT Express*, 10(1): 28-33.
- [22] Zhang H., Ji J., Ma H. et al. (2023). Wheat Seed Phenotype Detection Device and Its Application. *Agriculture*, 13, 706.
- [23] Zhao J., Kaga A., Yamada T. et al. (2023). Improved field-based soybean seed counting and localization with feature level considered [J]. *Plant Phenomics*, 5: 0026.

RESEARCH ON THE STEERING CHARACTERISTICS OF ELECTRO-HYDRAULIC COUPLED STEERING SYSTEM OF SELF-DRIVING TRACTOR

自动驾驶拖拉机电液耦合转向特性研究

Guangfei XU ¹⁾, Qun SUN ¹⁾, Meizhou CHEN ²⁾, Jian WU ^{1)*}, Jiwei FENG ³⁾, Peisong DIAO ²⁾, Chenqiang YIN ⁴⁾

¹⁾ College of Mechanical and Automotive Engineering, Liaocheng University, Liaocheng 252000, China;

²⁾ College of Agricultural Engineering and Food Science, Shandong University of Technology, Zibo 255049, China;

³⁾ School of Mechanical Engineering, Southeast University, Nanjing, 211189, China.

⁴⁾ School of Machinery and Automation, Weifang University, Weifang 261000, China;

Tel: +86-13666386200.; E-mail: wujian@cu.edu.cn (correspondent author: Wu jian)

DOI: <https://doi.org/10.35633/inmateh-73-51>

Keywords: self-driving tractor, E-HCSS, steering characteristics, multifactorial experiment

ABSTRACT

To solve the problem of poor steering performance of existing self-driving tractors based on electro-hydraulic coupled steering systems (E-HCSS) under multiple influencing factors, the research on electro-hydraulic coupled steering characteristics of self-driving tractors was carried out in this paper. Taking the electro-hydraulic coupled steering system as the research object, the E-HCSS test bench of the tractor was built, and the influencing factors affecting the responsiveness of the steering process were obtained through theoretical analysis: hydraulic fluid temperature, oil supply pressure and driving speed. The hydraulic fluid temperature, oil supply pressure and driving speed were taken as the test factors, and the steering system response time and response error were taken as the performance indexes for the single-factor steering test and orthogonal test. By establishing the regression mathematical model between the influencing factors and the indexes, the interactive influence of the factors on the indexes was analyzed, the optimal parameter combination was obtained, and the optimization results were verified. The test results indicated that the tractor electro-hydraulic coupling steering system could achieve good steering performance under the optimal parameter combination, and the optimal parameter combination was: hydraulic oil temperature 60°C, hydraulic oil pressure 15 MPa and driving speed 8 km/h. The study's results were as follows: hydraulic oil temperature 60°C, hydraulic oil pressure 15 MPa and driving speed 8 km/h. The study's results could provide a reference for the steering control of the self-driving tractor, the design of the self-driving steering system and the optimization of the parameters.

摘要

为了解决现有基于电液耦合转向系统的自动驾驶拖拉机受多重影响因素下的转向性能差的问题, 本文进行了自动驾驶拖拉机电液耦合转向特性研究。以电液耦合转向系统为研究对象, 搭建了拖拉机电液耦合转向试验台, 通过理论分析得到了影响转向过程响应能力的影响因素: 液压油液温度、供油压力及行驶速度。以油液温度、供油压力及行驶速度为试验因素, 以转向系统响应时间、响应误差为性能指标进行转向单因素试验及正交试验。通过建立各影响因素与指标之间的回归数学模型, 分析各因素对指标的交互影响, 获得最优参数组合, 对优化结果进行验证试验, 试验结果表明在最优参数组合下拖拉机电液耦合转向系统能够达到良好的转向性能, 最优参数组合为: 液压供油温度 60°C、液压供油压力 15MPa 及行驶速度 8km/h。研究结果可为自动驾驶拖拉机转向控制、自动驾驶转向系统设计及参数优化提供参考。

INTRODUCTION

Self-driving tractors are important technological means for the implementation of precision work and the development of modern agriculture. However, the influence of different factors on the steering performance of self-driving tractor is not clear which makes the self-driving control challenging (Fang S. et al., 2017).

There are two main existing structural steering systems for self-driving tractors. One is modified on the basis of the original tractor hydraulic power assist system, and a solenoid valve is connected in parallel. The steering control is carried out by controlling the opening of the solenoid valve (Lee C., 2022; Zardin B., 2018). Another is not to change the original hydraulic steering system, and the steering motor and the corresponding deceleration structure are added in the steering column or steering wheel.

Steering is realized by controlling the rotation of the motor and then driving the steering column and the hydraulic steering part (Xu G. *et al.*, 2020). Because the parallel solenoid valve needs to change the original oil circuit, the modification cost is higher, the implementation is difficult, so the second program is applied more often. However, the second program has two power sources—electric and hydraulic, so its steering performance is susceptible to the influence of various parameters within the steering system and other factors (Kralev J. *et al.*, 2019). Especially in the process of operation, multiple factors can seriously affect the steering performance of the self-driving tractor, which in turn affects the operation results (Lindhorst C., 2019).

Due to the unclear steering characteristics of electro-hydraulic coupled steering system (E-HCSS), the corresponding controller was designed to attenuate the multiple influences on the steering system as uncertainties and parameter perturbations to ensure the control of the tractor (Liu Y. *et al.*, 2020). (Xu G. *et al.*, 2021) proposed a path tracking control method based on E-HCSS considering external disturbances and uncertainties. (Zhao W. *et al.*, 2019) considered the energy loss and optimized the parameters of the E-HCSS. Due to the complex structure of the hydraulic system, the wide range of steering loads and the difficulty of control, (Du H. *et al.*, 2020), proposed an improved integral sliding mode control method to improve the steering control accuracy.

However, since the E-HCSS is a composite system involving mechanical, hydraulic, and electrical components, its system characteristics are subject to multidimensional changes due to multiple factors such as oil temperature, oil pressure, and driving speed (Tang B. *et al.*, 2015). Simplifying the influences on the steering system to uncertainties and parameters makes it difficult to ensure steering performance under tractor-specific characteristic factors. Therefore, it is necessary to explore the influencing factors of E-HCSS to clarify its steering characteristics and intrinsic steering coupling mechanism, so as to improve the steering performance (Feng J. *et al.*, 2023).

The motivation of this work is to find the optimal combination of performance parameters of E-HCSS. The working performance of E-HCSS always suffers from multiple factors including oil temperature, oil pressure, and driving speed, *et al.* To achieve better response time and response error of E-HCSS integrate in self-driving tractor, single factor test and orthogonal test with E-HCSS under steering condition are carried out and the optimal parameter combination is obtained which is not hitherto reported in the open literature. One of the advantages and contributions of the research is that it provides a way to find a relationship between self-driving performance and multiple parameters of E-HCSS—oil temperature, oil pressure and driving parameter—driving speed *etc.*

MATERIALS AND METHODS

Whole structure of E-HCSS

In order to carry out research on tractor E-HCSS characteristics and simulate the steering scenarios of tractors under actual working conditions, a tractor E-HCSS hardware-in-the-loop (HIL) test bench was constructed by using the hydraulic power steering system of the tractor as the substructure, and coupling the hydraulic pressure with the power assisting motor in the steering shaft (Xu G *et al.*, 2020). Fig. 1 shows the structure of the E-HCSS which mainly consists of steering module, hydraulic power module, power supply module, resistance loading module, human-machine interaction module, support module and so on.

Steering module mainly consists of full hydraulic steering system and motor steering system. The two are connected by a pipe column, which is mounted on a circular column support at an angle of the real vehicle, and the circular ball steering device is connected by a universal joint. The hydraulic power and an electric motor torque acting together to execute the steering signals from the controller of the self-driving tractor, and the hydraulic pressure provides a large steering power at low speeds, which reduces the loss of energy consumption.

Hydraulic power module mainly consists of 15 kW three-phase asynchronous motor, hydraulic pump, oil temperature controller, hydraulic pressure controller. The module is used to provide a hydraulic source with a maximum supply pressure of 20 MPa and a maximum flow rate of 14 L/min. The oil temperature controller can regulate the oil temperature and the hydraulic pressure controller can regulate the oil supply pressure. In order to improve the reliability of the hydraulic system, the pump station has a hydraulic oil filtering function.

The power supply module mainly provides the appropriate voltage for the various power modules of the test stand to keep the whole bench working properly.

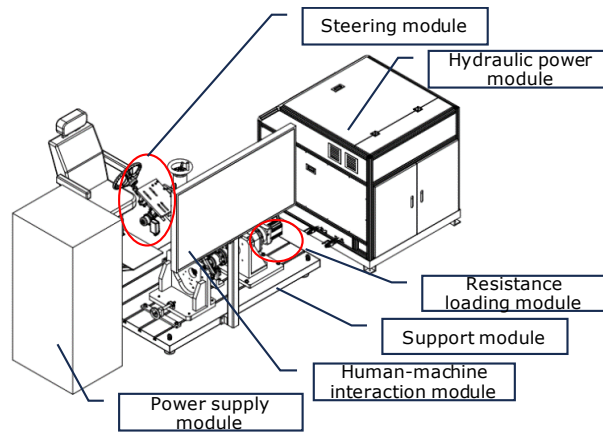


Fig. 1 - Structure drawing of tractor E-HCSS

The resistance loading module is mainly composed of servo motor, reducer, coupling assembly, pull pressure sensor, etc. It is mainly used to simulate the steering resistance loading provided for the electro-hydraulic coupled steering module to satisfy the real dynamics relationship, so as to make it closer to the real operation environment.

The human-computer interaction module mainly consists of a monitor, a seat, a steering wheel and so on. The monitor is used to display the running screen of the tractor model in the set operating environment in real time. It can provide an interface for human-computer interaction, and can be used for driving simulation.

The support module adopts cast iron platform structure, which is mainly composed of base and circular column module. Among them, the circular column module is mainly composed of screw, rotary table, handwheel, sliding block and so on. It is used in combination with the column fixture to realize the installation of different columns at different heights and angles.

Working principle of E-HCSS

The working principle of the E-HCSS is schematically shown in Fig. 2. Based on the original fully hydraulic steering system of the tractor, the steering motor is connected in series. The self-driving controller controls the rotation of the steering rod by controlling a motor connected in series to the upper end of the vehicle. Turning of the steering rod opens the rotary valve. The oil flowing through the rotary valve is fed into the hydraulic cylinder to generate hydraulic power. The power of the motor and the power of the hydraulic pressure work together to produce a steering force to overcome the steering resistance and the friction within the steering system.

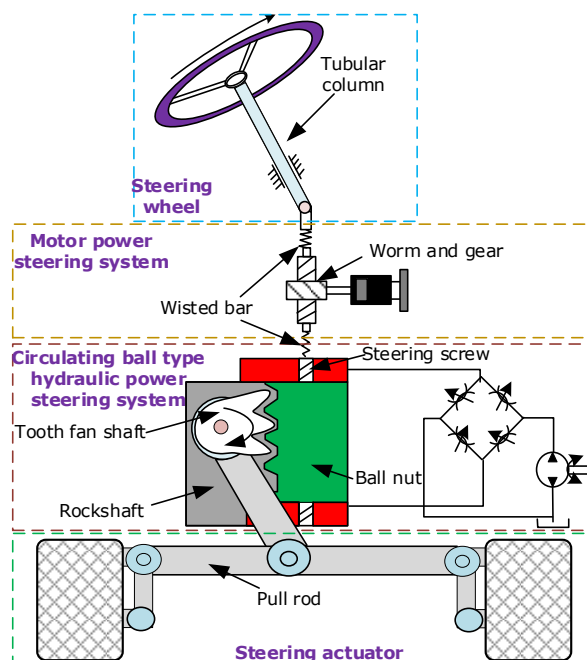


Fig. 2 - Schematic diagram of E-HCSS

Analysis of factors affecting steering system performance

The steering motor output torque T_a of the E-HCSS and the hydraulic power F_L of the hydraulic steering system work in concert to overcome the steering resistance T_r and the internal friction T_f so that the tractor can execute the steering command. The steering dynamics are modeled referring to (Shi G et al., 2023).

Under the joint action of motor power and hydraulic power, the control principle block diagram is shown in Fig. 3.

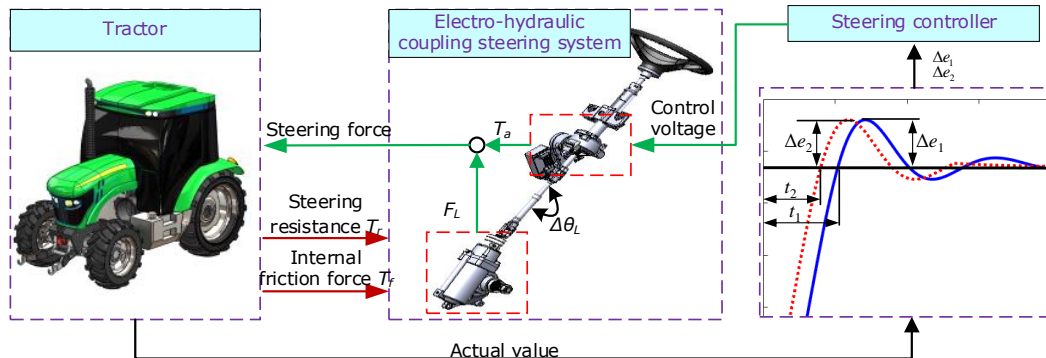


Fig. 3 - Control principle diagram of E-HCSS

It can be known from the dynamics relationship and Fig. 3 that hydraulic power F_L affects the dynamics relationship of the steering system. F_L will be affected by the oil supply pressure, oil temperature and other factors, which in turn affects the response time of the control system, $t_{1, 2, \dots}$ and the response error, $\Delta e_{1, 2, \dots}$, and steering resistance likewise affects the dynamics of the steering system relationships (He X et al., 2022). Furthermore, the steering resistance is related to the driving speed, which in turn can affect the response time and response error of the control system.

EXPERIMENTAL DATA ACQUISITION

Test methodology

In order to fully study the steering characteristics of the E-HCSS in the steering process, the hydraulic system's hydraulic oil temperature, oil supply pressure and driving speed are selected as the test factors, and the steering response time of the whole steering system operation as well as the response error are taken as the test indexes to carry out the tractor self-driving steering test. In order to test the accuracy of the built steering system, the test is carried out with different frequencies of 1 Hz, 2 Hz and 3 Hz corner inputs, and the corner response curve of the response is obtained as shown in Fig. 4. It can be seen that the system response is accurate and can be used in the study of corner control systems.

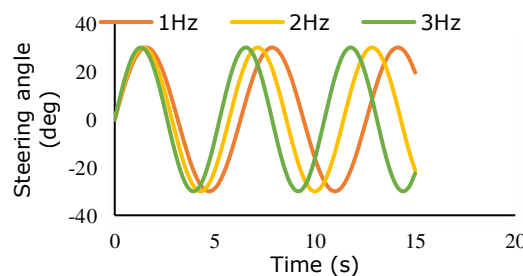


Fig. 4 - Schematic diagram of angle input at different frequencies in the steering system

Test equipment

To analyze the main factors affecting the performance of E-HCSS, a HIL test platform is built (Xu G et al., 2024) as shown in Fig. 5. Carsim contains various types of vehicle models with high degrees of freedom, so the tractor model of Carsim was used as a real tractor for data interaction and processing with NI/PXI. Corner tracking control program is written by Matlab/Simulink and compiled into Dspace/MicroAutoBox. The I/O interface of Dspace/MicroAutoBox receives the real signals such as motor current, front wheel angle, steering torque and so on from the sensor of E-HCSS, and drives the PMSM motor according to the final drive signal calculated by the corner controller to realize the steering control (He X et al., 2022). The PMSM electric power steering system is installed on the original hydraulic steering system.

The servo motor is used to simulate the steering resistance. The two monitors respectively display the road environment and real-time data. All the interaction data can be obtained from the computer. The key indicator parameters are shown in Table 1.



Fig. 5 - Tractor HIL steering test bench

Table 1

| Key parameters of the self-driving tractor E-HCSS test bench | | |
|--|--------------------------------------|----------------|
| Component modules | Key Parameters | Value |
| Resistance loading module | Torque loading range | 2000 N·m (MAX) |
| | Torque sensor range | 3000 N·m (MAX) |
| | Torque sensor accuracy | 0.5% FS |
| Hydraulic power module | Maximum assisting pressure | 20 MPa |
| | Pressure sensor range | 25MPa (MAX) |
| | Pressure sensor accuracy | 0.25%FS |
| | Maximum assisted flow | 14L/min |
| | Flow sensor range | 25L/min (MAX) |
| Electrohydraulic coupling steering module | Flow sensor accuracy | 0.5% FS |
| | Maximum torque of the steering motor | 240 Nm |
| | Maximum speed of steering motor | 8500 rpm |
| | Maximum current of steering motor | 315 A |

In order to realize the operation of the hardware and software systems, the HIL data flow and control structure of the E-HCSS is proposed as shown in Fig. 6.

The tractor model and operating environment model are developed in Carsim 8.02 and embedded into PXI, the path tracking program is written using MatLab2016/Simulink and compiled into MicroAutoBox, the proposed corner controller is run and the current signal is generated by computation, which is sent to the PMSM through the MicroAutoBox real-time module. The PMSM is used to drive the steering system to track the target corner. The tracking error obtained from Carsim8.02 is sent to the controller in the MicroAutoBox through the PXI/NI interface. At the same time, the real-time steering angle from the angle sensor is fed back to the controller through the MicroAutoBox real-time module to complete the closed-loop control (Xu G *et al.*, 2019).

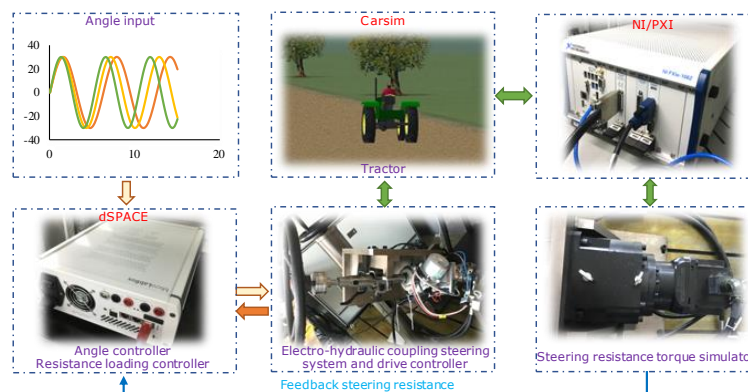


Fig. 6 - The data flow and control architecture of the HIL simulation system

RESULTS

Single factor test

Oil temperature

When the tractor is working, the hydraulic steering system oil temperature will also change with the change of the working load. The temperature change affects the oil flow characteristics and thus affect the steering characteristics of the steering system.

According to (Yin H *et al.*, 2024), it is known that the variation range of oil temperature of hydraulic system is generally 30~60°C. Therefore, the gradient of oil temperature variation is designed to be 30°C, 40°C, 50°C, 60°C, and 70°C, respectively. Record the system response time and response error during the autopilot test.

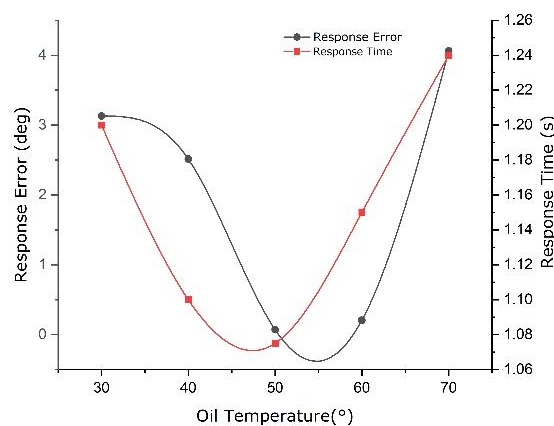
The temperature regulation of the hydraulic oil is carried out by AI-518P artificial intelligence temperature controller, as shown in Fig. 7.



Fig. 7- Artificial intelligence temperature controller

The controller has the function of oil temperature regulation and temperature measurement. Its measurement range is -50~1700°C. The measurement accuracy is 0.25 level, the resolution can be as low as 0.1°C and the response time is less than 0.5 seconds. The regulation mode adopts bit-type regulation and AI artificial intelligence regulation, which contains fuzzy logic PID regulation and parameter self-tuning function. At the same time, the controller is also equipped with an alarm function, which is divided into four ways: upper limit, lower limit, positive deviation and negative deviation.

It can be seen from Fig. 8 that the response error and response time decrease and then increase with the increase of oil temperature. The hydraulic oil of the steering system has higher viscosity and poorer flowability at lower temperatures, thus leading to poorer steering performance of the steering system. As the temperature increases, the viscosity of the oil decreases and the flowability gradually becomes better. Therefore, the steering performance improves, and the response error and response time are minimized at 50~60°C. The temperature continues to rise so that high temperatures lower the viscosity of the hydraulic fluid, increasing the hydraulic system's leakage and causing the hydraulic system's efficiency and response ability to decline. Considering the response time and response error, the oil temperature is 40~60°C for better performance.



Note: Oil supply pressure 12 MPa, driving speed 8 km/h

Fig. 8 - The effect of oil temperature on steering performance

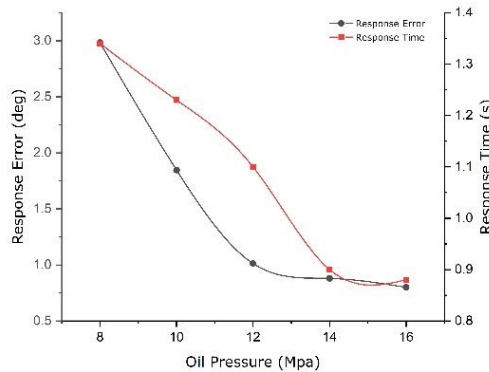
Oil supply pressure

The self-driving tractor will steer in real time according to the change of the path. When facing different steering conditions and steering amplitude, the oil supply pressure should also be changed in real time, and its oil supply pressure has a lot to do with the model and setting of the tractor at the time of production. The oil supply pressure is determined within a certain range once the initial settings of the tractor are determined. However, to better reduce the power consumption while meeting the applicable requirements, further experimental studies on the oil supply pressure are required. The gradient of oil supply pressure change is designed as 8 MPa, 10 MPa, 12 MPa, 14 MPa, 16 MPa. At the same time, the response time and error in the self-driving process are recorded.

MD-S800 series pressure controller is adopted as oil supply pressure regulation which has the advantages of intelligent self-diagnosis, prompting for error types, full-range adjustability of upper and lower limit control points, and simple adjustment methods. The controller has a hydraulic oil supply pressure regulation and pressure display function.

The controller is integrated with pressure measurement, display and control together. When the pressure reaches a predetermined value, the controller controls the controlled equipment to turn on or off to achieve the purpose of automation control. Its pressure range is 0~160 MPa, accuracy level is 1.0 and sampling frequency is 5 Hz.

It can be seen from Fig. 9 that as the oil pressure increases, the system response time and response error are decreasing and the steering performance becomes better. However, after exceeding 14 MPa, with the increase of oil pressure, the performance of the system does not change significantly. This depends on two main reasons. On one hand, the system itself must protect the hydraulic system and the steering system designed for the safety of pressure relief. After reaching a certain pressure, the oil pressure will not be converted into the steering power. On the other hand, there is a constraint in the steering system itself, even if the pressure is increased, it cannot be converted into the actual steering power. Considering the response time and response error, the oil supply pressure of 14~16 MPa has better performance.



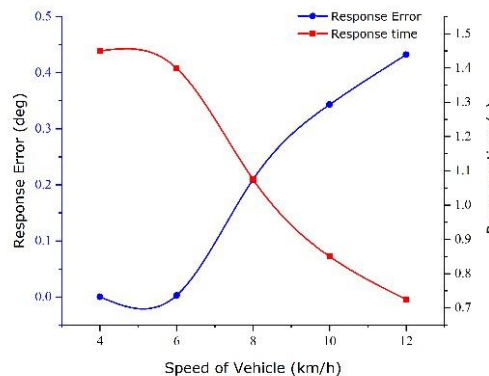
Note: Oil temperature 50°C, driving speed 8km/h

Fig. 9 - The effect of oil temperature on steering performance

Driving speed

Self-driving tractors are generally set to a fixed driving speed during operation. In addition to the power setting of the tractor itself, the driving speed also needs to be combined with the operation scene, and then there is no other reference basis, so that the tractor driving speed does not match the operation conditions frequently (Liang J et al., 2023; Wu J et al., 2022). Therefore, in order to find the driving speed that maximizes the performance of the tractor under the corresponding conditions, a single factor test of speed gradient variation was conducted with speed settings of 4 km/h, 6 km/h, 8 km/h, 10 km/h, and 12 km/h. At the same time, the response time and response error of the self-driving process were recorded.

It can be seen from Fig. 10 that the response error of the steering system gradually increases and the response time of the steering system gradually decreases as the vehicle speed increases. The response error and response time are almost unaffected by the change of vehicle speed within 4~6 km/h. At this time, the steering system response error is small at this driving speed. As the speed increases, the response error gradually increases, and the response time gradually decreases. The influence of driving speed on the two indicators has the opposite trend. Considering the response time and response error, better performance can be obtained under the driving speed of 6~10 km/h.



Note: Oil temperature 50°C, oil supply pressure 12 MPa

Fig. 10 - The effect of speed on steering performance

Orthogonal tests

By analyzing the single factor test on the influence of oil temperature, oil supply pressure and driving speed on the steering performance of the E-HCSS, the reasonable range of change is obtained when the steering performance is better: oil temperature 40~60°C, oil pressure 14~16 MPa, driving speed 6~10 km/h.

On this basis, in order to further clarify the optimal parameter combinations of multiple factors, a three-factor, three-level orthogonal test was designed, and orthogonal table L⁹(3⁴) was selected for the test. Each group of tests was repeated three times, and the factor level design is shown in Table 2. The experimental program and the results are shown in Table 3, with A, B, and C as the values of factor levels.

Table 2

| Factors and levels of orthogonal experiment | | | |
|---|------------------------|----------------------|------------------------|
| Level | Factors | | |
| | Oil temperature A (°C) | Oil pressure B (MPa) | Driving speed C (km/h) |
| 1 | 40 | 14 | 6 |
| 2 | 50 | 15 | 8 |
| 3 | 60 | 16 | 10 |

It can be seen from Table 3 that oil temperature, oil pressure, and driving speed have different degrees of influence on the performance of the steering system. For the metric of response time, the most influential factor is driving speed. Recommended combination level: oil temperature of 60°C, oil supply pressure of 15 MPa, driving speed of 6 km/h. For the index of response error, the most influential factor is the oil temperature, and the recommended combination level is oil temperature of 40°C, oil supply pressure of 14 MPa, and driving speed of 10 km/h.

To further analyze the significance of the effect of each factor on the evaluation indicators, *F*-test (Chen M et al., 2021) was performed for each factor using SPSS 26.0 software at a significance level of 0.05, and the analysis of variance is shown in Table 4.

Table 3

| Test scheme and results | | | | | | |
|-------------------------|---|------|-------|--------------|-------|----------|
| Serial number | Factor | | | Blank column | T / s | Δe (deg) |
| | A | B | C | | | |
| 1 | 3 | 3 | 1 | 1 | 1.38 | 0.23 |
| 2 | 1 | 2 | 3 | 2 | 0.94 | 2.54 |
| 3 | 3 | 1 | 3 | 3 | 0.96 | 0.89 |
| 4 | 1 | 3 | 2 | 3 | 1.09 | 2.12 |
| 5 | 2 | 3 | 3 | 1 | 0.89 | 0.71 |
| 6 | 3 | 2 | 2 | 2 | 1.15 | 0.54 |
| 7 | 2 | 2 | 1 | 2 | 1.35 | 0.62 |
| 8 | 2 | 1 | 2 | 3 | 1.01 | 0.83 |
| 9 | 1 | 1 | 1 | 1 | 1.39 | 2.50 |
| <hr/> | | | | | | |
| | <i>K</i> ₁ | 3.49 | 3.36 | 4.12 | | |
| | <i>K</i> ₂ | 3.42 | 3.44 | 2.79 | | |
| | <i>K</i> ₃ | 3.25 | 3.36 | 3.25 | | |
| | <i>R</i> | 0.08 | 0.027 | 0.443 | | |
| <i>t</i> | Primary and secondary factors C > A > B | | | | | |
| | Optimal combination A ₃ B ₂ C ₁ | | | | | |
| <hr/> | | | | | | |
| | <i>K</i> ₁ | 1.66 | 3.06 | 3.35 | | |
| | <i>K</i> ₂ | 7.16 | 3.7 | 4.14 | | |
| | <i>K</i> ₃ | 2.16 | 4.22 | 3.49 | | |
| | <i>R</i> | 1.83 | 0.387 | 0.263 | | |
| <i>Δe</i> | 3 | | | | | |
| | Primary and secondary factors A > B > C | | | | | |
| | Optimal combination A ₁ B ₁ C ₃ | | | | | |

Note: *K*₁~*K*₃ denote the sum of the values under each level of each factor, respectively; *R* is the extreme deviation

The results show that the effect of driving speed on the response time of the steering system is highly significant at 95% confidence level, and the effects of oil temperature and supply pressure are not significant. The effect of oil temperature on the response error of the steering system is highly significant, and the effect of oil temperature and supply pressure on the response error of the steering system is significant. The primary and secondary factors affecting the response time of the steering system are *C*, *A*, and *B*, and the optimal combination is $A_3B_2C_1$. While the primary and secondary factors affecting the response error of the steering system are *A*, *B*, and *C*, and the optimal combination is $A_1B_1C_3$. The oil temperature and oil supply pressure on the steering system's response time and response error have the same trend, and the driving speed has the opposite trend on the response time and response error. Considering the above laws and focusing on the response time, the optimal parameter combination $A_3B_2C_2$ is determined: the oil temperature is 60°C, the oil supply pressure is 15 MPa, and the driving speed is 8 km/h. The test is repeated five times under the combination and the average is taken. Afterwards, the system response time is 0.88 s, and the response error is 0.54°, which has good steering performance.

Table 4

| Variance analysis results | | | | | |
|---------------------------|-----------------|-------------------|---------------|----------|---------|
| Index | Variance source | Degree of freedom | Quadratic sum | F value | P value |
| <i>t</i> | <i>A</i> | 2 | 0.010 | 5.785 | 0.147 |
| | <i>B</i> | 2 | 0.001 | 0.810 | 0.552 |
| | <i>C</i> | 2 | 0.304 | 173.253 | 0.006** |
| | Error | 2 | 0.002 | | |
| Δe | <i>A</i> | 2 | 6.167 | 1468.254 | 0.001** |
| | <i>B</i> | 2 | 0.225 | 53.587 | 0.018* |
| | <i>C</i> | 2 | 0.118 | 28.206 | 0.034* |
| | Error | 2 | 0.004 | | |

Note: $P < 0.01$ (highly significant), $0.01 < P < 0.05$ (significant)

CONCLUSIONS

(1) The dynamics of the E-HCSS of a self-driving tractor were analyzed. Meanwhile, the main factors affecting the performance of the response time and response error were obtained as follows: hydraulic oil temperature, oil supply pressure and driving speed.

(2) By analyzing the influence of hydraulic oil temperature, oil supply pressure and driving speed on the steering performance of the steering system in a single factor test, the reasonable variation range of each factor was obtained in the case of better steering performance: the oil temperature was 40~60°C, the oil pressure was 14~16 MPa, and the driving speed was 6~10 km/h.

(3) Using 3-factor 3-level orthogonal test, it was obtained that the factors affecting the response time of the steering system were: driving speed>oil temperature>oil supply pressure, and the factors affecting the response error were: oil temperature>oil supply pressure>driving speed. The driving speed had opposite influence on the two performance indexes. Taking into account the overall consideration, the optimal parameter combination was determined as follows: oil temperature was 60°C, oil supply pressure was 15 MPa, driving speed was 8 km/h. At this time, the response time of the system was 0.88 s, and the response error was 0.54°. The verification test indicated that under this parameter combination, the steering system had better steering performance. It could provide a reference for the intelligent design of self-driving tractor.

ACKNOWLEDGEMENT

This work was supported by the Youth Project of Natural Science Foundation of Shandong Province (ZR2023QE091), Kcey Research and Development Program of Shandong Province (2022CXPT025); Natural Science Foundation of Shandong Province (ZR2022ME101), Key Laboratory of Vehicle Detection, Diagnosis and Maintenance Technology (JTZL2001), Natural Science Foundation of Shandong Province (ZR2023MF078).

REFERENCES

- [1] Chen, M. Z., Xu, G. F., Wei, M. J., Song, Z. C., Wang, W. J., Diao, P. S., & Teng, S. M. (2021). Longitudinal compressing and shearing properties of silage corn stalk in North China Plain (华北平原青贮玉米秸秆纵向压缩剪切特性研究). *INMATEH - Agricultural Engineering*, Vol. 65(3), pp. 47-56.
- [2] Du, H., Wang, L., Chen, J., Huang, H., & Feng, X. (2020). Integral sliding-mode tracking control for heavy vehicle electrohydraulic power steering system. *IEEE/ASME Transactions on Mechatronics*, Vol. 26(3), pp. 1455-1466.

- [3] Fang, S., Lu, Z., Wang, Z., Diao, X., Lu, Y., Gong, J., & Zhu, C. (2017). Design and prototype performance experiments of steering-by-wire hydraulic pressure system of tractor. *Transactions of the Chinese Society of Agricultural Engineering*, Vol. 33(10), pp. 86-93.
- [4] Feng, J., Yin, G., Liang, J., Lu, Y., Xu, L., Zhou, C., & Cai, G. (2023). A Robust Cooperative Game Theory based Human-machine Shared Steering Control Framework. *IEEE Transactions on Transportation Electrification*. Doi: 10.1109/TTE.2023.3332681.
- [5] He, X., Lou, B., Yang, H., & Lv, C. (2022). Robust decision making for autonomous vehicles at highway on-ramps: A constrained adversarial reinforcement learning approach. *IEEE Transactions on Intelligent Transportation Systems*, Vol. 24(4), pp. 4103-4113.
- [6] He, X., Yang, H., Hu, Z., & Lv, C. (2022). Robust lane change decision making for autonomous vehicles: An observation adversarial reinforcement learning approach. *IEEE Transactions on Intelligent Vehicles*, Vol. 8(1), pp. 184-193.
- [7] Kravec, J., Mitov, A., Slavov, T., & Angelov, I. (2019, October). Optimal three-loop cascade PI-P-PI controller for electro-hydraulic power steering system. *In IOP Conference Series: Materials Science and Engineering*, Vol. 664(1), pp. 012011.
- [8] Lee, C., Jeon, C. W., Han, X., Kim, J. H., & Kim, H. J. (2022). Application of electrohydraulic proportional valve for steering improvement of an autonomous tractor. *Journal of Biosystems Engineering*, Vol. 47(2), pp. 167-180.
- [9] Liang, J., Feng, J., Fang, Z., Lu, Y., Yin, G., Mao, X., & Wang, F. (2023). An energy-oriented torque-vector control framework for distributed drive electric vehicles. *IEEE Transactions on Transportation Electrification*, Vol. 9(3), pp. 4014-4031.
- [10] Lindhorst, C. (2019). Field Obstacle Identification for Autonomous Tractor Applications.
- [11] Liu, Y., Ji, X., Yang, K., He, X., Na, X., & Liu, Y. (2020). Finite-time optimized robust control with adaptive state estimation algorithm for autonomous heavy vehicle. *Mechanical Systems and Signal Processing*, Vol. 139, pp. 106616.
- [12] Marques, F., Flores, P., Pimenta Claro, J. C., & Lankarani, H. M. (2016). A survey and comparison of several friction force models for dynamic analysis of multibody mechanical systems. *Nonlinear Dynamics*, Vol. 86, pp. 1407-1443.
- [13] Shi, G., Song, M., Ju, C., Wang, S., & Qiao, P. (2023). Adaptive robust steering strategy for electro-hydraulic hybrid steering system based on backstepping method. *Proceedings of the Institution of Mechanical Engineers, Part D: Journal of Automobile Engineering*, 09544070231179073.
- [14] Tang, B., Jiang, H. B., Xu, Z., Geng, G. Q., & Xu, X. (2015). Dynamics of electromagnetic slip coupling for hydraulic power steering application and its energy-saving characteristics. *Journal of Central South University*, Vol. 22(5), pp. 1994-2000.
- [15] Wu, J., Kong, Q., Yang, K., Liu, Y., Cao, D., & Li, Z. (2022). Research on the steering torque control for intelligent vehicles co-driving with the penalty factor of human-machine intervention. *IEEE Transactions on Systems, Man, and Cybernetics: Systems*, Vol. 53(1), pp. 59-70.
- [16] Xu G., Diao P., He X., et al. (2021) Research on vehicle active steering control based on linear matrix inequality and hardware in the loop test scheme design and implement for active steering[J]. *Advances in Mechanical Engineering*, Vol. 11(11), pp. 1687814019892108.
- [17] Xu, G., Chen, M., He, X., Liu, Y., Wu, J., & Diao, P. (2024). Research on state-parameter estimation of unmanned Tractor—A hybrid method of DEKF and ARBFNN. *Engineering Applications of Artificial Intelligence*, Vol. 127, pp. 107402.
- [18] Xu, G., Chen, M., He, X., Pang, H., Miao, H., Cui, P., ... & Diao, P. (2021). Path following control of tractor with an electro-hydraulic coupling steering system: Layered multi-loop robust control architecture. *Biosystems Engineering*, Vol. 209, pp. 282-299.
- [19] Xu, G., Pang, H., Chen, M., Song, Z., Zhao, D., & Diao, P. (2020). Design of hardware in loop tractor electro-hydraulic coupling steering test platform *Transactions of the Chinese Society for Agricultural Machinery*, Vol. 1, pp. 525-534.
- [20] Yin, H., Wang, Y., Sun, W., & Wang, L. (2024). Fault diagnosis of hydraulic system based on DS evidence theory and SVM. *International Journal of Hydromechanics*, Vol. 7(1), pp. 1-15.
- [21] Zardin, B., Borghi, M., Gherardini, F., & Zanasi, N. (2018). Modelling and simulation of a hydrostatic steering system for agricultural tractors. *Energies*, Vol. 11(1), pp. 230.
- [22] Zhao, W., Zhou, X., Wang, C., & Luan, Z. (2019). Energy analysis and optimization design of vehicle electro-hydraulic compound steering system. *Applied Energy*, Vol. 255, pp. 113713.

RESEARCH ON PARAMETER MATCHING METHOD OF PURE ELECTRIC HORTICULTURAL MACHINERY DRIVELINE BASED ON WORKING CONDITION CHARACTERISTICS

考虑作业工况特性的纯电动园艺作业机械动力传动系统参数匹配方法研究

Dongyang WANG^{1,2}, Zhanyu LI¹, Jiangtao JI², Weixiang LIU², Zuohua DONG³, Hongmei ZHU¹, Lijun BAO⁴

¹⁾ College of Automotive and Transportation Engineering, Shenzhen Polytechnic University, Shenzhen/China;

²⁾ College of Agricultural Equipment Engineering, Henan University of Science and Technology, Luoyang/China;

³⁾ Changzhou Dongfeng Agricultural Machinery Group Co., Ltd., Changzhou/China

⁴⁾ Beijing Research Institute of Commercial Machinery, All China Federation of Supply and Marketing Cooperatives, Beijing/China

Tel: +86- 13728766480; E-mail: autolzy@szpu.edu.cn

DOI: <https://doi.org/10.35633/inmateh-73-52>

Keywords: Pure electric horticultural machinery, Driveline, Parameter Matching, Gear ratio optimization

ABSTRACT

To meet the economy requirement of the horticultural machinery, a two-speed transmission system was proposed based on the characteristics of the driving cycle of the horticultural machinery. Firstly, the test cycle of the horticultural machinery was established based on the data collector that fixed on the machinery. Secondly, the two-speed driveline system was designed. To reduce the energy consumption in the horticultural machinery working cycle, the gear ratio of the two-speed gear box was optimized with the goal of minimum energy consumption by the Genetic Algorithm. The optimized gear ratio were 11.6 and 9.62. The comparison of energy consumption between single gear ratio and two-speed gear ratio was made. The comparison result showed that the energy consumption can reduce 0.25% under one transportation test condition, the energy consumption can reduce 0.41% under one ploughing test condition, and the energy consumption can reduce 0.41% under one rotary test condition.

摘要

针对纯电动园艺作业动力机械使用周期内需具备田间道路行驶和满足不同作业需求的特点, 本研究考虑不同作业工况的经济性, 提出了一种两挡园艺作业动力机械动力传动系统。根据园艺作业动力机械的工作特点, 构建了作业工况模型, 以作业过程能耗最小为目标, 两挡变速箱的传动比为变量, 采用遗传算法对两挡位变速箱的传动比进行优化, 得到 1 挡和 2 挡的传动比分别为 11.6 和 9.62。并将优化后的传动比与单挡位的情况进行对比, 结果表明: 优化后的双挡位变速箱在单个运输测试工况下能耗降低 0.25%, 单个犁耕测试工况下, 能耗降低 0.41%, 单个旋耕测试工况下, 能耗降低 0.41%。

INTRODUCTION

Horticultural machinery is the main equipment used to develop family farming and yard economy, it can complete the task of ploughing, rotary tillage and transportation, other operations by equipping with different agricultural machinery. It can also be used in some urban public utilities. Most of the arable land in China is mainly based on family farming, and the types of crop planting and agronomy in different regions are different, therefore, farmers have a greater demand for horticultural machinery. They can not only carry out agricultural production activities during busy agricultural hours, but also carry out some transportation business activities in agricultural leisure time by using these power machinery (Cao Zhang *et al.*, 2015, Yiqi Huang *et al.*, 2007).

Pure electric power horticultural operation machinery has the advantages of clean, environmental protection, easy to control, and is the development direction of agricultural machinery in the future (Ali *et al.*, 2022). Electric driveline for agricultural tractors has been focused on by researchers (Rossi, C *et al.*, 2021). As the core device of pure electric horticultural operation machinery, the driveline system directly affects the performance of the dynamics and the fuel consumption (Kargar M. *et al.*, 2022, Lee T. *et al.*, 2023, Park J., 2022).

¹ Dongyang Wang, Lecture, Ph.D.Eng; Zhanyu Li, Assoc. Prof. Ph.D. Eng; Jiangtao Ji, Prof. Ph.D.Eng; Weixiang Liu, Ph. D Stud Eng; Zuohua Dong, Senior engineer, M.S. Eng; Hongmei Zhu, Assoc. Prof. Ph.D. Eng; Lijun Bao, Senior engineer, Ph.D. Eng .

Compared with fuel machinery, the motor in the pure electric power mechanical drive system has the characteristics of large starting torque, wide speed regulation range and good NVH (Noise, Vibration, Harshness), which is very suitable for yard, facility agriculture and field operations.

At present, the research on horticultural machinery mainly focuses on the configuration of the drive system and its parameter optimization. Researchers mainly analyzed the performance of single-motor drive and dual-motor drive tractor, and optimizes its key parameters.

Fang et al., (2017), designed a single-motor driven pure electric tractor driveline system based on the characteristics of agricultural tractors in Anhui Province, and he matched the power transmission parameters through simulation. But he did not optimize the key parameters in the transmission system. *Liu et al., (2022)*, proposed a two-way coupling device for pure electric tractors in view of the low power utilization rate of dual-motor driven tractors. They analyzed and optimized the topology of the coupling device. *Yu Liu, (2023)*, proposed a dual-motor driven pure electric tractor power coupling system in view of the problems existing in the current research on the parameter matching of pure electric tractor drivetrain, such as not considering the power efficiency distribution, excessive weight coefficient of static index optimization and ignoring dynamic load, and using a double-layer collaborative parameter optimization method to optimize the parameters of the power transmission system. *Gaoli Chen, (2023)*, proposed an improved undominated ranking genetic algorithm for the optimization parameters and complex constraints of the pure electric tractor power transmission system, and optimized the heat loss and total efficiency of the drive motor based on this method. *Xiaolei Cai et al., (2023)*, designed an electric tractor for greenhouse driven by brushless motor, and controlled the brushless DC motor. *Guoxiang Lu et al., (2020)*, proposed a method to realize multi-directional power output in view of the multi-directional power output requirements of horticultural tractors, based on which a multi-power take-off device was designed, and the structural parameters and performance of the device were simulated and optimized by three-dimensional modelling method. *Junxiang Zhang et al., (2020)*, proposed a driveline using two-speed transmission in view of the actual working characteristics of pure electric tractor, and optimized the gear transmission ratio with the power and working time of the electric tractor, the results show that the two-speed driveline can improve the overall operating performance of the electric tractor, but in this paper, the transmission ratio optimization only considers the optimization of ploughing and rotary tillage speed, and does not analyse the economy of the tractor under driving conditions.

To design a high efficiency and pure electric horticultural machinery driveline that satisfy different working cycle, a two-speed driveline system was proposed and the test working cycle of ploughing, rotary tillage, and transportation were established with the data that collected from the working machineries. The gear ratio of the two-speed transmission was optimized with the goal of minimum energy consumption by the genetic algorithm.

MATERIALS AND METHODS

Construction of test working conditions

The main operation methods of horticultural machinery include: ploughing, rotary tillage and transportation driving. It is necessary to construct test working conditions to analyze its operating conditions and load when matching the power parameters of horticultural operation machinery (*Jingwen Xiao, et al., 1998; Xiaosen Hou et al., 2019*). Therefore, the force analysis of each test working cycle was done first, and the test working cycle of ploughing, rotary tillage and transportation were established first.

Test working cycle of ploughing

The horticultural machinery will suffer the resistance force from the solid and the equipped agricultural machinery, when it does the ploughing work. Assuming the resistance force of agricultural machinery is F_p , its calculation equation can be expressed by equation (1).

$$F_p = Z \cdot k \cdot b_l \cdot h_k \quad (1)$$

where, k is the specific resistance of the soil, kPa; b_l is the width of a single ploughshare, cm; h_k for depth of the ploughing, cm; Z is the number of ploughshares.

When the horticultural machinery is operated in the field, it is generally a cyclic operating condition, and its main working process includes: acceleration, agricultural tools piercing into the soil, running with constant speed, agricultural tools unearthing and stopping, and in the stage of acceleration and deceleration the agricultural tools piercing into the soil and unearthing the soil. Therefore, it is necessary to construct a suitable test condition, according to the calculated load of ploughing operation and the speed of ploughing operation when matching the dynamic parameters of horticultural machinery.

And considering the reciprocating nature of horticultural machinery during operation, a test working condition (one-way ploughing length of 200 m as the test data) was established, as shown in Figure 1.

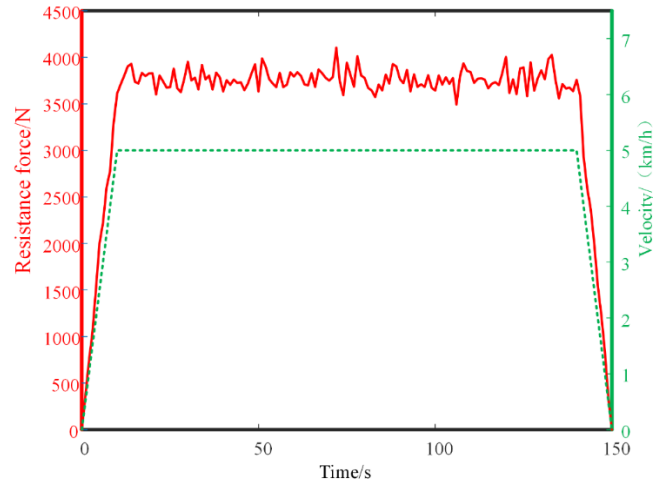


Fig. 1 - Test cycle of ploughing

Test conditions of rotary tillage operation

Force analysis of the rotary tillage knife is complicated, when the horticultural machinery is in the operation of rotary tillage, and many methods to calculate the power consumption of the rotary cultivator were proposed, such as unit analysis method, energy analysis method, specific work method, specific resistance method and other analysis methods. In practice, the consumption power of the rotary tillage is calculated by equation (2) (Junxiang Zhang et al., 2020).

$$N = 0.1 \cdot K_{\lambda} \cdot d \cdot v \cdot B \tag{2}$$

where N is the power consumption of the rotary cultivator, kW; v is the forward speed of the machinery, m/s; B is the width of the tillage cultivator, m; d is the depth of the tillage cultivator, cm; K_{λ} is the specific resistance of rotary tillage, N/cm².

Referring to the ploughing condition and agricultural machinery manual, the speed of the horticultural machinery was set to 5 km/h, and the test cycle of rotary tillage was established, which is shown in Figure 2.

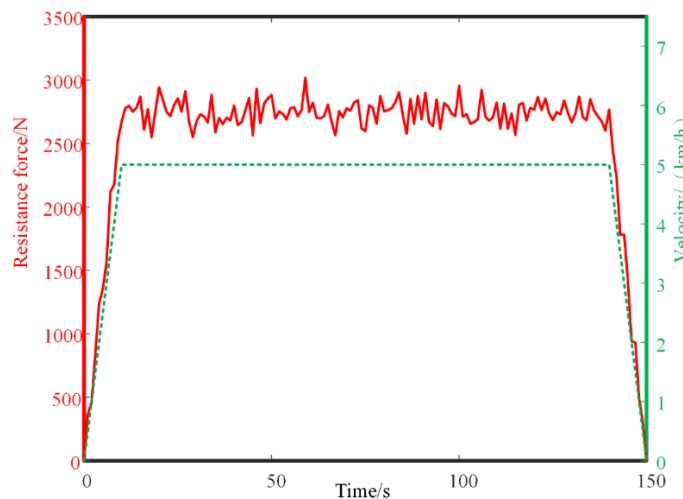


Fig. 2 - Test cycle of rotary tillage

Transportation test conditions

In addition to the operation in the field, the horticultural machinery also carries out transportation operations. During transportation, the machinery suffers the resistance from the air, slope, and soil. Assuming the resistance is F_r , it mainly includes acceleration resistance, F_j , rolling resistance, F_f , air resistance, F_w , and ramp resistance F_i .

$$F_r = F_f + F_w + F_i + F_j \tag{3}$$

where: $F_f = mgf \cos \theta$, $F_w = 0.5C_D A \rho v^2$, $F_i = mg \sin \theta$, $F_j = \delta m du/dt$, ρ is the air density, v is the vehicle speed, and δ is the vehicle rotation mass conversion coefficient.

From the above formula, it can be seen that in the case of knowing other structural parameters, the speed of the vehicle can be determined to determine the resistance of the power machinery transportation condition, according to the situation of the horticultural under the transportation condition, referring to the New European Driving Cycle (NEDC) cycle, the transportation test cycle can be established, which is shown in Figure 3.

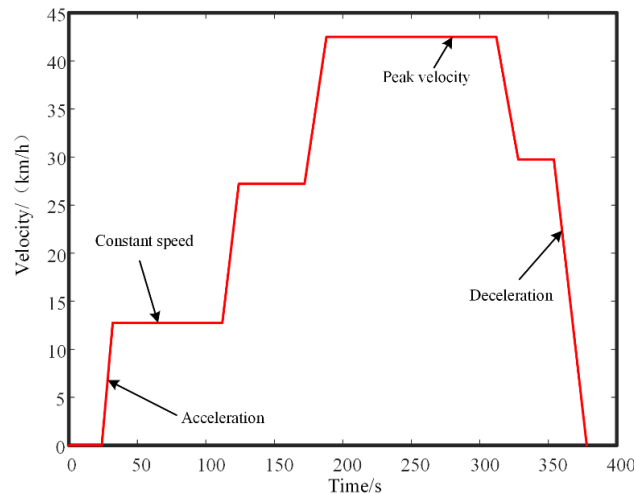


Fig. 3 - Test cycle of transportation

Design of pure electric horticultural machinery driveline system

The main function of horticultural machinery is to pull agricultural machinery in the field to operate at a constant speed, and under pure traction conditions, the working machinery is not only driven by the driving resistance during the driving process, but also by the traction of the agricultural tools, which can be shown by equation (4).

$$F_T = F_r + F_p \tag{4}$$

where F_T is the driving force of the horticultural machinery.

Calculation of motor power

All the power of the horticultural operation machinery comes from the electric motor, so the power of the motor should be higher than the demand power of several working conditions of the horticultural machinery. The power of the ploughing cycle can be calculated by equation (5).

$$P_p = (F_r + F_p) v_p / \eta_T / 1000 \tag{5}$$

where: P_p is the demand power under ploughing conditions, kW; v_p is the speed, m/s; η_T is the efficiency.

The power of rotary tillage can be calculated by equation (6).

$$P_N = N + F_r v_p / \eta_T / 1000 \tag{6}$$

where: P_N is the required power under rotary tillage conditions, kW.

The power required for transportation conditions can be calculated by equation (7).

$$P_r = F_r v_p / \eta_T / 1000 \tag{7}$$

where: P_r is the demand power under transportation conditions, kW.

Then the required power of the motor P_m is:

$$P_m \geq \max \{ P_p, P_r, P_N \} \tag{8}$$

Design of the battery

As the only power source of electric horticultural machinery, the power battery pack needs to meet the power demand and operation time demand of horticultural machinery.

First, in terms of power demand, it is necessary to satisfy Equation (9).

$$P_{m_max} \leq n_m P_b \eta_{bat} \tag{9}$$

where: P_{m_max} is the peak power of the motor, and n_m is the number of batteries that is calculated to meet the power demand. η_{bat} is the efficiency of the battery and motor controller, and P_b is the output power of a single battery, kW.

Secondly, in terms of the working time demand, it is necessary to satisfy Equation (10).

$$P_m t_w \leq \frac{n_h W_{bat}}{3.6 \times 10^{-6}} \tag{10}$$

where: n_h is the number of batteries calculated to meet the working time requirements, W_{bat} is the energy that can be released by a single battery, and t_w is the working time of the unit, h.

In the design of the power battery pack, the largest of the two n_h and n_m should be selected.

Design of the gearbox

Though the drive motor has the ability of zero speed starting, and can output constant torque below the rated speed, and has the characteristics of constant power above the rated speed compared with the traditional internal combustion engine, it is necessary to make the motor work in the high-efficiency area as much as possible (that is, near the rated speed of the motor). It is stipulated that when the motor is at rated speed, the corresponding vehicle speed is at rated speed, so the energy consumption of horticultural machinery can be reduced and the working time can be extended. The motor can work in the high efficiency area with more gears (Tao Liu, 2020; Yanni Chen et al., 2018; Kang Huang et al., 2020).

According to the principle that the driving force curve of adjacent two gears must have at least one intersection point in the design of multi-speed transmission, the number of the gears of the transmission can be calculated, as shown in equation (11).

$$\frac{v_{max}}{v_{rat}} \leq \beta^n \tag{11}$$

where, β is the coefficient of the motor expanding the constant power zone, the general value is 2~4, and n is the number of the gear.

From the above formula, the value range of the number of blocks can be obtained.

$$n \geq f(v_e, \beta) = \frac{\log\left(\frac{v_{max}}{v_e}\right)}{\log(\beta)} \tag{12}$$

According to the formula, the relationship between the rated vehicle speed and the transmission gear can be obtained.

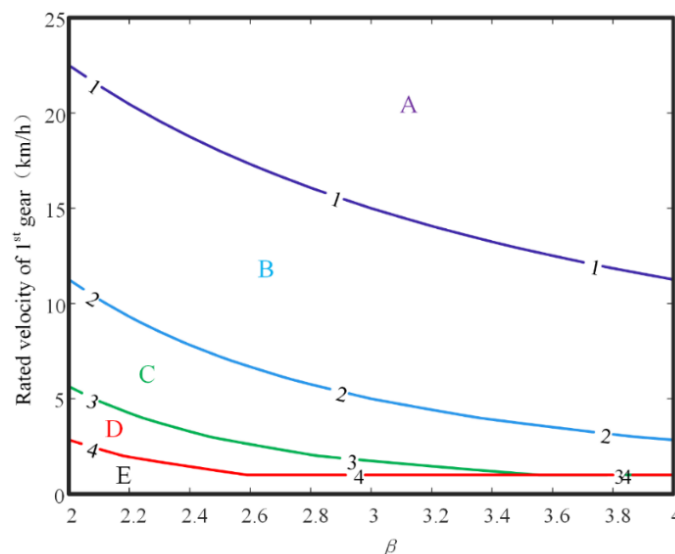


Fig. 4 - The relationship between the number of gears and the rated speed of 1st gear

Figure 4 showed relationship between the transmission gear number and the rated point speed of 1st gear. It can be seen from the figure that the gear number divides it into different areas, wherein area A represents the range of rated speed of 1st gear when selecting single gear, area B represents the range of rated point speed of 1st gear when two gears are set, area C means the range of 1st gear rated point speed when setting three gears, area D represents the range of 1st gear rated point speed when setting four gears, and area E represents the range of 1st gear rated point speed when setting five gears. Considering the wide range of values of the rated point speed of the first gear in the B area and the reduction of the complexity of the transmission system, it is possible to set two gears to improve the power and economy of the horticultural machinery.

Gear ratio parameters

According to the kinematic relationship of the vehicle driveline, the maximum gear ratio of the vehicle gearbox has the following relationship (equation (13)) with the peak speed of the motor and the maximum speed of the vehicle (Gözen E. et al., 2022).

$$i_{hg} \leq 0.377 \frac{n_{max} r_w}{v_{max}} \tag{13}$$

Among them, i_{hg} is the gear ratio of the highest gear of the transmission, r_w is the tire radius, and n_{max} is the peak speed of the motor.

Considering the characteristics of the motor, the maximum speed of the corresponding motor at the highest speed is generally 90%~95% of the peak speed, so the range of the 2-speed transmission ratio can be obtained by equation (14).

$$0.377 \frac{n_{max} r_w}{v_{max}} \times 90\% \leq i_2 \leq 0.377 \frac{n_{max} r_w}{v_{max}} \times 95\% \tag{14}$$

According to the principle that the driving force curves of adjacent two gears must have at least one intersection, their constraint relationship can be determined, as shown in equation (15).

$$\begin{cases} 0.377 \frac{n_e r_w}{i_1} \leq 0.377 \frac{n_e r_w}{i_2} \\ 0.377 \frac{n_e r_w}{i_2} \leq 0.377 \frac{n_{max} r_w}{i_1} \end{cases} \tag{15}$$

From the above equation, the relationship between the 1st gear ratio and the 2nd gear ratio can be obtained, which can be shown in equation (16).

$$i_2 < i_1 \leq i_2 \beta \tag{16}$$

Since the rated speed of the motor has been determined, the relationship between the 1st gear ratio and the rated point speed of 1st gear can be calculated by equation (17).

$$0.377 \frac{n_e r_w}{v_{e_min}} \geq i_1 \geq 0.377 \frac{n_e r_w}{v_{e_max}} \tag{17}$$

where: v_{e_min} is the minimum value of the 1st gear rated point speed range; v_{2_max} is the maximum value of the 1st gear rated point speed range.

Combining the above formula, the range of gear ratios of 1 and 2 gears can be obtained, as shown in Table 1.

Table 1

| Range of the gear ratio | |
|-------------------------|---------------------|
| Gear | Range of gear ratio |
| 1st | 9.42~20.54 |
| 2nd | 9.42~9.94 |

Optimization of the gear ratio considering the working cycle

Construction of composite working cycle

The main goal of the design of the gearbox is to reduce the energy consumption of the horticultural machinery under different working cycles (Baohua Zhou, 2010; Xuebing Yin et al., 2022; Li Y et al., 2020; Sun G.B. et al., 2021).

The gear ratio should be optimized with the goal of minimum energy consumption (Krüger B. et al., 2022; Peng H. et al.; 2022, Licun F. et al., 2007; Eckert J.J. et al., 2022, Zhu B. et al., 2013; Wang W. et al., 2019).

In this study the gear ratio should be optimized under different working cycles, therefore, the composite working cycle contains ploughing, rotary tillage and transportation. The composite working cycle should reflect the actual conditions of the horticultural machinery.

Considering the actual operating conditions of horticultural machinery, the composite working cycle (transportation + ploughing + transportation + rotary tillage + transportation) are constructed, which reflect the actual work flow of the horticultural machinery: go to the field, work (repeat process), and go to home. The constructed composite working cycle is illustrated in Figure 5.

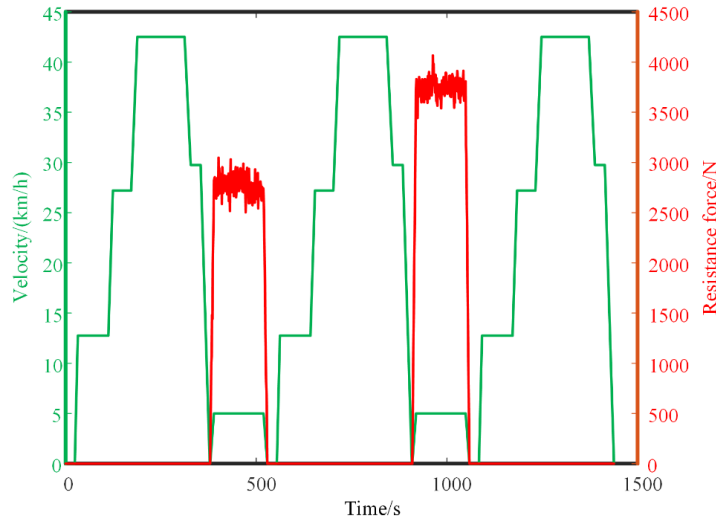


Fig. 5 - The composite working cycles (transportation + ploughing + transportation + rotary tillage + transportation)

RESULTS

Optimization of gear ratio of two-speed transmission based on genetic algorithm

The transmission ratio is optimized by genetic algorithm, the optimization process is shown in Figure 6. The simulation model was built with Matlab/Simulink, the working cycle built above was set in the model and the shift schedule and control strategy were made with Matlab/Stateflow, the energy consumption was chosen as the Fitness function. The maximum number of iterations was set to 50, and the optimization process and results are shown in Figure 7.

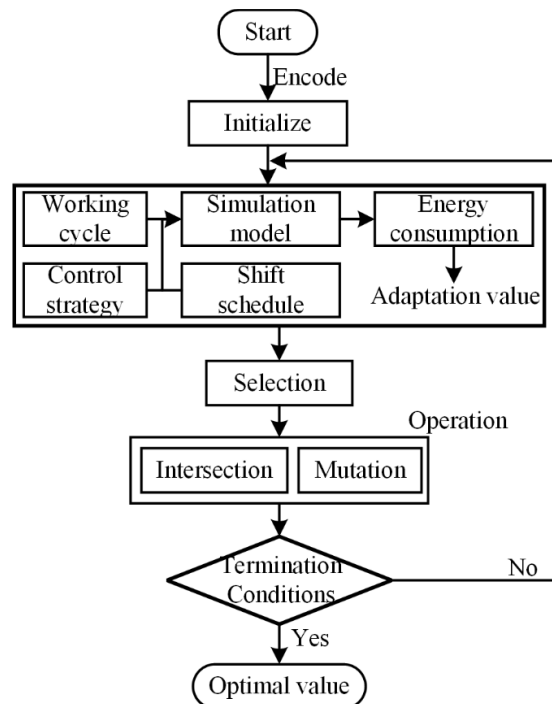


Fig. 6 - Work flow optimization of the gear ratio

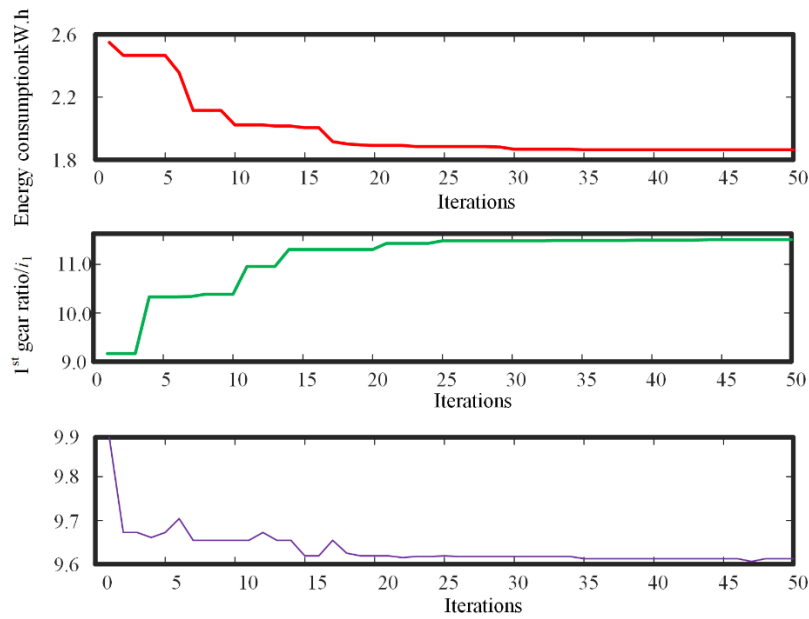


Fig. 7 - Optimization result of the gear ratio

It can be seen from figure 7 that the solution tends to converge when the number of iterations is 25, the first gear ratio finally converges to 11.6, the second gear ratio converges to 9.62, and the optimized gear ratio is shown in the table.

Table 2

Optimization result of the gear ratio

| 1st | 2nd |
|------|------|
| 11.6 | 9.62 |

To verify the optimization result, the optimized gear ratio was applied to different working cycle and the comparison was made with single gear. In this study, the single gear ratio was set to be $i_{ig} = 9.8$. and the comparison of different cycles were made as follows.

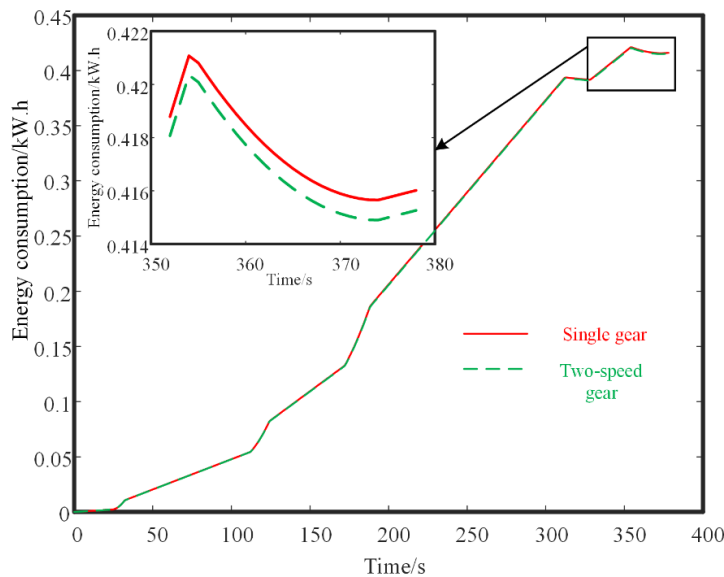


Fig. 8 - Comparison in one transportation test cycle

Figure 8 showed the comparison result under transportation cycle. It can be seen from the figure that the energy consumption of single gear is 4.16×10^{-1} kW.h in one test cycle. The energy consumption of two-speed gear is 4.15×10^{-1} kW.h, the energy consumption can be reduced by 0.25% in one transportation test cycle.

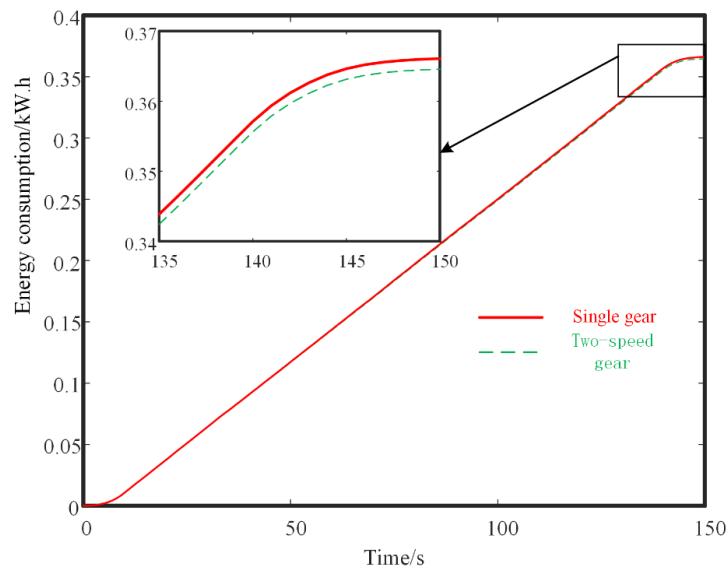


Fig. 9 - Comparison in one ploughing test cycle

Figure 2 showed the comparison result of ploughing test cycle. It can be seen from the figure that the energy consumption of two-speed gear is lower than the single gear. The energy consumption of single gear is 3.661×10^{-1} kW.h in one ploughing test cycle. The energy consumption of two-speed is 3.646×10^{-1} kW.h in one ploughing test cycle. The energy consumption can be reduced by 0.41% in one ploughing test cycle.

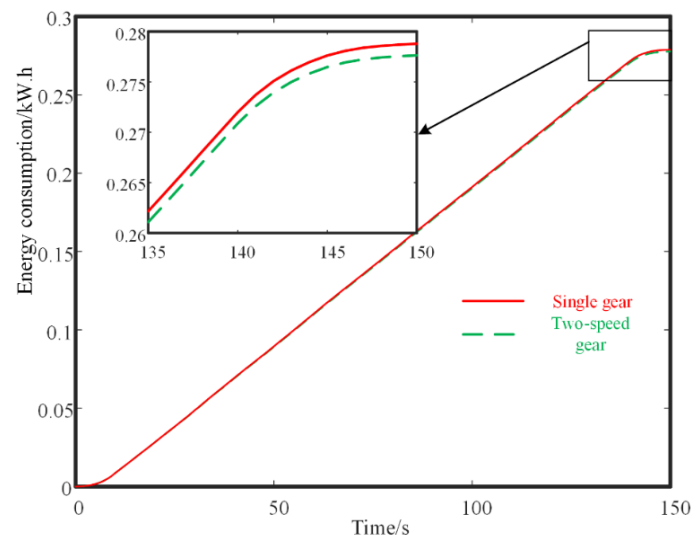


Fig. 10 - Comparison in one rotary tillage test cycle

Figure 10 shows the comparison result of rotary tillage test cycle. It can be seen from the figure that the energy consumption of single gear is 2.788×10^{-1} kW.h in one rotary tillage test cycle. The energy consumption of two-speed gear is 2.776×10^{-1} kW.h in one rotary tillage test cycle. The energy consumption can be reduced by 0.41% in one rotary tillage test cycle.

CONCLUSIONS

In this study, a two-speed transmission system was proposed based on the characteristics of the driving cycle of the horticultural machinery. Firstly, the test cycle of the horticultural machinery was established based on the data collector that fixed on the machinery. Secondly, the two-speed driveline system was designed. To reduce the energy consumption in the horticultural machinery working cycle, the gear ratio of the two-speed gear box was optimized with the goal of minimum energy consumption by genetic algorithm. The optimal gear ratio was obtained, and the comparison was made with the single speed gearbox, the comparison result showed that the energy consumption can be reduced 0.25, 0.41% and 0.41% under the transportation, ploughing and rotary tillage test cycle.

ACKNOWLEDGEMENT

This work is supported by the National Key R&D Program Project of China (No.2023YFD2001102), Shenzhen Polytechnic University Research Fund (No. 6023310012K), Scientific Research Project of Shenzhen Polytechnic University (No. 6021310021K) Shenzhen Polytechnic University Research Fund (No. 6024310003K).

REFERENCES

- [1] Ali, A. M., & Asfoor, M.S. (2022). Optimal Battery Sizing and Stops' Allocation for Electrified Fleets Using Data-Driven Driving Cycles: A Case Study for the City of Cairo. *IEEE Transactions on Transportation Electrification*, 9(1), 896-911. DOI: [10.1109/TTE.2022.3160615](https://doi.org/10.1109/TTE.2022.3160615)
- [2] Baohua Zhou. (2010), Study on parameters design and shifting control strategy for transmission system of electric vehicle (电动汽车传动系统参数设计及换挡控制研究). *Chongqing University*, Chongqing.
- [3] Cao Zhang, Sihong Zhu, and Junyang Yang, Songhui Gao, Xiaoting Deng. (2015). Matching design and performance analysis for driving system of solar garden tractor (太阳能园艺拖拉机驱动系统匹配设计与性能分析). *Transactions of the Chinese Society of Agricultural Engineering*, 31(11):24-30.
- [4] Eckert J.J., da Silva S.F., Santiciolli F.M., de Carvalho Á.C., Dedini, F.G. (2022), Multi-speed gearbox design and shifting control optimization to minimize fuel consumption, exhaust emissions and drivetrain mechanical losses. *Mechanism and Machine Theory*, 169, 104644. <https://doi.org/10.1016/j.mechmachtheory.2021.104644>
- [5] Fengxiang Lu, Jinguo Liu, Qinfang Tang, Houfei Xu, Rui Shan, Quan Zhen. (2020). Design and test of multi-power output device for garden tractor (园艺拖拉机多动力输出装置设计与试验). *Journal of Chinese Agricultural Mechanization* [J], 41(01):54-58. DOI: 10.13733/j.jcam.issn.2095-5553.2020.01.10.
- [6] Gaoli Chen. (2023). Multi-objective optimization and experiment study of electric tractor drive motor (电动拖拉机驱动电机的多目标优化及试验研究). *Journal of Agricultural Mechanization Research*, 45(10):250-255. DOI: 10.13427/j.cnki.njyi.2023.10.041.
- [7] Gözen, E., Çevirgen, M. S., Özgül, E., (2022). Transmission speed and ratio optimization for heavy-duty electric truck. *Heliyon*, 8(8). DOI:<https://doi.org/10.1016/j.heliyon.2022.e10028>
- [8] Jingwen Xiao. (1998) Test the power consumption of rotary cultivator with a comprehensive tester for automobile tractors (用汽车拖拉机综合测试仪测试旋耕机功耗). *Tractor & Farm Transporter*, (06):43-45.
- [9] Junxia Zhang, Jinzhe Yang, Guocai Ji, Zhonglin Li, Yueying Zhu. (2020). Multi-objective optimization of the transmission system parameters of electric tractors based on actual conditions (基于实际作业工况的电动拖拉机传动系统参数多指标同步优化). *Journal of Tianjin University of Science & Technology*, 35(03):63-68. DOI:10.13364/j.issn.1672-6510.20180211.
- [10] Kang Huang, Zhelien Liu, and Mingming Qiu, Yiran Zhang, Qiang Wang, Yan Ru. (2020). Multi Objective parameters decoupling optimization method of two-speed Evs (两挡纯电动汽车多目标参数解耦优化方法). *China Mechanical Engineering*, 31(06):746-755.
- [11] Kargar, M., Sardarmehni, T., Song, X. (2022). Optimal powertrain energy management for autonomous hybrid electric vehicles with flexible driveline power demand using approximate dynamic programming. *IEEE Transactions on Vehicular Technology*, 71(12), 12564-12575. DOI: [10.1109/TVT.2022.3199681](https://doi.org/10.1109/TVT.2022.3199681)
- [12] Krüger, B., Keinprecht, G., Filomeno, G., Dennin, D., Tenberge, P. (2022). Design and optimisation of single motor electric powertrains considering different transmission topologies. *Mechanism and Machine Theory*, 168, 104578. <https://doi.org/10.1016/j.mechmachtheory.2021.104578>
- [13] Lee, T., Choi, S.B. (2023). Real-time optimization of gear shift trajectories using quadratic programming for electric vehicles with dual clutch transmission. *IEEE Transactions on Vehicular Technology*, 72(7), 8647-8660. DOI: [10.1109/TVT.2023.3246179](https://doi.org/10.1109/TVT.2023.3246179)
- [14] Licun, Fang, Shiyin, Qin. (2007), Parameters optimization of hybrid electric vehicle based on multi-objective genetic algorithms. *Automotive Engineering*, 29(12), 1036-1040.
- [15] Li Y., Zhu B., Zhang N., Peng H., Chen Y. (2020). Parameters optimization of two-speed powertrain of electric vehicle based on genetic algorithm. *Advances in Mechanical Engineering*. 12(1), 1-16. <https://doi.org/10.1177/1687814020901652>

- [16] Mengnan Liu, Shuyuan Li, Liyou Xu, Yirong Zhao. (2022). Design and performance analysis of tractor bidirectional coupling electric drive system (拖拉机双向耦合电驱动系统设计与性能分析). *Transactions of the Chinese Society for Agricultural Machinery*, 53(04):423-431+449.
- [17] Park, J., Choi, S., Oh, J., Eo, J. (2022). Adaptive slip engagement control of a wet clutch in vehicle powertrain based on transmitted torque estimation. *Mechanical Systems and Signal Processing*, 171, 108861. <https://doi.org/10.1016/j.ymssp.2022.108861>
- [18] Peng H., Qin D., Hu J., Chen Z. (2022). Analysis of the influence of power coupling type and transmission type of the powertrain on the performance of single-motor hybrid electric vehicles. *Proceedings of the Institution of Mechanical Engineers, Part D: Journal of Automobile Engineering*, 236(6), 1285-1299. <https://doi.org/10.1177/09544070211033952>
- [19] Rossi, C., Pontara, D., Falcomer, C., Bertoldi, M., Mandrioli, R. (2021). A hybrid–electric driveline for agricultural tractors based on an e-CVT power-split transmission. *Energies*, 14(21), 6912. <https://doi.org/10.3390/en14216912>.
- [20] Shuping Fan, Ningning Wang, Kechuan Yi, Jieping Chen. (2017). Design and performance analysis of power system for pure electric tractor (纯电动拖拉机动力系统设计与性能分析). *Journal of Chinese Agricultural Mechanization*, 38(01):80-84.
- [21] Sun G.B, Y.J. Chiu, W.Y. Zuo, S. Zhou, J.C Gan, Y. Li, (2021). Transmission ratio optimization of two-speed gearbox in battery electric passenger vehicles. *Advances in Mechanical Engineering*. 13(6), 1-13. <https://doi.org/10.1177/16878140211022869>
- [22] Tao Liu. (2020). Research on design and control strategy of the horticultural electric tractor driving system (园艺电动拖拉机驱动系统设计与控制策略研究). *Jiangsu University*, Zhenjiang.
- [23] Wang W., Li J.Q., Sun F.C. (2019). Pseudo-spectral optimization of smooth shift control strategy for a two-speed transmission for electric vehicles. *Vehicle System Dynamics*, 1-26. <https://doi.org/10.1080/00423114.2019.1594316>
- [24] Xuebing Yin, Yong Chen, Qinglin Dai, Hai Liu, Naili Tian, Bolin He. (2022). Study on shift schedule of 2DCT for pure electric vehicle based on NSGA-II Algorithm and Fuzzy Control (基于 NSGA-II 算法和模糊控制的纯电动汽车 2DCT 换挡规律研究). *Automotive Engineering*, 44(10):1571-1580.
- [25] Xiaolei Cai, Xiaoyong Zhu, Zhiling Liao, Hongping Jia, Lei Xu. (2023). Design and test of electric tractor drive system used in greenhouse (温室大棚用电动拖拉机电驱系统设计与试验). *Journal of Agricultural Mechanization Research*, 45(11):222-228.
- [26] Xiaosen Hou, Xin Zhang, and Ong Zhou, Wenli Mao. (2019). Data Collection test for tractor working load Condition (拖拉机作业负载工况数据采集试验). *Tractor & Farm Transporter*, 46(01):6-8+12.
- [27] Yanni Chen. (2018). Study on design and drive control methods of powertrain for electric tractor (电动拖拉机动力系统设计与驱动控制方法研究). *China Agricultural University*, Beijing.
- [28] Yiqi Huang, Changying Ji, Shuping Yan. (2007). Research on horticultural tractors and their supporting tools (园艺拖拉机及其配套机具的研究). *Abstracts of the 2007 Annual Conference of the Chinese Society of Agricultural Engineering*, 1, Daqing.
- [29] Yu Liu. (2023). Design and Experimental study of dual motor drive system for electric tractor (电动拖拉机双电机驱动系统的设计及试验研究). *Journal of Agricultural Mechanization Research*, 45(11):247-252+258.
- [30] Zhu B., Zhang N., Walker P., Zhan W.Z., Zhou X.X., Ruan J.G. (2013). Two-Speed DCT Electric Powertrain Shifting Control and Rig Testing. *Advances in Mechanical Engineering*, (4):543-564. <https://doi.org/10.1155/2013/3239>

A PRIMARY INVESTIGATION OF SEPARATING ALFALFA STEMS AND LEAVES BY CHOPPING AND BLOWING METHOD

苜蓿切断-气吹茎叶分离方法初步研究

Bojun CAO¹⁾, Tianlin ZUO¹⁾, Bei WU^{*1,2)}, Tianci HUANG¹⁾, Huaiyuan QIAN¹⁾

¹⁾ Hunan Agricultural University, College of Mechanical and Electrical Engineering, Changsha/China;

²⁾ Hunan Key Laboratory of Intelligent Agricultural Machinery and Equipment, Changsha/China

Tel: +86 15802521582; E-mail: wubei@hunau.edu.cn

Corresponding author: Bei Wu

DOI: <https://doi.org/10.35633/inmateh-73-53>

Keywords: alfalfa, stems and leaves separation, chopping and blowing method, suspension velocity

ABSTRACT

The protein content of alfalfa leaves surpasses that of stems significantly, rendering harvested alfalfa following stems-leaves separation a valuable resource for livestock feed, thus ensuring the provision of high-quality raw materials for production. This study introduces a novel process for stems-leaves separation, alongside the establishment of a suspension velocity experiment rig aimed at investigating and determining the suspension velocity of alfalfa leaves, stems, and plants across various moisture levels. The relationship among various factors including different alfalfa components, the length of lateral branches, stem lengths, Moisture Content (MC), and suspension velocity was empirically derived through experimentation. In this study, the chopping and blowing method was proposed, where the alfalfa was cut into pieces according to a certain length, and then the alfalfa was blown apart by generating airflow through a fan. To comprehensively analyze the impact of airflow velocity and cutting length on the Separation Evaluation Index, a response surface mathematical model was developed. The empirical findings indicate optimal stems and leaves separation of alfalfa when the airflow velocity reaches 4.29556 m/s, paired with a cutting length of 33.7956 mm. Conclusively, this experiment validates the efficacy of the chopping and blowing separation method for alfalfa stems and leaves segregation, thereby offering valuable insights into alfalfa stems and leaves separation practices. The outcomes of this study hold significant reference value for the broader alfalfa agricultural domain.

摘要

苜蓿的叶片蛋白质含量远远高于茎秆，进行茎叶分离收获后的苜蓿可以作为畜牧饲料提供优质的生产原料。本文采用了一种全新的工艺进行茎叶分离，搭建了悬浮速度试验台，分别研究测定了苜蓿的叶片、茎秆、植株在不同含水率情况下的悬浮速度。通过试验得出了苜蓿的不同组分、侧枝长度、茎秆长度、含水率(MC)与悬浮速度的关系。本研究提出了切断-气吹分离方法，将苜蓿按照一定的长度将其切分，再通过风机产生气流将苜蓿吹分。建立了响应面数学模型，分析了气流速度和切断长度对分离评估指数(SEI)的影响。实验结果表明，在气流速度为4.29556m/s，切断长度为33.7956mm时，苜蓿的茎叶分离效果最好。本试验得出了切断-气吹分离法是苜蓿茎叶分离的一种可行方法，研究结果可以为苜蓿茎叶分离提供参考价值。

INTRODUCTION

Alfalfa is known as the "King of Forages" (Liu et al., 2023), due to its significant role in the forage production systems. While it is renowned for its protein richness, there's a notable disparity in the nutritive value between its stems and leaves. The protein content in the leaves often surpasses that of the stems by 2-2.5 times (Motsinger et al., 2021). However, traditional methods of utilizing alfalfa as feed, where the whole plant is used, have led to suboptimal nutrient utilization. Harvesting alfalfa with the separation of stems and leaves has emerged as a crucial technique for acquiring leaves protein (Lange et al., 2023). By focusing on separating the valuable leaves from the stems, this method enhances the potential for utilizing alfalfa's high-protein content more efficiently.

Presently, two primary modalities for separating alfalfa stems and leaves prevail: "post-harvest separation" and "direct separation in the field" (Zhang *et al.*, 2017). The former encompasses sieving, wind separation, and drying separation. The sieving technique employs vibrating screens to segregate dry, chopped forage stems and leaves. For instance, Pfister (1980) devised a technical solution involving striking, chopping, and sieving alfalfa post-harvest, subsequently segregating the fine leaves fraction from the coarse stem fraction. Wind separation exploits the differential aerodynamic properties of dry leaves and stems, with typical equipment categorized as vertical or horizontal. Gan-Mor, *et al.* (1986), demonstrated that horizontal wind separation yielded superior results, achieving a separation rate exceeding 90%. Bilanski, *et al.*, (1989), investigated the impact of material moisture content, feeding speed, wind speed, and other factors on the separation rate using horizontal wind separation equipment, offering an estimation formula for the separation rate of coarse proteins. Moreover, Bilanski, *et al.*, (1989), explored the drying separation method, achieving stems and leaves separation concomitant with artificial drying. Adapa, *et al.*, (2005), scrutinized the hot air separation method for cutting alfalfa, capable of simultaneously affecting the drying and stems and leaves separation of alfalfa. Beyond these conventional methods, some scholars have delved into stems and leaves separation techniques and equipment for post-harvest fresh forage (Siles *et al.*, 2015), aiming to transition from whole plant drying to leaf drying exclusively, thereby advancing energy conservation and efficiency goals. The "direct field separation" mode offers distinct advantages over the "post-harvest separation" approach, primarily in terms of operational simplicity and reduced nutrient loss of forage. This mode comprises two main methods: the stratified harvesting method and the segmented harvesting method. The layered harvesting method capitalizes on the natural distribution of alfalfa branches and leaves, which are predominantly concentrated in the upper part of the plant. This method involves harvesting alfalfa in staggered layers, both above and below. Yang Zhao (2015), delved into determining the optimal mowing height for stratified harvesting of alfalfa, optimizing the process for maximum efficiency. In 1964, some academics pioneered the concept of segmented harvesting of alfalfa stems and leaves (Currence, 1964; Currence and Buchele, 1967). Currence designed a double-drum alfalfa stems and leaves separation equipment, validating the feasibility of directly harvesting alfalfa leaves through field trials. These trials demonstrated that the collected leaves material had a higher nutritional value compared to whole alfalfa. Additionally, the alfalfa stems could be recovered after leaf harvesting, or left in the field to facilitate regrowth. In recent years, there has been a surge in research on alfalfa-segmented stems and leaves separation harvesting technology and equipment. Innovative solutions and joint harvesting equipment for forage stems and leaves separation have been continuously emerging (Pratt and Jackson, 2021; Liebhardt, *et al.*, 2022; Arinze, *et al.*, 2007), indicating a growing interest and investment in this field. This trend underscores the ongoing efforts to optimize harvesting techniques for alfalfa, aiming to enhance efficiency and preserve the nutritional quality of the forage. Research into the storage treatment of leaf material after segmental harvesting has been progressively undertaken. Digman, *et al.*, (2013), proposed a methodology involving pressing and dehydrating the leaf material before storage, aimed at addressing the challenge of post-harvest leaf material preservation. Some academics (Sikora, *et al.*, 2019; Muck, *et al.*, 2010; Bao, *et al.*, 2023), explored the technique of mixed silage comprising alfalfa leaves, stems, and corn. Andrzejewska, *et al.*, (2017), conducted a study on the silage production of alfalfa, incorporating the separation technology and equipment for oriental goat bean stems and leaves.

Currently, the development trend of the alfalfa harvesting method is "direct separation in the field". Shinnars *et al.* (2004, 2007), utilized a multi-tined rotor to strip the leaves directly in the field and obtained high leaf purity. This is a reliable way to separate alfalfa stems and leaves in the field. Additional mechanisms are needed on the machine to chop the stalks. In this study, by considering the combination of the chopping method in silage harvesting and the blowing method in alfalfa drying and separation, the chopping and blowing method was considered a potentially viable method of field alfalfa separation and harvesting. Before putting the methodology into practice, exploring the distinct suspension characteristics of each component of alfalfa is an important work. In this regard, Li, *et al.*, (2006), studied the effect of alfalfa moisture content on suspension velocity, and Wu, *et al.*, (2014), measured the suspension velocity of alfalfa at different growth periods. However, there are no reference data on the suspension velocity of different fractions of fresh alfalfa with different cutting lengths.

In this study, the feasibility and optimal process parameters of the chopping and blowing separation method under laboratory conditions have been initially investigated. A suspension velocity experiment bench was constructed, to determine the suspension velocity parameters of various fractions of alfalfa, varying lengths of lateral branches, and different lengths of stems across different moisture content gradients during the harvesting period.

Through experimentation, relationships between different fractions of alfalfa, lengths of lateral branches, stem lengths, MC, and suspension velocity were established. On this basis, an investigation focused on the separation of alfalfa stems and leaves using the chopping and blowing separation method was conducted aiming to discern the relationship between cutting length, airflow velocity, and the Separation Evaluation Index. The experimental findings can offer valuable insights for alfalfa stems and leaves separation research.

MATERIALS AND METHODS

Experiment equipment

The suspension speed of alfalfa was assessed using a custom-made suspension speed experiment bench, illustrated in Figure 1. During experimenting, the feeding gate and material net facilitate the placement of alfalfa materials, while the material blocking bag, designed as a net, prevents material displacement due to excessive airflow without impeding airflow discharge. The airflow velocity is measured by TES-1341 Thermal Anemometer with a range of 0-30 m/s and a resolution of 0.01 m/s.



Fig. 1 - Suspension speed experiment device

- 1- Material-blocking bag; 2 - Observation tube; 3 - Frame; 4- Rectification grille; 5 - Transition hose; 6- Damper;
7- Centrifugal fan; 8- Down regulator; 9- Material net; 10- Feeding door 11- Up regulator

The harvesting occurred during a period characterized by high temperatures and dry conditions, resulting in the alfalfa plants exhibiting weakened growth and smaller dimensions, with both leaves and stems being relatively diminutive. At the time of cutting, the average height of the harvested alfalfa was measured at 534.57 millimeters, with stem diameters falling within the range of 1.5 to 2.5 millimeters. Notably, the initial moisture content (MC) of the alfalfa material was recorded at 70.34%.

Theoretical analysis of suspended velocity

By Newtonian principles, suspension velocity denotes the fluid velocity at which particles of a solid or liquid are held in suspension within the fluid medium (Shehryar et al., 2019). Newton's law elucidates that the force exerted by the airflow upon the material was calculated as follows:

$$F = \frac{1}{2} k \gamma s v^2 \quad (1)$$

where: F is airflow force, [N]; γ is air density, [kg/m^3]; v is relative velocity of the material to the airflow, [m/s]; s is material in the direction of airflow velocity cross sectional area, [m^2]; k is resistance coefficient.

When the airflow force (F) on the material is equal to gravity, the material will be suspended in the airflow (Meibohm et al., 2017; Dana and Moghaddam, 2022). At this time, the absolute speed of the material is zero, and the magnitude of the airflow velocity is the suspension velocity of the material, so the suspension velocity of the material was calculated as follows:

$$v_f = \sqrt{\frac{mg}{k\gamma s}} \quad (2)$$

v_f is material suspension speed, [m/s]; m is the mass of material, [kg]; g is gravitational acceleration, [N/kg].

During the suspension of alfalfa material at a specified elevation within the observation tube, the assessment entails the extension of an experiment rod housing a thermal sensing element from the anemometer into the observation tube through the designated measurement orifice. Sequentially, the wind velocity at several measurement points is determined, and subsequently averaged for each assessment. The determination of measurement point placement is conducted employing the equal-area circle method.

As illustrated in Figure 2, the cross-section of the pipe is stratified into three segments based on area, with measurement points situated along the equidistant lines within each segment.

$$R_i = R_0 \times \sqrt{\frac{2i-1}{2n}} \quad (3)$$

where: R_i is equidistant radius, [m]; R_0 is radius of cross-sectional area of down regulator, [m]; n is equivalent fraction of cross-section of Down regulator.

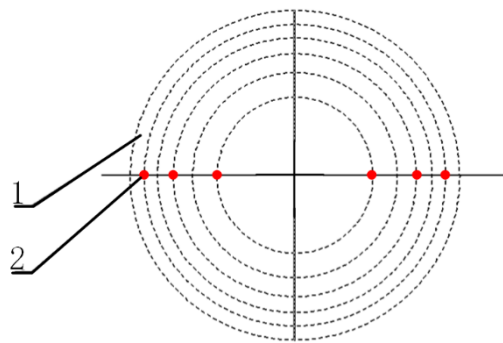


Fig. 2 - Position of measuring points
1- Pipe cross section; 2- Measuring points

Suspension velocity experiment of different components of alfalfa

Before commencing the experiment, alfalfa samples from the same batch were meticulously arranged on an elevated drying rack to ensure uniform distribution. For each experiment iteration, alfalfa was randomly selected, while the remaining samples underwent natural drying until reaching the requisite MC range. Throughout the experiment, the randomly chosen alfalfa samples were methodically sorted into three distinct components: leaves, stems (measuring 100 mm in length and 1.5 mm-2.5 mm in diameter), and whole plants (measuring 300 mm in length from tip to root). Each component comprised a minimum of 15 specimens, as depicted in Figure 3-a. These specimens were then positioned on the mesh material, with the feeding door subsequently closed. Initiating the experiment procedure entailed activating the fan and gradually adjusting the dampers to incrementally increase airflow until achieving a stable suspension of the material at a predetermined height within the observation tube. After airflow velocity measurement (We *et al.*, 2021), the fan was deactivated, and the material was removed. The MC of the leaf, stem, and plant specimens were independently measured thrice per group to ascertain the mean value. Suspension velocity assessments were repetitively conducted for 15 samples of alfalfa leaves, stems, and plants across varying MC gradients, with the resultant average value deemed the definitive outcome.

Suspension velocity experiment of alfalfa with different lengths of lateral branches

Before experimenting, the alfalfa experiment materials from the same batch were uniformly spread onto the suspension drying rack. A selection of alfalfa was then chosen for experimenting at a given interval, while the remaining materials were naturally air-dried to achieve the desired MC range. Throughout the experiment, a random assortment of alfalfa materials was manually segmented into six groups based on length categories: <60 mm, 80-120 mm, 120-160 mm, 160-200 mm, 200-240 mm, and >240 mm. It was ensured that each group contained a minimum of 15 specimens, as illustrated in Figure 3-b.

These six groups of sidestep samples were then positioned on the material net. Subsequently, the feeding door was sealed, the fan was activated, and the airflow was meticulously adjusted until the material could be suspended at a consistent height within the observation tube. The airflow rate was quantified, following which the fan was deactivated, and the material was withdrawn for MC analysis. This process was repeated thrice for each of the six sidestep sample groups to derive an average MC value.

Each of the six sample groups underwent three repetitions to calculate the average MC. Furthermore, within each MC gradient, the experiment was replicated with the six groups of alfalfa systems to measure the suspension speed of 15 samples. The resultant average value was deemed as the measurement outcome.

Suspension velocity experiment of alfalfa with different lengths of stems

Before conducting the test, the alfalfa test materials from the same batch were first evenly spread on an overhanging drying rack. A portion of the alfalfa was then selected for testing, while the remaining materials were allowed to naturally air-dry until they reached the desired MC range. During the test, the selected alfalfa materials were manually divided into eight groups based on stem lengths: 25 mm, 50 mm, 75 mm, 100 mm, 125 mm, 150 mm, 175 mm, and 200 mm. It was ensured that each group contained at least 15 specimens, as shown in Figure 3-c. These eight groups of stem samples were separately placed on the material net. The feeding door was closed, the fan was started, and the air valve was adjusted to gradually increase the airflow until the material could be stably suspended at a certain height in the observation tube. The airflow velocity was then measured, the fan was shut down, and the material was removed. For each of the eight groups of stem specimens, the MC was measured three times to obtain an average value. This process was repeated under each gradient of MC. Additionally, under each MC gradient, the experiment was repeated with the eight groups of stems to measure the suspension speed of 15 specimens per group. The final average value was then taken as the measurement result for each group.

Chopping separation experiment

Before the start of the experiment, the fresh alfalfa was randomly divided into nine groups manually. Each group of alfalfa will be cut according to different cutting lengths, and the lengths of the nine groups of cuttings are 10 mm, 15 mm, 20 mm, 25 mm, 30 mm, 35 mm, 40 mm, 45 mm, and 50 mm, ensuring that there are 15 specimens in each group. After the alfalfa is processed, it is chopped into alfalfa fractions of the same length, which consist of three fractions: leaves-stems connection fractions, pure leaves fractions, and pure stems fractions. The alfalfa fractions were then manually selected and separated strictly according to the three different fractions, and the contents of stems and leaves still adherent, pure leaves, and pure stems were counted in each set of trials. Each set of trials was repeated three times and the results were averaged.

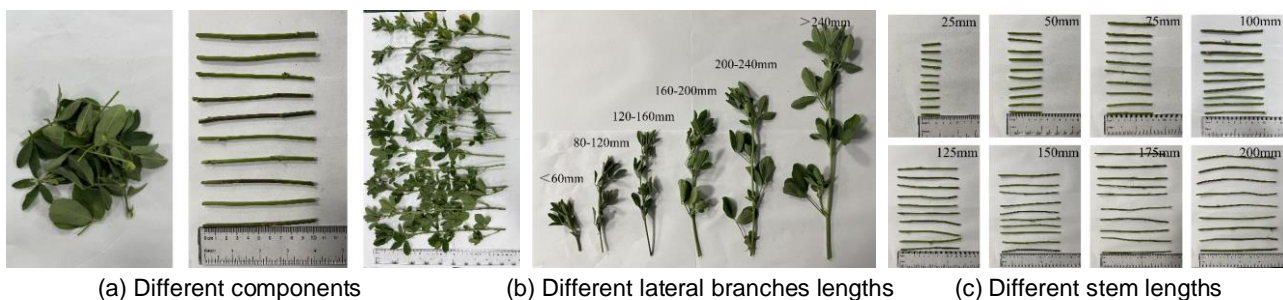


Fig. 3 - Different forms of alfalfa

Chopping and blowing separation experiment

In order to explore the optimal process parameters for chopping and blowing separation, the central composite design (CCD) of the response surface method was used to construct the experiment proposal. Response surface design is a statistically comprehensive experimental technique for dealing with the action of multiple variables on response, which can construct the regression fit with a limited number of trials. Previous experimental research identified airflow velocity and cutting length as influential factors affecting the separation of alfalfa stems and leaves. Accordingly, airflow velocity (X_1) and cutting length (X_2) were chosen as the test factors, with the Separation Efficiency Index (*SEI*) serving as the evaluation index.

According to the CCD method, five levels were selected for each test factor and experimental factor coding was employed, as outlined in Table 1. Design-Expert 12.0 software is used for Central Composite Design, there are 13 different groups of the experiment proposal as shown in Table 5. The different experimental groups contained both replicates (Test No. 6, 9, 8, 12, and 13) and different combinations of levels of each factor.

Table 1

| Level | Factors and levels | |
|----------|--|---------------------------------------|
| | Airflow velocity X ₁ [m/s] | Cutting length X ₂ [mm] |
| -1.41421 | 1.17 | 1.72 |
| -1 | 2 | 10 |
| 0 | 4 | 30 |
| 1 | 6 | 50 |
| 1.41421 | 6.83 | 58.28 |

Before the experiment begins, fresh alfalfa is manually divided into 13 groups according to the experimental plan shown in Table 1. An equal amount of alfalfa is selected for each trial. The alfalfa is first cut into small sections according to the length requirements specified in Table 1, and then thoroughly mixed. The segments of alfalfa are tested using a suspended velocity tester. During the experiment, the alfalfa is blown into two parts: one part is blown by the airflow into the material-blocking bag, while the other part remains on the material net without being blown away by the airflow. The pure leaves, pure stems, and leaves-stems connection of the two parts of alfalfa were sieved separately, and the leaves-stems connection fraction was further divided into pure leaves and pure stems. The masses of stems and leaves in both the retained and blown-away parts are recorded separately. Each of the 13 experimental groups is repeated twice, and the average values are taken as the results.

This paper introduces an index, Separation Evaluation Index (*SEI*), where $0 < SEI < 2$. A higher *SEI* indicates signifying a more effective stems and leaves separation. Conversely, a lower *SEI* indicates implying a less efficient stems and leaves separation.

$$SEI = \frac{m_{2L}}{m_{1L} + m_{2L}} + \frac{m_{2S}}{m_{1S} + m_{2S}} \quad (4)$$

where: m_{1L} is the total mass of leaves in the left-behind portion, [g]; m_{1S} is the total mass of stems in the left-behind portion, [g]; m_{2L} is the total mass of leaves in the blown-away portion, [g]; m_{2S} is the total mass of stems in the blown-away portion, [g].

RESULTS

Suspension velocity of different components of alfalfa

The experimental findings regarding the suspension velocities of distinct fractions of alfalfa across varying MC are presented in Figure 4-a. As the MC of alfalfa leaves decreased from 70% to 13%, the suspension velocity decreased from 2.21 m/s to 1.34 m/s. Similarly, a reduction in MC from 71% to 17% for alfalfa stems corresponded to a decrease in suspension velocity from 6.85 m/s to 4.01 m/s. Likewise, as the MC of whole alfalfa plants decreased from 67.75% to 13.33%, the suspension velocity diminished from 6.96 m/s to 3.0 m/s. Notably, the results reveal a significant disparity in suspension velocity among alfalfa leaves, stems, and whole plants. Specifically, alfalfa leaves exhibited a notably lower suspension velocity compared to both stems and whole plants. Conversely, the difference in suspension velocities between alfalfa stems and whole plants was negligible. Moreover, a consistent decrease in suspension velocities across all alfalfa components was observed with declining MC, indicating a linear relationship between suspension velocities and moisture levels.

Analysis of variance (ANOVA) was conducted on the experimental data about the suspension speed of various components of alfalfa under differing MC conditions, with the analysis outcomes presented in Table 2. Examination of the analysis results reveals that the P-values associated with the two factors, MC, and alfalfa components, are both less than 0.05. This observation underscores the highly significant impact that both factors exert on the suspension speed of alfalfa.

Table 2

ANOVA of alfalfa suspended velocity experiments with different alfalfa components at different MC.

| Source | SS | DF | MS | F | P-value |
|------------|----------|----|----------|----------|------------|
| MC | 16.14186 | 7 | 2.30598 | 8.40834 | 0.0004** |
| components | 50.63991 | 2 | 25.31995 | 92.32465 | < 0.0001** |
| Pure Error | 3.839488 | 14 | 0.274249 | | |
| Cor Total | 70.62126 | 23 | | | |

Suspension velocity of alfalfa with different lengths of lateral branches

The results depicted in Figure 4-b illustrate the findings from suspension velocity tests conducted on alfalfa with varying stem lengths under different MC conditions. When the length of alfalfa lateral branches decreased from over 240 mm to less than 60 mm, the suspension velocity of lateral branches with over 70% MC decreased from 5.33 m/s to 2.72 m/s. Similarly, for lateral branches with MC ranging between 50% and 60%, the suspension velocity decreased from 5.17 m/s to 2.65 m/s. Additionally, for lateral branches with MC between 20% and 30%, the suspension velocity decreased from 4.70 m/s to 2.19 m/s. A similar decreasing trend in suspension velocity was observed for lateral branches with moisture content below 20%, where the velocity decreased from 3.31 m/s to 2.02 m/s. It was observed that the suspension velocity of alfalfa lateral branches exhibited an increase corresponding to the increase in lateral branch length. Conversely, a decrease in suspension velocity was noted with a reduction in MC, while maintaining a consistent length of alfalfa lateral branches.

The experimental data about the suspension speed of alfalfa, considering varied lengths of lateral branches across different MC levels, underwent thorough analysis via ANOVA. Table 3 delineates the outcomes of this analysis. Upon scrutiny of the analysis results, it becomes apparent that the P-values associated with both factors, namely MC and lateral branch length, fell below the threshold of 0.05. This observation signifies the presence of statistically significant effects exerted by both factors on the suspension speed of alfalfa.

Table 3

ANOVA of alfalfa suspended velocity experiments with different lateral branch lengths at different MC

| Source | SS | DF | MS | F | P-value |
|------------------------|----------|----|----------|----------|------------|
| lateral branch lengths | 14.39204 | 5 | 2.878408 | 21.28784 | < 0.0001** |
| MC | 10.89201 | 3 | 3.63067 | 26.85135 | < 0.0001** |
| Pure Error | 2.028205 | 15 | 0.135214 | | |
| Cor Total | 27.31225 | 23 | | | |

Suspension velocity of alfalfa with different stem lengths

The levitation velocities of alfalfa stalks of various lengths under differing water contents are depicted in Figure 4-c. As the length of alfalfa stalks reduces from 200 mm to 25 mm, the suspension velocity decreases accordingly. Specifically, for stalks with a moisture content exceeding 60%, velocities decline from 10.06 m/s to 5.04 m/s, while for those with a moisture content below 20%, velocities decrease from 8.63 m/s to 4.51 m/s and 7.032 m/s to 3.17 m/s, respectively. A consistent trend emerges that the suspension velocity of alfalfa stalks decreases proportionally with diminishing water content. Notably, a linear correlation is observed between suspension velocity and stalk length, indicating that longer stalks exhibit greater suspension velocities.

ANOVA analysis was conducted to examine the suspension speeds of alfalfa stalks of different lengths and water contents, as presented in Table 4. Notably, both water content and stalk length yielded P-values below 0.05, indicating their significant impact on alfalfa suspension speed.

Table 4

ANOVA of alfalfa suspended velocity experiments with different stem lengths at different MC

| Source | SS | DF | MS | F | P-value |
|--------------|----------|----|----------|----------|------------|
| stem lengths | 49.30891 | 7 | 7.04413 | 39.06163 | < 0.0001** |
| MC | 22.30518 | 2 | 11.15259 | 61.84416 | < 0.0001** |
| Pure Error | 2.524673 | 14 | 0.180334 | | |
| Cor Total | 74.13876 | 23 | | | |

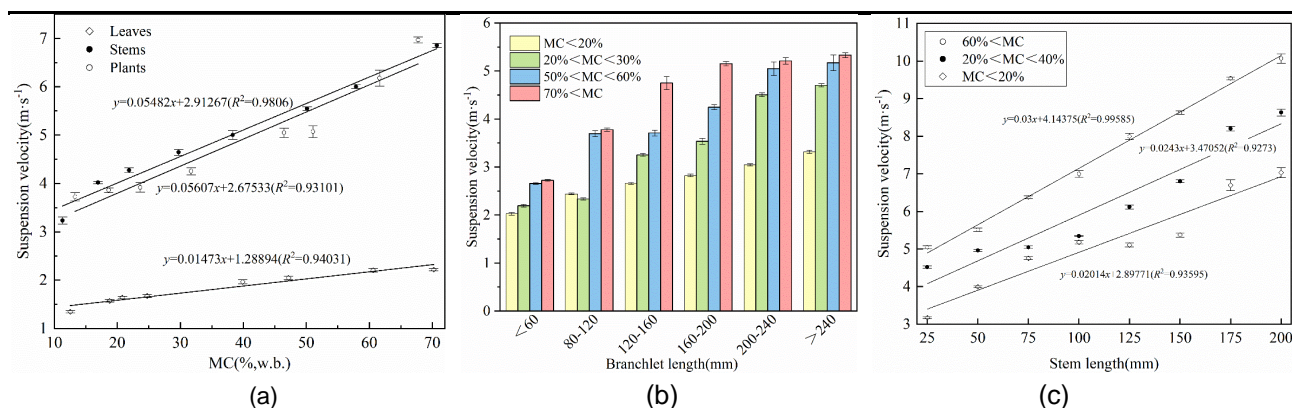


Fig. 4 - Results of the two-factor test

Chopping separation results

The results illustrated in Figure 5 elucidate the percentage composition of each component of alfalfa following separation at distinct cutting lengths. At a cutting length of 10 mm, the proportion of leaves-stems connection stood at 7.5%, whereas it escalated to 42.2% at a cutting length of 50 mm. Conversely, the proportion of pure stem was declining from 60.5% to 45.5%, and the proportion of pure leaf was diminishing from 31.9% to 12.3%. Analysis of the experimental data reveals discernible trends in the proportions of the leaves-stems connection, pure stems, and pure leaves in response to varying cutting lengths. As the cutting length increased, there was a notable augmentation in the proportion of the stem and leaf connection parts. Conversely, a contrasting trend was observed in the content of the pure stems and pure leaves, which exhibited a decrement with increasing cutting length. These results collectively indicate a significant influence of cutting length on the separation of stems and leaves in alfalfa. Notably, a smaller cutting length yielded more effective stem and leaf separation, as evidenced by the observed trends in component proportions.

Chopping and blowing separation results

As delineated in Table 5, the experimental design incorporated airflow velocity and cutting length as pivotal factors, with *SEI* serving as the response metric. Employing Design Expert 12.0 software, the experiment's outcomes were fitting via multiple regression and subsequent analysis via ANOVA, as detailed in Table 6. Notably, the analysis revealed a significant influence of both X_1 and X_2 on *SEI*, with the interaction term $X_1 X_2$ also exhibiting a noteworthy effect. The model's P-value <0.05 underscores its statistical significance, further reinforced by the non-significant misfit term ($P = 0.4426 > 0.05$), indicating a favorable model fit. Moreover, the Coefficient of Variation (CV) stood at 4.21%, signifying a commendable degree of precision, as corroborated by a noteworthy Adequacy Precision value of 15.4129, affirming the model's reliability. The determination coefficients R^2 and R^2_{adj} were calculated at 0.8245 and 0.9264, respectively. Similarly, the Predicted R^2 and R^2_{adj} were established at 0.8245 and 0.9264, demonstrating a minimal discrepancy between them, indicative of a robust fitting correlation. This congruence implies the model's utility for predictive purposes, as it accurately reflects the observed data trends.

The results of the regression analysis experiments are shown in Table 5, which were analyzed by Design Expert software for multiple regression and fitting. The multiple regression equations for airflow velocity, cutting length, and *SEI* were established.

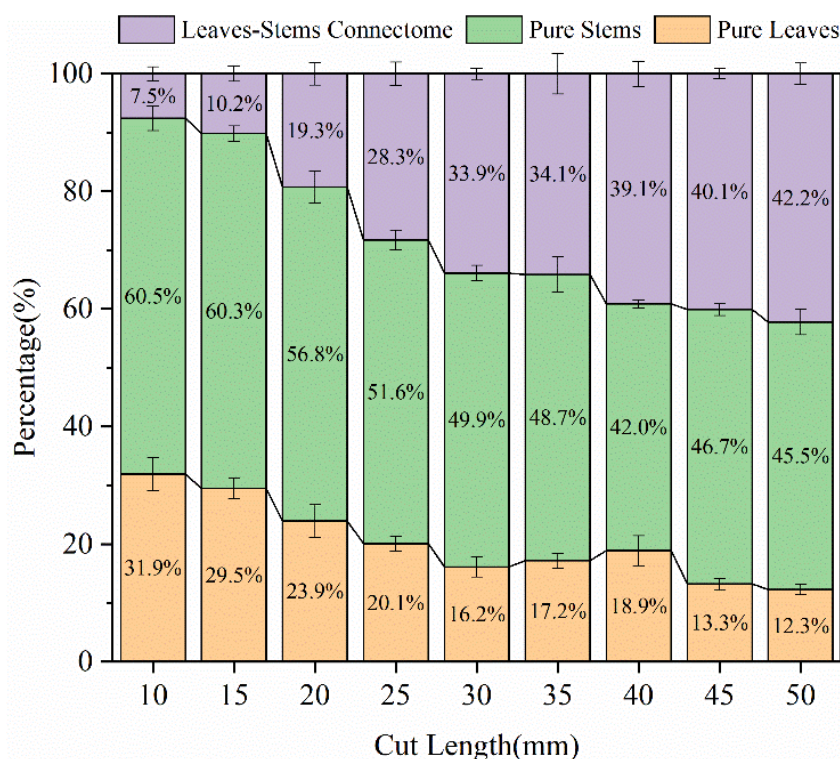


Fig. 5 - Content of alfalfa components under different cutting lengths

Table 5

| Experimental results and range analysis | | | |
|---|---------------------------------|------------------------------|--------|
| Test No. | Airflow velocity X_1 [m/s] | Cutting length X_2 [mm] | SEI |
| 1 | 1.17 | 30 | 1.0000 |
| 2 | 6.83 | 30 | 1.1048 |
| 3 | 4 | 1.72 | 1.4766 |
| 4 | 6 | 10 | 1.2565 |
| 5 | 2 | 10 | 1.2216 |
| 6 | 4 | 30 | 1.4995 |
| 7 | 2 | 50 | 1.1482 |
| 8 | 4 | 58.28 | 1.4408 |
| 9 | 4 | 30 | 1.5733 |
| 10 | 4 | 30 | 1.6582 |
| 11 | 6 | 50 | 1.4718 |
| 12 | 4 | 30 | 1.5980 |
| 13 | 4 | 30 | 1.5937 |

Table 6

| Variance analysis of test result of the separation evaluation index | | | | | |
|---|----------------|-------------------|-------------|----------|------------|
| Source of variation | Sum of squares | Degree of freedom | Mean square | F- Value | P-Value |
| Model | 0.5332 | 5 | 0.1066 | 31.19 | 0.0001** |
| X_1 | 0.0321 | 1 | 0.0321 | 9.39 | 0.0182* |
| X_2 | 0.001 | 1 | 0.001 | 0.3046 | 0.5982 |
| $X_1 X_2$ | 0.0208 | 1 | 0.0208 | 6.1 | 0.0429* |
| X_1^2 | 0.4751 | 1 | 0.4751 | 138.97 | < 0.0001** |
| X_2^2 | 0.0235 | 1 | 0.0235 | 6.89 | 0.0342* |
| Residual | 0.0239 | 7 | 0.0034 | | |
| Lack of Fit | 0.0109 | 3 | 0.0036 | 1.11 | 0.4426 |
| Pure Error | 0.013 | 4 | 0.0033 | | |
| Cor Total | 0.5571 | 12 | | | |

$$SEI = 1.58 + 0.0633X_1 + 0.0114X_2 + 0.0722X_1X_2 - 0.2613X_1^2 - 0.0582X_2^2 \tag{5}$$

where: X_1 is airflow velocity, [m/s]; X_2 is cutting length, [mm].

The influence of airflow velocity X_1 and cutting length X_2 on SEI is shown in Fig. 6.

When the airflow velocity $X_1 = 4.29556$, and cutting length $X_2 = 33.7956$, the SEI achieved a maximum value of 1.59029, indicating the best separation of alfalfa stem and leaves by chopping and blowing method under this condition. Conversely, the orthogonal rotation center combination of the control group in the experimental results indicates $X_1=4$ and $X_2=30$, and $SEI=1.60579$. The discrepancy in SEI values between these two data sets is merely 0.98%, affirming the model's predictive accuracy against experimental outcomes. This validation confirms that an airflow velocity of $X_1=4.3$ m/s and a cutting length of $X_2=34$ mm represent the optimal parameter combination for the alfalfa chopping and blowing separation method.

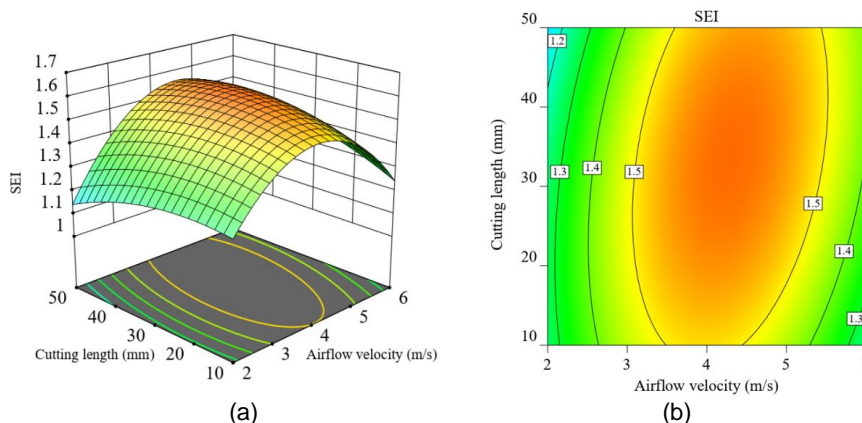


Fig. 6 - Response surface of the airflow velocity and cutting length to the separation evaluation index

Discussion

A chopping and blowing method was proposed in this study by considering the combination of the chopping method in silage harvesting and the blowing method in alfalfa drying separation, which was considered a potentially viable method of field alfalfa separation and harvesting. In order to explore the feasibility and optimal process parameters of the chopping and blowing separation method, this paper investigated the suspension velocity characteristics of alfalfa, and analyzed the effects of airflow velocities and cutting lengths on the separation of alfalfa stems and leaves by response surface experiment.

The suspension velocity of all alfalfa components decreased with the decrease of MC, and there was a linear relationship between the suspension velocity and MC. Under the same MC gradient, the suspension velocity of the whole plant was the largest, followed by the suspension velocity of stems, and the suspension velocity of leaves being the smallest. The greater the length of alfalfa lateral branches and stems, the greater their suspension velocity. The results of chopping separation experiment showed that a smaller cutting length yielded more effective stem and leaf separation.

Response surface test results confirmed the feasibility of the chopping and blowing separation method and obtained optimum airflow velocity and optimum cutting length. Currently, a reliable way to separate fresh alfalfa stems and leaves is stripping method that was proposed by *Shinners et al. (2004, 2007)*, which utilized a multi-tined rotor to strip the leaves directly in the field. However, the use of different evaluation metrics makes it difficult to compare the separation efficiencies directly. An indirect comparison can still be made. When using the Stripping method, test indicators were measured after drying, and the purity of dry leaves in the stripped component typically ranges from 50.2% to 89.5%, with a stem-leaf separation efficiency between 65.7% and 97.1%. In contrast, The Separation Evaluation Index (*SEI*) in this study was measured for wet samples. By further calculating the *SEI* results, the purity of fresh separated leaves ranged from 51.65% to 79.14%, with a stem-leaf separation efficiency between 58.05% and 79.47%. Considering that the water content of the stems in the samples should greatly exceed that of the leaves, the data of the separation results of these two separating method should be at essentially the same level.

It should be noted that there are still some limitations of this study. Although the feasibility of the chopping and blowing separation method under laboratory conditions has been demonstrated, there are still many issues to address before it is realized in the field. When harvesting in the field, the flow rate of alfalfa material will inevitably be much larger than that of the sample in the laboratory, and the length of alfalfa cutting can only fluctuate in a range, which does not guarantee the uniformity of the length of cut alfalfa. What's more, field conditions also have a great influence on machine operations. How to realize the chopping and blowing separation method by means of mechanical engineering, and promote the reliability as much as possible, is what needs to be further investigated.

CONCLUSIONS

(1) The suspension characteristics of different fractions of alfalfa, and different lengths of lateral branches and stems at different MC gradients were determined by setting up a test bench. The suspension velocity of alfalfa components decreased with the decrease of MC, and there was a linear relationship between suspension velocity and MC. At the same MC gradient, the suspension velocity of the plants was the largest, the stems were the second, and the leaves were the smallest. The greater the length of alfalfa lateral branches and stems, the greater the suspension velocity.

(2) Cutting length has a significant effect on the stems-leaves separation of alfalfa. Longer cutting lengths resulted in more content of adherent stems and leaves and less pure stems and pure leaves content in the chopped material. Instead, a smaller cutting length improves the separation of alfalfa stems and leaves.

(3) The central composite design (CCD) of the response surface method was used to study the effect of airflow velocity and cutting length on *SEI*. The optimum process parameters of the chopping and blowing method are as follows: the airflow velocity of 4.29556 m/s and cutting length of 33.7956 mm. The *SEI* is 1.59029 under this condition. These results can provide a reference basis for the determination of engineering solutions for alfalfa field separation and harvesting, such as the structure of the chopping device and the blowing device and the setting of operating parameters.

ACKNOWLEDGEMENT

The study was supported by Hunan Provincial Natural Science Foundation of China (2024JJ5194), Changsha Municipal Natural Science Foundation (kq2208071), the Scientific Research Fund of the Hunan Provincial Education Department (23A0181) and Postgraduate Scientific Research Innovation Project of Hunan Province (CX20230723).

REFERENCES

- [1] Adapa, P. K., Schoenau, G. J., & Arinze, E. A. (2005). Fractionation of alfalfa into leaves and stems using a three pass rotary drum dryer. *Biosystems Engineering*, Vol. 91, Issue 4, pp. 455-463.
- [2] Andrzejewska, J., Ignaczak, S., Albrecht, K. A., & Surucu, M. (2017). Fractional harvest of perennial legumes can improve forage quality and their exploitation. *Grassland Science in Europe*, Vol. 22, pp.509-511.
- [3] Arinze, E. A., Schoenau, G. J., & Adapa, P. (2007). Modeling the fractional drying and aerodynamic separation of alfalfa into leaves and stems in a rotary dryer. *Drying Technology*, Vol. 25, pp. 785-798.
- [4] Bilanski, W., Graham, W., Mowat, D., & Mkomwa, S. (1989). Separation of alfalfa silage into stem and leaf fractions in a horizontal airstream. *Transactions of the ASAE*, Vol. 32, Issue 5, pp.1684-1690.
- [5] Bao, X., Guo, G., Huo, W., Li, Q., Xu, Q., & Chen, L. (2023). Ensiling pretreatment fortified with laccase and microbial inoculants enhances biomass preservation and bioethanol production of alfalfa stems. *Science of The Total Environment*, Vol. 857, Issue 10, pp. 159442.
- [6] Currence, H. D. (1964). Development of a leaf-strip harvesting system for alfalfa. MSc Thesis, Iowa State University of Science and Technology, Ames/USA.
- [7] Currence, H. D., & Buchele, W., (1967). Leaf-strip harvester for alfalfa, *Agricultural Engineering*, Vol. 48, Issue 1, pp. 20.
- [8] Dana, M., & Ahmadi Moghaddam, P. (2022). Studying experimentally and numerically the rate of moisture loss in conditioned alfalfa using computational fluid dynamics. *Journal of Food Process Engineering*, Vol. 45, Issue 4, pp.14062.
- [9] Digman, M.F., Runge, T.M., Shinnars, K.J., & Hatfield, R.D. (2013). Wet fractionation for improved utilization of alfalfa leaves. *Biological Engineering Transactions*, Vol. 6, Issue 1, pp. 29-42.
- [10] Gan-Mor, S., Wiseblum, A., & Regev, R. (1986). Separation of leaves from stems with a perforated rotating drum under suction. *Journal of Agricultural Engineering Research*, Vol. 34, Issue 4, pp. 275-284.
- [11] Lange, M., Silva, L., Zambom, M., Soder, K., & Brito, A. (2023). Feeding alfalfa-grass or red clover-grass mixture baleage: Effect on milk yield and composition, ruminal fermentation and microbiota taxa relative abundance, and nutrient utilization in dairy cows. *Journal of Dairy Science*, Vol. 107, Issue 4, pp. 2066-2086.
- [12] Li, A., & Wang, C. (2006). Experimental Study on the Effect of Alfalfa's Length on Drying Rate and Floating Velocity (苜蓿段长度对干燥速度与悬浮速度影响的试验). *Transactions of the Chinese Society for Agricultural Machinery*, Vol. 37, Issue 8, pp.168-170.
- [13] Liebhardt, P., Maxa, J., Bernhardt, H., Aulrich, K., & Thurner, S. (2022). Comparison of a conventional harvesting technique in alfalfa and red clover with a leaf stripping technique regarding dry matter yield, total leaf mass, leaf portion, crude protein and amino acid contents. *Agronomy-Basel*, Vol. 12, Issue 6, pp.1408
- [14] Liu, Z., Lan, J., Li, W., & Ma, H. (2023). Reseeding improved soil and plant characteristics of degraded alfalfa (*Medicago sativa*) grassland in loess hilly plateau region. *Ecological Engineering*, Vol. 190, Issue 1, pp.106933.
- [15] Meibohm, J., Pistone, L., Gustavsson, K., & Mehlig, B. (2017). Relative velocities in bidisperse turbulent suspensions. *Physical Review*, Vol. 96, Issue 6, pp.1-6.
- [16] Motsinger, L. A., Young, A. Y., Feuz, R., Larsen, R., Brady, T. J., Briggs, R. K. (2021). Effects of feeding a novel alfalfa leaf pellet product (ProLEAF MAX) and alfalfa stems (ProFiber Plus) on performance in the feedlot and carcass quality of beef steers. *Translational Animal Science*, Vol. 5, Issue 3, pp. 1-11.
- [17] Muck, R. E., Shinnars, K. J., & Duncan, J. A. (2010). Ensiling Characteristics of Alfalfa Leaves and Stems, American Society of Agricultural and Biological Engineers, Pittsburgh/USA, Vol. 1.
- [18] Pfister, G. (1980). Alfalfa separator. USA, Patent, No. 4183471.
- [19] Pratt, C. A., & Jackson, A. S. (2021). Multipurpose leaf crop harvesting apparatus and processing method. USA, Patent, No.11026369.
- [20] Shehryar, A., Hassan, A., Hamid, A., Murilo dos Santos, C., Khan, A., & Ullah, A. (2019). Model for Predicting Solids Velocity Fluctuations in Sedimenting Suspensions. *Chemical Engineering & Technology*, Vol. 42, Issue 12, pp.2641-2648.
- [21] Shinnars, K.J., Herzmann, M.E., Binversie, B.N., & Digman, M.F. (2007). Harvest Fractionation of Alfalfa. *Transactions of the ASABE*, Vol.50, Issue 3, pp.713-718.

- [22] Shinnars, K.J., Herzmann, M.E., Binversie, N., & Digman, M.F. (2004). A preliminary investigation of harvest-fractionation of alfalfa. Paper presented at the 2004 ASAE Annual Meeting. Ottawa/ Canada.
- [23] Siles, J.A., González-Tello, P., Martín, M. A., & Martín, A. (2015). Kinetics of alfalfa drying: Simultaneous modelling of moisture content and temperature. *Biosystems Engineering*, Vol. 129, pp.185-196.
- [24] We, A. C. E., Aris, A., Zain, N. A. M., Muda, K., & Sulaiman, S. (2021). Influence of static mixer on the development of aerobic granules for the treatment of low-medium strength domestic wastewater. *Chemosphere*, Vol. 263, Issue 12, pp.128209.
- [25] Wu, M., Chen, S., Bian, L., & Li, J. (2014). Measurement and analysis on suspension velocity of cut medicago falcate components in different harvesting periods (不同刈割期秧草收割物悬浮速度的测定与分析). *Journal of Anhui Agricultural University*, Vol. 41, Issue 3, pp.507-512.
- [26] Yang, Z., & Su, D. (2015). Study on Layered Cutting Height in Alfalfa Layered Cutting (紫花苜蓿分层收获方法的分层刈割高度研究). *Chinese Journal of Grassland*, Vol. 37, Issue 2, pp.75-80.
- [27] Zhang, W., Grimi, N., Jaffrin, M. Y., Ding, L., & Tang, B. (2017). A short review on the research progress in alfalfa leaf protein separation technology. *Journal of Chemical Technology & Biotechnology*, Vol.92, Issue 12.

RESEARCH ON SIMULTANEOUS LOCALIZATION AND MAPPING METHOD FOR ORCHARDS BASED ON SCAN CONTEXT AND NDT-ICP FUSION SCHEME

基于扫描上下文和 NDT-ICP 融合方案的果园同步定位与绘图方法研究

Zhen QIN ¹⁾, Hongxia WANG ¹⁾, Pengcheng LV ^{*2)}

¹⁾ School of Information and Control Engineering of Qingdao University of Technology, Qingdao, China

²⁾ Shandong University of Technology, Collage of Agricultural Engineering and Food Science, Zibo, China

Tel: +86 13964379460; E-mail: wslpc1999@163.com

Corresponding author: Pengcheng LV

DOI: <https://doi.org/10.35633/inmateh-73-54>

Keywords: Loopback Detection; Scan Context; Point Cloud Alignment; SLAM

ABSTRACT

Simultaneous localization and mapping (SLAM) is one of the key technologies for agricultural robots to build maps and localize in complex orchard environments and realize unmanned autonomous operations. Due to the complexity of the orchard environment, the single canopy feature and the diffuse reflection of light caused by the leaves, etc., the map construction process of the orchard environment leads to mismatch and increases the cumulative error of the map construction. Aiming at the above problems, this paper proposes a navigation map construction method for orchard environment based on the fusion of Scan Context and NDT-ICP. The method firstly searches the Ring key quickly to get the candidate frames, and scores the similarity between the candidate frames and the current frame, and effectively detects the loopbacks by two-stage searching algorithm to reduce the false matches in the map of orchard environment. Meanwhile, a point cloud alignment method based on the fusion of normal distribution transform coarse alignment and iterative nearest point exact alignment is used to reduce the cumulative error of the orchard environment map. The results show that the improved algorithm compensates the drift of the point cloud map with higher mapping accuracy, better real-time performance, lower resource utilization, higher overlap between the trajectory estimation and the real trajectory, smoother loops, and a 4% reduction in CPU occupancy. In the complex orchard environment, the root mean square error and standard deviation of the trajectories of this paper's algorithm are 0.57 m and 0.19 m, which are 68% and 83% higher than those of the loop detection algorithms in the Lightweight Ground Optimized Lidar Trajectory Measurement and Multivariate Terrain Mapping (LeGO-LOAM), respectively. Accurate map construction and low drift pose estimation can be performed. The research algorithm effectively reduces the influence of mis-matching and large cumulative error in the process of map construction in the orchard environment, meets the demand for high-precision environmental mapping in the orchard environment, and provides technical support for promoting unmanned operation in the orchard environment.

摘要

同步定位与绘图 (SLAM) 是农业机器人在复杂果园环境中构建地图并进行定位、实现无人自主作业的关键技术之一。由于果园环境的复杂性、树冠的单一性和树叶对光线的漫反射等特点, 果园环境的地图构建过程中会出现不匹配现象, 增加了地图构建的累积误差。针对上述问题, 本文提出了一种基于 Scan Context 和 NDT-ICP 融合的果园环境导航地图构建方法。该方法首先快速搜索环键得到候选帧, 并对候选帧与当前帧的相似度进行评分, 通过两阶段搜索算法有效检测回环, 减少果园环境地图中的虚假匹配。同时, 采用基于正态分布变换粗配准和迭代最近点精确配准融合的点云配准方法, 降低果园环境地图的累积误差。结果表明, 改进后的算法可以弥补点云图的漂移, 具有更高的映射精度、更好的实时性、更低的资源利用率、更高的轨迹估计与真实轨迹重合度、更平滑的循环以及降低 4% 的 CPU 占用率。在复杂果园环境中, 本文算法的轨迹均方根误差和标准偏差分别为 0.57 米和 0.19 米, 比轻量级地面优化激光雷达轨迹测量和多元地形测绘 (LeGO-LOAM) 中的环路检测算法分别高 68% 和 83%。该算法有效降低了果园环境地图构建过程中的误匹配和大累积误差的影响, 满足了果园环境高精度环境测绘的需求, 为推进果园环境无人化作业提供了技术支撑。

INTRODUCTION

In recent years, with China's strong support for intelligent agriculture, China's first unmanned farm landed, which further promoted the rapid development of intelligent agricultural equipment technology.

The application of mobile robots in precision agriculture is becoming more and more widespread, autonomous mobile robots have a variety of functions such as environment perception, dynamic decision-making, path planning and autonomous navigation, and can perform specific tasks in unknown environments. Agricultural robotics technology has gained rapid development with the advancement of computers, LiDAR and other technologies. Instant localization and map construction is one of the key technologies of agricultural robot navigation technology, and it is also an important basis for automatic navigation. The continuous development of sensor technology, especially the rapid development of three-dimensional LiDAR in recent years, makes the instant localization and map construction technology having a great degree of improvement in map building accuracy and robustness. According to the type of sensor, SLAM technology can be divided into two categories: visual SLAM and laser SLAM. Among them, visual SLAM obtains environmental information with the help of visual sensors, low cost, simple structure, but large arithmetic capacity, easily affected by light, not applicable to farmland and other environments with obvious changes in light, laser SLAM technology is relatively mature, accurate ranging, less affected by light, and LiDAR compared to cameras, ultrasonic, infrared sensors, etc. has the advantages of strong anti-jamming ability, high accuracy, wide measurement range, etc., and is more suitable for orchard environments. At present, agricultural robots equipped with LiDAR to achieve local positioning and navigation method cannot provide global positioning information, Real Time Kinematic (RTK) global positioning method is mainly realized through the three-dimensional map building and repositioning. The main algorithms to achieve map building are Lidar Odometry and Mapping (LOAM) and Lightweight and Ground Optimized Lidar Odometry and Mapping (LeGO-LOAM). The LOAM algorithm, which lacks loopback detection and back-end map optimization, operates in the complex environment of the orchard with a serious lack of accuracy. Based on this, LeGO-LOAM algorithm adds loopback detection and graph optimization part. However, agricultural scenarios are a typical unstructured environment, which is characterized by inconspicuous features, uneven terrain, and dynamic changes of objects, which brings new challenges to the construction of maps in such scenarios, and the loopback detection and graph optimization part inevitably introduces problems such as map mismatch and large cumulative errors in orchard environments (Wang *et al.*, 2022).

Loopback detection, also known as closed-loop detection, is the ability of a robot to recognize that it has arrived at a scene so that the map closes the loop, usually using 3D descriptor matching, such as Fast Point Feature Histogram (FPFH), Fast Laser Region of Interest Transform (FLIRT) and Signature of Histograms of Orientation (SHOT) algorithms (Davison *et al.*, 2007). If the loopback detection is successful, it can significantly reduce the cumulative error and help the robot realize the obstacle avoidance navigation work more accurately and quickly. Therefore, loopback detection has become one of the most popular methods in recent years in the field of robotics research. Loop detection has become one of the hotspots in robotics research in recent years. With the development of deep learning, semantic information can be easily obtained from point cloud images, which can be used to assist SLAM loopback detection (Pire *et al.*, 2017). For example, SegMatch, a 3D point cloud segmentation matching based method, and SUMA++, a surf-based method, achieve amazing accuracy in highway scenes by dynamic removal (Zhou *et al.*, 2021).

In addition to loopback detection, point cloud alignment is also an important step in robot obstacle avoidance navigation. There are two commonly used 3D LiDAR point cloud alignment methods, Iterative Closest Point (ICP) and Normal Distribution Transform (NDT). Among them, the ICP algorithm is slower but more accurate, while the NDT algorithm is faster but less accurate. To address the problems of mis-matching of orchard environment maps and large cumulative errors introduced by the LeGO-LOAM algorithm, the Scan Context algorithm is used to optimize the LeGO-LOAM map detection module, taking into account the characteristics of Scan Context's high accuracy, low cost, high efficiency and robustness, and the NDT-ICP point cloud alignment algorithm to optimize the global map obtained from the loop to improve the accuracy, real-time and robustness of the map construction in the orchard environment, and the performance of the algorithm is evaluated with the KITTI dataset 00 sequential data and the field map construction test in the vineyard as an example to validate the performance of the proposed map construction method for the agricultural robots' localization and navigation, environment map construction and unmanned driving.

MATERIALS AND METHODS

LeGO-LOAM Algorithm

LeGO-LOAM is based on the improvements made to the LOAM algorithm in 2018. As illustrated in Fig. 1, the collected point cloud of the orchard environment is initially clustered and segmented, with the ground point cloud being isolated. Concurrently, a limited number of point cloud clusters are excluded (Zhang *et al.*,

2014). A two-step Levenberg-Marquardt (L-M) optimization method is employed to resolve the six-degree-of-freedom transformation between continuous frames. In the initial stage, the ground point cloud is employed to determine the planar transformation parameters (Rösmann et al., 2015). Subsequently, the edge and surface points within the segmented point cloud are matched to generate the bitmap transformation matrix, which is subsequently processed and aligned. Finally, the motion estimation drift correction is performed, and the final pose estimate is generated (Xue et al., 2023).

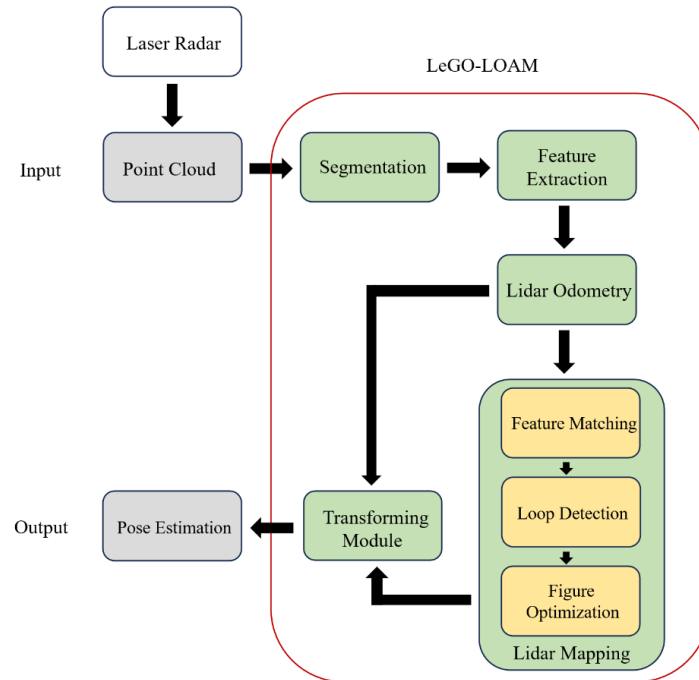
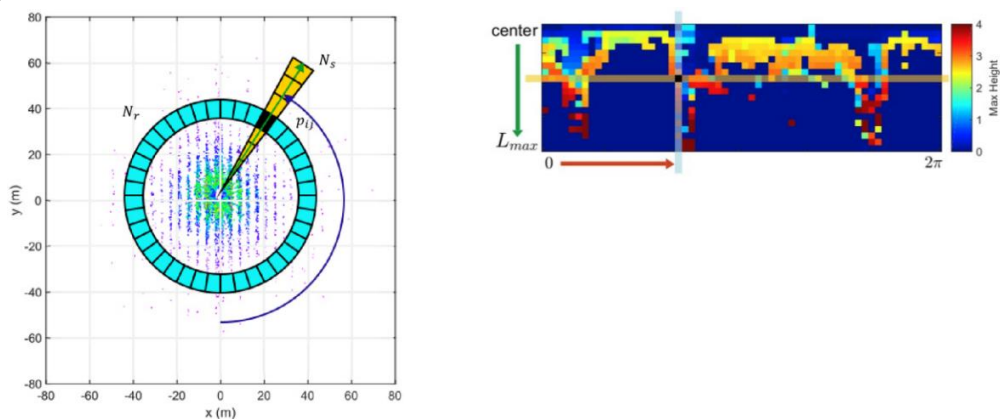


Fig. 1 – LeGO-LOAM algorithm flow

The LeGO-LOAM method cyclic algorithm is computationally intensive, inefficient in detection, and still produces significant cumulative errors in mapping large scenes at long distances (Shan et al., 2018).

Scan Context Loopback Detection Method

Scan context converts a 3D point cloud to 2.5D by dimensionality reduction and uses a search algorithm to match point cloud data from current and historical frames to enable loopback detection (Shan et al., 2020). Figure 2 shows the structure diagram of scan context global descriptor. For a frame of point cloud data scanned by LiDAR, the top view is obtained from the top of 3D point cloud (as shown in Figure 2a), and the polar coordinate system is established with the LiDAR position as its origin. Twenty rings are divided outward from origin, and each ring is divided into 60 equal parts, namely 1200 grids, taking the maximum height (Z value) of the points in each grid as the grid value. Then the top view is expanded radially into 20 rows and 60 columns of rectangular images (Figure 2b), the average values of each row and each column are calculated respectively, and the two vectors—ring key and sector are obtained as global descriptors (Dijkstra et al., 1959).



(a) Top view of one frame of point cloud

(b) Rectangular image expanded from the top view

Fig. 2 – Construction diagram of scan context global descriptor

The Scan Context loopback detection algorithm constructs a rectangular image using the scanned point cloud data, constructs a KD tree using the loopback key vectors, performs a nearest-neighbor search to find similar frames and their loopback key transitions that may be looped back to the current frame, calculates the similarity score, and filters out the similar frames that have higher scores; it then calculates the minimum offset and the similarity score on a sector-by-sector basis, and selects the frame that has the highest similarity score as a looped back frame, solves the attitude relationship between the current frame and the looped back frame, and realizes the loopback detection (Seet et al., 2004). This method is highly effective in detecting trajectory drift and can significantly reduce the accumulated errors in map construction and localization, enabling orchard robots to perform tasks such as obstacle avoidance navigation with greater accuracy and speed (Fox et al., 1997).

Improved Algorithm Principle

The ICP loopback detection method based on Euclidean distance is mainly adopted in the LeGO-LOAM algorithm, in this paper, the fusion algorithm of Scan Context and NDT-ICP is adopted instead of the ICP loopback detection method based on Euclidean distance in the LeGO-LOAM algorithm, and the positional constraints computed by the NDT-ICP are added into the GTSAM for the global positional optimization, at this time, we obtain The global map is more complete. The block diagram of the algorithm is shown in Fig. 3.

The system reads the point cloud data collected by LiDAR and projects the points as depth images. Then, the ground plane of the depth map is estimated, ground points are extracted, and each frame of the point cloud Pt is divided into different clusters labeled as segmentation points by the point cloud segmentation module. At the same time, the point cloud that cannot be clustered is re-clustered by obtaining three features: the label of the point, the row and column index in the depth map, and the distance value. After that, the feature extraction module is used to extract the edge feature point nF_e and the plane feature point nF_p based on the roughness c . The ranging module performs a two-step L-M optimization to obtain the attitude transformation matrix through the above two feature points to realize the spatial constraints between consecutive frames of the point cloud. The LiDAR mapping module matches the features in (F_e^t, F_p^t) with the surrounding point cloud Q^{-t-1} and further sends its own position to GTSAM for map optimization, at which point the radar estimates the pose update and optimizes the current map.

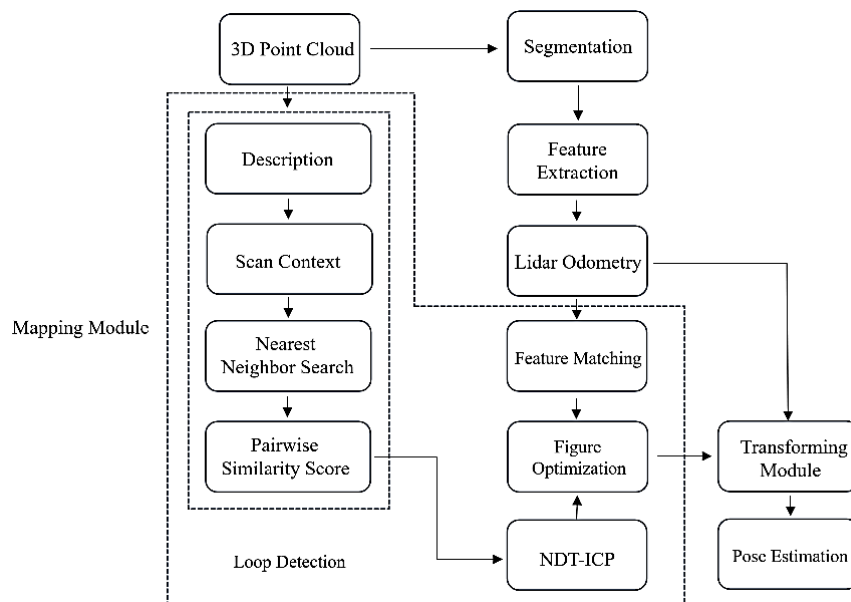


Fig. 3 – System architecture diagram of the improved algorithm in this paper

In order to obtain the relative position matrix between the matched point cloud frame and the loopback point cloud frame for back-end graph optimization, after confirming the loopback position, this paper chooses NDT-ICP to align the point cloud between the matched point cloud frame and the candidate point cloud frame of the orchard, and calculate the alignment score by the NDT-ICP method. If the alignment score is less than a given threshold, the repositioning is considered successful and the attitude constraints between the repositioned frame and the current frame are obtained. The constraints are added to GTSAM for map optimization and point cloud map update.

The transform fusion module fuses the position and location estimates from the LiDAR rangefinder module and the LiDAR mapping module and outputs the final position and location estimates.

Divide the orchard matching point cloud frame space into a number of identical cubes and satisfy that there are at least 5 points in the cube, the mathematical expressions for the mean μ and covariance matrix C of the points in the cube of each matching point cloud frame are:

$$C = \frac{1}{m} \sum_{k=1}^m I_k^q \tag{1}$$

$$\Sigma = \frac{1}{m-1} \sum_{k=1}^m I_k^q - \mu \quad I_k^q - \mu^T \tag{2}$$

where: m is the number of point clouds in the spatial cube of the matched point cloud frame; k is the point cloud serial number, $k = 1, 2, \dots, m$; I_k^q is the point cloud in the spatial cube of the matched point cloud frame of the orchard.

Probability density of each point location in the frame cube of the orchard matching point cloud:

$$p \ I^q = \exp \left(- \frac{I^q - \mu^T \sum_k^{-1} I^q - \mu}{2} \right) \tag{3}$$

Mapping the matched point cloud frames to the loopback detection frame coordinate system, each point mapping a transformed normal distribution:

$$p \ I_k^{q'} \sim \exp \left(- \frac{I_k^{q'} - \mu_k^T \sum_k^{-1} I_k^{q'} - \mu_k}{2} \right) \tag{4}$$

where:

$I_k^{q'}$ is the set of point clouds after I_k^q mapping; μ_k is the mean value of the point cloud set $I_k^{q'}$.

Summing the probability densities of each point, the mathematical expression for the parameters of the coordinate transformation is evaluated as

$$s(p) = \sum_k \exp \left(- \frac{I_k^{q'} - \mu_k^T \sum_k^{-1} I_k^{q'} - \mu_k}{2} \right) \tag{5}$$

Optimize $s(p)$ using the Hessian matrix method. Then, remap to the loopback detection frame coordinate system until the convergence condition is satisfied. The optimized loopback point set is $I_k^{c*'}$ and the matched point set I^q . The error between the orchard origin point set $I_k^{c*'}$ under the transformation matrix (R, t) and the orchard target point set I^q is denoted by $E(R, t)$. Then the problem of solving the optimal transformation matrix is transformed into the optimal solution (R, t) satisfying $\min E(R, t)$. where $E(R, t)$ is called the objective function, which represents the degree of difference between the two point sets. This objective function is expressed as

$$E(R, t) = \sum_{k=1}^n \left\| I_k^q - I_k^{c*'}.R + t \right\|^2 \tag{6}$$

where:

$I_k^{c*'}$ is the optimized loopback point set of the candidate point cloud frame I^c ; n is the number of points in the point set I_k^q ; R is the rotation parameter; t is the translation parameter.

In order to minimize the objective function, the optimal transformation matrix, i.e., R and t is solved. first, the corresponding closest point in the I^q point set is calculated for each point in the orchard's target point set, I^{c*} . The rotation parameter R and the translation parameter t are obtained using SVD decomposition so that the transformation matrix $E(R,t)$ is minimized. Using the rotation parameter R and translation parameter t obtained in the previous step for the point set I^{c*} , new transformed point set $I^{c''}$ is obtained. If the transformed point set $I^{c''}$ and I^q point set satisfy the requirement of the objective function, i.e., the average distance between the two point sets is less than a given threshold, then the iterative computation is stopped; otherwise, recalculate the new point set $I^{c''}$ as the new point set I^{c*} and continue iterating until the convergence condition is satisfied, and then obtain the optimal solution (R, t) with the relative positional matrix.

Test Equipment and Environment

At present, orchard robots are available in three main categories: legged, wheeled, and tracked. Each type has its own set of advantages and disadvantages in different environments. The legged inspection robot exhibits strong terrain adaptability, yet its intricate structure and sophisticated control system present significant technical challenges. Wheeled inspection robots are distinguished by their high speed, high efficiency, and low motion noise, yet they are constrained by complex terrain. The tracked inspection robot is equipped with a robust traction force, high applicability, and excellent stability in challenging terrain, such as outdoor, sandy, and muddy areas. In this paper, a tracked kinematic chassis was used to design an orchard robot for data acquisition and field trials in a complex outdoor orchard environment, as shown in Fig. 4(a). The hardware system mainly consists of a 3D LiDAR (Ouster-64), Global navigation satellite systems real-time kinematic (GNSS-RTK), and Jetson AGX Xavier with Ubuntu 20.04 operating system. Ouster-64 is a 64-line 3D LiDAR developed by Ouster Inc. in the United States. The GNSS-RTK used in this paper was developed by New Coordinate Intelligent Equipment Co. Ltd. in Zibo, Shandong Province, China, and the Jetson AGX Xavier was manufactured by NVIDIA Corporation in Santa Clara, California, USA.

The robot fixes the Ouster 64-line LiDAR at the centre of the crawler chassis through an aluminium radar bracket, and the centre of the LiDAR is 1 m away from the ground, which ensures that the LiDAR is not obstructed and guarantees the accuracy of the SLAM construction. In addition, two GNSS antennas are screwed to the strong magnetic suction cups and fixed in the forward direction and backward direction of the crawler chassis respectively, with a distance of 1 meter, to ensure that there is no obstruction above the antennas, so as to ensure that they can receive good positioning signals, and at the same time, ensure that the corresponding centres of the two GNSS antennas form the same line with the central axis of the crawler chassis, so as to ensure that the GNSS-RTK can collect the position of the orchard robots in real time. GNSS-RTK can collect the position information of the orchard robot in real time, and the accuracy reaches centimetre level. Finally, the Jetson AGX Xavier is installed and connected to the robot's underlying control driver board via a serial cable, to the GNSS-RTK positioning receiver via a USB cable, and to the LiDAR adapter box via an Ethernet cable. The tracked chassis of the orchard robot is powered by a bucking module that reduces the 48V voltage of the LiDAR to 24V and the 48V voltage of the Jetson AGX Xavier to 5V. Figure 5 shows the hardware connection diagram of the orchard robot.

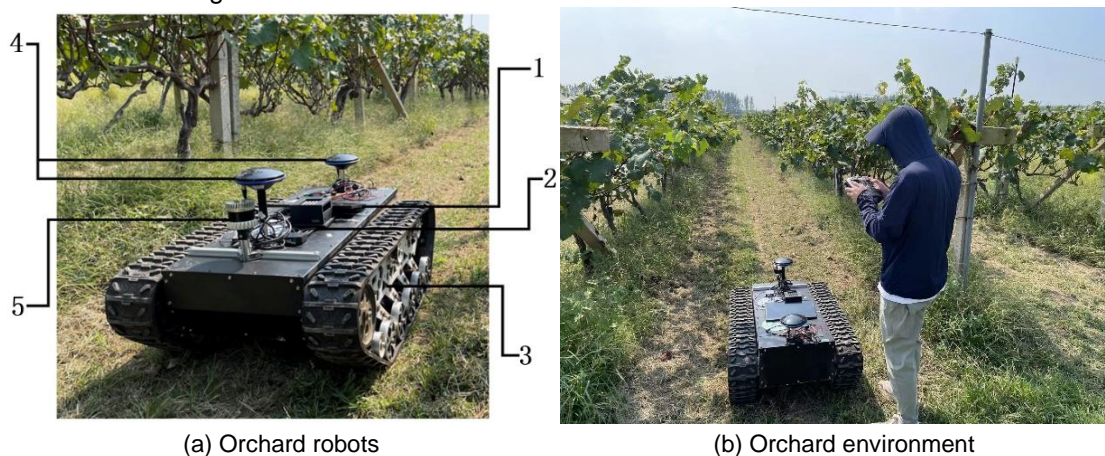


Fig. 4 – Field orchard environmental experiment

1. External Monitor; 2. Jetson AGX Xavier; 3. Crawler-Type Mobile Chassis; 4. Dual-Antenna GNSS-RTK; 5. 64-Line 3D LiDAR

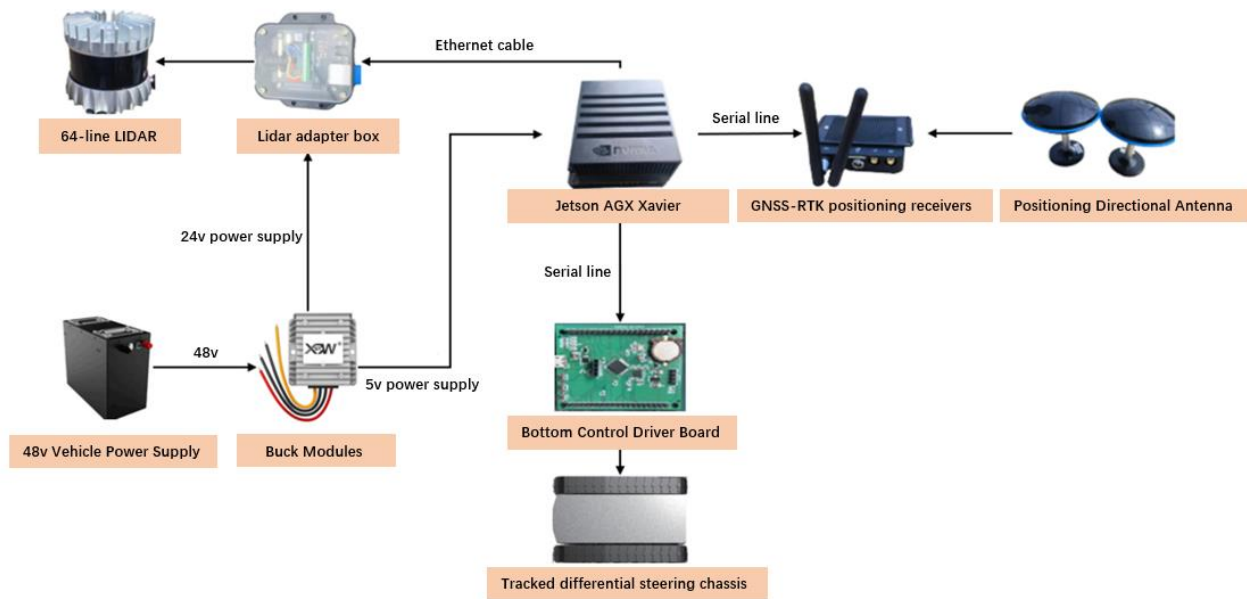


Fig. 5 – Hardware Connection Diagram of Orchard Work Robot

The data used for the experiments in this paper are the KITTI dataset in the field of automated driving and the dataset collected in the field of standardized plantation vineyard environment. Among them, the orchard environment dataset has a total length of 1707.635 m and a duration of 1166 s. The KITTI dataset 00 sequence, which has a total length of 3724.187 m, lasts for 570 s.

As shown in Fig. 4(b), in order to study the SLAM approach for orchard robots in orchard environments, we have used the KITTI dataset 00 sequence in the Grapevine Base in Huantai County, Zibo City, Shandong Province (N37.07420° and E117.91777°) in Zibo City, Shandong Province, where a 132-m × 144-m rectangular plot was selected for data collection. The cultivation pattern of the grape base is the ridge planting method, which means that grapes are planted in a single row on each ridge with a row spacing of 3 m. The cultivation pattern of the grape base is the ridge planting method. To collect the data, we need to scan the orchard environment with a LIDAR-equipped robot. The manually controlled orchard robot travels through the orchard at a speed of 0.5-1 m/s, and the 3D LIDAR records the point cloud data at a frequency of 10 Hz.

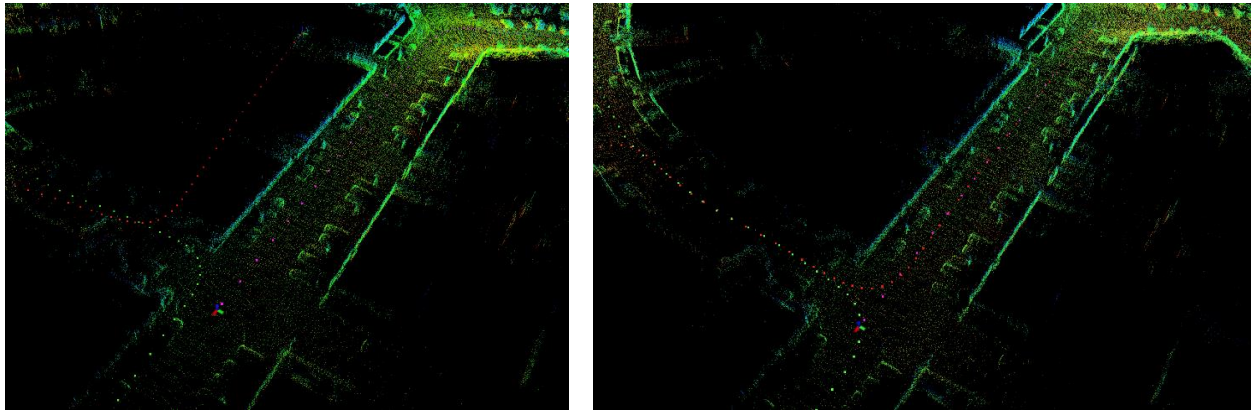
RESULTS

Experiment details

The experimental equipment used for the test was a Shenzhou laptop, its CPU model is I7-12650H, memory is 16G, the graphics chip is NVIDIA Geforce GTX4060, the system environment is Ubuntu20.04, ROS noetic, PCL 1.8, GTSAM 4.0.0, Python 3.6. The test dataset uses the KITTI dataset 00 sequence as well as our field-collected standardized vineyard environment dataset.

In the loopback detection experiment on the KITTI dataset, the vineyard point cloud map generated by the orchard robot based on the LeGO-LOAM algorithm is depicted in Fig. 6(a). Upon the orchard robot's return to the starting point, the end point of the radar odometer fails to form a closed loop with the starting point, resulting in a cumulative error in position estimation that causes the robot trajectory to deviate and the loopback detection to fail in this instance. The point cloud generated by this paper based on the scanning context fusion NDT-ICP loopback detection algorithm is shown in Fig. 6(b).

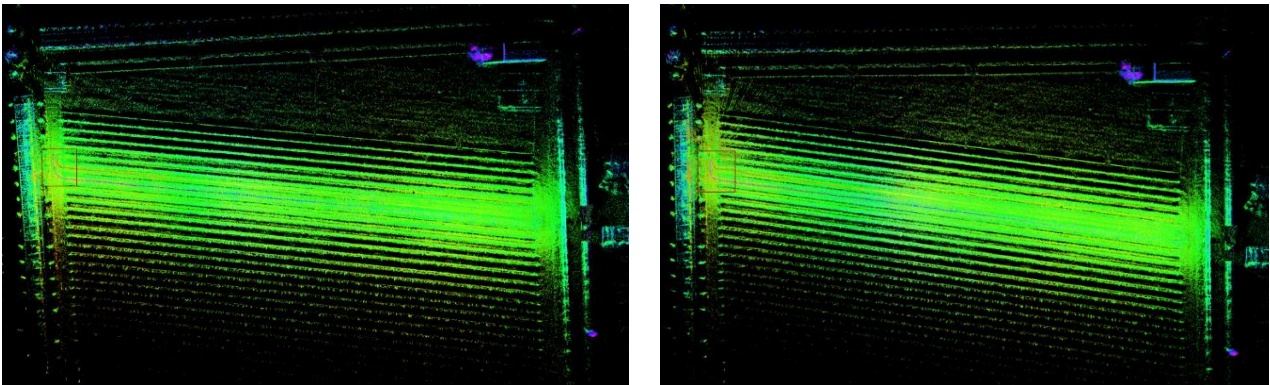
The robot is able to recognize the scene of the previously reached location after building the map and successfully performs loopback detection. Furthermore, we conducted a comparative analysis between LeGO-LOAM and the proposed algorithm on a standardized vineyard environment dataset, as illustrated in Fig. 7(a) and Fig. 7(b). This analysis revealed that the endpoints of the vineyard point clouds generated by LeGO-LOAM do not form a closed loop with the starting point, resulting in a failed loopback. In contrast, the vineyard point clouds generated by this paper's algorithm are successfully looped back, as illustrated by the red box.



(a) Loopback detection test failed

(b) Loopback detection test successful

Fig. 6 – KITTI dataset loopback detection test

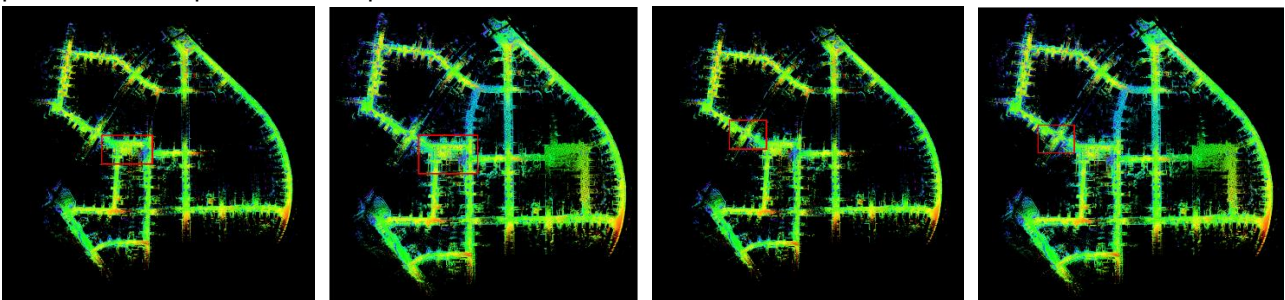


(a) Loopback detection test failed

(b) Loopback detection test successful

Fig. 7 – Vineyard dataset loopback detection test

Figure 8 shows the global point cloud map of KITTI dataset 00 sequence constructed by LeGO-LOAM and the improved algorithm in this paper. Figure 9 shows the local zoomed-in point cloud map of KITTI dataset 00 sequence constructed by LeGO-LOAM and the improved algorithm in this paper. It can be seen that when the LeGO-LOAM algorithm is used for mapping, the drift is serious, the effect is poor and the mapping is incomplete. When the algorithm in this paper is used for mapping, the mapping results are more complete and clearer than the LeGO-LOAM algorithm. Figures 8(b), (d) and 9(b), (d) show that it just makes up for the phenomenon of point cloud map drift.



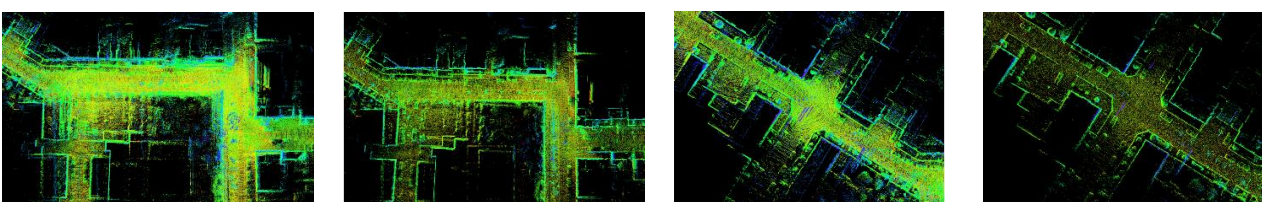
(a)

(b)

(c)

(d)

Fig. 8 – Global Map



(a)

(b)

(c)

(d)

Fig. 9 – Local zoom map

Test Analysis

In order to evaluate the effectiveness of the mapping method in this paper in the vineyard, the continuously acquired latitude and longitude information from GNSS is used as the trajectory truth in this paper to compare with the trajectory generated by the algorithm. The Root Mean Square Error (RMSE) and the Standard Deviation (STD) are often used as evaluation metrics for algorithms, so we use this as a reference.

The mathematical expression for root mean square error (RMSE) is:

$$RMSE = \sqrt{\frac{\sum_{a=1}^d X_a - X' ^ 2}{d}} \tag{7}$$

where: X' is the true value; X_a is the measured value; d is the number of positions; a is the positional ordinate, $a = 1, 2, \dots, d$.

The mathematical expression for standard deviation (STD) is:

$$std = \sqrt{\frac{\sum_{a=1}^d X_a - \bar{X} ^ 2}{d - 1}} \tag{8}$$

where \bar{X} is the mean value.

Three algorithms for motion trajectory estimation for the orchard test: LOAM, LeGO-LOAM and Ours. as shown in Fig. 10, the algorithm in this paper gives the best results, which are basically consistent with the real trajectory (ground truth).

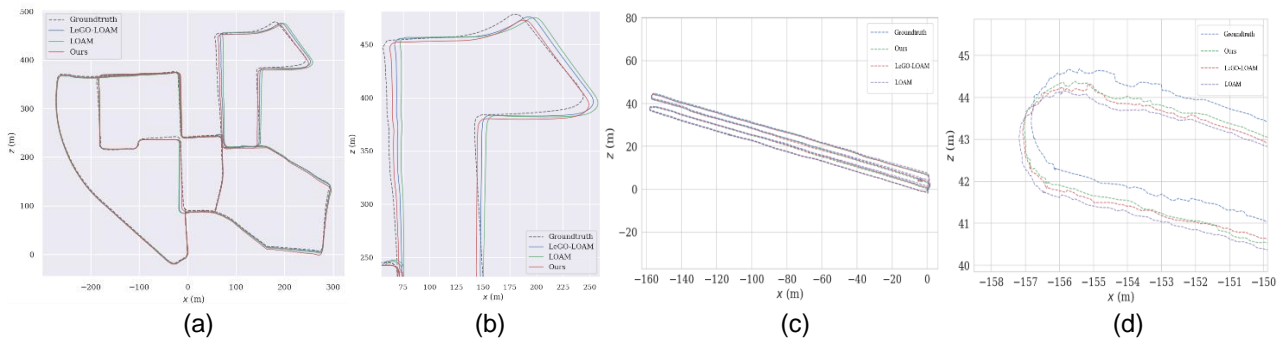


Fig. 10 – Trial traces versus real-value traces

(a). Global trajectory of the KITTI dataset; (b). Localized trajectories for the KITTI dataset; (c). Global trajectory of the Vineyard dataset; (d). Localized trajectories for the Vineyard dataset.

Table 1 gives the estimated path length, time consumption, CPU occupancy, RMSE, and STD for LOAM, LeGO-LOAM, and the algorithm in this paper (Ours), reflecting the real-time robustness and stability of the algorithms.

Table 1

| Test error comparison between different algorithms | | | | | | |
|--|-----------|------------|----------|--------------|----------|---------|
| Scene | Algorithm | Length (m) | Time (s) | CPU Rate / % | RMSE (m) | STD (m) |
| Kitti00 | LOAM | 3736.586 | 556.362 | 70 | 7.92 | 4.88 |
| | LeGO-LOAM | 3731.182 | 572.168 | 65 | 5.46 | 2.41 |
| | Ours | 3724.187 | 540.872 | 62 | 2.11 | 0.72 |
| Vineyard | LOAM | 1719.361 | 1181.271 | 77 | 2.88 | 1.31 |
| | LeGO-LOAM | 1712.846 | 1173.984 | 74 | 1.76 | 1.12 |
| | Ours | 1707.635 | 1166.323 | 71 | 0.57 | 0.19 |

In comparison to the LeGO-LOAM algorithm, the algorithm presented in this paper demonstrates a 4% reduction in CPU occupancy on average, an improvement in real-time performance, and a reduction in elapsed time of approximately 5%. The root mean square error and standard deviation of the algorithm presented in this paper in the KITTI 00 dataset are 2.11 meters and 0.72 meters, respectively. These values are reduced by 61% and 70%, respectively, in comparison to the LeGO-LOAM algorithm.

In the Vineyard dataset, the root mean square error and standard deviation of this algorithm are 0.57 m and 0.19 m, respectively, representing a reduction of 68% and 83%, respectively, in comparison to the LeGO-LOAM algorithm.

The experiments demonstrate that in a large-scale, standardized planting vineyard scenario, the orchard robot is capable of successfully looping back to detect multiple times, thereby greatly reducing the cumulative error and enhancing the efficiency of our algorithm. Furthermore, an examination of the KITTI dataset reveals that the algorithm has been optimized for real orchard scenarios. This is due to the fact that the algorithm is not constrained by the dimensions of the scene in question. The experimental results serve to illustrate the viability of our augmented algorithm in the context of orchard scenes.

CONCLUSIONS

This study addresses the context of complex orchard environments where simultaneous localization and mapping (SLAM) in large-scale scenarios often leads to loopback failures. To address these challenges, this paper presents a method for constructing navigation maps for orchard environments based on scanning context and NDT-ICP fusion. The method initially identifies potential frames by rapidly searching for ring keys, and then assesses the degree of similarity between candidate frames and the current frame. This approach enables the effective detection of loopbacks through the implementation of a two-stage search algorithm, thereby reducing the occurrence of false matches in the orchard environment map.

Furthermore, a point cloud alignment method based on the fusion of normal distribution transform coarse alignment and iterative nearest point exact alignment is employed to reduce the cumulative errors in the orchard environment map, and field experiments were conducted in the vineyard. The following conclusions were drawn from the study:

1. An improved SLAM algorithm incorporating Scan Context and NDT-ICP proposed in this paper has been tested on datasets and experimental test results show that the improved algorithm has higher mapping accuracy and lower time consumption and resource usage.

2. The mapping and position estimation performance of LOAM, LeGO-LOAM, and the enhanced algorithm of this paper were evaluated using the KITTI dataset 00 sequence with the vineyard dataset. The results demonstrated that the algorithm proposed in this paper exhibited enhanced performance in terms of reducing the drift of point cloud maps, improving the accuracy of the motion trajectory estimation, and providing a more seamless loop. Additionally, the estimated trajectory length was found to be more closely aligned with the real trajectory length. In comparison to the LeGO-LOAM algorithm, the CPU occupancy is reduced by 4% on average, the real-time performance is enhanced, and the time consumption is reduced by approximately 5%. In the KITTI 00 dataset, the root mean square error and standard deviation of the enhanced algorithm are 2.11 meters and 0.72 meters, respectively. In comparison to the LeGO-LOAM algorithm, these two values are reduced by 61% and 70%, respectively. In the vineyard dataset, the root mean square error and standard deviation of our enhanced algorithm are 0.57 m and 0.19 m, respectively, representing a reduction of 68% and 83%.

3. The prevailing approach to SLAM is largely reliant on mathematical models and the design of intricate algorithmic processes to process sensor data and generate localization maps. In the future, there is potential to explore the integration of deep learning and SLAM. This could enable the full exploitation of the strengths of deep learning in vision and semantics, thereby enhancing the localization and mapping accuracy of the SLAM system. Furthermore, the application of a deep learning model to extract and analyse the features of the sensor data could lead to improvements in the performance and applicability of mapping and localization.

ACKNOWLEDGEMENT

The project supported by the R&D of low-speed unmanned autonomous navigation controller Project under Grant (No.2022TSGC1175).

REFERENCES

- [1] Chang L., Shan L., Jiang C., Dai Y., et al. (2021) Reinforcement based mobile robot path planning with improved dynamic window approach in unknown environment. *Auton. Robot.* 45, 51–76.
- [2] Davison A., Reid I., Molton N., Stasse O., et al. (2007). MonoSLAM: Real-time single camera SLAM. *IEEE Trans. Pattern Anal. Mach.Intell.* 29, 1052–1067.
- [3] Dijkstra, E. W., et al. (1959) A note on two problems in connexion with graphs. *Numerische Mathematik.* 1, 269–271.

- [4] Fox, D., Burgard, W., & Thrun, S., et al. (1997) The dynamic window approach to collision avoidance. *IEEE Robotics & Automation Magazine*. 4(1), 23-33.
- [5] Pire T., Fischer T., Castro G., De Cristóforis P., Civera J., Berlles J., et al. (2017) S-PTAM: Stereo parallel tracking and mapping. *Robot. Auton. Syst.* 93, 27–42.
- [6] Rösmann C., Hoffmann F., Bertram T., et al. (2015) Timed-elastic-bands for time-optimal point-to-point nonlinear model predictive control. In *Proceedings of the 2015 European Control Conference (ECC)*, Linz, Austria, 15–17 July. 3352–3357.
- [7] Shan T., Englot B., et al. (2018) LeGO-LOAM: Lightweight and ground-optimized lidar odometry and mapping on variable terrain. *IEEE/RSJ International Conference on Intelligent Robots and Systems (IROS)*. 4758-4765.
- [8] Shan T., Englot B., Meyers D., et al. (2020) LIO-SAM: Tightly-coupled lidar inertial odometry via smoothing and mapping. *IEEE/RSJ international conference on intelligent robots and systems (IROS)*. 5135-5142.
- [9] Seet B., Liu G., Lee B., Foh C., Wong K., Lee K., et al. (2004) A-STAR: A mobile ad hoc routing strategy for metropolis vehicular communications. In *Proceedings of the Networking 2004: Networking Technologies, Services, and Protocols; Performance of Computer and Communication Networks; Mobile and Wireless Communications Third International IFIP-TC6 Networking Conference*, Athens, Greece, 9–14 May; Springer: Berlin/Heidelberg, Germany. 989–999.
- [10] Wang N., Han Y., Wang Y., et al. (2022) Research progress on full-coverage operational planning for agricultural robots (农业机器人全覆盖作业规划研究进展). *Transactions of the Chinese Society for Agricultural Machinery*, Vol. 53, Issue S1: 1-19.
- [11] Xue G, Li R, Zhang Z., et al. (2023) Research Status and Development Trend of SLAM Algorithm Based on 3D LiDAR (基于 3D 激光雷达的 SLAM 算法研究现状与发展趋势). *Information and Control*, vol. 52, Issue (01): 18-36.
- [12] Zhou Z., Cao J., Di S., et al. (2021) Overview of 3D LiDAR SLAM algorithms (3D 激光雷达 SLAM 算法综述). *Chinese Journal of Scientific Instrument*, vol. 42, Issue (09): 13-27.
- [13] Zhang J., Singh S., et al. (2014) LOAM: Lidar odometry and mapping in real-time. *Robotics: Science and Systems Conference*. 2(9): 1-9.

AGRICULTURAL PLANT PROTECTION UNMANNED AERIAL VEHICLE SPRAY PATH PLANNING BASED ON ANT COLONY ALGORITHM

基于蚁群算法的农业植保无人机作物喷洒路径规划

Mingda HE^{*1)}, Xinyan YANG²⁾

¹⁾ Chengdu Sport University, Chengdu, Sichuan, 610000, China

²⁾ Chengdu Normal University, Chengdu, 611130, China

E-mail: cdheminda@126.com

Corresponding author: Mingda He

DOI: <https://doi.org/10.35633/inmateh-73-55>

Keywords: Plant protection; UAV; Path optimization; Genetic algorithm; Spraying operations

ABSTRACT

The farmland in the southwestern mountainous areas of China is mostly hilly terrain with multiple obstacles, and traditional manual spraying operations are time-consuming and laborious. The use of agricultural plant protection unmanned aerial vehicle (UAV) can reduce the problem of high manual operation costs. To solve the problem of optimizing the spraying operation path of plant protection UAVs, this study focused on the complex agricultural environment in the southwestern mountainous areas of China. First, a 2D agricultural map model with multiple obstacles was constructed using MATLAB. Second, the optimization requirements for job paths were analyzed, and a path optimization model based on the grid graph method was studied, aiming to shorten the total flight distance and reduce the number of paths. By applying the genetic algorithm, efficient optimization of the spraying path of plant protection UAV was carried out. Simulation verification showed that the optimized path significantly shortened the flight distance, accelerated convergence speed, and effectively avoided local repeated paths, thereby greatly improving the spraying efficiency of plant protection UAV.

摘要

中国西南山区农田多为含多个障碍物的丘陵地貌，传统人工喷洒作业费时费力，借助农业植保无人机可以减少人工作业成本高的问题。为解决植保无人机喷洒作业路径优化问题，本研究针对中国西南山区复杂农田环境，首先利用 MATLAB 构建了含多障碍物的二维农田地图模型。随后，分析了作业路径优化需求，研究了基于网格图法的路径优化模型，旨在缩短总飞行距离并减少路径数量。通过应用遗传算法，对植保无人机喷洒路径进行了高效寻优。仿真验证显示，优化路径显著缩短了飞行距离，加快了收敛速度，有效避免了局部重复路径，从而大幅提升了植保无人机的喷洒作业效率。

INTRODUCTION

The application of agricultural plant protection unmanned aerial vehicle (UAV) in foreign countries was first introduced in the United States. The fixed wing UAV produced by Huff Daland Company in 1932 has already been used in the agricultural field. According to statistics, over 9,000 UAVs are used in agricultural fields in the United States, and over 60% of them use UAVs to assist in planting management work. However, American agricultural UAVs mainly rely on fixed wing aircraft and helicopters, combined with advanced remote sensing and flight control technology, which is in line with the flat terrain and large-scale planting characteristics of their farmland. Among Asian countries, Japan was one of the earliest to apply UAVs to agricultural production. In 1958, Japan began using manned UAVs to control pests, diseases, and weeds in farmland. In 1983, the method of manned and unmanned driving working together on farmland was proposed. By 1987, the world's first agricultural UAV had been born in Japan, making it the first country to use crop protection UAV for crop protection operations (Gago J. et al., 2020). Compared with large-scale farmland in the United States, Japan has a smaller per capita arable land area and complex terrain. In addition, the significant reduction in agricultural population and the high cost of manual labor caused by hilly terrain make the development of agricultural UAV in Japan relatively large. Japan's plant protection UAVs mainly rely on oil powered unmanned helicopters, and they have established a comprehensive plant protection service system around unmanned helicopters (Xu C. et al., 2020). They have rich experience in the research and management of specialized pesticides for UAV.

The labels of their specialized pesticides include parameters such as weather restrictions, flight altitude, spray volume, and drift volume, making it convenient for the promotion and use of drugs.

The application of UAVs in China's agricultural sector was relatively late compared with the United States and Japan. In 2010, the first commercial plant protection UAV appeared. In 2014, it began to enter a stage of rapid development. At present, China has over 100,000 types of agricultural crop protection UAVs, including fixed-wing and rotary-wing UAVs, with multi-rotor UAV being the main type in recent years. The well-known enterprise DJI UAV Company established DJI Agricultural Company in 2015, specializing in the agricultural field, and launched the T series of agricultural UAV. Its latest T50 can achieve the replacement of spraying and broadcasting modules to adapt to agricultural application scenarios. Its load capacity can reach up to 50 kg, and the dual atomization spraying system can make the droplets uniform and fine. When operating on fruit trees, centrifugal nozzles can be added to increase the spraying area and improve the adhesion rate of leaf back medicine. By carrying an active phased array radar and binocular vision system, terrain prediction and obstacle avoidance can be achieved. Some other companies have also launched similar plant protection UAVs (Zhang H., et al., 2021).

Given that the main rice planting areas in China are concentrated in the south, the terrain is mainly irregular mountains and hills. The traditional method of spraying rice paddies mainly relies on individual farmers carrying portable equipment, which has the characteristics of high manual labor intensity and low work efficiency. With the development of UAV technology, using agricultural plant protection UAV for spraying operations has become a trend in modern agriculture. Compared with traditional methods of plant protection operations, plant protection UAVs not only have the characteristics of small size, easy portability, high safety, and the ability to hover freely, but they also can vertically take off and land in small work areas, allowing UAVs to perform spraying operations on various terrains. Therefore, the rational utilization of agricultural plant protection UAV has become a hot topic worthy of research in the current field of agricultural plant protection.

As the application scope of plant protection UAV continues to expand, the working environment faced by UAVs will gradually become complex, and the number of tasks will continue to increase, which may lead to some problems in path planning, such as missed or repeated operations, high energy consumption, long working paths, and inability to effectively avoid obstacles. Path planning is an essential part to improve the operational efficiency and reduce losses of plant protection UAV. Reasonably planning the operation path is the key to achieving safe and efficient operation of plant protection UAVs. In this process, factors such as terrain characteristics, vegetation information, and aircraft performance should be combined to develop path planning algorithms suitable for different terrains and farmland types by combining plant protection UAV with artificial intelligence to achieve efficient and energy-saving plant protection operations. This not only effectively reduces labor costs in agricultural production but also helps reduce pesticide spraying omissions and repetitions, thereby improving agricultural production efficiency and quality and ensuring food security.

At present, scholars at home and abroad have conducted extensive research on the path planning problem of plant protection UAVs. The methods used in the research can be generally divided into two types: one is path planning based on intelligent bionic algorithms. Commonly used examples are grey wolf optimization algorithm, ant colony algorithm, and genetic algorithm. These algorithms are mainly inspired by the intelligent phenomenon of natural biological populations and optimization algorithms were proposed by imitating the behavior of social animals. These algorithms are widely used in path planning research due to their efficient optimization speed and the need to consider too much initial information of the problem. Another type is path planning algorithms based on graph search, such as Voronoi diagram (Asano H. et al., 2022), A* algorithm (Kong X. et al., 2020) and Dijkstra algorithm (Zhang and Bai, 2024). These algorithms have strong path search capabilities and usually obtain accurate solutions, but the computational complexity of these algorithms increases with the increase in environmental complexity, resulting in a significant decrease in path planning performance.

When conducting plant protection operations, UAVs need to spray uniform medication on crops in the target area to ensure the effectiveness of the operation. In plain areas, the trajectory planning of plant protection UAV is full coverage path planning based on 2D planes, mainly limited by the battery capacity, load capacity, operation range, and plot shape of the UAV. The main focus is on indicators such as non-plant protection operation duration, plant protection operation trajectory length, operation repetition rate, and omission rate. The full coverage trajectory planning algorithm needs to plan an optimal trajectory that avoids obstacles and traverses the entire area within the region, mainly using the unit decomposition method and grid method.

The unit decomposition method divides the working area of the UAV into multiple accessible sub areas, and the coverage of each subarea becomes a simple reciprocating motion. The grid method decomposes environmental information into squares based on the motion speed and spraying width of the UAV. Each square represents a certain size of land, and it can be divided into idle or occupied squares based on whether there are obstacles in the land. The UAV can then find the optimal route to traverse all squares.

At present, there are mainly two methods for 3D trajectory planning. One is to obtain the height of the UAV relative to the ground and predict the slope of the work site through onboard sensors without obtaining a 3D map in advance to ensure that the UAV always maintains a relative height with the ground and completes the entire operation. Some research provided accurate positioning for UAV through RTK modules and used laser sensors to achieve obstacle avoidance, achieving trajectory planning for UAV under hilly terraced fields (Wan Y. et al., 2022). Another approach is to obtain 3D terrain in advance and combine it with the constraints of the UAV itself for trajectory planning. And some other research rasterized the farmland based on its shape, height, and other information, established a 3D model of the farmland, and compared the planned trajectory of the same farmland on a 2D map and a 3D map. Their results showed deviations in the length of the trajectory and the position of the return point (Xie H. et al., 2021). Using a 2D map for shortest path planning and then combining the performance of the UAV with its operating altitude through a 3D map, the waypoint position during the UAV's flight process can be optimized, thereby ensuring the safety of the UAV in terrain with large altitude changes. In hilly and mountainous environments, the round-trip distance of plant protection UAVs in non-operational situations cannot be ignored. Reducing energy consumption outside of work can prolong the overall operation time of UAVs and improve their work efficiency (Lambertini A. et al., 2022).

In summary, the current path optimization problem of agricultural plant protection UAVs mostly utilizes various methods for 2D map drawing. It is proposed to integrate the genetic algorithm, neural network algorithm, particle swarm optimization algorithm, artificial potential field method, and other algorithms to obtain the optimal algorithm for plant protection UAVs (Liu Y. et al., 2022). On this basis, this study further designed a path optimization model based on the genetic algorithm for multi-obstacle avoidance scenarios in complex mountainous and hilly terrain to optimize the spraying operation path of agricultural plant protection UAV.

MATERIALS AND METHODS

The fitness function can calculate the cost of the track and compare the cost values of different tracks to determine the quality of the track. This article comprehensively balances three factors: track length, obstacle collision, and height change, and models the fitness function, as shown in formula (1):

$$F = \varphi_1 f_L + \varphi_2 f_C + \varphi_3 f_H \quad (1)$$

Among them: f_H represents the cost of height change, f_C represents the cost of obstacle collision, f_L represents the cost of track length, F represents the cost of track, $\varphi_1, \varphi_2, \varphi_3$ represents the weight values of different costs, and is a constant, and its proportion is related to the tasks performed by the drone.

Problem Description

The principle of path planning for commercial UAV is to traverse all points in point units to complete the task. The path planning of agricultural plant protection UAV is slightly different from commercial UAV. The purpose of the path planning is to start from the workstation, find a work path that traverses all grid lines in the target farmland area without crossing obstacles, and finally return to the work station. At this point, the task is completed. In summary, the goal of path planning for plant protection UAV is to find a Hamiltonian loop with the smallest weight, as shown in Fig. 1.

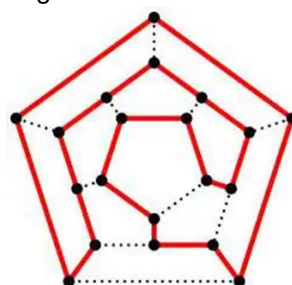


Fig. 1 - Hamiltonian circuit schematic diagram

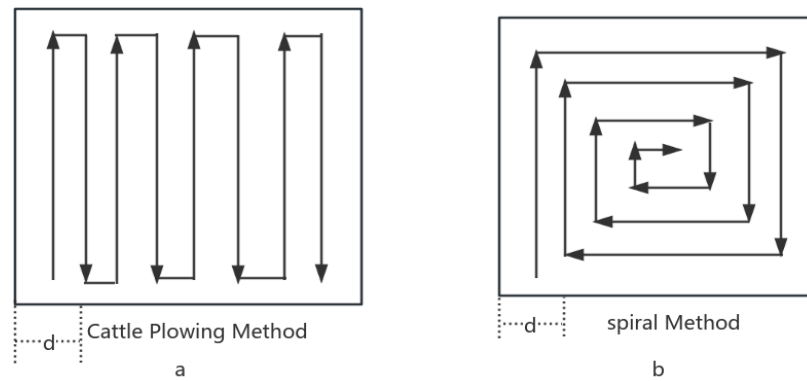


Fig. 2 -Schematic diagram of agricultural plant protection UAV operation coverage

The main problem faced by agricultural plant protection UAV serving farmland in southern China is how to achieve obstacle avoidance. The obstacles in agricultural areas come from two aspects. One is the actual obstacles in the agricultural area, such as power poles and signal towers; the other is the cruising altitude difference caused by the undulating terrain of hilly land. To address this issue, this study uses the ant colony algorithm to optimize the path of agricultural plant protection UAV while considering obstacle avoidance. As a result of the inability of plant protection UAVs to perform spraying operations when turning, to improve work efficiency, combined with the terrain characteristics of the target farmland area and the actual UAV model, this study abandoned the spiral (See Fig. 2 b) covering method and chose the cow plowing (See Fig. 2 a) method as the coverage method for plant protection UAV spraying operations.

Under the cow plowing method, the flight trajectory of the plant protection UAV is a unidirectional straight line. Therefore, the main method for optimizing its path is to determine the total sum of one-way paths, which is the total flight length. In addition, the UAV used in this study cannot perform operations during turns, so the optimization process should minimize the number of turns for the UAV.

Referring to XX's research, the total flight length S_{Bou} and total number of turns T_{Bou} of plant protection UAV are defined as Formulas (2) and (3), respectively.

$$S_{Bou} = L \cdot \text{ceil}\left(\frac{M}{d}\right) + d \cdot (\text{ceil}\left(\frac{M}{d}\right) - 1) \quad (2)$$

$$T_{Bou} = 2(\text{ceil}\left(\frac{M}{d}\right) - 1) \quad (3)$$

In the formula:

- M - The horizontal length of the work area;
- L - Vertical width of the work area;
- D - The maximum width of UAV operation.

Model Building

The path planning of plant protection UAV first requires a recognizable work environment information map. Currently, common model construction methods include grid graph method, visual graph method, and Voronoi graph method. Given the use of the ox plowing method in this study and considering the ease of achieving full coverage of farmland areas, the grid diagram method was chosen to simulate the establishment of a 2D operation plan for plant protection UAV via MATLAB simulation. When constructing the grid, the width of the UAV operation was set to a fixed spacing and then the path of the divided grid was planned based on environmental information. Compared with the two other modeling methods, the complexity of constructing a work environment using the grid graph method is relatively low, and the constructed graphics are clearer. To better implement the modeling process, this study determined the coordinates of the work area, as well as the coordinates of obstacles and workstations, to set or modify the work area of the plant protection UAV. MATLAB was used to establish a 2D environmental coordinate map including obstacles and workstations, as shown in Fig. 3.

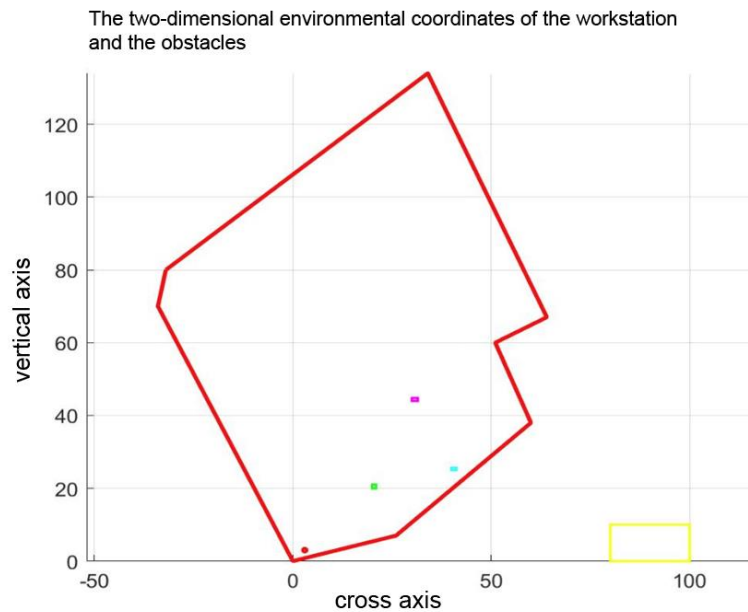


Fig. 3 - Two dimensional environmental coordinate map of plant protection area based on MATLAB simulation

In Fig. 3, the yellow area represents a dedicated workstation for UAV takeoff, landing, and maintenance. The red area is the experimental area selected for this study.

Design of Obstacle Avoidance Methods

Chinese farmland is mostly located in mountainous and hilly terrain, and common obstacles during spraying operations include telecommunications poles, large trees, and agricultural hardware facilities (Khalilpour S. A. *et al.*, 2020). These obstacles have different shapes and irregular distributions. During the process of using the ox plowing method, if there are no obstacles on the moving route, the plant protection UAV will walk between the two ends of the route during non-turning operations, with a distance of Euclidean distance. If there are obstacles on the moving route, the walking route of the plant protection UAV will be separated and obstacle avoidance is required (Yin X. *et al.*, 2021). Therefore, in the actual operation process, plant protection UAV must flexibly avoid obstacles according to their actual situation. On the basis of existing research findings, there are two principles for designing obstacle avoidance methods. One is to avoid crossing obstacles, that is, to stop moving forward when obstacles are detected. Another approach is to detour around obstacles. Considering the accuracy of grid graph simulation, this study adopted the obstacle avoidance design by bypassing obstacles. The principle of detour is shown in Fig. 4.

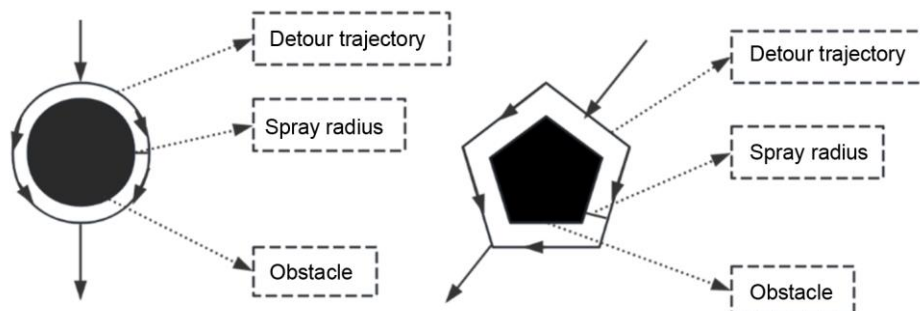


Fig. 4 - Schematic diagram of obstacle avoidance and detour for plant protection UAV

Calculation of Distance Matrix

The obstacle avoidance scheme used in this study requires calculating the shortest path between any two points on the map (Ampatzidis Y. *et al.*, 2020). For irregular obstacles, there are multiple detours to choose from. Appropriate algorithms must be used to select and calculate the distance between the pre-set endpoints of opposite obstacles, and a short path should be selected for the operation. Therefore, the key to designing obstacle avoidance methods is to determine the shortest distance between endpoints on the route.

The Floyd algorithm was used in this study to calculate the shortest path between any two points in the map. The Floyd algorithm has a time complexity of $O(n^3)$ and a spatial complexity of $O(n^2)$, which can limit the computational complexity to an allowable range (Xie P. et al., 2024). As a result of its compact triple-loop structure, the algorithm performs well in planning dense graphs and can handle problems with positive or negative edge weights. Compared with the Dijkstra algorithm, this algorithm has higher execution efficiency and is simple and effective.

In the Floyd algorithm, a directed graph is first constructed based on known conditions and the intrinsic relationships between nodes, and the shortest distance matrix d is generated based on the weight information between each node. In the distance matrix, $D(i, j)$ represent the weight of the shortest path directly connecting point i and point j . If point i and point j cannot be directly reached, $D(i, j)=\text{inf}$. In a directed graph, generally $D(i, j) \neq D(j, i)$.

The routing matrix P is used to record the information of intermediate nodes generated in the distance matrix d . When the sum of the weights of $d[i, k]$ and $d[k, j]$ is less than the previous weight of $d(i, j)$, update the weight of $P[i, j]$ to the intermediate node k . When the sum of the weights of $d[i, k]$ and $d[k, j]$ is greater than the weight of $d(i, j)$, the weight of $P[i, j]$ is not updated. At the end of the loop, the shortest path between any two points can be found in the routing matrix P . Finally, through the obtained routing matrix P , calculate the shortest path length from any point i to point j according to the constructed job area. Let the point set consisting of all endpoints of the grid line be V_1 , and the point set consisting of all vertices of obstacles be V_2 . The starting point of the UAV is v^* , and all the above points from the point set V , as shown in formula (4):

$$V = V_1 \cup V_2 \cup \{v^*\} \quad (4)$$

Calculate the distance matrix D between any two endpoints based on the point set V , as shown in formula (5), where $D_{ij} \in D$.

$$D_{ij} = \begin{cases} \sqrt{(x_i - x_j)^2 + (y_i - y_j)^2} & \text{Accessibility between } i \text{ and } j \\ M & \text{otherwise} \end{cases} \quad (5)$$

$M \in R^+$, A sufficiently large positive real number.

The distance D_{ij} calculated according to Formula (5) is the direct distance between any two points in the graph, that is, the distance between the two points without obstacles. Correspondingly, it is the indirect distance between two points, which is the shortest path when there are obstacles between the two points. When there are obstacles between two points, the Floyd algorithm proposed in this article needs to be used to calculate the shortest path of the detour. To achieve effective obstacle avoidance of UAV and achieve the optimization goal of minimizing the length of operations, this paper used the following algorithm to construct the shortest path matrix, as shown below:

Input: Point set V

Output: Shortest path matrix R between two points.

1) Calculate the direct distance D in point set V using formula (5).
2) Using the Floyd algorithm, calculate the shortest path matrix R between any two points in set V based on the distance matrix D .

3) Due to the fact that the vertices of obstacles do not necessarily belong to the vertices of the grid lines. Therefore, by removing all rows and columns corresponding to points ($V_2 - V_1$) included in V_2 but not in V_1 from R , the matrix R is obtained.

4) Output the shortest path matrix R .

RESULTS

Determination of the Shortest Path

The traditional ant colony algorithm was initially used to solve the traveling salesman problem, which requires traversing all points during planning (Tian H. et al., 2023). The path planning problem of plant protection UAV is based on line segments as the basic unit of operation, which requires traversing all grid lines in the operation area to complete the task of full coverage of the operation area. When using the ant colony algorithm for path planning, first, set the endpoints of the grid lines to ensure that the plant protection UAV can operate based on line segments.

When a UAV reaches a certain endpoint, the primary problem to be solved in path planning is how to select the other end point of the line segment that this endpoint is facing. On the basis of the above issues, this article proposes the following solutions for the application of the ant colony algorithm in plant protection UAV.

To ensure that the plant protection UAV traverses all grid lines in a basic unit of line segments, the first step is to process the line segments formed by the two endpoints of the grid lines. Therefore, this article processed the shortest path matrix R, as shown in Formula (6):

$$\overline{R}_{ij} = \begin{cases} 0 & i \neq j, \text{ Endpoints belonging to the same network cable} \\ R_{ij} & \text{otherwise} \end{cases} \quad (6)$$

After processing, the UAV will inevitably pass through another endpoint of the same grid line when it first reaches one end of the grid line. Thus, the plant protection UAV can traverse all line segments during operation and complete the full coverage task.

Ant Colony Algorithm Process

This study defined all grid lines as a set L , and any grid line $Li \in L, i=1,2,3,\dots,n$. The two endpoints of Li are v_{i1} and v_{i2} , respectively (where $v_{ij} \in V1, j=1, 2, V1$ is the set of points formed by all endpoints of the grid lines shown in the previous section). The specific implementation steps of the ant colony algorithm based path planning for plant protection UAV proposed in this article are as follows:

Step 1: Construct the operation map of the plant protection UAV.

Step 2: Initialize the number of ants m in the ant colony algorithm, the maximum number of iterations NC_{max} , the pheromone constant Q , the pheromone weight factor α , the heuristic function weight factor β , and the volatility coefficient ρ .

Step 3: Randomly select v_{ij} as the starting point for the ants, and set a variable *tabuk* to store the points that the ants have passed.

Step 4: The ant starts from point $v_i \in V1$ and selects the next point v_j from *Allowed_k* based on the concentration of pheromones on the path and the heuristic function. The calculation formula is shown in Formula (7).

$$P_{ij}^k(t) = \begin{cases} \frac{[\tau_{ij}(t)]^\alpha \times [\eta_{ij}(t)]^\beta}{\sum [\tau_{is}(t)]^\alpha \times [\eta_{is}(t)]^\beta} & s \in Allowed_k \\ 0 & \text{else} \end{cases} \quad (7)$$

In the formula:

$P_{ij}^k(t)$: The probability of ant k from point i to j at time t ;

$\tau_{ij}(t)$: The intensity of pheromones on the connection path from point i to point j at time t ;

α : Pheromone weight factor;

$\eta_{ij}(t)$: The expected degree of ant transfer from point i to point j ;

β : Heuristic function weight factor;

Allowed_k: Stores the points that ants are waiting to access;

Step 5: Check if there are any points in the *Allowed_k* that need to be accessed. If not, record the current route. Otherwise, return to step 4.

Step 6: When ants choose the next line segment to work on, they will release pheromones along their path, and the concentration of pheromones that have already walked along the path will evaporate over time. Therefore, when all ants traverse all line segments, the pheromone concentration on the job path must be updated, as shown in Formulas (8) and (9).

$$\begin{cases} \tau_{ij}(t+1) = (1 - \rho)\tau_{ij}(t) + \Delta\tau_{ij} \\ \Delta\tau_{ij}(t) = \sum_{k=1}^m \Delta\tau_{ij}^k(t) \end{cases} \quad (8)$$

$$\Delta\tau_{ij}^k(t) = \begin{cases} Q / L_k & , \text{ ant } K \text{ from } i \text{ to } j \\ 0 & \text{else} \end{cases} \quad (9)$$

In the formula:

$\rho(0 < \rho < 1)$: Volatility coefficient of pheromones;

$\Delta\tau_{ij}(t)$: The total concentration of pheromones released by all ants on paths i to j ;

$\Delta\tau_{ij}^k(t)$: The concentration of pheromones released by the k -th ant on paths i to j ;

Q : Constant, representing the total amount of pheromones released by ants in one cycle;

L_k : The path length of ant k after traversing all the job grid lines.

Step 7: Check if the number of times the ant has traversed has reached the maximum number of iterations. If it has, output the optimal solution. Otherwise, return to step 3.

The flowchart of the application of ant colony algorithm in plant protection UAV is shown in Fig. 5.

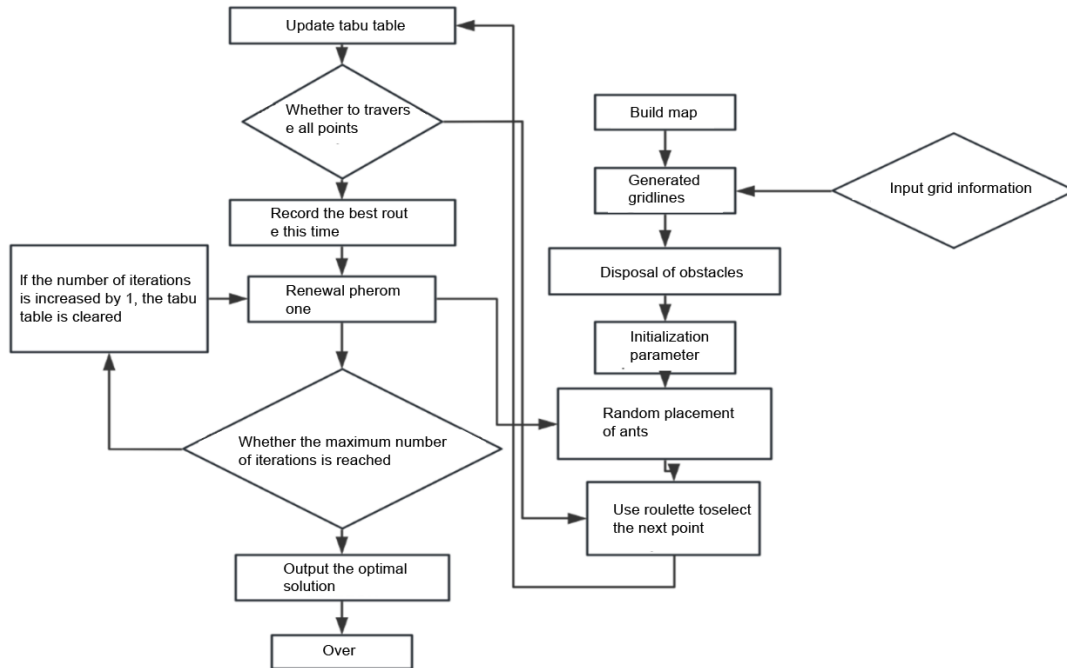


Fig. 5 - Algorithm flow

Simulation Results and Analysis

In general, changes in pheromone weight factor, number of ants, heuristic function weight factor, maximum number of iterations, pheromone volatility coefficient, and total pheromone quantity can all affect the optimization effect of ant colony algorithm. To date, there is no mathematical method that can directly solve for the most parameter settings, and the parameters need to be set through empirical or experimental methods. This study referred to the former research to set the parameters of the ant colony algorithm (Liu Lu et al., 2024; Tian H. et al., 2023), with specific values shown in Table 1.

Table 1

Parameter Settings of Ant Colony Algorithm

| Parameter | Parameter value setting |
|------------------------------|-------------------------|
| Maximum number of iterations | 500 |
| Ant count | 100 |
| Heuristic function weight | 10 |
| Pheromone weighting factor | 1.0 |
| Total amount of pheromones | 200 |
| Volatility coefficient | 0.9 |

The software system for this simulation experiment was WIN10 and M atlab2021; the hardware platform was Intel (R) Core (TM) i5-6200U CPU @ 2.30GHz, with 8GB of memory. The experimental plot is located in Guang'an, southwestern China, and its shape and obstacle distribution are shown in Figure 3. According to Figure 3, the coordinates of the plot are arranged counterclockwise as (-32, 80), (-34, 70), (0, 0), (26, 7), (60, 38), (51, 60), (64, 67), (34, 134), and the coordinates of the workstation are (-10, -40), (10, -40), (10, -50), (-10, -50). Adjust the unit as needed in meters. The relevant information about obstacles is shown in Table 2.

Table 2

| Obstacle Information | |
|-------------------------------|--|
| Obstacle name | Grid 2D coordinates |
| Basic farmland facilities | (40,27), (41,27), (41,28), (40,28) |
| Water storage well | The center coordinates are (3, 2) with a radius of 0.5 |
| Telecommunications facilities | (18,20), (19,20), (19,21), (18,21) |
| Power facilities | (35,44), (36,44), (36,45), (35,45) |

The spraying width of the local plant protection UAV was 6 m. Considering the departure position of the UAV from the workstation, it entered the experimental site in a 135° operation direction for work and finally returned to the UAV departure workstation. Therefore, in the simulation experiment, initial settings were made based on the above conditions, and the obstacle avoidance method of this study was adopted. The experimental results are shown in Fig. 6. The new path enabled the plant protection UAV to effectively avoid all obstacles and plans an optimal path from the starting point to traverse all trajectories before returning to the starting point, verifying the effectiveness of the proposed algorithm.

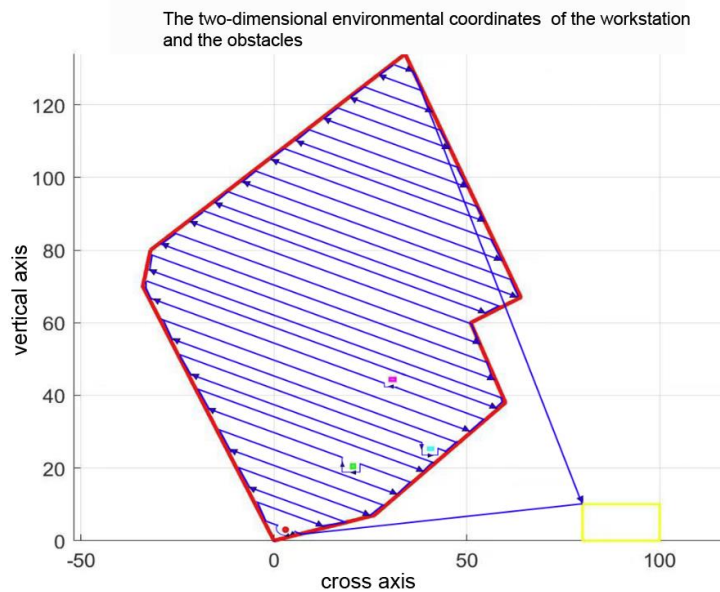


Fig. 6 - Results of Path Optimization Operation

The red curve in Fig. 6 represents the average path length planned by the ant colony algorithm, whereas the blue line represents the shortest path length. The graph shows that the ant colony algorithm had relatively small fluctuations in the overall average data when planning the path of plant protection UAV. The algorithm could quickly converge to the optimal path, as shown in Fig. 7.

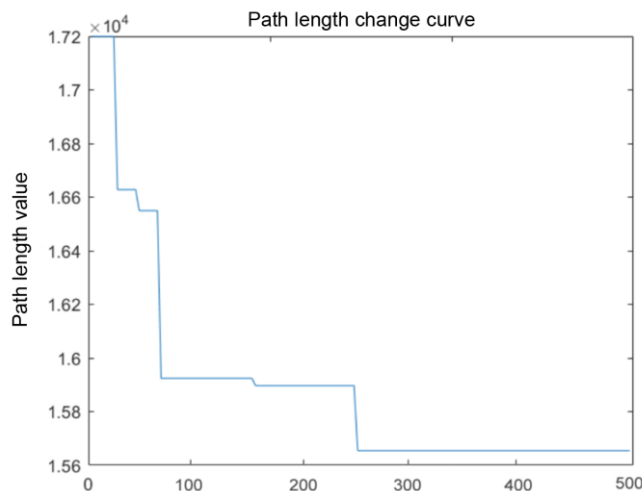


Fig. 7 - Algorithm iteration diagram

To further verify the performance of the ant colony algorithm in path planning of plant protection UAV, this paper compared the operation path of plant protection UAV with that of traditional cattle plowing method in the grid graph. Path planning of plant protection UAV with obstacles reduced the repetition of local paths compared with the traditional cattle plowing method (from 15% of repeated paths to 2.7% occasionally), and the spraying coverage rate was 100%. These data showed that the ant colony algorithm remarkably optimized the operation path of the plant protection UAV, effectively improving its operational efficiency. Further observation of the variance data of the shortest path planned by the ant colony algorithm in the table revealed that the optimal path length planned by the ant colony algorithm was relatively stable. The above analysis indicated that the ant colony algorithm was superior in path planning for plant protection UAV.

CONCLUSIONS

This study mainly optimized the spraying operation path of plant protection UAV in a certain farmland area of a southwestern city in China. First, considering reasonable obstacle avoidance, the shortest detour distance was calculated using the Floyd algorithm to construct the optimal path model for plant protection UAV. Second, the ant colony algorithm was used for experimental design, and MATLAB was used for simulation experiments. Results showed that the path planning method based on the ant colony algorithm proposed in this section was feasible, and its coverage range and total operation path were better than traditional ox plowing methods. Given the topography of the research object, the proposed approach is mainly applicable to farmland with small hilly terrain. When the land area is large, multiple plant protection UAVs may be simultaneously deployed for optimal path planning. In addition to mature applications in the agricultural field, UAV path planning has the feasibility of further expansion in commercial fields (such as UAV express delivery routes), cultural tourism, and sports (such as optimizing the performance paths of UAVs in sports stadiums and spraying operations on football fields). The limitations of further application of the results of this study mainly lie in two aspects: first, some geomorphic environmental wind fields in the mountainous areas of southwest China change greatly in real time, and the UAV may be interfered with in the process of plant protection operation; second, this study mainly considers the operation scenario of contiguous farmland area, and does not consider the operation scenario of non-contiguous multi-farmland area. In the future, the application of this path optimization model in plant protection operations of multiple farmland under complex wind field environment in mountainous areas will be further verified.

REFERENCES

- [1] Ampatzidis Y., Partel V., Costa L. (2020). Agroview: Cloud-based application to process, analyze and visualize UAV-collected data for precision agriculture applications utilizing artificial intelligence. *Computers and Electronics in Agriculture*, Vol. 174, pp. 105457. England.
- [2] Asano H., Okada H., Naila C. B., Katayama M. (2022). Voronoi-based UAV flight method for non-uniform user distribution in delay-tolerant aerial networks. *IEICE Transactions on Communications*, Vol. 105, Issue 11, pp. 1414-1423, Japan.
- [3] Gago J., Estrany J., Estes L., Fernie A. R., Alorda B., Brotman Y., Medrano H. (2020). Nano and micro unmanned aerial vehicles (UAVs): a new grand challenge for precision agriculture? *Current protocols in plant biology*, Vol. 5, Issue 1, pp. 20203, United States.
- [4] Khalilpour S. A., Khorrambakht R., Damirchi H., Taghirad H. D., Cardou P. (2020). Tip-trajectory tracking control of a deployable cable-driven robot via output redefinition. *Multibody System Dynamics*, Vol. 16, Issue 4, pp. 1-28, Netherlands.
- [5] Kong X., Pan B., Cherkashin E., Zhang X., Liu L., Hou J. (2020). Multi-constraint UAV fast path planning based on improved a* algorithm. *Journal of Physics: Conference Series*, Vol. 1624, Issue 4, pp.042009 (6pp), United Kingdom.
- [6] Lambertini A., Mandanici E., Tini M. A., Vittuari L. (2022). Technical challenges for multi-temporal and multi-sensor image processing surveyed by UAV for mapping and monitoring in precision agriculture. *Remote Sensing*, Vol. 14, Issue 19, pp. 4954, Switzerland.
- [7] Liu Lu., Shen Xiaowei., Ge Chao., Wang Hong. (2024). Plant protection drone path planning based on improved ant colony algorithm *Computer Simulation*, Vol.3, Issue 1, pp. 39-43, China.
- [8] Liu Y., Zhang P., Ru Y., Wu D., Wang S., Yin N., Liu Z. (2022). A scheduling route planning algorithm based on the dynamic genetic algorithm with ant colony binary iterative optimization for unmanned aerial vehicle spraying in multiple tea fields. *Frontiers in Plant Science*, Vol. 13, pp. 998962, Switzerland.

- [9] Tian H., Mo Z., Ma C., Xiao J., Jia R., Lan Y., Zhang Y. (2023). Design and validation of a multi-objective waypoint planning algorithm for UAV spraying in orchards based on improved ant colony algorithm. *Frontiers in Plant Science*, Vol. 14, pp. 1101828, Switzerland.
- [10] Wan Y., Zhong Y., Ma A., Zhang L. (2022). An accurate UAV 3-D path planning method for disaster emergency response based on an improved multiobjective swarm intelligence algorithm. *IEEE Transactions on Cybernetics*, Vol. 53, Issue 4, pp. 2658-2671, United States.
- [11] Xie H., Yang D., Xiao L., Lyu J. (2021). Connectivity-aware 3D UAV path design with deep reinforcement learning. *IEEE Transactions on Vehicular Technology*, Vol. 70, Issue 12, pp. 13022-13034, United States.
- [12] Xie P., Ma B., Wang B., Chen J., Xiao G. (2024). 3D path planning of the solar powered UAV in the urban-mountainous environment with multi-objective and multi-constraint based on the enhanced sparrow search algorithm incorporating the levy flight strategy. *Guidance, Navigation and Control*, Vol. 4, Issue 1, China.
- [13] Xu C., Liao X., Tan J., Ye H., Lu H. (2020). Recent research progress of unmanned aerial vehicle regulation policies and technologies in urban low altitude. *Ieee Access*, Issue 8, pp. 74175-74194, United States.
- [14] Yin X., Pan L., Cai S. (2021). Robust adaptive fuzzy sliding mode trajectory tracking control for serial robotic manipulators. *Robotics and Computer-Integrated Manufacturing*, Vol. 72, pp. 101884, England.
- [15] Zhang H., Wang L., Tian T., Yin J. (2021). A review of unmanned aerial vehicle low-altitude remote sensing (UAV-LARS) use in agricultural monitoring in China. *Remote Sensing*, Vol. 13, Issue 6, pp. 1221, Switzerland.
- [16] Zhang J., Bai J. (2024). Dijkstra algorithm based cooperative caching strategy for UAV -assisted edge computing system. *Wireless Networks*, Vol. 30, Issue 3, pp. 1201-1219, Netherlands.

APPLYING MACHINE LEARNING FOR ENVIRONMENTAL FACTOR PREDICTION ON DESIGNING IOT APPLIED HYDROPONIC SYSTEM

ỨNG DỤNG PHƯƠNG PHÁP HỌC MÁY ĐỂ DỰ ĐOÁN CÁC YẾU TỐ MÔI TRƯỜNG TRONG THIẾT KẾ HỆ THỐNG THỦY CANH IOT

Van-Tinh NGUYEN*, Tan-Hoang NGUYEN, Ngoc-Kien NGUYEN

School of Mechanical Engineering, Hanoi University of Science and Technology, Hanoi, Vietnam.

Tel: +840985800038; E-mail: tinh.nguyenvan@hust.edu.vn

DOI: <https://doi.org/10.35633/inmateh-73-56>

Keywords: Internet of Things, hydroponics, temperature prediction, machine learning, smart farming.

ABSTRACT

In IoT hydroponics, the integration of Internet of Things (IoT) and Machine Learning (ML) has opened up great opportunities to increase the productivity and smart system's management. With the collected data from sensors in the environment, the machine learning model would analyze and predict the trend of the environmental factors, this combination not only improves the outcome quality but also helps saving the resources. Integrating machine learning into an IoT hydroponics system could not only create a smart, autonomous and adaptable system to changing conditions of environment in real-time but also optimize resources for a cost-effective and productive hydroponic system. In this study, a novel method was presented for predicting environmental factors using Machine Learning algorithm for smart IoT hydroponic systems. By applying this method, an IoT hydroponic system can predict the trends of environmental factors which affects the plants such as temperature, moisture, pH levels.... The experiment results show that the accuracy of the predicted data is reliable, it reached 94.2% for a day and 92.6% for a week. These results could help users take proactive measures to improve the cultivation quality.

TÓM TẮT

Trong hệ thống thủy canh IoT, sự tích hợp của công nghệ kết nối vạn vật (IoT) và thuật toán học máy (ML) đã mở ra nhiều cơ hội để tăng năng suất và quản lý hệ thống. IoT cho phép thu thập dữ liệu từ các cảm biến trong môi trường, trong khi thuật toán học máy cung cấp khả năng phân tích và dự đoán dựa trên dữ liệu quá khứ. Sự kết hợp này không chỉ cải thiện chất lượng kết quả mà còn giúp tiết kiệm tài nguyên. Khả năng dự đoán của thuật toán học máy giúp người nông dân quản lý hệ thống một cách hiệu quả, tiết kiệm nguyên liệu đầu vào và duy trì các điều kiện lý tưởng cho cây trồng. Bài báo này trình bày một phương pháp mới để dự đoán nhiệt độ môi trường bằng thuật toán học máy, áp dụng cho hệ thống thủy canh IoT. Phương pháp này có thể dự đoán xu hướng thay đổi của các yếu tố môi trường dựa trên dữ liệu thời tiết có sẵn của một khu vực trong quá khứ. Kết quả thí nghiệm chỉ ra rằng độ chính xác của dữ liệu dự đoán đạt 94.2% cho một ngày và 92.6% cho một tuần. Nó có thể cung cấp trước thông tin cho người dùng thông qua giao diện trang web để họ có thể thực hiện các biện pháp chủ động nhằm cải thiện năng suất của quá trình thủy canh và đảm bảo chất lượng sản phẩm.

INTRODUCTION

Hydroponics is an agricultural method where plants are cultivated in a nutrient-rich liquid, essentially water. The core concept is to utilize water as a way to supply plants with essential elements and nutrients for optimal growth. The suitable amount of sunlight is maintained to facilitate the photosynthesis and respiration processes, therefore, promoting robust plant development and productivity. In traditional soil environments, plants can only absorb around 5% of nutrients from the soil, with the remaining 95% synthesized through the process of photosynthesis. The soil serves as a reservoir for nutrients, gradually utilized by plants as they grow. In hydroponics, nutrients are converted into a liquid form, the most easily absorbable state for plants during their growth. This eliminates the necessity for soil as a growth medium, as plants can readily assimilate nutrients from the liquid environment throughout their development. Another benefit of hydroponics is that it helps restricts contact with harmful worms and limits the need of using pesticides therefore, makes it safer for humans' health.

Based on the conditions of the applied environment, there are four main models of hydroponics: wick-based, static, recirculating and drip hydroponics. Wick-based hydroponics utilizes a wick to supply nutrients to the plant by placing one end of the wick into the nutrient solution, the other end touches the plant's roots, the wick will absorb water and nutrients to nourish the plant, ensuring it receives sufficient nutrients for growth. Static hydroponic model employs a container, tank, tray, or reservoir for the hydroponic solution, the plant support component is typically made of lightweight material at the top. Plant roots are submerged in the hydroponic solution. Recirculating model is quite similar to static one with a slight difference is that it uses a pumping machine to control the amount of the nutrient's liquid coming in and out of the tray following a certain cycle and therefore, the roots will not be drowned in the water all the time and make space for natural respiratory. In contrast to recirculating model, dripping hydroponics can use soil or other growing mediums as a substrate, but the irrigation water permeates instead of circulating back to the reservoir. When the moisture level in the garden falls below a threshold, the pump system is activated, or water is periodically pumped based on a predefined schedule. There have been many attempts to improve the tradition hydroponics systems such as developments of new hydroponic chemicals, installs devices to automatically control natural conditions in the systems entirely such as using LEDs to provide light in a specified spectrum that is beneficial for the plants' growth, pumping systems to control the water circulation, etc.... As technology evolves, the trend of utilizing cutting-edge techniques to monitor the growing process of the plants in the hydroponic garden is inevitable. The advanced hydroponic farming methods in 4.0 industrial revolution usually integrates sensors, smart and IoT technology for automatic monitoring and controlling the farming processes (Yanes *et al.*, 2020).

The challenges of applying IoT technology into the recirculation hydroponics is a precise supervision of factors such as pH, nutrients amount, temperature, air moisture and watering amount. These environmental indexes would be directly sent to the control center and the owner's smartphone. As a result, the technicians could provide suitable technical support to always make the best condition for growing plants. In automated mode, the system's component such as misting and rolling mechanisms, shading nets, and lighting on/off switches could automatically operate to provide light, temperature balance in the greenhouse can be maintained by opening/closing misting nozzles, adjusting the pH level in the nutrient solution, and dosing the fertilizer formula. Across the history of agriculture's automation, there have been many published research and completed IoT applied systems on cultivating plants. For example, Farhan Mohd Pu'ad *et al.* designed a IoT based water quality monitoring system for aquaponics (Farhan *et al.*, 2020), Chien Lee *et al.* developed a cloud-based IoT monitoring system for Fish metabolism and activity in aquaponics (Lee *et al.*, 2020) and Isabella Wibowo built an IoT based automatic water nutrition monitoring system (Isabella *et al.*, 2019). Maritel Dawa also designed and built an IoT based aquaponics management system which can adapt to climate change (Maritel *et al.*, 2022) while S. B. Dhal *et al.* introduced an IoT system designed for managing nutrient supply within a commercial hydroponic environment (Dhal *et al.*, 2022). There is the research on smart farming IoT platform based on edge and cloud computing of Zamora-Izquierdo and the colleagues (Zamora-Izquierdo *et al.*, 2019). R. Barosa applied image recognition technique on leaf to detect diseases along with IoT incorporated to collect and transfer data (Barosa *et al.*, 2019) and J. P. Mandap *et al.* used Raspberry Pi as network backbone to control and monitor aquaponics pH level, temperature, and dissolved oxygen (Mandap *et al.*, 2019). In addition, the machine learning algorithm is also integrated into the IoT hydroponic system to predict trends of the environment based on the historical data. Some remarkable papers can be mentioned such as the WPART method applied the machine learning technique to predict crop productivity and drought for proficient decision support making (Rezk *et al.*, 2021). Tanzila Saba's team developed a trust-based decentralized blockchain system with machine learning using IoT (Tanzila *et al.*, 2023). Plant disease diagnosing method using computer vision and deep learning models were proposed by Gaytri Bakshi and Silky Goel (Gaytri *et al.*, 2023). A weather monitoring system using OSSA and MA Techniques was developed by Rani Chandrabhan *et al.* (Rani *et al.*, 2023).

In this paper, a novel IoT applied hydroponics system was introduced to enhance the performance of planting process and be convenient for the farmers in use. The proposed approach combines the machine learning algorithm and IoT to predict trends of environment based on the available weather data. In addition, the state of the system would be continuously updated to the center unit and the warning text would be sent to the user. The remain of the paper is organized into four main sections. For details, the second section explains the design of the system and how the machine learning algorithm works. The fabrication of the prototype of the designed system will be described in the third section and the new features testing and results will be discussed in the fourth section. The final section consists of some conclusions of this research.

MATERIALS AND METHODS

Structure design of IoT hydroponics system

The above hydroponics system was designed with two cultivation layers, each layer has two hydroponic pipelines. Each pipeline has 4 holes to plant vegetables. The mechanical design has two main modules: the pipelines supporting aluminum frame and the water supply and misting system as presented in Fig. 1.



Fig. 1 – Overview of two-layer recirculating hydroponics system

The designed supporting frame is 1150 mm in height, 440 mm in width and 610 mm in length as shown in Fig. 2. The material of the frame is aluminum alloy 6063-T5 which has yield and tensile strength of 145 and 186 MPa, respectively. The aluminum framework utilizes 20x20 mm shaped aluminum bars interconnected by corner brackets and T-nuts. Four wheels are affixed at the bottom for mobility. The water supply and misting system is constructed using hydroponic tubes, PVC pipelines, M8 pumping tube, a 10 L and 25 L water tanks as shown in Fig. 3. The dissolved nutrient solutions will be contained in the large 25 L tank to circulate completely in the hydroponic tubes. The small 10 L tank will provide water for both the large tank and the mist spraying pipelines. Before fabrication, the frame is verified to ensure the technical requirements. The numerical simulation is implemented by SolidWorks software. Figure 4 shows the setting process where the down arrows express the external force from the gravity of the devices acting on the frame, the bottom of the frame is fixed. The simulation results are expressed in Fig. 5; as can be seen in Fig. 5a, the maximum stress is 0.001 MPa which is much less than the yield stress of 145 MPa while Figure 5b shows that the maximum displacement is 4.18×10^{-5} mm and is insignificant. In conclusion, the frame meets the technical requirements for fabrication.

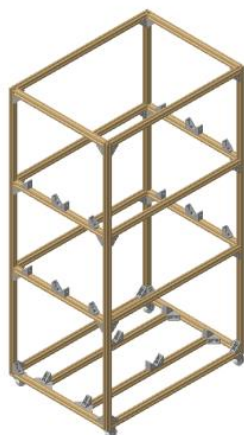


Fig. 2 – Pipelines supporting aluminum frame

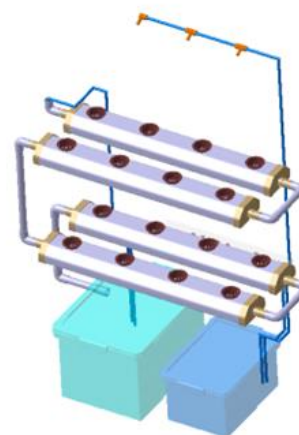


Fig. 3 – Water supply and misting system

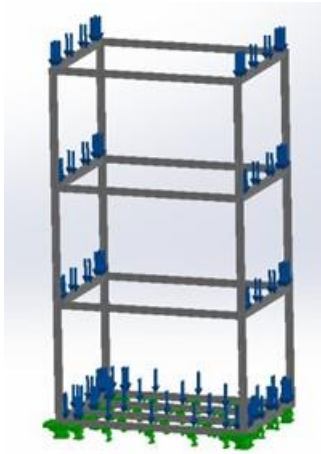


Fig. 4 – Setting process

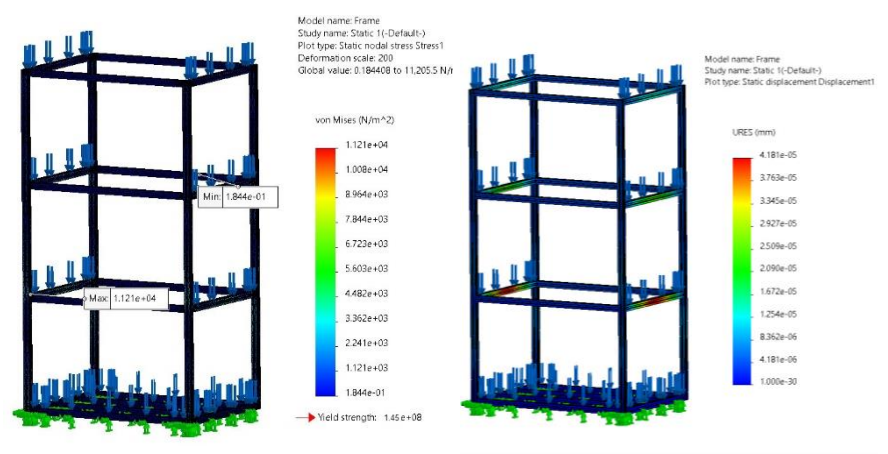


Fig. 5 – Simulation results: a) Stress graph; b) displacement

Design of control system

Overview of control system

The control system consists of three main modules: controller, programming module and peripheral module. The overview of the control system is shown in Fig. 6.

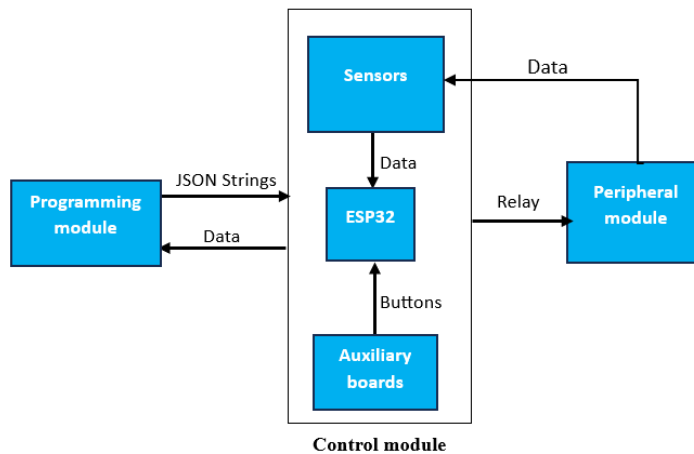


Fig. 6 – Overview diagram of control system

The embedded board and sensors module is the combination of the sensors and auxiliary boards to collect data from the peripheral module’s operating parameters along with the button signals from auxiliary boards to send to the main ESP32 board. The system incorporates various sensors, including the DHT22 temperature-humidity sensor, HC-SR04 ultrasonic sensor, TSL2561 light intensity sensor, and a pH sensor and an LCD display module with physical buttons included for control. The programming module uses Web Server programming to remotely control and monitor the system’s operation through the website. Peripheral devices consist of two power supply pumps, a misting pump, and two illumination bulbs. With the block model as described, the system can meet all the requirements of a modern IoT system: remote control via the web with a response time of under 1 second, the ability to monitor environmental parameters online, and the system can be controlled both through a physical control circuit and operate automatically based on programmed structures.

Controller and peripheral module

The IoT hydroponics system utilizes the ESP32 microcontroller with the DOIT V1 board version to read sensor data, send and receive data with a web server, while also controlling peripheral devices such as pumps and lights. The structural diagram of two modules is shown in Fig. 7.

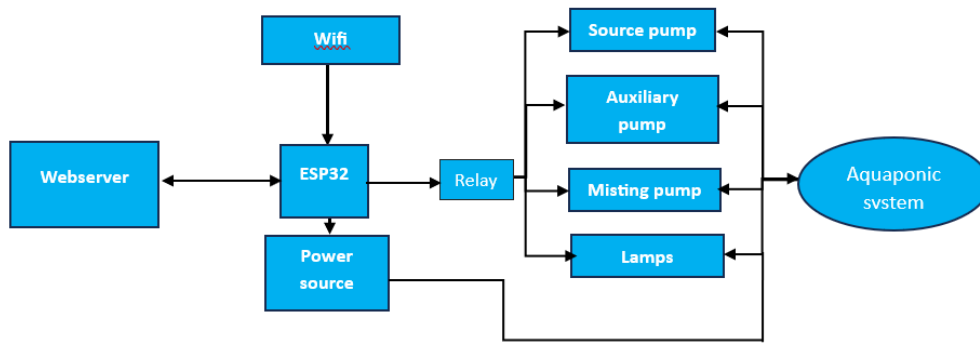


Fig. 7. Control and peripheral module’s block diagram

In the diagram, it can be observed that the ESP32 serves as the coordinating component for the entire system. With the advantage of being controllable at a minimum voltage of 3 V and optimal performance at 5 V through relays, it influences the operation of opening and closing peripheral devices, including power pumps, auxiliary pumps, misting pumps, and lights. The ESP32 directly receives input signals from various sensors, including temperature-humidity sensors, light sensors, water level sensors, and pH sensors. The microcontroller is connected to Wi-Fi to synchronize data with the Webservice data management system. Through the Webservice, an automatic alert system and remote control via a mobile phone can be seamlessly integrated.

Programming module designed for user interaction and environmental factors prediction

In this paper, the term “programming module” refers to the program designed for data storage, management and the website interface to communicate with the user. The server used to store the data of the sensor’s reading, designed websites and user account’s operation are called webservice. Web servers, whether hardware or software, manage data efficiently and ensure continuous operation for internet data delivery. Hardware servers store and deliver website files to end-users, accessed through domains. Software servers control user access, understanding website addresses and browser protocols like HTTP. The HTTP protocol facilitates communication, enabling browsers to request and receive files from the server. Server software, installed on suitable computers, allows users to access website information over the internet.

The structure of the programming block is described in Fig. 8. The data received from ESP32 of the controlling module will be stored in a MySQL database. The directory containing PHP script files manages the input and output of data from the database, redirects paths, handles user addition and deletion, and includes modules used in the project, particularly the design of the management interface for administrators.

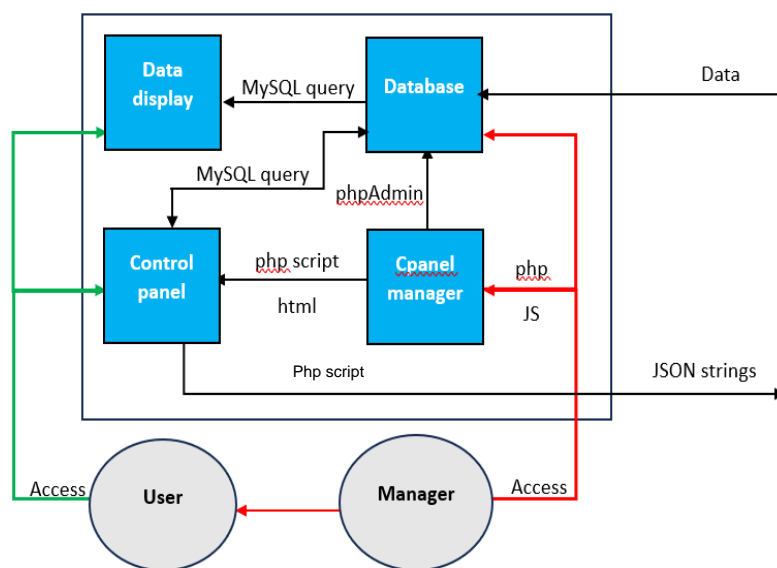


Fig. 8 – Web server programming module block diagram

The user can access the data by utilizing the control panel and monitoring the data display. MySQL query commands are used to extract data from the database. To access the data, the user will have to access the programmed website and login to the registered account. If the account belongs to a regular user, the interface will display modules for monitoring and control. If the selected module is a control module, pressing the buttons on the web will trigger the web to return a JSON string to control the ESP32. For other modules, when data is sent, it will be stored in the database, and simultaneously checked to see if the value exceeds the permissible threshold, triggering an email alert. For admin accounts, there will be an additional interface to modify settings and add/remove system modules.

For monitoring data and remote control in case there is sign of abnormality in the system, a custom website interface was designed for the user. For the admin account, the user interface will appear as in Fig. 9. In this system, some key factors that influence the plant's development such as temperature, humidity, pH level, and the amount of watering for the plants are measured and sent to the web for real-time monitoring. Simultaneously, the data is checked to ensure it falls within permissible thresholds. If the values exceed these limits and adversely affect plant growth, an email notification is promptly sent to the user through Gmail as shown in Fig. 10. The email subject corresponds to the management code of the IoT system, enabling users to quickly address the alert, especially when managing multiple hydroponic systems simultaneously. There are four tabs to display the data of temperature, humidity, pH level and water level.

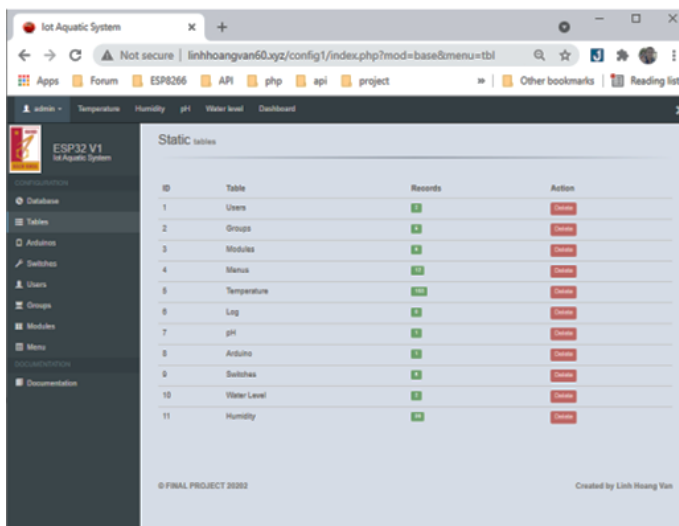


Fig. 9 – Admin's account website interface

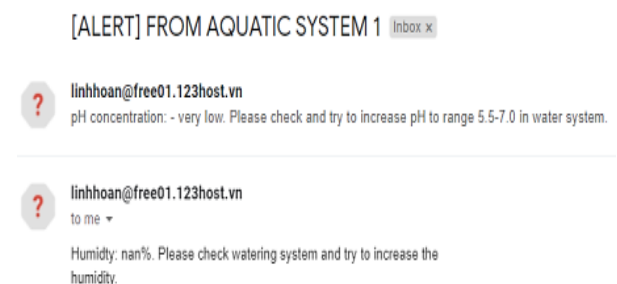


Fig. 10 – Warning email from the system

The novelty of the designed system is applying machine learning for the environmental factors (temperature, humidity, pH level) data prediction at hydroponic cultivation site which will allow users to take proactive measures. To apply machine learning for predicting these factors' parameters in the city requires a substantial amount of environmental data to achieve accuracy, ideally spanning over a year. The idea is to gather the environmental data from the available official sources (websites) and make prediction on the factors' parameters based on the variation trend of the built actual data graph and sensors' reading data of the system. This approach not only enhances reliability but also incorporates innovative technology to support users. Then, a machine learning algorithm based on the collected data will be implanted. The predicted temperature data will be displayed on the website. By integrating these steps, the system will provide users with accurate temperature predictions, leveraging machine learning and real-time weather data collected from IoT hydroponic systems. This not only increases reliability but also incorporates innovative technology to support users in making informed decisions about their cultivation practices.

RESULTS AND DISCUSSIONS

Fabrication of proposed system

To see how the idea works out, a real IoT aquaponic system was built for experimental determinations. It is tested by applying the machine learning algorithm for predicting temperature. The fabricated system has a total height of 1150 mm, 610 mm in length and 440 mm in width with three main floors.

The first floor contains two water tanks while plants will be planted on the second and third floor. The image of the fully assembled system can be found in Fig. 11.



Fig. 11 – Fully assembled IoT hydroponic system

The working principle for feeding water and misting is described in Fig. 12. As for the lighting, a large LED as shown in Fig. 13 is incorporated to provide light for plants on both floors. Since the LED takes power from AC 220V power source, it must have intermediate relays built in to adjust following the electrical signal sent from the control module. As shown in the diagram, pump 1 will take water from 10L tank and provide for the misting system while pump 3 will take water from 25L tank and pump up to the hydroponic tube, then the water will be recirculated back to the tank, pump 2 will pump water from 10 L to 25 L tank.

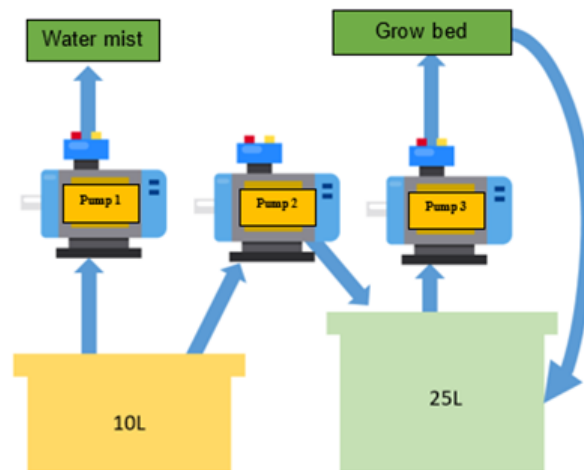


Fig. 12 – Diagram of working principle for feeding water and misting

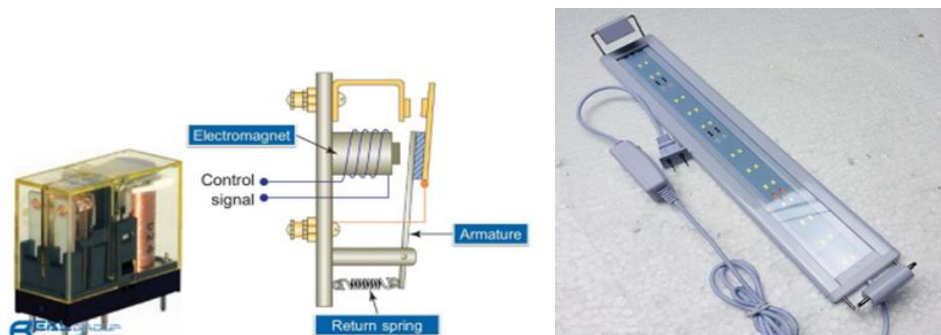


Fig. 13 – LED and intermediate relay

The chosen embedded programming board for controlling sensors and peripheral devices was ESP DOIT V1 – a dev kit developed by DOIT with BLE (Bluetooth Low Energy) along with Wi-Fi function available and multiple peripheral communication channels supported. The sensors’ reading will also be displayed on an LCD attached onto the control board, and the data will be processed and sent to Webserver through Wi-Fi. The control board and LCD are attached onto a PCB to avoid electrical signal jam in transmission. The assembled IoT control board is shown in Fig. 14.



Fig. 14 – Controller board

Implementation of the experiment

An experiment was conducted to test the ability of temperature prediction of the proposed method. Firstly, the system collected temperature data from January 1st, 2019 to March 31st, 2024 for training. Hourly live weather data collected by the IoT system could be monitored through the live weather data and the track table in the temperature tab on the user’s website which looks like in Fig. 15. Then, the predicted data was compared to the weather data stored on <https://www.wunderground.com> from April 1st to June 17th 2024. This website is among the top 10 largest weather data statistics websites globally, with an average monthly traffic of around 50 million visits (according to SimilarWeb statistics). The city chosen for the data collecting is Hanoi. The data comparison between the forecast and real data was made by cross-referencing the hourly collected data points with the actual temperature data graph. If the forecast data points matched the points on the actual data graph, then the experiment would prove its accuracy and the proposed system could be applied.

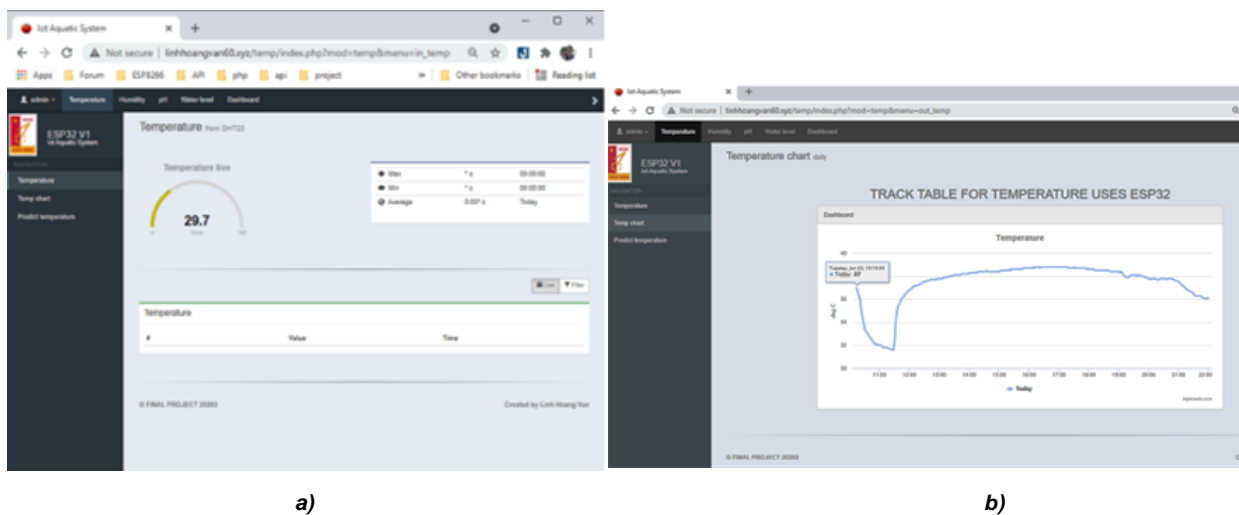


Fig. 15 – Hourly live weather
 a) Temperature live data; b) Track table

As a result, the accuracy of the predicted data in a day is 94.2% as shown in Fig. 16 and 92.6% in 7 days as shown in Fig. 17. As it can be seen, the measured points are remarkably close to the original data. Red dots represent the predicted results which are either close or coincidental to the actual temperature plot line. Difference between the predicted results and the actual temperature fluctuates within 0.2 to 0.5°C. Its accuracy decreased as the test time got longer.

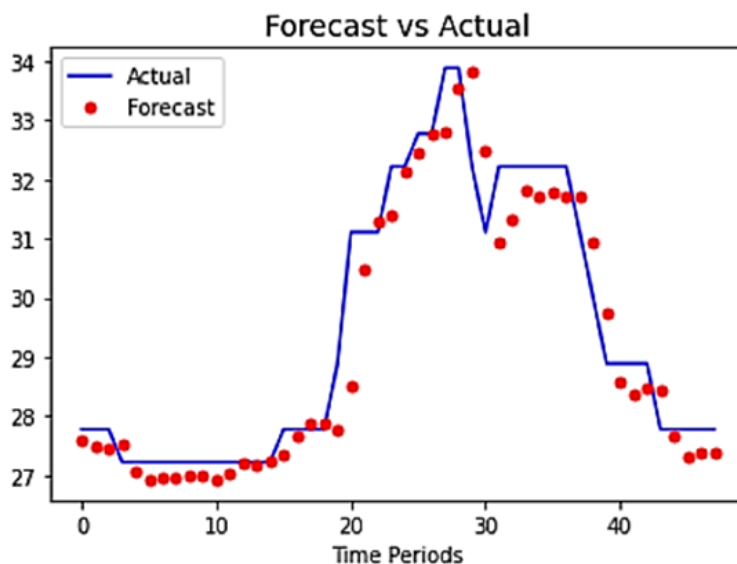


Fig. 16 – Predicted temperature in one day

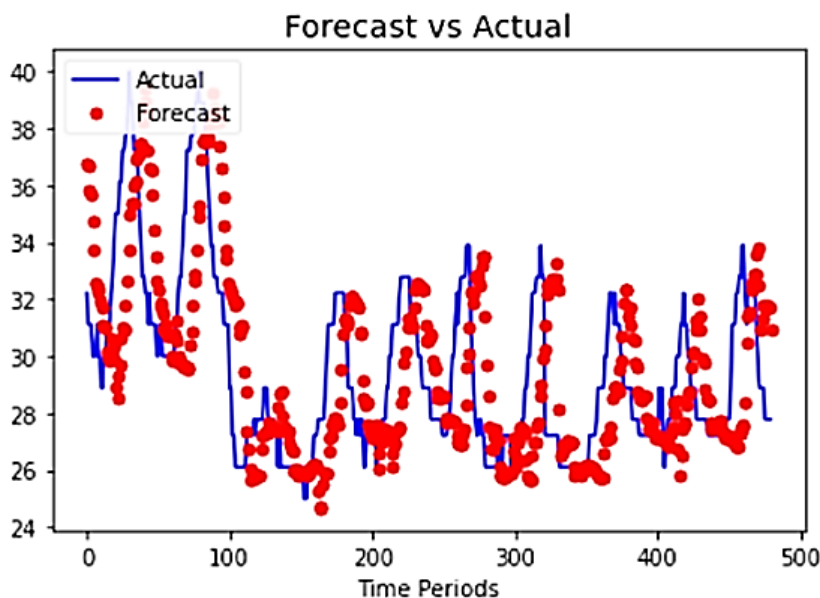


Fig. 17 – Predicted temperature in one week

In summary, the use of the machine learning model was enabled to predict the trends of the temperature of the environment that supports the farmers to provide the plants with the necessary adjustment of the technical system such as water, misting, and light to make the best condition for the development of the plants. In addition, this method utilized IoT technology to manage and process the information of the system where the data was stored online on Web server and the warnings were intermediately sent to the user via email if the value of any factors was over the threshold. The proposed system is developed for the small families and is suitable with the low-income countries such as Vietnam, Cambodia, Laos...

CONCLUSIONS

In this paper, a novel hydroponic system integrating machine learning algorithm and IoT to predict the temperature of the outdoor environment was presented. The proposed system was designed with three floors and is suitable for small families. The control system consisted of three main modules: web server programming, controller and peripheral modules. The programming module was to store the data, communicate with the user and apply the machine learning algorithm for the environmental factors' prediction.

The controller used ESP board controls sensors, peripheral equipment and sent the readings data to the webserver. The environmental indices and warnings were sent to the users through Gmail so that they could take proactive action. The experiment results showed that the accuracy of the predicted data were reliable, it reached 94.2% for a day and 92.6% for a week.

The limitations of the study are that the machine learning algorithm was currently applied to predict the temperature data only and the accuracy of the machine learning model needs improving, thus, the operation of the system was not optimized. Future research will focus on increasing the number of the forecasted output such as humidity and enhance the performance of the predicted model.

ACKNOWLEDGEMENT

This research was partially supported by the Asahi Glass Foundation: AGF.2024-03.

REFERENCES

- [1] Bakshi, G. & Goel, S. (2023). Computation Analysis of Multi-Class Plant Disease Diagnosis using Deep Learning Models, *IEEE 2nd International Conference on Industrial Electronics: Developments & Applications (ICIDEA)*, pp.597-602.
- [2] Barosa, R., Hassen, S. I. S. & Nagowah, L. (2019). Smart Aquaponics with Disease Detection. *Conference on Next Generation Computing Applications (NextComp)*, pp. 1–6.
- [3] Dhal, S.B., Jungbluth, K., Lin, R., Sabahi, S.P., Bagavathiannan, M., Braga-Neto, U. & Kalafatis, S. (2022). A Machine-Learning-Based IoT System for Optimizing Nutrient Supply in Commercial Aquaponic Operations. *Sensors*, 22, 3510.
- [4] Farhan, M. P. M., Azami S. K., & Mel, M. (2020). IoT based water quality monitoring system for aquaponics. *Journal of Physics: Conference Series*, 1502(1), 012020.
- [5] Lee, C., & Wang, Y.-J. (2020). Development of a cloud-based IoT monitoring system for Fish metabolism and activity in aquaponics. *Aquacultural Engineering*, 90, 102067.
- [6] Mandap, J. P., Sze, D., Reyes, G. N., Matthew Dumlao, S., Reyes, R. & Danny Chung, W. Y. (2019). Aquaponics pH Level, Temperature, and Dissolved Oxygen Monitoring and Control System using Raspberry Pi as Network Backbone. *IEEE Region 10 Conference*, pp. 1381–1386.
- [7] Maritel, D., Samson, M. L., & Maria, R. T. (2022). Internet of things (IoT) based aquaponics management system adaptive to climate change. *AIP Conference Proceedings*.
- [8] Rezk, N. G., Hemdan, E. E.-D., Attia, A.-F., El-Sayed, A., & El-Rashidy, M. A. (2021). An efficient IoT based smart farming system using machine learning algorithms. *Multimedia Tools and Applications. Multimed Tools Appl* 80, pp. 773–797.
- [9] Saba, T., Rehman, A., Lloret, J., Bahaj, S. A., & Lloret, J. (2023). Trust-based decentralized blockchain system with machine learning using Internet of agriculture things. *Computers and Electrical Engineering*, vol. 108.
- [10] Tiple, R. C., Akant, K. & Chandankhede, P. & Yadav, S. (2023). IoT based Weather Monitoring System Using OSSA & MA Techniques, *11th International Conference on Emerging Trends in Engineering & Technology - Signal and Information Processing (ICETET - SIP)*, pp.1-5.
- [11] Wibowo I. R. R. D., Ramdhani, M., Priramadhi, R. A., & Aprillia, B. S. (2019). IoT based automatic monitoring system for water nutrition on aquaponics system. *Journal of Physics: Conference Series*, 1367, 012071.
- [12] Yanes, A. R., Martinez, P., & Ahmad, R. (2020). Towards automated aquaponics: A review on monitoring, IoT, and smart systems. *Journal of Cleaner Production*, 263, 121571.
- [13] Zamora-Izquierdo, M. A., Santa, J., Martínez, J. A., Martínez, V., & Skarmeta, A. F. (2019). Smart farming IoT platform based on edge and cloud computing. *Biosystems Engineering*, 177, pp. 4-17.

DESIGN AND OPTIMIZATION OF A VACUUM SYSTEM FOR A LARGE STORAGE TANK CLEANING ROBOT

大型贮罐清理机器人吸尘系统的设计与研究

Yong TIAN¹⁾, Zhengtao WANG²⁾, Jian SONG¹⁾, Fuxiang XIE^{*1)}, Hongwei WANG¹⁾

¹⁾ School of Machinery and Automation, Weifang University, Shandong/ China;

²⁾ WindSun Science & Technology Co., Ltd., Shandong / China

Tel: +86-18863637275; E-mail: 20210007@wfu.edu.cn

DOI: <https://doi.org/10.35633/inmateh-73-57>

Keywords: Cleaning robot, EDEM, Gas-solid coupling, Structural optimization, Nozzle, Dust suction test

ABSTRACT

Taking the large storage tank as the cleaning object, a cleaning robot integrating shoveling, crushing, sweeping and dust-absorbing was developed, and its dust-absorbing system was analyzed and optimized. Firstly, Fluent-EDEM gas-solid coupling was utilized to simulate the dust-absorbing system. By analyzing the fluid distribution and particle trajectory, the internal structure of the dust collection box was optimized to reduce the dust particles entering the fan box. Then, by analyzing the structural parameters of the suction nozzle, the influence of the nozzle shoulder angle, nozzle length, and shoulder height on the dust-absorbing effect was explored, and the parameters were determined, so as to reduce the energy loss and increase the flow rate on both sides of the nozzle. Finally, through the dust suction test, different models of nozzles were tested for dust suction, and the wind speed at the nozzle was measured, and the leakage of dust particles on both sides of the nozzle was significantly reduced after optimization, which verified the reliability of the simulation results and provided a theoretical basis for the design of the sweeping robot.

摘要

以大型贮罐作为清理对象, 研制了一种集铲装、破碎、清扫、吸尘为一体的清理装置, 并对其吸尘系统进行研究。首先, 利用 Fluent-EDEM 气固耦合对吸尘装置进行仿真分析, 通过对集尘箱中的流体分布和颗粒轨迹进行分析, 完成了对集尘箱内部结构进行结构优化, 减少了进入风机箱的尘粒; 然后, 通过对吸嘴结构参数分析, 探究了吸嘴肩部夹角、吸嘴长度、肩部高度对吸尘效果影响, 确定了吸嘴吸尘性能最佳时的参数, 减少了能量损失, 增大吸嘴两侧的流速; 最后, 通过吸尘试验, 对不同型号吸嘴进行吸尘测试, 将吸尘前后效果进行对比, 得出优化后吸嘴两侧漏吸的尘粒明显减少。并对吸嘴处的风速进行测量, 将得到结果与仿真数据进行对比, 保证了验证仿真的可靠性, 从而为清扫机器人的设计提供理论基础。

INTRODUCTION

Currently, there are two main ways of cleaning large storage tanks. One is to utilize robotic arms carrying water spraying devices (Bogue and Robert, 2011; Buckingham and Graham, 2012; Dandan et al., 2015; Michal, 2012), and the other way is to utilize cleaning robots (Anonymous, 2012; Asafa et al., 2018; Azizi and Naderi, 2013; Nesaian and Karthikeyan, 2012; Song et al., 2020). In this study, a clean-up robot was designed to clean large tanks. As the last part of the cleaning operation, vacuuming collects the residues. In order to avoid secondary processing of the collected dust particles, the vacuuming device is required to not only collect, but also automatically pour the collected dust particles into a collection container.

At present, many researchers have done a lot of studies on the dust suction port used in various occasions, including various studies on the geometry of the dust suction port and the organization of the airflow inside the dust suction port. Chen (Chen, 2023) improved the geometric structure of the dust suction port on the basis of the traditional model of dust suction port. In order to increase the working efficiency of the dust suction port, side baffles perpendicular to the wings were added to the edges of the left and right wings, which is conducive to optimizing the direction of airflow through the bottom of the dust suction port, resulting in a smoother flow of airflow and improving the dust removal efficiency. Through the study of the suction port of the vacuum truck, Walter et al., (2012), found that changing the traditionally used straight up and down suction port into a new type of suction port with a certain angle had a better control effect on the internal dust-containing airflow, and the streamlined structural design allowed particulate matter to be discharged more quickly.

Yang *et al.*, (2012), analyzed the effect of the extended area outside the suction port on the dust removal performance through simulation experiments, which added a new research direction for the simulation experiments of the suction port.

Some scholars used discrete eddy method to test, and proved that the structural parameters of the dust hood flange length and tilt angle would have an impact on the dust absorption efficiency (Logachcv *et al.*, 2019). Lu *et al.*, (2023), used a reasonable turbulence model to analyze the factors causing the escape phenomenon and derived the trajectory of particles in industrial production. Huang, (2016), used numerical simulation to study the law of gas-solid two-phase flow under high temperature conditions, and found that the height of the dust hood from the heat source was a key factor affecting the escape of high-temperature dust, and proposed to change the dust hood from the heat source height offset and the ventilation of the dust hood could be effective in controlling the escape of high-temperature dust. Xi *et al.*, (2016), used Fluent to numerically simulate the gas-solid two-phase flow characteristics inside the dust suction port, and found that the increase of the inclination angle of the front baffle of the dust suction port and the pressure drop of the dust suction port could improve the dust suction efficiency. Wang and Tan, (2020), used Fluent to analyze the working process of the dust extraction hood, and concluded that the height of the dust extraction aperture from the ground and the height of the shoulder of the dust extraction port had an effect on the dust extraction efficiency.

Although a large number of researchers have optimized the inner cavity structure of the suction nozzle (Guo *et al.*, 2019; Huang *et al.*, 2019; Zhou *et al.*, 2024; Ye, 2023), the interaction of the influence of each parameter on the dust removal effect is not considered, and a single study of a certain factor can no longer meet the design requirements. Therefore, based on the dust suction system of the existing robot, Fluent is used to analyze the dust transport law and the influence of the structural parameters of the dust collection box and nozzle on the dust suction effect, to further optimize the structure of the nozzle and the dust collection box and to carry out engineering verification, so as to improve the performance of the dust suction system.

MATERIALS AND METHODS

Robot vacuuming system design

The overall structure of the robot is shown in Fig. 1(a). The residue is pulverized with a crushing device, and then the disturbed residue is sent to the collection container by a shoveling device. Fine particles are absorbed by the vacuuming device and sucked into the dust collection box through the suction nozzle at the bottom of the vehicle, and finally the absorbed residue is poured into the collection container, thus completing the whole residue cleaning and collection work.

As the final part of the cleaning operation, the main task of the dust suction is to clean and collect the residue concentrated by the cleaning. The structure of the dust suction device sketch is shown in Fig. 1(b). The working principle of the dust-absorbing device is to utilize the gas from the suction nozzle into the hose to bring the residual dust particles into the dust collection box, and then the gas passes through the top of the baffle into the fan box and is then discharged by the fan. Dust particles will continue to gather in the mouth of the tube and between the baffle plates.

The design of the nozzle is very important for the whole vacuuming system, and the rationality of the nozzle design largely determines the vacuuming efficiency. The main structural parameters of the nozzle of the vacuuming device designed in this paper are: nozzle outlet area S , nozzle length L , nozzle width B , nozzle height H and nozzle shoulder height H_1 , shoulder angle α , as shown in Fig. 1(c).



a) the cleaning robot

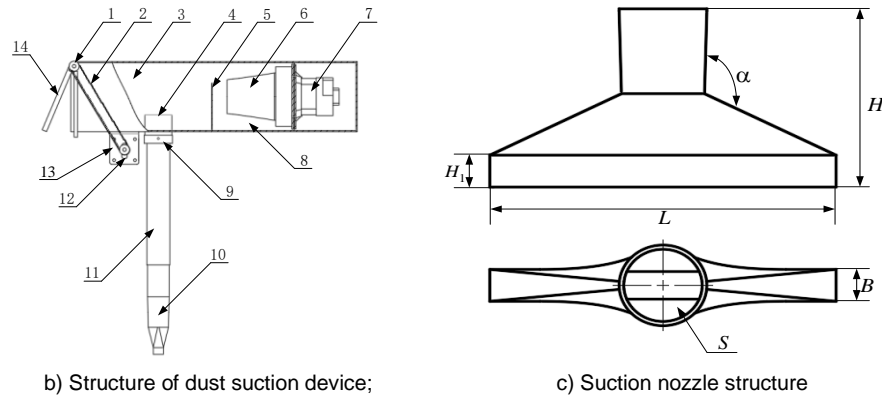


Fig. 1 - Structure of the cleaning robot

1- synchronous wheel, 2-synchronous belt, 3-dust collection box, 4-dust outlet pipe, 5-baffle plate, 6-filter, 7-electric fan, 8-fan box, 9-connecting sleeve, 10-suction nozzle, 11-hose, 12-helm, 13-seat, 14-seal plate

RESULTS

Simulation analysis and optimization of vacuum box

In the simulation, dust particles enter the dust collection box through the suction nozzle and hose. In the simulation process, the particle diameters are set as 0.5 mm, 1 mm, 1.5 mm, 2 mm and 2.5 mm. The number of each kind of particle generation is set to 100. The time step of FLUENT in the simulation process of this paper is set to 1E-04 s, and the number of time steps is 10000.

● **Structural analysis of dust collection box**

The rationality of the structural design of the dust container is analyzed by Fluent-EDEM coupled simulation (Lin *et al.*, 2023). The flow field in Fluent and the particle trajectory in EDEM are combined to analyze the structure of the dust collection box, as shown in Fig. 2(a).

As can be seen from Fig. 2(a), when the gas flow will enter the dust collection box from the pipeline, the gas flow rate at the entrance is obviously higher, and the gas flow is dispersed to both sides when it reaches the upper wall of the box. The gas flow velocity at the upper wall of the box is also significantly higher than other parts. Due to the higher gas flow rate above, the dust particles may cross the baffle plate with the gas flow into the fan box, and the vortex phenomenon appears on both sides of the dust particle inlet. As shown in Fig. 2(b), it can be seen that most of the particles are scattered in the dust collection box, but some of the particles enter into the fan box. The trajectory of the dust particles into the fan box can be clearly seen from the particle trajectory. Based on the velocity vector diagram, it can be seen that particles enter the box from the pipe opening. Due to the wind force of the fan, particles move towards the upper port of the fan box from the outlet.

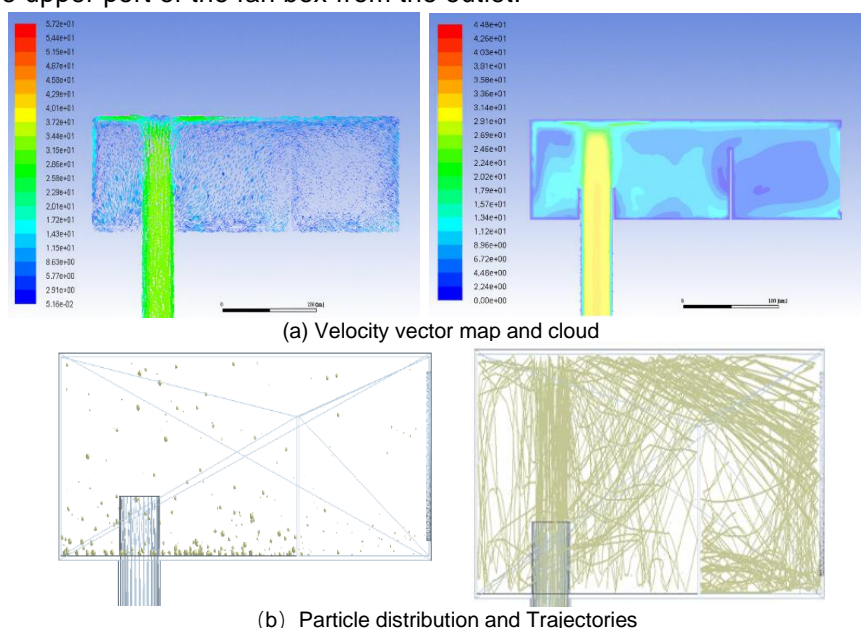


Fig. 2 - Velocity vector map and cloud

In order to better study the particles entering the blower box, and to provide data support for the subsequent optimization of the dust collection box, the particles entering the blower box are counted, as shown in Table 1. It can be seen that the smaller the particles are, the easier it is to enter the fan box. When the particle diameter is 2.5 mm, the particles entering the fan box obviously become less.

Table 1

| Probability of entry of different particles | | |
|---|-----------------------------|------------------------------|
| Particle diameter (mm) | Pre- opt Number (grains) | Post- opt Number (grains) |
| 0.5 | 57 | 31 |
| 1 | 30 | 18 |
| 1.5 | 19 | 8 |
| 2 | 9 | 4 |
| 2.5 | 6 | 0 |

● Structural optimization of dust collection box

In order to reduce the particles into the fan box, the internal structure of the box is optimized and improved. As shown in Fig. 3, a baffle plate is added above the tube outlet and the inlet of the fan box. When the particles enter the dust collection box from the tube outlet, the particles will slide downward due to the blocking of the plate fixed on the top.

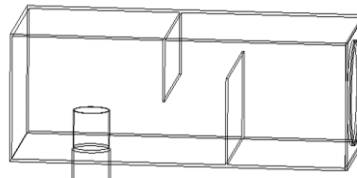
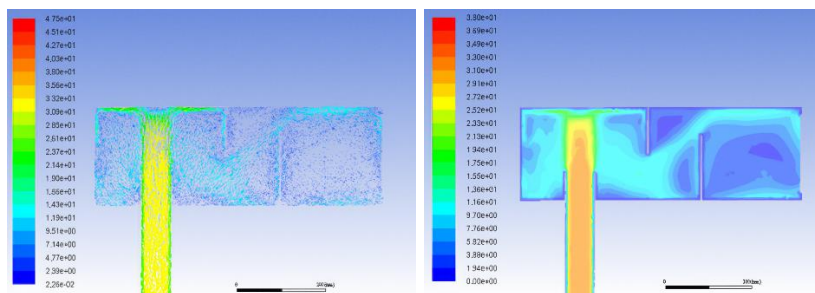
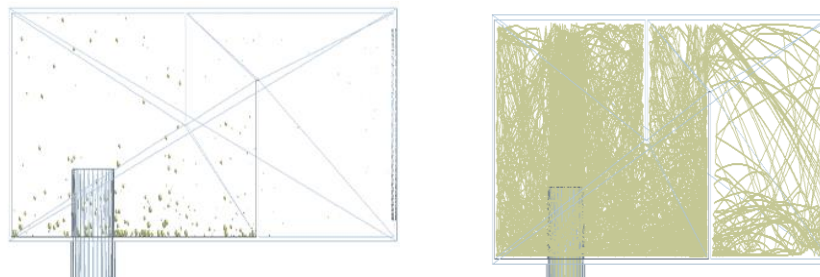


Fig. 3 - Structure of the optimized dust collection box



(a) velocity vector map and velocity cloud



(b) Optimized particle motion trajectories

Fig. 4 - Optimized fluid velocity vector map, velocity cloud and trajectories

The internal structure of the dust collection box is improved, and EDEM analysis is used to obtain the fluid velocity vector map and velocity cloud map inside the box, as shown in Fig. 4(a). From the fluid velocity vector map and velocity cloud diagram, it can be seen that the optimized fluid inside the box changes the direction. As shown in Fig. 4(b), it can be clearly seen that there are more dust particles gathered under the baffle, and the dust particles in the fan box are obviously reduced. The airflow enters into the fan box from the outlet bypassing the baffle plate. When particles reach the baffle from the tube opening, the particles will slide downward due to the existence of the baffle.

By counting the particles in the fan box, the number of different particles entering the fan box is obtained, as shown in Table 1. Comparing with the particles before the optimization analysis, it can be concluded that the quantity of particles entering the fan box is significantly reduced, and the most obvious is the particles with a size of 1.5 mm to 2 mm.

● Structural analysis and optimization of the suction nozzle

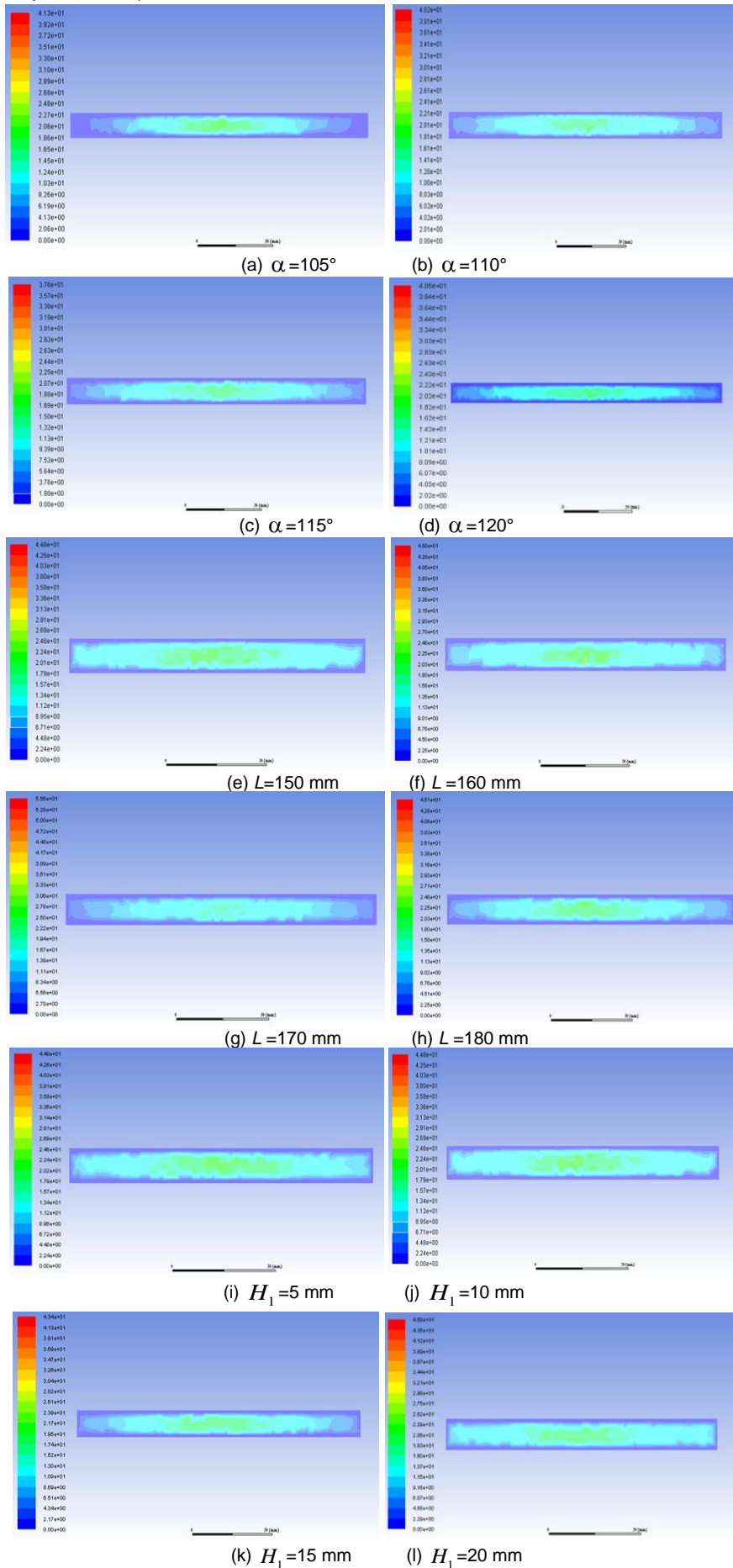


Fig. 5 - Air velocity distribution at nozzle inlet with different shoulder

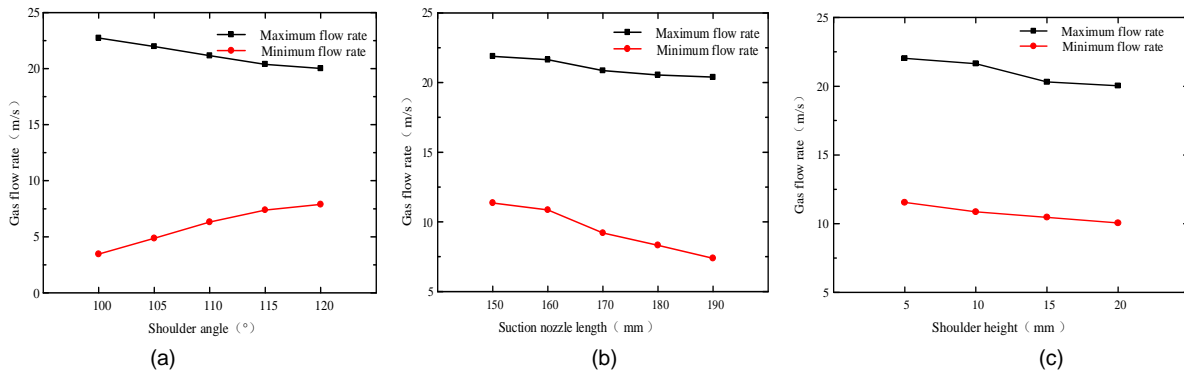


Fig. 6 - Gas flow rate graph

The rationality of the structural design of the suction nozzle is extremely important, and its structural parameters have a great influence on the dust suction efficiency. Through the simulation analysis of the structural design and performance of the nozzle, the stability of the flow field inside the nozzle is ensured.

As shown in Fig. 5(a-d), it can be seen that the flow rate in the center of the nozzle is larger, and the flow rate on both sides is smaller. With the change of the shoulder angle, the yellow area in the center of the nozzle and the light blue area on both sides have different changes, indicating that the shoulder angle has a greater influence on the airflow inside the nozzle. The maximum and minimum values of the gas flow at the entrance of the nozzle were chosen to analyze and compare, and observe the overall change rule of the flow rate under the change of shoulder angle, as shown in Fig. 6(a). The change of the shoulder angle has a greater effect on the flow rate on both sides of the nozzle and a smaller effect on the flow rate in the middle of the nozzle. The maximum and minimum flow velocities show a certain trend when the shoulder angle changes from 105° to 110°, and the change trend becomes smooth from 115° to 120°. The shoulder angle is selected 115° as the optimal parameter in this range.

Figure 5(d-h) shows the effect of changes in nozzle length on the airflow velocity at the nozzle inlet while maintaining a shoulder angle of 115°. Fig. 6(b) shows that the change of nozzle length mainly affects the gas flow velocity on both sides of the nozzle shoulder, and has less effect on the flow velocity in the middle of the nozzle. The gas flow velocity decreases slowly when the nozzle length is 150 mm to 160 mm, and the gas flow velocity decreases more when the nozzle length is 170 mm to 180 mm. Considering that the nozzle length not only affects the flow rate of the nozzle, but also affects the working width, the nozzle length of 160 mm is selected as the optimal parameter choice.

As shown in Figure 5(i-l), the airflow velocity distribution at the nozzle inlet at different shoulder heights was obtained through simulation, with a shoulder angle of 115° and a nozzle length of 160 mm. The airflow velocity values under different shoulder heights are compared and analyzed as shown in Fig. 6(c). It can be found that the maximum and minimum flow velocities show a decreasing trend with the increase of shoulder height. The shoulder height of 5 mm is selected as the optimal choice.

Analysis shows that the maximum and minimum flow rates at the nozzle are the highest when the shoulder angle is 115°, the nozzle length is 160 mm, and the shoulder height is 5 mm. The optimized cross-section of the vacuum device is shown in Fig. 7.

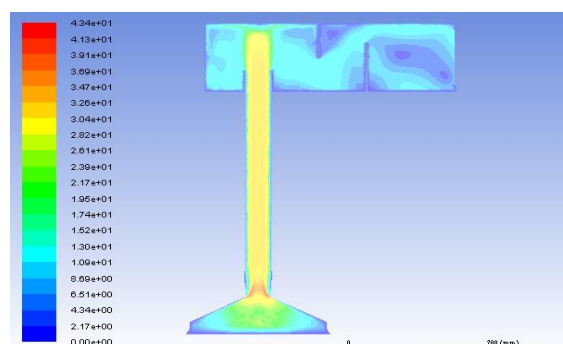


Fig. 7 - Velocity cloud of the optimized vacuum unit

Comparison of the number of dust particles entering the fan box before and after optimization are shown in Table 2. Comparison shows that the optimization of the nozzle structure reduces the number of dust particles entering the fan box, improves the airflow velocity at the nozzle inlet without changing the overall structure, reduces the occurrence of leakage, and improves the efficiency of dust suction.

Table 2

| Comparison of data before and after optimization | | |
|--|---------|----------|
| Projects | pre-opt | post-opt |
| Percentage of dust particles entering the fan box (%) | 31.84 | 16.05 |
| Maximum velocity of the cross-section at the suction inlet (m/s) | 20.01 | 22.03 |
| Minimum velocity of the cross-section at the suction inlet (m/s) | 7.89 | 11.54 |
| Differential flow rate at the suction port (m/s) | 12.12 | 10.49 |

Changing the internal structure of the dust collection box reduces the probability of dust particles entering the fan box by 15.75%. The flow rate at the inlet of the nozzle is the largest relative to 22.03 m/s and the minimum flow rate is the largest relative to 11.54 m/s, which can be taken as the optimal choice.

Sample machine test

● Analysis of suction nozzle flow rate

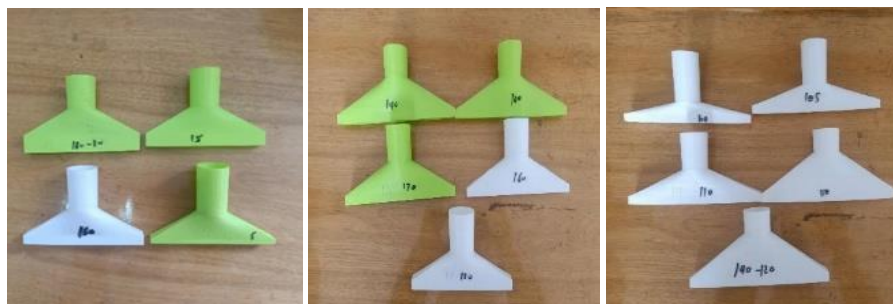
In order to detect the airflow at the entrance of the nozzle, a set of detection points are set up at the entrance of the nozzle to detect the size of the airflow velocity at three points at the entrance. The experimental error is used to analyze the reliability of the simulation results, and the error calculation formula is as follows:

$$\varphi = \left| \frac{H_a - H}{H_a} \right| \times 100\% \quad (1)$$

where, φ is the error, H_a is the experimental value, H is the simulation value.



(a) Dust Extraction Unit Test Stand



(b) Different height, lengths and angles

Fig. 8 - Dust Extraction Unit Test Stand and different sizes of suction nozzles

As shown in Fig. 8, a speed-adjustable conveyor belt is used to simulate the working conditions when the work is in progress, and the dust particles are evenly spread on the conveyor belt, so that the effect of the suction nozzle in picking up the dust particles can be more clearly observed.

Fig. 8(b) shows suction nozzles with different shoulder heights, different lengths, and different shoulder angles. Measurement points at the inlet of different nozzles were measured.

It can be seen from Table 3 that there are different errors between the measured data and the simulated data for each nozzle. For measurement point 1, the largest error value appears at the nozzle with model number 6, and its error value is 16.43%. For measurement point 2, the largest error occurs at the nozzle with serial number 3, and the error value is 16.72%. For measurement point 3, the largest error occurs at the nozzle of serial number 6, with an error value of 15.56%. The measurement data of the suction nozzle shows the same trend with the simulation data.

Table 3

| Serial No. | Nozzle type ($\alpha - L - H_1$) | Data of measurement points | | | | | |
|------------|---------------------------------------|----------------------------|-----------------|---------------------|-----------------|---------------------|-----------------|
| | | Gas flow speed (m/s) | | | | | |
| | | Measurement point 1 | Simulation data | Measurement point 2 | Simulation data | Measurement point 3 | Simulation data |
| 1 | 100-190-10 | 9.15 | 10.82 | 20.56 | 22.73 | 9.68 | 10.32 |
| 2 | 105-190-10 | 8.48 | 10.13 | 19.69 | 21.98 | 8.45 | 10.15 |
| 3 | 110-190-10 | 9.36 | 11.18 | 18.12 | 21.15 | 9.21 | 11.18 |
| 4 | 115-190-10 | 9.45 | 10.62 | 18.01 | 20.39 | 9.45 | 10.60 |
| 5 | 120-190-10 | 9.85 | 11.46 | 17.46 | 20.01 | 9.38 | 11.45 |
| 6 | 115-150-10 | 13.33 | 15.52 | 19.05 | 21.89 | 13.53 | 15.52 |
| 7 | 115-160-10 | 13.46 | 15.18 | 20.03 | 21.64 | 13.58 | 15.18 |
| 8 | 115-170-10 | 11.95 | 13.48 | 18.98 | 20.86 | 11.94 | 13.95 |
| 9 | 115-180-10 | 10.21 | 12.19 | 18.65 | 20.55 | 10.43 | 12.24 |
| 10 | 115-160-5 | 14.48 | 16.46 | 20.96 | 22.03 | 14.48 | 16.46 |
| 11 | 115-160-15 | 13.36 | 15.06 | 19.23 | 20.31 | 13.35 | 15.06 |
| 12 | 115-160-20 | 12.03 | 13.46 | 18.48 | 20.03 | 12.08 | 13.45 |

● **Sample machine performance test**



(a) 105-190-5



(b) 115-190-5

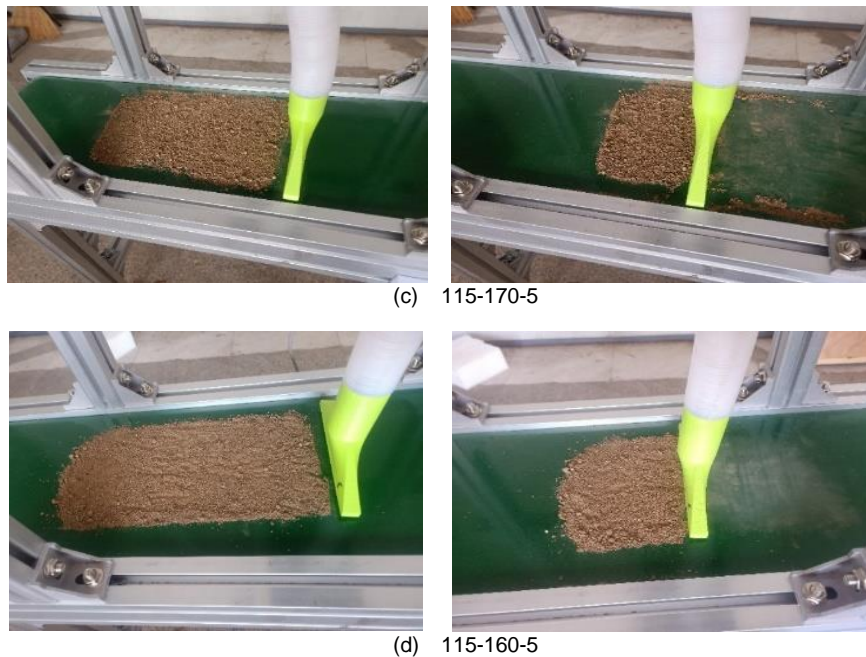


Fig. 9 - Comparative test of dust-absorbing effect

A quantity of 50 g of dust particles were taken from the test site and spread evenly on the conveyor belt of the test stand. Two types of nozzles were taken from the two parameters to analyze and compare. Take the suction nozzle model were 105-190-5, 115-190-5, 115-170-5, 115-160-5 as the object of the test. The speed of the conveyor belt was set to 0.1 m/s to simulate the forward speed of the cleaning robot, and the distance between the nozzle inlet and the conveyor belt was set to 10 mm. The effectiveness of different models of nozzles was investigated by observing the distribution of dust particles on the conveyor belt.

As shown in Fig. 9, the effect of the nozzles before and after vacuuming can be clearly seen from the conveyor belt. In Fig. 9(a) (b) (c), the nozzles all have the phenomenon of leakage of dust particles on both sides, and the degree of leakage on both sides of the nozzles is different with the change of the shoulder angle and nozzle length. Fig. 9(d) shows the optimized vacuuming effect, compared with other models of nozzles, there is no leakage of dust particles on both sides.

CONCLUSIONS

(1) The structure of the dust collection box was optimized. Through the comparative analysis of the data before and after the optimization, the dust particles entering the fan box were reduced by 15.75%.

(2) The shoulder angle optimal parameters were selected to increase the gas flow rate to improve the dust suction efficiency.

(3) Through the performance test of the cleaning robot, it was concluded that the leakage of dust particles on both sides of the suction nozzle was obviously improved.

ACKNOWLEDGEMENT

This research has received support from the Weifang Science and technology development plan project (2022GX005).

REFERENCES

- [1] Anonymous, (2012). Subsea 7 adds more Schilling Robotics HD Systems to ROV fleet. *Ocean News & Technology*, Vol. 18, pp. 58, USA.
- [2] Asafa, T., Afonja, T., Olaniyan, E., & Alade, H., (2018). Development of a vacuum cleaner robot. *Alexandria Engineering Journal*, Vol. 57, pp. 2911-2920, Egypt.
- [3] Azizi, M. R., & Naderi, D., (2013). Dynamic modeling and trajectory planning for a mobile spherical robot with a 3dof inner mechanism. *Mechanism & Machine Theory*, Vol. 64, pp. 251-261, Netherlands.
- [4] Bogue, & Robert, (2011). Robots in the nuclear industry: a review of technologies and applications. *Industrial Robot*, Vol. 38, pp. 113-118, United Kingdom.

- [5] Buckingham, R., & Graham, A., (2012). Nuclear snake-arm robots. *Industrial Robot*, Vol. 39, pp. 6-11, United Kingdom.
- [6] Chen, Y., (2023). *Optimization of aerodynamic performance and internal flow characteristics of high-speed centrifugal fans for vacuum cleaners* (吸尘器用高速离心式风机气动性能优化及内部流动特性研究). Master dissertation, Zhejiang University of Science and Technology, Zhejiang/China.
- [7] Dandan, K., Albitar, H., Ananiev, A., & Kalaykov, I., (2015). Motion control of siro: the silo cleaning robot. *International Journal of Advanced Robotic Systems*, Vol. 12, pp. 1, Australia.
- [8] Guo, H., Zhang, Z., & Ma, Y., (2019). Structure analysis and improvement of suction nozzle of sweeper (清扫车吸嘴结构分析及改进). *Development & Innovation of Machinery & Electrical Products*, Vol. 32, pp. 22-24, Beijing/China.
- [9] Huang, X., (2016). *Analysis and experimental research on underwater foreign object salvage robot system for nuclear reactor* (核反应堆水下异物打捞机器人系统分析与实验研究). PhD dissertation, Hebei University of Technology, Tianjin/China.
- [10] Huang, X., Ye, J., & Xiong, J., (2019). Optimized design and test of suction nozzle of small sweeper (小型清扫车吸嘴的优化设计与试验). *Machine Design & Research*, Vol. 35, pp. 168-172, Shanghai/China.
- [11] Lin, H., Xu, C., & Lu, Y., (2023). Simulation test and verification of material conveying for small and medium-sized air suction jujube picking machine based on CFD-DEM coupling (基于CFD-DEM耦合中小型气吸红枣捡拾机物料输送仿真试验与验证). *INMATEH - Agricultural Engineering*, Vol. 71, pp. 535-547, Romania.
- [12] Logachcv, K.I., Ziganshin, A.M., & Averkova, O.A., (2019). On the resistance of a round exhaust hood shaped by outlines of the vortex zones occurring at its inlet. *Building and Environment*. Vol. 151, pp. 338-347, United Kingdom.
- [13] Lu, Y., Zhang, B., & Chen, Z., (2023). Numerical simulation and optimization design of sweeper suction nozzle flow field (清扫车吸嘴流场仿真分析及优化设计). *Construction Machinery Technology & Management*, Vol. 4, pp. 75-78, Beijing/China.
- [14] Michal, V., (2012). Remote operation and robotics technologies in nuclear decommissioning projects-ScienceDirect. *Nuclear Decommissioning*, pp. 346-374, Netherlands.
- [15] Nesaian, K. P., & Karthikeyan, M. B., (2012). Design and development of vision based blockage clearance robot for sewer pipes. *IAES International Journal of Robotics & Automation*, Vol. 1, pp. 64-68, USA.
- [16] Song, Z., Zhou, C., & Zhang, S., (2020). Application of dredging robot in culvert dredging project (清淤机器人在暗涵疏浚工程中的应用). *Northwest Hydropower*, Vol. 4, pp.70-73, Shanxi/China.
- [17] Walter, S., Ulli-Beer, S., & Wokaun, A., (2012). Assessing customer preferences for hydrogen-powered street sweepers: a choice experiment. *International Journal of Hydrogen Energy*, Vol. 37, pp. 12003-12014, United Kingdom.
- [18] Wang, G., & Tan, Y., (2020). Structural optimization design of vacuum hood based on FLUENT-EDEM coupling (基于FLUENT-EDEM耦合的吸尘罩结构优化设计). *Journal of Vacuum Science and Technology*, Vol. 40, pp. 66-80, Beijing/China.
- [19] Xi, Y., Cheng, K., & Lou, X., (2016). Numerical analysis of the flow field of a blowback nozzle and study of dust suction efficiency (反吹式吸嘴流场数值分析及吸尘效率研究). *Journal of Southwest Jiaotong University*, Vol. 51, pp. 105-112, Sichuan/China.
- [20] Yang, C., Zhang, Y., & Yang, Z., (2012). Parameter design of vacuum cleaner suction port based on fluent simulation (基于流畅模拟得真空清扫车吸尘口的参数设计). *Journal of Central South University*, Vol. 09, pp. 3704-3710, Hunan/China.
- [21] Ye, J., (2023). *Structure Research and Performance Analysis of vacuum port of pure electric small sweeper* (纯电动小型扫地车吸尘口结构研究与性能分析). Master dissertation, Anhui University of Technology, Anhui/China.
- [22] Zhou, H., Zhang, C., Liu, T., Wang, Y., Fang, J., & Hu, A., (2024). Design and experiment of annular air-blowing assisted seed guiding device for corn no-till planter (玉米免耕播种机环形气吹辅助导种装置设计与试验). *INMATEH - Agricultural Engineering*, Vol. 73, pp. 50-62, Romania.

EXPERIMENTAL RESEARCH ON THE EXTRACTION OF POLYPHENOLS FROM NETTLE, LAVENDER AND SAGE USING THE PERCOLATION METHOD

CERCETĂRI EXPERIMENTALE PENTRU EXTRAȚIA POLIFENOLILOR DIN URZICĂ, LAVANDĂ ȘI SALVIE PRIN METODA PERCOLĂRII

Ana-Maria TĂBĂRAȘU^{1,2)}, Iuliana GĂGEANU^{*1)}, Nicolae-Valentin VLĂDUȚ¹⁾, Mihai-Gabriel MATAACHE¹⁾,
Dragoș-Nicolae ANGHELACHE^{*1)}

¹⁾INMA Bucharest / Romania; ²⁾POLITEHNICA University / Romania

Tel: +40762676642, E-mail: iulia.gageanu@gmail.com; Tel: +40728034500, dragos1989anghelache@gmail.com

DOI: <https://doi.org/10.35633/inmateh-73-58>

Keywords: percolation, polyphenols, antioxidant capacity, nettle, lavender, sage

ABSTRACT

This article presents the results of experimental research on the extraction of polyphenols from nettle, lavender, and sage using the percolation method. This technique is recognized for its efficiency in extracting bioactive compounds from plants. Polyphenols are a group of natural chemical compounds characterized by the presence of multiple phenolic groups in their molecular structure. They are predominantly found in plants and are recognized in various industries, including agriculture, for their antioxidant, antimicrobial, and antifungal properties. The antioxidant capacity of the extracts from nettle, lavender, and sage refers to the ability of these extracts to neutralize free radicals. The concentrations of polyphenols in the obtained extracts were measured using the Folin-Ciocalteu spectrophotometric method. The impact of pressure on total polyphenol content varied by plant species. Sage showed increased polyphenol content at higher pressures, indicating more efficient extraction with the proposed technology.

REZUMAT

Acest articol prezintă rezultatele cercetărilor experimentale privind extracția polifenolilor din urzică, lavandă și salvie, utilizând metoda percolării. Această tehnică este recunoscută pentru eficiența sa în extragerea compușilor bioactivi din plante. Polifenolii reprezintă un grup de compuși chimici naturali, caracterizați prin prezența multiplelor grupări fenolice în structura lor moleculară. Aceștia se găsesc predominant în plante și sunt recunoscuți în diverse industrii, inclusiv în agricultură pentru proprietățile lor antioxidante, antimicrobiene și antifungice. Capacitatea antioxidantă a extractelor din urzică, lavandă și salvie se referă la abilitatea acestor extracte de a neutraliza radicalii liberi. Concentrațiile de polifenoli din extractele obținute au fost măsurate folosind metoda spectrofotometrică Folin-Ciocalteu. Impactul presiunii asupra conținutului total de polifenoli a variat în funcție de specie. Salvia a arătat un conținut crescut de polifenoli la presiuni înalte, indicând o extracție mai eficientă cu tehnologia propusă.

INTRODUCTION

Medicinal and aromatic plants were the primary source of medicine for humans before the advent of civilization (Parvin *et al.*, 2023). Biologically, these plants are remarkable for their rich composition of active substances with recognized medicinal properties according to Western standards (Mendes *et al.*, 2023). These active substances are either produced and stored by the plants during their growing season or accumulate in response to stress conditions such as sudden climate changes, excess or insufficient soil water, nutrient deficiency, air pollution, etc. (Greff *et al.*, 2022). Among the bioactive compounds present in plants are polyphenols, which are especially recognized for their antioxidant properties (Pinto *et al.*, 2021). In agriculture, polyphenols protect crops from diseases and pests, enhance the quality and nutritional value of produce, and reduce the need for chemical pesticides, thereby promoting more sustainable agricultural practices (Stiller *et al.*, 2021).

Additionally, these types of plants are crucial for maintaining ecological balance and soil health, protecting other crops, and contributing to reducing the use of harmful chemicals through their efficient use as natural pesticides and organic fertilizers. Promoting ecological processes for extracting active principles from these plants is an important step towards sustainable agriculture, minimizing the environmental impact (Greff *et al.*, 2022).

Percolation is a widely used process for extracting compounds from plants. In this process, a solvent passes through a porous material, such as plant material, to extract the desired substances. This method is considered gentle as it occurs at room temperature, making it suitable for extracting thermosensitive compounds from plants (Zhang *et al.*, 2023). The percolation process can be conducted either by subjecting the plant material to high pressures or without using pressure variations. Studies have demonstrated that percolation under high pressures enhances the efficiency of extracting valuable compounds from plant materials by increasing solvent penetration and solute dissolution (Nenciu *et al.*, 2023). This method often leads to higher yields of target compounds, such as polyphenols, due to the improved extraction dynamics facilitated by elevated pressures. These compounds can then be used as biofertilizers in ecological agriculture, offering promising results for enhancing soil health and plant growth (Popescu *et al.*, 2023). Solid-liquid extraction under high pressure regimes enhances the extraction of specific compounds from the plant materials improving solvent penetration and compound solubility, leading to higher yields and faster extraction times (Butler *et al.*, 2004).

The three plants studied in this article—nettle, lavender and sage—were selected for their beneficial effects in horticulture, particularly as biofertilizers and biopesticides.

Nettle (*Urtica dioica*) –, is native to Europe and Asia, and was later spread to other parts of the world, including North America and North Africa. Although nettle has adapted to the climate and environmental conditions of many regions, Europe and Asia are still considered its regions of origin (Subba and Pradhan, 2022; Bhusal *et al.*, 2022). Nettle is a perennial plant that can grow between 0.4 and 4 meters tall (Subba and Pradhan, 2022; Bhusal *et al.*, 2022; Mueen Ahmed and Parsuraman, 2014; Devkota *et al.*, 2022), with oval or elongated, opposite leaves that have strongly serrated edges, a cordate base, and a pointed tip (Bhusal *et al.*, 2022; De Vico *et al.*, 2018; Subba and Pradhan, 2022). Nettle leaves are a rich source of bioactive compounds, including flavonoids, phenolic acids, essential amino acids, terpenoids, carotenoids, lutein, as well as vitamins, tannins, polysaccharides, sterols, and minerals (Kregiel *et al.*, 2018.; Devkota *et al.*, 2022; Koraqi, 2023). Nettle flowers are small, dioecious, and borne in separate inflorescences. They can be brown to greenish and appear in the axils of the upper leaves (De Vico *et al.*, 2018; Subba and Pradhan, 2022).

Nettle (*Urtica dioica*) - Figure 1, is used as a food additive in the food industry, in shampoos and lotions in the cosmetic industry, as supplements in the pharmaceutical industry (Koraqi, 2023), and its extracts are also used as biofertilizers/bioinsecticides in agriculture. In agriculture, nettle extracts act as biofertilizers and bioinsecticides, enhancing plant growth and soil fertility by improving nutrient absorption, stress resistance, and microbial activity. They also positively impact soil conductivity, boosting nutrient availability for plants (Maricic *et al.*, 2022).



Fig. 1 - Nettle (*Urtica dioica*)

Lavender (*Lavandula angustifolia*) - Figure 2, is a perennial plant in the Lamiaceae family and originates from Mediterranean regions, which is why it shows adaptability to dry and warm climates, preferring sandy soils and sunny locations (Oroian *et al.*, 2019; Adam, 2018; Kimbrough and Swift, 2006). Lavender grows as shrubs between 20 and 60 cm tall. It has leaves of various shapes, including sessile, linear, and lanceolate, and its stems are branched and irregular. The roots are woody, and the flowers, predominantly blue-violet, are spirally arranged and have a two-lipped form (Katarzyna, *et al.*, 2014; Fakhridinova *et al.*, 2020). Lavender

flowers are rich in various essential compounds such as phytochemicals (triterpenoids, phenolic acids, flavonoids) (Héral, et al., 2021), anthocyanins, phytosterols (Batiha et al., 2023), and essential oils (Kozuharova et al., 2023; Diass et al., 2023; Voicea, et al., 2022). The benefits of lavender extracts in agriculture are remarkable and can bring significant improvements in plant health and agricultural system efficiency (Crişan et al., 2023).

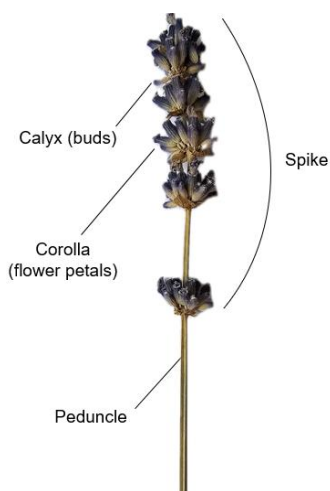


Fig. 2 - Lavender (*Lavandula angustifolia*)

Sage (*Salvia officinalis*) - Figure 3, is an aromatic and medicinal plant in the Lamiaceae family, originating from Mediterranean regions (Ghorbani and Esmailizadeh, 2017; Hamidpour et al., 2014; Ben Khader et al., 2017). Sage plants grow up to 60 cm tall, with grey-green leaves that are hairy on the underside, and they range from 3 to 6.5 cm long and 1.5 to 2.5 cm wide (Jakovljevic et al., 2019). The flower colour varies from red-violet-blue and they are grouped in panicles or racemes (Ben Akacha et al., 2023). The flowers, leaves, and stems of *Salvia officinalis* contain numerous chemical substances, the most important being polyphenols, alkaloids, fatty acids, terpenes, steroids, glycoside derivatives, and essential oils (Ghorbani and Esmailizadeh, 2017).

Extracts from *Salvia officinalis* can bring multiple benefits to agriculture. Through their antifungal and antibacterial action, these extracts help prevent and combat plant diseases, ensuring their health. Additionally, the antioxidant properties of sage protect plants against oxidative stress and promote their growth and development. By repelling insects and other harmful organisms, sage extracts protect crops, reducing the need for chemical pesticides (Speranza et al., 2023; Busato et al., 2022).

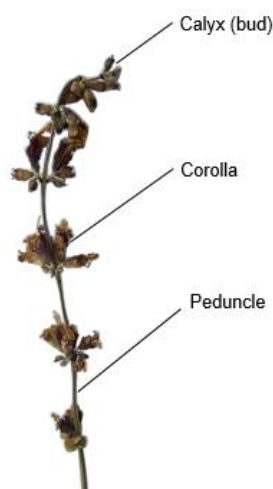


Fig. 3 - Sage (*Salvia officinalis*)

This paper presents experimental results obtained through the pressure percolation extraction method, obtaining extracts from nettle, lavender and sage and assessing their polyphenol content and antioxidant activity with the purpose of assessing the extracts' suitability to be used as amendments in agriculture.

MATERIALS AND METHODS

The plants used for experimentation in this study were: nettle (*Urtica dioica*), lavender (*Lavanda angustifolia*) and sage (*Salvia officinalis*).

To ensure the vegetal material for experiments, plants were harvested using a mechanized equipment. The plants were dried for 12 hours in a laboratory oven at 105°C and were cut at dimensions no larger than 3 cm using a plant cutting equipment.

The three plants were chosen because of their ecological and agricultural benefits. Nettle improves soil fertility, having the capacity to act as an organic fertilizer that stimulates plant growth. Lavender and sage are rich in essential compounds with properties to repel harmful insects, acting as natural pesticides that protect crops, thus eliminating the need for synthetic chemical substances.

The active principles from the medicinal and aromatic plants (nettle, lavender, sage) were extracted using the TIMATIC percolator (Figure 4).

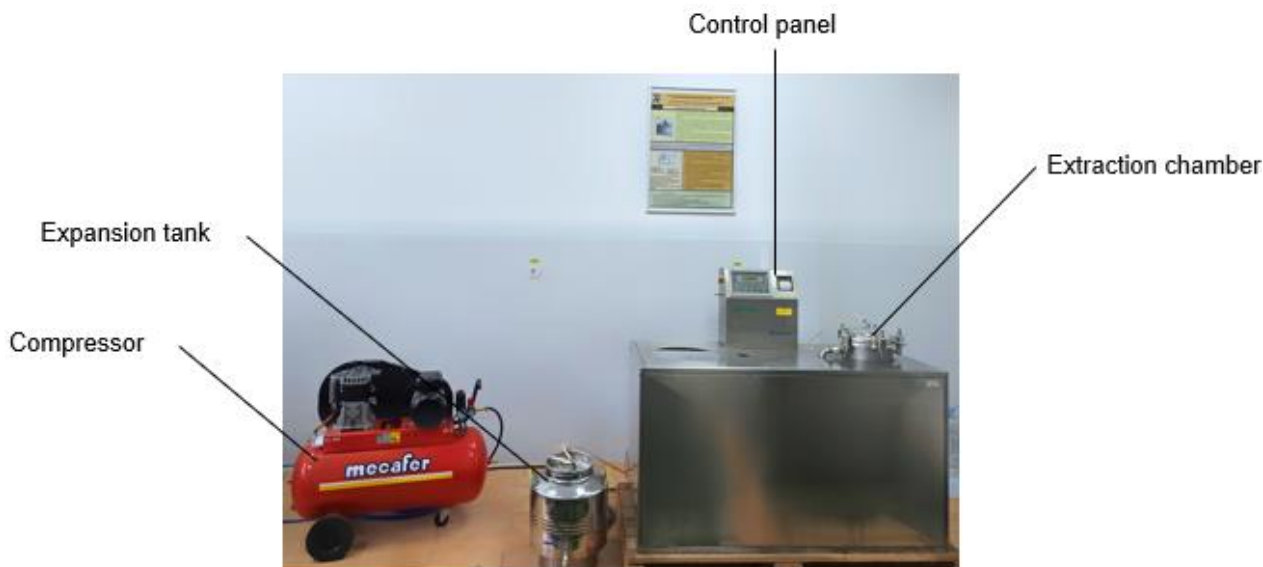


Fig. 4 - TIMATIC percolator

The TIMATIC Percolator model is a high-performance equipment designed for the extraction of active compounds from plants, combining automation with the ability for manual adjustments. It supports a maximum working pressure of 8 bar and operates efficiently within a temperature range of 5-45°C. Its maximum power consumption is 500 W, optimized to deliver high performance and energy efficiency under various operating conditions. The total extraction time, cycles, compression time (TP1) and decompression time (TP0) can be adjusted according to the user's requirements. It operates through a pressure percolation process in two distinct phases.

The equipment consists of the following main components: the extraction chamber - allocated for the introduction of plant batches, ensuring precise handling of the plant material; control panel - displays the extraction process parameters; expansion tank - used to release air from the system during priming operation and also serves as the reservoir from which the necessary amount of solvent for the entire process is drawn; compressor - used to regulate the pressure at which the extraction process takes place.

Each sample involved using 400 grams of dried plant material, with a solvent (water) volume of 12 litres, plus an additional 7 litres to ensure the proper functioning of the process and to eliminate air from the system. The moisture content of the plants before extraction was determined using the Shimadzu MOC63u moisture analyser, and the values obtained were as follows (Figures 5-7): 10.19% for nettle, 9.84% for lavender, and 10.29% for sage.



Fig. 5 - Moisture content of dried nettle



Fig. 6 - Moisture content of dried lavender



Fig. 7 - Moisture content of dried sage

The extraction process begins with the preparation of the plant material, which is weighed to ensure a correct ratio between the plant material and the solvent used. The weighed and dosed plants are then placed into a special cloth bag (Figure 8) and placed in the extraction chamber of the TIMATIC equipment (Figure 9). The solvent is added over the plant material up to the base of the compartment, after which the lid is closed and secured with clamps and nuts to ensure a tight seal.



Fig. 8 – Preparation of plant material: packing in special cloth bag and weighing



Fig. 9 – Sample prepared for introduction into the extraction chamber

The initiation of the percolator's operation involves using an expansion tank to eliminate air from the system and provide the necessary amount of solvent. After completing the preparatory operations, the percolator is started by setting the time and low/high pressure for the percolation operation.

During the extraction process, the percolator alternates between dynamic and static phases, controlling the pressure to facilitate the transfer of the extract into the solvent. The extraction process is optimized by alternately varying the high and low pressures, favouring the release of bioactive principles from the plants.

Finally, after the percolation process is complete, the DISCHARGE operation follows, in which the extract and active principles are collected in the expansion tank for subsequent use in various applications.

A total of 18 tests were performed using the percolator (6 for each type of plant used) at both low pressure (total extraction time – 60 min, number of percolations – 8, and 6 cycles) and high pressure (total extraction time – 60 min, number of percolations – 8, and 6 cycles).

For the low-pressure tests, each cycle included a compression time (TP1) of 4 minutes (at 5 bar pressure) and a decompression time (TP0) of 6 minutes. The decompression time was divided as follows: 1 minute at 0.06 bar, followed by 7 repetitions of 10 seconds at 0.06 bar and another 2 minutes and 30 seconds at the same pressure. These cyclic phases alternated with 8 repetitions of 10 seconds at 0.69 bar. This sequence was repeated for the following 5 cycles.

For the high-pressure tests, each cycle included a compression time (TP1) of 4 minutes (at 7 bar pressure) and a decompression time (TPO) of 6 minutes. The decompression time was divided as follows: 1 minute at 0.12 bar, followed by 7 repetitions of 10 seconds at 0.12 bar and another 2 minutes and 30 seconds at the same pressure. These cyclic phases alternated with 8 repetitions of 10 seconds at 0.87 bar. This sequence was repeated for the following 5 cycles.

Determining the total polyphenol content in the plant extracts (nettle, lavender, sage) was performed using the Folin-Ciocalteu spectrophotometric method. The method involves extracting the total polyphenols in a methanol: water mixture (1:1), treating them with the Folin-Ciocalteu reagent, and measuring the absorbance of the complex formed at a wavelength of $\lambda = 755$ nm. The quantification of phenolic compounds was based on the calibration curve of gallic acid, in the concentration range 0-0.2 mg/mL, with results expressed in mg GAE/100g.

The antioxidant capacity of the nettle, lavender, and sage extracts was determined using the DPPH (2,2-diphenyl-1-picrylhydrazyl) method, at a wavelength of $\lambda = 517$ nm. The Trolox calibration curve was created in the concentration range of 0-0.4375 mmol/L.

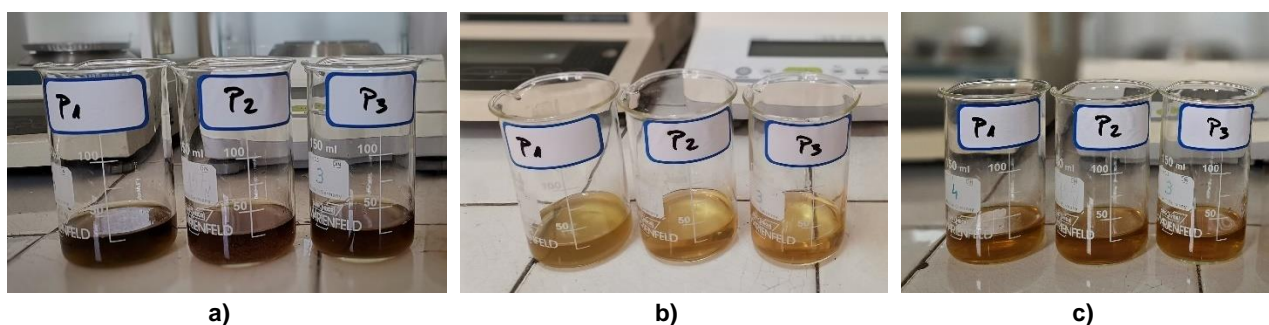


Fig. 10 – Extracts from: a) nettle; b) lavender; c) sage

RESULTS

Table 1 summarizes relevant information about the type of plant, the pressure used in percolation, the degree of plant chopping, extraction time, number of cycles, and number of percolations. This data is essential for evaluating the effectiveness of the extraction process in obtaining polyphenols from each type of plant.

Table 1

Input parameters for the extraction process of active principles from medicinal and aromatic plants

| Plant | Extraction method* | Chopping degree (cm) | Pressure (bar) | Time (min) | TP1 (min:sec) | TPO (min:sec) | Cycles | No. of percolations |
|----------|--------------------|----------------------|----------------|------------|---------------|---------------|--------|---------------------|
| NETTLE | P1 | 3 | 5 | 60 | 4 | 6 | 6 | 8 |
| | P2 | 3 | 5 | 60 | 4 | 6 | 6 | 8 |
| | P3 | 3 | 5 | 60 | 4 | 6 | 6 | 8 |
| | P4 | 3 | 7 | 60 | 4 | 6 | 6 | 8 |
| | P5 | 3 | 7 | 60 | 4 | 6 | 6 | 8 |
| | P6 | 3 | 7 | 60 | 4 | 6 | 6 | 8 |
| LAVENDER | P1 | 3 | 5 | 60 | 4 | 6 | 6 | 8 |
| | P2 | 3 | 5 | 60 | 4 | 6 | 6 | 8 |
| | P3 | 3 | 5 | 60 | 4 | 6 | 6 | 8 |
| | P4 | 3 | 7 | 60 | 4 | 6 | 6 | 8 |
| | P5 | 3 | 7 | 60 | 4 | 6 | 6 | 8 |
| | P6 | 3 | 7 | 60 | 4 | 6 | 6 | 8 |
| SAGE | P1 | 3 | 5 | 60 | 4 | 6 | 6 | 8 |
| | P2 | 3 | 5 | 60 | 4 | 6 | 6 | 8 |
| | P3 | 3 | 5 | 60 | 4 | 6 | 6 | 8 |
| | P4 | 3 | 7 | 60 | 4 | 6 | 6 | 8 |
| | P5 | 3 | 7 | 60 | 4 | 6 | 6 | 8 |
| | P6 | 3 | 7 | 60 | 4 | 6 | 6 | 8 |

*P1, P2, P3– Low-pressure percolation; P4, P5, P6 – High-pressure percolation;

The average results of the experimental analysis of polyphenol content and antioxidant capacity of extracts from the three types of plants are summarized and presented in Tables 2 and 3.

Table 2

Total polyphenol content of nettle, lavender, and sage extracts

| No. | SAMPLES | Total polyphenol content (mg GAE/100g) |
|------------------------|---------------|--|
| 1. | P1 (nettle) | 5.021±0.126 |
| 2. | P2 (nettle) | 5.227±0.114 |
| 3. | P3 (nettle) | 5.351±0.129 |
| Average results | | 5.199±0.123 |
| 4. | P4 (nettle) | 6.445±0.161 |
| 5. | P5 (nettle) | 6.219±0.170 |
| 6. | P6 (nettle) | 6.083±0.186 |
| Average results | | 6.249±0.172 |
| 7. | P1 (lavender) | 14.184±0.355 |
| 8. | P2 (lavender) | 14.471±0.201 |
| 9. | P3 (lavender) | 14.711±0.315 |
| Average results | | 14.455±0.290 |
| 10. | P4 (lavender) | 15.042±0.376 |
| 11. | P5 (lavender) | 15.094±0.282 |
| 12. | P6 (lavender) | 15.088±0.311 |
| Average results | | 15.074±0.323 |
| 13. | P1 (sage) | 17.23±0.43 |
| 14. | P2 (sage) | 17.05±0.22 |
| 15. | P3 (sage) | 17.31±0.11 |
| Average results | | 17.19±0.25 |
| 16. | P4 (sage) | 20.87±0.52 |
| 17. | P5 (sage) | 20.51±0.43 |
| 18. | P6 (sage) | 20.88±0.19 |
| Average results | | 20.75±0.38 |

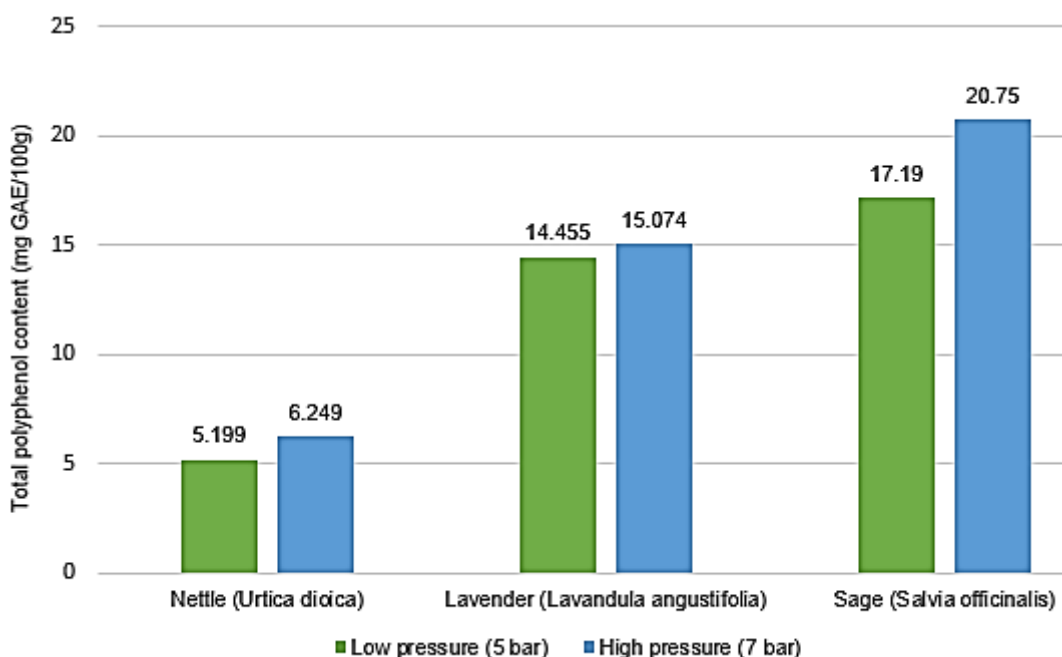


Fig. 11 – Graphical representation of average results obtained for total polyphenol content of nettle, lavender and sage extracts

The results in Figure 11 demonstrate that the effect of pressure on polyphenol extraction varies significantly depending on the type of plant. Data shows that the percolation method (at both 5 and 7 bar pressure) is more suitable for sage, as it more effectively extracts the polyphenols contained in the plant. When analyzed from a perspective of percentage extraction depending on the two pressures, the differences between the two pressure regimes are not significantly different.

Table 3

| Antioxidant capacity of nettle, lavender, and sage extracts | | |
|---|---------------|---------------------------------------|
| No. | SAMPLE | Antioxidant capacity (mg Trolox/100g) |
| 1. | P1 (nettle) | 11.760±0.294 |
| 2. | P2 (nettle) | 11.799±0.213 |
| 3. | P3 (nettle) | 11.802±0.344 |
| Average results | | 11.787±0.283 |
| 4. | P4 (nettle) | 11.088±0.277 |
| 5. | P5 (nettle) | 11.194±0.269 |
| 6. | P6 (nettle) | 11.207±0.302 |
| Average results | | 11.163±0.282 |
| 7. | P1 (lavender) | 38.563±0.964 |
| 8. | P2 (lavender) | 38.405±0.787 |
| 9. | P3 (lavender) | 38.221±0.555 |
| Average results | | 38.396±0.768 |
| 10. | P4 (lavender) | 28.578±0.714 |
| 11. | P5 (lavender) | 28.502±0.636 |
| 12. | P6 (lavender) | 29.495±0.622 |
| Average results | | 28.525±0.657 |
| 13. | P1 (sage) | 61.99±1.55 |
| 14. | P2 (sage) | 61.83±2.21 |
| 15. | P3 (sage) | 61.56±1.58 |
| Average results | | 61.79±1.78 |
| 16. | P4 (sage) | 66.21±1.66 |
| 17. | P5 (sage) | 66.11±1.59 |
| 18. | P6 (sage) | 66.02±1.18 |
| Average results | | 66.11±1.47 |

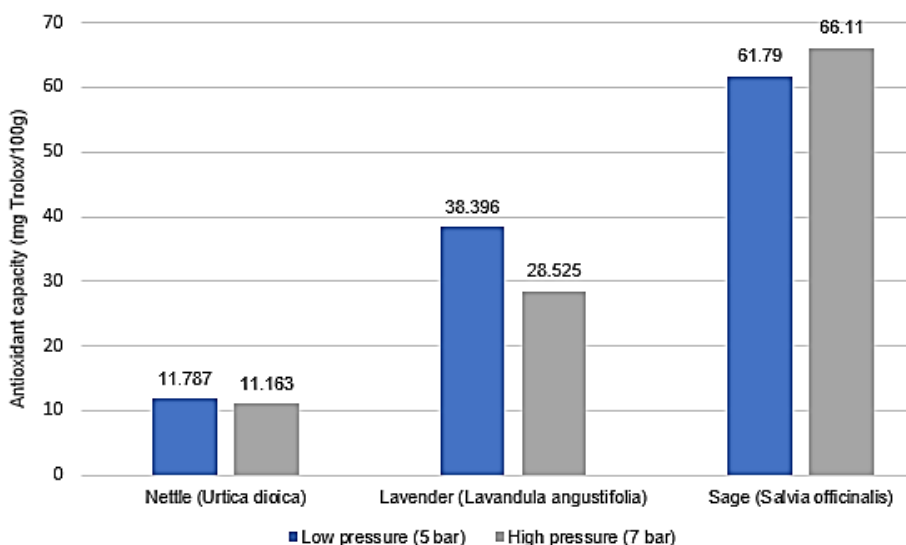


Fig. 12 – Graphical representation of average results obtained for the antioxidant capacity of extracts

According to Figure 12, the results of the antioxidant capacity analysis of nettle, lavender, and sage extracts obtained through percolation at different pressures show that sage has the strongest antioxidant capacity, regardless of pressure. The antioxidant capacity of lavender decreases at high pressure, while for nettle remains relatively constant. A possible explanation could be that high pressure percolation can induce stress on the delicate antioxidant compounds present in lavender, such as certain flavonoids and essential oils. These compounds are more sensitive to high pressure, leading to their degradation or structural alteration, which reduces their effectiveness as antioxidants.

CONCLUSIONS

The impact of pressure on the total polyphenol content varied depending on the plant species. For nettle and lavender, no significant differences were observed between low and high pressure, suggesting stability in

polyphenol content regardless of the applied pressure. In the case of sage, an increase in total polyphenol content was observed at higher pressures, indicative of a more efficient extraction at elevated pressures.

These findings suggest that the properties of the three types of plants can be utilized in various agricultural applications: sage for its robust antioxidant potential, and lavender and nettle for their antimicrobial and antifungal properties.

The results obtained underscore the importance of optimizing extraction conditions based on the plant species to maximize the extraction of various compounds such as polyphenols and the antioxidant activity of the obtained extracts.

ACKNOWLEDGEMENT

This research was supported by Project PN 23 04 02 01, Contract no.: 9N/ 01.01.2023 SUSTAIN-DIGI-AGRI, Innovative biofertilizer production technology used to restore soil biodiversity and reduce the effects of drought on agricultural lands.

REFERENCES

- [1] Adam K.L. (2018), Lavender Production, Markets and Agritourism. *ATTRA Sustain. Agric.*, 1–8. Available online: <https://ccsmallfarms.ucanr.edu/files/294700.pdf>
- [2] Batiha G.E-S., Teibo J.O., Wasef L., Shaheen H.M., Akomolafe A.P., Teibo T.K.A., Al-kuraishy H.M., Al-Garbeeb A.I., Alexiou A., Papadakis M., (2023), A review of the bioactive components and pharmacological properties of *Lavandula* species, *Naunyn-Schmiedeberg's Archives of Pharmacology*, 396:877–900, <https://doi.org/10.1007/s00210-023-02392-x>.
- [3] Ben Akacha B., Ben Hsouna A., Mekinic I.G., Ben Belgacem A., Ben Saad R., Mnif W., Kacániová M., Garzoli S., (2023), *Salvia officinalis* L. and *Salvia sclarea* Essential Oils: Chemical Composition, Biological Activities and Preservative Effects against *Listeria monocytogenes* Inoculated into Minced Beef Meat, *Plants*, 12, 3385, <https://doi.org/10.3390/plants12193385>.
- [4] Ben Khedher M.R., Ben Khedher S., Chaieb I., Tounsi, S., Hammami M., (2017), Chemical composition and biological activities of *Salvia officinalis* essential oil from Tunisia; *EXCLI Journal*, 16:160-173 – ISSN 1611-2156.
- [5] Bhusal K.K., Magar S.K., Thapa R., Lamsal A., Bhandari S., Maharjan R., Shrestha S., Shrestha J., (2022), Nutritional and pharmacological importance of stinging nettle (*Urtica dioica* L.): A review, *Heliyon*, <https://doi.org/10.1016/j.heliyon.2022.e09717>.
- [6] Busato I., Bertaiola O., Tundo S., Guarnerio C., Lucchetta M., Sella L., Pressi G., Favaron F.; (2022), A Phytocomplex Obtained from *Salvia officinalis* by Cell Culture Technology Effectively Controls the Grapevine Downy Mildew Pathogen *Plasmopara viticola*, *Plants*, Vol. 11, 2675, <https://doi.org/10.3390/plants11202675>.
- [7] Butler, M.S. (2004), The role of natural product chemistry in drug discovery. *J. Nat. Prod.* Vol. 67, 2141–2153. <https://doi.org/10.1021/np040106y>
- [8] Crişan I., Ona A., Vârban D., Muntean L., Vârban R., Stoie A., Mihăiescu T., Morea A., (2023), Current Trends for Lavender (*Lavandula angustifolia* Mill.) Crops and Products with Emphasis on Essential Oil Quality, *Plants*, Vol. 12, 357, <https://doi.org/10.3390/plants12020357>.
- [9] Devkota H.P., Paudel K.R., Khanal S., Baral A., Panth N., Adhikari-Devkota A., Jha N.K., Das N., Singh S.K., Chellappan D.K., Dua K., Hansbro P.M., (2022), Stinging Nettle (*Urtica dioica* L.): Nutritional Composition, Bioactive Compounds, and Food Functional Properties, *Molecules*, 27, 5219, <https://doi.org/10.3390/molecules27165219>.
- [10] De Vico G., Guida V., Carella F., (2018), *Urtica dioica* (Stinging Nettle): A Neglected Plant With Emerging Growth Promoter/Immunostimulant Properties for Farmed Fish, *Front. Physiol.*, 9, 285.
- [11] Diass K., Merzouki, M., Elfazazi K., Azzouzi H., Challioui A., Azzaoui K., Hammouti B., Touzani R., Depeint F., Gotor A.A., Rhazi L., (2023), Essential Oil of *Lavandula officinalis*: Chemical Composition and Antibacterial Activities, *Plants*, 12, 1571, <https://doi.org/10.3390/plants12071571>.
- [12] Fakhridinova D.K., Rakhimova T.R., Dusmuratova F.M., Duschanova G.M., Abdinazarov S.H., Samadov I.N., (2020), The Anatomical Structure of Vegetative Organs *Lavandula officinalis* Chaix in the Introduction of Tashkent Botanical Garden, *American Journal of Plant Sciences*, 11, 578–588, <https://doi.org/10.4236/ajps.2020.114043>.
- [13] Ghorbani A., Esmaeilzadeh, M., (2017), Pharmacological properties of *Salvia officinalis* and its components, *Journal of Traditional and Complementary Medicine*, Vol. 7, pp. 433-440, <http://dx.doi.org/10.1016/j.jtcme.2016.12.014>.
- [14] Greff B., Sáhó A., Lakatos E., Varga L., (2022), Biocontrol Activity of Aromatic and Medicinal Plants and Their Bioactive Components against Soil-Borne Pathogens, *Plants*, 12, 706, <https://doi.org/10.3390/plants12040706>.

- [15] Hamidpour M., Hamidpour R., Hamidpour S., Shahlari M., (2014), Chemistry, Pharmacology, and Medicinal Property of Sage (*Salvia*) to Prevent and Cure Illnesses such as Obesity, Diabetes, Depression, Dementia, Lupus, Autism, Heart Disease, and Cancer; *Journal of Traditional and Complementary Medicine*, Vol. 4, No. 2, pp. 82-88, DOI: 10.4103/2225-4110.130373.
- [16] Héral B., Stierlin É., Fernandez X., Michel T., (2021), Phytochemicals from the genus *Lavandula*: a review. *Phytochem Rev*, 751–771; <https://doi.org/10.1007/s11101-020-09719-z>.
- [17] Jakovljevic M., Jokic S., Molnar M., Jasic M., Babic J., Jukic H., Banjari I., (2019), Bioactive Profile of Various *Salvia officinalis* L. Preparations, *Plants*, Vol. 8, 55, doi:10.3390/plants8030055.
- [18] Kimbrough K.A., Swift C.E., (2006), *Growing Lavender in Colorado*; Colorado State University: Fort Collins, CO, USA.
- [19] Koraqi H., Qazimi B., Khalid W., Stanoeva J.P., Sehrish A., Siddique F., Česko C., Ali Khan K., Rahim M. A., Hussain I., Zongo E., (2023), Optimized conditions for extraction, quantification and detection of bioactive compound from Nettle (*Urtica dioica* L.) using the deep eutectic solvents, ultra-sonication and liquid chromatography-mass spectrometry (LC-DAD-ESI-MS/MS), *International Journal of Food Properties*, 26, 2171-2185, <https://doi.org/10.1080/10942912.2023.2244194>.
- [20] Kozuharova E., Simeonov V., Batovska D., Stoycheva C., Valchev H., Benbassat N., (2023), Chemical composition and comparative analysis of lavender essential oil samples from Bulgaria in relation to the pharmacological effects, *Pharmacia*, 70(2): 395–403, DOI 10.3897/pharmacia.70.e104404.
- [21] Kregiel D., Pawlikowska E., Antolak H., (2018), *Urtica* spp.: Ordinary Plants with Extraordinary Properties, *Molecules*, Vol. 23, 1664, doi:10.3390/molecules23071664.
- [22] Maricic B., Brkljaca M., Ban D., Palcic I., Franin K., Marcelic S., Ban S.G., (2022), Non-Aerated Common Nettle (*Urtica dioica* L.) Extract Enhances Green Beans (*Phaseolus vulgaris* L.) Growth and Soil Enzyme Activity, *Life*, Vol. 12, 2145, <https://doi.org/10.3390/life12122145>.
- [23] Mendes A., Oliveira A., Lameiras, J., Mendes-Moreira P., Botelho G., (2023), Organic Medicinal and Aromatic Plants: Consumption Profile of a Portuguese Consumer Sample, *Foods*, 12, 4145. <https://doi.org/10.3390/foods12224145>.
- [24] Mueen Ahmed KK., Parsuraman S., (2014), *Urtica dioica* L., (*Urticaceae*): A Stinging Nettle, *Sys Rev Pharm.*, Vol 5.
- [25] Nenciu, F., Fatu, V., Arsenoiaia, V., Persu, C., Voicea, I., Vladut, N.-V., Matache, M.G., Gageanu, I., Marin, E., Biris, S.-S., (2023), Bioactive Compounds Extraction Using a Hybrid Ultrasound and High-Pressure Technology for Sustainable Farming Systems. *Agriculture*, Vol. 13, 899. <https://doi.org/10.3390/agriculture13040899>.
- [26] Oroian C., Odagiu A., Racz C.P., Oroian I., Mureşan I.C., Duda M., Ilea M., Braşovean I., Iederan C., Marchiş Z., (2019), Composition of *Lavandula angustifolia* L. cultivated in Transylvania, Romania, *Not Bot Horti Agrobo*, 47(3):643-650, DOI:10.15835/nbha47311565.
- [27] Parvin S., Reza A., Das S., Miah M.U., Karim S., (2023), Potential Role and International Trade of Medicinal and Aromatic Plants in the World, *European Journal of Agriculture and Food Sciences*, Vol. 5, ISSN 2684-1827, pp. 89-99.
- [28] Pinto T., Aires A., Cosme F., Bacelar E., Morais M.C., Oliveira I., Ferreira-Cardoso J., Anjos R., Vilela A., Gonçalves B., (2021), Bioactive (Poly)phenols, Volatile Compounds from Vegetables, Medicinal and Aromatic Plants, *Foods*, 10, 106. <https://doi.org/10.3390/foods10010106>.
- [29] Popescu, E., Nenciu, F., Vladut, V., (2022), A new strategic approach used for the regeneration of soil fertility, in order to improve the productivity in ecological systems. *Scientific Papers-Series E-Land Reclamation Earth Observation & Surveying Environmental Engineering*, Vol.11, 277-284.
- [30] Seidler-Lozykowska K., Mordalski R., Kucharski W., Kedzia B., Bocianowski J., (2014), Yielding and quality of lavender flowers (*Lavandula angustifolia* Mill.) from organic cultivation. *Acta Sci. Pol. Hortorum Cultus*, 13, 173–183.
- [31] Speranza, B.; Guerrieri, A.; Racioppo, A.; Bevilacqua, A.; Campaniello, D.; Corbo, M.R.; (2023). Sage and Lavender Essential Oils as Potential Antimicrobial Agents for Foods; *Microbiology Research*, Vol.14, pp. 1089-1113, <https://doi.org/10.3390/microbiolres14030073>.
- [32] Stiller A., Garrison K., Gurdyumov K., Kenner J., Yasmin F., Yates P., Song B-H., (2021), From Fighting Critters to Saving Lives: Polyphenols in Plant Defense and Human Health, *International Journal of Molecular Sciences*, 22, 8995. <https://doi.org/10.3390/ijms22168995>.
- [33] Subba S., Pradhan K., (2022), A comprehensive review on common plants with remarkable medicinal properties: *Urtica dioica*, *Journal of Medicinal Plants Studies*, 10(6): 87-91.
- [34] Voicea, I., Fatu, V., Nenciu, F., Persu, C., Oprescu, R., (2022), Experimental research on bioinsecticide activity obtained by using an oleic extract from dwarf silver fir on some vegetable crops. *Sci. Pap. Ser. B Hort.* 66, 575–580.
- [35] Zhang M., Zhao J., Dai X., Li X., (2023), Extraction and Analysis of Chemical Compositions of Natural Products and Plants, *Separations*, 10, 598. <https://doi.org/10.3390/separations10120598>.

RESEARCH ON AGRICULTURAL LOGISTICS DISTRIBUTION PATH PLANNING CONSIDERING UAV ENDURANCE MILEAGE LIMIT

考虑无人机续航里程限制的农业物流配送路径规划研究

Yebiao XU *)

School of Economics and Management, Wuhan Railway Vocational College of Technology, Wuhan, Hubei/ China

Tel: +8613037141809; E-mail: xuybiao@126.com

Corresponding author: Yebiao XU

DOI: <https://doi.org/10.35633/inmateh-73-59>

Keywords: Agricultural engineering, unmanned aerial vehicle distribution, endurance mileage, path optimization, improved ant colony algorithm

ABSTRACT

To address the difficulties in logistics distribution in remote rural areas, a systematic planning of agricultural logistics distribution for UAV distribution was performed in this study. Considering the limit of cruising range, from the perspective of green routing, a multi-package distribution path planning model of UAV agricultural logistics considering the limitation of cruising range of unmanned aerial vehicle (UAV) was established to minimize total energy consumption. The task allocation was conducted according to the actual number of UAVs. Meanwhile, a mixed integer nonlinear programming model of task allocation was established. The improved ant colony algorithm was employed to solve the problem. The core idea was to exchange the pheromones of each ant subgroup, and subsequently to apply the insertion-based heuristic method and crossover and inversion operations to optimize the path. For the cases of remote areas in western China, the agricultural UAV distribution path planning considering the mileage limit contributes to saving resources and obtaining the lowest energy consumption distribution path. In addition, for the problem of agricultural logistics distribution path planning considering the mileage limit of UAV, the improved ant colony algorithm exhibits higher solution accuracy than the traditional ant colony algorithm.

摘要

为解决偏远农村地区物流配送存在的困难,对无人机配送进行农业物流配送系统性规划,考虑到续航里程限度,从绿色路由的角度,以最小化总能耗作为目标,建立了考虑无人机续航里程限制的无人机农业物流多包裹配送路径规划模型; 根据实际无人机数量进行任务分配,建立了任务分配混合整数非线性规划模型,采用改进蚁群算法求解,其核心思想是将各个蚂蚁子群的信息素进行交换,再采用基于插入的启发式方法和交叉、反转操作进行路径优化,经过对照实验。对于我国西部偏远地区的案例,考虑续航里程限制的农业无人机配送路径规划有利于节约资源,能得到能耗最低的配送路径; 对于考虑无人机续航里程限制的农业物流配送路径规划问题,本文设计的改进蚁群算法与传统蚁群算法相比,本文改进蚁群算法具有较高的求解精确度。

INTRODUCTION

Agricultural logistics distribution path planning has its own particularity. Agricultural products are fresh and seasonal, and are more sensitive to distribution distance and distribution efficiency. The allocation of goods in agricultural products warehouses should not be too frequent, and the profits of agricultural products themselves are not high. To ensure the interests of farmers, the cost of warehouse construction and distribution should be reduced as much as possible (Li et al., 2021). Recently, drone delivery has attracted considerable attention in the logistics industry. Numerous e-commerce companies and logistics suppliers have begun to test the application of drones to deliver packages. In China, Shunfeng and Jingdong took the lead in applying drones to deliver parcels to remote rural areas in places including Jiangxi and Shaanxi, and received government support. With the continuous improvement of civil unmanned aerial vehicle (UAV) control policies, UAVs will exert a vital role in distribution and emergency distribution in remote areas. Owing to the particularity of agricultural logistics distribution, refrigeration was needed to control the temperature during storage and transportation, which would produce a large amount of carbon dioxide (Dorling et al., 2017). Agricultural logistics distribution was characterized by high energy consumption and carbon emissions. Economic benefits and environmental impacts needed to be considered in this study.

Increasing attention had been paid to agricultural logistics distribution (Cheng et al., 2020). Therefore, reducing the cost of agricultural logistics distribution through agricultural logistics distribution path planning has been a focus of research.

An UAV is an aircraft that does not carry a pilot and is equipped with an autonomous flight control system. It has the characteristics of small size, low risk and easy to use, and is widely applied in military and civil fields. With the rapid development of the e-commerce industry, the pressure of logistics terminal distribution has also increased. Especially in mountainous areas, factors like scattered population and complex terrain lead to high logistics costs and long delivery time. In view of this situation, logistics drones came into being (Torabbeigi et al., 2020). However, China's UAV logistics is still in its infancy, and there have been some problems in the marketization of UAV logistics, bringing many challenges to the sustainable development of UAV agricultural logistics. By applying the emerging thing of drones to the field of agricultural logistics that was closely associated with life, the public inevitably questioned and worried about the safety of this new technology (Figliozzi et al., 2017). In addition, the high investment in technology research and development, personnel training and supporting system establishment of UAV agricultural logistics distribution also sets a higher threshold for enterprises to carry out UAV agricultural logistics business. The relevant policies and regulations and supervision mechanism system of UAV logistics are still in the stage of exploration and improvement. This study investigates the path planning of UAV agricultural logistics distribution from two aspects including the development of UAV technology and the standardized operation of UAV logistics.

Currently, few studies focus on the trajectory planning of logistics UAVs. UAV path planning was a satisfactory space flight path for UAV to successfully complete the flight mission by comprehensively considering topography, various threats, energy and fuel consumption and many other factors (Bug et al., 2018). At present, there were various path planning optimization algorithms, such as particle swarm optimization (Hong et al., 2021), ant colony algorithm (Buzzega et al., 2022), fish swarm algorithm (Song et al., 2021), and artificial potential field method (Chang et al., 2018). Among them, ant colony optimization (ACO) was widely used due to its strong robustness and fast search speed, while it revealed the disadvantages of low search efficiency, making it easy to fall into local optimum (Choi et al., 2017). To address the problem of path smoothing, Freitas et al. (2018) considered the influence of the number of UAV turns in the heuristic function, enhancing the global search ability of the algorithm and improving the smoothness of the path. However, the improved algorithm still has the disadvantages of slow initial convergence speed, making it easy to fall into local optimum (Freitas et al., 2018). Yang et al. (2015) proposed an ant colony algorithm with improved pheromone update rules based on the shortest path target. The performance of the algorithm is improved regarding running time and convergence speed. Nevertheless, only the shortest path is considered, and other factors including the safety and smoothness of the UAV track are not taken into consideration. Freitas et al. (2020) proposed a guiding factor considering the distance from the node to the target node and the distance from the node to the starting node. Through improving the guiding factor of the algorithm, the guiding effect of the heuristic function is enhanced. However, the algorithm is easy to fall into local optimum due to the influence of the initial distribution of pheromones (Freitas et al., 2020). Petrovska et al. (2013) proposed a method using geometric optimization. The adaptive parameter adjustment method is employed to improve the search ability of the ant colony algorithm and the interaction ability between individuals, effectively improving the traditional ant colony algorithm. Petrovska et al. (2013) proposed a geometric optimization method and adopted adaptive parameter adjustment method for improving the search ability and interaction ability of ant colony algorithm, which effectively improved the traditional ant colony algorithm's slow convergence speed, making it easy to fall into local optimality. However, the problem of slow search speed still existed in the initial stage of the algorithm. Williams et al. (2012) plan drone delivery within a fixed service radius from the warehouse. Each package has a customized delivery time and deadline. To minimize the number of drones, the scheduling decision support model and genetic algorithm are used to solve. Dell'Amico et al. (2021) considered the economic cost, delay penalty, safety and reliability, carried out the task allocation planning of multi-UAV cooperative distribution, and improved the quantum particle swarm optimization algorithm to solve the problem. The research on improving ant colony algorithm mainly includes: Wang et al. (2023) initialized the initial number of agricultural handling robots by scanning method, and the geometric center of the sub-path node was set as a virtual node. Then, the improved ant colony algorithm with embedded genetic operator was applied to solve the optimal path of connecting virtual nodes and the optimal result of sub-paths. Chu (2023) improved the problem that the classical artificial potential field method failed to reach the end point and local lock-in in agriculture through introducing the method of intermediate point and target relative distance.

Subsequently, the improved artificial potential field method was combined with the traditional ant colony algorithm, and the ant colony algorithm exerted a major role in the later period with the increasing pheromone concentration. *Fan (2023)* proposed an improved PSO algorithm based on A* algorithm, introduced a nonlinear convergence factor balance algorithm with global search and local development capabilities into the traditional PSO algorithm, and adopted population initialization for enhancing population diversity, and thus the improved PSO algorithm exhibited stronger model solving capabilities.

Considering the establishment of the energy consumption formula, restricting UAV cruising range and so on, *Ke et al. (2014)* established a drone delivery model from the perspective of time and budget, considered energy consumption and load constraints, and applied simulated annealing algorithm to solve the model. *Zhou et al. (2019)* applied the nonlinear energy consumption function to the modelling of multi-trip UAV routing problem with time windows, and designed a branch cutting algorithm to solve the problem. *Jung et al. (2021)* obtained the formula of UAV battery energy consumption by testing UAVs, and applied the formula to path constraints to address the multi-package delivery problem, aiming to minimize the number of UAVs. *Agatz et al. (2018)* performed targeted research on the MD4-3000 series of drones and applied them to solve distribution problems many times. *Zheng et al. (2020)* established a maximum coverage model of a limited charging point, uniquely allocating the demand point to the nearest charging facility, and constraining the flight path between the charging points, and thus the generated distribution network is topological. *Boccia et al. (2021)* established a multi-level location model for warehouses and charging facilities in order to minimize the total cost, and improved the genetic algorithm with greedy search to solve the model. *Liu et al. (2016)* applied the maximum coverage model of limited facility points to the scenario of UAV rescue material delivery, and established a three-stage heuristic (3SH) model to address the facility center location problem, material allocation problem, and the number of required UAVs in stages. *Bouman et al. (2018)* developed a UAV distribution optimization model for medical items, including charging station location, medical item supplier assignment for suburban clinics, and scheduling trips and distribution routes for drones to minimize the total service time. *Boysen et al. (2021)* aimed at maximizing the coverage demand point and performed the location of UAV charging facilities in two steps.

Concerning the shortcomings of the above research, this study further carried out research and established an agricultural logistics distribution route planning model considering the mileage limit of drones. To evaluate and make full use of battery energy, the energy consumption formula is established. The path planning is conducted with the lowest energy consumption as the goal. Considering that the weight of general express parcels is within 5 kg, and the load of drones commonly used in terminal distribution is 20 kg, this study investigates multi-package distribution considering the mileage limit of drones. This model improves the actual loading rate of drones, which contributes to saving space and resources and improving distribution efficiency.

MATERIALS AND METHODS

Problem Description

This study describes the scene of remote agricultural logistics distribution services in places including mountainous areas, islands, and grasslands and other places. In actual operation, agricultural logistics service providers provide drone distribution services for remote rural areas, with towns as distribution centers and villages as receiving units. Starting from the distribution center, the drone delivers the goods to the designated collection point in each village (hereinafter referred to as the demand point). In this study, the problem of agricultural logistics distribution path planning considering the limitation of UAV cruising range is investigated. Under the requirement that all demand points are covered, the total energy consumption of distribution is the lowest, and multiple UAV distribution tasks are obtained after solving the problem.

Problem hypothesis and parameter description

Problem hypothesis

- (1) Only a single distribution center is considered to provide agricultural logistics distribution services for multiple demand points within the distribution range.
- (2) All UAV models remain the same, and the battery weight does not change during the flight of the UAV.
- (3) This study only considers the energy consumption of UAV under ideal conditions, without considering the influence of weather and other factors.
- (4) The power consumption of UAV rising and falling is not calculated, respectively. Considering the battery safety factor $\mu=1.25$, the safe power of UAV is set to 80% of the maximum power that is: $Q = Q_{\max} / \mu$.

(5) Assuming that each demand point can only be delivered by one UAV, while one UAV can serve multiple demand points.

(6) The multi-package delivery model of UAV is defined by directed graph $G=(V, A)$, and the set of points is $V = D \cup C \cup R'$ and $(i, j) \in V$. Distribution center $D=\{v_0\}$, and the set of demand points $C=\{v_1, v_2, \dots, v_n\}$.

Parameter declaration

The relevant parameters of the agricultural logistics distribution path planning model considering the mileage limit of the UAV are shown in Table 1.

Table 1

| Model parameter description | | |
|-----------------------------|--|-----------------|
| Parameter | Parameter definition | Parameter units |
| D | The set of distribution centers, denoted by the following index o in the decision variable | — |
| C | The set of demand points | — |
| R | Set of candidate charging points | — |
| y_j | If the candidate charging point j is determined to be the charging point, then $y_j = 1$, otherwise $y_j = 0$ | — |
| x_{ij} | If the demand point i is uniquely assigned to the facility point $j, j \in D \cup R$, then; $x_{ij} = 1$, otherwise $x_{ij} = 0$ | — |
| d_{ij} | The distance between points i and j | km |
| c_{i0} | The total distance of the path from the demand point i to the distribution center | km |
| H | Unmanned aerial vehicle full range | km |
| λ_1 | The distance from the candidate facility point to the distribution center does not exceed λ_1 times of the full load range of the drone, $\lambda_1 = 0.8$ | — |
| λ_2 | The coverage of the facility point to the demand point is not more than λ_2 times the full range of the UAV, $\lambda_2 = 0.4$ | — |
| f | The energy consumed per unit distance of horizontal flight | W.h |
| m_t | Net weight of UAV without battery and cargo | kg |
| m_b | Battery weight of UAV | kg |
| m_l | The weight of cargo carried by UAV | kg |
| g | acceleration of gravity | N/kg |
| d | unit distance | m |
| η | energy transfer efficiency | — |
| \mathcal{G}_v | The ratio of lift to drag is a function of flight speed. | — |
| $f(m_l)$ | The energy consumed per unit distance in horizontal flight when the cargo weight is m_l | W.h |
| α | Formula parameters | — |
| β | Formula parameters | — |
| R' | The set of charging points and virtual charging points - | — |
| V | The set of all vertices, $V = D \cup C \cup R', (i, j) \in V$ | — |
| K | The set of UAVs, $k \in K$ | — |
| W_i | The demand for node $i, i \in C$ | kg |
| m_{ik} | The weight of the cargo when the k th drone leaves point $i, i \in V, k \in K$ | kg |
| q_{ik} | The remaining power of the k th drone when it leaves point $i, i \in V, k \in K$ | W.h |
| t_{ij} | The flight time of UAV from node i to node j | h |
| T_k | Time spent on the delivery of the k th drone | h |
| x_{ijk} | When the k th UAV passes through node j from node $i, x_{ijk} = 1$; otherwise $x_{ijk} = 0$ | — |
| N | Number of drones at distribution centers, $N = K $ | — |
| W | Maximum load capacity of UAV | kg |
| Q_{max} | Maximum power of UAV | W.h |
| Q | Maximum safe power of UAV, $Q = Q_{max} / \mu$ | W.h |
| μ | Battery safety factor, $\mu = 1.25$ | — |
| τ | The residence time of the UAV at the demand point or the charging point | h |
| v | UAV constant flight speed | m/s |

UAV agricultural logistics distribution model

UAV energy consumption formula

In this study, the energy consumption of UAV in horizontal flight state is defined as Equation (1):

$$f = \frac{(m_t + m_b + m_l)g}{3600\theta_v\eta}d \tag{1}$$

When the net weight and battery weight of the UAV are regarded as constant values, the energy consumption rate of the UAV per unit distance is only associated with the load capacity. The energy consumption Equation (1) is improved to obtain a new energy consumption Equation (2).

$$f = (\alpha m_1 + \beta)d = f(m_1)d \tag{2}$$

α is shown as Equation (3).

$$\alpha = g \frac{1}{3600J_v\eta}, \quad \beta = (m_t + m_b)g \frac{1}{3600J_v\eta} \tag{3}$$

UAV agricultural logistics distribution model considering endurance mileage

The combination of agricultural logistics distribution tasks is solved with the least total energy consumption and the delivery time of the corresponding tasks.

$$\text{Min} \sum_{k \in K} \sum_{i \in V} \sum_{j \in V} f(m_{ik})d_{ij}x_{ijk} \tag{4}$$

The meaning of Equation (4) is to minimize the total energy consumption of distribution. Among them, $f(m_{ik})$ indicates the energy consumption per unit distance of flight when the load capacity of the UAV is m_{ik} .

Constraint conditions are shown as follows:

$$\sum_{k \in K} \sum_{j \in V} x_{ijk} = 1, \forall i \in C \tag{5}$$

$$\sum_{j \in V} x_{ijk} \leq 1, \forall i \in R', \forall k \in K \tag{6}$$

$$\sum_{j \in V} x_{jik} - \sum_{j \in V} x_{ijk} = 0, \forall i \in V, \forall k \in K \tag{7}$$

$$\sum_{(i,j) \in E(U)} x_{ijk} \leq |U| - 1, \forall U \subseteq R' \cup C, U \neq \emptyset, \forall k \in K \tag{8}$$

Equation (5) suggests any requirement point, and there is only one UAV to visit once. Equation (6) indicates that for any charging point, the same UAV is accessed at most once. Equation (7) indicates that for any node, the number of visits and departures of the same UAV is equal. Equation (8) represents the sub-loop constraint, that is, no loop can appear in any non-empty subset composed of charging points and demand points.

The number of UAV departures is constrained to be:

$$\sum_{j \in R' \cup C} x_{ojk} \leq 1, \forall k \in K \tag{9}$$

Equation (9) limits the number of departures of each UAV to at most 1. The bearing weight constraint is presented as follows:

$$m_{ok} = \sum_{i \in V} \sum_{j \in C} w_j x_{ijk}, \forall k \in K \tag{10}$$

$$m_{ok} \leq W, \forall k \in K \tag{11}$$

$$m_{jk} = (1 - x_{ijk})m_{jk} + x_{ijk}(m_{ik} - w_j), \forall i \in V, \forall j \in C \cup R' \tag{12}$$

Equation (10) calculates the weight of each UAV 's cargo when it departs from the distribution center. Equation (11) constrains the weight of each drone's cargo when it departs from the distribution center. Equation (12) indicates that for any node $j (j \in C \cup R')$, the UAV flies from node i to node j , and the weight of the cargo when starting from node j is equal to the weight of the cargo when starting from node i minus the demand for node j .

The aim of this study is that the flight distance of the agricultural distribution UAV is affected by the power of the UAV, and the flight distance constraint is:

$$q_{jk} = (1 - x_{ijk})q_{jk} + x_{ijk}(q_{ik} - f(m_{ik})d_{ij}), \forall i \in V, \forall j \in C, \forall k \in K \tag{13}$$

$$q_{ik} = Q, \forall j \in D \cup R', \forall k \in K \tag{14}$$

$$x_{ijk}(q_{ik} - f(m_{ik})d_{ij} - f(m_{ik} - w_j)d_{jr}) \geq 0, \forall i \in V, \forall j \in C \cup R', \forall k \in K \tag{15}$$

Equation (13) indicates that for any demand point j , if the UAV flies from node i to node j , the electric quantity when starting from node j is equal to the electric quantity when starting from node i minus the flight energy consumption between nodes i and j . Equation (14) suggests that for any facility point, the electric quantity when the UAV leaves is equal to the maximum safe electric quantity. Equation (15) indicates that if the k^{th} UAV flies from node i to node j , the power of the UAV leaving node i should be enough to support the UAV to fly from node i to node j , and then from node j to the nearest facility point r from j . When j is a demand point, there must be a corresponding nearest facility point r . When the node j is a charging point, the nearest facility point r is the node j itself.

Equation (16) presents the calculation of the total flight time of each UAV:

$$T_k = \sum_{i \in V} \sum_{j \in V} (t_{ij} + \tau) x_{ijk}, \forall i \in V, \forall j \in V, \forall k \in K \tag{16}$$

Algorithm Design

Ant colony algorithm is a heuristic algorithm, which is essentially an iterative algorithm based on the positive feedback. There are two key node steps in the ant colony algorithm. One is the selection of the next node, and the other is the pheromone update rule. The common strategies for node selection include random selection, and roulette. In addition, the pheromone update strategy also has different methods. The original ant colony algorithm basically uses the global update strategy, that is, when all ants complete the search, the pheromone is updated. Subsequently, the elite strategy is introduced into the elite ant colony algorithm to improve the convergence. Under the elite strategy, there is no need to wait for all ants to complete the search, and only the pheromone is updated on the path of the optimal ants in each loop. Based on the basic ant colony algorithm, the maximum and minimum ant colony algorithm limits the concentration range of pheromone to a certain range, therefore increasing the possibility of searching for the optimal solution.

The core mechanism of ant colony algorithm

The basic ant colony algorithm is a kind of swarm intelligence bionic algorithm inspired by the path finding during the process of ant foraging. The basic idea of the algorithm is that the path of the ant indicates the feasible solution of the problem to be optimized, and all the paths of the whole ant population constitute the solution space of the problem to be optimized. The content of pheromone is determined by the length of the path. It indicates the longer the path, the lower the content of pheromone. The path selection of ants depends on the content of pheromone. Besides, it suggests the higher the content, the greater the probability that the path is selected. With the passage of time, most of the ants will eventually concentrate on a shorter path. Then, the path is the optimal solution of the optimization problem. The direction of each ant's progress is mainly related to two factors. One is pheromone, and the other is heuristic information. It shows the higher the content of pheromone on the path, the greater the possibility of ants choosing the path; the heuristic information is to guide each ant to determine the direction of the next step. Therefore, the key of ant colony algorithm lies in the construction of pheromone update model and heuristic function. The ant determines the direction of the next step according to the transition probability, which is expressed as following:

$$p_{i,j}^m(t) = \begin{cases} \frac{[\tau_{i,j}(t)]^\alpha [\eta_{i,j}(t)]^\beta}{\sum_{s \in allowed_i} [\tau_{i,s}(t)]^\alpha [\eta_{i,s}(t)]^\beta}, & j \in allowed_i \\ 0, & j \notin allowed_i \end{cases} \tag{17}$$

$$\tau_{i,j}(t+1) = (1 - \rho)\tau_{i,j}(t) + \sum_{m=1}^M \Delta\tau_{i,j}^m(t) \tag{18}$$

where $\eta_{i,j}(t)$ is the heuristic function, usually taking $\eta_{i,j}(t) = 1/d_{ij}$ (d refers to the Euclidean distance of the center of two nodes i, j). $\tau_{i,j}(t)$ is a pheromone. $allowed_i$ is the set of feasible adjacent nodes at node i ; m is the ant label; i denotes the current position node label; j is the node label of the next position to be transferred; t suggests the current number of iterations; α and β suggest the relative importance of pheromone and heuristic factors, respectively.

Pheromone is the key to the construction of ant colony algorithm. It indicates the shorter the path of ants, the higher the pheromone concentration, and the more it can play a guiding role for ants. With the passage of time, the pheromone will also evaporate, and thus it is essential to establish a pheromone update model. Common pheromone update models include ant week model, ant quantity model and ant density model.

$$\tau_{i,j}(t+1) = (1-\rho)\tau_{i,j}(t) + \sum_{m=1}^M \Delta\tau_{i,j}^m(t) \tag{19}$$

$$\Delta\tau_{i,j}^m(t) = \begin{cases} Q / L_m, & \text{If } m \text{ ants go through the path } (i, j) \\ 0, & \text{others} \end{cases} \tag{20}$$

where ρ is the pheromone volatilization factor, Q refers to a pheromone constant, L_m is the total length of the path passed by the m ant in this cycle, and m represents the total number of ants.

Generally, the ant colony algorithm program design is composed of two nested loops. The external cycle is a cycle of iterations, which is used to simulate the multiple explorations of the ant colony system. The internal loop is the loop of the single ant search process in the ant colony system, as displayed in Fig. 1.

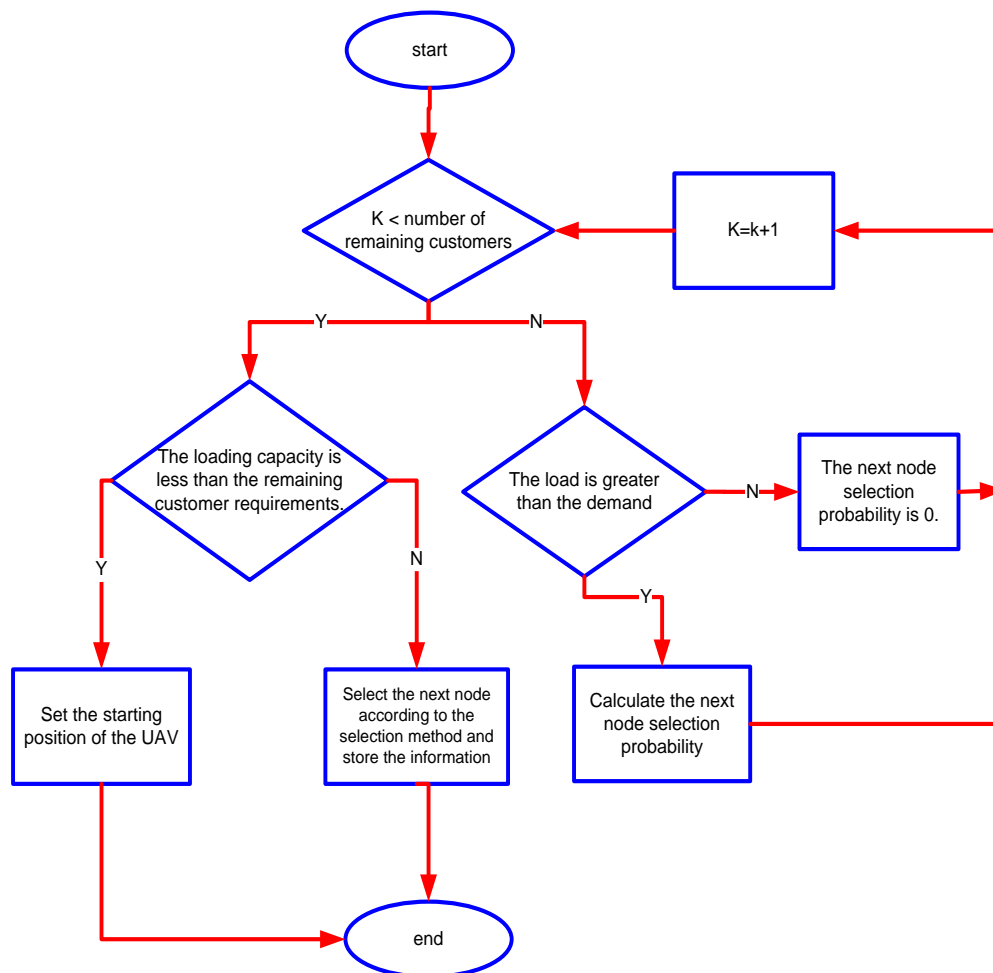


Fig. 1 – The basic process of ant colony algorithm

Considering the limitation of UAV load, when the cargo capacity of a single UAV fails to satisfy the needs of the next target customer, the UAV needs to return to the distribution center halfway. Its internal contains a cycle, that is, whether the UAV completes the traversal of all target customer nodes. The rule of UAV traversing the target customer is displayed in Fig. 2.

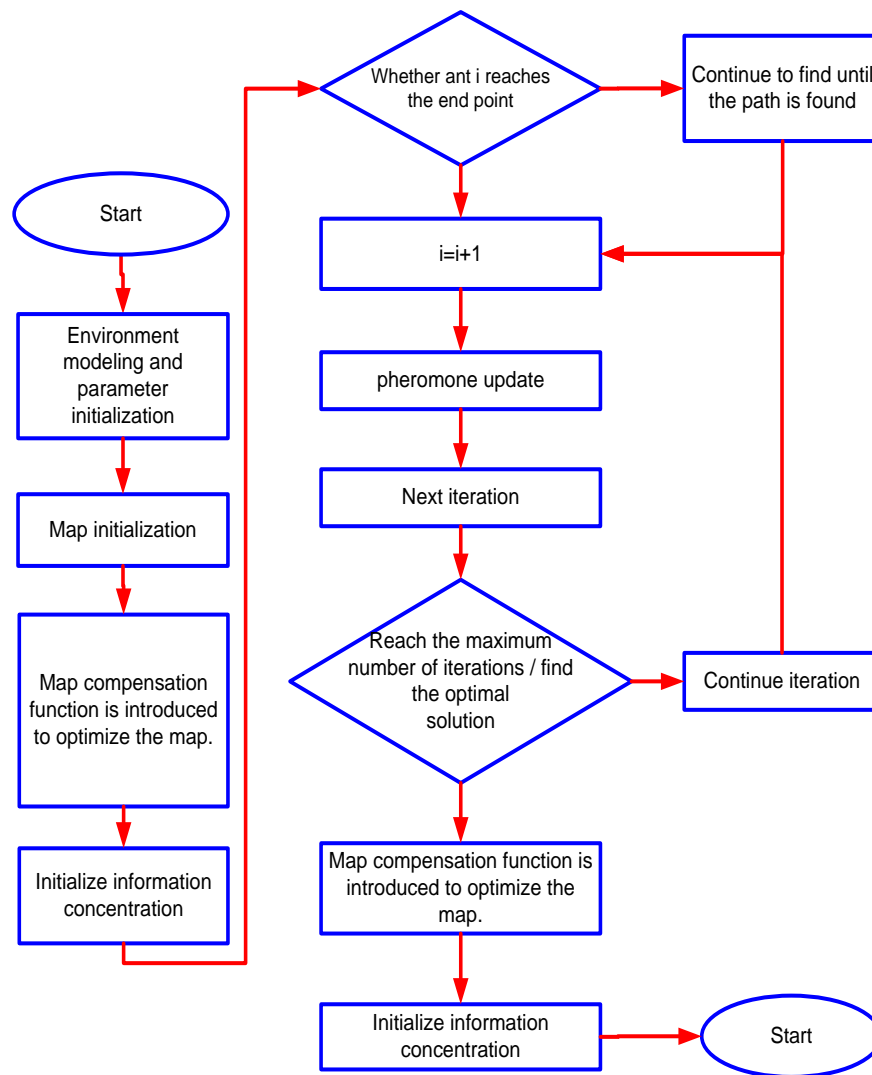


Fig. 2 – Traversal rules of agricultural logistics distribution UAV

Parameter design of improved ant colony algorithm

The optimization performance of ant colony algorithm is affected by key parameters including heuristic factors and pheromone volatilization rate. The parameters are closely related and exert a decisive role in the global search ability and solution efficiency of the ant colony algorithm. The ant colony algorithm uses fixed parameters, which has certain limitations. The information heuristic factor is set to α , and the empirical value range of the expected heuristic factor β is [0,5]. The value interval of pheromone volatilization rate ρ is [0, 1]. The parameters are coupled with each other and are associated with the research problem. When the scale of the problem to be dealt with is relatively large and the pheromone volatilization rate ρ is small, the random performance and global search ability of the algorithm will increase, and the overall convergence of the algorithm will be weakened. If ρ increases, the random performance and global search ability of the algorithm will be reduced, and the convergence speed of the algorithm will be slowed down. If the information heuristic factor α is too large, the randomness of the search is weakened, making the ants' search prematurely limited to local optimum. With the increase of the expected heuristic factor β , the ants are more likely to choose the local shortest path at a local point, which leads to the weakening of the randomness of the ants' search for the optimal path, making it easy to fall into local optimum. By contrast, it indicates the smaller the heuristic factor, the stronger the search ability, but the convergence decreases.

The idea of variable parameter has been widely used in control engineering including piecewise PID control, and parameter adaptive control. In summary, a simple idea is proposed, that is to ensure its search ability at the beginning of the algorithm iteration, maintain equilibrium in the middle of the algorithm iteration, and ensure its convergence performance at the end of the iteration. To realize the above ideas, the hyperbolic tangent function is introduced, and its mathematical expression is:

$$\tanh(x) = (e^x - e^{-x}) / (e^x + e^{-x}) \tag{21}$$

In the initial stage of the loop search, to search the global optimum in a wider range, ρ is controlled at a lower level. The pheromone on the path is low, and thus the information heuristic factor α is at a low level. In order to prevent directly falling into local optimum, the expected heuristic factor β is also at a low level. At the end of the loop search, both ρ and β are controlled at a higher level, maintaining a faster convergence speed.

The specific mathematical expression is shown in Equations (22)-(24):

$$\alpha = \alpha_{\max} - (\alpha_{\max} - \alpha_{\min}) \tanh[c_{\alpha}(Nc_{\max} - Nc)] \tag{22}$$

$$\beta = \beta_{\min} + (\beta_{\max} - \beta_{\min}) \tanh[c_{\beta}(Nc_{\max} - Nc)] \tag{23}$$

$$\rho = \rho_{\min} + (\rho_{\max} - \rho_{\min}) \tanh[c_{\rho}(Nc_{\max} - Nc)] \tag{24}$$

where c_{α} , c_{β} and c_{ρ} are adjustable parameters to control the range of α , β and ρ , Nc_{\max} is the set maximum number of iterations, Nc refers to the current number of iterations, α_{\max} and α_{\min} are the upper and lower limits of α , β_{\max} and β_{\min} represent the upper and lower limits of β ; ρ_{\max} and ρ_{\min} are the upper and lower limits of ρ .

To lower the computational pressure, the information heuristic factor α and the expected heuristic factor β are rounded. The rounding rules can be rounded or intercepted based on the rounding rules. After the rounding rules are introduced, the mathematical expressions of Eqs. 22 and 23 are shown in Eqs. 25 and 26, respectively:

$$\alpha = \text{Round}(\alpha_{\max} - (\alpha_{\max} - \alpha_{\min}) \tanh[c_{\alpha}(Nc_{\max} - Nc)]) \tag{25}$$

$$\beta = \text{Round}\{\beta_{\min} + (\beta_{\max} - \beta_{\min}) \tanh[c_{\beta}(Nc_{\max} - Nc)]\} \tag{26}$$

RESULTS

Experimental environment and parameter settings

In this study, Intel i7 processor and Matlab2014 b are used for experiments. The mutation probability of genetic algorithm is 0.1, the crossover probability is 0.9, and the genetic generation gap is 0.7. In the ant colony algorithm, the important factor of pheromone is 1, the constant coefficient Q is 1, the volatilization factor of information is 0.1, and the important factor of heuristic function is 5. The discount coefficient of the reinforcement learning algorithm is 0.9, and the learning rate is 0.2.

The three cost parameters are presented in Table 2.

Table 2

| Cost parameter table | | |
|--|----------------------------------|---------------|
| Parameter type check | Parameter name | Taking values |
| Underlying cost Transportation cost | The basic cost of sending UAVs | 500 yuan |
| | Unit distance loss of UAV | 6 yuan |
| Time cost | UAV running speed | 200 m/min |
| | UAV loading and unloading time | 5 min |
| | Maximum carrying capacity of UAV | 20 kg |

With Zhukou Town Center and other 20 villages in Taining County, Sanming City, Fujian Province as the research object. This study explores the problem of agricultural logistics distribution path planning considering the limitation of UAV endurance mileage. The location, demand, time window requirements, and basic demand information for the required service time of Zhukou Town Center and other 20 villages are shown in Table 3. Among them, '0' represents the distribution center, and '1 ~ 20' represents the village needing to be served.

Table 3

| Customer basic needs information | | | | | | | | |
|----------------------------------|-------------------|-------------------|------------------|--------------------------|------------|--------------------------|----------------------------|--------------------|
| Coding | Coordinate X (km) | Coordinate Y (km) | Coordinate Z (m) | Magnitude of demand (kg) | L*w*h (mm) | Expected time window (h) | Acceptable time window (h) | Service time (min) |
| A | 0.000 | 0.000 | 0 | 0 | 0 | 0 | 0 | 0 |
| B1 | 2.477 | 3.462 | 423 | 3 | 100*80*30 | 8:00-9:00 | 8:00-16:00 | 10 |
| B2 | 1.119 | 3.301 | 291 | 2 | 100*60*30 | 9:00-10:00 | 8:00-16:00 | 10 |
| B3 | 2.819 | 1.753 | 155 | 2 | 100*60*30 | 10:00-11:00 | 8:00-16:00 | 10 |
| B4 | 4.711 | 3.044 | 497 | 2 | 100*60*30 | 10:00-11:00 | 8:00-16:00 | 10 |
| B5 | 4.279 | 0.227 | 311 | 4 | 120*80*30 | 10:00-11:00 | 8:00-16:00 | 10 |
| B6 | 0.181 | 3.264 | 325 | 1 | 80*40*30 | 8:00-9:00 | 8:00-16:00 | 10 |
| B7 | 4.679 | 4.589 | 304 | 2 | 100*60*30 | 10:00-11:00 | 8:00-16:00 | 10 |
| B8 | 0.662 | 0.380 | 54 | 4 | 120*80*30 | 9:00-10:00 | 8:00-16:00 | 10 |
| B9 | 3.520 | 4.537 | 104 | 3 | 100*80*30 | 11:00-12:00 | 8:00-16:00 | 10 |
| B10 | 1.434 | 2.430 | 308 | 4 | 120*80*30 | 10:00-11:00 | 8:00-16:00 | 10 |
| B11 | 4.027 | 4.337 | 321 | 4 | 120*80*30 | 9:00-10:00 | 8:00-16:00 | 10 |
| B12 | 4.960 | 4.313 | 489 | 2 | 100*60*30 | 11:00-12:00 | 8:00-16:00 | 10 |
| B13 | 2.193 | 2.969 | 438 | 3 | 100*80*30 | 8:00-9:00 | 8:00-16:00 | 10 |
| B14 | 0.063 | 4.726 | 485 | 4 | 120*80*30 | 11:00-12:00 | 8:00-16:00 | 10 |
| B15 | 0.524 | 2.276 | 241 | 5 | 120*100*30 | 11:00-12:00 | 8:00-16:00 | 10 |
| B16 | 3.336 | 2.250 | 397 | 5 | 120*100*30 | 9:00-10:00 | 8:00-16:00 | 10 |
| B17 | 0.649 | 2.002 | 231 | 1 | 80*40*30 | 10:00-11:00 | 8:00-16:00 | 10 |
| B18 | 2.043 | 4.915 | 365 | 4 | 120*80*30 | 8:00-9:00 | 8:00-16:00 | 10 |
| B19 | 1.689 | 4.540 | 70 | 5 | 120*100*30 | 11:00-12:00 | 8:00-16:00 | 10 |
| B20 | 2.073 | 4.743 | 431 | 3 | 100*80*30 | 9:00-10:00 | 8:00-16:00 | 10 |

The technical parameters of the agricultural logistics distribution UAV were presented as follows: the weight of the empty aircraft was 42.5 kg (excluding batteries), 65 kg (including double batteries), the large take-off weight was 85 kg (standard cargo box, near sea level), the shape size was 2000 mm, the wheelbase was 2200 mm, the shape size was 1590 mm, the width was 1900 mm, and the height was 947 mm (arm expansion, blade folding).

Experiment and comparative analysis

In this study, an improved ant colony algorithm was employed to solve the agricultural logistics distribution path planning model considering the limitation of UAV cruising range. The maximum number of iterations was set to 200, and the cost of agricultural handling UAV was 300 yuan. A satisfactory solution could be obtained by solving the model, that was, three mobile drones were needed to complete the storage and

unloading tasks of agricultural products. The total travel distance of the drone was 55.086 km, and the total cost was 4055.09 yuan. The algorithm took 349.47 seconds. The improved ant colony algorithm path diagram was shown in Fig.3. The convergence curve of the improved ant colony algorithm embedded in the genetic algorithm was shown in Fig.4, and the calculation results were presented in Table 4.

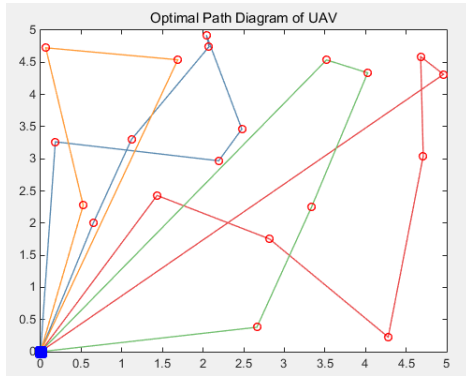


Fig. 3 – The path diagram of genetic algorithm

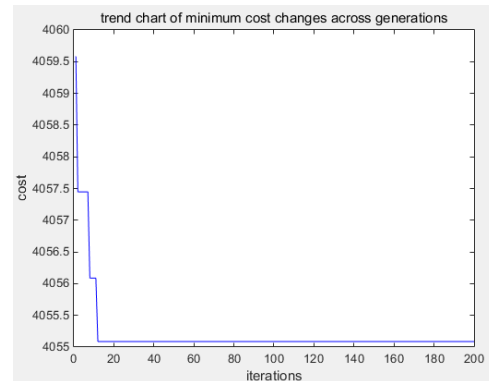


Fig.4 – Convergence curve of genetic algorithm

Table 4

| Optimal service path. | | | |
|-----------------------|--------------------------|------------|----------------------|
| Service path | Actual carrying capacity | Load limit | Capacity utilization |
| 0→6→13→1→18→20→2→17→0 | 17 | 20 | 85% |
| 0→10→3→5→4→7→12→0 | 15 | 20 | 75% |
| 0→8→16→11→9→0 | 15 | 20 | 75% |
| 0→19→14→15→0 | 14 | 20 | 70% |

To further demonstrate the effectiveness of the improved ant colony algorithm, this study also designed a traditional ant colony algorithm to solve the model. In the case of constant initial cost and parameters, solving the agricultural UAV path optimization model required 5 mobile UAVs, and the total travel of the UAV was 59.85 km. The total cost was 5059.85 yuan, and the algorithm took 365.31 seconds. The path diagram of the traditional ant colony algorithm was shown in Fig.5. The convergence curve of the traditional ant colony algorithm was displayed in Fig. 6, and the calculation results were presented in Table 5.

Table 5

| Optimal service path. | | | |
|-----------------------|--------------------------|------------|----------------------|
| Service path | Actual carrying capacity | Load limit | Capacity utilization |
| 0→6→18→1→13→10→0 | 15 | 20 | 75% |
| 0→2→20→11→16→17→0 | 15 | 20 | 75% |
| 0→3→5→4→7→12→9→0 | 15 | 20 | 75% |
| 0→14→19→15→0 | 14 | 20 | 70% |
| 0→8→0 | 4 | 20 | 20% |

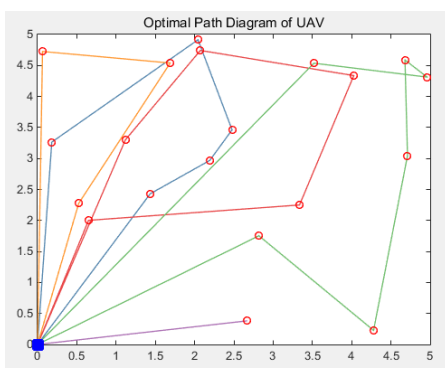


Fig. 5 – Path diagram of traditional algorithm

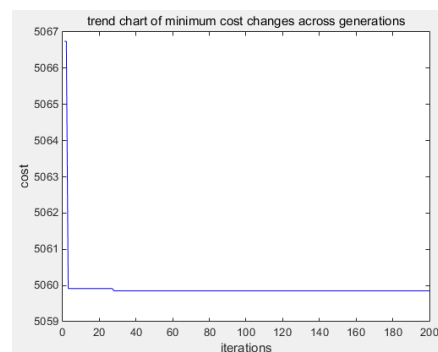


Fig. 6 – Convergence curve of traditional algorithm

Compared with the traditional ant colony algorithm, the improved ant colony algorithm embedded with genetic operator exhibited strong exploration and convergence, and the value of the objective function was better. The comparison of the two algorithms was shown in Table 6.

Table 6

| Comparison of two algorithms. | | | | | |
|----------------------------------|------------------|--------------|---------------------|-------------------|------------------------------|
| Algorithm | Number of drones | Average full | Distance of run(km) | Total cost (yuan) | The algorithm takes time (s) |
| improved ant colony algorithm | 4 | 76.25% | 55.09 | 4055.09 | 349.47 |
| traditional ant colony algorithm | 5 | 63% | 59.85 | 5059.85 | 365.31 |

It can be observed from Table 6 that the improved ant colony algorithm was superior to the traditional ant colony algorithm regarding the number of UAVs, average full load rate, driving distance, total cost and algorithm time. The traditional ant colony algorithm required 5 UAVs to complete the agricultural logistics distribution task considering the UAV 's cruising range limit, while the improved ant colony algorithm only needed 4 machines to complete the same task, with the efficiency being improved by 20%. Regarding full load rate, the average full load rate of the traditional ant colony algorithm agricultural UAV was 63 %, while the average full load rate of the improved ant colony algorithm to complete the same task was 76.25%, and the average full load rate was increased by 13.25%. Concerning the driving distance of the UAV, the total distance of the traditional ant colony algorithm agricultural UAV was 59.85 km, while the total distance of the improved ant colony algorithm to complete the same task was 55.09 km. In terms of the driving distance of the UAV, the total cost of the traditional ant colony algorithm agricultural UAV was 5059.85 yuan, while the total cost of the improved ant colony algorithm to complete the same task was 4055.09, regarding algorithm time, the convergence time of the traditional ant colony algorithm was 365.31 seconds, while the convergence time of the improved ant colony algorithm was 349.47 seconds.

CONCLUSIONS

To conclude, this study mainly investigated the path planning problem of agricultural logistics distribution for express parcel delivery by UAV in remote areas, and established the path planning model of agricultural logistics distribution considering the mileage limit of UAV. By comparing the optimal path of agricultural distribution without considering the mileage limit of drones and considering the mileage limit of drones, this study established a mathematical optimization model to minimize the total distribution cost of agricultural logistics under the constraints of customer demand for agricultural logistics, the maximum carrying capacity of agricultural drones, customer time window requirements, and drone endurance mileage restrictions. Aiming at the problems of slow convergence speed and the easiness to fall into local optimum of ant colony algorithm, the idea of variable parameters was introduced into ant colony algorithm. The parameters were automatically adjusted in the iterative process of the algorithm through hyperbolic tangent function to achieve the purpose of strong global search ability in the early stage of the algorithm and significant improvement of convergence speed in the later stage of the algorithm. Through simulation and comparative experiments, the effectiveness of the model and algorithm was verified, which could provide scientific method support for the cold chain logistics industry to achieve a win-win situation of economy and environmental protection. Additionally, the introduction of hyperbolic sine function was not only suitable for ant colony algorithm, but also could be introduced into optimization algorithms which were greatly affected by parameters. After introducing the hyperbolic sine function, the upper and lower limits of the algorithm parameters needed to be firstly determined. Therefore, how to quickly determine the upper and lower limits of the parameters was a work worthy of study. Meanwhile, the mechanism of the influence of ant colony algorithm parameters on its performance was still unclear and lacked systematic mathematical theoretical support. In the future, it is necessary to conduct more in-depth studies on the influencing mechanism of parameters on research results.

REFERENCES

- [1] Agatz, N., Bouman, P., Schmidt, M., (2018). Optimization Approaches for the Traveling Salesman Problem with Drone, *Transportation Science*, Vol. 52, pp. 965-981. United States.
- [2] Boccia, M., Masone, A., Sforza, A., Sterle, C., (2021). An Exact Approach for a Variant of the FS-TSP, *Transportation Research Procedia*, Vol. 52, pp. 51-58. Netherlands.

- [3] Bouman, P., Agatz, N., Schmidt, M., (2018). Dynamic Programming Approaches for the Traveling Salesman Problem with Drone, *Networks*, Vol. 72, pp. 528-542. United States.
- [4] Bug, P., Gordon, N., Staudenmaier, A.S., (2018). Fashion Business Case Study on the German Click & Collect Situation. *Contemporary Case Studies on Fashion Production, Marketing and Operations*, pp. 139-163, Germany.
- [5] Buzzega, Novellani, G.S., (2022). Last Mile Deliveries with Lockers: Formulations and Algorithms, *Soft Computing*, Vol. 27 pp. 12843–12861. United States.
- [6] Chang, Y.S., Lee, H.J., (2018). Optimal Delivery Routing with Wider Drone-Delivery Areas Along a Shorter Truck-Route, *Expert Systems with Applications*, Vol.104, pp. 307-317, United Kingdom.
- [7] Cheng, C., Adulyasak, Y., Rousseau, L.M., (2020). Drone Routing with Energy Function: Formulation and Exact Algorithm. *Transportation Research Part B: Methodological*, Vol.47, pp. 364-387, Netherlands.
- [8] Choi, D., Kim, D., Lee, K., (2021). Collision Avoidance of Unmanned Aerial Vehicles in an Urban Environment, *NAECON 2021-IEEE National Aerospace and Electronics Conference*, pp. 25-32. USA.
- [9] Dell'Amico, M., Montemanni, R., Novellani, S., (2021). Modeling the Flying Sidekick Traveling Salesman Problem with Multiple Drones, *Networks*, Vol.78, pp. 303-327, United States.
- [10] Dorling, K., Heinrichs, J., Messier, G.G., Magierowski, S., (2017). Vehicle Routing Problems for Drone Delivery. *IEEE Transactions on Systems, Man, and Cybernetics: Systems*, Vol.47, pp. 70-85, USA.
- [11] Figliozzi, M., (2017). Lifecycle Modeling and Assessment of Unmanned Aerial Vehicles (Drones) CO2 Emissions. *Transportation Research Part D: Transport and Environment*, Vol. 57, pp. 251-261, UK.
- [12] Freitas, J.C.D., Penna, P.H.V., (2018). A Randomized Variable Neighborhood Descent Heuristic to Solve the Flying Sidekick Traveling Salesman Problem, *Electronic Notes in Discrete Mathematics*, Vol.66, pp. 95-102, Netherlands.
- [13] Freitas, J.C.D., Penna, P.H.V., (2020). A Variable Neighborhood Search for Flying Sidekick Traveling Salesman Problem, *International Transactions in Operational Research*, Vol. 27, pp. 267–290. UK.
- [14] Hexia Chu. (2023). Analysis on path optimization of agricultural handling robots based on ant colony-improved artificial potential field method [J]. *INMATEH - Agricultural Engineering*, Vol. 71, No. 3 / 2023. 548-557
- [15] Hong, Y., Kim, S., Kim, Y., Cha, J., (2021). Quadrotor Path Planning Using A* Search Algorithm and Minimum Snap Trajectory Generation. *ETRI Journal*, Vol. 43, pp. 1013-1023, Korea.
- [16] Jung, S., Lee, H., Shim., D.H., Agha-Mohammadi, A.A., (2021). Collision-free Local Planner for Unknown Subterranean Navigation, *ETRI Journal*. Vol.43, pp.580-593. Korea.
- [17] Li, H., Zhang, H.H., Zhang, L.D., Liu, H., (2021). Multiple Logistics Unmanned Aerial Vehicle Collaborative Task Allocation in Urban Areas. *Systems Engineering and Electronics*, Vol. 43, pp. 3594-3602, Beijing/China.
- [18] Lijuan Fan. (2023). Agricultural UAV crop spraying path planning based on PSO-a* algorithm [J]. *INMATEH - Agricultural Engineering*, Vol. 71, No. 3 / 2023. 625-636
- [19] Liu, W., Anguelov, D., Erhan, D., Szegedy, C., Reed, S., Fu, C. Y., Berg, A.C., (2016). SSD: Single Shot Multibox Detector, *In Computer Vision—ECCV 2016: 14th European Conference*, pp. 21-37, Netherlands.
- [20] Lu, K., Wang, Z.Z., Yuan, S.Z., (2014). Automatic Landing on Carrier Method of Unmanned Air Vehicle, *In Proceedings of 2014 IEEE Chinese Guidance, Navigation and Control Conference*, pp. 299–302, Yantai/China.
- [21] Petrovska, O., Rechkoska-Shikoska, U., (2013). Aircraft Precision Landing Using Integrated GPS/INS System, *Transport Problems*, Vol.8, pp.17-25, Poland.
- [22] Song, K., Yeo, H., Moon, J.H., (2021). Approach Control Concepts and Optimal Vertiport Airspace Design for Urban Air Mobility (UAM) Operation, *International Journal of aeronautical and Space Sciences*, Vol. 22, pp. 982-994, Korea.
- [23] Torabbeigi, M., Lim, G. J., Kim, S. J., (2020). Drone Delivery Scheduling Optimization Considering Payload-Induced Battery Consumption Rates. *Journal of Intelligent & Robotic Systems*, Vol. 97, pp. 471-487, Netherlands.
- [24] Williams, P., Crump, M., (2012). Intelligent Landing System for Landing UAVs at Unsurveyed Airfields, *In 28th International Congress of the Aeronautical Sciences*, pp. 1-19. Australia.
- [25] Yang, S., Ying, J., Lu, Y., Li, Z., (2015). Precise Quadrotor Autonomous Landing with SRUKF Vision Perception, *2015 IEEE International Conference on Robotics and Automation (ICRA)*, 2196-2201. USA.

- [26] Zhen Wang, Keqing Qian, Xiaoli Zhu, et al. (2023). Analysis on handling path optimization of agricultural robots based on improved ant colony algorithm [J]. *INMATEH - Agricultural Engineering*, Vol. 70, No. 2 / 2023. 455-467
- [27] Zheng, Z., Bewley, T.R., Kuester, F., (2020). Point Cloud-Based Target-Oriented 3D Path Planning for UAVs, *In 2020 International Conference on Unmanned Aircraft Systems (ICUAS)*, pp. 790-798. Greece.
- [28] Zhou, B., Gao, F., Wang, L., Liu, C., Shen, S., (2019). Robust and Efficient Quadrotor Trajectory Generation for Fast Autonomous Flight, *IEEE Robotics and Automation Letters*, Vol. 4, pp. 3529–3536. United States.

DESIGN AND EXPERIMENT OF DOUBLE-ROW WHEEL SELF-PROPELLED CHINESE CABBAGE HARVESTER

双行轮式自走型大白菜收获机设计与试验

Wenyu TONG¹⁾, Yanwei YUAN¹⁾, Shenghe BAI^{1,2)}, Kang NIU¹⁾, Chengxu LV¹⁾, Liming ZHOU¹⁾

¹⁾ Chinese Academy of Agricultural Mechanization Sciences Group Co., Ltd,
National Key Laboratory of Agricultural Equipment Technology, Beijing 100083, China;

²⁾ China Agricultural University, Beijing 100083, China.

Tel: +86-15940594435; E-mail: 2020240027@stu.syau.edu.cn

DOI: <https://doi.org/10.35633/inmateh-73-60>

Keywords: Chinese cabbage; Harvester; Key components design; Harvest qualified rate; Field verification test

ABSTRACT

Aiming at the problems of low harvesting level of Chinese cabbage, high cost of manual operation and lack of special harvesting machinery, a double-row wheeled self-propelled Chinese cabbage harvester was designed on the basis of measuring the physical parameters of 'Zaofeng 01' Chinese cabbage varieties and combining with the main local planting patterns. It can complete the root cutting, pulling, clamping and conveying, packing and collecting of double-row Chinese cabbage at one time. Through the design and selection of the key working parts of the double-row wheel self-propelled Chinese cabbage harvester prototype, the key working parameters of the profiling device, the root cutting-pulling device and the clamping conveying device were determined. The kinematics analysis of the harvester in the profiling, cutting, pulling, clamping and conveying links was carried out, and the field operation performance test of the prototype was completed. The results showed that: when the rotation speed of the cutter was 280 r/min, the rotation speed of the clamping conveyor belt was 240 r/min, and the forward speed of the machine was 1.44 km/h, the maximum qualified rate of harvesting was 95.08 %, the minimum value was 90.65 %, and the average value was 93.79 %. At this time, the working performance of the working machine is stable, the harvesting effect is good, and all performance indicators meet the relevant design requirements and standards. The research results can provide reference for the development and structural improvement of Chinese cabbage low-loss harvesting equipment.

摘要

针对大白菜收获水平低、人工作业成本高、专用收获机械缺乏等问题，在测定“早丰 01”大白菜品种物理参数并结合当地主要种植模式基础上，设计了一种双行轮式自走型大白菜收获机，一次性可完成双行大白菜的切根、起拔、夹持输送、装箱收集等作业。通过对双行轮式自走型大白菜收获机样机关键作业部件进行设计选型，确定了仿形装置、切根-起拔装置、夹持输送装置的关键工作参数；对收获机在仿形、切根、起拔、夹持输送环节进行了运动学分析，并完成了样机田间作业性能试验。试验结果表明，当割刀转速为 280 r/min，夹持输送带转速为 240 r/min，机具前进速度为 1.44 km/h 时，采收合格率最大值为 95.08 %，最小值为 90.65 %，平均值为 93.79 %，此时作业机具工作性能稳定，收获效果良好，各项性能指标均达到相关设计要求和标准，研究成果可为大白菜低损收获装备开发及结构完善提供参考。

INTRODUCTION

Chinese cabbage is one of the staple vegetables in China. It has a wide range of cultivation areas. Because of its cold resistance, high yield, storage and transportation resistance, and long supply period, it is planted in all seasons in northern and southern China. The largest planting area is in the Yellow River Basin, and the smallest is in North China (Zhang *et al.*, 2021). In recent years, the planting area of Chinese cabbage is stable at about 1.8 million hm², and the total output is about 3.4 million tons (Cui *et al.*, 2021; Yang *et al.*, 2020). The cultivation of Chinese cabbage is rough, the planting mode is not uniform, and the individual differences of mature plants are large, which leads to the mismatch between the existing harvesting equipment and the planting agronomy, the high loss and damage of harvest, and the lack of special harvesting equipment designed for the physical characteristics of Chinese cabbage (Cui *et al.*, 2021; Bu L.X. *et al.*, 2020; Zhou *et al.*, 2023; Yao *et al.*, 2007; Zhao *et al.*, 2020). At present, Chinese cabbage is still mainly harvested manually. Therefore, it is urgent to develop a special harvesting equipment for Chinese cabbage that can closely fit the Chinese cabbage planting specifications and achieve low-loss combined harvesting, in order to reduce production costs, reduce farmers' labor burden, and improve the economic benefits of the Chinese cabbage industry.

Wenyu TONG, Ph.D. Stud. Eng.; Yanwei YUAN*, Prof. Ph.D. Eng.; Shenghe BAI, Ph.D. Stud. Eng.; Kang NIU, Prof. Ph.D. Eng.; Chengxu LV, Prof. Ph.D. Eng.; Liming ZHOU, Prof. Ph.D. Eng.

Kanamitsu M. et al., (1994), developed a hand-held Chinese cabbage harvester. In order to improve harvesting efficiency and reduce harvesting damage, a tractor side-suspended Chinese cabbage harvester was designed on this basis. The harvester mainly includes a pulling device, a clamping conveying device and a root cutting device. The harvesting process mainly adopts the method of first pulling, then cutting and then transporting. *Kim H.J. et al.*, (2020), of Chungnam University in South Korea developed a crawler self-propelled Chinese cabbage harvester, which uses double disc pulling device and double lateral clamping and conveying device to complete the functions of Chinese cabbage pulling, root cutting, conveying, header and so on. Aiming at the problems of easy blockage, leakage and high damage rate in the clamping and conveying process of Chinese cabbage harvester, the Agricultural Science Research Institute of Korea Rural Development Department (*Lee Y.S. et al.*, 2018), simulated and optimized the conveying device and determined the suitable conveyor belt material. *Wang Shengsheng et al.*, (2021), designed a flexible threshing device for cabbage seeds with a combination of flexible round-ended spike teeth and circular tube concave plate. *Yao Huiling et al.*, (2007), designed a spiral lifting device and a disc cutter with good sliding cutting performance in combination with the mechanical properties of the local main Chinese cabbage varieties to ensure that the roots and stems of Chinese cabbage can be smoothly transported backwards after being cut. A crawler self-propelled single-line Chinese cabbage harvester was designed by *Zhang Jing et al.* (2022). The machine adopts the method of cutting root first and then pulling out. It can realize many operations such as root cutting, clamping, longitudinal transportation lifting, lateral transportation and lateral loading of Chinese cabbage at one time. The field test effect is good.

Due to the intensive scale planting mode, many countries have conducted extensive research on the operation mode and performance of Chinese cabbage harvesters, mainly focusing on Japan, South Korea and other countries (*Li*, 2013). In China, due to the policy orientation of vegetable production and the upgrading of agricultural machinery and equipment, as well as the improvement and perfection of the management system of Chinese cabbage production, universities and scientific research institutions have carried out independent innovation on the basis of absorbing foreign advanced scientific and technological methods, and have successively carried out series of exploration and research on the theory and equipment of Chinese cabbage harvesting (*Zheng*, 2023). In summary, in recent years, Chinese cabbage harvesting equipment has gradually developed towards the direction of joint harvesting operations, especially for commercially promoted models, which generally require harvesting functions to integrate multiple functions such as harvesting, containerization, and transportation. The whole machine is more efficient, automated, and intelligent. However, due to the problems of many Chinese cabbage cultivars, low standardization of cultivation modes, and extensive agronomic management, most of the above models remain in the laboratory or prototype stage and are not used for actual production promotion. The development and promotion of Chinese cabbage harvesters still have a long way to go.

In view of the above problems, this paper takes the main variety of Chinese cabbage 'Zaofeng 01' as the research object, and improves the suitable mechanization scheme based on the agronomic requirements of Chinese cabbage planting in Yucheng City, Shandong Province. A double-row wheel self-propelled Chinese cabbage harvester integrating profiling root cutting, flexible clamping and vertical conveying is developed. The key components such as profiling device, root cutting-pulling device, clamping and conveying device are designed, and the working performance of the prototype is tested in combination with field verification test, in order to improve the level of mechanized harvesting equipment for Chinese cabbage.

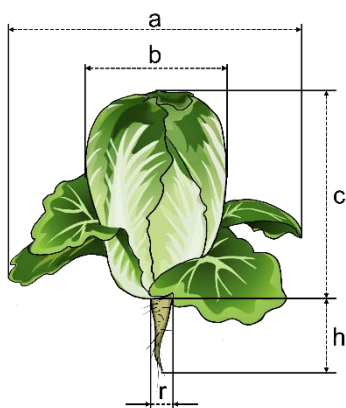
MATERIALS AND METHODS

Basic physical parameters and planting patterns of Chinese cabbage

● **Determination of basic physical parameters of Chinese cabbage**

In order to reduce the loss and improve the harvesting efficiency, the design of Chinese cabbage harvester needs to fully consider the basic physical parameters of Chinese cabbage. In this paper, the main cultivar of Chinese cabbage 'Zaofeng 0' was selected as the test object, and the basic physical parameters of 100 mature Chinese cabbages with no damage on the surface and complete rosette leaves and roots were selected by the principle of randomness, diagonal principle and classification principle. As shown in Figure 1, the measurement parameters include Chinese cabbage diameter, plant height, rhizome diameter, rhizome length, expansion degree and total mass.

The measurement results are shown in Table 1:



a - expansion degree; b - diameter; c - plant height; h - rhizome length; r - rhizome diameter

Fig. 1 - Determination of geometric characteristics of Chinese cabbage

Table 1

Measurement results of geometric characteristics of Chinese cabbage

| Chinese cabbage cultivars | Statistical indicators | Expansion degree /mm | Diameter /mm | Plant height /mm | Rhizome length /mm | Rhizome diameter /mm | Total mass/kg |
|---------------------------|--------------------------|----------------------|--------------|------------------|--------------------|----------------------|---------------|
| Zaofeng 01 | Average value | 543 | 155 | 164 | 60.55 | 28.36 | 2.77 |
| | Maximum value | 647 | 162 | 190 | 74.32 | 32.63 | 3.18 |
| | Minimum value | 438 | 148 | 138 | 50.68 | 42.57 | 2.35 |
| | Standard deviation | 104.5 | 7 | 3.41 | 11.87 | 7.29 | 0.42 |
| | Coefficient of variation | 0.19 | 0.05 | 0.07 | 0.20 | 0.26 | 0.15 |

● Planting pattern

There are two common planting patterns of Chinese cabbage: flat planting and ridge planting, ridge planting can provide a more stable growth environment for Chinese cabbage and reduce the adverse effects of external environmental factors on the quality of Chinese cabbage, such as soil erosion, weathering and water loss (Tong.,2023; Wang.,2020). At the same time, the Chinese cabbage in the ridge planting mode allows customizing the plant spacing and row spacing of Chinese cabbage according to the requirements of mechanized harvesting, reducing the hybrid and cross-growth between Chinese cabbage plants. This uniformity greatly improves the convenience of mechanized harvesting, thereby improving the harvesting efficiency of Chinese cabbage.

Therefore, combined with the local main varieties and planting patterns, the planting pattern of Yucheng City, Shandong Province was improved to obtain better mechanized harvesting effect. The specific planting requirements are as follows: Ridge planting, single ridge double row (ridge surface 1.1 m wide), row spacing 50-60 cm, plant spacing 45-50 cm (leaf expansion can cover all soil surface, reduce weed growth probability, reduce field management difficulty), ditch depth 15-30 cm, ditch width 20-30 cm.

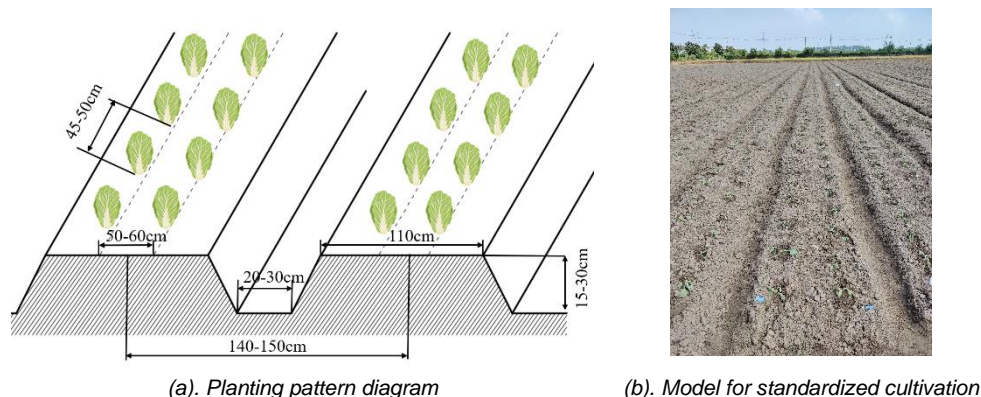
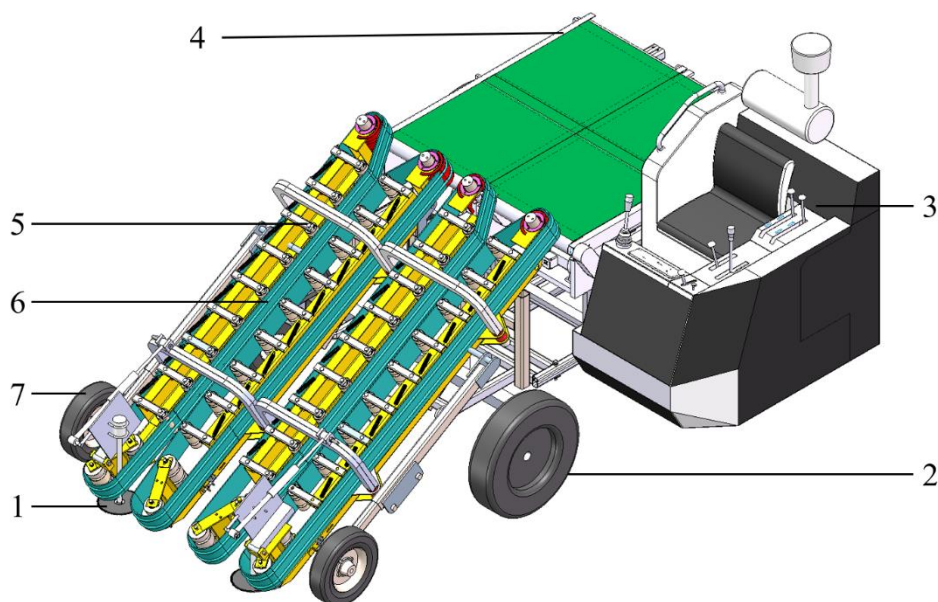


Fig. 2 - Ridge double row planting pattern diagram

The Complete machine structure and working principle of Chinese cabbage harvester

● Complete machine structure

The double-row wheeled self-propelled Chinese cabbage harvester is mainly composed of wheeled walking chassis, harvesting header and aggregate box. The Chinese cabbage harvesting platform is mainly composed of profiling device, root cutting-pulling device, clamping and conveying device, hydraulic transmission system and so on. The harvesting platform is placed on the wheeled walking chassis, hinged by the three-point suspension structure, and arranged longitudinally based on the symmetrical center surface. The schematic diagram of the whole structure of the Chinese cabbage harvester is shown in Figure 3.



1 - root cutting device; 2 - guide wheel; 3 - cockpit; 4 - transverse conveying platform; 5 - tension pulley; 6 - clamping conveyor belt; 7 - profiling device

Fig. 3 - Double wheel self-propelled Chinese cabbage harvester machine structure diagram

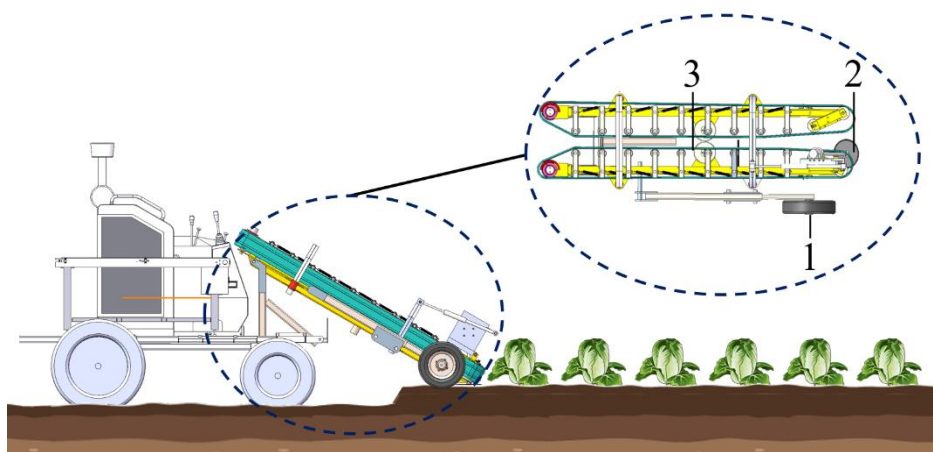
Table 2

Main parameters of harvester

| Technical Parameters | Numerical Value |
|-------------------------------------|--------------------------|
| Structural Forms | Self-propelled on wheels |
| Overall dimensions (L×W×H)/mm | 4100×2200×2500 |
| Auxiliary Power kW | 45 |
| Walking Speed/(km·h ⁻¹) | 2~3 |
| Number of Rows Harvested/- | 2 |
| Harvesting Row Spacing /mm | 450~650 |
| Working Width /mm | 1400 |
| Machine weight /kg | 1640 |

● Working Principle

The working area of the harvesting cutter is mainly divided into three parts: the profiling area, the root cutting-pulling area and the clamping conveying area. When the harvester is working, the height of the cabbage harvester cutting table needs to be adjusted first, so that the cutting tool is close to the ground, so that the roots can be cut accurately. During the whole operation process, the engine of the traveling chassis drives the directly connected hydraulic pump, which controls the hydraulic motors of the different working parts through the electronically controlled valve group. These hydraulic motors drive the various parts of the harvesting cutter to work in unison to realize a series of functions such as lifting, root cutting, gripping, conveying and collecting the cabbage. The whole process ensures effective cabbage harvesting and improves work efficiency at the same time.



1 - profiling area; 2 - root cutting- lifting area; 3 - clamping and conveying area

Fig. 4 - Working Principle

Profiling Area: in the process of advancing, the machine moves along the contour of the terrain and adapts to the changes in the undulation of the ground so that the cutter is always close to the ground, ensuring the consistency of cutting roots and improving the quality and efficiency of harvesting.

Root Cutting-Lifting Area: when the machine works, the cutter is attached to the land surface, placed under the cabbage outer wrapping leaves, through the synergistic effect of the machine forward and the cutter rotation, the cabbage is subjected to upward sustained traction, prompting the roots to separate from the soil, so as to complete the cabbage pulling up and cutting the root operation.

Clamping and Conveying Area: after completing the root cutting and pulling operation, the cabbage is steadily gripped and lifted by the tensioning mechanism and the clamping conveyor belt, this process is designed to reduce the risk of mechanical damage to the cabbage during the conveying and lifting phase and to smoothly feed the cabbage to the transverse conveying platform to complete the collection operation after removing the excess outer leaves of the cabbage.

Design of key components of Chinese cabbage harvester

● **Profiling device**

Profiling is the key process in the harvesting process of Chinese cabbage. Because the soil quality of Chinese cabbage growing environment is relatively soft, the ridge height and ridge surface fluctuate greatly. Therefore, a profiling device is designed to realize the real-time adjustment of the position of the harvesting header with the fluctuation of the ridge surface, so as to avoid the body tilt caused by the wheel sinking caused by the self-weight during the cross-ridge operation and the phenomenon that the position of the cutter is too high or too low during the harvesting process, which leads to the cutting of Chinese cabbage and the incomplete cutting of Chinese cabbage. The structure diagram and physical diagram of the profiling device are shown in figure 5.

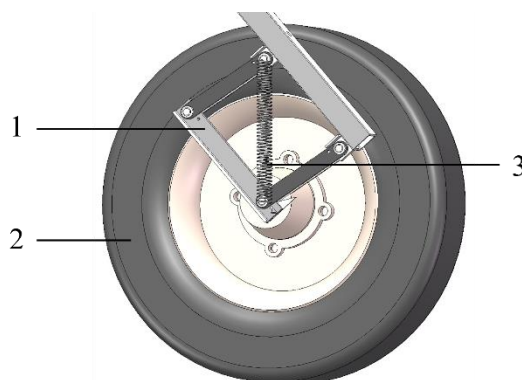


Fig. 5 - Schematic diagram of the structure of the profiling device

1 - profiling brackets; 2 - profiling wheel; 3 - profiling sprung

● **Swing arm design for profiling device**

In order to make the Chinese cabbage harvester cutting platform for harvesting operations as smooth as possible, the requirements of the imitation wheel force change as little as possible. The imitation device force sketch is shown in Figure 6, and the force equilibrium conditions are:

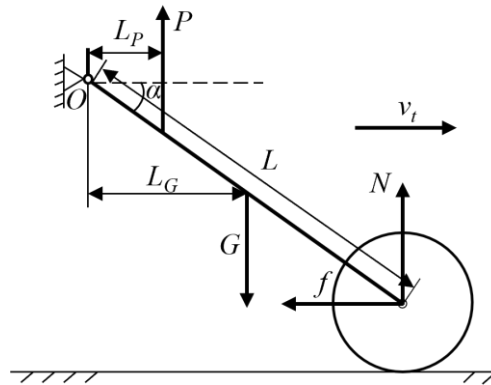


Fig. 6 - Force analysis diagram of the profiling device

$$\begin{cases} PL_p + NL \cos \alpha = GL_G + fL \sin \alpha \\ f = \mu N \\ F = \sqrt{N^2 + f^2} = N\sqrt{1 + \mu^2} \end{cases} \quad (1)$$

It can be obtained from Equation (1):

$$F = \frac{GL_G - PL_p}{L(\cos \alpha - \mu \sin \alpha)} \sqrt{1 + \mu^2} \quad (2)$$

where: P is the balance spring tension, [N];

N is the positive pressure of the ground on the profiling wheel, [N];

f is rolling resistance of profiling wheel, [N];

G is overall gravity of profiling device, [N];

μ is coefficient of rolling resistance;

F is the force of ground on profiling wheel, [N];

L is harvesting header length, [mm];

L_p is force arm of spring tension P to O point;

L_G is the force arm of the profiling device to point O as a whole;

α is the cutting table that can adjust the swing angle, [°].

It can be seen from Equation (2) that the force F of the ground to the profiling wheel is mainly related to the overall gravity G of the profiling device, the length L of the harvesting header and the swing angle α of the header. The overall gravity of the profiling device and the length of the harvesting header are fixed values. The position where the profiling wheel falls into the low-lying road and is not affected by the ground force is taken as the maximum force position of the profiling spring. At this time, the tension P of the profiling spring is balanced with the gravity G of the profiling device. In order to make the harvesting header work smoothly, the smaller the variation range of F should be, the smaller the variation range of the adjustable swing angle α of the header should be.

According to the design requirements of agricultural equipment profiling range requirements (*China Academy of Agricultural Mechanization Sciences. Handbook of Agricultural Machinery Design: Volume II*), the upper and lower profiling amount is generally $\pm (8 \sim 12)$ cm. As shown in Figure 7, when the harvesting header is at the upper and lower limit positions, the total profiling quantity can be expressed as:

$$h = L[\sin(\Delta\alpha_1 + \alpha_0) + \sin(\Delta\alpha_2 - \alpha_0)] \quad (3)$$

where: α_0 is the initial angle of adjustable swing arm of harvesting cutting table, [°];

$\Delta\alpha_1$ is the change from the initial position of the harvesting cutting table to the lowest swing Angle, [°];

$\Delta\alpha_2$ is the change from the initial position of the harvesting cutting table to the highest swing Angle,

[°].

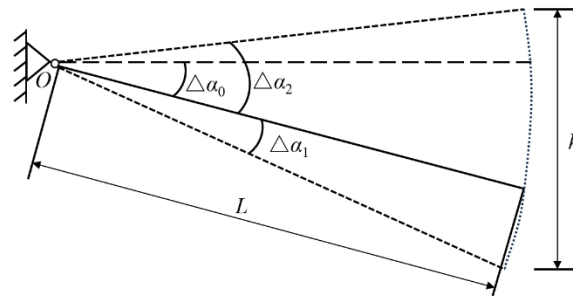


Fig. 7 - Harvesting cutting table contour diagram

According to Equation (2) and (3), under the condition that the total copying quantity h is constant, the longer the swing arm of the harvesting cutting table, the smaller the variation range of the adjustable swing Angle α , and the smaller the variation range of the force F of the ground facing the copying wheel, the more stable the harvesting cutting table will be during the harvesting operation. Therefore, in order to ensure the harvesting effect and the more stable the position change during the cutting table copying, the length of the swing arm of the copying device of Chinese cabbage harvesting cutting table designed in this paper is 1800 mm.

● Contour wheel diameter design

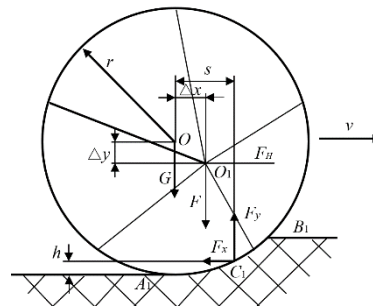


Fig. 8 - Force diagram of profiling wheel

The profiling effect of profiling wheel has a great correlation with its own diameter. The smaller the diameter is, the shorter the profiling time is, and the profiling effect is not ideal. If the diameter is too large, it is easy to produce the phenomenon of soil dragging.

In order to determine the reasonable diameter of the profiling wheel, it is necessary to analyze the force of the profiling wheel during the operation process. The schematic diagram of the force analysis is shown in Figure 8.

According to the torque relationship, it can be obtained :

$$\begin{cases} H(r - \Delta y) - F\Delta x + R_x h + R_y s = 0 \\ Gs - F(s - \Delta x) - H(r - \Delta y) = 0 \end{cases} \tag{4}$$

It can be obtained from Equation (4):

$$H(r - \Delta y) = F\Delta x - R_x h - R_y s = Gs - F(s - \Delta x) \tag{5}$$

where: F_H is the tractive force, [N];

G is the profiling wheel gravity, [N];

R is the profile wheel radius, [mm];

F is the gravity load of profiling wheel, [N];

h is the depth of subsidence from point C to the lowest point, [mm];

s —when the contour wheel sinks h , the forward length of the wheel, [mm];

F_x is the horizontal ground reaction force, [N];

F_y is the vertical ground reaction force, [N];

v is tool forward speed, [m/s];

Δx is the horizontal distance from the original center when copying the profile wheel, [mm];

Δy is the vertical distance from the original center when copying the profile wheel, [mm].

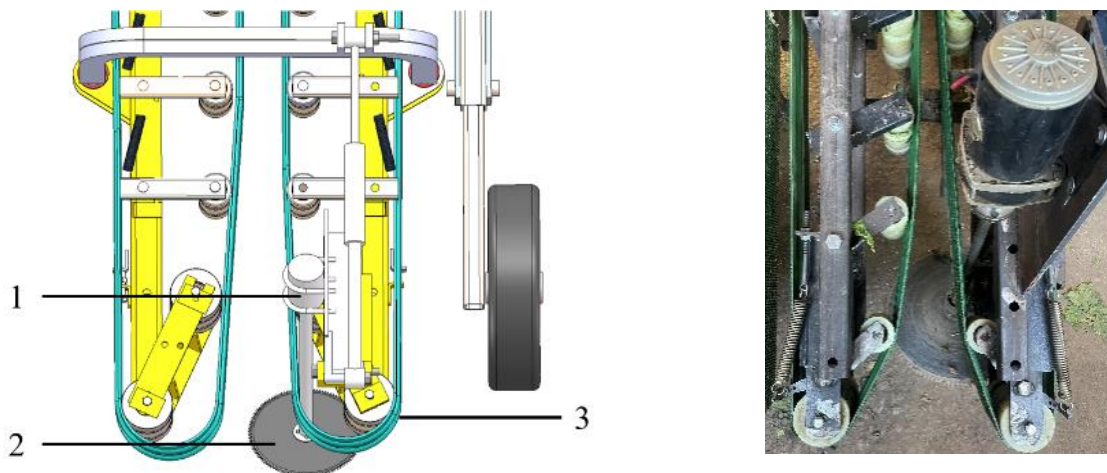
It can be seen from Equation (12) that when the traction and load are constant, at a certain speed, the eccentric distance of the central axis, that is, Δx and Δy is constant without considering the vibration of the spring. Under this condition, the smaller the wheel diameter is, the smaller the forward length s of the profiling wheel is, the smaller the profiling time t is, and the profiling effect is not ideal, which will lead to the phenomenon that the root cutting position is too high or too low. Therefore, the diameter of the profiling wheel is generally 200-500 mm (Hu et al., 1996). At the same time, in order to ensure that the profiling mechanism inside the profiling wheel has enough profiling stroke, the diameter of the profiling wheel is determined to be 400 mm after comprehensive consideration and analysis.

Design of root cutting-pulling device

● Root cutting device design

When the machine is pulling-cutting, the cutter is attached to the surface of the land. As the machine continues to move forward, the cutter extends into the bottom of the Chinese cabbage and rotates inward. After the front end of the clamping conveyor belt contacts the Chinese cabbage, the root of the Chinese cabbage is separated from the soil under the synergistic effect of the cutter and the front end of the conveyor belt, and the pulling-cutting operation of the Chinese cabbage is completed.

The root cutting device is shown in figure 9. Based on the planting mode of Chinese cabbage and the geometric size characteristics of the root of Chinese cabbage designed in this paper, a single disc saw-tooth root cutting device is adopted in this paper. In the cutting process, the saw-tooth disc cutter has the advantages of low speed drop value, high cutting ratio and high root cutting quality compared with other forms of disc cutter. It is installed at the center position deviating from the Chinese cabbage clamping and conveying route, in order to minimize the stress imbalance of Chinese cabbage in the cutting process.

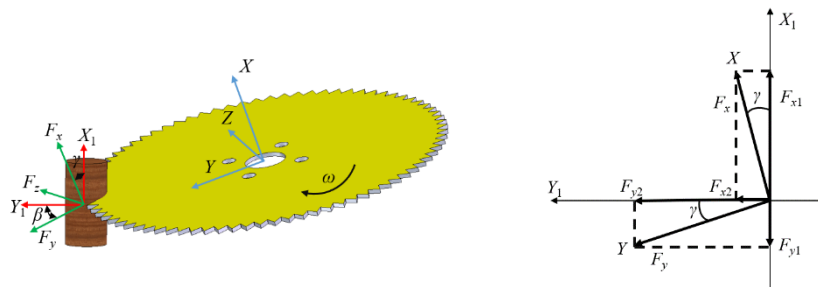


(a). 1 - root cutting device motor; 2 - saw-tooth disc cutter; 3 - clamping device. (b). The physical diagram of the root cutting device

Fig. 9 - Root cutting device

In the process of root cutting, the Chinese cabbage rhizome is subjected to the root cutting force F_x , F_y , F_z in the three directions of X axis, Y axis and Z axis, as shown in Figure 10a, and the stress analysis on the X axis and Y axis is shown in Figure 10b.

Due to the combined action of the cutter and the front end clamping force of the conveyor belt in the Z axis direction, most of the root cutting forces offset each other, but there is still a part of the cutting ability F_z . It can be seen from Figure 10b that the total longitudinal component force in the X_1 axis direction is the sum of the two components F_{x1} and F_{y1} in the opposite direction, so the total longitudinal component force is small, while the extraction of Chinese cabbage requires a large extraction force, and the rhizome is not easy to be pulled out. The total transverse component force on the Y_1 axis is the sum of the two component forces F_{x2} and F_{y2} with the same direction, and the total transverse component force is larger. Because the pitch angle γ is small, it can be seen that F_{x2} is small, so the total lateral component is mainly determined by F_{y2} , that is, it is mainly determined by F_y . Therefore, F_y can be approximated as a root-cutting force. In addition, considering the actual installation and use, the angle β of the vertical plane is set to zero, and only the influence of the same pitch angle γ is considered in order to determine the best cutting parameters.



(a). Three-dimensional force analysis (b). Force analysis of X and Y axis direction

Fig. 10 - Stress analysis diagram of Chinese cabbage rhizomes

The quality of Chinese cabbage root cutting is closely related to the root cutting force (Jiang., 2013). Therefore, by designing reasonable structural parameters of the cutting disc cutter and selecting the appropriate cutting angle, the stability of root cutting can be ensured. As shown in Figure 11, the Chinese cabbage rhizome to be cut is idealized as a positive circle, and its diameter is idealized as D_1 . When the serrated disc cutter works, the serrated mouth at the edge will clamp and cut the Chinese cabbage root. Combined with Figure 10b, the cutting force R_x and the clamping force Q_y are analyzed by the force analysis in the figure.

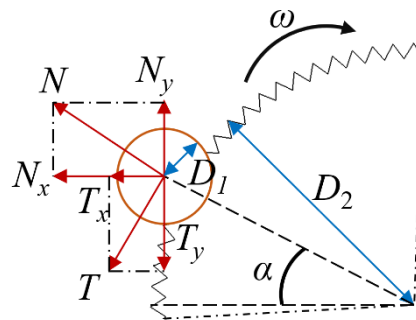


Fig. 11 - Force analysis diagram of root cutting process

The following equations are obtained by orthogonal decomposition:

$$F_y = R_x \tag{6}$$

$$\begin{cases} R_x = T_x + N_x \\ Q_y = T_y - N_y \end{cases} \tag{7}$$

where:

N - the horizontal component of the normal reaction force of the cutter on the rhizome is N_x , and the vertical component is N_y , [N];

T - the horizontal component of the friction force of the cutter is T_x , and the vertical component T_y , [N];

In order to make the Chinese cabbage rhizome be held by the cutter, the following conditions need to be met:

$$Q_y > 0 \tag{8}$$

It can be referred that $T_y > N_y$, and $T = N \cdot f$, which means:

$$N \cdot f \cos \alpha > N \cos \alpha \tag{9}$$

At this time, when $f > \tan \alpha$, saw-tooth disc cutter has good clamping performance:

$$\alpha = \arccos \frac{D_2}{D_2 + D_1} \tag{10}$$

where:

f is the friction coefficient between disc cutter and Chinese cabbage rhizomes, generally taking 0.4~0.7;

α is the angle between the normal reaction force of disc cutter on Chinese cabbage rhizome and X axis, [°];

D_1 is the diameter of the root of Chinese cabbage at the cutting place, [mm];

D_2 is the diameter of disc cutter, [mm].

In order to avoid the incomplete cutting of Chinese cabbage roots, the cutter keeps a certain distance from the conveying structure, so as to ensure the flatness and integrity of the roots. The diameter of the cutter head of the disc cutter designed in this paper is 225 mm, and the angle ' α ' $\approx 31.02^\circ$. At this time, $f > \tan\alpha$, which can well meet the requirements of clamping performance.

● **Motion Analysis of Pulling Process**

After the Chinese cabbage is cut by the cutter clamp, the Chinese cabbage is successfully completed under the synergistic effect of the front end of the conveyor belt and the internal rotation of the cutter, and is clamped by the conveyor belt for longitudinal lifting movement. The speed and force analysis of the Chinese cabbage pulling process are shown in Figure 12:

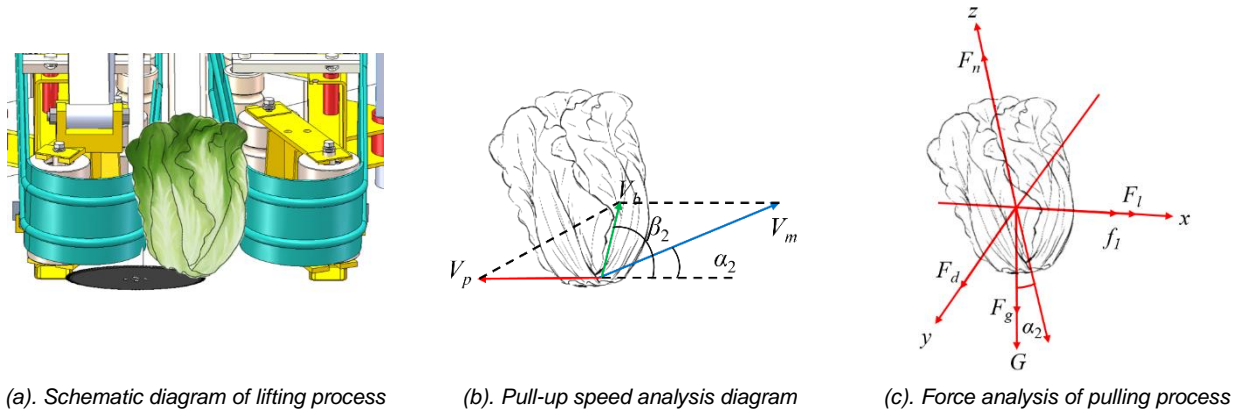


Fig. 12 - Analysis diagram of lifting process

Figure 12b shows the speed analysis diagram of Chinese cabbage during the pulling process. The direct relationship between speed and angle is as follows:

$$V_m \cos \alpha_2 > V_p \tag{11}$$

The movement of Chinese cabbage was analyzed, and the speed synthesis relationship of Chinese cabbage was as follows:

$$\vec{V}_b = \vec{V}_m + \vec{V}_p \tag{12}$$

According to the trigonometric function relationship, the following relationship can be obtained:

$$\frac{V_m}{V_p} = \frac{\sin \beta_2}{\sin(\beta_2 - \alpha_2)} = K \tag{13}$$

where:

V_p is the forward speed of Chinese cabbage harvester, [m/s];

V_m is the clamping speed of lower clamping, [m/s];

V_b is the moving speed of Chinese cabbage, [m/s];

α_2 is the angle between the working part of Chinese cabbage harvester and the ground, [°];

β_2 is the angle between the absolute speed of Chinese cabbage and the ground, [°].

According to the Equation (13), when K is less than 1, the β_2 angle is greater than 90° , which will lead to a forward movement trend of Chinese cabbage, resulting in a deviation of the cutting position. When K is greater than 1, β_2 is less than 90° , which will lead to a certain angle of Chinese cabbage plant tilted backwards, so that the axis of Chinese cabbage is perpendicular to the linear position where the header is located, which can improve the harvesting quality.

Therefore, the angle between the header and the ground of the Chinese cabbage harvester designed in this paper is 15° , and the K value is greater than 1, which meets the design requirements.

Figure 12c shows the force analysis when the cutter extends into the bottom of the Chinese cabbage and the conveyor belt holds the root of the Chinese cabbage during the pulling process of the Chinese cabbage:

$$\begin{cases} \sum F_x = F_d + f_1 - F_g \sin \alpha_2 - G \sin \alpha_2 \\ \sum F_z = F_n - G \cos \alpha_2 - F_g \cos \alpha_2 \end{cases} \quad (14)$$

Further derived:

$$\begin{cases} \sum F_x = 2\mu_1 F_d + \mu_2 F_n - F_g \sin \alpha_2 - mg \sin \alpha_2 \\ \sum F_z = F_n - mg \cos \alpha_2 - F_g \cos \alpha_2 \end{cases} \quad (15)$$

In order to make the Chinese cabbage be able to be pulled up smoothly, the conditions that need to be met are that the force of the Chinese cabbage in the x direction is greater than or equal to 0, and the force in the z direction is equal to 0. In the z direction, the Chinese cabbage is supported by the cutter to the Chinese cabbage. Force F_n and its own gravity G , soil cohesion F_g in the z direction, and F_n is a reaction force, its size changes with the change of the gravity of the Chinese cabbage and soil cohesion, so the force balance of Chinese cabbage in the z direction:

$$\begin{cases} 2\mu_1 F_d + \mu_2 F_n - F_g \sin \alpha_2 - mg \sin \alpha_2 \geq 0 \\ F_n - mg \cos \alpha_2 - F_g \cos \alpha_2 = 0 \end{cases} \quad (16)$$

Further derived:

$$\mu_2 \geq \frac{\sin \alpha_2 (F_g + mg) - 2\mu_1 F_d}{\cos \alpha_2 (F_g + mg)} \quad (17)$$

where:

F_n is the Chinese cabbage in the process of being pulled out by the cutter to the Chinese cabbage plant support, [N];

f_1 is the friction force on Chinese cabbage due to cutter rotation, [N];

F_d is the extrusion Pressure of Conveyor Belt on Root of Chinese Cabbage, [N];

F_1 is the pulling force of conveyor belt on Chinese cabbage, [N];

F_g is the soil Adhesion to Chinese Cabbage, [N];

G is the gravity of Chinese cabbage itself, [N];

μ_1 is the friction coefficient between Chinese cabbage and conveyor belt;

μ_2 is the friction coefficient between Chinese cabbage and cutter;

m is the quality of Chinese cabbage itself, [kg].

It can be seen from Equation (17) that the friction force of the cutter on Chinese cabbage is proportional to the support force. When the cutter inclination angle α_2 is 15° , the success rate of Chinese cabbage pulling and root cutting is the highest.

In summary, the saw-tooth disc cutter designed in this paper has a diameter of 225 mm, a thickness of 3 mm, a material of 65 Mn, and a cutter inclination angle of 15° . At this time, $f > \tan \alpha$, which can well meet the requirements of lifting and root cutting operations.

● Design of clamping conveying device

The double-row Chinese cabbage harvester designed in this paper adopts the new mechanism and new method of "vertical clamping with flexible conveying", and adopts the loss reduction method of flexible feeding and flexible clamping to improve the adaptability of Chinese cabbage with different ball diameters and realize the low loss conveying of Chinese cabbage.

The analysis of the movement process of Chinese cabbage in the clamping and conveying device is shown in figure 13, of which '1' is the Chinese cabbage feeding link, '2' is the clamping and conveying link, and '3' is the conveying and harvesting finished product link.

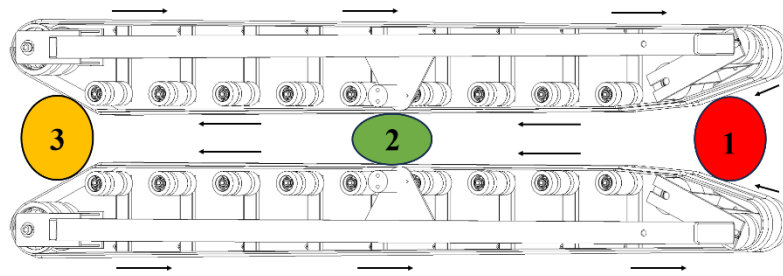


Fig. 13 - Chinese cabbage clamping conveying process

The motion analysis and force analysis of the Chinese cabbage feeding link are shown in Figures 14a and 14b.

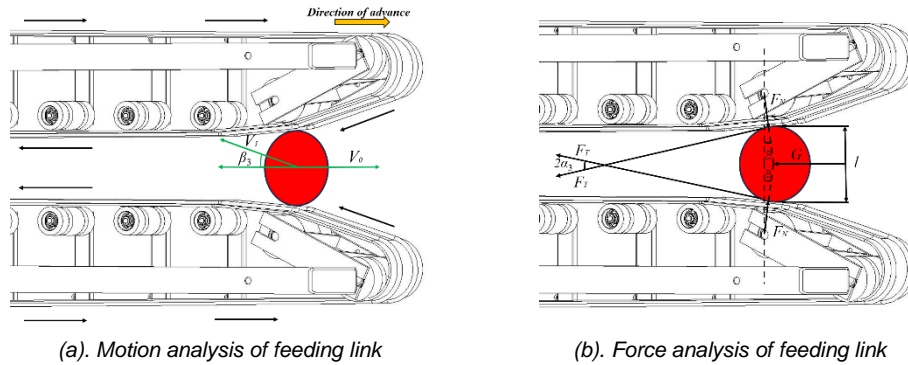


Fig.14 - Chinese cabbage feeding process

In order to make Chinese cabbage pass through the feeding inlet smoothly and enter the clamping and conveying device without blockage in the feeding link, the following conditions need to be met:

$$V_1 \sin \beta_3 > V_0 \tag{18}$$

$$\tan \alpha_3 \leq \frac{F_T}{T_N} = \mu \tag{19}$$

Further derived:

$$\mu \geq \sqrt{\frac{(D+d)^2 - (D+l)^2}{(D+l)^2}} \tag{20}$$

where:

V_1 is the clamping conveyor belt line speed, [m/s];

β_3 is the clamping conveyor belt lifting angle, [°];

α_3 is the angle between the extrusion pressure of Chinese cabbage and the horizontal direction, [°];

V_0 is the machine operation speed, [m/s];

F_T is the frictional force, [N];

F_N is the clamping conveyor tensioning wheel pressure on Chinese cabbage, [N];

μ is the Clamping conveyor belt and Chinese cabbage friction coefficient;

D is the tension wheel diameter, [mm];

d is the diameter of Chinese cabbage, [mm];

l is the tension wheel spacing, [mm].

The clamping position of the feeding inlet of the clamping conveyor should be the waist of Chinese cabbage. In this study, 'Zaofeng 01' Chinese cabbage was used as the research object. The single plant weight was 2.3~2.7 kg, and the ball diameter was 140~180 mm. The feeding inlet spacing of the clamping conveyor designed in this study was set to be adjustable spring type, and the minimum spacing was 120 mm. Therefore, the friction coefficient between the clamping conveyor belt and Chinese cabbage can be obtained by calculation:

$$\mu \geq \sqrt{\frac{(120+180)^2 - (120+140)^2}{(120+140)^2}} = 0.57 \tag{21}$$

The maximum extrusion pressure of Chinese cabbage is:

$$F_{N_{max}} = 2 \times \frac{G}{\mu} = 87.72N \tag{22}$$

At this time, the maximum extrusion pressure is far less than the extrusion pressure of 1166.06 N when the Chinese cabbage is damaged (Zhang, 2022), so the design of the clamping conveying device is reasonable.

The deformation of Chinese cabbage when clamping the conveying device interval is shown in Figure 15, and the local deformation of Chinese cabbage in the figure is analyzed as shown in Figure 16.

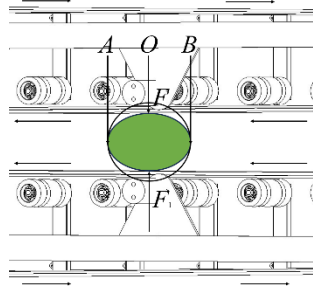


Fig.15 - Chinese cabbage pinching link deformation diagram

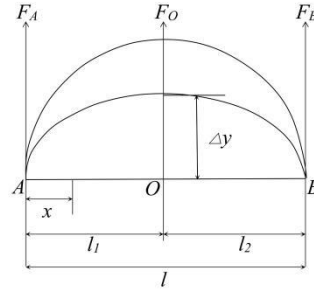


Fig.16 - Local deformation diagram of Chinese cabbage

It can be seen from Figure 15 that the extrusion force of Chinese cabbage at point O, the force of point A and point B are F_A and F_B respectively:

$$F_A = F_B = \frac{Fl_1}{l} \tag{23}$$

According to the equilibrium equation, the reaction force of point O is:

$$F_O = \frac{Fl_2}{l} \tag{24}$$

The deformation bending moment of Chinese cabbage is obtained as follows:

$$M_x = \frac{Fl_2}{l}x - F(x - l_1) \quad (l_1 \leq x \leq l) \tag{25}$$

In the ideal state, the bending moment on both sides of Chinese cabbage is the same, so the bending moment on one side is integrated:

$$EJ \frac{d^2 y}{dx^2} = \frac{Fl_2}{l}x \tag{26}$$

The winding curve equation can be obtained as follows:

$$y = \frac{Fl_2 x^2}{6lEJ} = x^2 - l_2^2 + l^2 \tag{27}$$

Because $x = l_1 = l_2$, so the Chinese cabbage clamping deformation deflection Δy is:

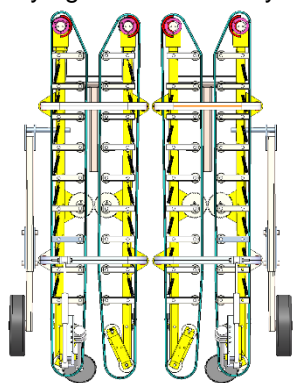
$$\Delta y = \frac{Fl_2 l_1 l}{6EJ} \tag{28}$$

where: E is the elastic modulus;
 J is the moment of inertia;
 l is the length of AB, [mm];
 l_1 is the length of AO, [mm];
 l_2 is the length of BO, [mm].

According to Equation (18), the speed of conveyor belt is closely related to the working speed of the machine. If the speed of conveyor belt and the working speed are too low, the conveying efficiency will be reduced, which will cause the feeding inlet to be blocked, resulting in the subsequent clamping not smooth, and the qualified rate of Chinese cabbage harvest will be reduced.

According to the preliminary experimental observation, the damage forms of Chinese cabbage in the process of clamping and conveying mainly include extrusion, wear, collision and other forms. The main reason is that the deformation of Chinese cabbage is too large under the action of belt, tension wheel and other components in the process of clamping and conveying, which in turn makes the deformation deflection Δy of Chinese cabbage larger, and Chinese cabbage is easy to be damaged, thus reducing the qualified rate of harvest. It can be seen from Equation (28) that the deformation deflection of Chinese cabbage is related to the elastic modulus. In order to minimize the damage of Chinese cabbage, the clamping and conveying device selects the conveyor belt of *XNBR* flexible material for clamping and conveying, as shown in Figure 17. While reducing the friction with Chinese cabbage, the deformation of Chinese cabbage by the tensioning mechanism is transferred to the flexible conveyor belt. In the process of clamping and conveying, the flexible conveyor belt absorbs part of the deformation deflection, and the deformation deflection of Chinese cabbage also becomes smaller, which plays a certain role in preventing damage to Chinese cabbage, and ensures that Chinese cabbage will not slide during the clamping and conveying process.

As shown in Figure 17, the center spacing of the Chinese cabbage clamping and conveying device designed in this paper is adjustable to a maximum of 240 mm, and the spacing of the feeding mechanism is between 140-200 mm, so as to ensure that the Chinese cabbage with different ball diameters passes through the clamping and conveying device smoothly.



(a). Clamping conveying mechanism



(b). Clamping conveying mechanism physical diagram

Fig.17 - Clamping device

Field experiment of Chinese cabbage harvester

● Test condition

As shown in Figure 18, the prototype of the double-row wheel self-propelled Chinese cabbage harvester developed in this paper was tested in Yucheng City, Shandong Province on November 16, 2023. The test site adopts the single ridge double row planting mode designed in this paper (ridge surface 1.1 m wide, row spacing 50~60 cm, plant spacing 45~50 cm, ditch depth 15~30 cm, ditch width 20~30 cm).

The test object was 'Zaofeng 01'. It took about 90 days from planting to harvest. The mature Chinese cabbage plant expansion was about 450~510 mm, the ball height was about 260~280 mm, the outer leaf was about 10~12 pieces, and the single ball quality range was 2.1~2.4 kg. Suitable for fertile clay loam or alluvial soil, soil pH value of about 6~7 is appropriate.



(a). Harvesting operation



(b). Planting pattern

Fig.18 - Field test

● Test method

Before the harvesting operation of the Chinese cabbage harvester, according to the Chinese cabbage varieties and planting patterns in the test site, the distance between the feeding inlets of the Chinese cabbage harvester and the height from the ground were adjusted, and the pre-test was carried out in the vegetable field outside the test site to ensure that the structure of the key components of the Chinese cabbage harvester remained optimized.

There are no relevant standards and regulations for the mechanical harvesting of Chinese cabbage. Therefore, this test refers to the Heading Chinese Cabbage Production Technical Specification (GB/Z26582-2011), combined with the Beet Harvesting Machinery Test Method (JB/T 6276-2007) and other relevant national standards. The relevant indicators of the test method select the harvesting pass rate as the standard for the harvesting test.

Mechanized harvesting standard of Chinese cabbage: When the Chinese cabbage leaf ball reaches tight real-time harvesting, 2 outer leaves (rosette leaves) are retained to protect the leaf ball during harvesting, so that the epidermis is clean without damage and no crack ball.

Harvest qualification rate: According to the production technical specifications of Chinese cabbage and the harvest quality requirements of stem and leaf vegetables, the harvest qualification rate of Chinese cabbage must meet the following conditions: (1) The mechanical root cutting section must be flat and cannot be broken or cut out of two sections; (2) The cutting position should be 15-20 mm above the outer leaf of Chinese cabbage, and the outer leaf should be cut off at the same time; (3) After harvest, 2-3 outer leaves were retained to protect the head; (4) There is no obvious cracking ball, extrusion damage, cutting damage and so on caused by mechanical harvesting operation. The formula of qualified rate of harvesting is as follows:

$$N = \frac{N_1}{N_0} \times 100\% \quad (29)$$

where: N is the harvest qualified rate, [%];

N_1 is the single determination test harvest Chinese cabbage qualified number, [tree];

N_0 is the total number of Chinese cabbages in single determination test, [tree].

Combined with the pre-test harvesting effect, the rotation speed of the cutter was adjusted to about 280 r/min, and the rotation speed of the clamping conveyor belt was about 240 r/min. Under the same test conditions, the forward speed of the machine was 1.08 km/h, 1.44 km/h, and 1.80 km/h, respectively. Three groups of field harvesting performance verification tests were carried out. In each test, the ridge surface with excellent growth status of Chinese cabbage was selected (about 60 m in length), and about 240~260 Chinese cabbages were planted on each ridge. Each group of tests was repeated five times. The number of qualified Chinese cabbages and the number of damages were counted, and the qualified rate and damage rate of harvest were calculated.

RESULTS AND DISCUSSION

Design results of key components of Chinese cabbage harvester

● Design results of profiling device

In order to realize the harvesting cutting platform with the ridge surface undulation real-time position adjustment, to avoid that the cutter position is too high or too low to cause the Chinese cabbage cut scattered and too low to cause the Chinese cabbage cut root incomplete phenomenon, this paper design of the Chinese cabbage harvesting cutting platform profiling device swing arm length of 1800 mm. At the same time, in order to ensure that the profiling wheel inside the profiling mechanism has enough profiling stroke, the profiling wheel diameter was determined to be 400 mm.

● Design results of root cutting-pulling device

In order to reduce the force imbalance in the process of cutting-pulling and improve the Chinese cabbage harvest qualification rate, a single disc saw-tooth root cutting device is adopted in this paper. In the cutting process, the saw-tooth disc cutter has the advantages of low speed drop value, high cutting ratio and high root cutting quality compared with other forms of disc cutter, the saw-tooth disc cutter designed in this paper has a diameter of 225 mm, a thickness of 3 mm, a material of 65 Mn, and a cutter inclination angle of 15°. At this time, $f > \tan\alpha$, which can well meet the requirements of lifting and root cutting operations.

● Design results of clamping conveying device

The double-row Chinese cabbage harvester designed in this paper adopts a new mechanism and new method of 'vertical clamping + flexible conveying'. In order to improve the adaptability of Chinese cabbage with different ball diameters and minimize the damage of Chinese cabbage, the material of the conveying

device in this paper is *XNBR* flexible material. At the same time, the center spacing of the Chinese cabbage clamping and conveying device designed in this paper is adjustable to a maximum of 240 mm, and the spacing of the feeding mechanism is between 140-200 mm, so as to ensure that Chinese cabbage with different ball diameters passes through the clamping and conveying device smoothly.

Field experiment statistics and analysis of test results

When the forward speed of Chinese cabbage harvester is 1.08 km/h, 1.44 km/h and 1.80 km/h, the harvesting results are shown in Table 3.

Table 3

| Harvesting test results statistics | | | | | | | |
|--------------------------------------|---------------|---|---------------------------|--|-------------------------------|-------------------------|---------------------------|
| Operating speed / km·h ⁻¹ | Serial number | Total number of test Chinese cabbage / tree | Number of cut-offs / tree | The number of split balls, abrasions, etc. /tree | Total number of damage / tree | Harvest qualified /tree | Harvest qualified rate /% |
| 1.08 | 1 | 258 | 4 | 14 | 18 | 240 | 93.02 |
| | 2 | 246 | 6 | 17 | 23 | 223 | 90.65 |
| | 3 | 227 | 9 | 5 | 14 | 213 | 93.83 |
| | 4 | 272 | 8 | 15 | 23 | 249 | 91.54 |
| | 5 | 246 | 5 | 15 | 20 | 226 | 91.87 |
| | mean value | | | | | | |
| 1.44 | 1 | 244 | 4 | 11 | 15 | 229 | 93.85 |
| | 2 | 238 | 3 | 12 | 15 | 223 | 93.70 |
| | 3 | 269 | 7 | 13 | 20 | 249 | 92.57 |
| | 4 | 257 | 6 | 10 | 16 | 241 | 93.77 |
| | 5 | 264 | 7 | 6 | 13 | 251 | 95.08 |
| | mean value | | | | | | |
| 1.80 | 1 | 242 | 3 | 25 | 28 | 214 | 88.43 |
| | 2 | 265 | 5 | 18 | 23 | 242 | 91.32 |
| | 3 | 284 | 9 | 30 | 39 | 245 | 86.27 |
| | 4 | 246 | 7 | 17 | 24 | 222 | 90.24 |
| | 5 | 229 | 4 | 16 | 20 | 209 | 91.27 |
| | mean value | | | | | | |

Discussion

According to the data of the harvesting test in Table 3, when the Chinese cabbage harvester was harvested at the forward speed of 1.08 km/h and 1.44 km/h, the qualified rate of Chinese cabbage harvest was greater than 90%, the maximum value was 95.08%, the minimum value was 90.65%, and the average qualified rate of harvest was 92.18% and 93.79% respectively. When the working speed of Chinese cabbage harvester was 1.80 km/h, the qualified rate of Chinese cabbage began to decline, with the maximum value of 91.32% and the minimum value of 86.27%. Analyze the reasons: when the machine operation speed is slow and moderate, at this time, the working parameters of the key components of the Chinese cabbage harvester are matched with the working speed of the machine, and the fit is high, so the qualified rate of Chinese cabbage harvesting is high ; when the operating speed of the Chinese cabbage harvester increases to 1.80 km/h, the operating speed of the machine is too fast, and the working time of the Chinese cabbage harvester is less when harvesting the Chinese cabbage, resulting in the previous Chinese cabbage not being completely cut. The root of the next Chinese cabbage has been cut and pulled, and the Chinese cabbage is squeezed between each other to feed the harvesting header to the inlet. At the same time, it will also cause damage to the mechanical structure of the Chinese cabbage harvester during the harvesting process, thereby reducing the test evaluation index. As shown in Figure 19, the harvesting effect of the Chinese cabbage harvester is very obvious, and there is no leakage phenomenon.



(a). Before harvesting



(b). After harvesting



(c). Harvesting qualified Chinese cabbage

Fig. 19 - Comparison of Chinese cabbage before and after harvesting

Figure 20 shows the damage types of Chinese cabbage during the harvesting process. The causes of Chinese cabbage damage were analyzed by field test results. First, the collision between the uprooting-cutting mechanism and Chinese cabbage caused the damage of Chinese cabbage. Second, due to the difference of individual physical characteristics, the position of Chinese cabbage is too high or too low after entering the clamping and conveying mechanism, so that the cutting position is not fixed and the Chinese cabbage is cut. Thirdly, the mutual extrusion of Chinese cabbage during the harvesting process will also cause damage.



Fig. 20 - The damage types of Chinese cabbage during harvesting

CONCLUSIONS

In this paper, based on the determination of the physical parameters of 'Zaofeng 01' Chinese cabbage varieties and combined with the main local planting patterns, a double-row wheeled self-propelled Chinese cabbage harvester was designed, which could complete the root cutting, pulling, clamping and conveying, packing and collecting of double-row Chinese cabbage at one time. Through the design and selection of the key working parts of the double-wheel self-propelled Chinese cabbage harvester prototype, the key working parameters of the profiling device, the root-cutting-pulling device, and the clamping and conveying device were determined. The specific conclusions are as follows:

(1) The basic physical characteristics of the main Chinese cabbage cultivar 'Zaofeng 01' in Yucheng City, Shandong Province were collected. The data of diameter, plant height, rhizome diameter, rhizome length, expansion degree and total mass were measured to provide data support for the design of key components of Chinese cabbage harvester.

(2) Based on the characteristics of local Chinese cabbage planting mode in Yucheng City, Shandong Province, the mechanization improvement was carried out. By optimizing the ridge height and customizing the row spacing and plant spacing of Chinese cabbage according to the basic physical shape of the main Chinese cabbage variety 'Zaofeng 01', the mechanical equipment can be operated smoothly and the loss and damage during the harvesting process can be reduced. According to the field verification test, the model significantly improved the efficiency and quality of mechanized harvesting of Chinese cabbage.

(3) A mechanized harvesting process of Chinese cabbage was proposed to improve the harvesting efficiency and reduce the loss. The structure of the prototype of the double-row wheel self-propelled Chinese cabbage harvester was determined, and its profiling device, lifting-cutting device, clamping and conveying device were designed and selected, and its dynamics and kinematics were analyzed. Finally, the key components were integrated to create a double-row wheel self-propelled Chinese cabbage harvester.

(4) The field performance test of the double-row wheel self-propelled Chinese cabbage harvester prototype showed that when the cutter speed was 280 r/min, the clamping conveyor belt speed was 240 r/min, and the forward speed of the machine was 1.44 km/h, the maximum harvesting pass rate was 95.08%, the minimum value was 90.65%, and the average value was 93.79%. The harvesting effect is the best at this time.

The follow-up research will further optimize the test to improve the qualified rate of Chinese cabbage harvest. The research results can provide reference for the development and structural improvement of Chinese cabbage harvesting equipment.

ACKNOWLEDGEMENT

This work was supported by the R&D and Demonstration of Key Technical Equipment for Intelligent Agricultural Machinery for Mountain Fruits and Vegetables (Project No. 2022YFD2001803).

REFERENCES

- [1] Bu LingXin., Chen ChengKun., Hu GuangRui., Adilet Sugirbay., Chen Jun., (2020). Technological development of robotic apple harvesters: a review. *INMATEH Agricultural Engineering*, 61(2), 151-164, DOI: <https://doi.org/10.35633/inmateh-61-17>. Bucharest / Romania.
- [2] Gongpei Cui, Yongzhe Wei., Xinmeng Zheng, Jingzheng Wang, Yongjie Cui, (2021). Design and experiment of transplanting machine for cabbage substrate block seedlings, *INMATEH-Agricultural Engineering*. 64 (2), pp. 375-384, DOI: <https://doi.org/10.35633/inmateh-64-37>. Bucharest / Romania.
- [3] Hu Y., Feng J., Qiao Y., Yu C., Luo W., Zhang K., Liu R., Han, R., (1996). Study on designing and testing of the drill unit with individual profiling press wheel. *Transactions of the Chinese Society for Agricultural Machinery*, 1996, 27(10): 53 – 57. China.
- [4] Jiang, L.Q. (2013). Simulation study of circular saw cutting process based on ANSYS/LS-DYNA (基于 ANSYS/LS-DYNA 的圆锯片锯切过程仿真研究). *Guangxi University*, Nanning/China.
- [5] Kanamitsu M., Yamamoto K., Shibano Y, et al. (1994). Development of a Chinese cabbage harvester (Part 3): development of height controller and field test of harvester. *Japan Agricultural Research Quarterly*, 56(2): 127-133. Japan.
- [6] Kim H.J., Yeongsoo C. (2020). Pulling performance of a self-propelled Chinese cabbage harvester and design of a preprocessing unit. *Journal of Agriculture Life Science*, 54(1): 99-108. Korea.
- [7] Lee Y.S., Jang B.E., Kim Y.J., et al. (2018). *Structural analysis of the transportation and the power transmission parts for design of a self-propelled and small-sized Chinese cabbage harvester*. Detroit, Michigan July 29-august. 2018. Korea.
- [8] Li Xiaoqiang, Wang Fene, Guo Weijun, Gong Ziwei, Zhang Juan, (2013). Analysis of influencing factors on cutting force of cabbage rhizomes (甘蓝根茎切割力影响因素分析). *Trans. CSAE*, 29(10): 42-48. Gansu/China.
- [9] Shengsheng Wang, Pan Chen, Jiangtao Ji, Mengqing Lu, (2021). Design and experiment study of flexible threshing unit for Chinese cabbage seeds, *INMATEH-Agricultural Engineering*. 65 (3), pp. 333-344, DOI: <https://doi.org/10.35633/inmateh-65-35>. Bucharest / Romania.
- [10] Tong Wenyu, Zhang Jianfei, Cao Guangqiao, Song Zhiyu, Ning Xiaofeng, (2023). Design and Experiment of a Low-Loss Harvesting Test Platform for Cabbage. *Agriculture*, 13, 1204. <https://doi.org/10.3390/agriculture13061204>. Nanjing/China.
- [11] Wang Jianjun, (2020). Production Status and Development Countermeasures of Chinese Cabbage in China(我国大白菜生产现状及发展对策). *China Fruit & Vegetable*, 40(07): 80-82+106. Shandong/China.
- [12] Yang Yating., Cui Zhichao, Gao Qingsheng, Guan Chunsong., Liu Xiancai., Chen Yongsheng., (2020). Present situation of Chinese cabbage mechanization production and development suggestions (大白菜机械化生产现状及发展建议). *China Veg*, 2020(11):9-16. Nanjing/China.
- [13] Yao, H.L. (2007). Study on key parts of Chinese cabbage harvester (大白菜收获机关键部件的研究), *China Agricultural University*, Beijing/China.
- [14] Zhang J., Wang J., Zheng CY., Du D.D., (2021). Relaxation characteristics for quality evaluation of Chinese cabbage[J]. *Journal of Food Engineering*, 2021, 306(3):110635. Zhejiang/China
- [15] Zhang, J. (2022). Research on physical and mechanical properties of headed Chinese cabbage and its crawler self-propelled harvesting equipment (结球大白菜物理力学特性与履带自走式收获机械的研究). *Zhejiang University*, Hangzhou/China.
- [16] Zhao, T.S. (2020). Study on the design and key technology of cabbage harvester (白菜收获机设计与关键技术研究). *Heilongjiang University*, Harbin/China.
- [17] Zhichao Cui, Chunsong Guan, Tao Xu, Jingjing Fu, Yongsheng Chen, Yating Yang, Qingsheng Gao, (2021). Experiment and parameter optimization of root-cutting for trimming post harvest cabbage, *INMATEH-Agricultural Engineering*. 63 (1), pp. 405-412, DOI: <https://doi.org/10.35633/inmateh-63-41>. Bucharest / Romania.
- [18] Zheng, Jinming, Wang Lin, Wang Xiaochan, Shi Yinyan, Yang Zhenyu, (2023). Parameter Calibration of Cabbages (*Brassica oleracea L.*) Based on the Discrete Element Method. *Agriculture*, 13(3): 555. <https://doi.org/10.3390/agriculture13030555>. Nanjing/China.

- [19] Zhou Liming, Zeng Yifan, Niu Kang, Yuan Yanwei., Bai Shenghe., Chen Kaikang., (2023). Analysis on root cutting mechanism of self-propelled Chinese cabbage harvester and optimisation of device parameters. *INMATEH - Agricultural Engineering*, 71(3), 70–82. <https://doi.org/10.35633/inmateh-71-05>. Bucharest / Romania.;
- [20] ***China Academy of Agricultural Mechanization Sciences. Handbook of Agricultural Machinery Design: Volume II [M]. *Beijing: China Agricultural Science and Technology Press*, 2007;
- [21] ***GB/Z 26582-2011; Production Technical Practice for Cabbage. China National GB Standard Research: Shenzhen, China, 2011.
- [22] ***JB/T 6276-2007; Test Method for Sugar Beet Harvesting Machinery. Ministry of Machinery and Electronics Industry of the People's Republic of China: Beijing, China, 2007.

SEED DISCHARGE PERFORMANCE TEST OF AIR SUCTION SEED DISCHARGER FOR SMALL VEGETABLE SEEDS

面向小粒蔬菜种子的气吸排种器排种性能试验

YanJun LI^{1,2)}, Yichao NING^{*2)}, Fuxiang XIE^{*1)}, Yang Bai¹⁾

¹⁾School of Machinery and Automation, Weifang University, Weifang/China;

²⁾ State Key Laboratory of Agricultural Equipment Technology, Beijing/China

Tel: 15584399067; E-mail: nyc9603@sina.com

Correspondent author: Yichao NING, Fuxiang XIE

DOI: <https://doi.org/10.35633/inmateh-73-61>

Keywords: small vegetable seeds, air-suction seed metering device, virtual simulation, experiment

ABSTRACT

Vegetable precision planting agronomy is suitable for my country's current vegetable planting system, and the air-suction vegetable precision planter is currently the most important work tool in my country. This paper designs a kind of air-absorbing vegetable precision sower for the problems of small vegetable seeds with small grains, poor mobility and high difficulty in achieving uniform sowing of small seeds. First, Fluent software is used to simulate and analyze the flow field of the air chamber in the seed metering device, and the pressure and velocity of the fluid in the air chamber are analyzed. Through the comparison of the pressure distribution cloud chart and the velocity distribution cloud chart, the influence of different apertures, holes, vacuum degree, and gas chamber depth on the flow field of the gas chamber is analyzed. The air suction seed discharger test bench was set up and orthogonal test was carried out, and the test results showed that the optimal parameter combination was 3.5 kPa vacuum degree of the air chamber, 2.4 mm diameter of the type hole, and 18 r/min rotational speed of the seed discharging disk. The high-speed photographic test was carried out under the optimal parameter combination, and the results showed that leakage of suction, adsorption of 1 seed, and adsorption of multiple seeds appeared in the process of suction, and it is important for the development of the air suction precision machine for small seeded vegetables with better performance. The results showed that the phenomenon of leakage, adsorption of 1 seed and adsorption of multiple seeds occurred in the process of seed suction, which provided a reference basis for the development of a better performance of the air-absorption precision planter for small seeds.

摘要

针对蔬菜播种存在播种劳动强度大、良种消耗多、播种质量有待提高等实际问题, 结合我国蔬菜精量播种农艺要求及种植体系, 本文设计了一种气吸式蔬菜精量排种器, 利用 Fluent 软件对排种器内气室流场进行模拟分析, 分析了气室内流体的压力和速度, 通过压力分布云图与速度分布云图的对比, 得出了真空度和排种盘型孔直径对气室流场的影响。搭建气吸排种器试验台进行正交试验, 试验结果表明, 最佳参数组合是气室真空度为 3.5kPa、型孔直径为 2.4mm、排种盘转速为 18r/min。在最佳参数组合下进行高速摄影试验, 结果表明, 在吸种过程中出现了漏吸、吸附 1 粒种子、吸附多粒种子的现象, 为研制出性能更优良的小粒种子蔬菜气吸精量播种机提供参考依据。

INTRODUCTION

With the continuous strengthening of China's science and technology, the overall level of agricultural mechanization technology in China has significantly improved. However, the mechanized planting technology of some small-seeded vegetable crops still needs to be improved (Tian et al., 2023). Vegetable seeders mainly have two types: mechanical and pneumatic. Mechanical seeders can generate static electricity, causing seeds to stick together and making precise sowing difficult (Qi et al., 2020). Moreover, improper structural design of the seeder may increase the seed breakage rate when considering mechanical seeding of small-seeded vegetables such as Chinese cabbage (Chen et al., 2019; Andrii et al., 2018). Although pneumatic seeders require complex maintenance and high cost, they can effectively reduce seed breakage rates and achieve higher seeding efficiency than mechanical seeders (Guan et al., 2018; Yazgi et al., 2007). This is why pneumatic seeders are becoming more and more deeply researched and widely applied in China (Jia, 2022; Huang et al., 2022; Zhang et al., 2022). Zhang et al., (2020), conducted Adams simulation analysis on the pneumatic single-pan double-row seeding device.

The simulation showed that the seed cannot fall when the honeycomb structure hole inclination angle is 2° . When the honeycomb structure hole inclination angle is 18° , the performance meets agronomic requirements and provides theoretical basis for the machining and manufacturing of the whole machine. *Liu et al.*, (2010), conducted experimental research on the influence of rotating speed and vacuum degree of the soybean pneumatic seeder on the seeding performance. *Liao Yitao et al.*, (2024), designed a positive-negative pressure combination seeder with 2 seeding discs that can simultaneously plant 8 rows of small cabbage and conducted a bench test, achieving an average qualified index of 91.32%, an average replanting index of 6.19%, and an average missed planting index of 2.49% when the seeding disc rotating speed was 30 r/min, the negative pressure was -3000 Pa, and the positive pressure was 300 Pa, meeting the agronomic requirements for small cabbage planting.

This article addresses the difficulties of achieving uniform homogeneous sowing of small vegetable seeds due to their small size and poor fluidity using ordinary seeders. Additionally, those seeders cannot meet the requirements of precise seeding operations for small vegetable seeds. For this reason, a seeder for small vegetable seeds with precise seeding capabilities is designed, and theoretical analysis of the overall structure of the pneumatic seeder is conducted. An ADAMS software is used for sowing trajectory simulation while a Fluent software is used for simulating the gas chamber airflow to analyze the changes of the gas chamber airflow under different vacuum degrees and apertures. A vegetable seed planter unit is built and seeding performance testing research is carried out to provide a reference for the development of new type seeders and precise seeding machines for vegetables.

MATERIALS AND METHODS

Analysis of Suction Process of Pneumatic Seeder

The structure of the seed discharger is shown in Fig. 1. During the suction process of the seeding machine, the force acting on the seed is quite complex. The frictional force acting on the seed in the filling zone is much greater than the weight of the seed itself. In order to ensure that the seed can be smoothly adsorbed onto the seeding plate, a force analysis is performed on the seed to calculate the minimum required air pressure (*Xu et al.*, 2022).

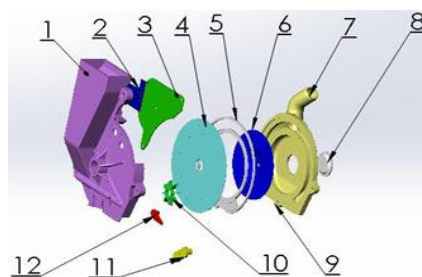


Fig. 1 – Assembly model seeding device

1. Seed box; 2. Seed stopper; 3. Seed scraper; 4. Seed discharge disc; 5. Sealing ring; 6. Sealing disc; 7. Negative pressure inlet; 8. Gasket; 9. Positive pressure hole; 10. Seed churn; 11. Seed paddle; 12. Seed churn holder

A three-dimensional Cartesian coordinate system is established with the center of mass of the seed as the origin. The i -axis represents the direction of the line velocity of the seeding plate rotation, the j -axis represents the direction of the centrifugal force acting on the seed, and the k -axis represents the direction perpendicular to the seeding hole of the seeding plate (*Zhang et al.*, 2021).

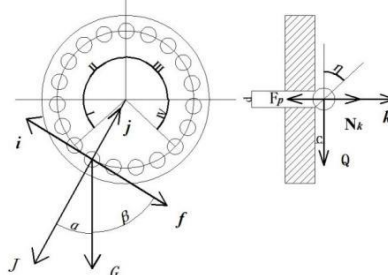


Fig. 2 – Force analysis of seed aspiration

I is the process of sucking seeds from the seed tray; *II* is clearing seeds from the seed tray; *III* is carrying seeds from the seed tray; *IV* is the process of casting seeds from the seed tray.

The force analysis of the seeding plate during the suction process is as follows:

$$\begin{cases} \sum F_i=0, N_i - f - G \cos \theta = 0 \\ \sum F_j=0, N_j - J - G \sin \theta = 0 \\ \sum F_k=0, N_k - F_p = 0 \\ \sum M=0, F_p \frac{d}{2} - QC = 0 \end{cases} \quad (1)$$

G - the weight of the seed [N];

J - the centrifugal force acting on the seed [N];

F - the combined frictional force and air resistance acting on the seed [N];

Q - the total force acting on the seed resulting from the combination of G , J and f [N];

N_i , N_j , N_k - the components of force acting on the seed from each seeding hole in the i , j , and k directions [N];

F_p - the force of adhesion acting on the seed [N];

C - the distance between the point of action of the seeding hole on the seed and the center of mass of the seed [m].

The force acting on the seed from each seeding hole on the seeding plate in the i - j plane N_{ij} can be calculated as follows:

$$N_{ij} = \sqrt{N_i^2 + N_j^2} = \sqrt{J^2 + G^2 + f^2 + 2G\sqrt{f^2 + J^2} \sin(\alpha + \beta)} \quad (2)$$

α - the angle between the direction of the weight of the seed and the direction of the centrifugal force acting on the seed [°];

β - the angle between the direction of the weight of the seed and the i -axis [°]

The force equilibrium at the suction hole yields:

$$\begin{aligned} F_p &= Q \frac{d}{2C} = Q \tan \eta = N_{ij} \tan \eta \\ &= \sqrt{J^2 + G^2 + f^2 + 2G\sqrt{f^2 + J^2} \sin(\alpha + \beta)} \tan \eta \end{aligned} \quad (3)$$

η - the angle between Q and the point on the seed where the seeding hole provides support to the seed [°];

d - the diameter of the seeding hole on the seeding plate [m].

The theoretical negative pressure value is:

$$P = \frac{F_p}{S} = \frac{4 * \sqrt{J^2 + G^2 + f^2 + 2G\sqrt{f^2 + J^2} \sin(\alpha + \beta)} \tan \eta}{\pi d^2} \quad (4)$$

P - the theoretical minimum negative pressure [kPa];

S - the area of the cylindrical seeding hole [m²].

In actual working conditions, irregularities in machinery vibrations and the shape of seeds may cause uncertainty. To ensure successful seed suction, the actual minimum negative pressure P_{min} should be:

$$P_{min} = K_1 K_2 K_3 P = \frac{4 * \sqrt{J^2 + G^2 + f^2 + 2G\sqrt{f^2 + J^2} \sin(\alpha + \beta)} \tan \eta}{\pi d^2} \quad (5)$$

K_1 - the reliability coefficient of seed suction [1.8-2.0];

K_2 - the stability coefficient of the seeding machine operation [1.6-2.0];

K_3 - the coefficient of influence of seed moisture content [1.1-1.2].

Analysis of the process by which the seeding plate carries seed

During the seed carrying stage, the entire seed planter operates smoothly without interference from other forces, and the negative pressure fluctuation is also small. When the seed carrying rotator rotates, the seed is only affected by air resistance without other forces interfering. The force situation is much smaller than that of the seed suction process. Since the fan is a constant pressure, the pressure inside does not change all the time.

At the same time, the negative pressure required for the seed-carrying process is much lower than that of the seed suction process, so it is not necessary to calculate the external force acting on the seed during the seed-carrying process, thus obtaining the required negative pressure (Li *et al.*, 2023).

Due to the existence of uncertain factors during the seed suction process, the actual air pressure value is much larger than the theoretical air pressure value, which may cause one type of hole in the seed plate to simultaneously adsorb multiple seeds (Liao *et al.*, 2018). Therefore, a seed clearing area is set between the seed suction area and the seed carrying area, and excess seeds are scraped off by the scraping plate when the seed adsorption becomes stable. The angle of the scraping plate can be adjusted at any time, and it can be adjusted according to different seeds and different models of seed discs to achieve the best sowing effect.

Fluent flow analysis of the seeder

The internal flow field of the air-suction seed planter was analyzed using Fluent software. The mesh model for the fluid simulation of the seed planter was established, and input and output boundary conditions were set (Chen *et al.*, 2018). By comparing and analyzing different vacuum degrees and different aperture sizes inside the planter, the internal pressure, velocity, and flow field were analyzed to discover the influence of different conditions on the internal pressure and flow velocity and achieve precision seeding (Tang *et al.*, 2022; Zang *et al.*, 2015).

The seed plate and vacuum chamber are key components of the seed planter and are shown in Fig 3. The hole design of the seed plate is circular, and the number of holes is 20, with an angle of 18° between every two holes. The size of the vacuum chamber is designed according to the size of the seed plate, and the diameter of the connecting suction tube is approximately 25 mm (Gong *et al.*, 2014). Due to the complexity of the internal structure of the seed planter, the internal model was simplified into three parts: the seed plate holes, seed chamber, and vacuum chamber, for the simulation analysis of the gas chamber flow field.



Fig. 3 – Structure of seed plate and vacuum chamber

Bench experiments

Yellow Sword 1 pelletized carrot seeds of Shouhe Company with water content less than 8% were used as test materials in the experiment (GB/T 6973-2005). The test equipment mainly consisted of conveyor belt, speed regulator, pneumatic device, and seed discharger as shown in Fig. 4. Other test auxiliary pieces of equipment are, rotational speed tester (3402, TACHO Hi Tester, Japan), wind pressure tester, camera, stopwatch, meter scale, and so on. High-speed photographic equipment used in Japan PHOTRON company produced FASTCAM-MiNi WX50 type675KM-16 high-speed camera, recording speed up to 67,500 frames per second (FPS), recording capacity of 16 G, the test was selected for the recording speed of 125 FPS.

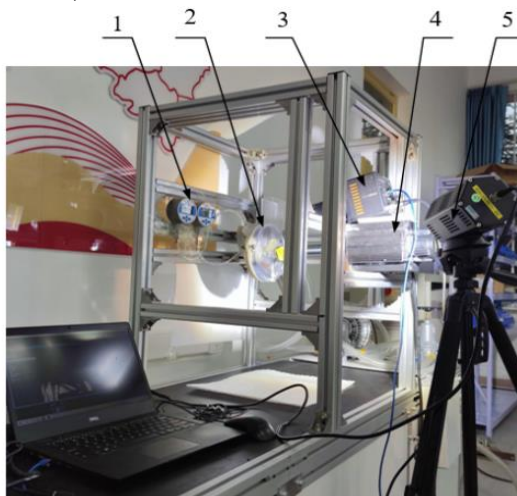


Fig. 4 – Test bench and test seeds

1. Digital display precision pressure gauge; 2. Pneumatic precision seed discharger;
3. High speed camera; 4. Servo motor; 5. LED flash light

Experiments indicators and experiments methods

The precision seed planter adopts the international standard ISO 7256/1-2004 "Seeders-Testing methods-Part 1: Single Seed Drills (Precision Seeders)," and combines it with the actual situation in China to select test indicators. The use of this standard can make the test results of different types of single seed (precision) seeders comparable (Biocca M. et al., 2019). In this standard, the three main performance indicators of the precision seed planter are the qualified planting rate, missed planting rate, and replanting rate.

Orthogonal experiments

Due to the influence of vacuum degree, hole diameter of tray and rotation speed of tray on the working performance of the seeder, the orthogonal test method was adopted to analyze the working performance of the seeder. Based on the results of single-factor tests, the rotational speed of the tray, vacuum degree of the chamber and hole diameter of the tray, which have significant effects on the test indicators, were selected for orthogonal tests. The range and variance analysis of the orthogonal test results were conducted to obtain the primary and secondary priority orders affecting the operating parameters of the test indicators, thus finding the optimal combination of operating parameters for the seeder and providing theoretical support for obtaining the optimal working state of the seeder (Kumar et al., 2012). Based on the single-factor test, the orthogonal test was conducted on three factors: the rotational speed of the tray A, the vacuum degree B, and the hole diameter C. The qualifying rate, re-broadcast rate, and leak broadcast rate of the seed were used as test indicators, with each level repeated 10 times and the results averaged. The level table of the orthogonal test factors is shown in table 1.

Table 1

| Factors and level of orthogonal test | | | |
|--------------------------------------|--------------------------|----------------------|----------------------|
| Level | Factors | | |
| | A. Seed reel speed r/min | B. Vacuum Level /kPa | C. Hole diameter /mm |
| 1 | 12 | 2.5 | 2.2 |
| 2 | 18 | 3 | 2.4 |
| 3 | 24 | 3.5 | 2.6 |

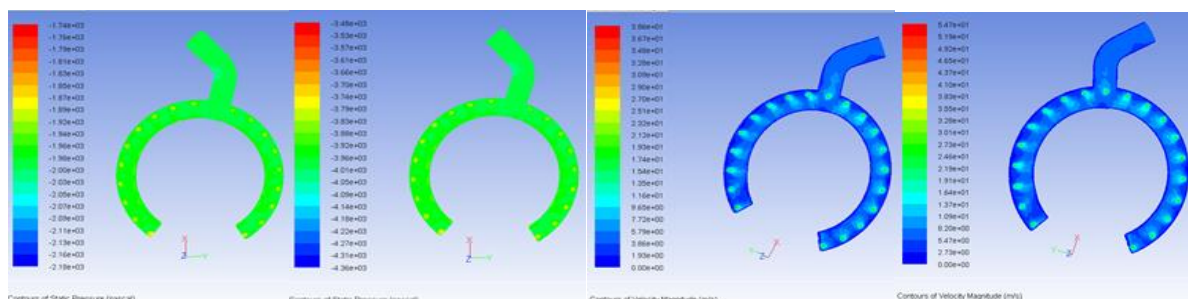
High-speed photography experiments

To observe the situation of seeds during the entire sowing process, a high-speed camera was used to record the seed suction process of the seeder, as the holes in the seeder rotate at a high speed and the human eye cannot see the situation of the holes adsorbing seeds (Elnesr et al., 2016).

RESULTS

Changes in flow field at different vacuities

Vacuum degree is an important factor affecting the flow field of the seed planter. Analyzing the changes of the internal flow field of the planter under different vacuum conditions and selecting the pressure of 2000 Pa and 4000 Pa as the two working conditions for comparative analysis, as shown in Fig 5.



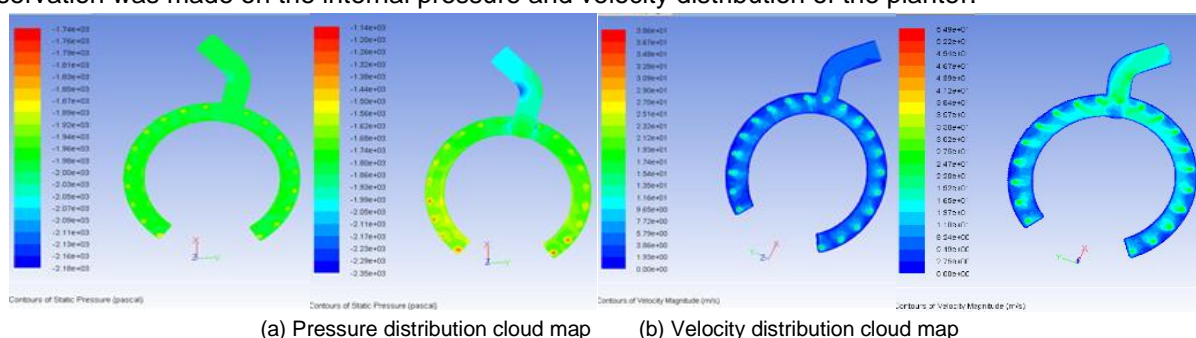
(a) Pressure distribution cloud map (b) Velocity distribution cloud map
Fig. 5 – Variation of flow field at different vacuum degrees

When the negative pressure inside the planter changes, there is no significant change in the internal pressure, and the overall trend is consistent, with relatively high pressure at each suction hole. Therefore, it can be judged that the pressure of the fan only affects the pressure of the flow field inside the planter, and has almost no effect on the flow field in the vacuum chamber.

In operation, only enough pressure is needed to provide stable negative pressure to ensure that the seeds are easily adsorbed. The gas velocity is related to the shape of the type hole on the planter, and the velocity is distributed circularly, and the velocity gradually decreases along the hole center. When the negative pressure inside the planter changes, the velocity distribution inside the planter near the hole is significantly higher, and the speed becomes smaller as it gets farther away from the hole position. There is gas flow at the type hole, and the velocity at various inner walls is basically close to zero. It can be concluded that the size of the pressure only affects the size of the velocity, and the velocity is proportional to the pressure. When the pressure value increases, the velocity value increases significantly. The figure shows the pressure distribution at different hole positions, where the pressure near the hole on the right side of the planter is relatively high, and the pressure near the bottom hole is relatively low. The reason for this phenomenon is that the type hole on the right side of the planter is closer to the pipeline of the fan, while the type hole near the bottom is farther away from the pipeline of the fan.

Changes in flow field at different aperture sizes

Comparative analysis was carried out between the 2 mm and 4 mm diameter type holes under the same simulation conditions when the pressure was set to 2000 Pa on the planter, as shown in Fig 6. The observation was made on the internal pressure and velocity distribution of the planter.



(a) Pressure distribution cloud map (b) Velocity distribution cloud map

Fig. 6 – Changes of flow field at different apertures

When the diameter of the type hole on the planter changes, the pressure distribution inside the planter will also change. When the diameter of the type hole increases, the pressure at the type hole also increases. This phenomenon is particularly evident at the bottom type hole of the planter, and there is a phenomenon of lower negative pressure at the bend of the upper pipe. The pressure distribution at other positions is relatively uniform. The larger the diameter of the type hole, the more obvious the influence on the internal pressure situation. Therefore, the diameter of the type hole affects the pressure, and the larger the diameter, the greater the pressure in the vacuum chamber. The gas velocity inside the planter is related to the diameter of the type hole on the planter. The larger the diameter of the type hole, the faster the internal gas velocity inside the planter. However, the gas velocities among the phases inside the planter are relatively consistent. For the same diameter, especially for larger diameters, the gas velocities at different positions are slightly different. The closer to the pipeline above, the faster the gas velocity. For different type holes, the larger the diameter, the faster the gas velocity in the upper pipe. The larger the diameter of the type hole, the greater the pressure at the hole.

In summary, when the diameter of the type hole on the planter is too large, gas leakage will occur and the pressure value will not continue to increase with the diameter. In addition, when the diameter of the type hole on the planter increases, the power required for the fan will also increase. Therefore, it is not recommended to choose too large type holes under the premise of meeting the sowing requirements. In this experiment, the vacuum degree of the planter is 2000 Pa, and the diameter of the type hole is 2 mm.

Orthogonal experiments

The orthogonal experimental design and the experimental results are shown in Table 2. According to the data in Table 3, it can be concluded from the range analysis of the qualified rate of the experimental indicators that $k_{A2} > k_{A3} > k_{A1}$, so it can be judged that A2 is the optimal level of factor A; $k_{B3} > k_{B2} > k_{B1}$, it can be judged that B3 is the optimal level of factor B; $k_{C1} > k_{C3} > k_{C2}$, it can be judged that C1 is the optimal level of factor C. Since the larger the qualified suction rate, the better the working performance of the pneumatic sowing mechanism, the optimal combination of the qualified suction rate is A2B3C1. Moreover, $2.86 > 1.41 > 1.19$, indicating that the factor that has the greatest impact on the qualified suction rate is the rotation speed of the pneumatic sowing plate, followed by the vacuum degree of the chamber, and finally the diameter of the holes.

Table 2

| Orthogonal test scheme and test results | | | | | | |
|---|---|---|-----------------------------------|-------------------|----------------|--|
| A | B | C | Suction seed qualification rate/% | Resorption rate/% | Leakage rate/% | |
| 1 | 1 | 1 | 87.19 | 6.99 | 5.82 | |
| 1 | 2 | 2 | 86.61 | 7.81 | 5.58 | |
| 1 | 3 | 3 | 88.36 | 5.47 | 6.17 | |
| 2 | 1 | 2 | 89.52 | 4.99 | 5.49 | |
| 2 | 2 | 3 | 89.6 | 4.2 | 6.2 | |
| 2 | 3 | 1 | 91.63 | 3.14 | 5.23 | |
| 3 | 1 | 3 | 87.55 | 6.87 | 5.58 | |
| 3 | 2 | 1 | 89.39 | 4.86 | 5.75 | |
| 3 | 3 | 2 | 88.50 | 5.81 | 5.69 | |

According to the range analysis of the missed suction rate of the experimental indicators, $k_{A1} > k_{A3} > k_{A2}$, it can be judged that A2 is the optimal level of factor A; $k_{B2} > k_{B3} > k_{B1}$, it can be judged that B1 is the optimal level of factor B; $k_{C3} > k_{C1} > k_{C2}$, it can be judged that C2 is the optimal level of factor C. Since the smaller the missed suction rate, the better the working performance of the pneumatic sowing mechanism, the optimal combination of the missed suction rate is A2B1C2, and $0.40 > 0.22 > 0.21$, indicating that the diameter of the holes has the greatest impact on the missed suction rate, followed by the rotation speed of the pneumatic sowing plate, and finally the vacuum degree of the chamber.

According to the range analysis of the repeated suction rate of the experimental indicators, $k_{A1} > k_{A3} > k_{A2}$, it can be judged that A2 is the optimal level of factor A; $k_{B1} > k_{B2} > k_{B3}$, it can be judged that B3 is the optimal level of factor B; $k_{C2} > k_{C3} > k_{C1}$, it can be judged that C1 is the optimal level of factor C. Since the smaller the repeated suction rate, the better the working performance of the pneumatic sowing mechanism, the optimal combination of the repeated suction rate is A2B3C1, and $2.65 > 1.48 > 1.21$, indicating that the rotation speed of the pneumatic sowing plate is the most important factor affecting the repeated suction rate, followed by the vacuum degree of the chamber, and finally the diameter of the holes.

Table 3

| Range analysis of orthogonal test results | | | | | | | | | | |
|---|----------|--------|--------|----------|-------|-------|----------|-------|-------|--|
| | η_1 | | | η_2 | | | η_3 | | | |
| | A | B | C | A | B | C | A | B | C | |
| K1 | 262.16 | 264.26 | 268.21 | 17.57 | 16.89 | 16.80 | 20.27 | 18.85 | 14.99 | |
| K2 | 270.75 | 265.60 | 264.63 | 16.92 | 17.53 | 16.76 | 12.33 | 16.87 | 18.61 | |
| K3 | 265.44 | 268.49 | 265.51 | 17.02 | 17.09 | 17.95 | 17.54 | 14.42 | 16.54 | |
| k1 | 87.39 | 88.09 | 89.40 | 5.86 | 5.63 | 5.60 | 6.76 | 6.28 | 5.00 | |
| k2 | 90.25 | 88.53 | 88.21 | 5.64 | 5.84 | 5.59 | 4.11 | 5.62 | 6.20 | |
| k3 | 88.48 | 89.50 | 88.50 | 5.67 | 5.70 | 5.98 | 5.85 | 4.81 | 5.51 | |
| R | 2.86 | 1.41 | 1.19 | 0.22 | 0.21 | 0.40 | 2.65 | 1.48 | 1.21 | |

The results of the orthogonal experiment analysis are shown in Table 4. According to the variance analysis of the qualified absorption rate, it can be found that $F_{0.1}(2,6)=3.46$ is obtained after consulting the F-table. Compared with the F value in Table 4, it can be concluded that the three factors have a certain impact on the qualified absorption rate. The rotational speed of the pneumatic seeding plate has a significant influence on the qualified absorption rate, while the vacuum degree of the air chamber and the diameter of the mold hole have an insignificant effect on the qualified absorption rate. According to the variance analysis of the leak suction rate, after consulting the F-table, it can be found that $F_{0.1}(2,6)=3.46$. Compared with the F value in Table 4, the three factors have a certain impact on the leak suction rate, but the vacuum degree of the air chamber, the rotational speed of the pneumatic seeding plate, and the diameter of the mold hole have an insignificant effect on the leak suction rate.

According to the variance analysis of the re-absorption rate, after consulting the F table, it can be found that $F_{0.1}(2,6)=3.46$. Compared with the F value in Table 4, the three factors have a certain impact on the re-absorption rate. The rotational speed of the pneumatic seeding plate has a significant influence on the re-absorption rate, while the vacuum degree of the air chamber and the diameter of the mold hole have an insignificant effect on the re-absorption rate.

In the single-factor experiment of the seedling planter, the effects of vacuum degree of the air chamber, diameter of the mold hole, and rotational speed of the pneumatic seeding plate on the working performance of the seedling planter were mainly analyzed. The range and variance analysis of the orthogonal experiment results were conducted, and the primary and secondary orders and the significant influence of the test indicators were obtained. Due to the requirements of the experiment, a higher qualified absorption rate needs to be obtained while reducing the leak suction rate and the re-absorption rate as much as possible. Based on the range analysis of the primary and secondary orders and the variance analysis of the significant impact, the optimal combination was finally determined as A2B3C1, that is, the rotational speed of the pneumatic seeding plate is 18 r/min, the vacuum degree of the air chamber is 3.5 kPa, and the diameter of the mold hole is 2.4 mm.

Table 4

Analysis of variance of orthogonal experiment results

| Source of variation | SS | | | df | | | MS | | | F | | |
|---------------------|----------|----------|----------|----------|----------|----------|----------|------------------|----------|----------|----------|----------|
| | η_1 | η_2 | η_3 | η_1 | η_2 | η_3 | η_1 | η_2 | η_3 | η_1 | η_2 | η_3 |
| A | 12.52 | 0.08 | 10.84 | 2 | 2 | 2 | 6.26 | 0.04 | 5.42 | 6.11 | 0.35 | 4.95 |
| B | 3.11 | 0.07 | 3.28 | 2 | 2 | 2 | 1.55 | 0.03 | 1.64 | 0.60 | 0.30 | 0.69 |
| C | 2.32 | 0.30 | 2.19 | 2 | 2 | 2 | 1.16 | $\frac{0.15}{3}$ | 0.09 | 0.42 | 1.93 | 0.43 |

High-speed photography experiments

Under the optimal combination parameters obtained from the orthogonal experiment, the rotational speed of the pneumatic seeding plate was selected as 18 r/min, the vacuum degree of the air chamber was 3.5 kPa, and the diameter of the mold hole was 2.4 mm for high-speed photography experiments to observe the grainy vegetable seeds' adsorption situation in the seed planter and summarize the adsorption characteristics of the seed planter.

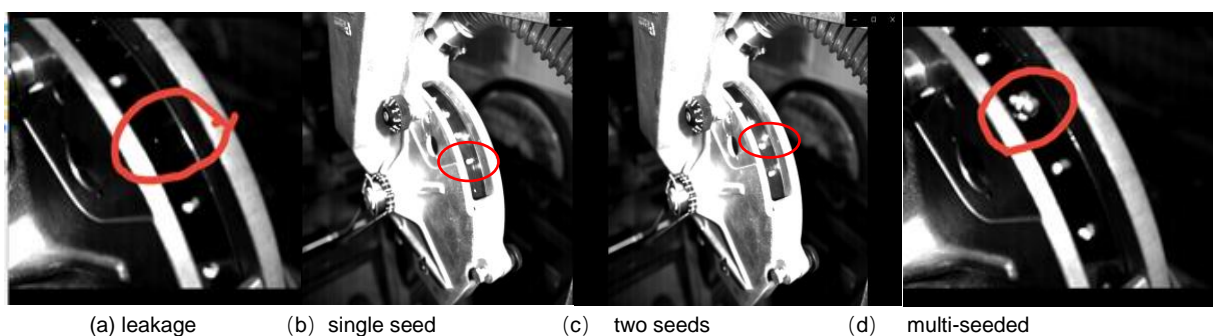


Fig. 7 – High-speed photography test results

The results of the high-speed photography experiments are shown in Fig 7. During the experiment, phenomena such as leak suction, adsorption of one seed, adsorption of two seeds, and adsorption of multiple seeds appeared. Through analysis, it was found that the leak suction phenomenon was caused by the unstable air chamber pressure. Adsorption of one seed is the main performance indicator of this type of seed planter, which can be achieved by adjusting parameters such as the rotational speed of the pneumatic seeding plate, the vacuum degree of the air chamber, and the diameter of the mold hole to achieve stability. The phenomenon of adsorption of multiple seeds is caused by uneven air chamber pressure, and later, the air chamber structure and the design of the sub-seeding needle need to be optimized to reduce the number of adsorbed seeds and achieve precision seeding.

CONCLUSIONS

(1) In this study, a kind of air-absorbing vegetable precision seed discharger was designed, the working principle of the seed discharger was clarified and its working process was analyzed theoretically, and the factors affecting the seed suction and seed carrying process of the seed discharger were obtained, as well as the size of the minimum negative pressure value of the air chamber required for the type of holes to be able to stably adsorb the seeds.

(2) Using Fluent software to theoretically analyze the flow field of the gas, establish a grid model for the simulation of the fluid inside the seeder, and obtain the pressure and velocity distribution cloud diagrams of different vacuum degrees and different aperture sizes inside the seeder, analyze the pressure, velocity and flow field inside the seeder, and provide a reference guide for the design of a better seeder.

(3) Using qualified rate, re-sowing rate, and missed rate as test indicators, orthogonal test and high-speed photography test were carried out, and the test results yielded the optimal parameter combinations, and the comprehensive balance of the test indexes, the seed discharge disk rotational speed of 18 r/min, the vacuum degree of the air chamber of 3.5 kPa, and the diameter of the type hole of 2.4 mm, the best effect of seed discharge. High-speed photography test showed that in the process of seed suction, there were leakage, adsorption of 1 seed, adsorption of 2 seeds and adsorption of more than 2 seeds.

ACKNOWLEDGEMENT

The authors were funded for this project by the State Key Laboratory of Agricultural Equipment Technology (NKL-2023-006) and Shandong Province Key R&D Program (Major Science and Technology Innovation Project)-Research and Development of High-Efficiency Production Equipment for Specialty Vegetables-2022CXGC010612.

REFERENCES

- [1] Biocca, M., Fanigliulo, R., Pochi, D., & Gallo, R. (2019). Dust drift mitigating devices applied on precision pneumatic seed drills: a mini-review. *INMATEH - Agricultural Engineering*, Vol. 58, no.2, pp. 273-284, Monterotondo/Italy;
- [2] Chen, Y., (2019). China vegetable production mechanization development report in 2018 (中国蔬菜生产机械化 2018 年度发展报告). *Journal of Chinese Agricultural Mechanization*, Vol. 40, no.4, pp. 1-6,18, Jiangsu/China;
- [3] Chen, M., Diao, P., Zhang, Y., Gao, Q., & Yang, Z., (2018). Design of pneumatic seed-metering device with single seed-metering plate for double-row in soybean narrow-row-dense-planting seeder (大豆窄行密植播种机单盘双行气吸式排种器设计). *Transactions of the CSAE*, Vol.21, no.21, pp.8-16, Shandong/China;
- [4] Elnesr, M.N., Alazba A.A., (2016). A spreadsheet model to select vegetables planting dates for maximum yield and water use efficiency[J]. *Computers and Electronics in Agriculture*. Vol.124, pp. 55-64, Riyadh/Saudi Arabia;
- [5] Guan, C., Cui, Z., Gao, Q., Yang, Y., Chen, Y., (2018). Research status of precision direct seeding technology and equipment for vegetables (蔬菜精量直播技术及装备的研究现状). *Chinese Vegetables*, Vol.12, pp. 9-15, Jiangsu/China;
- [6] Gong, Z., Chen, J., Li, Y., Li, J., (2014). Seed Force in Airflow Field of Vacuum Tray Precision Seeder Device during Suction Process of Seeds (吸盘式精密排种装置吸种过程气流场中种子受力研究). *Transactions of the Chinese Society for Agricultural Machinery*, Vol.45, no.6, pp.92-97+117, Jiangsu/China;
- [7] Huang, Y., Li, P., Dong, J., Chen, X., Zhang, S., (2022). Design and test of high-speed precision soybean metering device with side guide (大豆高速播种机侧置导引式精量排种器设计与试验). *Journal of Agricultural Machinery*, Vol.53, no.10, pp. 44-53, 75, Shanxi/China;
- [8] Jia, Y., (2022). Comparison of precision seed metering device and analysis of its development status (精量排种器对比及发展现状分析). *Agricultural Technology and Equipment*, Vol. 5, pp. 38-40, Hebei/China;

- [9] Kumar, G.V.P., Rasanna, H., (2012). Automatic feeding mechanism of a vegetable transplanter. *International Journal of Agricultural & Biological Engineering*, Vol. 5, no.2, pp. 1-8, 10, Assam/India;
- [10] Li, Y., Bai, Y., Zhang, X., Xie, F., (2023). Structural Design and Simulation Analysis of a Dual-row Pneumatic Vegetable Precision Planter. *Processes*, Vol. 11, no.6, pp. 1803, Shandong/China;
- [11] Liao, Y., Liao, Q., Wang, L., Zheng, J., Gao, L., (2018). Investigation on vacuum singulating effect influencing factors of pneumatic precision seed metering device for small particle size of seeds(气力式小粒径种子精量排种器吸种效果影响因素研究). *Transactions of the Chinese Society of Agricultural Engineering*, Vol. 34, no.24, pp. 10-17, Hubei/China;
- [12] Liao, Y., Liu, J., Liao, Q., Zheng, J., Li, T., (2024). Design and Test of Positive and Negative Pressure Combination Roller Type Precision Seed-metering Device for Rapeseed (正负气压组合滚轮式油菜精密排种器设计与试验). *Journal of Agricultural Machinery*, Vol. 55, no.5, pp. 63-76, Hubei/China;
- [13] Liu, W., Zhao, M., Wang, W., Zhao, S., (2010). Theoretical analysis and experiments of metering performance of the pneumatic seed metering device. *Transactions of the CSAE*, Vol. 26, no.9, pp. 133-138, Guangdong/China;
- [14] Qi, Y., Xiang, S., (2020). Research status and development trend of vegetable seeder at home and abroad (国内外蔬菜播种机的研究现状与发展趋势). *Journal of Chinese Agricultural Mechanization*, Vol. 41, no.1, pp. 205-208, Shandong/China;
- [15] Tang, H., Xu, C., Wang J., (2023). Method of straw ditch buried returning development of supporting machine and analysis of influencing factor. *Frontiers in Plant Science*, Vol. 13, pp. 967838. Harbin/China;
- [16] Tian, Y., Li, Y., Jiang, J., Li, C., Xie, F., (2023). Experimental study on seed compression characteristics of pak choi (青梗小白菜种子压缩载荷试验研究). *Agricultural Mechanization Research*, Vol. 45, no.6, pp. 152-158, Shandong/China;
- [17] Xu, M., (2019). Design and Experiment of Air Suction Carrot Seeder (气吸式胡萝卜播种机的设计与实验). MSc Thesis, *Shandong University of Science and Technology*, Shandong/China;
- [18] Yazgi A., Degirmencioglu A. (2007). Optimisation of the seed spacing uniformity performance of a vacuum-type precision seeder using response surface methodology. *Biosystems Engineering*, Vol. 97, no.3, pp. 347-356, Izmir/Turkey;
- [19] Yatskul A., Lemiere J.P. (2018). Establishing the conveying parameters required for the air-seeders. *Biosystems Engineering*, Vol. 166, no.2, pp. 1-12, Philadelphia/French;
- [20] Zang, G., Zang, Y., Luo, X., Wang Z., Zhang Q., Zhang, S., (2015). Design and indoor simulated experiment of pneumatic rice seed metering device. *International Journal of Agricultural & Biological Engineering*, Vol. 8, no.4, pp. 10-18, Guangdong/China;
- [21] Zhang, K., Ma, G., Li, J., Zhao, X., (2022). Material characteristics of vegetable seeds with small grain size and design of seed metering device. *INMATEH-Agricultural Engineering*, Vol. 68, no.3, pp. 789-797, Shandong/China;
- [22] Zhang K., Zhang L., Ding, Y., Liu, X., Zhao, X., (2021). Design and test of air-suction pepper seed metering device based on air supply and quantitative seed supply. *INMATEH-Agricultural Engineering*, Vol. 64, no.2, pp. 345-354, Shandong/China;
- [23] Zhang, X., Song, J., et al. (2020). Design and simulation analysis of pneumatic mechanical combined single disc and double row seed meter (气力机械组合式单盘双行排种器设计与仿真分析). *Journal of Chinese Agricultural Mechanization*, Vol. 41, no.3, pp. 30-34, Shandong/China;

A REVIEW OF INTELLIGENT HEADER TECHNOLOGY FOR GRAIN COMBINE HARVESTER

谷物联合收获机智能化割台技术研究综述

Jin WANG^{1,2)}, Fuqiang GOU^{1,2)}, Zhenjie QIAN¹⁾, Youliang NI¹⁾, Chengqian JIN^{*1,3)}

¹⁾ Nanjing Institute of Agricultural Mechanization, Ministry of Agriculture and Rural Affairs, Nanjing, Jiangsu / China

²⁾ Graduate School of Chinese Academy of Agricultural Sciences, Beijing / China

³⁾ School of Agricultural Engineering and Food Science, Shandong University of Technology, Zibo, Shandong / China

Tel: +8615366092900; E-mail: jinchengqian@caas.cn

DOI: <https://doi.org/10.35633/inmateh-73-62>

Keywords: Grain combine harvesters, intelligent header, agricultural machinery, height control systems

ABSTRACT

With the rapid advancement of agricultural mechanization, intelligent header technology has emerged as a pivotal element in optimizing the efficiency and quality of grain combine harvesters. This paper offers a comprehensive analysis of the current state of intelligent header technology, with a particular emphasis on the structure, working principles, contour-following mechanisms, and height control technologies. By integrating cutting-edge sensor technologies, advanced control algorithms, and optimized mechanical designs, intelligent headers can achieve precise control over height and posture, thereby significantly reducing crop losses and enhancing both harvesting efficiency and quality. Despite substantial progress, challenges remain in areas such as response speed, real-time performance, height measurement accuracy, and control algorithm effectiveness. Future research will likely concentrate on improving control system performance, refining component and system designs, and incorporating emerging technologies to better accommodate diverse crops and complex terrains. This paper also provides a critical evaluation of current limitations in intelligent header research and projects future trends, offering valuable theoretical and practical insights for optimizing header structures, minimizing losses, and enhancing intelligent functionalities. The ultimate aim is to drive continuous innovation and advancement in header technology for grain combine harvesters.

摘要

随着农业机械化技术的不断进步，智能割台技术已成为提升谷物联合收获机效率和质量的关键部件。本文全面分析了智能割台技术的发展现状，重点探讨了割台的结构与工作原理，以及仿形与高度智能化控制技术。通过整合先进的传感器技术、控制算法和机械结构优化，智能割台实现了对高度和姿态的精确控制，显著减少了作物损失，提升了收割效率和作业质量。尽管取得了显著进展，智能割台在响应速度、实时性、高度测量和控制算法方面还存在局限。展望未来，研究将集中在提升控制系统性能、优化部件与系统设计，并引入新技术以适应多样化的作物和复杂地形。本文还详细评述了当前智能割台研究的不足，并展望了未来的研究发展趋势，提供了割台结构优化、损失减少及智能化水平提升的理论与实践参考，旨在推动联合收获机割台技术的持续进步与创新。

INTRODUCTION

With the continuous advancement of modern agricultural mechanization, the deployment of grain combine harvesters has become increasingly prevalent. Among the critical components of these machines, the header plays an indispensable role in the harvesting process. Traditional headers, however, are often characterized by limited intelligence and imprecise control, resulting in substantial crop losses that significantly hinder harvesting efficiency and economic returns (Geng *et al.*, 2020; Golyapin *et al.*, 2021). In recent years, the development of intelligent headers has emerged as a focal point within both academia and industry. By integrating advanced sensor technologies, sophisticated control algorithms, and optimized mechanical designs, intelligent headers have achieved precise control over height and posture, leading to a marked reduction in crop losses and improvements in harvesting efficiency and quality. These technological advancements are particularly advantageous in complex terrains and under diverse crop conditions. The implementation of these innovations not only enhances the functionality of headers but also improves their adaptability across various operational environments (Goossens *et al.*, 2023; Wang *et al.*, 2024; Ji *et al.*, 2023).

The development of intelligent headers provides critical technical support for precision agriculture, fostering the optimization of operational processes and enhancing the economic and environmental sustainability of harvesting systems.

This review systematically examines the current state of intelligent header technology in grain combine harvesters. It delves into the structure and working principles of headers, explores contour and height control technologies and their applications, and investigates the intelligent control methods of key components. Additionally, it identifies existing challenges and limitations in the research on intelligent headers and anticipates future developmental trends, offering both theoretical insights and practical guidance for further research and technological implementation.

Header Structure and Working Principles

The combine harvester integrates the header, threshing unit, and intermediate conveyor system, enabling the simultaneous execution of cutting, threshing, separating, cleaning, and grain collection (Xu *et al.*, 2013). The header, located at the front end of the harvester, is one of its essential components (Tai *et al.*, 2020). As shown in Fig. 1, it comprises a reel, cutter, divider, and conveyor system. The primary function of the header is to sever crops and continuously convey them to the threshing unit, facilitating efficient harvesting (Zhou *et al.*, 2023; Liu, 2022). Currently, by replacing certain parts (such as the cutter, reel, and auger), the header can adapt to harvesting both rice and wheat as well as soybeans.

During operation, the header, functioning as the harvester's primary cutting mechanism (Nalobina *et al.*, 2019), initiates the process by directing crops into the cutting area via the divider. The reel then guides the grains towards the cutter, where the cutting occurs. Following this, the reel advances the cut crops onto the platform, where the auger accumulates them to the right side. Retractable fingers then feed the grains into the inclined conveyor. The conveyor chain transports the crops to the drum for threshing, completing the transition from harvesting to threshing in an efficient, continuous sequence (Wang *et al.*, 2022; Li *et al.*, 2014; Huang *et al.*, 2020).

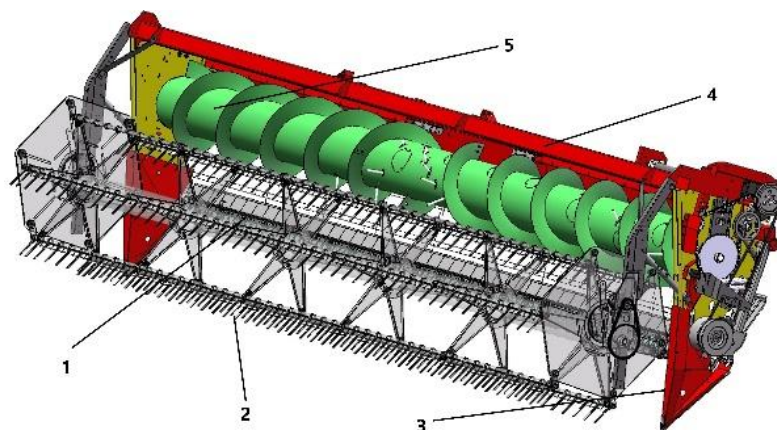


Fig. 1 - Schematic Diagram of the Header Structure
1. Cutter; 2. Reel; 3. Divider; 4. Header Frame; 5. Feeding Auger

Development of Contour Following and Height Control Systems for Cutting Headers

The header is a critical component of the combine harvester, with intelligent control being pivotal for optimizing harvesting efficiency and quality. Internationally, leading agricultural machinery companies are at the forefront of header development, particularly in areas such as power consumption, feed rate, reliability, and intelligent features. These advancements continually enhance the functionality and intelligence of headers (Wang *et al.*, 2021; Huawei *et al.*, 2022). In contrast, domestic researchers have concentrated on the adaptability of headers, achieving significant progress in contour following and height control. Innovations in height control systems and contour-following devices have effectively managed the operational posture of the header, minimized errors, and increased adaptability across various crops and environments (Tan *et al.*, 2023; Ji *et al.*, 2022). Currently, research is focused on optimizing the structure, working principles, and intelligent control systems of headers, with a particular emphasis on improving response speed and real-time performance. By integrating advanced control technologies and utilizing sensors such as image processing and ultrasonic distance measurement, researchers have significantly enhanced control precision and effectiveness. These innovations have not only optimized the header's structure but also reduced crop losses, thereby improving the overall performance of combine harvesters (Xie & Alleyne, 2011; Liu *et al.*, 2019; Lin *et al.*, 2021).

Research on Contour Following and Height Control Methods for Cutting Headers

The primary methods for controlling the height of headers in soybean harvesting equipment encompass manual, mechanical/electromechanical, hydraulic or pneumatic, and electro-hydraulic systems. Manual control, which relies on the operator's expertise, offers flexibility but is highly dependent on operator skill and is prone to inconsistency. Mechanical control employs linkages or cams to adjust the height automatically, offering reliability in simpler environments but limited adaptability in variable field conditions. Hydraulic or pneumatic control facilitates rapid and precise adjustments through hydraulic systems, making it well-suited for environments requiring swift responses to changes in terrain. However, its effectiveness can be limited by the complexity of the terrain and crop variability. Electro-hydraulic control, integrating sensors and electronic systems with hydraulic mechanisms, allows for intelligent, real-time adjustments that enhance precision and operational efficiency. This method, which often incorporates ground contour-following skids, represents a significant advancement in mechanized harvesting technology, aligning with future trends toward automation and precision agriculture (Pan et al., 2019; Li et al., 2016). The selection of an appropriate control method should be guided by specific operational requirements, with electro-hydraulic systems increasingly favored for their ability to optimize harvesting efficiency and accuracy in diverse conditions.

(1) Mechanical/Electromechanical Control

Li Zerui et al. (2024) designed a mechanical-hydraulic combined contour-following device for soybean headers, as illustrated in Fig. 2. The height contour-following function of the mechanical harvesting header primarily relies on a floating cutter. The floating cutter consists of a cutting blade, an elastic header base plate, and a four-bar linkage. During soybean harvesting, the lower base plate assembly maintains contact with the ground, allowing the floating cutter to move up and down with the terrain's undulations, ensuring close ground adherence for low-stubble harvesting. This design enables mechanical contour-following of the header height within a range of 0–70 mm (Li et al., 2024).

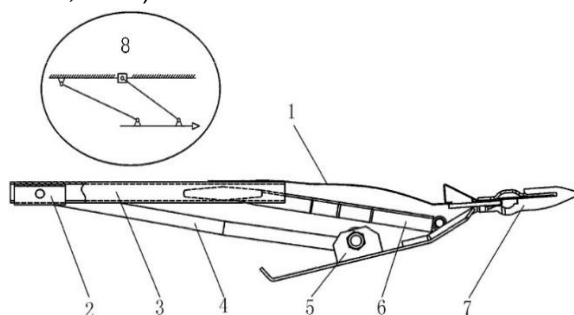


Fig. 2 - Schematic Diagram of the Floating Cutter Structure (Li et al., 2024)

1. Elastic Header Base Plate; 2. Mounting Plate; 3. Base Trough Plate; 4. Rotary Arm Assembly; 5. Lower Base Plate Assembly; 6. Limiting Plate Assembly; 7. Cutter; 8. Principle of Four-Bar Linkage Mechanism

(2) Hydraulic or Pneumatic Control

Wang Xibo et al. (1998) designed a suspended header with a hydraulic contour-following mechanism, as illustrated in Fig. 3. This mechanism primarily comprises mechanical and hydraulic components, without involving electronic controllers. An oil pump driven by a diesel engine sends oil through a pressure-reducing valve into a cylinder, where it pushes a piston rod acting on a buffer spring to adjust the header's height from the ground. It can achieve automatic contour-following on both flat and uneven surfaces but requires manual adjustment of bolts to adapt to different fields and stubble heights. Although the design enables automatic contour-following, the adjustment process is cumbersome, and the response speed of the hydraulic system significantly affects the contour-following performance (Wang & Yin, 1998).

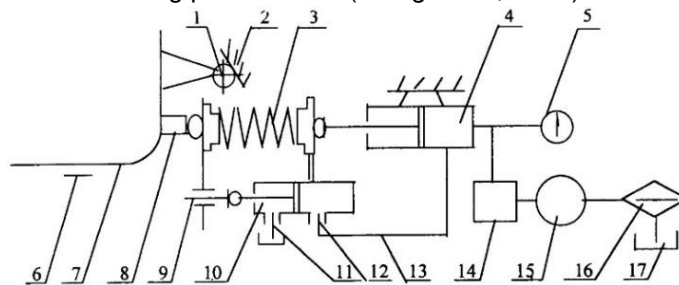


Fig. 3 - Schematic Diagram of the Hydraulic Profiling Mechanism for a Suspended Header (Wang & Yin, 1998)

1. Hinge; 2. Frame; 3. Buffer Spring; 4. Cylinder; 5. Pressure Gauge; 6. Profiling Plate; 7. Header; 8. Press Block; 9. Adjusting Bolt; 10. Quick Release Valve; 11. Oil Outlet; 12. Oil Inlet; 13. Pipeline; 14. Pressure Reducing Valve; 15. Oil Pump; 16. Oil Filter; 17. Oil Reservoir

(3) Electro-Hydraulic Control

Yi Fengyan *et al.* (2020) designed a header height control system based on an inclination sensor, which automatically adjusts the platform's angle by detecting changes in terrain angle. This system employs a hydraulic power model integrated with fuzzy control and PID control to achieve precise height control of the platform. The effectiveness of the algorithm was validated through simulations and experiments (Yi *et al.*, 2020). Ni Youliang *et al.* (2021) developed a height adjustment system for soybean harvester headers that combines a contour mechanism with hydraulic drive. This system utilizes angle sensors to make real-time, precise height adjustments to the header, as shown in Fig. 4. Field tests demonstrated that the adjustment error of the header can be controlled within 2 millimeters (Ni *et al.*, 2021). Liu Gangwei *et al.* (2023) designed an automatic height control system for soybean harvester headers, which integrates a contour mechanism, an ECU control unit, and a hydraulic system, enabling human-machine interaction via an industrial touch screen. Field trials indicated that the adjustment error of the header height in automatic mode was only 4 millimeters, with a coefficient of variation of 0.1, achieving a control accuracy of 93%, significantly surpassing manual operation and effectively enhancing the stability and operational quality of the harvester (Liu *et al.*, 2023). Yang Ranbing *et al.* (2022) developed an automatic header height adjustment system based on terrain monitoring. The system uses sensors to detect real-time changes in ground height and employs an improved PID algorithm (EVPIVS-PID) to dynamically adjust the hydraulic system, ensuring precise height control of the header (Yang *et al.*, 2022). Xie Yangmin *et al.* (2010) created an automatic header height control system for combine harvesters based on terrain following. By precisely setting state and cost functions, the system uses an optimal state feedback LQR controller to achieve height control (Xie *et al.*, 2010). Lopes G.T. *et al.* (2002) developed a header height control system that employs a Linear Quadratic Gaussian with Loop Transfer Recovery (LQG/LTR) method. This system aims to optimize combine harvester performance by precisely controlling header height, significantly improving the harvester's disturbance rejection capability on irregular terrain without increasing energy consumption (Lopes *et al.*, 2002). Wang Zhichao *et al.* (2024) designed a contour-following height control system for cutting platforms, which uses angle sensors to monitor ground undulations and employs an electro-hydraulic control strategy to automatically adjust the header height to various terrains. The system also incorporates integrated electro-magnetic proportional valves instead of traditional electro-hydraulic directional valves, achieving precise height adjustments through PWM signal control (Wang *et al.*, 2024).

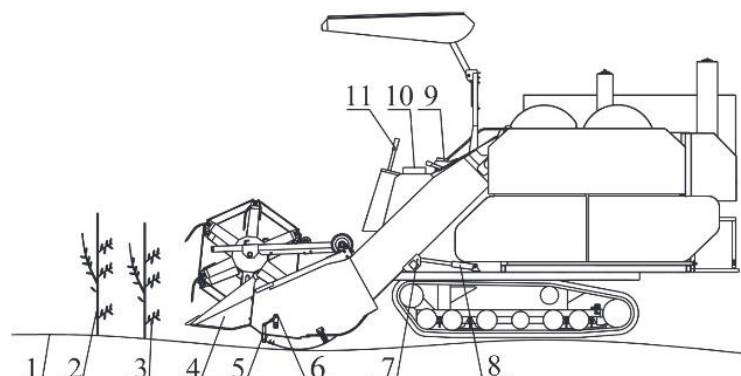


Fig. 4 - Schematic Diagram of the Header-Height Adjustment System for a Soybean Harvester (Ni *et al.*, 2021)

1. Ground; 2. Soybean plant; 3. Bottom pod of soybean; 4. Header; 5. Profiling mechanism; 6. Angular transducer; 7. Articulated mechanism; 8. Double-acting hydraulic cylinder; 9. Controller; 10. Solenoid directional valve; 11. IPC.

Research on Contour Following and Height Measurement Methods for Headers

Current methods for measuring the height of headers in soybean harvesting include ultrasonic distance measurement, image processing-based techniques, and multi-sensor integrated height measurement with contour-following technology. Ultrasonic distance measurement is advantageous in harsh harvesting environments due to its insensitivity to smoke and other particulate matter. However, when deployed as a standalone method, it is prone to significant errors, often failing to meet the stringent precision requirements necessary for optimal harvesting efficiency (Jia *et al.*, 2019). Image processing-based measurement utilizes computer vision to capture and analyze images of stubble, providing data to adjust the header height. Despite its potential for high precision, this method is vulnerable to system and environmental interferences and requires high-performance computational hardware, which can be a limiting factor (Jeught & Dirckx, 2019). Recent advancements in sensor technology have led to the development of multi-sensor integration, combining sensors that measure angles, displacement, and pressure with ultrasonic sensors.

This integrated approach facilitates more accurate distance measurement and enhances contour-following capabilities, offering robust real-time performance and wide applicability across diverse harvesting conditions. As a result, multi-sensor integrated height detection is emerging as a promising technology for the future, potentially setting new standards in precision and efficiency in agricultural mechanization (Nguyen *et al.*, 2020).

Through the combined efforts of domestic and international scholars and research institutions, these three methods have achieved significant advancements in contour following and height measurement for headers, laying a solid foundation for innovative research.

(1) Height Measurement Method Based on Ultrasonic Distance Measurement

Ultrasonic waves are non-contact mechanical waves that are not affected by light, dust, or electromagnetic interference, making them suitable for harsh harvesting environments. Compared to other detection methods, ultrasonic waves offer superior controllability and directionality. However, their sensors have a wide beam angle, and measurement accuracy can be influenced by field crops and changes in air density, potentially leading to errors (Gamarrá-Diezma *et al.*, 2015). Zhang Cong (2020) developed a contour-following system for headers based on ultrasonic array sensors and mechanical contour-following structures. This system utilizes an STM32 microcontroller for data processing, CAN bus communication, and closed-loop control. The least squares method was applied to enhance sensor measurement accuracy, and a fuzzy adaptive PID control strategy was designed to effectively adjust the header and achieve efficient ground contour-following (Zhang, 2020). Yang Shuming *et al.* (2008) designed a header height control system for combine harvesters based on ultrasonic sensors, as illustrated in Fig. 5. This system employs ultrasonic sensors for non-contact height detection of the cutting platform and uses an AT89C52 microcontroller to control the transceiver circuit and electro-hydraulic proportional directional valve. The system processes signals using the PID algorithm, thereby enabling automatic ground contour-following for the header (Yang *et al.*, 2008).

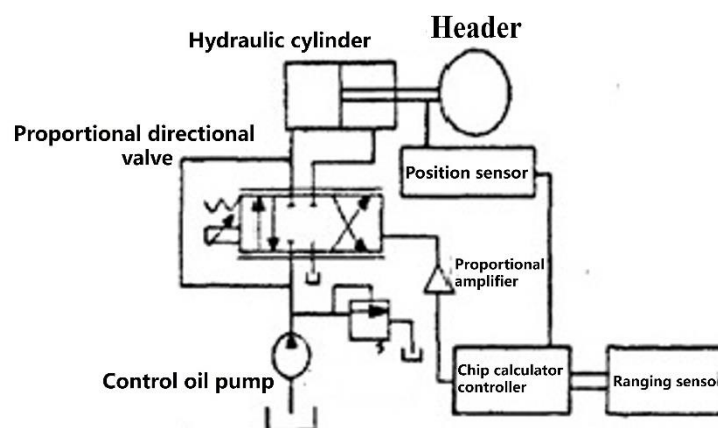


Fig. 5 - Schematic Diagram of the Header Height Measurement and Control System Based on Ultrasonic Sensors (Yang *et al.*, 2008)

(2) Measurement Method Based on Image Processing

The image processing method adjusts the header height by rapidly acquiring parameters, enabling accurate, robust, and quick determination of stubble height during detection, thus meeting the real-time requirements of harvesters. However, this method has several limitations: it needs to process a large volume of images, which can affect real-time performance; additionally, errors in acquiring and calibrating stubble height image signals and uncertainties from human factors in visual measurements can significantly impact the accuracy of stubble height measurement (Lida *et al.*, 2010). Wu Yuanyuan *et al.* (2017) designed an intelligent parameter acquisition system for leafy vegetable harvesters based on visual recognition and image processing. As shown in Fig. 6, the system first uses image preprocessing and robust regression methods to automatically acquire navigation parameters, enabling automatic adjustment of the harvester's operational direction. It then acquires stubble height through image processing, which serves as the parameter for adjusting the header height. The system achieved a navigation line recognition accuracy of 97% under natural light, with an average stubble height measurement error of 8 mm, providing technical support for the precise operation of autonomous leafy vegetable harvesters (Wu *et al.*, 2017).

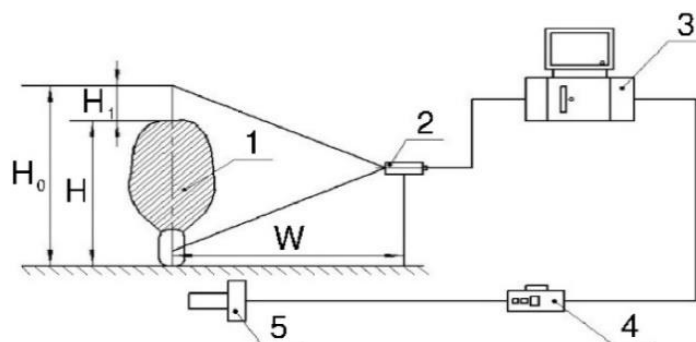


Fig. 6 – Schematic Diagram of the Header-Height Adjustment System for a Soybean Harvester (Wu et al., 2017)
1. Crop to be measured; 2. CCD Camera; 3. Computer; 4. Potentiometer; 5. Harvester Cutting Device

(3) Measurement Method Based on Multi-Sensor Integration

With the advancement of sensor technology, using sensors for header height monitoring and control has become a major trend in modern agricultural machinery development. This technology aims to enhance the operational efficiency and harvesting quality of agricultural machinery through more precise height monitoring. Research indicates that sensor applications in header height control include ground contour monitoring mechanisms and height feedback mechanisms based on angle sensors. For example, *Yang Ranbing et al. (2022)* designed an adaptive header height control system based on ground contour monitoring. This system uses angle sensors to monitor ground contours and employs electromagnetic proportional valves and PWM control technology for precise hydraulic cylinder adjustment. Experimental results demonstrated that the improved EVPIVS-PID algorithm dynamically adjusts PID parameters based on operational speed, ensuring stability in height control of the header. The stubble height error did not exceed 2 cm, meeting the speed requirements of 5–11 km/h for harvesting (*Yang et al., 2022*). *Ruan Mingjian et al. (2022)* developed an automatic header height control system for combine harvesters, with the schematic diagram shown in Fig. 7. The core components include a multi-sensor data fusion contour detection mechanism with angle and displacement sensors, a controller, and a proportional solenoid valve. The system uses a BP neural network to process sensor data and employs a fuzzy PID control algorithm to adjust the hydraulic cylinder height. Field tests showed that the average error for preset heights of 10 cm, 20 cm, and 30 cm was within 15 mm, effectively meeting the requirements for automatic height control (*Ruan et al., 2022*).

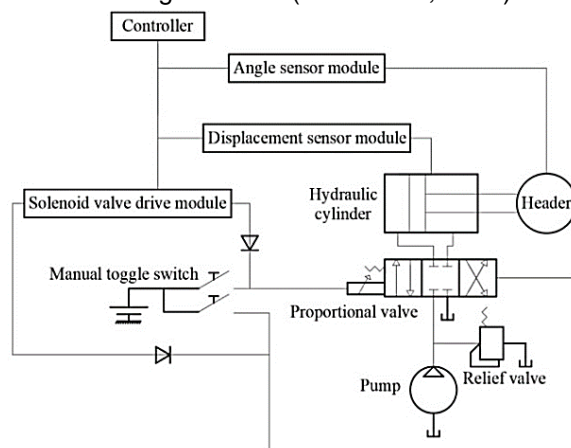


Fig. 7 – Working principle diagram of header height control (Ruan et al., 2022)

Research on Control Methods and Algorithms for Contour Following and Height Control Systems of Headers

In the control of combine harvester headers, mechanical structures serve as the foundation, while control methods and algorithms determine overall performance. PID control is known for its stability and reliability. Fuzzy control effectively handles imprecise information, addressing system uncertainties and nonlinearities, thereby enhancing disturbance rejection capabilities and adapting to variations in crop height and terrain. Robust feedback linearization control excels in managing system uncertainties and external disturbances, offering higher disturbance resistance and adaptability, which is essential for maintaining header stability in complex agricultural environments and improving harvesting efficiency and accuracy.

Neural network algorithms leverage self-learning and adaptation to automatically adjust control parameters using data, enhancing response speed and accuracy. Genetic algorithms optimize control parameters through simulated natural selection and mutation, achieving efficient control (Tulpule & Kelkar, 2014; Shojaei, 2021; Hanping et al., 2020). Thus, the selection and optimization of robust feedback linearization control and other advanced algorithms are critical in contour following and height control of headers, significantly boosting system performance when applied appropriately.

(1) Application Research of Traditional Control Methods and Algorithms

Traditional methods for header control primarily include PID control and fuzzy control, which have improved system accuracy, reduced height adjustment errors, and accelerated response times. De Keyser et al. addressed the challenge of inconvenient height adjustment during combine harvester operation by proposing an adaptive adjustment system with minimal error and rapid response, using PID and Model Predictive Control (MPC) algorithms. The system comprises a crop height detection device, header height detection device, hydraulic actuator, and control unit. Test results indicated that the system's height adjustment error was within 2 cm in the 0–2 cm range, significantly improving harvesting efficiency and reducing field crop loss (De Keyser et al., 2022). Zhou Dongdong et al. (2019) proposed a header height control system based on fuzzy logic algorithms, as illustrated in Fig. 8. This system consists of an angle displacement sensor for the header, a hydraulic actuator, and a control unit. Real-time detection and fuzzy control allow for automatic height adjustment of the header. Field tests demonstrated that the system exhibited good real-time performance, accuracy, and stability, maintaining the header height within the set range, thereby improving harvesting efficiency and reducing crop loss (Zhou et al., 2019). Zhang Meng (2020) designed an intelligent control system for corn harvester headers based on PID and fuzzy PID control algorithms, using the STM32F4ZGT6 microcontroller. The system includes a floating compression contour mechanism, a row-following mechanism, a speed monitoring module, and an electromagnetic valve drive module. The PID control algorithm achieved precise height control with an average error of only 3.25 mm, while the fuzzy PID control algorithm ensured accurate row following within the 0–4.2 km/h speed range. This study significantly enhanced the intelligence level of corn harvesters (Zhang, 2020).

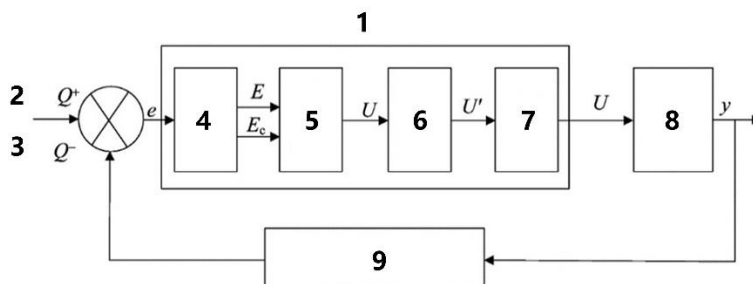


Fig. 8 – Schematic Diagram of the Header Height Fuzzy Control Principle (Zhou et al., 2019)

1. Fuzzy controller; 2. Cutting platform height; 3. Cutting platform height; 4. Fuzzification; 5. Fuzzy control algorithm; 6. Fuzzy decision; 7. Defuzzification; 8. Electromagnetic valve left and right relay energizing time; 9. Cutting platform height sensor

(2) Research on Innovative Control Methods and Algorithm Applications

In the study of the header height control system, scholars have proposed new methods with superior performance, in addition to further in-depth research on traditional algorithms such as PID. For instance, robust feedback linearization control has demonstrated excellence in handling uncertainties and external disturbances; neural networks have improved response speed through self-learning to adjust control parameters; and genetic algorithms have achieved more efficient control by simulating the natural evolution process through selection, crossover, and mutation operations. Kassen Daniel and Kelkar Atul (2017) proposed a header height control strategy based on robust feedback linearization control by constructing sensitivity equations and utilizing the current parameters of the hydraulic system control output. The research results indicate that the robust feedback linearization controller significantly outperforms the traditional PID controller in terms of header height tracking performance under various conditions, including different driving speeds, terrain sine amplitudes, and terrain periods (Kassen & Kelkar, 2017). Ji Kuizhou et al. (2022) designed an automatic header height adjustment system based on BP neural network multi-sensor data fusion, as illustrated in Fig. 9. They conducted simulation analysis of the hydraulic adjustment mechanism using AMESim software and employed fuzzy PID control to regulate the header height. Simulation and field test results demonstrate that the system achieves a header height error of less than 1.5 cm when harvesting rapeseed, millet, and rice (Ji et al., 2022).

Zhang Cong (2020) designed a fuzzy PID control system for header height optimized by a genetic algorithm, dynamically adjusting PID controller parameters through fuzzy rules to enhance the system's dynamic response capability and robustness against external disturbances. Simulation analysis using MATLAB and field tests show that the fuzzy adaptive PID control system can achieve fast and stable control under different terrain conditions, with a stubble height error of less than 1.5 cm (Zhang, 2020).

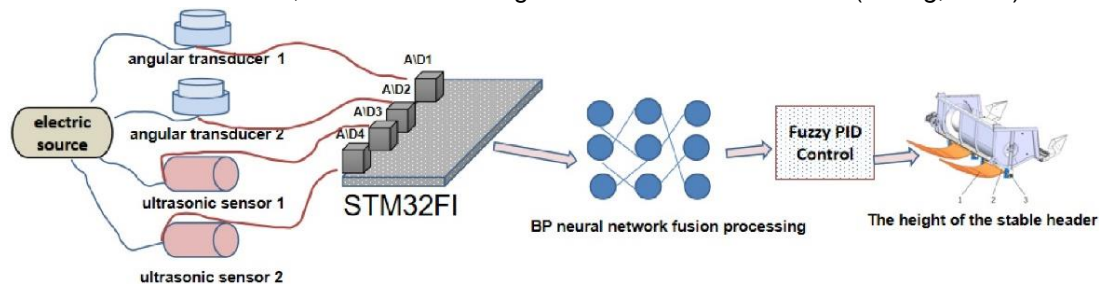


Fig. 9 – Schematic diagram of the header height measurement system (Ji et al., 2022)

Research on the Control System of Key Components of the Header

During combine harvester operations, header loss is a critical issue affecting overall harvest efficiency and economic benefits, accounting for the majority of total losses. Studies have shown that the motion patterns and working postures of core components such as the reel, cutter, and auger significantly impact the harvesting effect. Fine-tuning the control and structural optimization of these key components can significantly reduce header losses. Therefore, it is essential to study control systems that adjust the speed, angle, and synchronization of these components, optimizing their motion parameters and operating modes to ensure efficient harvesting. Additionally, the adoption of advanced sensor technologies and intelligent control algorithms is necessary to achieve real-time monitoring and dynamic adjustment of key components. This approach enhances operational performance and stability, thereby reducing header loss and improving harvesting efficiency and quality (Wang & Su, 2021; Wang et al., 2019; Yuan et al., 2023).

Current Research on Cutter (Sickle) Control Systems

The cutter is one of the key components of the header, functioning to cut the stalks through the reciprocating motion of the sickle driven by the cutting mechanism. Reciprocating cutters are widely used in combine harvesters due to their simple structure, high reliability, support for cutting, and high cutting quality. The frequency of the reciprocating motion of the sickle directly affects the harvest quality. Adjusting the sickle frequency to match the forward speed of the harvester effectively reduces re-cutting and missed cutting, thereby lowering power consumption from re-cutting and minimizing losses from missed cuts (Sheheda et al., 2021; Abdelmoteleb et al., 2009). To achieve precise adjustment of the sickle frequency, various control methods and algorithms have been studied and applied. Li Ying et al. (2021) designed a segmented control system for the cutter frequency of combine harvester headers. By constructing the sickle trajectory equation, the influence of forward speed and cutting frequency on the cutting area was analyzed, and the optimal cutting frequency range was determined using a segmented control method with regulation algorithms. Test results showed that the device adjusted the cutting frequency with a deviation within $\pm 0.8\text{Hz}$ and a maximum relative error of -8.6% , significantly reducing missed and repeated cutting, thus improving harvest quality and efficiency (Li et al., 2021). Yin Yanxin et al. (2021) studied a feedforward compensation control method for the cutting frequency of combine harvester sickles. By establishing a relationship model between sickle cutting frequency and cutting energy, the effects of wheat stem moisture content and cutting cross-sectional area on sickle cutting frequency were analyzed, making the actual field cutting frequency closer to the optimal value. Experimental results showed that this method reduced the maximum deviation by 28.33% , significantly improving harvesting performance (Yin et al., 2021). Guan Zhuohuai et al. (2020) proposed a cutting speed follow-up adjustment system based on a Proportional-Integral-Derivative (PID) control algorithm. Numerical simulation analysis of the sickle motion trajectory determined the optimal cutting speed ratio to be 1.1. Field tests indicated that the system controlled the sickle cutting speed error within 1.5% , with a response delay of 1.5 seconds, significantly reducing header and sickle losses (Guan et al., 2020).

Current Research on Reel Control Systems

The reel is an essential part of the header, used to direct grain towards the cutter, support stalk cutting, and clear the sickle to prevent clogging. The reel's rotational speed impacts operational quality; too low a speed results in untimely feeding, while too high a speed causes grain loss. Research on reel control systems helps stabilize reel speed, reducing crop impact and header loss, thereby improving header efficiency and

harvest quality (Zendehtel & Shamoradi, 2019). Yang Zhengtao et al. (2022) investigated the impact of reel speed on harvesting operations and proposed a reel control system based on a finite state machine algorithm. This system adjusts the reel speed in real time according to vehicle speed, grain density, and lodging conditions, ensuring the relative horizontal speed of the reel teeth is zero when contacting the crop, reducing crop impact, improving harvesting efficiency, and preventing clogging issues (Yang et al., 2022). Omid Mahmoud et al. (2010) designed an automatic reel speed control system using a fuzzy logic control algorithm. Sensors detect grain losses at the straw separator and upper sieve positions, and a programmable logic controller (PLC) processes the data and sends control commands to achieve precise reel speed adjustment (Omid et al., 2010). Cui Yong et al. (2018) developed an automatic reel speed control system using the 87C196KC microcontroller. The system controls the thyristor trigger using the cosine cross-intercept method, and combines motion and speed mathematical models to determine reel operating parameters and motor power. By adopting three-phase AC power and AC frequency conversion technology, along with voltage stabilization, synchronization, and amplification circuits, precise reel speed control was achieved (Cui et al., 2018). Du Juan et al. (2020) designed an automatic reel speed control device based on the PID control algorithm. The control principle diagram is shown in Fig. 10. The device measures the difference between actual and target speeds using sensors and sends control signals to achieve precise reel speed control, exhibiting high stability (Du et al., 2020).

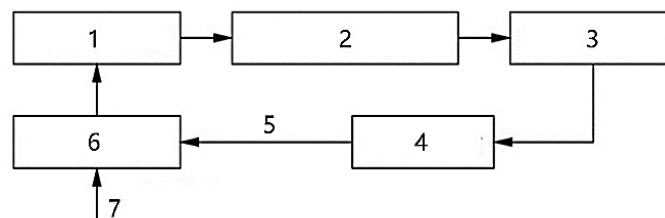


Fig. 10 – Block Diagram of the Automatic Reel Speed Control Principle (Du et al., 2020)

1. Motor driver; 2. Motor and transmission mechanism; 3. Reel main shaft; 4. Speed measurement;
5. Actual speed; 6. Speed controller; 7. Target speed

Issues and Challenges in the Intelligent Development of Headers

Despite significant advancements in the intelligent development of grain combine harvester headers, driven by continuous efforts from scholars and enterprises, there are still several issues and challenges in terms of structure and overall control. These challenges are primarily reflected in the following aspects:

Inadequate Intelligent Control and Response Speed

Current domestic research on intelligent control of headers mainly focuses on longitudinal height control, with relatively little attention to lateral height profiling and intelligent control. Although longitudinal control has made significant progress, headers still face issues with slow response speeds and insufficient real-time performance during actual operations. This is particularly problematic in complex terrains, where rapid adjustments in height and angle are necessary to prevent crop losses. Furthermore, there is limited research on the intelligent control of parameters such as reel speed and position adjustment, auger speed, and cutter frequency. This limits the system's application scope, thereby restricting harvest efficiency and quality. Therefore, it is essential to enhance the development of intelligent control systems for headers, improving response speed and real-time performance to minimize losses due to posture adjustments.

Limitations of Header Technology and Structure

A significant issue in the intelligent development of headers is the limitation of height measurement technology and control algorithms. Current measurement methods primarily rely on mechanical or laser sensors, which often lack precision and reliability in complex terrains and varying crop conditions. Mechanical sensors are prone to interference in uneven farmland environments, while laser sensors may fail due to changes in reflectivity, leading to inaccurate data. Moreover, existing control algorithms have limited capabilities in processing real-time data and dynamic adjustments, failing to fully consider the complexity of farmland environments and crop diversity. Introducing vision sensors based on image recognition and multi-sensor fusion technology, along with the development of more intelligent and adaptive control algorithms, is necessary. Additionally, the current header structure suffers from insufficient rigidity and adaptability, necessitating the use of lighter, more flexible materials and designs to enhance adaptability and operational efficiency.

Complexity and Reliability Issues of Header Systems

Although existing hydraulic and electro-hydraulic control systems are powerful, their complexity impacts the efficiency and reliability of header systems. Hydraulic control systems are prone to response delays and insufficient control precision during transmission, especially under high-intensity operating conditions, increasing the risk of equipment wear and failure. While electro-hydraulic control systems offer improvements in control precision and response speed, their complex hardware and software structures increase the failure rate and maintenance costs of header systems. To enhance overall performance, it is crucial to simplify the structure of hydraulic and electro-hydraulic control systems, adopting more reliable control components and techniques to improve system stability and usability, thereby advancing the intelligent level of combine harvester headers.

Future Trends in the Intelligent Development of Headers

The future trends in the intelligent development of headers include the following aspects: improving header control system performance and response speed through high-precision sensors and optimized control algorithms; continuously optimizing key components and control systems for energy efficiency; introducing new technologies and multifunctional designs to meet the harvesting needs of various crops and terrains; and enhancing vibration control and intelligent monitoring to improve harvest efficiency and reduce losses. These trends collectively drive headers toward greater efficiency, precision, and intelligence, achieving significant advancements in intelligent research.

High-Precision Sensors and Optimization of Control Algorithms

One important trend in the future development of intelligent headers is the installation of various high-precision sensors on header components to obtain more accurate and convenient parameters. Combining data from these sensors with optimized control methods and algorithms can significantly enhance the overall performance of header control systems, increasing control precision and response speed. Effective control systems verified through theoretical analysis, field experiments, and simulation software (such as MATLAB and ANSYS) show significant advantages in practical applications. Such high-precision, fast-response intelligent control systems ensure optimal performance of the header under various working conditions.

Optimization of Key Components for Energy Efficiency

Another critical trend is the continuous optimization of key header components (such as the reel) and the development of their control systems. Optimized headers can adjust parameter combinations promptly under different crops and working conditions, reducing loss rates during harvesting, lowering power consumption, and enhancing the adaptability and operational efficiency of grain combine harvesters. Future harvesters are expected to evolve toward high power, multifunctionality, and energy efficiency to meet the urgent needs of large-scale farmland and high-throughput harvesting.

New Technologies and Multifunctionality

The development trend of headers also includes the introduction of new technologies and the realization of multifunctionality. Internationally, headers have been designed to accommodate different cutting widths to meet regional and yield demands while improving header profiling structures to maintain consistent cutting heights on both flat and undulating terrains. Future developments will focus on how to universalize header chassis to install specialized headers, meeting the harvesting needs of various crops (such as soybeans and rapeseed). Additionally, addressing the issue of accumulation during harvesting is essential to improve efficiency and reduce losses.

Vibration Control and Intelligent Monitoring

Reducing vibrations generated during header operations is key to improving harvest efficiency and minimizing losses. The primary source of header vibrations is the cutter transmission system; thus, focused research on vibration reduction is necessary. Moreover, the development of headers should incorporate the application of global positioning systems (GPS) to gather information on crop yields and growing environments, optimizing the control of header height, reel height, harvester forward speed, and reel speed. Intelligent monitoring and control systems based on GPRS and GPS technology can detect the physical and mechanical properties of grains, intelligently adjusting the reeling device to enhance harvest efficiency and reduce loss rates. The development of new reeling device structures and materials using bionic technology will further improve the efficiency and lifespan of reeling devices.

CONCLUSIONS

This paper reviews the current state of intelligent header technology in combine harvesters, both domestically and internationally, detailing the types, characteristics, mechanical structures, operating principles, contour following, and height control advancements. The research indicates that China lags behind developed countries in the application of intelligent header technology. This lag is primarily due to the concentration of technological research and development within leading enterprises in developed countries and China's shortcomings in response speed and real-time capabilities of intelligent control systems. Additionally, regional disparities in agricultural mechanization and uneven research levels pose challenges for the adoption of intelligent header technology in China. To address these issues, this paper proposes strategies tailored to China's agricultural conditions, aiming to accelerate the development of intelligent header technology and enhance the operational efficiency and quality of grain combine harvesters in the country.

ACKNOWLEDGEMENT

We greatly appreciate the careful and precise reviews by the anonymous reviewers and editors. This research was funded by the National Key Research and Development Plan project (2021YFD2000503) and the National Natural Science Foundation of China (No. 32171911), and CAAS Center for Science in Smart Agriculture and Equipment (CAAS-SAE-202301).

REFERENCES

- [1] Abdelmoteleb, I. A., El-Gendy, H. A., Hassan, M. A. (2009). Combine header control. *Misr Journal of Agricultural Engineering*. Vol. 26, no. 3, pp. 1478-1500. Egypt. <https://doi.org/10.21608/mjae.2009.108719>
- [2] Cui, Y., Zhai, X., Tao, D. (2018). Design of Automatic Speed Control System of Combine Reel (联合收割机拨禾轮转速自动控制系统设计). *Journal of Agricultural Mechanization Research*. Vol.40, no.3, pp.128-132. Jiangsu / China. <https://doi.org/10.13427/j.cnki.njyi.2018.03.026>
- [3] De Keyser, R., Birs, I. R., Copot, D., Ghita, M., Muresan, C. I., Ionescu, C. M. (2022). Versatile solutions for the combine harvester header height control problem. *Proceedings of the 13th Asian Control Conference (ASCC 2022)*. pp. 221-226. South Korea. <https://doi.org/10.23919/ASCC56756.2022.9828248>
- [4] Du, J., Jiang, B., Yin, H., Zhang, L., Jin, C., Yin, X. (2020). Development of an automatic control system for the rotation speed of combine harvester reel (稻麦联合收获机拨禾轮转速自动控制装置研制). *Journal of Chinese Agricultural Mechanization*. Vol.41, no.12, pp.1-10. Shandong / China. <https://doi.org/10.13733/j.jcam.issn.2095-5553.2020.12.001>
- [5] Gamarra-Diezma, J. L., Miranda-Fuentes, A., Llorens, J., Cuenca, A., Blanco-Roldán, G. L., Rodríguez-Lizana, A. (2015). Testing accuracy of long-range ultrasonic sensors for olive tree canopy measurements. *Sensors*. Vol.15, no.2, pp.2902-2919. Spain. <https://doi.org/10.3390/s150202902>
- [6] Geng, A., Zhang, M., Zhang, J., Zhang, Z., Gao, A., Zheng, J. (2020). Design and Experiment of Automatic Control System for Corn Header Height (玉米收获机割台高度自动调控系统设计与试验). *Transactions of the Chinese Society for Agricultural Machinery*. Vol.51, no. S2, pp.118-125. Shandong / China. <https://doi.org/10.6041/j.issn.1000-1298.2020.S2.014>
- [7] Golyapin, V.Ya., Golubev, I.G., Buklagin, D.S. (2021). Global trends in the improvement of combine harvesters. *E3S Web of Conferences*. Vol.282, pp.07008. Russian. <https://doi.org/10.1051/e3sconf/202128207008>
- [8] Goossens, J., Lenaerts, B., Devos, S., Gryllias, K., De Ketelaere, B., Saeys, W. (2023). Anomaly detection on the cutter bar of a combine harvester using cyclostationary analysis. *Biosystems Engineering*. Vol.226, pp.169–181. Belgium. <https://doi.org/10.1016/j.biosystemseng.2023.01.013>
- [9] Guan, Z., Wu, C., Li, Y., Mu, S., Jiang, L. (2020). Cutting speed follow-up adjusting system of bidirectional electric drive side cutter for rape combine harvester. *Science Progress*. Vol.103, no.3, pp.1-19. Jiangsu / China. <https://doi.org/10.1177/0036850420935728>
- [10] Hanping, M., Jiahui, W., Gaoyong, X., Zhiyu, Z., Qinglin, L. (2020). Design and simulation of the operating speed regulation algorithm of plot cabbage seed combine harvester. *Journal of Advances in Agriculture*. Vol.11, pp.160–169. Jiangsu / China. <https://doi.org/10.24297/jaa.v11i.8862>

- [11] Huang, M., Li, Y., Chen, A., Xu, L. (2020). Design and Test of Double-Cutterbar Structure on Wide Header for Main Crop Rice Harvesting. *Applied Sciences*. Vol.10, no.13, pp.4432. Jiangsu / China. <https://doi.org/10.3390/app10134432>
- [12] Huawei, L., Ping, Z., Xiaohui, Y., Yujie, D., Keying, L., Guohai, Z. (2022). Research on the status and development of grain combine harvester cutting table intelligence in China (国内谷物联合收获机割台智能化现状与发展研究). *Journal of Chinese Agricultural Mechanization*. Vol.43, no.4, pp.189-197. Zibo, Shandong / China. <https://doi.org/10.13733/j.jcam.issn.2095-5553.2022.04.027>
- [13] Iida, M., Ikemura, Y., Suguri, M., Masuda, R. (2010). Cut-edge and stubble detection for auto-steering system of combine harvester using machine vision. *IFAC Proceedings Volumes*. Vol.43, pp.145–150. Japan. <https://doi.org/10.3182/20101206-3-JP-3009.00025>
- [14] Jeught, S. V. D., Dirckx, J. J. J. (2019). Deep neural networks for single shot structured light profilometry. *Optics Express*. Vol.27, no.17, pp.17091-17101. Belgium. <https://doi.org/10.1364/OE.27.017091>
- [15] Ji, K., Li, Y., Li, G., Wang, X., Wang, H. (2023). Design and test of height auto-control device of combine header (联合收获机割台高度自动调节装置设计与试验). *Journal of Agricultural Mechanization Research*. 2023(9), pp.85-94. Jiangsu / China. <https://doi.org/10.13427/j.cnki.njji.2023.09.021>
- [16] Ji, K., Li, Y., Zhang, T., Xia, S. (2022). Technology of adjusting the header height of the harvester by multi-sensor data fusion based on BP neural network. *INMATEH Agricultural Engineering*. Vol.68, no.3, pp.91-98. Bucharest / Romania. <https://doi.org/10.35633/inmateh-68-09>
- [17] Jia, L., Xue, B., Chen, S., Wu, H., Yang, X., Zhai, J., Zeng, Z. (2019). A high-resolution ultrasonic ranging system using laser sensing and a cross-correlation method. *Applied Sciences*. Vol.9, no.7, pp.1483. Tianjin / China. <https://doi.org/10.3390/app9071483>
- [18] Kassen, D., Kelkar, A. (2017). Combine harvester header height control via robust feedback linearization. *2017 Indian Control Conference (ICC)*, pp.1-6. India. <https://doi.org/10.1109/INDIANCC.2017.7846442>
- [19] Iida, M., Ikemura, Y., Suguri, M., Masuda, R. (2010). Cut-edge and stubble detection for auto-steering system of combine harvester using machine vision. *IFAC Proceedings Volumes*. Vol.43, pp.145–150. Japan. <https://doi.org/10.3182/20101206-3-JP-3009.00025>
- [20] Li, Q., Chen, G., Sun, Y., Sun, Y., Peng, Q. (2016). Study on corn harvester harvesting table height copying control. *J. Chin. Agric. Mech.* Vol.37, pp.43–47. Beijing / China.
- [21] Li, Y., Guan, Z., Chen, Y. (2021). Development and test of frequency subsection regulation system for combine harvester header cutter. *INMATEH Agricultural Engineering*. Vol.65, no.3, pp.283-292. Bucharest / Romania. <https://doi.org/10.35633/inmateh-65-30>
- [22] Li, Y., Li, Y., Xu, L., Hu, B., Wang, R. (2014). Structural parameter optimization of combine harvester cutting bench (联合收获机割台机架结构参数优化). *Transactions of the Chinese Society of Agricultural Engineering*. Vol.30, no.18, pp.30–37. Jiangsu / China. <https://doi.org/10.3969/j.issn.1002-6819.2014.18.004>
- [23] Li, Z., Xu, L., Xu, X., Xu, L., Chai, X. (2024). Design and simulation of a mechanical-hydraulic combined soybean header profiling device (机械-液压组合式大豆割台仿形装置设计与仿真). *Transactions of the Chinese Society for Agricultural Machinery*. Vol.55, no.5, pp.150-160. Jiangsu / China. <https://doi.org/10.13427/j.cnki.njji.2024.05.030>
- [24] Lin, X., Cai, J., Tong, L., Long, Z. (2021). Topology optimization design and modal analysis based on header frame of combine harvester. In *Proceedings of the 2021 2nd International Conference on Artificial Intelligence and Education (ICAIE)*, pp.204–208. China.
- [25] Liu, G. (2022). Research on profiling technology of soybean combine harvester header (大豆联合收获机割台仿形技术研究) (Master's thesis). *Chinese Academy of Agricultural Sciences, Nanjing Institute of Agricultural Mechanization*. Nanjing / China. <https://doi.org/10.27630/d.cnki.gznky.2022.000712>
- [26] Liu, G., Ni, Y., Yang, T., Qi, Y., Jin, C. (2023). Design and experiment of an automatic height control system for soybean harvester header (大豆收获机割台高度自动控制系统设计与试验). *Journal of Chinese Agricultural Mechanization*. Vol.44, no.6, pp.220-230. Zibo, Shandong / China. <https://doi.org/10.13733/j.jcam.issn.2095-5553.2023.06.022>
- [27] Liu, H., Reibman, A. R., Ault, A. C., Krogmeier, J. V. (2019). Video-based prediction for header-height control of a combine harvester. In *Proceedings of the 2019 IEEE Conference on Multimedia Information Processing and Retrieval (MIPR)*, pp.310–315. USA.

- [28] Lopes, G. T., Magalhães, P. S. G., Nobrega, E.G.O. (2002). Optimal header height control system for combine harvesters. *Biosystems Engineering*. Vol.81, no.3, pp. 261-272. Brazil. <https://doi.org/10.1006/bioe.2001.0016>
- [29] Nalobina, O. O., Vasylychuk, N. V., Bundza, O. Z., Holotiuk, M. V., Veselovska, N. V., Zoshchuk, N. V. (2019). A new technical solution of a header for sunflower harvesting. *INMATEH - Agricultural Engineering*. Vol.58, no.2, pp.129. Bucharest / Romania. <https://doi.org/10.35633/INMATEH-58-14>
- [30] Nguyen, T. H., Nguyen, T. M., Xie, L. (2020). Tightly-coupled ultra-wideband-aided monocular visual SLAM with degenerate anchor configurations. *Autonomous Robots*. Vol.44, no.11, pp.1519–1534. Singapore. <https://doi.org/10.1007/s10514-020-09944-7>
- [31] Ni, Y., Jin, C., Chen, M., Yuan, W., Qian, Z., Yang, T., Cai, Z. (2021). Computational model and adjustment system of header height of soybean harvesters based on soil-machine system. *Computers and Electronics in Agriculture*. Vol.183, pp.105907. Nanjing / China. <https://doi.org/10.1016/j.compag.2020.105907>
- [32] Omid, M., Lashgari, M., Mobli, H., Alimardani, R., Mohtasebi, S., Hesamifard, R. (2010). Design of fuzzy logic control system incorporating human expert knowledge for combine harvester. *Expert Systems with Applications*. Vol.37, no.8, pp.7080–7085. Iran. <https://doi.org/10.1016/j.eswa.2010.03.010>
- [33] Pan, Y., Zhao, Z., Liu, W., Meng, W. (2019). Research on header height automatic regulatory system. *In Proceedings of the 2019 Chinese Automation Congress (CAC)*, pp.203–206. IEEE: Hangzhou / China.
- [34] Ruan, M., Jiang, H., Zhou, H., Ye, J., Hu, J. (2022). Design and test of automatic control system for header height of combine harvester. *INMATEH Agricultural Engineering*. Vol.68, no.3, pp.569-578. Bucharest / Romania. <https://doi.org/10.35633/inmateh-68-56>
- [35] Sheheda, K., Shokarev, O., Kiurchev, S., Danchenko, M., Mykhailova, L. (2021). Results of research of combine harvester cutterbar. PhD Thesis. Ukraine.
- [36] Shojaei, K. (2021). Intelligent coordinated control of an autonomous tractor-trailer and a combine harvester. *European Journal of Control*. Vol. 59, pp. 82 - 98. Iran. <https://doi.org/10.1016/j.ejcon.2021.02.005>
- [37] Tai, J., Sun, H., Zhao, M., Yang, Z. (2020). Rapid design of maize ear harvester header based on knowledge engineering. *INMATEH Agricultural Engineering*. Vol.61, no.2, pp.296-303. Bucharest / Romania. <https://doi.org/10.35633/inmateh-61-29>
- [38] Tan, H., Wang, G., Zhou, S., Jia, H., Qu, M., Xiang, M., Gao, X., Zhou, Z., Li, H., Zou, Z. (2023). Design and experiment of header height adaptive adjustment system for maize (*Zea mays* L.) harvester. *Sustainability*. Vol.15, no.19, pp.14137. Changchun / China. <https://doi.org/10.3390/su151914137>
- [39] Tulpule, P., Kelkar, A. (2014). Integrated robust optimal design (IROD) of header height control system for combine harvester. *Proceedings of the American Control Conference (ACC)*, pp.2699-2704. Iran. <https://doi.org/10.1016/j.ejcon.2021.02.005>
- [40] Wang, G., Su, R. (2021). Research on ground profiling control of combine harvester based on the symmetric algorithm. *Journal of Physics: Conference Series*. Vol.1827, no.1, pp.012211. Jiangsu / China. <https://doi.org/10.1088/1742-6596/1827/1/012211>
- [41] Wang, H., Shen, H., Cao, S., Xu, X., Han, T., Guo, H. (2019). Hydraulic system design of combined harvester header and simulation of header lifting system. *IOP Conference Series: Earth and Environmental Science*. Vol.233, no.3, pp.032012. Jinan / China. <https://doi.org/10.1088/1755-1315/233/3/032012>
- [42] Wang, L., Li, S., Lv, D., Ekhlo, G. (2021). Multi-sensor signal acquisition and data processing analysis of combine harvester. *INMATEH Agricultural Engineering*. Vol.63, no.1, pp.335-344. Bucharest / Romania. <https://doi.org/10.35633/inmateh-63-34>
- [43] Wang, R., Chang, Y., Li, B., Lü, W., Liu, J. (2022). Design and experiment on the key components of millet combine harvester header (谷子联合收获机割台关键部件设计与试验). *Journal of Agricultural Mechanization Research*. 2022(10), pp.30-37. Luoyang / China. <https://doi.org/10.13427/j.cnki.njyi.2022.10.006>
- [44] Wang, X. B., Yin, K. H. (1998). Design of suspended header contour-following mechanism. *Rural Area Mechanization*. (4), Total Issue 44. Beijing / China.

- [45] Wang, Z., Yang, R., Chen, D., Wang, J., Li, X. (2024). Design of a Header Profile Height Control System Based on PID Regulation (基于PID调控的割台仿形高度控制系统的设计). *Research on Agricultural Mechanization*. Vol. 46, no. 2, pp.53-57. Qingdao / China. <https://doi.org/10.13427/j.cnki.njyi.2024.02.008>
- [46] Wu, Y., Shang, X., Zhang, C., Xie, X. (2017). Acquisition of operation parameters of intelligent leaf vegetable harvester under natural lighting (自然光照下智能叶菜收获机作业参数的获取). *Acta Agriculturae Zhejiangensis*. Vol.29, no.11, pp.1930-1937. Ningxia / China. <https://doi.org/10.3969/j.issn.1004-1524.2017.11.21>
- [47] Xie, Y., Alleyne, A. (2011). Integrated Plant and Controller Design of a Combine Harvester System. In *Proceedings of the ASME 2011 Dynamic Systems and Control Conference and Bath/ASME Symposium on Fluid Power and Motion Control*, pp.819-825. USA. <https://doi.org/10.1115/DSCC2011-5959>
- [48] Xie, Y., Alleyne, A., Greer, A., Deneault, D. (2010). Header Height Control of a Combine Harvester System. In *Proceedings of the ASME 2010 Dynamic Systems and Control Conference*, Vol.7, pp.345-353. USA. <https://doi.org/10.1115/DSCC2010-4088>
- [49] Xu, L., Li, Y., Tang, Z., Wang, L., Jiao, Z. (2013). 4LQZ-6 type tangential-flow combine harvester (4LQZ-6 型切向流联合收割机). *Transactions of the Chinese Society for Agricultural Machinery*. Vol.44, no.8, pp.94-98, 111. Beijing / China.
- [50] Yang, R., Wang, Z., Shang, S., Zhang, J., Qing, Y., Zha, X. (2022). The Design and Experimentation of EVPIVS-PID Harvesters' Header Height Control System Based on Sensor Ground Profiling Monitoring. *Agriculture*. Vol.12, no.2, pp.282. Haikou / China. <https://doi.org/10.3390/agriculture12020282>
- [51] Yang, S., Yang, Q., Yang, Y., Yang, S. (2008). Design of a combine harvester header height control system based on ultrasonic sensors (基于超声波传感器的割台高度控制系统设计). *Journal of Agricultural Mechanization Research*. Vol.3, pp.134-136. Beijing / China. <https://doi.org/10.13427/j.cnki.njyi.2008.03.035>
- [52] Yang, Z., Wang, H., Sun, H., Wang, P., Cao, Q. (2022). Experimental Study on Electric Harvesting of Combine Harvester. *Journal of Physics: Conference Series*. Vol.2218, pp.012064. Shanghai / China. <https://doi.org/10.1088/1742-6596/2218/1/012064>
- [53] Yi, F., Liu, J., Jiao, Z., Zhou, J. (2020). Study on height Control of Corn harvester in Hilly and mountainous area. In *2020 Chinese Automation Congress (CAC)*, pp.3272-3276. IEEE: Hangzhou / China. <https://doi.org/10.1109/CAC51589.2020.9327115>
- [54] Yin, Y., Qin, W., Zhang, Y., Chen, L., Wen, J., Zhao, C., Meng, Z., Sun, S. (2021). Compensation control strategy for the cutting frequency of the cutterbar of a combine harvester. *Biosystems Engineering*. Vol.204, pp.235-246. Beijing / China. <https://doi.org/10.1016/j.biosystemseng.2021.01.023>
- [55] Yuan, L., Lan, M., He, X., Wei, W., Wang, W., Qu, Z. (2023). Design and Experiments of a Double-Cutterbar Combine Header Used in Wheat Combine Harvesters. *Agriculture*. Vol.13, no.4, pp.817. Henan / China. <https://doi.org/10.3390/agriculture13040817>
- [56] Zendehtdel, N., Shamoradi, Y. (2019). Online control of combine reel height in presence of farm roughness using an on-off controller. *Tehnicki glasnik*. Vol.13, no.2, pp.104-109. Iran. <https://doi.org/10.31803/tg-20180926113107>
- [57] Zhang, C. (2020). Research on header profiling and crop height measurement methods for combine harvesters (收割机割台仿形与作物测高方法研究). *Southeast University Master's Thesis*. Nanjing / China. <https://doi.org/10.27014/d.cnki.gdnau.2019.002851>
- [58] Zhang, M. (2020). Research on the intelligent control system of corn harvester header (玉米收获机割台智能调控系统研究). *Shandong Agricultural University Master's Thesis*. Taian / China. <https://doi.org/10.27277/d.cnki.gsdnu.2020.001219>
- [59] Zhou, D., Jin, C., Ni, Y., Zhang, G. (2019). Design and experiment of a fuzzy control system for the header height of a combine harvester (联合收获机割台高度模糊控制系统的设计与试验). *Jiangsu Agricultural Sciences*. Vol.47, no.13, pp.264-267. Jiangsu / China. <https://doi.org/10.15889/j.issn.1002-1302.2019.13.063>
- [60] Zhou, Y., Luo, B., Liu, D., Liu, D., Qiu, Y., Zhou, Y. (2023). Design and experiment of a rapeseed header for the 4LZ-4.0 grain combine harvester (4LZ-4.0 谷物联合收获机油菜割台设计与试验). *Journal of Chinese Agricultural Mechanization*. Vol.44, no.9, pp.45-51. Zibo, Jiangxi/China. <https://doi.org/10.13733/j.jcam.issn.2095-5553.2023.09.004>

A REVIEW OF APPLICATION OF WATER JET TECHNOLOGY IN AGRICULTURE

水射流技术在农业领域的应用研究现状

Lixue ZHU¹⁾, Wenxuan LUO¹⁾, Hongnan HU^{*1)}, Shiang ZHANG¹⁾, Yifan SHI¹⁾, Shinian HUANG¹⁾College of Mechanical and Electrical Engineering, Zhongkai University of Agriculture and Engineering, Guangzhou 510225, China

* Correspondence: huhongnan@zhku.edu.cn; Tel.: +86-18301160669

DOI: <https://doi.org/10.35633/inmateh-73-63>**Keywords:** Water Jet; Agricultural Machinery; Jet Cutting; Jet Weeding; Post-harvest Processing**ABSTRACT**

Water jet technology, as a non-contact cutting and crushing technique, is commonly used in industries such as cleaning, rust removal, cutting, drilling, and mining. It enables a green and environmentally friendly production process by avoiding environmental pollution, heat generation, blade replacement, and sharpening issues. Cutting, cleaning, and crushing techniques are widely applied in various stages of agricultural production, but mostly through contact-based methods. The application of non-contact water jet technology in the agricultural field is still in its infancy. This paper summarized the current application status and research progress of water jet technology in different operational stages of agriculture, including sowing, management, field harvesting, and post-harvest processing. The specific requirements of key parameters for different operational objects and stages were analyzed. Furthermore, the challenges of the application of water jet technology in agriculture were discussed and the research development tendency was prospected. The review intended to provide references for the promotion and green sustainable development of water jet technology in the agricultural field.

摘要

水射流技术作为一种非接触式的切割破碎技术,常在工业中用于清洗、除锈、切割、钻孔、矿山开采等,可实现绿色环保的生产加工过程,避免污染环境、产生热量、刀片更换及磨利等问题。切割、清洗、破碎等技术被广泛应用于农业生产的各个环节,但多采用接触式方法,非接触式水射流应用在农业领域方兴未艾。本文总结了目前水射流技术在播种、管理、田间收获、采后加工等不同作业环节应用现状与研究进展;分析了不同作业对象及作业环节对射流关键参数的具体要求;探讨水射流技术在农业领域应用过程中存在的问题,并对未来的研究方向进行了展望,以期水射流技术在农业领域应用推广和绿色可持续发展提供参考。

INTRODUCTION

In agricultural production, various cutting and shredding processes are commonly involved, such as severing stalks during harvesting, drilling soil during seeding, cutting weeds during weed control, and post-harvest processing. Currently, the mainstream approach in these operations involved direct contact with crops or soil using blades or trenchers, exerting significant force to separate the products (Schuldt et al., 2018; Bremer et al., 2020; Ghosh et al., 2015). However, these methods suffered from drawbacks such as low cutting efficiency, limited precision, frequent tool replacements and wear, the need for regular maintenance and upkeep of tools, different wear reduction treatments for vulnerable parts, and the potential for microbial cross-contamination and high energy consumption due to continuous contact between the tools and agricultural products. Therefore, it is necessary to develop and apply specific cutting technologies in agricultural production and processing that offer higher processing efficiency and performance. With the emergence of advanced cutting technologies like ultrasonic vibration-assisted cutting, laser cutting, plasma cutting, and water jet cutting, attempts had been made to address the limitations of traditional cutting methods (Xu et al., 2022; Khatak, 2022; Krajcarz, 2014). These advanced cutting technologies were characterized by their high precision, high productivity, and green, safe, and sustainable features, that eliminated harmful chemicals, did not generate toxic gases or waste, and caused no pollution to the environment (Gupta, 2020; Deng et al., 2018). Water jet nozzles could achieve precise cutting and processing by allowing small movements and rotations, without compromising the material's quality and structure. Additionally, they prevent thermal deformation by avoiding high temperatures, preserving the material's original properties and shape. Furthermore, the absence of sparks and dust during operation significantly reduces the risk of worker injuries (Chen et al., 2008).

As a non-thermal processing technique, water jet technology is well-suited for handling agricultural materials and serves as an excellent alternative technology (Natarajan *et al.*, 2020).

Since the early 1960s, researchers have been studying water jet processing technology and its applications. In the initial stages of development, water jet technology utilized pure water jet with limited cutting capabilities, applicable only to soft materials such as wood, fabric, and rubber (Du *et al.*, 1978; Wilkins *et al.*, 1993; Hu *et al.*, 2014). In 1983, the United States manufactured ultra-high-pressure abrasive water jet cutting machines that the cutting capabilities of water jet technology significantly improved. With the development of ultra-high-pressure abrasive water jet cutting, it became possible to cut almost all materials, including metals, ceramics, and granite (Li *et al.*, 2009). Water jet technology has found applications in various industrial sectors such as machining, chemical engineering, aerospace, industrial cleaning, and marine engineering, encompassing cleaning, cutting, crushing, drilling, and other processes, supported by various technologies and theories (Lu *et al.*, 2011; Li *et al.*, 2008; Chen *et al.*, 2007; Zhang *et al.*, 2005). However, the research on water jet technology in the agricultural field is still relatively limited due to the diversity of agricultural materials. Moreover, the application of water jet in agriculture territory presented more complex challenges compared to factory environments, such as soil cutting and field harvesting.

When applying jet technology in the agricultural field, the predominant method is pure water jet. The parameters that affect its operational effectiveness can be classified into dynamic parameters such as jet pressure, flow rate, and power, structural parameters such as jet initial length and jet width, and engineering parameters such as operation time, movement speed, and jet impact angle. These parameters collectively influence the operational performance of water jet technology. Additionally, there are multiple evaluation metrics for water jet operations, including cutting depth, surface roughness, microbial counts, and raw material losses, which are important indicators for assessing operational quality. Overall, this review aims to explore the current research status and application potential of water jet technology in the agricultural field, considering the specific challenges posed by complex agricultural environments. The effects of various parameters on water jet performance will be investigated, and multiple performance indicators will be utilized to assess the quality of water jet operations.

The application of water jet technology in the agricultural field is primarily focused on four aspects: seeding, field management, harvesting, and post-harvest processing. In the seeding process, water jet technology enables precise seed placement and arrangement, thereby improving seed germination rates and seedling growth quality, ultimately increasing crop yield and quality. In field management, water jet technology can be used for soil moisture retention, weed removal, and precise water supply, facilitating precision farming and enhancing soil quality. For harvesting, water jet technology can be employed in crop picking, grass cutting, and other operations, offering efficiency, precision, and non-contact characteristics, which reduce labor costs and crop losses while improving harvesting efficiency. In post-harvest processing, water jet technology finds applications in cleaning, peeling, and cutting agricultural products. High-pressure water jet cutting, as a non-contact cutting technique, avoids blade dullness or contamination, effectively preventing cross-contamination and enhancing product hygiene, safety, freshness, shelf life, and added value. The research and practices in these application areas provide technical support and decision-making references for the sustainable development of agricultural production. The paper analyzes how to achieve specific functions, improve key indicators for different functions, and enhance operational quality and efficiency. Suggestions are provided for the development direction of water jet technology in specific functional applications, including deepening mechanistic research, adopting precision agriculture, and implementing intelligent control. Overall, this research aims to explore and advance the application of water jet technology in the agricultural sector, with the goal of promoting sustainable development in agriculture, enhancing operational quality, and increasing efficiency.

Water Jet Technology: Principles, Classifications, and Simulations

During the operation of a water jet system, purified water from the supply device is filtered, compressed, and mixed with the jetting medium in different ways (pre-mixing or post-mixing) to form the working fluid. Subsequently, the working fluid is ejected from a nozzle of a specific shape, generating a high-energy density jet in the form of a needle-like stream, which impinges on the surface of the target object. Under the continuous impact of the working fluid, the object undergoes cracking or fracturing until the cutting operation is completed. Therefore, water jet cutting is a dynamic destructive process (Cui *et al.*, 2022; Llanto, 2021; Pogrebnyak *et al.*, 2020; Folkes, 2009).

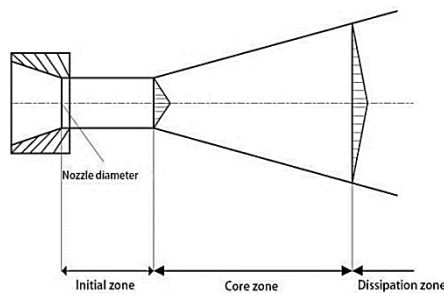


Fig.1 - Basic Structure of Water Jet

Water jet belongs to the typical fluid flow, and the jet will develop into a free jet after leaving the nozzle. Fig.1 divides the structure of a free jet into three sections: the initial zone, the core zone, and the dissipation zone (Yu, 2018). In the initial zone, the jet remains compact with constant density and velocity, known as the core region of the jet. In the core zone, both the dynamic pressure and axial velocity of the jet gradually decrease. Due to the pulsation exchange with the surrounding air, the jet spreads out in a fan shape. The velocity distribution follows a similarity law, and the average velocity distribution across the jet section can be described by the following relationship (Kang, 2016).

$$\frac{U}{U_c} = \left[1 - \left(\frac{y}{y_{1/2}} \right)^{1.5} \right]^2 \tag{1}$$

where:

U_c denotes the velocity along the axis of the jet, while $y_{1/2}$ represents the half-value width of the jet.

The region following the main region is the dissipation region, where the axial velocity and dynamic pressure of the jet are relatively low, and the previously dense jet transforms into a large number of atomized droplets. Due to the distinct characteristics of different jet regions, their applications also vary. The initial region of the water jet is generally used for cutting and crushing, the main region is primarily used for cleaning and rust removal, and the dissipation region is mainly used for dust removal and spraying.

Water jet technology can be classified into three types based on the working medium: pure water jet, abrasive water jet, and liquid water jet (Cheng et al., 2019; Lin et al., 2021; Li., 2009). The pure water jet is the traditional high-pressure water jet, where the working medium is solely water. The structure of high-pressure pure water jet cutting systems is relatively simple, but their cutting capabilities are limited and suitable only for soft materials such as paper, wood, rubber, carbon fiber fabric, etc. The abrasive jet involves adding abrasive particles like garnet or diamond, as well as solid abrasives like salt, ice, sugar grains, etc., to the working medium to enhance its cutting ability. The liquid water jet referred to a working medium that is a mixture of liquid media and water, primarily used in agricultural applications such as cutting soil for fertilization and sterilization (Nyord et al., 2008). Based on whether the jet medium has been mixed with water before entering the nozzle, it could be further classified into pre-mixing and post-mixing methods (Song, 2009). Pre-mixing referred to the mixing of abrasive or liquid jet media in a mixing device before entering the nozzle. Post-mixing involves mixing within the nozzle chamber itself, thereby requiring an additional inlet for the jet medium (as shown in Fig.2).

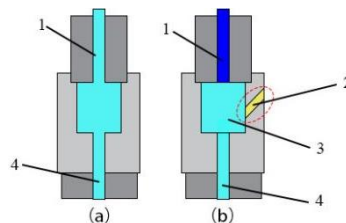


Fig.2 - Different jet nozzle structures of two mixing methods

(a) Pre-mixing jet nozzle; (b) Post-mixing jet nozzle

1. Fluid inlet; 2. Post-mixing medium inlet; 3. Mixing chamber; 4. Working fluid outlet

Currently, research methods for water jet applications in the agricultural field are mainly focused on traditional experimental approaches and optimization, with limited emphasis on simulation studies. Simulation research can assist in understanding the application effects of water jet technology in different processes, optimizing design parameters, improving efficiency, and reducing resource consumption.

Table 1

| Several Mainstream Water Jet Simulation Methods | | |
|---|--|--|
| Simulation methods | Principle of operation | Applications |
| Computational Fluid Dynamics (Zou et al., 2003; Song et al., 2019; Prisco et al., 2008; Kamarudin et al., 2016) | Simulate water jets by solving fluid flow equations on discretized grids | Study parameters such as velocity distribution, pressure distribution, and jet shape |
| Finite Element Method (Jianming et al., 2010; Jiang et al., 2020; Du et al., 2020) | Modeling the interaction between the fluid and the material as deformation and fracture behavior | Analyze the cutting effects and stress distribution on different materials |
| Discrete Element Method (Du et al., 2020; Horabik et al., 2016; Cheung et al., 2008; Zhao et al., 2013) | Discretizing the particle system into individual particles and simulating their interactions forces and motion rules | Study the interaction between particles or between particles and fluids |
| Smoothed Particle Hydrodynamics (Jianming et al., 2010; Jiang et al., 2020; Du et al., 2020; Vasudevan et al., 2022) | Simulation technique based on the particle method | Simulate the motion and interaction of fluids and solids |

Zou et al., (2023), employed the Euler Method-Volume of Fluid (VoF) model, a computational fluid dynamics (CFD) simulation method, to investigate the multiphase flow of air-water in abrasive water jet (AWJ) systems. The Euler-Lagrange method was further utilized to study the multiphase flow of abrasive particles. Valuable insights were provided to address the mixing issues in AWJ, improve abrasive acceleration processes, and extend nozzle lifespans. Song et al., (2019), used computational fluid dynamics methods to simulate the internal and external flow fields of nozzles. They compared and analyzed the velocity distribution in the flow fields of four commonly used conical convergent nozzles with different structures in water jet technology, as well as the impact pressures on target surfaces. Their findings concluded that the conical short-line nozzle is the most suitable nozzle for high-pressure water jet technology used in weld joint reinforcement. Wang Jianming et al., (2010), proposed a coupled Smoothed Particle Hydrodynamics (SPH)/Finite Element Method (FEM) approach to simulate abrasive water jet machining (AWJM) and analyze the material removal mechanisms. This method provided a useful approach for simulating AWJM and analyzing material removal mechanisms, which can be applied to optimize operational parameters and enhance process efficiency. Hongxiang Jiang et al. (2020), developed a numerical model for rock fragmentation using a coupled Smoothed Particle Hydrodynamics (SPH) and Finite Element Method (FEM). They simulated rock fragmentation under different conditions, investigated the assisting effect of high-pressure water jet on rock fragmentation, and evaluated the disturbance of water jet assistance on rock stress. The conclusion indicated that high-pressure water jet assistance could improve the working conditions of impact by reducing the peak stress on the punch head by more than 30%. Mingming Du et al. (2020), proposed a coupled SPH-DEM-FEM modeling approach to simulate the abrasive water jet (AWJ) machining process. The newly developed AWJ modeling method integrated SPH, DEM, and FEM into a single numerical model, enabling the reproduction of the actual high-speed response of workpieces and a better understanding of the incision formation process.

By establishing accurate simulation models, visual results such as flow field distribution, droplet trajectories, and pressure variations can be generated, which are advantageous for agricultural practitioners to gain a better understanding of the behavior and effects of water jets. This approach offers cost-effectiveness, improves efficiency in agricultural production and research, and promotes sustainability.

Application Status of Water Jet in the Agricultural Field

Seeding

Traditional seeding methods involve the use of arrow shovel-type trenchers, disc trenchers, and other tools. During operation, the seeding machine is driven forward by a tractor, and the pointed end forms a certain angle with the ground, facilitating soil penetration. The trench formed during the process is relatively even, but it comes with drawbacks such as high resistance, high energy consumption, significant soil disturbance, and susceptibility to wear, soil adhesion, and blockage caused by weed entanglement (Liu, 2021; Wang et al., 2018; Lu, 2020).

Experimental research conducted by Yang Yazhou *et al.*, (2010), on cutting corn straw with dynamic blades showed that the cutting performance deteriorates after the blades have been in operation for more than 660 minutes, necessitating blade replacement or sharpening. High-pressure water jet technology, as a non-contact cutting technique, can effectively address this challenge.

Fluid jet seeding is a high-pressure water jet technology for non-contact seed placement, offering advantages such as reduced energy consumption, fertilizer volatilization, soil disturbance, and environmental pollution (Zheng *et al.*, 2019). In 2001, Du Ruicheng proposed the concept of fluid jet seeding and designed an experimental device for water jet seed placement, verifying its feasibility on soil with a moisture content of 15.5% to 18.5%. Du Ruicheng *et al.* (2006) determined the parameter ranges for direct water jet seeding on leveled bare soil to be a water jet time of 0.6 seconds and a jet pressure of 0.5-0.6 MPa. For water jet seeding under plastic film, the parameter ranges were a water jet time of 0.6-1.0 seconds and a jet pressure of 1.8-2.0 MPa (as shown in Fig.3). These experimental findings demonstrated the feasibility of fluid jet seeding.

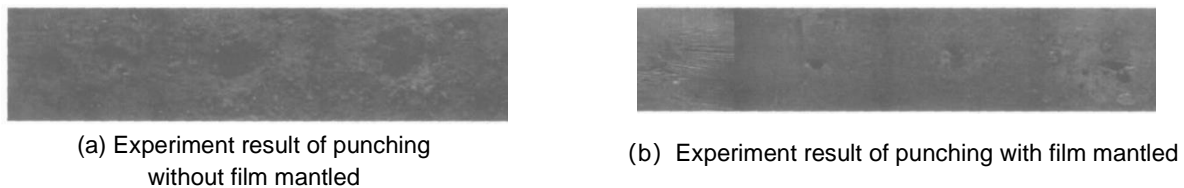


Fig. 3 - Experiment result of punching (Du *et al.*, 2006)

To achieve high-speed jet flow, Sun Jie designed the nozzle in the shape of a conical convergent-divergent tube and ensured that the nozzle outlet size satisfied two principles. Firstly, it needed to provide sufficient outlet velocity since a larger nozzle size would result in lower outlet velocity under constant pressure. Secondly, it needed to ensure smooth seed ejection, necessitating a nozzle diameter larger than the maximum radial diameter of the seeds (Sun, 2006).

Yang Zidong, (2010), designed a water content-controlled jet seeding device, which employed an AT89C51 microcontroller as the core and integrated various functional modules to complete the entire control process. Seed placement was achieved through water jet hole formation and pneumatic acceleration of seeds into the holes. The experimental results showed that the seed placement rate exceeded 98% when the seeding machine's moving speed was below 1 m/s. When the speed exceeded 2 m/s, the percentage of seeds properly placed in the holes reached 95%. This technology has pioneering and innovative significance for the study of non-contact seeding methods.

In recent years, conservation tillage has been widely promoted. The benefits of conservation tillage are mainly reflected in effective reduction of soil erosion, water and nutrient retention, increased soil organic matter content, simplified farming operations, cost reduction, and its crucial role in ensuring high and stable crop yields. No-tillage seeding is a key component of conservation tillage (Zhou, 2022). No-tillage seeding involves complex field conditions with abundant crop residues covering the surface. The tough and difficult-to-cut crop residues can lead to issues such as blockage and seed drying during the no-tillage seeding process, thereby affecting seeding efficiency and quality. Therefore, it is necessary to cut the crop stems to prevent blockages. In recent years, research on improving residue cutting and blockage prevention has mainly focused on optimizing the shape and structure of passive cutting disc devices. However, tool wear affects cutting efficiency and is an unavoidable issue in direct contact-based passive cutting methods.

Hu Hongnan *et al.* conducted a full factorial design with three operational parameters as variables to investigate the effect of pure water jet cutting parameters on the cutting performance of corn stalks (Hu *et al.*, 2019). A depth model for pure water jet cutting of corn stalks was established. The experimental results revealed that higher jet pressure, lower traverse speed, and shorter target distance led to improved cutting performance and increased cutting depth. According to the research findings, all the samples of corn stalks can be effectively cut when the isolation distance is less than 10 mm and the water jet pressure is 280 MPa (as shown in Fig.4).

Taking into account the field operating conditions, Hongnan Hu recommends using water jet pressure of 280 MPa or higher and maintaining a target distance between 10 mm and 15 mm for cutting corn stalks. These parameters are suggested for the cutting operation of corn stalks, considering the practical conditions encountered in agricultural fields.



Fig.4 - High speed photographs of maize stalks with different operation parameters(a-f), and (g) maize stalks after waterjet cutting (Hu et al., 2019)

T represents the top point of the maize stalks; *B* represents the bottom point of the maize stalks; *J* represents the deepest point of waterjet.

Additionally, Hongnan Hu employed the Arbitrary Lagrangian-Eulerian Finite Element Method (ALE-FEM) to simulate the process of water jet cutting of stalks. The accuracy of the model was verified through high-speed cameras. Building upon the simulation studies conducted by Hongnan Hu, further field experiments were carried out using an ultra-high-pressure water jet-assisted no-tillage planter (Hu et al., 2020). This field experiments demonstrated that, compared to the hoe-type furrow opener, the double-disc furrow opener combined with the ultra-high-pressure water jet (Fig.5) showed better performance. Optimization analysis indicated that when the water jet pressure ranged from 267 MPa to 280 MPa, the jet impact angle was between 80.2° and 90.0°, and the forward speed was between 4.00 km/h and 4.42 km/h, the straw cutting rate exceeded 95% when the non-contact jet cutting device and the double-disc furrow opener worked in conjunction, with no occurrence of blockage during the operation. Francesco Perotti (2021), conducted experimental research on abrasive water jet cutting of wheat straw and found that adding a small amount of abrasive powder to pure water jet can effectively enhance the cutting ability.



Fig. 5 - Non-contact jet cutting stalk-free tillage anti-blocking device (Hu et al., 2020)

Currently, high-pressure water jet has been applied in agricultural seeding and has achieved certain results. However, further optimization of the structure and water jet parameters is still needed in practical applications. Moreover, it is important to deepen the research on the mechanism of high-pressure jet cutting of plant stems and soil impact. This will contribute to reducing the size and weight of the entire machine, lowering costs, and offering extensive prospects and societal value. Continuous exploration and innovation are required in this field.

Field Management

Fertilization

In the field of crop fertilization, traditional methods such as broadcasting, furrow application, and foliar spraying have been found to have low fertilizer utilization efficiency, high soil disturbance, and potential environmental damage (Xiang et al., 2008). Deep placement of fertilizers has emerged as a promising direction for development. This method involves injecting liquid fertilizers directly into the soil using high-pressure water jets, allowing them to be deposited near the roots of crops. As a result, the efficiency of fertilizer utilization is significantly improved.

The use of liquid fertilizers eliminates issues related to uneven distribution, nutrient loss, and blockages associated with solid fertilizers. Compared to traditional fertilization methods, this approach minimizes soil disturbance while achieving high fertilizer utilization rates.

Studies conducted by *Lu Yulong et al. (2016)*, on the distribution of rice seedling root systems revealed that the main longitudinal range of rice seedling roots is within 0-50 mm. Therefore, a cutting depth of 50 mm is sufficient to meet the depth requirements for fertilization. *Niemoeller et al. (2011)*, investigated the feasibility of injecting pure water using high-pressure water jets. Experimental results showed that different injection depths can be achieved by adjusting various parameters of the high-pressure jet. In soil with an average moisture content of approximately 25%, an injection depth of 70-90 mm was achieved under the conditions of 40 MPa water pressure, 7.5 L/min volumetric flow rate, and 2 m/s propulsion velocity. It should be noted that soil moisture significantly influences the injection depth of the pure water jet under the same parameters. The experimental results demonstrated that the cohesion of the soil in dry conditions is considerably strong, and the injection depth increases with increasing soil moisture content. *Zheng Wenzhan et al. (2019)*, conducted design and experimental research on a jet-type fertilization machine for rice. The machine employed a high-pressure jet to introduce liquid fertilizer into a mixing chamber, where negative pressure generated by the mixing chamber allowed the liquid fertilizer to be sucked in. The fertilized mixture was then sprayed through a nozzle, representing a fertilization technique involving liquid and water mixing injection. Simulation experiments indicated that the cutting ability of the soil was strongest when the inlet and outlet diameters of the liquid fertilizer were 0.6 mm and 0.8 mm, respectively. The highest fertilization volume was achieved when the inlet and outlet diameters were both 1.0 mm. Under experimental conditions with a jet pressure of 12 MPa, forward velocity of 0.5-0.7 m/s, and fertilization target distance of 10-30 mm, the fertilization depth could reach 25-45 mm. Zheng Wenzhan also compared the yields obtained from different fertilization methods, and the results showed that the jet-type fertilization machine for deep placement had a significant yield-increasing effect compared to traditional broadcasting and topdressing operations.

The application of jet impact technology with appropriate pressure parameters for soil fertilization is a development direction with broad application prospects. It is of great significance in improving fertilizer utilization efficiency, reducing environmental pollution, and minimizing soil disturbance. Further research is needed to deepen our understanding of the mechanisms involved in jet impact on soil and to develop more comprehensive simulation models for jet impact on soil. This will provide a broader space for practical production applications and the future development of jet technology.

Weed Control

Chemical weed control methods pose challenges in terms of pollution, while biological weed control can disrupt the ecological balance, and traditional mechanical methods require regular sharpening, cleaning, and blade replacement (*Wang et al., 2016; Coleman et al., 2019; Colquhoun et al., 2019*). In contrast, high-pressure water jet weed control provides a new non-contact mechanical approach that can overcome these issues (*Zhang, 2012*). *Zhang Lin (2013)*, conducted experiments using *Artemisia annua* as the test subject and found that a water jet pressure of 13.5 MPa was sufficient to cut it. Among the four factors affecting hydro-cutting, the nozzle's lateral movement speed had the greatest impact, followed by water jet pressure, target distance, and nozzle diameter. *Ishida Yasumasa (2005)*, conducted experiments on cutting rice seedlings and found that the best cutting effect was achieved under the experimental conditions of a nozzle diameter of 0.4 mm, a water jet angle of 45 degrees with the seedlings, and the highest water jet pressure. *Assirelli et al., (2022)*, designed a high-pressure water jet weeder with four nozzles, each with a diameter of 0.16 mm, a constant water jet pressure of 100 MPa, and a movement speed of 1.2-2.6 km/h. Experimental studies showed that the weeding effect was directly related to the distance between the nozzle and the weeds, and comparative tests demonstrated that the high-pressure water jet weeder performed comparably to inter-row hoeing machines. The use of high-pressure water jet weed control is a promising and sustainable weed management solution. However, the experiments did not demonstrate effective capability in maintaining parallelism between the working head and the soil surface, directly affecting the weeding ability. Alberto Assirelli also pointed out that from the perspective of precision agriculture, the water quantity of the high-pressure water jet weeder can be quantitatively adjusted to intervene efficiently according to different operational requirements, even doubling the intervention at specific necessary points. To ensure the quality of the operation, Alberto Assirelli designed the weeder with a water jet pressure of 100 MPa, which may lead to excessive pressure and resource waste. However, many experimental studies have shown that high water jet pressures are not necessary for weed control operations and precise regulation of water usage can help reduce the size of agricultural machinery,

increase working hours, and improve efficiency (as shown in Fig.6) (Assirelli *et al.*, 2022; Schield, 1972). The adoption of new weed control technologies needs to demonstrate high efficiency, reliability, and proven economic feasibility.



Fig. 6 - Weed soil coverage (%) immediately after the Grass Killer test on 11 November 2020.
Left and right picture represent GK 2.7km h⁻¹ and GK 1.2km h⁻¹ forward speeds, respectively

Harvesting

Due to the complex field environment, there has been limited research on the application of high-pressure water jet in field harvesting of crops, and the depth of research is relatively shallow. As early as 1972, Schield (1972) verified the feasibility of water jet harvesting of lettuce and designed a horizontal jet cutting machine for harvesting lettuce crops. It was pointed out that when using a given nozzle system to cut different crops, the toughness of vascular fibers is more important than the stem diameter. To reduce the weight of mobile machines for harvesting sugar beets using high-pressure water jets, Juenemann *et al.*, (2010), studied jet spreading and impact during high-pressure water jet cutting of sugar beets. The experiments showed that almost all cutting water could be collected in a compact area. To achieve this, a compact water collection device was designed to recycle the cutting water, thereby reducing the amount of water that needs to be carried. The recovered cutting water contains impurities such as sludge and sugar, which do not meet the water quality requirements of the high-pressure pump. Therefore, an appropriate wastewater treatment process needs to be determined. Junemann *et al.*, (2011), pre-treated the wastewater by centrifugation for solid-liquid separation to counteract the clogging effect of the filter. Then, qualitative filter paper and quantitative membrane filters were used for filtration operations to ensure that the maximum particle size was below 0.5 μm or 1 μm . Regarding the removal of dissolved components, especially sugar, it can be achieved through reverse osmosis. Sugarcane mechanical harvesters use rotating base cutting machines for cutting operations, but the rotating cutting tool components are prone to entanglement with leaves, and materials such as stones and weeds in the field environment also accelerate blade wear. Therefore, high-pressure water jet cutting is considered an effective alternative. Valco pointed out that the cutting efficiency of sugarcane straw is mainly determined by the magnitude of the impact force rather than the erosion of the water jet on the material, and the erosion time-dependent effect is not the primary cutting mechanism for sugarcane (Valco, 1979). Valco *et al.* (1989), conducted cutting experiments on sugarcane under experimental conditions of nozzle diameter of 0.23-0.36 mm, nozzle pressure of 200-400 MPa, movement speed of 1.6-4.8 km/h, and target distance of 3-23 cm. It was concluded that the target distance had a significant impact on sugarcane cutting, while the nozzle pressure and nozzle size had a significant impact, and the influence of lateral movement speed was not significant.

Water jet cutting capacity and the sustainable working time of the nozzle system are important indicators for field harvesting equipment. These can be improved through methods such as using appropriate abrasives, increasing the utilization rate of cutting water, and adjusting machine parameters. Further research is needed in this area.

Post-harvest Processing

Cutting

Irwansyah *et al.* (2012), conducted experiments using high-pressure water jet cutting on samples of polycarbonate, polystyrene, and polyethylene with a thickness of 2mm, which have similar properties to agricultural products. The results showed that the water jet system has great potential for cutting materials

with suitable contour surfaces and can also improve the surface quality of cut food products. *Wulfkuehler et al.*, (2014), used a water jet with a nozzle diameter of 0.1 mm and water pressure of 250 MPa to cut red oak leaf lettuce. The experiments showed that compared to blade cutting, water jet cutting does not affect the microbiological, physiological, and sensory qualities of fresh cut lettuce. *Carreño-Olejua et al.*, (2010), conducted cutting experiments using a kitchen knife, a handheld slicer, and a high-pressure water jet. The water jet parameters used were pressure of 240 MPa, nozzle diameter of 0.1 mm, cutting speed of 5 mm/s, and distance of 15 mm. The experimental results showed that the surfaces of the specimens cut by water jet had better surface smoothness compared to traditional cutting tools and handheld slicers. *Alitavoli et al.*, (1998), conducted research on water jet cutting process planning for soft materials and identified control variables during the cutting process, including water jet pressure, transverse speed, nozzle diameter, and distance between the nozzle and the workpiece. *Becker et al.*, (1992), used a water jet cutting machine to slice potato tubers and observed the irregularities on the cut surface using non-specific protein staining. The study showed that among five samples with cutting pressures ranging from 69 to 345 MPa, the sample with the highest water jet pressure of 345 MPa exhibited the least irregularities in groove shape and depth on the potato cut surface. By controlling the water pressure, nozzle hole diameter, and cutting speed, the sub-surface damage depth was obtained. The results showed that regardless of water pressure or cutting speed, the smallest nozzle plate diameter resulted in the least cell damage and achieved the best cutting performance. As the cutting size increased, the influence of water pressure and cutting speed became more significant, and at lower cutting speeds and moderate water pressures, surface cell damage was more severe. In order to improve labor efficiency, *Lin, J. et al.*, (2017), designed an automatic strawberry calyx removal machine equipped with a jet pressure of 206.8 MPa, which combined color-based machine vision. Using Autodesk Inventor 2012 software to solve constraint equations, the optimal direction of strawberries was determined through dynamic simulation at a conveyor speed of 300 mm/s. Tests showed that when the machine processed medium-sized strawberries at a maximum speed of 2270 kg/h, the weight percentages of calyx-free berries, berries with calyx white shoulder, residual fruits, and reversed fruits were 49.6%, 18.2%, 8.1%, and 24.1%, respectively. Within a 95% confidence interval, the errors were 4.2%, 2.5%, 2.7%, and 4.3%, respectively. It is worth noting that reversed fruits can be fed back to the AVID machine for a second processing. This second processing will generate yields similar to the first processing, depending on the quality of the fruits. The results showed that it is a feasible and cost-effective option for automated industrial-scale calyx removal. To further improve product quality, they also suggested developing a more reliable multi-axis calyx removal system to accommodate a wider range of shapes and sizes.

When using pure water jet technology for cutting agricultural products, typically ultra-high-pressure jet pressures of 200 MPa or above are employed. Higher cutting pressures are advantageous for improving the cutting capability and quality of pure water jet cutting, including enhancing surface smoothness and reducing cell damage. Due to the atomization spray of the water jet column, it is preferable to minimize the distance between the nozzle and the target object. In terms of nozzle selection, using the smallest nozzle can achieve optimal cutting results. When performing cutting operations on specific agricultural products, water jet parameters should be adjusted according to their specific geometric shapes. It is particularly important to note that cost can be effectively reduced and economic benefits can be enhanced by lowering hydraulic parameters.

Peeling Processing

With the development of water jet technology, water jet has also been applied to the peeling process of agricultural products. Mainstream methods such as friction peeling, chemical peeling, and high-pressure steam peeling are difficult to meet production needs (*Chen et al.*, 2016; *Fadeyibi et al.*, 2020; *Singh et al.*, 1995). Friction peeling relies on friction to remove the skin of fruits and vegetables, which can easily damage the surface and affect color. Chemical peeling can alter the color of the skin and affect taste and color. High-pressure steam peeling can cause surface ripening, potentially affecting quality. However, using water jet peeling can avoid these problems.

The quality requirements for peeled lotus seeds are relatively high. In 2009, Cao Zhiqiang designed an integrated lotus seed shelling and peeling machine (*Cao*, 2009). In this machine, lotus seeds are individually washed and peeled using high-pressure water jets, achieving a peeling rate of over 97%. The processed lotus seeds have a quality comparable to manual processing, and the water consumption is only one-third of conventional methods. Most lotus seed shelling and peeling machines on the market use a bilateral structure. In response to the complexity and maintenance difficulties of bilateral machines, *Xu Xieqing et al.*, (2021), designed a lotus seed peeling machine with a single-sided structure.

Compared to bilateral machines, this single-sided structure machine is more compact, stable, and has reduced maintenance difficulties and machine failure rates. In addition, the issue of not being able to repeat processing on lotus seeds using lotus seed shelling and peeling machines often requires additional manual labor for hand peeling. *Xu Xieqing, (2014)*, designed a fresh lotus seed peeling machine based on water jet peeling that can repeat the processing of lotus seeds. This machine uses two symmetric water jets to strike the surface of the rotating lotus seed along its longitudinal axis in a clamped state, completing the peeling process. When using water jet peeling on lotus seeds, it is important to determine the range of jet impact force to ensure that the force is just enough to remove the skin without damaging the lotus flesh and affecting the quality. Based on multiple repeated experiments, it has been found that the maturity of lotus seeds has a significant impact on the peeling effect. Typically, the peeling pressure parameters for mature lotus seeds range from 0.6 to 0.8 MPa. In addition, water jet pressure, water jet angle, and processing speed are also key factors affecting the peeling effect. By using Design-expert software, the influence of these factors on various indicators can be determined and the operating parameters can be optimized. The water jet test pressure range for the fresh lotus seed peeling machine is 0.6 to 0.8 MPa, and the optimal operating parameter is determined to be 0.7 MPa. Experimental results show that the optimized fresh lotus seed peeling machine achieves a peeling rate of 92.63%, which basically meets the operational requirements.

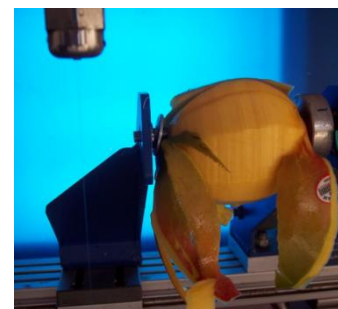
Carreño-Olejua conducted water jet cutting and peeling operations on agricultural products using an automated experimental setup. Under the condition of water jet pressure at the nozzle ranging from 292 to 308 MPa, they obtained the water jet cutting pressure variation graph by using the nozzle diameter and motor frequency as control variables. Based on this graph, they were able to perform cutting and peeling operations on agricultural products. The University of Applied Sciences of Konstanz, Germany, has applied for patents for several methods using this technology for fruit peeling. They have also conducted cutting tests on various geometrically shaped agricultural products such as apples, melons, mangoes, and pineapples, determining parameters such as traverse speed, spacing, material thickness of different agricultural products, and impact angle. *Olejua et al., (2009)*, combined robotics, water jet technology, and image processing techniques to achieve peeling and cutting operations on fruits such as cantaloupes, mangoes (as shown in Fig.7), and pineapples, demonstrating the potential of the system in terms of agricultural product processing quality. They suggested that the use of stereoscopic vision can be optimized as it can eliminate errors caused by eccentric fruits, thereby improving processing quality.



(a) Experiment setup of water-jet automation



(b) Cut of a mango cortex controlled by photography



(c) Final product

Fig.7 - Water Jet Cutting Mango (*Olejua et al., 2009*)

In the process of using waterjet technology for peeling agricultural products, particularly those with high-quality requirements, it is essential to conduct prior experimental research on their physical and mechanical characteristics. This research aims to determine suitable waterjet parameters and optimize them using specialized software. Currently, the application of waterjet technology for peeling agricultural products relies on specific structural designs and parameter ranges based on the physical and mechanical characteristics, as well as geometric shapes of different agricultural products. Integration with technologies such as image processing and robotics can further optimize the peeling process, minimize peel loss, and enhance peeling efficiency.

Summary and prospects

Water jet technology, as a non-contact advanced technique, holds great potential for various applications in the agricultural field. Its unique advantages include the absence of heat generation, blade wear,

and pollution. Extensive research has been conducted on the application of water jet technology in four key areas: sowing, field management, harvesting, and post-harvest processing. Water jet technology has become an important tool in agricultural production. However, its application in the agricultural sector is still in its early stages, especially in complex outdoor environments where weather conditions significantly affect its performance, posing challenges for implementation.

When targeting specific objectives, the parameters of water jet technology have varying degrees of influence, different ranges, and distinct research focuses. Currently, adjustments to jet parameters and working media are mainly achieved through experimental trials to enhance operation quality and efficiency, with limited emphasis on simulation studies. To further promote the application of water jet technology in agriculture, in-depth research should be conducted in the following three areas: Firstly, combining simulation and experimental investigations to deepen the understanding of the impact mechanism of water jet technology on agricultural products, soil, and other operational objects. This research will help clarify the evolution process of jet impacts and identify influential factors. Secondly, optimizing the design of agricultural machinery, adjusting parameters such as jet angles, movement speeds, and jet pressures. These optimizations will contribute to improving cutting capabilities, reducing equipment size, and lowering costs. Lastly, moving towards the development of intelligent agricultural equipment by integrating technologies such as machine vision, robotics, and image processing with water jet technology. This integration will enable real-time monitoring of the operational process and automatic adjustment of parameters, expanding the scope of technological convergence across multiple domains.

By delving into these research directions, the application of water jet technology in agriculture can be further enhanced, unlocking its full potential for improving productivity, efficiency, and sustainability in agricultural operations.

ACKNOWLEDGEMENT

This work was supported by National Natural Science Foundation of China (Grant No. 5220053533), the Basic and Applied Basic Research Project of Guangzhou Basic Research Plan (Grant No. 2023A04J1554) and Research and Application Demonstration of Mechanized Production Technology for Tuber Crops in Lingnan Region (Grant No. KA2201637).

REFERENCES

- [1] AlitaVoli, M., McGeough, J. A., (1998). An expert process planning system for meat cutting by high pressure water-jet. *Journal of Materials Processing Technology*, Vol. 84, pp. 130-135, United Kingdom.
- [2] Assirelli, A.; Ciaccia, C.; Giorgi, V.; Zucchini, M.; Neri, D.; Lodolini, E.M., (2022). An Alternative Tool for Intra-Row Weed Control in a High-Density Olive Orchard. *Agronomy*, Vol. 12, pp. 605, Switzerland.
- [3] Becker, R., Gary, G. M., (1992). Evaluation of a water jet cutting system for slicing potatoes. *Journal of Food Science*, Vol. 57, pp. 132-137, United States.
- [4] Bremer, F, Matthesen S., (2020). A review of research relating to food slicing in industrial applications. *Journal of Food Engineering*, Vol. 268, Netherlands.
- [5] Cao, Z., (2009, September 16). *A Lotus Seed Shelling and Peeling Integrated Machine* (一种莲子剥壳脱皮一体机). Patent, No. CN201308087, China.
- [6] Carreño-Olejua, R., Hofacker, W. C., Hensel, O., (2010), High-pressure water-jet technology as a method of improving the quality of post-harvest processing. *Food and bioprocess technology*, Vol. 3, pp. 853-860, Germany.
- [7] Chen, G., (2007). Characteristics and Applications of Numerical Control Ultra-High Pressure Water Jet Cutting Technology (数控超高压水射流切割技术的特点及其应用). *Machine Tool & Hydraulics*, Vol. 08, pp. 64-68, Guangdong/China.
- [8] Chen, G., (2008). Application of Ultra-High Pressure Water Jet Cutting Technology in Food Processing (超高压水射流切割技术在食品加工中的应用). *Machine Tool & Hydraulics*, Vol. 10, pp. 220-223, Guangdong/China.
- [9] Chen, H., Liu, Q., (2016). Research Progress on Potato Peeling Technology. *Food Industry*, Vol. 37, pp. 229-232, Shanghai/China.
- [10] Cheng, X., Zhang, S., Ma, L., Luo, Y., (2019). Current Application and Development Prospects of High-Pressure Water Jet Technology (高压水射流技术的应用现状与发展前景). *Hydraulic Pneumatics & Seals*, Vol. 39, pp. 1-6, Beijing/China.

- [11] Cheung, G., O'Sullivan, C., (2008). Effective simulation of flexible lateral boundaries in two-and three-dimensional DEM simulations. *Particuology*, Vol. 6, pp. 483-500, China.
- [12] Coleman, G. R. Y., Stead, A., Rigger, M. P., Xu, Z., Johnson, D., Brooker, G. M., ... Walsh, M. J., (2019). Using energy requirements to compare the suitability of alternative methods for broadcast and site-specific weed control. *Weed Technology*, Vol. 33, pp. 633-650, United States.
- [13] Colquhoun, J. B., Rittmeyer, R. A., Heider, D. J., (2019). Carrot weed management programs without linuron herbicide. *Weed Technology*, Vol. 33, pp. 490-494, United States.
- [14] Cui, D., Li, H., He, J., Wang, Q., Lu, C., Hu, H., Cheng, X., Wang, C., (2022). Applications of Water Jet Cutting Technology in Agricultural Engineering: A Review. *Applied Sciences*, Vol. 12, pp. 8988, Switzerland.
- [15] Deng, Z., Zhang, H., Fu, Y., Wan, L., Lv, L. (2018). Research on intelligent expert system of green cutting process and its application. *Journal of cleaner production*, Vol. 185, pp. 904-911. Netherlands.
- [16] Du, M., Wang, H., Dong, H., Guo, Y., Ke, Y., (2020). Numerical research on kerf characteristics of abrasive waterjet machining based on the SPH-DEM-FEM approach. *The International Journal of Advanced Manufacturing Technology*, Vol. 111, pp. 3519-3533, United Kingdom.
- [17] Du, R., Yang, Z., Zhang, J., Guo, Z., (2006). Design and Experiment of a Water-Jet Seeding Device for Creating Planting Holes (射水成穴播种试验装置的设计及试验). *Transactions of the Chinese Society for Agricultural Machinery*, Vol.07, pp. 52-55, Beijing/China.
- [18] DuPlessis, M. P., M. Hashish., (1978). High energy water jet cutting equations for wood. *Journal of Engineering for Industry*, Vol. 100, pp. 452-458, United States.
- [19] Fadeyibi, A., Faith, Ajao, O., (2020). Design and performance evaluation of a multi-tuber peeling machine. *AgriEngineering*, Vol. 2, pp. 55-71, Switzerland.
- [20] Folkes, J., (2009). Waterjet—An innovative tool for manufacturing. *Journal of Materials Processing Technology*, Vol. 209, pp. 6181-6189, Switzerland.
- [21] Ghosh, S., Rao, P. V. (2015). Application of sustainable techniques in metal cutting for enhanced machinability: a review. *Journal of Cleaner Production*, Vol. 100, pp. 17-34. Netherlands.
- [22] Gupta, K., (2020). A review on green machining techniques. *Procedia Manufacturing*, Vol. 51, pp. 1730-1736, Netherlands.
- [23] Horabik, J., Molenda, M., (2016). Parameters and contact models for DEM simulations of agricultural granular materials: A review. *Biosystems engineering*, Vol. 147, pp. 206-225, Netherlands.
- [24] Hu, H., Li, H., Wang, Q., He, J., Lu, C., Wang, Y., Wang, C., (2019). Performance of waterjet on cutting maize stalks: A preliminary investigation. *International Journal of Agricultural and Biological Engineering*, Vol. 12, pp. 64-70, Beijing/China.
- [25] Hu, H., Li, H., Wang, Q., He, J., Lu, C., Wang, Y., Liu, P., (2020). Anti-blocking performance of ultrahigh-pressure waterjet assisted furrow opener for no-till seeder. *International Journal of Agricultural and Biological Engineering*, Vol. 13, pp. 64-70, Beijing/China.
- [26] Hu, Y., Kang, Y., Wang, X., Li, X., Long, X., Zhai, G., Huang, M., (2014). Mechanism and experimental investigation of ultra-high pressure water jet on rubber cutting. *International Journal of Precision Engineering and Manufacturing*, Vol. 15, pp. 1973-1978, Korea.
- [27] Irwansyah, I., Ibrahim, M., Ferdiansyah, H., (2012). Influence of water-jet nozzle geometry on cutting ability of soft material. *Jurnal Rekayasa Kimia & Lingkungan*, Vol. 9, pp. 6-11, Indonesia.
- [28] ISHIDA, Y., OKAMOTO, T., IMOU, K., KAIZU, Y., (2005). A study on physical weeding using a water jet. *Journal of the Japanese Society of Agricultural Machinery*, Vol. 67, pp. 93-99, Japan.
- [29] Jiang, H., Zhao, H., Gao, K., Wang, O., Wang, Y., Meng, D (2020). Numerical investigation of hard rock breakage by high-pressure water jet assisted indenter impact using the coupled SPH/FEM method. *Powder Technology*, Vol. 376, pp.176-186, Netherlands.
- [30] Juenemann, D., Harms, H. H., (2010). Development of a water catcher for high pressure water jet cutting of agricultural goods. *Proceedings of the CIGR XVIIth World Congress of the International Commission of Agricultural and Biosystems Engineering*, pp. 13-17, Quebec City, QC, Canada.
- [31] Junemann, D., Harms, H. H., Lang, T., (2011). Water processing for high pressure water jet cutting of sugar beets. *Landtechnik*, Vol. 66, pp. 103-107, Germany.
- [32] Kamarudin, N. H., Rao, A. K. P., Azhari, A., (2016). CFD based erosion modelling of abrasive waterjet nozzle using discrete phase method. *IOP Conference Series: Materials Science and Engineering*, Vol. 114, United Kingdom.

- [33] Kang, C., (2016). *Fundamentals and Applications of High-Pressure Water Jet Technology* (高压水射流技术基础及应用), Machinery Industry Press, Beijing/China, pp. 14-16, ISBN 978-7-111-51825-9.
- [34] Khatak, P., (2022). Laser cutting technique: A literature review. *Materials Today: Proceedings*, Vol. 56, pp. 2484-2489. Netherlands.
- [35] Krajcarz, D. (2014). Comparison metal water jet cutting with laser and plasma cutting. *Procedia Engineering*, Vol. 69, pp. 838-843. Netherlands.
- [36] Li, X., Lu, Y., Zhao, Y., Kang, Y., Zhou, D., (2008). Study on Improving Permeability of Loose Coal Seam by High-Pressure Pulsed Water Jet (高压脉冲水射流提高松软煤层透气性的研究). *Journal of China Coal Society*, Vol. 33, pp. 1386-1390, Beijing/China.
- [37] Li, Z., Li, F., Wang, J., (2009). High-Pressure Water Jet Technology and Its Applications. *Mechanical Engineer*, Vol. 11, pp. 33-36, United States.
- [38] Lin J, Holmes M, Vinson R, et al., Lin, J., Holmes, M., Vinson, R., Ge, C., Pogoda, F. C., Mahon, L., ... & Tao, Y. (2017). Design and testing of an automated high-throughput computer vision guided waterjet knife strawberry calyx removal machine. *Journal of Food Engineering*, Vol. 211, pp. 30-38, United Kingdom.
- [39] Lin, Z. L., Lu, Q., Yi, X., Cheng, X., (2021). Development and Application of High-Pressure Water Jet Technology (高压水射流技术的发展与应用). *China Science and Technology Industry*, Vol. 5, pp. 46-47, Beijing/China.
- [40] Liu, H., (2021). *Design and Experiment of Deep Fertilization Subsoiling No-Tillage and Segmented Seeding Opener for Corn* (深施肥下玉米免耕分段式播种开沟器设计与试验), Master's thesis, Northeast Agricultural University, Heilongjiang/China.
- [41] Llanto, J. M., Tolouei-Rad, M., Vafadar, A., & Aamir, M., (2021). Recent progress trend on abrasive waterjet cutting of metallic materials: a review. *Applied Sciences*, Vol. 11, pp. 3344, Switzerland.
- [42] Lu, Y., Ma, B., (2011). Exploration and Application of High-Pressure Water Rust Removal Technology in Coal Mines (高压水除锈技术在煤矿的探索应用). *Mechatronics and Information*, Vol. 18, pp. 114-115, United Kingdom.
- [43] Lu, Y., (2016). *Design and Experimental Study on the Structure of Rice Jet Fertilizer Applicator* (水稻射流式施肥器结构设计与试验研究), Master's thesis, South China Agricultural University, Guangzhou/China.
- [44] Lu, Y., (2020). *Design and Experimental Research on High-Speed Bionic Furrow Opener* (高速仿生开沟器设计与试验研究), Master's thesis, Jilin University, Jilin/China.
- [45] Natarajan, Yuvaraj, et al., (2020). Abrasive Water Jet Machining process: A state of art of review. *Journal of Manufacturing Processes*, Vol. 49, pp. 271-322, United Kingdom.
- [46] Niemoeller, B., Harms, H. H., Lang, T., (2011). Injection of liquids into the soil with a high-pressure jet. *Agricultural Engineering International: CIGR Journal*, Vol. 13, Italy.
- [47] Nyord, T., Søgaard, H. T., Hansen, M. N., Jensen, L. S., (2008). Injection methods to reduce ammonia emission from Volatile liquid fertilisers applied to growing crops. *Biosystems Engineering*, Vol. 100, pp. 235-244, Netherlands.
- [48] Olejua, A. R. C., Hofacker, W. C., Hensel, O., (2009), Use of Image Analysis in Process Control of High Pressure Water-Jet Peeling and Cutting of Fruits, *American Society of Agricultural and Biological Engineers*, pp.1, Reno, Nevada.
- [49] Perotti, F., Annoni, M., Calcante, A., Monno, M., Mussi, V., Oberti, R. (2021). Experimental Study of Abrasive Waterjet Cutting for Managing Residues in No-Tillage Techniques. *Agriculture*, Vol. 11, pp. 392, Switzerland.
- [50] Pogrebnyak, A. Pogrebnyak, V. Perkun, I. Vasylyv, N., (2020). Influence of geometric and dynamic parameters of a water-polymer jet on characteristics of food products hydro-cutting process. *Ukrainian Food Journal*, Vol. 9, pp. 197-208, Ukraine.
- [51] Prisco, U., D'Onofrio, M. C., (2008). Three-dimensional CFD simulation of two-phase flow inside the abrasive water jet cutting head. *International Journal for Computational Methods in Engineering Science and Mechanics*, Vol. 9, pp. 300-319, United States.
- [52] Schield, M. L., (1972). Harvesting lettuce by severing with a water jet. United States.

- [53] Schuldt, S., Schneider, Y., Rohm, H., (2018). High-speed cutting of foods: Cutting behavior and initial cutting forces. *Journal of Food Engineering*, Vol. 230, pp. 55-62, Netherlands.
- [54] Singh, K. K., Shukla, B. D., (1995). Abrasive peeling of potatoes. *Journal of food engineering*, Vol. 26, pp. 431-442, Netherlands.
- [55] Song, G., Zheng, H., Wang, Y., Zheng, Y., Zhou, Y., Yao, B., (2019), Finite element analysis of nozzle selection based on high pressure water jet technology, IOP Conference Series: *Earth and Environmental Science*, Vol. 267, IOP Publishing.
- [56] Song, L., (2009). *Analysis of Factors Influencing the Characteristics of High-Pressure Water Jet Cutting and System Design* (高压水射流切割特性影响因素分析及系统设计), Master's thesis, Shenyang University of Technology, Shenyang/China.
- [57] Sun, J., (2006). *Development of a Mobile Fluid Jet Test Device and Experimental Study on Water-Jet Seeding* (移动式流体喷射试验装置研制及射水播种试验研究), Master's thesis, Shandong University of Technology, Shandong/China.
- [58] Valco, T. D., (1977). *High Pressure Water Jet Cutting of Sugarcane*, Master's thesis, Texas A&M University, United States.
- [59] Valco, T. D., Coble, C. G., Ruff, J.H., (1989). Water jet cutting of sugarcane. *Transactions of the ASAE*, Vol. 32, pp. 373-0378, United States.
- [60] Vasudevan, B., Natarajan, Y., Kumar, R. P., Chandra, K. U., Sikder, D., (2022). Simulation of AWJ drilling process using the FEA coupled SPH models: A preliminary study. *Materials Today: Proceedings*, Vol. 62, pp. 6022-6028, Netherlands.
- [61] Wang, C., Liu, C., Li, H., Wang, Q., He, J., Lu, C., (2018). Design and Experiment of Asymmetric Large and Small Disc Opener for Furrow Opening(非对称式大小圆盘开沟装置设计与试验). *Transactions of the Chinese Society of Agricultural Engineering*, Vol. 34, pp. 28-36, Beijing/China.
- [62] Wang, Z., Wang, B., Zhang, M., Dai, Y., Mo, Z., Luo. X., (2016). Synchronized Spray Weeding Technology and Dynamic Dissolution Characteristics of Herbicides (同步喷施除草技术及除草剂消解动态规律). *Transactions of the Chinese Society of Agricultural Engineering*, Vol. 32, pp. 59-64, Beijing/China.
- [63] Wang, J., Gao, N., Gong, W., (2010). Abrasive waterjet machining simulation by SPH method. *The International Journal of Advanced Manufacturing Technology*, Vol. 50, pp. 227-234, United Kingdom.
- [64] Wilkins, R. J., & Graham, E. E., (1993). An erosion model for waterjet cutting. *Journal of Engineering for Industry*, Vol. 115, pp. 57-61, United States.
- [65] Wulfkuehler, S., Stark, S., Dietz, J., Schmidt, H., Weiss, A., Carle, R. (2014). Effect of water jet cutting and moderate heat treatment on quality of fresh-cut red oak leaf lettuce (*Lactuca sativa* L. var. *crispa*). *Food and Bioprocess Technology*, Vol. 7, pp. 3478-3492, Germany.
- [66] Yan, X., Jin, J., He, P., Liang, M., (2008). Recent advances on the technologies to increase fertilizer use efficiency. *Agricultural Sciences in China*, Vol. 7, pp. 469-479, Beijing/China.
- [67] Xu, W., Wang, J., Deng, Y., Li, J., Yan, T., Zhao, S., ... & Liu, D. (2022). Advanced cutting techniques for solid food: Mechanisms, applications, modeling approaches, and future perspectives. *Comprehensive Reviews in Food Science and Food Safety*, Vol. 21, pp. 1568-1597, United States.
- [68] Xu, X., Rao, H., Li, T., Liu, M., (2014). Design and Experiment of Fully Automatic Lotus Seed Shelling and Peeling Machine (全自动莲子剥壳去皮机的设计与试验). *Transactions of the Chinese Society of Agricultural Engineering*, Vol. 30, pp. 28-34, Beijing/China.
- [69] Xu, X., Ding, W., Zhang, W., Liu, M., (2021). Design and Parameter Optimization of Fresh Lotus Seed Peeling Machine(鲜莲子去皮机设计与参数优化). *Transactions of the Chinese Society for Agricultural Machinery*, Vol. 52, pp. 338-349, Beijing/China.
- [70] Yang, Y., Xu, J., Wang, J., Zhang, Q., Liu, Q., (2010). Design and Experimental Study on the Wear of the Cutting Blades of a New Type of Corn Straw Crusher. *Journal of Jilin Agricultural University*, Vol. 32, pp. 468-472, Jilin/China.
- [71] Yang, Z., Du. R., Bai, T., (2010). Design and study on control system of water jet seeder by controlling seed and water respectively, *World Congress on Intelligent Control and Automation*, pp. 2998-3001, Jinan/China.
- [72] Yu, C., (2018). *Research on Dynamic Cleaning Technology for Granular Agricultural Products* (颗粒型农产品动态清洗技术研究), Master's thesis, Zhejiang University of Technology, Zhejiang/China.

- [73] Zhang, L., (2005). High-Pressure Water Cleaning Machine Rust Removal Technology for Metal Surfaces (金属表面高压水清洗机除锈技术). *Cleaning World*, Vol. 06, pp. 26-28, Beijing/China.
- [74] Zhang, L., (2012). *Theoretical and Experimental Study on Hydraulic Mowing* (水力割草理论及试验研究), Master's thesis, Hunan Agricultural University, Hunan/China.
- [75] Zhang, L., Li, M., Pei, Y., Liu, Z., (2013). Experiment on Cutting Resistance of Three Weeds (三种杂草切割阻力试验). *Journal of Hunan Agricultural University (Natural Sciences)*, Vol. 39, pp. 99-102, Hunan/China.
- [76] Zhao, J., Shan, T., (2013). Coupled CFD–DEM simulation of fluid–particle interaction in geomechanics. *Powder technology*, Vol. 239, pp. 248-258, Netherlands.
- [77] Zheng, W., (2019). *Design and Experimental Study on Rice Jet Fertilizer Applicator* (水稻射流式追肥机设计与试验研究), Master's thesis, South China Agricultural University, Guangzhou/China.
- [78] Zheng, W., Jiang, Y., Ma, X., Qi, L., (2019). Development of a liquid-jet nozzle for fertilizer injection in paddy fields using CFD. *Computers and electronics in agriculture*, Vol. 167, Netherlands.
- [79] Zhou, Z. H., (2022). Current Research Status and Development Trend of Anti-Clogging Technology for No-Tillage Seeders. *Farm Machinery Use and Maintenance*, Vol. 04, pp. 53-55, Heilongjiang/China.
- [80] Zou, X., Fu, L., Wu, L., Zuo, W., (2023). Research on Multiphase Flow and Nozzle Wear in a High-Pressure Abrasive Water Jet Cutting Head. *Machines*, Vol. 11, pp. 614, Switzerland.

DESIGN AND TESTING OF PEANUT SIEVING PROTOTYPE MACHINE

花生清选筛台架的设计与试验

Dongjie LI¹⁾, Jialin HOU^{*1)}, Dongwei WANG^{2,3)}, Zengcun CHANG¹⁾¹⁾ Shandong Agricultural University, College of Mechanical and Electrical Engineering/ China²⁾ Yellow River Delta Intelligent Agricultural Equipment Industry Academy, Shandong / China;³⁾ Qingdao Agricultural University, College of Mechanical and Electrical Engineering / China;

Tel: +86-0532-58957391; E-mail: 200701031@qau.edu.cn

Corresponding author: Hou Jialin

DOI: <https://doi.org/10.35633/inmateh-73-64>**Keywords:** Peanut; Impurity rate; Loss rate; Cleaning sieve; Combine harvester**ABSTRACT**

In order to address the high impurity and loss rates in the cleaning process of existing peanut combine harvesters, the design basis of the cleaning sieve was explored. Tests were conducted to determine the composition of the peanut picking fruit and the characteristics of the material suspension mixture. Additionally, the mechanical relationship between the fruit and miscellaneous mixtures and the cleaning sieve was investigated. The wind speed ranged from 8 m/s to 10 m/s, the vibration frequency ranged from 6 Hz to 8 Hz, and the inclination angle of the sieve ranged from 5° to 9°. The scavenger sieve platform was constructed and tested using Box-Behnken's central combination test method. The optimal combination of fan wind speed (9 m/s), sieve surface inclination angle (8°), and sieve vibration frequency (7 Hz) resulted in a pod impurity rate of 1.16% and a loss rate of 1.4%. The device significantly reduces impurity content and loss rate during peanut harvesting. The study's results can serve as a reference for improving the design of the peanut combine harvester cleaning mechanism and optimizing operating parameters.

摘要

针对现有花生联合收获机清选环节含杂率高、损失率大等问题，探究了清选装置设计依据，开展了花生摘果脱出物料的组成成分测定试验、混合物料悬浮特性试验，并探究了果杂混合物料与清选筛力学关系，确定风速为 8 m/s~10 m/s；振动频率为 6 Hz~8 Hz；清选筛倾角为 5°~9°。搭建形成清选筛台架并运用 Box-Behnken 的中心组合试验方法开展试验并优化，得最优参数组合风机风速为 9 m/s、清选筛倾角为 8°、清选筛振动频率 7 Hz，对应的荚果含杂率为 1.16%、清选损失率为 1.4%。该装置的作业效果显著降低了花生收获环节的含杂率和损失率，研究结果可为花生联合收获机清选机构的完善设计和作业参数优化提供参考。

INTRODUCTION

Peanut is one of the main oil crops in China, with increasing annual planting and production. Improving the quality of harvesting is crucial for farmers to achieve great economic benefits. In peanut harvesting machinery and equipment, the working effect of the cleaning sieve determines the loss rate and impurity rate of peanut harvesting. Therefore, the cleaning device plays a vital role in the working effect of the whole machine. In recent years, scholars both domestically and internationally have conducted numerous studies on the cleaning methods and theories of various crops.

The cleaning device can be classified into three types based on their principles: airflow type, sieve type, and airflow sieve combined cleaning device (Wang *et al.*, 2022). The principle of airflow sorting is to utilise the difference in floating characteristics of materials to sort them. Sieve-type sorting uses the physical characteristics of the material to sort it through the vibration principle. The airflow sieve combined cleaning device is a combination of the two methods and is widely used as a cleaning method in current peanut combine harvesters. Dongming Zhang analysed the motion mechanism of material particles in the wind sieve cleaning device using the lattice Boltzmann method (LBM). A simulation model was established to explore the flow field distribution of airflow through the static screen surface (Zhang *et al.*, 2023). In this text, Wang Bing discusses the occurrence of pod collision, bouncing, and friction during vibrating screen operation. The author conducts orthogonal and one-factor tests to determine the pod recovery coefficient and friction coefficient. The design of a non-blocking lap type finger popping sieve is also presented (Wang *et al.*, 2018).

Wan Xingyu’s research, the influence of the inlet and the MOG outlet air velocities on the high-velocity and low-velocity areas inside the cyclone separator was gained by the CFD approach. Furthermore, a prediction model built by the response surface experiment was utilized (Wan et al., 2023). Wang Bokai addressed the problems of high air-selection loss rate and high impurity rate of axial-flow peanut picker harvester in the harvesting process. Based on the physical characteristics of each type of particle in the peanut mixture and the air flow characteristics, a multi-wind system is designed and numerical simulations and tests are carried out (Wang et al., 2021). According to the analyses of previous studies, it was found that the structure and working parameters of the cleaning screen device have a significant effect on the performance of the harvester (Hou et al., 2023).

In summary, there are still shortcomings in the cleaning process of peanut combine harvesters. In order to address this drawback, this article takes the two ridges and four row peanut combine machine as the research object. It investigates the principle of pod and impurity separation in the sieving and windrowing processes. Its purpose is to analyse the conditions of pod and impurity movement in the sieving process, to design a sieving frame and to optimise the working parameters of the sieving frame. It is also intended to lay the foundation for the establishment of the theory and technical system of the combined peanut harvesting and cleaning system in China.

MATERIALS AND METHODS

Basis for designing the cleaning screen

To explore the basis for the design of the cleaning screen, the composition of the material after peanut picking, the relationship between the pods and miscellaneous blends and the cleaning screen, and the suspension characteristics of the blends were analysed (Wang et al, 2021, Lian et al, 2023, Yue et al, 2023, Wang et al, 2024).

The quality of the post-picking mixture was determined and the post-picking material mainly contained pods, seedling vines, miscellaneous leaves, peanut pod stalks, weeds, seedling membranes, soil, etc. The composition of the mixture obtained after harvesting is shown in Figure 1. In addition, the various components in the mixed materials will be classified and weighed, with their proportions shown in Table 1.



Fig.1 – Composition of impurities formed after picking peanuts

Table 1

The mass proportion of peanut pod and its components

| Materials | Peanut pods (%) | Stalks (%) | Seedling film, deflated pods (%) | Loam (%) |
|-----------|-----------------|------------|----------------------------------|----------|
| Sample 1 | 66.3 | 5.0 | 8.0 | 20.7 |
| Sample 2 | 70.2 | 4.8 | 7.6 | 17.4 |
| Sample 3 | 63.1 | 5.3 | 8.2 | 23.4 |
| Sample 4 | 66.8 | 5.5 | 8.5 | 19.2 |
| Sample 5 | 78.0 | 6.2 | 9.6 | 14.2 |
| averages | 68.9 | 5.36 | 8.38 | 18.98 |

By determining the composition of the material after peanut pod harvesting: peanut pods accounted for a range of 60% to 80%, seedling vines and stems accounted for a range of 4 % to 7 %, seedling membranes and shrivelled pods accounted for a range of 7 % to 10 %, and soil accounted for a range of 10 % to 30%.

The material after peanut harvesting is analysed and the material is varied and chaotic. As shown in Figure 2. If too much material is fed, it will cause clogging of the screen, loss of peanut shells and increase in impurities. Feeding too little material will result in a loss of power consumption of the screen. Therefore, a combination of air-screening and air-blowing cleaning methods was chosen.



Fig. 2 – Feeding material for primary cleaning

The cleaning process for peanut combine harvesters consists of two stages: vibration screening and air blowing with wind selection (Hu et al, 2023, Pang et al, 2023). The first stage ensures that peanut pods flow smoothly on the screen surface. During this stage, light impurities are selected based on their geometry. Air blowing wind selection is mainly used for screening surfaces that are difficult to screen and have more complicated impurities. The use of air separates the fruit. Therefore, the air blowing wind sieve combined with the cleaning sieve is a factor in peanut harvesting. This includes the design of the screen surface structure, the design of the eccentric vibration device, the inclination angle of the screen surface, the wind speed of the fan, and the fan's adaptive position. To investigate the impact of wind selection factors, a test was conducted to evaluate the floating characteristics of pods and miscellaneous mixtures. The test process is illustrated in Figure 3 and the results are presented in Table 3.



Fig. 3 – Test process

Table 2

The floating speed of peanut pods and their components

| Sample name | Floating speed of material (m/s) | | | | |
|-------------|----------------------------------|-------------|--------------|------------|-----------|
| | miscellaneous leaves | long stalks | short stalks | pod stalks | peanut |
| Ji Hua16 | 2.1~2.7 | 7.9~9.6 | 3.6~4.8 | 3.4~4.7 | 13.7~15.4 |
| Yu Hua14 | 1.1~1.6 | 7.1~9.7 | 3.1~5.2 | 2.8~3.9 | 11.4~14.2 |
| Da Baisha | 3.1~3.8 | 7.6~8.7 | 4.8~6.8 | 4.3~6.7 | 11.8~13.3 |

From Table 2, it can be concluded that: the floating speed of peanut pods ranges from 11.4 to 15.5 m/s, the floating speed of long stalks ranges from 7.1 to 9.6 m/s, the floating speed of short stalks ranges from 3.1 to 6.8 m/s, the floating speed of pod stalks ranges from 2.8 to 6.7 m/s, and the floating speed of seedling branches and leaves ranges from 1.1 to 3.8 m/s.

Cleaning is based on the physical properties that distinguish peanut pods from impurities. The speed of the material floating refers to the point at which the mixture of pod and impurities is subjected to an airflow force that opposes gravity. When the forces of gravity and airflow are in balance, the mixture of pod and impurities will be suspended in the air. The pod mixture is considered as a whole and moves within an airflow with a velocity of V moving diagonally upwards. The fan configuration is directed 23° upwards along the angle of inclination of the draft collector, as illustrated in Figure 4.

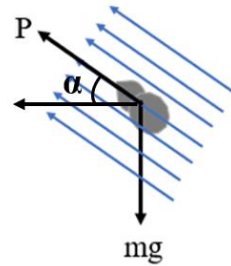


Fig. 4 – Schematic diagram of peanut and impurity wind

According to Newton's laws, the calculation formula is as follows:

$$P \sin \alpha = Gsp(V_1 - V_2)^2 \quad (1)$$

where:

G is the drag coefficient; p is the atmospheric air density, [g/m²]; α is the angle of airflow with horizontal direction, [°]; V_1 is the absolute velocity of the material, [m/s]; V_2 is the relative velocity of materials, [m/s]; s is the cross-sectional area of the material relative to the direction of air velocity, [m²].

Based on the above analysis, it can be concluded that: when $P \sin \alpha < mg$, the material is in falling movement; when $P \sin \alpha > mg$, the material is in rising movement; when $P \sin \alpha = mg$, the material gravity and the size of the wind force is balanced.

When the material is in equilibrium, the mathematical relationship is expressed as:

$$P = GpsV_2^2 = \frac{mg}{\sin \alpha} \quad (2)$$

The floating velocity of the material is expressed as:

$$V = \sqrt{\frac{mg}{\sin \alpha Gps}} \quad (3)$$

After measuring the buoyancy of different materials, a fan is used to remove light impurities such as fruit stalks and grass shavings. The equipment achieves the best separation effect when the wind speed is set between 8 m/s and 10 m/s.

Design of screen surface structure

To enhance work efficiency and quality, the basic structure of the sieve surface is optimized based on the traditional clearing device structure, as illustrated in Figure 5.

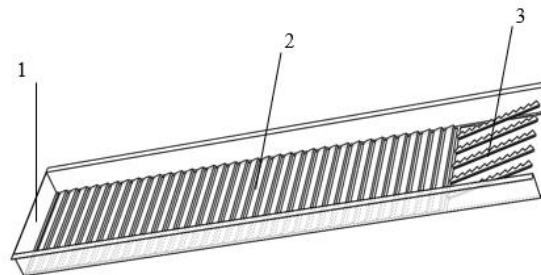


Fig. 5 – Schematic diagram of screen surface

1. Cleaning sieve racks; 2. Cleaning sieve surface; 3. Seedling discharge device

The length of the vibrating screen is primarily determined by the picking efficiency of the picking rollers. To calculate the length of the vibrating screen, use the following formula:

$$L = \frac{G_s}{bg_s} = \frac{G(1 - \delta k)}{bg_s} \quad (4)$$

where:

L is the vibrating screen length, [mm]; G_s is the weight of peanuts sieved per second, [kg/s]; G is the combine harvester feed weight per second, [kg/s]; δ is the share of impurities in post-pick material, [kg/s]; K is the scavenging performance factor, [0.6-0.9]; b is the vibrating screen width, [mm]; g_s is the weight of pods fed per second, [kg/s].

According to the formula, the width of the screen is 500 mm and the length is 1540 mm. In order to make the screen work optimally, the screen is of the stepped type. This design facilitates the breaking up of the soil. At the same time, it improves the flow of the material through the screen. The parameters of the stepped screen surface are as follows: the front part of the step is inclined upwards, the back part of the step is folded and extends vertically downwards to form a step unit, and each step unit formed is evenly distributed and welded to the support frame. The screen surface is connected to a cam device, using the impact force generated by the cam rotation to convey the material backwards. The gap between the two stepped corners of the sieve surface is smaller than the diameter of the peanut pods and larger than the diameter of the impurities, so that the impurities fall smoothly. The front and rear ends are each left with a welding allowance of 2 mm, so that the gap actually takes the value of 9 mm, the length of the drafter is 400 mm, the design improves the fluidity of the material in the sieve surface and reduces the loss rate of peanut pods and the impurity rate.

Design of vibration devices

The cleaning sieve's core component is the eccentric rotation device. This device uses the principle of eccentricity to drive the vibration of the cleaning screen body and materials. As a result, the vibration amplitude and frequency are influenced by the eccentric wheel device.



Fig. 6 – Structure diagram and prototype diagram of vibrating screen

The device operates by using the rotation of the eccentric wheel to drive the swing of the DE connecting rod. The DE rod is in a vertical state when the eccentric wheel C point reaches the farthest end. The D point is the limit point in the process of linkage swing, and the time for the D end to swing to the right is lower than the time to swing to the left.

The design aims to enable the material to move backward when it enters the cleaning sieve by causing the vibrating screen to swing back and forth. Additionally, the stepped shape of the screen surface ensures the fluidity of the material.

The cleaning sieve device's amplitude is determined by calculating the left and right swing displacement in the X direction and the up and down vibration displacement in the Y direction. The maximum and minimum moving distances of the cleaning sieve device in the horizontal direction were measured to be 2174.39 mm and 2081.42 mm, respectively, through testing.

$$A_1 = \frac{X_2 - X_1}{2} = \frac{2174.39 - 2081.42}{2} = 46.485 \quad (5)$$

The maximum travelling distance of the cleaning device in the vertical direction is 316.26 mm and the minimum travelling distance is 293.97 mm from Eq.:

$$A_2 = \frac{Y_2 - Y_1}{2} = \frac{316.26 - 293.97}{2} = 11.145 \quad (6)$$

where:

A_1 is the amplitude of scavenging device in horizontal direction, [mm]; A_2 is the amplitude of the cleaning device in the vertical direction, [mm]; X_1 is the minimum displacement of the sieving device in the X direction, [mm]; X_2 is the maximum displacement of the sieving device in the X direction, [mm]; Y_1 is the minimum displacement of the sieving device in Y direction, [mm]; Y_2 is the maximum displacement of the cleaning device in the Y direction, [mm].

The amplitude of vibration in the horizontal direction ranges from 40-60 mm according to the operating requirements of the cleaning device. The amplitude of vibration in the vertical direction is less than that in the horizontal direction. This meets the design requirements.

The vibration frequency of the cleaning device is directly proportional to the rotational speed of the main wheel, which is controlled by the motor in the eccentric device. Take the two ridges and four rows peanut combine harvester as an example, the rotational speed is calculated in the range of 400-500 r/min.

To calculate the vibration frequency, use the following formula:

$$T = \frac{60}{n} = 0.15 \sim 0.12 \tag{7}$$

$$f = \frac{1}{T} \approx 6 \sim 8 \tag{8}$$

where:

T is the time required for the active wheel to turn over one week, [s]; n is the rotational speed of the main wheel, [r]; f is the vibration frequency of cleaning sieve, [Hz].

The calculation shows that the device's frequency is between 6-8 Hz. In the peanut cleaning process, the frequency of the cleaning sieve has a significant impact on the operational performance of the entire machine. Therefore, it is necessary to further optimize this factor when determining the length of the cleaning device.

The eccentric wheel in the cleaning device uses the principle of eccentricity to provide vibration power for the screen surface, and the relative motion generated separates the pods from the impurities, which is a reciprocating simple harmonic motion. As shown in Figure 7 is the screening process movement sketch.

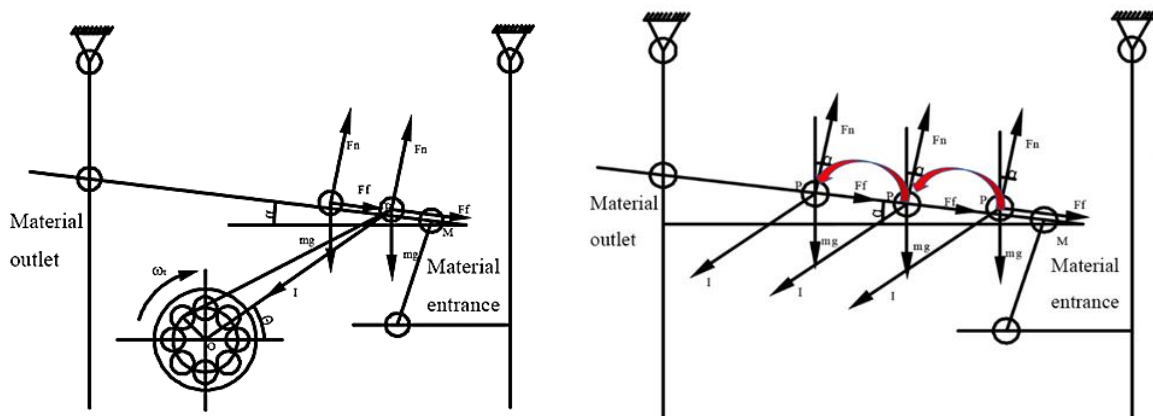


Fig. 7 – Sieve movement sketch

The expression for the motion of the clearing sieve is:

The displacement is expressed as:

$$x = -r \cos \omega t \tag{9}$$

The speed is expressed as:

$$V_x = r \omega \sin \omega t \tag{10}$$

The acceleration is expressed as:

$$a_x = r \omega^2 \cos \omega t \tag{11}$$

Based on the movement of pods and impurities on the sieve surface, the equation was analysed as:

$$F_f = \mu F_n = F_n \cdot \tan \varphi \tag{12}$$

$$F_n = mg \cos \alpha - I \sin(\alpha + \varepsilon) \tag{13}$$

$$I = mr \omega^2 \cos \omega t \tag{14}$$

At this time, the conditions of material movement on the surface of the clearing screen are:

$$I \cdot \cos(\alpha + \varepsilon) - mg \cdot \sin \alpha \geq F_f \quad (15)$$

The derivation yields Eq.16:

$$\frac{r\omega^2}{g} \cdot \cos \omega t \geq \frac{\sin(\varphi - \alpha)}{\cos(\alpha + \varepsilon - \varphi)} \quad (16)$$

where:

mg is the force of gravity of the material, [N]; F_f is the friction between the material and the sieve, [N]. F_n is the support force of the sieve on the material, [N]. I is the force of inertia of the material, [N]. φ is the angle of friction, °; α is the angle of inclination of the sieve, °; ε is the vibration direction angle, °.

Analysed by the formula, the motion state of the cleaning sieve is affected by the sieve surface inclination angle α . Therefore, the sieve surface inclination angle is an important factor affecting the effect of peanut cleaning, and the analysis obtained that the sieve surface inclination angle is within the range of 5°~9°.

RESULTS

Test analyses of cleaning devices

The test was conducted using a base feeding volume of 0.635 m/s for a two-ridged and four-row peanut combine harvester (Wang et al., 2013, Wang et al., 2017)). A test bench was constructed to verify the cleaning effect, as shown in Fig. 8. During the test, the wind speed and screen vibration frequency were controlled by adjusting the motor speed. The peanut impurity rate and crushing rate were used as indexes for test optimization.



Fig. 8 – Cleaning screen device test bench

The test equipment used included a variable frequency motor, speed controller, vernier callipers, and electronic scales, among other instruments. The peanut variety chosen for the test was the 'Yuhua 14' peanut pods outgrowth. The test was conducted at Yuanquan Machinery Co. in Yishui County, Shandong Province. To optimize the cleaning device's performance parameters, three main parameters that affect the cleaning effect were selected: centrifugal fan wind speed, sieve inclination angle, and vibration frequency.

Experimental programmer and results

Based on the operational requirements of the whole machine, the test aims to reduce the impurity rate and loss rate of peanut pods. According to the relevant test methods of peanut half-feed combine harvester, the impurity rate Z and loss rate Q of peanut pods are used as indicators to assess the operating effect of the cleaning device. Fan wind speed (Eq.3), sieve surface inclination angle (Eq.16), vibration frequency (Eq.8) as test factors, each test index can be expressed by the formula:

Peanut impurity rate:

$$Z = \frac{m'}{m} \times 100\% \quad (17)$$

where: m is the total mass of material, [kg]; m' is the mass of impurity after cleaning, [kg].

Peanut loss rate:

$$Q = \frac{v'}{v} \times 100\% \quad (18)$$

where:

v is the total mass of pods, [kg]; v' is the mass of pods lost after cleaning, [kg].

The test programme is based on Box-Behnken central combination theory. The centrifugal fan wind speed, the inclination angle of the cleaning device, and the vibration frequency were taken as the factors affecting the test. The test was conducted using a three-factor, three-level test method to verify the operational effectiveness of the cleaning and sorting device. The test code is shown in Table 3, and the test programme and data are shown in Table 4.

Table 3

| Levels of test factors | | | |
|------------------------|-----------------------------|--------------------------------------|---------------------------------|
| Code | Experimental factors | | |
| | Fan wind speed A / (m/s) | Sieve surface inclination B / (°) | Vibration frequency C / (Hz) |
| -1 | 8 | 5 | 6 |
| 0 | 9 | 7 | 7 |
| 1 | 10 | 9 | 8 |

Analysis of test results

Table 4

| Test protocol and response values | | | | | |
|-----------------------------------|----------------------|---|---|-------|-------|
| Serial number | Experimental factors | | | Z / % | Q / % |
| | A | B | C | | |
| 1 | 8 | 7 | 8 | 2.13 | 1.48 |
| 2 | 9 | 9 | 8 | 1.67 | 1.36 |
| 3 | 9 | 7 | 7 | 1.31 | 1.42 |
| 4 | 8 | 5 | 7 | 2.06 | 1.62 |
| 5 | 9 | 7 | 7 | 1.3 | 1.51 |
| 6 | 9 | 7 | 7 | 1.24 | 1.52 |
| 7 | 10 | 7 | 8 | 2.17 | 1.53 |
| 8 | 10 | 7 | 6 | 1.57 | 1.98 |
| 9 | 8 | 7 | 6 | 2.45 | 1.21 |
| 10 | 10 | 9 | 7 | 1.16 | 1.52 |
| 11 | 8 | 9 | 7 | 1.53 | 1.57 |
| 12 | 9 | 7 | 7 | 1.22 | 1.45 |
| 13 | 9 | 5 | 8 | 2.34 | 1.73 |
| 14 | 10 | 5 | 7 | 1.47 | 2.24 |
| 15 | 9 | 7 | 7 | 1.23 | 1.41 |
| 16 | 9 | 9 | 6 | 1.72 | 1.57 |
| 17 | 9 | 5 | 6 | 2.11 | 1.81 |

Multiple regression fitting analysis was carried out on the data in Table 5 using Design-Expert software. Response surface regression models of the test metrics on fan wind speed, device inclination, and frequency were established. The corresponding analysis of variance (ANOVA) was carried out using the equations. As shown in Table 5.

Table 5

| Detailed Analysis of Variance | | | | | | | | |
|-------------------------------|----------------------|-------------------|--------|---------|------------------|-------------------|-------|---------|
| Source | Impurity ratio Z / % | | | | Loss ratio Q / % | | | |
| | Sum of squares | Degree of freedom | F | P | Sum of squares | Degree of freedom | F | P |
| Model | 3.02 | 9 | 146.05 | <0.0001 | 0.93 | 9 | 31.75 | <0.0001 |
| A | 0.41 | 1 | 176.09 | <0.0001 | 0.24 | 1 | 74.13 | <0.0001 |

| Source | Impurity ratio Z / % | | | | Loss ratio Q / % | | | |
|----------------|----------------------|-------------------|--------|---------|------------------|-------------------|-------|---------|
| | Sum of squares | Degree of freedom | F | P | Sum of squares | Degree of freedom | F | P |
| B | 0.45 | 1 | 196.20 | <0.0001 | 0.24 | 1 | 73.07 | <0.0001 |
| C | 0.026 | 1 | 11.5 | 0.0116 | 0.028 | 1 | 8.48 | 0.0226 |
| AB | 0.012 | 1 | 5.26 | 0.0555 | 0.11 | 1 | 34.45 | 0.0006 |
| AC | 0.21 | 1 | 92.00 | <0.0001 | 0.13 | 1 | 39.78 | 0.0004 |
| BC | 0.02 | 1 | 8.52 | 0.0224 | 4.225E-003 | 1 | 1.30 | 0.2923 |
| A ² | 0.18 | 1 | 78.82 | <0.0001 | 0.046 | 1 | 13.98 | 0.0073 |
| B ² | 0.032 | 1 | 14.02 | 0.0072 | 0.12 | 1 | 38.01 | 0.0005 |
| C ² | 1.58 | 1 | 686.78 | <0.0001 | 1.078E-003 | 1 | 0.33 | 0.5832 |
| Residual | 0.016 | 7 | | | 0.023 | 7 | | |
| Lack of Fit | 9.100E-003 | 3 | | | 0.013 | 3 | | |
| Pure Error | 7.000E-003 | 4 | 1.73 | 0.2979 | 0.01 | 4 | 1.62 | 0.3178 |
| Cor Total | 3.04 | 16 | | | 0.95 | 16 | | |

Table 5 shows that the P-values of the test results for impurity content and loss rate are less than 0.01, indicating that the factors affecting these variables are highly significant. Additionally, the P-values of the loss-fitting terms were all greater than 0.05, demonstrating a good fit of the factors to the impurity content and loss rate of peanut pods. During the experiment analysis, the regression model for the experimental indicators was optimized. After removing insignificant terms in the analysis process, the optimized formula was obtained.

$$Z = 1.26 - 0.23A - 0.24B + 0.057C + 0.23AC - 0.07BC + 0.21A^2 + 0.087B^2 + 0.61C^2 \tag{11}$$

$$Q = 1.46 + 0.17A - 0.17B - 0.059C - 0.17AB - 0.18AC + 0.1A^2 + 0.17B^2 \tag{12}$$

Analysis of model interaction terms

Based on the results of Table 5, the effect of interaction between three factors, namely, fan air speed, clearing device inclination, and frequency, on the rate of impurity content and loss was evaluated. The response surface was plotted using software to further optimize the parameters as shown in Fig. 9.

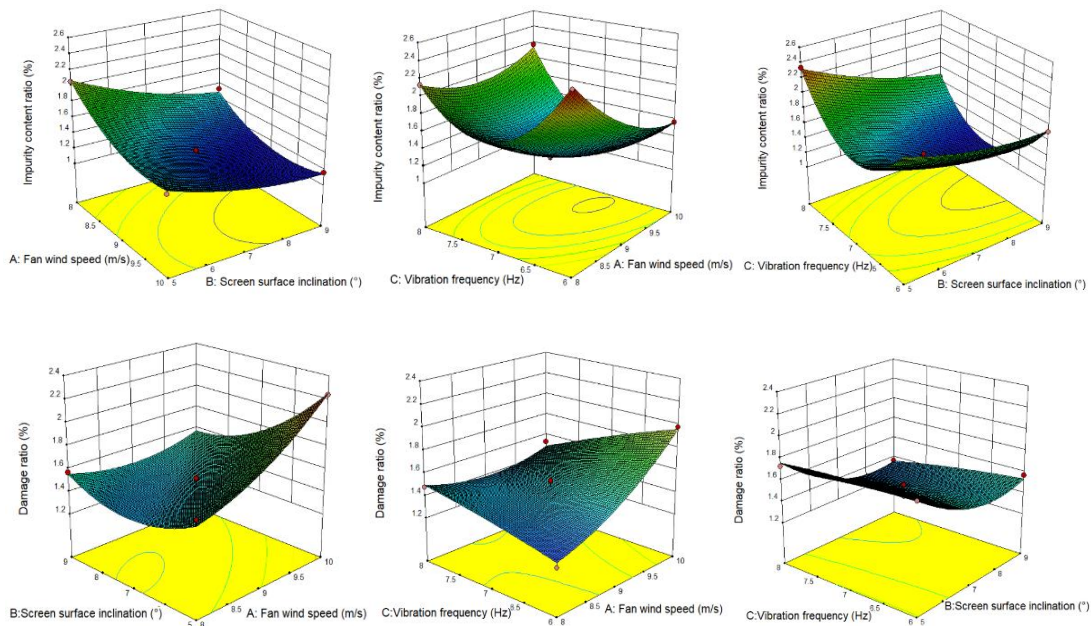


Fig. 9 – Effect of factor interactions on test indicators

The response surface analysis yields. The rate of peanut pod loss decreases as the inclination angle of the cleaning device increases, resulting in a gradual decrease in impurity rate. When the inclination angle of the cleaning device is small, the overall loss rate of peanut pods in the same period of time decreases

because the flow rate of the material in the device decreases. However, if the inclination angle of the cleaning device is too large, it may cause the material to bounce and result in losses. Centrifugal fan wind speed increases, the loss rate gradually increases, the impurity rate gradually decreases. Seedling discharge device below the configuration of the fan cleaning, when the airflow is too large, results in small quality peanut pods are blown out of the cleaning sieve, resulting in losses. Clearing vibration frequency increases, the loss rate of pods increases, and the impurity content is the first to decrease and then increase. The reason is that as the output frequency of the sieve increases, the peanut pods collide violently with the sieve surface, causing the peanuts to bounce and increasing the loss rate of pods.

Parameter optimised design

The separation effect of peanut impurity materials with different parameters was investigated, the optimal parameter combinations of the cleaning and sorting device were analysed, and the objective optimisation and optimal working parameters were determined.

$$\begin{cases} \min Z(A, B, C) \\ \min Q(A, B, C) \\ s.t. \begin{cases} 8 \leq A \leq 10 \\ 5 \leq B \leq 9 \\ 6 \leq C \leq 8 \end{cases} \end{cases} \quad (13)$$

The Design-Expert software was used to analyse the optimal parameter combinations to obtain the lowest impurity rate and loss rate. The optimal parameter combination is: fan wind speed 9 m/s, cleaning sieve inclination angle of 8 °, cleaning sieve vibration frequency of 7 Hz, then the pod impurity rate is 1.16 %, cleaning loss rate is 1.4 %.

CONCLUSIONS

(1) This article analyses the motion between the material and the sieve surface, and concludes that the wind speed range is from 8 m/s to 10 m/s, the vibration frequency range is from 6 Hz to 8 Hz, and the inclination angle of the sieve range is from 5 ° to 9 °.

(2) Bench tests showed that the optimal combination of parameters: fan speed of 9 m/s, inclination of the cleaning screen of 8 °, and vibration frequency of 7 Hz, resulted in a peanut impurity rate of 1.16 % and a cleaning loss rate of 1.4 %. The results of this device significantly reduced the impurity rate and loss rate during peanut harvesting, and it is suitable for half-feed combine harvesters.

ACKNOWLEDGEMENT

This research was funded by Shandong Province Key R&D Program (Major Science and Technology Innovation Project) Projects and High-performance seeding and harvesting key components and intelligent operation equipment creation (Grant NO.2021CXGC010813).

REFERENCES

- [1] Ciuperca R., Zaica A., Stefan V., Petcu P., Dumitrescu L., Cristea O. (2023). Research on detachment process and separation of frozen sea-buckthorn fruits from branches. *INMATEH - Agricultural Engineering*. Vol, 71, pp. 808-817, Bucharest. <https://doi.org/10.35633/inmateh-71-71>
- [2] Fletcher, S.M., Chen, C., Zhang, P. (2009). *Competitiveness of peanuts: United States versus China*. University of Georgia, Georgia.
- [3] Hou Y, Shang S, Li X., He X., Zheng H., Dong T., Li X., Yang S., Wang D. (2023). Discrete element method (EDEM) simulation and parameter optimization: Desing and testing of a low-loss and high-efficiency corn threshing device (离散元法 EDEM 仿真与参数优化: 低损高效玉米脱粒装置的设计与试验). *INMATEH - Agricultural Engineering*. Vol, 71, pp. 194-204, Qingdao/China.
- [4] Hu S., Chen L., Chen Z., Tan Y, Wang J, Lv X. (2023) Simulation and test of airflow field of double outlet cleaning device (双出风口清选装置气流场仿真及清选试验研究). *Journal of Northeast Agricultural University*, Vol. 54, pp. 67-79, Sichuan/China.
- [5] Lian G., Ma L., Feng W., Wei X., Cheng X., Zong W. (2023). Design and experiment of the cleaning device with double-layer vibrating air-sieve for edible sunflower seeds. (食葵籽粒双层振动风筛式清选装置

- 设计与试验) *Transactions of the Chinese Society of Agricultural Engineering*, Vol. 39, pp.55-65, Wuhan/China.
- [6] Pang J., Lin Y., Wang S., Du Z., Xie L., Chen X. (2023) Vibration analysis and structure optimization of grain cleaning screen based on VMD (基于 VMD 的谷物清选筛振动分析与结构优化). *Transactions of the Chinese Society of Agricultural Engineering*, Vol.39, pp. 1-9, Henan/China.
- [7] Wan X., Yuan J., Yang J., Liao Y., Liao Q. (2023). Effects of working parameters on the performance of cyclone separator for rapeseed combine harvester based on CFD (基于 CFD 的油菜籽联合收获机工作参数对旋风分离器性能的影响). *Int J Agric & Biol Eng*, Vol 167, pp. 128–135, Wuhan/China.
- [8] Wang B. (2018). *Pod-picking Mechanism and Screening Characteristic Research for Bottom-feeding Four Rows Peanut Combine Harvester* (四行半喂入花生联合收获摘果机理与筛选特性研究). Chinese Academy of Agricultural Sciences, Beijing/China.
- [9] Wang B., Hu Z., Peng B., Zhang Y., Gu F., Shi L., Gao X. (2017). Structure operation parameter optimization for elastic steel pole oscillating screen of semi-feeding four rows peanut combine harvester (半喂入四行花生联合收获机弹指筛结构运行参数优化). *Transactions of the CSAE*. Vol. 33, pp.20-28, Nanjing/China.
- [10] Wang B., Yu Z., Hu Z., Cao M., Zhang P., Wang B. (2021) Numerical Simulation and Experiment of Flow Field in Three Air Systems of Air Separation System of Peanut Pickup Harvester (花生捡拾收获机三风系风选系统流场数值模拟与试验). *Transactions of the Chinese Society for Agricultural Machinery*, Vol, 52, pp. 103-114, Beijing/China.
- [11] Wang D, Shang S. Li X., Gao D. (2013). Type L cleaning separation mechanism of peanut combine harvester (花生联合收获机 L 型输送清选分离机构研究). *Transactions of the Chinese Society for Agricultural Machinery*. Vol, 44, pp.68-74, Qingdao/China.
- [12] Wang F., Alym Memettsun Zhang J., Li Q., Xu L. (2024). Design and experiment of Pre-screening cleaning device for cornbined screen surface of corn grain harvester (玉米籽粒收获机组合筛面预筛分式清选装置设计与试验). *Journal of Agricultural Mechanization Research*, Vol, 55, pp.135-147 Xinjiang/Chian.
- [13] Wang S., Chen P., Ji J., Lu M. (2021). Design and experimental study of flexible threshing unit for Chinese cabbage seeds (大白菜种子柔性脱粒装置设计与试验). *INMATEH - Agricultural Engineering*. Vol. 65, pp. 333-344, Henan/China.
- [14] Wang Y. (2022). *Design of the Cleaning Device for the Peanut Combine Harvester and performance studies* (花生联合收获机清选装置的设计与性能研究). Hebei Normal University of Science & Technology, HeBei/China.
- [15] Yue Q, Tao G., Wang W., Zhang Z., Luo L., Xu Y. (2023). Design of grain in cleaning test bench (谷子清选试验台设计). *Agricultural Machinery Using & Maintenance*, Vol. 11, pp.1-4, Heilongjiang/China.
- [16] Zhang D. (2023). *Study on Working Mechanism and experimental research of Cleaning Device for Millet* (谷子风筛式清选装置筛分机理与试验研究). Heilongjiang Bayi Agricultural University, Heilongjiang/China.

ENGINEERING PROPERTIES OF COMMON BEAN (*PHASEOLUS VULGARIS* L.) IN PERSPECTIVE OF PHYSICAL AND FRICTIONAL PARAMETERS FOR THRESHING MACHINE DESIGN

/

የቦሎቄ (*Phaseolus vulgaris* L.) የምህንድስና ባህሪያት ለመውቁያ ማሽን ዲዛይን በአካላዊ እና ፍራክሽናል መለኪያዎች አንጻር

Biniam ZEWDIE¹⁾, Adesoji M. OLANIYAN²⁾, Amana WAKO¹⁾, Dereje ALEMU³⁾, Tamrat LEMA³⁾

¹⁾ School of Mechanical, Chemical, & Materials Engineering, Departments of Agricultural Machinery Engineering, Adama Science and Technology University, P.O. Box 1888, Adama, Ethiopia.

²⁾ Department of Agricultural and Bioresources Engineering, Faculty of Engineering, Federal University Oye-Ekiti, Ikole-Ekiti Campus, Post Code 370001, Ikole-Ekiti, Nigeria.

³⁾ Ethiopian Institute of Agricultural Research; Agricultural Engineering Research, Melkassa Agricultural Research Center, P.O.Box 436, Adama, Ethiopia

Tel: +2519-1040-8218/ +2519-1582-8327; email: nzq2001nzq@gmail.com

Corresponding author: Biniam Zewdie Ghebrekidan

DOI: <https://doi.org/10.35633/inmateh-73-65>

Keywords: Engineering properties, *Phaseolus vulgaris*, static coefficient, Threshing machine

ABSTRACT

When designing appropriate machinery systems, equipment, and infrastructures for interacting with, cultivating, gathering, and agriculture-related processing, it is required to have an understanding of the engineering characteristics of agricultural products. This unpredictability makes it difficult to design or develop machines that can efficiently and effectively manage a wide range of product characteristics. Experimental analysis was used to accomplish the study's objective, which was to investigate the implications of variation on the physical characteristics and frictional parameters of common beans (*Phaseolus vulgaris* L.) concerning the design of the threshing machine. One hundred bean seeds from each variety were randomly selected and their three primary dimensions were measured with a digital vernier caliper (least count 0.01 mm) and a micro-screw gauge in order to determine the dimensional parameters. The remaining parameters (elongation at the width, thickness, and vertical orientation, geometrical mean diameter, arithmetic mean diameter, square mean diameter, equivalent mean diameter, roundness, sphericity, flakiness ratio, aspect ratio, cross-sectional area, projected area, transverse surface area, and the seed volume) were calculated using mathematical models. Gravimetric characteristics true density and seed volumes were calculated using the toluene displacement method. The data were subjected to analysis of variance (ANOVA), and the Duncan multiple range test was used to separate the means. Significance was accepted at 95% confidence interval ($p < 0.05$). The results data are required for predicting loads in agricultural storage structures, and to establish useful sources for the development of machinery for handling, cleaning, storing, transporting and drying, among other things.

አገፅሮተ-ጥናት

ከግብርና ጋር ለተያያዙ ግንኙነቶች፣ ለማልማት፣ ለመሰብሰብ እና ለማቀነባበር ተስማሚ የሆኑ የማሽን ስርዓቶችን፣ መሰሪያዎች እና መሠረተ ልማቶችን ሲነድፉ። ይህ ያልተጠበቀ ሁኔታ ብዙ የምርት ባህሪያትን በብቃት ማስተዳደር የሚችሉ ማሽኖችን ለመንደፍ ወይም ለማምረት አስቸጋሪ ያደርገዋል። የሙከራ ትንታኔው የአውድማ ማሽን ዲዛይን በሚመለከት የቦሎቄ (*Phaseolus vulgaris* L.) አካላዊ ባህሪያት እና የግጭት መለኪያዎች ላይ ያለውን ልዩነት ለመመርመር ጥቅም ላይ ውሏል። ከእያንዳንዱ ዝርያ አንድ መቶ የቦሎቄ ዘሮች በዘፈቀደ ተመርጠዋል እና የሶስት ቀዳሚ ልኬቶቻቸው (ርዝመት፣ ስፋት፣ ውፍረት ሚዛን) በዲጂታል ቬሮኒየር ካሊፐር (ቢያንስ 0.01 ሚሜ) እና በማይክሮ-ስክራው መለኪያ መለኪያዎችን ይለካሉ። ቀሪዎቹ መመዘኛዎች (በስፋቱ፣ ውፍረት እና ቁመታዊ አቅጣጫ ማራዘም፣ ጂኦሜትሪያዊ አማካኝ ዲያሜትር፣ አርቲሜትክ አማካኝ ዲያሜትር፣ ካሬ አማካኝ ዲያሜትር፣ ተመጣጣኝ አማካኝ ዲያሜትር፣ ክብደት፣ ለልነት፣ የፍላኪነት ጥምርታ፣ ምጥጥነ ገጽታ፣ መስቀል-ክፍል አካባቢ፣ የታቀደ ቦታ፣ ተገለቢጦሽ የወለል ስፋት፣ እና የዘር መጠን) የሂሳብ ሞዴሎችን በመጠቀም ይሰላሉ። የግራቪሜትሪክ ባህሪያት እውነተኛ እፍጋት እና የዘር መጠን በቶሎኪን ማፈናቀል ዘዴ (ቲዲኤም) በመጠቀም ይሰላሉ። መረጃው የልዩነት ትንተና (ANOVA) ተደርገዋል፣ እና የዱንካን ባለብዙ ክልል ሙከራ ዘዴዎችን ለመለየት ጥቅም ላይ ውሏል። ትርጉሙ በ95% የመተማመን ልዩነት ($p < 0.05$) ተቀባይነት አግኝቷል። እነዚህ መረጃዎች የሚፈለጉትን በግብርና ማከማቻ መዋቅሮች ውስጥ ያሉ ሽክምትን ለመተንበይ ብቻ ሳይሆን ለሌሎች ነገሮች አያያዙ፣ ጽዳት፣ ማከማቻ፣ ማጓጓዣ እና ማድረቂያ ማሽኖች ልማት ጠቃሚ ምንጮችን ለማቋቋም ነው።

INTRODUCTION

The common bean is one of the primary worldwide sources of edible legumes (*Phaseolus vulgaris* L.). The leading producers are the US, China, Mexico, Brazil, India, and Mexico (FAO, 2020). In 2021, dry beans produced on 28 million hectares worldwide yielded over 20 million tons. Grain-based legumes are essential for nourishment for humans (Degirmencioglu et al., 2019), particularly for low-income people in underdeveloped countries (Fernando, 2021). Compared to grains, their protein content is almost 2-3 times higher (Wodajo et al., 2021), they are composed of a substantial amount of protein and are often referred to as "poor man's meat." For a sizable segment of the global populace, mostly in developing nations, they also provide an affordable and significant source of starch, dietary fiber, and protein (FAO, 2020).

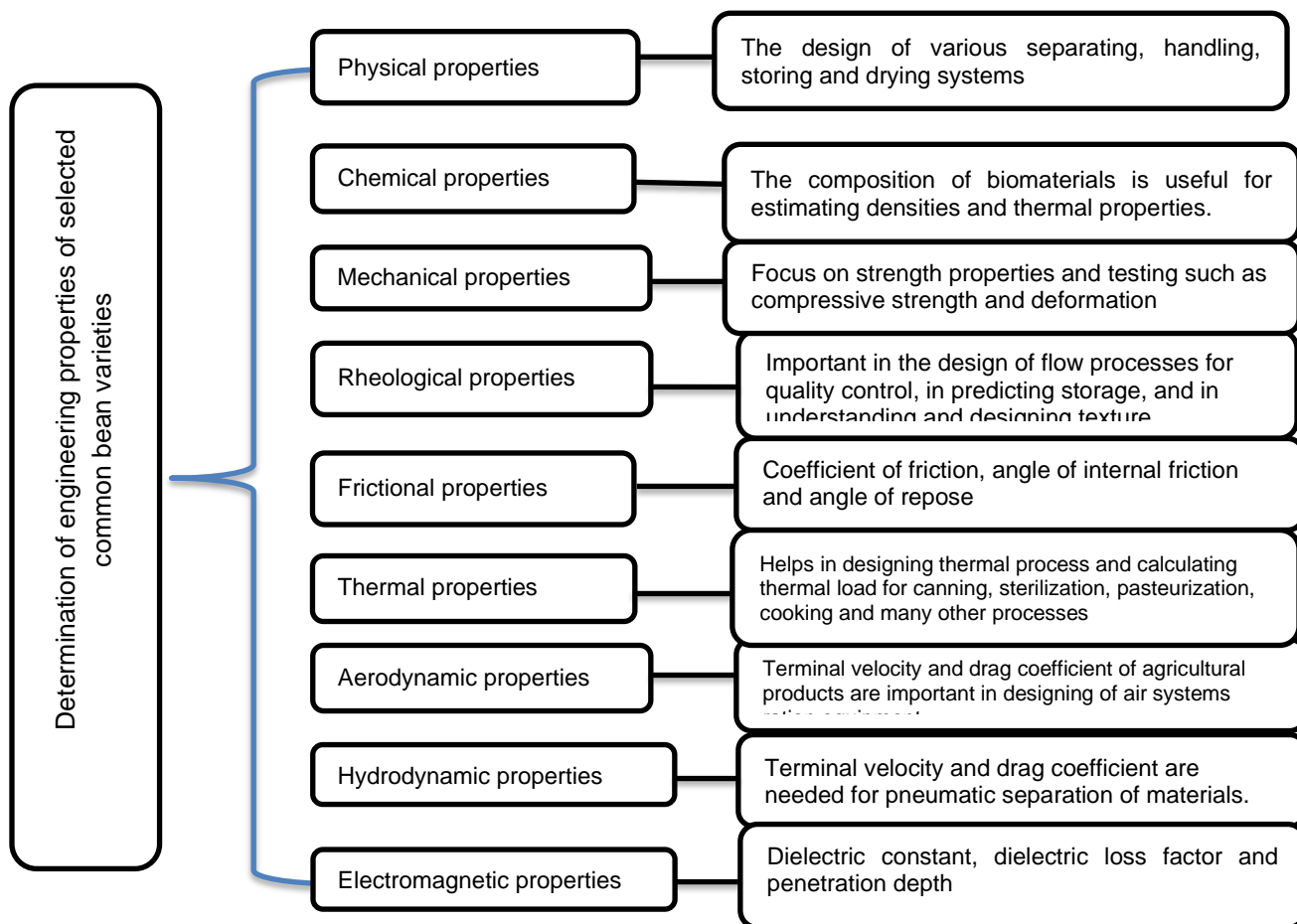
According to Amsalu et al. (2018), Ethiopia has been producing and exporting common beans for more than 50 years. The country produces red, white, black, and mottled varieties of common beans (Abera et al., 2020). The most widely available commercial kinds are pure red and white beans; as market demand increases, they are also being grown more frequently (Tekalign et al., 2022). Due to the increased demand for these commodities in the local and international markets, in recent years, there has been a discernible increase in nationwide production area and volume (Kefelegn et al., 2020). This illustrates how inefficient postharvest handling, primarily done by hand, persists in Ethiopia, considering the country's significant worldwide yield of common beans (Befikadu, 2018). To build appropriate systems, equipment, and infrastructures for interacting with, cultivating, gathering, and agriculture-related processing, comprehension of the engineering characteristics of agricultural products is essential (Fig.1).

Bayano-Tejero et al. (2023) state that when designing, cleaning, sizing, and grading machines, the three main dimensions of length, breadth, and thickness must be considered (Samrawit, 2023). Aspect ratio (Omobuwajo et al., 1999), projected area (Mirzabe et al., 2013), roundness (Baryeh, 2002), sphericity and surface area (Mohsenin, 1986; Baryeh, 2002), arithmetic mean diameter and geometric mean diameter (Baryeh, 2002; Mpotokwane et al., 2008), and Mohsenin (1986) computation of seeds' volume (V) were among the measurements taken. When developing the seed metering mechanism of seed drills (Önal and Ertuğrul, 2011), as well as transportation, sorting and sizing systems, bean seed size is a critical parameter (Nciri et al., 2014). Larger-seeded bean varieties absorb water more slowly and take longer to cook than smaller-seeded varieties (Sahin and Sumnu, 2006). During soaking, seed size affects electrical conductivity tests (Chhabra and Kaur, 2017).

Surface area plays a crucial role in heat and mass transfer processes such as drying and various thermal applications. An agricultural product's surface area usually indicates how it will behave in a flowing fluid and how easy it will be to remove unwanted contaminants from the product while cleaning it with a pneumatic tool (Omobuwajo et al., 1999). The surface area helps determine the agricultural products quality and quantity, color, respiration data, and aerodynamic calculations (Singh and Heldman, 2009).

The physical parameters alter the rate of moisture transfer and heat transfer in the approach, which makes them crucial properties in drying and ventilation processes. The bulk density determines the conveyor capacity and amount of produce storage needed. When separating materials, the actual density is taken into account. Grain hopper and storage equipment sizing is determined by porosity (Kakade et al., 2019). The engineering characteristics of agricultural materials are influenced by the moisture content, a physical parameter (Sahin and Sumnu, 2006; Bhise et al., 2014; Degirmencioglu and Srivastava, 1996; Singh and Heldman, 2009). Equipment design that is effective, affordable, and efficient depends on having a comprehension of the traits of agricultural materials at varying moisture levels (Chhabra and Kaur, 2017; Bhise et al., 2014). When constructing storage and solid flow mechanisms (Emrani and Berrada, 2023) and material handling equipment (Pawar et al., 2023), another essential consideration to take into account is the coefficient of resistance (Bako and Aguda, 2023). An essential factor in predicting pressure from seeds on walls (Amin et al., 2004) is the coefficient of friction (Bhise et al., 2014) between the seed and the wall.

Hence, agricultural products have inherent variability in their engineering parameters, including moisture contents, size, shape, surface area, sphericity, density (both bulk & true), porosity, volume of seed, coefficient (both static & dynamic), and angle of repose (Jahanbakhshi, 2018; Ertuğrul et al., 2022). This variability poses challenges in designing, modification, improvement, or development of machines efficiently and effectively. A lack of thorough data, inconsistent testing procedures, and a poor comprehension of the relationship between the agricultural product and the machine are a few additional challenges (Elijah et al., 2018). The aim of this article is to find out how the physical and frictional characteristics of common beans (*Phaseolus vulgaris* L.) influence the design of a thresher for a particular bean variety.



Model developed by Author, 2024

Fig. 1 – Conceptual study model of engineering properties common bean seeds

MATERIALS AND METHODS

Materials

Awash Melkassa Research Center, Oromia regional State, Ethiopia, provided three improved varieties of common beans that grow in several regions of the country: KAT-B1, KAT-B9, and SCR-15 (Fig. 2). One hundred bean seeds from each variety were randomly selected and their three primary dimensions were measured with a digital vernier caliper (least count 0.01 mm) and a micro-screw gauge in order to determine the dimensional parameters. For further investigation, the sample seeds were cleaned of foreign elements such as dust, stones, dirt, immature seeds, damaged seeds, and other contaminants. Then, in an airtight plastic vessel, the healthy seeds that had been chosen were kept at 5°C. The seeds were allowed to attain the room temperature before the test began.



KAT B1 (Katumani Bean 1)



KAT B9 (Katumani Bean 9)



SCR 15

Fig. 2 – Awash Melkassa Research Center's national common bean research programs improved varieties

Laboratory

All of the tests were carried out at the Agricultural Engineering Laboratories at Melkassa Agricultural Research Center (MARC), Haramaya University, and Adama Science & Technology University's; Science, Technology, Engineering, & Mathematics (ASTU STEM) Center's.

Methods - Experimental procedure

The dimensions of three hundred (100 for each variety) randomly chosen bean seeds were determined. Using an electronic vernier caliper with a precision of 0.01 mm, the three fundamental axial dimensions of *Phaseolus vulgaris* were measured. *Phaseolus vulgaris* mean diameters were computed as geometric mean (D_g), arithmetic mean (D_a), square mean (D_s), and equivalent mean (D_e) were determined using equations (1–4) (Fraser et al., 1978; Mohsenin, 1986; Baryeh, 2002; Haciseferogullari et al., 2003; Altuntas and Yildiz, 2007; Sundaram et al., 2014).

$$\text{Geometric Mean Diameter, mm} \quad D_g = \sqrt[3]{L \times W \times T} \quad (1)$$

$$\text{Arithmetic Mean Diameter, mm} \quad D_a = \frac{L + W + T}{3} \quad (2)$$

$$\text{Square Mean Diameter, mm} \quad D_{sq} = \sqrt{LW + WT + TL} \quad (3)$$

$$\text{Equivalent Mean Diameter, mm} \quad D_{eq} = \frac{D_g + D_a + D_s}{3} \quad (4)$$

Using equations (5–11) adopted by Mohsenin, (1986); Baryeh, (2002); Gupta et al., (2007); Sirisomboon et al., (2007); Mirzabe et al., (2013), the surface area, projected area, specific surface area, transverse surface area, cross-section area, and volume of the seeds were calculated.

$$\text{Surface Area seed, mm}^2 \quad A_s = \pi D_g^2 \quad (5)$$

$$A_s = (36\pi)^{\frac{1}{3}} V^{\frac{2}{3}} \quad (6)$$

$$\text{Projected Area, mm}^2 \quad A_p = \left(\frac{\pi}{4}\right) L * W \quad (7)$$

$$\text{Specific Surface Area, mm}^2 \quad S_s = A_s \rho_b / m \quad (8)$$

$$\text{Transverse Surface area, mm}^2 \quad A_t = \left(\frac{\pi}{4}\right) T * W \quad (9)$$

$$\text{Cross-Section Area, mm}^2 \quad CSA = \frac{\pi}{4} \left[\frac{(L + W + T)^2}{3} \right] \quad (10)$$

$$\text{Volume of the seed, mm}^3 \quad V = \frac{\pi B^2 L^2}{6(2L-B)} ; B = (WT)^{0.5} \quad (11)$$

where; $B = (WT)^{0.5}$; the seeds' width, W , and thickness, T , are measured in mm, L , length in mm.

Using the algorithms described by several references (Mohsenin, 1986; Omobuwajo et al., 1999; Baryeh, 2002; Chhabra and Kaur, 2017; Saporita et al., 2019), the flakiness ratio, aspect ratio, shape index, shape factor, sphericity, and roundness of the common beans were computed using the following equations (12–17).

$$\text{Flakiness Ratio} \quad R_f = T/W \times 100\% \quad (12)$$

$$\text{Aspect Ratio} \quad R_a = W/L \times 100\% \quad (13)$$

$$\text{Shape Index} \quad SI = L/\sqrt{(W * T)} \quad (14)$$

$$\text{Shape Factor} \quad SF = 4\pi P_A / P^2 \quad (15)$$

$$\text{Sphericity} \quad \varphi = \left(\frac{WT}{L^2} \right)^{1/3} \quad (16)$$

$$\text{Roundness} \quad R = \left\{ \frac{W/L + T/L + T/W}{3} \right\} \quad (17)$$

Using the following equations (18, 19, and 20) adopted by (Mohsenin, 1986), the elongation at the width orientation (Gupta et al., 2007), elongation at the thickness orientation (Mirzabe et al., 2013), and elongation at the vertical orientation (Chhabra and Kaur, 2017) of the *Phaseolus vulgaris* were determined.

$$\text{Elongation at the width orientation} \quad E_w = L/W \quad (18)$$

$$\text{Elongation at the thickness orientation} \quad E_t = L/T \quad (19)$$

$$\text{Elongation at the vertical orientation} \quad E_v = W/T \quad (20)$$

Determination of gravimetric parameters

The true density and seed volumes were determined using the liquid displacement technique. Water was not utilized since the seed absorbs water more readily than toluene (C₇H₈). To measure the amount of toluene displaced from the weighted seed, the amount of the product that was displaced was measured using a graduated scale on the cylinder. Once the weight of the seeds was divided by the volume of displaced toluene, their true density was found. Bulk density, true density, and porosity were calculated using equations 21–25, (Mohsenin, 1986; Desphande et al., 1993; Omobuwajo et al., 1999; Singh and Heldman, 2009; Saporita et al., 2019).

$$\text{Thousand Seed Mass (TSM)} \quad TSM = \frac{\text{Weight of sample, g}}{\text{Number of grains in sample}} \times 10 \quad (21)$$

$$\text{Bulk Density, kgm}^{-3} \quad \rho_b = \frac{\text{Weight of sample (g)}}{\text{Volume of occupied (cm}^3\text{)}} \quad (22)$$

$$\text{True Density, kgm}^{-3} \quad \rho_t = \frac{\text{Weight of the sample (g)}}{\text{Volume of toluene displaced (cm}^3\text{)}} \quad (23)$$

$$\text{Density Ratio, (\%)} \quad R_\rho = \left(\frac{\rho_b}{\rho_t} \right) \times 100(\%) \quad (24)$$

$$\text{Porosity, (\%)} \quad \varepsilon = \left(1 - \frac{\rho_b}{\rho_t} \right) \times 100(\%) \quad (25)$$

Determination of angle of repose

Two cylindrical diameter containers, one hollow and placed on top of a closed side, were used in the setup for the experiment for measurements of the repose angle (Fig. 3). Using equation (26) as provided by Baryeh (2002), Mohsenin (1986), Saporita et al. (2019), likewise the repose angle (α) and the apex height were taken into consideration were computed using the trigonometry rule.

Coefficient of static friction determination

Ten surfaces' coefficient of static friction was computed using the inclined plane approach. The angle of inclination (ϕ) was found using the protractor attached to the apparatus after the table had been gently raised to the horizontal at which the seeds began to slide. Equation (27) was utilized to compute the static friction coefficient (μ), following the method outlined by Mohsenin (1986) and Saporita et al. (2019), albeit with some adjustments.

Angle of repose/inclination: $\phi = \tan^{-1}\left[\frac{h}{b}\right]$ (26)

Coefficient of static friction $\mu = \tan\phi$ (27)

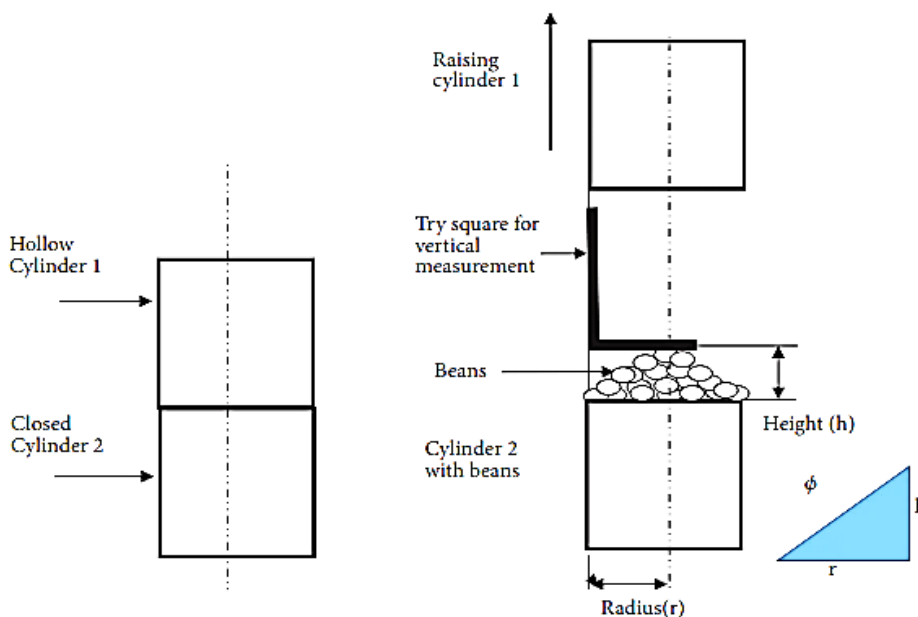


Fig. 3 – Experimental setup for repose angle measurements

Statistical Analysis

The standard deviation (SD) and mean of the results were displayed. Using IBM SPSS Statistics 27.0.1_IF026 and the Statistical Package for Social Science, version 22, way analysis of variance (ANOVA) was performed on the data.

RESULTS

Table (1a) shows a summary of the measured and determined dimensional parameters. For the three *Phaseolus vulgaris* (common bean) varieties KAT-B1, KAT-B9, and SCR-15, the physical parameter ANOVA values are shown in table 1a. The length, width, thickness, elongation ratios (at width, thickness, and vertical), arithmetic mean diameter, geometric mean diameter, square mean diameter, and equivalent mean diameter are among the physical parameters that are evaluated. The table displays the mean ± standard deviation, coefficient of variation, variance, maximum, minimum, and variance for each parameter. The findings verified that the seeds' longitudinal dimensions ranged from 8.25 to 15.67 mm, with an average mean value (amv) of 11.282 ± 0.995 mm; their width varied from 4.44 to 10.46 mm, with an amv of 7.24 ± 0.673 mm; their seed thickness ranged from 3.09 to 8.11mm, with an amv of 5.67 ± 0.794 mm; their elongation of width (Ew) varied from 1.024 to 2.748 mm, with an amv of 1.566 ± 0.136 mm; their elongation of thickness (Et) varied from 1.389 to 3.408 mm, with an amv of 2.037 ± 0.282 mm; and their elongation of vertical (Ev) varied from 0.671 to 2.104 mm, with an amv of 1.301 ± 0.152 mm. The significance of axial dimensions in machine design was emphasized by *Mohsenin (1986)*. However, symmetric projections towards process equipment adaption can be made by comparing the results with previous research on other seeds.

Table 1a

ANOVA values physical properties of selected *Phaseolus vulgaris* varieties

| Parameters | Variety | Mean | Max | Min | Variance | STDEV | CV% | Mean±STDEV |
|------------|---------|----------------------|--------|-------|----------|-------|---------------------|----------------------------|
| Length, mm | KAT-B1 | 11.521 ^{ns} | 15.670 | 9.050 | 1.195 | 1.093 | 9.487 ^{ns} | 11.521±1.093 ^{ns} |
| | KAT-B9 | 10.769 ^{ns} | 12.960 | 8.250 | 0.862 | 0.928 | 8.620 ^{ns} | 10.769±0.928 ^{ns} |
| | SCR-15 | 11.556 ^{ns} | 14.290 | 8.970 | 0.931 | 0.965 | 8.350 ^{ns} | 11.556±0.965 ^{ns} |

| Parameters | Variety | Mean | Max | Min | Variance | STDEV | CV% | Mean±STDEV |
|---|---------|---------------------|--------|--------|----------|-------|----------------------|----------------------------|
| Width W (mm) | KAT-B1 | 7.608* | 10.460 | 6.220 | 0.382 | 0.618 | 8.124* | 7.608±0.618* |
| | KAT-B9 | 6.795* | 8.310 | 4.440 | 0.493 | 0.702 | 10.334* | 6.795±0.702* |
| | SCR-15 | 7.317* | 8.910 | 5.940 | 0.488 | 0.699 | 9.548* | 7.317±0.699* |
| Thickness T (mm) | KAT-B1 | 6.213* | 8.110 | 4.660 | 0.291 | 0.540 | 8.685* | 6.213±0.540* |
| | KAT-B9 | 5.637* | 7.470 | 3.090 | 1.370 | 1.171 | 20.765* | 5.637±1.171* |
| | SCR-15 | 5.159* | 6.780 | 3.440 | 0.451 | 0.672 | 13.019* | 5.159±0.672* |
| Elongation at width E _w | KAT-B1 | 1.519* | 1.999 | 1.024 | 0.020 | 0.140 | 9.196* | 1.519±0.140* |
| | KAT-B9 | 1.593* | 2.748 | 1.298 | 0.022 | 0.149 | 9.342* | 1.593±0.149* |
| | SCR-15 | 1.586* | 1.832 | 1.238 | 0.014 | 0.120 | 7.560* | 1.586±0.120* |
| Elongation at thickness E _t | KAT-B1 | 1.866* | 2.663 | 1.493 | 0.050 | 0.225 | 12.034* | 1.866±0.225* |
| | KAT-B9 | 1.976* | 3.408 | 1.390 | 0.126 | 0.355 | 17.967* | 1.976±0.355* |
| | SCR-15 | 2.267* | 2.922 | 1.543 | 0.071 | 0.267 | 11.784* | 2.267±0.267* |
| Elongation at vertical E _v | KAT-B1 | 1.231* | 1.622 | 0.970 | 0.014 | 0.119 | 9.646* | 1.231±0.119* |
| | KAT-B9 | 1.241* | 2.104 | 0.671 | 0.040 | 0.199 | 16.020* | 1.241±0.199* |
| | SCR-15 | 1.431* | 1.802 | 1.088 | 0.020 | 0.140 | 9.763* | 1.431±0.140* |
| Arithmetic mean diameter (D _a), mm | KAT-B1 | 8.447 | 10.090 | 6.913 | 0.317 | 0.563 | 6.664 | 8.447±0.563 |
| | KAT-B9 | 7.734* | 9.563 | 5.853 | 0.712 | 0.844 | 10.911* | 7.734±0.884* |
| | SCR-15 | 8.011* | 9.517 | 6.427 | 0.434 | 0.659 | 8.222* | 8.011±0.659* |
| Geometric mean diameter (D _g), mm | KAT-B1 | 8.152 ^{ns} | 9.429 | 6.732 | 0.272 | 0.521 | 6.397 ^{ns} | 8.152±0.521 ^{ns} |
| | KAT-B9 | 7.421* | 9.280 | 5.592 | 0.827 | 0.909 | 12.255* | 7.421±0.909* |
| | SCR-15 | 7.571* | 8.924 | 5.985 | 0.439 | 0.662 | 8.747* | 7.571±0.662* |
| Square mean diameter (D _{sq}), mm | KAT-B1 | 14.357 | 16.786 | 11.811 | 0.865 | 0.930 | 6.478 ^{ns} | 14.357±0.930 ^{ns} |
| | KAT-B9 | 13.105 | 16.295 | 9.891 | 2.294 | 1.514 | 11.557 ^{ns} | 13.105±1.514 ^{ns} |
| | SCR-15 | 13.477 | 15.857 | 10.760 | 1.300 | 1.140 | 8.460 ^{ns} | 13.477±1.140 ^{ns} |
| Equivalent mean diameter (D _{eq}), mm | KAT-B1 | 10.319* | 12.092 | 8.485 | 0.448 | 0.670 | 6.490* | 10.319±0.670* |
| | KAT-B9 | 9.420* | 11.713 | 7.112 | 1.185 | 1.088 | 11.554* | 9.420±1.088* |
| | SCR-15 | 9.686 ^{ns} | 11.394 | 7.729 | 0.670 | 0.819 | 8.453 ^{ns} | 9.686±0.819 ^{ns} |

*Significant at $P \leq 0.05$, ns non-significant, CV = Coefficient of Variation, VARA = variance, STDEV = Standard deviation

The seeds' arithmetic mean diameter ranged from 5.853 to 10.793 mm, with an amv of 8.064 ± 0.688 mm; their geometrical mean diameter varied from 5.592 to 9.279 mm, with an amv of 7.715 ± 0.698 mm; their square mean diameter varied from 9.891 to 18.047 mm, with an amv of 13.646 ± 1.195 mm; their equivalent mean diameter varied from 7.112 to 12.994 mm, with an amv of 9.808 ± 0.859 mm; their roundness ranged from 0.537 to 0.760 mm, with an amv of 0.644 ± 0.056 ; their sphericity varied from 0.595 to 0.803 with an amv of 0.685 ± 0.044 ; their flakiness ratio varied from 0.594 to 0.966 with an amv of 0.784 ± 0.092 ; their aspect ratio varied from 0.539 to 0.847, with an amv of 0.643 ± 0.053 ; cross-sectional area varied from 76.403 to 156.528 mm² with the mean value of 154.477 ± 26.002 mm², the projected area ranged from 32.827 to 67.175 mm² with the amv of 64.508 ± 10.377 mm², the transverse surface area varied from 14.828 to 34.343 mm² with the mean value of 32.546 ± 6.683 mm², and the seed volume varied from 83.752 to 245.872 mm³ with the mean value of 241.744 ± 0.207 mm³, respectively.

The findings indicate that the three *Phaseolus vulgaris* varieties differ significantly ($p < 0.05$) in terms of width, thickness, elongation ratios, arithmetic mean diameter, geometric mean diameter, and equivalent mean diameter. There were not any significant variations in length, square mean diameter, or certain elongation ratios within the varieties. When it came to the physical parameters, KAT-B1 was typically the variety with the highest mean values, followed by SCR-15 and KAT-B9. With the exception of thickness in KAT-B9, which had a higher CV of 20.765%, the coefficient of variation (CV %) data indicate moderate variability within the bean samples for the majority of characteristics.

The values should be given for arithmetic, geometric, and sphericity were comparable to those of Ozturk *et al.*, (2009), Amin *et al.*, (2004), and Kumar and Sharma, (2021). Nonetheless, they were lower than those reported by Cetin (2007) and Altuntas and Yildiz (2007), but greater than common beans (Ozturk *et al.*, 2009) and lower than red kidney beans with speckles (Isik and Unal, 2007).

Table (1b) shows a summary of the measured and determined dimensional parameters. Surface area (A_s), projected area (A_p), area of transverse surface (A_t), cross-section area (CSA), volume (V), aspect ratio (R_a), flakiness ratio (R_f), sphericity (ϕ), and roundness are among the physical characteristics that are examined. The variations in the mean values between the three varieties are below the threshold for statistical significance ($p > 0.05$) for the remaining parameters, which include surface area, projected area, area of transverse surface, cross-section area, and volume.

Overall, the shape-related parameters (aspect ratio, flakiness ratio, sphericity, and roundness) and the size-related parameters (surface area, projected area, transverse surface area, cross-section area, and volume) of the three *Phaseolus vulgaris* varieties (KAT-B1, KAT-B9, and SCR-15) showed statistically significant differences.

Table 1b

ANOVA values physical properties of selected *Phaseolus vulgaris* varieties

| Parameters | Variety | Mean | Max | Min | Variance | STDEV | CV% | Mean \pm STDEV |
|--|---------|-----------------------|---------|---------|----------|--------|----------------------|------------------------------------|
| Surface area(A_s), mm^2 | KAT-B1 | 208.680 ^{ns} | 279.159 | 142.294 | 0.232 | 0.854 | 0.409 ^{ns} | 208.68 \pm 0.409 ^{ns} |
| | KAT-B9 | 172.927 ^{ns} | 270.398 | 98.199 | 2.148 | 2.597 | 1.502 ^{ns} | 172.927 \pm 1.502 ^{ns} |
| | SCR-15 | 180.007 ^{ns} | 250.038 | 112.462 | 0.604 | 1.377 | 0.765 ^{ns} | 180.007 \pm 1.377 ^{ns} |
| Projected Area (A_p), mm^2 | KAT-B1 | 69.018 ^{ns} | 96.439 | 46.320 | 101.650 | 10.082 | 14.608 ^{ns} | 69.018 \pm 10.082 ^{ns} |
| | KAT-B9 | 57.794 ^{ns} | 84.543 | 33.404 | 101.758 | 10.088 | 17.454 ^{ns} | 57.794 \pm 10.088 ^{ns} |
| | SCR-15 | 66.712 ^{ns} | 99.949 | 45.082 | 120.149 | 10.961 | 16.431 ^{ns} | 66.712 \pm 10.961 ^{ns} |
| Area of transverse surface(A_t), mm^2 | KAT-B1 | 37.198 ^{ns} | 52.962 | 25.452 | 25.659 | 5.065 | 13.618 ^{ns} | 37.198 \pm 5.065 ^{ns} |
| | KAT-B9 | 30.570 ^{ns} | 48.403 | 15.677 | 79.283 | 8.904 | 29.127 ^{ns} | 30.570 \pm 8.904 ^{ns} |
| | SCR-15 | 29.870 ^{ns} | 44.341 | 16.742 | 36.943 | 6.078 | 20.349 ^{ns} | 29.870 \pm 6.078 ^{ns} |
| Cross-Section Area(CSA), mm^2 | KAT-B1 | 168.786 ^{ns} | 239.758 | 112.555 | 505.740 | 22.489 | 13.324 ^{ns} | 168.786 \pm 22.489 ^{ns} |
| | KAT-B9 | 142.513 ^{ns} | 215.382 | 80.686 | 939.906 | 30.658 | 21.512 ^{ns} | 142.513 \pm 30.658 ^{ns} |
| | SCR-15 | 152.131 ^{ns} | 213.285 | 97.266 | 618.027 | 24.860 | 16.341 ^{ns} | 152.131 \pm 24.860 ^{ns} |
| Volume (V), mm^3 | KAT-B1 | 283.792 ^{ns} | 439.093 | 159.794 | 0.011 | 0.074 | 0.026 ^{ns} | 283.792 \pm 0.074 ^{ns} |
| | KAT-B9 | 214.079 ^{ns} | 418.585 | 91.609 | 0.296 | 0.394 | 0.184 ^{ns} | 214.079 \pm 0.394 ^{ns} |
| | SCR-15 | 227.360 ^{ns} | 372.209 | 112.277 | 0.044 | 0.152 | 0.067 ^{ns} | 227.360 \pm 0.152 ^{ns} |
| Aspect Ratio, R_a | KAT-B1 | 0.664* | 0.977 | 0.500 | 0.004 | 0.062 | 9.288* | 0.664 \pm 0.062* |
| | KAT-B9 | 0.632* | 0.770 | 0.364 | 0.002 | 0.047 | 7.377* | 0.632 \pm 0.047* |
| | SCR-15 | 0.634* | 0.808 | 0.546 | 0.002 | 0.050 | 7.807* | 0.634 \pm 0.050* |
| Flakiness Ratio, R_f | KAT-B1 | 0.820* | 1.030 | 0.617 | 0.006 | 0.076 | 9.218* | 0.820 \pm 0.076* |
| | KAT-B9 | 0.825* | 1.491 | 0.475 | 0.017 | 0.131 | 15.847* | 0.825 \pm 0.131* |
| | SCR-15 | 0.706* | 0.919 | 0.555 | 0.005 | 0.070 | 9.953* | 0.706 \pm 0.070* |
| Sphericity, ϕ | KAT-B1 | 0.711* | 0.838 | 0.576 | 0.002 | 0.043 | 6.116* | 0.711 \pm 0.043* |
| | KAT-B9 | 0.688* | 0.808 | 0.566 | 0.003 | 0.050 | 7.272* | 0.688 \pm 0.050* |
| | SCR-15 | 0.656* | 0.806 | 0.581 | 0.002 | 0.039 | 5.993* | 0.656 \pm 0.039* |
| Roundness | KAT-B1 | 0.675* | 0.776 | 0.541 | 0.002 | 0.049 | 7.250* | 0.675 \pm 0.049* |
| | KAT-B9 | 0.659* | 0.836 | 0.462 | 0.005 | 0.074 | 11.155* | 0.659 \pm 0.074* |
| | SCR-15 | 0.596* | 0.753 | 0.505 | 0.002 | 0.047 | 7.811* | 0.596 \pm 0.047* |

*Significant at $P \leq 0.05$, ^{ns}non-significant, CV = Coefficient of Variation, VARA = variance, STDEV = Standard deviation

Table 2 presents an overview of the outcomes the statistical description of gravimetric characteristics that were measured and determined. The average moisture content values were found to be $12.867 \pm 0.321\%$ on a dry basis, mass of one thousand seed (378.167 ± 31.608 kg), bulk density (793.40 ± 34.11 kgm⁻³), true density (1234.71 ± 34.03 kgm⁻³), and porosity ($35.714 \pm 3.17\%$) for selected varieties. Similar trends were reported for common beans by (Amin et al., 2004), faba beans by (Altuntas and Yildiz, 2007), barbania beans by (Cetin, 2007), white speckled red kidney beans by (Isik and Unal, 2007), and for red bean grain and common bean seed by (Saparita et al., 2019). Nevertheless, compared to the studies of Altuntas and Yildiz (2007) and Cetin (2007), these increases in the bulk and dimensions of the size variants as influenced by moisture content were smaller.

Table 2

Statistical description of gravimetric properties of selected *Phaseolus vulgaris*

| Variety | Mc db% | TSM, kg | Bulk Density, kgm ⁻³ | True Density, kgm ⁻³ | Density Ratio | Porosity, % |
|------------|--------------------------------|----------------------------------|---------------------------------|---------------------------------|---------------|--------------|
| KAT-B1 | 13.10 | 342.00 | 827.000 | 1217.0800 | 0.679495 | 32.0505 |
| KAT-B9 | 12.50 | 392.00 | 794.400 | 1273.9375 | 0.623578 | 37.6422 |
| SCR-15 | 13.00 | 400.50 | 758.800 | 1213.1000 | 0.625505 | 37.4495 |
| Mean | 12.867 ^{ns} | 378.167 ^{ns} | 793.400 ^{ns} | 1234.706 ^{ns} | 0.643* | 35.714* |
| Max | 13.100 | 400.500 | 827.000 | 1273.938 | 0.679 | 37.642 |
| Min | 12.500 | 342.000 | 758.800 | 1213.100 | 0.624 | 32.050 |
| Range | 0.600 | 58.500 | 68.200 | 60.837 | 0.056 | 5.592 |
| Variance | 0.103 | 999.083 | 1163.560 | 1158.303 | 0.001 | 10.076 |
| STDEV | 0.321 | 31.608 | 34.111 | 34.034 | 0.032 | 3.174 |
| CV% | 2.498 | 8.358 | 4.299 | 2.756 | 4.938 | 8.888 |
| Mean±STDEV | 12.867 ^{ns} ±0.321 | 378.167 ^{ns} ±31.608 | 793.40 ^{ns} ±34.11 | 1234.71 ^{ns} ±34.03 | 0.643*±0.032 | 35.714*±3.17 |

*Significant at $P \leq 0.05$, ns non-significant, CV = Coefficient of Variation, Mc = Moisture content, TSM = Thousand seed mass, STDEV = Standard deviation

Table 3 shows static coefficient of friction for different sliding surface materials with a single seed/minimum value and the remaining seeds/maximum value sliding on a selected surface. The static coefficient of friction on the iron sheet surface varied from 0.276 to 0.386 with average mean value (amv) of 0.344 ± 0.114 , on the stainless steel from 0.294 to 0.435 with amv of 0.355 ± 0.106 , on the galvanized iron from 0.317 to 0.434 with amv of 0.372 ± 0.110 , on the MDF sheet from 0.321 to 0.451 with amv of 0.373 ± 0.139 , on the aluminum from 0.319 to 0.480 with amv of 0.393 ± 0.26 , on the perforated sheet from 0.462 to 1.048 with amv of 0.639 ± 0.279 , on the painted sheet from 0.310 to 0.470 with amv of 0.412 ± 0.125 , on the glass from 0.320 to 0.440 with amv of 0.388 ± 0.105 , on the plastic from 0.333 to 0.447 with amv of 0.383 ± 0.095 and on the rubber from 0.374 to 0.575 were amv of 0.495 ± 0.172 , respectively. The moisture content and the coefficient of friction generally have a proportional relationship on all surfaces. Perforated sheet surfaces showed the highest static coefficients of friction, followed by rubber, plastic, plywood, glass, aluminum, galvanized iron, painted sheet, stainless steel and iron sheet surfaces. Similar patterns have been found for black-eyed peas (Desphande et al., 1993), cumin seed (Singh & Heldman, 2009), red kidney beans, soybeans, unshelled peanuts, black-eyed peas (Mohsenin, 1986), and lentil seeds (Saparita et al., 2019).

The table 3 shows the mean, variance, standard deviation, and coefficient of variation (CV %) for the angle of inclination (ϕ) and static coefficient of friction (μ_s) for different sliding surface materials and common bean genotypes. All the values shown are statistically significant at the $p \leq 0.05$ level. Compared to perforated sheet, rubber, plastic, plywood, glass, aluminum, galvanized iron, painted sheet, stainless steel and iron sheet surfaces, the angle of repose for common beans increased proportionally as the moisture content increased. The average mean value (amv) of the inclination in the following surfaces: iron sheet surface: 18.113 ± 5.813 , stainless steel: 19.057 ± 5.58 , galvanized iron: 19.00 ± 7.54 , MDF sheet: 19.557 ± 6.913 , aluminum: 19.667 ± 6.757 , perforated sheet: 28.667 ± 9.270 , painted sheet: 21.390 ± 6.367 , glass: 20.113 ± 4.87 , plastic: 18.777 ± 4.713 , and rubber: 24.163 ± 8.567 , respectively. Based on the results, the average suggested angle of repose for common bean seeds should be within 27.1° to 32.4° . According to Mohsenin (1986), the angle of repose for common bean seed was determined to be between 27.1° and 35.4° , which are still below the maximum angle of repose of 45° for the majority of agricultural commodities.

Table 3

Statistical description frictional properties of *Phaseolus vulgaris* on various types of sliding surface materials

| Surface | Common bean | Angle of inclination, ϕ | | | | | Static coefficient of friction, μ_s | | | | |
|------------------|-------------|------------------------------|-------|--------|--------------------|--------|---|-------|-------|------------------|--------|
| | varieties | Mean | VARA | STD EV | Mean \pm STDEV | CV% | Mean | VAR A | STDEV | Mean \pm STDEV | CV% |
| Iron sheet | KAT-B1 | 17.50* | 16.06 | 4.01 | 17.50 \pm 4.01* | 22.90* | 0.316* | 0.01 | 0.08 | 0.316 \pm 0.08 | 24.34 |
| | KAT-B9 | 18.67* | 56.89 | 7.54 | 18.89 \pm 7.54* | 40.41* | 0.341* | 0.02 | 0.15 | 0.341 \pm 0.15 | 43.16* |
| | SCR-15 | 18.17* | 34.72 | 5.89 | 18.17 \pm 5.89* | 32.44* | 0.330* | 0.01 | 0.11 | 0.330 \pm 0.11 | 34.59* |
| Stainless steel | KAT-B1 | 20.33* | 37.56 | 6.13 | 20.33 \pm 6.13* | 30.14* | 0.373* | 0.01 | 0.12 | 0.373 \pm 0.12 | 32.70 |
| | KAT-B9 | 17.67* | 32.00 | 5.66 | 17.67 \pm 5.66* | 32.02* | 0.320* | 0.01 | 0.11 | 0.320 \pm 0.11 | 34.03* |
| | SCR-15 | 19.17* | 24.50 | 4.95 | 19.17 \pm 4.95* | 25.82* | 0.349* | 0.01 | 0.10 | 0.349 \pm 0.10 | 27.79 |
| Galvanized Iron | KAT-B1 | 17.50* | 34.72 | 5.89 | 17.50 \pm 5.89* | 33.67* | 0.317* | 0.01 | 0.11 | 0.317 \pm 0.11 | 35.74* |
| | KAT-B9 | 18.33* | 26.89 | 5.19 | 18.33 \pm 5.19* | 28.28* | 0.333* | 0.01 | 0.10 | 0.333 \pm 0.10 | 30.23 |
| | SCR-15 | 19.00* | 56.89 | 7.54 | 19.00 \pm 7.54* | 39.70* | 0.351* | 0.02 | 0.15 | 0.351 \pm 0.15 | 43.51* |
| Plywood | KAT-B1 | 20.00* | 56.89 | 7.54 | 20.00 \pm 7.54* | 37.71* | 0.368* | 0.02 | 0.15 | 0.368 \pm 0.15 | 40.72* |
| | KAT-B9 | 19.17* | 46.72 | 6.84 | 19.17 \pm 6.84* | 35.66* | 0.350* | 0.02 | 0.13 | 0.350 \pm 0.13 | 38.29* |
| | SCR-15 | 19.50* | 40.50 | 6.36 | 19.50 \pm 6.36* | 32.64* | 0.357* | 0.02 | 0.13 | 0.357 \pm 0.13 | 35.15 |
| Aluminum | KAT-B1 | 19.17* | 53.39 | 7.31 | 19.17 \pm 7.31* | 38.12* | 0.351* | 0.02 | 0.14 | 0.351 \pm 4.01 | 40.90* |
| | KAT-B9 | 17.83* | 40.50 | 6.36 | 17.83 \pm 6.36* | 35.69* | 0.324* | 0.02 | 0.12 | 0.324 \pm 0.12 | 37.94* |
| | SCR-15 | 22.00* | 43.56 | 6.60 | 22.00 \pm 6.60* | 30.00* | 0.407* | 0.02 | 0.13 | 0.407 \pm 0.13 | 33.02* |
| Perforated sheet | KAT-B1 | 31.00* | 107.5 | 10.37 | 31.00 \pm 10.37* | 33.45* | 0.614* | 0.06 | 0.25 | 0.614 \pm 0.25 | 40.55 |
| | KAT-B9 | 28.17* | 76.06 | 8.72 | 28.17 \pm 8.72* | 30.96* | 0.544* | 0.04 | 0.20 | 0.544 \pm 0.20 | 36.29 |
| | SCR-15 | 26.83* | 76.06 | 8.72 | 26.83 \pm 8.72* | 32.50* | 0.513* | 0.04 | 0.19 | 0.513 \pm 0.19 | 37.50* |
| Painted sheet | KAT-B1 | 23.67* | 37.56 | 6.13 | 23.67 \pm 6.13* | 25.89* | 0.441* | 0.02 | 0.13 | 0.441 \pm 0.13 | 28.98 |
| | KAT-B9 | 20.17* | 53.39 | 7.31 | 20.17 \pm 7.31* | 36.23* | 0.371* | 0.02 | 0.15 | 0.371 \pm 0.15 | 39.19* |
| | SCR-15 | 20.33* | 32.00 | 5.66 | 20.33 \pm 5.66* | 27.82* | 0.373* | 0.01 | 0.11 | 0.373 \pm 0.11 | 30.20 |
| Glass | KAT-B1 | 20.67* | 18.00 | 4.24 | 20.67 \pm 4.24* | 20.53 | 0.378* | 0.01 | 0.08 | 0.378 \pm 0.08 | 22.38 |
| | KAT-B9 | 19.67* | 22.22 | 4.71 | 19.67 \pm 4.71* | 23.97* | 0.359* | 0.01 | 0.09 | 0.359 \pm 0.09 | 25.90 |
| | SCR-15 | 20.00* | 32.00 | 5.66 | 20.00 \pm 5.66* | 28.28* | 0.366* | 0.01 | 0.11 | 0.366 \pm 0.11 | 30.62 |
| Plastic/Maica | KAT-B1 | 19.67* | 18.00 | 4.24 | 19.67 \pm 4.24* | 21.57* | 0.359* | 0.01 | 0.08 | 0.359 \pm 0.08 | 23.32 |
| | KAT-B9 | 18.33* | 22.22 | 4.71 | 18.33 \pm 4.71* | 25.71* | 0.333* | 0.01 | 0.09 | 0.333 \pm 0.09 | 27.49 |
| | SCR-15 | 18.33* | 26.89 | 5.19 | 18.33 \pm 5.19* | 28.28* | 0.333* | 0.01 | 0.10 | 0.333 \pm 0.10 | 30.23 |
| Rubber | KAT-B1 | 24.83* | 46.72 | 6.84 | 24.83 \pm 6.84* | 27.52* | 0.467* | 0.02 | 0.15 | 0.467 \pm 0.15 | 31.15 |
| | KAT-B9 | 23.33* | 98.00 | 9.90 | 23.33 \pm 9.90* | 42.43* | 0.439* | 0.04 | 0.21 | 0.439 \pm 0.21 | 47.04* |
| | SCR-15 | 24.33* | 80.22 | 8.96 | 24.33 \pm 8.96* | 36.81* | 0.459* | 0.04 | 0.19 | 0.459 \pm 0.19 | 41.30 |

*Significant at $P \leq 0.05$, ns non-significant, CV = Coefficient of Variation, VARA = variance, STDEV = Standard deviation

CONCLUSIONS

In this study, the engineering properties of *Phaseolus vulgaris* seeds are determined that may provide opportunities to design construct and develop harvesting, handling, and processing machinery for *Phaseolus vulgaris* seeds by considering their physical and frictional characteristics. Experimental analysis was used to accomplish the study's objective, which was to investigate the implications of variation on the physical characteristics and frictional parameters of common beans (*Phaseolus vulgaris* L.) concerning the design of the threshing machine. The mean average values of physical parameters were determined by analyzing the experimental data: length (11.282 \pm 0.995 mm), width (7.24 \pm 0.673 mm), thickness (5.67 \pm 0.794 mm), elongation of width (1.566 \pm 0.136 mm), elongation of thickness (2.037 \pm 0.282 mm), elongation of vertical (1.301 \pm 0.152 mm), arithmetic mean diameter (8.064 \pm 0.688 mm), geometrical mean diameter (7.715 \pm 0.698 mm), square mean diameter (13.646 \pm 1.195 mm), equivalent mean diameter (9.808 \pm 0.859 mm), roundness (0.644 \pm 0.056), sphericity (0.685 \pm 0.044), flakiness ratio (0.784 \pm 0.092), aspect ratio (0.643 \pm 0.053), cross-sectional area (154.477 \pm 26.002 mm²), projected area (64.508 \pm 10.377 mm²), transverse surface area (32.546 \pm 6.683mm²), and the seed volume (241.744 \pm 0.207 mm³), respectively.

The static coefficient of friction varied between 0.276 and 0.386 on the surface of iron sheets, 0.294 to 0.435 on stainless steel, 0.317 to 0.434 on galvanized iron, 0.321 to 0.451 on medium density fiberboard, 0.319 to 0.480 on aluminum, 0.310 to 0.470 on painted sheets, 0.320 to 0.440 on glass, 0.333 to 0.447 on plastic, and 0.374 to 0.575 on rubber. Perforated sheet surfaces showed the highest static coefficients of friction, followed by rubber, plastic, plywood, glass, aluminum, galvanized iron, painted sheet, stainless steel, and iron sheet surfaces. These results data are frequently needed to establish a convenient reference required to develop equipment for handling, cleaning, storing, transporting, drying, and other processes, as well as for predicting loads in agricultural storage structures and resolving flow issues in agro-processing. More research ought to be done to investigate the enhanced *Phaseolus vulgaris* cultivars' moisture-dependent engineering characteristics.

ACKNOWLEDGMENTS

The author Biniam Zewdie Ghebrekidan would like to thank department of Agricultural Engineering & Food Process Engineering from Awash Melkassa Agricultural Research Center, Haramaya University, and Science, Technology, Engineering, & Mathematics (ASTU STEM) CENTER, Chemistry laboratory from Adama science & Technology University for the provision of the improved common bean seed varieties and laboratory facilities, respectively.

REFERENCES

- [1] Abera T. A., Heiskanen J., Pellikka P.K., Adhikari H., Maeda E.E. (2020). Climatic impacts of bushland to cropland conversion in Eastern Africa. *Science of the total environment*, 717, 137255.
- [2] Altuntaş E. and Yıldız M. (2007). Effect of moisture content on some physical and mechanical properties of faba bean (*Vicia faba* L.) grains. *Journal of Food engineering*, 78(1):174-183.
- [3] Amanuel T., Tadele T. and Belay A. (2022). Registration of Milkesa, large-red seed food type common bean (*Phaseolus vulgaris*) varieties for Midland Areas of Bale and East Bale, Southeast Ethiopia. *Journal of Plant Sciences*, 10(1): 46-50.
- [4] Amin M.N., Hossain M.A., Roy K.C. (2004). Effects of moisture content on some physical properties of lentil seeds. *Journal of Food Engineering*, 65(1): 83-87.
- [5] Amsalu B., Negash K., Shiferaw T., Tumssa K., Tsegaye D., Claude R.J. and Mukankusi C.M. (2018). Progress of common bean breeding and genetics research in Ethiopia. *Ethiopian Journal of Crop Science*, 6(3): 15-26.
- [6] Bako T., Aguda A.C. (2023). Effect of moisture content on the engineering properties of African yam bean (*Sphenostylis stenocarpa*) seed. *Journal of Horticulture and Postharvest Research*, 6(1), 15-26.
- [7] Baryeh E.A. (2002). Physical properties of millet. *Journal of Food Engineering*, 51(1): 39-46.
- [8] Bayano-Tejero S., Karkee M., Rodríguez-Lizana A., Sola-Guirado R.R. (2023). Estimation of harvested fruit weight using volume measurements with distance sensors: A case study with olives in a big box. *Computers and Electronics in Agriculture*, 205: 107620.
- [9] Befikadu D. (2018). Postharvest losses in Ethiopia and opportunities for reduction: a review. *International Journal of Sciences: Basic and Applied Research (IJSBAR)*, 38, 249-262.
- [10] Betelhem A., Menbere B., Amsalu N., Ruelle M.L., Alex M., Zemedede A., Zerihun W. (2020). Diversity, use and production of farmers' varieties of common bean (*Phaseolus vulgaris* L., Fabaceae) in southwestern and northeastern Ethiopia. *Genetic Resources and Crop Evolution*, 67(2): 339-356.
- [11] Bhise S.R., Kaur A. Manikantan M.R. (2014). Moisture dependent physical properties of wheat grain (PBW 621). *International Journal of Engineering Practical Research*, 3(2): 40-45.
- [12] Cetin M. (2007). Physical properties of barbutia bean (*Phaseolus vulgaris* L.). *Journal of Food Engineering*, 80(1): 353-358.
- [13] Chhabra N., Kaur A. (2017). Studies on physical and engineering characteristics of maize, pearl millet and soybean. *Journal of Pharmacognosy and Photochemistry*, 6(6): 01-05.
- [14] Degirmencioglu A., Srivastava A.K. (1996). Development of screw conveyor performance models using dimensional analysis. *Transactions of the ASAE*, 39(5): 1757-1763.
- [15] Degirmencioglu A., Mohtar R.H., Daher B.T., Ozgunaltay-Ertugrul G., Ertugrul O. (2019). Assessing the sustainability of crop production in the Gediz Basin, Turkey: a water, energy, and food nexus approach. *Fresen Environ Bull*, 28(4): 2511-2522.

- [16] Derese W., Shimelis A., Belay D. (2021). Geometric characteristics and mass-volume-area properties of haricot beans (*Phaseolus vulgaris* L.): Effect of Variety. *International Journal of Food Properties*, 24(1): 885-894.
- [17] Deshpande S.D., Bal S., Ojha T.P. (1993). Physical properties of soybean. *Journal of Agricultural Engineering Research*, 56(2): 89-98.
- [18] Dubale B. (2018). Postharvest losses in Ethiopia and opportunities for reduction: a review. *International Journal of Sciences: Basic and Applied Research (IJSBAR)*, 38: 249-262.
- [19] Elijah O., Rahman T.A., Orikumhi I., Leow C.Y., Hindia M.N. (2018). An overview of internet of things (iot) and data analytics in agriculture: Benefits and challenges. *IEEE Internet of things Journal*, 5(5): 3758-3773.
- [20] Emrani A., Berrada A. (2023). Structural behavior and flow characteristics assessment of gravity energy storage system: Modeling and experimental validation. *Journal of Energy Storage*, 72:108277.
- [21] Ertuğrul Ö., Yılar M., Kır H., Kömekçi C. (2022). Some physical, chemical, and germination properties of *Peganum harmala* L. seeds. *Journal of Food Process Engineering*, 45(2), e13967.
- [22] FAO (2020). Food and Agriculture Organization Crop Production and Trade Data, Available at <http://www.fao.org/faostat/en/#data/QC>
- [23] Fernando S. (2021). Production of protein-rich pulse ingredients through dry fractionation: A review. *LWT*, 141: p.110961.
- [24] Fraser B.M., Verma S.S., Muir W.E. (1978). Some physical properties of faba beans. *Journal of Agricultural Engineering Research*, 23(1): 53-57.
- [25] Gupta R.K., Arora G., Sharma R. (2007). Aerodynamic properties of sunflower seed (*Helianthus annuus* L.). *Journal of Food Engineering*, 79(3): 899-904.
- [26] Haciseferoğulları H., Gezer İ., Bahtiyarçay Y., Mengeş H.O. (2003). Determination of some chemical and physical properties of Sakız faba bean (*Vicia faba* L. Var. major). *Journal of Food Engineering*, 60(4): 475-479.
- [27] Isik E., Unal H. (2011). Some engineering properties of white kidney beans (*Phaseolus vulgaris* L.). *African Journal of Biotechnology*, 10(82): 19126-19136.
- [28] Jahanbakhshi A. (2018). Determine some engineering properties of snake melon (*Cucumis melo* var. flexuosus). *Agricultural Engineering International: CIGR Journal*, 20(1): 171-176.
- [29] Kakade A., Khodke S., Jadhav S., Gajabe M. and Othzes N. (2019). Effect of moisture content on physical properties of soybean. *International Journal of Current Microbiology and Applied Sciences*, 8(4): 1770-1782
- [30] Kefelegn N., Mekibib F., Dessalegn Y. (2020). Genetic advancement and variability of released common bean (*Phaseolus vulgaris* L.) varieties from 1974–2009 GC in Ethiopia. *Advances in Agriculture*, 2020, 1-7.
- [31] Kumar N., Sharma A.K. (2021). Study on engineering properties of chickpea (*Cicer arietinum*) seeds in relation to design of threshing mechanism. *The Pharma Innovation*, 10(9): 455-458.
- [32] Mirzabe A.H., Khazaei J., Chegini G.R. and Gholami O. (2013). Some physical properties of almond nut and kernel and modeling dimensional properties. *Agricultural Engineering International: CIGR Journal*, 15(2): 256-265.
- [33] Mohsenin N.N. (1986). *Physical properties of plant and animal materials: structure, physical characteristics and mechanical properties* (2. rev. and updated ed). Gordon and Breach
- [34] Mpotokwane S.M., Gaditlhatlhelwe E, Sebaka A and Jideani VA (2008). Physical properties of bambara groundnuts from Botswana. *Journal of food engineering*, 89(1): 93-98.
- [35] Nciri N., El-Mhamdi F., Ismail H.B., Mansour A.B., Fennira F. (2014). Physical properties of three white bean varieties (*Phaseolus vulgaris* L.) grown in Tunisia. *Journal of Applied Science and Agriculture*, 9(11 Special): 195-200.
- [36] Nigussie K., Frew M., Yigzaw D. (2020). Genetic Advancement and variability of released common bean (*Phaseolus vulgaris* L.) varieties from 1974–2009 GC in Ethiopia. *Advances in Agriculture*, 2020:1-7.
- [37] Omobuwajo T.O., Akande E.A., Sanni L.A. (1999). Selected physical, mechanical and aerodynamic properties of African breadfruit (*Treculia africana*) seeds. *Journal of Food Engineering*, 40.4 (1999): 241-244.
- [38] Ozturk I., Kara M., Yildiz C., Ercisli S. (2009). Physico-mechanical seed properties of the common Turkish bean (*Phaseolus vulgaris*) cultivars 'Hinis' and 'Ispir'. *New Zealand Journal of Crop and Horticultural Science*, 37(1): 41-50.

- [39] Önal İ., Ertuğrul Ö. (2011). Seed flow and in-row seed distribution uniformity of the top delivery type fluted roller for onion, carrot and canola seeds. *Journal of Agricultural Sciences*, 17(2011), 10-23.
- [40] Pawar P., Shinde V., Raut A., Suke S., Kolpe K., Manna A. (2023). An automated combined system for crop prediction and yield prediction using deep hybrid learning technique. In *2023 7th International Conference On Computing, Communication, Control and Automation (ICCUBEA)*. pp. 1-5. IEEE.
- [41] Sahin S., Sumnu S.G. (2006). Physical properties of foods: Springer science & Business media. *Journal of Applied Science and Agriculture*, 9(1):185-200.
- [42] Samrawit T. (2023). *Design and numerical analysis of rice grading machine for Ethiopian rice varieties* (Doctoral dissertation, Bahir Dar University).
- [43] Saporita R., Hidajat D.D., Kuala S.I. (2019). Statistical analysis on the geometric, physical and mechanical properties of dried robusta coffee cherry resulting from natural system processing. In *IOP Conference Series: Earth and Environmental Science*. Vol. 251, No. 1, p. 012041.
- [44] Singh R.P., Heldman D.R. (2009). *Psychrometrics*. In *Introduction to Food Engineering*, 4th ed, ed. R. P. Singh, and D. R. Heldman, 9, 571-593. Burlington, MA, USA: Academic Press.
- [45] Sirisomboon P, Kitchaiya P, Pholpho T and Mahuttanyavanitch W (2007). Physical and mechanical properties of *Jatropha curcas* L. fruits, nuts and kernels. *Biosystems engineering*, 97(2): 201-207.
- [46] Sundaram P.K., Singh A.K., Kumar S. (2014). Studies on some engineering properties of faba bean seeds. *Journal of AgriSearch*, 1(1):4-8.
- [47] Tekalign A., Tadesse T., Asmare B. (2022). Registration of Hora, Small-red Seed Food Type Common Bean (*Phaseolus vulgaris*) Varieties for Midland Areas of Bale and East Bale, Southeast Ethiopia. *Plant*, 10(1), 36-39.
- [48] Wodajo D., Admassu S., Dereje B. (2021). Geometric characteristics and mass-volume-area properties of haricot beans (*Phaseolus vulgaris* L.): Effect of Variety. *International Journal of Food Properties*, 24(1), 885-894.

ANALYSIS ON PATH OPTIMIZATION OF AGRICULTURAL WAREHOUSE LOGISTICS HANDLING ROBOT BASED ON POTENTIAL FIELD ANT COLONY ALGORITHM

基于势场蚁群算法的农业仓库物流搬运机器人路径优化研究

Yunyun WANG¹⁾, Mingzhe XIE^{*2)}

¹⁾ School of Management, Wuhan University of Technology, Wuhan, Hubei/ China

²⁾ School of Economics and Management, Ningbo University of Technology, Ningbo, Zhejiang/ China

Tel: +8613705846416; E-mail: xiemz13705846416@126.com

Corresponding author: Mingzhe Xie

DOI: <https://doi.org/10.35633/inmateh-73-66>

Keywords: Artificial potential field; ant colony algorithm; warehouse handling robot; obstacle avoidance; strategy gradient algorithm

ABSTRACT

In the layout of modern agricultural warehouse logistics handling industry, it was an inevitable way to realize industrial upgrading by replacing people with mobile robots. Aiming at the problems that the existing obstacle avoidance control algorithm of agricultural handling robot was easy to fall into local optimal solution, and the operation process of agricultural warehouse logistics handling robot was prone to collision, the obstacle avoidance control of agricultural warehouse logistics handling robot was studied. In addition, a control algorithm based on improved potential field ant colony was proposed. The moving trajectory of the agricultural warehouse logistics handling robot during the handling process was studied, and the spatial kinematics equation of the robot was given. The ant colony algorithm was used to optimize the classical artificial potential field algorithm to improve the global optimization ability and balance the interaction between gravity and repulsion. In the aspect of local area obstacle avoidance of agricultural storage and handling robots, the artificial potential field was optimized twice based on the strategy gradient algorithm. By analyzing the probability of the next action command, the randomness of the travel path selection when multiple robots work at the same time was improved. After testing, the path of the proposed control algorithm was the shortest, and under the condition of complex path planning, the number of collisions between robots was also significantly less than that of the traditional obstacle avoidance control algorithm. The practical application could meet the needs of improving the efficiency of warehouse logistics management.

摘要

在现代化农业仓库物流搬运产业布局中，通过移动机器人取代人来实现产业升级是一条必由之路。针对现有农业搬运机器人避障控制算法存在的路径寻优易陷入局部最优解，及农业仓库物流搬运机器人作业过程易发生碰撞等问题，对农业仓库物流搬运机器人的避障控制进行了研究，并提出一种基于改进势场蚁群的控制算法；对农业仓库物流搬运机器人搬运过程中的移动轨迹进行了研究，给出了机器人空间运动学方程；采用了蚁群算法对经典人工势场算法进行优化，提升全局寻优能力并平衡引力和斥力的相互作用关系；在农业仓储搬运机器人的局部区域避障方面，基于策略梯度算法对人工势场做二次优化，通过分析下一动作指令的发生概率，改善多机器人同时作业时行进路径选择的随机性；经测试，提出控制算法的路径最短，而且在复杂路径规划条件下，机器人之间发生碰撞的次数也显著少于传统避障控制算法，经实际应用能够满足提升仓储物流管理效率的需求。

INTRODUCTION

In the context of the rapid development of the logistics industry, the traditional manual or semi-manual warehouse logistics management methods obviously cannot meet the requirements of industry development. In recent years, with the advancement of robot technology, automation control technology and wireless sensor technology, warehouse logistics handling robots had been applied to warehouse logistics management activities on a large scale (Chu et al., 2019). Warehouse handling robots were introduced into logistics management activities, which could not only save labor handling costs, but also effectively improved the efficiency and accuracy of logistics turnover. Usually large warehouse logistics center, would use multiple logistics robot at the same time, the robot in the process of transportation and handling must avoid storage shelves, other transport robots and various uncertain obstacles (Yuan et al., 2021). This put forward higher requirements for the intelligent level of the warehouse handling robot, the economy of the transportation path selection and the emergency capability of the robot (Ru et al., 2019).

With the rapid development of sensor technology and servo drive technology, high-performance real-time control has been able to meet the relevant needs of industrial control. Based on this, the warehouse handling robot can gradually meet the requirements of positioning and handling of heavy-duty components in modern intelligent digital factories. With the continuous improvement of the performance of the handling robot, it has been well applied in the field of agricultural engineering.

Agricultural handling robot was an intelligent robot that can carry out autonomous path planning and complete specific agricultural warehouse handling tasks (Xu et al., 2021). As an indispensable part of the autonomous navigation of agricultural handling robots, path planning had received extensive attention from researchers. Its goal was to find a collision-free continuous solution that always meets specific performance indicators from the initial state to the target state. The quality of path cost and solution is an important factor to be considered when designing path planning algorithm (Zhang et al., 2021). The quality of path planning of agricultural warehousing and logistics robot determines whether the robots can cooperate with each other, and also determines the safety and efficiency of robot driving. Therefore, it is of great safety and economic significance to study the path planning of agricultural warehousing and logistics handling robots. How to solve the problem of path navigation and obstacle avoidance in a more complex, boundary and extreme environment, so that agricultural handling robots can better serve production and life, has become a new research topic in the field of intelligent mobile robot technology.

In recent years, relevant scholars have carried out cutting-edge academic research on the optimal scheduling problem of handling robots in mobile shelf warehouses, and have made some research progress. The representative achievements include: Lv et al. (2021) proposed a robot allocation rule based on the processing speed of the picking station, constructed a semi-open queuing network and used a two-stage approximation method for performance evaluation. Wang et al. (2020) developed a stylized performance evaluation model based on a multi-class closed queuing network model. Lv et al. (2020) expressed the robot scheduling problem as an asymmetric traveling salesman problem, and extended the model by adding customer order priority constraints. By analyzing the order picking operation process of e-commerce logistics distribution center, Shang et al (2022) proposed two operation modes of synchronous and asynchronous picking of multiple picking stations, and established a robot scheduling model under two picking modes. Bi et al. (2022) proposed a random scheduling strategy in the case of batch order tasks. Yang et al. (2020) established a mathematical model for the problem of order allocation and shelf selection for multiple picking stations. Tiseni et al. (2021) proposed two mathematical methods for the problem of order and shelf allocation to pickers, and established an integer programming model for the shelf sequencing problem of the picking station.

The research on agricultural handling robot navigation technology in academia has reached a relatively mature stage. Sarabu et al. (2019) proposed a novel method for planning the path of an agricultural handling robot towards a target in an unknown environment, utilizing sensors to detect new obstacles along the way. This method numerically solves the partial differential equation of heat conduction to synthesize artificial temperature gradients within the entire known environment, where the heat encountered during robot navigation contrasts with the 'cold' target. The temperature at all other points on the known environmental grid was numerically calculated and continuously updated to account for new obstacles (Sarabu et al., 2019). Sehestedt et al. (2010) proposed a multi-robot navigation method with heterogeneous capabilities. In this method, a single navigation had different translation and rotation speeds, accelerations, sensing distances and angles, while maintaining global connectivity to other robots. Xia et al. (2016) used unsupervised clustering to automatically detect the type of surrounding environment based on navigation complexity and limited the sampling space of local controllers. The methods described in the above literature all rely on laser to navigate and control the mobile robot. In a narrow environment, the movement of the robot is easily blocked by obstacles, resulting in the robot staying in place and the robot motion control is not flexible enough. According to the completeness of the agricultural robot's grasp of the working environment information, the robot path planning can be divided into global path planning and local path planning. Global path planning referred to planning a path from the starting point to the end point in a static environment when the environmental information was completely known (Zhang et al., 2017). Commonly used methods included fast search random tree, topology, and intelligent methods such as particle swarm optimization and ant colony algorithm (Dorigo et al., 2006). Local path planning referred to the planning of local driving paths in a dynamic environment when the environmental information was partially known. Common methods included rolling window method, artificial potential field method, and fuzzy strategy (Mirjalili et al., 2016). Inbarani et al., (2014), extended the 8-neighborhood grid to 24-neighborhood grid in the grid environment, and redefined the heuristic information and neighborhood selection probability.

The simulation results show that the proposed method has shorter planning path and better smoothness. Aiming at the problems existing in the A* algorithm, *Jahanbakht et al. (2021)* used the JPS algorithm to expand and jump the child nodes, which effectively improved the efficiency of the A* algorithm, and used the Bessel curve to improve the smoothness of the path. Aiming at the problems of local traps and unreachable targets in the artificial potential field method, *Patel et al. (2022)* proposed a multi-behavior strategy and a variable influence range potential field method, which had better planning performance in complex obstacle environments. The above research results have planned a better path in their respective settings, but the planning methods and planning objectives in different application scenarios are quite different. Therefore, the robot path planning problem is still a research hotspot of robot navigation.

Most of the existing warehouse logistics robot control algorithms were based on high-definition cameras (*Sawadwuthikul et al., 2022*), radar sensors (*Yu et al., 2021*), distance sensors (*Sami et al., 2020*), etc. to correct the route and avoid obstacles along the way. *Cai et al. (2020)* proposed an AGV (Automated Guided Vehicle) robot that could achieve autonomous navigation and obstacle avoidance on the basis of manually setting control procedures. However, there were some problems in the global path optimization of AGV robot, which was easy to fall into local optimization, and then to choose non-economic path (*Cai et al., 2020*). On the basis of neural network model and machine learning algorithm, *Zong et al. (2020)* proposed a path optimization algorithm based on Q learning, which selected a more economical path according to the instructions and avoided obstacles along the way. In summary, the artificial potential field model is an efficient global path optimization algorithm model, which has certain advantages in obstacle avoidance and global optimization. The principle of the artificial potential field algorithm is to simulate the force field in classical mechanics, that is, the gravitational force will be generated between the agricultural handling robot and the destination, attracting the agricultural handling robot to move towards the target point, and the repulsion will be generated between the robot and the obstacle, prompting the agricultural handling robot to avoid the obstacle. The agricultural handling robot will comprehensively evaluate the suction and repulsion, and choose the most economical path to move forward to the target. Based on the ant colony algorithm, this study optimizes the classical artificial potential field algorithm, overcomes the adverse effects of the repulsive potential field in the classical artificial potential field model, and improves the effect of global path optimization and obstacle avoidance.

MATERIALS AND METHODS

Spatial dynamics analysis

The agricultural storage and handling robot moves in three-dimensional space. Its position, direction, travel speed, acceleration, and steering angle in three-dimensional space have an important impact on obstacle avoidance and path selection. The robot searches the most economical optimization route in the global scope according to the pre-planned path planning, but it cannot avoid the occurrence of emergencies and needs to adjust the path temporarily. Therefore, the warehouse handling robot should also temporarily adjust the running speed and route according to the distribution of dynamic obstacles in the actual work, and actively avoid other robots to avoid collision with other robots. In this study, the four-wheel rear-drive rear-steering robot is taken as an example to analyze the spatial dynamics of the warehouse handling robot, as shown in Fig.1.

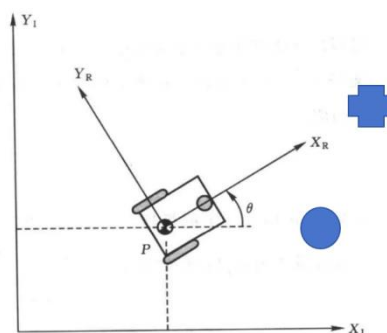


Fig. 1 – Spatial dynamics change of agricultural storage and handling robot

In the spatial coordinate system xOy , O' is the center of gravity of the storage and handling robot. A is the direction of the robot, β is the heading angle of the robot. If let $H = [x, y, \beta]^T$, $J = [v, \omega]^T$ (v and ω

are the speed and angular velocity of the robot respectively), the space kinematics equation of the robot is expressed as follows:

$$H = \begin{pmatrix} x \\ y \\ \beta \end{pmatrix} = \begin{pmatrix} \cos \beta & 0 \\ \sin \beta & 0 \\ 0 & 1 \end{pmatrix} J \tag{1}$$

The movement of the agricultural storage and handling robot includes two degrees of freedom, namely, the current position and direction of the robot. The movement also includes three output variables, namely, position, direction of motion and steering speed. In terms of the control of the robot 's trajectory, the real-time correction of the trajectory of the agricultural storage and handling robot is realized by controlling V and ω , and the obstacles in front are avoided in time. The spatial kinematics model of the storage and handling robot in the coordinate space is expressed as follows:

$$\begin{cases} \dot{x} = v \cos \beta \\ \dot{y} = v \sin \beta \\ \dot{\beta} = \omega \end{cases} \tag{2}$$

Because the four-wheeled warehouse handling robot is rear-wheel steering and rear-wheel drive in structural design, the position tracking and heading angle of the agricultural warehouse handling robot are synchronized, that is, the length and turning radius of the robot should be taken into account when the rear wheel is turned. At the same time, the heading angle is calibrated to ensure that the robot moves forward according to the specified path and can also avoid obstacles on the moving path. In order to better simulate the transportation and obstacle avoidance activities of agricultural storage and handling robots in warehouses, the target site is segmented based on the grille method. According to the volume of the storage robot and the size of the shelf, the entire warehouse site is divided into 46*46 small block areas, and then the robot 's travel channel is set according to the shelves and the placement of goods, and the size and location of obstacles (including moving obstacles such as shelves and other handling robots) are determined. Design the travel path and the trajectory of the robot. In large warehouse logistics centers, there are usually multiple warehouse handling robots working at the same time. For mobile agricultural warehouse handling robots, the three-dimensional shelves for storing items can be regarded as static obstacles, while other agricultural warehouse handling robots are regarded as moving obstacles.

Model construction

Assuming that the entire agricultural warehouse is a potential field, the current position coordinates of the agricultural warehouse handling robot are $P_o(x_o, y_o)$. The position coordinates of the target point are $P_d(x_d, y_d)$. The position coordinates of the obstacle are $P_b(x_b, y_b)$. Then the potential field function f_1 due to the existence of gravity, specifically expressed as follows:

$$f_1 = \frac{1}{2} \delta (P_o - P_d)^2 \tag{3}$$

Among them is the δ gravitational gain coefficient, then the relationship between the pure gravitational function relationship g_1 and f_1 between the agricultural storage and handling robot and the target point is as follows:

$$g_1 = -\nabla f_1 = -\delta \tau \|P_o - P_d\| \tag{4}$$

Where, τ is the direction vector pointing to the target point, $\|P_o - P_d\|$ is the shortest distance between two points (Euclidean distance). Similarly, the repulsion potential field function between the agricultural storage handling robot and the repulsion field is defined.

$$f_2 = \frac{1}{2} \delta \left(\frac{1}{\|P_o - P_b\|} - \frac{1}{\max|P_o - P_b|} \right) \tag{5}$$

Among them, $\|P_o - P_b\|$ is the Euclidean distance between the agricultural storage handling robot and the obstacle, $\max|P_o - P_b|$ is the maximum interference distance between the two. When $\|P_o - P_b\|$ exceeds $\max|P_o - P_b|$, the repulsion field is zero. In the artificial potential field environment, the final force of the agricultural storage and handling robot is the sum of the gravity of the object and the repulsion of the obstacle. The artificial potential field model is composed of the gravitational function of the potential field and the repulsion function of the potential field.

Under the action of artificial potential field, the storage and handling robot will choose the best path according to the gravity and repulsion. However, if there are many robots of the same type in the field, these agricultural storage and handling robots will be transformed into moving obstacles, and the repulsion between agricultural storage and handling robots will also change randomly, which will eventually lead to the failure of agricultural storage and handling robots to choose the best path or fall into the local optimal solution. Therefore, this study optimizes the artificial potential field algorithm based on the global perspective and uses the ant colony algorithm to form a new potential field ant colony algorithm, which can ensure that all mobile robots in the site can find the best path in the existing coordinate dimension.

The ant colony algorithm simulates the foraging behavior of ant individuals in the ant colony. Through the propagation of pheromones and the superposition of pheromone concentrations, an optimal foraging path with the highest pheromone concentration is selected. The advantages of ant colony algorithm are high fault tolerance and global optimization. The two most important core elements in the algorithm are individual transfer probability and individual pheromone concentration. Suppose that the ant individual (corresponding to the agricultural storage and handling robot) in the ant colony at time t starts from the starting point b to the target place c for food, the initial pheromone concentration is τ_{bc} , and the heuristic information along the way is ξ_{bc} , then the path transition probability $P_{bc}^A(t)$ of the individual is expressed as follows:

$$P_{bc}^A(t) = \frac{[\tau_{bc}(t)]^\xi [\xi_{bc}(t)]^\eta}{\sum [\tau_{bc}(t)]^\xi [\xi_{bc}(t)]^\eta} \quad (6)$$

In the formula, ξ and η are weight parameters related to pheromone concentration and heuristic information. The larger the parameter value is, the greater the role of pheromone in ant individual path optimization is. The pheromone concentration $\tau_{bc}(t)$ on the route at time t is related to the number of ants passing through the route, and the heuristic information $\xi_{bc}(t)$ at time t is related to the Euclidean distance from the individual to the target:

$$\xi_{bc}(t) = \frac{1}{d(b,c)} \quad (7)$$

In the formula, $d(b,c)$ is the Euclidean distance between the starting point and the target point. In the warehouse area delineated based on the grille method, each moving agricultural warehouse handling robot can be regarded as an ant individual. Each delivery and handling behavior is regarded as an iteration in the global scope. Each ant individual moves towards the moving target, resulting in different pheromone concentrations on different paths. In the process of simulating ant foraging activities, the best path is selected according to the change of pheromone concentration, while avoiding the interference of other agricultural warehouse handling robots in the local area.

Algorithm design

In the traditional ant colony algorithm, the reciprocal of the distance between the current node and the next node is usually used as the heuristic function. The distance heuristic function has low visibility to the end point and does not consider the actual multi-path situation. In view of the above situation, this study first introduces the artificial potential field method to reconstruct the distance heuristic function, which overcomes the blindness of the early search of the ant colony algorithm, and then comprehensively considers the three factors of path length, path smoothness and smoothness to construct a new multi-factor heuristic function:

$$\eta_{ij} = aL_{ij}(t) + bH_{ij}(t) + cT_{ij}(t) \quad (8)$$

In the formula, a , b , c are the weight coefficients, $L_{ij}(t)$ is the distance heuristic function introduced by the potential field method, $H_{ij}(t)$ is the gentleness heuristic function, and $T_{ij}(t)$ is the smoothness heuristic function. This heuristic function overcomes the limitation of traditional path planning with distance as the index.

Improvement of the heuristic function

(1) Distance heuristic function. A new distance heuristic function $L_{ij}(t)$ is constructed by using the resultant force F_s constructed by the artificial potential field method. Because the artificial potential field has a guiding effect on the robot, the convergence speed of the ant colony is faster, but it is easier to obtain the local optimal solution. For the ant colony algorithm is easy to fall into the local minimum, this study adds the coefficient α to improve the potential field force, as shown below:

$$\alpha = 1 - \frac{N_k}{N_{max}} \tag{9}$$

$$F_A = F_s \cdot \alpha \tag{10}$$

In the Equation (9), N_k is the number of iterations of the k-wave ants, N_{max} is the total number of iterations, and F_A is the improved potential force. Then the optimized distance heuristic equation is:

$$L_{ij}(t) = \begin{cases} \frac{\alpha F_A \cdot \cos \theta}{d_{ij} + d_{jg}}, & j \in a_k \\ 0, & \text{else} \end{cases} \tag{11}$$

In the formula, it is the distance from d_{ij} node i to node j , and d_{jg} is the distance from node j to the target point g . When the potential force becomes 0, the distance heuristic function is used to search to avoid the algorithm falling into a 'deadlock'.

(2) Smoothness heuristic function. In the actual working environment of the robot, too bumpy road surface is easy to cause the rollover of the robot, and will affect the moving speed and energy consumption of the robot, so this study adds the gentleness heuristic factor to the heuristic function to guide the robot to choose a gentler path, so as to improve the gentle performance of the path and get a higher quality path.

$$H_{ij}(t) = \frac{h_{max} - |h(i) - h(j)|}{h_{max} - h_{min} + Q} \frac{N_{max} - N_k}{N_{max}} M + N \tag{12}$$

$$h_{max} = \max\{ |h(i) - h[a_i]| \} \tag{13}$$

$$h_{min} = \min\{ |h(i) - h[a_i]| \} \tag{14}$$

In the formula, a_i represents the set of all reachable nodes near node i , h_{max} represents the maximum height difference between the current node i and the surrounding adjacent nodes, and h_{min} represents the minimum height difference between the current node i and the surrounding nodes. $h(i)-h(j)$ represents the height difference between node i and node j . N_{max} is the maximum number of iterations to prevent the denominator from being 0 when $h_{max}=h_{min}$, and M and N are stable correction parameters. When the ants choose a path with a smaller height difference, the greater the gentleness heuristic factor $H_{ij}(t)$, the gentler the path can be obtained.

(3) Smoothness heuristic function: In the process of path planning, the traditional ant colony algorithm tends to generate numerous inflection points, which can result in the robot needing to readjust its posture at these points, leading to unnecessary acceleration and deceleration, increased driving difficulty, and prolonged driving time for the robot. Therefore, in view of this phenomenon, the smoothness factor $T_{ij}(t)$ is added to the heuristic function, and the robot can choose the path with fewer turns.

$$T_{ij}(t) = \begin{cases} \rho u \frac{N_{max} - N_k}{N_{max}} + \sigma, & d_{mi} = d_{ij} \\ \frac{(1-\rho)u}{S(a_i)} \frac{N_{max} - N_k}{N_{max}}, & d_{mi} \neq d_{ij} \end{cases} \tag{15}$$

$$m = v_i(e-1) \tag{16}$$

In the formula, $\rho(0 \leq \rho \leq 1)$ represents the importance of the ant going straight, u represents the flexibility constant of the robot, N_{max} is the total number of iterations, σ is the turning correction constant, v_i represents the set of all passing nodes of the ant from the starting point to the node i , $S(a_i)$ represents the number of all nodes in the set, $e-1$ represents the penultimate element in the set, that is, the last node m of the node i , d_{mi}, d_{ij} represents the movement direction of the ant from node m to node i and node i to node j , respectively. When the direction is the same, it means that the robot does not have to turn, the heuristic function is larger, and the ant is guided to the path with fewer turns.

Optimization of the pheromone update

(1) Initial pheromone allocation principle. In the early stage of path search, the ant colony algorithm will make the positive feedback effect of the algorithm not obvious because of the small difference in pheromone concentration of each node, resulting in large blindness, poor convergence and long search time

in the early stage of the algorithm. In order to solve this problem, this study proposes an uneven distribution method of initial pheromone, which redistributes the initial pheromone value between all the nodes found by the algorithm and the target point, and the pheromone value of the remaining nodes remains unchanged, thereby improving the convergence speed and search time of the algorithm in the early stage.

$$\tau_i = \begin{cases} \phi D, & i \in P \\ 1, & \text{else} \end{cases} \quad (17)$$

In the formula, τ_i is the newly assigned initial pheromone value, $\phi(\phi > 1)$ is the initial pheromone concentration increase coefficient, D is the initial pheromone concentration, and P is the set of all nodes between the starting point and the target point. Because P contains the nodes in the optimal path, it is beneficial to improve the search speed of the search.

(2) Multi-factor pheromone update. Based on the results of multi-objective optimization, the pheromone update is determined by considering factors such as path smoothness, continuity, and overall path length.

The multi-factor pheromone update method is as follows:

$$\tau_{ij}(t+1) = (1-\phi)\tau_{ij}(t) + \phi\Delta\tau_{ij}^k(t) \quad (18)$$

$$\Delta\tau_{ij}^k(t) = \Delta\tau_{ij}^L(t) + \Delta\tau_{ij}^H(t) + \Delta\tau_{ij}^T(t) \quad (19)$$

$$\Delta\tau_{ij}^L(t) = \begin{cases} \frac{A \cdot Q}{L_{k(t)}}, & j \in a_i \\ 0, & \text{else} \end{cases} \quad (20)$$

$$\Delta\tau_{ij}^H(t) = \begin{cases} \frac{B \cdot Q}{100H_k(t)}, & j \in a_i \\ 0, & \text{else} \end{cases} \quad (21)$$

$$\Delta\tau_{ij}^T(t) = \begin{cases} \frac{C \cdot Q}{T_k(t)}, & j \in a_i \\ 0, & \text{else} \end{cases} \quad (22)$$

$$L_k(t) = \sum d(B, \dots, i, j, \dots, G) \quad (23)$$

$$H_k(t) = \sqrt{\frac{1}{p-1} \sum_{i=1}^p (h(i) - \bar{h})^2} \quad (24)$$

$$p = s(p), T_k(t) = c(B, \dots, i, j, \dots, G), d_{mi} \neq d_{ij} \quad (25)$$

In the formula, $\Delta\tau_{ij}^L(t)$, $\Delta\tau_{ij}^H(t)$ and $\Delta\tau_{ij}^T(t)$ represent the pheromone increments of the distance factor, the smoothness factor, and the continuity factor, respectively. In order to expand the influence of road conditions on the path, the height mean square error is increased by 100 times. A, B and C are the weights of each factor, which are used to adjust the adaptability of the robot in different environments, so as to achieve the optimal effect of the path. Q represents the pheromone strength, $L_{k(t)}$ represents the length of the path obtained by the artificial potential field method. The pheromone strength diminishes as the distance increases. $H_k(t)$ represents the height mean square error of the path, where $h(i)$ denotes the height of the current node, \bar{h} represents the average height, and p denotes the number of nodes. A smaller mean square error corresponds to a greater $\Delta\tau_{ij}^H(t)$, indicating stronger pheromone intensity for the path. $T_k(t)$ represents the number of turns in the path, and $c(B, \dots, i, j, \dots, G)$ records the turning nodes.

Improvement of the grid map

When the agricultural warehouse handling robot performs the handling task in the agricultural product warehouse, it has high safety requirements. Therefore, it is proposed that in the grid map, even the vertex of the obstacle cannot be touched, so that agriculture can ensure the absolute safety of the robot and obtain a path of better quality. The improved map information storage method is used to update the vertex anti-collision strategy, as shown in Fig. 2.

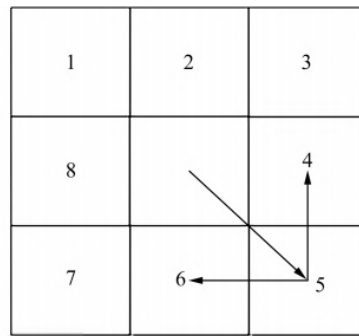


Fig. 2 – Improvement of the map information storage method to update the vertex anti-collision strategy

This study stipulates that the even number label is the robot's straight label, and the odd number label is the robot's oblique label. Only when there are no obstacles in the oblique direction and the two straight grids are perpendicular to the direction, can the oblique movement be carried out. As shown in Fig. 4, when turning to the 5th grid, when there are no obstacles in the 4th and 6th grids perpendicular to the 5th grid, the robot will carry out oblique transfer. In order to store the feasible information of the ant, the transfer distance matrix D is established as follows:

$$D(i, j) = \begin{cases} l, & \text{mod}(j, 2) = 0 \ \& \ G(i_1) = 0 \\ \sqrt{2}l, & \text{mod}(j, 2) = 1 \ \& \ G(i_2) = G(i') = G(i'') = 0 \\ \infty, & \text{else} \end{cases} \quad (26)$$

In the formula, i_1 is the straight grid, mod is the remainder function, i_2 is the oblique grid, i' and i'' are the grids in two directions perpendicular to the oblique grid, and l is the side length of the grid.

Selection of the experimental parameters

In this study, the simulation analysis is carried out in Matlab, and the path optimization of the agricultural warehouse logistics handling robot is verified in the 46×46 scale grid environment. The layout of the shelves and the scene diagram are shown in Fig. 3.

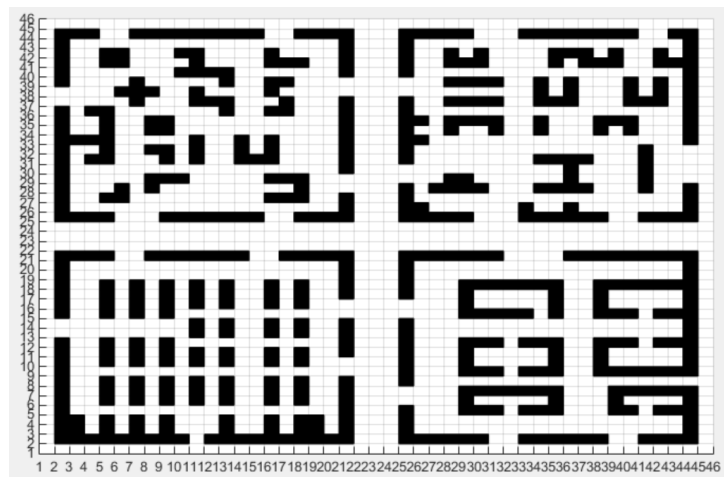


Fig. 3 – Warehouse site diagram based on grid method

The black square in Fig.4 represents the immovable shelf, and the white area is the channel. The length, width and height of the logistics handling robot used in the experiment are 0.9 m, 0.6 m and 0.4 m respectively. The warehouse logistics handling robot itself has the function of telescopic lifting, and the maximum bearing capacity is 0.5 tons.

RESULTS

Results analysis

In this study, two modes of warehouse area and cross warehouse area are set up to verify the model and algorithm, and the shortest path of the two algorithms in 46×46 environment is compared.

Analysis of the handling path of agricultural warehouse logistics robots in the warehouse area

The two algorithms are used to plan 10 times in a 46×46 environment, and the shortest paths planned by the two algorithms are selected for comparison. The potential field ant colony algorithm is used to carry the agricultural warehouse logistics robot in the warehouse area and the path is shown in Fig. 4. The traditional ant colony algorithm is used to carry the agricultural warehouse logistics robot in the warehouse area and the path is shown in Fig. 5.

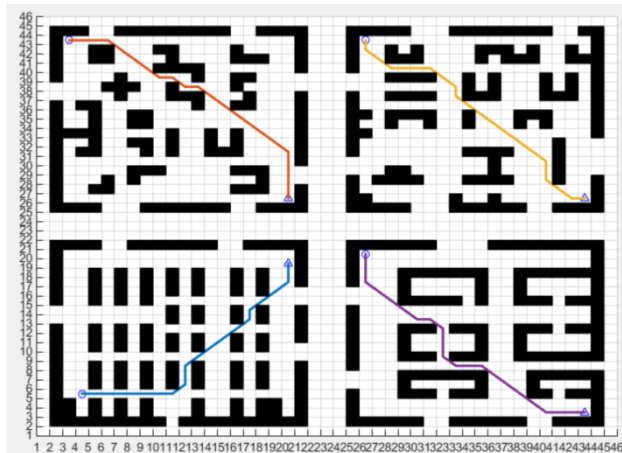


Fig. 4 - Potential field ant colony algorithm in warehouse area agricultural warehouse logistics robot handling path

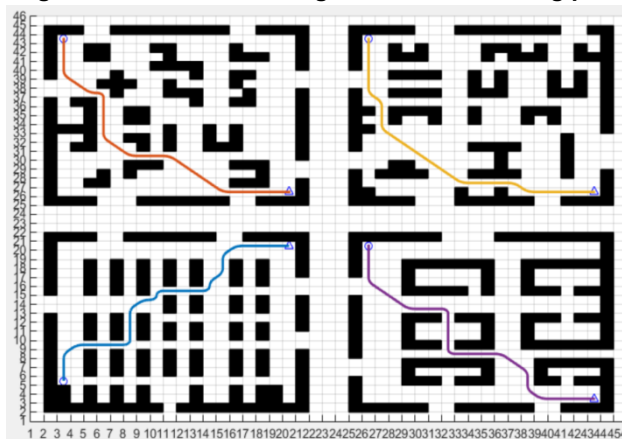


Fig. 5 – The traditional ant colony algorithm in the warehouse area of agricultural warehouse logistics robot handling path

Comparing the paths planned by the two algorithms in Fig. 5 and Fig. 6, it can be seen intuitively that the traditional algorithm has more inflection points and the corresponding length is larger. The potential field ant colony algorithm has fewer inflection points and shorter path length. In order to further compare, the length of the planned path, the number of inflection points, and the number of iterations of the two algorithms are counted, as shown in Table 1.

Table 1

Comparison of planning path results in each algorithm warehouse area

| Algorithm type | Warehouse area | Path length | Number of inflection points | Number of convergences |
|---|----------------|-------------|-----------------------------|------------------------|
| Potential field ant colony algorithm | Path 1 | 26.9706 | 6 | 76 |
| | Path 2 | 26.3848 | 8 | 77 |
| | Path 3 | 27.5563 | 8 | 79 |
| | Path 4 | 26.6820 | 6 | 75 |
| Traditional ant colony algorithm | Path 1 | 28.7872 | 15 | 90 |
| | Path 2 | 29.0018 | 16 | 91 |
| | Path 3 | 29.7441 | 13 | 90 |
| | Path 4 | 28.3184 | 15 | 92 |

Analysis of the handling path of agricultural warehouse logistics robots across warehouses

The two algorithms are used to plan 10 times in a 46×46 environment, and the shortest paths planned by the two algorithms are selected for comparison. The potential field ant colony algorithm is used to carry the agricultural warehouse logistics robot in the warehouse area and the path is shown in Fig. 6. The traditional ant colony algorithm is used to carry the agricultural warehouse logistics robot in the warehouse area and the path is shown in Fig. 7.

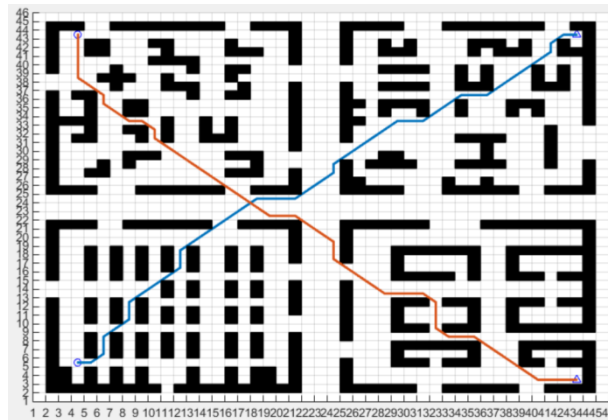


Fig. 6 – Potential field ant colony algorithm cross warehouse agricultural warehouse logistics robot handling path

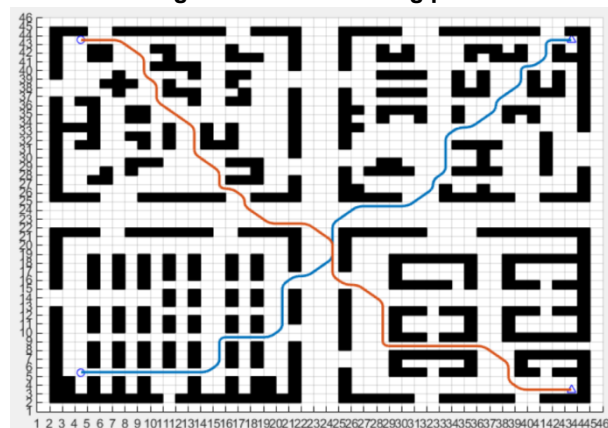


Fig. 7 – Traditional ant colony algorithm cross warehouse agricultural warehouse logistics robot handling path

From Fig.7 and Fig.8, it can be seen that the simulation experiment of the cross-warehouse handling path of the agricultural warehouse logistics robot is carried out in the grid environment. The differences between the two algorithms in the three dimensions of path length, number of corners and average number of iterations are compared. The experimental results are shown in Table 2.

Table 2

The comparison of the results of the cross-warehouse area planning path of each algorithm

| Algorithm type | Cross warehouse area | Path length | Number of inflection points | Number of convergences |
|---|----------------------|-------------|-----------------------------|------------------------|
| Potential field ant colony algorithm | Path 1 | 59.4264 | 18 | 85 |
| | Path 2 | 62.5980 | 18 | 88 |
| Traditional ant colony algorithm | Path 1 | 65.8400 | 36 | 101 |
| | Path 2 | 66.2972 | 39 | 106 |

It can be seen from Table 1 and Table 2 that the pheromone of the potential field ant colony algorithm uses the gradient initialization method, and the early search efficiency of the algorithm is high, which greatly reduces the number of algorithms. The pheromone gradient initialization method makes the ants more efficient in selecting the path, and the path planned by the ants is more concentrated in the optimal area. Based on the strategy gradient algorithm, the collision between the warehouse handling robot and the shelf is effectively avoided.

The strategy gradient algorithm will adjust the movement direction and speed of the robot in time according to the local obstacle distribution of the site, which not only ensures the overall progress of the path planned by the potential field ant colony algorithm, but also effectively realizes the obstacle avoidance of local moving obstacles. Based on the above analysis, it can be seen that the potential field ant colony algorithm has certain advantages in the path planning in the grid environment.

CONCLUSIONS

In recent years, with the rapid development of agriculture and logistics industry, the scale of the industry has expanded simultaneously, which objectively requires the management level and management efficiency of agricultural warehouses to be improved. At present, in order to cope with the large-scale, centralized and digital agricultural logistics management mode, agricultural warehouse handling robots are widely used in warehouse logistics management activities. When multiple warehouse handling robots work at the same time, while planning the travel path of each robot, it is also necessary to avoid local path conflicts between logistics robots, thereby avoiding collisions between logistics robots. In this study, the classical artificial potential field model was optimized, and the global optimization ability of ant colony algorithm was used to accurately determine the position of obstacle robot, and the economic path of robot was comprehensively planned from a macro perspective. At the same time, the strategy gradient algorithm was used to overcome the randomness in the local motion of the robot and avoid collisions due to path overlap. The experimental data showed that the obstacle avoidance ability, path planning ability and obstacle avoidance ability of the potential field ant colony algorithm were better than those of the traditional algorithm. It can be seen that the robot random planning algorithm based on local probability is an important research direction in the future, which is helpful to better realize the obstacle avoidance in complex scenes.

REFERENCES

- [1] Bi, H.B., Shang, W.L., Chen, Y.Y., & Wang, K.Z., (2022). Joint Optimization for Pedestrian, Information and Energy Flows in Emergency Response Systems with Energy Harvesting and Energy Sharing, *IEEE Transactions on Intelligent Transportation Systems*, Vol. 23, pp.22421-22435, United States.
- [2] Cai, Z., & Zheng, X., (2020). A Private and Efficient Mechanism for Data Uploading in Smart Cyber-Physical Systems, *IEEE Transactions on Network Science and Engineering (TNSE)*, Vol. 7, pp. 766-775, United States.
- [3] Chu, H., Li C.Y., Yang, K., & Wu, P.F., (2019). Research on Localization and Navigation Algorithm of Logistics Robot Based on Multi Sensor (多信息融合的物流机器人定位与导航算法的研究). *Machinery Design & Manufacture*, Vol. 4, pp. 240-243, Liaoning/China.
- [4] Dorigo, M., Birattari, M., & Stutzle, T., (2006). Ant Colony Optimization, *IEEE Computational Intelligence Magazine*, Vol. 1, pp. 28-39, United States.
- [5] Inbarani H.H., Azar A.T., & Jothi G., (2014). Supervised Hybrid Feature Selection Based on PSO and Rough Sets for Medical Diagnosis, *Computer Methods and Programs in Biomedicine*, Vol. 113, pp. 175-185, Netherlands.
- [6] Jahanbakht, M., Xiang, W., Hanzo, L., & Azghadi, M.R., (2021). Internet of Underwater Things and Big Marine Data Analytics—a Comprehensive Survey, *IEEE Communication Surveys and Tutorials*, Vol. 23, pp. 904-956, United States.
- [7] Lv, Z.H., Han, Y., Singh A.K., Manogaran G., & Lv, H.B., (2021). Trustworthiness in Industrial IoT Systems Based on Artificial Intelligence, *IEEE Transactions on Industrial Informatics*, Vol.17, pp. 1496-1504, United States.
- [8] Lv, Z., Kong, W., Zhang, X., Jiang, D., Lv, H., & Lu, X., (2020). Intelligent Security Planning for Regional Distributed Energy Internet, *IEEE Transactions on Industrial Informatics*, Vol. 16, pp. 3540-3547, USA.
- [9] Mirjalili, S., & Lewis, A., (2016). The Whale Optimization Algorithm, *Advances in Engineering Software*, Vol. 95, pp. 51-67, United Kingdom.
- [10] Patel, J., Sonar, P., & Pincioli, C., (2022). On Multi-Human Multi-Robot Remote Interaction: a Study of Transparency, Inter-Human Communication, and Information Loss in Remote Interaction, *Swarm Intelligence*, Vol. 16, pp. 107-142, United States.
- [11] Ru, F., Yu, Y.J., Wang, P., & Zhang, N., (2019). Path Planning Based on Multi-Optimization Rapidly-Exploring Random Tree Algorithm for Soccer Robot (基于多优化快速扩展随机树算法的足球机器人路径规划). *Science Technology and Engineering*, Vol. 28, pp. 189-195, Beijing/China.

- [12] Sami, H., Mourad, A., & El-Haj W., (2020). Vehicular-OBUs-as-on-Demand-Fogs: Resource and Context Aware Deployment of Containerized Micro-Services, *IEEE/ACM Transactions on Networking*, Vol. 28, pp. 778-790, United States.
- [13] Sarabu, H., Ahlin, K., & Hu, A., (2019). Graph-Based Cooperative Robot Path Planning in Agricultural Environments, *Proceedings of the 2019 IEEE/ASME International Conference on Advanced Intelligent Mechatronics (AIM)*, pp. 519-525, United States.
- [14] Sawadwuthikul, G., Tothong, T., Lodkaew, T., Soisudararat, P., & Dilokthanakul, N., (2022). Visual Goal Human-Robot Communication Framework with Few-Shot Learning: a Case Study in Robot Waiter System, *IEEE Transactions on Industrial Informatics*, Vol. 18, pp. 1883-1891, United States.
- [15] Sehestedt, S., Kodagoda, S., & Dissanayake, G., (2010). Robot Path Planning in a Social Context, *In 2010 IEEE Conference on Robotics, Automation and Mechatronics*, pp. 206-211, United States.
- [16] Shang, W., Gao, Z., Nicolo, D., Long, Y., Zhang, H., Guo, Z., & Ochieng, W., (2022). Benchmark Analysis for Robustness of Multi-Scale Urban Road Networks Under Global Disruptions, *IEEE Transactions on Intelligent Transportation Systems*, Vol. 24 pp. 15344-15354, United States.
- [17] Tiseni, L., Chiaradia, D., Gabardi, M., Solazzi, M., Leonardis, D., & Frisoli, A., (2021). UV-C Mobile Robots with Optimized Path Planning: Algorithm Design and on Field Measurements to Improve Surface Disinfection Against SARS-CoV-2, *IEEE Robotics & Automation Magazine*, Vol. 28, pp. 59-70, United States.
- [18] Wang, X., Pan, J.S., & Chu, S.C., (2020). A Parallel Multi-Verse Optimizer for Application in Multilevel Image Segmentation, *IEEE Access*, Vol. 8, pp. 32018-32030, United States.
- [19] Xia, C., Chen, X.M., & Xu, G.Y., (2016). The Path Planning Algorithm Studying about UAV Attacks Multiple Moving Targets Based on Voronoi Diagram, *International Journal of Control & Automation*, Vol. 9. pp. 281-292, Korea.
- [20] Xu, L., Fu, W.H., Jiang, W.H., & Li, Z.T., (2021). Mobile Robots Path Planning Based on 16-Directions 24-Neighborhoods Improved Ant Colony Algorithm (基于 16 方向 24 邻域改进蚁群算法的移动机器人路径规划). *Control and Decision*, Vol. 36, pp. 1137-1146, Liaoning/China.
- [21] Yang, S.M., Deng, B., Wang, J., Li, H.Y., Lu, M.L., Che, Y.Q., Wei, X.L., & Loparo, K.A., (2020). Scalable Digital Neuromorphic Architecture for Large-Scale Biophysically Meaningful Neural Network with Multi-Compartment Neurons, *IEEE Transactions on Neural Networks and Learning Systems*, Vol. 31, pp. 148-162. United States.
- [22] Yuan, F.L., & Zhu J.P., (2021). Optimal Path Planning of Mobile Robot Based on Improved Ant Colony Algorithm (基于改进蚁群算法的移动机器人最优路径规划). *Modern Manufacturing Engineering*, Vol. 1, pp. 38-47+65, Beijing/China.
- [23] Yu, T., Huang, J., & Chang, Q., (2021). Optimizing Task Scheduling in Human-Robot Collaboration with Deep Multi-Agent Reinforcement Learning, *Journal of Manufacturing Systems*, Vol. 60, pp. 487-499, United Kingdom.
- [24] Zhang, K., Liu, P.P., Kong, W.R., Zou, J., & Liu, M., (2017). An Improved Heuristic Algorithm for UCAV Path Planning, *Journal of Optimization*, pp. 8936164, United Kingdom.
- [25] Zhang, Z.W., Zhang, P., Mao, H.P., & Cheng, B.L., (2021). Path Planning of Mobile Robot Based on Improved A* Algorithm (改进 A*算法的机器人路径规划研究). *Electronics Optics & Control*, Vol. 28, pp. 21-25, Henan/China.
- [26] Zong, X., Luan, Y., Wang, H., & Li, S., (2021). A Multi-Robot Monitoring System Based on Digital Twin, *Procedia Computer Science*, Vol. 183, pp. 94-99, Netherlands.

DETECTION OF PESTICIDE RESIDUES IN WHITE TEA FRESH LEAVES BASED ON HYPERSPECTRAL AND ARTIFICIAL INTELLIGENCE MODELS

基于高光谱和人工智能模型白茶鲜叶农药残留检测

Weiqliang PI^{1,2}, Jingrui CHENG¹, Qinliang SUN^{1,2}, Guanyu LIU¹, Yong WANG¹, Rongyang WANG^{*1,2}

¹ Huzhou Vocational and Technical College, College of Intelligent Manufacturing and Elevator, Huzhou / China;

² Key Laboratory of Robot System Integration and Intelligent Equipment of Huzhou City, Huzhou / China

Tel: 15849125756; E-mail: piweiqliang20171@163.com

DOI: <https://doi.org/10.35633/inmateh-73-67>

Keywords: White tea, Hyperspectral, Pesticide residues, Deep learning

ABSTRACT

The detection of pesticide residues in white tea fresh leaves is an important step to ensure the quality safety of white tea finished products. Traditional detection methods are costly and inefficient to realize the demand for fast, low-cost, and accurate detection of pesticide residues in white tea fresh leaves. In this study, five types of white tea fresh leaf pesticide residue sample data were obtained using hyperspectral imaging technology for the high-frequency detected pesticides Glyphosate and Bifenthrin, and the SVM and 1D-CNN models were established to detect the samples after noise reduction processing and feature band screening methods. The study shows that the 1D-CNN model has better feature extraction ability, in which the SG-CARS-1D-CNN model has the highest detection accuracy, which is 94.62%, 95.12%, 94.35%, 94.95%, and 95.27% for the five type of species samples, respectively. This study provides pesticide residue detection for white tea fresh leaves based on the combination of hyperspectral data and an artificial intelligence model, which provides an intelligent, nondestructive, efficient, and high-precision pesticide residue detection model for white tea fresh leaves.

摘要

白茶鲜叶农药残留检测是保证白茶成品茶质量安全的重要环节。传统检测方法成本高、效率低，为了实现白茶鲜叶农药残留的快捷、低成本、准确的检测需求。本研究针对高频次被检出农药草甘膦和联苯菊酯，利用高光谱成像技术获得 5 类白茶鲜叶农药残留样本数据，经过降噪处理和特征波段筛选方法，建立支持向量机 (SVM) 和一维卷积神经网络模型 (1D-CNN) 对样本进行检测。研究表明，1D-CNN 模型具有更好的特征提取能力，其中 SG-CARS-1D-CNN 模型的检测精度最高，对 5 类种样本检测精度分别为 94.62%、95.12%、94.35%、94.95% 和 95.27%。本研究提供了一种基于高光谱数据与人工智能模型相结合的白茶鲜叶农药残留检测手段，为白茶鲜叶提供一种智能、无损、高效、高精度的农药残留检测模型。

INTRODUCTION

Tea is the second largest consumer beverage in the world, and China's tea production accounts for about 41.6% of the total global tea production, ranking first in the world, it is the largest consumer of tea in the world, as well as the second largest exporter of tea in the world (Huo et al., 2024).

Anji white tea is a specialty industry in Anji County, Huzhou City, Zhejiang Province, and has been selected as a national geographical indication product in China. Anji white tea is rich in tea polyphenols and tea pigments, which can enhance human immunity, and antioxidant, antimicrobial, and anticancer effects, which are beneficial to human health (Xia et al., 2024). According to the latest statistics, the planting area in the region is more than 200,000 mu, with an annual output of nearly 2,000 tons, an output value of nearly 3 billion yuan, and a comprehensive output value of 5 billion yuan (Mei et al., 2024).

Spraying pesticides is an important method of preserving the yield and increasing the yield of white tea. During the planting process of white tea, weeds competing for soil nutrients and insect pests nibbling have become two key factors affecting the yield of white tea. However, to simplify the management of weeds in the field, reduce labor costs, and increase tea production, some tea farmers have used organic pesticides, such as herbicides and insecticides, in the planting cycle of white tea (Lin et al., 2023). Some tea farmers are not trained in scientific management, and there is abuse and misuse of pesticides, which makes the pesticide residues of tea raw materials exceed the standard. Tea can be consumed directly after brewing in boiling water, and long-term consumption of tea with excessive pesticide residues can directly threaten the life and health of tea drinkers (Ali et al., 2021).

As food quality and safety have become more and more important to consumers, countries and regions such as the United States, Japan, Morocco, and the European Union have set strict Maximum Residue Limits (MRLs) for pesticides in tea (Luo *et al.*, 2023). In the past 10 years, more than 20 countries and regions have notified China of nearly 160 pesticide residues exceeding the MRLs in tea exported from China, which resulted in the return of tea exported from China and the denial of entry, causing huge economic losses. In the past decade, China has revised the National food safety Standard - Maximum Residue Limits of Pesticides in Food for five times (Yu *et al.*, 2024). Among them, the number of pesticide control categories for tea cultivation has been increased and the pesticide residue limits in tea have been reduced.

Excessive pesticide residues in tea are not only a problem of improper supervision of laws and regulations, but also a problem of insufficient detection means. After plucking, white tea leaves are purchased and processed by tea factories, and after withering and drying, they can be brought to the market (Xiang *et al.*, 2023). Therefore, efficient pesticide residue testing of white tea fresh leaves can ensure the food safety of finished tea from the processing source, and also reduce the loss of tea processing factories. This shows the importance of accurate, rapid, and nondestructive pesticide residue detection on white tea fresh leaves.

Currently, the most common methods for pesticide residue detection in tea are gas chromatography-mass spectrometry (Saitoshida *et al.*, 2015), liquid chromatography-mass spectrometry (Shizuka *et al.*, 2018; Ma *et al.*, 2018), and so on. The detection accuracy of the above means is high, but it requires standardized detection reagents, standardized detection processes, and professional detectors, and also has the limitations of destructive to samples, time-consuming, and high cost, etc. Currently, cumbersome detection means and high detection costs restrict the universality of pesticide residue detection in tea to a certain extent. As a supplement to gas chromatography and mass spectrometry detection technology, a non-contact, non-destructive, non-polluting, efficient, high-precision, intelligent means of pesticide residue detection in white tea is needed.

Spectroscopic analysis has gradually become a hot spot in the field of pesticide residue detection by its excellent performance, and the most widely used techniques are near-infrared spectroscopy (Arzu *et al.*, 2020), Raman spectroscopy (Mikac *et al.*, 2021), and hyperspectral imaging (Augustin *et al.*, 2023), etc. The spectral imaging technique is an emerging nondestructive testing technique with high spectral resolution, rich spectral bands, and integrated mapping. Hyperspectral imaging technology is an emerging non-destructive testing technology with high spectral resolution and rich spectral bands, which can provide rich spectral-spatial information. At present, hyperspectral imaging technology combined with traditional machine learning models has been applied in the detection of pesticide residues in agricultural products such as grains and vegetables. For example, pesticide residues such as Malathion and Chlorantraniliprole were detected on the surface of grain such as sorghum and corn (Lu *et al.*, 2021; Zhang *et al.*, 2023); pesticide residues such as imidacloprid and cypermethrin were detected on the surface of vegetables such as cucumber, broccoli, and spinach (Lu *et al.*, 2021; Wang *et al.*, 2024). However, research on hyperspectral pesticide residue detection models for tea using smarter deep learning models is significantly lagging behind other agricultural products.

In this study, white tea high-frequency detected pesticides as a research object, using hyperspectral imaging technology combined with noise reduction processing, and feature band screening, respectively, to establish machine learning and deep learning white tea fresh leaves pesticide residue detection model. The aim is to obtain a means of pesticide residue detection for white tea fresh leaves based on the combination of hyperspectral data and artificial intelligence modeling and to provide an intelligent, non-destructive, efficient, and high-precision pesticide residue detection method for white tea fresh leaves.

MATERIALS AND METHODS

Reagents and Samples

The fresh leaves of white tea used in this study were picked on the morning of April 8, 2024, in the white tea plantation of Anji County, Huzhou City, Zhejiang Province, China (30°28', 119°42' E). The tea plantation is a green tea plantation, i.e., no pesticide spraying or chemical fertilizer application. Two hundred white tea fresh leaves were selected as experimental samples.

The pesticides selected for this study were the high-frequency detected pesticides for white tea: the herbicide glyphosate and the insecticide bifenthrin. Glyphosate is one of the most widely used herbicides in the world and is very effective against perennial weeds. Bifenthrin is a new type of pyrethroid insecticide, which can effectively control aphids, mites, leafhoppers, and many other pests on tea trees.

Glyphosate reagent was used as bifenthrin standard (99.5% purity) from China National Pesticide Quality Supervision and Inspection Center (Shenyang); bifenthrin reagent was used as glyphosate standard (99% purity) from Shanghai Amperexperiment Technology Co. Concerning the latest Chinese national standard (Food Safety National Standard Maximum Residue Limits of Pesticides in Food), the maximum residue limits of tea were calculated to be 1MRLs, i.e., 1 mg/kg for glyphosate and 5 mg/kg for bifenthrin were calculated to be 1MRLs.

The two types of reagent standards were diluted to 1MRLs and 2MRLs to obtain four types of dilutions, i.e., the concentrations of glyphosate dilutions were 1 mg/kg and 2 mg/kg, respectively; the concentrations of bifenthrin dilutions were 5 mg/kg and 10 mg/kg, respectively, and the no-residue control was the laboratory grade one water. White tea leaves were immersed in the four types of dilutions, and 40 white tea leaves were immersed in each type of dilution so that the white tea leaves could fully absorb the pesticides, and a control group was formed with 40 white tea leaves immersed in laboratory grade I water.

Hyperspectral imaging techniques and sample data acquisition

The hyperspectral instrument is a Pika XC2 type hyperspectral instrument produced by Resonon Corporation of the United States, with a spectral range of 400 nm~1000 nm, a spectral resolution of 1.3 nm, the number of spectral channels is 447 bands, the number of spatial channels is 1600 bands, a scanning mode of linear push-scanning, and a selection of 23 mm lenses from Schneider, and the detailed technical parameters of hyperspectral imager are shown in Table 1.

Table 1

| Technical parameter of hyperspectral imager | |
|---|------------|
| Technical indicators | Parameter |
| Spectral range (nm) | 400 ~ 1000 |
| Spectral resolution (nm) | 1.3 |
| Number of spectral channels | 462 |
| Number of space channels | 1600 |
| Maximum frame rate (fps) | 165 |
| Camera shot | Schneider |
| Focal length (mm) | 23 |

The hyperspectral data acquisition platform is equipped with an alloy acquisition bracket to fix the hyperspectral imager; four halogen lamps are configured below the lens of the hyperspectral imager to simulate a natural light source; and a servomotor controls the linear movement speed of the sample tray and matches the frame rate of the hyperspectral imager. The hyperspectral data acquisition platform is shown in Figure 1.

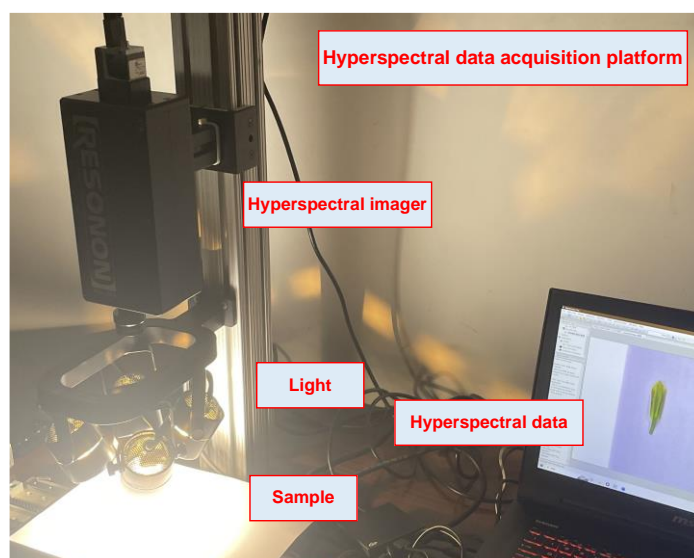


Fig. 1 - Hyperspectral data acquisition platform

To minimize the impact of ambient light on data quality, all light sources other than the four halogen lamps were turned off, curtains were used to block the external light and the computer screen light source, and the time of the collection experiment was set in the evening of the day when the tea leaves were collected. The hyperspectral data acquisition platform sequentially collected naturally dried white tea leaves after soaking in reagents, and a total of 200 hyperspectral data were collected.

Data preprocessing and regions of interest

A radiometric correction was performed using Spectral Pro software to convert the raw hyperspectral data DN to reflectance, and the radiometric correction equation is shown in Equation 1.

$$\lambda_t = \frac{DN_t - DN_d}{DN_w - DN_d} \times \lambda_w \tag{1}$$

where: λ_t is the reflectance of the degraded indicator feature in the original image, DN_t is the pixel luminance value of the degraded indicator feature in the original image, DN_w is the pixel luminance value of the standard whiteboard, and DN_d is the reflectance of the spectrometer under dark current.

The size of the radiometrically corrected image was 1000 lines×1600 samples×462 bands. To improve the efficiency of the subsequent data processing and at the same time to retain the continuity of the spatial information of the hyperspectral image, the bands with obvious noise effects were eliminated, and the consecutive 238 bands from band1-band227 (401.28 nm-701.37 nm) were retained with the Tea fresh leaf image as the center, cropping out the useless blank areas in the image, and finally obtaining 256 lines × 512 samples × 238 bands.

As shown in Fig. 2, five regions of interest (ROI) were selected inside the leaves of fresh tea leaves, and the size of the selected ROIs was 10 lines × 10 samples, totaling 100 pixels, and the average reflectance of the ROIs was calculated as the reflectance of the samples.

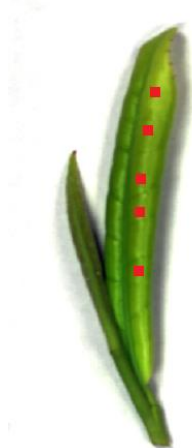


Fig. 2 - Selection of regions of interest for pesticide residues in white tea fresh leaves

The 5 classes of hyperspectral images are each selected 20 imaging effect better labeled regions of interest, a total of 100, a total of 500 ROIs are extracted, 80% of which are used as training samples, 20% of which are used as test samples, the distribution of the number of samples is shown in Table 2.

Table 2

| Distribution of pesticide residue sample size | | |
|---|--------------|-------------|
| Type of samples | Train sample | Test sample |
| Glyphosate-1MRLs (1mg/kg) | 80 | 20 |
| Glyphosate-2MRLs (2mg/kg) | 80 | 20 |
| Bifenthrin-1MRLs (5mg/kg) | 80 | 20 |
| Bifenthrin-2MRLs (10mg/kg) | 80 | 20 |
| No Residue (Laboratory Grade I water) | 80 | 20 |

Data Noise Reduction Processing

Hyperspectral raw data provides rich spectral information to provide a database for pesticide residue detection of white tea fresh leaves, but also contains a large amount of noise interference and sample gaps, as shown in Fig. 3(a). In this study, Savitzky-Golay (SG) smoothing and Moving Average (MA) smoothing methods were utilized for data Noise reduction processing.

Savitzky-Golay smoothing removes the interference of high-frequency noise from the data by polynomial least-squares fitting of the data within the moving window by a polynomial, which is set to $w=2$ in this study, and is shown in Equation 2; Moving Average smoothing calculates the mean fit by weighting the inter-spectral information, which can maximize the retention of the inter-band information of the spectrum while reducing the noise interference, and in this study, $w=2$ is set, which is calculated as shown in Equation 3 (Ma et al., 2023).

$$X_k^* = \frac{1}{H} \sum_{i=-w}^{i=w} X_{k+1} h_i \tag{2}$$

where: k is the center point of the window, h_i is the smoothing coefficient, $H = \sum_{i=-w}^{i=w} h_i$.

$$X_k^* = \frac{1}{2w+1} \sum_{i=-w}^{i=w} X_{k+1} \tag{3}$$

where: k is the center point of the window.

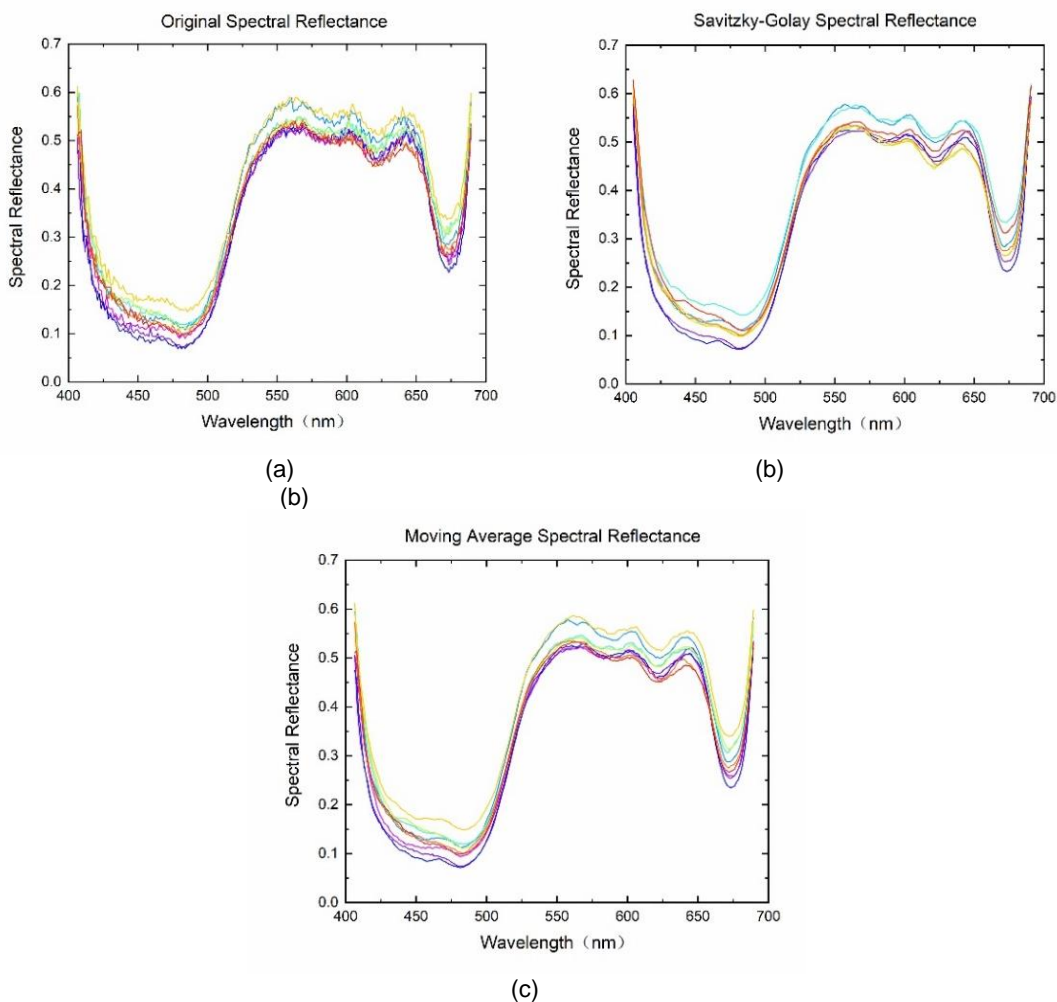


Fig. 3 - Noise Reduction Processing Spectral Curve
 (a) Original Spectral Reflectance; (b) S-G Spectral Reflectance; (c) MA Spectral Reflectance

As shown in Fig. 3, the spectral curves (Fig. 3-b, c) processed by the above two noise reduction methods have retained the spectral characteristics of the original spectral curves; compared with the original spectral curves (Fig. 3-a), they have become smoother, the noise interference has been significantly reduced, and the spectral difference between 420 nm-475 nm and 560 nm-620 nm has been enlarged, which possesses a good potential for data analysis.

Characteristic Band Screening

Hyperspectral data provides a large number of spectral bands, but too many spectral bands will lead to data redundancy, which is not conducive to further analysis of the data, in this study, Competitive Adaptive Re-weighted Sampling (CARS) and Successive Projections Algorithm (SPA) two Band feature extraction (Bfe) methods will be used for feature band screening to downsize the data (Wang et al., 2024).

CARS is a feature band screening method that combines Monte Carlo Sampling (MCS) and Partial Least Squares (PLS). In this study, the number of MCS is set to 50, cross-validation is performed 5 times, and the best feature band is obtained after 10 repetitions. SPA is a forward feature variable screening method that can effectively eliminate the original redundant information in spectral data. Based on the data processed by the two previous noise reduction methods, the number of feature bands after feature band screening is shown in Table 3, and the distribution of feature bands is shown in Fig. 4.

Table 3

| Number of characteristic bands screening | | |
|--|----------------------------|-----------------|
| Band feature screening | Noise reduction processing | Number of bands |
| CARS | SG | 32 |
| | MA | 40 |
| SPA | SG | 19 |
| | MA | 23 |

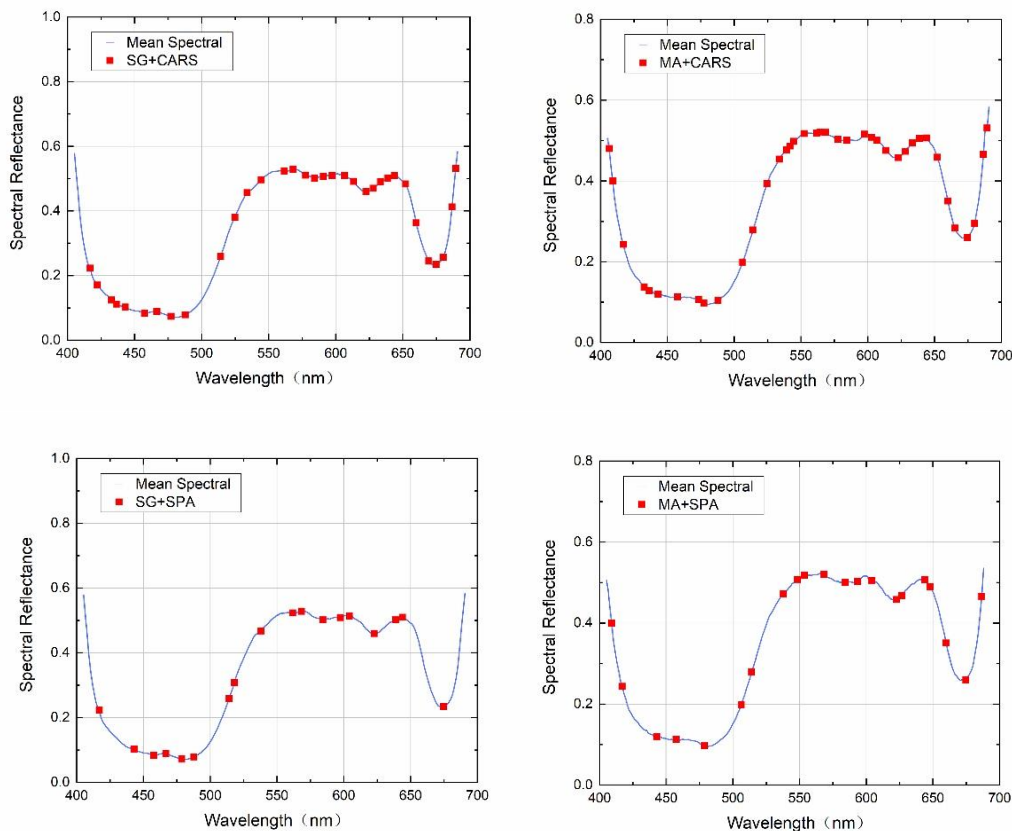


Fig. 4 - Distribution of characteristic bands

By comparison, it can be seen that the number of feature bands filtered by CARS is significantly larger than that of SPA, and combining the two noise reduction methods in the previous section, the number of bands filtered by MA-CARS is the largest, with 40 bands, and it is concentrated in the bands where the curvature of the spectral curve varies greatly; the number of bands filtered by SG-SPA is the smallest, 19 bands, and it is also distributed in the places where the curvature varies greatly, but it is more uniformly distributed compared

with that of CARS. The number of bands screened by SG-SPA is the least, 19, although they are also more distributed at the bands with larger curvature changes, compared with CARS.

Support Vector Machine Model

In this study, the classic model of machine learning-Support Vector Machine (SVM) will be used to detect the pesticide residue samples of white tea fresh leaves. SVM realizes the classification of different categories of samples by constructing the optimal hyperplane, which has the advantages of good small-sample detection ability, excellent generalization ability, avoiding dimensionality catastrophe, etc. The samples after noise reduction and feature band screening and the full band samples after noise reduction are used as input features of the SVM model.

The samples after noise reduction processing and feature band screening in the previous section and the full band samples after noise reduction processing are used as the input features of the SVM model, and the model performance evaluation of the SVM model Test sample detection is carried out by utilizing the precision of confusion matrix calculation (Equation 4).

$$\text{Accuracy} = \frac{Tp+Tn}{Tp+Tn+Fp+Fn} \times 100\% \quad (4)$$

where: T is the true target category; F is the false target category; p is the true prediction and n is the false prediction.

Table 4

| SVM test sample detection accuracy | | | | | | |
|------------------------------------|----------------------------|-----------------|-----------------|-----------------|-----------------|------------|
| Band feature screening | Noise reduction processing | Type of samples | | | | |
| | | Glyphosate-1MRL | Glyphosate-2MRL | Bifenthrin-1MRL | Bifenthrin-2MRL | No Residue |
| CARS | SG | 90.46% | 92.31% | 89.21% | 90.57% | 91.35% |
| | MA | 90.22% | 89.35% | 90.17% | 88.52% | 91.67% |
| SPA | SG | 91.54% | 92.37% | 90.18% | 91.86% | 92.83% |
| | MA | 91.37% | 91.92% | 90.02% | 90.77% | 91.42% |
| ALL | SG | 86.65% | 87.32% | 86.21% | 87.91% | 87.14% |
| | MA | 83.15% | 84.24% | 84.15% | 85.53% | 85.07% |

The detection accuracies of SVM models for different kinds of Test samples are shown in Table 4. It can be seen from the comparison that the detection accuracy of the samples with feature band screening is higher than that of the full band samples; compared with MA, the SG noise reduction process is more favorable to improve the detection accuracy; among them, the SG-SPA-SVM model has the highest detection accuracy, and the detection accuracies of the four kinds of pesticide residue samples are 91.54%, 92.37%, 90.18%, and 91.86%, and the detection accuracies of the no residue samples are 92.83%, which are 3.97%-5.69% higher than that of the full-band samples. The detection accuracy of the SG-SPA-SVM model is 92.83%, which is 3.97%-5.69% higher than that of the full-band samples.

Comprehensively, the SG-SPA-SVM model extracts fewer feature bands, but the band distribution is more reasonable. The method not only reduces redundant information and improves training efficiency, but also has excellent pesticide residue detection capability.

1D-CNN Model

In this study, deep learning methods will be also use to detect pesticide residue samples in white tea fresh leaves. The convolutional neural network has powerful data feature extraction ability and better generalization. In this study, a 1D-CNN model is built based on Pycharm, and the model structure is shown in Figure 5, which mainly consists of one input layer, six convolutional layers, and fully connected layers. The activation function is ReLU, the optimization algorithm is Adam, the initial learning rate is 0.001, and the pooling layer is Maxpool. The main parameters of the 1D-CNN model are shown in Table 5.

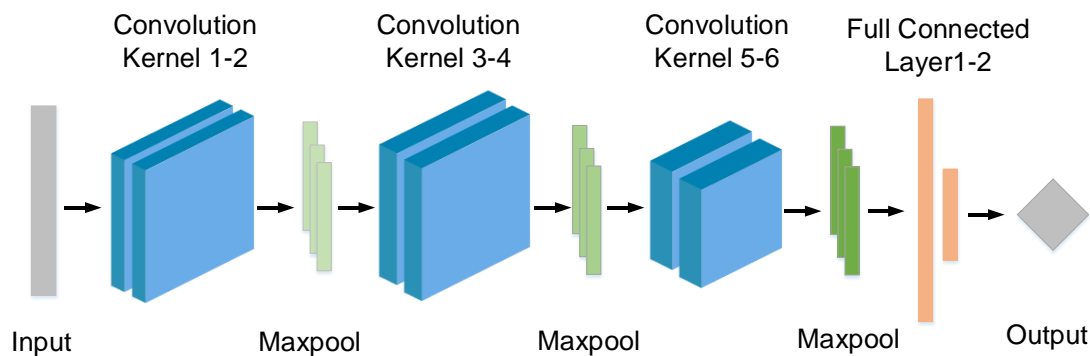


Fig. 5 - Schematic of 1D-CNN model structure

Table 5

| Main parameters of the 1D-CNN model | |
|-------------------------------------|---------------------------------------|
| Network layer | Parameters |
| Convolution layer 1-2 | Convolution kernel: 3×32×2, stride=1 |
| Convolution layer 3-4 | Convolution kernel: 3×64×2, stride=1 |
| Convolution layer 5-6 | Convolution kernel: 1×256×2, stride=1 |
| Full connected layer1-2 | Softmax: 1024-256 |

Table 6

| 1D-CNN model test sample detection accuracy | | | | | | |
|---|----------------------------|-----------------|-----------------|-----------------|-----------------|------------|
| Band feature screened | Noise reduction processing | Type of samples | | | | |
| | | Glyphosate-1MRL | Glyphosate-2MRL | Bifenthrin-1MRL | Bifenthrin-2MRL | No Residue |
| CARS | SG | 94.62% | 95.12% | 94.35% | 94.95% | 95.27% |
| | MA | 94.35% | 94.86% | 94.28% | 94.58% | 95.22% |
| SPA | SG | 93.26% | 93.54% | 93.62% | 93.89% | 93.72% |
| | MA | 93.42% | 93.36% | 93.57% | 93.92% | 93.68% |
| ALL | | 92.87% | 92.96% | 93.12% | 93.27% | 93.08% |

The samples after noise reduction processing and feature band screening in the previous section and the original samples are used as the input features of the 1D-CNN model respectively, and the obtained detection accuracies for different kinds of samples are shown in Table 6. It can be seen from the comparison that compared with the original samples, the samples with feature band screening have higher detection accuracy, CARS show better performance, and the SG-CARS-1D-CNN model has the highest detection accuracy, which is 94.62%, 95.12%, 94.35%, and 94.95% for four kinds of pesticide residue samples, and 95.27% for the no residue samples.

RESULTS

In this study, the white tea fresh leaf pesticide residue hyperspectral data samples were processed by means of noise reduction processing, feature band screening, etc., and the pesticide residue samples were detected using SVM and 1D-CNN models, respectively, and the detection accuracies of the models are shown in Table 7.

Table 7

| Comparison of SVM model and 1D-CNN model detection accuracy | | | | | | | |
|---|-----------------------|----------------------------|-----------------|-----------------|-----------------|-----------------|------------|
| Model | Band feature screened | Noise reduction processing | Type of samples | | | | |
| | | | Glyphosate-1MRL | Glyphosate-2MRL | Bifenthrin-1MRL | Bifenthrin-2MRL | No Residue |
| SVM | CARS | SG | 90.46% | 92.31% | 89.21% | 90.57% | 91.35% |

| Model | Band feature screened | Noise reduction processing | Type of samples | | | | |
|--------|-----------------------|----------------------------|------------------|------------------|------------------|------------------|------------|
| | | | Glyphosate -1MRL | Glyphosate -2MRL | Bifenthrin -1MRL | Bifenthrin -2MRL | No Residue |
| 1D-CNN | SPA | MA | 90.22% | 89.35% | 90.17% | 88.52% | 91.67% |
| | | SG | 91.54% | 92.37% | 90.18% | 91.86% | 92.83% |
| | | MA | 91.37% | 91.92% | 90.02% | 90.77% | 91.42% |
| | | SG | 86.65% | 87.32% | 86.21% | 87.91% | 87.14% |
| | | MA | 83.15% | 84.24% | 84.15% | 85.53% | 85.07% |
| | | SG | 94.62% | 95.12% | 94.35% | 94.95% | 95.27% |
| | CARS | MA | 94.35% | 94.86% | 94.28% | 94.58% | 95.22% |
| | | SG | 93.26% | 93.54% | 93.62% | 93.89% | 93.72% |
| | | MA | 93.42% | 93.36% | 93.57% | 93.92% | 93.68% |
| | | ALL | 92.87% | 92.96% | 93.12% | 93.27% | 93.08% |

Table 7 shows that the detection accuracy of the SG-SPA-SVM model is the best in the SVM model; the detection accuracy of the SG-CARS-1D-CNN model is the best in the 1D-CNN model; the detection accuracy of the 1D-CNN models is overall higher than that of SVM models; the SG noise reduction processing shows excellent potential in both kind of models.

Regarding the SVM models, feature band screening has a greater impact on the model detection accuracy, and the SG-SPA-SVM model improves the detection accuracy by 3.97%-5.69% compared to the SG-ALL-SVM model. Noise reduction processing has a smaller impact on the model detection accuracy, and the SG-SPA-SVM model improves the detection accuracy by 0.17%-1.41% compared to the MA-SPA-SVM model.

Regarding the 1D-CNN models, the ALL-1D-CNN model has shown promising detection potential; while noise reduction processing and feature band screening can further improve the detection accuracy of the model, the SG-CARS-1D-CNN model improves the accuracy compared to the ALL-1D-CNN model by 1.23% to 2.19%; compared with noise reduction processing, feature band screening can further improve the model detection accuracy.

CONCLUSIONS

In this paper, the white tea fresh leaf pesticide residue hyperspectral data samples were processed by means of noise reduction, feature band screening, etc., and the SVM and 1D-CNN models were utilized to realize the accuracy detection of white tea fresh leaf pesticide residue samples, respectively. The main results of this study are as follows:

1) Samples of pesticide residues in fresh white tea leaves were prepared, and hyperspectral data of the samples were collected; Through the combination of sample data noise reduction, feature band screening, and other means with deep learning, the optimal model for pesticide residue detection in fresh white tea leaves was obtained: The detection accuracy of SG-CARS-1D-CNN model for four pesticide residue samples was 94.62%, 95.12%, 94.35% and 94.95% respectively, and the detection accuracy of no residue samples was 95.27%.

2) By comparing the SVM models, the samples screened by feature bands can significantly improve the pesticide residue detection accuracy of the SVM model, and the noise reduction process can slightly improve the pesticide residue detection accuracy of the SVM model. Among them, the SG-SPA-SVM model has the highest detection accuracy, which is improved by 3.97%-5.69% compared with the SG-ALL-SVM model.

3) The deep learning 1D-CNN model has better feature extraction ability, and the original data without noise reduction processing and feature band screening show good detection accuracy in the ALL-1D-CNN model. Noise reduction processing and feature band screening can slightly improve the detection accuracy of the 1D-CNN model, in which the SG-CARS-1D-CNN model has the highest detection accuracy, with 4.62%, 94.86%, 94.28%, and 94.95% for the four pesticide residue samples, respectively, and 95.27% for the no residue samples, which is much better compared with the ALL-1D-CNN model, the detection accuracy was improved by 1.23%-2.19%.

In this study, the SG-CARS-1D-CNN model obtained has a good detection ability for pesticide residues in white tea fresh leaves, which provides a new method and means for the detection of pesticide residues in white tea fresh leaves based on hyperspectral data. It provides an accurate, rapid, and non-destructive detection idea for white tea fresh leaves pesticide residues, which is an effective supplement to the traditional detection means.

ACKNOWLEDGEMENT

This work was supported by the National Natural Science Foundation of China (52105283), the Huzhou Natural Science Foundation Project (2022YZ54), and the Huzhou Science and Technology Special Correspondent Project (2023KT33).

REFERENCES

- [1] Ali, H., Fereshteh, M., & Amin, M. K. (2021). Simultaneous multi-determination of pesticide residues in black tea leaves and infusion: a risk assessment study. *Environmental Science and Pollution Research*, Vol. 20(6), pp.13725-13735. <https://doi.org/10.1007/s11356-020-11658-3>
- [2] Arzu, Y., Gulgun, Y. T., & Huseyin, A. (2020). Determination of pesticide residual levels in strawberry (*Fragaria*) by near-infrared spectroscopy. *Journal of the Science of Food and Agriculture*, Vol. 100 (05): pp.1980-1989. <https://doi.org/10.1002/jsfa.10211>
- [3] Augustin, A., & Kiliroor, C. K. (2023). IoT-Based Pesticide Detection in Fruits and Vegetables Using Hyperspectral Imaging and Deep Learning. *Cognitive Computing and Cyber Physical Systems*, 536 (1): pp.74-83. https://doi.org/10.1007/978-3-031-48888-7_6
- [4] Huo, Z. H., Liu, C., Zhang, M., Chen, H. Q., & Liu, Z.H. (2024). Study on the Impact of Standards Differences in Pesticide Maximum Residue Limits on the Trade Efficiency of RCEP Members Exporting Tea from China: Based on the Stochastic Frontier Gravity Model (农药最大残留限量标准差异对我国茶叶出口 RCEP 成员国的贸易效率影响研究——基于随机前沿引力模型). *Journal of Tea Science*, Vol. 44 (03): pp.526-542. (In Chinese). <https://doi.org/10.13305/j.cnki.jts.2024.03.006>
- [5] Lin, W.P., Zheng, Z. Z., Ke, Z. F., Ma, Z. S., Zhang, T. J., Lin, Y. H., & Cao, X.J. (2023). Community and Malignant Species of Weeds at Tea Plantations in Chaozhou City (潮州茶区杂草类群调查与恶性杂草筛选). *Acta Tea Sinica*, Vol. 64 (03): pp.1-12. (In Chinese). <https://doi.org/10.20045/j.cnki.issn.2096-0220.2023.03.001>
- [6] Luo, D. W., Zhang, S., Hu, Z. H., Hu, H. M., Wang, F., & Luo, Z. Z. (2023). Study on 30 Pesticide Residues and Matrix Effects in Tea by SinChERS Purification Combined with UPLC-MS/MS Method (SinChERS 净化结合 UPLC-MS/MS 法测定茶叶中农药多残留的基质效应研究). *China Food Safety*, Vol. 21 (06): pp.1-5+18. (In Chinese). <https://doi.org/10.16043/j.cnki.cfs.2023.32.015>
- [7] Lu, X. H., Meng, Q. H., Tang, L., Huang, L., He, F. X., Wang, R. Y., & Zhang, K. Z. (2021). Application of hyperspectral technology in the detection of crop diseases and pesticide residues (高光谱成像在农产品疾病以及农药残留检测中的应用). *Journal of Food Safety and Quality*, Vol. 12 (11): pp.4566-4574. (In Chinese). <https://doi.org/10.19812/j.cnki.jfsq11-5956/ts.2021.11.036>
- [8] Ma, G. C., Zhang, M. L., Zhu, L., Chen, H. P. Liu, X., & Lu, C. Y. (2018). Facile synthesis of amine-functional reduced graphene oxides as modified quick, easy, cheap, effective, rugged and safe adsorbent for multi-pesticide residues analysis of tea. *Journal of Chromatography A*, Vol. 1531: pp.22-31. <https://doi.org/10.1016/j.chroma.2017.11.044>
- [9] Ma, S.B., & Guo, A. L. (2023). Non-destructive prediction of soluble solid content in kiwifruit based on vis/nir hyperspectral imaging. *INMATEH Agricultural Engineering*, Vol. 70 (2): pp.431-440. <https://doi.org/10.35633/inmateh-70-42>
- [10] Mei, Y., & Liang, X. (2024). Analysis of China's Tea Production, Sales, Import and Export Situation in 2023 (2023 年我国茶叶产销及进出口形势分析). *China Tea*, Vol. 46 (04): pp.18-26. (In Chinese).
- [11] Mikac, L., Kovačević, E., Ukić, S., Raić, M., Jurkin, T., Marić, I., Gotić, M., & Ivanda, M. (2021). Detection of multi-class pesticide residues with surface-enhanced Raman spectroscopy. *Spectrochimica Acta Part A: Molecular and Biomolecular Spectroscopy*, Vol. 252 (5): 119478. <https://doi.org/10.1016/j.saa.2021.119478>
- [12] Saitoshida, S., Nemoto, S., & Reshima, R. (2015). Multiresidue determination of pesticides in tea by gas chromatography-tandem mass spectrometry. *Journal of Environmental Science and Health*, Vol. 50 (11): pp.760-776. <https://doi.org/10.1080/03601234.2015.1058092>
- [13] Shizuka, S. S., Tomoko, H., Satoru, N., & Hiroshi, A. (2018). Multiresidue determination of pesticides in tea by liquid chromatography-high-resolution mass spectrometry: Comparison between Orbitrap and time-of-flight mass analyzers. *Food Chemistry*, Vol. 256 (4): pp.140-148. <https://doi.org/10.1016/j.foodchem.2018.02.123>

- [14] Wang, D., Luan, Y. Q., Tan, Z. J., & Wei, W. (2024). Pesticide Residue Detection in Broccoli Based on Hyperspectral Technology and Convolutional Neural Network. *Science and Technology of Food Industry*, Vol. 12 (11): 4566-4574. <https://doi.org/10.13386/j.issn1002-0306.2024020189>
- [15] Wang, X. H., Hao, M., Cao, X. T., & Zhang, Y. T. (2024). Detection of black heart disease in seed potato based on transmission spectroscopy technique. *INMATEH Agricultural Engineering*, Vol. 73 (2): pp.501-512. <https://doi.org/10.35633/inmateh-73-42>
- [16] Xia, C. Y., Yang, T. G., Zhai, J. W., Pu, L. L., Liu, Y. B., Wang, M., & Yang, H. (2024). Research progress of the impact of different varieties and process conditions on the quality of white tea quality formation (不同品种和工艺条件对白茶品质形成机制的影响研究进展). *Journal of Food Safety and Quality*, Vol. 64(02), pp.457-466. (In Chinese). <https://doi.org/10.19812/j.cnki.jfsq11-5956/ts.2024.04.013>
- [17] Xiang, L. H., Song, Z. S., Zhang, Y. G., Wang, L. L., Chen, J., & Chen, L. (2023). Effects of the leaf-spreading process on the quality of white tea during the withering of fresh tea shoots (茶鲜叶萎凋过程中摊青工艺对白茶品质的影响). *Transactions of the Chinese Society of Agricultural Engineering*, Vol. 39(07): pp.266-274. (In Chinese). <https://doi.org/10.11975/j.issn.1002-6819.202211049>
- [18] Yu, M. H., Zhang, T., Qin, Z. Y., Feng, Y. W., Yue, Y. Q., Yu, Z., Liang, P., Ni, D. J., & Zhang, D. (2024). Research Progress on Rapid Detection Technology for Pesticide Residues in Tea (茶叶中农药残留快速检测技术研究进展). *China Tea*, Vol. 46 (07): pp.1-10+32. (In Chinese).
- [19] Zhang, J. H., He, L., Hu, X. J., Peng, J. X., Xue, Q. Y., & Yan, S. C. (2023). Detection of pesticide residue types in sorghum based on hyperspectral imaging technology research. *Journal of Food Safety and Quality*, Vol. 12 (11): pp.4566-4574. <https://doi.org/10.19812/j.cnki.jfsq11-5956/ts.2023.20.016>

DESIGN AND EXPERIMENT OF AUTOMATIC FILM AND TAPE CUTTING SYSTEM FOR COTTON PRECISION FILM-LAYING HOLE SEEDER

棉花精量铺膜穴播机自动断膜带系统设计与试验

Shenghe BAI^{1,2)}, Yanwei YUAN^{1,2)}, Liang WEI²⁾, Gaoyong XING^{1,2)}, Liming ZHOU²⁾, Kang NIU²⁾, Bo ZHAO²⁾, Shuhui LI³⁾, Yuqi WANG²⁾, Wenyu TONG²⁾, Shuaiyang ZHANG²⁾, Lijing LIU^{1,2)}, Xuejun ZHANG⁴⁾, Yongliang YU⁵⁾

¹⁾ China Agricultural University, Beijing 100083, China

²⁾ Chinese Academy of Agricultural Mechanization Sciences Group Co., Ltd, National Key Laboratory of Agricultural Equipment Technology, Beijing 100083, China

³⁾ Gongzhuling City eight Wu town agricultural machinery technology extension service section, Ji Lin 136115, China

⁴⁾ College of Mechanical and Electrical Engineering, Xinjiang Agricultural University, Urumqi 830052, China

⁵⁾ Xinjiang Tiancheng Agricultural Machinery Manufacturing Co., Ltd., Tiemenguan 841007, China

Tel: +86-13815375524; E-mail: 13815375524@163.com

DOI: <https://doi.org/10.35633/inmateh-73-68>

Keywords: Cotton precision film-laying hole seeder; Automatic film and tape cutting; Wireless Control; Cut; Landfill

ABSTRACT

To achieve the process of automatic film cutting for cotton and improve the efficiency of cotton precision film hole seeding machine operation, this paper proposes a wireless handle button control method and designs an automatic film and tape cutting system for cotton precision film-laying hole seeder. The system includes electromagnetic integrated valve group, hole opener lifting hydraulic cylinder, membrane pressing hydraulic cylinder, multifunctional hydraulic cylinder for cutting film, strapping support hydraulic cylinder, hydraulic limit sensor, arc-shaped film cutting shovel reset sensor, wireless control handle for film cutting and film cutting controller. The system is based on the VisualTFT platform, equipped with a multi-functional touch screen. By integrating functions such as obtaining the forward distance of the machine, hydraulic control principles, and wireless control models for film cutting and burying, it achieves automatic cutting and burying of ground film and drip tape processes. The experiment verified the working performance of the automatic film cutting and feeding system of the cotton seed precision film mulching hole seeder and the results showed that the average monitoring accuracy of the machine's forward distance was 98.16%; the response time for controlling the film cutting belt and burying film belt was ≤ 0.78 s, and the execution time was ≤ 2.68 s; the success rate of cutting film strips was 100.00% and the success rate of burying film strips was above 98.33%, which met the operational requirements of automatic film strip cutting for precise cotton seeding film hole planting machines.

摘要

为实现棉花自动断膜带作业过程,提高棉花精量铺膜穴播机作业效率,提出无线手柄按键控制方式,设计了棉花精量铺膜穴播机自动断膜带系统,包括电磁一体化阀组、穴播器提升液压缸、压膜带液压缸、断膜带多功能液压缸、扎带支撑液压缸、液压限位传感器、弧形断膜带铲复位传感器、断膜带无线控制手柄及断膜带测控器等部分。基于 VisualTFT 平台,搭载多功能触摸屏,通过对机器前进距离获取、液压控制原理、断膜带无线控制模型等终端功能整体设计,实现了自动切断和填埋地膜、滴灌带过程。试验验证了棉花精量铺膜穴播机自动断膜带系统工作性能,结果表明:机器前进距离平均监测精度为 98.16%;断膜带及填埋膜带控制响应时间 ≤ 0.78 s,执行时间 ≤ 2.68 s;切断膜带成功率为 100.00%,填埋膜带成功率为 98.33%以上,符合实际棉花精量铺膜穴播机自动断膜带作业要求。

INTRODUCTION¹

Cotton is an important strategic commodity and economic crop in the country, with its planting area and output ranking among the top in the world (Liu W.J. et al., 2020). Xinjiang is the largest cotton-producing region in China, belonging to a typical arid and semi-arid area.

Shenghe BAI, Ph.D. Stud. Eng.; Yanwei YUAN*, Prof. Ph.D. Eng.; Liang WEI, M.S. Stud. Eng.; Gaoyong XING, Ph.D. Stud. Eng.; Liming ZHOU, Prof. Ph.D. Eng.; Kang NIU, Prof. Ph.D. Eng.; Bo ZHAO, Prof. Ph.D. Eng.; Shufeng LI, M.S. Stud. Eng.; Yuqi WANG, M.S. Stud. Eng.; Wenyu TONG, Ph.D. Stud. Eng.; Shuaiyang ZHANG, Ph.D. Stud. Eng.; Lijing LIU, Prof. Ph.D. Eng.; Xuejun ZHANG, Prof. Ph.D. Eng.; Yongliang YU, Prof. Ph.D. Eng.

The planting system adopts the precision hole seeding model with plastic film covering, which saves labor, reduces planting density, and improves efficiency. It is widely used because of its characteristics such as warming, moisturizing, and improving quality effects. It is an important way to realize the mechanized planting of cotton, which is of great significance for improving the quality and efficiency of cotton production (Yuan B.S. *et al.*, 2023; Zhang X.J. *et al.*, 2021; Zhang X.J. *et al.*, 2022). Therefore, the appropriate seeder is crucial for the precision hole seeding planting method with plastic film covering in Xinjiang agricultural areas.

Domestic and foreign scholars have conducted a large amount of research on precision hole seeding technology with plastic film mulching. In terms of cotton precision film mulching and hole seeding machine, it can be divided into pneumatic type and mechanical type according to the working principle. Yazgi *et al.*, (2014), studied the effect of different numbers of suction holes and operating speeds of the cotton vertical disc air-assisted planter on planting performance. Singh G. *et al.*, (2005), investigated the effects of seeding disc speed, vacuum level, and seed hole shape on cotton seeding quality. Academician Chen Xuegeng's team (Chen X.G. *et al.*, 2010; Lu Y.T. *et al.*, 2012) developed a precision cotton seed planter with air suction technology. It could achieve precise seed selection, cleaning, accurate sowing, and precise point seeding, solving the problems of air-suction precision hole seeder such as air leakage and high energy consumption. Zhang X.J. *et al.*, (2021), combined with the agronomic requirements of cotton seedling transplantation, designed a double-chamber rotary vertical round disc hole seeding planter for cotton. It solved the problems of poor sowing performance and high damage rate of the vertical round disc cotton planter. Wang J.K. *et al.*, (2006), Wang J.K., (2006), Wang J.K. *et al.*, (2011), designed a self-locking cotton seed precision planter with clamping mechanism. It added a protective device to reduce the problem of seed shedding caused by ground vibration and improved the overall stability of the seeding machine. Research on intelligent technology for mechanized cotton planting focused on automatic navigation and real-time monitoring of planting operation parameters (Chen H.Y. *et al.*, 2020; Zhang F. 2021; Zhao Y. *et al.*, 2018. Kaivosoja R. *et al.*, (2015), a GNSS error simulator being developed to improve tractor navigation and positioning accuracy. Erkan K. *et al.*, (2014), used distributed nonlinear predictive control method to solve the tractor trajectory tracking problem, which could improve control accuracy and robustness to environmental disturbances. Zhang X.J. *et al.*, (2022), developed a cotton precision dibbler seedling status monitoring system based on laser through-beam and Hall sensors; Cao Y. *et al.*, (2022), Cao Y. (2022), developed an automatic monitoring system for the seeding performance of cotton hole seeders using a high-speed CCD camera. Zhou Liming, (2014), developed a spiral capacitive seed sensor, which achieved the detection of seeding amount in precision cotton planters. In conclusion, the above research has laid a foundation for improving the performance of cotton seed metering and film mulching hole seeding machine, and has achieved good results. However, there are few reports on the research of cotton film cutting belts, and currently it mainly relies on manual operation, which affects the efficiency of machine operation and seriously hinders the rapid development of cotton precision film hole seeding machines.

To address the above issues, this article proposes a wireless remote control method using buttons for the cotton precision film mulch planting machine as the research platform. This article uses the STM32 microcontroller to build and develop an automatic film cutting system for cotton precision seeding and mulch punching machine and field performance verification tests are conducted to improve the quality of automatic film cutting and laying operation of cotton precision film hole seeding machine.

MATERIALS AND METHODS

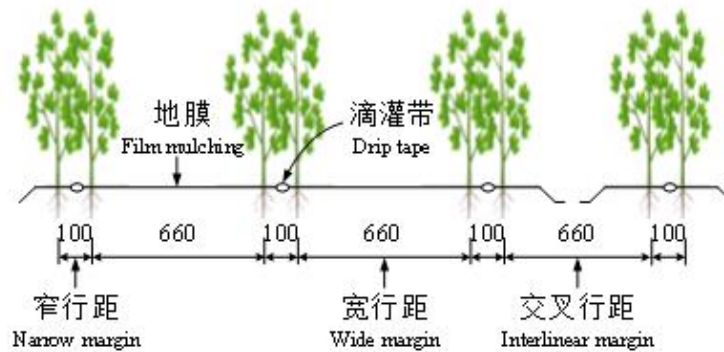
Overall design of cotton precision film mulching and hole seeding machine with film cutting and conveying unit

The cotton precision film laying and hole seeding machine with film cutting belt unit is mainly composed of two parts: mechanical structure and control system, which can be installed at the front or rear position of the hole seeder.

● **Mechanical structure**

The mechanical structure of the cotton precision mulch seed drill machine's breakage belt unit, located at the end of the cotton precision mulch seed drill machine, was selected as the research object. The narrow-wide spacing planting pattern is shown in Figure 1a. The unit position is shown in Figure 1b. This unit is composed of a frame, limit rods, curved breakaway strips, adjustable curved blades, and a fixed strap assembly, amongst other components (Figure 1b). This module can complete the separation and burial of drip irrigation film and plastic mulch in one go, thereby enhancing the efficiency of cotton seed drillers.

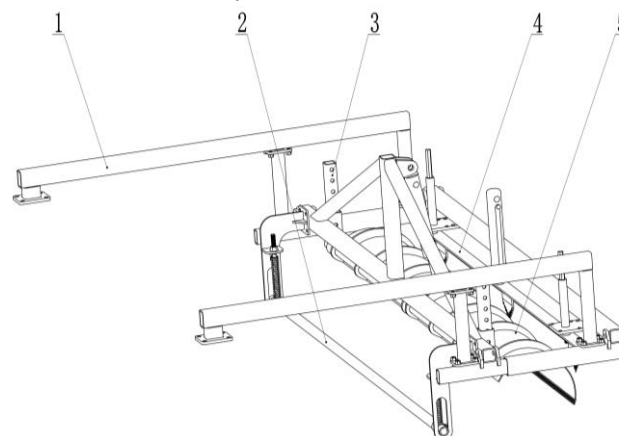
During operations, the machine is connected to a cotton precision-fertilizer-seeding machine via a setup. In this unit, the arc-shaped cutting blade is adjusted in depth by means of the adjustable arc-shaped shovel device prior to its insertion into the soil. The fixed tie assembly is first moved downward to ensure that the ground cover film and drip irrigation tape, which have already been laid out, do not shift during the breakage of the membrane. Subsequently, the curved breakaway strip is flipped down, completing the severance of the plastic film and drip irrigation strips connected to the machine. And then, a certain amount of soil is shoveled in, together with the limit rod, to firmly secure the plastic film and drip irrigation strip connected to the cotton precision seed drill machine, enabling the machine to shift its position for subsequent placement. The retaining strap assembly is repositioned in place. As the machinery is prepared for another round of mulching and drip irrigation, the curved breakaway strip is reset, and its interior soil is emptied out. It is ensured that it can hold down the newly laid plastic film and drip irrigation strips, completing the process of burying the plastic film and drip irrigation strips.



(a) Wide and narrow row planting pattern



(b) Installation position of unit mechanical structure



(c) Unit mechanical structure

Fig. 1 - Mechanical structure diagram of cotton precision film-laying hole seeder with film and tape cutting unit mechanical structure

1. Frame 2. Limit rods 3. Adjustable height mechanism for the curved blade 4. Fixed strap assembly 5. Curved ripper blade

● Control system

The overall structure of the cotton precision film hole seeding machine with automatic film cutting and control system is shown in Figure 2. The system mainly consists of an electromagnetic integrated valve group, a lift hydraulic cylinder for hole punching, a membrane pressing hydraulic cylinder, a multifunctional hydraulic cylinder for membrane cutting, a strap support hydraulic cylinder, hydraulic limit sensors, arc-shaped membrane cutting shovel reset sensors, wireless control handle for membrane cutting, and a measuring and control device for membrane cutting.

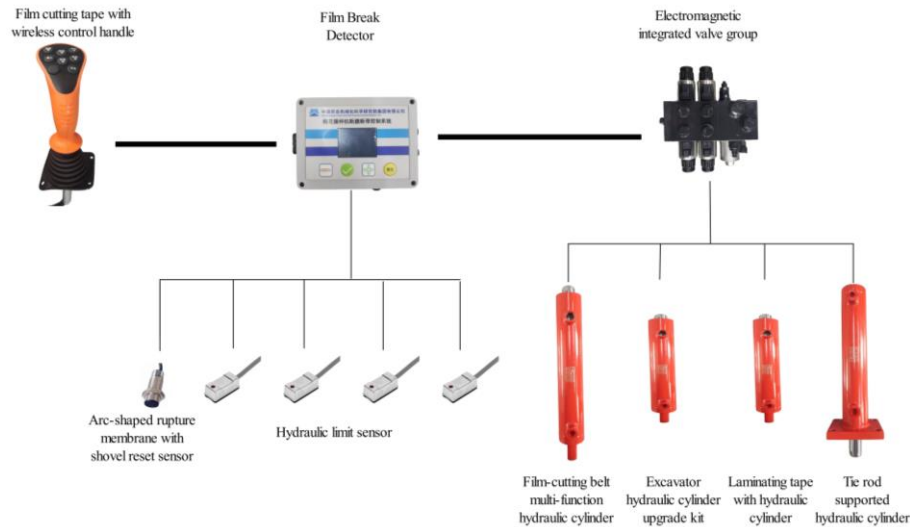


Fig. 2 - Overall Control System composition diagram of automatic film and tape cutting for cotton precision film-laying hole seeder

When the system starts working, first install the film cutting control terminal on the cotton precision film hole seeder frame through operation. It sets the distance parameter for the machine to move forward, and then initiates the reset operation of the arc-shaped film cutting shovel. This system completes the single-point 4-key action (① the hole opener raises the hydraulic cylinder and the zip tie support hydraulic cylinder extends out; ② the film pressing belt hydraulic cylinder and the film cutting belt multi-functional hydraulic cylinder extend; ③ the hole opener raises the hydraulic cylinder and the tie-down support hydraulic cylinder retracts; ④ the film pressing belt retracts with the hydraulic cylinder and the film cutting belt with the multi-function hydraulic cylinder) or single-point 2-key action (① the hole opener lifting hydraulic cylinder extends and the tie support hydraulic cylinder extends, the film pressing hydraulic cylinder extends, and the film cutting hydraulic cylinder extends; ② the hole puncher lifting hydraulic cylinder retracts, the tie support hydraulic cylinder retracts, the film pressing hydraulic cylinder retracts, and the film cutting multi-function hydraulic cylinder retracts) of the film cutting belt through the wireless control handle of the film cutting belt. The film cutting controller receives the wireless control handle button signal of the film cutting belt, and the received instructions correspond to the various oil circuit control signals mapped internally in the controller, analyzing whether it is a single-point 4-key action or a single-point 2-key action. If it is a single point 4-health action, the control valve group of the corresponding hydraulic cylinder control action is completed by combining the light-coupled output switch signal with the measuring controller. It controls the extension length of the hydraulic cylinder by detecting the signal from the hydraulic limit sensor. If the single-point 2-key action is completed after the first key is pressed to achieve automatic film cutting action, the arc film cutting belt shovel reset sensor signal needs to be waited for. It starts the next action when it reaches the set distance parameter for the machine to move forward, thus automatically completing the process of burying the plastic film and drip tape.

System hardware design

● Film Break Detector

The film tension controller is the core of the control system, consisting of a display control touch screen, controller, and membrane keyboard. It needs to receive and process signals from hydraulic limit sensors, arc-shaped film cutting shovel reset sensors, film cutting wireless control handles, etc. in real time.

It generates instructions in real time to control the switching of the oil circuit of the electromagnetic integrated valve group, thereby controlling the extension and retraction distances of each hydraulic cylinder. It sets the machine's forward distance parameters through manual key membrane keyboard or touch control touch screen. The controller uses the STM32F103RCT6 microcontroller produced by STMicroelectronics. It adopts the high-performance ARM® Cortex®-M3 core architecture, with 32-bit computing capability and interrupt masking feature. The display screen with touch control uses the serial display screen model DC24320M024 produced by Guangzhou Dacai. It has the advantages of good handling of workpiece movement and vibration, meeting the actual requirements of automatic film cutting with cotton precision film laying and hole seeding machine. The installation location is shown in Figure 3, and the performance parameters are shown in Table 1.



Fig. 3 - Installation diagram of film and tape cutting monitoring controller

Table 1

| Display control touch screen performance parameters | |
|---|-------------------|
| Parameter | Performance |
| Product Series | M Series |
| Central Processing Unit | 400MSOC processor |
| Size | 2.4 inches |
| Voltage | 5 V |
| Supporting PC software | VisualTFT® |
| Working frequency | 315 MHz |

● **Hydraulic limit sensor**

The extension distance of the hydraulic cylinder is an important detection parameter for automatic film cutting. The hydraulic limit sensors are installed on the multifunctional hydraulic cylinder with film breaking belt and the hydraulic cylinder with strapping support, located at the upper and lower limit positions of each hydraulic cylinder. It senses the extension position of the hydraulic cylinder through magnetic signal induction. This article features the contactless magnetic switch hydraulic limit position sensor produced by Zhiding Pneumatics. It has strong anti-interference ability and high cost performance. The installation location is shown in Figure 4, and the performance parameters are shown in Table 2.



Fig. 4 - Installation diagram of Hydraulic limit sensor

Table 2

Hydraulic limit sensor performance parameters

| Parameter | Performance |
|--------------------|---------------------------|
| Operating Voltage | 12-24 V wide voltage |
| Operating current | 2.5-100 mA |
| Temperature | -10-70°C |
| Action time | ≤1 ms |
| Protection circuit | Power Polarity Protection |
| Service life | Semi-permanent |
| Impact resistance | 1000 m/s ² |

● **Arc-shaped rupture membrane with shovel reset sensor**

The arc-shaped film strip shovel reset sensor uses a proximity switch sensor produced by Jingjiake. It features accurate detection and fast response speed. It detects metal from a distance, generates counting pulse signals, transmits them to the film strip controller, and calculates the distance the machine has traveled. The installation location is shown in Figure 5, and the performance parameters are shown in Table 3.



Fig. 5 - Installation diagram of Arcuate rupture membrane with shovel reset sensor

Table 3

Arcuate rupture membrane with shovel reset sensor performance parameters

| Parameter | Performance |
|-----------------------|------------------|
| Specifications | M12 non-embedded |
| Switching frequency | 1 KHz |
| Response Time | <0.5 ms |
| Delayed switch | <15% (Sr) |
| Repetitive accuracy | <3.0% (Sr) |
| Protection level | IP67 |
| Operating temperature | -25°C to +70°C |
| Connection method | D4 3*0.15 PVC 2M |

● **Electromagnetic integrated valve group**

The electromagnetic integrated valve group uses the electromagnetic multi-way valve produced by Hefei XieLi Hydraulic, which consists of one main oil passage and four branch oil passages. It includes directional solenoid valve, main relief valve, and flow divider valve. Each time it moves, the main oil supply must be opened and connected to the hydraulic interface of the tractor. The oil circuit is divided into four separate hydraulic cylinder extension and retraction circuits. It controls the hydraulic cylinder by switching the hydraulic oil circuit. It also adds dual hydraulic locks, main safety valves, and flow division function to prevent cylinder slippage and protect the entire machine system. It ensures that the working flow into the main valve does not exceed the standard, with the remaining flow being unloaded through the return oil, ensuring that there is no overheating on high-horsepower tractors. The installation location is shown in Figure 6, and the performance parameters are shown in Table 4.



Fig. 6 - Installation diagram of Electromagnetic integrated valve group

Table 4

Electromagnetic integrated valve group performance parameters

| Parameter | Performance |
|------------------------------------|---------------------|
| Rated flow | 50 L/min |
| Maximum flow rate of the work port | 40 L/min |
| Rated pressure | 31.5 MPa |
| Adjust pressure | 18 MPa |
| Operating Voltage | 12-24V wide voltage |
| Pressure loss | 0.7 MPa |

● **Hydraulic cylinder**

The hydraulic cylinder is connected to the electromagnetic integrated valve group via hydraulic oil pipes. The pressure film is connected with the hydraulic cylinder and the strap support hydraulic cylinder through the diversion valve, while the multifunctional hydraulic cylinder for film cutting is connected with the hydraulic cylinder for hole punching. Among them, the hydraulic cylinder for the film pressing belt and the multi-functional hydraulic cylinder for the film cutting belt are equipped with stainless steel double-acting hydraulic cylinders with magnetic ring induction produced by Zelco, matched with hydraulic limit sensors to detect the extension position of the hydraulic cylinder. The hydraulic double-acting oil cylinders for the film pressing with liquid hydraulic cylinder and the lifting hydraulic cylinder for the hole seeder are produced by Xingtai Tianjin. The installation location is shown in Figure 7, and the performance parameters are listed in Table 5.



Fig. 7 - Installation diagram of hydraulic cylinder

Table 5

Hydraulic cylinder performance parameters

| Name | Parameter | Performance |
|---|-----------|-------------|
| Film breakage detection multi-function hydraulic cylinder | Bore | 50cm |
| | Thrust | 3.9T |
| | Tension | 2.9T |
| Tie rod supported hydraulic cylinder | Bore | 50cm |
| | Thrust | 3.9T |
| | Tension | 2.9T |
| Laminating with hydraulic cylinder | Bore | 40cm |
| | Thrust | 3.12T |
| | Tension | 2.32T |
| Excavator hydraulic cylinder upgrade kit | Bore | 40cm |
| | Thrust | 3.12T |
| | Tension | 2.32T |

● **Film cutting tape with wireless control handle**

The wireless control handle for film cutting machine is produced by Henan Pengfei Intelligent Technology. It can complete single-point 4-key or single-point 2-key actions, with features of simple operation, reliable and stable performance, and good scalability. The installation location is shown in Figure 8, and the performance parameters are shown in Table 6.



Fig. 8 - Installation diagram of Wireless Control Handle for Film Cutting

Table 6

Wireless Control Handle for Film Cutting performance parameters

| Parameter | Performance |
|-------------------|---------------------|
| Key lifespan | 200,000 times |
| Operating Voltage | 12-24V wide voltage |
| Operating current | 50 mA |
| Working frequency | 315 MHz |

System Software Design

● **Overall design of terminal functions**

According to the functional requirements of the automatic film cutting control system, this paper designs the system implementation process. The principle of the drive circuit board is shown in Figure 9, and the implementation process is shown in Figure 10. Before starting the system, initialize the configuration, set system parameters, and obtain parameter values by parsing the corresponding protocol. Start the system and cyclically check the working status of each hardware component. After the control system is started, input the distance information of the machine's forward movement through the touch screen. It establishes the serial port connection relationship between the controller and the integrated electromagnetic valve group, hydraulic cylinder, hydraulic limit sensor, arc-shaped film breaker with shovel reset sensor, and the film breaker wireless control handle. The embedded host completes the automatic cutting and burying process of ground film and drip tape by obtaining the extension position of the hydraulic cylinder, the signal of the arc-shaped film cutting belt shovel reset, the signal of the wireless control handle button of the film cutting belt, and combining with the input parameters.

(1) Machine forward distance acquisition

The arc-shaped ruptured membrane belt shovel reset sensor is equipped with a Hall element inside. When the wheel hub passes through the sensor measurement area, a signal is generated due to the Hall effect. However, due to the slipping phenomenon of the ground wheel, the slip coefficient of the ground wheel must be considered.

The formula for calculating the actual distance traveled by the machine is as follows:

$$s = \frac{n\pi d(1 + \varepsilon)}{z} \tag{1}$$

where: s —Machine forward distance, m; n —Number of pulse signals; d —Wheel diameter, m; z —Number of wheel revolutions; ε —slip ratio, normally taken as 0.05~0.12 (Zhang J.C. et al., 2021).

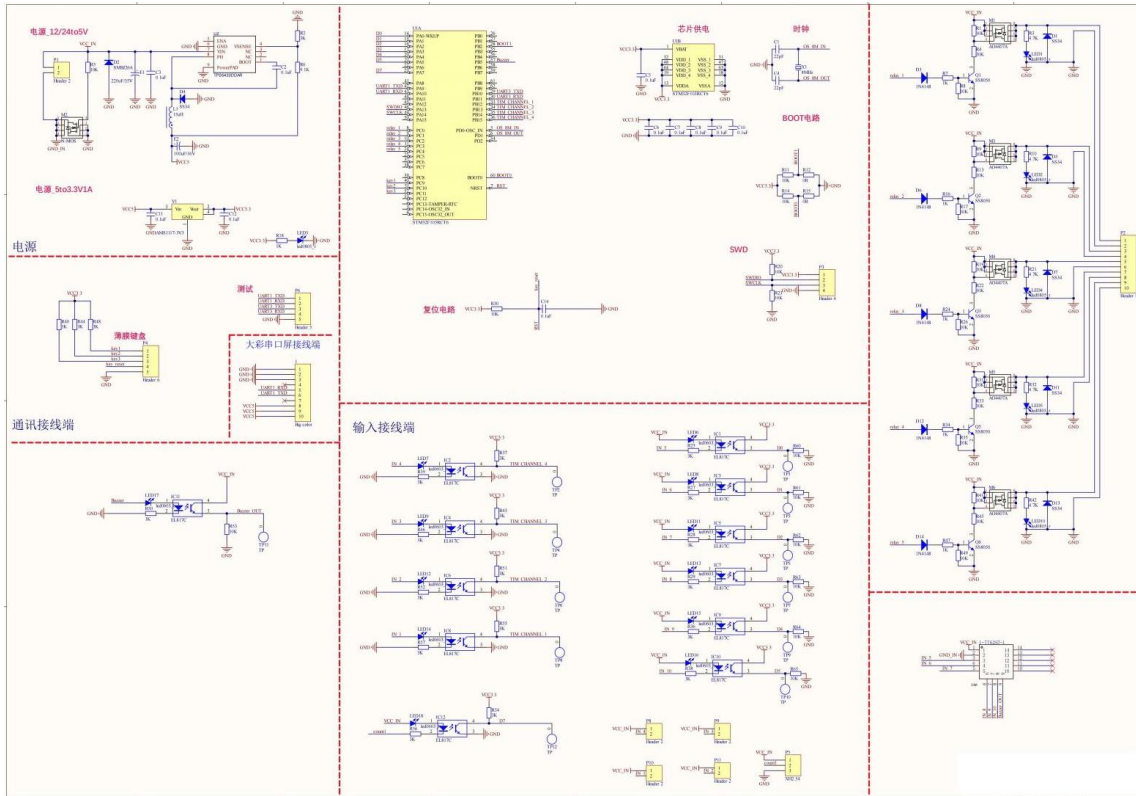


Fig. 9 - Schematic diagram of the driver circuit board

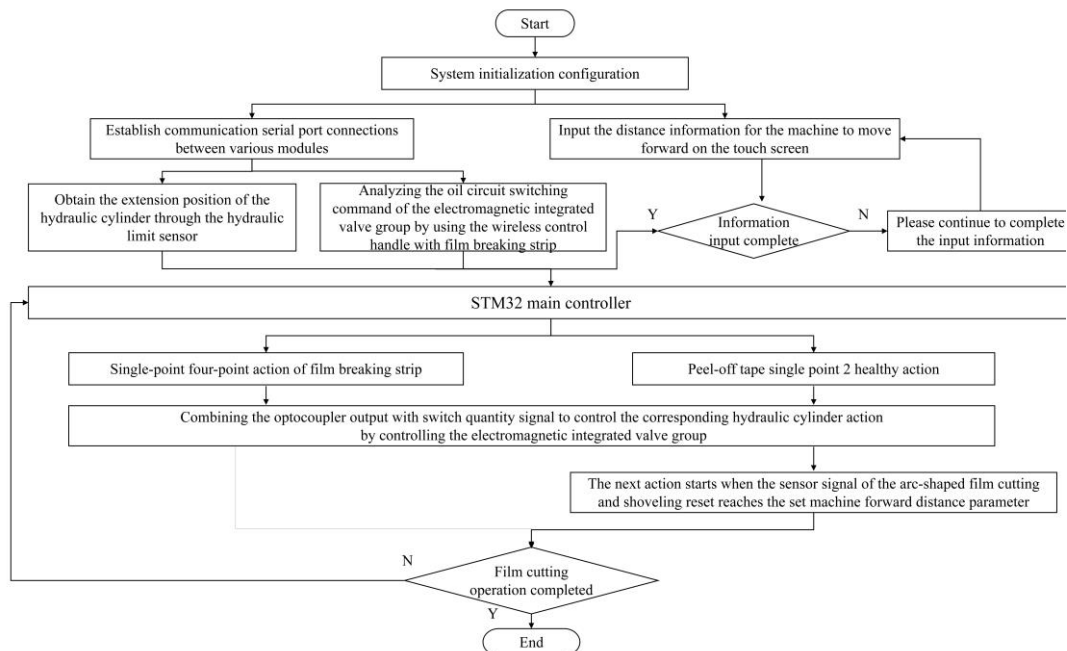


Fig. 10 - Control system implementation flowchart

(2) Hydraulic Control Principles

The hydraulic system is mainly composed of an electromagnetic integrated valve group, hydraulic cylinders, etc. Connect the main oil ports P and T of the integrated valve group to the tractor. The laminating tape hydraulic cylinder and the strapping support hydraulic cylinder are connected to the electromagnetic integrated valve group A1 and B1 for oil distribution. The multi-functional hydraulic cylinder with film cutting device and the lifting hydraulic cylinder with hole opener share the integrated electromagnetic valve group A2 and B2 oil outlets. It achieves the extension and retraction of the hydraulic cylinder through the directional valve. The hydraulic cylinder presses the film and drip tape to prevent rolling when cutting, ensuring the film and drip tape are securely held in place. The strap supports the hydraulic cylinder to tie down the drip tape and mulch film, ensuring that the laid mulch film and drip tape will not shift. Raise the hole opener to prevent the plastic film from wrapping around it. The multi-functional hydraulic cylinder with film cutting function completes the cutting, clamping, and connection of the film and drip tape to the machine, making it easier to re-lay after the machine is moved and then shovel a certain amount of soil to complete the burial process of the film and drip tape. The hydraulic control principle is shown in Figure 11.

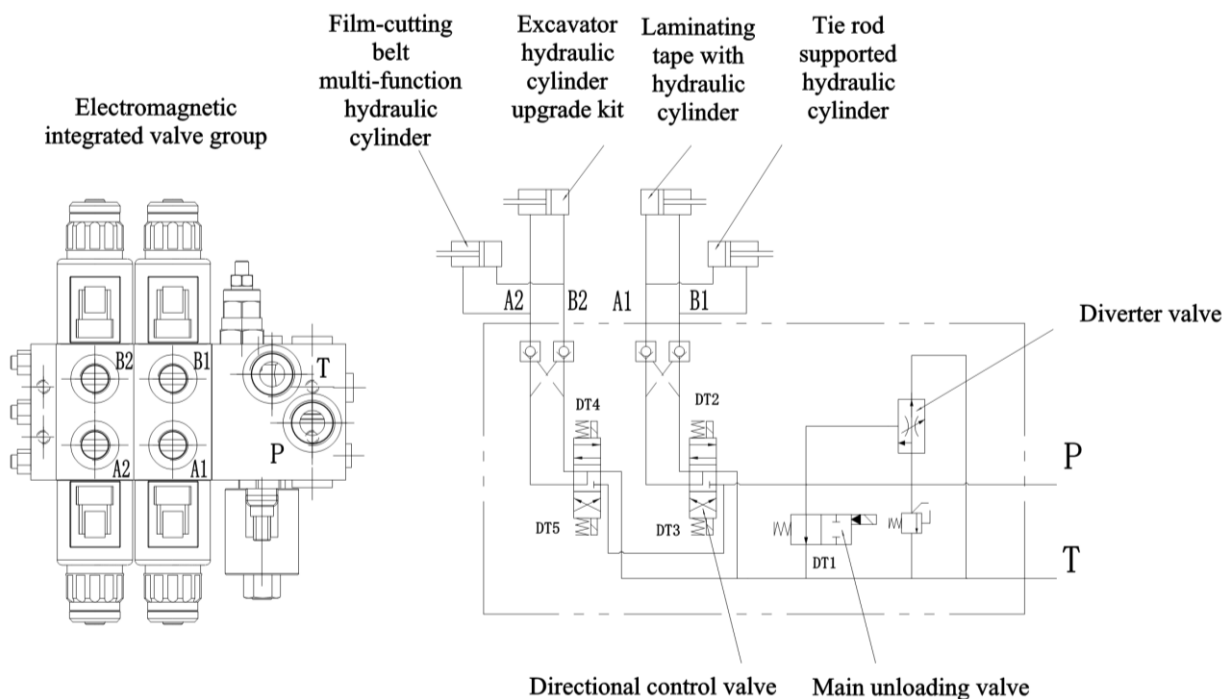


Fig. 11 - Hydraulic control schematic

(3) Film cutting with wireless control

The wireless control of the film cutting tape is achieved by first operating the transmission module through remote control, which controls the relay inside the receiving module of the film cutting tape controller to open or close, thereby enabling remote control of the electromagnetic integrated valve group. The receiving module has 8 input/output ports that can be collected. When the corresponding button on the joystick is pressed, the MCU receives an external interrupt signal indicating a change in the I/O status. After receiving the signal, the MCU triggers the corresponding electromagnetic integrated valve group to actuate, thereby driving the electromagnetic integrated valve group to complete the corresponding hydraulic cylinder extension or retraction process.

The transmission module is a 315M wireless transmission module, with a working frequency of 315 MHz. The transmission head uses SAW oscillation, which provides frequency stability and low temperature drift. When the ambient temperature is between $-25-85^{\circ}\text{C}$, the frequency drift is only $3\text{ ppm}/^{\circ}\text{C}$, suitable for multi-point remote control and data transmission systems, operating voltage between DC 3-5 V. The receiving module is a 351 MHz ASK superheterodyne decoding wireless receiving module, with a receiving sensitivity of -112 dBm , good selectivity, and suppression of spurious radiation. It operates at a voltage of 3-5 V.

The transmission module uses ASK modulation. When the data signal stops, the transmission current drops to zero. When the button is not pressed, the triode is cut off. The encoding integrated chip PT2262 is in power-off state, not transmitting signals. When the button is pressed, the transistor conducts, and the encoding integrated circuit PT2262 starts to work. According to the level of the data input terminal, the coding is performed, and a complete code word is composed of address code, data code, and synchronization code. The encoded signal is modulated through the 315M wireless data transmission module and transmitted to the surrounding space through the antenna. If the button is held down continuously, the transmitter module will continuously send out wireless signals.

It uses a 315M receiving module and decoding integrated chip PT2272-M4 in conjunction with D flip-flop 4013 and relay to form the receiving part circuit corresponding to the above-mentioned transmission module. When the wireless receiving module does not receive the 315 MHz signal in the space, it only outputs interference signals, all of which are low level. When the receiving module receives a 315 MHz signal, it processes it through amplification, frequency conversion, filtering, etc., and outputs a control signal. Only when the address pin of the PT2262 in the transmitting part matches, a high-level output is generated at the corresponding data pin. When the signal sent by the launch section is received, a rising edge of the level will be generated at the corresponding high level, and the controller will execute the action of the corresponding button's electro-magnetic integrated valve group.

● Display Interface

Based on the automatic film cutting control algorithm and flowchart, the system interface of the automatic film cutting control system for the precision cotton film laying and hole seeding machine is planned and designed on the VisualTFT platform. It is mainly used for displaying distance parameters, button single point interface, as shown in Figure 12. The execution distance parameter display interface allows the user to input the forward distance of the machine through touch operation. Automatically complete the process of burying the plastic film and drip tape when the set machine forward distance parameter is reached. The + and - buttons on the button single-point interface are used to increment or decrement the set forward distance of the machine. The ✓ button confirms the set distance for the machine to move forward, which will be maintained the next time the machine is turned on. The reset button resets the set forward distance of the machine and allows for reconfiguration.



Fig. 12 - System Settings Interface

Performance test design of monitoring system

● Experimental conditions

To verify the operation effect of the automatic film cutting control system for cotton precision seed furrow mulching machine, a cotton automatic film cutting control test was conducted on April 18, 2024 in Tiemenguan, Xinjiang. The supporting power is provided by the Dongfanghong 1504 tractor, using a cotton precision film hole seeder equipped with this system for automatic film cutting belt testing.

● Machine forward distance monitoring test

The field test sets the test distance at 10 meters, with manual measurement as the actual forward distance of the machine, and the value displayed on the human-machine interaction interface is the machine-measured forward distance. Five test distance points were selected from the test distance stage of 10 m, and each repeated test was conducted for 3 times. The average value was taken as the monitoring

test result of the machine advance distance. Calculate the monitoring accuracy by comparing the distance traveled by the machine with the actual value.

● **Control test of membrane strip and buried membrane strip**

To explore the accuracy and dynamic performance indicators of the automatic film cutting control of the cotton precision mulch hole seeder, automatic control performance tests and response tests were conducted. According to the national machinery industry standard JB/T7732-2006 "Film Mulching Seeder" (National Agricultural Machinery Standardization Technical Committee. 2006) and the national agricultural industry standard NY/T987-2006 "Quality of Film Mulching Hole Seeder Operation" (National Agricultural Machinery Standardization Technical Committee. 2006), the experimental process starts by powering on the system and resetting the data. Then start the machine to move forward, with distances of 200 m, 300 m, 400 m, 500 m, and 600 m respectively. The experiment was carried out in 5 groups, and the automatic film-breaking tape control system of cotton precision film-laying burrowing planter was started every 5 m. The repeatability test was carried out 3 times for each group, and the actual values of the successful times of film-breaking tape and the successful times of filling film tape were recorded.

During the automatic control response process of the film cutting tape and burial film tape, the response time and execution time both affect the performance of the test system. Therefore, the automatic control response test of the film cutting tape and burial film tape is set to be conducted 3 times, and the average value is taken as the result of the automatic control response test of the film cutting tape and burial film tape. The adjustment response time and execution time of the hydraulic cylinders for film pressing tape, tying tape support, multi-function hydraulic cylinder for film cutting tape, and hydraulic cylinder for hole opener lifting are recorded.

RESULTS AND ANALYSIS

Test results of machine forward distance monitoring

The test results of different machines' forward distance monitoring are shown in Table 7. The results indicate that the monitoring range of machine's forward distance was 96.53% to 99.60%, with an average monitoring accuracy of 98.16%.

The reasons for the error are: in the actual operation of the machine, due to the uneven surface of the cotton field, the machine is easily disturbed when the speed is slow; as the operating speed gradually increases, the impact of the uneven surface decreases.

Table 7

Test results of machine forward distance monitoring

| Actual distance traveled by the machine/m | Monitoring the distance traveled by the machine/m | Monitoring Accuracy/% | Average monitoring accuracy/% |
|---|---|-----------------------|-------------------------------|
| 2.02 | 2.09 | 96.53 | 98.16 |
| 4.15 | 4.05 | 97.59 | |
| 6.20 | 6.08 | 98.06 | |
| 8.10 | 8.18 | 99.01 | |
| 9.95 | 9.99 | 99.60 | |

Results of Control Tests for Geomembrane and Landfill Liner

The automatic control response test results of the film cutting tape and the burial film tape are shown in Table 8. Test results proves that the module meets the requirements of field operations.

Table 8

Response Test Results of Membrane Strips and Buried Membrane Strips

| Hydraulic cylinder | Stretch out | | Retract | |
|---|-----------------|------------------|-----------------|------------------|
| | Response Time/s | Execution time/s | Response Time/s | Execution time/s |
| Laminating with Hydraulic Cylinder | 0.65 | 1.16 | 0.63 | 1.20 |
| Tie rod supported hydraulic cylinder | 0.72 | 2.44 | 0.78 | 2.36 |
| Film-cutting tape multi-function hydraulic cylinder | 0.76 | 2.55 | 0.70 | 2.68 |
| Excavator hydraulic cylinder upgrade kit | 0.70 | 1.24 | 0.76 | 1.09 |

The field trial site was shown in Figure 13, the operation situation was shown in Figure 14, and the results were shown in Table 9. The test results show that the success rate of cutting film strips was 100.00%, and the success rate of burying film strips was above 98.33%, which meets the requirements for automatic cutting of film strips by the cotton seed precision film hole seeding machine. However, there is still room for improvement in the success rate and accuracy of the prototype film filling, and further research is needed on its working principle, hydraulic system, and control module to improve the accuracy of film cutting control.



Fig. 13 - Field test site



(a) Cutting film strip operation effect



(b) Effectiveness of landfill liner installation

Fig. 14 - Effectiveness of film cutting operation

Table 9

Test Results of Automatic Control Performance of Membrane Strips and Buried Membrane Strips

| Distance traveled by the machine/m | Total number | Number of successful membrane cutting operations | Number of successful landfill liner installations | Success rate of film breaking/% | Success rate of landfill liner/% |
|------------------------------------|--------------|--|---|---------------------------------|----------------------------------|
| 200 | 40 | 40 | 40 | 100 | 100 |
| 300 | 60 | 60 | 60 | 100 | 100 |
| 400 | 80 | 80 | 79 | 100 | 98.75 |
| 500 | 100 | 100 | 99 | 100 | 99.00 |
| 600 | 120 | 120 | 118 | 100 | 98.33 |

CONCLUSIONS

This article described an automatic film cutting belt control system designed for a precision film laying and hole seeding machine for cotton. Field tests were conducted to verify the reliability of the system operation.

(1) This article proposed a wireless joystick button control method, designed with the STM32 microcontroller as the core to control the cotton precision film laying hole opener system, which consisted of an electromagnetic integrated valve group, a hydraulic cylinder for lifting the seedling plate, a hydraulic cylinder for pressing the film, a multifunctional hydraulic cylinder for film cutting, a hydraulic cylinder for tying support, a hydraulic limit sensor, an arc-shaped film cutting shovel reset sensor, a wireless control joystick for film cutting, and a film cutting controller, aiming to improve the efficiency of cotton planting machines.

(2) Based on the VisualTFT platform, the software system developed for the automatic film cutting tape control system could complete the cutting and burying of drip tape and mulch film in one step through the wireless control module of the film cutting tape, achieving single-point 4-key action or single-point 2-key action.

(3) Field tests of the cotton precision film mulching and hole seeding machine with automatic film cutting and feeding system showed that the system worked stably and reliably. The average monitoring accuracy of the advance distance of the machine was 98.16%. The control response time of broken film belt and landfill film belt was ≤ 0.78 s, and the execution time was ≤ 2.68 s. The success rate of broken film tape was 100.00%, and the success rate of landfill film tape was more than 98.33%. The success rate of cutting film tape was 100.00%, and the success rate of landfill film tape was more than 98.33%, which was in line with the requirement of automatic cutting film tape of actual cotton precision film laying burrowing planter.

ACKNOWLEDGEMENT

This work was supported by the National Key Research and Development Program (Project No. 2022YFD2002400) and Key scientific and technological projects in key areas of Corps (Project No. 2023AB014).

REFERENCES

- [1] Cao Y., Guo W.S., Zhao P.F., Wang X.F., Wang L., Yang Q.N., (2022), Design of automatic detection system for cotton drill seed metering performance based on LabVIEW[J]. *Journal of Agricultural Mechanization Research*, 44(11): 135-141, Beijing / P.R.C.;
- [2] Cao Y., (2022), Design of Performance Testing System for Seed Metering of Dibbler Based on Machine Vision[D]. *Tarim University, Xinjiang / P.R.C.*;
- [3] Chen H.X., Han Y.C., Ma L., Yang B.F., LEI Y.P., Wang Z.P., Li Y.B., (2020), Application of smart agriculture in cotton production management[J]. *Cotton Science*, 32(03): 269-278, Henan / P.R.C.;
- [4] Chen X.G., Lu Y.T., (2010), Sowing performance of air-suction cylindrical cotton precision dibbler[J]. *Transactions of the Chinese Society for Agricultural Machinery (Transactions of the CSAM)*, 41(08): 35-38, Beijing / P.R.C.;
- [5] Erkan K., Erdal K., Herman R., Wouter S., (2014), Distributed nonlinear model predictive control of an autonomous tractor-trailer system[J]. *Mechatronics*, 24: 926-933, Oxford / UK.;
- [6] Kaivosoja J., Linkolehto R., (2015), GNSS error simulator for farm machinery navigation development[J]. *Computers and Electronics in Agriculture*, 119: 166-177, London / UK.;

- [7] Liu W.J., Fan Y.S., Dong Y.Q., Qu T., Zhu K., Liu Y.C., Wei F., (2020), Analysis and Suggestions on the Current Situation of Cotton Production in China[J]. *China Seed Industry*, (1): 21-25, Beijing / P.R.C.;
- [8] Lu Y.T., Li Y.X., Chen X.G., (2012), Design and experiment on air-suction cotton precision dibbler[J]. *Journal of Gansu Agricultural University*, 47(03): 129-133. Gansu / P.R.C.;
- [9] Singh R.C., Singh G., Saraswat D.C., (2005), Optimization of Design and Operational Parameters of a Pneumatic Seed Metering Device for Planting Cottonseeds[J]. *Biosystems Engineering*, 92(4): 429-438, San Diego, California / USA.;
- [10] Wang J.K. (2006), Study on Clamping and Self-Locking Cotton Precision Dibbler[D]. *Shihezi University*, Shihezi / P.R.C.;
- [11] Wang J.K., Kan Z., Wu J., Cha H.S., (2006), Design and experiment on clamping and self-locking cotton precision dibbler[J]. *Transactions of the Chinese Society for Agricultural Machinery (Transactions of the CSAM)*, (05): 54-56, 82. Beijing / P.R.C.;
- [12] Wang J.K., Guo K.Q., Lv X.M., Fu W., Qi C.S., (2011), Experiment and Improvement on Clamping Cotton Precision Seeding Dibbler[J]. *Transactions of the Chinese Society for Agricultural Machinery (Transactions of the CSAM)*, 42(04): 43-47, Beijing / P.R.C.;
- [13] Yazgla A., Degirmencioglu A., (2014), Measurement of seed spacing uniformity performance of a precision metering unit as function of the number of holes on vacuum plate[J]. *Measurement*, 56(10): 128-135, London / UK.;
- [14] Yuan B.S., Bai S.H., Niu K., Zhou L.M., Zhao B., Wei L.G., Liu L.J., (2023), Analysis on research progress of key technology and equipment of cotton planting mechanization[J]. *Transactions of the Chinese Society for Agricultural Machinery (Transactions of the CSAM)*, 39(06): 1-11, Beijing / P.R.C.;
- [15] Zhang X.J., Chen Y., Shi Z.L., Jin W., Zhang H.T., Fu H., Wang D.J., (2021), Design and experiment of double-storage turntable cotton vertical disc hole seeding and metering device[J]. *Transactions of the Chinese Society of Agricultural Engineering (Transactions of the CSAE)*, 37(19): 27-36, Beijing / P.R.C.;
- [16] Zhang X.J., Zhang H.T., Shi Z.L., Jin W., Chen Y., Yu Y.L., (2022), Design and experiments of seed pickup status monitoring system for cotton precision dibblers[J]. *Transactions of the Chinese Society of Agricultural Engineering (Transactions of the CSAE)*, 38(05): 9-19, Beijing / P.R.C.;
- [17] Zhang F., (2021), Analysis of the Application of Smart Agriculture in Cotton Production Management[J]. *Agricultural Engineering Technology*, 41(24): 33, 36, Henan / P.R.C.;
- [18] Zhang J.C., Yan S.C., Ji W.Y., Zhu B.G., Zheng P., (2021), Precision Fertilization Control System Research for Solid Fertilizers Based on Incremental PID Control Algorithm[J]. *Transactions of the Chinese Society for Agricultural Machinery (Transactions of the CSAM)*, 52(03): 99-106, Beijing / P.R.C.;
- [19] Zhao Y., Chen X.G., Wen H.J., (2018), Application of the development of precision agriculture and the China's Beidou satellite navigation System in agricultural production in The Xinjiang Production and Construction Corps[J]. *Journal of Shihezi University (Natural Science)*, 36(04): 397-404, Shihezi / P.R.C.;
- [20] Zhou L.M., (2014), Research on detection of yield and seeding rate of cotton based on capacitive method[J]. *China Agricultural University*, Beijing / P.R.C.;
- [21] Zhou L.M., Li S.J., Zhang X.C., Wang S.M., Yuan Y.W., Dong X., (2014), Detection of seed cotton mass flow based on capacitance approach[J]. *Transactions of the Chinese Society for Agricultural Machinery (Transactions of the CSAM)*, 45(06): 47-52, Beijing / P.R.C.;
- [22] ***National Agricultural Machinery Standardization Technical Committee., (2006), JB/T 7732-2006 Film planter[S]. *China Agriculture Press*, Beijing / P.R.C.;
- [23] ***National Agricultural Machinery Standardization Technical Committee., (2006), NY/T 987-2006 Quality of Film Mulching Seeder Operation[S]. *China Agriculture Press*, Beijing / P.R.C.;

CALIBRATION AND TESTING OF SALINE SOIL PARAMETERS BASED ON EDEM DISCRETE ELEMENT METHODOLOGY

基于 EDEM 离散元方法的盐碱土壤参数标定与测试

Xiaoning HE¹⁾, Shikuan MA¹⁾, Zhixin LIU¹⁾, Dongwei WANG¹⁾, Shuqi SHANG^{*1)}, Guanghui LI²⁾, Hongxiu LI²⁾

¹⁾ College of Electrical and Mechanical Engineering, Qingdao Agricultural University, Qingdao/ China ¹⁾

²⁾ Shandong Saline Modern Agriculture Co., Ltd, Dongying / China ²⁾

Corresponding author: Shuqi SHANG

Tel: +8618306391208; E-mail: 944286200@qq.com

DOI: <https://doi.org/10.35633/inmateh-73-69>

Keywords: EDEM; saline soil; Parameter calibration

ABSTRACT

In this study, saline soil parameters were calibrated based on EDEM discrete element method, soil density, soil elastic modulus, soil shear modulus, soil particle size distribution and Poisson's ratio were determined. The Hertz-Mindlin with Johnson-Kendall-Roberts (JKR) model was used to simulate the characteristics of soil stress and strain of particles under external forces. The JKR contact parameter between saline soil particles was used as a test factor, and the soil accumulation angle was used as a test index to carry out the saline soil contact parameter calibration test. It was finally determined that an elastic recovery coefficient of 0.262, a static friction coefficient of 0.263, a dynamic friction coefficient of 0.234, and a JKR surface energy of 10.084 were the optimal combinations of contact parameters for saline soils.

摘要

本研究基于 EDEM 离散元法对盐碱土壤参数进行标定, 通过测定土壤密度、土壤弹性模量、土壤剪切模量、土壤粒径分布及泊松比。采用 Hertz-Mindlin with Johnson-Kendall-Roberts 模型模拟颗粒在外力作用下的土壤应力与应变的特征。将盐碱土壤颗粒间的 Hertz-Mindlin with Johnson-Kendall-Roberts 接触参数作为试验因素, 以土壤堆积角作为试验指标, 进行盐碱土壤接触参数标定试验。最终确定弹性恢复系数 0.262、静摩擦系数 0.263、动摩擦系数 0.234、JKR 表面能 10.084 是盐碱土壤的最优接触参数组合。

INTRODUCTION

Studies have shown that analysing the interaction between saline soils and agricultural machinery is essential for developing agricultural machinery and equipment suitable for such lands (Xing et al., 2020; Xu et al., 2005; Abo-Elnor M. et al., 2004). The discrete element method can be used to simulate and analyse the interactions between agricultural bulk materials and machinery and equipment, which saves time and effort and provides more accurate data for the design of agricultural machinery and equipment due to its high visibility and accuracy compared to traditional field tests (Chen et al., 2021; Zeng et al., Yu et al., 2005; Tong J et al., 2010). In order to effectively predict the soil rheology under the interactions with touching soil components, parameter calibration and discrete element modelling of different types of soils are required, which have been studied by scholars at home and abroad. Song et al. (2022) and Han et al. (2021) determined the particle mechanics parameters of mulberry orchard soil and Xinjiang orchard deep applied bulk respectively, which can be used for the discrete element simulation analysis of the interaction between soil touching parts and soil of mulberry orchard tillage machinery in sandy loam soil and its structural optimization. Aikins et al. (2021), calibrated the contact parameters of Hysteretic Spring model and Linear Cohesion model for cohesive soil and verified their accuracy through the performance test of trencher. Qiu Y. et al. (2022), took brown soil as the research object and calibrated the relevant model parameters of brown soil by using EDEM simulation software, which provided basic data for the simulation study of cutting resistance of brown soil touching parts.

¹⁾ Xiaoning HE, Prof. Ph.D. Eng.; Shikuan MA, M.S. Stud. Eng.; Zhixin LIU, M.S. Stud. Eng.; Dongwei WANG, Prof. Ph.D. Eng.; Shuqi SHANG, Prof. Ph.D. Eng.

²⁾ Guanghui LI, M.S. Stud. Eng.; Hongxiu LI, M.S. Stud.

Luo *et al.*, (2018), proposed a method for the determination of the angle of repose of the bulk, through the JKR bonding model between the particles to reflect the matrix viscosity, and established a mapping relationship with the angle of repose. Zhang *et al.*, (2023) characterised the nature of the discrete elements of the soil in terms of several parameters by carrying out a stacking test with the angle of repose as the target. Tian *et al.*, (2021), used the Plackett- Burman test, the steepest climb test and so on to screen out the optimal range of values of the salient parameters, and then take the actual stacking angle as the target, and use the software optimisation function to optimise the salient parameters and get the optimal parameter combinations. Wang *et al.*, (2017), and Hao *et al.*, (2023), used the particle rheology parameter model for tyre compaction interaction simulation and rotary ploughing test to verify the validity of the calibrated results. Wang X. *et al.*, (2019), investigated the effect of different modelling particle radii on the interaction process by establishing a soil-plough interaction model, and obtained the optimal value of the particle radius of the soil model through the index of crushing and traction force and other indexes. Li J.W. *et al.*, (2019), calibrated the parameters of two kinds of clayey black soils with different water content in Northeast China, and provided simulation parameters for the design and optimisation of bionic drag reduction of touching parts of agricultural machinery under the operating conditions of clayey black soils in Northeast China.

Therefore, according to the characteristics of saline soil in Dongying City, based on the soil accumulation test, combined with experimental measurements, this study uses EDEM software to construct a soil simulation model, takes the accumulation angle as the evaluation index, and employs Design Expert software to determine the optimal values of soil simulation parameters, and carries out the calibration test of saline soil contact parameters, so as to provide the necessary discrete element simulation for the further research on the interaction between saline soil and soil touching components, basic parameters required for discrete element simulation.

MATERIAL AND METHODS

Particle modelling of saline soils

Five 100×100 cm sampling blocks were selected by five-point sampling method, as shown in Fig. 1. Soil particle size distribution determination, soil stacking angle determination and soil hardsetting determination were carried out at the sampling site for soil density determination, soil elastic modulus determination and soil shear modulus determination, respectively.

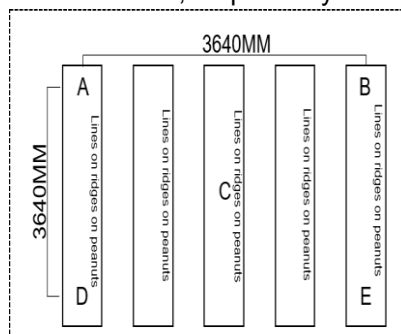


Fig. 1 – Field soil sampling

Density determination of saline soils

The cylinder method is chosen to determine the density of saline soils, the principle of the cylinder method is the ratio of the mass of the soil in the cylinder to the internal volume of the cylinder, the mass of the soil inside the cylinder can be weighed first after the mass of the cylinder and the soil and then subtracted from the mass of the cylinder itself, the formula for the calculation is:

$$\rho = \frac{m_1 - m_2}{V} \times 100\% \quad (1)$$

where:

ρ is the soil density, [%]; m_1 is the total mass of soil sample and ring cutter, [kg]; m_2 is the clean cylinder quality, [kg]; V is the ring cutter volume, [cm³].

Sampling in order to avoid different depths of the soil density is different, the depth of sampling will be divided into three levels, respectively, 0-5, 5-10, 10-15 cm. The same randomly take five samples in each layer, the average value, which can be obtained from the density of the soil layer, will be selected for five sampling. The five selected sampling blocks, are in accordance with the above steps for soil density determination test, the density data of different soil layers of each sampling block are shown in Fig. 2.

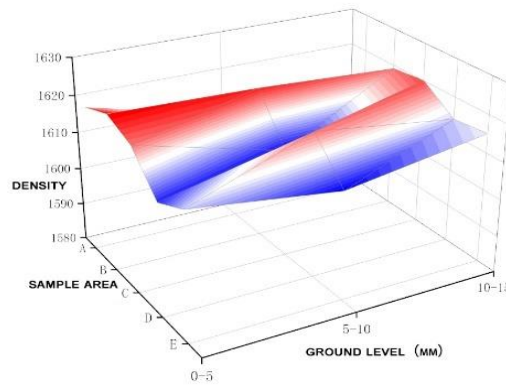


Fig. 2 – Soil Density by Survey Area

According to the data in Fig. 2, it can be seen that the location and depth 0-15 cm of saline soil have less effect on its soil density, so the soil density is taken as 1622.5 kg/m³.

Determination of shear modulus of saline soils

Soil shear modulus can be determined by straight shear test, the principle of soil direct shear test is based on Coulomb's law, given a vertical stress on the test soil sample, to determine the maximum shear force that can be withstood laterally by the test soil sample under the action of the vertical stress, so as to find out the coefficient of kinetic friction between saline and alkaline soils (Xiang et al, 2019).

This test is a fast shear test, using ZJ strain-controlled direct shear apparatus (referred to as direct shear apparatus in this paper). The test steps are as follows: four soil samples (soil samples) of saline-alkali soil were prepared by the ring knife of the direct shear apparatus in each sample area, and the ZJ strain-controlled direct shear apparatus was adjusted. As shown in Fig. 3, the water stone and the absorbent paper were placed in the interior of the shear box, and the ring knife with the soil sample was placed on the shear plate, and then the absorbent paper, the water stone and the shear box cover were placed in turn. The soil was pressed into the shear box with the box cover, and the pressure device was installed after the ring knife was removed, put the screws on the box cover and tighten the screws with a little force, rotate the handwheel clockwise, adjust the measuring force ring, set the percentage meter to zero, put the cover plate and the ball pressure frame in turn, and add weights to each group of soil specimens so that the vertical stress is 100 kPa, 200 kPa, 300 kPa, 400 kPa. Turn on the switch of the straight shear instrument so that the soil specimen is sheared in 3-5 minutes, and record the value of the gauge once every 1 s. Record the value of the recording gauge repeat the test 5 times and take the average value (Zhang et al, 2022).

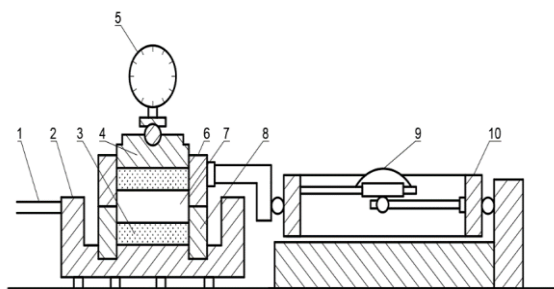


Fig. 3 – ZJ type strain control type straight shear instrument

1. axle; 2. base; 3. permeable stone; 4. piston; 5. gauge; 6. upper box; 7. soil sample; 8. lower box; 9. gauge; 10. gauge ring

The shear strength and the shearing displacement is given as:

$$\tau_0 = CR, \Delta L = tv \tag{2}$$

where:

τ_0 is the shear strength, [kPa]; C is the proving ring correction coefficient unit, 1.506; R is the proving ring readings, 0.01 mm; ΔL is the shear displacement, [mm]; t is the times, [s]; v is the shear rate, 0.08 mm/min.

Taking τ_0 as the vertical coordinate and ΔL as the horizontal coordinate, the relationship curve is obtained, as shown in Fig. 4.

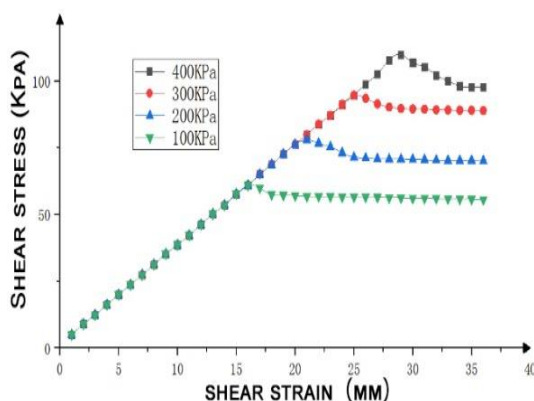


Fig. 4 – Shear Displacement-Shear Stress Relationship Curve

The magnitude of the measured soil shear strength is shown in Table 1. The shear modulus of saline soil is 3.76×10^7 Pa, it can be calculated from the shear displacement-shear stress relationship curve with Table 1:

$$G = \frac{\tau_0}{\Delta L} \tag{3}$$

Table 1

| Shear strength magnitudes | | | | |
|---|--------|-------|--------|--------|
| Vertical pressure (kPa) | 100 | 200 | 300 | 400 |
| Maximum deformation of measuring ring: | | | | |
| <i>R</i> (0.01 mm) | 33 | 48.5 | 68.5 | 91.5 |
| Shear strength | 49.698 | 73.04 | 103.16 | 137.80 |
| Quantitative force loop coefficient: <i>C</i> (kPa/0.01 mm) | | 1.506 | | |
| Gauge Ring Number | | 07439 | | |

Particle size distribution and Poisson's ratio of saline soil

The percentage of soil particle size distribution is the distribution ratio of soil particles in the field, and the soil texture can also be determined by the percentage of soil particle size distribution. The main steps of the soil particle size distribution percentage determination test are as follows: first, a certain number of soil samples needs to be taken and completely dried. The purpose of drying is to remove water from the soil in order to more accurately measure the particle size distribution of soil particles. Then, the JA21002 electronic precision balance (0.01 g) produced by Shanghai Jingtian Electronic Instrument Co., Ltd. was used to weigh and record the total mass of the sample. Finally, a series of standard sieves were used for screening, and the soil analysis sieve produced by Nanjing Soil Instrument Factory Co., Ltd. was used for screening. The apertures of each sieve were 2.0 mm, 1.0 mm, and 0.5 mm, respectively, fully vibrated for 20 minutes, and then the soil quality of each sieve surface was weighed by JA21002 electronic precision balance (He et al, 2021). The proportion of soil mass of each sieve to the total mass of the sample is calculated, which is the percentage of soil particle size distribution.

The calculation formula is:

$$x = \frac{m_i}{m_A} \times 100\% \tag{4}$$

where: *x* is the percentage by mass of soil particles of a given size, [%]; *m_i* is the mass of soil particles of a given size, [kg]; *m_A* is the total mass of soil sample, [kg].

Firstly, the soil pretreatment was carried out, and the collected soil was placed in a ventilated and dry room to air-dry for a period of time, and then the dried soil was crushed and passed through a standard sieve with a pore size of 2 mm, and stored in a container for spare.

Then the specific gravity meter method was used to determine the particle size distribution of the collected saline soil, the soil particle size percentage test was repeated five times for each sampling block, the average value of the soil particle size distribution percentage was calculated. After statistical analysis, the particle size distribution of saline soil in each sampling block is shown in Figure 5.

Table 2

| Name of soil particle composition and texture | | | | Soil condition |
|---|--------------------------|------------------------------|-------------------------|----------------|
| sampling area | Particle content / % | | | |
| | <0.002 mm (clay content) | 0.02~0.002 mm (silt content) | >0.02 mm (sand content) | |
| A | 12.7 | 30.6 | 56.7 | sandy loam |
| B | 11.8 | 32.1 | 56.1 | |
| C | 13.6 | 29.5 | 56.9 | |
| D | 12.2 | 31.9 | 55.9 | |
| E | 13.1 | 29.8 | 57.1 | |

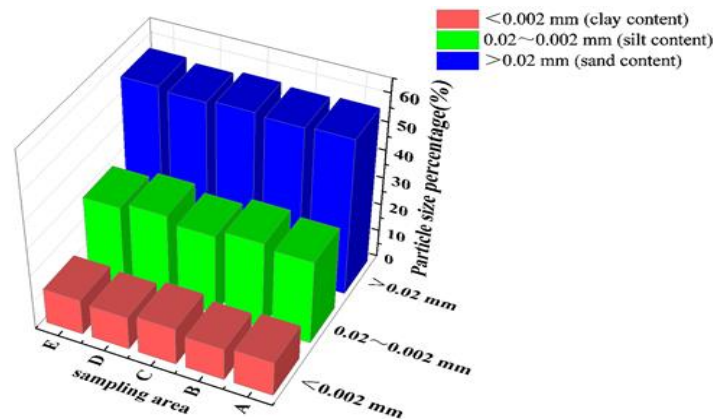


Fig. 5 – Saline soil particle size distribution

As can be seen from Figure 5, the saline soil grain size is mainly distributed in the >2 mm sandy loam interval, and the saline soil type can be obtained as chalky clay according to the International Soil Classification Standard.

The modulus of elasticity of soil is the instantaneous stress-strain modulus under un-lateralised conditions, and soil is not an ideal elastomer. A microcellular body taken from a laterally impermissible expansion compression soil sample was analysed under pressure in the Z-axis direction and was subjected to a positive stress of σ_z , and its positive stress in the horizontal direction was:

$$\sigma_x = \sigma_y = K_0 \sigma_z \tag{5}$$

Where:

K_0 is the coefficient of earth pressure at rest.

Analysing strain in the x-direction:

$$\epsilon_x = \frac{\sigma_x}{E_0} - \mu \frac{\sigma_y}{E_0} - \mu \frac{\sigma_z}{E_0} = 0 \tag{6}$$

The relationship between soil pressure coefficient and Poisson's ratio can be obtained by joining the two equations:

$$\mu = \frac{K_0}{(1+K_0)} \tag{7}$$

According to the type and state of the soil, the empirical value can be selected. The saline-alkali soil is silty clay, check 'mechanical soil dynamics' and 'soil mechanics', K_0 is 0.43, and the Poisson's ratio of the saline-alkali soil is 0.30.

Generate EDM particles

In conjunction with the determination of the soil intrinsic parameters, the saline soil intrinsic parameters were: density 1622.5 kg/m³, Poisson's ratio 0.30, shear modulus 3.76×10⁷ Pa. Simplified setting of the particle size and mass percentage of the soil were: 27% for 1 mm; 48.4% for 1.5 mm; and 24.6% for 2.0 mm.

Determination of particle contact models for saline soils

The JKR model can be used to simulate the characteristics of soil stress and strain of particles under external forces, which not only reflects the elasticity and plasticity of the particles, but also the bonding of the particles, which is shown schematically in Fig. 6.

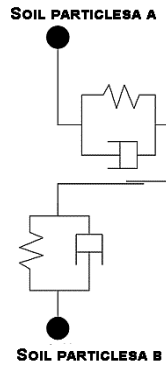


Fig. 6 – Schematic of soil particle contact modeling

To represent the cohesive force between particles, the normal elastic contact force of the JKR model is shown in Formula (8). The equivalent elastic modulus can be expressed by Formula (9). The equivalent contact radius is shown in Formula (10). The tangential overlap and normal overlap satisfy Formula (11).

$$F_{JKR} = -4\sqrt{\pi\gamma E^*} a^{\frac{3}{2}} + \frac{4E^*}{3R^*} a^3 \tag{8}$$

$$\frac{1}{E^*} = \frac{1-\nu_1^2}{E_1^*} + \frac{1-\nu_2^2}{E_2^*} \tag{9}$$

$$\frac{1}{R^*} = \frac{1}{R_1} + \frac{1}{R_2} \tag{10}$$

$$\delta = \frac{a^2}{R^*} - \sqrt{\frac{4\pi\gamma a}{E^*}} \tag{11}$$

where:

F_{JKR} is the JKR normal contact elastic force; E^* is the equivalent elastic modulus, [Pa]; R^* is the equivalent contact radius, [m]; a is the tangential overlap amount, [m]; γ is the surface tension, [N/m]; E_1^* is the elastic modulus of particle 1, [Pa]; E_2^* is the elastic modulus of particle 2; ν_1 is the Poisson's ratio of particle 1; ν_2 is the Poisson's ratio of particle 2; R_1 is the contact radius of particle 1, [m]; R_2 is the contact radius of particle 2, [m].

If there is no contact between the particles, the particles have a cohesive force that attracts each other. The maximum gap between the particles with non-zero cohesion is calculated according to Formula (12).

$$\delta_c^* = \frac{a_c^2}{R^*} - \sqrt{\frac{4\pi\gamma a_c}{E^*}} \quad a_c = \frac{9\pi\gamma R^{*2}}{2E^*} \left(\frac{3}{4} - \frac{1}{\sqrt{2}} \right) \tag{12}$$

where:

δ_c is the maximum normal gap when there is non-zero cohesion between particles, [m]; a_c is the maximum tangential gap when there is non-zero cohesion between particles, [m].

The saline-alkali soil has the characteristics of compaction and stratification. The Hertz-Mindlin with bonding contact model is selected for the saline-alkali compaction layer. As shown in Fig. 7, in this paper, the soil particle radius is set to 1 mm, and the particle bond radius is 2 mm. The normal stiffness per unit area of the model is 3.5×10^7 N/m³, the tangential stiffness per unit area is 2.4×10^7 N/m³, the critical normal stress is 3.1×10^7 Pa, and the critical tangential stress is 2.1×10^7 Pa.

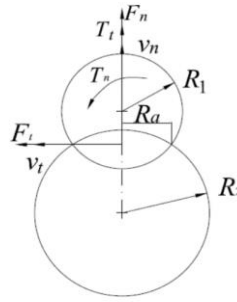


Fig. 7 – Force diagram of bonded bond

When the normal stress and tangential stress between soil particles reach a certain extreme value, the bonding bond between soil particles will break, assuming that the normal stress and tangential stress are σ_{max} and τ_{max} . According to Formula (13), when the bonding bond breaks, it satisfies Formula (14), so as to determine the critical normal stress and critical tangential stress at the time of fracture.

$$\begin{cases} \delta F_n = -v_n k_n A \delta_t \\ \delta F_t = -v_t k_t A \delta_t \\ \delta M_n = -w_n k_t A \delta_t \\ \delta M_t = -w_t k_t \frac{J}{2} \delta_t \\ A = \pi R_B^2 \\ J = \frac{1}{2} \pi R_B^4 \end{cases} \quad (13)$$

$$\begin{cases} \sigma_{max} < \frac{-F_n}{A} + \frac{2M_t}{J} R_B \\ \tau_{max} < \frac{-F_t}{A} + \frac{M_n}{J} R_B \end{cases} \quad (14)$$

where: F_n is the normal contact force, [N]; F_t is the tangential contact force, [N]; v_n is the normal velocity, [m/s]; v_t is the tangential velocity, [m/s]; k_n is the normal stiffness, [N/m]; k_t is the tangential stiffness, [N/m]; w_n is the normal angular velocity, [rad/s]; w_t is the tangential angular velocity, [rad/s]; A is the unit contact area, [mm²]; J is the moment of inertia, [mm⁴]; M_t is the normal torque between particles, [N·m]; M_n is the tangential torque between particles, [N·m]; δ_t is the time step, [s]; R_B is the particle bond radius, [mm].

Saline soil calibration test

The JKR contact parameters (coefficient of elastic recovery, coefficient of static friction, coefficient of kinetic friction, and JKR surface energy) between the saline soil particles were used as the test factors, and the soil stacking angle was used as the test index for the saline soil contact parameter calibration test (Wang et al, 2019). The experimental principle is shown in Fig.8. The inclination measuring instrument is placed above the soil plate, and the inclination measuring instrument is adjusted to 0°. Then the funnel of organic glass is placed on the test frame, so that the saline-alkali soil falls naturally from the upper end of the funnel under the action of gravity. After the soil falls off, the soil accumulation angle is measured. The soil accumulation angle was measured four times for each of the five sampling blocks, recorded and statistically analysed as shown in Fig. 9, which gives an actual soil accumulation angle of 36.6° with a standard deviation of 0.45.

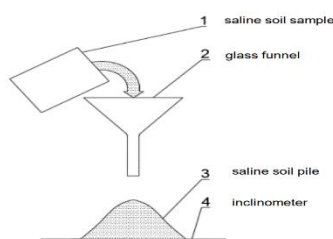


Fig. 8 – Principle of determination of accumulation angle of saline soil

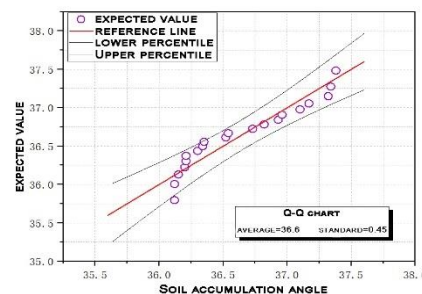


Fig. 9 – Statistical Analysis of Soil Stockpile Angles

Referring to the GEMM database in EDEM2021, the recommended range of values for the contact parameters was obtained based on the basic physical parameters of saline soils and the soil accumulation angle, with the factor codes as shown in Table 2, and the contact parameter calibration test was conducted for saline soils according to the four-factor quadratic orthogonal rotational combination test programme.

Table 2

| Code | A | B | C | D |
|------|------|-------|-------|-------|
| +2 | 0.40 | 0.30 | 0.45 | 14.5 |
| +1 | 0.33 | 0.238 | 0.363 | 11.75 |
| 0 | 0.26 | 0.175 | 0.275 | 9 |
| -1 | 0.19 | 0.113 | 0.188 | 6.25 |
| -2 | 0.12 | 0.05 | 0.10 | 3.5 |

Simulation test of soil accumulation angle

The simulation test of soil stacking angle was carried out in EDEM2021 at a ratio of 1:1. The other contact parameters in the simulation test were obtained by consulting the mechanical design manual, and the contact parameters between them can be obtained by referring to the relevant literature, and the simulation parameters are shown in Table 3.

Table 3

| analogue parameter | numerical value | analogue parameter | numerical value |
|----------------------------------|--------------------------|--|-----------------|
| Saline soil density | 1622.5kg/m ³ | Collision recovery coefficient between saline soil and -65Mn steel | 0.12 |
| Poisson's ratio for saline soils | 0.30 | Coefficient of static friction between saline soil-65Mn steel | 0.39 |
| Shear modulus of saline soils | 5.74×10 ⁶ Mpa | Sliding friction coefficient between saline soil-65Mn steel | 0.08 |
| 65Mn steel density | 7830kg/m ³ | Coefficient of recovery for collisions between saline soils and -glass | 0.15 |
| Poisson's ratio of 65Mn steel | 0.29 | Coefficient of static friction between saline soil-glass | 0.48 |
| 65Mn steel shear modulus | 7.9×10 ¹⁰ | Coefficient of sliding friction between saline soil-glass | 0.11 |
| Glass density | 1190 | gravitational acceleration (m/s ²) | 9.8 |
| Glass Poisson's ratio | 0.29 | time step: s | 1.20e-05 |
| Glass shear modulus | 1.28×10 ⁹ | simulation duration: s | 5 |

The simulation mimics the soil accumulation angle test, looking squarely at the X and Y axes and using the post-processing tool Protractor, the soil particles accumulation angle was measured, as shown in Fig. 10, and a total of four measurements were taken in each direction, and the average value was taken and recorded.

RESULTS

Simulation results

The simulation model of soil repose angle is shown in Fig.10. Among them, the funnel-shaped diversion curved wall adopts smooth glass material, its Poisson 's ratio is 0.24, the density is 1190 kg/m³, and the shear modulus is 1.28 × 10⁹ Pa. The selection range of soil contact parameters is shown in Table 3. The aggregate groups of soil samples in each plough layer were established by EDEM particle element function. In the process of settlement, it stabilizes the downflow by gravity acceleration, squeezes and deforms between aggregates, and forms a stacking effect on the receiving plate. Then, according to the four-factor quadratic orthogonal rotation combination test design method, the test scheme is compiled for the data in table 2, and the simulation test of soil accumulation angle measurement is carried out according to the test scheme. In order to avoid the error in each calculation process, each test group will be repeated three times. The average value is used as the test result. After determining the test result, the difference between the test result and the actual soil accumulation angle is made. The test scheme and its result are shown in table 4.

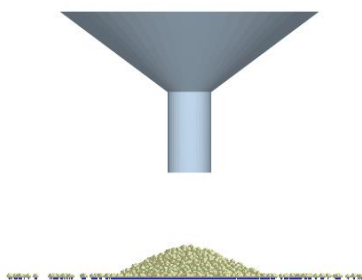


Fig. 10 – Soil accumulation angle simulation test

Table 4

| Test Program and Results | | | | | |
|--------------------------|------|------|------|----|------|
| NO. | A | B | C | D | 1 |
| 1 | 0.19 | 0.1 | 0.15 | 6 | 2.73 |
| 2 | 0.33 | 0.1 | 0.15 | 6 | 2.59 |
| 3 | 0.19 | 0.2 | 0.15 | 6 | 2.5 |
| 4 | 0.33 | 0.2 | 0.15 | 6 | 2.44 |
| 5 | 0.19 | 0.1 | 0.25 | 6 | 3.27 |
| 6 | 0.33 | 0.1 | 0.25 | 6 | 2.91 |
| 7 | 0.19 | 0.2 | 0.25 | 6 | 2.79 |
| 8 | 0.33 | 0.2 | 0.25 | 6 | 2.38 |
| 9 | 0.19 | 0.1 | 0.15 | 12 | 2.29 |
| 10 | 0.33 | 0.1 | 0.15 | 12 | 2.64 |
| 11 | 0.19 | 0.2 | 0.15 | 12 | 2.49 |
| 12 | 0.33 | 0.2 | 0.15 | 12 | 2.66 |
| 13 | 0.19 | 0.1 | 0.25 | 12 | 2.68 |
| 14 | 0.33 | 0.1 | 0.25 | 12 | 2.65 |
| 15 | 0.19 | 0.2 | 0.25 | 12 | 2.58 |
| 16 | 0.33 | 0.2 | 0.25 | 12 | 2.46 |
| 17 | 0.12 | 0.15 | 0.2 | 9 | 2.76 |
| 18 | 0.4 | 0.15 | 0.2 | 9 | 2.56 |
| 19 | 0.26 | 0.05 | 0.2 | 9 | 2.54 |
| 20 | 0.26 | 0.25 | 0.2 | 9 | 2.16 |
| 21 | 0.26 | 0.15 | 0.1 | 9 | 2.41 |
| 22 | 0.26 | 0.15 | 0.3 | 9 | 2.81 |
| 23 | 0.26 | 0.15 | 0.2 | 3 | 2.95 |
| 24 | 0.26 | 0.15 | 0.2 | 15 | 2.75 |
| 25 | 0.26 | 0.15 | 0.2 | 9 | 2.65 |
| 26 | 0.26 | 0.15 | 0.2 | 9 | 2.62 |
| 27 | 0.26 | 0.15 | 0.2 | 9 | 2.64 |

Analysis of test results

In order to analyse the test factors that have a significant effect on the simulated stacking angle, the test results were analysed by ANOVA, as shown in Table 5.

Table 5

| Analysis of Variance (ANOVA) for Soil Stockpile Angle Regression Tests | | | | |
|--|----------------|-------------------|--------|---------|
| Source of variance | Sum of squares | Degree of freedom | F | P |
| Model | 1.24 | 14 | 66.49 | <0.0001 |
| A-A | 0.0417 | 1 | 31.19 | 0.0001 |
| B-B | 0.2053 | 1 | 153.69 | <0.0001 |
| C-C | 0.198 | 1 | 148.2 | <0.0001 |
| D-D | 0.1014 | 1 | 75.89 | <0.0001 |
| AB | 0.0036 | 1 | 2.69 | 0.1266 |
| AC | 0.0961 | 1 | 71.93 | <0.0001 |
| AD | 0.1122 | 1 | 83.99 | <0.0001 |
| BC | 0.0812 | 1 | 60.79 | <0.0001 |
| BD | 0.1089 | 1 | 81.51 | <0.0001 |
| CD | 0.04 | 1 | 29.94 | 0.0001 |

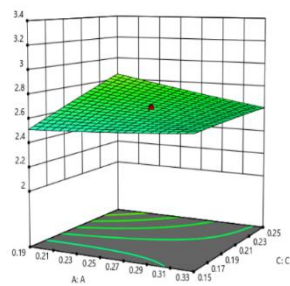
| Source of variance | Sum of squares | Degree of freedom | F | P |
|--------------------|----------------|-------------------|--------|---------|
| A ² | 0.0013 | 1 | 0.9487 | 0.3493 |
| B ² | 0.1039 | 1 | 77.77 | <0.0001 |
| C ² | 0.0005 | 1 | 0.3666 | 0.5561 |
| D ² | 0.065 | 1 | 48.67 | <0.0001 |
| Residual | 0.016 | 12 | | |
| Lack of fit | 0.0156 | 10 | 6.67 | 0.1373 |
| Pure error | 0.0005 | 2 | | |
| Cor total | 1.26 | 26 | | |

Based on the ANOVA, the regression equation for saline soil accumulation angle Y1 was established, and after transformation, the regression model was as follows:

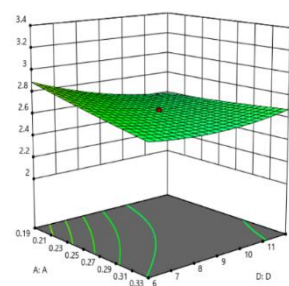
$$R_1 = 1.70 + 0.068A + 8.39B + 15.61C - 0.25D - 22.14A \times C + 0.39A \times D - 28.5B \times C + 0.55B \times D - 27.92B^2 + 0.006D^2 \tag{16}$$

From Table 5, it can be seen that the regression model p<0.001, indicating that the regression model for saline soil accumulation angle and soil hardsetting is extremely significant.

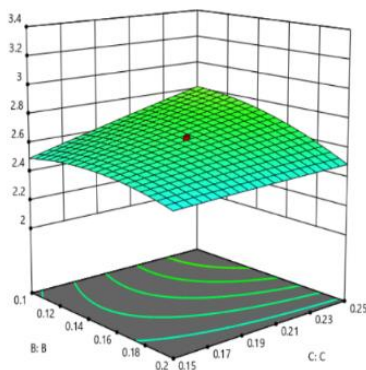
In order to explore the interaction effect of the four test factors on the response values, according to Table 5, the interaction of AC, AD, BC, and BD had a significant effect on the accumulation angle of saline soil with the response surface and contour distribution plots, as shown in Fig. 11.



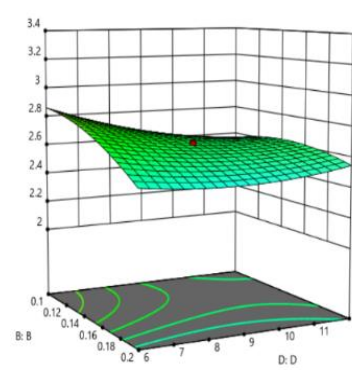
(a) Effect of AC on soil accumulation angle



(b) Effect of AD on soil accumulation angle



(c) Effect of BC on soil accumulation angle



(d) Effect of BD on soil accumulation angle

Fig. 11 – Saline soil accumulation angle interaction

The curvature of the response surface shows that the interaction term affects the soil accumulation angle in the order of AD>BD>AC>BC, and the interaction term affects the soil hardsetting in the order of AC>AD>BD. It can be seen in Fig. 11(a) that the soil accumulation angle increases slowly with the collision recovery coefficient, and increases with the coefficient of kinetic friction, and the two interact with each other, and the soil accumulation angle almost does not change with the increase of the two simultaneously. It can be seen in Fig. 11(b) that the soil accumulation angle decreases with the increase of surface energy, but after interacting with the collision recovery coefficient, the soil accumulation angle appears to decrease and then increase as both increase. Fig. 11(c) shows that the soil accumulation angle tends to increase and then decrease as the static friction coefficient increases, and increases as the kinetic friction coefficient increases. They cancelled each other out and had a small effect on the soil accumulation angle. Fig. 11(d) shows that the soil accumulation angle increases with the decrease of static friction coefficient and JRK surface energy.

Determination of optimal parameters

In order to determine the optimal combination of contact parameters for saline soils, the minimum value of the difference between the soil accumulation angle and the soil hardsetting and the actual difference was taken as the target value, and the constraint equations were:

$$\begin{cases} \text{Obj. } \{ \min Y_1 \\ \text{s. t. } \begin{cases} 0.12 \leq A \leq 0.40 \\ 0.05 \leq B \leq 0.30 \\ 0.10 \leq C \leq 0.45 \\ 3.50 \leq D \leq 14.5 \end{cases} \end{cases} \quad (17)$$

The results of obtaining the optimal solution are: coefficient of elastic recovery 0.262, coefficient of static friction 0.263, coefficient of kinetic friction 0.234, and JRK surface energy 10.084.

CONCLUSIONS

In this study, the soil parameters in the test field were measured, and the soil density was 1622.5, the shear modulus was 3.76×10^7 Pa, the percentage distribution of saline soil particle size was mainly distributed in the interval of >2 mm sandy loam, and the type of saline soil can be obtained as chalky sandy clay according to the International Soil Classification Standard, the Poisson's ratio was 0.30. Due to the strong adhesion and elastic plasticity of saline soil, JKR was chosen as the contact model for saline soil and the contact parameters between saline soil particles (elastic recovery coefficient, static friction coefficient, dynamic friction coefficient, JRK surface energy) were taken as the test factors, and the soil stacking angle was taken as the test index for the saline soil contact parameter calibration. The test was conducted, and the quadratic regression equation was fitted, ANOVA and interaction effect analysis were performed to determine the optimal parameter combinations as: elasticity recovery coefficient 0.262, static friction coefficient 0.263, kinetic friction coefficient 0.234, and JRK surface energy 10.084 J/m².

This study has a certain role in advancing the research on constructing saline and alkaline soil models and analysing the interaction mechanism between saline and alkaline soils and the soil-entry components of agricultural machinery, especially in advancing the research on the mechanical properties of soil particles and changes in physical properties of soil touching the soil components of agricultural machinery operations in the process of excavation, trenching and other operations, which is crucial for the development of agricultural machinery and equipment applicable to saline and alkaline soils. However, the research in this paper mainly provides a method for constructing a structural soil discrete element particle contact model and parameter calibration, and the model parameters have complexity and variability under the conditions of soil characteristics and water content in different regions, which need to be reconstructed and calibrated according to soil type, particle size composition, water content and other factors.

ACKNOWLEDGEMENT

The author was supported by the Shandong Province Technology Innovation Guidance Programme Project (YDZX2023005) and the Shandong Province Higher Educational Institutions Youth Creative Science, Technology Support Programme Project (2023KJ304) and the Youth Project of Natural Science Foundation of Shandong Province (ZR2022QE167).

REFERENCES

- [1] Abo-Elnor, M., Hamilton, R., Boyle, J.T. (2004). Simulation of soil-blade interaction for sandy soil using advanced 3D finite element analysis. *Soil and Tillage Research*, Vol. 75, pp 61-73, Cairo/Egypt.
- [2] Aikins, K. A., Ucgul, M., Barr, J. B., Jensen, T. A., Antille, D. L., & Desbiolles, J. M. (2021). Determination of discrete element model parameters for a cohesive soil and validation through narrow point opener performance analysis. *Soil and Tillage Research*, Vol. 213, pp 105-123, Toowoomba/Australia.
- [3] Chen, L., Mu, X., Peng, Z., (2021). Application of Discrete Element Method in Agricultural Engineering (离散元法在农业工程中的应用). *Agricultural Engineering*, Vol. 11, pp 29-34, Guangxi/China.
- [4] Han, S., Qi, J., Kan, Z., Li, Y., Meng, H., (2021). Parameters Calibration of Discrete Element for Deep Application of Bulk Manure in Xinjiang Orchard (新疆果园深施散体厩肥离散元参数标定研究). *Trans. Chin. Soc. Agric. Mach.*, Vol. 52, pp 101-108, Shihezi/China.
- [5] Hao, Z., Zheng, E., Li, X., Yao, H., Wang, X., Qian, S., Li, W., Zhu, M., (2023). Performance analysis of the soil-contacting parts for no-tillage planters and optimization of blade structure (免耕播种机旋耕刀耕作性能分析与结构优化). *Transactions of the CSAE*, Vol. 39, pp 1-13, Nanjing/China.

- [6] Li, J. W., Tong, J., Hu, B., Wang, H. B., Mao, C. Y., & Ma, Y. H. (2019). Calibration of parameters of interaction between clayey black soil with different moisture content and soil-engaging component in northeast China. *Transactions of the CSAE*, Vol. 35, pp 130-140, Shihezi/China.
- [7] Luo, S., Yuan, Q., Gouda, Shaban., Yang, L., (2018). Parameters Calibration of Vermicomposting Nursery Substrate with Discrete Element Method Based on JKR Contact Model (基于JKR粘结模型的蚯蚓粪基质离散元法参数标定). *Trans. Chin. Soc. Agric. Mach*, Vol. 49, pp 343-350, Wuhan/China.
- [8] Qiu, Y., Guo, Z., Jin, X., Zhang, P., Si, S., & Guo, F. (2022). Calibration and verification test of cinnamon soil simulation parameters based on discrete element method. *Agriculture*, Vol. 12, Luoyang/China.
- [9] Song, Z., Li, H., Yan, Y., Tian, F., Li, Y., Li, F., (2010). Calibration Method of Contact Characteristic Parameters of Soil in Mulberry Field Based on Unequal-diameter Particles DEM Theory (桑园土壤非等径颗粒离散元仿真模型参数标定与试验). *Trans. Chin. Soc. Agric. Mach*, Vol. 53, pp 21-33, Taian/China.
- [10] Tian, X., Cong, X., Qi, J., Guo, H., Li, M., Fan, X., (2021). Parameter Calibration of Discrete Element Model for Corn Straw-Soil Mixture in Black Soil Areas (黑土区玉米秸秆-土壤混料离散元模型参数标定). *Trans. Chin. Soc. Agric. Mach*, Vol. 52, pp 100-108, Changchun/China.
- [11] Tong, J., Mohammad, M. A., Zhang, J., Ma, Y., Rong, B., Chen, D., & Menon, C. (2010). DEM numerical simulation of abrasive wear characteristics of a bioinspired ridged surface. *Journal of Bionic Engineering*, Vol. 7, pp 175-181, Changchun/China.
- [12] Wang, X., Hu, H., Wang, Q., Li, H., He, J., Chen, W., (2017). Calibration Method of Soil Contact Characteristic Parameters Based on DEM Theory (基于离散元的土壤模型参数标定方法). *Trans. Chin. Soc. Agric. Mach*, Vol. 48, pp 78-85, Beijing/China.
- [13] Wang, X., Zhang, S., Pan, H., Zheng, Z., Huang, Y., & Zhu, R. (2019). Effect of soil particle size on soil-subsoiler interactions using the discrete element method simulations. *Biosystems Engineering*, Vol. 182, pp 138-150, Yangling/China.
- [14] Xing, J., Zhang, R., Wu P., Zhang, X., Dong, X., Chen, Y., Ru, S., (2020). Parameter calibration of discrete element simulation model for latosol particles in hot areas of Hainan Province (海南热区砖红壤颗粒离散元仿真模型参数标定). *Transactions of the CSAE*, Vol. 36, pp. 158-166, Hainan/China.
- [15] Xu, Z., & Wang, J., (2005). Advances in Finite Element Analysis of Soil Cutting (有限元法分析土壤切削问题的研究进展). *Trans. Chin. Soc. Agric. Mach*, Vol. 36, pp. 134-137, China.
- [16] Yu, J., Fu, H., Li, H., Shen, Y., (2005). Application of discrete element method to research and design of working parts of agricultural machines (离散元法及其在农业机械工作部件研究与设计中的应用). *Transactions of the CSAE*, Vol. 21, pp 1-6, Changchun/China.
- [17] Zeng, Z., Ma, X., Cao, X., Li, Z., Wang, X., (2021). Critical Review of Applications of Discrete Element Method in Agricultural Engineering (离散元法在农业工程研究中的应用现状和展望). *Trans. Chin. Soc. Agric. Mach*, Vol. 52, pp 1-20, Guangzhou/China.
- [18] Zhang, S., Zhao, H., Wang, X., Dong, J., Zhao, P., Yang, F., ... & Huang, Y. (2023). Discrete element modeling and shear properties of the maize stubble-soil complex. *Computers and Electronics in Agriculture*, Vol. 204, Yangling/China.

EXPERIMENTAL STUDY ON THE CLEANING PERFORMANCE OF BIONIC SCREEN BASED ON EARTHWORM MOTION CHARACTERISTICS

基于蚯蚓运动特征的仿生筛清选性能试验研究

Yongtao YU, Yanjun LI, Fuxiang XIE*, Jian SONG

College of Machinery and Automation, Weifang University, Weifang 261000, China

Tel: +86-182-6566-9383; E-mail: xfx608@126.com

Corresponding author: Fuxiang Xie

DOI: <https://doi.org/10.35633/inmateh-73-70>

Keywords: maize grain harvester, bionic screen for cleaning, cleaning performance, test, CFD-DEM

ABSTRACT

As the feeding mass of the combine harvester continues to be increased, the accumulation of the maize mixture on the screen more serious leading to a reduction in the screening efficiency of the cleaning screen. The maize mixture on the screen was quickly transported backward through a bionic screen based on the movements characteristics of earthworms to reduce accumulation. However, the influence of the main operating parameters of this bionic screen on the cleaning performance was not clear, so the main operating parameters affecting the loss percentage and impurity percentage of maize grain in the cleaning device of bionic screen were simulated using CFD-DEM. Analysis of variance, regression and response surface were carried out on the test data, and parameter optimization was carried out to obtain the optimal parameter combinations: the concave depth of the screen surface was 25 mm, the installation angle of the screen surface was -5.5° , and the airflow velocity at the inlet of the cleaning device was 12.3 m/s. At this time, the loss percentage of maize grain was 1.56%, and the impurity percentage of maize grain was 1.85%, which satisfied the requirements of national standards. The experiment provides a reference and basis for the subsequent investigation of the screening mechanism of the bionic screen.

摘要

随着联合收获机喂入量越来越大,玉米脱出物在筛上的堆积越发严重导致清选筛分效率降低。基于蚯蚓运动特征的仿生筛能够将筛上玉米脱出物快速向后运移从而减少堆积。但是此仿生筛主要作业参数对清选性能的影响尚不明确,为此采用 CFD-DEM 耦合方法对影响仿生筛清选装置玉米籽粒损失率和含杂率的主要作业参数进行了仿真试验。对试验数据进行方差分析、回归分析和响应面分析,并进行参数优化得到较优的参数组合为:筛面下凹深度 25 mm,筛面安装倾角 -5.5° ,入口气流速度 12.3 m/s,此时,玉米籽粒损失率为 1.56%,籽粒含杂率为 1.85%,清选性能满足相关标准要求。试验为后续仿生筛筛分机理的探究提供参考和依据。

INTRODUCTION

The mechanized harvesting of maize grain is a key link in the whole process of maize mechanization, which is of great significance to guarantee maize production and food security (Buryanov *et al.*, 2019; Zhao, 2023). The cleaning device is a key component of a maize grain combine harvester, and its operation performance affects multiple indicators such as the loss percentage of maize grain and the impurity percentage of maize grain (Wang *et al.*, 2021).

However, the feeding mass of maize grain harvesters continue to increase and has led to the accumulation of the maize mixture (a mixture of grains, stalks, and cobs that fall onto the vibrating screen after threshing by the threshing device) on the screen, which is a key problem that needs to be solved urgently for its improvement (Vlăduț *et al.*, 2022). While the working width of the combine harvester and corn yields continue to increase, the feeding mass continues to be increased, so that the accumulation of maize mixture becomes more serious (Ivan *et al.*, 2015). Therefore, based on the principle of bionics (Massah *et al.*, 2020), the earthworm as a bionic prototype, and the movement characteristics of the earthworm and the operating principle of the cleaning screen were integrated. A bionic screen for maize cleaning based on the movement characteristics of earthworms has been designed to solve the accumulation of maize mixture on the screen under the large feeding mass with continuous feeding (Wang *et al.*, 2021). However, the influence of the main operating parameters of this bionic screen on its cleaning performance needs to be further explored.

The dispersion, layering, and screening of particles on the cleaning screen are directly affected by their operating parameters, so scholars have conducted in-depth research. *Ma et al.* constructed a variable amplitude vibrating screen based on a planar reciprocating vibrating screen, and the effect of the rotation angle of the front swing bar on the throwing and backward movement of particles in front of the screen was investigated (*Ma et al., 2015; Ma, 2017; Ma, 2020*). *Kharchenko et al. (2019)* proposed a sieve with particle size activator to improve the efficiency of flat seed grain mixtures. *Mircea Costin et al., (2020)* designed a new constructive subassembly that would increase the performance of rotary sorters used for extracting various contaminants from seeds. *Li et al.* designed a stepped screen with a sliding finger structure arranged in a stepped pattern and with a certain angle at the end of each section, and the influence of the sliding finger angle on the accumulation of particles on the screen was analysed (*Li et al., 2022; Li, 2022*).

Numerical simulation is an effective method to study complex problems as the experimental process and results are fully visualized and the relevant details of the experiment can be effectively analysed. In the field of agricultural engineering, the computational fluid dynamics and discrete element method (CFD-DEM) coupling method is commonly used to numerically simulate the gas-solid two-phase flow motion of agricultural materials. *Xu et al., (2020)*, simulated the screening process of rice mixture using CFD-DEM, and a mathematical model was established to extract the particle centre velocity and dispersion of the rice mixture. *Yuan et al. (2019)*, simulated the screening process of rice mixture in a fan-inner cylinder using CFD-DEM, and the influence of the working and structural parameters of the cylinder screen on the particle movement and cleaning performance was analysed. *Feng et al., (2021)*, tracked the motion of particles through CFD-DEM, and the influence of the centroid position on the screening behaviour during collision between particles and screen holes was studied.

Based on this, the simulation experiment of the cleaning performance of the bionic screen was conducted through CFD-DEM, with the concave depth of the bionic screen surface, the installation angle of the screen surface, and the airflow direction angle as test factors, with the loss percentage of maize grain and the impurity percentage of maize grain as test indicators. The influence of the main operating parameters of the bionic screen on its cleaning performance was explored, and parameter optimization was carried out to obtain the optimal parameter combination of the bionic screen. The experiment provides a reference and basis for the subsequent investigation of the screening mechanism of bionic screen.

MATERIALS AND METHODS

Structure of bionic screen based on earthworm motion characteristics

The structure of the bionic screen is shown in Fig. 1, which mainly consists of a frame, cam drive mechanism, and screen plate. The side plates are fixed to the front and rear sides of the frame symmetrically, and the driveshaft is fixed on the side plates through the bearing seat. Cam drive mechanisms are installed at the front and rear ends of the driveshaft, respectively, and the screen plate is driven by the pin shaft hinged with the cam driving mechanism. The biomimetic principle and design basis of this bionic screen could be found in the preliminary research results of the project (*Wang et al., 2021*).

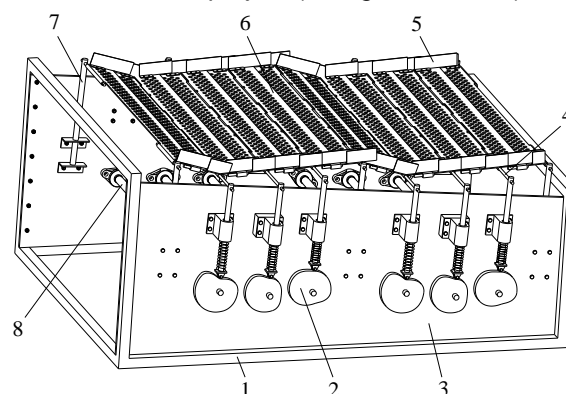


Fig. 1 - Structure diagram of bionic screen

1 - frame; 2 - cam drive mechanism; 3 - side plate; 4 - pin shaft; 5 - baffle; 6 - screen plate; 7 - support rod; 8 - driveshaft

Working principle of bionic screen

During the movement of the bionic screen, the screen surface is concave and reaches the lowest point. At this time, the screen surface becomes "V-shaped", and the screen surface was divided into four postures according to the different concave positions.

The screen surface is continuously changed from attitude 0 to attitude 3 by means of the interplay between the cam drive mechanisms. During operation, the fan is installed at the front of the bionic screen. The maize mixture is initially stratified and dispersed by the fan's airflow during the process of falling from the oscillation grain pan. The maize mixture is fed to the front of the bionic screen, then gathers at the lowest point of the bionic screen surface, and gradually migrates backward with the bionic screen surface to avoid accumulation. The follower is driven by the rotating cam to move up and down. Simultaneously, the combinations of the screen plate are driven by the followers to achieve continuous conversion between concave bending and flattening. The maize mixture falling on the bionic screen surface is thrown up, shaken, and loosened, so that the impurities and the grains are gradually stratified and dispersed on the screen surface.

Experimental materials

The Xianda 205 maize variety was used in the experiment. In the maize mixture, grains, stalks and cobs each account for 73.34%, 17.56%, and 9.10%, with moisture content ranging from 27.41% to 28.65%, 37.22% to 38.01% and 57.09% to 58.22%, respectively.

Foundation of model of bionic screen cleaning device

The length of the cleaning device is 1779 mm, the height is 500 mm, and the width is 105 mm (Yuan et al., 2022; Yuan, 2020). The height of the airflow inlet is 380 mm, and the height of the impurity outlet is 280 mm. The screen body is a round hole screen with a diameter of 15 mm. The length of the screen surface is 1500 mm.

Foundation of particle model of maize mixture

The three-dimensional modelling of simulated particles was carried out for each component of the maize mixture, and this contour was used as the basis for filling the spheres. To ensure accurate contouring of maize mixture while ensuring the computational speed of the computer (Zhang et al., 2020; Wang, 2020), the radius of the modelled spheres was selected as 1 mm. The simulation model of the maize mixture after the modelling was shown in Fig. 2.

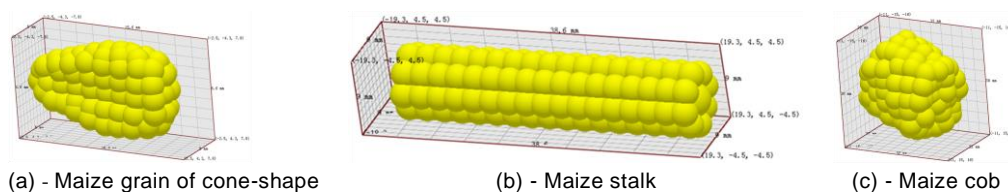


Fig. 2 - Simulation models of maize mixture

Setting of simulation parameters

The standard $k-\epsilon$ turbulence model was selected in Fluent, and the type of solver was set to pressure based unsteady state. The Hertz-Mindlin (no-slip) model was selected in EDEM. The angle of the air outlet of the fan was 25°, and the rotational speed of the cams were 90 r/min. The equations of motion of the screens were extracted by ADAMS, and the non-simple harmonic motion of the bionic screen was added to EDEM through API (Application Programming Interface). The numerical simulation experiment of bionic screen was conducted through CFD-DEM-API coupling. The moisture contents of maize grains, stalks and cobs was 27.91%, 37.62%, and 57.09%, respectively, and the parameters of mechanical properties of each component of the maize mixture are shown in Table 1 (Wang et al., 2018; Wang, 2015).

Table 1

| Mechanical properties of materials | | | |
|------------------------------------|------------------------------|---------------------|---------------|
| Material | Density [kg/m ³] | Shear modulus [MPa] | Poisson ratio |
| Maize grain | 1190 | 127 | 0.40 |
| Maize stalk | 150 | 100 | 0.42 |
| Maize cob | 650 | 109 | 0.45 |
| Screen surface (steel) | 7800 | 700 | 0.30 |

The parameters of properties interaction for each component of maize mixture are shown in Table 2 (Wang et al., 2018; Wang, 2015).

Table 2

| Interaction properties of materials | | | | | | | | | |
|-------------------------------------|-------------|-------------|-----------|----------------------|-------------|-----------|----------------------|---------|--------------------|
| Attributes of contact | Grain-Grain | Grain-Stalk | Grain-Cob | Grain-Screen (steel) | Stalk-Stalk | Stalk-Cob | Stalk-Screen (steel) | Cob-Cob | Cob-Screen (steel) |
| Recovery coefficient of collision | 0.44 | 0.35 | 0.28 | 0.61 | 0.26 | 0.29 | 0.43 | 0.27 | 0.39 |
| Rolling friction coefficient | 0.06 | 0.01 | 0.01 | 0.03 | 0.01 | 0.01 | 0.01 | 0.01 | 0.01 |
| Static friction coefficient | 0.50 | 0.32 | 0.73 | 0.53 | 0.32 | 0.47 | 0.45 | 0.97 | 0.43 |

Setting of particle factors

The particle factor is set above the oscillation grain pan, and the feeding mass of maize mixture is 7 kg/s. The feeding mass of maize mixture is 0.6338 kg/s after equal conversion based on the screen width of the simulation model and continued to feed for 3 s. The specific feeding mass of maize mixture is shown in Table 3.

Table 3

| Feeding mass of different components of maize mixture | | | | | |
|---|-------------------|----------------------------|----------------------------------|-----------|-----------------|
| Component | Category | Number of particles [unit] | Total number of particles [unit] | Mass [kg] | Total mass [kg] |
| Maize grain | Cone | 2835 | | 1.0424 | |
| | Spherical | 973 | 4282 | 0.2119 | 1.3994 |
| | Rectangle | 474 | | 0.1451 | |
| Maize stalk | 28 mm[a] cylinder | 573 | | 0.0458 | |
| | 36 mm cylinder | 789 | 2142 | 0.1088 | 0.3360 |
| | 44 mm cylinder | 468 | | 0.1012 | |
| | 52 mm cylinder | 312 | | 0.0802 | |
| Maize cob | 1/4 cylinder | 1374 | | 0.0840 | |
| | 1/2 cylinder | 105 | 1554 | 0.0344 | 0.1661 |
| | Whole cylinder | 75 | | 0.0477 | |
| Total | | | 7978 | | 1.9015 |

Note: [a] 28 mm, 36 mm, 44 mm, and 52 mm are the length of the cylinder.

Design of test

Based on the theoretical analysis and design process in the early stage, the factors that affect the cleaning performance of the bionic screen were obtained, including the concave depth of the screen surface, the cam rotation speed, the installation angle of the screen surface, the airflow velocity at the inlet of the cleaning device, and the airflow direction angle. The effective adjustment ranges for each factor are 25.0~75.0 mm, 60~120 r/min, -1.5° ~ -5.5° , 9.6~14.4 m/s, and 20.0° ~ 30.0° , respectively. The significant factors were removed based on pre-experiments (Wang *et al.*, 2022; Wang, 2021). The concave depth of the screen surface x_1 , the installation angle of the screen surface x_2 , and the airflow velocity at the inlet of the cleaning device x_3 were selected as factors. The loss percentage of maize grain y_1 and the impurity percentage of maize grain y_2 were selected as indicators, and a three-factor, five-level quadratic orthogonal rotation combination experiment was designed. The median of each factor is used as the zero level of the experiment, and the coding of the experimental factors is shown in Table 4.

Table 4

| Experimental factors and models | | | |
|---------------------------------|---|--|---|
| Level | Factor | | |
| | The concave depth of the screen surface x_1 [mm] | The installation angle of the screen surface x_2 [$^{\circ}$] | The airflow velocity at the inlet of the cleaning device x_3 [m/s] |
| 1.682 | 75.0 | -5.5 | 14.4 |
| 1 | 62.5 | -4.5 | 13.2 |

| Level | Factor | | |
|-------|---|---|---|
| | The concave depth of the screen surface x_1 [mm] | The installation angle of the screen surface x_2 [°] | The airflow velocity at the inlet of the cleaning device x_3 [m/s] |
| 0 | 50.0 | -3.5 | 12.0 |
| -1 | 37.5 | -2.5 | 10.8 |
| - | 25.0 | -1.5 | 9.6 |
| 1.682 | | | |

The total mass of feeding grain into the cleaning device was calculated by the proportion of maize grain to the maize mixture before simulation. At the end of the simulation experiment, the material under the screen and the quality of the grain were extracted, respectively. The loss percentage of maize grain and the impurity percentage of maize grain were calculated using equations (1) and (2), and each group of experiments was repeated 3 times to obtain the average value.

$$S_L = \frac{W_L}{W_Z} \times 100\% \tag{1}$$

$$Z_z = \frac{W_{za}}{W_h} \times 100\% \tag{2}$$

S_L - loss percentage of maize grain [%];

W_L - mass of maize grain lost [g];

W_Z - mass of all maize grain [g];

Z_z - impurity percentage of maize grain [%];

W_{za} - mass of impurities [g];

W_h - mass of sample (mixture of maize grain and impurities) [g].

RESULTS

Test results

The coupled CFD-DEM simulation of the maize mixture is shown in Fig. 3. In the figure, the yellow material is maize grains, the green material is maize stalks and the red material is maize cobs.

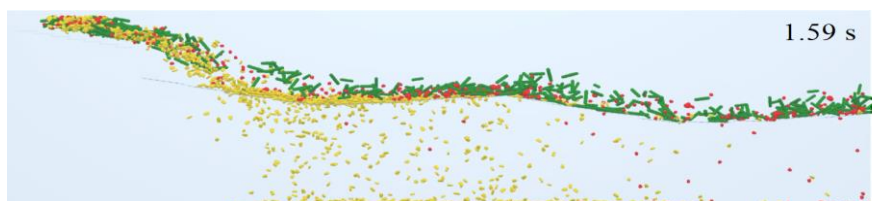


Fig. 3 - CFD-DEM coupled simulation of maize mixture

The results of the three-factor five-level quadratic orthogonal rotation combination test are shown in Table 5.

Table 5

Design scheme and the result of quadratic regression rotation combination

| Number | The concave depth of the screen surface x_1 [mm] | The installation angle of the screen surface x_2 [°] | The airflow velocity at the inlet of the cleaning device x_3 [m/s] | The loss percentage of maize grain y_1 [%] | Standard deviation | The impurity percentage of maize grain y_2 [%] | Standard deviation |
|--------|---|---|---|---|--------------------|---|--------------------|
| 1 | -1 (37.5) | -1 (-2.5) | -1 (10.8) | 0.87 | 0.11 | 4.09 | 0.30 |
| 2 | 1 (62.5) | -1 (-2.5) | -1 (10.8) | 1.28 | 0.13 | 2.96 | 0.26 |
| 3 | -1 (37.5) | 1 (-4.5) | -1 (10.8) | 1.66 | 0.22 | 2.51 | 0.19 |
| 4 | 1 (62.5) | 1 (-4.5) | -1 (10.8) | 3.02 | 0.14 | 1.53 | 0.22 |
| 5 | -1 (37.5) | -1 (-2.5) | 1 (13.2) | 2.12 | 0.20 | 2.06 | 0.18 |

| | | | | | | | |
|----|--------------|--------------|-------------|------|------|------|------|
| 6 | 1 (62.5) | -1 (-2.5) | 1 (13.2) | 2.37 | 0.18 | 2.17 | 0.26 |
| 7 | -1 (37.5) | 1 (-4.5) | 1 (13.2) | 2.74 | 0.15 | 1.82 | 0.15 |
| 8 | 1 (62.5) | 1 (-4.5) | 1 (13.2) | 2.93 | 0.21 | 1.74 | 0.17 |
| 9 | -1.68 (25.0) | 0 (-3.5) | 0 (12.0) | 0.65 | 0.08 | 3.01 | 0.34 |
| 10 | 1.68 (75.0) | 0 (-3.5) | 0 (12.0) | 1.51 | 0.12 | 2.16 | 0.23 |
| 11 | 0 (50.0) | -1.68 (-1.5) | 0 (12.0) | 0.62 | 0.09 | 3.54 | 0.35 |
| 12 | 0 (50.0) | 1.68 (-5.5) | 0 (12.0) | 1.95 | 0.23 | 2.46 | 0.24 |
| 13 | 0 (50.0) | 0 (-3.5) | -1.68 (9.6) | 2.69 | 0.24 | 3.5 | 0.26 |
| 14 | 0 (50.0) | 0 (-3.5) | 1.68 (14.4) | 4.48 | 0.32 | 0.95 | 0.09 |
| 15 | 0 (50.0) | 0 (-3.5) | 0 (12.0) | 1.28 | 0.06 | 3.15 | 0.21 |
| 16 | 0 (50.0) | 0 (-3.5) | 0 (12.0) | 1.15 | 0.08 | 2.98 | 0.26 |
| 17 | 0 (50.0) | 0 (-3.5) | 0 (12.0) | 0.97 | 0.11 | 3.13 | 0.22 |
| 18 | 0 (50.0) | 0 (-3.5) | 0 (12.0) | 1.11 | 0.10 | 2.89 | 0.19 |
| 19 | 0 (50.0) | 0 (-3.5) | 0 (12.0) | 0.82 | 0.08 | 3.34 | 0.27 |
| 20 | 0 (50.0) | 0 (-3.5) | 0 (12.0) | 1.26 | 0.11 | 2.65 | 0.19 |
| 21 | 0 (50.0) | 0 (-3.5) | 0 (12.0) | 0.89 | 0.08 | 3.62 | 0.29 |
| 22 | 0 (50.0) | 0 (-3.5) | 0 (12.0) | 0.73 | 0.12 | 3.46 | 0.29 |
| 23 | 0 (50.0) | 0 (-3.5) | 0 (12.0) | 1.07 | 0.17 | 2.89 | 0.25 |

Analysis and discussion of the results

The results were analysed by ANOVA using Design-Expert 8.0 software to test their significance. The regression equations of the loss percentage of maize grain and the impurity percentage of maize grain were obtained based on regression analysis, and the influence of the interaction terms on the experimental indexes were analysed by response surface.

The loss percentage of maize grain

(1) Variance and regression analysis

The results of ANOVA for loss percentage of maize grain are shown in Table 6, and the experimental model was highly significant ($p < 0.01$). The effect of concave depth of the screen surface x_1 , the installation angle of the screen surface x_2 and the airflow velocity at the inlet of the cleaning device x_3 on the loss percentage of maize grain were highly significant ($p < 0.01$). The interaction terms of concave depth of the bionic screen surface with airflow velocity at the inlet of the cleaning device x_1x_3 , installation angle of the screen surface with airflow velocity at the inlet of the cleaning device x_2x_3 , and the quadratic term of airflow velocity x_3^2 were significant on the loss percentage of maize grain ($p < 0.05$). The rest of the terms were not significant. The order of the effect of each factor on the loss percentage of maize grain was x_3, x_2, x_1 .

Table 6

| Source of variance | Sum of squares | df | Mean square | F-Value | p-Value |
|--------------------|----------------|----|-------------|---------|---------|
| Model | 20.68 | 9 | 2.30 | 59.06 | <0.0001 |
| x_1 | 0.98 | 1 | 0.98 | 25.16 | 0.0002 |
| x_2 | 2.59 | 1 | 2.59 | 66.55 | <0.0001 |
| x_3 | 2.94 | 1 | 2.94 | 75.65 | <0.0001 |
| x_1x_2 | 0.099 | 1 | 0.099 | 2.54 | 0.1347 |
| x_1x_3 | 0.22 | 1 | 0.22 | 5.68 | 0.0331 |
| x_2x_3 | 0.23 | 1 | 0.23 | 5.85 | 0.0309 |
| x_1^2 | 0.019 | 1 | 0.019 | 0.48 | 0.4989 |
| x_2^2 | 0.18 | 1 | 0.18 | 4.67 | 0.0500 |
| x_3^2 | 13.45 | 1 | 13.45 | 345.69 | <0.0001 |
| Residual | 0.51 | 13 | 0.039 | | |
| Lack of fit | 0.21 | 5 | 0.042 | 1.14 | 0.4118 |
| Error | 0.30 | 8 | 0.037 | | |
| Sum | 21.19 | 22 | | | |

From Table 6, the lack of fit of the model was not significant ($p > 0.05$), and the regression model was established. The insignificant terms were removed to obtain the regression equation of each factor on the loss percentage of maize grain as shown in equation (3).

$$y_1 = 1.03 + 0.27x_1 + 0.44x_2 + 0.46x_3 - 0.17x_1x_3 - 0.17x_2x_3 + 0.92x_3^2 \quad (R^2 = 0.9761) \quad (3)$$

(2) Analysis of the response surface of the interaction term

When the installation angle of the screen surface is -3.5° , there is an interaction between the concave depth of the bionic screen surface and the airflow velocity at the inlet of the cleaning device, as shown in Fig. 4(a). Under the condition of an airflow velocity at the inlet of the cleaning device, the loss percentage of maize grain increases with the increase of the concave depth of the bionic screen surface. The reason is that with the increase of the concave depth of the bionic screen, the horizontal velocity of the grains increases, and the probability of the grains passing through the screen gradually decreases, resulting in a gradual increase in the loss percentage of maize grain. Under the condition of a concave depth of the bionic screen surface, the loss percentage of maize grain first decreased and then increased with the increase of the inlet air velocity. The reason is that the airflow velocity at the inlet of the cleaning device affects the separation and migration of maize mixture along the screen surface. When the inlet airflow velocity is too small, the grains and impurities cannot be effectively separated, and the grains cannot be fully contacted with the screen surface, resulting in a high the loss percentage of maize grain.

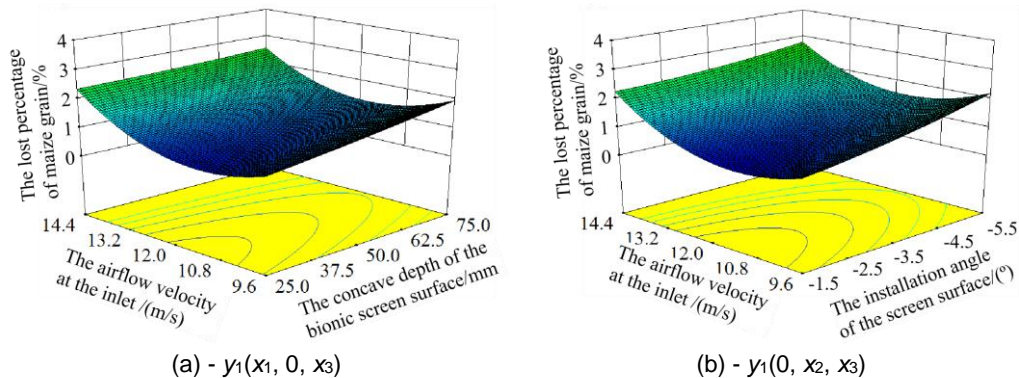


Fig. 4 - Response surface of effects of various factors on loss percentage of maize grain

When the concave depth of the screen surface is 50.0 mm, there is an interaction between the installation angle of the screen surface and the airflow velocity at the inlet of the cleaning device, as shown in Fig. 4(b). Under the condition of airflow velocity at the inlet of the cleaning device, the loss percentage of maize grain increases with the increase of the installation angle of the screen surface. The reason is that with the increase of the installation angle of the screen surface, the horizontal velocity of the grain gradually increases, and the probability of its penetration through the screen decreases, resulting in a gradual increase in the loss percentage of maize grain. Under the condition of installation angle of the screen surface, the loss percentage of maize grain first decreased and then increased with the increase of the inlet airflow velocity. The reason is that the grains and impurities cannot be effectively separated when the inlet airflow velocity is low. When the inlet airflow velocity is too high, the grains move backwards faster. In both cases, the probability of the grains passing through the screen is reduced.

The impurity percentage of maize grain

(1) Variance and regression analysis

The results of ANOVA for impurity percentage of maize grain are shown in Table 7, and the experimental model was highly significant ($p < 0.01$). The effect of concave depth of the screen surface x_1 , the installation angle of the screen surface x_2 and the airflow velocity at the inlet of the cleaning device x_3 on the impurity percentage of maize grain were highly significant ($p < 0.01$). The interaction terms of concave depth of the bionic screen surface with airflow velocity at the inlet of the cleaning device x_1x_3 , installation angle of the screen surface with airflow velocity at the inlet of the cleaning device x_2x_3 , the quadratic term of concave depth of the bionic screen surface x_1^2 , and the quadratic term of airflow velocity x_3^2 on the impurity percentage of maize grain were significant ($p < 0.05$). The rest of the terms were not significant. The order of the effect of each factor on the impurity percentage of maize grain was x_3, x_2, x_1 .

Table 7

ANOVA results for the impurity percentage of maize grain

| Source of variance | Sum of squares | df | Mean square | F-Value | p-Value |
|-----------------------------------|----------------|----|-------------|---------|---------|
| Model | 11.63 | 9 | 1.29 | 12.18 | <0.0001 |
| x₁ | 0.90 | 1 | 0.90 | 8.50 | 0.0120 |
| x₂ | 2.21 | 1 | 2.21 | 20.85 | 0.0005 |
| x₃ | 4.22 | 1 | 4.22 | 39.75 | <0.0001 |
| x₁x₂ | 0.0002 | 1 | 0.0002 | 0.0019 | 0.9660 |
| x₁x₃ | 0.57 | 1 | 0.57 | 5.40 | 0.0370 |
| x₂x₃ | 0.68 | 1 | 0.68 | 6.45 | 0.0246 |
| x₁² | 0.87 | 1 | 0.87 | 8.22 | 0.0132 |
| x₂² | 0.12 | 1 | 0.12 | 1.15 | 0.3036 |
| x₃² | 2.08 | 1 | 2.08 | 19.58 | 0.0007 |
| Residual | 1.38 | 13 | 0.11 | | |
| Lack of fit | 0.62 | 5 | 0.12 | 1.30 | 0.3529 |
| Error | 0.76 | 8 | 0.095 | | |
| Sum | 13.01 | 22 | | | |

From Table 7, the lack of fit of the model was not significant ($p>0.05$), and the regression model was established. The insignificant terms were removed to obtain the regression equation of each factor on the impurity percentage of maize grain as shown in equation (4).

$$y_2 = 3.13 - 0.26x_1 - 0.4x_2 - 0.56x_3 + 0.27x_1x_3 + 0.29x_2x_3 - 0.088x_1^2 - 0.36x_3^2 \quad (R^2 = 0.8940) \quad (4)$$

(2) Analysis of the response surface of the interaction term

When the installation angle of the screen surface is -3.5° , there is an interaction between the concave depth of the bionic screen surface and the airflow velocity at the inlet of the cleaning device, as shown in Fig. 5(a). Under the condition of airflow velocity at the inlet of the cleaning device, the impurity percentage of maize grain decreases with the increase of the concave depth of the bionic screen surface. The reason is that with the increase of the concave depth of the bionic screen surface, the horizontal velocity of maize stalk and cob gradually increases, and the probability of impurities remaining through the screen decreases, resulting in a gradual decrease in the impurity percentage of maize grain. Under the condition of concave depth of the bionic screen surface, the impurity percentage of maize grain gradually decreased with the increase of the airflow velocity at the inlet of the cleaning device. The reason is that with the increase of the airflow velocity at the inlet of the cleaning device, the separation effect of grains and impurities along the screen surface is better, so that the backward migration speed of impurities is faster and faster, so that the impurity percentage of maize grain gradually decreases.

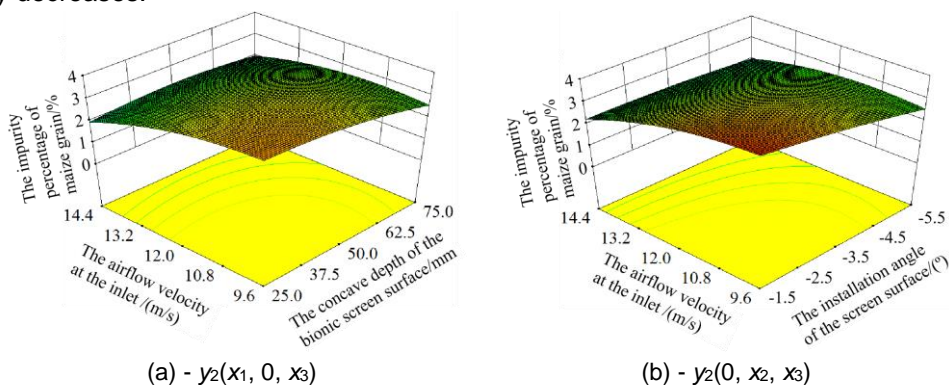


Fig. 5 - Response surface of effects of various factors on impurity percentage of maize grain

When the concave depth of the screen surface is 50.0 mm, there is an interaction between the installation angle of the screen surface and the airflow velocity at the inlet of the cleaning device, as shown in Fig. 5(b). Under the condition of airflow velocity at the inlet of the cleaning device, the impurity percentage of maize grain decreases with the increase of the installation angle of the screen surface. The reason is that with the increase of the installation angle of the screen surface, the horizontal speed of the impurities gradually increases, so that the impurity percentage of maize grain gradually decreases.

Under the condition of installation angle of the screen surface, the impurity percentage of maize grain decreased gradually with the airflow velocity at the inlet of the cleaning device. The reason is that with the increase of the airflow velocity at the inlet of the cleaning device, the impurities migrate backward on the screen faster and faster, so that the impurity percentage of maize grain gradually decreases.

Optimization of parameters

To obtain the best cleaning performance of the bionic screen, the multi-objective optimization algorithm of the Design-Expert 8.0 software was used to optimize the structural parameters and operating parameters of the bionic screen based on the multi-factor experiments. The objectives and constraints are as follows:

$$\begin{cases} \min y_1 \\ \min y_2 \\ 25\text{mm} \leq x_1 \leq 75\text{mm} \\ -1.5^\circ \leq x_2 \leq -5.5^\circ \\ 9.6\text{m/s} \leq x_3 \leq 14.4\text{m/s} \end{cases} \quad (5)$$

Optimization results: when the concave depth of the screen surface is 25 mm, the installation inclination angle of the screen surface is -5.5° , and the inlet airflow velocity is 12.3 m/s, the loss percentage of maize grain is 1.56%, and the impurity percentage of maize grain is 1.85%, which are all in line with the standard requirements (GB/T 21962, 2020; NY/T 1355, 2007).

Verification test of bench

The bench of the bionic screen cleaning device is shown in Fig. 6. The bench test is carried out to verify the results of the simulation test with the optimization results of the simulation test as the operation parameters.



Fig. 6 - Cleaning device of bionic screen

1 - fan; 2 - oscillation grain pan; 3 - bionic screen; 4 - high-speed camera; 5 - motor; 6 - computer; 7 - frequency converter.

Before the test, the maize mixture were evenly spread on the oscillation grain pan, and 21 kg of maize mixture were continuously fed in 3 s to ensure that the feeding mass of maize mixture was 7 kg/s. The loss percentage of maize grain and the impurity percentage of maize grain were calculated, and each group of experiments was repeated 5 times to obtain the average value. The average value of the loss percentage of maize grain was 1.64%, and the average value of the impurity percentage of maize grain was 1.86%. The maximum relative error between the measured values and the numerical simulation results does not exceed 5.13%, which is within the acceptable range. The accuracy of the numerical simulation was proven.

CONCLUSIONS

The main operating parameters that affect the loss percentage and impurity percentage of maize grain in the cleaning device of bionic screen were simulated using CFD-DEM. Analysis of variance, regression and response surface were carried out on the test data, and the optimal parameter combination was obtained.

(1) The effects of the concave depth of the bionic screen surface x_1 , the installation angle of the screen surface x_2 , and the airflow velocity at the inlet of the cleaning device x_3 on the loss percentage of maize grain and the impurity percentage of maize grain were analysed by the variance and interaction term response surface method. The order of the effect on the loss percentage and impurity percentage of maize grain was x_3 , x_2 , x_1 .

(2) The parameters of the bionic screen were optimized and its optimal combination of parameters was obtained as follows: the concave depth of the screen surface was 25 mm, the installation inclination angle of the screen surface was -5.5° , and the inlet airflow velocity was 12.3 m/s. At this time, the loss percentage of maize grain was 1.56%, and the impurity percentage of maize grain was 1.85%, which are all in line with the standard requirements.

(3) The validation experiment was conducted by the bench of bionic screen cleaning device, the average value of the loss percentage of maize grain of the bionic screen cleaning device was 1.64%, and the average value of the impurity percentage of maize grain was 1.86%. The maximum relative error between the measured values and the numerical simulation results does not exceed 5.13%, and the accuracy of the numerical simulation was proven.

ACKNOWLEDGEMENT

The work was supported financially by the Start-up Foundation for Doctoral Research of Weifang University (N0.2022BS30), and the Shandong Province Higher Education Institutions Young Innovation Team Talent Introduction Program.

REFERENCES

- [1] Feng, X., Gong, Z., Wang, L., Yu, Y., Liu, T., & Song, L., (2021). Behavior of maize particle penetrating a sieve hole based on the particle centroid in an air-screen cleaning unit. *Powder Technology*, Vol. 385, pp. 501-516, Switzerland.
- [2] GB/T 21962-2020 *Corn Harvesting Machinery (玉米收获机械)*. China.
- [3] Kharchenko, S., Kovalyshyn, S., Zavgorodniy, A., Kharchenko, F., Mikhaylov, Y., (2019). Effective sifting of flat seeds through sieve. *INMATEH - Agricultural Engineering*, Vol. 60, No. 1, pp. 17-26, Romania.
- [4] Li, Y., Xu, Y., Cui, T., Zhang, D., Fan, H., Gao, X., Su, Y., Qiao, M., & Song, Z., (2022). Improving particle dispersion characteristics with a novel cleaning screen: parameter design and numerical simulation. *Powder Technology*, Vol. 397, 116987, Switzerland.
- [5] Li, Y., Fan, H., Xu, Y., Cui, T., Su, Y., Qiao, M., Han, S., Qian, J., & Zheng, Z., (2022). CFD-DEM investigation of particle dispersion degree on a novel vibrating screen. *Powder Technology*, Vol. 404, 117497, Switzerland.
- [6] Ma, Z., Li, Y., Xu, L., (2015). Discrete-element method simulation of agricultural particle motion in variable-amplitude screen box. *Computers and Electronics in Agriculture*, Vol. 118, pp. 92-99, England.
- [7] Ma, Z., Li, Y., Xu, L., Chen, J., Zhao, Z., & Tang, Z., (2017). Dispersion and migration of agricultural particles in a variable-amplitude screen box based on the discrete element method. *Computers and Electronics in Agriculture*, Vol. 142, pp. 173-180, England.
- [8] Ma, Z., Han, M., Li, Y., Gao, H., Lu, E., Chandio, F., & Ma, K., (2020). Motion of cereal particles on variable-amplitude sieve as determined by high-speed image analysis. *Computers and Electronics in Agriculture*, Vol. 174, 105465, England.
- [9] Jafar, M., Fatemeh, H., Zeinab, H., Kwyvan, A., (2020). Experimental investigation of bionic soil-engaging blades for soil adhesion reduction by simulation armadillidium vulgare body surface. *INMATEH - Agricultural Engineering*, Vol. 60, No. 1, pp. 99-106, Romania.
- [10] NY/T 1355-2007 *Corn Harvester Operation Quality (玉米收获机作业质量)*. China.
- [11] Ivan, G., Vladut, V., Ganea, I., (2015). Improving threshing system feeding of conventional cereal harvesting combine, *Proceedings of the 43 International Symposium on Agricultural Engineering "Actual Tasks on Agricultural Engineering"*, pp. 431-440, Opatija/Croatia.
- [12] Mircea C., Nenciu F., Vladut, V., Gheorghe, G., Gageanu G., & Cujbescu D., (2020). Increasing the performance of cylindrical separators for cereal cleaning, by using an inner helical coil, *INMATEH – Agricultural Engineering*, Vol. 62, No. 3, pp. 249-258, Romania.
- [13] Buryanov, A., Chervyakov, I. (2019). Using combines for cleaning grain crops by non-traditional technologies, *INMATEH – Agricultural Engineering*, Vol. 59, No. 3, pp. 27-32, Romania.
- [14] Wang, L., Chai, J., Wang, H., Wang, Y., (2021). Design and performance of a countersunk screen in a maize cleaning device. *Biosystems Engineering*, Vol. 209, pp. 300-314, England.
- [15] Vlăduț N.-V., Biris S.-St., Cârdei, P., Găgeanu, I., Cujbescu, D., Ungureanu, N., Popa, L.-D., Perișoară, L., Matei, G., & Teliban, G.-C. (2022). Contributions to the Mathematical Modeling of the Threshing and Separation Process in An Axial Flow Combine, *Agriculture*, Vol. 12, No. 10, 1520, Slovak Republic.
- [16] Wang, L., Yu, Y., Zhang, S., Fen, X., & Song, L., (2021). Bionic design and performance test of maize grain cleaning screen through earthworm motion characteristics. *International Journal of Agricultural and Biological Engineering*, Vol. 14, No. 3, pp. 12-21, China.
- [17] Wang, W., Liu, W., Yuan, L., Qu, Z., He, X., & Lu, Y., (2020). Simulation and experiment of single longitudinal axial material movement and establishment of wheat plants model (小麦植株建模与单纵轴流

- 物料运动仿真与试验). *Transactions of the Chinese Society for Agricultural Machinery*, Vol. 51, No. s2, pp. 170-180, China.
- [18] Wang, L., Li, R., Wu, B., Wu, Z., & Ding, Z., (2017). Determination of the coefficient of rolling friction of an irregularly shaped maize particle group using physical experiment and simulations. *Particuology*, Vol. 38, No. 6, pp. 185-195, China.
- [19] Wang, L., Zhou, W., Ding, Z., Li, X., & Zhang, C., (2015). Experimental determination of parameter effects on the coefficient of restitution of differently shaped maize in three-dimensions. *Powder Technology*, Vol. 284, pp. 187-194, Switzerland.
- [20] Xu, L., Li, Y., Chai, X., Wang, G., Liang, Z., Li, Y., & Li, B., (2020). Numerical simulation of gas-solid two-phase flow to predict the cleaning performance of rice combine harvesters. *Biosystems Engineering*, Vol. 190, pp. 11-24, England.
- [21] Yuan, J., Wu, C., Li, H., Qi, X., & Shi, X., (2019). Screening motion of a fan-inner cylinder sieve for rice harvest exfoliants (水稻收获脱出物风机-内圆筒筛分运动研究). *Journal of Nanjing tech university (Natural Science Edition)*, Vol. 41, No. 3, pp. 361-369, Nanjing/China.
- [22] Yuan, J., Wang, J., Li, H., Qi, X., Wang, Y., & Li, C., (2022). Optimization of the cylindrical sieves for separating threshed rice mixture using EDEM. *International Journal of Agricultural and Biological Engineering*, Vol. 15, No. 2, pp. 236-247, China.
- [23] Yuan, J., Li, H., Qi, X., Hu, T., Bai, M., & Wang, Y., (2020). Optimization of airflow cylinder sieve for threshed rice separation using CFD-DEM. *Engineering Applications of Computational Fluid Mechanics*, Vol. 14, No. 1, pp. 871-881, China.
- [24] Zhang, R., Jiao, W., Zhou, J., Qi, B., Liu, H., & Xia, Q., (2020). Parameter calibration and experiment of rice seeds discrete element model with different filling particle radius (不同填充颗粒半径水稻种子离散元模型参数标定). *Transactions of the Chinese Society for Agricultural Machinery*, Vol. 51, No. s1, pp. 227-235, China.
- [25] Zhao, Z., Du, H., Yang, X., & Zhang, G., (2023). Numerical simulation and experiment on airflow field of corn seed harvester cleaning device. *INMATEH - Agricultural Engineering*, Vol. 69, No. 1, pp. 511-519, Romania.

CALIBRATION AND EXPERIMENTATION OF DISCRETE META-SIMULATION PARAMETERS OF ASTRAGALUS MEMBRANACEUS

黄芪离散元仿真参数的标定与试验

Xiangyu GAO^{1,2)}, Xuejie MA¹⁾, Xiangdong LIN^{*1)}, Qianqian SUN^{*1)}, Zhanfeng HOU^{*1,3)}, Xiaoming ZHANG^{*4)}

¹⁾ College of Mechanical and Electrical Engineering, Inner Mongolia Agricultural University, Inner Mongolia, Hohhot/ China

²⁾ Inner Mongolia First Machinery Group Corporation, Baotou/ China

³⁾ Inner Mongolia Engineering Research Center of Intelligent equipment for the entire process of forage and feed production, Inner Mongolia, Hohhot/ China

⁴⁾ Hohhot Agriculture and Animal Husbandry Technology Promotion Center, Hohhot, Inner Mongolia/ China

Corresponding author: Xiangdong Lin, Qianqian Sun, Zhanfeng Hou, Xiaoming Zhang

Tel: +8613171058429; E-mail: njau-hzf@163.com

DOI: <https://doi.org/10.35633/inmateh-73-71>

Keywords: astragalus membranaceus, angle of repose, relative error, parameter calibration, EDEM

ABSTRACT

This study is based on the discrete element method to calibrate the physical parameters of astragalus membranaceus. Plackett Burman test, steepest climb test, and Box Behnken test were used to screen for significant influencing factors and optimal levels, and a quadratic regression model was obtained for the relative error between the simulated and physical experiment resting angles. The results showed that the relative error between the simulated and physical test angles of repose was only 0.392%, which can provide a theoretical basis for the discrete element simulation test of the working process of the astragalus membranaceus picking machine.

摘要

本研究基于离散元法对黄芪物性参数进行标定, 采用 Plackett-Burman 试验, 最陡爬坡试验, Box-Behnken 试验筛选出显著影响因素及最优水平, 得到仿真试验休止角与物理试验休止角相对误差的二次回归模型。结果表明: 仿真试验休止角与物理试验休止角相对误差仅为 0.392%, 可为黄芪捡拾机工作过程的离散元仿真试验提供理论依据。

INTRODUCTION

Astragalus, a traditional Chinese herbal medicine, has been used medicinally for more than 2000 years and is one of the Chinese herbs with a large clinical dosage in traditional Chinese medicine. Astragalus is 50-100 cm long, with a thicker cylindrical rhizome part, light brownish-yellow or greyish-white in colour, and has a bean flavour when consumed (Kang et al., 2016; Wu et al., 2004; Huang et al., 2023; Shen et al., 2023).

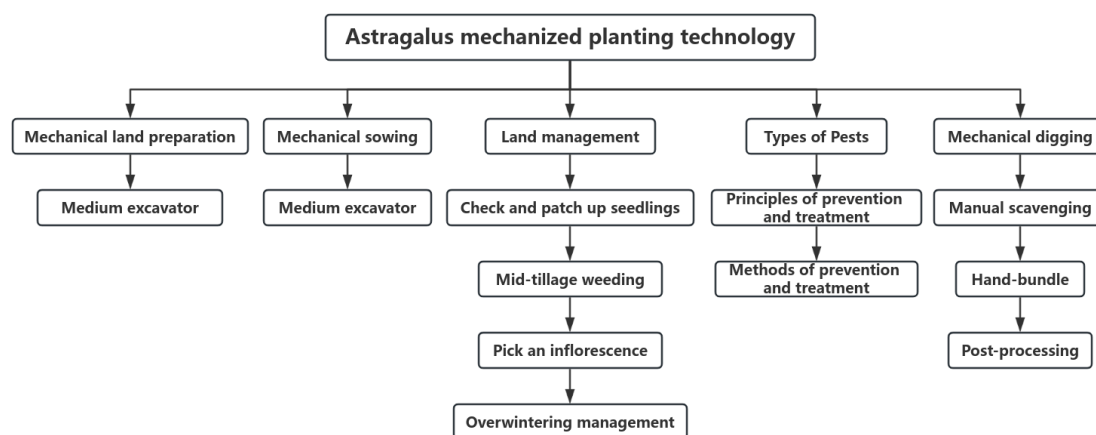


Fig. 1 - Mechanized planting of astragalus industry

As shown in Figure 1, some planting scale astragalus industry has basically realized the mechanized planting of astragalus, but in the harvesting stage of astragalus, due to the depth of astragalus planting up to 400 mm below ground, it adopts a segmented harvesting method, which is firstly dug by the astragalus harvester for astragalus, and then hiring the farmers to carry out the manual gleaning operation (Jiang et al., 2013; Zhang et al., 2006; Li et al., 2015). Artificial gleaning operation efficiency is low and the cost is high, so there is a need to develop and design a kind of astragalus gleaning machine applied to the astragalus industry, and to use the astragalus gleaning machine instead of the traditional manual gleaning operation, so as to reduce the amount of manual work, save cost, improve the efficiency of the astragalus gleaning operation, and achieve the mechanization of the astragalus industry (Cui et al., 2014; Zhao et al., 2017).

MATERIALS AND METHODS

Astragalus picker discrete element simulation model shown in Figure 2, astragalus picker in the working process, due to the operation of the picker components, there is a collision between the astragalus and the picker components, astragalus force including astragalus - astragalus, astragalus – steel; the force relationship is very complex, the magnitude of the astragalus collision force suffered by the astragalus will have a direct effect on the extent of damage to the astragalus epidermal skin, was shown in the use of the discrete element method of the astragalus picker work process. Numerical simulation of the working process of the astragalus picker using the discrete element method is conducive to revealing the working principle of the astragalus picker and further calibrating and optimizing the working parameters of the astragalus picker.

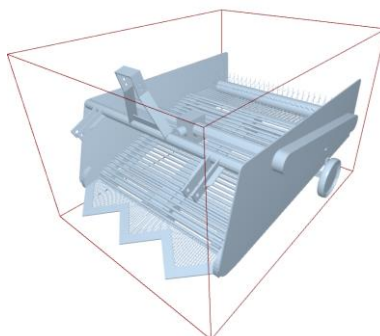


Fig. 2 - Discrete element modelling of astragalus picker

Before carrying out the research on the factors affecting the performance of the astragalus picker, since no researcher has calibrated and benchmarked the discrete element simulation parameters of the astragalus, it is necessary to calibrate the astragalus parameters to ensure the accuracy of the working parameter settings of the environment of the discrete element simulation software during the subsequent simulation experiments (Chen et al., 2018).

Determination of basic physical property parameters

First, the basic physical parameters of astragalus which are easy to measure were determined. Digital vernier callipers were used to determine the external dimensions of astragalus, and the parameters of the external dimensions of astragalus are shown in Table 1.

Table 1

| External dimension parameters of astragalus | |
|---|--------------|
| Projects/Unit | Target value |
| Astragalus length (mm) | 300~690 |
| Reed head diameter (mm) | 11~21 |
| Center Diameter (mm) | 10~18 |
| Root Diameter (mm) | 10~17 |

Table 2

| Basic physical parameters of astragalus segment | |
|---|-------------------|
| Projects/Unit | Target value |
| Overall dimensions (mm) | 25.7±6.3×11.3±1.3 |
| Mass (g) | 9.95±2.15 |
| Densities (kg·m ⁻³) | 0.912±0.159 |

Due to the large size of the astragalus, the error in measuring the physical parameters was large, so the astragalus was cut into astragalus segments of different sizes for the determination of astragalus. The weight of the astragalus segments was measured using an electronic balance, the length and diameter of the segments were measured using vernier callipers (LxD), and the density of the astragalus was measured using a measuring cylinder. The mean values of the measurement results are shown in Table 2.

As shown in Figure 3, the pressure deformation test of astragalus was carried out by using the texture instrument. Before the test started, the astragalus segment was placed horizontally on the test platform, the working parameters of the texture instrument were set, and loading was carried out at a speed of 5 mm/s in the thickness direction of astragalus, and when the deformation of the astragalus reached 30%, the loading was stopped and the press returned to the initial position. The thickness and width of the astragalus segments were measured before the test. The thickness and width of the astragalus segments were measured again after the press finished loading the astragalus in the thickness direction and returned to the initial position. Using equation (1), the Poisson's ratio of the astragalus was calculated according to the deformation of the astragalus segments in the width and thickness directions before and after loading.

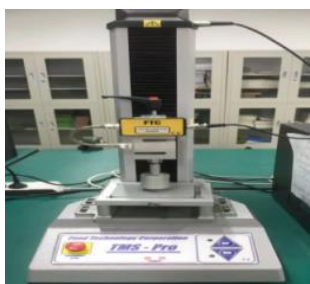


Fig. 3 - Texture analyzer

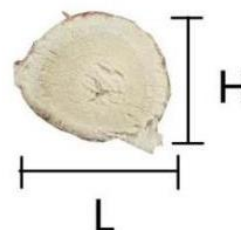


Fig. 4 - Diagram of astragalus membranaceus

$$\nu = \frac{|\varepsilon'|}{|\varepsilon|} = \frac{L_1 - L_2}{H_2 - H_1} \quad (1)$$

ν - the Poisson's ratio;

ε' - the transverse deformation;

ε - the longitudinal deformation;

L_1 - the width of astragalus before loading;

L_2 - the width after loading of astragalus;

H_2 - represents the thickness after loading of astragalus;

H_1 - represents the thickness of astragalus before loading.

Determination of exposure parameters

The contact parameters required when applying the discrete element method to study the law of motion of astragalus and the working principle of astragalus picker are static friction, rolling friction, and collision recovery coefficient between astragalus and astragalus; static friction, rolling friction, and collision recovery coefficient between astragalus and steel; and collision recovery coefficient between astragalus and rubber. In order to improve the accuracy of the contact parameters, a combination of physical tests and simulation tests will be used to determine the required contact parameters through physical tests, and the range of the required parameters to carry out the discrete element simulation tests will be determined by physical tests as a reference.

The physical test of the contact parameters was conducted using the cut and treated astragalus segments with a density of 0.912 g/cm³, and the material in contact with the astragalus was steel with a density of 7,850 kg/m³, a Poisson's ratio of 0.3, a shear modulus of 80 GPa, and a modulus of elasticity of 2.06×10⁵ MPa.

Determination of crash recovery coefficient

The collision recovery coefficient indicates the ability of the object under test to recover its original state after a collision, and is defined as the ratio between the velocity of the object under test after collision and separation and the velocity before the collision. In this paper, free-fall physical tests were used to determine the collision recovery coefficients between astragalus and astragalus, astragalus and steel, and astragalus and rubber, and the test setups are shown in Fig. 5.

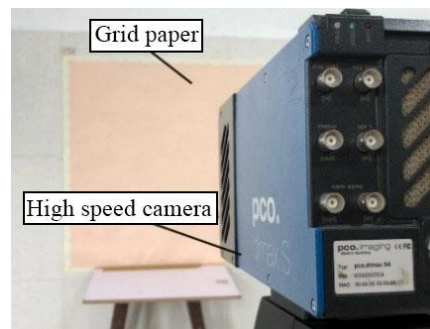


Fig. 5 - High speed camera

A high-speed camera was placed directly in front of the test bench and the tripod was adjusted to keep it horizontal, and the distance between the high-speed camera and the test bench was 780 mm. In order to facilitate the TEMA high-speed camera analysis software to capture the movement process of the astragalus, a piece of grid paper was arranged at the back of the test bench, so that the rebound height of the astragalus could be accurately observed.

Assuming that the astragalus is subjected only to gravity during its fall, the normal velocity of the astragalus before the collision is obtained from the kinetic energy theorem:

$$v_1 = \sqrt{2gh_1} \quad (2)$$

Normal velocity after collision separation:

$$v_2 = \sqrt{2gh_2} \quad (3)$$

From the definition of collision recovery coefficient, the collision recovery coefficient is obtained as:

$$e = \frac{|v_2|}{|v_1|} = \sqrt{\frac{h_2}{h_1}} \quad (4)$$

v_1 - the speed of astragalus before collision ;

v_2 - the velocity of astragalus after collision ;

h_1 - represents the astragalus fixed drop height ;

h_2 - represents the astragalus rebound height after collision (*Dai et al., 2021*).

In this physical test, the height of the falling astragalus was fixed at 400 mm, and different astragalus were selected to repeat the test, and the collision recovery coefficients between astragalus and rubber were obtained as 0.3142 ± 0.013 ; between astragalus and astragalus as 0.3 ± 0.1 ; and between astragalus and steel as 0.35 ± 0.05 .

Determination of static and rolling friction coefficients

The coefficient of static friction and the rolling friction coefficient between astragalus and astragalus, astragalus and steel were measured using CNY-1 type inclinometer (Figure 6).



Fig. 6 - CNY-1 inclinometer

In order to accurately measure the coefficient of static friction and coefficient of rolling friction between astragalus, before the test started, the astragalus and the test plane of the inclinometer were glued together by using transparent double-sided adhesive tape, and then the astragalus segments were placed along the length of the test plane of the inclinometer on the astragalus determination plane.

The test was conducted by slowly rotating the inclinometer test plane counterclockwise, immediately stopping rotating when the astragalus segment slides on the astragalus determination plane, recording the angle indicated by the inclinometer pointer at this time, through which the static friction coefficient and rolling friction coefficient between the astragalus can be calculated (Zhang *et al.*, 2018). When determining the coefficient of static friction and coefficient of rolling friction between astragalus and steel plate, it is only necessary to change the test plane to steel plate.

Through 20 test trials and taking the average value, the average values of static friction coefficient and rolling friction coefficient between astragalus and astragalus were obtained as 0.65 ± 0.03 and 0.53 ± 0.03 respectively, and the average values of static friction coefficient and rolling friction coefficient between astragalus and steel plate were obtained as 0.2 ± 0.1 , and 0.15 ± 0.05 respectively.

Determination of angle of repose of astragalus

According to the review of relevant literature, the test of measuring the angle of repose of astragalus segments was carried out by using the pumping plate method, the randomly selected astragalus was loaded into a closed cardboard box, the baffle plate on one side of the cardboard box was pumped vertically upward, so that the astragalus was free to slide down, and when the astragalus in the box was free to slide down and come to a standstill on the substrate, the astragalus heap was photographed with a camera, and a front-view picture of the heap of the astragalus was obtained, and the grayscale and binary processing was carried out for the picture by applying the software of Matlab. The image digitizing tool in Origin2018 software was applied to extract the boundary curve for fitting treatment, and the average value of the rest angle was obtained as 35.79° (Figure 7).

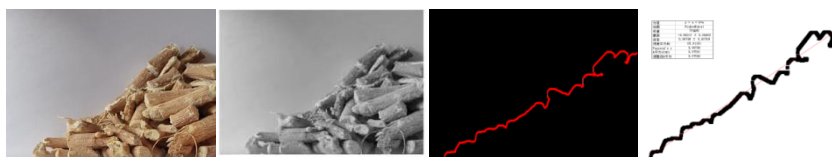


Fig. 7 - Image processing of astragalus accumulation

RESULTS

Parameter calibration for discrete meta-simulation of astragalus

According to Table 1 - astragalus external dimensions parameter list, the astragalus was modelled in Solidworks software, and the modelling file was imported into EDEM2018 software, and 121 basic spheres with a radius of 8 mm (the radius of the basic sphere is R_{min}) in the EDEM software library were used to fill out the simulation model of astragalus, which is shown in Figure 8.

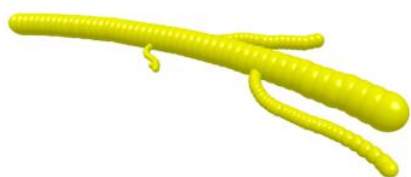


Fig. 8 - Whole plant model of astragalus



Fig. 9 - Segmental model of astragalus membranaceus

In the physical parameter calibration simulation test of astragalus, the astragalus segments after the cutting treatment were used, and according to Table 2, the average diameter of astragalus segments was obtained as 11 mm, and the average length was obtained as 25 mm, and the shape of astragalus segments was approximate to a cylinder, so the simulation model of astragalus segments was populated by using five basic spheres with a radius of 5.5 mm in the library of the EDEM2018 software as shown in Figure 9.

The modelling of the simulated angle of repose determination apparatus for astragalus was based on the actual angle of repose determination apparatus. Considering the feasibility of the experiment and the high efficiency of the software operation, discrete element models of astragalus segments with different sizes were used in the simulation. The total simulation time was set to 10 s, the time step was 7.43678×10^{-5} s, and the grid size was $3 \times R_{min}$. The working parameters of EDEM software were set as shown in Figure 10.

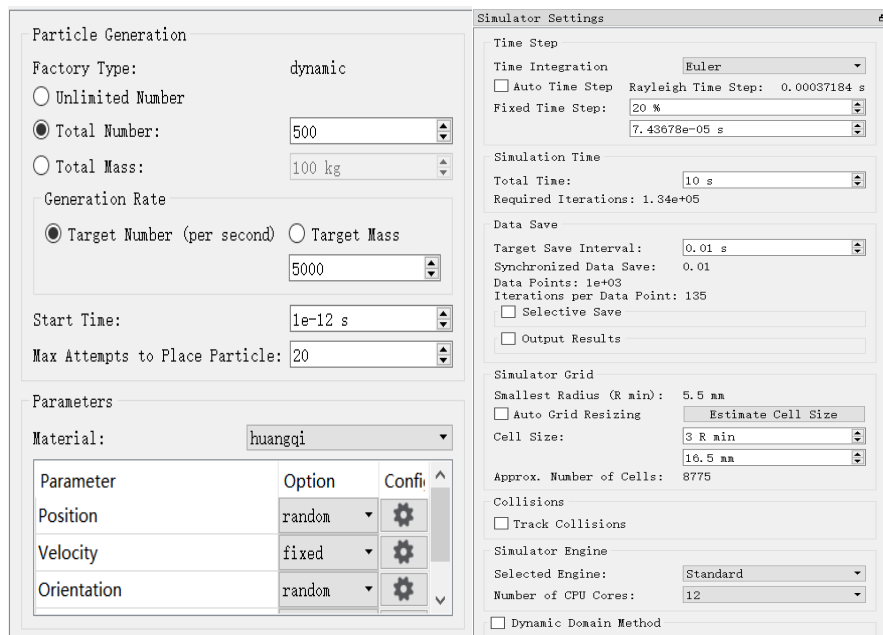


Fig. 10 - EDEM working parameter setting diagram

The particle dynamic generation plant was established in the inner position of the carton, and 500 astragalus segments were modelled to be generated in one second, and the plate on one side of the carton was withdrawn at 4s, and the astragalus segments were free to pour down under gravity, and the astragalus segments were stationary on the substrate after a period of 6s to form an astragalus pile, as shown in Fig. 11.

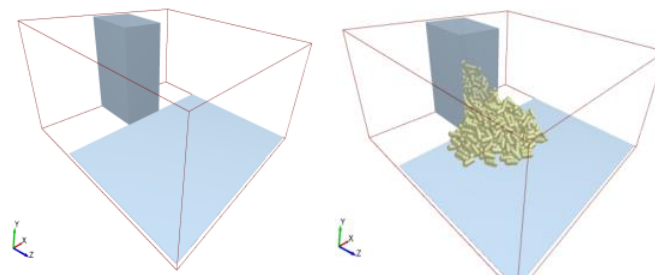


Fig. 11 - Simulation test of angle of repose of astragalus

**Discrete element simulation parameter calibration
Plackett-Burman test**

The Plackett-Burman test was designed using Design-Expert11 software, with the simulated resting angle of astragalus as the response value and the parameters measured in the physical test as the test parameters, and the maximum and minimum values of the measured results were coded as the +1 and -1 levels, and the parameters that had a significant effect on the resting angle of astragalus were derived from the results of the Plackett-Burman test. The Plackett-Burman test level coding table with test protocol and results are shown in Table 3 and Table 4.

Table 3

| Test parameters table | | | |
|-----------------------|--|----------------|-----------------|
| NO. | Test parameters | Low level (-1) | High level (+1) |
| A | Poisson's ratio | 0.22 | 0.28 |
| B | Astragalus-Astragalus collision recovery coefficient | 0.2 | 0.4 |
| C | Astragalus-Astragalus static friction coefficient | 0.62 | 0.68 |
| D | Astragalus-Astragalus rolling friction coefficient | 0.5 | 0.56 |
| E | Astragalus-steel collision recovery coefficient | 0.3 | 0.4 |
| F | Astragalus-steel static friction coefficient | 0.1 | 0.3 |
| G | Astragalus-steel rolling friction coefficient | 0.1 | 0.2 |

Table 4

Design and results of the Plackett-Burman experiment

| No. | Test Parameters | | | | | | | Repose angle θ (°) |
|-----|-----------------|----|----|----|----|----|----|------------------------------|
| | A | B | C | D | E | F | G | |
| 1 | 1 | 1 | -1 | 1 | 1 | 1 | -1 | 43.93° |
| 2 | -1 | 1 | 1 | -1 | 1 | 1 | 1 | 43.27° |
| 3 | 1 | -1 | 1 | 1 | -1 | 1 | 1 | 30.11° |
| 4 | -1 | 1 | -1 | 1 | 1 | -1 | 1 | 28.7° |
| 5 | -1 | -1 | 1 | -1 | 1 | 1 | -1 | 36.13° |
| 6 | -1 | -1 | -1 | 1 | -1 | 1 | 1 | 29.68° |
| 7 | 1 | -1 | -1 | -1 | 1 | -1 | 1 | 22.78° |
| 8 | 1 | 1 | -1 | -1 | -1 | 1 | -1 | 32.62° |
| 9 | 1 | 1 | 1 | -1 | -1 | -1 | 1 | 23.75° |
| 10 | -1 | 1 | 1 | 1 | -1 | -1 | -1 | 22.78° |
| 11 | 1 | -1 | 1 | 1 | 1 | -1 | -1 | 21.31° |
| 12 | -1 | -1 | -1 | -1 | -1 | -1 | -1 | 20.8° |

The results of the experiment were analysed by ANOVA using Design-Expert software, as shown in Table 5.

Table 5

The Plackett-Burman test parameter significance affects the results

| Parameters | Degree of freedom | Sum of squares | F-value | P-value |
|------------|-------------------|----------------|---------|---------|
| A | 4.04 | 1 | 0.5648 | 0.4941 |
| B | 97.13 | 1 | 13.59 | 0.0211 |
| C | 0.0936 | 1 | 0.0131 | 0.9144 |
| D | 0.7203 | 1 | 0.1008 | 0.7668 |
| E | 109.69 | 1 | 15.35 | 0.0173 |
| F | 475.27 | 1 | 66.49 | 0.0012 |
| G | 0.0560 | 1 | 0.0078 | 0.9339 |

Note: $0.01 < P < 0.05$, significant effect; $P < 0.01$, highly significant effect; $P > 0.05$, no significant effect.

As can be seen from Table 5, by carrying out the Plackett-Burman test, the astragalus-astragalus collision recovery coefficient (B), astragalus-Steel collision recovery coefficient (E) and astragalus-Steel static friction coefficient (F) were screened as significant factors.

Steepest climb experimental design

On the basis of Plackett-Burman test, the steepest climb test was conducted for the significance factors, and the relative error between the rest angle of the physical test and the rest angle of the simulation test was used as the evaluation index to determine the range of optimal intervals for the significance factors (Ma *et al.*, 2020), and the other parameters were averaged for the simulation test.

Table 6

Design and results of the steepest climbing test

| No. | Test Parameters | | | Repose angle θ (°) | Relative error (%) |
|-----|-----------------|------|------|------------------------------|--------------------|
| | B | E | F | | |
| 1 | 0.2 | 0.3 | 0.1 | 40.73° | 13.8% |
| 2 | 0.24 | 0.32 | 0.14 | 39.91° | 11.5% |
| 3 | 0.28 | 0.34 | 0.18 | 37.48° | 4.7% |
| 4 | 0.32 | 0.36 | 0.22 | 35.47° | 0.89% |
| 5 | 0.36 | 0.38 | 0.26 | 37.9° | 5.9% |
| 6 | 0.4 | 0.4 | 0.3 | 40.3° | 12.6% |

The design scheme and results of the steepest climb test are shown in Table 6. The Box-Behnken response surface design was carried out with level 4 as the centre point in the steepest climb test, and levels 3 and 5 as the low and high levels, respectively.

All other parameters in the simulation tests were averaged using physical test measurements: the Poisson's ratio of astragalus was taken to be 0.25, the coefficient of static friction between astragalus and astragalus was taken to be 0.65, the coefficient of rolling friction between astragalus and astragalus was taken to be 0.53, and the coefficient of rolling friction between astragalus and steel was taken to be 0.15 (Hou et al., 2021).

Box-Behnken experimental design

The Box-Behnken simulation test with significant contact parameters was designed using Design Expert11 software to calibrate the astragalus simulation parameters. The level 4 in the steepest climb test was taken as the centre point (0), and levels 3 and 5 were taken as the low level (-1) and high level (1), respectively, and the level coding table is shown in Table 7, and the Box-Behnken test design scheme and results are shown in Table 8.

Table 7

Significant exposure parameter level coding table

| Levels | Astragalus -Astragalus Collision coefficient of restitution | Astragalus -Steel plate Collision coefficient of restitution | Astragalus -Steel plate static friction coefficient |
|--------|---|--|---|
| -1 | 0.28 | 0.34 | 0.18 |
| 0 | 0.32 | 0.36 | 0.22 |
| +1 | 0.36 | 0.38 | 0.26 |

Table 8

Box-Behnken experimental design and results of significant contact parameters

| No. | Astragalus -Astragalus Collision coefficient of restitution | Astragalus -Steel plate Collision coefficient of restitution | Astragalus -Steel plate static friction coefficient | Repose angle θ (°) |
|-----|---|--|---|---------------------------|
| 1 | -1 | -1 | 0 | 40.69° |
| 2 | 1 | -1 | 0 | 34.67° |
| 3 | -1 | 1 | 0 | 34.51° |
| 4 | 1 | 1 | 0 | 38.3° |
| 5 | -1 | 0 | -1 | 34.99° |
| 6 | 1 | 0 | -1 | 34.78° |
| 7 | -1 | 0 | 1 | 36.75° |
| 8 | 1 | 0 | 1 | 34.57° |
| 9 | 0 | -1 | -1 | 37.23° |
| 10 | 0 | 1 | -1 | 33.04° |
| 11 | 0 | -1 | 1 | 34.51° |
| 12 | 0 | 1 | 1 | 35.97° |
| 13 | 0 | 0 | 0 | 36.13° |
| 14 | 0 | 0 | 0 | 35.72° |
| 15 | 0 | 0 | 0 | 35.75° |
| 16 | 0 | 0 | 0 | 34.72° |
| 17 | 0 | 0 | 0 | 35.91° |

Multiple regression analysis of the experimental results in the table was carried out using Design-Expert11 software to obtain a second-order regression model for the simulated resting angle of astragalus with three significance parameters with the equation:

$$\theta = 35.65 - 0.5775 \times A - 0.66 \times B + 0.22 \times C + 2.45 \times AB - 0.4925 \times AC + 1.41 \times BC + 0.7408 \times A^2 + 0.6557 \times B^2 - 1.11 \times C^2 \tag{5}$$

The p-value of the fitted model is less than 0.01, the coefficient of determination R² is 0.9717, the corrected coefficient of determination R²adj is 0.9354, both close to 1, and the signal-to-noise ratio (Adeq precision) is 22.7736, which indicates that the angle of repose regression model is highly significant and predicts the target angle of repose; and the coefficient of variation, C.V. = 1.25%, is low, which indicates that the equations are well fitted . As shown in Table 9, it is indicated that the regression model is extremely significant, can reliably and realistically reflect the real situation, and can be used for further analysis of target angle of repose prediction.

Table 9

Analysis results of Box-Behnken test

| Source of variation | Mean Square | Degree of freedom | Sum of Squares | P-value |
|---------------------|-------------|-------------------|----------------|---------|
| Model | 5.38 | 9 | 48.45 | 0.0001 |
| B | 2.67 | 1 | 2.67 | 0.0083 |
| E | 3.48 | 1 | 3.48 | 0.0042 |
| F | 0.3872 | 1 | 0.3872 | 0.2081 |
| BE | 24.06 | 1 | 24.06 | <0.0001 |
| BF | 0.9702 | 1 | 0.9702 | 0.0642 |
| EF | 7.98 | 1 | 7.98 | 0.0004 |
| B ² | 2.31 | 1 | 2.31 | 0.0116 |
| E ² | 1.81 | 1 | 1.81 | 0.0200 |
| F ² | 5.23 | 1 | 5.23 | 0.0014 |
| Residual | 0.2013 | 7 | 1.41 | |
| Lack of Fit | 0.0772 | 3 | 0.2317 | 0.8498 |
| Pure Error | 0.2944 | 4 | 1.18 | |
| Sum | | 16 | | |

Note: $0.01 < P < 0.05$, significant effect; $P < 0.01$, highly significant effect; $P > 0.05$, no significant effect.

Simulation parameter calibration and experimental verification

In the optimization module of Design-Expert11 software, the second-order regression equation (Eq. 5) was optimized and solved using the angle of repose of 35.79° measured in the physical tests as the target value, and a set of parameters similar to the data of the physical tests was obtained: the collision recovery coefficient of astragalus-astragalus was 0.32, the collision recovery coefficient of astragalus-Steel was 0.36, and the coefficient of static friction of astragalus-Steel was 0.22. The values of the remaining non-significant parameters were taken as the average of the physical test measurements.



Fig. 12 - Test comparison of repose angle of astragalus membranaceus

To check whether the optimal parameter combinations could meet the simulation test results, the above parameters were input into EDEM2018 software to carry out the validation test, and the validation test was repeated three times, and the resulting angles of repose of astragalus were 35.51° , 36.01° , and 35.43° , with an average value of 35.65° . The relative error between the simulation test result of angle of repose under the optimal parameter combination (35.65°) and the angle of repose measured in the physical test (35.79°) was 0.392%, which verified the reliability and authenticity of the simulation test. The test comparison is shown in Figure 12.

The basic physical property parameters and contact parameters of astragalus were measured by physical tests, and the average values of collision recovery coefficient, static friction coefficient and rolling friction coefficient between astragalus were obtained as 0.3 ± 0.1 , 0.65 ± 0.03 , 0.53 ± 0.03 , respectively; and the average values of collision recovery coefficient, static friction coefficient and rolling friction coefficient between astragalus and steel were obtained as 0.35 ± 0.05 , respectively, 0.2 ± 0.1 , 0.15 ± 0.05 . The Plackett-Burman test was carried out to screen astragalus-astragalus collision recovery coefficient, astragalus-steel collision recovery coefficient and astragalus-steel static friction coefficient as significant factors affecting the angle of repose of astragalus.

CONCLUSIONS

Based on the physical property parameters measured in physical experiments, simulation experiments were conducted to establish a second-order regression model for the relative error between the simulated and physical experiment angles of repose. The optimal simulation parameters for astragalus membranaceus were obtained: astragalus membranaceus- astragalus membranaceus collision recovery coefficient of 0.32, astragalus membranaceus-steel collision recovery coefficient and static friction coefficient of 0.36 and 0.22, respectively.

The relative error between the average angle of repose in the astragalus membranaceus simulation experiment and the average angle of repose in the physical experiment is 0.392%, which further verifies the authenticity and feasibility of the simulation experiment and calibrated simulation parameters, providing a basis for subsequent research.

ACKNOWLEDGEMENT

This work was funded by the Key R&D and achievement transformation plan project of Inner Mongolia (2023YFDZ0006), the Program for improving the Scientific Research Ability of Youth Teachers of Inner Mongolia Agricultural University (BR220128), the Research Program of science and technology at Universities of Inner Mongolia Autonomous Region (NJZZ23046), and the High-level Talent Introduction and Research Launch Project of Inner Mongolia Agricultural University (NMGIRT2403).

REFERENCES

- [1] Chen, L., Chen, Z., Hou, Z., et al. (2018). Experimental study of pilling coating parameters of forage seeds based on vibration action. *Research on agricultural mechanization*, 40(10):189-193. China.
- [2] Cui, Z. (2014). Uses of Astragalus and the application of its cultivation and planting techniques. *Heilongjiang Pharmaceuticals*, 27(04):821-825. China.
- [3] Dai, N., Hou, Z., Qiu, Y., et al. (2021). Calibration and testing of discrete meta-simulation parameters for red clover seeds. *Journal of Hebei Agricultural University*, 44(06):92-98. China.
- [4] Hou, Z., Chen, L., Chen, Z., et al. (2021). Research on the movement law and parameter optimization of pelletized coating of forage seed. *Research on agricultural mechanization*, 43(11):184-191. China.
- [5] Hou, Z., Dai, N., Chen, Z., et al. (2020). Determination of physical property parameters of iceplant seeds and calibration of parameters for discrete element simulation. *Journal of Agricultural Engineering*, 36(22):36-42. China.
- [6] Huang, S., Shen, Y., Ou, C. (2023). Astragalus membranaceus and Panax notoginseng saponins improves intestinal L-arginine absorption and protects against intestinal disorder in vivo. *Food Science and Technology Research*, 29(2):129-140. China.
- [7] Jiang, L., Zhang, D., Hao, X., et al. (2013). Overview of Astragalus development in Inner Mongolia. *Disease Surveillance and Control*, 7(03):165-166. China.
- [8] Kang, Q., Yuan, H., Hu, Y., et al. (2016). Benefits and Prospects of Herbal Medicine Astragalus in Heilongjiang Province. *Heilongjiang Agricultural Science*, 08:118-121. China.
- [9] Li, F., Liu, F., Liu, S., et al. (2015). Discussion on the items and methods to be measured for ultrasonic cleaning of traditional Chinese medicine Astragalus membranaceus. *Journal of Animal Husbandry and Veterinary Medicine*, 34(05):45-49. China.
- [10] Liu, M., Hou, Z., Ma, X., et al. (2022). Discrete element-based simulation parameter calibration and testing of alfalfa seeds. *Jiangsu Agricultural Science*, 50(06):168-175. China.
- [11] Ma, Y., Song, C., Xuan, C., et al. (2020). Parameter calibration of discrete element model for alfalfa straw compression simulation. *Journal of Agricultural Engineering*, 36(11):22-30. China.
- [12] Shen M., Wang Y., Liu Z., et al. (2023). Inhibitory Effect of Astragalus Polysaccharide on Premetastatic Niche of Lung Cancer through the S1PR1-STAT3 Signalling Pathway. *Evidence-Based Complementary and Alternative Medicine*, 2023, 1-10. China.
- [13] Wang, Y., Liang, Z., Zhang, D., et al. (2016). Discrete element-based calibration of interspecies contact parameters for corn seed particle models. *Journal of Agricultural Engineering*, 32(22):36-42. China.
- [14] Wu, F., Chen, X., et al. (2004). A review on the pharmacological effects of Astragalus membranaceus. *Chinese herbal medicine*, 03:232-234. China.
- [15] Zhang, L., Guo, B., Zhu, S., et al. (2006). Survey Report on Astragalus Germplasm Resources. *Chinese herbal medicine*, 2006(08):771-773. China.
- [16] Zhang, T., Liu, F., Zhao, M., et al. (2018). Determination of physical parameters of corn stover contact and calibration by discrete element simulation. *Journal of China Agricultural University*, 23(4):120-127. China.
- [17] Zhao, S. (2017). Prospect analysis and large-scale mechanized planting technology of astragalus. *Special economic flora and fauna*, 20(04):25-27. China.

OPTIMIZATION OF JOINT SAND BARRIER SPACING AND CHARACTERIZATION OF WIND AND SAND FLOW STUDY BASED ON CFD NUMERICAL SIMULATION

基于 CFD 数值模拟的联合沙障间距优化与风沙流特征研究

Ming YAN¹⁾; Afang JIN ^{*1)}; Wenxiu GAO ¹⁾

¹⁾ College of Mechanical Engineering, Xinjiang University, Urumqi 830046/ China;

Tel: + 86-18999869949; E-mail: jinaf3500_xju@xju.edu.cn

DOI: <https://doi.org/10.35633/inmateh-73-72>

Keywords: Agricultural security, numerical simulation, wind tunnel experiment, wind sand, combined sand barrier, optimal spacing

ABSTRACT

Strong wind and sand activities will seriously damage the ecological restoration and agricultural safety production on the edge of desert areas, resulting in irreversible economic losses. To prevent and protect the agroecological environment in the wind-blown sand area, this paper constructs a combination of double-row vertical nylon net sand barrier and grass grid sand barrier. The protection benefits of double-row vertical nylon net sand barrier and grass grid under different spacing conditions are analyzed through numerical simulation and wind tunnel experiment, and the layout conditions with optimal spacing are obtained. The results show that when the spacing between the double-row vertical sand barrier and grass grid is 5H-10H, the airflow velocity behind the double-row vertical sand barrier cannot be fully developed, the increase of airflow velocity is small, and the average wind prevention efficiency is above 85%. The effective protection distance completely covers the entire combined sand barrier area, and a large number of sand particles near the surface are fixed to the grass grid, so the sand resistance rate is over 77%. The combined sand barrier has a good cooperative protection effect and achieves efficient wind prevention and sand fixation. The wind tunnel experiment verifies the reliability of the results. It also realizes efficient wind prevention and sand fixation under extreme wind and sand, and avoids sand burial on farmland and ecological restoration areas caused by extreme wind and sand weather.

摘要

强烈的风沙活动会对沙漠地区边缘地带的生态恢复建设和农业安全生产形成严重破坏,造成不可逆转的经济损失。为预防保护风沙地区的农业生态环境,本文构建了双排高立式尼龙网沙障+草方格联合沙障,通过数值模拟和风洞实验,分析双排高立式尼龙网沙障与草方格不同间距条件下的防护效益,得到了最优间距的布设工况。结果表明,当双排高立式沙障与草方格间距为 5H-10H 时,双排高立式沙障后气流速度无法充分发育,气流速度增大幅度较小,平均防风效率达到 85% 以上,有效防护距离完全覆盖整个联合沙障区域,近地表沙粒大量被固定至草方格内,阻沙率达到 77% 以上,联合沙障协同防护作用较好,实现高效的防风固沙。经风洞实验测试,验证了结果的可靠性。实现了在极端风沙天气下高效的防风固沙,避免极端风沙天气对农田和生态修复区造成沙埋。

INTRODUCTION

China has most extensive desert distribution in the world, mainly concentrated in Xinjiang, Gansu, Inner Mongolia, and Qinghai (Xiao J., 2016). Wherever the strong air currents carrying sand particles pass, large areas of farmland are buried by sand or blown away by wind erosion through sand burial, wind erosion, and wind attacks, resulting in the deterioration of the ecological environment and severe losses to people's lives and property (Zhenghua Z., 2006; Ming W., 2007).

Protective measures are divided into sand-blocking and sand-fixing measures to protect the ecological restoration area around the desert plants and farmland from sandstorms, generally in the oasis edge of the deployment of protective measures. Mechanical sand barriers have the advantages of anti-aging, anti-wind-sand, industrial production, convenient construction, in some fields with serious wind-sand disasters, such as industry and mining, transportation and national defense, the use of mechanical sand barriers can achieve rapid results (Maolin W., Ling S. et al., 2024).

Among the sand-fixing sand barriers, the most typical one is the grass grid sand barrier. Grass grid plays an irreplaceable role in wind prevention and sand fixation, precipitation interception, water evaporation reduction and nutrition for sand and soil (Jiayuan D, Xiangyun Q, 2019). One of the direct functions of grass grid sand barrier is to increase the surface aerodynamic roughness Z_0 , the aerodynamic roughness of Z_0 is hundreds to thousands of times larger than the surface of quicksand, thus significantly reducing the ground surface wind speed, making it lower than the sand generating wind speed, and maintaining the stability of the sand surface in the grid (Junling X., 1982; Yingxin L., 1987; Jiguo Z., 1987; Dong, Chen et al., 2002). Another direct effect is to physically block the aeolian sand flow and promote the rapid settlement of the transit aeolian sand flow (Congmao K., 2000; Yizheng Y., Guangting C. et al., 2006; Guoping Z., Hejun Z. et al., 2008).

Qu Jianjun (Jianjun Q., 2001; Jianjun Q., 2002) conducted wind tunnel simulation experiments on the effect of nylon mesh sand prevention, and found that nylon mesh sand barrier fence is more efficient than wooden sand barrier fence, which is a high-quality new material for sand prevention. The results show that the double row of wind grids is the best through numerical simulation and wind tunnel tests, combined with economy and effective shielding distance (Fang, Wu et al., 2018). Dong, Chen et al., (2023), pointed out that double-row and three-row wind fences are the most effective in reducing wind speed, which was confirmed in subsequent studies (Cornelis and Gabriels, 2004). For the line spacing, Papesch, (1992), and Wu, Zou et al., (2013), recommended 6-8 H (H is the height of the wind fence) as being the best.

Guangpu J., Hejun Z. et al., (2020), showed in the experiment that the distance between the double-row sand barriers at the height of 150 cm was 20 m when the wind speed increased to more than 15 m/s, there was basically no sand accumulation on the lee side of the double-row sand barriers, and the high-vertical sand barriers gradually lost their protective effect. There is a certain relationship between the height of sand barriers and the protection distance. Wang Xunming et al. (1997; 1999), found in the analysis of the benefits of the Tarim Desert highway sand prevention system that laying vertical nylon net sand barriers with a height of 1.1 m on flat sandy land can achieve a protection range of about 10 m. Xu et al. 's numerical simulation analysis found that there were a series of non-uniformly distributed eddies in the grass grid, which would carry sand particles near the grass belt and accumulate them, promoting the formation of concave surfaces (Xu, Zhang et al., 2018). Based on the aerodynamic principle of sand movement, Wang Zhenting (Zhenting W., 2002) obtained the analytical formula for the optimal correlation between the surface height of wheat grass and the side length of the grid by using numerical simulation. Qiu, Lee et al., (2004), used a computational fluid dynamics (CFD) model to simulate the wind speed profiles of wheat grass sand barriers of different specifications. Considering the cost and protection benefits comprehensively, it is suggested to set the sand barriers with a specification of 1m×1m and a height of 10-20 cm. Zhang, Li et al., (2016), observed the wind speed and sand transport rate of bare sand. They paved grass square sand barriers through field comparison, and found that the height of 20 cm sand barriers can improve the surface roughness by more than 0.02 m, and the sand transport rate above the sand barriers changes with the height of the contour in the form of a weevil.

The combined sand barrier and grass grid have the function of blocking solid combination, which can produce better protective efficiency. Through wind tunnel experiment and numerical simulation, Xin, Zhang et al., (2023), studied the optimal porosity and opening type of the second sand barrier in the combination of double-row nylon mesh high vertical sand barrier and grass grid sand barrier, and found that when the second high vertical sand barrier had a horizontal opening, the second high vertical sand barrier destroyed the continuous flow of particles from the first sand fence. Thus, most of the sand is deposited on the leeward side and in the grass grid, improving the wind and sand prevention efficiency. Peng, Jin et al., (2023), used the computational fluid dynamics method and the Eulerian-Eulerian two-fluid model to simulate the wind protection effect and the airflow characteristics of the newly developed double-row reed-nylon mesh combination sand barrier, which is made of different materials, and combines the advantages of both, improving the construction efficiency and service life for deserts. It also provides a more economical and efficient reference for the layout of windscreen sand facilities around railways and highways in desert areas.

To sum up, domestic and foreign scholars have a large research foundation for the study of wind and sand resistance performance and mechanism of single sand barrier and sand-fixation barrier. It also has accumulated profound experience in the application of various technical means in continuous in-depth research. However, the effect of combined sand barrier and how it can be used it in engineering measures are still mainly based on engineering experience. So, there is a lack of systematic experimental and theoretical research and few studies on the protection ability of the protection system under extreme wind and sand environment. To avoid destroying ecological restoration areas and farmland economic losses, we study the wind and sand prevention facilities in this kind of extreme weather.

Therefore, this paper takes the combination of double-row high vertical nylon net sand barrier and straw checkerboard barrier as the research object, the numerical simulation as the primary research method, the wind tunnel test as the verification method, the maximum field wind speed as the inlet wind speed condition, studies the protection benefits under the conditions of different spacing between double-row high vertical nylon net sand barrier and grass grid, and obtains the layout conditions with the optimal spacing. It provides a theoretical basis for the design of sand control projects in desertification ecological restoration areas.

MATERIALS AND METHODS

Overview of the study area

Minqin County of China is located in the northeast of Hexi Corridor, the lower reaches of the Shiyang River basin, the south adjacent to Wuwei, southwest adjacent to Jinchang, east, west, north three sides, surrounded by Tengger Desert and Badain Jaran Desert (Yanli Z., 2011). The study area is a temperate continental arid climate, with northwest winds throughout the year, with an average wind ≥ 12 m/s and the instantaneous wind ≥ 17 m/s, the gale weather above grade 8 is more frequent, the maximum wind speed is 11, the average gale days in the county are 27.8 days, the maximum is 63 days, the sand storm is 25 days, the sand blowing is 37.5 days, and the sand-driving wind speed is 4.5, the average yearly temperature is 7.7°C , the annual average precipitation is 48-185 mm, and the rainfall is mainly concentrated in July to September. So, the soil desertification phenomenon in the territory is severe, the desert area is vast, the desert vegetation is sparse, the composition types are scarce, and the vegetation structure is simple (Fugui H., Ming Z. et al., 2009; Cuicui J., Xuemei Y. et al., 2021). Minqin Oasis is the front line of desertification resistance in northern China, and an ecological fortress to protect the unimpeded flow of the Eurasian Continental Bridge, which needs effective wind and sand blocking facilities to protect, so it is necessary to rationally configure according to the degree of sand damage in different areas.



Fig. 1 – The current situation of farmland around the desert in Minqin County, China
a) The desert invades the farmland; b) the locals erect sand retaining walls.

Numerical simulation

Theoretical governing equation

This paper, uses the Euler two-phase fluid model to study the near-surface aeolian sand movement with different double rows of vertical sand barriers and grass grid spacing. In this model, the gas phase and solid phase are regarded as continuous media that exist together and permeate each other, and the sum of their volume fractions is 1. That's to say: $\alpha_g + \alpha_s = 1$. Gas-solid two-phase flow follows mass conservation and momentum conservation equations, respectively, and the governing equations are as follows:

Gas-phase mass conservation equations:

$$\frac{\partial}{\partial t}(\alpha_g \rho_g) + \nabla(\alpha_g \rho_g v_g) = 0 \quad (1)$$

Sand-phase mass conservation equations:

$$\frac{\partial}{\partial t}(\alpha_s \rho_s) + \nabla(\alpha_s \rho_s v_s) = 0 \quad (2)$$

The gas-phase momentum conservation equation:

$$\frac{\partial}{\partial t}(\alpha_g \rho_g U_g) + \nabla(\alpha_g \rho_g U_g U_g) = -\alpha_g \nabla p + \nabla \tau_g + \alpha_g \rho_g g + K_{gs}(U_g - U_s) \quad (3)$$

Sand-phase momentum conservation equations:

$$\frac{\partial}{\partial t}(\alpha_s \rho_s U_s) + \nabla(\alpha_s \rho_s U_s U_s) = -\alpha_s \nabla p - \nabla p_s + \nabla \tau_s + \alpha_s \rho_s g + K_{sg}(U_s - U_g) \tag{4}$$

Gas-solid interaction forces:

$$f_{sg} = \frac{3 C_D \alpha_s \alpha_g \rho_g}{4d} |U_r| U_r \alpha_g^{-2.65} \tag{5}$$

In this equation, α_g, α_s are the volume fractions of the gas and sand phases, t is the time, ρ_g, ρ_s are the densities of the gas and sand phases, respectively, v_g, v_s are the velocity vectors of the gas and sand phases, respectively; U_g, U_s , are the velocities of the gas and sand phases, respectively, and τ_g, τ_s are the surface stress tensors of the gas and sand phases, respectively; p is the same pressure shared by the two phases. p_s is the pressure of the sand phase, and g is the acceleration of gravity, so $K_{gs} = K_{sg}$, and they are the momentum exchange coefficients of the gas and solid phases, respectively. C_D is the drag coefficient; U_r is the relative velocity between the gas and solid phases; and d is the diameter of the sand grain.

The standard $k-\epsilon$ turbulence model was used in this study. Air is defined as an incompressible flow without heat exchange. According to the multiphase fluid theory, with the gas phase as the dominant phase, the sand phase as the dilute phase, and the volume fraction of the sand phase as 0.02, the turbulence is considered to be fully developed.

Turbulent kinetic energy equation:

$$\rho \frac{\partial(k)}{\partial t} + \rho u_i \frac{\partial(k)}{\partial x_i} = \frac{\partial}{\partial x_j} \left[\left(\mu + \frac{\mu_t}{\sigma_k} \right) \frac{\partial k}{\partial x_j} \right] + G_k - \rho \epsilon \tag{6}$$

Turbulent dissipation rate equation (TDR):

$$\rho \frac{\partial(\epsilon)}{\partial t} + \rho u_i \frac{\partial(\epsilon)}{\partial x_i} = \frac{\partial}{\partial x_j} \left[\left(\mu + \frac{\mu_t}{\sigma_\epsilon} \right) \frac{\partial \epsilon}{\partial x_j} \right] + C_{1\epsilon} G_k \frac{\epsilon}{k} - C_{2\epsilon} \rho \frac{\epsilon^2}{k} \tag{7}$$

In this equation, u_i is the velocity component along the i direction; t is time. ρ is the air density. k is the turbulent kinetic energy. ϵ is the turbulent dissipation rate. μ is the dynamic viscosity. μ_t is the turbulent viscosity. G_k is the turbulent kinetic energy generated by the mean velocity gradient. $\sigma_k, \sigma_\epsilon$ are the Trump constants corresponding to the turbulent kinetic energy and the dissipation rate, σ_k is 1.0, σ_ϵ is 1.3, $C_{1\epsilon}$ and $C_{2\epsilon}$ are constants, $C_{1\epsilon}$ is 1.44, $C_{2\epsilon}$ is 1.92.

Geometric modeling and meshing

This model mainly studies the changes in wind-sand flow in the same horizontal section and vertical section, so a two-dimensional model is adopted to simplify the calculation. The size of the flow field in the calculation domain is set as 100m×15m, the positive direction of the X-axis is the direction of the wind-sand flow, the positive direction of the Y-axis is the direction perpendicular to the ground, and the ground at the entrance is the coordinate O point. The calculation domain of the combined sand barrier is shown in Figure 2. The common double rows of high vertical nylon mesh sand barriers and grass grid sand barriers with a porosity of 30% were taken. Among them, the height of the high vertical nylon net sand barrier is 1.5 m. The grass grid sand barrier is composed of a 1m×1m sand-fixing structure, the overall height of the grass grid sand barrier is 0.2 m, and 10 rows are set up in total. In order to simulate the change characteristics of the concentration of Aeolus sand in the Aeolus grid barrier, the Aeolus grid sand barrier model was added to the Aeolus flow model on a flat bed. Here, the permeability of the Aeolus grid and the influence of flexible materials, such as wheat grass on the wind field or such as swaying or vibration, are not considered and the Aeolus grid sand barrier is treated as a rigid body (Xianpan X., 2015). Therefore, the wind tunnel experiment also uses a rigid plastic grid instead. A double-row vertical sand barrier and grass grid combined sand barrier model with spacing D of 7.5 m (5H), 15 m (10H), 22.5 m (15H), and 30 m (20H) is established under different working conditions.

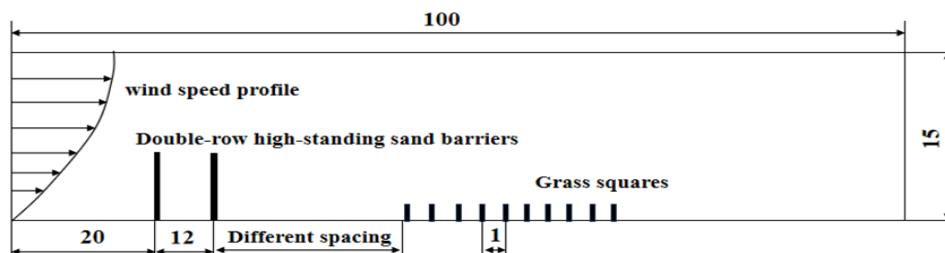


Fig. 2 – Schematic diagram of the computational domain of the joint sand barriers (unit: m)

Considering that the flow field area is large enough, and the influence of the vertical sand barrier on the flow field is mainly the porosity and height, the vertical sand barrier is designed as a wall with no thickness in order to improve the quality of mesh delineation and computational efficiency (Chang L., Hailong W. et al., 2023). The model is meshed by CFD software, the grid type is a Quad (quadrilateral) grid, and the maximum grid size is controlled within 0.2. According to the movement characteristics of wind-blown sand flow, the movement of wind-blown sand flow near the surface is more intense. The grid around the surface and the combined sand barrier is properly encrypted, and 10 boundary layers are set at the bottom, with an increase rate of 1.2. The left and right edges are encrypted at the same time according to the ratio of 1.01, the top is sparse, the bottom is dense, and the total number of grids is about 1.3×10^6 .

Boundary condition definition and calculation parameters

The left side of the model is defined as the velocity-inlet, and the wind speed adopts the logarithmic equation of the wind profile. On the right side of the model is a pressure-outlet, with fully developed outflow boundary conditions. The top and sides of the boundary are set as symmetry boundaries, and the ground and sand barriers are defined as non-slip walls. Generally, the particle size carried by the wind-blown sand flow ranges from 0.075 to 0.25 mm. In this paper, the particle size carried by the wind-blown sand flow is 0.1 mm, the sand density is 2600 kg/m^3 , and the motion viscosity coefficient of the sand particle is $\mu = 0.047 P_s \cdot s$ (Guowei, Ning et al., 2021). According to statistics, the flow density of wind sand is on the $10^{-5} \text{ g} \cdot \text{m}^{-3}$ order of magnitude, and the sand phase is sparse, so the initial sand phase volume fraction is 0.02 (Liangying L., Zhizhong T. et al., 2024).

$$V = \frac{V_*}{k} \ln \frac{y}{z_0} \quad (7)$$

In this equation, V is the horizontal wind speed at y height [$\text{m} \cdot \text{s}^{-1}$] and y are the height of the entrance boundary from the bottom surface. And k are the von Karman constants, taking 0.4. V_* is the friction wind speed, [$\text{m} \cdot \text{s}^{-1}$] and z_0 is the surface roughness, also the height at which the average wind speed near the ground is 0. Generally, 1/30 of the average particle size of the sand on the bed surface is taken.

Wind tunnel experiment

The wind tunnel test was carried out by the small direct flow wind tunnel experiment platform of Intelligent Manufacturing Modern Industry College of Xinjiang University. It consists of five parts: power section, rectification section, sand supply device, test section and diffusion section. The scale of the model is 1:20. The wind tunnel inlet axis simulation indicates wind speed $v_{\infty m} = \sqrt{\frac{1}{20}} v_{\infty 0} = 0.224 v_{\infty 0}$. $v_{\infty 0}$ is prototype indicator wind speed. Considering the wind speed in the field is $30 \text{ m} \cdot \text{s}^{-1}$, so the wind speed indicated in this paper is $v_{\infty m} = 7 \pm 0.05 \text{ m} \cdot \text{s}^{-1}$.



Fig. 3 – Real picture of the wind tunnel

The model was fixed at 1 m away from the sand source, and the inlet wind speed was 7 m/s. Before the experiment, the wind speed at different heights was measured by Pitot tubes. Rough elements are used to generate turbulent boundary layers. In order to ensure a sufficient supply of sand source, the supply length of the sand bed along the flow direction was 0.3 m, and the sand was continuously supplied. The experiment started and continued to blow sand for about 50 minutes. The multi-gradient sand collecting instrument was used to collect sand particles, and the sand collecting instrument was placed 3H behind the combined sand barrier, and the sand accumulation amount under four different spacing distributions was measured respectively. By comparing the sand accumulation amount with that in the open field (same wind speed and sand source, but no wind prevention and sand fixation facilities), the influence of four working conditions on the post-model sand accumulation distribution was studied. The test arrangement is shown in Figure 4.

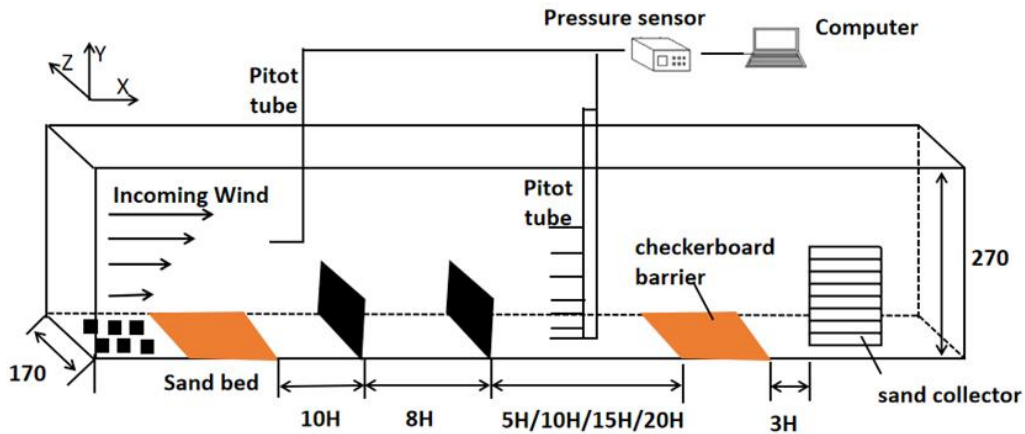


Fig. 4 – Wind tunnel test layout (unit: mm)



Fig. 5 – The layout of wind tunnel experiment

The simulated results of numerical simulation usually need to be verified with wind tunnel tests or field investigations, to ensure the reliability of numerical simulation results. In this paper, the same size model as the wind tunnel test is established for numerical simulation reliability verification under the air field conditions. Based on the solution parameters set in the previous paper, the changes in horizontal wind speed at different heights are simulated and compared with the results of the wind tunnel test.

As shown in Figure. 6, it is found through comparison that the wind speed contour lines of numerical simulation and wind tunnel experiment have good consistency to a certain extent, and there are only some differences at lower heights, but they do not affect the specific calculations. Thus, the parameter selection in this paper is reasonable and accurate, which can provide a precise parameter basis for the subsequent analysis.

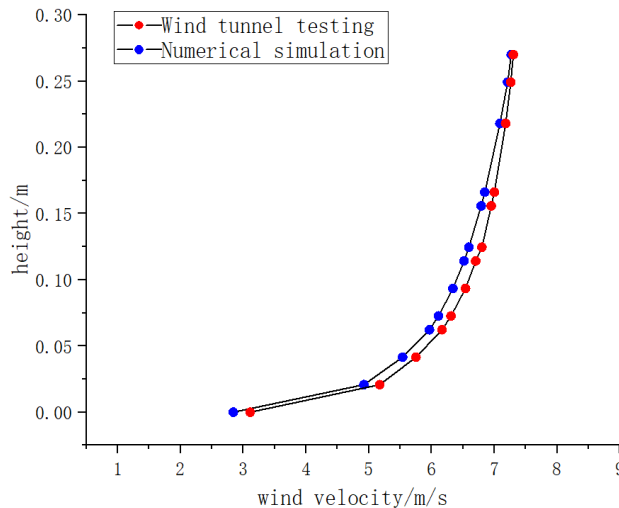


Fig. 6 – Comparison of wind speed profiles from wind tunnel experiments and numerical simulations

RESULTS

Numerical simulation results and analysis

Distribution characteristics of the flow field around the sand barrier

From Figure 7, it can be found that, due to the presence of sand barriers, the airflow deceleration zone is formed on the windward side of the first sand barrier when the wind-driven sand flow enters the flow field, and then most of the airflow rises along the sand barrier to form the airflow acceleration zone. Due to the effect of the sand barrier on airflow collection, the airflow high-speed zone is formed on the sand barrier. The kinetic energy of the other part of the air passing through the pores is reduced, and the direction of the lower part of the air is changed by the action of the mesh plate, forming a large elliptical eddy current region. The distribution characteristics of the flow field around the sand barrier in the four working conditions before the second sand barrier are almost the same, but there is no big difference. The airflow passes through the grass grid sand barrier, forming a low speed-zone in the sand barrier, and finally, the speed gradually recovers at a distance.

Under the four working conditions, due to the different spacing between the high vertical sand barrier and the grass grid barrier, the influence of the low-speed zone behind the second high vertical sand barrier on the grass grid is different. When the spacing is 5H and 10H, the distance between the second vertical sand barrier and the grass grid is relatively close, and a vortex zone of 6 m~8 m is formed between them. The grass grid is basically covered in the low-speed zone, and the wind speed is close to 0, so the sand particles cannot start, and the sand consolidation effect is good. When the spacing is 15H and 20H, the distance between the second vertical sand barrier and the grass grid is far away, and there is a certain range of speed recovery area, the sand is easy to start again, and the grass grid cannot play its sand-fixing role.

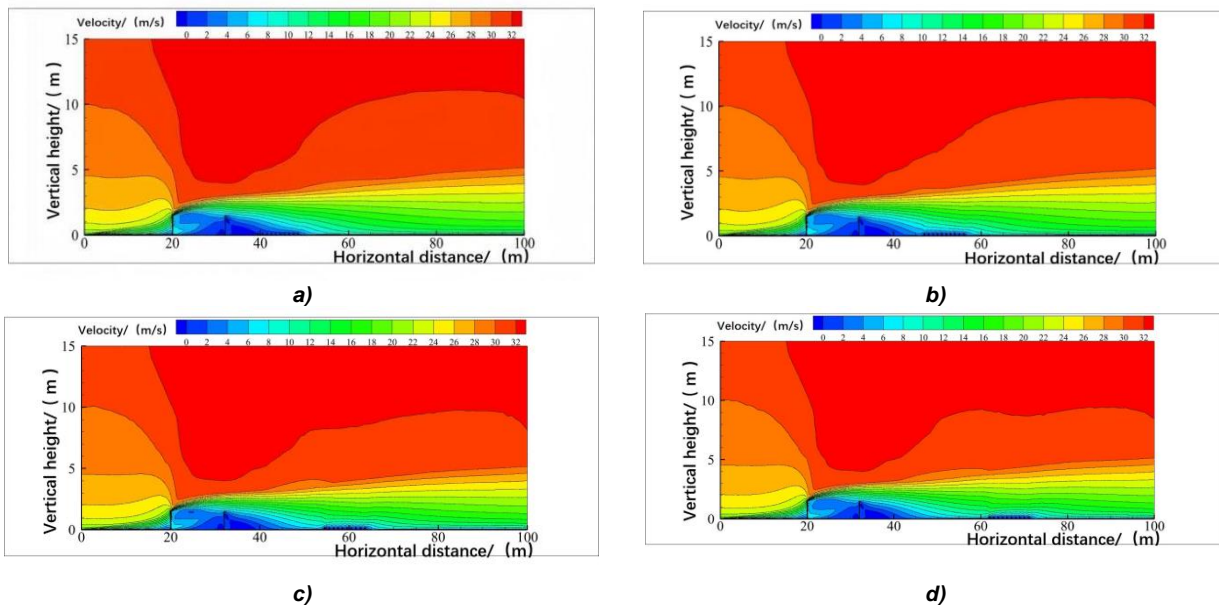


Fig. 7 – Characteristic cloud map of flow field distribution
 a) $D=5H$; b) $D=10H$; c) $D=15H$; d) $D=20H$.

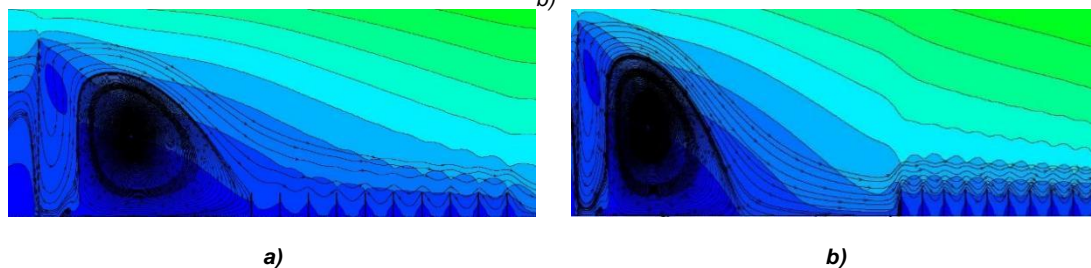


Fig. 8 – Vortex flow diagram
 a) $D=5H$; b) $D=10H$.

Variation characteristics of horizontal wind speed around sand barriers

The wind-sand flow generally moves close to the surface in the desert, and the near-surface wind speed has a significant effect on the movement of sand particles. Studying the changing trend of air flow around near-surface sand barriers can better analyze the mechanism of sand blocking and fixation (Zhibao D, 2005).

Figure 9 shows the horizontal velocity diagrams around the double-row high vertical nylon mesh sand barriers and grass square joint sand barriers with four spacings at different heights when the inlet velocity is 30 m/s. As can be seen from Figure 9, the sand-carrying wind speed continues to decrease from the entrance, decreases to the minimum value after the second high vertical sand barrier, increases slightly after moving away from the second high vertical sand barrier, and decreases significantly within the height range after encountering the grass grid, and then increases gradually. By comparing the changes in horizontal wind speed under different working conditions, it can be found that within 7 m from the entrance to the second high vertical sand barrier, the change law and amplitude of air velocity are basically the same, and the air velocity is greatly reduced. However, with the increase of spacing, the airflow behind the second vertical sand barrier can fully develop, and the speed increases gradually before reaching the grass grid sand barrier, and the increased amplitude is small in the first and second working conditions. From the third working condition, the increase is obviously greater than the sand-generating wind speed, which is not conducive to the full play of the wind prevention and sand consolidation effect of the grass grid behind. In addition, when the airflow reaches the grass grid, the wind speed is at a small value in the height range, and the wind speed changes less with the increase of the spacing.

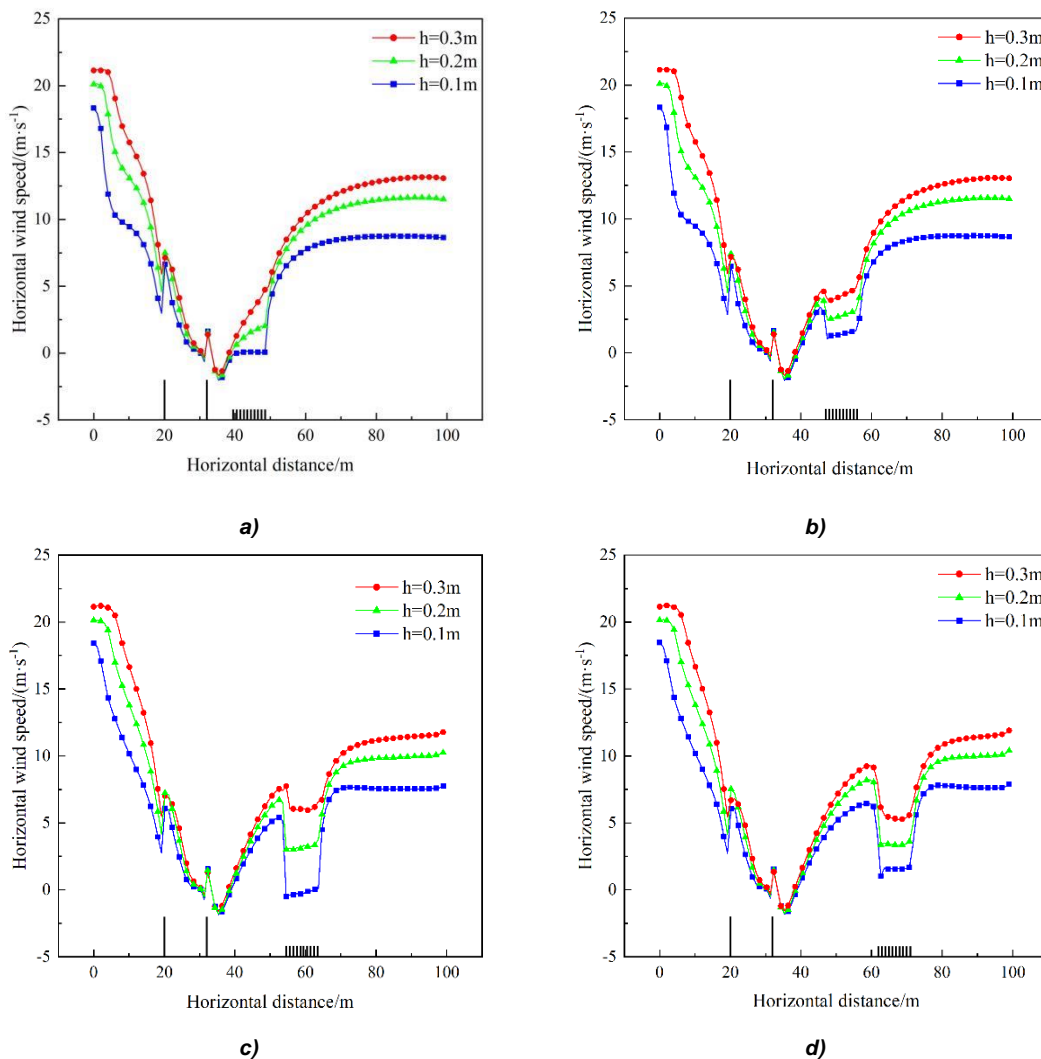


Fig. 9 – Horizontal wind speed map:
 a) $D=5H$; b) $D=10H$; c) $D=15H$; d) $D=20H$.

Windproof efficiency

The wind-proof efficiency of the sand barrier reflects the protective effect of the sand barrier. The greater the wind-proof efficiency, the stronger the block of the sand barrier on the wind sand flow, and the transport of sand particles can be prevented. By extracting the horizontal wind speed at different heights from the flow field, it can be seen that the sand barrier reduces the surrounding wind speed. Therefore, the following formula is used to represent the wind prevention efficiency of the sand barrier (Tao, Jianjun et al., 2017; Tao, Jianjun et al., 2017):

$$\Phi_{xy} = \left[1 - \frac{V_{xy}}{V'_{xy}} \right] \times 100 \% \tag{9}$$

In this equation, Φ_{xy} is the windproof efficiency of the sand barrier, [%]. X is the length from the first sand barrier, [m]. Y is the height from the ground, [m]. When there is sand barrier protection, V_{xy} is the wind speed at point (x, y), [m/s]. When there is no sand barrier protection, V'_{xy} is the wind speed at point (x, y), [m/s].

As shown in Figure 10, when the wind speed from the surface of 0.1 m, 0.2 m, 0.3 m height is taken to calculate the windproof efficiency of the joint sand barriers under different working conditions, it can be found that the closer the windproof efficiency is to the ground, the greater the windproof efficiency is. And it can also be found that the change rule of windproof efficiency at different heights is similar, but there are differences in the windproof efficiency under different working conditions. When the spacing is 5H and 10H, the average windproof efficiency of the combined sand barrier reaches more than 85%, but when the spacing continues to increase, the average windproof efficiency decreases to less than 80%, and the windproof efficiency decreases significantly. When 60% of the wind protection efficiency is taken to determine the effective protection distance, it can be found that the effective protection distance completely covers the entire combined sand barrier area under the conditions of 5H, 10H and 15H, but under the conditions of 20H, the effective protection distance cannot cover the grass grid sand barrier at the height of 0.2 m and 0.3 m.

Table 1

| Wind prevention efficiency of combined sand barriers at different spacing | | | | |
|---|--------|--------|---------|--------|
| | D=5H | D=10H | D=15H | D=20H |
| 0.1 m | 93.28% | 90.59% | 88.77 % | 82.79% |
| 0.2 m | 90.24% | 87.86% | 84.06% | 79.12% |
| 0.3 m | 87.86% | 85.66% | 80.29% | 76.46% |
| average | 90.46% | 88.04% | 84.37% | 79.45% |

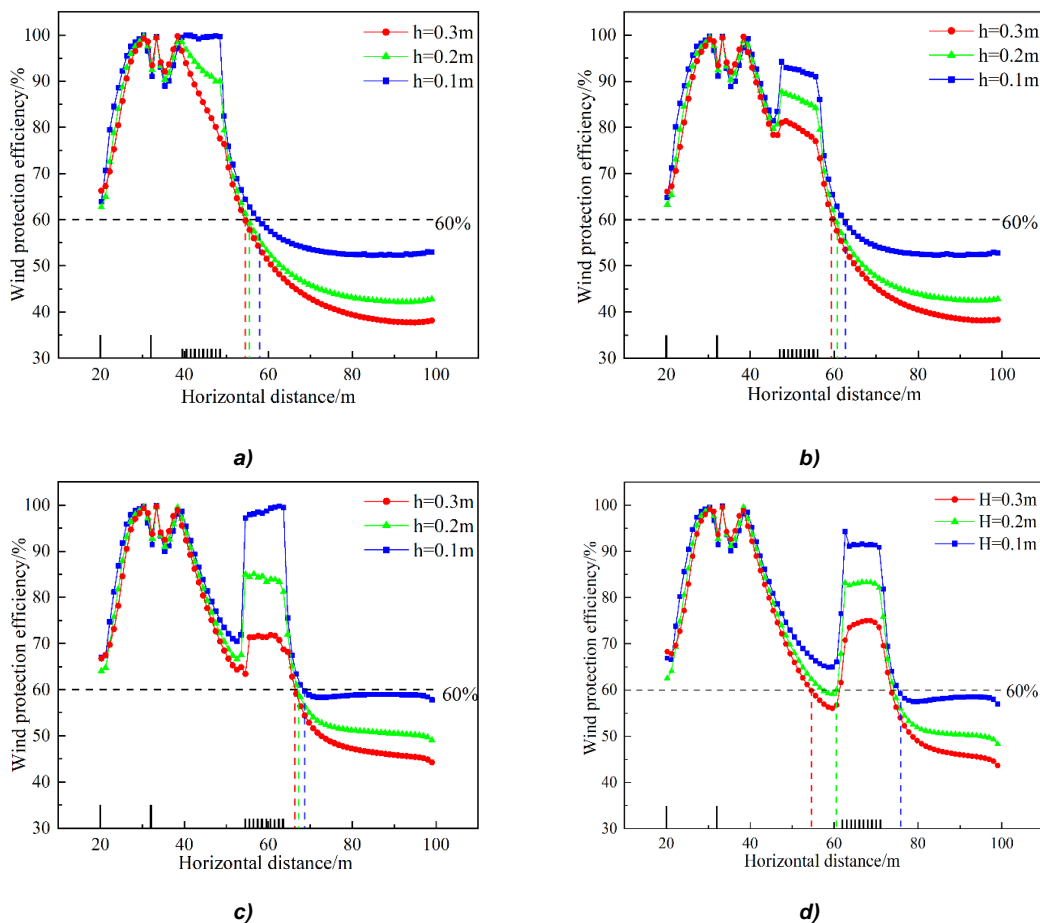


Fig. 10 – Chart of wind protection efficiency and effective protection distance: a) D=5H; b) D=10H; c) D=15H; d) D=20H.

Location distribution of sediment deposition movement

The mass difference between the airflow and the sand particles is large. When the running wind sand flow encounters obstacles or pressure differences, local resistance will be generated to reduce the wind speed, and at the same time, the energy of the airflow to transport the sand particles will be weakened, causing some sand particles to deposit. The volume distribution of sand particles in the flow field is shown in Figure 11. The larger the volume fraction of sand particles is, the more sand particles are deposited.

It can be found that under different working conditions when the sand-carrying wind passes through the high vertical sand barrier, a large number of sand grains are deposited behind the high vertical sand barrier because the wind speed is greatly reduced to below the sand-generating wind speed. However, due to the different spacing between the grass grid and the high vertical sand barrier, the sand fixation effect of the grass grid is different. Under the conditions of 5H and 10H spacing, due to the close distance between the grass grid and the high vertical sand barrier, there is no space for the wind flow to develop fully after leaving the high vertical sand barrier, and the air flow speed is still low. Coupled with the obstruction effect of the grass grid, a large number of near-surface sand particles are fixed into the grass grid, and the combined sand barrier has a good synergistic protection effect. Under the conditions of 15H and 20H spacing, due to the distance between the grass grid and the high vertical sand barrier, the wind-sand flow can fully recover after leaving the high vertical sand barrier, the airflow speed increases and carries most of the near sand particles up and continues to move backward. So, the sand accumulation in the grass grid is very small, the sand consolidation effect of the grass grid is ineffective, and the synergistic protection effect of the combined sand barrier is poor.

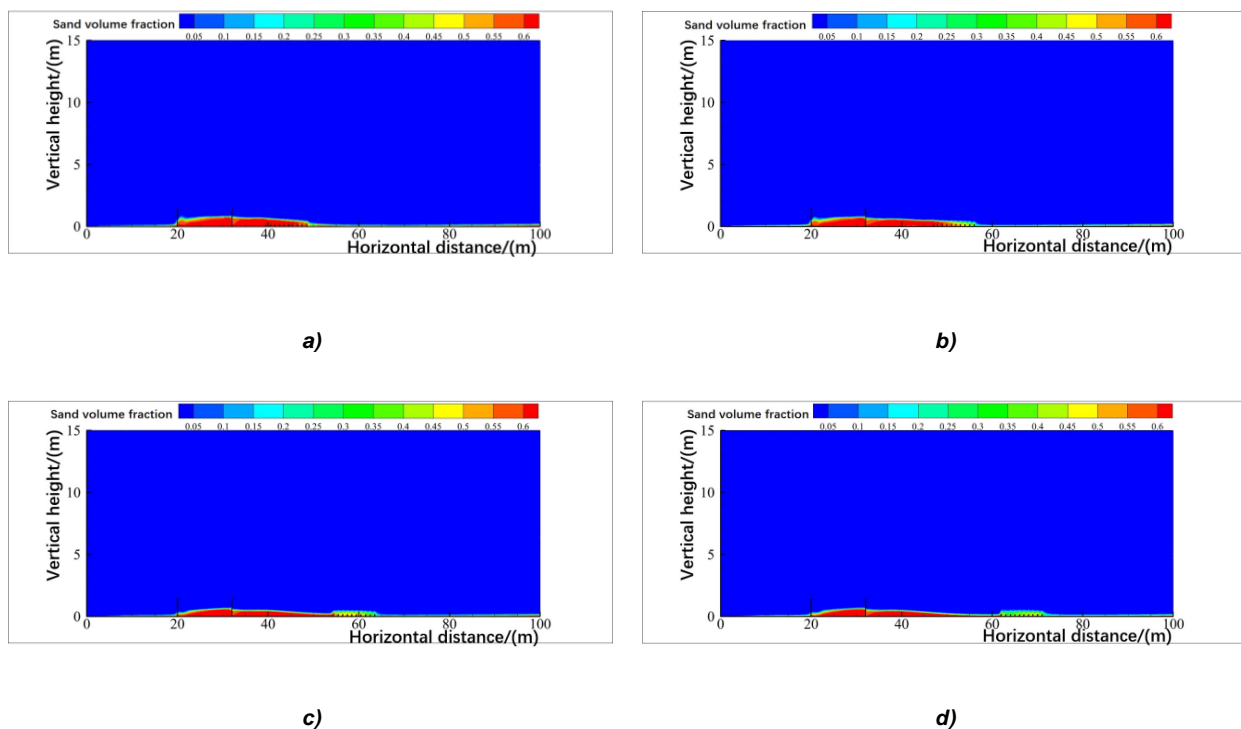


Fig. 11 – Cloud map of sand accumulation around the joint sand barrier

a) $D=5H$; b) $D=10H$; c) $D=15H$; d) $D=20H$.

The results and analysis of the wind tunnel experiment

The distribution characteristics of sand accumulation in the wind tunnel test are shown in Figure 12. It can be found that the high vertical sand barrier plays a full role in preventing sand, and a large number of sand particles are deposited near the high vertical sand barrier. As the distance between the grass grid sand barrier and the high vertical sand barrier increases, the proportion of the area covered by sand accumulation between the second sand barrier and the grass grid gradually decreases, and the sand accumulation in the grass grid gradually decreases. However, the accumulation of sand near the high vertical sand barrier has mostly stayed the same. The sediment distribution characteristics of the wind tunnel test under four conditions are basically consistent with the numerical simulation results, which verifies the reliability of the numerical simulation results.

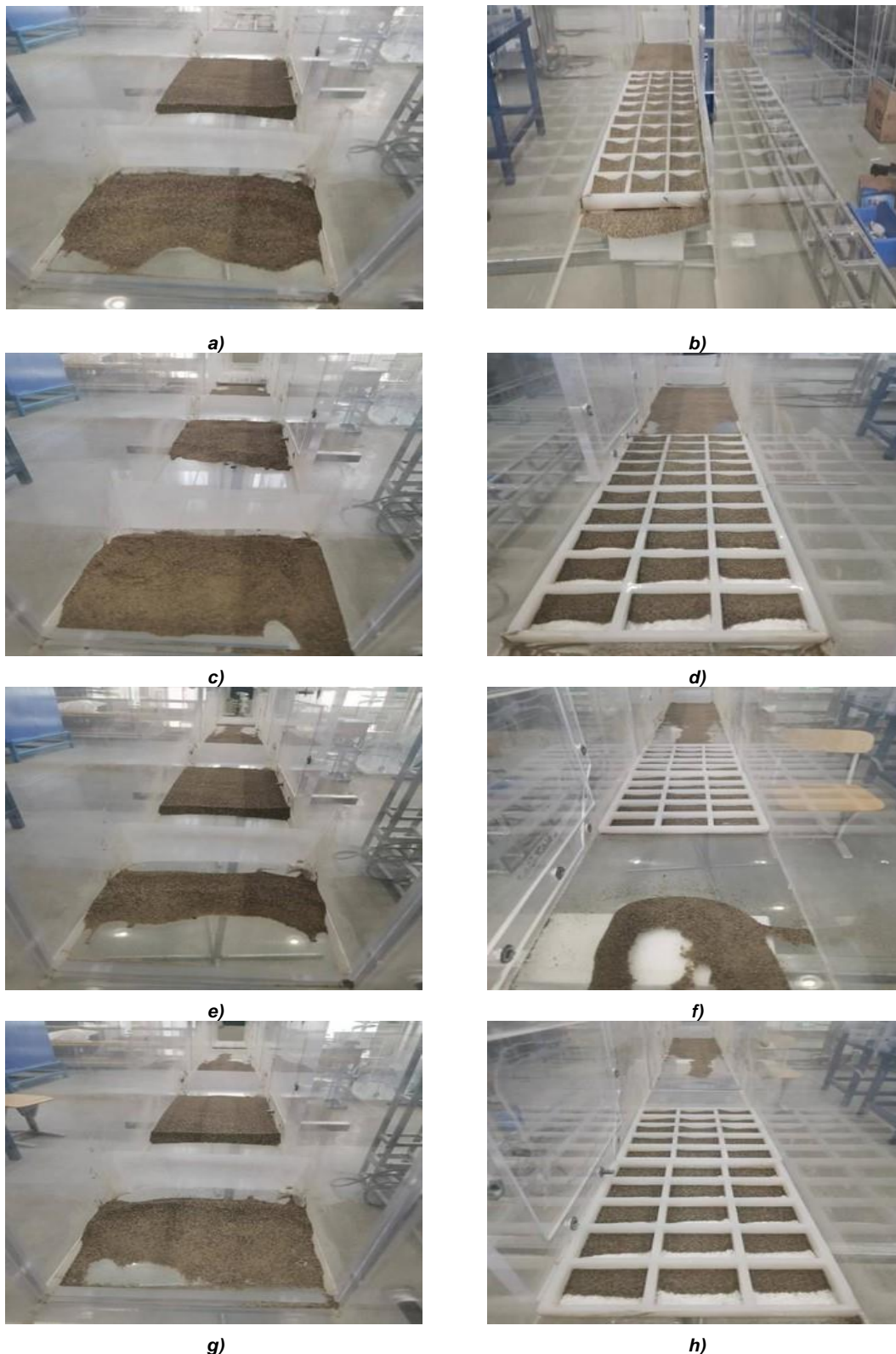


Fig. 12 – The distribution of sand accumulation in joint sand barriers at different spacings:
 a) $D=5H$; b) $D=5H$; c) $D=10H$; d) $D=10H$; e) $D=15H$; f) $D=15H$; g) $D=20H$; h) $D=20H$.

After about 50 min of continuous sand blowing at 7 m/s for the joint sand barrier model with different spacing distributions, the amount of sand coming from the cavity collected by the sand collecting instrument and the amount of sand coming from the combined sand barrier placed (3H on the lee side) were drawn as a bar chart, as shown in Figure 13. It can be found that with the increase of the distance between the grass grid sand barrier and the high vertical sand barrier, the amount of sediment intercepted by the combined sand barrier gradually increases, but when $D=15H$, the amount of sediment accumulated by the sand collecting instrument behind the combined sand barrier increases sharply. It shows that when $D=5H$ and $10H$, the combined sand barrier can cut more sand, and the protection efficiency is better.

In order to quantify the protective benefits of joint sand control measures in wind tunnel tests, the concept of sand barrier retention rate is introduced. This concept introduces itself by assuming the erosion process of ground sandy materials as a superimposed effect of pure wind shear stress and sandy wind impact abrasion (Liu, Hou et al., 2019). This method can quantitatively evaluate the influence of sand barriers on particle retention of sand material. That is, when the eroded sand grains pass through the sand barrier, the proportion of the trapped sand grains accounts for the total sand grains. The specific formula is as follows:

$$n = \frac{W-Q}{W} \times 100\% \tag{10}$$

In this equation: n is the retention rate of the sand barrier; W is the desert sediment transport flux of the same altitude layer under the same wind speed, [g/cm²]. Q is the remaining sand transport flux after the influence of sand barrier, [g/cm²].

By calculating, it can be found that with the increase of the spacing, the sand-blocking rate of the combined sand barrier decreases gradually. The sand-blocking rate of the combined sand barrier for 5H, 10H, 15H and 20H is 78.25%, 77.11%, 71.09% and 67.73%, respectively, indicating that the sand blocking effect of the combined sand barrier shows a decreasing trend with the increase of the spacing. By comparing the sand accumulation results of wind tunnel experiment with those of numerical simulation, it can be seen that the flow field law and sand accumulation distribution law obtained by numerical calculation and analysis are similar to the variation trend of sand accumulation law measured by wind tunnel test. And there is a corresponding relationship, which further confirms the correctness of the numerical calculation results.

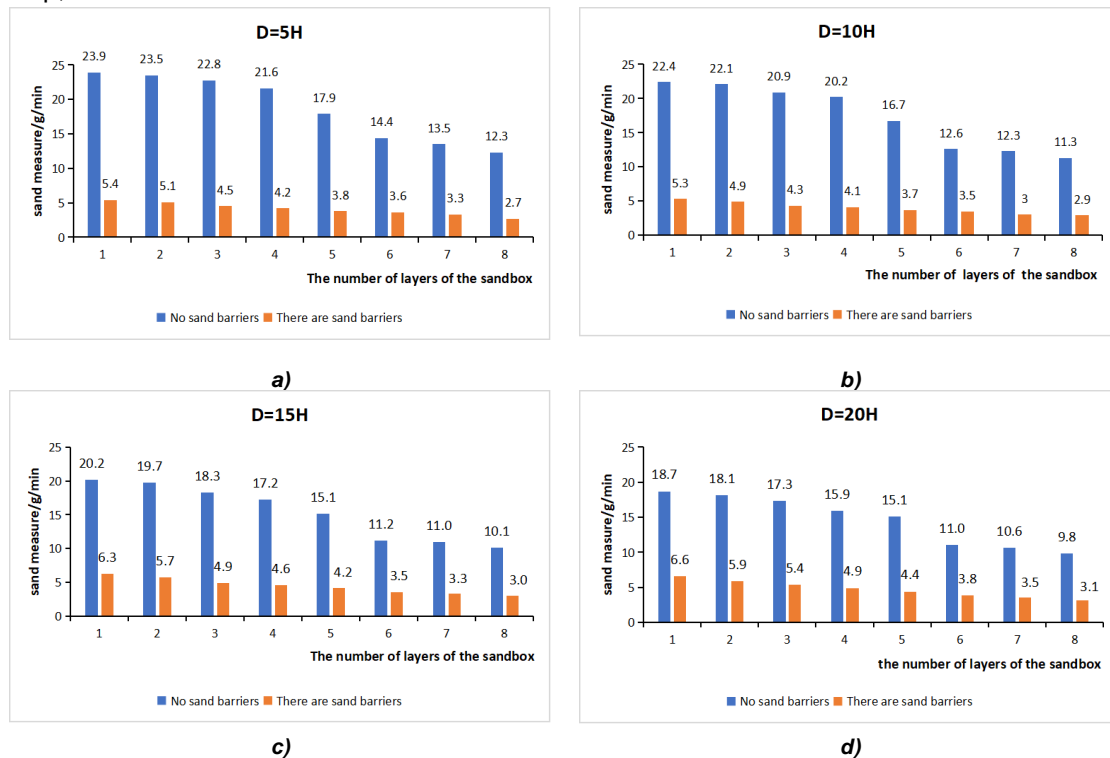


Fig. 13 – Sand trapping capacity of joint sand barriers at different spacings: a) D=5H; b) D=10H; c) D=15H; d) D=20H.

CONCLUSIONS

In this study, the wind-sand flow field characteristics and protection effect around the double-row nylon mesh high vertical sand barriers and grass square joint sand barriers under extreme wind-sand environment were analyzed by Fluent numerical simulation. Then the wind tunnel test was used to verify the numerical simulation results, and the following conclusions were drawn.

1. When the distance between the double-row vertical sand barrier and the grass grid was 5H and 10H, the airflow velocity behind the double-row vertical sand barrier could not fully develop, and the low-speed area behind the double-row vertical sand barrier was basically covered with grass grid; when the spacing between the double-row vertical sand barrier and the grass grid was 15H and 20H, the airflow behind the double-row vertical sand barrier produced a certain speed recovery zone, and the airflow low-speed zone could not cover the grass grid;

2. When the spacing was 5H and 10H, the average windproof efficiency of the combined sand barrier reached more than 85%, and the effective protection distance completely covered the entire combined sand barrier area. When the spacing continued to increase, the average windproof efficiency decreased to less than 80%, and the effective protection distance could not cover the grass grid sand barrier;

3. When the spacing was 5H and 10H, the increase of airflow velocity behind the second vertical sand barrier was slight, and a large number of near-surface sand particles were fixed in the grass grid, then the sand resistance rate was over 70%, and the combined sand barrier had a good synergistic protection effect. As the distance continued to increase, the air velocity behind the second high vertical sand barrier gradually increased, even more than the sand-driving wind speed. The airflow carried most of the near-sand particles up and continued to move backward, and the sand accumulation in the grass grid was very slight. So, the sand resistance rate decreased and the synergistic protection effect of the combined sand barrier was poor.

In order to better protect the agricultural and ecological restoration areas at the edge of the desert in the Minqin area of China from wind and sand, it is recommended that the spacing between the double-row high-standing sand barriers and the grass checkered sand barrier should be 5H to 10H. Meanwhile, many farmlands, ecological restoration areas, and other agricultural areas around the desert in Northwest China are affected by strong sandstorms all year round, resulting in a decline in agricultural yield, low plant survival rate, and huge economic losses. It is hoped that this study can provide some theoretical and technical support for the design of sand control projects in farmland and ecological restoration areas in the desert areas of Northwest China.

ACKNOWLEDGMENTS

The authors were funded for this project by the National Natural Sciences Foundation of China (NSFC), Grant/Award Number: 12362033.

REFERENCES

- [1] Chang L., Hailong W., Jing S. (2023). Research on the optimization of design parameters for comprehensive windbreak and sand fixation systems (综合防风固沙体系设计参数优化研究). *Journal of The China Railway Society*, Vol. 42, pp. 135-144. Beijing/China.
- [2] Cuicui J., Xuemei Y., Fang C., et al. (2021). Spatio-temporal evolution of photosynthetic/non-photosynthetic vegetation coverage in typical arid areas of Minqin, Gansu Province (典型干旱区甘肃民勤光合-非光合植被覆盖度时空演变分析). *Journal of Changchun Institute of Technology(Natural Science Edition)*, Vol. 22, pp. 127-135. Changchun/China.
- [3] Cornelis W.M., Gabriels D. (2004). Optimal windbreak design for wind-erosion control. *Journal of Arid Environments*, Vol. 61, pp. 315-332, United States.
- [4] Congmao K. (2000). Research on the Prediction and Forecasting Model of Sand Hazards in Grass (Branches) Grid Sand Barrier (草(枝条)方格沙障沙害预测预报模型的研究). *Journal of Nanchang Institute of Technology*, Vol. 02, pp. 49-59, Jiangxi/China.
- [5] Dong G., Chen T., Ren C., et al. (2023). Wind tunnel investigation of wind reduction effect under porous fences protection. *Journal of Wind Engineering and Industrial Aerodynamics*, Vol. 02, pp. 232, United States.
- [6] Dong Z., Chen G., He X., et al. (2002). Controlling blown sand along the highway crossing the Taklimakan Desert. *Journal of Arid Environments*, Vol. 57, pp. 329-344, United States.
- [7] Fang H., Wu X., Zou X., et al. (2018). An integrated simulation-assessment study for optimizing wind barrier design. *Agricultural and Forest Meteorology*, Vol. 263, pp. 198-206, United States.
- [8] Fugui H., Ming Z., Fengzhao C., et al. (2009) Characteristics of sand and dust weather and its influencing factors in the Shazhou area of Minqin County over the past 50 years (民勤沙区 50 多年来沙尘天气特征及其影响因素). *Arid Zone Research | Arid Zone Res*, Vol. 26, pp. 889-894. Wulumuqi/China.
- [9] Guowei X., Ning H., Jie Z., et al. (2021). Investigations into the design of sand control fence for Gobi buildings. *Aeolian Research*, Vol. 49, pp. 100662, United States.
- [10] Guangpu J., Hejun Z., Haibing W., et al. (2020). Numerical simulation and experiment of wind and sand movement characteristics around high vertical nylon mesh sand barriers (高立式尼龙网沙障周围风沙运动特性的数值模拟与试验). *Transactions of the Chinese Society of Agricultural Engineering*, Vol. 36, pp. 109-117, Beijing/China.

- [11] Guoping Z., Hejun Z., Lianxiu X., et al. (2008). Study on the windbreak and sand blocking benefits of sand willow barriers (沙柳沙障防风阻沙效益的研究). *Journal of Soil and Water Conservation*, Vol. 02, pp. 38-42, Beijing/China.
- [12] Jia Y., Xiang Y. (2019). Application of Grass Square Grid Sand Barrier in Wind Prevention and Sand Fixation (草方格沙障在防风固沙中的应用). *Construction & Design for Project*, Vol. 21, pp. 205-207, Beijing/China.
- [13] Jianjun Q. L., et al. (2002). Research on the Sand Control Effect of Nylon Mesh Fence (尼龙网栅栏防沙效应研究). *Journal of Lanzhou University*, Vol. 02, pp. 171-176. Lanzhou/China.
- [14] Jianjun Q. L., et al. (2001). Wind tunnel simulation experiment on sand prevention effect of nylon mesh fence (尼龙网栅栏防沙效应的风洞模拟实验). *Journal of Desert Research*, Vol. 21, pp. 276-280, Lanzhou/China.
- [15] Jiguo Z. (1987). Change of surface morphology after shifting sand control in Shapotou area, southeast edge of Tengger Desert (腾格里沙漠东南缘沙坡头地区流沙治理后地表形态变化). *Journal of Desert Research*, Vol. 1, pp. 12-20, Lanzhou/China.
- [16] Jun L., Renhua W. (1982). Discussion on the width of semi concealed wheat straw grid sand barrier protection belt (半隐蔽式麦草方格沙障防护带宽度的探讨). *Journal of Desert Research*, Vol. 2, pp. 20-27, Lanzhou/China.
- [17] Liu H., Hou Z., Chen Z., et al. (2019). Effects of standing stubble on the interception of soil erosion particles. *Land Degradation & Development*, Vol. 30, pp. 328-336, United States.
- [18] Mao L., Ling S., Jie L., et al. (2024). Wind tunnel experiment on windproof effect of double row nylon sand blocking net grass grid combined sand barrier (双排尼龙阻沙网-草方格联合沙障防风效应的风洞实验). *Journal of Desert Research*, Vol. 44, pp. 9-17, Lanzhou/China.
- [19] Ming W. (2007). *Large-eddy Simulation of Three Dimensional Turbulent Aeolian Motion and Numerical Simulation of Evolution of Sand Ripples* (三维湍流风沙运动的大涡模拟及沙漠地貌的数值模拟). Master's dissertation. Hohai university, Nanjing.
- [20] Peng H., Jin A., Zhang S., et al. (2023). Numerical Simulation and Parameter Optimization of a New Reed-Nylon Net Combined Sand Fence. *Sustainability*, 15(18). Vol. 15, pp. 13920, United States.
- [21] Papesch A.J.G. (1992). Wind tunnel test to optimize barrier spacing and porosity to reduce wind damage in horticultural shelter systems. *Journal of Wind Engineering and Industrial Aerodynamics*, Vol. 44, pp. 2631-2642, United States.
- [22] Qiu G.Y., Lee I-B, Shimizu H., et al. (2004). Principles of sand dune fixation with straw checkerboard technology and its effects on the environment. *Journal of Arid Environments*, Vol. 56, pp. 449-464, United States.
- [23] Tao W., Jianjun Q., Yuquan L., et al. Wind tunnel test on the effect of metal net fences on sand flux in a Gobi Desert. *Journal of Arid Land*, Vol. 9, pp. 888-889, United States.
- [24] Tao W., Jianjun Q., Yuquan L., et al. (2017). Shelter effect efficacy of sand fences: A comparison of systems in a wind tunnel. *Aeolian Research*, Vol. 30, pp. 32-40, United States.
- [25] Wu X., Zou X., Zhang C., et al. (2013). The effect of wind barriers on airflow in a wind tunnel. *Journal of Arid Environments*, Vol. 97, pp. 73-83, United States.
- [26] Xin G., Zhang J., Fan L., et al. (2023). Numerical Simulations and Wind Tunnel Experiments to Optimize the Parameters of the Second Sand Fence and Prevent Sand Accumulation on the Subgrade of a Desert Railway. *Sustainability*, Vol. 15, pp. 12761, United States.
- [27] Xu B., Zhang J., Huang N., et al. (2018). Characteristics of Turbulent Aeolian Sand Movement Over Straw Checkerboard Barriers and Formation Mechanisms of Their Internal Erosion Form. *Journal of Geophysical Research: Atmospheres*, Vol. 123, pp. 6907-6919, United States.
- [28] Xiao J. (2016). *The Numerical Simulation Research on Response Rules of Wind-Blown Sand Two Phase Flow to Railway Embankment and the Wind-break Retaining Sand Wall* (风沙两相流对铁路路堤及防风沙墙响应规律的数值模拟研究). Master's dissertation. Lanzhou Jiaotong University, Lanzhou.
- [29] Xianpan X. (2015). *numerical simulation of dispersion characteristics of sand particles in straw checkerboard barriers* (沙粒在草方格沙障内弥散特征的数值模拟). Master's dissertation, Lanzhou university, Lanzhou.

- [30] Xunming W., Zhiwen H., Zhibao D. (1999). The Benefit of the Prevention System along the Desert Highway in Tarim Basin (塔里木沙漠公路沿线机械防沙体系效益分析). *Journal of Desert Research*, Vol. 19, pp. 120-127. Lanzhou/China.
- [31] Xunming W. (1997). Benefit evaluation of mechanical sand prevention system along Tarim Desert Highway and preliminary exploration of reasonable width of sand prevention belt (塔里木沙漠公路沿线机械防沙体系效益评价及防沙带合理宽度的初步探讨). *Journal of Arid Land Resources and Environment*, Vol. 11, pp. 29-36, Neimeng/China.
- [32] Yanli Z. (2011). *Research on Ecological Security Synthetic Assessment of Minqin* (民勤县生态安全综合评价研究). Master's dissertation, Beijing Agricultural University, Beijing.
- [33] Yingxin L. (1987). Establishment and Benefits of Sand Prevention System for Shapotou Section of Baolan Railway (包兰铁路沙坡头地段铁路防沙体系的建立及其效益). *Journal of Desert Research*, Vol. 7, pp. 1-11, Lanzhou/China.
- [34] Zhang C., Li Q., Zhou N., et al. (2016). Field observations of wind profiles and sand fluxes above the windward slope of a sand dune before and after the establishment of semi-buried straw checkerboard barriers. *Aeolian Research*, Vol. 20, pp. 59-70, United States.
- [35] Zheng H. (2006). *Study of new sand-fixing materials and the field integrated sand-fixing technology* (固沙用新材料及野外固沙综合技术研究). Master's dissertation. Lanzhou university, Lanzhou.
- [36] Zhengyi Y., Guangting C., Zhiwen H., et al. (2006). The decline process of sand prevention function of mechanical sand prevention system (机械防沙体系防沙功能的衰退过程). *Journal of Desert Research*, Vol. 26, pp. 226-231, Lanzhou/China.
- [37] Zhibao D.Z. (2005). Research Achievements in Aeolian Physics in China for Last Five Decades(II) (中国风沙物理研究 50a(II)). *Journal of Desert Research*, Vol. 25, pp. 795-815. Lanzhou/China.
- [38] Zhenting W. (2002). A simple model for size analysis of grass square grid sand barrier (草方格沙障尺寸分析的简单模型). *Journal of Desert Research*, Vol. 22, pp. 229-232. Lanzhou/China.

RESEARCH REGARDING AGRICULTURAL BIONIC BLADE DEVELOPMENT BASED ON THE MECHANISM OF THE CUTTING-SAWING MOTION OF THE CAMPONOTUS MANDIBLE

基于弓背蚁上颚切-锯运动机理的农业仿生刀开发研究

Zhu ZHAO^{1,2)}, Dongli SHUI¹⁾, Fengbo LIU¹⁾, Bintong ZHAO³⁾, Zhongnan WANG*¹⁾

¹⁾ Liaoning Agricultural Technical College, Yingkou / China;

²⁾ Tacheng Vocational and Technical College, Tacheng / China;

³⁾ College of Engineering, Shenyang Agricultural University, Shenyang / China

Tel: +86-0417-7020545; E-mail: zhaosynd@163.com Corresponding author: Wang Zhongnan

DOI: <https://doi.org/10.35633/inmateh-73-73>

Keywords: Bionic blade, cutting-sawing motion, mandible, finite element analysis

ABSTRACT

Aiming at issues such as low instantaneous grasping ability, unsatisfactory cutting quality, and proneness to damage of the blades for existing agricultural mechanical harvesters, by observing the physiological structure and movement characteristics of the ant's mandible and by bionic design theory, a bionic blade was designed and a study was performed to optimize its performance. In this paper, *Camponotus* ant species was selected as the research object to observe the movement of the right mandibular teeth. It was concluded that the movement of the ant's mandibular teeth has a cutting-sawing motion. A comparative analysis was carried out using the flat blade and the mandibular teeth blade, uncovering that the mandibular teeth movement formed a sliding cut with a variable sliding cutting angle. The mandibular teeth were beneficial for clamping the target and boosting the instantaneous grasping force. The fourth tooth of the mandible was selected as the bionic prototype, from which the contour curve was extracted and analyzed, followed by the design of the bionic blade. Through the finite element method, the influence laws of parameters such as the tooth pitch, structural angle, and blade inclination angle on the stress field and deformation of the bionic blade were analyzed under two force application circumstances: along the inclination direction of the tooth edge and on the blade face direction. The results showed that when the applied force was along the tooth edge inclination, the total deformation of the bionic blade initially decreased and then increased with the tooth pitch increase. The maximum equivalent stress of the bionic blade rose gradually with the tooth pitch increase, and the total deformation decreased with the increase of the inclination angle of the tooth. The equivalent stress diminished with the rise in the inclination angle. With the increase of the structural edge angle, the total deformation of the bionic blade rose gradually. When the force was applied along the blade face direction, the deformation and stress values of the blade were significantly lower than those when the force was along the tooth edge inclination. The research findings can offer theoretical references for the design of bionic blades for harvesters.

摘要

针对现有收割机用刀具瞬时抓取能力低、切割质量不理想、刀具易损坏等问题，通过观察蚂蚁上颚生理结构和运动特征，依据仿生设计理论，设计仿生刀刃来优化其性能。本文选取弓背蚁为研究对象，观察右侧上颚齿运动，得出蚂蚁上颚齿的运动为一种切-锯运动。选择平刃与上颚齿刃进行对比研究，得出上颚齿运动过程形成滑切，且滑切角是变化的，上颚齿有助于钳住目标，提高瞬时抓取力。选取上颚第四齿为仿生原型，提取分析上颚齿的轮廓曲线，设计仿生刀刃。利用有限元方法，分析作用力沿着齿刃倾斜方向和刀面方向两种情形下，刀刃齿距、构造刃角和刀刃倾斜角等参数对仿生刀应力场和形变的影响规律。结果表明：当作用力沿齿刃倾斜方向时，仿生刀总变形量随着齿距的增加，呈现先变小后变大趋势，最大等效应力随着齿距增加而呈现逐渐增大趋势；总变形量随着齿刃倾斜角增加，呈现逐渐减小趋势；仿生刀等效应力随着齿刃倾斜角增加，呈现逐渐减小趋势；随着构造刃角增加，仿生刀总变形量呈现逐渐增大趋势。当作用力沿着刀面方向时，刀片形变和应力值都远远小于作用力沿齿刃倾斜方向的形变和应力值。研究结果可为收获机用仿生刀具设计提供理论参考。

¹⁾ Zhao Zhu, Prof. Ph.D. Eng.; Shui Dongli, Lab.Techo. MA. Eng.; Liu Fengbo, Prof. Ph.D. Eng.; Zhao Bintong, MA. Stud. Eng.; Wang Zhongnan, Lab.Techo. MA. Eng.

INTRODUCTION

During agricultural harvesting processes, the blade acts as the "tooth" of the harvester, and its performance and quality directly determine the working quality of the harvester and the straw treatment effect (Ren et al., 2023; Zhang et al., 2022). The characteristics of crops vary significantly, and the cutting situations are complex (Guo et al., 2024). There are issues such as low instantaneous grasping ability of straw, unsatisfactory cutting quality, and proneness to damage for the cutting knives of harvesters (He et al., 2023). Under the demand of developing a low-carbon, it is of great significance to research and develop high-quality and highly adaptive cutting blades for harvesters.

Bionics is a field that focuses on the complex and refined structures of evolved or coevolved living organisms that are highly adaptable to their environment (Liang et al., 2016). As an interdisciplinary subject, bionics is applied in agricultural machinery research and plays a vital role in enhancing the operational performance of agricultural machinery equipment (Chen et al., 2021; Yu et al., 2024; Zhao et al., 2023). Meanwhile, it can provide new research ideas and methods to improve the performance of crushing blades. By analyzing the geometric shape of the mandible of herbivorous insects, such as crickets and locusts, researchers have extracted the curve of the mandible tooth to design bionic stubble blades and have experimentally demonstrated that such blades can reduce resistance and energy consumption (Zhao et al., 2020; Jia et al., 2013). Tong et al. studied the mouthparts of *Cyrtotrachelus longimanus* Fabricius and found that the contour curve of the maxillary incisors was close to the standard circular arc. Based on their analysis results, a bionic vegetable cutting blade was designed (Tong et al., 2017). Test results indicated that the designed bionic vegetable cutting blade could significantly reduce energy consumption and effectively improve the cutting. Tian et al. designed a bionic blade based on the morphological characteristics of the mandible cutting teeth of longhorn beetles. Bench test results showed that the designed bionic blade could significantly reduce the maximum cutting force and power consumption (Tian et al., 2017). Du et al. designed three bionic cutting blades based on the mandible shape and structure of crickets. Compared with ordinary cutting blades, the bionic cutting blades are more suitable for cutting tea stalks (Du et al., 2018). In conclusion, analyzing the geometric structure and shape profile of chewing mouthparts of certain insects for bionic crushing blade design has become an effective way to improve the performance of agricultural machinery working parts.

Ants are one of the most widely distributed and numerous insect species on Earth (Paul et al., 2003). They possess a unique and hard mandible structure for carrying food and providing considerable bite force to cut branches and leaves and crush food at high speed (Ma et al., 2022). Ants have well-formed mandible teeth, which are excellent bionic prototypes for designing a new type of crushing blade. The purpose of this study is to clarify the sawing motion characteristics of the right mandibular teeth of ants, elaborate the mechanism of the cutting-sawing motion of the ant's mandible, and provide a basis for the design of bionic blades. By employing the finite element method to analyze the structural parameters and acquire the influence laws of key parameters such as the tooth pitch, the inclination angle, and the structural edge angle on the total deformation, stress, and strain of the bionic blade under different forces, research results can provide a reference for the design of bionic knives for harvesters.

MATERIALS AND METHODS

Analysis of cutting principle of *camponotus*

Camponotus japonicus (class insect: hymenoptera, formicidae), commonly known as carpenter ant, has a propensity for cutting leaves and exhibits excellent crushing capabilities. Accordingly, *camponotus japonicus* was selected as the research object in this study. The analysis route of the geometric features of mandible is shown in Figure 1.

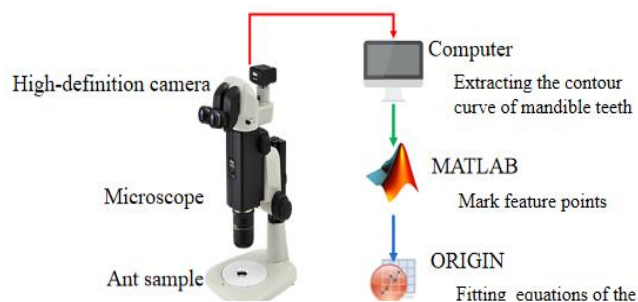


Fig. 1 - Analysis route of the ant mandible

The ants analyzed in this study were captured from a corn field in Gaizhou County, Liaoning Province, China. A total ant samples were measured and analyzed. The measurement results of the structural parameters of the samples are presented in Table. Microscope and Image View software were utilized to capture the video of the mandible movement of the ant, and the Free Video software was employed to convert the video into pictures frame by frame. Figure 2 presents the opening and closing process of the ant's mandible. From I to VI, the palate opens, reaching the maximum at time VI, and from VII to XI, the mandible closes.

Table 1

The structural parameters of ants

| Ant species | Camponotus |
|---------------------|------------|
| weight/mg | 15.4±0.30 |
| body length/mm | 11.45±0.30 |
| maxillary length/mm | 1.57±0.18 |
| head width/mm | 3.13±0.27 |
| head length/mm | 3.05±0.35 |

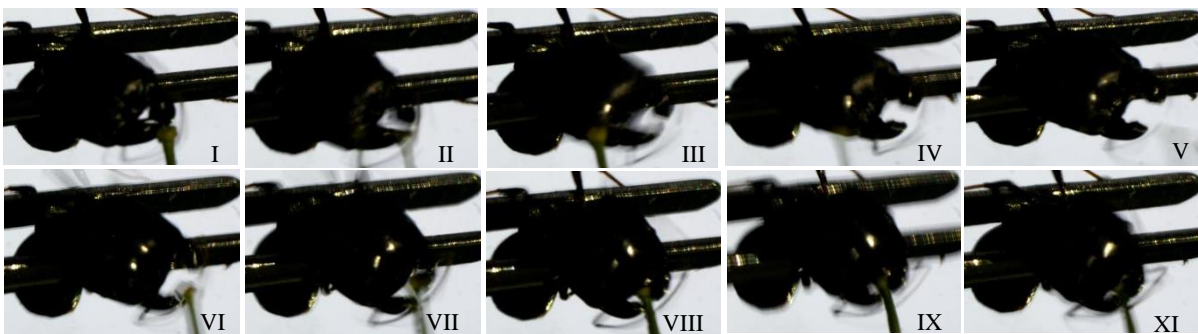
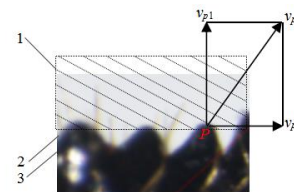


Fig. 2 -The moving process of the ant's maxilla

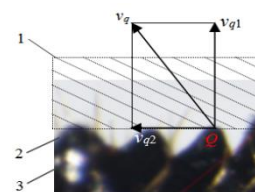
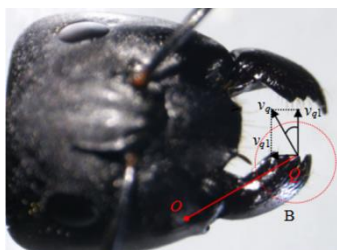
The analysis of the movement of the right maxillary closure is illustrated in Figure 3. The axis of the maxillary motion is positioned at point O . The initial point of the cutting force rests at the end point of the maxillary teeth, and the end point of a specific tooth is regarded as point P . The movement of P comprises moving to the left side of the upper jaw and the outer side of the oral cavity. The speed of the movement towards the left palate is defined as the cutting speed of the right palate and is denoted by v_{p1} , the velocity of the movement away from the outer part of the mouth is designated the sawing velocity of the right upper jaw and is expressed by v_{p2} . Consequently, the absolute movement of the maxillary palate is a cut-saw movement.



1. The Object; 2. Maxillary tooth blade; 3. The maxillary tooth
Magnified view of Area A

Fig. 3 - Analysis of the maxillary moving process distant from the mouthparts

As shown in Figure 4, the movement process of the maxilla towards the mouth-part is illustrated. The rotation axis of the maxilla movement is at point O . The initial application point of the cutting force is at the end point Q of the maxillary tooth. The movement of point Q of the maxillary tooth comprises two parts: approaching the left maxilla and the inner side of the mouth-part.



1. The Object; 2. Maxillary tooth blade; 3. The maxillary tooth
Magnified view of Area B

Fig. 4 - Analysis of maxillary moving process close to mouthparts

In order to further investigate the principle underlying the cutting and sawing movement of the mandibular teeth of the ant, a comparative study was carried out between the flat blade and the mandibular blade. As illustrated in Figure 5, the blade cuts the object at a speed of v_p , the cutting mode of the flat-blade blade is tangent. When the mandibular blade cuts, the absolute speed of the contact point is v_p . Taking the adjacent points P_1 and P_2 , the absolute speed of P_1 can be decomposed into the normal direction velocity v_{p1} and the tangential velocity of the point v_{p1}' . The absolute movement direction of P_1 is neither parallel nor perpendicular to the cutting line of the tooth profile, thereby forming a sliding cut. Similarly, point P_2 also constitutes a sliding cut on the tooth edge line, and the sliding cutting angle of this point is τ_{p2} . The sliding cutting of the tooth edge of the upper jaw is a type of cut-saw motion.

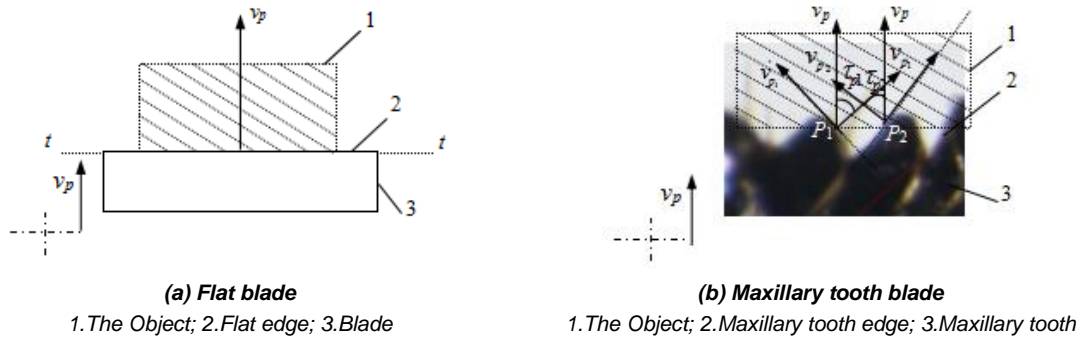


Fig. 5 - Comparative analysis of cutting motion between flat and ant mandibular edge

As depicted in Figure 6, during the cutting process of the object using the flat-edge blade, a sliding cut is formed. The sliding cutting angles at point O and point O' are identical, and the sliding cutting angle of the flat-edge cutting remains fixed. Any section of the curve of the maxillary tooth can be taken to analyze the sliding cutting angle during the cutting process of the bionic edge. At time t_1 , two points O_1 and O_1' on the bionic edge cut the object, and at time t_2 , two points O_2 and O_2' perform the cutting. It is ascertained that the sliding cutting angles of $O_1, O_1', O_2,$ and O_2' are respectively $\tau_{01}, \tau_{01'}, \tau_{02},$ and τ_{02}' .

From time t_1 to t_2 , the sliding cutting angle demonstrates an overall increasing tendency. The sliding cutting angle during the cutting process is variable, or the cut-saw motion relationship is dynamically altering. Hence, the maxillary tooth edge of the ant is beneficial for cutting objects and possesses superior cutting performance compared to the flat edge.

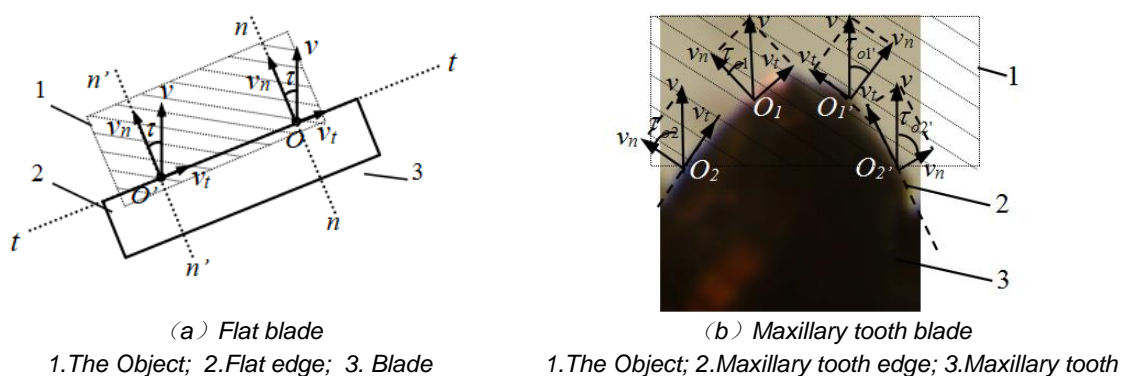


Fig. 6 - Comparative analysis of slip cutting angle between flat and ant mandibular edge

Furthermore, the external contour of the maxillary tooth of the ant enables it to have increased contact with the object to be cut during the cutting process, which is conducive to the cutting operation. Through evolution and natural selection, the tooth structure and arrangement of the maxilla of the ant have proved advantageous for both fighting and food processing, and also have significant reference value for the bionic design of the blade in the harvester.

Geometrical characteristics of ant mandible teeth

For morphology measurements, the ant samples were placed in a plastic test tube containing 10 ml of absolute ethanol until they became inactive. In this experiment, the mandible teeth were observed using a research-grade stereo microscope (NSZ818, magnification ranging from 14 to 60, Yongxin Co., Ltd.).

Ants usually crush food with the right mandible, disregarding individual differences. Details of the ant's right mandible are shown in Figure 7. The mandible was observed to have five teeth with a relatively uniform size and distribution, and the tooth exhibited a smooth surface and an arc-shaped profile.

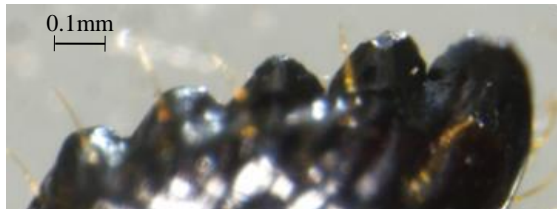


Fig. 7 - The image of right maxillary tooth

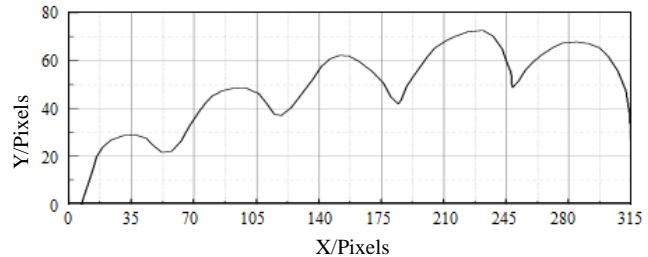


Fig. 8 - Extracted positive contour curve of maxillary tooth

Based on the previous research findings of the research group (Zhao et al., 2022), the forward boundary contour image and the side boundary contour image of the mandible were provided (as shown in Figure 8), and the mathematical model of the forward contour curve and side profile was established. After analyzing the mathematical model, the structural parameters of the fourth tooth of the mandible of the ant were chosen as biomimetic elements. The tooth size is a significant parameter for the structural characteristics of the mandible. To optimize the structural characteristics of the mandible, the ratio of height W_0 to root width W is defined as w . Subsequently:

$$w = \frac{W_0}{W} \tag{1}$$

Where: w is the ratio of height W_0 to root width W .

The geometric dimensions of the teeth were measured by using an image acquisition system configured with a research-grade stereo microscope NSZ818, as shown in Table 2.

Table 2

The geometric dimension of maxillary tooth

| Tooth Name | Root Width/ μm | Root Height/ μm | Ratio of Height to Width |
|--------------|---------------------------|----------------------------|--------------------------|
| Fourth Tooth | 150.643 | 75.83 | 0.5055 |

Because the actual size of the teeth is extremely small, it is necessary to optimize the structural characteristics of the bionic teeth. The distance values of the bionic blade are 1.5, 3, and 4.5 mm, which are applied in the design of the bionic blade.

Construction of the simulation and optimization model of bionic teeth blade

In order to improve the reliability and accuracy of the results, the bionic blade model was appropriately simplified to evade the influence of blade geometry and other factors (Liu et al., 2018). As for the simplified bionic blade structure model, it is shown in Figure 9.

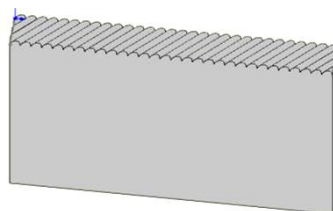


Fig. 9 - Simplified geometric model of blade

The blade structure angle is set at 26° , the tooth edge is inclined at 15° , the direction of the action force is selected in two ways: along the blade direction and the blade tilt direction, and the tooth pitches of the bionic blade are 1.5, 3, and 4.5 mm respectively, to explore the influence of the bionic blade tooth pitch on the stress field and deformation of the bionic blade.

The blade structure angle is set at 26°, the blade tooth pitch is 3 mm, and the direction of the action force is selected in two ways: along the blade direction and the blade tilt direction. The inclination angles of the teeth are respectively selected as 0°, 7.5°, 15°, 22.5°, 30°, 37.5°, and 45° to explore the influence of the inclination angle of the teeth on the stress field and deformation of the bionic blade.

The blade tooth pitch is set as 3 mm, the inclination angle of the teeth is 30°, and the force direction is selected along the blade direction and the blade tilt direction. The blade structure angle is set at 14°, 20°, 26°, 32° and 38°, to explore the influence of the blade structure angle on the stress field and deformation of the bionic blade.

The material parameters commonly utilized in engineering are offered by ANSYS software, and the material of the blade is selected as steel T10. A variety of distinct mesh division approaches exist in ANSYS software. During this analysis process, Face Meshing division and Body Sizing control are adopted, and ElementSize is specified as 1.0 mm to acquire the finite element mesh model of the blade.

The actual installation mode of the bionic blade is threaded connection. To mitigate the influence of threaded holes on the simulation test results, the threaded holes are omitted in the simplified model, and the opposite edge of the blade is chosen as the fixed constraint application surface. Neglecting air friction, a uniform load is applied to the blade, the maximum load on the simplified bionic model is set at 2000 N, and the loading is static (Xue et al., 2016). The load direction is classified into the direction along the tooth edge inclination (referred to as direction 1) and the direction along the blade surface (referred to as direction 2), as shown in Figure 10.

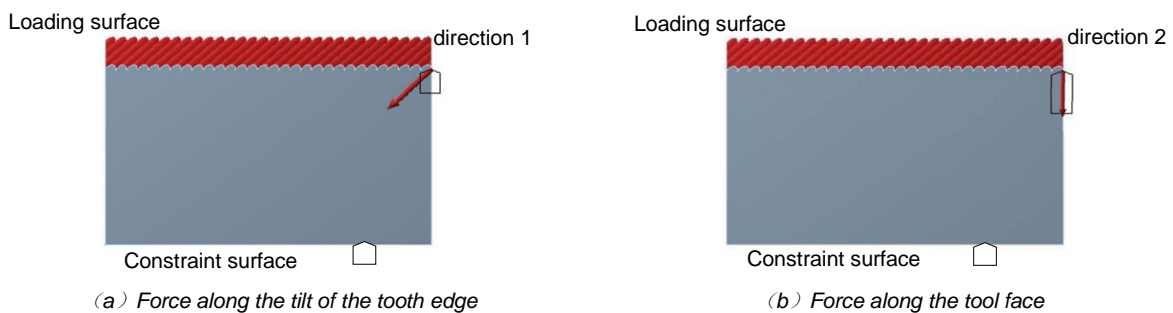


Fig. 10 - Diagram of constraints and loads

RESULTS AND ANALYSIS

Analysis of the Influence of Tooth Pitch Parameters on the Deformation and Stress Field of the Bionic blade

The effect of teeth pitch parameters on the deformation and stress field of the bionic blade is shown in Figure 11, 12, 13.

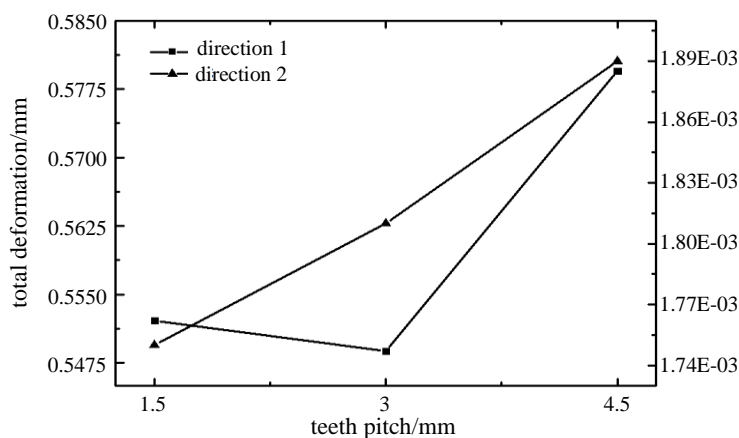


Fig. 11 - Rule of total deformation of blade with teeth pitch

As illustrated in Figure 11, when the force is applied along direction 1, the total deformation of the bionic blade exhibits a trend that initially decreases and subsequently increases with the increase of the tooth pitch.

The total deformation of the bionic blade with a 3 mm tooth pitch amounts to 0.54878 mm, representing a 5.3% reduction compared to that of a 4.5 mm tooth pitch. When the force is applied along direction 2, the total deformation of the bionic blade rises in tandem with the increase in the tooth pitch. The total deformation of the bionic blade with a tooth pitch of 4.5 mm escalates by 7.67% when contrasted with that of a 1.5 mm tooth pitch. By comparing the total deformation of the blade under the two conditions, it is discovered that the total deformation of the blade along direction 1 is considerably larger than that along direction 2.

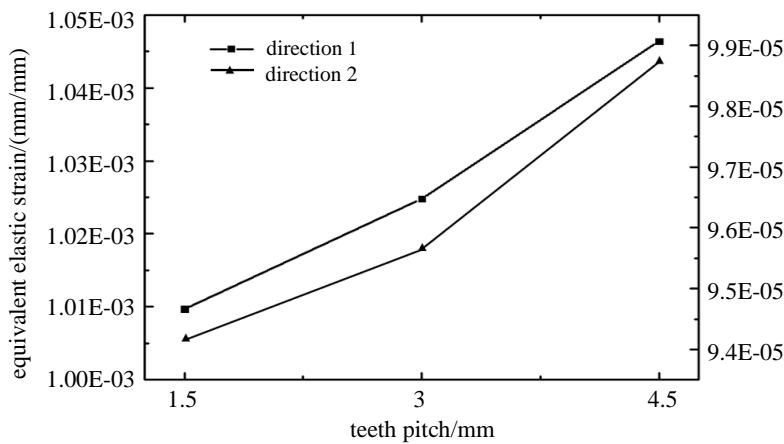


Fig. 12 - Rule of equivalent elastic strain of blade with teeth pitch

As can be discerned from Figure 13, when the force is applied in both direction 1 and direction 2, the equivalent strain of the bionic blade gradually ascends with the increase in tooth pitch. When the force is applied along direction 1, the equivalent strain of the bionic blade with a tooth pitch of 1.5 mm reaches 1.0097×10^{-3} , and the equivalent stress of the bionic blade is reduced by 3.5% in comparison with that of a 4.5 mm tooth pitch. When the force is applied along direction 2, the equivalent strain of the bionic blade with a 1.5 mm tooth pitch amounts to 9.4171×10^{-5} , and the equivalent stress of the bionic blade is reduced by 4.64% when compared to that of a 4.5 mm tooth pitch.

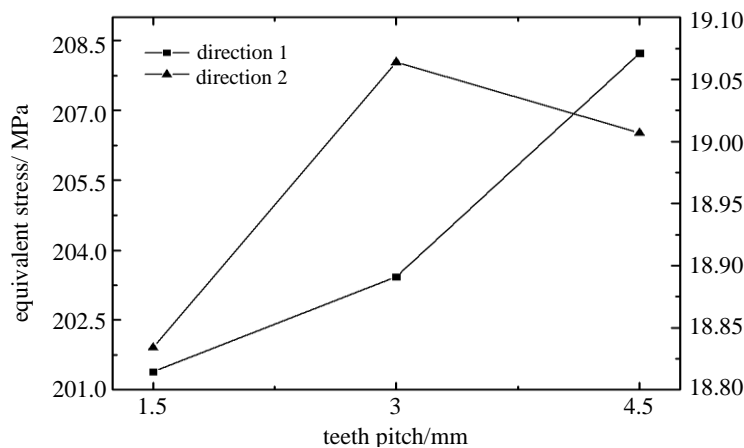


Fig. 13 - Rule of equivalent stress of blade with teeth pitch

As can be seen from Figure 13, when the force is applied along direction 1, the maximum equivalent stress of the bionic blade gradually increases with the increase in tooth pitch. The maximum equivalent stress of a bionic blade with a 4.5 mm blade pitch is 208.23 MPa, which is 3.3% higher than that of a bionic blade with a 1.5 mm blade pitch. When the force is applied along direction 2, the maximum equivalent stress of the bionic blade initially increases and subsequently decreases with the increase in the tooth pitch. The maximum equivalent stress of the bionic blade with a 3 mm tooth pitch is 19.064 MPa, and the maximum equivalent stress of the bionic blade is increased by 1.2% compared to that with a 1.5 mm tooth pitch.

The influence of the inclination angle of the tooth on the deformation and stress field of the bionic cutter

Figures 14, 15, and 16 show the effect of the inclination angle of the tooth on the deformation and stress field of the bionic blade. As can be seen from Fig. 14, when the force is applied along direction 1, the total deformation of the bionic blade gradually decreases as the inclination angle of the tooth edge increases. The total deformation of the bionic blade at an inclination angle of 45° of the tooth is decreased by 29.31% compared with that at 0°. When the applied force is along Direction 2, the total deformation of the bionic blade initially increases and then decreases with the increase in the inclination angle of the tooth. When the inclination angle of the tooth is 30°, the total deformation of the blade is 1.818×10^{-3} mm.

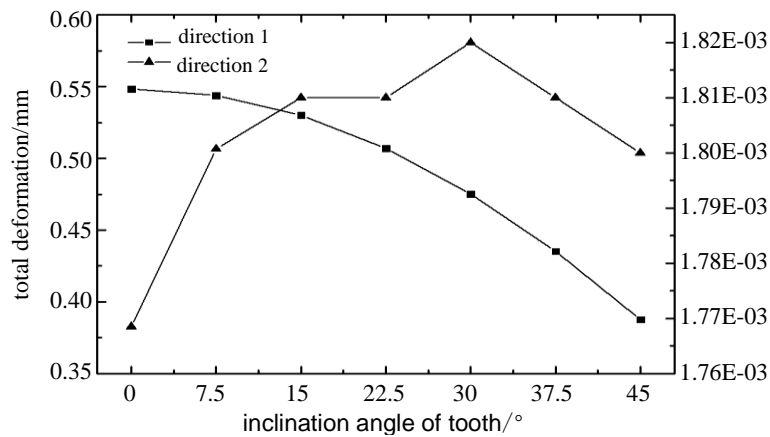


Fig. 14 - Rule of total deformation of blade with inclination angle of tooth

As can be observed from Figure 15, when the force is applied along Direction 1, the equivalent strain of the bionic blade gradually decreases with the increase in the inclination angle of the tooth. The equivalent strain of the bionic blade with a tooth inclination angle of 45° is reduced by 13.77% compared to that of the bionic blade with a tooth inclination angle of 0°. When the applied force is in Direction 2, the equivalent strain of the bionic blade initially decreases and then increases with the increase in the inclination angle of tooth.

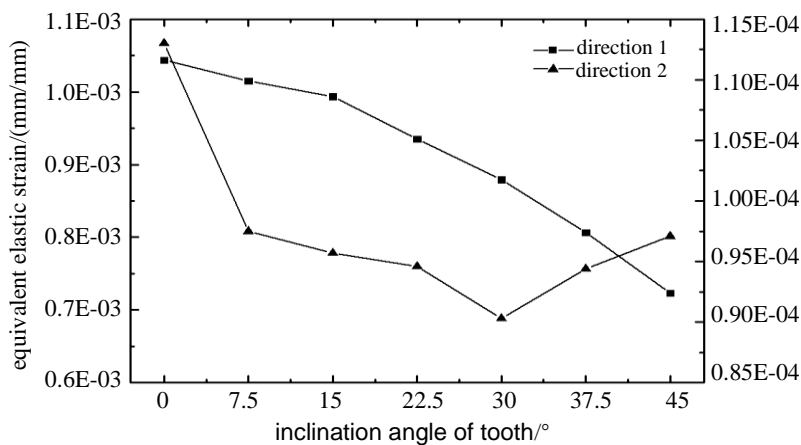


Fig. 15 - Rule of equivalent elastic strain of blade with inclination angle of tooth

As can be seen from Figure.16, when the force is applied along Direction 1, the equivalent stress of the bionic blade gradually decreases with the increase of the tooth inclination angle. The equivalent stress of a bionic blade with a 45° tooth inclination angle is 144.23 MPa, which is 30.16% less than that of a bionic blade with a 0° tooth inclination angle.

When the applied force is along Direction 2, the total deformation of the bionic blade initially decreases and then increases with the increase in the tooth inclination angle. Among them, when the tooth inclination angle is 22.5°, the maximum equivalent stress of the blade is the minimum, being 17.706 MPa.

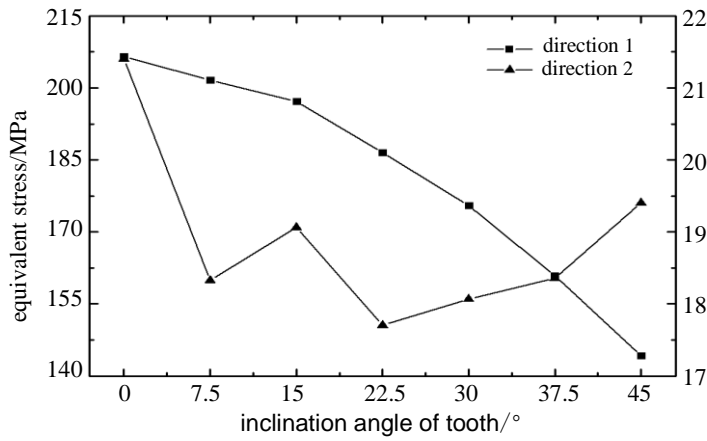


Fig. 16 - Rule of equivalent stress of blade with inclination angle of tooth

Effect of structural Angle of bionic blade on deformation and stress field

The influence of the structural edge Angle on the stress field and deformation of the bionic blade is shown in Figure 17, 18 and 19.

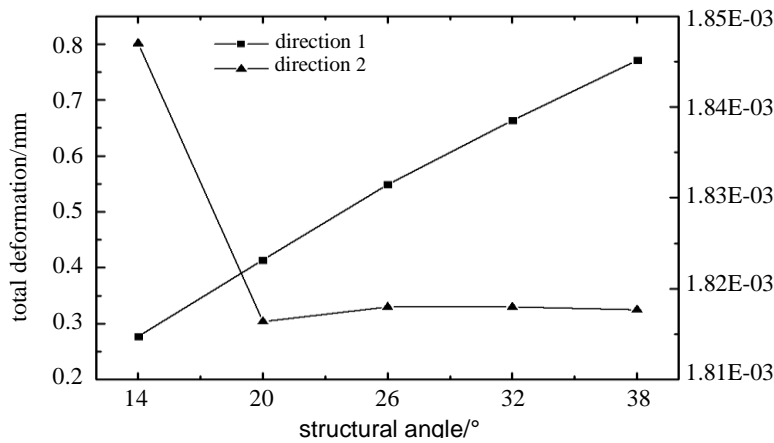


Fig. 17 - Rule of total deformation of blade with structural angle

As the force is along Direction 1, with the increase of the structural edge angle, the total deformation of the bionic blade shows a gradual increasing trend. The total deformation of the structural edge angle of 38° is increased by 64% compared to that of 14°. As the force is along Direction 2, with the increase of the structural edge angle, the total deformation of the bionic blade exhibits a trend of rapid decline initially and then basically maintains a stable tendency.

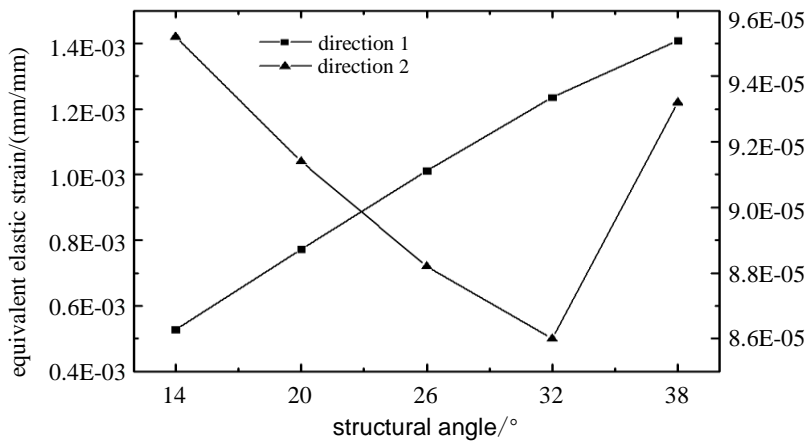


Fig. 18 -Rule of equivalent elastic strain of blade with structural angle

When the force is along Direction 1, the equivalent strain of the bionic blade shows a gradual increase with the increase in the structural edge angle, and the equivalent strain of the 38° structural edge angle is 64% higher than that of 14°. When the force is along Direction 2, with the increase in the structural edge angle, the equivalent strain of the bionic blade shows a trend of first decreasing and then increasing rapidly. The equivalent strain of the blade with a 32° structural edge angle is the smallest, which decreases by 9.6% compared to that of 14°.

As the force is along Direction 1, with the increase of the structural edge angle, the maximum stress of the bionic blade shows a gradual increasing trend, and the total deformation of the 38° structural edge angle is increased by 62.4% compared to that of 14°. As the force is along Direction 2, with the increase of the structural edge angle, the total deformation of the bionic blade presents a trend of rapid decline at first and then basically stabilizes. The maximum equivalent stress is minimum when the structural edge angle is 32°, and it is 14.8% less than that of the 14° blade.

The total deformation, equivalent strain, and equivalent stress values of the bionic blade vary significantly when the force is applied in Direction 1 and Direction 2. The deformation and stress values of the blade when the force is along Direction 2 are much smaller than those when the force is along Direction 1.

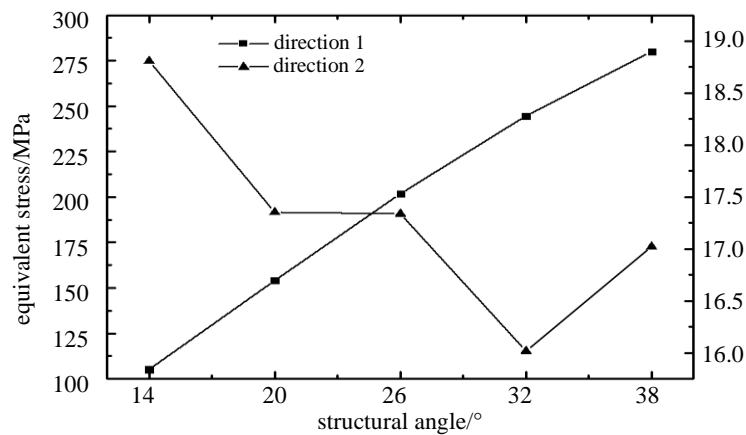


Fig. 19 -Rule of equivalent stress of blade with structural angle

CONCLUSIONS

In this study, the movement and the geometric structure of the mandible teeth of ants were studied, and the characteristic profiles of tooth-4 were utilized in the design of a bionic blade. The models of the blade were developed for analyzing the parameters of the bionic blade through ANSYS. Based on the simulation test results, the following conclusions are drawn.

(1) The movement characteristics of the ant's mandible were studied using research-grade microscopes and high-speed photography techniques. It was clarified that the right maxillary teeth of the ant demonstrated a cutting movement approaching the left maxilla and a sawing movement towards the side of the mouthparts (or away from the side of the mouthparts) during the cutting process. The combined effect of the cutting and sawing movements of the ant's maxillary teeth revealed the tooth-edge cutting mechanism of the cutting-sawing movement of the ant's mandible.

(2) The bionic blade was designed with the following parameters: tooth pitch of 1.5 mm, 3 mm, and 4.5 mm; tooth edge inclination angle ranging from 0 to 45°; and structural edge angle ranging from 14 to 38°. Based on the finite element analysis of the bionic blade structural parameters, the influence laws of the tooth pitch, the inclination angle of the blade edge, and the structural edge angle on the total deformation, stress, and strain of the bionic cutter were obtained. Based on the finite element analysis of the structural parameters of the bionic blade, the influence laws of the tooth pitch, the inclination angle, and the structural edge angle on the total deformation, stress, and strain of the bionic blade were obtained.

ACKNOWLEDGEMENT

This research was funded by the doctoral research project of Liaoning Natural Science Foundation in 2024 (2024-BS-287), the "Enterprise Doctor Dual Innovation Plan of Yingkou City" project in 2023 (YKSCJH2023-015), and the scientific effort of Liaoning Agricultural Technical College (Lnz202216, LnzKA202310).

REFERENCES

- [1] Chen Pan, Xu Pengfei, (2021), Simulation analysis and mechanism study on drag reduction of “Bionics” groove (“仿生学”沟槽减阻仿真分析及机理研究), *Aeroengine*, Vol.47, Issue2, pp.28-32, Shen Yang / P.R.C;
- [2] Du Zhe, Hu Yongguang, Wang Sheng, (2018), Simulation and Experiment of Reciprocating Cutter Kinematic of Portable Tea Picking Machine (便携式采茶机切割器运动仿真与试验), *Transaction of the Chinese Society for Agricultural Machinery*, Vol.49, Issue S1, pp.221-226, Bei Jing/ P.R.C;
- [3] Guo Sijia, Liu Xinzhu, Liu Xiangdong et al., (2024), Experimental Study of Mechanical Properties of Corn Straw in Cold Region (寒地玉米秸秆力学特性研究), *Journal of Agricultural Mechanization Research*, Vol.46, Issue 6, pp.170-174, Hei Longjiang / P.R.C;
- [4] He Zhitao, Ding Huiling, Li Jian, et al., (2023), Review of researches on stalk cutting (秸秆切割问题研究综述), *Machinery Design & Manufacture*, Issue8, pp.277-284, Liao Ning/ P.R.C;
- [5] Jia Honglei, Li Changing, Zhang Zhihong et al., (2013), Design of bionic saw blade for corn stalk cutting. *Journal of Bionic Engineering*, Vol.10, Issue 4, pp.497-505, Ji Lin / P.R.C;
- [6] Liang Yunhong, Ren Luquan, (2016), Preliminary study of bionics in human life (人类生活及其仿生学初探). *Journal of Jilin University*, Vol.46, Issue 4, pp.1373-1384, Ji Lin / P.R.C;
- [7] Liu Dong, Xiao Hongru, Jin Yue et al., (2018), Finite element analysis of stalk cutting of Chinese little greens based on ANSYS and verification Test (基于 ANSYS 的鸡毛菜茎秆切割的有限元分析及验证试验), *Journal of Agricultural Science and Technology*, Vol.20, Issue11, pp.85-93, Bei Jing / P.R.C;
- [8] Ma Mingjie, Zhu Biru, Hu Yi, (2022), Research progress on ant symbiotic microorganisms (蚂蚁共生微生物研究进展), *Scientia Sinica (Vitae)*, Vol.52, Issue8, pp.1212-1225, Bei Jing /P.R.C;
- [9] Paul J., Roces F. et al., (2003), Fluid intake rates in ants correlate with their feeding habits, *Journal of Insect Physiology*, Vol.49, Issue4, pp.347-357, Würzburg / Germany;
- [10] Ren Jiahui, Zhi Teng, Li Fatang, et al., (2023), Design and simulation of the disc-cutting picking device of sisal hemp (圆盘切割式剑麻采摘装置设计与仿真), *Journal of Chinese Agricultural Mechanization*, Vol.44, Issue1, pp.77-84, Nan Jing/ P.R.C;
- [11] Tian Kunpeng, Li Xiangwang, Shen Chen, et al., (2017), Design and test of cutting blade of cannabis harvester based on longicorn bionic principle (天牛仿生大麻收割机切割刀片设计与验), *Transactions of the Chinese Society of Agricultural Engineering*, Vol.33, Issue5, pp.56 – 61, Bei Jing / P.R.C;
- [12] Tong Jin, Xu Shun et al., (2017), Design of a bionic blade for vegetable chopper, *Journal of Bionic Engineering*, Vol.14, Issue1, pp.163-171, Ji Lin / P.R.C;
- [13] Xue Zhong, Zhang Yanlin, Zhang JiN et al., (2018), Compressive test and simulation of cassava stems based on ANSYS (基于 ANSYS 的木薯茎秆静力学仿真研究), *Journal of Agricultural Mechanization Research*, Vol.38, Issue6, pp.116-121, Hei Longjiang / P.R.C;
- [14] Yu Yongtao, Li Yanjun, Xie Fuxiang et al., (2024), Experimental study on the cleaning performance of bionic screen based on earthworm motion characteristics (基于蚯蚓运动特征的仿生筛清选性能试验研究), *INMATEH-Agricultural Engineering*, Vol.73, Issue 2, pp.834-844, Bucharest / Romania;
- [15] Zhang Xuening, You Yong, Wang Decheng et al., (2022), Design and experiment of a combined root-cutting and ditching device, *INMATEH-Agricultural Engineering*, Vol.66, Issue 1, pp.383-392, Bucharest / Romania.
- [16] Zhao Jiale, Guo Mingzhuo, Lu Yun et al., (2020), Design of bionic locust mouthparts stubble cutting device. *Int J Agric & Biol Eng*, Vol.13, Issue1, pp.20-28, Ji Lin / P.R.C;
- [17] Zhao Ping, Yu Tiankuo, Xu Guofa et al., (2023), Design and drag reduction performance analysis of a potato harvest shovel based on the surface texture characteristics of pangolin scale (基于穿山甲鳞片表面纹理特征的马铃薯挖掘铲设计及减阻性能分析), *INMATEH-Agricultural Engineering*, Vol.70, Issue 2, pp.21-36, Bucharest / Romania.
- [18] Zhao Zhu, Wang Zhongnan, Zhao Bintong et al., (2022), Design and research of a cutting blade for corn stalks based on a bionic principle, *INMATEH-Agricultural Engineering*, Vol.68, Issue3, pp.711-722, Bucharest / Romania.

WRITING INSTRUCTIONS

Article Types

Three types of manuscripts may be submitted:

1. **Regular articles:** These should describe new and carefully confirmed findings, and experimental procedures should be given in sufficient detail for others to verify the work. The length of a full paper should be the minimum required to describe and interpret the work clearly (max.10 pages, even number);
2. **Reviews:** Submissions of reviews and perspectives covering topics of current interest are welcome and encouraged (max.12 pages, even number).

Manuscripts should be written in English (American or British usage is accepted, but not a mixture of these) and submitted **electronically** at the following e-mail addresses: ***inmatehjournal@gmail.com***

Please be sure to include your full affiliation and e-mail address (see Sample manuscript)

The authors are responsible for the accuracy of the whole paper and references.

There are allowed 2 papers by each first author.

The text layout should be in single-column format. To avoid unnecessary errors it is strongly advised to use the "spell-check" and "grammar check" functions of your word processor.

Review Process

All manuscripts are reviewed by 2 members of the Scientifically Review Office. Decisions will be made as rapidly as possible and the journal strives to return reviewers' comments to authors in approx.3 weeks.

The editorial board will re-review manuscripts that are accepted pending revision.

NOTE:

Submission of a manuscript implies: that the work described has not been published before (excepting as an abstract or as part of a published lecture or thesis) that it is not under consideration for publication elsewhere.

1. REGULAR ARTICLES

- Manuscripts should be concise, in **1.15 line spacing**, and should have 2 cm all over margins. The font should be **Arial 10 pt.** Ensure that each new paragraph is clearly indicated, using **TAB at 1 cm.**
- Title will be **Arial 12 pt.** and explicit figures will be **Arial 9 pt.**
- Text will be written in English.
- Chapters' titles are written by **Arial 10 pt, Bold, Uppercase** (e.g. **INTRODUCTION, MATERIALS AND METHODS**), between chapters is left a space for 10 pt. At the beginning of each paragraph, TAB of 1 cm.
- The paper body will be written in **Arial 10 pt., Justify alignment.**

TITLE **Arial 12 pt., Uppercase, Bold, Center** (in English language) and **Bold Italic** (in native language).

Should be a brief phrase describing the contents of the paper. Avoid long titles; a running title of no more than 100 characters is encouraged (without spaces).

AUTHORS **ARIAL 9, Bold, Centre alignment**

Under the paper's title, after a space (enter) 9 pt., write **authors' names** and **affiliations (Arial 8 pt.-Regular)**

When the paper has more than one author, their name will be followed by a mark (Arabic numeral) as superscript if their affiliation is different. **Less than 6 authors.**

Corresponding author's name (next row), (**Arial 8 pt.**). Should be added also: phone, fax and e-mail information, for the paper corresponding author (**font: 8 pt., Italic**).

KEYWORDS (**In English**) about 4 to 7 words that will provide indexing references should be listed (**title: Arial 10pt, bold italic, text Arial 10 pt., italic**).

A list of non-standard **Abbreviations** should be added. In general, non-standard abbreviations should be used only when the full term is very long and used often. Each abbreviation should be spelled out and introduced in parentheses the first time it is used in the text. Standard abbreviations (such as ATP and DNA) need not to be defined.

ABSTRACT (**in English and Native language, Arial 10 pt.**), the title **bold**; the text of abstract: **italic**) should be informative and completely self-explanatory, briefly present the topic, state the scope of the experiments, indicate significant data, and point out major findings and conclusions. The Abstract should be max.250 words. Complete sentences, active verbs, and the third person should be used, and the abstract should be written in the past tense. Standard nomenclature should be used and abbreviations should be avoided. No literature should be cited.

INTRODUCTION (**Arial 10 pt.**) should provide a clear statement of the problem, the relevant literature on the subject, and the proposed approach or solution. It should be understandable to colleagues from a broad range of scientific subjects. We should refer to the current stage of researches performed in the field of the paper to be published, by quoting up-to-date specialty studies, preferably published after 2006, excepting certain referential specialty

books/studies, especially papers issued in magazines/journals/conferences/ISI quoted symposia or in other international data bases, which are well known and available.

MATERIALS AND METHODS (*Arial 10 pt.*) should be complete enough to allow experiments to be reproduced. However, only truly new procedures should be described in detail; previously published procedures should be cited, and important modifications of published procedures should be mentioned briefly. Methods in general use need not be described in detail.

RESULTS (*Arial 10 pt.*) should be clearly presented. The results should be written in the past tense when describing findings in the authors' experiments. Results should be explained, but largely, without referring to the literature. Discussion, speculation and detailed interpretation of data should not be included in the Results, but should be put into the Conclusions section.

CONCLUSIONS (*Arial 10 pt.*) The main conclusions drawn from results should be presented in a short Conclusions section. Do not include citations in this section.

Formulae, symbols and abbreviations: Formulae will be typeset in Italics (preferable with the Equation Editor of Microsoft Office 2003) and should be written or marked as such in the manuscript, unless they require a different styling. They should be referred to in the text as Equation (4) or e.g. (4). The formulae should be numbered on the right side, between brackets (*Arial 10 pt.*):

$$P = F \cdot v \quad (1)$$

Terms of the equation and the unit measure should be explained, e.g.

P is the power, [W];

F – force, [N];

v – speed, [m/s]

SI units must be used throughout.

Tables should be self-explanatory without reference to the text. The details of the methods used in the experiments should preferably be described in the legend instead of in the text. The same data should not be presented both in table and graph form or repeated in the text.

Table's title will be typed *Arial 9 pt, Bold, Centered*

In the table, each row will be written Arial 9 pt, single-spaced throughout, including headings and footnotes.

The table should be numbered on the right side, *Arial 10 pt.*

Figures (*Arial 9 pt., Bold, Center*) should be typed in numerical order (Arabic numerals). Graphics should be high resolution (e.g. JPEG). Figure number is followed by what represent the figure or graph e.g.:

Fig.1 – Test stand

Legend: *Arial 8 pt, Italic, Center, e.g.:*

1 - plansifter compartments; 2- break rolls; 3 – semolina machines; 4 – reduction rolls; 5 – flour

ACKNOWLEDGMENTS (*Arial 10 pt.*) of people, grants, funds etc should be brief (*if necessarily*).

REFERENCES (*Arial 10 pt.*)

(*In alphabetical order, in English and in the original publication language.*)

Minimum 10 references, last 10 years, minimum 3 references from the last 2 years

It can be used “*References*” tool from the *Word Editor*. **APA Style (American Psychological Association)** <https://apastyle.apa.org/style-grammar-guidelines/references/examples>

All references must be provided in English

Authors are fully responsible for the accuracy of the references.

References should be **alphabetically**, with complete details, as follows:

Examples:

Books: <https://apastyle.apa.org/style-grammar-guidelines/references/examples/book-references>

Jackson, L. M. (2019). *The psychology of prejudice: From attitudes to social action* (2nd ed.). American Psychological Association. <https://doi.org/10.1037/0000168-000>

Kesharwani, P. (2020). *Nanotechnology based approaches for tuberculosis treatment*. Academic Press.

Sapolsky, R. M. (2017). *Behave: The biology of humans at our best and worst*. Penguin Books.

Torino, G. C., Rivera, D. P., Capodilupo, C. M., Nadal, K. L., & Sue, D. W. (2019). *Microaggression theory: Influence and implications*. John Wiley & Sons. <https://doi.org/10.1002/9781119466642>

In text:

- **Parenthetical citations:** (Jackson, 2019; Sapolsky, 2017)
- **Narrative citations:** Jackson (2019) and Sapolsky (2017)

Journal Article:

<https://apastyle.apa.org/style-grammar-guidelines/references/examples/journal-article-references>

Grady, J. S., Her, M., Moreno, G., Perez, C., & Yelinek, J. (2019). Emotions in storybooks: A comparison of storybooks that represent ethnic and racial groups in the United States. *Psychology of Popular Media Culture*, 8(3), 207–217. <https://doi.org/10.1037/ppm0000185>

In text:

- **Parenthetical citation:** (Grady et al., 2019)
- **Narrative citation:** Grady et al. (2019)

Conference or Symposium:

<https://apastyle.apa.org/style-grammar-guidelines/references/examples/conference-proceeding-references>

Duckworth, A. L., Quirk, A., Gallop, R., Hoyle, R. H., Kelly, D. R., & Matthews, M. D. (2019). Cognitive and noncognitive predictors of success. *Proceedings of the National Academy of Sciences, USA*, 116(47), 23499–23504. <https://doi.org/10.1073/pnas.1910510116>

In text:

- **Parenthetical citation:** (Duckworth et al., 2019)
- **Narrative citation:** Duckworth et al. (2019)

Dissertation / Thesis:

<https://apastyle.apa.org/style-grammar-guidelines/references/examples/published-dissertation-references>

Zambrano-Vazquez, L. (2016). *The interaction of state and trait worry on response monitoring in those with worry and obsessive-compulsive symptoms* [Doctoral dissertation, University of Arizona]. UA Campus Repository. <https://repository.arizona.edu/handle/10150/620615>

In text:

- **Parenthetical citations:** (Kabir, 2016; Miranda, 2019; Zambrano-Vazquez, 2016)
- **Narrative citations:** Kabir (2016), Miranda (2019), and Zambrano-Vazquez (2016)

<https://apastyle.apa.org/style-grammar-guidelines/references/examples/unpublished-dissertation-references>

Harris, L. (2014). *Instructional leadership perceptions and practices of elementary school leaders* [Unpublished doctoral dissertation]. University of Virginia.

In text:

- **Parenthetical citation:** (Harris, 2014)
- **Narrative citation:** Harris (2014)

Patents: Names and initials of authors, year (between brackets), patent title (Italic), patent number, country:

Grant, P. (1989). *Device for Elementary Analyses*. Patent. No.123456. USA.

Legal regulations and laws, organizations:

<https://apastyle.apa.org/style-grammar-guidelines/references/examples/iso-standard-references>

International Organization for Standardization. (2018). *Occupational health and safety management systems—Requirements with guidance for use* (ISO Standard No. 45001:2018). <https://www.iso.org/standard/63787.html>

Occupational Safety and Health Administration. (1970). *Occupational safety and health standards: Occupational health and environmental control: Occupational noise exposure* (OSHA Standard No. 1910.95). United States Department of Labor.

<https://www.osha.gov/laws-regs/regulations/standardnumber/1910/1910.95>

In text:

- **Parenthetical citations:** (International Organization for Standardization, 2018; Occupational Safety and Health Administration, 1970)
- **Narrative citations:** International Organization for Standardization (2018) and Occupational Safety and Health Administration (1970)

Web references: The full URL should be given in text as a citation, if no other data are known. If the authors, year, and title of the documents are known and the reference is taken from a website, the URL address has to be mentioned after these data.

Citation in text

Please ensure that every reference cited in the text is also present in the reference list (and vice versa).

Do not cite references in the Abstract and Conclusions !.

Unpublished results, personal communications as well as URL addresses are not recommended in the references list.

Making personal quotations (one, at most) should not be allowed, unless the paper proposed to be published is a sequel of the cited paper. Articles in preparation or articles submitted for publication, unpublished, personal communications etc. should not be included in the references list.

Citations style

Text: All citations in the text may be made directly (or parenthetically) as bellow.

- **single author:** the author's name (without initials, unless there is ambiguity) and the year of publication: "as previously demonstrated (*Brown, 2010*)".
- **two authors:** both authors' names and the year of publication: (*Adam and Brown, 2008; Smith and Hansel, 2006; Stern and Lars, 2009*)
- **three or more authors:** first author's name followed by "et al." and the year of publication: "As has recently been shown (*Werner et al., 2005; Kramer et al., 2000*) have recently shown"

Citations of groups of references should be listed first alphabetically, then chronologically.

Units, Abbreviations, Acronyms

- Units should be metric, generally SI, and expressed in standard abbreviated form.
- Acronyms may be acceptable, but must be defined at first usage.

2. REVIEWS

Summaries, reviews and perspectives covering topics of current interest in the field, are encouraged and accepted for publication.

Reviews do not have the requirements for regular articles. However, should include: (*) an introductory chapter, (**) a careful and critical presentation of the relevant aspects of the topic approached and (***) emphasis of the aspects that aren't known and require further research to progress.



Edited by: INMA Bucharest

6, Ion Ionescu de la Brad Blvd., sect. 1, Bucharest, ROMANIA

Tel: +4021.269.32.60; Fax: +4021.269.32.73

[https:// inmateh.eu](https://inmateh.eu)

e-mail: inmatehjournal@gmail.com

